Available online at www.sciencedirect.com
ScienceDirect
Organic Electronics 9 (2008) 1–13
Organic Electronics
www.elsevier.com/locate/orgel

Transparent flexible conductor of poly(methyl methacrylate) containing highly-dispersed multiwalled carbon nanotube

Dong Ouk Kim [a], Min Hye Lee [a], Jun Ho Lee [a], Tae-Woo Lee [b], Kwang Jin Kim [c], Young Kwan Lee [d], Taesung Kim [e], Hyouk Ryeol Choi [e], Ja Choon Koo [e], Jae-Do Nam [a,*]

[a] *Department of Polymer Science and Engineering, SAINT, Sungkyunkwan University, Suwon 440-746, Republic of Korea*
[b] *Samsung Advanced Institute of Technology (SAIT), Suwon, Republic of Korea*
[c] *Department of Mechanical Engineering, University of Nevada, Reno, NV 89557, USA*
[d] *Department of Chemical Engineering, Sungkyunkwan University, Suwon 440-746, Republic of Korea*
[e] *School of Mechanical Engineering, Sungkyunkwan University, Suwon 440-746, Republic of Korea*

Received 5 June 2007; received in revised form 6 July 2007; accepted 10 July 2007
Available online 1 August 2007

Abstract

Multiwalled carbon nanotubes (MWCNTs) were incorporated into a poly(methyl methacrylate) (PMMA) solution to develop a transparent and flexible composite conductive film. Monitoring the MWCNT-granule size in the PMMA solutions as well as after the film casting, the self-aggregation of MWCNTs was thoroughly investigated to provide a highly-dispersed polymeric conductor. In addition to the degree of acid treatment of MWCNTs, the dipole moment of solvent and the random-coil length of polymer were considered to be the key factors for the MWCNTs to retain the highly-dispersed state in the polymer matrix after solidification. Investigating several solvent systems, dimethylformamide was found to have the best dispersing capability for the MWCNT/PMMA system to give a surface electrical conductivity up to 10^{-2} S/cm at ca. 3.0 wt% of MWCNT, which was considered to be well above what had been reported for such a low level of MWCNT loading, with a light transmittance over 95%. Finally, the polymer-rich layer, which is usually formed on the coating surface due to the surface tension and wetting characteristics of the MWCNT/PMMA mixture, was mechanically peeled off to give an increase in electrical conductivity of nearly two orders of magnitude.

PACS: 72.60.+g; 72.80.−r; 73.25.+i; 74.25.Gz; 78.66.−w

Keywords: Multiwalled carbon nanotubes (MWCNTs); Conductive polymer film; Dispersion; Conductivity; Percolation

1. Introduction

Since carbon nanotubes were first reported in 1991 by Iijima [1], they have been intensively

* Corresponding author. Tel.: +82 31 290 7285; fax: +82 31 292 8790.
E-mail address: jdnam@skku.edu (J.-D. Nam).

1566-1199/$ - see front matter © 2007 Elsevier B.V. All rights reserved.
doi:10.1016/j.orgel.2007.07.004

investigated due to their mechanical, chemical and electrical properties [2–4]. Carbon nanotubes (CNTs) are considered as functional additives in polymeric composites systems. In particular, when compared with other spherical-shaped conductive filling materials such as carbon black and silver particle, their relatively large length/diameter aspect ratios help the composite systems show a high electric conductivity at low concentrations of the carbon nanotubes, due to their low percolation threshold [5,6]. Although CNTs have excellent properties in nature, their dispersion characteristics specifically incorporated in various binding systems still remain as a challenge to be required for the optoelectronic device fabrication and assembly processes.

Curran et al. reported the electrical conductivity as about 10^{-4} S/cm at 35 wt% loading of single-walled carbon nanotubes (SWCNT) in poly(*m*-phenylenevinylene-co-2,5-dioctoxy-p-phenylenevinylene) [6]. It was reported that the poly(phenyleneethynylene) (PPE)-functionalized SWCNT was soluble in organic solvents and the electrical conductivity of PPE-SWCNT/polycarbonate composite system reached 4.81 S/cm at 7 wt% of SWCNT loading [7]. Recently, there was a report on the SWCNT/PMMA composite system giving the electrical conductivity of 10^{-6} S/cm at 2 wt% of SWCNT loading [8]. For MWCNT/polyimide composite systems, Ogasawara et al. reported 10^{-4}–10^{-2} S/cm of electrical conductivity with 3.3–14.3 wt% of MWCNT loading [9], and Zhu et al. reported 10^{-10}–10^{-5} S/cm at around 1–12 wt% of MWCNT loading [10]. The electrical conductivity of a water-soluble composite system, MWCNT/PVA(poly vinyl alcohol), was reported as 10^{-2} S/cm with 3 wt% of MWCNT loading [11]. For transparent applications, the electrical conductivity of the H_2O_2-treated MWCNT/polycarbonate(PC) composite system was 10^{-1} S/cm at 7 wt% loading of peroxide-treated MWCNT [12]. The electric sheet resistivity of the MWCNT/PMMA composite system reached 10^3 Ω/square at 1 wt% of MWCNT loading using UV-ozone treatment for MWCNT [13].

Reviewing previously-reported results, CNT/polymer composite systems show a wide range of electrical conductivities in a wide range of CNT loading, which makes it difficult to identify the key factors of the electrical threshold. It is often found that different researchers provide different values of electrical conductivity and light transmittance for the same material systems. Furthermore, it should be pointed out that those reported values are not always reproduced by different researchers. Those discrepancies in electrical conductivities may be due to the non-uniform spatial distribution of carbon nanotubes in the states of liquid mixtures or solidified forms. As well known, CNTs are hardly dispersed and easily agglomerate to form various-sized granules, which could influence the electrical conductivity and transparency to a great extent. The agglomerated CNTs usually require additional amount of CNT loading to reach the electrical percolation state and the CNT-agglomerated spots could become a serious defect in various optoelectronic applications.

The percolation threshold for the electrical conductivity has been investigated to depend on the aspect ratio [14], alignment [15], and dispersion [16]. In particular, MWCNTs have an extremely large surface area with the van der Waals attraction and, thus, they easily self-aggregate in polymeric solutions [17–19]. There have been many attempts to obtain a homogeneous, fine, and stable dispersion of carbon nanotubes in polymeric composites [20,21]. Several mechanical and chemical techniques have been introduced, despite the lack of understanding of the dispersion and stability of nanotubes in polymeric solutions [8]. The mechanical dispersion methods include a high shear mixing known as melt blending, which is relatively easier than the other methods, yet not efficient, because of the high viscosity of the composites even at low concentrations of the nanotubes [22]. In the case of chemical techniques, the open-end functionalization method is most widely used, which involves refluxing the CNTs in nitric acid, whereupon the carboxylic groups which are formed on the CNT surfaces are converted into other functional groups via standard condensation reactions [23,24]. Functionalization techniques of the CNT sidewalls have been reported to use such organic reagents as azomethine ylides, carbenes, nitrenes, aryl radicals and diazonium to disperse CNTs in various polymer systems [25–30]. However, the CNT dispersion is yet to be understood in different solvents and different polymers in relation with the functionalization of CNT sidewalls.

Although CNTs look dispersed well in the solution state right after the physical mixing, they often give CNT sediments or floating granules after being placed still for a time being. Unless there is a good compatibility among the solvent, polymer and CNTs, we believe that the CNT

granule size grows in the polymeric solution with time to reach a critical granule size for sedimentation. In addition, although a well-dispersed CNT mixture is used, the CNTs could easily agglomerate to form CNT grains while being solidified by the solvent evaporation in the drying process of film casting.

In this study, we carefully investigated the MWCNT dispersion in various PMMA polymer solutions by measuring the dispersed granule size of MWCNT using a dynamic light scattering technique, which was correlated well with visual observation and light transmittance of the solution mixtures. The acid treatment conditions and different solvent type were studied in relation with the electrical conductivity, aggregated-MWCNT granule, and light transmittance of coated thin films. The surface morphology of MWCNT/PMMA coating was mechanically modified by peeling off the polymer-rich layer subsequently to give an enhanced electrical pathway of MWCNTs.

2. Experimental

2.1. Multiwalled carbon nanotubes

The multiwalled CNTs synthesized by the thermal chemical vapor deposition (CVD) method were purchased from Iljin Nanotech Co., Korea. The diameters, lengths of the carbon nanotubes and number of multiwalled shells were measured by TEM (JEM-3011 TEM, JEOL Tokyo, Japan) to give about 10–20 nm in outer diameter, 1–10 μm in length, and ca. 17 walls (Fig. 1). The impurity content estimated by thermo-gravimetric analysis was approximately 5 wt% (TGA, DuPont, Ltd., TGA 2910, USA).

The MWCNTs were heat treated in an oxygen-flowing environment to remove amorphous carbon impurities. The optimum heat treatment temperature was determined by using TGA to prevent the thermal degradation of the carbon nanotubes. The pre-treatment time, treatment temperature, ramping and oxygen flow rate were 1 h, 663 K, 5 K/min and 40 standard cubic centimeters per minute (SCCM), respectively.

After the heat treatment, an acid treatment was used to remove metallic catalyst impurities. The MWCNTs were sonicated for several hours in a (3:1) mixture of concentrated sulfuric (98%) and hydrochloric (100%) acid at a frequency of 20 kHz. The sonication time was 12, 18, and 24 h. Finally, the MWCNTs were subjected to centrifugation at a speed of 12,000 rpm for 20 min and then rinsed with water repeatedly using a PTFE filter with a pore size of 0.2 μm. The Raman spectra were obtained using an FT-Raman spectrometer (Model: FRA 106/S, Bruker Optics, Germany) to check the effects of the acid treatment time on the efficiency of functionalization.

2.2. Polymer matrix systems

5 wt% of polymethylmethacrylate (PMMA) ($M_w = 350{,}000$ g/mol, 1.15 g/cm^3, Sigma–Aldrich) was dissolved in four different solvent systems: chloroform, toluene, tetrahydrofuran (THF), and dimethylformamide (DMF) with a mechanical stirrer. The purified MWCNTs were dispersed in a 5 wt% solution of PMMA for four different solvent systems and sonicated for several hours at a frequency of 20 kHz. For comparison, in this study, a semi-crystalline transparent polymer, PVDC copolymer (poly(vinylidene chloride-co-acrylonitrile-co-methyl

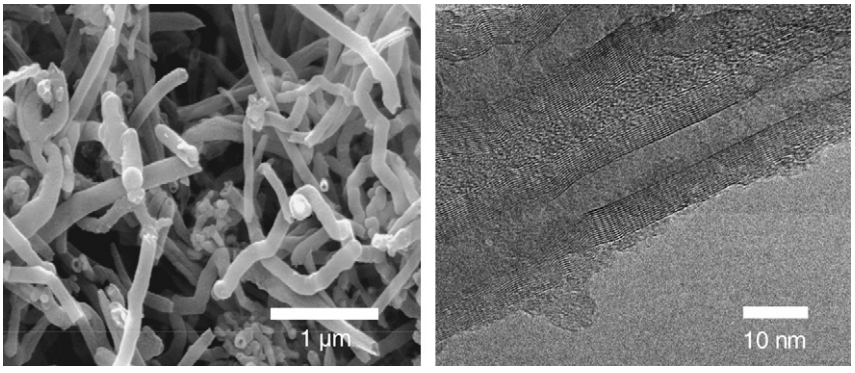

Fig. 1. SEM and TEM micrographs of MWCNTs.

methacrylate)) ($M_w = 90{,}000$ g/mol, 1.68 g/cm^3, Sigma–Aldrich), was investigated using DMF as a solvent (PVDC/DMF weight ratio: 0.05, MWCNTs/PVDC weight ratio: 0.005).

2.3. MWCNT dispersion

The solution dispersion of the MWCNTs was visually examined using optical microscopy (Olympus Inc., Japan) and UV–Vis–NIR spectroscopy (Model: Cary 50, Varian Inc., USA). Dynamic light scattering (DLS, Model: DLS-7000, Otsuka Electronics, Japan) experiments were performed for the MWCNT/PMMA/DMF mixture having a MWCNT/PMMA weight ratio as 0.025 and a PMMA/DMF weight ratio as 0.0006. The dilute mixture was aged at ambient temperature for two weeks to evaluate the stability of the dispersion before the DLS experiments.

2.4. Electrical conductivity

The MWCNT/PMMA/DMF mixtures were prepared for the measurement of electrical conductivity maintaining the PMMA/DMF weight ratio at 0.05 varying the MWCNT contents with respect to PMMA from 0 wt% to 3.0 wt% in increments of 0.5 wt%. Thin composites films were cast on the surface of the poly(ethylene terephthalate) (PET) film as well as glass plate using a solvent casting method. Prior to the solvent casting, the PET film was treated with an oxygen plasma (250 W and 150 mTorr, 30 s.) and the glass plate was cleaned and coated with hexamethyldisilazane (Model: AZ AD Promoter-K, AZ Electronics Materials, Luxembourg) to enhance the adhesion between the composite films and the substrates. The electrical conductivity was monitored by a 4-point type probe (Model: Universal probe, Jandel Inc., USA) connected to a current/voltage source-measure unit (Model: Keithley 236, Keithley Instruments Inc., USA). The contact pressures between the probe needle and the film surface were carefully controlled by means of a tension knob to prevent the surface from being damaged by the needle. The contact pressure was approximate 15 g/cm^2.

The MWCNT/PMMA composites films were mechanically polished using micro-fiber pad and alumina powder (diameter: 0.3 μm, Model: XL16756, Excel technologies Inc., USA) to enhance the electrical contact between the MWCNTs and the probes of the 4-point probe instrument. The surface morphology of the polished surface was investigated by scanning electron microscopy (Model S-2400, Hitachi Inc., Japan).

3. Results and discussion

3.1. Effects of acid-treatment time

The Raman spectra of the carbon nanotubes are shown in Fig. 2. The prominent D (at around 1290 cm^{-1}) and G (at around 1590 cm^{-1}) band peaks clearly indicate the intrinsic characteristics of the carbon nanotubes. The carbon nanotubes exhibit a strong tangential mode band at ca. 1590 cm^{-1} and a weak band at ca. 1290 cm^{-1}, which is attributed to the sp-3 hybridized carbon in the hexagonal framework of the nanotube walls [31]. As the acid treatment time increases from 12 to 24 h, the peak intensity increases in the region around 3300 cm^{-1} (more exactly: 3370–3470 cm^{-1}), which corresponds to the O–H stretching in carboxylic groups on the MWCNT surface. There is an apparent increase in the peak intensity at 3300 cm^{-1} with the acid treatment time of MWCNTs. As the acid treatment time increases, the CNT length is decreased and, subsequently, the probability of functionalization tends to increase [23]. Accordingly, our results demonstrate that the MWCNTs are shortened and their sidewalls are substantially functionalized by the acid treatment after 24 h.

3.2. Dispersion of MWCNT/polymer solution mixtures

In this study, MWCNT dispersion was investigated for four different types of solvent (chloroform, toluene, THF and DMF) and two polymer systems (PMMA and PVDC). When a black and uniform ink-type appearance is observed, the MWCNTs can be regarded as being dispersed well in the polymer solutions. On the other hand, if the MWCNT dispersion is not good, some of the MWCNTs are sedimented at the bottom of the solution mixture and the color becomes lighter black.

The MWCNT/polymer solution mixtures are compared in Fig. 3a and b before and after sonication, respectively. Fig. 3c shows the aged mixtures after 24 h of sonication treatment. As shown in Fig. 3a, all the acid-treated MWCNTs are not dis-

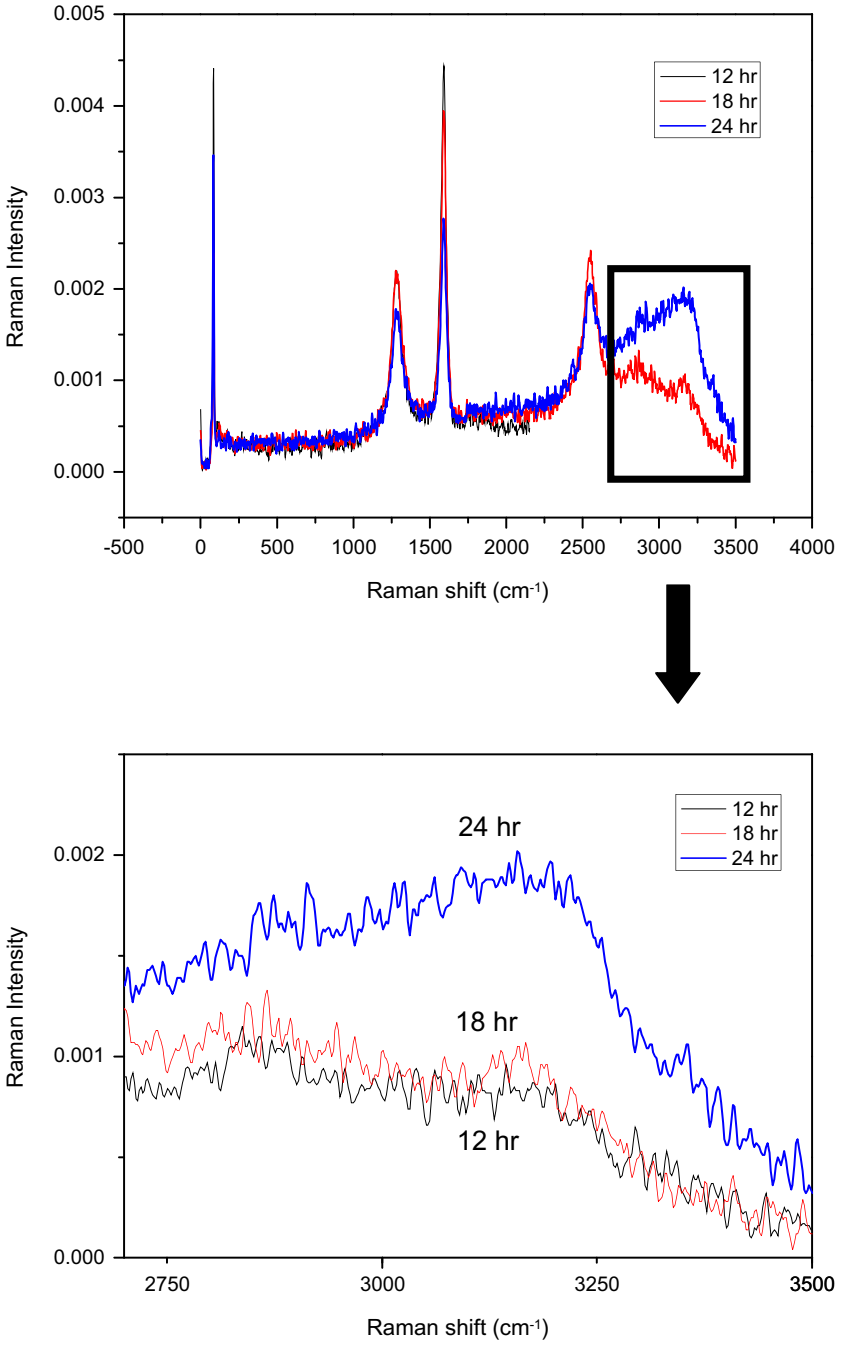

Fig. 2. Raman spectra of MWCNTs for various acid treatment conditions.

persed in the organic solvents before the sonication treatment to form granules at the bottom of the bottles as the arrow indicated in figures. After sonication in Fig. 3b, the MWCNTs look as being dispersed well in all the polymer solutions, although there are a slight difference in color and uniformity among samples. At a glance, the sonication process seems to be an efficient way in dispersing MWCNTs in organic solvents. However, after 24 h of aging following the sonication process, the MWCNTs begin to agglomerate and sediment as can be observed in Fig. 3c for the samples in chloroform, toluene, and THF. These three solvent systems exhibit different colors and different amounts of

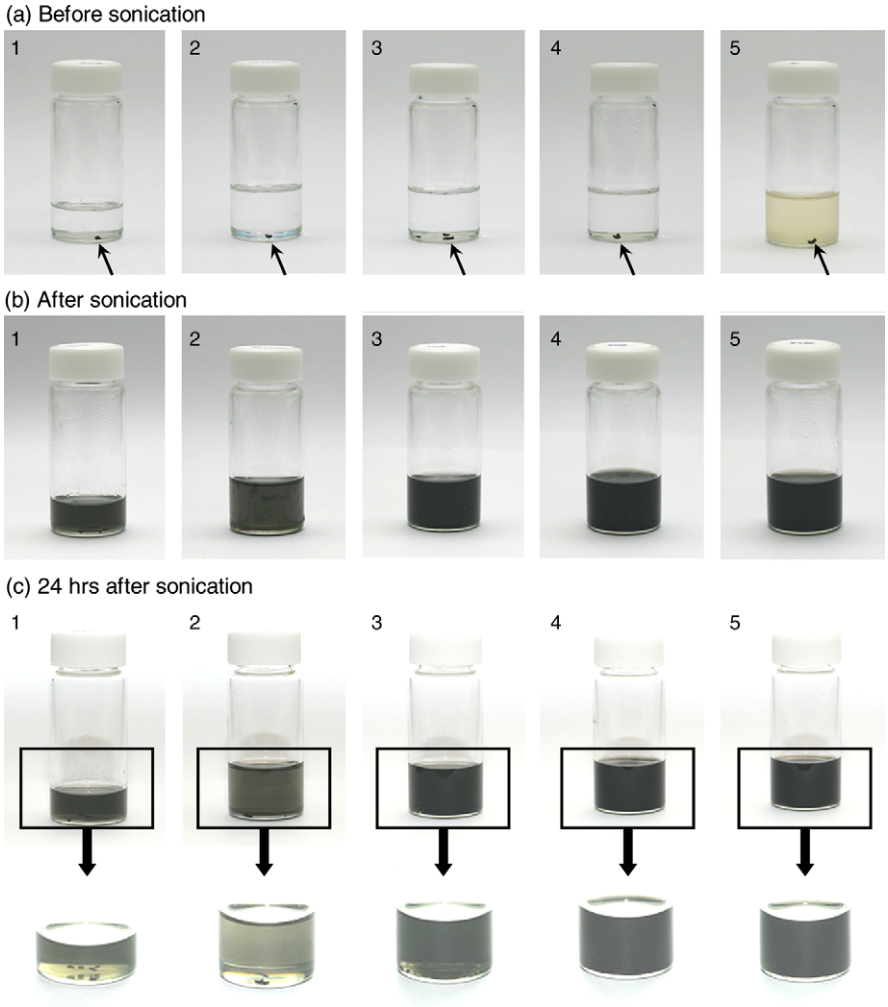

Fig. 3. Visual observation of MWCNT polymer mixtures (a) before sonication, (b) after sonication, and (c) aged for 24 h after sonication. The samples indicated are 1: MWCNT/PMMA/chloroform, 2: MWCNT/PMMA/toluene, 3: MWCNT/PMMA/THF, 4: MWCNT/PMMA/DMF and 5: MWCNT/PVDC/DMF.

sedimentation, indicating different dispersing capability. Apparently, the DMF system shows no sedimented MWCNT granules and maintains as a homogeneous mixture after 24 h of aging. The order of dispersion capability in the visual examination, which is based on the color and amount of sedimentation, is DMF > THF > chloroform > toluene. The physical dispersion of sonication, which is most commonly used in CNT dispersion, usually provides a good-looking mixture for a short period of time, but the long-term stability should be checked for following downstream fabrication processing.

Further evaluation of the MWCNT dispersion was performed using UV–Vis–NIR transmittance and optical microscopy. The UV–Vis–NIR transmittances of samples in Fig. 3c, which are aged for 24 h after sonication, are compared in Fig. 4. A well-dispersed mixture provides darker color in visual observation, which should correspond to a lower value in transmittance intensity. Low transmittance is due to the diffusion of light by the well-dispersed particles in the solution mixture, indicating that MWCNTs are well-dispersed. The DMF system, which was darkest in color in Fig. 3c, exhibits 89% of transmittance at 380 cm^{-1} of wavenumber (Fig. 4), whereas the chloroform and toluene systems show pale gray and about 95% of transmittance. According to Fig. 4, the order of transmittance intensity is toluene > chloroform > THF > DMF, which apparently agrees with the order of the dispersion capability examined in visual observation.

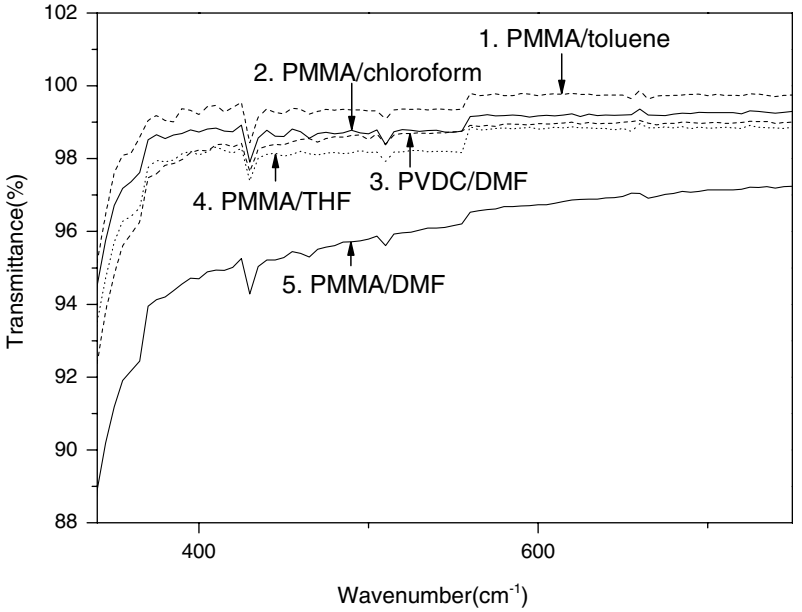

Fig. 4. Visible-ray transmittance of MWCNT polymer mixtures indicating 1: MWCNT/PMMA/toluene, 2: MWCNT/PMMA/chloroform, 3: MWCNT/PVDC/DMF, 4: MWCNT/PMMA/THF, 5: MWCNT/PMMA/DMF.

The optical microscopy images for the MWCNT/polymer film are shown in Fig. 5 for the samples corresponding to those examined in Fig. 3b. The chloroform (Fig. 5a) and toluene (Fig. 5b) mixtures show noticeable MWCNTs agglomerates in PMMA mixture. The MWCNT agglomerate size in chloroform and toluene are relatively smaller than that in THF (Fig. 5c). There are no agglomerates observed in the MWCNT/PMMA/DMF mixture, indicating that DMF have the best dispersion ability among the solvents, which agrees well with results in visual observation and light transmittance. Although DMF is the best solvent for PMMA, it is not the case for the PVDC polymer system as seen in Fig. 5e. In the MWCNT/PVDC/DMF system, MWCNTs look well-dispersed in visual examination (Fig. 3) and transmittance (Fig. 4), but a loosely-agglomerated granules can be observed in Fig. 5e. Accordingly, it

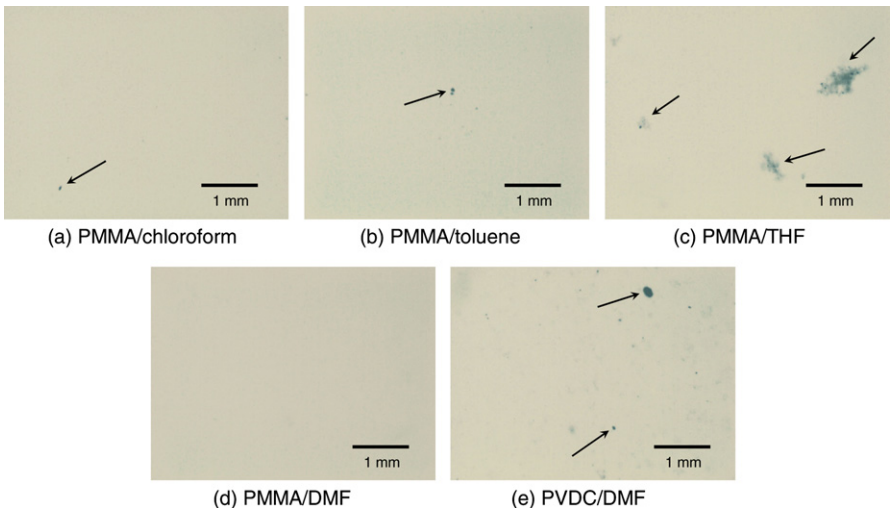

Fig. 5. Optical micrographs of MWCNT polymer mixtures coated on glass substrate comparing (a) MWCNT/PMMA/chloroform; (b) MWCNT/PMMA/toluene; (c) MWCNT/PMMA/THF; (d) MWCNT/PMMA/DMF and (e) MWCNT/PVDC/DMF. All samples were prepared at the same mixing ratios of MWCNTs/PMMA as 0.005, and polymer/solvent as 0.05.

should be mentioned that different polymer gives different dispersion for the same solvent to be used in CNT mixtures.

DMF turns out to be the most effective solvent system to disperse the MWCNTs in the PMMA solution among four different types of solvents investigated in this study. DMF and THF are classified as polar aprotic solvents, whereas toluene and chloroform are classified as non-polar (lipophilic) solvents, which may be represented by the dipole moment. The dipole moment values of these four solvents are 3.820 D for DMF, 1.750 D for THF, 1.040 D for chloroform and 0.375 D for toluene [32]. Although detailed mechanism is not clear yet, it may be reasonably speculated that the dipole–dipole interaction among the solvent molecule, carboxylic groups in MWCNT, and polar groups in PMMA chains. The order of the dipole moment values consists with the dispersion capability estimated by visual observation and transmittance measurement. Subsequently, we consider that the solvent polarity is closely associated with the MWCNT dispersion in PMMA solution.

From the viewpoint of physical interaction of polymer chains and MWCNTs, the MWCNT dispersion in polymers may be evaluated by comparing the dimensions of the polymer chain and MWCNT in the molecular level [8]. The average radius of gyration of the isolated PMMA chains in a dilute solution may be expressed as $\langle S^2\rangle = a(M_w)^b$, where $\langle S^2\rangle$ is the mean-squared radius of gyration in the unit of 0.01 nm^2. M_w is the molecular weight of PMMA, and the constants a and b for PMMA are 0.0713 and 1.0098, respectively [8]. Using the above equation, the average diameter of a random coil may be estimated by $2\langle S^2\rangle^{1/2}$. For the PMMA system with $M_w = 350{,}000$ g/mol in this work, the average diameter of PMMA coil may be estimated to be 34 nm. However, the molecular weight of PVDC used in this study is 90,000 g/mol, which gives the estimated average diameter of PVDC random coil is 7.3 nm. Consequently, the average diameter of PMMA coil is about 3.4 times larger than that of the carbon nanotubes (ca. 10 nm), whereas that of the PVDC random coil is even shorter than the diameter of the carbon nanotubes. Therefore, it may be reasonable to mention that the PMMA coil is long enough to be capable of wrapping up the carbon nanotubes effectively to prevent the agglomerations of nanotubes bundles, which is not the case with PVDC. This consideration agrees with the observed dispersion of PMMA and PVDC systems in color (Fig. 3), transmittance (Fig. 4) and agglomerates (Fig. 5).

As a result, dispersion of MWCNTs in polymer seems substantially influenced by polymer type, molecular weights (or chain lengths) of polymer, and the polarity of solvent. However, the precise dispersion control and interaction mechanism is far from being clearly understood and further study is required for various polymer/solvent systems.

3.3. Dynamic light scattering (DLS) analysis

The degree of CNT dispersion has been measured by the dynamic light scattering (DLS) method in ethanol [33] and DI water [34,35] to estimate the length distribution of dispersed carbon nanotubes [36,37]. DLS detects the intensity fluctuation of the scattered light due to the Brownian motion of the dispersed particles. The estimation of the size of objects is made from the measured intensity, $I(\tau, t)$, to give the auto-correlation function, $G_2(\tau)$, viz: $G_2(\tau) = [I(t) \times I(t+\tau)]/[I(t)]^2$, where t is the detecting time and the τ is correlation time. The normalized first-order auto-correlation function, $g_1(\tau)$ is given by $g_1(\tau) = \sqrt{G_2(\tau) - 1}$. Subsequently, the function $g_1(\tau)$ is related to the diffusion coefficient of the particles, viz: $g_1(\tau) = B\exp(-D(\tau)q^2)$, where q is the scattering vector ($q = 4\pi n \times \sin(\theta/2)/\lambda$) and D is diffusion constant. Here, n is the refractive index, θ is the scattering angle, and λ is the wavelength in a vacuum. Finally, the size of the dispersed particles is calculated from the diffusion coefficient through the Stokes–Einstein equation, $R = k_B T/6\pi\eta D$, where R is the particle radius, k_B is the Boltzman constant, T is the absolute temperature, and η is the solvent viscosity. In this way, the final size distributions of our MWCNT/PMMA/DMF mixtures were obtained from the function $G_2(\tau)$ by the inverse Laplace transformation [35]. Accordingly, the number of particles and the laser intensities are shown in Fig. 6 for the MWCNT mixtures after 12, 18 and 24 h of acid-treatment.

In DLS measurement, the agglomerated MWCNT bundles may well give a relatively larger size than the well-dispersed nanotubes. Accordingly, it is reasonable to suppose that the size distributions in Fig. 6, which are represented in terms of the number and intensity of the particles, reflect the degree of MWCNT dispersion. As seen in Fig. 6, the average diameter of the acid-treated MWCNTs decreases with the acid treatment time to give 224.4, 84.8 and 55.6 nm for 12, 18, and 24 h of acid

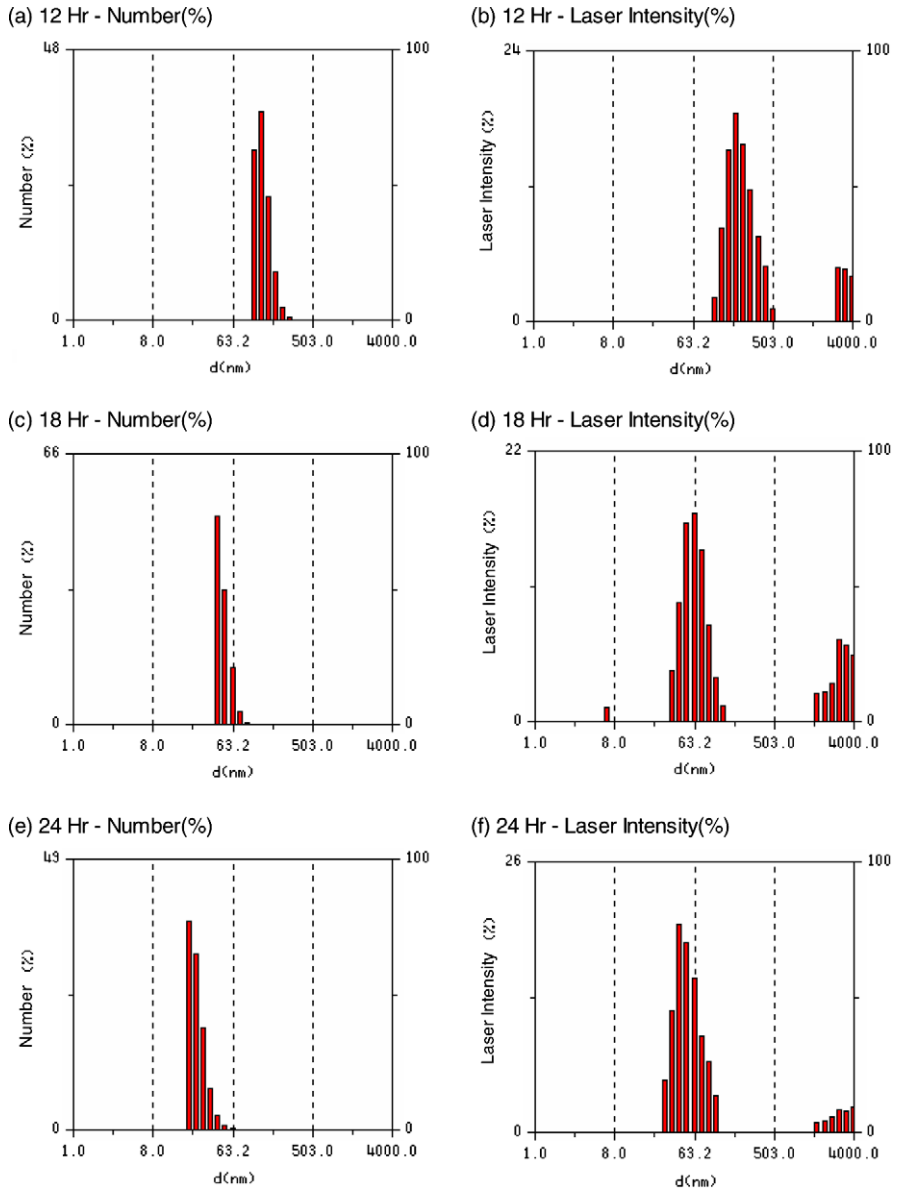

Fig. 6. DLS size distribution of carbon nanotubes dispersed in PMMA/DMF solution (MWCNTs/PMMA weight ratio at 0.025 and PMMA/DMF weight ratio at 0.0006) expressed as the number of particles and laser intensity for the acid treatment times of 12 h (a and b), 18 h (c and d) and 24 h (e and f).

treatment, respectively. It clearly demonstrates that the MWCNT dispersion is improved by the acid-treatment time.

3.4. Dispersion and percolation of carbon nanotubes in polymer matrix

Fig. 7a shows the electrical conductivity and transparency of the MWCNT/PMMA composite films cast from DMF in the glass substrate as a function of MWCNT loading. The conductivities of the MWCNT/PMMA films cast from chloroform, toluene and THF solutions (Fig. 5) were not measurable because they were less than 10^{-16} S/cm, which was the lowest limit of our instrument. Those composite films cast from DMF containing less than 1.0 wt% of MWCNTs were non-conductive (<ca. 10^{-16} S/cm). The electrical conductivity at around 2.0 wt% of MWCNT loading is 3.84×10^{-4} S/cm, which increases up to 10^{-2} S/cm

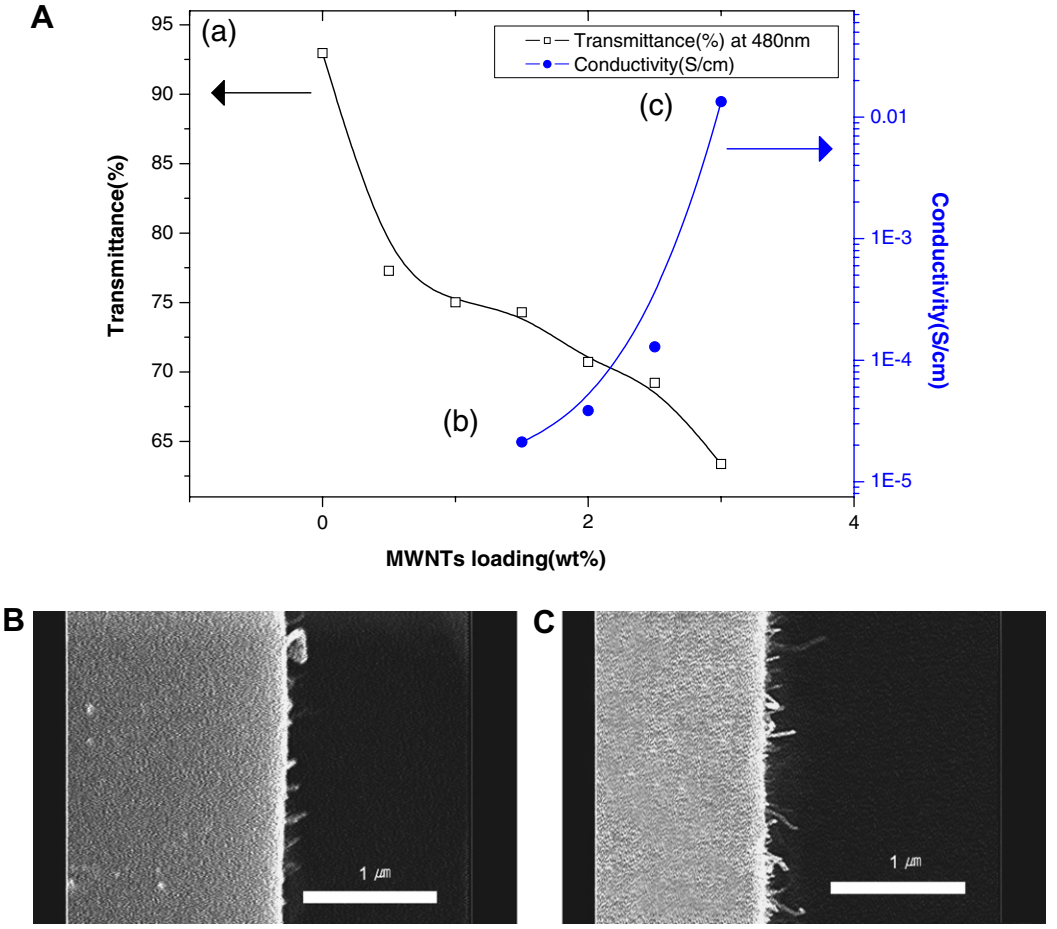

Fig. 7. Transmittance and electrical conductivity of MWCNT/PMMA composites plotted as a function of MWCNT weight fraction (a), and SEM micrographs of fractured surfaces for the 1.5 wt% (b) and 3.0 wt% composite film (c).

at 3.0 wt% of MWCNT loading, which lies among the highest in such a low loading density of MWCNTs [6,8]. We believe that the well-dispersed MWCNT/PMMA solution desirably provides a percolated state of MWCNTs at a low loading density in the PMMA matrix. Although CNT is an effective conductive filler, the electrical conductivity can be ensured by a good dispersion of CNTs in the states of both liquid mixture and solidified composite. We believe that the high conductivity achieved in our MWCNT/PMMA composite is ascribed to good dispersion of the MWCNTs carefully confirmed in both solution mixture and cast film.

The SEM micrographs of the fractured surface of MWCNT/PMMA composite films are shown in Fig. 7b and c for the MWCNT loadings of 1.5 and 3.0 wt%, respectively. As can be seen, the well-dispersed MWCNTs are pulled-out from the fractured surface and the number of pulled-out MWCNTs increases with the increased loading density. No agglomerated MWCNT bundles were observed on the fractured surface, demonstrating that the MWCNTs should be well dispersed in the PMMA matrix.

3.5. Elimination of polymer-rich surface by mechanical polishing

As represented in the schematic in Fig. 8, even when the electrical percolation is made by the well-dispersed carbon nanotubes inside the composite film, the probing electrodes may not touch the MWCNTs at the surface due to the polymer-rich layer formed on the free surface. As schematically seen in Fig. 8a, the polymer-rich layer is usually formed at the liquid–gas interface during the solvent-casting process. When the liquid-phase PMMA/MWCNT mixture is cast as a thin film on

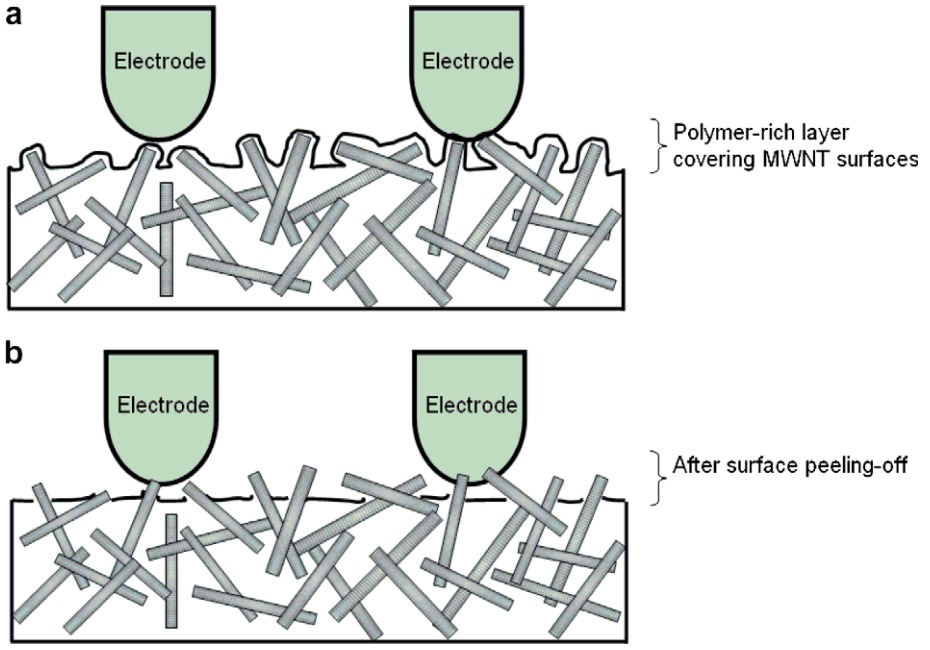

Fig. 8. Schematic of MWCNT exposure on the surface caused by mechanical polishing to eliminate the polymer-rich region on the cast film (a) before and (b) after polishing.

a substrate, the composite morphology near the surface may well be different from that in the bulk because of the surface tension and gravity force. When the polymer solution and MWCNTs have good wetting characteristics, namely having suitable free surface energies, the MWCNTs on the free surface may well be wet (or covered) with the polymer. In addition, the density of the MWCNTs is usually higher than that of the polymer solution and, thus, the MWCNTs may sediment underneath the

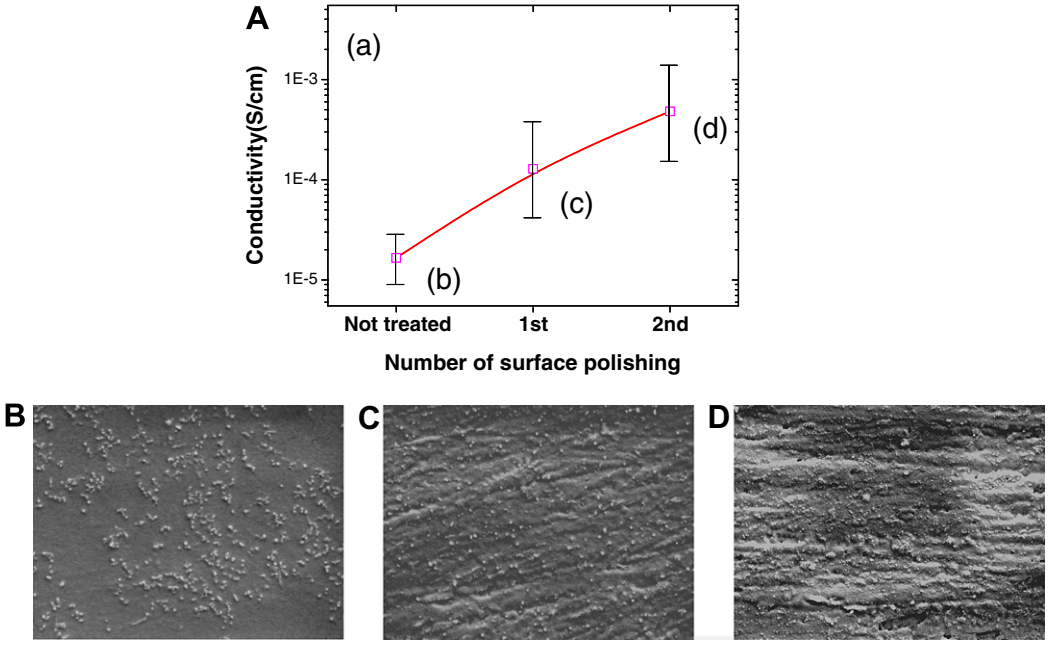

Fig. 9. Electrical conductivity of MWCNT/PMMA composites as a function of repeated mechanical polishing (a), and surface micrographs of composites film comparing (b) before polishing, (c) after 1st polishing, and (d) after 2nd polishing.

coating surface [38]. As a result, MWCNTs tend to be covered with the polymer-rich layer on the surface. Accordingly, the surface peel-off of the polymer-rich layer could improve the surface conductivity of the MWCNT composites. As schematically shown in Fig. 8b, the electrical contact between the probing electrodes and surface-exposed MWCNTs may be substantially improved simply by polishing the polymer-rich surface in a mechanical way. This consideration is supported by Fig. 9, which shows the electrical conductivity of the MWCNT composites subjected to mechanical polishing. The conductivity is elevated from about 10^{-5} S/cm to 10^{-3} S/cm with a repeated mechanical polishing for the MWCNT loading of 1.5 wt%. The SEM micrographs in Fig. 9b–d, compare the MWCNTs exposed on the surface before and after the mechanical polishing. Before the mechanical polishing, the MWCNTs appear to be covered with PMMA on the surface (Fig. 9b). With mechanical polishing, the number of MWCNTs exposed on the surface apparently increases to give more opportunity for the probing elctrode to come into contact with the MWCNTs at the surface. In our experiments, the electrical conductivity was increased by approximately two orders of magnitude simply by eliminating the polymer-rich layer by mechanical polishing, without increasing the MWCNT loading.

4. Conclusion

Investigating MWCNT dispersion in different solvents and polymers, a polar aprotic solvent, DMF, showed good dispersion characteristics for the MWCNT/PMMA composites system. Increasing the acid treatment time enhanced the dispersion of the MWCNTs, because of the improved dipole interaction with the polymer and solvent. By using an adequate solution system and controlled functionalization of the carbon nanotube sidewalls, a noticeable improvement of the electrical conductivity was obtained up to 10^{-2} S/cm with 3.0 wt% of MWCNT loading. Furthermore, the polymer-rich layer on the coating surface was eliminated by mechanical polishing to give an increment of electrical conductivity approximately by the three orders of magnitude.

Acknowledgements

This work was supported by Grant No. R01200600010348020006 from the Basic Research Program of the Korea Science & Engineering Foundation. We also appreciate the instrumental and technical support from the Samsung Advanced Institute of Technology through SAINT, Sungkyunkwan University.

References

[1] S. Iijima, Nature 354 (1991) 56.
[2] A.G. Rinzler, J.H. Hafner, P. Nikolaev, L. Lou, S.G. Kim, D. Tomanek, Science 269 (1995) 1550.
[3] W.A. de Heer, A. Chatelain, D. Ugarte, Science 270 (1995) 1179.
[4] P.G. Collins, A. Zettl, H. Bando, A. Thess, R.E. Smalley, Science 278 (1997) 100.
[5] S. Frank, P. Poncharal, Z.L. Wang, W.A. de Heer, Science 280 (1998) 1744.
[6] S.A. Curran, P.M. Ajayan, W.J. Blau, D.L. Carroll, J.N. Coleman, A.B. Dalton, Adv. Mater. 10 (1998) 1091.
[7] R. Ramasubramaniam, J. Chen, H. Liu, Appl. Phys. Lett. 83 (2003) 2928.
[8] F. Du, R.C. Scogna, W. Zhou, S. Brand, J.E. Fischer, K.I. Winey, Macromolecules 37 (2004) 9048.
[9] T. Ogasawara, Y. Ishida, T. Ishikawa, R. Yokota, Compos. Part. A. 35 (2004) 67.
[10] B. Zhu, S. Xie, Z. Xu, Y. Xu, Compos. Sci. Technol. 66 (2006) 548.
[11] Y. Bin, M. Mine, A. Koganemaru, X. Jiang, M. Matsuo, Polymer 47 (2006) 1308.
[12] Y.T. Sung, M.S. Han, K.H. Song, J.W. Jung, H.S. Lee, C.K. Kim, Polymer 47 (2006) 4434.
[13] E. Najafi, J.Y. Kim, S.H. Han, K. Shin, Colloid. Surf. A: Physicochem. Eng. Aspect. 284–5 (2006) 373.
[14] M.B. Bryning, M.F. Islam, J.M. Kikkawa, A.G. Yodh, Adv. Mater. 17 (2005) 1186.
[15] F. Du, J.E. Fischer, K.I. Winey, J. Polym. Sci.: Part B: Polym. Phys. 41 (2003) 3333.
[16] S. Barrau, P. Demont, E. Perez, A. Peigney, C. Laurent, C. Lacabanne, Macromolecules 36 (2003) 9678.
[17] J. Rong, Z. Jing, H. Li, M. Sheng, Macromol. Rapid. Commun. 22 (2001) 329.
[18] M.F. Islam, E. Rojas, D.M. Bergey, A.T. Johnson, A.G. Yodh, Nano. Lett. 3 (2003) 269.
[19] S.J. Park, M.S. Cho, S.T. Lim, H.J. Choi, M.S. Jhon, Macromol. Rapid. Commun. 24 (2003) 1070.
[20] J. Liu, M.J. Casavant, M. Cox, D.A. Walters, P. Boul, W. Lu, A.J. Rimberg, K.A. Smith, D.T. Colbert, R.E. Smalley, Chem. Phys. Lett. 303 (1999) 125.
[21] K.D. Ausman, R. Piner, O. Lourie, R.S. Ruoff, M. Korobov, J. Phys. Chem. B. 104 (2000) 8913.
[22] P. Poetschke, A.R. Bhattacharyya, A. Janke, H. Goering, Compos. Interf. 10 (2003) 389.
[23] Y.P. Sun, K. Fu, Y. Lin, W. Huang, Acc. Chem. Res. 35 (2002) 1096.
[24] C.A. Dyke, J.M. Tour, Chem. Eur. J. 10 (2004) 812.
[25] V. Georgakilas, K. Kordatos, M. Prato, D.M. Guldi, M. Holzinger, A. Hirsch, J. Am. Chem. Soc. 124 (2002) 760.
[26] Y. Chen, R.C. Haddon, S. Fang, A.M. Rao, P.C. Eklund, W.H. Lee, J. Mater. Res. 13 (1998) 2423.

[27] J. Chen, M.A. Hamon, H. Hu, Y. Chen, A.M. Rao, P.C. Ecklund, Science 282 (1998) 95.
[28] M. Holzinger, O. Vostrowsky, A. Hirsch, F. Hennrich, M. Kappes, R. Weiss, Angew. Chem. Int. Ed. 40 (2001) 4002.
[29] J.L. Bahr, J.P. Yang, D.V. Kosynkin, M.J. Bronikowski, R.E. Smalley, J.M. Tour, J. Am. Chem. Soc. 123 (2001) 6536.
[30] J.L. Bahr, J.M. Tour, Chem. Mater. 13 (2001) 3823.
[31] Y. Ying, R.K. Saini, F. Liang, A.K. Sadana, W.E. Billups, Org. Lett. 5 (2003) 1471.
[32] R.L. David, Handbook of Organic Solvents, CRC Press, Boca Raton, 1994.
[33] L. Zhao, L. Gao, Colloid. Surf. A: Physicochem. Eng. Aspects 224 (2003) 127.
[34] L. Jiang, L. Gao, J. Sun, J. Colloid. Interf. Sci. 260 (2003) 89.
[35] J.Y. Lee, J.S. Kim, K.H. An, K. Lee, K.Y. Kim, D.J.D.J. Bae, J Nanosci. Nanotech. 5 (2005) 1045.
[36] M. Sano, A. Kamino, J. Okamura, S. Shinkai, Langmuir 17 (2001) 5125.
[37] X. Gao, T. Hu, L. Liu, Z. Guo, Chem. Phys. Lett. 370 (2003) 661.
[38] L.H. Sperling, Introduction to Physical Polymer Science, John Wiley & Sons, Hoboken, 2006.

Available online at www.sciencedirect.com
ScienceDirect
Organic Electronics 9 (2008) 14–20
Organic Electronics
www.elsevier.com/locate/orgel

Bottom-contact poly(3,3‴-didodecylquaterthiophene) thin-film transistors with reduced contact resistance

Qin Jia Cai [a], Mary B. Chan-Park [a,*], Jun Zhang [b,c], Ye Gan [b,c], Chang Ming Li [b,c,1], Tu Pei Chen [d], Beng S. Ong [e]

[a] School of Chemical and Biomedical Engineering, Nanyang Technological University, 62 Nanyang Drive, Singapore 637459, Singapore
[b] School of Chemical and Biomedical Engineering, Nanyang Technological University, 70 Nanyang Drive, Singapore 637457, Singapore
[c] Center for Advanced Bionanosystems, Nanyang Technological University, 70 Nanyang Drive, Singapore 637457, Singapore
[d] School of Electrical and Electronic Engineering, Nanyang Technological University, 50 Nanyang Avenue, Singapore 639798, Singapore
[e] Materials Design and Integration Laboratory, Xerox Research Centre of Canada, Mississauga, Ontario, Canada L5K 2L1

Received 22 June 2007; received in revised form 7 July 2007; accepted 10 July 2007
Available online 21 July 2007

Abstract

A dramatic, ~20-fold, reduction in the contact resistance of the bottom-contact poly(3,3‴-didodecylquaterthiophene) (PQT-12) thin-film transistors was achieved through a simple treatment of gold (Au) source and drain electrodes. The Au electrode treatment involved simply immersing the Au electrodes into Piranha solution prior to the deposition of the organic semiconductor. This treatment led to significant improvement of device performance. Channel length scaling analysis indicates that the contact resistance is reduced by about one order of magnitude, resulting in enhancement of estimated field-effect mobility by about a factor of five. Transport characteristic analysis suggests that the improved efficiency of charge carrier injection is probably due to increased dopant density of PQT-12 at the electrode/PQT-12 interface.

PACS: 73.40.Cg; 73.40.Sx; 73.61.Ph

Keywords: Poly(3,3‴-didodecylquaterthiophene); Contact resistance; Thin-film transistors; Electrodes; Treatment; Interface

1. Introduction

Solution-processable organic thin-film transistors (OTFTs) have attracted great interest due to their potential application for large-area, flexible, and ultralow-cost electronics [1–3]. In the operation of OTFTs, charge transport strongly depends on two interfaces: (i) interfaces between organic semiconductors and dielectric and (ii) interfaces between source and drain (S–D) electrodes and organic semiconductors. In the former interfaces, charge transport takes place in the organic semiconductor layer and in the latter interfaces, charge carriers are injected into and extracted from the semiconductors. To improve device performance, the molecular ordering of organic semiconductors has been

* Corresponding author. Tel.: +65 67906064; fax: +65 6792 4762 (M.B. Chan-Park).
E-mail addresses: mbechan@ntu.edu.sg (M.B. Chan-Park), ecmli@ntu.edu.sg (C.M. Li).
[1] Tel.: +65 67904485; fax: +65 67911761.

1566-1199/$ - see front matter
doi:10.1016/j.orgel.2007.07.002

manipulated at the interface between organic semiconductor and dielectric by substrate surface chemistry [4–7], resulting in improved charge transport in the organic semiconductors. On the other hand, the contact properties at the interfaces between the electrodes and organic semiconductors have also been tailored to improve the carrier injection efficiency [8–10], giving rise to improved device performance.

The S–D electrodes need to be chemically stable and energetically compatible with the organic semiconductors to form Ohmic contacts for efficient charge injection. To achieve high performance OTFTs, gold (Au) electrodes have usually been used because of their high conductivity, excellent operational stability, and particularly their high work function, which enables efficient hole injection from Au into most p-type organic semiconductors, such as pentacene and poly(3-hexylthiophene). Recently, interfacial studies by photoemission spectroscopy have shown that the contact formation between organic semiconductor and Au could result in a significant energy barrier (0.5–1.0 eV) for hole injection [11–14]; such a barrier is associated with contact resistance in the device operation [15–18]. The contact resistance may affect the device performance. The effect of the contact resistance depends on the magnitude of the contact resistance relative to that of the channel resistance, and usually is substantial in OTFTs of short channel length [15]. The reduction of contact resistance in TFTs of poly(3,3‴-didodecylquaterthiophene) (PQT-12), a novel high performance polymeric semiconductor with strong environmental stability, will be helpful to improve the performance of devices made from it. This is especially so since it has a high ionization potential (5.2–5.3 eV) (0.1–0.2 eV higher than that of regioregular poly(3-hexylthiophene) – a common organic semiconductor) [19,20]. No study on the contact resistance of PQT-12 TFTs has been reported yet.

In this work, we report a dramatic reduction of the contact resistance between the poly(3,3‴-didodecylquarterthiophene) (PQT-12) and Au source–drain (S–D) electrodes for bottom-contact OTFTs. By simply dipping Au electrodes into Piranha solution (70% H_2SO_4 + 30% H_2O_2), the magnitude of contact resistance in the operation of the OTFTs was reduced ~20-fold. The analysis of current transport over the electrode/PQT-12 interfaces suggests that the improved carrier injection efficiency is probably attributable to an increased dopant density of PQT-12 at the electrode/PQT-12 interface by the electrode treatment. Bottom-contact OTFTs with Piranha-treated Au (AuP) electrodes show significantly improved field-effect mobility over OTFTs with untreated Au electrodes.

2. Experimental

A series of bottom-contact OTFTs (schematically shown in Fig. 1) were fabricated on a heavily n-doped silicon (Si) wafer, on which the S–D electrodes were made of Au (~50 nm) with a titanium adhesion layer (~1 nm). The electrodes were patterned using the lift-off technique. The silicon wafer was used as gate electrode. A thermally grown SiO_2 layer of about 100 nm on the Si wafer served as the gate dielectric. For OTFTs with untreated Au electrodes, the electrodes were cleaned successively with ultrasonication in acetone, methanol, and de-ionized water. The wafer surface with patterned Au electrodes was cleaned with oxygen plasma. For OTFTs with AuP electrodes, Au electrodes were additionally treated by immersing Au electrode-patterned wafer into a Piranha solution for 15 min, rinsed with de-ionized water, and dried with nitrogen. Subsequently, both untreated and treated electrode-patterned wafers were immersed into 3 mM solution of octyltrichlorosilane in hexane at room temperature for 15 min, rinsed with hexane and isopropanol, and dried with nitrogen gas. Finally, PQT-12 semiconductor layers of about 60 nm were deposited on both Au electrode patterns by spin-coating a dispersion of PQT-12 nanoparticles in dichlorobenzene. The semiconductor layer was then dried, annealed at 125 °C for 30 min, and cooled to room temperature overnight in vacuum. The OTFTs were charac-

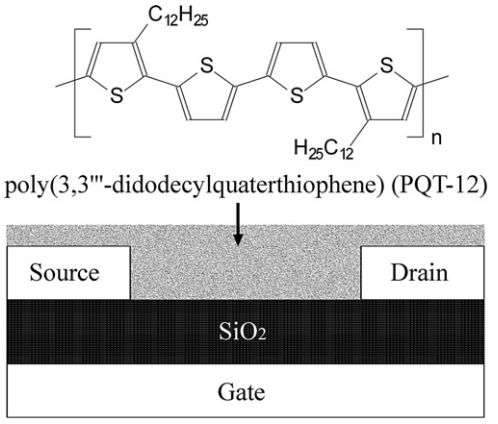

Fig. 1. Schematic depiction of a bottom-contact poly(3,3‴-didodecylquaterthiophene) (PQT-12) thin-film transistor with untreated Au or AuP S–D electrodes.

terized under ambient condition using an Agilent 4157B Semiconductor Parameter Analyzer System. The atomic force microscopy (AFM) experiments were conducted with a Nanoscope IIIa MultiMode scanning probe microscope (Digital Instruments) in tapping mode with a scan rate of 0.5 Hz.

3. Results and discussion

Fig. 2 shows the output characteristics of devices with untreated Au and AuP S–D electrodes, respectively. The device characteristics followed the metal–oxide–semiconductor field-effect transistor (MOSFET) gradual channel model. As shown in Fig. 2a, the output characteristics of the device with untreated Au electrodes showed a pronounced curvature at low V_{DS}, indicating the existence of contact resistance arising from the energy barrier for carrier injection. The corresponding device had a mobility μ of only about 0.01 $cm^2\,V^{-1}\,s^{-1}$, together with a current on/off ratio of about 10^4 and a threshold voltage V_T of about -2 V. The mobility μ was estimated using the relation in the saturated regime given by

$$\mu = \frac{2L}{WC_i}\left(\frac{\partial\sqrt{I_{DS}}}{\partial V_{GS}}\right)^2, \tag{1}$$

where I_{DS} is the drain current, C_i is the capacitance per unit area of the gate dielectric layer, and V_{GS} is the gate voltage. V_T of the device was determined from the relationship between the square root of I_{DS} at the saturated regime and V_{GS} of the device by extrapolating the measured data to $I_{DS} = 0$. On the other hand, the output characteristics of the device with AuP electrodes show no curvature at low V_{DS} but a linear current-voltage relationship at $V_{DS} < V_{GS}$, with much (~6-fold) higher saturation currents. The corresponding device exhibited an increased mobility of about 0.05 $cm^2\,V^{-1}\,s^{-1}$, with current on/off ratio of about 10^5 and a threshold voltage of about -3 V. The improved performance of devices with AuP electrodes was generally observable in the experiments. When AuP electrodes on wafer substrate were plasma-cleaned, the mobility of the device was reduced to a value close to that of device with untreated Au electrodes. The pronounced curvature associated with the high contact resistance at low V_{DS} reappeared. These results indicate that the device performance of bottom-contact PQT-12 TFTs has been significantly improved by simple treatment of Au S–D electrodes with Piranha solution.

To understand the relationship between the device performance of OTFTs and the contact resistance, the dependence of device resistance on the channel length was studied in the linear operation regime (source–drain voltage $\ll$ gate voltage), where there should be the most pronounced contact effect. At low drain voltage, device "on" resistance, R_{on}, can be expressed as [21,22]

$$R_{on} = \left.\frac{\partial V_{DS}}{\partial I_{DS}}\right|_{V_{DS}}^{V_{GS}} = R_{Ch} + R_C = \frac{L}{W\mu_i C_i(V_{GS} - V_T)} + R_C, \tag{2}$$

where R_{Ch} and R_C are the channel resistance and the contact resistance, respectively. Fig. 3 shows a plot

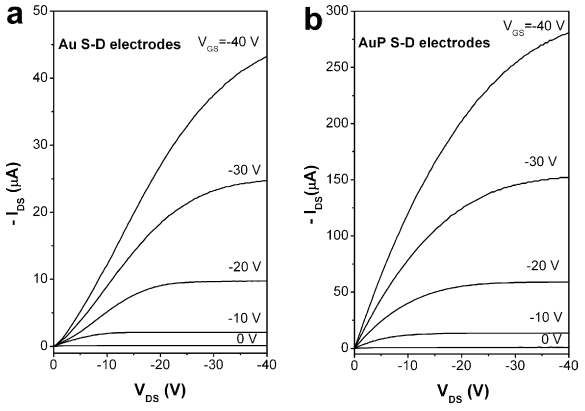

Fig. 2. Source–drain current I_{DS} versus source–drain voltage V_{DS} as a function of gate voltage V_{GS} for bottom-contact PQT-12 TFTs with (a) untreated Au and (b) AuP S–D electrodes. The channel length and width are, respectively, 20 and 10,000 μm.

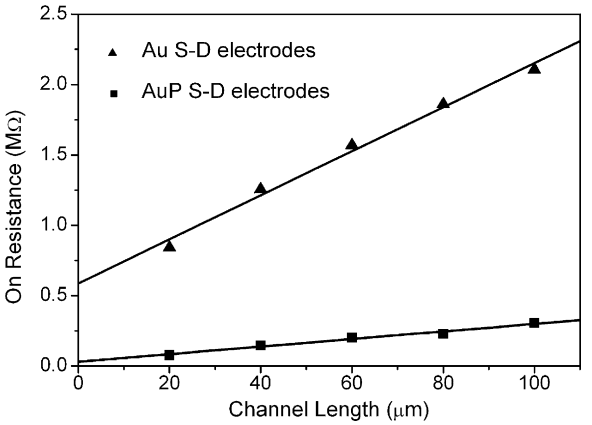

Fig. 3. Relationship between the "on" resistance and channel length at -40 V gate voltage for bottom-contact PQT-12 TFTs with untreated Au and AuP S–D electrodes.

of R_{on} as a function of channel length L at the gate voltage of -40 V and the drain voltage of -2 V. The experimental data are well expressed by Eq. (2) in first order, with R_{on} linearly depending on L. The contact resistance was determined by extrapolating the relationship of R_{on} versus L to $L = 0$. The contact resistance of the OTFTs with untreated Au electrodes was about 0.6 MΩ. The R_C/R_{Ch} ratio is about 1.9 at channel length of 20 μm. In sharp contrast, the devices with AuP electrodes have much lower contact resistance of about 30 kΩ. The R_C/R_{Ch} ratio is only about 0.6 at channel length of 20 μm. The channel length scaling analysis presented here suggests that the simple treatment of Au S–D electrodes by Piranha solution significantly decreases the contact resistance for bottom-contact PQT-12 TFTs, resulting in improved device performance.

Typically, current transport over an energy barrier at a metal/semiconductor interface is dominated by thermionic emission over the barrier at room temperature. The current transport characteristics over the barrier can be expressed as [23,24]

$$J \propto \exp\left(-\frac{q\phi_B}{kT}\right)\exp\left(\frac{q\Delta\phi}{kT}\right), \tag{3}$$

$$\text{where} \quad \Delta\phi = \left[\frac{q^3 N_A (V + V_{bi} - kT/q)}{8\pi^2 \varepsilon_s}\right]^{1/4}. \tag{3a}$$

T is the absolute temperature, q is the electron charge, ϕ_B is barrier height, k is Boltzmann's constant, $\Delta\phi$ is Schottky-barrier lowering due to the combined effects of the image force and applied electric fields, N_A is the dopant density, V is the applied voltage, V_b is the built-in potential, and ε_S is the semiconductor permittivity. According to Eqs. (3) and (3a), the logarithm of the current density should scale linearly with the fourth root of applied voltage neglecting the term $V_{bi} - kT/q$, with a slope depending on the dopant density.

Fig. 4a shows the current versus the fourth root of applied voltage (positive bias) characteristics of planar Au/PQT-12 and AuP/PQT-12 diodes at room temperature. The electrical current under positive bias can be attributed to hole injection current from electrode contacts into PQT-12 semiconductor. The diodes were fabricated by depositing PQT-12 thin-films between coplanar electrode contacts with a channel width of 800 μm and a channel length of 1 μm on oxide Si wafer as the OTFTs. Short channel length was used to study the charge transport over the electrode/PQT-12 interfaces since charge transport in diodes with short channel length could be mainly interface-limited and provide information about the charge transport over a Schottky-barrier. As shown in Fig. 4a, the experimental data above the lower range of applied voltage are well described by Eqs. (3) and (3a). The injection current over the AuP/PQT-12 interfacial barrier has a significantly higher value. The slope of the fitting line for AuP/PQT-12 is about 30% steeper than that for Au/PQT-12, suggesting the dopant density of PQT-12 at AuP/PQT-12 interface is higher than that at Au/PQT-12 interface. This difference is evidently due to the Piranha-treatment of Au surface,

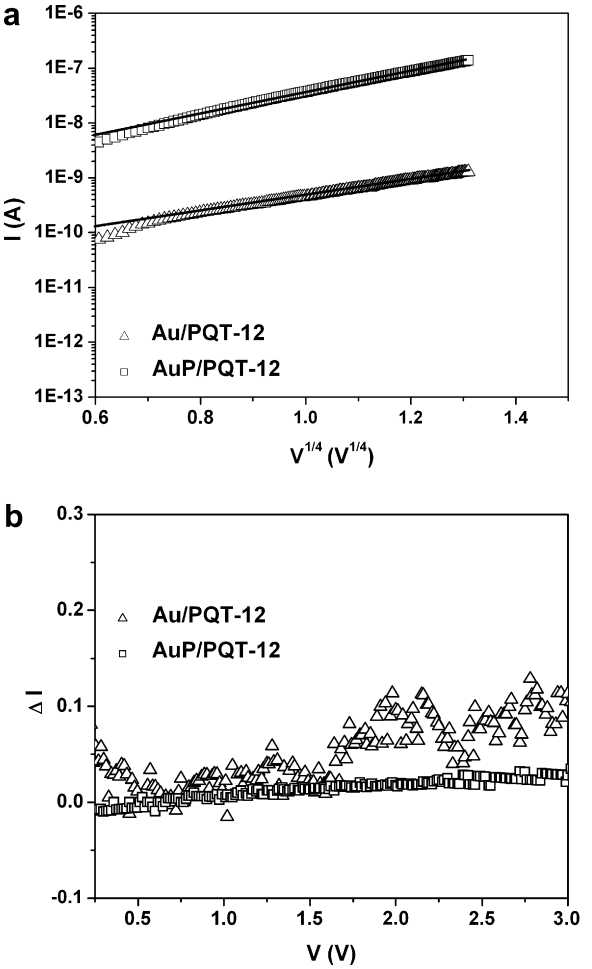

Fig. 4. (a) Current versus the fourth root of applied voltage (positive bias) characteristics of planar Au/PQT-12 and AuP/PQT-12 diodes with a length of 1 μm and a width of 800 μm fabricated on oxide Si wafer as the OTFFs at room temperature. Solid lines are fitting lines for experimental data. The departures of the data from the model at low V may reflect the terms that were neglected in Eqs. (3) and (3a) to yield the log-linear relationship. (b) ΔI–V characteristics of respective planar Au/PQT-12 and AuP/PQT-12 diodes.

which probably results in a trace amount of sulfate and bisulfate species adsorbed on the Au surface [25]. Sulfate and bisulfate species may be acceptors for the PQT-12 and increase the dopant density of PQT-12 at the electrode/PQT-12 interface. Higher dopant density at the electrode/semiconductor interface can give rise to more lowering of the Schottky-barrier for charge carrier emission under a bias, resulting in improved charge injection efficiency in the operation of bottom-contact PQT-12 TFTs.

Fig. 4b shows the ΔI–V characteristics of respective planar Au/PQT-12 and AuP/PQT-12 diodes. $\Delta I = 2(I_p - I_n)/(I_p + I_n)$ is the relative current difference between I_p and I_n, where I_p is hole current injected from an electrodes contact into PQT-12 semiconductor under positive bias and I_n is electron current injected from an electrode contact into PQT-12 semiconductor. ΔI of AuP/PQT-12 interface is slightly smaller than that of the Au/PQT-12 interface in Fig. 4b. Since I_p and I_n depend on the respective hole injection barrier and electron injection barrier at the electrode/PQT-12 interfaces, the results in Fig. 4b suggest that the AuP electrodes could not give lower hole injection barrier height than untreated Au electrodes. The improved hole injection efficiency due to the Piranha-treatment,

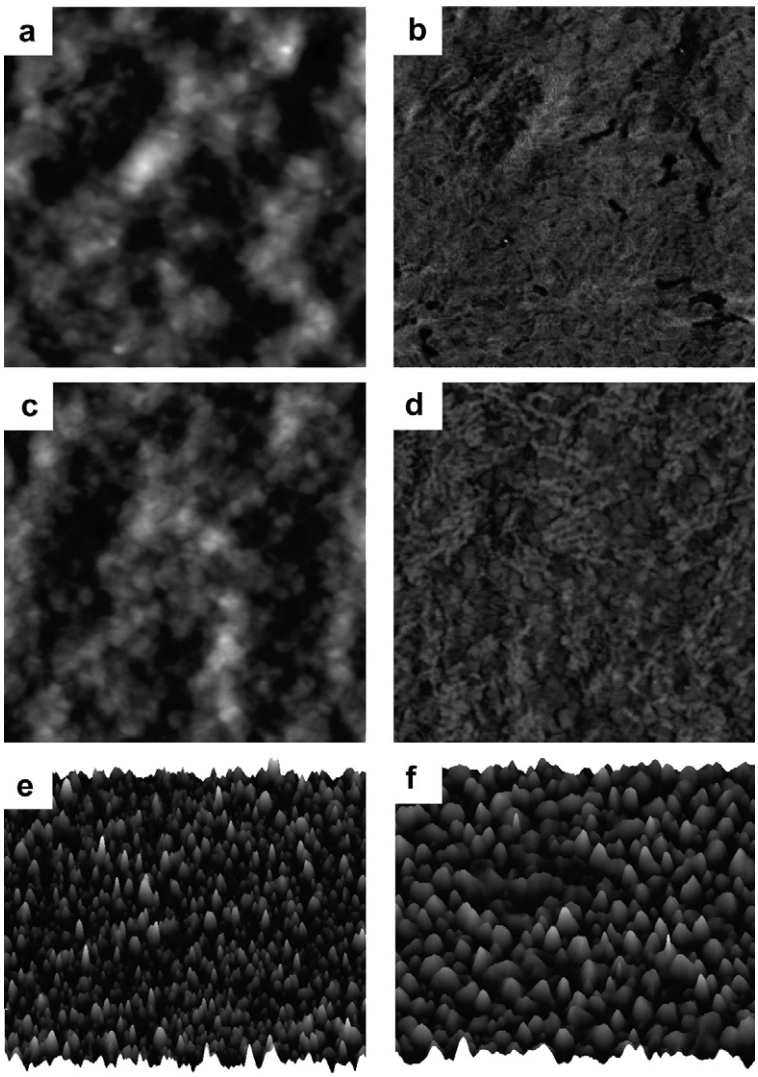

Fig. 5. (a) and (b) are, respectively, AFM topography and phase images (1 μm × 1 μm) of PQT-12 thin-film on Au surface after annealing; (c) and (d) are, respectively, AFM topography and phase images (1 μm × 1 μm) of PQT-12 thin-film on AuP surface after annealing; (e) and (f) are, respectively, AFM topography images (1 μm × 1 μm) of Au and AuP surfaces. Height scale (z): $z = 20$ nm in (a) and (c); 10° in (b) and (d); 10 nm in (e) and (f).

shown in Fig. 4a, could not attributed to lowering of hole injection barrier.

It has been shown that the film morphologies of organic semiconductors bordering the bottom electrodes are critically importance for the device performance of OTFTs [1,8,26]. Improved molecular ordering (crystalline) of organic semiconductors in proximity of the bottom electrodes may improve charge injection from electrodes into organic semiconductors and device performance of OTFTs. AFM was used to investigate the morphologies of PQT-12 thin-films on untreated Au and AuP surfaces. PQT-12 solution was found to easily spread and showed very good wetting on Au and AuP surfaces, suggesting good wetting of PQT-12 on edges of the bottom electrodes and electrode/PQT-12 interfaces for bottom-contact PQT-12 TFTs. Fig. 5a and b shows the AFM topography and phase images of PQT-12 film on untreated Au surface and Fig. 5c and d shows the AFM topography and phase images of PQT-12 film on AuP surface after postdeposition annealing. After deposition and postdeposition annealing, both PQT-12 films on Au and AuP surface are featureless and show amorphous or disorder morphological properties (Fig. 5b and d), which is probably due to the interaction between the PQT-12 and electrode surface [8,27]. No improved film morphology of PQT-12 on AuP surface is clearly observable and conclusive.

Fig. 5e and f shows the AFM topography images of Au and AuP surfaces. AFM analysis shows that untreated Au and AuP surfaces had surface roughness values (root mean square average of height deviations taken from the mean data plane (R_q)) of ~0.85 nm and ~0.96 nm, respectively, suggesting that the Piranha-treatment of Au surfaces did not significantly change the surface rough of electrode surfaces. The AFM images show extensive gold nano-domain on untreated Au and AuP surfaces. The size of nano-domains on AuP surface is significantly larger than that on untreated Au surface, suggesting that the interfacial area of AuP/PQT-12 contacts is smaller than that of Au/PQT-12 contacts. In addition, the average surface area of single nano-domain on AuP is evidently bigger than that on untreated Au surface, suggesting local field-effects around rough edges of AuP surface could not account for the improved charge injection of AuP electrodes. The AFM results suggest that film morphologies of PQT-12 on electrode surfaces and evolved surface morphologies of electrode due to Piranha-treatment show no clear correlation with the improved charge injection of bottom AuP electrode contacts.

4. Conclusions

In summary, dramatic reduction of contact resistance for bottom-contact PQT-12 thin-film transistors was achieved by treating the Au electrodes with Piranha solution prior to the organic semiconductor deposition. The reduction of the contact resistance is probably due to an increased dopant density of PQT-12 at the electrode/PQT-12 interface, which may resulted from the electrode treatment by Piranha solution. The OTFTs with Piranha-treated Au S–D electrodes showed significantly enhanced field-effect mobility over the OTFTs with untreated Au S–D electrodes.

Acknowledgements

The authors thank Dr. Qin Zhou and Mr. Zhisong Lu for the AFM characterizations. This work is financially supported by Singapore A*STAR under Grant No. 052 117 0031.

References

[1] C.D. Dimitrakopoulos, P.R.L. Malenfant, Adv. Mater. 14 (2002) 99.
[2] M.M. Ling, Z. Bao, Chem. Mater. 16 (2004) 4824.
[3] T.D. Anthonopoulos, C. Tanase, S. Setayesh, E.J. Meijer, J.C. Hummelen, P.W.M. Blom, D.M. de Leeuw, Adv. Mater. 16 (2004) 2174.
[4] H. Sirringhaus, N. Tessler, R.H. Friend, Science 280 (1998) 1741.
[5] A. Salleo, M.L. Chabinyc, M.S. Yang, R.A. Street, Appl. Phys. Lett. 81 (2002) 4383.
[6] Y. Wu, P. Liu, B.S. Ong, T. Srikumar, N. Zhao, G. Botton, S. Zhu, Appl. Phys. Lett. 86 (2005) 142102.
[7] Y.Y. Lin, D.J. Gundlach, S.F. Nelson, T.N. Jackson, IEEE Trans. Electron. Dev. 18 (1997) 606.
[8] I. Kymissis, C.D. Dimitrakopoulos, S. Purushothaman, IEEE Trans. Electron. Dev. 48 (2001) 1060.
[9] T. Maeda, H. kato, H. Kawakami, Appl. Phys. Lett. 89 (2006) 123508.
[10] B.H. Hamadani, D.A. Corley, J.W. Ciszek, J.M. Tour, D. Natelson, NanoLetters 6 (2006) 1303.
[11] P.G. Schroeder, D.B. France, J.B. Park, B.A. Parkinson, J. Appl. Phys. 91 (2002) 3010.
[12] J.E. Lyon, A.J. Cascio, M.M. Beerbom, R. Schlaf, Y. Zhu, S.A. Jenekhe, Appl. Phys. Lett. 88 (2006) 222109.
[13] N. Koch, A. Vollmer, S. Duhm, Y. Sakamoto, T. Suzuki, Adv. Mater. 19 (2007) 112.
[14] M. Grobosch, M. Knupfer, Adv. Mater. 19 (2007) 688.
[15] D. Gamota, P. Brazis, K. Kalyanasundaram, J. Zhang (Eds.), Printed Organic and Molecular Electronics, Kluwer, Dordrecht, Netherlands, 2004, and references therein.

[16] E.J. Meijer, G.H. Gelinck, E. van Veenendaal, B.-H. Huisman, D.M. Leeuw, T.M. Klapwijk, Appl. Phys. Lett. 82 (2003) 4576.
[17] L. Bürgi, T.J. Richards, R.H. Friend, H. Sirringhaus, J. Appl. Phys. 94 (2003) 6129.
[18] B.H. Hamadani, D. Natelson, Appl. Phys. Lett. 84 (2004) 443.
[19] B.S. Ong, Y. Wu, P. Liu, S. Gardner, J. Am. Chem. Soc. 126 (2004) 3378.
[20] B.S. Ong, Y. Wu, P. Liu, S. Gardner, Adv. Mater. 17 (2005) 1141.
[21] S. Luan, G.W. Neudeck, J. Appl. Phys. 72 (1992) 766.
[22] M. Lefenfeld, G. Blanchet, J.A. Roger, Adv. Mater. 14 (2003) 1188.
[23] S.M. Sze, Physcis of Semiconductor Devices, second ed., Wiley, New York, 1981.
[24] D.B.A. Rep, A.F. Morpurgo, T.M. Klapwijk, Org. Electron. 4 (2003) 201.
[25] P. Zelenay, L.M. Rice-Jackson, A. Wieckowski, J. Electroanal. Chem. 283 (1990) 389.
[26] Q. Cao, Z.T. Zhu, M.G. Lemaitre, M.G. Xia, M. Shim, J.A. Rogers, Appl. Phys. Lett. 88 (2006) 113511.
[27] Z.Y. Yang, H.M. Zhang, C.J. Yan, S.S. Li, H.J. Yan, W.G. Song, L.J. Wan, Proc. Natl. Acad. Sci. USA 104 (2007) 3707.

Available online at www.sciencedirect.com
ScienceDirect
Organic Electronics 9 (2008) 21–29
Organic Electronics
www.elsevier.com/locate/orgel

Lower hole-injection barrier between pentacene and a 1-hexadecanethiol-modified gold substrate with a lowered work function

Kipyo Hong, Jong Won Lee, Sang Yoon Yang, Kwonwoo Shin, Hayoung Jeon, Se Hyun Kim, Chanwoo Yang, Chan Eon Park *

Polymer Research Institute, Department of Chemical Engineering, Pohang University of Science and Technology, SAN 31, Hyoja-dong, Nam-Gu, Pohang, 790-784, Republic of Korea

Received 2 May 2007; received in revised form 9 July 2007; accepted 12 July 2007
Available online 8 August 2007

Abstract

We used ultraviolet photoemission spectroscopy (UPS) to study the hole injection barrier at the interface between pentacene and a gold surface treated with 1-hexadecanethiol (HDT). Through these UPS in-situ experiments, we found that the energy barrier between HDT-modified gold and pentacene was 0.74 eV. This energy barrier was 0.11 eV smaller than that between bare gold and pentacene, despite the work function of HDT-modified gold being 1.08 eV lower than that of bare gold. This result does not follow the typical trend, whereby decreasing the work function of a metal increases the energy barrier. The observed behavior can be explained by two factors. First, the bare gold substrate exhibited a large interface dipole, whereas the HDT-modified gold did not. And second, pentacene on the HDT-modified gold substrate had a lower ionization energy than pentacene on bare gold. This finding can be explained in terms of the polarization energy related to the more crystalline structure of pentacene on the HDT-modified gold substrate, which was established by X-ray diffraction analysis. For comparison, we also measured the injection barrier between the amorphous organic semiconductor, *N*,*N*′-diphenyl-*N*,*N*′bis(1-naphthyl-1,1′-biphenyl-4,4′-diamine (α-NPD)), and HDT-modified gold.

PACS: 73.20.-r; 61.05.cp; 79.60.-i

Keywords: Hole-injection barrier; Pentacene; Crystalline; Gold; 1-hexadecanethiol, Self-assembled monolayer

1. Introduction

In organic devices such as organic field effect transistors (OFETs) and organic light emitting diodes (OLEDs), the metal–organic semiconductor interface plays a crucial role in determining the device performance. The key parameter at this interface is the injection barrier between the metal and the organic semiconductor, which is determined by the energy difference between the metal work function and the ionization energy of the organic material [1,2]. The lower this barrier, the more efficient

* Corresponding author. Tel.: +82 54 279 2269; fax: +82 54 279 8298.
E-mail address: cep@postech.ac.kr (C.E. Park).

1566-1199/$ - see front matter © 2007 Elsevier B.V. All rights reserved.
doi:10.1016/j.orgel.2007.07.006

the injection of holes across the interface and hence the better the device performance. Campbell et al. demonstrated that the metal work function can be controlled by covering the metal with a self-assembled monolayer (SAM) that forms a highly ordered two-dimensional layer with molecular dipoles oriented in the desired direction [3–5]. Generally, modifying a metal by applying a perfluorinated thiolate SAM, which exhibits a negative dipole oriented away from the metal surface, increases the work function, leading to a lower hole-injection barrier from the metal to the organic semiconductor. By contrast, modifying a metal with an alkyl thiolate SAM lowers the work function, resulting in a higher hole-injection barrier (Fig. 1) [3,4,6,7]. These effects of SAMs have been demonstrated in studies using ITO, gold, silver or copper as the metal, and poly[2-methoxy,5-(2′-ethyl-hexyloxy)-1,4-phenylene vinylene] (MEH-PPV) [3,4, 8,9], poly(9,9-dioctylfluorene-co-bis-*N*,*N*′-4-butylphenyl)-bis-*N*, *N*′-4-butylphenyl-1,4-phenylenediamine (PFB) [10] or *N*,*N*′-bis(3-methylphenyl)-*N*,*N*-diphenyl-1,1-biphenyl-4,4′-diamine (TPD) [11,12] as the organic semiconductor; all of these semiconductors are amorphous materials. In addition, in the case of pentacene, which is polycrystalline, researchers have reported that modification of the source/drain electrodes of pentacene OFETs with an alkyl thiol SAM enhances the device performance [13,14]. However, the origin of this beneficial effect is not clear, because alkyl thiol SAMs lower the work function of the metal, and a lower work function is known to increase the hole-injection barrier, which would be expected to degrade rather than improve the device performance. The seemingly counterintuitive effect of modifying the source/drain electrodes of pentacene OFETs with alkyl thiols is supported by the findings of Wan et al. in a study of *N*,*N*′-diphenyl-*N*,*N*′bis(1-naphthyl-1,1′-biphenyl-4, 4′-diamine (α-NPD)) on contaminated gold substrates. They found that the contaminated gold substrate has a lower work function, but that this leads to a lower hole-injection barrier due to the smaller interface dipole on the contaminated gold surface [15]. However, contrary to the findings of Wan et al., several studies have found that the hole-injection barrier between amorphous polymers or small molecules and a metal is higher for a metal whose work function is lowered by SAM modification compared to the bare metal. Thus, the result of Wan et al., although supportive, cannot fully explain the improved performance of pentacene OFET devices in which the source/drain electrode is modified with an alkyl thiol SAM.

In the present study, we used photoemission spectroscopy (PES) to study the injection barrier at the interface between a pentacene layer and a gold-coated surface treated with 1-hexadecanethiol (HDT). HDT is known to form SAMs on gold surfaces and has a 2.3D dipole along the molecular axis [6], leading to a lowering of the metal work function when HDT molecules are adsorbed. Our findings indicate that even though the presence of the HDT SAM on the gold surface lowers the work function by 1.07 ± 0.01 eV, the hole-injection barrier is smaller for pentacene on HDT-modified gold than for pentacene on the bare gold surface. We discuss how the injection barrier could be lowered at

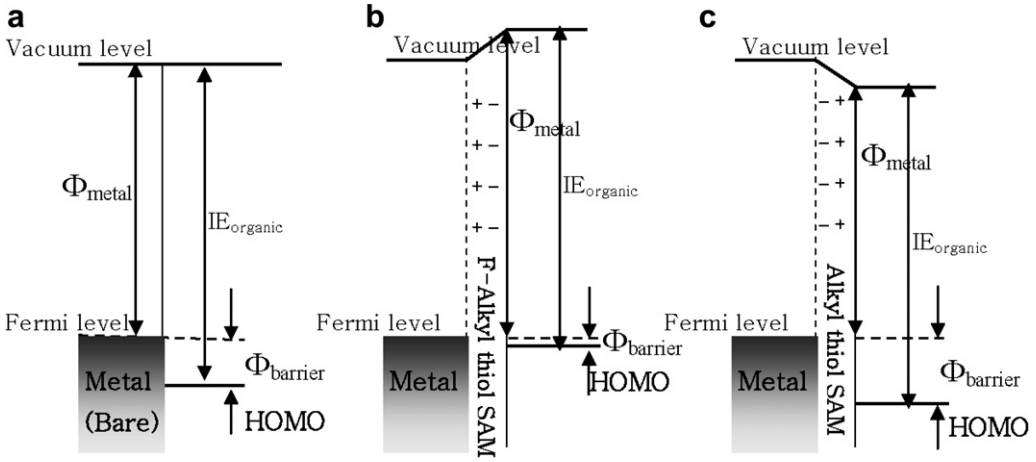

Fig. 1. Schematic energy level diagram of metal/organic interfaces with SAM modification. (a) metal/organic, (b) metal modified with fluorinated alkyl thiol/organic, and (c) metal modified with alkyl thiol/organic.

the interface between pentacene and a HDT-modified gold substrate in terms of the interface dipole and the crystallinity of the pentacene film. For comparison with the behavior of crystalline pentacene, we additionally measured the injection barrier between the amorphous semiconductor, α-NPD, and HDT-modified gold.

2. Experimental

As a substrate, we used a 200 nm thick gold-coated wafer (INOSTEK, Korea), which was prepared by gold-sputtering on SiO_2 with adhesion layer (30 nm thick Cr). We prepared two types of substrates, bare and HDT-modified gold substrates. For preparation of HDT-modified gold substrate, gold-coated wafer was washed with acetone and cleaned using an UV/ozone cleaner, GCS-1700 (AHTECH LTS, Korea) for 30 minutes. After cleaning, this was immediately immersed in a 1×10^{-3} M solution of HDT (Aldrich) in ethanol and left for 3 days in a sealed jar. The substrate was then rinsed with ethanol, sonicated in ethanol for 2 min to thoroughly remove physically adsorbed molecules, and dried with a N_2 flow. After this procedure, HDT-modified and bare gold substrates were loaded into a UHV chamber (base pressure $\sim 10^{-10}$ Torr) equipped with an electron analyzer and thermal evaporator at the 4B1 beam line in the Pohang Accelerator Laboratory (PAL). For bare gold substrate, the same cleaning procedure as the case for HDT-modification was carried out. However, carbon and oxygen contaminants on bare gold were detected from XPS spectra even after both wet and UV/ozone cleaning. Therefore, argon ion sputtering was carried out to completely remove carbon and oxygen contamination on the bare gold after sample loading in UHV chamber. The cleanliness of the resulting surface was confirmed by verifying that the C1s and O1s peaks were not present in the XPS spectra of the bare gold substrate.

Pentacene (Aldrich) and α-NPD (Chung Wha Sa Co., Korea) were deposited at a rate of 0.1 Å/s at room temperature. When the thickness of the pentacene or α-NPD film reached 0.4, 1.6, 6.4 or 25.6 nm, the sample was characterized in-situ using ultraviolet photoemission spectroscopy (UPS), 21.2 eV (He I, He discharge lamp was used) in normal emission mode. In addition, a −7.0 eV bias was applied to improve the transmission of low kinetic energy electrons and to ensure the determination of the energy of the low kinetic energy edge. For the XRD experiments, a 20 nm thick pentacene film was deposited on a gold or HDT-modified gold substrate at 0.1 Å/s, and the experiment was performed at the 10C1 beam line (wavelength ~1.54 Å) of the PAL.

3. Results

Figs. 2a and b show the UPS (He I) energy distribution curves (EDCs) for pentacene on the bare vac-

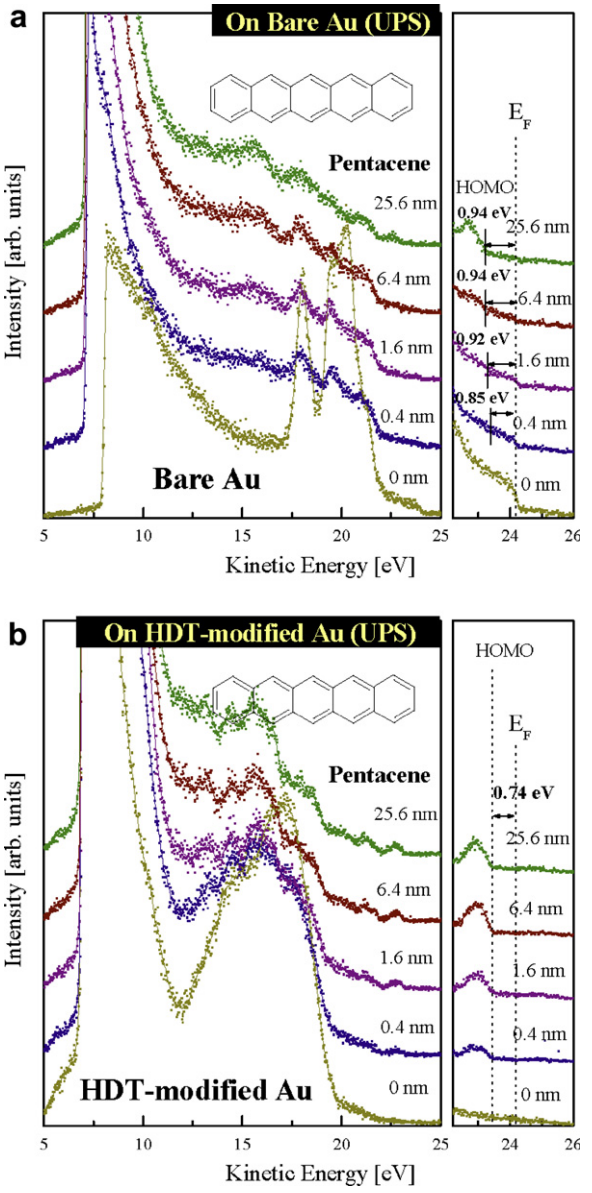

Fig. 2. UPS EDCs of (a) pentacene deposited on gold, and (b) pentacene deposited on HDT-modified gold. The left side shows the full spectra, and the right side shows a magnified view of the region where the gold Fermi edge and the HOMO peak of pentacene are observed.

uum-deposited gold substrate and on the HDT-modified gold substrate, respectively. The cut-off at the left-hand part of each EDC (E_k^{cut}) corresponds to electrons that have just enough energy to escape from the solid, and thus gives information on the position of the vacuum level. The maximum kinetic energy (E_k^{max}) at the right-hand part of each EDC corresponds to electrons from the highest occupied level and therefore gives information on the position of the Fermi level (E_F) for gold and the highest occupied molecular orbital (HOMO) for pentacene. E_k^{max} and E_k^{cut} were determined through linear extrapolation of the UP spectra. The hole-injection barrier, Φ_B, the work function of the metal, Φ_m, and the ionization energy (I) were obtained using $\Phi_B = E_k^{max(metal)} - E_k^{max(organic)}$, $\Phi_m = h\nu - (E_k^{max(metal)} - E_k^{cut(metal)})$ and $I = h\nu - (E_k^{max(organic)} - E_k^{cut(organic)})$, respectively [1,2]. Using this approach, the work functions of bare gold and HDT-modified gold were determined to be 5.09 ± 0.01 eV and 4.02 ± 0.02 eV, respectively. Although we confirmed the absence of contamination or impurities by examining XPS spectra, the work function of the bare gold substrate was slightly lower than the literature value [16], probably due to surface roughness [17,18]. From the UPS data, the hole-injection barrier was determined to be 0.85 eV for pentacene on bare gold and 0.74 eV for pentacene on the HDT-modified gold substrate. Hole-injection barrier (0.85 eV) between pentacene and bare gold in this study seems to be higher than that reported in some previous literatures [19]. However, one can find that the hole-injection barriers from the previous studies on pentacene on bare gold substrate have shown controversial values ranging from 0.5 to 1.0 eV [20–24]. We think these differences could come from the combination of many possible reasons such as a preparation method of gold substrate (sputtering or thermal evaporation), pentacene layer thickness, and polymorphisms of pentacene film [19–25].

In addition, we did not observe a shift of the vacuum level on HDT-modified gold, but found that the vacuum level shifted as much as 0.88 eV on bare gold (Fig. 2). Furthermore, the I of pentacene on HDT-modified gold was 4.74 eV, which was about 0.4 eV smaller than that of pentacene on bare gold.

Figs. 3a and b show the UPS (HeI) EDCs for α-NPD on a bare vacuum-deposited gold substrate and on a HDT-modified gold substrate, respectively. From the UPS EDCs, the hole-injection barriers for α-NPD on bare gold and HDT-modified gold were determined to be 1.03 eV and 1.22 eV,

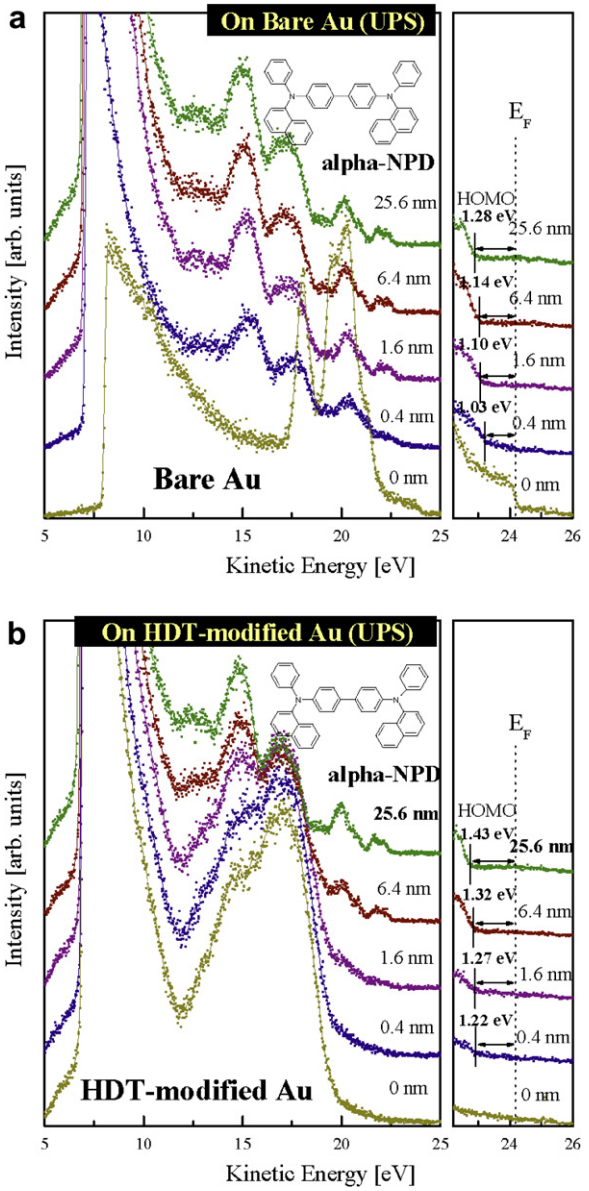

Fig. 3. UPS EDC of (a) α-NPD deposited on gold, and (b) α-NPD deposited on HDT-modified gold. The left side shows the full spectra and the right side shows a magnified view of the region where the gold Fermi edge and the HOMO peak of α-NPD are observed.

respectively. Also, in contrast to pentacene, the I of α-NPD was almost the same on both substrates; specifically, the Is were 5.23 ± 0.05 eV on bare gold and 5.26 ± 0.03 eV on HDT-modified gold, which are similar to the value of 5.3 eV reported previously [26]. Fig. 4 summarizes the UPS results for pentacene and α-NPD on bare gold and HDT-modified gold substrates, and Fig. 5 shows the positions

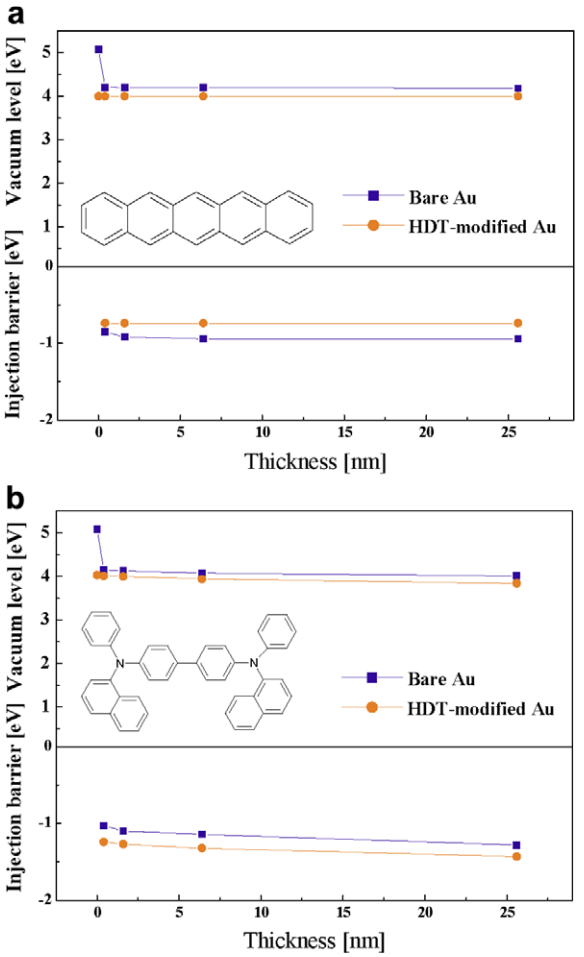

Fig. 4. (a) Hole-injection barrier and vacuum level position of pentacene on bare gold and HDT-modified gold, and (b) hole-injection barrier and vacuum level position of α-NPD on bare gold and HDT-modified gold.

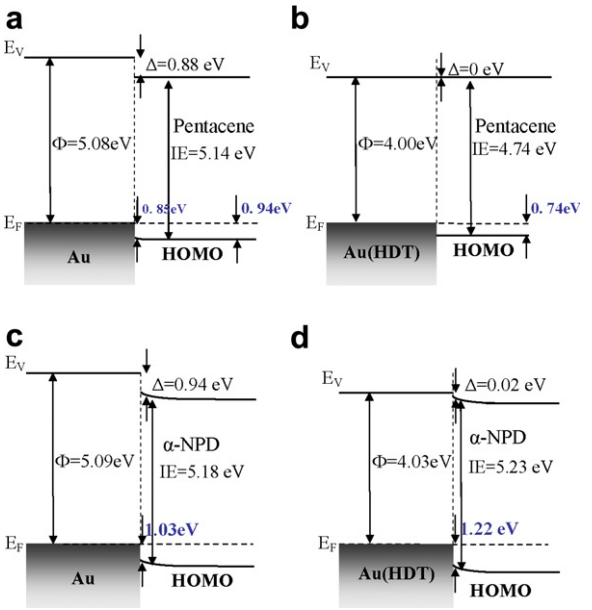

Fig. 5. (a) Band diagram of the interface between pentacene and gold, (b) band diagram of the interface between pentacene and HDT-modified gold (6.4 nm thick pentacene layer), (c) band diagram of the interface between α-NPD and gold, and (d) band diagram of the interface between α-NPD and HDT-modified gold (0.4 nm thick α-NPD layer).

of the molecular levels obtained from the UPS measurements.

4. Discussion

Here we have shown that bare gold and HDT-modified gold substrates have work functions of 5.09 ± 0.01 and 4.02 ± 0.02 eV and injection barriers at the interface between pentacene and the substrate of 0.85 and 0.74 eV, respectively. The observed effect, that HDT-modification decreases both the work function and the injection barrier, does not conform to the usual trend whereby decreasing the work function of a metal leads to an increase in the hole-injection barrier. The observation of a smaller injection barrier on HDT-modified gold despite this substrate having a lower work function can be explained by two factors.

The first factor is the absence of the large vacuum level shift that is typically observed during the early stages of pentacene deposition on bare gold. The shift in the vacuum level as a result of deposition of an organic film derives from the interface dipole between the metal and the adjoining film. When a pentacene film is deposited on bare gold, the interface dipole is 0.88 eV and the vacuum level is shifted substantially. When, however, a pentacene film is deposited on a HDT-modified gold substrate, there is no dipole at the interface and hence the vacuum level shift is negligible. Our finding that the interface dipole is absent for pentacene on a HDT-modified gold substrate is consistent with previous findings for α-NPD on a contaminated gold surface, which has a lower work function but leads to a lower hole-injection barrier due to a smaller interface dipole on the contaminated gold surface [15]. Generally, in the case of a nonreactive interface between a metal and a semiconductor, the continuum of metallic states in close proximity with the semiconductor induces a density of gap states at the semiconductor interface. This density of states around the charge neutrality level (CNL) and the difference

between the CNL and Fermi level determines the interface dipole and charge injection barrier. Thus, for the system considered here, if the Fermi level of gold is below the CNL of pentacene, electron transfer associated with the induced density of interface states (IDIS) will occur from the pentacene to the metal, leading to the formation of an interface dipole, which manifests as a downward vacuum level shift from the metal to the organic material [27,28]. If the IDIS is high, the Fermi level at the interface will be pinned at the CNL of pentacene, leading to the generation of an interface dipole. In contrast, a low IDIS would lead to behavior close to the Schottky–Mott limit, which is known as vacuum level alignment [15,28].

A theoretical calculation by Vázquez et al. showed that the IDIS is reduced from 1.5×10^{14} to $0.5 \times 10^{14}\ eV^{-1}cm^{-2}$ with the increase of distance from 2.8 to 3.5 Å between gold and 3,4,9,10-perylenetetracarboxylic dianhydride (PTCDA) [29,30]. This reduced IDIS give a rise to weakly-pinned Fermi level around the CNL, and as a result, an interface energetic becomes closer to vacuum level alignment [15]. In the system considered here, the HDT molecules form a layer on the gold surface with a thickness of about 20 Å [31], and this layer keeps the pentacene film apart from the gold substrate. Given the finding of Vázquez et al., that increasing the separation between gold and PTCDA by just 0.7 Å reduces the IDIS by a factor of three, we can assert that the 20 Å separation caused by the HDT layer is sufficient to preclude local orbital exchange and potential correlation, and thus leads to a drastic reduction in the IDIS. Since the IDIS determines the degree to which the system differs from vacuum alignment [28], the lower IDIS for pentacene on HDT-modified gold compared to pentacene on bare gold will lead to a smaller vacuum level shift, and thus to a lower hole-injection barrier.

Although the small vacuum level shift on the HDT-modified gold will contribute to a lowering of the hole-injection barrier, this effect is not sufficient to fully account for the observed lowering of the hole-injection barrier for pentacene on a HDT-modified gold substrate. In Fig. 6, the black solid line indicates the band diagram determined from the UPS data, and the gray dotted line indicates the HOMO level predicted based on the assumption of constant ionization. If we simply assume that the *I* of pentacene on HDT-modified gold is the same as that of pentacene on bare gold, the hole-injection barrier between pentacene and HDT-modified gold

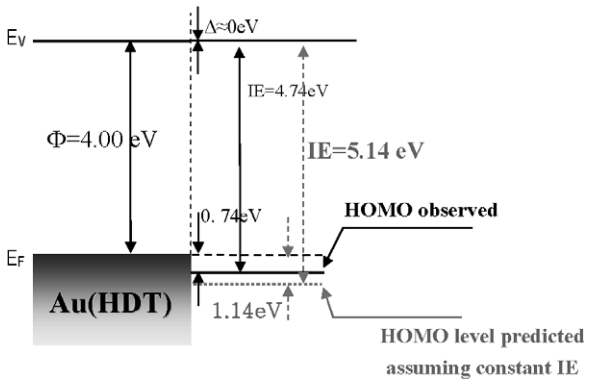

Fig. 6. Band diagram of the interface between pentacene and HDT-modified gold. Black lines indicate the band diagram generated from UPS data, and gray lines indicate the bands predicted assuming that the ionization energy of pentacene on HDT-modified gold is the same as that of pentacene on bare gold (i.e., 5.14 eV).

would be 1.14 eV, which is greater than that between pentacene and bare gold (Fig. 5). Thus, under this assumption, the modified metal exhibits a lowered work function and a larger hole-injection barrier compared to the bare metal. This behavior conforms to the usual trend observed for many systems. For example, this behavior is observed in the UPS results obtained in the present work for α-NPD on HDT-modified and bare gold substrates (Figs. 5c and d). Similarly, a higher hole-injection barrier between a SAM-treated metal with a lowered work function and an amorphous semiconductor has been observed in several studies [3,4,8,10,12]. However, whereas amorphous semiconductors have the same *I* on both the modified and bare substrates, the *I* of pentacene on a HDT-modified gold substrate is 4.74 eV, compared to 5.14 eV on bare gold, and hence the hole-injection barrier on the HDT-modified gold substrate is smaller than that on bare gold. That is, the smaller hole-injection barrier on the HDT-modified gold cannot be explained only by the smaller interface dipole on the HDT-modified gold, but it is also result of the polycrystalline nature of the pentacene film affecting the *I* of the film. This effect on the *I* is one of the major factors underlying the smaller hole-injection barrier on the HDT-modified gold substrate compared to the bare gold substrate, and is a feature distinguishing pentacene from the amorphous organic semiconductor, α-NPD.

The *I* of an organic compound in the solid phase derives from both the intrinsic *I* of each molecule and the polarization energy of surrounding mole-

cules [32–34]. When ions are generated in a solid organic semiconductor by photoemission, the surrounding molecules rapidly form induced dipoles and stabilize the ions; the energy associated with this stabilization is the polarization energy. Because of this polarization, the I of organic compounds such as pentacene is smaller in the solid phase than in the gas phase. The reduction in I due to polarization is observed as an energy shift of the spectral bands in the UPS EDC [32–35]. The polarization energy (P^+) can be expressed crudely as $P^+ \propto \alpha\rho^{4/3}$, where α is the average molecular polarizability and ρ is the molecular packing density in the solid [30]. Thus the polarization energy can be calculated as the difference between the I of the solid phase and that of the gas phase. Using a value of 6.58 eV for the gas phase I of pentacene, determined from the spectrum in the literature [36], we find that the polarization energy for pentacene is 1.44 eV on bare gold and 1.84 eV on HDT-modified gold (Figs. 5a and b). Since P^+ is proportional to ρ in the relation above, differences in the P^+ for pentacene layers on different substrates arise from the crystallinity of the deposited pentacene layer. This idea is supported by the previous result by Sato et al. that I can be varied with the molecular packing density (ρ) of pentacene films on gold substrates [33]. Sato el al. have reported that I of pentacene deposited on bare gold at room temperature showing less molecular packing density is 5.15 eV, and I of pentacene was reduced to 4.85 eV by increasing substrate temperature (353 K), in turn, enhancing molecular packing of pentacene film [33]. Our result shows that I of pentacene film on HDT-modified gold (4.74 eV) is smaller than that on bare gold (5.14 eV). This result is closely related to the difference in the molecular packing density of pentacene film on each substrate. However, in contrast to pentacene, α-NPD has almost the same I on the HDT-modified and bare gold substrates, and therefore has similar polarization energies on these substrates. This means that the α-NPD film has a similar molecular packing density on both substrates, consistent with its amorphous nature.

We additionally carried out XRD experiments on 20 nm thick pentacene films vacuum-deposited on bare gold and HDT-modified gold substrates. Figs. 7a and b show the out-of-plane and in-plane XRD patterns, respectively. The XRD data indicate that the pentacene film on the HDT-modified gold substrate is polycrystalline of pentacene molecules with c axis perpendicular to the substrate as inferred from (00k) peaks in the out-of-plane direction. Only thin-film phase characterized by an interplanar spacing of 15.43 Å was observed in this case [37]. Also, we found from in-plane XRD patterns that pentacene molecules on the HDT-modified gold are arranged with a herringbone geometry, and the domains in the pentacene crystal, over which structural order is maintained, are randomly oriented about the a and b axis parallel to the surface. By contrast, the pentacene film on the bare gold is also polycrystalline, but the domains in the polycrystalline film on bare gold are randomly oriented as indicated from in-plane and out-of-plane XRD patterns: the pentacene molecules on the bare gold did not show any ordered structure (00k) in the out-of-plane direction, but did show some crystalline lying parallel to the surface in the in-plane pattern, as inferred from (00k) peaks. From the XRD patterns, we calculated the coherence length (the distance over which order is maintained). The

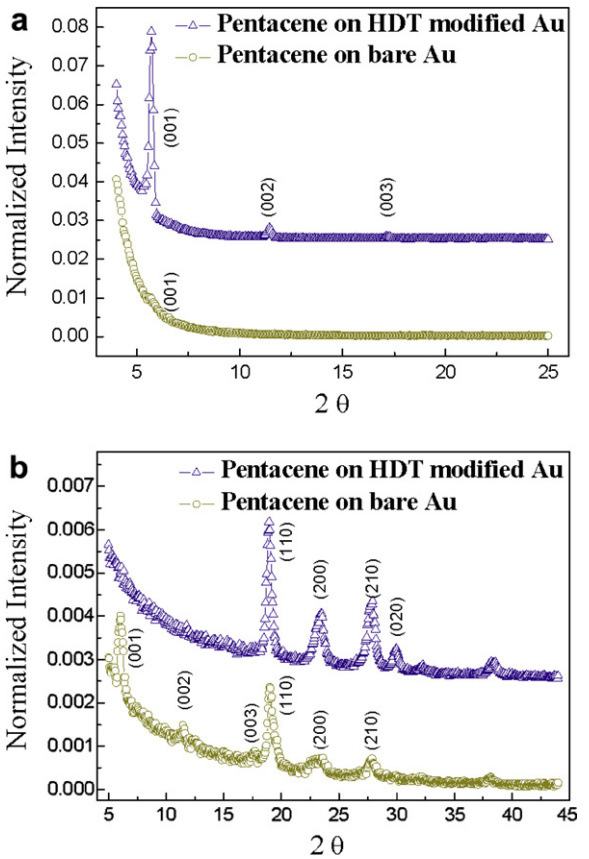

Fig. 7. (a) Out-of-plane mode and (b) in-plane mode X-ray diffraction patterns of pentacene on gold and HDT-modified gold substrates.

coherence length in the (1 1 0) direction was determined to be about 13 nm on the bare gold substrate and 17 nm on the HDT-modified gold substrate, as determined from the half width of each (1 1 0) peak using Scherrer's formula [37]. Given that the coherence length is proportional to the size of the domains, the present results indicate that larger domains were present on the HDT-modified gold substrate. The smaller domain size on the bare gold substrate implies that the pentacene film on this substrate will contain a greater number of defects such as vacancies. A higher defect density indicates less ordered packing, and thus a lower value of ρ for pentacene on the bare gold. Since the pentacene film on the HDT-modified gold substrate showed a more ordered structure, the polarization energy of this pentacene will be larger and hence the I will be lower. This reasoning would explain our finding from the UPS EDCs that the pentacene film on a HDT-modified gold substrate had a smaller I than the film on a bare gold substrate.

5. Conclusion

We have shown here that although the work function of HDT-modified gold is 1.08 eV lower than that of bare gold, the energy barrier between pentacene and HDT-modified gold was 0.11 eV lower than that between pentacene and bare gold. This unusual behavior appears to be due to HDT modification of gold causing a reduction in the IDIS, which leads to a very small vacuum level shift between pentacene and gold. However, our observation of a smaller injection barrier between pentacene and HDT-modified gold cannot be explained only by a reduction in the IDIS. We also established that a pentacene film on a HDT-modified gold substrate has a higher crystallinity than that on a bare gold substrate. This enhanced crystallinity leads to a smaller I, and thus to a lower injection barrier between pentacene and HDT-modified gold compared to bare gold. By contrast, the I of the amorphous organic semiconductor, α-NPD, is almost the same on both substrates, resulting in a higher hole-injection barrier on the HDT-modified gold substrate. The smaller injection barrier between pentacene and HDT-modified gold suggests that the performance of pentacene OFETs could be improved by HDT-modification of the gold surface in the device. This effect would be consistent with previous reports that SAM modification of the gold surface in pentacene OFETs improves the device performance even though it lowers the metal work function [13,14].

Acknowledgements

This work was supported by the Information Display R&D Center as part of the 21st Century Frontier R&D Program funded by the Ministry of Commerce, Industry and Energy of Korea. The authors are grateful to the Pohang Accelerator Laboratory for access to synchrotron radiation at the 4B1 and 10C1 beam lines.

References

[1] H. Ishii, K. Sugiyama, E. Ito, K. Seki, Adv. Mater. 11 (1999) 605.
[2] D. Cahen, A. Kahn, Adv. Mater. 15 (2003) 271.
[3] I.H. Campbell, J.D. Kress, R.L. Martin, D.L. Smith, N.N. Barashkov, J.P. Ferraris, Appl. Phys. Lett. 71 (1997) 3528.
[4] I.H. Campbell, S. Rubin, T.A. Zawodzinski, J.D. Kress, R.L. Martin, D.L. Smith, N.N. Barshkov, J.P. Ferraris, Phys. Rev. B 54 (1996) 14321.
[5] A. Ulman, Chem. Rev. 96 (1996) 1533.
[6] D.M. Alloway, M. Hogmann, D.L. Smith, N.E. Gruhn, A.L. Graham, R. Colorado, Jr., V.H. Wysocki, T.R. Lee, P.A. Lee, N.R. Armstrong, J. Phys. Chem. B 107 (2003) 11690.
[7] R.W. Zehner, B.F. Parsons, R.H. Hsung, L.R. Sita, Langmuir 15 (1999) 1121.
[8] B.D. Boer, A. Hadipour, M.M. Mandoc, T.V. Woudenbergh, P.W.M. Blom, Adv. Mater. 17 (2005) 621.
[9] J.H. Cho, W.H. Lee, Y.D. Park, W.K. Kim, S.Y. Kim, J.L. Lee, K. Cho, Electrochem. Solid-State Lett. 9 (2006) G147.
[10] S. Khodabakhsh, D. Poplavskyy, S. Heutz, J. Nelson, D.D.C. Bradley, H. Murata, T.S. Jones, Adv. Funct. Mater. 14 (2004) 1205.
[11] R.A. Hatton, M.R. Willis, M.A. Chesters, F.J.M. Rutten, D. Briggs, J. Mater. Chem. 13 (2003) 38.
[12] S.F.J. Appleyard, S.R. Day, R.D. Pickford, M.R. Willis, J. Mater. Chem. 10 (2000) 169.
[13] I. Kymissis, C.D. Dimitrakopoulos, S. Purushothaman, IEEE Trans. Electron. Dev. 48 (2001) 1060.
[14] S.H. Kim, J.H. Lee, S.C. Lim, Y.S. Yang, T. Zyung, Jpn. J. Appl. Phys. 1A/B (2004) L60.
[15] A. Wan, J. Hwang, F, Amy, A. Kahn, Org. Electron. 6 (2005) 47.
[16] D.R. Lide, Handbook of Chemistry and Physics, 75th ed., CRC Press, Boca Raton, Fl, USA, 1995.
[17] K. Wandelt, in: P. Wissman (Ed.), Thin Metal Films and Gas Chemisorption, Elesevier, New York, USA, 1987.
[18] H. Ishii, K, Seki, in: W.R. Salaneck, K. Seki, A. Kahn, J.J. Pireaux (Eds.), Conjugate Polymer and Molecular Interfaces, Marcel Dekker, NY, USA, 2002, ch. 10.
[19] F. Amy, C. Chan, A. Kahn, Org. Electron. 6 (2005) 85.
[20] N. Koch, A. Kahn, J. Ghijsen, J. Pireanx, J. Schwartz, R. Johnson, A. Elschner, Appl. Phys. Lett. 82 (2003) 70.
[21] S. Kang, Y. Yi, C. Kim, S. Cho, M. Noh, K. Jeong, C. Whang, Synth. Met. 156 (2006) 32.

[22] P.G. Schroeder, C.B. France, J.B. Park, B.A. Parkinson, J. Appl. Phys. 91 (2002) 3010.
[23] K. Ihm, B. Kim, T.H. Kang, K.J. Kim, M.H. Joo, T.H. Kim, S.S. Yoon, S. Chung, J. Appl. Phys. 89 (2006) 033504.
[24] A. Vollmer, O.D. Jurchescu, I. Arfaoui, I. Salzmann, T.T.M. Palstra, P. Rudolf, J. Niemax, J. Pflaum, J.P. Rabe, N. Koch, Eur. Phys. J. E17 (2005) 339.
[25] N. Koch, A. Vollmer, S. Duhm, Y. Sakamoto, T. Suzuki, Adv. Mater. 19 (2007) 112.
[26] N. Koch, S. Duhm, J.P. Rabe, Phy. Rev. Lett. 95 (2005) 237601.
[27] F. Flores, C. Tejedor, J. Phys. C: Solid State Phys. 20 (1987) 145.
[28] A.M. Cowley, S.M. Sze, J. Appl. Phys. 36 (1965) 3212.
[29] H. Vazquez, R. Oszwaldowski, P. Pou, J. Ortega, R. Perez, F. Flores, A. Kahn, Europhys. Lett. 65 (2004) 802.
[30] H. Vazquez, F. Flores, R. Oszwaldowski, J. Ortega, R. Perez, A. Kahn, Appl. Surf. Sci. 234 (2004) 107.
[31] C.D. Bain, E.B. Troughton, Y.T. Tao, J. Evall, G.M. Whitesides, R.G. Nuzzo, J. Am. Chem. Soc. 111 (1989) 321.
[32] N. Sato, K. Seki, H. Inokuchi, J. Chem. Soc. Faraday Trans. 77 (1981) 1621.
[33] N. Sato, K. Seki, H. Inokuchi, Y. Harada, Chem. Phys. 109 (1986) 157.
[34] H. Fukagawa, H. Yamane, T. Kataoka, S. Kera, M. Nakamura, K. Kudo, N. Ueno, Phys. Rev. B 73 (2006) 245310.
[35] C. Shen, A. Kahn, I. Hill, in: W.R. Salaneck, K. Seki, A. Kahn, J.J. Pireaux (Eds.), Conjugate Polymer and Molecular Interfaces, Marcel Dekker, NY, USA, 2002, ch. 11.
[36] P.A. Clark, F. Brogli, E. Heilbronner, Helv. Chim. Acta 55 (1972) 1415.
[37] R. Ruiz, A.C. Mayer, G.G. Malliaras, B. Nickel, G. Scoles, A. Kazimirov, H. Kim, R.L. Headrick, Z. Islam, Appl. Phys. Lett. 85 (2004) 4926.

Available online at www.sciencedirect.com
ScienceDirect
Organic Electronics 9 (2008) 30–38
Organic Electronics
www.elsevier.com/locate/orgel

Dual enhancing properties of LiF with varying positions inside organic light-emitting devices

Kyul Han [a,*], Yeonjin Yi [b,*], Won Jun Song [c], Sang Wan Cho [a], Pyung Eun Jeon [a], Hyunbok Lee [a], Chung-Nam Whang [a], Kwangho Jeong [a]

[a] *Institute of Physics and Applied Physics and Atomic-Scale Surface Science Research Center, Yonsei University, 134 Sinchon-dong, Seodaemun-gu, Seoul 120-749, South Korea*

[b] *Division of Advanced Technology, Korea Research Institute of Standards and Science, 1 Doryong-Dong, Yuseong-Gu, Daejeon 305-340, South Korea*

[c] *Corporate R&D Center, Samsung SDI Company Limited 428-5, Gongse-dong, Giheung-gu, Yongin-si, Gyeonggi-do 446-577, South Korea*

Received 3 June 2006; received in revised form 16 July 2007; accepted 20 July 2007
Available online 3 August 2007

Abstract

A multilayer organic light-emitting device (OLED) has been fabricated with a thin (0.3 nm) lithium fluoride (LiF) layer inserted inside an electron transport layer (ETL), aluminum tris(8-hydroxyquinoline) (Alq_3). The LiF electron injection layer (EIL) has not been used at an Al/Alq_3 interface in the device on purpose to observe properties of LiF. The electron injection-limited OLED with the LiF layer inside 50 nm Alq_3 at a one forth, a half or a three forth position assures two different enhancing properties of LiF. When the LiF layer is positioned closer to the Al cathode, the injection-limited OLED shows enhanced injection by Al interdiffusion. The Al interdiffusion at least up to 12.5 nm inside Alq_3 rules out the possible insulating buffer model in a small molecule bottom-emission (BE) OLED with a thin, less than one nanometer, electron injection layer (EIL). If the position is further away from the Al cathode, the Al diffusion reaches the LiF layer no longer and the device shows the electroluminescence (EL) enhancement without an enhanced injection. The suggested mechanism of LiF EL efficiency enhancer is that the thin LiF layer induces carrier trap sites and the trapped charges alters the distribution of the field inside the OLED and, consequently, gives a better recombination of the device. By substituting the Alq_3 ETL region with copper phthalocyanine (CuPc), all of the electron injection from the cathode of Al/CuPc interface, the induced recombination at the Alq_3 emitting layer (EML) by the LiF EL efficiency enhancer, and the operating voltage reduction from high conductive CuPc can be achieved. The enhanced property reaches 100 mA/cm^2 of current density and 1000 cd/m^2 of luminance at 5 V with its turn-on slightly larger than 2 V. The enhanced device is as good as our previously reported non-injection limited LiF EIL device [Yeonjin Yi, Seong Jun Kang, Kwanghee Cho, Jong Mo Koo, Kyul Han, Kyongjin Park, Myungkeun Noh, Chung Nam Whang, Kwangho Jeong, Appl. Phys. Lett. 86 (2005) 213502].

* Corresponding authors. Tel.: +82 2 2123 3845; fax: +82 2 392 1592.
E-mail addresses: kyulhan@phya.yonsei.ac.kr (K. Han), yeonjin@kriss.re.kr (Y. Yi).

1566-1199/$ - see front matter
doi:10.1016/j.orgel.2007.07.005

PACS: 72.80.Le; 77.84.Jd; 85.60.Jb

Keywords: Organic light-emitting device; Lithium fluoride; Alq_3; CuPc

1. Introduction

Since the report of Tang and VanSlyke [1] with multilayer organic light-emitting devices (OLEDs), tremendous efforts have been made to improve the device performance. The Cambridge group [2] reported polymer light-emitting devices (PLEDs) and this had stimulated the synthesis research in the polymer field. To increase the OLED performances, carrier injection and transport mechanisms for both small molecular organic materials and polymers have been widely investigated. A modification at the interface between an organic material and an electrode increases the carrier injection into the organic material from the electrode, and one of the famous examples is the insertion of lithium fluoride (LiF) at the interface of an aluminum (Al) cathode and an organic electron transport layer (ETL). The role of the LiF electron injection layer (EIL) has long been in a dispute [3] since its introduction [4,5]. Its injection mechanism models are mainly categorized into two: one is the insulating buffer model [6] and the other is the interfacial chemistry model [7,8]. The insulating buffer model attributes LiF injection enhancement to its insulating property which takes more electric field when biased and hence allows tunneling injection with less barrier height. For the interfacial chemistry model, chemical reactions at the interface of LiF and Al layers or aluminum tris(8-hydroxyquinoline) (Alq_3), LiF and Al layers are the causes of the enhancement. The subsequent observed phenomena include the LiF dissociation [8], Alq_3 anion formation with Li doping [9], the surface potential reduction with the interface dipole [10], the protection of organic materials from the metal cathode [7], etc. A recent study by Jin et al. showed that the electron injection enhancement is only with an Al/LiF (0.6 nm) cathode but not with a silver (Ag)/LiF (0.6 nm) [11]. Another study by Wang et al., however, opposed the result and showed that a Ag/LiF (3.0 nm) cathode can also increase the electron injection by varying the LiF thicknesses [12]. The significances of two studies are that they are each supporting differently one of the two categorized models.

2. Experiments

Here, we have conducted an experiment to classify the role of LiF inside an OLED. Our control device (CD) has the configuration of Al (100.0 nm)/Alq_3 (50.0 nm)/alpha-*N*,*N*′-bis(naphthalene-1-yl)-*N*,*N*′-bis(phenyl)benzidine (α-NPB) (50.0 nm)/indium tin oxide (ITO) (70.0 nm), which does not have a LiF EIL at the Al/Alq_3 interface on purpose. The 0.3 nm thin LiF layer has been inserted inside an Alq_3 ETL. Inserting LiF at one forth, half or three forth position inside Alq_3 of CD gives our device configurations of Al (100.0 nm)/Alq_3 (12.5 nm)/LiF (0.3 nm)/Alq_3 (37.5 nm)/NPB (50.0 nm)/ITO (70.0 nm), Al (100.0 nm)/Alq_3 (25.0 nm)/LiF (0.3 nm)/Alq_3 (25.0 nm)/NPB (50.0 nm)/ITO (70.0 nm), and Al (100.0 nm)/Alq_3 (37.5 nm)/LiF (0.3 nm)/Alq_3 (12.5 nm)/NPB (50.0 nm)/ITO (70.0 nm). Other devices substituting the ETL part of Alq_3 by copper phthalocyanine (CuPc) has also been prepared. The Fig. 1 depicts CD and each configuration of our devices.

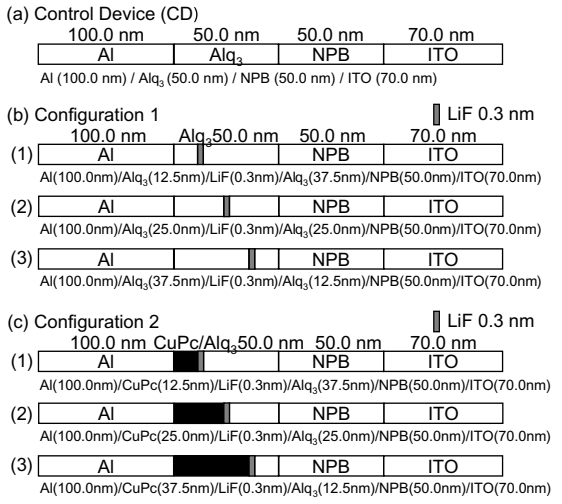

Fig. 1. The control device (CD) and two different configurations of organic light-emitting devices in the experiment. (a) The first configuration is characterized as thin (0.3 nm) LiF layers at one forth, half or three forth position of Alq_3 inside CD. (b) The second configuration has a CuPc electron transport layer (ETL) substitution of the first configuration.

In our experiment, the multi-structure OLED was fabricated on a commercial ITO glass substrate. Four Knudsen cells (K-cells) were used for thermal evaporation in ultrahigh vacuum (UHV) chamber kept below 10^{-7} Torr. Each cell contains a boron nitride (BN) crucible, each filled with Alq_3, α-NPB, CuPc, and LiF. The deposition rate of Alq_3, NPB and CuPc was fixed at 0.1 nm/s and for LiF at 0.02 nm/s. The Al cathode was deposited from a titanium diboride (TiB_2) boat by thermal evaporation and its deposition rate was above 1 nm/s. Current density–luminance–voltage (C–L–V) characteristics were measured with a Keithely 237 source measure unit and a photodiode calibrated by a PR650 spectrophotometer in a glove box under nitrogen gas atmospheres. The emission spectra of OLEDs were measured with an Ocean Optics, Inc. PC2000 Spectrometer.

3. Results and discussions

The interfacial chemistry model, as in the 0.6 nm Al/LiF cathode of Jin et al., does not require a complete cover of a LiF EIL layer. However, LiF, when deposited with thickness of several nanometers, is definitely an insulator. The Fig. 2 shows the current density of a LiF EIL OLED, Al/LiF (x nm)/Alq_3 (50.0 nm)/NPB (50.0 nm)/ITO device at 10 V with the LiF thickness variation, and the sharp increase

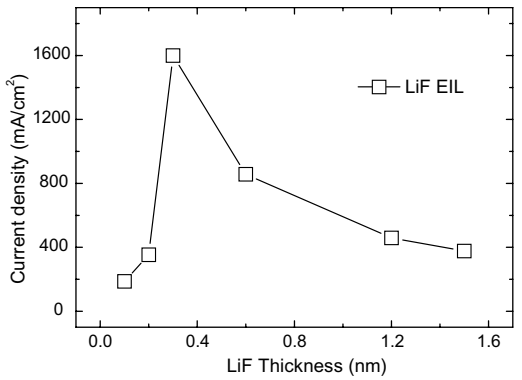

Fig. 2. LiF thickness versus current density graph of Al/LiF (x nm)/Alq_3 (50.0 nm)/NPB (50.0 nm)/ITO devices at an applied voltage of 10 V. An OLED with a LiF electron injection layer (EIL) has an optimized thickness of a 0.3 nm LiF layer with its maximum current density of 1600 mA/cm^2. The LiF EIL shows its injection enhancement with an incomplete cover of the 0.3 nm LiF layer and for the complete cover of LiF with thicker LiF layer, the insulating effect of LiF is dominant with both of the decrease in the luminance (not shown) and the current density in the device.

of the current density is within one nanometer. The optimized thickness with the sharp increase in electron injections lessens as the thickness of the LiF EIL increases. In the model, the steep increase owes to some chemical interactions such as, for example, the Li dissociation. It is doubtful whether the thickness of several tenth of a nanometer of LiF can form a complete cover of a layer and the studies supporting the model generally have the device configurations of LiF thickness less than one nanometer [7,8]. One more important condition of the LiF interfacial chemistry model is the existence of the Al cathode. The referenced devices all include Al cathodes and as shown by Jin et al., the LiF injection enhancement occurs with Al cathodes but not with Ag cathodes.

For the insulating buffer model, the complete cover of the insulator layer has to be presumed and the referenced results of the model have shown thicknesses of several nanometers of their insulator thicknesses. Kim et al. [6] have shown the device with Al/PMMA (2 nm)/MEHPPV (90 nm)/ITO, and Wang et al. [12] have shown the device with Ag/LiF (3.0 nm)/Alq_3/NPB/ITO. Even though the latter case seems to rule out the condition of the Al cathode existence in the interfacial chemistry model, there exists the LiF thickness difference of an order which makes the Ag/LiF (3.0 nm) cathode enhancement a different one from the interfacial chemistry model enhancement. For the Al/LiF (0.3 nm) cathode, it is doubtful to have the complete cover of a layer required as in the insulating buffer model; furthermore, our experiment with varying the 0.3 nm LiF layer inside organic materials makes the insulating buffer model even more unrealistic in the Al/LiF (0.3 nm) cathode.

From Fig. 3, the current density–luminance–voltage (C–L–V) characteristic curves of Configuration 1 show that both the electron injection and the luminance have been increased in Al (100.0 nm)/Alq_3 (12.5 nm)/LiF (0.3 nm)/Alq_3 (37.5 nm)/NPB (50.0 nm)/ITO (70.0 nm) device (▽ plots) compared to the control device (CD) of Al (100.0 nm)/Alq_3 (50.0 nm)/NPB (50.0 nm)/ITO (70.0 nm) (□ plots); By inserting 0.3 nm LiF layer inside CD at the 12.5 nm position away from the Al cathode, the current density has been increased to 370 mA/cm^2 from 60 mA/cm^2 at 10 V. Our devices follow the bottom-emission (BE) structure OLED and the Al cathode is the last layer being deposited. Yet, the Al (100.0 nm)/Alq_3 (25.0 nm)/LiF (0.3 nm)/Alq_3 (25.0 nm)/NPB (50.0 nm)/ITO (70.0 nm) and Al

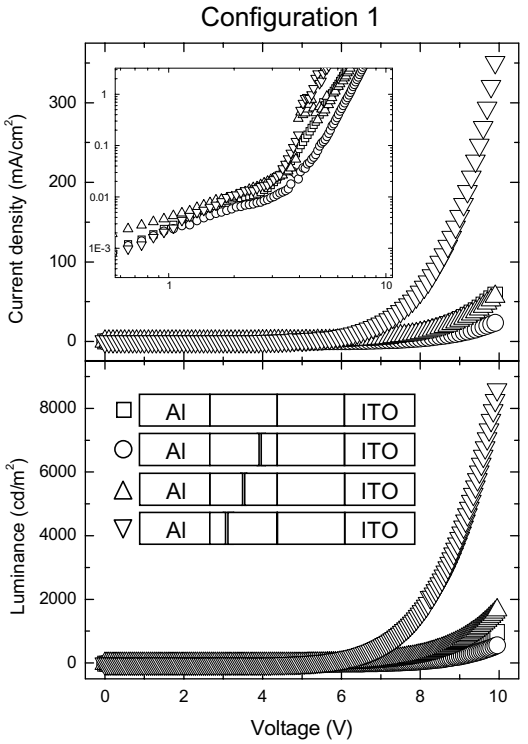

Fig. 3. Current density–luminance–voltage (C–L–V) characteristics of Configuration 1. The inset is the closer look in the current density–voltage (C–V) relation in log–log scale near turn-on voltage values. The device of ▽ plots is clearly less injection-limited than others and the enhancement is from the strong Al interdiffusion ranging at least up to 12.5 nm into Alq_3. A different enhancement is observed in the devices of △ and ○ plots in which the recombination of electrons and holes is enhanced without the electron injection enhancement.

(100.0 nm)/Alq_3 (37.5 nm)/LiF (0.3 nm)/Alq_3 (12.5 nm)/NPB (50.0 nm)/ITO (70.0 nm) devices (△ and ○ plots of Fig. 3) do not show any such enhancement. This Al has an implication to the enhanced electron injection. It can be inferred that the deposited Al diffuses inside the Alq_3 region reaching partially to 12.5 nm away from the cathode, which has accounted to the electron injection enhancement in the device. The fact that the Al diffusion is partial can be confirmed when the electron injection level is compared to the level of the injection in the LiF EIL device of Al (100.0 nm)/LiF (0.3 nm)/Alq_3 (50.0 nm)/NPB (50.0 nm)/ITO (70.0 nm) device, a non-injection limited device from our previous report [13], showed the current density of 1670 mA/cm^2 at 10 V and the value is four times larger than the value of the device with LiF at 12.5 nm position, 370 mA/cm^2. So far, there has not been a report on the depth of the Al diffusion to Alq_3 in a BE structure OLED. This data, however, gives a glimpse of the Al diffusion range. A study by Arndt et al. showed a Au morphology on diindenoperylene thin films (DIP, $C_{32}H_{16}$) with TEM [14]. The morphology of Al on Alq_3 might have a similar nucleation and short-circuiting of Al on Alq_3 by interdiffusion partially up to the distance of 12.5 nm (see Fig. 4). At the 25.0 nm range away from the Al cathode, the Al diffusion is not effective, and the devices with LiF layers each at 25.0 nm and 37.5 nm position away from the cathode (△ and ○ plots in Fig. 3) show no such enhancement in electron injections.

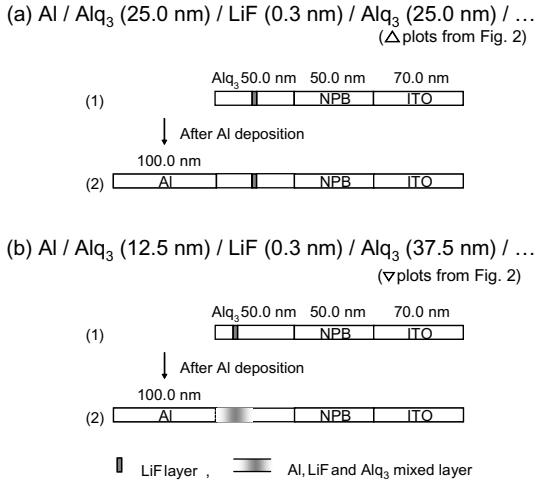

Fig. 4. The schematic picture of (a) a untouched LiF layer and (b) an Al, LiF and Alq_3 mixed layer after Al deposition in the respective devices of △ and ▽ plots from Fig. 2. The strong Al interdiffusion and the mixed layer formation in (b) is the reason of the partial injection enhancement which is better than the CD and less than the LiF EIL device.

The strong interdiffusion of Al into Alq_3 layer and incomplete cover of the LiF layer make the insulating buffer model not proper when considering a small molecule BE OLED with a thin (less than a nanometer) LiF EIL. Considering LiF layer as an indicator of diffusion depth of Al when thermally deposited onto Alq_3, the Al partially interdiffuses to 12.5 nm as discussed above. For the LiF EIL device of Al/LiF (0.3 nm)/Alq_3/NPB/ITO, it is best described as having Al interdiffuses into LiF (0.3 nm) and partial Alq_3 layers, and the interfacial chemistry is the source of an electron injection.

The elimination of the insulating buffer layer effect, however, has to be careful when considering the insulator as thick as a few nanometers as in

the cases of Kim et al.'s [6] and the Wang et al.'s [12] reports. As pointed out in Fig. 2, in fact, as the LiF thickness grows larger, the layer would have a complete cover of a layer and LiF might show its insulating effect dominantly. For the device with a thicker insulator layer, we observe the field range higher for the device to reach a certain current density. With the Kim et al.'s report, the field range is rather high around 10^6 V/cm at 100 mA/cm^2 current density; yet, the range of field at 100 mA/cm^2 in a device with a thin EIL lies below 10^5 V/cm including our device for the same current density. In Wang et al.'s report, the organic part thickness of the device, which is typically around 100 nm, is even thicker to be 150 nm thus the applied field is again higher to have the same current density inside the device. Hence, in a higher field with a thick insulator layer, the tunneling with the insulating buffer layer effect is most probable, and the elimination of the insulating buffer model must be limited to a BE OLED with an EIL as thin as a few tenth of a nanometer.

On the other hand, the LiF insertion at different positions shows a different enhancing property of LiF. Seeing △ and ○ plots of the Fig. 3, for the devices having LiF layer at 25.0 nm and 37.5 nm from the Al cathode, the current density injections are not enhanced compared to CD (□ plots) but the luminance is increased for the device with LiF at 25.0 nm (△ plots). The luminance of the device with LiF at 37.5 nm (○ plots) is not higher than that of CD. Yet, the luminance has been increased compared to its current density level which can be clearly seen when the electroluminescence (EL) efficiency is drawn versus the current density as in Fig. 5. In the figure, the LiF EIL device (◊ plots) is a non-injection limited device with both the high electron injection and the subsequent high electron and hole recombination rate. By inserting LiF in the hole dominant CD, the LiF EIL device is a non-injection limited device with affluent electron injections in its cathode and has the highest EL efficiency [4,5]. For the device with LiF at 12.5 nm position (▽ plots), due to the partial Al diffusion and the partial interfacial chemistry, the electron injection is partially enhanced and the EL efficiency is higher than that of CD but lower than that of the LiF EIL device. For those devices with LiF at 25.0 nm and 37.5 nm positions (△ and ○ plots) are enhanced in different manner; the electron injection is not enhanced but the recombination rate is enhanced compared to CD.

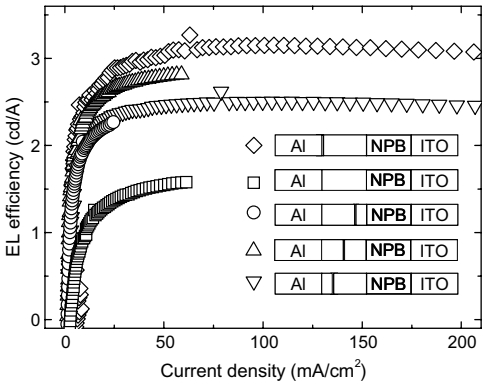

Fig. 5. Current density versus electroluminescence (EL) efficiency graph. The devices of ○ and △ plots have lower current densities (an injection-limited device) but have high EL efficiency compared to CD (□ plot). The devices with ▽ and ◇ plots are injection enhanced ones and, at the same time, have high EL efficiencies compared to CD. The LiF EIL device (◇ plot), Al/LiF (0.3 nm)/Alq_3 (50.0 nm)/NPB (50.0 nm)/ITO device is shown as a reference.

To see the indiffusion pattern of the electron injections and the corresponding EL efficiencies with varying LiF insertion positions, an additional experiment has been carried. OLEDs with LiF respective insertions at every multiple of 3.1 nm step position have been fabricated and their current densities at the operation voltage of 8 V and maximum EL efficiencies of respective devices are shown in Fig. 6. Newly bought organic materials and ITO substrates have given the CD with the current density of 230 mA/cm^2 at 8 V and the EL efficiency of 0.84 cd/A (dashed lines in Fig. 6). The LiF EIL device is the device with LiF at 0 nm position and the LiF position is the distance of a LiF insertion away from the Al cathode, as before. The Al interdiffusion is again confirmed to be at least over 12.5 nm range; the corresponding decreases of the electron injections and the EL efficiency of the devices with increased LiF position ends at the position 12.5 nm. The dual enhancing properties, i.e., injection enhancing and EL efficiency enhancing properties of LiF change smoothly from one another under 12.5 nm and over 12.5 nm positions and the device EL efficiencies do not reach the CD level of 0.84 cd/A (dark dashed line in Fig. 6).

Reduction of the current density in the device with LiF insertions inside Alq_3 layer at 25.0 nm and 37.5 nm positions, where Al does not diffuse, hence the interfacial chemistry of LiF is definitely not possible, explains the existence of trap sites by the thin layers (see the reduction of current densities

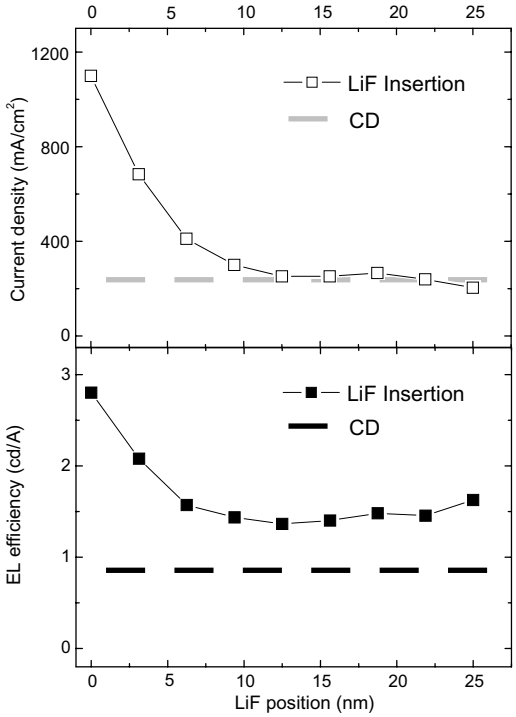

Fig. 6. LiF (0.3 nm) insertion position versus respective current density at an applied voltage of 8 V and maximum EL efficiency graphs (Al/Alq_3 (x nm)/LiF (0.3 nm)/Alq_3 (50.0–x nm)/NPB (50.0 nm)/ITO devices). The indiffusion pattern of the electron injections is shown up to 12.5 nm distance range from the Al cathode. The LiF has another enhancing property, an EL efficiency enhancer, which has taken over the EL efficiency increase of the devices from the current density injection enhancement, which is ineffective beyond the distance 12.5 nm. The maximum EL efficiency and current density levels of CD (Al/Alq_3 (50.0 nm)/NPB (50.0 nm)/ITO) is 0.84 cd/A and 230 mA/cm^2 at an applied voltage of 8 V, respectively.

of △ and ○ plots of Fig. 3 compared to CD). Comparing the emission spectra of CD and the LiF at 25.0 nm position device (Fig. 7), a possible role of a blocking layer by the thin layers can be eliminated. If they were effective blocking layers, a different recombination center, other than the NPB/Alq_3 interface, would have been formed thus a different emission spectrum would have been detected as an evidence of different light extractions in the device. The normalized emission spectra at an applied voltage of 7 V are identical as in Fig. 7. A suggested explanation of the EL efficiency enhancement of the devices is that trap charges provided by the insertions indeed lessen the current injections of the devices; yet, the existence of trap charges alters the field distribution in the OLED and more recombination is induced at the NPB/Alq_3 interface.

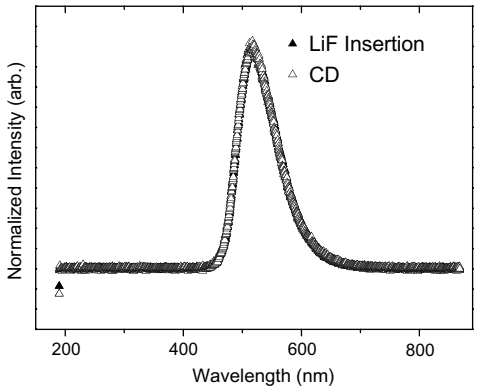

Fig. 7. The emission spectra of CD and the Al/Alq_3 (25.0 nm)/LiF (0.3 nm)/Alq_3 (25.0 nm)/NPB (50.0 nm)/ITO device at an applied voltage of 7 V. The identical spectra eliminate the possible role of the thin LiF blocking layer.

Evidence [15,16] has been reported that the existence of charges can have a "field screening" effect and we propose that the screening of the field by trap charges has prevented the well-known exciton quenching at the organic/cathode interface with the increase of the applied field; more excitons are confined at the NPB/Alq_3 interface. Although the exact mechanism of LiF EL efficiency enhancer is not clear, the phenomenon has a following application in the OLEDs.

A following device scheme with the use of LiF EL efficiency enhancer was considered. We adopted CuPc for an ETL and the device scheme is illustrated in Configuration 2 of Fig. 1. A similar device scheme was first introduced by Hung and Mason with a structure of MgAg/CuPc (40 nm)/Al (0.6 nm)/LiF (0.3 nm)/Alq_3 (35 nm)/NPB (120 nm)/ITO [17]. According to Hung and Mason, the CuPc layer has the higher electron mobility than the Alq_3 layer and can well be substituted for an ETL. The Al/LiF bilayer was inserted to make a better alignment between CuPc and Alq_3 LUMO levels and without its presence an enhanced device property was not acquired. The report suggested that the barrier between CuPc and Alq_3 LUMO limits the device electroluminescence efficiency and non-emissive recombination is formed in the CuPc region. The 0.6 nm Al deposition onto 0.3 nm LiF was adopted for the injection enhancement between CuPc and Alq_3. The overall enhancement of the CuPc was recovered after the substitution of the bilayer, preventing the exciton quenching inside CuPc. The report added that the voltage reduction in the OLED is the consequence of the substitution

of CuPc. In our scheme, the 0.3 nm LiF single layer has been adopted instead of the (0.6 nm) Al/(0.3 nm) LiF bilayer. The LiF without the assistance of Al inside an organic material, as discussed before, is an insulator and provides trap charges only but their existence can give better recombination through the field variations. In our device, with the insertion of a LiF single layer, the device property has been recovered as in the report of Hung and Mason. We suggest that the role of LiF is same as the EL efficiency enhancer as in devices of Configuration 1 and the trapped carriers provided variations of fields inside the OLED and more recombination is induced inside Alq_3 emitting layer (EML).

In Fig. 8, the C–L–V characteristics of Configuration 2 are shown. The Al (100.0 nm)/CuPc (25.0 nm)/LiF (0.3 nm)/Alq_3 (25.0 nm)/NPB (50.0 nm)/ITO (70.0 nm) and Al (100.0 nm)/CuPc (37.5 nm)/LiF (0.3 nm)/Alq_3 (12.5 nm)/NPB (50.0 nm)/ITO (70.0 nm) devices (△ and ○ plots of Fig. 8) show both current density and luminance enhancement compared to CD (□ plots). The devices show their turn-on voltages around at 2 V and all other devices of configurations in Fig. 1 show their turn-on around at 3 V (see the inset of Figs. 3 and 8, which is a closer look of the turn-on voltages in log–log scale). The significance of the devices of Configuration 2 is that the Al cathode is used not in conjunction with a LiF EIL and they showed a comparable enhanced device property to the LiF EIL device. Due to their limited EML region of Alq_3 (12.5 nm and 25.0 nm), their C–L–V relations can not be obtained properly above 6 V. From Fig. 8, the current densities of the devices are around 100 mA/cm^2 with their luminances above 1000 cd/m^2 at 5 V, which is comparable to our LiF EIL device. The high current densities should not be misunderstood as the result of LiF EL efficiency enhancer; they owe much to the voltage reduction by the CuPc ETL from Hung and Mason.

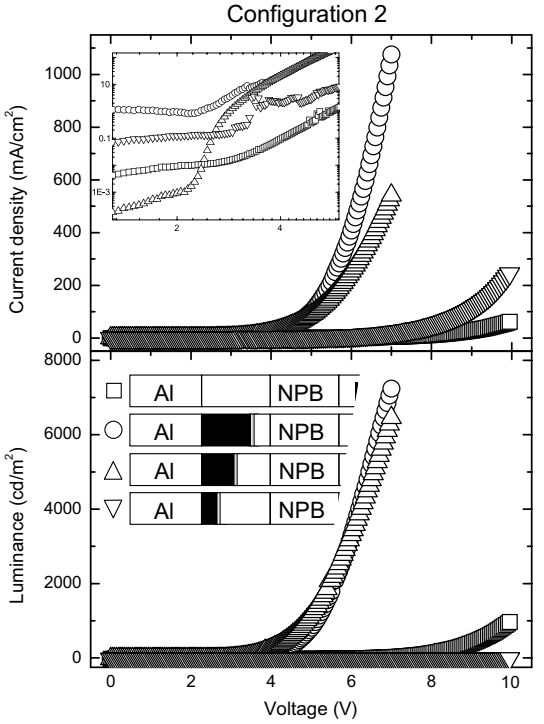

Fig. 8. Current density–luminance–voltage (C–L–V) characteristics of Configuration 2. The inset is the closer look in the current density–voltage (C–V) relation in log–log scale near turn-on voltage values. The devices of ○ and △ plots are benefited from the copper phthalocyanine (CuPc) substitution and both current densities and luminances are enhanced. For the devices, the turn-on voltages are lower around 2 V; the voltage reduction is achieved by CuPc substitutions. The device of ▽ plots is affected by the previously discussed Al interdiffusion in Configuration 1 which penetrates into CuPc up to 12.5 nm.

To explain the voltage reduction stated by Hung and Mason, a simple case of two dielectric materials, material 1 and material 2, in series between parallel plates is considered. To maintain a same current density, J, the current densities inside each material, J_1 and J_2 has to be equal to a value J ($J_1 = J_2 = J$). J is the multiple of the conductivity of a dielectric material, σ and the applied electric field to it, E ($J = \sigma E$). The equation, $\sigma_1 E_1 = \sigma_2 E_2$ is hence equated (σ_1 and E_1, for the material 1 and σ_2 and E_2, for the material 2) and this gives us a simple relation that when two dielectric materials are put in series, a dielectric material with relatively higher conductivity will have lower electric field applied to it and vice versa (for relative $\sigma_1 \uparrow \sigma_2 \downarrow$, $E_1 \downarrow E_2 \uparrow$ and for $\sigma_1 \downarrow \sigma_2 \uparrow$, $E_1 \uparrow E_2 \downarrow$). CuPc has higher electron mobility than that of Alq_3 according to Hung and Mason, and hence the conductivity, σ of CuPc is higher than that of Alq_3. From the $\sigma_1 E_1 = \sigma_2 E_2$ relation, the electric field in CuPc would be less than the electric field in Alq_3 and as in Fig. 9b, the CuPc ETL substituted device for the same voltage, V can have higher current density in its device compared to CD in Fig. 9a which has a pristine Alq_3. Since the slope of Alq_3 energy level corresponds to the E-field, the slope in Fig. 9b is steeper than the slope of CD in Fig. 9a. The device of with CuPc ETL has more current density in Alq_3 and will generate more light compared to CD. By drawing CD differently, with the same slope of Fig. 9b and c is drawn, which has the

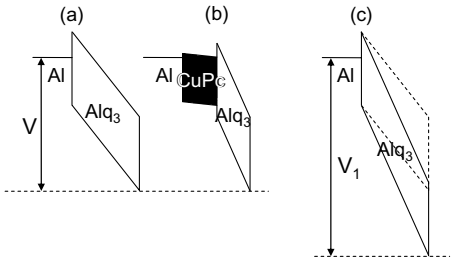

Fig. 9. Voltage reduction in an OLED with a copper phthalocyanine (CuPc) substitution. The LUMO and HOMO levels are −3.0 eV and −5.7 eV, for Alq_3 and −3.6 eV and −5.2 eV, for CuPc. The Al workfunction is −3.7 eV. The more conductive CuPc substitution in (b), the more field is distributed in aluminum tris(8-hydroxyquinoline) (Alq_3) than that in CuPc. For the same applied voltage V, the (b) device has more field in Alq_3 than the pristine Alq_3 of CD in (a), meaning more current density in the (b) device. The (c) device is CD with the same slope of an Alq_3 energy level in (b). This gives an impression of how much voltage reduction is achieved in the (b) device with the CuPc substitution compared to the (c) device.

same current flow as in Figure (b). The applied voltage V_1 in the CD of Fig. 9c gives us an impression of how much voltage reduction is achieved in the device with the CuPc substitution and which gives the high current density. It seems Al/CuPc electron injection is not poor; otherwise, CuPc experiencing lesser field would have not made enough electron injection from the Al cathode into CuPc, for the electron injection mechanisms such as Fowler–Nordheim tunneling and Richardson–Schottky thermionic emissions are field dependent in OLEDs.

A remark has to be made in explaining the Configuration 2. The device of Al (100.0 nm)/CuPc (12.5 nm)/LiF (0.3 nm)/Alq_3 (37.5 nm)/NPB (50.0 nm)/ITO (70.0 nm) (∇ plots in Fig. 8) shows the enhanced current density higher than CD but the luminance is null in reading. This is in accord with the strong Al interdiffusion, which is at least 12.5 nm for Al into Alq_3 from Configuration 1, and gives an approximately same Al diffusion range for CuPc. The deposited Al forms a mixed layer of CuPc, LiF and Al itself up to 12.5 nm, and the ill-defined CuPc ETL, LiF, and Alq_3 interfaces does not give the expected voltage reduction as in other devices. CuPc acting as an exciton quencher in the device is also a good agreement from the previous report [18].

4. Conclusions

The dual enhancing properties of thin 0.3 nm LiF layer inside a small molecule BE OLED has been observed by varying the position of the LiF layer. The last deposited Al cathode has strong interdiffusion into organic materials of both Alq_3 and CuPc at least up to 12.5 nm. This strong interdiffusion gives special weight to the interfacial chemistry model of the LiF EIL than the insulator buffer model. Yet, this seems limited to thin EILs less than one nanometer and devices with thicker EIL can be described by the insulating buffer model. When LiF is inside organic materials and out of reach from Al, LiF is an insulator and acts as an EL efficiency enhancer. The LiF thin layer traps carriers and reduces the overall current density inside an OLED but the trapped carriers provided variations of fields inside the OLED and hence give better recombination in the device. Using the CuPc ETL substitution in conjunction with the LiF EL efficiency enhancer, a better device property has been achieved. The device enhancement is originated from the high Al/CuPc cathode interface electron injection, the high conductivity of CuPc, and the high recombination of electrons and holes induced inside the Alq_3 EML by the LiF EL efficiency enhancer. The device property is comparable to the device with a LiF EIL.

Acknowledgement

This work was supported by Seoul Science Fellowship of the Seoul Metropolitan Government, the Korea Research Foundation Grant funded by Korea Government (MOEHRD, Basic Research Promotion Fund) (KRF-2005-015-C00130), and BK21 project of the Korea Research Foundation (KRF).

References

[1] C.W. Tang, S.A. VanSlyke, Appl. Phys. Lett. 51 (1987) 913.
[2] J.H. Burroughes, D.D.C. Bradley, A.R. Brown, R.N. Marks, K. Mackay, R.H. Friend, P.L. Burns, A.B. Holmes, Nature 347 (1990) 539.
[3] Takahiro Yokoyama, Daisuke Yoshimura, Eisuke Ito, Hisao Ishii, Yukio Ouchi, Kazuhiko Seki, Jpn. J. Appl. Phys. 42 (2003) 3666.
[4] L.S. Hung, C.W. Tang, M.G. Mason, Appl. Phys. Lett. 70 (1997) 152.
[5] G.E. Jabbour, Y. Kawabe, S.E. Shaheen, J.F. Wang, M.M. Morrell, B. Kippelen, N. Peyghambarian, Appl. Phys. Lett. 71 (1997) 1762.
[6] Young-Eun Kim, Heuk Park, Jang-Joo Kim, Appl. Phys. Lett. 69 (1996) 599.
[7] M.G. Mason, C.W. Tang, L.-S. Hung, P. Raychaudhuri, H. Madathil, D.J. Giesen, L. Yan, Q.T. Le, Y. Gao, S.-T. Lee, L.S. Liao, L.F. Cheng, W.R. Salaneck, D.A. dos Santos, J.L. Brédas, J. Appl. Phys. 89 (2001) 2756.

[8] H. Heil, J. Steiger, S. Karg, M. Gastel, H. Ortner, H. von Seggern, M. Stößel, J. Appl. Phys. 89 (2001) 420.
[9] Junji Kido, Toshio Matsumoto, Appl. Phys. Lett. 73 (1998) 2866.
[10] Hisao Ishii, Kiyoshi Sugiyama, Eisuke Ito, Kazuhiko Seki, Adv. Mater. 11 (1999) 605.
[11] Y.D. Jin, X.B. Ding, J. Reynaert, V.I. Arkhipov, G. Borghs, P.L. Heremans, M. Van der Auweraer, Org. Electron. 5 (2004) 271.
[12] X.J. Wang, J.M. Zhao, Y.C. Zhou, X.Z. Wang, S.T. Zhang, Y.Q. Zhan, Z. Xu, H.J. Ding, G.Y. Zhong, H.Z. Shi, Z.H. Xiong, Y. Liu, Z.J. Wang, E.G. Obbard, X.M. Ding, W. Huang, X.Y. Hou, J. Appl. Phys. 95 (2004) 3828.
[13] Yeonjin Yi, Seong Jun Kang, Kwanghee Cho, Jong Mo Koo, Kyul Han, Kyongjin Park, Myungkeun Noh, Chung Nam Whang, Kwangho Jeong, Appl. Phys. Lett. 86 (2005) 213502.
[14] Arndt C. Dürr, Franck Schreiber, Marion Kelsch, Heinz D. Carstanjen, Helmut Dosch, Adv. Mater. 14 (2002) 961.
[15] P.A. Lane, J.C. deMello, R.B. Fletcher, M. Bernius, Appl. Phys. Lett. 83 (2003) 3611.
[16] Frank Rohlfing, Toshiki Yamada, Tetsuo Tsutsui, J. Appl. Phys. 86 (1999) 4978.
[17] L.S. Hung, M.G. Mason, Appl. Phys. Lett. 78 (2001) 3732.
[18] L.S. Hung, C.W. Tang, Appl. Phys. Lett. 74 (1999) 3209.

Available online at www.sciencedirect.com
ScienceDirect
Organic Electronics 9 (2008) 39–44
Organic Electronics
www.elsevier.com/locate/orgel

Switching between different conformers of a molecule: Multilevel memory elements

Bikas C. Das, Amlan J. Pal *

Department of Solid State Physics, Indian Association for the Cultivation of Science, Kolkata 700 032, India

Received 21 May 2007; received in revised form 22 June 2007; accepted 24 July 2007
Available online 15 August 2007

Abstract

We report voltage-driven electrical bistability in an organic semiconductor, namely Ponceau SS. Conductance switching to different levels or "multilevel switching" in devices based on thin-films is due to different density of high-conducting molecules. In a monolayer of Ponceau SS, we have observed one low-conducting and two high-conducting states. This is due to three configurable planes of the molecule exhibiting at least two stable high-conducting conformers. Apart from establishing conductance switching to be a molecular phenomenon, the multilevel conductance in a monolayer shows that a single molecule can exhibit multilevel memory application.

PACS: 73.61.Ph; 82.37.Gk; 85.35.−p; 85.65.+h

Keywords: Conductance switching; Memory phenomenon; Multilevel memory; Molecular multilevel memory

1. Introduction

With the success of organic semiconductors in thin-film transistors [1], light-emitting devices [2], sensors [3] and photovoltaic solar cells [4], the materials are being considered for electronic memory elements [5–14]. Apart from acting as switching elements in integrated-circuits, the conjugated organics are expected to offer high-density memory applications to meet the need of the future. During the last few years, several classes of organic materials exhibited such applications, which occurred due to electrical bistability. In general, a suitable voltage changes the conformer of a molecule [5,15]. When both the conformers are stable with a large difference in their conductivities, the molecules exhibit electrical bistability. It is manifested as two current values at a voltage, with the preceding voltage pulse determining the conducting state. By controlling the density of high-conducting molecules in a device, multilevel conductivity has also been achieved in organic memory devices [13,14].

In devices based on thin-films of organic materials with electrode metals having low electronegativity, the bistability sometimes arises due to reversible growth of metal filaments through redox reactions [16]. When individual molecules (or a 2D molecular layer) with noble metal electrodes exhibit electrical

* Corresponding author. Tel.: +91 33 24734971; fax: +91 33 24732805.
E-mail address: sspajp@iacs.res.in (A.J. Pal).

1566-1199/$ - see front matter © 2007 Elsevier B.V. All rights reserved.
doi:10.1016/j.orgel.2007.07.008

bistabilty, the phenomenon is explained in terms of conformational change [5] and/or electroreduction of the molecule [17]. The bistability in such cases is hence a molecular phenomenon. With a suitable material, such systems may yield multilevel conductivity for multibit memory storage. The chosen molecules will then have to possess several stable conformers. In this article, we introduce such a molecule, which, due to its multiplaner structure, yields multilevel conductivity with associated memory phenomenon in the molecular scale.

2. Experimental

The molecule for the present work is Ponceau SS (Acid red 150), which was purchased from Aldrich Chemical Co. Molecular structure of the molecule is shown in the inset of Fig. 1. Both monolayer and spin-cast thin-films of the material were deposited and characterized. Devices based on spun-cast films of Ponceau SS were fabricated on indium tin oxide (ITO) coated glass substrates (sheet resistance = 12 Ω/□). Ponceau SS in methanol (2 mg/ml) was spun at a speed of 1000 rpm resulting in a film thickness of about 70 nm. The films were dried in vacuum at 60 °C for 12 h. Aluminum (Al) was thermally evaporated at a pressure of 1×10^{-6} Torr to act as the top electrode. Area of a typical device was 6 mm^2.

The devices were placed in a shielded vacuum chamber before current–voltage (I–V) characteristics were recorded at room temperature with a Keithley 486 picoammeter and Yokogawa 7651 dc source. I–V characteristics were recorded at two sweep directions (from $+V_{Max}$ to $-V_{Max}$ and from $-V_{Max}$ to $+V_{Max}$) and also in voltage loops (from 0 to $+V_{Max}$ to $-V_{Max}$ to $+V_{Max}$). Here V_{Max} represents amplitude of voltage up to which bias was swept. For read-only memory (ROM) and random-access memory (RAM) applications, voltage pulse of suitable amplitude and width were generated by fast switching transistors triggered by a PC.

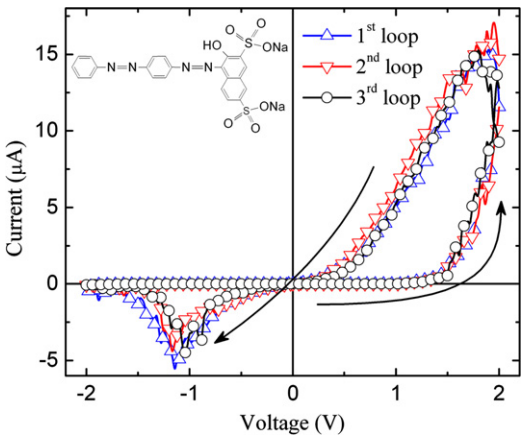

Fig. 1. I–V characteristics of a device based on spun-cast film of Ponceau SS in three loops. Inset shows the molecular structure of a Ponceau SS molecule.

To obtain a monolayer of Ponceau SS via electrostatic assembly, layer-by-layer (LbL) films were deposited with poly(allylamine hydrochloride) (PAH) as a polycation. A deprotonated n-type Si(1 1 1) substrate (resistivity = 3–10 mΩ cm) was first dipped in the polycationic bath (pH 6.5) for 15 min followed by through rinsing in deionized water baths. The Si substrate was then dipped in the Ponceau SS bath (5 mM) for 15 min followed by the same rinsing protocol in a separate set of water baths. This resulted in a monolayer of Ponceau SS due to electrostatic binding through its SO_3^- moieties. The dipping sequence was repeated to obtain multilayer films (on quartz) to record electronic absorption spectra.

Before recording scanning tunneling microscope (STM) images, the films were annealed in vacuum at 100 °C. Pt/Ir tip of the STM was lowered till a current of 0.5 nA was achieved at 0.5 V. The tip position was then fixed to measure a set of I–V characteristics. Bias was swept in both directions. In certain cases, a suitable voltage pulse was applied before recording the I–V characteristics. Measurements were carried at room temperature and in ambient condition.

3. Results and discussion

3.1. Conductance switching

Fig. 1 shows a typical I–V plot for a spun-cast film of Ponceau SS sandwiched between ITO and Al electrodes. Ponceau SS exhibits electrical bistability. The I–V characteristics depend on the voltage sweep direction. The magnitude of device current at a voltage is higher during the sweep from a positive voltage as compared to that from a negative one. In other words, a suitable positive bias induces a higher conducting state. The higher state is retained even when the bias is removed from the devices terming the bistability as a memory-switching phenomenon. The On/Off ratio, the ratio between current values during the two voltage-sweeps, reaches up to 3000. When the bias was applied in loops,

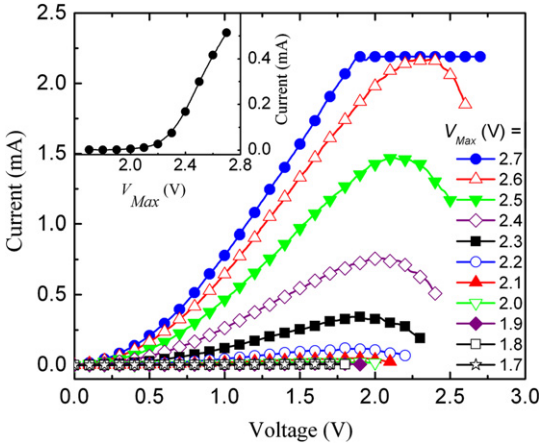

Fig. 2. *I–V* characteristics of a device based on spun-cast film of Ponceau SS from different $+V_{Max}$s. For $V_{Max} = 2.7$ V, current value reached the limit of measuring instrument during the voltage sweep. Inset shows current at 0.8 V as a function of V_{Max}.

the *I–V* characteristics retraced for both the conducting states showing (high) reproducible nature of the electrical bistability in Ponceau SS.

The degree of bistability, or the conductivity of the high-state depends on the amplitude of V_{Max}. Plots for $+V_{Max}$ to 0 V for different V_{Max} are shown in Fig. 2. The inset of the plot summarizes the results showing the dependence of device current (at a voltage) as a function of V_{Max}. The plot shows the current (at 0.8 V) increases with V_{Max} – the rate of rise initially being low – giving rise to multilevel conductivity. Such dependence in a thin-film device may be due to switching of more number of molecules by the application of higher voltage amplitude. It may also arise if the molecule has more than one high-conducting (stable) conformers.

3.2. Multilevel memory

Multilevel memory has indeed been observed in this system. To demonstrate multilevel read-only memory (MROM), we applied different pump voltages and probed the states by applying a small voltage. Fig. 3a shows the current under probe voltage as a function of time after a suitable pump voltage pulse was applied. Here, pump voltages were ±1.8, ±2.2 and ±2.6 V (width = 10 s). While the positive voltages induced high-conducting states, the negative ones reinstated the low-state. The figure shows that current under probe voltage for the high-state depends on the magnitude of preceding pump pulse. In probing the low-conducting state, the current remained unaltered for the three cases. It further shows that we could successfully reinstate the low-conducting state every time, showing reproducibility of conductance switching. Here, the low-state may be referred to as (0 0), whereas the high-conducting states pumped by +1.8, +2.2 and +2.6 V may be termed as (0 1), (1 0) and (1 1), respectively, resembling two-bit memory elements in a single device.

Fig. 3b shows that multilevel random-access memory (MRAM) applications can also be observed in these devices. We "write" the three high-conducting states and "erase" them to the low-state every time. After establishing one of the four states, it is "read" by the application of a small voltage. In effect, the device undergoes a "write-read-erase-read" voltage pulse sequence with "write" pulse amplitude of +1.8, +2.2 and +2.6 V (width = 10 s). While the "erase" pulse has a value of –2.6 V (width 10 s), +0.8 V was applied as "read" voltage pulse. The results show that the current

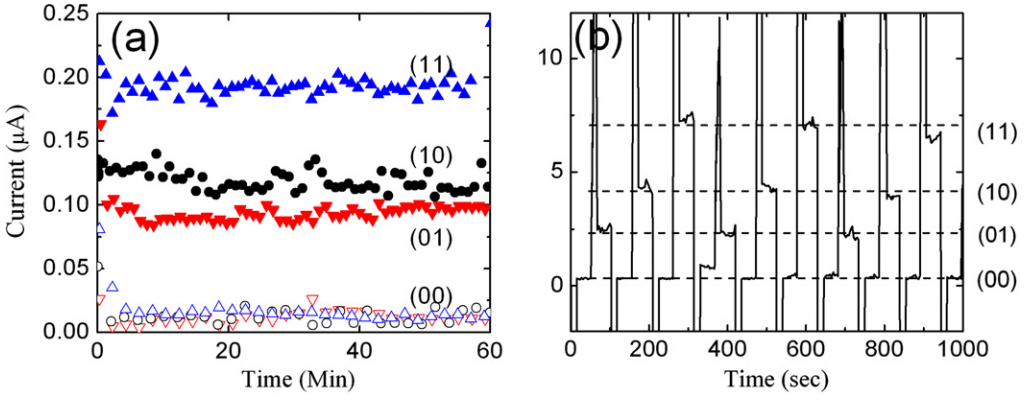

Fig. 3. (a) Multilevel Read-Only Memory of a device based on spun-cast film of Ponceau SS. Current was read under +0.8 V pulse (width 2 s; duty cycle = 17 %); for (1 1), current values were divided by six for comparison. (b) Multilevel Random-Access Memory application of the same device. Current under "write-read-erase-read" voltage sequence is presented.

under the probe voltage for the low- and three high-conducting states differed distinctively. The four states, namely (0 0), (0 1), (1 0) and (1 1), can hence be achieved and probed in a device for RAM applications between two-bits. The results further show reversible nature of conductance switching to the three high-conducting states.

3.3. Formation of a monolayer

Though the multilevel memory in devices based on Ponceau SS may arise due to varied density of high-conducting molecules, we investigated the possibility of more than two stable conformers in Ponceau SS. In doing so, we chose a monolayer of Ponceau SS on doped Si(1 1 1) wafers deposited via electrostatic assembly, so that progressive switching along the depth of the device does not occur. Topographic image of the bare wafer and monolayer of Ponceau SS are presented in insets (a) and (b) of Fig. 4, respectively. A clear difference between the images is certainly due to deposition of Ponceau SS during electrostatic adsorption via binding through the two SO_3^- groups.

To further confirm deposition of Ponceau SS during LbL deposition, we recorded electronic absorption spectra of the films on quartz substrate. Since the value of absorbance for a monolayer was low, we confirmed film formation by monitoring its progress during multilayer deposition. Electronic absorption spectra of different number of layers of LbL films are shown in Fig. 4. All the spectra show a peak at 515 nm – the intensity of the band increasing with number of layers deposited. The band at 515 nm is very close to that in Ponceau SS solution (516 nm). Such a low shift further shows that Ponceau SS did not form aggregates in LbL films. The inset (c) of Fig. 4 shows the absorbance of the film at 515 nm as a function of number of Ponceau SS layers. A linear plot through the origin with a slope of unity confirms that the Ponceau SS molecules were adsorbed uniformly during deposition of every layer via LbL assembly.

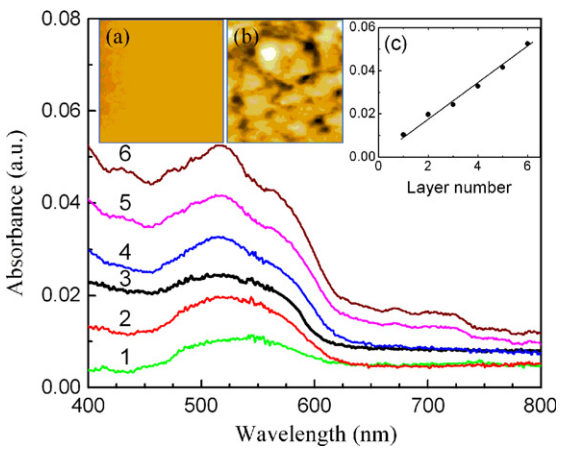

Fig. 4. Electronic absorption spectra of LbL films of Ponceau SS for different number of layers. Insets show topographic STM image of (a) a bare Si substrate and (b) a monolayer of Ponceau SS on Si. The STM measurements were recorded in a constant current mode (0.5 nA) at a 0.5 V bias. The displayed scan area is 85 nm × 85 nm in both the cases. Inset (c) shows absorbance at 515 nm as a function of number of layers.

3.4. Multilevel memory in a monolayer

We characterized the 2D array of Ponceau SS by STM tip. Here since Ponceau SS molecules are attached to the substrate by electrostatic binding via the two SO_3^- groups, the two planes containing benzene rings connected through $N{=}N$ remains freely configurable (to reach a local low-energy configuration). To record I–V characteristics of the low- and other possible different high-conducting states, we first applied a suitable voltage pulse and then scanned I–V characteristics in a small voltage range in loops. V_{Max} for the I–V characteristics ranged from ±1.0 to ±1.5 V. In this experiment, while the width of the pulse was kept the same (10 ms), the amplitude of the pulse varied up to 8.5 V (Fig. 5). The figure shows that the current in the forward bias depends strongly on the preceding "write" voltage pulse. There was however little difference in the reverse bias current. At any forward voltage, higher current was observed when amplitude of the "write" pulse was higher. The increase in current was not monotonic (in contrast to the case of the device based on spun-cast film) with the amplitude of the pulse. The I–V plots were clubbed or "bunched". The results are summarized in inset (a) of Fig. 5 as a plot of current (at 0.8 V) as a function of amplitude of the preceding voltage pulse. The current shows three steps. By the application of a reverse bias pulse, the low-conducting state was induced. Depending on the amplitude of voltage pulse, two distinctively different probe current was observed. This shows that multiple conducting states in a monolayer can be achieved due to different high-conducting configurations of a single molecule. In other words, one low- (0 0) and at least two high-conducting states (two of 0 1, 1 0, 1 1) could be observed in a single Ponceau SS molecule. Absence

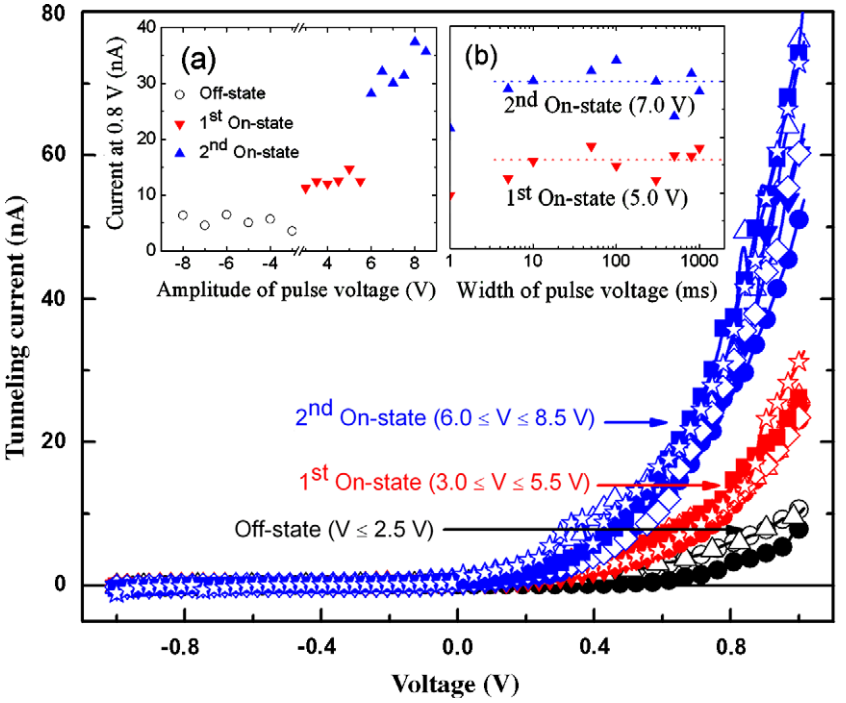

Fig. 5. *I–V* characteristics with a STM tip of a monolayer of Ponceau SS. Voltage-sweeps were carried out after application of voltage pulse of different amplitudes. For the off-state, pulse amplitude was up to 2.5 V. For the first and second on-states, the amplitude ranged from 3.0 to 5.5 V and 6.0 to 8.5 V, respectively. Insets show (a) tunneling current at +0.8 V as a function of amplitude of preceding voltage pulse (fixed width of 10 ms) and (b) tunneling current at +0.8 V as a function of width of preceding voltage pulse (amplitude being 5.0 and 7.0 V representing first and second on-states, respectively).

of a monotonic increase in inset (a) of Fig. 5 shows that even though the STM measurements involve a number of molecules in parallel, different high-conducting states did not arise due to switching of more number of molecules in the 2D plane. We may add that by application of a suitable negative voltage pulse, the pristine low-conducting state can always be reinstated showing reproducibility of switching in a monolayer or a molecule of Ponceau SS. Control experiments on only bare Si wafer yielded much higher current as compared to that with Ponceau SS monolayer. The observation of electrical bistability in a monolayer with STM tip further excludes the possibility of metal filament formation upon diffusion of metal cations.

To verify if the width of voltage pulse has any role in inducing different high-conducting states, we have carried out the following experiment. By keeping the amplitude of voltage pulse the same, we varied the width of the pulse that precedes the *I–V* sweep. Inset (b) of Fig. 5 shows the current at +0.8 V (from *I–V* sweep) as a function of pulse width that ranged from 1 to 1000 ms. Measurements were carried out for the two high-states by applying 5.0 and 7.0 V amplitude pulses, respectively. The figure shows that the current did not depend on the width of the preceding pulse. In each of the two high-conducting states, all the molecules must have switched to a particular configuration by the application of a pulse width of more than 5 ms. The high-state induced by a 7.0 V pulse cannot be achieved by applying a 5.0 V pulse of very long width. Similarly, a very short pulse of 7.0 V cannot induce an equivalent state induced by a 5.0 V pulse. From the insets of Fig. 5, we conclude that the amplitude of voltage pulse is the key factor in obtaining different conformer or conducting state in a molecule.

4. Conclusions

In summary, we have shown that Ponceau SS molecules exhibit multilevel memory-switching property. When a monolayer of the molecule is characterized by STM, the molecules exhibit one low- and two high-conducting states. The three states arise due to different conformers of the molecules. Amplitude of voltage pulse determines the conformer or corresponding high-state of the

molecule. The width of the pulse has little or no effect in the 1–1000 ms range. In thin-film based devices, amplitude of voltage pulse determines the density of high-conducting molecules and hence the level of high-conducting states. Such devices exhibit multilevel ROM and RAM phenomena. Our results show that while in a spun-cast film based device multilevel memory is a bulk property, for a monolayer of Ponceau SS, it appears due to different conformers of a single molecule itself. The results open up a route to achieve multilevel memory elements in the molecular scale.

Acknowledgments

B.C.D. acknowledges CSIR Junior Research Fellowship No. 09/080(0504)/2006-EMR-I, Roll No. 503982. The Department of Science and Technology, Government of India, financially supported the work through Ramanna Fellowship SR/S2/RFCMP-02/2005.

References

[1] A. Dodabalapur, Mater. Today 9 (2006) 24.
[2] Z.L. Shen, P.E. Burrows, V. Bulovic, S.R. Forrest, M.E. Thompson, Science 276 (1997) 2009.
[3] S.D. Evans, S.R. Johnson, Y.L.L. Cheng, T.H. Shen, J. Mater. Chem. 10 (2000) 183.
[4] H. Hoppe, N.S. Sariciftci, J. Mater. Res. 19 (2004) 1924.
[5] Z.J. Donhauser, B.A. Mantooth, K.F. Kelly, L.A. Bumm, J.D. Monnell, J.J. Stapleton, D.W. Price, A.M. Rawlett, D.L. Allara, J.M. Tour, P.S. Weiss, Science 292 (2001) 2303.
[6] D. Ma, M. Aguiar, J.A. Freire, I.A. Hummelgen, Adv. Mater. 12 (2000) 1063.
[7] A. Bandhopadhyay, A.J. Pal, J. Phys. Chem. B 107 (2003) 2531.
[8] M. Kushida, H. Inomata, H. Miyata, K. Harada, K. Saito, K. Sugita, Jpn. J. Appl. Phys., Part 2 42 (2003) L622.
[9] L.P. Ma, Q.F. Xu, Y. Yang, Appl. Phys. Lett. 84 (2004) 4908.
[10] M. Terai, K. Fujita, T. Tsutsui, Jpn. J. Appl. Phys., Part 1 45 (2006) 3754.
[11] M. Caironi, D. Natali, M. Sampietro, C. Bertarelli, A. Bianco, A. Dundulachi, E. Canesi, G. Zerbi, Appl. Phys. Lett. 89 (2006) 243519.
[12] T. Iimori, T. Naito, N. Ohta, J. Am. Chem. Soc. 129 (2007) 3486.
[13] M. Lauters, B. McCarthy, D. Sarid, G.E. Jabbour, Appl. Phys. Lett. 87 (2005) 231105.
[14] B. Mukherjee, A.J. Pal, Appl. Phys. Lett. 85 (2004) 2116.
[15] A. Bandyopadhyay, A.J. Pal, Appl. Phys. Lett. 84 (2004) 999.
[16] S. Ssenyange, H.J. Yan, R.L. McCreery, Langmuir 22 (2006) 10689.
[17] A.O. Solak, S. Ranganathan, T. Itoh, R.L. McCreery, Electrochem. Solid-State Lett. 5 (2002) E43.

Available online at www.sciencedirect.com
ScienceDirect
Organic Electronics 9 (2008) 45–50
Organic Electronics
www.elsevier.com/locate/orgel

Improved performance of polymer light-emitting devices based on blend of MEH–PPV and vinyl copolymer with 1,3,4-oxadiazole chromophores

Kun-Ming Yeh, Yun Chen *

Department of Chemical Engineering, National Cheng Kung University, Tainan, Taiwan

Received 12 April 2007; received in revised form 27 July 2007; accepted 8 August 2007
Available online 15 August 2007

Abstract

We have developed a simple method to overcome the intrinsic defect of well-known poly[2-methoxy-5-(2′-ethylhexoxy)–*p*-phenylenevinylene] (MEH–PPV), i.e. rampant inter-chain interaction and imbalanced hole and electron fluxes, by blending with copolymer of polystyrene containing pendant aromatic 1,3,4-oxadiazole (PSOXD12). The addition of PSOXD12 reduces the inter-chain interaction and balances charge carrier transport simultaneously. Photoluminescence (PL), PL excitation and electroluminescence (EL) spectra of the blends reveal that the inter-chain interactions, such as aggregation and excimer/exciplex, are reduced markedly due to the presence of PSOXD12. Enhanced EL device performance has been achieved (16,261 cd/m^2, 4.79 cd/A) as a result of both reduced inter-chain interaction and balanced charge transport.

PACS: 79.60.Fr; 85.60.Jb; 83.80.Tc

Keywords: Light-emitting diodes; Blend; Inter-chain interaction

1. Introduction

Electroluminescence (EL) from small organic molecules [1] and polymers [2] forms the basis for their use in light-emitting diodes (OLEDs and PLEDs). Polymeric EL materials have drawn great attention in recent years because of their advantages of good processability, simple fabrication by solution processes, and good thermal stability. However, some major hindrances, arising from the inter-chain interaction and charge imbalance between hole and electron, still need to be overcome. In general, the emission spectra of conjugated polymers are usually broad and red-shifted compared with single chain emission due to the formation of inter-chain emissive species, such as aggregation and excimer/exciplex, which generally reduce the efficiency and degrade the color purity dramatically. Many methods have been developed to overcome these defects, such as chemical structure modification [3], solvent selection [4], and polymer blending. For example, Yang et al. achieved enhanced devices performance by blending emitting poly[2-methoxy-5-(2′-ethylhexoxy)–*p*-phenylenevin-

* Corresponding author. Tel.: +886 6 2085843; fax: +886 6 2344496.
E-mail address: yunchen@mail.ncku.edu.tw (Y. Chen).

1566-1199/$ - see front matter © 2007 Elsevier B.V. All rights reserved.
doi:10.1016/j.orgel.2007.08.001

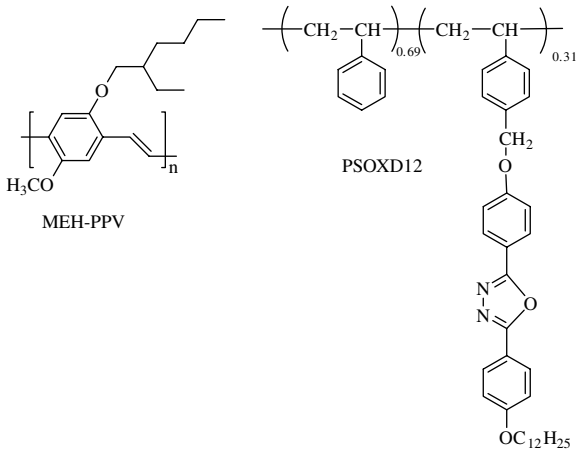

Fig. 1. Molecular structures of MEH–PPV and PSOXD12.

ylene] (MEH–PPV, Fig. 1) with an inert polystyrene (PS), which had been attributed to the dilution effect and reduced inter-chain interaction [5]. On the other hand, electron-injection in most of conjugated EL polymers is much more difficult than hole-injection, resulting in imbalanced electron and hole injection from negative and positive contacts, respectively, and a shift of the recombination zone toward the region near the interface of the polymer/cathode [6]. In addition, in common conjugated EL polymers, the electron mobility is much smaller than hole mobility. To overcome this problem, it is necessary to balance the injection/transport rates of opposite charges and decrease the barriers of charge injection from the opposite contacts [7]. Aromatic 1,3,4-oxadiazole-based compounds have been demonstrated to facilitate electron-transport and injection due to their high electron affinity [8–10].

In this work, a simple method was developed to reduce inter-chain interaction and improve charge balance between hole and electron simultaneously. Combination of aromatic 1,3,4-oxadiazole and inert polystyrene leads to a vinyl copolymer PSOXD12 (Fig. 1) with pendant electron withdrawing chromophores, which is efficient in enhancing electron-transport/injection. In addition, the incorporation of polystyrene segment in PSOXD12 have an advantage of improving solubility of rigid aromatic 1,3,4-oxadiazole. Compared with small molecular 1,3,4-oxadiazole derivatives, such as 2-(4-biphenyl)-5-(4-*tert*-butylphenyl)1,3,4-oxadiazole (PBD), using polymer-attached 1,3,4-oxadiazole should be effective in preventing recrystallization processes. Therefore, simple blending of MEH–PPV with PSOXD12 results in depressed inter-chain interaction and reduced full width at half maximum (FWHM) in PL and EL spectra when compared with the neat MEH–PPV. Moreover, significantly improved device performance (16261 cd/m^2, 4.79 cd/A) has been achieved by using blend of MEH–PPV and PSOXD12 (50/50) as emitting layer. This finding offers simple method of improving device performance by using commercially available MEH–PPV without modifying its chemical structure.

2. Experiment

The MEH–PPV and PSOXD12 were prepared following a synthetic procedure described elsewhere [11,12], and identified by ^{1}H NMR, FT-IR, and elemental analysis (EA). Their chemical structures are shown in Fig. 1. The polymers were soluble in common organic solvents, such as toluene, chloroform, and 1,1,2,2-tetrachloroethane. The glass transition temperatures (T_g) of the polymers were measured using a differential scanning calorimeter (DSC), Perkin–Elmer DSC-7, under nitrogen atmosphere at a heating rate of 10 °C/min.

PL and PL excitation spectra of polymer films were obtained using a Hitachi F-4500 fluorescence spectrophotometer. Field emission scanning electron microscope (FE-SEM) image was recorded on a JEOL JSM-6700F HR-FESEM at an acceleration voltage of 5 kV. The EL device configuration was ITO/PEDOT:PSS/polymer blends/Al. The PLEDs were fabricated on pre-cleaned indium tin oxide (ITO) substrates with a sheet resistance of 14 Ω/□. The poly(3,4-ethylenedioxythiophene):poly(styrene sulfonate) (PEDOT:PSS) was first coated onto ITO glass as the hole-injection layer and annealed at 150 °C for 0.5 h in a dust-free atmosphere. A thin layer of the polymer blend was spin-coated onto the PEDOT layer from its solution in toluene (ultra resi-analyzed grade) to obtain uniform and pinhole-free films. Finally, the aluminum cathode was deposited onto the polymer film via thermal evaporation under 10^{-5} Torr. The film thickness of emissive layers were about 75–100 nm as measured by an atomic force microscope (AFM), Veeco/Digital Instrument Scanning Probe Microscope (tapping mode) with Nanoscope IIIa controller. For the measurements of device characteristics, current density–voltage–luminance (J–V–L) changes were measured using a power supply (Keithley 2400) and a fluorescence spectrophotometer (Ocean Optics usb2000), and the luminance

was further corrected by SpectraScan PR650 spectrophotometer. The active area of the EL device, defined by the overlap of the ITO and the cathode electrodes, was 4 mm^2.

3. Results and discussion

EL polymers with high glass transition temperature (T_g) are generally believed to prevent morphology deformation and degradation when used as emitting or electron-transport layers in PLEDs [3]. Accordingly, the relaxation of MEH–PPV chains are also expected to be retarded by blending with more-rigid PSOXD12, which possess much higher T_g (135 °C) than MEH–PPV (75 °C).

Fig. 2 shows the PL spectra of neat MEH–PPV films measured at 300 K and 77 K and its blend films with PSOXD12 at 300 K. The inset shows the spectral intensity at 630 nm, originated from the formation of inter-chain interaction, versus variable blend ratios. The blend films were spin-coated on the quartz substrate from toluene solution (10 mg/mL). Table 1 summarizes PL and EL data of the blend films. The spectrum of neat MEH–PPV film at 300 K shows emission maximum at 581 nm with a shoulder at approximately 630 nm. It has been demonstrated that the shoulder located at ca. 630 nm is attributed to inter-chain interaction [5,13]. With increasing content of PSOXD12, the emission maximum remains almost the same (ca. 580 nm) between the weight ratios of MEH–PPV/PSOXD12 = 100/0 and 80/20 and then blue-shifts slightly (6 nm) at MEH–PPV/PSOXD12 = 50/50. Moreover, the FWHM of the PL spectra reduces from 66 nm (neat MEH–PPV) to 45 nm at MEH–PPV/PSOXD12 = 50/50, indicating that higher color purity can be obtained by simple blending of MEH–PPV with PSOXD12. The most important result is that the PL spectral intensity located at 630 nm decreases from 0.47 to 0.2 as the weight ratio of PSOXD12 is increased from 0 to 50, suggesting that the inter-chain interaction is reduced markedly due to the dilution effect. Similar result has been reported by Yang et al. [5] for MEH–PPV/PS blends. The PL spectrum of MEH–PPV at 77 K was also measured for the purpose of comparison [14]. The emission peak shows 17 nm red-shift relative to that at 300 K, which is due to the decrease of thermal disorder and results in extended conjugation. The spectral intensity (0.17) at 650 nm (originate from inter-chain interaction) is slightly lower than that of MEH–PPV/PSOXD12 blend (50/50, 0.20) located at 630 nm at 300 K. Fig. 3 shows the EL spectra of neat MEH–PPV films and its blend films with PSOXD12, measured at a current density of 300 mA/cm^2, for the devices with a configuration of ITO/PEDOT:PSS/MEH–PPV + PSOXD12/Al. The inset shows plot of the spectral intensity at 630 nm versus blend ratios. With the increase of PSOXD12 concentration, the spectrum peak at ca. 590 nm blue-shift (14 nm) gradually to 575 nm. The spectral intensity of the shoulder at 630 nm depends on concentration

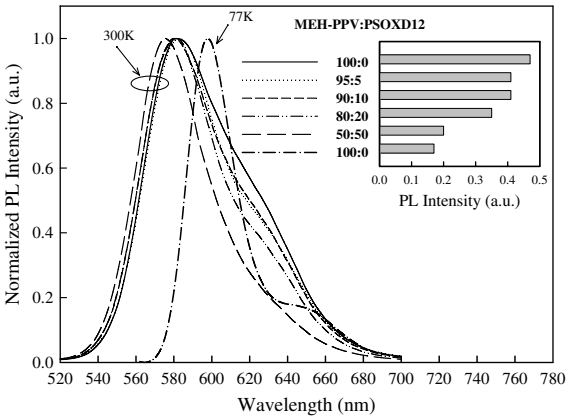

Fig. 2. PL spectra of films from neat MEH–PPV and blends of MEH–PPV and PSOXD12 at different weight ratios. The inset shows plot of the spectral intensity (at 630 nm) versus variable blend ratios.

Table 1
PL and EL spectral data of the blend films (MEH–PPV and PSOXD12)

MEH–PPV:PSOXD12 (weight ratio)	λ_{PL} (nm)	$FWHM_{PL}$ (nm)	PL Int.[a] (a.u.)	λ_{EL} (nm)	$FWHM_{EL}$ (nm)	EL Int.[a] (a.u.)
100:0	581	66	0.47	589	81	0.79
95:5	581	56	0.41	587	76	0.67
90:10	580	56	0.41	587	75	0.68
80:20	580	52	0.35	583	70	0.56
50:50	575	45	0.20	575	60	0.40
100:0 (77 K)	598	29	0.17[b]	–	–	–

[a] The intensity of PL or EL spectra at 630 nm.
[b] The intensity of PL spectrum at 650 nm.

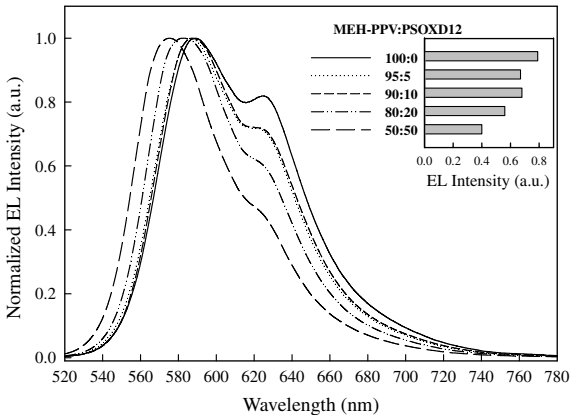

Fig. 3. EL spectra of corresponding devices measured at a current density of 300 mA/cm^2 The inset shows plot of the spectral intensity (at 630 nm) versus blend ratios.

and decreases from 0.79 to 0.4 as the weight percent of PSOXD12 is increased from 0 to 50. Moreover, the spectral width (FWHM) is compressed obviously at equivalent weight ratio (from 81 nm to 60 nm as shown in Table 1), indicating that the inter-chain interaction in MEH–PPV can be effectively suppressed with high concentration of PSOXD12. Both PL and EL spectra are originated exclusively from radiation relaxation of excited MEH–PPV molecules, because no emission of aromatic 1,3,4-oxadiazole chromophores is detected, suggesting no phase separation is formed in the blends. FE-SEM was employed to further investigate the morphology of the blend films to confirm the absence of phase separation. Fig. 4 shows the FE-SEM micrograph of the blend film with MEH–PPV/PSOXD12 = 50/50 and clearly the film exhibits homogeneous phase. The PL and EL spectral blue-shift in MEH–PPV/PSOXD12 blends is attributed to the conformation change in MEH–PPV chain caused by the presence of PSOXD12 [15]. In an attempt to elucidate the origin of main PL emission at 580 nm, the PL excitation analysis of neat MEH–PPV films and its blend films with PSOXD12 were monitored at 580 nm, and the excitation spectra are depicted in Fig. 5. The excitation spectrum of neat MEH–PPV film shows a peak at 530 nm with a shoulder located at approximately 480 nm. With the increase of PSOXD12 concentration, the shoulder grows gradually to form as a new peak at 20% of PSOXD12. The new peak is even stronger than long-wavelength peak at 530 nm when 50% PSOXD12 is incorporated. The results also support the earlier argument that the inter-chain interaction (aggregation) is reduced markedly due to dilution effect.

Fig. 6 shows the energy level diagram of the neat MEH–PPV and MEH–PPV/PSOXD12 blends. The lowest unoccupied (LUMO) and highest occupied molecular orbital (HOMO) levels of PSOXD12 are −3.10 eV and −5.77 eV [12], respectively, which are much lower than MEH–PPV (−2.7 eV and −5.02 eV). This means that the hole is mainly injected into MEH–PPV, while the electron is injected into PSOXD12 under device operation. The electron-injection barrier between cathode and emitting layer reduces from 1.6 eV (neat MEH–PPV) to 1.2 eV (MEH–PPV/PSOXD12 blends). The blend (MEH–PPV/PSOXD12) may induce the formation of type-II heterojunction due to reduced HOMO and LUMO levels of PSOXD12, which readily retard the formation of exciton. However, in fully-conjugated polymers, such as MEH–PPV, electron mobility is much slower than hole mobility, leading to imbalance in carriers transport. The

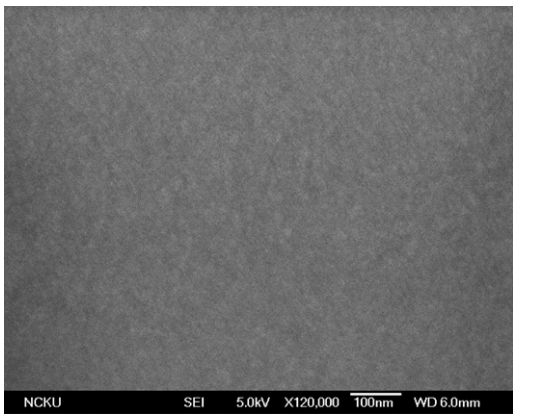

Fig. 4. SEM micrograph of polymer blend from MEH–PPV and PSOXD12 (w/w = 50/50).

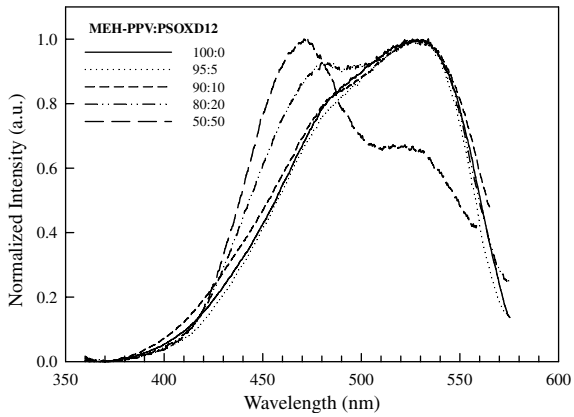

Fig. 5. PL excitation spectra (monitored at 580 nm) of neat MEH–PPV and its blend with PSOXD12 at different weight ratios.

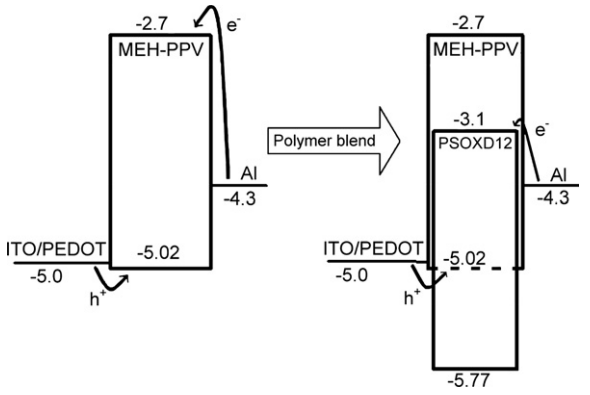

Fig. 6. Energy band diagram by blending of MEH–PPV and PSOXD12.

1,3,4-oxadiazole groups in PSOXD12 possess electron-transport and hole-blocking ability, which is helpful to balance the transport of opposite charge carriers and to reduce the consumption of hole in the cathode. Therefore, the origins of enhanced device efficiency are not only due to the dilution of MEH–PPV by PSOXD12, but also to enhanced electron-transport. Fig. 7 shows the plots of current density and luminance versus bias for EL devices using the MEH–PPV/PSOXD12 blends as emitting layer. With the increase of PSOXD12 content in the blend with MEH–PPV, the maximum luminance of the EL devices increases gradually. However, the turn-on voltage, which is defined as the voltage required for the luminance of 1 cd/m^2, shifts to higher voltage from 2.5 V (neat MEH–PPV) to 4.0 V (MEH–PPV/PSOXD12 blends). This is probably due to the hole-blocking property of aromatic 1,3,4-oxadiazole groups, leading to a need of additional bias to overcome this barrier [16,17]. The maximal current efficiency of the devices is enhanced smoothly from 1.45 cd/A to 4.79 cd/A as the weight ratio of PSOXD12 is increased from 0 to 50%. Fig. 8 shows the EL spectra of the device from MEH–PPV/PSOXD12 blend (80/20) measured at different bias. The EL spectra are almost the same under different operation voltage, revealing the stability of blend device.

In summary, as a result of both reduced inter-chain interaction and balanced charge transport, enhanced device performance has been achieved. Both luminance and current efficiency of the blend devices increases gradually with weight percent of PSOXD12. The maximal current efficiency (4.79 cd/A) and luminance (16261 cd/m^2) of the EL device using MEH–PPV/PSOXD12 blend (50/50) as emitting layer are much higher than those of neat MEH–PPV (1.45 cd/A, 5860 cd/m^2) [12], respectively.

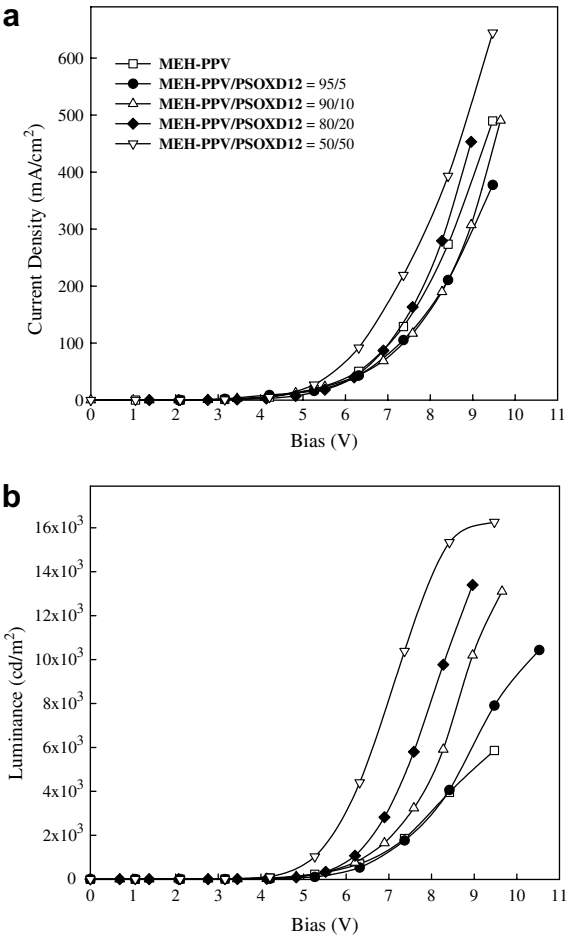

Fig. 7. Current density-bias (J–V) and luminance-bias (L–V) characteristics for the EL devices (ITO/PEDOT:PSS/MEH–PPV+PSOXD12/Al).

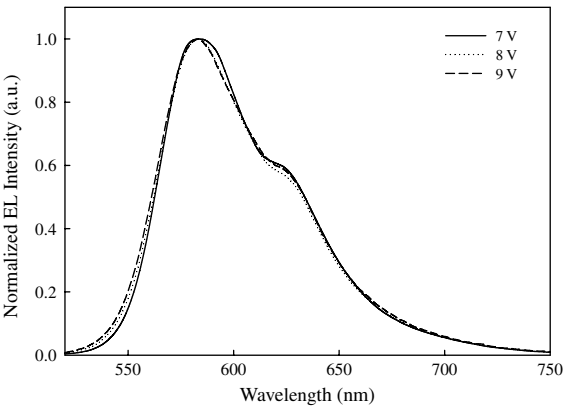

Fig. 8. EL spectra of the device from MEH–PPV/PSOXD12 blend (80/20) measured at different bias.

4. Conclusions

In summary, we developed a simple method to reduce inter-chain interaction and improve charge balance between hole and electron simultaneously by blending MEH–PPV with vinyl copolymer PSOXD12 containing pendant aromatic 1,3,4-oxadiazole. Both PL and EL emissions show sharper spectra and higher color purity than those of neat MEH–PPV, which has been attributed to reduced inter-chain interaction with increasing concentration of PSOXD12. The FWHM of PL and EL spectra are compressed considerably from 66 and 81 nm to 45 and 60 nm, respectively. PL excitation analysis also supports the depression of the inter-chain interaction (aggregation) with increasing content of PSOXD12. Besides, the addition of PSOXD12 also improves charge transport balance due to its high electron affinity. As a result of both reduced inter-chain interaction and balanced charge transport, improved device performance has been achieved.

Acknowledgement

This work was supported by National Science Council of Taiwan, Republic of China through the Project NSC 94-2216-E-006-002.

References

[1] C.W. Tang, S.A. VanSlyke, Appl. Phys. Lett. 51 (1987) 913.
[2] J.H. Burroughes, D.D.C. Bradley, A.R. Brown, R.N. Marks, K. Mackey, R.H. Friend, P.L. Burns, A.B. Holmes, Nature 347 (1990) 539.
[3] S.-H. Jin, M.-Y. Kim, J.Y. Kim, K. Lee, Y.-S. Gal, J. Am. Chem. Soc. 126 (2004) 2474.
[4] R. Traiphol, P. Sanguansat, T. Srikhirin, T. Kerdcharoen, T. Osotchan, Macromolecules 39 (2006) 1165.
[5] G. He, Y. Li, J. Liu, Y. Yang, Appl. Phys. Lett. 80 (2002) 4247.
[6] H. Meng, W.L. Yu, W. Huang, Macromolecules 32 (1999) 8841.
[7] N.C. Greenham, S.C. Moratti, D.D.C. Bradley, R.H. Friend, A.B. Holmes, Nature 365 (1993) 628.
[8] C. Adachi, T. Tsutsui, S. Saito, Appl. Phys. Lett. 55 (1989) 1489.
[9] Y. Cao, I.D. Parker, G. Yu, C. Zhang, A.J. Heeger, Nature 397 (1999) 414.
[10] S.-W. Hwang, Y. Chen, Macromolecules 35 (2002) 5438.
[11] B.R. Hsieh, Y. Yu, A.C. Vanlaeken, H. Lee, Macromolecules 30 (1997) 8094.
[12] K.-M. Yeh, Y. Chen, J. Polym. Sci.: Part A: Polym. Chem. 45 (2007) 2259.
[13] Y.J. Shi, J. Liu, Y. Yang, J. Appl. Phys. 87 (2000) 4254.
[14] Z. Yu, P.F. Barbara, J. Phys. Chem. B 108 (2004) 11321.
[15] Y. Zhang, J. Peng, Y. Mo, Y. Cao, Appl. Phys. Lett. 85 (2004) 5170.
[16] Y.-Z. Lee, X. Chen, S.-A. Chen, P.-K. Wei, W.-S. Fann, J. Am. Chem. Soc. 123 (2001) 2296.
[17] H.-J. Su, F.-I. Wu, Y.-H. Tseng, C.-F. Shu, Adv. Funct. Mater. 15 (2005) 1209.

Available online at www.sciencedirect.com
ScienceDirect
Organic Electronics 9 (2008) 51–62
Organic Electronics
www.elsevier.com/locate/orgel

Influence of plasma treatment of ITO surface on the growth and properties of hole transport layer and the device performance of OLEDs

Z.H. Huang [a,*], X.T. Zeng [a], X.Y. Sun [a], E.T. Kang [b], Jerry Y.H. Fuh [c], L. Lu [c]

[a] *Surface Technology Group, Singapore Institute of Manufacturing Technology, 71 Nanyang Drive, Singapore 638075, Singapore*
[b] *Department of Chemical and Biomolecular Engineering, National University of Singapore, 10 Kent Ridge Crescent, Singapore 119260, Singapore*
[c] *Department of Mechanical Engineering, National University of Singapore, 10 Kent Ridge Crescent, Singapore 119260, Singapore*

Received 3 May 2007; received in revised form 3 July 2007; accepted 15 August 2007
Available online 26 August 2007

Abstract

Surface energy of indium tin oxide (ITO) surfaces treated by different plasmas, including argon (Ar–P), hydrogen (H_2–P), carbon tetrafluoride (CF_4–P), and oxygen (O_2–P), was measured and analyzed. The initial growth mode of hole transport layers (HTLs) was investigated by atomic force microscope observation of thermally deposited 2 nm thick *N*,*N*′-bis(1-naphthyl)-*N*,*N*′-diphenyl-1,1′-biphenyl-4,4′-diamine (NPB) on the plasma treated ITO surfaces. The results show that different plasma treatments of ITO influence the growth of HTLs in significantly different ways through the modification of surface energy, especially the polar component. The O_2–P and CF_4–P were found to be most effective in enhancing surface polarity through decontamination and increased dipoles, leading to more uniform and denser nucleation of NPB on the treated ITO surfaces. It was further found that increased density of nucleation sites resulted in a decreased driving voltage of OLEDs. Under the same fabricating conditions, a lowest driving voltage of 4.1 V was measured at a luminance of 200 cd/m^2 for the samples treated in CF_4–P, followed by the samples treated in O_2–P (5.6 V), Ar–P (6.4 V), as-clean (7.0 V) and H_2–P (7.2 V) plasma, respectively. The mechanisms behind the improved performance were proposed and discussed.

PACS: 81.65.-b; 68.37.Ps; 68.35.Md; 64.60.qj; 85.60.Jb

Keywords: Plasma; Indium tin oxide; Morphology; OLEDs; Surface treatment; Surface energy

1. Introduction

Indium tin oxide (ITO) is commonly used as an anode in organic light emitting diodes (OLEDs) due to its high conductivity, transparency in visible wavelength range, wide energy band gap and relatively high work function. OLED devices with

* Corresponding author.
E-mail address: zhhuang@SIMTech.a-star.edu.sg (Z.H. Huang).

1566-1199/$ - see front matter © 2007 Elsevier B.V. All rights reserved.
doi:10.1016/j.orgel.2007.08.002

as-deposited ITO, however, were found to have many problems, such as shorting, unstable I–V characteristics and indium penetration into organic layers after device operation, causing degradation in device performance [1]. To mitigate these problems, various surface treatment processes using UV ozone [2,3], gas plasma [4–6], acids [7,8], hydrogen peroxide [9], and electrochemistry [10] have been adopted to modify the ITO surface properties such as work function, surface roughness, surface energy, carrier concentration and mobility, and surface sheet resistance. Among these methods, the oxidative treatments (e.g., oxygen plasma and UV ozone) were found to be most effective in improving OLED device performance in terms of driving voltage, luminance efficiency, and stability [4,8,11,12]. The work function hypothesis is often used to explain the mechanism behind, in particular to explain the reduced device driving voltage [13–17].

Besides the work function, other surface properties were also found to play an important role in influencing the device performance [5,18,19]. It was reported that the increased surface energy would provide a better adhesion of the polymer layer and reduce the interfacial tension between polymer and substrate [6]. This would lead to an improved charge carrier injection through the interface, and thereby the OLED performance due to the better electronic contact between the two materials. Other experimental results [10,20] showed that the devices fabricated on ITO substrates with similar work functions but different surface morphologies (e.g., roughness) exhibited markedly different performance. Chen et al. recently reported their experimental results using different hole injection layers (HILs) with different levels of high occupied molecular orbital (HOMO), and concluded that the energy barrier difference between the ITO/HIL interface was not the main factor in determining the hole injection efficiency from the ITO anode to HIL [21]. Instead, they proposed that the morphology of HIL and therefore the contact of HIL/HTL would play a decisive role in the device performance.

Another point to note is that the increased work function due to plasma treatment decays over time and returns to its original value within hours [22–24]. The ultimate cause of this erratic increase of work function is yet to be understood. Possible explanations include the diffusion of high concentration oxygen on ITO surface into the ITO bulk [25] and/or adsorption of ambient carbon during handling [26,27]. It is reasonable to deduce that if the increase of ITO work function induced by oxygen plasma treatment is the governing factor, the improvements of OLED performance would be diminished correspondingly with the decay of ITO work function. However, there has been no such report on device instability attributed to the oxygen plasma treatment. In other words, no close correlation has been found between the work function and the device stability [11,28].

Therefore, more experimental work is needed to understand the mechanisms behind the improved device performance by surface treatments. This work was aimed to study the effects of gas plasma treatment on ITO surface and the correlated dependence of device performance. Four different types of plasmas, namely, hydrogen (H_2–P), argon (Ar–P), oxygen (O_2–P), and carbon tetrafluoride (CF_4–P) were used in this work. Ultra thin HTLs of N,N'-bis(1-naphthyl)-N,N'-diphenyl-1,1′-biphenyl-4,4′-diamine (NPB) were deposited on the ITO samples plasma treated, respectively. The surface polarity of ITO, morphology of NPB, and the performance of OLEDs made thereof were characterized. The results showed that ITO surface polarity controls the nucleation and the initial growth of HTL. The morphology of initially formed HTL on ITO surface is closely influenced by the gas plasma used via the change of surface energy, especially the polar component. The samples with highly uniform HTLs on ITO surfaces treated by O_2–P and CF_4–P were observed to have the best improvements in OLED performance. The results suggest that the performance enhancement is the consequence of the high quality interface between ITO surface and HTL.

2. Experiment

The ITO-coated glass (Präzisions Glas and Optik GmbH) with an initial sheet resistance of 10 Ω/□ was used as the substrate for surface characterizations and also for device fabrication. After a routine cleaning process, involving a sequence of sonication in detergent solution, ethanol and de-ionized (DI) water, the ITO glass samples were transferred into a parallel plate type plasma system (MARCH PX-1000) for plasma treatment at room temperature using Ar, H_2, CF_4, and O_2, respectively. In the plasma chamber, two electrode plates were fixed with a distance of 10 mm, and the samples were placed on the bottom plate. The plasma treatment was carried out for 3 min at an rf (13.56 MHz) power of 600 W, where process pressure was main-

tained at 30 Pa. The control ITO sample without plasma treatment is referred to as-clean sample. Surface energy values of treated and untreated ITO surfaces, as a sum of dispersion and polar components [29], were calculated using the geometric-mean method [30] from contact angles measured with water and glycerol. The contact angle is the angle formed between a liquid droplet and a flat surface when the liquid droplet is at rest and in thermal equilibrium with the surface. A pipette was used to deliver a constant volume of about 0.045 cm^3 of pre-filtered distilled water and glycerol on the ITO surface. A traveling microscope with a miniature protractor eyepiece was used to determine the contact angle. All contact angle measurements were performed at 20 °C under 60% relative humidity. Five samples for each treatment were prepared for the contact angle measurements and the average values from the five samples were used for calculation of the surface energy. In order to understand the influence of ITO surface modifications by gas plasmas on nucleation and initial growth of HTL thin films, ultra thin NPB was deposited onto ITO substrates pre-treated with different gas plasmas. Two nanometers thick NPB ultra thin films was deposited on both treated and untreated ITO surfaces by thermal evaporation under the same conditions as described below. The surface morphology of the ultra thin NPB films on ITO surfaces has been studied using a Digital Instruments Nanoscope IIIA AFM. The images for the morphological studies had a scan size of $2 \times 2\ \mu m^2$. Non-contact AFM with tapping mode was used as the contact mode is not appropriate due to its constant force applied which is sufficient to physically distort the organic films. All AFM results are shown in phase mode to provide a clearer picture of the organic film morphology. The OLED panels with a structural configuration of ITO/NPB/Alq_3/LiF/Al [Alq_3 = tris(8-hydroxyquinolato) aluminum] were subsequently deposited by the conventional thermal evaporation technique. The process starts with the evaporation of a 60 nm thick NPB as the hole transport layer, followed by a 60 nm thick Alq_3 as the electron transport and light emissive layer, at a deposition rate of 0.2 nm/s. After the deposition of organic layers, a 0.6 nm thick LiF electron injection layer and a 150 nm thick Al layer were deposited immediately as the cathode at rates of 0.03 and 0.3 nm/s, respectively. The Al cathodes were deposited through a shadow mask to form devices with active area of 0.09 cm^2. The film thickness was monitored by a quartz thickness monitor. To ensure the valid comparison of the experimental results, all the functional layers were deposited successively on the differently treated samples at a pressure of 1×10^{-4} Pa during one vacuum run. Basic characterization of the OLED devices involved measuring the device light output and current as a function of the applied voltage (*L–I–V*). The voltage was supplied by a computer driven Keithley 2400 source using a linear staircase of 0.2 V with a 0.2 s delay between measurements, and the current was measured by a Keithley 2000 multimeter. The luminous output from the light emission area of 0.09 cm^2 was collected with a calibrated silicon photodiode. In addition, the power efficiency (lm/W) and EL efficiency (cd/A) were calculated using the same system. All the *L–I–V* characteristics were carried out in a dark box and ambient atmosphere at room temperature.

3. Results and discussion

3.1. Influence on ITO surface energy

Table 1 summarizes the surface energies of ITO samples treated with different plasmas in terms of polar and dispersion components, total surface energy, and polarity that is defined as the ratio of the polar component to total surface energy [6]. The results show that, the total surface energy of ITO was remarkably increased by Ar–P, O_2–P and CF_4–P treatments in the order of CF_4–P > O_2–P > Ar–P and slightly reduced by H_2–P treatment, compared to the as-clean ITO sample. It should be noted that the Ar–P, O_2–P and CF_4–P increase polar component, in the order of CF_4–P > O_2–P > Ar–P, but decrease dispersion component. On the contrary, H_2–P renders the highest dispersion

Table 1
Surface energies and polarities for different plasma treatments of the ITOs

Sample	Contact angle (°)		γ_s^p (mJ/m^2)	γ_s^d (mJ/m^2)	$\gamma_s = \gamma_{s_2}^p + \gamma_s^d$ (mJ/m^2)	$\chi_p = \gamma_s^p/\gamma_s$
	Water	Glycerol				
As-clean	40.7	34.3	36.6	19.8	56.4	0.65
H_2–P	42.6	34.8	34.1	21.2	55.3	0.62
Ar–P	23.0	21.3	50.2	17.1	67.3	0.75
O_2–P	7.9	21.8	62.4	11.8	74.2	0.84
CF_4–P	11.9	27.3	65.1	9.5	74.6	0.87

The total surface energy γ_s is the sum of the polar (γ_s^p) and dispersion (γ_s^d) components ($\gamma_s = \gamma_s^p + \gamma_s^d$) and the polarity χ_p is the ratio of the polar component to the total surface energy ($\chi_p = \gamma_s^p/\gamma_s$) [6].

component and the lowest polar component in total surface energy. CF_4–P yields the maximum polarity of 0.87 and hydrogen plasma, on the opposite, the minimum polarity of 0.62, compared to 0.65 of the as-clean ITO.

Our results show that plasma treatments change ITO surface energy mainly through its polar component. It is interesting to understand how the plasma treatment changes the surface polarity. It is generally accepted that there are two origins of the polar component in surface energy, the surface dipole and the hydrogen bonding. The former is the predominating factor in influencing work function [31]. As-clean ITO surface is suspected to have various chemical species [24,32], such as M, M–O–M, M–OH, as well as CH_x, where M denotes metallic atoms (i.e., In and Sn in this study) and CH_x the organic contaminants. These species form various dipoles and have different concentrations on ITO surface, which collectively contribute to the polar component in surface energy. M–O–M bond is more hydrophobic [33] than its corresponding metallic bond due to its symmetric structure and thus low polarity.

In contrast, the dangling bond of M–O is extremely polar, but their concentration may be negligible because of its high reactivity. Experimental studies showed that M–O–M has tendency to be incompletely hydrolyzed [34–36]. Therefore, OH groups on ITO surface are considerable, which have been estimated in the order of one OH group per 1 nm^2 of ITO surface [37]. The polarity of M–OH bond is believed to be in the same order of M, which is supported by the fact that work function of ITO is independent of dehydroxylation and rehydroxylation [31]. Besides dipoles, hydrogen bonds have considerable contribution to the ITO surface energy [38] due to the existence of M–O–M and M–OH species as well as the usage of probe solvents (e.g., water and glycerol) during measurement of contact angle. In addition, contamination of ITO surface must be considered, which might also influence the ITO surface energy [6,13,23]. The organic contaminants are insulating and have lower polarity due to their more covalent bond features. A fractional coverage of ITO surface with such hydrocarbon contaminants will decrease surface energy through reducing the exposure of M–O–M and M–OH species, and therefore the dipoles and hydrogen bonds.

For Ar plasma treatment, there should be no chemical reaction due to the inert property of Ar. However, the Ar ion bombardment has been proved to be capable of removing hydrocarbon contaminants from ITO surface [4], and makes more polar species exposed. Although Ar plasma also remove OH group (i.e., dehydroxylation), the treated sample is easily rehydrolyzed in presence of water [31], leading to zero net change in OH group once exposed to humid air. Therefore, the increase in polarity after Ar plasma can be attributed to the decontamination effect instead of dehydroxylation and rehydroxylation. An increase of 13.6 mJ/m^2 or ~37.2%, in polar component after Ar plasma, as shown in Table 1, indicates that the as-clean ITO surface used in this study is heavily contaminated. Once the majority of the contaminants are removed by Ar plasma, the real ITO surface is exposed with surface energy of about 50.2 mJ/m^2 in polar component. Thus the decontamination by Ar plasma is effective to promote hole injection, which agrees with the results from other research groups [4,39,40], although it does not change work function [4,5,10,38]. Theoretically, the value of ITO work function should be enhanced with a contamination layer due to its insulating property, and therefore, the decontamination by Ar plasma seems to lower the work function. However, more fresh surface areas with more dipoles are exposed after removing the contaminants, and therefore the positive effect on work function can offset the loss due to the decontamination. This may explain why Ar plasma increases ITO surface polarity instead of work function. It should be pointed out that other factors might be also considered to elucidate the contrary results. For instance, the contamination layer may not be uniform or continuous over ITO surface. On the other hand, the measurement scales of UPS and/or Kelvin probe, which are usually used for determination of work function, are much smaller than that of surface energy via contact angle.

When reductive H_2 plasma is applied, the hydrogen ion bombardment may cause some clusters of hydrocarbon contaminants to spread over the ITO surface, leading to more surface areas contaminated and therefore more hydrophobic ITO surface. Furthermore, physical adsorption of a hydrogen atom onto M–O–M surface may result in a negative dipole as well. As shown in Table 1, however, minor change of the surface polarity after H_2 plasma (lowered by only 0.3) implies that a fraction of M–O–M or M–OH may be reduced into M with higher surface energy that partially compensate the negative effect of the plasma treatment on polarity. This is supported by the fact that dispersion component is

raised after H_2 plasma, by about 1.4 mJ/m^2. Because London dispersion force increases with the size of surface atoms in question, more concentration of larger metals such as In and Sn firmly results in higher dispersion component in surface energy and lower work function due to the relative deficiency of oxygen atoms. Significant drop of ITO work function by H_2 plasma has been reported by several research groups [8,12,41].

In contrast, hydrocarbon contaminants on ITO surface will be effectively removed by O_2–P [40], which contribute to the high surface polarity for the same reason as Ar plasma. More importantly, O_2 plasma converts the M–OH or M-OOH into M–O$^{\cdot}$ through –OH group oxidation chemistry [31]. Because M–O$^{\cdot}$ can be stabilized by "resonance" delocalization of unpaired spin density among lattice oxygen, it would be expected to be stable even in presence of water. By virtue of the electron deficiency of the oxygen-based radical, this oxidation increases the ITO surface dipole layer, leading to higher polarity. Other hypotheses have also been proposed to elucidate the increase in polarity by O_2–P, such as adsorption of oxygen anions [13,38] and water absorption. However, hydroxylation or dehydroxylation has been proved not to be a primary factor in determining the work function of ITO, which is highly related to surface dipole [31]. Therefore, O_2–P increases surface polarity possibly through removing contaminants and producing highly polar and stable M–O$^{\cdot}$ species. Of course, hydrogen bonding is also a considerable factor.

Compared to the instance of O_2–P, CF_4–P is a more oxidative treatment and can definitely remove hydrocarbon contaminants from ITO surface. Furthermore, the released fluorine atoms or ions during CF_4–P treatment possibly produce M–F bond [39,42], through oxidation of –OH groups or direct substitution for O in M–O–M bond. The higher negativity of F and asymmetric structure of M–F bond provide ITO surface with more positive dipole and stronger hydrogen bonding than M–O$^{\cdot}$, which might be the reason for the highest surface polarity of 0.87, as shown in Table 1. Moreover, as M–F is not hydrolysable, CF_4–P treated ITO surface should be more stable than that of O_2–P.

To further understand the influencing factors on surface polarity, Si wafer samples with 2 nm native oxide were also treated by the same plasmas as described above and the surface energies are listed in Table 2. It is surprisingly found that unlike ITO, minor changes in surface polarity of SiO_2 were observed after various plasma treatments. As Si has the similar negativity with In and Sn, i.e., 1.8 for Si vs. 1.7 for In and 1.8 for Sn, minor difference in permanent dipole should exist between Si–O–Si and In–O–In or Sn–O–Sn. The higher phenomenal effects of ITO surface to plasma treatment suggest that other factors also contribute to the formation of dipole layer and/or the surface polarity. Besides their crystal structures, the most considerable difference between SiO_2 and ITO is that SiO_2 is an insulator but ITO a conductor with considerable free electrons. The delocalized electrons in ITO take an important role in stabilizing M–O$^{\cdot}$ species. As a result, the highly polar species may not exist on SiO_2 surface due to its deficiency of free electrons. In addition, polycrystalline ITO contains more defects than single crystal Si wafer, which may also influence the responsive behavior of ITO to plasma treatment.

Table 2
Surface energies and polarities of the Si with 2 nm native oxide and the ITOs after different plasma treatments

Silicon sample	γ_s^p (mJ/m^2)	γ_s^d (mJ/m^2)	$\gamma_s = \gamma_s^p + \gamma_s^d$ (mJ/m^2)	$\chi_p = \gamma_s^p/\gamma_s$ (mJ/m^2)
S1-as-clean	50.2	17.1	67.3	0.75
S2-Ar plasma	54.0	18.1	72.1	0.75
S3-H_2 plasma	53.3	14.5	67.8	0.79
S4-O_2 plasma	55.9	17.0	72.9	0.77
S5-CF_4 plasma	42.8	12.1	54.9	0.78

The total surface energy γ_s is the sum of the polar (γ_s^p) and dispersion (γ_s^d) components ($\gamma_s = \gamma_s^p + \gamma_s^d$) and the polarity χ_p is the ratio of the polar component to the total surface energy ($\chi_p = \gamma_s^p/\gamma_s$) [6].

In addition to the significant modification of the polar component in ITO surface energy, plasma treatment also alters dispersion component but in a reversed trend, which has not been discussed in previous literature. London dispersion force is proportional to the polarizability of surface molecules or atoms, and the larger the atom, the greater the polarizability. With H_2–P treatment the ITO surface exposes more metallic atoms (In and/or Sn) with greater polarizability, leading to strong dispersion force. In contrast, CF_4–P treatment offers ITO surface rich of fluorine with small polarizability, leading to weak dispersion force. In evidence, changes in dispersion component of surface energy suggest that the composition of ITO surface may be altered after plasma treatments.

As well-known, plasma treatments change not only surface energy but also ITO work function

based on dipole theory [6,13,14]. However, no direct correlation between the surface energy and the work function has been found for ITO surface and the dominant factor controlling the hole injection is still under dispute. For instance, Ar plasma increases ITO surface polarity and hole injection, as shown in this study, but does not change work function as documented in literature. Moreover, oxidative plasma treatments of ITO improve the devices stability, which could not be explained by the work function hypothesis. These suggest that the hole injection seems to be more closely correlated with the ITO surface polarity that, as well-known, controls the evolution of HTL film.

3.2. Influence on nucleation and growth of NPB films

As-deposited ITO film by DC magnetron sputtering features with a so called "grain–subgrain" surface morphology and polycrystalline structure, as shown in Fig. 1a (height mode) or b (phase mode). Each "grain" (200–600 nm in size) consists of a cluster of 10–40 nm sized subgrains, which are highly aligned in crystalline orientation. More discussions on their crystallinity features are reported in Ref. [43].

Our results from AFM observation and analysis show that plasma treatments do not significantly change the ITO morphologies, being the same as the previous report [44], with the rms surface roughness value kept in the range of 3–4 nm. As the phase mode AFM offers a clearer image of the material phases with less topographic information, as seen in Fig. 1, the phase mode was used in this work to study the NPB nucleation and growth on ITO surface.

Fig. 2 shows the phase AFM images of 2 nm NPB thin film deposited on as-clean ITO surface (a), and pre-treated ITO surfaces by Ar–P (b), H_2–P(c), CF_4–P(d), and O_2–P(e). It can be seen that the surface coverage with 2 nm thick NPB highly depends on the type of plasma treatment. The CF_4–P treated sample has the highest coverage, followed by the O_2–P, Ar–P, as-clean, and H_2–P treated samples. For the as-clean, Ar–P and H_2–P treated ITO surfaces, island-like morphology is observed, although there is slight difference in shape and distribution. Basically, the islands discontinuously distribute along grain boundaries, but the wetting features of NPB on the three substrates are clearly different, with wettability in an order of Ar–P > as-clean > H_2–P. On the contrary, CF_4–P and O_2–P treatments of ITO led to more uniform NPB thin film coverage without conglomeration, and the NPB film seems to grow in two-dimensional mode. In this case, NPB film covers not only the grain boundaries but also the subgrain boundaries, although subgrains are not fully covered. It is observed that the CF_4–P treatment led to a more subgrain coverage by NPB film compared with O_2–P treatment. Considering the fact that deposition rate and substrate temperature strongly influence the surface morphology of organic films [45,46], the NPB of a given thickness was deposited onto the ITO samples in discussion in the same

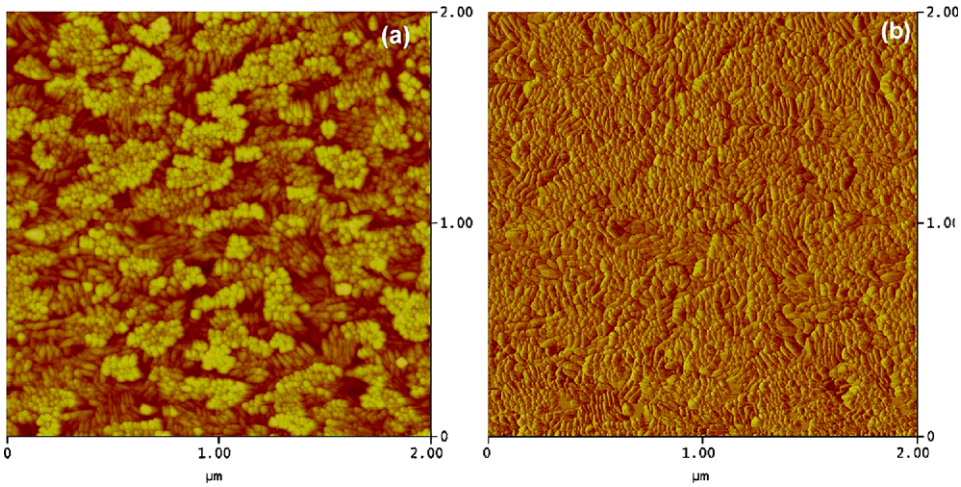

Fig. 1. AFM image of as-clean ITO thin film deposited by dc magnetron sputtering: (a) height mode and (b) phase mode.

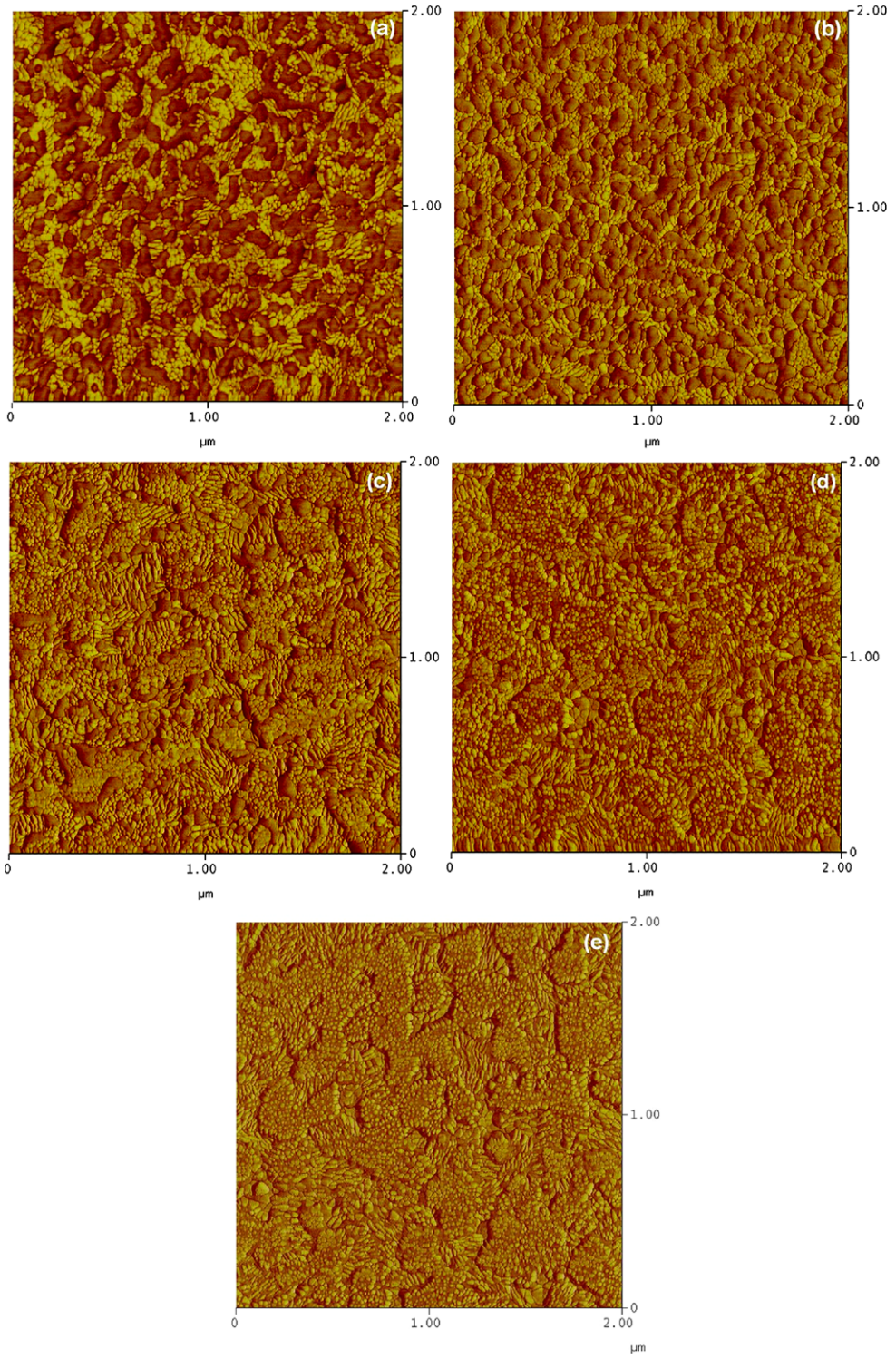

Fig. 2. AFM images (phase) of 2 nm thick NPB on ITO surfaces with different plasma treatments: (a) as-clean; (b) Ar–P; (c) H_2–P; (d) CF_4–P; and (e) O_2–P.

batch and thus the morphological difference should be caused mainly by the different plasma treatments.

Much of the surface structure observed in thin films grown from the vapor phase may be attributed

to the surface energy of substrate and film, as well as the interfacial energy. In general, the higher surface energy of substrate is beneficial to a smooth growth of the film (i.e., layer growth mode) and a strong bonding of the film to substrate, whereas island growth mode is corresponding to a relatively low surface energy of the substrate. In most thin film deposition processes, nucleation of the product phase occurs heterogeneously at some preferential sites on the substrate, such as grain boundaries [47], subgrain boundaries [48], dislocations [49], or other surface defects [50–52], where the surface energy is remarkably higher than the rest of the surface. When the substrate is not uniform in surface energy, the adsorbed molecules or particles are locked or irreversibly trapped on to the surface defects and grow into stable nuclei [51,53], because the energy barrier for nucleation is significantly lower at high surface energy areas. On the other hand, the arrived species on the lower surface energy sites tend to migrate towards active sites and finally add onto the stable nuclei. In this case, the bonding energy between two deposited atoms is greater than the average bonding energy between one deposited atom and substrate atom [54], resulting in thin film growth in island mode [55,56]. As a result, the coverage of lower energy areas will mainly rely on the lateral growth or spreading of islands instead of dense nucleation. This is the case when 2 nm NPB deposited onto the as-clean and Ar–P and H_2–P treated ITO surface, as shown in Fig. 2a–c.

As DC sputtered polycrystalline ITO is characterized with a nano-scaled grain–subgrain structure, from micro-point of view, surface energy over ITO surface should be accordingly varied from place to place. Therefore, NPB film normally grows on ITO surface in island growth mode, as previously reported [41]. In addition, contamination also has influence on size, shape, density, distribution, and wetting condition of the NPB islands. For instance, Ar plasma treatment provides more nucleation sites and better wetting condition due to its decontamination effect. It should be noted that although the NPB coverage is increased up to 50%, the effect of Ar plasma treatment on promoting nucleation sites seems not to be as significant as expected. This suggests that except for decontamination and/or surface refreshment, Ar plasma does not significantly change the ITO surface conditions in terms of energy states and chemical composition. It is believed that Ar plasma treatment of ITO can promote NPB nucleation, but the effect is limited. In contrast, H_2 plasma results in reduced nucleation sites, poor wetting of NPB film, and thus lower coverage (~20%), which might be caused by the lower polarity induced by the reductive treatment.

The O_2 and CF_4 plasma treatments, on the contrary, significantly increased the ITO surface polarity due to the effective removal of contaminants and the formation of M–O· and M–F species and therefore high density of dipoles. As the oxidative reactions are not selective but uniform over ITO surface, the strong dipoles overwhelm the effect of original defects along the grain and subgrain boundaries, leading to less fluctuation in surface energy and fewer preferential nucleation sites over ITO substrate. In other words, surface defects such as grain boundaries are no longer preferential for NPB nucleation. On the other hand, the high surface polarity increases the diffusion energy barrier of the arrived NPB molecules and decreases the interfacial energy between ITO and NPB, which makes the arrived molecules "frozen" or "locked" onto ITO surface. As a result, the strong adherence of the nuclei to high energy surface creates high density of nucleation sites or small islands, as shown in Fig. 2d and e. The islands coalesce and become a continuous layer at the thinner nominal film thickness [57], leading to film growth like in two-dimensional mode [55].

3.3. Influence on device performance

Fig. 3a and b shows, respectively, the current–voltage (I–V) and luminance–voltage (L–V) characteristics of the devices with ITO substrates pre-treated by different plasmas. In comparison with the control sample (as-clean), both the I–V and L–V curves shift to the lower voltage region for the devices with ITO pre-treated by Ar–P, O_2–P and CF_4–P, but to the higher voltage region for the device with H_2-plasma treated ITO. For instance, the operating voltages at luminance of 200 cd/m^2 are 4.1, 5.6, 6.4, 7.0, and 7.2 V for the samples of CF_4–P, O_2–P, Ar–P, as-clean, and H_2–P, respectively.

Fig. 4a shows the current efficiency vs. current density of the devices. Compared with the control sample (as-clean), current efficiency is in principle unchanged for Ar–P and H_2–P treatments, but lowered by O_2–P and CF_4–P treatments. For instance, at a given current density of ~30 mA/cm^2, current efficiencies of devices with as-clean, Ar–P, H_2–P, O_2–P, and CF_4–P treated ITO substrates are 2.88,

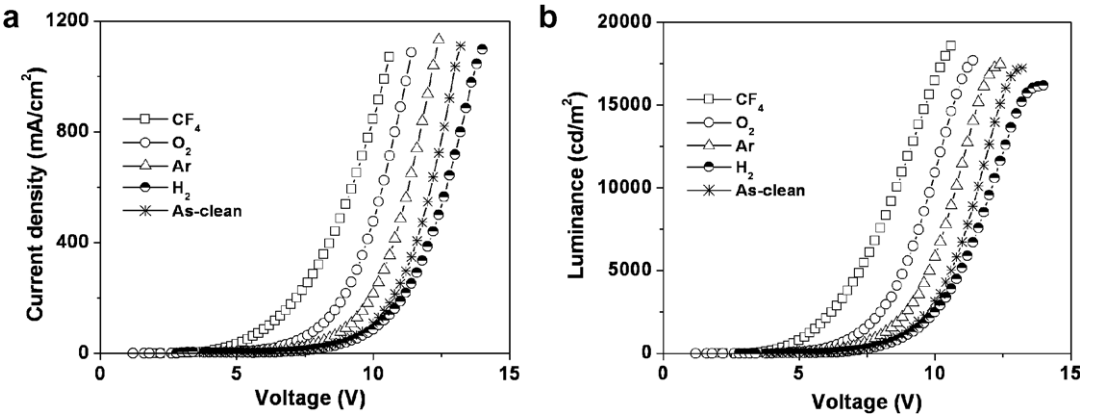

Fig. 3. *I–V* (a) and *L–V* (b) characteristics of the devices made with ITO treated by different plasmas.

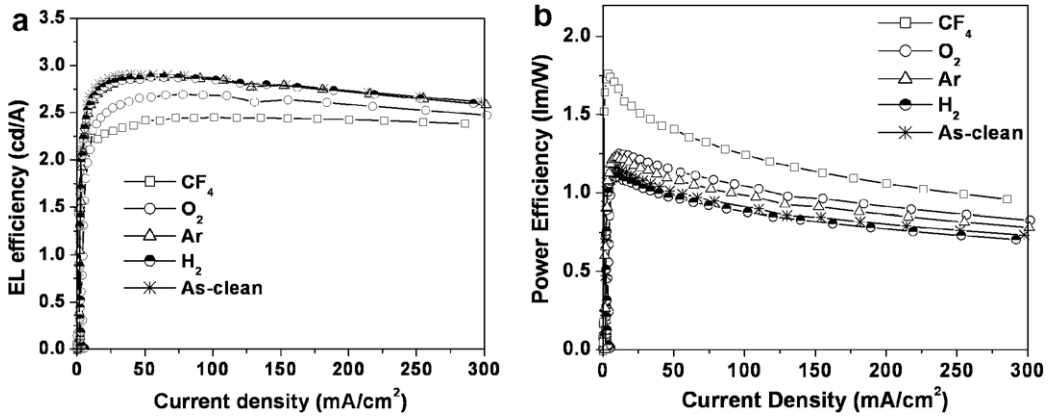

Fig. 4. Current efficiency (a) and power efficiency (b) vs. current density curves of devices made with ITO electrochemically treated at different voltages.

2.84, 2.80, 2.55 and 2.34 cd/A, respectively. It is interesting to note that these results do not agree with the earlier reported results in Ref. [5], where EL efficiency is raised by O_2–P and lowered by H_2–P [5].

In contrast to current efficiency, the power efficiency shows totally different influence, as shown in Fig. 4b, where the device with CF_4–P treatment is prominent over the measurable current density range. At about 11 mA/cm^2, maximum power efficiencies are obtained for the devices with as-clean, Ar–P, H_2–P, and O_2–P treated ITO substrates in an order of O_2–P (1.25 lm/W) > Ar–P (1.22 lm/w) > as-clean (1.14 lm/W) > H_2–P (1.09 lm/W). However, the corresponding power efficiency for device with CF_4–P treatment is up to 1.67 lm/W which is ~34% higher than that of O_2–P, although the value is not the maximum point of power efficiency.

As the cathode for electron injection was the same in all the devices and the samples were fabricated in the same batch, the marked changes in *I–V* and *L–V* characteristics, current efficiency and power efficiency suggest that the device performance was highly sensitive to the plasma pre-treatments. In other words, hole injection across ITO/NPB interface, which has been modified by the plasma treatments, dominates the device performance. In the present study, *I–V* curve shift can be viewed as a direct indicator of the change of hole injection efficiency. The results in Fig. 3b suggest that O_2 and CF_4–P treatments promotes the hole injection from ITO to HTL, while H_2–P treatment depressed the hole injection efficiency, which is consistent with the previous findings that reducing treatments increase the required drive voltage whereas oxidative treatments decrease it. As for

Ar–P, our results show that the treatment is moderately helpful to enhance the hole injection, which is similar to the results reported by Wu et al. [4], although there were other reports showing the negligible or even negative effect [5,6].

The influence of plasma treatments on electroluminescence efficiency is more complex, as the efficiency depends on not only the hole injection from anode but also the electron injection from cathode. As well-known, besides the intrinsic quantum efficiency of the light emitting materials, charge injection balancing exhibits a remarkable impact on the external quantum efficiency. For an electron injection limited device, excess hole injection will contribute to the device current but not the electron–hole recombination, leading to a lower current efficiency. It is known from the results shown in Fig. 4a that the devices in this study are electron injection limited. The considerable decrease of the operating voltage by the O_2–P and CF_4–P treatments of ITO indicates a remarkable improvement of hole injection, as shown in Fig. 3. Therefore, the excess hole injection should be responsible to the lower current efficiencies due to the unbalanced charge injection and/or the recombination zone shift closer to the Al cathode [58]. For a hole injection limited device, the influence of plasma treatments on efficiency may be concluded differently, where the treatments raising hole injection should enhance the current efficiency of OLED devices. This may explain the controversial reports in literatures on the dependence of efficiency upon the same surface treatment.

Power efficiency is another important performance indicator of OLED devices. It is clear that with the same luminance, power efficiency depends on not only the current density but also the driving voltage. Lowered driving voltage can significantly raise power efficiency, which causes the difference between current and power efficiencies in this study. For instance, compared with the control sample, the operating voltage (at 200 cd/m^2) after CF_4–P treatment is reduced by about 2.9 V. The considerable drop of driving voltage overwhelms the negative effect from the excess hole injection, leading to significant increase of power efficiency from 1.14 to 1.67 lm/W, or ~46%.

3.4. Discussion on hole injection efficiency

The performance of OLEDs is strongly influenced by the properties of the interface between the organic layers and electrodes [59]. A good electrical contact between the two materials is expected to enhance the charge carrier injection through the interface [6,33,38]. It is believed that a good contact is formed at the nucleation sites of NPB on ITO, compared with the neighboring areas, in terms of mechanical, electrical and electronic properties. At such good contact spots (or active spot), the charge (hole) injection barrier would be lower, giving rise to a lower resistance to current flow. If this phenomenological model stands logical, then the density of nucleation sites (thus the density of active hole injection spots) would significantly influence the hole transportation properties at the interface, which will determine the device performance specifications such as driving voltage, current efficiency and device reliability. A higher density of active spots would result in a lower driving voltage, or vice versa. It should be pointed that the actual situation is much more complicated, as the electrical properties of the active spots vary cross the surface due to the surface inhomogeneity. The charge carriers may also be injected at other areas around the said active spots. However, the voltage required to activate such hole injection would be higher due to the higher interface barrier caused by poorer electrical contact.

This may explain the results shown in Figs. 3 and 4 based on the observations of NPB nucleation on different ITO substrates as discussed in section 3.2. For as-clean and H_2 plasma treated ITO surfaces, the preferential nucleation sites are mainly located on the grain boundaries, leading to lower density of active spots for carriers passing through at a given voltage. Furthermore, the grain boundaries are intrinsically amorphous in structure which has higher barrier for charge injection [60]. As the nucleation sites of NPB film on as-clean, H_2, as well as Ar plasma treated ITO surfaces are mainly located on grain boundaries, the effectiveness of the active spots along the grain boundaries on hole injection would be discounted. The shadow effect existing in evaporation deposition may be also a concern in generating additional defects such as voids or weak interface, particularly when the film growth is in strong island growth mode as shown in Fig. 2a–c, which will reduce the effective contact area [61] between ITO and NPB leading to a low hole injection efficiency. It is speculated that hole injection and thus current flow will highly localized on the good contact areas or active spots, which may cause problem in device reliability, such as dark spots, particularly when operated at high driving voltage.

In contrast, O_2–P and CF_4–P significantly "passivate" the ITO surface through removing the active sites [44] on the grain boundaries. In other words, the high surface polarities obtained by O_2–P and CF_4–P can effectively suppress the preference of grain boundaries for nucleation. As a result, denser and more uniform nucleation sites exist across the ITO surface, leading to more active spots for hole injection at lower driving voltage. Furthermore, the plasma treatment induced better wetting surface, as shown in Fig. 2d and e, can effectively suppress the formation of voids and therefore increase the actual contact areas. The increased good contact areas or active spots will effectively mitigate the current localization, leading to improved reliability.

4. Conclusions

Surface energy study of ITO as OLED electrode demonstrated that different plasma treatments influence the polarity of ITO surface in a remarkably different way, which controls the nucleation and initial growth of NPB and, as a result, determine the device performance of OLED. The polarity value is 0.87, 0.84, 0.75, 0.65, and 0.62 for CF_4–P, O_2–P, Ar–P, as-clean, and H_2–P, respectively. The AFM studies of the surface morphology of ultrathin NPB films demonstrate that the higher the ITO surface polarity, the larger the NPB film coverage. Under the same fabricating conditions, a lowest driving voltage of 4.1 V was measured at a luminance of 200 cd/m^2 for the samples treated in CF_4–P, followed by the samples treated in O_2–P (5.6 V), Ar (6.4 V), as-clean (7.0 V) and H_2–P(7.2 V), respectively. This suggests that there should be high correlations between the ITO surface polarity after plasma treatment, the NPB nucleation, and the OLED performances.

Acknowledgement

Authors thank Ms. Liu Yuchan for assistance in experiment.

References

[1] S.T. Lee, Z.Q. Gao, L.S. Hung, Appl. Phys. Lett. 75 (1999) 1404.
[2] S.A. Van Slyke, C.H. Chen, C.W. Tang, Appl. Phys. Lett. 69 (1996) 2160.
[3] L.S. Hung, C.W. Tang, M.G. Mason, Appl. Phys. Lett. 70 (1997) 152.
[4] C.C. Wu, C.I. Wu, J.C. Sturm, A. Kahn, Appl. Phys. Lett. 70 (1997) 1348.
[5] K. Furukawa, Y. Terasaka, H. Ueda, M. Mtsumura, Synth. Met. 91 (1997) 99.
[6] J.S. Kim, R.H. Friend, F. Cacialli, J. Appl. Phys. 86 (1999) 2774.
[7] F. Nüesch, E.W. Forsythe, Q.T. Le, Y. Gao, L.J. Rothberg, J. Appl. Phys. 87 (2000) 7973.
[8] F. Li, H. Tang, J. Shinar, O. Resto, S.Z. Weisz, Appl. Phys. Lett. 70 (1997) 2741.
[9] T. Osada, Th. Kugler, P. Bröms, W.R. Salaneck, Synth. Met. 96 (1998) 77.
[10] Z.H. Huang, X.T. Zeng, E.T. Kang, Jerry Y.H. Fuh, L. Lu, X.Y. Sun, Electrochem. Solid State Lett. 9 (6) (2006) H39–H42.
[11] J.S. Kim, M. Granström, R.H. Friend, N. Johanson, W.R. Salaneck, F. Cacialli, J. Appl. Phys. 84 (1998) 6859.
[12] F. Cacially, J.S. Kim, T.M. Brown, J. Morgado, M. Granström, R.H. Friend, G. Gigli, R. Cingolani, L. Favaretto, G. Barbarella, R. Daik, W.J. Feast, Synth. Met. 109 (2000) 7.
[13] M.G. Mason, L.S. Hung, C.W. Tang, S.T. Lee, K.W. Wong, M. Wang, J. Appl. Phys. 86 (1999) 1688.
[14] S.F.J. Appleyard, M.R. Willis, Opt. Mater. 9 (1998) 120.
[15] J.S. Kim, F. Cacialli, A. Cola, G. Gigli, R. Cingolani, Appl. Phys. Lett. 75 (1999) 19.
[16] V. Christou, M. Etchells, O. Renault, P.J. Dobson, O.V. Salata, G. Beamson, R.G. Egdell, J. Appl. Phys. 88 (2000) 5180.
[17] H.Y. Yu, X.D. Feng, D. Grozea, Z.H. Lu, R.N. Sodhi, A.-M. Hor, H. Aziz, Appl. Phys. Lett. 78 (2001) 2595.
[18] A. Andersson, N. Johansson, P. Bröms, N. Yu, D. Lupo, R. Salaneck, Adv. Mater. 10 (1998) 859.
[19] Y.-H. Liau, N.F. Scherer, K. Rhodes, J. Phys. Chem. B 105 (2001) 3282.
[20] N.G. Park, M.Y. Kwak, B.O. Kim, O.K. Kwon, Y.K. Kim, B. You, T.W. Kim, Y.S. Kim, Jpn. J. Appl. Phys. (Part 1) 41 (2002) 1523.
[21] S.-F. Chen, C.-Wu. Wang, Appl. Phys. Lett. 85 (2004) 765.
[22] P.M.S. Monk, C.M. Man, J. Mater. Sci.: Mater. Electron. 10 (1999) 101.
[23] S.K. So, W.K. Choi, C.H. Cheng, L.M. Leung, C.F. Kwong, Appl. Phys. A 68 (1999) 447.
[24] A. Berntsen, Y. Croonen, R. Cuijpers, B. Habets, C. Liedenbaum, H. Schoo, R.J. Visser, J. Vleggaar, P.v.d. Weijer, Proc. SPIE 3148 (1997) 264.
[25] K. Otsuka, T. Yasui, A. Morikawa, Bull. Chem. Soc. Jpn. 56 (1983) 2161.
[26] J.A. Chaney, P.E. Pehrsson, Appl. Surf. Sci. 180 (2001) 214.
[27] Z. Ovadyahu, B. Ovryn, H.W. Kraner, J. Electrochem. Soc. 130 (1983) 917.
[28] C. Adachi, K. Nagai, N. Tamoto, Appl. Phys. Lett. 66 (1995) 2679.
[29] E. Ruckenstein, S.V. Gourisandkar, J. Colloid Interf. Sci. 109 (1986) 557.
[30] S. Wu, Polymer Interface and Adhesion, Marcel Dekker Inc., New York, 1982, pp. 171–178.
[31] D.J. Milliron, I.G. Hill, C. Shen, A. Kahn, J. Schwartz, J. Appl. Phys. 87 (2000) 572.
[32] T. Ishida, H. Kobayashi, Y. Nakato, J. Appl. Phys. 73 (1993) 4344.
[33] J.S. Kim, F. Cacialli, R. Friend, Thin Solid Films 445 (2003) 358.

[34] K.L. Purvis, G. Lu, J. Schwartz, S.L. Bernasek, J. Am. Chem. Soc. 122 (2000) 1808.
[35] A.R. Span, E.L. Bruner, S.L. Bernasek, J. Schwartz, Langmuir 17 (2001) 948.
[36] L.-Q. Wang, K.F. Ferris, P.X. Skiba, A.N. Shultz, D.R. Baer, M.H. Engelhard, Surf. Sci. 440 (1999) 60.
[37] S.K. Vanderkam, E.S. Gawalt, J. Schwartz, A.B. Bocarsly, Langmuir 15 (1999) 6598.
[38] J.S. Kim, M. Granström, R.H. Friend, N. Johansson, W.R. Salaneck, A. Cola, G. Gigli, R. Cingolani, F. Cacialli, Mat. Res. Soc. Symp. Proc. 558 (2000) 427.
[39] I.-M. Chan, F.C.-N. Hong, Thin Solid Films 444 (2003) 254.
[40] M. Ishii, T. Mori, H. Fujikawa, S. Tokito, Y. Taga, J. Lumin. 87 (2000) 1165.
[41] Q.T. Le, E.W. Forsythe, F. Nuesch, L.J. Rothberg, L. Yan, Y. Gao, Thin Solid Films 363 (2000) 42.
[42] B. Choi, H. Yoon, H.H. Lee, Appl. Phys. Lett. 76 (2000) 412.
[43] M. Kamei, Y. Shigesato, S. Takaki, Thin Solid Films 259 (1995) 38.
[44] N.D. Popovich, S.-S. Wong, S. Ufer, V. Sakhrani, D. Paine, J. Electrochem. Soc. 150 (2003) H255–H259.
[45] M. Mandai, K. Takarda, K. Takarda, T. Aoki, T. Fujinami, Y. Nakanishi, Y. Hataneks, Synth. Met. 91 (1997) 12.
[46] L.F. Cheng, L.S. Liao, W.Y. Lai, X.H. Sun, N.B. Wong, C.S. Lee, S.T. Lee, Chem. Phys. Lett. 319 (2000) 418.
[47] C.S. Smith, Trans. ASM 45 (1953) 533.
[48] T. Furuhara, T. Maki, Mater. Sci. Eng. A 312 (2001) 145.
[49] J.W. Cahn, Acta Metall. 5 (1953) 169.
[50] Y. Han, D. Kim, J.-S. Cho, Y.-W. Beag, S.-K. Koh, Thin Solid Films 496 (2006) 58.
[51] C. Ratsch, J.A. Venables, J. Vac. Sci. Technol. A 21 (2003) S96.
[52] J.N. Barisci, R. Stella, G.M. Spinks, G.G. Wallace, Synth. Met. 124 (2001) 407.
[53] M. Harsdorff, Thin Solid Films 90 (1982) 1.
[54] Q.D. Wu, Vacuum 41 (1990) 1431.
[55] J.A. Venables, G.D.T. Spiller, M. Hanbücken, Rep. Prog. Phys. 47 (1984) 399.
[56] R. Kern, G. LeLay, J.J. Métois, Curr. Top. Mater. Sci. 3 (1979) 139.
[57] Y. Han, D. Kim, J.S. Cho, Y.W. Beag, S.K. Koh, V.S. Chernysh, J. Appl. Phys. 97 (2005) 24910.
[58] J. Morgado, A. Charas, N. Barbagallo, Appl. Phys. Lett. 81 (2002) 933.
[59] S. Fujita, T. Sakamoto, K. Ueda, K. Ohta, S. Fujita, Jpn. J. Appl. Phys. 36 (1997) 350.
[60] D.M. Sherman, J.S. Maa, T.E. Hutchinson, J. Vac. Sci. Technol. 10 (1973) 155.
[61] N.D. Popovich, S.-S. Wong, B.K.H. Yen, H.-Y. Yeom, D.C. Paine, Anal. Chem. 74 (2002) 3127.

Available online at www.sciencedirect.com
ScienceDirect
Organic Electronics 9 (2008) 63–69
Organic Electronics
www.elsevier.com/locate/orgel

Suppressive effect of a self-assembled monolayer on the polycrystallization of naphthyl-substituted diamine derivative thin film

Tatsuo Mori [a,*], Shunsuke Nishino [a], Takao Nishikawa [b], Satoshi Ogawa [b]

[a] Department of Electrical Engineering and Computer Science, Graduate School of Engineering, Nagoya University, Furo-cho, Chikusa-ku, Nagoya 464-8603, Japan
[b] Faculty of Engineering, Iwate University, 4-3-5 Ueda, Morioka-shi, Iwate 020-8551, Japan

Received 24 May 2007; received in revised form 15 August 2007; accepted 20 August 2007
Available online 26 August 2007

Abstract

We observed the polycrystallization process of a naphthyl-substituted diamine derivative (NPD) thin film on a self-assembled monolayer (SAM)-modified indium–tin–oxide (ITO) substrate. Fluorine-substituted SAM suppressed the growth of the polycrystalline region. After estimating the surface morphology of the polycrystalline region using AFM measurement, correlation between the molecular migration rate on the substrate, the rearrangement rate at the growth point, and the provision rate from the amorphous region clarified the polycrystallization growth mechanism for the NPD thin film. The formation of a channel around the polycrystalline region and the molecular migration rate on the substrate play important roles in polycrystalline region growth.

PACS: 68.35.bm; 68.55.am; 68.35.Ja

Keywords: Polycrystallization; Hole-transport material; Self-assembled monolayer; Surface migration rate

1. Introduction

Since the wide an rapid practical application of organic light-emitting diodes (OLEDs) [1], expectations have been created for the possible realization of organic electronic devices. Commercial OLEDs and practical organic field-effect transistors (OFETs) are often fabricated using a vacuum-deposition method. To produce devices with high performance and durability, it is important not only to optimize the function-separated device, but also to retain that structure. In general, although the initial film structure of vacuum-deposited organic thin films is emphasized, the change of film structure over time has been little reported [2]. Especially, in such heavy (continuous and bright) uses as television and lighting sources, the temperature of emitting devices increases to 80 °C due to Joule heating [3,4]. Through examination of the polycrystallization of a naphthyl-substituted diamine derivative (NPD)

* Corresponding author. Tel.: +81 052 789 4429; fax: +81 052 789 5306.
E-mail address: tmori@nuee.nagoya-u.ac.jp (T. Mori).

1566-1199/$ - see front matter © 2007 Elsevier B.V. All rights reserved.
doi:10.1016/j.orgel.2007.08.003

and its suppression by the organic alloy method [5–9], we have become interested in the surface modification of an indium–tin–oxide (ITO) substrate. For example, Sato et al. reported on the relationship between fabrication condition, polycrystallization, and molecular packing for silole derivative [10].

A self-assembled monolayer (SAM) is an effective material for use in organic electronic devices because it can be fabricated easily, allowing control of the surface electronic state of the substrates. Gundlach et al. reported that a well-ordered naphthacene thin film and the enhancement of carrier mobility for an OFET are obtainable by the vacuum deposition of naphthacene on an octadecyltrichlorosilane-formed SiO_2 gate insulator [11]. Kobayashi et al. showed that the carrier density of an OFET is controllable by changing the type of SAM [12]. For OLEDs, Campbell et al. reported that the carrier injection from the metal to the organic layer is controllable by forming an interfacial dipole layer because of the introduction of a SAM between Ag and poly[2-methoxy, 5-(2′-ethylhexyloxy)-1,4-phenylene vinylene] (MEH-PPV) [13]. Sano et al. showed that degradation of the Alq3 layer can be suppressed by the introduction of a SAM between ITO and NPD. They explained that the decrease in excess hole density by increasing the barrier height of the hole injection to NPD improves the carrier balance in Alq3 [14]. We investigated the effects of SAM introduction on the NPD polycrystallization process.

For this study, we vacuum-deposited NPD after forming two kinds of SAM on an ITO substrate. We then we investigated their polycrystallization phenomena.

2. Experimental

We used *N*,*N*′-di(1-naphthyl)-*N*,*N*′-diphenyl-1,1′-diphenyl-1, 4′-diamine) (NPD), and employed a special ITO substrate with a roughness, $R_a = 0.9$ nm for OLEDs (Giomatic). The ITO substrates were cleaned using UV-ozone treatment (5 min; Nippon Laser and Electronics Lab.) after ultrasonic washing in pure water, acetone, and 2-propanol. It is very important to clean the substrate surface adequately before SAM deposition. We used (heptadecafluoro-1,1,2,2-tetrahydrodecyl)triethoxysilane (F-SAM) and *n*-decyltriethoxysilane (CH_3-SAM) as SAM materials. Two kinds of SAM were fabricated as a gas-phase. Detailed fabrication procedure was described in the reference [12] including Nishikawa and Ogawa. As the other reference, we used copper-phthalocyanine (CuPc)-deposited ITO substrate. The organic thin films were prepared using vacuum deposition of ca. 0.2 nm/s under 0.8–1×10^{-3} Pa at room temperature.

We measured the contact angle of pure water using an automatic contact angle meter (CA-VP, Kyowa Interface Science Co., Ltd.). We stored the specimens in an environmental chamber (LHL-113; Espec Co.) in which the temperature and relative humidity were controlled in an air atmosphere. After removing the specimens from the environmental chamber temporarily, we observed the NPD film prepared on an ITO substrate using a polarizing microscope (Opti Photo-2; Nikon Co.) equipped with a polarizing unit. Conventional photographs were also taken (Digital Sight, DS-L1; Nikon Co.). In addition, atomic force microscopy (AFM) images were obtained using a nanoscale hybrid microscope (VN-8010; Keyence Co.).

3. Experimental results and discussions

Fig. 1 shows the dependence of contact angle on the deposition time of a SAM-coated ITO substrate. Both contact angles of F-SAM and CH_3-SAM increased rapidly with the absorption of SAM molecules on the ITO surface. The angles increased gradually with deposition time and became saturated after 120 min. Final contact angles of F-SAM and CH_3-SAM are estimated respectively as 110.4° and 102.5°. Table 1 shows both contact angles along with those reported previously [12,15]. Our values in this work almost match the

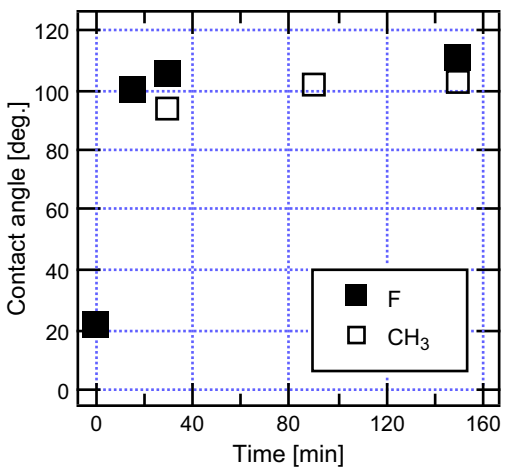

Fig. 1. Dependence of contact angles on deposition time of a SAM-coated ITO substrate.

Table 1
Comparison of contact angles with those of other reports

Specimen	This work	Ref. [8]	Ref. [11]
F-SAM	110.4°	108.8°	110°
CH_3-SAM	102.5°	105.1°	100°

values reported in the other groups' papers. Therefore, a SAM can be formed on an ITO surface as well as on an SiO_2 surface. In addition, the layer quality of the SAM on the ITO surface is regarded to be equivalent to that on SiO_2. For this study, we used SAM-coated ITO substrates after keeping them for 150 min in gas-phase SAM.

Fig. 2 shows polarizing microscopic photographs of 50-nm-thick NPD films deposited on bare, CuPc-, F-SAM-, and CH_3-SAM-coated ITO substrates. In fact, CuPc is often used as a hole-injection layer for OLEDs. We have previously reported that the polycrystallization process of NPD progresses slowly when the NPD thin film is deposited on the CuPc layer [4]. The introduction of an organic layer between NPD and the ITO substrate can suppress growth of the polycrystalline region. The polycrystalline regions appear after about one day. Although the results are not shown, all NPD thin films were in an amorphous state immediately after fabrication because all polarizing microscopic images appeared as dark areas. However, it was found that the NPD thin film deposited on F-SAM is only slightly crystallized. The degree of suppression of polycrystallization for CH_3-SAM is equal to that for CuPc. Fig. 3 shows the radius of the polycrystalline region vs. storage time of the NPD thin film on various substrates at temperatures less than 40 °C at 70% RH. The polycrystalline

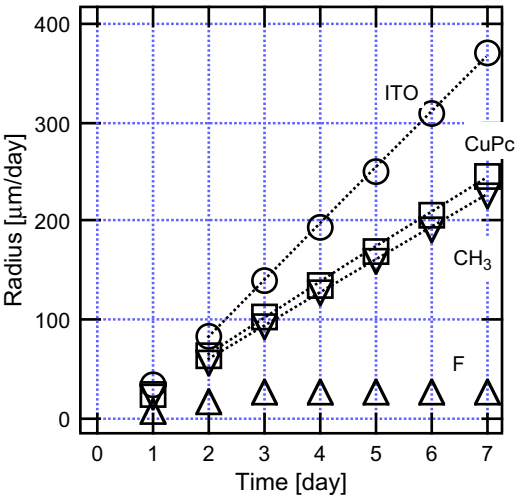

Fig. 3. The radius of polycrystalline region vs. storage time of NPD thin film on various substrates at 40 °C, with 70% RH.

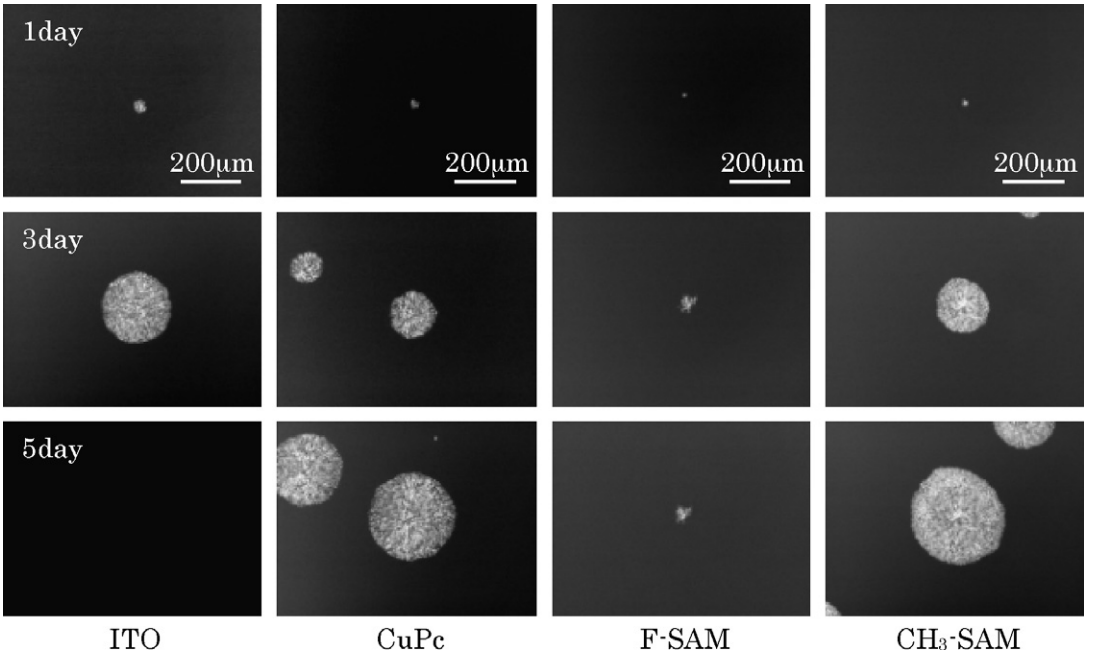

Fig. 2. Polarizing microscopic photographs of 50-nm-thick NPD films deposited on bare, CuPc-, F-SAM-, and CH_3-SAM-coated ITO substrates (639 × 853 μm).

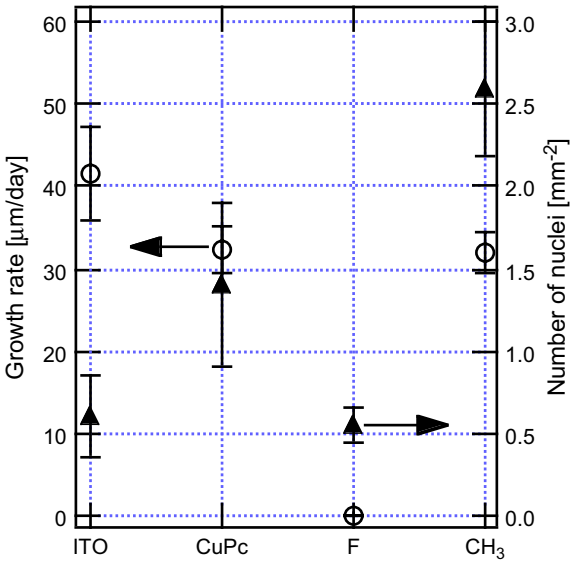

Fig. 4. Growth rate and number of nuclei of the polycrystalline region for NPD thin films on various substrates.

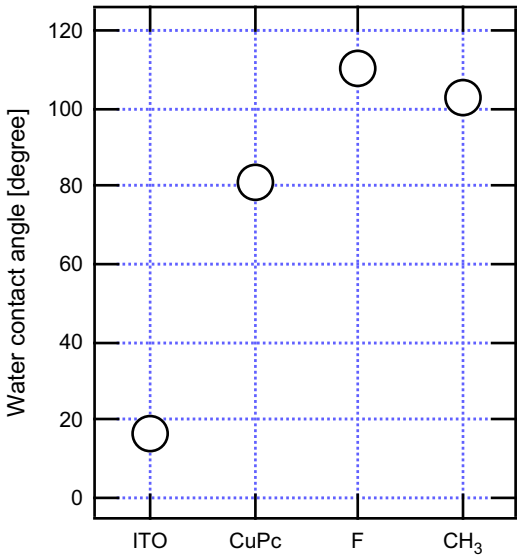

Fig. 5. Contact angles of water for substrates before deposition of the NPD thin film.

region growth rate is constant under a constant storage condition. Fig. 4 shows the growth rate and number of nuclei of the polycrystalline region for an NPD thin film on various substrates. The growth rate of NPD on ITO is ca. 42 μm/day. The growth rates of both CuPc and CH_3-SAM are ca. 32 μm/day; they are lower than that on ITO. For the NPD thin film on F-SAM, the formation of nuclei was observed, but the growth rate was impossible to estimate. The density of nuclei of NPD thin film's nuclei on F-SAM, 0.55 mm^{-2}, is equal to that on ITO, 0.6 mm^{-2}. On the other hand, those of both CuPc and CH_3-SAM are higher than that on ITO. For that reason, the formation of nuclei is thought to depend on the interface condition contacted on NPD thin film.

Fig. 5 shows the contact angles of water for substrates before the deposition of the NPD thin film. Although the contact angle on the UV-ozone-cleaned ITO is ca. 14° and the substrate is hydrophilic, those on CuPc, CH_3-SAM, and F-SAM, which are hydrophobic, are ca. 81°, 103°, and 110°, respectively. The formation of nuclei is thought not to correlate with substrate hydrophobicity. Measurements of the surface morphology of all substrates and deposited NPD thin films using AFM revealed no differences among the samples.

Next, we specifically address the morphology of polycrystalline region after polycrystallization. Fig. 6 shows AFM images of an edge of the polycrystalline region for NPD thin films deposited on various substrates. The polycrystalline regions of NPD molecules on three substrates other than F-SAM are regarded as having similar morphologies. However, the polycrystalline region of NPD molecules on F-SAM shows a unique progression of crystallization. The NPD crystal typically grows and arborizes in the usual polycrystalline region, but the NPD crystal on F-SAM was unbranched. Consequently, the polycrystalline region does not spread because of the decrease in the growing front; also, it grows as a single fibril. Fig. 7 shows enlarged AFM images of a single growing fibril of NPD thin film deposited on F-SAM. This crystal fibril grows ca. 3 μm after 1 day from the first observation, but it grows only slightly at 2 days and thereafter. However, the channel between the crystal and an amorphous region debouches with time because the dark area around the crystal becomes larger.

We have previously proposed a polycrystallization model of NPD molecules in an NPD thin film [8]. However, because it is difficult to clarify the generation of nuclei directly through observation, we specifically examined the growth process of polycrystalline region in the present study. First, results show that no underlayer has any interaction with NPD molecules existing less than 50 nm distant from the underlayer. The NPD molecules located on the NPD layer surface are thought to behave similarly in all specimens. Fig. 8 shows a conceptual diagram of the polycrystalline region growth: panel

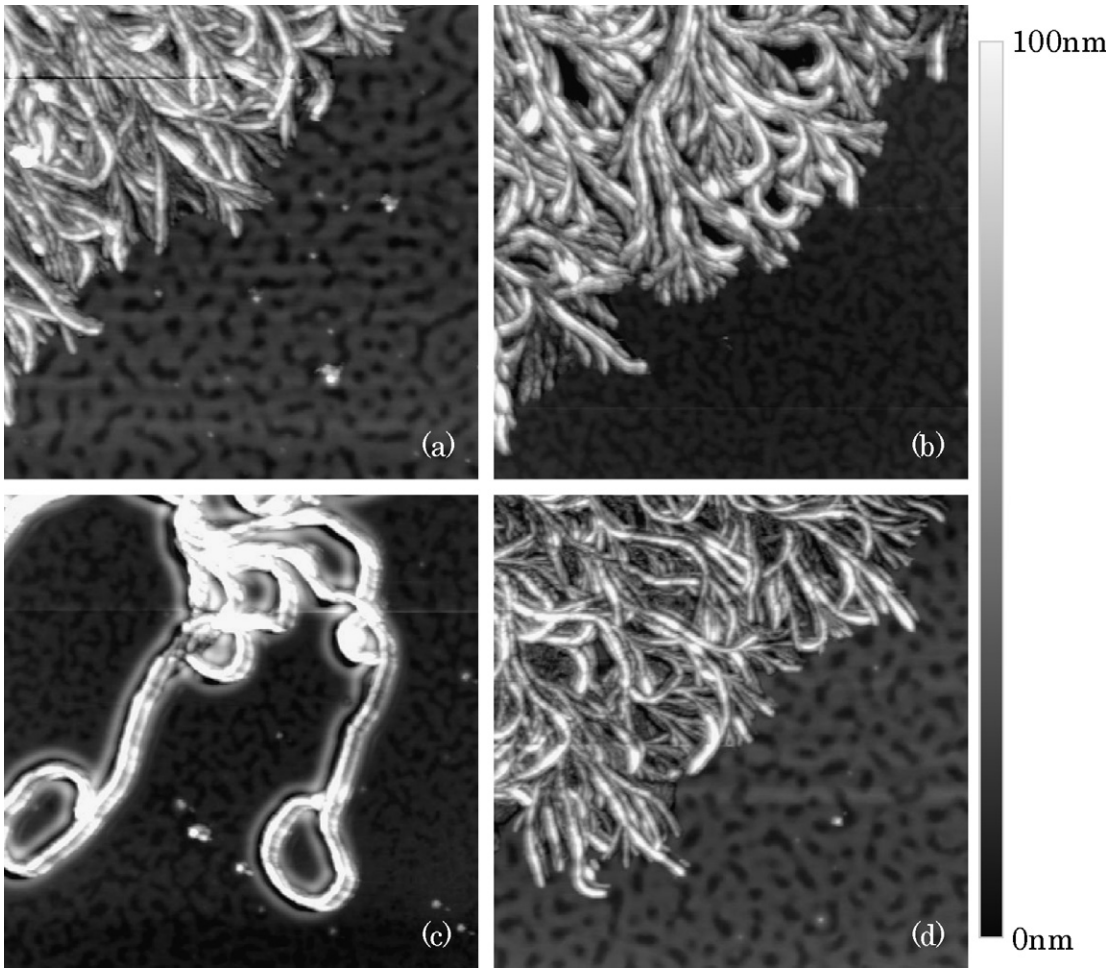

Fig. 6. AFM images of an edge of the polycrystalline region for NPD thin films deposited on various substrates: (a) bare ITO, (b) CuPc, (c) F-SAM, and (d) CH_3-SAM (20×20 μm).

(a) shows the situation with a channel around the fibril; panel (b) shows the situation without. Crystal growth is thought to be controlled by three factors: the provision rate from NPD amorphous region, v_p, the migration rate on the substrate, v_S, and the rearrangement rate of the growing front, v_R. Another factor, the migration rate on the NPD layer, is defined as v_N. The roughness of deposited NPD films is $R_a =$ ca. 0.7 nm in all specimens. Therefore, we infer that no deep pinhole penetrates into the ITO substrate in any NPD layer. In the initial stage of polycrystallization, a small polycrystalline region is thought to exist on and/or contact the amorphous region of the NPD. Fig. 8b shows that NPD molecules will be provided to the growing front by migration on the NPD layer surface if the growing front contacts an amorphous region in both the above cases. In this case, v_R corresponds to v_N. When rearrangement of the molecule at the growing front proceeds at a slower rate than the migration of the NPD molecule, the growth rate is expected to be controlled by v_N and the growing front is predicted to be in constant contact with the amorphous region. If that were true, the polycrystallization process of the NPD layer would be independent of the lower material for ITO. In reality, the polycrystalline region growth rate for NPD affects the underlayer material.

The NPD molecules near the growth front are absorbed to the polycrystalline region when the rearrangement of molecules at the growth front occurs at a higher rate than that of the NPD molecule migration. Consequently, the underlayer surface appears and a channel is formed around the growth front. At that time, the polycrystallization process is affected by the migration rate on substrate

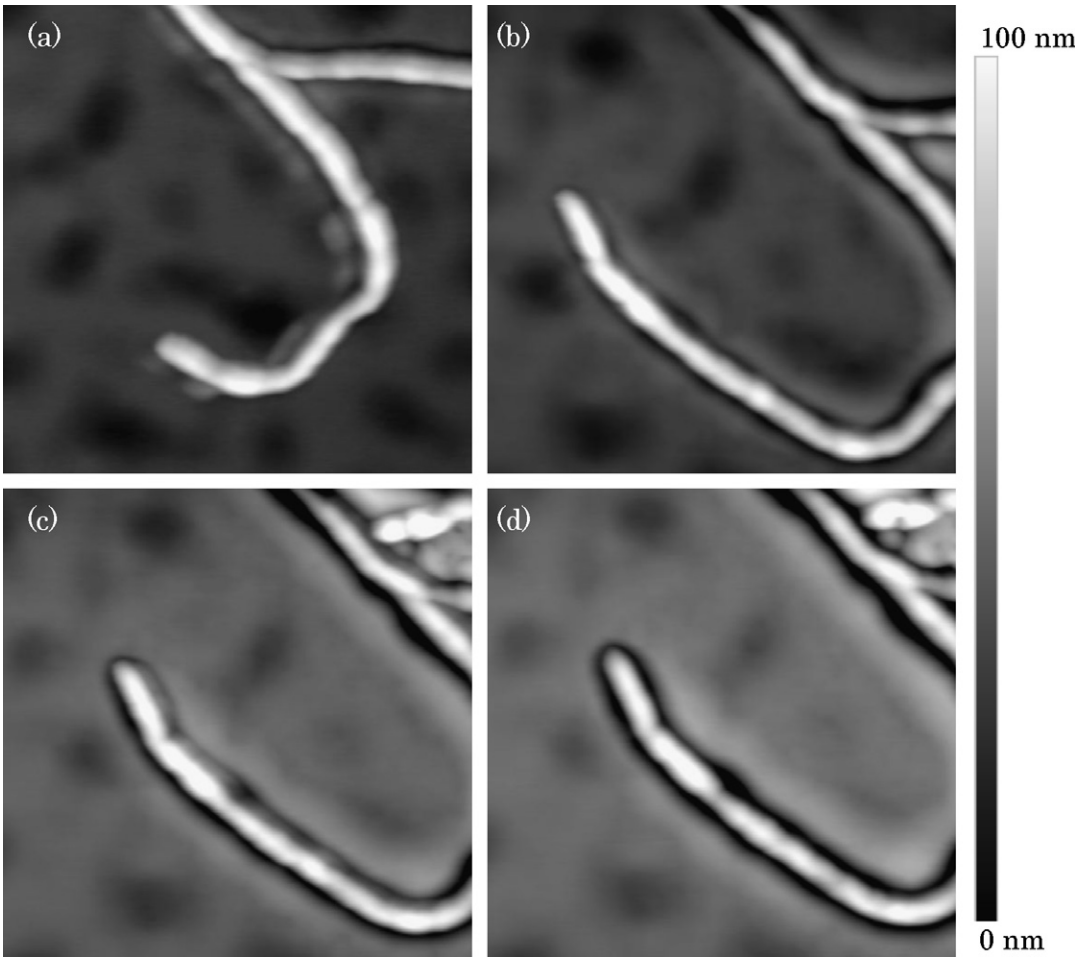

Fig. 7. Enlarged AFM images of a single growing fibril of NPD thin film deposited on F-SAM: (a) start day, (b) after 1 day, (c) after 2 days, and (d) after 3 days (5×5 μm).

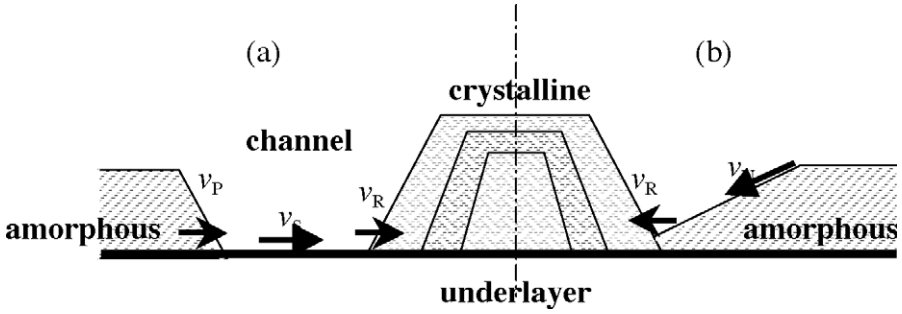

Fig. 8. Conceptual diagram of polycrystalline region growth (a) with and (b) without a channel around the fibril: the provision rate from the NPD amorphous region, v_p; the migration rate on substrate, v_S; the rearrangement rate of growing front, v_R; and the migration rate on NPD layer, v_N.

(underlayer), v_S. Fig. 8a shows that the growth of the polycrystalline region is controlled by both rates: v_p, and v_S. Only the NPD polycrystallization on F-SAM is thought to be suppressed when it is assumed that the v_S on F-SAM is much lower than the v_S on the others. This mechanism is supported by the fact that the channel around a fibril becomes larger over time.

4. Conclusions

We observed the NPD thin film polycrystallization process on two kinds of SAM. The introduction of a SAM between an ITO and NPD layer suppressed NPD polycrystallization. The polycrystalline region for the NPD thin film on F-SAM grew only slighty and the crystal fibril of the polycrystalline region on F-SAM was not branched. Because of the decrease in the growth front, the polycrystalline region did not spread. We discussed the rate balance of the provision, migration, and rearrangement of NPD molecules. The suppression of polycrystallization on F-SAM was thought to be caused by the formation of a channel around the polycrystalline region and the low molecular migration rate on the substrate.

Acknowledgements

This research was partially supported by the Ministry of Education, Culture, Sports, Science and Technology and a Grant-in-Aid for Scientific Research (B), 2006, No. 18360146.

References

[1] C.W. Tang, S.A. VanSlyke, Appl. Phys. Lett. 51 (1987) 913–915.
[2] E.-M. Han, L.-M. Do, N. Yamamoto, M. Fujihira, Thin Solid Films 273 (1996) 202–208.
[3] H. Tsuji, A. Oda, J. Kido, T. Sugiyama, Y. Furukawa, Ext. Abst. The 66th Autumn Meeting, 2005 The Japan Society of Applied Physics, 7a-R-11 (in Japanese).
[4] H. Tsuji, A. Oda, J. Kido, T. Sugiyama, Y. Furukawa, in: Polymer Processing Society, 22nd Annual Meeting, PPS22 (2006) SP7. 07.
[5] T. Kato, T. Mori, T. Mizutani, Thin Solid Films 393 (2001) 109–113.
[6] T. Mori, Y. Iwama, J. Photopolym. Sci. Technol. 18 (2005) 59–63.
[7] Y. Iwama, T. Mori, T. Mizutani, IEE J. Trans. FM 125 (2005) 699–704 (in Japanese);
Y. Iwama, T. Mori, T. Mizutani, Elect. Eng. Jpn. 156 (2006) 1–8.
[8] T. Mori, Y. Masumoto, J. Photopolym. Sci. Technol. 19 (2006) 209–214.
[9] T. Mori, S. Oda, N. Ooishi, Y. Masumoto, Jpn. J. Appl. Phys. 46 (2007) 5954–5959.
[10] N. Sato, R.J. Murdey, in: The 3rd Workshop on Advanced Spectroscopy of Organic Materials for Electronic Applications (ASOMEA III), Vadstena (Sweden) 2–5, 2005.
[11] D.J. Gundlach, J.A. Nichols, L. Zhou, T.N. Jackson, Appl. Phys. Lett. 80 (2002) 2925–2927.
[12] S. Kobayashi, T. Nishikawa, T. Takenobu, S. Mori, T. Shimoda, T. Mitani, S. Shimotani, N. Yoshimoto, S. Ogawa, Y. Iwase, Nat. Mater. 3 (2004) 317–322.
[13] I.H. Campbell, S. Rubin, T.A. Zawodzinski, J.D. Kress, R.L. Martin, D.L. Smith, N.N. Barashkov, J.P. Ferrais, Phys. Rev. B 54 (1996) 14321–14324.
[14] J. Sano, Y. Kinoshita, H. Murata, Ext. Abst. 66th Autumn Meeting, 2005, The Japan Society of Applied Physics, 8p-R-9 (in Japanese).
[15] H. Sugimura, K. Ushiyama, A. Hozumi, O. Takai, Langmuir 16 (2000) 558–888.

Available online at www.sciencedirect.com
ScienceDirect
Organic Electronics 9 (2008) 70–76
Organic Electronics
www.elsevier.com/locate/orgel

Gate insulators and interface effects in organic thin-film transistors

F.A. Yildirim [a,*], R.R. Schliewe [a], W. Bauhofer [a], R.M. Meixner [b], H. Goebel [b], W. Krautschneider [c]

[a] Institute of Optical and Electronic Materials, Hamburg, University of Technology, Eissendorfer Strasse 38, D-21073 Hamburg, Germany
[b] Department of Electronics, Helmut-Schmidt-University/University of Federal Armed Forces, Holstenhofweg 85, D-22043 Hamburg, Germany
[c] Institute of Nanoelectronics, Hamburg University of Technology, Eissendorfer Strasse 38, D-21073 Hamburg, Germany

Received 15 May 2007; received in revised form 12 September 2007; accepted 13 September 2007
Available online 29 September 2007

Abstract

This paper presents a detailed characterization of different thermosetting polymers to be used as gate dielectrics in organic thin-film transistors. Selected materials yield smooth films with good insulation properties and offer attractive processing conditions. Bottom-gate transistors were prepared using these dielectrics and compared to hybrid transistors with surface-treated SiO_2 as the dielectric. Gate bias induced leakage and solvent effects were investigated by preparing metal/insulator/semiconductor devices. Poly(3-hexylthiophene) (P3HT) transistors with organic dielectrics exhibited higher channel conductivity and lower mobility values with respect to P3HT-hybrid transistors and pentacene transistors. The importance of dielectric/semiconductor interface was discussed by comparing the performances of pentacene and P3HT transistors produced on different dielectrics.

PACS: 85.30.Tv; 73.61.Ph; 77.84.Jd

Keywords: Organic thin-film transistor; P3HT; Polymer dielectric; Interface; Solvents

In the last two decades, there has been great amount of research on solution-processing of polymeric layers for organic thin-film transistors. In addition to the efforts for the synthesis of soluble, high mobility semiconductors, the research on materials and their processing for the gate dielectric has increased explicitly, due to a better understanding of the influence of gate dielectric on device operation [1–9]. It is desired that the dielectric should be a good insulator and as thin as possible in order to decrease the operating voltages. On the other hand, it is reported many times that the interface between dielectric and semiconductor is of great importance [3,5,7]. Recently, there were also reports on detailed investigation of the electrical characteristics of solution-processed OTFTs, considering

* Corresponding author. Tel.: +49 40 42878 3854; fax: +49 40 42878 2229.
E-mail address: a.yildirim@tuhh.de (F.A. Yildirim).

1566-1199/$ - see front matter
doi:10.1016/j.orgel.2007.09.005

both bulk and interface effects of gate dielectrics on device performance [10–12].

In this work, four different thermosetting materials were examined for application in OTFTs: Benzocyclobutene (BCB-Cyclotene, DOW Chemical), epoxy-based SU-8 photoresist (Microchem) and Norland Optical Adhesive (NOA74), and epoxy-based coating EL37A (Beck Electrical Insulation). In addition to the fact that these materials form smooth films by spin-coating, they also satisfy most of the criteria mentioned above. The aim of this research is not only to improve the performance of transistors but also to discuss the factors that influence the device performance considering materials aspects. Additionally, two of these organic materials, SU-8 and EL37A, were introduced as dielectrics to the field of organic electronics. BCB has already been successfully used in organic transistors but it suffers from very high curing temperature 250 °C [13]. The other materials mentioned above were selected for lower curing temperatures or UV-curing properties, which is important for the simple and cheap processing of transistors.

In the bottom-gate configuration the active semiconductor layer is deposited on the dielectric layer. Therefore, properties of the dielectric/semiconductor interface are defined by the dielectric surface. For that reason, it is important to test the surface of the dielectrics for roughness variation due to solvent exposure, with the solvents used for the semiconductor [5]. For the electrical characterization of the dielectrics metal/insulator/metal (MIM) capacitors were built. Dielectric properties and the effects of solvents on these properties were examined. In order to understand the gate bias induced leakage and its effects on transistors, metal/insulator/semiconductor (MIS) capacitors were also prepared. After these tests, bottom-gate OTFTs were produced with these dielectrics using two different semiconductors. Regioregular poly(3-hexylthiophene) (rr-P3HT) (Merck Chemicals), which was deposited from different solvents and pentacene (Aldrich), which was evaporated were used for comparison. In Fig. 1, schematic structures of MIM and MIS capacitors, as well as an organic bottom-gate transistor can be seen. Finally, the results were compared to hybrid transistors with surface-treated SiO_2 as the dielectric.

Production of the devices started with the evaporation of chromium/gold (5 nm/35 nm) layers on glass slides by electron beam evaporation. Dielectric layers were all deposited in a clean-room atmosphere by spin-coating. Viscosities of the solutions and the spin parameters were adjusted to get films of 1–2 μm thickness on glass substrates. Thinner films lead to the problem of increased leakage currents, therefore they were not taken into consideration. Process parameters of the resins are listed in Table 1.

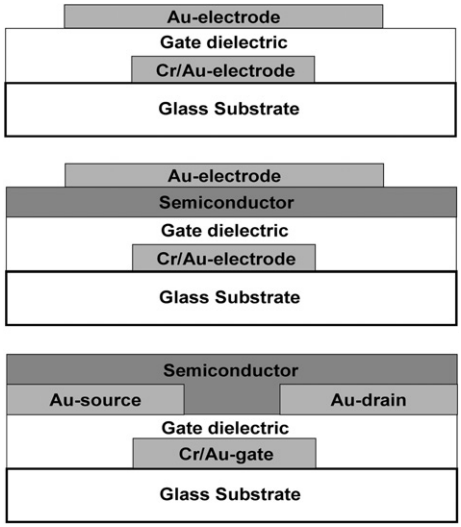

Fig. 1. Metal/insulator/metal (MIM), metal/insulator/semiconductor (MIS) and bottom-gate transistor structures.

Surface roughnesses of the films were investigated, before and after solvent exposure, with a white-light interferometer, Zygo LOT New-View 100 (WIM), by using a 40× lens. This test was conducted on all four dielectrics with four different solvents, which are used to dissolve the semiconductor P3HT. These solvents and their boiling points are as follows: Xylene (140 °C), chloroform (61 °C), toluene (110 °C) and 1,2,4-trichlorobenzene (TCB) (214 °C). After they were dropped on the dielectric layers, the films were dried on a hot-plate at 140 °C for 2 h. The surfaces were then examined once more for their roughness. Additionally, contact angle values of the dielectric layers with water and diiodomethane were measured and surface energies were determined by the method defined by Owens and Wendt [14] (Table 1).

Rms-roughness values of the dielectric films measured by WIM, before and after the exposure to solvents, generally showed no considerable variation. The films, even after prolonged exposure, withstand the solvents showing small amounts of variation in the roughness values. Only in the case of BCB layer upon exposure to TCB, the rms-roughness increased to 3 nm which can be considered as an exception for

Table 1
Processing conditions and measured properties of selected dielectric materials

Polymer	UV exposure	Curing conditions	Dielectric constant (20 Hz/100 kHz)	Resistivity (MIM) (Ω m)	RMS-roughness (nm)	Contact angle with water (°)	Surface energy γ_s (mJ m^{-2})
BCB	–	250 °C–60 min (vacuum)	3.3/3.0	3.2×10^{13}	1	93	34.3
SU-8	1 min	150 °C–30 min	4.0/3.8	1.0×10^{12}	1	80	41.5
NOA 74	30 min	–	4.8/4.0	1.2×10^{12}	1	60	43.1
EL37A	–	160 °C–60 min	4.0/3.3	1.7×10^{13}	1	96	32.1

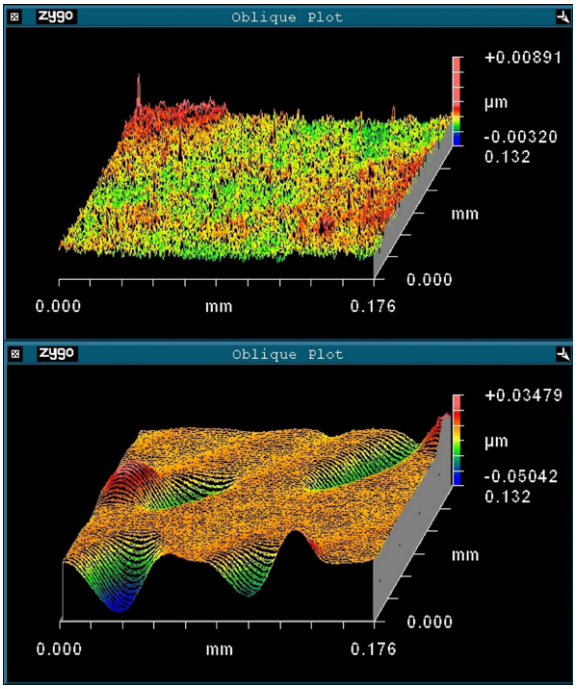

Fig. 2. WIM pictures of BCB surface: before and after exposure to TCB. Rms-roughness increased from 1 to 3 nm, whereas PV roughness increased from 12 to 48 nm.

those samples. Also the peak-to-valley (PV) roughness increased from 12 nm to 48 nm. (Fig. 2) This indicates a slight swelling of the dielectric film which did not appear to be detrimental to insulating properties, during the measurements made on MIM-devices. It might have affected the field effect mobility by causing a mixture at the dielectric/semiconductor interface. However, in this study effect of PV-roughness on mobility was not observed, therefore not discussed any further.

In order to form the MIM-capacitors a layer of gold was thermally evaporated on the dielectric films. In the MIM-configuration, leakage currents passing through the films were measured at 80 V over time. By using Ohm's law and the general formula for resistance, the specific volume resistivities of the films were calculated (Table 1). Since the solution-processing conditions will apply during the transistor production, effects of the used solvents on the resistivity of the dielectric films were investigated. Also by means of an LCR-Meter HP 4282A, capacitance values were measured and dielectric constant values of the films were determined. For MIS-capacitors and transistors, semiconductor P3HT was deposited by spin-coating from the solvents mentioned before. Solutions of 0.3–0.6 wt% were filtered (0.2 µm pore size PTFE) and coated onto the dielectrics, followed by the annealing step. The MIS-capacitors were then tested for leakage currents to compare with MIM-devices.

Leakage current values of 10–50 pA were measured at 80 V from the MIM-capacitors of all 4 dielectrics, where the areas of capacitors were approximately 1 mm^2. After dropping the solvents and drying the films, measured leakage currents increased slightly, showing values between 17 and 75 pA. Therefore, the layers proved to be good insulators even after the solvent exposure. However, when the same leakage test was conducted in the MIS-configuration, the observed currents increased up to values from 1 nA to 10 nA. Although the insulators were the same and solvents for the semiconductor did not affect the dielectrics considerably, the leakage current increased. The observation was confirmed by depositing P3HT films from four different solvents on NOA74 and EL37A dielectrics, so that the measurement was independent of solvent effects (Fig. 3). It can be concluded that the current through the dielectric increases when a semiconductor layer replaces an electrode. This phenomenon was already reported in the work of Raja et al. It was explained by the increased amount of charge injection into the dielectric, due to the displacement of dopant ions or impurities in the semiconductor [15]. Dependence of leakage current on the doping state of the semiconductor was also investigated in MIS-devices. An extra annealing step was applied under vacuum so that the unintentional doping level

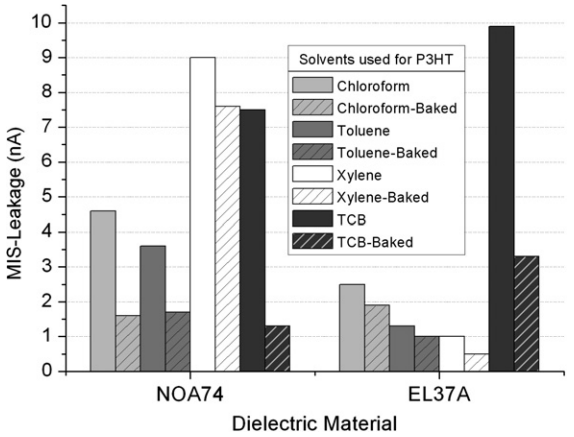

Fig. 3. Leakage currents flowing at 80 V measured from Au/dielectric/P3HT MIS-devices. P3HT was deposited from four different solvents on two different dielectric materials. Currents decreased with decreased doping level in all of the cases.

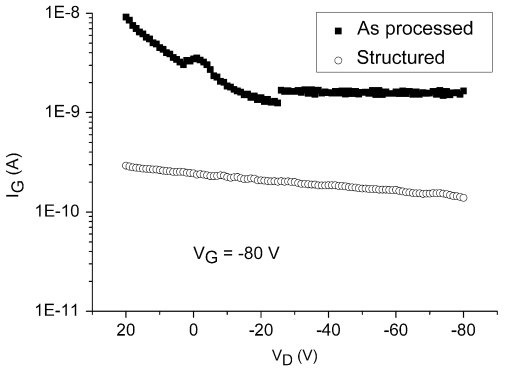

Fig. 4. Leakage currents flowing through the gate dielectric during the measurement of output characteristics of a pentacene transistor with BCB dielectric. Current decreases due to structuring of semiconductor.

of the P3HT layer was minimized [15]. In every case, lower leakage currents were obtained in the de-doped states, which also support the previous efforts (Fig. 3). This effect explains the increased leakage in the transistors. The current does not flow directly from S/D electrodes into the dielectric, but from semiconductor. Therefore, part of the semiconductor overlapping with the gate electrode should be as small as possible.

Four different bottom-gate transistors were prepared with four different dielectric layers, by using a shadow mask for the source and drain electrodes. Channels of length 25 μm and width of 1–2 mm (Fig. 1) were formed. Hybrid transistors of same channel sizes were prepared on Si-wafers where the dielectric layer was a SiO_2 (300 nm thick) layer with a hexamethyldisilazane (HMDS) treatment. For this treatment, Si-wafer was first laid into 25% ammonia solution followed by the exposure to HMDS vapour at 100 °C, where contact angle with water increased from 50° to 85°. P3HT was used as semiconductor layer and spin-coated from three different solvents; chloroform, xylene and TCB. They were then annealed as stated above, for the capacitors. Evaporated pentacene (Aldrich) was also used as semiconductor, for comparison. The evaporation of pentacene took place at around 2×10^{-5} mbar. In order to decrease leakage-currents outside the channel area, the semiconductor around this area was carefully removed by a scalpel. This simple structuring of the semiconductor resulted in a considerable reduction in gate current (Fig. 4).

Electrical characteristics of the transistors were measured by Agilent 4156C Semiconductor Parameter Analyzer. Threshold voltages of the transistors were determined by extrapolating the tangent to the plot $I_D^{1/2}$ vs. V_G to the V_G-axis where V_D was −80 V. Saturation field-effect mobility values were calculated from the slope of the transfer curves ($V_D = -80$ V) by using the equation for transconductance g_m. These conventional methods were used in order to get a comparison between transistors. It does not consider the differences in transistor characteristics which may affect the evaluation [16]. In Fig. 5 there is a comparison of a hybrid transistor with another having NOA74 dielectric. A common observation in almost all of the devices having organic dielectric is that they exhibit higher off-current values, I_D ($V_G = 0$ V), than their hybrid counterparts, which indicates a high conductivity. It was possible to turn the channel off by applying positive voltages to the gate. It can also be observed from the comparison of transfer characteristics in Fig. 5 that the threshold voltage was shifted to positive values where NOA74 was the dielectric. Mobility was slightly higher in the hybrid transistor, most probably due to the proper interface leading to a better chain ordering in P3HT. Increased conductivity can be explained by the purity/doping state of the films. Whereas mobility is generally related to the quality of the dielectric/semiconductor interface and the ordering of the semiconductor [7,11]. Almost all of the P3HT-transistors having an organic dielectric suffered from unintentional doping at the interface. This might be due to the impurities originating from the dielectric during the solution-processing of the semiconductor.

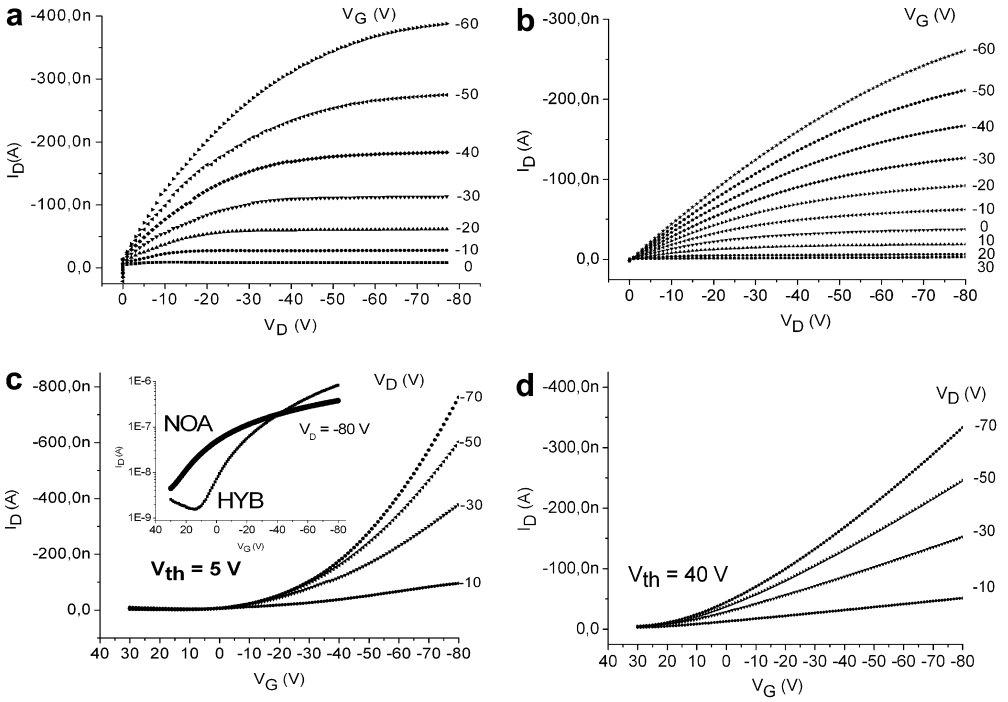

Fig. 5. Comparison of electrical characteristics of a transistor with NOA gate dielectric, shown in the graphs (b) and (d), with a hybrid transistor shown in parts (a) and (c). In the inset of part (c) a comparison of transfer curves for $V_D = -80$ V is given. On/off current ratios of 523.6 and 83.6 can be calculated from this plot for hybrid and NOA transistors, respectively.

Solution-processed transistors generally exhibited the highest mobility where the semiconductor P3HT was deposited from the solvent TCB. This is known to be due to the effect of high boiling point of TCB. Slow evaporation of the solvent lets the film more time to order during the drying stage [17]. The values increased with increasing boiling point of the solvent for almost every dielectric. However, it can be observed by comparing the output characteristics in Fig. 6 that in some cases the conductivity values ($V_G = 0$ V) were also higher where the mobility was higher. A relationship between mobility and conductivity was already discussed in previous studies [18,19]. The threshold voltage values in Table 2 imply the doping state of the transistors. Therefore, it can be said that transistors showing a high mobility value together with a low threshold voltage exhibit a proper dielectric/semiconductor interface and a highly ordered semiconductor.

In case of pentacene, measured field-effect mobility values were approximately two orders of magnitude higher than those with P3HT, as expected. (Table 2) It was observed that the mobility values of pentacene transistors decreased with increasing surface energy of the dielectric; as discussed by Yang et al. [20] NOA74-pentacene combination probably suffers from a bad interface, exhibiting improper transistor characteristics. NOA74 also had the highest surface energy. However, a direct dependence of mobility on dielectric surface energy cannot be concluded here since the dielectrics not only have different surface energies but also different chemical groups. Additionally, when the output characteristics of pentacene transistors with BCB and EL37A dielectrics are compared, it can be seen that the saturation behaviour of the drain-current is better where the conductivity is lower. Threshold voltage of BCB-pentacene combination was −21 V, whereas that of EL37A combination was −2 V. Therefore, the first one showed a better saturation (Fig. 6). Transfer characteristics of transistors using different semiconductors are presented in Fig. 7. High mobility leads to higher currents (at high V_G) and low conductivity (at low V_G) brings a high on–off current ratio in case of pentacene. Both of the P3HT semiconductors presented higher off-currents with this dielectric. Drain currents were higher in case of TCB chosen as the solvent.

In conclusion, four organic dielectric materials were investigated for usage in organic transistors. Three of them offer lower temperature or UV-pro-

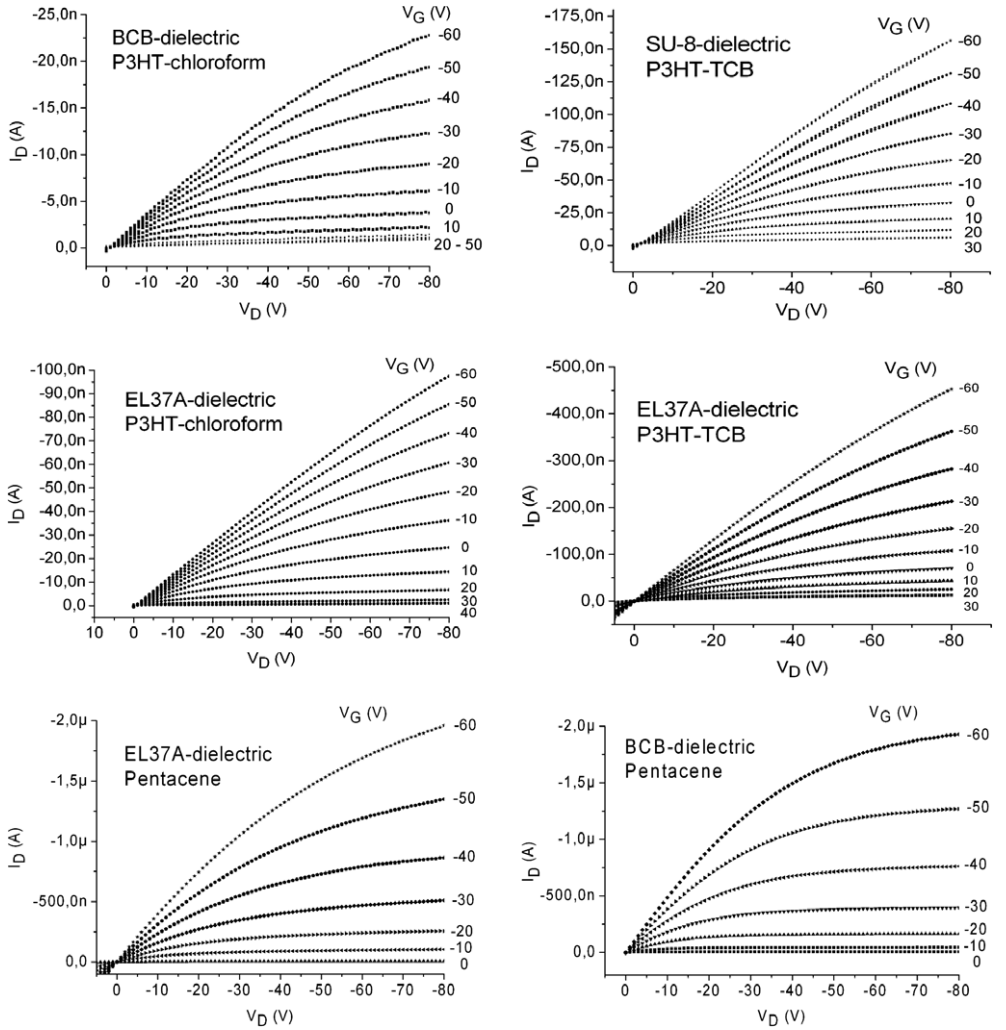

Fig. 6. Output characteristics of selected transistors with organic dielectrics and different semiconductors. Devices with pentacene semiconductor exhibited higher mobility values and higher on/off current ratios.

Table 2
Dielectric capacitance values presented with threshold voltages and saturation field-effect mobility values of different transistors

Dielectric material	Capacitance (nF/cm^2)	Vth/saturation field-effect mobility (cm^2/V s)			
		P3HT-CHL	P3HT-XYL	P3HT-TCB	Pentacene
SiO_2	11.5	$+5$ V/3.2×10^{-4}	$+19$ V/ 5.5×10^{-4}	$+8$ V/1.3×10^{-3}	-10 V/0.1
BCB	2.7	$+32$ V/5.6×10^{-5}	–	–	-21 V /2.1×10^{-2}
SU-8	2.7	$+75$ V/6.2×10^{-5}	$+59$ V/ 9.5×10^{-5}	$+64$ V/3.3×10^{-4}	$+16$ V/1.2×10^{-2}
NOA74	3.0	$+30$ V/5.7×10^{-4}	$+72$ V/ 1.7×10^{-5}	$+24$ V/6.1×10^{-4}	$+25$ V/2.3×10^{-3}
EL37A	2.7	$+35$ V/1.2×10^{-4}	$+67$ V/2.2×10^{-4}	$+32$ V/8.0×10^{-4}	-2 V /2.3×10^{-2}

cessing conditions. It was observed that these three thermosetting resins exhibit smooth films and good insulation properties and therefore they are suitable for OTFTs. With this, it was also shown that chemically resistant dielectric films do not necessarily require very high processing temperatures. Therefore, further research on such materials is surely very interesting for organic electronics. All-polymer transistors that use NOA74 as the dielectric and P3HT layer as the semiconductor were already produced successfully with laser ablation [21].

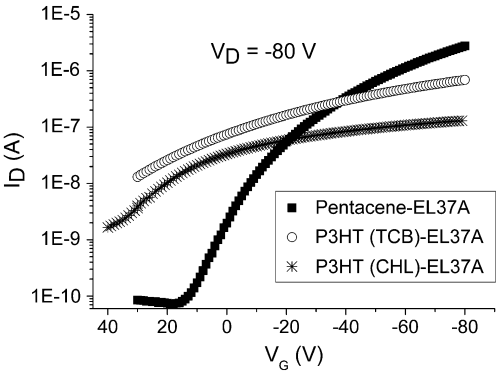

Fig. 7. Comparison of transfer characteristics of transistors with the following semiconductors: P3HT deposited from chloroform, P3HT deposited from TCB, and evaporated pentacene. They were using the same organic dielectric, EL37A. They exhibited on/off current ratios of 32.5, 53.1 and 3.7×10^4, respectively.

P3HT transistors with polymer dielectrics exhibited higher conductivity values than both SiO_2 hybrid transistors and all pentacene transistors did. Pentacene generally yields a lower conductivity with respect to P3HT. This is because of high purity of pentacene films where vacuum evaporation allows a clean film production. In case of hybrid transistors, however, solution-processed semiconductor/dielectric interface was playing the most important role. The comparison of the organic devices with hybrid transistors indicates that the performance of P3HT transistors could be improved by improving the interface. It was also shown that the performance of the devices depends significantly on solvent choice. Solvent used for the semiconductor determines both the microstructure of the semiconductor and the formed semiconductor/dielectric interface. Therefore, materials selection for a gate-dielectric in OTFTs should be made for a selected semiconductor–solvent combination. Surface treatments or additional layers could be applied to improve the device performance, but this brings complexity to the production by adding another step. Alternatively, as presented in this work, a systematic materials selection and understanding interface issues also help improving the transistor performance.

Acknowledgements

The authors thank Christian Recknagel, Martin Gruhlke and Hendrik Rothe for the WIM-investigations at the Department of Measurement and Informations Technology, from the Helmut-Schmidt-University/University of Federal Armed Force, Hamburg. Also the students Asanka Weerasinghe, Cihan Ucurum, Christopher Kofi Nyakey, Senthilkumar Sandrasekaran, Peter Schertling, Rocco Wille and Borislav Garkov are acknowledged for their contributions to the work in various parts of it.

References

[1] M. Halik, H. Klauk, U. Zschieschang, G. Schmid, W. Radlik, W. Weber, Adv. Mater. 14 (2002) 1717.
[2] Th.B. Singh, N. Marjanovic, P. Stadler, M. Auinger, G.J. Matt, S. Gunes, N.S. Sariciftci, J. Appl. Phys. 97 (2005) 083714.
[3] S.Y. Park, M. Park, H.H. Lee, Appl. Phys. Lett. 85 (2004) 2283.
[4] M. Halik, H. Klauk, U. Zschieschang, G. Schmid, C. Dehm, M. Schütz, S. Maisch, F. Effenberger, M. Brunnbauer, F. Stellacci, Nature 431 (2004) 963.
[5] J. Park, S.Y. Park, S.-O. Shim, H. Kang, H.H. Lee, Appl. Phys. Lett. 85 (2004) 3283.
[6] A. Fachetti, M.-H. Yoon, T.J. Marks, Adv. Mater. 17 (2005) 1705.
[7] J. Veres, S. Ogier, G. Lloyd, D. de Leeuw, Chem. Mater. 16 (2004) 4543.
[8] H.E. Katz, X.M. Hong, A. Dodabalapur, R. Sarpeshkar, J. Appl. Phys. 91 (2002) 1572.
[9] B. Stadlober, M. Zirkl, M. Beutl, G. Leising, S. Bauer-Gogonea, S. Bauer, Appl. Phys. Lett. 86 (2005) 242902.
[10] H. Jia, G.K. Pant, E.K. Gross, R.M. Wallace, B.E. Gnade, Org. Electron. 7 (2006) 16.
[11] H.G.O. Sandberg, T.G. Bäcklund, R. Österbacka, M. Shkunov, D. Sparrowe, I. McCulloch, H. Stubb, Org. Electron. 6 (2005) 142.
[12] Y.H. Noh, S.Y. Park, S.-M. Seo, Hong H. Lee, Org. Electron. 7 (2006) 271–275.
[13] L.L. Chua, P.K.H. Ho, H. Sirringhaus, R.H. Friend, Appl. Phys. Lett. 84 (2004) 3400.
[14] D.K. Owens, R.C. Wendt, J. Appl. Polym. Sci. 12 (1969) 1741.
[15] M. Raja, G. Lloyd, N. Sedghi, S. Higgins, W. Eccleston, Mater. Res. Soc. Symp. Proc. 725 (2002) 161.
[16] G. Horowitz, R. Hajlaoui, H. Bouchriha, R. Bourguiga, M. Hajlaoui, Adv. Mater. 10 (1998) 923.
[17] J.F. Chang, B. Sun, D.W. Breiby, M.M. Nielsen, T.I. Sölling, M. Giles, I. McCullough, H. Sirringhaus, Chem. Mater. 16 (2004) 4772.
[18] A.R. Brown, C.P. Jarrett, D.M. de Leeuw, M. Matters, Synthetic Met. 88 (1997) 37.
[19] M. Raja, G.C.R. Lloyd, N. Sedghi, W. Eccleston, R. Di Lucrieza, S.J. Higgins, J. Appl. Phys. 92 (2002) 1441.
[20] S.Y. Yang, K. Shin, C.E. Park, Adv. Funct. Mater. 15 (2005) 1806.
[21] R.M. Meixner, R. Wille, P. Schertling, H. Goebel, H. Harde, K.-H. Steiglich, F.A. Yildirim, W. Bauhofer, W. Krautschneider, Org. Electron. 7 (2006) 586.

Available online at www.sciencedirect.com
ScienceDirect
Organic Electronics 9 (2008) 77–84
Organic Electronics
www.elsevier.com/locate/orgel

Bipyridyl substituted triazoles as hole-blocking and electron-transporting materials for organic light-emitting devices

Musubu Ichikawa [a,*], Soichi Fujimoto [a], Yuta Miyazawa [a], Toshiki Koyama [a], Norimasa Yokoyama [b], Tetsuzo Miki [b], Yoshio Taniguchi [a]

[a] *Department of Functional Polymer Science, Shinshu University, 3-15-1 Tokita, Ueda, Nagano 386-8567, Japan*
[b] *Hodogaya Chemical Co., Ltd., 45 Miyukigaoka, Tsukuba, Ibaraki 305-0841, Japan*

Received 9 July 2007; received in revised form 29 August 2007; accepted 3 September 2007
Available online 14 September 2007

Abstract

We have demonstrated bipyridyl substituted triazole derivatives (Bpy-TAZs) as an electron-transporting material for organic light-emitting devices (OLEDs). Substitution of triazole with bipyridyl is a good way to improve electron-transporting ability of triazoles with keeping good hole-blocking ability, which is a useful property of triazole derivatives. A Bpy-TAZ has high electron mobility of above 10^{-4} cm^2/V s. Moreover, by employing one of Bpy-TAZs as a hole-blocking and electron-transporting material for phosphorescent OLEDs, lower operation voltage was achieved with keeping the same external quantum efficiency of electroluminescence (almost 10%) as compared with the conventional hole-blocking and electron-transporting bilayer consisting of bathocuproine and tris (8-hydroxyquinolinato) aluminum.

PACS: 72.80.Le; 73.61.Ph; 85.60.Jb

Keywords: Amorphous material; Hole blocking; Electron transporting; Triazole; Electroluminescent device; OLED; Phosphorescent device; Mobility; Pyridine

1. Introduction

Organic light-emitting devices (OLEDs) have been received much attention due to their potential applications for thin flat television, mobile displays, lightings, optical communication light sources, and so on. OLEDs are generally composed of functionally divided organic multi-layers, e.g. hole transporting (HT), emissive, and electron transporting (ET) layers, and so on [1,2]. In the last decade, many kinds of amorphous molecular semiconductor materials [3,4], working as HT materials [5–9] and ET materials [10–15], have been proposed, and HT molecular semiconducting materials have become practical due to their high charge carrier mobility and excellent operational durability. On the other hand, there have been scarcely reports on ET organic semiconducting amorphous materials with high performance (high-speed transportation of electrons, easy injection of electrons from the cathode, and good operational durability) [13]. Tris (8-hydroxyquinolinato) aluminum(III) (Alq), which

* Corresponding author. Tel.: +81 268 21 5498; fax: +81 268 21 5413.
E-mail address: musubu@shinshu-u.ac.jp (M. Ichikawa).

1566-1199/$ - see front matter © 2007 Elsevier B.V. All rights reserved.
doi:10.1016/j.orgel.2007.09.002

is the historical material reported in the first bright OLED by Tang et al. in 1987 [1], is still conventionally used as an ET material regardless of its slow electron mobility [17] because it exhibits high operational durability. However, as a reflection of the imbalanced performance between ET and HT materials, electron-feeding from the cathode into an emissive layer controls device characteristics. Consequently, the development of efficient ET organic amorphous semiconducting materials is a challenge of high priority.

Efficient ET materials provide some advantages, such as lowering the operating voltage and power consumption. Moreover, if the ET materials have wide band gaps, in other words, deeper highest occupied molecular orbitals (HOMO), such ET materials can also work as hole blocking (HB) materials. The complete confinement of a hole in an emissive layer by the HB layer raises the quantum efficiencies of electroluminescence (EL). Recently, we have developed a new electron-transporting material family with very high electron mobility: bipyridyl substituted oxadiazoles. The new ET materials show excellent ET properties with electron mobility of above 10^{-3} cm^2/V s and good thermal stability with high glass transition temperature (T_g) of above 100 °C [18,19]. As the result, using the new materials as electron-transporting materials leaded to lower operation voltage, lower power consumption, and longer lifetime. Consequently, substitution of conventionally well-known electron-transporting molecular skeletons with pyridine and/or bipyridyl will be a valuable way to create new electron-transporting material with high performance. Here we demonstrate another pyridyl substituted material family: bipyridyl triazoles (Bpy-TAZs), which work as efficient electron-transporting materials and also good hole-blocking materials. In addition, the materials can be utilized for phosphorescent OLEDs.

2. Experimental

2.1. Materials

Fig. 1 shows chemical structures of the newly developed materials abbreviated as Bpy-TAZs. These materials are synthesized from the corresponding hydrazide intermediates by ring formation reaction with an aryl amine as shown in Scheme 1. For example, Bpy-TAZ-01 was synthesized from Bpy2-Hyd with 4-*tert*-butylaniline in *o*-dichlorobenzene. The reactions quantitatively proceeded. They

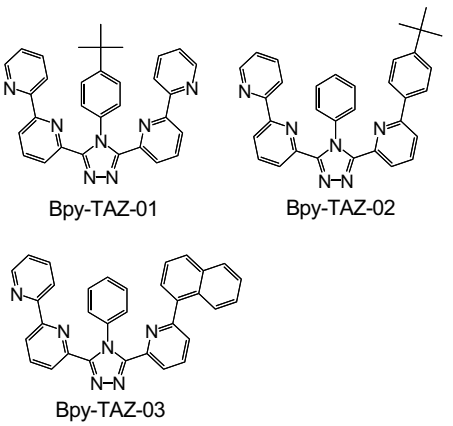

Fig. 1. Chemical structures of Bpy-TAZs.

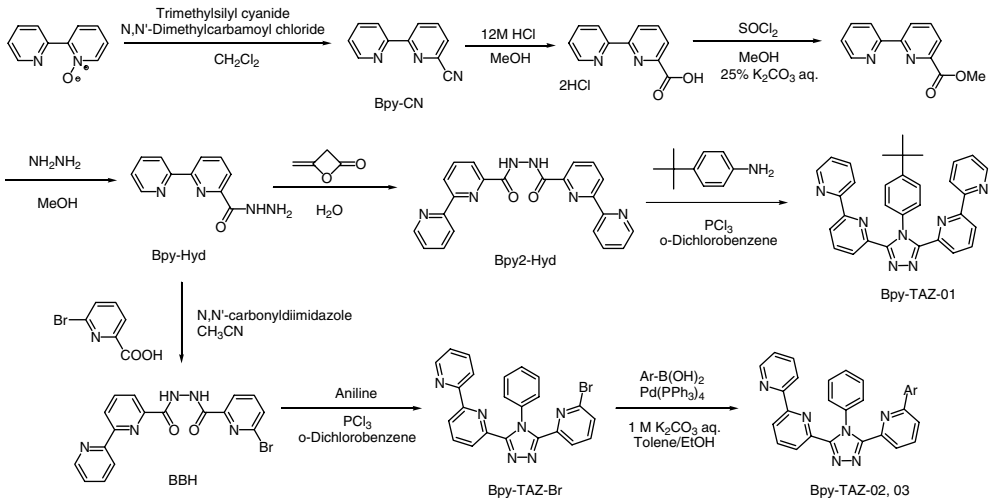

Scheme 1. Synthetic routes of Bpy-TAZs.

were purified by silica gel column chromatography to give white crystals, whose structures were confirmed by ^{1}H NMR, ^{13}C NMR, mass spectroscopy and elemental analysis. Further purification was carried out with temperature gradient sublimation in a flow stream of pure argon gas before use. Note that other OLED materials were from industrial companies as sublimation grades, and then used without further purification.

2.2. Synthesis

2.2.1. [2,2′]Bipryridinyl-6-carboxylic acid hydrazide (Bpy-Hyd)

[2,2′]Bipryridinyl-6-carbonitrile (Bpy-CN) was synthesized from 2,2′-dipyridyl-*N*-oxide (10.0 g, 58.1 mmol), trimethylsilyl cyanide (8.70 mL, 69.7 mmol) and *N*,*N*-dimethylcarbamoyl chloride (6.40 mL, 69.7 mmol) in absolute dichloromethane (100 mL) for 5 days at room temperature by following a previously reported reaction [18]. Note that all reagents used in this study were commercially available. Bpy-CN was converted to carboxylic acid with conc. HCl in methanol, and then methyl-esterificated with thionyl chloride in dewatered methanol. Finally, Bpy-Hyd was synthesized from the methyl ester (43.7 g, 204 mmol) with hydrazine (12.8 mL, 408 mmol) in methanol (400 mL). δ_H (270 MHz, $CDCl_3$): 9.12 (1H, s), 8.70 (1H, d, *J* 4.3 Hz), 8.58 (1H, d, *J* 7.8 Hz), 8.37 (1H, d, *J* 8.1 Hz), 8.09 (1H, d, *J* 7.6 Hz) 7.96 (1H, t, 7.7 Hz), 7.84 (1H, t, *J* 6.9 Hz), 7.35 (1H, t, *J* 5.6 Hz), 4.16 (2H, d, *J* 4.3 Hz).

2.2.2. 3,5-Bis([2,2′]Bipyridin-6-yl)-4-(4-tert-butylphenyl)-[1,2,4]triazole (Bpy-TAZ-01)

First, [2,2′]Bipyridinyl-6-carboxylic acid *N*′-([2,2′]bipyridinyl-6-carbonyl)-hydrazide (Bpy2-Hyd) was synthesized from Bpy-Hyd (3.70 g, 17.3 mmol) with 4-methylene-oxetan-2-one (7.63 g, 90.8 mmol) in chloroform (139 mL) at the reflux under N_2. After hexane-washing the precipitation obtained by removing chloroform from the solution, Bpy2-Hyd was obtained by a hydrolysis with 70-mL-water of the precipitation (1.45 g) in diglyme (50 mL) at 120 °C under N_2. Finally, Bpy-TAZ-01 was synthesized from Bpy2-Hyd (1.18 g, 2.98 mmol) with 4-*tert*-butylaniline (2.81 mL, 17.9 mmol) in *o*-dichlorobenzene (30 mL) at 100 °C for 1 h under N_2 adding phosphorus trichloride (0.286 mL, 3.27 mmol). White powder (0.91 g) of Bpy-TAZ-01 was obtained by NH-silica-gel chromatography (chloroform:hexane = 2:1). δ_H (270 MHz, $CDCl_3$): 8.58 (2H, d, *J* 3.8 Hz), 8.40 (2H, dd, *J* 7.8, 1.1 Hz), 8.31 (2H, dd, 8.1, 1.1 Hz), 7.94 (2H, t, 7.8 Hz), 7.53(2H, dt, 7.6, 1.6 Hz), 7.46–7.43 (2H, m), 7.34–7.19 (8H, m), 1.27 (9H, s). δ_C (68 MHz, $CDCl_3$): 155.08, 154.85, 154.04, 150.99, 148.59, 146.04, 137.53, 136.24, 134.75, 127.11, 125.49, 124.33, 123.49, 120.83, 120.73, 34.63, 31.43. MS (EI): *m*/*z* 509 (M^+). Elemental analysis calculated for $C_{32}H_{27}N_7$: C, 75.42; H, 5.34; N, 19.24. Found: C, 75.63; H, 5.44; N, 18.98.

2.2.3. [2,2′]Bipryridinyl-6-carboxylic acid N′-(6-bromopyridine-2-carbonyl)hydrazide (BBH)

First, an intermediate product was synthesized from *N*,*N*′-carbonyldiimidazole (29.4 g, 181 mmol) with 6-bromopicolinic acid (35.0 g, 173 mmol) in dewatered acetonitrile (350 mL) for 30 min at 35 °C. After cooling the solution to room temperature, add 700 mL acetonitrile and Bpy-Hyd (35.3 g, 165 mmol), and stir the mixture for 3 h at 40 °C. BHH white powder (53.2 g) was obtained from the mixture after washing with water and cooled acetonitrile. δ_H (270 MHz, $CDCl_3$): 10.48 (1H, s), 10.23 (1H, s), 8.70 (1H, d, *J* 4.6 Hz), 8.64 (1H, dd, *J* 8.0, 1.2 Hz), 8.47 (1H, d, 7.8 Hz), 8.22 (1H, dd, *J* 7.6, 1.1 Hz), 8.17 (1H, dd, *J* 7.6, 1.1 Hz), 8.02 (1H, t, *J* 7.8 Hz), 7.87 (1H, dt, J 7.8, 1.8 Hz), 7.76 (1H, t, *J* 7.7 Hz), 7.68 (1H, dd, *J* 8.1, 1.1 Hz), 7.37 (1H, ddd, *J* 7.5, 4.7, 1.4 Hz).

2.2.4. 3-([2,2′]Bipyridin-6-yl)-5-[6-(4-tert-butylphenyl)prydin-2-yl]-4-phenyl-[1,2,4]triazole (Bpy-TAZ-02)

BpyTAZ-Br was synthesized as a shared intermediate product for both Bpy-TAZ-02 and -03 from BBH with aniline. Initially, aniline (41.2 mL, 452 mmol) and phosphorous trichloride (7.25 mL, 82.9 mmol) in absolute *o*-dichlorobenzine (500 mL) was stirred under nitrogen stream for 1 h at 100 °C, and then BBH (30.0 g, 75.3 mmol) was added to the mixture. After that, the mixture was continuously stirred for 1.5 h at 140 °C. BpyTAZ-Br was obtained from the mixture by conventional procedures, and then, Bpy-TAZ-02 was synthesized from BpyTAZ-Br (3.00 g, 6.59 mmol) with 4-*tert*-butylphenylboronic acid (1.76 g, 9.88 mmol) in degassed toluene/ethanol (80 mL:20 mL) under Ar stream by Suzuki coupling with tetrakis(triphenylphosphine)palladium (0) (0.381 g, 0.329 mmol) and 1-M-K_2CO_3-aquaous solution (22.5 g, 19.8 mmol) for 3 h at 72 °C (reflax). After cooling the mixture, precipitation was filtered, washed with water, tolene, and methanol, and then, white powder of

Bpy-TAZ-02 (2.70 g) was obtained by solving and concentrating the precipitation with chloroform. δ_H (270 MHz, $CDCl_3$): 8.58 (1H, d, J 4.0 Hz), 8.37–8.35 (2H, m), 8.24 (1H, d, J 7.8 Hz), 7.92 (1H, t, J 7.8 Hz), 7.84 (1H, t, 7.8 Hz), 7.68 (1H, d, J 8.1 Hz), 7.54–7.41 (6H, m), 7.31–7.19 (5H, m), 7.10 (1H, d, J 8.1 Hz), 1.33 (9H, s). δ_C (68 MHz, $CDCl_3$): 155.85, 155.09, 154.83, 154.27, 152.17, 148.72, 146.53, 146.18, 138.23, 137.63, 137.33, 136.17, 135.19, 129.08, 127.97, 127.80, 126.37, 125.12, 124.13, 123.68, 122.37, 121.22, 120.84, 119.81, 113.65, 34.69, 31.32. MS (EI): m/z 508 (M^+). Elemental analysis calculated for $C_{33}H_{28}N_6$: C, 77.93; H, 5.55; N, 16.52. Found: C, 78.38; H, 5.68; N, 16.26.

2.2.5. 3-([2,2′]Bipyridin-6-yl)-5-[6-(1-naphthyl)-prydin-2- yl]-4-phenyl-[1,2,4]triazole (Bpy-TAZ-03)

Bpy-TAZ-03 was synthesized from BpyTAZ-Br (3.00 g, 6.59 mmol) with naphthylene-1-boronic acid (1.70 g, 6.59 mmol) in degassed toluene/ethanol (80 mL:20 mL) under Ar stream by Suzuki coupling with tetrakis(triphenylphosphine)palladium (0) (0.381 g, 0.329 mmol) and 1-M-K_2CO_3-aquaous solution (22.5 g, 19.8 mmol) for 2 h at 72 °C (reflax). After cooling the mixture, precipitation was filtered, washed with water, tolene, and methanol, and then, white powder of Bpy-TAZ-03 (2.12 g) was obtained by recrystallizing from a mixture of tolene and methanol. δ_H (400 MHz, $CDCl_3$): 8.55 (1H, d, J 4.0 Hz), 8.37 (2H, dd, J 7.9, 2.4 Hz), 8.23 (1H, d, J 7.0 Hz), 7.90 (2H, t, J 7.8 Hz), 7.85 (2H, t, J 8.9 Hz), 7.81 (1H, d, J 8.6 Hz), 7.55 (1H, d, J 7.1 Hz), 7.48–7.42 (2H, m), 7.41–7.36 (2H, m), 7.34 (3H, dt, J 7.4, 7.1, 1.4 Hz), 7.27 (2H, d, J 7.0 Hz), 7.17 (1H, ddd, J 7.5, 4.8, 1.1 Hz), 6.99 (1H, d, J 8.0 Hz), 6.89 (1H, dd, J 7.1, 1.1 Hz). δ_C (101 MHz, $CDCl_3$): 158.33, 155.61, 155.38, 155.10, 154.33, 149.23, 147.46, 146.66, 138.21, 138.13, 137.83, 137.21, 136.64, 134.07, 131.08, 129.27, 129.18, 128.70, 128.66, 128.24, 126.87, 126.07, 125.71, 125.60, 125.37, 124.43, 124.14, 123.29, 121.65, 121.33. MS (EI): m/z 502 (M^+). Elemental analysis calculated for $C_{33}H_{22}N_6$: C, 78.87; H, 4.41; N, 16.72. Found: C, 79.08; H, 4.52; N, 16.39.

2.3. Device fabrication and measurements

All OLEDs were fabricated on 150-nm-thick layers of indium-tin oxide (ITO) commercially precoated onto glass substrates with a sheet resistance of 14 Ω/sq. The solvent cleaned ITO surface was treated by O_2-plazma for 5 min just before loading the substrates into a high-vacuum chamber (base pressure below $\sim 6 \times 10^{-4}$ Pa), where organic layers, 0.5-nm-thick LiF, and 200-nm-thick aluminum cathode layers were deposited via thermal evaporation. Deposition rates are, respectively, 0.6 Å/s for organic materials, 0.1 Å/s for LiF, and 6 Å/s for Al. The current density-applied voltage-luminance characteristics of OLEDs were measured with a commercial apparatus (Precise Gauge, EL1003) with a Keithley 2400 source meter.

^{1}H NMR spectra were recorded either on a JEOL JNM-EX270 spectrometer (270 MHz) or a Bruker AVANCE spectrometer (400 MHz). Elemental analysis was carried out with Yanaco MT-3 CHNcoder. Thermal analysis was performed on Seiko Instruments DSC-6200 at a heating rate of 10 °C/min for differential scanning calorimetry (DSC) under nitrogen gas. Ultraviolet (UV) and visible absorption spectra and fluorescence spectra were recorded with a Shimadzu UV-3150 spectrophotometer and a JASCO FP-750 spectrofluorometer, respectively. The highest occupied molecular orbital (HOMO) energy was determined with a Riken Keiki AC-3 photoelectron emission spectrometer, where the HOMO energy was defined as being equal to the ionization potential measured by photoelectron emission spectroscopy. Optical band gaps were determined by a spectral onset of each UV–vis absorption spectrum, and then the lowest unoccupied molecular orbital (LUMO) energies were obtained with the HOMO energy and the optical band gap. The spectroscopic measurements were carried out with thin-films prepared by thermally evaporated on quartz substrates.

Electron mobility was measured by conventional time-of-flight (TOF) technique. 500-ps-duration optical pulse from a nitrogen gas laser ($\lambda = 337$ nm, Lasertechnik Berlin, MSG-800) was used as an excitation light for TOF. Test samples were prepared by thermal evaporation in vacuum and encapsulated with a fresh desiccant under highly inert atmosphere of N_2 at the dew point of almost −60 °C and O_2 concentration of below 10 ppm. We employed a 100-nm-thick fullerene C_{60} layer as a charge generation layer for the optical excitation.

3. Results and discussion

3.1. Thermal and electronic properties

Fig. 2 shows DSC curves of Bpy-TAZ-03. An endothermic peak due to melting was observed at

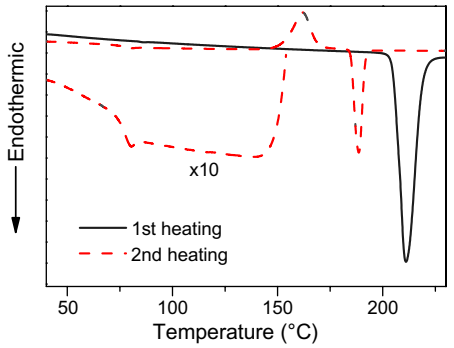

Fig. 2. DSC curves of Bpy-TAZ-03 in first and second heating.

211 °C in a first heating of Bpy-TAZ-03 powder. A baseline shift due to the glass transition and an exothermic peak at 162 °C due to crystallizing were observed in a second heating. The DSC results confirm that Bpy-TAZ-03 can form a stable glassy state with glass transition temperature (T_g) of 74 °C. This T_g value is rather lower than that (94 °C) of NPB (see Fig. 5) a practical HT material, but higher than that (64 °C) of another generally used HT material TPD (*N*,*N*′-diphenyl-*N*,*N*′-di(*m*-tolyl)benzidine).

UV–vis absorption and fluorescence spectra of a neat thin film of Bpy-TAZ-03 are shown in Fig. 3. The absorption maximum of the material is 304 nm and the material emits bright UV fluorescence. The band gap of 3.6 eV for Bpy-TAZ-03 from the absorption spectrum is very wide. This wide band gap characteristics results from the weak π-conjugations of triazole. LUMO level of Bpy-TAZ-03 (2.7 eV) in neat solid is low enough to easily accept electrons from a cathode metal. This nature is caused by substitution of triazole with pyridine.

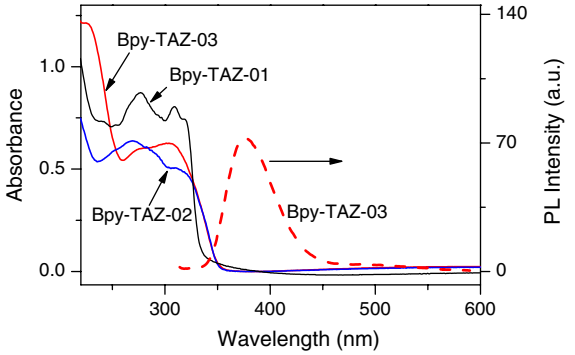

Fig. 3. UV and visible absorption spectra of Bpy-TAZs thin-films. The thicknesses of the films are, respectively, 130 nm for Bpy-TZA-01, 90 nm for -02, and 90 nm for -03. PL spectrum of the Bpy-TAZ-03 film was also shown in the figure (right axis).

In addition, HOMO level of Bpy-TAZ-03 (6.3 eV) is sufficiently deep to suppress hole-leakage from the emissive layer to the cathode via the Bpy-TAZ-03 layer, and the hole confinement in the emissive layer leads to high quantum efficiencies of EL. Bpy-TAZ-03 can be utilized as efficient electron-transporting and hole-blocking materials with rather high thermal stability. In addition, the other Bpy-TAZs also show similar absorption-spectroscopic characteristics as presented in the figure. Note that optical interference by the sample thin-film causes broad absorption around 500–600 nm.

The thermal and electronic properties of Bpy-TAZs were summarized in Table 1. Only Bpy-TAZ-03 has T_g, and evaporated thin-films of Bpy-TAZ-03 have a thermal stability. On the other hand, Bpy-TAZ-01 and 02 have no T_g. No T_g and higher melting points (T_m) of Bpy-TAZ-01 and Bpy-TAZ-02 indicate that they have higher crystallinity than Bpy-TAZ-03. However, high T_m of Bpy-TAZ-01 means that Bpy-TAZs will have good thermal stability; in other words, no decomposition occurs in vacuum evaporation. As we can see from the table, introduction of asymmetric diversities and a naphthyl substituent gave a good amorphous nature to the materials in common with other amorphous organic semiconductors. Consequently, we believe that it should be successful to obtain another Bpy-TAZ with higher T_g for improving thermal and long-time stabilities of its amorphous state by carrying out some chemical modifications.

3.2. OLED properties

Fig. 4 shows current density–voltage ($J-V$) characteristics of OLEDs with Bpy-TAZs as electron-transporting materials. The figure also shows reference devices with no Bpy-TAZ. Structures of the devices and used chemicals are shown in Fig. 5. As shown in Fig. 4, Bpy-TAZs excepting for Bpy-TAZ-01 show higher performance than the TAZ01 reference device: the conventional triazole compound [20] The Bpy-TAZ-02 device showed comparable $J-V$ characteristics with the Alq reference

Table 1
Thermal and electronic properties of Bpy-TAZs

Bpy-TAZ-	HOMO (eV)	LUMO (eV)	Band gap (eV)	T_m (°C)	T_g (°C)
01	6.7	2.9	3.8	316	NA
02	6.3	2.7	3.6	268	NA
03	6.3	2.7	3.6	211	74

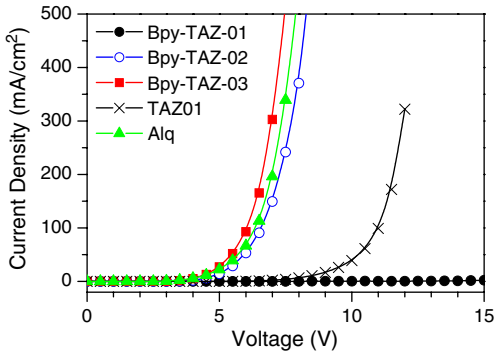

Fig. 4. Current density–voltage characteristics of OLEDs with Bpy-TAZs as electron-transporting materials, showing together the reference devices with Alq and TAZ01.

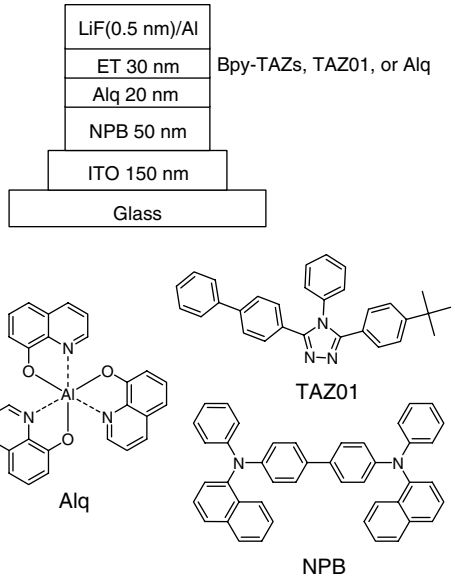

Fig. 5. Device structure of OLEDs with different ET materials and chemical structures of materials used.

device. Therefore, it is concluded that substitution of triazole with pyridyl is a valuable way to enhance the electron-transporting property of triazole derivatives. Furthermore, the Bpy-TAZ-03 device shows higher current efficiency (4.4 cd/A) than the Alq device (3.9 cd/A). This higher efficiency indicates strong hole-blocking nature of the compound. As generally known, hole-blocking is a valuable property of triazoles. Note Bpy-TAZ-01 briefly: the Bpy-TAZ-01 device shows quite bad performance, and we think that the reason must be instability of the amorphous state of Bpy-TAZ-01, not intrinsic inferior natures of electron injection and transport of this molecule, because the Bpy-TAZ-01 layer was completely hazed at the device fabrication, in other words, easily re-crystallized.

As elucidated in the above paragraph, Bpy-TAZs, especially Bpy-TAZ-03, exhibited good performance as not only an electron-transporting material but also a hole-blocking material. So we try to utilize Bpy-TAZ-03 as a double function (electron-transporting and hole-blocking) material. As well known the recent high efficient phosphorescent OLEDs have both hole-blocking layer and electron-transporting layer. In particular, the hole-blocking layer is important to obtain high quantum efficiency because hole-leakage seriously reduces the efficiency. Moreover, it is more important to consider the triplet energy dissipation from the emissive layer to the hole-blocking layer for attaining high quantum efficiency. At present there is only few materials to be utilized as hole-blocking materials for phosphorescent OLEDs, for example, bathocuproine (BCP), bis (2-methyl-8-quinolinolato) (*p*-phenylphenolato) aluminum (BAlq), and so on.

Fig. 6 shows $J-V$ characteristics of phosphorescent OLEDs with Bpy-TAZ-03 as a hole-blocking and electron-transporting material, showing together a reference device, where structures of the device and chemicals are shown in Fig. 7. As we can see from Fig. 6, the phosphorescent OLED with Bpy-TAZ-03 exhibited much lower operation voltage than that of the reference which had a conventional double layer made up with BCP and Alq

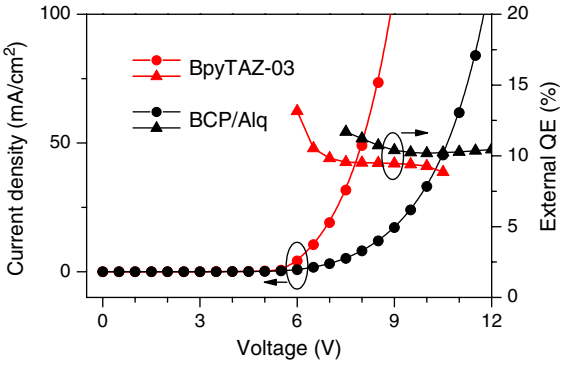

Fig. 6. $J-V$ (left axis) and external quantum efficiency (QE)-V (right axis) characteristics of the phosphorescent OLED with Bpy-TAZ-03 as a hole-blocking and electron-transporting material, showing together a reference device with the conventional structure.

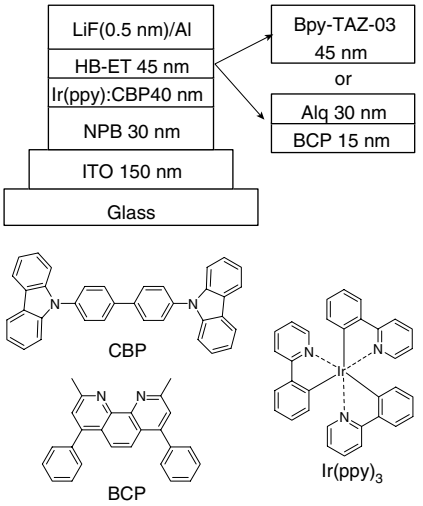

Fig. 7. Device structure of phosphorescent OLEDs with Bpy-TAZ-03 as a hole-blocking and electron-transporting layer, and chemical structures of used other chemicals in the OLEDs.

layers for hole-blocking and electron-transporting functions [21] Since both devices shows high external quantum efficiency of almost 10 % as shown in the figure, Bpy-TAZ-03 is useful as a hole-blocking and electron transporting materials for phosphorescent OLEDs.

3.3. Electron mobility

Finally, we would like to briefly discuss electron mobility in Bpy-TAZ-03 thin-film. Fig. 8 shows the transient electron photocurrent waveform obtained by TOF measurement. We obtained the transit time (t_T) of 9.70 μs from the transient photocurrent, where t_T was defined as the kink point of the the transient photocurrent. Hence, electron mobility (μ) was determined to be 8.0×10^{-5} cm^2/V s at the electric field ($E = V/D$) of 680 kV/cm with the following equation:

$$\mu = Dd/(t_T V), \quad (1)$$

where V, D, and d are, respectively, the applied voltage, the distance between the two electrodes, and the thickness of Bpy-TAZ-03 layer. This mobility is two-fold higher than that of Alq of 1.3×10^{-6} cm^2/V s at approximately same electric field from the literature [22] This high mobility probably caused the better current density–voltage curve of the Bpy-TAZ-03 device than the Alq reference device. In addition, the waveform in Fig. 8 has the well-defined plateau, implying that electron-transportation in Bpy-TAZ-03 thin-film is non-dispersive. The degree of carrier transport dispersion can be described by the tail broadening parameter W, defined as [23]

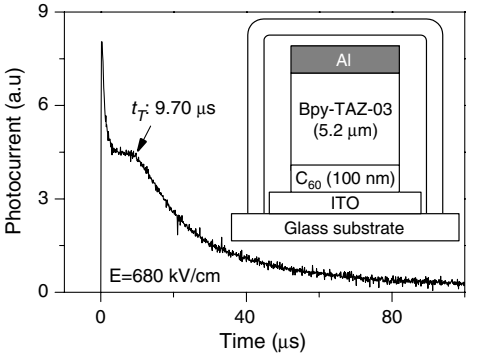

Fig. 8. Electron transient photocurrent of TOF measurement of Bpy-TAZ-03 at the applied voltage of 360 V to the Al cathode. The inset shows device structure used.

$$W = (t_{1/2} - t_0)/t_{1/2}, \quad (2)$$

where t_0 is the time of the kink and $t_{1/2}$ is the time when the transient photocurrent reaches half of its plateau value. For the transient photocurrent, we calculate $W = 0.57$, indicating a relatively-small dispersion of the electron packet during transport across the sample. As a summary, Fig. 9 shows electron mobility *vs.* square root of applied electric field for several materials including Bpy-TAZ-03. As you can see from the figure, Bpy-TAZ-03 shows almost 2-folder higher mobility than Alq for a wide electric field range from 400 to 2000 kV/cm. The mobility is over 10^{-4} cm^2/V s above 720 kV/cm. This high mobility is comparable to that of a representative ET material with high electron mobility: a

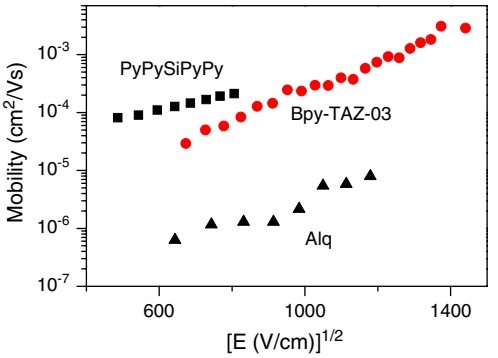

Fig. 9. Electric field dependence of electron mobility of Bpy-TAZ-03, Alq, and PyPySiPyPy. Data for Alq and PyPySiPyPy were referred from the literature by Murata (see text).

silole derivative, 2,5-bis(6′-(2′,2″-bipyridyl))-1,1-dimethyl-3,4-diphenylsilole (PyPySiPyPy)[22,24]

4. Conclusion

In conclusion, we have demonstrated bipyridyl substituted triazole derivatives (Bpy-TAZs) as electron-transporting materials for OLEDs. Substitution of triazole with bipyridyl is a good way to improve electron-transporting ability of triazoles with keeping good hole-blocking ability, which is a useful property of triazole derivatives. By employing Bpy-TAZ-03 as a hole-blocking and electron-transporting material for phosphorescent OLEDs, lower operation voltage was achieved with holding the comparable high external quantum efficiency to the OLED with the conventional BCP/Alq of almost 10%. At present, the glass transition temperature of Bpy-TAZ-03 is not high enough, but we believe that another Bpy-TAZ with higher T_g should be prepared keeping its high electron mobility by means of some chemical modifications. Now further experiments are in progress.

Acknowledgements

The authors thank Mr. S. Hayashi and Mr. N. Yokoyama of Hodogaya Chem. for helpful advise to the synthesis of the materials, and also thank Dr. Y. Nakajima and Mr. D. Yamashita of Riken Keiki for measuring the ionization potential of compounds with their photoelectron spectroscopic equipment (Riken Keiki AC-3). This work was supported by the Cooperative Link for Unique Science and Technology for Economy Revitalization (CLUSTER) of the Japan's Ministry of Education, Culture, Sports, Science and Technology. It was also supported by the Ministry's 21st Century COE program.

References

[1] C.W. Tang, S.A. VanSlyke, Appl. Phys. Lett. 51 (1987) 913.
[2] C. Adachi, T. Tsutsui, S. Saito, Appl. Phys. Lett. 57 (1990) 531.
[3] Y. Shirota, J. Mater. Chem. 10 (2000) 1.
[4] U. Mitschke, P. Baeuerle, J. Mater. Chem. 10 (2000) 1471.
[5] S.A. VanSlyke, C.H. Chen, C.W. Tang, Appl. Phys. Lett. 69 (1996) 2160.
[6] M. Thelakkat, H.-W. Schmidt, Adv. Mater. 10 (1998) 219.
[7] K. Katsuma, Y. Shirota, Adv. Mater. 10 (1998) 223.
[8] H. Tanaka, S. Tokito, Y. Taga, A. Okada, Chem. Commun. (1996) 2175.
[9] M. Ichikawa, K. Hibino, N. Yokoyama, T. Miki, T. Koyama, Y. Taniguchi, Synth. Met. 156 (2007) 1383.
[10] C. Adachi, T. Tsutsui, S. Saito, Appl. Phys. Lett. 55 (1989) 1489.
[11] Y. Hamada, C. Adachi, T. Tsutsui, S. Saito, Jpn. J. Appl. Phys. 31 (1992) 1812.
[12] K. Tamao, M. Uchida, T. Izumizawa, K. Furukawa, S. Yamaguchi, J. Am. Chem. Soc. 118 (1996) 11974.
[13] M. Uchida, T. Izumizawa, T. Nakano, S. Yamaguchi, K. Tamao, K. Furukawa, Chem. Mater. 13 (2001) 2680.
[14] J. Bettenhausen, P. Strohriegl, Adv. Mater. 8 (1996) 507.
[15] S.B. Heidenhain, Y. Sakamoto, T. Suzuki, A. Miura, H. Fujikawa, T. Mor, S. Tokito, Y. Taga, J. Am. Chem. Soc. 122 (2000) 10240.
[16] R.G. Kepler, P.M. Beeson, S.J. Jacobs, R.A. Anderson, M.B. Sinclair, V.S. Valencia, P.A. Cahill, Appl. Phys. Lett. 66 (1995) 3618.
[17] M. Ichikawa, T. Kawaguchi, K. Kobayashi, T. Miki, K. Furukawa, T. Koyama, Y. Taniguchi, J. Mater. Chem. 16 (2006) 221.
[18] M. Ichikawa, N. Hiramatsu, N. Yokoyama, T. Miki, S. Narita, T. Koyama, Y. Taniguchi, Phys. Status Solidi RRL 1 (2007) R37.
[19] J. Kido, C. Ohtaki, K. Hongawa, K. Okuyama, K. Nagai, Jpn. J. Appl. Phys. 32 (1993) L917.
[20] M.A. Baldo, S. Lamansky, P.E. Burrows, M.E. Thompson, S.R. Forrest, Appl. Phys. Lett. 75 (1999) 4.
[21] H. Murata, G.G. Malliaras, M. Uchida, Y. Shen, Z.H. Kafafi, Chem. Phys. Lett. 339 (2001) 161.
[22] L.B. Schein, Philos. Mag. B 65 (1992) 795.
[23] S. Tabatake, S. Naka, H. Okada, H. Onnagawa, M. Uchida, T. Nakano, K. Furukawa, Jpn. J. Appl. Phys. 41 (2002) 6582.

Available online at www.sciencedirect.com
ScienceDirect
Organic Electronics 9 (2008) 85–94
Organic Electronics
www.elsevier.com/locate/orgel

Enhanced cyanine solar cell performance upon oxygen doping

Bin Fan [a], Roland Hany [a], Jacques-Edouard Moser [b], Frank Nüesch [a,*]

[a] *Laboratory for Functional Polymers, Swiss Federal Laboratories for Materials Testing and Research, Empa, Überlandstrasse 129, CH-8600 Dübendorf, Switzerland*

[b] *Photochemical Dynamics Group, Institute of Chemical Sciences and Engineering, Ecole Polytechnique Fédérale de Lausanne, CH-1015 Lausanne, Switzerland*

Received 29 July 2007; received in revised form 25 September 2007; accepted 30 September 2007
Available online 13 October 2007

Abstract

The effect of exposing cyanine–fullerene C_{60} bilayer solar cells to ambient atmosphere is investigated. For exposure times of a few hours and concomitant light soaking, the device performance experiences a drastic power efficiency increase going from 0.14% to 1.2% measured at 30 mW/cm^2 simulated solar irradiation. The 10-fold enhancement is attributed to the photoinduced doping involving oxygen and water leading to the formation of reactive superoxide anions and mobile holes in the cyanine layer. The influence of water and dry oxygen are investigated separately. While water deteriorates the device performance, dry oxygen leads only to a partial increase of efficiency. Annealing does not ameliorate the performance of doped devices. Although then the cyanine layer features more crystallinity, the considerable morphological changes cause diffusional loss in charge carrier collection. Doping of not annealed devices brings a sizeable efficiency enhancement that highlights the importance of charge carrier transport in cyanine dye based solar cells.

PACS: 72.80.Jc; 84.60.Jt; 78.40.Me; 73.61.Ph; 27.40.tw; 78.30.Jw; 73.50.Pz

Keywords: Organic optoelectronic devices; Photovoltaic cells; Solar cells; Cyanine dyes; Fullerene; C_{60}; Doping; Oxygen; Annealing; Charge transport; Superoxide anion; Conductivity

1. Introduction

Cyanine dyes were developed at the beginning of the 20th century, mainly as sensitizers for silver halide emulsions in the photographic process [1]. Above all, cyanines exhibit extraordinarily high extinction coefficients and tunable absorption spectra throughout the visible and near infrared domain. Because of their unique optical properties, they have more recently been applied in non-linear optics [2–4], in data storage devices [5], as fluorescent probes in biomolecules [6] or as contrast agents in optical imaging of tissue [7]. Redox properties of cyanine dyes have also been extensively studied with respect to their role as sensitizer or desensitizer for silver halides [8]. The wide range of oxidation and reduction potentials allows cyanines to act as electron donors as well as electron acceptors in photoinduced electron transfer processes.

* Corresponding author. Tel.: +41 44 823 4740.
E-mail address: frank.nueesch@empa.ch (F. Nüesch).

1566-1199/$ - see front matter
doi:10.1016/j.orgel.2007.09.008

Combined advantages of optical and electronic properties make cyanines an interesting material class for solar cell applications. Numerous works report on cyanines used in dye sensitized solar cells [9–14]. Power efficiencies greater than 5% and current densities exceeding 21 mA/cm^2 at AM 1.5 simulated solar irradiation have been found. Despite these promising results, photoinduced degradation of related polymethine dyes due to titanium dioxide catalysed decomposition reactions has been reported [15,16] and might also be a concern for cyanines. This degradation pathway can be avoided in solid all-organic solar cell devices, which also allow cost efficient fabrication processes. Only few works report on organic solar cells using solid cyanine films as active material [17–19]. So far, these devices have shown rather modest efficiencies which could be related to inefficient charge transport.

Different approaches to increase charge transport in organic solar cells have been proposed. Crystallinity can be induced by annealing and often leads to enhanced charge transport [20–23]. Another way to improve charge transport relies on enhancing the conductivity of the organic film. Based on the pioneering work on semiconducting and metallic polymers [24], electrical conductivity has been induced by doping various optoelectronic materials with oxidizing or reducing agents [25–27]. This strategy has been used to fabricate organic p–i–n junction [28] and Schottky barrier solar cells [29]. In some cases enhancing the bulk film conductivity in organic photovoltaic cells proved to be beneficial for device efficiency [30,31].

In this work we investigate the effect of exposing cyanine dye–C_{60} bilayer devices to ambient atmosphere under light irradiation. The drastic increase of performance upon short exposure to air is explored by separately looking at the influence of water and oxygen. The impact of light irradiation during air exposure on the device characteristics is analysed in order to get insight into the reaction mechanism. Finally the effect of annealing is discussed.

2. Experimental

2.1. Materials

Cyanine dye 1,1′-diethyl-3,3,3′,3′-tetramethylcarbocyanine perchlorate (Cy-5) was synthesized in our laboratory and recrystallized in ethanol before use. Poly(3,4-ethylenedioxythiophene)–poly(styrenesulfonate) (PEDOT:PSS, Bayer), fullerene C_{60} (SES Research, 99.95% purity) and tetrafluoropropanol (TFP, Fluka) were used as received. The chemical structures of the organic compounds used in this work are shown in Fig. 1.

2.2. Cyclic voltammetry

Cyclic voltammetry measurements were recorded on a PGStat 30 potentiostat (Autolab) using a three cell electrode system with a glassy carbon working electrode, a platinum counter electrode and an Ag/AgCl (0.1 M tetrabutyl ammonium chloride in acetonitrile) reference electrode. Redox potentials of Cy-5 were measured in acetonitrile and referenced to the ferrocene/ferrocenium couple. To relate the electrochemical potentials to the corresponding vacuum levels, the potential of 0.69 V vs NHE was taken for ferrocene and the NHE value of −4.48 eV vs vacuum was adopted from the literature [32]. Redox potentials of C_{60} referenced to ferrocene/ferrocenium were taken from the literature [33]. Therefore the same relationship between the electrochemical scale and the physical scale was applied to obtain the vacuum reduction and oxidation potentials. The highest occupied molecular orbital energy level of PEDOT:PSS was adopted from the literature [34]. Fig. 1 summarizes lowest unoccupied molecular orbital (LUMO) and highest occupied molecular orbital (HOMO) energy levels of the different materials used in this work.

2.3. Device fabrication and characterization

Solar cell devices were fabricated on patterned indium-tin-oxide coated glasses (ITO, 140 nm, 20 Ω/square) that were cleaned in ethanol, acetone and detergent ultrasonic baths. A 90 nm thick PEDOT:PSS layer was deposited by spin-coating and heated in vacuum at 150 °C for 10 min to get rid of residual water. A 40 nm thick Cy-5 layer was then spin-coated from a 5 mg/ml solution in TFP on top of PEDOT:PSS, followed by vapour depositon of a 40 nm thick C_{60} layer under high vacuum. Finally a 70 nm thick aluminium cathode was vapour deposited through a shadow mask, defining four separate solar cell devices with an active device area of 0.031 cm^2. The full device fabrication sequence leading to the ITO/PEDOT:PSS/Cy-5/C_{60}/Al architecture was carried out under inert atmosphere. To study doping effects, devices were exposed to ambient atmosphere for several hours in the dark or under room light irradiation of 5 mW cm^{-2}. In

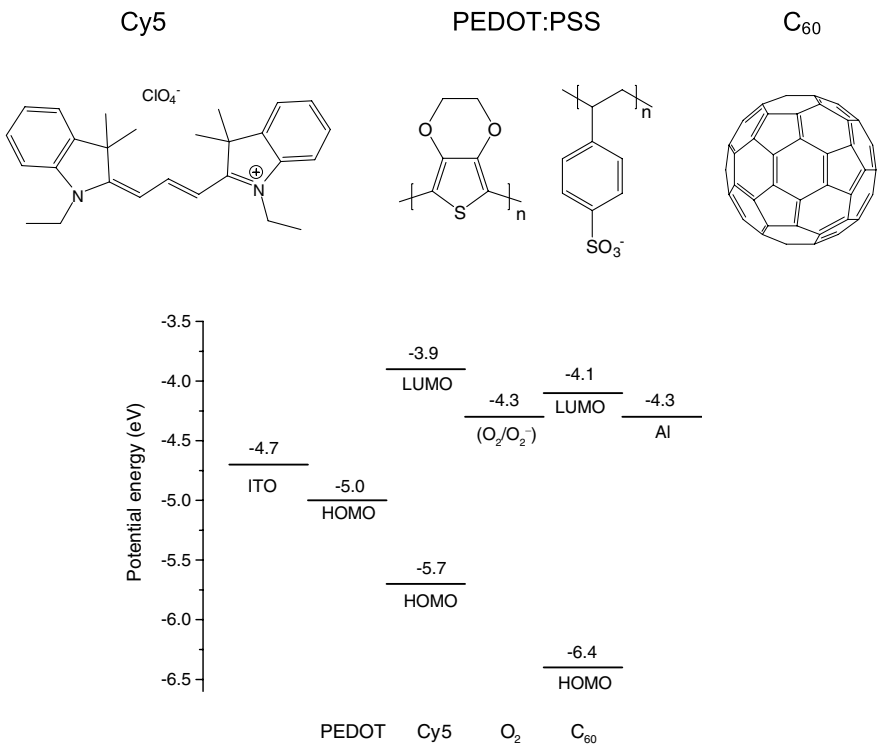

Fig. 1. Chemical structures of the materials used in this work. The HOMO and LUMO energy levels, the workfunctions of the electrodes as well as the reduction potential of triplet oxygen are also indicated.

order to investigate the effect of water separately, samples were placed in a glass decicator under the same irradiation conditions. A special measurement cell was constructed to characterize devices that were subjected to a flow of water saturated nitrogen. Doping was also studied for annealed devices. In this case the completed devices were heated in a vacuum oven at 100 °C for various durations.

Thicknesses of the organic films were measured using an Ambios XP-1 profilometer, while morphology analyses were carried out on an Nanosurf Mobile S atomic force microscope in tapping mode employing rectangular silicon cantilevers (Mikromasch, Nanosensors). Optical absorption spectra were measured with a Varian Cary 50 spectrophotometer.

Photovoltaic device performance was characterized under nitrogen atmosphere or in air using a monochromator (Oriel 74000) with a xenon lamp light source to obtain the incident photon-to-current conversion efficiency (IPCE) according to $\mathrm{IPCE} = 1240 \times J_{SC} \times \lambda^{-1} \times P_{in}^{-1}$ where J_{SC} (mA/cm^2) is the short-circuit current-density, P_{in} (mW cm^{-2}) the incident light intensity at wavelength λ (nm). Current–voltage characteristics were recorded using a Keithley 2400 source-measure unit. Simulated solar spectra with irradiation intensities of 30 mW/cm^2 or 47 mW/cm^2 were obtained from the same xenon discharge lamp using an AM1.5G filter set (Oriel). Power efficiencies were calculated as $\eta = \mathrm{FF} \times J_{SC} \times V_{OC} \times P_{in}^{-1}$, where $\mathrm{FF} = V_m \times J_m \times V_{OC}^{-1} \times J_{SC}^{-1}$ is the fill factor, V_m (V) and J_m (mA/cm^2) are the current-density and voltage at maximum power output, V_{OC} (V) is the open-circuit voltage.

2.4. Four probe measurements

Electrical conductivity measurements of thin Cy-5 films were performed by a standard four-probe method. The glass substrates comprised four finger-like gold electrodes separated by a channel distance of 10 μm. A current of 10 nA was applied at the outer electrodes while the voltage was measured at the inner electrodes.

3. Results and discussion

In order to investigate the effect of exposing ITO/PEDOT:PSS/Cy-5/C_{60}/Al devices to ambient

atmosphere, solar cells were first characterized in nitrogen atmosphere without being exposed to the ambient atmosphere at any time. Since the device fabrication procedure excludes any contact with air, it can be assumed that freshly prepared devices only contain low amounts of residual water and oxygen. Then they were exposed to air for several hours and characterized in regular time intervals. Fig. 2 shows the effect of air soaking on device performance, by indicating the variation of short-circuit current and open-circuit voltage. A steep rise in V_{OC} can be observed within the first two hours leading to an increase from 0.47 V to 0.60 V. At longer exposure times V_{OC} gradually saturates at 0.73 V. With some retardation, the short-circuit current follows the rise of the open-circuit voltage, reaches a maximum at 1.8 mA/cm^2 and starts to drop. At exposure times of a few days, the device characteristics severely degrade and ultimately drop-off below the initial value.

The maximum power efficiency is reached for devices that were soaked in air and light for a duration of 3 h. The IPCE doubles with respect to the initial value (Fig. 3a) and the current increases in a spectacular way leading to a power efficiency of 1.2%. As can be inferred from Table 1 the fill factor also rises from 0.19 to 0.27, indicating increased charge carrier collection.

Different mechanisms may be invoked to explain the rise in device performance. Oxygen could assist charge generation in the cyanine layer and augment photocurrent generation in the bulk. This hypothesis can be discarded based on the Cy-5 thickness dependence of the external quantum efficiency. At

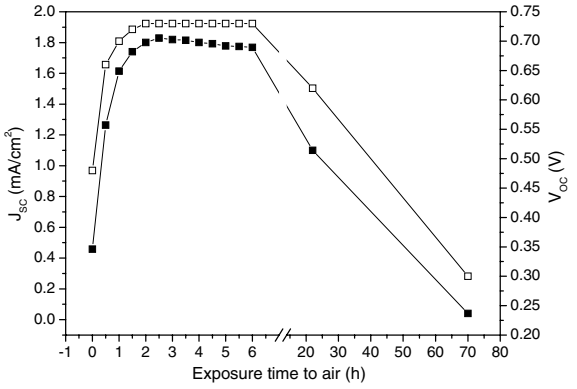

Fig. 2. Variation of the short-circuit current J_{SC} (full squares) and the open-circuit voltage V_{OC} (empty squares) of ITO/PEDOT:PSS/Cy-5/C_{60}/Al devices as a function of exposure time to ambient atmosphere and white light irradiation.

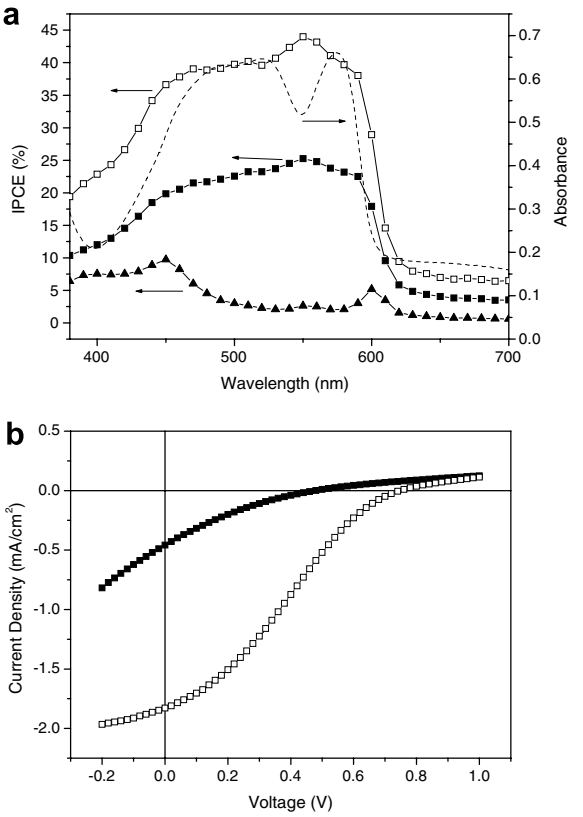

Fig. 3. ICPE and absorbance (a) and current–voltage characteristics (b) of ITO/PEDOT:PSS/Cy-5 (40 nm)/C_{60} (40 nm)/Al devices right after fabrication (full squares) and after being exposed to ambient atmosphere and white light irradiation for 3 h (empty squares). Additionally a device using a 100 nm thick Cy-5 layer that was also exposed to air is shown in (a) (full triangles). Devices were measured at an irradiation intensity of 30 mW cm^{-2}.

Table 1
Photovoltaic characteristics of ITO/PEDOT:PSS/Cy-5/C_{60}/Al devices measured just after fabrication (fresh) and soaked in ambient atmosphere under white light irradiation of 5 mW cm^{-2} for the duration of 3 h (air)

	V_{OC} (V)	J_{SC} (mA/cm^2)	FF	η (%)
Fresh	0.47	0.46	0.189	0.14
Air	0.73	1.83	0.274	1.2

The devices were measured at a white light irradiation intensity of 30 mW cm^{-2}.

thicknesses above 50 nm, the IPCE does not follow the absorption spectrum but shows a marked filter effect with a minimum in the spectral region where Cy-5 absorbs strongly and two maxima at the absorption edges of the cyanine (see Fig. 3a). This behaviour is similar to non-exposed devices that were reported in a previous work [19]. At a thick-

ness of 40 nm the filter effect is still apparent in the IPCE maximum corresponding to the local minimum in the absorption spectrum at 550 nm (see Fig. 3a).

Doping by oxygen is therefore proposed as an explanation for the tenfold increase in power efficiency upon air exposure. By looking at the current–voltage curve measured in the dark, a marked increase in the forward current is observed upon air soaking while the reverse current lowers significantly (Fig. 4). This results in a rectification ratio of 151 measured at ±1.5 V, which is a fundamental change as compared to the almost symmetrical current–voltage curve obtained for freshly prepared devices. According to the energy level diagram in Fig. 1, electrons can easily be injected from the Al cathode under forward bias and are blocked at the C_{60}–cyanine heterointerface, while holes would face a significant injection barrier at the PEDOT:PSS electrode. Therefore the current onset is mainly determined by the injection of holes at the anode. Under reverse bias, holes can hardly be injected from the Al cathode into C_{60}, and electrons face a considerable injection barrier at the interface between PEDOT:PSS and Cy-5. Similarly to the forward bias situation, injection from the PEDOT:PSS electrode again determines the current-onset under reverse bias.

Rectification of the current–voltage characteristics upon doping with oxygen has indeed been observed in the literature and has been attributed to Schottky barrier formation at the metal electrode [35]. In the present work, p-type doping induced by oxygen would give rise to a Schottky barrier at the anode, favouring hole injection and inhibiting electron injection (Fig. 4a). Note that Cy-5 is a cationic dye with a rather mobile perchlorate counter-anion that can significantly augment charge carrier injection under forward bias due to ion accumulation at the anode. By using fast current–voltage scans, ion motion can be significantly reduced. The reverse current, however, is only slightly affected by ion motion and is therefore a better probe for the formation of a Schottky barrier.

The question still remains regarding the doping mechanism in Cy-5 based devices. To scrutinize the reaction of the cyanine layer in ambient atmosphere, the devices were submitted to air in the dark for 0.5 h. Measured in the dark, the current-density under reverse bias is not reduced to the same amount as under illumination (Fig. 5). Moreover the current is lowered both under forward and reverse bias, if exposed to air for longer durations. As will be shown below, the decreased current–density can be attributed to the effect of water only. Therefore the mechanism of doping leading to rectified current–voltage characteristics must be photoinduced.

In a next step, devices were exposed to dry oxygen under white light irradiation to analyse the effect of oxygen only. In this case, the current–voltage characteristics in the dark show an intermediate behaviour (Fig. 6a). The rectification ratio rises from 1 to 30 after being placed in the decicator and irradiated with 5 mW/cm^2 light for 3 h. Solar cell performance increases substantially but never reaches the performances achieved by the simultaneous action of oxygen and water (Fig. 6b). It

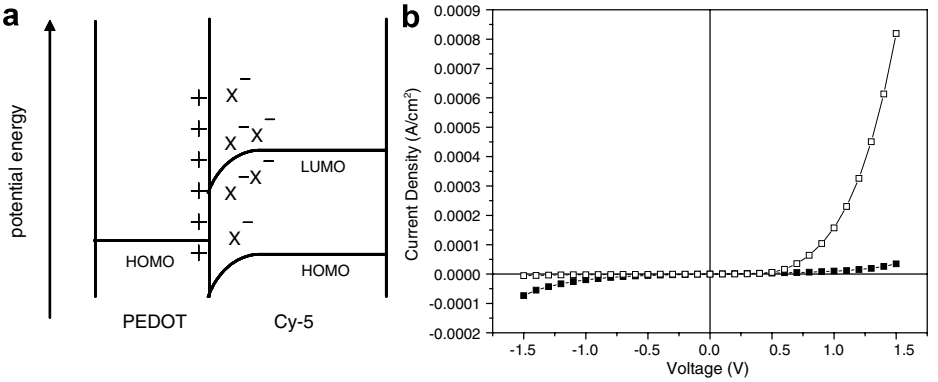

Fig. 4. Schematic drawing of Schottky barrier formation at the PEDOT:PSS interface induced by p-type doping with oxygen (a). The anionic species corresponding to the photochemically created oxygenated complex are labelled as X^-, positive charge carriers are marked as plus signs. Figure (b) shows the dark current for a freshly prepared cell (full squares) and a cell that was exposed to ambient atmosphere and white light (empty squares) for 3 h.

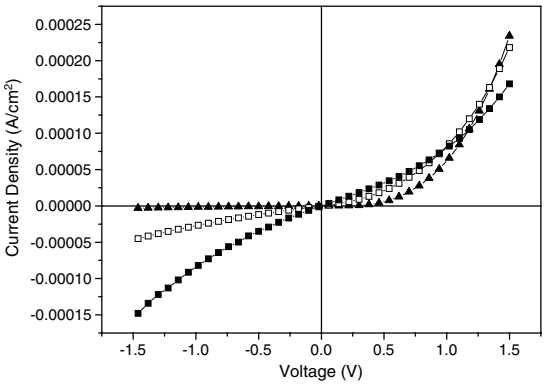

Fig. 5. Current–voltage characteristics of ITO/PEDOT:PSS/Cy-5/C_{60}/Al devices measured in the dark just after being fabricated (full squares), after being exposed to ambient atmosphere for 0.5 h in the absence of light (open squares) and under white light irradiation (full triangles).

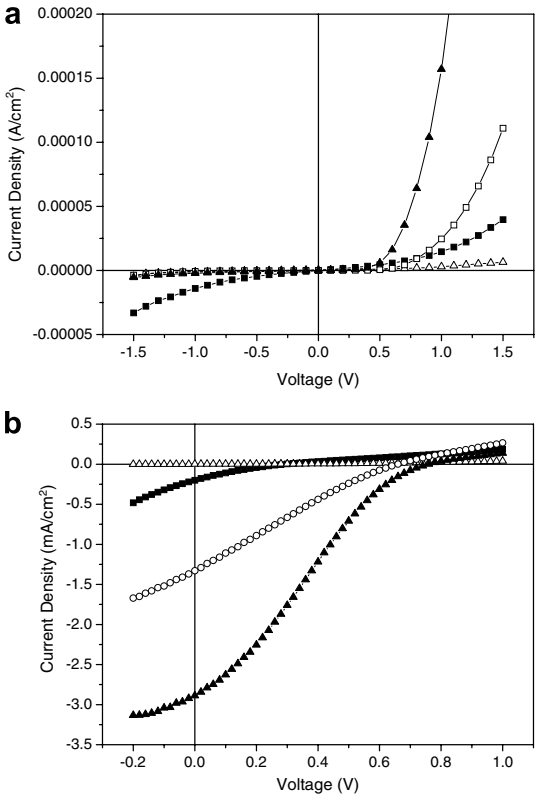

Fig. 6. Current–voltage characteristics of ITO/PEDOT:PSS/Cy-5/C_{60}/Al devices just after being fabricated (full squares), after being exposed under white light irradiation to dry air for 3 h (empty squares), to ambient atmosphere for 3 h (full triangle) as well as to water saturated nitrogen for 1 h (empty triangles). (a) Dark current. (b) Devices measured at a simulated solar irradiation intensity of 47 mW cm^{-2}.

has to be noted that some water contamination occurred during the transfer of the devices from the glove box to the decicator which may already favour the doping process. Nevertheless, light irradiation occurred under dry atmosphere. The experimental findings therefore emphasize the beneficial effect of water in the doping process.

Water alone, however, has a detrimental effect on all device characteristics. When the cell is exposed to water saturated nitrogen, the current–voltage characteristics measured in the dark gradually decreases both under forward and reverse bias to reach roughly a 10 times smaller current after being immersed in the flow cell for 1 h. The photovoltaic effect reached the noise level of our measurement unit and could no longer be detected (see Fig. 6b). It appears that water can not be the only factor leading to doping. As was shown in the literature, water is absorbed by the hygroscopic PEDOT:PSS layer, thereby decreasing the conductivity of the latter and introducing a large serial resistance to the device [36]. The same phenomenon is likely to occur in the devices described here.

With a view to further improve device performance, fresh ITO/PEDOT:PSS/Cy-5/C_{60}/Al devices were annealed in a vacuum oven at 100 °C for 30 min. Indeed, a clear rise in the J_{SC} is observed (Fig. 7a). It can be attributed to a higher mobility due to increased crystallinity of the cyanine film leading to higher charge carrier mobility. Surprisingly, the open-circuit voltage drops by 100 mV and the fill factor decreases from 0.19 to 0.17, which is contrary to what can be expected from increased charge carrier mobility. In order to find an explanation for this behaviour the morphologies of the devices were analyzed by atomic force microscopy using tapping mode. To avoid peeling-off the cathode thereby possibly destroying the top surface layer, we analyzed the surface area of the organic multilayer that was not covered by aluminium. Non-annealed devices show a fine, granulated structure that homogeneously covers the entire surface (Fig. 7c). In analogy to other bilayer devices using a thin fullerene acceptor layer, this structure is attributed to small C_{60} spheres on top of the cyanine layer [37]. After annealing, the sphere like features are no longer homogeneously distributed over the surface. Instead, larger rectangular shapes appear additionally to the small spheres, and in some cases the former protrude to the top surface. These larger crystallites are attributed to cyanine aggregates. Similar morphological changes may occur in the film

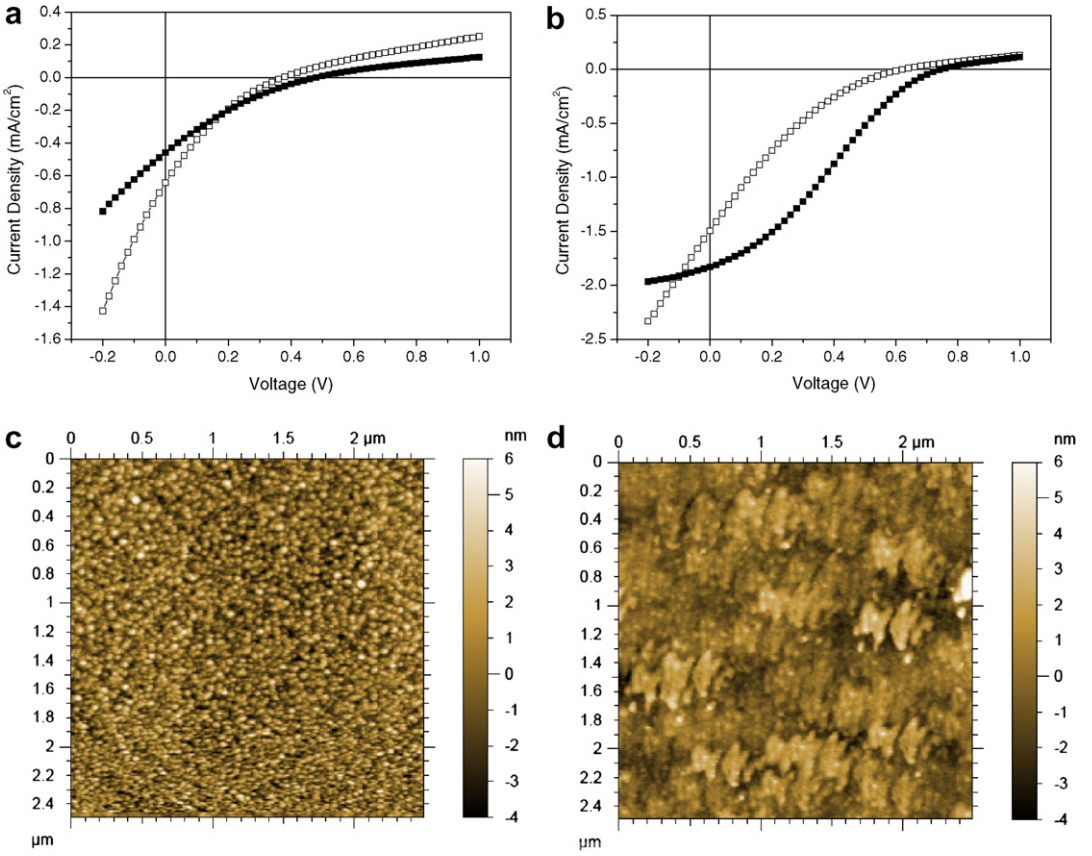

Fig. 7. Current–voltage characteristics of ITO/PEDOT:PSS/Cy-5/C_{60}/Al devices with (empty squares) and without (full squares) being annealed in a vacuum oven at 100 °C for 30 min. Undoped (a) and doped (b) devices were measured at a simulated solar irradiation intensity of 30 mW cm^{-2}. Atomic force microscopy images show the morphology of above doped devices measured on top of the organic layers that were not covered by aluminium for non-annealed (c) and annealed (d) devices.

areas covered by aluminium, giving rise to cyanine and C_{60} channels that are in direct contact with both anode and cathode. Such a film morphology would allow charge carrier diffusion to both electrodes, which becomes particularly unfavourable for charge carrier collection in the case of low drift fields, i.e. when the applied voltage approaches the open-circuit voltage. As a consequence, lowered open-circuit voltage and fill factor are expected, which may explain the behaviour of annealed devices.

For doped devices the fill factor also decreases upon annealing, from 0.27 to 0.16 for not-annealed and annealed devices, respectively (Fig. 7b). Differently to undoped devices, the short-circuit current is lower for annealed cells as compared to non-annealed ones. However, J_{SC} can be increased after placing the devices under vacuum for 12 h. As can be inferred from Fig. 8, the short-circuit current rises up to a maximum and then decreases rapidly.

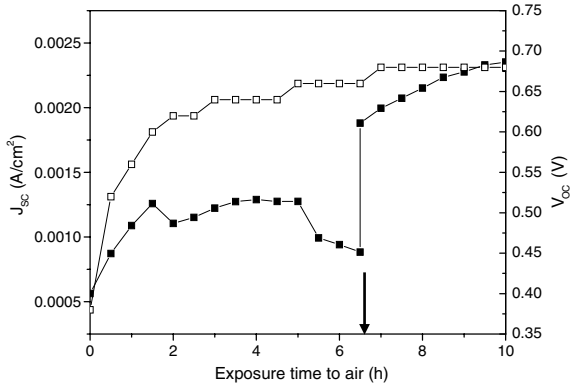

Fig. 8. Variation of short-circuit current J_{SC} (full squares) and open-circuit voltage V_{OC} (empty squares) of an annealed ITO/PEDOT:PSS/Cy-5/C_{60}/Al device as a function of exposure time to ambient atmosphere and white light irradiation. The device was annealed in vacuum at 100 °C for 30 min before being soaked in air. The vertical arrow indicates the time at which the device was pumped in a vacuum chamber for 12 h.

This decrease is attributed to the uptake of water by the hygroscopic PEDOT:PSS layer leading to a higher series resistivity. The inhomogeneous, crystalline film morphology opens larger channels in the thin film where water can penetrate more easily. Pumping desorbs water from PEDOT:PSS and restores the short-circuit current.

Above experimental findings demonstrate that photoinduced doping occurs, when devices are soaked in ambient atmosphere for several hours. So far, the precise reaction mechanism has not been addressed. Formation of a rectifying Schottky barrier strongly indicates that doping occurs in the cyanine layer. Moreover, the higher fill factor suggests that hole transport in the cyanine layer is increased. The possibility that the reaction of air with C_{60} under illumination is responsible for the observed efficiency rise can also be discarded since it has recently been shown that this reaction leads to a decrease of device performance [38]. Photochemical reactions of cyanine dyes with oxygen have indeed been reported in the literature, both in solution and in thin solid films. Self-sensitized energy transfer from the triplet excited state of a cyanine dye to triplet oxygen $O_2(^3\Sigma_g^-)$ leading to reactive singlet oxygen $O_2(^1\Delta_g)$ was found to be responsible for photofading of the dye in solution. Evidence was brought indirectly by using a spin trap [39] or by detecting the ketonic reaction products using NMR [40]. Self-sensitized photobleaching due to triplet–triplet energy transfer has also been observed in thin Cy-5 films by monitoring the singlet oxygen emission in the near infrared [41].

Photochemical reaction involving the energy transfer mechanism, however, can not account for the doping process, i.e. the generation of free charge carriers. Electron transfer from the photoexcited state of the cyanine dye to triplet oxygen is also energetically possible given that the redox potential for the reduction of triplet oxygen is at −0.16 eV vs NHE [42] as compared to the reduction potential of −0.59 eV vs NHE for Cy-5. The photoinduced electron transfer process has indeed been observed for a cyanine dye in solution by using spin trapping to detect transient superoxide anion O_2^- species [43]. In one of the works both the electron transfer process and the energy transfer process from photoexcited cyanine to oxygen were observed [39]. Active oxygen species have also been generated from photoexcited fullerene C_{60} [44]. Interestingly, the authors observed efficient generation of singlet oxygen $O_2(^1\Delta_g)$ in nonpolar solvents such as benzene and benzonitrile, while O_2^- and subsequent formation of hydroxyl radicals were detected instead in polar solvents such as water. Based on above discussion, both energy and electron transfer reaction mechanisms may be present in the photooxygeneation of Cy-5 solid films. If water is coadsorbed together with oxygen, the electron transfer path is favored leading to increased production of positive charge carriers and superoxide anions that further react to yield anionic cyanine oxidation products.

To verify that free charge carriers are indeed generated during the photodoping process, the conductivity of Cy-5 films was directly measured by four probe technique. Cyanine films were drop-cast on glass substrates patterned with four finger-like gold electrodes separated by a channel length of 10 microns. Fig. 9 presents the conductivity change after exposure to ambient atmosphere in the dark as well as under 5 mW/cm^2 white light irradiation. In both cases the conductivity was measured in absence of light. Very clearly there is a strong increase of the conductivity for the irradiated films, while the films kept in the dark show a relatively small variation. This corroborates our hypothesis that photoinduced doping of the cyanine layer occurs during exposure to ambient atmosphere and simultaneous white light irradiation. The conductivity rise in the four probe experiment is much faster than the performance rise observed in solar cells which can be attributed to the oxygen and water barrier effect of the aluminum cathode of the devices. After an exposure time to ambient atmosphere and light of 10 min, the conductivity of Cy-5 films starts to decrease. We have assigned

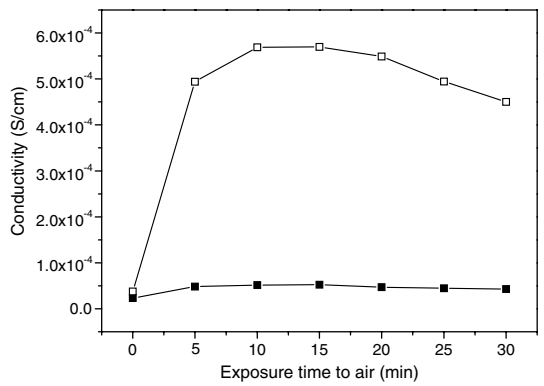

Fig. 9. Conductivity measurements of Cy-5 films as a function of exposure time to ambient atmosphere in the dark (full squares) and under white light irradiation (empty squares). In both cases, conductivity measurements were performed in the absence of light.

this effect to the degradation of the cyanine film in the vicinity of the gold electrodes. Bubble formation could be observed which may come from hydrogen gas evolution following electrochemical reduction of water during the conductivity measurement.

4. Conclusions

We have demonstrated a tenfold increase in power efficiency of cyanine based heterojunction solar cells by doping the cyanine film in the presence of oxygen, water and light. This raises the efficiency of cyanine based thin film solar cells above the 1% benchmark. The encouraging results highlight the potential of cyanine dyes and the importance to increase charge carrier transport in thin cyanine films. Charge carrier doping is a possible way to achieve high performance. Although promising, the air doping method presents some drawbacks. While water adsorption in PEDOT:PSS leads to increased serial resistivity, photochemical reaction with oxygen can also yield ketonic species acting as charge trapping defects and lowering device efficiency. Well defined chemical doping employing carefully chosen oxidizing agents could therefore even further improve cyanine based devices.

Acknowledgements

We acknowledge financial support of this work by the Swiss Competence Center for Energy and Mobility CCEM-CH as well as "swisselectric research". Matthias Nagel is thanked for his help in cyclic voltammetry measurements. Thomas Geiger is acknowledged for the synthesis of the cyanine dye. We thank Dr. Kappenberger and the Swiss SPM User Laboratory at Empa for support with the AFM measurements.

References

[1] T.H. James, The Theory of the Photographic Process, fourth ed., Macmillan, New York, 1977.
[2] U. Lawrentz, W. Grahn, K. Lukasznk, C. Klein, R. Wortmann, A. Feldner, D. Scherer, Chemistry – A European Journal 8 (7) (2002) 1573–1590.
[3] O.I. Tolmachev, N.V. Pilipchuk, O.D. Kachkovsky, Y.L. Slominski, V.Y. Gaywronsky, E.V. Shepelyavyy, S.V. Yakunin, M.S. Brodyn, Dyes and Pigments 74 (1) (2007) 195–201.
[4] M. Del Zoppo, A. Bianco, G. Zerbi, Synthetic Metals 124 (1) (2001) 183–184.
[5] H. Mustroph, M. Stollenwerk, V. Bressau, Angewandte Chemie – International Edition 45 (13) (2006) 2016–2035.
[6] J.H. Flanagan, S.H. Khan, S. Menchen, S.A. Soper, R.P. Hammer, Bioconjugate Chemistry 8 (5) (1997) 751–756.
[7] K. Licha, Contrast Agents for Optical Imaging. In: Contrast Agents II, vol. 222, 2002, pp. 1–29.
[8] R.O. Loutfy, J.H. Sharp, Photographic Science and Engineering 20 (4) (1976) 165–174.
[9] C.P. Chen, B.M. Zhou, D.H. Lu, G.G. Xu, Journal of Photographic Science 43 (4) (1995) 134–135.
[10] Y.S. Chen, Z.H. Zeng, C. Li, W.B. Wang, X.S. Wang, B.W. Zhang, New Journal of Chemistry 29 (6) (2005) 773–776.
[11] S.L. Li, K.J. Jiang, K.F. Shao, L.M. Yang, Chemical Communications (26) (2006) 2792–2794.
[12] K. Sayama, S. Tsukagoshi, T. Mori, K. Hara, Y. Ohga, A. Shinpou, Y. Abe, S. Suga, H. Arakawa, Solar Energy Materials and Solar Cells 80 (1) (2003) 47–71.
[13] Q.H. Yao, F.S. Meng, F.Y. Li, H. Tian, C.H. Huang, Journal of Materials Chemistry 13 (5) (2003) 1048–1053.
[14] M. Liang, W. Xu, F.S. Cai, P.Q. Chen, B. Peng, J. Chen, Z.M. Li, Journal of Physical Chemistry C 111 (11) (2007) 4465–4472.
[15] J. Yang, C.C. Chen, H.W. Ji, W.H. Ma, J.C. Zhao, Journal of Physical Chemistry B 109 (46) (2005) 21900–21907.
[16] T.X. Wu, T. Lin, J.C. Zhao, H. Hidaka, N. Serpone, Environmental Science and Technology 33 (9) (1999) 1379–1387.
[17] F.A. Castro, A. Faes, T. Geiger, C.F.O. Graeff, M. Nagel, F. Nuesch, R. Hany, Synthetic Metals 156 (14–15) (2006) 973–978.
[18] F.S. Meng, K.C. Chen, H. Tian, L. Zuppiroli, F. Nuesch, Applied Physics Letters 82 (21) (2003) 3788–3790.
[19] F. Nuesch, G. Tornare, L. Zuppiroli, F.S. Meng, K.C. Chen, H. Tian, Solar Energy Materials and Solar Cells 87 (1–4) (2005) 817–824.
[20] S. Cho, K. Lee, J. Yuen, G.M. Wang, D. Moses, A.J. Heeger, M. Surin, R. Lazzaroni, Journal of Applied Physics 100 (11) (2006) 114503.
[21] P. Peumans, S. Uchida, S.R. Forrest, Nature 425 (6954) (2003) 158–162.
[22] Y. Shao, S. Sista, C.W. Chu, D. Sievers, Y. Yang, Applied Physics Letters 90 (10) (2007) 103501.
[23] X.N. Yang, J. Loos, S.C. Veenstra, W.J.H. Verhees, M.M. Wienk, J.M. Kroon, M.A.J. Michels, R.A.J. Janssen, Nano Letters 5 (4) (2005) 579–583.
[24] A.J. Heeger, Angewandte Chemie – International Edition 40 (14) (2001) 2591–2611.
[25] B.A. Gregg, S.G. Chen, H.M. Branz, Applied Physics Letters 84 (10) (2004) 1707–1709.
[26] J.G. Xue, S.R. Forrest, Physical Review B 69 (24) (2004).
[27] A. Nollau, M. Pfeiffer, T. Fritz, K. Leo, Journal of Applied Physics 87 (9) (2000) 4340–4343.
[28] J. Drechsel, B. Mannig, F. Kozlowski, M. Pfeiffer, K. Leo, H. Hoppe, Applied Physics Letters 86 (24) (2005) 244102.
[29] G.A. Chamberlain, Journal of Applied Physics 53 (9) (1982) 6262–6269.
[30] A.C. Arias, M. Granstrom, D.S. Thomas, K. Petritsch, R.H. Friend, Physical Review B 60 (3) (1999) 1854–1860.
[31] K. Nakayama, Y. Matsui, M. Yokoyama, Japanese Journal of Applied Physics Part 1 – Regular Papers Brief Communications and Review Papers 44 (1B) (2005) 633–635.
[32] C.P. Kelly, C.J. Cramer, D.G. Truhlar, Journal of Physical Chemistry B 111 (2) (2007) 408–422.

[33] T. Suzuki, Y. Maruyama, T. Akasaka, W. Ando, K. Kobayashi, S. Nagase, Journal of the American Chemical Society 116 (4) (1994) 1359–1363.
[34] N. Koch, A. Kahn, J. Ghijsen, J.J. Pireaux, J. Schwartz, R.L. Johnson, A. Elschner, Applied Physics Letters 82 (1) (2003) 70–72.
[35] T.D. Anthopoulos, T.S. Shafai, Applied Physics Letters 82 (10) (2003) 1628–1630.
[36] K. Kawano, R. Pacios, D. Poplavskyy, J. Nelson, D.D.C. Bradley, J.R. Durrant, Solar Energy Materials and Solar Cells 90 (20) (2006) 3520–3530.
[37] A. Geiser, B. Fan, H. Benmansour, F. Castro, J. Heier, B. Keller, K.E. Mayerhofer, F. Nüesch, R. Hany, Solar Energy Materials and Solar Cells (2007) accepted for publication.
[38] M. Rusu, J. Strotmann, M. Vogel, M.C. Lux-Steiner, K. Fostiropoulos, Applied Physics Letters 90 (15) (2007) 153511.
[39] P. Chen, J. Li, Z.G. Qian, D.S. Zheng, T. Okasaki, M. Hayami, Dyes and Pigments 37 (3) (1998) 213–222.
[40] G.W. Byers, S. Gross, P.M. Henrichs, Photochemistry and Photobiology 23 (1) (1976) 37–43.
[41] H. Horiuchi, S. Ishibashi, S. Tobita, M. Uchida, M. Sato, K. Toriba, K. Otaguro, H. Hiratsuka, Journal of Physical Chemistry B 107 (31) (2003) 7739–7746.
[42] P. Wardman, Journal of Physical and Chemical Reference Data 18 (4) (1989) 1637–1755.
[43] C.P. Chen, B.M. Zhou, D.H. Li, G.G. Xu, Journal of Photochemistry and Photobiology A – Chemistry 89 (1) (1995) 25–29.
[44] Y. Yamakoshi, N. Umezawa, A. Ryu, K. Arakane, N. Miyata, Y. Goda, T. Masumizu, T. Nagano, Journal of the American Chemical Society 125 (42) (2003) 12803–12809.

Available online at www.sciencedirect.com
ScienceDirect
Organic Electronics 9 (2008) 95–100
Organic Electronics
www.elsevier.com/locate/orgel

Full color and monochrome passive-matrix polymer light-emitting diodes flat panel displays made with solution processes

Qiaoli Niu, Yuxuan Shao, Wei Xu, Lei Wang, Shaohu Han, Nanliu Liu, Junbiao Peng, Yong Cao, Jian Wang *

Institute of Polymer Optoelectronic Materials and Devices, South China University of Technology, and Key Lab of Specially Functional Materials, Ministry of Education, Guangzhou 510640, PR China

Received 15 August 2007; received in revised form 27 September 2007; accepted 2 October 2007
Available online 17 October 2007

Abstract

1.5 in. diagonal red, green, and blue monochrome passive-matrix (PM) polymer light-emitting diodes (PLED) flat panel displays (FPDs) with format 96×64 were fabricated by spin-coating technology with device structure of ITO/PEDOT/Emissive layer/Ba/Al. During spin-coating process, by rearranging the location and the direction of the panel with respect to the center of the spinner, the piling of organic materials under the cathode separator was significantly reduced, resulting in a more uniform light emission. The final display showed neither dead pixels nor dead lines. Current efficiencies of 1.37, 9.5 and 1.44 cd/A, and CIE color coordinates of $(0.62, 0.37)$, $(0.37, 0.60)$ and $(0.15, 0.13)$, for red, green, and blue monochrome displays, respectively, have been achieved. Further, 1.5 in. full color PM PLED FPDs with format $96 \times \mathrm{RGB} \times 64$ was successfully fabricated by inkjet printing technology. The current efficiency was about 0.75 cd/A at full screen white with color coordinates located at $(0.34, 0.35)$. A color gamut of 50% NTSC was obtained. For all the displays, the 5-point uniformity was more than 80%.

PACS: 85.60.Jb; 85.60.Pg

Keywords: Polymer light-emitting diodes; Passive-matrix displays; Full color displays; Spin-coating; Inkjet

After only a little more than one decade's research and development, organic light-emitting diode (OLED) technology has evolved from attractive to practical for flat panel display industry. Offering lightweight, thin panel thickness, wide view angle, high self-electroluminescent efficiencies, and less power consumption, OLED technology is being considered as the next generation flat panel display technology to replace liquid crystal. There are two variations of the OLED technology. One is so called "small molecule" (SmOLED) technology, which was first invented at Eastman Kodak Co. in the late 1980s [1]. The other is "polymer" (PLED) based technology [2,3]. Though FPDs based on both technologies have

* Corresponding author. Tel.: +86 (20) 8711 4525; fax: +86 (20) 8711 0606.
E-mail address: jianwang@scut.edu.cn (J. Wang).

1566-1199/$ - see front matter © 2007 Elsevier B.V. All rights reserved.
doi:10.1016/j.orgel.2007.10.001

been demonstrated and commercialized, PLED based displays are more promising for large size, high definition, high resolution displays, due to their processing advantages in device manufacture.

The main difference in process between SmOLEDs and PLEDs is that SmOLEDs are commonly fabricated by vacuum deposition, whereas PLEDs are made by solution processing which is a simpler and cheaper process. To pattern fine structures for full color displays, shadow mask is typically used in SmOLED fabrication. The shadow mask process becomes challenging for large size and high resolution display panels. In contrast, full color PLED pixels can be patterned with one of printing techniques such as inkjet printing [4,5], screen printing [6,7], dye diffusion [6], laser induced thermal transfer [8–10], or be patterned with the photolithographic process [11,12]. The solution process is typically carried out at low or room temperature, allowing a device being made onto a flexible, organic substrate [13]. Full color PLED displays made with inkjet process have been demonstrated with excellent image qualities [14,15].

For OLED devices, film qualities of organic layers are of extreme importance in order to achieve high device performances. Obtaining uniform pinhole free films with optical quality is a challenging task. In this paper, we modified the spin-coating process by rearranging the position and direction of the substrate with respect to the spinner center. After the modification, the materials' pileup along the cathode separator was significantly reduced, leading to a more uniform light emission and a larger fill factor for 1.5 in. monochrome PLED display. For RGB full color display, the red emission intensity was increased by printing green materials onto red subpixels after the red had been printed. With additional green materials as energy transfer media, complete energy transfer from blue to red was accomplished. 1.5 in. full color PLED FPDs were successfully fabricated by using inkjet printing technology.

The monochrome displays have a format of 96×64 with pitch size of 0.33 mm × 0.33 mm, while full color displays have a format of $96 \times \mathrm{RGB} \times 64$ with same pitch size as that of monochrome panel. The specifications of both displays are summarized in Table 1. All the panel substrates were made and provided by Truly Semiconductors Ltd.

The red, green and blue polymer light-emitting materials used in the experiments were polyfluorene and its derivatives, which were synthesized in our lab. The hole transport materials PEDOT (P4083) was purchased from Bayer Corp. The glass substrates provided by Truly Semiconductors Ltd. have a 150 nm transparent indium–tin–oxide (ITO) layer on top with 10 Ω/□ sheet resistance. The ITO columns were patterned through conventional photolithography. To make a display, the substrate was cleaned first by UV ozone for 15 min. After the deposition of PEDOT layer by spin-coating, it was baked at 90 °C for 2 h inside vacuum oven to remove the residual water. The thickness of the PEDOT layer was around 50 nm. Following PEDOT baking, the emissive polymer layer was prepared by spin-casting from solutions in *p*-xylene containing about 10 mg/ml polymer by weight to make a monochrome display. No baking was performed after spin-coating emissive layer. Cathode layer consisting of 4 nm barrium (Ba) and 200 nm aluminum (Al) was deposited on top of organic layers by vacuum evaporation at pressure below 1×10^{-6} Torr. Before testing, the display panel was encapsulated by a thin glass cap with desiccants inside.

Table 1
Specifications of 1.5 in. PM PLED displays

	Monochrome	Full color
Display area	31.66 mm × 21.11 mm, 1.25 in. × 0.83 in. (1.5 in. in diagonal)	
Number of pixels	96×64	$96 \times 3 \times 64$
Pixel pitch	0.33 mm × 0.33 mm	0.33 mm × 0.33 mm
Panel resolution	77 dpi	77 dpi
Fill factor	FF = 77%	FF = 58%
Grey level	16	$32 \times 32 \times 64 = 65\,536$

To make a full color display, blue emissive layer was spin-coated instead of printed following PEDOT deposition. The common blue layer functioned as a receiving layer to reduce the leaking current [16]. The red and green polymer solutions in 1,2-dichlorobenzene were printed into red and green subpixels in a sequence on top of the blue layer by inkjet printer JetLab II from MicroFab Technologies, Inc. No annealing or nitrogen flow was carried out to accelerate the film drying process. The cathode layer and encapsulation layer were formed through same processes as those described in monochrome panel making. To drive the panel, driver chips SSD1332T1R1 and SSD1325T3R1 purchased from Solomon Systech Ltd. were bonded to the color and monochrome panels, respectively, and controlled by periphery circuits designed in our lab.

To define the cathode rows, we used photoresist to form cathode separators perpendicular to the

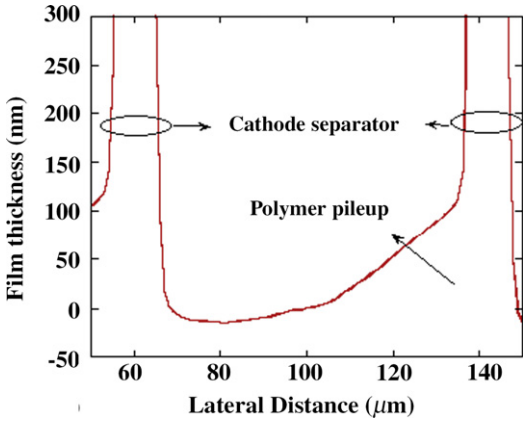

Fig. 1. Polymer pileup inside a single pixel.

ITO columns. During the spin-coating process, those separators would block the spreading of the organic solutions, causing materials pileup under the separators. Fig. 1 shows the polymer pileup inside a single pixel. Due to materials pileup, only partial area of a single pixel could emit lights during operation, leading to higher operating voltage and shorter lifetime.

The most commonly used location of the substrate on the spinner is at the center of the spinner shown in Fig. 3a, B. In addition to causing the materials pileup inside each single pixel, this spinning location also caused the degree of materials pileup inside each pixel nonuniform across the whole panel. The outskirt region of the panel has more serious materials pileup than the center region as illustrated in Fig. 2. In addition, in the panel's upper region, the materials accumulated at the bottom side of the cathode separator, while in the panel's bottom region, the materials accumulated at the upper side of the cathode separator. To overcome such technical difficulties and make a more uniform light-emitting display, we have changed the position and the direction of the panel with respect to the center of the spinner to find optimal spin-coating conditions. Three different positions have been tested, as shown in Fig. 3a.

The locations of the substrates on the spinner are described as the following:

A: The middle of the first row (from the bonding area) is at the center of the spinner and the cathode separators are horizontal;
B: The substrate was at the center of the spinner (the most commonly used position);
C: The middle of the substrate's right side is at the center of the spinner and the cathode separators are vertical.

In spin mode A, since the centrifugal force on the polymer solution was perpendicular to the cathode separators, the blocking and piling of polymer by

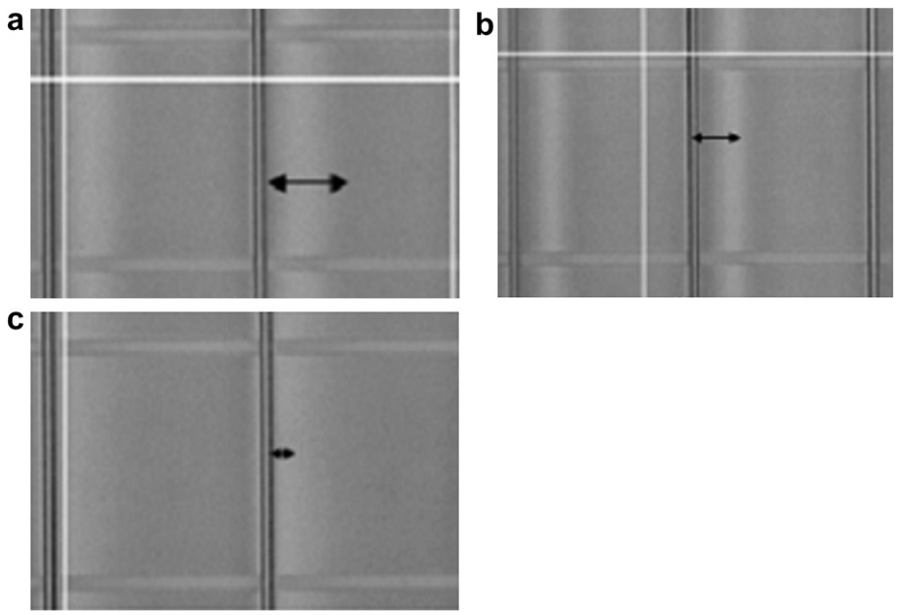

Fig. 2. Microscopic photos of the polymer pileup (thicker area) marked by ↔ at different regions of the panel: (a) farthest from the center; (b) near the center; (c) at the center.

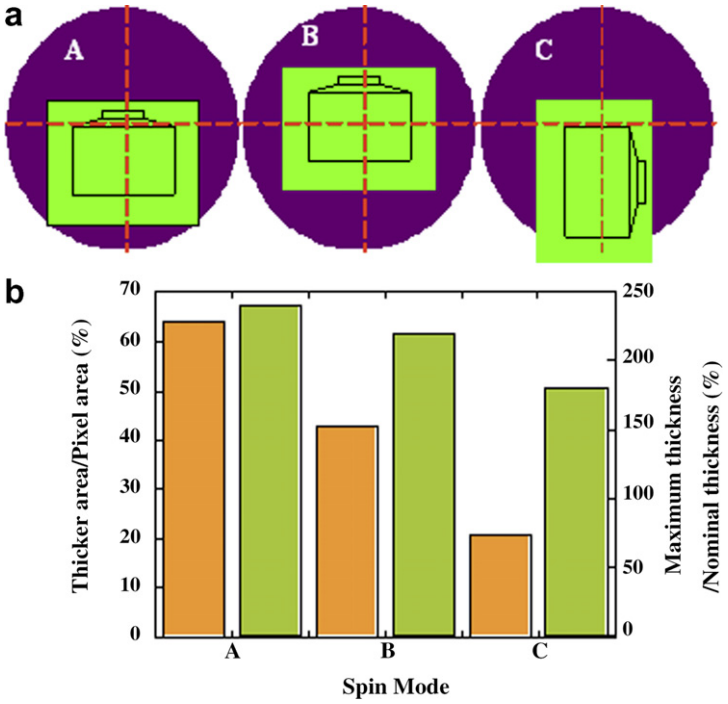

Fig. 3. (a) Three spin modes: A, B, and C; (b) the characterizations of the non-uniformity of polymer film spin-coated by spin mode A, B, and C, inside a single pixel.

cathode separators were the most serious. Inside one single pixel, the film became thicker along the direction of the centrifugal force. The thicker film area occupied about 64% of the whole pixel area, translating to 40% light emission during operation. The maximum thickness of the polymer is almost two and half times the nominal thickness. In spin mode B, the polymer solution blocking by the cathode separators was reduced due to the reduction of the centrifugal force (proportional to the square of the radius). As a result, the thicker area percentage was decreased to 43%, while the ratio of the maximum thickness to the nominal thickness is about 2.2. In spin mode C, since the centrifugal force on the polymer solution is parallel to the separators, the polymer blocking by the cathode separators is the minimum. The 21% thicker area percentage, and 180% maximum thickness to nominal thickness are the smallest ratios achieved among the three spin-coating modes. Highly efficient monochrome PLED FPDs with high polymer film qualities were fabricated by using spin-coating mode C. The display showed neither dead pixels nor dead lines. Current efficiencies of 1.37, 9.5 and 1.44 cd/A, and CIE color coordinates of (0.62, 0.37), (0.37, 0.60) and (0.15, 0.13), for red, green, and blue monochrome displays, respectively, have been achieved. Five-point uniformity test showed spin-coating mode C gave the best light emission uniformity across the whole display panel. The brightness uniformity of all the monochrome displays reached 80%.

Since the real emission area of each single pixel was doubled by employing spin mode C compared to that by spin mode A, the actual luminance from each single pixel was reduced to half in order to obtain a certain panel brightness. OLED lifetime dependence on the luminance takes a power law in which the exponent n is the acceleration coefficient [17,18], as shown in the following equation. Our experiments showed that n was 1.65 for PPV family conjugated polymers [19]. As a result, the reduction of the actual luminance by half will extend the panel lifetime by a factor of 3.

$$L^n \times \tau_{1/2} = \text{constant} \tag{1}$$

To make full color PLED FPDs, the red and green polymer solutions in 1,2-dichlorobenzene were inkjetted into red and green subpixels sequentially on top of the common blue receiving layer. The energy transfer from the blue polymer to the green and red polymers will make the green and red subpixels emit

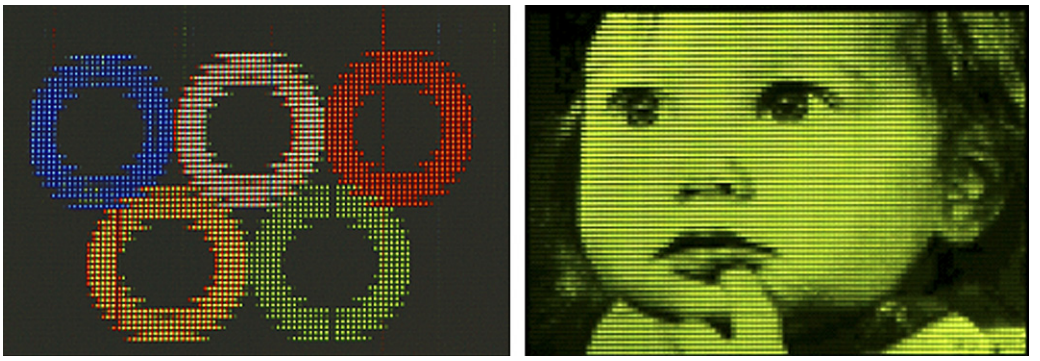

Fig. 4. The photographs of 1.5 in. full color and monochrome PM PLED FPDs.

green and red lights, respectively. However, the energy transfer from blue to red was incomplete, causing the red subpixels emit mixed red and blue lights. To accomplish full energy transfer in red subpixels while keeping printing processes still simple, first, we printed red polymer solutions into red subpixels on top of blue. Second, we printed green materials into both green and red subpixels. The red subpixels now contained three kinds of materials: spin-coated blue, printed red, and printed green. With additional green materials as the energy transfer media, the blue emission was totally quenched and the red emission was significantly enhanced. The full color display panel's luminous efficiency was about 0.75 cd/A at full screen white with color coordinates located at (0.34, 0.35). Due to the pure red emission, a color gamut of 50% NTSC was obtained. The 5-point uniformity of the full color display was 80% as same as that of those monochrome displays. Photos of pictures displayed on the color and monochrome PLED FPDs are shown in Fig. 4.

1.5 in. diagonal red, green, and blue monochrome PM PLED FPDs with format 96×64 were fabricated by modified spin-coating technology. The light emission uniformity and efficiency were significantly improved by rearranging the location and direction of the substrate with respect to the center of the spinner. Luminous efficiencies of 1.37, 9.5 and 1.44 cd/A for red, green, and blue monochrome displays, respectively, have been achieved. 1.5 in. full color PM PLED FPDs with format $96 \times \mathrm{RGB} \times 64$ was successfully fabricated by inkjet printing technology. By printing green materials into the red subpixels, complete energy transfer from blue to red was accomplished through green. The luminous efficiency was about 0.75 cd/A at full screen white with color coordinates located at (0.34, 0.35). The color gamut was 50%NTSC. The five-point uniformity of all the displays was over 80%.

Acknowledgements

We thank Mingliang Sun and Ergang Wang for providing the materials. This research was supported by the National Natural Science Foundation of China (#90201031, #50573024), Key Project of Science and Technology, Ministry of Education, (#104208) and the State 973 Project (#2002CB 613405).

References

[1] C.W. Tang, S.A. VanSlyke, Appl. Phys. Lett. 51 (1987) 913.
[2] J.H. Burroughes, D.D.C. Bradley, A.R. Brown, R.N. Marks, K. Mackay, R.H. Friend, P.L. Burns, A.B. Holmes, Nature 347 (1990) 539.
[3] D. Braun, A.J. Heeger, Appl. Phys. Lett. 58 (1991) 1982.
[4] T.R. Hebner, C.C. Wu, D. Marcy, M.H. Lu, J.C. Sturm, Appl. Phys. Lett. 72 (1998) 519.
[5] S.-C. Chang, J. Liu, J. Bharathan, Y. Yang, J. Onohara, J. Kido, Adv. Mater. 11 (1999) 734.
[6] F. Pschenitzka, J.C. Sturm, Appl. Phys. Lett. 74 (1999) 1913.
[7] D.A. Pardo, G.E. Jabbour, N. Peyghambarian, Adv. Mater. 12 (2000) 1249.
[8] S.T. Lee, J.Y. Lee, M.H. Kim, M.C. Suh, Tae Min Kang, Y.J. Choi, J.Y. Park, J.H. Kwon, H.K. Chung, J. Baetzold, E. Bellmann, V. Savvateev, M. Wolk, S. Webster, SID 02 Digest 784 (2002).
[9] M.B. Wolk, P.F. Baude, J.M. Florczak, F.B. McCormick, Y. Hsu, US Patent # 6,114,088, 2000.
[10] M.B. Wolk, P.F. Baude, F.B. McCormick, Y. Hsu, US Patent # 6,194,119, 2001.
[11] C.D. Müller, A. Falcou, N. Reckefuss, M. Rojahn, V. Wiederhirn, P. Rudati, H. Frohne, O. Nuyken, H. Becker, K. Meerholz, Nature 421 (2003) 829.

[12] M. Gather, A. Kohnen, K. Meerholz, H. Becker, A. Falcou, SID 06 Digest 909 (2006).
[13] G. Gustafsson, Y. Cao, G.M. Treacy, F. Klavetter, N. Colaneri, A.J. Heeger, Nature 357 (1992) 477.
[14] SID 2002 Advance Program, <http://www.sid.org/conf/sid2002/sid2002.html>, 2002.
[15] Samsung SDI, IMID Exhibition, Asia Display/IMID'04, Daegu, Korean, August 23–24, 2004.
[16] G. Yu, G. Srdanov, M. Stainer, J.G. Innocenzo, R. Sun, US Patent # 7,098,060, 2006.
[17] C. Féry, B. Racine, D. Vaufrey, H. Doyeux, S. Cinà, Appl. Phys. Lett. 87 (2005) 213502.
[18] Rico Meerheim, Karsten Walzer, Martin Pfeiffer, Karl Leo, Appl. Phys. Lett. 89 (2006) 061111.
[19] Wei Xu, Degree of Master Thesis, South China University of Technology, 2007.

Available online at www.sciencedirect.com
ScienceDirect
Organic Electronics 9 (2008) 101–110
Organic Electronics
www.elsevier.com/locate/orgel

Iminodibenzyl-substituted distyrylarylenes as dopants for blue and white organic light-emitting devices

Meng-Huan Ho [a,*], Chia-Ming Chang [a], Ta-Ya Chu [b], Teng-Ming Chen [a], Chin H. Chen [c]

[a] Department of Applied Chemistry, National Chiao Tung University, Hsinchu 300, Taiwan, ROC
[b] Department of Electrophysics, National Chiao Tung University, Hsinchu 300, Taiwan, ROC
[c] Display Institute, Microelectronics and Information Systems Research Center, National Chiao Tung University, Hsinchu 300, Taiwan, ROC

Received 21 March 2007; received in revised form 9 July 2007; accepted 28 September 2007
Available online 9 October 2007

Abstract

A series of highly efficient blue materials based on iminodibenzyl-substituted distyrylarylene (IDB-series) fluorescent dyes using the concept of steric-compression have been designed and synthesized by means of a rigidized and over-sized ring. The steric-compression effect can shorten the effective conjugation length (chromophore) of the molecule and the added phenyl moiety in the core can alleviate the propensity for molecular aggregation. These materials also possess high glass transition temperature over 100 °C. The blue IDB-Ph device achieved a maximum external quantum efficiency of 4.8% with a Commission Internationale de l'Eclairage ($CIE_{x,y}$) coordinate of (0.16, 0.28). When applied in two-element white OLED system, the IDB-Ph doped device achieved a luminance efficiency of 11.0 cd/A with a $CIE_{x,y}$ color coordinate of (0.29, 0.36).

PACS: 78.55.Kz; 78.60.Fi; 85.60.Jb

Keywords: Iminodibenzyl; Distyrylarylenes; Fluorescent blue material; Organic electroluminescent device

1. Introduction

Recently, owing to their unique electrical and optical properties, various functional devices using organic materials have been developed in a variety of applied fields [1]. Since the initial work by Tang and Van Slyke [2], interest in organic light-emitting diodes (OLEDs) has been steadily growing. In particular, OLEDs have been the subject of intensive investigation because of their successful commercialization in various full-color displays [3,4]. Materials development continues to play a pivotal role in this technology as OLED materials have to function often not only as a charge transporter but also an efficient light emitter. Morphology stability of various layers is another issue that needs to be addressed to assure sufficient long operational lifetime for the devices [5,6].

To date, white organic light-emitting devices (WOLEDs) have drawn intensive studies due to their potential applications in full-color display

* Corresponding author.
E-mail address: kinneas.ac94g@nctu.edu.tw (M.-H. Ho).

1566-1199/$ - see front matter
doi:10.1016/j.orgel.2007.09.006

fabrication with color filters [7], in backlight for liquid crystal display as well as in solid-state lightings [8]. One of the best known methods to achieve WOLEDs is the two-color system of sky blue and yellow or orange emission, which has been widely reported [9–11]. In this system, it has been shown that performance of WOLEDs can be improved significantly by adopting sky blue fluorescent materials with high efficiency, optimized color, and long operational stability. To this end, there have been a number of efficient blue fluorescent dyes developed in the past several years [12–15], especially the di(styryl)- amine-based blue dopant, DSA-Ph [16] and BUBD-1 [17] which, upon doping in the morphologically stable host material, 2-methyl-9,10-di(2-naphthyl)anthracene (MADN), their device performances achieved an EL efficiency of 9.7 cd/A with $CIE_{x,y}$ of (0.16, 0.32) and 13.2 cd/A with $CIE_{x,y}$ of (0.16, 0.30) at 20 mA/cm^2, respectively.

In this paper, we disclose a newly designed series blue dopants based on the 7-membered *N*-heterocyclic core structure of iminodibenzyl-distyrylarylene (IDB). It has been reported that when general aromatic amino-substituents (e.g. diphenyl amine) of hole transport material are replaced with the *iminodibenzyl* groups, the thermal properties can be improved and the emission wavelength would be blue-shifted [18,19]. Hence, we decided to introduce the iminodibenzyl groups into the highly fluorescent distyrylarylene structure. From *ab initio* density functional theory (DFT) using B3LYP/6-31* level of basis sets, we also found that the emission wavelength could be shifted to slightly deeper blue with increasing the number of phenyl moiety in the center core. We expect these new blue materials will be potentially useful in producing a deep blue emission with a properly matched host and a two-element white OLED system as well.

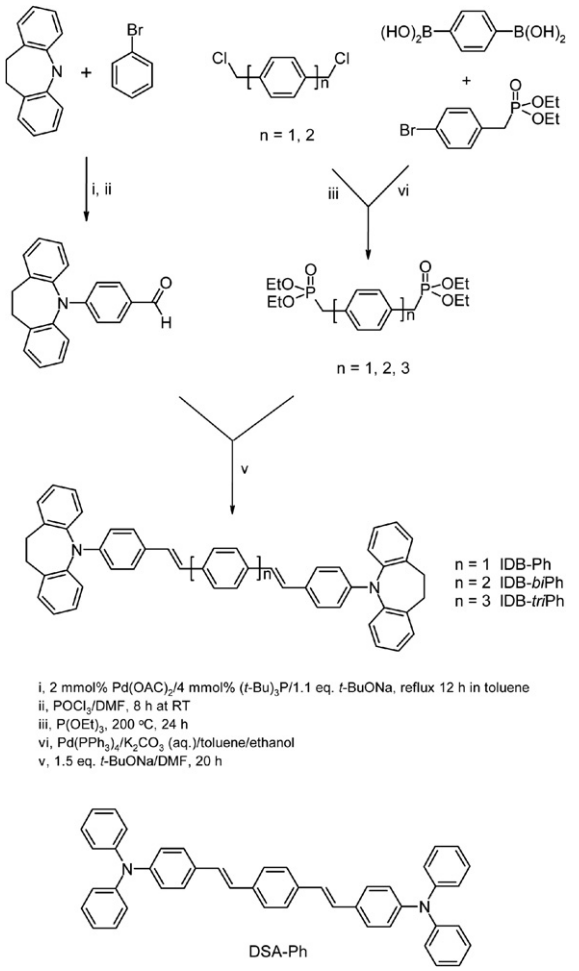

Scheme 1. Synthetic routes of IDB-series materials and structure of DSA-Ph.

2. Experimental

2.1. Synthesis

The synthetic routes of iminodibenzyl-substituted distyrylarylene derivatives (IDB-series) are shown in Scheme 1. The intermediate 4-(iminodibenzyl)-benzoaldehyde was prepared by coupling iminodibenzyl (IDB) and 4-bromobenzene with a palladium-catalyzed aromatic amination reaction [20]. After the reaction was completed, 9-phenyl-iminodibenzyl was purified by column chromatography and then mixed with phosphoryl chloride in DMF at room temperature for 8 h under nitrogen [21]. The mixture was quenched with sodium acetate and water to precipitate the gray solid and purified by recrystallization twice from ethanol to afford the intermediate as colorless crystal.

On the other hand, a mixture of *p*-xylylene dichloride and neat triethyl phosphite was heated at 200 °C for 24 h under nitrogen. After cooling to room temperature, the reaction mixture was purified by bulb to bulb distillation to afford tetraethyl *p*-(xylylene)diphosphonate [22]. The tetraethyl biphenyl-4,4′-diylbis(methylene)diphosphonate was synthesized from 4,4′-bis(chloromethyl)-biphenyl with same procedure. The tetraethyl triphenyl-4,4″-diybis(methylene)diphosphonate was synthesized by adding aqueous K_2CO_3 (2.0 M, 20 mL) to

a solution of diethyl-4-bromobenzyl phosphonate (4.5 mmol) and 1,4-benzenediboronic acid (1.9 mmol) in toluene (60 mL) and ethanol (10 mL). The mixture was degassed and tetrakis(triphenylphosphine) palladium (3.9 mol%) was added in one portion under an atmosphere of N_2 and then heated under reflux for 24 h [23]. After the solution cooled, the solvent was evaporated under vacuum and the product was extracted with ethyl acetate. The organic solution was washed with water several times and dried with anhydrous $MgSO_4$, followed by recrystallization from ethanol.

Finally, the IDB-series materials were readily synthesized by Horner–Wadsworth–Emmons reaction according to a known procedure [24]. To a solution of 4-(iminodibenzyl)-benzoaldehyde (2.1 mmol) and the appropriate phosphonate (1 mmol) in DMF cooled in an ice bath, sodium *tert*-butoxide (1.5 mmol) was added and stirred at 25 °C for 20 h. The mixture was then poured into water, and the precipitated product was collected and washed with methanol. The crude product was purified by chromatography to give pure IDB-series material as a yellow solid. The final products were purified by temperature gradient sublimation before using in subsequent studies.

tetraethyl *p*-(xylylene)diphosphonate. ^{1}H NMR (300 MHz, $CDCl_3$): δ/ppm 1.19 (t, 12H), 3.08 (d, 4H), 3.99-4.03 (m, 8H), 7.23 (s, 4H).

tetraethyl biphenyl-4,4′-diylbis(methylene)diphosphonate. ^{1}H NMR (300 MHz, $CDCl_3$): δ/ppm 1.22 (t, 12 H), 3.14 (d, 4H), 4.00–4.04 (m, 8H), 7.35 (d, 4H), 7.51 (d, 4H).

tetraethyl biphenyl-4,4″-diylbis(methylene)diphosphonate. ^{1}H NMR (300 MHz, $CDCl_3$): δ/ppm 1.24 (t, 12H), 3.19 (d, 4H), 4.03–4.08 (m, 8H), 7.23–7.64 (m, 12H).

IDB-Ph. ^{1}H NMR (300 MHz, $CDCl_3$): δ/ppm 3.00 (s, 8H), 6.56 (d, 4H), 6.82–6.97 (m, 4H), 7.21–7.43 (m, 24H). FAB-MS: $m/z = 668$ (M^+). Anal. for $C_{50}H_{40}N_2$: Calcd: C, 89.78; H, 6.03; N, 4.19. Found: C, 89.14; H, 5.83; N, 3.66.

IDB-biPh. ^{1}H NMR (300 MHz, $CDCl_3$): δ/ppm 3.00 (s, 8H), 6.59 (d, 4H), 6.89–7.08 (m, 8H), 7.23–7.60 (m, 24H). FAB-MS: $m/z = 744$ (M^+). Anal. for $C_{56}H_{44}N_2$: Calcd: C, 90.29; H, 5.95; N, 3.76. Found: C, 89.72; H, 5.82; N, 3.46.

IDB-triPh. ^{1}H NMR (300 MHz, $CDCl_3$): δ/ppm 3.00 (s, 8H), 6.56(d, 4H), 6.87–7.06 (m, 8H), 7.20–7.66 (m, 28H). FAB-MS: $m/z = 820$ (M^+). Anal. for $C_{62}H_{48}N_2$: Calcd: C, 90.70; H, 5.89; N, 3.41. Found: C, 89.91; H, 5.83; N, 2.95.

2.2. Characterization of material properties

All IDB-series materials were further purified via train sublimation and fully characterized with satisfactory spectroscopic data. UV–Vis and solution photoluminescence spectra were recorded in toluene by Hewlett Packard 8453 and Acton Research Spectra Pro-150, respectively. Electrochemical properties were studied by cyclic voltammetry using CHI 604 A. The energy gap can be calculated from the edge of UV–Vis absorption peak. Melting points (T_m), Glass transition temperatures (T_g) of the respective compounds were measured by differential scanning calorimetry (DSC) under nitrogen atmosphere using a SEIKO SSC 5200 DSC Computer/thermal analyzer.

2.3. Geometry optimization

The ground-state structures of IDB-series materials were optimized by using *ab initio* density functional theory (DFT) with the B3LYP (Becke three-parameter Lee–Yang–Parr) [25,26] exchange correlation function with 6-31G* basis sets, in Gaussian 03 program [27].

2.4. Device fabrication

The structures of blue and white devices and materials applied in this study are shown in Fig. 1. In the device fabrication, CF_x, *N*,*N*′-bis-(1-naphthyl)-*N*,*N*′-diphenyl,1,1′-biphenyl-4,4′-diamine (NPB), *tris*(8-quinolinolato)aluminium (Alq_3), and LiF were used as hole injection [28], hole transport, electron transport and electron injection materials, respectively. The emitting layer (EML) of blue-doped devices is composed of blue IDB dopants doped in the stable blue host material of MADN with each optimized concentration. In two-element WOLED device, the sky-blue light emission was generated by doping 7% highly fluorescent IDB-Ph into MADN while the yellow emission was derived from the doping 4% 2,8-di(*t*-butyl)-5,11-di [4-(*t*-butyl)phenyl]-6,12-diphenylnaphthacene (TBRb) [29] in NPB to obtain a white emission.

After a routine cleaning procedure, the indium-tin-oxide (ITO)-coated glass was loaded on the grounded electrode of a parallel-plate plasma reactor, pretreated by oxygen plasma, and then coated with a polymerized fluorocarbon film. Devices were fabricated under the base vacuum of about 10^{-6} torr in a thin-film evaporation coater following

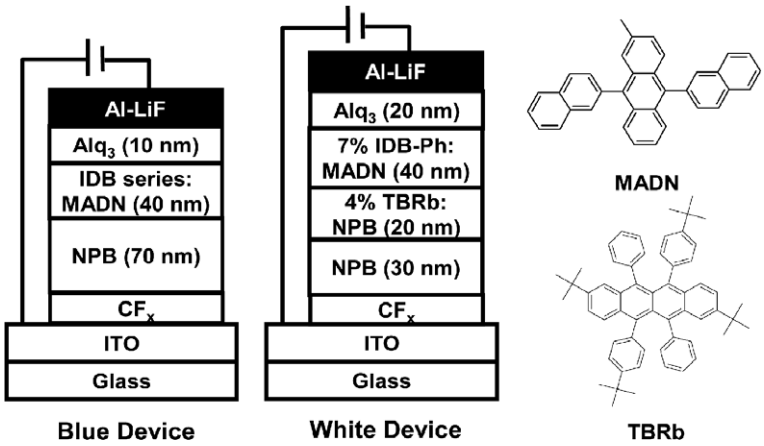

Fig. 1. Structures of MADN, TBRb, blue and white devices.

a published protocol [30]. In the evaporation of EML, the fluorescent dopant was co-deposited with host molecule at its optimal molar ratio. After the thermal deposition of the organic layers and without a vacuum break, the ultra thin layer of 1 nm of LiF followed by 200 nm of Al was deposited through a patterned shadow mask on top of the organic layers using separately controlled sources to complete the cathode. All devices were hermetically sealed prior to testing. The active area of the EL device, defined by the overlap of the ITO and the cathode electrodes, was 9 mm^2. The current–voltage–luminance characteristics of the devices were measured with a diode array rapid scan system using a Photo Research PR650 spectrophotometer and a computer-controlled programmable dc source. The device lifetime measurements were performed in a glove box at a constant drive current density of 20 mA/cm^2.

3. Results and discussion

3.1. Luminescence in solution

The photo-physical, electrochemical and thermal properties of DSA-Ph and IDB-series materials are summarized in Table 1. Fig. 2 compares the absorption and photoluminescence (PL) spectra of DSA-Ph and IDB-series materials in toluene. The features of the lowest absorption band and fluorescence of IDB-Ph are very similar to those of DSA-Ph, except they are blue-shifted. The emission wavelength of IDB-Ph is 449 nm which is blue-shifted around 9 nm with respect to that of DSA-Ph. From the conformational structures of DSA-Ph and IDB-Ph optimized by the density functional theory method using B3LYP/6-31* level of basis sets shown in Fig. 3, we found that the orthogonality between the distyrylarylene core and the phenyl group of iminodibenzyl substituent is higher than that between the core and phenyl group of diphenylamine substituent in the ground state. We attributed that the phenomenon is due to the rigid iminodibenzyl substituent which would increase the steric strain and cause the iminodibenzyl moiety to twist slightly out of the plane defined by the π–π conjugation of the distyrylarylene core. For example, the angle between the stilbene core and the phenyl group of iminodibenzyl (66°) is higher than that between the core and phenyl group of diphenylamine (42°). As a result, the effect of steric-compression would be the reason for the

Table 1
The photo-physical, electrochemical and thermal properties of DSA-Ph, IDB-Ph, IDB-biPh and IDB-triPh

Material	$\lambda_{abs,max}$ (nm)	$\lambda_{em,max}$ (nm)	HOMO (eV)	LUMO (eV)	Band gap (eV)	T_g (°C)	T_m (°C)
DSA-Ph	410	458	5.4	2.7	2.7	89	172
IDB-Ph	408	449	5.2	2.4	2.75	119	325
IDB-biPh	402	447	5.2	2.4	2.75	131	335
IDB-triPh	398	443	5.1	2.3	2.8	137	344

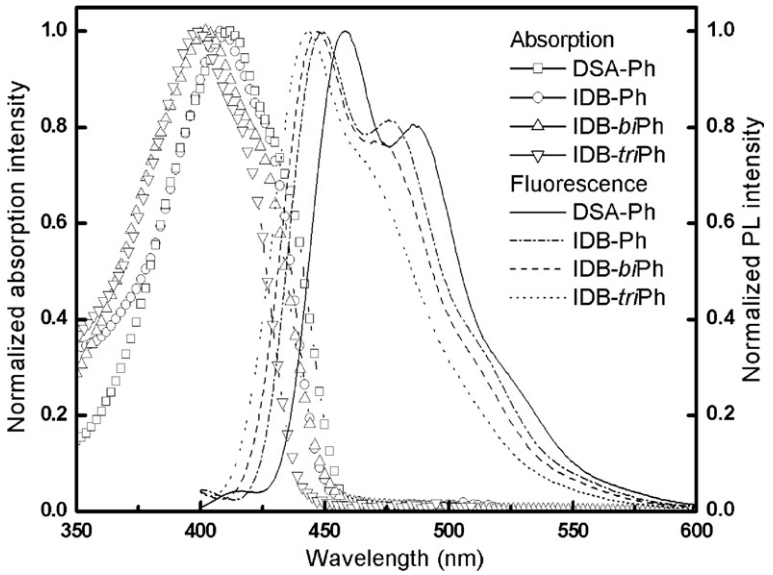

Fig. 2. Normalized absorption, photoluminescence (PL) spectra of DSA-Ph and IDB-series materials.

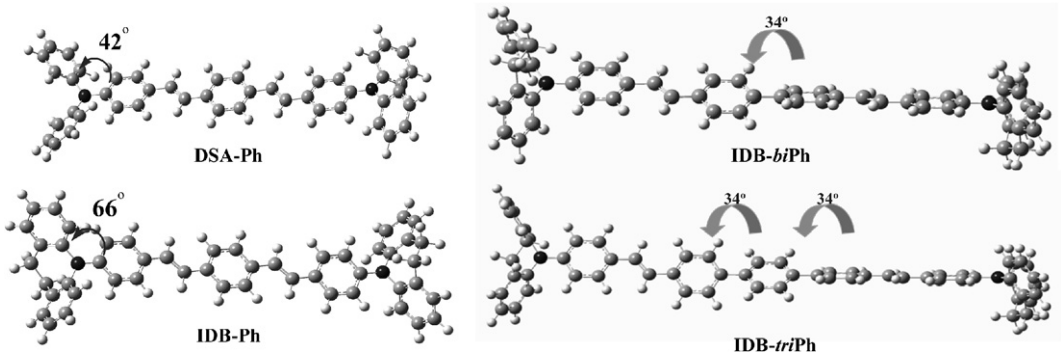

Fig. 3. Conformational Structures of DSA-Ph and IDB-series materials [DFT with B3LYP/6-31G(d)].

hypsochromic-shifted emission wavelength of IDB-Ph as compared to DSA-Ph.

It was also found that IDB-biPh and IDB-triPh (with emission λ_{max} 447 nm and 443 nm, respectively) have a slightly blue-shifted emission wavelength with respect to IDB-Ph, which means the optical spectra can be slightly shifted to shorter wavelength with the increasing phenyl moiety in the molecular core. This *hypsochromic*-shifted phenomenon can also be rationalized from the conformational structures of IDB-series materials shown in Fig. 3, in which the added phenyl moiety appears to enlarge the twist angle between two (styryl)iminodibenzyl chromophores and further decrease the π–π conjugation. As a result, the effective conjugation length (chromophore) of the molecule is slightly shortened and causes the emission wavelength to deeper blue region.

3.2. Luminescence in the solid state

In order to investigate the energy-transfer between host material (MADN) and dopant (IDB-series materials), we measured the solid-state emission spectra of various doping concentration of IDB materials doped in MADN thin films (excited with 400 nm, $\lambda_{ex,max}$ of MADN). As shown in Fig. 4a, the IDB-Ph emission can be clearly observed at 5% doping concentration and the emission of MADN around 430 nm essentially quenched confirming that the Förster energy-transfer from MADN to IDB-Ph is efficient. Moreover, when

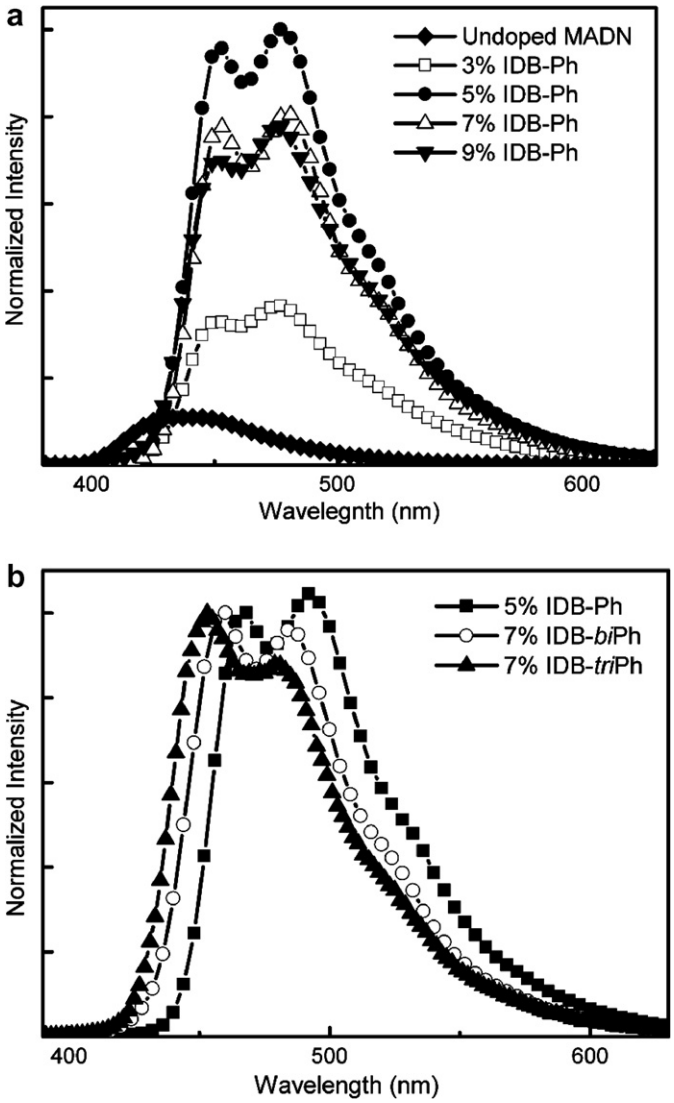

Fig. 4. (a) Solid state emission spectra of IDB-Ph/MADN thin films. (b) Normalized solid state emission spectra of IDB-series/MADN thin films.

doping concentration is up to 7%, the IDB-Ph emission intensity would be decreased and the intensity of long wavelength shoulder tends to grow with increasing doping concentration and appears to be even higher than that of the main peak. This phenomenon is primarily due to the molecular aggregation propensity of IDB-Ph with the flat stilbene-based center core, especially at high doping concentration.

The emission spectra of IDB-biPh/MADN and IDB-triPh/MADN thin films reveal the same results as there are also efficient Förster energy-transfer between IDB-biPh/MADN and IDB-triPh/MADN, respectively. Fig. 4b depicts the normalized solid-state emission spectra of IDB-series materials/MADN thin films. The solid-state emission spectra were similar to those recorded in toluene solution shown in Fig. 2. It is observed that the solid-state emission spectra become broader and the intensity of long wavelength shoulder become higher when compared with the solution PL spectra. Interestingly, the intensity of long wavelength shoulder and the full width at half maximum (FWHM) of solid-state emission spectra can be decreased with the increasing phenyl moiety in the molecular core. (The FWHM of solid-state emission of IDB-series

materials are $1.32 \times 10^5\ cm^{-1}$, $1.43 \times 10^5\ cm^{-1}$, $1.47 \times 10^5\ cm^{-1}$, respectively.) It was also found that the optimal doping concentration of IDB-biPh and IDB-triPh is 7% which is higher than that of IDB-Ph. Based on these results, we conclude that the introduction of added phenyl moiety can enlarge the twist angle in the center core and thus can alleviate the propensity for molecular aggregation. Therefore, the added phenyl moiety in the center core can be expected to further improve the color purity of blue-doped devices.

3.3. Electrochemical and thermal properties

The HOMO energy level of each material can be obtained by cyclic voltammetry and the energy-gap can be calculated from the edge of UV–Vis absorption peak. The measured HOMO energy levels of IDB-series materials are about 5.1–5.2 eV and are smaller than that of DSA-Ph (5.4 eV). This phenomenon can be rationalized by the strong donor characteristic of iminodibenzyl group, which has a small ionization potential (I_p) [31] and oxidation potential [32] and consequently causes the LUMO energy level of IDB-series dopants are much decreased to 2.3–2.4 eV.

We used differential scanning calorimetry (DSC) to investigate the thermal properties of IDB-series materials. The thermal characteristics of IDB-series materials are also summarized in Table 1. The glass transition temperature (T_g) of IDB-Ph, IDB-biPh and IDB-triPh are found at 119 °C, 131 °C and 137 °C, respectively, which are all much higher than that of DSA-Ph (89 °C). This result indicates that the steric iminodibenzyl substituent and the added phenyl moiety would not only affect the emission wavelength but also improve the material thermal stability. As a result, these IDB-series materials can form amorphous thin films that are more stable than that of DSA-Ph, and they are more promising in terms of their thermal stability for application in OLEDs.

3.4. Blue device performance

The EL efficiency of the undoped MADN is 1.5 cd/A at 20 mA/cm^2 with a $CIE_{x,y}$ color coordinate of (0.15, 0.10). When doped with IDB-Ph, IDB-biPh and IDB-triPh at their optimal doping concentrations of 5%, 7% and 7%, the EL efficiencies are increased to 9.1, 6.3, and 3.7 cd/A with $CIE_{x,y}$ color coordinate of (0.16, 0.28), (0.15, 0.24) and (0.13, 0.20), respectively. Their optimal doping levels are consistent with those of their corresponding solid-state thin film fluorescence yield. The overall EL performances of the new blue dopants doped devices are summarized in Table 2. The device performance indicates that the IDB-series materials are useful in producing blue OLED devices with high efficiency. The maximum external quantum efficiency (EQE) of IDB-Ph doped device is close to the theoretical limit of 4.8% and the half-decay lifetime ($t_{1/2}$) is 700 h with an initial brightness of 1976 cd/m^2 monitored in a dry box. Assuming the scalable law of Coulombic degradation [29] for driving at L_0 of 100 cd/m^2, the half-decay lifetime ($t_{1/2}$) of the IDB-Ph doped device is projected to be over 13,000 h.

Fig. 5 shows the normalized EL spectra of these blue-doped devices. The EL spectra peak and FWHM of dopants IDB-Ph, IDB-biPh and IDB-*tri*Ph are 461 nm, 460 nm, 456 nm and $1.39 \times 10^5\ cm^{-1}$, $1.47 \times 10^5\ cm^{-1}$, $1.67 \times 10^5\ cm^{-1}$, respectively, that are in good agreement with their corresponding solid-state emission spectra. Most importantly, the intensity of long wavelength shoulder is indeed suppressed with the increasing number of phenyl moiety at the molecular core which further improves the CIE y value to deeper blue (from 0.28 to 0.20).

3.5. Two-element white OLED device performance

We also introduced the new sky-blue emitter, IDB-Ph, into the white OLED structure incorporating a dual-layered emitting layer (EML) of blue and yellow to compose the white emission additively. Within the device structure, NPB doped with TBRb was used as the yellow emission layer. The performances of IDB-Ph doped WOLED are summarized

Table 2
Performance of IDB-series doped blue devices and two-element WOLED devices at 20 mA/cm^2

Blue dopant	Voltage (V)	Yied (cd/A)	Pow. Eff. (lm/W)	EQE (%)	$CIE_{x,y}$
Blue device					
IDB-Ph	5.9	9.1	4.9	4.8	(0.16, 0.28)
IDB-biPh	5.9	6.3	3.3	3.7	(0.15, 0.24)
IDB-triPh	6.8	3.7	1.7	2.5	(0.13, 0.20)
Two-element WOLEDs					
IDB-Ph	6.5	11.0	5.3	4.8	(0.29, 0.36)

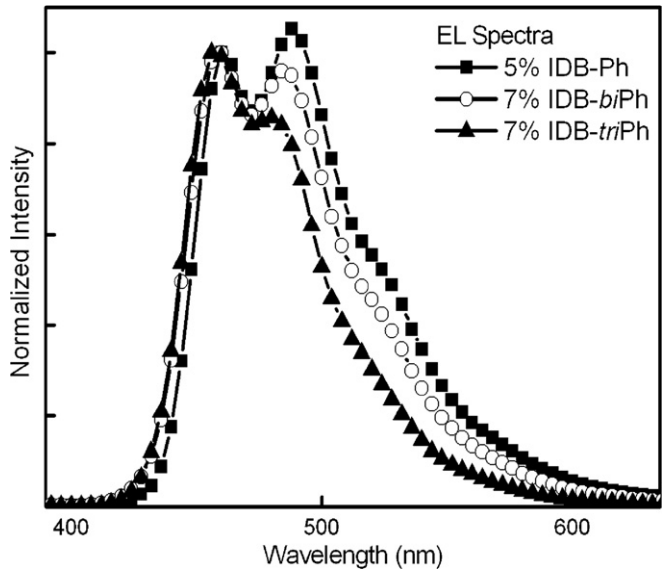

Fig. 5. Normalized EL spectra of IDB-series doped blue devices at 20 mA/cm^2.

in Table 2. The IDB-Ph doped WOLED can achieve an EL efficiency of 11.0 cd/A and 5.3 lm/W with a $CIE_{x,y}$ color coordinate of (0.29, 0.36) which are all better than the reported DSA-Ph doped WOLED [11]. The inset of Fig. 6 shows the EL spectra of IDB-Ph deoped WOLED, it covers a wild range of visible region, clearly indicating the emissions of IDB-Ph and TBRb with a dominant peak at 464, 488, and 564 nm, respectively. It is evident that there is no obvious EL color shift with increased driving currents from 20 mA/cm^2 to 200 mA/cm^2. Fig. 6 shows the operational lifetime of the IDB-Ph doped WOLED under a constant current density of 20 mA/m^2 monitored in a dry box. The t_{80} (the time for the luminance to drop to 80% of initial luminance) and initial luminance (L_0) is 420 h with an initial brightness of 2198 cd/m^2 monitored in a dry box. Assuming the scalable law of Coulombic degradation [29] for driving at L_0 of 100 cd/m^2, the half-decay lifetime ($t_{1/2}$) of

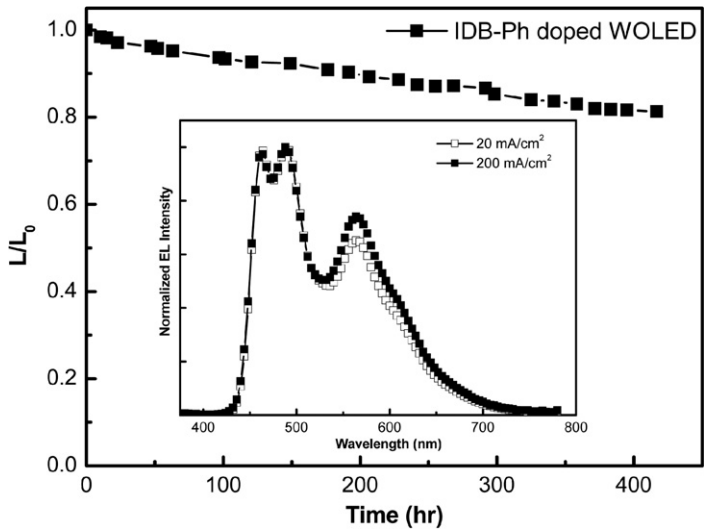

Fig. 6. Device operational stability of the IDB-Ph doped WOLED. Inset: The normalized EL spectra of IDB-Ph doped WOLED at various current densities.

the IDB-Ph doped device is projected to be over 42,000 h.

These results indicate that the two-element WOLED performance can really be significantly enahnced both in device efficiency and $CIE_{x,y}$ color coordinates by replacing DSA-Ph to IDB-Ph. The improved result is due to the new blue emitter, IDB-Ph, which emits deeper blue light with higher efficiency and better thermal stability than that of DSA-Ph. Therefore, when this new blue emitter was used in a two-element WOLED system, it can achieve a high EQE of 4.8% and generate a more balanced white $CIE_{x,y}$ color coordinates.

4. Conclusions

By molecular engineering of the di(styryl)amine-based structure, we have designed and synthesized a series of highly efficient blue dopants based on the iminodibenzyl-substituted distyrylarylene (IDB-series) compounds. The steric-compression effect can shorten the effective conjugation length (chromophore) of the molecule and the added phenyl moiety in the core can alleviate the propensity for molecular aggregation. These materials also possess high glass transition temperature over 100 °C. When doped in the stable blue host material, MADN, the maximum external quantum efficiency of IDB-Ph doped device is close to the theoretical limit of 4.8% with a $CIE_{x,y}$ color coordinate of $(0.16, 0.28)$. When IDB-Ph was used in a two-element WOLED system, the doped device achieved a luminance efficiency of 11.0 cd/A at 20 mA/cm^2 with a $CIE_{x,y}$ color coordinate of $(0.29, 0.36)$. The white device achieved a half-decay lifetime ($t_{1/2}$) of 42,000 h at an initial brightness of 100 cd/m^2.

Acknowledgements

This work was supported by grants from Chunghwa Picture Tubes, Ltd. (CPT) of Taoyuan, Taiwan. and National Science Council of Taiwan. We thank e-Ray Optoelectronics Technology Co., Ltd. of Taiwan for generously supplying some of the OLED materials studied in this work.

References

[1] M. Pope, C. Swenberg, Electronic Processes in Organic Crystals and Polymers, Oxford Science Publcations, New York, 1999.
[2] C.W. Tang, S.A. Van Slyke, Appl. Phys. Lett. 51 (1987) 913.
[3] U. Mitschke, P. Bauerle, J. Mater. Chem. 10 (2000) 1471.
[4] L.S. Hung, C.H. Chen, Mater. Sci. Eng. R 39 (2002) 143.
[5] S. Tokido, H. Tanaka, K. Noda, A. Okada, T. Taga, Appl. Phys. Lett. 70 (1997) 1929.
[6] P. Fenter, F. Schreiber, V. Buloviæ, S.R. Forrest, Chem. Phys. Lett. 277 (1997) 521.
[7] J. Kido, K. Nagai, K. Okutama, Appl. Phys. Lett. 64 (1994) 815.
[8] Y. Sun, N.C. Giebink, H. Kanno, B. Ma, M.E. Thompson, S.R. Forrest, Nature 440 (2006) 908.
[9] M. Li, W.L. Li, J.H. Niu, B. Chu, B. Li, X.Y. Sun, Z.Q. Zhang, Z.Z. Hu, Solid-State Electron. 49 (2005) 1956.
[10] D. Gupta, M. Katiyar, Opt. Mater. 28 (2006) 295.
[11] Y.S. Wu, S.W. Hwang, H.H. Chen, M.T. Lee, W.J. Shen, C.H. Chen, Thin Solid Film 488 (2005) 265.
[12] W.J. Shen, R. Dodda, C.C. Wu, F.I. Wu, T.H. Liu, H.H. Chen, C.H. Chen, C.F. Shu, Chem. Mater. 16 (2004) 930.
[13] S. Tao, Z. Peng, X. Zhang, P. Wang, C.S. Lee, S.T. Lee, Adv. Funct. Mater. 15 (2005) 1716.
[14] Y.H. Kim, H.C. Jeong, S.H. Kim, K. Yang, S.K. Kwon, Adv. Funct. Mater. 15 (2005) 1799.
[15] B.K. Shah, D.C. Neckers, J. Shi, E.W. Forsythe, D. Morton, Chem. Mater. 18 (2006) 603.
[16] M.T. Lee, H.H. Chen, C.H. Tsai, C.H. Liao, C.H. Chen, Appl. Phys. Lett. 85 (2004) 3301.
[17] M.F. Lin, L. Wang, W.K. Wong, K.W. Cheah, H.L. Tam, M.T. Lee, C.H. Chen, Appl. Phys. Lett. 89 (2006) 121913.
[18] B.E. Koene, D.E. Loy, M.E. Thompson, Chem. Mater. 10 (1998) 2235.
[19] D.F. O'Brien, P.E. Burrows, S.R. Forrest, B.E. Koene, D.E. Loy, M.E. Thompson, Adv. Mater. 10 (1998) 1108.
[20] M. Watanabe, M. Nishiyama, T. Yamamoto, Y. Koie, Tetrahedron Lett. 41 (2000) 481.
[21] M.J. Plater, T. Jackson, Tetrahedron 59 (2003) 4673.
[22] B. Iorga, F. Eymery, P. Savignac, Tetrahedron 55 (1999) 2671.
[23] A. Suzuki, Pure. Appl. Chem. 57 (1985) 1749.
[24] J.M. Kauffman, G. Moyna, J. Org. Chem. 68 (2003) 839.
[25] A.D. Becke, J. Chem. Phys. 98 (1993) 5648.
[26] C. Lee, W. Yang, R.G. Parr, Phys. Rev. B 37 (1988) 785.
[27] M.J. Frisch, G.W. Trucks, H.B. Schlegel, G.E. Scuseria, M.A. Robb, J.R. Cheeseman, J.A. Montgomery Jr., T. Vreven, K.N. Kudin, J.C. Burant, J.M. Millam, S.S. Iyengar, J. Tomasi, V. Barone, B. Mennucci, M. Cossi, G. Scalmani, N. Rega, G.A. Petersson, H. Nakatsuji, M. Hada, M. Ehara, K. Toyota, R. Fukuda, J. Hasegawa, M. Ishida, T. Nakajima, Y. Honda, O. Kitao, H. Nakai, M. Klene, X. Li, J.E. Knox, H.P. Hratchian, J.B. Cross, C. Adamo, J. Jaramillo, R. Gomperts, R.E. Stratmann, O. Yazyev, A.J. Austin, R. Cammi, C. Pomelli, J.W. Ochterski, P.Y. Ayala, K. Morokuma, G.A. Voth, P. Salvador, J.J. Dannenberg, V.G. Zakrzewski, S. Dapprich, A.D. Daniels, M.C. Strain, O. Farkas, D.K. Malick, A.D. Rabuck, K. Raghavachari, J.B. Foresman, J.V. Ortiz, Q. Cui, A.G. Baboul, S. Clifford, J. Cioslowski, B.B. Stefanov, G. Liu, A. Liashenko, P. Piskorz, I. Komaromi, R.L. Martin, D.J. Fox, T. Keith, M.A. Al-Laham, C.Y. Peng, A. Nanayakkara, M. Challacombe, P.M.W. Gill, B. Johnson, W. Chen, M.W. Wong, C. Gonzalez, J.A. Pople, Gaussian 03, Revision A.1, Gaussian, Inc., Pittsburgh PA, 2003.
[28] L.S. Hung, L.R. Zheng, M.G. Mason, Appl. Phys. Lett. 78 (2001) 673.

[29] Y.S. Wu, T.H. Liu, H.H. Chen, C.H. Chen, Thin Solid Film 496 (2006) 626.
[30] S.A. Van Slyke, C.H. Chen, C.W. Tang, Appl. Phys. Lett. 69 (1996) 2160.
[31] H.J. HainK, J.E. Adams, J.R. Huber, Ber. Bunsenges, Phys. Chem. 78 (1974) 436.
[32] S.N. Frank, A.J. Bard, J. Electrochem. Soc. 122 (1975) 898.

Available online at www.sciencedirect.com
ScienceDirect
Organic Electronics 9 (2008) 111–118
Organic Electronics
www.elsevier.com/locate/orgel

PTCDA on Au(1 1 1), Ag(1 1 1) and Cu(1 1 1): Correlation of interface charge transfer to bonding distance

S. Duhm [a], A. Gerlach [b], I. Salzmann [a], B. Bröker [a], R.L. Johnson [c], F. Schreiber [b], N. Koch [a,*]

[a] *Institut für Physik, Humboldt-Universität zu Berlin, Newtonstr. 15, D-12489 Berlin, Germany*
[b] *Institut für Angewandte Physik, Universität Tübingen, Auf der Morgenstelle 10, D-72076 Tübingen, Germany*
[c] *Institut für Experimentalphysik, Universität Hamburg, Luruper Chaussee 149, D-22761 Hamburg, Germany*

Received 29 June 2007; received in revised form 2 October 2007; accepted 10 October 2007
Available online 25 October 2007

Abstract

The electronic structure at the interfaces of 3,4,9,10-perylene tetracarboxylic dianhydride (PTCDA) and the metal surfaces Au(1 1 1), Ag(1 1 1) and Cu(1 1 1) was investigated using ultraviolet photoelectron spectroscopy (UPS). By combining these results with recent X-ray standing wave data from PTCDA on the same substrates clear correlation between the electronic properties and the interface geometry is found. The charge transfer between the molecule and the metal increases with decreasing average bonding distance along the sequence Au–Ag–Cu. Clear signatures of charge-transfer-induced occupied molecular states were found for PTCDA on Ag(1 1 1) and Cu(1 1 1). As reported previously by Zou et al. [Y. Zou et al., Surf. Sci. 600 (2006) 1240] a new hybrid state was found at the Fermi-level (E_F) for PTCDA/Ag(1 1 1), rendering the monolayer metallic. In contrast, the hybrid state for PTCDA/Cu(1 1 1) was observed well below E_F, indicating even stronger charge transfer and thus a semiconducting chemisorbed molecular monolayer. The hybridisation of molecular and Au electronic states could not be evidenced by UPS.

PACS: 73.61.Ph; 73.20.−r; 68.43.−h

Keywords: Organic/metal interface; Photoelectron spectroscopy; Energy level alignment; Charge transfer; Bonding distance; Electronic structure

1. Introduction

The energy level alignment at organic/metal interfaces is a key issue for the performance of devices in the field of *organic electronics* [1,2]. Two rather simple models are often employed to describe limiting cases of the energy level alignment mechanism: (i) the Schottky–Mott limit, where the energies of the molecular orbitals (MOs) are strictly determined by the work function of the metal substrate involving vacuum level alignment, and (ii) Fermi-level pinning, where the energies of the

* Corresponding author. Tel.: +49 30 2093 7819; fax: +49 30 2093 7632.
E-mail address: norbert.koch@physik.hu-berlin.de (N. Koch).

1566-1199/$ - see front matter © 2007 Elsevier B.V. All rights reserved.
doi:10.1016/j.orgel.2007.10.004

MOs are pinned relative to the Fermi-level (E_F) of the metal by charge transfer between the substrate and adsorbate [3,4]. However, these models do not incorporate the complex processes determining the energy level alignment at organic/metal interfaces, where other mechanisms like the chemical interaction between substrate and adsorbate [5,6], the electron push-back effect [1,7–9], interface dipoles [1,10,11], or the adsorption-induced geometry of the molecules [12–14] play important roles. Hence, in order to obtain a deeper understanding of energy level alignment mechanisms at organic/metal interfaces it is helpful to study the electronic interface properties of a structurally well characterized system.

An interesting model molecule in this context is 3,4,9,10-perylene tetracarboxylic dianhydride [PTCDA, Fig. 1]. The electronic as well as the geometric structure of PTCDA on different metal substrates has been studied in detail [15–28]. It is known that PTCDA can react strongly with metals *via* electron transfer [15–18], resulting in anionic molecular species. Despite the manifold possible interactions at the interface, PTCDA multilayers exhibit the same hole injection barrier (HIB) on a variety of polycrystalline metal substrates, covering a wide range of work functions (ca. 3.7–5.2 eV). For PTCDA on Mg, In, Sn and Au, [19] as well as for PTCDA on Au and Co, [20] the molecular levels have been investigated by ultraviolet photoelectron spectroscopy (UPS). For PTCDA on Au, Al and Sn the HIBs have been determined from current–voltage measurements in model devices [21]. Structural information for PTCDA adsorbed on single crystalline substrates Au(1 1 1), Ag(1 1 1) and Cu(1 1 1) has been obtained by means of low and high energy electron diffraction, scanning tunneling microscopy (STM) and X-ray diffraction [22,23,27,29]. Recent X-ray standing wave (XSW) studies have shown different adsorption geometries for PTCDA on Au(1 1 1) [12], Ag(1 1 1) [12–14] and Cu(1 1 1) [14]. In addition to different average bonding distances of PTCDA on these metal surfaces, significant deviations from the planar bulk-conformation of the organic molecule were found. To obtain deeper insight in bonding mechanisms at organic/metal interfaces it is necessary to compare these data with the interfacial electronic structure of PTCDA on these three metal substrates. For PTCDA/Ag(1 1 1) it is already known that hybridisation of unoccupied and occupied molecular orbitals with Ag 4d-bands occurs in the monolayer [15,30], accompanied by electron transfer from the metal to the molecule. This well characterized system may act as a reference for PTCDA/Au(1 1 1), where the bonding is expected to be weaker than on Ag(1 1 1) [16,24,31] and for PTCDA/Cu(1 1 1) [27,28], where a stronger chemical interaction is expected [14,32]. We have performed UPS measurements on PTCDA/metal interfaces with Au(1 1 1), Ag(1 1 1), and Cu(1 1 1) substrates. These data reveal a correlation between the adsorption geometry and the interface electronic structure, leading to deeper insight into this interesting model system. In addition, the electronic structure of multilayer PTCDA has been measured on each substrate. Despite the remarkable differences in adsorption geometry and interfacial electronic structure for monolayers, the multilayer electronic structure and energy level alignment are virtually identical for all three cases.

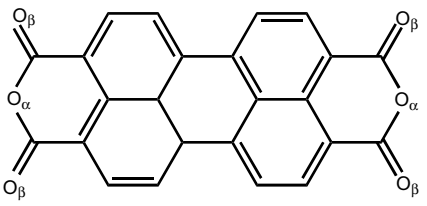

Fig. 1. Chemical structure of PTCDA, the indices mark the anhydride (O_α) and the carboxylic (O_β) oxygen.

2. Experimental details

Photoemission experiments were performed at the FLIPPER II end-station at HASYLAB (Hamburg, Germany) [33]. The interconnected sample preparation chambers (base pressure 2×10^{-9} mbar) and analysis chamber (base pressure 2×10^{-10} mbar) allowed sample transfer without breaking the ultrahigh vacuum. The Au(1 1 1), Ag(1 1 1) and Cu(1 1 1) single crystals were cleaned by repeated Ar-ion sputtering and annealing cycles (up to 550 °C). PTCDA was evaporated using resistively heated pinhole sources, at evaporation rates of about 1 Å/min. The film mass thickness was monitored with a quartz crystal microbalance. Hence, the values for PTCDA coverages corresponds to nominal film thicknesses. However, depending on the specific growth mode a nominal coverage of 2–3 Å corresponds to a monolayer on all three substrates. Spectra were recorded with a double-pass cylindrical mirror analyzer in off-normal

emission and an acceptance angle of 24° with an energy resolution of 200 meV and a photon energy of 22 eV. The secondary electron cut-offs (SECO) [for determination of the sample work function (ϕ) and the ionization energy] were measured with the sample biased at −3.00 V. All preparation steps and measurements were performed at room temperature. The error of all given values of binding energies and SECO positions is estimated to ±0.05 eV.

3. Results

The thickness dependent evolution of the photoemission spectra for PTCDA on the three different (1 1 1)-substrates is shown in Fig. 2.

The deposition of up to 2 Å PTCDA on Au(1 1 1) resulted in the attenuation of the Au derived photoemission features and the growth of a shoulder centered at 1.80 eV binding energy (BE) on the low binding energy side of the Au 5d-bands. In analogy to earlier studies [31,34], we attribute this feature to the HOMO (highest occupied molecular orbital) of PTCDA. No indication for another molecular adsorption-induced photoemission feature close to E_F was found. Increasing the coverage up to 48 Å led to a continuous shift of this feature to 2.55 eV BE. At this multilayer coverage, the spectrum fully agrees with PTCDA spectra on polycrystalline Au reported previously [20,34]. For 1 Å PTCDA/Au(1 1 1) the sample work function decreased by 0.20 eV compared to pristine Au(1 1 1) ($\phi_{Au} = 5.15$ eV), and by further 0.25 eV at a coverage of up to 48 Å (i.e., −0.45 eV total vacuum level shift).

For the Ag(1 1 1) substrate the deposition of 1 Å PTCDA resulted in several new photoemission features; a peak centered at 0.2 eV BE directly below the Fermi-edge of the metal (L′) and another peak

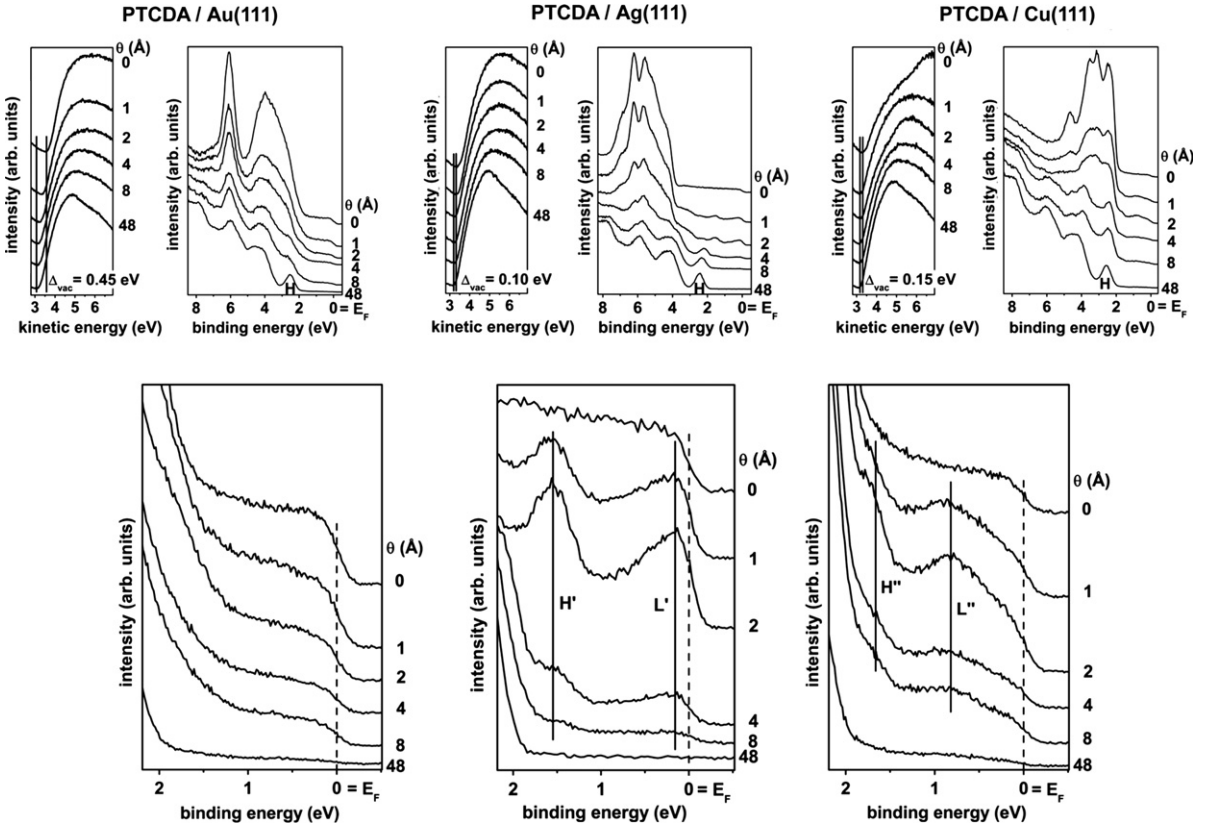

Fig. 2. Thickness dependent UPS spectra of PTCDA on Au(1 1 1), Ag(1 1 1) and Cu(1 1 1). θ denotes the layer thickness. A coverage of about 3 Å corresponds to monolayer coverage. The first row displays in each case the secondary electron cut-off spectra and the survey spectra. H marks in each case the HOMO of multilayer PTCDA. The second row shows the corresponding spectrum in the region close to the Fermi-energy (E_F) on an enlarged scale. H′ marks the HOMO and L′ the LUMO-derived interface states in the case of PTCDA/Ag(1 1 1), H″ and L″ the same for PTCDA/Cu(1 1 1). Δ_{vac} denotes the decrease in the vacuum level between the pristine metal and multilayers of PTCDA.

centered at 1.55 eV BE (H′). Increasing the coverage up to 2 Å led to enhanced intensity of both peaks. However, for 4 Å PTCDA coverage the intensity of the two peaks L′ and H′ decreased and a new peak centered at 2.20 eV BE emerged. Increasing the coverage up to the final value of 48 Å led to a shift of this peak to 2.45 eV BE, while the two low BE peaks vanished. ϕ of pristine Ag(1 1 1) was 4.90 eV. For sub-monolayer coverage ϕ decreased by only 0.10 eV and stayed constant for higher coverages.

The deposition of up to 2 Å PTCDA on Cu(1 1 1) also resulted in two new photoemission features in the region near to E_F, i.e., a broad peak centered at 0.80 eV BE (L″) and another peak centered at 1.70 eV BE (H″). At higher coverages the intensities of these peaks decreased and at 48 Å PTCDA coverage these peaks and the metal Fermi-edge were no longer visible. However, similar to the case of PTCDA/Ag(1 1 1) a new peak centered at 2.55 eV BE emerged at multilayer coverage. ϕ of clean Cu(1 1 1) was 4.90 eV. The work function was decreased by 0.15 eV for a coverage of 1 Å PTCDA and stayed essentially constant for further PTCDA deposition.

The work function at monolayer coverage was 4.75 eV on all three substrates, regardless of the shape of the photoemission spectrum. The HOMO positions of all multilayer samples were virtually identical, with the peaks centered at 2.55 eV for PTCDA/Au(1 1 1) and PTCDA/Cu(1 1 1), and at 2.45 eV BE for PTCDA/Ag(1 1 1). Consequently, the PTCDA ionization energies (measured from the HOMO-onset to the vacuum-level) were identical on all three substrates within the error bar of ±0.05 eV, namely 6.80 eV on Au(1 1 1), 6.85 eV on Ag(1 1 1) and 6.75 eV on Cu(1 1 1).

4. Discussion

In the following we will discuss our photoemission results in the light of previous knowledge about the properties of PTCDA/metal interfaces. We will make particular relation to recently reported bonding distance values, which will finally allow to arrive at a comprehensive picture of PTCDA/metal interface energetics.

It has been suggested that the interaction between a conjugated organic molecule and a Au(1 1 1) surface should be rather weak [16,24]. Consequently, no clear signature of molecule-metal reaction-induced peaks within the energy gap region of PTCDA was observed in the spectra of PTCDA/Au(1 1 1), even at sub-monolayer coverage (Fig. 2). The shift of the HOMO between monolayer and multilayer of 0.75 eV towards higher binding energies seems unusually large for weakly interacting conjugated organic molecules on metals. Usually, the screening of the photo-hole by the metal charge density results in shifts up to 0.40 eV between mono- and multilayer coverage of molecules on metals [35,36]. The position of the HOMO in the monolayer (1.80 eV BE) is in good agreement with scanning tunneling spectroscopy (STS) data, where a HOMO position of 1.90 eV BE was measured [24]. In contrast, another STS study found the HOMO centered at 2.18 eV BE for monolayer PTCDA/Au(1 1 1) and at 2.32 eV BE for 2–3 layers PTCDA/Au(1 1 1) [31]. As an explanation for this discrepancy, different tip–surface interactions and/or tunneling distances were suggested [24]. A monolayer of PTCDA on Au(1 1 1) forms well ordered domains with two distinct structures, but only modification is observed in the second and subsequent layers [37,38]. A recent STS study of the unoccupied states of PTCDA/Au(1 1 1) reported differences in the position of the lowest unoccupied molecular orbital (LUMO) of up to 0.35 eV depending on the adsorption domain of PTCDA [39]. The authors suggested hydrogen-bond-mediated intermolecular interaction to be responsible for the different peak positions. By analogy, differences of the same order of magnitude should be possible for occupied states. The area-averaged UPS spectra reveal both peaks, but the peak at higher BE may be masked by the dominant Au 5d emission. However, the differences in the electronic structure of the two monolayer adsorption domains, coupled with the polarization effect of the photo-hole can explain the 0.75 eV shift of the PTCDA HOMO between mono- and multilayer. UPS data of multilayer PTCDA on polycrystalline Au report the HOMO peak centered at 2.60 eV BE [34] or 2.35 eV BE [20], respectively. Considering the structural differences between Au(1 1 1) and polycrystalline Au, our value is in good agreement with the literature.

The absence of clear molecule-derived photoemission features in the energy gap region may thus be interpreted as indicative of physisorption of PTCDA on Au(1 1 1). However, the small decrease of ϕ by only 0.45 eV induced by a monolayer of PTCDA on Au(1 1 1) compared to the pristine substrate may indicate a stronger interaction than only physisorption. The electron push-back effect fre-

quently leads to a larger decrease of ϕ (in the range of 1 eV) for molecules physisorbed on Au surfaces [1,8]. Molecules chemisorbed on a metal via electron transfer (from the metal to the molecule) induce an additional contribution to the total interface dipole, which can partially or totally cancel the push back effect [6,40]. If the charge transfer for PTCDA/Au(1 1 1) were very small, the experimental observation would merely be limited by the fact that the newly induced density of states is simply too low to be detected [41]. Moreover, detailed theoretical work for PTCDA/Au(1 1 1) suggested significant molecular level broadening and interface electron density rearrangement induced by the metal proximity [42], which could be regarded as another way of describing a "soft" chemisorption process.

PTCDA on Ag(1 1 1) exhibits a strong chemical interaction, accompanied by electron transfer from Ag to PTCDA [15,16]. Following earlier reports, the (sub-)monolayer peaks in the energy gap of PTCDA are assigned to hybrid states of the Ag 4 d-bands and the LUMO (now partially filled L′), HOMO (now the H′), and the HOMO-1 states of neutral PTCDA [15,30]. At elevated temperatures PTCDA/Ag(1 1 1) grows in the Stranski–Krastanov mode, but at room temperature the growth becomes more layer-by-layer like [43,44]. Consequently, these interface states are no longer visible in the UPS signal for higher PTCDA coverages. The LUMO-derived interface peak (L′) is located directly at the Fermi-level, thus a monolayer PTCDA on Ag(1 1 1) is metallic [15]. The peak emerging at 2.20 eV BE at a coverage of 4 Å was assigned to the HOMO of neutral molecules [15]. The shift of the HOMO peak to 2.45 eV BE for 48 Å PTCDA coverage can be attributed to different polarization energies of PTCDA for the monolayer and multilayers [31]. The decrease in ϕ between the pristine metal and monolayer PTCDA is much smaller than for PTCDA/Au(1 1 1), also indicative of a stronger chemical interaction between the substrate and the adsorbate.

The observation of interface states for a monolayer of PTCDA on Cu(1 1 1) shows that strong chemical interaction occurs at this interface. As the behavior of the SECO is similar to PTCDA/Ag(1 1 1), we conclude that significant electron transfer from the metal to the molecule takes place as well. Thus, peak L″ is assigned to the (partially) filled LUMO and H″ from the HOMO of the neutral PTCDA molecule. However, these interface states of PTCDA on Cu(1 1 1) are centered at significantly higher binding energies than for PTCDA/Ag(1 1 1). The energetic differences indicate that the hybridization of the molecular levels and the Cu 3d-bands is different from the case of PTCDA/Ag(1 1 1). Because the peaks are shifted to higher binding energies, stronger bonding of PTCDA to Cu(1 1 1) is likely. For monolayer PTCDA on Cu(1 1 1) the LUMO-derived interface state (L″) is located clearly below the Fermi-level, i.e., a monolayer of PTCDA on Cu(1 1 1) is expected to be semiconducting, in contrast to the metallic molecular layer on Ag(1 1 1). Since PTCDA on Cu(1 1 1) grows in the Stranski-Krastanov mode [27], the interface state photoemission is not completely attenuated by overlayer material in the UPS spectra at multilayer coverages. The position of the HOMO of the multilayer is consistent with UPS data for PTCDA on polycrystalline Cu, where a HOMO position of 2.47 eV BE has been reported [20].

The electronic structure of PTCDA on the different substrates exhibits remarkable differences, ranging from "soft" chemisorption (on Au) to strong hybridization of metal bands and molecular orbitals, yielding metallic (on Ag) or semiconducting monolayers (on Cu). It is now interesting to see how these differences in the electronic structure are reflected in the adsorption geometry and bonding distance of PTCDA on the metal substrates (or, of course, *vice versa*). In Fig. 3 the binding models of PTCDA on Au(1 1 1), Ag(1 1 1) and Cu(1 1 1), are summarized schematically. The PTCDA energy levels in the interface region are compared to those in PTCDA multilayers (Fig. 3a) and the binding positions d_H of the carbon and oxygen atoms of PTCDA adsorbed on the three noble metals (Fig. 3b), using the results from X-ray standing wave studies [12–14].

The comparably weak PTCDA/Au(1 1 1) interaction is reflected in both the electronic structure and the adsorption geometry. In the UPS spectra no LUMO-derived features appeared at the PTCDA/Au(1 1 1) interface. The XSW results report an average carbon bonding distance of PTCDA on Au(1 1 1) ($d_H = 3.27$ Å) [12] close to the molecular stacking distance measured in PTCDA single crystals ($d_{(102)} = 3.22$ Å) [45], which also suggests a rather weak interaction. For PTCDA on Ag(1 1 1) a clear LUMO-derived peak (L′) appeared in the interface region directly at the Fermi-edge, which leads to the metallic character of adsorbed PTCDA. The interface electronic structure of PTCDA on Ag(1 1 1) has already been discussed in detail

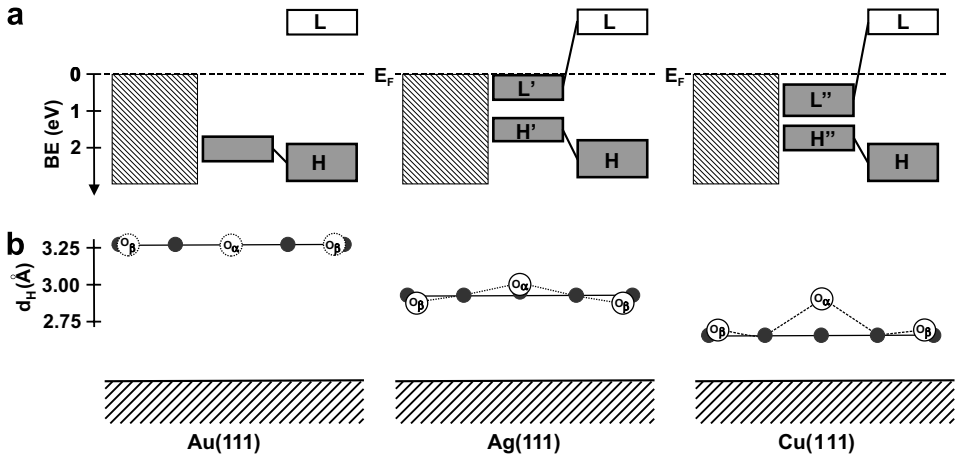

Fig. 3. (a) Schematic energy level diagram of PTCDA on Au(1 1 1), Ag(1 1 1) and Cu(1 1 1). The shaded area corresponds to the metal electron density, gray bars to occupied and open bars to unoccupied molecular orbitals. From left to right, the pristine metal, the interface region with the LUMO and HOMO derived interface states labeled L′ and H′ for the metallic case of PTCDA/Ag(1 1 1) and L″ and H″ for the semiconductive case of PTCDA/Cu(1 1 1) and multilayer PTCDA (H and L) are shown. The positions of the LUMOs are estimated from the transport gap, measured with (inverse) photoemission for PTCDA/Ag [31]. (b) Schematic binding positions of PTCDA on the three different substrates as measured in [12–14]. The position of the oxygen atoms in PTCDA/Au(1 1 1) was not measured with XSW, however a merely planar adsorption geometry of PTCDA on Au(1 1 1) might be assumed [22,23].

[15,30] and is presented here for completeness. The adsorption geometry with an average carbon bonding distance of $d_H = 2.86$ Å [13,14] directly supports the strong chemical interaction of PTCDA with Ag(1 1 1). In addition, PTCDA on Ag(1 1 1) shows a nonplanar adsorption geometry with the carboxylic oxygens (O_β) bent towards and the anhydride oxygens (O_α) bent away from the metal surface with respect to the carbon plane. On the Cu(1 1 1) substrate the higher binding energy of the LUMO-derived peak (L″) compared to PTCDA/Ag(1 1 1) nicely correlates with the even smaller bonding distance of PTCDA carbons ($d_H = 2.66$ Å) [14]. In addition, the PTCDA bending on Cu is also different than on Ag, as all of the oxygen atoms are bent away from the surface with respect to the PTCDA carbon plane.

Making an overall comparison of UPS and XSW results, a direct correlation between the adsorption geometry and strength of chemical bonding can be found. With increasing metal reactivity the chemical interaction, as revealed by the interfacial electronic structure, increases and the carbon bonding distance decreases accordingly. The distortion of the PTCDA molecules in the case of the strongly interacting systems PTCDA/Ag(1 1 1) and PTCDA/Cu(1 1 1) is not yet fully understood [14]. However, it can be speculated that the different molecular conformations (i.e., bending of the carboxylic oxygens) are directly related to the amount of charge transferred to the molecule, evidenced by the metallic-type monolayer PTCDA on Ag(1 1 1) and the semiconducting-type on Cu(1 1 1). This open question may be the topic of further ab initio calculations.

In the following, we consider the properties of the PTCDA multilayers on the three different substrates. The PTCDA ionization energies were found to be essentially the same on all three substrates. Despite the obvious differences in the (sub-)monolayer spectra, the hole injection barriers of multilayer PTCDA on all three substrates are virtually identical. Considering the work functions of PTCDA monolayers on the three substrates this finding is no longer surprising, since ϕ for all three monolayer PTCDA/metal systems is the same. Particularly for PTCDA on Ag(1 1 1) and Cu(1 1 1) the chemisorbed monolayer must be regarded as a modified metal substrate for the multilayer growth. The molecular levels of PTCDA in the multilayer are thus aligned relative to the modified substrate ϕ as in other organic heterostructures [6,46]. Therefore the observation of the nearly equal HIBs on all three substrates irrespective of the initial clean metal substrate work function cannot be interpreted in terms of "classical" Fermi-level pinning in the framework of organic/metal interfaces, where besides a small charge transfer between the metal and the adsorbate no chemical interaction occurs and a small density of interface states is able to pin the molecular orbitals [3,4]. Reactive PTCDA

is possibly a special case, which is not compatible with the existing energy level alignment models. The three-layer model (metal–chemisorbed monolayer–multilayer) can explain our findings, but the reason for the constant work functions of the PTCDA/metal systems remains open. An alternative approach may be provided by the calculations of charge neutrality levels (CNL) [42,47]. In the case of PTCDA on Au(1 1 1), a CNL level is found (2.45 ± 0.10) eV above the center of the PTCDA HOMO level, the CNL again is located 0.02 eV above E_F [42]. This result is in good agreement with our measured HOMO positions. Vázquez et al. [42,47] stated that changes in the bonding distance of PTCDA and distortions in the range of the experimentally measured values on the different substrates have no significant influence on the position of the CNL. Therefore, also for PTCDA/Ag(1 1 1) and PTCDA/Cu(1 1 1) the CNL theory should be applicable. It should be interesting to see in future work, whether this theory, which was designed for chemically weakly interacting systems, can successfully describe the physics at these interfaces.

5. Conclusion

We have demonstrated chemisorption with different interaction strength of PTCDA on the substrates Au(1 1 1), Ag(1 1 1) and Cu(1 1 1) using photoemission. Our results confirm the results from recent XSW studies and reveals the correlation between the strength of the chemical interaction and the average bonding distance. Taking PTCDA on Ag(1 1 1) as a reference we find that PTCDA binds more strongly to Cu(1 1 1) and less strongly to Au(1 1 1). For PTCDA on Au(1 1 1) no additional states are observed in the energy gap and the bonding distance is large. For PTCDA on Cu(1 1 1) the LUMO-derived interface state is more tightly bound than on Ag(1 1 1), the bonding distance is smaller, and the PTCDA molecule is distorted. Multiple layers of PTCDA on all three substrates have the same hole injection barrier since the work function of PTCDA monolayers is identical in all three cases.

Acknowledgements

N.K. acknowledges financial support by the Emmy Noether-Program (DFG), F.S. and A.G. by the EPSRC and the DFG.

References

[1] A. Kahn, N. Koch, W.Y. Gao, J. Polym. Sci. B 41 (2003) 2529.
[2] H. Ishii, K. Sugiyama, E. Ito, K. Seki, Adv. Mater. 11 (1999) 605.
[3] N. Koch, A. Vollmer, Appl. Phys. Lett. 89 (2006) 162107.
[4] H. Fukagawa, S. Kera, T. Kataoka, S. Hosoumi, Y. Watanabe, K. Kudo, N. Ueno, Adv. Mater. 19 (2007) 665.
[5] X. Crispin, V. Geskin, A. Crispin, J. Cornil, R. Lazzaroni, W.R. Salaneck, J.-L. Bredas, J. Am. Chem. Soc. 124 (2002) 8131.
[6] N. Koch, S. Duhm, J.P. Rabe, A. Vollmer, R.L. Johnson, Phys. Rev. Lett. 95 (2005) 237601.
[7] N. Koch, A. Elschner, J. Schwartz, A. Kahn, Appl. Phys. Lett. 82 (2003) 2281.
[8] G. Witte, S. Lukas, P.S. Bagus, C. Wöll, Appl. Phys. Lett. 87 (2005) 263502.
[9] E. Ito, H. Oji, H. Ishii, K. Oichi, Y. Ouchi, K. Seki, Chem. Phys. Lett. 287 (1998) 137.
[10] K. Seki, E. Ito, H. Ishii, Synthetic Met. 91 (1997) 137.
[11] S. Kera, Y. Yabuuchi, H. Yamane, H. Setoyama, K.K. Okudaira, A. Kahn, N. Ueno, Phys. Rev. B 70 (2004) 085304.
[12] S.K.M. Henze, O. Bauer, T.-L. Lee, M. Sokolowski, F.S. Tautz, Surf. Sci. 601 (2007) 1566.
[13] A. Hauschild, K. Karki, B.C.C. Cowie, M. Rohlfing, F.S. Tautz, M. Sokolowski, Phys. Rev. Lett. 94 (2005) 036106.
[14] A. Gerlach, S. Sellner, F. Schreiber, N. Koch, J. Zegenhagen, Phys. Rev. B 75 (2007) 045401.
[15] Y. Zou, L. Kilian, A. Schöll, T. Schmidt, R. Fink, E. Umbach, Surf. Sci. 600 (2006) 1240.
[16] M. Eremtchenko, D. Bauer, J.A. Schaefer, F.S. Tautz, New J. Phys. 6 (2004) 4.
[17] Y. Hirose, A. Kahn, V. Aristov, P. Soukiassian, V. Bulovic, S.R. Forrest, Phys. Rev. B 54 (1996) 13748.
[18] G. Gavrila, D.R.T. Zahn, W. Braun, Appl. Phys. Lett. 89 (2006) 162102.
[19] I.G. Hill, A. Rajagopal, A. Kahn, Y. Hu, Appl. Phys. Lett. 73 (1998) 662.
[20] E. Kawabe, H. Yamane, K. Koizumi, R. Sumii, K. Kanai, Y. Ouchi, K. Seki, Mater. Res. Soc. Symp. Proc. 965 (2007) S09.
[21] R. Agrawal, S. Ghosh, Appl. Phys. Lett. 89 (2006) 222114.
[22] P. Fenter, F. Schreiber, L. Zhou, P. Eisenberger, S.R. Forrest, Phys. Rev. B 56 (1997) 3046.
[23] T. Schmitz-Hübsch, T. Fritz, F. Sellam, R. Staub, K. Leo, Phys. Rev. B 55 (1997) 7972.
[24] N. Nicoara, E. Román, J.M. Gómez-Rodríguez, J.A. Martín-Gago, J. Méndez, Org. Electron. 7 (2006) 287.
[25] M. Schneider, E. Umbach, M. Sokolowski, Chem. Phys. 325 (2006) 185.
[26] V. Shklover, F.S. Tautz, R. Scholz, S. Sloboshanin, M. Sokolowski, J.A. Schaefer, E. Umbach, Surf. Sci. 454–456 (2000) 60.
[27] T. Wagner, A. Bannani, C. Bobisch, H. Karacuban, M. Stöhr, M. Gabriel, R. Möller, Org. Electron. 5 (2004) 35.
[28] T. Wagner, A. Bannani, C. Bobisch, H. Karacuban, R. Möller, J. Phys. Condens. Mat. 19 (2007) 056009.
[29] B. Krause, A.C. Dürr, F. Schreiber, H. Dosch, O.H. Seeck, J. Chem. Phys. 119 (2003) 3429.

[30] F.S. Tautz, M. Eremtchenko, J.A. Schaefer, M. Sokolowski, V. Shklover, E. Umbach, Phys. Rev. B 65 (2002) 125405.
[31] E.V. Tsiper, Z.G. Soos, W. Gao, A. Kahn, Chem. Phys. Lett. 360 (2002) 47.
[32] A. Schmidt, T.J. Schuerlein, G.E. Collins, N.R. Armstrong, J. Phys. Chem. 99 (1995) 11770.
[33] R.L. Johnson, J. Reichardt, Nucl. Instrum. Methods 208 (1983) 791.
[34] I.G. Hill, A. Kahn, Z.G. Soos, R.A. Pascal Jr., Chem. Phys. Lett. 327 (2000) 181.
[35] N. Koch, G. Heimel, J. Wu, E. Zojer, R.L. Johnson, J.-L. Bredas, K. Müllen, J.P. Rabe, Chem. Phys. Lett. 413 (2005) 390.
[36] I.G. Hill, A.J. Mäkinen, Z.H. Kafafi, J. Appl. Phys. 88 (2000) 889.
[37] I. Chizhov, A. Kahn, G. Scoles, J. Cryst. Growth 208 (2000) 449.
[38] L. Kilian, E. Umbach, M. Sokolowski, Surf. Sci. 600 (2006) 2633.
[39] J. Kröger, H. Jensen, R. Berndt, R. Rurali, N. Lorente, Chem. Phys. Lett. 438 (2007) 249.
[40] N. Koch, S. Duhm, J.P. Rabe, S. Rentenberger, R.L. Johnson, J. Klankermayer, F. Schreiber, Appl. Phys. Lett. 87 (2005) 101905.
[41] S. Duhm, H. Glowatzki, V. Cimpeanu, J. Klankermayer, J.P. Rabe, R.L. Johnson, N. Koch, J. Phys. Chem. B 110 (2006) 21069.
[42] H. Vázquez, R. Oszwaldowski, P. Pou, J. Ortega, R. Pérez, F. Flores, A. Kahn, Europhys. Lett. 65 (2004) 802.
[43] B. Krause, A.C. Dürr, K. Ritley, F. Schreiber, H. Dosch, D. Smilgies, Phys. Rev. B 66 (2002) 235404.
[44] B. Krause, F. Schreiber, H. Dosch, A. Pimpinelli, O.H. Seeck, Europhys. Lett. 65 (2004) 372.
[45] M. Möbus, N. Karl, T. Kobayashi, J. Cryst. Growth 116 (1992) 495.
[46] I.G. Hill, A. Kahn, J. Appl. Phys. 84 (1998) 5583.
[47] H. Vázquez, W. Gao, F. Flores, A. Kahn, Phys. Rev. B 71 (2005) 041306.

Available online at www.sciencedirect.com
ScienceDirect
Organic Electronics 9 (2008) 119–128
Organic Electronics
www.elsevier.com/locate/orgel

Switching in polymeric resistance random-access memories (RRAMS)

H.L. Gomes [a,*], A.R.V. Benvenho [a], D.M. de Leeuw [b], M. Cölle [b], P. Stallinga [a], F. Verbakel [c], D.M. Taylor [d]

[a] Universidade do Algarve, Centre of Electronic Optoelectronics and Telecommunications (CEOT), Campus de Gambelas, 8000 Faro, Portugal
[b] Philips Research Laboratories, Professor Holstlaan 4, 5656 AA Eindhoven, The Netherlands
[c] Laboratory of Macromolecular and Organic Chemistry, Eindhoven University of Technology, P.O. Box 513, 5600 MB Eindhoven, The Netherlands
[d] School of Electronic Engineering, University of Wales, Dean Street, Bangor, Gwynedd LL57 1UT, UK

Received 17 July 2007; received in revised form 28 September 2007; accepted 11 October 2007
Available online 24 October 2007

Abstract

Resistive switching in aluminum-polymer-based diodes has been investigated using small signal impedance measurements. It is shown that switching is a two-step process. In the first step, the device remains highly resistive but the low frequency capacitance increases by orders of magnitude. In the second step, resistive switching takes place. A tentative model is presented that can account for the observed behavior. The impedance analysis shows that the device does not behave homogenously over the entire electrode area and only a fraction of the device area gives rise to switching.

PACS: 73.40.Sx; 84.37.+q; 73.61.Ph; 85.65.+h

Keywords: Organic memory; Switching; Impedance spectroscopy; Oxide; Traps

1. Introduction

Electrically switchable solid state memories have been demonstrated in diodes using a variety of organic materials. The key feature of these memories is the ability to switch their resistance between two or more stable states simply by applying voltage pulses. Many devices exhibit sufficiently fast switching capability, low switching threshold voltages giving ON/OFF current ratios up to 10^6 and long retention times, thus opening interesting perspectives for applications in the domain of resistance random access memories (RRAMs).

Several memory architectures have been reported. Bistable organic diodes made of a single organic layer between two metal electrodes [1–17], nanoparticles embedded into an organic matrix [18–21], organic layers with granular metals [22–25] and transistor type memories [26,27].

We also reported bistable resistance characteristics in metal/polymer/metal diodes [28]. We showed

* Corresponding author. Tel.: +351 289 800 900.
E-mail address: hgomes@ualg.pt (H.L. Gomes).

1566-1199/$ - see front matter
doi:10.1016/j.orgel.2007.10.002

that the current is transported through filaments and that the formation of a thin aluminum oxide layer was crucial for the fabrication of reliable switching devices. Multi-level stages can be obtained depending on the number of filaments. Recently, our findings were corroborated by Karthäuser and co-workers [29] who elegantly showed that switching characteristics can be obtained simply by depositing an aluminum film directly onto the substrate and without the need for an organic layer. Previously, Oyamada et al. [12] had also concluded that the aluminum electrode is responsible for electrical switching. As long ago as 1990, Sato et al. [30] proposed that the contact between the aluminum and the semiconductor plays an essential role. This inference was supported by the experimental fact that no observable switching effect could be found when other electrode metals such as nickel or gold were employed instead of aluminum. Similar results were reported by Beck et al. [31].

In practice, since the memory effect seems intimately related to the presence of oxide, the switching in binary oxides and perovskite-type oxides is clearly relevant. In these materials switching is attributed to deep trapping processes. For instance, trapped charges in nanometer-thin insulating layers of Al_2O_3 were reported to exhibit a remarkable resistance to annihilation by opposite polarity carriers passing through the oxide [32]. Retention times are estimated to be as long as 10 years [33].

Much knowledge about carrier trapping in interfacial oxide layers in a variety of devices has been provided by small signal impedance spectroscopy. It is thus surprising that detailed studies of the impedance characteristics in switching devices have not been conducted. The scarce reports [30,34,35] do, however, show a behavior common to all memory device architectures: the switching is always accompanied by an increase in the device capacitance at low frequencies and explained as a trapping process. Simon et al. [36] have been shown that the trapped charge gives rise to inductive effects. Another study interpreted the impedance data in terms of different density of highly conducting molecules [37]. Here, we report a systematic and detailed analysis of the impedance changes occurring in the devices as they are formed and subsequently programmed into high conductance states. We show that prior to resistive switching, the device undergoes a dramatic increase in the capacitance. In spite of this change, the device still behaves as an insulator and no appreciable dc currents can be measured. Switching to higher conducting levels can then be triggered by a subsequent voltage pulse.

The frequency dependence of the admittance reveals that the observed changes are located at the aluminum/polymer interface. The initial capacitance change is caused by a trap filling mechanism occurring at the aluminium/polymer interface. These traps were likely created in a previous process, the so-called "forming", a term first used by Simmons and Verderber [38] in 1967. Since then, the term "forming" has been used by a number of authors to describe a permanent change in the oxide, induced by a once-only voltage or current pulse in oxide-based memories [39–42]. Memory switching can only be initiated after this forming stage. The results described in this contribution were on devices that had already been formed.

2. Experimental

The structure of the electrically-bistable device studied here and the schematic flat-band diagram are presented in Fig. 1. The polymer used as the active layer was poly(spirofluorene) (PFO) for which the electron affinity, $\chi = 2.2$ eV, ionization potential, $I_p = 5.1$ eV and energy gap, $E_g = 2.9$ eV [16]. The aluminium (Al) and barium (Ba) electrodes have workfunctions $\phi_{Al} = 4.3$ eV and

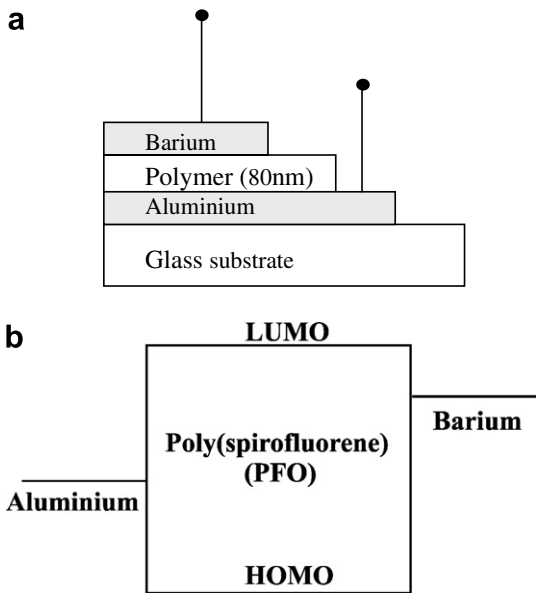

Fig. 1. Schematic diagram showing: (a) the physical structure of the memory device (top electrode is Ba, Al) and (b) the energy levels of the structure.

$\phi_{Ba} = 2.7$ eV, respectively. The methods used for fabrication of these electron-only diodes were described in Ref. [28]. The polymer thickness was 80 nm and both metal electrodes were 30 nm thick. The top electrode is 5 nm Ba with 100 nm Al. Effective device areas were either 0.01 or 0.09 cm^2. The aluminum electrode was treated with UV/O_3 plasma treatment before polymer deposition. The current–voltage (I–V) curves were obtained using a Keithley 487 picoammeter/voltage source and capacitance–frequency and capacitance–voltage (C–V) curves were obtained using a Fluke PM 6306 RLC meter. In all the measurements, voltages are referenced such that the Ba/Al electrode is held at local ground, while the bias is applied to the Al electrode.

3. Results and discussion

3.1. Current–voltage characteristics

Fig. 2 shows typical current–voltage (I–V) characteristics obtained for two programmed states. The lower I–V curve corresponds to the "OFF state" and the higher curve to what we designate the "fully-ON state". In between, multilevel stages can be observed, see Ref. [28]. The different conductive states can be programmed by application of a voltage pulse, for example 3–5 V for 5 s. The process is totally electrically reversible, as described previously [28]. In the OFF state, the I–V curves can sometimes exhibit rectification properties as in Fig. 2. Current–voltage characteristics corresponding to the OFF state frequently show a shoulder at low positive bias at about the built-in voltage (see Fig. 2). This plateau/shoulder has often been observed in polymeric light emitting diodes (PLEDs) and will be discussed later when treating the capacitance–voltage (C–V) characteristics.

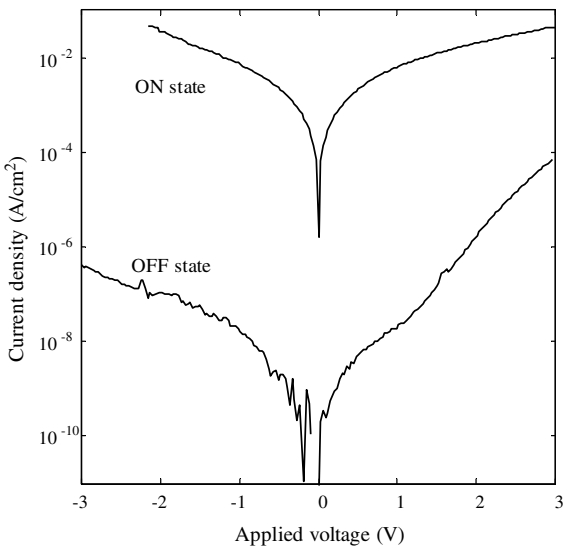

Fig. 2. Typical current density vs. voltage characteristics of an Al/ polysprirofluorene/BaAl device. The lower curve corresponds to the OFF state and the upper curve to a high ON state. The switch between the states is done by an external voltage pulse.

3.2. Small signal impedance characteristics

The OFF state and the ON-state observed in the I–V characteristics are associated with corresponding changes in the impedance characteristics. However, the changes do not occur simultaneously, capacitance changes precede changes in the current–voltage characteristics.

The changes occurring in the frequency-dependence of the admittance of devices in the OFF and ON states is shown in Fig. 3a. When the devices are OFF they behave as simple parallel plate capacitors with capacitance (C) and dielectric loss (G/ω) almost independent of frequency (f), where G is the conductance and $\omega = 2\pi f$, is the angular frequency. As no free carriers are able to follow the modulation of the external voltage at high frequencies, the material system behaves like a passive dielectric medium.

If the devices are submitted to voltage ramps (0.1 V/s) within a small range (e.g. ± 5 V) a dramatic increase in capacitance at low frequencies may be induced. The rise in capacitance is accompanied by the appearance of a relaxation process with a cut-off frequency near 200 kHz, see Fig. 3a.

In this work, we chose to induce the capacitance change by cycling a triangular voltage ramp from 0 V to 5 V to 0 V with a scan speed of 0.1 V/s until the change was observed. We found this procedure more reliable than applying a voltage pulse, which can also induce the state. However, a voltage pulse frequently also induces resistive changes. The several device stages can also be observed when the device is switching from full ON to OFF states. However, we have not found a procedure to address the different states in a controllable way.

The OFF state also shows evidence of a weak relaxation frequency occurring near 1 MHz as shown in Fig. 3a. The high frequency dispersion here is likely to be caused by a small contact resistance. Once the device is triggered to the high capacitive state the associated relaxation, which occurs at

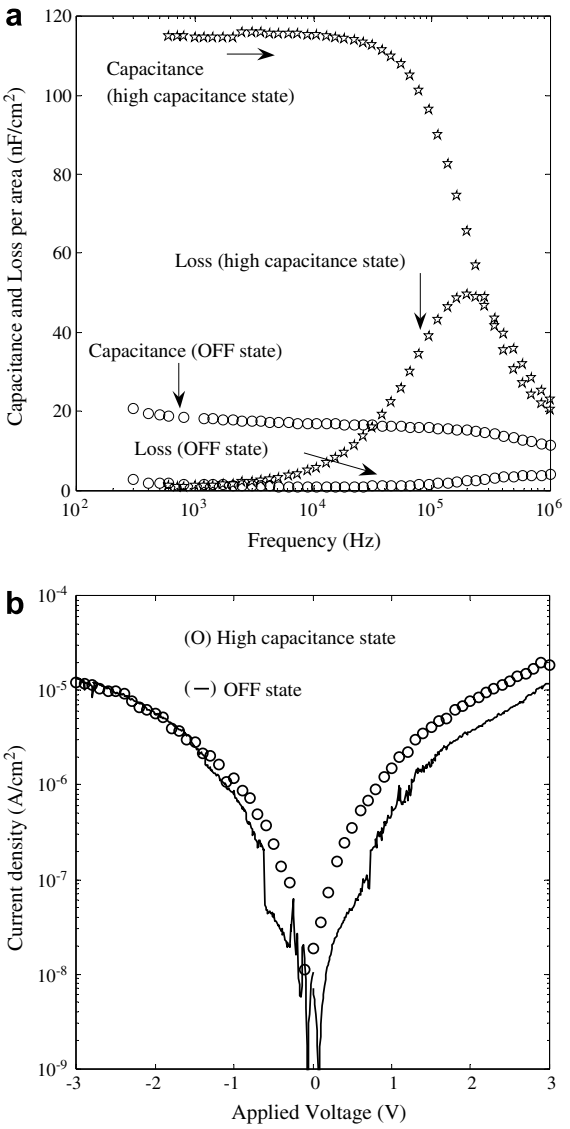

Fig. 3. (a) Frequency dependence of the measured capacitance (C) and the loss (G/ω) for an OFF state and for a high capacitance state. (b) The corresponding current voltage characteristics.

200 kHz, completely swamps the relaxation due to contact effects.

Crucially, the increase in device capacitance does not cause major changes in the current–voltage characteristics as shown in Fig. 3b. While there is some evidence for partial switching above about ±0.5 V, the device is still considered to be in a low-conductance OFF state even though the currents are higher than in Fig. 2. This is further confirmed by the low-frequency (<1 kHz) behaviour of the loss curves for both the OFF and high capacitance states. At low frequencies, the DC resistance, R_{DC} of the device contributes a component, $1/2\pi R_{DC}$, to the overall loss. As seen in Fig. 3a, despite a major change in capacitance (from ~20 to ~120 nF/cm^2) the loss curves simply merge together as the frequency decreases with only a slight increase to ~3.6 nF/cm^2 observed at ~300 Hz. Attributing this to the DC leakage through the device we estimate R_{DC} to be ~14.6 MΩ. The capacitance increase is thus a process that occurs prior to the onset of significant switching. Later, we will show that when the samples are programmed to high conductance states this is always accompanied by an increase in the low frequency loss (G/ω).

Once the device is in the high capacitance state, it can switch to higher conductive states (multi-level states) by applying a voltage pulse (typically 5–11 V for 5 s). Changes are now observed both in the current–voltage characteristics and in the ac conductance while the low-frequency capacitance remains constant. This behavior is seen in Fig. 4 where the capacitance (C) and loss (G/ω) for two ON states are presented. The higher conductive state yields a higher loss at low frequencies which rises as $1/f$ as expected for a dc resistance. The changes in the device are now purely resistive. The dispersion centered on 200 kHz is typical of the Maxwell–Wagner relaxation process [43] observed in two-layer dielectric structures and can

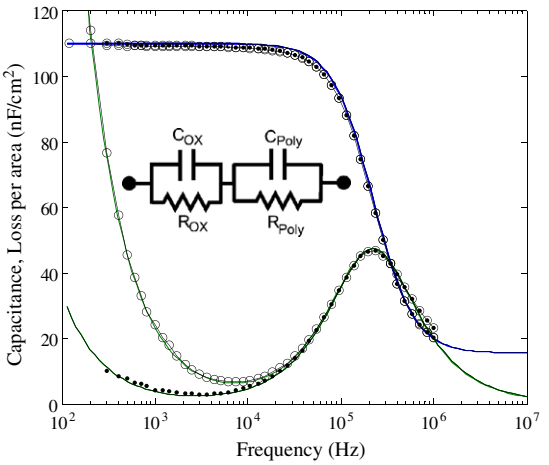

Fig. 4. Experimentally measured admittance (points) and theoretical fits (continuous lines) for two multi-level ON states using the equivalent circuit in the inset. The fitting parameters are shown in Table 1. The changes are purely resistive and only located in the high capacitive layer of the sample; only R_{OX} changes.

be modeled, therefore, by the double RC circuit in the inset of Fig. 4. This circuit exhibits dispersion in capacitance centered around a relaxation frequency, f_R, given by

$$f_R = \frac{1/R_{POLY} + 1/R_{OX}}{2\pi(C_{POLY} + C_{OX})}, \quad (1)$$

which for $R_{OX} \gg R_{POLY}$ reduces to

$$f_R = \frac{1}{2\pi R_{POLY}(C_{POLY} + C_{OX})}. \quad (2)$$

In this case it is seen that f_R is sensitive to R_{POLY} and will move to higher frequencies as R_{POLY} decreases.

Without discussing, for the moment, the physical origin of the components in the circuit, we use this conceptual model to fit the experimental data in Fig. 4. The fitting parameters are shown in Table 1, from which it can readily be seen that the changes are purely resistive and only located in the high capacitive layer of the sample; only a decrease in R_{OX} from 500 MΩ/cm^2 to 70 MΩ/cm^2 is required to provide a good fit to the data. As can be seen, the relaxation frequency of the main dispersion (controlled essentially by R_{POLY}) is unaffected.

The electrical characteristics described up to now are typical for devices in the ON state with current densities in the order of 10 mA/cm^2. However, devices programmed to higher conductances, with current densities in the order of 0.1–1.0 A/cm^2 exhibit a different low frequency impedance response as shown in Fig. 5. The capacitance now increases rapidly with decreasing frequency. However, this increase is accompanied by a reduction in the capacitance in the previously constant capacitance region below the relaxation frequency. These effects are not yet clearly understood; we assume that they are related to the high currents passing through the device.

Table 1
Parameter values used to fit the experimental capacitance (C) and loss (G/ω) curves shown in Fig. 4

Circuit elements	C_{OX} (nF/cm^2)	R_{OX} (MΩ/cm^2)	C_{POLY} (nF/cm^2)	R_{POLY} (kΩ/cm^2)
State ON (a)	110	500	18	56
State ON (b)	110	70	18	56
State OFF	≫18	>2000	18	≫1000

Also given for comparison are the capacitance and resistance corresponding to the OFF state as shown in Fig. 3a. In the OFF state in Fig. 3a, however, since $f_R \ll 100$ Hz, then R_{POLY} must be ≫1000 kΩ and that C is dominated by C_{POLY} which is much less than C_{OX}.

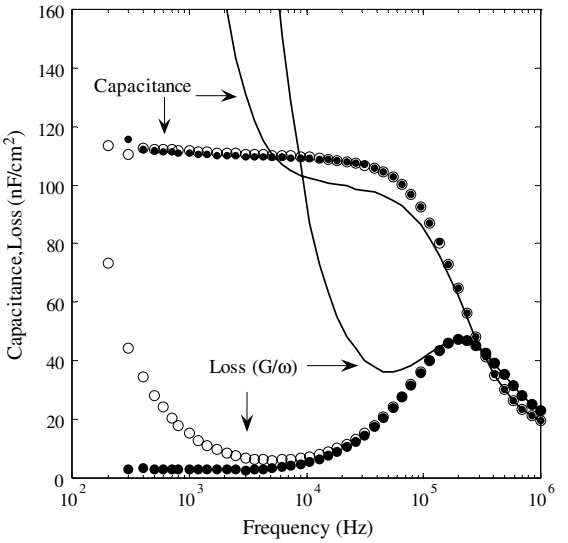

Fig. 5. The capacitance behavior when the device is programmed into very high conducting states. These states exhibit very high loss at low frequencies.

In summary, there are two major steps in the switching behavior as observed in the device admittance characteristics:

(a) *Capacitive switching:*
Capacitance switching is the first step. It has a signature in the capacitance but goes unnoticed in the I–V characteristics. The frequency response of the admittance shows that the device undergoes a change from a pure, capacitor-like behavior to a double-layer structure behavior following a significant reduction in the polymer resistance.

(b) *Resistive switching:*
Once the capacitive state is induced, the device can be programmed to a number of multi-level ON-states using voltage pulses of increasing magnitude. The changes in admittance are now purely resistive. Simulations using the equivalent circuit approach confirm that the resistive changes occur only in the high capacitance layer of the device.

3.3. Capacitance–voltage characteristics

Switched devices also exhibit three different types of C–V plots corresponding to the three different states of the sample, i.e. the OFF state, the capacitive

state and multi level ON-states. In the OFF state, the device capacitance exhibited a voltage-independent capacitance (not shown) confirming that, in this state, the device behaves as a pure capacitor. In the multi-level ON-states, the capacitance has a maximum at zero bias which decreases for both positive and negative applied bias. Such behavior is seen in Fig. 6. The AC conductance–voltage plot in the inset shows that the device exhibits a high conductance which depends symmetrically on applied voltage. The decrease in capacitance with increasing bias in the ON state is likely to be caused by the collapse of the oxide resistance shunting the capacitance as the bias increases.

Often when the device has suffered a capacitive switching but is still in the OFF state, the C–V plot can also show anomalous behavior, see Fig. 7. Here, the capacitance decreases at ~1 V but then increases sharply for increasing positive voltage above 2 V. When this bias dependence is observed the corresponding I–V characteristics exhibit a shoulder or a knee as observed in Fig. 2. The dip in the C–V plot and the shoulder in the I–V curve both occur at a similar voltage (between 1 and 2 V) suggesting that they are correlated. Such behavior is only observed when the device rectifies as the conductance curve in the inset of Fig. 7 (recorded simultaneously with the C–V plot) clearly shows.

Inductive dips in C–V plots have often been reported in the literature of inorganic based devices

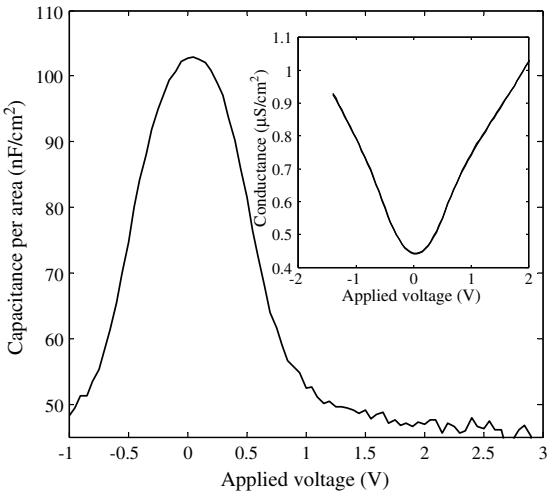

Fig. 6. Capacitance–voltage curve recorded when the sample is in the ON state. The conductance vs. voltage plot is represented in the inset showing that the device has a high and symmetrical conductance–voltage characteristic. The measurements were recorded at a frequency of 100 Hz.

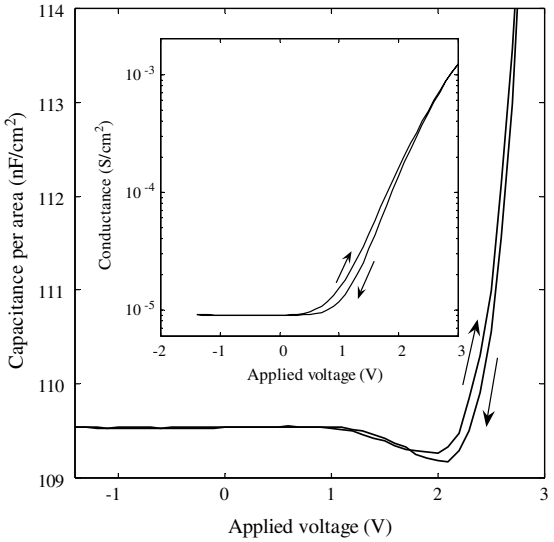

Fig. 7. Capacitance–voltage characteristic showing an inductive dip. The inset shows that this behavior is accompanied by a rectifying conductance–voltage curve. The conductance was recorded simultaneously with the capacitance at a frequency of 900 Hz.

and recently for polymeric light emitting diodes, where even negative capacitances have been reported [44–48]. In PLEDs, the observation of negative differential capacitance has been attributed to space-charge limited transport [49,50], but in a similar way, it can also be explained by inductive effects due to minority carriers. The underlying physics has been well described by Misawa for pn junctions [51] and by Green and Shewchun for Schottky barriers [52] and MIS tunneling diodes [53]. When the current is minority-carrier dominated and the frequency is high, the current cannot follow the voltage instantaneously; the current starts lagging behind the voltage and a shift of the phase of the current relative to the voltage occurs. If the phase shift is large, this effect can even imitate negative capacitance. It must be noted that this is not a true capacitance in the sense that the device can store charge, but is rather an as-measured capacitance caused by a phase shift of the ac current. The important aspect of this behavior is that it is expected to occur when a thin insulating interfacial layer or a dipole layer exists between the electrode and the semiconductor.

Since there are no depletion layers in the device, the increase of capacitance after the dip deserves some comment. In forward bias, above the dip in the C–V plot, both the majority and minority carri-

ers contribute to the total device current. But the minority carriers are still a significant fraction of the total current. This minority carrier density will give rise to a diffusion capacitance. This contribution to the device capacitance increases with the applied bias in a similar way to the diffusion capacitance increase in a pn junction after the collapse of the depletion layer [54,55].

3.4. Phenomenological model

3.4.1. Capacitive switching

In this section, we propose a tentative model to explain the admittance data. Supported by the results discussed earlier, we assume that there is a thin oxide layer at the aluminum electrode. In the OFF state, the resistances of both the oxide and the polymer are high so that the AC equivalent circuit of the device reduces to two ideal capacitors in series and may be represented by the band diagram in Fig. 8a. As expected, the device capacitance displays a nearly flat frequency response. The weak dispersion appearing near 1 MHz in Fig. 3a we attribute to a resistance arising from the contacts and interconnecting tracks and cables in series with the geometric capacitance.

Under bias stress, either from the direct application of a pre-set voltage or from voltage cycling, the oxide layer undergoes an irreversible migration of atomic species, a process known in the literature as "forming". We suggest that this forming process creates hole traps in the oxide or at the polymer/oxide interface. As long as the traps are unfilled, the barrier for conduction through the oxide is high and the device remains in the low conductance OFF state.

When positive bias is applied to this electron only device, electrons injected from the Ba electrode drift through the polymer and accumulate at the polymer/oxide interface (Fig. 8b). Several consequences now follow: (i) the field across the oxide increases, thus encouraging hole (minority carrier) injection from the aluminum electrode into the oxide where most become trapped while the remainder are injected into the polymer, (ii) the presence of extrinsic charge carriers, both electrons and holes, in the polymer reduces its resistance and (iii) hole trapping in the oxide encourages further accumulation of electrons at the interface, creating a dipole layer of increasing polarization.

As the concentration of extrinsic carriers in the polymer increases, R_{POLY} becomes sufficiently low to shunt C_{POLY} giving rise to the large increase in low-frequency capacitance (capacitance switching) and the frequency dispersion seen in Fig. 3a.

3.4.2. Non-uniform switching

Assuming that the changes described above occur uniformly over the diode area and that

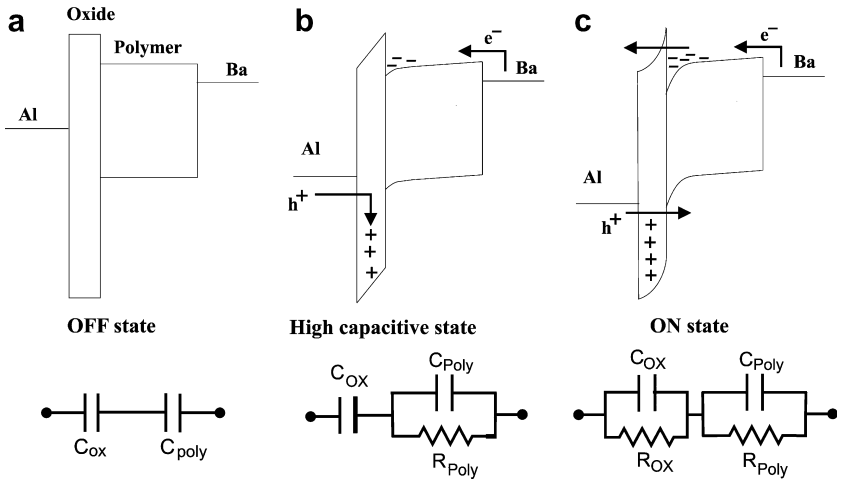

Fig. 8. Energy-band diagram (not to scale) and the respective equivalent circuit model as the device switches from an OFF state to a higher conductive state. (a) Equilibrium band diagram, the AC equivalent circuit of the device reduces to two ideal capacitors. (b) When positive bias is applied electrons injected from the Ba electrode drift through the polymer and accumulate at the polymer/oxide interface. R_{POLY} becomes sufficiently low to shunt C_{POLY} giving rise to the large increase in low-frequency capacitance (capacitance switching) and the frequency dispersion. (c) Higher voltages lead to increased electrical stress across the oxide reducing the oxide resistance R_{OX}, which is the current limiting layer controlling the low-frequency loss in Figs. 3a and 5 following capacitive switching.

$R_{POLY} \ll R_{OX}$, then the low frequency capacitance should increase to >600 nF/cm^2, consistent with an oxide layer <10 nm thick. However, the measured low-frequency capacitance at ~110 nF/cm^2 is much lower.

From the I–V plots in Fig. 3b we note that capacitance switching is accompanied by a small but significant increase in DC current through the device, suggesting that R_{OX} decreases as well as R_{POLY}. Such a decrease may be anticipated as the trapped hole and accumulated electron concentrations both increase. Fields in the oxide become highly non-linear, modifying the band diagram as shown in Fig. 8c so that interface conditions are conducive for electron tunneling from the polymer into the oxide, thus reducing R_{OX}. Therefore, we must now consider the full expression for the low-frequency capacitance of the device, i.e.

$$C = \frac{C_{POLY} + \beta^2 C_{OX}}{(1+\beta^2)} \quad (3)$$

where $\beta = R_{OX}/R_{POLY}$. Thus, if $C_{POLY} = 18$ nF/cm^2 and $C_{OX} = 600$ nF/cm^2, to yield a measured low-frequency capacitance of 110 nF/cm^2 then $\beta = 0.43$. Inserting this value into Eq. (1) requires that $R_{OX} = 890\ \Omega$ and $R_{POLY} = 2\ k\Omega$ to give a relaxation frequency $f_R = 200$ kHz in Figs. 3a and 5. Ascribing these values to the DC resistance of the device yields a DC current density of 35 mA/cm^2 at 1 V, which is significantly higher than observed after capacitive switching. We may conclude, therefore, that the device does not behave homogenously over the entire electrode area.

The admittance data can be explained however when we assume a patchy conductance in the polymer film. The corresponding equivalent circuit for a film composed of two areas of different polymer conductivity is now given in Fig. 9. In this case, only that fraction of the device area with a low polymer resistance (Region 1) gives rise to the Maxwell–Wagner dispersion seen in Figs. 3a and 4, the rest of the device area (~83%) remaining in the high resistance state. Applying Eqs. (2) and (3) we now conclude that for the conductive region, $R_{POLY1} = 770\ \Omega$ which is close to the value required to fit the plots in Fig. 4 (see Table 1). This model requires that the condition $R_{OX1} \gg R_{POLY1}$ still applies in this region of the device so that the oxide layer limits the current through the device. Noting the values of R_{OX} in Table 1, the DC currents expected at 1 V are ~20 μA/cm^2 and 140 μA/cm^2 for the two switched

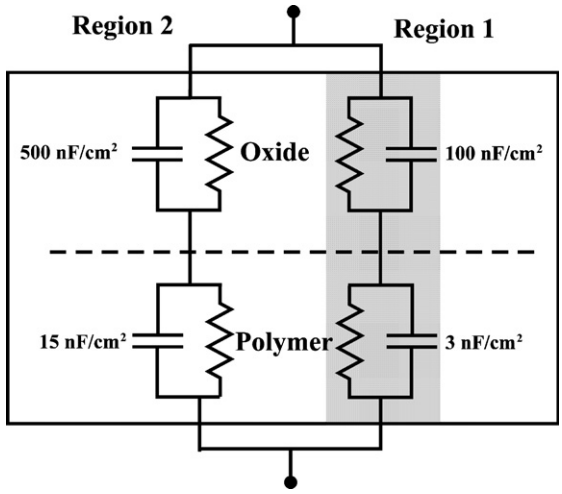

Fig. 9. Equivalent circuit for a film composed of two areas of different polymer conductivity. In this case, only that fraction of the device area with a low polymer resistance (Region 1) gives rise to the Maxwell–Wagner dispersion seen in Figs. 3a and 5, the rest of the device area, (~83%) remaining in the high resistance state (Region 2).

states and consistent, therefore, with the range of currents observed experimentally between the fully OFF and fully ON states (Fig. 2).

A further possibility is that the oxide layer is not uniform. To explain the capacitance data in Figs. 3a and 4 we must now assume that over ~83% of the device area (Region 2), the oxide capacitance is shunted by an oxide resistance that is much smaller than that of the corresponding area of polymer. Applying Eq. (2) to this fraction of the device and (i) replacing R_{POLY} with R_{OX2} and (ii) noting that the relaxation time of this part of the device must lie well below the measurement range, i.e. $f_R \ll 100$ Hz if the oxide in this region is not to contribute to the measured capacitance, then we may deduce that $R_{OX2} \gg 30\ M\Omega$. Since $R_{POLY2} \gg R_{OX2}$ the expected DC current densities at an applied voltage of 1 V from this part of the device will be much less than 3 μA/cm^2 and closer to that expected for the fully OFF state suggesting that the premise on which this model is founded is likely to be unsound.

Of the models proposed above, that based on a non-uniform polymer conductivity is the most plausible. However, the microscopic origin is as yet unknown.

Clearly, further work is necessary to clarify fully the nature of capacitive switching. Nevertheless, the general principles have been established. The device is described by a two layer model. The resistive switching reported by other workers is now seen

to be preceded by capacitive switching in which the conductance of one of the layers, probably that of the polymer, must increase substantially to explain the Maxwell–Wagner dispersion. The increased electric field now appearing across the oxide due to electron accumulation enhances minority carrier (hole) injection from the Al electrode, which is the likely cause of the dip in the C–V plots and the shoulder in the forward I–V characteristic observed in some devices after capacitive switching. Higher voltages lead to increased electrical stress across the oxide, further reducing the oxide resistance, which we surmise is the current limiting layer controlling the low-frequency loss in Figs. 3a and 4 following capacitive switching.

If, indeed, the conductance of the polymer is not homogeneous, the additional rise in capacitance and accompanying increase in loss in the fully ON state in Fig. 5 may simply reflect increased contributions from previously non-conducting regions of the device.

4. Conclusions

Summarizing, this admittance study shows that switching is a two-stage process. Initially, hole injection must be switched on at the aluminum electrode, we assume that this occurs as a result of electron trapping near the aluminum electrode. Hole injection will fill states in the aluminum oxide creating a dipole layer at the oxide/polymer interface. The high field across the oxide increases, thus encouraging injection of extrinsic charges into the polymer. The polymer resistance decreases substantially shunting the polymer capacitance and giving rise to a Maxwell–Wagner dispersion. We have termed this first step capacitive switching. Higher external applied voltages lead to increased electrical stress across the oxide reducing the oxide resistance and causing resistive switching.

The admittance data analysis also shows that the device does not behave homogenously over the entire electrode area, only a relatively small fraction of the device area (20%) gives rise to switching, the rest of device area remains in a high resistance state.

Acknowledgements

We gratefully acknowledge the financial support received from the Fundação para a Ciência e Tecnologia (FCT) through the research Unit no. 631, Center of Electronics Optoelectronics and Telecommunications (CEOT), the EC (Project Poly-Apply IST-IP-507143) and the Engineering and Physical Sciences Research Council, UK (Grant No. GR/S97040/01).

References

[1] J.R. Koo, S.W. Pyo, J.H. Kim, S.Y. Jung, S.S. Yoon, T.W. Kim, Y.H. Choi, Y.K. Kim, Synth. Metals 156 (2006) 298.
[2] Q. Lai, Z. Zhu, Y. Chen, Appl. Phys. Lett. 88 (2006) 133515.
[3] H.S. Majumdar, J.K. Baral, R. Österbacka, O. Ikkada, H. Stubb, Org. Electron. 6 (2005) 188.
[4] J. Chen, D. Ma, Appl. Phys. Lett. 87 (2005) 023505.
[5] M. Lauters, B. McCartthy, D. Sarid, G.E. Jabbour, Appl. Phys. Lett. 87 (2005) 0231105.
[6] F.L.E. Jakobsson, X. Crispin, M. Berggren, Appl. Phys. Lett. 87 (2005) 063503.
[7] T. Graves-Abe, J.C. Sturm, Appl. Phys. Lett. 87 (2005) 133502.
[8] Y.S. Lai, C.-H. Tu, D.-L. Kwong, J.S. Chen, Appl. Phys. Lett. 82 (2005) 122101.
[9] J. Chen, D. Ma, Appl. Phys. Lett. 87 (2005) 023505.
[10] C.A. Richter, D.R. Stewart, D.A.A. Ohlberg, R.S. Williams, Appl. Phys. A. 80 (2005) 1355.
[11] B. Mukherjee, A.J. Pal, Appl. Phys. Lett. 85 (2005) 2116.
[12] T. Oyamada, H. Tanaka, K. Matsushige, H. Sasabe, C. Adachi, Appl. Phys. Lett. 83 (2003) 1252.
[13] A. Bandhopadhyay, A.J. Pal, Appl. Phys. Lett. 82 (2003) 1215.
[14] A. Bandhopadhyay, A.J. Pal, J. Phys. Chem. B. 107 (2003) 2531.
[15] L.P. Ma, J. Liua, Y. Yang, Appl. Phys. Lett. 80 (2002) 2927.
[16] D.M. Taylor, C.A. Mills, J. Appl. Phys. 90 (2001) 306.
[17] D. Ma, M. Aguiar, J.A. Freire, I.A. Hümmelgen, Adv. Mater. 12 (2000) 1063.
[18] J.H. Jung, J.Y. Jin, I. Lee, T.W. Kim, H.G. Roh, Y.-H. Kim, Appl. Phys. Lett. 88 (2006) 112107.
[19] R.J. Tseng, J. Huang, J. Ouyang, R.B. Kaner, R.B. Yang, Nano Lett. 5 (2005) 1077.
[20] J. Ouyang, Chih-Wei Chu, D. Sieves, Y. Yang, Appl. Phys. Lett. 86 (2005) 123507.
[21] L. Ma, S. Pyo, J. Ouyang, Q. Xu, Y. Yang, Appl. Phys. Lett. 82 (2003) 1419.
[22] L.D. Bozano, B.W. Kean, V.R. Deline, J.R. Salem, J.C. Scott, Appl. Phys. Lett. 84 (2004) 2997.
[23] L.D. Bozano, B.W. Kean, M. Beinhoff, K.R. Carter, P.M. Rice, J.R. Salem, J.C. Scott, Adv. Funct. Mater. 15 (2005) 1933.
[24] S.M. Pyo, L.P. Ma, J. He, Q. Xu, Y. Yang, Y. Gao, J. Appl. Phys. 98 (2005) 054303.
[25] D. Tondelier, K. Lmimouni, D. Vuillaume, C. Fery, G. Hass, Appl. Phys. Lett. 85 (2005) 5763.
[26] K.N. Naryanan, U.R. de Bettignies, S. Dabos-Seignon, J.M. Nunzi, Appl. Phys. Lett. 85 (2004) 1823.
[27] R. Schoeder, L.A. Majewski, M. Grell, Adv. Mater. 16 (2004) 633.
[28] M. Cölle, M. Büchel, D.M. de Leeuw, Org. Electr. 7 (2006) 305.
[29] S. Karthäuser, B. Lüssem, M. Weides, M. Alba, A. Besmehn, R. Oligschlaeger, R. Waser, J. Appl. Phys. 100 (2006) 094504.

[30] C. Sato, S. Wakamatsu, K.T.K. Ishii, J. Appl. Phys. 68 (1990) 6537.
[31] A. Beck, J.G. Bednorz, Ch. Gerber, C. Rossel, D. Widmer, Appl. Phys. Lett. 77 (2000) 139.
[32] V.V. Afanasev, A. Stesmans, Appl. Phys. Lett. 80 (2002) 1261.
[33] M. Spech, H. Reisinger, F. Hofmann, T. Schulz, E. Landgrave, R.J. Luyken, W. Röner, M. Grieb, L. Risch, Solid State Electron. 49 (2005) 716.
[34] A. Bandyopadhyay, A.J. Pal, J. Phys. Chem. B. 109 (2005) 6084.
[35] J. Ouyang, C.W. Chu, R.J.H. Tseng, A. Prakash, Y. Yang, Proc. IEEE 93 (2005) 1287.
[36] D.T. Simon, M.S. Griffo, R.A. Dipietro, S.A. Swanson, S.A. Carter, Appl. Phys. Lett. 89 (2006) 1333510.
[37] B. Mukherjee, A.J. Pal, Chem. Phys. Lett. 401 (2005) 410.
[38] J.G. Simmons, R.R. Verderber, Proc. Royal. Soc. A 301 (1967) 77.
[39] G. Dearnaley, D.V. Morgan, A.M. Stoneham, J. Non-Cryst. Solids 4 (1970) 593.
[40] A.L. Pergament, V.P. Malinenko, O.I. Tulubaeva, L.A. Aleshina, Phys. Status Solid A 201 (2004) 1543.
[41] J.O. Orwa, S.R.P. Silva, J.M. Shannon, Electr. Lett. 41 (2005) 98.
[42] K.R. Kim, I.S. Park, J.P. Hong, S.S. Lee, B.L. Choi, J. Ahn, J. Korean Phys. Soc. 49 (2006) S548.
[43] V. Hippel, A. Robert, Dielectrics and Waves, Wiley, New York, 1954.
[44] L.S.C. Pingree, B.J. Scott, M.T. Russell, T.J. Marks, M.C. Hersam, Appl. Phys. Lett. 86 (2005) 073509.
[45] F.A. Castro, P.R. Bueno, C.F.O. Graeff, F. Nüesch, L. Zuppiroli, L.F. Santos, R.M. Faria, Appl. Phys. Lett. 87 (2005) 013505.
[46] H.H.P. Gommans, M. Kemerink, R.A.J. Janssen, Phys. Rev. B. 72 (2005) 235204.
[47] J. Bisquert, G.G. Belmonte, A. Pitarch, H.J. Bolink, Chem. Phys. Lett. 422 (2006) 184.
[48] P. Stallinga, H.L. Gomes, H. Rost, A.B. Holmes, R.H. Friend, J. Appl. Phys. 89 (2001) 1713.
[49] H.C.F. Martens, W.F. Pasveer, H.B. Brom, J.N. Huiberts, P.W.M. Blom, Phys. Rev. B 63 (2001) 125328.
[50] D.M. Taylor, IEEE Trans. Dielectr. Electr. Insulat. 13 (2006) 1063.
[51] T. Misawa, J. Phys. Soc. Jpn. 12 (1957) 882.
[52] M.A. Green, J. Shewchun, Solid State Electr. 16 (1973) 1141.
[53] M.A. Green, J. Shewchun, J. Appl. Phys. 46 (1975) 5185.
[54] S.M. Sze, Physics of Semiconductor Devices, second ed., Wiley, New York, 1981.
[55] M. Shur, Physics of Semiconductor Devices, Prentice-Hall, New Jersey, 1990.

Available online at www.sciencedirect.com
ScienceDirect
Organic Electronics 9 (2008) 129–135
Organic Electronics
www.elsevier.com/locate/orgel

Carrier mobility in two-dimensional disordered hopping systems

E.V. Emelianova [a,c,*], M. van der Auweraer [b,c], G.J. Adriaenssens [a], A. Stesmans [a,c]

[a] Semiconductor Physics Laboratory, K.U. Leuven, Celestijnenlaan 200D, B-3001 Heverlee-Leuven, Belgium
[b] Laboratory for Molecular Dynamics and Spectroscopy, K.U. Leuven, Celestijnenlaan 200F, B-3001 Heverlee-Leuven, Belgium
[c] Institute for Nanoscale Physics and Chemistry (INPAC), Belgium

Received 7 June 2007; received in revised form 10 September 2007; accepted 15 September 2007
Available online 22 September 2007

Abstract

A model of the equilibrium 2D hopping mobility in a disordered organic semiconductor is formulated for arbitrary charge carrier densities and arbitrary temperatures. The calculated dependence of the 2D mobility upon inverse temperature is compared with experimental data obtained on 2D carrier transport in poly(3-hexylthiophene) thin film field-effect transistors.

PACS: 72.80.Le; 73.50.Dn

Keywords: Hopping mobility; Transport energy; Organic semiconductors; Thin films

1. Introduction

Because of the important role of organic polymers as inexpensive and promising materials for micro-electronic devices such as light-emitting diodes (OLEDs), photovoltaic and thin-film devices, thin-film transistors, etc. [1], charge carrier transport in those materials has been investigated over the last decades by many authors [2–6]. It is well known that in disordered organic materials conduction occurs by way of charge carrier hopping within a positionally random and energetically disordered system of localized states [3]. While the general principles of such hopping transport have been well known and accepted for years, many important aspects of the process such as, for instance, the influence of large carrier concentrations on the charge carrier mobility or the role of (deep) traps, have only been examined analytically more recently [7–9].

Upon doping with acceptor-type or donor-type atoms or molecules, the density of free carriers can be significantly increased in organic polymers and its conductivity can be varied and controlled over a very wide range. High carrier density can be achieved by (electro)chemical doping of the polymer [10] or by accumulation of carriers in a sufficiently strong gate field of a metal–insulator–semiconductor structure (field-effect doping [11]). This property of organic polymers is used in field-effect transistors (FETs). Despite of the number of recently developed

* Corresponding author. Address: Semiconductor Physics Laboratory, K.U. Leuven, Celestijnenlaan 200D, B-3001 Heverlee-Leuven, Belgium. Tel.: +32 16 32 7173; fax: +32 16 32 7987.
E-mail address: zhenia.emelianova@fys.kuleuven.be (E.V. Emelianova).

1566-1199/$ - see front matter
doi:10.1016/j.orgel.2007.09.004

models describing hopping transport of charge carriers in highly doped systems [6,7,9,10], the mechanism of charge carrier transport in organic FETs where a thin film of conjugated molecules acts as a semiconducting layer, remains of a high interest [12–14]. It was recently experimentally proven that in thin-film FETs the first layers next to dielectric interface dominate the charge transport [13]. As in thin-film transistors the charge carrier mobility is usually one or two orders of magnitude smaller than in organic single crystals [13], and decreasing upon decreasing the temperature, one can try to apply a model for hopping in a two-dimensional (2D) system of localized sites to describe conductivity in those layers rather than the conventional three-dimensional (3D) hopping model. In the present paper we formulate an analytic model of a weak-field charge carrier mobility in a 2D hopping system with positional and energetic disorder. The effect of a high carrier concentration on the equilibrium weak-field 2D carrier hopping is examined. An analytical formula to calculate the 2D field-effect hopping mobility, dependent upon temperature, charge carrier concentration and the features of the density of localized states (DOS) in organic material is derived. The temperature and carrier concentration dependencies of the 2D mobility are calculated for a Gaussian DOS distribution. The results were compared with those obtained for the 3D mobility in a hopping system with the identical material parameters. The theoretical results are used to fit experimental data obtained on 2D carrier transport in poly(3-hexylthiophene) (P3HT) thin-film field-effect transistors [12].

2. Theory

Most hopping models are based on the Miller-Abrahams [15] expression for the rate $v\ (r, E_s, E_t)$ of carrier jumps, over the distance r between an initially occupied starting state of the energy E_s to a vacant target site of the energy E_t. This expression can be written as

$$v(r, E_s, E_t) = v_0 \exp[-u(r, E_s, E_t)],$$
$$u(r, E_s, E_t) = 2\gamma r + \frac{\eta(E_t - E_s)}{kT}, \tag{1}$$

where u is the hopping parameter, v_0 the attempt to jump frequency, γ the inverse localization radius, T the temperature, k the Boltzmann constant, and η the unity step function. In a 2D hopping system carrier jumps from a fixed starting site to a target site can be characterized by the hopping parameter u defined by Eq. (1). In a positionally random system of localized states, the average number of target sites for a starting site of energy E_s, $n(E_s, u)$, whose hopping parameters are not larger than u can be calculated in 2D as

$$\begin{aligned} n(E_s, u) &= 2\pi \int_0^{u/2\gamma} dr r \int_{-\infty}^{E_s + kT(u-2\gamma r)} dE_t g(E_t) \\ &= \pi \left(\frac{u}{2\gamma}\right)^2 \left[\int_{-\infty}^{E_s} dE_t g(E_t) \right. \\ &\quad \left. + \int_{E_s}^{E_s + kTu} dE_t g(E_t) \left(1 - \left(\frac{E_t - E_s}{kTu}\right)\right)^2 \right], \end{aligned} \tag{2}$$

where $g(E)$ is density-of-states (DOS) distribution function that describes the number of states per unit surface per unit energy. Its dimension is $\mathrm{cm}^{-2}\,\mathrm{eV}^{-1}$.

The first term in the right-hand side of Eq. (2) gives the number of target states that are deeper than the starting site and the second one describes the number of shallower states. Using the formalism that was developed in [6] for estimating the hopping parameter as $\langle u \rangle(E_s) = \int_0^\infty du \exp[-n(E_s, u)]$, one can estimate the average squared jump distance, $\langle r^2 \rangle(E_s)$, as

$$\begin{aligned} \langle r^2 \rangle(E_s) &= \frac{1}{2} \left(\frac{\langle u \rangle}{2\gamma}\right)^2 \left[\int_{-\infty}^{E_s} dE_t g(E_t) \right. \\ &\quad \left. + \int_{E_s}^{E_s + kT\langle u \rangle} dE_t g(E_t) \left(1 - \left(\frac{E_t - E_s}{kT\langle u \rangle}\right)\right)^4 \right] \\ &\quad \times \left[\int_{-\infty}^{E_s} dE_t g(E_t) + \int_{E_s}^{E_s + kT\langle u \rangle} dE_t g(E_t) \right. \\ &\quad \left. \times \left(1 - \left(\frac{E_t - E_s}{kT\langle u \rangle}\right)\right)^2 \right]^{-1}. \end{aligned} \tag{3}$$

The equilibrium 2D hopping mobility μ can be then evaluated by averaging the hopping rates over E_s and using the Einstein relation relating the mobility to the diffusion coefficient as was done for a 3D hopping system in [6]:

$$\mu = \frac{ev_0}{kT} \int_{-\infty}^{\infty} dE_s \exp\left[-\langle u \rangle(E_s)\right] \langle r^2 \rangle(E_s) f(E_s), \tag{4}$$

where the functions $n(E_s, u)$ and $\langle r^2 \rangle(E_s)$ are calculated using Eqs. (2) and (3) and $f(E_s)$ is the normalized energy distribution function of localized carrier in a 2D hopping system. The choice of the form of the function $f(E_s)$ depends upon the carrier density

in the hopping system and will be described below in the text.

The 2D hopping carrier mobility can be also calculated by means of the effective transport energy concept [16]. This concept is based on the fact that all the carriers localized in a deep tail of the DOS function will eventually have to jump to one of the shallower states whose energy is close to some universal value which is traditionally referred to as the transport energy, E_{tr}. A very interesting feature of this model is that, for a sufficiently steep decaying DOS, the value of E_{tr} is independent of the energy of the initially occupied state E_s.

Under thermal equilibrium conditions practically all carriers occupy relatively deep hopping sites. Therefore, the nearest vacant target hopping site for most carriers will have a higher energy and hopping is controlled by energetically upward carrier jumps that allow to neglect the first term in the right-hand side of Eq. (2). Carrying out the replacement $\varepsilon = E_s + kTu$ and taking into account that the upward carrier jump from a starting site is possible if there is at least one hopping neighbour, i.e. $n(E_s, E_{tr}) = 1$, leads to the following transcendental equation for the energy ε:

$$\int_{E_s}^{\varepsilon} dE_t g(E_t)[\varepsilon - E_t]^2 = \frac{1}{\pi}(2\gamma kT)^2. \tag{5}$$

If at E_s and lower energies the DOS distribution decreases with energy faster than $|E|^{-3}$, the lower bound of the integration does not affect the result of the integration appreciably and the major contribution to the integral comes from sites with energy around ε. Physically this means that target sites for thermally assisted upward carrier jumps are located around the transport energy $\varepsilon = E_{tr}$, independent of the energy of starting sites. Therefore from Eq. (5) one can obtain the expression for the transport energy in a 2D hopping system in transcendental form

$$\int_{-\infty}^{E_{tr}} dE_t g(E_t)[E_{tr} - E_t]^2 = \frac{1}{\pi}(2\gamma kT)^2. \tag{6}$$

In analogy to the calculations made by Arkhipov et al. [6] the average squared jump distance of a carrier to a site at the effective transport level in a 2D hopping system can be approximated by

$$\langle r^2 \rangle = \left[\int_{-\infty}^{E_{tr}} dE g(E)\right]^{-1}. \tag{7}$$

Averaging rates of carrier jumps to the effective transport level and using the Einstein relation yields the following expression for the equilibrium 2D hopping carrier mobility

$$\mu = \frac{ev_0}{kT}\int_{-\infty}^{E_{tr}} dE f(E) \times \exp\left(-\frac{E_{tr} - E}{kT}\right)\left[\int_{-\infty}^{E_{tr}} dE g(E)\right]^{-1}, \tag{8}$$

where $f(E)$ represents the normalized energy distribution of localised carriers.

In practice, the 2D hopping mobility was experimentally observed in organic thin-film FETs where the charge carrier density is very high. Recently reported values of mobility in thin-film FET are up to a few times 10^{-1} cm^2 V^{-1} s^{-1} [12,13]. The typical surface carrier density accumulated under the gate insulator is of the order of 10^{11}–10^{12} cm^{-2}. Since the carrier density is comparable with the density of localized states, the hopping sites in the deep tail of the DOS distribution can be fully filled by charged carriers. Such filling affects the energy distribution of both localized carriers and vacant hopping sites. Therefore, the field and temperature dependencies of the hopping mobility must be very sensitive to the density of charge carriers. In the case of high carrier density the thermal equilibrium energy distribution of localized carriers is given by a product of the Fermi–Dirac function and the DOS distribution as

$$f(E) = \frac{g(E)}{1 + \exp[(E - E_F)/kT]} \times \left[\int_{-\infty}^{\infty} dE \frac{g(E)}{1 + \exp[(E - E_F)/kT]}\right]^{-1}, \tag{9}$$

where the Fermi energy E_F is determined by the total charge carrier density p via following transcendental equation

$$p = \int_{-\infty}^{\infty} dE \frac{g(E)}{1 + \exp[(E - E_F)/kT]}. \tag{10}$$

It is worth to note that in case of rather high density of charge carriers the classical Einstein relation used to derive the Eqs. (4) and (8) should be replaced by its generalized form [17]

$$\mu = D\frac{e}{kTp}\int_{-\infty}^{\infty} dE g(E) \times \frac{\exp[(E - E_F)/kT]}{(1 + \exp[(E - E_F/kT)])^2}. \tag{11}$$

Even for a comparatively high doping level or strong injection one still may neglect the effect of

filling if it occurs only in a very deep tail of the DOS far below E_F. In that case 2D hopping mobility depend upon charge carrier concentration p as

$$\mu = \frac{ev_0}{kTp^2}\int_{-\infty}^{\infty} dE g(E)\frac{\exp\left[(E-E_F)/kT\right]}{\left(1+\exp\left[(E-E_F/kT)\right]\right)^2} \times \int_{-\infty}^{E_{tr}} dE \frac{g(E)}{1+\exp\left(\frac{E-E_F}{kT}\right)} \times \exp\left(-\frac{E_{tr}-E}{kT}\right)\left[\int_{-\infty}^{E_{tr}} dE g(E)\right]^{-1}. \quad (12)$$

When one has to take into account the effect of filling of localized states, one should use the density of vacant hopping sites $g_v(E) = g(E) - pf(E)$ rather than the DOS function $g(E)$ in Eq. (6). In this case of high carrier concentration the transport energy in 2D hopping system will be dependent upon charge carrier concentration and can be obtained from:

$$\int_{-\infty}^{E_{tr}} dE \frac{g(E)}{1+\exp\left[-(E-E_F)/kT\right]}\left[E_{tr}-E\right]^2 = \frac{1}{\pi}(2\gamma kT)^2. \quad (13)$$

It should be mentioned that one can use the Eqs. (12) and (13) to calculate the 2D hopping mobility if the effective transport energy, calculated from Eq. (13) is well above the position of E_F [6]. If $E_{tr} - E_F \sim kT$ one should use Eqs. (2)–(4), and (11) to calculate the 2D hopping mobility where the DOS function $g(E)$ is replaced by function $g_v(E)$ and the carrier distribution function is given by Eq. (9).

3. Results and discussion

The transport energy in a 2D disordered hopping system was calculated from Eq. (6) with the Gaussian DOS distribution

$$g(E) = \frac{N_t^{2D}}{\sqrt{2\pi}\sigma}\exp\left[-\frac{E^2}{2\sigma^2}\right], \quad (14)$$

where N_t^{2D} is the total density of 2D hopping sites and σ is the standard deviation of the hopping sites distribution. The temperature dependence of E_{tr} for a 2D and a 3D systems, parametric in the charge carrier concentration, is shown in Fig. 1. The temperature dependence of the 3D transport energy was calculated from Eqs. (4)–(6) in [18] for a DOS distribution described by Eq. (14) with for both systems the same value of $\sigma = 0.1$ eV, and with a 3D total density of intrinsic sites equal to $N_t^{3D} = [N_t^{2D}]^{3/2}$ were used. The inverse localization radius was taken $\gamma = 3.5\,\mathrm{nm}^{-1}$ for both hopping systems. In the 2D hopping system the energy of most probable jump lies higher than that in the 3D system because the number of neighbours with

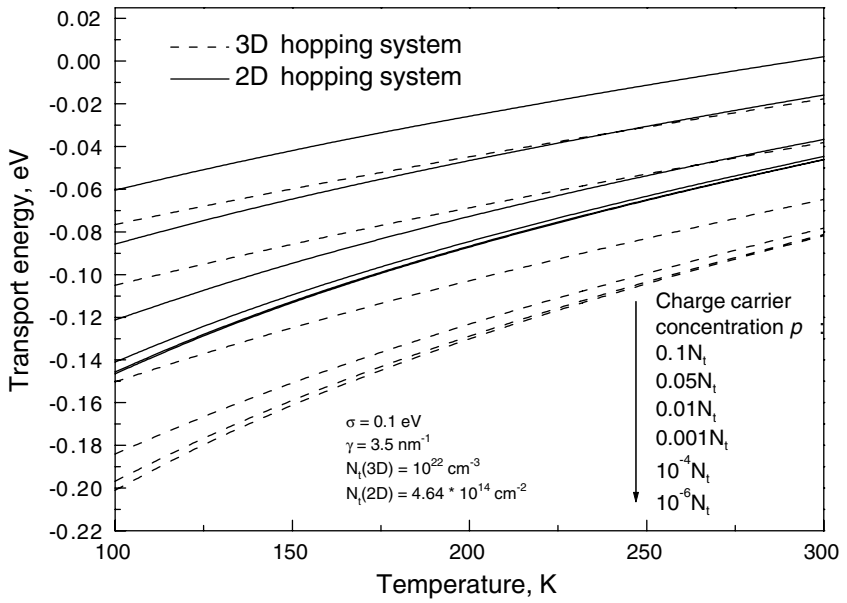

Fig. 1. Temperature dependence of the transport energy in 2D (straight lines) and 3D (dashed lines) hopping systems with a Gaussian DOS distribution of localized states parametric in charge carrier concentration. The total density of intrinsic sites in the 3D system was taken as $N_t^{3D} = [N_t^{2D}]^{3/2}$ while the other system parameters are identical for both systems.

the same hopping parameter is effectively less in 2D than in 3D. In other words, the rate of upward jumps to a neighbouring hopping site with a minimum possible value of the hopping parameter u is higher in the 3D system than in the 2D hopping system. This fact is illustrated in Fig. 2 where the 2D and 3D mobilities are plotted vs. the inverse temperature. The temperature dependence of the mobility is stronger in the 2D hopping system and the value of the 2D mobility is always less than in 3D because, even at a higher position of E_{tr}, the density of hopping sites near the transport energy is still significantly less in a 2D system. Furthermore in a 2D system the rate of the upward jumps decreases faster with decreasing temperature than in a 3D system. This result is in accordance with Monte-Carlo simulations [3] where the constant c in the expression $\mu \sim \exp[-(c\sigma/kT)^2]$, describing the temperature dependence of the hopping mobility, increases from about 0.67 to 1 when the dimensionality decreases from 3 to 1. For high values of the charge carrier concentration corresponding to $p = 0.01N_t^{2D,3D}$ the trap-filling effect leads to a conductivity controlled by carrier hopping from the Fermi level and the mobility reveals an Arrhenius-like behaviour, even around room temperature, as illustrated by the insert in Fig. 2. In the case of a diluted system the conductivity is due to jumps of carriers localized above the Fermi level and obeys the $\log(\mu) \sim 1/T^2$ law.

The theoretical results were used to fit experimental data on two-dimensional charge transport in a thin-film of the conjugated polymer poly(3-hexylthiophene) P3HT [12]. Self organization in P3HT results in a lamellar structure with two-dimensional sheets formed by interchain stacking of the conjugated chains. Depending on processing conditions the lamellae can adopt two different orientation – parallel and normal to the substrate [12,19]. Experimental data on the field-effect mobility in P3HT samples with different regioregularity vs. inverse temperature are shown in Fig. 3. One should note that the 2D mobility in a system with a Gaussian DOS distribution Eq. (14) decreases monotonically with decreasing temperature (see Fig. 2) and never saturates at low temperatures even if the effect of filling of localized states is taken into account. The saturation behavior of the experimental curves at low temperature hardly could be described assuming only a singe Gaussian DOS. At low temperature the conductivity behavior can be interpreted by a jumps to the transport level from a rather narrow disorder-induced localized states that occur below the high-mobility electronic states [12]. To take into account these deeper states we used two-Gaussian

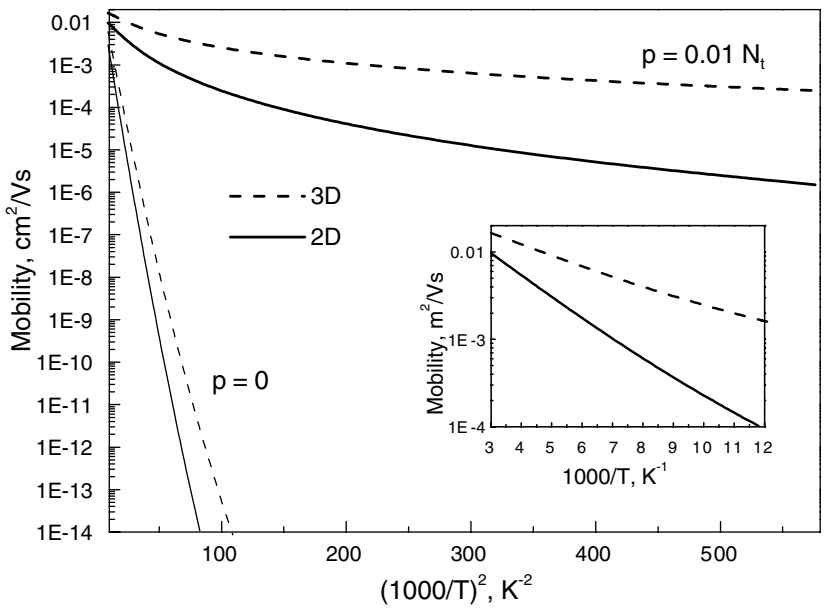

Fig. 2. Hopping mobility vs square inverse temperature for 2D and 3D hopping systems for high (1% of total density of intrinsic states) and low (10^{-10} density of intrinsic states) charge carrier concentrations. The total density of intrinsic sites in the 3D system was taken as $N_t^{3D} = [N_t^{2D}]^{3/2}$ and the other system parameters while identical for both systems. The insert shows an Arhenius-like behaviour of 2D and 3D mobilities at high carrier concentration.

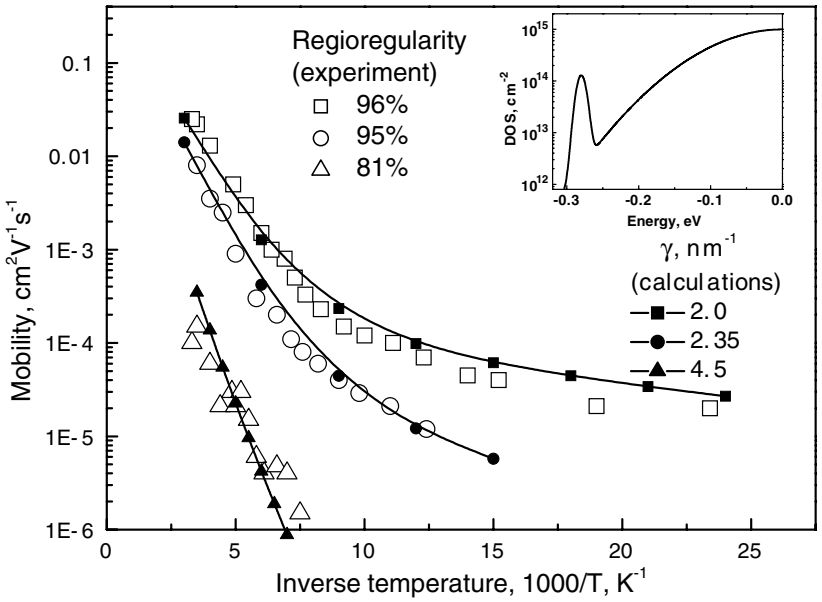

Fig. 3. Experimental data on the field-effect mobility in P3HT samples with different regioregularity [12] vs. inverse temperature together with the theoretical curves calculated from Eq. (10). The inverse localization radius is the only changed fitting parameter. The following set of material parameters has been used for the calculation: $N_t = 2\times10^{14}$ cm^{-2}, $N_d = 2\times10^{12}$ cm^{-2}, $p = 1\times10^{-3}$ ($N_t + N_d$), $\sigma = 0.08$ eV, $\sigma_1 = 0.006$ eV, $E_d = 0.28$ eV, $\nu_0 = 10^{13}$ s^{-1}. The insert shows a double Gaussian DOS distribution Eq. (14) that was used to calculate the theoretical curves from Eqs. (10), (12) and (13).

DOS distribution that incorporates both intrinsic DOS and the deeper localized states to fit experimental data (see the insert in Fig. 3):

$$g(E) = \frac{N_t^{2D}}{\sqrt{2\pi}\sigma}\exp\left[-\frac{E^2}{2\sigma^2}\right] + \frac{N_d}{\sqrt{2\pi}\sigma_1}\exp\left[-\frac{(E-E_d)^2}{2\sigma_1^2}\right], \quad (15)$$

where N_d is the total density of disorder-induced localized states, E_d is the energy of their maximum and σ_1 is the Gaussian variation of deep-sites. The numerical values of the fitting parameters are mentioned on the captions to Fig. 3. The experimental values of the mobility strongly depend upon the level of regioregularity of the sample. According to Sirringhaus [12] a high level of regioregularity of the sample (up to 91%) would correspond to a mainly parallel orientation of the microcrystalline domain while a normal orientation would be a feature of low regioregularity. For a mostly parallel orientation of ordered domains the direction of π–π stacking is parallel to substrate and coincident with the carrier transport direction. The carrier transport occurs either along the chains (where the coupling is strong) or in the stacking direction (where the transfer distance is very short). That corresponds to the rather large value of the apparent localization radius (small γ) as obtained from the curve fitting (see Fig. 3).For lower values of regioregularity the inter-chain interaction effect is weaker in the direction of carrier transport what corresponds to a smaller value of the localization radius (or a larger 2D-γ) In this case even excursion of the carriers in the direction of the π–π-stacking, perpendicular to the transport plane can not be excluded giving the transport some 3D-character. As the developed model considers (to avoid a too large number of parameters) the transfer distances isotropic, the stronger interactions in the case of 2D transport in considered P3HT system [12] are accounted for by a smaller apparent inverse localization radius γ in the 2D system.

It should be noted that according to existing literature [6,7,9] and to limit the number of parameters no distinction is made between the centre-to-centre distance of the hopping sites and the edge-to-edge jump distance. It is actually the latter which is relevant for the weakening of the wavefunction overlap. Although this has a limited influence on the calculations above, it will influence the combination of the values ν_0 and γ necessary to obtain realistic values of the 2D mobilities or to fit the experimental values of the mobilities and their

temperature dependence. The recovered values of γ are quite small to what is found in literature. Already for electron transfer assisted by σ-bonds values between 6.8 and 10.9 nm^{-1} are found for γ [20–23]. This discrepancy in inverse localisation radius values is to some extent due to the strong correlation that exists in the Miller-Abrahams model for the rate of carrier jump between γ and the fixed parameter v_0. For v_0 we used a value of 1×10^{13} s^{-1} [6,7,9,24] which was accepted elsewhere for the development of models for charge transport and charge generation in conjugated polymers.

4. Conclusion

The present paper derives analytical expressions for calculation of the 2D hopping mobility and its dependence on temperature, charge carrier concentration and DOS distribution. The formalism is applicable to an arbitrary DOS distribution and to arbitrarily high charge carrier densities. If the energy of the most probable carrier jump is not well above the Fermi level for a hopping system with high charge carrier concentration, i.e. when $E_{tr} - E_F \sim kT$, one should use Eqs. (2)–(4), and (11) instead of Eqs. (12) and (13) to calculate the 2D hopping mobility.

Acknowledgements

E.V. Emelianova would like to thank A.K. Kadashchuk for discussions and H. Bässler for usefull comments. The FWO and the K.U.Leuven Research Fund through GOA 2006/2 are acknowledged for financial support.

References

[1] G. Hadzijoannou, P. van Hutten (Eds.), Semiconducting Polymers, Wiley, Weinheim, 2000.
[2] P.M. Borsenberger, L. Pautmeier, H. Bässler, J. Chem. Phys. 94 (1991) 5447.
[3] H. Bässler, Phys. Status Solidi B 15 (1993) 175.
[4] M.A. Abkowitz, J.S. Facci, W.W. Limburg, J.F. Yanus, Phys. Rev. B 46 (1992) 6705.
[5] L.B. Schein, Philos. Mag. B 65 (1992) 795.
[6] V.I. Arkhipov, P. Heremans, E.V. Emelianova, G.J. Adriaenssens, H. Bässler, J. Phys.: Condens. Matter 14 (2002) 9899.
[7] V.I. Arkhipov, E.V. Emelianova, P. Heremans, H. Bässler, Phys. Rev. B 72 (2005) 235202.
[8] I.I. Fishchuk, A.K. Kadashchuk, A. Vakhnin, Yu. Korosko, H. Bässler, B. Souharke, U. Scherf, Phys. Rev. B 73 (2006) 115210.
[9] W.F. Pasveer, J. Cotaar, C. Tanase, R. Coehoorn, P.A. Bobbert, P.W.M. Blom, D.M. de Leeuw, A.M.J. Michels, Phys. Rev. Lett 94 (2005) 206601.
[10] M. Pope, S.E. Swenberg, Electronic Processes in Organic Crystals and Plymers, 2nd ed., Oxford University Press, Oxford, 1999.
[11] S.M. Sze, Physics of Semiconductor Devices, 2nd ed., Woley, New York, 1981.
[12] H. Sirringhaus, P.J. Brown, R.H. Friend, et al., Lett. Nature 401 (1999) 685–688.
[13] F. Dinelli, M. Murgia, P. Levy, M. Cavallini, F. Biscarini, D.M. de Leeuw, Phys. Rev. Lett. 92 (2004) 116802.
[14] H. Shimotani, G. Diguet, Y. Iwasa, Appl. Phys. Lett. 86 (2005) 022104.
[15] A. Miller, E. Abrahams, Phys. Rev. 120 (1960) 745.
[16] V.I. Arkhipov, E.V. Emelianova, G.J. Adriaenssens, Phys. Rev. B 64 (2001) 125125.
[17] Y. Roichman, N. Tessler, Appl. Phys. Lett. 80 (2002) 1948.
[18] V.I. Arkhipov, P. Heremans, E.V. Emelianova, G.J. Adriaenssens, H. Bässler, Appl. Phys. Lett. 82 (2003) 3245.
[19] Y. Kim, S. Cook, S.M. Tuladhar, S.A. Choulis, J. Nelson, J.R. Durrant, D.D.C. Bradley, M. Giles, I. Mcculloch, C.-S. Ha, M. Ree, Lett. Nature Mater. 5 (2006) 197–203.
[20] N. Hush, M.N. Paddon-Row, E. Cotsaris, H. Oevering, J.W. Verhoeven, Chem. Phys. Lett. 117 (1985) 8.
[21] M. Van der Auweraer, G. Biesmans, B. Verschuere, F.C. De Schryver, F. Willig, Langmuir 3 (1987) 992–1000.
[22] J. Miller, in: V. Balzani (Ed.), "Supramolecular Photochemistry, NATO ASI Series C, vol. 214, Reidel Publishing Company, Dordrecht, 1987, p. 241.
[23] J.W. Verhoeven, in: J. Jortner, M. Bixon (Eds.), Electron Transfer-From Isolated Molecules to Biomolecules, Part One, Advances in Chemical Physics, vol. 106, John Wiley & Sons, 1999, p. 603.
[24] V.I. Arkhipov, E.V. Emelianova, H. Bässler, Chem. Phys. Lett. 372 (2003) 886.

Available online at www.sciencedirect.com
ScienceDirect
Organic Electronics 9 (2008) 136–142
Organic Electronics
www.elsevier.com/locate/orgel

Letter

Sequentially doped blue electrofluorescent organic light-emitting diodes

Y. Divayana, X.W. Sun *

School of Electrical and Electronic Engineering, Nanyang Technological University, Nanyang Avenue, Singapore 639798, Singapore

Received 12 August 2007; received in revised form 21 October 2007; accepted 22 October 2007
Available online 30 October 2007

Abstract

We report on a blue fluorescent [4,4′-bis(9-ethyl-3-carbazovinylene)-1-1′-bisphenyl] organic light-emitting diode with a sequentially doped device architecture introduced recently. The emission layer consists of a few repeating cells, similar to a multiple quantum well structure, which are made of sequentially evaporated host and guest layers. An external quantum efficiency as high as 2.8% photons/electron was obtained, comparable with that fabricated using the conventional doping method. Without degrading the efficiency, devices with varied emission spectra (peak wavelength shifted from 472 to 488 nm) were produced by simply varying the guest layer thickness. The spectrum shift is due to changes in local order or aggregate state, or both.

PACS: 32.50.+d; 33.50.-j; 71.35.-y

Keywords: Organic light-emitting diode; Tunable spectrum; Doping; Aggregation

1. Introduction

Doping has generally being used in organic light-emitting diodes (OLED) to increase the external quantum efficiency (EQE) for phosphorescent [1] and fluorescent [2] devices and is performed by co-evaporating the host and guest material at the same time; doping enables isolation of the emitting molecules to reduce the aggregation effect in solid state [3]. One problem with conventional doping is that precise control of the evaporation rates of both host and guest materials are crucial to ensure optimal performance. Uniform deposition rates of organic materials are difficult to achieve because the organic materials are typically thermal insulators. In a conventional evaporation boat, only the fraction of organic material in contact with the resistively heated boat is heated, creating pockets in the source that occasionally collapse under gravity, resulting in rapid changes in deposition rate [4]. Therefore, it is not an easy task considering batch-to-batch manufacturing [5]. Recently, we have reported red fluorescent OLED fabricated by sequential doping, which relies on thickness rather than rate control, where host and guest materials are sequentially deposited as cells [6]. The emission layer (EML)

* Corresponding author. Tel.: +65 6790 5369; fax: +65 6793 3318.
E-mail address: exwsun@ntu.edu.sg (X.W. Sun).

1566-1199/$ - see front matter
doi:10.1016/j.orgel.2007.10.006

consists of a few repeating cells, similar to a multiple quantum well structure.

Here, we report on a blue OLED with sequential doping. Besides achieving a high efficiency close to the conventional doping method, devices with different emission spectra can be realized without altering the efficiency by simply varying the thickness of the guest layer. This capability is unique to sequential doping as both the thicknesses of guest and host layers can be controlled separately. In contrast, the conventional doping only allows one parameter, the doping concentration, to be varied. It is also the purpose of this paper to highlight this unique feature of sequential doping.

The inset of Fig. 1a shows the architecture of the blue fluorescent OLED fabricated using sequential doping. In co-evaporation, guests are randomly dispersed in the matrix of host molecules. By keeping the doping concentration low (~0.1–5%), almost all guest molecules are isolated from each other, preventing the formation of aggregate states. By doing so, a device with high EQE (2.8% photons/electron) can be realized. In sequential doping, a similar isolation effect can be achieved by separating the guest molecules with host layers. However, as

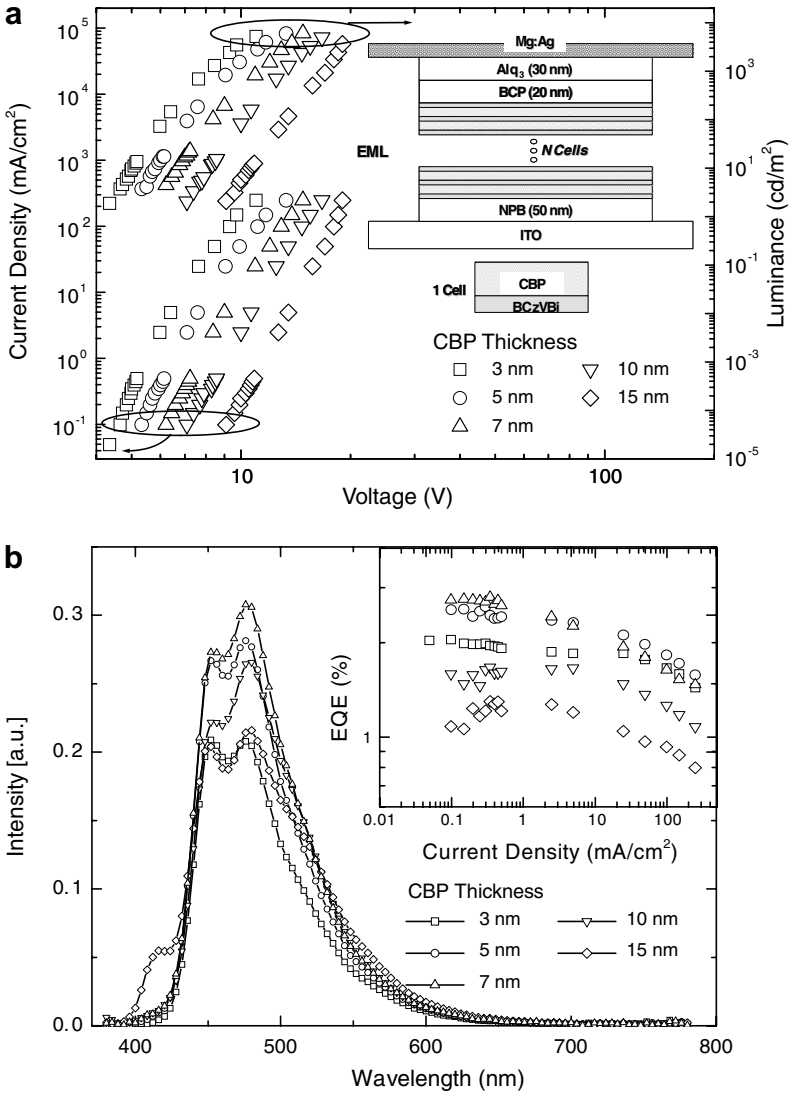

Fig. 1. (a) Current density and luminance versus voltage for devices with various CBP thicknesses. (b) Normalized emission spectrum for the device in (a). The inset in (a) shows the architecture of the blue OLED fabricated by the sequential doping method. The inset in (b) shows EQE versus current density for the devices in (a). Symbols in (a) also apply in (b).

guests are deposited as a thin layer, aggregation effects are unavoidable but can be minimized [6].

2. Experimental

Here, we employed *N*,*N*′-di(naphth-2-yl)-*N*,*N*′-diphenyl-benzidine (NPB) as the hole transporting layer, 4,4′-bis(*N*-carbazolyl)biphenyl (CBP) as the host, 4,4′-bis(9-ethyl-3-carbazovinylene)-1-1′-bisphenyl (BCzVBi) as the guest, and 2,9-dimethyl-4,7-diphenylphenanthroline (BCP) as the hole blocking layer and tris-(8-hydroxyquinoline) aluminum (Alq_3) as the electron transporting layer.

The routine cleaning procedure, including ultrasonication in acetone, ethanol, and rinsing in deionized water, was firstly carried out to clean ITO glass (50 Ω/square). Before deposition, the ITO was treated by oxygen plasma at 10 Pa for 2.5 min. The ITO substrates were then transferred to the main chamber under high vacuum for devices fabrication. The main chamber is equipped with 10 sources, each of which is heated by a tantalum heater. The opening and closing of shutters controls the deposition sequences. The deposition rate and thickness are measured by a crystal sensor quartz oscillator combined with a frequency meter. In order to obtain large-area uniformity and abrupt interface, the chamber is equipped with three sets of shutters, i.e. besides the shutters for each crucible, there are also a big shutter between the crucibles and substrates and a small shutter under each substrate. The thickness/rate crystal sensor is installed in the center of the substrate holders, which features planetary rotation, and the rotation rate can be adjusted. Evaporation of organic materials and metals was carried out in a high vacuum condition of about 2×10^{-4} Pa at deposition rate of 0.5–4 Å/s. Electroluminescence spectra of the fabricated devices were measured with a PR650 Spectra Scan spectrometer. We assumed the emission pattern was Lambertian, and calculated the EQE from the luminance, current density and EL spectrum [7]. All measurements were carried out at room temperature under ambient atmosphere without any encapsulation.

3. Results and discussion

For the first step of optimization, we varied the thickness of the host layer while fixing the guest layer thickness. We fabricated devices with a structure of NPB/[BCzVBi (0.5 nm)/CBP (*x* nm)] (6 cells)/BCzVBi (0.5 nm)/BCP/Alq_3, where *x* was varied from 3, 5, 7, 10–15 nm. Fig. 1a shows the current density and luminance versus voltage curves for devices with various values of *x*. As expected, the current density drops with the increase of the CBP thickness, as thicker structure leads to a higher operating voltage. The luminance also follows the trend of the current density.

The emission spectra for various devices at a current density of 5 mA/cm^2 are shown in Fig. 1b. The inset of Fig. 1b shows the external quantum efficiency (EQE) of the respective devices in Fig. 1a. A maximum EQE of 2.8% photons/electron was obtained for a device with 7 nm of CBP layer. The EQE is comparable to that of OLED fabricated by the conventional doping method using the same materials [8]. Current and power efficiency reaches 4.5 cd/A and 2.3 lm/W, respectively, at a current density of 100 μA/cm^2 for the optimized device. Devices with CBP thickness larger than 7 nm, besides having a lower efficiency, also emit an additional peak at 420 nm, as shown in Fig. 1b. This indicates that the efficiency loss is originated from an incomplete energy transfer from the host to the guest molecules, which led to the host emission [9]. In contrast, the device with thin layers of CBP which shows a similar lower EQE, show no sign of host emission. This suggests that the exciton quenching occurred via an escalating interaction among guest layers which may introduce another non-radiative recombination pathway [6]. Interaction between the active BCzVBi layers can be activated by dipole–dipole coupling (Förster process) type interaction, due to its long range capability [10]. However unlike the known Förster process which involves the electronic state of the excited donor and ground acceptor, the process occurring here is between the excited donors and the vibrational mode of the acceptor [6]. This is because the known Förster process would not result in efficiency loss, while the later introduces a new non-radiative decay channel [6]. As the thickness of the CBP is reduced, the active layers of BCzVBi become closer to one another resulting in the increase of the non-radiative energy transfer rate between the active layers.

In addition to the variation of the host thickness, we also varied the thickness of the guest layer. It is found that a variation of guest thickness is able to shift the emission spectrum without degrading the device EQE. We fabricated devices with a structure of NPB/[BCzVBi (*y* nm)/CBP (7 nm)] (6 cells)/BCzVBi (*y* nm)/BCP/Alq_3, where *y* was varied from

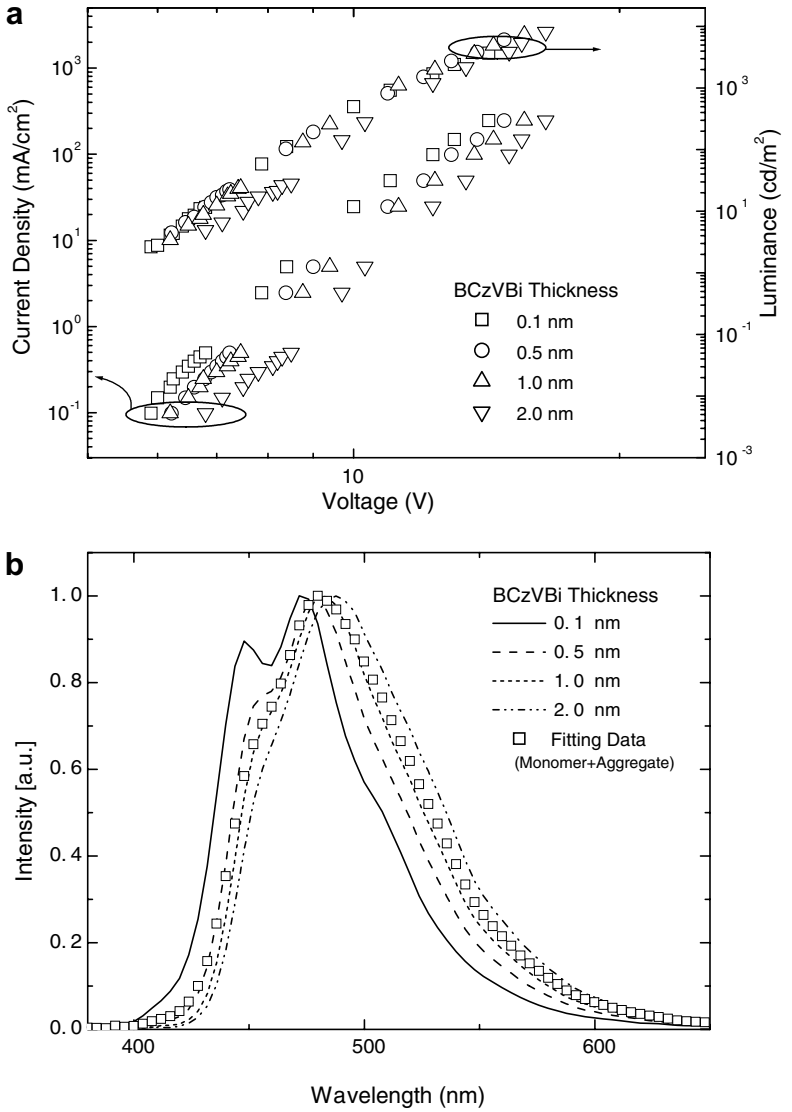

Fig. 2. (a) Current density and luminance versus voltage for devices with various BCzVBi thicknesses. (b) Normalized emission spectrum for device in (a), fitting data shown in square are obtained from a linear combination of monomer and aggregate emissions with $f = 0.7$.

0.1, 0.5, 1, 1.5–2 nm. Fig. 2a shows the current density and luminance versus voltage curves for devices for various values of y. The operating voltage slightly shifts toward higher values with the increase of BCzVBi thickness, which illustrates that the guest material alters the current transportation. The luminance curves on the other hand do not show much change, except for a BCzVBi thickness of 2 nm. Maximum luminance for device with 2 nm and 0.1 nm of BCzVBi is 8165 cd/m^2 and 3697 cd/m^2, respectively. Current and power efficiency reaches 5.3 cd/A and 2.5 lm/W, respectively, at a current density of 100 μA/cm^2 for a device with 2 nm of BCzVBi layer. This seemingly indicates that the device with thicker guest layer emits light more efficiently. However, as we will see later, the increase in luminance is accompanied by a shift in the emission peak. The shift of the emission spectrum to longer wavelengths resulted in the seemingly better device performance. In Table 1, we summarized the performances of the device with various thicknesses of BCzVBi. Table 1 also tabulates the equivalent guest concentration by conventional doping which produces a similar emission spectrum with that fabricated by the sequential doping method. Details of the calculation are explained later in the paper.

Table 1
Summary of performances for devices with various BCzVBi thicknesses

Thickness of BCzVBi (nm)	EQE (%) @ $J = 100$ μA/cm^2	Current efficiency (cd/A) @ $J = 100$ μA/cm^2	Power efficiency (lm/W) @ $J = 100$ μA/cm^2	Operating voltage @ $J = 100$ μA/cm^2	CIE (x, y)	Fraction of aggregate (f)	Peak of emission spectrum (nm)	Corresponding conventional doping concentration (%)
0.1	1.4	1.9	1	5.9	0.15, 0.17	0	472	0.005–0.01 (monomer)
0.5	2.6	4.5	2.3	6.2	0.15, 0.24	0.4	478	0.625–1.25
1.0	2.5	4.7	2.3	6.3	0.16, 0.29	0.7	482	5–10
2.0	2.5	5.3	2.5	6.8	0.18, 0.34	1	488	40–80

Fig. 2b plots the emission spectrum for devices in Fig. 2a. The emission peak shifts from 472 to 488 nm for thicknesses of BCzVBi of 0.1–2 nm, respectively. In term of Commission Internationale de l′Eclairage (CIE) coordinate, it shifts from deep blue $(x, y) = (0.15, 0.17)$ to slightly greenish blue $(x, y) = (0.18, 0.34)$. As the photopic response is higher at a green wavelength [11], a device that emit slightly greener would have higher luminance value compared to that of pure blue. This explains why the device with thick BCzVBi appears to have a higher luminous efficiency. In the inset of Fig. 3, we plotted the EQE for all devices in Fig. 2. Except for the device with 0.1 nm of BCzVBi, the EQE shows almost the same value irrespective of the guest thickness with a maximum EQE of 2.8% photons/electron. This indicates that the aggregate state does not alter the EQE. The device with 0.1 nm of BCzVBi exhibits lower EQE because of the inadequate number of guest molecules available for emission. From the emission spectrum, it can be seen clearly that the device with 0.1 nm BCzVBi has an additional peak at 420 nm, which shows an incomplete host–guest energy transfer.

The shift in emission spectrum is obviously related to the aggregation of the BCzVBi molecules. Molecule aggregation may shift the emission wavelength by a few different mechanisms, the solid state solvation effect [12], increase in local order [13], and increase in electronic aggregate state (dimer or excimer) [3]. Here, we discuss the likeliness of each mechanism to explain the observed spectrum shift.

The solid state solvation effect occurs due to an increase in the local electric field (permittivity) of

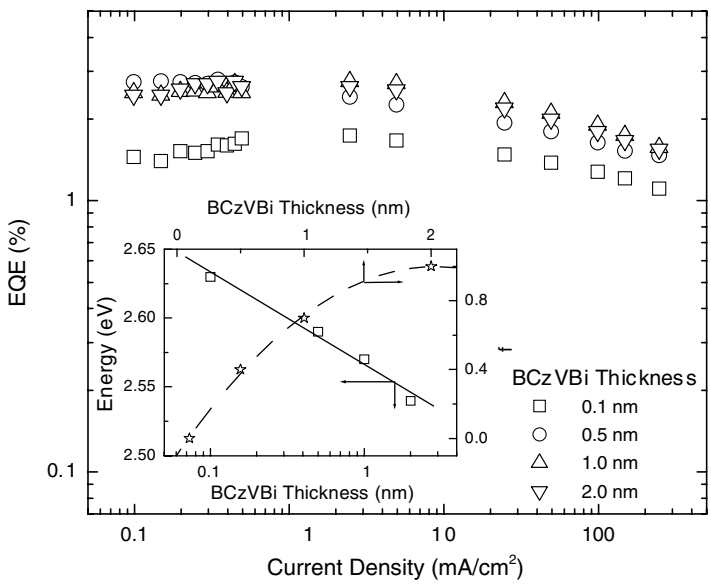

Fig. 3. EQE for devices with various thicknesses of BCzVBi with six cells as emission layer. Inset shows the logarithmic plot of emission peak and fraction of aggregation (f) versus BCzVBi thickness.

the thin film, which results in a wavelength shift [12]. Provided that the host and guest molecules have different dipole moments, a variation of the concentration of either molecule would change the local electric field, hence the permittivity. In other words, an emission shift is expected if either the host or the guest layer thickness changes, i.e. an increase in thickness of the guest layers has a similar effect, though weaker, with reduction of host thickness. However, for our case, a spectrum shift is only observed for devices with a variation of the guest layer. A variation of the host thickness only changes the EQE of the device, but does not change in emission spectrum. Hence, the solid state solvation effect can be eliminated from the rationale behind the spectrum shift.

An alternative explanation of the emission shift is the increase in local order due to thicker structure of the active molecules. In the literature, an increase in local order resulted in a logarithmic shift in the emission spectrum with the size of the order-domain [13]. Order-domain is defined as the average area of molecular aggregate where molecules are correlated by the dipole–dipole interaction. For our case the thickness of the guest layer corresponds linearly to the dimension of the order-domain. In the inset of Fig. 3, we plotted the peak energy (emission spectrum) as a function of guest layer thickness. A logarithmic shift is clearly observed. This signifies that the shift in the emission spectrum is due to an increase in the local order of the active molecules. Based on this model, we can calculate the corresponding guest concentration for a device fabricated by conventional doping which produces a similar emission spectrum to that fabricated by sequential doping. As mentioned above, the shift in emission spectrum is caused by the increase in the order-domain. In conventional doping, the size of the order-domain (R) is related with the doping concentration (η) by $R^3 \propto \eta$ [13]. Assuming that the emission of the device with 1 nm of BCzVBi (with peak emission at 482 nm) corresponds to the conventional doping concentration of 5–10% [14–16], we can extrapolate the corresponding guest doping concentration by conventional doping for devices with other thicknesses of BCzVBi proportionally (Table 1). The emission from the device with a BCzVBi layer of 0.1 nm can be considered as monomer emission due to its low corresponding guest concentration of 0.005–0.01% for conventional doping.

Another way to understand the shift in the emission spectrum is the following: we divide the emission spectrum into two separate entities, one of which is pure monomer emission ($g_{\mathrm{Monomer}}(\lambda)$), and the other emission of a purely aggregate electronic state ($g_{\mathrm{Aggregate}}(\lambda)$) (such as dimers or excimers),

$$g(\lambda) = (1-f)g_{\mathrm{Monomer}}(\lambda) + fg_{\mathrm{Aggregate}}(\lambda) \quad (1)$$

where f is the fraction of the aggregate emission. As the thickness of the guest layer increases, an increase in the fraction (f) of aggregate emission is expected. The fitting of emission spectrum as combination of monomer and aggregation [17] is shown as square in Fig. 2b, where a good fit is achieved. In the inset of Fig. 3, we also plotted the fraction of aggregate (f) as a function of guest thickness. The fraction of aggregate emission increases and eventually saturates with the increase of the guest layer thickness. This is reasonable, as at a certain guest thickness, the emission spectrum should not shift any more.

Both models, the local order and electronic aggregate, are able to fit well with the data obtained in the experiment. This coincidence may occur only if the dipole–dipole coupling is weak and the aggregate peak only slightly red-shifts compared to that of the monomer. The exact origin of the emission shifts, however, remains inconclusive; it can be either the local order or electronic aggregate, or both.

In the picture of local order, the drop in efficiency with an increase in order-domain is usually discussed in terms of material impurity [13]. For our case, the absence of efficiency loss for thick guest layers that is accompanied by an emission shift indicates that the purity of the BCzVBi is very high. Our discussion on electronic aggregate state indicates that the dimer or excimer of the BCzVBi molecule has a high photo-yield relatively to the monomer [3].

It is worth mentioning that the device structure has the potential for further optimization, such as the usage of LiF/Al or CsF/Al cathodes and the reduction in the number of cells [6] in order to further reduce the operating voltage and the complexity of the device.

4. Conclusion

In conclusion, we have fabricated a blue OLED with the sequential doping method. A device with EQE of 2.8% photons/electron is reported, similar to that achieved by the conventional doping method. A variation of guest thickness is shown to shift the emission spectrum without sacrificing the

EQE. The mechanism which governs the emission shift is concluded to be due to either the local order or electronic aggregate, or both, but not the solid state solvation effect.

Acknowledgement

Financial support from Research Grant (M48040154) of Nanyang Technological University, Singapore is greatly acknowledged.

References

[1] M.A. Baldo, D.F. O'Brien, Y. You, A. Shoustikov, S. Sibley, M.E. Thompson, S.R. Forrest, Nature 395 (1998) 151.
[2] C.W. Tang, S.A. VanSlyke, C.H. Chen, J. Appl. Phys. 65 (1989) 3610.
[3] M. Pope, C.E. Swenberg, Electronic Processes in Organic Crystals and Polymers, second ed., Oxford University Press, Oxford, 1999, p. 39.
[4] S.R. Forrest, Nature 428 (2004) 911.
[5] C.T. Chen, Chem. Mater. 16 (2004) 4389.
[6] Y. Divayana, X.W. Sun, Appl. Phys. Lett. 90 (2007) 203509.
[7] Y. Divayana, X.W. Sun, B.J. Chen, G.Q. Lo, C.Y. Jiang, K.R. Sarma, Appl. Phys. Lett. 89 (2006) 173511.
[8] Y. Sun, N.C. Giebink, H. Kanno, B. Ma, M.E. Thompson, S.R. Forrest, Nature 440 (2006) 908.
[9] The emission peak corresponds to NPB emission. This is occurred because the excess excitons in CBP transfer their energy to the NPB layer.
[10] T. Förster, Discuss. Faraday Soc. 27 (1959) 7.
[11] M.A. Baldo, PhD Dissertation, Princeton University, 2001.
[12] C.F. Madigan, V. Bulovic, Phys. Rev. Lett. 91 (2003) 247403.
[13] M.A. Baldo, Z.G. Zoos, S.R. Forrest, Chem. Phys. Lett. 347 (2001) 297.
[14] C. Hosokawa, H. Higashi, H. Nakamura, T. Kusumoto, Appl. Phys. Lett. 67 (1995) 3853.
[15] Y. Kishigami, K. Tsubaki, Y. Kondo, J. Kido, Synth. Met. 153 (2005) 241.
[16] H. Kanno, Y. Sun, S.R. Forrest, Appl. Phys. Lett. 89 (2006) 143516.
[17] We assumed pure monomer (aggregate) emission for the devices with 0.1 (2.0) nm of BCzVBi.

Available online at www.sciencedirect.com
ScienceDirect
Organic Electronics 9 (2008) 143–148
Organic Electronics
www.elsevier.com/locate/orgel

Letter

Organic field-effect transistors (OFETs) of highly oriented films of dithiophene-tetrathiafulvalene prepared by zone casting

M. Mas-Torrent [a,b,*], S. Masirek [c], P. Hadley [b,d], N. Crivillers [a], N.S. Oxtoby [a], P. Reuter [d], J. Veciana [a], C. Rovira [a,*], A. Tracz [c,*]

[a] Institut de Ciència de Materials de Barcelona (CSIC), Campus de la Universitat Autònoma de Barcelona, 08193 Bellaterra, Spain
[b] Kavli Institute NanoScience Delft, Delft University of Technology, Lorentzweg 1, 2628 CJ Delft, The Netherlands
[c] Centre of Molecular and Macromolecular Studies, Polish Academy of Sciences, 90-363 Łódź, Sienkiewicza 112, Poland
[d] Institute of Solid State Physics, Graz University of Technology, Petersgasse 16, 8010 Graz, Austria

Received 9 May 2007; received in revised form 17 September 2007; accepted 21 September 2007
Available online 12 October 2007

Abstract

We report on the preparation of large area coverage of well-oriented films of dithiophene-tetrathiafulvalene (DT-TTF) from solution by using the zone casting technique. The X-ray analysis shows that the molecules are highly ordered in the films with the stacking direction parallel to the substrate. We further demonstrate that it is possible to prepare organic field-effect transistors (OFETs) employing these films. The devices reveal a remarkable OFET mobility with a maximum value of 0.17 cm^2/V s. The fact that the films are prepared from solution makes these devices eminently suitable for low-cost electronics.

PACS: Semiconductor devices; Materials sciences

Keywords: Organic field-effect transistors; Thin film; Tetrathiafulvalene; X-ray diffraction

Great interest in organic devices has emerged recently due to their potential in applications in modern microelectronics [1,2]. The performance of the best organic field-effect transistors (OFETs) is of the same order as that of amorphous silicon. The highest OFET mobilities have been found for single-crystalline materials [3–8]. However, crystals are not suitable for fabricating large-scale thin films and, in order to effectively exploit organic semiconductors as active components in electronic devices, it is crucial to develop new easy methods to prepare films of these organic molecules. Most of the devices exhibiting high OFET performance are currently prepared by evaporation of the organic layer, which is a relatively expensive process [9,10]. To promote, therefore, the development and utility of organic semiconductors, there is a clear need to find

* Corresponding authors. Address: Institut de Ciència de Materials de Barcelona (CSIC), Campus de la Universitat Autònoma de Barcelona, 08193 Bellaterra, Spain. Tel.: +34 935801853; fax: +34 935805729.
E-mail addresses: mmas@icmab.es (M. Mas-Torrent), cun@icmab.es (C. Rovira), atracz@cbmm.lodz.pl (A. Tracz).

1566-1199/$ - see front matter © 2007 Elsevier B.V. All rights reserved.
doi:10.1016/j.orgel.2007.09.007

materials that can be solution-processed and, simultaneously, achieve a high OFET mobility [11–14]. Hence, considerable effort is currently being devoted to synthesising soluble precursors or derivatives of the organic semiconductor materials (e.g. oligothiophene, acenes) [15–19]. Recently, we reported that crystals of the organic material dithiophene-tetrathiafulvalene (DT-TTF, Fig. 1) have a very high field-effect charge carrier mobility of up to 1.4 cm^2/V s [3,4]. These crystals were formed by a simple drop casting method, making this material interesting to investigate for possible applications in low-cost electronics. Here, we report on the preparation of large area coverage of well-ordered films of DT-TTF by zone casting and further demonstrate that it is possible to prepare OFETs employing these films.

The conductivity in ordered organic materials is typically anisotropic as it strongly depends on the electronic coupling between the neighboring molecules in the different crystallographic directions. For this reason, in the preparation of organic films for electronic devices, it is essential to grow them with directed order. The zone casting technique, developed in 1981 in Łódź, was specially designed for the preparation of oriented, anisotropic layers of soluble molecular materials on substrates that are not pre-oriented [20,21]. This technique consists of the deposition of a material from solution on a moving substrate. The solution is continuously supplied to the evaporation zone by a flat nozzle, the solvent evaporates from the meniscus zone, and the solute is deposited on the moving substrate. The solution supply rate, substrate velocity, initial solute concentration, solvent evaporation rate, and crystallization rate must be optimized to obtain well-ordered films. This technique was used for the preparation of oriented networks of nanowires of tetrathiotetracene-tetracyanoquinodimethane embedded in amorphous [22] or semicrystalline [23] polymeric matrices. Aligned films of discotic hexabenzocoronenes and a TTF bearing long alky chains were also obtained by this method [24,25] and, furthermore, such films could be used for fabricating OFETs [25–27]. However, this technique has never been applied to the preparation of films based on classical low-molecular-weight organic semiconductors which are not liquid crystal materials nor have long pendant chains that promote the film ordering.

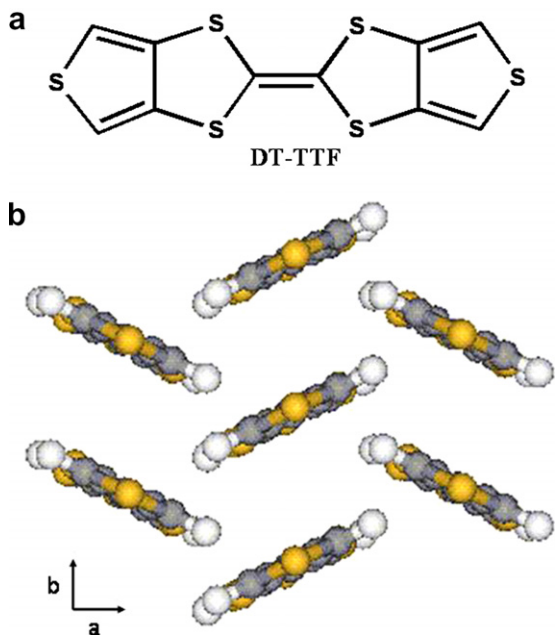

Fig. 1. (a) Molecular structure of dithiophene-tetrathiafulvalene (DT-TTF). (b) Crystal structure of DT-TTF viewed along the *c*-axis.

The high OFET performance and solubility of DT-TTF prompted us to study the preparation of oriented films of this small molecule. Zone casting films of DT-TTF were prepared from toluene solutions at concentration of 1.2 mg/ml on a silicon wafer with a 200 nm thick layer of oxide. The substrates were cleaned for one minute in nitric acid and rinsed in de-ionized water, acetone and isopropanol. The film was deposited using a specially constructed zone-casting apparatus, equipped with controlled linear stage and independently-controlled solution and substrate heaters. The solution and the substrate temperature was 60 °C. The fabrication was performed in ambient atmosphere and the substrate velocity was 30 μm/s. Fig. 2 shows an optical micrograph (taken in reflected light) of a zone cast DT-TTF film. It consists of parallel ribbons growing on the substrate along the casting direction. We were aiming at obtaining single-crystalline plates of DT-TTF on Si/SiO_2. However, DT-TTF readily crystallizes and as soon as the evaporation from the meniscus starts, many nucleation centers appear at the contact line resulting in growth of arrays of ribbon like crystals parallel to the casting direction. Between the needles the underlying substrate was observed, nevertheless, the coverage of the substrate is high. Closer inspection using AFM revealed that the crystalline ribbons are ca. 300 nm thick (Fig. 3).

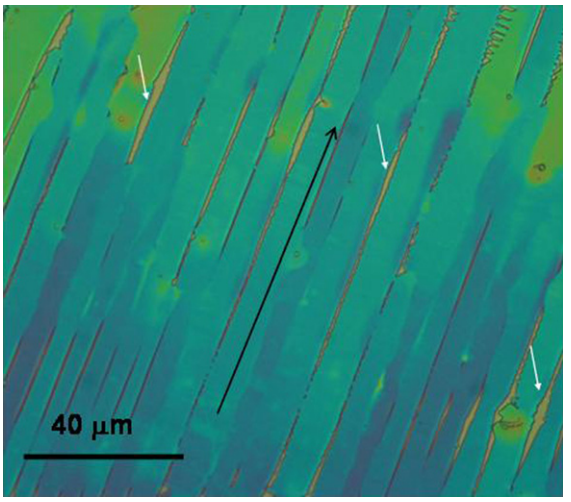

Fig. 2. Optical micrograph (reflected light) of DT-TTF films prepared by zone casting on a Si/SiO_2 substrate. The black arrow indicates the casting direction. White arrows indicate some of the places on the substrate not covered by the organic layer.

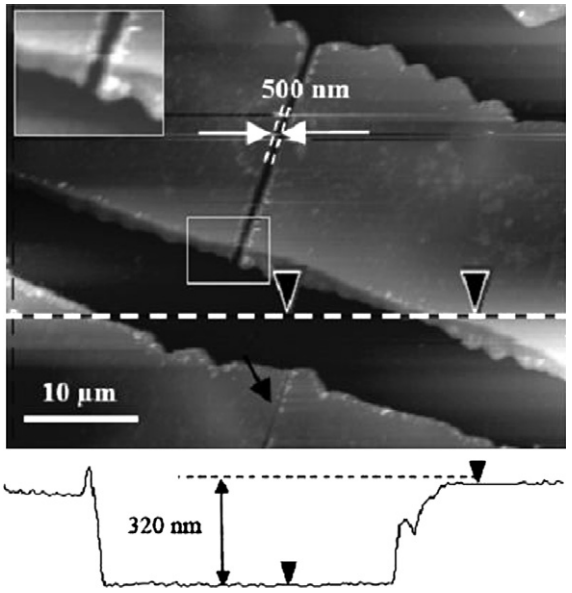

Fig. 3. AFM image of defected crystalline ribbons of DT-TTF zone cast on silicon wafer. A crack perpendicular to the ribbon going through the whole thickness is seen in the center of the image. A narrower crack in the neighboring ribbon below is indicated by the black arrow. The profile, shown at the bottom, scanned along the dotted white line reveals the thickness of the crystalline ribbons is about 300 nm.

Although the idea of the zone casting seems very simple it is rather difficult to optimize the conditions allowing the formation of layers with the desired morphology. The wetting instabilities at the solution-substrate interface (dewetting, stick-slip motion, fingering instabilities, etc.) that appear within a certain range of casting conditions lead to the formation of various morphological structures [28]. Commonly observed instability in the zone casting process is the stick-slip motion of the three-phase contact line on the moving substrate (pinning–depinning process) during the solvent evaporation. Instead of compact continuous layers, stripes of the solute perpendicular to the casting direction are formed. Under some conditions the stick-slip motion and the periodic solidification (or crystallization) along the meniscus edge occur simultaneously leading to complicated patterns. The examples of such layers obtained from DT-TTF solutions are shown in Fig. 4. The electrical properties of such layers were not investigated.

In order to study the orientation of the molecules in the zone cast films, powder X-ray experiments were performed. DT-TTF molecules crystallize forming uniform stacks along the *b* axis with an interplanar distance of 3.56 Å (Fig. 1b) [29]. In addition, the long axis of the crystals was determined to be the crystallographic *b* axis, that is, the stacking direction, which corresponds also to the conducting channel of the previously fabricated DT-TTF single crystal OFETs [3]. To develop DT-TTF films that work as OFETs, it will be essential that the molecular arrangement in the films is similar to that in the crystalline form. The X-ray powder diffraction patterns of the films indicate the presence of only (0 0 l) reflections, which points to the fact that the molecules are highly ordered with the crystallographic *c**-axis perpendicular to the substrate. This means that, similar to the high mobility DT-TTF single crystal OFETs, the stacking direction is parallel to the substrate, which is encouraging for the preparation of electronic devices.

OFETs were prepared on the zone cast films by evaporating gold electrodes on the films through a shadow mask (top-contact configuration). Devices with a channel length and width of 80 µm and 2 mm, respectively, were prepared. The study of the electrical characteristics of the device was performed in air by using the evaporated gold electrodes as source and drain contacts and the silicon substrate as a gate. Fig. 5 shows the collected mobility values, calculated in the linear regime, of various zone cast films. Due to the fact that the films were not completely homogenous along the conducting channels, we found that there was a scattering in the charge carrier mobilities obtained. The average

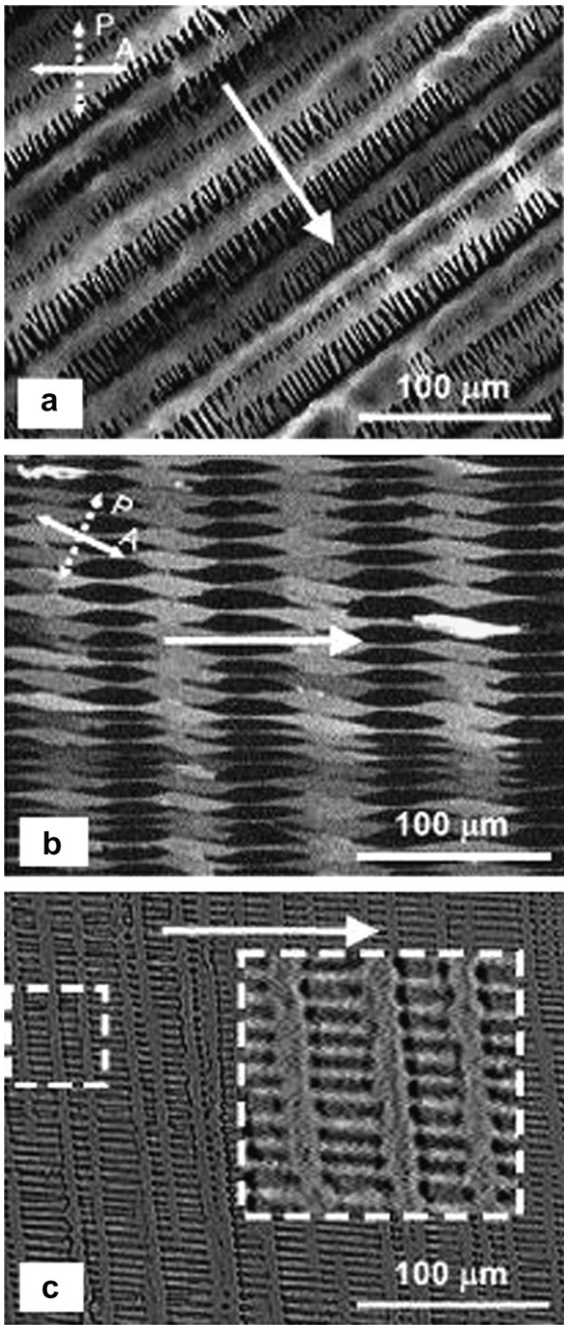

Fig. 4. Optical micrographs (crossed polarizers) of microcrystalline patterns of crystalline DT-TTF zone cast on glass from 1.2 mg/ml solution in toluene at a temperature of 65 °C, at different casting rates: (a) 6 μm/s; (b) 10 μm/s and (c) 16 μm/s. White arrow indicates the casting direction.

mobility observed was 0.05 cm^2/V s. The highest OFET mobility found was 0.17 cm^2/V s, which is one order of magnitude lower than the maximum mobility obtained for a single crystal DT-TTF but

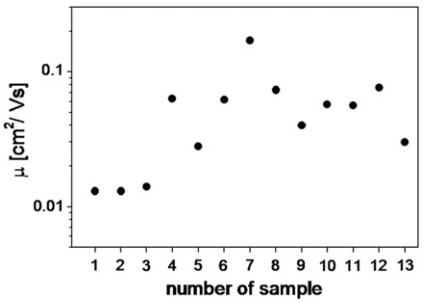

Fig. 5. Mobility values obtained for the zone cast films investigated.

of the same order as some of the measured DT-TTF single crystals OFETs (Fig. 6) [3,4]. In addition, we note that the intrinsic mobility of this material could be higher since it is well-known that contact resistances between organic semiconductors and metals can strongly influence the transport properties of electronic devices [30]. Fig. 6a shows the source–drain current (I_{SD}) versus the applied

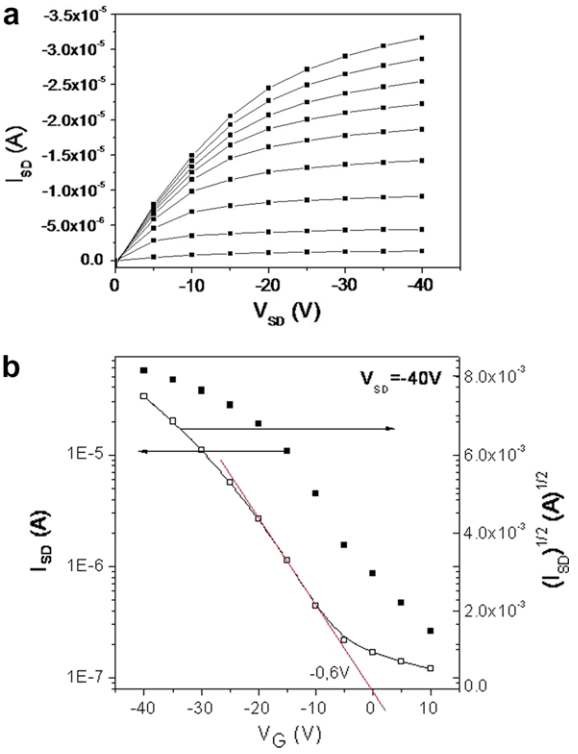

Fig. 6. (a) I_{SD} versus V_{SD} at V_G (from top to bottom) −40, −35, −30, −25, 20, −15, −10, −5 and −0 V. This device exhibited a mobility of 0.17 cm^2/V s. (b) For the same device as in Fig. 6a, I_{SD} *versus* V_G at $V_{SD} = -40$ V.

source–drain voltage (V_{SD}) across the two electrodes for different gate voltages (V_G). As expected for a p-type material [1–4], as a more negative V_G is applied, more holes are induced in the semiconductor and the conductivity increases. The transfer characteristics (I_{SD} versus V_G at fixed $V_{SD} = -40$ V) for this device are shown in Fig. 6b. The threshold voltage of this device is −0.6 V. That is, it is necessary to apply a gate voltage lower than −0.6 V to induce conductivity in the film. The devices exhibited high OFF current, probably due to the doping of the film with oxygen. We believe that this effect would be reduced if the films showed fewer defects. These results are very promising since the fact that the films are deposited from solution makes these devices eminently suitable for low-cost integrated circuit technology.

The fabrication of OFETs with a bottom-contact configuration was also attempted by performing the zone casting experiments on a Si/SiO_2 substrate with prefabricated electrodes. Unfortunately, the film formation was interrupted near the gold edges and, thus, no measurements could be performed. We believe that this was caused by the substrate inhomogeneity due to the presence of the protruding electrodes.

In summary, we successfully demonstrated that it is possible to prepare ordered films of DT-TTF from solution by zone casting. We also show for the first time the application of the zone casting technique for preparing films of low-molecular weight semiconductors. Although future work will be devoted to improve the film formation, the results obtained so far allow us to conclude that DT-TTF is a highly promising material for applications due to its facile processability and OFET performance.

Acknowledgements

C.R., J.V., M.M.-T., N.C. and N.S.O. thank the support of EU by the 6FP NAIMO Integrated Project No NMP4-CT-2004-500355, DGI, Spain (Project EMOCIONa, CTQ2006-06333/BQU) and DGR; Generalitat de Catalunya (Centre de Referencia CeRMAE and Project 2001SG00362). A. T. thanks the support of KBN Project T08E04423 (2002–2005) and Marie Curie RTN-THREADMILL (MRTN-CT-2006-036040). Prof. J. Ulanski and Dr. P. Miskiewcz (Technical University of Lodz) are kindly acknowledged for the help in electrical characterization of OFET devices.

References

[1] C.D. Dimitrakopoulos, P.R.L. Malenfant, Adv. Mater. 14 (2002) 99.
[2] Y.M. Sun, Y.Q. Liu, D.B. Zhu, J. Mater. Chem. 15 (2005) 53.
[3] M. Mas-Torrent, M. Durkut, P. Hadley, X. Ribas, C. Rovira, J. Am. Chem. Soc. 126 (2004) 984.
[4] M. Mas-Torrent, P. Hadley, S.T. Bromley, X. Ribas, J. Tarres, M. Mas, E. Molins, J. Veciana, C. Rovira, J. Am. Chem. Soc. 126 (2004) 8546.
[5] V.C. Sundar, J. Zaumseil, V. Podzorov, E. Menard, R.L. Willett, T. Someya, M.E. Gershenson, J.A. Rogers, Science 303 (2004) 1644.
[6] R.W.I. De Boer, T.M. Klapwijk, A.F. Morpurgo, Appl. Phys. Lett. 83 (2003) 4345.
[7] M. Ichikawa, H. Yanagi, Y. Shimizu, S. Hotta, N. Suganuma, T. Koyama, Y. Taniguchi, Adv. Mater. 14 (2002) 1272.
[8] V.Y. Butko, X. Chi, D.V. Lang, A.P. Ramirez, Appl. Phys. Lett. 83 (2003) 4773.
[9] H. Yanagi, Y. Araki, T. Ohara, S. Hotta, M. Ichikawa, Y. Taniguchi, Adv. Funct. Mater. 13 (2003) 767.
[10] S.F. Nelson, Y.-Y. Lin, D.J. Gundlach, T.N. Jackson, Appl. Phys. Lett. 72 (1998) 1854.
[11] Y. Li, Y. Wu, S. Gardner, B.S. Ong, Adv. Mater. 17 (2005) 849.
[12] Z. Bao, Adv. Mater. 12 (2000) 227.
[13] H.E. Katz, Chem. Mater. 16 (2004) 4748.
[14] M.M. Ling, Z. Bao, Chem. Mater. 16 (2004) 4824.
[15] P.T. Herwig, K. Müllen, Adv. Mater. 11 (1999) 480.
[16] G.H. Gelink, H.E.A. Huitema, E. van Veenendaal, E. Cantatore, L. Schrijnemakers, J.B.P.H. van der Putten, T.C.T. Geuns, M. Beenhakkers, J.B. Giesbers, B.-H. Huisman, E.J. Meijer, E. Mena Benito, F.J. Touwslager, A.W. Marsman, B.J.E. van Rens, D.M. de Leeuw, Nature Mater. 3 (2004) 106.
[17] M.M. Payne, S.R. Parkin, J.E. Anthony, C.-C. Kuo, T.N. Jackson, J. Am. Chem. Soc. 127 (2005) 4986.
[18] A.R. Murphy, J.M.J. Fréchet, P. Chang, J. Lee, V. Subramanian, J. Am. Chem. Soc. 126 (2004) 1596.
[19] A. Azfali, C.D. Dimitrakopoulos, T.O. Graham, Adv. Mater. 15 (2003) 2066;
K.P. Weidkamp, A. Afzali, R.M. Tromp, R.J. Hamers, J. Am. Chem. Soc. 126 (2004) 12740.
[20] A. Tracz, J. Ulanski, T. Pakula, M. Kryszewski, Patent PRL-131986, 1981.
[21] A. Tracz, T. Pakula, J.K. Jeszka, Mater. Sci. – Poland 22 (2004) 415.
[22] L. Burda, A. Tracz, T. Pakula, J. Ulanski, M. Kryszewski, J. Phys. D – Appl. Phys. 16 (1983) 1737.
[23] A. Tracz, E. El Shafee, J. Ulanski, J.K. Jeszka, M. Kryszewski, Synth. Met. 37 (1990) 175.
[24] A. Tracz, J.K. Jeszka, M.D. Watson, W. Pisula, K. Mullen, T. Pakula, J. Am. Chem. Soc. 125 (2003) 1682.
[25] P. Miskiewicz, M. Mas-Torrent, J. Jung, S. Kotarba, I. Glowacki, E. Gomar-Nadal, D.B. Amabilino, C. Rovira, J. Veciana, B. Krause, D. Carbone, J. Ulanski, Chem. Mater. 18 (2006) 4724.
[26] P. Miskiewicz, A. Rybak, J. Jung, I. Glowacki, J. Ulanski, Y. Geerts, M. Watson, K. Mullen, Synth. Met. 137 (2003) 905.

[27] W. Pisula, A. Menon, M. Stepputat, I. Lieberwirth, U. Kolb, A. Tracz, H. Sirringhaus, T. Pakula, K. Mullen, Adv. Mater. 17 (2005) 684.
[28] A. Tracz, S. Masirek, M. Klos, Israel Journal of Chemistry, 47 (3), in press.
[29] C. Rovira, J. Veciana, N. Santalo, J. Tarres, J. Cirujeda, E. Molins, J. Llorca, E. Espinosa, J. Org. Chem. 59 (1994) 3307.
[30] B.H. Hamadani, D. Natelson, Appl. Phys. Lett. 84 (2004) 443.

Available online at www.sciencedirect.com
ScienceDirect
Organic Electronics 9 (2008) 149–154
Organic Electronics
www.elsevier.com/locate/orgel

Letter

Conductive atomic force microscopy (C-AFM) analysis of photoactive layers in inert atmosphere

Alexander Alexeev [a], Joachim Loos [b,*]

[a] Nanotechnology-MDT Co, Moscow, Russia
[b] Eindhoven University of Technology, Department of Chemical Engineering and Chemistry, Laboratory of Materials and Interface Chemistry, and Laboratory of Polymer Technology, and Soft Matter Cryo-TEM Research Unit, P.O. Box 513, 5600 MB Eindhoven, The Netherlands

Received 9 August 2007; received in revised form 12 October 2007; accepted 14 October 2007
Available online 24 October 2007

Abstract

Conductive atomic force microscopy (C-AFM) measurements have been performed on the MDMO-PPV/PCBM system which is potentially interesting for applications as active layer in polymer solar cells (PSCs). It is demonstrated that C-AFM analysis performed in air for ambient conditions provides only inadequate information about the local electrical properties. The main reason is that the samples chemically degrade when in contact with air. Moreover, we speculate that also the adsorbed water layer interferes with reliable nanoscale electrical measurements. In contrast, when performed in inert atmosphere C-AFM analysis offers consistent results of e.g. the *I–V* characteristics with lateral resolution better than 50 nm, and is able to detect local heterogeneities of these *I–V* characteristics at the sample surface.

PACS: 07.79.Lh; 68.37.Ps; 73.61.−r

Keywords: Conductive atomic force microscopy; Polymer solar cell; Morphology; Photoactive layer; Inert atmosphere

1. Introduction

In general, performance measurements of polymer solar cells (PSCs) are carried out on operational devices having at least the size of square millimetres to centimetres. On the other hand, the characteristic length scale determining the functional behaviour of the bulk heterojunction photoactive layer is in the order of 10 nm (exciton diffusion length) to about 100–200 nm (layer thickness) [1–3]. The morphological requirement for the photoactive layer in a high-performance PSC is nanoscale phase separation, which provides large interface area for exciton dissociation and, at the same time, continuous pathways for free charge carrier transport to the appropriate electrodes. Further, it is well-known that the local organisation dominantly controls the functional behaviour of devices. Thus, it is necessary to obtain property data of nanostructures with nanometre resolution to be able to establish structure-property relations that link length scales from local nanostructures to macroscopic devices.

* Corresponding author. Tel.: +31 40 2473034.
E-mail address: j.loos@tue.nl (J. Loos).

1566-1199/$ - see front matter
doi:10.1016/j.orgel.2007.10.003

In this respect, a very useful analytical tool is conductive atomic force microscopy (C-AFM) [4,5]. Because AFM uses the interaction force between probe and sample surface as feedback signal, both topography and conductivity of the sample can be mapped independently. Theoretically, the resolution of C-AFM is as small as the tip-sample contact area, which can be in the few nanometre range. C-AFM is widely used for the characterization of electrical properties of organic semiconductors. For example, single crystals of sexithiophene have been studied [6], where the *I–V* characteristics of the samples were measured. Several electrical parameters such as grain resistivity and tip-sample barrier height were determined from these data. In another study, the hole transport in thin films of MEH-PPV was investigated and the spatial current distribution and *I–V* characteristics of the samples were discussed [7]. Recently, the distribution of electrical characteristics of polymer blends was studied by C-AFM [8–11].

It is well-known that the performance of most PSC as well as of organic electronic systems in general, drops dramatically after short-time exposure to air, especially when illuminated by light [12]. While some groups have already taken care to perform their C-AFM measurements in a dry nitrogen atmospheres thereby achieving good correlation with device properties [8], it is more common to perform C-AFM in air under ambient conditions. It is the purpose of our study to clearly demonstrate that the local electrical properties of nanostructures in the photoactive layer of PSCs changes when C-AFM measurements are performed at ambient conditions; and as consequence the obtained results are not comparable with data gained from device characterisation. At the same time, we would like to point out that C-AFM measurements performed in the inert atmosphere of a glove box provide more reliable information on electrical properties of organic nanostructures and allow establishing structure-property relations of functional polymer systems at the nanometre length scale.

2. Experimental

2.1. Materials

For the present study, 1-(3-methoxycarbonyl)propyl-1-phenyl-[6,6]-methanofullerene (PCBM) [13] was synthesized in the University of Groningen, the Netherlands, and poly[2-methoxy-5-(3′,7′-dimethyloctyloxy)-1,4-phenylenevinylene] (MDMO-PPV) [14] was obtained from Philips Research Eindhoven, the Netherlands. The molecular weight of the MDMO-PPV was 570 kg/mol as determined by GPC using polystyrene standards. Poly(ethylenedioxythiophene)-poly(styrenesulfonate)(PEDOT:PSS) was purchased from Bayer AG, Germany. The energy level diagram for materials used in this work is presented in Fig. 1.

2.2. Specimen preparation

The samples studied consist of a glass substrate with an ITO layer (kindly provided by Philips Research, the Netherlands), a spin-coated PEDOT:PSS layer (Baytron-P, Bayer) and a spin-coated photoactive layer. The latter is based on a 1:4 blend by weight (MDMO-PPV/PCBM) initially dissolved in toluene. The spin coating conditions were optimized such that the thicknesses of the photoactive layers were below 100 nm. These samples represent working photovoltaic devices, except for the missing metal back electrode. All sample preparation steps were performed in a glove box (Unilab, MBRAUN, Germany). We are aware that applying toluene as solvent forces large scale phase separation between MDMO-PPV and PCBM, which provides photoactive samples better suited for C-AFM investigations but not for optimum performance in PSCs.

2.3. Characterization

For AFM measurements Solver P47H and NTegra-Aura were used (both NT-MDT, Russia). The cantilevers used were CSC12 (Micromash, Estonia) coated with an additional Au-layer for conductivity measurements. A typical force constant of the cantilevers was about 0.65 N/m, and the radius was below 50 nm. C-AFM experiments were performed with AFM installed in a glove box, which had a

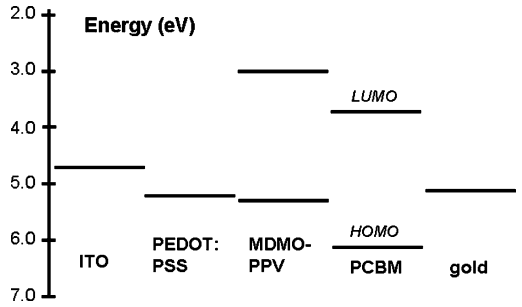

Fig. 1. Energy level diagram for the materials used in present work (energy levels according to Ref. [15]).

nitrogen atmosphere with oxygen and water levels below 1 ppm; only few experiments were carried out at ambient conditions. The ITO layer was grounded during all C-AFM measurements performed in the glove box. The C-AFM measurements for ambient conditions in air were performed with grounded tip.

3. Results and discussion

MDMO-PPV/PCBM is one of the systems best studied for applications as photoactive layer in high-efficient PSCs; efficiencies of about 2.5% have been reported for optimized preparation conditions [16]. Further, it has been demonstrated that the performance of devices having these compounds as blend in their photoactive layers decreases immediately when exposed to air [17]. For this reason, we have chosen the blend MDMO-PPV/PCBM as a model system for our C-AFM experiments.

Fig. 2 shows a series of C-AFM images obtained at ambient conditions in air of a thin PCBM/MDMO-PPV film spin-coated from toluene solution. For such preparation conditions PCBM and MDMO-PPV phase segregate, and PCBM forms large nanocrystalline domains embedded in the MDMO-PPV matrix [15,18]. All images were acquired with a tip coated with a gold layer. The topography image (Fig. 2a) shows that the PCBM domains (bright areas) have maximum diameters of about 500 nm. Phase segregation is responsible for the high roughness of the film: the PCBM domains stick out of the film plane few tens of nanometres.

Figs. 2b and c represent the current distribution image for bias voltages at the tip of −2.3 V (Fig. 2b) and +10 V (Fig. 2c), respectively, measured at the same sample area as the topography image. For negative bias at the tip good contrast is obtained between the electron donor (p-type

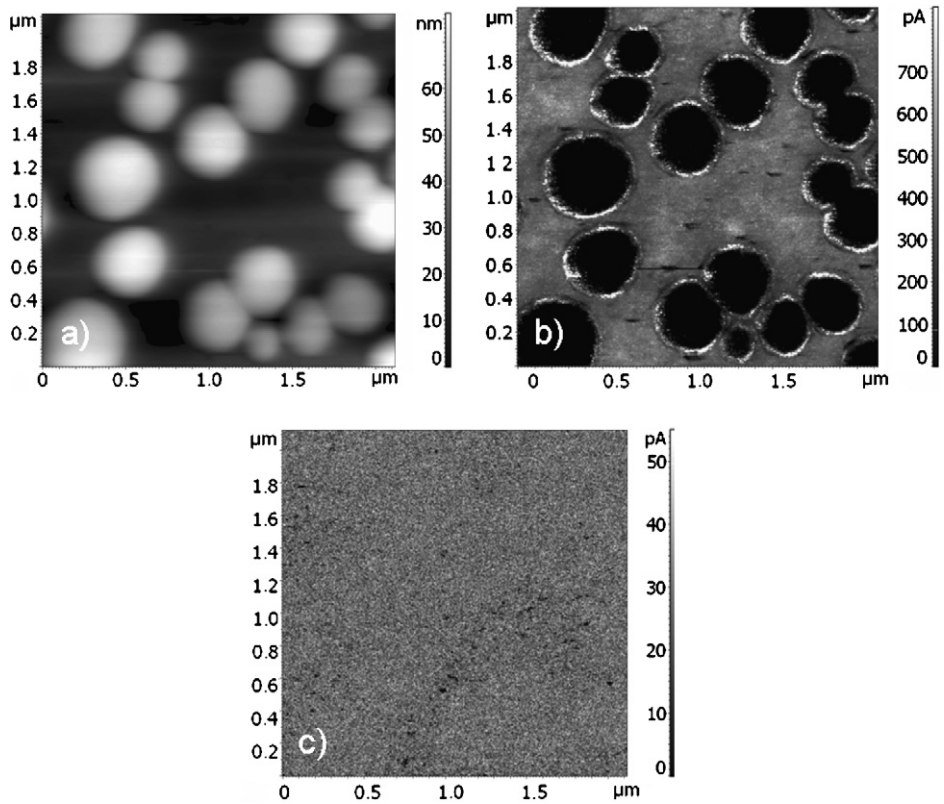

Fig. 2. C-AFM image series acquired at ambient conditions in air of a thin PCBM/MDMO-PPV film spin-coated from toluene solution: (a) topography image, and current distribution images of the same area for (b) a negative bias at the tip of −2.3 V, and (c) for a positive bias at the tip of +10 V. The very slight contrast (c) is caused by some superposition with topography information during the current measurements.

semi-conductor) and the electron acceptor (n-type semi-conductor) materials in the sample. From the corresponding energy level diagram (Fig. 1) it follows that the difference between the HOMO level of MDMO-PPV and the Fermi levels of both electrodes (ITO/PEDOT:PSS and Au-tip) is rather small so that we expect ohmic contacts for hole injection and strong energy barriers for electrons [6,19]. Therefore a hole only current through the MDMO-PPV is expected for both polarities of voltage in a ITO/PEDOT:PSS/MDMO-PPV/Au-tip structure. On the other hand, we can conclude that areas of low current level correspond to the electron acceptor materials, i.e. PCBM (Fig. 2b). This interpretation is in accordance with the above-mentioned topographical observations (Fig. 2a). For positive bias at the tip, however, no differences between the two phases can be obtained, and the measured overall current level is below the noise level of our experimental setup.

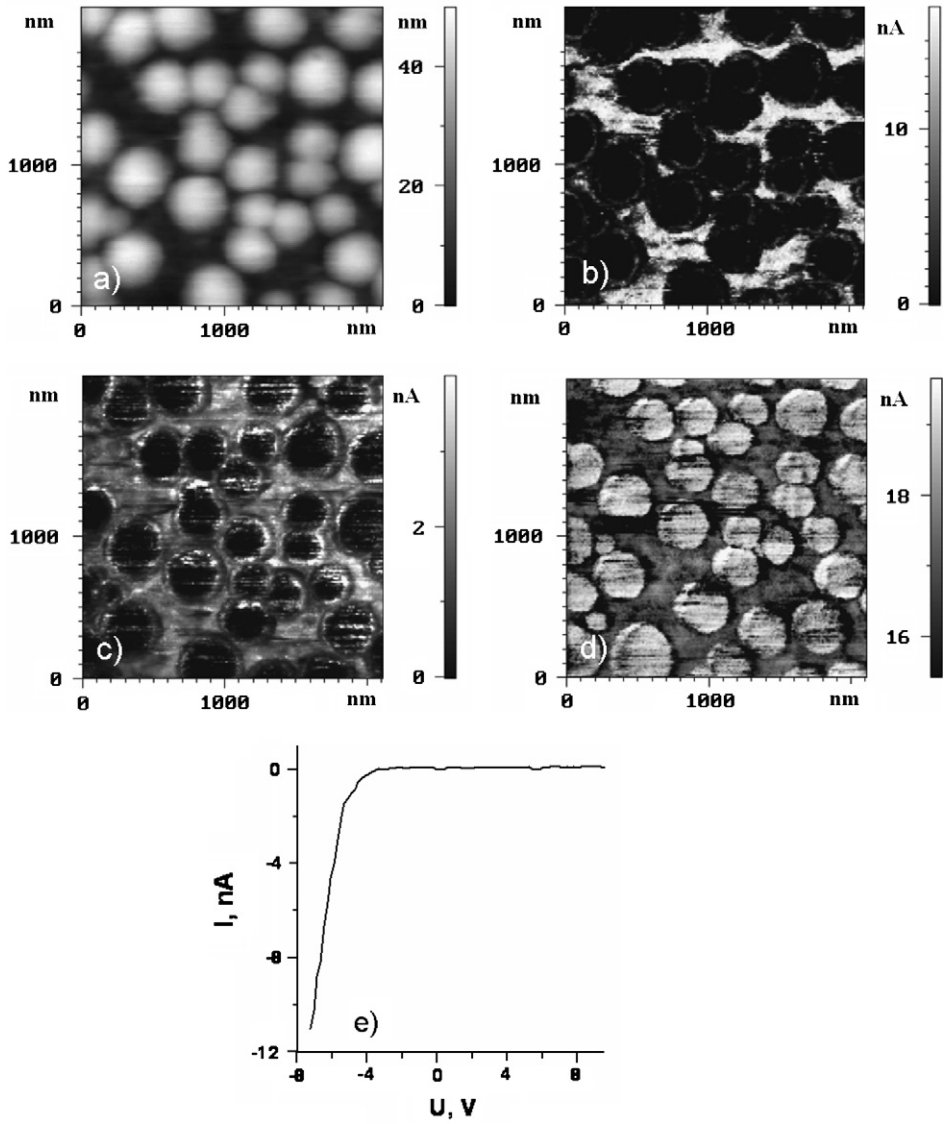

Fig. 3. (a) Topography of a PCBM/MDMO-PPV thin film sample obtained in contact mode; (b)–(d) C-AFM images acquired in the inert and water free atmosphere of a glove box showing the current distribution of the same sample area for (b) a positive bias at the tip of +10.0 V, (c) for a negative bias at the tip of −5 V, and (d) for a negative bias at the tip of −10 V, (e) *I–V* curve obtained on pure PCBM film spin-coated on glass/ITO/PEDOT:PSS.

Since the materials under investigation are sensitive to oxygen and at ambient conditions the always-present water layer on top of the sample surface interferes with nanometre scale electrical measurements, which has been reported recently for the case of surface potential measurements [20], we have performed additional C-AFM experiments on the same MDMO-PPV/PCBM system but in inert atmosphere. For this purpose, we have assembled the C-AFM setup in a glove box filled with nitrogen atmosphere and an oxygen and water level below 1 ppm.

Fig. 3 presents C-AFM measurements of a MDMO-PPV/PCBM sample for such an experimental setup with lateral resolution better than 50 nm. For negative bias at the tip of −5 V similar features are observed as discussed for Fig. 2b (Fig. 3c): the dark areas represent PCBM domains with low current embedded in the MDMO-PPV matrix showing higher current. Contrary to measurements performed in air, also for the positive bias value at the tip of +10 V good contrast between the phases is observed (Fig. 3b). Beside some little drift of the area probed during the two successive C-AFM measurements with positive and negative bias, PCBM domains can be recognised as dark areas embedded in the bright MDMO-PPV matrix in Fig. 3b and c. Around the PCBM domains ring-like structures are seen having higher current (Fig. 3b–d and Fig. 2b), which might be caused by more efficient charge collection at the domain interface [11]. Probably, an existing mixed-phase of PCBM and MDMO-PPV at the interface may enhance charge mobility, as reported for blends of polythiophene with polyethylene or polystyrene [21]. For negative bias at tip of −10 V the contrast of the current image is inversed: the current through the PCBM-rich phase is higher than the current through the matrix (Fig. 3d). Such contrast changes can be explained by analysing corresponding *I–V* measurements performed on a pure PCBM film: current above the noise level is detected only at high negative bias on tip (Fig. 3e).

4. Conclusions

C-AFM is a reliable analysis technique providing local information of electrical properties of functional polymer systems, when applied in inert atmosphere. In air most samples chemically degrade, and the present molecular water layer interferes with adequate measurements. Applying C-AFM on the functional blend MDMO-PPV/PCBM reliable current contrast images of the PCBM domains embedded in the MDMO-PPV matrix are acquired with lateral resolution better than 50 nm. Details of the interface between the two components are visualised and discussed. Currently, investigations of various photoactive layer systems are in progress applying higher lateral resolution in the order of 10–20 nm to identify features having similar length scale as the exciton diffusion length.

Acknowledgements

We would like to thank Svetlana v. Bavel for her support for sample preparation. Part of the work is embedded in the research program of the Dutch Polymer Institute (DPI projects #326 and #524), and additional financial support is appreciated by the Ministry of Economic Affairs of the Netherlands via the Technologische Samenwerkings project QUANAP (SenterNovem TSGE3108).

References

[1] G. Yu, A.J. Heeger, J. Appl. Phys. 78 (1995) 4510.
[2] J.J.M. Halls, C.A. Walsh, N.C. Greenham, E.A. Marseglia, R.H. Friend, S.C. Moratti, A.B. Holmes, Nature 376 (1995) 498.
[3] G. Yu, J. Gao, J.C. Hummelen, F. Wudl, A.J. Heeger, Science 270 (1995) 1789.
[4] C. Shafai, D.J. Thomson, M. Simard-Normandin, G. Mattiussi, P.J. Scanlon, Appl. Phys. Lett. 64 (1994) 342.
[5] P. De Wolf, J. Snauwaert, T. Clarysse, W. Vandervorst, L. Hellemans, Appl. Phys. Lett. 66 (1995) 1530.
[6] T.W. Kelley, C.D. Frisbie, J. Vac. Sci. Technol. B 18 (2000) 632.
[7] H.-N. Lin, H.-L. Lin, S.-S. Wang, L.-S. Yu, G.-Y. Perng, S.-A. Chen, S.-H. Chen, Appl. Phys. Lett. 81 (2002) 2572.
[8] C. Ionescu-Zanetti, A. Mechler, S.A. Carter, R. Lal, Adv. Mater. 16 (2004) 385.
[9] A. Alexeev, J. Loos, M.M. Koetse, Ultramicroscopy 106 (2006) 191.
[10] O. Douheret, L. Lutsen, A. Swinnen, M. Breselge, K. Vandewal, L. Goris, J. Manca, Appl. Phys. Lett. 89 (2006) 032107.
[11] D.C. Coffey, O.G. Reid, D.B. Rodovsky, G.P. Bartholomew, D.S. Ginger, Nano Lett. 7 (2007) 738.
[12] J. Morgado, R.H. Friend, F. Cacialli, Synt. Met. 114 (2000) 189.
[13] J.C. Hummelen, B.W. Knight, F. LePeq, F. Wudl, J. Yao, C.L. Wilkins, J. Org. Chem. 60 (1995) 532.
[14] H. Becker, H. Spreitzer, W. Kreuder, E. Kluge, H. Schenk, I. Parker, Y. Cao, Adv. Mater. 12 (2000) 42.
[15] H. Hoppe, N.S. Sariciftci, J. Mat. Chem. 16 (2006) 45.
[16] C.J. Brabec, N.S. Sariciftci, J.C. Hummelen, Adv. Funct. Mater. 11 (2001) 15.
[17] F. Padinger, T. Fromherz, P. Denk, C. Brabec, J. Zettner, T. Hierl, N. Sariciftci, Synth. Met. 121 (2001) 1605.
[18] X. Yang, J.K.J. van Duren, R.A.J. Janssen, M.A.J. Michels, J. Loos, Macromolecules 37 (2004) 2151.

[19] N. Koch, A. Elschner, J. Schwartz, A. Kahn, Appl. Phys. Lett. 82 (2003) 2281.
[20] H. Sugimura, Y. Ishida, K. Hayashi, O. Takai, N. Nakagiri, Appl. Phys. Lett. 80 (2002) 1459.
[21] S. Goffri, C. Müller, N. Stingelin-Stutzmann, D.W. Breiby, C.P. Radano, J.W. Andreasen, R. Thompson, R.A.J. Janssen, M.M. Nielsen, P. Smith, H. Sirringhaus, Nat. Mater. 5 (2006) 950.

Available online at www.sciencedirect.com
ScienceDirect
Organic Electronics 9 (2008) 155–163
Organic Electronics
www.elsevier.com/locate/orgel

Efficient blue emitting organic light emitting diodes based on fluorescent solution processable cyclic phosphazenes

Henk J. Bolink [a,*], Eva Barea [b], Rubén D. Costa [a], Eugenio Coronado [a], Sundarraj Sudhakar [c,d], Changgua Zhen [c], Alan Sellinger [c,1]

[a] *Instituto de Ciencia Molecular (ICMol), Universidad de Valencia, P. O. Box 22085, 46071 Valencia, Spain*
[b] *Departament de Física, Universitat Jaume I, E-12071, Castelló, Spain*
[c] *Institute of Materials Research and Engineering (IMRE), 3 Research Link, Singapore 117602, Republic of Singapore*
[d] *Global Research Center, Singapore – Laboratory for Nanostructured Surfaces, BASF South East Asia Pte Ltd., 61 Science Park Road, # 03-01 The Galen, Science Park III, Singapore 117525, Republic of Singapore*

Received 14 September 2007; received in revised form 16 October 2007; accepted 17 October 2007
Available online 25 October 2007

Abstract

Solution processable blue fluorescent dendrimers based on cyclic phosphazene (CP) cores incorporating amino-pyrene moieties have been prepared and used as emissive layers in organic light emitting diodes (OLEDs). These dendrimers have high glass transition temperatures, are monodisperse, have high purity via common chromatographic techniques, and form defect-free amorphous films via spin/dip coating. The solution processable blue light emitting OLEDs reach current efficiencies of 3.9 cd/A at brightness levels near 1000 cd/m^2. Depending on the molecular bridge used to attach the fluorescent dendron to the inorganic core, the emission wavelength changes from 470 to 545 nm, corresponding to blue and green light respectively. Via dilution experiments we show that this shift in emission wavelength is likely associated with molecular stacking of the amino-pyrene units.

PACS: 85.60.Jb

Keywords: Dendrimer; OLED; Blue fluorescence

1. Introduction

The field of organic and polymeric light emitting diodes (OLEDs) has progressed quickly since the initial reports by Tang and VanSlyke [1] and Friend and coworkers [2] in 1987 and 1990, respectively [3]. Despite OLED displays having reached the commercialization level, there is still a need for materials development with regard to efficiency, colour purity and stability. This is true for multi-layered OLED's prepared via vacuum evaporation and even more so for architectures prepared using solution processing. The latter technique offers a more economically viable production route, thus it is of great interest for the more widespread application of OLED

* Corresponding author. Fax: +34 9 6354 4859.
E-mail addresses: henk.bolink@uv.es (H.J. Bolink), alan-sellinger@imre.a-star.edu.sg (A. Sellinger).
[1] Fax: +65 6872 0785.

1566-1199/$ - see front matter © 2007 Elsevier B.V. All rights reserved.
doi:10.1016/j.orgel.2007.10.005

technology. One of these opportunities is in the area of active OLED materials related to charge transport and emission. For these active materials, both small molecules and polymers are currently the preferred candidates. Small molecules are advantageous as they can be highly purified and vacuum deposited in multi-layer stacks, both important for device lifetime and efficiency. However, vacuum deposition techniques generally require expensive equipment, imposes a limitation to achievable display size, and complicates the production of full colour displays at high volume using traditional masking technologies. Polymers are generally of lower purity than small molecules but can access full colour and larger display sizes at much lower costs using solution-based deposition techniques such as spray coating, ink jet and screen printing [4,5].

On the other hand dendrimers and oligomers, lying in the molecular weight range between 1000–10,000 g/mol, combine the properties of both small molecules and polymers for application in OLEDs. For example, dendrimers can be purified to a high degree using chromatographic techniques, are soluble in common solvents, and allow synthetic versatility for tuning charge transport [6–15] and emissive [16–23] properties. The attachment of conjugated, charge transporting or light emitting moieties to dendritic structures decreases the possibility of aggregate and/or eximer formation that can reduce device efficiency [24]. Finally dendrimers of different emission colours can be physically blended with one another without phase separation for possible application in white lighting.

Cyclic phosphazenes (CP) are an interesting class of materials with a planar non-delocalized cyclic ring consisting of alternating N and P atoms. The inorganic phosphazenes have been well studied in both the cyclic and linear forms by several groups due to their diverse properties including excellent hydrolytic stability, thermal stability, flame retardant properties, and liquid crystalline behaviour to name a few [25–30]. The CP core serves many advantageous purposes towards useful materials for solution processable OLED materials. First, the chemistry to prepare functionalized CP cores is very straightforward. Second, the functionalized CP cores are very stable and do not breakdown even under very aggressive chemical conditions. Third, the functional groups are projecting in 3 dimensions thus producing a rigid spherical core from which to attach the dendrons of interest. These rigid spheres have been shown to promote amorphous properties that are known to be important for OLED devices [31].

In extension of our previous work, we report here four types of amino-pyrene containing CP dendrimers and their use as the light emitting layer in simple solution processable OLEDs. We show that depending on the dendritic molecular architecture it is possible to prevent aggregation of the fluorescent amino-pyrene groups in the solid film and optimize blue electroluminescence.

2. Results and discussion

The synthetic scheme used for the preparation of a series of dendrimers is shown in Fig. 1.

2.1. Synthesis and characterisation

As outlined in Fig. 1, the synthesis of the CP dendrimers begins from the commercially available hexachlorocyclic triphosphazene (**1**) [31]. In the first step (**1**) was reacted with 4-bromophenol or 4-bromo-4′-hydroxy biphenyl to obtain the corresponding hexasubstitued 4-bromophenoxy CP (**2**) or 4-bromo-biphenyloxy CP (**3**) in good yields (>90%) as reported in our earlier work. Compounds (**2**) and (**3**) were then reacted under Buchwald–Hartwig amination conditions with the selected secondary arylamines in the presence of Pd[P(tBu)$_3$] and NaOtBu to yield the desired CP dendrimers (**4a**–**b**) and (**5a**–**b**) in good yields (>80%). The corresponding *N*-aryl-*N*-pyrene-amines were prepared from the reaction of aniline or *p*-tolylamine with 1-bromopyrene also using the Buchwald–Hartwig amination procedure. Formation of the desired CP dendrimers was determined by NMR (^{1}H, ^{13}C, ^{31}P), GPC and MALDI-TOF mass spectroscopy (see supporting information). All the dendrimers synthesized in this study were soluble in common organic solvents facilitating their characterization and solution processability for subsequent device fabrication.

The photophysical properties of the dendrimers were characterized using UV/vis and fluorescence spectroscopy and the results are presented in Table 1.

In general, the photoluminescence spectra obtained from thin films are slightly red shifted with respect to the spectra obtained in solution. This is most likely due to a change in the dielectric constant of the medium going from a solution to a solid thin film. In the case of a pure film of **5a**, however, the shift is more pronounced indicating

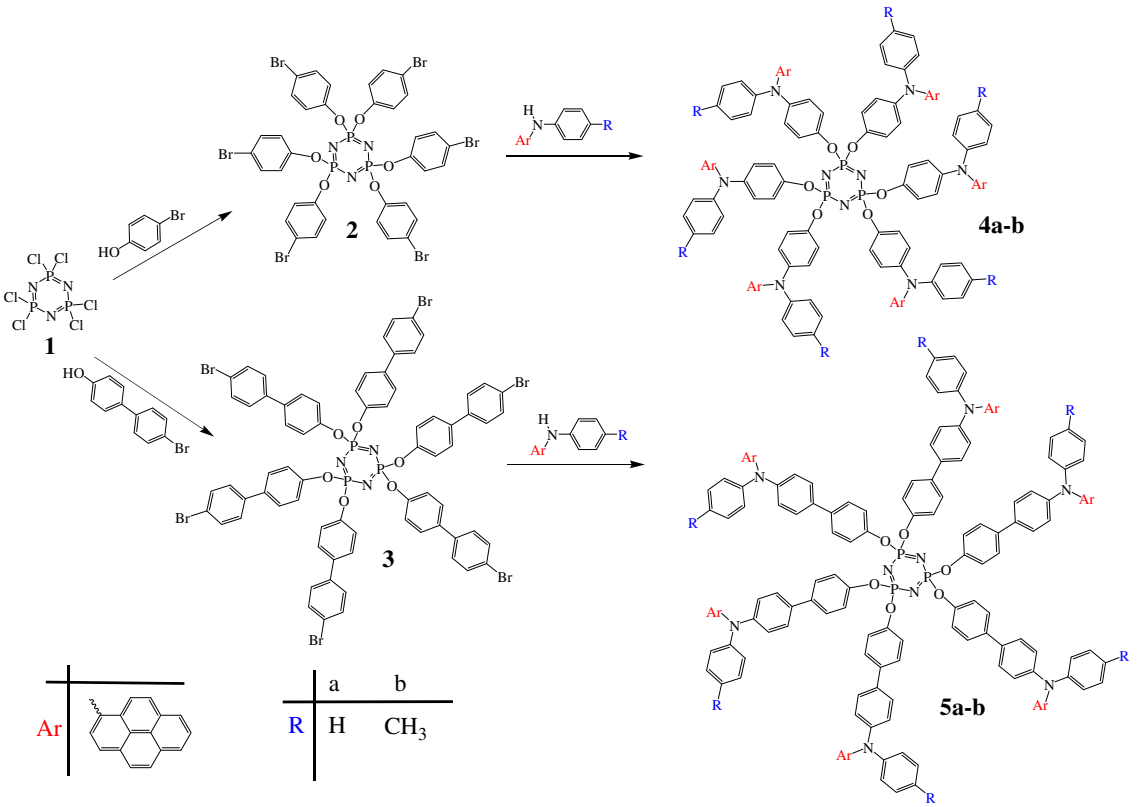

Scheme 1.

Table 1
Photophysical and thermal properties of CP dendrimers

	Molecular weight	λ_{em} (nm)[a]	$\lambda_{em,film}$ (nm)	PLQE[b]	T_g[c] (°C)	T_d[d] (°C)
4a	2441.6	470	481[e]	0.80	173	436
5a	2898.2	476	484[e], 519[f]	0.67	191	459
4b	2525.8	479	484[e]	0.83	168	490
5b	2982.4	484	489[e]	0.68	183	483

[a] Measured in CH_2Cl_2.
[b] Photoluminescent quantum efficiency, measured in CH_2Cl_2 using quinine sulfate as standard.
[c] T_g and T_m were obtained from DSC measurements.
[d] T_d was obtained from TGA and reported as temperature at 5% weight loss using 10 °C/min ramp cycle.
[e] 5% in polystyrene.
[f] Pure film.

the occurrence of an additional effect. Such a large shift is indicative of the formation of aggregates, which should diminish at decreasing concentration. Indeed the spectra of thin polystyrene films doped with 1, 5 and 20 wt.% of **5a** shows the peak of the emission spectrum at 478, 489 and 505 nm, respectively. The PL spectrum of a pure film of dendrimer **5a** has a maximum at 519 nm. This clearly shows that with increasing concentration the formation of aggregates increases which results in a red shift of the emission spectrum (see Fig. SI-2). The same concentration dependent photoluminescence experiments were performed for dendrimers **4a** and **4b**, where only a very slight (<10 nm) red shift was observed going from 1% to 20% (Figs. SI-1 and SI-3). This shows that a slight modification of the dendritic architecture can prevent the formation of aggregates and hence assures that the emission is originating from isolated aminopyrene dendrons.

The thermal properties of the CP dendrimers were evaluated using TGA and DSC. The thermal properties of the compounds depended strongly on the pendent group although all decomposition temperatures in nitrogen were in excess of 425 °C. Interestingly all the dendrimers in the present study showed only T_g's with no observable T_m's, which confirms the amorphous nature of these materials. The biphenyl series (**5**) have slightly higher T_g's than the phenyl series (**4**), which is due to the presence of the rigid biphenyl ring that links the CP core to the amine.

Cyclic voltammetric studies were carried out to understand the electro-chemical properties of the synthesized compounds. A reversible oxidation of the triarylamine was shown in cyclic voltammetry for all compounds. As was shown previously, the electro-chemical properties are very similar to their small molecule analogues demonstrating that the CP core does not influence this property [31]. The electro-chemical data together with the UV band edge were used to obtain the highest occupied molecular orbital (HOMO) and lowest unoccupied molecular orbital (LUMO) energy levels respectively (Table 2).

2.2. OLED device characterization

Simple OLEDs were fabricated utilizing the dendrimers as light emitting layers (50 nm) by spin-coating a toluene solution containing the dendrimer on an indium tin oxide (ITO) coated patterned substrate. Previously, a 100 nm thick PEDOT:PSS (obtained from HC-Starck) was deposited to enhance the hole injection and the device stability [32]. The organic layers were covered by a thin (5 nm) layer of barium protected by a 80 nm layer of silver that serves as the cathode and were deposited via thermal vacuum deposition. These simple bi-layer devices did not result in efficient electroluminescence. This is indicative of a hole dominated device in which the recombination occurs in close vicinity of the cathode, resulting in a large quenching of the excitons and hence a poor light emission. Such a hole dominated device is expected as the barrier for hole injection is negligible (difference between the HOMO of the dendrimers to the work function of the PEDOT is less than 0.1 eV) and due to the high concentration of arylamine groups in the dendrimer structures. The latter groups are well known hole transporting molecules and hence it is expected that the hole mobility is dominant in these dendrimer systems [33]. To verify this, the hole mobility was estimated from the current density versus voltage curves using the space-charge limited transport model on hole-only devices, in which gold was used as the cathode [34,35]. For the dendrimer **4** series, mobilities ranging from 0.2 to 6×10^{-5} $cm^2/V\,s$ were found which is not especially high, however, larger than the normally observed electron mobilities. In comparison, the mobility of dendrimer **5a** was significantly lower, in the range of 1×10^{-8} $cm^2/V\,s$. The observed decrease in mobility for dendrimer **5a** is indicative of the occurrence of charge trapping in these films possibly originating from aggregate formation of the amino-pyrene units. These observations explain therefore the low efficiencies observed for the simple OLED devices structure. Hence, to separate the recombination zone from the cathode and to prevent the loss of holes by recombination at the cathode a 20 nm layer of 1,3,5-tris(2-*N*-phenylbenzimidazolyl) benzene (TPBI) electron transport layer was thermally evaporated [36].

The three layer OLED devices based on the dendrimers, **4a**, **4b** and **5b** all show similar performances. The turn-on voltages for light emission is around 2.5 V which is low considering the built-in potential for these devices of approximately 2.4 eV. This low turn-on voltage confirms the earlier

Table 2
Electro-chemical properties of the CP dendrimers

Compound	UV/vis absorption band edge (nm)	$E_{oxonset}$ [V][a]	HOMO [eV][b]	LUMO [eV][c]	HOMO-LUMO Gap [eV][d]
4a	438	0.84	−5.24	−2.41	2.83
5a	444	0.83	−5.23	−2.44	2.79
4b	449	0.79	−5.19	−2.43	2.76
5b	459	0.78	−5.18	−2.48	2.70

[a] Measured in CH_2Cl_2.
[b] Calculated from CV data.
[c] Calculated from CV data and UV/vis absorption spectra band edge.
[d] Calculated from UV/vis absorption spectra band edge.

Table 3
Performance of ITO/PEDOT:PSS/emitting layer/TPBI/Ba/Ag OLED devices at a driving voltage of 8 V

Emitting layer	Current density (A/m^2)	Luminance (cd/m^2)	External quantum efficiency (%)	Current efficiency (cd/A)	Power efficiency (lm/W)	λ_{max}(nm)	Colour coordinate (x, y)
4a	1910	3615	0.72	1.89	0.74	485	0.207, 0.324
4a[a]	*245*	*954*	*1.40*	*3.90*	*1.50*	*486*	*0.207, 0.324*
5a	17.7	12.9	0.23	0.72	0.28	548	0.349, 0.557
4b	358	728	0.69	2.00	0.79	493	0.246, 0.500
5b	5390	1107	0.09	0.21	0.08	570	0.407, 0.478

[a] OLED with an emitting layer thickness of 80 nm.

assumption that the barrier for hole injection is low. Additionally, as light emission can only occur when both holes and electrons have been injected it implies that the injection of electrons is also almost barrier free. The maximum light emission is achieved for dendrimer **4a**, in which luminance levels of 3600 (8 V) and 11,000 cd/m^2 (12 V) are reached. The efficiency associated with this high brightness device is 1.89 cd/A. In a device using a slightly thicker dendrimer layer (80 versus 50 nm) the total brightness is less, however in this device the current efficiency reaches 3.9 cd/A, which is high for a singlet emitting blue emitter [37]. Furthermore, the device exhibits only a small decline over a quite large voltage range, indicating that the hole and electron recombination remains efficient even at higher voltages. This data shows that these dendrimers hold promise as efficient emitters for solution processable OLEDs Table 3.

The OLED device using dendrimer **5a**, however, shows a strikingly different behaviour, the turn-on voltage is higher by almost one volt and the current density and luminance values are orders of magnitude lower than for the devices using the other dendrimers. The lower current density is indicative of a significant level of traps and the lower light output can be a direct result from this low current density. However, to be able to discuss this unusual result it is necessary to analyse the electroluminescent spectra of the four devices.

The light emission of the **4a** and **4b** dendrimer containing OLEDs is blue whereas the emission colour of the OLED based on the **5a** and **5b** dendrimers is green. The emission maximum of the dendrimer **5a** containing OLED lies at 545 nm, which is substantially red shifted with respect to the emission spectra of the dendrimer obtained in solution (427 nm), but rather close to the emission observed after photoexcitation of a pure film of **5a** (520 nm). This corroborates the assumption made earlier that the emission originates from aggregates and not from isolated amino-pyrene dendrons. Such aggregates generally show red shifted emission due to the stabilization of the HOMO and LUMO levels. The change in emission can be due to the formation of dimers and/or excited state dimers (excimers). In view of the large change in current density for dendrimer **5a** based OLEDs, it seems likely that the dimer is formed in the ground state and acts as a hole trapping site. This is in agreement with the low hole mobility observed from the hole-only devices. The formation of aggregates is strongly dependent on the exact molecular architecture and on the average distance between the groups responsible for the aggregation in the thin film. Therefore to verify if blue emission can be obtained from dendrimers **5a** and **5b,** we prepared OLEDs using the large bandgap polymer poly(*N*-vinylcarbazole) (PVK) [38] in combination with 2-(4-biphenyl)-5-(4-*tert*-butylphenyl)-1,3,4-oxadiazole (PBD) (to improve the electron transporting properties) to which small amounts (5% and 25% by weight) of the selected dendrimer were added as the emitting species. As a comparative experiment the dendrimers **4a** and **4b** were also used in the PVK:PBD host based OLEDs Fig. 1.

The emission spectra obtained from the different OLED architectures is depicted in Fig. 2. The emission of the PVK:PBD OLED device containing 5 wt.% of dendrimer **5a** has an emission maximum at 471 nm, blue shifted with as much as 77 nm compared with the emission obtained from the OLED employing dendrimer **5a** as the single component emitting layer. Additionally, this coincides with the emission spectrum obtained after photoexcitation of a polystyrene film containing 5 wt.% of the dendrimer **5a**. The CIE colour coordinates for this emission spectrum are: $x = 0.157$, $y = 0.209$ which corresponds to a deep blue colour. Upon increasing the percentage of dendrimer **5a** in the PVK:PBD blend the emission maximum shifts towards the red and coincides with that obtained for the OLED

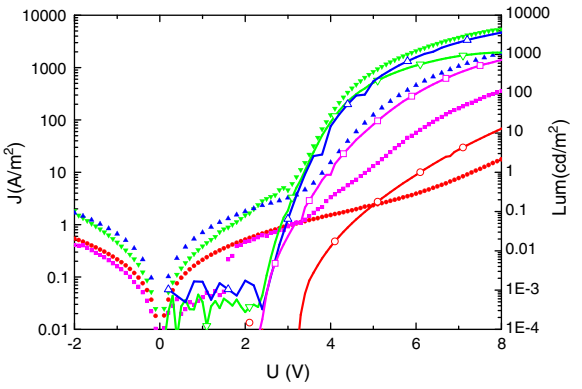

Fig. 1. Current density (symbols) and luminance (lines) for ITO/PEDOT:PSS/dendrimer/TPBI/Ba/Ag OLED devices containing the dendrimers; **4a** (blue, up triangles), **5a** (red, circles), **4b** (magenta, squares) and **5b** (green, down triangles). (For interpretation of the references in colour in Figs. 1 and 2 legends, the reader is referred to the web version of this article.)

with a 100% dendrimer emitting layer. These results show that upon decreasing the dendrimer concentration, the interaction of the amino-pyrene emitting units is reduced and hence the emission is originating from the amino-pyrene dendron. However, upon increasing the concentration aggregates seem to be forming that cause a red shift in the emission spectrum and act as trapping sites, reducing the current density of the device. The device efficiency when using PVK:PBD as hosts were lower than for the devices based on the pure dendrimer emitting layers. Proper selection of the host matrix would likely increase the efficiencies to much higher levels.

The emission spectrum of the OLED using a 100% dendrimer **4a** as the emitting layer is rather broad due to a contribution of a lower energy emission band around 534 nm. This lower energy emission contribution seems not associated with the generation of aggregates as the same emission spectrum is observed for a device in which the **4a** dendrimer is dispersed in a PVK:PBD matrix. The resulting CIE colour coordinates are: $x = 0.229$, $y = 0.392$ which is a greenish-blue colour. This puts the observed higher device efficacies in perspective as the emission is not completely in the blue but has a considerable component in the green part of the visible spectrum where the sensitivity of the human eye is higher, thus resulting in a higher candela value. To have a colour independent value of the device efficiency, the external quantum efficiency was determined as 1.4 photons/electrons. Although this value is somewhat lower than the best singlet emitting systems, we are confident higher efficiencies can be obtained after further optimization of the hybrid dendrimers and devices architectures. A comment is in order concerning the anomalous performance of dendrimer **5b**, which has a very broad electroluminescent spectrum, however a comparable current density and luminance versus the voltage curve. The broad emission spectrum is like in the **5a** case probably due to the formation of aggregates, which disappear when the dendrimer is diluted in a PVK:PBD matrix. Nevertheless, the aggregates apparently are not operating as trapping sites as the current density is rather high. At this time, the difference from the very small structural modifications on the dendrimer structure have on the device

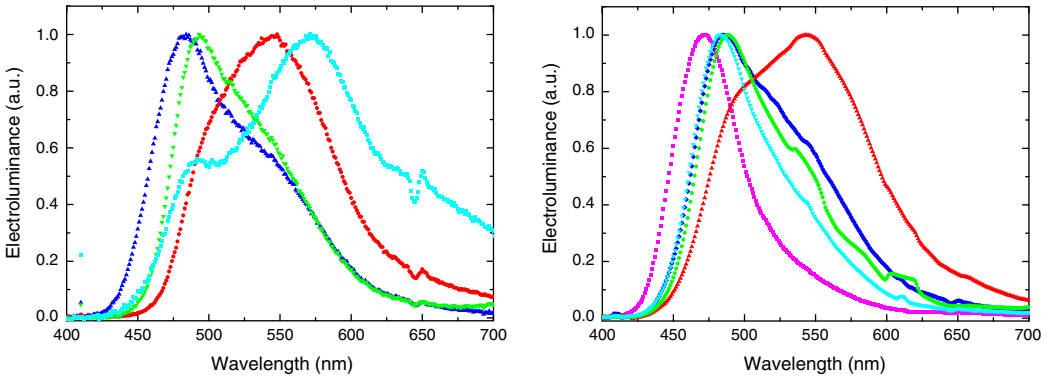

Fig. 2. Electro-luminance spectra obtained from two types of OLEDs, one using the dendrimer alone as the emitting layer (left), **4a** (blue up triangles), **5a** (red, circles), **4b** (green, down triangles), **5b** (cyan, squares), and one using a blend of PVK:PBD:dendrimer as the emitting layer (right), **4a** −5 wt.% blue diamonds, **5a** −5 wt.% magenta squares, **5a** −25 wt.% red up triangles, **4b** −5 wt.% green circles and **5b** −5 wt.% cyan down triangles. The device architecture is: ITO/PEDOT:PSS/emitting layer/TPBI/Ba/Ag.

performance is not fully understood and is the topic of further analysis. It has recently been found that local nano-phase crystallization can occur in solid films of small (in general) amorphous molecules, which can also in our case be the origin of such drastic differences in device performances [39,40].

3. Experimental

3.1. Materials and methods

All materials used for the synthesis of the CP dendrimers were commercial products (Aldrich, Fluka, TCI, Strem, Acros, Avocado) and were used as received. Dry toluene (Aldrich) was used for all the amination reactions. All the reactions were carried out using Schlenk techniques in an argon atmosphere.

3.2. Instruments

^{1}H and ^{13}C NMR data were recorded on a Bruker DPX 400 MHz spectrometer with chemical shifts referenced to $CDCl_3$. MALDI-TOF was performed on a Bruker Autoflex MALDI Tandem TOF/TOF mass spectrometer. Dithranol or *trans*-2-[3-(4-*tert*-butylphenyl)-2-methyl-2-propenylidene] malononitrile (DCTB) were used as the matrix and silver trifluoromethanesulfonate (AgTFA) as the ion source when necessary. Differential scanning calorimetry (DSC) was carried out under nitrogen on a Thermal Analysis DSC 2920 module (scanning rate of 10 °C min^{-1}. Thermal gravimetric analysis (TGA) was carried out using a Thermal Analysis TGA 2050 module (heating rate of 10 °C min^{-1}). All GPC analyses were performed on a Waters Alliance 2690 system equipped with photodiode array (Waters 996) and evaporative light scattering detectors (Waters 2420) and THF as solvent. The system was calibrated using polystyrene standards. Cyclic voltammetry experiments were performed using an Autolab potentiostat (model PGSTAT30) by Echochimie. All CV measurements were recorded in dicholoromethane with 0.1 M tetrabutylammonium hexafluorophosphate as supporting electrolyte (scan rate of 50 mV/s). The experiments were carried at room temperature with a conventional three electrode configuration consisting of a platinum wire working electrode, a gold counter electrode and a Ag/AgCl in 3 M KCl reference electrode. The measured potentials were converted to versus SCE (saturated calomel electrode) and the corresponding ionization (IP) and electron affinity (EA) values were derived from the onset redox potentials, based on −4.4 eV as the SCE energy level relative to vacuum ($EA = E_{redonset} + 4.4$ eV, $IP = E_{oxonset} + 4.4$ eV). UV–vis spectra were recorded on a Shimadzu model 2501-PC UV–VIS spectrometer and photoluminescence (PL) spectra were measured on a Perkin-Elmer spetrofluorometer. The solution spectra were measured from dichloromethane solutions and the thin film spectra were recorded from thin film obtained by spin-coating dichloromethane solutions on quartz glass plates.

3.3. Device preparation

PEDOT:PSS was purchased from HC-Starck, TPBI was obtained from Sensient GmbH, poly(N-vinylcarbazole) (PVK), 2-(-4-biphenyl)-5-(4-*tert*-butylphenyl)-1,3,4-oxadiazole (PBD) and solvents used were obtained from Aldrich. The pre-patterned ITO glass plates were extensively cleaned, using chemical and UV–Ozone methods, just before the deposition of the organic layers. The thickness of the films was determined using an Ambios XP1 profilometer, resulting in a 100 nm and an 70 nm thick PEDOT:PSS and PVK:PBD:dendrimer film, respectively. TPBI was thermally evaporated to a layer thickness of 20 nm using temperature controlled sources and an evacuation chamber integrated in an inert atmosphere glovebox (<0.1 ppm O_2 and H_2O). In a separate evaporation chamber integrated in the same inert atmosphere glovebox the barium and silver metals were evaporated. The base pressure for both evaporators is $<1 \times 10^{-6}$ mbar. Current density and luminance versus voltage were measured using a Keithley 2400 source meter and a photodiode coupled to a Keithley 6485 pico-ampmeter using a Minolta LS100 to calibrate the photocurrent. External quantum efficiencies (EQE) were determined using an integrated sphere coupled to an UDT instruments S370 Optometer. An Avantes luminance spectrometer was used to measure the EL spectrum. Devices were characterized in inert atmosphere.

4. Conclusion

In conclusion, efficient fluorescent temperature stable hybrid dendrimers were developed and used to prepare solution processable OLEDs. Depending on the exact nature of the dendrimer used, the device emitted blue or green light. The emission of

green light was associated with the formation of ground state aggregates, as the green emitting OLED showed orders of magnitude lower current densities. When the dendrimer was dispersed in small concentrations into a hole and electron transporting matrix, deep blue emission was observed. Maximum device efficiencies of 1.4% and 3.9 cd/A were obtained for greenish-blue light emitting OLEDs. These results show the potential of this new type of dendritic emitting structures for solution processed and hybrid (solution and thermally evaporated) OLED devices.

Acknowledgements

We thank the Institute of Materials Research and Engineering (IMRE), the Agency for Science, Technology and Research (A*STAR), the Spanish Ministry of Education and Science (MEC) (MAT2007-61584 and CSD2007-00010), and the Generalitat Valenciana. A.S. thanks Mr. Teck Lip Tam, Dr. Mui Siang Soh and Ms. Soon Yee Chang for characterization support. H.J.B. acknowledges the support of the Program "Ramon y Cajal" of the MEC. R.D.C. thanks the MEC for a FPU grant.

Appendix A. Supplementary data

Supplementary data associated with this article can be found, in the online version, at doi:10.1016/j.orgel.2007.10.005.

References

[1] C.W. Tang, S.A. VanSlyke, Appl. Phys. Lett. 51 (1987) 913.
[2] J.H. Burroughes, D.D.C. Bradley, A.R. Brown, R.N. Marks, K. Mackay, R.H. Friend, P.L. Burn, A.B. Holmes, Nature 347 (1990) 539.
[3] Frost and Sullivan. Strategic Assesment of World Organic LED Markets. 1–30, 2007.
[4] D.A. Pardo, G.E. Jabbour, N. Peyghambarian, Adv. Mater. 12 (2000) 1249.
[5] B. de Gans, P.C. Duineveld, U.S. Schubert. Adv. Mater. 16 (2004) 203.
[6] M. Thelakkat, Macromol. Mater. Eng. 287 (2002) 442.
[7] J. Louie, J.F. Hartwig, J. Am. Chem. Soc. 119 (1997) 11695.
[8] J.S. Cho, A. Kimoto, M. Higuchi, K. Yamamoto, Macromol. Rapid. Commun. 26 (2005) 597.
[9] J.S. Cho, A. Kimoto, M. Higuchi, K. Yamamoto, Macromol. Chem. Phys. 206 (2005) 635.
[10] J.S. Cho, K. Takanashi, M. Higuchi, K. Yamamoto, Syn. Metals 150 (2005) 79.
[11] K. Katsuma, Y. Shirota, Adv. Mater. 10 (1998) 223.
[12] Y. Shirota, J. Mater. Chem. 10 (2000) 1.
[13] T.W. Kwon, M.M. Alan, S.A. Jenekhe, Chem. Mater. 16 (2004) 4556.
[14] N. Satoh, J.S. Cho, M. Higuchi, K. Yamamoto, J. Am. Chem. Soc. 125 (2003) 8104.
[15] J. Pei, J.L. Wang, X.Y. Cao, X.H. Zhou, W.B. Zhang, J. Am. Chem. Soc. 125 (2005) 9944.
[16] P.W. Wang, Y.J. Lui, C. Devadoss, P. Bharathi, J.S. Moore, Adv. Mater. 8 (1996) 237.
[17] A.W. Freeman, S.C. Koene, P.R.L. Malenfant, M.E. Thompson, J.M.J. Frechet, J. Am. Chem. Soc. 122 (2000) 12385.
[18] J.A. Barron, S. Bernard, P.L. Houston, H.D. Abruna, J.L. Ruglovsky, G.G. Malliars, J. Phys. Chem. A. 107 (2003) 8130.
[19] M. Halim, J.N.G. Pillow, I.D.W. Samuel, P.L. Burn, Adv. Mater. 11 (1999) 371.
[20] S.C. Lo, N.A.H. Male, J.P.J. Markham, S.W. Magennis, P.L. Burn, O.V. Salata, I.D.W. Samuel, Adv. Mater. 14 (2002) 975.
[21] T.D. Anthopoulos, J.P.J. Markham, E.B. Namdas, I.D.W. Samuel, S.-C. Lo, P.L. Burn, Appl. Phys. Lett. 82 (2003) 4824.
[22] G.J. Richards, J.P.J. Markham, S.-C. Lo, E.B. Namdas, S. Sharma, P.L. Burn, I.D.W. Samuel, Adv. Funct. Mater. 15 (2005) 1.
[23] T. Tsuzuki, N. Shirasawa, T. Suzuki, S. Tokito. Highly efficient multifunctional phosphorescent dendrimers consisting of an iridium-complex core and charge-transporting dendrons for organic light emitting devices, in: A.C. Arias, N.B.L. Tessler, J.A. Emerson, (Eds.), 871E (Organic Thin-Film Electronics), Materials Research Society Symposium Proceedings, 2005, pp. I2.8.1–I2.8.6.
[24] D. Marsitzky, J.C. Scott, J.P. Chen, V.Y. Lee, R.D. Miller, S. Setayesh, K. Mullen, Adv. Mater. 13 (2001) 1096.
[25] H.R. Allcock, Phosphorus Nitrogen Compounds. Cyclic, Linear and High Polymeric Systems, Academic Press, 1972.
[26] H.R. Allcock, Chemistry and Applications of Polyphosphazenes, John Wiley & Sons, 2003.
[27] M. Gleria, R. De Jaeger, Top. Curr. Chem. 250 (2005) 165.
[28] G.A. Carriedo, F.J.G. Alonso, P.G. Elipe, E. Brillas, A. Labarta, L.J. Julia, Org. Chem. 69 (2004) 99.
[29] J. Barbera, M. Bardaji, J. Jimenez, A. Laguna, M.P. Martinez, L. Oriol, J.L. Serrano, I. Zaragozana, J. Am. Chem. Soc. 127 (2005) 8994.
[30] G.A. Carriedo, F.J. Garcia Alonso, P.A. Gonzales, P. Gomez-Elipe, Polyhedron 18 (1999) 2853.
[31] S. Sundarraj, A. Sellinger, Macromol. Rapid Comm. 27 (2006) 247.
[32] R.E. Gill, P. van de Weijer, C.T.H. Liedenbaum, H.F.M. Schoo, A. Berntsen, J.J.M. Vleggaar, R.J. Visser, Opt. Mater. 12 (1999) 183.
[33] P.M. Borsenberger, D.S. Weis, Organic Photoreceptors for Xerography, Marcel Dekker, New York, 1998.
[34] J. Bisquert, G. Garcia-Belmonte, E. Barea, H.J. Bolink, Phys. Stat. Sol. (2006) 1.
[35] W.F. Pasveer, J. Cottar, C. Tanase, R. Coehoorn, P.A. Bobbert, P.W.M. Blom, D.M. de Leeuw, C.J. Michels, Phys. Rev. Lett. 94 (2005) 206601.
[36] E.A. Plummer, A. van Dijken, J.W. Hofstraat, L. De Cola, K. Brunner, Adv. Funct. Mater. 15 (2005) 281.
[37] R.J. Tseng, R.C. Chiechi, F. Wudl, Y. Yang, Appl. Phys. Lett. 88 (2006) 093512.

[38] X.H. Yang, D. Neher, Appl. Phys. Lett. 84 (2004) 2476.
[39] D.R. Blasini, J. Rivnay, D.M. Smilgies, J.D. Slinker, S. Flores-Torres, H.D. Abruña, G.G. Malliaras, J. Mater. Chem. 17 (2007) 1458.
[40] J.D. Slinker, J. Rivnay, J.B. Moskowitz, J.S. Parker, S. Bernhard, H.D. Abruña, G.G. Malliaras, J. Mater. Chem. 17 (2007) 2976.

Available online at www.sciencedirect.com
ScienceDirect
Organic Electronics 9 (2008) 164–170
Organic Electronics
www.elsevier.com/locate/orgel

Inkjet printed surface cell light-emitting devices from a water-based polymer dispersion

Gernot Mauthner [a,b], Katharina Landfester [c], Anton Köck [d], Hubert Brückl [d], Michael Kast [d], Christoph Stepper [d], Emil J.W. List [a,b,*]

[a] *Christian Doppler Laboratory Advanced Functional Material, Institute of Solid State Physics, Graz University of Technology, Petersgasse 16, A-8010 Graz, Austria*
[b] *Institute of Nanostructured Materials and Photonics, JOANNEUM RESEARCH GmbH, Franz-Pichler-Straße 30, A-8160 Weiz, Austria*
[c] *Organic Chemistry III/Macromolecular Chemistry, University of Ulm, Albert-Einstein-Allee 11, D-89069 Ulm, Germany*
[d] *ARC, Nano System Technologies, Donau-City-Street 1, A-1220 Vienna, Austria*

Received 16 October 2007; accepted 23 October 2007
Available online 30 October 2007

Abstract

We report on the fabrication of polymer light-emitting diodes (PLEDs) and light-emitting electrochemical cells (LECs) in planar surface cell geometry (anode as well as the cathode are made of gold; interelectrode spacing: 1 μm) by means of inkjet printing. The active material for PLEDs is an aqueous poly[2-methoxy-5-(2-ethylhexyloxy)-1,4-phenylenevinylene] (MEH-PPV) dispersion, and for LECs blends thereof with poly(ethylene oxide) (two different molecular weights: 100,000 g/mol (PEO-100,000) and 30,000 g/mol (PEO-30,000)) and lithium-triflate, building the solid state electrolyte. The surface PLEDs reveal very poor device performance with extremely high current and light emission onset voltages. However, adding the solid state electrolyte to the luminescent material, leading to the device type of an LEC, distinctly improves the performance obtaining onset voltages slightly above 3 V and remarkable enhanced light output. Due to the exchange of the high molecular weighted PEO-100,000 by the PEO-30,000, which leads to an elimination of the undesired bead-on-a-string effect during the inkjet printing process, the reproducibility of the device fabrication can be conspicuously improved. Additionally, the location of the light emission zone of a surface LEC can be easily determined, since one has a direct view between the electrodes. For such a device the light generation occurs near the cathode.

Keywords: Inkjet; Light-emitting polymer device; LEC

1. Introduction

In the middle of the 20th century it was demonstrated that a new material class – organic semiconductors– can be used to achieve electroluminescence (EL) [1]. Especially organic conjugated polymers reveal the paramount advantage of excellent processability, since these materials are soluble in common

* Corresponding author. Address: Christian Doppler Laboratory Advanced Functional Material, Institute of Solid State Physics, Graz University of Technology, Petersgasse 16, A-8010 Graz, Austria.
E-mail address: e.list@tugraz.at (E.J.W. List).

1566-1199/$ - see front matter © 2007 Elsevier B.V. All rights reserved.
doi:10.1016/j.orgel.2007.10.007

organic solvents due to functionalization with side-chains. For this reason polymer solutions can be easily processed by spin- or drop-casting, screen-printing [2–4], inkjet printing [5–8], etc. In particular the inkjet printing process used as material deposition technique reveals a number of advantages. Three major benefits are: (1) Precise material deposition on the substrate at well defined positions which means that selective structuring of devices is possible. Thus this technique is appropriate for the deposition of different polymers in a controlled pattern on a substrate, which is necessary, e.g., for the fabrication of full-color displays. (2) Low material consumption and less material wastage can be achieved compared to standard methods like spin-casting, which is connected with the reduction of device costs. (3) Furthermore, the fabrication of large-area devices is facilitated.

Yet the fabrication of polymer light-emitting devices (polymer light-emitting diodes [9] (PLEDs) and polymer light-emitting electrochemical cells [10,11] (LECs)) by using inkjet printing as deposition method of polymer-based solutions involves several challenges to solve like the bead-on-a-string effect [12] induced by high molecular linear polymer chains during the droplet formation of the ink at the printhead nozzles or the coffee-stain effect [13], which appears at the drying process of the droplet on the substrate. On the other hand, inkjet printing provides the possibility of utilizing substrates with alternative electrode geometries like the surface cell structure [14–20] for fabrication of cheap lighting applications beyond the display market.

In contrast to conventional PLEDs, LECs require additionally to the conjugated polymer a solid state electrolyte for their operation. Due to the electrolyte the working principle differs strongly from that of PLEDs, which operate due to charge carrier tunneling and/or thermionic injection [21]. Since the ionic species of the solid state electrolyte migrate under the influence of an applied electric field towards the corresponding electrodes, the LECs working principle is based on electrochemical doping of the conjugated polymer at the electrodes (electrochemical p-doping close to the anode and electrochemical n-doping close to the cathode) and the formation of a pin-junction type structure [11]. i represents the intrinsic region between the doped zones, where the exciton formation and light emission zone is located [22].

The presented results show that the problematic inkjet printing related issue the bead-on-a-string effect induced by the interaction of long linear polymer chains can be eliminated by utilizing a dispersion of the polymer (the diameter of the polymer colloids used in this study is in the range of 100 nm), or, if available, to use a soluble polymer with a low molecular weight. Another benefit can be exploit when utilizing the dispersion approach, namely that water, which is environmental friendly, can be used as dispersing agent for polymers which generally are only soluble in common organic solvents (simplifies the handling during device preparation) [23]. It is demonstrated that on the one hand inkjet printing is a powerful technique for the deposition of the pristine aqueous poly[2-methoxy-5-(2-ethylhexyloxy)-1,4-phenylenevinylene] (MEH-PPV) dispersion and blends thereof used in this study, and on the other hand that when fabricating light-emitting devices in surface cell geometry (interelectrode spacing resulting in device thickness of 1 μm) by inkjet printing only the device type of the LEC reveals characteristics of good quality.

2. Experimental

Water-based solutions of a poly(ethylene oxide) with a molecular mass of 30,000 g/mol (PEO-30,000), a poly(ethylene oxide) with a molecular mass of 100,000 g/mol (PEO-100,000), and lithium-triflate (LiTf) were fabricated for blending with the aqueous dispersion of semiconducting MEH-PPV (molecular weight: M_n 70,000–100,000) colloids (c-MEH-PPV). The diameter of the MEH-PPV colloids is in the range of 100 nm. The interdigital electrodes of the utilized planar surface cell structures consist of gold and have an interelectrode spacing of 1 μm. The surface PLEDs were fabricated by inkjet printing of the pure MEH-PPV dispersion with a final concentration of 11 mg/ml. For the preparation of the polymer dispersion, a 2.5 wt.% polymer solution in chloroform were added to an aqueous sodium dodecyl sulfate (SDS) (100 mg SDS/10 g of water) solution. After stirring 1 h for pre-emulsification, the miniemulsion was prepared by sonicating the mixture for 2 min (Branson Sonifier W450, 90% amplitude, ½ in. tip). The samples were left under stirring for 30 min at 62 °C to evaporate the chloroform from the liquid droplets in order to obtain an aqueous dispersion. To eliminate the excess of surfactant and concentrate the samples, they were ultrafiltered in centrifuge tubes (Amicon Ultra-4 centrifugal

filter, 10,000 molecular weight cut-off). Surface LECs (SLECs) were prepared by inkjet printing of the blends c-MEH-PPV/PEO-35,000/LiTf and c-MEH-PPV/PEO-100,000/LiTf (weight ratio 20:10:4 in each case). The concentration of c-MEH-PPV in the blend solutions was 7 mg/ml. The substrate temperature at the printing process was 50 °C for both device types. The surface light-emitting devices investigated in the study were fabricated by a single-nozzle inkjet printer using the jetting device Microfab [24] MJ-AT-01 with an orifice of 50 μm. After the device fabrication the active layers were dried in argon atmosphere and subsequently in vacuum at elevated temperature. All devices were operated and characterized under argon atmosphere at room temperature. EL spectra were taken with a CCD-spectrometer (Oriel 77400). Current/voltage characteristics ($I(V)$) were recorded with a Keithly source measure unit and for the luminance/voltage characteristics ($L(V)$) an integrating sphere in combination with a photodiode was used. The $I(V)$ and $L(V)$ characteristics were recorded with a scan speed of 0.2 V per 300 ms.

3. Results and discussion

In Fig. 1a, an image of an interdigital surface electrode structure, which is utilized in the following studies, is shown. The anode as well as the cathode is made of gold; the interelectrode gap has the form of a meander and is 1 μm wide. Fig. 1b depicts a schematic of the surface cell electrode structure covered with inkjet printed lines forming the active layer of the light-emitting device in surface cell geometry.

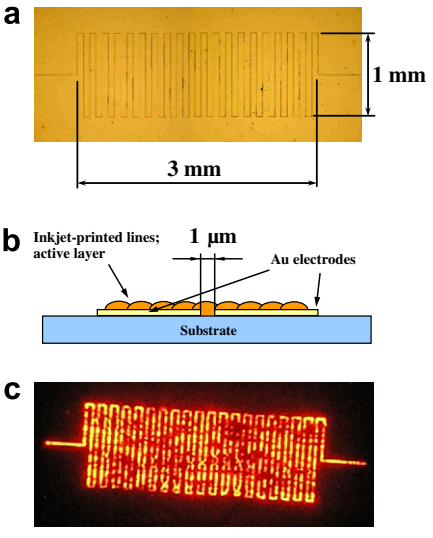

Fig. 1. (a) Interdigital surface electrode structure recorded with an optical microscope. Interelectrode spacing: 1 μm (b) Schematic of the surface cell electrode structure covered with inkjet printed lines forming the active layer of the light-emitting device. (c) Electroluminescence of an inkjet printed c-MEH-PPV SLEC.

First surface PLEDs were fabricated by inkjet printing from an aqueous MEH-PPV dispersion. Fig. 2a displays the droplet formation of the pristine dispersion of MEH-PPV nanospheres printed by the single-nozzle printer. The dispersion is well jettable and the droplets are formed within the first 50 μs after leaving the nozzle. Such a beneficial behavior is in contrast to a conventional MEH-PPV (M_n: 70,000–100,000) solution having an identical polymer concentration like the dispersion, since this solution suffers by the bead-on-a-string effect [13] at the inkjet printing process (figure is not shown here).

In Fig. 3a, a typical $I(V)$ and $L(V)$ characteristic of an inkjet printed c-MEH-PPV surface PLED is depicted. The current and light emission onsets were found at approximately 55 V. Obviously, the current and the luminance reveal an extremely low ascent when further increasing the bias, which is a

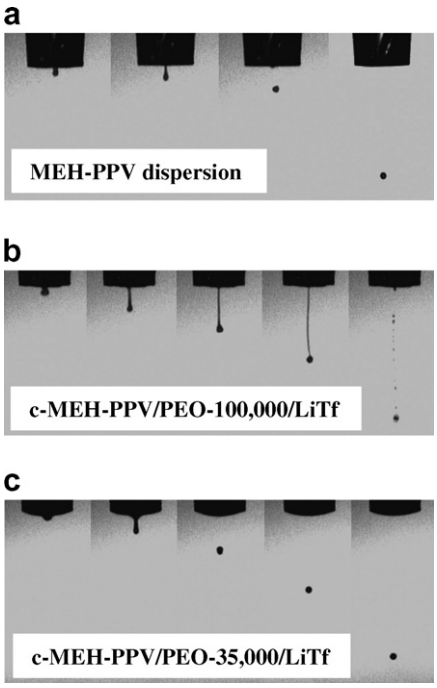

Fig. 2. Drop formation of: (a) the MEH-PPV dispersion at 0, 20, 50, 200 μs and of the blend systems, (b) c-MEH-PPV/PEO-100,000/LiTf and (c) c-MEH-PPV/PEO-35,000/LiTf at 0, 20, 50, 100, and 200 μs after leaving the printer nozzle.

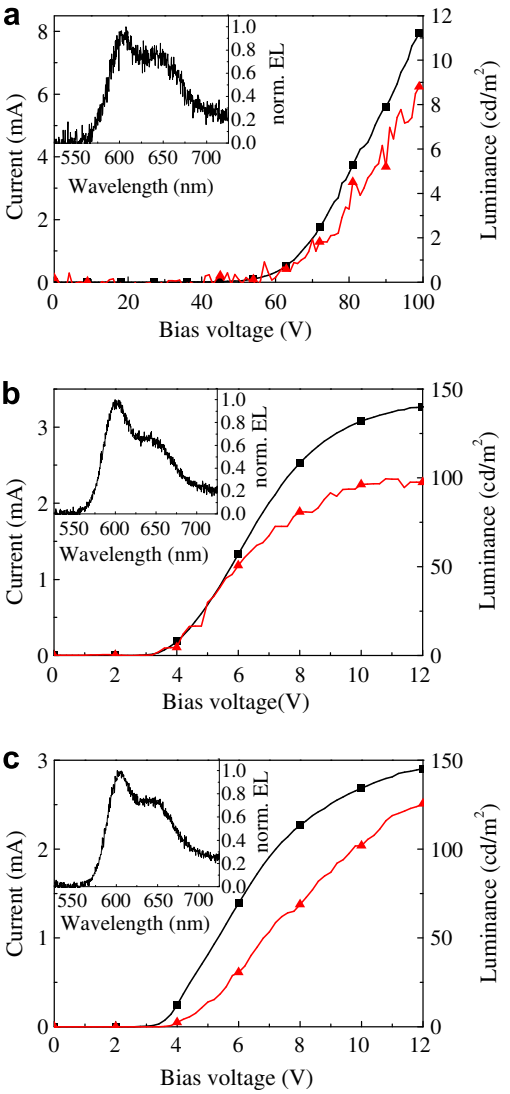

Fig. 3. (Squares) $I(V)$ and (triangles) $L(V)$ characteristics of surface cell light-emitting devices fabricated by inkjet printing: (a) c-MEH-PPV surface PLED, (b) c-MEH-PPV/PEO-100,000/LiTf surface LEC, and (c) c-MEH-PPV/PEO-35,000/LiTf surface LEC. The insets show the EL spectra of the corresponding devices.

result of the intrinsic behavior of this device type under these operation conditions. At a drive voltage of 100 V the current and the luminance reach 8 mA and 12 cd/m^2, respectively. The obtained EL intensity is unexpected low when considering the high current through the device. This feature indicates that the main part of the current stems from holes, since the energetic injection barrier generated by the highest occupied molecular orbital (HOMO) of the MEH-PPV and the Fermi level of the gold anode is rather low, which is in contrast to the electron injection barrier created by the lowest unoccupied molecular orbital (LUMO) of the polymer and the Fermi level of the gold cathode (see Fig. 4b) [25]. Consequently, a highly unbalanced charge carrier injection occurs, leading to a low rate of singlet exciton formation and recombination, respectively. Conventional PLEDs produced from the polymer MEH-PPV in sandwich structure (ITO/MEH-PPV/Ca/Al) turn on at voltages around 3 V [26]. However, in these instances the electrode spacing is sub-100 nm, but what is of even greater importance is the fact that by using calcium as cathode (work-function ~2.9 eV) the electron injection is strongly improved, which leads to a more balanced electron and hole injection. The consequence for devices with interelectrode spacing of 1 μm is that the emission onset voltage should be at least 10 times larger ($E = V/d$; E: electrical field, V: bias

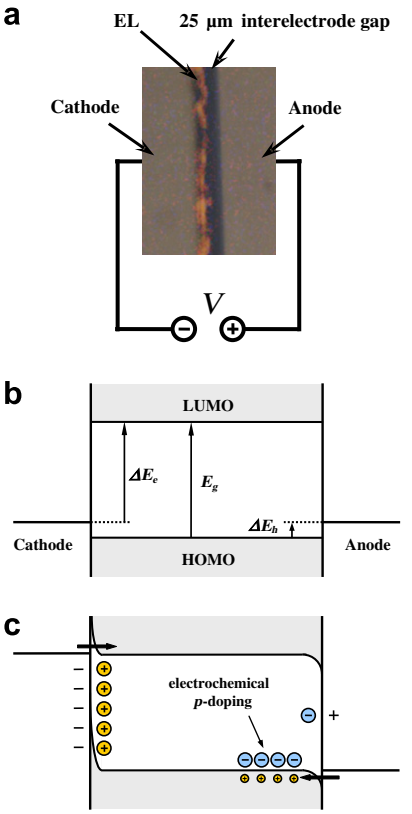

Fig. 4. (a) Image of the light emission of a SLEC fabricated by inkjet printing. Interelectrode spacing: 25 μm. Bias voltage: 70 V. Schematic electron energy diagrams of: (b) an unbiased SLEC ($V = 0$ V) and (c) an SLEC at a bias of $V = E_g/e$, consisting of a gold anode and a gold cathode, which results in the asymmetric barrier heights for electron injection ΔE_e and hole injection ΔE_h. Large circles: cations and anions; small circles: positive polarons.

voltage, *d*: device thickness), when applying the same electrode materials (indium tin oxide (ITO) and calcium (Ca)), in order to generate the identical electric field in the active layer. However in the case of the interdigital electrodes the anode as well as the cathode were made of gold (work-function ~5.1 eV, which is in the range of the commonly used hole injecting electrode ITO), which means that the electron injection is extremely problematic, and the EL onset voltage ought to be further strongly increased. The extreme case would be that the electron injection is totally hindered by the large injection barrier resulting in a sole hole current, which means that no EL can be generated. An auxiliary reason why the device operates at the stated voltages could be residual ionic impurities provided by a surfactant of the dispersion, which is needed for its stabilization, leading to a slight electrochemical doping of the polymer near the electrodes and an enhanced charge carrier injection. The inset of Fig. 3a shows the EL spectrum of the surface PLED. The shape of the spectrum is typical for MEH-PPV and the EL peak maximum is found at 606 nm.

The results presented before indicate that for light generation from a surface cell light-emitting device with large interelectrode gaps at acceptable low bias voltages the PLED exhibits the wrong fundamental working principle. An alternative device type is the LEC, which possesses the paramount advantage of an enhanced and more balanced charge carrier injection due to electrochemical doping of the polymer at the electrodes. The active layers of the surface LECs were produced by inkjet printing of the MEH-PPV dispersion blended with PEO-100,000 and the alkali metal salt LiTf in the weight ratio of c-MEH-PPV:PEO-100,000:LiTf = 20:10:4 (PEO-100,000 and LiTf build the solid state electrolyte).

In Fig. 2b, the droplet formation of the aqueous c-MEH-PPV/PEO-100,000/LiTf ink at the printer nozzle is shown. Obviously, this mixture is not as well jettable as the pure dispersion shown in Fig. 2a. Within the first 100 μs the droplet forms a long thread as a result of the bead-on-a-string effect, which is induced by the interaction of the long flexible linear PEO-100,000 chains. After 200 μs the droplet detaches the nozzle, however, small satellite droplets are generated from the liquid tail. Nevertheless, the inkjet printing process remained 'stable' during the entire device fabrication, meaning that the formation of the satellite droplets does not alter with time. In Fig. 3b, the $I(V)$ and $L(V)$ characteristics of a SLEC fabricated by inkjet printing of the c-MEH-PPV/PEO-100,000/LiTf ink are shown. The current and the light emission onset are found at 3.2 V, which is relatively close to the optical bandgap of the MEH-PPV. Further increasing of the driving voltage leads to a steep increase of the current and the luminance, which is typical for LECs. At a bias of 12 V the luminance reaches its maximum of approximately 100 cd/m^2, correlated with a current through the device of 3.3 mA. The inset of Fig. 3b depicts the normalized EL spectrum of the SLEC. The EL peak maximum is located at 602 nm. The hypsochromic shift of 4 nm in comparison to the surface PLED's EL peak maximum can be attributed to smaller self-absorption due to a distinctly lower amount of c-MEH-PPV in the active layer.

When comparing the performance of the two device types investigated, it can be found that the onset voltages for both the current and the light emission can be distinctly reduced; from 55 V for the PLED to around 3 V in the case of the LEC. Additionally the EL intensity emitted from the SLEC is unequally larger. These facts emphasize the necessity of the electrochemical doping process and the related efficient charge carrier injection, thus the usage of the LEC for such surface cell lighting applications.

To improve not only the inkjet printing process but also the reproducibility and the performance of the devices, a closer look concerning the utilized ink has to be done. Since the droplets of the aqueous c-MEH-PPV/PEO-100,000/LiTf solution generate during the inkjet printing process the bead-on-a-string structure (see Fig. 2b), whereas the pure MEH-PPV dispersion is well jettable (see Fig. 2a), it is evident that the jetting problem arises from the PEO-100,000 chains. A reasonable strategy to avoid this effect is to make a change from the high molecular weighted PEO-100,000 to the lower molecular weighted PEO-35,000, leading to the novel ink of c-MEH-PPV, PEO-35,000, and LiTf. Fig. 2c displays the droplet formation of the aqueous c-MEH-PPV/PEO-35,000/LiTf (weight ratio 20:10:4) blend solution at the nozzle of the inkjet printer after different times of ejection. The solid content of the mixture is identical with that of the former solution. Obviously the PEO exchange results in a well jettable ink and the droplet formation is similar to that of the pure MEH-PPV dispersion.

In Fig. 3c, the $I(V)$ and $L(V)$ characteristics of a c-MEH-PPV/PEO-35,000/LiTf SLEC fabricated by

inkjet printing are illustrated. The current onset is found at a bias of 3.1 V and the light emission starts slightly later at 3.4 V. Further increasing of the driving voltage leads to a strong increase of the current and the luminance and at a bias of 12 V the current and the luminance are about 2.9 mA and 125 cd/m^2. The inset of Fig. 3c depicts the normalized EL spectrum of the SLEC. The EL peak maximum is located at a wavelength of 603 nm, which matches almost exactly with that of the SLEC investigated before indicating a similar thickness of the active layers. In Fig. 1c, an image of such a SLEC under operation is shown. The inhomogeneous EL emission is a composition of various reasons: deviations in the active layer thickness due to the coffee-stain effect, phase-separation between the hydrophobic c-MEH-PPV and the hydrophilic polymer electrolyte, and small differences in the interelectrode spacing of the device.

Basically, the two types of surface LECs (containing PEO-100,000 and PEO-35,000) reveal comparable device performances. However, in the latter case a larger luminance was obtained at a bias of 12 V, which can be attributed to morphological differences of the active layer induced by the different PEO chains length. Additionally to the slightly improved performance, the indispensable advantage of an advanced device fabrication process due to the elimination of the bead-on-a-string effect has to be highlighted. Without this feature no defined and reproducible performance of the surface LECs can be achieved.

The device type of the surface LEC can be excellently used for investigations concerning the light emission zone, since one has a direct view between the electrodes. Fig. 4a shows an image of a surface LEC with an anode/cathode spacing of 25 μm from the ink c-MEH-PPV/PEO-35,000/LiTf SLEC fabricated by inkjet printing under operation (applied bias: 70 V; the high bias needed for the device operation is a result of the PEO/LiTf nature, which tends to be crystalline at room temperature [27]). Obviously the light generation occurs near the cathode. This feature is a result of the utilized high work-function metal gold for both electrodes, consequently the energetic injection barrier for holes ΔE_h is significantly lower than that for electrons ΔE_e (see the corresponding electron energy diagram for an unbiased SLEC ($V = 0$ V) in Fig. 4b) and no internal built-in voltage can be generated. Since the number of ions required for compensating the hole injection barrier is significantly smaller than that to compensate the barrier for electrons, and in order to preserve the electro-neutrality in the bulk, also electrochemical p-type doping of the polymer at the anode towards the center of the device takes place (see Fig. 4c). This effect causes a shift of the light emission zone from the center of the device (holds only for SLECs with equal energy barrier heights for electron and hole injection, and the assumption of identical electron and hole mobility in the conjugated polymer) to the cathode side. Such a behavior has been also observed for other types of SLECs [17].

4. Conclusion

In summary, we have pointed out some key issues of the fabrication of light-emitting devices in surface cell geometry by means of inkjet printing, concerning an applicable ink and the appropriate device type. The superior advantages of the aqueous MEH-PPV dispersion has to be emphasized, which are the environmental friendliness and the absence of the bead-on-a-string effect typical for high molecular weight conjugated polymers during the printing process. Surface PLEDs fabricated from c-MEH-PPV by inkjet printing reveal very poor device performance with extremely high current and light emission onset voltages (50–60 V). However, surface LECs show distinctly improved performance with onset voltages for the current as well as for the luminance slightly above 3 V and remarkable enhanced light output. These facts inevitably lead to the necessity of the usage of the LEC principle, i.e., the electrochemical doping process, for such surface cell lighting applications.

Acknowledgements

The CDL-AFM gratefully acknowledges the continuous support of AT&S AG.

References

[1] M. Pope, H. Kallmann, P. Magnante, J. Chem. Phys. 38 (1963) 2042.
[2] K. Mori, T.L. Ning, M. Ichikawa, T. Koyama, Y. Taniguchi, Jpn. J. Appl. Phys. 39 (2000) L942.
[3] Z.N. Bao, Y. Feng, A. Dodabalapur, V.R. Raju, A.J. Lovinger, Chem. Mater. 9 (1997) 1299.
[4] S.E. Shaheen, R. Radspinner, N. Peyghambarian, G.E. Jabbour, Appl. Phys. Lett. 79 (2001) 2996.
[5] T.R. Hebner, J.C. Sturm, Appl. Phys. Lett. 73 (1998) 1775.
[6] T.R. Hebner, C.C. Wu, D. Marcy, M.H. Lu, J.C. Sturm, Appl. Phys. Lett. 72 (1998) 512.
[7] L.M. Leung, C.F. Kwong, C.C. Kwok, S.K. So, Displays 21 (2000) 199.

[8] Y. Yang, S.C. Chang, J. Bharathan, J. Liu, J. Mater. Sci. Mater. Electron. 11 (2000) 89.
[9] J.H. Burroughes, D.D.C. Bradley, A.R. Brown, R.N. Marks, K. Mackay, R.H. Friend, P.L. Burn, A.B. Holmes, Nature 347 (1990) 539.
[10] Q. Pei, G. Yu, C. Zhang, Y. Yang, A.J. Heeger, Science 269 (1995) 1086.
[11] Q. Pei, Y. Yang, G. Yu, C. Zhang, A.J. Heeger, J. Am. Chem. Soc. 118 (1996) 3922.
[12] R.P. Mun, J.A. Byars, D.V. Boger, J. Non-Newton. Fluid Mech. 74 (1998) 285.
[13] R.D. Deegan, O. Bakajin, T.F. Dupont, G. Huber, S.R. Nagel, T.A. Witten, Nature 389 (1997) 827.
[14] D.J. Dick, A.J. Heeger, Y. Yang, Q. Pei, Adv. Mater. 8 (1996) 985.
[15] U. Lemmer, D. Vacar, D. Moses, A.J. Heeger, T. Ohnishi, T. Noguchi, Appl. Phys. Lett. 68 (1996) 3007.
[16] M.D. McGehee, D. Vacar, U. Lemmer, D. Moses, A.J. Heeger, Phys. Rev. B 70 (2004) 115212.
[17] L. Edman, M.A. Summers, S.K. Buratto, A.J. Heeger, Phys. Rev. B 70 (2004) 115212.
[18] J. Gao, J. Dane, Appl. Phys. Lett. 83 (2003) 3027.
[19] J. Dane, J. Gao, Appl. Phys. Lett. 85 (2004) 3905.
[20] Y. Kaminorz, E. Smela, T. Johansson, L. Brehmer, M.R. Andersson, O. Inganäs, Synth. Met. 113 (2000) 103.
[21] A. Kraft, A.C. Grimsdale, A.B. Holmes, Angew. Chem., Int. Ed. 37 (1998) 402.
[22] D.L. Smith, J. Appl. Phys. 81 (1997) 2869.
[23] K. Landfester, R. Montenegro, U. Scherf, R. Güntner, U. Asawapirom, S. Patil, D. Neher, T. Kietzke, Adv. Mater. 14 (2002) 651.
[24] www.microfab.com.
[25] I.D. Parker, J. Appl. Phys. 75 (1994) 1656.
[26] S.H. Kwon, S.Y. Paik, J.S. Yoo, Synth. Met. 130 (2002) 55.
[27] J.-H. Shin, A. Dzwilewski, A. Iwasiewicz, S. Xiao, A. Fransson, G.N. Ankah, L. Edman, Appl. Phys. Lett. 89 (2006) 013509.

Available online at www.sciencedirect.com
ScienceDirect
Organic Electronics 9 (2008) 171–182
Organic Electronics
www.elsevier.com/locate/orgel

Green and blue-green phosphorescent heteroleptic iridium complexes containing carbazole-functionalized β-diketonate for non-doped organic light-emitting diodes

Zhiwei Liu, Zuqiang Bian *, Lang Ming, Fei Ding, Hongyan Shen, Daobo Nie, Chunhui Huang *

Beijing National Laboratory for Molecular Sciences (BNLMS), State Key Laboratory of Rare Earth Materials Chemistry and Applications, College of Chemistry and Molecular Engineering, Peking University, Beijing 100871, PR China

Received 15 May 2007; received in revised form 4 August 2007; accepted 4 September 2007
Available online 8 September 2007

Abstract

Two novel iridium complexes both containing carbazole-functionalized β-diketonate, $Ir(ppy)_2(CBDK)$ [bis(2-phenylpyridinato-*N*,C^2)iridium(1-(carbazol-9-yl)-5,5-dimethylhexane-2,4-diketonate)], $Ir(dfppy)_2(CBDK)$ [bis(2-(2,4-difluorophenyl)pyridinato-*N*,C^2)iridium(1-(carbazol-9-yl)-5,5-dimethylhexane-2,4-diketonate)] and two reported complexes, $Ir(ppy)_2(acac)$ (acac = acetylacetonate), $Ir(dfppy)_2(acac)$ were synthesized and characterized. The electrophosphorescent properties of non-doped device using the four complexes as emitter, respectively, with a configuration of ITO/*N*,*N*′-diphenyl-*N*,*N*′-bis(1-naphthyl)-1,1′-diphenyl-4,4′-diamine (NPB) (20 nm)/iridium complex (20 nm)/2,9-dimethyl-4,7-diphenyl-1,10-phenanthroline (BCP) (5 nm)/tris(8-hydroxyquinoline)aluminum (AlQ) (45 nm)/$Mg_{0.9}Ag_{0.1}$ (200 nm)/Ag (80 nm) were examined. In addition, a most simplest device, ITO/$Ir(ppy)_2(CBDK)$ (80 nm)/$Mg_{0.9}Ag_{0.1}$ (200 nm)/Ag (80 nm), and two double-layer devices with configurations of ITO/NPB (30 nm)/$Ir(ppy)_2(CBDK)$ (30 nm)/$Mg_{0.9}Ag_{0.1}$ (200 nm)/Ag (80 nm) and ITO/$Ir(ppy)_2(CBDK)$ (30 nm)/AlQ (30 nm)/$Mg_{0.9}Ag_{0.1}$ (200 nm)/Ag (80 nm) were also fabricated and examined. The results show that the non-doped four-layer device for $Ir(ppy)_2(CBDK)$ achieves maximum lumen efficiency of 4.54 lm/W and which is far higher than that of $Ir(ppy)_2(acac)$, 0.53 lm/W, the device for $Ir(dfppy)_2(CBDK)$ achieves maximum lumen efficiency of 0.51 lm/W and which is also far higher than that of $Ir(dfppy)_2(acac)$, 0.06 lm/W. The results of simple devices involved $Ir(ppy)_2(CBDK)$ show that the designed complex not only has a good hole transporting ability, but also has a good electron transporting ability. The improved performance of $Ir(ppy)_2(CBDK)$ and $Ir(dfppy)_2(CBDK)$ can be attributed to that the bulky carbazole-functionalized β-diketonate was introduced, therefore the carrier transporting property was improved and the triplet–triplet annihilation was reduced.

PACS: 78.66.-w

Keywords: Iridium complex; Carbazole; Non-doped OLED; Blue and green

* Corresponding authors. Tel./fax: +86 10 62757156.
E-mail address: chhuang@pku.edu.cn (C. Huang).

1566-1199/$ - see front matter © 2007 Elsevier B.V. All rights reserved.
doi:10.1016/j.orgel.2007.09.001

1. Introduction

Organic light-emitting diodes (OLEDs) have attracted great attention in the past decades because of their potential advantages in low-power emissive, flexible, cost competitive, flat panel displays. Recently, the photophysics of phosphorescent materials has been the subject of extensive studies because both singlet and triplet excited states participated to the emission leading to the internal quantum efficiency potentially as high as 100% [1–4]. Among the phosphorescent emitters such as iridium, platinum, ruthenium, and osmium complexes, the best performing phosphorescent materials have been shown to be those based on iridium complexes. Up to now, high brightness and efficiency were achieved by using a host:dopant systems to improve energy transfer and avoid triplet–triplet annihilation [5–15]. In contrast, high-performance phosphorescent OLEDs fabricated by a much simplified, non-doped method are rare and their typical performances both in brightness and efficiency are far from satisfactory [16–19].

In pursuit of highly electroluminescent efficiency iridium complexes, many different classes of homoleptic ($Ir(C^{\wedge}N)_3$) and heteroleptic ($Ir(C^{\wedge}N)_2(LX)$) iridium complexes have been developed, where $C^{\wedge}N$ is a monoanionic cyclometalating ligand (e.g., 2-phenylpyridine, 2,4-difluorophenylpyridine) and LX is an ancillary ligand (e.g., acetylacetonate, picolinate). It has been well demonstrated that structural changes in the skeleton as well as the substituent groups of the cyclometalating ligand afford significant color tuning and efficiency improving of electrophosphorescence. Therefore, many studies have been enthusiastically investigated on the design and synthesis of novel cyclometalating ligands [20–29].

In our previous work, we have changed the ancillary ligand from acetylacetonate (acac) to a carbazole-functionalized β-diketonate and designed a red phosphorescent emission iridium complex, $Ir(DBQ)_2(CBDK)$ [bis-(dibenzo[*f*,*h*]quinoxalinato-*N*,C^2)iridium(1-(carbazol-9-yl)-5,5-dimethylhexane-2,4-diketonate)]. The performance of non-doped device based on this complex showed that improved hole transporting property which benefits exciton transportation could lead to highly efficient non-doped OLEDs, and consequently the device fabrication will be simplified and the danger of the phase separation, which potentially exist in the long-playing device operation, will be avoided [30–33].

Encouraged by the fact that the functionalized β-diketonate can play such an important role to iridium complex and with an effort to design high efficiency non-doped green and blue OLEDs, herein two complexes both containing carbazole-functionalized β-diketonate, $Ir(ppy)_2(CBDK)$ [bis(2-phenylpyridinato-*N*,C^2)iridium(1-(carbazol-9-yl)-5,5-dimethylhexane-2,4-diketonate)] and $Ir(dfppy)_2(CBDK)$ [bis(2-(2,4-difluorophenyl)pyridinato-*N*,C^2)iridium(1-(carbazol-9-yl)-5,5-dimethylhexane-2,4-diketonate)] were synthesized. For comparison, two reported complexes, $Ir(ppy)_2(acac)$ and $Ir(dfppy)_2(acac)$ were also synthesized and the related devices were fabricated under the same conditions. Data show that the lumen efficiency of the device using $Ir(ppy)_2(CBDK)$ (or $Ir(dfppy)_2(CBDK)$) as emitter is far higher than that of $Ir(ppy)_2(acac)$ (or $Ir(dfppy)_2(acac)$). In addition, a most simplest device and two double-layer devices involved $Ir(ppy)_2(CBDK)$ were also fabricated and data show that the designed iridium complex both have good hole transporting ability and electron transporting ability.

2. Experimental

2.1. General information

^1H NMR spectra were recorded on an ARX-400 NMR spectrometer, chemical shift data for each signal were reported in ppm units with tetramethylsilane (TMS) as internal reference, where $\delta(TMS) = 0$. Elemental analyses were performed on a VARIO EL instrument. The UV–vis absorption spectra were measured with Shimadzu UV-3100 spectrometer. The photoluminescence (PL) spectra and phosphorescence decay lifetimes were recorded on an Edinburgh Analytical Instruments FLS920 spectrometer after removing the oxygen in the solution by vacuum technique (3 or 4 freeze–pump–thaw cycles).

2.2. Materials

The synthetic procedure of HCBDK has been reported in a previous paper [30], $Ir(ppy)_2(acac)$ and $Ir(dfppy)_2(acac)$ were synthesized according to the literature [7]. Tris(8-hydroxyquinolinolinolato)aluminium (AlQ) was prepared by published methods. Both *N*,*N*′-diphenyl-*N*,*N*′-bis(1-naphthyl)-1,1′-diphenyl-4,4′-diamine (NPB) and 2,9-dimethyl-4,7-diphenyl-1,10-phenanthroline (BCP) were purchased from Aldrich. NPB, BCP and AlQ were all subjected to gradient sublimation prior to use.

2.3. $Gd(CBDK)_3 \cdot 2EtOH$

To a round-bottomed flask (50 mL), HCBDK (0.307 g, 1.00 mmol) and NaOH (0.040 g, 1.00 mmol) were mixed in 10 mL ethanol and refluxed for 15 min, then it was added dropwise to 10 mL ethanol solution of $GdCl_3 \cdot 6H_2O$ (0.124 g, 0.33 mmol) under stirring. The mixture was refluxed for 2 h and then poured into water. The crude product was collected by filtration and purified by recrystallization in dichloromethane–petroleum ether. Yield: 86%. Anal. Found (calcd.) for $C_{64}H_{72}GdN_3O_8$: C, 65.73 (65.78); H, 6.29 (6.21); N, 3.59 (3.60).

2.4. $C^{\wedge}N_2Ir(\mu\text{-}Cl)_2IrC^{\wedge}N_2$ dimer complexes

Cyclometalated Ir^{III}-μ-chloro-bridged dimers were synthesized according to the Nonoyama route, by refluxing $IrCl_3 \cdot 3H_2O$ with 2–2.5 equiv. of cyclometalating ligand in a 3:1 mixture of 2-ethoxyethanol and water [34].

2.5. $Ir(C^{\wedge}N)_2(LX)$ complexes

Synthesis of $Ir(C^{\wedge}N)_2(LX)$ involved the following steps: cyclometalated Ir^{III}-μ-chloro-bridged dimer complex (0.5 mmol), HLX (1.1 mmol) and sodium carbonate (5.0 mmol) were refluxed in 15 mL of 2-ethoxyethanol in an N_2 atmosphere for 10 h. After cooling to room temperature, the mixture was poured into water. The rude product which was collected by filtration was then chromatographed on a silica column to obtain the pure $Ir(C^{\wedge}N)_2(LX)$.

2.6. $Ir(ppy)_2(CBDK)$

Yield: 72%. ^1H NMR (400 MHz, $CDCl_3$): δ/ppm 8.39–8.41 (d, 1H); 8.25–8.27 (d, 1H); 8.05–8.07 (d, 2H); 7.85–7.87 (d, 1H); 7.76–7.78 (d, 1H); 7.73–7.74 (t, 1H); 7.66–7.68 (t, 1H); 7.58–7.60 (d, 1H); 7.49–7.51 (d, 1H); 7.32–7.36 (t, 2H); 7.19–7.22 (t, 4H); 6.65–6.99 (m, 6H); 6.37–6.39 (d, 1H); 6.25–6.27 (d, 1H); 5.02 (s, 1H); 4.68–4.73 (d, 1H); 4.53–4.57 (d, 1H); 0.55 (s, 9H). Anal. Found (calcd.) for $C_{42}H_{36}IrN_3O_2$: C, 62.49 (62.51); H, 4.41 (4.50); N, 5.28 (5.21).

2.7. $Ir(dfppy)_2(CBDK)$

Yield: 81%. ^1H NMR (400 MHz, $CDCl_3$): δ/ppm 8.14–8.19 (t, 4H); 8.04–8.06 (d, 2H); 7.69–7.76 (m, 2H); 7.30–7.34 (t, 2H); 7.16–7.22 (q, 4H); 6.97–7.01 (t, 1H); 6.86–6.90 (t, 1H); 6.28–6.37 (m, 2H); 5.63–5.69 (t, 2H); 5.17 (s, 1H); 4.58–4.73 (q, 2H); 0.63 (s, 9H). Anal. Found (calcd.) for $C_{42}H_{32}F_4IrN_3O_2$: C, 57.30 (57.39); H, 3.52 (3.67); N, 4.72 (4.78).

2.8. Cyclic voltammetry and the estimation of HOMO and LUMO energy levels

Electrochemical measurements were recorded on a computer-controlled EG&G Potentiostat/Galvanostat model 283 at room temperature under atmosphere. Cyclic voltammetry (CV) measurements were carried out in a HPLC grade CH_2Cl_2 solution containing Bu_4NPF_6 (0.1 M) as supporting electrolyte with a platinum button working electrode, a platinum wire counter electrode, and an Ag/AgCl reference electrode. The concentration of the compounds used in the experiments was 1×10^{-3} M. The scan rate was 50 mV s^{-1}. The reference electrode was calibrated to be 0.456 V versus the standard hydrogen electrode with a ferrocene standard solution. The highest occupied molecular orbital (HOMO)/lowest unoccupied molecular orbital (LUMO) levels were calculated by assuming the energy level of ferrocene/ferrocenium to be −4.8 eV [35].

2.9. OLED fabrication and measurements

The devices were fabricated by sequentially depositing organic layers in one run under high vacuum ($<8 \times 10^{-5}$ Pa) thermal evaporation onto a precleaned indium-tin oxide (ITO) glass substrate with a sheet resistance of 7 Ω/sq. A shadow mask with a rectangle (3×3 mm) openings was used to define the cathode of a 200 nm thick layer of $Mg_{0.9}Ag_{0.1}$ alloy, with an 80 nm thick Ag cap. The thickness of the deposited layer and the evaporation speed of the individual materials were monitored in vacuum with a quartz crystal monitor. All electric testing and optical measurements were performed under ambient conditions. The electroluminescence (EL) spectra and luminance were measured with a Spectra Scan PR650 at atmosphere. The current–voltage (I–V) and luminance–voltage (L–V) characteristics were measured with a computer controlled Keithley 2400 Sourcemeter.

3. Results and discussion

3.1. X-ray crystal structure

Single crystal of Ir(dfppy)$_2$(CBDK) was prepared by slow evaporation of a mixed chloroform and ethanol solution. The Ir(dfppy)$_2$(CBDK), which consists of two cyclometallated 2,4-difluorophenylpyridine fragments and one carbazole-functionalized β-diketonate ligand has a distorted octahedral geometry around the iridium atom, as depicted in Fig. 1. There are several weak interactions in the crystal of Ir(dfppy)$_2$(CBDK). First of all, the phenylpyridine ligand is nearly parallel to the carbazole ring of the same molecule. It is clearly shown by the rather short π–π interaction of 3.78 Å (Fig. 1). The second kind of interaction attributed to hydrogen bonding can be easily seen in the intermolecular packing diagram of Ir(dfppy)$_2$(CBDK) (Fig. 2). Although those interactions are weak, they are notable because they possibly play a role in the radiationless quenching of the phosphorescent emission [17].

3.2. Phosphorescence spectra of $Gd(CBDK)_3 \cdot 2EtOH$

The complex Gd(CBDK)$_3 \cdot$ 2EtOH was synthesized for the determination of phosphorescence spectra owing to enhanced phosphorescence–fluorescence ratios and thus to study the triplet level of CBDK. As shown in Fig. 3, the spectrum of Gd(CBDK)$_3 \cdot$ 2EtOH at 77 K include two parts, the band shorter than 400 nm can be assigned to the fluorescence emission which are similar to the emission detected at room temperature, while the emission longer than 400 nm that appears only at low temperature can be assigned to the phosphorescence emission. Since the phosphorescence emission band was representing the fall from the phosphorescent state to a number of vibrational states of the ground state, the band at 412 nm, which is corresponding to the blue side of the phosphorescence spectra can be assigned to be the $0 \rightarrow 0$ transition. Thus the triplet level for CBDK was deduced to be 24,200 cm^{-1} (3.00 eV), which is a little lower than that of acac anion, 25,300 cm^{-1} (3.14 eV) [36], but higher than the triplet energy level of Ir(dfppy)$_2$ [37] and Ir(ppy)$_2$ [7] fragments. The data mentioned above predicate that introducing CBDK to these two fragments would no influence on their phosphorescence spectra [7].

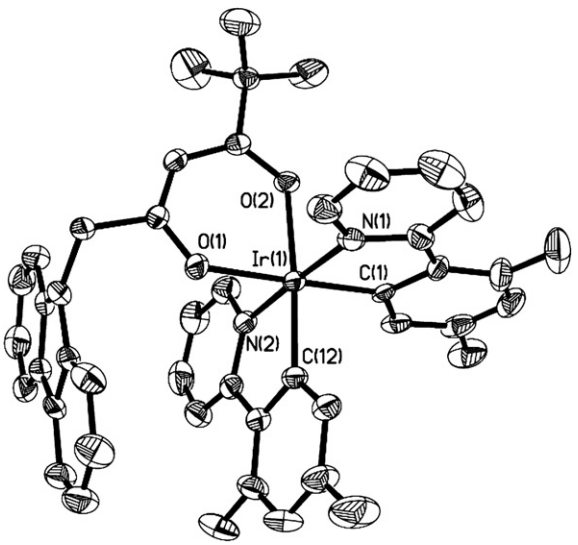

Fig. 1. ORTEP diagram of Ir(dfppy)$_2$(CBDK), the hydrogen atoms are omitted for clarity.

3.3. UV–vis absorptions and photoluminescent properties of iridium complexes

The UV–vis absorption and photoluminescence of Ir(ppy)$_2$(CBDK) compared with Ir(ppy)$_2$(acac) that recorded in dichloromethane at room temperature are shown in Fig. 4a, and these of Ir(dfppy)$_2$(CBDK) compared with Ir(dfppy)$_2$(acac) are shown in Fig. 4b. The photoluminescence spectra comparisons of the four iridium complexes in solid state are presented in Fig. 5.

The UV–vis absorption spectra of Ir(ppy)$_2$(CBDK) and Ir(dfppy)$_2$(CBDK) are different to these of Ir(ppy)$_2$(acac) and Ir(dfppy)$_2$(acac) mainly in the absorptions attributing to the different β-diketonate ligand (see Fig. 4a and b). The absorptions at 343, 329, 293, 283 and 237 nm for Ir(ppy)$_2$(CBDK) and Ir(dfppy)$_2$(CBDK) appear to be CBDK ligand-based transitions that resemble to the absorptions of the free CBDK. While the absorptions attribute to the cyclometalated ligand and MLCT transitions for Ir(ppy)$_2$(acac) and Ir(dfppy)$_2$(acac) complexes still can be found in absorption spectra of Ir(ppy)$_2$(CBDK) and Ir(dfppy)$_2$(CBDK), respectively. It can be seen from the photoluminescence spectra that Ir(ppy)$_2$(CBDK) and Ir(dfppy)$_2$(CBDK) have the similar emission to Ir(ppy)$_2$(acac) and Ir(dfppy)$_2$(acac), respectively. The Ir(ppy)$_2$(CBDK) and Ir(dfppy)$_2$(CBDK) have maximum emission bands at 521 and 487 nm with

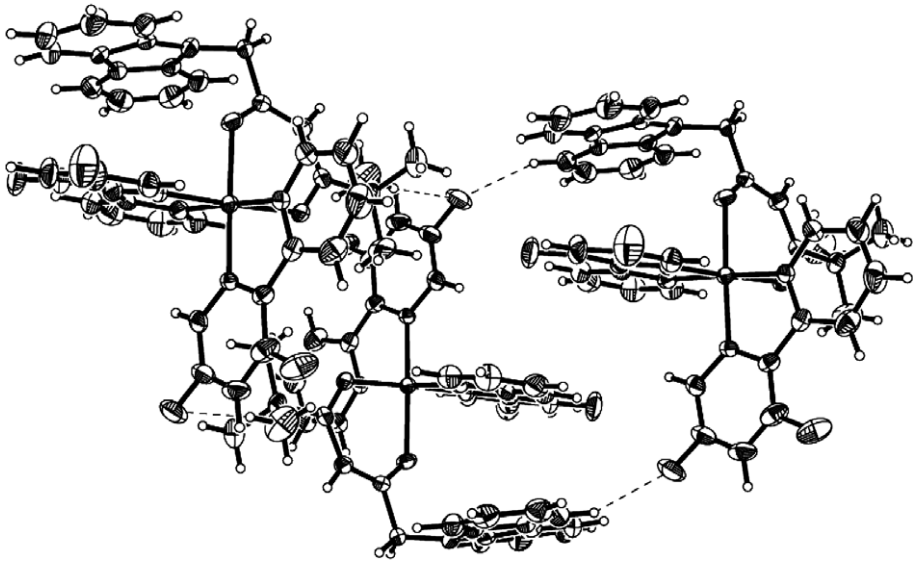

Fig. 2. Portion of the crystal-packing diagram of Ir(dfppy)$_2$(CBDK) showing the non-bonding interactions.

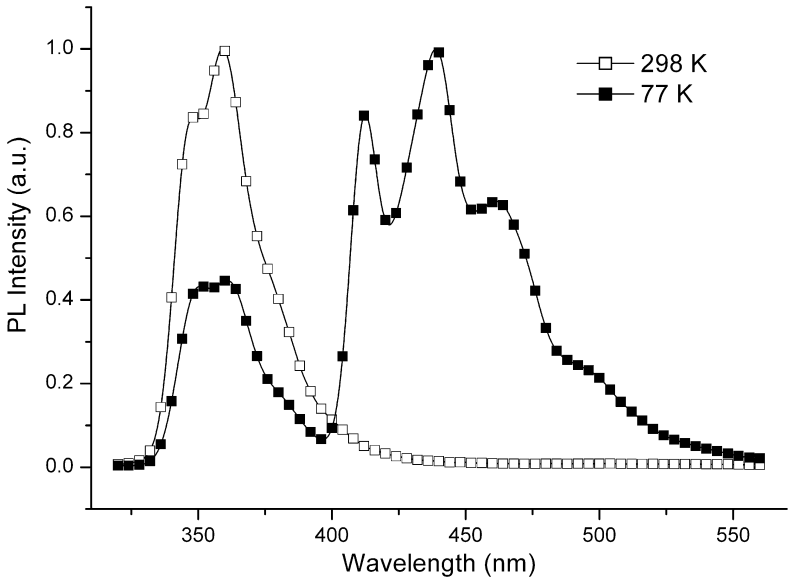

Fig. 3. Emission spectra of Gd(CBDK)$_3$ in ethanol (1×10^{-5} mol/L) at 298 and 77 K.

decay lifetimes of 0.9 and 1.0 μs, respectively, which are similar to that of corresponding Ir(ppy)$_2$(acac) and Ir(dfppy)$_2$(acac), maximum emission bands at 519 and 483 nm with decay lifetimes of 1.1 and 1.3 μs. Citing the quantum yield of 0.34 [38] and 0.62 [37] for complexes Ir(ppy)$_2$(acac) and Ir(dfppy)$_2$(acac) as standard materials, respectively, the phosphorescence quantum yields for Ir(ppy)$_2$(CBDK) and Ir(dfppy)$_2$(CBDK) were measured to be 0.19 and 0.20, respectively. The relatively low phosphorescence quantum yield for Ir(ppy)$_2$(CBDK) may attribute to the introduction of CBDK, which have a lower triplet energy level than acac anion, while the low quantum yield for Ir(dfppy)$_2$(CBDK) may also attribute to the intra-/intermolecular interaction.

The solid state photoluminescence spectra of Ir(ppy)$_2$(CBDK) and Ir(dfppy)$_2$(CBDK) are similar to these of Ir(ppy)$_2$(acac) and Ir(dfppy)$_2$(acac), respectively. The maximum emission bands for

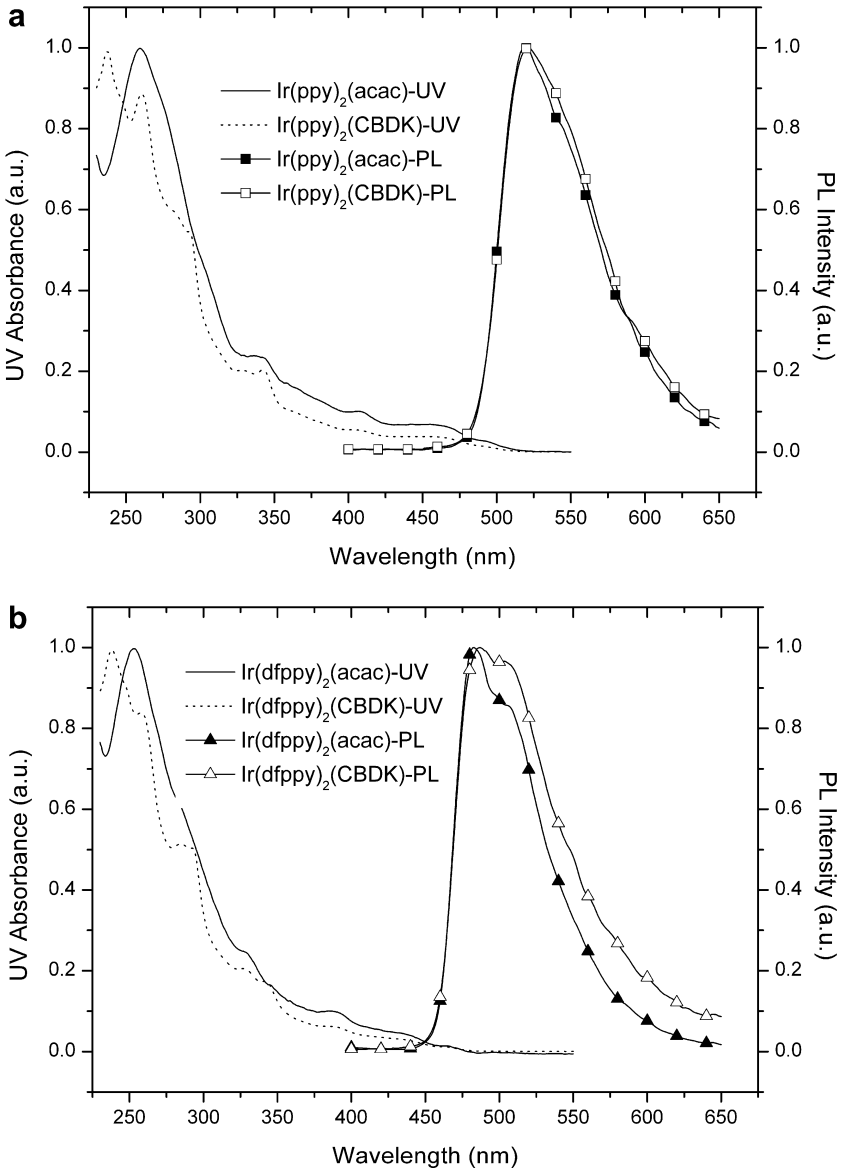

Fig. 4. The UV–vis absorption spectra and photoluminescence spectra of (a) $Ir(ppy)_2(CBDK)$ compared with $Ir(ppy)_2(acac)$, (b) $Ir(dfppy)_2(CBDK)$ compared with $Ir(dfppy)_2(acac)$ in CH_2Cl_2 (1×10^{-5} mol/L).

$Ir(ppy)_2(CBDK)$ and $Ir(ppy)_2(acac)$ in solid state are both centered at 542 nm, which are 21 and 23 nm red-shifted comparing with their maximum emission bands in CH_2Cl_2 solution, respectively. The maximum emission bands for $Ir(dfppy)_2(CBDK)$ and $Ir(dfppy)_2(acac)$ in solid state are centered at 522 and 514 nm, respectively, which are 35 and 31 nm red-shifted comparing to the corresponding spectra in solution. These spectra data are well agree with what we predicted, that appropriately modification of the β-diketonate while remaining of the structure of the cyclometalating ligand has only a little influence on the photoluminescence spectra of the iridium complexes.

3.4. Electrochemical properties

The highest occupied molecular orbital (HOMO) and lowest unoccupied molecular orbital (LUMO) energy level of material is one of the most important factors when they are used in OLEDs. Herein, the HOMO and LUMO energy levels of those iridium complexes were estimated according to the electrochemical performance and UV–vis absorp-

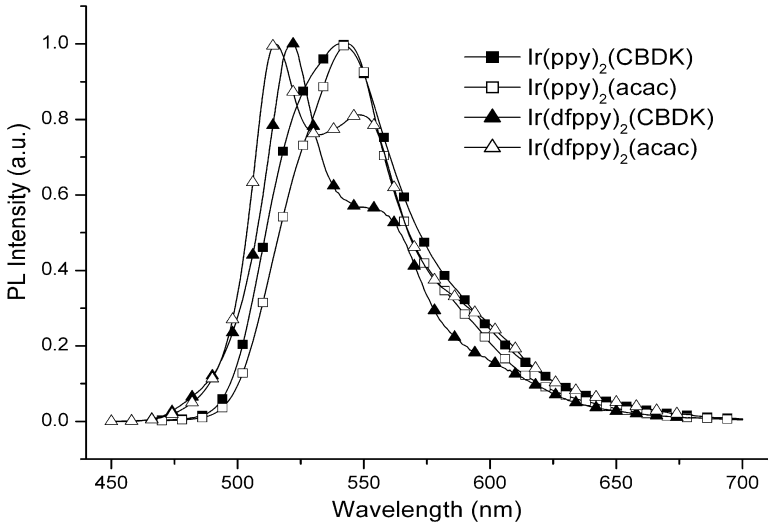

Fig. 5. The photoluminescence spectra of $Ir(ppy)_2(CBDK)$ and $Ir(dfppy)_2(CBDK)$ compared with $Ir(ppy)_2(acac)$ and $Ir(dfppy)_2(acac)$ in solid state, respectively.

tion spectra. The cyclic voltammograms of $Ir(ppy)_2(CBDK)$, $Ir(ppy)_2(acac)$, $Ir(dfppy)_2(CBDK)$ and $Ir(dfppy)_2(acac)$ are shown in Fig. 6. The electrochemical data and energy levels are summarized in Table 1.

As shown in Fig. 6 and Table 1, the oxidation potentials for $Ir(ppy)_2(CBDK)$ and $Ir(ppy)_2(acac)$ were observed to be 0.71 and 0.63 V and thus the HOMO energy levels of the two complexes were estimated to be 5.03 and 4.95 eV, respectively. Estimated from the UV–vis absorption spectra, they nearly have the same band gap of 2.25 eV, thus the LUMO energy levels are 2.78 and 2.70 eV for $Ir(ppy)_2(CBDK)$ and $Ir(ppy)_2(acac)$, respectively, from which we can see that the HOMO and LUMO energy levels of $Ir(ppy)_2(CBDK)$ and $Ir(ppy)_2(acac)$ are similar. However, when examined $Ir(dfppy)_2(CBDK)$ and $Ir(dfppy)_2(acac)$, the oxidation potentials were observed to be 1.02 and 0.34 eV, and thus the HOMO energy levels of the two

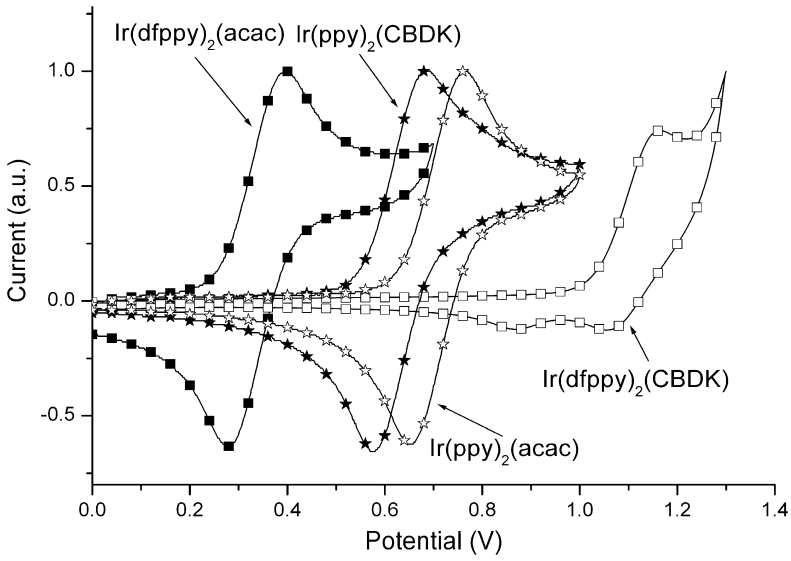

Fig. 6. Cyclic voltammograms of $Ir(ppy)_2(CBDK)$ and $Ir(dfppy)_2(CBDK)$ compared with $Ir(ppy)_2(acac)$ and $Ir(dfppy)_2(acac)$ in a CH_2Cl_2 solution containing 0.1 M Bu_4NPF_6 at a scan rate of 50 mV/s.

Table 1
Electrochemical potentials and energy levels of the iridium complexes

Iridium complex	E^{oxa} (V)	E_g[b] (eV)	HOMO[c] (eV)	LUMO[d] (eV)
$Ir(ppy)_2(CBDK)$	0.71	2.25	5.03	2.78
$Ir(ppy)_2(acac)$	0.63	2.25	4.95	2.70
$Ir(dfppy)_2(CBDK)$	1.02	2.39	5.34	2.95
$Ir(dfppy)_2(acac)$	0.34	2.39	4.66	2.27

[a] Oxidation potentials measured by cyclic voltammetry with ferrocene as the standard.
[b] Band gap estimated from the UV–vis absorption spectra.
[c] Calculated from the oxidation potentials.
[d] Deduced from the HOMO and E_g.

complexes were estimated to be 5.34 and 4.36 eV, respectively. Although they have the same band gap of 2.39 eV, the LUMO energy levels for $Ir(dfppy)_2(CBDK)$ and $Ir(dfppy)_2(acac)$ were deduced to be 2.95 and 2.27 eV, respectively. As investigated above, the triplet energy of CBDK that deduced to be 3.00 eV is more close to the triplet MLCT energy of $Ir(dfppy)_2$ (2.64 eV) than that of $Ir(ppy)_2$ (2.47 eV) fragment, there may have a different distribution of the HOMO over the $Ir(dfppy)_2(CBDK)$ which lead to such a difference in HOMO and LUMO energy. All the data deduced above indicate that the energy level of $Ir(ppy)_2(CBDK)$ and $Ir(dfppy)_2(CBDK)$ are matching to fabricate devices.

3.5. Electroluminescent properties

In order to understand the electroluminescent (EL) properties of these iridium complexes, four non-doped four-layer devices I–IV using $Ir(ppy)_2(CBDK)$, $Ir(ppy)_2(acac)$, $Ir(dfppy)_2(CBDK)$ and $Ir(dfppy)_2(acac)$, respectively, as emitter were fabricated with the same configuration of ITO/ NPB (20 nm)/iridium complex (20 nm)/BCP (5 nm)/AlQ (45 nm)/$Mg_{0.9}Ag_{0.1}$ (200 nm)/Ag (80 nm), in which NPB was used as the hole transporting material, BCP and AlQ were used as hole blocking layer and electron transporting layer, respectively. The chemical structures of the materials and the structure of the EL devices are shown in Fig. 7.

When $Ir(ppy)_2(CBDK)$ or $Ir(ppy)_2(acac)$ was used, respectively, as emitting layer, both devices I and II emit green light with emission peaking around 525 nm under different driving voltages. The CIE chromaticity coordinates are the same of $x = 0.36$, $y = 0.60$ for device I at 8 V and device II at 17 V. There are no characteristic emission peaks from NPB or AlQ, indicating that the emission originates predominantly from the iridium complex.

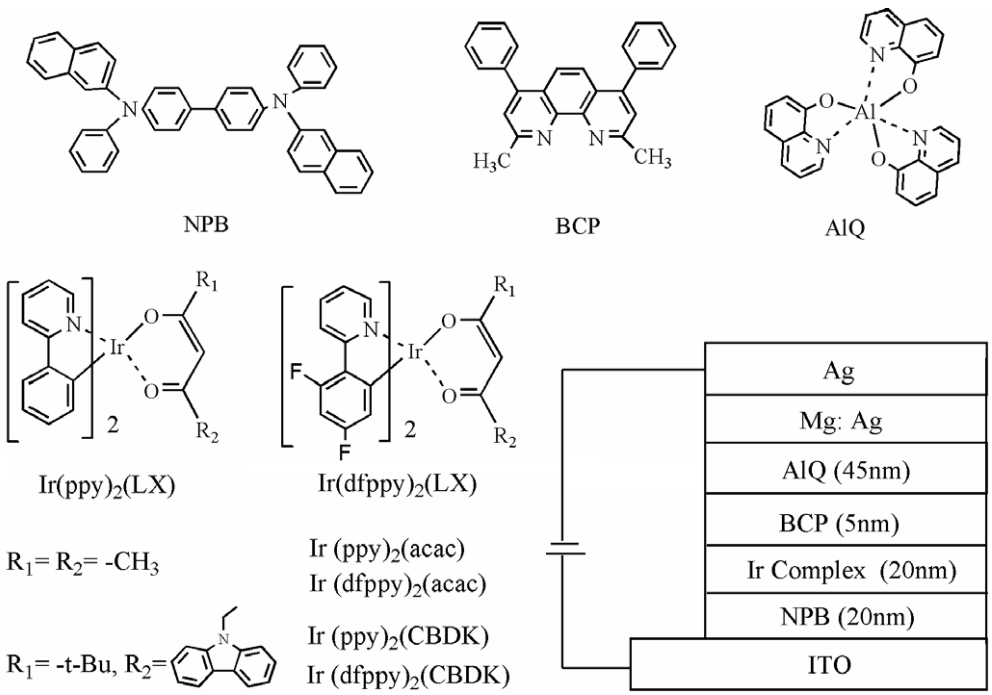

Fig. 7. Chemical structures of the materials used and the configuration of the EL devices.

And the fact that they have similar EL spectra (Fig. 8a and b, insert) shows that appropriately modification of the β-diketonate has only a little influence on the EL spectrum of the iridium complex. However, their electroluminescence performances are quite different. Device I has a lower turn-on voltage (4 V, 2.95 cd/m^2) compared with device II (8 V, 0.62 cd/m^2), the relatively low turn-on voltage is originate from improved hole transporting ability, which benefitting for exciton recombination. Device I exhibits the highest brightness of 9121 cd/m^2 at 14 V, the highest power efficiency and current efficiency are 4.54 lm/W (4 V, 2.95 cd/m^2, 0.051 mA/cm^2), 6.34 cd/A (5 V, 10.66 cd/m^2, 0.168 mA/cm^2), respectively, while device II displays the highest brightness of 4569 cd/m^2 at 19 V, the highest power efficiency and current efficiency are 0.53 lm/W (12 V, 97.2 cd/m^2, 4.8 mA/cm^2), 2.01 cd/A (12 V), respectively. In addition, when the brightness of the device I increased to 998.9 cd/m^2 (17.56 mA/cm^2), it still has a power efficiency of 1.98 lm/W (current efficiency of 5.68 cd/A). While the current density increased to 170.5 mA/cm^2 (5570 cd/m^2), the device still has a power efficiency of 0.86 lm/W (current efficiency of 3.27 cd/A). Even at the highest brightness, the current efficiency of 1.67 cd/A is kept.

When Ir(dfppy)$_2$(CBDK) or Ir(dfppy)$_2$(acac) was used as emitting layer, respectively, both devices III and IV emit blue-green light with an emission

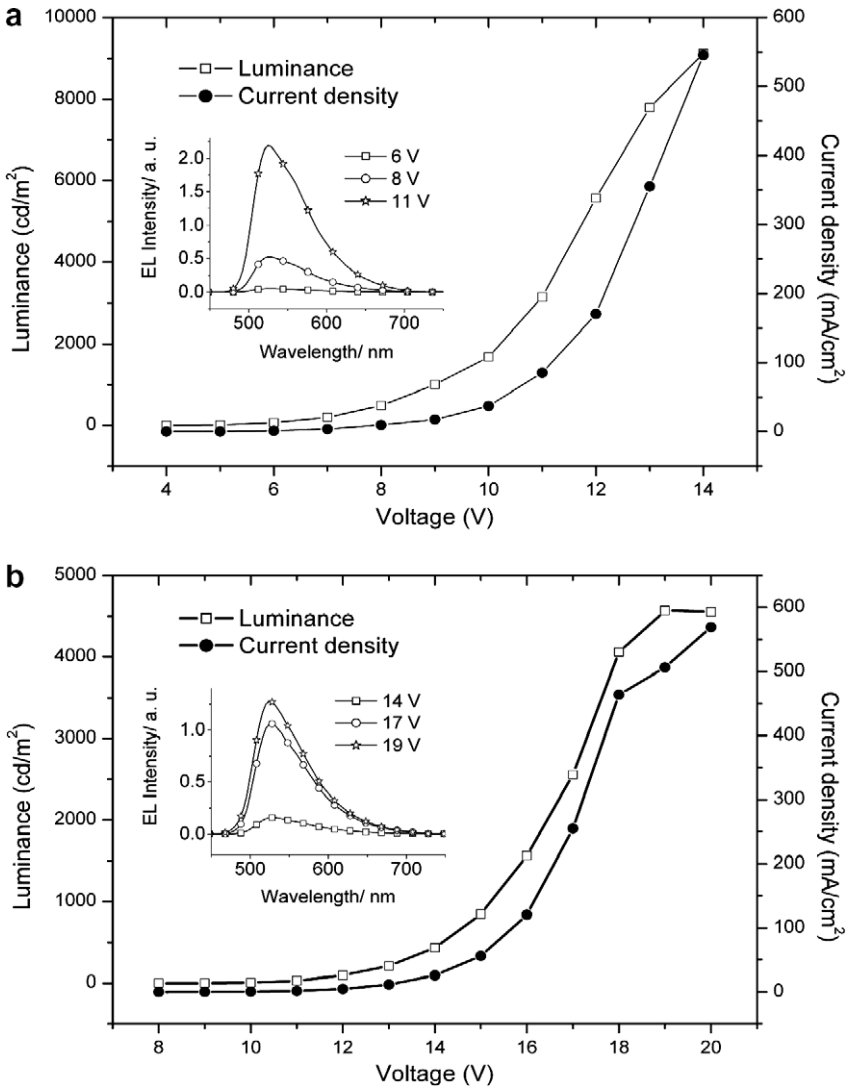

Fig. 8. Current density–luminance–voltage curves, EL spectra of device I (a – Ir(ppy)$_2$(CBDK) was used as emitter) and device II (b – Ir(ppy)$_2$(acac) was used as emitter).

peaking around 510 nm under different driving voltage. The CIE chromaticity coordinates are the same of $x = 0.29$, $y = 0.50$ for device III at 12 V and device IV at 17 V. Similar to the performance of devices I and II, only the emission originates from the iridium complex was observed and nearly the same EL spectra (Fig. 9c and d, insert) were detected when examined devices III and IV. In addition, the electroluminescence performance of deviced III and IV are also quite different. Device III has a lower turn-on voltage (6 V, 1.04 cd/m^2) compared with device IV (11 V, 0.82 cd/m^2). Device III exhibits the highest brightness of 1416 cd/m^2 at 15 V, the highest power efficiency and current efficiency are 0.51 lm/W (6 V, 1.04 cd/m^2, 0.106 mA/cm^2), 1.35 cd/A (7 V, 5.17 cd/m^2, 0.38 mA/cm^2), respectively, while device IV displays the highest brightness of 515 cd/m^2 at 19 V, the highest power efficiency and current efficiency are as low as 0.06 lm/W (14 V, 8.1 cd/m^2, 2.8 mA/cm^2) and 0.28 cd/A (14 V), respectively. The two sets data compared above show that the device performance can be greatly improved when the ancillary ligand acac was replaced by CBDK.

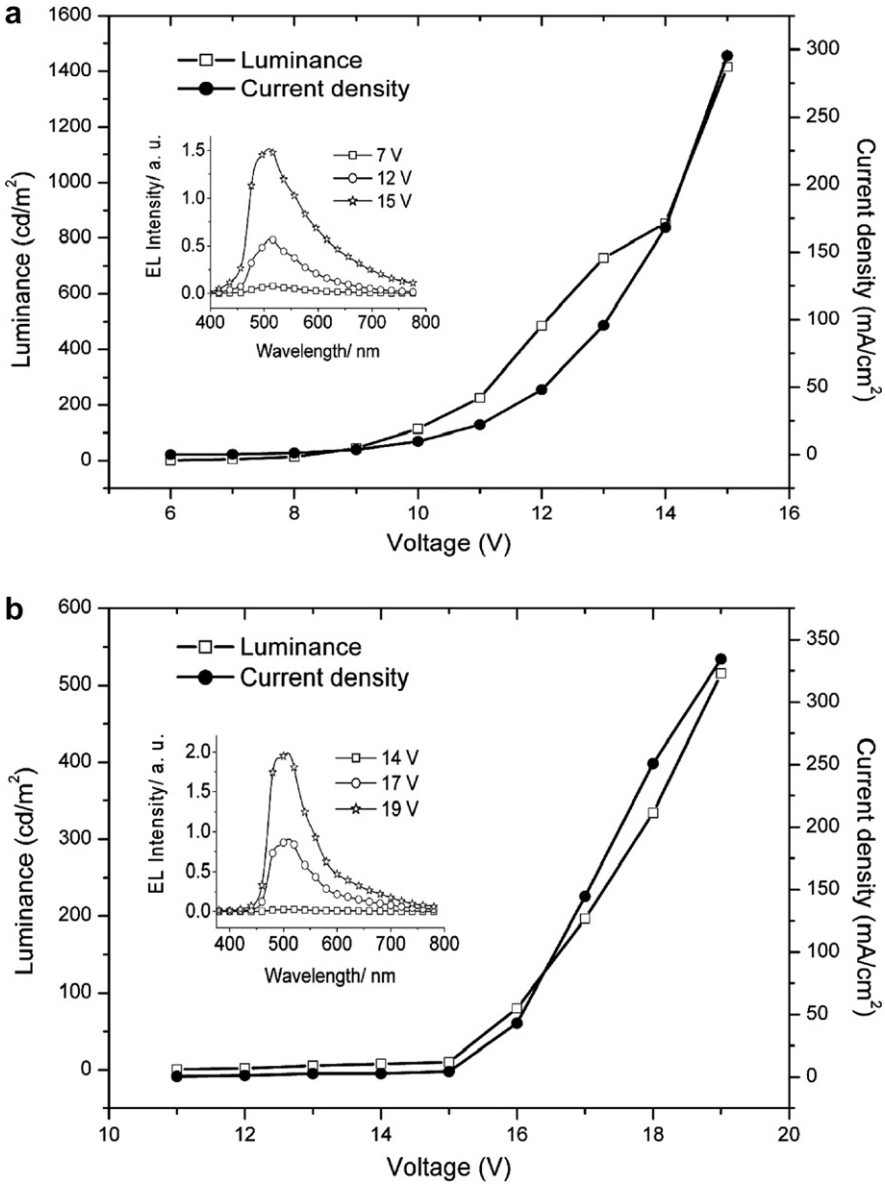

Fig. 9. Current density–luminance–voltage curves, EL spectra of device III (c – Ir(dfppy)$_2$(CBDK) was used as emitter) and device IV (d – Ir(dfppy)$_2$(acac) was used as emitter).

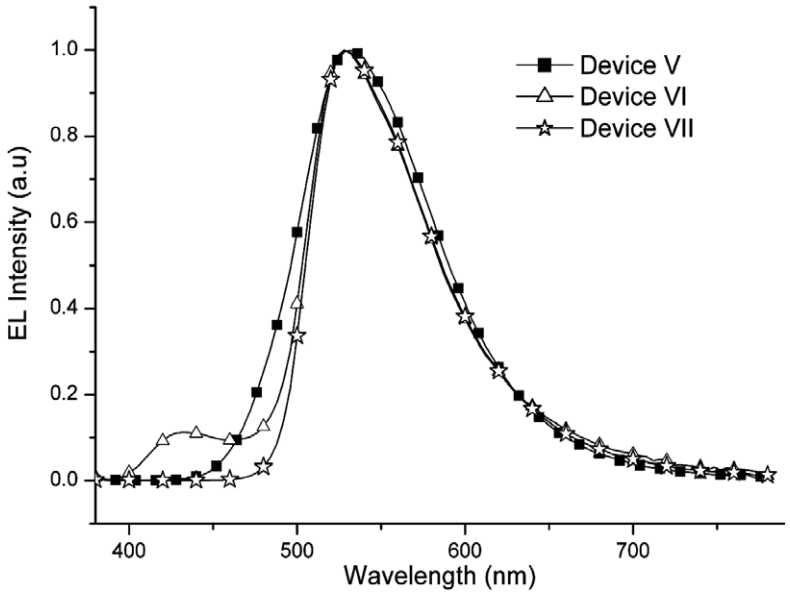

Fig. 10. EL spectra of devices V–VII.

Among the four iridium complexes, $Ir(ppy)_2$-(CBDK) has been demonstrated with the best performance, and thus the electroluminescent performance of $Ir(ppy)_2$(CBDK) was further studied. Two double-layer devices, ITO/$Ir(ppy)_2$(CBDK) (30 nm)/AlQ (30 nm)/$Mg_{0.9}Ag_{0.1}$ (200 nm)/Ag (80 nm) (device V), ITO/NPB (30 nm)/$Ir(ppy)_2$-(CBDK) (30 nm)/$Mg_{0.9}Ag_{0.1}$ (200 nm)/Ag (80 nm) (device VI) and a most simplest device VII, ITO/Ir-$(ppy)_2$(CBDK) (80 nm)/$Mg_{0.9}Ag_{0.1}$ (200 nm)/Ag (80 nm) were fabricated. Data show device V emits green light from AlQ, which indicate that $Ir(ppy)_2$-(CBDK) has a good hole transporting ability. Device VI exhibits two emission bands at 430 and 528 nm, originate from NPB and the iridium complex, respectively, indicate that the excitons were combined at the interface of the two layers, which shows that $Ir(ppy)_2$(CBDK) also has a good electron transporting ability. Device VII has a turn-on voltage (5 V, 1.15 cd/m^2) and a highest brightness of 179 cd/m^2 at 9 V. The device emits green light with an emission peaking around 525 nm from $Ir(ppy)_2$(CBDK) without any hole or electron layer, supporting the effect of CBDK from another view again. The EL spectra of devices V–VII are shown in Fig. 10.

4. Conclusions

This study reports the synthesis, photophysical and electrochemistry properties of two novel iridium complexes both containing carbazole-functionalized β-diketonate, discusses their application in non-doped OLEDs. Data show that devices based on the modified iridium complexes have remarkably improvement of electroluminescent performance, which can be attributed mainly to an improved hole transporting property that benefits the exciton transport.

Acknowledgements

We thank the National Basic Research Program (2006CB601103), and the NNSFC (20021101, 20423005, 20471004, 90401028, 50372002, 20671006) for financial support.

References

[1] M.A. Baldo, D.F. O'Brien, Y. You, A. Shoustikov, S. Sibley, M.E. Thompson, S.R. Forrest, Nature 395 (1998) 151.
[2] M.A. Baldo, S. Lemansky, P.E. Burrows, M.E. Thompson, S.R. Forrest, Appl. Phys. Lett. 76 (1999) 4.
[3] A. Kohler, J.S. Wilson, R.H. Friend, Adv. Mater. 14 (2002) 701.
[4] S.R. Forrest, Org. Electron. 4 (2003) 45.
[5] J.P. Duan, P.P. Sun, C.H. Cheng, Adv. Mater. 15 (2003) 224.
[6] X.W. Chen, J.L. Liao, Y.M. Liang, M.O. Ahmed, H.E. Seng, S.A. Chen, J. Am. Chem. Soc. 125 (2003) 636.
[7] S. Lamansky, P. Djurovich, D. Murphy, F. Abdel-Razzaq, H.-E. Lee, C. Adachi, P.E. Burrows, S.R. Forrest, M.E. Thompson, J. Am. Chem. Soc. 123 (2001) 4304.
[8] W. Lu, B.X. Mi, M.C.W. Chan, Z. Hui, N.Y. Zhu, S.T. Lee, C.M. Che, Chem. Commun. (2002) 206.
[9] B.W. D'Andrade, J. Brooks, V. Adamovich, M.E. Thompson, S.R. Forrest, Adv. Mater. 14 (2002) 1032.

[10] M. Buda, G. Kalyuzhny, A.J. Bard, J. Am. Chem. Soc. 124 (2002) 6090.
[11] E.S. Handy, A.J. Pal, M.F. Rubbner, J. Am. Chem. Soc. 121 (1999) 3525.
[12] C.M. Elliott, F. Pichot, C.J. Bloom, Lonn S. Rider, J. Am. Chem. Soc. 120 (1998) 6781.
[13] X.Z. Jiang, Alex K.-Y. Jen, B. Carlson, L.R. Dalton, Appl. Phys. Lett. 80 (2002) 713.
[14] X.Z. Jiang, Alex K.-Y. Jen, B. Carlson, L.R. Dalton, Appl. Phys. Lett. 81 (2002) 3125.
[15] C. Adachi, M.A. Baldo, M.E. Thompson, S.R. Forrest, J. Appl. Phys. 90 (2001) 5048.
[16] V.V. Grushin, N. Herron, D.D. LeCloux, W.J. Marshall, V.A. Petrov, Y. Wang, Chem. Commun. (2001) 1494.
[17] Y.H. Song, S.J. Yeh, C.T. Chen, Y. Chi, C.S. Liu, J.K. Yu, Y.H. Hu, P.T. Chou, S.M. Peng, G.H. Lee, Adv. Funct. Mater. 14 (2004) 1221.
[18] Y. Wang, N. Herron, V.V. Grushin, D.L. Cloux, V. Petrov, Appl. Phys. Lett. 79 (2001) 449.
[19] R.J. Holmes, B.W. D'Andrade, S.R. Forrest, X. Ren, J. Li, M.E. Thompson, Appl. Phys. Lett. 83 (2003) 3818.
[20] A. Tsuboyama, H. Iwawaki, M. Furugori, T. Mukaide, J. Kamatani, S. Igawa, T. Moriyama, S. Miura, T. Takiguchi, S. Okada, M. Hoshino, K. Ueno, J. Am. Chem. Soc. 125 (2003) 12971.
[21] S. Lamansky, P. Djurovich, D. Murphy, F. Abdel-Razzaq, R. Kwong, I. Tsyba, M. Bortz, B. Mui, R. Bau, M.E. Thompson, Inorg. Chem. 40 (2001) 1704.
[22] T.D. Anthopoulos, M.J. Frampton, E.B. Namdas, P.L. Burn, I.D.W. Samuel, Adv. Mater. 16 (2004) 557.
[23] S.J. Yeh, M.F. Wu, C.T. Chen, Y.H. Song, Y. Chi, M.H. Ho, S.F. Hsu, C.H. Chen, Adv. Mater. 17 (2005) 285.
[24] J. Li, P.I. Djurovich, B.D. Alleyne, I. Tsyba, N.N. Ho, R. Bau, M.E. Thompson, Polyhedron 23 (2004) 419.
[25] M.K. Nazeeruddin, R. Humphry-Baker, D. Berner, S. Rivier, L. Zuppiroli, M. Graetzel, J. Am. Chem. Soc. 125 (2003) 8790.
[26] Y.M. You, S.Y. Park, J. Am. Chem. Soc. 127 (2005) 12438.
[27] C.S.K. Mak, A. Hayer, S.I. Pascu, S.E. Watkins, A.B. Holmes, A. Kohler, R.H. Friend, Chem. Commun. (2005) 4708.
[28] H.Y. Zhen, C.Y. Jiang, W. Yang, J.X. Jiang, F. Huang, Y. Cao, Chem. Eur. J. 11 (2005) 5007.
[29] S. Bettington, M. Tavasli, M.R. Bryce, A. Beeby, H. Al-Attar, A.P. Monkman, Chem. Eur. J. 13 (2007) 1423.
[30] Z.W. Liu, M. Guan, Z.Q. Bian, D.B. Nie, Z.L. Gong, Z.B. Li, C.H. Huang, Adv. Funct. Mater. 16 (2006) 1441.
[31] J.R. Gong, L.J. Wan, S.B. Lei, C.L. Bai, X.H. Zhang, S.T. Lee, J. Phys. Chem. B 109 (2005) 1675.
[32] C. Buchgraber, A. Pogantsch, S. Kappaun, J. Spanring, W. Kern, J. Polym. Sci. Pt. A: Polym. Chem. 44 (2006) 4317.
[33] J.S. Kim, P.K.H. Ho, C.E. Murphy, R.H. Friend, Macromolecules 37 (2004) 2861.
[34] M. Nonoyama, Bull. Chem. Soc. Jpn. 47 (1974) 767.
[35] J. Pommerehne, H. Vestweber, W. Guss, R.F. Mahrt, H. Bässler, M. Porsch, J. Daub, Adv. Mater. 7 (1995) 551.
[36] W.F. Sager, N. Filipescu, F.A. Serafin, J. Phys. Chem. 69 (1964) 1092.
[37] J. Li, P.I. Djurovich, B.D. Alleyne, M. Yousufuddin, N.N. Ho, J.C. Thomas, J.C. Peters, R. Bau, M.E. Thompson, Inorg. Chem. 44 (2005) 1713.
[38] S. Lamansky, P. Djurovich, D. Murphy, F. Abdel-Razaq, R. Kwong, I. Tsyba, M. Bortz, B. Mui, R. Bau, M.E. Thompson, Inorg. Chem. 40 (2001) 1704.

Available online at www.sciencedirect.com
ScienceDirect
Organic Electronics 9 (2008) 183–190
Organic Electronics
www.elsevier.com/locate/orgel

Effects of solution-processed polymer interlayers on hole injection and device performance of polymer light-emitting diodes

M. James Harding [a], Dmitry Poplavskyy [b,1], V.-E. Choong [b], Alasdair J. Campbell [a,*], Franky So [b,2]

[a] *Department of Physics, The Blackett Laboratory, Imperial College London, South Kensington Campus, London, SW7 2AZ, UK*
[b] *OSRAM Opto Semiconductors Inc., 3870, North First Street, San Jose, CA 95134, USA*

Received 5 April 2007; received in revised form 12 September 2007; accepted 13 September 2007
Available online 20 September 2007

Abstract

We present studies of current density and photometric efficiency using three well known, commercially available polyphenylenevinylene and polyfluorene based light-emitting polymers (LEPs) with different interlayers. The thin, spin-coated interlayers of poly(9,9-dioctyl-fluorene-co-*N*-(4-butylphenyl)-diphenylamine) (TFB) and poly[9,9-dioctyl-fluorene-co-(bis-*N*,*N*′-(3-carboxyphenyl)-bis-*N*,*N*′-phenylbenzidine)] (BFA) are placed between the poly(3,4-ethylenedioxythiophene)/polystyrenesulphonic acid (PEDOT:PSS) anode and the LEP. It is found that despite having very similar HOMO levels (±0.1 eV) to the LEPs, the interlayers alter both the hole injection efficiency and the photometric efficiency of PLED devices. The increase or decrease of these depends on the particular interlayer-LEP combination involved, but there is a strong, general correlation between poorer hole injection resulting in a higher photometric efficiency. We attribute the variation in hole injection to the altered morphology and contact area at the anode interfaces, with the possible involvement of mobility-dependant space-charge effects or charge trapping. The dominant process in improving the photometric efficiency must be better electron-hole current balance, and/or the shift of the recombination zone to a more favourable position with less exciton quenching. The interlayers do not act as electron blocking layers, but hole injection enhancement by electron injection does seem to occur. These results show that interlayers can both increase and decrease device performance, depending on the interlayer-LEP combination involved.

PACS: 73.61.Ph; 85.60.Jb; 72.80.Le; 73.40.Lq

Keywords: Polymer; Light-emitting diode; Interlayer; Injection

* Corresponding author. Tel.: +44 0 2075947567; fax: +44 0 2075813817.
E-mail address: alasdair.campbell@imperial.ac.uk (A.J. Campbell).
[1] Address: Innovalight, Inc., 3303 Octaius Dr Ste 104, Santa Clara, CA 95054, USA.
[2] Address: Department of Materials Science and Engineering, University of Florida, Gainesville, FL 33611-6400, USA.

1566-1199/$ - see front matter
doi:10.1016/j.orgel.2007.09.003

1. Introduction

Solution-processable organic electronic devices, such as polymer light-emitting diodes (PLEDs), organic solar cells and transistors hold great promise of becoming a commercial success due to their ease of processing, low material cost, flexibility and a number of other advantages over their inorganic-based counterparts. Understanding of interfaces between different layers within a device is of vital importance for further improvements in device performance and operational lifetime.

PLEDs normally employ a layer of poly(3,4-ethylenedioxythiophene)/polystyrenesulphonic acid (PEDOT:PSS) that is used to planarize the underlying indium-tin-oxide (ITO) surface, as well as to enhance hole injection into the active light-emitting polymer (LEP) layer. While the PEDOT:PSS layer does indeed enhance hole injection into most LEPs [1], it still does not provide a fully ohmic contact to a number of LEPs [2–5], implying that further enhancement of hole injection is possible. Enhancement of hole injection could potentially lead to higher efficiencies and lower operating voltages. In addition, proximity of the PEDOT:PSS layer to the recombination zone within the LEP can result in additional quenching of excitons thus leading to the reduction in device efficiency.

One of the recent approaches to tackle the above problems was to use an additional thin layer (a so called interlayer) of a solution-processable hole conducting polymer between the PEDOT:PSS and the LEP layer [6–9]. Bernius et al. used a relatively thick (80 nm) poly[9,9-dioctyl-fluorene-co-(bis-*N*,*N*′-(3-carboxyphenyl)-bis-*N*,*N*′-phenylbenzidine)] (BFA) layer to improve the device efficiency of a higher ionization potential (5.8 eV) green-emitting fluorine copolymer PLED by enhancing hole injection and transport [9]. Morgado et al. used a 35 nm thick layer of poly(*p*-phenylene vinylene) (PPV) to improve PLED performance of a green-emitting fluorine based polymer blend, attributing this improvement primarily to electron blocking by the PPV layer [10]. However, PPV has the disadvantage of needing an additional thermal conversion step. Kim et al. used a relatively thin (10 nm) poly-(9,9-dioctyl-fluorene-co-*N*-(4-butylphenyl)-diphenyl- amine) (TFB) interlayer with the same green-emitting blend and other polymers and observed a dramatic enhancement of PLED efficiency, which was attributed mainly to reduction of exciton quenching due to the presence of the interlayer [7]. Choulis et al. used a thin (10 nm) TFB interfacial layer to dramatically enhance hole injection into the blue-emitting polymer poly(9,9-dioctyl-fluorene) (PFO), which was attributed to a favorable position of the interlayer HOMO level between that of PEDOT:PSS and the LEP [6]. The same TFB interlayer was also used to enhance the performance of electrophosphorescent solution-processed LEDs, again due to better hole injection [11]. More recently, Lee et al. used thicker (25 nm) PFB and PVK layers to improve blue-emitting PLEDs, attributing this to either improved hole injection and relating it to the mobility of the interlayer or electron blocking by the interlayer [12]. These reports indicate that such an interlayer, when spin-coated onto the PEDOT:PSS and annealed, remains insoluble and thus is preserved when a subsequent LEP layer is spin-coated on top of it [6,7,9,11,12].

It should however be noted that in nearly all of these reports the interlayer HOMO level lies between the HOMO levels of PEDOT:PSS and the LEP, so that enhancement of hole injection due to a reduced energy barrier would be expected in these systems [6,7,9–11]. However, when the HOMO levels of PEDOT:PSS, interlayer and LEP are close to each other, the effect of the interlayer on hole injection becomes more complicated as interfacial morphology and transport will tend to dominate over any injection barriers [12]. The purpose of our study is to investigate the effect of two different thin interlayers (10 nm) with similar HOMO levels on hole injection and device performance of PLEDs. We use three different LEPs of different chemical structure and with HOMO levels close to those of the interlayer. We show that the presence of an interlayer between PEDOT:PSS and LEP can either enhance or reduce hole injection, depending on the interlayer-LEP combination, and can vary the PLED efficiency. This implies the importance of interfacial morphology and interfacial transport for hole injection into PLEDs.

2. Experimental details

The LEPs under study in this work are Sumitomo's LUMATION™ 1300 Green and LUMATION™ Blue and Merck OLED Gmbh's SuperYellow. The interlayers are TFB and BFA, provided by the Dow Chemical Company.

The HOMO levels of these interlayers are 5.33 eV and 5.28 eV, respectively, [9]. The HOMO levels of the Green LEP, the Blue LEP and SuperYellow are 5.4 eV [4], 5.2 eV [13] and 5.3 eV [14], respectively. These are within 0.1 eV of each of the LEPs used, suggesting that any benefit/loss derived from the interlayer is not due to the relative energy levels. Modeling indicates that below 0.3–0.4 eV charge injection into organic semiconductor diodes is no longer limited by injection barriers, and we are well within this regime [15,16].

The devices consist of the organic layers sandwiched between two electrodes. The anode consists of a layer of indium tin oxide (ITO) on a glass substrate. The ITO is oxygen plasma treated for 15 min to increase its workfunction. This layer is coated with a 60 nm layer of the hole-transporting PEDOT:PSS (Baytron P – CH8000 – H.C.Starck GmbH), giving the anode a workfunction of around 5.1 eV [17]. The TFB interlayers were prepared from 0.5% by weight toluene solutions, the BFA from 0.5% cyclohexanone solution. The solutions were spin-coated onto the PEDOT:PSS anode at 1200 rpm for 30 s. This yielded a layer of ~10 nm in thickness. The layer was then baked at 200 °C for 30 min. To ensure the TFB interlayer was not mixing with the LEP a subsequent washing step was introduced for a selection of devices, washing the layer in toluene at 1000 rpm for 30 s. This step made no difference to any of the devices, suggesting the interlayers were insoluble with subsequent layers. The LEPs were spun from toluene solutions yielding layers of 75 nm thickness. The devices were then transferred into a thermal evaporator, where the cathode was evaporated at a pressure of less than 10^{-6} mbar. To study the effects of the interlayers on hole current we fabricated hole-only devices – devices fabricated with a blocking contact as a cathode to ensure no injection of electrons into the LUMO of the LEP. For the hole-only devices we used Au as a cathode. The dual carrier devices had cathodes consisting of 5 nm of barium capped by 200 nm of aluminum. All devices were made entirely in a nitrogen glove box ($O_2 < 0.1$ ppm. $H_2O < 1$ ppm), and were encapsulated with a glass coverlid and getter (desiccant) prior to being removed from the glove box environment. Current–voltage–luminance (IVL) measurements were carried out using a computer controlled Keithley 237 source-measure unit, and a calibrated photodiode.

3. Results and discussion

3.1. Interlayer effects on current–voltage characteristics

Fig. 1 shows the hole-only (a) and dual carrier (b) *JV* characteristics of the LUMATION™ Blue LEP with and without interlayers. Clearly the interlayers effect the hole currents, as shown in Fig. 1a. The TFB interlayer enhances the hole current across most of the studied voltage range. In contrast, the BFA interlayer results in an enhanced hole current only at low voltages, while the current is reduced at higher voltages.

The HOMO levels of the interlayers are lower than the LUMATION™ Blue LEP. The energy barriers to hole injection from TFB and BFA are −0.13 and −0.08 eV, respectively. They are therefore not expected to have any significant effect on the hole currents. If anything, a slight reduction in hole injection might be expected due to the barriers between PEDOT:PSS and TFB and BFA of 0.18 and 0.23 eV, respectively. This is compared to a PEDOT:PSS/LUMATION™ Blue LEP barrier of 0.1 eV. However, in this case both TFB and BFA

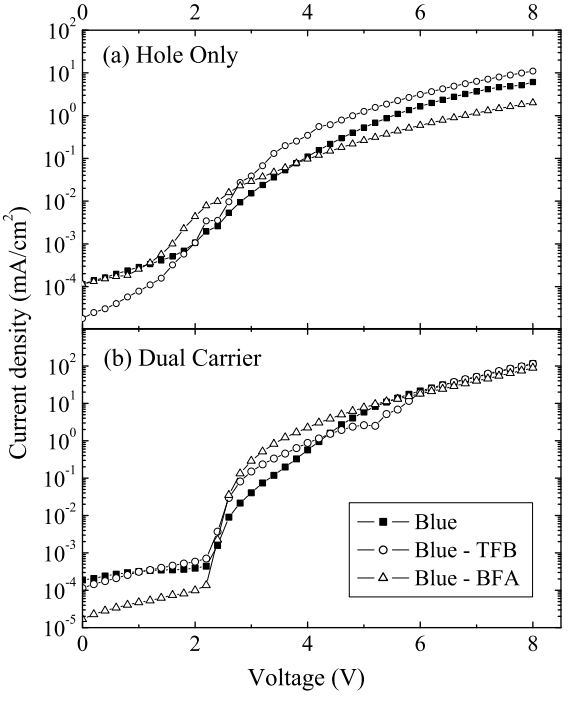

Fig. 1. Current–voltage (*IV*) characteristics of (a) the hole-only and (b) the dual carrier Blue devices with different interlayers.

would have a reduced hole current compared to the pure LUMATION™ Blue LEP. This is not observed in Fig. 1a. As expected, the injection barriers are not controlling the hole current.

The TFB device is about one order of magnitude higher in current than the BFA device. This is unlikely to reflect any difference in the PEDOT:PSS/interlayer energy barrier as it is only 0.05 eV.

Fig. 1b demonstrates the effect of interlayers on currents in dual carrier devices, which, unlike hole-only devices, contain electron-injecting electrodes. Qualitatively, currents at low voltages are affected in the same way as in the hole-only devices, where both interlayers show enhancement in current, although in this case BFA is above TFB. However, this changes at higher voltages and currents for all three devices become practically the same, in sharp contrast to what is observed for the hole-only devices (see Fig. 1a) where TFB *enhances* the hole-only current by about ×2 and BFA *reduces* the hole-only current by about ×4 at a voltage of 8 V.

In dual carrier devices the total current is given by the addition of electron, hole and recombination currents at any given point, and this will involve interactions between the local carrier densities, electric field and recombination rate [16,18–21]. Hence, it cannot be taken as a simple addition of electron and hole currents. If one or both contacts are ohmic, the presence of carriers of opposite sign will greatly increase any space-charge limited currents [16,21–23]. Also, electron trapping at the PEDOT:PSS interface has also been shown to improve hole injection in some PLEDs [3,24].

Measurements of PLEDs of the LUMATION™ Blue LEP with no interlayer have a recombination zone close to the anode, suggesting that they are dominated by the injection and transport of electrons at higher voltages [25]. However, non-optimized electron injecting contacts for the Blue LEP are used in this work, so the electron currents will be lower. The dual carrier currents in Fig. 1b at 8 V are one order of magnitude greater than even the TFB hole-only device in Fig. 1a. This suggests that the electron currents are larger than the hole currents. However, this increase is also likely to be because the injection of electrons boosts the injection and density of holes. Certainly at lower voltages the total current is strongly affected by the presence of the interlayers, while currents at higher voltages are relatively unaffected. It also implies that the interlayers cannot act as strong electron blocking layers at the anode.

Fig. 2 shows *JV* measurement results for hole-only (a) and dual carrier (b) SuperYellow (SY) devices with and without interlayers.

Hole-only currents, presented in Fig. 2a, are adversely affected by both interlayers for all voltages studied, with the BFA interlayer resulting in the strongest reduction of the hole current. At 8 V the hole current is reduced by a factor of 2 for TFB, and a factor of 10 for BFA compared to the device with no interlayer. Given the HOMO levels, the energy barriers to hole injection into the SY LEP from PEDOT:PSS, TFB and BFA are 0.2, −0.03 and 0.02 eV, respectively. Similar to the Blue LEP, the HOMO level of SY is well aligned with the HOMO levels of the interlayers. The barrier to injection from PEDOT:PSS is the largest, and yet this gives the largest current. This shows very clearly that the variations in hole injection cannot be attributed to changes in the injection barriers.

It should be pointed out that in this case the LEP and the interlayers are chemically different, since the SY polymer is a poly(phenylenevinylene)-based copolymer while the interlayers are polyfluorene-based. Such differences may result in poor intermix-

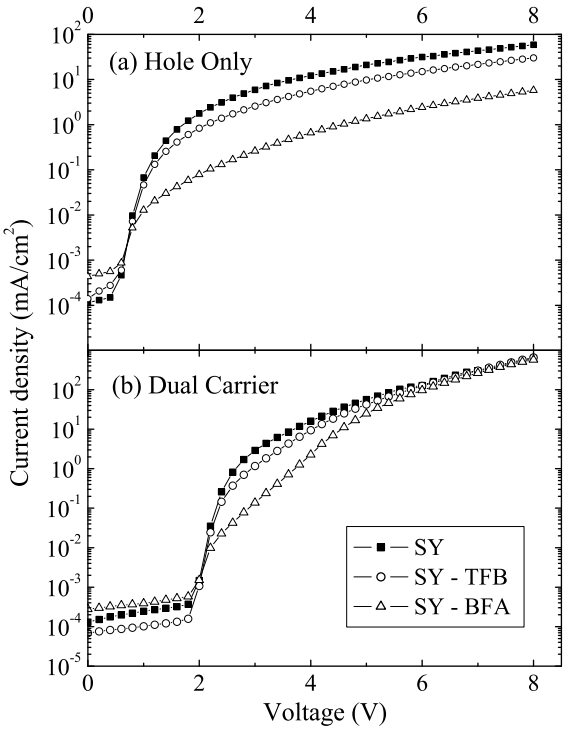

Fig. 2. Current–voltage (*IV*) characteristics of (a) the hole-only and (b) the dual carrier SuperYellow (SY) devices with different interlayers.

ing at the interface, both for TFB and BFA, and thus in a reduced hole injection efficiency. We have shown that non-uniform hole injection from PEDOT:PSS into the Green LEP below results in a reduced hole current [4]. If the physical contact between the interlayer and the LEP is poor it may also result in non-uniform injection, again leading to a reduced hole current. This is consistent with the similar shapes of the *JV* curves with and without interlayers, suggesting a change in the injecting area but not in the injection mechanism.

Dual injection currents in SY, shown in Fig. 2b, reveal very similar behavior to that of the Blue LEP. Indeed, the differences in current density at low voltages are the same as those for the corresponding hole-only devices, while at higher voltages the currents become practically identical. This behavior is consistent with earlier results that the current in dual carrier SY PLEDs are dominated by the hole current at low voltages, but that at higher voltages the electron current component either dominates and/or greatly increases the hole current [26,27]. This is strongly supported by the fact that all the dual carrier currents at 8 V in Fig. 1b are one order of magnitude larger than the largest hole-only current at 8 V in Fig. 1a, which is for the non-interlayer device. It also implies that the interlayers cannot act as strong electron blocking layers at the anode in this LEP, despite the lower LUMO level (of order 0.3–0.4 eV) compared to BFA and TFB.

Fig. 3 shows the *JV* characteristics for (a) hole-only and (b) dual carrier Green LEP devices. From Fig. 3a we see that the effect of the BFA interlayer is to reduce the hole current across the whole studied voltage range, while the TFB interlayer reduces hole current at low voltages (up to 4 V) and enhances hole current at higher voltages. Given the HOMO levels the energy barriers to hole injection into the Green LEP from PEDOT:PSS, TFB and BFA are 0.3, 0.07 and 0.12 eV respectively. Therefore, as in the cases of the Blue LEP and SY, these are not expected to limit hole injection. Indeed, the hole current for the BFA device is about a factor of four times lower than the non-interlayer device, while the injection barrier is 0.18 eV larger.

Unlike with the other LEPs, both BFA and TFB are expected to act as shallow hole traps in the Green LEP with an energy depth of about 0.1 eV. This could explain why hole injection is actually *reduced* at low voltages in the interlayer devices. Any such traps would be confined to a narrow interfacial region at the interlayer/LEP boundary. At low voltages the traps will be empty, and thus will reduce the injected current. As the voltage is increased the traps will be gradually filled and thus the injection efficiency will be increased. However, this would mean that any additional intermixing at the boundary due to the solubility of TFB would not affect the trap density compared to BFA.

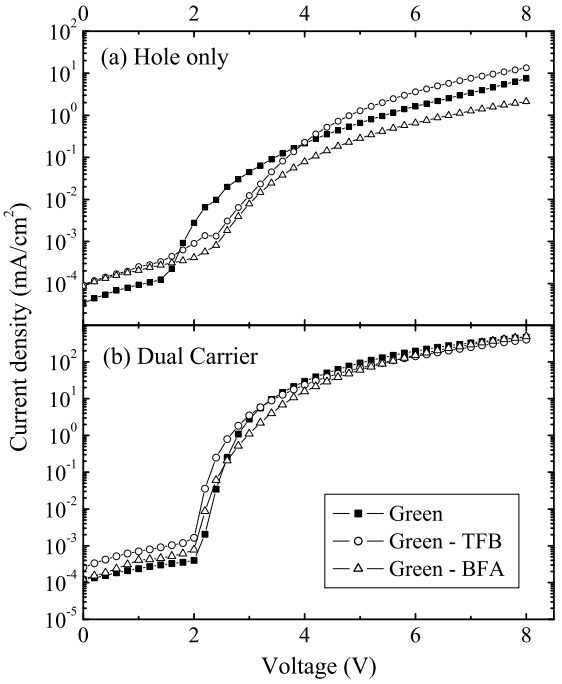

Fig. 3. Current–voltage (*IV*) characteristics of (a) the hole-only and (b) the dual carrier Green devices with different interlayers.

Dual carrier currents in the Green LEP devices are much less affected by the presence of the interlayers, as shown in Fig. 3b. Again, similarly to the previous cases, there is practically no difference between the devices with and without interlayers at higher voltages, while some small differences are still observed in the low voltage range. Previous measurements of single-carrier diodes of this Green LEP have shown that the electron-only current is an order of magnitude higher than the hole-only current [4]. The observed relative insensitivity of the dual injection current for the Green LEP devices to the presence of the interlayers, along with its magnitude, is consistent with the characteristics being dominated by the electron current. However, the effect of electrons in the device may again increase the hole currents. The results additionally imply that the interlayers cannot act as strong electron blocking layers at the anode.

Finally, inspection of all of the results in Figs. 1a, 2a and 3a show that the hole-only currents for all the devices with TFB interlayers are always higher than those with BFA interlayers. Between 4 and 8 V this is by about an order of magnitude and is irrespective of the LEP involved. This suggests that hole injection from PEDOT:PSS into TFB is better than into BFA. This must be due to either better physical contact, less or more interfacial intermixing, less charge trapping, a higher hole mobility, or some combination of these factors.

3.2. Interlayer effects on PLED efficiencies

Fig. 4 shows photometric efficiency versus current density measurements taken from the same dual carrier Blue devices used in Fig. 1. The overall efficiencies are relatively low due to the BaAl cathode not being optimal for this material, and can be further improved by using a cathode with higher electron injection efficiency. However, if device efficiency can be improved by injecting more electrons, the dual carrier device currents in Fig. 1b must involve a substantial contribution from holes. Indeed, the carrier balance in the recombination zone cannot be optimal, but must involve too many holes.

In Fig. 4, the efficiency of the BFA device is highest, followed by the non-interlayer device and then the TFB device. This immediately indicates that a decrease in exciton quenching due to the interlayer cannot be the dominant effect, as otherwise the BFA device would have a similarly high efficiency as the TFB device. Instead, the efficiencies appear to follow the inverse behaviour of the hole currents over the same bias range (between about 5.5 V and 8 V). This strongly suggests that decreasing the hole current increases the efficiency. This is consistent with the above observation about the efficiency of these devices: there being too many holes and too few electrons in the recombination zone. Hence, the hole currents in the dual carrier devices must be strongly increased by the presence of electrons in the device, whether by better injection due to electron trapping at the anode, cancellation of bulk space-charge limitations in the injected carrier densities, or removal of carriers by recombination. However, the differences in efficiency (of order ×2 between TFB and BFA) are not as great as the differences in hole current (of order ×7) at the same bias range. Hence, the differences between hole-injecting electrodes will be diminished in the dual carrier devices.

Fig. 5 shows photometric efficiencies of SY dual injection devices as a function of current density. The BFA device is the highest, then the TFB device and then the non-interlayer device. Again this follows the inverse behaviour of the hole currents over the same bias range. A decrease in hole injection increases the efficiency. This can be understood in exactly the same way as the Blue LEP devices. The differences in efficiency (of order ×1.25 between BFA and the non-interlayer device) are not as great as the differences in hole current (of order ×10) at the same bias range. Therefore, the differences between different hole-injecting electrodes will be diminished in the dual carrier devices.

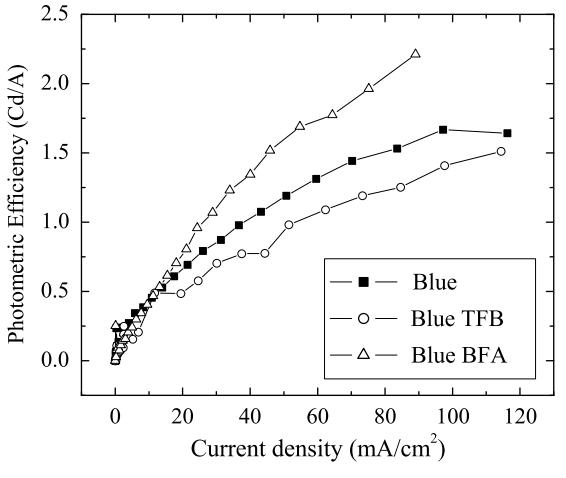

Fig. 4. Photometric efficiency of Blue PLEDs with different interlayers as a function of current density.

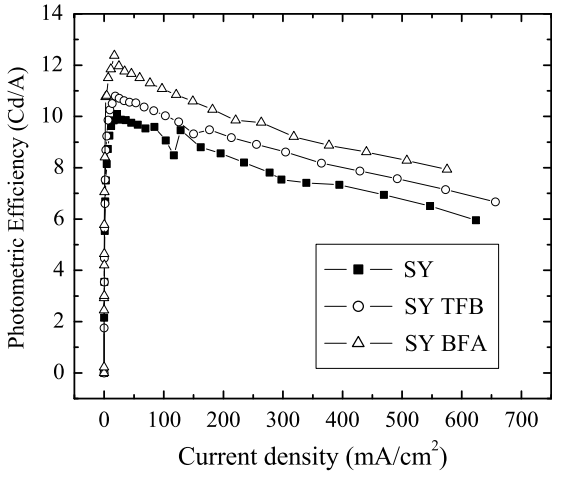

Fig. 5. Photometric efficiency of SuperYellow dual injection devices with different interlayers as a function of current density.

Fig. 6 shows the results of efficiency measurement for the Green LEP dual carrier devices. The situation is more complex. The interlayer devices follow the same trends shown for the Blue and SY devices. The BFA device is higher than the TFB device, the efficiency again following the inverse behaviour of the hole currents over the same bias range. A decrease in hole injection again seems to increase the efficiency. However, the efficiency of the non-interlayer device decreases with increasing current density, being initially higher than both interlayer devices, falling below the BFA device at about 100 mA/cm^2, and then decreasing to the TFB value at about 400 mA/cm^2. As the non-interlayer devices hole injection at higher biases in Fig. 1a lies between that of TFB and BFA, over most of the measured range in Fig. 6 it does still follow the trend of a reduced hole current equating with better efficiency. However, the interlayers must change the process of hole injection at the anode for the Green LEP. The variation of hole injection with applied bias, how it is effected by injected electrons, the position of the recombination zone, and variations in exciton quenching levels with position will then determine the differences in the shape and magnitude of the efficiency-current density characteristics in Fig. 6. Again, the differences in efficiency (of order ×1.25 between BFA and the TFB device) are not as great as the differences in hole current (of order ×8) at the same bias range. The differences between different hole-injecting electrodes are again diminished in the dual carrier devices.

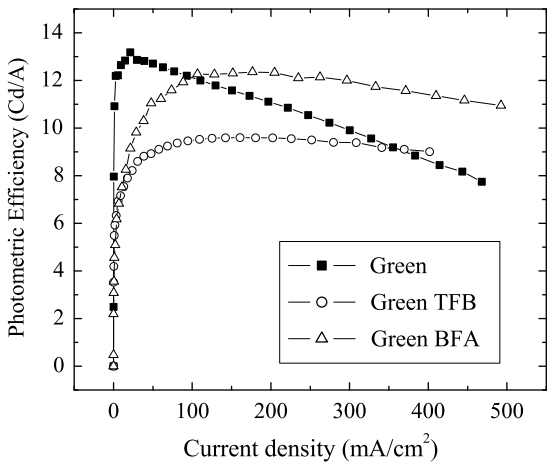

Fig. 6. Photometric efficiency of Green dual injection devices with different interlayers as a function of current density.

Therefore, for all three types of LEP with the two different polymer interlayers a lower hole injection efficiency can be equated with a higher photometric efficiency. The large dual carrier currents compared to the hole-only currents therefore support the model of hole injection enhancement due to the presence of electrons. Device efficiencies, which are expected to be strongly affected by changes in hole injection efficiency, are however much less affected. The reduction in exciton quenching at the PEDOT:PSS/LEP interface due to the interlayer is more difficult to identify.

4. Conclusions

We have shown how hole injection into PLEDs can be varied by using hole conducting interlayers even when the interlayer HOMO level is within 0.1 eV of the LEP. Depending on the interlayer and LEP combination, hole injection can be either enhanced or reduced. This must depend on the level of physical contact, chain intermixing and hole trapping at the interlayer interfaces, and any mobility dependant space-charge effects. This result shows that interfacial morphology and charge transport, apart from energetic alignment, can alter charge injection. The device photometric efficiency has an inverse relationship with the hole injection efficiency, indicating that a reduction in hole injection improves carrier balance in these devices. The size of the dual carrier currents however indicate that hole injection enhancement must occur due to the presence of electrons in the bulk and/or trapped at the anode. In dual carrier devices such enhancement effects must also reduce the differences in hole injection efficiency compared to the single carrier devices. Electron blocking does not seem to play a role, and any changes due to the interlayers reducing exciton quenching at the PEDOT:PSS interface are difficult to identify. However, the interlayers can improve PLED photometric efficiency by up to 25%, and if they do not have a negative effect on device lifetime they will have a strong future in this technology.

Acknowledgements

We thank the UK Engineering and Physical Research Council (grant GR/S14078/01) for financial support. We thank Sumation for the polymers used in this study.

References

[1] A.J. Campbell, D.D.C. Bradley, H. Antoniadis, M. Inbasekaran, W.W. Wu, E.P. Woo, Appl. Phys. Lett. 76 (2000) 1734–1736.

[2] D. Poplavskyy, T. Kreouzis, J. Nelson, A.J. Campbell, D.D.C. Bradley, Mater. Res. Soc. Sym. Proc. 725 (2002) 67–77.

[3] D. Poplavskyy, J. Nelson, D.D.C. Bradley, Appl. Phys. Lett. 83 (2003) 707–709.

[4] D. Poplavskyy, W. Su, F. So, J. Appl. Phys. 98 (2005) 014501.

[5] A.J. Campbell, D.D.C. Bradley, H. Antoniadis, J. Appl. Phys. 89 (6) (2001) 3343.

[6] S.A. Choulis, V.-E. Choong, A. Patwardhan, M.K. Mathai, F. So, Adv. Mater. 16 (2006) 1075.

[7] J.-S. Kim, R.H. Friend, I. Grizzi, J.H. Burroughes, Appl. Phys. Lett. 87 (2005) 023506.

[8] W. Su, D. Poplavskyy, F. So, H. Clearfield, D. Welsh, W. Wu, SID Symposium Digest of Technical Papers 36 (2005) 1871.

[9] M. Bernius, M. Inbasekaran, E. Woo, W. Wu, L. Wujkowski, J. Mater. Sci.: Mater. Electron. 11 (2000) 111–116.

[10] J. Morgado, R.H. Friend, F. Cacialli, Appl. Phys. Lett. 80 (2002) 2436–2438.

[11] S.A. Choulis, V.-E. Choong, M.K. Mathai, F. So, Appl. Phys. Lett. 87 (2005) 113503.

[12] T.W. Lee, M. Kim, S.Y. Kim, S.H. Park, O. Kwon, T. Noh, Appl. Phys. Lett. 89 (2006) 123505.

[13] R. Khan, D.D.C. Bradley, M. Webster, J. Auld, A. Walker, Appl. Phys. Lett. 84 (6) (2004) 921.

[14] H. Becker, H. Spreitzer, W. Kreuder, E. Kluge, H. Schenk, I. Parker, Y. Cao, Adv. Mater. 12 (1) (2000) 42.

[15] P.S. Davids, I.H. Campbell, D.L. Smith, J. Appl. Phys. 82 (12) (1997) 6319.

[16] G.G. Malliaras, J.C. Scott, J. Appl. Phys. 85 (10) (1999) 7426.

[17] T.M. Brown, J.S. Kim, R.H. Friend, F. Cacialli, R. Daik, W.J. Feast, Appl. Phys. Lett. 75 (1999) 1679.

[18] B.K. Crone, P.S. Davids, I.H. Campbell, D.L. Smith, J. Appl. Phys. 84 (2) (1998) 833.

[19] J.C. Scott, S. Karg, S.A. Carter, J. Appl. Phys. 82 (1997) 1454.

[20] G.G. Malliaras, J.C. Scott, J. Appl. Phys. 83 (1998) 5399.

[21] P.W.M. Blom, M.J.M. de Jong, S. Breedijk, Appl. Phys. Lett. 71 (7) (1997) 930.

[22] A.J. Campbell, Conduction in Organic Materials, in: T. Richardson (Ed.), Functional Organic and Polymeric Molecular Materials, Wiley & Sons, Chichester, 1999, pp. 201–232 (Chapter 8).

[23] B.K. Crone, P.S. Davids, I.H. Campbell, D.L. Smith, J. Appl. Phys. 84 (1998) 833.

[24] P.J. Brewer, P.A. Lane, J. Huang, A.J. deMello, D.D.C. Bradley, J.C. deMello, Phys. Rev. B 71 (2005) 205–209.

[25] T. van Woudenbergh, J. Wildeman, P.W.M. Blom, J.J.A.M. Bastiaansen, B.M.W. Langeveld-Vos, Adv. Funct. Mater. 14 (2004) 677–683.

[26] J. Burroughes, presented at the FPD International 2004 (<http://cn.fpdisplay.com/forum/images/upfile/2005347488.pdf>).

[27] D. Poplavskyy, unpublished.

Available online at www.sciencedirect.com
ScienceDirect
Organic Electronics 9 (2008) 191–197
Organic Electronics
www.elsevier.com/locate/orgel

Ambipolar transport in transparent and flexible all-organic heterojunction field effect transistors at ambient conditions

P. Cosseddu [a,b,*], A. Bonfiglio [a,b], I. Salzmann [c], J.P. Rabe [c], N. Koch [c]

[a] INFM-University of Cagliari, Department of Electric and Electronic Engineering, Piazza d'Armi, 09123 Cagliari, Italy
[b] CNR-INFM-S3 nanoStructures and bioSystems at Surfaces, Via Campi 213/A, 41100 Modena, Italy
[c] Humboldt-Universität zu Berlin, Institut für Physik, Newtonstr. 15, 12489 Berlin, Germany

Received 17 September 2007; received in revised form 25 October 2007; accepted 31 October 2007
Available online 22 November 2007

Abstract

We report on the realization of fully flexible and transparent n-type and ambipolar all-organic OFETs. A double layer, pentacene-C60 heterojunction, was used as the semiconductor layer. The contacts were made with poly(ethylenedioxythiophene)/poly(styrenesulfonate) (PEDOT:PSS) and patterned by means of Soft Lithography MicroContact Printing (μCP). Interestingly, as demonstrated by atomic force microscopy and X-ray diffraction investigations, growing C60 on a pre-deposited pentacene buffer layer leads to a clear improvement in the morphology and crystallinity of the deposited film allowing to obtain n-type conduction despite the very high electron injection barrier at the interface between PEDOT:PSS and C60. As a result, it was possible to realize n-type and ambipolar all-organic OFETs by optimizing the thicknesses of the pentacene buffer layer. All devices, measured in air, worked in accumulation mode with mobilities up to 1×10^{-2} cm^2/V s and 3.5×10^{-4} cm^2/V s for p-type and n-type regimes, respectively. This is particularly interesting because it demonstrates, also for n-type and ambipolar transistors, the possibility of avoiding problems normally associated to metal contacts: the lack of mechanical robustness, flexibility, and the unfeasibility of realizing contacts with low cost techniques like printing or soft lithography. These results confirm the importance of the substrate properties for the ordered growth of organic semiconductors, which determines the transport properties of organic materials.

PACS: 68.55.am; 85.30.Tv; 85.30.Pq

Keywords: Organic field effect transistors; Ambipolar transport; Fullerene; Pentacene; Flexible electronics

1. Introduction

Over the past few years, organic field effect transistors (OFETs) have attracted considerable attention since they offer the opportunity to produce low cost large-area devices on plastic substrates, opening an entirely new market segment. Many applications have already been reported, such as

* Corresponding author. Address: INFM-University of Cagliari, Department of Electric and Electronic Engineering, Piazza d'Armi, 09123 Cagliari, Italy. Tel.: +39 0706755769; fax: +39 0706755782.
E-mail address: piero.cosseddu@diee.unica.it (P. Cosseddu).

1566-1199/$ - see front matter © 2007 Elsevier B.V. All rights reserved.
doi:10.1016/j.orgel.2007.10.011

organic flexible displays, smart tags, and sensors [1–3]. One characteristic of almost all-organic semiconductors is that, even in their undoped state, often only unipolar transport, i.e. either holes (in most cases) [4,5] or electrons [6–8], can be realized. In several cases, the work function of metals employed for contact fabrication dictated the polarity of charge transport [9]. The simultaneous transport of both types of carriers, however, could lead to a simplification in the design of complementary logic circuits, allowing at the same time to reduce power dissipation and to increase noise margins. As a consequence, a lot of efforts have been made towards the fabrication and optimization of ambipolar OFETs. Recently, solution-processed ambipolar OTFTs and organic inverters using interpenetrating blends [10–12] or small-bandgap polymer [10] have been reported. As for organic small molecules, OTFTs based on a heterostructure, first reported by Dodabalapur et al. [13], have exhibited ambipolar transport characteristics [14–17] showing high mobility (both in the p- and n-type regime) and very good stability under ambient conditions [11,18–23]. However, most ambipolar OFETs are still assembled on silicon substrates, just few examples of devices realized on plastic exist, and all of them were realized using metal contact as source and drain electrodes. In an industrial perspective, using conductive polymers instead of metals would be highly required, since they offer the possibility to be deposited and patterned with very low cost techniques suitable for mass production as ink jet printing and/or soft lithography [24,25]. Nevertheless, obtaining efficient ambipolar transport using conductive polymer contacts is a non-trivial challenge, in particular because of the very high electron injection barriers usually present at interfaces between them and the most common n-type organic semiconductors. As a result, all previous attempts to achieve ambipolar charge injection and transport with conductive polymer contacts in organic transistors failed.

In principle, most organic semiconductors may allow both kinds of charge carriers transport [26–29]. Therefore, the realization of either n- or p-type conduction in OFETs is expected to depend mainly on the metal employed as source and drain electrodes enabling the injection of the desired type of charge carrier into the semiconductor layer. The efficiency of charge injection strongly depends on the interplay of metal electrode work functions with the ionization energy as well as electron affinity of the respective organic compounds [30], i.e., the energetic position of the transport levels derived from the lowest unoccupied molecular orbital (LUMO) and highest occupied molecular orbital (HOMO). Recently, Takenobu et al. [9] showed that the choice of an appropriate pair of high and low work function metals as source and drain electrodes can lead to an improvement and balance of carrier injection into the channel. However, the impact of electrode work function is still under debate, as reports exist on efficient n-type OFETs despite high electron injection barriers [31,32] employing gold electrodes, while it was also difficult to obtain n-type conduction even in devices with low work function electrodes [1].

In some cases, electron trapping at the interface between the gate dielectric and the organic semiconductor is regarded as cause for the lack of n-type conduction. Chua et al. [29] have suggested that, in SiO_2 based devices, electron conduction is inhibited by a high concentration of hydroxyl groups acting as electron traps at the interface. Another important issue was discussed by Itaka et al. [33], who demonstrated that controlling the wetting of a substrate by a molecular overlayer can improve the crystalline quality of organic semiconductor films, which in turn is favorable for efficient charge transport. They showed that depositing a thin pentacene layer (1 or 2 monolayers) prior to the deposition of a C60 layer leads to an increase of the n-type mobility if compared to a single C60 layer device.

In the present paper, we report on the realization of fully flexible and transparent, all-organic n-type and ambipolar OFETs on a plastic substrate using conducting polymer contacts. It will be shown that modifying the interface between gate dielectric and the organic semiconductor by means of organic planar heterojunctions, leads to an improvement of the crystallinity of the deposited active layer which, in turn, allows to overcome the very high electron injection barrier between the conductive polymer and the active layer, leading to obtain n-type and ambipolar charge transport.

2. Experimental

A poly(ethyleneterephtalate) (PET) sheet with 1.6 μm thickness, (Mylar®, Du Pont), adapted to a plastic frame, was used as gate insulator and as mechanical support for the whole device. This polymer is characterized by a dielectric constant similar

to that of SiO_2 ($k_e \approx 3.0$), high resistivity (surface resistivity $10^{16}\ \Omega^{-2}$) and low permeability to oxygen, hydrogen, water and CO_2. Moreover, it can be used as a flexible mechanical support for the realization of completely flexible electronic devices. Conducting poly(ethylenedioxythiophene):polystyrenesulfonate (PEDOT:PSS; Baytron P CPP 105D, H.C. Stark GmbH) was used as electrode material. Gate electrodes were made by spin coating, while source and drain contacts were patterned by means of soft lithography (MicroContact printing, μCP). A poly(dimethylsiloxane) (PDMS) stamp, reproducing the pattern of source and drain electrodes, was used to transfer the PEDOT:PSS pattern onto the substrate in order to obtain the final structure. In our case, electrodes with $W = 5$ mm and $L = 75$ μm (where W and L are the channel width and length, respectively) were used. However, electrode dimensions can be easily lowered, due to the high resolution achievable with PDMS, which is able to reproduce features on the order of 100 nm [34]. All details about the printing procedure by means of μCP can be found in Ref. [25]. All devices were realized in "top contact" configuration by printing the source and drain electrodes after the organic semiconductor deposition, since this structure already allowed to obtain unipolar p-type OFETs with mobilities up to 0.1 cm^2/V s and I_{on}/I_{off} ratios around 10^5 [35]. As n-type material we employed C60. Where indicated, we used pentacene ($C_{22}H_{14}$) as a buffer layer prior to C60 film deposition. Pentacene and C60 were evaporated from resistively heated Al_2O_3 crucibles in a custom-built vacuum chamber (base pressure 5×10^{-8} mbar). The film thickness and the deposition rate (0.5 nm/min in all cases) were monitored by a quartz crystal microbalance placed next to the sample. The structure of our fully flexible and transparent device is depicted in Fig. 1.

Drain-source current (Ids) measurements were carried out at room temperature in air. An Agilent HP 4155 Semiconductor Parameter Analyzer, provided with gold tips for contacting the electrodes, was used to control the gate voltage (V_{gs}) and the drain-source voltage (V_{ds}) and to measure the drain-source current (I_{ds}) (the source being the common ground).

X-ray diffraction measurements were performed at the beamline W1.1 at the synchrotron radiation source HASYLAB (Hamburg, Germany) using a wavelength of 0.11808 nm. In order to achieve a flat substrate surface, Mylar® foil was fixed on quartz

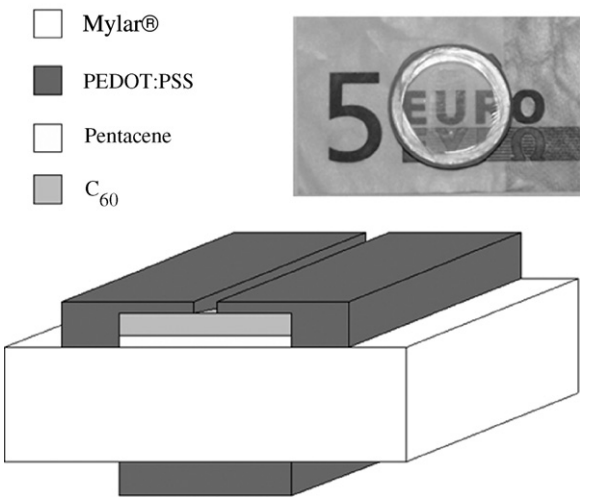

Fig. 1. Schematic of the ambipolar device structure. In the inset a picture of the transparent film assembled on a circular frame with the final device assembled on it, demonstrating the transparency of the resulting structure.

coupons (area 1 cm^2) using double-sided adhesive tape. The vacuum-deposition process was identical to the case of OFET preparation described above.

Scanning force microscopy (SFM) measurements were performed in Tapping Mode™ with a Nanoscope III device (Veeco Instruments).

3. Results and discussion

At first, all-organic top contact OFETs were fabricated by employing a single C60 layer as semiconductor. However, no n-type behavior was obtained in such configurations. One possible reason for this could be the rather large electron injection barrier at the PEDOT:PSS/C60 interface. In fact, the hole injection barrier at the PEDOT:PSS/C60 interface was reported to be 1.0 eV under ultrahigh-vacuum conditions [36], which yields an electron injection barrier at this interface of 1.5 eV, considering the electronic gap of C60 as 2.5 eV [37]. Note that in our case the C60 layer was exposed to air prior to PEDOT:PSS printing, and therefore the reported value for the electron injection barrier is to be considered only as an estimation. In addition, a poor structural and morphological quality of the C60 layer on bare Mylar® could also be invoked as a cause for device failure. In fact, the high surface roughness of Mylar® (measured root mean square roughness = 1.2 nm), can cause a high concentration of structural defects (i.e., charge traps) within the active layer, thus inhibiting electron transport

through the channel. Moreover, it is known from literature that electron trapping can be pronounced when using a polar gate dielectric as PET [29], thus inhibiting electron transport. All these assumptions prompted us to modify the interface between the gate dielectric and the organic layer by using a buffer film, in the present case a thin pentacene film. Interestingly, the electrical characteristics of devices using a pentacene buffer layer of 3 nm nominal thickness showed clear n-type device behavior, as can be seen in Fig. 2. Despite the possibly high electron injection barrier (see above) we found evidence for a field effect, and the electron mobility (obtained from the transfer characteristics in the saturation regime) was ca. 4×10^{-5} cm^2/V s. This indicates that the presence of a pentacene buffer layer improves the structural quality of the C60 film, and consequently reduces charge trapping within the channel. Also, electron trapping at the interface with the polar insulator surface could be partially avoided. This clearly demonstrates that the structural quality of the active layer and charge trapping at the insulator/organic semiconductor interface are likely more important parameters than the electrode/organic injection barrier height for achieving n-type charge transport.

Note that despite the presence of the 3 nm pentacene layer, no p-type conduction was observed. Since pentacene exhibits pronounced island growth on rough substrates such as Mylar®, we expect no closed layer over the entire gate dielectric surface to be formed at this low nominal thickness. Therefore, the absence of a continuous percolation path is most probably the reason for the lack of hole conduction in the channel.

We circumvented this problem by fabricating devices with pentacene buffer layers of nominally 10 nm thickness. As can be clearly seen from the output characteristics, recorded both in the p-type and n-type regime (Fig. 3), this strategy led to ambipolar device behavior. Note that in addition to the emergence of hole transport across the channel for a continuous pentacene layer also a clear increase of the electron mobility could be obtained. All devices were assembled in top contact configuration, i.e., source and drain are printed on the C60 layer. Consequently, the electronic structure of the metal/semiconductor interface does not change. The improvement of the n-type transport should be thus attributed to the fact that C60 grows more uniformly and crystalline if the pentacene buffer layer covers the whole insulator surface, as will be shown by means of X-ray diffraction (XRD) and scanning force microscopy (SFM). Moreover, it is worth to underline that the presence of a continuous buffer layer allows, in this case, to eliminate electron trapping at the interface with the polar gate dielectric.

Despite the high electron injection barrier and the fact that all devices were measured in air, we obtained hole mobilities up to 1×10^{-2} cm^2/V s, and electron mobilities up to 3.5×10^{-4} cm^2/V s. Only few examples of n-type or ambipolar devices stable in air can be found in the literature [11,22,23], while the majority of them have been obtained only in controlled atmosphere [17–21].

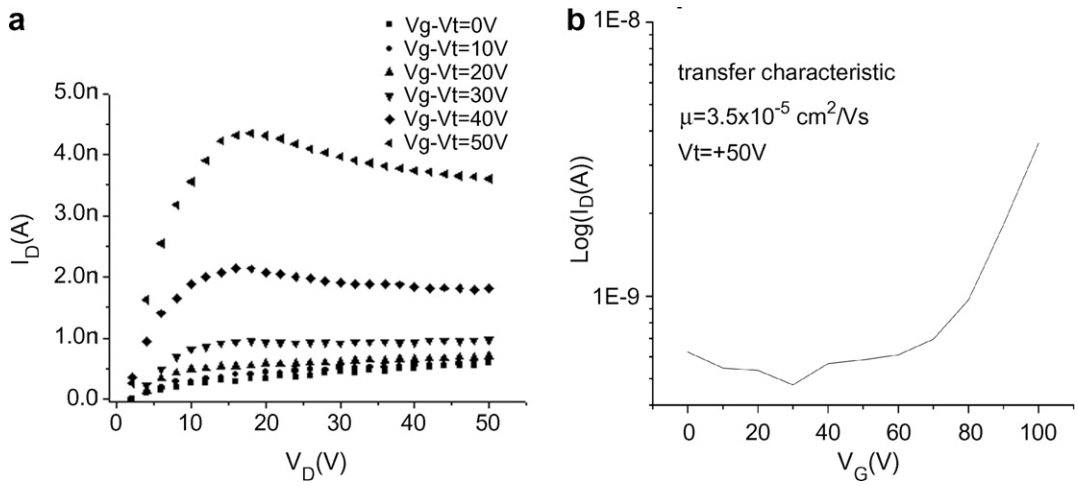

Fig. 2. Typical output (a) and transfer (b) characteristics of top contact FETs realized with a 3 nm pentacene buffer layer and a 30 nm C60 layer. The device works as a unipolar n-type FET.

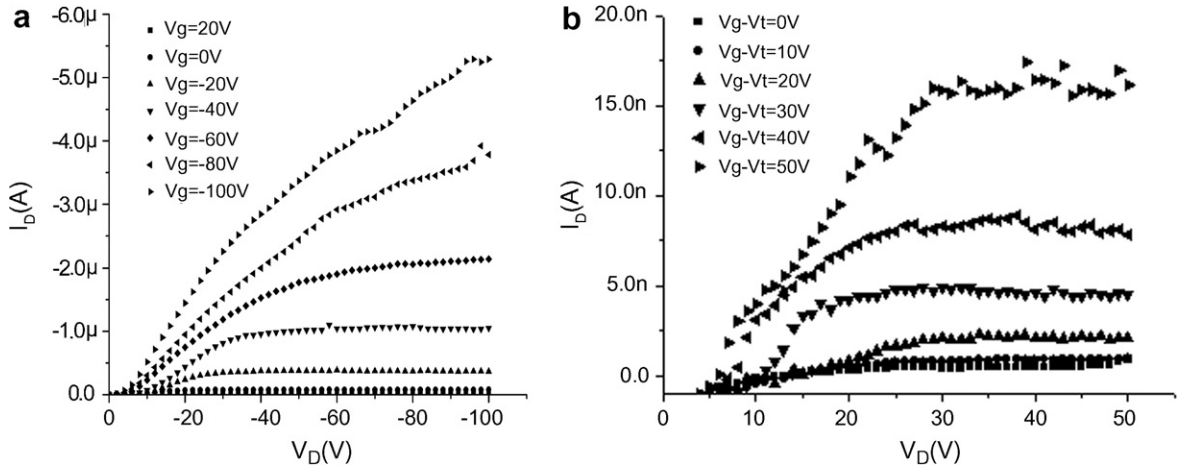

Fig. 3. Electrical characteristics of a top contact all-organic ambipolar FET realized with a 10 nm pentacene buffer layer and a 30 nm C60 layer. (a) Output characteristics of the device working in p-type mode and (b) output characteristic of the device working in n-type mode. A clear improvement in the recorded drain current (at the same $V_g - V_t$ values) can be noticed if compared to Fig. 2a.

However, from the analysis of the output characteristics reported in Fig. 3, one notices a parasitic contact resistance effect (detectable for low source/drain voltages), in the n-type regime (presumably due to the high electron injection barrier at the PEDOT:PSS/C60 interface) and in the p-type regime (probably due to the presence of a resistive path for the injected holes through the C60 layer before reaching the channel).

Interestingly, despite the increase in the electron mobility, a threshold voltage shift towards higher positive values ($\Delta V_T = +25$ V) was also detected when using a thicker pentacene buffer layer. It is noteworthy that passing from 3 nm to 10 nm of pentacene buffer layer, the interface between the n-type semiconductor and the gate dielectric dramatically changes. In the first case we have a very complex interface, where C60 is interfaced both with pentacene islands and with the gate dielectric (Mylar®). In the latter, we have a complete interface between C60 and pentacene. A complex interface morphology could strongly influence the threshold voltage of the final devices, as reported by Opitz et al. [38]. Moreover, Kang et al. [39] reported an upward band bending (inducing a depletion of electrons at the interface) on both sides of the pentacene/C60 interface. Tentatively, this phenomenon could be the reason for the observed threshold voltage shift in the n-type regime.

In order to go deeper inside the observed electrical behaviors, we performed specular X-ray diffraction scans on both 60 nm thick C60 films deposited directly on Mylar® (Fig. 4c) as well as on Mylar®

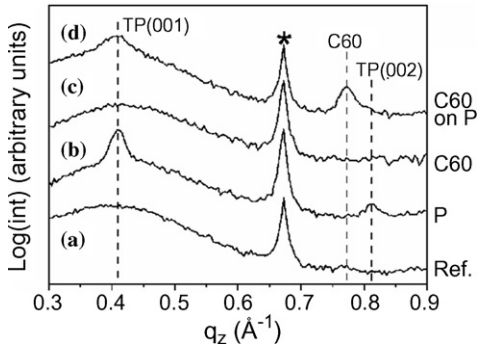

Fig. 4. Specular X-ray diffraction scans on the Mylar®/tape/quartz substrate as reference (a), a film of 20 nm pentacene (b), a layer of 60 nm C60 (c) and a film of 60 nm C60 on 10 nm pentacene (d). Pre-coverage of the substrate with pentacene leads to crystalline growth of C60. TP(hkl) denotes reflections of planes (hkl) originating from the pentacene thin film phase (see text). The star marks a substrate contribution.

pre-covered with a layer of nominally 10 nm pentacene (Fig. 4d). A 20 nm thick pentacene film was firstly investigated (Fig. 4b). For the pure pentacene film, the peak at a momentum transfer (q_z) value of 0.4085 Å^{-1} (lattice spacing $d = 1.538$ nm) and its weak second order peak at 0.813 Å^{-1} can be assigned to reflections of the (0 0 1) and (0 0 2) net planes of a well known pentacene polymorph that is usually referred to as *pentacene thin film phase* [1,40,41]. The 60 nm thick film of C60 deposited directly on Mylar® does not show any Bragg peaks, in contrast to the film of equal nominal thickness deposited on a 10 nm thick pentacene pre-coating. We find a peak at $q_z = 0.7720$ Å^{-1} (lattice spacing

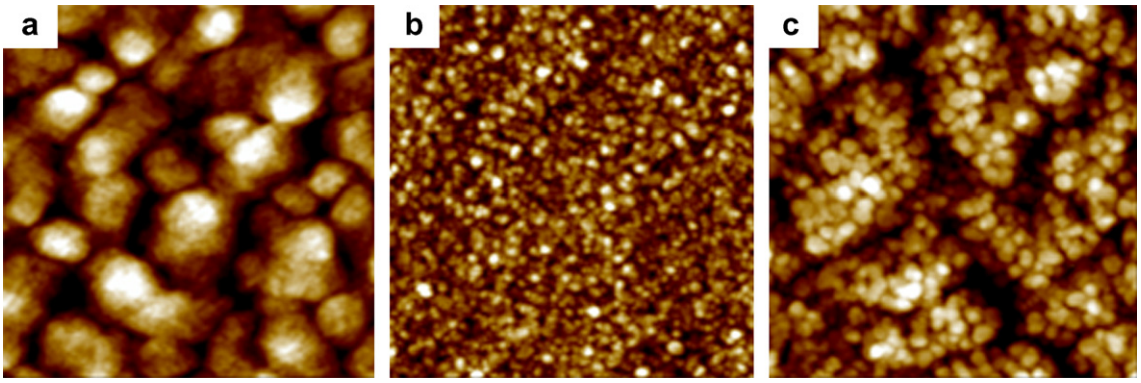

Fig. 5. Scanning force microscopy (SFM) micrographs of $1 \times 1\ \mu m^2$ showing: 20 nm pentacene on bare Mylar® (a); 60 nm C60 on bare Mylar® (b); 60 nm C60 on 10 nm pentacene on Mylar® (c). The pre-coverage of the substrate with pentacene leads to an increase in the average grain size. The color range represents 0–20 nm in (a) and (c), and 0–10 nm in (b).

$d = 0.814$ nm) that can be assigned to the (1 1 1) reflection of cubic C60 polymorphs [42,43] as well as to the (0 0 2) reflection of hexagonally grown C60 [43]. This result is in agreement with previous findings for C60 vacuum-deposition on sapphire, where crystalline growth of C60 took place exclusively after pre-coverage of the substrate with a monolayer of pentacene [33]. However, a film of 30 nm C60 on 3 nm pentacene, which corresponds to nominally two monolayers of upright standing pentacene, did not exhibit any indication of crystalline C60 growth in X-ray diffraction (not shown). We attribute this to the pronounced island growth of pentacene on Mylar® due to the high surface roughness of the substrate. The nominally 20 nm thick film of pentacene (Fig. 4 curve b) exhibits an out-of-plane crystalline coherence length of 30 ± 5 nm as estimated from the (0 0 1) reflection using the Scherrer formula [44]. Therefore, the 3 nm pentacene film can be regarded as far from being closed, leaving large substrate areas uncovered for the subsequent C60 growth and thus increasing its amorphous proportion, which is detrimental for device performance.

Further interesting conclusions can be drawn from the analysis of SFM micrographs reported in Fig. 5. The C60 morphology on bare Mylar® (Fig. 5b) is characterized by a granular appearance with a grain density of $\sim 3000\ \mu m^{-2}$ and grain diameters <30 nm. From Fig. 5c we can clearly notice that with a pentacene buffer layer, the nucleation of C60 grains on top of the underlying pentacene islands leads to a reduction of the grain density by a factor of about 3 and to a significant increase in the C60 average grain size. Together with our finding of crystalline C60 growth from XRD, this explains the increase of the electron mobility we observed in the OFETs characteristics.

4. Conclusions

In summary, we fabricated fully flexible and transparent all-organic n-type and ambipolar OFETs on plastic substrates by employing a double layer architecture comprising pentacene and C60 as active layers. We confirmed the importance of the substrate quality for controlling transport properties and even the type of charge carrier transport in organic semiconductor thin films. It was shown that the use of a pentacene buffer layer on the dielectric polymer leads to n-type conduction of the device due to the improvement of the order in the C60 layer. Moreover, an increase of the pentacene layer thickness leads to ambipolar device behavior, and also increases the electron mobility in C60 by one order on magnitude.

Acknowledgments

The authors acknowledge financial support by the European Commission under the IST Integrated Project no. 26987 "PROETEX", and the Deutsche Forschungsgemeinschaft (Sfb448). NK acknowledges support by the Emmy Noether-Program (DFG).

References

[1] C.D. Dimitrakopoulos, P.R.L. Malenfant, Adv. Mater. 14 (2002) 99.
[2] R.G. Nuzzo, PNAS 98 (2001) 4827.
[3] R.H. Reuss, B.R. Chalamala, A. Moussessian, M.G. Kane, A. Kumar, D.C. Zhang, J.A. Rogers, M. Hatalis, D. Temple,

G. Moddel, B.J. Eliasson, M.J. Estes, J. Kunze, E.S. Handy, E.S. Harmon, D.B. Salzman, J.M. Woodall, M. Ashraf Alam, J.Y. Murthy, S.C. Jacobsen, M. Olivier, D. Markus, P.M. Campbell, E. Snow, in: Proceeding of IEEE, Special issue on Flexible Electronics Technology, Part 1: Systems & Applications, vol. 93, 2005.
[4] S.F. Collins, G.W. Baxter, S.A. Wade, T. Sun, K.T.V. Grattan, Z.Y. Zhang, A.W. Palmer, J. Appl. Phys. 84 (1998) 4649.
[5] Y.-Y. Lin, D.J. Gundlach, S.F. Nelson, T.J. Jackson, IEEE Electron Device Lett. 18 (1997) 606.
[6] N. Tessler, N.T. Harrison, D.S. Thomas, R.H. Friend, Appl. Phys. Lett. 73 (1998) 732.
[7] S. Kobayashi, T. Takenobu, S. Mori, A. Fujiwara, Y. Isawa, Appl. Phys. Lett. 82 (2003) 4581.
[8] S.A. Wade, S.F. Collins, G.W. Baxter, J. Appl. Phys. 94 (2003) 4743.
[9] T. Takenobu, T. Takahashi, J. Takeya, Y. Iwasa, Appl. Phys. Lett. 90 (2007) 013507, and references therein.
[10] E.J. Meijer, D.M. de Leeuw, S. Setayesh, E. van Veenendaal, B.H. Huisman, P.W.M. Blom, J.C. Hummelen, U. Scherf, T.M. Klapwijk, Nat. Mater. 2 (2003) 678.
[11] A. Babel, J.D. Wind, S.A. Jenekhe, Adv. Funct. Mater. 14 (2004) 891.
[12] Y. Hayashi, H. Kanamori, I. Yamada, A. Takasu, S. Takagi, K. Kaneko, Appl. Phys. Lett. 86 (2005) 052104.
[13] A. Dodabalapur, H.E. Katz, L. Torsi, R.C. Haddon, Science 269 (1995) 1560.
[14] A. Dodabalapur, H.E. Katz, L. Torsi, R.C. Haddon, Appl. Phys. Lett. 68 (1996) 1108.
[15] C. Rost, D.J. Gundlach, S. Karg, W. Riess, J. Appl. Phys. 95 (2004) 5782.
[16] J. Wang, H.B. Wang, X.J. Yan, H.C. Huang, D.H. Yan, Chem. Phys. Lett. 407 (2005) 87.
[17] S.D. Wang, K. Kanai, Y. Ouchi, K. Seki, Org. Electron. 7 (2006) 457.
[18] T.D. Anthopoulos, C. Tanase, S. Setayesh, E.J. Meijer, J.C. Hummelen, P.W.M. Blom, D. de Leeuw, Adv. Mater. 16 (2004) 2174.
[19] T. Takahashi, T. Takenobu, J. Takeya, Y. Iwasa, Appl. Phys. Lett. 88 (2006) 033505.
[20] E. Kuwahara, Y. Kubozono, T. Hosokawa, A. Fujiwara, Appl. Phys. Lett. 85 (2004) 4765.
[21] T.B. Singh, N. Marjanovic, P. Stadler, M. Auinger, G.J. Matt, S. Günes, N.S. Sariciftci, J. Appl. Phys. 97 (2005) 083714.
[22] H. Wang, J. Wang, X. Yan, J. Shi, H. Tian, Y. Geng, D. Yan, Appl. Phys. Lett. 88 (2006) 133508.
[23] T.D. Anthopoulos, S. Setayesh, E. Smits, M. Cölle, E. Cantatore, B. de Boer, P.W.M. Blom, D. de Leeuw, Adv. Mater. 18 (2006) 1900.
[24] T. Kawase, T. Shimoda, C. Newsome, H. Sirringhaus, R.H. Friend, Thin Solid Films 438 (2003) 279.
[25] P. Cosseddu, A. Bonfiglio, Appl. Phys. Lett. 88 (2006) 023506.
[26] E.C.P. Smits, T.D. Anthopoulos, S. Setayesh, E. van Veenendaal, R. Coehoorn, P.W. Blom, B. de Boer, D.M. de Leeuw, Phys. Rev. B 73 (2006) 205316.
[27] S. Seo, B.-N. Park, P.G. Evans, Appl. Phys. Lett. 88 (2006) 232114.
[28] T. Yasuda, T. Goto, K. Fujita, T. Tsutsui, Appl. Phys. Lett. 85 (2004) 2098.
[29] L.-L. Chua, J. Zaumseil, J.-F. Chang, E.C.-W. Ou, P.K.-H. Ho, H. Sirringhaus, R.H. Friend, Nature 434 (2005) 194.
[30] A. Kahn, N. Koch, W.Y. Gao, J. Polym. Sci. B 41 (2003) 2529.
[31] A. Facchetti, M. Mushrush, H.E. Katz, T.J. Marks, Adv. Mater. 15 (2003) 33.
[32] T.B. Singh, F. Meghdadi, S. Gunes, N. Marjanovic, G. Horowitz, P. Lang, S. Bauer, N.S. Sariciftci, Adv. Mater. 17 (2005) 2315.
[33] K. Itaka, M. Yamashiro, J. Yamaguchi, M. Haemori, S. Yaginuma, Y. Matsumoto, M. Kondo, H. Koinuma, Adv. Mater. 18 (2006) 1713.
[34] B. Michel, A. Bernard, A. Bietsch, E. Delamarche, M. Geissler, D. Junker, H. Kind, J.-P. Renault, H. Rothuizen, H. Schmid, P. Shmidt-Winkel, R. Stutz, H. Wolf, IBM J. Res. Dev. 45 (2001) 697.
[35] P. Cosseddu, A. Bonfiglio, Thin Solid Films 515 (2007) 7551.
[36] F.J. Zhang, A. Vollmer, J. Zhang, Z. Xu, J.P. Rabe, N. Koch, Org. Electron. 8 (2007) 606.
[37] Y. Tanaka, K. Kanai, Y. Ouchi, K. Seki, Chem. Phys. Lett. 441 (2007) 63.
[38] A. Opitz, M. Bronner, W. Brutting, J. Appl. Phys. 101 (2007) 063709.
[39] S.J. Kang, Y. Yi, C.Y. Kim, K. Cho, J.H. Seo, M. Noh, K. Jeong, K.-H. Yoo, C.N. Whang, Appl. Phys. Lett. 87 (2005) 233502.
[40] S. Fritz, S. Martin, C. Frisbie, M. Ward, M. Toney, J. Am. Chem. Soc. 126 (2004) 4084.
[41] M. Oehzelt, R. Resel, C. Suess, R. Friedlein, W.R. Salaneck, J. Chem. Phys. 124 (2006) 054711.
[42] S. Liu, Y.J. Lu, M.M. Kappes, J.A. Ibers, Science 254 (1991) 408.
[43] J.L. de Boer, S. van Smaalen, V. Petricek, M. Dusek, M.A. Verheijen, G. Meijer, Chem. Phys. Lett. 219 (1994) 469.
[44] P. Scherrer, Nachr. Ges. Wiss. Göttingen, 98, 26 September 1918.

Available online at www.sciencedirect.com
ScienceDirect
Organic Electronics 9 (2008) 198–208
Organic Electronics
www.elsevier.com/locate/orgel

Al_2O_3 as gate dielectric for organic transistors: Charge transport phenomena in poly-(3-hexylthiophene) based devices

L. Fumagalli [a], D. Natali [a], M. Sampietro [a], E. Peron [b], F. Perissinotti [b], G. Tallarida [b], S. Ferrari [b,*]

[a] *Dipartimento di Elettronica e Informazione, Politecnico di Milano, unità IIT, P.za L. da Vinci 32, 20133 Milano, Italy*
[b] *Laboratorio MDM – CNR-INFM, I-20041 Agrate Brianza (MI), Italy*

Received 29 June 2007; received in revised form 30 October 2007; accepted 3 November 2007
Available online 17 November 2007

Abstract

We studied organic thin film transistors based on poly-(3-hexylthiophene) having as gate dielectric Al_2O_3, which was prepared by atomic layer deposition (ALD) technique, that provides films with very good electrical properties, roughness below 1 nm and compatibility with virtually any type of substrate, including polymeric ones. High-*k* gate oxides such as Al_2O_3 are advantageous since they enable a reduction of operating voltages, but when used in conjunction with organic semiconductors, they induce worse transport properties if compared to low-*k* dielectrics. To address this issue, we focused on the interface between the gate dielectric and the active material and we explored the effects of functionalizing the Al_2O_3 surface by means of self-assembled monolayers (SAM). We studied and compared a set of SAMs differing in the ligand groups and in the chain lengths. We show that the most important parameter is the SAM chain length, the longer SAM being more effective in giving better charge carrier mobility. The microscopical origins of this finding are analyzed exploiting and comparing the dependence of the mobility on the gate voltage in the transistors based on the variously functionalized Al_2O_3. With *n*-octadecyltrichlorosilane (OTS) the mobility reaches the value of 10^{-2} cm^2/V s, comparable to the mobility on transistors with properly functionalized SiO_2 gate dielectric.

PACS: 73.61.Ph; 85.30.Tv; 85.30.Dc; 81.16.Dn; 77.84.Bw

Keywords: Organic electronics; High-*k* dielectrics; Organic thin film transistor

1. Introduction

Organic semiconductors are considered as a replacement for amorphous silicon in thin film transistor (TFT) applications, since they show comparable electrical properties and potential advantages for their processability and compatibility with plastic substrates. While a lot of work has been devoted to the study and improvement of the semiconductor materials and of their deposition procedure, the role of the dielectric and of the semiconductor/dielectric interface in the determination of the performances of the OTFT [1–3] has been realized only recently. Considering that the channel in organic TFT is

* Corresponding author. Tel.: +39 039 6036383; fax: +39 039 6881175.
E-mail address: ferrari@petroceramics.com (S. Ferrari).

1566-1199/$ - see front matter © 2007 Elsevier B.V. All rights reserved.
doi:10.1016/j.orgel.2007.11.001

limited to the first one or two monolayers [4], it is not surprising that the dipole moment [1], the templating effect [5] and the charged mobile impurities [6] of the dielectric strongly affect the charge transport process in the semiconductor channel.

Among the dielectric materials, aluminium oxide (Al_2O_3) appears to be promising due to its high dielectric constant (between 7.5 and 9.5), its robustness and its possibility to be prepared on different type of substrates with easy processing conditions. The Al_2O_3 as gate dielectric for organic semiconductors has been investigated in a number of papers in conjunction with pentacene [7,8] as well as regioregular poly-(3-hexylthiophene) (RR-P3HT) [4,9,33].

In contrast to SiO_2, where it has been demonstrated that the mobility depends mainly on the structural order of the polymer at the interface [10–12], for the Al_2O_3 there are indications that other factors might affect the mobility in the transistor. In particular the higher polarity of the Al_2O_3 surface might cause an increase in the disorder in the localized states of the semiconductor, thus affecting the mobility [1]. Such an effect appears to have detrimental effects more on polymeric semiconductors than on crystalline molecular ones, because hopping between localized states is the dominant transport mechanism in the former.

The use of self-assembled monolayers (SAMs) on the Al_2O_3 surface contributes to a considerable improvement of the transistor mobility in both p-type [11] and n-type [2] transistors. Nevertheless, in the case of polymeric semiconductors, and of RR-P3HT in particular, used in conjunction with high-k oxides, all reports refer to mobilities below 10^{-2} cm^2/V s, even when SAMs are used to improve the semiconductor/insulator interface. In particular, for devices based on Al_2O_3 as gate insulator, the highest mobility ever reported is 5×10^{-3} cm^2/V s [9].

In order to elucidate the mechanism for mobility reduction using Al_2O_3 as a dielectric, we present the result of a systematic study of the influence of the SAMs on the mobility in OTFT based on RR-P3HT. We selected two groups of SAMs, alkylsilanes and alkyl phosphonic acids, which differ for their binding group, and in each group we tested molecules of different chain lengths, going from a single methyl group up to a octadecyl chain.

To correlate SAM structural order with the OTFT mobility we carried out a structural characterisation of the SAM and the electrical characterisation of the OTFTs.

2. Experimental details

The Al_2O_3 based devices (see Fig. 1a) were fabricated on a substrate of Si covered with a 100 nm thick thermally grown SiO_2. The gate electrode was realized using standard photolithography with three metal layers deposited in the same evaporation run: Ti/Au/Ti with an overall thickness of 60 nm (see Fig. 2); the titanium interlayers are necessary to achieve a good adhesion between the gold film and the oxides. The Al_2O_3 thin films, used as gate insulators, were grown by atomic layer deposition in a flow type reactor (F-120 ASM-microchemistry Finland). The precursors were TMA (trimethyl aluminium) and H_2O and they were injected into the growth chamber by N_2. The growth temperature was 125 °C and the final film thickness of about 50 nm. The oxide film grown with ALD is totally amorphous and uniform (see Fig. 2), with a surface roughness of 0.5 nm (Fig. 3); it has good insulating properties with a measured dielectric constant of about 7. Gold source and drain electrodes were defined by standard photolithography; channel lengths varied from 3 to 18 μm. Before the deposition of the semiconducting layer, Al_2O_3 was functionalized with different SAMs (Fig. 4): bis (2-ethylhexyl) phosphate (97%) (BEHP), *n*-octylphosphonic acid (98%) (NOPA), *n*-octadecylphosphonic acid (93%) (OPA), *n*-octyltrichlorosilane (98%) (NOTS), *n*-octadecyltrichlorosilane (mixture of isomers, 95%) (OTS), all obtained from Alfa Aesar; dimethyldichlorosilane (99.9%) (DDS) was purchased from Aldrich. All these materials and the solvents 2-propanol (semiconductor grade), chloroform (HPLC grade), acetone (semiconductor grade) (Aldrich) were used without any further purification. Toluene (HPLC grade, Aldrich) was distilled over metal sodium before use. Dielectrics have been carefully cleaned with acetone and 2-propanol, dried with nitrogen flow and baked on hot plate at 120 °C for 2 min. Just before the introduction in the solutions, the substrates were treated

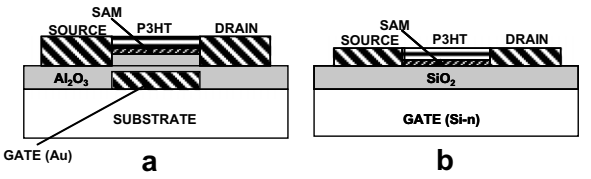

Fig. 1. Schematic cross-section of the devices used in this study: Al_2O_3 based device (a) and SiO_2 based device (b).

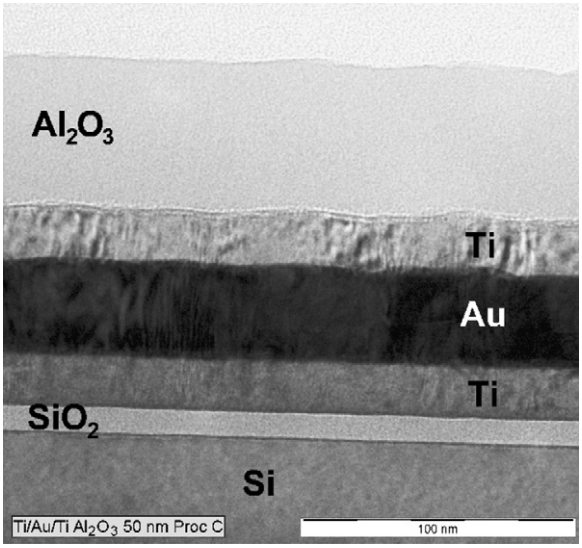

Fig. 2. TEM cross-section of Al_2O_3 (50 nm) on a Ti (15 nm)/Au (30 nm)/Ti (15 nm) stack. The atomic layer deposition technique offers highly uniform and conformal Al_2O_3 layers. Al_2O_3 was employed as gate insulator and Ti/Au/Ti stack as gate electrode in Al_2O_3 based TFTs.

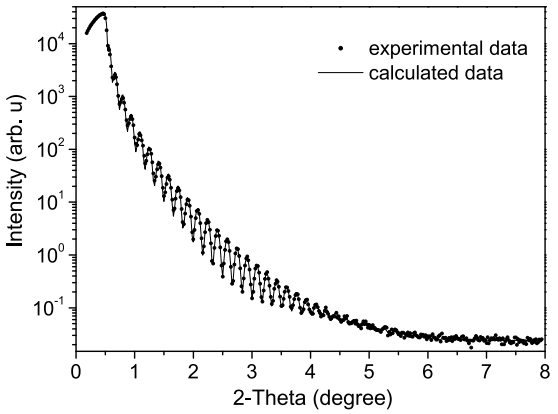

Fig. 3. XRR profile and simulation of Al_2O_3 film grown by ALD on SiO_2 at 125 °C. The calculated thickness is 52 nm, the roughness is 0.5 nm and the density is 3.2 g cm^{-3}.

by an oxygen plasma (10 W, 1 mbar, 5 min). Recipes were specific for each SAM: for BEHP, NOPA and OPA the substrates were dipped in the appropriate dilute solution for 1 h (NOPA and OPA 5 mM in 2-propanol, BEHP 2 mM in toluene), rinsed for 5 min with the same solvents of solutions and then put on hot plate at 150 °C for 10 min; for DDS the substrates were dipped in the solutions (1:10 in chloroform) for 15 min, rinsed for 5 min in fresh chloroform and dried on the hot plate at 120 °C for 2 min; for OTS and NOTS the substrates were

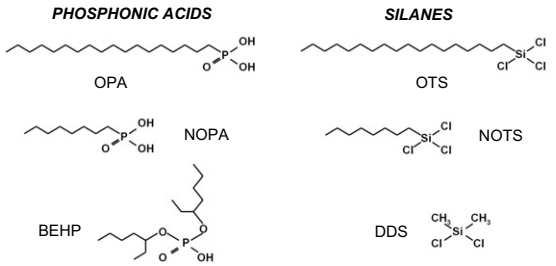

Fig. 4. Chemical structure of the molecules used to obtain SAMs on Al_2O_3 and SiO_2 substrates. These molecules were chosen so that the dependence of TFTs performances could be studied depending on chain length and binding group.

put into a chamber under a nitrogen atmosphere in which a fresh prepared solution (2 mM in anhydrous toluene) was introduced. The substrates were then taken out after 1 h, rinsed for 5 min with toluene and chloroform and baked on hot plate at 150 °C for 10 min. All functionalized substrates were finally placed in dry box until use. The functionalized Al_2O_3-based OTFTs were compared with a benchmark TFT having a 130 nm thick DDS-functionalized SiO_2 dielectric, a low resistivity Si-p+ gate and a pattern of Ti/Pt about 40 nm thick for the source and drain contacts (Fig. 1b). RR-P3HT (Aldrich) was fractionated and purified by a sequence of organic solvent extraction ($MW = 52483\,D$, $MN = 23961\,D$ and $D = 2.19$). RR-P3HT films were spin-coated from a 0.5 wt% solution in toluene onto flat and FET substrates in order to achieve a thickness of about 30 nm. X-ray reflectivity data were collected using laboratory X-ray source equipped with a monochromatic Cu Kα. The degree of coverage of the surface and the uniformity of SAMs were studied by atomic force microscopy (AFM) in "non-contact" mode using a platinum covered silicon tip under ambient condition. Electrical measurements have been performed in vacuum at 10^{-5} mbar after about 24 h of permanence in vacuum using a Keithley 4200 Modular DC Source/Monitor.

3. Results and discussion

3.1. Morphological and structural characterisation of SAMs

The morphological characterisation of all the SAM considered in this study were obtained by AFM. To measure the thickness of SAM films, we try to exploit non-uniformities in the film coverage and to measure the step-height there, but in many

Table 1
Thickness t and rms roughness σ of the oxide/SAM systems considered in this study

Substrate	SAM	t (nm)		σ (nm)
		Literature	Experimental	Experimental
Al_2O_3	NOTS	1.05 [28]	–	0.2
	OTS	2.5 [29]	1.1	0.4
	BEHP	–	0.8	0.3
	NOPA	1.0 [8]	1.0	0.2
	OPA	2.1 [30]	2.0	0.7
SiO_2	DDS	–	0.4	0.2

Data of the third column are obtained from literature, while data in the last two columns were obtained from AFM measurements, the thicknesses being estimated from the depth of the pinholes present in SAM.

cases, especially with long chain SAMs, the very high surface homogeneity made this a difficult task. SAM thickness is reported in Table 1. Fig. 5 shows the AFM pictures of a selected set of different SAMs on Al_2O_3 and on SiO_2.

It was not possible to extract meaningful thickness measurements from the short chain silane-based SAMs, namely DDS and NOTS, due to the film homogeneity. As to the short chain phosphonic-based SAM, BEHP, which has branched chains, has a certain tendency to agglomerate as shown by the presence of particles (Fig. 5c), whereas NOPA, which has non-branched chain, is very smooth and homogeneous (not shown for brevity). In both OPA and OTS-functionalized surfaces, no uncovered areas were found beside the rare pinholes, in some (but not all) of the AFM scanned areas. The typical size for such pinholes is of few nanometers. The OTS SAM is very smooth and homogeneous (root mean square (rms) roughness σ is 0.4 nm) with a low density of particles, that we attributed to OTS aggregates, as shown in Fig. 5a (phase images, not shown,

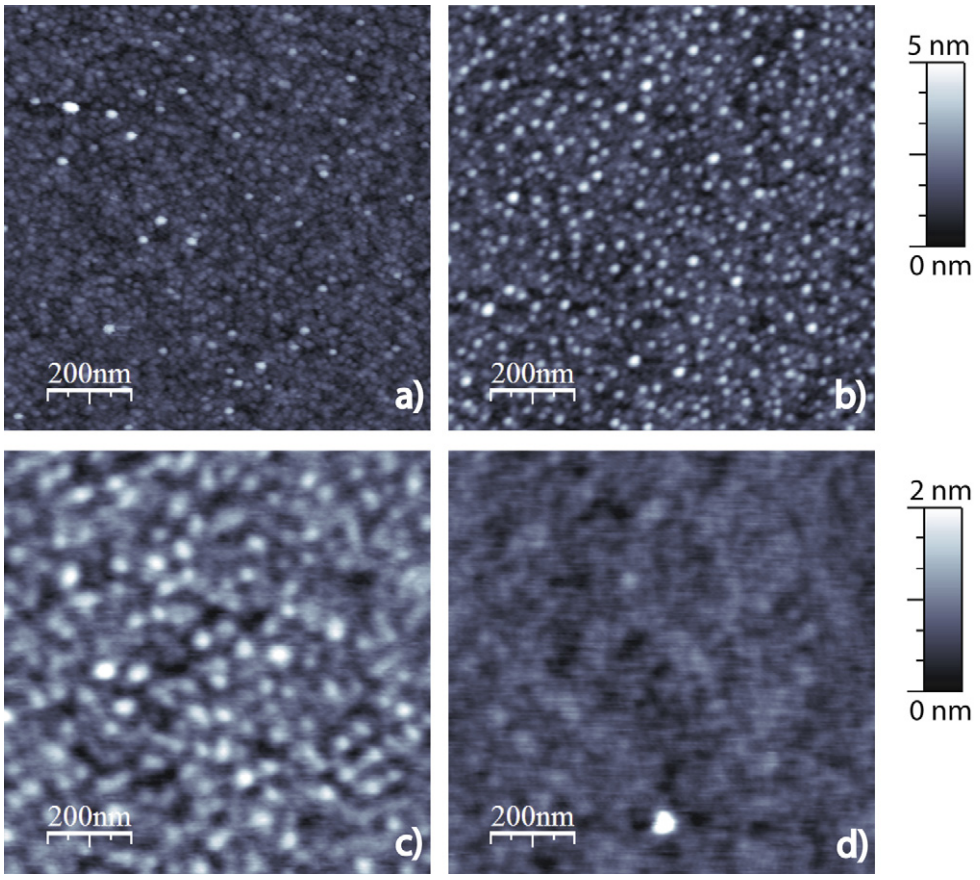

Fig. 5. AFM pictures showing the surface morphology of SAMs on Al_2O_3 and SiO_2 surfaces. (a) OTS on Al_2O_3; (b) OPA on Al_2O_3; (c) BEHP on Al_2O_3; (d) DDS on SiO_2. Information about the topography of SAMs are reported in Table 1.

indicate that the interaction of the AFM tip with the aggregates is the same as the rest of the surface, thus suggesting chemical similarity). The measured OTS film thickness (1.1 nm), is lower than the data reported in the literature (2.5 nm). This can be attributed to the fact that the steps used to measure the SAM thickness, are not between ordered SAM and uncovered surface, but rather between SAM domains with a different degree of order, where alkyl chains are either standing perpendicular to the surface or laying flat on it, as observed earlier [13]. The OPA SAM, shown in Fig. 5b, has a rms roughness of 0.7 nm slightly higher than OTS. It has a higher density of aggregates, which are typically structures with a thickness ranging from 2 to 4 nm and with lateral dimension going from 5 to 20 nm. Nevertheless such structures are affecting only marginally the overall rms roughness.

Finally, DDS self-assembled layers on SiO_2 (Fig. 5d) are very homogeneous and smooth.

3.2. Structural characterisation of P3HT films

Fig. 6 shows X-ray Bragg–Brentano profiles of the P3HT films deposited on the differently functionalized Al_2O_3 surfaces. The profiles were fitted using the matrix method formalism for the reflectivity part [14], while the diffraction peaks were fitted using gaussian curves. All P3HT films are about 35 nm thick with a roughness of 1–2 nm. The films deposited on bare and short chain SAMs (BEHP, NOPA, DDS, NOTS) coated surfaces do not show any diffraction peak, suggesting that the film is either amorphous or, at least, grains aligned with the $\langle 100 \rangle$ plane parallel to the surface are below the detection limit of our apparatus (only NOPA shown for brevity in Fig. 6).

On the other hand, the profiles of the P3HT films deposited on OTS and OPA show a broad diffraction peak that can be related to the $\langle 100 \rangle$ reflection of the P3HT. The appearance of the $\langle 100 \rangle$ diffraction peak in the out-of-plane direction is therefore specific of films spun cast on long chain SAMs. The long chain SAMs are forming a well ordered structure on the oxide surface with the alkyl chains aligned (almost) vertically on the oxide surface. Such organization is promoting in turn the organization of the hexyl chains of the P3HT on the oxide surface, favoring the formation of P3HT crystals aligned in the $\langle 100 \rangle$ direction in the out-of-plane direction. Eventually the short chain SAMs (and even less the branched ones), where the olefinic chains can not arrange in a well ordered manner [15], are not effective in inducing crystalline order in the P3HT layer. Such an effect has been observed previously on SiO_2 surfaces [18], where significant differences in the polymer organization, between HMDS and OTS-functionalized surfaces were observed.

From the position of the maxima, located at 0.34 ($Å^{-1}$) and 0.36 ($Å^{-1}$) for P3HT films on OPA

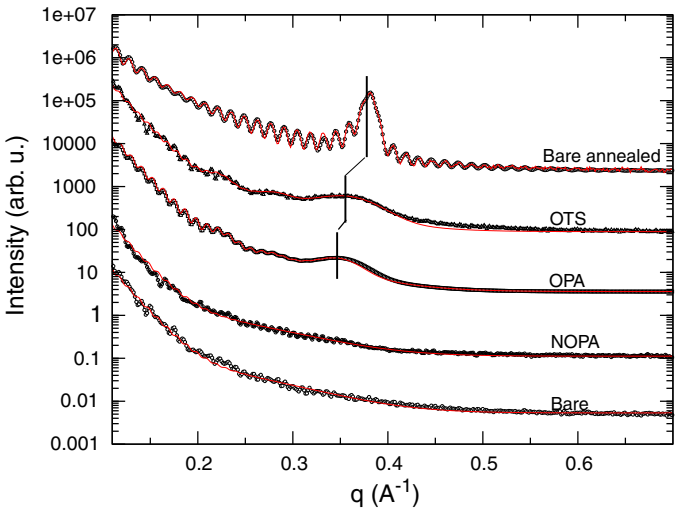

Fig. 6. XRD spectra of the RR-P3HT thin films on functionalized Al_2O_3 surfaces. A highly crystalline film on bare Al_2O_3, obtained by annealing, is also shown for comparison. The solid lines represent fits to the reflectivity/diffraction data based on refined structural models. The different data are offset by a factor 100 for clarity.

and OTS respectively, interplanar distances of 18 Å and 17.6 Å can be deduced. These values are typical for P3HT films of high molecular weight (MW = 52 kD in our case) [12,18], but higher than those observed for highly crystallized films. In fact, by annealing at 240 °C (i.e. at P3HT melting point) in nitrogen atmosphere and then cooling down slowly, we obtained highly crystallised films displaying an intense and sharp peak at 0.38 ($Å^{-1}$), as seen in Fig. 6, which corresponds to an interplanar distance of 16.5 Å [17] (film deposited on bare Al_2O_3).

Comparing the interplanar distances for P3HT on OTS and OPA with the crystallised sample, a better organization in the former can be hypothesized. Indeed as seen in Fig. 5a and b, the lower surface roughness and aggregates density observed in OTS might be more effective in promoting order in the P3HT film.

3.3. Electrical characterisation

The transistors using the different SAMs have been electrically characterised by measuring their transfer and their output characteristic curves in the saturation regime. As an example, measurements of devices functionalized with OPA and OTS are given in Fig. 7. For all kind of SAM we observed output characteristic curves with a well defined saturation region and more than quadratic transfer characteristic curves. This can be explained assuming a gate voltage (V_G) dependent mobility, which reflects the increase of the mobility on the accumulated carrier density (Q') usually found in organic semiconductors. This dependence can be modelled as a power law [19,20]:

$$\mu = k \cdot (V_G - V_T)^{\gamma} = k' Q'^{\gamma} \quad (1)$$

Using this expression the drain current in the saturation region can be written as

$$I_D = \frac{1}{\gamma + 2} k C_{OX} \frac{W}{L} (V_G - V_T)^{\gamma+2} \quad (2)$$

We have fitted our experimental transfer characteristic curves according to Eq. (2) and the extracted relevant parameters are summarised in Table 2. For each SAM-functionalized TFT, the parameters extracted from various devices have been averaged out and the standard deviation is also reported. For the mobility (calculated at $V_G = -15$ V) the best values have been also reported. The I_{on}/I_{off} ratio is always very high, ranging between 10^4 and 10^5 and there are no differences between functionalized and bare samples, except for the OTS sample in which the RR-P3HT underwent a light non-intentional doping [34].

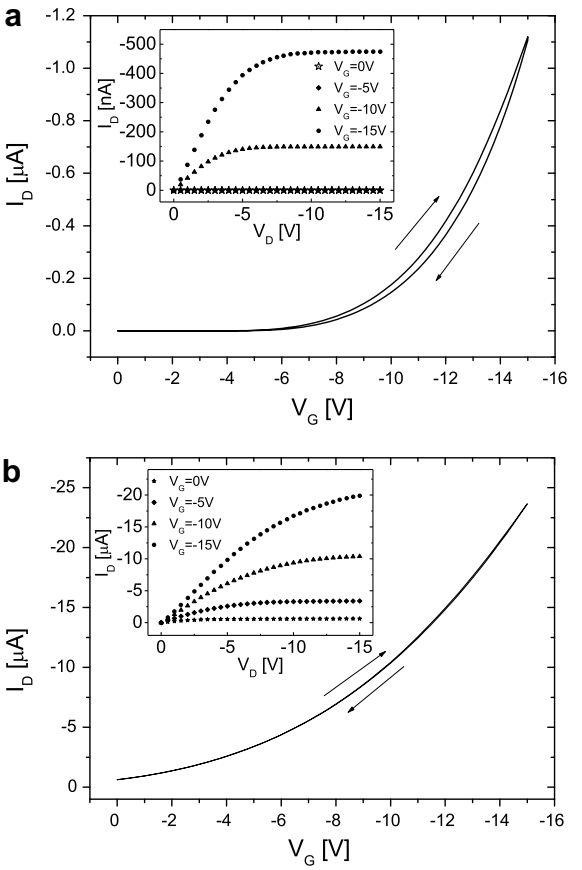

Fig. 7. Transfer characteristic curve of Al_2O_3 based TFT ($L = 12$ μm, $W = 1.6$ mm) functionalized with OPA (a) and with OTS (b), measured at $V_D = -15$ V. In the inset the output characteristics are shown, measured for V_G ranging from 0 V to −15 V.

Fig. 8 summarises the average *mobility*. With respect to the bare Al_2O_3, the use of BEHP, DDS and NOTS does not improve the mobility, which is around few 10^{-4} cm^2/V s, and NOPA gives only a slight improvement (less than a factor 2). A sizeable boost is achieved with long chain SAMs: OPA, which reaches a mobility of 10^{-3} cm^2/V s, and OTS, which reaches 0.83×10^{-2} cm^2/V s. This is in agreement with results reported in Section 3.1, where it was shown that only with OPA and OTS a certain degree of crystallinity is displayed in the RR-P3HT. The value obtained on OTS is the highest ever reported for Al_2O_3 based TFTs and it is very close to the one measured on our DDS-functionalized SiO_2 based devices (about

Table 2
Summary of the electrical properties of Al_2O_3 based transistors with modified surface dielectrics

Sample	Best mobility ($cm^2/V\,s$)	Average mobility ($cm^2/V\,s$)	V_{th} (V)	I_{on}/I_{off} at $V_G = -15$ V
Bare Al_2O_3	4.1×10^{-4}	$(3.0 \pm 1.15) \times 10^{-4}$	-3.6 ± 1.14	$(7 \pm 3) \times 10^4$
Al_2O_3 + BEHP	3.4×10^{-4}	$(2.6 \pm 0.3) \times 10^{-4}$	-5.7 ± 0.6	$(1.0 \pm 0.5) \times 10^5$
Al_2O_3 + NOPA	6.9×10^{-4}	$(5.1 \pm 0.5) \times 10^{-4}$	-3.4 ± 0.3	$(8 \pm 3) \times 10^4$
Al_2O_3 + OPA	2.0×10^{-3}	$(1.2 \pm 0.2) \times 10^{-3}$	-2.1 ± 0.5	$(1.1 \pm 0.1) \times 10^5$
Al_2O_3 + DDS	3.7×10^{-4}	$(2.6 \pm 0.3) \times 10^{-4}$	-4.4 ± 0.5	$(1.0 \pm 0.3) \times 10^5$
Al_2O_3 + NOTS	2.3×10^{-4}	$(2.0 \pm 0.1) \times 10^{-4}$	-2.9 ± 0.3	$(1.0 \pm 0.3) \times 10^5$
Al_2O_3 + OTS	9.2×10^{-3}	$(8.3 \pm 0.4) \times 10^{-3}$	$+5.6 \pm 0.2$	54 ± 7
SiO_2 + DDS	1.2×10^{-2}	$(8.8 \pm 0.7) \times 10^{-3}$	-1.8 ± 0.4	$(8 \pm 2) \times 10^3$

Mobilities extracted at $V_G = -15$ V.

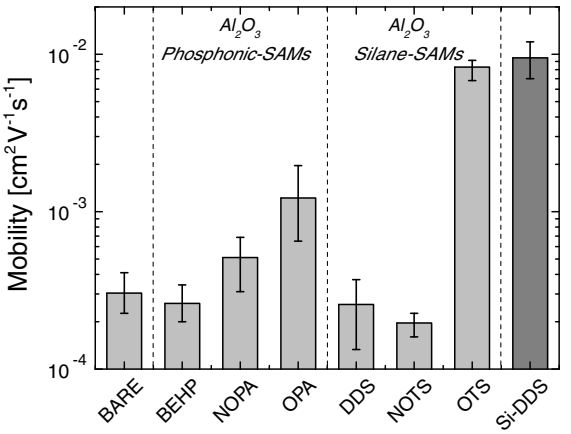

Fig. 8. Mobility values extracted at $V_G = -15$ V in the saturation region from transistors using bare and functionalized Al_2O_3 dielectrics (light gray). Functionalized SiO_2 (dark gray) dielectric also given for reference.

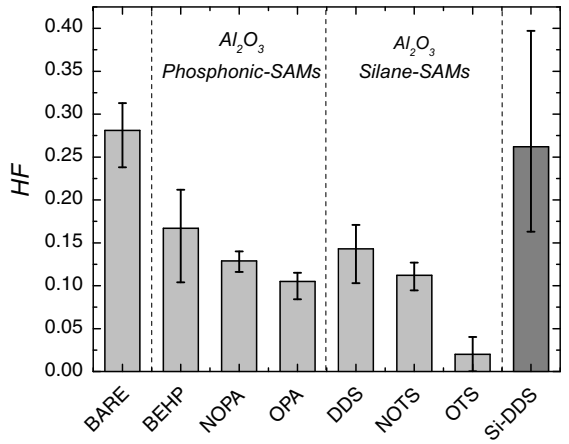

Fig. 9. Hysteresis factor (HF) as a function of the SAM in Al_2O_3 based devices (light gray) and in SiO_2 (dark gray), given for reference.

10^{-2} $cm^2/V\,s$, also shown in Fig. 8), and in general is close to the mobility reported in the literature for high MW RR-P3HT spin cast on SiO_2. This demonstrates that by means of a proper functionalization, high mobilities can be obtained with Al_2O_3.

To measure the *hysteresis* in the transfer characteristics curves, a *hysteresis factor* (HF) has been defined as the area of the hysteresis normalised to the area of the forward voltage scan. Hysteresis is considerably reduced by SAM, as can be appreciated in the summary plot of Fig. 9, particularly in the case of long chain SAMs. Bare Al_2O_3 devices have an HF of 0.28, which is reduced to 0.1 in OPA-functionalized devices, while hysteresis becomes practically negligible in OTS-functionalized devices with an HF value comprised between 4×10^{-2} and 2.5×10^{-4}.

The origin of hysteresis in organic TFTs has not been clarified yet [21]. It has been reported, in carbon nanotubes based transistor, that it is related to the presence of water on the insulator surface, which introduces traps with very long release time [22]. In our case the relatively large HF in the bare Al_2O_3 is in agreement with the polar and hygroscopic character of this insulator. The introduction of SAMs gives to the surface a less polar character, diminishes its water content and hence the hysteresis. The HF dependence upon chain length can be explained by considering that functionalization leaves some surface hydroxyl groups un-reacted: since longer chain SAMs are more dense and compact, they have a lower density of residual OH groups, as it has been recently shown by FT-IR studies [23].

4. Mobility: analysis of the dependence on the charge density

In order to better understand the large difference between the mobility in RR-P3HT on bare and functionalized Al_2O_3, we exploit the power law

dependence of the mobility on the accumulated charge density. In fact, from the parameters k' and γ of Eq. (2), relevant information on the electronic structure of the active material can be extracted. To this extent, we re-extracted the mobility in the *linear regime* of operation of TFTs, where the longitudinal electric field is moderate ($V_{DS} = -1$ V, $V_G = -10$ V), to minimise the dependence of k' and γ on the electric field [24,25] which could obscure the extraction of the intrinsic electronic structure of the active material [26]. The mobilities as function of the charge density are plotted in Fig. 10.

4.1. Broadness of the density of states

The parameter γ, which is the slope of μ versus Q' on a double logarithmic plot, depends on the energy spreading of the density of states (DOS): in the framework of the theory developed by Vissenberg and Matters [20], the DOS is modelled as an exponential function $g(\epsilon) = \frac{N_t}{kT_0}\exp(\frac{\epsilon}{kT_0})$ and γ is related to the DOS characteristic temperature T_0 by the following relation: $\gamma = 2(\frac{T_0}{T} - 1)$. We take kT_0 as an index of the DOS broadness. Therefore from γ we can estimate the DOS broadness, and this indicates the degree of energetic disorder in the semiconductor: in fact if the DOS is broader, a larger energetic disorder is present.

The values of DOS broadness kT_0 for RR-P3HT deposited on the various SAMs are shown in Fig. 11. If we consider separately silane and phosphonic-based SAMs, we observe that a trend is present for the two groups: the DOS broadness diminishes going from bare to functionalized Al_2O_3, and further diminishes on the longer chain SAMs.

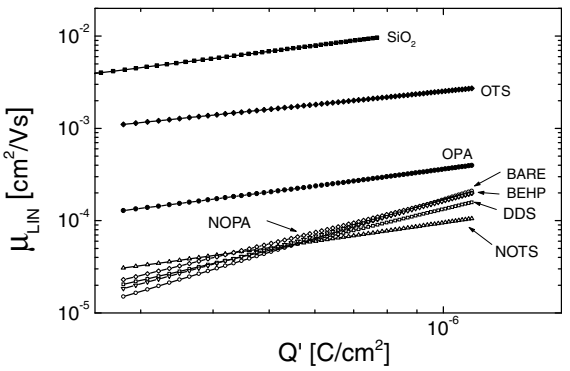

Fig. 10. Mobility as a function of Q' for RR-P3HT deposited on bare Al_2O_3, functionalized Al_2O_3 and on DDS–SiO_2. The reported curves are an average of the mobility extracted from various devices in the linear regime.

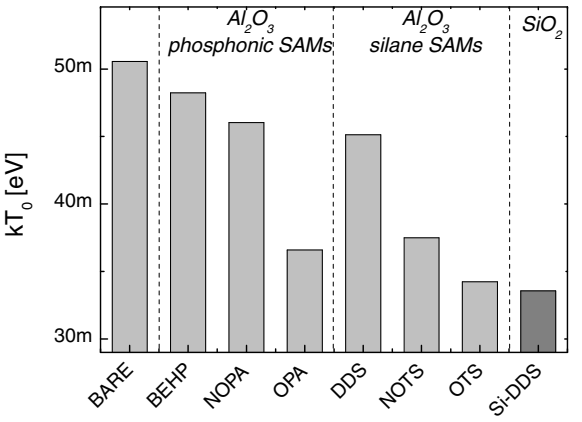

Fig. 11. DOS broadness for RR-P3HT deposited on bare, functionalized Al_2O_3 (light gray) and on DDS–SiO_2 (dark gray).

Indeed, OPA and OTS, whose structural data indicates partial crystallinity, are characterised by the least broad density of states. Apart from structural reasons, another mechanism could explain the observed trend in kT_0: being an high-k oxide, Al_2O_3 is expected to have a high density of surface disordered permanent dipoles. These are the sources of a disordered electric potential landscape which interacts with RR-P3HT enhancing the broadness of its density of states [1]. This effect is less intense the larger is the distance between the RR-P3HT and the Al_2O_3 surface, which explains the observed trend.

4.2. Effective wavefunction overlap

As to k', it is shown in the Appendix how to extract from it an interval of possible values for the effective wavefunction overlap α^{-1}, which determines the ease of the hopping process between adjacent sites.

The possible intervals for the effective wavefunction overlap α^{-1} for the various SAMs are reported in Fig. 12. It can be seen that bare Al_2O_3 and the various SAMs have approximately the same range of values, with the remarkable exception of OTS which has a larger α^{-1}. The fact that the bare substrate and short chain SAMs are similar, is in good agreement with the structural characterisation given in Section 3.1. As to long chain SAMs, the result for RR-P3HT on OTS is in agreement with its XRR spectrum, which shows a lower interplanar distance in the out-of-plane direction, which points to a more close-packed arrangement for the polymer chains and hence supports a larger effective wavefunction overlap. On the other hand, the poor result of

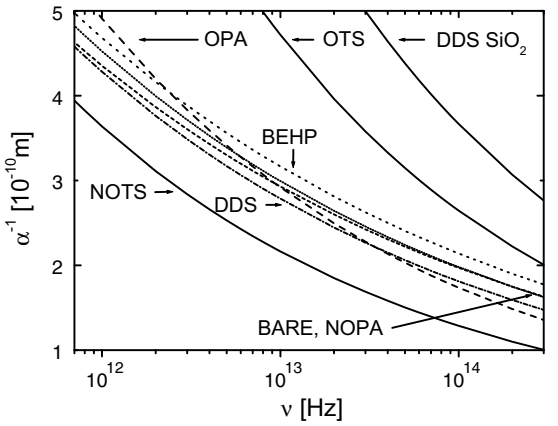

Fig. 12. Effective wavefunction overlap α^{-1} as function of the attempt to escape frequency ν for RR-P3HT deposited on bare Al_2O_3, functionalized Al_2O_3 and on DDS–SiO_2 ($N_t = 10^{26}$ m^{-3}).

OPA can be surprising if compared to its promising structural characteristics. We conclude that crystals which are present in RR-P3HT on OPA as revealed by XRR analyses, are immersed in an amorphous RR-P3HT matrix which dominates the transport properties. The consequent limited degree of connectivity between crystals could be traced back to the higher density of aggregates and surface roughness of OPA SAM. Indeed, it has been recently shown that mobility in polymers can be highly sensitive to the surface microroughness [35,36].

4.3. SAM effect on the mobilities

Using results for kT_0 and α^{-1}, we can give a more detailed explanation of the SAM effects on RR-P3HT mobilities. Short chain SAMs do not give any improvement with respect to bare Al_2O_3, because they have both a disordered DOS and a poor effective wavefunction overlap (NOTS is less disordered than other short chain SAMs but has a very low effective wavefunction overlap). OTS is the best one because it combines both a low energetic disorder and a good effective wavefunction overlap, whereas OPA gives a certain improvement with respect to the bare Al_2O_3 thanks to its limited DOS broadness, whereas it has a α^{-1} which is not different from bare Al_2O_3.

4.4. Comparison between OTS–Al_2O_3 and DDS–SiO_2

Finally, we compare our best result on Al_2O_3, functionalized with OTS SAM, to our benchmark reference SiO_2 functionalized with DDS. In Fig. 8 OTS–Al_2O_3 and DDS–SiO_2 were shown to yield similar mobilities, but this occurs when they are compared at the same applied gate voltage: taking into account the larger dielectric constant of Al_2O_3 and its smaller thickness, at the same applied gate voltage the charge density on Al_2O_3 is about four times larger than on SiO_2. When compared at the same accumulated charge density Q', as in Fig. 10, the former has a lower mobility than the latter. Looking at Fig. 11, it can be seen that OTS–Al_2O_3 and DDS–SiO_2 have the same degree of energetic disorder: if disordered surface dipoles are present on the surface of Al_2O_3, their effect becomes negligible when the active channel is moved away from the interface with a long chain SAM such as OTS. On the other hand, from Fig. 12 it can be seen that OTS–Al_2O_3 has an effective wavefunction overlap α^{-1} which is smaller than DDS–SiO_2. This difference is the origin for the observed mobility difference, and highlights the specificity of Al_2O_3 which, even after a long chain functionalization, still yields performances which are inferior to a short chain functionalized SiO_2.

5. Conclusions

We performed a systematic study of the effect of SAM on the electrical properties of transistors using ALD Al_2O_3 as gate dielectric and RR-P3HT as semiconductor. SAMs differing in the polar head group and alkyl chain length were investigated. We showed that the length of the SAM is the most important parameter in improving transistor performance, and that longer SAMs, most notably OTS, give better results. From a detailed study of the dependence of the mobility on the accumulated charge density, the improvement induced by OTS could be traced back to a reduction of the broadness of the density of states in conjunction with an improvement of the effective wavefunction overlap with respect to the bare Al_2O_3. With respect to functionalized SiO_2, OTS-functionalized Al_2O_3 equals functionalized SiO_2 in terms of broadness of the density of states, but still suffers from a lower effective wavefunction overlap. Nevertheless, exploiting the high dielectric constant of Al_2O_3 and developing transistors with a sufficiently thin dielectric, a mobility of 0.8×10^{-2} cm^2/V s could be measured, a result which is comparable to that of SiO_2 based transistors.

Acknowledgements

This work was supported financially by Fondazione CARIPLO, through TESEO and PROTEO projects. The authors are indebted with Giovanna Scarel for the ALD growth, Claudia Wiemer for assistance in XRR analysis and Mario Alia for device fabrication from MDM Laboratory, with Alberto Bolognesi and Paolo Di Gianvincenzo from CNR-ISMAC for RR-P3HT purification, with Sergio Masci from Politecnico di Milano for wafer bonding and Giuseppe Pavia from STMicroelectroncis for TEM analysis.

Appendix

In Eq. (1), the parameter k' can be rewritten as

$$k' = \sigma_0(\alpha^{-1})^{\frac{3}{2}\gamma+3} f(\gamma) \tag{A.1}$$

where $f(\gamma)$ is a known function which depends only on γ, α^{-1} is the effective wavefunction overlap, and σ_0 is the so-called conductivity prefactor [20]. According to Ref. [27], the parameter σ_0 can be estimated as

$$\sigma_0 = \frac{e^2}{kT} N_t^{\frac{1}{3}} \nu \tag{A.2}$$

where ν is the attempt to escape frequency and N_t is the total density of states per unit volume. Substituting Eq. (A.2) in Eq. (A.1), we find

$$k' = \left[\frac{e^2}{kT} f(\gamma)\right] N_t^{\frac{1}{3}} \nu (\alpha^{-1})^{\frac{3}{2}\gamma+3} \tag{A.3}$$

There are three unknowns in k', namely α, N_t and ν, whereas the term between square brackets is known. Indeed, N_t is reported in the literature to be in the range 10^{26}–$10^{27}\,m^{-3}$, and since it appears in Eq. (A.3) raised to one third, the dependence of k' on this parameter is weak [27]. On the other hand, ν is reported to be in the range 10^{12}–10^{14} Hz, thus having a larger impact on k'. Therefore we solve Eq. (A.3) for α^{-1} and we plot this quantity as a function of ν. Restricting to the ranges where α^{-1} and ν are physically significant, that is $10^{12}\,Hz < \nu < 10^{14}$ Hz and α^{-1} below a few Å, we can estimate an interval of possible values for α^{-1}.

Results are shown in Fig. 12 for $N_t = 10^{26}\,m^{-3}$ (no significant differences occur by taking $N_t = 10^{27}\,m^{-3}$).

References

[1] J. Veres, S.D. Ogier, S.W. Leeming, D.C. Cupertino, S.M. Khaffaf, Advanced Functional Materials 13 (2003) 199.
[2] L.-L. Chua, J. Zaumsell, J.-F. Chang, E. Ou, P. Ho, H. Sirringhaus, R. Friend, Nature 434 (2005) 194–199.
[3] A. Facchetti, M.-H. Yoon, T.J. Marks, Advanced Materials 17 (2005) 1105–1125.
[4] Guangming Wang, Daniel Moses, Alan J. Heeger, Hong-Mei Zhang, Mux Narasimhan, R.E. Demaray, Journal of Applied Physics 95 (1) (2004) 316–322.
[5] R.A. Street, J.E. Northrup, A. Salleo, Physical Review B 71 (16) (2005) 165202.
[6] H.G.O. Sandberg, T.G. Backlund, R. Osterbacka, H. Stubb, Advanced Materials 16 (13) (2004) 1112–1115.
[7] K.P. Pernstich, S. Haas, D. Oberhoff, C. Goldmann, D.J. Gundlach, B. Batlogg, A.N. Rashid, G. Schitter, Journal of Applied Physics 96 (11) (2004) 6431–6438.
[8] T.W. Kelley, L.D. Boardman, T.D. Dunbar, D.V. Muyres, M.J. Pellerite, T.P. Smith, Journal of Physical Chemistry B 107 (2003) 5877–5881.
[9] L.A. Majewski, R. Schroeder, M. Grell, P.A. Glarvey, M.L. Turner, Journal of Applied Physics 96 (10) (2004) 5781–5787.
[10] Jui-Fen Chang, Baoquan Sun, Dag W. Breiby, Martin M. Nielsen, Theis I. Sölling, Mark Giles, Iain McCulloch, Henning Sirringhaus, Chemistry of Materials 16 (2004) 4772–4776.
[11] D.H. Kim, Y.D. Park, Y. Jang, H. Yang, Y.H. Kim, J.I. Han, D.G. Moon, S. Park, T. Chang, C. Chang, M. Joo, C.Y. Ryu, K. Cho, Advanced Functional Materials 15 (2005) 77–82.
[12] H. Sirringhaus, P.J. Brown, R.H. Friend, M.M. Nielsen, K. Bechgaard, B.M.W. Langeveld-Voss, A.J.H. Spiering, R.A.J. Janssen, E.W. Meijer, P. Herwing, D.M. De Leeuw, Nature 401 (6754) (1999) 685.
[13] J.T. Woodward, A. Ulman, D.K. Schwartz, Langmuir 12 (1996) 3626–3629.
[14] J. Daillant, A. Gibaud, X-ray and Neutron Reflectivity: Principles and Applications, Springer, 1999.
[15] A. Lio, D.H. Charych, M. Salmeron, Journal of Physical Chemistry B 101 (1997) 3800–3805.
[17] R. Joseph Kline, Michael D. McGehee, Ekaterina N. Kadnikova, Jinsong Liu, Jean M.J. Fréchet, Michael F. Toney, Macromolecules 38 (8) (2005) 3312–3319.
[18] R. Joseph Kline, Michael D. McGehee, Michael F. Toney, Nature Materials 5 (2006) 222–228.
[19] G. Horowitz, P. Lang, M. Mottaghi, H. Aubin, Advanced Functional Materials 14 (11) (2004) 1069.
[20] M. Vissenberg, M. Matters, Physical Review B 57 (20) (1998).
[21] G. Gu, M. Kane, J. Doty, A. Firester, Applied Physics Letters 87 (2005) 243512.
[22] W. Kim, A. Javey, O. Vermesh, Q. Wang, Y. Li, H. Dai, Nano Letters 3 (2) (2003) 193.
[23] S. Brandriss, S. Margel, Synthesis and characterization of self-assembled hydrophobic monolayer coatings on silica colloids, Langmuir 9 (1993) 1232–1240.
[24] Y. Roichman, Y. Preezant, N. Tessler, Physica Status Solidi A 201 (6) (2004) 1246.
[25] K.D. Meisel, W.F. Pasveer, J. Cottaar, C. Tanase, R. Coehoorn, P.A. Bobbert, P.W.M. Blom, D.M. de Leeuw, M.A.J. Michels, Physica Status Solidi C 3 (2) (2006) 267.
[26] In contrast to the saturation region (Section 3.3), transfer characteristic curves in the linear regime do not behave as power law as it would be expected in case of ideal transistor

operation. We ascribed this to the presence of contact resistances and we analyzed and extracted TFT parameters according to the method reported in Ref. [32]. Contact resistances were generally in the range of a few MΩ, except for OTS which had contact resistance of few kΩ. The different behavior between saturation, where no contact resistances could be detected, and linear region, can be explained taking into account a dependence of the contact resistances on the electric field. In saturation the longitudinal electric field is high and the contact resistances magnitude is so small to give negligible effects.

[27] R. Coehoorn, W.F. Pasveer, P.A. Bobbert, M.A.J. Michels, Physical Review B 72 (2005) 155206.

[28] S. Kobayashi, T. Nishikawa, T. Takenobu, S. Mori, T. Shimoda, T. Mitani, H. Shimotani, N. Yoshimoto, S. Ogawa, Y. Iwasa, Nature Materials 3 (2004) 317–322.

[29] Mingji Wang, Kenneth M. Liechti, Qi Wang, J.M. White, Langmuir 21 (5) (2005) 1848–1857.

[30] Nikhil Tambe, Bharat Bhushan, Nanotechnology 16 (2005) 1458–1549.

[32] D. Natali, L. Fumagalli, M. Sampietro, Journal of Applied Physics 101 (2007) 014501.

[33] The positive sign of the threshold voltage for RR-P3HT on Al_2O_3 + OTS is a consequence of the light non-intentional doping occured to the sample: since a non-negligible current already flows at $V_G = 0$ V, to switch the device off a positive gate voltage has to be applied.

[34] The doping of RR-P3HT was accidental, because previous experiments with SAM OTS yielded transistors with on/off ratio higher than 10^3, and it is not related with OTS itself, but due to contamination of RR-P3HT before spin-coating.

[35] L.-L. Chua, P.K.H. Ho, H. Sirringhaus, R. Friend, Advanced Materials 16 (2004) 1609.

[36] M.L. Chabinyc, R. Lujan, F. Endicott, M.F. Toney, I. McCulloch, M. Heeney, Applied Physics Letters 90 (2007) 233508.

Available online at www.sciencedirect.com
ScienceDirect
Organic Electronics 9 (2008) 209–219
Organic Electronics
www.elsevier.com/locate/orgel

Contact effects in organic thin film transistors with printed electrodes

Amare Benor, Dietmar Knipp *

Jacobs University Bremen, School of Engineering and Science, 28759 Bremen, Germany

Received 10 June 2007; received in revised form 18 October 2007; accepted 25 October 2007
Available online 23 November 2007

Abstract

The influence of contact effects on the performance of pentacene thin film transistors with printed electrodes was investigated. The electrodes of the transistor were realized by a combination of microcontact printing and selective dewetting/wetting. Printing of silane based self-assembled monolayers on glass or silicon substrates allows for the modulation of the surface energy, so that polymers or resists can be selectively deposited in the hydrophilic regions of the substrate, whereas the hydrophobic regions stay uncoated. A poly methyl methacrylate (PMMA) resist was selectively deposited in the hydrophilic regions. The resists structures were used as a template to pattern electrodes of pentacene thin film transistors by a lift-off process. The transistors exhibit charge carrier mobilities of 0.2 cm^2/V s, low threshold voltages, and high on/off ratios of 10^6. The pentacene transistors with printed drain and source electrodes were compared to devices patterned by optical lithography. In particular the influence of the drain and source contacts on the charge carrier mobility of the devices will be discussed. A simple model will be presented which takes the influence of contact effects into account when describing the electrical behavior of the transistors.

PACS: 72.80.Le; 73.40.Cg; 73.40.Sx; 73.61.Ph.

Keywords: Microcontact printing; Organic thin film transistor; TFT; Pentacene; Selective dewetting; Self-assembled monolayers

1. Introduction

Organic and polymeric electronics has attracted much attention in recent years. Due to low processing temperatures the materials can be fabricated on low cost substrates like glass or flexible foils. The prospect of flexible, unbreakable, extremely low-weight electronics at relatively low cost has stimulated a lot of research and development on organic thin film transistors (oTFTs) [1–3], flexible displays media [4], and organic sensor arrays [5,6]. Besides the new materials alternative patterning methods have been developed, which are compatible with organic materials and large area electronics. The most notable methods are microcontact printing (μCP) [7] and nanoimprint lithography (NIL) [8]. Both techniques offer novel and inexpensive routes in patterning microstructures over large areas. In the case of microcontact printing a self-assembled monolayer (SAM) is printed onto a substrate to pattern semiconductors or metals, or to modify surfaces

* Corresponding author.
E-mail address: d.knipp@jacobs-university.de (D. Knipp).

1566-1199/$ - see front matter © 2007 Elsevier B.V. All rights reserved.
doi:10.1016/j.orgel.2007.10.012

[9–12]. Furthermore, self-assembled monolayers can be used as template to selectively grow films of organic small molecules [13,14].

In this study microcontact printing was combined with selective dewetting/wetting to realize electrodes of organic thin film transistors. In the first step the substrate is functionalized by a printed silane based self-assembled monolayer (SAM). The functionalized substrate facilitates the selective deposition of polymers or resists on the surface. The resists structures are comparable to conventional resist structures patterned by optical lithography. The resist structures allow for the patterning of metallic or semiconducting micro and nanostructures over large areas by a lift-off or an etching process. In our study metal electrodes were patterned by using a lift-off process. The process was applied to realize electrodes of organic thin film transistors. The fabrication of the pentacene thin film transistor will be described in Section 2. The electrical properties of the pentacene thin film transistors will be presented in Section 3. Furthermore, the transistor will be compared to organic transistors realized by optical lithography. In particular the influence of the drain and source contacts on the charge carrier mobility of the organic transistors will be discussed. A simple model will be presented which allows for determining the contact resistance of organic transistors. The microcontact printing approach will be compared with optical lithography in terms of its applicability in organic electronics (Section 4). Finally the results will be summarized in Section 5.

2. Microcontact printing and selective wetting

Microcontact printing is a versatile additive printing process in which self- assembled monolayers are selectively transferred to rigid or flexible substrates. The μCP process is carried out by an elastomeric and flexible stamp. The stamp is fabricated by replica casting of a polydimethylsiloxane (PDMS) prepolymer against a master, which exhibits a relief structure on its surface. The master can be prepared by optical or electron beam lithography depending on the required feature size. After casting the elastomer against the master the stamp is cured before being separated from the master. A detailed description of the fabrication process of the master and the elastomeric stamp is given in Ref. [7]. Afterwards the stamp is coated by a solution, which contains the self-assembled molecules. Finally, the stamp is brought in conformal contact with the substrate. The molecules in solution are transferred to the substrate, where they form a self-assembled monolayer.

The most prominent self-assembled monolayers are thiol based self-assembled monolayers, which can be printed on noble metals (see Fig. 1a). Self-assembled monolayers like eicosanethiol and hexadecanethiol act as etch mask, which facilitates the direct patterning of metals by a wet chemical etching process [10–12]. However, patterning of metal films by thiol SAMs is restricted to materials like silver, gold and copper. Such materials might be compatible with organic electronics but they are not compatible with silicon large area electronics. Typical metals used in silicon large area electronics are aluminum, chromium or tungsten. Therefore, the use of thiol self-assembled monolayers is not applicable to silicon large area electronics.

Alternatively we developed an approach in which printed silane based SAMs are combined with the selective deposition of polymers or resists. The approach facilitates a universal route in patterning a variety of materials on substrates like glass or oxidized silicon wafers. Once the resist is selectively deposited over the substrate, different materials can be patterned by a lift-off or an etching process (see Fig. 1b). In this study the approach was used to realize drain and source electrodes of pentacene thin film transistors.

We used the silane based self-assembled monolayer octadecyltrichlorosilane (OTS) for our experiments. OTS can be printed on glass or silicon wafers. The OTS molecules modulate the surface energies, so that polymers or resists can be selectively deposited on the surface. The schematic process flow is shown in Fig. 1b. Before printing the SAMs on the substrate, the silicon wafers or glass substrates were cleaned by H_2O_2 and H_2SO_4. The cleaning procedure results in the formation of an –OH terminated surfaces. Such –OH terminated surfaces are hydrophilic. A solution of OTS ($CH_3(CH_2)_{17}SiCl_3$) in hexane was used as "ink" for the printing process. The solution was spin coated on an elastomeric PDMS stamp. The stamp is used to transfer the OTS molecules on the silicon surface. In the printed regions the OTS molecules form Si–O–Si bonds to the substrates. The OTS covered regions turn hydrophobic, while the unexposed regions stay hydrophilic. Water contact angle measurements showed complete wetting in the hydrophilic regions, whereas the hydrophobic regions exhibit contact angles of 90–113° [15].

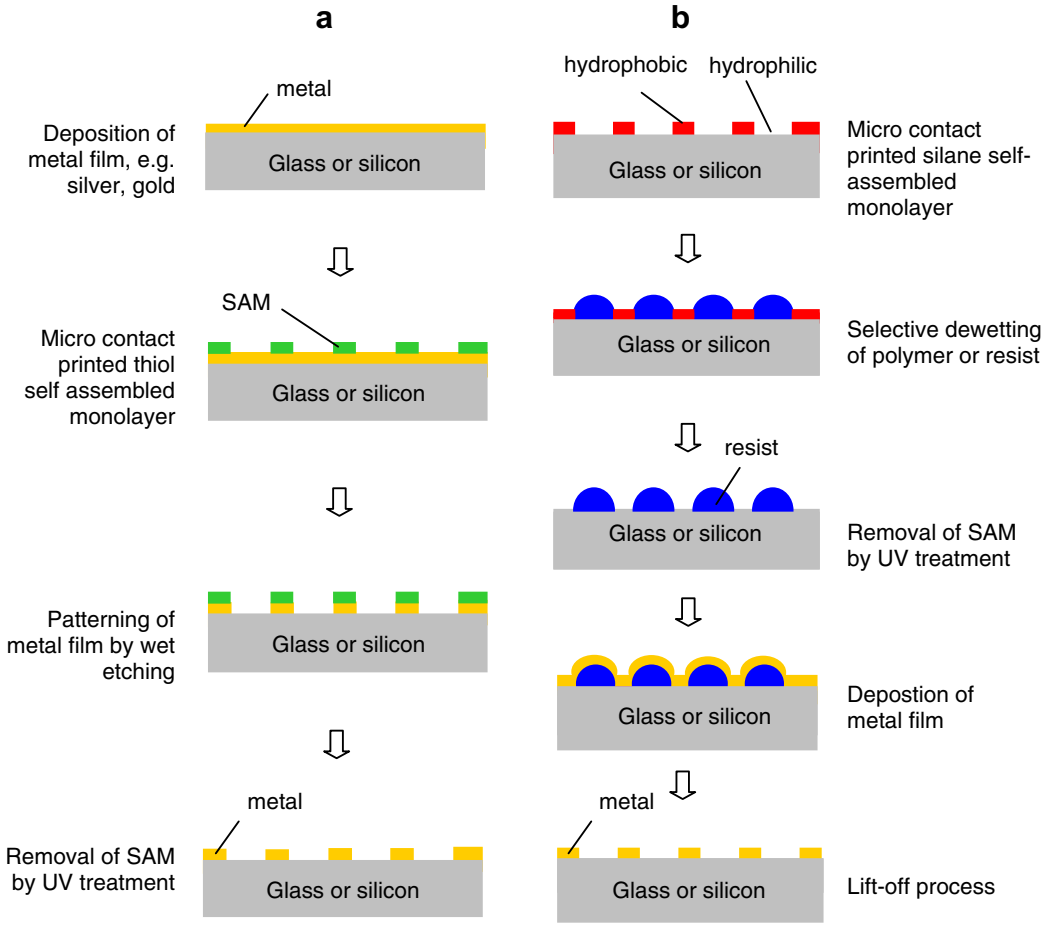

Fig. 1. Patterning of noble metals like silver, gold or copper by microcontact printing of thiol based self-assembled monolayers (SAMs) and subsequent wet etching (left). Patterning of metal or semiconducting films by a lift-off process (right). The resist structures were prepared by microcontact printing of silane based self-assembled monolayers and selective dewetting/wetting.

After prepatterning the substrate by the SAMs the sample was dip coated or spin coated by a diluted resist like (polymethyl methacrylate, PMMA). The resist selectively wets the hydrophilic regions of the substrate, whereas the hydrophobic regions stay uncoated. Subsequently, the OTS SAMs were removed by a UV exposure. In the following the resist pattern was used to lift-off different metal films like chromium and gold. The patterned gold films are later on used as drain and source electrodes in organic thin film transistors. An optical micrograph of the realized metal structures is shown in Fig. 2. The micrographs show silicon substrates before (Fig. 2a) and after patterning the gold film (Fig. 2b). The dark areas in Fig. 2a correspond to the regions covered by the resist (PMMA), whereas the bright regions are uncoated (silicon substrate). The patterned metal electrodes after carrying out the lift-off process are shown in Fig. 2b. In this particular case a thin gold film (20 nm) was patterned by the lift-off process. To improve the adhesion of the film on the substrate a 3 nm thick titanium film was evaporated prior to the gold film. The patterned metal film can be used as electrodes, interconnects or micro coils. The combination of microcontact printing and selective dewetting can be used as universal approach to pattern metals and semiconducting films. A resolution of $\sim$2 μm was achieved for thin metal films ($<$50 nm). The resolution of the process depends mainly on the resist profile on the substrate. The formation of the resist profile on the substrate again depends on several factors including the surface energies of the substrate, the viscosity of the resist, the dipping or spinning procedure of the resist [16,17].

Besides PMMA other materials like PEDOT:PSS (poly(3,4-ethylenedioxythiophene)-polystyrene-

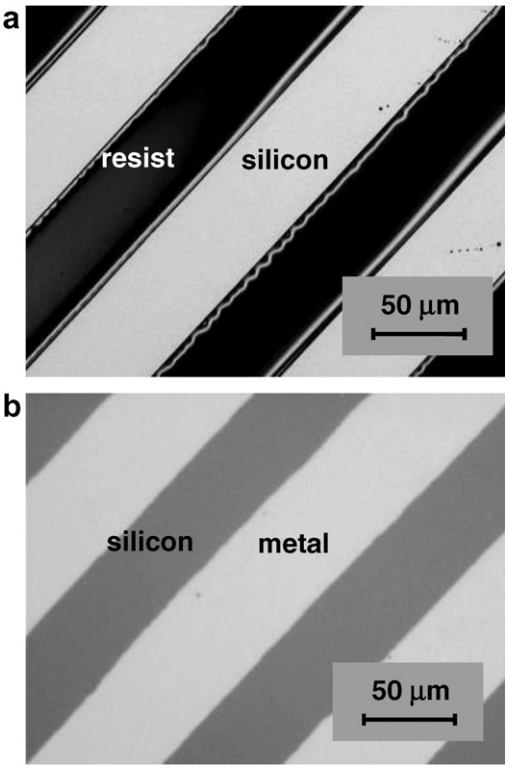

Fig. 2. Optical micrograph of a poly methyl methacrylate (PMMA) pattern on an oxidized silicon substrate (a), and a patterned gold film on an oxidized silicon substrate (b). The resist structures were prepared by microcontact printing of silane based self-assembled monolayers (e.g. octadecyl-trichlorosilane) and selective dewetting/wetting. The gold patterns were realized by a lift-off process.

sulfonate) or prepolymer polyurethane were patterned by selective dewetting [15]. The patterned conductive polymer PEDOT PSS can be used directly as drain and source electrodes of the pentacene thin film transistor. However, the achieved resolution of the process was only in the range of 30 μm. Small features down to 1 μm were patterned by using other resist materials like (prepolymer polyurethane). The resolution of the process was determined by the resolution of the stamp used for microcontact printing. Submicrometer structures can be fabricated by using electron beam lithography in preparing the master. However, lifting-off metal films by such resist patterns was not possible. The spherical resist profile on the substrate does not allow for lifting-off very small structures. Alternatively the process can be used to pattern the underlying film by a dry or a wet chemical etching process.

3. Organic thin film transistors

3.1. Device fabrication

The schematic cross-section of a pentacene thin film transistors is shown in Fig. 3. The bottom drain and source electrodes of the organic thin film transistors were realized by the combination of microcontact printing and selective wetting, which was described in Section 2. Gold electrodes with a thickness of 20 nm were used to form the drain and source electrodes of the transistor. Organic TFTs with a channel length of 20–140 μm, and a channel width of 4000 μm were realized. In order to evaluate the printing process a highly doped silicon wafer was used as substrate and gate electrode. The gate dielectric of the transistor was formed by a 100 nm thick thermal oxide layer. Before depositing the organic semiconductor the oxide surface and the gold electrodes were treated by hexamethyldisilazane (HMDS) and 2-mercapto-5-nitrobenzimidazole (MNB) SAMs, respectively. Treating the silicon dielectric by HMDS leads to an increase of the charge carrier mobility of the transistors by a factor of 2–3 [18]. Treating the gold electrodes by MNB leads to an improved charge injection, so that the drain and source contact resistance is reduced by 20–50% [19]. The pentacene molecules (Fig. 3a) were deposited by organic molecular beam deposition (OMBD). A further description of the deposition conditions is given in Ref. [20].

3.2. Transistor characteristics

The transfer curves of a pentacene TFT with printed drain and source electrodes is shown in

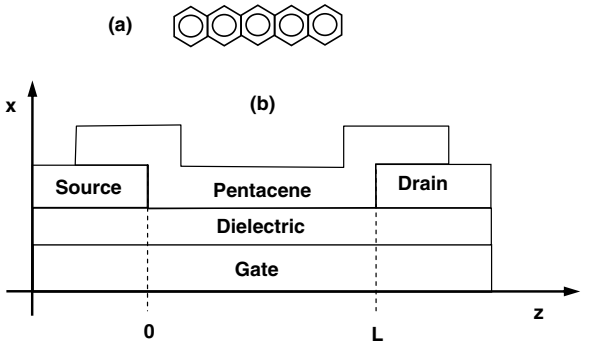

Fig. 3. A schematic cross-section of a pentacene thin film transistor. The source and drain electrodes were patterned by microcontact printing and selective dewetting/wetting.

Fig. 4. The transfer curves were measured for drain–source voltages of −1 V and −10 V. The transistor exhibits an on/off ratio – defined as the ratio of the drain–source current in the on-state ($V_{GS} = V_{DS} = -10$ V) and the off-state ($V_{GS} < 5$ V) – of approximately six orders of magnitude. A threshold voltage of 0.2 V was determined by extending the tangent to the drain current in the linear region and extracting the gate voltage at the intersection with the gate voltage axis. The drain–source current of the thin film transistor in the linear region is described by

$$I_{DS} = \frac{W}{L} C_G \cdot \mu_{eff} \cdot V_{DS} \cdot \left(V_{GS} - V_T - \frac{V_{DS}}{2} \right), \qquad (1)$$

where W and L are the width and the length of the channel. C_G is the gate capacitance per unit area, and V_{GS}, V_{DS} and V_T are the gate–source, drain–source and threshold voltages, respectively. The transistor operates in the linear region if $V_{DS} < V_{GS} - V_T$. Based on Eq. (1) the effective charge carrier mobility of the transistors in the linear region can be determined by

$$\mu_{eff} = \frac{1}{V_{DS} C_G} \cdot \frac{L}{W} \cdot \frac{\partial I_{DS}}{\partial V_{GS}}. \qquad (2)$$

The effective charge carrier mobility of the device as a function of the gate–source voltage is shown in Fig. 5 for a transistor with printed drain and source electrodes. The channel length was 40 μm. The charge carrier mobility reaches a maximum of 0.20 cm^2/V s for a gate–source voltage of −3.5 V. Additional the effective mobility is plotted for a pentacene TFT with drain and source electrodes patterned by optical lithography. The transistor with drain and source electrodes patterned by optical lithography is considered as a standard or reference structure. The effective mobility of the transistor with standard electrodes is 2–3 times higher than the effective mobility of the transistor with printed electrodes. Furthermore, the effective mobility of the transistor with standard electrodes is constant for gate–source voltages more negative than −5 V. If the transistor behaves like an ideal transistor, which can be described by Eq. (1), the effective charge carrier mobility should be independent of the gate voltage and the device geometry. Such behavior can be observed for the transistor with drain and source electrodes patterned by optical lithography. The device mobility is independent of the gate–source voltage, so that the derived device mobility is constant in the linear region of operation. This is not the case for the transistor with printed drain and source electrodes.

The device charge carrier mobility of the transistor with printed electrodes drops with decreasing gate–source voltages. The drop of the device charge carrier mobility gate–source voltages can be caused by traps in the pentacene film [21,22], scattering of

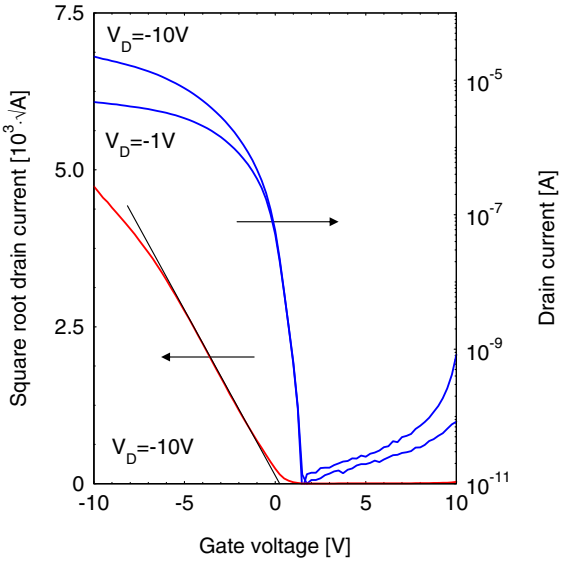

Fig. 4. Transfer curves of a pentacene thin film transistor with printed drain and source contacts fabricated by microcontact printing and selective dewetting.

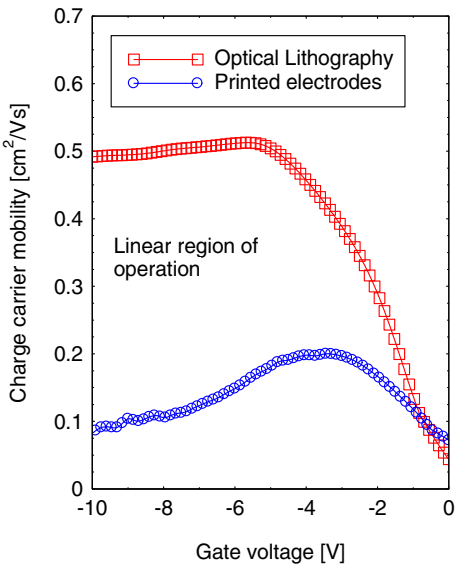

Fig. 5. Charge carrier mobility in the linear region of operation for pentacene transistors with drain and source electrodes prepared by printing and optical lithography.

charges at the semiconductor dielectric interface or the influence of contacts effects on the device performance [23,24]. As pentacene TFTs fabricated on different dielectrics exhibit the same behavior scattering processes at the dielectric play a minor role in describing the electronic transport of polycrystalline pentacene thin film transistors. Measurements of transistors with different channel lengths reveal that the extracted device charge carrier mobility strongly depends on the channel length [23–25]. The charge carrier mobility is significantly reduced for transistors with short channel lengths. The experimental results reveal that the drain and source contact have a distinct influence on the device performance. Therefore, it can be expected that the drop of the charge carrier mobility in Fig. 5 as function of the gate–source voltage is caused by the influence of the drain and source contacts.

3.3. Contact effects

In the following the influence of the contacts on the device mobility of the oTFTs is described. It is assumed that the contact effects can be described by an ohmic contact resistance. Even though the real contact behavior might be non-ohmic, a certain degree of inaccuracy might be accepted since the assumption of an ohmic contact behavior allows for providing an analytical relationship between the charge carrier mobility and the contact effects. In order to account for the influence of the contact on the drain–source current in the linear region the drain–source voltage, V_{DS}, in Eq. (1) is replaced by $V_{DS} - I_{DS}R_C$, where R_c corresponds to the sum of the drain and source contact resistances. Thus, the drain–source current can be described by

$$I_{DS} = \frac{W}{L} C_G \mu_0 (V_{DS} - I_{DS}R_C) \cdot \left(V_{GS} - V_T - \frac{V_{DS}}{2} + \frac{I_{DS}R_C}{2} \right). \quad (3)$$

Eq. (3) can be simplified by assuming that $V_{GS} - V_T$ is significantly larger than $V_{DS}/2 - I_{DS}R_C/2$, so that the drain–source current can be expressed by

$$I_{DS} \approx \frac{W}{L + W\mu_0 C_G R_C (V_{GS} - V_T)} \mu_o C_G V_{DS} (V_{GS} - V_T). \quad (4)$$

Subsequently an expression for the effective mobility, μ_{eff}, of the transistors as a function of the channel length and the contact resistance can be defined by [23]:

$$\mu_{eff} = \mu_0 \frac{L}{L + W\mu_0 C_G R_C (V_{GS} - V_T)}. \quad (5)$$

In the following the transfer curve of the transistor with printed drain and source electrodes was fitted by Eq. (1) and (4) to determine the intrinsic charge carrier mobility, the threshold voltage and the contact resistance of the pentacene thin film transistor. The drain–source current was fitted for gate–source voltages more negative than −2 V. For gate–source voltages less negative than −2 V the transistor operates in the saturation region ($V_{GS} \geqslant V_{DS} + V_T$). A good agreement between the experimental data and the fit was achieved if the influence of the contacts was taken into account (Eq. (4)). Eq. (1) does not allow for the description of the drain–source current in the linear region of operation. Taking the contact resistance into account a charge carrier mobility of $\mu_0 = 0.3\ cm^2/V\ s$, a threshold voltage of $V_T = -1$ V and a contact resistance of 12 kΩ cm was determined for a transistor with a channel length of 40 μm.

A summary of the different device parameters is given in Table 1 and 2. Table 1 provides the device parameters directly extracted from the experimental data. Table 2 states the device parameters by fitting the experimental data with and without contact effects.

Eq. (5) was used to describe the drop of the charge carrier mobility as a function of the gate–source voltage in Fig. 6b. The drop of the charge carrier mobility can be described by using the parameters stated in Table 2. The same procedure was applied to transistors with electrodes patterned by optical lithography. In this case a threshold voltage of ∼−1.5 V and a charge carrier mobility of $\sim 0.5\ cm^2/V\ s$ were determined. The contact resistance of the device was reduced by a factor of 20–30 leading to contact resistances of 0.6 kΩ cm. The extracted parameters are again listed in Table 2.

In the saturation region the transfer curve of the transistors is described by

$$I_{DS} = \frac{W}{2L} C_G \cdot \mu_{eff} \cdot (V_{GS} - V_T)^2. \quad (6)$$

Eq. (6) is valid for $V_{DS} \geqslant V_{GS} - V_T$. The transistor in Fig. 4 exhibits a maximum saturation mobility of $0.18\ cm^2/V\ s$ and threshold voltage of 0.3 V. The charge carrier mobility in the saturation region of the transistor can be calculated according to

Table 1
Extracted device parameters of pentacene thin film transistors with printed drain and source electrodes (left) and electrodes patterned by optical lithography (right)

	Experiment	
Linear region		
Parameter [Dim.]	Charge carrier mobility [$cm^2/V\,s$]	Threshold voltage [V]
Measurement	0.20/0.45	−0.8/−1.0
Saturation region		
Parameters	Charge carrier mobility [$cm^2/V\,s$]	Threshold voltage [V]
Measurement	0.18/0.50	0.2/−1.3

Table 2
Transistor parameters determined by fitting the experimental data using the classical transistor model and an extended transistor model, which takes the influence of drain and source contacts into account. The parameters are given for the transistors with printed drain and source electrodes (left) and transistors with electrodes patterned by optical lithography (right)

	Transistor model /transistor model including contacts		
Linear region			
Parameter [Dim.]	Charge carrier mobility [$cm^2/V\,s$]	Threshold voltage [V]	Contact resistance [$k\Omega\,cm$]
Standard	0.15/045	0.1/−0.5	–
With contacts	0.30/0.52	−1.0/−0.55	12/0.6
Saturation region			
Parameter [Dim.]	Charge carrier mobility [$cm^2/V\,s$]	Threshold voltage [V]	Contact resistance [$k\Omega\,cm$]
Standard	0.11/0.50	1.3/−0.8	–
With contacts	0.30/0.55	−0.3/−0.9	11.2/0.4

$$\mu_{\text{eff}} = \frac{1}{C_G}\cdot\frac{2L}{W}\cdot\left(\frac{\partial\sqrt{I_{DS}}}{\partial V_{GS}}\right)^2. \tag{7}$$

The device mobility in the saturation region as a function of the gate–source voltage is plotted in Fig. 7b. Again a distinct drop of the charge carrier mobility is observed with decreasing gate–source voltages.

In order to derive an expression for the drain–source current in the saturation region taking the contact effects into account, the drain–source voltage, V_{DS}, in Eq. (3) was substituted by $V_{GS} - V_T$ Thus, the following expression for the drain–source current in the saturation region can be derived.

$$I_{DS} = \frac{W}{2L}C_G\mu_0[(V_{GS}-V_T)^2 - I_{DS}^2R_C^2]. \tag{8}$$

In order to derive an analytical expression for the charge carrier mobility in the saturation region the drain–source current in Eq. (8) can be substituted by Eq. (4) for $V_{DS} = V_{GS} - V_T$, which will lead to the following approximation of the drain–source current in the saturation region:

$$I_{DS} \approx \frac{W}{2L}C_G\mu_0\left[(V_{GS}-V_T)^2 - \left(\frac{\mu_0 WC_GR_C(V_{GS}-V_T)^2}{L+WR_CC_G\mu_0(V_{GS}-V_T)}\right)^2\right]. \tag{9}$$

Based on Eq. (9) the following expression for the effective charge carrier in the saturation region can be derived:

$$\mu_{\text{eff}} = \mu_0\left[1-\left(\frac{W\mu_0C_GR_C(V_{GS}-V_T)}{L+WR_CC_G\mu_0(V_{GS}-V_T)}\right)^2\right] \tag{10}$$

The fit of the transfer curve in the saturation region is shown in Fig. 7a. According to Eq. (9) a charge carrier mobility of 0.3 $cm^2/V\,s$, a threshold voltage of −0.3 V, and a contact resistance of 11.2 $k\Omega\,cm$ were extracted. Again a good agreement between the experimental data and the fit was achieved if the influence of the contacts was taken into account. The extracted parameters for the charge carrier mobility and the contact resistance in the linear and the saturation region are almost identical (Table 2).

To study the origin of the high contact resistance of the transistors with printed electrodes atomic force microscope (AFM) measurements of the electrodes were taken. Fig. 8 shows atomic force microscope images of pentacene films at the edge between the channel and the contact region. Fig. 8a exhibits the image of a pentacene film prepared on a photo lithographically patterned drain and source electrode. Fig. 8b shows a pentacene film prepared on top of a drain and source electrode patterned by

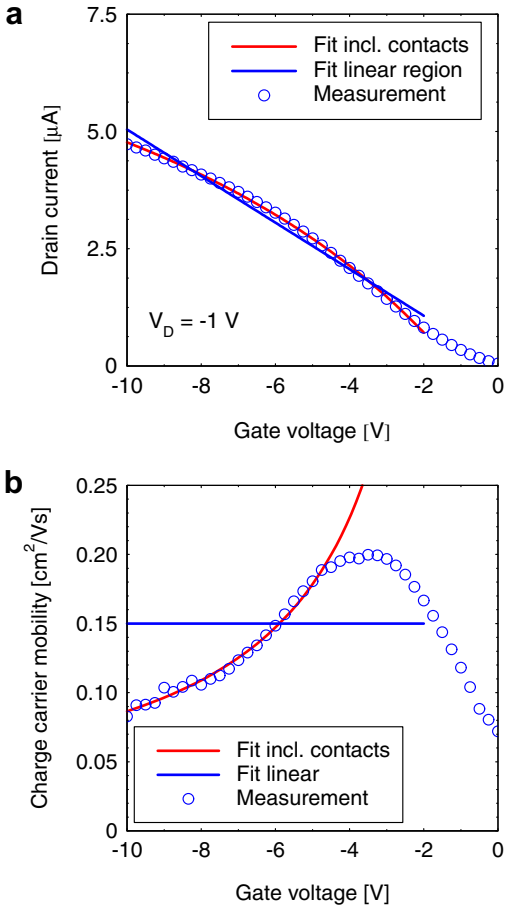

Fig. 6. Measured and simulated drain–source current (a) and charge carrier mobility (b) of a pentacene thin film transistor with printed drain and source contacts in the linear region of operation.

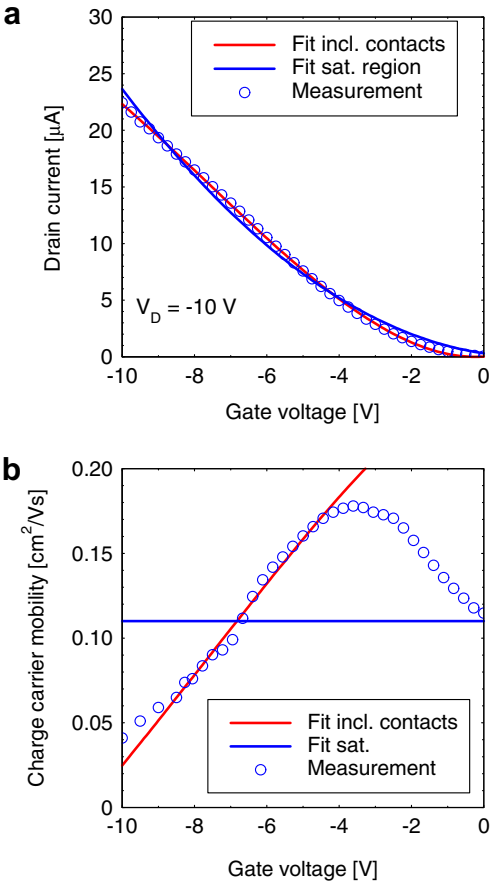

Fig. 7. Measured and simulated drain–source current (a) and charge carrier mobility (b) of a pentacene thin film transistor with printed drain and source contacts in the saturation region of operation.

microcontact printing and selective wetting. The thickness of the pentacene film (10–15 nm) and the drain and source electrodes (20 nm) is identical for both samples. The AFM images in Fig. 8 show the typical morphology of polycrystalline pentacene films. The pentacene crystals exhibit a dendritic structure with average crystal diameters of 1 μm in the channel region. The channel region was treated by HMDS prior to the deposition of the pentacene film. The drain and source electrodes were treated by a MNB self-assembled monolayer before bringing down the pentacene molecules. The SAM treatment leads to the formation of a highly ordered pentacene film on top of the gold electrodes. The pentacene crystals exhibit an average diameter of 300 nm. A comparison of the AFM images reveals that the formation of the pentacene film at the edge of the electrode is different for the two samples. A clustering of pentacene molecules can be observed for the sample with printed electrodes (Fig. 8b). The clustering might be caused by the formation of a burr-like structure at the edge of the printed electrode. A schematic cross-section of the sample is shown in Fig. 8c and d to illustrate the influence of the burr-like structure on the formation of the pentacene film. The selective wetting process leads to the formation of an arc-like resist pattern on the substrate. The arc-like structure prevents a complete lift-off of the deposited metal in the channel region. The high contact resistance of the transistor is caused by the poor injection of holes in the pentacene film due to poor step coverage of the pentacene film at the edge of the transistor. The pentacene film is very thin, so that the pentacene molecules just form a contact with the titanium rather that the gold film.

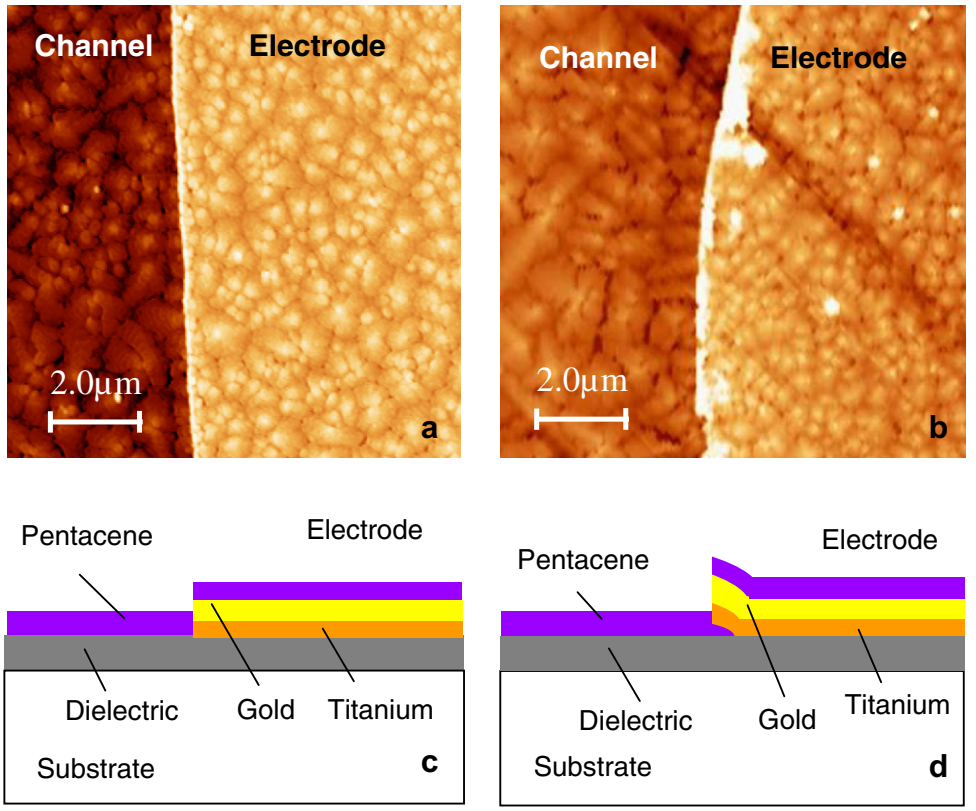

Fig. 8. Atomic force microscope (AFM) image of polycrystalline pentacene films prepared on a silicon dioxide dielectric treated with a hexamethyldisilazane (HMDS) self-assembled monolayer (SAM) and a gold drain/source electrode treated by 2-mercapto-5-nitrobenzimidazole (MNB) SAMs, respectively. The drain/source electrodes were patterned by optical lithography (a) and microcontact printing in combination with selective dewetting/wetting (b) Cross- section of a pentacene thin film transistor with drain/source electrodes patterned by optical lithography (c) and microcontact printing in combination with selective dewetting/wetting (d).

4. Discussion

Microcontact printing is a very versatile printing technology, which opens up new opportunities in micro and nanofabrication of electronic and photonics devices on large areas. In this study microcontact printing was combined with selective dewetting/wetting to pattern polymers or resists. Subsequently the resist structures were used to pattern electrodes of organic transistors by a lift-off process. The selective dewetting/wetting process allows for the patterning of submicrometer structures. However, the resists profile on the surface forms an arc-like structure (see Fig. 1b), which limits the resolution of the subsequent lift-off process, so that submicrometer structures cannot be fabricated. In this study metal electrodes were realized for organic thin film transistors. The electrical performances of the organic transistors is comparable to the electrical performance of oTFTs prepared by optical lithography, even thought the devices exhibit an increased contact resistance, which leads to a reduction of the extracted device charge carrier mobility. The contact resistance is increased due to the formation of a burr-like structure at the edge of the electrodes, which limits the injection of charges in the channel of the transistor. The influence of the contacts on the charge carrier mobility in the linear and the saturation region was described by a simple model, which accounts for the influence of the drain and source contacts.

The influence of the contact effects on the device operation is not only limited to electrodes prepared by a printed approach. In general, it is well known that the performance of organic transistors is limited by the injection of charges in the channel via metal electrodes [2]. Different models have been proposed to describe contact effects in organic thin film transistors ranging from simple ohmic contacts [24], to gate–source voltage dependent contact resistances

[23,26–28] to anti- parallel connected Schottky diodes [23]. Recent results show that the contacts between pentacene and noble metals like gold, silver and platinum can be described by Schottky barriers or Schottky diodes [30]. However, different barrier heights and different dipole moments were determined by different authors [30,31]. The barrier height and the dipole moment are influenced by the contact geometry (top versus bottom drain and source contacts), potential SAM treatments of the electrodes and environmental conditions [25,29]. In particular moisture has a distinguished influence on the injection of charges [22]. Therefore, the simple model presented in this manuscript provides only an estimate of the contact resistance. The contact resistance is the only free parameter in this model. Other models typically require several fitting parameters. Furthermore, the presented model allows for describing the gate voltage depended charge carrier mobility, which confirms the assumption of an ohmic contact resistance. Nevertheless, further investigations are needed to identify and describe the charge injection in the pentacene films. Scanning probe [32,33] and four probe measurements [34] should provide insights in the charge injection mechanism and the contact behavior.

First results in which microcontact printing in combination with selective wetting was used to pattern front electrodes of silicon large area electronic devices like thin film solar cells or thin film detectors exhibit promising results. Therefore, the presented approach facilitates a universal route in patterning a variety of materials on substrates like glass or silicon wafers.

5. Summary

In summary, microcontact printing is a promising technology for large area electronic and photonic applications. In this study the combination of microcontact printing and selective wetting was applied to realize metallic microstructures. The approach is based on the selective wetting of resists on hydrophilic and hydrophobic prepatterned substrates. Polymers and resists can be selectively deposited in the hydrophilic regions, while the hydrophobic regions remain uncovered. In this study the selectively patterned resist structures were used to pattern different metal structures like electrodes, interconnects and micro coils by a lift-off process. Printed drain and source electrodes were used to fabricate pentacene thin film transistors. The transistors exhibit charge carrier mobilities of 0.2 cm^2/V s and on/off ratios of 10^6. The electrical performances of the organic transistors is comparable to the electrical performance of oTFTs prepared by optical lithography, even thought the devices exhibit an increased contact resistance, which leads to a reduction of the charge carrier mobility. The contact resistance is increased due to the formation of a burr-like structure at the edge of the electrodes, which limits the injection of charges in the channel of the transistor. The electrical characteristic of the transistors was described by a simple transistor model, which takes the influence of the contacts into account.

Acknowledgement

The authors like to acknowledge Veit Wagner, Arne Hoppe for scientific discussions and Hany Elgala for technical assistance in electron beam evaporation.

References

[1] C.D. Dimitrakopoulos, P.R.L. Malenfant, Adv. Mater. 14 (2002) 99.
[2] G. Horowitz, J. Mater. Res. 19 (2004) 1946.
[3] D. Knipp, R.A. Street, J. Non-Cryst. Solids 338–340 (2004) 595.
[4] G.H. Gelink, H.E. Huitema, E. van Veenendaal, E. Cantatore, L. Schrijnemakers, J.B.P.H. Van Der Putten, T.C.T. Geuns, M. Beenhakkers, J.B. Giesbers, B.-H. Huisman, E.J. Meijer, E.M. Benito, F.J. Touwslager, A.W. Marsman, B.J.E. Van Rens, D.M. de Leeuw, Nature Mater. 3 (2004) 106.
[5] R.A. Street, M. Mulato, R. Lau, J. Ho, J. Graham, Z. Popovic, J. Hor. Appl. Phys. Lett. 78 (2001) 4193.
[6] T. Someya, Y. Kato, S. Iba, H. Kawaguchi, T. Sakurai, IEEE Trans. Electr. Dev. 52 (11) (2005) 2502.
[7] Y. Xia, G.M. Whitesides, Annu. Rev. Mater. Sci. 28 (1996) 153.
[8] L.J. Guo, P.R. Krauss, S.Y. Chou, Appl. Phys. Lett. 71 (1997) 1881.
[9] A. Kumar, H. Biebuyck, G.M. Whitesides, Langmuir 10 (1994) 1498.
[10] Y. Xia, E. Kim, G.M. Whitesides, J. Electrochem. Soc. 143 (3) (1996) 1070.
[11] Y. Xia, E. Kim, M. Marksich, G.M. Whitesides, Chem. Mat. 8 (3) (1996) 601.
[12] M. Leufgen, A. Lebib, T. Muck, U. Bass, V. Wagner, T. Borzenko, G. Schmidt, J. Geurts, L.W. Molenkamp, Appl. Phys. Lett. 84 (2004) 1582.
[13] S. Steudel, D. Janssen, S. Verlaak, J. Genoe, P. Heremans, Appl. Phys. Lett. 85 (2004) 5550.
[14] A.L. Briseno, S. Mansfeld, M.M. Ling, R.J. Tseng, S.H. Liu, C. Reese, M. Roberts, Y. Yang, F. Wudl, Z. Bao, Nature 444 (2006) 913.

[15] A. Benor, A. Hoppe, V. Wagner, D. Knipp, Thin Solid Films 515 (2007) 7679.
[16] A.A. Darhuber, S.M. Troian, J.M. Davis, S.M. Miller, S. Wagner, J. Appl. Phys. 88 (9) (2000) 5119.
[17] A. Benor, V. Wagner, D. Knipp, J. Vac. Sci. & Technol. B 25 (2007) 1321.
[18] S. Kobayashi, T. Nishikawa, T. Takenobu, S. Mori, T. Shimoda, T. Mitani, H. Shimotani, N. Yoshimoto, S. Ogawa, Y. Iwasa, Nature Mater. 3 (2004) 317.
[19] I. Kymissis, D. Dimitrakopoulos, S. Purushothaman, IEEE Trans. Electr. Dev. 48 (2001) 1060.
[20] D. Knipp, T. Muck, A. Benor, V. Wagner, J. Non-Cryst. Solids 352 (2006) 1774.
[21] K.P. Pernstich, D. Oberhoff, C. Goldmann, B. Batlogg, Appl. Phys. Lett. 89 (2006) 213509.
[22] A.R. Völkel, R.A. Street, D. Knipp, Phys. Rev. B. 66 (2002) 195336.
[23] P.V. Necliudov, M.S. Shur, D.J. Gundlach, T.N. Jackson, J. Appl. Phys. 88 (2000) 6594.
[24] H. Klauk, G. Schmid, W. Radlik, W. Weber, L. Zhou, C.D. Sheraw, J.A. Nichlos, T.N. Jackson, Solid-State Electr. 47 (2003) 297.
[25] D. Knipp, A. Benor, V. Wagner, T. Muck, J. Appl. Phys. 101 (2007) 044504.
[26] G. Horrowitz, M.E. Hajlaoui, R. Hajlaoui, J. Appl. Phys. 87 (2000) 4456.
[27] R.A. Street, A. Salleo, Appl. Phys. Lett. 81 (2002) 2887.
[28] J. Zaumseil, K.W. Baldwin, J.A. Rogers, J. Appl. Phys. 93 (2003) 6117.
[29] E.J. Meijer, G.H. Gelinck, E. van Veenendaal, B.H. Huisman, D.M. de Leeuw, T.M. Klapwijk, Appl. Phys. Lett. 82 (2003) 4576.
[30] L. Diao, C.D. Frisbie, D.D. Schroepfer, R.P. Ruden, J. Appl. Phys. 101 (2007) 0145510.
[31] N. Koch, A. Kahn, J. Ghijsen, J.J. Pireeaux, J. Schwartz, R.L. Johnson, A. Elschner, Appl. Surf. Sci. 82 (2003) 70.
[32] K. Seshardi, C.D. Frisbie, Appl. Phys. Lett. 78 (2001) 993.
[33] L. Bürgi, T.J. Richards, R.H. Friend, H. Sirringhaus, J. Appl. Phys. 94 (2003) 6129.
[34] R. Chesterfield, J.C. McKeen, C.R. Newman, C.D. Frisbie, P.C. Ewbank, K.R. Mann, L.L. Miller, J. Appl. Phys. 95 (2004) 6396.

Available online at www.sciencedirect.com
ScienceDirect
Organic Electronics 9 (2008) 220–226
Organic Electronics
www.elsevier.com/locate/orgel

Electric field and temperature dependence of the hole mobility in a bis-fluorene cored dendrimer

S. Gambino [a], I.D.W. Samuel [a,*], H. Barcena [b,c], P.L. Burn [b,c]

[a] Organic Semiconductor Centre, SUPA, School of Physics and Astronomy, University of St Andrews, North Haugh, St Andrews, Fife KY16 9SS, UK
[b] Department of Chemistry, University of Oxford, Chemistry Research Laboratory, Mansfield Road, Oxford OX1 3TA, UK
[c] Centre for Organic Photonics & Electronics, School of Molecular & Microbial Sciences, University of Queensland, St Lucia 4072, Australia

Received 12 November 2006; received in revised form 29 October 2007; accepted 3 November 2007
Available online 17 November 2007

Abstract

Time-of-flight mobility measurements on a first generation, bis(fluorene)-cored dendrimer are reported. A charge generation layer was used enabling measurements to be performed on spin-coated films, comparable to those used in devices such as organic light-emitting diodes. The results are compared with spin-coated polyfluorene films. The temperature and electric field dependence of the mobility of the dendrimer was studied and found to be in excellent agreement with the Gaussian disorder model, with an energetic disorder parameter, σ, of 74 meV and a positional disorder parameter, Σ, of 2.6.

PACS: 72.80.Le; 73.50.Pz; 85.60.Jb; 73.50.Dn

Keywords: Organic light-emitting diode; Charge transport; Time of flight; Dendrimer; Fluorene

1. Introduction

There is considerable current interest in the physics of organic semiconductors and the application of these materials in devices such as light-emitting diodes [1–5], solar cells [6–8] and field-effect transistors [9,10]. For all these applications, charge transport plays a very important role in device operation and a detailed understanding of it at the materials level is needed. Materials for organic light-emitting diodes can be divided into three main classes: small molecules [1,11–13], conjugated polymers [2,12–15] and light-emitting dendrimers [4,16–19]. Small molecules are generally deposited by evaporation, whereas conjugated polymers and dendrimers are normally processed from solution. Charge transport in small molecules and conjugated polymers has been extensively studied [20–24], but much less is known about it in light-emitting dendrimers [5,25–27]. In this paper we report a detailed study of charge transport in a blue fluorescent light-emitting dendrimer, and compare the results with a closely related conjugated polymer.

* Corresponding author. Tel.: +44 1334463114; fax: +44 1334463104.
E-mail address: idws@st-and.ac.uk (I.D.W. Samuel).

1566-1199/$ - see front matter © 2007 Elsevier B.V. All rights reserved.
doi:10.1016/j.orgel.2007.11.002

Light-emitting dendrimers consist of a core, conjugated dendrons, and surface groups. The dendrimer studied in the present work (G1F) is shown in the inset of Fig. 2, and consists of a bis(fluorene) core, *meta*-linked biphenyl dendrons, and 2-ethylhexyloxy surface groups. It has been successfully used to make deep-blue OLEDs with reasonable efficiency [28]. The core chromophore is closely related to the widely studied polymer poly[(9,9-dioctylfluoren-2,7-diyl) (PFO), and we make a direct comparison of the charge transport in the two materials in this paper.

Time-of-flight mobility measurements, in which a sample is photoexcited and the transit time of the charge carriers across the film is measured, provide a powerful way of studying charge transport [29–31]. They are most commonly made on films a few microns thick to ensure that the excitation light is absorbed in a layer that is thin compared with the total thickness of the film [23,24]. However, such films are much thicker than those used in OLEDs, and are prepared by techniques such as blade-coating, dip-coating or solution-casting, instead of the spin-coating commonly used to make OLEDs. This is a concern as the properties of organic semiconductors, and in particular film morphology, can be very sensitive to the preparation method used [32–34]. Differences in morphology mean that thin films of PFO have dispersive charge transport, whilst thicker films show non-dispersive behaviour [35]. Accordingly in the present study we have used a charge generation layer in order to be able to work with much thinner films that can be prepared by spin-coating [36], and are therefore comparable to films used in OLEDs. The same spin-coating solvent (chloroform) was used for the dendrimer and for PFO to make the results directly comparable. The charge generation layer gives a well-defined region of charge generation, which is needed for time-of-flight measurements. Working with thinner films also means that transit times are much faster, and so in order to obtain good time-resolution and good sensitivity, we built a transimpedance amplifier based around a Texas Instruments OPA 655 chip.

Non-dispersive charge transport has been reported in PFO and in a brief study on the bis(fluorene) dendrimer. However, a detailed understanding of charge transport requires temperature-dependent measurements in order to determine, for example, positional and energetic disorder parameters. We report such a study here and show that the results can be interpreted in terms of Bässler's Gaussian disorder model [37].

2. Experiment

Charge-generation-layer time-of-flight [36,38,39] (CGL-TOF) measurements were performed on 300 nm thick G1F films spin-coated onto cleaned ITO substrates (sheet resistance 20 Ω/□) from a 45 mg/ml chloroform solution. Subsequently 10 nm of a perylene dye derivative (Lumogen Red) charge generation layer was evaporated onto the device. The device was completed by deposition of 100 nm of aluminium to give an active pixel area of approximately 5.6 mm^2. A similar procedure was used for the preparation of PFO films, which were also spin-coated from 45 mg/ml chloroform solution. The PFO was from H.W. Sands, and had a number average molecular weight of 86,000 with a polydispersity of 5.8. The excitation wavelength of 580 nm was chosen to pass through the film under study and to be absorbed by the perylene dye (see Fig. 1). Charge carriers were generated within the perylene layer by excitation (0.5 μJ) from a 500 ps pulse of a dye laser at a wavelength of 580 nm. The highest occupied molecular orbital of the Lumogen Red was estimated from cyclic voltammetry measurements to be 6.2 eV from the vacuum level, enabling hole injection into the fluorene layer. The packet of charge carriers was then swept through the device under an applied field, and the transit time (t_{tr}) measured using a digital storage oscilloscope. The aluminium electrode was biased positively and the photocurrent signal detected from the ITO. The applied bias led to the electrons photogenerated in the perylene dye layer being removed from the device at the aluminium electrode and

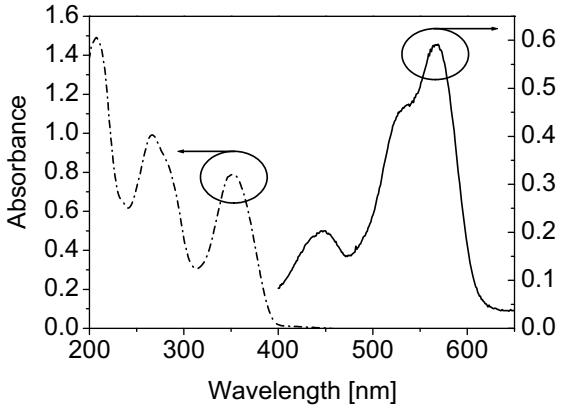

Fig. 1. Absorption spectra of the first generation bis(fluorene)-cored dendrimer (G1F) thin film (dotted line) and a Lumogen Red thin film (solid line).

holes being injected into the dendrimer from the perylene dye and consequently swept across the device to be collected at the ITO electrode. Thus the measured photocurrent transients are hole currents.

Hole mobilities, μ, were deduced from the transit times t_{tr} via the relation $\mu = d^2/(Vt_{tr})$, where d is the film thickness and V is the applied voltage. The sample was mounted in a vacuum cryostat at controlled temperature. The signal to noise ratio is the limiting factor for obtaining data at low temperatures and low applied electric fields. We were able to perform measurements at very low fields and temperatures using a custom-made transimpendance amplifier. The RC time constant of the measurement circuit was always selected to be $\leqslant 20\ t_{tr}$. The total charge injected into the film was kept around 2–3% CV in all cases, where C is the capacitance of the device and V is the applied voltage.

Since either variation of solvent or casting technique [24] can affect charge transport in conjugated polymer films, we spin-coated PFO of thickness $\approx$1.2 μm from a chloroform solution onto ITO coated glass substrates. Semitransparent aluminium electrodes of 30 nm thickness were then deposited by thermal evaporation (at 10^{-6} mbar) through a shadow mask onto PFO film yielding sandwich structures with an active area, defined by the electrode overlap, of $\approx$5.6 mm^2. Optical excitation of the carrier packet was achieved by illumination through the Al electrode using a 20 μJ short duration (500 ps) light pulse from a N_2 laser (337 nm).

3. Results

Fig. 2 shows a typical room temperature hole current transient on a linear scale for the first generation bis(fluorene)-cored dendrimer (G1F). The plot shows an initial current spike followed by a clear constant-current plateau. This corresponds to non-dispersive hole transport with a time-independent drift velocity. The subsequent drop in the current is caused by the holes reaching the ITO electrode, where they are discharged.

Carrier transit times, t_{tr}, were evaluated at each of a range of different bias fields from the intersection point of the asymptotes to plateau and to the long tail. Fig. 3 shows the field dependent mobility at temperatures from 195 to 335 K at intervals of 20 K. At the lower fields, the mobility decreases as the field increases, reaching a minimum at $E \approx 10^5$ V/cm. At higher fields ($E \geqslant 10^5$ V/cm),

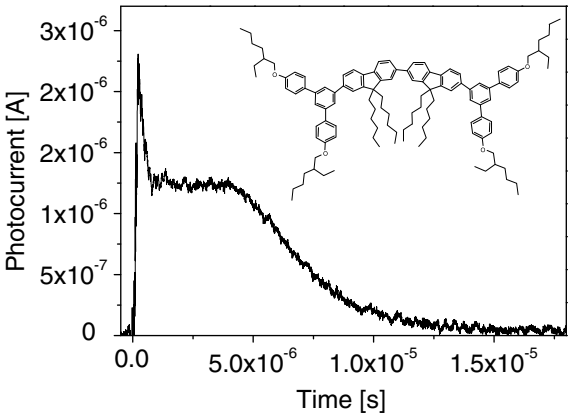

Fig. 2. Typical room temperature TOF hole transient for a first generation bis-fluorene dendrimer (G1F). G1F film of thickness $d = 300$ nm, $E = 1.6 \times 10^5$ V/cm. Also shown is the structure of G1F.

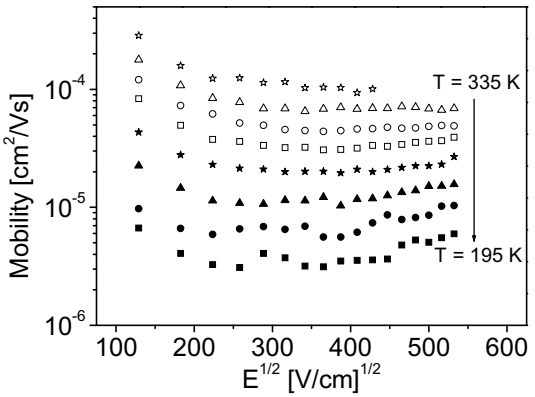

Fig. 3. The field dependent mobility at temperatures from 195 to 335 K at intervals of 20 K.

the mobility increases weakly with increasing field, and is consistent with the Poole–Frenkel relation (Eq. (1)):

$$\ln[\mu(E)/\mu_{E=0}] = SE^{1/2} \tag{1}$$

where S is the slope and $\mu_{(E=0)}$ is the zero-field mobility.

The zero-field mobilities obtained for various temperatures from Fig. 3 are plotted against $1/T^2$ in Fig. 4. A linear relationship is observed for $\ln(\mu)$ against $1/T^2$ as expected in the Gaussian disorder model (GDM)[37] (Eq. (2))

$$\mu_{(E=0)} = \mu_0 \exp(-(T_0/T)^2) \tag{2}$$

where μ_0 is the mobility at infinite temperature and T_0 is a characteristic temperature of the material investigated. T_0 is obtained from the slope of Fig. 4 and is 579 K.

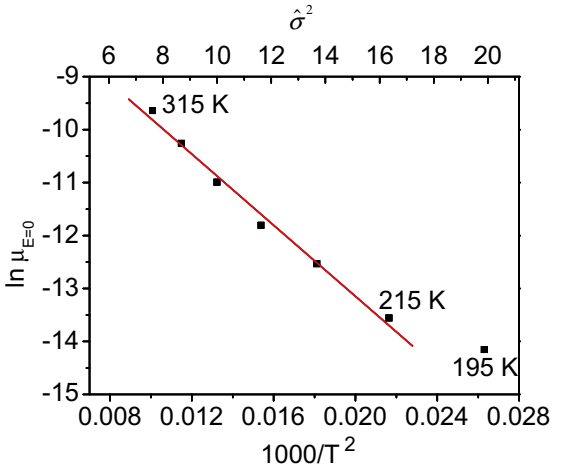

Fig. 4. The zero field mobility plotted against $1/T^2$ in order to determine energetic disorder parameter.

The two central parameters of the disorder formalism are σ, the energy width of the hopping site manifold, and Σ, the positional disorder due to a distribution of intersite distances. The width of the Gaussian density of states is related to T_0 by $T_0 = 2\sigma/3k$, where k is the Boltzmann constant and this gives a value of $\sigma = 74 \pm 4$ meV.

The deviation from the straight line in the plot of $\ln(\mu)$ against $1/T^2$ between 215 K and 195 K (see Fig. 4) is attributed to the onset of the non-dispersive to dispersive transition (ND–D). This can be clearly seen in the shape of the photocurrent transients as a function of temperature (see Fig. 5). As temperature is decreased, the photocurrent plateau becomes less distinct and disappears below 215 K. The width of the tail also increases upon decreasing the temperature. The temperature dependence of the mobility is expected to change at the non-dispersive to dispersive transition temperature T_c according to Eq. (3)

$$(\sigma/kT)^2 = 44.8 + 6.7 \log L \tag{3}$$

where L is the thickness of the sample in centimetres [31,37]. With a thickness of 300 nm and $\sigma = 74$ meV, the onset of the ND–D transition for G1F should occur at 228 K according to Eq. (3), which is similar to that observed experimentally.

In the Gaussian disorder model, the influence of the positional disorder parameter, Σ on the electric field dependence of the mobility is given by

$$\mu \propto \exp\{C\lfloor \sigma^2/(kT)^2 - \Sigma^2 \rfloor E^{1/2}\} \tag{4}$$

where C is a constant. The value of Σ was determined by plotting the slope S (determined using Eq. (1)) in the higher field regime (>10^5 V/cm) for various temperatures against $\hat{\sigma}^2$, where $\hat{\sigma}^2 = (\sigma/kT)^2$. The result is shown in Fig. 6 for the temperature range 195–315 K, and by fitting to the linear region of this plot [37], we extract Σ from the intercept. This analysis yielded a positional disorder parameter of 2.6 for the G1F films.

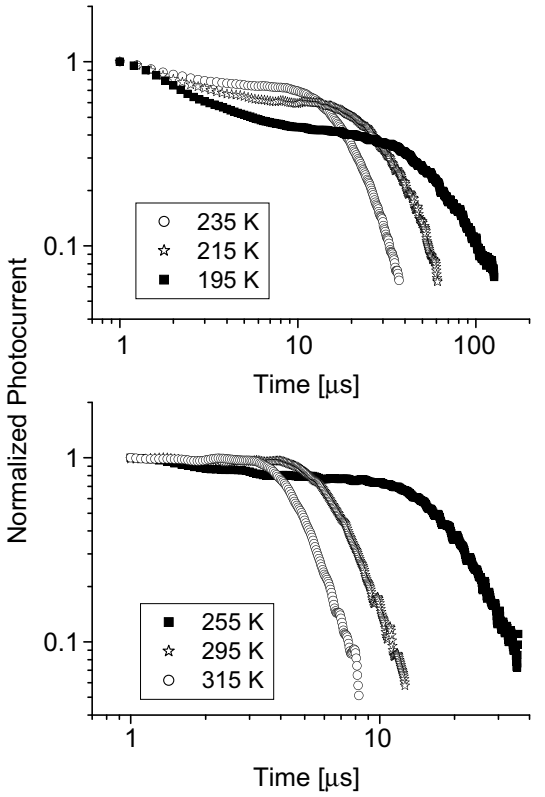

Fig. 5. The photocurrent transients for temperatures in the range 195–315 K, for G1F films. The electric field is 1.6×10^5 V/cm.

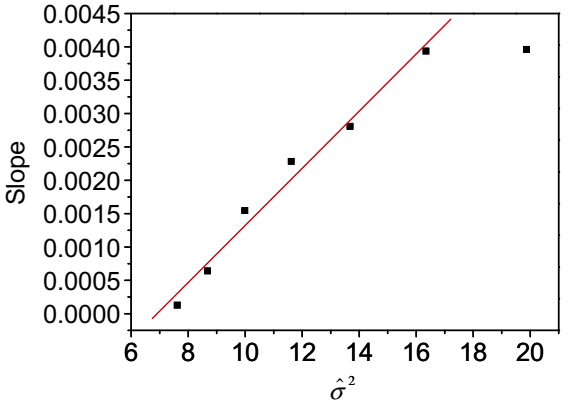

Fig. 6. The slope, S, at different temperatures is plotted against $\hat{\sigma}^2$ to obtain the positional disorder parameter, Σ.

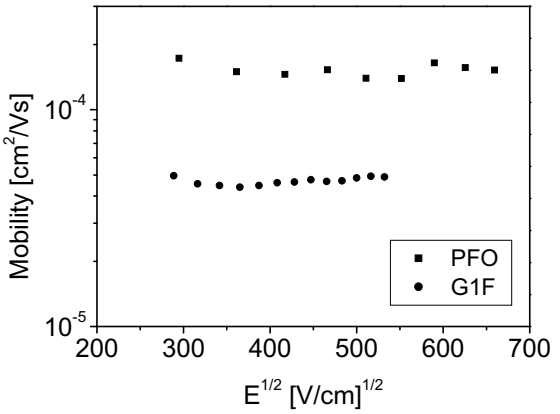

Fig. 7. Comparison of field dependent hole mobilities at room temperature for PFO and G1F. Data are plotted on a log-linear scale as function of the square root of the electric field.

In order to compare charge transport in fluorene based polymers and dendrimers, room temperature hole mobility measurements of PFO were also performed, with the results plotted in Fig. 7. It is clear that both materials show a weak field dependence at room temperature. PFO hole mobilities are in the range of 1–2 $\times$ 10^{-4} cm^2/V s for an applied electric field ranging from 8.7×10^4 to 4.3×10^5 V/cm, in good agreement with those previously reported [23]. The G1F hole mobility values were in the range of 4–5 $\times$ 10^{-5} cm^2/V s for applied electric fields ranging from 1–3 $\times$ 10^5 V/cm.

4. Discussion

TOF measurements were used to characterize both the magnitude of the mobility and the nature of charge transport. We first consider the nature of charge transport in G1F. The form of the current transient for G1F signifies that hole transport is highly non-dispersive in this dendrimer, as previously reported for room temperature measurements, [5] but in contrast to other dendrimers [25,26]. The study of a very thin sample, of order of a few hundred nanometers thickness, using a CGL-TOF demands a measurement circuit with fast response and sufficient sensitivity because of the short transit time. By using a transimpedance amplifier we were able to get a very good signal to noise ratio even at very low electric field. This allowed us to perform TOF measurements on thinner samples, at lower electric field, and to detect a photocurrent transient characterized by a clearer plateau compared to previous results on G1F [5]. A well defined plateau is a clear manifestation of the average velocity of charge carriers within the sample and not of the fastest ones. As a consequence mobility values determined in this work, are more representative of the average carrier properties.

We next consider the field and temperature dependence of the mobility. The weak electric-field dependence of the mobility (see Fig. 3) is an indication that positional disorder is large in the G1F films. In the presence of larger positional disorder, charge carriers can then detour around the next energetically favourable charge-transporting site by diffusion, and may travel against the direction of the applied field more easily [37], thus making the mobility smaller. As a result, the dependence of mobility on applied field becomes less prominent as the positional disorder increases. Furthermore, as temperature increases, the slope of the field-dependent mobility decreases for materials with large positional disorder. At vanishing energetic disorder ($\sigma/kT \to 0$), i.e. increasing temperature, charge transport is approaching a hopping system with isoenergetic sites in which the field does not affect intersite jump rate. This is because the thermal voltage ($\frac{kT}{q}$) reduces the average barrier height for jumps to higher energy sites in the field direction. In this case the mobility will approach the $\mu \propto E^{-1}$ law expected for a pure hopping system in which backward transitions are excluded. This behavior is observed in the G1F devices, where Fig. 3 shows that the slope S gradually decreases as the temperature increases. Furthermore the change in slope at higher temperature (335 K) in the high field regime ($E > 10^5$ V/cm) is due to the decrease of the energetic disorder parameter ($\hat{\sigma}$). This simply reflects the saturation of the drift velocity with field [37].

The temperature transition from non-dispersive to dispersive (that is, there is no longer a plateau in the photocurrent transients) charge transport behaviour, means that below the changing temperature (see Fig. 5), the carriers will cross the sample before relaxing to their mean energy. In contrast to previous results on a *fac*-tris(2-phenylpyridyl)iridium(III) cored dendrimer with three of the same dendrons as attached to G1F [27], G1F exhibits a non-dispersive transport mechanism even at low temperatures. Furthermore the enhanced dispersion of the TOF transient at lower temperature results from a broad distribution of hopping rates.

The transition temperature, $T_c = 215$ K, can be seen more clearly by plotting the mobility at zero field versus $1/T^2$ (Fig. 4). The deviation from the straight line in the plot of $\ln(\mu)$ against $1/T^2$ is

attributed to the onset of the non-dispersive to dispersive transition [37]. It is noteworthy how this value is strikingly close to the value of 228 K predicted by the Gaussian disorder model (Eq. (3)).

We now turn to the energetic disorder parameter. The σ value is consistent with a well ordered conjugated material, leading to a value of $\hat{\sigma} = 2.9$ at 295 K, in agreement with Bässler's Monte Carlo simulations [37,39], where photocurrent transients reveal a plateau of variable temporal length (that is, a non-dispersive transient) for $\hat{\sigma} \leqslant 3.5$.

We finally consider how the field dependent mobility of the G1F dendrimer compares with PFO. The dendrimer does not have the extended conjugation of PFO, but its mobility (4.6×10^{-5} $cm^2/V\,s$ at a field of 2.1×10^5 V/cm) is close to that of the PFO ($1.5 \times 10^{-4}\,cm^2/V\,s$ also measured at 2.1×10^5 V/cm) and higher than the value measured for other conjugated polymers (e.g. MEH-PPV [40], mobility $3.9 \times 10^{-6}\,cm^2/V\,s$ at a field of 2.1×10^5 V/cm).

The same weak field dependence of both materials investigated, suggests that in G1F the charge transport mechanism is similar to PFO and it involves the same kind of transporting sites (that is, the fluorene units). In the study of the *fac*-tris(2-phenylpyridyl)iridium(III) cored dendrimer with phenylene based dendrons [27] it was shown that charge transport was by hopping between the dendrimer cores, with the phenylene dendrons just acting as spacers, and hence charge transport through the film of G1F is expected to be by hopping between the chromophore containing the bis(fluorene) core in G1F.

5. Conclusions

The mobility of G1F is approaching that of PFO, showing that extensive conjugation is not needed for solution-processed materials to achieve mobilities suitable for OLED applications. We have shown that CGL-TOF using a suitable transimpedance amplifier is a powerful tool for the study of charge transport in spin-coated films. We have found that GDM, which has been widely applied to a variety of polymers and doped polymers to understand how material properties affect transport, gives a perfect description of dendrimer charge transport. G1F is a "text book" example of the main features of a hopping system with Gaussian DOS. This is demonstrated by the $\ln(\mu) \propto E^{1/2}$ behaviour within a limited field interval ($E > 10^5$ V/cm), the slope parameter (S) changing sign below a certain value of $\hat{\sigma}$, that is, above a certain temperature, and finally a non-dispersive charge transport behaviour for an energetic disorder parameter $\hat{\sigma} \leqslant 3.5$.

Acknowledgement

We are grateful to P. Ferreira for determining the HOMO level of lumogen red.

References

[1] C.W. Tang, S.A. VanSlyke, Appl. Phys. Lett. 51 (1987) 913–915.
[2] J.H. Burroughes, D.D.C. Bradley, A.R. Brown, R.N. Marks, K. Mackay, R.H. Friend, P.L. Burn, A.B. Holmes, Nature 347 (1990) 539.
[3] M.A. Baldo, D.F. O'Brien, Y. You, A. Shoustikov, M.E. Thompson, S.R. Forrest, Nature 395 (1998) 151.
[4] S.-C. Lo, N.A.H. Male, J.P.J. Markham, S.W. Magennis, P.L. Burn, O.V. Salata, I.D.W. Samuel, Adv. Mater. 14 (2002) 975.
[5] J.P.J. Markham, T.D. Anthopoulos, I.D.W. Samuel, G.J. Richards, P.L. Burn, C. Im, H. Bässler, Appl. Phys. Lett. 81 (2002) 3266.
[6] C.W. Tang, Appl. Phys. Lett. 48 (1986) 183.
[7] G. Yu, J. Gao, J.C. Hummelen, F. Wudl, A.J. Heeger, Science 270 (1995) 1789.
[8] J.J.M. Halls, C.A. Walsh, N.C. Greenham, E.A. Marseglia, R.H. Friend, S.C. Moratti, A.B. Holmes, Nature 376 (1995) 498.
[9] H. Sirringhaus, N. Tessler, R.H. Friend, Science 280 (1998) 1741.
[10] F. Garnier, R. Hajlaoui, A. Yassar, P. Srivastava, Science 265 (1994) 1684.
[11] C.W. Tang, S.A. VanSlyke, C.H. Chen, J. Appl. Phys. 65 (1989) 3610.
[12] M. Pope, C.E. Swenberg, Electronic Processes in Organic Crystals, Oxford University Press, 1999.
[13] R. Farchioni, G. Grosso, Organic Electronic Materials, Springer, 2001.
[14] R.H. Partridge, Polymer 24 (1983) 755.
[15] E.M. Conwell, in: H.S. Nalwa (Ed.), Handbook of Organic Conductive Molecules and Polymers, Conductive Polymers: Transport, Photophysics and Applications, vol. 4, Wiley, 1997.
[16] J.M. Lupton, I.D.W. Samuel, R. Beavington, P.L. Burn, H. Bässler, Adv. Mat. 13 (2001) 258.
[17] M. Halim, I.D.W. Samuel, J.N.G. Pillow, P.L. Burn, Synth Met. 102 (1999) 1113.
[18] M. Halim, J.N.G. Pillow, I.D.W. Samuel, P.L. Burn, Adv. Mat. 11 (1999) 371.
[19] J.N.G. Pillow, M. Halim, J.M. Lupton, P.L. Burn, I.D.W. Samuel, Macromol. 32 (19) (1999) 5985–5993.
[20] R.G. Kepler, P.M. Beeson, S.J. Jacobs, R.A. Anderson, M.B. Sinclair, V.S. Valencia, P.A. Cahill, Appl. Phys. Lett. 66 (1995) 618–3620.
[21] G.G. Malliaras, Y. Shen, D.H. Dunlap, H. Murata, Z.H. Kafafi, Appl. Phys. Lett. 79 (2001) 2582–2584.
[22] H.H. Fong, K.C. Lun, S.K. So, Chem. Phys. Lett. 353 (2002) 407–413.

[23] M. Redecker, D.D.C. Bradley, M. Inbasekaran, E.P. Woo, Appl. Phys. Lett. 73 (1998) 1565.
[24] A.R. Inigo, H.C. Chiu, W. Fann, Y.S. Huang, U.S. Jeng, T.L. Lin, C.H. Hsu, K.Y. Peng, S.A. Chen, Phys. Rev. B 69 (2004) 075201.
[25] J.M. Lupton, I.D.W. Samuel, R. Beavington, M.J. Frampton, P.L. Burn, H. Bässler, Phys. Rev. B 63 (2001) 155206.
[26] J.M. Lupton, I.D.W. Samuel, R. Beavington, M.J. Frampton, P.L. Burn, H. Bässler, Synth. Met. 121 (2001) 1703.
[27] J.P.J. Markham, I.D.W. Samuel, S.-C. Lo, P.L. Burn, M. Weiter, H. Bässler, J. Appl. Phys. 95 (2004) 438.
[28] J.P.J. Markham, PhD thesis, University of St Andrews (2003).
[29] R.G. Kepler, Phys. Rev. 119 (1960) 1226.
[30] W.E. Spear, J. Non-Cryst. Solids 1 (1968) 197–214.
[31] P.M. Borsenberger, D.S. Weiss, Organic Photoreceptors for Xerography, M. Dekker, New York, 1998.
[32] T.-Q. Nguyen, R.C. Kwong, M.E. Thompson, B.J. Schwartz, Appl. Phys. Lett. 76 (2000) 2454.
[33] T.-Q. Nguyen, R.Y. Yee, B.J. Schwartz, J. Photochem. Photobiol. A: Chem. 144 (2001) 21–30.
[34] Y. Shi, J. Liu, Y. Yang, J. Appl. Phys. 87 (2000) 4254–4263.
[35] T. Kreouzis, D. Poplavskyy, S.M. Tuladhar, M. Campoy-Quiles, J. Nelson, A.J. Campbell, D.D.C. Bradley, Phys. Rev. B 73 (2006) 235201.
[36] C. Im, H. Bässler, H. Rost, H.H. Horhold, J. Chem. Phys. 113 (2000) 3802.
[37] H. Bässler, Phys. Status Solid B 175 (1993) 15.
[38] P.M. Borsenberger, L. Pautmeier, H. Bässler, J. Chem. Phys. 95 (1991) 1258.
[39] P.M. Borsenberger, L.T. Pautmeier, H. Bässler, Phys. Rev. B 46 (1992) 12145.
[40] S. Gambino, PhD thesis, Università degli studi di Palermo (2006).

Available online at www.sciencedirect.com
ScienceDirect
Organic Electronics 9 (2008) 227–233
Organic Electronics
www.elsevier.com/locate/orgel

Photoluminescent and electroluminescent properties and ultra-fast spectrometric studies of dihydroheptacenes

Rajib Mondal [a], Brigitte Wex [b,1], Bipin K. Shah [a,2], Bilal R. Kaafarani [c], Evgeny O. Danilov [a], Ghassan E. Jabbour [b,*], Douglas C. Neckers [a,*]

[a] *Center for Photochemical Sciences*[3], *Bowling Green State University, Bowling Green, OH 43403, United States*
[b] *School of Materials and Flexible Display Center, Arizona State University, Tempe, AZ 85284, United States*
[c] *Department of Chemistry, American University of Beirut, Beirut, Lebanon*

Received 3 May 2007; received in revised form 9 October 2007; accepted 26 October 2007
Available online 24 November 2007

Abstract

Photophysical and electrochemical properties of 7,16-dihydroheptacenes (**1**–**3**) were investigated in detail. Although their HOMO–LUMO gaps are higher than 3 eV, the organic light-emitting diodes containing **1** as the emitting dopant showed green electroluminescence ($\lambda_{max} \sim 515$ and 550 nm) even at a concentration of the dopant as low as 1%. The green electroluminescence of **1** appears to be originating from an electromeric state (an intermolecular ion pair). The maximum brightness of 190 cd/m^2 was observed at a current density of 34 mA/cm^2 at operating voltage of 19 V for the device containing 1% **1**, and overall performance of the devices decreased with an increase in the doping concentration of **1**.

PACS: 42.70.−a; 85.60.Jb

Keywords: Dihydroheptacenes; Photoluminescence; Electroluminescence; Excimer; Electromer

1. Introduction

Development of new fluorescent materials has become an active area of research because of their potential use in the electroluminescent displays [1–4]. Anthracene is one of the earliest reported luminescent materials and emits violet both in the solid state and in solution. Anthracene derivatives have been used successfully as blue emitters in commercial organic light-emitting diodes (OLEDs) [5]. 7,16-Dihydroheptacenes are a new class of light-emitting materials that have the anthracene chromophore. We recently designed, synthesized, and studied several 7,16-dihydroheptacenes including

* Corresponding authors. Tel.: +1 419 372 2034; fax: +1 419 372 0366.
E-mail addresses: jabbour@asu.edu (G.E. Jabbour), neckers@photo.bgsu.edu (D.C. Neckers).
[1] Present address: Division of Natural Sciences, Lebanese American University, Byblos, Lebanon.
[2] Present address: Department of Chemistry, Pittsburg State University, Pittsburg, KS 66762, United States.
[3] Contribution number 632 from Center for Photochemical Sciences.

1566-1199/$ - see front matter © 2007 Elsevier B.V. All rights reserved.
doi:10.1016/j.orgel.2007.10.013

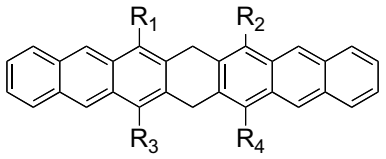

1. R_1, R_2, R_3, R_4 = phenyl
2. R_1, R_4 = phenyl;
R_2, R_3 = *p*-*tert*-butylphenyl
3. R_1, R_2, R_3, R_4 = *p*-*tert*-butylphenyl

Chart 1. Structures of 7,16-dihydroheptacene derivatives (**1**–**3**).

[7,16-dihydro-6,8,15,17-tetraphenylheptacene (**1**), 7,16-dihydro-6,15-bis-(*p*-*tert*-butylphenyl)-8,17-diphenylheptacene (**2**), and 7,16-dihydro-6,8,15,17-tetrakis-(*p*-*tert*-butylphenyl)heptacene (**3**)] (Chart 1) [6].

Compounds **1**–**3** show blue emission ($\lambda_{em} = 420$–428 nm) in dilute solution and in a poly(methylmethacrylate), [PMMA], matrix [6]. Their radiative ($k_R^0 \sim 6 - 8 \times 10^7\ s^{-1}$) and nonradiative ($k_{NR}^0 \sim 3 - 3.6 \times 10^8\ s^{-1}$) rate constants of deactivation from the singlet surface were found to be similar to those of anthracene ($k_R^0 \sim 2 \times 10^8\ s^{-1}$ and $k_{NR}^0 \sim 6 \times 10^8\ s^{-1}$). These compounds also showed high stability and retained colour purity after aging under ambient condition and annealing at 110 °C for more than 24 h [6].

In this article, we report the electrochemical characteristics of **1**–**3** and the performance of **1** in OLED devices. The device containing **1** as active emitting layer shows green emission (510 and 550 nm) with a maximum external quantum efficiency of 0.26%. The characteristics of these devices are unusual in that the emission does not come from the molecular units even at a dopant concentration as low as 1% or from the excimer [7] or exciplex formation [8]. It rather comes from the electromer. This prompted us to investigate and understand the nature of light-emitting species involved in photoluminescence (PL) and electroluminescence (EL) processes of this class of material. Detailed transient spectroscopic studies of **1**–**3** are also discussed.

2. Experimental

2.1. Fabrication and characterization of OLEDs

The OLED devices were fabricated on ITO-coated glass substrates with a nominal sheet resistance of 20 Ω/sq which had been ultrasonicated in acetone, methanol, and 2-propanol, dried in a stream of nitrogen, and then plasma-etched for 60 s. Poly(3,4-ethylenedioxythiophene) (PEDOT):PSS Al4083 (12 ± 2 nm) was deposited by spin-casting (spin rate: 6000 rpm, 30 s; and then thermal curing for 10 min at 190 °C). The emissive layer (102 ± 3 nm) consisted of the host PVK:PBD (1:1) matrix (poly(*N*-vinylcarbazole), 2-*tert*-butylphenyl-5-biphenyl-1,3,4-oxadiazole; 12 mg/mL) and dopant **1** at different concentrations (device 1 – 1%, device 2 – 5%, device 3 – 10%, and device 4 – 0%). This layer was also formed by spin-casting (spin rate: 1000 rpm; acceleration: 3000 rpm/s; 60 s). Subsequently, layers of LiF (~1 nm), aluminum (~30 nm), and silver (~150 nm) were deposited thermally. The vacuum system had an operating pressure of about 10^{-6} Torr.

Current–voltage and light output characteristics of the devices were measured in forward bias. Device emission was measured using a silicon photodetector at a fixed distance from the sample. The response of the detector had been calibrated in this setup where the total power emitted in the forward direction was measured with a NIST traceable integrating sphere. In this case, the external quantum efficiency represents the ratio of the photons measured in the forward direction and the total charge injected in the device. All device measurements were done in a nitrogen glove box.

2.2. Electrochemical measurements and estimation of HOMO and LUMO energies

Cyclic voltammetry measurements were carried out with an Electrochemical Workstation using a three-electrode cell assembly (platinum working electrode) at room temperature. The dichloromethane solutions of the samples containing 0.1 M of the recrystallized supporting electrolyte tetrabutylammonium hexafluorophosphate were used. All potentials are referred against $Ag/AgNO_3$ as the reference electrode, which was calibrated against the ferrocene/ferrocenium (Fc/Fc^+) redox system. The Fc couple potential was determined to be +0.161 vs. Ag/Ag^+. The energy level of the Fc/Fc^+ redox system is estimated to be 4.8 eV below the vacuum level, determined from −4.6 eV for the standard electrode potential (E) of normal hydrogen electrode (NHE) on the zero vacuum level scale and a value of 0.2 V for Fc vs. NHE.

2.3. Ultra-fast spectrometry

The system for the ultra-fast transient absorption spectrometric experiments consisted of a Ti:sapphire

laser (Spectra-Physics, Hurricane), the output of which was typically 1 mJ/pulse (fwhm <100 fs) at a repetition rate of 1 kHz. The Hurricane output was 800 nm. An optical parametric amplifier (OPA-800 C, Spectra-Physics) was used to obtain the 340 nm excitation wavelength. A total of 85% of the fundamental laser output was used to generate the required excitation wavelength whereas 8% of the output was used for white light generation. A 3 mm thick sapphire plate (Crystal Systems, Inc., HEML UX grade) was used for continuum generation.

Prior to generating the probe continuum, the amplified fundamental was passed to a delay line (Newport) that provided an experimental time window of 1.4 ns. The energy of the probe pulses was <0.5 μJ at the sample. The pump beam was typically arranged to be 5 μJ/pulse with spot size of 1–2 mm diameter at the sample. The angle between pump and probe beam was 5–7°. The sample cell had an optical path of 2 mm. Both beams were coupled into 400 μm fiberoptic cables after the sample cell and thereafter input into a CCD spectrograph (Ocean Optics, S2000 UV–vis) for time resolved spectral information (425–800 nm). Typically, 5000 excitation pulses were averaged to obtain the transient spectrum at a particular delay time. The CCD spectrograph, the delay line, and the shutters were driven by a computer-controlled system.

In-house LabView (National Instruments) software allowed automatic spectral acquisition over a series of delay line settings. Kinetic traces at appropriate wavelengths were assembled from the accumulated spectral data. Sample solutions were prepared to have a absorption of 0.8–1.0 at the excitation wavelength in the 2 mm cell and were used without deaeration. All measurements were carried out at room temperature, 22 ± 2 °C.

2.4. Geometry optimization

The Gaussian 03 program package [24] was used for DFT calculations to optimize the geometries and calculate the HOMO and LUMO of **1**.

3. Results and discussion

3.1. Photoluminescence

Two anthracene moieties are attached to one another via two methylene bridges in the molecules of **1–3**. The spectroscopic properties of **1–3** are comparable with those of anthracene, indicating that absorption and emission are due to the anthracene moieties [6]. Dilute solutions of these compounds showed blue emission ($\lambda_{em} = 420 - 428$ nm) in common organic solvents. They also showed blue emission in the PMMA matrix with the quantum efficiency of fluorescence (Φ_F) ranging 0.37–0.44.

Photoluminescence of **1–3** were observed to be concentration dependent. For example, additional peaks centered at 480 and 510 nm become predominant in the fluorescence spectra of **1** (Fig. 1) at higher concentration (1.1×10^{-3} M or higher in dichloromethane), while these peaks were absent in the fluorescence spectra recorded at lower concentration (5.5×10^{-4} M solution; $\lambda_{em} = 402$ and 424 nm). Since no change in absorption was found in these concentration ranges, the red shift of about 80–85 nm in the emission spectra can be considered due to an excimer [9]. The latter is formed by the interaction of an excited molecule with an unexcited counterpart [10]. Moreover, self quenching occurs in these compounds and emission becomes very weak at very high concentration (>1.0×10^{-2} M) (see Supporting information).

The crystal structure indicates that the molecule of **1** is V-shaped with an angle of 131.51° between the two anthracene arms (Fig. 2). Crystal molecular packing shows that the adjacent planar anthracene moieties of two molecules are parallel and are closely spaced. The possibility of such a close proxim-

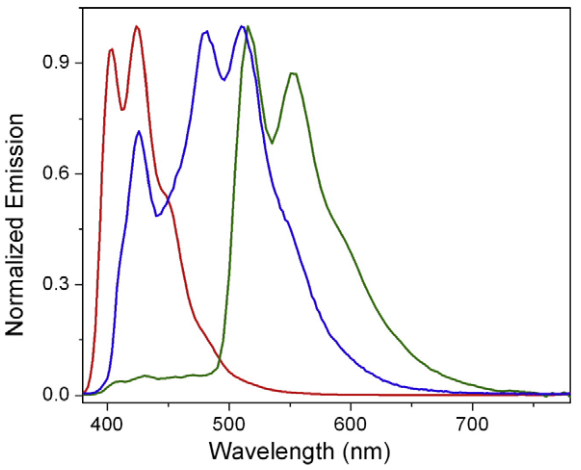

Fig. 1. Normalized emission spectra of compound **1** (a) red: PL spectra in dichloromethane, 5.5×10^{-4} M; (b) blue: PL spectra in dichloromethane, 5.5×10^{-3} M; and (c) green: EL spectra of (5% of **1** doped in 1:1 PVK:PBD). (For interpretation of the references to colour in this figure legend, the reader is referred to the web version of this article.)

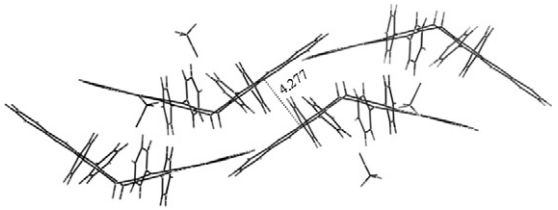

Fig. 2. X-ray crystal structure of **1**: a view showing molecular packing and π–π interaction between two anthracene moieties (distance = 4.277 Å).

ity between two molecules seems to be the reason for the excimer formation at higher concentration. The distance between the two parallel anthracene moieties was found to be about 4.277 Å.

3.2. Electrochemical properties

The cyclic voltammetry (CV) graphs of **1**–**3** (graphs provided in Supporting information) were obtained with a positive scan from 0 to 1.7 V and negative scan from 0 to −2.0 V with the compounds in 0.1 M tetrabutyl ammonium hexafluorophosphate in anhydrous dichloromethane. The CV measurements revealed three oxidation potentials ($E_{1/2}$) of **1** at +1.07 V, +1.25 V, and +1.54 V without any reduction potential. The $E_{1/2}$ of **2** and **3** are similar to that of **1** (Table 1). It is well known that anthracene (+1.16 and +1.50 V) and 9,10-diphenylanthracene (+1.22 and +1.60 V) show two reversible monoelectronic oxidation potentials [11,12]. The first oxidation (~1.20 V) is due to the generation of a radical cation, which undergoes second monoelectronic oxidation to form a dication at higher potentials (~1.50 V). Similar formation of monocation and dication seems responsible for the oxidation potentials of **1**–**3**. The observation of three distinctive oxidation potentials in the case of **1**–**3** may be due to the two spatially separated anthracene rings, which are not electrochemically equivalent.

The HOMO energy levels of **1**–**3** were estimated from the CV measurements and by comparison of their oxidation potentials with that of ferrocene (4.8 eV below the vacuum level) [13]. LUMO levels were estimated from the onset of the absorption spectra [14]. The HOMO–LUMO energy gaps ($E_{H\text{-}L}$) of **1**–**3** were found to be in the range of 3.01–3.06 eV (Table 1). We optimized the structure of **1** using density functional theory (DFT) method [B3LYP/6-31G(d)]. The HOMO of **1** appears to be localized on the anthracene moieties, while the LUMO is more distributed in the molecule and

Table 1
Electrochemical properties and HOMO–LUMO energy gaps ($E_{H\text{-}L}$) of **1**–**3**

Compound	$E_{1/2(ox1)}$[a] (V)	$E_{1/2(ox2)}$[a] (V)	HOMO[a] (eV)	LUMO[b] (eV)	$E_{H\text{-}L}$ (eV)
1	+1.07, +1.25	+1.54	−5.87	−2.81	3.06 (3.43)[c]
2	+1.04, +1.22	+1.50	−5.84	−2.80	3.04
3	+1.04, +1.24	+1.53	−5.84	−2.83	3.01

[a] Determined from cyclic voltammetry (solvent-dichloromethane).
[b] Estimated from the onset of the absorption spectra.
[c] Calculated using density functional theory (DFT) method [B3LYP/6-31G(d)].

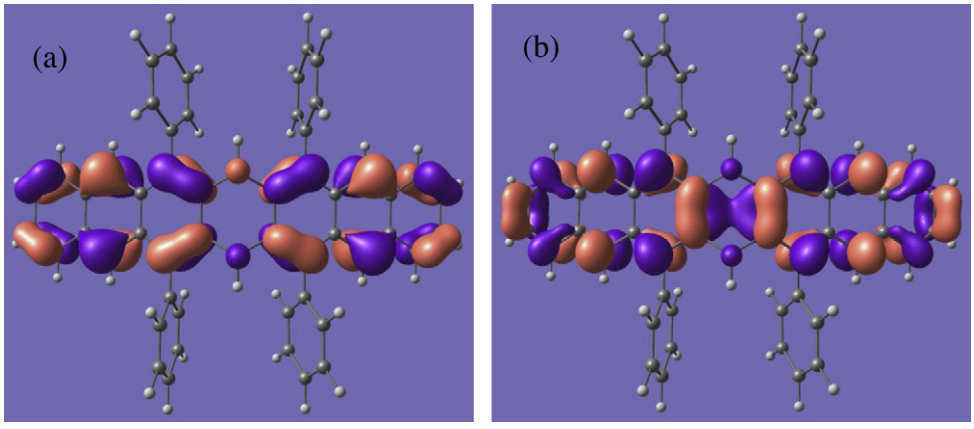

Fig. 3. (a) HOMO and (b) LUMO of the geometry optimized structure of **1** [B3LYP/6-31G(d)].

has a significant contribution from the central methylene bridge (Fig. 3). A similar diffused LUMO was also calculated for fused pyrazines that are structurally similar to dihydroheptacenes [15]. The DFT calculated $E_{H\text{-}L}$ value for **1** (3.43 eV) is close to the electrochemically estimated value (3.06 eV).

3.3. Electroluminescence and device characteristics

OLED devices consisting ITO/PEDOT:PSS (~12 nm)/emissive layer (~102 nm)/LiF (~1 nm)/Al (30 nm)/Ag (~150 nm) layers were constructed. A 1:1 mixture of poly(*N*-vinylcarbazole), (PVK, a hole-transporting material) and 2-*tert*-butylphenyl-5-biphenyl-1,3,4-oxadiazole (PBD, an electron-transporting material) was used as the host material, while different concentrations of **1** were used as emissive dopants. Devices 1, 2, 3, and 4 contained 1%, 5%, 10%, and 0% of **1**, respectively. The EL spectrum of the device 2 is shown in Fig. 1.

The device 4 (undoped) exhibited very weak blue emission (peak centered at 440 nm) originating from the host materials (Fig. 4) [16]. The device 1 showed intense peaks centered at 515 nm and 550 nm, with smaller peaks centered at 404 and 424 nm. The latter peaks are residual molecular emission from **1** and emission from the host materials. The intensity of those lower wavelength peaks gradually diminishes as the weight percent of the dopant increased from 1% to 10%. Interestingly, the higher wavelength peaks (515 and 550 nm) are not due to the excimer of **1**, because they are considerably red shifted than the emission of the excimer (480 and 510 nm). This shift may be explained on the basis of the formation of electromer of **1**, which was observed in all devices (device 1–3), irrespective of the amount of the dopant used [17]. An electromer represents an intermolecular electron-hole entity, which can be represented as $Emitter^{+}/Emitter^{-}$.

While excimer formation is facilitated by the short inter-ion distance and efficient π orbital overlap, electromer formation is believed to depend on the inter-ion separation and steric hindrance present in the molecule [19,20]. It has been suggested that large molecules with small chromophoric units facilitate formation of efficient electromers, as the charge separation on localized excited states becomes the major pathways for electromeric emission [18,20]. Nevertheless, anthracene is also known to exhibit electromeric emission at 540 nm [18]. Electromer emission was observed when 20% of anthracene was doped in neutral polycarbonate binder. It is interesting to note that electromeric emission was observed even from the device that contained only 1% of **1**.

At higher doping concentration (device 3 containing 10% of **1**), the electromeric emission became very weak. This may be due to the high concentration quenching, where the emitted light can be absorbed by neighboring molecules or the excitons are de-excited via energy transfer mechanisms. In the case of **1**, a dopant concentration of 1–5% seemed to give the optimal result.

The current–voltage (*I–V*) and voltage–luminescence (*V–L*) curves for devices 1–4 are shown in Figs. 5 and 6, respectively. The maximum brightness of 190 cd/m^2 was observed at a current density of 34 mA/cm^2 at operating voltage of 19 V for device 1. The external quantum efficiency was found to be maximum for device 2 (0.26%), while that was

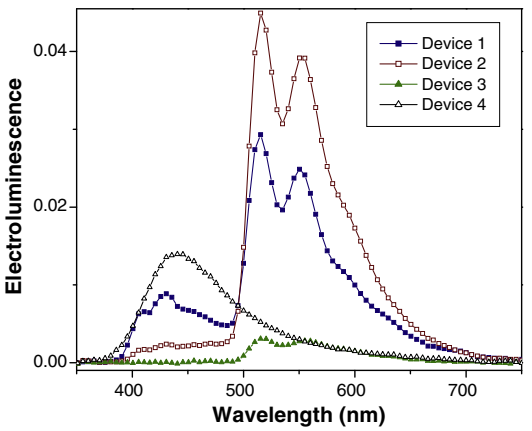

Fig. 4. EL spectra of the devices with the structure of ITO/PEDOT:PSS/PVK:PBD, **1**/LiF/Al/Ag: (device 1, 2, 3, and 4 containing 1%, 5%, 10%, 0% of **1**, respectively).

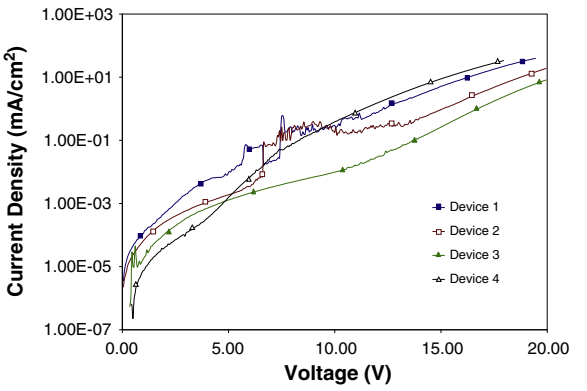

Fig. 5. Current density–voltage (*I–V*) curves for devices 1, 2, 3, and 4.

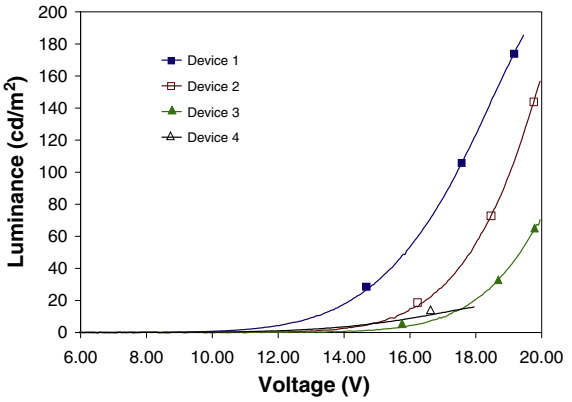

Fig. 6. Voltage–luminance (*V*–*L*) curves for devices 1, 2, 3, and 4.

lower for device 1 (0.22%) and 3 (0.19%). The operating voltage was also higher for device 3, while that was lower for device 1. This indicates that overall device performance decreased with an increase in the doping concentration of **1**.

3.4. Transient spectroscopy

We also performed transient spectroscopic studies to understand the photophysical behavior of **1**–**3**. The $S_n \leftarrow S_1$ absorption spectra obtained by ultra-fast pump-probe experiments (instrument response function ~150 fs) of **1** are presented in Fig. 7. Excitation of a degassed solution of **1** (1×10^{-4} M in dichloromethane) at 340 nm produced a broad transient absorption in the 500–650 nm region, which is assigned to the S_1 state of **1** because of its similarity with the reported S_1 absorption of anthracene [21]. Similar spectra were recorded in the case of **2** and **3** in dichloromethane.

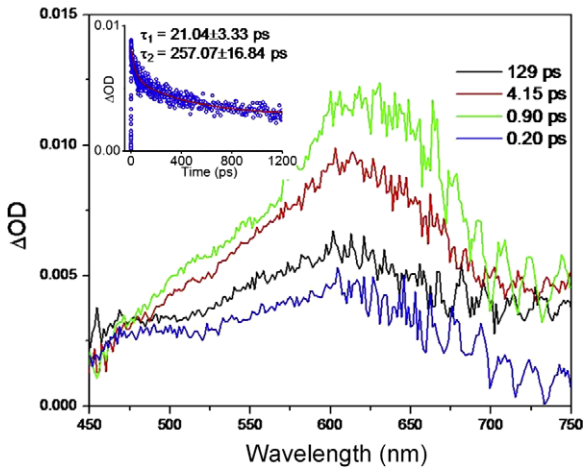

Fig. 7. Transient absorption spectra obtained from ultra-fast pump-probe experiments of **1** in dichloromethane (1×10^{-4} M), recorded 0.20 ps (blue), 0.90 ps (green), 4.15 ps (red), and 129 ps (black) after the laser pulse (excitation at 340 nm). Inset: decay profile monitored at 570 nm. (For interpretation of the references to colour in this figure legend, the reader is referred to the web version of this article.)

Table 2
Vibrational relaxation time (τ_1) and lifetimes of the S_1 state (τ_2) of **1**–**3** recorded in dichloromethane

Compound	τ_1 (ps)	τ_2 (ps)
1	21 ± 03	257 ± 17
2	9 ± 1	229 ± 10
3	16 ± 1	330 ± 18

The time profile monitored at 570 nm for **1** showed bi-exponential decay. Similar bi-exponential decays were observed in the case of **2** and **3** monitored at 580 nm. These lifetimes (τ_1 and τ_2) are summarized in Table 2. The shorter decay times (τ_1) can be assigned to the reorganization of the aromatic ring systems or vibrational relaxation on the S_1 surface. Longer lifetimes calculated to be in the range of 0.23–0.33 ns can be assigned as the lifetimes of the S_1 state of **1**–**3**. There are no differences among **1**–**3** in terms of the absorption and the lifetimes of their S_1 states.

It is also noted that about 40% of the S_1 molecules of **1** do not come back to the S_1 state after they are excited to a certain S_n level as indicated by decay profile not coming back to the zero level (see the decay profile provided in the inset of Fig. 7). This may suggest that about 40% of the excited S_1 state decomposes. Although the experiments were performed under argon, a small amount of diffused oxygen may be reacting with the excited S_1 state causing its decomposition. It is also known that a T_2 state is isoenergetic to the S_1 state in the case of anthracene and similar other polyaromatic hydrocarbons [22,23]. Thus, it may also be possible that a fraction of the excited S_1 molecules intersystem cross into the T_2 state, thus finding an alternate channel to relax than to come to the S_1 state.

4. Conclusions

7,16-Dihydroheptacenes containing the phenyl and *tert*-butylphenyl groups at the 6,8,15, and 17 positions were studied as emitting materials for OLEDs. Their dilute solutions showed blue emission ($\lambda_{max} \sim 420$ nm) while at higher concentration they showed excimer emission ($\lambda_{max} \sim 480$ and 510 nm). Interestingly, the OLED devices containing **1** showed

green emission ($\lambda_{max} \sim 515$ and 550 nm) that is even further red shifted than the emission of excimer. This indicates that an inter-ion pair, electromer, is responsible for the electroluminescence. Moreover, the electromer of **1** was observed to form at higher inter-ion separation distance than 10 Å, which is considered to be optimal distance. Pump-probe experiments of **1**–**3** revealed that the S_1 state shows a broad absorption (~500–650 nm) in dichloromethane with a lifetime of ~0.23–0.33 ns.

Acknowledgements

This work was supported, in part, by the Ohio Department of Development Wright Photoscience Laboratory (TECH 03-054), by the Office of Naval Research (NOOO 14-05-1-0372), and the Army Research Laboratory (DAAD 19-03-2-0032). The authors greatly appreciate this support. R.M. thanks the McMaster Endowment for a research fellowship. B.R.K. thanks the University Research Board (URB) of the American University of Beirut for a Faculty Development Fund. The work at Arizona State University was done in the facilities of the Flexible Display Center.

Appendix A. Supplementary data

Supplementary data associated with this article can be found, in the online version, at doi:10.1016/j.orgel.2007.10.013.

References

[1] J. Shinar, in: Organic Light-Emitting Devices, Springer-Verlag, New York, 2003.
[2] K. Müllen, U. Scherf, in: Organic Light-Emitting Devices. Synthesis, Properties and Applications, Wiley-VCH Verlag GmbH & Co. KGaA, Weinheim, 2006.
[3] R.F. Service, Science 310 (2005) 1762.
[4] R.H. Friend, R.W. Gymer, A.B. Holmes, J.H. Burroughes, R.N. Marks, C. Taliani, D.D.C. Bradley, D.A. Dos Santos, J.L. Brédas, M. Lögdlund, W.R. Salaneck, Nature 397 (1999) 121.
[5] J. Shi, C.W. Tang, Appl. Phys. Lett. 80 (2002) 3201.
[6] R. Mondal, B.K. Shah, D.C. Neckers, J. Org. Chem. 71 (2006) 4085.
[7] E.L. Williams, K. Haavisto, J. Li, G.E. Jabbour, Adv. Mater. 19 (2007) 197.
[8] J.-F. Wang, Y. Kawabe, S.E. Shaheen, M.M. Morrell, G.E. Jabbour, P.I. Lee, J. Anderson, N.R. Armstrong, B. Kippelen, E. Mash, N. Peyghambarian, Adv. Mater. 10 (1998) 230.
[9] Broadness of the excimer emission is not an essential feature. See T. Seko, K. Ogura, Y. Kawakami, H. Sugino, H. Toyotama, J. Tanaka, Chem. Phys. Lett. 291 (1998) 438.
[10] K.-Y. Lai, T.-M. Chu, F.C.-N. Hong, A. Elangovan, K.-M. Kao, S.-W. Yang, T.-I. Ho, Surf. Coat. Technol. 200 (2006) 3283.
[11] A. Doménech, I. Casades, H. Garcia, J. Org. Chem. 64 (1999) 3731.
[12] R.E. Visco, E.A. Chandross, J. Am. Chem. Soc. 86 (1964) 5350.
[13] J. Pommerehne, H. Vestweber, W. Guss, R.F. Mahrt, H. Bässler, M. Porsch, J. Daub, Adv. Mater. 7 (1995) 551.
[14] K.R.J. Thomas, J.T. Lin, Y.-T. Tao, C.-W. Ko, J. Am. Chem. Soc. 123 (2001) 9404.
[15] T. Kobayashi, S. Kobayashi, Eur. J. Org. Chem. (2002) 2066.
[16] B. Luszczynska, E. Dobruchowska, I. Glowacki, J. Ulanski, F. Jaiser, X. Yang, D. Neher, A. Danel, J. Appl. Phys. 99 (2006) 024505.
[17] J. Kalinowski, G. Giro, M. Cocchi, V. Fattori, P. Di Marco, Appl. Phys. Lett. 76 (2000) 2352.
[18] J. Kalinowski, G. Giro, M. Cocchi, V. Fattori, R. Zamboni, Chem. Phys. 277 (2002) 387.
[19] G. Giro, M. Cocchi, V. Fattori, G. Gardret, G. Ruani, M. Murgia, M. Cavallini, F. Biscarini, R. Zamboni, T. Loontjens, J. Thies, D.A. Leigh, A.F. Morales, R.F. Mahrt, Synth. Metals 122 (2001) 27.
[20] G. Giro, M. Cocchi, V. Fattori, G. Gardret, G. Ruani, M. Cavallini, F. Biscarini, R. Zamboni, T. Loontjens, J. Thies, D.A. Leigh, A.F. Morales, R.F. Mahrt, Synth. Metals 122 (2001) 63.
[21] J. Sepiol, J. Lumin. 36 (1986) 115.
[22] N.J. Turro, Modern Molecular Photochemistry, University Science Books, Sausalito, CA, 1991.
[23] B.K. Shah, D.C. Neckers, J. Shi, E.W. Forsythe, D. Morton, Chem. Mater. 18 (2006) 603.
[24] Gaussian 03, see Supporting information.

Available online at www.sciencedirect.com
ScienceDirect
Organic Electronics 9 (2008) 234–240
Organic Electronics
www.elsevier.com/locate/orgel

5,6,11,12-Tetrachlorotetracene, a tetracene derivative with π-stacking structure: The synthesis, crystal structure and transistor properties

Xialiou Chi [a,*], Dawen Li [b], Huaqiang Zhang [c], Yongsheng Chen [c,*], Vanessa Garcia [a], Celina Garcia [a], Theo Siegrist [b]

[a] Department of Chemistry, Texas A&M University – Kingsville, Kingsville, TX 78363, USA
[b] Bell Laboratories, Alcatel–Lucent Technologies, 600 Mountain Avenue, Murray Hill, NJ, 07974, USA
[c] Key Laboratory for Functional Polymer Materials and Center for Nanoscale Science & Technology, Institute of Polymer Chemistry, College of Chemistry, Nankai University, Tianjin 300071, China

Received 14 August 2007; received in revised form 8 November 2007; accepted 15 November 2007
Available online 26 December 2007

Abstract

An important parameter for applications of organic semiconductor in devices is their charge-carrier mobility. It has been predicted theoretically that forming face-to-face π-stacks at the molecular level may increase the charge-carrier mobility due to enhanced electronic couplings. To achieve different molecular arrangements, we recently synthesized and crystallized a tetracene derivative, 5,6,11,12-tetrachlorotetracene. The X-ray crystal structure shows that the molecules form slip π-stacks in contrast to herringbone type tetracene. Comparison of electrostatic potential maps of tetrachlorotetracene and the parent tetracene molecule shows that the slip-stack packing structure is favored in terms of electrostatic forces due to the substituents in tetrachlorotetracene crystals. Single crystal field-effect transistors based on tetrachlorotetracene crystals show p-type behavior with a field-effect mobility of 1.7 cm^2/V s, which is among the best values reported for organic field-effect transistors. These results, together with several recent findings, may serve as guidance in search of new organic semiconductors with high performance.

PACS: 73.90.+f

Keywords: Organic; Single crystal; Field-effect transistor; Mobility; Stacking

1. Introduction

One of the key physical parameters for successful use of organic semiconductor devices is the charge-carrier mobility, i.e. the efficiency of charge transport. The effective mobility of a transistor device can be improved by optimizing a number of factors including the purity and structural quality of the active organic layer, the quality of the dielectric layer, the interfaces between the different layers, and in the case of thin-film devices, film morphology, etc. [1,2].

* Corresponding authors. Tel.: +1 361 595 9971.
E-mail addresses: kfxc000@tamuk.edu (X. Chi), yschen99@nankai.edu.cn (Y. Chen).

1566-1199/$ - see front matter © 2007 Elsevier B.V. All rights reserved.
doi:10.1016/j.orgel.2007.11.009

An alternative way to increase the intrinsic charge-carrier mobility is to design new molecular materials with high intrinsic mobility, and the recent development of organic single crystal field-effect transistors (FETs) provides a convenient method for measuring the mobilities in organic materials [3]. Theoretically, high mobility can be achieved through strong intermolecular electronic coupling [4–8], and for planar carbon-based organic molecules, the intermolecular electronic coupling may be maximized in a face-to-face stack of the π-electron systems (π-stack) [4,6]. For instance, rubrene (I) may be considered such a molecule with a crystal structure showing a slip-stack arrangement [9]. Within each stack, the rubrene molecules are displaced along the long axis of the tetracene backbone, while there is virtually no displacement along the short axis (perpendicular to the long axis), resulting in an overlap of approximately 60% of the tetracene backbone (π-electron systems) with adjacent molecules. In comparison, unsubstituted tetracene or pentacene adopt herringbone-type packing arrangements [10] with an edge-to-face pattern, and thus the π–π overlap is not maximized. Single crystal rubrene field-effect transistors revealed anisotropic charge-carrier mobilities, with the highest reported value of approximately 20 $cm^2/V\,s$ in the stacking direction [11], consistent with quantum chemical calculations of the anisotropic transfer integrals [9]. Despite the recent progress on new materials with π-stack patterns [12–16], experimental evidence that such structures can have higher mobilities than herringbone-packed solids is still scant [6]. One of the problems is the lack of suitable molecules for the study. It is therefore necessary to synthesize novel molecules that form π-stack arrangements and to study their electronic transport properties. The results may then serve as guidance in search of high performance organic semiconductors.

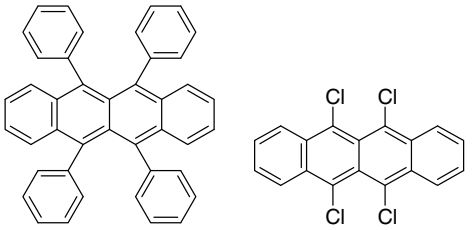

I II

We recently synthesized and crystallized a tetracene derivative, 5,6,11,12-tetrachlorotetracene (II). The synthetic procedure was established 30 years ago [17], but the crystal structure and the transport properties were never reported. In this paper, we describe the crystal structure and FET properties based on this material. In particular, we show that the molecule crystallizes in a slip-stack pattern with a high mobility along the stacking direction, and we further performed quantum mechanical calculations to investigate the origin of the slip-stack arrangements of this tetracene derivative.

2. Experimental section

The synthesis of II followed a previously published procedure [17] with the synthetic Scheme 1 shown below. Refluxing a mixture of 6,11-dihydroxy-5,12-naphthacenedione (Aldrich) and PCl_5 in $POCl_3$ affords hexachloro intermediate in 53% yield, which is then refluxed with NaI in DMF giving molecule II in 73.4% yield. The crude product can be recrystallized from acetic acid to give red transparent needles.

Single crystals for both X-ray and electronic transport measurements were subsequently grown by horizontal physical vapor phase transport in a stream of high purity argon using a modified apparatus previously described by Laudise et al. [18]. Here, two glass tubes of different diameters were used, with the outer tube wrapped with two rope-heaters defining source zone and crystal growth zone, respectively. A glass tube of smaller diameter served as the sample container. The source temperature was held at 215 °C, and the argon flow rate was 19 ml/min. Typical needle-like crystals showed dimensions of 1–8 mm in length, 0.1–0.5 mm in width, and 0.05–0.1 mm in thickness.

The crystals were analyzed using an Oxford-Diffraction Xcalibur2 CCD X-ray diffractometer, using graphite monochromated MoKα radiation. CCDC 634428 contains the supplementary crystallographic data for this paper [19].

The charge transport properties were measured using field-effect transistors fabricated on single crystals [3]. The needle-like habit of the crystals allowed measuring the charge transport along the a-axis, and therefore, along the π-stacks. We used graphite ink to paint source and drain electrodes while a Parylene-N film served as gate dielectric [20–23]. The gate material was again graphite ink. Parylene-N was deposited on top of the crystal in a home-made reactor, and its thickness was determined with a profilometer. The channel capacitance was then calculated from the measured thickness and the tabulated dielectric constant of Parylene

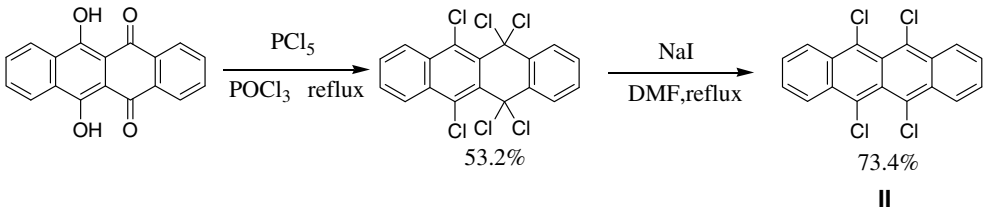

Scheme 1. Synthesis of tetrachlorotetracene (II).

N ($\varepsilon = 2.65$). Typical FET dimensions of the channel lengths (l) and widths (w) were 0.5 mm 0.3 mm, respectively. The FET characteristics were measured using a probe station and a HP 4155A semiconductor parameter analyzer.

Quantum chemical calculations were carried out using the Spartan 04 program. All calculations were performed using B3LYP hybrid density functional theory at the 6-31 + G* level, including the geometry optimization, the HOMO energy level and the electrostatic potential (ESP) maps.

3. Results and discussion

3.1. X-Ray crystal structure

Tetrachlorotetracene crystallizes in a monoclinic unit cell with space group symmetry $P2_1/n$. Fig. 1a and b show the molecular structure of a single molecule in different orientation while the molecular packing is shown in Fig. 2. The four benzene rings of the tetracene backbone are not quite coplanar but adopt a "Z" shape (Fig. 1b). The two pairs of chlorine atoms point in the opposite directions: one pair attaching to the same benzene ring (left to the center) points upwards while the other pair of the neighboring benzene ring (right to the center) points downwards. The dihedral angle of the carbon–chlorine bonds in each side of the molecule is about 33°. The molecules form isolated stacks along the a-axis, with an inter-planar distance of 3.58 Å (Fig. 3), slightly larger than the sum of the van der Waals radii. Fig. 3 is a projection diagram depicting the overlap between two neighboring molecules within a stack. There are slight shifts along both the long and short molecular axes (of the tetracene backbone), with a displacement of 0.6 Å and 1 Å along short and long molecular axis, respectively; the latter is much shorter than the value found in rubrene (6.1 Å). These shifts make it possible for eight pairs of carbon atoms to be superimposed between two neighboring molecules (Fig. 3). The stacks are isolated, with no π–π interaction between them, and the closest carbon–carbon distance is found to be 3.83 Å. Thus, the crystal structure indicates that this molecule forms a one-dimensional crystal with strongest interaction along the a-axis, consistent with the needle-like habit of the red crystals.

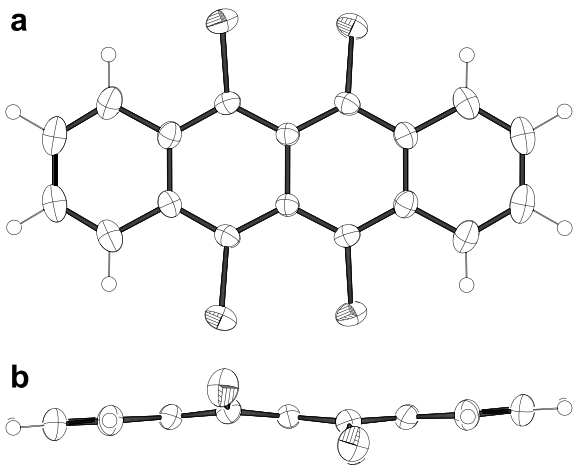

Fig. 1. X-ray crystal structure of tetrachlorotetracene (a) view perpendicular to the molecular plane (b) side view of tetrachlorotetracene showing non-planarity of the molecule.

3.2. Computational studies

The calculated bond lengths and bond angles are all in good agreement with the single crystal structure data, with the largest difference in bond lengths being 0.014 Å (~1%). The predicted structure reproduces the "Z" shape (Fig. 4) and the orientation of the two pairs of chlorine atoms. The dihedral angle of the carbon–chlorine bonds on each side of the molecule is 35° compared to 33° found in the crystal structure (Fig. 1b). Thus, the observed crystal/molecular structure matches well with the calculated structure of the tetrachlorotetracene molecule in the gas phase. The solid-state packing has therefore little effect on the molecular conformation (structure) in the crystal.

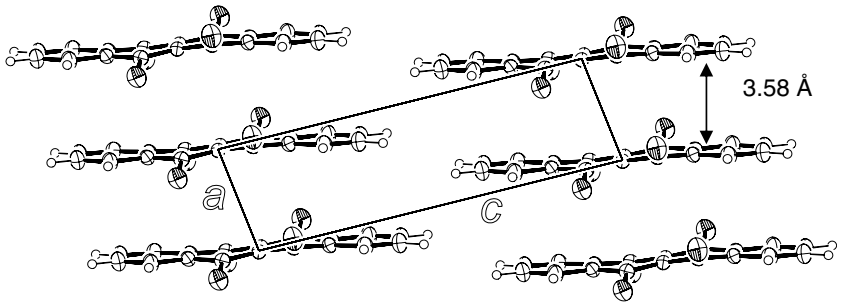

Fig. 2. The stacking pattern of tetrachlorotetracene along a axis.

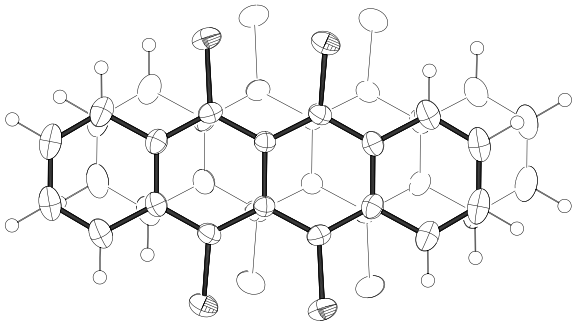

Fig. 3. Projection diagram of two neighboring molecules within a stack. Black thick lines are used to identify the molecule on the top while thin lines are used for the molecule below it.

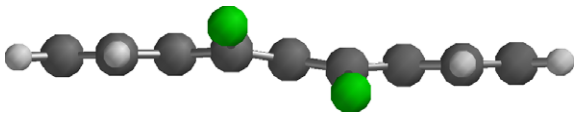

Fig. 4. Calculated structure of tetrachlorotetracene.

The calculated HOMO energy level of tetrachlorotetracene is 0.52 eV lower than that of the parent tetracene molecule, indicating that the addition of chlorine atoms to the parent tetracene should increase the stability of the system towards oxidation. This is consistent with our observation that a solution of tetracene loses its orange color rapidly, while tetrachlorotetracene can be recrystallized from several organic solvents without protection. Both enhanced solubility and stability found in this material are important parameters for large-area applications where inexpensive fabrication methods such as solution processing are desired.

A simple model proposed by Hunter and Sanders [24] suggests that an aromatic system can be pictured as a positively charged σ-framework sandwiched between two negatively charged π-electron clouds, and that the net favorable π–π interactions between molecules are actually the result of π-σ attractions that overcome π–π repulsions. Therefore, the electrostatic force rather than the π–π overlap controls the geometry of molecules in a crystals [24]. Electrostatic interactions can be qualitatively predicted by drawing electrostatic potential (ESP) maps, which were recently used to explain the slip-stack arrangements observed in several fluorinated thiophene and selenophene-based polymers [25]. Such ESP maps combine electrostatic potential and electron density surfaces, and thus convey which regions of a molecule are electron rich (indicated in red) and which are electron poor (indicated in blue), as shown in Fig. 5 for both tetracene and tetrachlorotetracene.

In the parent tetracene molecule (Fig. 5a), the π electrons have the highest probability to be found above (and below) the four aromatic rings (red), while the edge of the molecule (where the hydrogen atoms are located) is electron-deficient (blue). One can imagine that stacking of tetracene molecules is energetically unfavorable due to the repulsive force of the π-electrons, but would otherwise provide an efficient overlap. Therefore, polyacenes, including tetracene and pentacene, adopt a herringbone structure instead of face-to-face stacks. In contrast, for tetrachlorotetracene (Fig. 5b), the electron density on the surface of the tetracene backbone is significantly reduced and the electron rich regions only exist at the two ends (red) of the ring system. This redistribution of the π electrons may favor a slip-stack arrangement so that the electron rich region is paired with the electron poor region, while maintaining optimal space filling. Also notice that the locations of carbon atoms bear the highest electron densities while the centers of the benzene rings are electron-deficient (Fig. 5b). This may explain the slip-stack overlap geometry illustrated in Fig. 3, where the centers of the benzene rings of one

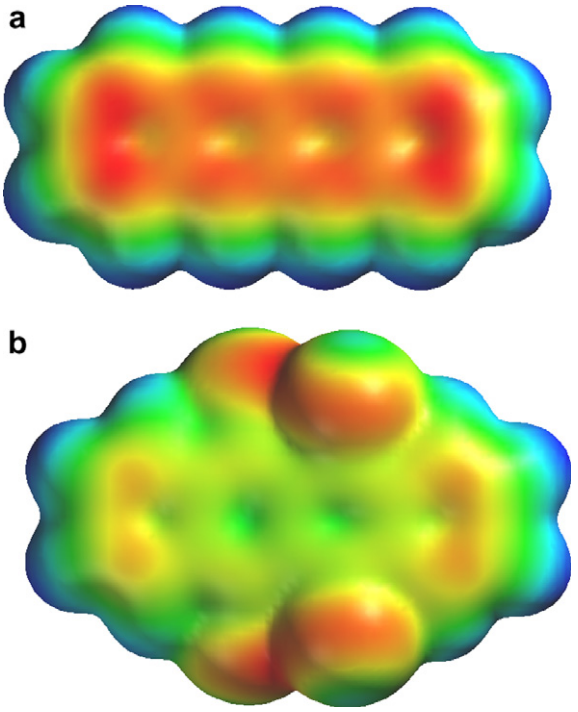

Fig. 5. ESP surface plots for (a) tetracene (b) and tetrachlorotetracene.

molecule are almost superimposed on the carbon atoms of the other molecule, thus optimizing the electrostatic forces between the stacked molecules.

3.3. Single crystal field-effect transistor

Typical output and transfer characteristics of single crystal FET transistors at room temperature are shown in Figs. 6 and 7, respectively. The negative gate bias required indicates that holes are the charge-carriers (p-type semiconductor). At low drain–source voltage V_{ds}, the drain current exhibits a nonlinear dependence on V_{ds}, suggesting non-Ohmic contact behavior. At higher voltages, however, saturation is observed as V_{ds} becomes comparable to V_{gs}, indicating that the contact resistance does not dominate the transconductance in this region. From the transfer characteristics in Fig. 7 we extracted an on/off current ratio of $\sim 10^4$, a field-effect mobility of 1.7 cm^2/V s, and a threshold voltage of $V_t \sim -12$ V. The fairly large threshold voltage indicates a large trap density, which could be a significant factor in reducing the FET-mobility. Therefore, the intrinsic p-type mobility in tetrachlorotetracene single crystal is likely to be higher than 1.7 cm^2/V s. Occasionally, a field-effect mobility as high as 5 cm^2/V s was observed, but was not clearly reproducible.

A number of techniques have been used to measure the charge-carrier mobility in organic single crystals [3], and in some cases different results for the same material have been reported [26]. Furthermore, the chemical purity and quality of the crystal also affect the observed mobility [27]. However,

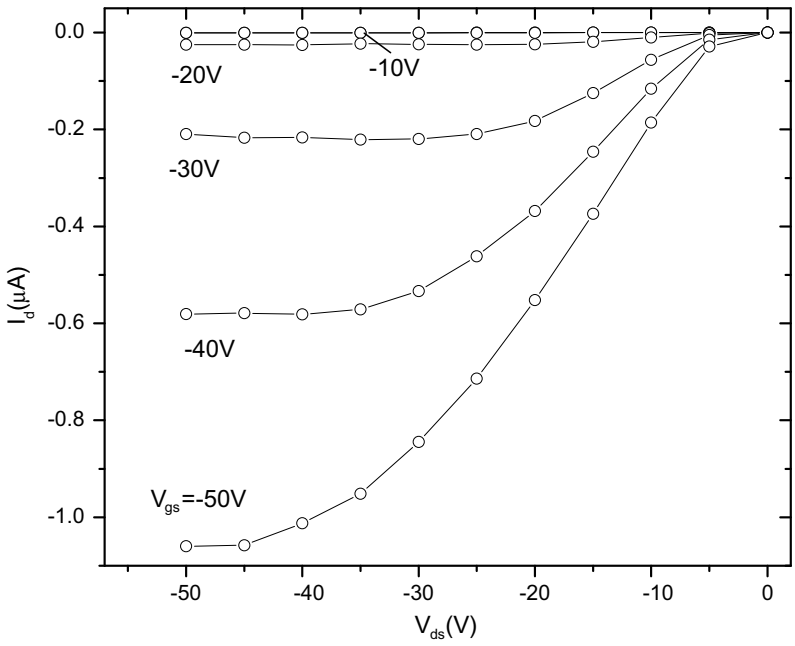

Fig. 6. Output characteristics of a typical tetrachlorotetracene single crystal field-effect transistor.

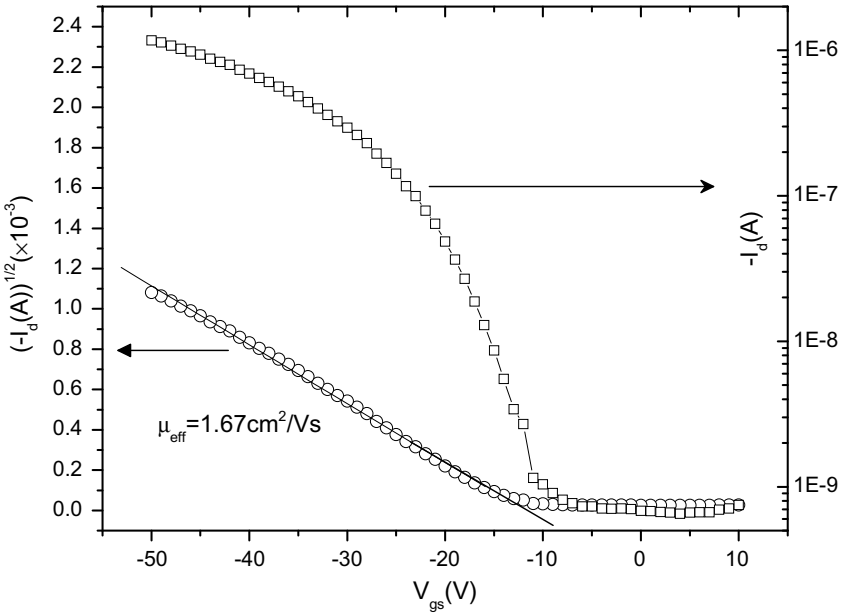

Fig. 7. Transfer characteristics of a typical tetrachlorotetracene single crystal field-effect transistor.

among three types of tetracene derivatives we have measured using the same technique, (parent) tetracene, tetrachlorotetracene (title compound) and tetraphenyltetracene (rubrene), both rubrene and the tetrachlorotetracene crystals showed significantly higher mobility than parent tetracene crystal [28]. Note that both tetrachlorotetracene and rubrene adopt slip-stack pattern whereas in parent tetracene crystal there is little π–π overlap between parallel molecules. Furthermore, the tetrachlorotetracene used in this study was purified only once before crystallization from the gas phase. Therefore, our results provide further evidence that π-stacking allows efficient charge-carrier transport along a stack and that molecules crystallizing in stack patterns promise high charge-carrier mobility, consistent with a recent report [14]. Although we have not yet performed thin-film transistor measurement on the title compound, the present results already give important information in designing new organic semiconductors with high charge-carrier mobility. Furthermore, the results indicate that for thin-film transistors, high mobility can be achieved when the molecules stack at the gate–semiconductor interface along the channel direction.

4. Conclusion

The tetracene derivative, 5,6,11,12-tetrachlorotetracene, crystallizes in isolated slip-stacks with enhanced π–π overlap within the stacks, but little interactions between them. ESP surface maps show that the slip-stack arrangement is favored by the modification of electrostatic potential surface of the tetracene backbone due to the chlorine atoms compared to the parent tetracene molecule (herringbone). A hole mobility in single crystal FETs as high as 1.7 cm^2/V s was achieved along the stack direction. Our next step is to test and optimize thin-film transistor of the title compound, and to synthesize other molecules with stacking patterns to move towards the high mobility limit in organic semiconductors.

Acknowledgments

This research was supported in part by DOE under Award No. DE-FG02-04ER46118, DOD/DMEA under Award No. DMEA-H94003-06-2-0608, and an award from Research Corporation. We thank Drs. A. P. Ramirez and Woo-Young So at Bell Laboratories, Alcatel–Lucent Technologies, for their help and suggestions.

References

[1] C.D. Dimitrakopoulos, P.R.L. Malenfant, Adv. Mater. 14 (2002) 99.
[2] D. Gamota, B. Paul, K. Kalyanasundaram, J. Zhang (Eds.), Printed Organic and Molecular Electronics, Kluwer Academic Publishers, Norwell, 2004.

[3] R.W.I. de Boer, M.E. Gershenson, A.F. Morpurgo, V. Podzorov, Phys. Stat. Solid (A) 201 (2004) 1302.
[4] J.-L. Bredas, J.P. Calbert, D.A. da Silva Filho, J. Cornil, Proc. Natl. Acad. Sci. USA 99 (2002) 5804.
[5] J.-L. Bredas, D. Beljonne, V. Coropceanu, J. Cornil, Chem. Rev. 104 (2004) 4971.
[6] M.D. Curtis, J. Cao, J.W. Kampt, J. Am. Chem. Soc. 126 (2004) 4318.
[7] M. Mas-Torrent, P. Hadley, S.T. Bromley, X. Ribas, J. Tarres, M. Mas, E. Molins, J. Veciana, C. Rovira, J. Am. Chem. Soc. 126 (2004) 8546.
[8] C.R. Newman, C.D. Frisbie, D.A. da Silva Filho, J.-L. Bredas, P.C. Ewbank, K.R. Mann, Chem. Mater. 16 (2004) 4436.
[9] D.A. da Silva Filho, E.-G. Kim, J.-L. Bredas, Adv. Mater. 17 (2005) 1072.
[10] G.R. Desiraju, A. Gavezzotti, J. Chem. Soc., Chem. Commun. 621–623 (1989).
[11] V. Podzorov, E. Menard, A. Borissov, V. Kiryukhin, J.A. Rogers, M.E. Gershenson, Phys. Rev. Lett. 93 (2004) 086602.
[12] J.E. Anthony, J.S. Brooks, D.L. Eaton, S.R. Parkin, J. Am. Chem. Soc. 123 (2001) 9482.
[13] T.M. Pappenfus, R.J. Chesterfield, C.D. Frisbie, K.R. Mann, J. Casado, J.D. Raff, L.L. Miller, J. Am. Chem. Soc. 124 (2002) 4184.
[14] H. Moon, R. Zeis, E. Borkent, C. Besnard, A.J. Lovinger, T. Siegrist, C. Kloc, Z. Bao, J. Am. Chem. Soc. 126 (2004) 15322.
[15] D.E. Janzen, M.W. Burand, P.C. Ewbank, T.M. Pappenfus, H. Higuchi, D.A. da Silva Filho, V.G. Young, J.-L. Bredas, K.R. Mann, J. Am. Chem. Soc. 126 (2004) 15295.
[16] Q. Miao, X. Chi, S. Xiao, R. Zeis, M. Lefenfeld, T. Siegrist, M.L. Steigerwald, C. Nuckolls, J. Am. Chem. Soc. 128 (2006) 1340.
[17] K. Balodis, R. Medne, O. Neiland, L.M. Kozlova, Z. Klavina, I. Mazeika, A.P. Gaukhman, Zh. Org. Khim. 21 (1985) 2423.
[18] R.A. Laudise, C. Kloc, P.G. Simpkins, T. Siegrist, J. Crystal Growth 187 (1998) 449.
[19] The supplementary crystallographic data can be found at www.ccdc.cam.ac.uk.
[20] V. Podzorov, V.M. Pudalov, M.E. Gershenson, Appl. Phys. Lett. 82 (2003) 1739.
[21] V.Y. Butko, X. Chi, D.V. Lang, A.P. Ramirez, Appl. Phys. Lett. 83 (2003) 4773.
[22] V.Y. Butko, X. Chi, A.P. Ramirez, Solid State Commun. 128 (2003) 431.
[23] R. Zeis, C. Besnard, T. Siegrist, C. Schlockermann, X. Chi, C. Kloc, Chem. Mater. 18 (2006) 244.
[24] C.A. Hunter, J.K.M. Sanders, J. Am. Chem. Soc. 112 (1990) 5525.
[25] D.J. Crouch, P.J. Skabara, J.E. Lohr, J.J.W. McDouall, M. Heeney, I. McCulloch, D. Sparrowe, M. Shkunov, S.J. Coles, P.N. Horton, M.B. Hursthouse, Chem. Mater. 17 (2005) 6567.
[26] C. Goldmann, S. Haas, C. Krellner, K.P. Pernstich, D.J. Gundlach, B. Batlogg, J. Appl. Phys. 96 (2004) 2080.
[27] O.D. Jurchescu, J. Baas, T.T.M. Palstra, Appl. Phys. Lett. 84 (2004) 3061.
[28] Using the same techniques we measured transistor properties of single crystals of tetracene and rubrene. The results vary with the purity and crystal qualities. The highest mobility we obtained for rubrene and tetracene were 15 cm^2/V s and 1.0 cm^2/V s, respectively.

Available online at www.sciencedirect.com
ScienceDirect
Organic Electronics 9 (2008) 241–252
Organic Electronics
www.elsevier.com/locate/orgel

Fluorene trimers with various 9,9′-substituents: The synthesis, characteristics, condensed state structures, and electroluminescence properties

Shi Tang [a], Meirong Liu [a], Ping Lu [a], Gang Cheng [b], Ming Zeng [a], Zengqi Xie [a], Hai Xu [a], Huiping Wang [a], Bing Yang [a], Yuguang Ma [a,*], Donghang Yan [a]

[a] *Key Laboratory for Supramolecular Structure and Materials of Ministry of Education, Jilin University, Changchun, China*
[b] *National Laboratory of Integrated Optoelectronics, Jilin University, Changchun, China*

Received 11 February 2007; received in revised form 24 October 2007; accepted 25 October 2007
Available online 19 November 2007

Abstract

The four fluorene-based trimers with various aromatic and alkyl substituents (**T1**–**T4**) are synthesized and characterized. These oligomers show the similar electronic absorption and emission characteristics (e.g., absorption peak at 351 nm, and highly efficient deep blue emission at 394 nm in solution), indicating that the major electronic properties of the core chromophore are essentially independent of the substituents. However, the condensed state structures and thermal properties of four trimers are found to be different from each other, from crystalline (full alkyl (**T1**) or full aromatic (**T2**) substituted trimers) to amorphous (mixed aromatic and alkyl (**T4**) substituted trimers). The effect of different condensed state structures on electroluminescence device properties is presented: The blue light-emitting devices with accordant structure of ITO/PEDOT:PSS/TCTA (40 nm)/trimers (40 nm)/BCP (10 nm)/Alq_3 (20 nm)/LiF/Al exhibit different EL efficiency (2.9% of **T2**, 1.8% of **T3** and 2.7% of **T4**). Using amorphous **T4**, the white light-emitting device of ITO/TCTA (40 nm)/rubrene (0.1 nm)/**T4** (8 nm)/Alq_3(52 nm)/LiF/Al is fabricated with high efficiency (6.15 cd A^{-1}), high brightness (9500 cd m^{-2}) and good white light CIE coordinates (0.32, 0.37).

PACS: 28.52.Fa; 61.05.cp; 65.90.+i; 73.40.lq; 73.61.ph

Keywords: Fluorene; Oligomers; Organic electroluminescence

1. Introduction

Organic conjugated materials have attracted considerable attention due to potential applications toward photonic and optoelectronic displays [1]. Many features of the materials, such as photoluminescence efficiency, thermo- and electrochemical-stability are relative to their device applications. In this content, the condensed state structures of the materials are also key points for the feasibility of their applications especially in electroluminescent (EL) devices [2], because the change of surface

* Corresponding author. Tel.: +86 431 85618480; fax: +86 431 85193421.
E-mail address: ygma@jlu.edu.cn (Y. Ma).

1566-1199/$ - see front matter © 2007 Elsevier B.V. All rights reserved.
doi:10.1016/j.orgel.2007.10.010

structure (crystalline formation or ambulatory interface) of organic film due to Joule heating during device operation is an important cause of the degradation of EL devices [3]. Therefore, it is obvious that developing organic materials with high thermal and condensed state stability is the fundamental task for practical applications [4]. Most of the organic conjugated materials with low molecular weights generally tend to crystallize readily, which limit their applications for EL devices due to the present of grain boundaries and resultant bad surface [5]. In the meanwhile, Shirota et al. [6] have demonstrated that a few of organic molecular materials could exhibit amorphous properties similarly with polymers, so called amorphous materials or molecular glasses, which means low molecular-weight organic compounds readily form stable amorphous glasses above room temperature. Such amorphous molecular materials may form uniform amorphous films without generation of structure defects by different techniques, exhibiting great potential in optoelectronic devices. Considerable effort has been made to develop the functional molecular glass materials with highly thermal and amorphous stability in the solid state, including dendritic macromolecules [7], starburst materials [8], tetrahedral-shaped molecules [9] and spiro-linked compounds [10]. Salbeck et al. [11] firstly used spiro-linked to modify steric demand of materials with desired electronic or optical properties to change their condensed state structures and thermal properties without altering major electronic properties of the core chromophore. Recently, Wong and Wu et al. [12] reported a series of optoelectronic materials constructed by spirobifluorene building blocks, which exhibited high EL efficiency and extraordinary ambipolar carrier transport properties. Furthermore, fluorene-based oligomers with well-defined structure have been widely employed because they may function as model-compounds for poly-2,7-(9,9′-dialkyl)fluorenes (PFs) [13] and as active materials in organic light-emitting devices [14]. In addition, the facile process of functionalizing the C-9 position of the fluorene moieties provides the opportunity to improve the physical properties of resulting fluorene derivatives. Aiming at improving the condensed state structures of fluorene oligomers, a series of fluorene-based trimers with different substitutes at C-9 position of fluorene moieties are synthesized (Chart 1). Herein we report the structures of four trimers and intriguing changes of their condensed state from crystalline to glass, and their potential applications in optoelectronic devices.

2. Results and discussion

2.1. Preparation and characterization

The detailed synthesis of four trimers, **T1**–**T4**, are depicted in Scheme 1, where the spiro-linked diphenyl and hexyl groups are substituted at the C-9 position of fluorene moieties, respectively. Introduction of rigid spiro-linked diphenyl groups is expected to not only serve as an effective insulating spacer blocking interaction between the chain's backbones, but also improves the thermal stability. The hexyl groups may increase flexibility and solubility of compounds. The synthetic route is based on a Suzuki Pd-catalyzed coupling reaction between boronic ester and bromide of fluorene. Here, synthesis of compounds **1** and **2** are not described redundantly,

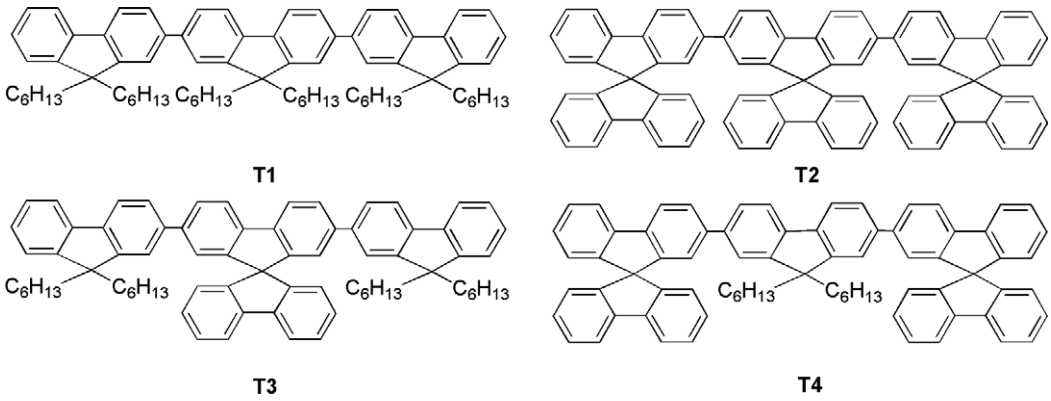

Chart 1. The molecular structures of the trimers **T1**–**T4**.

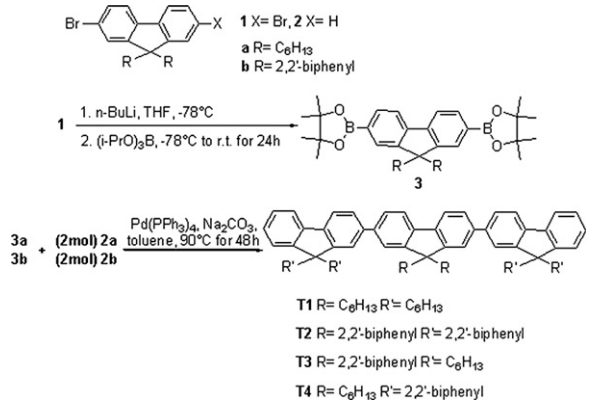

Scheme 1. The synthetic routes of the trimers **T1**–**T4**.

because their preparation is following the reported literatures [10,12]. Treatment of **1a** and **1b** with excess amount of *n*-BuLi and subsequent reaction with 2-isopropoxy-4,4,5,5-tetramethyl-1,3,2-dioxabrorolane can afford diboronic ester **3a** and **3b**, respectively. Finally, Suzuki coupling reaction between diboronic ester **3a** or **3b** and monobromide **2a** or **2b** in the Na_2CO_3 and toluene can obtain relevant fluorene trimers **T1**–**T4** with acceptable yields of 50–72%. All trimers are verified by ^1H and ^{13}C NMR spectroscopy, MALDI-TOF mass spectrometry, as well as elemental analysis. The ^1H NMR spectra of **T3** and **T4** in aromatic range are shown in Fig. 1, while characterization of other **T1** and **T2** is in agreement with previous literatures [12,15]. Here, the aromatic peaks of all cases can be clearly assigned and they confirm the purity of each trimers. Additional definitive evidence for the trimers molecular structures is obtained from MALDI-TOF mass spectrometry. The deviation between the calculated and experimentally measured value is no more than one tenth mass unit. For example, the molecular formula of **T4** is $C_{75}H_{62}$. The calculated molecular weight is 962.5 and we obtained the value 962.6, as shown in Fig. 2. The other three trimers all showed the correct molecular weight consistent with calculated value.

2.2. Photophysical properties

Fig. 3 illustrates the absorption and emission spectra of **T1**–**T4** in dilute THF solution and in film on a quartz substrate, and the more detailed data is summarized in Table 1. These four kinds of trimers show the very similar photophysical properties. The absorption spectrum of four trimers in both THF solution and films show maxima absorption peaks at 351 nm, which is attributed to π–π^* transition of the central backbone chromophore. The absorption of high-energy band at 310 nm is caused by the absorption of the peripheral fluorene units in compounds **T2**–**T4**, and the peak intensity at 310 nm is gradually enhanced with increasing of number of peripheral fluorene unit in trimers. All trimers in solution exhibit very strong deep blue fluorescence

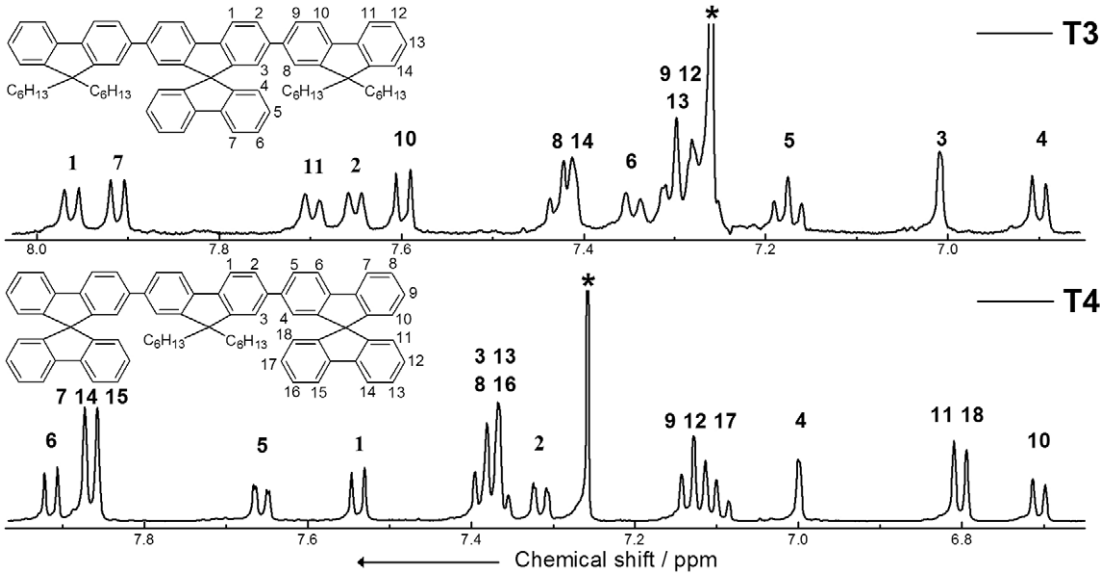

Fig. 1. The ^1H NMR spectrum of **T3** and **T4** in $CDCl_3$ in aromatic range at room temperature.

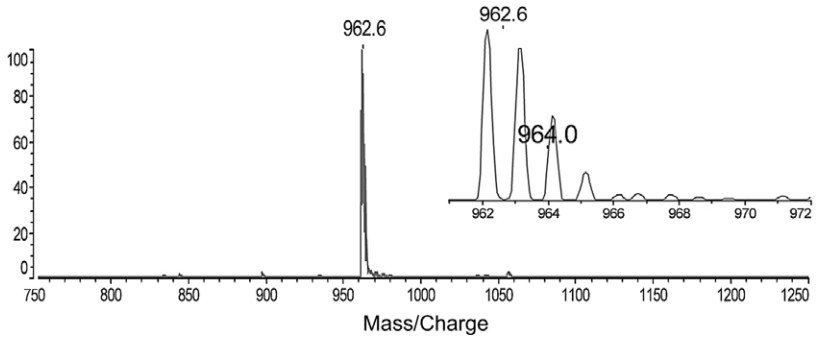

Fig. 2. The MALDI-TOF mass spectrum and corresponding to the "molecular ion" of **T4**.

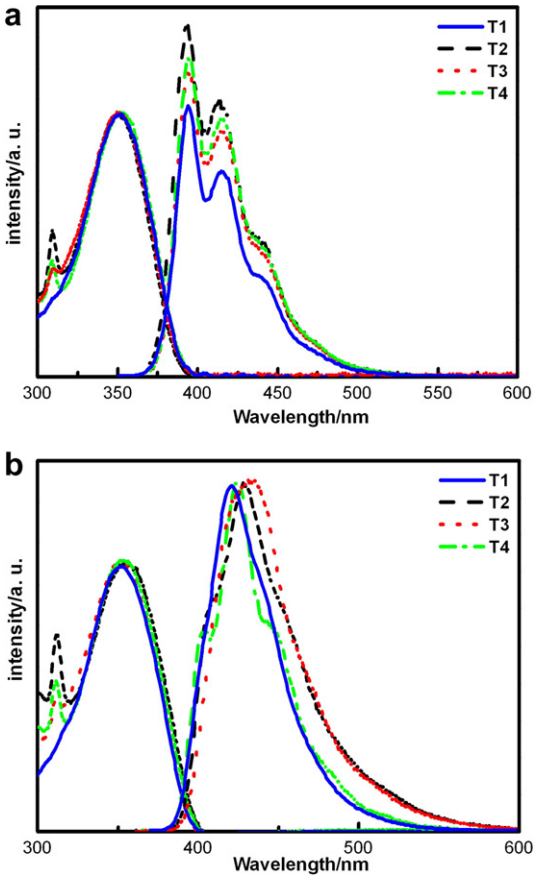

Fig. 3. The normalized UV/Vis and PL spectra of **T1**–**T4** in solution (a) and in films (b). All the films (~100 nm) are fabricated by spin-coated method.

with λ_{max} at 394 nm and shoulder peaks at 414 nm and 435 nm as excitation under 350 nm light, which features the typical characteristics of the conjugated fluorene derivatives [16]. By using quinine sulphate in 1 M sulphuric acid as standard, the trimers in the solution show higher measured quantum yield (about 90%), besides **T1** (70%) due to strong interaction between hexyl side-chains of fluorene. From Fig. 3b, the emission of trimers in films shows a slight red shift (λ_{max} at 422–433 nm) compared to that in solution, however, the whole spectrum still locate at deep blue region. The red-shift between solution and solid-state in PL spectra commonly is assigned to self-absorption effect or aggregation effect. However, in our molecular structure, the rigid spiro-linked diphenyl groups serve as an effective insulating spacer blocking interaction between the backbones. To demonstrate our molecular design, we gain single crystal structure of **T3**. As indicated in Fig. 4, the backbone's phenyl rings in two adjacent molecules have less overlapped area, and the closest distance between the phenyl ring planes is 3.95 Å. Hence π–π interaction between chromophores difficultly occurs. Another, the relative peak intensity of PL spectra in solid-state is changed compared with PL spectra in solution (see Fig. 3b). The peak at 394 nm and first shoulder peak 414 nm are obviously weakened and second shoulder peak at 435 nm is enhanced, indicating emission from high-energy band is absorbed by itself. As a whole, the optical properties of all trimers have only slight difference, indicating that the electronic structures of fluorene oligomers are essentially independent of the substituents.

The material stability is the most problem in fluorene-based derivatives, because it nearly associated with lifetime and color purity in light-emitting diodes. To investigate the difference of stability between the trimers with different substituents, their photostability in the films is tested. Fig. 5 illustrates the emission spectra of the pristine films and the subsequent photodegradation under air for two representative trimers with all aromatic and all alkyl side chains. For the trimer (**T1**) with all alkyl sub-

Table 1
Summary of physical properties of four trimers

Trimer	T_g[a] (°C)	T_m[b] (°C)	T_d[c] (°C)	$\lambda_{1,max,abs}$[d] (nm)	$\lambda_{2,max,abs}$[e] (nm)	$\lambda_{1,maxPL}$[d] (nm)	$\lambda_{2,maxPL}$[e] (nm)	Q_{PL}[f] in solution (%)	Q_{PL}[g] in films (%)	HOMO/ LUMO[h] (eV)
T1	25	105	357	351	351	394	422	70	65	−5.57/−2.10
T2	na[i]	440	460	351	351	394	428	93	85	−5.67/−2.30
T3	80	169	368	351	351	394	433	86	78	−5.64/−2.30
T4	132	na[j]	387	351	351	394	424	85	82	−5.63/−2.23

[a] Glass phase transition temperature by DSC.
[b] Melting temperature by DSC.
[c] Decomposition temperature by TGA.
[d] In dilute THF solutions (~1.0×10^{-4} M/L).
[e] In films (~100 nm) by spin-coated method.
[f] Using quinine sulphate in 1 M sulphuric acid as standard.
[g] Measurement in calibrate integrating sphere.
[h] Highest occupied molecular orbital and lowest unoccupied molecular orbital by CV.
[i] No T_g detectable, only exhibit a distinct T_m.
[j] No T_m detectable, only show a clear T_g.

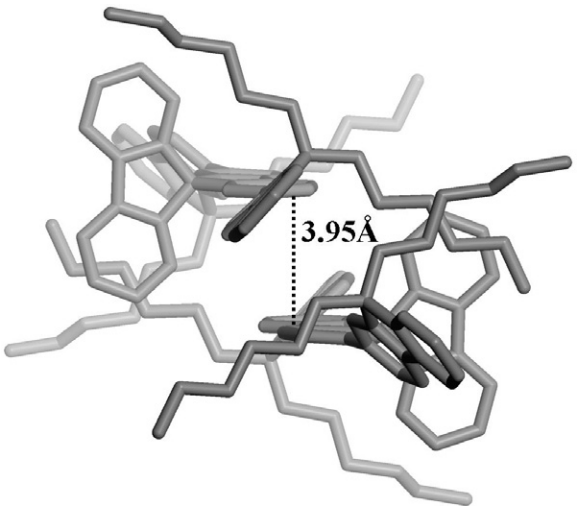

Fig. 4. The illustration of the molecular stacking of **T3**.

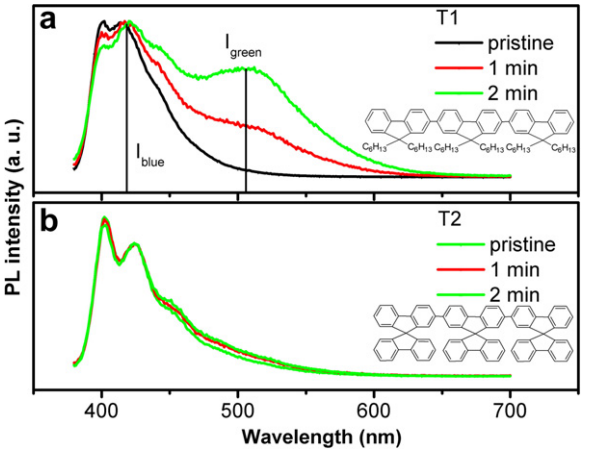

Fig. 5. The normalized emission spectra of a pristine film and the subsequent photodegradation under air for the trimers with different side chain units. All the films are excited with UV light of 360 nm wavelength.

stituents, the low-energy emission bands around 510 nm are emerging after degradation and the intensity increase with the increase of the degradation time. When alkyl substitution is replaced by the aromatic substitution (**T2**), the low-energy emission bands cannot be observed in the given degradation period. According to recent reports by List and Scherf [17] the green emission at 510 nm generally is due to the formation of ketonic defects in PFs and LPPP (lader-type poly(*p*-phenylene)) backbone. Above, the result combined with our other studies [18] reveal that the aromatic structures can effectively restrain the effect of photodegradation due to alkyl oxidation, hence improve material stability.

2.3. Condensed state structures and thermal properties

The powder X-ray diffraction analysis exhibits condensed state structures of the trimers in the solid state. As shown in the Fig. 6, the four trimers show very different condensed state features. The crystalline capacity is gradually weakened from **T1** to **T4**. In this content, the XRD patterns of **T2** and **T3** show significant crystalline peaks as well as an amorphous halo, suggesting that the **T2** and **T3** are semicrystalline compounds [19]. In particular, the relatively broad and random scatter peaks for **T4** are shown, demonstrating the non-crystalline amorphous nature of**T4** in solid state. This is likely

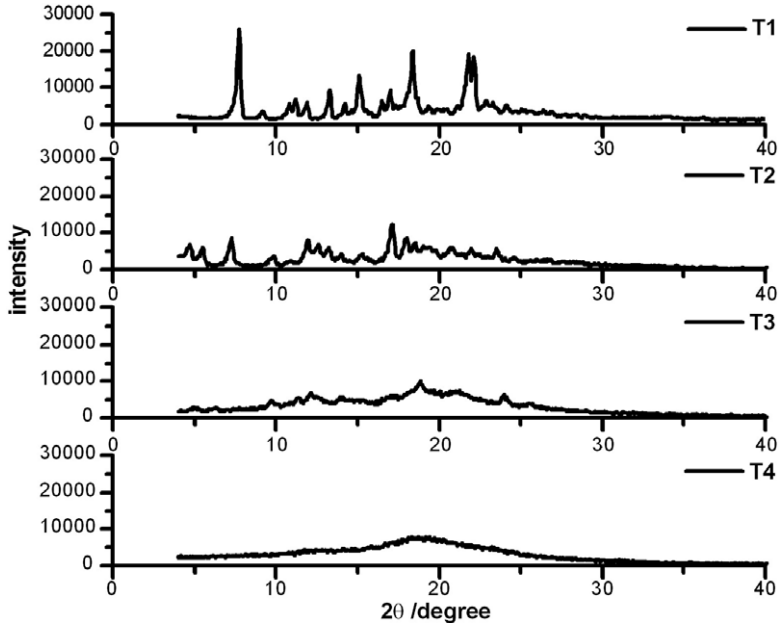

Fig. 6. Comparison of X-ray powder diffraction patterns for four trimers. All samples were tested under the same condition and all intensities were scaled relative to the largest peak in pattern **T1** (each pattern was at its original intensity).

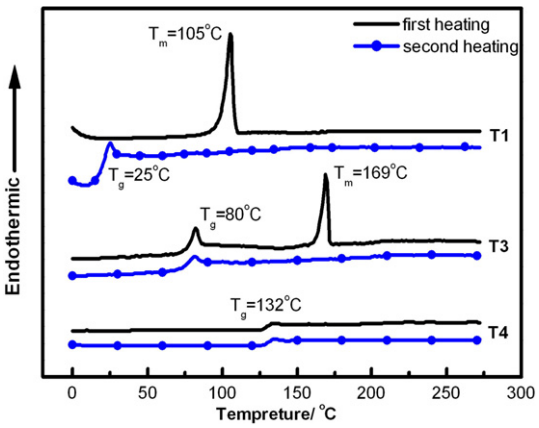

Fig. 7. DSC scans of **T1**, **T3** and **T4** with the first and second heating at rate of 10 °C/min. All trimers almost are not found thermodynamic change as cooling.

due to the mixed aromatic and alkyl substitutes, which disturb the crystallization.

The condensed state structures of these trimers in solid state are validated in advance by differential scanning calorimetry (DSC) analysis (Fig. 7). All samples of trimers are obtained by precipitation from organic solvent without further thermodynamically disposal. When sample **T1** is heated, a sharp endothermic peak is observed at 105 °C due to melting of sample, corresponding to the melting temperature (T_m). This indicates **T1** have strong crystalline nature. And then isotropic liquid is quickly cooled down on standing in liquid nitrogen, an amorphous glass is spontaneously formed via supercooled liquid. When amorphous glass sample is heated again, a glass phase transition (T_g) is observed at 25 °C. The DSC curve of **T3** exhibits a glass phase transition (T_g) at 80 °C as well as a sharp endothermic peak (T_m) at 169 °C as heating in the first cycle. Such characteristic feature in DSC measurement indicates that the **T3** exists as both crystalline and amorphous nature ca. semicrystalline feature, which is in agreement with XRD analysis of **T3**. When the sample is heated again, only glass phase transition (T_g) is observed at 80 °C, which means a glass is formed when rapidly cooling down. It should be noted that endothermic melting peak of **T1** and **T3** disappeared in the second and further reheating cycles, which indicate that a stable amorphous phase can be formed by the fast cooling. However, the T_g of compound **T1** and **T3** is not enough high for practical application. In contrast, the DSC analysis for **T4** shows only a glass phase transition (T_g) at 132 °C without other phase transitions even at first heating cycle, and very stable thermo-behaviors are found during the repeated heating and cooling. This indicates that the **T4** is a more stable amorphous material in nature, as we known, which is sel-

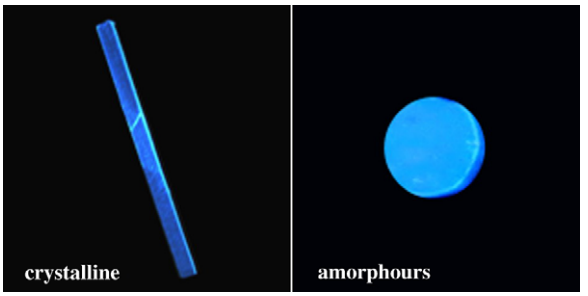

Fig. 8. The crystalline solid of **T2** (left, acicular crystal) and amorphous solid of **T4** (right, glass) under an ultraviolet lamp (365 nm).

dom among reported low molecular-weight organic compounds. After such kind of up and down scans in DSC experiments, **T4** is found to change from powder-like solid to transparent glass-like solid as shown in Fig. 8. In DSC experiments for highly crystalline compound **T2**, we did not obtain an intact DSC curve because of its high T_m up to 440 °C which is very close to its decomposition temperature T_d of 460 °C. Fig. 8 show a needle-like crystal of **T2** obtained from solvent evaporation for comparison with amorphous glass of compound **T4**. Although compound **T2** has high fluorescence efficiency and high thermo-stability, which may benefit to high-performance EL device, its intense crystallization tendency may result in the film with a quite rough surface.

2.4. Electroluminescent properties

A series of EL devices based on these trimers are fabricated [20], except **T1**, which is not suitable for OLEDs applications since its low T_g (25 °C). Considering the large energy gap (~3.4 eV) of these trimers, it is difficult to find appropriate carrier-transport materials, because energy levels matching for injecting one type of carriers and appropriate carrier-transport properties or energy levels for blocking the opposite type of carriers must be possess. Previously, the compound 4,4′,4″-tri(*N*-carbazolyl)triphenylamine (TCTA) is found to be suitable hole-transporting material for oligofluorene based device because of its relatively high hole mobility and large energy gap (3.3 eV) [12]. Thus the EL devices of **T2**, **T3** and **T4** are fabricated by utilizing them as an emissive layers in a standard device structure ITO/PEDOT:PSS/TCTA (40 nm)/trimers (40 nm)/BCP (10 nm)/Alq_3 (20 nm)/LiF (0.5 nm)/Al (150 nm), where the conducting polymer polyethylene dioxythiophene/polystyrene sulphonate (PEDOT:PSS) is used as the hole-injection layer, TCTA as a hole-transporting layer, BCP (2,9-dimethyl-4,7-diaphenyl-1,10-phenanthroline) as an exciton-blocking layer, and Alq_3 (aluminum tris(8-hydroxyquinolate)) as a electron transporting layer (Fig. 9). These devices all exhibit similar EL emission, and the representative EL spectra of **T4** is shown in inset of Fig. 10. The peaks of the EL spectra of these devices are at 408 nm and 428 nm, showing deep blue color using non-doping structures with the CIE coordinates of (0.16, 0.07), (0.17, 0.09) and (0.16, 0.07), respectively, which are close to blue standards (0.14, 0.08) of the National Television Standards Committee (NTSC). Furthermore, their EL spectra are stable with increasing voltage during operation and the long wavelength emission is not observed in our devices.

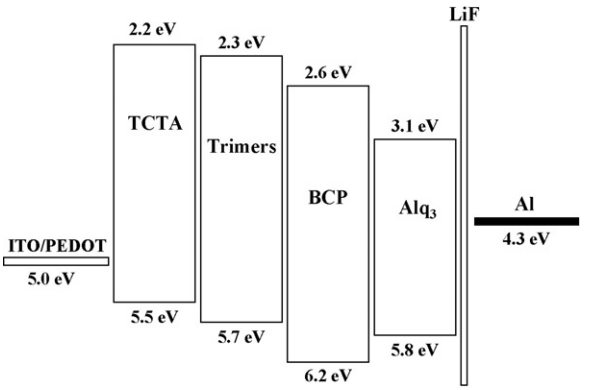

Fig. 9. Band diagram of ITO/PEDOT:PSS/TCTA/trimers/BCP/Alq_3/LiF/Al.

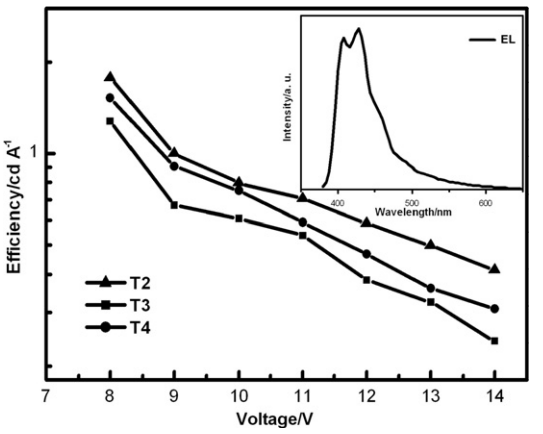

Fig. 10. EL efficiency–voltage characteristics of devices using **T2**, **T3** and **T4**. Insert is The EL spectra of **T4**.

This phenomenon can be attributed to the non-planar molecular structure of the spirobifluorene, because it can effectively restrain photodegradation due to alkyl oxidation, hence reduce green emission and improve color purity [18].In fact, the EL spectra of trimers show some blue-shift compared to their PL spectra, which is attributed to the thin films with 30 nm in devices can effectively restrain a strong self-absorption phenomenon arising a great spectral red-shift, compared with the thick films with ~100 nm in PL measurement. In addition to the deep blue emission, EL efficiencies of these devices are rather high (Fig. 10). The maximum values for **T2**, **T3** and **T4** are 1.77, 1.27 and 1.52 cd A^{-1} at 8 V, corresponding to external quantum efficiencies of 2.9%, 1.8% and 2.7%, respectively (detailed data for EL performance are shown in Table 2). The devices using **T2**, **T3** and **T4** exhibit a maximum luminance of 805, 380 and 772 cd m^{-2}, respectively (Fig. 11). In particular, the device using **T4** as emission layer shows a considerable brightness at lower voltage as compared with **T2** and **T3**. For example, at 10 V, the brightness is 710 cd m^{-2} for **T4**, and about 100 cd m^{-2} for **T2** and **T3**, presumably due to amorphous feature of **T4**. It is obvious that the devices using **T2** and **T4** exhibit higher device performance because of highly thermal and condensed state stable emitter. In view of the fact that such EL performances are obtained from neat blue emissive layers, these EL efficiencies are fairly high for deep blue OLEDs.

Considering their high EL efficiency and color saturation, these trimers can be excellent candidates for white light emitting devices with simple structure. After optimizing device structure, the devices composing of ITO/PEDOT:PSS/TCTA (40 nm)/rubrene (0.1 nm)/trimers (8 nm)/Alq_3 (52 nm)/LiF (0.5 nm)/Al (150 nm) are fabricated, where 5,6,11,12-tetraphenylnaphthacene (rubrene) is used as yellow light emitter, which composes with trimers' blue emission to make white light emitting. These devices using **T2**, **T3** and **T4** exhibit a maximum EL efficiency of 7.07 cd A^{-1}, 5.25 cd A^{-1} and 6.15 cd A^{-1}, respectively. The maximum luminance for **T2**, **T3** and **T4** are 12,350 cd m^{-2}, 7363 cd m^{-2} and 9500 cd m^{-2}, respectively (detailed data for EL performance are shown in Table 3). However, it is key

Table 2
Performances of devices having structures ITO/PEDOT:PSS/TCTA/trimers/BCP/Alq_3/LiF/Al

Trimer	Max efficiency (cd/A)	η_{ext}[a] (%)	Max brightness (cd/m^2)	Brightness @ 10 V (cd/m^2)	CIE @ 10 V (x, y)
T2	1.77	2.9	805	100	0.16, 0.07
T3	1.27	1.8	380	99	0.17, 0.09
T4	1.52	2.7	772	711	0.16, 0.07

[a] External quantum efficiency in device.

Table 3
Performances of white emission devices having structures ITO/PEDOT:PSS/TCTA/rubrene/trimers/Alq_3/LiF/Al

Trimer	Max efficiency (cd/A)	Max brightness (cd/m^2)	CIE @ 15 V (x, y)
T2	7.07	12,350	0.41, 0.46
T3	5.25	7363	0.40, 0.45
T4	6.15	9500	0.32, 0.37

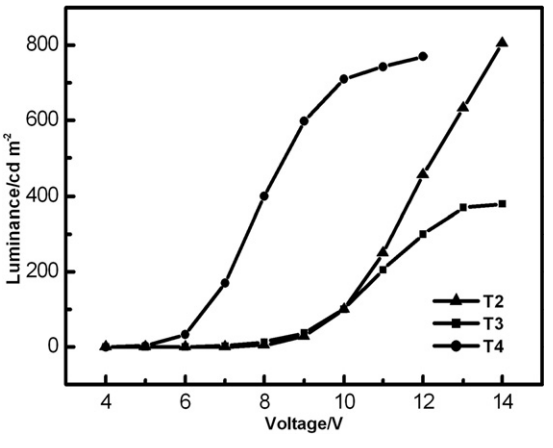

Fig. 11. Luminance–voltage characteristics of devices using **T2**, **T3** and **T4**.

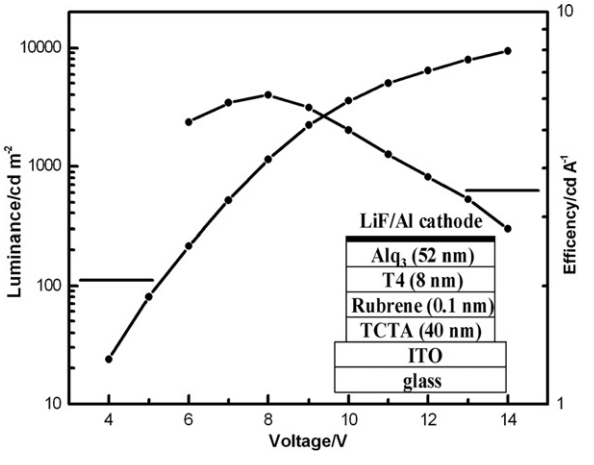

Fig. 12. Luminance–voltage and EL efficiency–voltage characteristics of white LEDs.

that the only device using **T4** shows white emission with CIE coordinates of (0.32, 0.37) as compared with CIE coordinates of (0.41, 0.46) and (0.40, 0.45) for **T2** and **T3**, respectively. The luminance–voltage and EL efficiency–voltage characteristics of **T4** based white device are shown in Fig. 12. Among these trimers, only **T4** exhibits good performance both for blue and white LEDs, indicating that material with stable amorphous feature and high T_g is the desirable molecular design for OLEDs applications. However, we believe that the most important influence of condensed state structure on OLED is stability and lifetime of devices, and the corresponding works is in present.

3. Conclusions

In summary, we have synthesized a series of fluorene-based trimers with different substituents, which exhibit strong deep blue emission both in solid state and EL devices. These trimers with the same backbone and different substituents 9-C of fluorene exhibit very different condensed state structures from a crystalline to amorphous glass, providing a new instance of molecular structure impacting on its condensed state structure. The present results also demonstrate that the devices using highly thermal and condensed state stable emitter exhibit higher device performance.

4. Experimental

4.1. General information and materials

Commercial grade reagents were used without further purification unless otherwise stated. Tetrahydrofuran (THF) and diethyl ether were dried and purified by fractional distillation over sodium/benzophenone. Column chromatography was performed using silica gel (200–300 mesh). The ^1H and ^{13}C NMR spectra were recorded on AVANCZ 500 spectrometers at 298 K by utilizing deuterated chloroform ($CDCl_3$) as solvent and tetramethylsilane (TMS) as standard. All the compounds were characterized by Flash EA 1112, CHNS–O elemental analysis instrument. The mass spectra were recorded using an APPLIED BIOSYSTEMS QSTAR instrument and a Krotos MALDI-TOF mass system. Thermogravimetric analysis (TGA) was conducted on a Perkin–Elmer Thermal Analysis system under a heating rate of 20 °C/min and a nitrogen flow rate of 80 ml/min. The differential scanning calorimeter (DSC) analysis was determined using a NETZSCH (DSC-204) instrument at 10 °C/min under nitrogen flushing. The powder X-ray diffraction was detected with a Rigaku X-ray diffractometer (D/max r A, using Cu Kα radiation of wavelength 1.542 Å). UV–Vis absorption spectra were recorded on UV-3100 spectrophotometer. Fluorescence measurements were carried out with RF-5301PC. Quantum yield was determined in THF solution and was calculated by comparing emission with that of the standard solution of quinine sulphate in 1 M sulphuric acid ($\Phi = 0.545$) at room temperature. Cyclic voltammetry (CV) were performed with a BAS 100 W Bioanalytical Systems, using a glass carbon disk ($\Phi = 3$ mm) as working electrode, platinum wire as auxiliary electrode, with porous ceramic wick, Ag/Ag^+ as reference electrode, standardized for the redox couple ferricinium/ferrocene. Cyclic voltammetric studies were carried out containing 0.1 M [*n*-NBu_4][BF_4] dried in an oil pump vacuum at 80 °C as supporting electrolyte. The procedure was performed at room temperature and nitrogen atmosphere was maintained over the solution during measurements.

4.2. Synthesis

4.2.1. 2,7-Bis(4,4,5,5-tetramethyl-1,3,2-dioxaborolan-2-yl)-9,9′-dihexanelyfluorene (*3a*)

To a solution of **1a** (8 g, 10 mmol) in THF (120 ml) at −78 °C was added 13.75 ml (22 mmol) *n*-butyllithium. The mixture was stirred at −78 °C, warmed to room temperature for 15 min, and then cooled again to −78 °C for 15 min, 2-isopropoxy-4,4,5,5-tetramethyl-1,3,2-dioxabrorolane (7.9 ml, 35 mmol) was added rapidly to the solution, and the resulting mixture was warmed to room temperature and stirred for 24 h. Some water was poured into the solution and then organic layer was extracted with diethyl ether several times. The organic phase was dried over anhydrous magnesium sulphate. After filtration the solution was removed by rotary evaporation, the residue was purified by column chromatography (silica gel, hexane) to give a white solid (yield 65%). ^1H NMR (500 MHz, $CDCl_3$): δ 7.81–7.79 (d, 2H, Ar-H), δ 7.74–7.73 (d, 2H, Ar-H), δ 7.71 (s, 2H, Ar-H), δ 2.01–1.99 (m, 4H, CH_2), δ 1.39 (s, 24H, CH_3), δ1.08–0.98 (m, 12H, Ar-H), δ 0.75–0.73 (m, 6H, CH_3), δ 0.55–0.54 (m, 4H, CH_2). MS (*m*/*z*) 586.5. Anal. Calcd for $C_{37}H_{56}B_2O_4$: C, 75.78; H, 9.62. Found: C, 75.50; H, 9.86.

*4.2.2. 2,7-Bis(4,4,5,5-tetramethyl-1,3,2-dioxaborolan-2-yl)-9,9′-spirofluorene (**3b**)*

The procedure was followed to prepare **3a** from **1a** (0.711g, 1.5 mmol) to afford a white solid (yield 55%). ^{1}H NMR (500 MHz, $CDCl_3$): δ 7.88–7.83 (m, 6H, Ar-H), δ 7.37–7.34 (t, 2H, Ar-H), δ 7.13 (s, 2H, Ar-H), δ 7.10–7.07 (t, 2H, Ar-H), δ 6.70-6.68 (d, 2H, Ar-H), δ 1.22 (s, 24H, CH_3). MS (m/z) 567.6. Anal. Calcd for $C_{37}H_{38}B_2O_4$: C, 78.2; H, 6.74. Found: C, 77.66; H, 6.80.

General procedure for the preparation of **T1**, **T2**, **T3** and **T4** is based on the Suzuki coupling reaction between diborolan-compound **3a** or **3b** with corresponding bromo-compounds **2a** or **2b**. Toluene and a 2.0 M/L aqueous solution of Na_2CO_3 (toluene/water at a 3:2 ratio) were added to the mixture of the (1:1 equiv) and $Pd(PPh_3)_4$ (1% mol). The reaction mixture was stirred at 90 °C for 2 days under a nitrogen atmosphere. The resulting solution was added some water and then was extracted with chloroform several times. The organic phase was dried over anhydrous magnesium sulphate. After filtration and solvent evaporation, the liquid was purified by column chromatography on silica gel.

T1: The title compound was prepared from **3a** (484 mg, 0.82 mmol) and **2a** (677 mg, 1.64 mmol) and purified with column chromatography using petroleum ether/CH_2Cl_2 as the eluent to afford a white solid (yield 52%). ^{1}H NMR (500 MHz, $CDCl_3$): δ 7.82–7.80 (d, 2H, Ar-H), δ 7.79–7.78 (d, 2H, Ar-H), δ 7.75–7.73 (d, 2H, Ar-H), δ7.67–7.66 (m, 4H, Ar-H), δ 7.64 (s, 2H, Ar-H), δ 7.62 (s, 2H, Ar-H), δ 7.38–7.30 (m, 6H, Ar-H), δ 2.08–2.01 (m, 12H, CH_2), δ 1.15–1.07 (m, 36H, CH_2), δ 0.78–0.76 (m, 30H, CH_2CH_3). ^{13}C NMR (500 MHz, $CDCl_3$): δ 151.8, 151.5, 151.0, 140.8, 140.6, 140.3, 140.0, 127.0, 126.8, 126.1, 126.0, 122.9, 121.5, 121.4, 119.9, 119.8, 119.7, 55.3, 40.4, 31.5, 29.7, 23.8, 22.5, 14.0. Anal. Calcd for $C_{75}H_{98}$: C, 90.12; H, 9.88. Found: C, 89.16; H, 9.80. MALDI-TOF-MS (M^+) 998.7 (100%).

T2: The title compound was prepared from **3b** (170.4 mg, 0.3 mmol), and **2b** (237.2 mg, 0.6 mmol) and purified with column chromatography using petroleum ether/CH_2Cl_2 as the eluent to afford a white solid (yield 67%). ^{1}H NMR (500 MHz, $CDCl_3$): δ 7.83–7.81 (d, 6H, Ar-H), δ 7.78–7.76 (d, 2H, Ar-H), δ 7.72–7.70 (d, 2H, Ar-H), δ 7.68–7.66 (d, 2H, Ar-H), δ 7.35–7.30 (m, 12H, Ar-H), δ 7.08–7.03 (m, 8H, Ar-H), δ 6.82 (s, 2H, Ar-H), δ 6.77 (s, 2H, Ar-H), δ 6.70–6.69 (m, 6H, Ar-H), δ 6.65–6.63 (d, 2H, Ar-H). ^{13}C NMR (500 MHz, $CDCl_3$): δ 149.6, 149.3, 149.1, 148.7, 148.6, 141.8, 141.2, 141.0, 140.9, 140.8, 140.5, 128.0, 127.9, 127.8, 127.8, 127.7, 127.7, 127.6, 127.1, 124.2, 124.1, 123.9, 122.6, 122.5, 120.0, 119.9, 66.1. Anal. Calcd for $C_{75}H_{44}$: C, 95.31; H, 4.69. Found: C, 94.01; H, 5.37. MALDI-TOF-MS (M^+) 944.5 (100%).

T3: The title compound was prepared from **3b** (94 mg, 0.165 mmol) and **2a** (150 mg, 0.364 mmol) and purified with column chromatography using petroleum ether/CH_2Cl_2 as the eluent to afford a white solid (yield 72%). ^{1}H NMR (500 MHz, $CDCl_3$): δ 7.97–7.95 (d, 2H, Ar-H), δ 7.91–7.90 (d, 2H, Ar-H), δ 7.70–7.69 (d, 2H, Ar-H), δ 7.65–7.64 (d, 2H, Ar-H), δ 7.60–7.59 (d, 2H, Ar-H), δ 7.43–7.41 (m, 4H, Ar-H), δ 7.35–7.33 (d, 2H, Ar-H), δ 7.31–7.28 (t, 6H, Ar-H), δ 7.19–7.16 (t, 2H, Ar-H), δ 7.00 (s, 2H, Ar-H), δ 6.90–6.89 (d, 2H, Ar-H), δ 1.95–1.92 (m, 8H, CH_2), δ 1.09–0.99 (m, 24H, CH_2), δ 0.74–0.72 (m, 12H, CH_3), δ 0.61–0.58 (m, 8H, CH_2). ^{13}C NMR (500 MHz, $CDCl_3$): δ 151.3, 150.0, 149.9, 148.8, 141.9, 141.5, 140.7, 140.6, 140.3, 139.8, 127.9, 127.8, 127.2, 126.9, 126.7, 126.0, 124.3, 122.8, 122.5, 121.2, 120.2, 120.1, 119.6, 55.1, 40.3, 31.3, 29.6, 22.7, 22.5, 14.0. Anal. Calcd for $C_{75}H_{80}$: C, 91.78; H, 8.22. Found: C, 91.62; H, 8.24. MALDI-TOF-MS (M^+) 980.5 (100%).

T4: The title compound was prepared from **3a** (175.8 mg, 0.3 mmol) and **2b** (248.7 mg, 0.63 mmol) and purified with column chromatography using petroleum ether/CH_2Cl_2 as the eluent to afford a white solid (yield 50%). ^{1}H NMR (500 MHz, $CDCl_3$): δ 7.92–7.90 (d, 2H, Ar-H), δ 7.87–7.85 (d, 6H, Ar-H), δ 7.66–7.63 (d, 2H, Ar-H), δ 7.54–7.53 (d, 2H, Ar-H), 7.40–7.35 (m, 8H, Ar-H), δ 7.32–7.30 (d, 2H, Ar-H), δ 7.14–7.08 (m, 6H, Ar-H), 7.00 (s, 2H, Ar-H), δ 6.81–6.80 (d, 4H, Ar-H), δ 6.71–6.69 (d, 2H, Ar-H), δ 1.91–1.88 (m, 4H, CH_2), δ 1.03–0.93 (m, 12H, CH_2), δ 0.70–0.67 (m, 6H, CH_3), δ 0.56 (m, 4H, CH_2). ^{13}C NMR (500 MHz, $CDCl_3$): δ 151.6, 149.4, 149.3, 148.8, 141.9, 141.5, 141.4, 141.0, 139.9, 139.8, 127.8, 127.7, 127.1, 126.1, 124.2, 124.0, 122.6, 121.3, 120.2, 120.0, 119.7, 66.1, 55.2, 40.2, 31.3, 29.5, 23.6, 22.4, 13.9. Anal. Calcd for $C_{75}H_{62}$: C, 93.51; H, 6.49. Found: C, 93.54; H, 6.48. MALDI-TOF-MS (M^+) 962.1 (100%).

4.3. OLED device fabrication

OLEDs based on the trimers were fabricated and investigated. Indium tin oxide (ITO)-coated

glasses with a sheet resistance of about 100 Ω/□ were used as the substrates and carefully cleaned before the deposition of organic materials. Organic layers were deposited by high-vacuum ($<10^{-6}$ Torr) thermal evaporation. A LiF buffer layer and a 150-nm-thick Al cathode were vapour-deposited at a background pressure of 10^{-6} Torr onto the organic films subsequently. The layer thickness and the deposition rate of organic and inorganic materials were monitored in situ by an oscillating quartz thickness monitor. Electroluminescent (EL) spectra and 1931 CIE coordinates of the devices were measured by a PR650 spectroscan spectrometer. The luminance–current density–voltage characteristics were recorded simultaneously with the measurement of the EL spectra by combing the spectrometer with a Keithley model 2400 programmable voltage–current source. All the measurements were carried out at room temperature under ambient conditions.

Acknowledgments

We are grateful for financial support from National Science Foundation of China (Grant Numbers 20125421, 90101026, 20474024, 50473001, 50303007, 50473006), and by Ministry of Science and Technology of China (Grant Number 2002CB6134003) and PCRIT.

References

[1] J.S. Miller, Adv. Mater. 5 (1993) 671;
J. Roncali, Chem. Rev. 92 (1992) 711;
A. Kraft, A.C. Grimsdale, A.B. Holmes, Angew. Chem., Int. Ed. 37 (1998) 402.
[2] H. Aziz, Z.D. Popovic, Chem. Mater. 16 (2004) 4522.
[3] M.D. Joswick, I.H. Campbell, N.N. Barashkov, J.P. Ferraris, J. Appl. Phys. 80 (1996) 2883;
L.-M. Do, M. Oyamada, A. Koike, E.-M. Han, N. Yamamoto, M. Fujihira, Thin Solid Films. 273 (1996) 209;
L.-M. Do, E.M. Han, Y. Niidome, M. Fujihira, T. Kanno, S. Yoshida, A. Maeda, A.J. Ikushima, J. Appl. Phys. 76 (1994) 5118;
Y. Kuwabara, H. Ogawa, H. Inada, N. Nona, Y. Shirota, Adv. Mater. 6 (1994) 667.
[4] W.-L. Yu, J. Pei, W. Huang, A.J. Heeger, Adv. Mater. 12 (2000) 828;
D.-C. Shin, Y.-H. Kim, H. You, S.-K. Kwon, Macromolecules 36 (2003) 3222;
D. Vak, B. Lim, S.-H. Lee, D.-Y. Kim, Org. Lett. 7 (2005) 4229;
C. Ego, A.C. Grimsdale, F. Uckert, G. Yu, G. Srdanov, K. Müllen, Adv. Mater. 14 (2002) 809.
[5] E.-M. Han, L.-M. Do, N. Yamamoto, M. Fujihira, Thin Solid Films 273 (1996) 202;
C. Adachi, K. Nagai, N. Tamoto, Appl. Phys. Lett. 54 (1989) 1145;
K.A. Higginson, X.-M. Zhang, F. Papadimitrakopoulos, Chem. Mater. 10 (1998) 1017.
[6] Y. Shirota, J. Mater. Chem. 10 (2000) 1;
D. Mutaguchi, K. Okumoto, Y. Ohsedo, K. Moriwaki, Y. Shirota, Org. Electron. 4 (2003) 49;
K. Okumoto, Y. Shirota, Chem. Mater. 15 (2003) 699;
H. Doi, M. Kinoshita, K. Okumoto, Y. Shirota, Chem. Mater. 15 (2003) 1080;
H. Utsumi, D. Nagahama, H. Nakano, Y. Shirota, J. Mater. Chem. 12 (2002) 2612.
[7] P.W. Wang, Y.J. Liu, C. Devadoss, P. Bharathi, J.S. Moore, Adv. Mater. 8 (1996) 237.
[8] Y. Shirota, T. Kobata, N. Noma, Chem. Lett. (1989) 1145.
[9] S.J. Wang, W.J. Oldham, R.A. Hudack, G.C. Bazan, J. Am. Chem. Soc. 122 (2000) 5695.
[10] J. Pei, J. Ni, X.-H. Zhou, X.-Y. Cao, Y.-H. Lai, J. Org. Chem. 67 (2002) 8104;
D. Katsis, Y. Geng, J.J. Ou, S.W. Culligan, A. Trajkovska, S.H. Chen, L.J. Rothberg, Chem. Mater. 14 (2002) 1332;
H. Tian, B. Chen, P.-H. Liu, Chem. Lett. 30 (2001) 990.
[11] J. Salbeck, M. Schörner, T. Fuhrmann, Thin Solid Films 417 (2002) 20;
J. Salbeck, N. Yu, J. Bauer, F. Weissortel, H. Bestgen, Synth. Met. 91 (1997) 209.
[12] K.-T. Wong, Y.-Y. Chien, R.-T. Chen, C.-F. Wang, Y.-T. Lin, H.-H. Chiang, P.-Y. Hsieh, C.-C. Wu, C.H. Chou, Y.O. Su, G.-H. Lee, S.-M. Peng, J. Am. Chem. Soc. 124 (2002) 11576;
C.-C. Wu, T.-L. Liu, W.-Y. Hung, Y.-T. Lin, K.-T. Wong, R.-T. Chen, Y.-M. Chen, Y.-Y. Chien, J. Am. Chem. Soc. 125 (2003) 3710;
H.-W. Lin, C.-L. Lin, H.-H. Chang, U.-T. Lin, C.-C. Wu, Y.-M. Chen, R.-T. Chen, Y.-Y. Chien, K.-T. Wong, J. Appl. Phys. 95 (2004) 881;
C.-C. Wu, T.-L. Liu, Y.-T. Lin, W.-Y. Hung, T.-H. Ke, K.-T. Wong, T.-C. Chao, Appl. Phys. Lett. 85 (2004) 1172;
C.-C. Wu, W.-G. Liu, W.-Y. Hung, T.-L. Liu, K.-T. Wong, Y.-Y. Chien, R.-T. Chen, T.-H. Hung, T.-C. Chao, Y.-M. Chen, Appl. Phys. Lett. 87 (2005) 052103;
T.-C. Chao, Y.-T. Lin, C.-Y. Yang, T.S. Hung, H.-C. Chou, C.-C. Wu, K.-T. Wong, Adv. Mater. 17 (2005) 992;
K.-T. Wong, R.-T. Chen, F.-C. Fang, C.-C. Wu, Y.-T. Lin, Org. Lett. 7 (2005) 1979;
C.-C. Wu, Y.-T. Lin, K.-T. Wong, R.-T. Chen, Y.-Y. Chien, Adv. Mater. 16 (2004) 61;
K.-T. Wong, Y.-L. Liao, Y.-T. Lin, H.-C. Su, C.-C. Wu, Org. Lett. 7 (2005) 5131.
[13] H.S. Lee, T. Tsutsui, Thin Solid Films 363 (2000) 76;
Y. Geng, A. Trajkovska, S.W. Culligan, J.J. Ou, H.M.P. Chen, D. Katsis, S.H. Chen, J. Am. Chem. Soc. 125 (2003) 14032.
[14] S.W. Culligan, Y. Geng, S.H. Chen, K. Klubek, K.M. Vaeth, C.W. Tang, Adv. Mater. 15 (2003) 1176.
[15] P.K. Tsolakis, J.K. Kallitsis, Chem. Eur. J. 9 (2003) 936.
[16] Q. Hou, Q. Zhou, Y. Zhang, W. Yang, R. Yang, Y. Cao, Macromolecules 37 (2004) 6299;
J. Teetsov, M.A. Fox, J. Mater. Chem. 9 (1999) 2117;
K.-H. Weinfurtner, F. Weissortel, G. Harmgarth, J. Salbeck, Proc. SPIE-Int. Soc. Opt. Eng. 3476 (1998) 40.

[17] E.J.W. List, R. Guentner, P.S.D. Freitas, U. Scherf, Adv. Mater. 14 (2002) 374;
L. Romaner, A. Pogantsch, P.S.D. Freitas, U. Scherf, M. Gaal, E. Zojer, E.J.W. List, Adv. Funct. Mater. 13 (2003) 597;
L. Romaner, G. Heimel, H. Wiesenhofer, P.S.D. Freitas, U. Scherf, J.-L. Brédas, E. Zojer, E.J.W. List, Chem. Mater. 16 (2004) 4667;
X.H. Yang, F. Jaiser, D. Neher, P.V. Lawson, J.-L. Brédas, E. Zojer, R. Güntner, P.S.D. Freitas, M. Forster, U. Scherf, Adv. Funct. Mater. 14 (2004) 1097.

[18] L. Liu, S. Tang, M. Liu, Z. Xie, W. Zhang, P. Lu, M. Hanif, Y. Ma, J. Phys. Chem. B. 110 (2006) 13734;
L. Liu, S. Qiu, B. Wang, W. Zhang, P. Lu, Z. Xie, M. Hanif, Y. Ma, J. Shen, J. Phys. Chem. B. 109 (2005) 23366.

[19] J. Jayaseharan, K. Kishore, G. Nalini, T.N. Gururow, J. Polym. Sci. Part A: Polym. Chem. 37 (1999) 4033.

[20] G. Cheng, Y. Zhang, Y. Zhao, S. Liu, S. Tang, Y. Ma, Appl. Phys. Lett. 87 (2005) 151905;
Y. Zhang, G. Cheng, Y. Zhao, J. Hou, S. Liu, S. Tang, Y. Ma, Appl. Phys. Lett. 87 (2005) 241112.

Available online at www.sciencedirect.com
ScienceDirect
Organic Electronics 9 (2008) 253–261
Organic Electronics
www.elsevier.com/locate/orgel

Characterization of indium tin oxide surfaces after KOH and HCl treatments

S. Gardonio [a], L. Gregoratti [a,*], D. Scaini [a], C. Castellarin-Cudia [a], P. Dudin [a,b,c], P. Melpignano [b], V. Biondo [b], R. Zamboni [c], S. Caria [c], M. Kiskinova [a]

[a] *Sincrotrone Trieste, Area Science Park, SS14-Km163.5, 34012 Trieste, Italy*
[b] *Centro Ricerche Plast-Optica, via Jacopo Linussio 1, 33020 Amaro (UD), Italy*
[c] *Istituto per lo Studio dei Materiali Nanostrutturati CNR, via P. Gobetti 101, 40129 Bologna, Italy*

Received 3 September 2007; received in revised form 27 November 2007; accepted 2 December 2007
Available online 8 December 2007

Abstract

The extraction of the light produced by an organic light emitting diode has been made possible by the use of transparent conductive materials which should have well defined electronic and optical properties. All the requirements are satisfied by indium tin oxide which has rapidly become the most common conductive substrate used for the growth of organic light emitting sources. Atomic force microscope, conventional X-ray photoemission spectroscopy and scanning photoemission spectromicroscopy have been used to investigate the morphology and the chemical properties of commercial thin indium tin oxide films after several treatments commonly used prior to the organic layer growth for smoothing/cleaning/patterning the surface. Unambiguous smoothing effects of the potassium hydroxide-based solutions have not been observed while Si contaminations of the surfaces have been found after the application of different patterning procedures.

PACS: 79.60.−I; 85.60.Jb; 68.37.−d; 68.37.Ps

Keywords: X-ray photoelectron spectra in surface analysis; Light-emitting diodes; Surfaces microscopy; Degradation process; Atomic force microscope; Indium tin oxide

1. Introduction

Indium tin oxide (ITO) films are transparent conductors that have been deeply investigated in the last decade because of their applications in the design of optoelectronic devices. ITO films combine many technological properties such as high transparency for visible light, good electrical conductivity and excellent substrate adherence. Most of the organic light emitting diodes (OLED) use ITO as anode layer for the injection of the current into the hole transport organic layers. The typical thickness of the OLED organic multilayer stack is of about 100 nm; this makes them susceptible of failures caused by possible ITO-substrate-device imperfections. Commercial available ITO substrates are characterised by the presence on the surface of

* Corresponding author. Tel.: +39 0403758025; fax: +39 0403758565.
E-mail address: luca.gregoratti@elettra.trieste.it (L. Gregoratti).

1566-1199/$ - see front matter © 2007 Published by Elsevier B.V.
doi:10.1016/j.orgel.2007.12.002

hillocks which can have heights comparable with the organic layer thickness; it has been shown that such spikes can compromise the functionality of the devices [1]. Therefore, there is a large demand for smoothed ITO surfaces to improve life expectancy of electroluminescent devices. Another critical parameter for optoelectronic devices is the current injection efficiency; it is strongly linked to the work function of the electrode which in turn is extremely sensitive to the morphology and chemical state of the anodic surface [2–5].

Thin films of ITO can be prepared by various techniques including thermal evaporation deposition [6], direct current and radio frequency magnetron sputtering [7,8], electron beam evaporation [9], spray pyrolysis [10], chemical vapour deposition [11], dip-coating technique [12] and pulsed laser deposition [13]. In addition a large variety of preparation and post-deposition treatments have been reported in literature, the most investigated ones being: mechanical cleaning [14], wet cleaning [2,14–20], dry cleaning, such as oxygen or argon plasma treatment [14,16,19–22] and UV–ozone irradiation [23]. Detailed characterizations have demonstrated that both the surface roughness and the presence of spikes along the film strictly depend from the growth methods and surface treatments [7,13–18,20–23]. Despite the efforts to determine the chemical and physical properties of the ITO surfaces after the treatments, there is no general agreement on the ideal procedure to produce the best ITO film for OLED devices. It should be mentioned that in order to smooth the ITO surface other approaches have been proposed which, to a large extend, circumvent the problem. For example in Ref. [24] the deposition of a thin polymeric layer decreases the initial roughness of the ITO surface. Such a method is very effective for the ITO surface smoothing and for the substantial improvement of the device lifetime stability. However the most commonly used polymer film, namely poly(3,4-ethylenedioxythiophene)–poly(styrenesulfonate) (PEDOT–PSS), used both as buffer and as hole transport layer, is highly hydrophilic. This film property requires a very careful device encapsulation in order to avoid the device damage due the moisture penetration through the polymer film.

Etching with potassium hydroxide (KOH)-based solutions is among wet treatments the most common post-deposition treatment used to: (i) remove the carbon contamination [5], (ii) modify the ITO work function [5] and (iii) reduce the surface roughness [1,25] without any evident chemical modification of the surface [5]. If the KOH efficiency in the removal of C contamination is well established, controversy results can be found on its property to reduce the surface roughness. For ITO samples grown by sputtering [1] it has been shown that a long etching time (24 h) reduces occasional spikes even higher than 50 nm without compromising the sheet resistance and film thickness, while in the case of ITO film prepared by sol gel spin coating a very short KOH etching time (above 40 s) seems to increase the surface roughness [25].

In the fabrication of OLED KOH and hydrochloric acid (HCl) are also used as etching liquids in the photolithographic patterning processes of transparent electrodes [26]. The most diffused process consists of five steps: (i) resist spin coating, (ii) optical photolithography with UV light, (iii) KOH solution developing, (iv) HCl etching and (v) acetone removal of photoresist. Another diffused patterning process is the HCl etching of ITO surface patterned with varnish. The influence of the etching rate on the resulting morphology of the borders of the etched regions and the evaluation of the resulting electro-optical properties of the ITO substrates have been widely investigated in the last decade [25–29], although very few information are available on the chemical composition of the ITO film after the patterning process. Since the ITO surface structure and its chemical composition are of crucial importance for the OLED growth and performance, adequate spectroscopic and microscopic characterization of the surface after patterning treatments are needed.

Here we present a systematic study of the chemical composition and topography of ITO commercial films exposed to KOH etching for different times and after the different steps of the patterning process. Chemical composition has been investigated at two different spatial scales: with conventional X-ray photoemission spectroscopy (XPS) averaging the probed area over few square millimetres and with synchrotron based Scanning Photoelectron Spectro-microscopy (SPEM) capable of 150 nm lateral resolution in order to detect chemical changes at microscopic level. The topography has been investigated by using the atomic force microscope (AFM) at a spatial resolution of 1 nm.

2. Experimental

ITO commercial coated glasses, from UNAXIS corporation, have been selected for this investigation.

The nominal thickness and sheet resistance of the ITO films were 160 nm and 30 Ω/sq^{-1}, respectively.

Different ITO surface samples treatments were performed and analysed. In order to study the effects of KOH in the smoothing of pristine ITO surfaces, three samples have been etched for 8, 16 and 24 h, respectively in a saturated KOH–isopropanol solution and then rinsed with de-ionised (DI) water and blow-dried in N_2. The effects of KOH and HCl etching on ITO surface in the patterning processes have been analysed by preparing four different samples (Sample A–D) following steps reported in Table 1.

XPS measurements were performed using a VG Escalab MKII apparatus provided with a Mg Kα source (1254 eV) and with a 150° spherical electron energy analyser. The photon beam radiate a circular area of about 5 mm diameter at an angle of 60° out of the surface normal while photoelectrons are collected 20° out of it with a total energy resolution of about 1.2 eV. With the Mg Kα source the probing depth did not exceed 10 nm. SPEM investigation was carried out at the experimental station of the ESCA microscopy beamline at the ELETTRA Synchrotron Light Source facility [30]. In SPEM the X-ray beam is focused into a small spot of 150 nm diameter by means of zone plates. Photoelectrons are detected and energy filtered by a hemispherical electron analyzer equipped with a 48-channel detector. SPEM measurements can be performed in two complementary operation modes: imaging and microspot photoelectron spectroscopy (μ-XPS) [31]. In the imaging mode, the sample is scanned with respect to the focused beam simultaneously collecting photoelectrons within an energy window, usually corresponding to the elemental core level of interest. In the μ-XPS mode conventional spectra of the energy distribution curve are measured from micro-spot selected from the images, providing detailed information about the local chemical composition. The geometrical setup of the SPEM (normal incidence of the photon beam on the sample and take-off angle of 30°) enhances the surface sensitivity, e.g. the probing depth in the present study, where a photon energy of 650 eV was used, did not exceed 2 nm.

All the AFM images were made by a commercial NT-MDT Solver Pro microscope at the ELETTRA Nanostructure Laboratory. The instrument is furnished with a $50 \times 50 \times 5$ μm closed loop scanner. The topographic images were done in contact mode using silicon rectangular cantilever (MikroMasch, spring costant: 0.6–1.0 N/ma) at a resolution of 256×256 pixels. A laser is focused on the back of the cantilever and deflected to a four-segment photosensitive detector, which can monitor the vertical deflection and the twisting of the cantilever as the tip scans across the surface. The height resolution during scanning was about 0.06 Å.

3. Results

The morphology of a pristine ITO surface at the nanometric scale has been analysed by means of AFM. In (Fig. 1a) a representative 3D reconstruction of an AFM picture of 16×16 μm^2 area of pristine ITO is shown together with a 1×1 μm^2 area 2D map (Fig. 1b). The surface is characterised by a grainy structure where the grain size ranges from few tens to few hundreds of nanometers with occasional spikes of maximum height of 20 nm with respect to the average value; the measured average roughness (R_a) is 2.64 nm. A 64×64 μm^2 In 3d core level map of a pristine ITO surface is shown in

Table 1
Steps followed for the ITO surface preparation of samples A, B, C and D

Step	Sample A	Sample B	Sample C	Sample D
1	Spin coating deposition of photoresist[a] on ITO surface	Same as sample A	Surface coverage with commercial varnish[b]	Same as sample C
2	Surface coverage with mask and exposure to UV radiation	None	None	None
3	Developing of photoresist with KOH solution (1%) for 2 min and then rinse in DI water	Same as sample A	None	None
4	Etching with acid solution[c] for 3 min	None	Etching with acid solution[c]	None
5	Rinsing in DI water and removal of resist with acetone	None	Removal of varnish with acetone	Same as sample C

[a] AZ4562 from CLARIANT.
[b] Toluensulfonamido fenolformaldeide.
[c] Composition of acid solution: 6% acetic acid, 31% chloridric acid and 63% water.

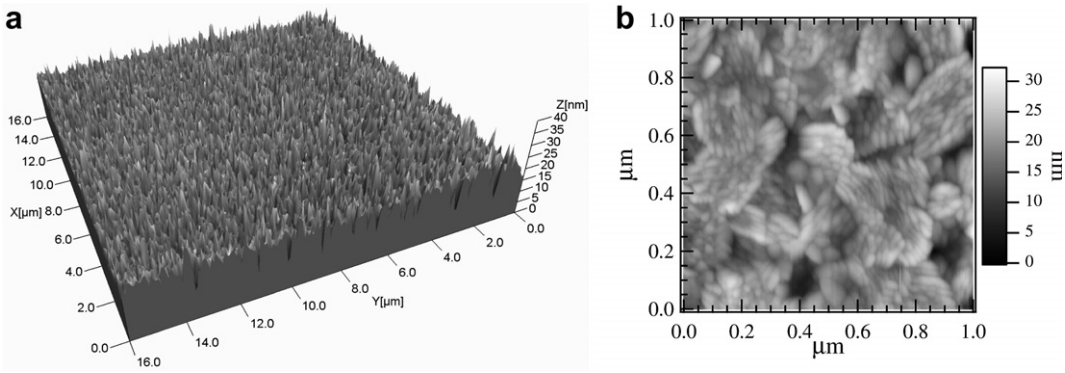

Fig. 1. AFM image of a (a) 16 μm × 16 μm and (b)1 μm × 1 μm area on pristine ITO surface.

Fig. 2a. The In content is not homogenous; major darker spots of a diameter of about 0.5 μm are randomly distributed while weaker variations in the contrast are present over all the surface. The local XPS μ-spectra at most representative regions are shown in Fig. 2b. The μ-spectra collected on a dark spot (indicated as point 1 in Fig. 1a) is compared to that acquired on the flatter background region (point 2) showing the presence of a higher C concentration while in the surrounding region In is dominant. It must be remarked that the enhanced surface sensitivity of the spectro-microscopy measurements amplifies the signal from the surface contaminations of the unclean ITO surface. The other peaks visible in the spectra are the main photoemission and Auger lines of In, Sn and O. A detailed analysis of the pristine ITO In 3d core level has been already reported in Ref. [32].

In Fig. 3a and b the 3D and 2D images, respectively of a 16 × 16 μm^2 and 1 × 1 μm^2 area of a pris-

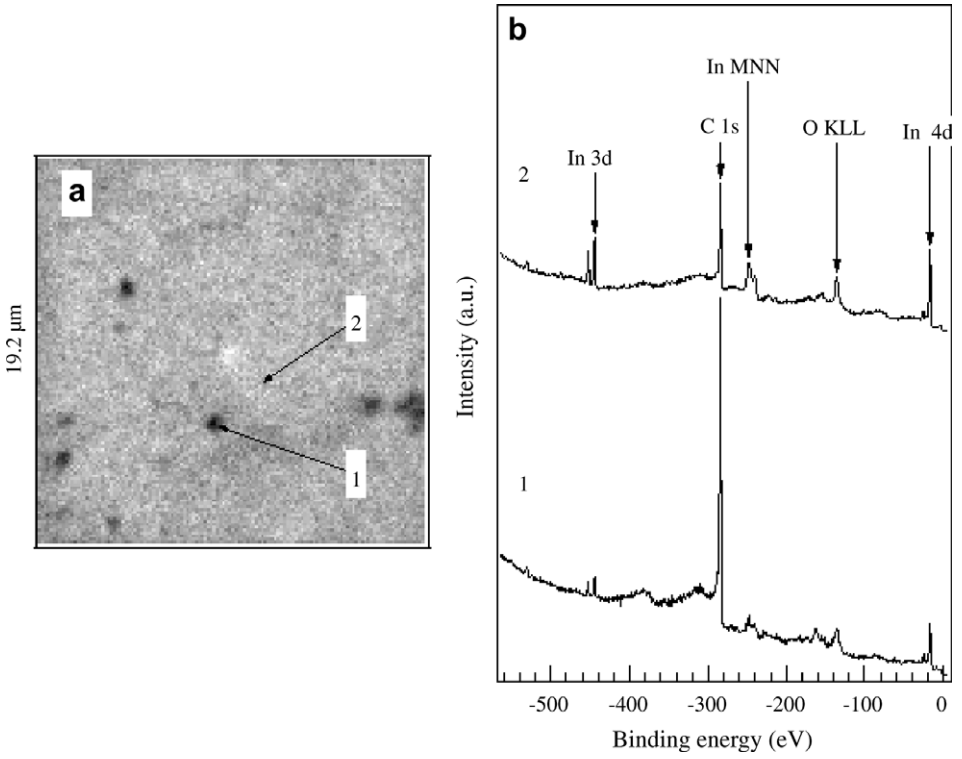

Fig. 2. (a) In 3d map of pristine ITO surface; (b) XPS μ-spectra collected at point 1 and 2 indicated in the map (a).

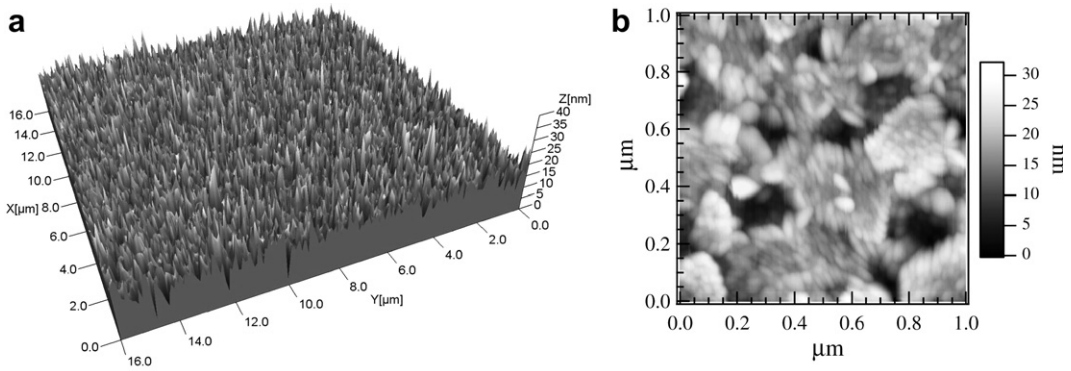

Fig. 3. AFM maps of a (a) 16 × 16 μm and (b) 1 × 1 μm area on a ITO sample etched on KOH–isopropanol saturated solution for 24 h.

tine ITO sample exposed for 24 h in a saturated KOH + isopropanol solution are shown. The duration of the etching is the same used in Ref. [1] for ITO samples grown by sputtering. The topography of the surface looks very similar to that of the pristine sample shown in Fig. 1: occasional spikes of the order of 20 nm with respect to the average are still present and the average roughness ($R_a = 3.5$ nm) is of the same order of magnitude of the pristine sample. The variation of the chemical composition of the ITO sample after KOH etching with respect to the pristine one has been determined by both laterally resolved and conventional XPS measurements.

The In 3d core level map of the etched ITO surface is shown in Fig. 4a. The In distribution is similar to that of the pristine surface; major darker

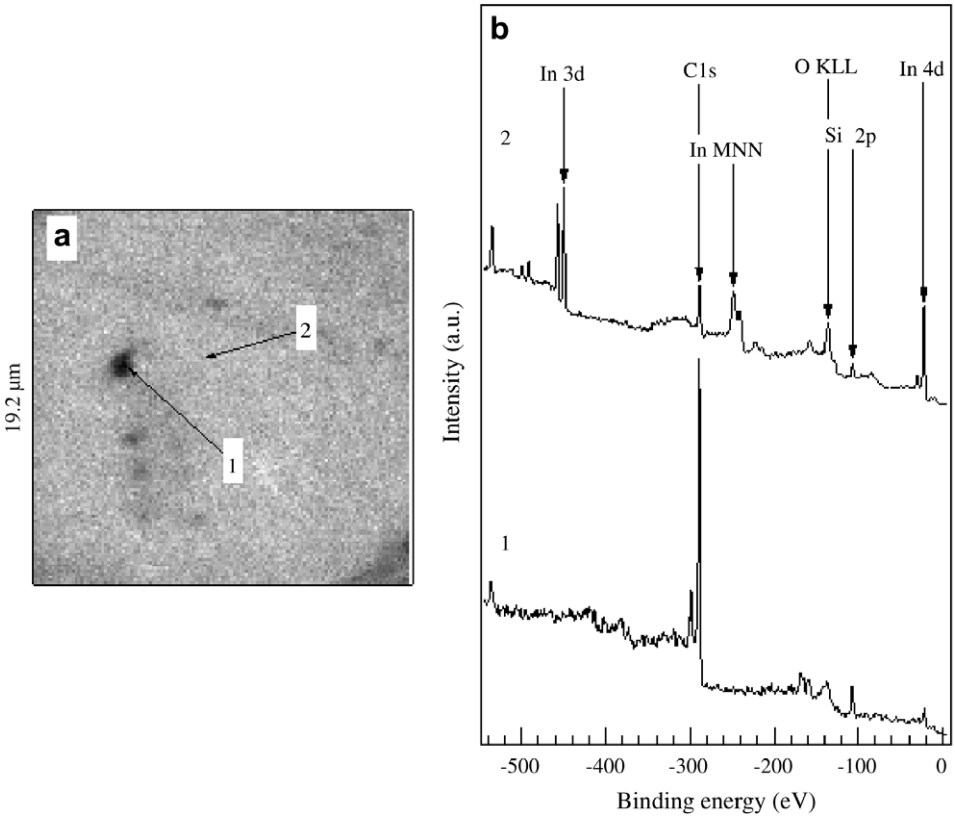

Fig. 4. (a) In 3d map of KOH etched ITO surface; (b) XPS μ-spectra collected at point 1 and 2 indicated in the map (a).

spots are randomly distributed while weaker variations in the contrast are present over the entire surface. The local XPS μ-spectra at most representative regions are shown in Fig. 4b. The μ-spectra collected on a dark spot (indicated as point 1 in the Fig. 4a) is compared to that acquired on the flatter background region (point 2) showing the presence in the dark spot of a higher C concentration, while in the uniform region In is dominant. The small peak close to the C 1s at ~300 eV of BE can be attributed either to a local charge induced on some part of the defected region or to a K contamination of the defect. Due to our limited spatial resolution it was not possible to investigate more in detail such defective particles. The C content on the flatter background region is lower than that detected on the pristine sample. The most relevant difference between the treated and the pristine sample is the appearance of the Si signal after the etching.

The same pristine and etched samples have been measured also with a conventional XPS system characterised by a larger detected area and a deeper probing depth with respect to μ-XPS. The survey spectra collected on the two surfaces are shown in Fig. 5. Due to the deeper probing depth of the conventional XPS, the C contribution, mainly coming from surface ad-layers, is negligible while the Si contamination, visible at a closer inspection of the In 4s region of spectrum b, is shown in the inset.

The concentration of Si with respect to In on the etched surfaces, roughly estimated by taking into account the Si 2p and In 4d core level intensity normalized by the corresponding core level cross section [33] and geometrical factors, is about 15%. A similar intensity of Si has been also measured in the ITO films exposed for 8 and 16 h to the KOH etching. A closer analysis of the In 3d and O 1s core level, not shown here, has not revealed any variation in their lineshape in the presence of Si.

A systematic study of the appearance of Si on the ITO surfaces has been performed by analysing four different samples prepared in different ways as described in Table 1. The photoemission spectra acquired by conventional XPS are shown in (Fig. 6) For samples A, B, and C a Si signal with an intensity close to that measured for the ITO sample etched by KOH for 24 h (see inset of (Fig. 5)) has been detected. In sample D, no Si contribution is observed. From the comparison of the preparation procedures reported in (Table 1) it can be immediately noticed that samples where some Si was detected have been protected with resist (sample A and B) or varnish (sample C) before their exposure to KOH or HCl. In order to probe the homogeneity of such protective layers before the chemical etching an AFM investigation on such films has been performed. Resist is homogenously distributed over the ITO surface with occasional spikes of few

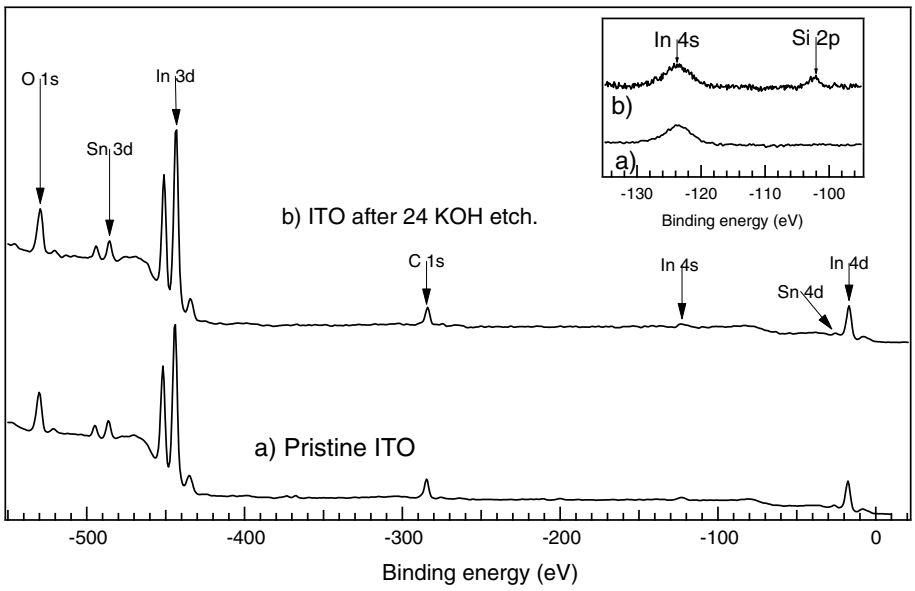

Fig. 5. XPS spectra acquired on (a) a pristine ITO and on (b) an ITO sample etched for 24 h with a saturated KOH–isopropanol solution. In the inset the same spectra are shown in a shorter energy range.

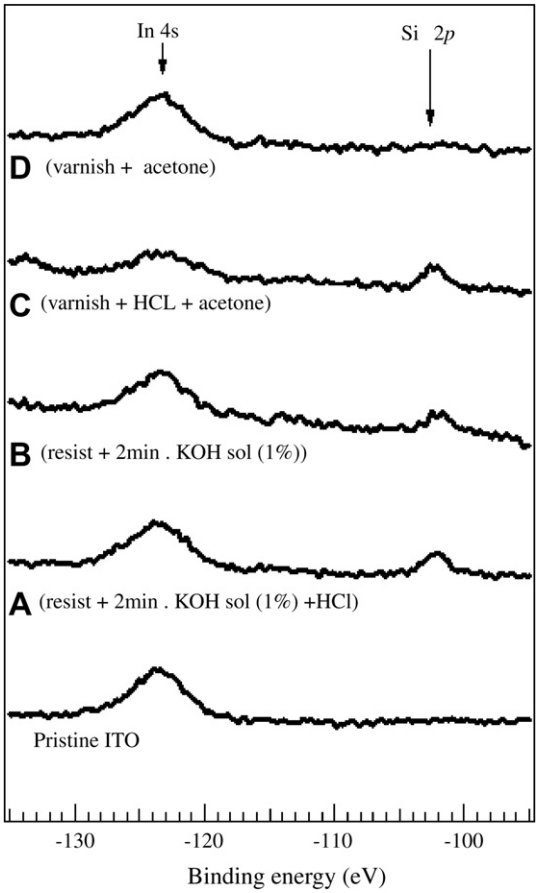

Fig. 6. XPS spectra of pristine ITO sample and of ITO surface surfaces prepared following A, B, C and D procedure described in Table 1.

nanometers height, while the varnish layer is characterized by the presence of randomly distributed holes of about 300 nm diameter width; the depth of such holes is higher than 60–70 nm which was the limited depth range of the AFM during the scanning.

4. Discussion

The commercial pristine ITO films here studied are characterised by a grainy structure with a grain size ranging from few to several tens of nanometer. The photoemission maps, despite their lower spatial resolution if compared with AFM measurements, clearly show a chemical heterogeneity of the surface; two distinct features can be identified from the photoemission maps: few sub-micrometric well defined C-rich spots and a smooth variation of the In content over the probed area visible also in the corresponding O map not shown here. The presence of the C-rich spots in the ITO film surface can be attributed to contaminations of the raw materials used for the fabrication of the ITO or induced during the growing phase. A large sampling of the ITO surface has provided an indication of the density of the larger C-rich spots which is one spot every $\sim 20 \times 20\ \mu m^2$. The variations of the In concentration over the surface are limited to few percent of the average value and could arise from a different stoichiometry of the ITO or to different atomic terminations of the grains.

The KOH etching of our pristine ITO samples did not produce a significant change in the surface roughness and in the height and density of the spikes. A systematic comparison of these results with similar experiments published elsewhere is not possible. In Ref. [1], for instance, the authors report on a strong decrease of the number of spikes after a similar etching treatment, but the initial height of such spikes was much higher (up to 100 nm) than in our case. Also, authors of Ref. [18] mention an unchanged surface and an average roughness very close to our values after a 5 min long chemical etching but the acidic solution used for the treatment had different composition.

XPS measurements indicate that the chemical state of In, O and Sn atoms remain the same after KOH exposure, as shown in Ref. [5] by Auger measurements as well. The appearance of Si in the photoemission spectra of the active ITO area after KOH and/or HCl treatments was never reported in the literature. The different Si/In ratio measured with the two photoemission probes indicates a surface nature of this contamination confirmed by the total disappearance of any Si trace after a light Ar^+ sputtering of the ITO surface etched for 24 h in KOH. The laterally resolved photoemission maps and μ-XPS spectra show a homogenous distribution of the Si contamination over the surface. On the other hand the limited spatial resolution of the SPEM is overcame by AFM mapping which even at the nanometric scale did not reveal the presence of any foreign particles suggesting the presence of Si as distributed atoms.

As shown by the photoemission spectra of (Fig. 6) Si is detected whenever KOH or HCl is used in contact with the sample. No signal is, in fact, visible on sample D where the varnish cap was simply removed by acetone. It has been shown that once HCl reaches the ITO layer it starts to erode preferentially the amorphous ITO grain boundaries

[34,35]; in our case such erosion did not produce any significant change in the morphology of the ITO film as shown in the AFM maps.

Three different possible mechanisms could give rise to the appearance of Si in the photoemission spectra: (i) the complete erosion of ITO film, (ii) the diffusion of Si into the ITO matrix and (iii) the erosion of bottom glass surface by KOH and/or HCl solution with the subsequent dispersion of Si contaminant in the liquid and its deposition on the ITO surface. Simple considerations on case (i) suggest that if a strong erosion process occurs, it will decrease the film thickness in such a way that different AFM morphology will be detected; moreover it is likely to expect modifications to the chemical state of O, Sn and In surface atoms; additionally the Si signal should increase linearly with the KOH exposure time. On the other hand a KOH induced Si diffusion into the ITO matrix, case (ii), is an unlike event even if it could not be unambiguously proved by XPS and AFM analysis since it is a process that will not necessarily modify the pristine ITO morphology, thickness and surface chemical state of In, Sn or O. A Si diffusion through the ITO matrix mediated by the etching solutions should in principle produce a gradient of the Si content through the entire film thickness. In this case a light sputtering should not eliminate completely the Si from the surface as was in our case. The hypothesis (iii) seems to be the most appropriate for the interpretation of the different experimental results obtained. The commercial bottom glass here used most probably has not been optimized against chemical etching and ITO surface contamination occurs during its exposure to KOH and/or HCl solution containing glass derived contaminants such as Si. As here systematically shown this occurs not only when ITO is treated with KOH with long time exposure, but also when the ITO surface is exposed to KOH due to the patterning procedure.

5. Conclusions

The morphological and chemical characterization of commercial ITO substrates has been performed in order to evaluate any modification induced by some classical smoothing/cleaning and patterning procedures. No significant morphological modifications have been observed after several KOH-based solutions baths. A surface heterogeneous chemical composition has been observed at a submicron scale lateral resolution together with randomly distributed micron-sized C-rich islands on the pristine samples and after the baths. On the other hand commonly used patterning procedures have produced a Si contamination of the ITO surface. Despite its relevant concentration on the surface we have demonstrated that Si contaminates only the surface of the ITO; this excludes any bulk diffusion process moving the Si from the glassy substrate onto the ITO surface. Since the thickness of the ITO is not significantly changed, as demonstrated also by the unchanged electrical film resistance, keeping the glass underneath fully masked to the photoemission signal we have attributed the contamination to a partial and selected erosion of the glassy substrate due to the acid and basic solutions used for the smoothing/patterning of the surface which disperses silicon molecules in the solutions wetting the ITO surface. The presence of Si on the surface of ITO can modify the work function compromising the operation of the optoelectronic device. Even if at our lateral resolution, which is greater than the average ITO grain size, the Si contamination appears uniform it can not be excluded it is more heterogeneously distributed at a smaller scale.

References

[1] G. Liu, J.B. Kerr, S. Johnson, Synth. Metal 144 (2004) 1 (and Refs. therein).
[2] F. Nüesch, L.J. Rothberg, E.W. Forsythe, Quoc Toan. Le, Yongli Gao, Appl. Phys. Lett. 74 (1999) 880.
[3] H.Y. Yu, X.D. Feng, D. Grozea, Z.H. Lu, R.N.S. Sodhi, A.-M. Hor, H. Aziz, Appl. Phys. Lett. 78 (2001) 2595.
[4] S.Y. Kim, J.-L. Lee, Appl. Phys. Lett. 88 (2006) 112106.
[5] J.A. Chaney, S.E. Koh, C.S. Dulcey, P.E. Pehrsson, Appl. Surf. Sci. 218 (2003) 259.
[6] A. Salehi, Thin Solid Films 324 (1999) 214.
[7] K. Zhang, F. Zhu, C.H.A. Huan, A.T.S. Wee, J. Appl. Phys. 86 (1999) 974.
[8] K. Zhang, F. Zhu, C.H.A. Huan, A.T.S. Wee, Thin Solid Films 376 (2000) 255.
[9] J.K. Sheu, Y.K. Su, G.C. Chi, M.J. Jou, C.M. Chang, Appl. Phys. Lett. 72 (1999) 3317.
[10] S. Major, K.L. Chopra, Sol. Energy Mater. 17 (1988) 319.
[11] J. Hu, R.G. Gordon, J. Appl. Phys. 72 (1992) 5381.
[12] K. Nishio, T. Sei, T. Tsuchiya, J. Mater. Sci. 31 (1996) 1761.
[13] H. Kim, A. Piqué, J.S. Horowitz, H. Mattoussi, H. Murata, Z.H. Kafafi, D.B. Chrisey, Appl. Phys. Lett. 74 (1999) 3444.
[14] J.S. Kim, M. Granström, R.H. Friend, N. Johansson, W.R. Salaneck, R. Daik, W.J. Feast, F. Cacialli, J. Appl. Phys. 84 (1998) 6859.
[15] J.M. Nel, C.M. Demanet, K.T. Hillie, F.D. Auret, H.L. Gaigher, Appl. Surf. Sci. 134 (1998) 22.
[16] G. Wantz, L. Hirsch, N. Huby, L. Vignau, J.F. Silvain, A.S. Barriére, J.P. Parneix, Thin Solid Films 485 (2005) 247.

[17] C. Suess, F.P. Wenzl, G. Jakopic, M. Wuchse, S. Muellegger, N. Koch, A. Haase, K. Lamprecht, M. Schatzmayr, C. Mitterbauer, F. Hofer, G. Leising, Surf. Sci. 507 (2002) 473.
[18] T.P. Nguyen, P. Le Rendu, N.N. Dinh, M. Fourmigué, C. Mézière, Synthetic Metal 138 (2003) 229.
[19] J.S. Kim, R.H. Friend, F. Cacialli, Appl. Phys. Lett. 74 (1999) 3084.
[20] J.S. Kim, R.H. Friend, F. Cacialli, Thin Solis Films 445 (2003) 358.
[21] Huei-Tzong Lu, Meiso Yokoyama, J. Crystal Growth 260 (2004) 186.
[22] C. Heck et al., Nucl. Instr. Meth. Phys. Res. B 242 (2006) 140.
[23] Y. Fukushi, H. Kominami, Y. Nakanishi, Y. Hatanaka, Appl. Surf. Sci. 244 (2005) 537.
[24] Ch. Jonda, A.B.R. Mayer, U. Stolz, A. Elschner, A. Karbach, J. Mater. Sci. 35 (22) (2000) 5645.
[25] Y.-H. Yun, J.-W. Choi, S.-C. Choi, J. Ceramic Process. Res. 5 (2004) 395.
[26] M. Hoheisel, A. Mitwalsky, C. Mrotzek, Phys. Stat. Sol. 123 (1991) 461.
[27] M. Inoue, T. Matsuoka, Y. Fujita, A. Abe, Jpn. J. Appl. Phys. 2 (1989) 274.
[28] T. Ratcheva, M. Nanva, Thin Solid Films 141 (1986) L87.
[29] Z. Calahorra, E. Minami, R.M. White, R.S. Muller, J. Electrochem. Soc. 136 (1989) 1839.
[30] M. Marsi, L. Casalis, L. Gregoratti, S. Günther, A. Kolomakov, J. Kovac, D. Lonza, M. Kiskinova, J. Electron. Spectrosc. Rel. Phenom. 84 (1997) 73.
[31] L. Gregoratti, A. Barinov, E. Benfatto, G. Cautero, C. Fava, P. Lacovig, D. Lonza, M. Kiskinova, R. Tommasini, S. Maehl, W. Heichler, Rev. Sci. Instrum. 75 (1) (2004).
[32] P. Melpignano, A. Baron-Toaldo, V. Biondo, S. Priante, R. Zamboni, M. Murgia, S. Caria, L. Gregoratti, A. Barinov, M. Kiskinova, Appl. Phys. Lett. 86 (2005) 41105.
[33] J.J. Yeh, Atomic Calculation of Photoionization Cross-Sections and Asymmetry Parameters, Gordon and Breach Science Publishers, Langhorne, PE (USA), 1993.
[34] M. Hoheisel, A. Mitwalisky, C. Mrotzek, Phys. Status Solidi (a) 123 (1991) 461.
[35] B.S. Chiou, J.-H. Lee, J. Mat. Sci.: Mat. Electron. 7 (1996) 241.

Available online at www.sciencedirect.com
ScienceDirect
Organic Electronics 9 (2008) 262–266
Organic Electronics
www.elsevier.com/locate/orgel

Letter

Improved performance in n-channel organic thin film transistors by nanoscale interface modification

Chih-Wei Chu [a,b,*], Chao-Feng Sung [c], Yuh-Zheng Lee [c], Kevin Cheng [c]

[a] Research Center for Applied Sciences, Academia Sinica, Taipei 11529, Taiwan
[b] Department of Photonics, National Chiao-Tung University, Hsinchu 300, Taiwan
[c] Industrial Technology Research Institute, Hsinchu 300, Taiwan

Received 16 July 2007; received in revised form 22 November 2007; accepted 27 November 2007
Available online 26 December 2007

Abstract

We demonstrate that the electrical properties of n-channel thin film transistors can be enhanced by inserting a nanoscale interfacial layer, namely, cesium carbonate (Cs_2CO_3), between organic semiconductor and source/drain electrodes. Devices with the Cs_2CO_3/Al electrode showed a reduction of contact resistance, not only with respect to Al, but also compared to Ca. The improvement is attributed to the reduction in the energy barrier of electron injection and the prevention of unfavorable chemical interaction between the organic layer and the metal electrode. High field-effect mobility of 0.045 cm^2/V s and on/off current ratios of 10^6 were obtained in the [6,6]-phenyl C60 butyric acid methyl ester-based organic thin film transistors using the Cs_2CO_3/Al electrodes at a gate bias of 40 V.

PACS: 73.40.Cg

Keywords: n-Type; Organic thin film transistors; Nanoscale interface modification

In recent years, there has been a worldwide interest in developing organic thin film transistors (OTFTs) due to their potential application in display drivers, radio frequency identification tags, and smart cards [1–3]. Great progress has been achieved so far in p-type OTFTs, whose electronic properties have already reached the level of hydrogenated amorphous silicon (a-Si:H). For example, field effect mobilities greater than 1 cm^2/V s and high on/off current ratio ($>10^6$) have been obtained in pentacene-TFTs [4]. However, the development of n-type OTFTs with comparable performance remains a key issue in terms of meeting the requirements for practical applications. Although a large number of studies have focused on improving the intrinsic electrical properties of n-type materials [5,6] and their applications, [7,8] devices still exhibit limited life span. This could be attributed to the instability of single component π-electron materials, which can easily undergo surface oxidation/deoxidation and chemical interaction with metal electrodes. Moreover, low work function metals, used to reduce energy barriers and promote electron injection [9,10], are diffi-

* Corresponding author. Address: Research Center for Applied Sciences, Academia Sinica, Taipei 11529, Taiwan. Tel.: +886 2 2789 8000.
E-mail address: gchu@gate.sinica.edu.tw (C.-W. Chu).

1566-1199/$ - see front matter © 2007 Elsevier B.V. All rights reserved.
doi:10.1016/j.orgel.2007.11.008

cult to process because of their susceptibility to atmospheric moisture and oxygen. These factors henceforth indicate that the property of organic–metal electrode interface play an important role in obtaining high performance n-type OTFTs; however, engineering of the interface has not received much attention in n-type OTFTs [11].

An alternative approach for replacing the reactive metal as an electrode is to insert a thin layer of alkali metal halides [12] and carboxylates [13], in various attempts at improving the charge injection from an Al cathode to an emitting layer for organic light emitting diodes (OLED). Similarly, the source/drain (S/D) contacts in the OTFTs have significant influence on device operation. For example, their contribution to the contact resistance arise from mismatching work functions, and/or interaction between the metal electrodes and the organic semiconductor [14,15]. Recently, it has been reported that Cs_2CO_3 is one of the best electron injection materials among a wide range of metal electrodes, and can be used as an electron injection layer for OLED by thermal and solution deposition [13,16]. In this letter, we present the conclusion that the performance of the [6,6]-phenyl C60 butyric acid methyl ester (PCBM)-based n-type OTFTs with an bi-layer S/D electrodes is greatly improved over the bare Al, and calcium electrodes. The performance enhancement of our devices is achieved by using a nanoscale interfacial modification layer made of Cs_2CO_3. The presence of a Cs_2CO_3 layer at the organic/Al interface significantly reduces the contact barrier and provides protection against diffusion and chemical interaction between organic layer and metal electrodes.

The devices were fabricated on ITO-coated glass substrates (10–20 Ω/sq sheet resistance). ITO-coated glass substrate was used as the gate electrode. After routine solvent cleaning, the substrates were treated with UV-ozone for 15 min. The cleaned ITO substrates were then covered with 750-nm-thick polymer dielectric insulator, prepared by spin-coating a solution of poly-4-vinylphenol (11 wt%) and poly(melamineco-formaldehyde) (4 wt%) in propylene glycol monomethyl ether acetate (PGMEA). The substrate was then prebaked at 100 °C for 5 min, followed by baking at 200 °C for 20 min, to cross-link the polymer. The thickness of the PVP films was 680 nm. The resulting capacitance per unit area of the film, C_i, was 5.47 nF/cm^2. The semiconductor layer, consisting of a 50-nm-thick layer of PCBM (purchased from Solenne B.V.), was spun over the cross-linked PVP from a 1 wt% ratio chloroform solution in a nitrogen environment inside a glove box. Prior to S/D electrode deposition, the device was thermally annealed on a hot plate at 70 °C for a period of 20 min. Finally, Cs_2CO_3 (Sigma–Aldrich, 99% purity) was deposited by a Knudsen cell (k-cell), a molecular beam epitaxy single-filament effusion cell from Veeco/Applied Epi, and Al was thermally evaporated onto the PCBM film through a shadow mask to form the S/D electrodes. The thicknesses of Cs_2CO_3 and Al films were 1 nm and 80 nm, respectively. A schematic cross-section of our top-contact OTFTs is presented in the inset of Fig. 1a with a channel length of 170 μm and width of 2 mm. For comparison, Ca, Al, and Au were investigated as alternative to the Cs_2CO_3/Al as S/D contacts. All thermal evaporations were done under a pressure of less than

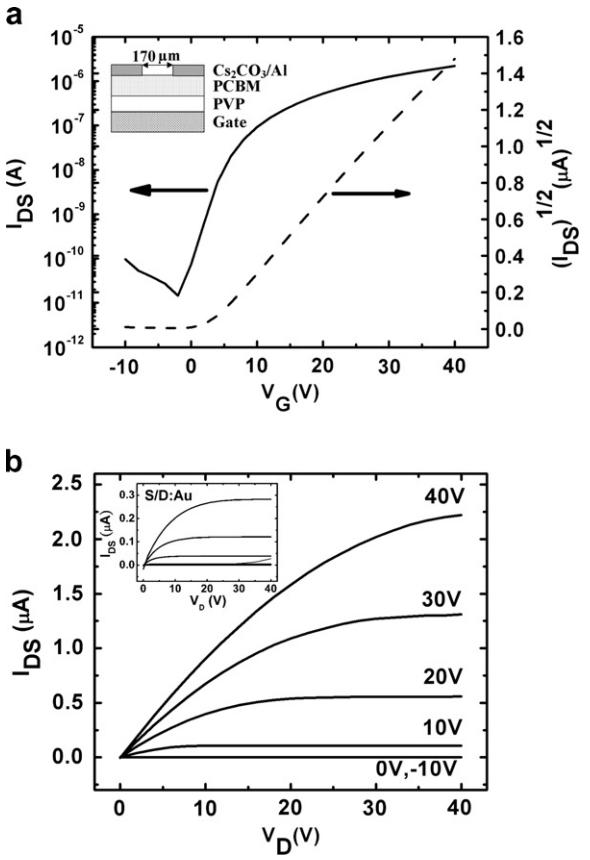

Fig. 1. (a) Typical transfer characteristics of the OTFT with Cs_2CO_3/Al electrodes at a constant drain voltage of 40 V. Inset: schematic structure of a top-contact OTFT. (b) Source/drain current–voltage characteristics of the OTFT with Cs_2CO_3/Al electrodes. Inset: source/drain current–voltage characteristics of the OTFT with Au electrode.

6×10^{-6} torr and the film thickness was monitored with a quartz oscillator. The electrical measurements of the devices were performed in a nitrogen environment inside a glove box using a Keithley 4200 semiconductor parameter analyzer and HP 4980A Precision LCR meter.

Typical transfer and output curve characteristics of the PCBM OTFTs, with Cs_2CO_3/Al S/D electrodes, are shown in Fig. 1a and b, respectively. The device exhibited typical n-channel characteristics with good linear/saturation behavior, without any apparent negative drain current resulting from gate leakage at $V_{DS} = 0$ V and significant low gate leakage ($<4 \times 10^{-9}$ A) even at $V_G = 40$ V. Strong field-effect modulation of the channel conductance was observed, with on/off current ratios (I_{on}/I_{off}) as high as 10^6 (measured between gate voltage, $V_G = -10$–40). The field-effect mobility (μ) and threshold voltage (V_T) were extracted from the measured transfer curve by comparing it with the standard transistor's current–voltage equation in the saturation regime: $I_{DS,sat} = (WC_i/2L)\mu(V_G - V_T)$ [2,17] where $I_{DS,sat}$ is the saturated drain current. The μ and the V_T of the OTFT were found to be 4.45×10^{-2} cm^2/V s and -2.3 V, respectively.

It has been proposed that PCBM has much lower electron affinity compared to C_{60} [18]. In addition, the energy level of lowest occupied molecular orbital (LUMO) for PCBM is 3.7 eV [19]. Therefore, the electron injection current can be limited by the selection of electrode materials. As shown in the idealized transfer characteristics for different materials for the S/D electrodes, Fig. 2, the slope for Cs_2CO_3/Al devices results in higher μ and lower V_T, not only with respect to Al ($\Phi = 4.1$ eV), but also compared to Ca ($\Phi = 2.8$ eV). The device with Ca and Al electrodes had similar I_{on}/I_{off} compared to the device with Cs_2CO_3/Al electrode, while the decreased slope of the transfer characteristics corresponded to the decrease in field-effect mobilities. For further demonstrated the electron current is contact-limited. We have fabricated the devices with Au ($\Phi = 5.0$ eV) as S/D electrodes. The output curve characteristic for the PCBM OTFTs with Au is shown in the inset of Fig. 1b. Due to the large energy level mismatch between Au work function and LUMO level of PCBM, the injection of electrons from Au to PCBM is a difficult process. The mobility for the PCBM OTFTs with Au was determined from the transfer curve characteristics (saturation region) to be 0.0081, which is smaller by quintuple of magnitude than that of the PCBM OTFTs with Cs_2CO_3/Al as electrodes. Thus, the increase of the field effect mobilities with decreasing work-function suggests that the contact effect lowers the extrinsic field-effect mobility than the intrinsic value. The summary of parameters for the devices made in this study is given in Table 1.

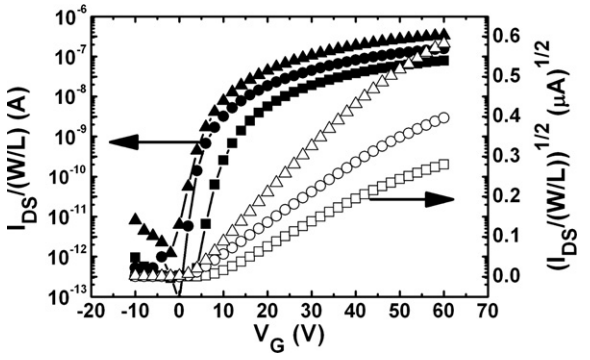

Fig. 2. Idealized I_{SD}–V_G (solid) and $(I_{SD})^{1/2}$–V_G (open) plots for different materials as the source/drain contacts at V_D=40 V. Cs_2CO_3/Al (triangles); Ca/Al (circle); Al (square).

Although the work-function of Ca is lower than the LUMO level of PCBM, with no energy barrier, and with a thin layer Cs_2CO_3 between PCBM and electrode, mobility is more than doubled compared to that obtained with the Ca electrodes. It was reported that the lowering of the vacuum level of organic semiconductors was observed with a thin layer of Cs_2CO_3 by an ultraviolet photoelectron spectrometer [20,21]. The energy offset between the Fermi level of the electrode and the LUMO of semiconductors at interface is greatly reduced. Therefore, the improvement of the device performance is attributed to Cs_2CO_3 lowering the barrier for electron injection from Al to the LUMO level of PCBM. Moreover, earlier studies on Cs_2CO_3 indicated that Cs_2CO_3 decomposes into cesium oxide during thermal evaporation [22]. With a metal oxide as a buffer layer, it will consume most of the interface of metal and leave the

Table 1
Summary of the performance of the PCBM OTFTs with different source/drain electrodes materials

S/D electrode	μ (cm^2/V^{-1} s)	V_t (V)	S (V/decade)	On/off ratio
Au	0.0081	4.87	1.81	10^3
Al	0.0120	3.15	1.80	10^6
Ca/Al	0.0227	0.74	1.45	10^6
Cs_2CO_3/Al	0.0445	−2.30	1.39	10^6

The values are an average of ten different devices with practical standard deviation.

organic semiconductor intact [23]; therefore, Cs_2O could serve as a protective agent for PCBM against metal-induced degradation and a better interface (absence of reactive Ca), hence further minimizing contact resistance. Fig. 3 shows the contact resistance (R_C), obtained according to the method in Ref. [24], (extracted at $|V_{SD}| = 4$ V and in linear regime) as a function of the V_G with different materials as S/D electrodes. The R_C of Ca electrode decreased from 8×10^8 to 3×10^8 Ω as V_G varied from 10 to 40 V. In contrast, the R_C of Cs_2CO_3/Al electrode was insensitive with V_G, and is decreased more than twofold compared to the Ca electrode. The change of potential drop at the organic–metal electrode interface due to the variation of R_C will change the distribution of the electric field in the vertical direction, which influences the V_T (the higher the contact resistance, the larger the V_T) [25]. Hence the decrease of R_C due to the introduction of the Cs_2CO_3 in our OTFTs will lead to the reduction of V_T, as can be seen in Table 1. This result demonstrates that the introduction of the Cs_2CO_3 in our OTFTs played an important role in the enhancement of the device performance.

Recently, Li et al. reported that Cs_2CO_3 is decomposed to metallic Cs during thermal evaporation, as measured with the quartz crystal microbalance [26]. However, contrary to the observation of Li et al., we found that the 230-nm-thick Cs_2CO_3 film has a capacitance of about 6.9 nF/cm^2 at 1 kHz with good insulator properties. In addition, the pressure in the vacuum chamber had increased rapidly as the k-cell temperature raised above 690 °C which we believe was due to the formation of Cs_2O and CO_2 [23,27]. Since Cs_2CO_3 layer was deposited by thermal evaporation, the small amount of metallic Cs might also be introduced into the film during thermal evaporation. However, the proportion of the Cs within the composite film is quite low, and Cs would absorb the residual oxygen in vacuum to form Cs_2O; the electrical conductivity of the composite film is still in the insulating region. Hence, as-deposited Cs_2CO_3 film is a dielectric with good insulating properties. With the presence of a thin Cs_2CO_3 layer, the energy barrier for electrons from Al to PCBM could be greatly lowered by the larger potential drop, resulting in increasing the injection of electrons via tunneling. As the Cs_2CO_3 becomes thicker, it leads to slowing down of tunneling probability. As can be seen in Fig. 4, the transfer characteristics of the devices are dependent on the thickness of Cs_2CO_3 layer. The device with 1 nm thick Cs_2CO_3 exhibits the highest mobility. With the further incremental thickness of Cs_2CO_3 layer, mobility has gradually decreased.

In conclusion, we have demonstrated that the performance of PCBM-based n-channel OTFTs can be improved by inserting a thin Cs_2CO_3 film between the PCBM and S/D electrode. The current and the field-effect mobility were significantly improved, when compared to Ca as S/D electrodes. The improvement in device performance is due to improved electron injection at the interface, resulting from the narrowed and lowered tunneling barrier by the insertion of the Cs_2CO_3 layer. In addition, it also serves as a protective agent against unfavorable chemical reaction between the organic layer and the metal electrode. Further improvement of the device performance can be achieved by optimizing fabrication conditions.

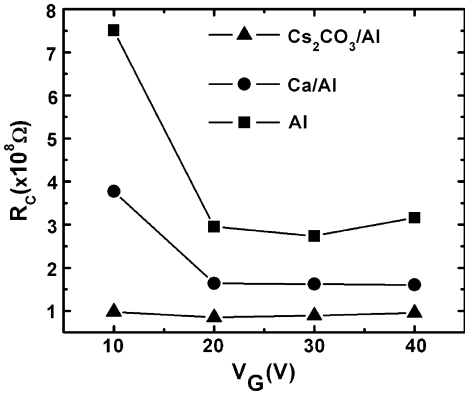

Fig. 3. Contact resistance vs. gate voltage for different materials as the source/drain contacts.

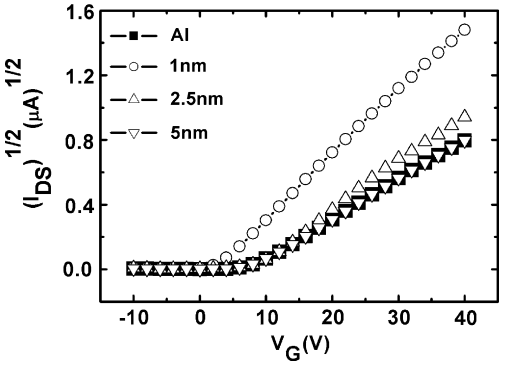

Fig. 4. $(I_{SD})^{1/2}$–V_G plots of OTFTs with a variety of Cs_2CO_3 thickness. Thicknesses of the Cs_2CO_3 layers are indicated.

Acknowledgements

Financial support from Academia Sinica, the National Science Council, ROC (NSC-95-2218-E-001-003) and the Ministry of Economic Affairs, ROC is deeply appreciated.

References

[1] P. Mach, S.J. Rodriguez, R. Nortrup, P. Wiltzius, J.A. Rogers, Appl. Phys. Lett. 78 (2001) 3592.
[2] B. Crone, A. Dodabalapur, Y.-Y. Lin, R.W. Filas, Z. Bao, A. LaDuca, R. Sarpeshkar, H.E. Katz, W. Li, Nature (London) 403 (2000) 521.
[3] P.F. Baude, D.A. Ender, M.A. Haase, T.W. Kelley, D.V. Muyres, S.D. Theiss, Appl. Phys. Lett. 82 (2002) 3964.
[4] Y. Lin, D.J. Gundlach, S.F. Nelson, T.N. Jackson, IEEE Trans. Electron Dev. 18 (1997) 606.
[5] S. Kobayashi, T. Takenobu, S. Mori, A. Fujiwara, Y. Iwasa, Appl. Phys. Lett. 82 (2003) 4581.
[6] T. Yasuda, T. Goto, K. Fujita, T. Tsutsui, Appl. Phys. Lett. 85 (2004) 2098.
[7] C. Waldauf, P. Schilinsky, M. Perisutti, J. Hauch, C.J. Brabec, Adv. Mater. 15 (2003) 2084.
[8] Th.B. Singh, N. Marjanović, G.J. Matt, N.S. Sariciftci, R. Schwödiauer, S. Bauer, Appl. Phys. Lett. 85 (2004) 5409.
[9] T.D. Anthopoulos, C. Tanase, S. Setayesh, E.J. Meijer, J.C. Hummelen, P.W.M. Blom, D.M. de Leeuw, Adv. Mater. 16 (2004) 2174.
[10] T.W. Lee, Y.H. Byun, B.W. Koo, I.N. Kang, Y.Y. lyu, C.H. Lee, L.S. Pu, S.Y. Lee, Adv. Mater. 17 (2005) 2180.
[11] X. Yan, J. Wang, H. Wang, H. Wang, D. Yan, Appl. Phys. Lett. 89 (2006) 053510.
[12] L.S. Hung, C.W. Tang, M.G. Mason, Appl. Phys. Lett. 70 (1997) 152.
[13] T. Hasegawa, S. Miura, T. Moriyama, T. Kimura, I. Takaya, Y. Osato, H. Mizutani, SID Int. Symp. Dig. Tech. Papers 35 (2004) 154.
[14] F.C. Chen, T.H. Chen, Y.S. Lin, Appl. Phys. Lett. 90 (2007) 073504.
[15] N.J. Watkins, L. Yan, Y.L. Gao, Appl. Phys. Lett. 80 (2002) 4384.
[16] J. Huang, G. Li, E. Wu, Q. Xu, Y. Yang, Adv. Mater. 18 (2006) 114.
[17] S.M. Sze, Physics of Semiconductor Devices, Wiley, New York, 1981.
[18] C.J. Brabec, N.S. Sariciftci, J.C. Hummelen, Adv. Funct. Mater. 11 (2001) 15.
[19] C.J. Brabec, A. Cravino, D. Meissner, N.S. Sariciftci, M.T. Rispens, L. Sanchez, J.C. Hummelen, T. Fromherz, Thin Solid Films 403–404 (2002) 368.
[20] C.I. Wu, C.T. Lin, Y.H. Chen, M.H. Chen, Y.J. Lu, C.C. Wu, Appl. Phys. Lett. 88 (2006) 152104.
[21] J.S. Huang, T. Watanabe, K. Ueno, Y. Yang, Adv. Mater. 19 (2007) 739.
[22] T.R. Briere, A.H. Sommer, J. Appl. Phys. 48 (1977) 3547.
[23] C.W. Chu, S.H. Li, C.W. Chen, V. Shrotriya, Y. Yang, Appl. Phys. Lett. 87 (2005) 193508.
[24] D.K. Schroder, Semiconductor material and device characterization, second ed., John Wiley & Sons, New York, 1998.
[25] L. Torsi, A. Dodabalapur, H.E. Katz, J. Appl. Phys. 78 (1995) 1088.
[26] Y. Li, D.Q. Zhang, L. Duan, R. Zhang, L.D. Wang, Y. Qiu, Appl. Phys. Lett. 90 (2007) 012119.
[27] S.T. Melnychuk, M. Seidl, J. Vac. Sci. Technol. A 9 (1991) 1650.

Available online at www.sciencedirect.com
ScienceDirect
Organic Electronics 9 (2008) 267–272
Organic Electronics
www.elsevier.com/locate/orgel

Letter

Effects of methyl substitution of metal (II) bis(2-(2-hydroxyphenyl) benzothiazolate) chelates on optical properties

Xu Bingshe [a,b,*], Xu Huixia [a,b], Chen Liuqing [a,b], Fang Xiaohong [a,c], Liu Xuguang [a,d], Wang Hua [a,b]

[a] *Key Laboratory of Interface Science and Engineering in Advanced Materials, Taiyuan University of Technology, Ministry of Education, Taiyuan, Shanxi 030024, China*
[b] *College of Materials Science and Engineering, Taiyuan University of Technology, Taiyuan, Shanxi 030024, China*
[c] *College of Mining Engineering, Taiyuan University of Technology, Taiyuan, Shanxi 030024, China*
[d] *College of Chemistry and Chemical Engineering, Taiyuan University of Technology, Taiyuan, Shanxi 030024, China*

Received 8 August 2007; received in revised form 23 October 2007; accepted 25 October 2007
Available online 17 November 2007

Abstract

The influence of methyl substitution on three-position of metal (II) bis(2-(hydroxyphenyl)benzothiazolate) on thermal stability, photophysical, electronic structure, and electrochemical properties was investigated. Experimental results show that methylated complexes were more thermally stable and had 10–20 nm red shift in emission wavelength. Quantum chemistry calculation indicated that the methyl substitution affects mostly the highest occupied molecular orbitals charge distribution. In addition, the introduction of electro-donating methyl group can produce a decrease in the energy of the lowest unoccupied molecular orbitals.

PACS: 72.80.LE; 78.60.Fi; 74.25.Jb; 82.80Fk; 87.15ag

Keywords: BTZ; Photoluminescence; Electronic structure; Photophysic; DFT

1. Introduction

Since Tang and Vanslyke's demonstration of the electroluminescence of organic molecules [1], organic electroluminescent devices (OLEDs) have been the subject of increasing interest due to their potential impact on lighting industry and back lighting application [2,3]. In order to optimize the device structure and explore the marketable OLEDs, researchers are synthesizing high-performance emitting materials with desirable properties. So far, many new materials with RGB (red, green, blue) emission have been developed to meet this requirement [4–6]. However, in contrast to green-light-emitting materials,

* Corresponding author. Address: Key Laboratory of Interface Science and Engineering in Advanced Materials, Taiyuan University of Technology, Ministry of Education, Taiyuan, Shanxi 030024, China. Tel.: +86 0351 6014852; fax: +86 0351 6010311.
E-mail address: xubs@public.ty.sx.cn (X. Bingshe).

1566-1199/$ - see front matter © 2007 Published by Elsevier B.V.
doi:10.1016/j.orgel.2007.10.009

blue-light-emitting materials still need to be further improved in performance [7]. Due to their high energy levels, excellent blue-light-emitting materials can not only realize blue-light emission, but also facilitate white and other color emission by adding another dopant emitter [8]. It is thus important to develop high-performance blue-light-emitting materials with good stability and high fluorescence efficiency.

The complex with 2-(2-hydroxyphenyl)benzothiazolate (BTZ) ligand is a kind of small molecular emitter, and can provide obvious practical advantages, such as easy purification, high thermal stability, easy sublimation, and good formation of film. It is well known that $Zn(BTZ)_2$ is one of the best white electroluminescent material used in fabricating OLEDs [9–11] and $Be(BTZ)_2$ is an excellent blue-emitting material, with emission peak at 440 nm [12].

Both the semiconductive and emissive properties of the BTZ complexes are largely defined by the HOMO/LUMO levels and their lowest $\pi \rightarrow \pi^*$ electron transitions. Previous physical and theoretical studies provided an insight into the distribution of the HOMO/LUMO densities in BTZ ligand [11]. According to the results of density functional theory (DFT) calculation performed on $Zn(BTZ)_2$, the HOMO orbital was located almost on phenoxide side, correspondingly the LUMO density was found at benzothiazolate and phenoxide rings. It seems logical that substitution with appropriate functional group at phenoxide ring wound result in changes in the HOMO levels.

The previous studies on the modification of tris(8-quinolinolate)aluminum (Alq_3) indicated that introduction of electron-donating groups (EDGs) to phenoxide ring can cause a decreased HOMO level [13]. However, it should be noted that the thermal stability of substituted chelates are not desirable due to steric hindrance. In this paper, how the methyl group introduced into C-3 position of phenoxide ring affects the electronic nature of BTZ complexes was described. (The structures of complexes in this paper are illustrated in Fig. 1.)

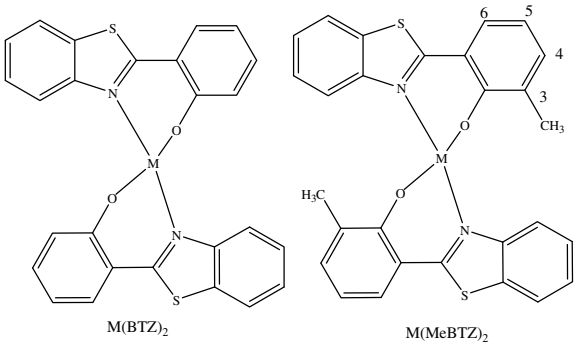

Fig. 1. Metal (M = Zn, Be) bis(2-(2-hydroxyphenyl)benzothiazolate) chelates used in this study.

2. Experimental

All reactants and solvents were obtained commercially and were used without further purification. $Zn(BTZ)_2$ and $Be(BTZ)_2$ were prepared in our laboratory. All materials were purified by high-vacuum gradient-temperature sublimation before analysis. C, H, and N microanalysis were carried out with an Elemental Vario EL Elemental analyzer. ^{1}H NMR data were recorded with Switzerland Bruker DR × 300 NMR spectrometers. FT-IR spectra were determined with a Nicolet 7199B spectrometer.

Thermal analysis was conducted using STA 409PC thermogravimeter. Pure polycrystalline samples were placed in an aluminum pan and heated at a heating rate of 10 °C/min in dry argon gas at a flow rate of 30 ml/min. All the calculations were performed using the density functional theory (DFT) [14] with the Dmol3 program. The geometry optimization was carried out on the DND basis set for all atoms and GGA level.

2.1. Synthesis of ligands

BTZ was synthesized on the basis of literature method. ^{1}H NMR (300 MHz, $CDCl_3$): δ 12.5(1H, S), 8.02(1H, *d*), 7.9(1H, *d*), 7.7(2H, *m*), 7.5(1H, *d*), 7.45(1H, *d*), 7.14(1H, *m*), 6.99(1H, *d*). The similar procedure was used to prepare MeBTZ and the as-synthesized product was recrystallized from ethanol in a yield of about 75%. ^{1}H NMR (300 MHz, $CDCl_3$): δ 1.768(1H, s), 1.955–1.975(2H, s), 6.803–6.800(2H, s), 7.037–7.156(2H, m), 7.279–7.331(2H, m); Anal. calcd for $C_{14}H_{11}SNO$: C, 69.68; H, 4.59; N, 5.80; found: C, 70.76; H, 5.365; N, 5.307; FT-IR (KBr) cm^{-1}: 3054, 2915, 2855, 2350, 1618, 1506, 1438, 1242, 1085, 761, 628.

2.2. Synthesis of complexes

$BeSO_4{\cdot}4H_2O$ (1.2 mmol) was dissolved in 20 ml of deionized water in a flask. MeBTZ (2.4 mmol) was dissolved in 40 ml of ethanol in another flask. The $BeSO_4{\cdot}4H_2O$ solution was slowly poured into the MeBTZ solution while stirring. $Be(MeBTZ)_2$ was

precipitated after the mixed solution was adjusted to pH 9–10 using triethylamine at room temperature. ^{1}H NMR (300 MHz, $CDCl_3$) δ 2.459(6H, s), 6.928–6.978(4H, m), 7.304–7.590(4H, m), 7.859–7.886(4H, d), 7.952–7.979(2H, d); MALDI-TOF m/z: [MH^+] calcd for $C_{28}H_{20}BeS_2N_2O_2$, 489.11; found, 489.1; Anal. calcd for $C_{28}H_{20}BeS_2N_2O_2$: C, 68.69; H, 4.12; N, 5.72; found: C, 68.77, H, 4.17; N, 5.71; FT-IR (KBr) cm^{-1}: 3042, 2914, 1670, 1618, 1506, 1438, 1242, 1085, 761, 628.

The same procedure was employed to obtain $Be(BTZ)_2$ and its single crystal was grown by vacuum sublimation. The colorless single crystal was collected with typical size of $0.20 \times 0.20 \times 0.10$ mm. The crystal data for $Be(BTZ)_2$ are monoclinic, $a =$ 24.522(3) Å, $b = 12.0546(14)$ Å, $c = 14.7981$ (17) Å, $\beta = 93.476(2)°$ and space group $C2/c$. Crystallographic data have been deposited with the Cambridge Crystallographic Data Centre as supplementary publication No. CCDC-620423.

$Zn(MeBTZ)_2$ was synthesized from the reaction between MeBTZ and $Zn(CH_3COO)_2 \cdot 2H_2O$ in ethanol solution. The mixed solution was heated in reflux and stirred for 2 h. The yellow powder of $Zn(MeBTZ)_2$ was filtered. ^{1}H NMR (300 MHz, DMSO) δ 1.902(6H, s), 6.488(4H, d), 7.137(2H, s), 7.408–7.527(4H, m), 8.062(2H, d), 8.273(2H, d); MALDI-TOF m/z: [MH^+] calcd. for $C_{28}H_{20}ZnS_2N_2O_2$, 544.03; found: 545.3; Anal. calcd for $C_{28}H_{20}ZnS_2N_2O_2$: C, 61.59; H, 3.69; N, 5.13; found: C, 61.40; H, 3.70; N, 5.12; FT-IR (KBr) cm^{-1}: 3043, 2926, 1653, 1458, 1412, 1225, 1088, 669, 482.

$Zn(BTZ)_2$ was synthesized by the reaction between BTZ and $Zn(CH_3COO)_2 \cdot 2H_2O$.

3. Results and discussion

$Zn(BTZ)_2$ and $Be(BTZ)_2$ were found to be reasonably stable upon exposure to air and exhibit high thermal stability. Their melting temperatures (T_m) and endothermic transiting points are shown in Table 1. A single endothermic transition was observed at 280 °C with only 1% weight loss prior to decomposition at 453 °C for $Zn(BTZ)_2$. The onset temperature of endothermic transition (T_{el}) appeared at 217 °C for $Be(BTZ)_2$ with T_m of 224 °C and decomposition point (T_d) of 455 °C.

Table 1
Thermal analysis data for four metal chelates (T_{el} onset: the onset of endothermic transition; T_m: melting temperature; T_d: decomposition temperature)

Metal chelate (°C)	$Zn(BTZ)_2$	$Zn(MeBTZ)_2$	$Be(BTZ)_2$	$Be(MeBTZ)_2$
T_{el} onset	280	277	217	290
T_m	287	284	224	296
T_d	453	505	455	483

The TG, DTG, and DSC curves of the C-3 methyl-substituted complexes are illustrated in Fig. 2. All complexes in our study exhibited similar thermal behavior, that is, only one endothermic transition occured prior to decomposition. Compared with $Zn(BTZ)_2$, the decomposition point of $Zn(MeBTZ)_2$ increased to 505 °C. However, the endothermic transition onset point decreased to 277 °C. For the beryllium chelates, the melting temperature of $Be(MeBTZ)_2$ was located at 296 °C and endothermic transition occurred at 290 °C. The C-3 methyl-substituted derivatives had higher T_{el} and T_m than corresponding matrix (in Table 1), suggesting that methylation of the BTZ ligand increased intermolecular interactions.

Table 3 summarizes the photophysical data of all metal chelates. Absorption and emission spectra are illustrated in Fig. 3. The absorption bands are located at blue and ultraviolet region of 229–450 nm. The 250–260 nm bands, which are $s_0 \rightarrow s_1$ transition, are attributed to the local $\pi \rightarrow \pi^*$ transition of the deprotonated ligands [12]. The broad bands of 330–375 nm, which correspond to the transition of HOMO − 1 to LUMO, can be assigned to a phenoxido-to-thiazolyl $\pi \rightarrow \pi^*$ transition. The maximal absorption bands, which are associated with the transition from the corresponding HOMO to LUMO, are mainly caused by the charge transition from metal to ligand. The observed red-shifted bands of methyl-substituted complexes indicate that the methyl group introduced into the phenoxide has a significant effect on electronic transition energies. The emission spectra of C-3 methyl-substituted derivatives in solution with a concentration of 1×10^{-5} mol/L and in powder at room temperature have distinct redshift. For instance, the maximum emission wavelength, λ_{max}, of $Be(MeBTZ)_2$ powder is red-shifted from 465 to 475 nm. This result can be explained by the electronic and steric effects resulted from the methyl substitution. In addition, the emission spectra of powder and solution are similar with the slight red-shift for powder. The shift is probably due to the difference in dielectric constant of the environment [15].

As for the methyl-substituted complexes, excited state is formed by the transition from methyl group to phenoxide ring. Because their electron cloud was

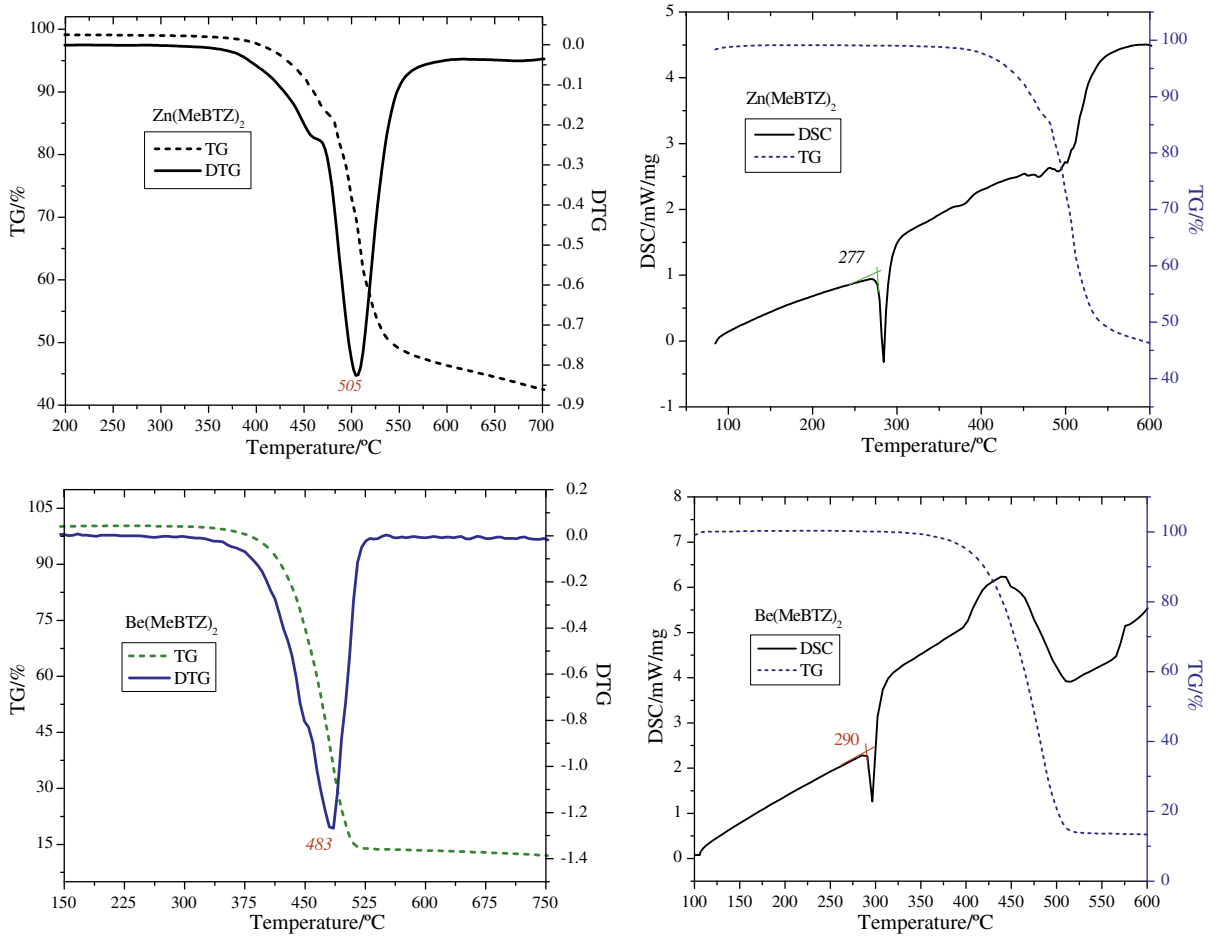

Fig. 2. TG, DTG, and DSC curves of $Zn(MeBTZ)_2$ and $Be(MeBTZ)_2$ (under a dry argon gas flow at a heating rate of 10 °C/min).

parallel to the orbits of aromatic rings, the conjugate system was amplified and the degree of rigidity was increased. When a methyl group is attached to the electron-rich phenoxide ring it causes redshift in absorption and emission, and better thermal stability.

The interpretation of observed spectral features is greatly assisted by molecular orbital energies, furnished detailed description of orbitals, including spatial characteristics, nodal patterns, and individual atom contributions. With the assistance of quantum chemical calculations, the electronic structures of the complexes are obtained and presented in Table 2, involving HOMO, HOMO − 1, LUMO, and LUMO + 1. The methyl group has only contribution to HOMO and HOMO − 1. In addition, the contributions of Be^{2+} ions for all orbitals in beryllium complexes are vacancy. On the other hand, different results are observed for HOMO, HOMO − 1 and LUMO of zinc complexes, which are also localized on Zn^{2+}. Therefore, the 380 nm shouder band on the absorption spectra of zinc complexes can be assigned to the ligand-to-metal-charge-transfer (LMCT) transitions.

The optical transition responsible for photoluminescence in metal (2-(2-hydroxyphenyl)benzothiazolate) is centered on the organic ligand. This transition is attributed to a $\pi \rightarrow \pi^*$ charge transfer from the electron-rich phenoxide ring (HOMO) to the electron deficient benzothiazolate ring (LUMO). To investigate the electronic effects caused by the addition of methyl group, the energy of HOMO and LUMO (E_{HOMO}, E_{LUMO}) were calculated by DFT. The values are list in Table 3. As can be seen, the methyl-substituted complexes show lower E_{HOMO} and E_{LUMO}. This can be ascribed to the great electron-donating ability of methyl group. Therefore, the observed red-shifted absorption and emission spectra of the methylated complexes can be probably attributed to steric factor with a contribution from the

Table 2
Molecular orbital amplitude plots of four materials

	HOMO	HOMO − 1	LUMO	LUMO + 1
$Be(BTZ)_2$				
$Be(MeBTZ)_2$				
$Zn(BTZ)_2$				
$Zn(MeBTZ)_2$				

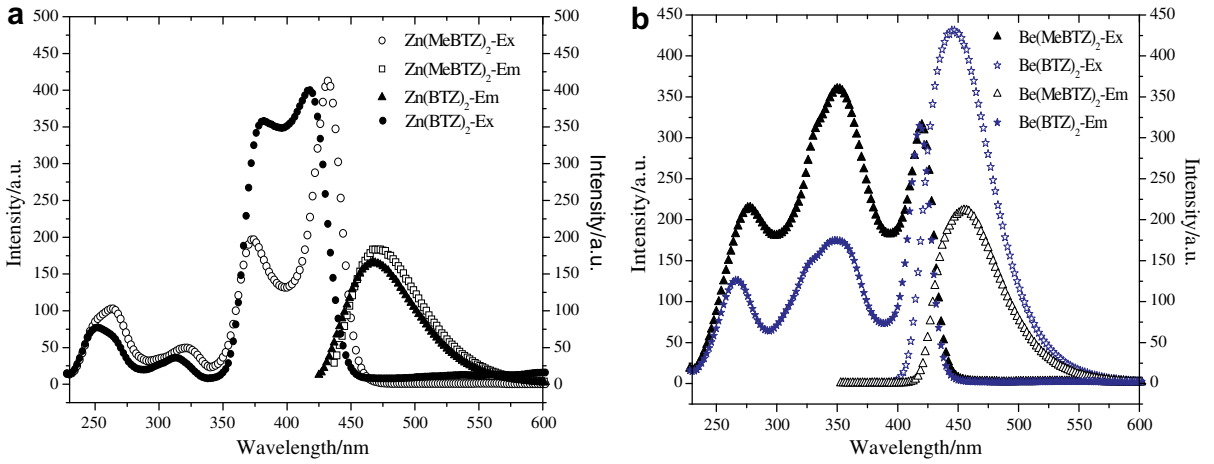

Fig. 3. Absorption and emission spectra of a: $Zn(BTZ)_2$ (Ex (●) and Em (▲)) and $Zn(MeBTZ)_2$ (Ex (○) and Em (□)) in CH_2Cl_2; b: $Be(BTZ)_2$ (Ex(⋆)and Em (⋆)) and $Be(MeBTZ)_2$ (Ex (▲) and Em (△)) in THF (Ex: Excitation; Em: emission).

strong electron-donating effect of the methyl group. As expected, the lower energy gap (E_g) bands were obtained by $E_g = E_{HOMO} - E_{LUMO}$ [16].

4. Conclusions

In summary, a detailed study of the effect on thermal stability, photophysical properties, electronic structure, and electrochemical properties of methylation of bis(2-(2-hydroxyphenyl)benzothiazolate) chelates was presented. As revealed by TG and DSC analysis, the methylated complexes exhibited good thermal stabilities. The red-shifted absorption and emission spectra were attributed to the steric factor from the electron-donating methyl group. Calculation of the location and distribution

Table 3
Photophysical and electrochemical data for four materials (E_m: emission; FWHM: full wave at half maximum; CIE: the commission internationalde de L'Eclairage; E_{HOMO}: energy of HOMO; E_{LUMO}: energy of LUMO; E_g: energy gap)

Metal chelates	Absorption	E_m (λ_{max})		FWHM	CIE		E_{HOMO}	E_{LUMO}	E_g
	(nm)	Solution	Powder	(nm)	X	Y	(eV)	(eV)	(eV)
$Zn(BTZ)_2$	251, 313, 382, 416	466	478	53.4	0.1846	0.3875	−5.051	−2.731	2.32
$Zn(MeBTZ)_2$	262, 323, 372, 431	473	507	62.9	0.2379	0.5914	−4.958	−2.678	2.28
$Be(BTZ)_2$	266, 349, 416	444	465	46.5	0.1663	0.2473	−5.076	−2.778	2.29
$Be(MeBTZ)_2$	277, 350, 420	456	475	60.4	0.1551	0.2796	−4.975	−2.717	2.25

of the orbitals showed that the methyl group has contribution to HOMO and HOMO − 1. Meanwhile, for the electrochemical properties, the methyl derivatives exhibited lower oxidation and reduction potentials, and optical band gaps decrease correspondingly.

Acknowledgments

This work was financially supported by National Natural Scientific Foundation of China (20671068); Natural Science Foundation of Shanxi Province (20041066); Shanxi Scientific Research Foundation for Returned Scholars (200523); Scientific and Technical Key Project of Shanxi (2006031121).

References

[1] C.W. Tang, S.A. VanSlyke, Appl. Phys. Lett. 51 (1987) 913.
[2] M. Wohlgenannt, Kunj Tandon, S. Mazumdar, S. Ramasesha, Z.V. Vardeny, Nature 409 (2001) 494.
[3] S.R. Forrest, Nature 428 (2004) 911.
[4] T. Karatsu, R. Hazuku, M. Asuke, A. Nishigaki, S. Yagai, Y. Suzuri, H. Kita, A. Kitamura, Org. Electron. 8 (2007) 357.
[5] B.S. Xu, Y.Y. Hao, X.H. Fang, H. Wang, X.G. Liu, Appl. Phys. Lett. 90 (2007) 053903.
[6] B.S. Xu, H. Wang, Y.Y. Hao, Z.X. Gao, H.F. Zhou, J. Lumin. 122–123 (2007) 663.
[7] E. Holder, B.M.W. Langeveld, U.S. Schubert, Adv. Mater. 17 (2005) 1109.
[8] M. Mazzeo, V. Vitale, F. Della Sala, M. Anni, G. Barbarella, L. Favaretto, G. Sotgiu, R. Cingolani, G. Gigli, Adv. Mater. 17 (2005) 34.
[9] Y. Hamada, T. Sano, H. Fujii, Y. Nishio, H. Takahashi, K. Shibata, Jpn. J. Appl. Phys. 35 (1996) L1339.
[10] T. Sano, Y. Nishio, Y. Hamada, H. Takahashi, T. Usuki, K. Shibata, J. Mater. Chem. 10 (2000) 157.
[11] G. Yu, S.W. Yin, Y.Q. Liu, Z.G. Shuai, D.B. Zhu, J. Am. Chem. Soc. 125 (2003) 14816.
[12] Y.P. Tong, S.L. Zheng, X.M. Chen, Inorg. Chem. 44 (2005) 4270.
[13] L.S. Sapochak, A. Padmaperuma, N. Washton, F. Endrino, G.T. Schmett, J. Marshall, D. Fogarty, P.E. Burrows, S.R. Forrest, J. Am. Chem. Soc. 123 (2001) 6300.
[14] Y. Kan, G.S. Wu, L.D. Wang, Y. Qiu, Int. J. Quantum Chem. 98 (2004) 325.
[15] J. Salbeck, N. Yu, J. Bauer, F. Weissörtel, H. Bestgen, Synth. Met. 91 (1997) 209.
[16] V. Promarak, M. Lchikawa, D. Meunmart, T. Sudyoadsuk, S. Saengsuwan, T. Keawin, Tetrahedron Lett. 47 (2006) 8949.

Available online at www.sciencedirect.com
ScienceDirect
Organic Electronics 9 (2008) 273–278
Organic Electronics
www.elsevier.com/locate/orgel

Letter

High-efficiency fluorescent white organic light-emitting device with double emissive layers

Yu Wang [a,b,c], Yu-Lin Hua [a,b,c,*], Xiao-Ming Wu [a,b,c], Li-Juan Zhang [a,b,c], Qing-Chuan Hou [a,b,c], Qian Liu [a,b,c]

[a] *Institute of Physical Material, Tianjin University of Technology, Tianjin 300384, PR China*
[b] *Tianjin Key Laboratory of Photoelectric Materials and Devices, Tianjin 300384, PR China*
[c] *Key Laboratory of Display Materials and Photoelectric Devices, Ministry of Education, Tianjin 300191, PR China*

Received 29 August 2007; received in revised form 30 November 2007; accepted 11 December 2007
Available online 23 December 2007

Abstract

The authors demonstrate a fluorescent white organic light-emitting device (WOLED) with double emissive layers. The yellow and blue dyes, 5,6,11,12-tetraphenylnaphthacene and *N*-(4-((*E*)-2-(6-((*E*)-4-(diphenylamino)styryl)naphthalen-2-yl)vinyl)phenyl)-*N*-phenylbenzenamine, are doping into the same conductive host material, *N*,*N*′-dicarbazolyl-4-4′-biphenyl). The maximum luminance and power efficiency of the WOLED are 14.6 cd/A and 9.5 lm/W at 0.01 mA/cm^2, with the maximum brightness of 20 100 cd/m^2 at 17.8 V. The Commission International de L'Éclairage coordinates change slightly from (0.27, 0.37) to (0.28, 0.36), as the applied voltage increases from 6 V to 16 V. The high efficiencies can be attributed to the balance between holes and electrons.

PACS: 85.60.Jb; 78.60.Fi

Keywords: Efficiency; Balance; Holes and electrons; White organic light-emitting

1. Introduction

White organic light-emitting devices (WOLEDs) have attracted a great deal of attention of the application potential as full color displays, backlight units for liquid crystal display, and general illuminant lighting sources. To achieve highly efficient WOLEDs, various approaches have been tried, such as configuring the multiple-emissive-layer structures [1], inserting the hole-injecting layer [1,2], adding the exciton-blocking layer [3], using high electron mobility [4], adopting double host [5] and so on. Generally, WOLEDs are classified into phosphorescent and fluorescent devices by materials used. The maximum luminance and power efficiency of phosphorescent WOLEDs have reached 38.2 cd/A [6] and 33.2 lm/W [7], as compared to 12.8 cd/A [2] and 9 lm/W [8] for small-molecular fluorescent

* Corresponding author. Address: Institute of Physical Material, Tianjin University of Technology, Nankai District, Tianjin 300384, PR China. Tel.: +86 022 60215378; fax: +86 022 60215796.
E-mail address: yulinhua@tjut.edu.cn (Y.-L. Hua).

1566-1199/$ - see front matter © 2007 Elsevier B.V. All rights reserved.
doi:10.1016/j.orgel.2007.12.004

WOLEDs. Recently, Lai et al. [4] reported a type of fluorescent WOLEDs of double emissive layer with maximum power efficiency of 8.7 lm/W. By doping 4′-bis[*N*-(1-naphthyl)-*N*-phenyl-amino]biphenyl (NPB) or 4,7-diphenyl-1,10-phenanthroline (BPhen) into the blue emissive layer, they realized efficiency enhancement and voltage reduction. However, this method complicated the fabrication of WOLEDs, because it is technological difficult to accurately control the concentration through the different evaporation rates especially for the multiple dyes. To reduce the complicated of fabrication, the conventional devices with only single host could be considered. But the maximum luminance and power efficiency of WOLEDs with conventional double emissive layers reported are only 12.8 cd/A [2] and 9 lm/W [8].

In this letter, we demonstrate a structure of indium tin oxide (ITO)/NPB/*N*,*N*′-dicarbazolyl-4-4′-biphenyl (CBP): 5,6,11,12-tetraphenylnaphthacene (Rubrene)/CBP: *N*-(4-((*E*)-2-(6-((*E*)-4-(diphenylamino) styryl)naphthalen-2-yl)vinyl)phenyl)-*N*-phenylbenzenamine (N-BDAVBi)/bis(2-methyl-8-quinolinolato)(*para*-phenylphenolato)aluminium(III) (BAlq)/LiF/Al, where ITO with a sheet resistance of 20 Ω/□ is used as anode and NPB is used as 50-nm-thick hole-transporting layer while BAlq is used as 30-nm-thick exciton-blocking and electron-transport layer. The yellow and blue dye, Rubrene and N-BDAVBi (purchased from Rubipy Scientific Inc.), is doped in the host material, CBP, and LiF(0.8 nm)/Al(120 nm) is used as cathode. The energy level diagram and the chemical structure of the material adopted in this device are shown in Fig. 1. This WOLED exhibits the maximum luminance and power efficiency of 14.6 cd/A and 9.5 lm/W, respectively.

2. Experimental

Our ITO glasses are cleaned in an ultrasonic bath by the following sequence: in de-ionized water, acetone and isopropyl alcohol. Thereafter, precleaned ITO is dry in an oven. Organic layers are deposited onto a precleaned ITO glass substrate by thermal evaporation in BOC Edwards Auto 500 thermal evaporation coating system at 3×10^{-4} Pa, followed by a LiF buffer layer, and an Al cathode in the same vacuum run. Deposition rates and thickness of the layers are monitored by an oscillating quartz monitor. The evaporating rates are kept at 1–2 Å/s for organic layers and LiF layer and 5 Å/s

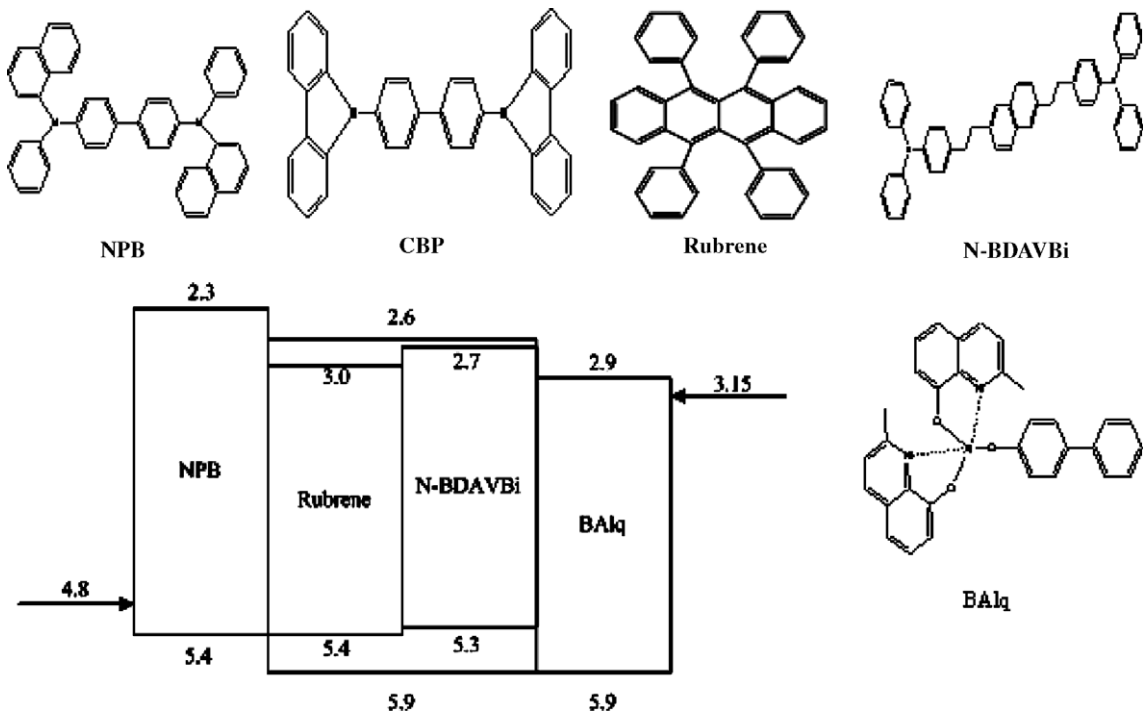

Fig. 1. Chemical structures of the employed organics and the corresponding energy level diagram.

for Al cathode without breaking vacuum, respectively. Electroluminescent (EL) spectra and Commission Internationale De L'Éclairage (CIE) coordinates of these devices are measured by a PR650 spectra scan spectrometer. The luminance-current, density-voltage characteristics are recorded simultaneously with the measurement of EL spectra by combining the PR650 spectra scan spectrometer with a Keithley model 2400 programmable voltage–current source. Absorption and photoluminescence (PL) spectra of the organic materials are measured with JASCO V-570 and FluoroMax-P spectrometer. The energy levels of the materials are determined by Ecochemie μAutolab III electrochemical station through cyclic voltammogram measurements and the absorption spectra of the solid films. All the measurements are carried out at room temperature in air without encapsulation.

3. Results and discussion

In general, the EL spectra and the CIE coordinates of the white light-emitting device are strongly influenced by the concentration of the dyes as well as the thickness of each emissive layer. First, we consider the most suitable concentration for the different dyes. As shown in Fig. 2, the normalized EL spectra of the devices shows two main emission peaks at 476 nm and 564 nm originating from N-BDAVBi and Rubrene, respectively. With the concentration of Rubrene increased, the yellow emission is enhanced. As a result, the CIE coordinates of the device at 1000 cd/m^2 changed from (0.23, 0.38) at 1 wt% Rubrene to (0.24, 0.33) at 2 wt% Rubrene and to (0.29, 0.37) at 5 wt% Rubrene (white device). In a word, the CIE coordinates of the device depend on the concentration of the Rubrene. However, it seems that the efficiency of 5 wt% Rubrene is a little higher than the device with only 2 wt% Rubrene doped in tris(8-hydroxyquinoline) aluminum (Alq_3) [2]. It should be mentioned that a strong dependence of luminance efficiency on the Rubrene concentration is observed. For instance, the maximum luminance efficiency changed from 7.1 cd/A at 1.3 mA/cm^2 to 7.8 cd/A at 58.6 mA/cm^2 and 14.6 cd/A at 0.01 mA/cm^2, as the concentration of Rubrene is increased from 1 wt% to 2 wt% and 5 wt%. This may be attributed to the incomplete Förster energy transfer from CBP to Rubrene because of the little overlap between the photoluminescence (PL) spectrum of the CBP [9] and the absorption spectrum of the Rubrene [10].

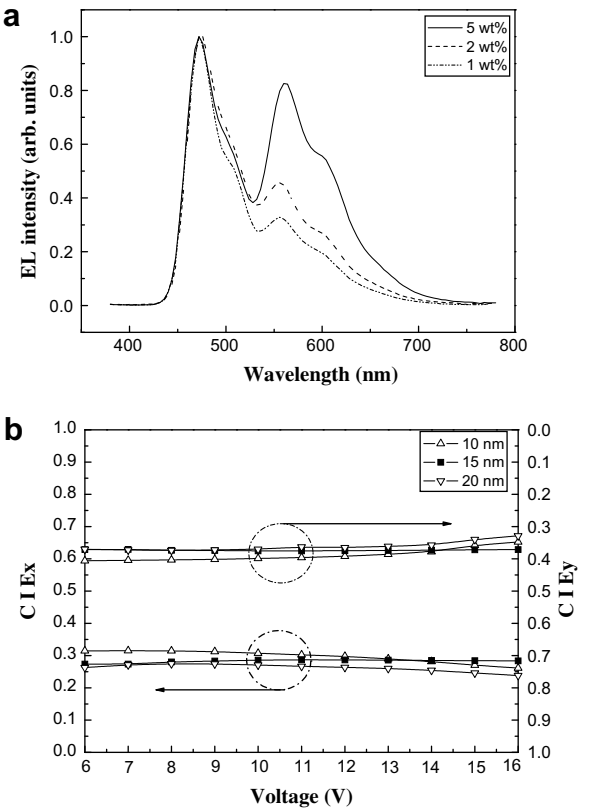

Fig. 2. (a) EL Spectra of the devices with the ITO/NPB/CBP: Rubrene (x wt%)/CBP: N-BDAVBi (2 wt%)/BAlq/LiF/Al structure, where $x = 1$ wt%, 2 wt%, 5 wt% and (b) $CIE_{x,y}$ coordinates of the devices with the ITO/NPB/CBP: Rubrene (20 nm)/CBP: N-BDAVBi (y nm)/BAlq/LiF/Al structure, where $y = 10$, 15, 20.

In another hand, the optimal doping concentration for the blue fluorescent dye, N-BDAVBi, is 2 wt%, which is determined from a single emissive layer device (ITO/NPB/CBP: N-BDAVBi (30 nm)/BALq/LiF/Al), whose maximum luminance efficiency is 8 cd/A. In this blue device, large densities of holes (p) and electrons (n) pile up at both NPB/CBP and CBP/BALq interfaces, thus resulting in the higher exciton formation probability ($\sim n \times p$) as compared with that at just one interface. The detailed experiments about these characteristics of N-BDAVBi will be published in another paper. As for the WOLEDs, the blue emission is mainly originated by the excitons at the CBP/BALq interface, as well the recombination zone of the yellow dye is around the NPB/CBP interface. When the Rubrene concentration is very light (1 wt% or 2 wt%), the number of the excitons formed at the NPB/CBP interface is limited and the device shows predominate blue emission (Fig. 2), thus resulting in

the lower efficiency compared with the blue device. By increasing the Rubrene concentration, the number of the excitons contributed to the yellow emission increases, corresponding to an improvement of overall efficiencies of the WOLEDs. Based on these results, we fixed the concentrations of blue and yellow fluorescent dyes for 2 wt% and 5 wt%, respectively.

Next, we consider the variant of CIE coordinates with the thickness of the blue emissive layer. To control the whole thickness of the device, we fix the thickness of yellow emissive layer for 20 nm. Fig. 2b presents the graph of the variation of CIE coordinates for various thicknesses of the blue emissive layer with the applied voltages increasing from 6 V to 16 V. It can be seen that the thicker the blue emissive layer, the weaker the yellow emission originated from Rubrene. As a result, both CIE_x and CIE_y decrease gradually. These can be understood as following. Some holes injected from anode will be trapped by N-BDAVBi but mostly accumulate at the interface between CBP and BAlq because of the hole-blocking property of BAlq. When the thickness of blue emissive layer increases, the number of the electrons reaching the yellow emissive layer will reduce in contrast to the increasing electrons staying at the blue emissive layer, because of the preferred hole-transporting property of CBP. In sequence, the exciton formation probability in the blue emissive layer will increase accordingly. As a consequence, the blue emission will enhance with the yellow emission reducing, corresponding to both CIE_x and CIE_y decreasing.

When the thickness of blue emissive layer is kept at 15 nm, the CIE coordinates of the devices change slightly from (0.27, 0.37) to (0.28, 0.36). It means that the device has achieved a good balance between hole and electron currents arriving at the recombination zone. In contrast, when the thickness of the blue emissive layer varies, the CIE coordinates depend significantly on the voltage. This can be ascribed to the shift of the recombination zone, resulting from the difference between the mobility of hole and electron carriers [11]. In conclusion, the optimized thickness of the yellow and blue emissive layer is 20 nm and 15 nm, respectively.

From Fig. 3, we can see the turn-on voltage of the WOLED is 4.4 V (for 1 cd/m^2) and the maximum brightness is 20 100 cd/m^2 at 17.8 V. Fig. 4 depicts the maximum luminance and power efficiency of the device is 14.6 cd/A and 9.5 lm/W at 0.01 mA/cm^2. The high-efficiency is attributed to

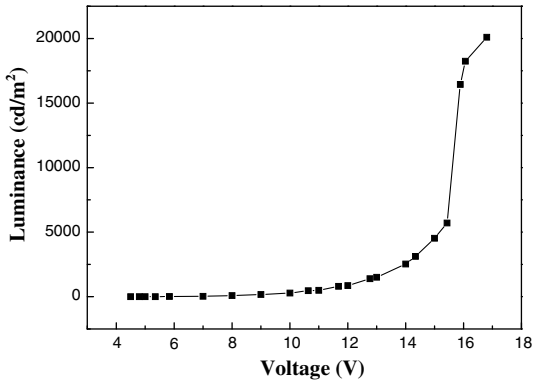

Fig. 3. Luminance vs. voltage characteristics of the white device.

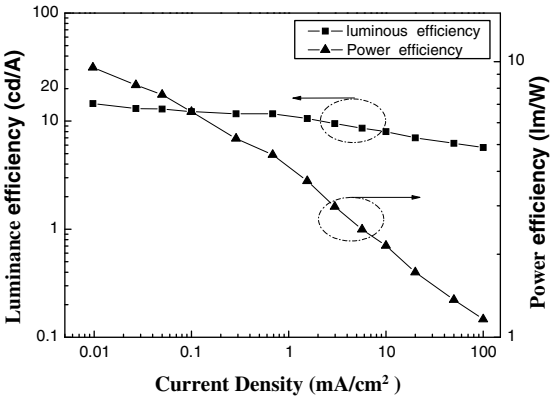

Fig. 4. Luminance efficiency and power efficiency vs. current density characteristics of the white device.

the balance of hole and electron currents, as well as an effective confinement of carriers within the emitting layers.

The high-efficiency can be further explained in terms of the alignments of the energies of organic materials used in the device (as shown in Fig. 1). Here, it is worthy to pay attention to what the Matsushin [12] has pointed out – when the highest occupied molecular orbital (HOMO) level of a guest molecule was aligned to that of the hole-transporting material, *N*,*N*′-diphenyl-*N*,*N*′-bis(3-methylphenyl)-[1,1′-biphenyl]-4,4′-diamine (TPD), a device reached the highest hole injection efficiency and current density due to the largest overlap area of density-of-states distributions of the hole-transporting and guest molecules [12]. Fortunately, NPB is a derivative of TPD. Although there is 0.5 eV energy barrier between the of NPB at 5.4 eV and CBP at 5.9 eV, we can also expect the highest hole injection efficiency from NPB to Rubrene (5.4 eV). Due to the very

high hole mobility of over 0.1 cm^2/V S of Rubrene [13], enough holes will inject to the following dye, N-BDAVBi. In sequence, the holes are effectively confined in the emissive layer because of the hole-blocking property of BAlq, leading to the exitons confined in the recombine zone with the high-efficiency shown. But when the current density increases gradually, the efficiency decreases accordingly. This is due to singlet-heat annihilation and singlet–singlet annihilation [14], which generated Joule heat and caused singlet–singlet exciton collisions.

To verify the hole-blocking property of BAlq, following devices have been designed. According to the conventional approach, the improvement of electron injection should lead to an increased efficiency. As a consequence, considering the relative low LUMO level of Alq_3 (3.0 eV [15]), we expect device A (ITO/NPB/CBP: Rubrene/CBP: N-BDAVBi/BAlq (10 nm)/Alq_3 (30 nm)/LiF/Al) to enhance the injection of electrons into the emissive layers by means of electron cascading. However, the maximum luminance and power efficiency of device A are only 7.7 cd/A at 3.3 mA/cm^2 and 2.7 lm/W at 0.64 mA/cm^2. A probable explanation for the decreased efficiencies is that the 10-nm thickness of BAlq is not thick enough to efficiently confine the holes and some holes transport to the subsequent layer, thus resulting in the low efficiencies. In order to investigate this, we fabricate device B with the structure of ITO/NPB/CBP: Rubrene/CBP: N-BDAVBi/BAlq: CBP/LiF/Al. Due to the high hole and electron mobility of CBP of 2×10^{-3} and 3×10^{-4} cm^2/V S at the applied field of 0.5 MV/cm [16], CBP doping into BAlq is expected to increase the holes-transporting to the BALq: CBP layer. Indeed, as the concentration of CBP doping in BAlq changes from 1 wt% to 5 wt% and to 8 wt%, the corresponding maximum luminance efficiency reduces from 12.5 cd/A at 0.12 mA/cm^2 to 8.6 cd/A at 0.37 mA/cm^2 and to 7.7 cd/A at 0.71 mA/cm^2. Therefore, we can confirm that the low efficiencies of device A are attributed to some holes-transporting to subsequent layer, leading to the cathode quenching caused by non-radiative energy transfer as well as the outcoupling problems [17]. As for our WOLEDs, it seems that the holes are effectively confined in the emissive layers by the 30-nm-thick BALq. As a result, the electrons will predominately recombine with the holes in the emissive layers and subsequently the balance of hole and electron currents is improved, corresponding to the high-efficiency of 14.6 cd/A.

4. Conclusions

In summary, we have demonstrated a high-efficiency WOLED by doping yellow and blue fluorescent dyes in CBP, separately. Comparing the performances of different concentration of the yellow dye and the various thicknesses of the blue emissive layer, we have obtained the optimized structure of ITO/NPB (50 nm)/CBP: Rubrene (5 wt%, 20 nm)/CBP: N-BDAVBi (2 wt%, 15 nm)/BAlq (30 nm)/LiF/Al. The maximum luminance and power efficiencies of the WOLEDs are 14.6 cd/A and 9.5 lm/W at 0.01 mA/cm^2, with the maximum brightness of 20 100 cd/m^2 at 17.8 V. The quite stable white emission in CIE coordinates slightly varies from (0.27, 0.37) to (0.28, 0.36) as the applied voltage increases from 6 V to 16 V. The high efficiencies are ascribed to the balance of holes and electrons, as well as an effective confinement of carriers within the emitting layers.

Acknowledgements

This work is supported by the National Natural Science Foundation of China (NSFC) (Grant No. 60576038), the Natural Science Key Foundation of Tianjin (Grant No. 06TXTJJC14603), the International Joint Project between NSFC and Royal Society and the Key Discipline of Material Physics and Chemistry of Tianjin.

References

[1] G. Cheng, Y. Zhang, Y. Zhao, Y. Lin, C. Ruan, S. Liu, T.Y. Ma, Y. Cheng, Appl. Phys. Lett. 89 (2006) 043504.
[2] T.H. Liu, Y.S. Wu, M.T. Lee, H.H. Chen, C.H. Liao, C.H. Chen, Appl. Phys. Lett. 85 (2004) 4304.
[3] D.F. O'Brien, M.A. Baldo, M.E. Thompson, S.R. Forrest, Appl. Phys. Lett. 74 (1999) 0442.
[4] S.L. Lai, M.Y. Chan, M.D. Fung, C.S. Lee, S.T. Lee, Appl. Phys. Lett. 90 (2007) 203510.
[5] Y.C. Tsai, J.H. Jou, Appl. Phys. Lett. 89 (2006) 243521.
[6] Y. Sun, N. Giebink, H. Kanno, B. Ma, M.E. Thompson, S.R. Forrest, Nature (in London) 440 (2006) 908.
[7] J.H. Seo, J.H. Seo, J.H. Park, Y.K. Kim, J.H. Kim, G.W. Hyung, K.H. Lee, S.S. Yoon, Appl. Phys. Lett. 90 (2007) 203507.
[8] Q.X. Tong, S.L. Lai, M.Y. Chan, J.X. Tang, H.L. Kwong, C.S. Lee, S.T. Lee, Appl. Phys. Lett. 91 (2007) 023503.
[9] L. Zou, V. Savvate'ev, J. Booher, C.H. Kim, J. Shinar, Appl. Phys. Lett. 79 (2001) 2282.

[10] S. Tao, C.S. Lee, S. Lee, X. Zhang, Appl. Phys. Lett. 91 (2007) 013507.
[11] C. Chen, H. Meng, Appl. Phys. Lett. 86 (2005) 201102.
[12] T. Matsushin, K. Goushi, C. Adachi, Chem. Phys. Lett. 435 (2007) 327.
[13] V. Podzorov, S.E. Sysoev, E. Loginova, V.M. Pudalov, M.E. Gershenson, Appl. Phys. Lett. 83 (2003) 3504.
[14] H. Nakanotani, H. Sasabe, C. Adachi, Appl. Phys. Lett. 86 (2005) 213506.
[15] Y.M. Kim, Y.W. Park, J.H. Choi, B.K. Ju, J.H. Jung, J.K. Kim, Appl. Phys. Lett. 90 (2007) 033506.
[16] J.W. Kang, S.H. Lee, H.D. Park, W. Jeong, K.M. Yoo, Y.S. Park, J.J. Kim, Appl. Phys. Lett. 90 (2007) 223508.
[17] F. Nüesch, D. Berner, E. Tutiš, Michel Schaer, C. Ma, X. Wang, B. Zhang, L. Zuppiroli, Adv. Funct. Mater. 15 (2005) 323.

Available online at www.sciencedirect.com
ScienceDirect
Organic Electronics 9 (2008) 279–284
Organic Electronics
www.elsevier.com/locate/orgel

Deep blue light-emitting diode based on high molecular weight poly(9,9-dioctylfluorene) with high efficiency and color stability

Shin-Rong Tseng [a], Shiuan-Yi Li [a], Hsin-Fei Meng [a,*], Yi-Hsiang Yu [b], Chia-Ming Yang [b], Hua-Hsien Liao [b], Sheng-Fu Horng [b], Chian-Shu Hsu [c]

[a] *Institute of Physics, National Chiao Tung University, Hsinchu 300, Taiwan, ROC*
[b] *Department of Electrical Engineering, National Tsing Hua University, Hsinchu 300, Taiwan, ROC*
[c] *Department of Applied Chemistry, National Chiao Tung University, Hsinchu 300, Taiwan, ROC*

Received 15 July 2007; received in revised form 15 November 2007; accepted 19 November 2007
Available online 18 December 2007

Abstract

A highly efficient deep blue polymer light-emitting diode based on poly(9,9-dioctylfluorene) is demonstrated. The performance is found to increase significantly with the molecular weight. Two different molecular weights are compared, one is 71,000 and the other is 365,000. The electroluminescent efficiency and color stability are improved by slightly doping hole traps into the emission layer and bilayer structure. The maximum efficiency is 3.8 cd/A with the corresponding external quantum efficiency of 3.7% at deep blue with Commission Internationale de L'Eclairage (CIE) coordinate at (0.15, 0.09). Stable blue emission is maintained up to 6600 cd/m^2 without growth of green shoulder in emission spectrum.

Keywords: Polymer light-emitting diodes; Blocking layer; Molecular weight; Deep blue; Stability

Conjugated polymer light-emitting diodes (PLED) have generated a great deal of interest due to their easy solution process, potentially high emission efficiency and many optoelectronic applications. Therefore, they are viewed as the material for light-weight large-area flat panel display of the new generation. One promising way for display application is using the white PLED combined with color filters. For this purpose highly efficient blue PLED is critical to achieve white PLED through energy transfer by using the blue emitters as the host and red/green emitter as the dopants [1,2]. Deep blue PLED is more essential than the sky blue one in making white light. However the deep blue material still remains a challenge due to their large band gap and difficulty in charge balance. Up to now, the highest reported efficiency for deep blue PLED is about 3 cd/A by the Covion company with unavailable chemical structure [3]. The most well-known and commonly used materials for deep blue PLED are polyfluorene (PF) and its derivatives due to their high photoluminescence quantum efficiency [4–7]. However, they

* Corresponding author. Tel.: +886 35731955.
E-mail address: meng@mail.nctu.edu.tw (H.-F. Meng).

1566-1199/$ - see front matter © 2007 Elsevier B.V. All rights reserved.
doi:10.1016/j.orgel.2007.11.003

still suffer from low electroluminescence (EL) efficiency due to the poor charge balance caused by the difficulty in electron injection and transport. In addition, the color is unstable due to the formation of excimer in its liquid crystalline phase and ketone defect in the presence of oxygen [8,9]. Among all the PF derivative poly(9,9-dioctylfluorene) (PFO) is archetypical and the easies to synthesize. It would greatly reduce the barriers to make high-performance blue PLED using simply PFO. The optical and morphological properties of PFO have been shown to depend sensitively on the molecular weight [10]. In general the higher molecular weight implies better stability and purity of the material. The low molecular weight polymers are also known to have poor color stability due to easier chain motions under device operation. Removal of the low molecular weight components is known to improve the performance [11]. So far the efficiency remains far lower than the Covion material even with molecular weight control. In this work we employ a high molecular weight PFO with MW up to 365,000 to demonstrate a deep blue PLED with efficiency as high as 3.8 cd/A with corresponding external quantum efficiency 3.7%, which is even better than the Covion blue PLED. Color stability is also improved relative to the low molecular weight counterpart. High molecular weight is found to enhance the electron current resulting in a better charge balance. Moreover, the efficiency is significantly enhanced by the doping of hole traps [12]. Instead of using a cross-linking polymer [13], a soluble hole-transport layer (HTL) is added by buffer liquid method [14] to increase the efficiency.

In this letter, three types of device are fabricated, including the doped host–guest emission layer (EML) in single layer structure (type I), HTL/EML bilayer device (type II), and HTL/host–guest EML bilayer device (type III). Fig. 1A shows the schematic energy profile for type I devices and Fig. 1B for type II. Low molecular weight PFO (MW = 71,000) and high molecular weight HMW-PFO (MW = 365,000) purchased from American Dye Source (ADS) are chosen as light-emitting polymers without any further purification. Poly[(9,9-dioctylfluorenyl-2,7-diyl)-co-(4,4′-(*N*-(4-*sec*-butylphenyl))diphenylamine)] (TFB, MW = 197,000, purchased from ADS) are chosen as dopant for type I devices and HTL for the bilayer devices (type II and type III). Single layer PLEDs based on PFO and HMW-PFO without any TFB are made as standard devices. All PLED devices

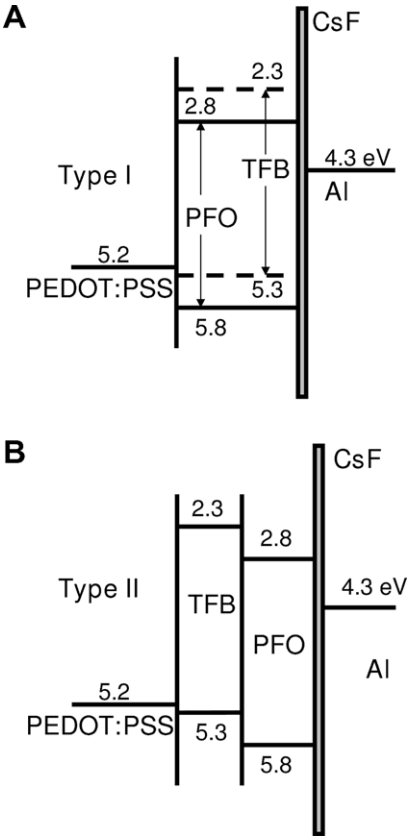

Fig. 1. Schematic electronic energy profile for the (A) type I (PFO: 1 wt% TFB) device structure (B) type II (TFB/ PFO) device structure. The numbers are in eV.

are fabricated on glass substrates with poly-(3,4-ethylenedioxythiophene):poly-(styrenesulfonate) (PEDOT:PSS) layer on a patterned ITO layer. For type I devices 1 wt% of TFB is blended into PFO and HMW-PFO individually as the dopant. The film is formed by spin-coating and baking at 120 °C in vacuum (10^{-3} torr) for 40 min to remove the solvent. For type II and type III devices TFB dissolved in toluene is spin-coated to make a 30 nm thin film then baked at 180 °C in vacuum for 40 min. PFO and HMW-PFO are also dissolved in toluene and spin-coated to make bilayer devices (type II and III) by a liquid buffer layer to prevent the dissolution problem [14]. For the bilayer structure, PFO layer is baked in vacuum at 120 °C for 1 h to remove the residual 1,2-propylene glycol liquid buffer and organic solvent. Except for the PEDOT:PSS layer all the fabrication processes are carried out in the glove box to reduce oxygen adsorption of PFO. CsF (2 nm)/Al (100 nm) are deposited as cathode by thermal evaporation [15].

Finally all devices are packaged in the glove box. The film thickness is measured by Kosaka ET4000 Surface Profiler. The EL efficiency is measured by photo research PR650 spectrophotometer integrated with Keithley 2400 multimeter. The PL efficiency is measured by an integrating sphere system. Ionization potential (IP) is measured by cyclic voltammetry and electron affinity (EA) is calculated by IP plus band gap determined by the ultraviolet absorption spectrum. Below we present the low molecular weight results first and the high molecular weight results latter.

Fig. 2 shows the results of PFO-based devices. The maximum efficiency of type I (PFO: 1 wt% TFB) device are 2.3 cd/A with the corresponding EQE of 1.99%, which is three times higher than that of the standard PFO device (EQE = 0.63%) without TFB doping. This indicates that TFB plays the role of hole trap in the host–guest EML and the effective hole mobility is reduced. The efficiency is enhanced due to the better carrier balance. The maximum efficiency of type II device (TFB/PFO) is 1.64 cd/A with the corresponding EQE of 1.29%, which is also two times higher compared to the standard one. As seen in Fig. 1B, at the interface between TFB and PFO there is a hole barrier from the TFB side and electron barrier from the PFO side. The recombination zone is hence expected to concentrate in the PFO region near the interface, unlike the case of single layer PFO where the recombination zone is expected to be near the cathode due to the low electron mobility. The cathode quenching effect in the bilayer structure is therefore less severe than the single layer case, thus explaining the improved efficiency in type II even without any doping. The type III device (TFB/PFO: 1 wt% TFB) combines the functions of type I and type II devices. The maximum efficiency of type III is 1.5 cd/A with the corresponding EQE of 1.18%. The efficiency of type III does not get better than type I or type II device. Compared with device I, the HTL in device III may cause too much hole injection and destroy the balance already established by TFB doping. Compared with device II, the holes in device III may be less confined at the interface due to the easy injection from HTL into the TFB dopants to cause more cathode quenching.

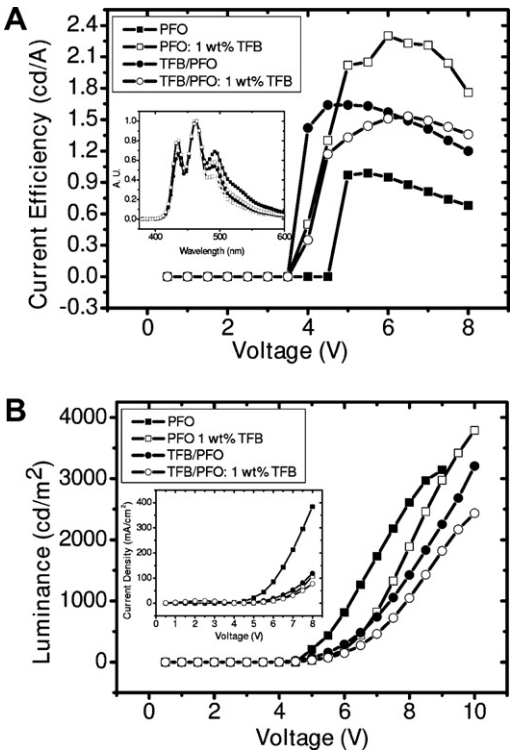

Fig. 2. The performances of PFO devices: standard PFO device (solid square), type I (PFO: 1 wt% TFB) device (open square), type II (TFB/PFO) device (solid circle) and type III (TFB/PFO: 1 wt% TFB) device (open circle). (A) The current efficiency. Insets are the EL spectra. (B) The luminance. Inset is the current density.

Now we turn to the case of high molecular weight PFO with MW equal to 356,000. The basic physical picture and the relative efficiencies of the device types are the same as the low molecular weight PFO. However the absolute values of the performance parameters are greatly enhanced by the increasing molecular weight. The results of HMW-PFO devices are shown in Fig. 3. The maximum efficiency of type I device (HMW-PFO: 1 wt% TFB) is 2.8 cd/A for thickness of 100 nm with the corresponding EQE of 2.04%. When the thickness is reduced to 60 nm, the maximum efficiency is enhanced to the remarkable value of 3.8 cd/A with the corresponding EQE of 3.7% and power efficiency of 2.6 l m/W. The emission color is deep blue with Commission Internationale de L'Eclairage (CIE) coordinate = (0.15, 0.09). It is well-known that the main limiting factor for the blue polymer LED is the electron transport. Because of the small electron affinity electrons in PFO are highly susceptible to the impurities, with either chemical or structural nature, which commonly causes electron trap states inside the energy gap. High molecular weight polymers usually implies low impurity level after the synthesis. In addition, in the high molecular weight polymer there are much less chain ends which

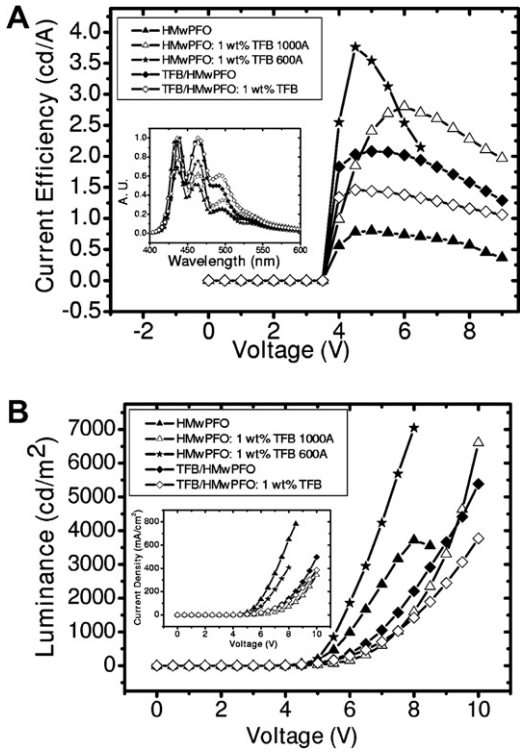

Fig. 3. The performances of HMW-PFO devices: standard HMW-PFO device (solid triangle), type I (HMW-PFO: 1 wt% TFB) device of thickness 100 nm (open triangle), type I (HMW-PFO: 1 wt% TFB) device of thickness 60 nm (solid star), type II (TFB/PFO) device (solid rhombus) and type III (TFB/PFO: 1 wt% TFB) device (open rhombus). (A) The current efficiency. Insets are the EL spectra. (B) The luminance. Inset is the current density.

themselves are considered as some kind of traps [10]. Moreover, the chain entanglement and thermal as well mechanical stability are improved by the larger molecular weight and may result in less structural defects like aggregation formation. It is quite intriguing that the reduction of the thickness has such a dramatic effect on the efficiency. Apparently the high electric field helps the electron injection and mobility, especially for the high molecular PFO with less traps, therefore in the thin samples the charge balance and enhance the efficiency are improved despite of the concurrent negative effect of more cathode quenching. The maximum efficiency of type II (TFB/HMW-PFO) device is 2.1 cd/A with corresponding EQE of 1.8% which are slightly higher than the low molecular weight counterpart. The maximum efficiency of type III (TFB/HMW-PFO: 1 wt% TFB) is 1.4 cd/A with corresponding EQE of 1.1% roughly the same as the low molecular weight counterpart. The luminance at a given voltage for HMW-PFO is however always much higher than low molecular weight PFO, supporting the assumption of higher electron current.

In addition to efficiency, another equally critical issue for blue PLED is the color stability at higher voltage. As discussed above polyfluorene is known to have the tendency to show pronounced green emission at the shoulder of the spectrum due to either aggregate or ketone defects. As a result it is commonly observed that the emission spectrum suddenly changes from blue to green beyond some critical voltage. The maximal luminance below which there is no spectral shift can be taken as a measure for the color stability. As shown in Table 1, in general HMW-PFO shows a much higher maximal luminance compared with PFO. In particular, type I device with 100 nm thickness sustains stable deep blue emission up to almost 7000 cd/m^2. Such brightness is more than enough for most of the display and lighting applications. Note also that the color stability of the three types are all enhanced relative to the standard single layer sample. We suspect

Table 1
Performance of PLEDs in this work

Label	Max. current efficiency (cd/A)	Max. EQE (%)	Max. power efficiency (l m/W)	Max. luminance (cd/m^2)
PFO	1.0 (at 5.5 V)	0.63	0.6 (5 V)	2967 (at 8.5 V)
PFO: 1 wt% TFB	2.3 (6 V)	1.99	1.3 (5 V)	3788 (10 V)
TFB/PFO	1.6 (5 V)	1.29	1.1 (4.5 V)	3205(10 V)
TFB/PFO: 1 wt% TFB	1.5 (6.5 V)	1.18	0.8 (5 V)	2435 (10 V)
HMW-PFO	0.8 (5 V)	0.62	0.5 (5 V)	3554 (8.5 V)
HMW-PFO: 1 wt% TFB (100 nm)	2.8 (6 V)	2.04	1.5 (5 V)	6604 (10 V)
HMW-PFO: 1 wt% TFB (60 nm)	3.8 (4.5 V)	3.7	2.6 (4.5 V)	4235 (7 V)
TFB/HMW-PFO	2.1 (5 V)	1.8	1.4 (4 V)	5388 (10 V)
TFB/HMW-PFO: 1 wt% TFB	1.4 (5 V)	1.1	1.0 (4 V)	3773 (10 V)

The Max. luminance is defined as the highest luminance before the growth of green peak in emission spectrum.

that with either TFB blending or bilayer structure the recombination zone of the device is moved away from the cathode where a higher concentration of oxygen or other defects are present and the polymers are less stable under electroluminescence.

The mechanisms for the efficiency improvement are clarified by further experiments. Fig. 4A gives the direct evidence that TFB plays the role of hole trap by measuring the hole currents of hole-only devices with and without blending TFB. The hole current is reduced about one order of magnitude with a light TFB doping of 1 wt%. In addition, electron-only devices for PFO and HMW-PFO are compared. The results are shown in Fig. 4B. The effective work function of CsF/Al is 2.6 eV [16]. It there forms a Ohmic contact with PFO whose electron affinity is 2.8 eV, and the current is bulk-limited instead of injection limited. In the inset we calculate the electron mobility by using space-charge-limited current (SCLC) voltage–current relation $J_{\mathrm{SCLC}} = \frac{9}{8}\varepsilon\mu_{\mathrm{e}}\frac{(V-V_{\mathrm{bi}})^2}{L^3}$. J is the current density, ε is the permittivity of the polymer, μ_{e} is the electron mobility, V is driving voltage, V_{bi} is the built-in voltage, and L is the polymer thickness. Both the current and the electron mobility of HMW-PFO is higher than that of PFO. This might be due to the greater chain length of HMW-PFO for longer intrachain transport and the reduced impurities which act as electron traps as discussed above. Finally we compare the photoluminescence (PL) quantum efficiency. The PL efficiency is 40% for PFO and 50% for HMW-PFO. More surprisingly the PL efficiency is enhanced to 75% by slightly doping TFB into HMW-PFO, which might be attributed to the decrease of the aggregation formation in polyfluorene [17].

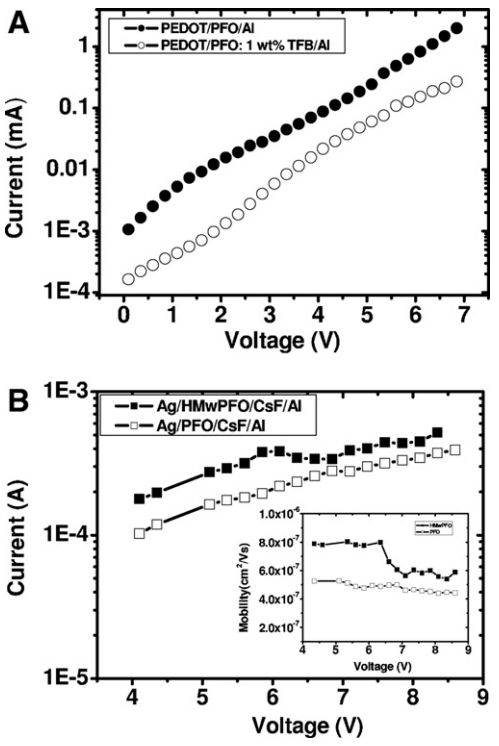

Fig. 4. (A) Hole-only currents of PFO (solid circle) and PFO: 1 wt% TFB (open circle) devices. (B) Electron-only currents of HMW-PFO (solid square) and PFO (open square) devices. Inset is calculated electron mobility.

In conclusion, the PLED performance for PFO with high molecular weight up to 360 K is superior to the ordinary low molecular weight PFO. The high molecular weight implies a higher electron mobility and better color stability at high luminance. By blending a hole-transport polymer TFB into PFO as the hole trap to enhance the charge balance, the efficiency reaches as high as 3.8 cd/A (3.7%) in the deep blue for high molecular weight PFO. Maximal stable blue emission is also doubled by the molecular weight control. The originally unpromising PFO now reaches a even better performance than the Covion blue polymers with closed chemical structures.

Acknowledgements

This work was supported by the National Science Council and the Excellence Project of the Ministry of Education of the Republic of China.

References

[1] M. Granstrom, O. Inganas, Appl. Phys. Lett. 68 (1996) 147.
[2] B. Hu, F. Karasz, J. Appl. Phys. 93 (2003) 1995.
[3] C.D. Muller, A. Falcou, N. Reckefuss, M. Rojahn, V. Wiederhirn, P. Rudati, H. Frohne, O. Nuyken, H. Becker, K. Meerholz, Nature 421 (2003) 829.
[4] U. Scherf, E.J.W. List, Adv. Mater. 14 (2002) 477.
[5] M. Gross, D.C. Müller, H.G. Nothofer, U. Scherf, D. Neher, C. Bräuchle, K. Meerholz, Nature 405 (2000) 661.
[6] T. Miteva, A. Meisel, W. Knoll, H.G. Nothofer, U. Scherf, D.C. Müller, K. Meerholz, A. Yasuda, D. Neher, Adv. Mater. 13 (2001) 565.
[7] D.C. Müller, T. Braig, H.G. Nothofer, M. Arnoldi, M. Gross, U. Scherf, O. Nuyken, K. Meerholz, Chem. Phys. Chem. 1 (2000) 207.
[8] D.D.C. Bradley, M. Grell, X. Long, H. Mellor, A. Grice, Proc. SPIE 3145 (1998) 254.
[9] E.J.W. List, R. Guentner, P.S.D. Freitas, U. Scherf, Adv. Mater. 14 (2002) 374.

[10] K. Hosoi, T. Mori, T. Mizutani, T. Yamamoto, N. Kitamura, Thin Solid Films 438–439 (2003) 201.
[11] K.H. Weinfurtner, H. Fujikawa, S. Tokito, Y. Taga, Appl. Phys. Lett. 76 (2000) 2502.
[12] D. Sainova, T. Miteva, H.G. Nothofer, U. Scherf, I. Glowacki, J. Ulanski, H. Fujikawa, D. Neher, Appl. Phys. Lett. 76 (2000) 1801.
[13] D. Müller, T. Braig, H. Nothofer, M. Arnoldi, M. Gross, U. Scherf, O. Nuyken, K. Meerholz, Chem. Phys. Chem. 4 (2000) 207.
[14] S.R. Tseng, S.C. Lin, H.F. Meng, H.H. Liao, C.H. Ye, H.C. Lai, S.F. Horng, C.S. Hsu, Appl. Phys. Lett. 88 (2006) 163501.
[15] T.M. Brown, R.H. Friend, I.S. Millard, D.J. Lacey, J.H. Burroughes, F. Caciallia, Appl. Phys. Lett. 79 (2001) 174.
[16] T.M. Brown, F. Cacialli, J. Polym. Sci.: Part B 41 (2003) 2649.
[17] J. Huang, W.J. Hou, J.H. Li, G. Li, Y. Yang, Appl. Phys. Lett. 89 (2006) 133509.

Available online at www.sciencedirect.com
ScienceDirect
Organic Electronics 9 (2008) 285–290
Organic Electronics
www.elsevier.com/locate/orgel

High electron mobility triazine for lower driving voltage and higher efficiency organic light emitting devices

Richard A. Klenkler [a,*], Hany Aziz [b], An Tran [c], Zoran D. Popovic [a], Gu Xu [a]

[a] Department of Materials Science and Engineering, McMaster University, 1280 Main Street West, Hamilton, Ontario, Canada L8S 4L8
[b] Department of Electrical and Computer Engineering, University of Waterloo, 200 University Avenue West, Waterloo, Ontario, Canada N2L 3G1
[c] Department of Electrical Engineering, Carleton University, 1125 Colonel By Drive, Ottawa, Ontario, Canada K1S 5B6

Received 1 August 2007; received in revised form 14 November 2007; accepted 19 November 2007
Available online 18 December 2007

Abstract

The triazine compound 4,4′-bis-[2-(4,6-diphenyl-1,3,5-triazinyl)]-1,1′-biphenyl (BTB) was developed for use as an electron transport material in organic light emitting devices (OLEDs). The material demonstrates an electron mobility of $\sim 7.2 \times 10^{-4}$ cm^2 V^{-1} s^{-1} at a field of 8.00×10^5 V cm^{-1}, which is 10-fold greater than that of the widely used material tris(8-hydroxyquinoline) aluminum (AlQ_3). OLEDs with a BTB electron transport layer showed a ~1.7–2.5 V lower driving voltage and a significantly increased efficiency, compared to those with AlQ_3. These results suggest that BTB has a strong potential for use as an OLED electron transport layer material.

PACS: 72.80.Le; 78.60.Fi; 73.50.−h; 73.61.−r

Keywords: Organic device; Charge transport; Electron mobility; Triazine; OLED

1. Introduction

Tris(8-hydroxyquinoline) aluminum (AlQ_3) is the electron transport material (ETM) used in the vast majority of small-molecule based organic light emitting devices (OLEDs). This has been the case since Tang and VanSlyke first reported a bi-layer OLED employing AlQ_3 and a diamine hole transport material (HTM), over twenty-five years ago [1]. Although subsequent advancements in OLED technology included the development of better performing HTMs that gradually replaced the earlier ones [2–6], AlQ_3 continues to be widely used. It has remained despite the increasing realization that alternative ETMs with higher electron mobility are necessary for reducing OLED driving voltage and increasing efficiency. The situation arose, perhaps, from the difficulty to develop materials that can surpass AlQ_3 in electron mobility yet still show adequate electrochemical stability – especially in anionic states formed during electron transport processes – and the ability to form a good contact with the cathode metal. Numerous materials, including

* Corresponding author. Tel.: +1 905 822 7091.
E-mail address: klenklar@mcmaster.ca (R.A. Klenkler).

1566-1199/$ - see front matter © 2007 Elsevier B.V. All rights reserved.
doi:10.1016/j.orgel.2007.11.004

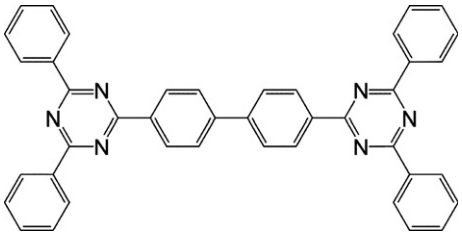

Fig. 1. Molecular structure of BTB electron transport material.

various oxidiazoles, triazoles, and triazines [7–9], have been tested, and more recently, some materials with higher electron mobility, such as bathophenanthroline (BPhen) [10], have shown promise. Nevertheless, AlQ_3 still remains by far the most commonly used OLED ETM. Alternate approaches to reduce the device driving voltage have also been pursued. Among these approaches, doping the electron transport layer (ETL) with an n-type dopant has been particularly successful [11,12]. However, the approach requires co-deposition of the ETM and dopant; therefore, it lacks the inherent simplicity of using a single material. In addition, there has been speculation that such dopants may play a role in limiting the stability of these devices.

In this article, we present results from a study of the novel ETM 4,4′-bis-[2-(4,6-diphenyl-1,3,5-triazinyl)]-1,1′-biphenyl (BTB) for which the molecular structure is depicted in Fig. 1 [13]. The material is found to demonstrate an electron mobility of $\sim 7.2 \times 10^{-4}\,cm^2\,V^{-1}\,s^{-1}$ at a field of $8.00 \times 10^5\,V\,cm^{-1}$, which is an order of magnitude higher than that of AlQ_3. Replacing AlQ_3 with BTB as the ETL material in green emitting OLEDs leads to a significant decrease in the device turn-on voltage. At a brightness of $100\,cd\,m^{-2}$ the driving voltage of a device with a BTB ETL was 3.25 V, ~1.70 V lower than its counterpart with an AlQ_3 ETL. At this brightness, the power conversion efficiency of the two devices was 10.18 and $4.60\,lm\,W^{-1}$, respectively.

2. Experimental

2.1. Synthesis of BTB

4,4-Biphenyldicarbonyl chloride (11.52 g, 41.28 mmol), 1,2-dichlorobenzene (80 mL), thionyl chloride (2.0 mL), and aluminum chloride (11.56 g, 86.69 mmol) were placed in a 500 mL round-bottom flask. While stirring, benzonitrile (17.28 mL, 169.25 mmol) was added slowly, and the resulting reaction mixture was heated under argon to 150 °C for 30 min. The temperature of the reaction was reduced to 120 °C then ammonium chloride (9.05 g, 169.25 mmol) was added. The reaction mixture was then stirred at 170 °C for an additional 20 h. The reaction was then cooled to room temperature after which it was poured into 400 mL of methanol and stirred for 30 min. The precipitates were collected by filtration, washed with methanol, and then dried. The crude product was then purified twice by sublimation to produce the desired material as a white solid (yield: 46%). Melting point (m.p.): 362 °C. ^1H NMR (300 MHz, $CDCl_3$–CF_3COOD) δ [ppm]: 7.76 (t, $J = 7.8$ Hz), 7.92 (t, $J = 7.8$ Hz), 8.10 (d, $J = 8.6$ Hz), 8.63 (d, $J = 8.4$ Hz), 8.84 (d, $J = 8.6$ Hz). ^{13}C NMR (300 MHz, $CDCl_3$–CF_3COOD) δ [ppm]: 129.1, 129.3, 130.3, 130.4, 130.9, 131.9, 137.8, 147.8, 169.1, 169.4. IR (KBr): 1129.1, 129.3, 130.3, 130.4, 130.9, 131.9, 137.8, 147.8, 169.1, 169.4. IR (KBr) [cm^{-1}]: 1588, 1564, 1525, 1445, 1368, 842, 827, 765, 690, 645.

2.2. Fabrication of devices

Devices for mobility; current density, voltage, luminance (*J–V–L*); and stability measurements were prepared in a manner similar to that described by Tang and VanSlyke in which successive layers of material were vapor deposited on to an ITO patterned, UV light cleaned glass substrate [1]. The structures of the devices used in each measurement are shown in Figs. 2–4, and similar parameters

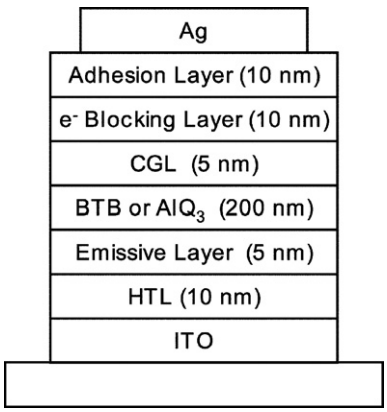

Fig. 2. Structural diagram of the devices used to measure the bulk electron mobility of BTB and AlQ_3 by the photoinduced electroluminescence method. Where, Ag is the silver cathode, CGL is the charge generator layer, and ITO is the indium tin-oxide anode.

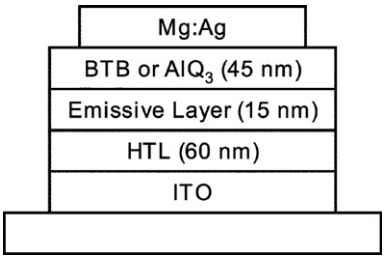

Fig. 3. Structural diagram of the organic light emitting devices used for the current density, voltage, luminance measurements.

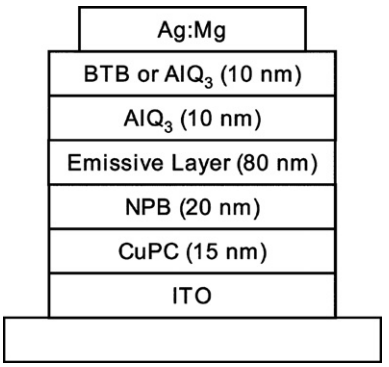

Fig. 4. Structural diagram of the organic light emitting devices used for the stability (luminance vs. time) measurements.

(e.g. evaporation rates) were used in the preparation of each.

Devices for the mobility measurements (Fig. 2) were prepared in the following manner. First, 10 nm of hole transporting NPB was deposited at a rate of 0.1 nm s^{-1}, followed by a 5 nm emissive electroluminescent layer consisting of AlQ_3 and C545T coumarin dye, co-deposited at 0.35 and 0.003 nm s^{-1}, respectively (where, NPB is *N*,*N*′-di-(naphthalene-1-yl)-*N*,*N*′-diphenyl-benzidine and C545T is 10-(2-benzothiazolyl)-2,3,6,7-tetrahydro-1,1,7,7-tetramethyl 1-1*H*,5*H*,11*H*-(1)-benzopyropyrano(6,7,8-*i*,*j*)quinolizin-11-one). The C545T containing layer was included due to its widely know effect of improving recombination efficiency, which thus increases measurement signal strength. Next, a 200 nm layer of either BTB or AlQ_3 was deposited at either 0.2 nm s^{-1} or 0.35 nm s^{-1}, respectively. It is in these electron transporting layers that mobility was measured. Following the BTB or AlQ_3 a 5 nm layer of CuPC charge generator was deposited at 0.15 nm s^{-1} (where, CuPC is copper phthalocyanine). Next, 10 nm layers of NPB and AlQ_3 were deposited successively, at 0.12 nm s^{-1} and 0.35 nm s^{-1}. This last layer of NPB served as an electron blocking layer [14], and the final layer of AlQ_3 served the sole purpose of improving adhesion of the cathode [14,15]. Finally, a Ag cathode of 90 nm was deposited at 0.1 nm s^{-1}.

Similarly, OLEDs for the *J*–*V*–*L* measurements (Fig. 3) were prepared by depositing 60 nm of NPB followed by a 15 nm emissive layer of co-deposited AlQ_3 and C545T, and then a 45 nm layer of either BTB or AlQ_3. Finally, a two layer cathode consisting of a 120 nm layer of co-deposited Mg and Ag (at a 10:1 ratio) followed by a 90 nm capping layer of Ag was deposited.

The OLEDs for the stability measurements (Fig. 4) were prepared by first depositing 15 nm of CuPC followed by 20 nm of NPB. Next, an 80 nm emissive layer consisting of rubrene, NPB, and AlQ_3 was co-deposited at 0.004, 0.498, and 0.498 nm s^{-1}, respectively (where, rubrene is 5,6,11,12-tetraphenylnaphthacene). Then a 10 nm layer of AlQ_3 was deposited followed by a 10 nm layer of either AlQ_3 or BTB, which formed the ETL. Finally, a two layer cathode consisting of a 120 nm layer of co-deposited Mg:Ag (10:1) followed by a 90 nm capping layer of Ag was deposited.

Lastly, it should be noted that microscopic examination of all the devices showed the films to be smooth and featureless, suggesting an amorphous morphology.

3. Results and discussion

3.1. Electron mobility

In this study, we used the recently reported photo-induced electroluminescence (EL) mobility measurement technique [14]. The method is based on measuring optically induced electroluminescence transients and allows testing the charge transport properties in sub-micron thin films that more closely resemble those used in an OLED. In these devices (Fig. 2) the thin film (~200 nm) of the material to be tested is placed between a charge generating layer (CGL) and an emissive electroluminescent layer. The three organic layers are sandwiched between an indium tin-oxide anode and a blocking cathode (the device structure further included interface thin layers at the two contacts as outlined in the experimental section). The charge carrier mobility is calculated from the average transient time that carriers – photogenerated in the CGL by a laser pulse – take to reach the emissive layer while in an externally applied electric field. The results of the measurements are shown in Fig. 5. As can be seen,

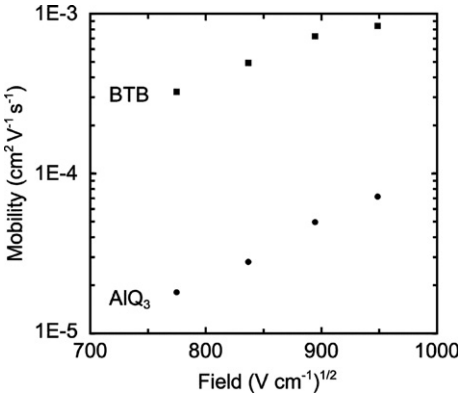

Fig. 5. Mobility as a function of field for 200 nm thin films of BTB and AlQ_3 electron transport material. Each point represents the average mobility, determined from 3 individual devices.

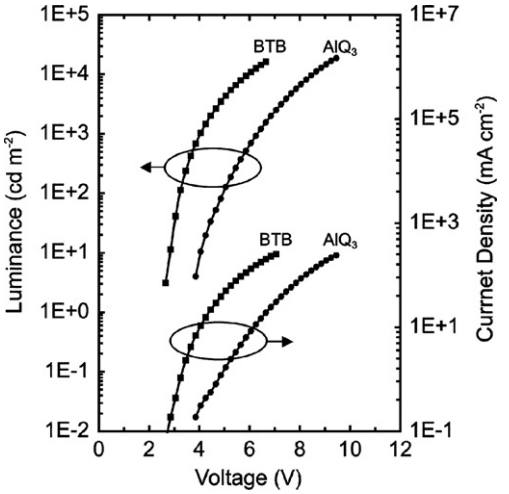

Fig. 6. Luminance and current density as a function of voltage, for organic light emitting devices containing either BTB or AlQ_3 electron transport layers.

BTB exhibits an order of magnitude higher electron mobility (μ_e) than AlQ_3 across the entire range of applied fields (E). As expected, both materials exhibited Poole–Frenkel behavior ($\log \mu_e \propto E^{1/2}$), which is typical of charge transport in amorphous organic systems at moderate fields [16]. In absolute terms, BTB has approximately a factor of 10 stronger field dependency than AlQ_3.

3.2. Brightness and efficiency

To investigate the effect that using BTB instead of AlQ_3 has on OLED performance, we tested OLEDs with ETLs of either of these materials. In these devices (Fig. 3) NPB served as a hole transport layer, 0.6% C545T-doped AlQ_3 served as the emissive layer, and ITO and Mg:Ag served as the anode and cathode, respectively. Under forward bias the BTB devices gave bright and uniform green electroluminescence that was essentially identical to that of the AlQ_3 devices ($CIE_{(x,y)}$ coordinates were (0.317, 0.638) and (0.311, 0.631) for the BTB and AlQ_3 ETL OLEDs, respectively). Fig. 6 shows the results of J–V–L measurements performed on these devices. A numerical summary and analysis of the results is shown in Table 1. As can be seen in Fig. 6, for a given luminance the OLED devices containing a BTB ETL have a ~1.70–2.50 V lower driving voltage compared to their AlQ_3 counterparts. The lower driving voltage has the effect of increasing the device efficiency, which is noted in Table 1 by the calculated values for electroluminescence efficiency (η_{EL}) and power conversion efficiency (η_P). For example, at a brightness of 100 cd m^{-2} the driving voltage of a device with a BTB ETL was 3.25 V, which is ~1.70 V lower than its counterpart with an AlQ_3 ETL. At this brightness the power conversion efficiency of the two devices was 10.18 and 4.60 lm W^{-1}, respectively. Conversely, at a fixed current density the luminance for the BTB OLEDs was greater than that of those containing AlQ_3 (luminance values at 25 mA cm^{-2} are shown in Table 1). The observation can be attributed to the improved electron/hole balance and the subsequent increase in electron/hole recombination efficiency that in part results from the use of a higher electron mobility material. However, for a more complete picture, the electron injection energy barrier from the Mg:Ag cathode into the BTB ETL must be considered, as well. Earlier experiments (data not shown here) showed that the inclusion of a very thin (10 nm) BTB injection

Table 1
Numerical summary and analysis of the current density, voltage, luminance measurement results shown in Fig. 6. Where, ETL is the electron transport layer material, J is current density, L is luminance, V is voltage, η_{EL} is electroluminescence efficiency, and η_P is power conversion efficiency

ETL	J (mA cm^{-2})	L (cd m^{-2})	V (V)	η_{EL} (cd A^{-1})	η_P (lm W^{-1})
BTB	0.95	100	3.25	10.53	10.18
AlQ_3	1.38	100	4.95	7.25	4.60
BTB	10.30	1000	4.05	9.71	7.53
AlQ_3	12.15	1000	6.30	8.23	4.10
BTB	25.00	2300	4.51	9.20	6.41
AlQ_3	25.00	2040	6.86	8.16	4.74

layer at the Mg:Ag cathode of a bilayer NPB (60 nm)/AlQ_3 (75 nm) based OLED lead to a decrease in driving voltage from 7.7 to 7.4 V, despite the added thickness of the additional layer. This observation suggests that the lowest unoccupied molecular orbital (LUMO) of BTB is somewhere between 3.0 eV (LUMO of AlQ_3) [17] and 3.7 eV (work function of Mg:Ag) [18]. Further, photoluminescence measurements (data not shown here) show BTB to have a bandgap (E_g) of ~3.1 eV. It follows that the BTB highest occupied molecular orbital (HOMO) energy level will be between 6.1 and 6.8 eV (from LUMO + E_g). Given that electron injection from the Mg:Ag cathode into BTB requires less voltage, the superior OLED *J–V–L* characteristics can be attributed to both the higher mobility and greater injection efficiency of BTB as compared to AlQ_3.

Finally, it should be noted that the BTB devices show an interesting trend of diminishing improvement in efficiency over the AlQ_3 devices with increasing current density. The reasons behind this behavior are still unclear; however, the correlation of this effect with BTB layer thickness (data not shown here) may suggest that it is due to a difference in the space charge limited conduction behavior between BTB and AlQ_3.

3.3. Stability

To investigate the stability of BTB as an ETL, we tested the material in a mixed emissive layer OLED [3,19]. The mixed emissive layer structure was chosen due to its known improved stability over the simplified device structure used for the *J–V–L* measurements. Hence, the use of a mixed emissive layer structure is more suitable when comparing performance over an extended period of time. In these mixed emissive layer devices (Fig. 4) CuPC served as a buffer layer [3], NPB served as a hole transport layer, a 0.4% rubrene-doped 50:50 mix of NPB and AlQ_3 served as the emissive layer [19], and ITO and Mg:Ag served as the anode and cathode, respectively. The layers of either AlQ_3 or BTB adjacent to the cathode served as the ETLs, where AlQ_3 was used as a reference. To avoid possible complexation between NPB and BTB at the emissive/BTB contact, a thin interfacial layer of AlQ_3 (10 nm thick) was introduced on top of the emissive layer. For ease of comparison, this additional layer was also included in the AlQ_3 ETL device. The stability of the OLEDs was assessed by measuring their luminance as a function of time at a fixed average current density of 31.25 mA cm^{-2} at 100 °C. The higher temperature was used to further accelerate the test where, according to our previous report the half-life at room temperature is typically nine times that at 100 °C for a device of this architecture driven at 31.25 mA cm^{-2} [20]. The results, shown in Fig. 7, revealed that both devices have comparable long-term stability. Thus, replacing the AlQ_3 ETL with one of BTB has almost no effect on overall stability. Microscopic examination of the OLEDs after the test, again, showed the films to be smooth and featureless, suggesting no change in the amorphous morphology. The high stability of these devices can partially be attributed to the high morphological stability of BTB, which, based on our differential scanning calorimetry measurements, has a glass transition temperature of 137 °C.

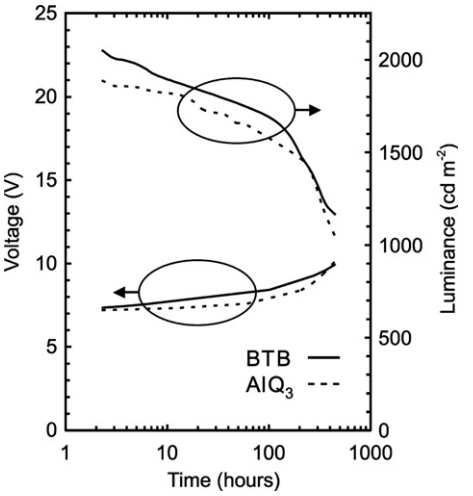

Fig. 7. Luminance as a function of time, for organic light emitting devices containing either BTB or AlQ_3 electron transport layers.

4. Conclusions

In summary, the bulk mobility of physically vapor deposited (PVD) thin-films of BTB and AlQ_3 were measured by the photoinduced EL method [14]. As well, a comparison of the *J–V–L* characteristics of OLEDs prepared with either a BTB or AlQ_3 ETL was made. It was found that the mobility of the BTB films was one order of magnitude larger than that of AlQ_3, for example mobility values of 7.2×10^{-4} and 4.9×10^{-5} cm^2 V^{-1} s^{-1} at a field of 8.00×10^5 V cm^{-1} for BTB and AlQ_3, respectively. Due to its higher electron mobility,

using BTB to replace AlQ_3 as an ETL in OLEDs results in a significant decrease in device driving voltage and, as a consequence, enhances device efficiency. The results here suggest that BTB indeed has a strong potential as an ETL in OLEDs, especially for applications where low power consumption is important. Although the exact reasons behind the high electron mobility of BTB are still uncertain, the difference in mobility may be due to the potentially flatter molecular structure of BTB relative to AlQ_3 [21]. A flatter structure would allow for increased molecular stacking, and as a result a larger degree of inter-molecular π–π orbital overlapping; thus, decreasing the inter-molecular hopping distance for charge carriers.

Acknowledgements

The authors gratefully acknowledge the assistance of Dr. Nan-Xing Hu and Jennifer Coggan.

References

[1] C.W. Tang, S.A. VanSlyke, Appl. Phys. Lett. 51 (1987) 913.
[2] Y. Shirota, Y. Kuwabara, H. Inada, Appl. Phys. Lett. 65 (1994) 807.
[3] S.A. VanSlyke, C.H. Chen, C.W. Tang, Appl. Phys. Lett. 69 (1996) 2160.
[4] S. Tokito, H. Tanaka, K. Noda, A. Okada, Y. Taga, IEEE Trans. Electron. Dev. 44 (1997) 1239.
[5] S. Okutsu, T. Onikubo, M. Tamano, T. Enokida, IEEE Trans. Electron. Dev. 44 (1997) 1302.
[6] D.F. O'Brien, P.E. Burrows, S.R. Forrest, B.E. Koene, D.E. Loy, M.E. Thompson, Adv. Mater. 10 (1998) 1108.
[7] M. Thelakkat, H.-W. Schmidt, Polym. Adv. Technol. 9 (1998) 429.
[8] T. Ishi-i, K. Yaguma, T. Thiemann, M. Yashima, K. Ueno, S. Mataka, Chem. Lett. 33 (2004) 1244.
[9] T. Yamamoto, S. Watanabe, H. Fukumoto, M. Sato, T. Tanaka, Macromol. Rapid Commun. 27 (2006) 317.
[10] S. Naka, H. Okada, H. Onnagawa, T. Tsutsui, Appl. Phys. Lett. 76 (2000) 197.
[11] M. Pfeiffer, S.R. Forrest, K. Leo, M.E. Thompson, Adv. Mater. 14 (2002) 1633.
[12] G. He, M. Pfeiffer, K. Leo, M. Hofmann, J. Brinstock, R. Pudzich, J. Salbeck, Appl. Phys. Lett. 85 (2004) 3911.
[13] N.-X. Hu, S. Xie, Z.D. Popovic, B. Ong, A.-M. Hor, US Patent 5 942 340, 1999.
[14] R.A. Klenkler, G. Xu, H. Aziz, Z.D. Popovic, Appl. Phys. Lett. 88 (2006) 101.
[15] H. Aziz, Z.D. Popovic, N.-X. Hu, A.-M. Hor, G. Xu, Science 283 (1999) 1900.
[16] D.M. Pai, B.E. Springett, Rev. Mod. Phys. 65 (1993) 163.
[17] D. Kolosov, V. Adamovich, P. Djurovich, M.E. Thompson, C. Adachi, J. Am. Chem. Soc. 124 (2002) 9945.
[18] B.J. Chen, X.W. Sun, K.S. Wong, X. Hu, Opt. Exp. 13 (2005) 26.
[19] Z.D. Popovic, H. Aziz, C.P. Tripp, N.-X. Hu, A.-M. Hor, G. Xu, Proc. SPIE 3476 (1998) 68.
[20] H. Aziz, Z.D. Popovic, N.-X. Hu, Appl. Phys. Lett. 81 (2002) 370.
[21] A. Ranganathan, B.C. Heisen, I. Dix, F. Meyer, Chem. Commun. (2007) 3637.

Available online at www.sciencedirect.com
ScienceDirect
Organic Electronics 9 (2008) 291–295
Organic Electronics
www.elsevier.com/locate/orgel

Small polymeric nano-dot enhanced pure-white organic light-emitting diode

Jwo-Huei Jou [a,*], Mao-Feng Hsu [a], Wei-Ben Wang [a], Chi-Ping Liu [a], Zhao-Chin Wong [a], Jing-Jong Shyue [b], Chung-Che Chiang [c]

[a] Department of Materials Science and Engineering, National Tsing Hua University, Hsin-Chu 300, Taiwan, ROC
[b] Research Center for Applied Sciences, Academia Sinica, Taipei 115, Taiwan, ROC
[c] Department of Applied Chemistry, National Chi Nan University, Nantou Hsien 545, Taiwan, ROC

Received 15 September 2007; received in revised form 18 November 2007; accepted 25 November 2007
Available online 3 December 2007

Abstract

Marked efficiency improvement of a spin-coated phosphorescent pure-white organic light-emitting diode was obtained by incorporating a novel small polymeric nano-dot (PND) in the hole-transporting layer. The resultant device efficiency strongly depended on the concentration and size of the PND used. The resultant power efficiency at 100 cd/m^2, for example, was increased from 6.8 to 23.7 lm/W, an increase of 350%, as 14 wt% PND of 8 nm in size was employed. The improvement may be attributed to a better carrier-injection balance resulted from hole trapping on the PND.

Keywords: OLED; Efficiency; Nano dot

1. Introduction

Organic light-emitting diodes (OLEDs), particularly white OLEDs, are increasingly attracting interest because of their potential as flat-panel displays and for liquid crystal display backlighting and area illumination [1–4]. These applications require highly efficient white OLEDs. Numerous approaches have been reported to improve the efficiency, such as the use of electroluminescence (EL) efficient phosphorescent and/or fluorescent materials [4], coupled with appropriate device architectures. Efficient devices typically possess thin device thickness, low carrier-injection barrier, effective carrier/exciton confinement, highly efficient host-to-guest energy transfer and balanced carrier injection [4–14]. Recently, the incorporation of quantum- or nano-dot in the emissive or another layer has been found to be effective for some OLED devices [13–18]. However, the mechanism of this improvement is not yet clear. A homogeneous distribution of the embedded nano-dots may also be crucial, which restrains the use of a dry process for their incorporation. In order to obtain high efficiency, OLED devices must frequently be kept relatively thin, which would consequently limit the use of large nano-dots.

In this letter, we present a pure-white OLED with marked efficiency improvement obtained by incorporating small polymeric nano-dot (PND) in

* Corresponding author.
E-mail address: jjou@mx.nthu.edu.tw (J.-H. Jou).

1566-1199/$ - see front matter © 2007 Elsevier B.V. All rights reserved.
doi:10.1016/j.orgel.2007.11.005

hole-transporting layer (HTL), poly(ethylenedioxythiophene): poly(styrene sulfonic acid) (PEDOT:PSS). The effects of the size and concentration of the PND on the EL characteristics of the resultant devices were examined. The resultant power efficiency at 100 cd/m^2, for example, was increased from 6.8 to 23.7 lm/W, an increase of 350%, when 14 wt% PND of 8 nm in size was employed.

2. Experimental

Fig. 1 shows the schematic energy-level diagram of the white OLEDs studied. The device comprises a 1250 Å anode layer of indium tin oxide (ITO), a 350 Å HTL of PEDOT:PSS doped with PND, a 400 Å white emissive layer, a 360 Å electron-transporting layer (ETL) of 2,2′,2″-(1,3,5-benzenetriyl)-tris(1-phenyl-1-*H*-benzimidazole) (TPBi), a 7 Å electron-injection layer of lithium fluoride (LiF) and a 1500 Å cathode layer of aluminum (Al). The white emissive layer was composed of a molecular host of 4,4′-bis(carbazol-9-yl) biphenyl (CBP) doped with 0.3 wt% red dye of bis[2-(2′-benzothienyl)-pyridinato-N,C$^{3\prime}$] (acetyl-acetonate) iridium (III) [Btp$_2$Ir(acac)], 0.08 wt% green dye of tris(2-phenylpyridine) iridium (III) [Ir(ppy)$_3$] and 14 wt% blue dye of bis(3,5-difluoro-2-(2-pyridyl)-phenyl-(2-carboxypyridyl)) iridium (III) (FIrpic).

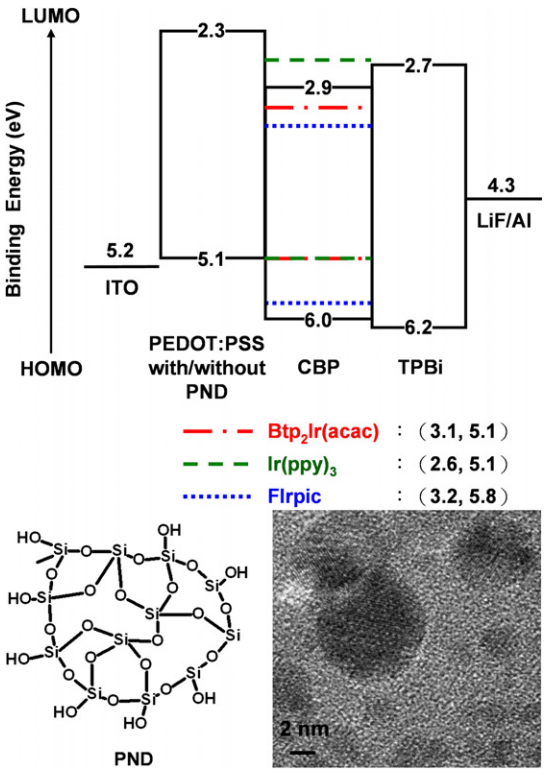

Fig. 1. Schematic energy-level diagram of the white OLEDs. Also shown are the molecular structure and TEM image of the studied PND.

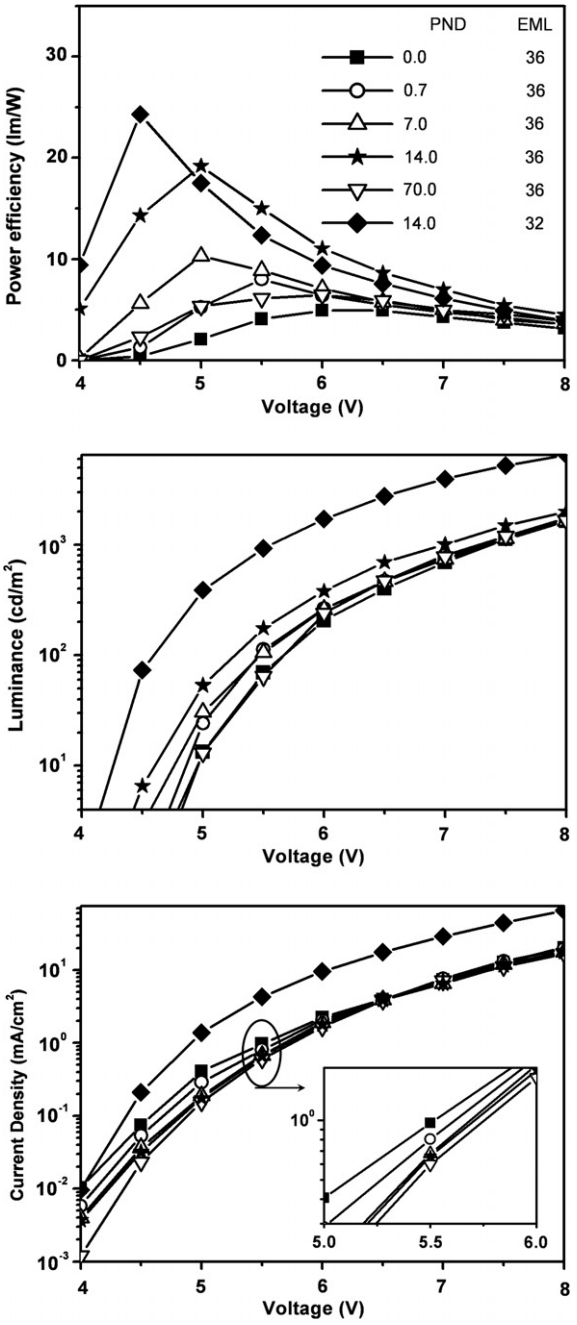

Fig. 2. Doping concentration effects of the 8 nm PND on the power efficiency, current density and luminance of the white OLEDs.

Table 1
The effects of size and concentration of PND and thickness of ETL on the EL characteristics of the white OLEDs

Concentration of PND (wt%)	Size of PND (nm)	Thickness of ETL (nm)	Power efficiency (lm/W)[b]		CIE 1931 chromatic coordinates (x, y)	
			At 100 cd/m^2	Max.	At 100 cd/m^2	At 1000 cd/m^2
0.0	–	36	4.3 ± 0.2	4.9 ± 0.2	(0.333, 0.356)	(0.315, 0.355)
0.7	8	36	7.6 ± 0.3	8.1 ± 0.3	(0.333, 0.356)	(0.316, 0.356)
7.0	8	36	8.9 ± 0.3	10.3 ± 0.3	(0.332, 0.356)	(0.316, 0.355)
14.0	8	36	17.6 ± 0.3	19.2 ± 0.3	(0.332, 0.356)	(0.316, 0.356)
70.0	8	36	6.2 ± 0.2	6.5 ± 0.3	(0.333, 0.357)	(0.315, 0.356)
0.0	–	32	6.8 ± 0.2	6.8 ± 0.3	(0.324, 0.357)	(0.310, 0.353)
10.5	8	32	18.8 ± 0.3	19.3 ± 0.3	(0.324, 0.358)	(0.310, 0.353)
14.0	8	32	23.7 ± 0.3	24.3 ± 0.3	(0.323, 0.357)	(0.310, 0.352)
17.5	8	32	19.9 ± 0.3	21.0 ± 0.3	(0.323, 0.357)	(0.313, 0.355)
21.0	8	32	17.3 ± 0.3	18.2 ± 0.3	(0.323, 0.357)	(0.310, 0.356)
7.0	8[a]	36	8.9 ± 0.3	10.2 ± 0.3	(0.331, 0.358)	(0.314, 0.356)
7.0	15[a]	36	7.7 ± 0.3	8.7 ± 0.3	(0.332, 0.357)	(0.315, 0.356)
7.0	30[a]	36	6.9 ± 0.2	7.5 ± 0.3	(0.331, 0.358)	(0.314, 0.355)

[a] These devices were fabricated from two different batches.
[b] Power efficiency was calculated as an average of the data taken from four separated emissive areas on the same glass substrate.

The PNDs were prepared by hydrolysis and condensation of sodium metasilicate [19]. To examine the size effect, PNDs with sizes of 8, 15 and 30 nm were synthesized. Fig. 1 also shows a schematic illustration of the molecular structure and transmission electron microscopic (TEM) image of one of the synthesized PNDs. The resultant PNDs also exhibited negative charge as determined by the value of their zeta potential measured with a Nano ZS ZEN-3600.

The luminance and CIE chromatic coordinates of the resulted OLEDs were measured by using Minolta CS-100 luminance-meter. A Keithley 2400 electrometer was used to measure the current–voltage (I–V) characteristics. All the devices were characterized without encapsulation and all the measurements were carried out in the ambient condition. The emission area of all the resultant devices was 25 mm^2 and only the luminance in the forward direction was measured.

3. Result and discussion

Fig. 2 shows the power efficiency of the white OLEDs with and without the incorporation of the 8 nm PND. The power efficiency increased as the doping concentration of PND first increased. Without the incorporation of PND, the power efficiency at 100 cd/m^2, for example, was 4.3 lm/W. The power efficiency became 7.6 lm/W as 0.7 wt% PND was added. It was further increased to 17.6 lm/W as 14.0 wt% PND was incorporated. By increasing the PND concentration to 70.0 wt%, the power efficiency dropped to 6.2 lm/W. By fixing the PND concentration at 14 wt%, a highest power efficiency 23.7 lm/W was obtained by changing the thickness of the ETL from 36 to 32 nm. Relatively high sample-to-sample reproducibility on the power efficiency data was obtained as shown in Table 1.

Fig. 2 also shows the effects of PND concentration on the current density and luminance of the

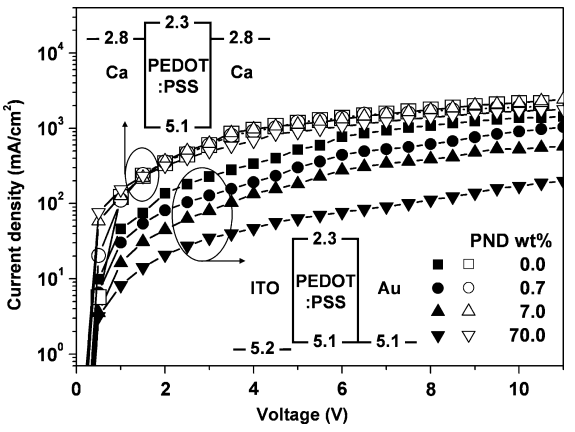

Fig. 3. Doping concentration effects of the 8 nm PND on the current density of the devices. The hole-injection layers of PEDOT:PSS doped with x wt% PND were sandwiched by high-work-function electrode pairs, ITO and gold, and the low-work-function electrode pairs, calcium. Insets: schematic energy-level diagrams of the devices.

white OLEDs. The current density continuously decreased as the PND concentration increased, indicating that the PND had effectively reduced the injection of hole carrier. The incorporation of titanium oxide nano-dot in a separated layer of a green OLED was found to enhance the injection of hole caused by tunneling effect as revealed by the marked increase of current density and decrease of turn-on voltage [11–13]. However, in the present work the turn-on voltage herein did not change much with the change of PND concentration, revealing the absence of tunneling effect. The size of the PND, 8 nm, was much smaller than the 35 nm thickness of the PEDOT:PSS HTL, so that the PND was presumably well embedded within the HTL. The turn-on voltage described herein was defined as the voltage at which the luminance is equal to or greater than 10 cd/m^2. The resultant luminance, especially at voltage between 4 and 6 V, did not decrease, but increased obviously until the PND concentration was above 14.0 wt%. This indicates that higher carrier-recombination efficiency was resulted from the addition of nano-dot to the device, since its corresponding current density was comparatively lower than that of its counterpart without nano-dot incorporation.

The reason why the incorporation of PND in the HTL of PEDOT:PSS reduced the injection of hole, but not electron, can be revealed by the difference in I–V characteristics of the devices consisting only of a HTL of PEDOT:PSS sandwiched by high- and low-work-function electrode pairs, as shown in Fig. 3. As also shown in the figure, the device with the low-work-function electrode pair, calcium, possesses relatively low injection barrier to electron (0.5 eV) but relatively high injection barrier to hole (2.3 eV). Thus any measured current density should be mainly attributed to electron transport. Regardless of the addition amount, the addition of PND had little effect on the current density of the device with a calcium electrode pair, indicating that the PND had no effect on the injection of electron.

The device with the high-work-function electrode pair, ITO and gold, possesses relatively low injection barrier to hole (−0.1 eV) but relatively high injection barrier to electron (2.8 eV), so that any measured current density should be mainly attributed to hole transport. Actually, the current density of the device with the high-work-function electrode pair of ITO and gold markedly decreased as the concentration of PND increased, proving that the PND could effectively reduce the injection of hole into the HTL. The reason why the PND could reduce hole injection may be attributed to its negative charge character on surface, whose zeta potential was −5.8 mV as determined at 8 wt% in a THF suspension.

The size effect of PND on the EL characteristics is shown in Table 1. By fixing the PND concentration at 7.0 wt%, for example, the power efficiency at 100 cd/m^2 increased from 6.9 to 8.8 lm/W as the size of PND decreased from 30 to 8 nm. It is plausible that the smaller PND may have exhibited higher surface charge density, enabling the trapping of more holes and leading to a more balanced carrier injection. However, further investigation is needed to clarify the real cause. Regardless of their size, the incorporation of PND showed little effect on the resultant chromaticity of the white device at 100 or 1000 cd/m^2. The chromaticity coordinates at 100 cd/m^2, for examples, were nearly the same, (0.331, 0.358), (0.332, 0.357) and (0.331, 0.358), for the devices incorporated with 8, 15 and 30 nm PNDs.

Table 2
Doping concentration effects of the 8 nm PND on the EL characteristics of the OLEDs of ITO/PEDOT:PSS with x wt% PND/first emissive layer/second emissive layer/TPBi/LiF/Al

Device	First emissive layer	Second emissive layer	Concentration of PND (wt%)	CIE 1931 chromatic coordinates (x, y)	
				At 5.5 V[a]	At 7.5 V[b]
I	FIrpic (blue)	$Btp_2Ir(acac)$ (red)	0.0	(0.481, 0.327)	(0.459, 0.327)
			0.7	(0.477, 0.322)	(0.457, 0.320)
			7.0	(0.475, 0.321)	(0.456, 0.320)
			70.0	(0.474, 0.320)	(0.454, 0.319)
				At 7.5 V[a]	At 10.5 V[b]
II	$Btp_2Ir(acac)$ (red)	FIrpic (blue)	0.0	(0.267, 0.311)	(0.283, 0.312)
			0.7	(0.268, 0.310)	(0.285, 0.312)
			7.0	(0.269, 0.311)	(0.285, 0.317)
			70.0	(0.271, 0.313)	(0.288, 0.317)

[a] The voltage is defined as the resultant value obtained at luminance $\geqslant$100 cd/m^2.
[b] The voltage is defined as the resultant value obtained at lumina.

Although the incorporation of PND showed little effect on the chromaticity of the white device, the recombination zone was actually shifted toward the anode as PND was added. The recombination zone shift can be evidenced by investigating the effect of adding PND on the chromaticity of the OLED devices with two separated emissive layers, one blue and one red. As shown in Table 2, systematic chromatic variation was stronger as the content of PND was increased. The chromaticity coordinates at 100 cd/m^2, for example, were (0.481, 0.327), (0.477, 0.322), (0.475, 0.321) and (0.474, 0.320) for Device I with 0, 0.7, 7.0 and 70 wt% incorporated PND, respectively. The blue shift confirmed that the recombination zone would shift toward the blue emissive layer, which was closer to the anode, as PND was incorporated. Similarly, Device II showed red shift as PND was incorporated. In Device II, the red emission layer was closer to the anode. The red shift in Device II also confirmed the recombination zone to be shifted toward the anode as PND was added.

4. Conclusion

In conclusion, a novel small PND was synthesized and added in the hole-transporting layer, PEDOT:PSS, to markedly improve the efficiency of a phosphorescent pure-white organic light-emitting diode. The device efficiency was strongly dependent on the concentration and size of the PND. The resultant power efficiency at 100 cd/m^2, for example, was increased from 6.8 to 23.7 lm/W, an increase of 350%, as 14 wt% PND of 8 nm in size was employed. This improvement may be attributed to a better carrier-injection balance resulted from hole trapping on the added PND, which exhibited negative charge on surface and hence facilitated hole trapping in the hole-transporting layer.

Acknowledgement

This work was financially supported under NSC95-2221-E-007-128-MY3, AFOSR-AOARD-05-0488 and BD96013P.

References

[1] J. Kido, M. Kimura, K. Nagai, Science 267 (1995) 1332.
[2] R. Duggal, J.J. Shiang, C.M. Heller, D.F. Foust, Appl. Phys. Lett. 80 (2002) 3470.
[3] S.R. Forrest, Org. Electron. 4 (2003) 45.
[4] W. D'Andrade, S.R. Forrest, Adv. Mater. 16 (2004) 1585.
[5] M.T. Lee, C.H. Liao, C.H. Tsai, C.H. Chen, Adv. Mater. 17 (2005) 2493.
[6] L.S. Hung, C.H. Chen, Mater. Sci. Eng. R 39 (2002) 143.
[7] V.I. Adamovich, S.R. Cordero, P.I. Djurovich, A. Tamayo, M.E. Thompson, B.W. D'Andrade, S.R. Forrest, Org. Electron. 4 (2003) 77.
[8] Z.Y. Xie, L.S. Hung, S.T. Lee, Appl. Phys. Lett. 79 (2001) 1048.
[9] J.H. Jou, Y.S. Chiu, C.P. Wang, R.Y. Wang, H.C. Hu, Appl. Phys. Lett. 88 (2006) 193501.
[10] C.O. Poon, F.L. Wong, S.W. Tong, R.Q. Zhang, C.S. Lee, S.T. Lee, Appl. Phys. Lett. 83 (2003) 1038.
[11] F. Zhu, B. Low, K. Zhang, S. Chua, Appl. Phys. Lett. 79 (2001) 1205.
[12] Z.B. Deng, X.M. Ding, S.T. Lee, W.A. Gambling, Appl. Phys. Lett. 74 (1999) 2227.
[13] Z.F. Zhang, Z.B. Deng, C.J. Liang, M.X. Zhang, D.H. Xu, Displays 24 (2003) 231.
[14] J.-M. Caruge, J.E. Halpert, V. Bulovic, M.G. Bawendi, Nano Lett. 6 (2006) 2991.
[15] S.A. Carter, J.C. Scott, P.J. Brock, Appl. Phys. Lett. 71 (1997) 1145.
[16] V. Bliznyuk, B. Ruhstaller, P.J. Brock, U. Scherf, S.A. Carter, Adv. Mater. 11 (1999) 1257.
[17] Y.K. Kim, K.Y. Lee, O.K. Kwon, D.M. Shin, B.C. Sohn, J.H. Choi, Syn. Met. 111–112 (2000) 207.
[18] C.C. Oey, A.B. Djurisic, C.Y. Kwong, C.H. Cheung, W.K. Chan, J.M. Nunzi, P.C. Chui, Thin Solid Films 492 (2005) 253.
[19] Y.G. Hsu, K.H. Lin, I.L. Chiang, Mater. Sci. Eng. B 87 (2001) 31.

Available online at www.sciencedirect.com
ScienceDirect
Organic Electronics 9 (2008) 296–302
Organic Electronics
www.elsevier.com/locate/orgel

Processable and multichromic polymer of bis-3-hexylthiophene substituted 4-*tert*-butylphenyl quinoxaline

Funda Ozyurt, E. Gorkem Gunbas, Asuman Durmus, Levent Toppare *

Department of Chemistry, Middle East Technical University, 06531 Ankara, Turkey

Received 18 October 2007; received in revised form 16 November 2007; accepted 23 November 2007
Available online 4 December 2007

Abstract

A new polythiophene derivative, poly-2,3-bis(4-*tert*-butylphenyl)-5,8-bis(4-hexylthiophen-2-yl)quinoxaline (PHTQ) was synthesized by both chemical and electrochemical polymerization and its electrochemical properties were reported. The monomer was electrochemically polymerized in the presence of tetrabutylammonium hexafluorophosphate ($TBAPF_6$) as the supporting electrolyte in dichloromethane–acetonitrile (5:95, v:v). Nuclear magnetic resonance (^1H NMR) and Fourier transform infrared (FTIR) were utilized for the characterization of the monomer and the soluble polymer. The polymer was further characterized by gel permeation chromatography (GPC). Spectroelectrochemistry and switching ability of the polymer were investigated by UV–vis spectrophotometer and cyclic voltammetry. The polymer revealed three distinctive colors upon doping which indicated that the polymer is multichromic. *tert*-Butyl group on the pendant phenyl rings and hexyl groups on thiophene eased the solution processability of the electrochromic polymer. The electrochemical and spectral properties of the chemically synthesized polymer were investigated via spray coating on ITO glass slides.

PACS: 65.40.Gk; 82.45.Aa; 78.20.Jq; 82.35.Cd

Keywords: Processable conducting polymers; Multichromism; Electrochemical polymerization

1. Introduction

A reversible optical change in a material caused by an applied voltage, for both organic and inorganic species is broadly defined as electrochromism [1]. Generation of absorption bands at different regions of the visible and NIR regions upon switching between redox states causes this phenomenon. Electrochromism is one of the most popular application of conjugated polymers together with applications like light-emitting diodes (LEDs) [2], solar cells (SCs) [3] and sensors [4]. Although many conjugated polymers revealed electrochromism, for realization of commercial device applications urgent need for processable polymers have arisen. There are vast amount of methods to develop soluble conducting polymers but most common and effective ones were shown to be synthesis of soluble precursors that forms conductive coating upon heating [5] and introduction of long alkyl side chains [6] in

* Corresponding author. Fax: +90 3122103200.
E-mail address: toppare@metu.edu.tr (L. Toppare).

1566-1199/$ - see front matter © 2007 Elsevier B.V. All rights reserved.
doi:10.1016/j.orgel.2007.11.006

the polymer backbone. Although introduction of alkyl side chains enhance the ease of processing it also modify the electronic properties of the resulting polymers [7]. Many key properties like oxidation potential of the monomer and the polymer [8], stability of the oxidized state [9] and band gap [10] can be changed upon introducing strong electron-donating alkoxy side chains.

When soluble, processable EC polymers were shown to be potentially useful materials [11–14], electropolymerization has always been the most powerful method for investigation of potential electrochromism in conducting polymers. Structural modification of the monomer repeat unit is used to tune the band gap and achieve multicolor electrochromic polymers through homopolymerization. Polyaniline has multiple colored forms depending on the oxidation state of the polymer film which include leucoemeraldine (bright yellow), emeraldine (green), and pernigraniline (dark blue) [15–17]. Attaching EDOT (3,4-ethylenedioxythiophene) moieties through the 3- and 6-positions of carbazole also results in a polymer that exhibits three-colored multichromism [18]. The multichromism revealed by these kind of systems occurs due to a conjugation break along the polymer which results in the formation of radical cation and dication oxidized states. Multicolored electrochromism observed in a homopolymer is a promising property since these type of materials can be utilized as active layers in many device applications especially in the information systems.

In this study, we present the synthesis and characterization of a monomer, 2,3-bis(4-*tert*-butylphenyl)-5,8-bis(4-hexylthiophen-2-yl) quinoxaline (HTQ) which was polymerized to give a solution processable, three-colored multichromic polymer. Electrochemical homopolymerization of HTQ was achieved using $TBAPF_6$ as the supporting electrolyte from a 10^{-2} M monomer solution in a mixture of dichloromethane (DCM) and acetonitrile (ACN) (5:95, v:v). Chemical polymerization of PHTQ was achieved using iron (III) chloride as the oxidant. The band gap (E_g) was calculated as 1.75 eV. The polymer was obtained as a red–purple powder and can be easily dissolved in common organic solvents. The good solubility can be partially attributed to the two hexyl side chains attached to thiophene units. The CV and FTIR studies were done to characterize the resulting polymer. Sequentially, we studied the optoelectrochemistry and measured the L, a, and b values of the homopolymer coated on ITO.

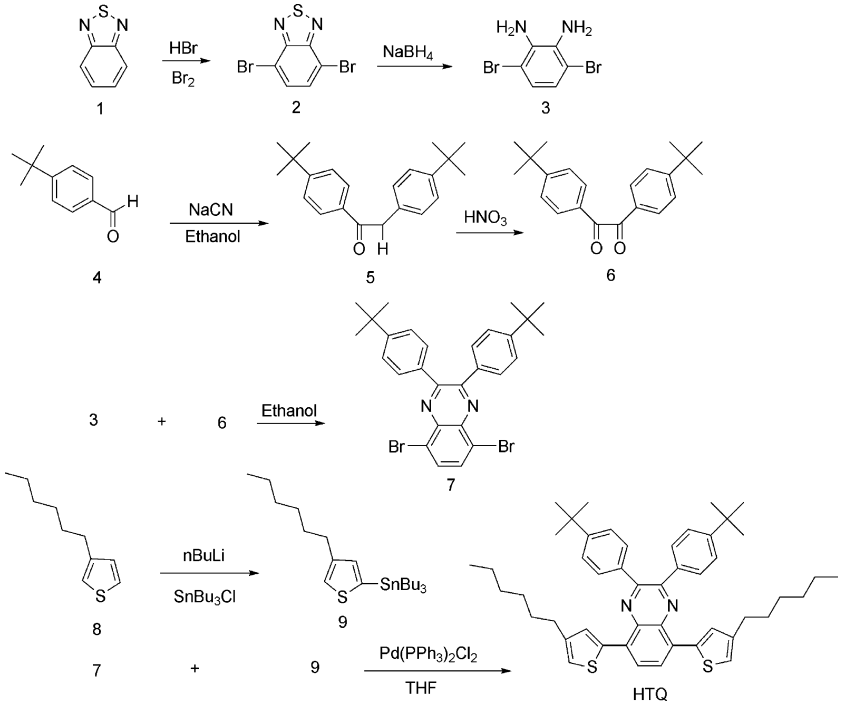

Scheme 1. Synthetic route for monomer HTQ.

2. Results and discussion

2.1. Monomer synthesis

2,1,3-Benzothiadiazole was brominated to completion in a mixture of HBr/Br_2 mixture (yield: 95%) and reduced by excess amount of $NaBH_4$ to give 3,6-dibromo-1,2-phenylenediamine as pale yellow solid. Condensation reaction of 3,6-dibromo-1,2-phenylenediamine and 1,2-bis(4-*tert*-butylphenyl)ethane-1,2-dione was performed in ethanol to afford 2,3-bis(4-*tert*-butylphenyl)-5,8-dibromoquinoxaline in very high yields. The organotin compound was synthesized by lithiation of an equal molar of 3-hexylthiophene which followed by addition of tributyltin chloride in the corresponding mixture. The Stille coupling reaction of 2,3-bis(4-*tert*-butylphenyl)-5,8-dibromoquinoxaline with tributyl(4-hexylthiophen-2-yl)stannane was achieved in anhydrous THF in the presence of catalytic amount of $Pd(PPh_3)_2Cl_2$ (Scheme 1).

The reaction proceeded quite nicely to yield the title compound HTQ in high yields and purity.

2.2. Electropolymerization

To directly synthesize and investigate potential electrochromic characteristics of the polymer film, electrochemical polymerization was carried out. For electrochemical synthesis of PHTQ, 0.1 M tetrabutylammonium hexafluorophosphate ($TBAPF_6$) was used as the supporting electrolyte in dichloromethane (DCM): acetonitrile (ACN) (5/95, v/v) solvent mixture. The irreversible oxidation of HTQ was observed clearly on the first cycle at 1.3 V versus Ag wire pseudo reference electrolyte. Fig. 1 shows the repeated cyclic voltammogram of HTQ on ITO at 100 mV/s. Polymer redox couple reveal the formation of an electroactive polymer film (PHTQ) with an oxidation potential of 1.1 V and a reduction potential of 0.76 V. Current response versus scan rate graph (Fig. 2) showed a linear relation which proves that the PHTQ film was electroactive and well adhered to the ITO electrode. Additionally, linear relation between anodic peak potentials and scan rate indicates that electrochemical processes are not diffusion limited and are reversible [19].

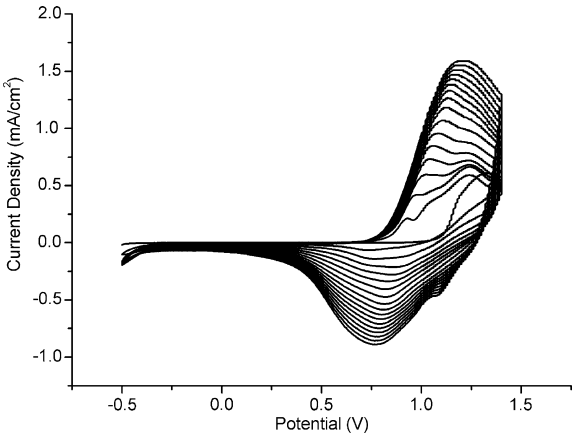

Fig. 1. Repeated potential scan electropolymerization of HTQ at 100 mV/s in 0.1 M $TBAPF_6$/DCM/ACN on ITO electrode.

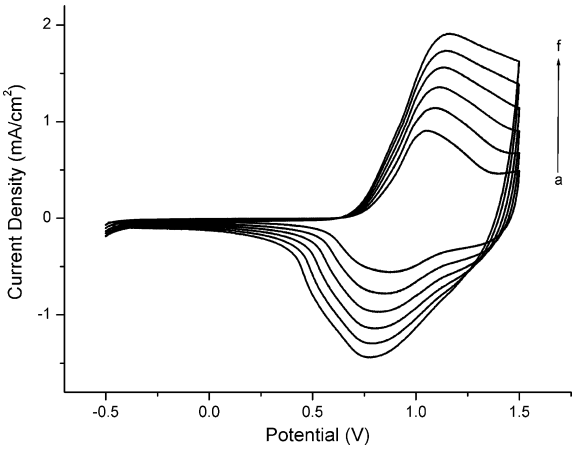

Fig. 2. Scan rate dependence of PHTQ film in $TBAPF_6$/ACN (a) 100, (b) 150, (c) 200, (d) 250, (e) 300 mV/s.

2.3. Chemical polymerization

A typical oxidative polymerization of HTQ was achieved using iron(III) chloride in a mixture of nitromethane and chloroform [20].

After the addition of $FeCl_3$ the solution turned into a dark green solution immediately. The solution was stirred for 4 h at room temperature and washed with methanol and dedoped with a hydrazine solution to yield a saturated red color polymer with high solubility in common organic solvents. A saturated chloroform solution was prepared and the polymer was spray-coated on ITO glass for electrochemical characterization. The polymer revealed similar cyclic voltammogram as seen in Fig. 3. The oxidation and reduction potentials were found to be almost the same with those given for the film synthesized electrochemically. The scan rate dependence of the chemically synthesized polymer (cPHTQ) was also

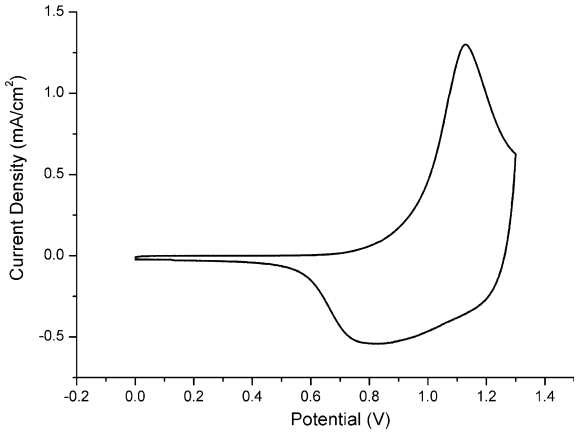

Fig. 3. Cyclic voltammogram of chemically produced PHTQ that spray-coated on ITO glass at 100 mV/s in 0.1 M $TBAPF_6$/DCM/ACN.

investigated. The linear relation between the anodic peak potentials and scan rate showed that the electrochemical processes are not diffusion limited and reversible for cPHTQ (Fig. 4). GPC measurements reveal that the heterogeneity index of the chemically polymerized polymer was higher compared to that of the electrochemically synthesized one. This is due to the rather more controlled polymerization on the surface of metal electrode in electrochemical polymerization.

2.4. Spectroelectrochemistry

To investigate the optical changes upon doping, spectroelectrochemistry studies were performed. PHTQ was coated on ITO glass slides and spectral changes were investigated by UV–vis-NIR spectrometer in a monomer-free 0.1 M $TBAPF_6$ solution via incrementally increasing applied potential between 0.4 V and 1.2 V. As illustrated in Fig. 5, the donor–acceptor type polymer, PHTQ reveals two distinct absorption bands centered at 345 nm and 538 nm. At the reduced state, polymer has a red–purple color (Y: 144, x: 0.407, y: 0.319) and upon successive oxidation, intensities of both absorption bands gradually decrease leaving a residual tail centered at 350 nm. Additionally a low intensity absorption centered between 430 nm and 600 nm and an absorption at around 800 nm (due the formation of polaronic band) are formed. All these absorptions in the visible region resulted in a green color in the oxidized state (Y: 255 x: 0.314 y: 0.373). Upon further oxidation the absorptions at 345 and 538 nm depletes totally and the absorption at 800 nm increases to greater extend resulted in a dark gray color (Y: 243, x: 0.304 y: 0.349).

The electronic band gaps of the polymer were calculated as 1.75 eV and 2.46 eV for the two transitions observed at 345 nm and 538 nm (Fig. 5) The increase in absorption centered at 800 nm corresponds to the formation of polaronic bands.

Spectroelectrochemistry of the chemically synthesized polymer was also investigated. A very similar spectrum was obtained for the chemically synthesized polymer at different applied potentials. The maximum absorption wavelength for both bands was found to be almost the same with the ones synthesized electrochemically. Colorimetry studies were performed to determine the Y, y, x

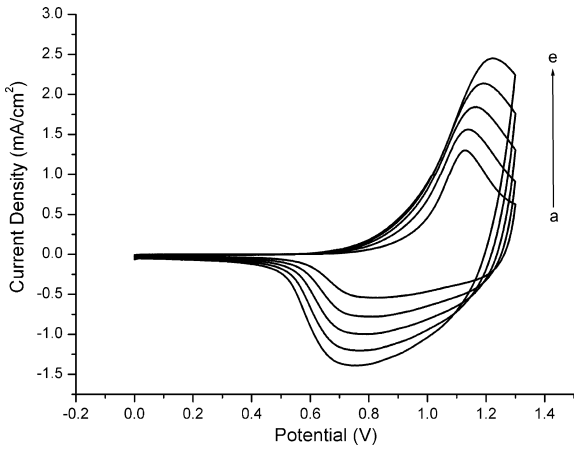

Fig. 4. Scan rate dependence of cPHTQ film in $TBAPF_6$/ACN (a) 100, (b) 150, (c) 200, (d) 250, (e) 300 mV/s.

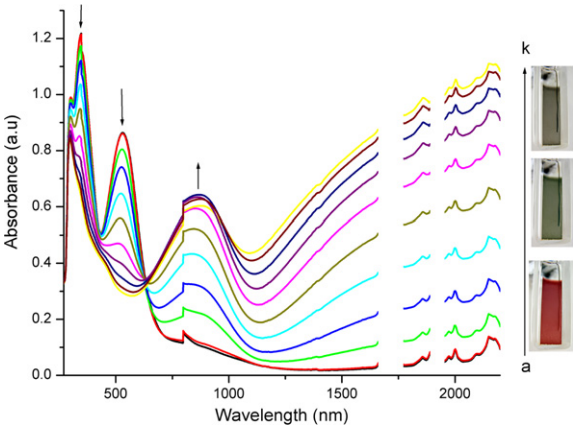

Fig. 5. Spectroelectrochemistry of PHTQ film on an ITO coated glass slide in monomer-free, 0.1 M $TBAPF_6$/ACN electrolyte-solvent couple at applied potentials (V): (a) 0.4, (b) 0.6, (c) 0.8, (d) 0.9, (e) 1.0, (f) 1.05 (g) 1.1, (h) 1.125, (i) 1.15 (j) 1.175 (k) 1.2.

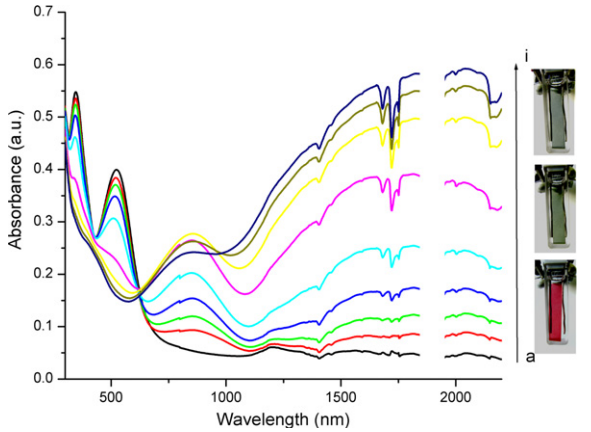

Fig. 6. Spectroelectrochemistry of cPHTQ film on an ITO coated glass slide in monomer-free, 0.1 M $TBAPF_6$/ACN electrolyte-solvent couple at applied potentials (V): (a) −0.5, (b) 0.85, (c) 0.9, (d) 0.95, (e) 1.0, (f) 1.05 (g) 1.1, (h) 1.15, (i) 1.2.

coordinates of the colors. As seen in Figs. 5 and 6 both polymers revealed very similar colors (see Table 1).

2.5. Kinetic study

The capability of a polymer to switch rapidly and demonstrating a remarkable color change are essential properties for an electrochromic polymer. Electrochromic switching is proven to be one of the most efficient and easiest ways to observe these properties.

The % transmittance (T%) at different wavelengths including the λ_{max} of the polymer was measured using a UV–vis-NIR spectrophotometer when the applied potential was switched between 0.4 V and 1.2 V with a period of 5 s. The optical contrast for PHTQ was measured as the difference between T% in the neutral and oxidized states and calculated as 10% and 25% at 345 and 538 nm, respectively (Fig. 7).

Polymer switches between its reduced and oxidized states in less than 2 s at both absorption maxima (345 and 538 nm). PHTQ has an excellent optical contrast of 46% in the NIR region which

Table 1
Colorimetry studies of PHTQ

Potential (V)	Color	Y	x	y
0.4	Red–purple	144	0.407	0.319
1.0	Green	255	0.314	0373
1.2	Dark gray	243	0.304	0.349

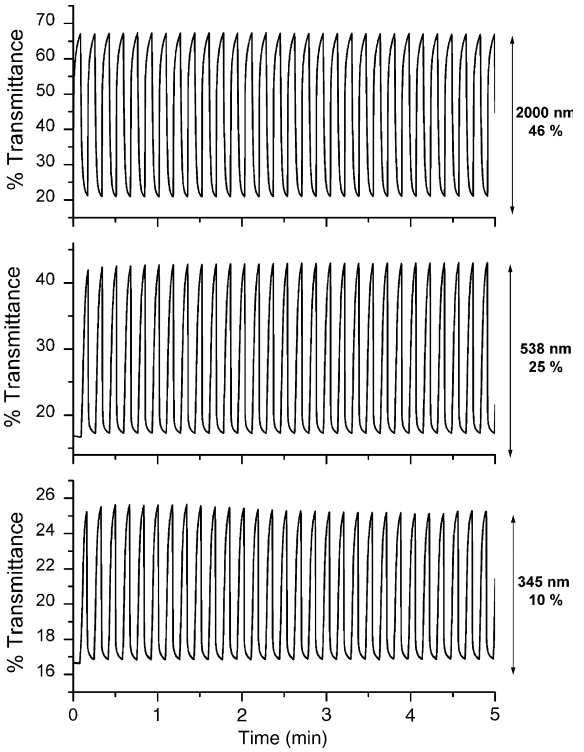

Fig. 7. Electrochromic switching, optical absorbance change monitored at 345 and 538 nm and 2000 nm for PHTQ in 0.1 M $TBAPF_6$/ACN.

makes this polymer a good candidate for NIR electrochromic device applications.

3. Conclusion

2,3-Bis(4-*tert*-butylphenyl)-5,8-bis(4-hexylthiophen-2-yl)quinoxaline (HTQ) was synthesized via Stille coupling reaction. PHTQ was synthesized by means of both electrochemical and chemical polymerization methods and electrochromic properties of both polymers were investigated in detail. PHTQ showed satisfactory optical contrasts in the visible region with three distinctive colors upon doping. The polymer showed an excellent optical contrast of nearly 50% in the NIR region which makes this solution processable polymer a remarkable choice for NIR device applications. The switching times of the polymer both in the visible and NIR regions were shown to be less than 2 s. Multichromic soluble polymer, PHTQ, also stands for an excellent choice for many electrochromic device applications. In addition, deep red fluorescence in the dedoped state makes this polymer a promising candidate as an active layer in plastic solar cells.

4. Experimental section

4.1. Materials

All chemicals were purchased from Aldrich except for THF which was purchased from Across. 4,7-Dibromobenzo[1,2,5]thiadiazole [21], 3,6-dibromo-1,2 phenylenediamine [22], 1,2-bis(4-*tert*-butylphenyl)-2-hydroxyethanone [23], 1,2- bis(*tert*-butylphenyl) ethane-1,2-dione [23], tributyl(4-hexylthiophen-2-yl)stannane [24] were synthesized according to literature procedure.

4.2. Monomer synthesis

4.2.1. 2,3-Bis(4-tert-butylphenyl)-5,8-dibromoquinoxaline:

A solution of 3,6-dibromo-1,2-phenylenediamine (1.0 g, 3.8 mmol) and 1,2-bis(4-*tert*-butylphenyl)ethane-1,2-dione (1.223 g, 3.8 mmol) in EtOH (40 ml) was refluxed overnight by with a catalytic amount of paratoluenesulfonic acid (PTSA). The mixture was cooled to 0 °C. The precipitate was isolated by filtration and washed several times with EtOH to afford the desired compound. (1.5 g, 72%). ^{1}H NMR (400 MHz, $CDCl_3$): δ: 1.22 (s, 18 H), 7.27 (d, 4 H, $J = 8.26$ Hz), 7.54 (d, 4 H, $J = 8.30$ Hz), 7.72 (s, 2 H). ^{13}CNMR (100 MHz, $CDCl_3$): δ: 31.30, 34.81, 123.65, 125.31, 129.98, 132.76, 135.25, 139.21, 152.90, 154.10, MS: *m*/*e* 552 (M^+).

4.2.2. 2,3-Bis(4-tert-butylphenyl)-5,8-bis(4-hexylthiophen-2-yl)quinoxaline:

2,3-Bis(4-*tert*-butylphenyl)-5,8-dibromoquinoxaline (400 mg, 0.8 mmol) and tributyl(4-hexylthiophen-2-yl)stannane (1832 mg, 4 mmol) were dissolved in dry THF (100 ml), the solution was purged with argon for 30 min and $PdCl_2(PPh_3)_2$ (120 mg, 0.171 mmol) was added at room temperature under argon atmosphere. The mixture was stirred at 100 °C under argon atmosphere for 15 h, cooled and concentrated on the rotary evaporator. The residue was subjected to column chromatography to afford an orange solid (320 mg, 55%).

^{1}H NMR (400 MHz, $CDCl_3$): δ: 0.83 (t, 6H), 1.27 (m, 30H), 1.64 (m, 4H), 2.60 (t, 4H, $J = 7.3$ Hz), 7.02 (s, 2 H), 7.30(d, 4H, $J = 8$ Hz), 7.65(d, 4H, $J = 8$ Hz), 7.66 (s, 2H), 7.96(s, 2H), MS: *m*/*e* 727 (M^+).

^{13}C NMR (400 MHz, $CDCl_3$): δ: 13.11, 21.65, 28.12, 29.62, 30.28, 30.80, 33.73, 122.51, 124.07, 125.65, 127.07, 129.13, 130.14, 134.97, 136.12, 137.65, 141.81, 150.40, 151.11.

4.3. Polymer synthesis

Oxidative polymerization of HTQ was achieved by $FeCl_3$ in a 50 ml mixture of nitromethane and chloroform (90/10, v/v) containing 10^{-2} M monomer. The monomer to oxidizing agent ratio was 1:4. The mixture was stirred for 4 h at room temperature. The solution immediately turned to dark green which is the color of the electrochemically produced film in the oxidized state. The polymer was washed with methanol several times, dissolved in a mixture of THF and 50% aqueous solution of hydrazine and stirred overnight at room temperature for complete dedoping. A deep red solution was obtained. THF was evaporated under reduced pressure. Chloroform was added to residue and the organic phase was extracted several times with water. Combined organic phases were evaporated and the residue was washed with acetone several times to remove unreacted monomer. The polymer was then dried under vacuum to give the title compound in high yields (90–95%).

^{1}H NMR (400 MHz, $CDCl_3$): δ: 0.77, 1.25, 1.66, 2.73, 7.18, 7.30, 7.68, 7.89, 8.09.

GPC (cPHTQ), $M_n = 26{,}951$, $M_w = 56{,}892$, HI = 2.11.

(PHTQ), $M_n = 22{,}458$, $M_w = 38, 403$, HI = 1.71.

IR (drift) v: 555, 837, 1072, 1153, 1280, 1350, 1473, 1539, 1631, 2877, 2966 cm^{-1}.

4.4. Equipments

A Voltalab potentiostat was used for all electrochemical studies. Electropolymerization was performed in a three-electrode cell consisting of a indium tin oxide doped glass slide (ITO) as the working electrode, platinum wire as the counter electrode, and Ag wire as the reference electrode. ^{1}H and ^{13}C NMR spectra were recorded in $CDCl_3$ on Bruker Spectrospin Avance DPX-400 Spectrometer. Chemical shifts were given in ppm downfield from tetramethylsilane. Varian Cary 5000 UV–vis spectrophotometer was used to perform the spectroelectrochemical studies of the polymer. Colorimetry measurements were done via Minolta CS-100 Spectrophotometer. FT-IR spectra were obtained using a Varian 5000 FT-IR spectrometer. Number average molecular weight was determined by gel perme-

ation chromatography (GPC) using a Polymer Laboratories GPC 220.

Acknowledgement

Authors gratefully thank DPT-2005K120580, METU and TUBA grants.

References

[1] A.A. Argun, P.H. Aubert, B.C. Thompson, I. Schwendeman, C.L. Gaupp, J. Hwang, N.J. Pinto, D.B. Tanner, A.G. MacDiarmid, J.R. Reynolds, Chem. Mater. 16 (2004) 4401.
[2] J.H. Burroughes, D.D.C. Bradley, A.R. Brown, R.N. Marks, K. Mackay, R.H. Friend, P.L. Burns, A.B. Holmes, Nature 347 (1990) 539.
[3] N.S. Sariciftci, D. Braun, C. Zhang, V. Srdanov, A.J. Heeger, G. Stucky, F. Wudl, Appl. Phys. Lett. 62 (1993).
[4] J.J. Miasik, A. Hooper, B.C. Tofield, J. Chem. Soc. Faraday Trans. 1 (85) (1986) 1117.
[5] F.R. Denton III, A. Sarker, P.M. Lahti, R.O. Garay, F.E. Karasz, J. Polym. Sci. Part A: Polym. Chem. 30 (1992) 2233.
[6] K. Yoshino, P. Love, M. Onoda, R. Sugimoto, Jpn. J. Appl. Phys. Part 2: Lett. 27 (1988) L2388.
[7] G. Sonmez, I. Schwendeman, P. Schottland, K. Zong, J.R. Reynolds, Macromolecules 36 (2003) 639.
[8] G. Heywang, F. Jonas, Adv. Mater. 4 (1992) 116.
[9] R. Hanna, M. Leclerc, Chem. Mater. 8 (1996) 1512.
[10] G. Sonmez, H.B. Sonmez, C.K.F. Shen, R.W. Jost, Y. Rubin, F. Wudl, Macromolecules 38 (2005) 669.
[11] A. Cirpan, A.A. Argun, C.R.G. Grenier, B.D. Reeves, J.R. Reynolds, J. Mater. Chem. 13 (2003) 2422.
[12] F. Wang, M.S. Wilson, R.D. Rauh, P. Schottland, B.C. Thompson, J.R. Reynolds, Macromolecules 33 (2000) 2083.
[13] D.M. Welsh, L.J. Kloeppner, L. Madrigal, M.R. Pinto, B.C. Thompson, K.S. Schanze, K.A. Abboud, D. Powell, J.R. Reynolds, Macromolecules 35 (2002) 6517.
[14] H. Meng, D. Tucker, S. Chaffins, Y. Chen, R. Helgeson, R. Dunn, F. Wudl, Adv. Mater. 15 (2003) 146.
[15] R. Mortimer, J. Electrochim. Acta 44 (1999) 2971.
[16] J.C. Lacroix, K.K. Kanazawa, A. Diaz, J. Electrochem. Soc. 136 (1989) 1308.
[17] J.-C. Ching, A.G. MacDiarmid, Synth. Met. 13 (1986) 193.
[18] (a) J.L. Reddinger, G.A. Sotzing, J.R. Reynolds, Chem. Commun. (1996) 1777;
(b) G.A. Sotzing, J.L. Reddinger, A.R. Katritzky, J. Soloducho, R. Musgrave, J.R. Reynolds, Chem. Mater. 9 (1997) 1578.
[19] G. Sonmez, H. Meng, Q. Zhang, F. Wudl, Adv. Funct. Mater. 13 (2003) 726.
[20] J. Rodriguez, H.J. Grande, T.F. Otero, in: H.S. Nalwa (Ed.), Handbook of Organic Conductive Molecules and Polymers, vol. 2, John Wiley & Sons, New York, 1997, p. 415.
[21] A.B. Da Silveria Neto, A. Lopes Sant'Ana, G. Ebeling, S.R. Goncalves, E.V.U. Costa, H.F. Quina, J. Dupont, Tetrahedron 61 (2005) 10975.
[22] Y. Tsubata, T. Suzuki, T. Miyashi, Y. Yamashita, J. Org. Chem. 57 (1992) 6749.
[23] G.Y. Han, P.F. Han, J. Perkins, H.C. McBay, J. Org. Chem. 46 (1981) 4695.
[24] Q. Hou, Q. Zhou, Y. Zhang, W. Yang, R. Yang, Y. Cao, Macromolecules 37 (2004) 6299.

Available online at www.sciencedirect.com
ScienceDirect
Organic Electronics 9 (2008) 303–309
Organic Electronics
www.elsevier.com/locate/orgel

Electronically controlled pH gradients and proton oscillations

Joakim Isaksson [a], David Nilsson [b], Peter Kjäll [c], Nathaniel D. Robinson [a], Agneta Richter-Dahlfors [c], Magnus Berggren [a,*]

[a] Department of Science and Technology, Campus Norrköping, Linköpings universitet, SE-601 74 Norrköping, Sweden
[b] Acreo AB, Bredgatan 34, SE-602 21 Norrköping, Sweden
[c] Microbiology and Tumor Biology Center, Karolinska Institutet, SE-171 77 Stockholm, Sweden

Received 31 July 2007; received in revised form 21 November 2007; accepted 28 November 2007
Available online 15 December 2007

Abstract

An organic electronic ion pump, including poly(3,4-ethylenedioxythiophene) as the active material has been used to electronically control the transport of protons between two electrolytes and to change the pH of the target solution from 7 to 3 in a few minutes. The number of transported protons equals the time-integrated current between the two addressing electrodes. If no voltage is applied the leakage due to diffusion is not detectable, which indicates an overall proton delivery on/off ratio exceeding 1000. Locally, the pH drop can be even larger and the relationship between the proton delivery rate of the pump and proton diffusion in the electrolyte forms pH gradients. If the device is instead addressed with short pulses, local pH oscillations are created. The transport of protons presented here can be extended to other small sized ions, which in combination with the biocompatibility of the delivery surface make the device promising for cell communication studies and lab-on-a-chip applications.

PACS: 81; 82.35Cd; 82.45−h; 87

Keywords: Electronic ion pump; Conjugated polymer; pH; Ion oscillations

1. Introduction

In biology, intra- and intercellular communication depend to a large extent on spatially as well as temporally regulated ion fluxes and gradients [1,2]. Such ionic signals often have an oscillatory character, thus creating specificity for diverse cellular mechanisms. This is exemplified by neurotransmitter exocytosis, which is triggered within microseconds and, at the other end of the scale, cell proliferation and fertilization with periodicities of several hours [3].

Living organisms are critically dependent on the physiological proton concentration. The intracellular pH levels of the cytosol and different organelles are crucial for the function of most macromolecules in our body and membrane gradients, created by proton pumps [4], are necessary for the cellular metabolism via the respiratory chain. The pH is typically close to 7 [5,6] but can vary depending on specific functions of intracellular compartments.

* Corresponding author. Tel.: +46 11 363637; fax: +46 11 363270.
E-mail address: magbe@itn.liu.se (M. Berggren).

1566-1199/$ - see front matter © 2007 Elsevier B.V. All rights reserved.
doi:10.1016/j.orgel.2007.11.011

In e.g. the phagosomes of immune cells, the pH can be as low as 5.5 to create a lethal environment for pathogenic microorganisms [7,8]. Also, as studied by e.g. Wolf and coworkers [6,9], the pH in the extracellular microenvironment is an important regulator of many cellular functions and interactions and can decrease to five close to tumor cells. The most acidic extracellular environment in the body is the stomach, where the very high proton concentration (pH 2) helps in the digestion of food [10].

Apart from actuating cellular responses, induced gradients and fluctuations in pH have many other potential applications regarding e.g. peptide organization [11], interfacial properties [12] and isoelectric separation [13].

Similarly to biological systems, electrochemical organic electronic devices utilize ions as information carriers [14,15]. Conjugated polymer–polyelectrolyte systems, which can work as both ionic conductors and electron-to-ion transducers are therefore well-suited materials for electronic control of biological systems. In addition, the inherent biocompatibility [16,17] of many such polymers in combination with the ease (ultimately low cost) of manufacturing on flexible and transparent substrates, make them promising candidates for single-use bioelectronic applications. Conjugated polymer electrodes have therefore been explored extensively in the delivery devices to offer electronic control of the release of charged species [18–21]. Particular interest has been devoted to electrically trigger the delivery of bio-relevant ions to regulate various physiological mechanisms and overall signaling in biological systems. These electrodes typically operate according to the principle that the charged (bio-)molecule is to a varying extent imprisoned inside the polymer bulk, as predicted by the oxidation state of the conjugated polymer [21–23]. When the electrode is electrochemically switched, its volume, water content and charging character changes, and the coupling to the source molecule is altered. So, in one oxidation state the molecule can more freely diffuse out from the polymer and induce desired effects in the adjacent biological system. However, such electrodes typically suffer from a number of limitations. First, the spontaneous ion exchange in between the electrode and the target fluid is high independently of the oxidation state of the polymer. This reduces the on/off ratio. Also, the electrodes can in general store a rather low overall concentration of the charged source species. This limits these electrodes to applications, in which the source species has strong therapeutic effect already at very low concentrations. Third, there is little correlation between the electronic signal (current or voltage) applied to the electrode and the amount of ions emitted out from the polymer surface, which makes it difficult to deliver an exact dose. The ultimate drug delivery electrode must fulfill several requisites, the most important ones are: perfect match between the addressing signal and the release rate over time and the possibility to entirely shut off the release of charged species during desired moments [19]. With such characteristics, the electronic delivery device can produce oscillations of the source species at high enough concentrations matching the signaling levels of biology.

We have in earlier work [24] developed an organic electronic ion pump to, as a first step, gain electronic control of ion homeostasis of individual neuronal cells. Here, we utilize the organic electronic ion pump to create electronically controlled pH gradients and local oscillations on single plastic chips, without the need for mechanical valves and pumps that create convection at the point of delivery. The ion pump includes a delivery electrode that can be regenerated via electrophoretic transport of protons from an acidic source. In this configuration, we obtain improved delivery rates as well as on/off ratios as compared to prior work.

2. The ion pump

The basis of the organic electronic ion pump is a plastic foil covered with a 200 nm thin film of the conjugated polymer poly(3,4-ethylenedioxythiophene) (PEDOT) doped with polystyrene sulfonate (PSS). This polymer–polyelectrolyte system is a very common material for use in electrochemical devices since it is stable in the oxidized state and has a relatively high ionic and electronic conductivity [25,26]. Examples of such devices made from PEDOT:PSS or similar materials include displays and smart windows [27–29], transistors and logic circuits [30], surface wettability switches [31,32] and sensors [33,34], all of which could potentially be integrated on the same plastic sheet.

In the case of the ion pump used here, the film of PEDOT:PSS was patterned into four electrodes, labelled A–D, as shown in Fig. 1a. The region between electrode B and C has been chemically over-oxidized and is therefore ionically but no longer electronically conducting [35]. On top of the polymer film, a hydrophobic layer of SU-8

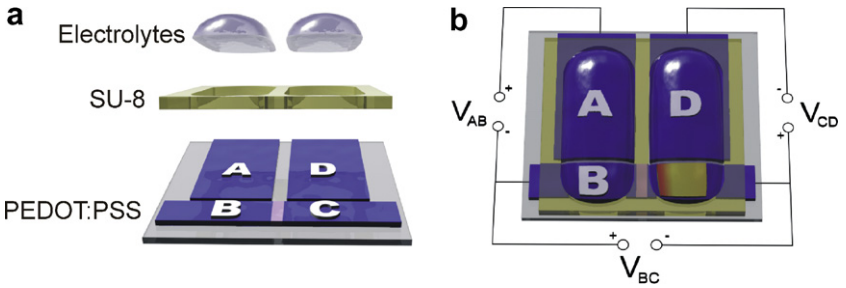

Fig. 1. Sketch of the ion pump. (a) With the layers separated. The pink region between B and C is electronically but not ionically insulating. (b) The assembled device with applied potentials and a pH paper above C to study changes in pH.

was added, with openings for the two electrolytes that cover the A–B and C–D electrodes, respectively. In this configuration, the AB electrolyte is the source electrolyte that contains the ions to be transported, here protons from a 1 M HCl solution with pH 0. The CD electrolyte is the target for the ions that move through the polymer film between B and C when a potential is applied. In the experiments presented here, the CD electrolyte was a 0.1 M KCl solution with pH 5 or 0.1 M $CaCl_2$ with pH 7 (both in equilibrium with air).

When a potential is applied between two PEDOT:PSS electrodes in an electrochemical cell with ions (cations are denoted M^+ below) available, the electrodes are oxidized (positively biased) and reduced (negatively biased) according to the following half-reaction (reduction left to right, oxidation right to left):

$$PEDOT^+PSS^- + M^+ + e^- \rightarrow PEDOT^0 + M^+PSS^-$$

As long as the electrochemical reaction occurs, an electric field, in which ions will move, exists between the electrodes. The potential between B and C (typically between 2 and 10 V) creates such an electric field that electrophoretically drives ions between the electrolytes (separated by the SU-8 barrier), through the polymer–polyelectrolyte film. If cations are relatively mobile in the PEDOT:PSS film, which is saturated with water prior to the experiment, they will migrate to the CD electrolyte when the potential is applied. The same process also occurs to some extent for mobile anions, such as OH^- (highly basic solution in AB), if the potentials are reversed. As soon as the ions reach the CD electrolyte edge, vertical diffusion through the 200 nm film release them into the liquid, at a line at the boundary between the left side of the CD electrolyte and the C electrode.

The over-oxidized channel between electrodes B and C constitutes the path for ions to move between the electrolytes. One or several miniaturized electrodes and channels can be created to increase the spatial resolution of the device (we have in prior work delivered K^+ to single cells on a 50 μm line) but in the experiments presented here, only one broad (4 mm) channel was used. However, in order to enlarge the capacity of the ion pump, electrodes A and D are utilized to regenerate electrodes B and C, respectively. By constantly keeping B and C in a moderately oxidized state with V_{AB} and V_{CD}, a continuous high rate of ion transport can be maintained. Consequently, since A and D determine the capacity of the device, they can be made larger and thicker than B and C, without compromising the spatial resolution of the device. The operational lifetime of the devices is explored in greater detail in Ref. [24].

Experiments with K^+ and Ca^{2+} have shown that the ion pump can be used to create very high (tenths of mM) local ionic concentrations when potentials are applied and have no detectable leakage at all before it is switched on (on/off is >300 for K^+) [24]. Also, since every electron that passes between B and C corresponds to one transported ionic charge, Q_{BC} (integrated I_{BC}) is an accurate measure of the number of cations that have been delivered to the CD electrolyte.

As a very simple approach to macroscopically detect the delivery and diffusion of protons in the CD electrolyte, a pH indicator paper was placed in the electrolyte drop, on top of the C electrode before running the device, as shown in Fig. 1b.

3. Materials and methods

3.1. Device manufacturing

The substrate, PEDOT:PSS coated by AGFA-Gevaert on a polyethylene terephthalate (PET)

substrate, commercially available as Orgacon™ EL-300, was cleaned with acetone and de-ionized water and dried in an oven at 110 °C before processing. The layer of PEDOT:PSS was patterned by etching the regions not covered with Shipley 1818 photoresist with a O_2/CF_4 plasma. The photoresist was then removed. In the second processing step the conducting polymer marked pink in Fig. 1 was chemically over-oxidised. A patterned opening of the photoresist (Shipley 1818) was exposed to a 1% NaOCl aqueous solution for 10 s and then rinsed in water. The NaOCl over-oxidised the PEDOT in the exposed region and thus rendered the film electronically (but not ionically) non-conducting. The photoresist was removed and the top layer of SU-8 (SU-8 2010, MicroChem) was patterned using standard photolithography.

3.2. Device operation

The V_{BC} and V_{CD} potentials were applied with a Keithley 2602 source meter and controlled through a Labview program, which also measured the current. The V_{AB} potential was applied with an external power supply and that current was not measured. The reservoir (AB) and target electrolytes (CD) were deposited (150 μl) with micropipettes. The AB electrolyte was HCl with pH 0 and CD was KCl with pH 5 or $CaCl_2$ with pH 7. Spatially resolved proton transport was studied with ordinary pH paper (Merck) placed in the CD electrolyte above the C electrode. The impermeable backside of the paper was peeled of before use. Judging from the color change of the PEDOT:PSS underneath and the current levels when potentials are applied, the presence of the paper does not seem to interfere with the electrochemical switch of the C electrode. The part of the pH paper used for spatially resolved measurements was yellow at pH 5 and dark red at pH 2. Pictures of the paper were acquired with a Scalar USB camera. When the average pH of the entire CD electrolyte was analyzed, 100 μl liquid was withdrawn and placed on a stripe of pH paper.

3.3. Image analysis

Images of the pH paper were analyzed in a simple Matlab program. The levels of the green channel changed the most when the pH paper switched color and was therefore used to evaluate pH. Only the direction along the C electrode (from the B–C channel towards the C contact, left to right in Fig. 1b) was analyzed, i.e. each value is the mean of all intensities along a column of pixels. The intensity of the green channel was very approximately calibrated to pH values with solutions of known pH. Reference points that did not change pH were used to correct the images from fluctuations in surrounding light and effects from the color change of the underlying PEDOT:PSS upon oxidation and reduction. The pH in the liquid was assumed to be uniform immediately ($t = 0$) after deposition onto the device.

4. Results and discussion

When the potentials shown in Fig. 1b are applied ($V_{AB} = V_{CD} = 1$ V and $V_{BC} = 10$ V), protons from the AB electrolyte are delivered through the B–C channel and released into the CD electrolyte. During 10 min, the pH of KCl in CD drops from 5 to 3 or if $CaCl_2$ is used in CD, from 7 to about 3, i.e. a large part of the physiologically interesting pH range is covered. This alteration in pH is of course only a rough estimate of the exact number of transported protons but the concentration of free protons has increased with approximately 1 mM in both cases. That corresponds to 150 nmol of transported ions (electrolyte volume is 150 μl). The integrated B–C current was ~15 mC, i.e. 155 nmol of electrons (15 mC divided by the charge of one electron and Avogadro's number), which means that the efficiency of the device is close to 100%. This is also what we see when e.g. K^+ is transported and the concentrations are measured more accurately, e.g. with atomic absorption spectroscopy. Results from extensive studies on the relationship between the addressing voltage and the amount of delivered cations were recently published [24]. If no potentials are applied, no change in pH is detected. Thus, the on/off of the device is at least 1000 (probably higher locally) when pumping protons.

Maybe more interesting than the pH of the entire electrolyte is to study what happens locally, close to the line where ions (protons) are released. Fig. 2a shows the pH distribution along the C electrode (each point is the average of all pixels in a column) at different times when the potentials ($V_{AB} = V_{CD} = 1$ V and $V_{BC} = 5$ V) are constantly applied. Fig. 2b shows examples of what the pH paper look like at different time points when the potentials are applied (on these particular photos, the impermeable backside of the paper was not removed). It is

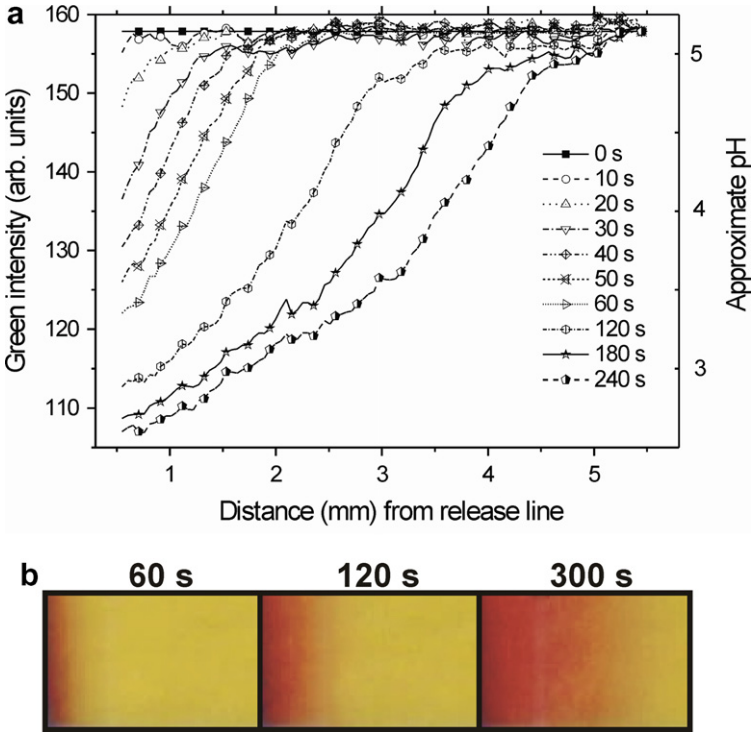

Fig. 2. pH gradient along electrode C. (a) Change in pH at constantly applied potentials ($V_{AB} = V_{CD} = 1$ V, $V_{BC} = 5$ V). (b) Examples of photographs of pH paper (in this case with white backside to improve contrast) at different time scales with the same potentials as above applied.

evident from Fig. 2 that the delivery of new ions is faster than the diffusion process that balances the pH in the entire CD electrolyte. The pH close to the line of release constantly decreases as more and more protons are transported. At the same time, the proton concentration is evened out by diffusion and the pH gradient stretches along 5 mm of the 7 mm wide C electrode, already after 4 min.

The faster the protons (or other ions) are supplied, the steeper the gradient, which means that it is possible to tune the shape of the gradient by balancing the transport rate (by adjusting voltages and times) with the diffusion rate in the receiving electrolyte.

As mentioned in the introduction, many biological signals are oscillatory with specific frequencies. Therefore, we tested to drive the ion pump with short pulsed signals to create local oscillations. The column of pixels closest (~0.5 mm into the electrolyte) to the release line was analyzed during each run and the results of 15 s pulses with $V_{BC} = 10$ V and 10 s pulses with $V_{BC} = 5$ V are presented in Fig. 3a and b, respectively.

Protons drift from the AB reservoir to the CD target electrolyte through the channel, which in part consists of over-oxidised PEDOT:PSS. The channel is hydrated and proton transport is expected to occur primarily in the PSS (polyelectrolyte) phase. We assume the following: the addressing potential difference ($V_{BC} = 10$ V) all drops linearly along the 2 mm long channel, protons are the only charge carriers transported through the channel and the measured I_{BC} current only reflects proton migration. Then, we find that the proton conductivity (1)

$$\sigma_{proton} = (I_{BC}/A_{channel})/(E/1_{channel}) \quad (1)$$

has a value of at least 0.125 S/cm. $A_{channel}$ (2×10^{-6} cm^2) and $l_{channel}$ (0.2 cm) are the channel area and length, respectively and we assume (see Fig. 3a) that the current through the channel is at least 50 μA.

The experiment in Fig. 3 shows that it is possible to create ion concentration oscillations by matching the pulses with ion diffusion in the electrolyte. The period time of the oscillations created here is about

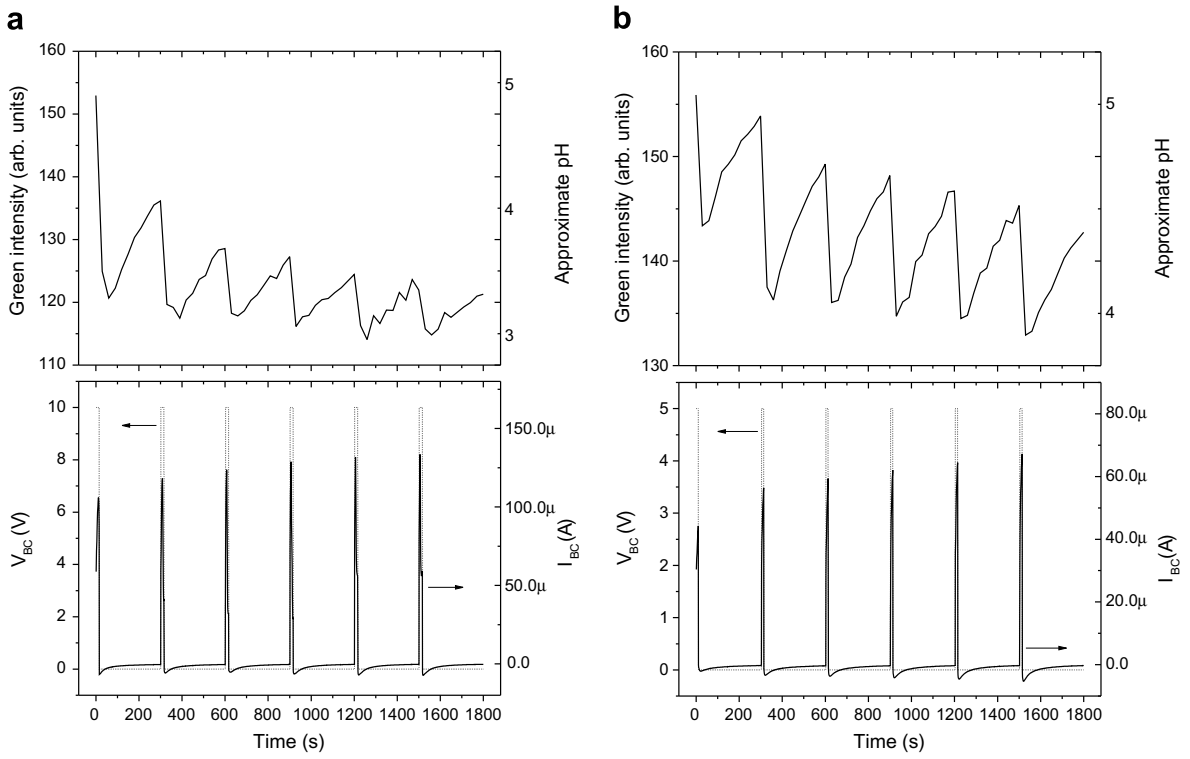

Fig. 3. Short pulses can be used to create oscillations in the CD electrolyte close to the release line. $V_{AB} = V_{CD} = 1$ V during the pulses, otherwise 0 V. (a) 15 s pulses with $V_{BC} = 10$ V. (b) 10 s pulses with $V_{BC} = 5$ V.

5 min. This corresponds very well to the time scale observed in many cell signaling events, such as ion controlled gene transcription [3,36].

5. Conclusions

An organic electronic ion pump, using PEDOT:PSS as the active material, can be used to electronically control the delivery of protons to a receiving electrolyte. Ordinary pH indicator paper in the electrolyte is a simple way to detect changes in pH and gradients stretching along several mm. By adjusting the applied voltages and pulse times, it is possible, not only to control the shape of pH gradients, but also to create local ion concentration oscillations. Such gradients and oscillations in ion concentration are highly interesting for various kinds of cell signaling studies as well as lab-on-a-chip applications and should not be restricted to protons, since the same behaviour apply for other mobile ions such as e.g. K^+ and Ca^{2+}. The amount of transported ions can be counted by integrating the current between the transport electrodes and the on/off ratio is around 1000 for protons. All these characteristics make the organic electronic ion pump a very promising device for future drug delivery applications. Conducting polymer electrodes have been explored for drug delivery applications in the past. In those earlier devices the electrochemically triggered release function occurs from the same volume, within the polymer film, as the drug molecules themselves are stored. Typically, this limits the scenario to applications for which low dose levels and high spontaneous diffusion (losses) can be accepted. In the organic delivery device, reported here, ions from a separate storage chamber migrate, via electrical addressing, to the delivery electrode. This suppresses high levels of spontaneous leakage and enables us to choose applications which require high delivered doses.

Acknowledgements

This research was funded by grants from the Swedish Foundation for Strategic Research (SSF) through the Bio-X and OBOE projects, Knut and Alice Wallenberg Foundation, and the Royal Swedish Academy of Sciences (Göran Gustafsson Prize).

Thanks to Annelie Eveborn at Acreo for manufacturing of devices.

References

[1] M.J. Berridge, M.D. Bootman, P. Lipp, Nature 395 (1998) 645.
[2] R.E. Dolmetsch, R.S. Lewis, C.C. Goodnow, J.I. Healy, Nature 386 (1997) 855.
[3] M.J. Berridge, M.D. Bootman, H.L. Roderick, Nature Reviews Molecular Cell Biology 4 (2003) 517.
[4] K. Faxen, G. Gilderson, P. Adelroth, P. Brzezinski, Nature 437 (2005) 286.
[5] V.A. Verriere, D. Hynes, S. Faherty, J. Devaney, J. Bousquet, B.J. Harvey, V. Urbach, Journal of Biological Chemistry 280 (2005) 35807.
[6] B. Wolf, M. Kraus, U. Sieben, Biosensors and Bioelectronics 12 (1997) 301.
[7] L.R. Prost, M.E. Daley, V. Le Sage, M.W. Bader, H. Le Moual, R.E. Klevit, S.I. Miller, Molecular Cell 26 (2007) 165.
[8] B.E. Steinberg, N. Touret, M. Vargas-Caballero, S. Grinstein, PNAS 104 (2007) 9523.
[9] M. Lehmann, W. Baumann, M. Brischwein, R. Ehret, M. Kraus, A. Schwinde, M. Bitzenhofer, I. Freund, B. Wolf, Biosensors and Bioelectronics 15 (2000) 117.
[10] G.J. Tortora, S.R. Grabowski, Principles of Anatomy and Physiology, John Wiley & Sons, New York, 2000.
[11] A. Aggeli, M. Bell, L.M. Carrick, C.W.G. Fishwick, R. Harding, P.J. Mawer, S.E. Radford, A.E. Strong, N. Boden, Journal of the American Chemical Society 125 (2003) 9619.
[12] X. Zhu, J. De Graaf, F.M. Winnik, D. Leckband, Langmuir 20 (2004) 1459.
[13] E.L. May, A.C. Hillier, Analytical Chemistry 77 (2005) 6487.
[14] A. Lisowska-Oleksiak, K. Kazubowska, A. Kupniewska, Journal of Electroanalytical Chemistry 501 (2001) 54.
[15] M. Vázquez, P. Danielsson, J. Bobacka, A. Lewenstam, A. Ivaska, Sensors and Actuators, B: Chemical Sensors and Materials 97 (2004) 182.
[16] P.M. George, A.W. Lyckman, D.A. LaVan, A. Hegde, Y. Leung, R. Avasare, C. Testa, P.M. Alexander, R. Langer, M. Sur, Biomaterials 26 (2005) 3511.
[17] X. Wang, X. Gu, C. Yuan, S. Chen, P. Zhang, T. Zhang, J. Yao, F. Chen, G. Chen, Journal of Biomedical Materials Research – Part A 68 (2004) 411.
[18] M.R. Abidian, D.H. Kim, D.C. Martin, Advanced Materials 18 (2006) 405.
[19] L.M. Lira, S.I.C. de Torresi, Electrochemistry Communications 7 (2005) 717.
[20] L.M. Low, S. Seetharaman, K.Q. He, M.J. Madou, Sensors and Actuators B-Chemical 67 (2000) 149.
[21] L.L. Miller, Reactive Polymers, Ion Exchangers, Sorbents 6 (1986) 341.
[22] P.M. George, D.A. LaVan, J.A. Burdick, C.Y. Chen, E. Liang, R. Langer, Advanced Materials 18 (2006) 577.
[23] K. Kontturi, L. Murtomaki, P. Pentti, G. Sundholm, Synthetic Metals 92 (1998) 179.
[24] J. Isaksson, P. Kjäll, D. Nilsson, N. Robinson, M. Berggren, A. Richter-Dahlfors, Nature Materials 6 (2007) 673.
[25] B.L. Groenendaal, F. Jonas, D. Freitag, H. Pielartzik, J.R. Reynolds, Advanced Materials 12 (2000) 481.
[26] G. Heywang, F. Jonas, Advanced Materials 4 (1992) 116.
[27] P. Andersson, D. Nilsson, P.-O. Svensson, M. Chen, A. Malmstrom, T. Remonen, T. Kugler, M. Berggren, Advanced Materials 14 (2002) 1460.
[28] H.W. Heuer, R. Wehrmann, S. Kirchmeyer, Advanced Functional Materials 12 (2002) 89.
[29] Q.B. Pei, G. Zuccarello, M. Ahlskog, O. Inganäs, Polymer 35 (1994) 1347.
[30] D. Nilsson, N.D. Robinson, M. Berggren, R. Forchheimer, Advanced Materials 17 (2005) 353.
[31] J. Isaksson, C. Tengstedt, M. Fahlman, N. Robinson, M. Berggren, Advanced Materials 16 (2004) 316.
[32] L. Robinson, A. Hentzell, N.D. Robinson, J. Isaksson, M. Berggren, Lab on a Chip 6 (2006) 1277.
[33] J. Mabeck, G. Malliaras, Analytical and Bioanalytical Chemistry 384 (2006) 343.
[34] Z.T. Zhu, J.T. Mabeck, C.C. Zhu, N.C. Cady, C.A. Batt, G.G. Malliaras, Chemical Communications 13 (2004) 1556.
[35] P. Tehrani, A. Kanciurzewska, X. Crispin, N.D. Robinson, M. Fahlman, M. Berggren, Solid State Ionics 177 (2007) 3521.
[36] P. Uhlén, Å. Laestadlus, T. Jahnukalnen, T. Söderblom, F. Bäckhed, G. Celsi, H. Brismar, S. Normark, A. Aperia, A. Richter-Dahlfors, Nature 405 (2000) 694.

Available online at www.sciencedirect.com
ScienceDirect
Organic Electronics 9 (2008) 310–316
Organic Electronics
www.elsevier.com/locate/orgel

High-performance solution-processed polymer space-charge-limited transistor

Yu-Chiang Chao [a], Hsin-Fei Meng [a,*], Sheng-Fu Horng [b], Chain-Shu Hsu [c]

[a] *Institute of Physics, National Chiao Tung University, Hsinchu 300, Taiwan, ROC*
[b] *Department of Electrical Engineering, National Tsing Hua University, Hsinchu 300, Taiwan, ROC*
[c] *The Department of Applied Chemistry, National Chiao Tung University, Hsinchu 300, Taiwan, ROC*

Received 19 July 2007; received in revised form 22 November 2007; accepted 27 November 2007
Available online 15 December 2007

Abstract

We demonstrate a polymer non-field-effect transistor in a vertical architecture with an Al grid embedded in a polymer sandwiched between another two electrodes. The Al grid containing high density of self-assembled submicron openings is fabricated by a non-lithography method. This device modulates the space-charge-limited current of a unipolar polymer diode with the Al grid. The operating voltage of the device is as low as 4 V, the on/off ratio is higher than one hundred, and the current gain is 10^4. The current density is higher than 1 mA/cm^2.

PACS: 85.30.De; 73.61.Ph

Keywords: Space-charge-limited current; Vertical transistor

1. Introduction

An explosion of interests in flexible electronics made from organic semiconductors gave rise to extensive research on polymer light-emitting diodes (PLED), polymer field-effect transistors (FET), polymer chemical sensors and polymer solar cells. One of the key components of the flexible electronics is the polymer FET, a horizontal device with source and drain electrodes in the same plane. Its operating voltage usually exceeds 20 V due to low carrier mobility. The characteristics of polymer FETs can be strengthened by increasing the mobility [1], utilizing a self-assemble monolayer as gate dielectrics [2] and reducing the channel lengths to the submicron [3]. Horizontal organic FETs with submicron channel lengths made by electron-beam lithography [4], nanoimprint lithography [5] and soft contact lamination [6] have been demonstrated. Vertical organic FETs, whose channel length was determined by the thickness of an insulating layer between source and drain, have been made by solid-state embossing [7], excimer laser [8] and photolithography [9]. However, the inherently low mobility as well as the incompatibility between conventional submicron lithography and organic

* Corresponding author. Tel.: +886 3 5731955.
E-mail address: meng@mail.nctu.edu.tw (H.-F. Meng).

1566-1199/$ - see front matter © 2007 Elsevier B.V. All rights reserved.
doi:10.1016/j.orgel.2007.11.012

materials pose great limitation on the device performance and the fabrication process for polymer FET. The unique advantages of organic materials such as low-cost and large-area solution process are so far not fully explored for high-performance FET. Vertical non-field-effect transistors with multilayer structures give another route to circumvent the limits of both horizontal and vertical field-effect transistors. In vertical non-field-effect transistors, the channel length can be easily defined by the total thickness of the organic layers, and the current is modulated by a conductive layer embedded in the organic materials. Various device operating principles were proposed with different types of conductive layers such as a thin metal film [10–12], a strip-type metal film [13,14], a mesh gate electrode [15–17], and a porous conducting polymer network [18]. The remaining problems are the low current density, low on/off ratio as well as the complex fabrication process. One promising direction is to turn a vacuum tube triode into a solid-state device with current limited by the space-charge-limited current (SCLC), following the initial attempt of Shockley [19] in 1952. Vacuum tube triode is a three terminal device which consists of cathode and anode for electron emission and collection as well as the grid for current modulation. The on and off state of the vacuum tube triode is determined by whether the emitted electrons encounter a large energy barrier between cathode and anode or not. Recently, we demonstrated the polymer space-charge-limited transistor (SCLT) which functions similar to the vacuum tube triode [20]. A metal with random openings made by non-lithographic method is used as the grid. The output current density is however only about 0.01 mA/cm^2 due to the difficulty in realizing high opening density. In this work we solve that difficulty and the current density is significantly raised by two orders of magnitudes to as high as 1 mA/cm^2, which is nearly enough to drive a high-efficiency phosphorescent organic LED with the same area.

The schematic device structure and the energy band diagram are shown in Fig. 1. Poly(3,4-ethylenedioxythiophene):poly(styrenesulfonate) (PEDOT:PSS), with a work function of 5.2 eV, was used as an Ohmic contact for hole injection into the highest occupied molecular orbital (HOMO) of poly(3-hexylthiophene) (P3HT) at 5.1 eV. As the transistor is on, the injected holes can pass through the openings on Al grid and collected by Al collector electrode. The Al grid, functions similarly to the grid in vacuum tube triode, is an Al film with a high density of random submicron openings. The polystyrene spheres are used as the shadow mask for Al deposition to form Al grid, and the openings are formed at the positions of the spheres. The current density is proportional to the opening density. We form Al grid with high opening density using controlled assembly of polystyrene spheres on hydrophobic polymer surface, resulting a much higher current density.

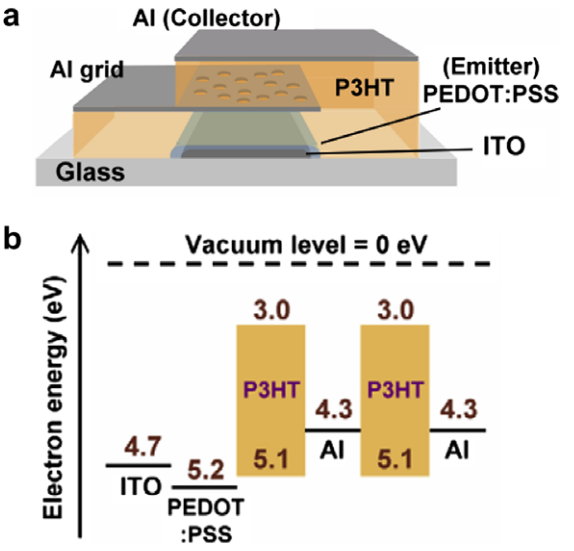

Fig. 1. (a) Device structure of polymer SCLT with an Al grid with random submicron openings. (b) Energy band diagram of polymer SCLT. The energies are indicated in eV. The solid line is the Fermi level of Al and PEDOT:PSS. The LUMO and HOMO energy for P3HT are 3 and 5.1 eV. The thickness between PEDOT and Al grid is 200 Å, and 300 Å between grid and Al collector.

2. Experimental

The device is fabricated on a cleaned indium–tin-oxide (ITO) glass substrate with a layer of 400 Å PEDOT:PSS. After baking in glove box at 200 °C for 10 min, P3HT is spin coated from chlorobenzene solution (1.5 wt.%) on the PEDOT:PSS layer and anneal at 200 °C for 10 min. A spin rinsing with xylene is used to remove the remaining soluble part of P3HT, even though the P3HT annealing condition has been chosen to have an almost fixed thickness after spin rinsing. After depositing the polystyrene spheres on the P3HT surface with the method described in the next section, the 150 Å Al grid is evaporated. After removing the polystyrene spheres by an adhesive tape, a layer of 300 Å P3HT is spin

coated from xylene solution (1.3 wt.%). An Al film of 300 Å is finally deposited to complete the device. The device active area is 1 mm^2.

A variety of self-assembly strategies of polystyrene spheres have been developed for hydrophilic surface to form two dimensional colloidal arrays [16,17,21,22]. A major problem to achieve a high density of separated colloid spheres is the hydrostatic attraction among the spheres. Fujimoto et al. [16] rinsed the samples in 98 °C water to avoid the sphere aggregation on the hydrophilic glass substrate. However, for the hydrophobic surface of the polymer like P3HT, modifications of these strategies are necessary. We use ethanol to dilute the polystyrene spheres (Sigma–Aldrich) for decreasing the contact angle since its alkyl group improves the adhesion between polymer and polystyrene ethanol solution. The polystyrene spheres are absorbed on the P3HT film surface by submerging the film in a polystyrene spheres ethanol solution for tens of seconds. The key procedure in the fabrication is that the substrate is then transferred to a beaker with boiling isopropanol solution for 10 s. Similar to the method of Fujimoto et al. [16], the substrate is finally blown dry immediately in a unidirectional nitrogen flow. After the Al deposition as Al grid, the polystyrene spheres are removed by an adhesive tape (Scotch, 3 M) without damage to the metal. The atomic force microscopy (AFM, Digital Instruments D3100) images of the Al grid with 1000 Å and 2000 Å opening diameter are shown in Fig. 2. The boiling isopropanol treatment is a critical step to achieve a high density yet separated array of holes, required for vacuum tube triode as well as SCLT. When the substrate is submerged in polystyrene solution, the charged polystyrene spheres are absorbed on the P3HT surface without aggregation due to the electrostatic repulsion force. Without the boiling isopropanol treatment, the polystyrene spheres are easy to aggregate during the drying process and cause unwanted non-uniform and connected distribution (Fig. 2f). This may be attributed to the capillary force which pulls spheres into aggregates before the spheres are immobile when the solvent is vaporized. The importance of the boiling isopropanol treatment is presumed to increase the evaporation rate of the solvent during the nitrogen blow dry such that the spheres do not have enough time to move to one another and form aggregate during evaporation. Another possible advantage of the boiling solvent is that it partially melts the spheres and glues the spheres on the surface. With the boiling isopropanol treatment, the opening density on the Al grid indeed increases dramatically, and the openings remain separated. The opening density on the Al grid increases with increasing solution concentration and submerging time (Fig. 2a–d). However, the amount of openings with irregular shape and size also increases (Fig. 2e). This may be due to the high capillary force between spheres with very short distance when the sphere density is high, or due to the unabsorbed spheres in the fluid over the film. One way to remove these unabsorbed spheres is gently rinsing the surface with ethanol or isopropanol before boiling isopropanol treatment. In spite of some occurrence of the unwanted irregular openings, the condition to prepare Al grid with maximum opening density with minimum unwanted openings can be found by tuning the solution concentration and submerging time. The benefit of this method is the possibility to process large-areas in a short processing time without photolithography.

3. Results and discussions

The characteristics of polymer SCLT with opening diameters of 1000 Å and 2000 Å on Al grid are shown in Fig. 3a and c. First note there is one major difference on the grid current I_G between vacuum tube and SCLT. The grid electrode in vacuum tube is not heated so the possibility for the electrons to enter the vacuum by thermal excitation from the grid is practically zero. There is therefore no need to consider the current gain which is defined as the ratio between the collector current and grid current. However in SCLT the carriers in the Al grid are blocked only by the Schottky barrier of 0.8 eV between Al and P3HT. In fact the grid current is the reverse current of the Al/P3HT Schottly diode which is small but not zero. The current gain is therefore an important value to be maximized. As shown in Fig. 3b and d, the grid current I_G of our devices is in the order of 10^{-9} A which is much smaller than I_C. The current gain I_C/I_G is as large as 10^4. For fixed collector voltage the collector current I_C is modulated by the grid voltage V_G. The emitter is the common ground. V_G is limited to be no more negative than −1 V otherwise the emitter-grid diode would turn on and cause large I_G. The positive V_G is used to introduce energy barrier for holes at the openings, and the off current can be reduced by increasing V_G until a large leakage current between the grid and collector occurs. The

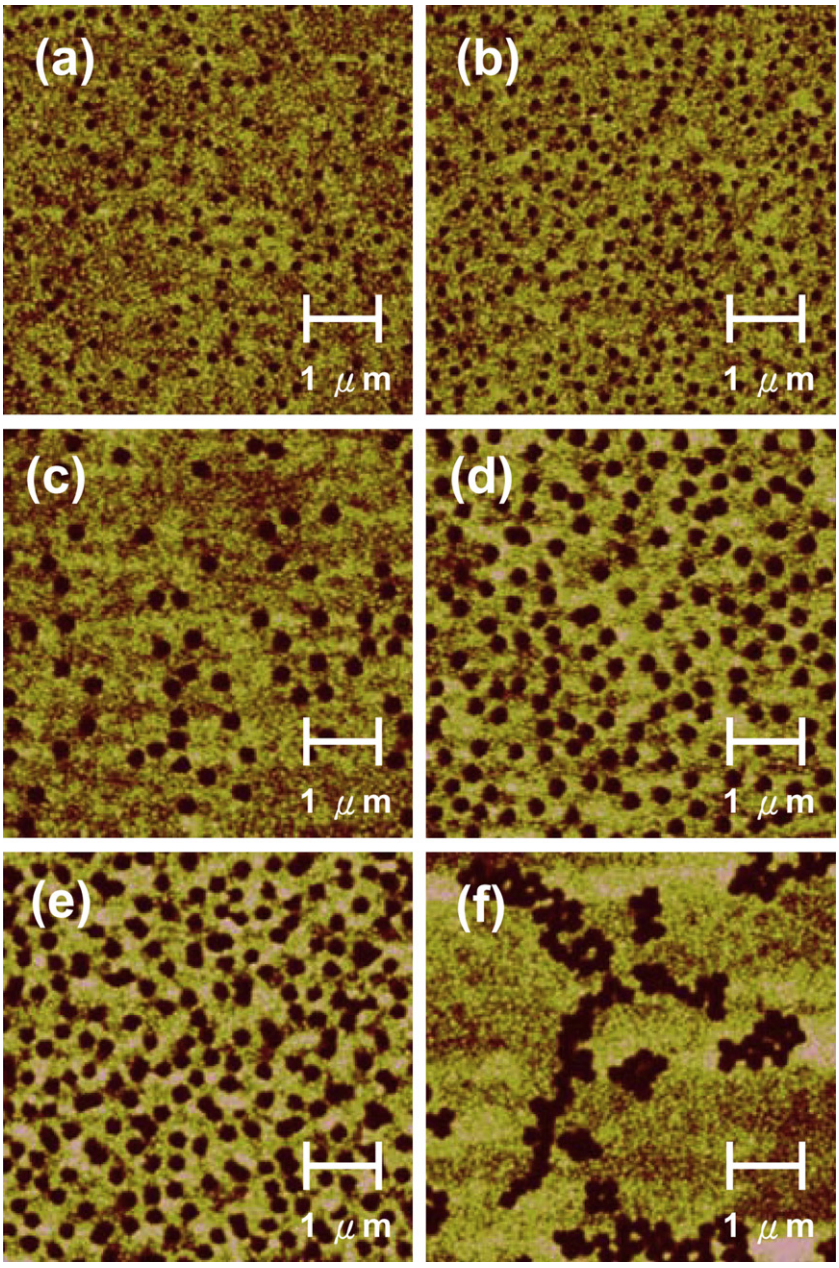

Fig. 2. Al grid with opening diameter of 1000 Å prepared by submerging the substrate in (a) 0.05 wt.%, and (b) 0.1 wt.% polystyrene solutions for 20 s with the boiling isopropanol treatment. Al grid with opening diameter of 2000 Å prepared by submerging the substrate in (c) 0.08 wt.%, (d) 0.24 wt.% and (e) 0.4 wt.% polystyrene solutions for 40 s with the boiling isopropanol treatment. (f) Same condition in (e) but without the boiling isopropanol treatment. The height scale is 30 nm for each image and the dimensions of the image is $5 \times 5\ \mu m^2$.

on/off ratio of I_C is 123 and 116 at $V_C = -4$ V, respectively, for transistors with opening diameters of 1000 Å and 2000 Å on Al grid. The highest I_C output is 1.14×10^{-5} A in Fig. 3c, corresponding to 1.14 mA/cm^2 for active area of 1 mm^2. Note the total output current can be easily scaled up by using a larger area. In order to look for the signature of SCLC, the device characteristics in double logarithmic scale with fixed V_G are shown in the inset of Fig. 3a and c. Three regions belonging to ohmic, trap filling and SCLC can be distinguished [23]. The slope of $\log I - \log V$ is equal to 1 for ohmic conduction, while the slope is equal to 2 for SCLC. The dashed lines with slope equal to 1 and 2 are

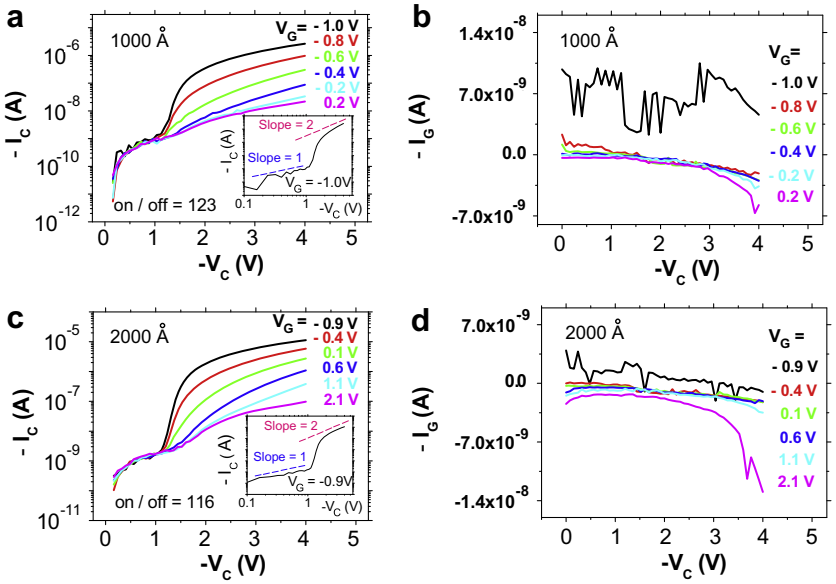

Fig. 3. The electric characteristics of the polymer SCLT with various grid voltages applied. The ITO electrode is commonly grounded and the Al collector is negatively biased at V_C with respect to ITO. The negative collector current I_C means the holes are collected by the Al collector and flows out from the transistor. The gate current I_G is no more than a few nA for all measurements. (a) The collector current as a function of the collector voltage. During the fabrication procedure, the 0.05 wt.% solution of polystyrene spheres with diameters of 1000 Å is used. The submerging time is 20 s. The inset shows the characteristics in double logarithmic of the device with V_G equal to −1 V. (b) The grid current as a function of the collector voltage of the transistor with same fabrication procedure described in (a). (c) The collector current as a function of the collector voltage. During the fabrication procedure, the 0.08 wt.% solution of polystyrene spheres with diameters of 2000 Å is used. The submerging time is 40 s. The inset shows the characteristics in double logarithmic of the device with V_G equal to −0.9 V. (d) The grid current as a function of the collector voltage of the transistor with same fabrication procedure described in (c).

drawn in the inset of Fig. 3a and c for indication. Indeed, the current follows the SCLC once the barrier at the opening is suppressed by a negative enough V_C. At low voltage there is always a small ohmic current. The polymer diode has a turn-on voltage where the current switches from a small leakage ohmic current into a quadratic SCLC current. The turn-on voltage is determined by both the level of the leakage and the difference between the work functions of the cathode and anode. For our diode it is about 1 V as shown in Fig. 3.

The operation mechanism of the polymer SCLT can be understood as the quadratic space-charge-limited current between the emitter and the opening modulated by the grid potential. As in vacuum tube, the potential at the center of the opening is a linear combination of grid and collector potential $\lambda V_G + V_C$, the factor λ depends on the device geometry and increases with the ratio between the opening diameter and the grid-collector distance. The SCLC between the emitter and the opening is therefore approximately $C\,\varepsilon\mu\,(\lambda V_G + V_C)^2/L^3$, where ε is the polymer dielectric constant and L is the emitter-grid distance. If the potential across the opening were uniform, the factor C would be the standard SCLC value of 9/8. The overall effect of non-uniform potential in our case can be absorbed into a numerical factor C. Because of the higher electric field the space between the grid and the collector does not limit the collector current so the emitter-opening current given above is actually the output current.

The above analysis is based on the assumption that all the space charge and potential profiles are determined by the injected carriers instead of background doping. The active semiconductor P3HT is an intrinsic semiconductor without intentional doping. It is well known the main source of unintentional doping of P3HT is oxygen. The samples are fabricated in our glove box with oxygen level below 1 ppm. There are reports on the doping level of P3HT around 10^{15} cm^{-3} without particular attention on oxygen doping [24]. The sample fabrication process is carefully controlled to minimize the oxygen and water contamination. The water and oxygen level inside the glove box are both below 1 ppm. Dehydrated ethanol (≤0.2% water, Riedel-de-Haën)

is used for the polystyrene sphere deposition. The vacuum in the grid evaporation chamber is 10^{-7} torr, so most of the adsorbed oxygen molecules during ethanol immersion are expected to be removed by the high vacuum. Moreover the sample is annealed at 200 °C in vacuum after the spin coating of the second P3HT film. It is known that thermal treatment will significantly de-dope P3HT [25]. We therefore believe our doping level is below 10^{15} cm^{-3}. Even for 10^{15} cm^{-3} the calculated Debye–Huckel screening length is 700 Å which is larger than the total thickness of the SCLT. The electric field provided by the collector voltage is therefore not screened. The quadratic I_C–V_C relation indicates that the space charge is dominated by the injection carrier. This is also an evidence that the doping is not important for the device operation here.

The grid control of the current can be further illustrated by looking at the spatial distribution of the current across the opening. In general only some region near the center of the opening has negative potential for the holes to pass through. Near the edge the effect of the grid is so strong that a potential barrier forms despite of the negative potential of the collector. The current is therefore confined in an area controlled by the grid potential. As the transistor is in the on state, there is no barrier in all the area. The emitter–collector path through A position at the center and the path through B position near the edge of the opening have the potential profiles as the curves (x) and (y) in Fig. 4b, respectively. Assuming that the collector current is roughly a superposition of the currents of many small diodes given by the paths through different positions, the small diodes at position A contributing to a high current (A^{ON}) and those at position B are just about to be turned on (B^{ON}), as indicated in Fig. 4c. On the other hand as the device is in the off state, the grid potential is positive and there is a potential barrier at the B position as the curve (z) in Fig. 4b, and the small diodes there is reverse biased (B^{OFF}). As for A position, if it also has the potential profile like curve (z) in Fig. 4b, the off current comes from small diodes at position A will be small. However, if the potential profile is as the curve (y), there will be an undesirable leakage current from the barely-on small diode at A (A^{OFF}). Theoretically an even more positive grid potential can always drive it into

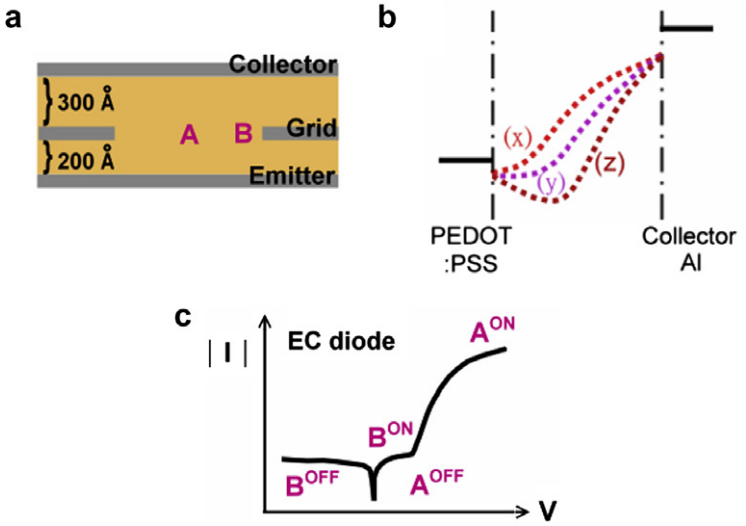

Fig. 4. (a) The device structure near one opening of polymer SCLT. Position A is at the center of the opening, while position B is near the grid. (b) The potential profile along the emitter–collector path through the opening when V_C is fixed at a negative value. (x), (y), (z) are the potential profile along the path for various conditions. Curve (x) is a potential profile without energy barrier for hole as in the case of a simple emitter–collector diode without the grid. Curve (z) is a potential profile with energy barrier for hole for a positive enough grid potential V_G. The barrier for hole diminishes while V_G drops from positive to negative as indicated by (y). Different position in the opening has different potential profile, which result from different $\lambda V_G + V_C$. (c) The schematic current–voltage curve of EC diode with the structure ITO/PEDOT/P3HT/Al. There is a turn-on voltage for the forward bias direction. The path through position A in on or off state are denote as A^{ON} or A^{OFF} in the diode IV curve. The double-sided arrow means off-state could be either reverse bias or small forward bias before turn-on. The state of the path through B is also shown. Because of the proximity to the positive biased grid B path can never be fully turned on as A.

curve (z), but in practice breakdown of the grid/polymer Schottky junction may happen first.

4. Conclusion

In summary, we demonstrate the vertical polymer space-charge-limited transistor with high current density, high on/off ratio, high current gain, and low operation voltage. A non-lithography method is introduced for the desired high opening density on the metal grid embedded in the polymer. This non-field-effect device opens a new possibility for high-performance organic electronics with easy large-area solution process and vertical integration with organic light-emitting diodes without demanding a very high carrier mobility.

Acknowledgement

This work is supported by the National Science Council of the Republic of China under Contract No. NSC96-2112-M-009-036.

References

[1] I. Mcculloch, M. Heeney, C. Bailey, K. Genevicius, I. Macdonald, M. Shkunov, D. Sparrowe, S. Tierney, R. Wagner, W. Zhang, M.L. Chabinyc, R.J. Kline, M.D. Mcgehee, M.F. Toney, Nature Mater. 5 (2006) 328.
[2] M. Halik, H. Klauk, U. Zschieschang, G. Schmid, C. Dehm, M. Schütz, S. Maisch, F. Effenberger, M. Brunnbauer, F. Stellacci, Nature 431 (2004) 963.
[3] J.Z. Wang, Z.H. Zheng, H.W. Li, W.T.S. Huck, H. Sirringhaus, Nature Mater. 3 (2004) 171.
[4] Y. Zhang, J.R. Petta, S. Ambily, Y. Shen, D.C. Ralph, G.G. Malliaras, Adv. Mater. 15 (2003) 1632.
[5] M.D. Austin, S.Y. Chou, Appl. Phys. Lett. 81 (2002) 4431.
[6] J. Zaumseil, T. Someya, Z. Bao, Y.-L. Loo, R. Cirelli, J.A. Rogers, Appl. Phys. Lett. 82 (2003) 793.
[7] N. Stutzmann, R.H. Friend, H. Sirringhaus, Science 299 (2003) 1881.
[8] R. Parashkov, E. Becker, G. Ginev, T. Riedl, M. Brandes, H.-H. Johannes, W. Kowalsky, Appl. Phys. Lett. 85 (2004) 5751.
[9] R. Parashkov, E. Becker, S. Hartmann, G. Ginev, D. Schneider, H. Krautwald, T. Dobbertin, D. Metzdorf, F. Brunetti, C. Schildknecht, A. Kammoun, M. Brandes, T. Riedl, H.-H. Johannes, W. Kowalsky, Appl. Phys. Lett. 82 (2003) 4579.
[10] M.S. Meruvia, I.A. Hümmelgen, M.L. Sartorelli, A.A. Pasa, W. Schwarzacher, Appl. Phys. Lett. 84 (2004) 3978.
[11] Y.C. Chao, S.L. Yang, H.F. Meng, S.F. Horng, Appl. Phys. Lett. 87 (2005) 253508.
[12] K.I. Nakayama, S.Y. Fujimoto, M. Yokoyama, Appl. Phys. Lett. 88 (2006) 153512.
[13] K. Kudo, D.X. Wang, M. Iizuka, S. Kuniyoshi, K. Tanaka, Thin Solid Films 331 (1998) 51.
[14] Y. Watanabe, K. Kudo, Appl. Phys. Lett. 83 (2005) 223505.
[15] N. Hirashima, N. Ohashi, M. Nakamura, K. Kudo, IPAP Conf. Series 6 (2005) 158.
[16] K. Fujimoto, T. Hiroi, M. Nakamura, e-J. Sci. Nanotech. 3 (2005) 327.
[17] K. Fujimoto, T. Hiroi, K. Kudo, M. Nakamura, Adv. Mater. 19 (2007) 525.
[18] Y. Yang, A.J. Heeger, Nature 372 (1994) 344.
[19] W. Shockley, Proc. IRE 40 (1952) 1289.
[20] Y.C. Chao, H.F. Meng, S.F. Horng, Appl. Phys. Lett. 88 (2006) 223510.
[21] Y. Xia, B. Gates, Y. Yin, Y. Lu, Adv. Mater. 12 (2000) 693.
[22] C. Werdinius, L. Österlund, B. Kasemo, Langmuir 19 (2003) 458.
[23] Z. Chiguvare, V. Dyakonov, Phys. Rev. B 70 (2004) 235207.
[24] E.J. Meijer, A.V.G. Mangnus, C.M. Hart, D.M. de Leeuw, T.M. Klapwijk, Appl. Phys. Lett. 78 (2001) 3902.
[25] B. Mattis, P. Chang, V. Subramanian, Synth. Met. 156 (2006) 1241.

Available online at www.sciencedirect.com
ScienceDirect
Organic Electronics 9 (2008) 317–322
Organic Electronics
www.elsevier.com/locate/orgel

Enhancement of the field-effect mobility of poly(3-hexylthiophene)/functionalized carbon nanotube hybrid transistors

Yeong Don Park [a], Jung Ah Lim [a], Yunseok Jang [a], Minkyu Hwang [a], Hwa Sung Lee [a], Dae Ho Lee [a], Hwa-Jeong Lee [b], Jong-Beom Baek [b], Kilwon Cho [a,*]

[a] *Department of Chemical Engineering, Polymer Research Institute, Pohang University of Science and Technology, Pohang 790784, Republic of Korea*
[b] *School of Chemical Engineering, Chungbuk National University, Cheongju 361-763, Republic of Korea*

Received 9 July 2007; received in revised form 15 November 2007; accepted 27 November 2007
Available online 26 December 2007

Abstract

With the aim of enhancing the field-effect mobility of poly(3-hexylthiophene) (P3HT) field-effect transistors (FETs), we added functionalized multiwalled carbon nanotubes (CNTs) to the P3HT solution prior to film formation. The nanotubes were found to be homogeneously dispersed in the P3HT films because of their functional groups. We found that at the appropriate CNT concentration (up to 10 wt% CNT), the P3HT FETs have a high field-effect mobility of 0.04 $cm^2 V^{-1} s^{-1}$, which is an improvement by a factor of more than 10. This remarkable increase in the field-effect mobility over that of the pristine P3HT film is due to the high conductivity of the CNTs which act as conducting bridges between the crystalline regions of the P3HT film, and the reduction in the hole-injection barrier due to the low work function of CNTs, which results in more efficient carrier injection.

Keywords: Carbon nanotube; Polythiophene; Organic transistor; Field-effect mobility

1. Introduction

Carbon nanotubes (CNTs) are now being used in organic electronics as electrodes [1,2], semiconductors [3,4], and in blends with other conjugated polymers [5–7]. CNTs provide high conductivity, but their uses are restricted due to their insolubility and the difficulties of producing homogeneous films. The successful homogeneous dispersion of CNTs in polymer films and facilitated charge conduction using functionalized CNTs have recently been reported [8–11].

The high field-effect mobility, stability, and solution processability of regioregular poly(3-hexylthiophene)s (P3HTs) [12–14] have stimulated considerable interest in the utilization of these

* Corresponding author. Tel.: +82 54 279 2270; fax: +82 54 279 8269.
E-mail address: kwcho@postech.ac.kr (K. Cho).

1566-1199/$ - see front matter © 2007 Elsevier B.V. All rights reserved.
doi:10.1016/j.orgel.2007.11.007

fascinating polymers as active materials in organic field-effect transistors (OFETs) [15–19]. Further, self-organized regioregular P3HT has a supramolecular two-dimensional structure that is of special interest because in this structure the one-dimensional electronic properties of its π-conjugated polymer chains are modified by the increased interchain stacking that results from their π–π interactions [20–22]. However, the charge-carrier mobilities of macroscopic samples of solution-processed conjugated polymer films are generally limited because of their low crystallinity by the rate of hopping between polymer chains in disordered regions of such films. Therefore we prepared surface-functionalized CNTs with the aim of obtaining homogeneously dispersed CNT−P3HT films in which the dispersed CNTs play a key role as conducting bridges connecting the films' tiny fibrillar crystals. In this paper, we show that high field-effect mobilities can be achieved in P3HT−CNT hybrid transistors by simply blending the P3HT solution with a certain amount of functionalized CNTs. We also studied the effects of the functionalized CNTs on the electrical characteristics of the OFETs.

2. Experimental

93% regioregular P3HT ($M_n = 45$–50 kg/mol) was purchased from Rieke Metals and multiwalled carbon nanotubes (MWNTs) were purchased from Iljin Nanotech Co. The outer diameter and length of the CNTs were 20–30 nm and 10–50 μm, respectively. The MWNTs were hydroxylbenzoyl-functionalized (Fig. 1a) with an established procedure [23]. 4-Hydroxyl benzoic acid (0.50 g, 3.62 mmol), CNTs (0.50 g), polyphosphoric acid (83% assay, 20 g), and P_2O_5 (5.0 g) were placed in a resin flask.

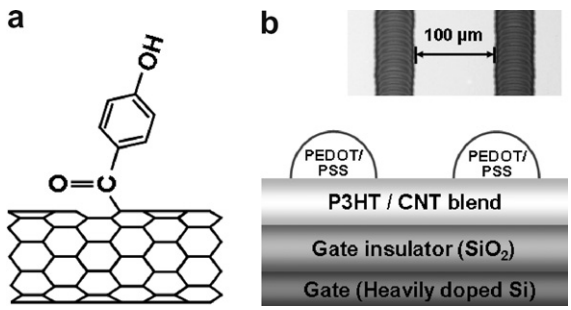

Fig. 1. (a) Molecular structure of a functionalized carbon nanotube. (b) Schematic view of a P3HT–CNT FET. The inset shows an optical micrograph of inkjet-printed source and drain electrodes ($L = 100$ μm).

The flask was immersed in an oil bath and heated at 80 °C for 1 h and then 100 °C for 1 h. The reaction mixture was heated and its temperature maintained around 130 °C for 72 h with nitrogen flow. After cooling the mixture to room temperature, water was added. After suction filtration, Soxhlet extraction was carried out for three days, and the product was freeze dried for 48 h to afford 0.65 g (69.7% yield) of a dark black powder. Three or four hydroxyl benzoic acid groups were introduced for every one hundred carbons of the CNTs; this functionalization of the CNTs was analyzed with transmission electron microscopy (TEM), Fourier-transform infrared spectroscopy (FT-IR), and thermogravimetric analysis (TGA). The molecular structure of a functionalized CNT is shown in Fig. 1a.

Highly doped Si was used as the transistor substrate as well as the gate electrode. A thermally grown silicon dioxide (SiO_2) layer with a thickness 300 nm was employed as the gate dielectric. MWNTs at various concentrations (5, 10, 20, and 30 wt% with respect to P3HT) were added to 0.5 wt% P3HT solutions in dichlorobenzene. A simple spin-coating method was used to fabricate P3HT thin films with a thickness of 25–35 nm. We used a water-based ink of the conducting polymer poly(3,4-ethylenedioxythiophene) doped with polystyrene sulfonic acid (PEDOT/PSS) (from Bayer AG, Bytron P) for the source–drain electrodes (channel length 100 μm, channel width 1000 μm). A line of PEDOT/PSS droplets was deposited on top of the P3HT film by using inkjet printing (Fig. 1b) [24]. Fig. 1b shows a schematic cross-section of a P3HT−CNT hybrid transistor fabricated as described above. All the measurement results were obtained at room temperature in ambient conditions using Keithley 2400 and 236 source/measure units.

3. Results and discussion

The morphology of a crystalline semiconducting film in an FET is closely related to its electrical properties. Scanning electron microscopy (SEM) observations were carried out to provide images of the top surfaces of the blend films. Fig. 2 shows SEM images of the P3HT−CNT thin films. The pristine P3HT film is featureless (Fig. 2a). Due to the functional groups of the CNTs, the nanotubes are homogeneously dispersed in the polymer matrix at low CNT concentrations (Fig. 2b and c).

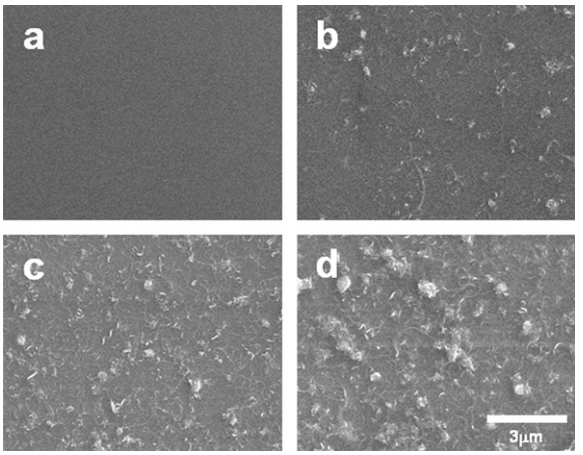

Fig. 2. Field emission scanning electron microscopy images of P3HT films with various CNT concentrations: (a) 0 wt%, (b) 5 wt%, (c) 10 wt% and (d) 20 wt%.

However, the P3HT–CNT films are inhomogeneous due to the aggregation of CNTs at high CNT concentrations (see Fig. 2d). We conclude that functionalized CNTs can be homogeneously dispersed in the polymer matrix at low concentrations.

To investigate the variation of the molecular structure of P3HT thin films as a function of the CNT concentration, grazing-incidence X-ray diffraction (GIXD) measurements were carried out on the spin-coated films [13,21,22]. Fig. 3 shows the out-of-plane X-ray diffraction patterns for the P3HT films with various CNT concentrations. In the case

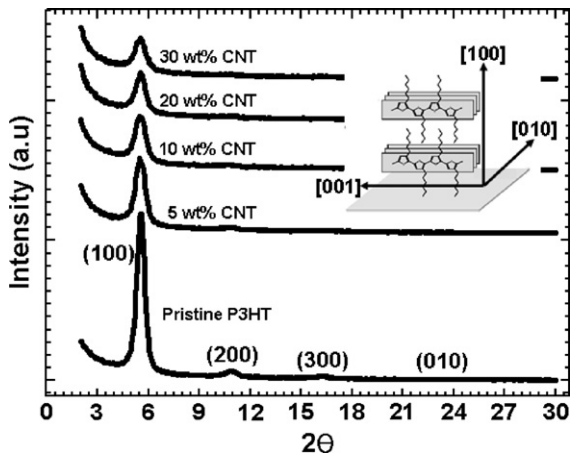

Fig. 3. Out-of-plane grazing-incidence angle X-ray diffraction intensities as a function of the scattering angle 2θ for P3HT thin films on SiO_2/Si substrates with various CNT concentrations. The inset shows a schematic representation of the edge-on structure of the P3HT crystals.

of the pristine P3HT thin film, the intensity of the (100) reflection due to lamellar layer structure (16.4 Å) is strong (Fig. 3), but the intensity of the (010) reflection due to π–π interchain stacking (3.8 Å) is very weak. The crystallinity of P3HT films spin-coated from dichlorobenzene solution is typically greater than that of the P3HT films spin-coated from dichloromethane or chloroform solutions: the (100), (200), and (300) reflections are more intense for dichlorobenzene, which has a higher boiling point, due to its slow evaporation rate. However, as the amount of CNTs added to the solution increases, the intensity of the first Bragg peak (100) is significantly reduced, even though the total film thickness increases slightly, as was found with ellipsometry. We speculate that the well-dispersed CNTs disturb the molecular ordering of the P3HT film.

To determine the relationship between the CNT concentration and the electrical properties, the field-effect mobilities of the P3HT films were measured using a top-contact FET geometry. Fig. 4a shows typical source–drain current (I_{DS}) vs. source–drain voltage (V_{DS}) plots at various gate voltages for the pristine P3HT and P3HT–CNT (10 wt%) FETs, operating in accumulation mode. The addition of 10 wt% CNT increases the drain current of the FET by a factor of about 7, from 1.4 to 9.5 μA. However, the P3HT–CNT FETs with >20 wt% CNTs exhibit poor output characteristics, with no saturation behavior and increased off-currents ($V_G = 0$) (Fig. 4b). The average field-effect mobility of each transistor was calculated in the saturation regime ($V_{DS} = 80$ V) by plotting the square root of the drain current versus the gate voltage (Fig. 4c) and fitting the data to the following equation: [25]

$$I_{DS} = \frac{WC_i}{2L}\mu(V_{GS} - V_T)^2$$

where $C_i = 10.8 \times 10^{-9}$ F cm^{-2}, $W = 1000$ μm, and $L = 100$ μm.

Fig. 4d shows the field-effect mobilities and on–off ratios of the P3HT−CNT FETs spin-coated from dichlorobenzene and chloroform solutions. The field-effect mobility of the FET with 10 wt% CNT (4.0×10^{-2} cm^2 V^{-1} s^{-1}) is more than 10-fold greater than that of the pristine P3HT FET (2.8×10^{-3} cm^2 V^{-1} s^{-1}) spin-coated from dichlorobenzene solution, which has a low field-effect mobility mainly because of very low film thickness (~25 nm) [26]. This remarkable increase in the field-effect mobility upon the addition of CNTs is probably due to the high conductivity of CNT the CNTs, which

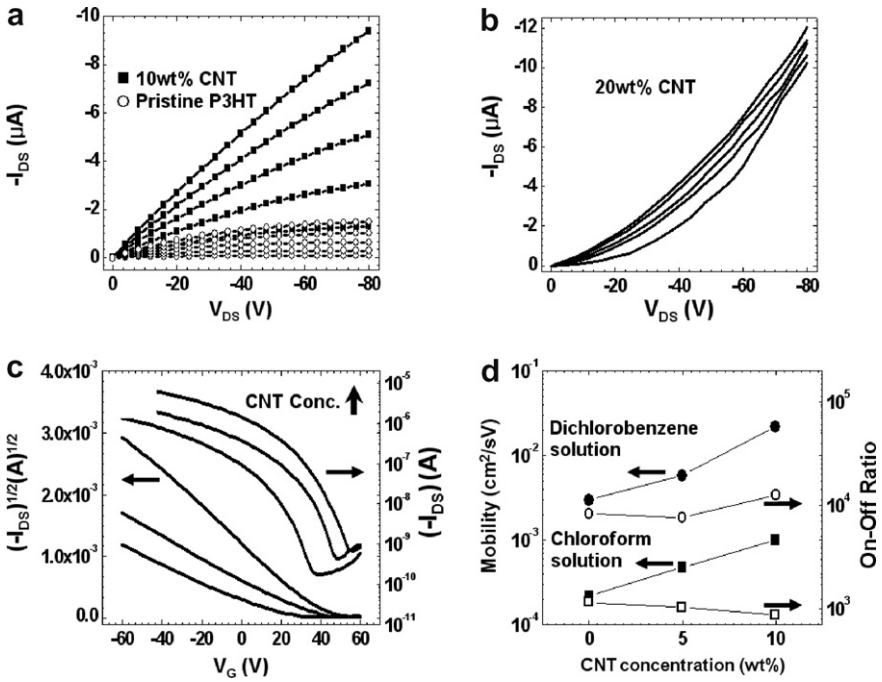

Fig. 4. Current-voltage characteristics of the FETs (100 μm long and 1000 μm wide): (a) pristine P3HT (○) and P3HT blended with 10 wt% CNT (■) and (b) P3HT blended with 20 wt% CNT. V_G was varied from 0 to −80 V. (c) Plot of I_{DS} versus V_G at a fixed V_{DS} of −80 V on both linear (left axis) and log (right axis) scales for devices as a function of the CNT concentration. The CNT concentration increases in the direction of the arrows. (d) Field-effect mobility (left axis) and on–off ratio (right axis) obtained in the saturation regime of the P3HT−CNT FETs as a function of the CNT concentration.

act as conducting bridges connecting the crystals in the P3HT film, although the molecular ordering of the P3HT chains dramatically decreases with the addition of the CNTs. However, at high CNT concentrations (>20 wt% of CNT) the FETs exhibit metallic behavior and no field-effect transistor characteristics due to the percolation of CNTs.

Furthermore, we also investigate the effects of the addition of the CNTs on the hole-injection barrier, because the energy levels of the interface between the electrode and the semiconductor are likely to be changed by the addition of the CNTs. To investigate the variation of the electronic structure of the P3HT−CNT films as a function of CNT concentration, we performed X-ray photoelectron spectroscopy (XPS) using synchrotron radiation techniques [27–29]. Fig. 5a shows the variation in the valence band maximum (VBM) of the P3HT

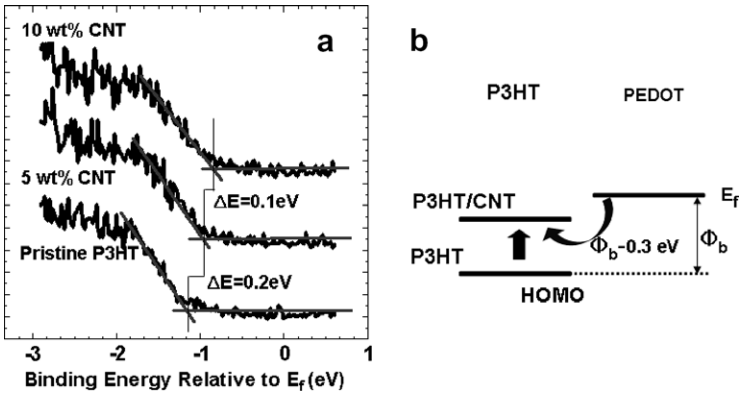

Fig. 5. (a) Changes in the valence band spectra of the P3HT films as a function of CNT concentration. (b) Energy level diagram of the interfaces between P3HT and PEDOT.

films with CNT concentrations. The spectra were recorded using a photon energy of 80 eV, and the measured VBM was calibrated with that of a clean Au surface. From the spectra obtained for pristine P3HT, P3HT with 5 wt% CNT, and P3HT with 10 wt% CNT, their HOMO levels were found to be 1.2 eV, 1 eV, and 0.9 eV, respectively. Thus the VBM at the surface of the P3HT film with 10 wt % CNT is shifted by about 0.3 eV to a lower binding energy with respect to that of pristine P3HT, which is due to the lower work function of the CNTs [30–32]. Therefore the hole-injection barrier for the P3HT–10 wt% CNT film is about 0.3 eV smaller than that for a pristine P3HT film.

A schematic energy level diagram of the electrode/semiconductor interface and the hole-injection barrier is shown in Fig. 5b. P3HT thin films containing CNTs have significantly different characteristics to pristine P3HT films. In particular, the hole-injection barrier in P3HT with 10 wt% CNT is significantly smaller, which enhances carrier injection.

4. Conclusions

In conclusion, to enhance the field-effect mobility of regioregular P3HT, we blended various amounts of functionalized CNTs with P3HT in solution, and compared the results obtained for these systems with those for the pristine P3HT thin film. We found that the molecular ordering of P3HT is disturbed by the addition of the CNTs, but that the P3HT films have a higher field-effect mobility, on average 0.04 $cm^2 V^{-1} s^{-1}$. This remarkable increase in the field-effect mobility over that of the pristine P3HT film is due to the high conductivity of the CNTs, which act as conducting bridges connecting the crystals in the P3HT film. In addition, the hole-injection barrier decreases with increases in the CNT concentration, which results in more efficient carrier injection. This approach to enhancing the electrical properties of semiconducting polymer materials should prove useful to the development of robust and practical polymer devices for a wide range of commercial applications.

Acknowledgements

This work was supported by a Grant (F0004022-2007-23) from the Information Display R&D Center under the 21st Century Frontier R&D Program, ERC Program (R11-2003-006-03005-0) of the MOST/KOSEF, and the Regional Technology Innovation Program of the MOCIE (RTI04-01-04), POSTECH Core Research Program, and the Pohang Acceleratory Laboratory for providing the synchrotron radiation source at the 3C2, 4B1, 8A2, 8C1, and 10C1 beamlines used in this study.

References

[1] H. Ago, K. Petritsch, M.S.P. Shaffer, A.H. Windle, R.H. Friend, Adv. Mater. 11 (2005) 1281.
[2] Z. Wu, Z. Chen, X. Du, J.M. Logan, J. Sippel, M. Nikolou, K. Kamaras, J.R. Reynolds, D.B. Tanner, A.F. Hebard, A.G. Rinzler, Science 305 (2004) 1273.
[3] Q. Cao, M.G. Xia, M. Shim, J.A. Rogers, Adv. Funct. Mater. 16 (2006) 2355.
[4] Y. Li, D. Mann, M. Rolandi, W. Kim, A. Ural, S. Hung, A. Javey, J. Cao, D. Wang, E. Yenilmez, Q. Wang, J.F. Gibbons, Y. Nishi, H. Dai, NanoLetters 4 (2004) 317.
[5] J. Wang, J. Dai, T. Yarlagadda, Langmuir 21 (2005) 9.
[6] E. Kymakis, I. Alexandrou, G.A.J. Amaratunga, J. Appl. Phys. 93 (2003) 1764.
[7] X.Z. Bo, N.G. Tassi, C.Y. Lee, M.S. Strano, C. Nuckolls, G.B. Blanchet, Appl. Phys. Lett. 87 (2005) 203510.
[8] X. Wang, H. Liu, Y. Jin, C. Chen, J. Phys. Chem. B 110 (2006) 10236.
[9] B. Pradhan, S.K. Batabyal, A.J. Pal, Appl. Phys. Lett. 69 (1996) 4108.
[10] Y. Qin, J. Shi, W. Wu, X. Li, Z.X. Guo, D. Zhu, J. Phys. Chem. B 107 (2003) 12899.
[11] G. Viswanathan, N. Chakrapani, H. Yang, B. Wei, H. Chung, K. Cho, C.Y. Ryu, P.M. Ajahan, J. Am. Chem. Soc. 125 (2003) 9258.
[12] A. Facchetti, M.H. Yoon, T.J. Marks, Adv. Mater. 17 (2005) 1705.
[13] H. Sirringhaus, P.J. Brown, R.H. Friend, M.M. Nielsen, K. Bechgaard, B.M.W. Langeveld-Voss, A.J.H. Spiering, R.A.J. Janssen, E.W. Meijer, P. Herwig, D.M. de Leeuw, Nature 401 (1999) 685.
[14] M.J. Panzer, C.D. Frisbie, Adv. Funct. Mater. 16 (2006) 1051.
[15] B.K. Crone, A. Dodabalpur, R. Sarpeshkar, A. Gelperin, H.E. Katz, Z. Bao, J. Appl. Phys. 91 (2001) 10140.
[16] S. Kobayashi, T. Nishikawa, T. Takenobu, S. Mori, T. Shimoda, T. Mitani, H. Shimotani, N. Yoshimoto, S. Ogawa, Y. Iwasa, Nature Mater. 3 (2004) 317.
[17] R. Österbacka, C.P. An, X.M. Jiang, Z.V. Vardeny, Science 287 (2000) 839.
[18] A.R. Murphy, J.M.J. Fréchet, Chem. Rev. 107 (2007) 1066.
[19] A. Facchetti, Mater. Today 10 (2007) 28.
[20] C.D. Dimitrakopoulos, P.R.L. Malenfant, Adv. Mater. 14 (2002) 99.
[21] Y.D. Park, D.H. Kim, Y. Jang, J.H. Cho, M. Hwang, H.S. Lee, J.A. Lim, K. Cho, Org. Electron. 7 (2006) 514.
[22] R.J. Kline, M.D. McGehee, E.N. Kadnikova, J. Liu, J.M.J. Fréchet, Adv. Mater. 15 (2003) 1519.
[23] H.J. Lee, S.J. Oh, J.Y. Choi, J.W. Kim, J. Han, L.S. Tan, J.B. Baek, Chem. Mater. 17 (2005) 5057.
[24] Y.D. Park, D.H. Kim, Y. Jang, M. Hwang, J.A. Lim, K. Cho, Appl. Phys. Lett. 87 (2005) 243509.
[25] G. Horowitz, Adv. Mater. 10 (1998) 365.

[26] H. Jia, S. Gowrisanker, G.K. Pant, R.M. Wallace, B.E. Gnade, J. Vac. Sci. Technol. A 24 (2006) 1228.
[27] Y.D. Park, J.H. Cho, D.H. Kim, Y. Jang, H.S. Lee, K. Ihm, T.H. Kang, K. Cho, Electrochem. Solid State Lett. 9 (2006) G317.
[28] P. Dannetun, M. Boman, S. Stafström, W.R. Salaneck, R. Lazzaroni, C. Fredriksson, J.L. Brédas, R. Zamboni, C. Taliani, J. Chem. Phys. 99 (1993) 664.
[29] D. Schmeiβer, Synth. Met. 138 (2003) 135.
[30] P. Liu, Y. Wei, K. Jiang, Q. Sun, X. Zhang, S. Fan, Phys. Rev. B 73 (2006) 235412.
[31] H. Ago, T. Kugler, F. Cacialli, K. Petritsch, R.H. Friend, W.R. Salaneck, Y. Ono, T. Yamabe, K. Tanaka, Synth. Met. 103 (1999) 2494.
[32] A.D. Pasquier, H.E. Unalan, A. Kanwal, S. Miller, M. Chhowalla, Appl. Phys. Lett. 87 (2005) 203511.

Available online at www.sciencedirect.com
ScienceDirect
Organic Electronics 9 (2008) 323–327
Organic Electronics
www.elsevier.com/locate/orgel

Integrating organic light-emitting diode and field-effect-transistor in a single device

Bin Wei [a], Jun Wang [a,*], Chong Li [b], Aoi Shimada [b], Musubu Ichikawa [b], Yoshio Taniguchi [b], Taketomi Kamikawa [c]

[a] *Key Laboratory of Advanced Display and System Applications, Ministry of Education, Shanghai University, P.O. Box 143, 149 Yanchang Road, Shanghai University, Shanghai 200072, PR China*
[b] *Department of Functional Polymer Science, Shinshu University, 3-15-1 Tokida, Ueda, Nagano 386-8567, Japan*
[c] *Institute of Frontier Device, Seiko Epson Corporation, 281 Fujimi, Fujimi-machi, Suwa-gun, Nagano 399-0293, Japan*

Received 10 July 2007; received in revised form 30 November 2007; accepted 30 November 2007
Available online 14 December 2007

Abstract

We have investigated organic light-emitting diodes (OLEDs) with a structure of field-effect-transistor (FET) using MgAg as source and drain electrodes, respectively. These devices were found to present both a typical switchable behavior of FET and an electro-optical transfer characteristic of OLEDs. Five organic layers were employed in devices that were expected to play each role for OFET and OLED, respectively. In a result, the FET unipolar behavior has been demonstrated experimentally. Furthermore, FET characteristics were discussed based on an equivalent circuit.

PACS: 85.30.Tv; 72.80.Le; 85.60.Jb

Keywords: Field-effect transistors; Organic light-emitting diodes; Equivalent circuit

1. Introduction

Organic semiconductor devices have received much attention due to intensive applications of organic light-emitting diodes (OLEDs) in lightening, flat panel displays, and optically pumped organic thin films in stimulated emission [1–3]. Besides, organic field-effect transistors (OFETs) based on organic thin film or single crystals (such as tetracene, pentacene or rubrene) are also one of these topics that have attracted great attention in these years [4–7]. Furthermore, some research groups have reported field-effect transistor (FET) driven OLEDs and organic light-emitting transistors (OLETs) [8–12]. Since transistors can control the amount and the species (hole or electron) of injection carriers by the third electrode and employing OLETs will make drive circuits of displays simpler than using organic light-emitting diodes, OLETs are expected to become promising in the fields of high performance light-emitting devices. However, since the emission in OLETs mainly radiate toward the edge of film or crystal under wave-guided, the light

* Corresponding author.
E-mail address: wangj@shu.edu.cn (J. Wang).

1566-1199/$ - see front matter © 2007 Elsevier B.V. All rights reserved.
doi:10.1016/j.orgel.2007.11.010

intensity is relatively weak and emission spectrum is difficult to observe [13]. Furthermore, the integration of two kinds of devices (OFET and OLED) on a substrate has been reported [14].

In this paper, we reported an OLED with a FET structure by which will overcome the disadvantages of OLETs, such as edge emission and light quenching near metal drain electrode. Compared to TFT driven OLEDs, our devices present both a unipolar FET behavior and an electro-optical transfer characteristics of OLEDs. The FET behavior has been observed from an OLED with a strong surface emission mode.

2. Experimental

We have developed a type of OLED with a FET structure, as shown in Fig. 1. For top – contact configuration we defined, as shown in Fig. 1, a indium–tin-oxide (ITO) glass substrate with 150 nm was served as a gate electrode, and a 150 nm of MgAg as both drain and source electrode. The structure of organic layers in devices is 2,5-bis(6N-(2′, 2″-bipyridyl))-1,1-dimethyl-3,4-diphenylsilole (PyPySPyPy, 80 nm)/bathocuproine (BCP, 10 nm)/tris(8-hydroxyquinoline)aluminum (Alq_3, 30 nm)/4,4′-bis[*N*-(1-napthyl)-*N*-phenyl-amino]-biphenyl (NPB, 60 nm)/tris [2-naphthyl (phenyl) amino] triphenylamine (2-TNATA, 220 nm). We selected 2-TNATA to function as a hole injection and transport layer, and PyPySPyPy as electron transport layer, due to their relatively high carrier mobility [15,16], for which the devices with 400 nm of organic layers can be operated under high voltages without degradation. In addition, the BCP was employed as a hole block layer to prevent hole leak into electron transport layer. These organic layers and MgAg electrode (9:1 mass ratio) were processed by thermal deposition. The deposition rates were typically 0.1 nm/s and 0.5 nm/s for organic materials and metal cathode, respectively.

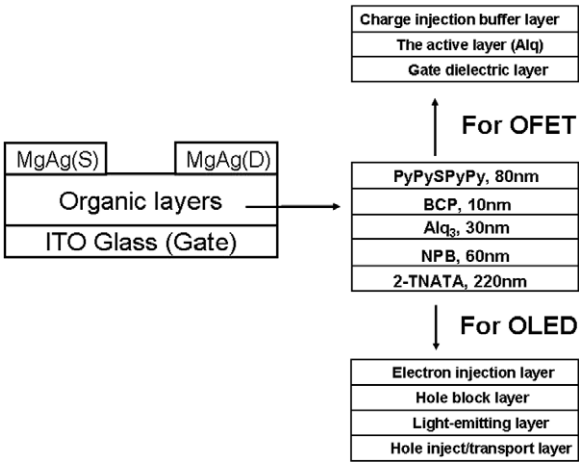

Fig. 1. Configuration of OLEDs with a FET structure of top-contact. Four organic layers act as different function are shown in OFET and OLED.

A shadow mask with one thin tungsten line of diameter 30 μm was carefully mounted on the organic layers to form a top-contact configuration. On the other hand, we fabricated a bottom-contact configuration with a very thin channel on ITO. We have etched line ITO to achieve a drain and a source electrode by the following procedures. First, we used electron beam (EB) lithography (Tokyo technology Co. Ltd.) to form a narrow pattern with an order of μm on a cleaned nonluminescent glass substrate (beam current is 250 pA, exposure time is 0.75 μs, lithography field is the order of μm^2, resolution is 0.02 μm/pixel). In addition, EB resist (ZEP520A) was used to carry out processing procedure. Next, a thick LiF layer with 300 nm was thermally deposited on the glass substrate with EB pattern. Then the substrate was immersed in *N*,*N*-dimethylacetamide solvent and ultrasonic wave treatment was carried out to remove LiF onto EB resist. Subsequently, opaque metal Cr was deposited onto the substrate and then LiF was liftoffed by a treatment in hot water with ultrasonic wave for 30 min. Finally, photoresist agent has been spin-coated with under UV exposure prior to using the completed Cr mask having narrow channels onto an ITO substrate, and then we etched the substrate in mixed acid for 35 min and obtained an ITO pattern with a very narrow channel.

The electric characteristics of devices were measured with two source electrometers (Advantest, R6245) in vacuum (10^{-3} Pa or less) environment at room temperature. Two Au wires as probes were placed onto gate and drain contact carefully by observing optical microscope (Keyence digital HF microscope VH-8000). We investigated the device characteristics by scanning V_D from 0 to 20 V at a constant of V_G (15 V) with a step of 0.5 V (ITO as gate contact for bottom configuration and drain contact for top configuration).

3. Results and discussion

These devices exhibited typical OLED characteristics when applied voltage on source and gate con-

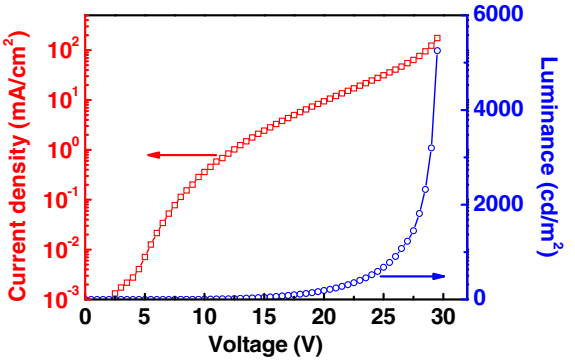

Fig. 2. The luminescent characteristics of OLED in current studies.

tact. The luminescence characteristics of OLED were shown in Fig. 2. An OLED (size: 4 mm^2) with ITO as an anode and MgAg (Source contact in OFET) as a cathode has been presented from electro-optical characteristics. Results found that the turn-on voltage to observe the luminescence of 0.1 cd/m^2 is 7.5 V, and maximum luminance of 5252.1 cd/m^2 was realized at 29.5 V. The current density and luminance are 0.36 mA/cm^2 and 6.3 cd/m^2 at 10 V, 2.42 mA/cm^2 and 46.0 cd/m^2 at 15 V. The function of each layer in devices was also showed in Fig. 1.

It is noted that typical transistor characteristics can be clearly observed, too. When applied positive drain and gate voltage, electrons are injected into organic layers from MgAg contact. Fig. 3 shows the family curves ($I_D - V_D$) of our devices. The linear and saturation regime may be observed with the increase of V_D. Electrons are injected from the source contact, and extracted from drain contact. The depletion region under drain contact is gradually enlarged with the increase of V_D, which leads to the form of saturation current. From the transfer curves ($I_D - V_G$), the switch characteristics of transistors are displayed with the increase of V_G. Here, electrons are accumulated at the interface of Alq_3 and NPB/2-TNATA by applying positive gate voltage. Therefore, current devices with OLED structure also showed typical characteristics of field-effect transistors although conventional gate insulator and active layer have not been defined in current devices. According to the configuration and operation mechanism of FET, the five organic layers are believed to act as different function. The upper two layers (BCP and PyPySPyPy) will serve as two charge (electrons) injection layers, the light-emitting layer (Alq_3) as the active layer in transistors, and the last two layers (NPB/2-TNATA) as the gate dielectric layer as shown in Fig. 1. Thus, these devices exhibit also transistor behavior. Furthermore, noted that electron accumulation mode is operated by using MgAg as source/drain contact for easy electrons injection due to its low work function. Finally, a similar device with ITO as source and drain contact and MgAg as gate electrode in inversion structure displays hole accumulation mode due to easy hole injection. Despite of the output current of device is low when compared with conventional organic transistors, which is due to low mobility of Alq_3 [17], however, in this work we focused on the performance of OLEDs while a TFT behavior was expected to obtain. Moreover, similar to the organic light-emitting transistors with PN-hetero-boundary carrier recombination sites [18], we consider Alq_3 functioning mainly as carrier recombination and emissive layer. The typical device characteristics will be significant that present a new path for organic light-emitting transistors. Further optimizations about devices performance

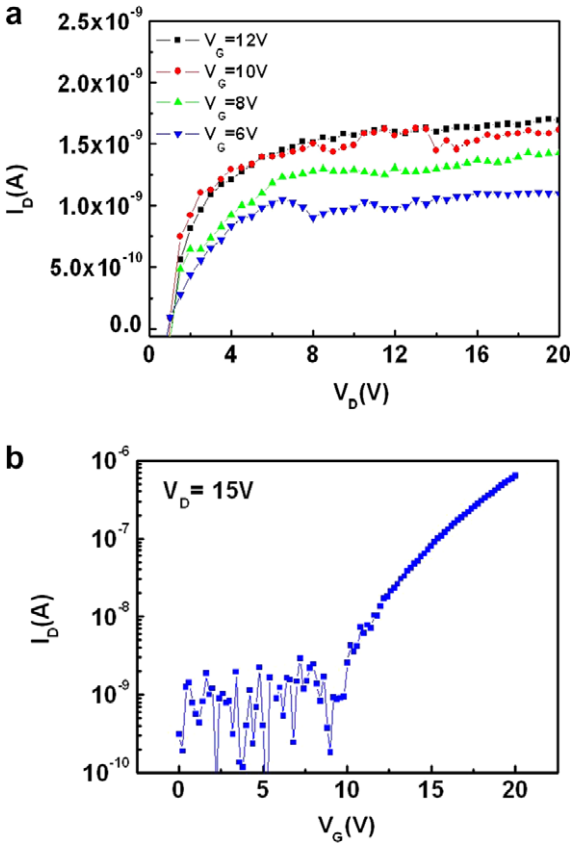

Fig. 3. The typical transistor characteristics of OLEDs with a FET structure. (a) Family curves and (b) transfer characteristics.

are in progress, such as using the molecular π-conjugated oligomers with good carrier transport and photonic properties as a transistor to replace Alq_3 due to their cooperative interaction between aligned molecules.

In Fig. 3a, I_D was obtained with increasing the V_D at a constant of V_G. In this case, the quantity of accumulated charge carriers at the interface between semiconductor/insulator resulted from constant gate voltage (V_G). On the other hand, the I_D in Fig. 3b, was different from that in Fig. 3a, due to the trap effect of organic semiconductors in OFETs, in which more trapped carriers can be released with the successive increase of V_G (particularly for amorphous materials). Therefore, the difference of I_D between Figs. 3a and b is attributed to different voltage (either gate or drain bias) process.

We have established an equivalent circuit to discuss the FET behavior. Similar to one OLED [17], the equivalent circuit of the device with top-contact configuration used in this study can be schematically described in Fig. 4a. The internal resistance of organic layer for source-drain contact, source-gate contact and drain-gate contact in device was assumed to be R, R_1, R_2, respectively. We described

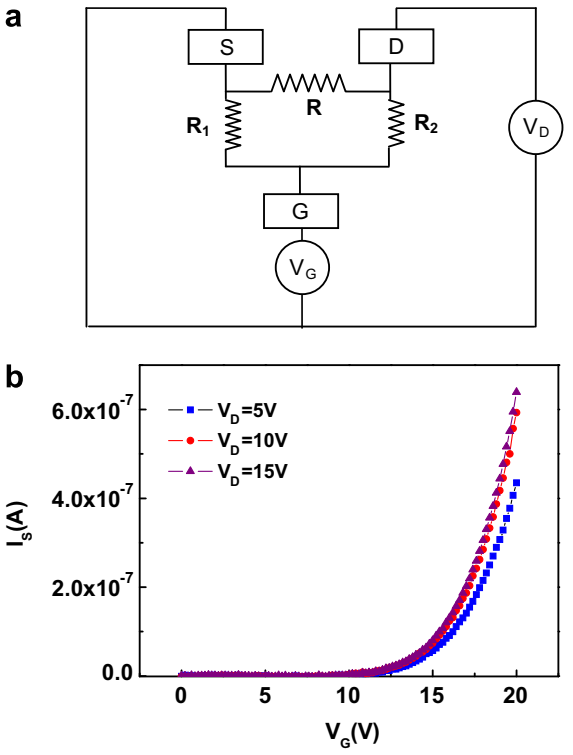

Fig. 4. (a) Equivalent circuit of an OLED with a top-contact FET configuration and (b) electric modulation characteristics.

the currents of three contacts, I_D, I_G and source current (I_S) using the following expression:

$$I_G = \frac{V_G}{R_1} + \frac{V_G - V_D}{R_2} \quad I_D = -\frac{V_G - V_D}{R_2} + \frac{V_D}{R}$$
$$I_s = -\frac{V_G}{R_1} - \frac{V_D}{R} \qquad (1)$$

The expression suggests that the OLED-current (V_G/R_1) and OFET-current (V_D/R) are mutually rivaled. However, the change magnitude of each type of current was varied with the change in the channel length of organic layer adjacent to the drain and source cathodes.

In Eq. (1), the I_S is considered to be equal to the negative of the sum of I_D and I_G, which have been recorded experimentally. We plotted the relative change of I_S at some $V_D = V$ with respect to the value of I_S at $V_D = 0$ V against the gate voltages, as shown in Fig. 4b. It was clearly observed the V_D dependence of I_S at a low drain voltage region, as described by Eq. (1), although the value of I_S is at the order of μA. This demonstrates that a FET behavior has been obtained in addition to OLED characteristics, particularly at the low drain voltage condition. Moreover, it is noted that the I_S will reach a saturated state when drain voltage increases up to when OLED characteristics is more significant.

4. Conclusion

In summary, we have reported the characteristics of OLED with an FET structure. The typical FET behaviors in an OLED were obtained from these devices. The unique electric characteristics of both OFET and OLED were analyzed. The five layers of organic semiconductors are believed to play different role in OFET and OLED, respectively. Furthermore, its mechanism is presented based on an equivalent circuit. The works to investigate the change in recombination zone of device and improve device performance are in process.

Acknowledgements

This work was supported by the Cooperative Link for Unique Science and Technology for Economy Revitalization (CLUSTER) of the Ministry of Education, Culture, Sports, Science and Technology, Japan, and shanghai excellent teacher program. The corresponding author (J. Wang) would like to thank the funding support from Shanghai Rising-Star Program (07QA14023).

References

[1] V.G. Kozlov, V. Bulovic, P.E. Burrows, S.R. Forrest, Nature (London) 389 (1997) 362.
[2] M. Berggren, A. Dodabalapur, R.E. Slusher, Appl. Phys. Lett. 71 (1997) 2230.
[3] B. Wei, N. Kobayashi, M. Ichikawa, T. Koyama, Y. Taniguchi, T. Fukuda, Opt. Exp. 14 (2006) 9436.
[4] V.C. Sundar, J. Zaumseil, V. Podzorov, E. Menard, R.L. Willett, T. Someya, M.E. Gershenson, J.A. Rogers, Science 303 (2004) 1644.
[5] V. Podzorov, E. Menard, A. Borissov, V. Kiryukhin, J.A. Rogers, M.E. Gershenson, Phys. Rev. Lett. 93 (2004) 086602-1.
[6] J. Wang, H.B. Wang, X.J. Yan, H.C. Huang, D. Jin, J.W. Shi, Y.H. Tang, D.H. Yan, Adv. Fuct. Mater. 16 (2006) 824.
[7] J. Wang, H.B. Wang, X.J. Yan, H.C. Huang, D.H. Yan, Chem. Phys. Lett. 407 (2005) 87.
[8] M. Ichikawa, H. Yanagi, Y. Shimizu, S. Hotta, N. Suganuma, T. Koyama, Y. Taniguchi, Adv. Mater. 14 (2002) 1272.
[9] A. Hepp, H. Heil, W. Weise, M. Ahles, R. Schmechel, H. von Seggern, Phys. Rev. Lett. 91 (2003) 157406.
[10] M. Ahles, A. Hepp, R. Schmechel, H. von Seggern, Appl. Phys. Lett. 84 (2004) 428.
[11] C. Rost, S. Karg, W. Riess, M.A. Loi, M. Murgia, M. Muccini, Appl. Phys. Lett. 85 (2004) 1613.
[12] T. Oyamada, H. Sasabe, C. Adachi, S. Okuyama, N. Shimoji, K. Matsushige, Appl. Phys. Lett. 86 (2005) 86.
[13] K. Nakamura, M. Ichikawa, R. Fushiki, T. Kamikawa, M. Inoue, T. Koyama, Y. Taniguchi, Jpn. J. Appl. Phys. 44 (2005) L1367.
[14] C.C. Chu, C.W. Chen, S.H. Li, E.H.E. Wu, Y. Yang, Appl. Phys. Lett. 86 (2005) 253503.
[15] K. Okumoto, Y. Shirota, J. Lumin. 87 (2000) 1171.
[16] S. Tabatake, S. Naka, H. Okada, H. Onnagawa, M. Uchida, T. Nakano, K. Furukawa, Jpn. J. Appl. Phys. 41 (2002) 6582.
[17] B. Wei, K. Furukawa, J. Amagai, M. Ichikawa, T. Koyama, Y. Taniguchi, Semicond. Sci. Technol. 19 (2004) L56.
[18] N. Suganuma, N. Shimoji, Y. Oku, K. Matsushige, MRS Proceed. 965E (2006) 0965-S03–0965-S14.

Available online at www.sciencedirect.com
ScienceDirect
Organic Electronics 9 (2008) 328–332
Organic Electronics
www.elsevier.com/locate/orgel

N-type field-effect transistor based on a fluorinated-graphene

Tomohiko Mori *, Yoshihiro Kikuzawa, Hisato Takeuchi

Toyota Central Research and Development Laboratories, Inc., Nagakute, Aichi 480-1192, Japan

Received 20 August 2007; received in revised form 29 November 2007; accepted 10 January 2008
Available online 20 January 2008

Abstract

A fluorinated-graphene, 2,5,8,11,14,17-hexafluoro-hexa-*peri*-hexabenzocoronene (6F-HBC), has been synthesized. 6F-HBC was deposited by vacuum sublimation as an active layer in an organic field-effect transistor (OFET). The OFET with 6F-HBC performed as an n-type semiconductor, while that with hexa-*peri*-hexabenzocoronene (HBC) performed as a p-type semiconductor. The electron field-effect mobility and on/off ratio for 6F-HBC were 1.6×10^{-2} cm^2/Vs and 10^4, respectively. Hexafluoro-substituting reduces both the highest occupied molecular orbital and lowest unoccupied molecular orbital levels by 0.5 eV, which is suitable for electron injection from the electrode. 6F-HBC has a face-to-face structure which is a preferable crystal structure for carrier transport.

PACS: 61.66.Hq; 68.03.Hj; 61.10.Nz

Keywords: OFET; Hexabenzocoronene; Graphene

1. Introduction

Organic field-effect transistors (OFETs) have attracted considerable attention recently, because of their use in lightweight, low-cost, large-area and flexible electronic products, such as flat-panel displays, smart cards and radio-frequency (rf) tags [1].

Graphenes, of well-defined size and shape, such as hexa-*peri*-hexabenzocoronene (HBC) and their derivatives, are interesting molecules for use as an active layer in OFETs [2,3]. Graphenes are rich in π electrons, and graphenes of well-defined size and shape are expected to have a high degree of overlap of the π electrons of neighboring molecules, which would impart high charge carrier mobility. HBC derivatives actually exhibit some of the highest values for intrinsic hole charge carrier mobility of up to 1 cm^2/Vs in the bulk sample, using a pulse-radiolysis time-resolved microwave conductivity (PR-TRMC) technique, which makes them promising candidates for organic electronic devices [2].

Considering the production of bipolar transistors and complimentary circuits, n-type organic semiconductors should have similar physical and electrical properties except for the type of carriers. To date, most of the organic molecules reported for OFETs have been p-type semiconductors, and only a few molecules have also been found to function as n-type semiconductors. It is known that for a material to transport electrons (n-type) requires access to

* Corresponding author. Tel.: +81 561 71 7185; fax: +81 561 63 5328.
E-mail address: tomohiko@mosk.tytlabs.co.jp (T. Mori).

1566-1199/$ - see front matter © 2008 Elsevier B.V. All rights reserved.
doi:10.1016/j.orgel.2008.01.002

the lowest unoccupied molecular orbital (LUMO) level for electron injection. Therefore, molecules with strong electron-withdrawing groups are good candidates as n-type semiconductors. In fact, good performance of n-type organic semiconductors has been obtained by the introduction of fluoro or fluoroalkyl substituents into pentacene [4] and oligothiophene derivatives [5], which are known as hole-transporting systems.

In the present study, 2,5,8,11,14,17-hexafluoro-hexa-*peri*-hexabenzocoronene (6F-HBC) was synthesized as a potential n-type semiconductor for OFETs. An OFET with 6F-HBC was fabricated, and the performance as n-type semiconductor is presented. The crystal structure of the bulk and the crystalline morphology of the film were measured using powder X-ray diffraction and grazing incidence X-ray diffraction (GIXD), respectively.

2. Experimental methods

The chemical structures of HBC and 6F-HBC are shown in Fig. 1. HBC and 6F-HBC were synthesized by a previously reported method [6] from substituted starting materials.

The configuration of the OFET device is a top-contact structure, as shown in Fig. 2. Heavily doped n-type single-crystal silicon wafer ($< 0.02\,\Omega\,\mathrm{cm}$) covered with a 300 nm thick film of thermally grown SiO_2 (SiO_2) was used as the substrates for the OFET. The silicon wafer also serves as the gate electrode. The thermally grown SiO_2 provides a good gate insulator with high breakdown voltage and low defect concentration. A 20 nm active layer of 6F-HBC was deposited on the SiO_2 layer by vacuum evaporation at a rate of 0.1 nm/min under a pressure of 1×10^{-5} Pa. The OFET was completed by evaporating Ca/Al (1 nm/100 nm) layers through a shadow mask to form the source and drain contacts, and forming a 100 nm Al layer on the back side of the wafer to the contact gate. The channel length and width were 200 and 5000 μm, respectively. After annealing the OFET in a vacuum chamber at 150 °C for 1 h, in order to remove the influence of oxygen and humidity which presumably traps negative carriers, the OFET characteristics were measured using an HP4145B parameter analyzer.

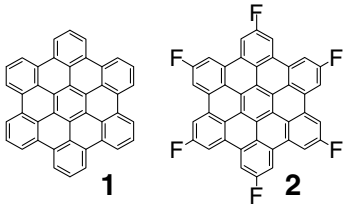

Fig. 1. The chemical structures of hexa-*peri*-hexabenzocoronene (HBC) and 2,5,8,11,14,17-hexafluoro-hexa-*peri*-hexabenzocoronene (6F-HBC).

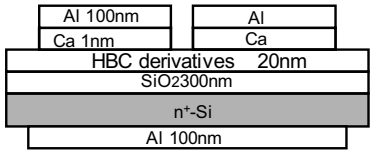

Fig. 2. Schematic structure of the OFET device investigated in this study.

Crystalline structures were measured using powder X-ray diffraction (XRD). Powder samples were sealed in a glass capillary of 0.3 mmϕ. Powder XRD data were collected at the Japan Synchrotron Radiation Research Institute (SPring-8), using beamline BL19B2, X-ray energy of 12.4 keV, and an imaging plate. The structure and crystallinity of the films were characterized by out-of-plane XRD, in-plane XRD and atomic force microscope. XRD (θ–2θ) scans were acquired using a Rigaku RINT 2200 system with Cu Kα radiation. In-plane XRD was performed at SPring-8, using beamline BL46XU at an incident angle of 0.13° and X-ray energy of 12.0 keV. The AFM system used in this study was a Nanoscope IIIa + D3100 (Digital Instrument, Inc., Santa Barbara, CA). The measurement was performed in the tapping mode and in air at room temperature.

3. Results and discussion

Fig. 3 shows the (a) output and (b) transfer characteristics of the OFET with a 6F-HBC active layer. It is seen that the application of a positive voltage to the gate increases the positive drain current. This indicates that the OFET with 6F-HBC performs as an n-type transistor, in contrast to a p-type transistor of HBC [3]. The field-effect mobilities were calculated using the I_D values in the saturation regions. The electron field-effect mobility and on/off ratio for 6F-HBC were $1.6 \times 10^{-2}\,\mathrm{cm^2/Vs}$ and 10^4, respectively. The electron mobility of 6F-HBC was comparable to the hole mobility of HBC ($3.3 \times 10^{-2}\,\mathrm{cm^2/Vs}$), which was obtained under the optimized condition of a 150 °C substrate temperature.

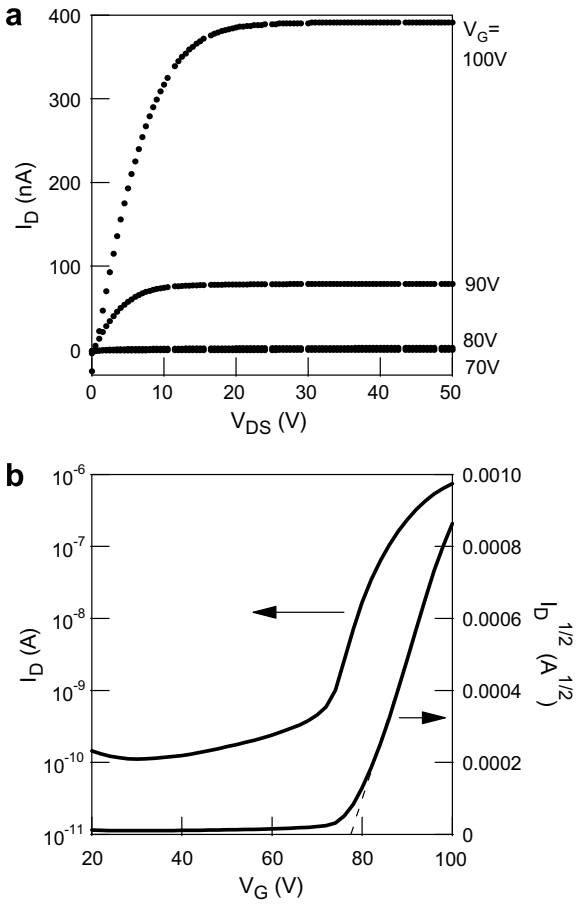

Fig. 3. (a) Drain current (I_D) versus drain voltage (V_D) characteristics as a function of the gate voltage (V_G) for a 6F-HBC OFET and (b) I_D and $I_D^{1/2}$ versus V_G plots at $V_D = 40$ V for the same OFET.

The HOMO levels of the HBC and 6F-HBC films were determined using a photoelectron spectrometer (Riken Keiki Co. Ltd., AC-2). Those of HBC and 6F-HBC were at 5.4 and 5.9 eV, respectively. The LUMO levels of HBC and 6F-HBC films were deduced from the band gaps obtained from the UV/Vis absorption spectra and the HOMO levels. The band gaps of HBC and 6F-HBC were both 2.7 eV. The LUMO levels of HBC and 6F-HBC were 2.7 and 3.2 eV, respectively. Therefore, hexafluoro-substitution reduces both the HOMO and LUMO levels by 0.5 eV, which is suitable for electron injection from the electrode.

Fig. 4 shows powder, out-of plane and in-plane XRD patterns of HBC and 6F-HBC deposited on SiO_2/Si substrates. The out-of-plane XRD patterns exhibit only one set of Bragg reflections from the same family of lattice planes. The layer spacings obtained from the first reflection peaks were 1.21 nm for HBC and 1.22 nm for 6F-HBC. The in-plane lattice parameters (A, B) and the angle between them (Γ) were determined from in-plane XRD patterns, and the results are displayed in Table 1.

The lattice spacing of HBC (1.21 nm) was consistent with the (0 0 1) spacing, $d_{001} = 1.19$ nm, of the reported single-crystal structure: monoclinic, space group $P2_1/a$, $a = 1.8431$ nm, $b = 0.5119$ nm, $c = 1.2929$ nm, $\beta = 112.57°$ [7]. The peaks in the in-plane XRD pattern of HBC are indexed to a rectangular in-plane unit cell with dimensions $A = 1.853$ nm, $B = 0.511$ nm, and $\Gamma = 90°$. The

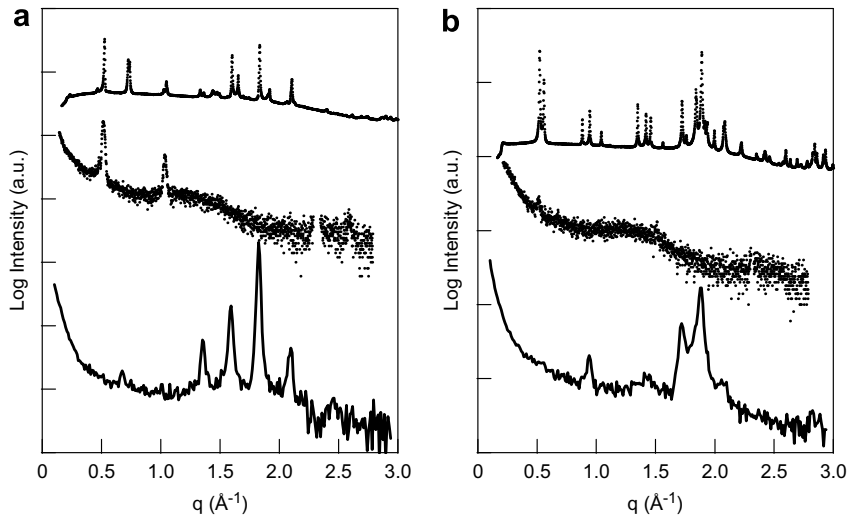

Fig. 4. (Top) Powder XRD patterns, (middle) out-of plane and (bottom) in-plane XRD patterns of (a) HBC and (b) 6F-HBC thin films on SiO_2/Si substrates.

Table 1
The in-plane lattice parameters (A, B), the angle between them (Γ), and the layer spacing (d) for the films of HBC and 6F-HBC

Compound	A (nm)	B (nm)	d_{001} (nm)	Γ (°)
HBC	1.853	0.511	1.21	90
6F-HBC	1.348	0.370	1.22	96.3

in-plane unit cell is consistent with the ab plane of bulk HBC. The absence of (10), (30) reflections agrees with a herringbone structure in the ab plane of space group $P2_1/a$.

The crystal structure of 6F-HBC was determined from the powder XRD pattern: monoclinic, space group $P1$, $a = 2.291$ nm, $b = 1.432$ nm, $c = 0.370$ nm, $\alpha = 90°$, $\beta = 98.9°$, $\gamma = 90°$. The peaks in the in-plane XRD pattern of 6F-HBC are indexed to a unit cell with dimensions; $A = 1.348$ nm, $B = 0.370$ nm, and $\Gamma = 96.3°$. The cell is consistent with the (1 −1 0) plane. The half length of 1 1 0 agrees with 1.348 nm, and the length of 0 0 1 agrees with 0.370 nm. The angle between 1 1 0 and 0 0 1 was calculated as 97.5°, which agrees with the observed angle of 96.3°. The out-of-plane XRD pattern for 6F-HBC shows 1 1 0 Bragg reflections. Since the direction of 1 1 0 is slightly different from the perpendicular of the film and the small rectangular grains with the average size of 200 nm as shown in Fig. 5, the intensity of the 1 1 0 peak is weak.

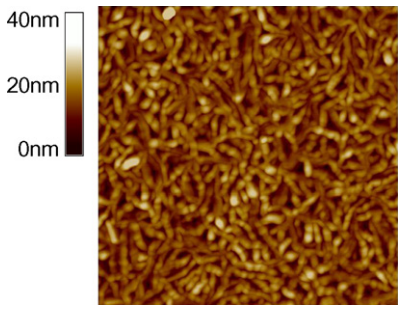

Fig. 5. 2 μm × 2 μm AFM image of 6F-HBC thin film on SiO_2/Si substrate.

In order to determine the molecular packing from the powder XRD pattern, the state-of-the-art software package Reflex Plus was used, which is based on the Powder Solve approach [8] Fig. 6 shows the molecular packing diagrams for HBC and 6F-HBC. Interestingly, 6F-HBC has a face-to-face structure, while HBC has a herringbone structure. The large van der Waals radius of fluorine would appear to change the crystal structure from herringbone to face-to-face.

Curtis et al. have recently made a structural analysis of some common organic semiconductors, discussing the correlation between solid-state packing and transport [9]. Theoretically, a face-to-face π stacking structure is expected to provide more efficient orbital overlap and thereby facilitate carrier

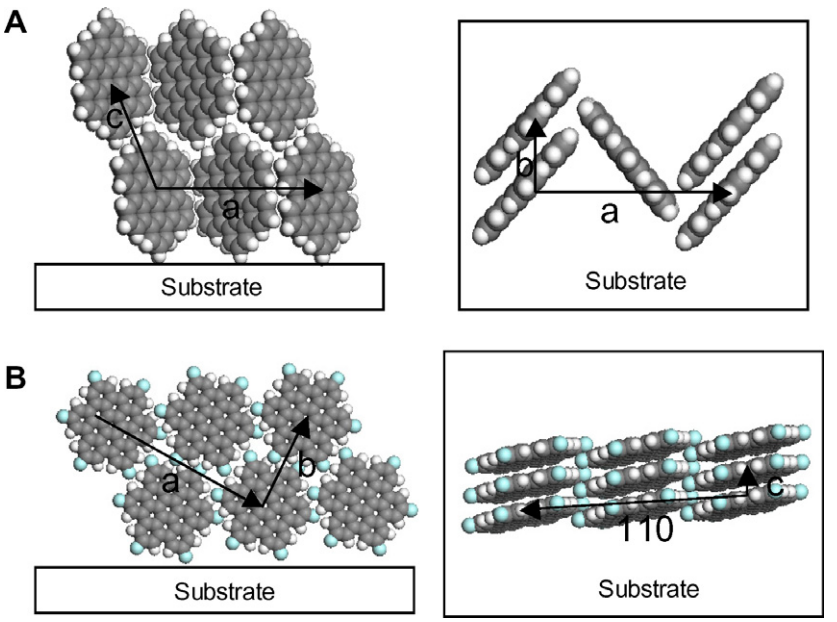

Fig. 6. Molecular packing diagrams of (a) HBC and (b) 6F-HBC.

transport. Therefore 6F-HBC has a preferable crystal structure for carrier transport.

4. Conclusion

In conclusion, OFET with 6F-HBC performed as n-type semiconductor. The electron field-effect mobility and on/off ratio for 6F-HBC were $1.6\times 10^{-2}\,cm^2/Vs$ and 10^4, respectively. In-plane and out-of-plane XRD have been performed to study the thin film structure of HBC and 6F-HBC. The data indicated that 6F-HBC has a face-to-face structure, which is a preferable crystal structure for carrier transport. The effect of the large van der Waals radius of fluorine would change the crystal structure from herringbone to face-to-face.

References

[1] C.D. Dimitrakopoulos, P.R.L. Malenfant, Adv. Mater. 14 (2002) 99.
[2] A.M. van de Craats, J.M. Warman, A. Fechtenkötter, J.D. Brand, M.A. Harbison, K. Müllen, Adv. Mater. 11 (1999) 1469.
[3] T. Mori, H. Takeuchi, H. Fujikawa, J. Appl. Phys. 97 (2005) 066102.
[4] Y. Sakamoto, T. Suzuki, M. Kobayashi, Y. Gao, Y. Fukai, Y. Inoue, F. Sato, S. Tokito, J. Am. Chem. Soc. 126 (2004) 8138.
[5] M. Yoon, S. DiBenedetto, A. Facchetti, T. Marks, J. Am. Chem. Soc. 127 (2005) 1348.
[6] M.D. Watson, A. Fechtenkötter, K. Müllen, Chem. Rev. 101 (2001) 1267.
[7] R. Goddard, M.W. Haenel, W.C. Herndon, C. Krüger, M. Zander, J. Am. Chem. Soc. 117 (1995) 30.
[8] Materials Studio (version 3.2), Accelrys Inc., San Diego, 2005.
[9] M. Curtis, J. Kao, J. Kampf, J. Am. Chem. Soc. 126 (2004) 4318.

Available online at www.sciencedirect.com
ScienceDirect
Organic Electronics 9 (2008) 333–338
Organic Electronics
www.elsevier.com/locate/orgel

Bulk and interface properties of molybdenum trioxide-doped hole transporting layer in organic light-emitting diodes

Won-Ju Shin [a], Je-Yun Lee [a], Jae Chang Kim [a], Tae-Hoon Yoon [a,*], Tae-Shick Kim [b], Ok-Keun Song [b,*]

[a] School of Electrical Engineering, Pusan National University, Busan 609-735, South Korea
[b] R&D Center, Samsung SDI, Gongse-dong, Giheung-gu, Yongin, Gyeonggi-do 449-577, South Korea

Received 28 August 2007; received in revised form 28 November 2007; accepted 3 December 2007
Available online 8 December 2007

Abstract

Effects of doping molybdenum trioxide (MoO_3) in *N*,*N*′-diphenyl-*N*,*N*′-bis(1,1′-biphenyl)-4,4′-diamine (NPB) are studied at various thicknesses of doped layer (25–500 Å) by measuring the current–voltage characteristics, the capacitance–voltage characteristics and the operating lifetime. We formed charge transfer complex of NPB and MoO_3 by co-evaporation of both materials to achieve higher charge density, lower operating voltage, and better reliability of devices. These improved performances may be attributed to both bulk and interface properties of the doped layer. The authors demonstrated that the interface effects play more important role in lowering the operating voltage and increasing the lifetime.

Keywords: OLED; Metal oxide; Charge transfer complex; Interface; Stability

Since Tang and Vanslyske demonstrated stable and efficient double-layered organic light-emitting diodes (OLEDs) in 1987, various efforts have been made to enable their practical applications to flat panel displays and lighting devices [1–13]. Performances of OLEDs are considered relatively good enough for small-sized displays, but power consumption and operating lifetime are still critical issues for large-sized displays.

High power efficiency of OLEDs can be achieved by higher external quantum efficiency and lower operating voltage. The external quantum efficiency is usually determined by internal quantum efficiency and light extraction efficiency, both of which are strongly dependent on electroluminescent materials and device structures. Low operating voltage can be achieved by reducing Ohmic losses of charge injection at the interface, and increasing charge transporting ability at bulk. Several approaches for high power efficiency, such as modulating the work function of electrodes [2,3] and inserting an effective buffer layer between the organic layer and the metal electrode [4–6], have been studied.

* Corresponding authors.
E-mail addresses: thyoon@pusan.ac.kr (T.-H. Yoon), ok.song@samsung.com (O.-K. Song).

1566-1199/$ - see front matter © 2007 Elsevier B.V. All rights reserved.
doi:10.1016/j.orgel.2007.12.001

Doping of the charge transporting layer can also be one of the most effective methods to reduce the operating voltage. Alkali or alkaline earth metals [7–9], or cationic dyes [10], were introduced as n-dopant into the electron transfer layer (ETL). In addition, p-dopant materials, such as $FeCl_3$ [11], $SbCl_5$ [12], and tetrafluorotetracyano-quinodimethane (F4-TCNQ) [13,14], were introduced into the hole transporting layer (HTL) to achieve a low operating voltage device. However, some of doping materials show problems such as material toxicity, high temperature for evaporation and cross contamination during evaporation. Cross contamination is quite fatal to the stability of devices.

Doping of metal oxides can be one of the most effective methods to lower the operating voltage and to improve stability without contamination problems. Various metal oxides have been recently reported as an effective p-dopant in HTL to improve power efficiency [15–18]. Although various studies have been tried to improve power efficiency by introducing a p-type metal oxide into HTL, detailed mechanisms of the lower voltage and stability have not yet been sufficiently understood.

In this paper, we investigated effects of doping MoO_3 on charge injection from the indium-tin-oxide (ITO) anode to the NPB layer at ITO/NPB interface, and the charge transporting ability in the bulk of MoO_3-doped NPB. In addition, the effects on operational stability from doping MoO_3 in NPB were also investigated.

Charge transfer (CT) complexes can be easily formed by doping MoO_3 in NPB. These contribute to an increase in the cationic charge carrier density in NPB, resulting in lower operating voltage and higher power efficiency. To discriminate interface effects from bulk effects of CT complexes in NPB, we systematically varied the thickness and concentration of the MoO_3-doped layer and monitored the operating voltage and reliability of the devices.

All devices used in this work were fabricated on ITO glass with a sheet resistance of 15 Ω/□ and a thickness of 1500 Å. Oxygen plasma treatment was used to remove excess moisture on the active area. For a doped layer, MoO_3 and NPB were co-evaporated from different sources in the same chamber. Pure NPB and tris-(8-hydroxyquinoline) aluminum (Alq_3) were subsequently deposited by conventional thermal evaporation at the rate of 1 Å/s. 10-(2-Benzothiazolyl)-2,3,6,7-tetrahydro-1,1,7,7,-tetramethyl-1H,5H,11H-[1] benzopyrano [6,7,8-ij] quinolizin-11-one (C545T) was used as a green dopant with a concentration of 5.0% in the emitting layer. The pressure of the vacuum chamber was kept at $\sim 2 \times 10^{-6}$ torr during evaporation. All devices were encapsulated with BaO in a dry nitrogen glove box. The lifetime measurements were carried out at a DC current density of 50 mA/cm^2. HP 4192A was used for capacitance–voltage (C–V) measurements at the room temperature.

A charge transfer complex is usually formed by an electron transfer from the highest occupied molecular orbital of the host materials to the lowest occupied molecular orbital of the dopant material. If we consider NPB as having an ionization potential level of 5.0–5.5 eV and MoO_3 as having a high work function of about 5.3–5.5 eV, then a charge transfer complex can be easily formed as proved by absorption spectra [5]. Fig. 1 shows the absorption spectra of NPB and MoO_3-doped NPB films at various doping concentrations. The broad absorption band around 1400 nm can be clearly observed only from MoO_3-doped NPB films, and its intensity increases as the MoO_3 doping concentration increases. This indicates that a CT complex can be easily formed and generate extra free holes with no applied current to a device. This result is similar to those on CT complexes discussed in other literatures [11,12].

To verify the effects of p-doping MoO_3 in NPB on electrical properties, a series of hole-only devices of ITO/NPB (1000 Å)/Al and ITO/5, 10, 25, 50% MoO_3-doped NPB (1000 Å)/Al were fabricated, and their electrical properties were measured. As shown in Fig. 2a, significantly improved current density–voltage (J–V) characteristics were observed when MoO_3 was doped in a NPB layer. These results might be attributed to the decrease of the injection energy barrier height and the increase of extra free charge carriers by the formation of the CT complex between MoO_3 and NPB.

We estimated the hole carrier density of the MoO_3-doped layer from C–V measurements. From the standard Schottky–Mott analysis [19], the capacitance can be described as

$$\frac{1}{C^2} = \frac{2(V_{bi} - V)}{A^2 q \varepsilon \varepsilon_0 N_A} \quad (1)$$

where q is elementary charge, V_{bi} is the built-in potential, ε is the relative dielectric constant, ε_0 is the vacuum permittivity, A is active area of device, and N_A is active concentration of charge carriers. The relative dielectric constant ε is assumed to

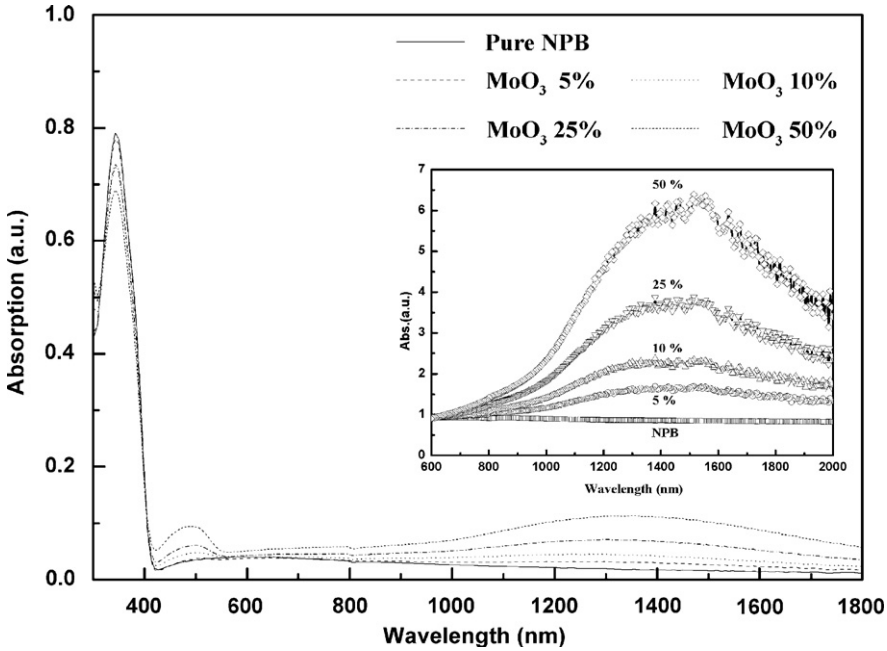

Fig. 1. Absorption spectra of pure NPB and MoO_3-doped NPB films at various MoO_3 concentrations. Inset: relative intensity of charge transfer complex bands.

be 3. Fig. 2b shows the linear increase of $1/C^2$ versus the bias voltage. The fitted lines are in good agreement with the experimental data, and the hole carrier density can be easily extracted from the slope. The calculated charge carrier density values of $0.79 \times 10^{19}\,cm^{-3}$, $0.97 \times 10^{19}\,cm^{-3}$ and $1.23 \times 10^{19}\,cm^{-3}$ were obtained for MoO_3 concentrations of 5%, 10%, and 25% in NPB, respectively. The charge carrier densities of the doped layer are much higher than that of the pure NPB layer ($1.97 \times 10^{14}\,cm^{-3}$) [20].

The increase in charge carrier density by doping MoO_3 in NPB can contribute to lower operating voltage (or higher conductivity) of the devices. To investigate the contribution of the MoO_3-doped NPB layer to the performance of OLEDs, we fabricated green emitting devices of ITO/MoO_3-doped NPB(x Å)/NPB($700 - x$ Å)/C545T doped Alq_3(300 Å)/Alq_3(400 Å)/LiF(10 Å)/Al(800 Å) with differing MoO_3-doped NPB thickness ($x = 0$, 25, 50, 100, 150, 300, 500 Å). The thickness of the MoO_3-doped layer was systematically varied to discriminate interface effects from bulk effects. The total thickness of the HTL (doped and pure NPB) was kept to a constant value of 700 Å by adding a pure NPB layer, which prevents exitons in the EML from being quenched by blocking the diffusion of MoO_3 into the EML [21].

Fig. 3a shows J–V characteristics and luminance-J (inset) of the device at various thicknesses of 5% MoO_3-doped NPB layer. The control device has the NPB thickness of 700 Å without MoO_3 dopant. It can be seen that the hole current increases significantly as the thickness of the doped NPB layer increases, while luminous efficiencies become slightly lowered. This is due to the unbalanced charge effects as shown in the inset of Fig. 3a [22]. Fig. 3b shows the operating voltages of the devices versus the thickness of the MoO_3-doped layers at two different MoO_3 concentrations of 5% and 10%. The operating voltage decreased from 10.2 V to 8.4 V at a fixed current density of 100 mA/cm^2 while a 10% MoO_3-doped layer with the thickness of 100 Å was inserted. The operating voltage shows a lower value with a higher concentration of MoO_3.

It is noteworthy that two different slopes are clearly observed. The operating voltage shows rapid decrease with the increase of the doped layer thickness when it is thinner than 100 Å. However, further increase of the doped layer when it is thicker than 100 Å shows a relatively slow decrease of the operating voltage. We assumed that the interface and bulk effects were responsible for the rapid drop of the operating voltage in devices with thinner doped layers, and for the slow drop in devices with thicker

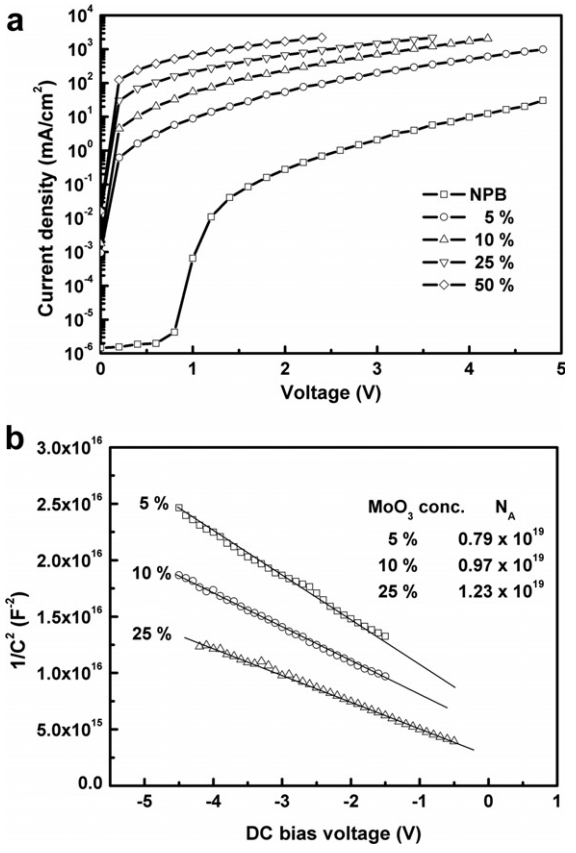

Fig. 2. (a) J–V characteristics and (b) $1/C^2$ vs V_{bias} plots of 1000 Å NPB films at various MoO_3 doping concentrations. For C–V measurements, 0.1 V signal oscillating at 100 kHz was added to dc bias.

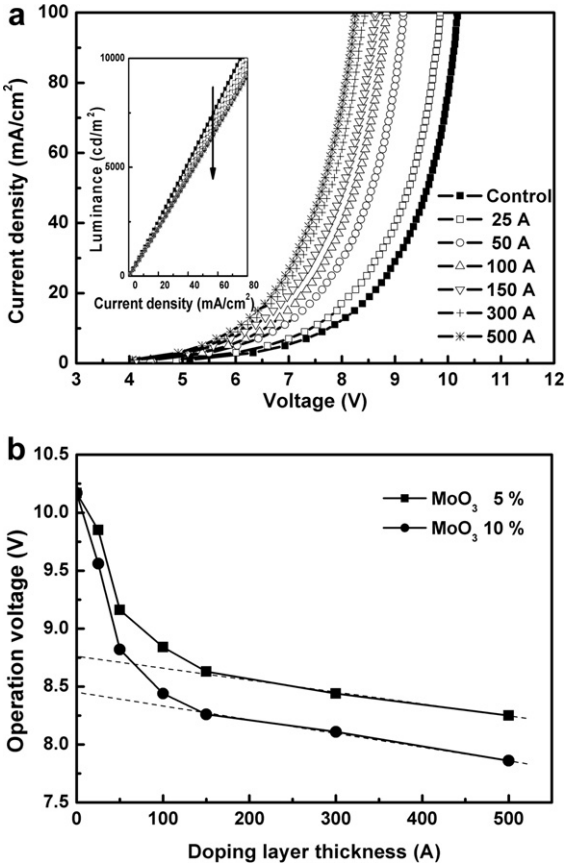

Fig. 3. (a) J vs V characteristics and luminous efficiency (inset) of a green device at various thicknesses of 5% MoO_3-doped NPB layer. (b) The operating voltage at a DC current of 100 mA/cm^2 of a green device with 5% and 10% MoO_3-doped NPB layer.

layers, respectively. These results indeed indicate that a partial doping of metal oxide in the HTL might be very effective for voltage reduction. The slow drop in devices with thicker layers can be explained by the reduced bulk resistance of the NPB layer due to the electrical doping effects, which reduce the hoping activation energy [23].

More complicated mechanisms could be involved in the rapid drop of the operation voltage when the doped layer is thinner than 100 Å. In addition to the electrical doping effects, MoO_3 itself can be an excellent hole injection layer. You et al. recently reported an improved hole injection and stability by introducing a thin layer of MoO_3 between ITO and HTL [24]. MoO_3 can exist in the form of a CT complex ($MoO_3^- : NPB^+$) in MoO_3-doped layers. The dipole of CT complex could also reduce the charge injection energy barrier at the ITO/NPB interface. Although it is somewhat difficult to describe detailed mechanisms, it is evidently apparent that the interface effects are directly involved in reducing the operating voltage and are a more dominant factor. In particular, the doped layer thickness of ~100 Å might be enough to achieve a sufficient reduction of the operating voltage.

In addition to voltage reduction, we observed a significantly improved stability of devices with a MoO_3-doped NPB layer. Fig. 4a shows the experimental results of the operating lifetime at various thicknesses of 5% MoO_3-doped layers. Fig. 4b shows the half lifetimes versus the doped layer thickness. All measurements were made at a DC current density of 50 mA/cm^2. Fig. 4a clearly shows that the MoO_3-doped layer contributes to improve the stability of the devices.

It is quite interesting to note that the increased stability shows a trend similar to the voltage reduction at various doped layer thicknesses. The lifetime was improved rapidly when the doped HTL

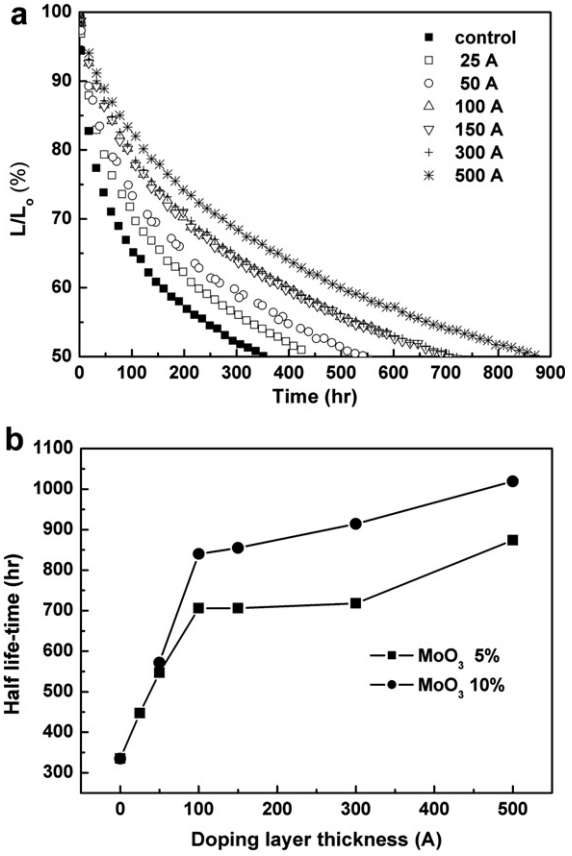

Fig. 4. Lifetime test results of a green device with pure and MoO_3-doped NPB layers. (a) Output intensity of the device as a function of time with the doped NPB layer thickness as a parameter. Doping concentration is 5%. (b) Operating lifetime vs doped NPB layer thickness. Doping concentration is 5% or 10%.

thickness was increased up to 100 Å, while improved slowly when the thickness was increased from 100 Å to 500 Å. The lifetime of the devices with a doped layer thickness of 500 Å and a doping concentration of 5% was 870 h. The lifetime increased to 1010 h when the doping concentration was 10%. These values were much longer than the 335 h of the control device. The charge balance in EML is in general one of the most important factors in determining the stability of OLEDs. However, improved stability in this work cannot be explained simply by the charge balance mechanism since we broke the hole–electron charge balance by increasing the excess hole current as mentioned above.

You et al. achieved a significantly improved stability by introducing a thin layer of MoO_3 layer between ITO and HTL, and ascribed the results to the MoO_3 layer to avoid the crystallization of NPB [24]. We believe that MoO_3-doped NPB is effective in avoiding the crystallization of pure NPB, just as other doping system showed [16]. The morphology stability of NPB that has been enhanced by doping MoO_3 must be one of the reasons for improved stability. It is, however, more interesting that an improvement in stability, shown in Fig. 4b, exhibits a tendency very similar to that of voltage reduction shown in Fig. 3b. This behavior clearly indicates that the improvement in stability might be related to the lower operating voltage leading to weak Joule-heating effects. This strongly suggests that the interface effects of the MoO_3-doped HTL play a more important role in determining device stability.

In summary, we demonstrated that MoO_3 acts as an efficient p-dopant in NPB by the formation of CT complexes. Significantly improved stability and reduced operating voltage were achieved by introducing a thin layer of MoO_3-doped NPB between ITO and NPB. The contribution of interface effects was discriminated from bulk effects. In addition, we found that the interface effects play a major role in lowering the operating voltage and enhancing the stability of OLEDs with a MoO_3-doped HTL.

Acknowledgment

This study was supported by Mobile Display Center, Samsung SDI.

References

[1] C.W. Tang, S.A. Vanslyke, Appl. Phys. Lett. 51 (1987) 913.
[2] C.C. Wu, C.I. Wu, J.C. Sturm, A. Kahn, Appl. Phys. Lett. 70 (1997) 1348.
[3] C. Ganzorig, K.J. Kwak, K. Yagi, M. Fujihira, Appl. Phys. Lett. 79 (2001) 272.
[4] S.A. Vanslyke, C.H. Chen, C.W. Tang, Appl. Phys. Lett. 69 (1996) 2160.
[5] S. Tokito, K. Noda, Y. Taga, J. Phys. D: Appl. Phys. 29 (1996) 2750.
[6] I.H. Hong, M.W. Lee, Y.M. Koo, H. Jeung, T.S. Kim, O.K. Song, Appl. Phys. Lett. 87 (2005) 063502.
[7] J. Kido, T. Matsumoto, Appl. Phys. Lett. 73 (1998) 2866.
[8] G. Parthasarathy, C. Shen, A. Kahn, S.R. Forrest, J. Appl. Phys. 89 (2001) 4986.
[9] J.S. Huang, M. Pfeiffer, A. Werner, J. Blochwitz, K. Leo, S. Liu, Appl. Phys. Lett. 80 (2002) 139.
[10] A. Werner, F. Li, K. Harada, M. Pfeiffer, T. Fritz, K. Leo, Appl. Phys. Lett. 82 (2003) 4495.

[11] J. Endo, T. Matsumoto, J. Kido, Jpn. J. Appl. Phys. 41 (2002) 358.
[12] C. Ganzorig, M. Fujihira, Appl. Phys. Lett. 77 (2000) 4211.
[13] X. Zhou, M. Pfeiffer, J. Blochwitz, A. Werner, A. Nollau, T. Fritz, K. Leo, Appl. Phys. Lett. 78 (2001) 410.
[14] W. Gao, A. Kahn, Appl. Phys. Lett. 79 (2001) 4040.
[15] C.W. Chu, C.W. Chen, S.L. Lee, E.H.E. Wu, Y. Yang, Appl. Phys. Lett. 86 (2005) 253503.
[16] S.Y. Chen, T.Y. Chu, J.F. Chen, C.Y. Su, C.H. Chen, Appl. Phys. Lett. 89 (2006) 053518.
[17] H. Ikeda, J. Sakata, M. Hayakawa, T. Aoyama, T. Kawakami, K. Kamata, Y. Iwaki, S. Seo, Y. Noda, R. Nomura, S. Yamazaki, SID '06 Digest, 2006, p. 932
[18] D.-S. Leem, H.-D. Park, J.-W. Kang, J.-H. Lee, J.W. Kim, J.-J. Kim, Appl. Phys. Lett. 91 (2007) 011113.
[19] S.M. Sze, Physics of Semiconductor Devices, second ed., Wiley Interscience, New York, 1981.
[20] M.T. Hsieh, C.C. Chang, J.F. Chen, Appl. Phys. Lett. 89 (2006) 103510.
[21] G. He, M. Pfeiffer, K. Leo, Appl. Phys. Lett. 85 (2004) 3911.
[22] H. Aziz, Z.D. Popovic, N.X. Hu, A.M. Hor, G. Xu, Science 283 (1999) 1900.
[23] I.M. Chan, E.C. Hong, Thin Solid Films 450 (2004) 304.
[24] H. You, Y. Dai, Z. Zhang, D. Ma, J. Appl. Phys. 101 (2007) 026105.

Available online at www.sciencedirect.com
ScienceDirect
Organic Electronics 9 (2008) 339–346
Organic Electronics
www.elsevier.com/locate/orgel

Comparison of two cohost systems for doped red organic light-emitting devices in an effort to improve the efficiency and the lifetime

Young Gu Lee [a,1], Sung Kee Kang [a], Tae Sik Oh [b], Ho-Nyeon Lee [c], Soonil Lee [d,*], Ken Ha Koh [d]

[a] *Display Device and Processing Laboratory, Samsung Advanced Institute of Technology, P.O. Box 111, Suwon 440-600, Republic of Korea*
[b] *Division of Electronic Engineering, Sunmoon University, Asan 336-708, Republic of Korea*
[c] *Department of Display and Electronic Information Engineering, Soon Chun Hyang University, Asan 336-745, Republic of Korea*
[d] *Division of Energy Systems Research, Ajou University, Suwon 443-749, Republic of Korea*

Received 2 August 2007; received in revised form 3 December 2007; accepted 7 December 2007
Available online 23 December 2007

Abstract

Blue-emitting 2-methyl-9,10-di(2-napthyl)anthracene (MADN) and yellow-emitting 5,6,11,12-tetraphenylnaphthacene (rubrene) were used as cohost materials together with tris(8-hydroxyquinolinato)aluminum (Alq_3) to form emission layers doped with the red dopant molecule 4-(dicyanomethylene)-2-*t*-butyl-6-(1,1,7,7-tetramethyljulolidyl-9-enyl)-4H-pyran (DCJTB). DCJTB-doped red organic light-emitting diodes based on both cohost systems showed remarkable improvements in terms of efficiency compared to DCJTB-doped Alq_3 single-host devices. With 2% DCJTB doping, the respective efficiencies of Alq_3 single-host, Alq_3 (60%)/rubrene (40%)-, and Alq_3 (20%)/MADN (80%)-cohost devices were 1.79, 4.44 and 5.42 cd/A at 20 mA/cm^2. Unlike Alq_3/rubrene-cohost devices, which experienced substantial current-induced quenching, Alq_3/MADN-cohost devices showed only a slight efficiency change at high current densities. At the luminance of 7680 cd/m^2, which was the benchmark for a practical passive-matrix OLED array with 64 scan-lines, an aperture ratio of 50%, and a polarizer transmittance of 50%, the power efficiency of the 2% DCJTB Alq_3/MADN-cohost device was 4.1 and 1.5 times better than that of Alq_3 single-host and Alq_3/rubrene-cohost devices, respectively. Moreover, the half-decay lifetime of the Alq_3/MADN-cohost device, measured as 14,000 h at an initial luminance of 1000 cd/m^2, was 4.4 and 1.9 times longer than the respective half-decay lifetimes of Alq_3 single-host and Alq_3/rubrene-cohost devices.

PACS: 85.60.−q; 85.60.Jb; 78.60.Fi; 78.66.Qh

Keywords: Organic light-emitting diode; Cohost system; Doped red device; OLED

1. Introduction

In general, red organic light-emitting diodes (OLEDs) experience drawbacks such as low

* Corresponding author. Tel.: +82 31 219 2582; fax: +82 31 219 1748.
E-mail address: soonil@ajou.ac.kr (S. Lee).
[1] At also the Department of Information Display, Ajou University, Suwon 442-749, Korea.

1566-1199/$ - see front matter © 2007 Elsevier B.V. All rights reserved.
doi:10.1016/j.orgel.2007.12.003

light-emitting efficiency, luminance-quenching due to intermolecular interactions, and poor color purity. One means of overcoming these problems involves using judicially selected host-dopant systems that can take advantage of energy transfer from the host to the dopants. A tris(8-hydroxyquinolinato)aluminum (Alq_3) host doped with 4-(dicyanomethylene)-2-*t*-butyl-6-(1,1,7,7-tetramethyljulolidyl-9-enyl)-4H-pyran (DCJTB) is an example of a host-dopant emitting layer (EML) for red OLEDs [1,2] with good color coordinates. However, such devices have been shown to have low luminance efficiency (<2 cd/A), and are not free from the current-induced quenching phenomenon under high-current driving conditions [3,4]. To alleviate the problems associated with doped red OLEDs, either multi-doped EML with a single-host material or doped cohost systems are used. An example of an EML utilizing multiple dopants is an Alq_3 host doped with the 2% red dopant 4-dicyanomethylene-2-methyl-6-(2-(2,3,6,7-tetrahydro-1H,5H-benzo[ij]-quinolizin-8-yl)vinyl)-4H-pyran (DCM2) and the 5% emitting-assist dopant 5,6,11,12-tetraphenylnaphthacene (rubrene) [5]. Another example is an Alq_3 host doped with 5% rubrene, 2% DCJTB, and 6% *N*,*N*′-bis(1-naphthyl)-*N*,*N*′-diphenyl-1,1′-biphenyl-4,4′-diamine (NPB) [6]. A device with a triple-dopant EML had a luminance efficiency rating of 2.8 cd/A at 20 mA/cm^2 and $CIE_{x,y}$ color coordinates of (0.65, 0.34).

A prototypical cohost device fabricated by Liu et al., which showed power and luminance efficiency values of 2.1 lm/W and 4.4 cd/A, respectively, $CIE_{x,y}$ color coordinates of (0.65, 0.35) and a half-life of 3500 h used an EML consisting of Alq_3 (60%)/rubrene (40%)-cohost doped with 2% DCJTB [7]. It was reported that the removal of excess holes at a high current density via a large amount of rubrene contributed not only to an improvement in the efficiency, but also to stable device operation by suppressing the formation of $[Alq_3]^+$. However, the excessive amount of rubrene was ultimately detrimental, as the luminance-quenching effect diminished the efficiency. Slight modifications of the Alq_3/rubrene-cohost devices were outlined in Liu et al. [8,9]. A device with an EML of Alq_3 (35%)/rubrene (65%) doped with 1% DCJTB and having a luminance efficiency of 5.62 cd/A, $CIE_{x,y}$ color coordinates of (0.64, 0.36) and the half-life of 1,179 h at 70 °C was fabricated by Brown et al. [8]. A 4-(dicyanomethylene)-2-methyl-6-(*p*-dimethylaminostyryl)-4H-pyran (DCM) doped Alq_3/rubrene-cohost device with a luminance efficiency of 5.49 cd/A, $CIE_{x,y}$ color coordinates of (0.64, 0.36) and a half-life comparable to those of the DCJTB-doped EMLs was reported by Wen et al. [9].

In this work, 2-methyl-9,10-di(2-napthyl)anthracene (MADN), a wide band-gap blue-host material

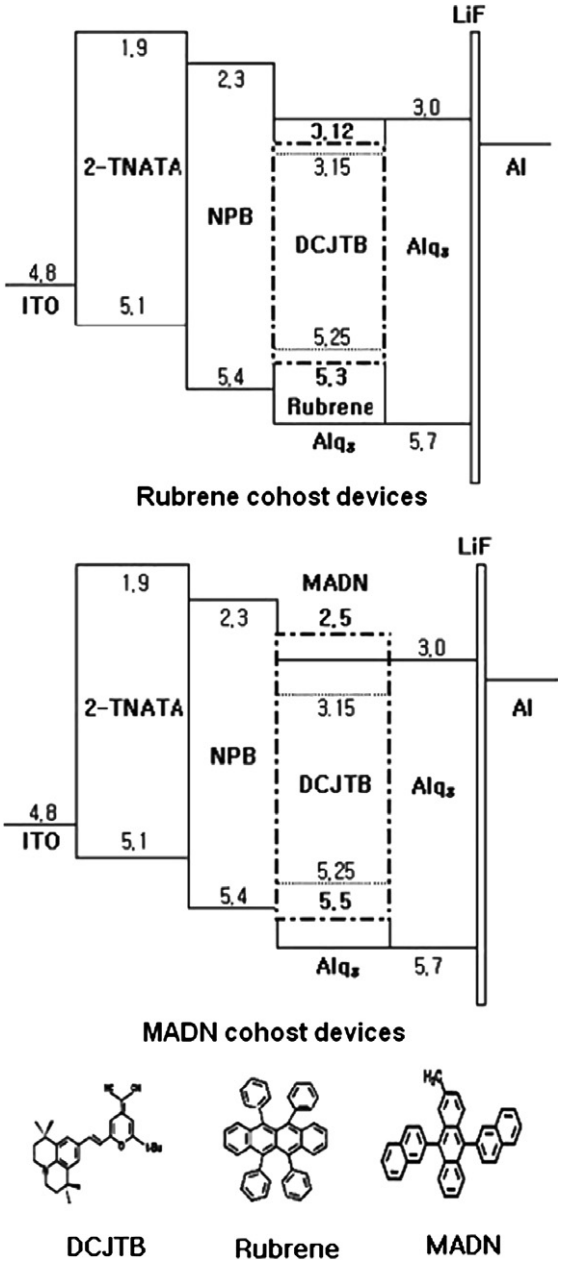

Fig. 1. Energy diagram of Alq_3/rubrene- and Alq_3/MADN-cohost devices doped with DCJTB and the molecular structures of DCJTB, rubrene, and MADN.

with robust thin-film morphology [10,11], was tested as a new cohost material for use in conjunction with Alq_3. Several red OLEDs with a DCJTB-doped Alq_3/MADN-cohost EML were fabricated using various mixing fractions of MADN while maintaining fixed levels of the DCJTB-doping fraction and the EML thickness. The performance of these DCJTB-doped Alq_3/MADN-cohost devices were compared with those of similarly fabricated DCJTB-doped Alq_3/rubrene-cohost devices. The motivation of this investigation was to improve the efficiency, operational stability, and lifetime of doped red OLEDs based on cohost systems. High luminance efficiency without significant current-induced quenching is essential for passive-matrix organic light-emitting diode (PMOLED) given that a decrease of the luminance efficiency at a high current density requires a significantly increased power consumption, consequently resulting in a substantial decrease in the lifetime of PMOLED arrays.

2. Experimental

Indium–tin-oxide (ITO) coated glasses were used as substrates for the fabrication of the devices. The ITO film used as an anode electrode was 150 nm thick and had a sheet resistance of 10 Ω/□. The ITO surface underwent an O_2 plasma treatment before the deposition of the organic and cathode layers. 4,4′,4″-tris(2-naphthylphenyl-phenylamino)-triphenylamine (2-TNATA), NPB, DCJTB-doped Alq_3/MADN (or Alq_3/rubrene), Alq_3, and a double-layer of LiF and Al were deposited sequentially to form a hole injection layer (HIL), a hole transport layer (HTL), an EML, an electron transport layer (ETL), and a cathode electrode, respectively. The multilayer structure of the fabricated red electroluminescent (EL) device was ITO/2-TNATA(60 nm)/NPB(30 nm)/DCJTB-doped cohost/Alq_3/LiF(0.8 nm)/Al(150 nm). The energy diagram of the fabricated DCJTB-doped cohost devices are shown in Fig. 1 together with the molecular structures of DCJTB, rubrene, and MADN. The square active area defined by the overlap of the ITO anode and the cathode was $2 \times 2\ mm^2$. All fabricated devices were hermetically sealed via glass encapsulation with getter. Keithley 238 was used as a source-measurement unit and PR650 was used as the luminance meter when measuring the current–voltage–luminance (I–V–L) characteristics.

3. Results and discussion

3.1. Alq_3/rubrene-cohost devices

Fig. 2(a) shows the luminance efficiencies for a series of Alq_3/rubrene-cohost devices doped with 2% DCJTB with respect to the current density. The respective thickness of the cohost EML and ETL were fixed at 30 and 33 nm. It was clear that the efficiencies of the Alq_3/rubrene-cohost devices were superior to that of the Alq_3 single-host device with an identical DCJTB-doping concentration (Device 1–1). In addition, the rubrene concentration of 40–50% was found to be optimal for the highest efficiency; the efficiency was reduced at a high current density regardless of the rubrene concentration. A reduction in the efficiency under high-current drive conditions was observed as in other devices

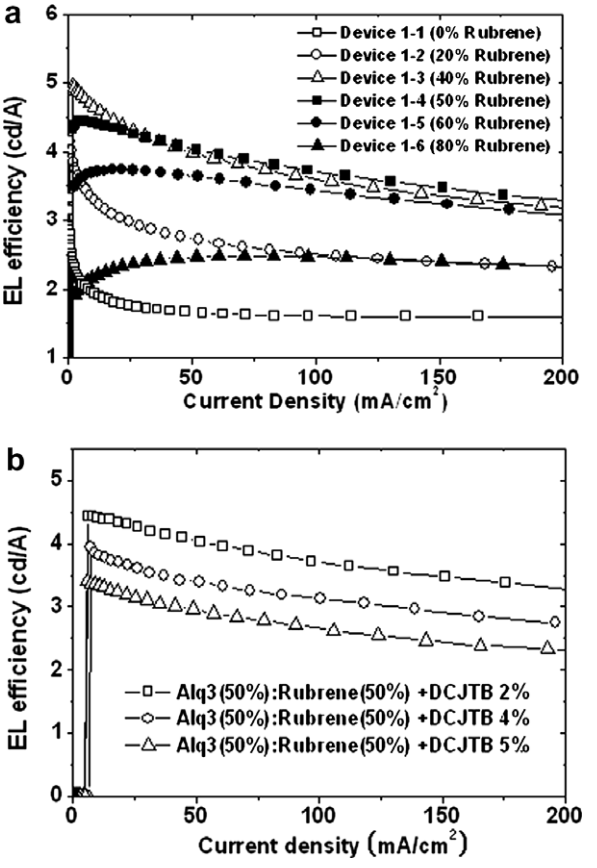

Fig. 2. (a) Luminance efficiencies for a series of Alq_3/rubrene-cohost devices doped with 2% DCJTB with respect to the current density. (b) Efficiency variations of Alq_3(50%)/rubrene(50%)-cohost devices with respective DCJTB doping concentrations of 2%, 4%, and 5%.

with different EML and ETL thicknesses. Fig. 2(b) shows current-density-dependent variations of efficiencies for three Alq_3 (50%)/rubrene (50%) devices with respective DCJTB doping concentrations of 2%, 4%, and 5%. It was found that the efficiencies of 4%- and 5%-doped devices were inferior to that of the 2%-doped device throughout the measured current-density range. This indicated that concentration quenching due to DCJTB dopants was a factor that limited the performance of doped cohost devices. Moreover, it was evident that the 2%-doped device was less susceptible to current-induced quenching. It is important to note that the efficiencies of 4.32, 3.68, and 3.22 cd/A at 20 mA/cm^2 were reduced by 14.4%, 15.2%, and 17.3% as the current density was increased to 100 mA/cm^2 for the 2%-, 4%- and 5%-doped devices, respectively.

The details of the EL performance for a series of Alq_3/rubrene-cohost devices doped with 2% DCJTB are listed in Table 1, and the variations of the luminance efficiency and drive voltage with respect to the rubrene fraction are plotted in Fig. 3(a) and (b). At a current density of 20 mA/cm^2, the maximum luminance efficiency was measured as 4.44 cd/A for a rubrene fraction of 40% (Device 1–3), which was more than twice of that of the DCJTB-doped Alq_3 single-host device (Device 1–1). However, the efficiency of the same device was reduced to 3.62 cd/A at 100 mA/cm^2. It is interesting to note that current-induced quenching was prominent around the rubrene-fraction for maximum efficiency; this became smaller at higher fractions. Previously, it was argued that a small fraction of rubrene may assist dopants and contribute to improving the efficiency via a cascading energy transfer [5,11,12]. Additionally, it has been shown that a large amount of rubrene removes excess holes and hinders the formation of quenching species. In this case, excessive rubrene would result in luminescence quenching

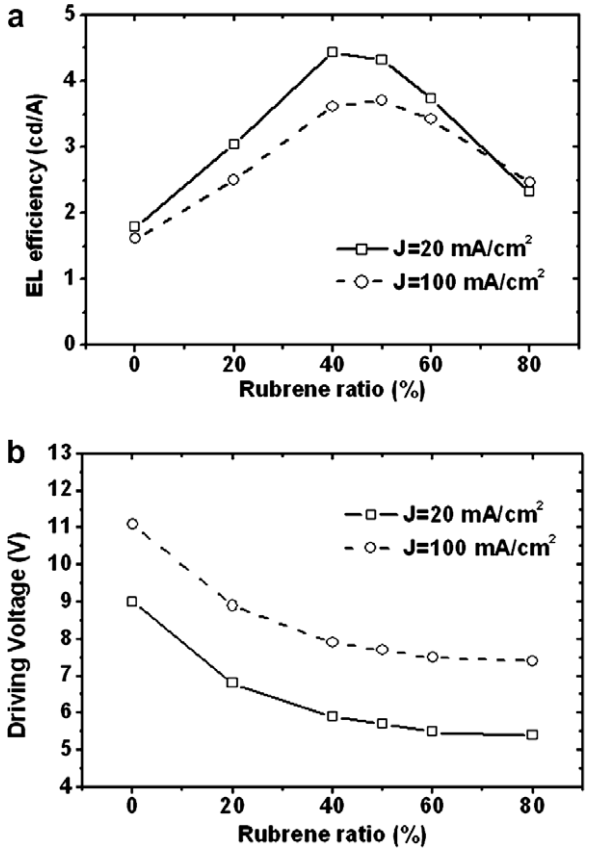

Fig. 3. Variations of (a) the luminance efficiency and (b) the drive voltage with respect to the rubrene fraction of a series of 2%-DCJTB doped Alq_3/rubrene-cohost devices at current densities of 20 and 100 mA/cm^2.

that is independent of the carrier density [7]. Alternatively, factors such as the rubrene-fraction-dependent variations in the charge-transfer and recombination regions in EML [13], the occurrence of balanced carrier injection and transport, and efficient energy transfers to DCJTB around a rubrene-fraction of 40% cannot be ruled out. The $CIE_{x,y}$

Table 1
Details of EL performance for a series of Alq_3/rubrene-cohost devices doped with 2% DCJTB at the current densities of 20 and 100 mA/cm^2

Device	Rubrene ratio (%)	$J = 20$ mA/cm^2			$J = 100$ mA/cm^2			$\frac{\eta_{20}-\eta_{100}}{\eta_{20}}$ (%)
		Bias (V)	η_{20} (cd/A)	CIE (CIE_x, CIE_y)	Bias (V)	η_{100}(cd/A)	CIE (CIE_x, CIE_y)	
1–1	0	9.0	1.79	(0.63, 0.37)	11.1	1.61	(0.62, 0.38)	10.1
1–2	20	6.8	3.04	(0.65, 0.35)	8.9	2.51	(0.64, 0.35)	17.4
1–3	40	5.9	4.44	(0.64, 0.35)	7.9	3.62	(0.64, 0.36)	18.5
1–4	50	5.7	4.32	(0.64, 0.36)	7.7	3.70	(0.63, 0.36)	14.4
1–5	60	5.5	3.74	(0.63, 0.37)	7.5	3.42	(0.63, 0.37)	8.6
1–6	80	5.4	2.32	(0.59, 0.40)	7.4	2.46	(0.59, 0.40)	-6.0

color coordinates of devices with 40–50% rubrene were in the range of (0.64, 0.36)–(0.63, 0.36). These values were closer to the national-television-system-committee (NTSC) standard of (0.67, 0.33) compared to the values of an Alq_3 single-host device.

Unlike the luminance efficiency, the drive voltage was found to decrease monotonically as the rubrene fraction increased. Compared to the drive voltage of an Alq_3 single-host device doped with 2% DCJTB, that of an Alq_3/rubrene-cohost device with the equivalent doping level was reduced by as much as 3.6 V. It is reasonable to assume that the large bipolar mobility of rubrene was responsible for the observed reduction of the drive voltage. Another interesting observation was the nearly constant 2-V offset independent of rubrene concentration between the drive voltages for current densities of 20 and 100 mA/cm^2. The constant drive-voltage offset throughout the rubrene concentration in cohost EML indicated that the currents in these devices were controlled by the spatial charge distribution, which depended on carrier mobility, rather than by injection barriers. Moreover, rubrene was likely to be a major current carrying component while being comparable to or less efficient than Alq_3 in transferring energy to DCJTB.

3.2. Alq_3/MADN-cohost devices

Fig. 4(a) and (b) show variations of the luminance efficiency and drive voltage with respect to the MADN fraction of a series of Alq_3/MADN-cohost devices doped with 2% DCJTB. The respective thicknesses of the cohost EML and ETL were fixed at 35 and 30 nm. The maximum efficiency of 5.42 cd/A at 20 mA/cm^2, which was observed from the device with a MADN fraction of 80% (Device 2–3), was approximately 1 cd/A larger than that of an Alq_3/rubrene-cohost device with the same drive current density. Another prominent difference between the EL performance of Alq_3/MADN and the Alq_3/rubrene-cohost devices was the current-induced quenching behavior. For a MADN fraction of 80% (Device 2–3), the reduction of efficiency compared to that at 20 mA/cm^2 was only 3.1% when operated at 100 mA/cm^2. The amounts of the reduction in efficiency, corresponding to the increase of the current density from 20 to 100 mA/cm^2, of all other Alq_3/MADN devices with 2% DCJTB doping were as low as that of the Alq_3(20%)/MADN(80%) device.

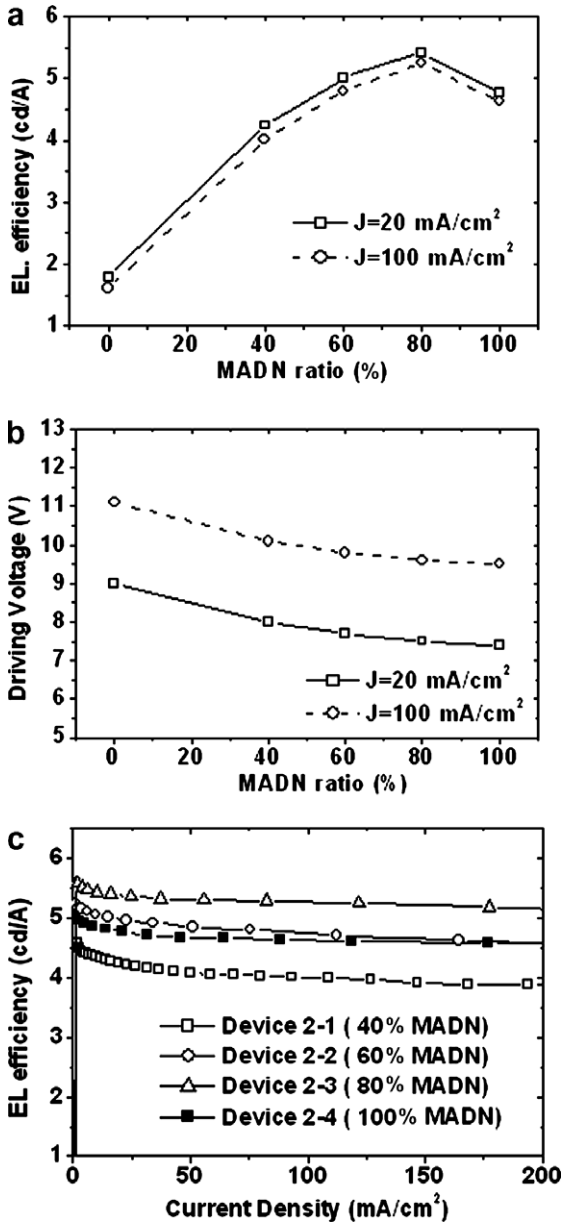

Fig. 4. Variations of (a) the luminance efficiency and (b) the drive voltage with respect to MADN fraction at current densities of 20 and 100 mA/cm^2, and (c) luminance efficiencies with respect to the current density of a series of Alq_3/MADN-cohost devices doped with 2% DCJTB.

Fig. 4(b) shows the variation of the driving voltage with respect to the MADN fraction at two different current densities. As in the case of an Alq_3/rubrene-cohost device, a monotonic decrease of the drive voltage was observed with respect to the increase of the MADN fraction. It is proposed that the good bipolar mobility of MADN [10,14] was

responsible for the observed reduction of the drive voltage corresponding to the increase of the MADN fraction. However, the maximum reduction of the drive voltage compared to that of the Alq_3 single-host device doped with 2% DCJTB was only 1.6 V, which is much smaller than the 3.6 V value of Alq_3/rubrene-cohost devices with identical doping levels, as the charge mobility of MADN, in particular the hole mobility, is not as good as that of rubrene. Alq_3/MADN devices doped with 2% DCJTB also showed a constant drive-voltage offset of 2 V, regardless of the MADN fraction, between current densities of 20 and 100 mA/cm^2. This indicates that the currents in the Alq_3/MADN devices doped with 2% DCJTB were controlled by the spatial charge distribution as were the identically doped Alq_3/rubrene devices. It is important to note that the hole mobility of MADN is ~3 orders of magnitude smaller than that of rubrene and ~2 orders of magnitude larger than that of Alq_3. More importantly, MADN is a bipolar transport material with nearly equal mobility for electrons and holes [10,14]. Therefore, it is conceivable that more balanced carrier injection and transport, and consequently the carrier balance in EML were realized for Alq_3/MADN-cohost devices at a larger MADN fraction. This is attributed to good luminance efficiency. Moreover, it was likely that MADN was more efficient in transferring energy to DCJTB.

Fig. 4(c) shows the current-density-dependent variations of the luminance efficiencies for a series of Alq_3/MADN-cohost devices doped with 2% DCJTB. The details of the EL performance of these Alq_3/MADN-cohost devices are listed in Table 2. Here, the Alq_3/MADN-cohost devices are less susceptible to current-induced quenching up to a current density of 200 mA/cm^2; consequently, the (20%)/MADN(80%) device (Device 2–3) maintained efficiency over 5.2 cd/A throughout the measured current-density range. As shown in Fig. 5, the EL spectra of this device (Device 2–3) did not

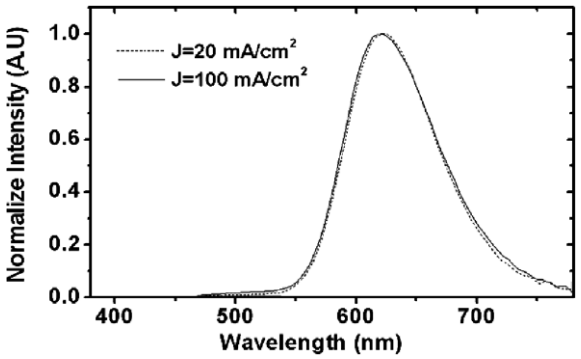

Fig. 5. Comparison of the EL spectra of the Alq_3(20%)/MADN(80%)-cohost device doped with 2% DCJTB (Device 2–3) at current densities of 20 and 100 mA/cm^2.

change significantly as the current density increased: from 20 to 100 mA/cm^2. However, the $CIE_{x,y}$ color coordinates of the Alq_3/MADN-cohost devices were not as suitable as those of Alq_3/rubrene-cohost devices. Nevertheless, the $CIE_{x,y}$ color coordinates of the highest efficient device (Device 2–3 with 80% MADN) were in the range of (0.63, 0.37)–(0.63, 0.38) which were sufficient for use as red organic light-emitting devices.

Fig. 6(a) and (b) show, respectively, the luminance-dependent variations of EL and the power efficiencies of the Alq_3 single-host device (Device 1–1), and the Alq_3(50%)/rubrene(50%) (Device 1–4) and Alq_3(20%)/MADN(80%) (Device 2–3) cohost devices doped with 2% DCJTB. As shown in Fig. 6(a), the efficiencies of 5.38, 4.28, and 1.64 cd/A were achieved at a luminance of 1000 cd/m^2 from the MADN-cohost (Device 2–3), rubrene-cohost (Device 1–4) and Alq_3 single-host (Device 1–1) devices, respectively. It was interesting to find that only the MADN-cohost device (Device 2–3) remained stable and maintained EL efficiency over 5.2 cd/A up to a luminance of 15,000 cd/m^2. In the case of the rubrene-cohost device (Device 1–4), the EL efficiency degraded monotonically as

Table 2
Details of EL performance for a series of Alq_3/MADN-cohost devices doped with 2% DCJTB at the current densities of 20 and 100 mA/cm^2

Device	MADN ratio (%)	$J = 20$ mA/cm^2			$J = 100$ mA/cm^2			$\frac{\eta_{20}-\eta_{100}}{\eta_{20}}$ (%)
		Bias (V)	η_{20} (cd/A)	CIE (CIE_x, CIE_y)	Bias (V)	η_{100} (cd/A)	CIE (CIE_x, CIE_y)	
2-1	40	8.0	4.24	(0.64, 0.36)	10.1	4.01	(0.63, 0.37)	5.4
2-2	60	7.7	5.01	(0.63, 0.36)	9.8	4.80	(0.63, 0.37)	4.2
2–3	80	7.5	5.42	(0.63, 0.37)	9.6	5.25	(0.63, 0.38)	3.1
2–4	100	7.4	4.77	(0.60, 0.39)	9.5	4.63	(0.59, 0.40)	2.9

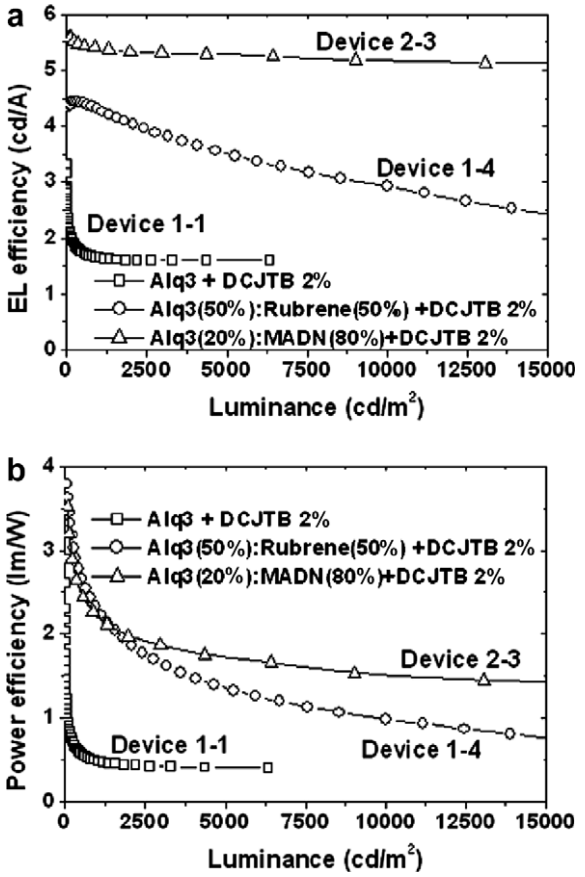

Fig. 6. Luminance-dependent variations of (a) the EL and (b) power efficiencies of Alq_3 single-host (Device 1–1), and Alq_3(50%)/rubrene(50%) (Device 1–4) and Alq_3(20%)/MADN(80%) (Device 2–3) cohost devices doped with 2% DCJTB.

the luminance level was increased, and reduced to 3.52 cd/A at a luminance of 5000 cd/m^2. Furthermore, the Alq_3 single-host device (Device 1–1) was completely degraded and emitted no light when the luminance level was increased to over 6000 cd/m^2.

As shown in Fig. 6(b), the initially rapid decreases of the power efficiencies of these devices were followed by relatively slower reductions. For a luminance value over 1000 cd/m^2, the power efficiency of Device 2–3 was higher than that of Device 1–4 and the power-efficiency gap widened as the luminance of these devices increased. For example, the power efficiencies of Device 2–3, Device 1–4, and Device 1–1 at a luminance of 1000 cd/m^2 were 2.30, 2.20, and 0.49 lm/W, respectively. However, at a luminance of 5000 cd/m^2, the respective power efficiencies of Device 2–3 and Device 1–4, and Device 1–1 were 1.70 and 1.34, and 0.40 lm/W. The large difference in the power efficiency at a higher luminance has great implications on the power consumption of real PMOLED arrays. Eq. (1) describes the relationship between the luminance of a sub-pixel and a PMOLED array for primary colors such as red, green or blue.

$$L_{\text{sub-pixel}} = 3 \times \left(\frac{L_{\text{panel}} \times N_{\text{scan}}}{T_{\text{Polarizer}} \times AR} \right) \quad (1)$$

Here, L_{panel} is the effective luminance of a primary color for a real PMOLED array with polarizer, N_{scan}, $T_{\text{polarizer}}$ and AR are respectively the number of scan-lines, the transmittance of the polarizer and the aperture ratio of the sub-pixel. $L_{\text{sub-pixel}}$ is the peak luminance of a sub-pixel without taking the polarizer and aperture into account. It is important note that the value of $L_{\text{sub-pixel}}$ is the target luminance that should be achieved from a test device to realize a real PMOLED array with luminance L_{panel} for a primary color. For example, in a PMOLED array with 64 scan-lines, an aperture ratio of 50%, and a polarizer transmittance of 50%, 7680 cd/m^2 must be achieved from a red test device to realize a PMOLED array with a red luminance value of 10 cd/m^2. According to Fig. 6(b), the respective power efficiencies of devices using the Alq_3 single-host (Device 1–1), the 50% rubrene-cohost (Device 1–4), and the 80% MADN-cohost (Device 2–3) are 0.39, 1.1 and 1.6 lm/W, respectively, at a luminance of 7680 cd/m^2. These power efficiencies indicate that a PMOLED array with an Alq_3 single-host and 50% rubrene cohost would consume 4.1 and 1.5 times more power compared, respectively, to a PMOLED array with an 80% MADN-cohost.

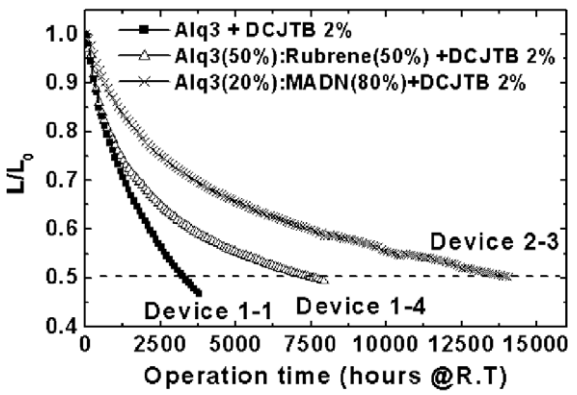

Fig. 7. Temporal variation of the luminance (L) of the Alq_3 single-host (Device 1–1), 50% rubrene-cohost (Device 1–4), and 80% MADN-cohost (Device 2–3) devices starting at an initial luminance (L_0) of 1000 cd/m^2.

Fig. 7 shows the results of the lifetime measurement of the Alq_3 single-host (Device 1–1), the 50% rubrene-cohost (Device 1–4), and the 80% MADN cohost (Device 2–3) devices. The lifetime measurements were made at room temperature after setting the initial luminance of all three devices at 1000 cd/m^2. It is worth emphasizing that the half-decay lifetime of the 80% MADN-cohost device (Device 2–3) was 14,000 h, which was 1.9 and 4.4 times longer than that of the Alq_3/rubrene-cohost and the Alq_3 single-host devices: 7500 h for Device 1–4 and 3200 h for Device 1–4. It is conceivable that in addition to the higher power efficiency of MADN-cohost devices over other devices, the more robust thin-film morphology of MADN was beneficial for the stable operation of the MADN-cohost device [10].

4. Conclusion

The characteristics of DCJTB-doped red OLED devices with either an Alq_3/rubrene or Alq_3/MADN-cohost EML were investigated in this study. Given that concentration quenching due to DCJTB dopants was persistent despite using the cohost EML, the DCJTB doping concentration was limited to 2%. Between the two cohost systems tested, the Alq_3/MADN-cohost had superior luminance and power efficiencies compared to the other system. Moreover, Alq_3/MADN-cohost devices were much less susceptible to current-induced quenching and showed much longer half-decay lifetime for luminance. The measured half-decay lifetime of 14,000 h with an initial luminance of 1000 cd/m^2 is equivalent to an extrapolated lifetime of 140,000 h at an initial luminance of 100 cd/m^2. It is proposed that the wide bandgap, balanced bipolar transport properties, and stable thin-film morphology of the MADN contributed to the aforementioned improvements of the DCJTB-doped red OLED devices.

Acknowledgement

SL acknowledges the financial support by the ABRL Program of KOSEF through Grant No. R14-2002-062-02000-0.

References

[1] C.H. Chen, C.W. Tang, J. Shi, K.P. Klubek, Micromol. Symp. 125 (1997) 49.
[2] C.H. Chen, C.W. Tang, J. Shi, K.P. Klubek, Thin Solid Films 363 (2000) 327.
[3] Z.Y. Xie, L.S. Hung, S.T. Lee, Appl. Phys. Lett. 79 (2001) 1048.
[4] Ralph H. Young, Ching W. Tang, Alfred P. Marchetti, Appl. Phys. Lett. 80 (2002) 874.
[5] Y. Hamada, H. Kanno, T. Tsujioka, H. Takahashi, T. Usuki, Appl. Phys. Lett. 75 (1999) 1682.
[6] T.K. Hatwar, G. Rajeswaran, J. Shi, Y. Hamada, H. Kano, H. Takahashi, in: Proceedings of EL'00, Hamamatsu, Japan, 2000, pp. 31.
[7] T.H. Liu, C.Y. Iou, C.H. Chen, Appl. Phys. Lett. 83 (2003) 5241.
[8] C. Brown, D. Kondakov, J. SID 323 (2004).
[9] S.W. Wen, T.H. Liu, SID '04 Digest 784 (2004).
[10] M.T. Lee, Y.S. Wu, H.H. Chen, C.H. Tsai, C.H. Liao, C.H. Chen, SID '04 Digest 710 (2004).
[11] J. Feng, F. Li, W. Cao, G. Cheng, W. Xie, S. Liu, Appl. Phys. Lett. 81 (2002) 2935.
[12] H. Kanno, Y. Hamada, H. Takahashi, IEE J. Selected Topics Quant. Electron. 10 (1) (2004) 30.
[13] T.K. Hatwar, C.T. Brown, L. Cosimbescu, M. Ricks, J. Spindler, W. Begley, J.R. Vargas, Proc. SPIE 5519 (2004) 30.
[14] S.W. Wen, M.T. Lee, C.H. Chen, IEEE/OSA J. Display Technol. 1 (2005) 90.

Available online at www.sciencedirect.com
ScienceDirect
Organic Electronics 9 (2008) 347–354
Organic Electronics
www.elsevier.com/locate/orgel

The effect of annealing/quenching on the performance of polymer light-emitting electrochemical cells

Salima Alem, Jun Gao *

Department of Physics, Engineering Physics and Astronomy, Queen's University, Kingston, Ontario, Canada K7L 3N6

Received 18 October 2007; received in revised form 11 December 2007; accepted 14 December 2007
Available online 28 December 2007

Abstract

We report the effect of thermal annealing and quenching on the film morphology and device performance of polymer light-emitting electrochemical cells (LECs). The polymer films of LECs consist of a luminescent polymer, an ion-conducting polymer, and a lithium salt. The LECs studied have an extremely large planar configuration, which enables time-resolved fluorescence imaging of both doping and emission profiles of the devices. Annealing at temperatures above 350 K leads to the disappearance of many visible "white dots" initially present in the LEC film, and a much smoother surface. Annealed and quenched devices exhibit dramatically improved initial and peak current, peak electroluminescence (EL) intensity, doping propagation speed and response time. In addition, the emission zone of annealed devices is more centered than un-annealed devices. These improvements are attributed to the melting of electrolyte domains in the LEC film, which leads to better film quality and enhanced ion conductivity. Our results demonstrate that the simple annealing/quenching technique can be used to achieve the desired phase morphology in LEC films, which are often severely phase-separated due to incompatibility between the luminescent polymer and the electrolyte polymer.

PACS: 85.60.Jb; 78.60.Fi; 82.35.Rs

Keywords: Polymer light-emitting electrochemical cell; Poly(ethylene oxide); Post-annealing

1. Introduction

A polymer light-emitting electrochemical cell (LEC) is a solid-state polymer light-emitting device whose operating mechanism is analogous to that of traditional *p–n* junction light-emitting diode (LED) [1]. The active material of an LEC is a mixed electronic/ionic conductor consisting of a luminescent polymer and a solid-state polymer electrolyte. The latter typically consists of polyethylene oxide (PEO) and a salt. When a sufficiently large voltage is applied to the device, electrons and holes are injected into the luminescent polymer and subsequently compensated by the insertion of cations and anions between the polymer chains. As a result, the luminescent polymer is electrochemically doped to *p* type on the anode side and *n* type on the cathode side greatly increasing electrical conductivity. The propagation of the *p* and *n*-doped regions leads to the formation of a true *p–n* junction, which is

* Corresponding author.
E-mail address: jungao@physics.queensu.ca (J. Gao).

1566-1199/$ - see front matter © 2007 Elsevier B.V. All rights reserved.
doi:10.1016/j.orgel.2007.12.006

accompanied by the onset of the electroluminescence, caused by the radiative recombination of the injected electrons and holes.

The LEC operating mechanism described above is consistent with a large body of experimental results [2–11] and has recently been vividly confirmed by the fluorescence imaging of extremely large planar LECs [12,13]. An LEC offers an alternative approach to achieving electroluminescence from conjugated luminescent polymers in addition to the widely studied polymer light-emitting diodes (PLEDs) [14]. Moreover, *in situ* electrochemical doping leads to some unique device characteristics among polymer-based devices. LEC characteristics such as insensitivity to electrode work function and interelectrode spacing are highly desirable and difficult to achieve in a PLED.

Unfortunately, LECs also suffer from drawbacks such as a short operational lifetime and a slow turn-on response, compared to PLEDs in which undoped polymers are used. So far the fastest and longest-lasting LECs are "frozen-junction" LECs, realized by first turning on the devices at room temperature and then cooling to below the glass transition temperature of polymer electrolyte to freeze out the ion motion [15–17]. Alternatively, it has been shown that the response time and lifetime of an LEC can be significantly improved by controlling the phase morphology of the polymer blend film. The ideal morphology of an LEC film is a nano-scale interpenetrating network of luminescence polymer and ion-conducting polymer [18]. However, this is difficult to achieve since the luminescent polymers used in LECs are generally nonpolar while the solid electrolyte such as PEO is strongly polar. The admixture of the two polymers tends to be severely phase-separated due to their incompatibility and the minimum gain in entropy when polymers are mixed.

Several approaches have been used to control the phase morphology of LEC films with some success. This includes the synthesis of bi-functional conjugated polymers that are both ionically and electronically conductive. This was done by grafting the semiconducting polymer backbone with ion-transporting side groups such as oligo(ethylene oxide) [5,19–21], or by inserting ion-solvating segments within the main polymer chains [22–24]. Additionally, a bipolar high boiling point surfactant has been used as an additive to facilitate the mixing of polymers and to ensure maximum interfacial surface area between these two phases [18]. Electrolytes other than PEO have also been used to improve the film quality in LECs. A successful example is crown ether, which forms stable complexes with alkali metal cations that are soluble in nonpolar solvents. Sandwich LECs based on crown ether and lithium salt were demonstrated with good quantum efficiency and fast response [25].

Here we report the effect of annealing/quenching on the film morphology and device performances of PEO-based LECs. Post-deposition thermal processing has been widely used in polymer LEDs and polymer-based solar cells [26–32]. In those cases the positive effect of annealing was attributed to the improved contact between the polymer and the electrode by reducing free volume or pores in the interface and improving the degree of interchain interactions. Our LEC films are annealed at temperatures below the glass transition temperature (T_g) of the luminescent copolymer, but above the melting point (T_m) of the polymer electrolyte, and subsequently quenched to preserve the desirable morphology formed. We observed significantly improved turn-on response and EL intensity. Moreover, our studies are performed on planar LECs with an interelectrode spacing of 1 mm. The millimeter-scale planar LECs afford us an interelectrode view of the device operation with great spatial and temporal resolution. Using time-lapse imaging, dramatic changes in film morphology, doping propagation speed, doping uniformity, EL intensity, and the position of emission zone have been observed.

2. Experimental

In this study poly[(9,9-dioctyl-2,7-divinylene-fluorenylene)-alt-co-{2-methoxy-5-(2-ethyl-hexyloxy)-1,4-phenylene}], a green-emitting fluorene copolymer, was used as the luminescent polymer. The polymer electrolyte consists of poly(ethylene oxide) (PEO) and lithium trifluoromethanesulfonate (LiTf). The molecular weights of the fluorene copolymer and PEO are 3×10^3 and 2×10^6, respectively. The luminescent material and the polymer electrolyte were dissolved in their common solvent, cyclohexanone, with a concentration of 5% and 2% (w/v), respectively. Suitable amounts of these master solutions were then mixed together to form an LEC solution with a fluorene copolymer, PEO and LiTf ratio of 5:5:1 in weight. The LEC solution was stirred and heated at 50 °C for 1 h and cooled to room temperature before use.

The LEC solution was then spin cast onto 15×15 mm^2 sapphire substrates at 1500 rpm. The resulting polymer blend films, which had a thickness of approximately 600 nm, were dried on a hotplate at 50 °C for at least 2 h. Aluminum (100 nm) was at last thermally evaporated on top of the LEC films through a shadow mask to realize planar LECs with 1 mm interelectrode spacing. All device processing procedures were performed inside a MBraun double glove-box/evaporator system filled with dry nitrogen.

The annealing, quenching and testing of the finished devices were all performed in a microscopy cryostat under 10^{-5} torr vacuum, provided by a turbo-pump backed by a diaphragm pump. Thermal paste was used to ensure good heat transfer between the sapphire substrate and the copper cold finger of the cryostat. The devices were annealed before testing at temperatures ranging from 330 to 400 K for 5 min and then quickly cooled down to 315 K. The rate of cooling varied from 25 to 43 K/min.

The LECs were kept at 315 K for 35–40 min before any voltage bias was applied to ensure thermal equilibrium. A Keithley 237 source measurement unit was used to turn on the LECs while simultaneously recording the device current. A Hamamatsu amplified photodiode was used to measure EL intensity. A Nikon D200 digital camera with a Tamron 90 mm 1:1 macrolens at ISO 200 sensitivity was used to image the devices through the quartz cryostat window.

3. Results and discussion

Fig. 1 displays the surface of un-annealed and annealed LEC films viewed under an optical microscope and room light. The aluminum electrodes were deposited before any annealing/quenching procedure was performed, and the imaging was carried out with the films maintained at a constant temperature of 315 K. The LEC films appear yellowish green[1] in color. Visible in Fig. 1a are many white dots embedded in the un-annealed LEC film. Annealing at 330 K does not have discernable effect on film morphology, as shown in Fig. 1b. On the other hand, LEC films annealed at or above 350 K have a significantly reduced number of white dots. Annealing at 400 K led to the most uniform-looking film, and the white dots have all but disappeared. Considering the following characteristic temperatures of the materials used in the LECs: T_g(fluorene copolymer) > 623 K, T_g(PEO) $= 206$ K, T_m(PEO) $= 340$ K and T_m(LiTf) > 573 K, the white dots are mostly likely PEO-rich electrolyte domains and their disappearance upon annealing at above 350 K is due to melting. Recently Shin et al. performed differential scanning calorimetry (DSC) measurement on LEC films containing MEH-PPV, PEO and LiTf of similar weight ratio [33]. They observed a significant melting transition at $T = 331$ K which they attributed to the melting of crystalline PEO–LiTf domain. In addition, they showed that the cooling rate affected the crystallinity of the electrolyte, with the heat-quenched sample exhibiting a crystallization event at 276 K prior to melting which is absent in the slow-cooled sample. These observations led us to believe that the white dots initially present in the LEC films were mostly crystalline PEO domains which may also contain LiTf.

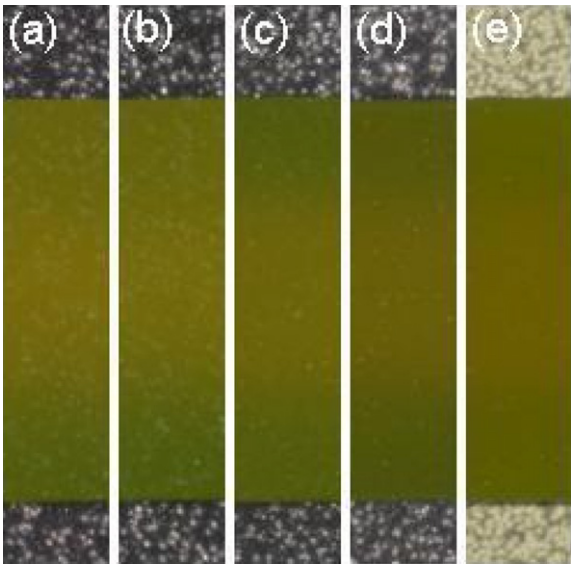

Fig. 1. Surface morphology of un-annealed (a) and annealed (b–e) LEC films imaged under room light at 315 K. Annealing temperature and duration: (b) 330 K, 5 min, (c) 350 K, 5 min, (d) 380 K, 5 min, (e) 400 K, 8 min. The LEC films consist of a fluorene copolymer, PEO, and LiTf salt. All annealed films were cooled from their respective annealing temperatures to 315 K with a cooling rate ranging from 25 to 43 K/min. The top and bottoms portions of each film are covered by aluminum electrodes. The interelectrode spacing is 1 mm.

Consistent with the dramatic change in surface morphology, annealing/quenching also has strong effects on the device performance of LECs. The

[1] For interpretation of color in Fig. 1, the reader is referred to the web version of this article.

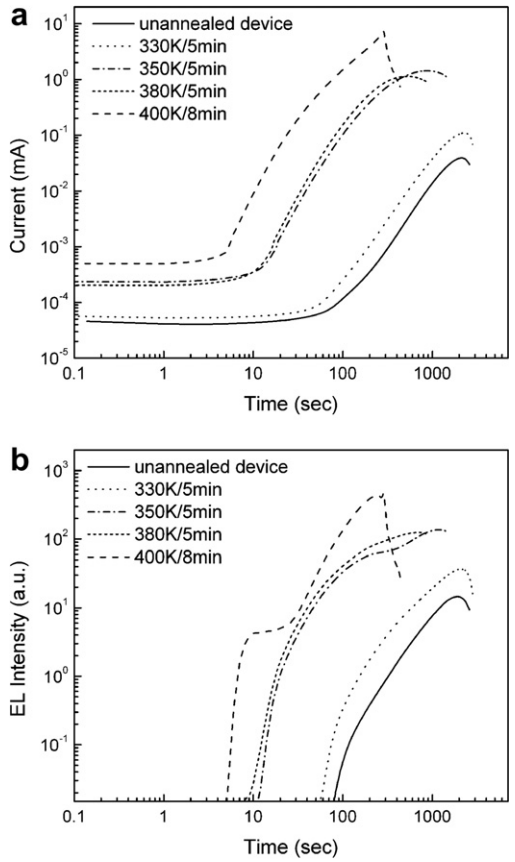

Fig. 2. Time evolution of device current (a) and EL intensity (b) of the un-annealed and annealed devices. All devices were maintained at 315 K. A 400 V bias was applied at time zero.

devices were turned on by applying a 400 V bias at 315 K, and the time evolution of device current and EL intensity of both un-annealed and annealed devices are shown in Fig. 2. The EL and current turn-on response of these extremely large planar devices are much slower than sandwich cells, making it easier to observe the effects of annealing/quenching at various temperatures. In all devices the onset of EL coincides with a sharp increase in device current, indicative of the initial formation of a light-emitting *p–n* junction [12]. Subsequently both device current and EL intensity would increase by several orders of magnitude as the devices become more conductive and charge injection become more efficient with increasing doping level. The overall current level and EL intensity increase with the annealing temperature. On the other hand, the onset of EL occurs sooner with increasing annealing temperature. The device annealed at 400 K displayed detectable EL after only 5 s, which is more than 10 times faster than that of the un-annealed device. We notice that annealing at 330 K had a measurable effect on device performance, but clearly annealing at above the melting temperature of PEO resulted in the most significant improvement in device performance.

Table 1 summarizes the device characteristics extracted from Fig. 2. We first notice that the initial device currents of devices annealed at above the melting point of PEO are 3–10 times higher than in un-annealed device and the device annealed at 330 K. Since the initial device current in an LEC is largely ionic, this observation suggests that the annealing/quenching process makes the device much more ion-conductive. Several factors may have contributed to the increase in ion conductivity. The melting of isolated PEO domains (white dots) facilitates ion transport via improved percolation. The annealing/quenching process also converts crystalline PEO into amorphous PEO which is mainly responsible for the ion conduction in PEO-based electrolytes [34].

Higher ion conductivity leads to faster and heavier doping, and therefore higher peak current and peak EL intensity. The peak device current reached

Table 1
Device performance parameters of un-annealed and annealed planar LECs

Annealing temperature	Current			Luminance			*p*-doping speed (μm/s)	*n*-doping speed (μm/s)
	Initial (nA)	Maximal (mA)	$T[I_{max}]$ (s)	Turn-on (s)	Maximal (a.u.)	$T[L_{max}]$ (s)		
Un-annealed	40.5	0.039	2115	82	14.6	1880	$6.40 + 0.01$	$3.00 + 0.01$
330 K	52.6	0.11	2280	56	37	2093	$8.6 + 0.1$	6.10 ± 0.01
350 K	233.6	1.4	885	12	136.8	1171	$27.0 + 3.0$	$20.3 + 0.1$
380 K	202	1.1	513	7	125.3	687	$37.2 + 0.5$	$25.3 + 0.4$
400 K	494.1	7.3	282	5	460	285	33.0 ± 0.0	$27.1 + 1.9$

$T[I_{max}]$ is the time to reach maximum current.
$T[L_{max}]$ is the time to reach maximum EL intensity.

over 1 mA in devices annealed at or above 350 K, compared to a mere 0.039 mA for the un-annealed device. Due to the extremely small cross-sectional area of the planar device configuration, the in plane peak current density is close to 15 A/cm^2 in the device annealed at 400 K. The peak EL intensity is also higher in devices with higher peak current. However, for reasons to be explained below, the relative EL efficiency (EL intensity/current) of the device actually decreases with annealing temperature. Not only are the peak current and EL intensity much higher in devices annealed at higher temperatures, the time it takes to reach these values, $T[I_{max}]$ and $T[L_{max}]$, respectively, are also significantly reduced.

Also included in the table are the average speeds of *p*- and *n*-doping propagation, extracted from successive fluorescence images taken during the turn-on process. The devices that underwent time-lapse fluorescence imaging were identical to those measured with a photodiode (Fig. 2) and were turned on by applying the same voltage bias and temperature. Both *p*- and *n*-doping propagation speeds increase with annealing temperature until 380 K. In the 400 K-annealed device the *p*-doping propagation speeds is slightly lower that of the 380 K-annealed device, and the *n*-doping propagation speed is slightly higher than that of the 380 K-annealed device. As a result, the 400 K-annealed device has nearly identical *p*- and *n*-doping propagation speeds. The dramatic increase in doping propagation speeds explains why the EL onset time decreases with annealing temperature.

Since the onset of EL coincides with the initial formation of the *p*–*n* junction, the EL onset time can also be calculated by dividing the interelectrode

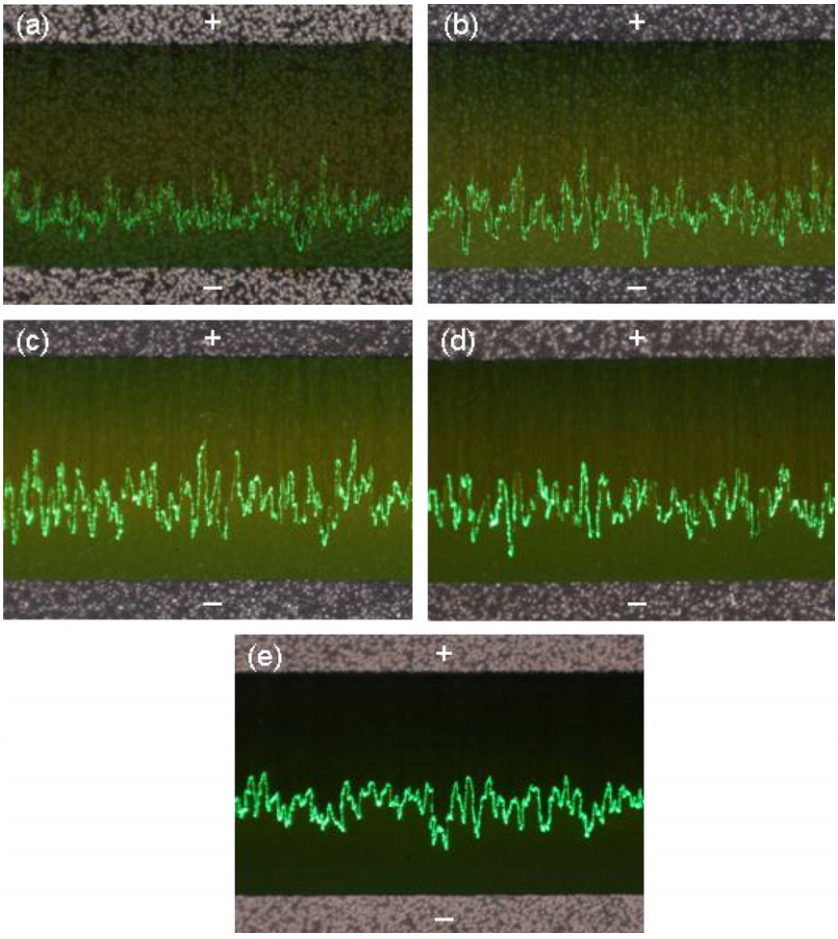

Fig. 3. Un-annealed (a) and annealed planar LEC exhibiting maximum EL. Annealing temperature (b) 330 K, (c) 350 K, (d) 380 K, (e) 400 K. The devices were subjected to a 400 V bias at 315 K and imaged under room light.

spacing (1 mm) by the sum of *n*- and *p*-doping propagation speeds. The calculated EL onset time for the un-annealed, 330, 350, 380, and 400 K-annealed devices are 106.4, 68, 21.1, 16, and 16.6 s, respectively. These values are slightly higher than the measured turn-on times (displayed in Table 1), due to the fact that the calculated turn-on time is estimated from the average doping propagation speeds while the jagged doping profile lead to the formation of a localized light-emitting *p–n* junction at an earlier time.

Fig. 3 shows the images of the devices that have been fully turned on. The devices were all under a voltage bias of 400 V at 315 K and imaged under room light. The highly uneven emission zone observed in all five devices is characteristic of millimeter-sized planar LECs, caused by highly uneven doping propagation along the length of the device. Nevertheless, it is very clear that the brightness of the emission zone increases with annealing temperature. The emission zone is much more centered in the 400 K-annealed device than in un-annealed or 330 K-device, owning to the more balanced *p*- and *n*-doping propagation speeds. A centered emission zone is preferred over an off-centered one, especially in sandwich devices, because it prevents metal-induced quenching of the light emission and the formation of shorts by runaway doping [35].

Another major observation in Fig. 3 is the progressive darkening of the non-emitting regions of the polymer film with the increase of annealing temperature. This darkening of the polymer film is directly caused by the *in situ* electrochemical doping process, which quenches the photoluminescence of the polymer [36]. The degree of PL quenching is therefore an indication of the doping level. The 400 K-annealed device is the most heavily and uniformly doped, which explains its high current level. By contrast, the un-annealed and the 330 K-annealed devices display lower levels of doping as shown by their lighter shade. Doping and PL quenching also make the white dots, which are electrolyte domains that cannot be doped, more visible by increasing the overall contrast of the polymer films. It can be seen that the density of the white dots decreases with annealing temperature. The heavy PL quenching of devices annealed at higher temperatures has a negative effect on their relative EL efficiency (EL intensity/current). This drawback can be overcome by relaxing an as-formed *p–n* junction into a more efficient *p–i–n* junction [37].

The dramatic effects of annealing/quenching described above are not limited to LEC films containing large, visible PEO domains. A second series of LECs were prepared, annealed and tested following the same procedures as for previous devices, with the exception that the LEC solution was not heated before film casting. The lower solution temperature resulted in visibly more uniform as-cast LEC films that did not show any large white dots under an optical microscope. Nevertheless, similar improvements to device current, EL, and turn-on time have been observed following the annealing/quenching treatment. Fig. 4 compares the time evolution of device current and EL intensity between an un-annealed device and a 400 K-annealed device. The peak current and peak EL intensity of the annealed device are ~1200 and 194 times higher than those of the un-annealed device. The annealed device also displays much faster EL turn-on (7 s) than the un-annealed device (103 s). The images of the fully turned on devices are shown in the inset of Fig. 4. Again we observe heavy doping and a more centered emission zone in the annealed device.

Scanning electron microscope (SEM) imaging reveals the effect of annealing/quenching on the topography of LEC films cast from unheated solution, as shown in Fig. 5. The surface of the annealed device is much smoother that of the as-cast film. This again can be attributed to the melting of (smaller) PEO domains. The fast cooling rate is necessary to prevent the PEO from precipitating out of the

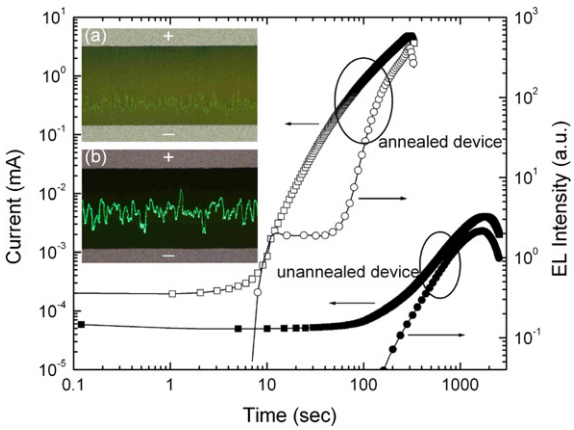

Fig. 4. Time evolution of device current and EL intensity of an un-annealed planar LEC and a planar LEC annealed at 400 K for 5 min. Both devices were subjected to a 400 V bias at 315 K. The inset shows the photographs of the two devices at near maximum emission. The polymer films were spin cast from unheated LEC solution.

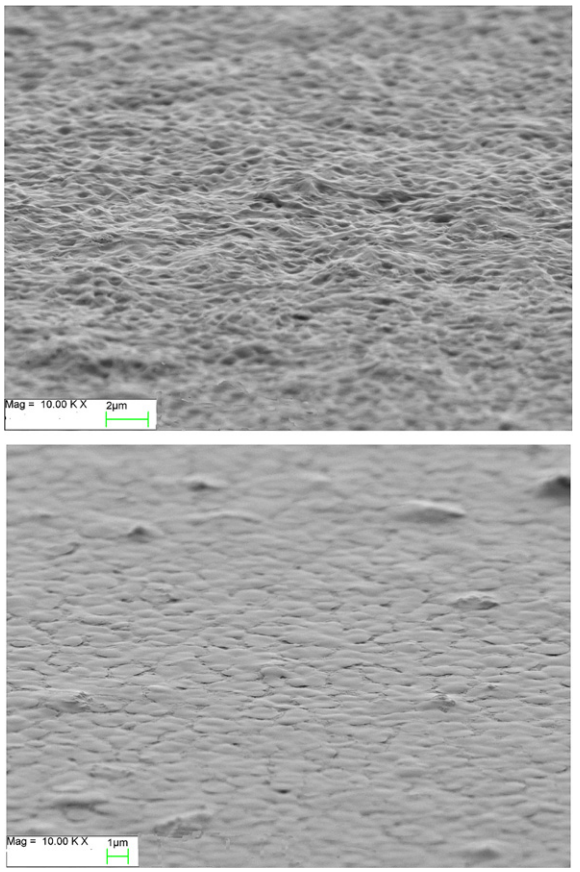

Fig. 5. Scanning electron microscopy micrographs of un-annealed (top) and annealed (400 K/5 min) (bottom) LEC films containing fluorene copolymer, PEO, and LiTf.

polymer mixture when it is cooled to 315 K. However, fast cooling creates a large temperature gradient normal to the polymer film. This is likely responsible for the formation of cracks, visible in Fig. 5b, giving rise to a surface topography resembling a dry riverbed.

The improvement in device performance remains the same, regardless of whether the aluminum electrodes were deposited before or after the annealing/quenching procedure. This confirms that film morphology change, rather than the modification at the electrode/polymer interface is mainly responsible for the dramatic effect on the doping process and device performance. The effect of annealing/quenching is also independent of the luminescent polymer used as we have observed similar improvement in device performance in MEH-PPV-based LECs following the same thermal treatment. The surface morphology of the MEH-PPV LEC films did not exhibit visible difference after annealing. However, the maximum current of the annealed (5 min at 400 K) device was 5.3 mA, compared to 0.11 mA for the un-annealed device. Finally, It should be mentioned that the LEC films imaged under SEM (Fig. 5) were stored in a glove-box for three days before imaging. The observed large difference in surface morphology between the annealed film and the control film indicates the effects of annealing/quenching are not short-term.

4. Conclusions

The effects of annealing/quenching on PEO-based planar light-emitting electrochemical cells have been demonstrated. Annealing above the melting point of PEO dramatically improve the film morphology as well as the performance of planar LECs. This is attributed to the melting of crystalline PEO domains and better mixing of PEO and the luminescent polymer at high temperatures. The fast cooling freezes the film morphology achieved and is as important as the annealing step. The simple thermal processing technique demonstrated here provides an effective, ''thermodynamic'' approach to solving the compatibility problem in multi-component polymer LECs.

Acknowledgements

The authors would like to thank American Dye Source, Inc. for providing the luminescent materials used in this work. The research is supported by the Natural Sciences and Engineering Research Council of Canada (NSERC).

References

[1] Q.B. Pei, G. Yu, C. Zhang, Y. Yang, A.J. Heeger, Science 269 (1995) 1086–1088.
[2] Q.B. Pei, Y. Yang, G. Yu, C. Zhang, A.J. Heeger, Journal of the American Chemical Society 118 (1996) 3922–3929.
[3] G. Yu, Y. Yang, Y. Cao, Q. Pei, C. Zhang, A.J. Heeger, Chemical Physics Letters 259 (1996) 465–468.
[4] D.J. Dick, A.J. Heeger, Y. Yang, Q.B. Pei, Advanced Materials 8 (1996) 985–987.
[5] Y. Yang, Q.B. Pei, Journal of Applied Physics 81 (1997) 3294–3298.
[6] Y.F. Li, J. Gao, G. Yu, Y. Cao, A.J. Heeger, Chemical Physics Letters 287 (1998) 83–88.
[7] I.H. Campbell, D.L. Smith, C.J. Neef, J.P. Ferraris, Applied Physics Letters 72 (1998) 2565–2567.
[8] J. Gao, A.J. Heeger, I.H. Campbell, D.L. Smith, Physical Review B 59 (1999) R2482–R2485.
[9] S. Tasch, L. Holzer, F.P. Wenzl, J. Gao, B. Winkler, L. Dai, A.W.H. Mau, R. Sotgiu, M. Sampietro, U. Scherf,

Mullen, A.J. Heeger, G. Leising, Synthetic Metals 102 (1999) 1046–1049.
[10] J. Morgado, R.H. Friend, F. Cacialli, B.S. Chuah, H. Rost, S.C. Moratti, A.B. Holmes, Synthetic Metals 122 (2001) 111–113.
[11] L. Edman, M.A. Summers, S.K. Buratto, A.J. Heeger, Physical Review B 70 (2004) 115212.
[12] J. Gao, J. Dane, Applied Physics Letters 84 (2004) 2778–2780.
[13] Y.F. Hu, C. Tracy, J. Gao, Applied Physics Letters 88 (2006) 123507.
[14] R.H. Friend, R.W. Gymer, A.B. Holmes, J.H. Burroughes, R.N. Marks, C. Taliani, D.D.C. Bradley, D.A. Dos Santos, J.L. Bredas, M. Logdlund, W.R. Salaneck, Nature 397 (1999) 121–128.
[15] J. Gao, G. Yu, A.J. Heeger, Applied Physics Letters 71 (1997) 1293–1295.
[16] G. Yu, Y. Cao, M. Andersson, J. Gao, A.J. Heeger, Advanced Materials 10 (1998) 385–388.
[17] J.H. Shin, S. Xiao, A. Fransson, L. Edman, Applied Physics Letters 87 (2005) 043506.
[18] Y. Cao, G. Yu, A.J. Heeger, C.Y. Yang, Applied Physics Letters 68 (1996) 3218–3220.
[19] T. Johansson, W. Mammo, M.R. Andersson, O. Inganas, Chemistry of Materials 11 (1999) 3133–3139.
[20] J. Morgado, R.H. Friend, F. Cacialli, B.S. Chuah, S.C. Moratti, A.B. Holmes, Journal of Applied Physics 86 (1999) 6392–6395.
[21] C.C. Ho, K.M. Yeh, Y. Chen, Polymer 45 (2004) 8739–8749.
[22] Q.J. Sun, H.Q. Wang, C.H. Yang, G.F. He, Y.F. Li, Synthetic Metals 128 (2002) 161–165.
[23] H.C. Ko, D.K. Lim, S.H. Kim, W. Choi, H. Lee, Synthetic Metals 144 (2004) 177–182.
[24] F. Verbakel, S.C.J. Meskers, R.A.J. Janssen, Chemistry of Materials 18 (2006) 2707–2712.
[25] Y. Cao, Q.B. Pei, M.R. Andersson, G. Yu, A.J. Heeger, Journal of the Electrochemical Society 144 (1997) L317–L320.
[26] T. Zyung, S.D. Jung, D.H. Hwang, Synthetic Metals 117 (2001) 223–225.
[27] T. Ahn, H. Lee, S.H. Han, Applied Physics Letters 80 (2002) 392–394.
[28] J. Liu, T.F. Guo, Y. Yang, Journal of Applied Physics 91 (2002) 1595–1600.
[29] Y.H. Niu, Q. Hou, Y. Cao, Applied Physics Letters 81 (2002) 634–636.
[30] J. Kim, J. Lee, C.W. Han, N.Y. Lee, I.J. Chung, Applied Physics Letters 82 (2003) 4238–4240.
[31] Y. Kim, S.A. Choulis, J. Nelson, D.D.C. Bradley, S. Cook, J.R. Durrant, Journal of Materials Science 40 (2005) 1371–1376.
[32] P.A.C. Quist, T.J. Savenije, M.M. Koetse, S.C. Veenstra, J.M. Kroon, L.D.A. Siebbeles, Advanced Functional Materials 15 (2005) 469–474.
[33] J.H. Shin, A. Dzwilewski, A. Iwasiewicz, S. Xiao, A. Fransson, G.N. Ankah, L. Edman, Applied Physics Letters 89 (2006) 013509.
[34] F.M. Gray, Polymer Electrolytes, The Royal Society of Chemistry, NY, Weinheim Germany, Cambridge UK, 1997.
[35] J.H. Shin, S. Xiao, L. Edman, Advanced Functional Materials 16 (2006) 949–956.
[36] A.L. Holt, J.M. Leger, S.A. Carter, The Journal of Chemical Physics 123 (2005) 044704.
[37] Y.G. Zhang, Y.F. Hu, J. Gao, Applied Physics Letters 88 (2006) 163507.

Available online at www.sciencedirect.com
ScienceDirect
Organic Electronics 9 (2008) 355–368
Organic Electronics
www.elsevier.com/locate/orgel

Charge transport in disordered organic solids: A Monte Carlo simulation study on the effects of film morphology

S. Raj Mohan, M.P. Joshi *, Manoranjan P. Singh

Laser Physics Applications Division, Raja Ramanna Centre for Advanced Technology, Indore, MP 452 013, India

Received 2 July 2007; received in revised form 16 December 2007; accepted 16 December 2007
Available online 14 January 2008

Abstract

The influence of ordered regions (micro crystallites and aggregates) in the other wise disordered polymer host matrix on field and temperature dependence of mobility (μ) has been simulated. Increase in concentration of ordered regions leads to increase in magnitude of mobility and in high field regime the saturation of the mobility occurs at lower electric field strength. The influence of different mean and standard deviation of Gaussian density of states (DOS) of ordered regions on the field dependence of mobility was studied and found to be significant only at higher concentrations. Weak influence of these parameters at low concentrations is attributed to the strong interface effects due to the difference in the standard deviation of DOS of two regions (host and ordered region) and shallow trapping effect by ordered regions. For all the parameters of ordered regions under investigation the temperature dependence of mobility ($\log \mu$) and the slope of $\log \mu$ vs. $E^{1/2}$ plot show $1/T^2$ dependence.

PACS: 72.80.Le; 72.80.Lg; 71.55.Jv; 73.61.Ph; 68.55.−a

Keywords: Molecularly doped polymers; Disordered system; Morphology; Electronic transport; Aggregation; Monte Carlo simulation

1. Introduction

Thin films of conjugated organic solids (both molecular and polymers) have gained tremendous importance due to their potential applications in developing various optoelectronic devices like organic light emitting diodes (OLED), organic field effect transistors (OFET), organic solar cells etc [1,2]. A better understanding and control of morphology of disordered organic solid films is of prime importance because the performance of several organic devices have been shown to be highly sensitive to film morphology and processing conditions [3–8]. Often, the active layers of devices, e.g. spin cast films of molecularly doped polymers (MDP) and conjugated polymers, are not purely disordered or amorphous rather they are partially ordered. Ordered regions (e.g. molecular aggregation and crystallization in MDP or oriented polymer chains in conjugated polymers) are formed either unintentionally due to processing conditions and aging or intentionally incorporated via annealing. Compared

* Corresponding author. Fax: +91 731 2488300.
E-mail address: mukesh@cat.ernet.in (M.P. Joshi).

1566-1199/$ - see front matter © 2007 Elsevier B.V. All rights reserved.
doi:10.1016/j.orgel.2007.12.005

to purely amorphous films the partially ordered polymer films show an improvement in carrier mobility (μ) and charge transport properties. Therefore a careful control of deposition parameters and processing conditions [3,9–12] are generally employed to improve the structural order in these materials.

Charge transport in these films occur through a mixture of ordered and less ordered regions, which is against the assumptions made in hopping charge transport models developed for completely isotropic and disordered medium [13–15]. In these models of charge transport the influence of film morphology of the active layers, which has profound effect on charge transport, is not considered well. The presence of ordered regions can in-fact reduces the overall energetic disorder in the material and enhances the mobility. It has been shown that with improvement in structural order in the film the nature of charge transport changes from dispersive to non-dispersive [16]. The field dependence of mobility also shows large variations. For example, the field dependence of mobility in partially ordered samples generally show a Poole–Frenkel type behavior but in some cases either very weak field dependence or even negative field dependence, at low temperatures, of mobility have been observed [17–20]. In our previous report [18], we reported difference in field dependence of mobility compared to earlier reports on similar system [15]. Fig. 1(a) shows the electric field dependence of mobility obtained from our study in *N*-*N*′-diphenyl-*N*-*N*′-bis(3-methylphenyl)-1-1-biphenyl-4,4′-diamine (TPD) dispersed in Polystyrene at 20:80 proportions by weight. Mobility was measured using small signal time of flight (TOF) transient photoconductivity technique. Compared to earlier report [15] we observed a higher magnitude in mobility as well as the saturation of mobility when field is increased. In addition, we have also observed that the slope of field dependence of mobility, at intermediate field regime, changes from positive to negative at lower temperature. The values of both energetic ($\sigma = 0.053$ eV) and positional disorder ($\Sigma = 2.51$) were also low when data was analyzed using Gaussian disorder model (GDM). The observed difference in field dependence of mobility was attributed to the low value of energetic disorder. The reason for the low value of energetic disorder was attributed to the different morphology of our sample resulting from the aggregation of TPD. Aggregates, which spread through out the sample, were confirmed using scanning electron microscope (SEM) images of the sample (shown in the inset of Fig. 1a). Earlier studies on similar system reporting high values of σ and Σ also report no crystallization/aggregation of TPD. Temperature dependence of mobility in these partially ordered films has also been a matter of discussion whether $\log \mu$ follows $1/T$ or $1/T^2$ [10,21]. As shown in Fig. 1b, we however observed $1/T^2$ dependence of mobility. Therefore a proper understanding of charge transport in these partially ordered materials is yet to be obtained which is important for developing appropriate model for explaining the charge transport mechanism as well as for controlling the morphology of active layers for design of efficient devices.

In this study we perform Monte Carlo simulation to investigate the influence of ordered regions on the charge transport when incorporated in an otherwise disordered host medium. We simulate transport in energetically inhomogeneous medium by considering regions of sub-micron sized domains of lower energetic disorder distributed uniformly over the region of high energetic disorder. The problem is similar to charge transport in samples like molecularly doped polymers (MDP) where sub-micron sized microcrystallization/aggregation of dopants occur unintentionally or intentionally [18,22] or when partial structural ordering (like alignment of polymer chains) takes place in amorphous polymer films [4,6,10]. Our observation of aggregates of TPD doped polymers and the significant influence of these aggregates (of size $\sim$100 nm) on charge transport [18] also motivated us to simulate the charge transport mechanism in these partially ordered films and provide justification for our experimental results. In earlier simulation study by Rakhmanova et al. [23] on charge transport in similar energetically inhomogeneous system showed that temperature dependence of mobility follow $1/T$ rather than $1/T^2$. They assumed a complete energetically inhomogeneous lattice such that at every jump site the energetic disorder parameter is obtained randomly from two different Gaussian distributions of different widths. Here we consider two spatially extended regions of different energetic disorder parameter. In our simulation, the morphology of the disordered host lattice is therefore altered by randomly incorporating sub-micron sized cuboids with narrow energetic distribution of localized states (representing ordered region). Simulation is performed for various electric field strength and temperature by changing the concentration of

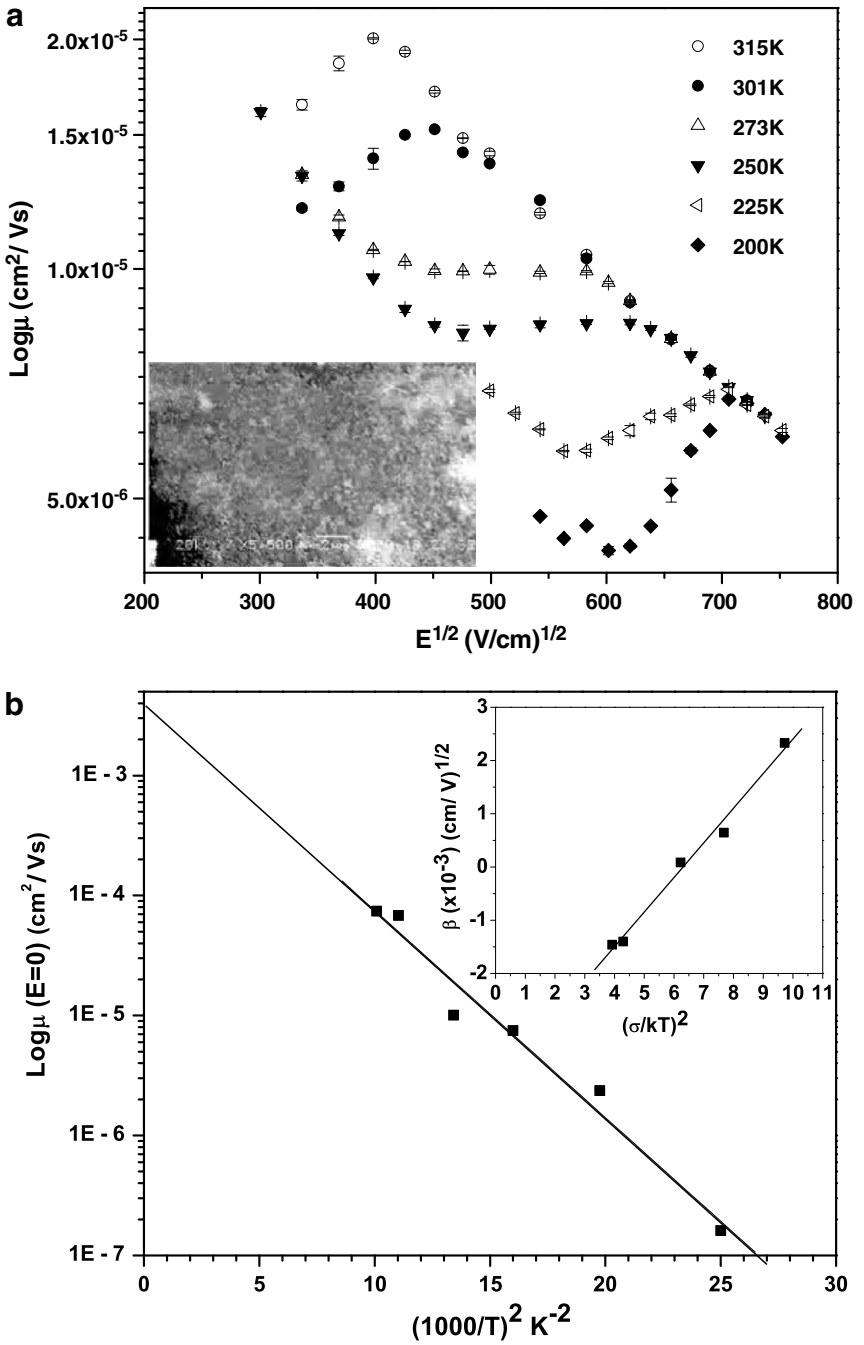

Fig. 1. (a) Log μ vs. $E^{1/2}$ plot of TDP doped Polystyrene, with 20:80 wt%, at various temperatures. Inset shows the SEM image of sample showing aggregation of TPD. (b) Log μ (at $E = 0$) vs. T^{-2} and the inset show the β vs. $(\sigma/kT)^2$ plot, where β is the slope of high field region of log μ vs. $E^{1/2}$ plot.

ordered regions, standard deviation and mean energy of density of states (DOS) of ordered regions. The influence of these parameters is important because the variation in these parameters is common as the degree of order obtained in the active layers vary depending on the processing conditions.

The incorporation of ordered regions leads to increase in magnitude of mobility with increase of concentration of ordered regions while at high field

regime the saturation of mobility occurs at lower electric field strength. The influence of parameters like standard deviation and mean energy of DOS of ordered regions is found to be significant only at high concentration of ordered regions. This is rationalized on the basis of interface trap effects due to difference in standard deviation of DOS of ordered region and host lattice. The temperature dependence of mobility and the slope of $\log\mu$ vs. $E^{1/2}$ plot at intermediate field regime follow $1/T^2$ as predicted by Gaussian disorder model (GDM) [14].

2. Simulation procedure

The Monte Carlo simulation is based on the commonly used algorithm reported by Schönherr et al. [24]. A lattice of $70 \times 70 \times 300$, along x-, y- and z-direction, with lattice constant $a = 6$ Å was used for computation. z-Direction is considered as the direction of the applied field. The size of the lattice is judged on the basis of our aim to change the morphology of the sample and also by taking into account the available computational resources. The site energies of lattice were taken randomly from a Gaussian distribution of mean ~5.1 eV (mean hole transport level with respect to vacuum) and standard deviation $\sigma = 75$ meV, which gives the energetic disorder parameter $\hat{\sigma} = \sigma/kT$. The value for σ was chosen close to the experimental values observed in TPD based MDPs. Simulation was performed on this energetically disordered lattice with the assumption that the hopping among the lattice sites are controlled by Miller–Abrahams equation [25] in which the jump rate v_{ij} from the site i to site j is given by

$$v_{ij} = v_0 \exp\left(-2\gamma a \frac{\Delta R_{ij}}{a}\right) \times \begin{pmatrix} \exp\left(-\frac{\varepsilon_{i\text{full}} - \varepsilon_{j\text{full}}}{kT}\right), & \varepsilon_j > \varepsilon_i \\ 1, & \varepsilon_j < \varepsilon_i \end{pmatrix} \quad (1)$$

where E is the applied electric field, $\Delta R_{ij} = |R_i - R_j|$ is the distance between sites i and j, $\varepsilon_{i\text{full}}$ and $\varepsilon_{j\text{full}}$ are the effective energies of the site i and j ($\varepsilon_{i\text{full}} = \varepsilon_i - eER_i$ and $\varepsilon_{j\text{full}} = \varepsilon_j - eER_j$), a is the intersite distance, k is the Boltzmann constant, T is the temperature in Kelvin and $2\gamma a$ is the wave function overlap parameter which controls the electronic exchange interaction between sites. Throughout the simulation we assume $2\gamma a = 10$ [14a,24]. Jump rates on the basis of Miller–Abrahams equation is considered to be more valid for the present study because the use of polaronic models requires unacceptable values of polaron binding energies or transfer integrals when site energies are uncorrelated [13,26], as in present simplified case.

With the aim to determine transit time, the time taken by the carrier to cover the entire sample length defined in the simulation, carrier residing randomly the first plane ($z = 0$) was allowed to move in the lattice under the action of applied field. Hopping of carrier from site i to site j was performed on the basis of the probability (P_{ij}) that a carrier jumps from the present site i to any site j around within a cube of size $7 \times 7 \times 7$ (343 sites). A random number u_r from a uniform distribution is chosen and this decides to which site the carrier should jump because each site is given a length in random number space according to P_{ij}. Time taken by the carrier for jumping from site i to j is then calculated. By adding time for all the jumps made when carrier covers the desired sample length, the transit time of the carrier is then determined. Using boundary condition along x-, y- and z-direction the simulation was always performed for a sample of length $L \sim 4$ μm along the field direction. The sample length was chosen so as to make sure that carrier will attain thermal equilibrium during its transit [14a]. Whenever boundary condition was used the lattice configuration was changed to ensure that the carriers do not move again through the same lattice. In the present study we calculated the mobility from the average transit time obtained after averaging over 150 carriers with one lattice configuration for each carrier. Simulation was preformed for various electric field and temperature by introducing one carrier at a time.

Film morphology was varied by incorporating cuboids of so called ordered regions (representing molecular aggregates/microcrystallites in MDPs or regions of oriented polymer chains in conjugated polymers) of varying size that are placed randomly inside the otherwise disordered host lattice. Sizes of ordered regions were limited to a maximum size of $12 \times 12 \times 100$ nm along x-, y- and z-directions. The maximum size was chosen so as to simulate the charge transport in a situation that is close to experimentally observed TPD aggregates [18]. The ordered regions are placed only either along the direction or perpendicular to the field direction. The ordered regions may sometimes overlap each other but it is always ensured that ordered region occupy the required volume

fraction of the host lattice. Whenever overlap occurs, the amount of the overlap is detected and this region is not counted again so as to maintain the volume fraction occupied by the ordered cuboids. To perform this task all host lattice points are initially set to some fixed numerical value (zero). When a cuboid is placed the lattice points occupied by cuboid are assigned with numerical value different from the host lattice. While placing a second cuboid, by checking the numerical value assigned to lattice points that are going to be occupied by the second cuboid we can ensure whether the second cuboid is overlapping with the already placed one or not.

The energetic disorder inside the ordered region was kept low compared to the host lattice. This is justified because the aggregates are more ordered regions and hence to simulate the charge transport the cuboids must be of low energetic disorder compared to host lattice. The site energies inside the ordered regions were also taken randomly from another Gaussian distribution (The ordered regions and host lattice are identified from the values assigned to the lattice points). Aggregation of dopants, for example, can also lead to change in the energy gap (shift in HOMO, LUMO levels) and can change the mean energy of Gaussian distribution. The mean energies of ordered regions were chosen such that their difference from the mean energy of host lattice is in the order of kT. Simulations were performed by varying the concentration of such ordered regions (varying the percentage of volume of lattice occupied by ordered region) and the standard deviation and mean of Gaussian distribution from which the site energies of ordered regions were assigned.

3. Results and discussion

Fig. 2 shows the field dependence of mobility simulated for a lattice having DOS with standard deviation $\sim$75 meV (the host lattice), parametric with various values of energetic disorder parameter ($\hat{\sigma}$). At low field strength the mobility shows saturation while at intermediate field strength the mobility increases with increase of electric field in $\log\mu$ vs. $E^{1/2}$ fashion. This is because the applied field tilts the density of states that lead to the decrease of energetic barrier which the carriers encounter [14]. When temperature is increased carriers gain thermal energy and hence the effect of energetic disorder decreases which results in decrease of the slope of $\log\mu$ vs. $E^{1/2}$ curve at intermediate field strengths. At higher electric field strength, the drift velocity of charge carrier saturates and mobility attains a maximum value and decreases with further increase of electric field in $1/E$ fashion. At higher temperature, the drift velocity saturates at low electric field strength leading to the saturation of mobility [14]. Inset of Fig. 2 shows the remarkable difference in the field dependence of mobility for a lattice having DOS with standard deviation 60 meV, 40 meV and 2 meV. With decrease in energetic disorder it is observed that mobility increases and the slope of mobility curve, at intermediate field strength, changes from positive to negative.

To study the influence of embedded micro crystals/aggregation of dopants, the simulation was performed after incorporating ordered regions inside the host lattice (as explained in simulation procedure). Fig. 3 shows the field dependence of mobility, at $\sim$248 K, parametric with the concentration of ordered regions having DOS with standard deviation $\sim$40 meV and mean energy lower by $\sim kT$ compared to mean energy of host lattice. Magnitude of mobility at all regimes of electric field except the high field regime increases with increase in the concentration of ordered regions concomitant with decrease of slope at the intermediate field regime. In high field regime, the incorporation of ordered regions leads to the saturation of the mobility at lower electric field strength. When the concentration of ordered region is increased, the saturation of mobility also occurs at lower electric field strength. These observed features in the field dependence of the mobility, after embedding the ordered regions in the host lattice, can be rationalized on the basis of decrease in effective energetic disorder parameter of the transport medium. At low value of effective energetic disorder the energetic barrier seen by the carriers will be less which results in higher mobility but a weaker field dependence. This explains the increase in magnitude of mobility and decrease in the slope of $\log\mu$ vs. $E^{1/2}$ curve at intermediate field regime with increase in concentration of ordered regions in the host lattice. The low value of energetic disorder also can lead to saturation of drift velocity and mobility at lower electric field strengths. These simulated results support our experimental observation (as shown in Fig. 1) and explanation provided on the basis of low value of energetic disorder that resulted from a different morphology persisted in our sample due to the aggregation of TPD. Similarly, the change in slope at intermediate field

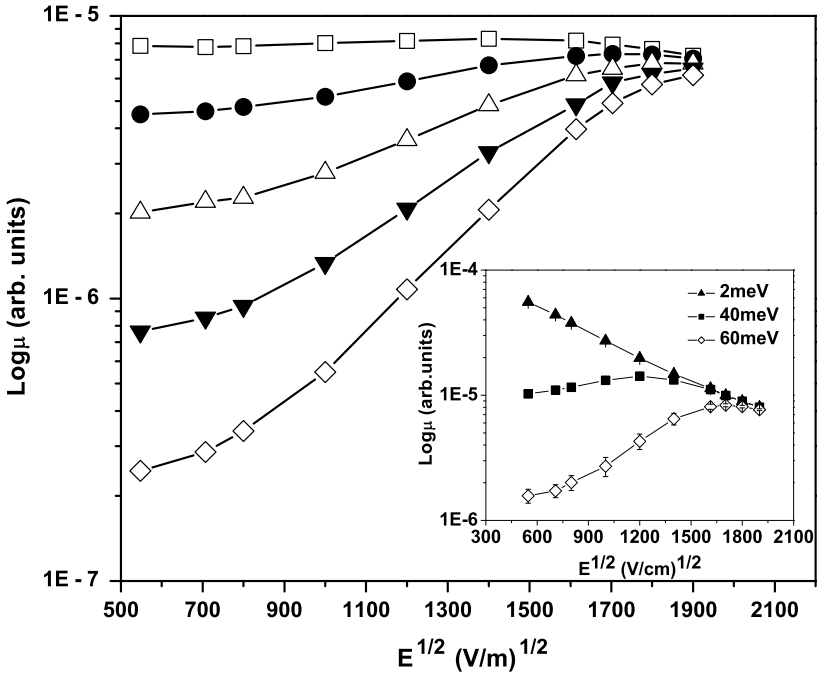

Fig. 2. Field dependence of mobility of host lattice with $\sigma = 75$ meV parametric with energetic disorder parameter 1.5 (□), 2 (●), 2.5 (△), 3 (▼), 3.5 (◇). Inset shows the field dependence of mobility for a lattice with 60 meV (–◇–), 40 meV (–■–) and 2 meV (–▲–), at 248 K.

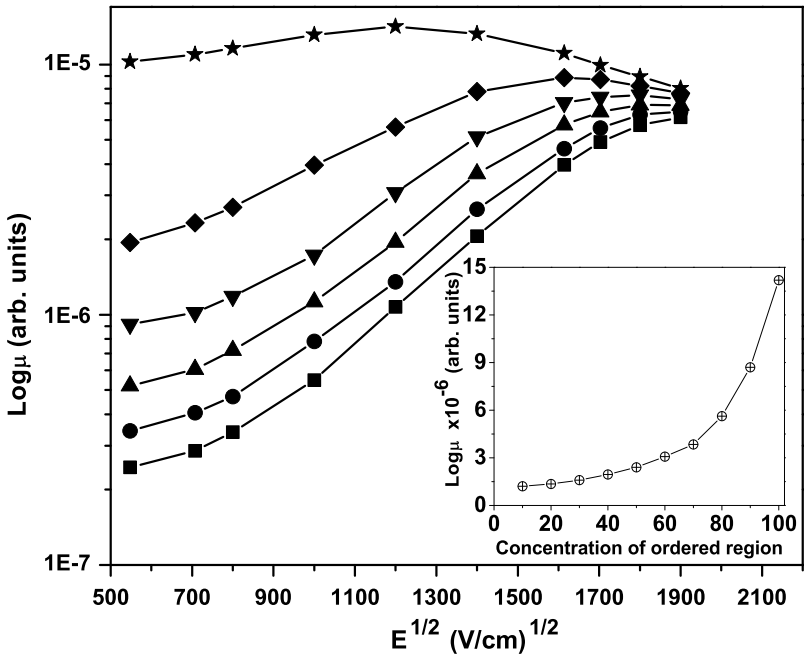

Fig. 3. Field dependence of mobility of host lattice, at 248 K, with 100% (★), 80% (♦), 60% (▼), 40% (▲), 20% (●) and 0% (■) concentration of embedded ordered regions having DOS with standard deviation ~40 meV. Inset shows the variation of mobility with the concentration of embedded ordered regions having DOS with standard deviation ~40 meV, at 248 K and field = 1.44×10^6 V/cm.

regime from positive to negative occurring at lower temperatures can also be explained from the weaker field dependence of mobility as observed from the simulated data. With the incorporation of ordered region in host lattice the slope of $\log \mu$ vs. $E^{1/2}$ plot at intermediate field regime changes from positive to

negative at lower temperatures (figure not shown) compared to purely disordered lattice. The temperature at which this change occurs decreases when the disorder inside the ordered region is lower and also when the concentration of ordered region is high.

From Fig. 3 it is clear that the magnitude of mobility attained even for concentration of ordered region as high as 80% is ~8–10 times less than that of a host lattice with DOS same as that of ordered region (but without any crystallites). Inset of Fig. 3 shows the variation of mobility (at ~248 K and field $\sim 1.44 \times 10^6$ V/cm) with concentration of ordered region, having DOS with standard deviation ~40 meV. A remarkable increase in the mobility was observed only when the concentration of the ordered regions was greater than ~60%. According to percolation theory this is expected to occur at ~25–30% concentration [27]. The observation of large threshold and weakly percolating transport is due to the fact that when group of carriers moves in a mixture of high and low mobility regions then only few carriers may find very low resistance paths (paths containing very low fraction of low mobility material) with short transit time and overall high mobility only for those carriers. To obtain further insight into this aspect the path of the 250 carriers, for various concentration of ordered region inside the host lattice, was followed and the fraction of the path occupied by the ordered region was calculated. Simulation was performed with one configuration for each carrier. From the histogram, shown in Fig. 4 for various concentrations of ordered region inside the host lattice, it is clear that very few low resistant paths (paths with fraction of ordered regions >0.95) with high mobility exist in our simulation studies. The number of such low resistance paths is very less compared to those paths where the fraction of low mobility region is considerable, i.e. high resistant (low mobility) paths. Hence on averaging over number of carriers the mobility value will be dominated by contribution from those high resistant paths which results in low magnitude of average mobility compared to uniform lattice with DOS of standard deviation same as that of ordered region. Moreover, the interface effect that occurs at the interface between ordered region and host lattice due to the difference in standard deviation of DOS also decrease the mobility. Interface effects will be discussed later in this paper. Increase in fraction of low resistant paths with increase of concentration of ordered region in the host lattice also supports the improvement in the mobility with increase in concentration of ordered region in host lattice.

The standard deviation and mean energy of DOS for ordered regions also influence the charge transport, especially its field and temperature dependence. Influence of disorder inside the ordered region on charge transport properties is investigated by performing simulation by varying the standard deviation of DOS inside the ordered region and the concentration of such ordered regions. Fig. 5 shows comparison of the field dependence of mobility for various values of the concentration and the standard deviation of DOS of ordered regions. Higher mobility is expected when ordered regions have a low value energetic disorder. It was, however, observed that the field dependence of mobility did not vary significantly with the change in the energetic disorder of the ordered region as long the concentration was below 60%. As we show below this happens because of the presence of the interface between the ordered region and the host lattice which acts like a "trap" for a carrier. Once carrier enter the ordered region, where the energetic disorder is low and mobility high, it spends less time to traverse the entire length of ordered region along the field direction. However at other interface the carrier face energetic barrier and may undergo several back and forth jumps before it proceeds forward through the host lattice. Thus, at the second interface carrier looses some part of the time that it has gained while traversing inside the ordered region. The interface effect is more prominent for ordered regions with very low energetic disorder. Hence on average the total transit time of a carrier (the time taken to traverse the entire lattice), effectively the carrier mobility, for different values of energetic disorder inside the ordered region may not vary appreciably as long as its concentration is low. To elucidate this interface effect a single ordered region was sandwiched between regions of high energetic disorder (as shown in the inset of Fig. 6). Region 2 is the ordered region while the regions 1 and 3 are regions with $\sigma = 75$ meV (all regions are of same dimension, $70 \times 70 \times 150$). Carrier transit time is recorded from the first plane of the first region. From the time carrier first enters and first comes out from the region 2, the transit time of the carrier inside the region 2 (ordered region) was calculated. Similarly from the time carrier first comes out of region 2 and the time it reached the other end of the lattice, the transit time

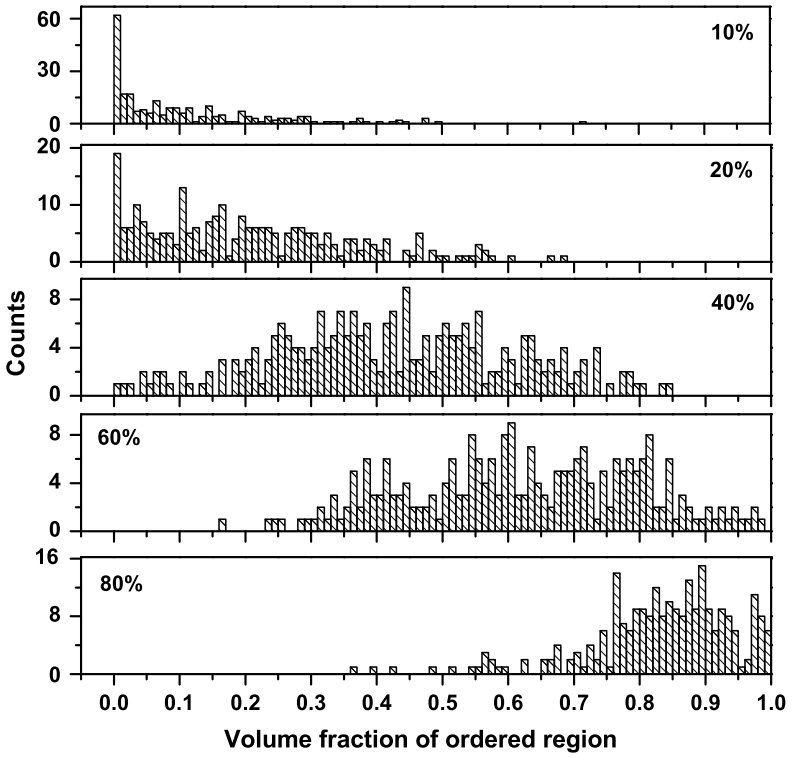

Fig. 4. Histograms showing the fraction of ordered regions in independent paths followed by 250 carriers with each configuration for each carrier, for different concentration of ordered region inside the host lattice, at 248 K and field = 1.44×10^6 V/cm. Standard deviation of the DOS of ordered regions were taken to be ~40 meV.

of the carrier in region 3 was also calculated. Simulation was performed by varying disorder inside the region 2. The time was calculated after averaging over 2000 carriers with one configuration for each carrier. Fig. 6 shows the typical values of carrier transit time in region 2 and 3 for various values of energetic disorder in region 2. The dependence of carrier transit time in region 3 on the energetic disorder in region 2 was clearly observed. Carrier transit time in region 3 increases with decrease of energetic disorder inside the region 2. This observation can be completely attributed to the interface effects. When the disorder inside the region 2 decreases then barrier seen by the carrier at the interface of region 2 and 3 increases. Basically at the interface the carrier will hop back and forth several times before moving forward through the region 3. This results in the increase of carrier transit time in the region 3. Transit time of carrier inside region 2 increases with increase of energetic disorder inside the region 2 as expected from GDM. This observation supports our explanation of almost independent nature of field dependence of mobility on the energetic disorder inside ordered regions, up to 60% concentration of ordered regions (as shown in Fig. 5), on the basis of interface effects. At high concentration, due to close vicinity of ordered regions, carrier spends most of the time in the ordered regions with less interface effects. Therefore mobility will be higher when the ordered region has lower energetic disorder and vice versa. Thus at higher concentrations charge transport is mainly governed by the energetic disorder inside the ordered region. This behavior was shown in our simulation for high concentrations of ordered regions (shown in Fig. 5 for 80% of ordered region in our study).

These interface effects are expected to play important role if site energies at each jump site were chosen randomly from a narrow and broad Gaussian distribution. This was the model chosen in earlier reported simulation study [23]. This we refer as joint distribution case. In this case interface effect can occur throughout the lattice while in case when host lattice is embedded with spatially extended ordered region (as in this study), the interface effect

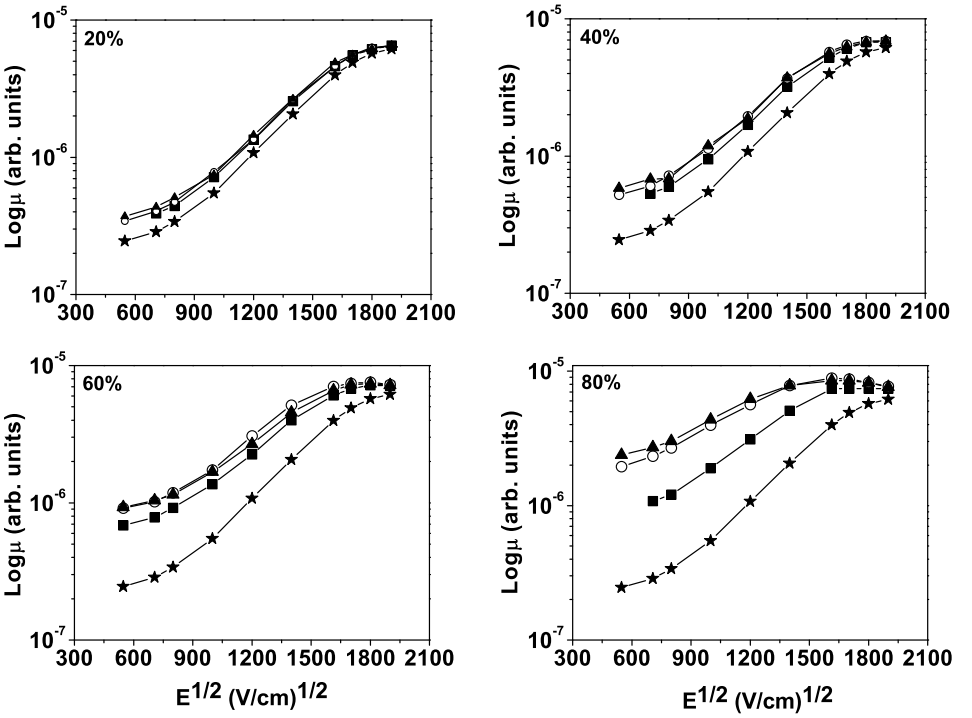

Fig. 5. Field dependence of mobility, at 248 K, of a host lattice embedded with ordered regions having DOS with standard deviation ~2 meV (▲), 40 meV (○) and 60 meV (■) at various concentrations. For comparison the field dependence of host lattice without embedded ordered regions is also shown (★).

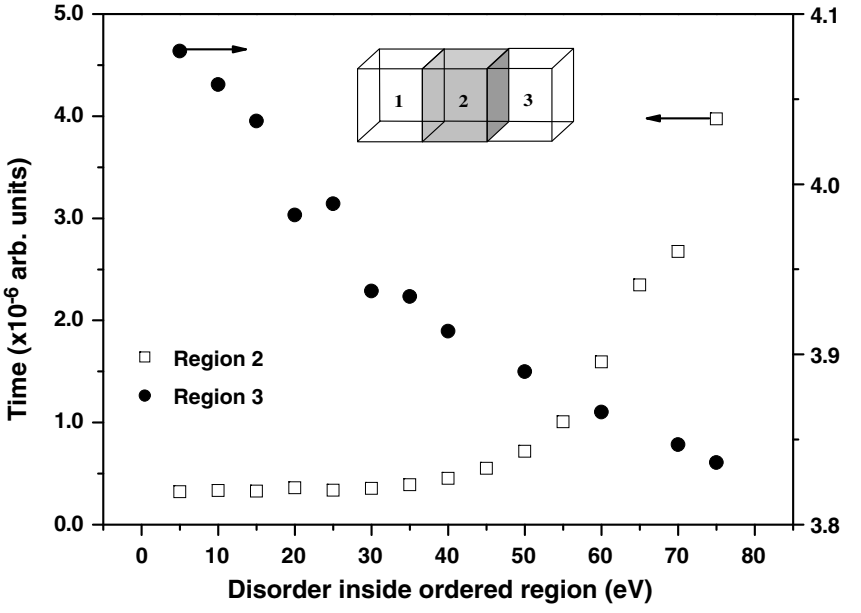

Fig. 6. Dependence of transit time of carrier in the region 3 (●) ($\sigma = 75$ meV) and region 2 (□) (for the sample shown in the inset) on the standard deviation of DOS of region 2 (ordered region), at 248 K and field = 1.44×10^6 V/cm.

occurs only at the boundary between host and ordered regions. To understand the differences in two cases we made a comparison of field dependence of mobility in the two cases with two different volume fractions. To ensure similar volume fraction in the two cases we provided a suitable weighting

factor (40% and 80%) in the joint distribution case. As shown in Fig. 7, the influence of higher interface effect is seen when the site energies of host lattice were chosen and assigned randomly from a narrow (standard deviation = 40 meV) and broad Gaussian distribution (standard deviation = 75 meV), the case of joint distribution. In joint distribution case, the magnitude of mobility was found to be low at all field values, except at high field regime. This is because interface effects is more and occur through out the lattice, which results in higher transit time and hence lower magnitude of mobility. When field strength increases the interface effect also decreases and hence at high field values both cases provide similar magnitude of mobility. Thus it is clear that one can have higher magnitude of mobility when lattice is embedded with ordered region or domains with low disorder than when site energies at each jump site are chosen randomly from a narrow and broad Gaussian distribution. This study suggests that in case of mixing two materials of different mobility, it is probably advantageous to have micro crystallites or domains of high mobility regions rather than randomly mixing the two at molecular level.

Simulations were also performed for different mean energy for DOS of ordered region compared to the host lattice. As explained in earlier section that the mean energy may change (normally decrease) upon aggregation or crystallization. Also, there are examples of molecular species of low ionization potential dispersed in hole transporting host material. It has been shown that in such system the dopants act as trap at low concentration while at high concentration the entire charge transport occurs through hopping among dopant species [28]. We performed simulation for three cases: (1) the mean energy of ordered region less than that of host lattice, (2) the mean energy of ordered region same as that of host lattice, and (3) the mean energy of ordered region higher than that of host lattice. Simulation was performed for a given concentration of ordered region and varying the mean energy in the order of kT. We chose two different concentrations of ordered regions, 20% and 80%. As shown in Fig. 8, at low field and low concentration, mobility is little higher for case (1) than for case (2) and smaller for case (3). With increasing concentration of ordered regions this difference in mobility is seen more prominently. While at high

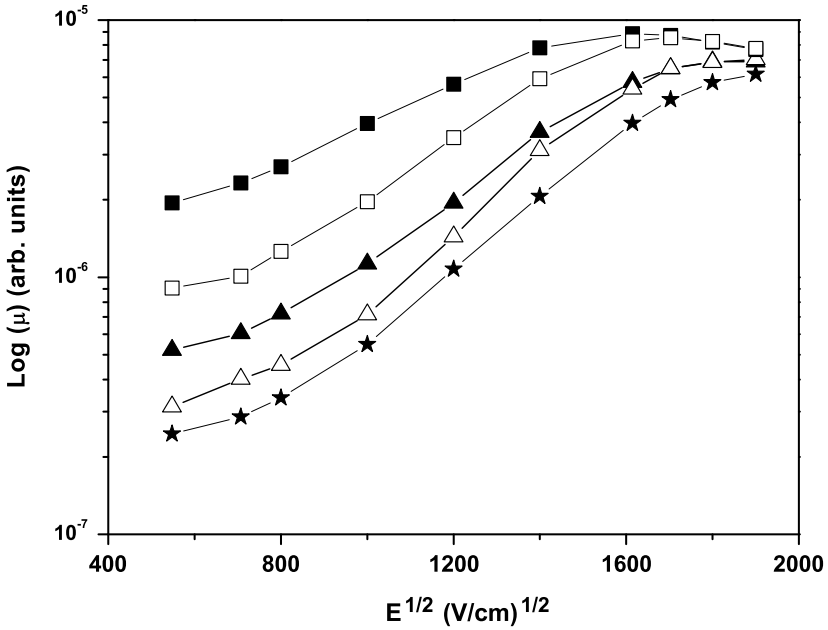

Fig. 7. Comparison of field dependence of mobility for two cases of energetic inhomogeneity (1) when host lattice is embedded with ordered regions (parameters kept same as in case of Fig. 3) and (2) when the site energies of host lattice were chosen and assigned randomly from a narrow (standard deviation = 40 meV) and broad Gaussian distribution (standard deviation = 75 meV) (the joint distribution case), at $T = 248$ K. Volume fraction was kept same in both cases and simulation is performed for 40% (▲) and 80% (■) volume fraction. Filled symbols represent case (1) and open symbols represent case (2). For comparison the field dependence of host lattice without embedded ordered regions (constant $\sigma = 75$ meV) is also shown (★).

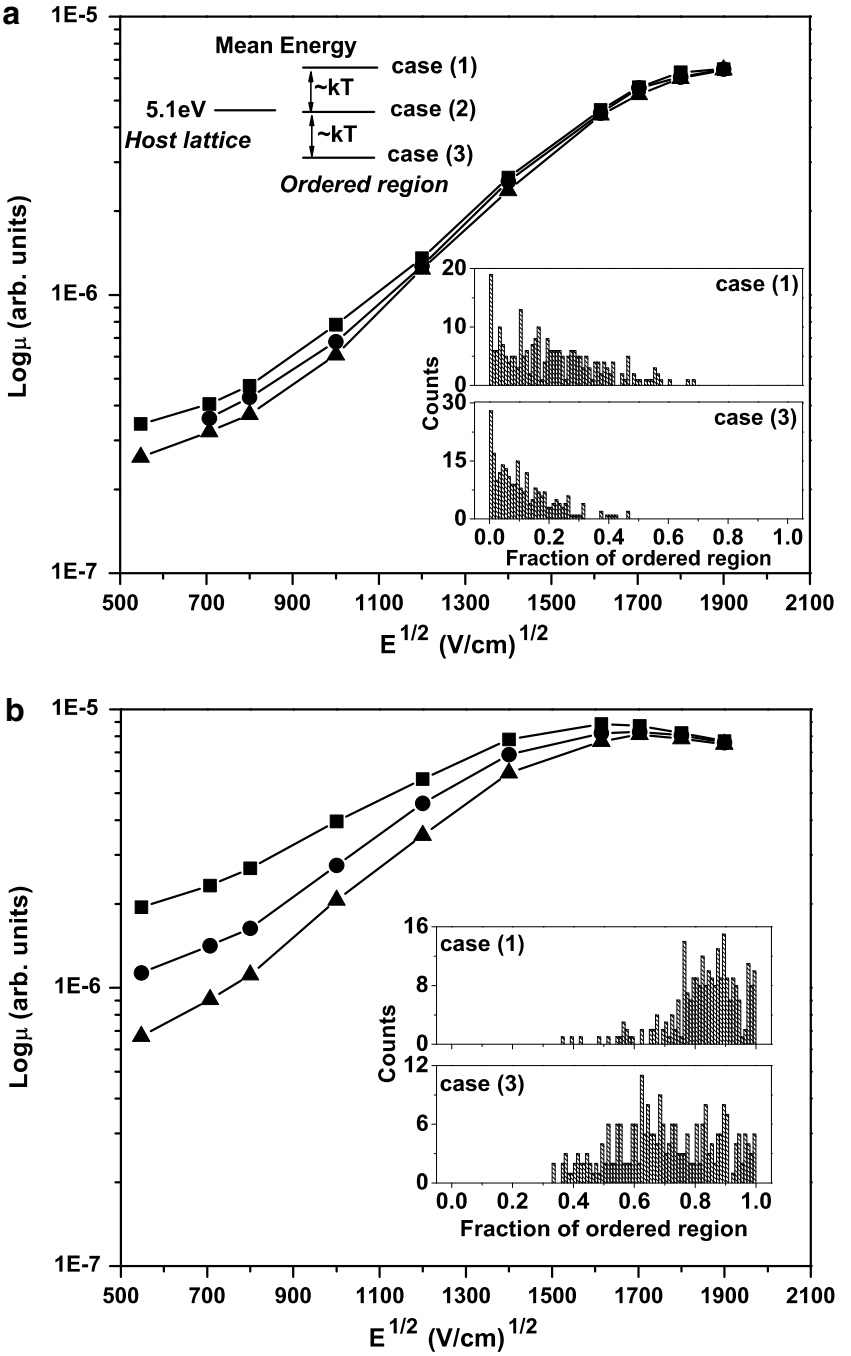

Fig. 8. Field dependence of mobility of a host lattice, at 248 K, with (a) 20% and (b) 80% concentration of embedded ordered regions having DOS with standard deviation 40 meV and mean energy varying in the order of kT compared to mean energy of DOS of host lattice. Case (1) (■), case (2) (●) and case (3) (▲). Mean energy of DOS of the host lattice is taken as 5.1 eV. Inset of each figure shows the fraction of ordered regions in the independent paths followed by 250 carriers in a host lattice embedded with respective concentration of ordered regions having DOS with standard deviation 40 meV, at 248 K and 1.44×10^6 V/cm.

field regime the field dependence of mobility in all the cases are nearly same. The observed differences in mobility for three cases are due to the fact that at all concentrations the low mean energy regions act as shallow traps. The low mean energy regions are either high mobility ordered region or low

mobility host regions. For example, in case (1) the low mean energy regions are high mobility ordered regions. Shallow trapping in ordered region also helps the carrier in finding more suitable paths inside the ordered region so as to move fast along the field direction. While in case (3) the low mean energy region is the host lattice of low mobility values. At very high concentrations (e.g. 80%) carrier will spend good amount of its transit time mostly inside the ordered region therefore the effects of shallow traps are seen more clearly as large difference in mobility behavior. In case (3) even at such high concentration the trapping effect due to the host lattice is still effective. This trapping mechanism due to difference in mean energy of DOS is an additional trapping mechanism that coexists at interface due to difference in standard deviation of DOS. Thus the mobility in case (3) is low compared to case (1) and (2). This mechanism is further get clarified from the histogram shown in inset of the respective Fig. 8a and b. This histogram shows the fraction of the ordered region in the different paths followed by carriers, for case (1) and case (3), at the respective concentrations. It is clear from histogram that carriers find more number of least resistant paths in case (1) than in case (3) which results in higher mobility for case (1).

Temperature dependence of mobility shown by such partially ordered active layers may be different from the predictions of GDM because of the fact that charge transport now occurs through ordered and disordered regions. Fig. 9 shows temperature dependence of zero field mobility and slope of $\log\mu$ vs. $E^{1/2}$ curve at intermediate field regime for a host lattice with $\sigma = 75$ meV (data represented by ■, without any ordered regions). The observed $1/T^2$ dependence is as predicted by the GDM. Even when ordered regions of lower energetic disorder and at different concentrations are incorporated in the host lattice the temperature dependence of mobility still show fit better with $1/T^2$ than $1/T$ (data represented by ○ and △ in Fig. 9). In contrast to prediction by Rakhmanova et al. [23] our simulations predict $1/T^2$ dependence for mobility. The absence of $1/T$ dependence of mobility in our simulation is because of the different degree of inhomogeneity in the two lattices. In the present study the ordered regions have sub-micron sized spatial extensions and inhomogeneity is seen only at interfaces. When carrier is either inside the ordered region or in the host lattice it moves in a region with site energies decided by a single Gaussian and transport in both the region should follow GDM. Due to large spatial extension of two regions the energetic inhomogeneity seen by

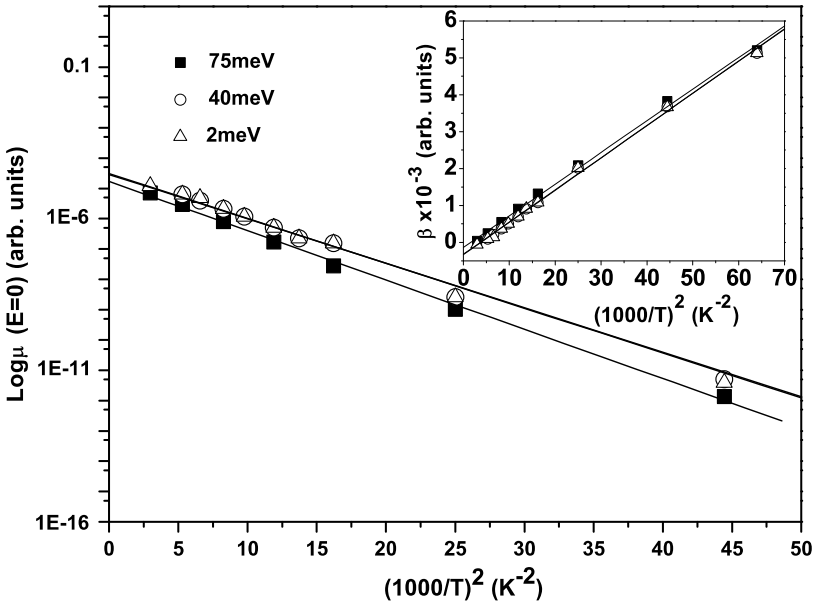

Fig. 9. Temperature dependence of zero field mobility for host lattice having DOS with standard deviation (■) 75 meV. Data (○) and (△) are temperature dependence for a host lattice with 40% of sites occupied by ordered regions having DOS with standard deviation 40 meV and 2 meV, respectively. Inset of figure shows the temperature dependence of slope of $\log\mu$ vs. $E^{1/2}$ curve (β) at intermediate field for the respective cases.

the carrier must be less compared to the simulated lattice used in Ref. [23]. Only at the interface of two regions carrier see energetic inhomogeneity. Hence the absence of $1/T$ dependence of mobility in our simulation can be attributed to low amount of energetic inhomogeneity in the lattice. Our simulation suggests that the charge transport in the lattice investigated occurs in a manner similar to prediction by GDM.

4. Conclusion

We studied the influence of embedded ordered regions on the charge transport in otherwise disordered amorphous systems. This is similar to the case of aggregation of dopants in molecularly doped polymers or when the microcrystals are deliberately embedded inside the conjugated polymer matrix. The effect of embedded ordered regions is seen as decrease of overall energetic disorder in the system. This decrease in energetic disorder results in the increase of over all mobility, decrease of slope of $\log\mu$ vs. $E^{1/2}$ curve at intermediate field regime and in high field regime the saturation of mobility at lower field strengths. The magnitude of the mobility increases with increase in concentration of ordered regions. The simulation results support our experimental observations and explanations provided on the basis of low energetic disorder present in the sample due to aggregation of TPD. Mobility is higher when ordered regions have low energetic disorder and low mean energy compared to the host lattice. The influence of standard deviation and mean energy of the DOS of ordered region on the field dependence of mobility was seen as trapping effects which occurs at the interface between ordered region and host lattice. At low concentration of ordered regions the field dependence of mobility do not show any significant change with standard deviation and mean energy of DOS of ordered regions. A remarkable influence of these parameters was observed only at high concentrations. The temperature dependence of mobility and the slope of $\log\mu$ vs. $E^{1/2}$ curve follow $1/T^2$ dependence than $1/T$ dependence. This is attributed to low inhomogeneity seen by the carrier in the simulated lattice. Simulation also suggests that one can have higher mobility with less inhomogeneity for carrier transport by having spatially extended ordered regions inside the lattice. From the simulation, the importance of concentration, energetic disorder and mean of DOS of ordered region to be incorporated in charge transport models is justified. Our study also suggests that in case of mixing two materials of different mobility it is advantageous to have micron or sub-micron sized regions of high mobility material rather than random or uniform mixing of the two.

Acknowledgements

Authors are grateful to S.C. Mehendale for the support and encouragement. S. Raj Mohan is grateful to Department of Atomic Energy (DAE), India, for providing Senior Research Fellowship. SRM like to thank J. Jayabalan, Aparana Chakravarti and V.K. Dixit of RRCAT for fruitful discussions.

References

[1] J. Shinar, V. Savvateev, in: J. Shinar (Ed.), Organic Light Emitting Devices: A Survey, Springer-Verlag, New York, 2004.
[2] G. Hadziioannou, Paul F. van Hutten, Semiconducting Polymers: Chemistry, Physics and Engineering, Wiley-VCH, Weinheim, 2000.
[3] H. Sirringhaus, P.J. Brown, R.H. Friend, M.M. Nielsen, K. Bechgaard, B.M.W. Langeveld-Voss, A.J.H. Spiering, R.A.J. Janssen, E.W. Meijer, P. Herwig, D.M. de Leeuw, Nature 401 (1999) 685.
[4] D. Fichou, J. Mater. Chem. 10 (2000) 571.
[5] J.M. Frost, F. Cheynis, S.M. Tuladhar, J. Nelson, Nano Lett. 6 (2006) 1674.
[6] C. Melzer, M. Brinkmann, V.V. Kransikov, G. Hadziioannou, ChemPhysChem 6 (2005) 2376.
[7] W. Ma, C. Yang, X. Gong, K. Lee, A.J. Heeger, Adv. Funct. Mater. 15 (2005) 1617.
[8] A. Andreev, F. Quochi, F. Cordella, A. Mura, G. Bongiovanni, H. Sitter, G. Hlawacek, C. Teichert, N.S. Sariciftci, J. Appl. Phys. 99 (2006) 034305.
[9] A. Kadashchuk, A. Andreev, H. Sitter, N.S. Sariciftci, Y. Skryshevski, Y. Piryatinski, I. Blonsky, D. Meissner, Adv. Funct. Mater. 14 (2004) 970.
[10] A. Salleo, T.W. Chen, A.R. Völkel, Y. Wu, P. Liu, B.S. Ong, R.A. Street, Phys. Rev. B 70 (2004) 115311.
[11] S. Cho, K. Lee, J. Yuen, G. Wang, D. Moses, A.J. Heeger, M. Surin, R. Lazzaroni, J. Appl. Phys. 100 (2006) 114503.
[12] H. Sirringhaus, R.J. Wilson, R.H. Friend, M. Inbasekaran, W. Wu, E.P. Woo, M. Grell, D.D.C. Bradley, Appl. Phys. Lett. 77 (2000) 406.
[13] L.B. Schein, Philos. Mag. B 65 (1992) 795.
[14] (a) H. Bässler, Phys. Status Solidi (b) 175 (1993) 15; (b) M. Jaiswal, R. Menon, Polym. Int. 55 (2006) 1371.
[15] S. Huen, P.M. Borsenberger, Physica B 216 (1995) 43.
[16] T. Kreouzis, D. Poplavskyy, S.M. Tuladhar, M. Campoy-Quiles, J. Nelson, A.J. Campbell, D.D.C. Bradley, Phys. Rev. B 73 (2006) 235201.
[17] M. Redecker, D.D.C. Bradley, M. Inbasekaran, E.P. Woo, Appl. Phys. Lett. 74 (1999) 1400.
[18] S. Raj Mohan, M.P. Joshi, Solid State Commun. 139 (2006) 181.

[19] S.J. Martin, A. Kambili, A.B. Walker, Phys. Rev. B 67 (2003) 165214.
[20] A.J. Mozer, N.S. Sariciftci, Chem. Phys. Lett. 389 (2004) 438.
[21] D. Hertel, H. Bässler, U. Scherf, H.H. Hörhold, J. Chem. Phys. 110 (1999) 9214.
[22] (a) D.M. Russel, C.J. Newsome, S.P. Li, T. Kugler, M. Ishida, T. Shimoda, Appl. Phys. Lett. 87 (2005) 222109;
(b) F. Khan, Ah-Mee Hor, P.R. Sundararajan, J. Phys. Chem. B 108 (2004) 117;
(c) F. Khan, P.R. Sundararajan, Org. Electron. 7 (2006) 410.
[23] S.V. Rakhmanova, E.M. Conwell, Appl. Phys. Lett. 76 (2000) 3822.
[24] G. Schönherr, H. Bässler, M. Silver, Philos. Mag. 44 (1981) 47.
[25] A. Miller, E. Abrahams, Phys. Rev. 120 (1960) 745.
[26] P.E. Parris, V.M. Kenkre, D.H. Dunlap, Phys. Rev. Lett. 87 (2001) 126601.
[27] M. Sahimi, Applications of Percolation Theory, Taylor & Francis, London, 1994.
[28] M. Stolka, J.F. Yanus, D.M. Pai, J. Phys. Chem. 88 (1984) 4707.

Available online at www.sciencedirect.com
ScienceDirect
Organic Electronics 9 (2008) 369–376
Organic Electronics
www.elsevier.com/locate/orgel

High sensitivity organic photodiodes with low dark currents and increased lifetimes

Marc Ramuz *, Lukas Bürgi, Carsten Winnewisser, Peter Seitz

CSEM SA, Badenerstrasse 569, 8048 Zürich, Switzerland

Received 16 July 2007; received in revised form 25 January 2008; accepted 26 January 2008
Available online 2 February 2008

Abstract

Organic semiconductors hold the promise for large-area, low-cost image sensors and monolithically integrated photonic microsystems. This requires the availability of photodiodes offering at the same time high quantum efficiency, low noise and long lifetimes. Although published structures of organic photodiodes offer high external quantum efficiencies (EQE) of up to 76% [F. Padinger, R.S. Rittberber, N.S. Sariciftci, Effects of postproduction treatment on plastic solar cells, Advanced Functional Materials 13 (2003) 1, P. Schilinsky, C. Waldauf, C.J. Brabec, Recombination loss analysis in polythiophene based bulk heterojunction photodetectors, Applied Physics Letters 81 (20) (2002) 3885], [1,2] they normally suffer from short lifetimes of only a few hundred hours as well as large dark currents. In our work the lifetime of a poly(3-hexylthiophene) (P3HT) and [6,6]-phenyl-C61 butyric acid methyl ester (PCBM) heterojunction photodiode structure was increased to several thousand hours by omitting the widely used poly(3,4-ethylenedioxythiophene):poly(styrenesulfonic acid) (PEDOT:PSS) anode layer. In addition, a simple model of optical interference and absorption effects was used to find the optimum thickness that combines high quantum efficiency with low dark current. As a result, we report on organic photodiodes with state-of-the-art EQE of 70% at 0 V bias, an on/off current ratio of 10^6 at -1 V and 40 mW/cm^2 illumination, dark current densities below 10 nA/cm^2 at -1 V, and a lifetime of at least 3000 h.

PACS: 73.61.Ph; 73.50.Gr; 73.50.Td

Keywords: Organic electronics; Polymer photodetectors; Lifetime; Bulk heterojunction

1. Introduction

Our information society has a seemingly insatiable need for microelectronic devices which are increasingly smaller and cheaper, while offering at the same time more functionality. This need spurred research for alternative processing methods for semiconductors. In particular, the novel field of organic semiconductors appears very promising for many applications: Compared to their inorganic counterparts, organic semiconductor materials and devices offer numerous desirable properties and technological advantages, i.e. their mechanical flexibility [3,4], the large area of the produced devices and systems, the simplicity of processing and, consequently, their low cost. Among the earliest and

* Corresponding author. Tel.: +41 44 497 1450; fax: +41 44 497 1400.
E-mail address: marc.ramuz@csem.ch (M. Ramuz).

1566-1199/$ - see front matter © 2008 Elsevier B.V. All rights reserved.
doi:10.1016/j.orgel.2008.01.007

potentially most significant devices that were studied are photovoltaic (PV) cells [5–7] and, more recently, organic photodetectors (oPDs) [8,9]. In contrast to oPDs, solar cells must have a high conversion efficiency over the entire solar spectrum, which reaches significantly into the near-IR. To date, there are no organic materials with acceptable quantum efficiencies in the IR, which explains why organic solar cells currently show power efficiencies of typically 5% [10,11]. Although PVs and PDs are in many ways similar devices, they nevertheless have to fulfill a different set of requirements. For PDs the spectral region of interest is often quite narrow, and the important parameters are the photocurrent and the dark current, where the dark current should only be a very small fraction of the photocurrent. The numerous synthesis possibilities to obtain new organic materials with tailored electro-optical properties provide a great diversity of photodetectors (PDs), adapted for each application. The possibility to use additive print technologies to deposit these materials opens the possibility to fabricate large area or/and specifically shaped PDs. Furthermore, oPDs can be easily monolithically integrated with other optical/electronic devices to form integrated systems with smart functionality [12].

One of the most interesting structures for oPDs is the bulk heterojunction [13,14], which can be achieved by mixing an electron donor and an electron acceptor in an appropriate solvent and subsequently spin-casting the resulting solution. Bulk heterojunctions have proven to be a very successful concept to overcome the short exciton diffusion length of organic semiconductors. However, this structure enhances the disorder and hampers collection of photogenerated charge carriers. Therefore, creating a bi-continuous and interpenetrating network between the donor and acceptor phase is of key importance. The use of high boiling point solvents and low spin speeds turned out to be a successful approach to increase the molecular order and thus the collection efficiency of charge carriers [15].

Despite the significant improvements reported in the last years, bulk heterojunction PDs still show limitations such as low response speed, comparatively high dark currents and rather low chemical stability. The latter often compromises the inherent simplicity of solution processing in that it enforces device fabrication to be carried out in inert atmosphere and a superior device encapsulation scheme.

In this paper, we show how to improve the performance and stability of P3HT:PCBM bulk heterojunction photodiodes by optimizing and simplifying their device structure. Systematic optimization in terms of EQE, on/off ratio and device stability resulted in polymer PDs with state-of-the-art EQE of 70% at 0 V, an improved dark current density <10 nA/cm^2 at -1 V and significantly increased lifetimes of above 3000 h.

2. Experimental details

In this work, polymer heterojunction photodiodes based on poly(3-hexylthiophene) (P3HT) as donor and [6,6]-phenyl-C61 butyric acid methyl ester (PCBM) as acceptor were investigated (Fig. 1). Regioregular head-to-tail coupled P3HT and PCBM were purchased from Merck Chemicals Ltd. and Nano-C Inc., respectively, and used without further purification.

The devices were fabricated and characterized under nitrogen atmosphere (< 5 ppm O_2, < 1 ppm H_2O). The device architecture and the energy band diagram [16] are illustrated in Fig. 2. The glass substrates with a 75 nm layer of indium tin oxide (ITO) were purchased from Thin Film Devices Inc.

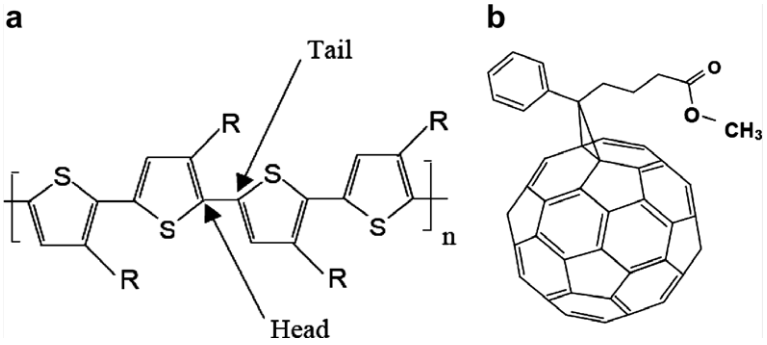

Fig. 1. Molecular structure of (a) P3HT and (b) PCBM.

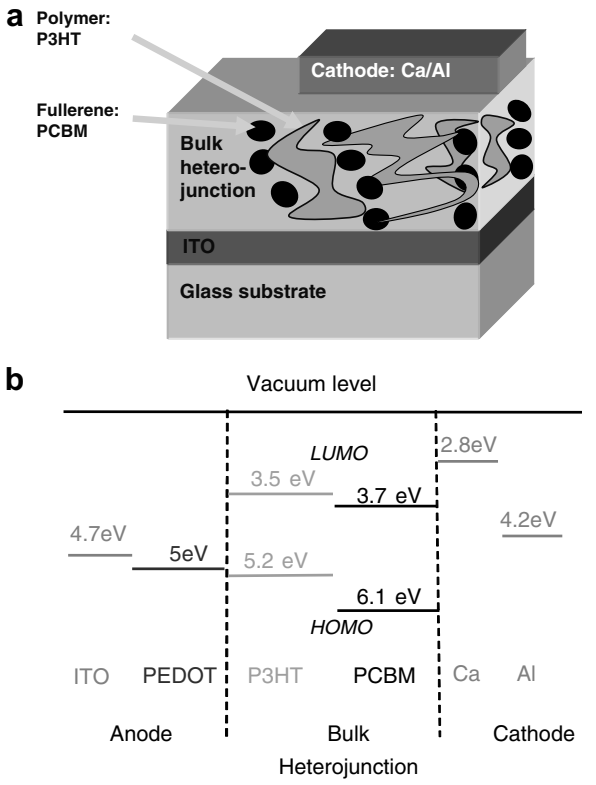

Fig. 2. (a) Schematic device architecture and (b) energy band diagram of the bulk heterojunction PD.

Careful substrate (i.e. ITO) cleaning turned out to be an important step for achieving a significant enhancement of device lifetime: First, the substrates were cleaned under a shower of deionized water (DIW), followed by a 10 min ultrasonic bath in DIW and another 10 min ultrasonic bath in acetone (purity $\geqslant$ 99%). Then the substrates were blow-dried with pure nitrogen and subject to an O_2 plasma (Oxford Plasmalab, 80 W, 20% partial pressure of O_2) for 2 min. A final ultrasonic bath in isopropanol (purity $\geqslant$ 99%) followed by blow-drying with pure nitrogen finished the cleaning cycle. For those devices that do include a PEDOT:PSS layer, a 60 nm thick film of BAYTRON P VP AI 4083 was spin-cast at 1500 rpm onto the ITO in a next step, followed by annealing at 180 °C for 15 min.

At this stage the substrates were transferred into the nitrogen glove-box system, where the deposition of the active organic blend was carried out. The two organic materials were dissolved in 1,2-dichlorobenzene (if not otherwise stated) at a concentration of 60 mg/ml, from which a 1:1 by weight (if not otherwise stated) blend was mixed. The solution was spin-cast onto the substrate at low spin speed (800 rpm) during 180 s, resulting in an organic active layer of 240 nm thickness. The choice of 1,2-dichlorobenzene as solvent and a low spin speed are known to favor self organization [15]. After drying the organic layer at 80 °C for 10 min, the metallic cathode – consisting of 3 nm calcium followed by an aluminum or silver capping layer of 50–70 nm thickness – was evaporated in a vacuum chamber. Pixel area is 2×2 mm^2.

I–V measurements were performed using a Hewlett-Packard 4145B semiconductor parameter analyzer. Inorganic blue light emitting diodes (Kingbright L7104QBC-D), with a peak wavelength at 468 nm, were used to illuminate the PDs with an intensity of typically 40 mW/cm^2 during the photocurrent measurements. The illuminated area is restricted to a beam diameter of 1 mm by an aperture.

The external quantum efficiency (EQE) versus wavelength was measured with an optical radiation measurement system from Optronic Laboratories Inc. For these measurements the PDs were backside encapsulated and taken out of the nitrogen glove-box system, where the EQE-versus-wavelength measurement was performed.

Operational lifetime measurements of the PDs were performed in a dedicated lifetime tester inside the N_2 glove-box under the following conditions:

(a) Continuous N_2 atmosphere (O_2 level <5 ppm, H_2O level <1 ppm)
(b) Temperature: $T_R = 22 \pm 1$ °C
(c) Continuous blue LED illumination Kingbright L7104QBC-D, $\lambda_{max} = 468$ nm, $\Delta\lambda_{FWHM} = 25$ nm) with 5 mW/cm^2
(d) Constant bias voltage $V = -1$ V
(e) The photocurrent I_{ph} was measured every 30 min.
(f) At the beginning and approximately every 500 h the lifetime test was interrupted for approximately 15 min, and the $I(V)$ characteristic of the PDs were measured inside the glove-box. From the $I(V)$ characteristic the On/Off ratio was determined at a bias voltage of $V = -1$ V.

3. Modeling

In order to increase the dynamic range of a PD, the on/off ratio has to be enhanced by reducing for instance the dark current. The simplest method

to realize this is to employ a thicker active layer. In the case of solution-processed PDs this can, for example, be achieved by increasing the concentration of the solution. We analyze the influence of the oPD's thickness on its EQE with the following simplified model, for which the oPD is assumed to consist of the active polymer layer of thickness d sandwiched between a transparent anode and a metallic cathode [17,18] (Fig. 3).

We assume normal incidence and a constant absorption coefficient α. In point A at a distance x from the mirror the electric field amplitude E of the electromagnetic radiation is given by

$$E = E_0 e^{-ikx}\left(e^{-\frac{\alpha}{2}(d-x)} + r \times e^{\frac{\alpha}{2}(d+x)} \times e^{i2kx}\right) \quad (1)$$

where $r = |r| \cdot e^{i\cdot\varphi_r}$ is the complex reflection coefficient of the metal cathode (mirror), $k = \frac{2\pi}{\lambda}n$ is the wave vector, λ denotes the wavelength and n the refractive index of the polymer blend. Assuming that the local absorption in the polymer semiconductor is proportional to the square of the absolute value of the electric field amplitude E, we obtain the following expression for the total absorbed power A in the polymer layer:

$$A \propto \int_0^d |E|^2 dx$$

$$A \propto |E_0|^2 \cdot \left[\frac{1}{\alpha}.(1-e^{-\alpha d}) \cdot (1 + |r|^2 e^{-\alpha d}) + |r| \frac{\lambda}{2\pi \cdot n} e^{-\alpha d} \cdot \left(\sin\left(\frac{4\pi.n}{\lambda} d + \varphi_r\right) - \sin\varphi_r\right)\right] \quad (2)$$

It follows from Eq. (2) that the total absorption oscillates with varying device thickness d with a period equal to $\frac{\lambda}{2n}$. If we assume that the fraction of absorbed photons that leads to charge carriers in the external circuit is independent of wavelength and polymer thickness, i.e. EQE $\propto A$, we can conclude that as a consequence of the interference effects in front of the metallic cathode the EQE also shows oscillations with varying thickness according to Eq. (2). From this equation the device thickness difference between two EQE maxima is calculated to $\Delta d = \frac{\lambda}{2n}$.

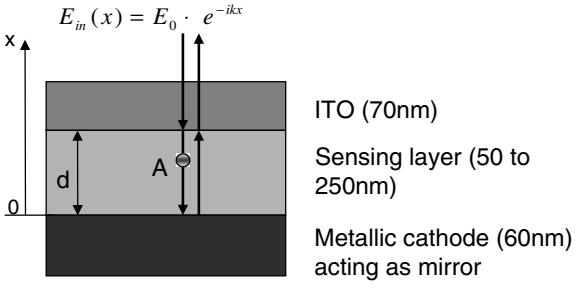

Fig. 3. Simple model of the interference effect in an oPD.

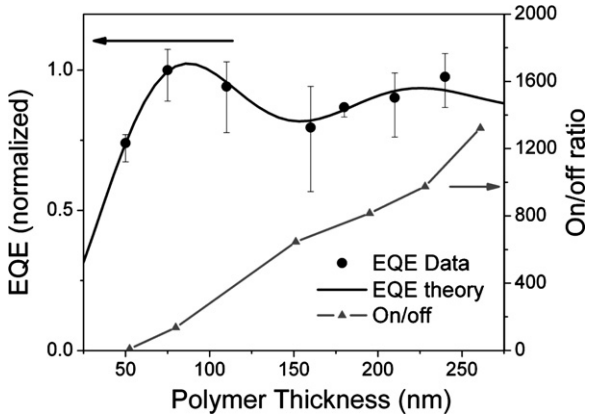

Fig. 4. EQE and on/off ratio, measured at –1 V and wavelength illumination of 468 nm, as a function of the thickness d of the active polymer layer. PD structure: ITO(70 nm)/PEDOT(60 nm)/PCBM:P3HT (1:1)/Ca(3 nm)/Ag(50 nm).

To validate the simple theory we have determined the EQE of a series of polymer PDs of varying active layer thickness d (PCBM:P3HT ratio of (1:1)). As seen from Fig. 4, Eq. (2) reproduces the main features of the experimental data. For the fit of Fig. 4 |r| was fixed at 1 – aluminum is highly reflecting in the visible –, n was set to 1.6 – a typical value for the polymers under consideration – and the absorption coefficient α was measured to be 10^5 cm^{-1} and agrees well with values from the literature [16]. That remaining two fit parameters are an overall proportionality factor E_0 and the phase shift φ_r. The fitted value for φ_r becomes 1.3 π.

As seen in Fig. 4, the EQE, measured at –1 V, exhibits maxima at around 70 nm and 240 nm active layer thicknesses. That means the photocurrent lonely decreased by 5%, however the dark current is reduced by a factor 10 between a 240 nm and 70 nm thick device, which can be seen from the on/off ratio plotted in Fig. 4. Thus one can strongly reduce the dark current by using a 240 nm thick active layer while at the same time sacrificing only a few percent of the device's external quantum efficiency.

4. Results and discussion

Up until now, the P3HT:PCBM bulk heterojunction has been carefully optimized mainly in view of

photovoltaic applications [19]. Thus, short circuit current, open-circuit voltage and fill factor have been in the center of attention. On the other hand, the specifications of a PD include the following different key figures: high sensitivity at the operating wavelength, low noise, low-operating voltage and high response speed. As with photovoltaic cells, reliability under the required operating conditions is a key factor in the case of photodiodes, too.

In the following, the systematic optimization of the P3HT:PCBM bulk heterojunction for photodiode applications in the visible part of spectrum are described. A blending ratio of (1:1) between P3HT:PCBM has been used. This ratio gives an improved balance of electron and hole mobilities [15].

4.1. Bulk optimization

The choice of the solvent used for the deposition process can influence the device performance in many ways, not least because it has a strong effect on the resulting (sub-)micrometer phase structure of the film. We have tested a variety of different solvents (including chloroform, xylene, chlorobenzene and 1,2-dichlorobenzene) we found that 1,2-dichlorobenzene yields devices with the best performance. Fig. 5 compares the EQE of devices processed from chlorobenzene and 1,2-dichlorobenzene. The EQE of PDs processed from 1,2-dichlorobenzene is about 10% larger than the one of equivalent devices processed from chlorobenzene. Furthermore, the solubility of P3HT and PCBM is highest in 1,2-dichlorobenzene; solutions of up to 60 mg/ml at room temperature can be prepared. This solution allows one to achieve thicker films from 1,2-dichlorobenzene than from any other solvent tested in this study. The targeted 240 nm active layer thickness was thus most easily achieved from 1,2-dichlorobenzene, which is another reason why 1,2-dichlorobenzene was the solvent of choice. The increased EQE of devices fabricated from 1,2-dichlorobenzene solutions can be rationalized by improved charge separation and transport properties of the interpenetrating network that forms during the deposition process. The larger boiling point of 1,2-dichlorobenzene (180 °C) than e.g. the one of chlorobenzene (131 °C) and the concomitant lower evaporation rate leaves the system more time for structural ordering during the drying process, leading to a higher degree of self organization and thus improved charge transport properties [15].

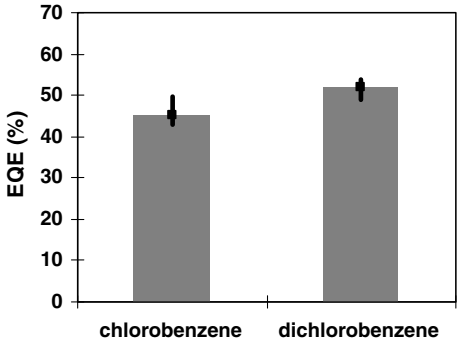

Fig. 5. Influence of the solvent on the EQE. PD structure: ITO(70 nm)/PEDOT(60 nm)/PCBM:P3HT (1:1, 80 nm)/Ca(3 nm)/Ag(50 nm).

Fig. 6a shows an I–V curve of an optimized photodiode of the following device structure: ITO(70 nm) / PEDOT (50 nm)/PCBM:P3HT (1:1, 240 nm)/Ca(3 nm)/Al(60 nm). The on/off ratio and the corresponding dark currents are 3×10^4 and 300 nA/cm^2, respectively, both measured at a

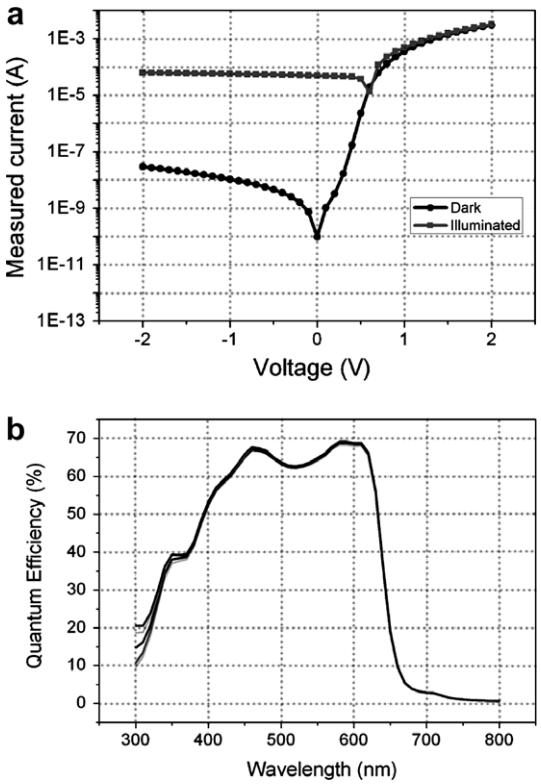

Fig. 6. (a) $I(V)$ characteristics of a 2×2 mm^2 PD measured in the dark and under (40 mW/cm^2) illumination at 468 nm. (b) EQE at 0 V as a function of wavelength. Curves of seven different pixels on one device are plotted. PD structure: ITO(70 nm)/PEDOT(60 nm)/PCBM:P3HT (1:1, 240 nm)/Ca(3 nm)/Ag(50 nm).

reverse bias of –1 V. Note that the illuminating beam has a diameter of 1 mm, while the pixel area is $2 \times 2\,mm^2$. So the on/off ratio measured on the *I–V* characteristic has to be multiply by a factor of 5. The EQE of our devices is above 60% for a wide range of the optical spectrum as seen in Fig. 6b.

4.2. Frequency response

Fig. 7 shows the frequency response of one of our photodiodes, measured by illuminating the device with a pulsed blue LED (468 nm, 6 μW) and acquiring the resulting photocurrent with a lock-in amplifier. At 0 V applied bias the 3 dB attenuation of the response occurs at a frequency of $f_{3dB} = 62$ kHz. For higher frequencies the photocurrent rolls off as $\frac{1}{f^2}$. Although f_{3dB} increases with increasing reverse bias (data not shown), the values for the P3HT:PCBM heterojunctions are more than three orders of magnitudes smaller than the ones of optimized small molecule photodiodes [20]. Further device optimization and different driving schemes (e.g. under strong reverse bias) will lead to a somewhat improved response speed of P3HT:PCBM diodes, nevertheless these devices will be limited to applications requiring modest response frequencies of <1 MHz.

4.3. Anode optimization

In many organic optoelectronic devices – organic light-emitting diodes or photovoltaic cells, for example – a doped hole injection layer is inserted between the transparent anode and the active layer. Apart from serving as a planarization layer, the main function of this layer is to ensure an energetic match of the anode work function and the lowest occupied molecular orbital of the active layer and by this it promotes hole injection from the anode into the active layer under forward bias conditions (see energy diagram in Fig. 2b). As opposed to light-emitting diodes or photovoltaic cells, a photodiode is operated under reverse bias conditions, i.e. holes and electrons are collected by – rather than injected at – the anode and the cathode, respectively.

Fig. 8 shows an *I*(*V*) characteristic of P3HT:PCBM heterojunction photodiodes without PEDOT:PSS hole-injection layer. We find that omitting the standard PEDOT:PSS layer does not adversely affect the photocurrent under reverse bias. Without a PEDOT:PSS layer, the built-in electric field is too weak to fully extract photogenerated charges if no bias is applied. As can be seen from Fig. 8 the photocurrent at 0 V is $2{,}6 \times 10^{-5}$ A in contrast to 4×10^{-5} A at –1 V. A negative bias is required to maintain a large photocurrent collection efficiency which results in an higher EQE.

It should be noted, that PEDOT:PSS-free structures are not favorable for solar cell applications, since the open circuit voltage, the current at 0 V, and the fill factor are resulting in a low power efficiency. On the other hand, photodiodes are normally operated at a trade-off reverse bias, which ensures good quantum efficiency while still keeping the dark current low.

However, the PEDOT:PSS-free photodetector devices show a considerable improvement in on/off ratio (see Fig. 8) of almost two orders of magnitude

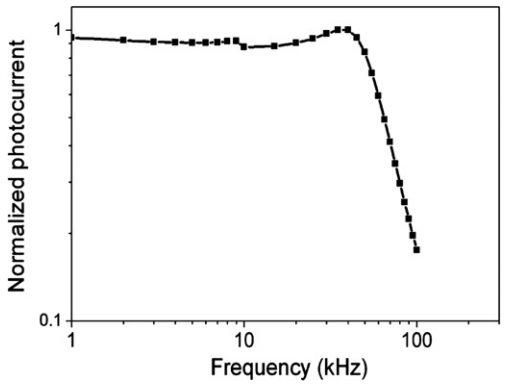

Fig. 7. Frequency response of a P3HT:PCBM bulk heterojunction photodiode without applied voltage and wavelength illumination of 468 nm. PD structure is ITO/PEDOT:PSS (60 nm)/PCBM:P3HT (1:1, 240 nm)/Ca(3 nm)/Ag(50 nm).

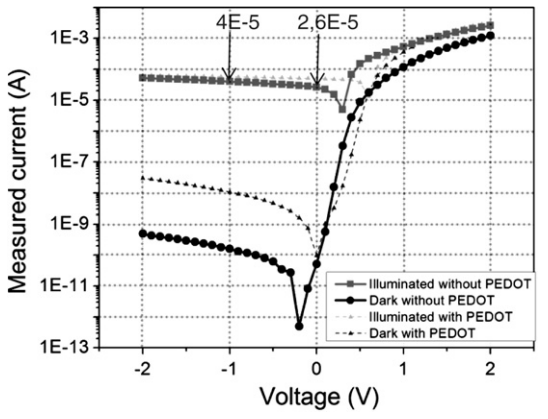

Fig. 8. *I*(*V*) characteristics of a $2 \times 2\,mm^2$ PD fabricated according to our process without PEDOT layer measured in the dark and under ($40\,mW/cm^2$) illumination at 468 nm. PD structure: ITO(70 nm)/PCBM:P3HT (1:1, 240 nm)/Ca(3 nm)/Al(60 nm).

with a ratio value of 9×10^5 measured at –1 V. This improvement is related to the reduction of the dark current, which is as low as 10 nA/cm^2 in the PEDOT:PSS-free devices. The unfavorable quality and/or the weak stability of the PEDOT:PSS/ITO interface is a possible explanation for the reduction of the dark current when no PEDOT:PSS is used. This layer is known to etch the ITO [21], resulting in ionic dopants generation that can migrate to the active layer.

4.4. Detector noise

To quantify the detector noise, a good figure of merit to use is the noise equivalent power (NEP) [22]. The NEP is defined as the minimum incident power required in order to generate a photocurrent equal to the noise current of the photodetector at a specified frequency (f), and within a specific bandwidth (B). The NEP for a detector is calculated by the following formula:

$$\mathrm{NEP} = \frac{I_\mathrm{N}}{\Re(\lambda)} \tag{3}$$

where I_N is the noise current in A/Hz$^{1/2}$ and $\Re$ is the responsivity equal to 0.25 A/W at the wavelength of 468 nm. The NEP given in Eq. (3) is in units of Watts/Hz$^{1/2}$. Since the power to current conversion of a diode depends on the wavelength, the NEP is always quoted at a particular wavelength. For a reverse biased photodiode the shot noise is the dominant component and the thermal noise contribution can be neglected. The shot noise for the dark current is defined by [22]:

$$I_\mathrm{s} = \sqrt{2ei_\mathrm{D}B} \tag{4}$$

where e is the unit charge (1.6×10^{-19} coulombs), i_D the dark leakage current and B the bandwidth.

With typical values of our diodes ($i_\mathrm{D} = 1.6 \times 10^{-10}$ A and $B = 1$ Hz) a shot noise current of 7.16×10^{-15} A/Hz$^{1/2}$ is obtained, which translates into a dark current NEP of 2.8×10^{-14} W/Hz$^{1/2}$ for our device area $A = 2 \times 2$ mm^2. For comparison with detectors of different area, we introduce the specific detectivity parameter defined by

$$D^* = \frac{\sqrt{A}}{\mathrm{NEP}} \tag{5}$$

where D^* is the specific detectivity (cm $\times$ Hz$^{1/2}$/W^{-1}) and A the surface area (0.04 cm^2).

A high D^* indicates the ability to detect lower levels of radiant power. This factor produces a figure of merit which is area independent. We obtain a specific detectivity of 7×10^{12} cm $\times$ Hz$^{1/2}$/W for our organic photodiode, which is comparable to a common inorganic silicon photodiode like for instance a Hamamatsu S2551 with a specific detectivity of 1.5×10^{13} cm $\times$ Hz$^{1/2}$/W.

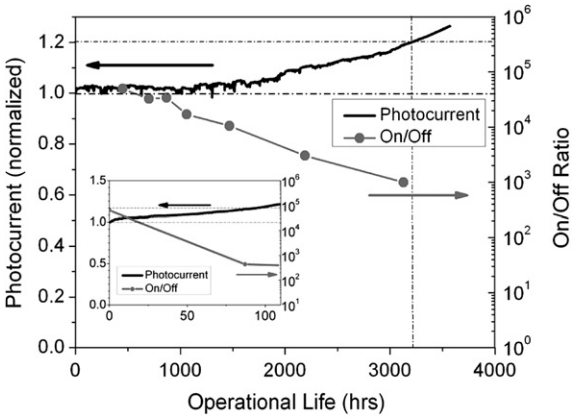

Fig. 9. Stability of the PDs without PEDOT:PSS layer. The normalized photocurrent, measured at –1 V and wavelength illumination of 468 nm, is plotted as a function of operating time at room temperature in N_2 atmosphere. The on/off ratio of the device is also displayed (right axis). PD structure: ITO(70 nm)/PCBM:P3HT (1:1, 240 nm)/Ca(3 nm)/Al(60 nm). Inset: Equivalent stability measurement for a device with PEDOT:PSS layer. PD structure for the device shown in the inset: ITO (70 nm)/PEDOT:PSS (60 nm)/PCBM:P3HT (1:1, 240 nm)/Ca(3 nm)/Al(60 nm).

4.5. Lifetime

As just described, a main advantage of the PEDOT:PSS-free devices is their reduced dark current. However, an equally important aspect of omitting the PEDOT:PSS layer is our finding that the operational lifetime of the photodiodes is considerably increased in devices without a PEDOT:PSS layer. In Fig. 9 the normalized photocurrent, measured at –1 V, of a PEDOT:PSS-free diode is plotted as a function of operating hours. The photocurrent is stable for more than 1500 h. After approximately 1800 h the photocurrent starts to increase gradually. (This rise of the photocurrent is currently not understood and is subject of further investigations). The on/off ratio decreases monotonically but is larger than 10^3 over the entire measuring period of 3000 h (four months). When comparing this with the inset of Fig. 9, which shows similar operational lifetime measurements performed on a photodiode with a PEDOT:PSS layer, it is evident that omitting

the PEDOT:PSS is largely beneficial to the device's operational lifetime [9].

It is clear from the above that the absence of PEDOT:PSS layer does not reduce the quantum efficiency of the photodiodes when we applied negative voltage. Moreover in this configuration the dark current level is drastically reduced and the lifetime increased.

5. Conclusions

In conclusion, we have optimized the P3HT:PCBM bulk heterojunction diode in terms of its photodiode (rather than photovoltaic cell) performance. We have shown that while increasing the thickness of the active layer from 70 nm to 240 nm does not significantly alter the photodiode's quantum efficiency, it results in a 10-fold decrease of the dark current. By omitting the PEDOT:PSS layer the dark current has been reduced by factor of ~100. Furthermore device lifetimes were considerable increased by omitting the PEDOT:PSS layer, too. In return, a negative voltage has to be applied to maintain the EQE high. Overall, solution-processed organic photodiodes with state-of-the-art EQE of between 60 and 70% over a wide range of the visible part of the spectrum, dark current densities below 10 nA/cm^2 at –1 V, specific detectivities of 7×10^{12} cm $\times$ $Hz^{1/2}/W$, and lifetimes above 3000 h have been demonstrated.

References

[1] F. Padinger, R.S. Rittberber, N.S. Sariciftci, Effects of postproduction treatment on plastic solar cells, Advanced Functional Materials 13 (2003) 1.
[2] P. Schilinsky, C. Waldauf, C.J. Brabec, Recombination loss analysis in polythiophene based bulk heterojunction photodetectors, Applied Physics Letters 81 (20) (2002) 3885.
[3] G. Gustafsson, Y. Cao, G.M. Treacy, F. Klavetter, N. Colaneri, A.J. Heeger, Flexible light-emitting diodes made from soluble conducting polymers, Nature 357 (1992) 477.
[4] C. Brabec, F. Padinger, J.C. Hummelen, R.A.J. Janssen, N.S. Sariciftci, Realization of a large area flexible fullerene – conjugated polymer photocells: a route to plastic solar cells, Synthetic Metals 102 (1999) 861.
[5] A.K. Ghosh, T. Feng, Merocyanine organic solar cells, Journal Applied Physics 49 (12) (1978) 5982.
[6] B. O'Regan, M. Grätzel, A low-cost high-efficiency solar cell based on dye-sensitized colloidal TiO_2 films, Nature 353 (1991) 737.
[7] S.R. Forrest, The limits to organic photovoltaic cell efficiency, Materials Research Society 30 (2005) 28.
[8] P. Peumans, A. Yakimov, S.R. Forrest, Small molecular weight organic thin-film photodetectors and solar cells, Journal of Applied Physics 93 (2003) 3693.
[9] P. Schilinsky, C. Waldauf, J. Hauch, C.J. Brabec, Polymer photovoltaic detectors: progress and recent developments, Thin Solid Films 451–452 (2004) 105.
[10] W. Ma, C. Yang, X. Gong, K. Lee, A.J. Heeger, Thermally stable, efficient polymer solar cells with nanoscale control of the interpenetrating network morphology, Advanced Functional Materials 15 (2005) 1617.
[11] B.P. Rand, J. Li, J. Xue, R.J. Holmes, M.E. Thompson, S.R. Forrest, Organic double-heterostructure photovoltaic cells employing thick tris(acetylacetonato)ruthenuim(iii) exciton-blocking layers, Advanced Functional Materials 17 (2005) 2714.
[12] Lukas Bürgi, Reto Pfeiffer, Mario Mücklich, Peter Metzler, Michael Kiy, Carsten Winnewisser, Optical proximity and touch sensors based on monolithically integrated polymer photodiodes and polymer LEDs, Organic Electronics 7 (2006) 114.
[13] G. Yu, J. Gao, J.C. Hummelen, F. Wudl, A.J. Heeger, Polymer photovoltaic cells: enhanced efficiencies via a network of internal donor–acceptor heterojunctions, Science 270 (1995) 5243.
[14] J.J.M. Halls, C.A. Walsh, N.C. Greenham, E.A. Marseglia, R.H. Friend, S.C. Moratti, A.B. Holmes, Efficient photodiodes from interpenetrating polymer networks, Nature 376 (1995) 498.
[15] J. Huang, G. Li, Y. Yang, Influence of composition and heat traitment on the vharge transport properties of poly(3-hexylthiophene) and [6,6]-phenyl c61-butiric acid methyl ester blends, Applied Physic Letters 87 (2005) 112105.
[16] S. Sensfuss, M. Al-Ibrahim, A. Konkin, G. Nazmutdinova, U. Zhokhavets, G. Gobsch, D.A.M. Egbe, E. Klemm, H.-K. Roth, Characterisation of potentiel donor acceptor pairs for polymer solar cells by ESR, optical and electrochemical investigations, Proceedings of SPIE 5215 (2004) 129.
[17] L.A.A. Pettersson, L.S. Roman, O. Inganäs, Modeling photocurrent action spectra of photovoltaic devices based on organic thin films, Journal of Applied Physics 86 (1) (1999) 487.
[18] H. Hoppe, N. Arnold, D. Meissner, N.S. Sariciftci, Modeling of optical absorption in conjugated polymer/fullerene bulk-heterojunctiom plastic solar cells, Thin Solid Films 451 (2004) 590.
[19] P. Schilinsky, C. Waldauf, C.J. Brabec, Performance analysis of printed bulk heterojunction solar cells, Advanced Function Material 16 (2006) 1669.
[20] P. Peumans, V. Bulović, S.R. Forrest, Efficient, high-bandwidth organic multilayer photodetectors, Applied Physics Letters 76 (2000) 3855.
[21] M.P. de Jong, L.J. Ijzendoorn, M.J.A. de Voigt, Stability of the interface between indium–tin–oxide and poly(3,4-ethylenedioxythiophene)/poly(styrene-sulfonate) in polymer light-emitting diodes, Applied Physics Letters 77 (2000) 2255.
[22] S.M. Sze, Physics of Semiconductor Devices, second ed., Wiley-Interscience Publication, 1981.

Available online at www.sciencedirect.com
ScienceDirect
Organic Electronics 9 (2008) 377–384
Organic Electronics
www.elsevier.com/locate/orgel

Non-radiative decay mechanisms in blue phosphorescent iridium(III) complexes

Ruth E. Harding [a], Shih-Chun Lo [b], Paul L. Burn [b,c,*], Ifor D.W. Samuel [a,*]

[a] Organic Semiconductor Centre, School of Physics and Astronomy, University of St. Andrews, St. Andrews, North Haugh, Fife KY16 9SS, UK
[b] Department of Chemistry, University of Oxford, Chemistry Research Laboratory, Mansfield Road, Oxford OX1 3TA, UK
[c] Centre for Organic Photonics and Electronics, School of Molecular and Microbial Sciences, University of Queensland, Queensland 4072, Australia

Received 11 November 2007; received in revised form 27 January 2008; accepted 30 January 2008
Available online 9 February 2008

Abstract

By using phosphorescent emitters, organic light emitting displays can be up to four times more efficient than those of fluorescent materials. Full colour displays based on phosphorescent materials have not been achieved thus far due to the poor efficiency of blue phosphorescent emitters. We show that there is a correlation between non-radiative decay of phosphorescence and vibrational coupling for related blue emissive materials containing similar iridium(III) complex chromophores. The materials had solution photoluminescence quantum yields (PLQYs) of up to 55% at room temperature with Commission Internationale de l'Eclairage co-ordinates of (0.155, 0.16). Stronger vibrational coupling was found to lead to an increased non-radiative decay rate and decreased PLQY. The activation energy for non-radiative decay was found to depend on the environment with the non-radiative decay rate being decreased when the emissive materials were placed in a solid host.

PACS: 78.55.Kz

Keywords: Phosphorescent; Vibrational coupling; Blue; Non-radiative decay; Dendrimers

1. Introduction

By using phosphorescent emitters, displays based on organic light-emitting diodes can potentially have an internal quantum efficiency of unity, since both singlet and triplet excitations are utilised, rather than fluorescent materials where only singlet excitations are emissive [1]. The higher efficiency available to phosphorescent emitters increases their attractiveness to a wide market and in particular mobile applications and lighting. For full colour displays saturated red, green, and blue emitters are required. Efficient red and green phosphorescent materials based on iridium(III) complexes have been made. However, rapid non-radiative decay is generally

* Corresponding authors. Address: Organic Semiconductor Centre, School of Physics and Astronomy, University of St. Andrews, St. Andrews, North Haugh, Fife KY16 9SS, UK. Tel.: +61 7 3346 7614; fax: +61 7 3346 9273 (P.L. Burn), tel.: +44 01334 463114; fax: +44 01334 463104 (I.D.W. Samuel).
E-mail addresses: p.burn2@uq.edu.au (P.L. Burn), idws@st-andrews.ac.uk (I.D.W. Samuel).

1566-1199/$ - see front matter © 2008 Elsevier B.V. All rights reserved.
doi:10.1016/j.orgel.2008.01.009

observed for deep or saturated blue phosphorescent materials [2–4], hindering efforts to make full colour organic displays based only on phosphorescent emitters.

The purpose of this article is to provide insight into the non-radiative decay mechanisms that occur in blue emissive iridium(III) complexes based on *fac*-tris(1-methyl-5-phenyl-3-propyl-[1,2,4]triazolyl)-iridium(III) (TrzPhIr) [5], one of very few blue phosphorescent materials that emit with solution CIE as low as (0.16, 0.20) at room temperature, and an alternative to carbene based ligands [2]. Understanding the non-radiative decay process is the first step in enabling efficient deep blue phosphorescent materials to be designed. In this paper, we further investigate the luminescence properties of the TrzPhIr complexes. We report the effect of dendronisation on the photophysical properties of the blue emissive monofluorinated complex **1** comparing the effect of the addition of biphenyl dendrons (**2**, **3**) [6–8], as well as the attachment of different numbers of fluorine atoms (**4**, **5**, and **6**) (Fig. 1) to improve the understanding of the non-radiative decay mechanisms in blue phosphorescent iridium(III) complexes. We show that the PLQY varies with vibrational coupling (Huang-Rhys factor) for **1**, **2**, and **3**. We study the effect of the environment (solution versus solid-state) on the phosphorescence

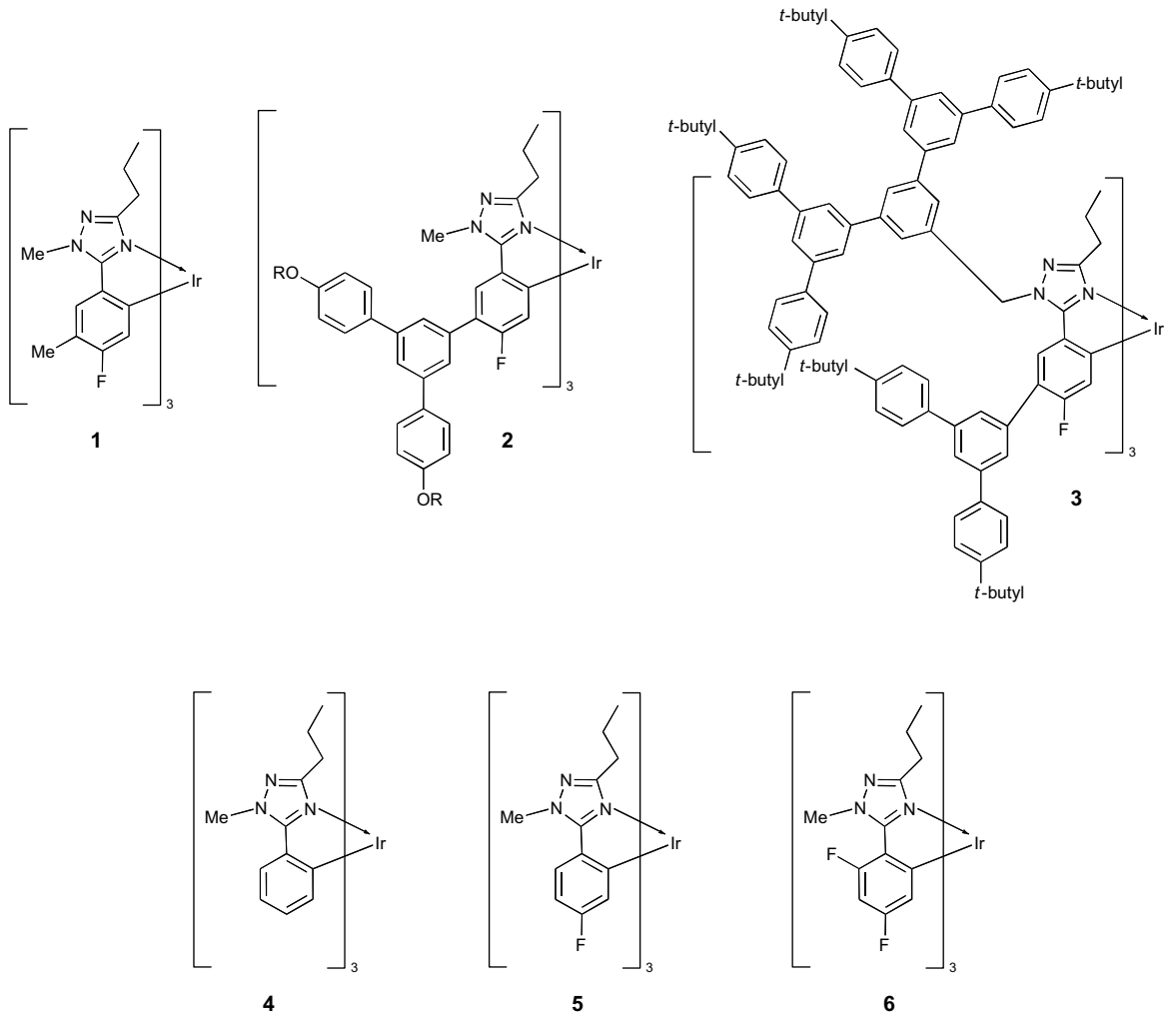

Fig. 1. Structures of the materials studied: **1** mono-fluorinated complex, **2** first generation mono-dendronised (one dendron per ligand) dendrimer with biphenyl based dendrons and R = 2-ethylhexyl, and **3** first/second generation doubly-dendronised (two dendrons per ligand) dendrimer with biphenyl based dendrons and *t*-butyl surface groups. **4–6** a family of fac-tris(phenyltriazolyl)iridium(III) complexes with different degrees of fluorination.

of **4**, **5**, and **6**, and discuss the implications for making highly efficient deep blue phosphorescent materials.

2. Experimental

For room temperature solution measurements, samples were dissolved in spectroscopic grade toluene in quartz degassing cuvettes, degassed by three freeze–pump–thaw cycles, sealed under vacuum, and warmed to room temperature in a bath of tepid water. The optical density (OD) of the samples and standard were similar and small ($\leqslant$0.1 at $\geqslant$360 nm). For low temperature solution measurements, sample preparation was identical except that spectroscopic grade anhydrous 2-methyltetrahydrofuran was used as the solvent and larger quartz degassing cuvettes were used. For room temperature and low temperature film measurements, poly(methylmethacrylate) (PMMA) was dissolved for 24 h in chlorobenzene solution at a concentration of 100 mg/ml using a magnetic stirrer, 6 wt% of the sample was then added and dissolved for 10 min prior to spin coating on a clean fused silica disc at a speed of approximately 1000 rpm for 60 s. Photoluminescence spectra were recorded using a Jobin Yvon Fluoromax 2 fluorimeter, set to a band pass of 1 nm for both excitation and detection. The excitation wavelength was 360 nm, and spectra were corrected for the instrumental response. PLQYs were measured by a relative method using quinine sulfate in 0.5 M sulphuric acid as a standard [9]. The error in this method is estimated to be approximately 10%.

Photoluminescence transient decays were measured by a time-correlated single-photon counting (TCSPC) system. Excitation was at 393 nm by a pulsed nitride diode laser (Picoquant LDH 400) giving 10 pJ/pulse at a pulse repetition rate of 100 kHz, focussed onto the sample to a spot size of 300 μm by 120 μm. The emitted light was dispersed in a monochromator with an entrance slit and detected with a cooled Hamamatsu micro-channel plate photomultiplier tube RU-3809 U-50. The average number of photons collected per pulse was 0.05 or less. The apparatus response function was $\approx$0.5 ns (FWHM) in the shortest time window. The measured lifetime was obtained by fitting a single exponential decay to the measured transient for solution measurements or a two exponential decay for film measurements. For optical measurements below room temperature, the sealed quartz cuvettes or films were placed in an Oxford instruments "DN" cryostat with fused silica windows. The sample was cooled by liquid nitrogen or cold nitrogen gas. The temperature inside the sample chamber was adjusted by a combination of manually adjusting the nitrogen flow rate and heating the sample chamber with a heater, controlled by an Oxford instruments intelligent temperature controller, so that a stable temperature was obtained. A period of 30 min was left before each measurement to allow the sample to come to thermal equilibrium with the sample chamber. Fourier transform Raman spectra were measured on powder samples using a Perkin–Elmer system 2000 spectrometer with excitation at 8000 cm^{-1}.

3. Results and discussion

The first part of this study involved determining the effect of dendrons on the emissive properties of the chromophore. The room temperature solution photoluminescence (PL) spectra of **1**, singly dendronised **2** and doubly dendronised **3** complexes are shown in Fig. 2. It can be seen that the energy corresponding to the 0–0 transition is very close at 2.84 eV for **1**, 2.82 eV for **2**, and 2.81 eV for **3**, showing that the position and structure of the dendrons is such that they do not extend the conjugation length of the ligand. Hence the emissive core is essentially the same for **1**–**3**. However, there is a different degree of vibrational coupling seen in the spectra from the relative height of the peaks at $\sim$2.82 eV and $\sim$2.65 eV (the 0–0 and 0–1 transition), respectively. The degree of vibrational coupling is often

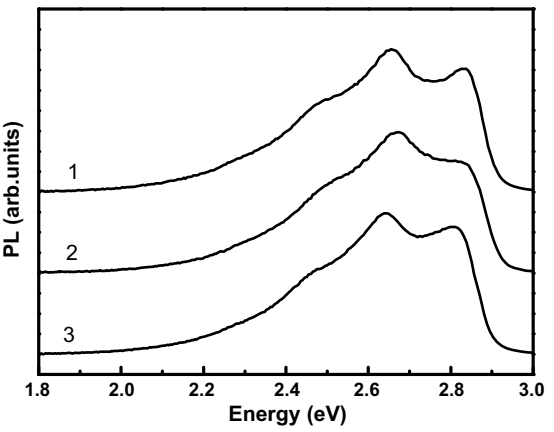

Fig. 2. PL spectra at room temperature of mono **2** and doubly **3** dendronised materials and the parent chromophore **1**. Spectra are displaced vertically for clarity.

quantified by the Huang-Rhys 'S' factor, which can be estimated by measuring the height of the 0–1 peak (~2.65 eV) divided by the height of the 0–0 peak (~2.82 eV) [10] if the width of the two peaks are the same, which applies for the single mode approximation. In this case however, the 0–0 peak is in fact narrower than the 0–1 peak which reflects the fact that more than one mode is present. Hence the actual Huang-Rhys factor will be higher than estimated by this single mode approximation, but it is nevertheless sufficient for identifying trends in these materials since the emissive core is nearly identical and therefore the vibrational modes which couple to the optical transition will be very similar. The peak to peak energy between 0–0 and 0–1, taken as the energy of the single dominant mode, is 1350 cm^{-1}. In the Raman data of **1** the dominant peaks were seen at 1457, 1536 and 1596 cm^{-1} but smaller peaks were also seen at 662 cm^{-1}, 864–865 cm^{-1} (doublet), whilst several small peaks were seen around 1082 cm^{-1} and around 1273 cm^{-1}, there is also a series of very small peaks between 179 and 454 cm^{-1}. The PL 0–0 peak to 0–1 peak energy of 1350 cm^{-1} should be a convolution of those modes which contribute to the PL spectrum, of which the dominant modes of the Raman spectrum at 1457, 1536 and 1596 cm^{-1} are likely to involve C–C stretches due to their similar energies to those modes of $Ru(bpy)_3^{2+}$ at 1450, 1563 and 1608 cm^{-1} [11].

In conjunction with PLQY, lifetime measurements are usually very useful for getting information about the excited states of molecules. Fig. 3 shows the PL decay of degassed solutions of **1**–**3** and Table 1 gives the solution PLQY and fitted solution lifetime values for **1**, **2**, and **3** along with the calculated radiative and non-radiative decay rates. The lifetime for the dendrimers, **2** and **3** is much longer than for the core molecule, **1**, and the PLQY of the dendrimer **3** is higher than that of **1** whilst the PLQY of **2** is lower than that of **1**. The meta linkage of the dendrons means that there is not electron delocalisation from the core to the dendrons, so, the chromophores of **1**–**3** are very similar,

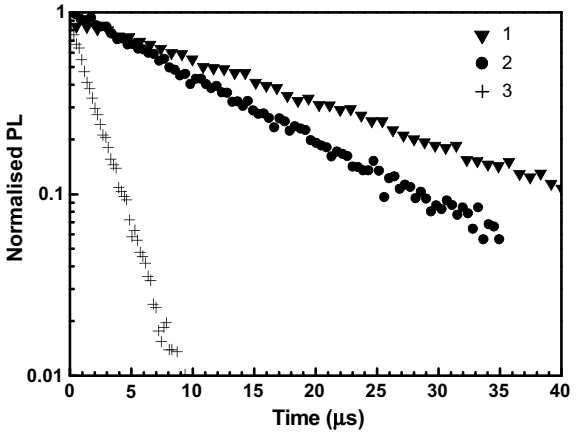

Fig. 3. Photoluminescence intensity as a function of time for complex **1**, **2**, **3** in solution at room temperature.

as confirmed by their very similar emission energy. They are therefore expected to have the same radiative decay rate. However the dendrimers have much longer lifetime and lower radiative and non-radiative decay rates. The increase in measured lifetime in the dendrimers, with respect to the core molecule, is caused by reversible energy transfer from the triplet level of the core to the triplet level of the dendrons. This is similar to the delayed phosphorescence observed for a FIrpic:CBP blend film [12]. We do not observe any PL spectral component attributed to the dendrons therefore the radiative decay rate associated with a triplet on the dendron is negligible. The PLQY of **3** is higher than that of **1**, suggesting that non-radiative decay on the dendrons of **3** is small compared to that of the core. The dendrons are very similar in both **2** and **3**, and so weak non-radiative decay on the dendrons is also expected for **2**. The dendrons simply act as a reservoir for excitations, with the efficiency of the PL determined by the core. The core and the dendrons have separate excited triplet states and can be treated as distinct. We can then associate a radiative and non-radiative decay of the emissive core in the dendrimer, but these differ from the measured rates for the dendrimers. The long lifetimes of

Table 1
PLQYs (%) and the Huang-Rhys factor estimated from the height of the 0–1 peak (~2.65 eV or ~465 nm) divided by the height of the 0–0 peak (~2.82 eV or ~438 nm) for complexes **1**–**3** (see Fig. 2) in degassed MeTHF solution at room temperature

Complex	PLQYs (%)	Lifetime (μs)	Radiative decay rate (10^5 s^{-1})	Non-radiative decay rate (10^5 s^{-1})	Oxidation potential (eV)	HOMO level (eV)	Estimated Huang-Rhys factor
1	40	1.25	3.2	4.8	0.41	5.79	1.16
2	26	19.9	0.13	0.50	0.54	5.92	1.26
3	55	11.6	0.47	0.39	0.58	5.96	1.11

the dendrimers are due to the dendrons acting as reservoirs for excitations.

Out of the series of molecules, the doubly dendronised **3** has the highest PLQY (55%) and lowest Huang-Rhys factor (vibrational coupling), while **2** has the lowest PLQY and the largest Huang-Rhys factor. Thus we observe an inverse correlation between vibrational coupling and PLQY for a series of molecules with the same emissive core. We expect that the radiative decay rates of the cores are the same in all three complexes since the structure of the core is the same for **1**–**3**. In a study of Ir molecules with the same core but different substituents, a correlation was found between the HOMO level and the radiative decay rate [13]. Effectively a correlation was also found by Li et al. between the HOMO level and the radiative decay rate [4]. In our case, we have the same core with different dendrimers substituted, however only a small variation in HOMO level was found from 5.79 to 5.96 eV for **1**–**3** (Table 1). We compare this with Li et al. where a variation of 0.14 V in oxidation potentials between compounds **1** and **2** led to a difference of the radiative decay rate of $2.7–2.0 \times 10^{-5}\ s^{-1}$. In our case we have a variation of 0.17 V in oxidation potential between **1** and **3** so the radiative decay rates of the emissive cores are not expected to by more than 40% and which, if the non-radiative decay rate was constant would lead to an increase in PLQY by only 20% rather than the 37.5% increase observed between **1** and **3**.

A room temperature solution PLQY of 55% for doubly dendronised complex **3** with CIE co-ordinates of (0.16, 0.16) with PL peaks at 441 and 469 nm (2.81 and 2.64 eV) compares favourably to Yang et al.'s 50% PLQY for their material with PL peaks at 450 and 479 nm [14].

Since the core chromophores of **1**–**3** are expected to have a similar radiative decay rate and we therefore attribute the differences in PLQY in this family of materials to the difference in non-radiative decay rate of the emissive core. Based on previous reports the differences in non-radiative decay rate could either arise from the presence of higher excited state d-orbitals [15] or increased vibrational decay [16]. Given the similar nature of the emissive chromophores of **1**, **2**, and **3** the ligand field strength should be the same for all three complexes. Thus the energy difference between a higher energy d-orbital and the emissive excited state should be the same for all three complexes and hence such an orbital could not account for the differencess in PLQY. The fact that metal d-orbitals are not directly the cause of the non-radiative decay is strengthened by molecular orbital calculations which show that related complexes with C_3 symmetry do not have higher energy empty molecular orbitals with predominantly d-character [5]. Therefore, the difference in PLQY should arise from vibrational decay.

Vibrational non-radiative decay from the radiative excited state is caused by coupling of vibronic states of the excited state potential energy surface to isoenergetic levels of the ground state. An increase in vibronic coupling as measured by the Huang-Rhys factor results in higher vibrational non-radiative decay. This is because the transition probability is increased by an increased overlap between initial and final states, caused by an increased displacement between the potential surfaces and the Huang-Rhys factor is proportional to the square of the displacement [17]. For **1**, **2**, and **3,** we see an inverse correlation between Huang-Rhys factor and PLQY (Table 1), that is, the PLQY increases with a decrease in the Huang-Rhys. This indicates that a decrease in vibrational coupling leads to a decrease in the non-radiative decay from the radiative excited state. Thus changes in vibronic coupling account for the differences in PLQY (see Table 1).

In the second part of this study, the effect of changing the host material on the photophysics of triazole complexes is investigated. PL lifetimes of complexes **4**, **5**, and **6** were measured in 2-methyltetrahydrofuran (MeTHF) [5] and as guests in poly(methylmethacrylate) (PMMA). We find that the difference in PLQY of the three complexes arises, as is the case for **1**, **2**, and **3**, from differences in the non-radiative decay rate caused by differences in vibrational coupling. Table 2 summarises the fitted PL lifetimes and estimated Huang-Rhys factors for the non-fluorinated **4**, mono-fluorinated **5** and di-fluorinated **6** iridium(III) complexes in solution and PMMA host at room temperature. Fig. 5 shows the PL decays for **6** in the solution at room temperature, at 77 K and in the solid host at room temperature. A bi-exponential decay was found for all molecules in the solid host. We can rule out triplet-triplet annihilation as the explanation of the fast decay component because it is expected to occur only above an excitation density of $2 \times 10^{17}\ cm^{-3}$ [18], compared to our excitation density of $\sim 5 \times 10^{16}\ cm^{-3}$. Since the radiative decay rate depends on overlap between the excited and ground state wavefunctions, we expect that the radiative

Table 2
PL lifetimes fitted by a single exponential decay in degassed MeTHF solution, average PL lifetimes fitted by a double exponential decay in a 6 wt% blend in PMMA and the Huang-Rhys factor estimated from the height of the 0–1 peak divided by the height of the 0–0 peak for complexes **4**–**6** in degassed MeTHF and a 6 wt% blend in PMMA

Complex	Lifetime (μs) in MeTHF at room temperature	1st lifetime component τ_1 (μs) in PMMA at room temperature	A_1, (τ_1 amplitude) in PMMA at room temperature	2nd lifetime component τ_2 (μs) in PMMA at room temperature	A_2, (τ_2 amplitude) in PMMA at room temperature	Estimated Huang-Rhys factor in MeTHF at room temperature	Estimated Huang Rhys factor in PMMA at room temperature
4	1.1	0.91	0.2	1.5	0.72	0.94	1.10
5	0.9	0.91	0.25	2.5	0.6	1.20	1.37
6	0.1	0.34	0.47	1.5	0.49	1.25	1.35

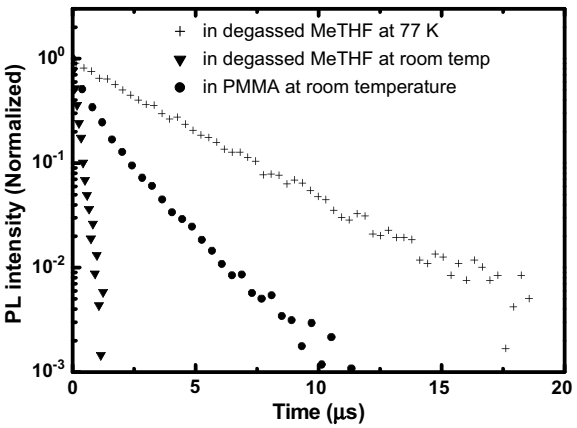

Fig. 4. Photoluminescence (PL) intensity as a function of time for complex **6** in degassed MeTHF at room temperature and 77 K and in a PMMA host.

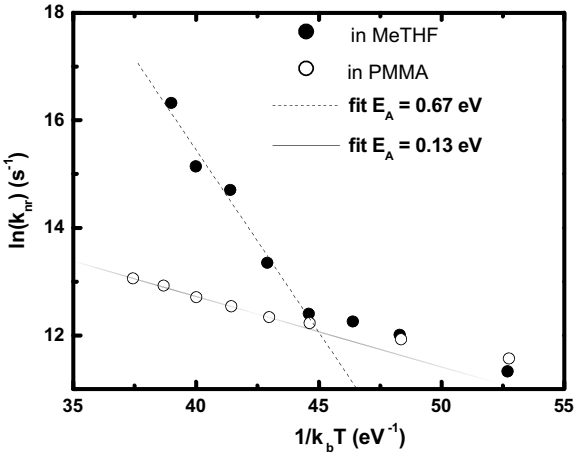

Fig. 5. Arrhenius (activation energy) plot of **6** dissolved in MeTHF or in solid host of PMMA.

decay rate of the molecules does not change as we go into the solid host [19] therefore the difference in decay in the solid host compared to the solution is attributed to a difference in non-radiative decay rates. For all three complexes, **4**, **5**, and **6**, the non-radiative decay was found to decrease when they were put into a solid host, consistent with the observations of Sajato et al. [2]. For device applications this is excellent news as there is the potential for higher device efficiencies than those predicted simply from solution PLQYs. The move from solution to the solid-state has two potential effects on the properties of the complexes; first, the solid host will inhibit vibrations associated with the non-radiative decay of the PL, and second, the host may also prevent the complexes from relaxing fully in the excited state, meaning the energy surface of the excited state could both be more curved and have less displacement with respect to the ground state, leading to less overlap of vibronic wavefunctions. In practice the vibrational relaxation is not completely inhibited and the Huang-Rhys factor actually increases slightly in the PMMA blends of **4**, **5**, and **6** even though the non-radiative decay rate decreases (Table 2).

To understand this apparent dichotomy it is important when considering vibrationally induced non-radiative decay from the excited state to understand how the vibrationally allowed electronic coupling between the isoenergetic ground and excited vibronic states occurs. That is, not all vibrational modes 'promote' the electronic coupling. Important promoting mode vibrations are expected to be metal ligand vibrations because these increase the overlap between the metal dπ and ligand π^* orbitals [20]. This increases spin orbit coupling, which is necessary to induce even a non-radiative decay from the triplet excited state to the isoenergetic (vibrationally excited) singlet (electronic) ground state. Modes involving metal-ligand vibrations are low energy vibrations (due to high mass of ligand and metal), which are observable at low intensities below about

400 cm^{-1} [11,20] in the Raman spectra. We propose these important promoting modes, since they are movements of the whole ligand with respect to the metal, are hindered in the solid-state, therefore decreasing the non-radiative decay rate in the solid-state with respect to solution. We attribute the non exponential decay to a range of conformations in the solid host, which have a range of non-radiative decay rates due to the promoting modes being more or less hindered in each conformation.

In order to investigate non-radiative decay mechanisms further, the temperature dependence of **6** was studied in PMMA and compared with that previously measured for MeTHF [5]. The PL decay as a function of time for the di-fluorinated complex **6** at room temperature in degassed MeTHF at 77 K (frozen solution) and at room temperature as a 6 wt% blend in PMMA are shown in Fig. 4. In the case of **6** in MeTHF, the lifetime was found by fitting a single exponential decay to the PL decay as a function of time. When **6** was in the PMMA host a bi-exponential decay curve was fitted and the long decay component lifetime was selected, assuming the long decay component arises from a subset of complexes with a given conformation. The PL decay of **6** in the PMMA film was found to be slower than in degassed MeTHF solution at room temperature (Fig. 4) and at 77 K the decay was even slower. The measured PL lifetime of **6** in MeTHF increases from 0.15 to 3.4 μs between 290 K and 200 K, and below 200 K is constant, while in PMMA the lifetime increases from 1.35 μs at 310 K to 3.7 μs at 77 K. In analysing these data we have assumed that the radiative decay rate is constant over the temperature range and that it is identical in PMMA and MeTHF.

The non-radiative decay rates extracted from the PL decay measurements were plotted in an Arrhenius plot (Fig. 5) and the data between 270 K and 300 K, which show the most change in non-radiative decay, were fitted to find activation energies for non-radiative decay. From the temperature dependent studies on **6**, we found that when blended with PMMA, **6** has a different activation energy for non-radiative decay compared with when in MeTHF (0.67 ± 0.06 eV versus 0.13 ± 0.07 eV). Therefore non-radiative decay via thermal activation to a higher excited state is not a sensible explanation, since PMMA and MeTHF are both inert 'hosts'. That is if the activation energy is determined solely by the ligand field strength, which is not affected by moving from MeTHF to PMMA, then the activation energy for non-radiative decay should be the same.

The Arrhenius behaviour for molecule **6** in solution was attributed to thermally activated vibrational decay in the strong coupling limit [5]. This behaviour is limited to high temperatures [21] and therefore high activation energies. The activation energy would be lowered if the excited state vibrational modes shifted to lower frequency with respect to those in the ground state as this would mean the displaced excited state potential energy was shallower and would intersect at a lower energy with the ground state potential energy. However, the possible shift in frequency is likely to be only a few percent and would not explain the low activation energy observed here in the solid state. According to Yersin and Donges, the exciton may be localised on a single ligand, if the distortion energy gained by localisation is larger than the energy gained by delocalisation due to metal mediated electronic ligand–ligand coupling [22]. If the exciton is localised, there would then be an activation energy for exciton transfer between ligands. Since this transfer would involve metal-ligand vibrations, which are considered to be important promoting modes, it is likely to induce non-radiative decay. This could then be the origin of the observed Arrhenius activated non-radiative decay, where the activation energy is equal to the localisation energy on the ligand minus the coupling energy gained by delocalisation. The differences in energy between solution and solid state may result from a lower distortion energy for localisation on a single ligand in the solid state since there is expected to be less vibronic coupling on the metal ligand vibrational modes.

4. Conclusions

We have shown that the Huang-Rhys factor is a useful tool in evaluating the luminescence properties of blue phosphorescent materials and vibrational coupling plays an important role in non-radiative decay of the luminescence. The results strongly suggest that vibrational decay occurs directly to the ground state without a higher energy excited state being involved. The luminescence of the blue materials was found to be higher in the solid state, and this was attributed to a reduction of the metal-ligand vibrations in the solid state. Finally, the change in Huang-Rhys factor suggests that the

addition of dendrons changes the excited state conformation of the chromophore. In the case of the doubly dendronised material, this improves the luminescence properties of the material, possibly by making the dendrimer more rigid due to steric constraints [16].

Acknowledgements

We are grateful to J.D. Woollins for access to the Raman spectrometer and to G. Tsiminis for assistance with beam-profile measurements. We thank CDT Oxford, the EPSRC and SHEFC for financial support.

References

[1] M.A. Baldo, D.R. O'Brien, Y. You, A. Shoustikov, S. Sibley, M.E. Thompson, S.R. Forrest, Nature 395 (1998) 151.
[2] T. Sajoto, P.I. Djurovich, A. Tamayo, M. Yousufuddin, R. Bau, M.E. Thompson, R.J. Holmes, S.R. Forrest, Inorganic Chemistry 44 (2005) 7992.
[3] C.H. Yang, S.W. Li, Y. Chi, Y.M. Cheng, Y.S. Yeh, P.T. Chou, G.H. Lee, C.H. Wang, C.F. Shu, Inorganic Chemistry 44 (2005) 7770.
[4] J. Li, P.I. Djurovich, B.D. Alleyne, M. Yousufuddin, N.N. Ho, J.C. Thomas, J.C. Peters, R. Bau, M.E. Thompson, Inorganic Chemistry 44 (2005) 1713.
[5] S.C. Lo, C.P. Shipley, R.N. Bera, R.E. Harding, A.R. Cowley, P.L. Burn, I.D.W. Samuel, Chemistry of Materials 18 (2006) 5119.
[6] P.L. Burn, S.-C. Lo, I.D.W. Samuel, Advanced Materials 19 (2007) 1675.
[7] T.D. Anthopoulos, S.-C. Lo, E.B. Namdas, P.L. Burn, I.D.W. Samuel, Advanced Materials 17 (2005) 1945.
[8] N.A.H. Male, S.-C. Lo, J.P.J. Markham, S.W. Magennis, P.L. Burn, O.V. Salata, I.D.W. Samuel, Advanced Materials 14 (2002) 975.
[9] J.N. Demas, G.A. Crosby, Journal of Physical Chemistry 75 (1971) 991.
[10] D.P. Rillema, C.B. Blanton, R.J. Shaver, D.C. Jackman, M. Boldaji, S. Bundy, L.A. Worl, T.J. Meyer, Inorganic Chemistry 31 (1992) 1600.
[11] P.K. Mallick, G.D. Danzer, D.P. Strommen, J.R. Kincaid, Journal of Physical Chemistry 92 (1988) 5628.
[12] C. Adachi, R.C. Kwong, P. Djurovich, V. Adamovich, M.A. Baldo, M.E. Thompson, S.R. Forrest, Applied Physics Letters 79 (2001) 2082.
[13] S. Okada, K. Okinaka, H. Iwawaki, M. Furugori, M. Hashimoto, T. Mukaide, J. Kamatani, S. Igawa, A. Tsuboyama, T. Takiguchi, K. Ueno, Dalton Transactions (2005) 1583.
[14] C.H. Yang, Y.-M. Cheng, Y. Chi, C.-J. Hsu, F.-C. Fang, K.-T. Wong, P.-T. Chou, C.-H. Chang, M.-H. Tsai, C.-C. Wu, Angewandte Chemistry 46 (2007) 2418.
[15] T.J. Meyer, Pure and Applied Chemistry 58 (1986) 1193.
[16] J.A. Treadway, B. Loeb, R. Lopez, P.A. Anderson, F.R. Keene, T.J. Meyer, Inorganic Chemistry 35 (1996) 2242.
[17] N.H. Damrauer, T.R. Boussie, M. Devenney, J.K. McCusker, Journal of the American Chemical Society 119 (1997) 8253.
[18] E.B. Namdas, A. Ruseckas, I.D.W. Samuel, S.-C. Lo, P.L. Burn, Applied Physics Letters 86 (2005) 091104.
[19] E.B. Namdas, A. Ruseckas, I.D.W. Samuel, S.-C. Lo, P.L. Burn, Journal of Physical Chemistry B 108 (2004) 1570.
[20] J.V. Caspar, T.J. Meyer, Journal of Physical Chemistry 87 (1983) 952.
[21] R. Englman, J. Jortner, Molecular Physics 18 (1970) 145.
[22] H. Yersin , D. Donges, Low-lying electronic states and photophysical properties of organometallic Pd(II) and Pt(II) compounds. Modern research trends presented in detailed case studies, in: Transition Metal and Rare Earth Compounds: Excited States, Transitions, Interactions Ii, 2001, p. 81.

Available online at www.sciencedirect.com
ScienceDirect
Organic Electronics 9 (2008) 385–395
Organic Electronics
www.elsevier.com/locate/orgel

Oriented growth of rubrene thin films on aligned pentacene buffer layer and its anisotropic thin-film transistor characteristics

Wei-Shan Hu [b], Shou-Zheng Weng [a], Yu-Tai Tao [a,b,*], Heng-Jui Liu [c], Hsin-Yi Lee [c]

[a] *Institute of Chemistry, Academia Sinica, Taipei 115, Taiwan, ROC*
[b] *Department of Chemistry, National Tsing-Hua University, Hsin-chu, Taiwan, ROC*
[c] *National Synchrotron Radiation Research Center, Hsinchu 300, Taiwan, ROC*

Received 25 December 2007; received in revised form 11 January 2008; accepted 12 January 2008
Available online 26 January 2008

Abstract

Oriented growth of polycrystalline rubrene thin film on oriented pentacene buffer layer was investigated. The oriented pentacene buffer layer was created by thermal evaporation of pentacene on a rubbed polyvinylalcohol (PVA) surface. The pentacene layer in turn induced the oriented growth of rubrene crystals upon thermal deposition. The structures of successive layers were characterized by using grazing incidence X-ray diffraction (GIXD) and atomic force microscopy. Highly oriented rubrene crystallites with the *a*-axis aligning along the surface normal and the (0 0 2) plane preferentially oriented 45° away from the rubbing direction were found. In contrast, the rubrene thin film deposited on PVA or rubbed-PVA substrate without a pentacene buffer layer only gave amorphous phases. With the aligned pentacene/rubrene film as the active layer of organic field-effect transistor, anisotropic mobilities were observed. The highest field-effect mobility (0.105 cm^2/V s) was observed along the direction 45° away from the rubbing direction and is ~4 times higher than that for similar device prepared on unrubbed PVA. The direction was consistent with the GIXD observation that a large number of rubrene crystallites are having their [0 0 2] direction aligning in this direction. A favourable C–H$\cdots\pi$ interaction between an oriented pentacene layer and the rubrene layer on the control of molecular orientation in the conduction channel of the OFET is suggested.

Keywords: Organic field-effect transistors; Oriented growth; Rubrene; Pentacene

1. Introduction

Organic electronic devices such as organic field-effect transistors (OFETs), organic light-emitting diodes (OLEDs) and organic solar cells have drawn wide attention for their great potential in fabricating flexible electronics for display and energy conversion purposes. As the major driving component of flexible electronics, field-effect transistors based on organic materials are critical for the success of the ultimate device integration. Field-effect mobility is one of the most important parameters that determine the practicality of an OFET. However, the

* Corresponding author. Address: Institute of Chemistry, Academia Sinica, Taipei 115, Taiwan, ROC, Tel.: +886 2 27898580; fax: +886 2 27831237.
E-mail address: ytt@chem.sinica.edu.tw (Y.-T. Tao).

1566-1199/$ - see front matter © 2008 Elsevier B.V. All rights reserved.
doi:10.1016/j.orgel.2008.01.003

field-effect mobility for most organic-based devices still cannot catch up with that of the silicon-based devices. Many efforts were devoted to the improvement of field-effect mobility of organic materials in recent years. While the intrinsic electronic property of an organic molecule is important, the electronic coupling between molecules, particularly in molecular thin films and crystals, are also crucial to the measured mobility. The electronic coupling between organic molecules is highly dependent on the packing and arrangement of the molecules within the crystal and can be very anisotropic due to the directionality of molecular orbitals involved in the electronic coupling. Therefore, control of the orientation of the molecular crystallites with respect to the conduction channel is a promising approach to improve the device performance. Rubrene single crystal has been reported to give a mobility as high as 20 cm^2/V s and anisotropy in charge transport in rubrene single crystal was also revealed so that mobility along *b*- and *c*-axes can differ by a factor of four [1]. While the high mobility is exciting, it is generally a very challenging task to grow and handle a large single crystal transistor. [2,3]. On the contrary, the deposition of rubrene thin films by conventional thermal evaporation technique, which can generate large area thin films with ease, only results in poor crystallinity or amorphous phase with very low mobility [4]. Recently, a thin pentacene buffer layer between the inorganic substrate and the deposited rubrene (as well as other material such as fullerene) thin films was found to greatly improve the crystallinity of the deposited rubrene [5–7]. The results imply a strong interaction and correlation between pentacene buffer layer and the molecules deposited on top. While organic–organic "heteroepitaxy" is believed to be important in multilayers of different organics [8], strong orientation effect can exist even if there is incommensurate relationship between the contacting crystal planes [9]. Pentacene was found to grow on various insulating surfaces with their c^*-axis parallel to the surface normal [10]. This (0 0 1) plane in contact with the deposited rubrene molecules induces the rubrene to grow into layers with the *a*-axis parallel to the surface normal. Nevertheless, the pentacene thin film deposited on isotropic substrate surface composes of grains with randomly oriented *a*-/*b*-axes parallel to the substrate plane. In view of the high anisotropy of charge transport in single crystal rubrene, it is interesting to have a polycrystalline rubrene thin film with preferred orientation of the crystallites in the surface plane. An oriented pentacene template layer may serve the role of directing growth. Recently, we and others have demonstrated polycrystalline pentacene films deposited on a rubbed polymer surface showed preferred crystal orientation [11,12]. Furthermore, the field-effect mobility of pentacene film deposited on a rubbed polymer or a rubbed self-assembled monolayer of *n*-alkyltrichorosilane on SiO_2 showed high anisotropy with respect to the rubbing direction [13,14]. In this study, we used aligned pentacene buffer layer prepared on rubbed polyvinylalcohol (PVA) film to induce a preferred "in-plane" orientation of rubrene crystallites deposited on top. The structures of the polycrystalline films were shown by grazing incidence X-ray diffraction (GIXD) to be specifically oriented with respect to the rubbing direction on the underlying polymer. Anisotropic mobilities of the films were also observed.

2. Experimental

2.1. Sample preparation

The *n*-doped Si/SiO_2 substrates were cleaned by a Piranha solution (H_2SO_4:H_2O_2 = 4:1, v/v). Polyvinylalcohol (30 mg/mL in DI water) was spin-coated on to silicon substrate at 5000 rpm for 1 min. The thickness of the PVA film was measured by AFM to be around 50 nm. The PVA film was gently rubbed with a flammel cloth in a single direction at near constant speed of 5 cm/s and a force of $\sim$0.9 g/cm^2 over 100 cm and used as an alignment layer in pentacene/rubrene deposition [15]. The AFM micrograph of the rubbed PVA showed aligned grooves no deeper than 5 nm. Commercially obtained pentacene (Aldrich Chemical Co.) was used as received. A 10 nm pentacene layer was deposited at a rate of 0.5 Å/s onto the substrate held at 50 °C in a vacuum of 1×10^{-5} Torr. The film thickness was monitored by quartz crystal thickness monitor. Rubrene (50 nm) was then deposited at a rate of 0.5 Å/s onto the pentacene buffer layer held at 75 or 90 °C during deposition process. Control experiment showed that pentacene film subjected to these temperatures essentially remained on the substrate during the rubrene deposition.

2.2. Grazing incidence angle X-ray diffraction

The grazing incidence X-ray diffraction experiments were performed at wiggler beamline BL-

17B1 at the National Synchrotron Radiation Research Center (NSRRC), Taiwan. Incident X-rays were focused vertically with a mirror and made monochromatic to an energy of 8 keV with a Si (1 1 1) double-crystal monochromator; the sagittal bend of the second crystal focused the X-rays in the horizontal direction. With two pairs of slits between the sample and the detector, the typical scattering vector resolution in the vertical scattering plane was set to $\sim 1 \times 10^{-3}\,\mathrm{nm}^{-1}$ in these experiments. A grazing incidence angle below the critical angle of total reflection for the film was chosen to enhance the sensitivity of measurement.

2.3. Atomic force microscopy

Atomic force microscopy (AFM) measurements were carried out under ambient conditions using a Digital Instruments Nanoscope IIIa microscope. Images were captured by tapping mode with a silicon tip at 300 kHz frequency.

2.4. Device fabrication and measurement

FET devices were fabricated on a silicon wafer with 300 nm-thick thermally grown SiO_2 layer as the gate dielectric and the highly *n*-doped silicon as the gate electrode. The 60 nm-thick gold source and drain electrodes were deposited on the organic films (top contact) through a shadow mask. The channel length (L) and width (W) are 50 and 500 μm, respectively. The electrical characteristics of the devices were measured in the air using a computer-controlled Agilent 4156C semiconductor parameter analyzer. The field-effect mobility of the OFET device was calculated from the saturation region according to the following equation:

$$I_{ds,sat} = (WC_{tot}/2L)\mu_{sat}(V_{gs} - V_{th})^2, \quad (1)$$

where W and L are the channel width and length, respectively, C_{tot} is the capacitance per unit area of the PVA coated SiO_2 insulator as calculated by $1/C_{tot} = 1/C_{oxide} + 1/C_{PVA}$, V_{gs} is the gate voltage and V_{th} is the threshold voltage.

3. Results and discussion

3.1. Structure of the oriented pentacene/rubrene heteroepitaxy film

PVA film was prepared as described in Section 2. After rubbing with a flammel cloth, the surface exhibited a smooth morphology, with grooves that were no more than 2 nm deep and a RMS roughness around 1.6 nm, as revealed by AFM (Fig. 1a). Pentacene buffer layer was prepared by thermal evaporation of 10 nm pentacene molecules onto the rubbed PVA (R-PVA) surface. The substrate temperature was kept at 50 °C during the deposition process. The AFM shows two distinct morphologies, one with large platelets, resulted from two-dimensional growth of pentacene molecules with molecular long axes near normal to the surface. The other with long rod-like grains which oriented perpendicular to the rubbing direction, presumably resulted from flat-lying pentacene crystals growing preferably in lateral direction (vide infra).

Powder X-ray diffraction of the film showed a "thin film phase" pentacene layer with (0 0 1) diffraction peak at $2\theta = 5.7°$ (or a d-spacing of 15.5 Å),

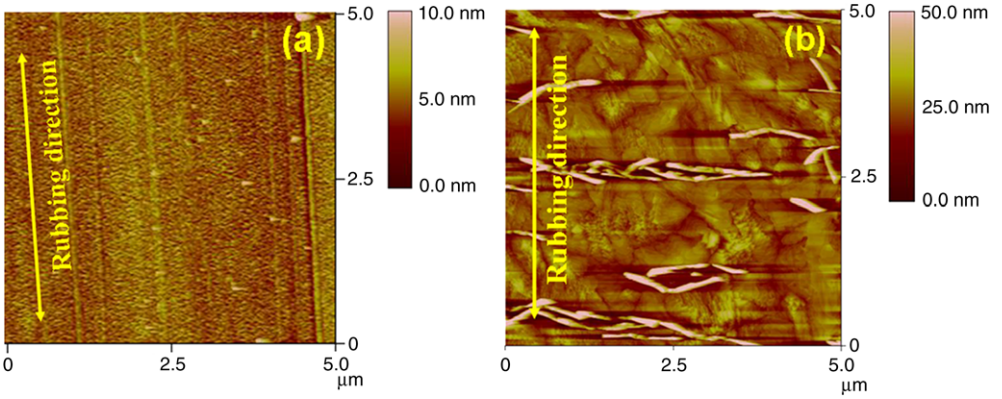

Fig. 1. AFM micrographs of (a) R-PVA surface and (b) 10 nm pentacene on the R-PVA surface. The arrows indicate the direction of rubbing.

which suggested the pentacene molecules were aligning with their long molecular axes near perpendicular to the surface. In-plane alignment of the pentacene crystallites within the layer was characterized by GIXD using synchrotron radiation. The in-plane diffraction was performed with two measurement set-ups: one with the incident X-ray beam aligned parallel to the rubbing direction (azimuthal angle $\varphi = 0°$, with the in-plane scattering vector q perpendicular to the rubbing direction, as shown in Fig. 2a) at a grazing incidence angle of 0.18°; the other with the incidence X-ray aligned perpendicular to the rubbing direction ($\varphi = 90°$, with the in-plane scattering vector q parallel to the rubbing direction, as shown in Fig. 2b) at the same grazing incidence angle. The in-plane θ–2θ scan was then measured with an incidence angle of 0.18°, less than the critical angle of total reflection, enabling information acquisition on lattice spacings parallel to the substrate surface. The pentacene (1 1 0) diffraction peak at 2θ of 19.3° was greatly enhanced when the in-plane θ–2θ scan was carried out with incidence X-ray parallel to the rubbing direction (Fig. 3, black line). When the in-plane θ–2θ scan was carried out with incidence X-ray perpendicular to the rubbing direction, the pentacene (0 0 1) diffraction peak was found and the (1 1 0) peak was greatly reduced (Fig. 3, red line). The fact that (0 0 1) peak was found when q was parallel to the rubbing direction implies that some pentacene molecules were lying flat with their long molecular axis parallel to the rubbing direction, similar to an earlier observation for *p*-hexaphenyl [16] or pentacene [12] film deposited on rubbed polymethylene surface. Nevertheless, the majority of pentacene molecules are having their long molecular axes stand near vertical to the surface, as shown by the wide-angle θ–2θ scan results in the inset, with the (1 1 0) plane of the crystallites aligned preferentially along the rubbing direction. Further azimuthal scans of the pentacene film were carried out by fixing the detector at 2θ of 19.3° for the pentacene (1 1 0) diffraction while rotating the sample 180° around the substrate normal in order to probe the distribution of (1 1 0) planes of the pentacene crystals on the surface. The results are shown in Fig. 4. It was found that besides the directions parallel to the PVA rubbing direction at $\varphi = 0°$ and 180°, there are two other angles, at $\varphi = 78.2°$ and $\varphi = 101.8°$, respectively, also giving strong diffraction intensities. The two angles are symmetrical with respect to the PVA rubbing direction. The results suggest that the pentacene [1 1 0] direction (the normal of (1 1 0) plane) of pentacene crystallites aligned perpendicular to the rubbing direction "or" 11.8° away in either direction from the rubbing direction in the surface plane. That the directions are symmetrical with respect to the rubbing direction may imply

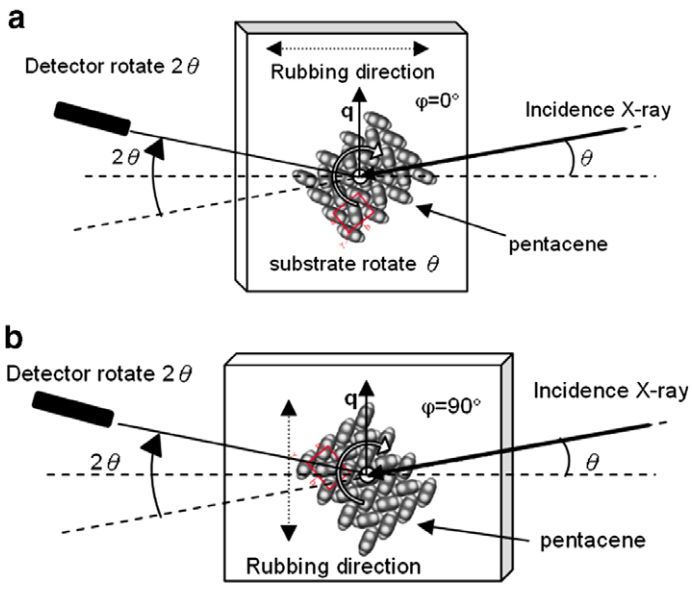

Fig. 2. Geometries of in-plane grazing incidence X-ray diffraction experiments with (a) the in-plane scattering vector q oriented perpendicular to the rubbing direction or (b) the in-plane scattering vector q oriented parallel to the rubbing direction.

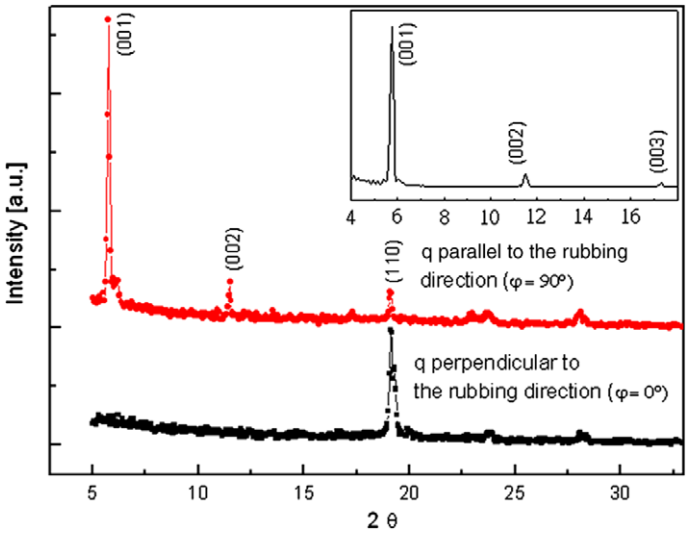

Fig. 3. GIXD pattern of pentacene buffer layer on rubbed PVA surface with $\varphi = 0°$ (black line) and $\varphi = 90°$ (red line). The inset shows the standard wide angle θ–2θ scan of pentacene buffer layer.

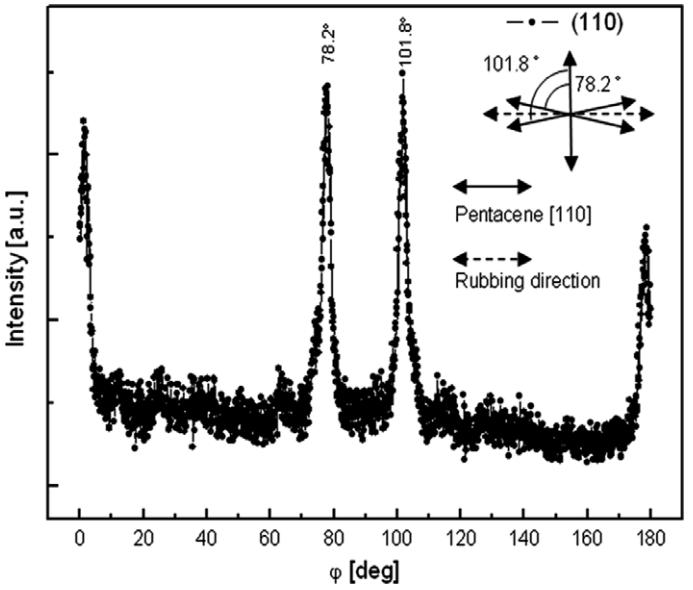

Fig. 4. GIXD (1 1 0) azimuthal scan pattern of pentacene buffer layer on rubbed PVA surface.

the twin growth of pentacene crystals on the rubbed surface. That the (1 1 0) plane aligned preferentially in more than one direction (along the rubbing direction or 78.2° away from it) implies there are more than one direction on the rubbed PVA surface interact favourably with the [1 1 0] direction of pentacene crystal lattice.

The insertion of a pentacene buffer layer has much influence on the affinity of the substrate to the rubrene molecules and the rubrene film deposited on the pentacene layer exhibited high crystallinity and order in the surface normal direction as shown by the θ–2θ powder X-ray diffraction pattern. The lattice parameters of orthorhombic rubrene unit cell were reported to be $a = 26.86$ Å, $b = 7.193$ Å, and $c = 14.433$ Å [17,18]. Fig. 5 shows θ–2θ XRD pattern of 50 nm rubrene deposited on a 10 nm pentacene/R-PVA surface at a substrate temperature of 90 °C. Diffraction peaks at $2\theta = 6.63$, 13.25, and 19.85 are assigned to be the (2 0 0),

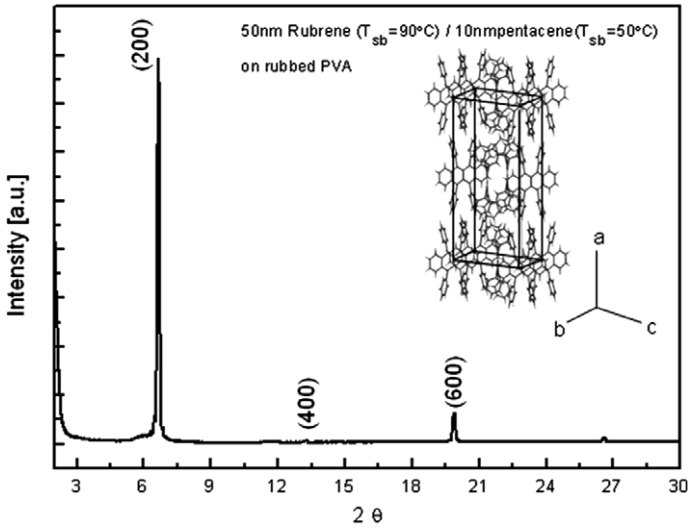

Fig. 5. θ–2θ X-ray diffraction patterns of 50 nm rubrene films deposited on 10 nm pentacene/rubbed PVA surface.

(400), and (600) planes of rubrene crystal. The diffraction peaks associated with pentacene were much suppressed due to the overcoating of a thicker layer of rubrene. Yet they are discernible upon expansion of the *Y*-axis. The *d*-spacing calculated from the lowest angle peak is 13.34 Å, which is the half of the *a*-axis of the rubrene unit cell. The result suggests that the (200) and higher order planes are parallel to the substrate and the *a*-axis of rubrene unit cell is perpendicular to the substrate surface. In contrast, rubrene thin film deposited on PVA film without a pentacene buffer layer only yielded amorphous phase. The grazing incidence X-ray diffraction results on 50 nm rubrene on 10 nm pentacene buffer layer-modified PVA/R-PVA are shown in Fig. 6. Diffraction pattern at three azimuthal angles at $\varphi = 0°$, 45°, and 90° with respect to the PVA rubbing direction were measured. The diffraction intensity of (002) planes of rubrene crystals showed an orientation-dependence and gave the highest intensity when measured at $\varphi = 45°$. Whereas the intensity measured at $\varphi = 0°$ and 90° are not much different from that obtained from a rubrene film deposited on the unrubbed PVA film. Further azi-

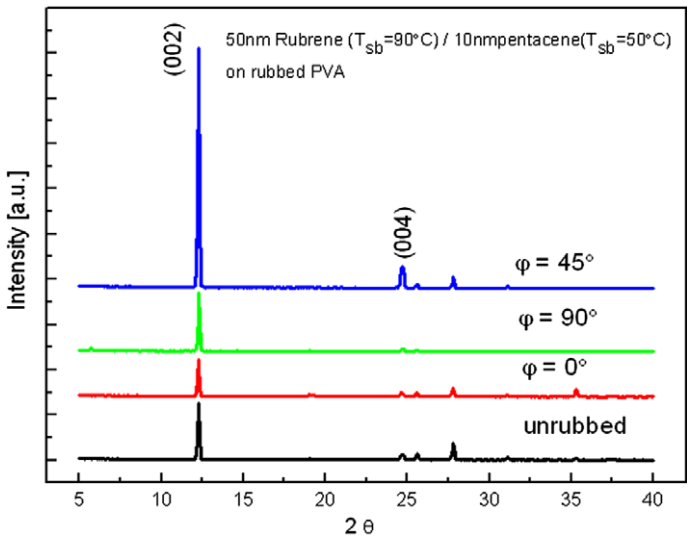

Fig. 6. GIXD pattern of 50 nm rubrene/10 nm pentacene on rubbed PVA and unrubbed PVA surfaces. at $\varphi = 0°$, 45° and 90° with respect to the rubbing direction.

muthal scans were performed with the detector held at the rubrene (002) reflection while rotating the sample 180° around the sample normal successively. The results are shown in Fig. 7. The red line shows the azimuthal scans with respect to the PVA rubbing direction for rubrene film deposited at 90 °C. The intensity of the rubrene (002) diffraction was highly dependent on the azimuthal angle φ. The angles at which high diffraction intensity were obtained can be divided into two sets which are symmetric to $\varphi = 90°$, i.e., $\varphi = 18.5°$ (and 161.5°), 39.6° (and 140.4°), 45.1° (and 134.9°) and 82.1° (97.9°). This indicates that the (002) plane of the rubrene crystals preferentially aligned in several directions that are symmetrical with respect to the PVA rubbing direction. The most intense (002) diffraction peak was found at $\varphi = 45.1°$ (and the corresponding 134.9°), consistent with the results shown in Fig. 6. Some other directions are also enhanced, meaning some crystallites also have their (002) plane aligned along these directions. For comparison, a 50 nm rubrene/10 nm pentacene film deposited on an unrubbed PVA surface under the same deposition condition gave a constant intensity during the same azimuthal scan experiments, shown by the green line in Fig. 7. Thus, an unaligned pentacene buffer layer will not induce preferred alignment of rubrene (00*l*) plane in the sample layer. Interestingly, the orientation distribution of the (002) plane changed when the rubrene was deposited at 75 °C, shown by the black line in Fig. 7. The highest intensity shifted to $\varphi = 39.6°$ (and 140.4°), together with some smaller preference in the direction of $\varphi = 18.5°$ and 82.1°. It should be noted that the distribution of the rubrene (002) plane was still symmetrical with respect to the PVA rubbing direction. The GIXD results clearly show that a rubbed PVA induced oriented growth of pentacene crystals, in at least two preferred directions, one with [1 1 0] direction perpendicular to the rubbing direction and another with [1 1 0] direction turned away from the rubbing direction by 11.8°. The rubbed polymer surface is expected to have an average alignment of polymer backbones as well as grooves [12]. More than one directed growth of pentacene were obtained. The rubrene crystals adopted even more possible orientations. The GIXD of pentacene layer shows that besides differently oriented "upright" pentacene crystals, there are also some crystallites lying flat, providing additional growth motif. A rubrene molecule has two phenyl rings sticking up and two phenyl rings sticking down from the tetracene moiety. When this molecule is landing on the substrate and in contact with an oriented pentacene crystal, the C–H···π type hydrogen bonding interaction involving the two para hydrogen atoms of the two lower phenyl rings in rubrene and the somewhat tilted pentacene molecule may play an important role in the initial disposition of the rubrene molecule. Fig. 8(a) shows the

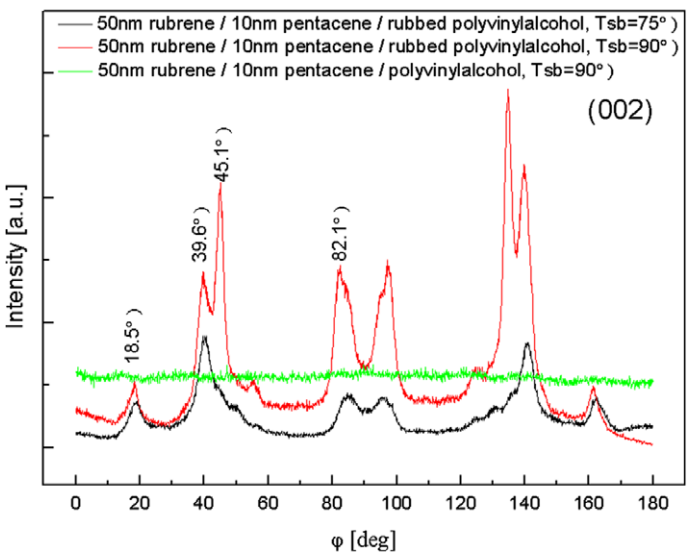

Fig. 7. Azimuthal GIXD pattern of (002) plane for 50 nm rubrene thin film on pentacene buffer layer/rubbed PVA surface. The red line is for rubrene deposited at $T_{sb} = 90$ °C and the black line for $T_{sb} = 75$ °C. The green line is for 50 nm rubrene/10 nm pentacene on unrubbed PVA surface.

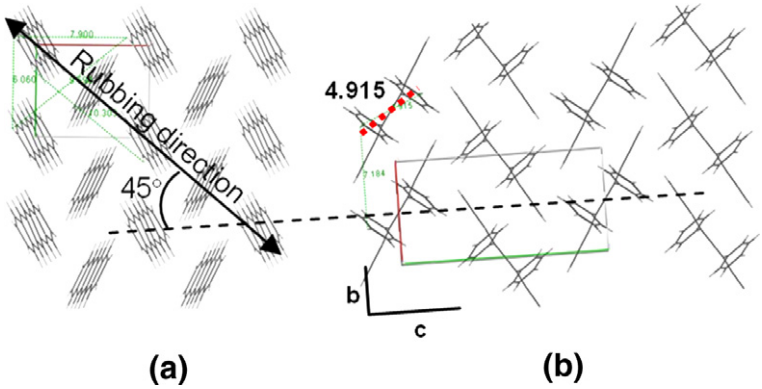

Fig. 8. (a) The top view of the lattice of pentacene crystal and its correlation with the rubbing direction. (b) The rubrene lattice with (002) plane rotates 45° off the rubbing direction.

pentacene crystal lattice with the (110) plane aligned parallel to the rubbing direction, as viewed from the top of the surface. Fig. 8(b) shows the rubrene lattice with the (002) plane rotated 45.1° from the rubbing direction. The distance between the two para hydrogen atoms is 4.915Å, which is about half of the *ab* diagonal of the pentacene unit cell. Aligning a rubrene molecule along this direction may give more favourable interaction and influence the initial growth direction of the rubrenes on pentacene layer. Thus the pentacene underlayer serves as nucleation sites. Although a complete lattice match was not obtained when overlapping the two lattice planes, many favourable C–H$\cdots\pi$ interactions can be approached. This may be the reason for the oriented growth. The presence of multiple directions in the crystal orientation also reflects the lacking of complete matching of the two lattices and the two orientations adopted by the rubrene molecules in a single crystal allow growth along various directions. A number of reports indicated that complete incommensurism or lattice mismatch can still lead to epitaxy growth of organic crystallites in the organic–organic interface [8,9]. The morphologies of the rubrene/pentacene on PVA alignment layer was examined by atomic force microscopy. Fig. 9(a) shows the AFM micrograph of a 50 nm rubrene deposited on 10 nm pentacene buffer layer on unrubbed PVA surface at a deposition temperature of 75 °C. Randomly oriented rod-like crystals were observed, with their long crystal axes lying parallel to the surface. The crystals were about 1 μm in length and 0.25 μm in width. The shapes of the crystals were similar but smaller than the millimeter-sized, needle-like rubrene single crystals reported previously [19]. Fig. 9(b) shows the micrograph of 50 nm rubrene deposited on 10 nm pentacene buffer layer on R-PVA surface. The grains in the rubrene film were much larger and oriented more specifically with respect to the PVA rubbing direction. In the 5 μm AFM image, the rod-like crystal oriented in a direction that was consistent with the GIXD (002) azimuthal rotation scan. The results also imply that the long axis of the rubrene crystal was in the same direction of rubrene [002] direction. Fig. 9(c) shows the 2×2 μm^2 AFM image of 50 nm rubrene/10 nm pentacene film on R-PVA surface. A smooth and well-packed terrace structure of rubrene was found. The sectional profile analysis on the step height, shown in Fig. 9(d), gave 13.3Å,. The result was consistent with the synchrotron XRD of *d*-spacing of 13.3 Å for rubrene (200) plane and thus the rubrene (*h*00) planes are parallel to the substrate surface. The larger grain sizes of the rubrene film on the pentacene/R-PVA layer may be explained by better connectivity of oriented crystallites of rubrene, induced by a rather smooth and orientationally ordered pentacene buffer layer.

3.2. Characterization of the aligned rubrene/pentacene transistor

FET devices were fabricated on a silicon wafer with 300 nm-thick, thermally grown SiO_2 layer as the gate dielectric and highly *n*-doped silicon as the gate electrode. A rubbed PVA layer served as the alignment layer. The field-effect mobilities along three different directions with respect to the rubbing direction were measured: parallel to the rubbing direction ($\varphi = 0°$), perpendicular to the rubbing direction ($\varphi = 90°$) and 45° from the rubbing direction ($\varphi = 45°$). The 50 nm rubren/10 nm pentacene

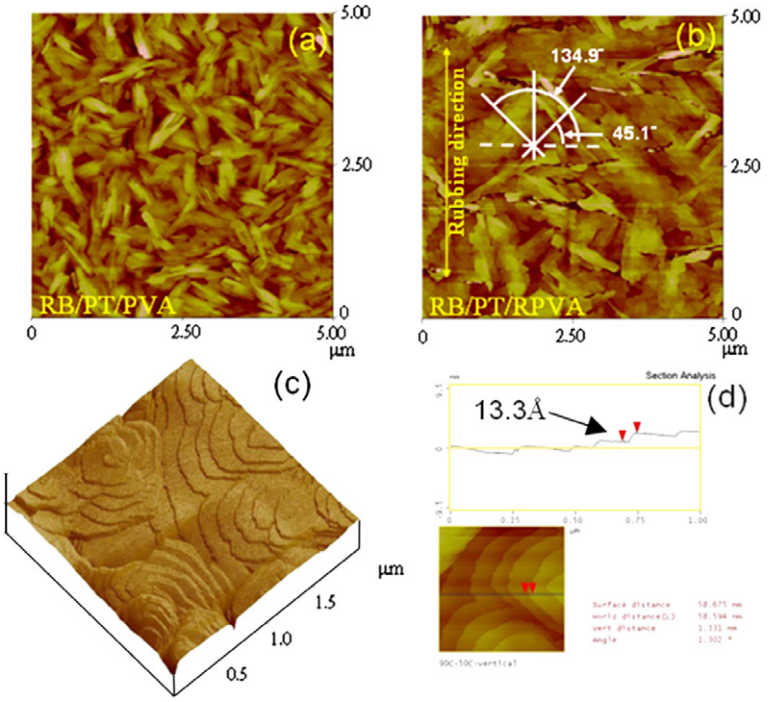

Fig. 9. AFM images of 50 nm rubrene/10 nm pentacene on (a) unrubbed PVA and (b) rubbed PVA surface (5 μm × 5 μm). (c) Terrace structure of the rubrene film on pentacene/R-PVA surface (2 μm × 2 μm). (d) The sectional profile analysis on the step height of the rubrene terrace.

film deposited on unrubbed PVA surface was also prepared as a control. A typical p-type OFET I–V curve was obtained (Fig. 10). The I–V characteristics are summarized in Table 1. The highest mobility for the rubrene/pentacene/R-PVA device was found along $\varphi = 45°$ direction and reached 0.105 $cm^2/V\,s$. The mobility along this direction is higher than that measured along the rubbing direction (0.079 $cm^2/V\,s$, $\varphi = 0°$) and that perpendicular to the rubbing direction (0.021 $cm^2/V\,s$, $\varphi = 90°$). The mobility

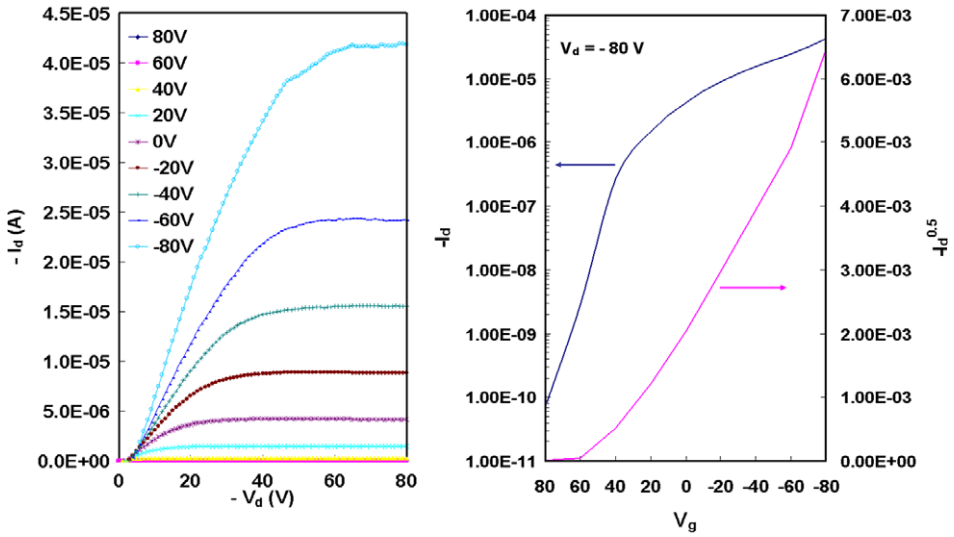

Fig. 10. (a) Drain current (I_d) versus drain voltage (V_d) of OFET with 50 nm rubrene/10 nm pentacene on R-PVA measured at $\varphi = 45°$ direction. (b) $-I_d^{1/2}$ versus gate voltage, V_g, and $\mathrm{Log}_{10}(-I_d)$ versus V_g plots under drain saturation condition ($V_d = -80$ V).

Table 1
Electrical characteristics of rubrene/pentacene organic FETs on PVA alignment film

Substrate	μ_{eff} (cm^2/V s)	On/Off
Unrubbed PVA	0.024	10^4
$\varphi = 0°$, ∥	0.079	10^5
$\varphi = 45°$	0.105	10^6
$\varphi = 90°$, ⊥	0.021	10^5

φ, the angle between source/drain conducting channel direction and PVA rubbing direction; μ_{eff}, room temperature field-effect hole mobility; On/Off, drain current on/off ratio and V_{th}, threshold voltage.

observed was due to the rubrene layer as the control experiment on the 10 nm pentacene/R-PVA device gave a scattered mobility in the range between 3×10^{-3} and 10^{-5} cm^2/V s, presumably due to the thinness of the film. Rubrene single crystal has been shown to possess anisotropic mobility within the *bc* planes of the crystal both experimentally [1] and theoretically [20]. The large electronic coupling along *b*-axis results in a more efficient conducting direction. In the current sample, the direction along $\varphi = 45°$ shows the highest amount of rubrene crystals with [0 0 2] vector oriented in this direction. The amount of rubrene crystals with *b*-axis and *c*-axis oriented in the conduction channel were equal to each other due to the twofold symmetry about the rubbing direction, as shown in Fig. 11. The

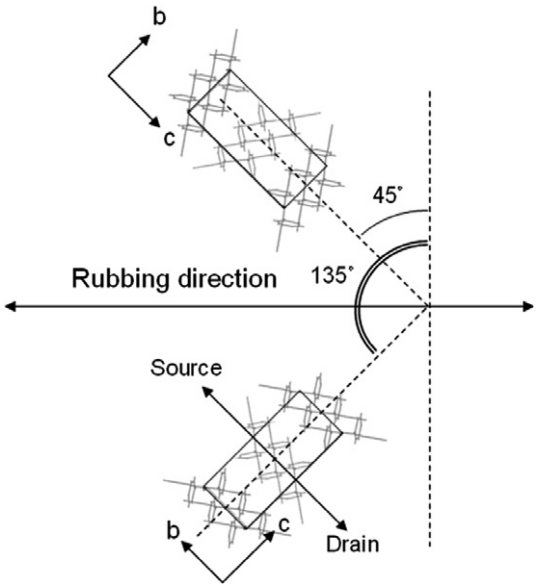

Fig. 11. The relationship between rubrene crystals orientation at $\varphi = 45°$ and 135° on the rubbed PVA with pentacene buffer layer and the charge conduction channel (source to drain) aligned 45° away from the PVA rubbing direction.

properly aligned rubrene crystals with *b*-axis orientated to the conduction channel increased the overall conduction. However, when conduction channel was made perpendicular to the rubbing direction, the mobility (0.021 cm^2/V s) was lower than parallel direction (0.079 cm^2/V s). The measured mobility is nevertheless far less that measured for a single crystal rubrene. The polycrystalline nature of the film and thus numerous grain boundaries and possibly the rough surface of rubbed PVA as the dielectric layer also hamper the charge transport.

4. Conclusions

We have demonstrated the use of a pre-rubbed polyvinylalcohol to induce a preferentially aligned pentacene crystallite layer, which in turn lead to an oriented growth of crystallites of rubrene film, all by thermal evaporation. The GIXD provide evidences of preferred orientation in the two organic layers. The pentacene buffer layer showed a preferred in-plane orientation of the crystallites with their [1 1 0] direction perpendicular to the rubbing direction or in the directions 11.8° away from the rubbing direction on either sides. The rubrene thin film deposited next to the pentacene buffer layer exhibited high crystallinity with the *a*-axis oriented perpendicular to the substrate surface and the (0 0 2) plane populated at several angles that are also symmetrical relative to the rubbing direction. The most preferred direction of the rubrene [0 0 2] director was 44.9° away from the rubbing direction in the surface plane. The maximization of C–H···π interactions may dictate the specific direction of the initial growth of crystals, even though a long range matching of the lattice (organic–organic epitaxy) is not found. Another consequence of the oriented growth is the larger grains formed compared to that on an unrubbed PVA surface. A higher propensity of merging of crystallites and orientationally ordered packing are suggested to be the origin of larger grain sizes. The field-effect mobility measured at 45° off the rubbing direction reached 0.105 cm^2/V s and was higher than other directions or four times higher than that ofnunaligned film. The rubrene crystals with *b*-axis properly orientated along the conduction channel gave improved overall conduction. Multiple orientations allowed in the current system may stem from the complex or mixed structure of a rubbed polymer system. Further simplification of the alignment system for orienting crystals is being pursued in the laboratory.

Acknowledgements

Financial support from National Science Council, Taiwan, the Republic of China through project NSC-95-2113-M-026-MY3 and Academia Sinica are gratefully acknowledged.

References

[1] (a) V.C. Sundar, J. Zaumseil, V. Podzorov, E. Menard, R.L. Willett, T. Someya, M.E. Gershenson, J.A. Rogers, Science 303 (2004) 1644;
(b) R.W.I. De Bore, M.E. Gershenson, A.F. Morpurgo, V. Podzorov: Phys. Status Solidi 201 (2004) 1302;
(c) C. Reese, Z. Bao, Adv. Mater. 19 (2007) 4535.
[2] A.L. Briseno, R.J. Tseng, M.-M. Ling, E.H.L. Falcao, Y. Yang, F. Wudl, Z. Bao, Adv. Mater. 18 (2006) 2320.
[3] A.L. Briseno, S.C.B. Mannsfeld, M.M. Ling, S. Liu, R.J. Tseng, C. Reese, M.E. Roberts, Y. Yang, F. Wudl, Z. Bao, Nature 444 (2006) 913.
[4] H.H. Fong, S.K. So, W.Y. Shm, C.F. Lo, Y.S. Wu, C.H. Chen, Chem. Phys. 298 (2004) 119.
[5] K. Itaka, M. Yamashiro, J. Yamaguchi, M. Haemori, S. Yaginuma, Y. Matsumoto, M. Kondo, H. Koinuma, Adv. Mater. 18 (2006) 1713.
[6] M. Haemori, J. Yamaguchi, S. Yaginuma, K. Itaka, H. Koinuma, Jpn. J. Appl. Phys., Part 1 44 (2005) 3740.
[7] J.H. Seo, D.S. Park, S.W. Cho, C.Y. Kim, W.C. Jang, C.N. Whang, K.-H. Yoo, G.S. Chang, T. Pedersen, A. Moewes, K.H. Chae, S.J. Cho, Appl. Phys. Lett. 89 (2006) 163505.
[8] M. Oehzelt, G. Koller, J. Ivanco, S. Berkebile, T. Haber, R. Resel, F.P. Netzer, M.G. Ramsey, Adv. Mater. 18 (2006) 2466.
[9] M. Campione, A. Sassella, M. Moret, A. Papagni, S. Trabattoni, R. Resel, O. Lengyel, V. Marcon, G. Raos, J. Am. Chem. Soc. 128 (2006) 13378.
[10] K. Itaka, N. Myojin, M. Yamashiro, J. Yamaguchi, H. Koinuma, Jpn. J. Appl. Phys., Part 1 44 (2005) 6249.
[11] M. Brinkmann, S. Graff, C. Straupé, J.-C. Wittmann, C. Chaumont, F. Nuesch, A. Aziz, M. Schaer, L. Zuppiroli, J. Phys. Chem. B 107 (2003) 10531.
[12] W.-S. Hu, Y.-T. Tao, H.-J. Liu, H.-Y. Lee, L.-J. Fan, Y.-W. Yang, Langmuir 23 (2007) 12901.
[13] M.L. Swiggers, G. Xia, J.D. Slinker, A.A. Gorodetsky, G.G. Malliaras, R.L. Headrick, B.T. Weslowski, R.N. Shashidhar, C.S. Dulcey, Appl. Phys. Lett. 79 (2001) 1300.
[14] S.-Z. Weng, W.-S. Hu, C.-H. Kuo, Y.-T. Tao, L.-J. Fan, Y.-W. Yang, Appl. Phys. Lett. 89 (2006) 172103.
[15] A. Cossy-Favre, J. Diaz, Y. Liu, H.R. Brown, M.G. Samant, J. Stöhr, A.J. Hanna, S. Anders, T.P. Russell, Macromolecules 31 (1998) 4957.
[16] W.-S. Hu, Y.-F. Lin, Y.-T. Tao, Y.-J. Hsu, D.-H. Wei, Macromolecules 38 (2005) 9617.
[17] O.D. Jurchescu, A. Meetsma, T.T.M. Palstra, Acta Crystallogr. B 62 (2006) 330.
[18] B.D. Chapman, A. Checco, R. Pindak, T. Siegrist, C. Kloc, J. Crystal Growth 290 (2006) 479.
[19] E. Menard, A. Marchenko, V. Podzorov, M.E. Gershenson, D. Fichou, J.A. Rogers, Adv. Mater. 18 (2006) 1552.
[20] D.A. Silva Filho, E.-G. Kim, J.-L. Brédas, Adv. Mater. 17 (2005) 1072.

Available online at www.sciencedirect.com
ScienceDirect
Organic Electronics 9 (2008) 396–400
Organic Electronics
www.elsevier.com/locate/orgel

Letter

Charge transport properties in liquid carbazole

J.-C. Ribierre, T. Aoyama, T. Muto, Y. Imase, T. Wada *

Supramolecular Science Laboratory, RIKEN (The Institute of Physical and Chemical Research), 2-1 Hirosawa, Wako, Saitama 351-0198, Japan

Received 17 August 2007; accepted 19 January 2008
Available online 1 February 2008

Abstract

The hole mobility in 9-(2-ethylhexyl)carbazole so-called liquid carbazole, in poly(*N*-vinylcarbazole) (PVK) and in their blends is determined by time-of-flight experiment using a phthalocyanine charge generation layer. With an applied electric field of 2.5×10^5 V/cm, mobilities of 4×10^{-6} cm^2/Vs and 6×10^{-7} cm^2/Vs are measured in liquid carbazole and PVK, respectively. The enhancement of the charge carrier mobility in liquid carbazole is attributed to both a larger transfer integral and changes in the distribution of the excimer trapping sites. The results show the potential interest of liquid carbazole for electroactive applications in optoelectronics.

PACS: 72.80.Le; 73.50.−h; 73.61.Ph; 78.66.Qn

Keywords: Charge transport; Carbazole derivatives; Time-of-flight

Carbazole molecules have been intensively studied in the last decades and still show great promise for technological applications in optoelectronics, mainly due to their photoconductive properties [1–6]. Polymers with a carbazole group such as poly(*N*-vinylcarbazole) (PVK) have been widely used as photoconductive layers in xerographic industry. Carbazole derivatives have also been successfully incorporated in efficient photorefractive [1,2], photovoltaic [3] and electroluminescent [4–6] devices. In addition to their good charge transport properties, many of these compounds are blue-emitting materials and can be used as energy donor in blends with other conjugated organic molecules [7].

In this manuscript, we study the charge transport and fluorescence properties of 9-(2-ethylhexyl)carbazole (EHCz) so-called liquid carbazole. This molecule presents a very low glass transition temperature (T_g) and is liquid at room temperature. Liquid carbazole was first used as "solvent" in ellipsometry measurements to determine the electric field induced birefringence on solution of photorefractive polymer composites [8]. More recently, by varying the concentration of EHCz in a PVK host, an optimization of the photorefractive performances in C_{60} sensitized polymers was demonstrated [9]. This work provides evidence that the potential interest for the use of this soft material in optoelectronics could have been

* Corresponding author. Tel.: +81 484679378; fax: +81 484624647.
E-mail address: tatsuow@postman.riken.jp (T. Wada).

1566-1199/$ - see front matter © 2008 Elsevier B.V. All rights reserved.
doi:10.1016/j.orgel.2008.01.005

seriously underestimated. Time-of-flight (TOF) measurements [10] show that the hole mobility in EHCz is one order of magnitude higher than in PVK. By tuning the concentration of liquid carbazole in PVK blends, it is possible to finely control both T_g and the charge transport properties. We also find that the slope of the logarithm of mobility against the square root of the electric field does not depend significantly on the concentration of liquid carbazole. The constancy of this slope and the high charge carrier mobility together with the blue emission shown in its photoluminescence spectrum make liquid carbazole an attractive candidate for applications in optoelectronics.

As shown in the inset of Fig. 1, for the PVK based samples, a 200 nm thick vanadylphthalocyanine (VOPc) charge generation layer (CGL) was evaporated under vacuum onto 1 mm thick aluminum substrate at a pressure of 3×10^{-4} Pa. A conversion [11] of the VOPc into its phase II was achieved by heating the samples at 250 °C for 1 h. The PVK and its various mixtures with EHCz were dissolved in chlorobenzene at a concentration of 60 mg/ml and deposited onto the VOPc layer by drop casting to yield homogeneous films of 20–30 μm thickness with a good optical quality. Twenty four hours were typically needed to obtain dry films. Then, in order to eliminate the presence of residual solvent, the films were placed in a vacuum chamber at 60 °C for one night. It should be noted that the VOPc layer was not affected by the chlorobenzene.

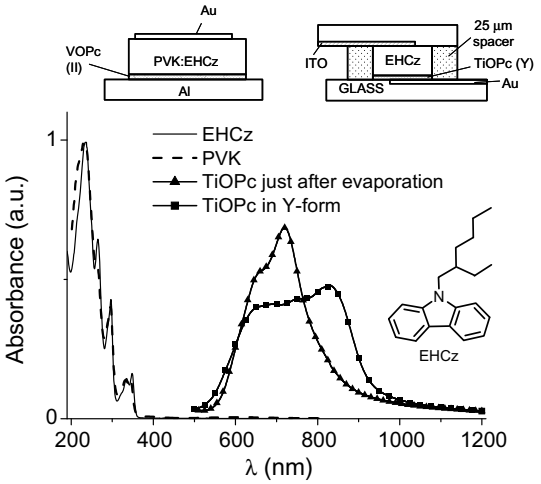

Fig. 1. Absorption spectra of EHCz, PVK, TiOPc in the crystalline phase just after the evaporation and in Y-form. In the inset are shown the schematic representations of our samples for the TOF measurements and the chemical structure of EHCz.

Finally, a thin and semitransparent gold electrode was evaporated on the top of our devices through a mask, defining an active pixel area of around 1.13 cm^2.

For the pure EHCz, another sample geometry was developed because of the liquid state of this compound. Sandwich type cell with a structure similar to that shown in the inset of Fig. 1 was prepared. The thick gold electrode with an active area around 0.28 cm^2 and then a titanylphthalocyanine (TiOPc) layer were deposited by evaporation under vacuum onto a glass substrate. Conversion of the TiOPc into Y-form [12] was achieved by solvent treatment in chlorobenzene and water vapors during 24 h in order to obtain a better charge photogeneration. The indium tin oxide (ITO) coating the glass substrate had a resistivity of 10 Ω cm^2. The 25 μm thickness of the sample was controlled by using spacers and verified by using a laser scanning microscope. The empty cell was then filled with the EHCz by capillarity. It should be noticed that no solvent was used during the preparation of this device.

The absorption spectra of EHCz, PVK and TiOPc measured in thin films are shown in Fig. 1. Both EHCz and PVK are fully transparent in the visible range of wavelength and strongly absorb the ultraviolet light. The peaks observed at 335 and 348 nm are characteristic of the carbazole monomer unit. The spectral position of these transitions and their relative absorption intensities are not deeply altered when changing from the EHCz to the PVK which means that there is no ground-state interaction among carbazole groups. In our TOF experi-

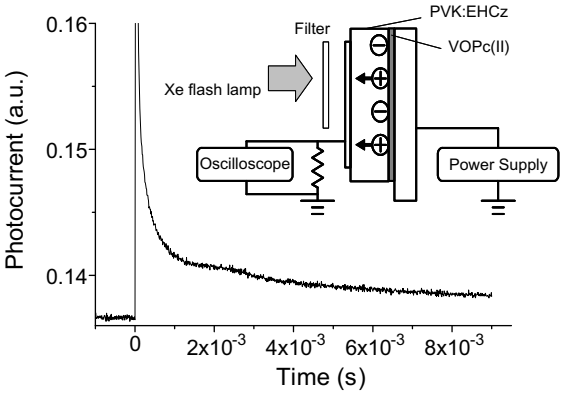

Fig. 2. Transient photocurrent in EHCz obtained by TOF technique with an applied electric field of 27 V/μm. In the inset, schematic representation of our TOF experiment.

ments, as illustrated in the inset of Fig. 2, the phthalocyanine CGL's were excited by a xenon flash lamp from 600 to 800 nm using appropriate filters. By considering the absorption spectra given in Fig. 1, the light in our experimental configuration is mainly absorbed by the CGL, producing a photocarrier sheet in our samples. The photocurrent signal is then detected using a 50 kΩ resistance input of a digital storage oscilloscope. The resistance–capacitance RC time constant of the system is estimated to less than 7.5 μs which was fast enough to accurately determine the charge carrier mobility in our samples.

Fig. 2 shows the photocurrent transient due to hole transport, measured at room temperature in EHCz with an applied electric field of 27 V/μm. This curve presents the features normally observed in photoconductive polymers: an initial spike associated to electronic relaxation of the charge carriers towards their density of states distribution, a plateau of variable temporal length and a long lasting tail on the trailing edge generally attributed to a dispersive transport. The plateau region leads to a well-defined inflection point demarcating the transit time τ_t of the packet. This transit time which corresponds to the time for the charge carrier packet to travel across the device, was determined from the intersection of the asymptotes to the plateau and the trailing edge of the transients in log–log scale. Mobility was then calculated from the classical expression $\mu = L/(\tau_t E)$, where L is the sample thickness, E is the magnitude of the applied electric field and τ_t is the transit time. Furthermore, by changing the polarity of the electric field applied across the sample, no photocurrent induced by electron transport was observed. It is well known that the conduction in most of carbazole derivatives is entirely dominated by holes and that hole transport occurs in these materials by hopping between carbazole units.

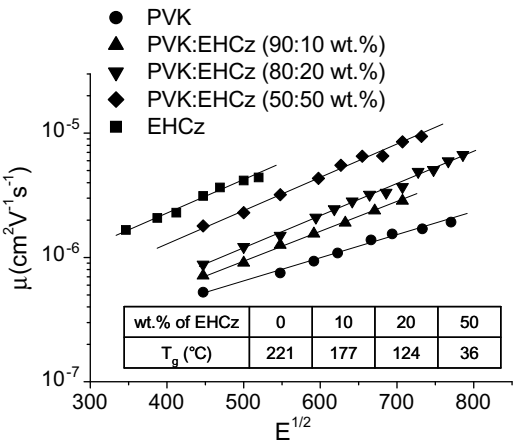

Fig. 3. Electric field dependence of the hole drift mobility in PVK, EHCz and their blends. Solid lines are the fits obtained from Eq. (1). In the inset, the table gives T_g versus the concentration of liquid carbazole in PVK:EHCz systems.

Fig. 3 shows the hole mobility in several PVK:EHCz blends as a function of the applied electric field. The hole mobility in PVK is strongly field and temperature dependent varying typically from 10^{-8} to 10^{-5} cm^2/(Vs) according to the temperature and the electric field [13]. The mobilities that we measured in PVK are in good consistency with this range of values. The mobility is found to gradually increase with the concentration of liquid carbazole and is one order of magnitude higher in EHCz than in PVK. In term of equations, the carrier drift mobility in polymers can be expressed as [14,15]:

$$\mu = \alpha_0 \rho^2 \exp\left(-\frac{2\rho}{\rho_0}\right) \exp\left(-\frac{\Delta_0}{kT}\right) \times \exp\left[\beta\sqrt{E}\left(\frac{1}{kT} - \frac{1}{kT_0}\right)\right] = \mu_0 \exp\left[\beta\sqrt{E}\left(\frac{1}{kT} - \frac{1}{kT_0}\right)\right] \quad (1)$$

where μ_0 and α_0 are fitting parameters, ρ is the distance between hopping sites, ρ_0 is the wave function decay constant, Δ_0 is the zero electric field activation energy, β and T_0 are parameters that characterize the electric field dependence. This equation has been already used to describe the field dependence of the carrier mobility in PVK based materials [15]. Consistently, we found that the mobility in liquid carbazole and in its blends with PVK increases exponentially with $\sqrt{E}$. The incorporation of liquid carbazole in the PVK host allows subtle control of charge transport without major modifications to the energy levels of the system. The HOMO level of EHCz is assumed here to be the same as that of PVK because for both the active moieties consist in carbazole group. We attribute the enhancement of the mobility in liquid carbazole to a larger wave function decay constant ρ_0, which leads to a larger transfer integral and a shorter effective distance between the carbazole hopping sites. The amplitude of the transfer integral is known to be extremely sensitive to the molecular packing and depends on the strength of the π–π interactions between conjugated

molecules or molecular groups. The low T_g of EHCz implies much larger and faster molecular motions than in PVK and this can induce a larger overlap between the wave function of adjacent carbazole units. The table in the inset of Fig. 3 displays the T_g value of the PVK blends, measured by differential scanning calorimetry at 10 °C/min. The enhancement of the charge carrier mobility with decreasing T_g can be assigned to a gradual increase of the transfer integral with the concentration of liquid carbazole. Fig. 3 also shows that the slope coefficient β does not depend significantly on the concentration of liquid carbazole. This parameter is related to the dipole moment [16] of the charge transporting molecules and thus does not strongly vary in our carbazole-based materials. The observed enhancement of the charge carrier mobility without any change in β indicates the strong potential of liquid carbazole to be used as a host material for displays and photorefractive devices.

Fig. 4 shows the photoluminescence (PL) spectra of EHCz, PVK and their blends. The broad and structureless emission spectrum of PVK exhibits a maximum at 408 nm. The feature of the PL spectrum in PVK is well assigned to the formation of excimers in which two interacting carbazole pendants, one of which is electronically excited, achieve an overlapping sandwich like configuration [17]. The emission spectrum in EHCz is found sharper than in PVK and three peaks are distinguished at 389, 409 and 433 nm. From previous works [17,18], these peaks are associated to a partial and total overlap of two carbazole groups. While there is a large dispersion of overlap degree between carbazole rings in PVK under the restriction based on the covalent bonding of polymer backbone, only stable dimers are formed in EHCz under the thermal equivalent states based on its softness. Fig. 4 shows the evolution of the PL spectra as a function of the liquid carbazole concentration and thus as a function of T_g. The changes in the shape of the PL spectra and in the relative strengths of the peaks can be associated to gradual variations in the distribution of the overlap degrees between the carbazole groups. Excimer states in PVK are known to act as trap for mobile holes leading to a significant decrease of their drift mobility [19,20]. Therefore, the PL spectra of the PVK:EHCz blends suggest that the enhancement of the charge carrier mobility in liquid carbazole can also be induced by the effects of T_g on the excimer trapping sites. It is worth noting that the variations observed in the PL spectra imply as well significant changes in the transfer integral.

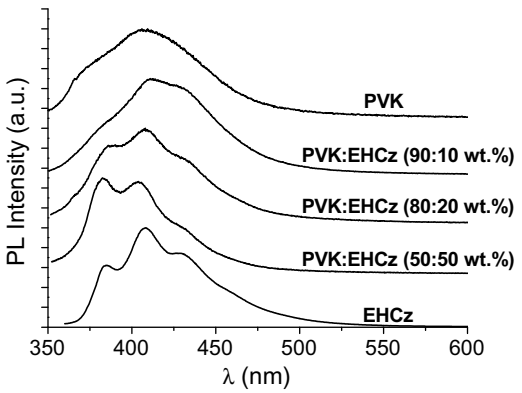

Fig. 4. Photoluminescence spectra of EHCz, PVK and their blends. The films of PVK, PVK:EHCz (90:10 wt.%), PVK:EHCz (80:20 wt.%), PVK:EHCz (50:50 wt.%) and EHCz were excited at 345, 346, 347, 348 and 357 nm, respectively.

In conclusion, we have demonstrated that the hole mobility in EHCz is one order of magnitude higher than in PVK and that the charge transport properties of PVK:EHCz blends can be finely tuned by changing the concentration of the liquid carbazole. We explain the enhancement of the hole mobility in EHCz by the influence of T_g on both the transfer integral and the excimer trapping sites. Based on its charge transport and fluorescence properties, we believe that liquid carbazole is an interesting candidate for various optoelectronic applications and could even provide a good opportunity to develop a new type of devices based on its unique liquid state.

References

[1] K. Meerholz, B.L. Volodin, Sandalphon, B. Kippelen, N. Peyghambarian, Nature 371 (1994) 497.
[2] Y. Zhang, T. Wada, S. Sasabe, J. Mater. Chem. 8 (1998) 809.
[3] Y. Wang, Nature 356 (1992) 585.
[4] J. Kido, K. Hongawa, K. Okuyama, K. Nagai, Appl. Phys. Lett. 63 (1993) 2627.
[5] J. Kido, H. Shionoya, K. Nagai, Appl. Phys. Lett. 67 (1995) 2281.
[6] Y. Liu, M. Nishiura, Y. Wang, Z. Hou, J. Am. Chem. Soc. 128 (2006) 5592.
[7] K. Brunner, A. van Dijken, H. Börner, J.J.A.M. Bastiaansen, N.M.M. Kiggen, B.M.W. Langeveld, J. Am. Chem. Soc. 126 (2004) 6035.
[8] E. Hendrickx, B.D. Guenther, Y. Zhang, J.F. Wang, K. Staub, Q. Zhang, S.R. Marder, B. Kippelen, N. Peyghambarian, Chem. Phys. 245 (1999) 407.
[9] J.-C. Ribierre, T. Aoyama, T. Kobayashi, T. Sassa, T. Muto, T. Wada, J. Appl. Phys. 102 (2007) 033106.

[10] P.M. Borsenberger, D.S. Weiss, Organic Photoreceptors for Imaging Systems, Springer, NY, 1993, p. 273.
[11] A. Yamashita, T. Maruno, T. Hayashi, J. Phys. Chem. 97 (1993) 4567.
[12] J. Mizuguchi, G. Rihs, H.R. Karfunkel, J. Phys. Chem. 99 (1995) 16217.
[13] W.D. Gill, J. Appl. Phys. 43 (1972) 5052.
[14] A. Peled, L.B. Schein, D. Glatz, Phys. Rev. B 41 (1990) 10835.
[15] W.D. Gill, J. Appl. Phys. 43 (1972) 5033.
[16] A. Hirao, H. Nishizawa, Phys. Rev. B 56 (1997) R2904.
[17] G.E. Johnson, J. Chem. Phys. 62 (1975) 4697.
[18] K. Okamoto, A. Itaya, S. Kusabayashi, Chem. Lett. (1974) 1167.
[19] W. Klopffer, J. Chem. Phys. 50 (1969) 2337.
[20] M. Yokoyama, K. Akiyama, N. Yamamori, H. Mikawa, S. Kusabayashi, Polym. J. 17 (1985) 545.

Available online at www.sciencedirect.com
ScienceDirect
Organic Electronics 9 (2008) 401–406
Organic Electronics
www.elsevier.com/locate/orgel

Letter

Organic light emitting diodes with highly conductive micropatterned polymer anodes

C. Piliego *, M. Mazzeo, B. Cortese, R. Cingolani, G. Gigli

National Nanotechnology Laboratory of INFM-CNR, and Istituto Superiore Universitario di Formazione Interdisciplinare-sezione Nanoscienze, Via per Arnesano Km.5, 73100 Lecce, Italy

Received 2 September 2007; received in revised form 11 December 2007; accepted 22 December 2007
Available online 18 January 2008

Abstract

We use a soft lithography technique to pattern a high conductive poly(3,4-ethylene dioxythiophene):poly(styrene sulfonate) (PEDOT:PSS) acting as anode in organic light emitting diodes. In this method all the polymer layers except for the desired pattern are lifted up from the substrate surface. We are able to define the emissive zones of our devices on a large area in a cheap and fast way. By comparing the devices realized using the patterned polymeric anode with an untreated indium tin oxide substrate, we obtained current efficiency values that have the same order of magnitude: this is the first step for the realization of low cost devices suitable for flexible substrates.

PACS: 73.61.Ph

Keywords: Organic light emitting diodes; Displays; Patterning; Polymeric anodes

Organic light emitting diodes (OLEDs) have recently attracted much attention for their application in display systems because of the advantages of self-emission, wide viewing angle, high brightness, high contrast and potentially low cost. OLED based next generation displays will be ultra thin, power efficient and mechanically flexible [1–3].

Although indium tin oxide (ITO) is frequently used as the transparent electrode in flexible displays, its mechanical flexibility is limited, and cracks readily occur when the substrate is bent, inserting defects in the device [4].

This is not the only obstacle for the use of ITO in future generation OLEDs; a few of the limitations are: the diffusion of oxygen and indium into proximate charge transporting/emissive layers [5], significant absorption in the blue region [6], a relatively low work function (4.7 eV) [7], corrosion susceptibility and a large increase in the price of indium [8]. Furthermore, fabrication of any devices requires patterning of the substrate: for ITO the most frequently used method is photolithography, using chemically intensive etching steps and cleaning procedures which determine the overall processing cost.

* Corresponding author. Tel.: +39 0832 298228; fax: +39 0832 298238.
E-mail address: piliclau@mailing.unile.it (C. Piliego).

1566-1199/$ - see front matter © 2008 Elsevier B.V. All rights reserved.
doi:10.1016/j.orgel.2007.12.007

Therefore, it is of great interest to find a low cost and transparent organic material, which at the same time is feasible for flexible substrates, highly conductive and easily patternable. The goal is to employ a generally applicable technology that allows for the production of inexpensive patterns for polymeric conductors in high performance, fully plastic electronic devices. Among conducting polymers poly(3,4-ethylenedioxythiophene):poly(styrene-sulfonate) PEDOT:PSS has emerged as a promising material for electrodes in optoelectronic devices. It has many advantages over other conducting polymers such as high transparency in the visible range and excellent thermal stability [9]. It can also be processed in an aqueous solution. Consequently PEDOT:PSS has been widely used as a hole injection layer for the molecular stack deposited on it. It also reduces the roughness of the ITO layer [10]. PEDOT:PSS shows more favorable properties than ITO, such as easy deposition, low surface roughness and low cost. However, until now its use as an anode in electronic devices has been limited by its low conductivity: PEDOT:PSS (Baytron P, Bayer Corporation) has a conductivity of less than $10\ S\ cm^{-1}$, depending on the type of coating formulation [11].

The recently developed PEDOT:PSS formulation Baytron PH 500, (hereafter referred to as PH500) from H.C. Stark solves this problem: if dimethylsulfoxide (DMSO) is added to the aqueous dispersion it can reach a conductivity value higher than $300\ S\ cm^{-1}$ [11], opening the possibility of fabricating ITO free OLEDs on flexible substrates.

In this letter we apply the lift-up soft lithography technique [12] to pattern a polymeric electrode of highly conductive PEDOT-PH500: we are able, in a simple and direct way, to define the emissive zone of our OLEDs with different sizes and shapes on a micrometric scale.

In the lift-up technique a mold with protruding features is brought in conformal contact with the PEDOT:PSS layer and after few seconds is removed. The polymer that is in contact with the protruding features adheres to the mold and becomes detached from the substrate, leaving the desired pattern on the surface.

Since the thickness determines the resistance of the layer [13], lift-up seems to be the more suitable method for the patterning of PEDOT:PSS used as an anode. In fact on the contrary to other soft lithography techniques [12] applied to PEDOT:PSS, such as micro molding in capillaries and micro contact printing, the lift up method is applicable on a large area, and allows good control of the thickness of the polymer layer on the surface. The same method was used by Inganäs and co-workers [12] to pattern a layer of PEDOT:PSS mixed with glycerol: in this case the fracture in the polymeric film during the lift-up occurred in the low cohesive material of glycerol, leading to a less defined profile when the line size is 10 μm. Also the conductivity of the PEDOT:PSS mixed with glycerol ($80\ S\ cm^{-1}$) is not enough to run an array of diodes connected through the same polymeric anode.

In this letter we reduced these problems.

We spin-coated an aqueous polymer dispersion of Baytron PH500 containing 5% of DMSO onto a pre-cleaned glass substrate. By using a spin-coating rate of 1700 rpm for 30 s [14] it is possible to obtain a thickness of almost 100 nm, which is enough to guarantee a good conductivity (about $360\ S\ cm^{-1}$) [15]. In addition, applying this rate the film is still wet when the substrate is removed from the spin coater and it is ready to undergo the imprinting process. Since the film must remain wet during the entire procedure, it is left to dry only for a minute and is then put in contact with the stamp for 30 s at 80 °C (Fig. 1a). The stamps were prepared by casting polydimethylsiloxane (PDMS) (Sylgard 184) with a curing agent in the ratio of 10:1 against silicon template realized by photolithography. The PDMS mold was cured for 1 h at 140 °C in order to minimize changes in its physical and mechanical properties, as well as to avoid transfer of PDMS on the PEDOT layer during contact. Before using the stamp it was exposed to plasma oxygen to render the surface hydrophilic and to facilitate contact with the water-based solution [16].

Conformal contact of the PDMS mold with the polymeric layer is essential for the patterning technique in order to ensure that there are no gaps or air bubbles trapped between the mold and the PEDOT-PH500 layer. As shown in the third step of Fig. 1(a), when the mold is removed the regions of PEDOT-PH500 layer that were in contact with it, become detached, resulting in the patterned anode. The patterned PEDOT-PH500 layer was then heated at 140 °C for 10 min to completely remove the solvent.

An appealing feature of this method is that it is very fast when compared with the multiple-step photolithographic processes used for ITO. It takes only a few minutes to obtain a patterned polymeric anode on a large area with good resolution.

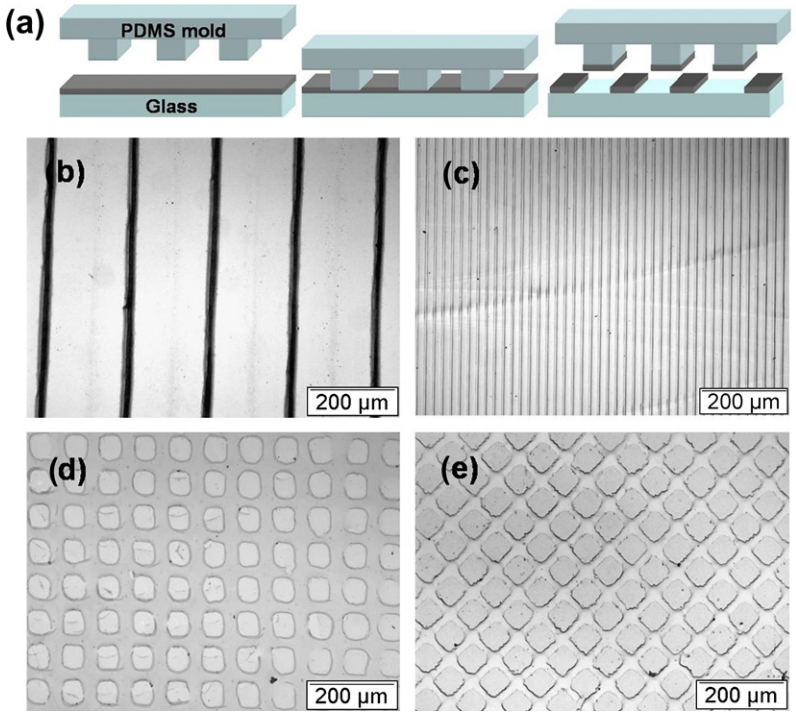

Fig. 1. (a) Schematic illustration of lift-up process: PEDOT-PH500 layer deposited on glass is detached from the substrate after conformal contact with the PDMS mold. (b–e) Patterned PEDOT-PH500 film on glass substrate: (b) 25 μm wide lines of PEDOT-PH500 separated by 160 μm, (c) 3 μm wide lines separated by 15 μm, (d) square holes of size 60 × 60 μm and spacing 15 μm, (e) square pillars of size 60 × 60 μm and spacing 15 μm.

Furthermore, the completely cured PDMS mold can be used repeatedly after having been cleaned with deionized water.

Another advantage is that during the process no pressure is applied for the patterning, avoiding the risk of deformations, buckles or collapses of the mold. The absence of applied pressure allows us to obtain good pattern fidelity even for small feature sizes on a large area.

The lift-off process works because the adhesion between the PDMS mold, treated with a plasma, and the DMSO-doped PEDOT-PH500 layer is stronger than the adhesion between the film and the glass substrate [17].

The work of adhesion W_{12} between materials 1 and 2 can be calculated with a harmonic-mean equation as follows:

$$W_{12} = 4\left(\frac{\gamma_1^d\gamma_2^d}{\gamma_1^d + \gamma_2^d} + \frac{\gamma_1^p\gamma_2^p}{\gamma_1^p + \gamma_2^p}\right) \quad (1)$$

where the superscripts d and p are for the dispersion and the polar components of the surface tension γ, respectively. For PEDOT-PH500 detachment we calculated the work of adhesion based on previous equation and contact angles [18]: $W_{\mathrm{PEDOTPH500/Glass}} = 135.73\ \mathrm{mJ/m_2} < W_{\mathrm{PEDOTPH500/PDMS}} = 145.48\ \mathrm{mJ/m^2}$. Clearly, selective lift-off of regions of the film is to be expected.

Shown in Fig. 1b–e is the PEDOT-PH500 layer patterned by the lift-up technique: we are able to realize stripes of different dimensions, (the smallest are 3 μm wide in Fig. 1c), as well as pillars and holes (Fig. 1d–e).

A three-dimensional atomic force microscopy (AFM) image (Fig. 2a) of the film shows that the lines obtained have smooth and vertical sidewalls. The sectional profile (Fig. 2b) indicates that the polymer thickness is about 140 nm, enough to guarantee good conductivity.

This technique is very appealing for the fabrication of ITO-free OLEDs: we realized a green device using the patterned PEDOT-PH500 as anode. We deposited a layer with the optimized thickness, able to guarantee good conductivity and at the same time good transmittance in the visible range (about 85%). After the optimization of the patterning process we realized a standard device, using thermal evaporation deposition, in order to test the performances and to compare the results with the ITO anode.

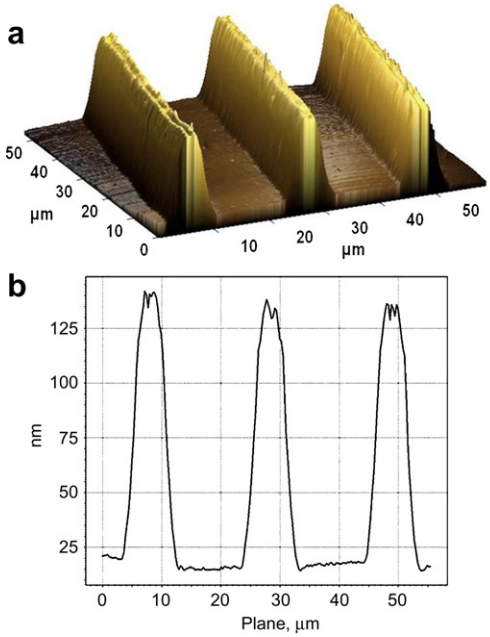

Fig. 2. (a) Three-dimensional AFM image of a group of lines (8 μm wide separated by 10 μm) and (b) sectional profile of the patterned polymer film.

The organic layers are 40 nm of *N*,*N*′-diphenyl-*N*,*N*′-bis(1-naphthylphenyl)-1,1′-biphenyl-4,4′-diamine (α-NPD), as a hole transporting layer and 50 nm of tris-(8-hydroxyquinoline) aluminum (Alq_3) as the active layer. A cathode consisting of 0.5 nm of LiF followed by 150 nm of Al was deposited on the organic stack.

Fig. 3 shows the confocal microscope images of the green light emitted from the devices. For the various geometries and scales (lines with different width in Fig. 3a–c and squared holes, with a side of 60 μm in Fig. 3d), light is emitted only from the areas where PEDOT-PH500 is present after the patterning process. The OLEDs are biased with a constant voltage of 10 V, and the electroluminescence is collected by a charge coupled device (CCD) color camera coupled to a confocal laser scanning microscope. The high contrast between the dark zones and the emissive zones confirms that the detachment process works and no residue remains on the glass substrate after the patterning.

In order to examine the effect of patterning on the device performance we compared the same devices fabricated using: PEDOT-PH500, patterned PEDOT-PH500, and ITO with and without plasma oxygen treatment as anodes. The comparison between the electroluminescent spectra (Fig. 4a) shows that the polymeric anode does not change the emission: the marginal difference is due to the different refractive index and absorption coefficient of ITO and PEDOT-PH500.

The device with the PEDOT-PH500 anode shows on average a lower turn on voltage (10 cd/m^2 between 4 and 4.2 V) with respect to the ITO anode

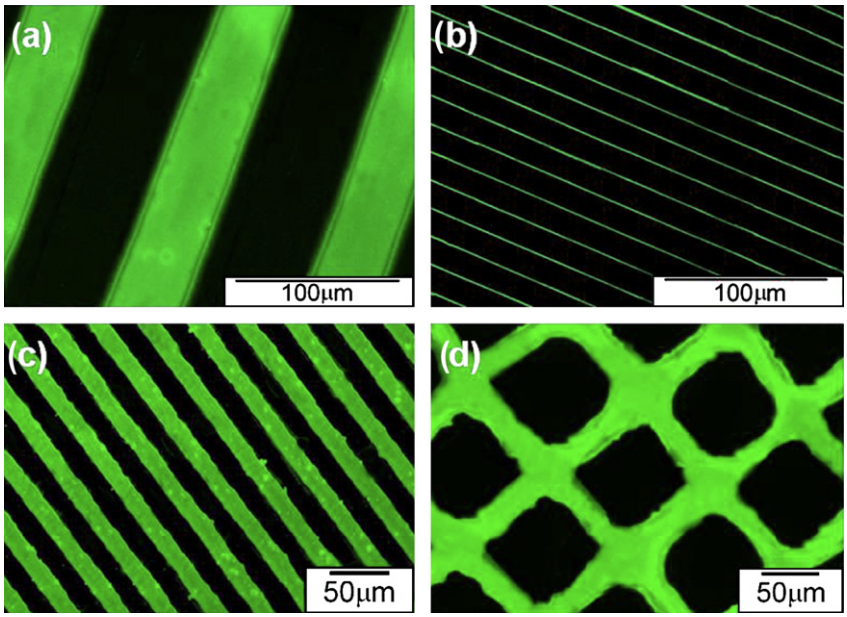

Fig. 3. Confocal microscope images of the emission from OLED device fabricated by lift-up: (a) 55 μm wide lines of PEDOT-PH500 separated by 70 μm, (b) 3 μm wide lines separated by 15 μm, (c) 15 μm wide lines separated by 15 μm, and (d) square holes of size 60 ×60 μm and spacing 15 μm.

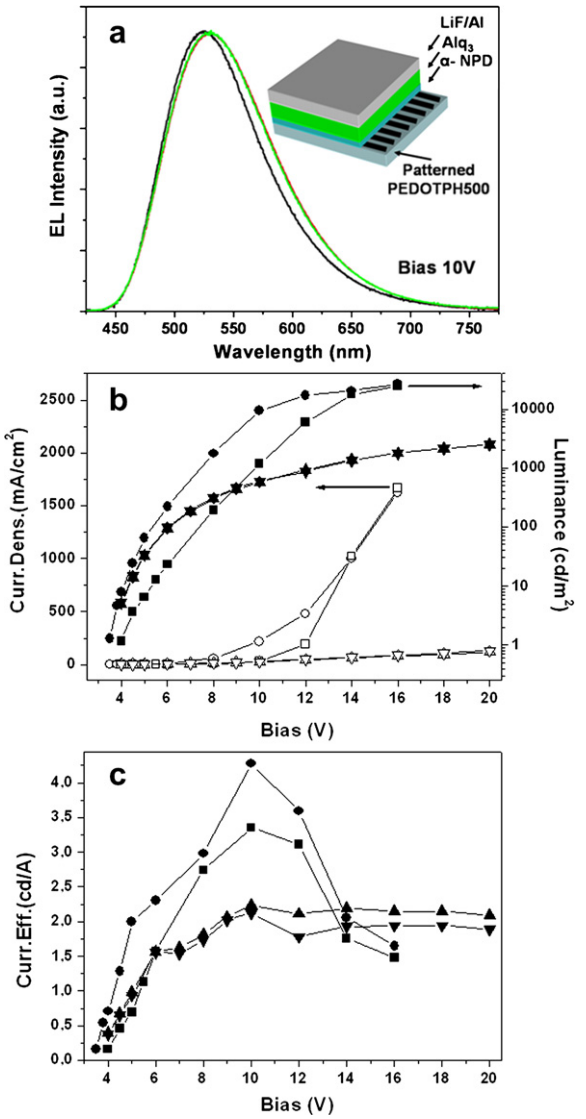

Fig. 4. (a) Electroluminescent spectra, black line ITO, red line unpatterned PEDOT-PH500, green line patterned PEDOT-PH500. Inset: device structure. (b) Characteristic of patterned OLED and reference devices: ITO anode with plasma oxygen treatment (circles); ITO anode without plasma oxygen treatment (square), PEDOT-PH500 anode (triangle pointing up), patterned PEDOT-PH500 (triangle pointing down); open symbols are current density–voltage measurements, while solid symbols are luminance–voltage measurements. (c) Current efficiency: ITO anode with plasma oxygen treatment (circles); ITO anode without plasma oxygen treatment (square), PEDOT-PH500 anode (triangle pointing up), patterned PEDOTPH500 (triangle pointing down).

(10 cd/m^2 between 5 and 5.5 V) without the oxygen plasma treatment. This means that intrinsically this material presents a lower energy barrier for hole injection with respect to the ITO. The polymer work function is ca. 5.0 eV [14], which is higher than that of ITO (typically 4.5–4.7 eV). After the plasma oxygen treatment a turn-on voltage of 4–4.5 V was also observed for the ITO substrates.

The standard device on ITO with plasma oxygen reaches a maximum current efficiency of 4.27 cd/A at 10 V (9411 cd/m^2 with a current density of 35 mA/cm^2). At the same voltage the maximum current efficiency of the PEDOT-PH500 anode is 2.23 cd/A (571 cd/m^2 with 25.5 mA/cm^2). The patterned device was realized using a mold with lines of 15 μm separated by spaces of 15 μm (Fig. 3c). It shows a turn on voltage of 4–4.2 V and a current efficiency of 2,12 cd/A (corresponding to 599 cd/m^2 with 28.3 mA/cm^2), which is comparable with the unpatterned PEDOT-PH500: this indicates that the lift-up process does not affect the performances. The current density of the patterned device is calculated considering that the current flows only where the PEDOT-PH500 is present.

By placing the emitting layer between a p-doped and an n-doped layer for electron and hole transport (p-i-n OLEDs), Fehse et al. [14] have already demonstrated that the performances of devices using PEDOTPH 500 as an anode can even surpass that of ITO-based OLEDs.

In conclusion we have presented a simple, but effective method to pattern highly conductive PEDOT-PH500 anodes. Since the method is based only on a distinction of contact and non-contact zones between the PDMS mold and the underlying PEDOT-PH500 layer, we obtain good resolution with small feature sizes also .We are able to obtain various geometries and define the emissive zones of our devices on a large area in an economic and fast way.

Our results open up a new way for the development of low cost plastic electronics. Highly conductive, easy patternable polymeric anodes could potentially lead to the replacement of ITOs for the realization of flexible and economic OLED based displays.

References

[1] B. Geffroy, P. le Roy, C. Prat, Poly. Int. 55 (2006) 572.
[2] M.C. Gather, A. Köhnen, A. Falcou, H. Becker, K. Meerholz, Adv. Funct. Mater. 17 (2007) 191.
[3] P. Görrn, M. Sander, J. Meyer, M. Kröger, E. Becker, H.-H. Johannes, W. Kowalsky, T. Riedl, Adv. Mater. 18 (2006) 738.
[4] R. Paetzold, K. Heuser, D. Henseler, S. Roeger, G. Wittmann, A. Winnacker, Appl. Phys. Lett. 82 (2003) 3342.
[5] S.T. Lee, Z.Q. Gao, L.S. Hung, Appl. Phys. Lett. 75 (1999) 1404.

[6] H.C. Lee, O. Ok Park, Vacuum 80 (2006) 880.
[7] D.J. Milliron, I.G. Hill, C. Shen, A. Kahn, J. Schwartz, J. Appl. Phys. 87 (2000) 572.
[8] Source: www.idtechex.com/printedelectronicsworld (09 July 2007).
[9] L. Groenendaal, F. Jonas, D. Freitag, H. Pielartzik, J.R. Reynolds, Adv. Mater. 12 (2000) 481.
[10] Ch. Jonda, A.B.R. Mayer, U. Stolz, A. Elschner, A. Karbach, J. Mater. Sci. 35 (2000) 5645.
[11] Baytron homepage. <http://www.baytron.com> (accessed November, 2007).
[12] T. Granlund, T. Nyberg, L. Stolz Roman, M. Svensson, O. Inganäs, Adv. Mater. 12 (2000) 269.
[13] D. Hohnholz, H. Okuzaki, A.G. MacDiarmid, Adv. Funct. Mater. 15 (2005) 51.
[14] K. Fehse, K. Walzer, K. Leo, W. Lövenich, A. Elschner, Adv. Mater. 19 (2007) 441.
[15] We spin coated a layer of PEDOT PH500 mixed with 5% of DMSO resulting in a thickness of about 100 nm on a glass substrate of 2 cm × 2 cm and then we baked it at 140 °C for 10 min. We then evaporated four small squared Aluminium areas (2 mm × 2 mm) in the four corners of the substrate for the electrical contacts. We measured the sheet resistance with the four-point probe method (van der Pauw method) and then we calculated the film conductivity.
[16] J. Ng Lee, C. Park, G.M. Whitesides, Anal. Chem. 75 (2003) 6544.
[17] S. Wu, Poly Interface and Adhesion, Dekker, New York, 1982.
[18] The contact angles of water and diidomethane with the PDMS mold after the oxygen plasma treatment, are 23° and 54.3°, respectively, with the spin coated PEDOT-PH500 layer 34° and 31°, and with the glass substrate after the cleaning procedure 33° and 46°. Calculated dispersion and polar component surface tensions of PDMS mold, PEDOT-PH500, and glass are: $\gamma^{d,PDMS} = 30.04\ mJ/m^2$, $\gamma^{p,PDMS} = 39.26\ mJ/m^2$, $\gamma^{d,PEDOT-PH500} = 39.66\ mJ/m^2$, $\gamma^{p,PEDOT-PH500} = 31.08\ mJ/m^2$, $\gamma^{d,GLASS} = 32.59\ mJ/m^2$ and $\gamma^{p,GLASS} = 33.16\ mJ/m^2$. The surface tension of diiodomethane at 20 °C was calculated from Ref. [17] and the values of other surface tensions at 20 °C are as follows: $\gamma^{d,water} = 22.6\ mJ/m^2$, $\gamma^{p,water} = 50.2\ mJ/m^2$, $\gamma^{d,diiodomethane} = 49\ mJ/m^2$ and $\gamma^{p,diiodomethane} = 1.8\ mJ/m^2$. Contact angles of water and diiodomethane on the different substrates were measured in atmosphere at room temperature using the sessile drop method of a contact angle goniometer (Dataphysics OCA 20). A drop of 3 μl was deposited on the surface and each reported angle is calculated on the average of six measurements in different points on the sample.

Available online at www.sciencedirect.com
ScienceDirect
Organic Electronics 9 (2008) 407–412
Organic Electronics
www.elsevier.com/locate/orgel

Letter

Interface studies of Aluminum, 8-hydroxyquinolatolithium (Liq) and Alq_3 for inverted OLED application

Youjong Lee [a], Joohyung Kim [a], Soonnam Kwon [a], Chang-Ki Min [b], Y. Yi [b], J.W. Kim [b], Bonki Koo [c], MunPyo Hong [a,*]

[a] Department of Display Semiconductor, Korea University, Chungnam 339-700, Republic of Korea
[b] Korea Research Institute of Standards and Science, 1 Doryong-Dong, Daejon 305-340, Republic of Korea
[c] Global Display Co., Ltd., 505-12, Mongne-dong, Ansan city, Kyunggi-do, Republic of Korea

Received 6 September 2007; received in revised form 18 December 2007; accepted 3 January 2008
Available online 9 January 2008

Abstract

This study examined the interfaces of Alq_3 on a thin 8-hydroxyquinolatolithium (Liq) layer deposited on aluminum using X-ray and ultraviolet photoemission spectroscopy. A thin layer of Liq reacted with the underlying aluminum surface. As a result, the molecular orbital features of Alq_3 shifted to a higher binding energy and a new gap state was created. This effect is believed to lower the barrier height for electron injection. An organic light emitting device with a structure of ITO/Al/Liq/Alq_3/NPB/WO_3/Al was fabricated.The device performance showed characteristics that were consistent with the results of the photoemission studies. It is proposed that Al/Liq can be used as an efficient electron injection layer for inverted organic light emitting devices.

PACS: 73.20.At; 73.40.−c

Keywords: OLED; IBOLED; EIL; Liq

1. Introduction

Organic light emitting devices (OLED) have been one of the most interesting subjects over the last decade due to their potential applications to large area flat panel displays e.g. televisions. In order for OLED to be applied to large area displays, an active matrix driving method needs to be developed for OLED. The development of an inverted OLED is one of the efforts to match OLED to the existing n-type amorphous silicon thin film transistor (a-Si TFT) technology. Inverted OLED consists of a bottom cathode (in contrast to a bottom anode in normal OLED) followed by the formation of an electron transport layer, light emission layer, hole transport layer and anode. The inverted OLED enables a direct connection between the bottom cathode and the n-type TFT drain line, which results in a decrease in driving voltage and improved stability [1,2].

* Corresponding author. Tel.: +82 41 860 1321; fax: +82 41 865 0939.
E-mail address: goodmoon@korea.ac.kr (M. Hong).

1566-1199/$ - see front matter © 2008 Elsevier B.V. All rights reserved.
doi:10.1016/j.orgel.2008.01.001

The bottom cathode of inverted OLED can be transparent or reflective, depending on the direction of the emitting light. If the light is emitted to the top direction of the substrate, the device is known as an inverted top emission OLED (ITOLED) [3–5]. On the other hand, the device is called an inverted bottom emission OLED (IBOLED) if the light is emitted to the bottom direction of the substrate [6]. Due to the difficulty in forming a transparent electrode onto an organic layer, this study focused on IBOLED for inverted device applications. Therefore, the bottom electrodes were formed on ITO, which was used as the transparent current carrier.

The bottom electrode should be chosen among materials that allow easy electron injection into the electron transporting layer [7–9]. Another requirement of a bottom electrode is the possibility of mass production, which suggests the exclusion of reactive metals, such as alkali metals or alkaline earth metals. Aluminum was chosen for the bottom electrode due to its wide applications to mass production. In addition, a thin layer of 8-hydoxyquinolatolithium (Liq) [10,11] was inserted between Al and Alq_3 to enhance the injection of electrons. Recently, Liq has been widely used instead of LiF in the OLED industry on account of its superior evaporation property and insensitivity to thickness control. To the best of the authors' knowledge, there are no reports on photoemission related to Liq. In this report, several IBOLED devices were made using various bottom cathodes for comparison. X-ray and ultraviolet photoelectron spectroscopy (XPS and UPS, respectively) were used to determine the role of Liq in the enhancement of electron injection.

2. Experimental

The devices were fabricated on ITO coated glass substrates, which had been patterned, cleaned by chemicals and undergone a UV ozone treatment before being inserted into the fabrication chamber. The device fabrication chamber consisted of two parts, a metal chamber and organic chamber, which were connected via a vacuum manipulator. The inserted ITO glass was transferred to a metal chamber and thin layer of metal was deposited onto the ITO surface by thermal evaporation. The substrate was then transferred to the organic chamber to deposit the organic layers, including Liq, Alq_3 and NPB. After successive deposition of the organic layers, the substrate was transferred back to the metal chamber to deposit the WO_3 and Al thin films. The device characteristics were measured using a Photo Research PR650 spectrometer and a Keithley 236 source measure unit.

The photoemission was examined using a VG electron spectroscope equipped with a magnesium source (1253.6 eV) for XPS analysis and an unfiltered He I (21.2 eV) gas discharge lamp for UPS analysis. The base pressure of the analysis chamber was $< 5 \times 10^{-10}$ torr and the preparation chamber pressure during evaporation was $< 1 \times 10^{-7}$ torr. The UPS spectra were taken with a sample bias of -10 V. The ITO coated glass was cleaned before being inserted into the introduction chamber for almost all measurements. However, Au and Ag foils were used as substrates for the Au and Ag measurements. The Au or Ag foils were cleaned by Ar ion bombardment before the measurement or vacuum deposition. The organic materials including Alq_3 and Liq were evaporated in a quartz tube that was wound by tungsten wire for heating. The aluminum was evaporated by directly heating the tungsten wire. All layer thicknesses were monitored and determined using a quartz crystal microbalance.

3. Result and discussion

Fig. 1 shows the current density curves versus voltage of the six devices with different cathodes. The current efficiency curves versus current density for the six devices are shown in the inset. Table 1 shows the numerical results of the devices. Each device was completed by the successive vacuum deposition of

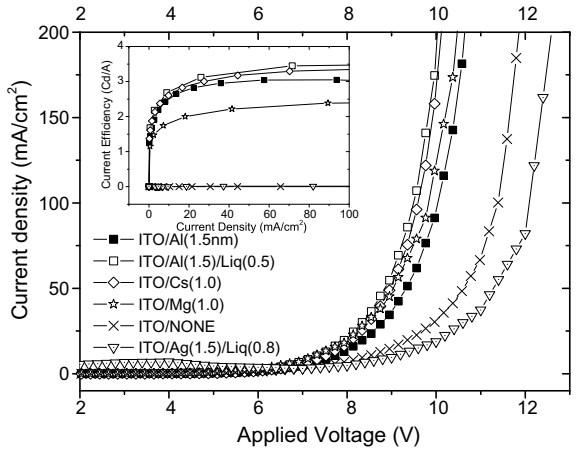

Fig. 1. *J–V* characteristics of inverted bottom emission OLEDs as a function of the cathode material. The device structure: ITO/Cathode/Alq_3/NPB/WO_3/Al.

Table 1
Performance of the devices shown in Fig. 1

Cathode	Bias (V)	Current density (mA/cm^2)	Luminance (Cd/m^2)	LE (Cd/A)
ITO/Al (1.5 nm)	9.5	57.6	1751	3.04
ITO/Al (1.5)/ Liq (0.5)	9	57.1	1902	3.33
ITO/Cs (1.0)	8.9	44.4	1407	3.17
ITO/Mg (1.0)	8.9	41.5	920	2.21
ITO/None	10.5	44.3	0	0
ITO/Ag (1.5)/ Liq (0.8)	11	38	5.1	0.01361

Alq_3 (60 nm)/NPB(60 nm)/WO_3(4 nm)/Al (60 nm). WO_3 was used as the hole injection layer that was evaporated by direct heating of the tungsten boat [12,13]. The device with no cathode, i.e., the device with an ITO/Alq_3/NPB/WO_3/Al structure showed no light emission but exhibited a considerable current, which is an indication of a hole only device. In addition, the device with the Ag/Liq cathode showed slight light emission and a current efficiency of only 0.018 Cd/A. This is contrast to the result of the device using Al/Liq as the cathode. The devices with the Al/Liq, Cs and Mg cathodes showed excellent characteristics. Cs and Mg were introduced by several authors as efficient electron injecting materials for inverted devices [6,7]. However, Cs and Mg are very reactive to ambient air exposure, which is not good for mass production. From the viewpoint of mass production, aluminum and Liq are stable materials and are thus suitable for mass production. The device exhibited a luminance of 6500 Cd/m^2 and a current efficiency of 3.5 Cd/A at an applied voltage of 9.5 V and a current density of 100 mA/cm^2. The turn on voltage and maximum luminance was 4.5 V and 21,000 Cd/m^2, respectively.

In order to check the effect of oxidation of the Al layer before the deposition of Liq, three devices were made under the same condition except for the time interval between Al layer formation and Liq layer deposition. The first device was made immediately after depositing the Al on ITO. The second and third device was made after 1 h and 10 h later. The first and second device showed similar results but the third device showed significant degradation, which contained many dark spots, low current injection, and low luminance efficiency.

The above results were based on device with a 1.5 nm thick Al layer. This thickness was chosen to satisfy both current injection enhancement and optical transparency. Fig. 2 shows the measured EL spectra at various tilted angles. In addition, the luminance curves as a function of the viewing angles are shown in the inset. The device with the 1.5 nm thick Al did not show a micro-cavity effect, which is an important requirement for a wide viewing angle.

Fig. 3a shows the evolution of the UPS spectra of the system consisting of Alq_3 on Liq over an aluminum layer. First, fresh Al was evaporated onto ITO, and the UPS spectrum was taken. Second, a 0.5 nm Liq layer was deposited onto the Al layer, and the UPS spectrum was taken. Finally, Alq_3 layers were deposited onto Liq layer up to a 3 nm thickness. The UPS spectrum of the 0.5 nm Liq film over the Al layer showed two small peaks around 3.9 eV and 2.1 eV. These two peaks are the highest occupied molecular orbital (HOMO) and gap state of Liq, respectively. However, the peak height of the HOMO is very small and the underlying aluminum features do not disappear. Fig. 3c presents the magnified spectrum showing different tendency with the spectra of Liq over Ag or Au. In the case of Liq over Ag or Au, after deposition of a 0.5 nm Liq layer, the sharp Ag (near 4 eV) or Au (near 2.5 eV) valence band peaks disappeared and molecular orbital features of Liq dominated. The molecular orbital features of Liq are similar to those of Alq_3. No gap state could be seen in the spectrum, which is in contrast to the result of Liq on the Al layer. This suggests a reaction between Liq and the underlying aluminum layer. As shown in Fig. 3a, the HOMO peak and gap state peak of Alq_3 began to grow after the deposition of an additional 0.3 nm Alq_3. The inset in Fig. 3a shows the evolution of the gap state

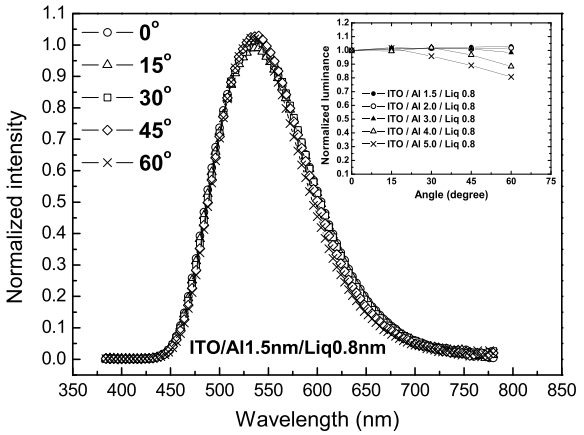

Fig. 2. Measured EL spectra at angles ranging from 0 to 60, and (inset) measured luminance with at measurement angles ranging from 0 to 60.

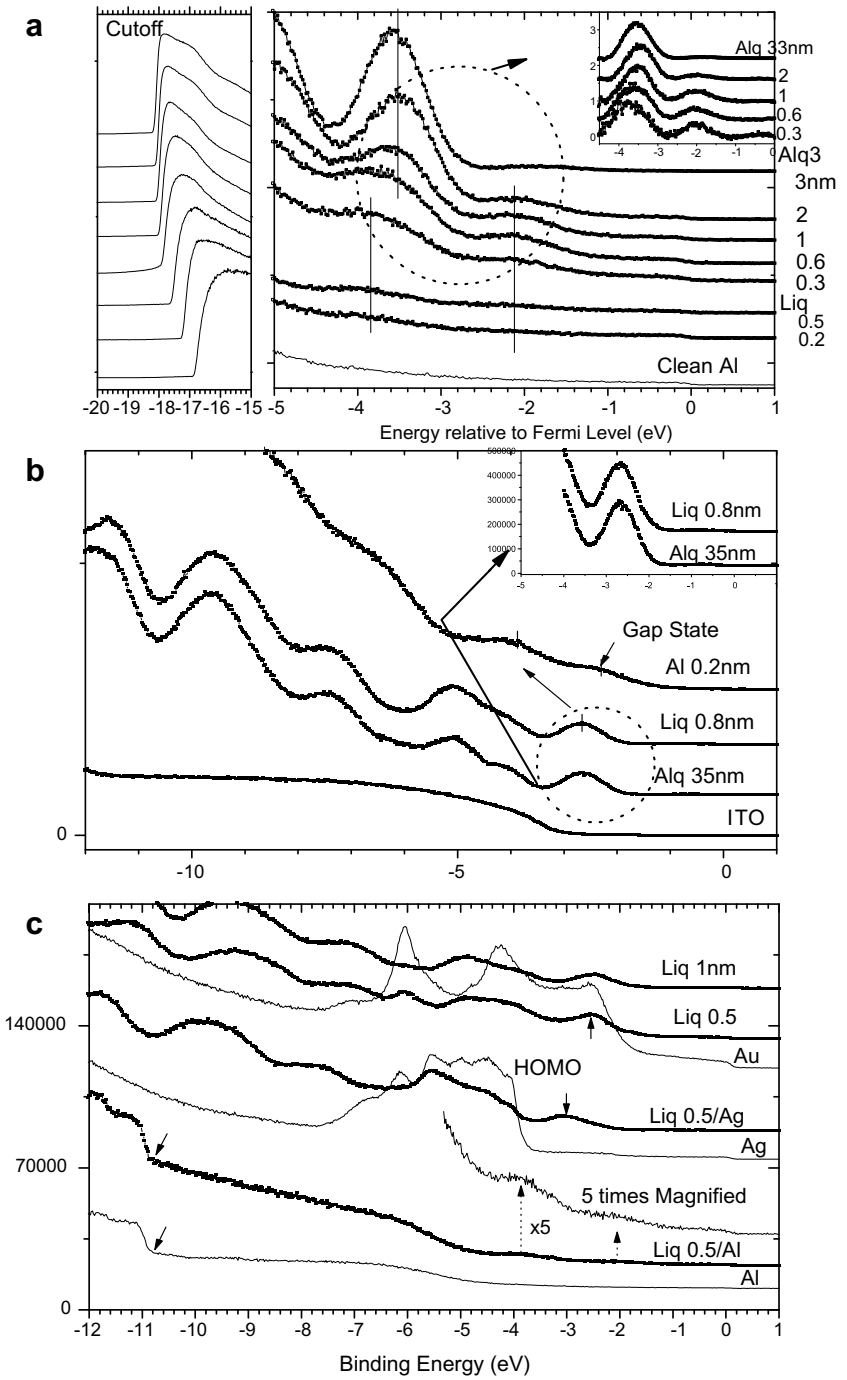

Fig. 3. Evolution of the valence band spectra. (a) Alq_3 deposition over Liq over Al, (b) Al deposition over Liq on Alq_3 and (c) Liq deposition over Au, Ag and Al.

height compared with the HOMO peak height. All the HOMO peaks were normalized after subtracting the baseline. The gap state appeared to disappear after depositing a 2 nm Alq_3 layer, which demonstrates that the peak located at approximately 2.1 eV is an interface state. In addition, the peak position of the HOMO level shifted to a lower binding energy as a function of the Alq_3 thickness. In the case of a gap state, the peak position did not move but just disappeared. This suggests that the gap

state formed by a chemical reaction between Liq and Al shifted the Alq_3 molecular levels down.

Fig. 3b shows the evolution of the UPS spectra after the deposition of Liq and aluminum onto the Alq_3 layer, which is the reverse stack of Fig. 3a. The initial HOMO peak of Alq_3 at 2.77 eV was not changed by the deposition of a 0.8 nm Liq layer except for the small shift in the cutoff to a higher binding energy (0.15 eV), which was not shown in the figure. The inset in Fig. 3b compares the magnified HOMO level of Alq_3 with that of Liq 0.8 nm over Alq_3, where no change could be resolved. Upon deposition of 0.2 nm Al, the HOMO peak of Alq_3 shifted by 1.3 eV to a higher binding energy, and a new gap state appeared at approximately 2 eV. This resembles the UPS spectrum of 0.5 nm Liq on aluminum shown in Fig. 3a, in which a small HOMO peak and a gap state peak of Liq appeared. In addition, the spectra evolution is quite similar to the report of Al on LiF/Alq_3 [14], where the authors suggested that Li is liberated from LiF and reacts with Alq_3 to form a radical anion.

Fig. 4a shows the change in the XPS N (1s) spectrum caused by the deposition of aluminum onto the Liq/Alq_3 layer. The single feature of the N (1s) peak for the Liq 0.8nm/Alq_3 layer becomes two peaks after the deposition of aluminum with a separation of approximately 1.5 eV. But the other peaks including O (1s), C (1s) and Al (2p) did not show any split (not shown in the figure). These results are similar to the results of Al deposition on LiF/Alq_3 and Li doping on Alq_3 [14,15]. The main peaks for N (1s), O (1s), C (1s), and Al (2p) were shifted to a higher binding energy by approximately 0.7 eV, 1.0 eV, 0.5 eV, and 0.7 eV, respectively (not shown in the figure). This indicates a consistent tendency with the shift in the HOMO level shown above in Fig. 3b. The above results dif-

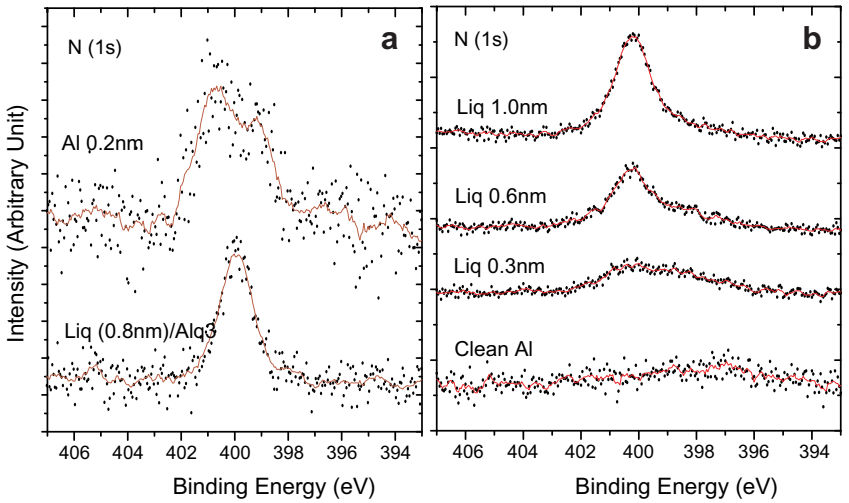

Fig. 4. (a) Change in the N (1s) spectrum of Liq/Alq_3 layers caused by the deposition of Al, (b) Evolution of the N (1s) spectrum as a function of Liq deposition onto Al. The dots are raw data points and the solid lines were obtained by an average of adjacent 5 points.

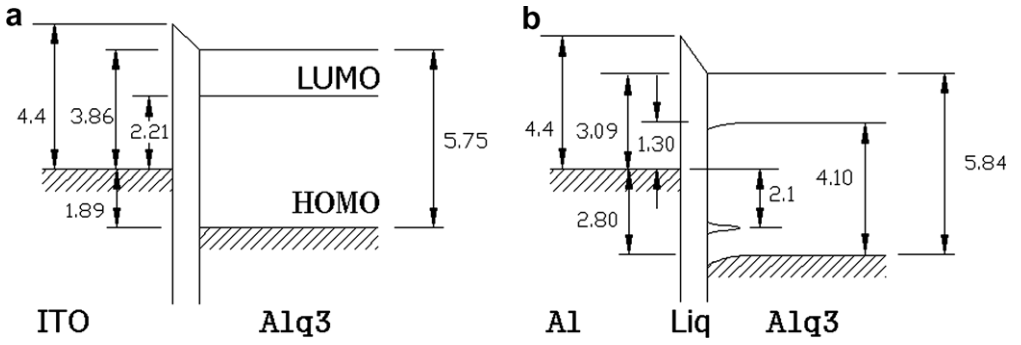

Fig. 5. Energy diagram of (a) interface between ITO and Alq_3, (b) interfaces between Al, Liq and Alq_3.

fer from previous work on Al/Alq_3, where all the four peaks did not show any significant split [14]. Fig. 4b shows the evolution of N (1s) spectrum during the deposition of Liq on Al. This is a reverse stack of Fig. 4a. The N (1s) spectrum shows two broad peaks until 0.3 nm Liq is deposited. After 0.6 nm deposition of Liq, the main peak with a higher binding energy overwhelms the small peak with lower binding energy. This spectrum evolution is similar to that shown in Fig. 4a. The lower binding energy peaks were assigned to the peaks originating from Liq molecules, which had reacted with Al.

Fig. 5 shows the energy diagrams calculated from the values of high binding energy cutoff and HOMO position. Fig. 5a shows an energy diagram of the interface between ITO and Alq_3, in which the electron barrier could be inferred as 2.21 eV based on the assumption that the transport energy gap of Alq_3 is approximately 4.1 eV [16,17]. Fig. 5b shows the energy diagram of Al/Liq/Alq_3 with a barrier height of 1.3 eV. The electron injection barrier was reduced by 0.91 eV by inserting a cathode buffer layer of Al/Liq.

4. Conclusion

A thin Liq film on a thin aluminum film can be used as an efficient electron injecting layer in inverted OLED. The device result showed excellent characteristics that were comparable to a device using Cs as the electron injecting layer. A thin aluminum layer with a thickness up to 1.5 nm did not show any micro-cavity effect or decrease in luminance. From the UPS results, the calculated barrier height of ITO/Alq_3 and (ITO)/Al/Liq/Alq_3 was 2.21 eV and 1.3 eV, respectively. The improved device characteristics can be explained by a decrease in barrier height. UPS and XPS suggest that the Liq reacted with the underlying aluminum layer. This reaction caused a chemical change in Liq, which might have resulted in the liberation of Li ions. As a result, the HOMO peak of the subsequent Alq_3 layer shifted to a higher binding energy. The increase in the binding energy of HOMO is responsible for the decrease in barrier height.

Acknowledgement

This Work Supported Partially by The Second Brain Korea 21 Program Endorsed by The Korea Ministry of Education.

References

[1] V. Bulovi, P. Tian, P.E. Burrows, M.R. Gokhale, S.R. Forrest, Appl. Phys. Lett. 70 (1997) 2954.
[2] X. Zhou, M. Pfeiffer, J.S. Huang, J. Blochwitz-Nimoth, D.S. Qin, A. Werner, J. Drechsel, B. Maennig, K. Leo, Appl. Phys. Lett. 81 (2002) 922.
[3] C. Qiu, H. Chen, Z. Xie, M. Wong, H.S. Kwok, Appl. Phys. Lett. 80 (2002) 3485.
[4] C.W. Chen, C.L. Lin, C.C. Wu, Appl. Phys. Lett. 85 (2004) 2469.
[5] Ho Won Choi, Soo Young Kim, Woong Kwon Kim, Jong Lam Lee, Appl. Phys. Lett. 87 (2005) 082102.
[6] Ta-Ya Chu, Jenn-Fang Chen, Szu-Yi Chen, Chao-Jung Chen, Chin H. Chen, Appl. Phys. Lett. 89 (2006) 053503.
[7] Takayuki Uchida, Toshifumi Mimura, Masao Ohtsuka, Toshio Otomo, Mieko Ide, Azusa Shida, Yutaka Sawada, Thin Solid Films 496 (2006) 75.
[8] S.T. Zhang, X.M. Ding, J.M. Zhao, H.Z. Shi, J. He, Z.H. Xiong, H.J. Ding, E.G. Obbard, Y.Q. Zhan, W. Huang, X.Y. Hou, Appl. Phys. Lett. 84 (2004) 425.
[9] F. Li, H. Tang, J. Anderegg, J. Shinar, Appl. Phys. Lett. 70 (1997) 1233.
[10] Christoph Schmitz, Hans-Werner Schmidt, Mukundan Thelakkat, Chem. Mater. 2000 (2000) 3012.
[11] Xinyou Zheng, Youzhi Wu, Runguang Sun, Wenqing Zhu, Xueyin Jiang, Zhilin Zhang, Shaohong Xu, Thin Solid Films 478 (2005) 252.
[12] Chih-Wei Chu, Sheng-Han Li, Chieh-Wei Chen, Vishal Shrotriya, Yang Yanga, Appl. Phys. Lett. 87 (2005) 193508.
[13] M.D. Hill, R.G. Egdell, J. Phys. C: Solid State Phys. 16 (1983) 6205.
[14] Quoc Toan Le, Li Yan, Yongli Gao, M.G. Mason, D.J. Giesen, C.W. Tang, J. Appl. Phys. 87 (2000) 375.
[15] N. Johansson, T. Osada, S. Stafstrom, W.R. Salaneck, V. Parente, D.A. Dos Santos, X. Crispin, J.L. Bredas, J. Chem. Phys. 111 (1999) 2157.
[16] I.G. Hill, A. Kahn, Z.G. Soos, R.A. Pascal Jr., Chem. Phys. Lett. 327 (2000) 181.
[17] T. Schwieger, H. Peisert, M. Knupfer, M.S. Golden, J. Fink, Phys. Rev. B 65 (2001) 033204.

Available online at www.sciencedirect.com
ScienceDirect
Organic Electronics 9 (2008) 413–417
Organic Electronics
www.elsevier.com/locate/orgel

Letter

Improvement of mechanical and electrical stabilities of flexible organic thin film transistor by using adhesive organic interlayer

Y.G. Seol [a], N.-E. Lee [a,*], S.H. Park [b], J.Y. Bae [b]

[a] School of Advanced Materials Science and Engineering, Center for Advanced Plasma Surface Technology, Sungkyunkwan University, Suwon, Kyunggi-do 440-746, Republic of Korea
[b] Department of Polymer Science and Engineering, Sungkyunkwan University, Suwon, Kyunggi-do 440-746, Republic of Korea

Received 20 November 2007; received in revised form 2 February 2008; accepted 7 February 2008
Available online 14 February 2008

Abstract

A newly synthesized organic material, oligo(3-methylsulfanylthiophene), was applied as an adhesive interlayer between the gold source/drain electrodes and the pentacene semiconductor layer in flexible, bottom-gated, organic thin film transistors (OTFTs). The cyclic bending tests showed that the electrical properties of the devices with the thermally evaporated interlayer were more stable than those of the device with no interlayer. The interlayer also reduced the contact resistance between Au and the pentacene layer. These results indicate that the interlayer is very useful in enhancing the mechanical and electrical stabilities of the OTFTs under repetitive mechanical bending as well as the electrical performance.

PACS: 72.20.Jv; 82.35.Gh; 85.30.Tv

Keywords: Organic thin film transistor; Oligo(3-methylsulfanylthiophene); Flexible devices; Cyclic bending; Interlayer; Contact resistance

In order to realize flexible electronic systems including radio-frequency identification tags [1–4], low-cost sensors [5–7], and flexible displays [1,3,8–12], utilizing organic thin film transistors (OTFTs), it is essential to achieve a good mechanical flexibility of each layer with no cracking and excellent adhesion between the layers without delamination during repetitive mechanical bending. Using all organic layers in flexible devices may allow acceptable mechanical flexibility [13]. Since the performance of all-organic TFTs has been limited by the low conductivity of the organic conductors as well as by the low dielectric constant and high leakage characteristics of the organic gate dielectrics [4,13], however, hybrid OTFTs employing both organic and inorganic materials have been more extensively investigated for high performance. In this case, improvement and control of adhesion properties in between dissimilar materials for good flexibility of the OTFTs are of great technical importance.

* Corresponding author. Tel.: +82 32 290 7398; fax: +82 31 290 7410.
E-mail address: nelee@skku.edu (N.-E. Lee).

1566-1199/$ - see front matter © 2008 Elsevier B.V. All rights reserved.
doi:10.1016/j.orgel.2008.02.003

In an inverted-staggered OTFT with the top-contact structure, the adhesion between Au source/drain (S/D) electrodes and pentacene layer is limited due their poor chemical interactions [14,15] and the large contact resistance limits device performance [16–18]. Adhesion improvement between metal electrodes and polymeric substrate using plasma treatment of the substrate and insertion of metal adhesion layer has been reported [14,15]. However, the plasma treatment of the pentacene layer for adhesion improvement between the pentacene and the Au source/drain electrodes in top contact structure is not applicable due to plasma-induced damage. Extensive studies of the interlayer between the metal electrode and organic semiconductor layer in organic light-emitting diodes have been performed in order to improve the injection efficiency of carriers [19,20]. Recently, there have been some experimental reports on the use of an organic semiconductor layer or self-assembled monolayer (SAM) between the Au electrode and organic semiconductors to reduce the contact resistance in OTFTs [21–23]. However, no research on improving adhesion and reducing contact resistance between the Au electrode and the pentacene layer simultaneously has been reported for flexible OTFTs. In this work, we show that the insertion of a newly synthesized adhesive organic interlayer, oligo(3-methylsulfanylthiophene) (OMST), in between the Au electrode and the pentacene layer was effective in improving the adhesion and device characteristics.

For synthesis of OMST interlayer, thiophene monomer or halogenated thiophene monomer with alkyl sulfonyl substituent can be made by oxidative coupling or reductive coupling. Mixture of iron (III) chloride (6.23 g) and chloroform (40 ml) were stirred for 30 min by magnetic stirring. After that, 3-methylsulfanylthiophene (1 g) was slowly added using a syringe in the solution and stirred for 12 h. After being left overnight, the remaining iron (III) chloride was removed by Soxhlet extraction with methanol and acetone and then one more Soxhlet extraction was performed with chloroform and the resulting specimen was dried in a vacuum oven.

OTFTs with pentacene layer (≅75 nm), gold S/D electrodes (≅80 nm), cross-linked PVP (poly-4-vinyl phenol) gate dielectric layer (350–400 nm), and electroplated Ni gate electrode (≅150 nm) were fabricated on 125-μm-thick PI film (Du Pont; Kapton®) [15]. The OMST interlayer (≅60 nm) was deposited through shadow mask on the pentacene by thermal evaporation at a deposition rate of 0.1 nm/s and was found to grow on the pentacene in interconnected islands with an average size of 1.4 μm. The average size of the interconnected islands was measured by field-emission scanning electron microscopy (FE-SEM) after deposition of the OMST interlayer on the pentacene layer. There was a difficulty in controlling the deposition rate smaller than 0.1 nm/s.

The mechanical flexibility and adhesion properties were tested by cyclic bending tests with a bending radius of 5 mm using a custom-built cyclic bending machine and by tape tests, respectively. Delamination and cracking were examined by optical microscopy, FE-SEM, and dual beam focused ion beam (FIB)–FESEM (NOVA 200). The electrical characteristics of the OTFTs before and after the cyclic bending test were evaluated in an ambient atmosphere without any protection after preparation using an HP 4145B semiconductor parameter analyzer.

The optical images of the devices following total 60 tension/compression cycles in different directions are shown in Fig. 1. The bent non-interlayer device (Fig. 1a) showed a higher crack density in the Au electrodes compared to the interlayer devices (Fig. 1b). The crack formation was apparently accompanied by delamination of the Au electrodes from the pentacene layer. The size of cracks was also much larger for the non-interlayer device compared to the interlayer device.

The FIB–FESEM cross-sectional images (the insets in Fig. 1a and b) of the non-interlayer and interlayer devices with the cyclic bending of 100,000 times in tension mode showed a clear difference in delamination. The non-interlayer device showed delamination at the Au/pentacene interface, while the interlayer device showed delamination at the pentacene/PVP interface. The tape test results using 3M Scotch™ Magic™ tapes also gave the same results. These results indicate improved integrity of the Au/interlayer/pentacene structure compared to that of the Au/pentacene structure probably because sulfur in the interlayer helped the chemical binding of the interlayer with Au [24].

Electrical characteristics of the bended devices (channel length $L = 35$ μm and channel width $W = 800$ μm) with and without the OMST interlayer were measured in tension mode as a function of the bending cycles and the results are compared in Fig. 2. Analysis of the unbent OTFT devices indicated that the insertion of the 60-nm interlayer increased the drain current on/off ratio (I_{on}/I_{off})

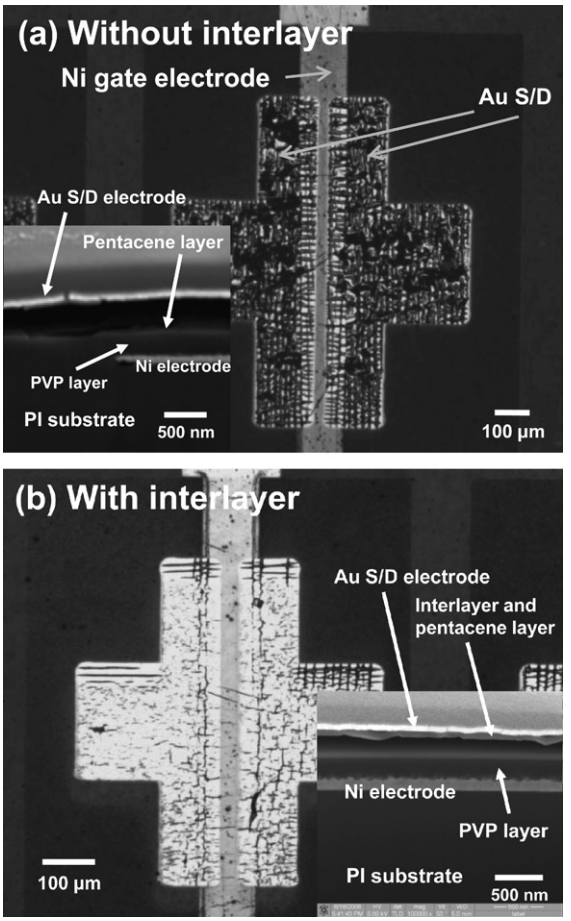

Fig. 1. Surface optical microscopy images and cross-sectional FIB–FESEM images (insets) of the cyclically bent devices: (a) without interlayer and (b) with 60-nm interlayer. The device in the optical images underwent total 60 tension and compression cycle in parallel and perpendicular directions to the channel. The device in the FIB–FESEM images underwent 100,000 tension bending cycles and the direction of bending was perpendicular to the direction of the channel.

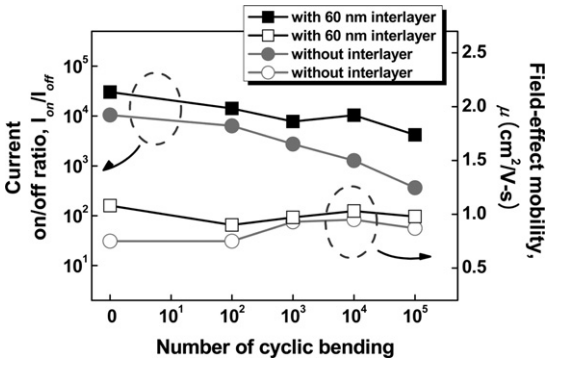

Fig. 2. Electrical characteristics of top-contact OTFTs with cyclic bending in tension mode was show variation of current on/off ratio ($I_{on/off}$) versus the number of bending cycles and field-effect mobility, μ, versus the number of bending cycles.

from $\cong 9 \times 10^3$ to 4×10^4, the field-effect channel mobility (μ) from 0.75 to 1.08 cm^2/V s, and lowered the threshold voltage (V_T) from -14 to -12.8 V. The device with the 120-nm thick interlayer showed reduction in the I_{on} and the μ values and with cyclic bending of 30 times the device characteristics degraded more rapidly compared to the device with the 60-nm interlayer (not shown). The electrical characteristics of the OTFT with the 60-nm-thick interlayer were improved compared to that with no interlayer.

The variation in the $I_{on/off}$ values of the cyclically bent devices in Fig. 2 indicated that the $I_{on/off}$ value of the interlayer device was gradually decreased but at a slow rate with the cyclic bending compared to that of the non-interlayer device. We found that the variation in the $I_{on/off}$ values was dominated by an increase in the off-current caused by accelerated degradation of the pentacene layer with cyclic bending. The change in the μ values of the interlayer device was less with cyclic bending compared to the non-interlayer device. The data in Fig. 2 show that the electrical characteristics of the interlayer device were always more stable and superior to those of the non-interlayer device under cyclic bending.

To understand the clear improvement gained in the electrical properties by introduction of the OMST interlayer, the contact resistance R_C was measured at a low $V_{SD} = -6$ V following the method reported in another report [16]. On average, the contact resistance was significantly reduced by inserting the interlayer, as shown in Fig. 3. The reduced contact resistance led to increase in the sat-

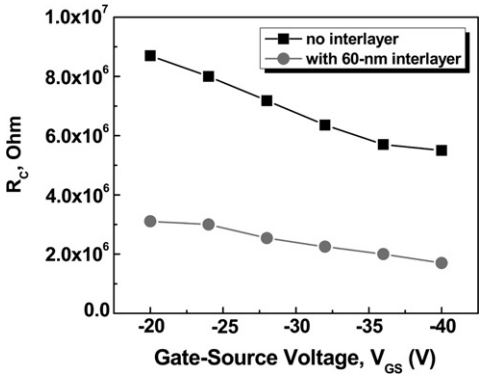

Fig. 3. Contact resistance, R_C, values for various gate voltages at low $V_{SD} = -6$ V.

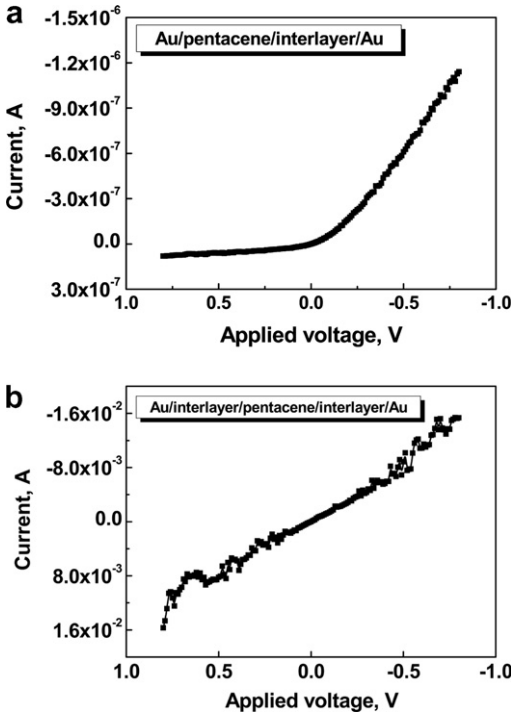

Fig. 4. *I–V* characteristics of the hole-only devices measured in two different structures: (a) Au/pentacene(70 nm)/interlayer(60 nm)/Au, and (b) Au/interlayer(60 nm)/pentacene(70 nm)/interlayer(60 nm)/Au.

urated on-current (I_{on}) of the device from 1.2×10^{-5} to 3.4×10^{-5} A at $V_G = -40$ V, which was considered to have been caused by increased carrier injection at the Au and pentacene interface due to the reduced energy barrier [21].

The results of the contact resistance measurements were consistent with the *I–V* characteristics of the hole-only devices (Fig. 4). The effect of the interlayer on the *I–V* characteristics was measured in two different structures: (a) Au/pentacene(70 nm)/interlayer(60 nm)/Au, and (b) Au/interlayer(60 nm)/pentacene(70 nm)/interlayer(60 nm)/Au. When the interlayer was introduced between the layers on both sides of the Au electrodes, the *I–V* electrical characteristics were changed to a linear relationship showing Ohmic contact property from Schottky contact property on one side because of the reduced energy barrier with the interlayer introduction. Furthermore, the current from the structure (a) with the interlayer at both sides was increased by three orders of magnitude at the same applied voltage compared to that of the device from the structure (b) with the interlayer at only one side.

In order to understand the reduction in the contact resistance with the 60-nm interlayer introduction, contact potential difference (CPD) were measured by Kelvin probe force microscopy (KFM) with the Au tip [25,26]. Fig. 5a and b shows the structure of the samples for the measurement of CPD, CPD image, and CPD distribution at each layer. It can be observed from Fig. 5a that the CPD of the pentacene layer deposited on the interlayer/Au was greatly decreased compared to that of

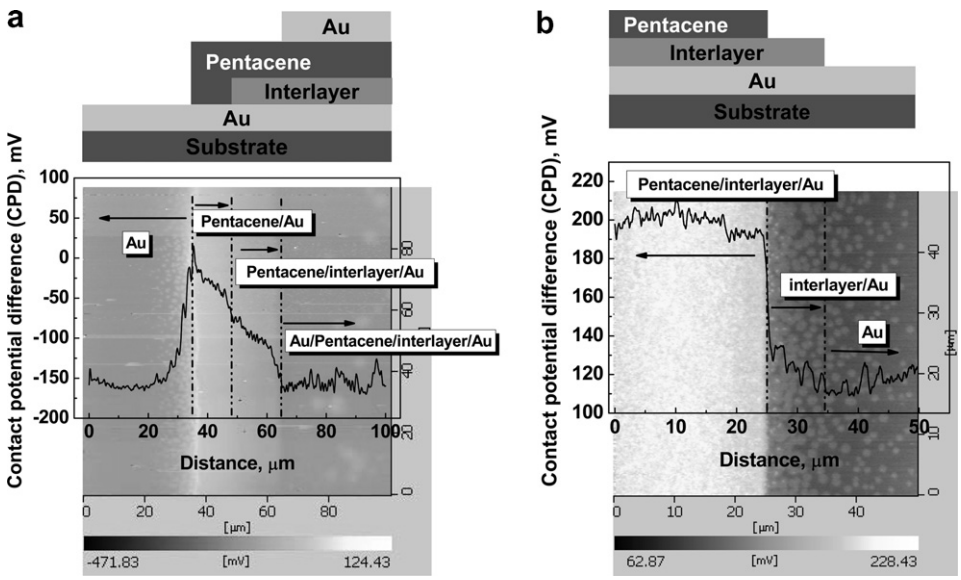

Fig. 5. Structure of the samples for measurement of CPD, CPD image, and CPD distribution at each layer for (a) Au/pentacene/interlayer/Au and (b) pentacne/interlayer/Au. The observed dots in (a) and (b) are ascribed to the islanded morphology of the pentacene and interlayer, respectively, evaporated using the shadow mask.

the pentacene deposited on the Au. The change in the CPD at the interface of the Au and pentacene was 160 mV. When the 60-nm interlayer was inserted between the layers in Fig. 5b, the CPD changes between the Au and the interlayer, and between the pentacene and the interlayer, were 20 and 60 mV, respectively, [27–29]. The decrease in the injection barrier for holes, from 160 to 80 mV, with the introduction of the interlayer reduced contact resistance in Fig. 3 and led to the Ohmic behavior of the contact.

In this work, the mechanical and electrical characteristics of OTFTs with a newly synthesized, organic OMST interlayer were studied under cyclic bending. Use of the interlayer between the Au S/D electrode and the pentacene layer was effective in reducing the contact resistance by mitigating the injection barrier for holes, while the mechanical flexibility of the OTFTs was also improved, leading to improved device performance and electrical stability against the cyclic mechanical deformation. Even though the device characteristics were improved by using the organic interlayer, delamination at the organic–organic interface, such as at the interface of the pentacene–PVP gate dielectrics layer, and cracking of the Au S/D electrodes continued to occur. Therefore, further investigation of cracking and delamination in flexible OTFT devices should be conducted and high performance, mechanically flexible materials such as electrodes and gate dielectric layers need to be developed.

Acknowledgement

This work was supported through the Korea Science and Engineering Foundation (Grant No. R01-2004-000-10839-0) and in part through the Center of Excellence program of the Korea Science and Engineering Foundation (Grant No. R-11-2000-086-0000-0).

References

[1] J.R. Sheats, J. Mater. Res. 19 (2004) 1974.
[2] R. Rotzoll, S. Mohapatra, V. Olariu, R. Wenz, M. Grigas, K. Dimmlerb, O. Shchekin, A. Dodabalapur, Appl. Phys. Lett. 88 (2006) 123502.
[3] T.W. Kelley, P.F. Baude, C. Gerlach, D.F. Ender, D. Muyres, M.A. Haase, D.E. Vogel, S.D. Theiss, Chem. Mater. 16 (2004) 4413.
[4] W. Clemens, W. Fix, J. Ficker, A. Knobloch, A. Ullmann, J. Mater. Res. 19 (2004) 1963.
[5] B. Crone, A. Doadbalapur, A. Gelperin, L. Torsi, H.E. Katz, A.J. Lovinger, Z. Bao, Appl. Phys. Lett. 78 (2001) 2229.
[6] I. Manunza, A. Bonfiglio, Biosens. Bioelectron. 22 (2007) 2775.
[7] T. Someya, T. Sekitani, S. Iba, Y. Kato, H. Kawaguchi, T. Sakurai, Proc. Natl. Acad. Sci. 101 (2004) 9966.
[8] J.A. Rogers, Z. Bao, A. Dodabalapur, IEEE Electron Dev. Lett. 21 (2000) 100.
[9] P. Mach, S.J. Rodriguez, R. Nortrup, P. Wiltiuz, J.A. Rogers, Appl. Phys. Lett. 78 (2001) 3592.
[10] C.D. Sheraw, L. Zhou, J.R. Huang, D.J. Gunbdlich, T.N. Jackson, M.G. Kane, I.G. Hill, M.S. Hammond, J. Campi, B.K. Greening, J. Francl, J. West, Appl. Phys. Lett. 80 (2002) 1088.
[11] Y.-H. Kim, S.-K. Park, D.-G. Moon, W.-K. Kim, J.-I. Han, Displays 25 (2004) 167.
[12] B. Comiskey, J.D. Albert, H. Yshizawa, J. Jacobson, Nature 394 (1998) 253.
[13] H. Rost, J. Ficker, J.S. Alonso, L. Leenders, I. McCulloch, Synth. Met. 145 (2004) 83.
[14] J.G. Lee, Y.G. Seol, N.-E. Lee, Thin Solid Films 515 (2006) 805.
[15] Y.G. Seol, J.G. Lee, N.-E. Lee, Org. Electron. 8 (2007) 513.
[16] P.V. Necliudov, M.S. Shur, D.J. Gundlach, T.N. Jackson, Solid-State Electron. 47 (2003) 259.
[17] T. Maeda, H. Kato, H. Kawakami, Appl. Phys. Lett. 89 (2006) 123508.
[18] I. Yagi, K. Tsukagoshi, Y. Aoyagi, Appl. Phys. Lett. 84 (2004) 813.
[19] S.-F. Chen, C.-W. Wang, Appl. Phys. Lett. 85 (2004) 765.
[20] C. Adachi, T. Tsutsui, in: J. Shinar (Ed.), Organic Light-Emitting Devices, Springer, New York, 2004.
[21] F.C. Chen, L.-J. Kung, T.-H. Chen, Y.-S. Lin, Appl. Phys. Lett. 90 (2007) 073504.
[22] S.Y. Park, Y.H. Noh, H.H. Lee, Appl. Phys. Lett. 88 (2006) 113503.
[23] N. Yoneya, M. Noda, N. Hirai, K. Nomoto, M. Wada, J. Kasahara, Appl. Phys. Lett. 85 (2004) 4663.
[24] J.A. Rodriguez, J. Dvorak, T. Jirsak, G. Liu, J. Hrbek, Y. Aray, C. González, J. Am. Chem. Soc. 125 (2003) 276.
[25] T.A. Beierlein, W. Brütting, H. Riel, E.I. Haskal, P. Müller, W. Reiß, Synth. Met. 111–112 (2000) 295.
[26] J.S. Kim, B. Lägel, E. Moons, N. Johansson, I.D. Baikie, W.R. Salaneck, R.H. Friend, F. Cacialli, Synth. Met. 111–112 (2000) 311.
[27] W.R. Salaneck, M. Fahlman, J. Mater. Res. 19 (2004) 1917.
[28] S. Braun, W. Osikowicz, Y. Wang, W.R. Salaneck, Org. Electron. 8 (2007) 14.
[29] I.-S. Park, S. Park, J. Oh, J. Lee, Org. Electron. 8 (2007) 382.

Available online at www.sciencedirect.com
ScienceDirect
Organic Electronics 9 (2008) 418
Organic Electronics
www.elsevier.com/locate/orgel

Corrigendum

Corrigendum to "Electron transport through polycyclic hydrocarbon molecules: a study of shot noise contribution to the power spectrum" [Organic Electronics 8 (2007) 575]

Santanu K. Maiti

Theoretical Condensed Matter Physics, Division Saha Institute of Nuclear Physics, 1/AF, Bidhannagar, Kolkata 700 064, India

Received 30 January 2008; accepted 1 February 2008
Available online 15 February 2008

The author would like to acknowledge and cite the following published works:

(1) D. Walter, D. Neuhauser, R. Baer. Quantum interference in polycyclic hydrocarbon molecular wires, Chem. Phys. 299 (2004) 139. doi:10.1016/j.chemphys.2003.12.015.

(2) Kamil Walczak, Current fluctuations of polymeric chains, Phys. Stat. Sol. (b) 241 (2004) 2555. doi:10.1002/pssb.200302036.

(3) Kamil Walczak, The role of quantum interference in determining transport properties of molecular bridges, Cent. Eur. J. Chem. 2 (2004) 524. doi:10.2478/BF02476205.

DOI of original article: 10.1016/j.orgel.2007.04.004
E-mail address: santanu.maiti@saha.ac

doi:10.1016/j.orgel.2008.02.004

Available online at www.sciencedirect.com
ScienceDirect
Organic Electronics 9 (2008) 419–424
Organic Electronics
www.elsevier.com/locate/orgel

Improving charge injection in organic thin-film transistors with thiol-based self-assembled monolayers

Patrick Marmont [a], Nicolas Battaglini [a], Philippe Lang [a], Gilles Horowitz [a,*], Jaehyung Hwang [b], Antoine Kahn [b], Claire Amato [c], Patrick Calas [c]

[a] *ITODYS, Université Paris Diderot, CNRS, 1 rue Guy de la Brosse, 75005 Paris, France*
[b] *Department of Electrical Engineering, Princeton University, Princeton, NJ 08540, USA*
[c] *Laboratoire Organisation Moléculaire, Evolution et Matériaux Fluorés, Université Montpellier II, CNRS, Place E. Bataillon, 34095 Montpellier Cedex 05, France*

Received 16 October 2007; received in revised form 8 January 2008; accepted 8 January 2008
Available online 26 January 2008

Abstract

The aim of this work is to improve charge injection by interposing an appropriately oriented dipole layer between contact and semiconductor in organic thin-film transistors (OTFTs). OTFTs are fabricated with pentacene semiconductor and gold source and drain contacts. The contacts are modified with self-assembled monolayers (SAMs) made of alkane or fluorinated alkane thiols. Ultraviolet photoelectron spectroscopy (UPS) shows a respective decrease and increase of the work function of the electrodes. Consistent with these results, we observe an increase and a decrease, respectively, of the contact resistance of the OTFTs, and a further decrease when shortening the length of the fluorinated molecule.

PACS: 73.40.Cg; 78.30.Jw; 79.60.Fr; 81.16.Dn

Keywords: Organic thin-film transistor; Self-assembled monolayers; Contact resistance; Ultraviolet photoelectron spectroscopy; Atomic force microscopy

1. Introduction

Source and drain contact resistance has been identified as a major limitation in organic thin-film transistors (OTFTs) [1]. In p-channel devices, charge injection from the electrodes into the organic semiconductor is controlled by the hole barrier height, which, according to the conventional Mott–Schottky (MS) model, is given by the difference between the semiconductor ionization potential and metal work function. However, this simple image is rarely observed in real junctions, where the presence of an interface dipole may substantially shift the energy levels of the semiconductor with respect to the metal Fermi level. As an example, MS rule would predict the hole barrier at a clean Au-pentacene contact close to zero, while the actual magnitude is 0.85 eV [2]. Several surface treatments have been reported to improve charge injection from metal electrodes into organic semiconductors. This includes selective

* Corresponding author.
E-mail address: horowitz@univ-paris-diderot.fr (G. Horowitz).

1566-1199/$ - see front matter © 2008 Elsevier B.V. All rights reserved.
doi:10.1016/j.orgel.2008.01.004

doping of the semiconductor near the contact [3,4] and oxidative treatment of the electrodes [5]. An alternative way is to purposely introduce on top of the electrode a counterbalancing dipole [6], for example with a self-assembled monolayer (SAM), that is, a single molecular layer that spontaneously forms when dipping the substrate in a solution of an appropriate reactive surfactant. However, while this concept has proven its usefulness in diodes, where the area of the contacts is dominant on the overall size of the device [7,8], the validity of its extension to thin-film transistors is still controversial, probably because in that case the contact area is substantially reduced as compared to that of the conducting channel. This can be exemplified by a recent work by Bock and coworkers [9] where the gold source and drain electrodes of pentacene OTFTs were modified with antrhacene-2-thiol SAMs. A careful analysis of the current–voltage curves through the Transfer Line Method (TLM) clearly indicated that the enhanced performance had to be attributed to better charge transport in the pentacene film due to morphological improvement, while no change of the contact resistance were detected. On the other hand, Asadi and coworkers [10] recently reported evidence for modified hole injection in organic polymer semiconductors upon modification of the source and drain electrodes with non-fluorinated and fluorinated alkyl thiols, while no alteration was recorded in the mobility of the semiconductor film.

The aim of this work is to tune the work function of gold source and drain electrodes with thiol-based SAMs. To adapt the direction and magnitude of the dipole moment, the molecule was chosen among alkanes and fluorinated alkanes. Ultraviolet photoelectron spectroscopy (UPS) is used to validate the concept in terms of work function of the modified gold electrodes. Transistors are then fabricated and characterized with various SAMs. It is found that alkane SAMs have a detrimental effect on hole injection, whereas fluorinated SAMs improve it, in good agreement with the UPS data.

2. Results and discussion

2.1. Fabrication and characterization of the SAMs

The molecules used are decanethiol CH_3–$(CH_2)_9$–SH (DT), and two fluorinated molecules, 1H,1H,2H,2H-perfluorodecanethiol CF_3–$(CF_2)_7$–$(CH_2)_2$–SH (PFDT) and 1H,1H,2H,2H-perfluorohexanethiol CF_3–$(CF_2)_3$–$(CH_2)_2$–SH (PFHT). The fabrication of the SAMs is detailed in the experimental section. In depth characterization of the organization of the SAMs was performed through surface infrared spectroscopy. The infrared spectrum of PFDT is shown in Fig. 1. Perfluoroalkane chains have a helix structure [11]. In the CF_2 stretching mode region, the band at ca. 1220 cm^{-1} (E1, ν_{eq}) and 1335 cm^{-1} (A1, ν_{ax}) are polarized perpendicular and parallel to the helix axis, respectively [12]. The intensity of the former (ν_{eq}) decreases with the adsorption time, whereas that of the latter (ν_{ax}) increases, thus giving evidence for that the molecule tends to straighten up on the substrate with increasing adsorption time.

Because the subsequent deposition of the pentacene film is performed under reduced pressure and moderately high temperature, it might result in desorption or disorganization of the SAM. Accordingly, surface infrared spectroscopy was also carried out after deposition of the pentacene. In all cases, only minute changes of the spectra were observed, thus bringing evidence for the stability and robustness of the monolayers. As an example, a mere shift by 1 cm^{-1} of the $\nu_a(CH_2)$ asymmetrical mode was recorded with DT, indicating a very slight disorganisation of the SAM.

2.2. UPS measurements

The He I UPS spectra taken from the clean Au reference surface and from DT/Au and PFDT/Au are compared in Fig. 2. The Fermi steps and salient features of the Au valence band remain visible on the two SAM-covered samples, consistent with the limited thickness of the molecular layers (13.7 Å

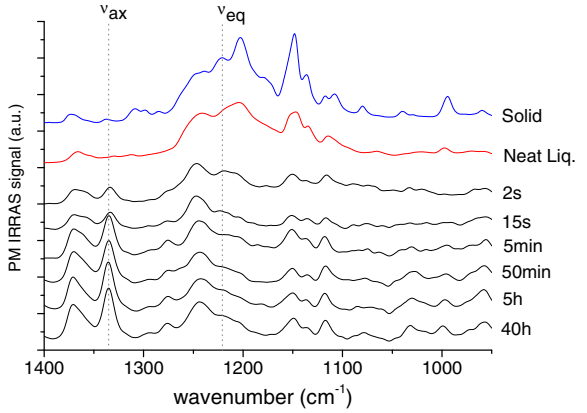

Fig. 1. Infrared (PMIRRAS) spectra of PFDT SAMs on gold for various immersion times. The spectra of the solid and the neat liquid are shown for comparison.

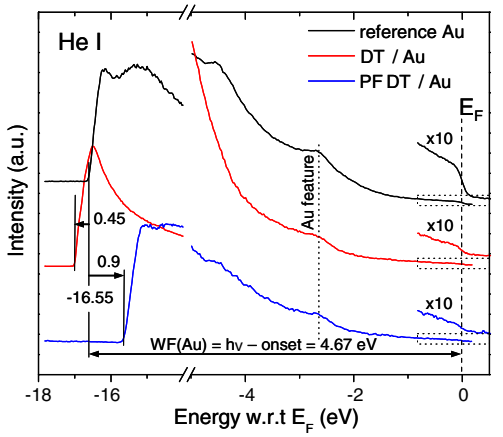

Fig. 2. UPS spectra (He I, $h\nu = 21.22$ eV) of the bare Au substrate and of the Au/DT and Au/PFDT samples. The Fermi step is visible on all three samples. The onset of photoemission (left most part of each spectrum) is used to determine the Au work function (4.67 eV) and the vacuum shift due to the molecular dipole.

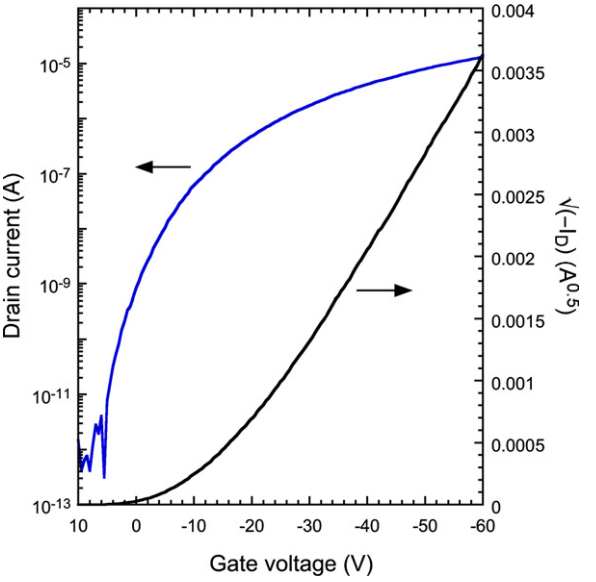

Fig. 3. Saturation transfer characteristic of a typical pentacene transistor at $V_D = -60$ V. Source and drain electrodes are modified with PFHT. Channel length and width are $L = 20$ μm and $W = 200$ μm. The saturation mobility is estimated from the slope or the square root current vs. gate voltage curve.

and 14.3 Å, respectively). The key features are the shifts of the onset of photoemission with respect to that of clean Au, toward higher and lower binding energies for DT/Au and PFDT/Au, respectively. The former denotes a decrease of the Au work function by 0.45 eV and the latter an increase by 0.9 eV, in accord with the known (and opposite) directions of the molecular dipoles of DT and PFDT [3]. These data are in good agreement with Kelvin probe measurements on similar SAM-modified gold [10].

2.3. Characterization of the transistors

A typical transfer characteristic in the saturation regime is given in Fig. 3. The mobility μ was estimated from Eq. (1), where W and L are the width and length of the channel, C_i the capacitance of the gate dielectric and V_T the threshold voltage

$$I_{Dsat} = \frac{W}{2L}\mu C_i (V_G - V_T)^2. \quad (1)$$

Table 1 gives the saturation mobility as a function of the nature of the SAM. We note that the mobility is lowered by an alkane thiol, while it is enhanced by fluorinated SAMs.

The mobility extracted from the saturation current is an *effective* mobility that includes both charge transport in the semiconductor and charge injection and removal at electrodes. To get deeper insight on what causes its variation, we estimated the contact resistance R_c with the Transfer Line Method (TLM) [13]. For this, the transfer characteristic in the linear regime ($V_D = -5$ V for V_G ranging from +30 to −60 V) was measured on devices with various channel length ($L = 2$, 5, 10, 15 and 20 μm) prepared in the same run. From these characteristics, the threshold voltage was first extracted from the peak of the second derivative of the gate voltage dependent drain current, as described previously [14]. The next step consisted of calculating the width corrected total resistance $R \times W = (V_D/I_D) \times W$ as a function of $V_G - V_T$. According to the TLM, this resistance can be decomposed into the contact resistance R_c in series with the channel resistance, as given in Eq. (2)

$$R \times W = R_c \times W + \frac{L}{\mu C_i (V_G - V_T)}. \quad (2)$$

A representative example of the length dependent resistance for various values of $V_G - V_T$ is shown in Fig. 4. The contact resistance corresponds to

Table 1
Saturation mobility of bare and SAM-modified pentacene transistors

SAM	None	DT	PFDT	PFHT
Mobility ($cm^2/V\,s$)	0.040	0.016	0.065	0.105

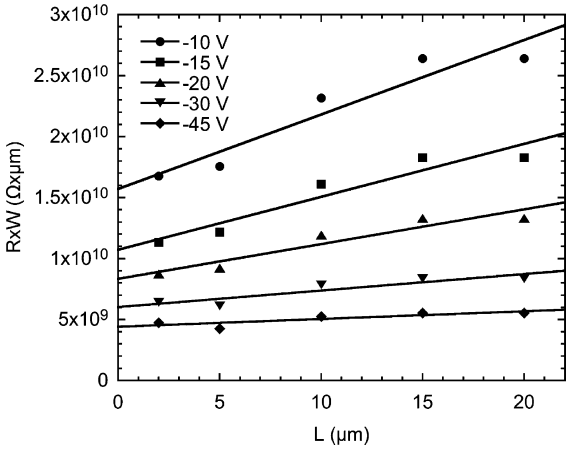

Fig. 4. Representative example of width normalized resistance vs. channel length curves, with untreated gold electrodes. The resistance is estimated from the transfer characteristic at a drain voltage of −5 V. The five curves correspond to five different values of $V_G - V_T$ (−10, −15, −20, −30 and −45 V). The straight lines are least-square fits to Eq. (2). The contact resistance corresponds to the extrapolation of the straight line to zero channel length.

the extrapolation of the straight line to zero channel length. Fig. 5 shows the gate voltage dependent contact resistance as obtained from a least-square fitting of the length dependent resistance to Eq. (2). We note that R_c decreases as $V_G - V_T$ increases,

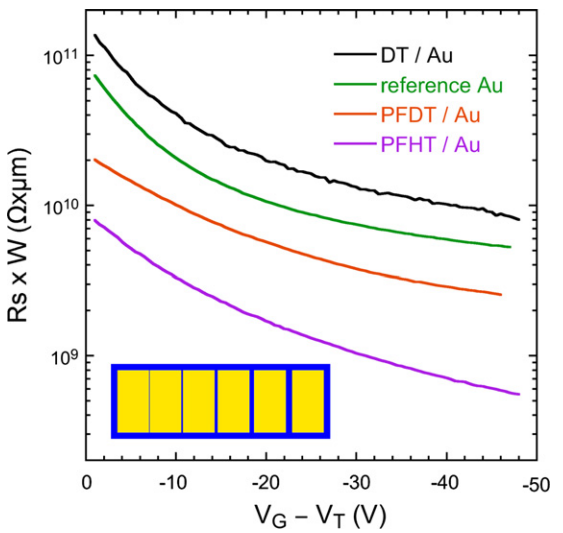

Fig. 5. Width normalized contact resistance of unmodified and SAM-modified transistors as estimated from the Transfer Line Method. The data were extracted from transfer characteristics recorded in the linear regime ($V_D = -5$ V) on devices with various channel lengths, as illustrated in Fig. 4. The inset is an image of the substrates, with channel lengths 2, 5, 10, 15 and 20 μm and a channel width of 200 μm.

in agreement with previous reports [13]. More importantly, the resistance follows the same trend as the effective mobility, thus inferring that the variation of the latter can be attributed to charge injection rather than charge transport in the transistor channel. This is also in good agreement with the UPS data. As compared to its value on bare gold, the contact resistance undergoes an average two-fold increase with DT, and a respective average decrease by a factor of two with PFDT and seven with PFHT. Because PFDT and PFHT have very similar dipole moment, we attribute the further reduction in contact resistance occurring with the shorter molecule to the lower series resistance of the respective SAM.

2.4. Morphological characterization

Fig. 6 shows AFM images (intermittent contact mode, scan size: 5 × 5 μm^2) of 8 nm thick pentacene layers deposited on gold substrates modified with the various SAMs used in this work. The substrates were held at 54 °C during deposition. The images clearly show that the morphology of the pentacene layer only depends on the presence or absence of a

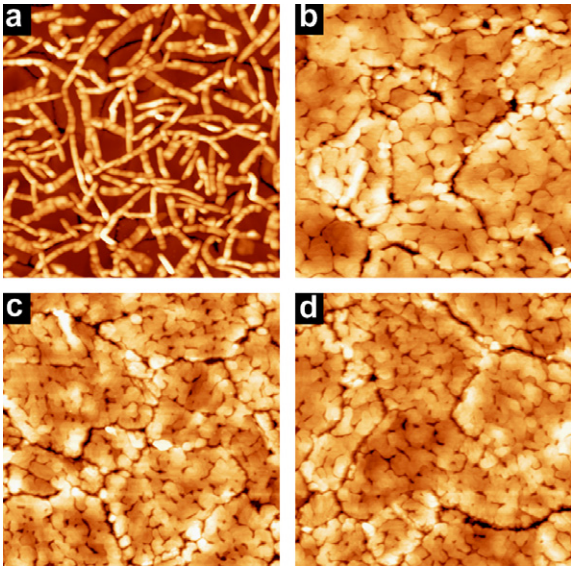

Fig. 6. AFM images (intermittent contact, scan size: 5 × 5 μm^2) of 8 nm-thick pentacene films deposited on polycrystalline gold substrates (typical grain size: 2 μm) held at a temperature of 54 °C for various surface treatments. (a) Bare gold (*z*-scale: 100 nm); (b) gold with DT SAM (*z*-scale: 35 nm); (c) gold with PFDT SAM (*z*-scale: 35 nm); (d) gold with PHDT SAM (*z*-scale: 40 nm). The morphology of the pentacene film does not depend on the nature of the SAM, but rather on its presence or absence.

SAM. No difference is observed when changing the SAM from alkyl to fluoro-alkyl. This is consistent with the general statement that the morphology is mainly sensitive to the surface energy of the surface on which the film is deposited. The rod-like morphology on bare Au is attributed to the tendency of the pentacene molecules to orient flat on the high-energy surface, while the molecules are nearly perpendicularly aligned on low-energy SAM-modified substrates [15]. As a matter of fact, alkyl and fluoro-alkyl modified gold substrates have very similar surface energy, as checked from contact angle measurements. This inclines us to attribute the reduction of the contact resistance to a dipolar rather than morphological origin. Further structural studies (e.g., X-ray diffraction) are currently under course to get a deeper insight of the effect of the substrate on the crystal structure of the pentacene films.

3. Conclusion

Thiol SAMs were grafted on the gold source and drain electrodes of pentacene-based organic transistors. Infrared spectroscopy shows that the molecules are preferentially oriented perpendicular to the electrodes. Photoelectron spectroscopy indicates that the work function of gold is reduced with an alkane chain, while it is increased in the case of a fluorinated molecule, in good agreement with the direction of the dipolar moment of the respective molecules. The change in the respective contact resistance, as estimated by TLM, is also in agreement with this trend. Morphological characterization through AFM shows that the structure of the pentacene films only depends on the presence or absence of a SAM on the gold substrate and not on the nature of the SAM, which seems to rule out any morphological explanation for the improved charge injection. It was also found that the contact resistance displayed further reduction by shortening the length of the molecules.

4. Experimental section

DT and PFDT were purchased from Aldrich and used without further purification. PFHT was synthesized as described earlier [16].

4.1. SAM fabrication and characterization

Gold substrates were rinsed in pure ethanol, dried in an argon flow, rapidly flamed in an H_2 torch and cooled down under argon. They were then dipped in a 0.5 mM ethanol solution of thiol for various adsorption times (2 s to 40 h) and immediately and thoroughly rinsed sequentially in ethanol and dichloromethane, and blown dry with argon.

PMIRRAS spectra (5000 scans at a spectral resolution of $8\ cm^{-1}$) were recorded with a Nicolet MAGNA-IR 860 as described previously [17]. The polarized light was reflected from the sample at an angle of about 80°.

4.2. UPS

The samples, packaged in inert atmosphere since formation of the SAM, were introduced in the photoemission chamber without ambient exposure. UPS was done with the He I photon line ($h\nu = 21.22$ eV) from a He-discharge lamp. The resolution of the UPS measurement was 150 meV. The Fermi level of the sample and system was measured on a Au surface prepared in situ via Ar^+ sputtering. The vacuum level of each sample, central to the determination of the work function vs. direction and magnitude of the SAM dipole, was measured from the onset of photoemission [18].

4.3. Fabrication and characterization of the transistors

Bottom contact transistors were fabricated on highly doped p-type silicon wafers with a 300 nm thick thermally grown SiO_2 layer that acted as the gate dielectric. Source and drain electrodes were patterned using conventional lithography, with sputtered Ti and Au, defining channels with various lengths ($L = 2$, 5, 10, 15 and 20 μm) and constant width ($W = 200$ μm). A 30 nm thick pentacene layer was deposited in an Edwards vacuum evaporating system at a base pressure of 1×10^{-6} mbar and a rate of 0.3 Å/s, with a substrate held at a temperature of 70 ± 3 °C. Current–voltage curves were recorded in air on a manual probe station connected to a Keithley 4200 semiconductor characterization system.

Morphological characterization was carried out with a commercial AFM operating in the intermittent contact mode on samples specially prepared for that purpose. The substrates consisted of polycrystalline gold surfaces that were prepared exactly the same way as the transistors and on top of which 8 nm of pentacene was evaporated.

Acknowledgements

Work at Princeton University was supported by the National Science Foundation (DMR-0408589), the Princeton MRSEC of the National Science Foundation (DMR-0213706) and the Department of Energy (DE-FG02-04ER46165). P.M. acknowledge the PhD scholarship from the French Ministère de l'Education Nationale. We thank Dr. Anne Anthore (MPQ, Université Paris Diderot) for providing the patterned Si substrates and Mr. M. Shafique for his help in AFM measurements.

References

[1] D. Natali, L. Fumagalli, M. Sampietro, J. Appl. Phys. 101 (2007) 014501.
[2] N. Koch, A. Kahn, J. Ghijsen, J.-J. Pireaux, J. Schwartz, R.L. Johnson, A. Elschner, Appl. Phys. Lett. 82 (2003) 70.
[3] C. Vanoni, S. Tsujino, T.A. Jung, Appl. Phys. Lett. 90 (2007) 193119.
[4] F. Fujimori, K. Shigeto, T. Hamano, T. Minari, T. Miyadera, K. Tsukagoshi, Y. Aoyagi, Appl. Phys. Lett. 90 (2007) 193507.
[5] B. Stadlober, U. Haas, H. Gold, A. Haase, G. Jakopic, G. Leising, N. Koch, S. Rentenberger, E. Zojer, Adv. Funct. Mater. 17 (2007) 2687.
[6] I.H. Campbell, S. Rubin, T.A. Zawodzinski, J.D. Kress, R.L. Martin, D.L. Smith, N.N. Barashkov, J.P. Ferraris, Phys. Rev. B 54 (1996) 14321.
[7] R.A. Hatton, M.R. Willis, M.A. Chesters, F.J.M. Rutten, D. Briggs, J. Mater. Chem. 13 (2003) 38.
[8] B. de Boer, A. Hadipour, M.M. Mandoc, T. Van Woudenbergh, P.W.M. Blom, Adv. Mater. 17 (2005) 621.
[9] C. Bock, D.V. Pham, U. Kunze, D. Kafer, G. Witte, A. Terfort, Appl. Phys. Lett. 91 (2007) 052110.
[10] K. Asadi, F. Gholamrezaie, E.C.P. Smits, P.W.M. Blom, B. de Boer, J. Mater. Chem. 17 (2007) 1947.
[11] C.A. Alves, M.D. Porter, Langmuir 9 (1993) 3507.
[12] H. Fukushima, S. Seki, T. Nishikawa, H. Takiguchi, K. Tamada, K. Abe, R. Colorado Jr., M. Graupe, O.E. Shmakova, T.R. Lee, J. Phys. Chem. B 104 (2000) 7417.
[13] J. Zaumseil, K.W. Baldwin, J.A. Rogers, J. Appl. Phys. 93 (2003) 6117.
[14] M. Mottaghi, G. Horowitz, Org. Electron. 7 (2006) 528.
[15] W.S. Hu, Y.T. Tao, Y.J. Hsu, D.H. Wei, Y.S. Wu, Langmuir 21 (2005) 2260.
[16] C. Amato, P. Calas, J. Fluorine Chem. 124 (2003) 169.
[17] N. Karsi, P. Lang, M. Chehimi, M. Delamar, G. Horowitz, Langmuir 22 (2006) 3118.
[18] D. Cahen, A. Kahn, Adv. Mater. 15 (2003) 271.

Available online at www.sciencedirect.com
ScienceDirect
Organic Electronics 9 (2008) 425–431
Organic Electronics
www.elsevier.com/locate/orgel

The effect of thiophene sequence separation on air-stable organic thin-film transistor materials

Shusuke Kanazawa, Musubu Ichikawa *, Youki Fujita, Ryu Koike, Toshiki Koyama, Yoshio Taniguchi

Faculty of Textile Science and Technology, Department of Functional Polymer Science, Shinshu University, Ueda, Nagano 386-8567, Japan

Received 29 November 2007; received in revised form 17 January 2008; accepted 17 January 2008
Available online 1 February 2008

Abstract

The relationship between thiophene sequences and organic thin-film transistor (OTFT) characteristics was studied to determine their effect on ionization potential, molecular orientation, and air stability. Two types of molecular structures were used: continuous sequence and divided sequence thiophenes. The length of thiophene sequence did not affect FET characteristics but did affect ionic potential and air stability. Furthermore, materials with divided thiophene sequences showed no change in OTFT characteristics when exposed to air. These results suggest that separation of thiophene sequences can improve air stability, which is a problem of thiophene-based materials.

PACS: 73.61.Ph

Keywords: Thiophene derivatives; Organic transistors; Ionization potential; Air stability; Thiophene sequence

1. Introduction

Organic thin-film transistors (OTFTs) have been the subject of a lot of recent research because they can be used in active matrix switching devices in flat panel displays due to their low cost, large area process ability, and flexibility [1–5]. Various organic semiconducting materials have been used in the active layers of OTFTs. Of these, thiophene-based derivatives are among the most attractive materials because their molecular structures can be easily modified using various organic synthesis methodologies such as introduction of substituents. For example, regio-regular poly(3-hexylthiophene) is a representative thiophene-based material that has performed well in polymer TFTs [6] and organic solar cells [7]. Thiophene oligomers, which consist of several thiophene rings, have been reported to have charge carrier mobilities comparable to that of amorphous silicon [8–11]. Research has also been done on improving their electrical characteristics using crystal growth [12,13] including by self-assembly from solution [14]. Thiophene oligomers are also known as good photonic materials due to their excellent π-conjugation [15,16]. However, over time, atmospheric moieties such as oxygen tend to

* Corresponding author. Tel.: +81 268 21 5417; fax: +81 268 21 5413.
E-mail address: musubu@shinshu-u.ac.jp (M. Ichikawa).

1566-1199/$ - see front matter © 2008 Elsevier B.V. All rights reserved.
doi:10.1016/j.orgel.2008.01.006

degrade the performance of most of these materials. This undesirable feature is due their low ionization potential (I_p), which causes high electron donation. It has been reported that longer thiophene sequences tend to reduce the I_ps of thiophene materials [17,18]. However, longer thiophene sequences can improve charge transport ability because their molecular interactions are strong [19,20]. Therefore, keeping a high I_p in materials with several thiophenes in a molecule is an important issue that must be addressed by designing thiophene-based materials that combine high mobility and good stability. To make the design of such a material possible, we studied the relationship between molecular structure and carrier transport characteristics. We investigated the four-thiophene molecules shown in Fig. 1 and demonstrated that split-sequence thiophenes have both large I_ps and good charge transport ability. A split-sequenced oligothiophene with single phenylene has been reported by Ponomarenko et al. [17], here we demonstrate the effect on I_p again using biphenyl-splitting oligothiophene and clearly show the TFT stability in the air and briefly discuss the difference between one-phenyl and two-phenyls.

We studied the four four-thiophene materials shown in Fig. 1. Quaterthiophene (4T), which simply consists of four thiophenes, is a common p-type organic semiconductor. P4T and 4TC2P have two more phenylene rings than 4T. As can be seen in Fig. 1, P4T and 4TC2P are isomers of each other. In 4TC2Pme is identical to 4TC2P except that the α-positions of both of its end-thiophenes are methyl. These materials all have four thiophenes.

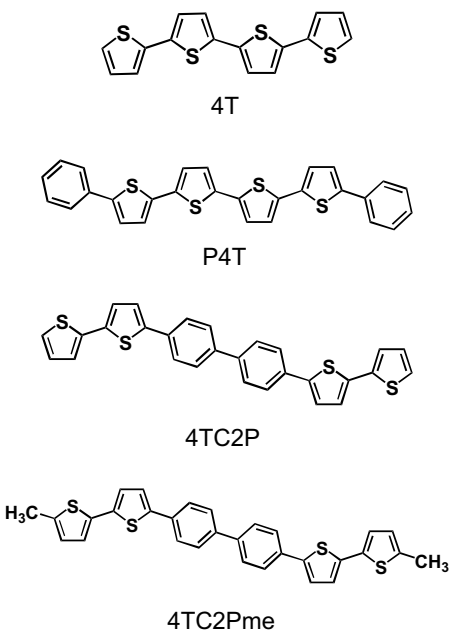

Fig. 1. Chemical structures of materials used.

2. Results and discussion

2.1. Ionization potentials and band gaps of the materials

Fig. 2 shows the photoelectron emission yield spectra of films of the materials. Their I_p values, which were estimated based on these spectra, are listed in Table 1. 4T and P4T showed similar I_ps in the lower energy range of about 5.2 eV, and 4TC2P and 4TC2Pme showed similar values in the higher energy range of about 5.5 eV. We think this difference arises from the lengths of the thiophene sequences, not from the total number of thiophenes in the molecules. That is, the biphenyl-splitting makes I_p 0.3 eV higher than fully linked compounds. One the other hand, it was 0.1 eV higher in the case of the single-phenyl splitting [17]. So it can be mentioned that biphenyl-splitting can work more efficiently for increasing I_p. The band gaps of the materials, estimated based on the edges of longer UV–vis spectra wavelengths (not shown), are also listed in Table 1. Band gaps fell into the same two groups; materials with separated thiophene chains (4TC2P and 4TC2Pme) had larger gaps because of their limited π-conjugation development. This indicates that the linkage conditions of thiophene chains are important factors in the materials. 4TC2P and 4TC2Pme, which had high I_ps

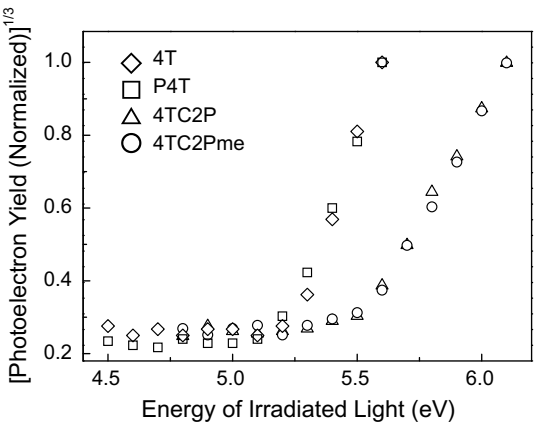

Fig. 2. Photoelectron emission yield spectra of materials.

Table 1
Energies of I_p and band gap of materials

	I_p (eV)	Band gap (eV)
4T	5.24	2.53
P4T	5.20	2.53
4TC2P	5.52	2.62
4TC2Pme	5.53	2.62

values, can be expected to be air-stable OTFT materials.

2.2. Molecular orientation in the thin-film state

Fig. 3 shows the results of X-ray diffraction (XRD) measurements of the materials. As can be seen in Fig. 3a, the pattern for 4T peaked at $2\theta = 6.00°$($d = 14.7$ Å) i.e., the perpendicular orientation of the molecule. Other peaks, which appeared at $2\theta = 11.8°$, $2\theta = 17.6°$, $2\theta = 23.4°$, correspond to higher order diffraction of $d = 14.7$ Å. This is the same as a molecular orientation that has been reported for 4T film [21]. As can be seen in Figs. 3b–d, the other three materials showed similar tendencies. The molecular orientation of 4TC2P can be demonstrated using the unit cell shown in Fig. 4. According to the cell parameters, the XRD pattern of 4TC2P (Fig. 3c), it can be understood that peaks at $2\theta = 7.00°$ ($d = 12.7$ Å), 10.5° ($d = 8.45$ Å), 14.0° ($d = 6.32$ Å), 17.5° ($d = 5.06$ Å) and 21.1° ($d = 4.21$ Å) correspond, respectively, to lengths of $c/2$, $c/3$, $c/4$, $c/5$, and $c/6$. These progressive peaks indicate that, like 4T molecules, 4TC2P molecules align perpendicularly in the film. However, it is thought that the peak at $2\theta = 19.4°$ ($d = 4.58$ Å) arises from polymorphism because it does not match any of the axes of the 4TC2P unit cell. We think this polymorphism is based on lying orientation because peaks that correspond to the c-axis of 4TC2P showed a shift in the 4TC2Pme spectrum due to the length of methyl. However, the polymorphism peak also appeared at the same degree in 4TC2P. This feature can also be found in the results for P4T, so it can be concluded that there may be both perpendicular and lying molecular orientations in the three materials other than 4T.

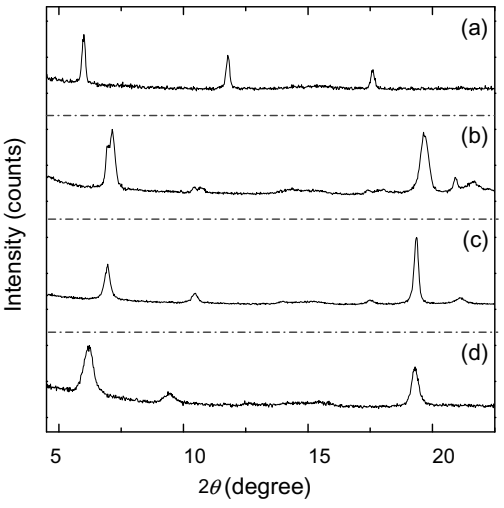

Fig. 3. XRD patterns of (a) 4T, (b) P4T, (c) 4TC2P, and (d) 4TC2Pme films.

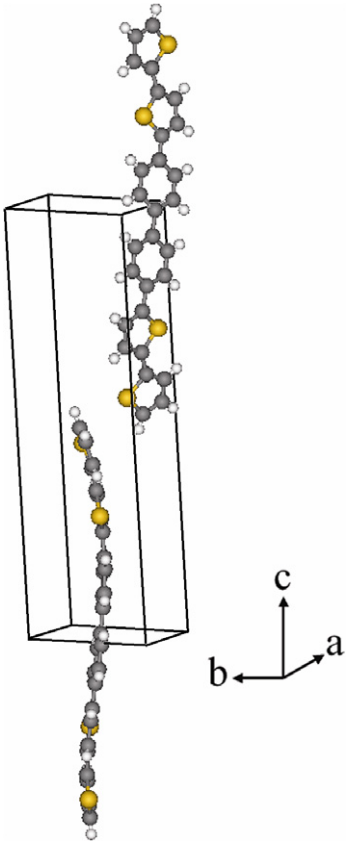

Fig. 4. 4TC2P unit cell. (Crystal class: monoclinic, Space group: *P21*, Cell Constants: $a = 5.816$ Å; $b = 7.2527$ Å; $c = 25.2863$ Å; $\beta = 96.265°$; CCDC number: 673710, the crystallographic data can be obtained free of charge from the Cambridge Crystallographic Data Centre via www.ccdc.cam.ac.uk/data_request/cif.)

2.3. OTFT characteristics

Fig. 5 shows characteristics of 4TC2P and 4TC2Pme. Like 4T and P4T OTFTs, both devices showed p-type behavior. Table 2 shows the field-

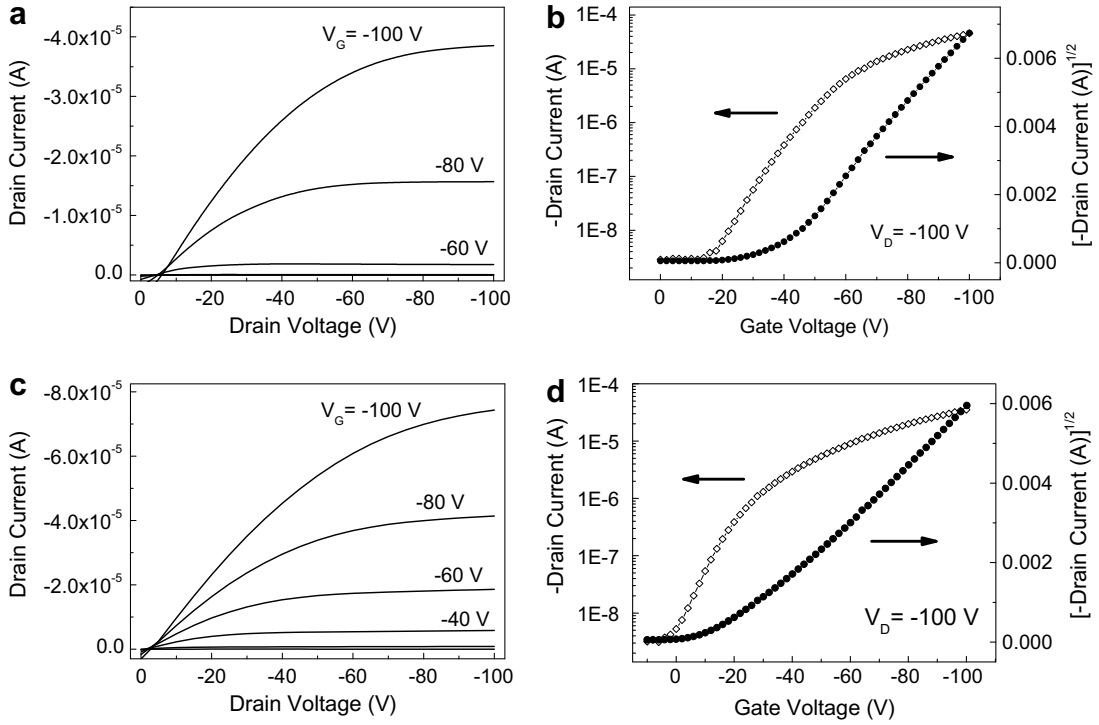

Fig. 5. I_D–V_D characteristics and I_D–V_G characteristics of (a, b) 4TC2P and (c, d) 4TC2Pme.

Table 2
Characteristics of oligomer material OTFTs in vacuum

	μ_{FET} (cm^2/Vs)	V_{th} (V)	ON/OFF ratio	Subthreshold slope (V/decade)
4T	3.7×10^{-2} (3.1×10^{-2})	–30 (–33)	10^4 (10^4)	8 (7)
P4T	5.3×10^{-2} (5.4×10^{-2})	–25 (–30)	10^4 (10^4)	8 (10)
4TC2P	2.1×10^{-2} (2.6×10^{-2})	–36 (–40)	10^4 (10^4)	9 (7)
4TC2Pme	5.2×10^{-2} (4.7×10^{-2})	–21 (–20)	10^4 (10^4)	8 (8)

Characteristics in atmosphere are shown in parentheses.

effect mobilities (μ_{FET}), threshold voltages (V_{th}), ON/OFF ratios, and subthreshold slopes of all the fabricated devices. The μ_{FET}s were calculated from the saturated drain current (I_D) with Eq. (1), where C_i is the specific capacitance of the insulator, L is channel length, V_G is gate voltage, and W is channel width.

$$I_D = \mu_{FET} \frac{WC_i}{2L}(V_G - V_{th})^2 \quad (1)$$

We first measured OTFT characteristics in vacuum conditions (about 2×10^{-2} Pa). While the ON/OFF ratios and the subthreshold slopes showed no major change for any of the devices, the V_{th}s showed two different tendencies. The materials with no substituents on their end-thiophenes (4T and 4TC2P) showed higher V_{th}s, and the substituted materials (P4T and 4TC2Pme) showed lower ones. Thus, it can be concluded that materials with substituents in the α-positions of their end-thiophenes are better OTFT materials because of their lower V_{th}. However, the μ_{FET}s of all four OTFTs are about the same. This indicates that the carrier transport properties of materials with the same number of thiophenes are about the same even if they fully link to each other or divide into two parts.

The next thing we measured was characteristics of the devices when they were exposed to air. The measurements were done immediately after exposing the devices to the atmosphere. The OTFT characteristics when the devices were exposed to air are shown in Table 2, where it can be seen that all of the

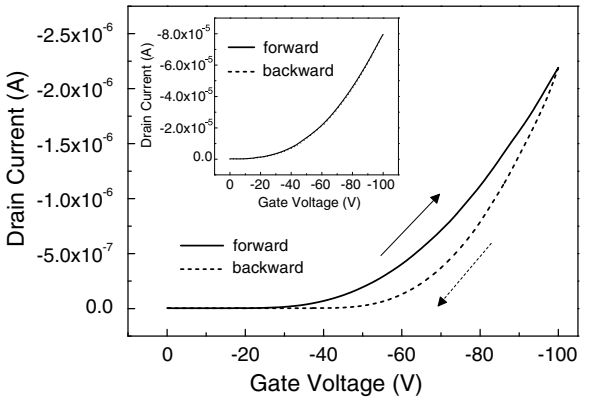

Fig. 6. Forward (solid line) and backward (dotted line) I_D–V_D characteristics of 4TC2P OTFTs and (inset) 4TC2Pme OTFTs.

devices worked as well as in the vacuum condition. However, the 4TC2P device had significant hysteresis, as shown in Fig. 6. In contrast, as in the vacuum condition, the 4TC2Pme OTFT had no hysteresis (Fig. 6 inset). This difference suggests that the lack of substituents on both end-thiophenes degrades performance of OTFT materials. This notion is supported by the V_{th} behavior of other devices: 4T showed hysteresis but P4T did not. In addition, the similar result is previously reported using other thiophene derivatives [22]. Therefore, the high reactivity of the α-position of both end-thiophenes must be important.

We also measured the OTFT characteristics of these devices continuously for ten days to investigate the stability of the devices when they were left in the atmosphere. Fig. 7 shows storage time dependences for (a) V_{th} and (b) μ_{FET} of the devices made of 4T, 4TC2P, and 4TC2Pme. As expected, the 4TC2P and 4TC2Pme devices showed no change in V_{th} during the measurements, while the V_{th} of the 4T device decreased. This air stability must be due to the higher I_p caused by the divided thiophene linkage. However, the 4TC2P and 4TC2Pme devices showed different μ_{FET} behaviors, i.e., the μ_{FET} of the 4TC2Pme device did not change but that of 4TC2P decreased to about 20% of its initial value. The structural difference between the two materials is in their end-thiophenes. The μ_{FET} of 4T, incidentally, also decreased. Therefore, to make thiophene materials air-stable, it is important both to maintain a large I_p and to substitute active α-positions for the end-thiophenes. As mentioned above, we successfully demonstrated that molecular structures like 4TC2Pme, with separated thiophene chains and substituted end-thiophenes, are air-stable thiophene derivatives.

3. Conclusion

We investigated the relationship between air-stability and molecular structure in materials that contain four thiophenes and whose molecular orientations in the thin-film state were about the same. I_ps were classified by type of thiophene chain, i.e., fully linked or divided. OTFTs made of these materials showed two tendencies with regard to air-stability. First, OTFTs made of materials with no substituents on the end-thiophenes, showed hysteresis in I_D–V_G characteristics. Second, materials with fully linked thiophenes showed changes in switching performance over time. This means that 4TC2Pme, which has two separate thiophene chains and substituents at both ends of the molecule, has both the normal advantages of thiophenes and significant stability as carrier transport material exposed to air.

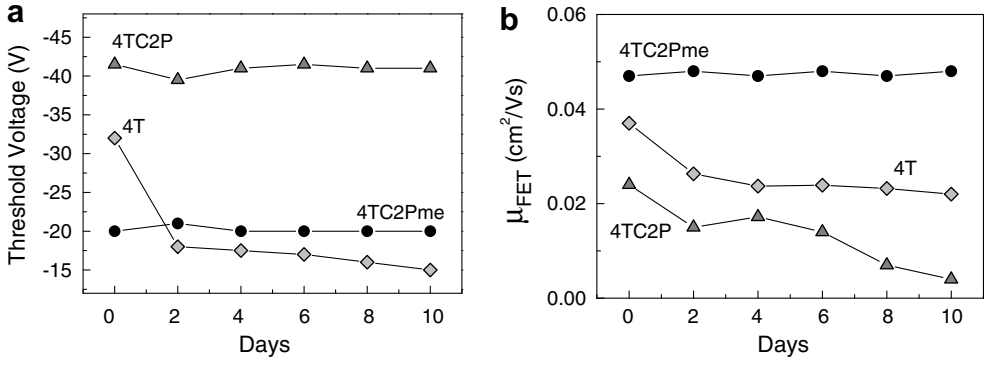

Fig. 7. Storage time dependences of (a) threshold voltage and (b) field-effect mobility of (◇) 4T, (△) 4TC2P, and (●) 4TC2Pme OTFTs.

4. Experimental

4.1. Synthesis

All reactions were carried out in an Ar environment. Solvents were purified according to the standard methods before use. A ^{1}H NMR (400 MHz) spectrum was recorded on a Bruker AVANCE-400 spectrometer, and chemical shifts (δ) were given in ppm relative to tetramethylsilane (TMS) as an internal standard. High-resolution mass (HRMS) measurements were carried out on a Jeol MS-700 spectrometer. The 4T was purchased from Sigma–Aldrich, and the P4T was prepared as recommended in the literature [23].

4.2. Preparation of 4TC2P

To a solution of 4,4′-diiodobiphenyl (1.0 g, 2.5 mmol) and 5-(4,4,5,5-tetramethyl-1,3,2-dioxaborolan-2-yl)-2,2′-bithiophene (1.8 g, 6.2 mmol) in toluene (40 mL) was added a 10% aqueous K_2CO_3 (30 ml). The contents were bubbled with nitrogen for 30 min to remove soluble oxygen, then tetrakis(triphenylphosphine) palladium(0) (0.028 g, 0.024 mmol, $Pd(Ph_3)_4$) was added and the solution refluxed for 18 h. After the solution was cooled to room temperature, the precipitate was filtrated and sequentially washed with toluene, distilled water, and methanol to produce crude 4TC2P, which was purified by the sublimation method described below. HRMS (EI) calcd for $C_{28}H_{18}S_4$ $[M]^+$ 482.0291 found 482.0316.

4.3. Preparation of 4TC2Pme

4TC2Pme was prepared from 5-(4,4,5,5-tetramethyl-1,3,2-dioxaborolan-2-yl)-5′-methy-l-2,2′-bithiophene (100 mg, 0.33 mmol, this compound was synthesized as described in the next section "Preparation of 5-(4,4,5,5-tetramethyl-1,3,2-dioxaborolan-2-yl)-5′-methyl-2,2′-bithiophene"), 4,4'-diiodobiphenyl (66.3 mg, 0.16 mmol), and $Pd(PPh_3)_4$ (11.3 mg, 0.0098 mmol) in a manner similar to a to that described above. HRMS (EI) calcd for $C_{30}H_{22}S_4$ $[M]^+$ 510.0604, found 510.0609.

4.4. Preparation of 5-(4,4,5,5-tetramethyl-1,3,2-dioxaborolan-2-yl)-5′-methyl-2,2′-bithiophene

To a solution of 5-methyl-2,2′-bithiophene (420 mg, 2.3 mmol) and *N,N,N′,N′*-tetramethylenediamine (0.38 mL, 2.56 mmol) in THF (50 mL) was added dropwise a 1.6 mol/L *n*-BuLi in hexane (1.6 mL, 2.56 mmol) at –78 °C. After being stirred for 15 min, 2-isopropoxy-4,4,5,5-tetramethyl-1,3,2-dioxaborolane (0.48 g, 2.56 mmol) was added and stirred for 1 h, then reacted for 24 h at room temperature.

Saturated aqueous NH_4Cl (three drops) was added to a reaction mixture to quench an excess *n*-BuLi and extracted with ethyl acetate. The organic phase was washed with brine and then dried over anhydrous $MgSO_4$. The solvent was removed under the reduced pressure. The residue was purified by the silica gel column-chromatography (eluent: hexane) to give 5-(4,4,5,5-tetramethyl-1,3,2-dioxaborolan-2-yl)-5′-methyl-2,2′-bithiophene (60%). ^{1}H NMR ($CDCl_3$) δ: 1.35 (s, 12H, CH_3), 2.48 (s, 3H, CH_3), 6.64 (d, 1H, Ar-H, $J = 3.6$ Hz), 7.03 (d, 1H, Ar-H, $J = 3.6$ Hz), 7.15 (d, 1H, Ar-H), 7.50 (d, 1H, Ar-H).

The 4T, P4T, 4TC2P, and 4TC2Pme were used for other experiments after further purification by thermal gradient sublimation.

4.5. Fabrication and measurement

We fabricated top-contact OTFTs made of the organic materials (4T, P4T, 4TC2P, and 4TC2Pme). The OTFTs were prepared on heavily doped n-type silicon wafers with 400 nm thick thermally grown SiO_2, which were used as a gate electrode and a gate dielectric (specific capacitance of 7.5 nF/cm^2), respectively. The organic materials were thermally evaporated at the rate of 0.4 Å/s onto room temperature substrates. The pressure in the evaporation chamber was 4.0×10^{-6} Torr, and the organic layers were 60 nm thick. Finally, Au was thermally evaporated onto the organic layers through a shadow mask to form source and drain electrodes. The channel length and width were 30 μm and 2 mm, respectively. OTFT characteristics were measured in a vacuum (below 5×10^{-2} Pa) and in the atmosphere using two KEITHLEY 2410 source meters.

The photoelectron emission yield spectra were measured with a Riken-Keiki AC2 at an irradiation light power of 10 nW/cm^2. The sample films of the organic materials were prepared by vacuum evaporation in the same conditions as were used to fabricate OTFTs on glass substrates whose surface was covered with indium thin oxide. The organic films were 100 nm thick.

The X-ray diffraction patterns were measured with a Rigaku Rotaflex using Cu Kα radiation at $\theta/2\theta$ geometry. The sample films, which all had thicknesses of 100 nm, were evaporated onto silicon wafers with SiO_2 in the same conditions as were used for TFT fabrication. The X-ray was generated from a 150 mA-electron beam accelerated at 40 kV. The crystal structure was analyzed with a Bruker AXS APEXII from Bruker AXS Japan Co., Ltd.

Acknowledgements

This work was supported by the Cooperative Link for Unique Science and Technology for Economy Revitalization (CLUSTER) and CLUSTER (the second stage), programs of the Japanese Ministry of Education, Culture, Sports, Science and Technology. The authors thank Bruker AXS Japan Co. Ltd. for analyzing the crystal structure of the 4TC2P.

References

[1] G. Horowitz, D. Fichou, X. Peng, Z. Xu, F. Garnier, Solid State Commun. 72 (1989) 381.
[2] G. Horowitz, M.E. Hajlaoui, Adv. Mater. 12 (2000) 1046.
[3] C.D. Dimitrakopoulos, P.R.L. Malenfant, Adv. Mater. 14 (2002) 99.
[4] C.D. Sheraw, L. Zhou, J.R. Huang, D.J. Gundlach, T.N. Jackson, M.G. Kane, I.G. Hill, M.S. Hammond, J. Campi, B.K. Greening, J. Francl, J. West, Appl. Phys. Lett. 80 (2002) 1088.
[5] F. Eder, H. Klauk, M. Halik, U. Zschieschang, G. Schmid, C. Dehm, Appl. Phys. Lett. 84 (2004) 2673.
[6] H. Yang, T.J. Shin, L. Yang, K. Cho, C.Y. Ryu, Z. Bao, Adv. Funct. Mater. 15 (2005) 671.
[7] Y. Kim, S. Cook, S.M. Tuladhar, S.A. Choulis, J. Nelson, J.R. Durrant, D.D.C. Bradley, M. Giles, I. Mcculloch, C.-S. Ha, M. Ree, Nature Mater. 5 (2006) 197.
[8] M. Ichikawa, H. Yanagi, Y. Shimizu, S. Hotta, N. Suganuma, T. Koyama, Y. Taniguchi, Adv. Mater. 14 (2002) 1272.
[9] K. Nakamura, M. Ichikawa, R. Fushiki, T. Kamikawa, M. Inoue, T. Koyama, Y. Taniguchi, Jpn. J. Appl. Phys. 43 (2004) L100–L102.
[10] B. Wex, B.R. Kaafarani, R. Schroeder, L.A. Majewski, P. Burckel, M. Grell, D.C. Neckers, J. Mater. Chem. 16 (2006) 1121–1124.
[11] Y. Sun, Y. Liu, Y. Ma, C. Di, Y. Wang, W. Wu, G. Yu, W. Hu, D. Zhu, Appl. Phys. Lett. 88 (2006) 242113.
[12] J. Ackermann, C. Videlot, P. Dumas, A.E. Kassmi, R. Guglielmetti, V. Safalov, Org. Electron. 5 (2004) 213–222.
[13] S. Kanazawa, M. Ichikawa, T. Koyama, Y. Taniguchi, ChemPhysChem 7 (2006) 1881–1884.
[14] M. Funahashi, F. Chang, N. Tamaoki, Adv. Mater. 19 (2007) 353.
[15] M. Ichikawa, R. Hibino, M. Inoue, T. Haritani, S. Hotta, T. Koyama, Y. Taniguchi, Adv. Mater. 15 (2003) 213.
[16] C.V. Ackermann, T. Isoshima, A. Yassar, T. Wada, H. Sasabe, D. Fichou, Synth. Met. 156 (2006) 154–161.
[17] S.A. Ponomarenko, S. Kirchmeyer, M. Halik, H. Klauk, U. Zschieschang, G. Schmid, A. Karbach, D. Dreschsler, N.M. Alpatova, Synth. Met. 149 (2005) 231–235.
[18] A.J. Mäkinen, I.G. Hill, M. Kinoshita, T. Noda, Y. Shirota, Z.H. Kafari, J. Appl. Phys. 91 (2002) 5456.
[19] M. Halik, H. Klauk, U. Zschieschang, G. Schmid, S. Ponomarenko, S. Kirchmeyer, W. Weber, Adv. Mater. 15 (2003) 917.
[20] C.V. Ackermann, J. Ackermann, H. Brisset, K. Kawamura, N. Yoshimoto, P. Raynal, A.E. Kassmi, F. Fages, J. Am. Chem. Soc. 127 (2005) 16346.
[21] J. Vrijmoeth, R.W. Stok, R. Veldman, W.A. Schoonveld, T.M. Klapwijk, J. Appl. Phys. 83 (1998) 3816.
[22] C.V. Ackermann, J. Ackermann, K. Kawamura, N. Yoshimoto, H. Brisset, P. Raynal, A.E. Kassmi, F. Fages, Org. Electron. 7 (2006) 465–473.
[23] S. Hotta, S.A. Lee, T. Tamaki, J. Heterocycl. Chem. 37 (2000) 25.

Available online at www.sciencedirect.com
ScienceDirect
Organic Electronics 9 (2008) 432–438
Organic Electronics
www.elsevier.com/locate/orgel

Fabrication and characterization of pentacene-based transistors with a room-temperature mobility of 1.25 cm^2/Vs

Hoon-Seok Seo, Young-Se Jang, Ying Zhang, P. Syed Abthagir, Jong-Ho Choi *

Department of Chemistry and Center for Electro- and Photo-Responsive Molecules, Korea University, Anam-Dong, Seoul 136-701, South Korea

Received 20 November 2007; received in revised form 30 January 2008; accepted 30 January 2008
Available online 9 February 2008

Abstract

Pentacene-based transistors produced by a novel neutral cluster beam deposition method were characterized, and the effects of the surface pretreatments were examined. Atomic force microscopy and X-ray diffraction showed that the cluster beams were quite efficient in growing high-quality, crystalline thin films on SiO_2 substrates at room-temperature without any thermal post-treatment, and that an amphiphilic surfactant, octadecyltrichlorosilane (OTS), enhances the packing density and crystallinity significantly. The observed field-effect mobilities (μ_{eff}) were among the best reported thus far: 0.47 and 1.25 cm^2/Vs for the OTS-untreated and -pretreated devices, respectively. The device performance was found to be consistent with the estimated trap density and activation energy, which were derived from the transport characteristics for the temperature dependence of μ_{eff} in the range of 10−300 K.

PACS: 73.40.−c; 73.61.Ph

Keywords: Pentacene; Neutral cluster beam deposition (NCBD); Organic thin-film transistor; Octadecyltrichlorosilane (OTS); Temperature dependence of field-effect mobility (μ_{eff})

1. Introduction

The recent advances in organic-based semiconductor electronics have led to them being viewed as potential alternatives to traditional silicon-based devices. The macroscopic properties of organic crystalline solids formed by weak van der Waals interactions are governed by the individual molecules, which makes the concept of molecular engineering feasible. The promising applications of these solids include optoelectronic devices such as thin-film transistors, light emitting diodes, photovoltaic cells, etc. Some of these transistors have comparable performance to that of hydrogenated amorphous Si devices. This is well illustrated by the devices fabricated using fused-ring polycyclic aromatic hydrocarbons such as pentacene, a π-conjugated molecule consisting of five aligned condensed benzene rings [1–13].

The preparation of good thin-film crystals is essential for fabricating high-quality, organic thin-film transistors. The neutral cluster beam deposition

* Corresponding author. Tel.: +82 2 3290 3135; fax: +82 2 3290 3121.
E-mail address: jhc@korea.ac.kr (J.-H. Choi).

1566-1199/$ - see front matter © 2008 Published by Elsevier B.V.
doi:10.1016/j.orgel.2008.01.008

(NCBD) method used in this study is a less popular, but quite useful deposition scheme [14]. In recent years, we have reported a series of optoelectronic devices fabricated using the NCBD approach [15–20]. Neutral cluster beams consisting of weakly bound molecules (Fig. 1) are produced when organic molecules evaporated by resistive heating undergo adiabatic expansion in a high vacuum. The unique characteristics of these beams are their high translational kinetic energy and directionality. The collision of cluster beams with a room-temperature substrate induces facile decomposition of the clusters into individual molecules and the subsequent energetic migration of these molecules results in the formation of smooth, uniform thin films. The NCBD scheme allows for a significant improvement in the surface morphology, crystallinity, and packing density of these films. In particular, the distinctive advantage of this method lies in the fact that thin-film formation proceeds on a substrate maintained at room temperature. The absence of thermal post-treatment is of very practical significance in terms of the device fabrication. Such a favorable procedure cannot be achieved by conventional vapor deposition techniques.

This paper reports our characterization study of pentacene-based, top-contact transistors prepared on room-temperature SiO_2 substrates using a novel NCBD method. The pretreatment effects of an amphiphilic surfactant, octadecyltrichlorosilane (OTS), on the device performance as well as the transport mechanisms in the temperature range of 10−300 K are reported. The transistor characteristics, which were found to be among the best reported thus far, are also discussed.

2. Experimental

For the fabrication of the top-contact transistors, a highly doped, n-type Si wafer coated with an Al layer was used as the gate electrode, and a thermally grown 2000 Å-thick SiO_2 layer was used as the gate dielectric [15]. Fig. 1 shows a schematic diagram of the process. The substrates were first cleaned by a series of successive ultrasonic treatments in acetone, hot trichloroethylene, acetone, HNO_3, methanol and deionized water in order and then blown with dry N_2 [21]. The substrates were finally exposed to UV (wavelength of 254 nm) for 15 min. For the OTS pretreatment, the cleaned substrates were

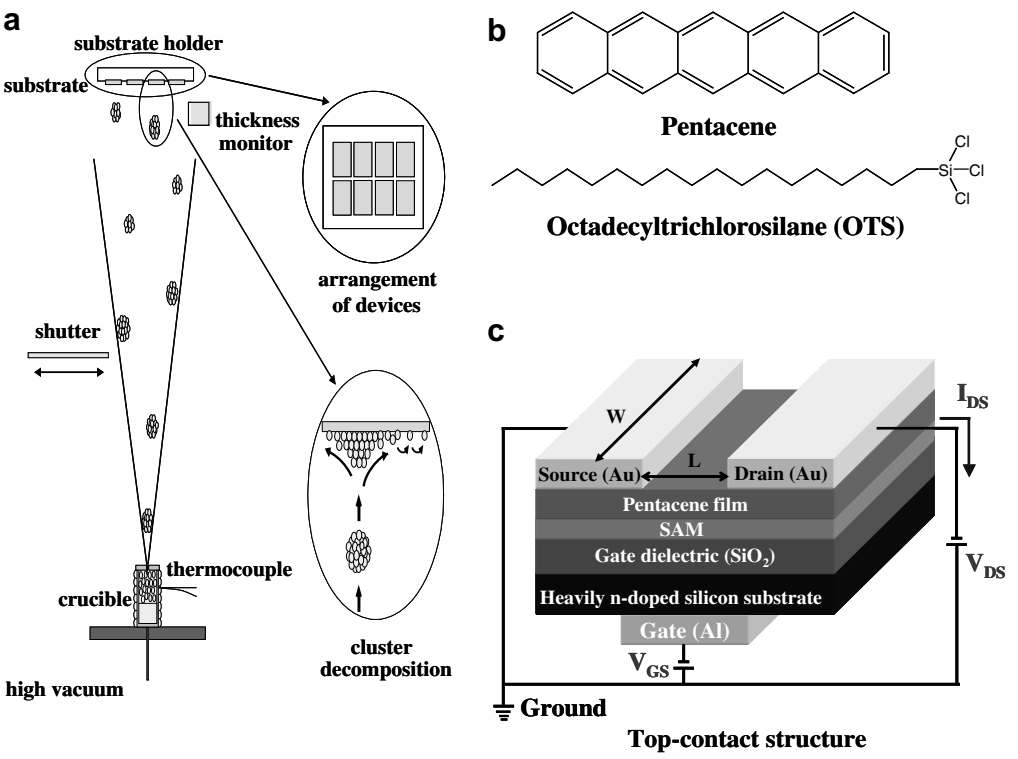

Fig. 1. (a) A schematic diagram of the NCBD apparatus. (b) Molecular structures of the pentacene and octadecyltrichlorosilane (OTS). (c) A schematic cross-sectional view of the top-contact transistor with its bias condition.

immersed in a 1×10^{-4} M solution of OTS (Aldrich Co.) in *n*-hexane [22]. Pentacene (TCI Co.) was deposited using a homemade NCBD apparatus. The system is described in detail elsewhere [14]. The chamber consisting of an evaporation crucible, a drift region, and a substrate was pumped by a 10 in. baffled diffusion pump. The pentacene sample was placed inside the enclosed cylindrical crucible cell with a diameter of 1.0 mm and a 1.0 mm-long nozzle, and sublimated at 460 K by resistive heating. The pentacene vapor then underwent adiabatic supersonic expansion into the drift region at a working pressure of about 3×10^{-6} Torr. The resultant neutral pentacene cluster beams were deposited directly onto the room-temperature SiO_2 layers with an average thickness of ca. 500 Å at a deposition rate 1 Å/s.

The thickness, morphology, crystallinity and contact angle were examined using an alpha step surface profile monitor, atomic force microscopy (AFM), X-ray diffraction (XRD) and a contact angle goniometer, respectively. The current–voltage characteristics and their temperature dependence were measured using an optical probe attached to an HP4140B *p*A meter-dc voltage source unit, and a 10 K-closed cycle refrigerator for more than 100 devices over a wide range of temperatures from 300 K down to 10 K.

3. Results and discussion

3.1. Morphological and structural properties

Fig. 2 shows 2-dimensional AFM micrographs of the OTS-untreated and -pretreated pentacene films at a nominal thickness of 500 Å. Both films were covered completely with grain crystallites with a dendritic structure. The diameter distributions and square roughness ranged from 0.25 to 0.30 μm and ~55 Å for the OTS-untreated films, respectively and 0.16 to 0.26 μm and ~30 Å for the OTS-pretreated films, respectively. The pretreated pentacene films showed a lower roughness and a higher packing density, which indicates that the amphiphilic OTS surfactant creates favorable deposition conditions for the non-polar pentacene cluster beams at the interface. This result is also consistent with the contact angle measurements. The OTS pretreatment increased the surface contact angle with water from 44° to 108°. This remarkable increase indicates that the pretreated surface becomes highly non-polar after the surfactant pretreatment. Therefore, the unfavorable lattice mismatch is significantly reduced through interactions with the OTS molecules, which are capable of simultaneously forming bonds with the hydrophobic pentacene and the hydrophilic SiO_2 at the interface.

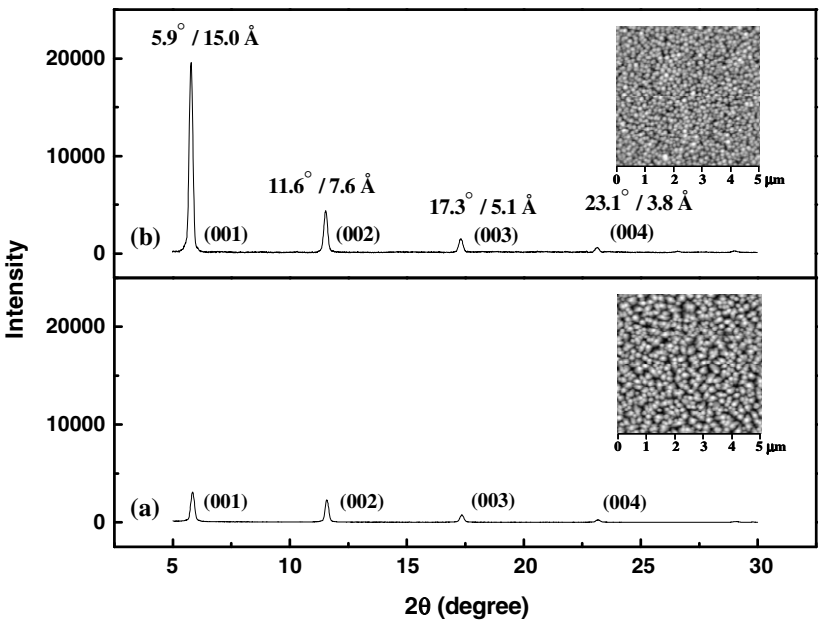

Fig. 2. Comparison of the XRD patterns and 2-D AFM micrographs (5×5 μm^2) of 500 Å-thick pentacene thin films prepared on the (a) untreated and (b) OTS-pretreated SiO_2 substrates at room temperature.

The effect of the surface pretreatment was examined by XRD. The diffraction patterns shown in Fig. 2 were assigned to the triclinic thin-film phase, which corresponds to a kinetically favored, metastable phase. The peaks could be fitted to a series of (0 0 l) reflection lines, and the interplanar spacing, d_{00l}, was determined to be 15.0 Å for both films. The more distinctive first- and higher-order multiple peaks with excellent signal-to-noise ratio in Fig. 2b indicate the presence of enhanced crystallinity in the OTS-pretreated films. Furthermore, compared with recent studies carried out by several groups using thermal evaporation [22,23], the superior surface morphology and crystallinity observed in this study demonstrate the unique capacity of the NCBD scheme to produce uniform, smooth films consisting of submicrometer-sized crystallites on room-temperature substrates without any thermal annealing processes.

3.2. Device performance

A comparative characterization of the performance of NCBD-based devices was carried out. The pentacene active layers exhibited a p-type behavior: the majority carriers were holes. The transistors were examined in accumulation mode. Fig. 3a demonstrates the typical plot of the drain-source current (I_{DS}) as a function of the drain-source voltage (V_{DS}) at various gate voltages (V_{GS}). The overall characteristics are well described by the standard field-effect transistor equations. The inset in Fig. 3a shows the I_{DS} at low V_{DS}, and the observed linear behavior indicates good ohmic contact between the gold electrodes and pentacene active layers [24]. From the $I_{DS}^{1/2}$ vs. V_{GS} and $\log(I_{DS})$ vs. V_{GS} plots, several device parameters such as the μ_{eff}, current on/off ratio (I_{on}/I_{off}), threshold voltage (V_T) and subthreshold slope $SS = V_{GS}/\log(I_{DS})$ can be derived. Here, μ_{eff} can be calculated in the saturation regime from the following equation:

$$\mu_{eff} = \frac{2L(I_{DS})}{WC_i(V_{GS} - V_T)^2} \text{ (saturation regime)},$$

where C_i is the capacitance per unit area of the SiO_2 gate dielectric insulator (for a thermally grown 2000-Å-thick SiO_2, $C_i = 17.25$ nF/cm^2) and the transistor dimensions have a channel width (W) of 500 μm and a length (L) of 660–1400 μm.

Table 1 lists the various parameters derived. In particular, the observed mobilities were among the best reported thus far: 0.47 and 1.25 cm^2/Vs for the OTS-untreated and -pretreated devices, respectively. In contrast, Pernstich et al. and Zhang et al. recently reported an effect of organosilane surfactants on the device performance and obtained room-temperature carrier mobilities of 0.4 and 0.6 cm^2/Vs for the OTS-pretreated devices prepared on the SiO_2 substrates, respectively, [12,13].

One of the critical factors determining the performance is the quality of the as-deposited thin films. The formation of active layers with higher structural organization will definitely result in more efficient charge-carrier transport through a face-to-face intermolecular interaction between the π–π stacks. The excellent mobilities observed were attributed mainly to the formation of such high-quality, NCBD-based thin films. Here, it should be noted that although the NCBD scheme was applied to room-temperature substrates, the cluster beams resulted in the growth of closely packed, nanometer-sized grain crystallites without any thermal post-treatment. Especially, after the OTS pretreatment, the amphiphilic surfactant enhanced the degree of molecular ordering and the resulting π–π overlap, leading to a significant increase in hydrophobicity, packing density and crystallinity of the films, as demonstrated by the contact angle, AFM and XRD results. Such favorable improvement was reflected in the outstanding device characteristics. Another desirable feature of the OTS pretreatment is the reduction of the subthreshold slope. The SS value is generally governed by the material properties, and the lower SS value observed indicates that the pretreatment improves the quality of the NCBD-based pentacene active layers.

3.3. Transport characteristics

The temperature dependence of the field-effect mobility (μ_{eff}) and the total trap density also support the aforementioned device features. Fig. 3b represents the typical plot of the mobility over a wide range of temperatures from 300 K down to 10 K for the NCBD-based transistors. μ_{eff} tends to be temperature-independent as the temperature is increased in region I (10 K $< T <$ 40 K), whereas μ_{eff} increases exponentially in region II (40 K $< T <$ 300 K). Region I can be described by a so-called tunneling mechanism occurring at the Au–pentacene interfaces. On the other hand, region II corresponds to an activated transport mechanism, where the conduction of hole carriers is governed by the

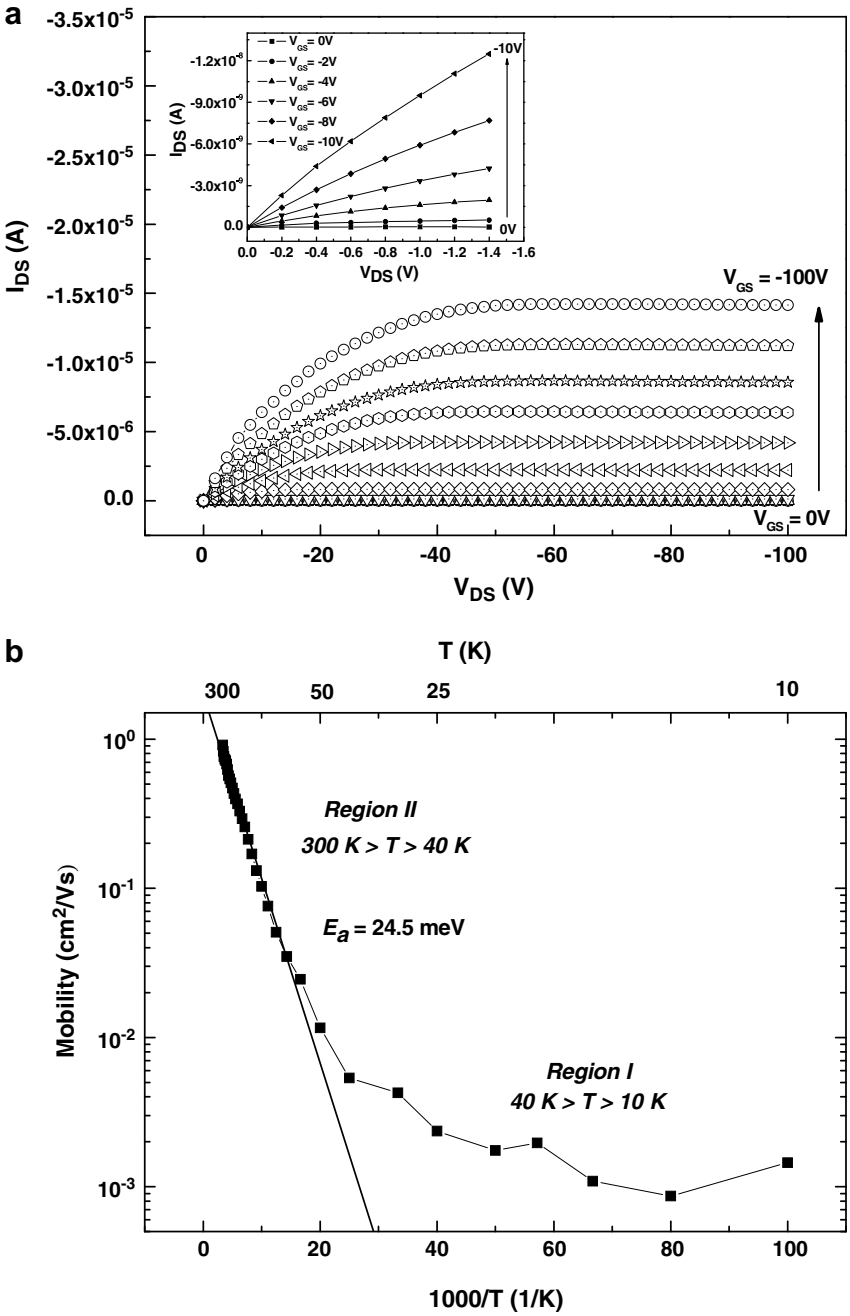

Fig. 3. (a) Current–voltage characteristics at various gate voltages for the OTS-pretreated pentacene-based transistors prepared using the NCBD method. The inset shows the I_{DS} in the low V_{DS} region. (b) An Arrhenius plot of the saturation mobility of the OTS-pretreated transistors in the temperature range of 10–300 K.

overcoming of shallow traps present in the pentacene active layer.

As shown by the solid line, region II is well fitted by the Arrhenius relation $\mu_{eff} \propto \exp(-E_a/kT)$, where E_a and k are the activation energy and Boltzmann constant, respectively. From the slope of the logarithmic plot, E_a was estimated to be 45.7 and 24.5 meV for the OTS-untreated and -pretreated devices, respectively (Table 1). The activation energies in this study were relatively lower than those

Table 1
Summary of the NCBD-based transistor characteristics for root-mean-square roughness (R_{rms}), field-effect mobility (μ_{eff}), threshold voltage (V_T), subthreshold slope SS = V_{GS} /log(I_{DS}), current on/off ratio (I_{on}/I_{off}), activation energy (E_a) and trap density (N_{trap})

	R_{rms} (Å)	μ_{eff} (cm^2/Vs)	V_T (V)	SS (V/dec)	I_{on}/I_{off}	E_a (meV)	N_{trap} ($10^{12}/cm^2$)
OTS-untreated	55	0.47	−19.6	5.7	10^4	45.7	1.7
OTS-pretreated	30	1.25	−35.5	3.4	10^5	24.5	0.8

The transistor dimensions have a channel width (W) of 500 μm and a length (L) of 1400 μm.

reported elsewhere, particularly in the OTS-pretreated system. Minari et al. reported an E_a of 54.8 meV in OTS-pretreated pentacene devices prepared by thermal evaporation [24]. The low E_a is also consistent with the estimated total trap densities N_{trap} of 1.7×10^{12} and $0.8 \times 10^{12}/cm^2$ for the OTS-untreated and -pretreated devices, respectively. Here, N_{trap} is expressed by the following relationship:

$$N_{trap} = \frac{C_i|V_T - V_{TO}|}{e},$$

where V_{TO} is the turn-on voltage and e is the elementary charge [12]. Those low densities are in sharp contrast with the higher density of $5.2 \times 10^{12}/cm^2$ reported by Zhang et al. in the OTS-pretreated devices [13]. The origin of the E_a lies mainly in the traps produced by the structural disorders and/or defects in the thin films [25]. It was clearly demonstrated that the lower E_a and trap density observed were strongly correlated with the improved quality of the as-deposited NCBD-based films, ultimately leading to the efficient carrier transport in the well-connected intergrains and the excellent mobilites in the pentacene-based transistors.

4. Conclusions

Pentacene-based, top-contact transistors were fabricated on two kinds of substrates, both at room temperature, using the NCBD method; OTS-untreated and -pretreated SiO_2. Both active layers without a thermal post-treatment consisted of high-quality, crystalline pentacene thin films with uniform, smooth surfaces. In particular, the total trap density and temperature dependence of μ_{eff} in the range of 10−300 K showed that the amphiphilic OTS pretreatment decreased the trap density and activation energy for carrier transport significantly by reducing the amount of structural disorder. The derived field-effect mobilities were among the best reported thus far: $\mu_{eff} = 0.47$ and $1.25\ cm^2/Vs$ for the OTS-untreated and -pretreated devices, respectively. The fabrication of several organic-based transistor devices using various types of π-conjugated molecules and surfactants through the NCBD method is currently underway. These studies are expected to provide further insight into the interactions at the interfaces at the molecular level as well as the structure-performance relationship.

Acknowledgments

H.-S. Seo is grateful for the Seoul Science Fellowship. This work was supported by the Korea Science and Engineering Foundation (KOSEF) through the National Research Lab. Program funded by the Ministry of Science and Technology (No. M10500000023-06J0000-02310).

References

[1] M.M. Ling, Z. Bao, Chem. Mater. 16 (2004) 4824.
[2] H. Klauk, M. Halik, U. Zschieschang, G. Schmid, W. Radlik, W. Weber, J. Appl. Phys. 92 (2002) 5259.
[3] T.W. Kelley, P.F. Baude, C. Gerlach, D.E. Ender, D. Muyres, M.A. Haase, D.E. Vogel, S.D. Theiss, Chem. Mater. 16 (2004) 4413.
[4] Y. Sun, Y. Liu, D. Zhu, J. Mater. Chem. 15 (2005) 53.
[5] J.K. Lee, J.M. Koo, S.Y. Lee, T.Y. Choi, J.Y. Kim, J.H. Choi, Opt. Mater. 21 (2002) 451.
[6] G. Horowitz, J. Mater. Chem. 9 (1999) 2021.
[7] F. Dinelli, M. Murgia, F. Biscarini, D.M. De Leeuw, Synth. Met. 146 (2004) 373.
[8] S. Yaginuma, J. Yamaguchi, K. Itaka, H. Koinuma, Thin Solid Films 486 (2005) 218.
[9] K. Itaka, T. Hayakawa, J. Yamaguchi, J. Koinuma, Appl. Phys. A 79 (2004) 875.
[10] T.W. Kelley, D.V. Muyres, P.F. Baude, T.P. Smith, T.D. Jones, Mater. Res. Soc. Symp. Proc. 771 (2003) L6.5.
[11] P.V. Necliudov, S.L. Rumyantsev, M.S. Shur, D.J. Gundlach, T.N. Jackson, J. Appl. Phys. 88 (2000) 5395.
[12] K.P. Pernstich, S. Haas, D. Oberhoff, C. Goldmann, D.J. Gundlach, B. Batlogg, A.N. Rashid, G. Schitter, J. Appl. Phys. 96 (2004) 6431.
[13] X.-H. Zhang, B. Domercq, X. Wang, S. Yoo, T. Kondo, Z.L. Wang, B. Kippelen, Org. Electron. 8 (2007) 718.
[14] J.-Y. Kim, E.-S. Kim, J.-H. Choi, J. Appl. Phys. 91 (2002) 1944.
[15] P.S. Abthagir, Y.-G. Ha, E.-A. You, S.-H. Jeong, H.-S. Seo, J.-H. Choi, J. Phys. Chem. B. 109 (2005) 23918, In comparison to the procedure described in the Ref. [15], there were three modifications in the present experiment. Firstly, we changed the procedure for cleaning the SiO_2

substrates as described in the text. Previously the substrates were simply cleaned by successive ultrasonic treatments in acetone, methanol and deionized water in order. Secondly, the thickness of thermally grown gate dielectric was changed from 1000 to 2000 Å. Thirdly, the channel length and width of the devices were changed from 1000 and 200 μm to 500 and 1400 μm, respectively. It was believed that all of those combined modifications increased the present device performance significantly.

[16] H. Lim, J.-H. Choi, J. Chem. Phys. 124 (2006) 014710.
[17] Y.-G. Ha, E.-A. You, B.-J. Kim, J.-H. Choi, Synth. Met. 153 (2005) 205.
[18] E.-A. You, Y.-G. Ha, Y.-S. Choi, J.-H. Choi, Synth. Met. 153 (2005) 209.
[19] M. Kim, B.-H. Jeon, J.-Y. Kim, J.-H. Choi, Synth. Met. 135–136C (2003) 743.
[20] H. Lim, B.-J. Kim, J.-H. Choi, Synth. Met. 135–136C (2003) 81.
[21] S.J. Kang, M. Noh, D.S. Park, H.J. Kim, C.N. Whang, C.-H. Chang, J. Appl. Phys. 95 (2004) 2293.
[22] D. Guo, S. Entani, S. Ikeda, K. Saiki, Chem. Phys. Lett. 429 (2006) 124.
[23] Y.-Y. Lin, D.J. Gundlach, S.F. Nelson, T.N. Jackson, IEEE Trans. Electron Devices 44 (1997) 1325.
[24] T. Minari, T. Nemoto, S. Isoda, J. Appl. Phys. 99 (2006) 034506.
[25] J.-G. Park, R. Vasic, J.S. Brooks, J. Appl. Phys. 100 (2006) 044511.

Available online at www.sciencedirect.com
ScienceDirect
Organic Electronics 9 (2008) 439–444
Organic Electronics
www.elsevier.com/locate/orgel

Factors influencing local potential drop in bottom-contact organic thin-film transistor using solution-processible tetrabenzoporphyrin

Mingsheng Xu [a,*], Akira Ohno [b], Shinji Aramaki [b], Kazuhiro Kudo [c], Masakazu Nakamura [c,*]

[a] Venture Business Laboratory, Chiba University, 1-33 Yayoi-cho, Inage-ku, Chiba 263-8522, Japan
[b] Mitsubishi Chemical Group Science and Technology Research Center, Inc., 1000 Kamoshida-cho, Aoba-ku, Yokohama 227-8502, Japan
[c] Department of Electrical and Electronics, Chiba University, 1-33 Yayoi-cho, Inage-ku, Chiba 263-8522, Japan

Received 18 August 2007; received in revised form 22 January 2008; accepted 2 February 2008
Available online 15 February 2008

Abstract

By exploiting atomic-force-microscope potentiometry, we have studied the local potential distribution in the solution-processible tetrabenzoporphyrin (BP) bottom-contact thin-film transistor under controlled atmospheres. It is found that abrupt and big potential drops mainly appeared at the domain boundaries and cracks in the BP film when the transistor was under operation, indicating a dominant influence of domain boundary and crack on the device performance. Exposure of the device to O_2 drastically reduced the potential drops at some boundaries, which is the main reason for the improved device performance by O_2 exposure.

PACS: 85.30.Tv; 73.40.Ns; 68.55.Jk; 68.37.Ps; 61.72.Ww

Keywords: Organic thin-film transistors; Potential distribution; Solution-based processes; Atomic-force-microscope potentiometry

1. Introduction

Understanding and control of the relation between the electronic transport properties and morphology of organic semiconductors is crucial for further improving device performance of organic thin-film transistors (OTFTs). Although it has been shown by potential measurements that domain structures in highly-ordered polythiophene monolayers [1] and pentacene grain boundary [2,3], and contacts at the interface between source/drain electrodes and organic active layer [4–6] influence carrier transport and injection properties, the nature of domain boundary and the formation of contact [7] in real devices are still not so clear. The demands for cheap, flexible and light-weigh devices drive the development of OTFTs using solution-processible fabrication methods. However, it is difficult to control material organization/molecular orientation when the devices are fabricated by solu-

* Corresponding authors.
E-mail addresses: XU.Mingsheng@nims.go.jp (M. Xu), nakamura@faculty.chiba-u.jp (M. Nakamura).

1566-1199/$ - see front matter © 2008 Elsevier B.V. All rights reserved.
doi:10.1016/j.orgel.2008.02.005

tion-based processes, which is crucial for charge transport. It is found that ambient atmosphere seriously affects performance of pentacene OTFTs as the ambient molecules interact with pentacene or form traps [8,9]. Towards commercialization of OTFT-based technology, the environmental stability of organic electronic devices must be understood and controlled.

It has been reported that the OTFTs using tetrabenzoporphyrin (BP) film as active layer, converted from the solution-coated 1,4:8, 11:15, 18:22, 25-tetraethano-29H, 31H-tetrabenzo[b, g, l, q]porphine (CP) precursor, show high mobility [10]. However, different domains were found in the BP films formed via solution methods in contrast to more ordered structures prepared by thermal deposition. In this work, we report the effects of both morphologic features and atmospheres on the potential distribution in a solution-processible BP bottom-contact (BC) OTFT by using an atomic-force-microscope potentiometry (AFMP) [4]. By the AFMP technique, we found that abrupt and big potential drops mainly occurred at the domain boundaries and cracks in the BP film, suggesting a dominant influence of the domain boundary and crack on the device performance. In contrast to the exposure to N_2, exposing the device to O_2 led to different responses of domain boundaries and enhanced carrier transport, possibly indicating that O_2 in this BP transistor formed an acceptor level.

2. Experimental

The BP BC-OTFT with a channel length of 10 μm and a channel width of 5000 μm was fabricated on a highly doped *n*-Si substrate with thermally grown 300 nm SiO_2. The source/drain (S/D) electrodes, Au (100 nm) along with 5 nm-Cr as adhesive layer, were patterned by using photolithography and lift-off techniques. BP film was fabricated by heating a solution-processed CP amorphous film, detail of which and the AFMP measurement can be found in our previous publications [4,10]. The field effect characterization in Fig. 1a and b was carried out in N_2 by using Agilent Technologies E5272A. Prior to the potential measurements under dry N_2, the device was out-gassed (about 1×10^{-3} Pa) for more than 14 h. After finishing measurements under N_2, the chamber was re-evacuated for more than 30 min, and then measurements were performed under dry O_2 after the device had been exposed to O_2 for more than 60 min.

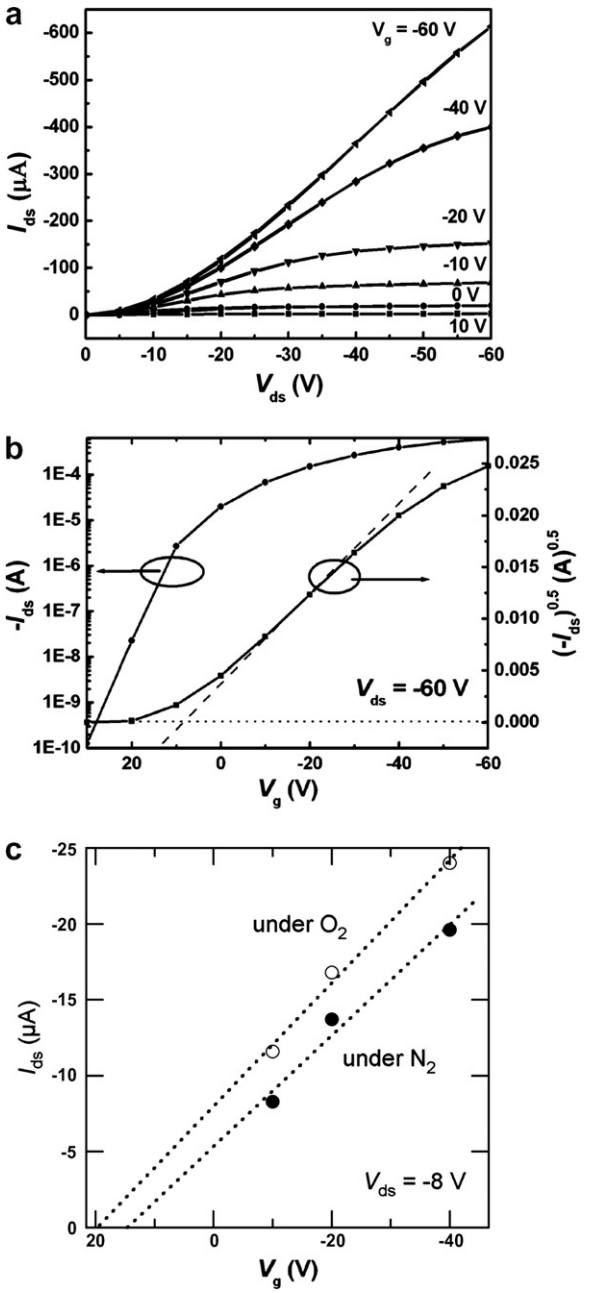

Fig. 1. (a) Output and (b) transfer characteristics of the BP bottom-contact transistor measured in N_2. (c) A comparison of transfer characteristics of the BP transistor operated in N_2 and O_2 as recorded during AFMP measurements.

3. Result and discussion

Fig. 1a and b show the output and transfer characteristics of a BP BC-OTFT measured under N_2. The saturation mobility (@ $V_{ds} = -60$ V) is estimated to be about 0.05 cm^2/Vs (the capacitance,

$C_0 = 10$ nF cm^{-2}), which is the typical value of BP bottom-contact transistors. The on/off ratio is above 10^6 between -60 V and 30 V of V_g, and the threshold voltage (V_{th}) is about 15 V. In the small bias range of the output characteristic, non-linear behavior is observed, which might stem from grain boundaries instead of the energy-level offset between the metal and organic as discussed later. Fig. 1c shows the transfer characteristics recorded during AFMP measurements at V_{ds} of -8 V under N_2 and O_2, which will be discussed later in detail. We hereafter will discuss the potential distribution under linear-regime operation judging from the output characteristics in Fig. 1a, i.e., under the condition of $V_{ds} = -8$ V and V_g of the range from -10 to -40 V. Since there exists an about -5 V threshold for V_{ds} due to the non-linear output characteristics, V_{ds} of -8 V is appropriate to be used for analyzing the barrier-like behavior at the grain boundaries.

Fig. 2a–d contrast the topographic and corresponding surface potential maps of the BP device characterized in Fig. 1 by operating the transistor with $V_{ds} = -8$ V and $V_g = -20$ V under dry N_2 and O_2, respectively. It is obvious from the topographic image that the BP film exhibits two kinds of domain structures, smooth and rough appearances with cracks among them. Geometrical edges of the S/D electrodes are also clearly observed. From the potential maps, we can discern very fine potential distribution around domain boundary, crack and contact.

Fig. 3a shows the surface potential profile along the '1' line of Fig. 2a and b measured under N_2. Abrupt and big potential drops occurred at the domain boundaries between the smooth domain and the rough one, which might indicate different orientations of BP crystals in the two kinds of domains [11]. Different orientations could result in ineffective electronic overlap between adjacent

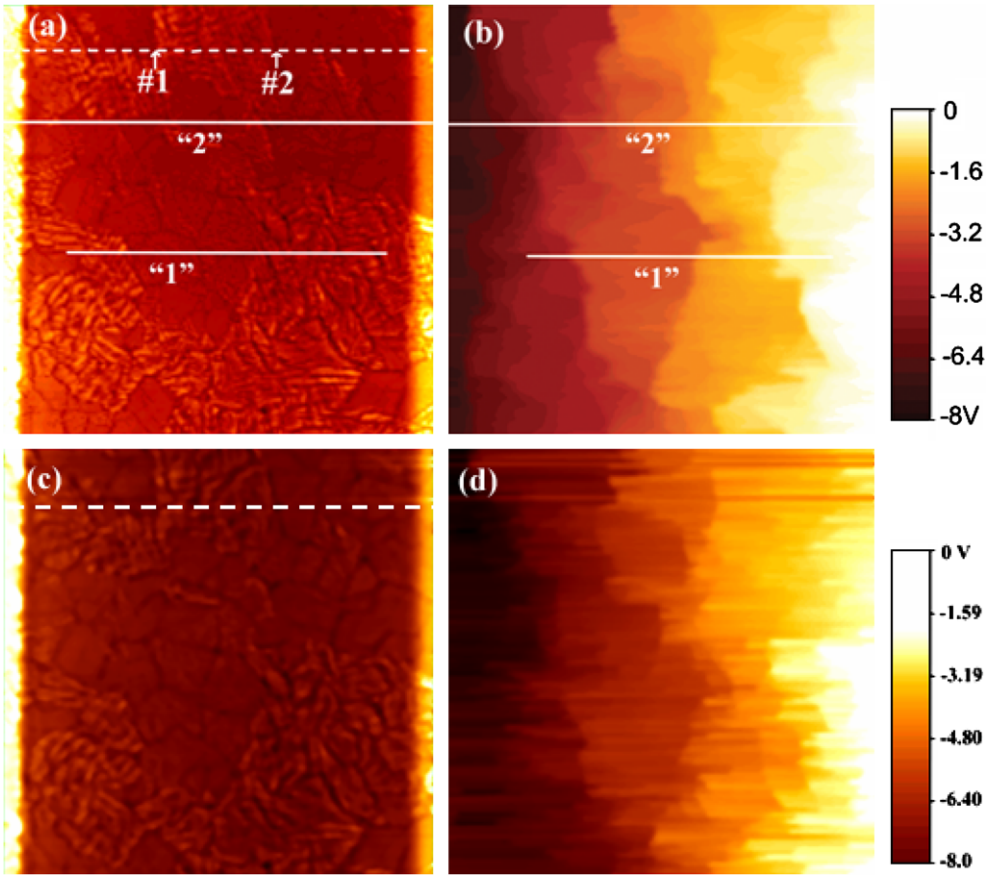

Fig. 2. (a) Topographic image and (b) corresponding potential mapping measured under N_2 with $V_{ds} = -8$ V and $V_g = -20$ V. (c) Topographic image and (d) corresponding potential mapping measured under O_2 with $V_{ds} = -8$ V and $V_g = -20$ V at the same sample area as in (a).

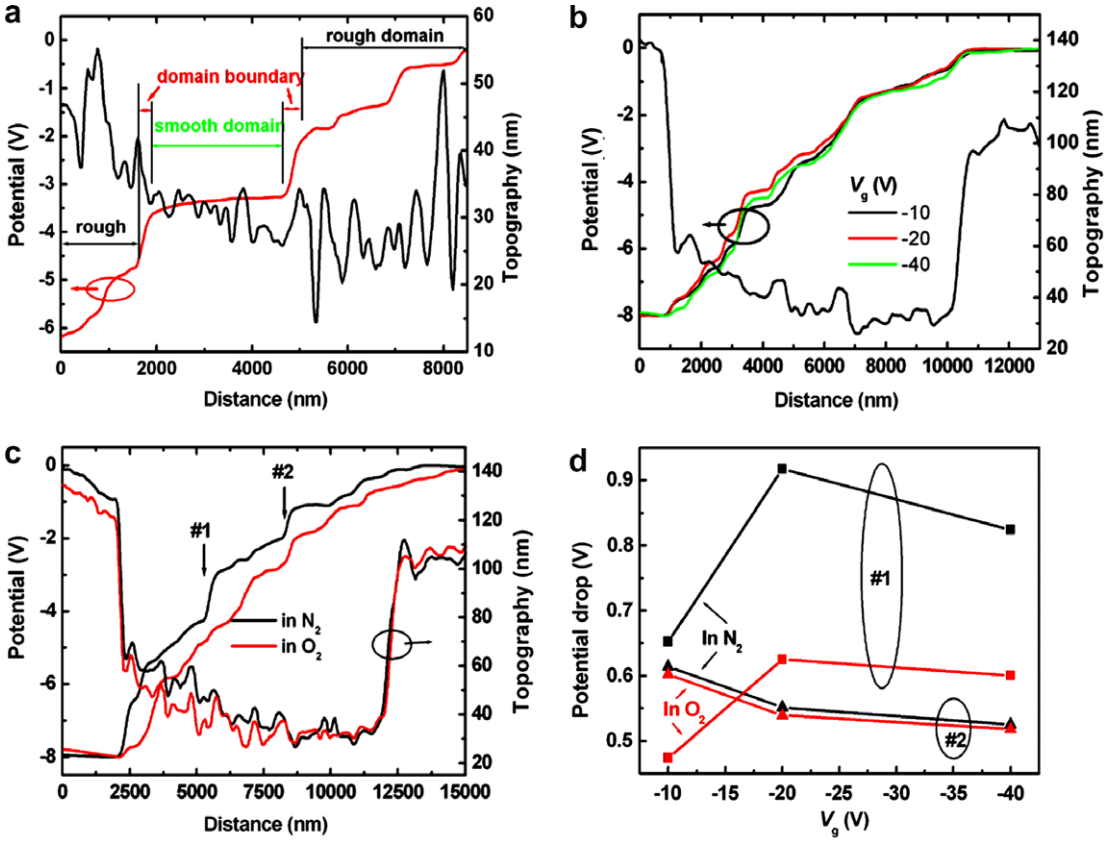

Fig. 3. (a) Potential profile along the '1' line of Fig. 2a measured with $V_{ds} = -8$ V and $V_g = -20$ V under N_2, highlighting the effect of domains. (b) Gate bias dependent potential distribution along the '2' line of Fig. 2a with $V_{ds} = -8$ V. (c) Comparison of potential profiles along the dash-line in Fig. 2a measured under N_2 and O_2 with the device operating with $V_g = -20$ V and $V_{ds} = -8$ V. (d) Comparison of gate voltage dependent potential drops measured under N_2 and O_2 at two domain boundaries marked in Fig. 2a.

domains [1] and thus the domain boundaries are much more resistive for carrier transport [3]. Furthermore, it seems that the smooth domains show a smaller slope potential profile as compared to the rough domains, suggestive of higher conductivity of the smooth domains, whereas the steeper potential profile of the rough domains was presumably caused by disordered structures. The possible structural difference among the cracks and boundaries led to different potential drops at cracks and domain boundaries exhibiting energy or spatial barrier for carrier transport [3], different gate bias dependence and different sensitivity to oxygen as discussed below. Fig. 3b shows the gate bias ($V_g = -10$, -20 and -40 V) dependent surface potential profiles along the '2' line of Fig. 2a and b measured when the device was operated with V_{ds} of -8 V under dry N_2. It is found that the potential drops at the drain-electrode/BP contact (left-hand side in Fig. 2a), the cracks, the domain boundaries and the source-electrode/BP contact (right-hand side in Fig. 2a) depend on the gate bias. However, the whole profiles show a complicated dependence. In particular, we will address the dependence of two domain boundaries below. Based on the potential profile measured along the '2' line in Fig. 2b with V_g of -20 V, the applied negative 8.0 V between the source and the drain electrodes was divided by the drain-electrode/BP, source-electrode/BP, cracks and boundaries, and bulk as 0.54, 0.17, 4.69, and 2.60 V, respectively. The results imply that the device performance of the BP BC-OTFT is predominated (nearly 60% of applied V_{ds}) by cracks and domain boundaries in the channel, while the contact is not highly resistive when compared to the cracks and boundaries. By considering ionization energy ($\sim$ 5.08 eV) of BP [12] and assuming no shift of vacuum level [13], we can draw the energy band diagram for the BP TFT with Au ($E_F = \sim$ 5.1 eV) source/drain electrodes as shown in Fig. 4a, which depicts that no serious carrier injection barrier exists. The non-linear behavior in

the output characteristic measured under N_2 and small potential drop at the source contact in the potential profile therefore may result from grain boundaries and/or cracks adjacent to the contacts due to discontinuous growth of BP film on/near the S/D electrodes. All these suggest that the limiting factor of the device is connectivity and different orientation among neighboring domains across the channel, whereas the injection barrier is not a major problem since the channel does not have a large conductance.

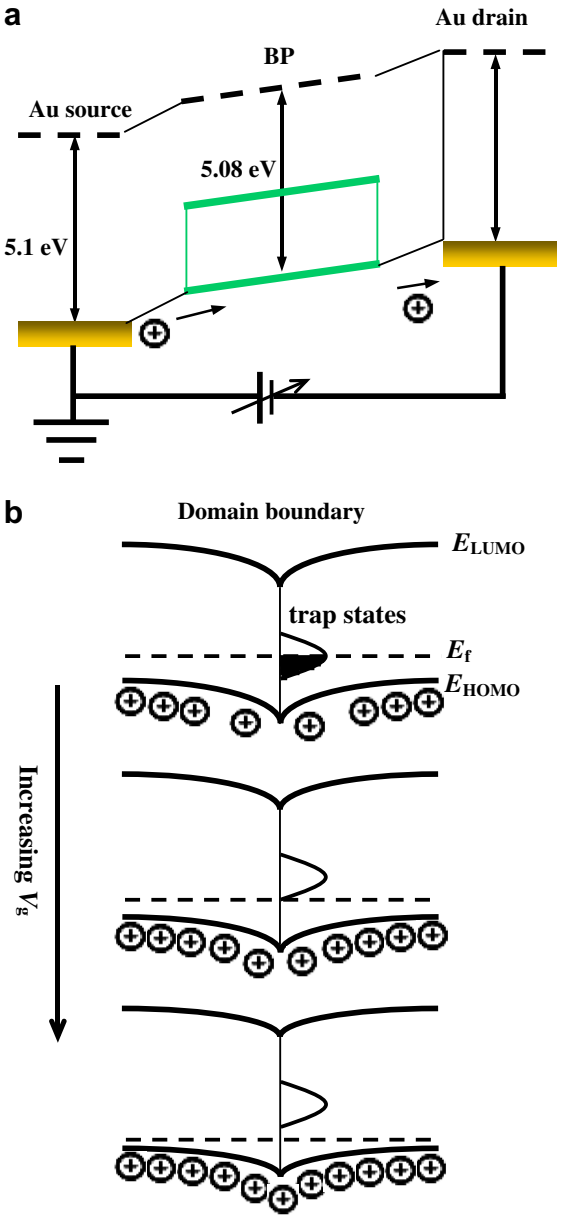

Fig. 4. (a) Schematic of energy band diagram of BP transistor with Au source and drain electrodes. (b) Change in potential barrier height at domain boundary with gate voltage.

Fig. 3c compares the potential profiles measured under N_2 and O_2 along the dash-line in Fig. 2a and c with the device biased at V_{ds} of −8.0 V and V_g of −20 V. Although difference is present at the drain/BP contact, we focus on the channel region since the contact is not the most important limiting factors of the device performance as discussed above. In general, as shown in Fig. 3c, when the device was operating under O_2, the potential drop at the domain boundaries is not steeper as compared with that under N_2. From the transfer characteristics in Fig. 1c, the linear mobility of the device operated under N_2 and O_2 is about 0.009 cm^2/Vs and 0.011 cm^2/Vs, respectively. In addition, the shift of V_{th} toward normally-on direction (from about 15 V under N_2 to 20 V under O_2) after exposure to O_2 might reflect an influence of O_2 exposure on carrier density of the film. The enhancement of mobility when the device was exposed to O_2 is in agreement with the results of Shea et al. [14]. The improvement of device performance is believed to stem from the smaller potential drops at boundaries under O_2 as observed on the potential profile (Fig. 3c), which may be partly due to the carrier doping effect of O_2 on the entire film. Moreover, as discussed below, there exist other factors that suggest a more obvious influence of O_2 on the gap states at the boundaries.

Let us concentrate on #1 and #2 domain boundaries in the dash-line as marked in Fig. 2a. Fig. 3d shows a plot of potential drop changes upon applying different gate bias under N_2 and O_2. Firstly, different gate bias dependence of the domain boundary is observed. In the case of #2 domain boundary, the potential drop reduced with increase in negative gate voltage, which is easily understood from the illustration in Fig. 4b. As gate voltage increased negatively, the number of accumulated carriers (holes in this case) increased and they gradually occupied the grain boundary states, and finally released the pinning of Fermi level. In contrast, a different gate bias dependence is observed at #1 boundary, which is not clearly understood based on the fundamental mechanisms of a field effect transistor. One possible reason for this non-monotonic V_g dependence is a dense discrete shallow trap which pins the Fermi level only after a negative V_g is applied. Secondly, for both boundaries the potential drops are smaller when the device was operating under O_2 than under N_2 at each gate bias as discussed above. Thirdly, the

two domain boundaries exhibit different response to O_2 exposure. The differences of the potential drops at #1 and #2 boundaries under N_2 and O_2 are estimated to be 0.29 V (=0.92 − 0.63 V, in N_2) and 0.01 V (=0.55 − 0.54 V, in O_2), respectively. Although the nature of the domain boundaries, i.e., energy and density of the boundary states, is not very clear at this stage, oxygen usually acts as an acceptor in *p*-type organic semiconductors and the increase of acceptor density narrows the depletion-width in domain boundary. By considering that #1 and #2 boundaries had nearly equal resistance in N_2 at $V_g = -10$ V, both depletion-width narrowing and V_{th} shifting should lead to almost same potential drops as a function of V_g for both the boundaries. However, #1 and #2 boundaries exhibited different responses to O_2 exposure. Based on the comparison of potential drops under N_2 and O_2, it is reasonable to conclude that the different degrees of the influence of O_2 exposure on #1 and #2 boundaries is due to different origins of the traps. And the shallower traps in #1 were rather directly decreased by O_2, which adsorbed at the boundary, and probably diffused into the film and in turn reached the channel.

4. Conclusion

We have found that the dominant factors influencing the BP BC-OTFT fabricated by a solution-based process are the domain boundaries and cracks in the BP film by using atomic-force-microscopy potentiometry under N_2 and O_2 atmospheres. Different dependences of domain boundaries on gate bias and on ambient gasses were observed. The observation of a smaller potential drop at domain boundary under O_2 than that under N_2 indicates that the exposure to O_2 could form acceptor levels which effectively weaken the Fermi level pinning at some of the boundaries. Adsorbed O_2 thus facilitates carrier transport in the BP device.

References

[1] T. Hassenkam, D.R. Greve, T. Bjornholm, Adv. Mater. 13 (2001) 631.
[2] K. Seshadri, C.D. Frisbie, Appl. Phys. Lett. 78 (2001) 993.
[3] M. Nakamura, H. Ohaguri, H. Yanagisawa, N. Goto, N. Ohashi, K. Kudo, in: Proceedings of the International Symposium Super-Functionality Organic Devices IPAP Conference Series, vol. 6, 2005, p. 130.
[4] M. Nakamura, N. Goto, N. Ohashi, M. Sakai, K. Kudo, Appl. Phys. Lett. 86 (2005) 122112.
[5] L. Burgi, H. Sirringhaus, R.H. Friend, Appl. Phys. Lett. 80 (2002) 2913.
[6] K.P. Puntambekar, P.V. Pessavento, C.D. Frisbie, Appl. Phys. Lett. 83 (2003) 5539.
[7] M. Grobosch, M. Knupfer, Adv. Mater. 19 (2007) 754.
[8] Z.T. Zhu, J.T. Mason, R. Dieckmann, G.G. Malliaras, Appl. Phys. Lett. 81 (2002) 4643.
[9] C.R. Kagan, A. Afzali, T.Q. Graham, Appl. Phys. Lett. 86 (2005) 193505.
[10] S. Aramaki, Y. Sakai, N. Ono, Appl. Phys. Lett. 84 (2004) 2085.
[11] S. Aramaki, Y. Sakai, R. Yoshiyama, K. Sugiyama, N. Ono, J. Mizuguchi, Proceedings of SPIE 5522 (2004) 22.
[12] I. Hill, A. Rajagopal, A. Kahn, Y. Hu, Appl. Phys. Lett. 73 (1998) 662.
[13] P.B. Shea, A.R. Johnson, N. Ono, J. Kanicki, IEEE Trans. Electron Dev. 52 (2005) 1497.
[14] P.B. Shea, J. Kanicki, Y. Cao, N. Ono, Appl. Phys. Lett. 87 (2005) 173506.

Available online at www.sciencedirect.com
ScienceDirect
Organic Electronics 9 (2008) 445–451
Organic Electronics
www.elsevier.com/locate/orgel

Enhancement of electrical characteristics of electrospun polyaniline nanofibers by embedding the nanofibers with Ga-doped ZnO nanoparticles

Jin Hyung Jun [a], Kyungah Cho [a], Junggwon Yun [a], Kwang S. Suh [b], TaeYoung Kim [b], Sangsig Kim [a,*]

[a] *Department of Electrical Engineering and Institute for Nano Science, Korea University, 5-1 Anam-dong, Seongbuk-gu, Seoul 136-701, Republic of Korea*
[b] *Department of Materials Science and Engineering, Korea University, 5-1 Anam-dong, Seongbuk-gu, Seoul 136-701, Republic of Korea*

Received 23 November 2007; received in revised form 30 January 2008; accepted 2 February 2008
Available online 9 February 2008

Abstract

Polyaniline nanofibers embedded with undoped ZnO nanoparticles (NPs) or Ga-doped ZnO (ZnO:Ga) NPs were fabricated and their structural and electrical properties were investigated. The uniform distribution of the NPs inside the polyaniline nanofibers was confirmed by transmission electron microscopy analysis. Polyaniline nanofibers embedded with ZnO:Ga-NPs showed their higher conductivities, compared with polyaniline nanofibers embedded with undoped ZnO-NPs. Single nanofibers electrospun from a mixture of a polyaniline solution with a 30 vol% ZnO:Ga-NPs dispersed-solution showed approximately five times higher conductivity than those electrospun from the polyaniline solution alone. This observation indicates that the embedding of the ZnO:Ga-NPs significantly enhances the electrical characteristics of the polyaniline nanofibers.

PACS: 72.80.Le; 72.60.+g; 73.63.Bd

Keywords: Conductivity; Electrospinning; Nanoparticles; Polyaniline

1. Introduction

Polymer-based devices have been attracted considerable attention in the fields of flexible functional and large-area electronics. In the fabrication of polymer electronics, recent studies have been focused on the electrospinning method as a versatile way of preparing polymer nanofibers [1–3]. Polymer nanofibers play a significant role as functional units in the fabrication of various electronics. Up to now, polymer nanofiber-based devices have been intensively studied in a wide range of applications, from textiles and tissue to sensors and optoelectronics [4–8]. However, the relatively low conductivity of

* Corresponding author. Tel.: +82 2 3290 3245; fax: +82 2 3290 3894.
E-mail address: sangsig@korea.ac.kr (S. Kim).

1566-1199/$ - see front matter © 2008 Elsevier B.V. All rights reserved.
doi:10.1016/j.orgel.2008.02.001

polymers, as compared to that of inorganic materials, is an obstacle to the realization of electronic devices based on polymer nanofibers, despite the advantages of polymer nanofibers such as their low cost, flexibility and light weight. Polymer nanofibers would be more readily applicable if their conductivities were enhanced.

The electrical characteristics of organic electronic materials have often been enhanced by adding inorganic materials with high conductivity [9,10]. Based on this concept, we developed a simple method of remarkably increasing the conductivities of polymer nanofibers. This simple method is based on the incorporation of heavily doped n-type inorganic nanomaterials into p-type polymer nanofibers. The essence of this idea is to bring about the type conversion of the polymer nanofibers from p- to n-type in order to increase both the mobility and concentration of the major carriers within them. Polyaniline (PANi) nanofibers were used in this work as representative conducting polymer nanofibers with conjugated bonds, and undoped ZnO nanoparticles (NPs) or Ga-doped ZnO (ZnO:Ga) NPs were utilized as n-type inorganic NPs; note that undoped ZnO materials are normally n-type. The embedding of undoped ZnO-NPs or ZnO:Ga-NPs into the PANi nanofibers was performed to increase the conductivities of the PANi nanofibers. In this study, PANi nanofibers and undoped ZnO-NPs or ZnO:Ga-NPs-embedded PANi nanofibers were fabricated first by electrospinning, and the electrical characteristics of each of the single nanofibers were investigated. (For simplicity, undoped ZnO-NPs will be written as ZnO-NPs henceforth).

2. Experimental

PANi solution was produced as follows. One grams of commercial emeraldine salt PANi ($C_6H_8N_2$, Sigma–Aldrich Inc.) and 1.29 g of camphorsulfonic acid (HCSA) were dissolved in 100 ml chloroform as the solvent, and the solution was stirred for 6 h using a magnetic stirrer, resulting in a light-green solution. HCSA was used not only to protonate PANi, but also to induce the solubility of PANi in the chloroform solvent [11]. The resultant solution was filtered using a 0.20 μm mixed-cellulose-ester filter, and the volume of the filtered solution was about 80 ml. Then 0.16 g of poly(ethylene-oxide) [PEO, $(C_2H_4O)\cdot nH_2O$, Sigma–Aldrich Inc.] with a molecular weight of 900,000 was added to the filtered solution, and this solution was stirred for 2 h using a magnetic stirrer. The reason for adding the PEO to the filtered solution was to enable the solution to be easily transformed into nanofibers during the electrospinning [12] henceforth, a mixture of PANi and PEO is labeled PANi for convenience.

Solutions dispersed with ZnO-NPs or ZnO:Ga (5 wt%) NPs were prepared as follows. One hundred milliliter of a methanol-based 0.1 M NaOH solution was first heated to 65 °C on a hot plate, and 2.19 g of zinc acetate dihydrate [$(C_2H_3O_2)_2Zn\cdot 2H_2O$, Sigma–Aldrich Inc.] was then added. In a few seconds, ZnO-NPs were formed in the solution whose color became clearer. The addition of 0.157 g of gallium(III) nitrate hydrate [$Ga(NO_3)_3\cdot xH_2O$, Sigma–Aldrich Inc.] to 100 ml of the ZnO-NPs solution at 65 °C led to the dispersion of the ZnO:Ga (5 wt%) NPs in the solution. To confirm the Ga doping into the ZnO-NPs, the solution was spin-coated on a Si substrate, and the NPs dispersed on the substrate were analyzed by X-ray photoelectron spectroscopy (XPS, Physical Electronics PHI 5700 ESCA spectrometer) with an Al Kα ($h\upsilon = 1486.6$ eV) X-ray source.

After the preparation of the PANi solution and the NPs-dispersed-solution, these two solutions were volumetrically mixed at ratios of 10, 20, 30, or 40 vol% of the NPs-dispersed-solution (hereafter, these solutions are referred to as the 9:1, 8:2, 7:3, and 6:4 PANi/NPs solutions, respectively), and the mixed solutions were stirred vigorously with a magnetic stirrer. The PANi-only solution and the PANi- and NPs-mixed solutions were electrospun to fabricate PANi-only nanofibers and NPs-embedded PANi nanofibers, respectively. Ten milliliter of the polymer solutions were placed in a syringe with a metal capillary tip having an inner diameter of 0.15 mm and the feeding rate of the solutions during the electrospinning was maintained at 1 ml/h by a mechanical syringe pump. The electrospinning was performed using a commercial electrospinning system (NNC-SP200, NanoNC, Korea), and the applied voltage and distance between the metal tip and collector in the electrospinning process were 4 kV and 10 cm, respectively. A metallic plate wrapped with Al foil was used as the collector. NPs-embedded PANi nanofibers were obtained by the electrospinning of the 9:1, 8:2, 7:3, and 6:4 PANi/NPs solutions (hereafter, these nanofibers are referred to as the 9:1, 8:2, 7:3, and 6:4 PANi/NPs nanofibers, respectively). The nanofibers were investigated using transmission electron microscopy

(TEM, FEI Technai G2 F30) to examine their structural properties, including the shapes and diameters of the nanofibers, and to confirm the presence of NPs within them. The current density–voltage (J–V) measurement for the nanofibers was performed with an HP4155 C semiconductor parameter analyzer. All electrical measurements were conducted at room temperature in a vacuum.

3. Results and discussion

High resolution TEM (HRTEM) analysis and XPS measurement were made to confirm the successful formation of ZnO-NPs and ZnO:Ga-NPs. The HRTEM image of ZnO-NPs is shown in Fig. 1a. The crystalline NPs with a diameter of 3–5 nm were indicated by light-gray colored arrows, and those NPs were identified indeed to be ZnO by energy dispersive X-ray (EDX) analysis. XPS spectrum obtained from a solid film composed of ZnO:Ga-NPs is plotted in Fig. 1b. While the peaks corresponding to Zn or O ions are present in the entire energy range of the spectrum, a weak peak corresponding to the Ga 2p core level is seen at 1118.6 eV [13], this peak is more clearly shown in the inset of Fig. 1b. The presence of this peak at a binding energy of 1118.6 eV in the XPS spectrum indicates the successful doping of Ga ions into the ZnO-NPs through their substitution into the Zn sites, since the peak position of elemental Ga ions is known to be at around 1117 eV [14].

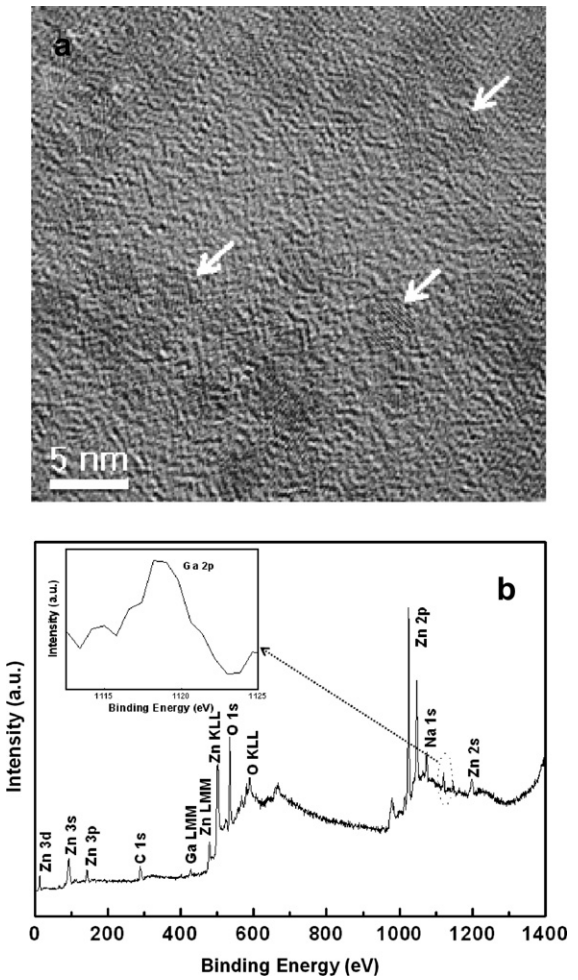

Fig. 1. (a) TEM image of synthesized ZnO-NPs, and (b) XPS spectrum of the spin-coated ZnO:Ga film. The inset in (b) shows the Ga 2p core level present at a binding energy of 1118.6 eV.

Fig. 2 shows the TEM images of (a) a PANi-only nanofiber, (b) a ZnO-NPs-embedded PANi nanofiber, and (c) a ZnO:Ga-NPs-embedded PANi nanofiber; note that images (b) and (c) were taken from the 7:3 PANi/ZnO-NPs and PANi/ZnO:Ga-NPs nanofibers, respectively. TEM image (a) demonstrates that the PANi nanofiber with a diameter of about 600 nm contains irregularly shaped and distributed pores. The formation of these pores is caused by the fast evaporation of the solvent [15]. TEM images (b) and (c) show that the diameters of the 7:3 PANi/NPs nanofibers are about 350 nm. These diameters are smaller than that of the PANi nanofiber. This is because the diameter of the electrospun nanofibers decreases as the viscosity of the polymer solution decreases [16,17]. When the NPs-dispersed alcohol-based solution and polymer (PANi) solution were mixed, the viscosity of the mixed solution decreased noticeably at a certain volumetric ratio with an accompanying/due to the increase in the volume of the NPs-dispersed-solution. In addition, the diameters of the 9:1 and 8:2 PANi/NPs nanofibers were 600 and 480 nm, respectively. The diameters of the 9:1 PANi/NPs nanofibers were the same as those of the PANi nanofibers, and those of the 8:2 PANi/NPs nanofibers were larger than those of the 7:3 PANi/NPs nanofibers. This observation supports our suggestion that the reduction in the diameter of the PANi/NPs nanofibers results from the decrease in the viscosity of the polymer solution due to the increase in the volume of the NPs-dispersed-solution.

HRTEM images of the PANi/NPs nanofibers were obtained to confirm the embedding of the NPs into the nanofibers. Fig. 3 shows the HRTEM images of (a) a PANi-only nanofiber, (b) a 7:3 PANi/ZnO-NPs nanofiber, and (c) a 7:3 PANi/

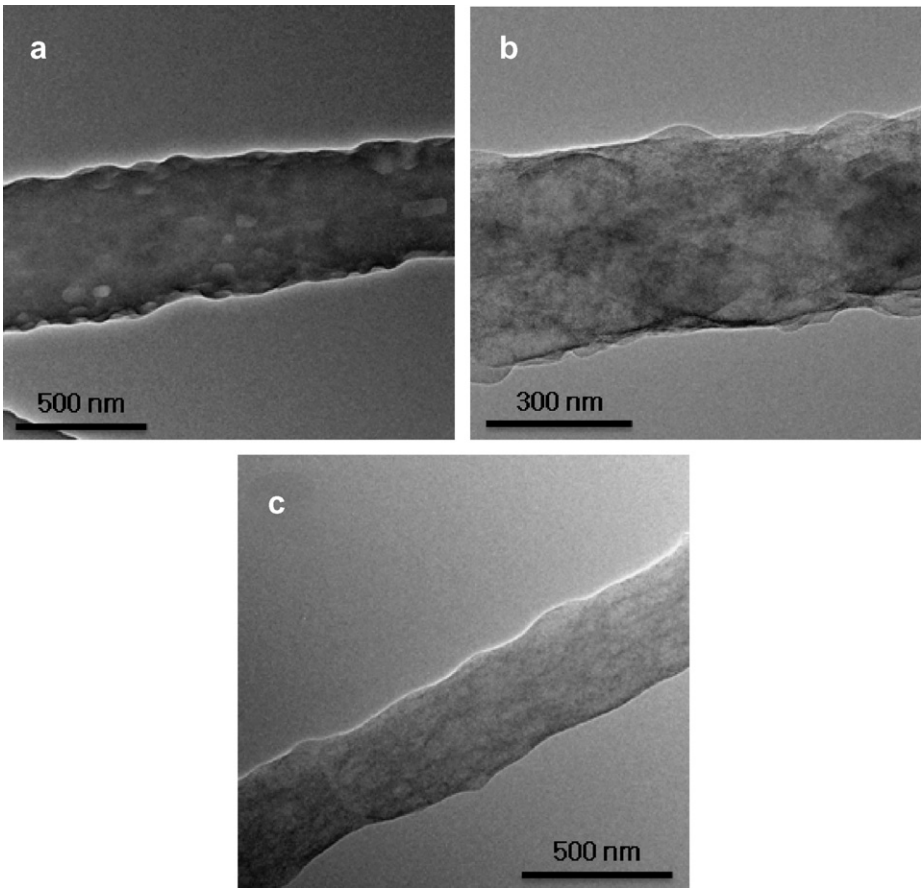

Fig. 2. TEM images of: (a) a PANi nanofiber, (b) a ZnO-NPs-embedded PANi nanofiber, and (c) a ZnO:Ga-NPs-embedded PANi nanofiber. Note that images (b) and (c) were taken from the 7:3 PANi/ZnO-NPs and PANi/ZnO:Ga-NPs nanofibers, respectively.

ZnO:Ga-NPs PANi nanofiber. In Figs. 3b and c, the crystallites with a diameter of 3–5 nm are indicated with light-gray colored arrows. Since there were no evident crystallites in the HRTEM image (a) of the PANi-only nanofiber, the crystallites seen in the HRTEM images (b) and (c) correspond to ZnO and ZnO:Ga-NPs, respectively. In addition, since the NPs have darker contrast than the fiber matrix does, it can also be concluded that the NPs are well distributed over the nanofibers when considering the contrast of the low magnification TEM images in Fig. 2.

Fig. 4 shows the electrical properties of the electrospun nanofibers. First of all, for all of the different nanofibers under study, a single nanofiber was suspended across two gold electrodes with a separation of 20 μm on top of a thermally oxidized Si substrate to investigate its electrical properties. The optical image of a single nanofiber lying on the patterned substrate is shown in Fig. 4a, and a schematic cross-sectional diagram of the structure is shown in the inset of this figure. For the selected nanofiber, the channel length is about 22 μm. Note that for each of the single nanofibers under study, the channel length was measured accurately to estimate its conductivity. Fig. 4b shows the J–V curves obtained in vacuum from single PANi/NPs nanofibers with a ratio of 7:3; for comparison, the J–V curve (marked by solid squares) taken from a single PANi nanofiber was added to these three figures. In addition, for a more accurate and direct comparison, the conductivities of the nanofibers (Fig. 4c) were estimated by calculating their resistivities which were derived from the slopes of linear-fitted I–V curves at applied voltages ranging from 0 to 5 V; their effective lengths were considered for the estimation. The conductivity of the PANi-only nanofiber measured in a vacuum is 2.8×10^{-7} S/cm. This magnitude is much lower than those reported by other research groups [12,18,19]. The conductiv-

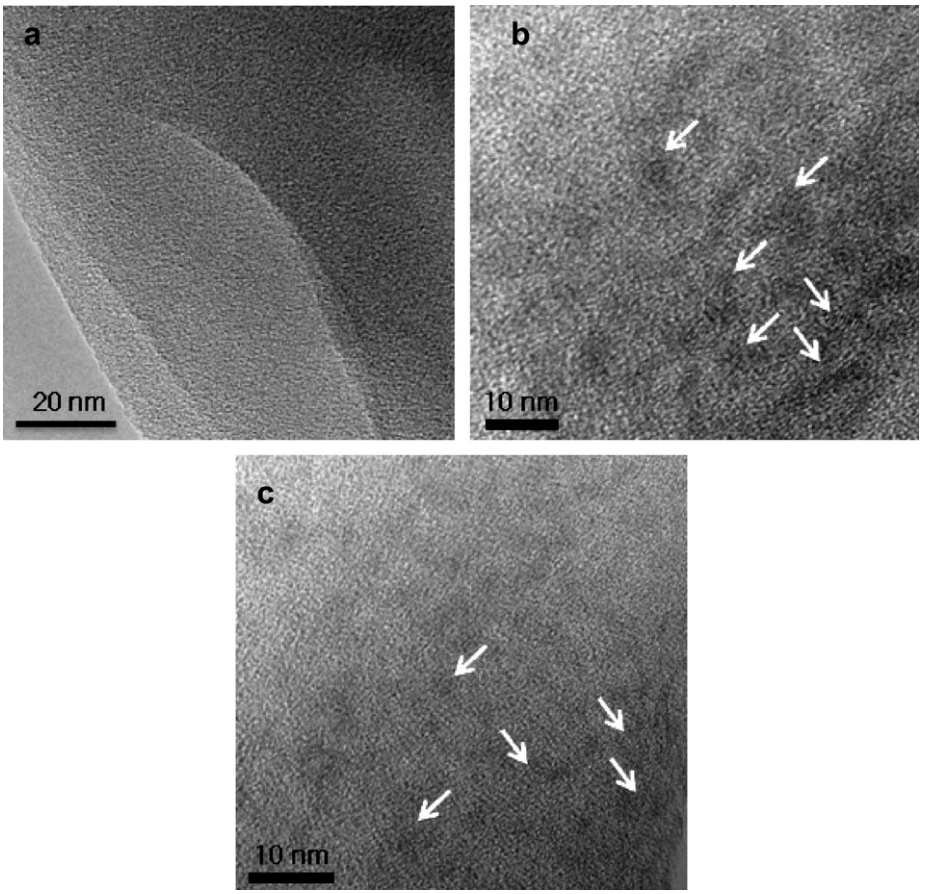

Fig. 3. HRTEM images of: (a) a PANi nanofiber, (b) a 7:3 PANi/ZnO-NPs nanofiber, and (c) a 7:3 PANi/ZnO:Ga-NPs PANi nanofiber. The light-gray colored arrows indicate NPs.

ity of the PANi nanofiber is significantly dependent on the measuring ambient. In particular, PANi is a moisture sensitive polymer [20]. The conductivity of the PANi-only nanofiber increased by about five-orders of magnitude (4.8×10^{-2} S/cm) when the measurement was made in air instead of in a vacuum.

The conductivity of the 9:1 PANi/ZnO-NPs nanofiber measured in a vacuum is slightly lower (2.7×10^{-7} S/cm) in magnitude than that of the PANi-only nanofiber. This observation can be explained by the charge compensation of the major charge carriers in the nanofiber. PANi is known to have p-type characteristics [21] and ZnO-NPs to have n-type characteristics [10]. The embedding of the ZnO-NPs into the PANi nanofiber results in the provision of electrons from the n-type ZnO-NPs to the p-type PANi nanofiber due to the larger electron affinity (4.4 eV) of PANi semiconducting materials than that (4.2 eV) of ZnO semiconducting ones (see the energy diagram drawn in the inset of Fig. 4c [22,23]). The provision of electrons from the n-type ZnO-NPs compensates for the holes (major charge carriers) in the p-type PANi nanofiber. The reduction of the whole concentration due to the charge compensation leads to a decrease in the conductivity of the nanofiber. Furthermore, the conductivity of the 9:1 PANi/ZnO:Ga-NPs nanofiber was estimated to be 2.0×10^{-7} S/cm, which is lower than that of the 9:1 PANi/ZnO-NPs nanofiber. The lower conductivity of the 9:1 PANi/ZnO:Ga-NPs nanofiber originates from the greater compensation of holes in the p-type PANi nanofiber, since ZnO:Ga-NPs provide a larger number of electrons than ZnO-NPs; Ga ions act as n-type dopants in ZnO semiconductors [24,25].

In contrast to the 9:1 PANi/ZnO-NPs and PANi/ZnO:Ga-NPs nanofibers, the current density and conductivity of the 8:2 PANi/NPs nanofibers were higher than those of the PANi-only nanofiber, as

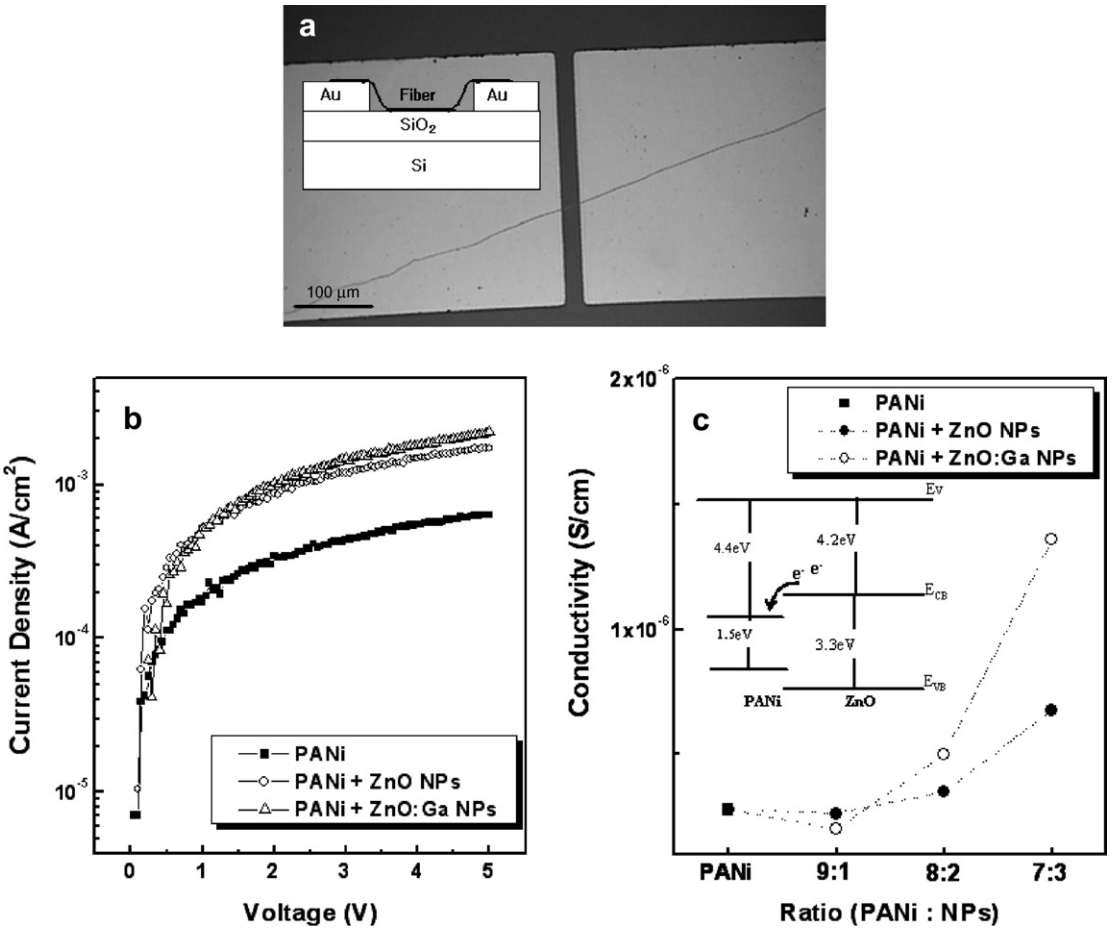

Fig. 4. (a) Optical image of a single nanofiber lying on the patterned substrate, the J–V curves of a single PANi/NPs nanofiber with a ratio of (b) 7:3, and (c) the estimated conductivities of the nanofibers. A schematic cross-sectional diagram of the single nanofiber lying on the patterned substrate is shown in the inset of (a). The J–V curves (marked by solid squares) taken from a single PANi-only nanofiber are included in (b), and the band diagrams of PANi and ZnO are drawn in the inset of (c).

shown in Fig. 4c. In the 8:2 PANi/NPs nanofibers, more electrons are transferred from the NPs to the PANi nanofibers, compared with the 9:1 PANi/NPs nanofibers. The higher current density and conductivity of the 8:2 PANi/NPs nanofibers compared to those of the PANi-only nanofiber indicate that excess electrons remain in the PANi nanofibers after the complete compensation of holes by the transferred electrons. Accordingly, we suggest that in the PANi/NPs nanofibers obtained from the NPs-dispersed-solutions with a mixed ratio of 20 vol%, the majority of the carriers in the nanofiber change from holes to electrons; in other words, the type conversion of the nanofibers from p-type to n-type occurs. This hypothesis is supported by the observation that the conductivity (5.0×10^{-7} S/cm) of the 8:2 PANi/ZnO:Ga-NPs nanofiber is higher than that of the 8:2 PANi/ZnO-NPs nanofiber. Furthermore, the current density and conductivity of the 7:3 PANi/NPs nanofibers shown in Figs. 4b and c, respectively, are much larger than those of both the other PANi/NPs nanofibers and the PANi-only nanofiber. The experimental results on the 7:3 PANi/NPs nanofibers are consistent with the type conversion of the nanofibers caused by the embedding of the n-type NPs. In particular, the conductivity of the 7:3 PANi/ZnO:Ga-NPs nanofiber of 1.4×10^{-6} S/cm is the highest among all the single nanofibers fabricated in this study. The conductivity of the 7:3 PANi/ZnO:Ga-NPs was remarkably enhanced compared with that of the PANi-only nanofiber. This remarkable enhancement in conductivity is due to both the higher mobility of electrons than that of holes and the increased electron

concentration, according to the equation of conductivity expressed as

$$\sigma = nq\mu$$

where n and μ are the concentration and mobility of the charge carriers. On the basis of our analysis of the electrical properties of the NPs-embedded PANi nanofibers, we suggest the embedding of n-type ZnO:Ga-NPs as an efficient and useful method of improving the electrical characteristics of p-type polymer nanofibers.

4. Conclusions

The electrical characteristics of PANi nanofibers embedded with ZnO- and ZnO:Ga-NPs were investigated in this work. The doping of Ga ions into the ZnO-NPs and the embedding of ZnO-NPs into the PANi nanofibers were confirmed by the XPS and HRTEM studies, respectively. The current density and conductivity of the 9:1 PANi/NPs nanofibers were lower in magnitude than those of the PANi-only nanofibers, indicating that the addition of a relatively small amount of NPs to the PANi nanofibers causes a drop in their conductivity due to the resulting charge compensation. In contrast, the current density and conductivity of the 8:2 PANi/NPs nanofibers were higher in magnitude than those of the PANi-only nanofibers, while those of the 7:3 PANi/NPs nanofibers were enhanced even more. The doping of Ga ions into the ZnO-NPs enhances the electrical characteristics of all of the PANi/NPs nanofibers. This remarkable enhancement in their conductivity is explained by the type conversion of the nanofibers from p-type to n-type. The increase in the number of NPs and the doping of Ga ions into the NPs in the PANi nanofibers increase the concentration of electrons transferred from the NPs into the PANi nanofibers, leading to the type conversion. Consequently, the conductivity of the NPs-embedded nanofibers increases due to both the higher mobility of electrons than that of holes and the increased electron concentration.

Acknowledgments

This work was supported by the National R&D Project for Nano Science and Technology (10022916-2006-22), the Center for Integrated-Nano-Systems (CINS) of the Korea Research Foundation (KRF-2006-005-J03601), the "System-IC2010" project of the Korea Ministry of Commerce, Industry and Energy, the Korea Science and Engineering Foundation (KOSEF) through the National Research Lab. Program (R0A-2005-000-10045-02 (2007)), the Nano R&D Program (M10703000980-07M0300-98010), and the Small and Medium Business Administration (SMBA) through the Technology Innovation Project for SMEs (S1010024).

References

[1] F. Dong, Z. Li, H. Huang, F. Yang, W. Zheng, C. Wang, Mater. Lett. 61 (2007) 2556.
[2] S.F. Fennessey, R.J. Farris, Polymer 45 (2004) 4217.
[3] R. Kessick, G. Tepper, Appl. Phys. Lett. 83 (2003) 557.
[4] J. Venugopal, S. Ramakrishna, Appl. Biochem. Biotech. 125 (2005) 147.
[5] S.-Y. Jang, V. Seshadri, M.-S. Khil, A. Kumar, M. Marquez, P.T. Mather, G.A. Sotzing, Adv. Mater. 17 (2005) 2177.
[6] M. Li, Y. Guo, Y. Wei, A.G. MacDiarmid, P.I. Lelkes, Biomaterials 27 (2006) 2705.
[7] H.Y. Liu, H.B. Liu, G.D. Peng, P.L. Chu, Opt. Commun. 266 (2006) 132.
[8] W.A. Daoud, J.H. Xin, Y.S. Szeto, Sensor. Actuat. B–Chem. 109 (2005) 329.
[9] R.J. Tseng, J. Ouyang, C.-W. Chu, J. Huang, Y. Yang, Appl. Phys. Lett. 88 (2006) 123506.
[10] J. Ouyang, C.-W. Chu, C.R. Szmanda, L. Ma, Y. Yang, Nat. Mater. 3 (2004) 918.
[11] Y. Cao, P. Smith, A.J. Heeger, Synth. Met. 48 (1992) 91.
[12] I.D. Norris, M.M. Shaker, F.K. Ko, A.G. MacDiarmid, Synth. Met. 114 (2000) 109.
[13] C.X. Xu, X.W. Sun, B.J. Chen, Appl. Phys. Lett. 84 (2004) 1540.
[14] J. Chastain, Handbook of X-ray Photoelectron Spectroscopy, first ed., Perkin–Elmer Corporation – Physical Electronics Division, Minnesota, 1992.
[15] M. Bognitzki, W. Czado, T. Frese, A. Schaper, M. Hellwig, M. Steinhart, Adv. Mater. 13 (2001) 70.
[16] P.K. Baumgarten, J. Colloid Interf. Sci. 36 (1971) 71.
[17] H. Fong, I. Chun, D.H. Reneker, Polymer 40 (1999) 4585.
[18] A.G. MacDiarmid, W.E. Jones Jr., I.D. Norris, J. Gao, A.T. Johnson Jr., N.J. Pinto, J. Hone, B. Han, F.K. Ko, H. Okuzaki, M. Llaguno, Synthetic Met. 119 (2001) 27.
[19] Y. Zhou, M. Freitag, J. Hone, C. Staii, A.T. Johnson Jr., N.J. Pinto, A.G. MacDiarmid, Appl. Phys. Lett. 83 (2003) 3800.
[20] G.F. Li, C. Martinez, S. Semancik, J. Am. Chem. Soc. 127 (2005) 4903.
[21] N.J. Pinto, A.T. Johnson Jr., A.G. MacDiarmid, C.H. Mueller, N. Theofylaktos, D.C. Robinson, F.A. Miranda, Appl. Phys. Lett. 83 (2003) 4244.
[22] P.R. Somani, S. Radhakrishnan, J. Solid State Electrochem. 7 (2003) 166.
[23] H. Kobayashi, H. Mori, T. Ishida, Y. Nakato, J. Appl. Phys. 77 (1995) 1301.
[24] V. Bhosle, A. Tiwari, J. Narayan, J. Appl. Phys. 100 (2006) 033713.
[25] C.-L. Hsu, Y.-R. Lin, S.-J. Chang, T.-H. Lu, T.-S. Lin, S.-Y. Tsai, I.-C. Chen, J. Electrochem. Soc. 153 (2006) G333.

Available online at www.sciencedirect.com
ScienceDirect
Organic Electronics 9 (2008) 452–460
Organic Electronics
www.elsevier.com/locate/orgel

A host material containing tetraphenylsilane for phosphorescent OLEDs with high efficiency and operational stability

Jae-Wook Kang [a,1], Deug-Sang Lee [b], Hyung-Dol Park [a], Ji Whan Kim [a], Won-Ik Jeong [a], Young-Seo Park [a], Se-Hyung Lee [a], Kyungmoon Go [b], Jong-Soon Lee [b], Jang-Joo Kim [a,*]

[a] *Department of Materials Science and Engineering and OLED Center, Seoul National University, Seoul 151-744, Republic of Korea*
[b] *Organic Synthesis Group, Dongwoo Fine-Chem co., LTD. Pyeongtaek 451-822, Republic of Korea*

Received 27 December 2007; received in revised form 4 February 2008; accepted 5 February 2008
Available online 13 February 2008

Abstract

A host material containing tetraphenylsilane moiety, 9-(4-triphenylsilanyl-(1,1′,4,1″)-terphenyl-4″-yl)-9*H*-carbazole (TSTC), was synthesized for green phosphorescent organic light emitting diodes. The tetraphenylsilane moiety was introduced to provide high triplet energy level, thermal and chemical stability, and glassy properties leading to high efficiency and operational stability of the devices. $Ir(ppy)_3$ based OLEDs using the TSTC host and DTBT (2,4-diphenyl-6-(4′-triphenylsilanyl-biphenyl-4-yl)-1,3,5-triazine) hole blocking layer (HBL) resulted in the maximum external quantum efficiency of 19.8% and the power efficiency of 59.4 lm/W. High operational stability with a half lifetime of 160,000 h at an initial luminance of 100 cd/m^2 was achieved from an electrophosphorescent device using TSTC host and BAlq HBL.

PACS: 72.80.Le; 78.60.Fi; 85.60.Jb

Keywords: Phosphorescent OLED; High efficiency; Operational stability; Tetraphenylsilane containing host

1. Introduction

Organic light emitting diodes (OLEDs) have been a subject of intense academic and industrial research for the last two decades due to their potential application in displays and solid state lighting. Phosphorescence materials are attractive for OLEDs due to their ability of highly efficient emission through harvesting of both singlet and triplet excitons [1–9]. Utilization of phosphorescent dyes as the light emitting material in OLEDs requires proper host materials [10]. Good host materials in phosphorescent OLEDs should possess higher triplet energy than that of the guest molecule to prevent exothermic energy transfer from the emissive dopant to the host material and good morphological stability to improve the operational stability of the device. A number of materials have been reported

* Corresponding author.
E-mail address: jjkim@snu.ac.kr (J.-J. Kim).
[1] Present address: Department of Surface Technology, Korea Institute of Materials Science (KIMS), Changwon 641-831, Republic of Korea.

1566-1199/$ - see front matter © 2008 Elsevier B.V. All rights reserved.
doi:10.1016/j.orgel.2008.02.002

as the host for highly efficient green emitting phosphorescent devices, which include 4-4′-*N*-*N*′dicarbazolylbiphenyl (CBP), bathcuproin (BCP), triazole, and oxadiazole derivatives [11,12]. Among them, CBP has been widely utilized for fabricating green-emitting OLEDs, while $Ir(ppy)_3$ is the most popular dopant. Nevertheless, these green-emitting phosphorescent OLEDs are still unable to achieve the desired high efficiency combined with high operational stability. $Ir(ppy)_3$ doped OLEDs employing the BCP hole blocking layer result in low stability of half lifetime of <700 h at an initial luminance (L_0) of 600–1200 cd/m^2 [2,13] where half-life, $T_{1/2}$, is defined as the time for the luminance to decay to $0.5L_0$.

In this study, we synthesized a new host material containing tetraphenylsilane, 9-(4-triphenylsilanyl-(1,1′,4,1″)-terphenyl-4″-yl)-9*H*-carbazole (TSTC), and used as the host for green electrophosphorescent devices. The tetraphenylsilane moiety is expected to provide high LUMO level, thermal and chemical stability, and glassy properties [14,15], resulting in high efficiency and operational stability of a device. $Ir(ppy)_3$ based OLEDs employing the new host material and DTBT (2,4-diphenyl-6-(4′-triphenylsilanyl-biphenyl-4-yl)-1,3,5-triazine) hole blocking layer (HBL) resulted in the maximum external quantum efficiency (η_{ext}) of 19.8% and the power efficiency (η_p) of 59.4 lm/W. High operational stability of $T_{1/2} = 160{,}000$ h at $L_0 = 100$ cd/m^2 was achieved using the host and BAlq HBL.

2. Experimental

2.1. Synthesis of host material (TSTC)

As indicated in Scheme 1, the TSTC was prepared by Suzuki–Miyamura coupling reaction of 4-triphenylsilylphenylboronic acid and 9-(4′-bromobiphenyl)-carbazole for use as a host material in the electrophosphorescent device.

Triphenyhl silyl chloride, 1,4-dibromo benzene, *n*-butyl lithium, trimethyl borate, 4-bromobenzaldehyde, carbazole, 1,4-dibromobiphenyl, copper(I) iodide, *trans*-1,2-diaminocyclohexane and tetrakis-(triphenylphosphine)palladium(0) were purchased from Aldrich Chemical Co. and used without further purification. Tetrahydrofurane, diethyl ether, 1,4-dooxane, and toluene were purchased from Oriental Chemical Industries and dried over calcium hydride before use.

Synthesis of 4-bromophenyl-triphenyl silane [1]. To a 500 ml, three-neck flask equipped with addition funnel and a mechanical stirrer were added dried ether (100 ml) and 1,4-dibromobenzene (9.6 g, 0.0407 mol). *n*-BuLi (26 ml, 1.6 M in hexane) was added to the reaction mixture which was cooled to −78 °C. The reaction mixture was stirred at room

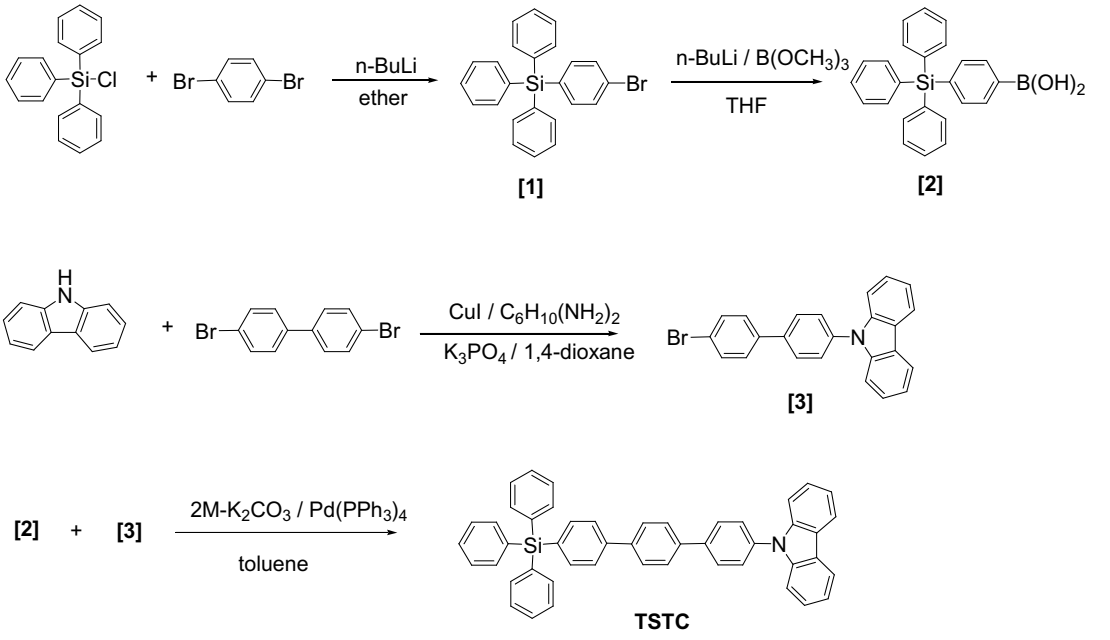

Scheme 1. Synthetic route to TSTC

temperature for 30 min. Ether (100 ml) solution dissolved triphenyl silyl chloride (10 g, 0.034 mol) was added to reaction mixture slowly through an addition funnel at −78 °C. The solution was stirred at room temperature for 1 h. The reaction mixture was poured into water and then this aqueous solution was extracted with diethyl ether. The extracts were washed with water and dried over $MgSO_4$. The crude product was purified by silica gel chromatography using hexane to obtain the white powder. The yield was 70%. ^{1}H NMR (300 MHz, $CDCl_3$) δ [ppm]: 7.54 (d, 8H, Ar–H), 7.43 (d, 2H, Ar–H), 7.36 (m, 9H, Ar–H).

4-Phenyl boronic acid triphenyl silane [2]. Dried THF (250 ml) and 4-bromotriphenyl silane [1] (8.3 g, 0.02 mol) were added into 500 ml three neck flask equipped with a condenser and mechanical stirrer under nitrogen. *n*-BuLi (20 ml, 1.6 M in hexane) was added to the reaction mixture which was cooled to −78 °C. The reaction mixture was stirred at −78 °C for 1 h. After lithiation, trimethyl borate (4.2 g, 0.04 mol) was rapidly added to the reaction mixture which was cooled to −78 °C. The solution was stirred at room temperature for 3 h. The reaction mixture was poured into a mixture of ice and water. The mixture was acidified with 2 N-HCl and extracted with ethyl acetate, and organic phase was washed tree times with water, dried over $MgSO_4$. The crude product was purified by chromatography on silica gel using ethyl acetate/hexane (1:2) as the eluent to obtain the white powder. The yield was 50%. ^{1}H NMR (300 MHz, $CDCl_3$) δ [ppm]: 8.20 (d, 2H, Ar–H), 7.60 (d, 2H, Ar–H), 7.56 (m, 7H, Ar–H, –OH), 7.43 (m, 10H, Ar–H).

9-(4′-bromobiphenyl)-carbazole [3]. Carbazole (10 g, 0.06 mol) and 1,4-dibromobiphenyl (18.7 g, 0.06 mol), copper iodide (0.4 g, 1.92 mmol), *trans*-1,2-diaminocyclohexane (2.3 g, 19.8 mmol) and 1,4-dioxane (150 ml) were added into 500 ml round flask equipped with a condenser and mechanical stirrer. The reaction mixture was heated to 100 °C for 15 h. After completion of the reaction, the crude product was purified by chromatography on silica gel using ethyl acetate/hexane (1:4) as the eluent to obtain the white powder. The yield was 32%. ^{1}H NMR (300 MHz, $CDCl_3$) δ [ppm]: 7.55 (d, 2H, Ar–H), 7.50 (m, 4H, Ar–H), 7.40 (m, 4H, Ar–H), 7.30 (d, 2H, Ar–H), 7.08 (t, 2H, Ar–H), 7.00 (t, 2H, Ar–H).

9-(4-Triphenylsilanyl-[1,1′,4,1″]-terphenyl-4″-yl)-9H-carbazole (TSTC). 9-(4'-bromobiphenyl)-carbazole (6 g, 0.015 mol), tetrakis(triphenylphosphine)palladium(0) (0.17 g, 0.15 mmol), 2 M-K_2CO_3 (60 ml) and toluene (200 ml) were added to a 500 ml three neck flask under nitrogen. The prepared 4-phenyl boronic acid triphenyl silane (5.7 g, 0.015 mol) was added to the solution and heated to 110 °C for 5 h. After cooling to room temperature, the reaction mixture was diluted with diethyl ether and organic phase was washed with water. After drying over $MgSO_4$, the solvent was removed. The resulting crude product was passed through flash column chromatography to remove impurities and recrystallized from ethanol to obtain a white solid product. The yield of product was 74%. ^{1}H NMR (300 MHz, $CDCl_3$) δ [ppm]: 8.18 (d, 2H, AR–H), 7.88 (d, 2H, Ar–H), 7.80 (m, 3H, Ar–H), 7.69 (m, 12H, Ar–H), 7.44 (m, 12H, Ar–H), 7.33 (m, 2H, Ar–H).). MS (ESI) (calcd for $C_{48}H_{35}NSi$, 653.2; found, 654) m/e: 654, 636, 584, 520, 487, 449, 392, 331, 271.

2.2. Characterization of materials

Absorption spectra of solutions were recorded with VARIAN Cary® 5000 UV–vis spectrophotometer from 250 to 700 nm. Photoluminescence (PL) spectra were measured in a system comprising a He:Cd CW laser (Melles-Griot 45MRS802-230) and a monochromator with a photomultiplier tube (Acton Research P2/PD-471). Phosphorescence spectra at 12 K were measured by using an ICCD camera (Princeton Instruments 7397-0005) with a Nd-YAG laser (Continuum Surelite 11-10) as the excitation source. Excitation laser power was few tens of μJ, which is close to the detection limit of phosphorescenece emission. Cyclic voltametry were carried out with a potentiostat (Princeton Applied Research model VSP) using a three electrode cell assembly comprising a Ag/Ag^+ as the reference electrode and Pt as the counter and working electrodes, respectively. Measurements were carried out in N_2-saturated *N*,*N*-dimethylformamide (for BCP and DTBT) and dichloromethane (for BAlq, CBP, TSTC and $Ir(ppy)_3$) solution with tetrabutylammonium hexafluorophosphate (0.1 M) as a supporting electrolyte. The potential was calibrated with NPB as a reference. The HOMO level of the BCP and DTBT were obtained from the measurement of the LUMO level and the optical bandgap of the materials, respectively [15]. Current density–voltage–luminescence characteristics of OLEDs were measured with a Keithley 2400 source meter and SpectraColorimeter PR650.

3. Results and discussion

3.1. Characterization of the host material

The TSTC was prepared by a Suzuki–Miyamura coupling reaction of 4-triphenylsilylphenylboronic acid and 29-(4′-bromobiphenyl)-carbazole (Scheme 1). The HOMO level of the material measured by the cyclic voltammetry technique was 6.0 eV, which is almost the same as the CBP. Fig. 1 shows the absorption and fluorescence spectra of TSTC and CBP film and phosphorescent spectra of TSTC film measured at 12 K. The energy gap of the TSTC film obtained from the absorption edge of the spectra was 3.5 eV, which is higher than that of CBP (3.2 eV). As a result, the LUMO level of the TSTC is higher (0.3 eV) than CBP. This high LUMO level will have significant effect on the electron mobility in the $Ir(ppy)_3$ doped layer and the efficiency of the devices as will be discussed later. It is interesting to note that the TSTC emits fluorescence at longer wavelength than CBP even though the HOMO–LUMO energy gap of TSTC is higher than the CBP film. The triplet energy level (E_T) of TSTC host estimated from the phosphorescence peak was 2.4 eV as shown in the inset of Fig. 1. The E_T of TSTC host is lower than that of commonly used CBP host ($E_T = 2.56$ eV) and similar to that of green phosphorescent dopant such as $Ir(ppy)_3$ ($E_T = 2.42$–2.46 eV) [16,17]. Even though the triplet energy level of the TSTC host is a little lower than the $Ir(ppy)_3$ dopant, it does not reduce the light emitting efficiency very much by the energy transfer as will be demonstrated by high efficiency using the host material. The HOMO, LUMO and triplet energy levels of the material are summarized in Table 1 and compared with CBP and hole blocking materials used for the fabrication of OLEDs.

3.2. Phosphorescent OLEDs

The OLEDs are fabricated by thermal evaporation onto a cleaned glass substrate precoated with indium tin oxide (ITO) without breaking the vacuum. Prior to organic layer deposition, ITO substrates were degreased in acetone and IPA followed by the exposure to UV–ozone flux for 10 min. All organic layers were grown by thermal evaporation at the base pressure of $<5 \times 10^{-8}$ Torr in the following order: hole transporting layer (HTL)/emitting layer (EML)/hole blocking layer

Table 1
Summary of the material properties

Materials	HOMO energy (eV)	LUMO energy (eV)	$E_T$energy (eV)
NPB	5.4	2.3	2.3 [2]
$Ir(ppy)_3$	5.4	2.9	2.42–2.46 [16,17]
TSTC	6.0	2.5	2.4
CBP	6.0	2.9	2.56 [2]
DTBT	6.6	3.1	2.44 [15]
BCP	6.3	2.8	2.50 [2]
BAlq	5.9	2.9	2.18 [19]

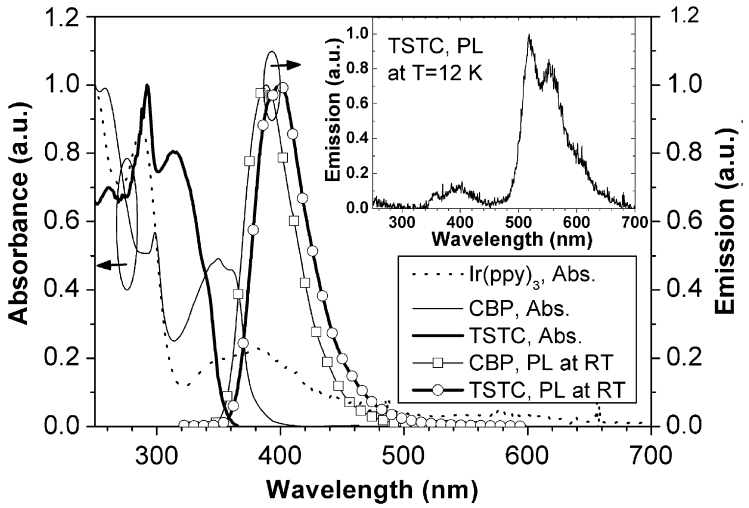

Fig. 1. Absorption and emission spectra of CBP and TSTC films, and emission spectrum of $Ir(ppy)_3$ at room temperature (RT). The inset shows the phosphorescent spectrum of TSTC film at $T = 12$ K.

(HBL)/electron transporting layer (ETL)/cathode. 40-nm-thick NPB was used as the HTL, 30-nm-thick TSTC or CBP doped with 6 wt.% $Ir(ppy)_3$ as the EML, 10-nm thick DTBT (2,4-diphenyl-6-(4′-triphenylsilanyl-biphenyl-4-yl)-1,3,5-triazine) [15], BCP or BAlq as the HBL and 40-nm-thick Alq_3 as the ETL, respectively. Finally, the cathode consisting of a 1-nm-thick LiF and a 100-nm-thick layer of Al were deposited onto the sample surface. The schematic diagram of the device structure and the chemical structures of the materials are shown in Fig. 2.

Fig. 3 exhibits the current density–voltage–luminance (J–V–L) characteristics of the phosphorescent OLEDs where 6 wt.% $Ir(ppy)_3$ was doped into CBP and TSTC with three different HBLs. The J–V–L characteristics of the TSTC:$Ir(ppy)_3$ devices are very similar to the CBP:$Ir(ppy)_3$ devices with the same HBL, indicating that most of the device characteristics can be explained by the properties of hole blocking materials [15]. It is noteworthy, however, that the maximum η_{ext} and η_p with TSTC host and DTBT HBL are much higher than those of commonly used CBP host and BCP HBL, respectively, as shown in Fig. 4 and summarized in Table 2. When we employ TSTC host and DTBT HBL, the peak η_{ext} and η_p reaches to 19.8% and 59.4 lm/W (at 64.3 cd/A and 0.002 mA/cm^2). The control devices adopting CBP host and BCP HBL showed the peak η_{ext} of 14.5% and η_p of 40.0 lm/W (at 49.1 cd/A and 0.004 mA/cm^2), which are similar to the recently reported results [3–5,15]. The devices with DTBT and BCP hole blocking layers with the same host gave higher efficiency than BAlq especially at low current densities, which can be explained by better hole blocking ability of DTBT and BCP coming from the lower HOMO levels than BAlq [15]. The reason why the high quantum efficiency could be obtained from the devices using TSTC host can be understood based on the trapping of both electrons and holes in the dopant sites because of the lower LUMO and higher HOMO levels of the dopant than the host. In contrast the CBP host has the same LUMO level as the dopant so that electrons are not trapped at the dopant sites and the direct exciton formation on the dopant site is less efficient than TSTC host.

More significant improvement in the device performance by using TSTC as the host for $Ir(ppy)_3$ comes from the device lifetime. The stability of the devices using various HBLs and EML hosts was examined at various luminances of 100–5000 cd/m^2 under constant currents at room temperature and the results are shown in Fig. 5 and Table 2. The operational lifetime of the devices differ by more than two orders of magnitude depending on hole blocking and host materials. The devices with the BAlq hole blocking layer gave the longest lifetime among the three HBLs even though the devices with the BCP and DTBT HBLs show higher efficiency

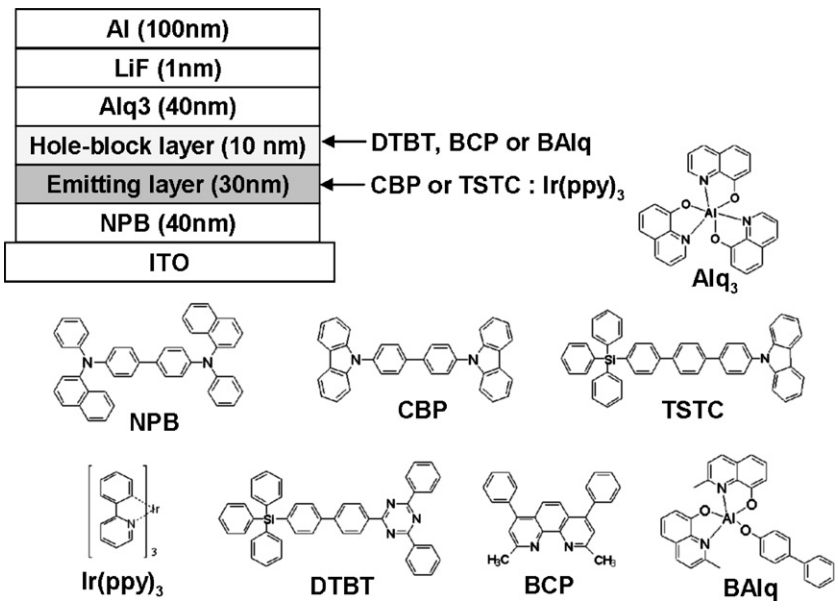

Fig. 2. The electrophosphorescent device structure and the chemical structure of the materials used in the devices.

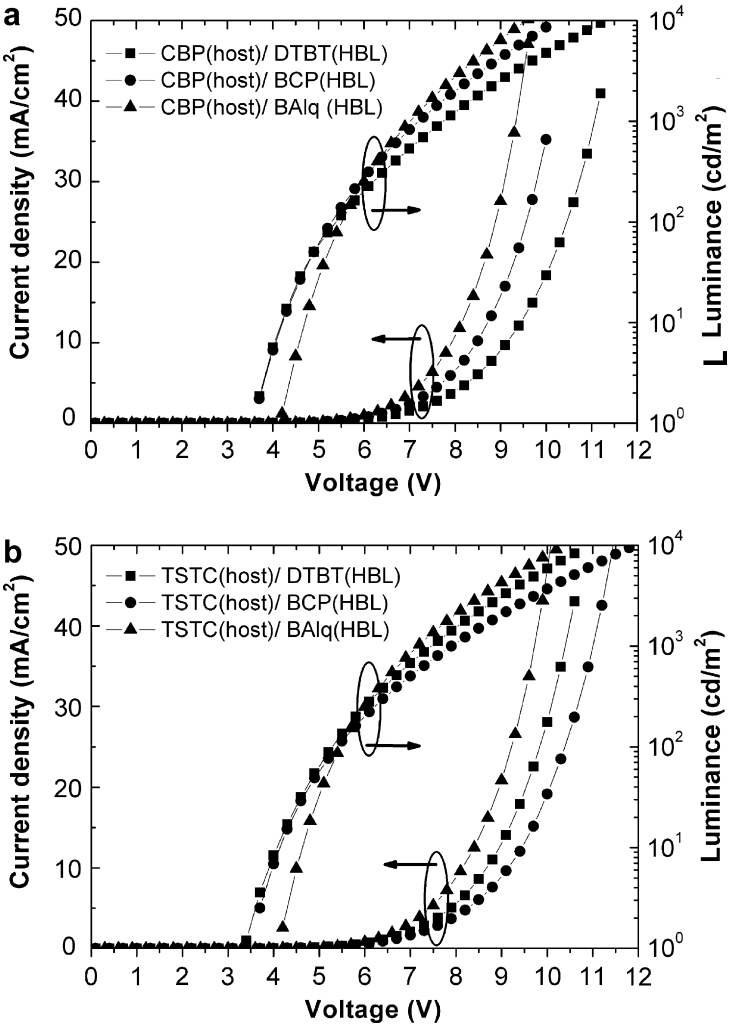

Fig. 3. Current density–voltage (J–V) and luminescence–voltage (L–V) characteristics for (a) CBP and (b) TSTC host with three different hole–block materials, respectively.

than BAlq HBL. It is worthwhile to note that the devices using the TSTC host show much longer lifetime than the devices with CBP host if the same HBL is employed for the devices. For instance, the device with the TSTC host and BAlq HBL shows $T_{1/2} = \sim$10,000 h at $L_0 = 500$ cd/m^2 which is much longer than 2550 h obtained from the device with the CBP host and BAlq HBL. The result is a significant improvement over that reported by Watanabe et al. of $T_{1/2} \sim 4000$ h at $L_0 = 570$ cd/m^2 for an Ir(ppy)$_3$ based device [13].

All devices exhibit linear relationships in $\log T_{1/2}$ vs $\log L_0$ as previously suggested [7,18]. The half lifetime of phosphorescent OLEDs with the BAlq HBL was estimated to be $T_{1/2} = 160{,}000$ for TSTC host when extrapolated to $L_0 = 100$ cd/m^2 using $T_{1/2} \propto (1/L_0)^{\alpha}$, which is much longer than 37,000 h for the CBP host. This result indicates that the triphenyl silane moiety in TSTC host improved thermal stability and glassy property resulting in the increase of operational stability. It is interesting to note that the slope in the $\log T_{1/2}$ vs $\log L_0$ plot is smaller for the devices with BCP than the devices with other HBLs of DTBT and BAlq3, where the latter devices give almost the same slope in the figure. Furthermore the devices with the TSTC host give almost five times improvement in the lifetime regardless of the initial luminance and the hole blocking material in the devices. Those observations need more study to understand and are under investigation now. Since the device stability is one of the most serious problems in OLEDs, we believe that

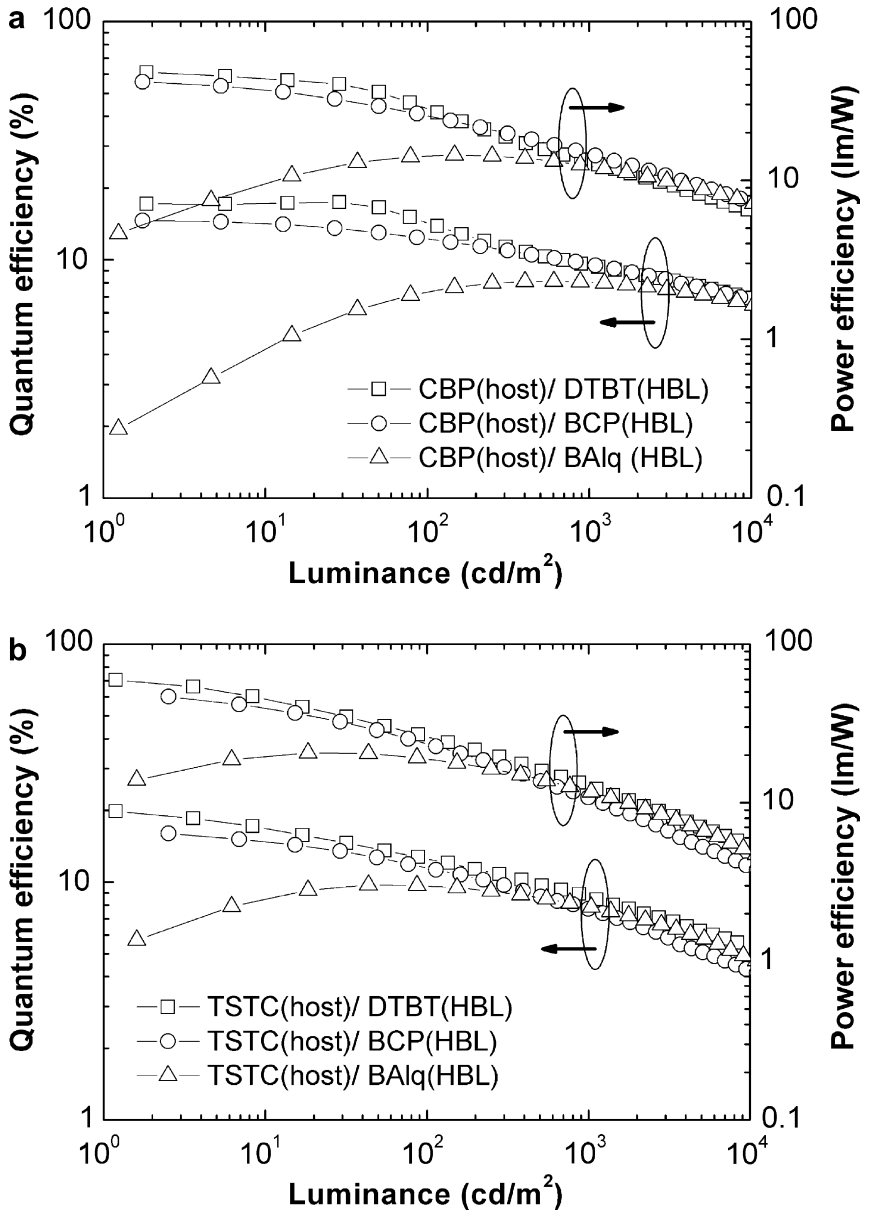

Fig. 4. The external quantum efficiency and power efficiency of OLEDs as a function of luminance using 6 wt.% $Ir(ppy)_3$:CBP and 6 wt.% $Ir(ppy)_3$:TSTC as the emitting layers with three different hole–block layers, respectively.

Table 2
Summary of device performances

Devices	η_{ext}[a] (%)	η_p[a] (lm/W)	η_{ext}[b] (%)	η_p[b] (lm/W)	$T_{1/2}$[c] (h)
CBP(host)/DTBT(HBL)	17.5	47.8	14.3	28.5	7000
CBP(host)/BCP(HBL)	14.5	40.0	12.2	25.4	1500
CBP(host)/BAlq(HBL)	8.1	14.4	7.4	14.3	37,000
TSTC(host)/DTBT(HBL)	19.8	59.4	12.5	26.0	–
TSTC(host)/BCP(HBL)	16.0	46.7	11.5	23.7	4800
TSTC(host)/BAlq(HBL)	9.7	20.6	9.6	18.9	160,000

[a] Peak values of the devices.
[b] Values collected at 100 cd/m^2.
[c] Half lifetime extrapolated to the initial luminance of 100 cd/m^2 (as shown in Fig. 5).

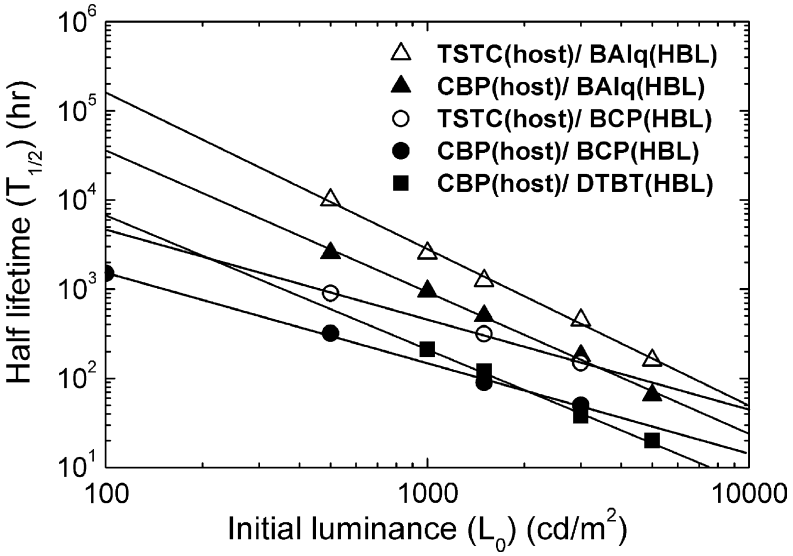

Fig. 5. The time for the luminance to decay to half of initial luminance ($T_{1/2}$) *vs* initial luminance (L_0). Extrapolated lifetime of 160,000 h at 100 cd/m^2 can be obtained for TSTC(host)/BAlq(HBL) based device.

this prolonged lifetime by employing the TSTC host is a significant contribution to OLEDs.

4. Conclusion

In summary, we synthesized a new host material containing tetraphenylsilane group, TSTC, and demonstrated phosphorescent OLEDs with high efficiency and operational stability. The tetraphenylsilane moiety was introduced to provide high LUMO level, thermal and chemical stability, and glassy properties, leading to high efficiency and operational stability of the devices. Ir(ppy)$_3$ based OLEDs using the DTBT HBL and TSTC host resulted in the maximum η_{ext} of 19.8% and the η_p of 59.4 lm/W. High operational stability with the operational half lifetime of 160,000 h at $L_0 =$ 100 cd/m^2 was achieved using the TSTC host and BAlq HBL.

Acknowledgment

This work was supported by the Ministry of Commerce, Industry and Energy through the OLED center and Cavendishi-KAIST-cooperation Program.

References

[1] M.A. Baldo, S. Lamansky, P.E. Burrows, M.E. Thompson, S.R. Forrest, Appl. Phys. Lett. 75 (1999) 4.
[2] V.I. Adamovich, S.R. Cordero, P.I. Djurovich, A. Tamayo, M.E. Thompson, B.W. D'Andrade, S.R. Forrest, Org. Electron. 4 (2003) 77.
[3] J.-W. Kang, S.-H. Lee, H.-D. Park, W.-I. Jeong, K.-M. Yoo, Y.-S. Park, J.-J. Kim, Appl. Phys. Lett. 90 (2007) 223508.
[4] H.J. Peng, X.L. Zhu, J.X. Sun, X.M. Yu, M. Wong, H.S. Kwok, Appl. Phys. Lett. 88 (2006) 033509.
[5] M. Ikai, S. Tokito, Y. Sakamoto, T. Suzuki, Y. Taga, Appl. Phys. Lett. 79 (2001) 156.
[6] C. Adachi, R. Kwong, P. Djurovichi, V. Adamovichi, M. Baldo, M.E. Thompson, S.R. Forrest, Appl. Phys. Lett. 79 (2001) 2082.
[7] R.C. Kwong, M.R. Nugent, L. Michalski, T. Ngo, K. Rajan, Y.-J. Tung, M.S. Weaver, T.X. Zhou, M. Hack, M.E. Thompson, S.R. Forrest, J.J. Brown, Appl. Phys. Lett. 81 (2002) 162.
[8] C. Wang, G. Jung, Y. Hua, C. Pearson, M.R. Bryce, M.C. Petty, A.S. Batsanov, A.E. Goeta, J.A.K. Howard, Chem. Mater. 13 (2001) 1167.
[9] D. Kolosov, V. Adamovichi, P. Djurovichi, M.E. Thompson, C. Adachi, J. Am. Chem. Soc. 124 (2002) 9945.
[10] P.-I. Shih, C.-H. Chien, C.-Y. Chuang, C.-F. Shu, C.-H. Yang, J.-H. Chen, Y.J. Chi, Mater. Chem. 17 (2007) 1692.
[11] C. Adachi, M.A. Baldo, S.R. Forrest, M.E. Thompson, Appl. Phys. Lett. 77 (2001) 904.
[12] H. Inomata, K. Goushi, T. Masuko, T. Konno, T. Imai, H. Sasabe, J.J. Brown, C. Adachi, Chem. Mater. 16 (2004) 1285.
[13] T. Watanabe, K. Nakamura, S. Kawami, Y. Fukuda, T. Tsuji, T. Wakimoto, S. Miyahuchi, Proc. SPIE 4105 (2000) 175.
[14] Y. You, C.-G. An, D.-S. Lee, J.-J. Kim, S.Y. Park, J. Mater. Chem. 16 (2006) 4706.
[15] J.-W. Kang, D.-S. Lee, H.-D. Park, Y.-S. Park, J.W. Kim, W.-I. Jeong, K.-M. Yoo, K. Go, S.-H. Kim, J.-J. Kim, J. Mater. Chem. 17 (2007) 3714.

[16] X. Ren, J. Li, R.J. Holmes, P.I. Djurovich, S.R. Forrest, M.E. Thompson, Chem. Mater. 16 (2004) 4743.
[17] H. Inomata, K. Goushi, T. Masuko, T. Konno, T. Imai, H. Sasabe, J.J. Brown, C. Adachi, Chem. Mater. 16 (2004) 285.
[18] S.A. Van Slyke, C.H. Chen, C.W. Tang, Appl. Phys. Lett. 69 (1996) 2160.
[19] I. Tanaka, Y. Tabata, S. Tokito, J. Appl. Phys. 99 (2006) 073501.

Available online at www.sciencedirect.com
ScienceDirect
Organic Electronics 9 (2008) 461–465
Organic Electronics
www.elsevier.com/locate/orgel

Disorder-mediated ordering by self-interfactant effect in organic thin film growth of pentacene on silicon

P. Kury [a,*], K.R. Roos [b], D. Thien [a], S. Möllenbeck [a], D. Wall [a], M. Horn-von Hoegen [a], F.-J. Meyer zu Heringdorf [a]

[a] FB Physik and Center for NanoIntegration (CeNIDE), Universität Duisburg-Essen, D-47057 Duisburg, Germany
[b] Physics Department, Bradley University, Peoria, IL 61625, USA

Received 19 June 2007; received in revised form 20 November 2007; accepted 6 February 2008
Available online 20 February 2008

Abstract

We have studied the morphology of pentacene films on different silicon surfaces with orientations between Si(1 1 1) and Si(0 0 1). Pentacene molecules are immobile on the Si surface, covering and passivating reactive defect sites. Molecules deposited on top of a closed amorphous wetting layer exhibit isotropic diffusion with diffusion lengths of several tens of micrometers. Neither steps, nor the surface structure affect the film morphology. The wetting layer thus acts as an interfactant, and isolates the molecular film from the substrate, explaining the high quality of pentacene films.

PACS: 68.35.bm; 68.35.Ct; 68.35.Fx; 68.37.Ef; 68.37.Nq; 68.37.Ps; 68.43.Jk; 68.47.Fg; 68.55.A-; 68.55.am

Keywords: Organic semiconductor; Epitaxy; Surfactant; Interfactant

The growth of organic layers on surfaces has attracted significant attention in recent years, based on the tremendous potential of these materials for novel applications. Pentacene, $C_{22}H_{14}$, a molecule consisting of five aromatic rings, is one of the most promising organic semiconductors [1], a direct consequence of its high charge carrier mobility [2]. Several aspects of the growth of pentacene are very similar to those well-known for inorganic species such as the applicability of classic nucleation theory [3–5]. But also fundamental deviations from the canonical picture of atomic beam epitaxial growth are to be expected due to the fact that molecules in general are saturated entities with many degrees of freedom for conformation and possible binding geometry. Pentacene, for instance, binds covalently to silicon substrates, resulting in a wetting layer of flat laying molecules between film and substrate [6–9,12]. The interaction of pentacene molecules within subsequent layers, however, is of van der Waals type. In light of the previous observation, that predeposition of cyclohexene on Si did not change the pentacene film morphology, the role of the wetting layer with its complicated interfacial chemistry during growth is called into question.

In this letter we report on the unique growth mode observed for thin pentacene films on Si

* Corresponding author. Tel.: +49 201 2438742.
E-mail address: peter.kury@uni-due.de (P. Kury).

1566-1199/$ - see front matter © 2008 Elsevier B.V. All rights reserved.
doi:10.1016/j.orgel.2008.02.006

substrates. We demonstrate that neither an increase of the surface step density nor the transition from a threefold to a twofold symmetry surface changes the growth mode and morphology of pentacene films. We interpret this as a direct consequence of a disordered wetting layer: We have found that the molecular pentacene diffusion length is nearly zero on bare silicon surfaces. Surface defects like steps and grain boundaries are covered after the wetting layer has been deposited, and are therefore "invisible" to subsequently deposited pentacene molecules, as evidenced by their nearly infinite diffusion length on top of the wetting layer. We characterize this unique, dramatic change in the surface diffusion parameters in this system as a self-interfactant effect. The resulting size of pentacene crystallites can be as large as several 10 μm, while the typical distance between one-dimensional defects like steps or (7×7) grain boundaries on a Si(1 1 1) surface is about 100–500 nm, and the step separation on a Si(0 0 1) surface is even smaller. Thus, the isolation between film and substrate by the self-interfactant layer is responsible for the fact that the defect density of the pentacene film is lower than the one of the silicon substrate surface.

Photoelectron emission microscopy (PEEM) experiments were carried out in an Elmitec PEEM III with imaging energy analyzer and in an IBM type I low energy electron microscope (LEEM). In both cases, the sample was illuminated with a mercury discharge lamp. Scanning tunneling microscopy (STM) images were acquired using an Omicron VT-STM, mounted in an Omicron Multiprobe S analysis system. All experiments were performed under ultrahigh vacuum (UHV) conditions with base pressures below 2×10^{-10} mbar. Atomic force microscopy (AFM) topographs were taken in non contact mode with a Veeco Dimension 3100. The various silicon substrates were doped with either phosphorus or boron in different concentrations, all samples had resistivities above 0.5 Ω cm, corresponding to dopant concentrations below $5 \times 10^{16}\,\mathrm{cm}^{-3}$. We have confirmed the expected absence of an influence of the dopant concentration on the film morphology with Si(1 1 1) samples of different doping levels. Prior to the transfer into the UHV the samples were wiped clean with ethanol and degassed at 800 K for several hours under high vacuum conditions. The native oxide was then removed in UHV by repeated flash annealing to 1500 K. Pentacene was deposited at room temperature (RT) from a custom made effusion cell with a ceramic crucible. The total amount of deposited material was monitored with a quartz crystal microbalance and deposition rates between 0.5 and about 2.0 molecular layers (ML, $1\,\mathrm{ML} = 8.1 \times 10^{13}\mathrm{cm}^{-2}$) per hour were used.

In order to systematically investigate the dependence of the growth on substrate properties such as step density, symmetry and reconstruction, we chose several different silicon substrates starting with a well oriented Si(1 1 1) surface and ending – with approximately equidistantly increasing vicinality in (11n) direction – at the Si(0 0 1) surface. The selected surfaces show very different properties concerning reconstruction, step density and roughness. The point of origin is the Si(1 1 1) surface with its complicated (7×7) reconstruction consisting of dimers, adatoms and a stacking fault [13]. With a miscut of eight degrees, a Si(1 1 1) surface is produced where the average step distance is about the size of the (7×7) unit cell. Thus, a mixture of (7×7) and metastable reconstructions with similar structures such as the (5×5) and (3×3) are observed, depending on the local step separation. The Si(1 1 2) surface is not stable and exhibits facets with (1 1 1) and (3 3 7) orientations [14]. Approximately in the middle between Si(1 1 1) and Si(0 0 1) is the Si(1 1 3) oriented surface. This surface is thermodynamically stable and shows a complicated reconstruction whose structure is still under debate [15–17]. Si(1 1 n) surfaces with $n > \approx 4$ can be described as Si(0 0 1) terraces plus atomic or double layer surface steps [18]: The Si(1 1 5) surface shows a mixture of rebonded and non-rebonded double-steps, the Si(1 1 9) surface is a strongly misoriented Si(0 0 1) with a (2×1) single domain reconstruction separated by D_B double steps [19,20]. Finally a well oriented Si(0 0 1) with step distances of several hundred nm is also used. This surface shows a (2×1) dimer reconstruction with two alternating rotational domains, separated by single atomic steps [21]. All these surfaces show different step morphologies, surface structures and surface symmetries, namely threefold and twofold. Therefore, substantial differences in the growth mode of any deposit are to be expected.

PEEM images of pentacene islands grown on the various substrates are shown in Fig. 1. The one molecular layer height pentacene islands of the first layer appear bright due to a reduced work function [8] and the substrate covered with a pentacene wetting layer appears dark. The islands are each single crystalline as we have confirmed for the (0 0 1) and

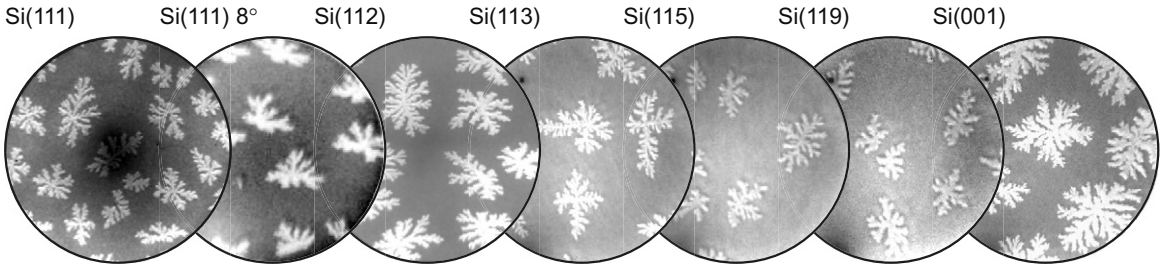

Fig. 1. PEEM images of pentacene islands grown at room temperature on different oriented silicon substrates. No difference in the shape is visible. The field of view is 50 μm for all images.

(1 1 1) orientation with micro-spot low energy electron diffraction (LEED) in the LEEM. During further deposition the islands grow and one-dimensional grain boundaries between rotational domains will be formed where the islands touch each other. Therefore, the defect density due to grain boundaries is the same as the island density on the surface. Though there are some differences of island sizes and densities due to small variations of substrate temperature and deposition fluxes from experiment to experiment, the fractal morphology of the islands is the same for all substrates and does not depend on step density or substrate atomic structure. This is in contradiction to the common belief that the structure and defect density of the initial substrate is crucial for the quality of the deposited film [22]. Instead, all islands show a very similar fractal shape. This shape has been shown to originate from the high diffusive mobility of the pentacene molecules and a hit and stick attachment to existing islands [3], leading to a situation similar to diffusion limited aggregation (DLA) [23]. Therefore, in order to quantify the "very similar shape" of the pentacene islands, we have calculated the fractal dimension of many islands on the different substrates via a box-counting algorithm. As shown in Fig. 2, the fractal dimension of the islands does not change with varying substrate orientation within the errors bars and for all surfaces is in the range of $D \approx 1.50$–1.70 typical for a DLA cluster. Any anisotropy in the diffusion should result in a change of the fractal dimension of the islands [10]. In addition to the very similar shape, there is no preferred orientation of the islands visible in Fig. 1, even on the highly stepped surfaces.

The atomic force microscopy topograph shown in Fig. 3, taken of a thin pentacene film on Si(1 1 1) shortly after nucleation of the first molecular islands, further demonstrates the lack of influence of the steps on the pentacene first layer

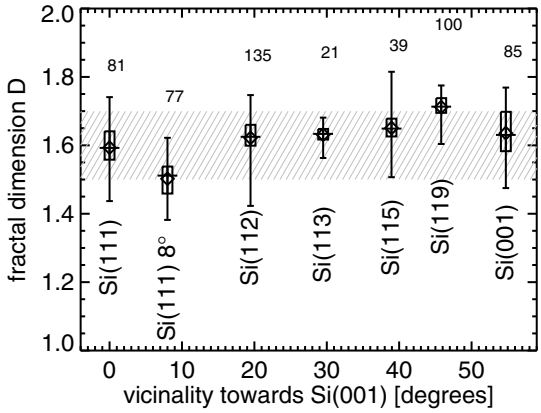

Fig. 2. Quantitative analysis of the morphology of the pentacene first layer islands on different substrates in terms of their fractal dimension. For each substrate orientation the extreme, mean, median and quartile values are shown as a box and whisker plot. The numbers above the data points denote the number of islands analyzed. Fractal dimension of the islands does not depend on the substrate orientation.

growth. A preferential nucleation of pentacene islands as described in reference [11] is not apparent. The dendritic islands are able to overgrow not only the 3.14 Å high atomic steps, but also step-bunches of up to more than ten atomic steps without having their shape affected. Atomic scale investigations on the adsorption geometry and structure of pentacene on silicon surfaces with scanning tunneling microscopy have been done up to now only for very low coverages in the sub-ML regime for Si(0 0 1) [12,24]. Little is known about the structure of the closed wetting layer. Our scanning tunneling microscopy data in Fig. 3b shows a pentacene wetting layer deposited on a Si(1 1 1) surface as well as one single pentacene molecule on the clean Si(1 1 1) surface in the same scale for comparison in the inset. The coverage is similar to the images in Fig. 1 where islands are already growing in the first molecular layer. The wetting layer between the first layer islands covers the initial surface

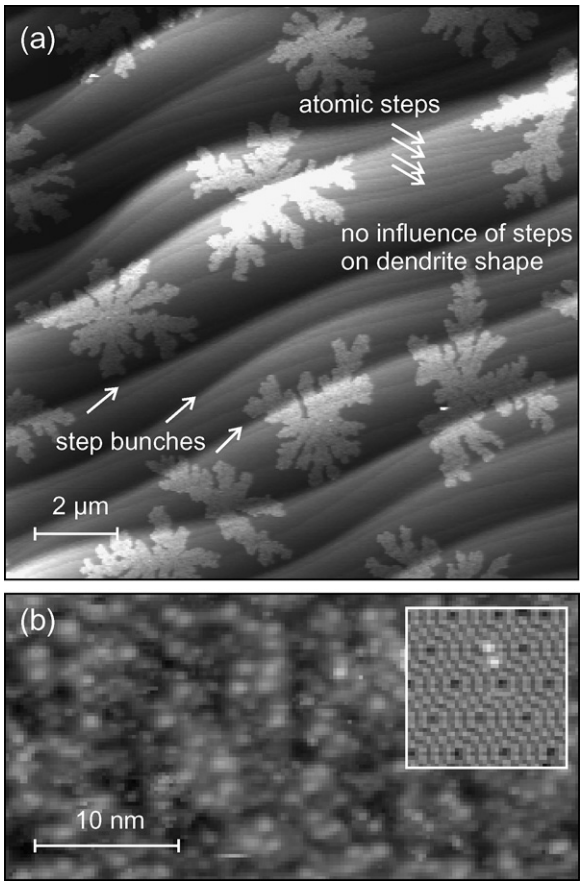

Fig. 3. (a) Non contact atomic force microscopy of first layer pentacene islands on Si(1 1 1). Steps and step bunches do not affect their dendritic shape. The average height of the step bunches is 2.5 nm, corresponding to eight atomic Si steps. (b) Scanning tunneling microscopy image of a closed wetting layer of pentacene on Si(1 1 1). The crystal symmetry of the substrate is no longer apparent through the isotropic, disordered wetting layer; no features are visible in the 2D pair correlation function (not shown) of this image. Tunneling parameters are $U_T = -1.37$ V, $I_T = 30$ pA. The small inset shows a single pentacene molecule on the initial (7×7) reconstructed surface and is of the same scale as the large image.

completely, no remains of the (7×7) reconstruction or other footprints of the substrate structure are visible: it shows an amorphous structure with no orientational or translational symmetry.

On top of this wetting layer diffusion lengths of up to a few hundreds of micrometers – depending on substrate temperature and deposition flux – are found even at RT, as derived from the separation of the dendritic islands of the first molecular layer in PEEM. In contrast, single adsorbed molecules on clean silicon can be imaged for hours in an STM at RT without any noticable diffusion. The completion of the wetting layer literally changes the diffusion length of a pentacene molecule from "zero" on the clean surface to "infinite" on the wetting layer. High diffusion lengths are always desirable in epitaxial growth for achieving high film qualities. In heterogrowth the manipulation and modification of the surface diffusion has been achieved by the deposition of surface active species classified as surfactants [25] or interfactants [26,27], depending on whether the adlayer floats on top of the growing film or remains buried at the interface. Pentacene acts qualitatively different as it provides its own diffusion enhancement mechanism. Furthermore, the wetting layer isolates the pentacene film from the substrate and its structural properties, and it even passivates steps so that the first molecular layer can grow over them in a carpet-like mode as sketched in Fig. 4. The islands in the first molecular layer show no preferred orientation and all possible rotational crystallites can be formed. In this sense, pentacene acts as its own interfactant: It passivates reactive sites on the initial surface and covers them during the formation of the wetting layer. The fact that neither step density nor surface symmetry affects the film morphology is a new concept and shows a fundamental difference between atomic and organic species. Atomic steps usually display a dramatic reactivity [28] and play an important role in the nucleation and capture of atomic adsorbates. Epitaxial growth always takes place via attachment of ad-species to surface steps, leading to step decoration in heterogrowth. Also,

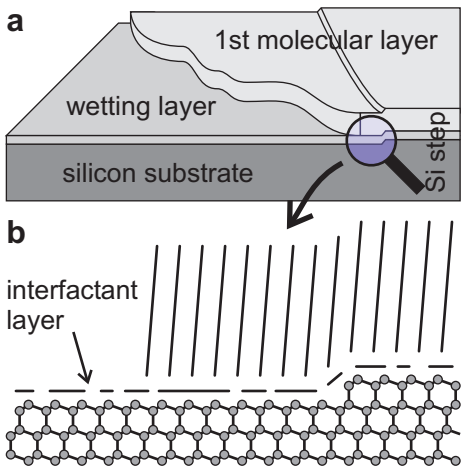

Fig. 4. Schematic sketch of the interaction between the different layers. The wetting layer with flat laying molecules is bound strongly via covalent bonds to the substrate. The molecules of the first layer interact by van der Waals forces with the wetting layer and each other. The wetting layer acts as an interfactant layer by isolating the first molecular layer from the substrate.

the reduced symmetry of the substrate makes vicinal surfaces with a significant step density perfectly suited as templates for the formation of nanoscopic or even mesoscopic structures by self-organization [29], which can, for example, be driven by a diffusion anisotropy [30]. In pentacene thin film growth, however, steps on the surface are completely ignored by the dendritic islands of the first molecular layer and do not play any role for its morphology. This is especially surprising since atomic surface steps have an electronic structure different from the flat surface, and a strong dependence of the pentacene growth mode on the electronic structure of the substrate has been found [31]. Thus pentacene itself creates its own optimized template for further growth, combining very large diffusion lengths, very few defects and no predestinated symmetry.

The possibly dramatic influence of a disordered wetting layer on island formation has also recently been shown for Pb/Si(1 1 1) [32]. In contrast to earlier work on the growth of organic semiconductors where a disordered interface layer was considered as an oddity [33] for one specific surface, we argue from the thorough analysis of our data that the non-crystalline structure and disorder of the wetting layer is in fact the key to high quality organic films if the molecules bind covalently to the substrate. Otherwise it is not plausible that a deposited heterofilm can have a lower defect density than the initial substrate. The self-interfactant effect is probably not limited to pentacene and can hold for other organic molecules as well. This is an explanation for the recent successful attempt to grow crystalline rubrene films on a pentacene buffer layer [34]. It should be possible to use the amorphous pentacene wetting layer as a template for thin film growth of other molecular semiconductors as well, leading to high quality films and making single grain transistors of many other materials possible.

Financial support by the Deutsche Forschungsgemeinschaft under SFB 616 is gratefully acknowledged. P. Kury thanks Kevin Kimberlin for assistance with the STM measurements. K.R. Roos acknowledges support from the National Science Foundation under contracts DMR-0320908 and DMR-0511811, and from an award from the Research Corporation.

References

[1] R. Ruiz, D. Choudhary, B. Nickel, T. Toccoli, K.C. Chang, A.C. Mayer, P. Clancy, J.M. Blakely, R.L. Headrick, S. Iannotta, et al., Chem. Mater. 16 (2004) 4497.
[2] C.D. Dimitrakopoulos, D.J. Mascaro, IBM J. Res. Dev. 45 (2001) 11.
[3] F.-J. Meyer zu Heringdorf, M.C. Reuter, R.M. Tromp, Nature 412 (2001) 517.
[4] F.-J. Meyer zu Heringdorf, M.C. Reuter, R.M. Tromp, Appl. Phys. A 78 (2004) 787.
[5] B. Stadlober, U. Haas, H. Maresch, A. Haase, Phys. Rev. B 74 (2006) 165302.
[6] R.J. Hamers, S.K. Coultier, M.D. Ellison, J.S. Hovis, D.F. Padowitz, M.P. Schwartz, Acc. Chem. Res. 33 (2000) 617.
[7] K.P. Weidkamp, C.A. Hacker, M.P. Schwartz, X. Cao, R.M. Tromp, R.J. Hamers, J. Phys. Chem. B 107 (2003) 11142.
[8] G. Hughes, D. Carty, A.A. Cafolla, Surf. Sci. 582 (2005) 90.
[9] D. Choudhary, P. Clancy, D.R. Bowler, Surf. Sci. 578 (2005) 20.
[10] R.C. Ball, R.M. Brady, G. Rossi, B.R. Thompson, Phys. Rev. Lett. 1406 (1985) 55.
[11] V. Ignatescu, J.-C. M. Hsu, A.C. Mayer, J.M. Blakely, G.G. Malliaras, Appl. Phys. Lett. 89 (2006) 253116.
[12] M. Kasaya, H. Tabata, T. Kawai, Surf. Sci. 400 (1998) 367; M. Kasaya, H. Tabata, T. Kawai, Surf. Sci. 406 (1998) 302.
[13] K. Takayanagi, Y. Tanishiro, M. Takahashi, S. Takahashi, J. Vac. Sci. Technol., A 3 (1985) 1502.
[14] A.A. Baski, L.J. Whitman, Phys. Rev. Lett. 74 (1995) 956.
[15] W. Ranke, Phys. Rev. B 41 (1990) 5243.
[16] J. Dabrowski, H.J. Müssig, G. Wolff, Phys. Rev. Lett. 73 (1994) 1660.
[17] C.Y. Chang, Y.C. Chou, C.M. Wei, Phys. Rev. B 59 (1999) R10453.
[18] A.R. Laracuente, L.J. Whitman, Surf. Sci. 545 (2003) 70.
[19] E. Pehlke, J. Tersoff, Phys. Rev. Lett. 67 (1991) 1290.
[20] E. Pehlke, J. Tersoff, Phys. Rev. Lett. 67 (1991) 465.
[21] D.J. Chadi, Phys. Rev. Lett. 59 (1987) 1691.
[22] J. Fraxedas, Adv. Mater. 14 (2002) 1603.
[23] S.B. Lee, J. Korean. Phys. Soc. 47 (2005) 577.
[24] G. Hughes, J. Roche, D. Carty, T. Cafolla, K.E. Smith, J. Vac. Sci. Technol., B 20 (2002) 1620.
[25] M. Copel, M.C. Reuter, E. Kaxiras, R.M. Tromp, Phys. Rev. Lett. 63 (1989) 632; M. Horn-von Hoegen, F.K. LeGoues, M. Copel, M.C. Reuter, R.M. Tromp, Phys. Rev. Lett. 67 (1991) 1130.
[26] T. Schmidt, E. Bauer, Phys. Rev. B 62 (2000) 15815.
[27] C.V. Ramana, P. Masse, R.J. Smith, B.S. Choi, Phys. Rev. Lett. 90 (2003) 066101.
[28] P. Kratzer, E. Pehlke, M. Scheffler, M.B. Raschke, U. Höfer, Phys. Rev. Lett. 81 (1998) 5596; E. Pehlke, P. Kratzer, Phys. Rev. B 59 (1999) 2790.
[29] F.-J. Meyer zu Heringdorf, T. Schmidt, S. Heun, R. Hild, P. Zahl, B. Bessel, E. Bauer, M. Horn-von Hoegen, Phys. Rev. Lett. 86 (2001) 5088.
[30] K.R. Roos, K.L. Roos, M. Horn-von Hoegen, F.-J. Meyer zu Heringdorf, J. Phys. 17 (2005) 1407.
[31] G.E. Thayer, J.T. Sadowski, F. Meyer zu Heringdorf, T. Sakurai, R.M. Tromp, Phys. Rev. Lett. 95 (2005) 256106.
[32] M. Hupalo, M.C. Tringides, Phys. Rev. B 75 (2007) 235443.
[33] M. Eremtchenko, R. Temirov, D. Bauer, J.A. Schaefer, F.S. Tautz, Phys. Rev. B 72 (2005) 115430.
[34] M. Haemori, J. Yamaguchi, S. Yaginuma, K. Itaka, H. Koinuma, Jpn. J. Appl. Phys. 44 (2005) 3740.

Available online at www.sciencedirect.com
ScienceDirect
Organic Electronics 9 (2008) 466–472
Organic Electronics
www.elsevier.com/locate/orgel

Fabrication micro-tube of substituted Zn–phthalocyanine in large scale by simple solvent evaporation method and its surface photovoltaic properties

Yan Luo [a,c,*], Junshan Gao [a,b], Chuanwei Cheng [a], Yufeng Sun [a], Xiguang Du [a,b,*], Guoyue Xu [a], Zhenling Wang [c]

[a] College of Material Science and Technology, Nanjing University of Aeronautics and Astronautics, Nanjing 210016, PR China
[b] Faculty of Chemistry, Northeast Normal University, Changchun 130021, PR China
[c] Key Laboratory of Rare Earth Chemistry and Physics, Changchun Institute of Applied Chemistry, Chinese Academy of Sciences, Changchun 130022, PR China

Received 7 July 2007; received in revised form 12 January 2008; accepted 10 February 2008
Available online 4 March 2008

Abstract

Micro-tubular structure of tetra(2-isopropyl-5-methylphenoxy) substituted Zn–phthalocyanine (**T2**) has been obtained in large scale by simple solvent evaporation method. FE-SEM micrographs indicate that most of the micro-tubes are in hollow rectangular shape. XRD measurement demonstrated that the walls of the micro-tubes are arranged in highly ordered nanoscopic structure. Both the XRD measurement and the UV–vis absorption spectrum of the micro-tubes indicated an *H*-aggregate of the substituted Zn–phthalocyanine molecules (**2**) in the micro-tubes. Formation mechanism of micro-tube has been proposed. Field-induced surface photovoltage spectrum (EFISPS) inferred that (**T2**) has p-type character.

PACS: 72.40.+w; 62.23.St

Keywords: Phthalocyanine; Self-assembly; Micro-tube; Surface photovoltage spectrum

1. Introduction

Phthalocyanines (Pcs) and their derivatives have been of great interest due to their special electronic and optical properties. They have potential applications for photovoltaic cell, chemical sensors, laser recording materials, light-emitting diodes, organic field effect transistors, microelectronics and even biomedical applications [1–5]. Recently, fabrication of Pcs into 1D structures by self-assembly and self-organization method has attracted great interest. For example, Nolte and coworkers reported the fiber structure of phthalocyanine derivatives that possess one central phthalocyanine core, four crown ether rings [6–10] as well as rod-like donor–acceptor phtha-

* Corresponding authors. Address: College of Material Science and Technology, Nanjing University of Aeronautics and Astronautics, Nanjing 210016, PR China. Tel.: +86 25 84234867 (Y. Luo).
E-mail addresses: maggiely2000@yahoo.com.cn (Y. Luo), xgdu@nenu.edu.cn (X. Du).

1566-1199/$ - see front matter © 2008 Elsevier B.V. All rights reserved.
doi:10.1016/j.orgel.2008.02.008

locyanine nanoaggregates [11]. There are also other 1D self-organization structures of Pcs reported by other groups [12–21]. Although Pcs prefer to aggregate into columnar structures by π–π stacking, the manipulation of 1D tubular structure of Pcs by self-assembly method, however, have not been reported and is still an increasing interest in chemistry and nanotechnology.

Here we report the synthesis and large scale fabrication of tetra(2-isopropyl-5-methylphenoxy) substituted Zn–phthalocyanine micro-tubular structure (**T2**) by simple solvent evaporation method. Both the XRD measurement and the UV–vis absorption spectrum of the micro-tubes indicated an *H*-aggregate of the Zn–phthalocyanine molecules in the micro-tubes. The formation mechanism for the micro-tubular structure (**T2**) is proposed. In order to judge the conduction type of (**T2**), the surface electronic property of (**T2**) was investigated by surface photovoltage spectrum (SPS) and field-induced surface photovoltage spectrum (EFISPS).

2. Experimental

2.1. Materials

4-Nitrophthalonitriles (>98%) were prepared according to the literature [22], 2-isopropyl-5-methylphenol, $LiOH \cdot H_2O$, NaCl, petroleum ether, aether, pentan-1-ol, dimethylsulfoxide (DMSO), 1,8-diazabicyclo(5,4,0)-undec-7-ene (DBU), methanol and $Zn(CH_3COO)_2 \cdot 2H_2O$ were purchased from Beijing Fine Chemical Company. Pentan-1-ol was distilled from Na prior to use. DMSO was pre-dried over BaO and distilled under reduced pressure. All other reagents and solvents are used without further purification. Column chromatography purifications were preformed on silica gel unless otherwise stated.

2.2. Measurements

^{1}H NMR spectrum were recorded on a Varian Unity 500 spectrometer. FT-IR spectra were obtained from KBr pressed pellets using a Magna 560 infrared spectrophotometer. MS spectra were obtained on a QUSTAR-TOF mass spectrometer or a LDI-1700-TOF mass spectrometer. The UV–vis absorption spectra were taken on a Cary 100 UV–vis spectrometer. Elemental analyses were performed on a Flash EA1112 Elemental Analyzer. The morphology of the samples was inspected using a field mission scanning electron microscope (FE-SEM, XL 30 Philips) as well as high-resolution electron microscope (HRTEM, FEI-Technai $G^2$20, operated at 200 keV). X-ray diffraction (XRD) measurements were performed with a Rigaku-Dmax 2500 diffractometer with Cu Kα radiation at 40 kV and 200 mA. All the measurements were performed at room temperature (RT). For photovoltage measurements, the (**T2**) sample was pressed between two slices of ITO glass used as transparent front and back electrodes. Surface photovoltage spectra (SPS) was measured with a laboratory-built apparatus using light source monochromator-lock-in detection technique. Monochromatic light was obtained by passing light from a 500 W xenon lamp through a double-prism monochromator (Hilger and Watts, D300). A lock-in amplifier (Brookdeal, 9503-3C), synchronized with a light chopper, was employed to amplify the photovoltage signal. The spectra were normalized to unity at their maxim, and the characteristic bands of the xenon lamp were subtracted by a computer. For electric-field-induced surface photovoltage spectroscopy (EFISPS) measurements, the electric field direction from the irradiated surface to the bulk was defined as positive. The measurement was performed at atmospheric pressure and room temperature and the sample has not gotten further treatments.

2.3. The synthesis of phthalonitrile derivative (*1*)

6.92 g 4-nitrophthalonitriles (40 mmol) was added to anhydrate DMSO (80 mL) and 1.10 g 2-isopropyl-5-methylphenol (40 mmol) was added to the above solution under stirring. After the reaction mixture being stirred for 10 min, 4.20 g $LiOH \cdot H_2O$ (25 mmol) was added over a 2 h period and the mixture was then stirred for 14 h at r.t. The mixture was then poured into 800 mL NaCl solution (0.4 M) and stirred till a yellow solid appeared. Then the product was collected by vacuum filtration. The obtained crude product was purified by column chromatography with petroleum ether–anhydrate Et_2O (9:1) as the mobile phase giving colorless crystals of phthalonitrile derivative (**1**). Yield: 8.41 g (76.1%).

^{1}H NMR (500 MHz, $CDCl_3$): $\delta = 7.708$ (d, 1H, $J = 8.5$ Hz, Ar*H*), 7.295 (d, 1H, $J = 8.5$ Hz, Ar*H*), 7.219 (s, 1H, Ar*H*), 2.958 (m, 1H, C*H*), 2.331 (s, 3H, ArCH_3), 1.154 (d, 6H, $J = 6.5$ Hz, 2CH(CH_3)$_2$). IR (KBr): 2229 cm^{-1} (C≡N), 1246 vs cm^{-1} (C–O–C). MS (QUSTAR-TOF): *m/z* calcd for [M+Na$^+$]: 299.1160; found: 298.9497 (an isotopic cluster peak) [M+Na$^+$]. UV–vis ($CHCl_3$): $\lambda_{max} = 261, 297, 306$ nm.

2.4. Synthesis of tetra(2-isopropyl-5-methylphenoxy) substituted Zn–phthalocyanine (2)

The synthesis of substituted Zn–phthalocyanine (**2**) are reported by us previously [23] as shown in Scheme 1. Following are the details: a mixture of 1 g phthalonitrile derivative (**1**) (4 mmol), 1 mmol $Zn(CH_3COO)_2 \cdot 2H_2O$ and 2 mL DBU were added to 8 mL pentan-1-ol under stirring at N_2 atmosphere. Then the mixture was heated at 140 °C for 24 h. After the mixture cooled down, it was poured into 20–40 mL methanol giving blue-green solid. The collected solid was purified by column chromatography with Et_2O–petroleum ether (1:3) as the mobile phase to give pure Zn–phthalocyanine derivatives (**2**). Yield: 35%.

^{1}H NMR (500 MHz, $CDCl_3$): $\delta = 7.340$ (br s, 12H, Ar*H*), 7.044 (br s, 12H, Ar*H*), 3.452 (br s, 12H, 4ArCH_3), 1.394 (br s, 24H, 4CH(CH_3)$_2$). MS (LDI-1700-TOF): *m*/*z* calcd for [M+H$^+$]: 1169.4; found: 1169.5 [M+H$^+$]. UV–vis ($CHCl_3$): λ_{max} (log ε) = 348 (4.28), 352 (4.28), 615 (3.82), 683 nm (4.52). Anal. calcd for $C_{72}H_{64}N_8ZnO_4$ (1168.4): C, 73.98; H, 5.52; N, 9.59; found: C, 73.62; H, 5.26; N, 9.30.

2.5. Micro-tube (T2) preparation

The above synthesized Zn–phthalocyanine derivatives (**2**) was dissolved in chloroform solution (1×10^{-6} M) and evaporated for 3 days giving the solid material of (**T2**) depositing on quartz slip.

3. Results and discussion

3.1. Morphologies

Fig. 1a and b shows the typical FE-SEM micrographs of the solid material (**T2**). Low magnification FE-SEM micrograph reveals that large quantities of micro-fiber materials were formed in large areas on the quartz slip (Fig. 1a). Most of them are arranged in flower-like microstructures. The fibers are in length of 100–300 μm. High magnification image showing that the overall surface of the substrate is covered by uniformly distributed hollow tubular structures with open ends (Fig. 1b). Most of the micro-tubes have rectangular framed (Fig. 1b). The width of the tubes is 2–3 μm, but their lengths can be in the range of 3–4 μm. The tubes have a

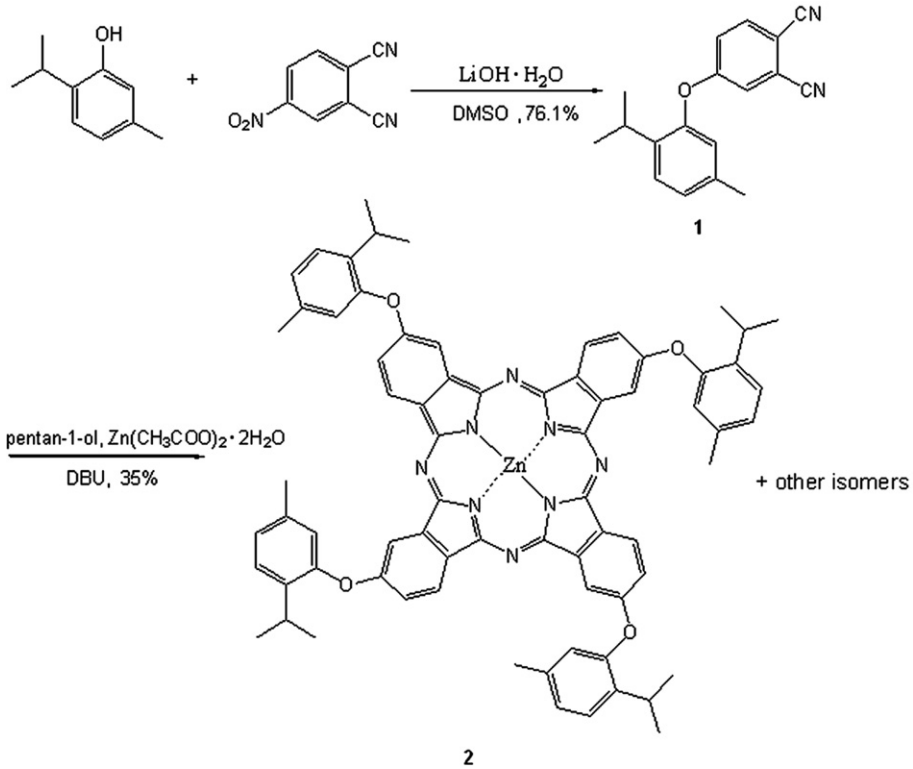

Scheme 1. Synthesis and chemical structure of tetra(2-isopropyl-5-methylphenoxy) substituted Zn–phthalocyanine (**2**).

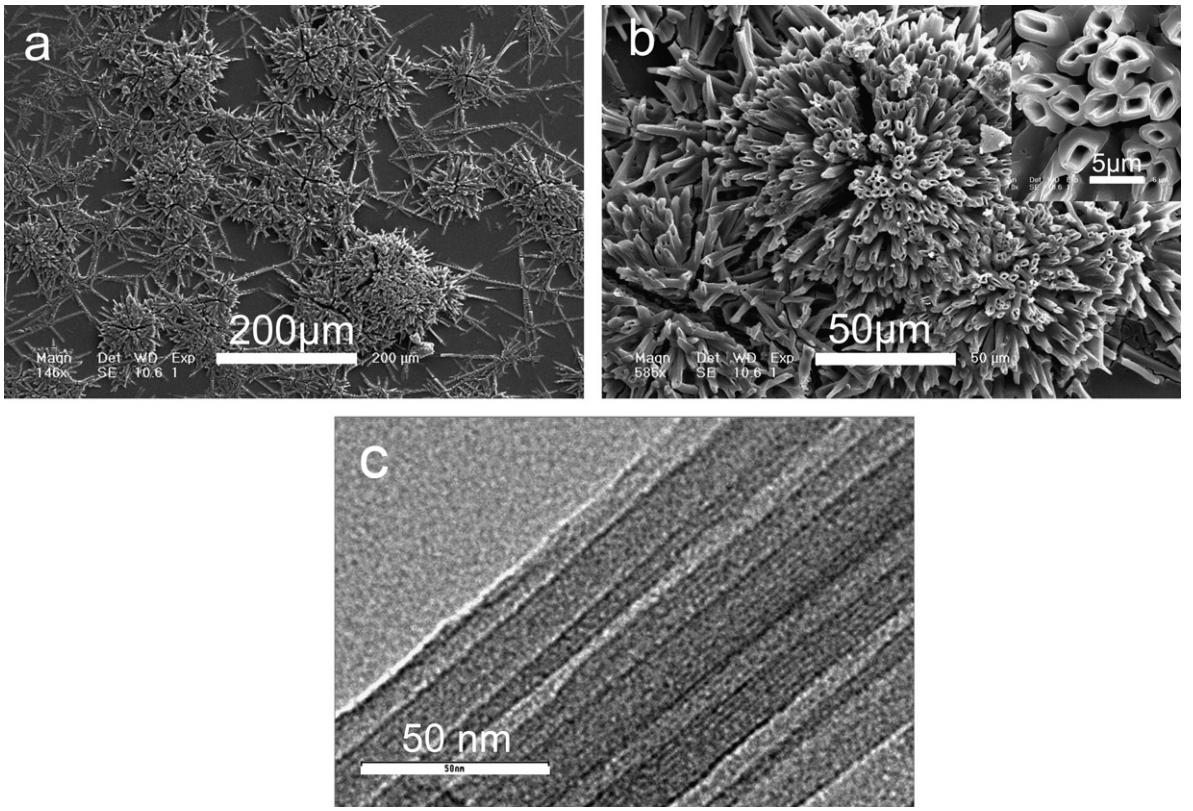

Fig. 1. Typical low (a) and high (b) magnification FE-SEM micrographs of solid material (**T2**) obtained after solvents evaporation as well as (c) HRTEM micrograph of the sample.

uniform, completely hollow structure without filling or blockage. A scanning electron microscopy (SEM) image at a higher magnification clearly indicates that the wall thickness of the tubes is 0.5–1 μm (Fig. 1b, inset). Fig. 1c is the typical HRTEM micrograph of the sample. From the HRTEM micrograph of the sample, we can see that the sample is arranged in lamellar structure. Our fails on getting the electron diffraction patterns of the sample on the lamellar walls indicates that the sample is in amorphous state in the walls.

3.2. XRD

To demonstrate the molecular packing of (**T2**) within the assembled morphologies, X-ray powder diffraction (XRD) spectrum of micro-tube (**T2**) was performed, as shown in Fig. 2. The XRD pattern of (**T2**) shows two well-resolved reflections at 4.8° ($d = 1.9$ nm) and 5.4° ($d = 1.7$ nm) indicating that the substituted Zn–phthalocyanine molecules are arranged in highly long-range ordered lamellar

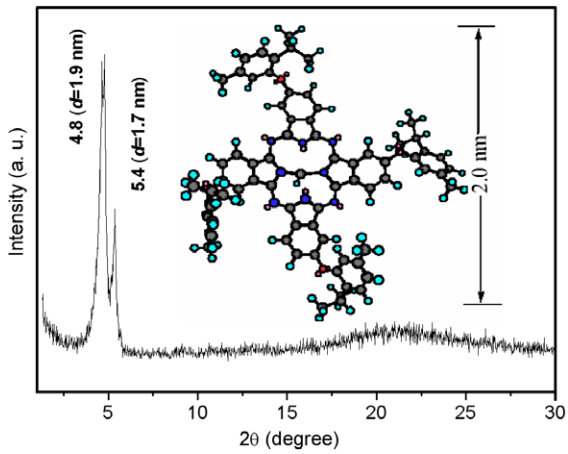

Fig. 2. XRD pattern the micro-tube (**T2**) deposited on the quartz slip. Inset is the optimized structure and dimension of tetra(2-isopropyl-5-methylphenoxy) substituted Zn–phthalocyanine (**2**).

structure in accordance to the observation of the HRTEM micrographs of the sample. Two stacking style in (**T2**) can be assumed through the two reflec-

tions. From the size of a single molecule of (**2**) (Fig. 2, inset, optimized with the MM2 force field using the Chem3D program, Cambridge Soft Corp.), the molecules are deduced to be packing at angles of almost 72° and 52°, respectively, to the stacking lamellar, i.e., *H*-aggregation of the substituted Zn–phthalocyanine molecules in the walls of the (**T2**). The lack of several periodic reflections in a ratio of 1:1/2:1/3:1/4, etc. may be due to two different stacking styles in the sample. The broad peak at 21° should be due to the reflection from the quartz substrate as well as the amorphous state of the sample. But the structure of the sample has not thoroughly been established and the present tube structure is made of multi-walled lamellar structure like as multi-walled carbon nanotubes. Further studies should be needed.

3.3. UV–vis spectra

Fig. 3 demonstrates the UV–vis absorption spectrum of 1D packed micro-tube of (**T2**) in comparison with solution of (**2**) (1×10^{-5}) in chloroform. In the UV–vis absorption spectrum of dilute solution of (**2**) (Fig. 3a), there are three groups of absorption bands at 550–750 nm, 300–450 nm and 230–300 nm, respectively. The band from 550 to 750 nm are characteristic Q-band absorption of phthalocyanine. In this band group, the two well-resolved absorption peakings at 683 and 615 nm should be assigned to Q_{0-0} and Q_{0-1} bands of (**2**) monomers, respectively [24]. The detected band at ca. 650 nm in-between them should be assigned to the aggregated band due to the dimmers and multimers. Band of 300–450 nm belongs to the typical Soret-band (B-band) absorption of phthalocyanine. The third band group from 230 to 300 nm should be due to the benzene rings absorption of the substituted 2-isopropyl-5-methylphenoxy moieties of (**2**). Compared with the solution spectrum of (**2**), line broadening was observed for Q-band (550–750 nm) absorption of micro-tube of (**T2**), as shown in Fig. 3b. Because the Q-band absorption is related the front orbitals of the metal–phthalocyanine rings, thus this indicates a tight packing between the Zn–phthalocyanine rings (**2**) by strong π–π interaction in micro-tube of (**T2**). There is almost no shift of the Soret-band (B-band) peaking at 345 nm for the micro-tube of (**T2**) by comparing with the absorption spectrum of (**2**) solution. Because B-bands are related to the front orbitals of the central metals in the metal–phthalocyanines, thus this means that the surrounding conditions of the central Zn ions are not changed in the micro-tube of (**T2**) which excludes the formation of Zn–O coordination bond between the neighbour phthalocyanines. Compared with the solution spectrum of (**2**), line broadening was observed for the third band group (230–300 nm) of the micro-tube of (**T2**), as shown in Fig. 3b. This indicates a tight packing between the benzene rings of the substituted 2-isopropyl-5-methylphenoxy moieties of (**2**).

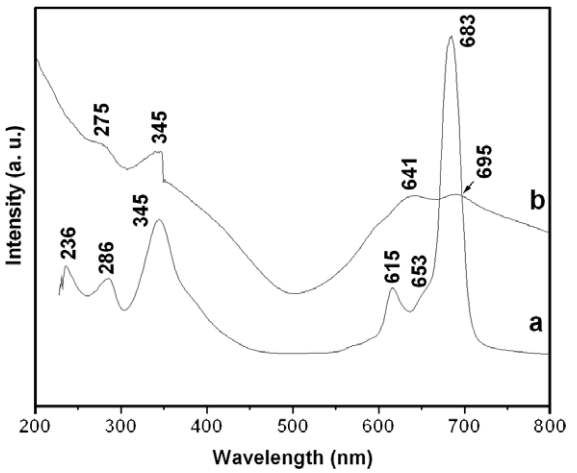

Fig. 3. The normalized UV–vis absorption spectra of (**2**) in dilute solution of chloroform (1×10^{-5}) (a) and the micro-tube (**T2**) deposited on the quartz slip (b).

3.4. Formation mechanism

In order to explore the formation mechanism of the tubular structure of (**T2**), we also measured the absorption spectra of (**2**) solution in different concentration. Fig. 4A and B is the normalized Q and 230–300 nm band group electron absorption spectra of (**2**) with different concentration in $CHCl_3$. As we can see, Fig. 4A and B shows that both the Q-band and 230–300 nm band group are changed with a isobestic point by improving the concentration of (**2**). This indicates that there exist both the strong π–π interaction between the phthalocyanine rings and the strong π–π interaction between the benzene rings of the substituted 2-isopropyl-5-methylphenoxy moieties of (**2**) with the increasement of the concentration of (**2**) and both these interactions are responsible for the formation of tubular structure of (**T2**). Thus based on the above discussion, a possible formation mechanism was proposed. The 2-isopropyl-5-methylphenoxy moieties of molecular

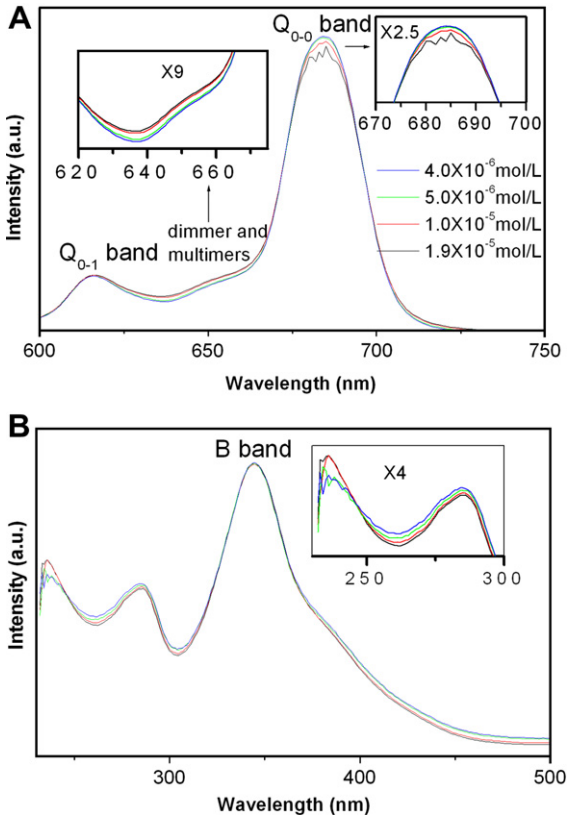

Fig. 4. (A) Q-band and (B) 230–300 nm band group electron absorption spectra of (**2**) with different concentration in $CHCl_3$ (normalized to the same intensity at 345 nm; insets are absorption peakings expanding to different magnitudes).

(**2**) act as hands for the formation of tubular structure of (**T2**) by π–π interaction between the benzene rings. First, with the evaporation of $CHCl_3$, millions of tetra(2-isopropyl-5-methylphenoxy) substituted Zn–phthalocyanine (**2**) molecules arranged into micro-rings structure hands in hands (see Fig. 5). Then by employing the micro-rings as seeds, micro-tube of (**T2**) were formed by preferentially packing of substituted Zn–phthalocyanine (**2**) rings along the direction of π–π stacking. That is, the driving force for one-dimensional tubular self-assembly is the cooperation of π–π stacking interaction between the four 2-isopropyl-5-methylphenoxy peripheral moieties and the phthalocyanine rings of (**2**). Other effect such as large steric hindrance of the 2-isopropyl-5-methylphenoxy which allows for the Zn–phthalocyanine rings to pack along the π–π stacking direction to form the tubular structure should also dedicate to the growth of tubular structure of (**T2**).

3.5. Electric-field-induced surface photovoltage spectroscopy

Fig. 6 illustrates the EFISPS of the tetra(2-isopropyl-5-methylphenoxy) substituted Zn–phthalocyanine micro-tube (**T2**) sample. Line (b) in Fig. 6 shows the surface photovoltaic (SPV) response of (**T2**). Referred to the UV–vis absorption spectrum (Line a), the SPV response resembles the absorption spectrum well and exhibits characteristic Soret-band and Q-band of (**T2**), lying in 200–300 nm and 600–700 nm, respectively. Fig. 6c and d shows the SPV response of (**T2**) with different external electric fields. The SPV value was always positive. It is clear that the response intensity was enhanced when a positive

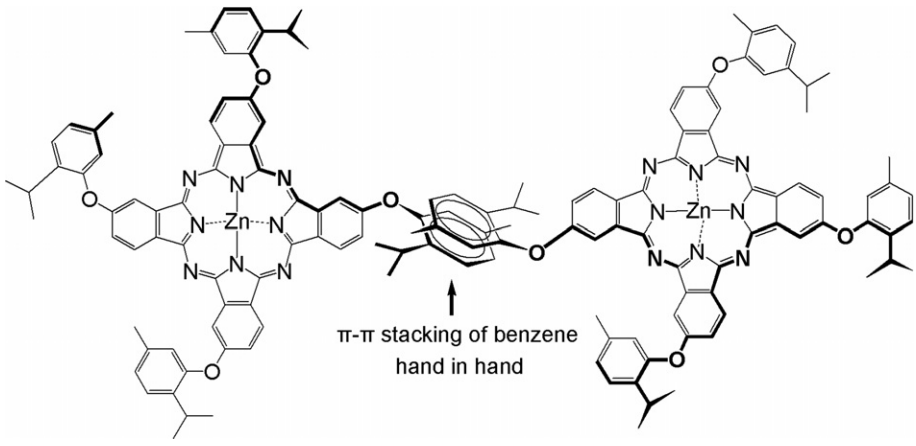

Fig. 5. Substituted Zn–phthalocyanine (**2**) molecules arranged hand in hand by employing the π–π stacking interaction between the 2-isopropyl-5-methylphenoxy peripheral moieties.

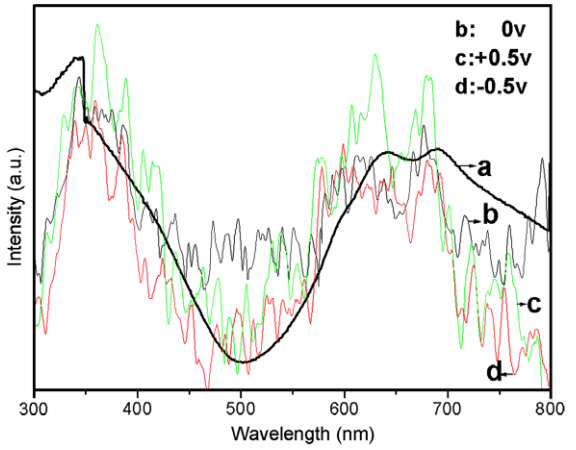

Fig. 6. SPS of the micro-tube sample (**T2**) under different external electric field (b: 0 V, c: +0.5 V, d: −0.5 V) as compared with its UV–vis spectrum (a).

bias was applied to the ITO electrode and was weaken when negative bias was applied. According to the principle of field effect, the effects of the electric field on the SPV response mainly exhibit that the electric field acts on the mobile direction and diffusive distance of the photogenerated charge carriers [25]. For a p-type semiconductor, the surface band bending is usually downward, when the photogenerated electrons move toward its surface and holes diffuse toward its bulk. The SPV response should be positive. When a positive electric field is applied on the semiconductor surface, the SPV response increases since the external field is consistent with the built-in field. On the contrary, when a negative electric field is applied, the SPV response is weakened [25]. Thus the EFI-SPS demonstrates that the tubular structure of tetra(2-isopropyl-5-methylphenoxy) substituted Zn–phthalocyanine (**T2**) behaves as p-type semiconductor.

4. Conclusion

In summary, large scale fabrication of substituted Zn–phthalocyanine micro-tube (**T2**) has been successfully achieved through a simple self-assembling process by evaporation of $CHCl_3$ solutions of (**2**). The p-type character of **T2** inferred by field-induced surface photovoltage spectrum (EFI-SPS) indicates that the micro-tube could be an ideal system of promising candidates for the dimensionally confined optoelectronic function on the mesoscopic scale.

Acknowledgments

This project is financially supported by the National Natural Science Foundation of China (20472014, 90505008), Natural Science Foundation of Jiangsu Province of China (BK2005126, BK2005127), China Postdoctoral Science Foundation and Jiangsu Planned Projects for Postdoctoral Research Funds. We would like to take this opportunity to express our appreciation on the valuable comments of the reviewer.

References

[1] B. Crone, A. Dodabalapur, Y.-Y. Lin, R.W. Filas, Z. Bao, A. Laduca, R. Sarpeshkar, H.E. Katz, W. Li, Nature 403 (2000) 521.
[2] B. Kessler, Appl. Phys. A 67 (1998) 125.
[3] P. Peumans, S. Uchida, S.R. Forrest, Nature 425 (2003) 158.
[4] A.P. Suzette, R. Anne, S.C. Winslow, Science 287 (2000) 1503.
[5] A. Ioannides, J.P. Dodelet, J. Phys. Chem. B 101 (1997) 510.
[6] J. Sly, P. Kasák, E. Gomar-Nadal, C. Rovira, L. Górriz, P. Thordarson, D.B. Amabilino, A.E. Rowan, R.J.M. Nolte, Chem. Commun. (2005) 1255.
[7] C.F. van Nostrum, S.J. Picken, A.-J. Schouten, R.J.M. Nolte, J. Am. Chem. Soc. 117 (1995) 9957.
[8] C.F. van Nostrum, Adv. Mater. 8 (1996) 1027.
[9] H. Engelkamp, S. Middelbeek, R.J.M. Nolte, Science 284 (1999) 785.
[10] P. Samori, H. Engelkamp, P. de Witte, A.E. Rowan, R.J.M. Nolte, J.P. Rabe, Angew. Chem. Int. Ed. 40 (2001) 2348.
[11] A. de la Escosura, M.V. Martínez-Díaz, P. Thordarson, A.E. Rowan, R.J.M. Nolte, T. Torres, J. Am. Chem. Soc. 125 (2003) 12300.
[12] M T.M. Choi, P.P.S. Li, D.K.P. Ng, Tetrahedron 56 (2000) 3881.
[13] C.L. Donley, W. Xia, B.A. Minch, R.A.P. Zangmeister, A.S. Drager, K. Debesny, D. O'Brien, N.R. Armstrong, Langmuir 19 (2003) 6512.
[14] R. Rai, A. Saxena, A. Ohira, M. Fujiki, Langmuir 21 (2005) 3957.
[15] S.D. Wang, X. Dong, C.S. Lee, S.T. Lee, J. Phys. Chem. B 108 (2004) 1529.
[16] R. Rotomskis, R. Augulis, V. Snitka, R. Valiokas, B. Liedberg, J. Phys. Chem. B 108 (2004) 2833.
[17] M. Kimura, H. Ueki, K. Ohta, K. Hanabusa, H. Shirai, N. Kobayashi, Chem. Eur. J. 10 (2004) 4954.
[18] W. Tong, A.B. Djurišić, A.M.C. Ng, W.K. Chan, Thin Solid Films 515 (2007) 5270.
[19] Z.L. Yang, H.T. Pu, Mater. Chem. Phys. 94 (2005) 202.
[20] S.-C. Suen, W.-T. Whang, F.-J. Hou, B.-T. Dai, Org. Electron. 7 (2006) 428.
[21] M. Wang, Y.-L. Yang, K. Deng, C. Wang, Chem. Phys. Lett. 439 (2007) 76.
[22] J.G. Young, W. Onyebuagu, J. Org. Chem. 55 (1990) 2155.
[23] C. Ma, D. Tian, X. Hou, Y. Chang, F. Cong, H. Yu, X. Du, G. Du, Synthesis 5 (2005) 741.
[24] A.W. Snow, N.L. Jarvis, J. Am. Chem. Soc. 106 (1984) 4706.
[25] X. Hou, X. Du, C. Ma, Y. Li, Q. Zhang, X. Wang, Y. Chang, W. Jiang, C. Chang, S. Shan, G. Du, Synth. Met. 150 (2005) 305.

Available online at www.sciencedirect.com
ScienceDirect
Organic Electronics 9 (2008) 473–480
Organic Electronics
www.elsevier.com/locate/orgel

Electrical characterization of mica as an insulator for organic field-effect transistors

X.F. Lu, L.A. Majewski, A.M. Song *

School of Electrical and Electrical Engineering, University of Manchester, Manchester M60 1QD, United Kingdom

Received 20 July 2007; received in revised form 9 November 2007; accepted 6 February 2008
Available online 10 March 2008

Abstract

Electrical properties of conjugated polymer films, including poly(3-hexylthiophene)-2,5-diyl (P3HT), poly(3,3‴-didodecylquarterthiophene) (PQT-12), and poly(triarylamine) (PTAA), on mica substrates have been studied. The test structure was similar to a standard organic field-effect transistor but with a 150-μm-thick commercially available mica gate insulator/substrate, which allowed to obtain a field-effect mobility of P3HT as high as 0.08 cm^2/Vs in the linear regime in ambient air. The influence of interface treatment, thermal annealing, and measurement conditions on the electrical properties of the P3HT films has been characterized and analyzed. We also studied the time dependence of the carrier concentration and mobility before and after a thermal annealing process. The results indicate that mica is a promising insulator for organic field-effect transistors, apart from already being one of the common thin-film materials widely used in electric capacitors.

PACS: 73.61.Ph; 73.40.Qv; 81.05.Lg; 85.30.Tv

Keywords: Organic field-effect transistor; Mica; Conducting polymer; Mobility; Gate dielectric; Substrate

1. Introduction

Since the early report by Koezuka and co-workers [1], organic field-effect transistors (OFETs) using conjugated polymers as the active layer have been the focus of intense research effort. It is envisaged that the advantages of solution-based organic semiconductors, such as potentially low cost, structural flexibility, and ability to process at low temperatures and over large areas, should lead to broad applications of organic electronics [2,3]. Encouraging examples of ink-jet printed logic circuits [4–6] and organic active-matrix drivers for displays [7,8] have been demonstrated. As a result of the ever-improving organic semiconductors [9–11], the performance-limiting factors of state-of-the-art OFETs are often now the substrate, gate insulator,the quality of source/drain contacts, and electrical stability of the devices [12,13]. The criteria on dielectrics for OFETs are rather strict. Apart from many similar requirements to inorganic transistors [14], OFET substrates and gate insulators also have to fulfill demands specific to organic electronics, such as the mechanical flexibility and thermal stability

* Corresponding author.
E-mail address: A.Song@manchester.ac.uk (A.M. Song).

1566-1199/$ - see front matter © 2008 Elsevier B.V. All rights reserved.
doi:10.1016/j.orgel.2008.02.007

[15,16]. It is also highly desirable that their surfaces are not only smooth but also have a relatively small amount of surface charge traps, because charge carriers in OFETs mainly transport close to the interface [17,18]. Moreover, they should be inert to common chemical solvents used for depositions of organic semiconductors. Polymeric materials, such as poly(vinyl phenol) (PVP) [19], poly(vinyl alcohol) (PVA) [20], poly(methylmethacrylate) (PMMA) [4,21], and benzocyclobutene (BCB) [22,23], have often been used as the gate dielectric in OFETs. However, although they can be processed from solution to form fairly smooth, low-polarity, and flexible films, their use in OFETs is often limited by the lower field-effect mobility than in the transistors made using inorganic gate dielectrics/substrates due to various reasons, and also by the insufficient stability to chemical solvents [16,24]. As a result, inorganic insulators such as thermally grown silicon dioxide are still commonly employed as the OFET gate insulator and/or substrate in research laboratories, despite being not flexible, being sensitive to processing history, and requiring high processing temperatures. SiO_2 has a relatively low dielectric constant ($k = 3.9$), which translates to high OFET gate voltages in order to obtain a high drive current. Recently, metal oxides such as Al_2O_3, Gd_2O_3, HfO_2, Ta_2O_5 or TiO_2 that display higher k values have been used [25,26].

Mica is a material widely used in electronics industry as, e.g., thin dielectric films in capacitors, and in electrical industry as an insulator. Mica is the generic name for naturally occurring minerals that belong to a family of hydrous potassium alumino-silicates. Micas possess a combination of chemical, physical, electrical, thermal, and mechanical properties not found in any other material. Thermally, micas possess excellent stability, are fire proof, and can resist temperatures in the range of 600–900 °C. Chemically, they are exceptionally stable and are described as being virtually inert to various solvents, alkalies, and acids except strong hydrofluoric and concentrated sulphuric acids. Electrically, they exhibit high dielectric strength, uniform dielectric constant, low power loss (high Q factor), and high electrical resistivity. Mechanically, micas are relatively flexible but maintain a robust strength within the film plane. In addition, due to their asymmetrical crystal structure, micas have a perfect cleavage, which leads to an atomically flat interface. When it is sufficiently thin (<1 μm), micas are also highly flexible and optically transparent [27]. Apparently, many of the above properties are favorable to OFETs. Moreover, it was long established that even mica films as thin as 300 nm were helium-tight and could hold atmospheric pressure [28]. This, in combination with the good optical transparency, may be interesting also to organic light-emitting devices and organic displays.

Here, we investigate the feasibility of using muscovite mica [$KAl_2(AlSi_3)O_{10}$ $(OH)_2$ from Agar Scientific Limited] as a possible substrate/gate dielectric for OFETs. Among various types of micas, muscovite mica is the most commonly used material for electrical insulation and has a high dielectric breakdown strength ($E_{Br} > 10$ MV/cm), a high dielectric constant ($k = 6.0 \sim 9.0$) [29], and a low dielectric loss [30]. Although mica sheets down to about a 100 nm in thickness can be prepared by, for instance, making use of the fact that the adhesion of certain thermoplastic resins to mica is stronger than the mutual cohesion of the molecular planes of mica [28], the thickness of the mica slides that we have obtained commercially is 150 μm [31], circa 1000 times thicker than a typical SiO_2 gate insulator layer in OFETs, for easy handling by tweezers in clean rooms. Nevertheless, this still allowed us to measure a few useful OFET parameters such as the carrier mobility in the linear regime. In order to exam the general applicability of mica as a substrate and/or gate insulator for polymer OFETs, electrical properties of three types of common semiconducting polymers on mica substrates have been studied in an OFET-like structure. Field-effect mobilities of 0.08 cm^2/Vs in poly(3-hexylthiophene)-2,5-diyl (P3HT), 0.04 cm^2/Vs in poly(3,3‴-didodecylquarterthiophene) (PQT-12 synthesized using Xerox formula [32]), and 0.003 cm^2/Vs in poly(triarylamine) (PTAA from Merck UK) have been observed. The effect of a thermal annealing process in over-pressured nitrogen gas environment has also been studied in time-dependent experiments.

2. Experimental details

It has long been established that the electrical properties of polythiophene layer, especially in OFETs, are strongly influenced by many factors: the surface energy of the dielectric layer, the nature (particularly the evaporation rate) of solvent used, the molecular weight and the purity of the polymer, as well as the history of its processing and thermal post-treatments of the film [12,33,34]. In addition,

due to the undesirable interactions with oxygen (i.e. a very rapid doping by airborne O_2) [35] and moisture [36,37], many semiconducting polymers, such as P3HT, are not electrically stable in ambient conditions and OFETs based on them typically degrade rather quickly [37]. Recently, we demonstrated that electrical stability of bottom-contact polythiophene OFETs might be improved from minutes to a few hours via certain device fabrication procedures [38]. These include the use of a high-boiling point solvent (1,2,4-trichlorobenzene, TCB), surface treatment with a highly hydrophobic self-assembled monolayer (*n*-octadecyltrichlorosilane, OTS), and annealing the devices in an over-pressured nitrogen gas. The improved stability allows us to characterize the electrical properties of polymer layers on the mica film in ambient air in this work.

All samples were fabricated in the so-called bottom-gate, bottom-contact OFET-like architecture (for simplicity, the samples shall still be referred to as OFETs in the following), as shown in Fig. 1. The gate insulator/substrate was a 150-μm-thick mica film, about three orders of magnitude thicker than that in a typical OFET that utilized SiO_2 as the gate insulator, which as mentioned earlier was due to the commercial availability and ease of handling in the cleanroom. No separate substrate was necessary because of the large thickness of the mica film. In all cases, the mica substrates were decreased with the following reagent grade solvents: trichloroethylene, acetone, and methanol. Subsequently, aluminum back gate contacts were deposited on the back surface of the mica substrates by means of thermal evaporation under vacuum ($<10^{-6}$ Torr). 50-nm-thick Au (99.99%, Cookson precious metals) source and drain contacts, defining channel length $L_{SD} = 20$, 30, 50, and 70 μm, respectively, and channel width $W_{SD} = 2000$ μm, were then patterned using the standard photolithography. All samples were subject of OTS surface treatment. The slides were immersed in solution of OTS-18 (+90%, Aldrich) in cyclohexane for 10 min at 10 °C. As OTS does not form a layer on Au, the SAM treatment was not expected to affect the performance of the source and drain contacts [39,40]. The regioregular P3HT (Aldrich, molecular weight $= 7.85 \times 10^4$ Daltons) solution was made by dissolving in TCB (99%, Aldrich) to obtain a 1% solution. For devices based on PQT-12 and PTAA, the processing steps are the same as that of devices based on P3HT. Due to the symmetrical molecular structure of PTAA, its solubility in nonpolar solvents is higher than that in polar solvents [41]. Thus, toluene was used as solvent for PTAA instead of TCB. Finally, all three types of semiconductor polymer films were formed by spin coating onto OTS-modified mica substrates at 2000 rpm for 120 s in air.

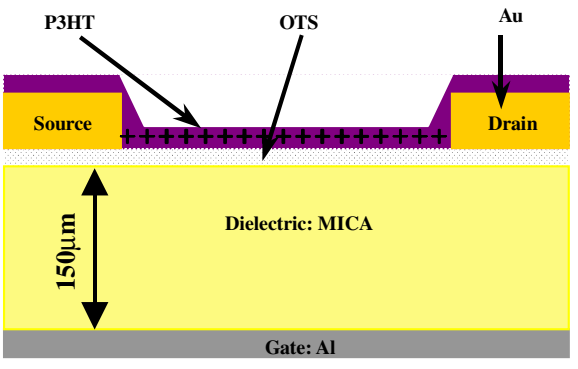

Fig. 1. Schematic diagram of a bottom-gate OTFT-like structure.

With the recently developed photolithography processes for semiconducting polymers [42,43], where UV exposure on the device active region was avoided, the semiconductor polymer layer was patterned by plasma etching into the shape of conducting channel between ohmic contacts. After a conducting polymer layer was spin-coated, photoresist (S1813) was spun onto it. After exposure and development, areas of the polymer layer that were not covered by S1813 were removed via plasma etching for 45 s with a power of 30 W. Finally, the S1813 layer was removed by immersing into acetone and methanol.

For electrical characterizations, the OFETs were contacted via Karl Süss MicroTech PH100 miniature probe heads to an Agilent E5270B precision measurement mainframe that controlled and recorded source–drain and gate voltages and currents, respectively. Additionally, in order to obtain a higher mobility as well as to investigate the electrical stability of the studied OFETs under ambient conditions, all devices were de-doped via thermal annealing at 100 °C in a chamber filled with over-pressured nitrogen gas after the initial measurements on the "as prepared" devices. Using the above procedures, a large number of devices (>20) for each type of semiconducting polymer were fabricated and measured. All investigated OFETs showed similar results to the ones reported here.

3. Results and discussion

Before determining the carrier mobility in the conducting polymer films, we first carried out measurements to determine whether there was a serious carrier injection barrier and hence a large contact resistance (R_C). Fig. 2 shows the dependence of the drain current (I_D) on the drain voltage (V_D) at a back-gate voltage of $V_G = -100$ V in three typical devices based on P3HT, PQT-12, and PTAA. Only the data at a back gate voltage of $V_G = -100$ V are shown here because the drain currents at other gate voltages ($V_G = +100$ V and 0 V) only differed by up to a few percent, due to the large thickness of the mica gate dielectric (150 μm). The application of 100 V to the gate of our mica-based devices roughly corresponds to about 0.1 V in an OFET with a common 200 nm thin SiO_2 gate insulator layer. In order to completely switch the transistors on and off, an enormous gate voltage ~100,000 V would have to be applied, which is far beyond our experimental limit. As such, it is not possible to measure the full transfer characteristics of the devices. Nevertheless, we will show in this work that we are still able to extract useful device parameters, such as the carrier mobility.

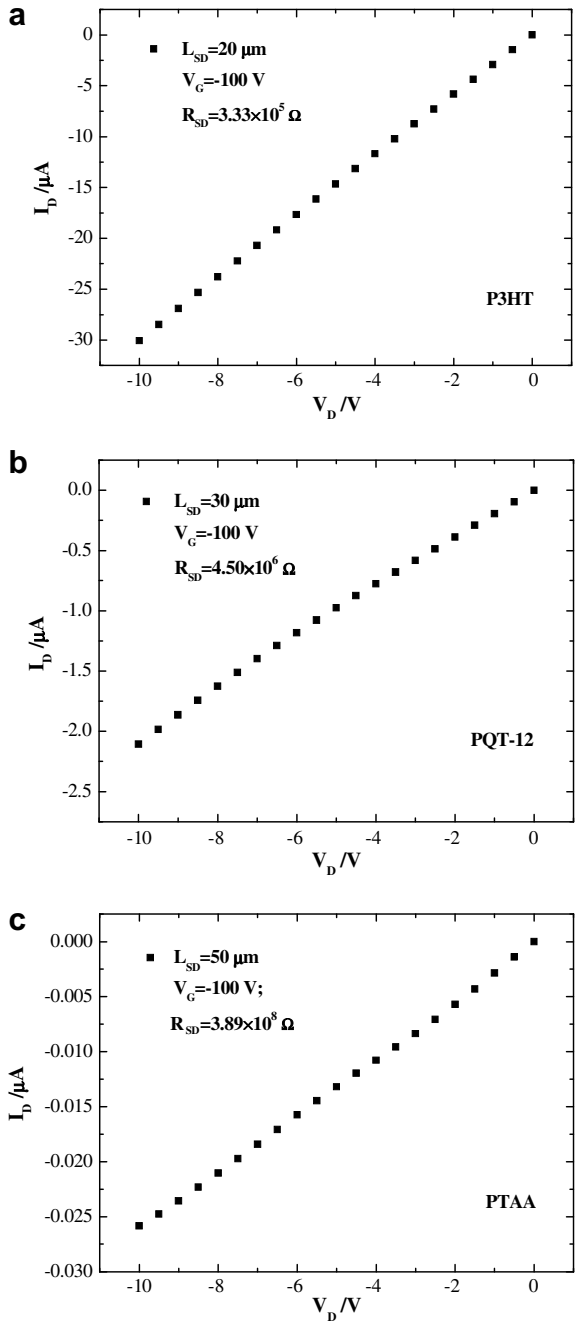

Fig. 2. I_D versus V_D curves of (a) a P3HT-based device, (b) a PQT-12 based device, (c) a PTAA-based device.

Within the experimental range of source/drain voltage (V_{SD}), a rather good linear relation was observed in all devices including with a zero or positive back-gate voltage. The derivation from a perfect linear line was likely due to a non-zero but insignificant injection barrier at the contacts. To further study this, we measured the total source–drain resistance (R_{SD}) of the P3HT and PQT-12 devices as a function of L_{SD}, as shown in Fig. 3a and b. The measurement was taken after annealing treatment on the device. Results of PTAA based devices are not shown here since a dewetting effect often occurred in the device fabrication with large L_{SD}. A good linear dependence of R_{SD} on L_{SD}, shown by the dashed linear fitting line, was clearly demonstrated. The values of the cross points of the linear fit at the $L_{SD} = 0$ axis in both figures indicate that the contact resistance was rather small particularly in devices with large L_{SD} (50 and 70 μm). The contact resistance (R_C) shown in Fig. 2b is larger than that in Fig. 2a, which is expected due to the lower injection barrier between the highest occupied molecular orbital (HOMO) state in P3HT (4.8 eV)and the work function of Au (4.83 eV) than that between PQT-12 (5.05 eV) and Au [44–46].

After obtaining the fairly good linear dependence of I_D on V_D in Fig. 2 and the insignificant role of R_C in Fig. 3, the carrier mobility in the linear regime was determined from the change of I_D with V_G. Because of the large thickness of the gate insulator, an enormous V_G (~100,000 V) would have to be applied to switch the transistor completely on and

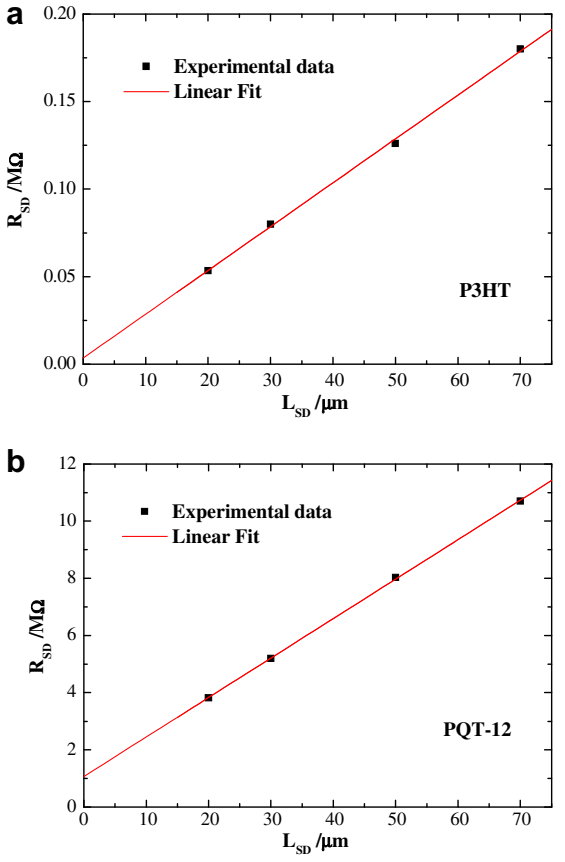

Fig. 3. A typical R_{SD} dependence on L_{SD} after annealing treatment in over-pressured nitrogen. (a) P3HT-based devices, (b) PQT-12 based devices.

off (i.e., to reach a high on/off ratio), which is beyond our experimental limit. In our experiments, V_G was ranged from +100 to −100 V, which was roughly equivalent to +0.1 to −0.1 V if a 200-nm-thick SiO_2 gate insulator had been used instead. Nevertheless, this allowed us to extract the carrier field-effect mobility (μ) in the linear regime by using the standard formula [14]

$$\left(\frac{\partial I_D}{\partial V_G}\right)_{V_D=\text{const}} = \frac{W_{SD} C_i}{L_{SD}} \mu V_{SD}, \quad (1)$$

in which C_i is the capacitance of the gate insulator per unit area. The I_D versus V_G curves in Fig. 4 allows a good estimate of the mobility, which is 0.082 cm^2/Vs in the P3HT device, 0.043 cm^2/Vs in the PQT12 device, and 0.003 cm^2/Vs in the PTAA device, respectively. The reason for the slight derivation from ideal linear curves is unknown, but it was possibly due to the charging effect in the measurement setup given the high device resistance and parasitic capacitance. The P3HT mobility is in the same order of magnitude of the best-achieved values in ambient air to date. PTAA showed the lowest mobility, which was expected because PTAA is an

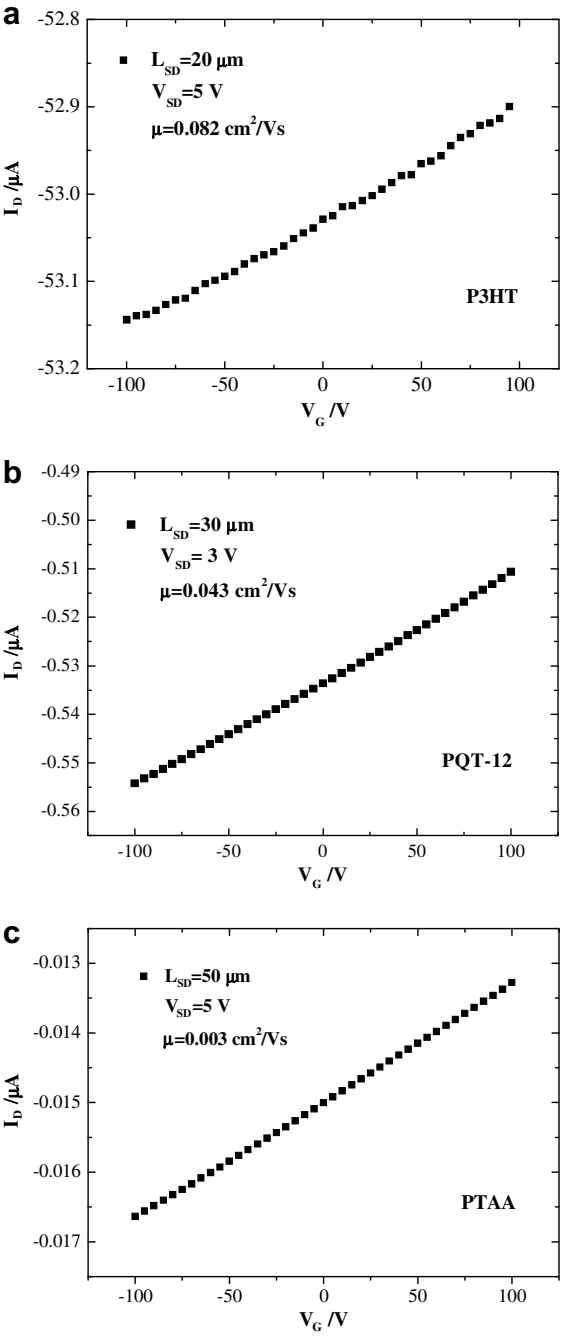

Fig. 4. I_D versus V_G curves of devices with OTS treatment. (a) A device based on P3HT; (b) a device based on PQT-12; (c) a device based on PTAA.

amorphous semiconductor. Separate experiments were performed using commercial SiO_2 substrates of 250 nm thick with the same solution and processing steps (results not shown here), and very similar carrier motilities were obtained.

Since the devices were fabricated and measured in ambient air conditions, we also characterized the time dependence of the devices. We found that P3HT-based devices generally deteriorate significantly after a few hours, in agreement with previous studies [35]. This makes controlled experiments difficult. In contrast, PTAA showed excellent ambient air stability. Focused experiments have therefore been performed on devices based on PQT-12. The change of the field-effect mobility as a function of time is displayed in Fig. 5a. Measurements started immediately after the device was prepared. After measuring for 6 h under ambient conditions, an annealing treatment was performed in over-pressured nitrogen atmosphere. During the annealing treatment, the device was heated up to 100 °C and slowly cooled down to room temperature. Application of thermal annealing treatment has been reported to enhance device performance and stability [47,48]. In ambient air, donor–acceptor complex or charge transfer complex (CTC) is induced by the interaction of oxygen with long π-conjugation lengths in the polymer film. With a low degree of doping, the oxygen dopant serves to increase conductivity of polymer film via production of localized states within the π–π^* gap, which induce counterions that help delocalize and stabilize the positive charge carriers on the polymer. A too high degree of doping, however, may introduce very strong scattering. As such, the conductivity can decrease with the degree of doping [49,35]. As the fabrication processes including the solution making were carried out in ambient air, the polymer film was expected to have been doped by oxygen. Via the thermal annealing, oxygen dopants are removed from the polymer film, and the densification and morphology improvement of the film are also expected, which serve to retard the diffusion of oxygen into the film [35,50]. Therefore, both mobility and the stability of the device are expected to be improved [38].

From Fig. 5a, it can be observed that before the annealing treatment was performed, the mobility increased slowly with time. After the device was annealed at the sixth hour, the device was measured again in ambient air. The mobility was found to have been enhanced dramatically by the annealing process, and then largely remained stable in the next 30 h. The improved mobility and stability were in good agreement with earlier studies [35,47,50].

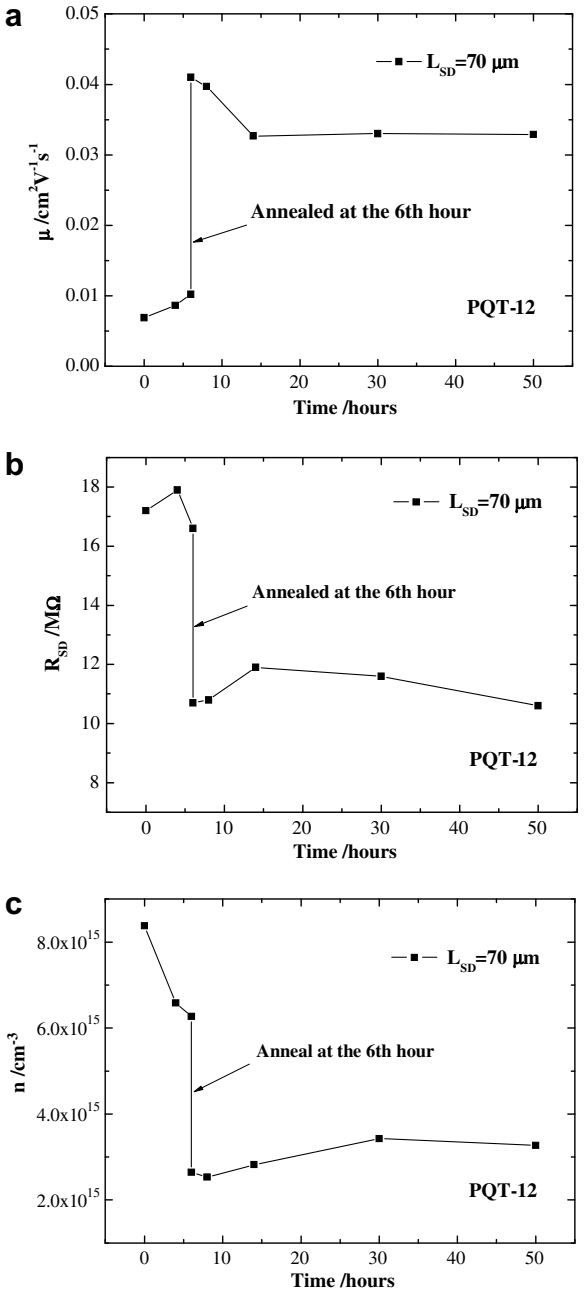

Fig. 5. Stability test of a device based on PQT-12 before and after annealing treatment in over-pressured nitrogen. (a) μ versus time, (b) R_{SD} versus time, (c) carrier concentration n versus time. Note that annealing treatment was performed at the sixth hour. Similar results were obtained on devices with different L_{SD} values. Dots represent experimental results and the lines are for the guide of the eyes.

To further study the physical properties of the film as a function of time before and after the annealing process, the dependence of R_{SD} on time was also measured and is shown in Fig. 5b. After the annealing treatment was performed, the resistances decreased dramatically and then remained rather stable in the next 30 h. The abrupt drop of R_{SD} after annealing was consistent with the changes of mobility in Fig. 5a. With the negligible R_C according to the results in Fig. 3 in devices with a 70 μm L_{SD}, the relation between the total resistance and mobility of a certain device can be given by [51]:

$$R_{SD} \approx R_{CH} = \frac{L_{SD}}{W_{SD}\mu ne}, \quad (2)$$

where n stands for the carrier density in the film assuming a uniform distribution. Hence, the change of carrier concentration can be deduced from the resistance and mobility values, which is depicted in Fig. 5c. A dramatic drop of the carrier concentration was observed after the annealing treatment, which indicated that the oxygen concentration was reduced due to the de-doping of the polythiophene layer. For about 30 h after the annealing treatment, the carrier concentration maintained stable, which may be largely due to the improved semicrystalline structure of the PQT-12 layer, which is more resistive to oxygen penetration into the film [50]. Moreover, it is worth noting that the carrier concentration kept increasing slowly for about 8 h after annealing treatment, which was expected due to the slow doping of oxygen with the sample placed in ambient air.

It is interesting to discover that immediately after the fabrication by oxygen plasma etching, the carrier concentration actually increased with time. This was initially rather surprising, since the carrier concentration was only expected to increase in ambient air. Separate experiments (not shown here) indicated that the edges of the polymer film were rather heavily doped during the plasma etching process to pattern the OFET channel. Except the region close to the edges, the PQT-12 film was protected by the photoresist during the plasma etching [42]. The edges of the OFET channel were nevertheless exposed to energetic oxygen molecules and more crucially to reactive oxygen ions in the plasma etching chamber. After the oxygen plasma etching, the devices were measured in ambient air, which had a much lower concentration of oxygen, particularly oxygen ions, than in the plasma etching chamber. As a result, excessive oxygen could be released from the film, which resulted in the reduction of the carrier concentration near the edge of the polymer film. Because Eq. (2) does not treat the edges and the central OFET channel separately but rather yields the average carrier concentration over the whole PQT-12 film, the obtained effective carrier concentration reduces as a function of time.

4. Conclusions

In summary, polymer-based OFET structures using mica as the substrate/gate insulator have been fabricated and characterized, showing carrier mobilities in the same order of magnitude as the best values reported to date in devices that were fabricated and measured in ambient air. Time dependent experiments up to 50 h after the sample preparation were performed on devices based on PQT-12. Our work shows that mica, which has been widely used in electronic industry particularly in capacitors, may be a useful thin-film material for OTFT devices.

Acknowledgements

This work was supported by the Engineering and Physical Science Research Council (EPSRC), the Royal Society, UMIP Ltd., and BTG International plc. The authors wish to thank M. F. McGowan for technical help.

References

[1] A. Tsumura, K. Koezuka, T. Ando, Appl. Phys. Lett. 49 (1986) 1210.
[2] G. Horowitz, J. Mater. Res. 19 (2004) 1946.
[3] C.D. Dimitrakopoulos, P.R.L. Malenfant, Adv. Mater. 14 (2002) 99.
[4] J.A. Rogers, Z. Bao, A. Makhija, P. Braun, Adv. Mater. 11 (1999) 741.
[5] G.H. Gelinck, T.C.T. Geuns, D.M. de Leeuw, Appl. Phys. Lett. 77 (2000) 1487.
[6] P.F. Baude, D.A. Ender, M.A. Haase, T.W. Kelley, D.V. Muyers, S.D. Theiss, Appl. Phys. Lett. 82 (2003) 3964.
[7] H.E.A. Huitema, G.H. Gelinck, J.B.P.H. van der Putten, K.E. Kuijk, C.M. Hart, E. Cantatore, P.T. Hervig, A.J.J.M. van Breemen, D.M. de Leeuw, Nature (London) 414 (2001) 599.
[8] C.D. Sheraw, L. Zhou, J.R. Huang, D.J. Gundlach, T.N. Jackson, M.G. Kane, I.G. Hill, M.S. Hammond, J. Campi, B.K. Greening, J. Francl, J. West, Appl. Phys. Lett. 80 (2002) 1088.
[9] I. McCulloch, M. Heeney, C. Bailey, K. Genevicius, I. Macdonald, M. Shkunov, D. Sparrowe, S. Tierney, R.

Wagner, W. Zhang, M. Chabinyc, R.J. Kline, M.D. Mcgehee, M.F. Toney, Nat. Mater. 5 (2006) 328.
[10] Z. Bao, A. Dodabalapur, A.J. Lovinger, Appl. Phys. Lett. 69 (1996) 4108.
[11] H. Sirringhaus, N. Tessler, R.H. Friend, Science 280 (1998) 1741.
[12] H. Sirringhaus, Adv. Mater. 17 (2005) 2411.
[13] J. Zaumseil, H. Sirringhaus, Chem. Rev. 107 (2007) 1296.
[14] S.M. Sze, Semiconductor Devices: Physics and Technology, Second ed., Wiley, New York, 2002.
[15] J. Veres, S.D. Ogier, G. Lloyd, D. de Leeuw, Chem. Mater. 16 (2004) 4543.
[16] A. Facchetti, M.H. Yoon, T.J. Marks, Adv. Mater. 17 (2005) 1705.
[17] J. Veres, D. Ogier, W. Leeming, D.C. Cupertino, S.M. Khaffaf, Adv. Funct. Mater. 13 (2003) 199.
[18] I. Yagi, K. Tsukagoshi, Y. Aoyagi, Appl. Phys. Lett. 86 (2005) 103502.
[19] M. Halik, H. Klauk, U. Zschieschang, T. Kriem, G. Schmid, W. Radlik, K. Wussow, Appl. Phys. Lett. 81 (2002) 289.
[20] P. Parashkov, E. Becker, G. Ginev, T. Riedl, H.H. Johannes, W. Kowalsky, J. Appl. Phys. 95 (2004) 1594.
[21] S. Uemura, M. Yoshida, S. Hoshino, T. Kodzasa, T. Kamata, Thin Solid Films 438 (2003) 378.
[22] L.L. Chua, P.K.H. Ho, H. Sirringhaus, R.H. Friend, Appl. Phys. Lett. 84 (2004) 3400.
[23] L.L. Chua, J. Zaumseil, J.F. Chang, E.C.W. Ou, P.K.H. Ho, H. Sirringhaus, R.H. Friend, Nature (London) 434 (2005) 194.
[24] L.L. Chua, P.K.H. Ho, H. Sirringhaus, R.H. Friend, Adv. Mater. 16 (2004) 1609.
[25] L.A. Majewski, R. Schoreder, M. Grell, Adv. Mater. 17 (2005) 192.
[26] L.A. Majewski, M. Grell, S.D. Ogier, J. Veres, Org. Electron. 4 (2003) 27.
[27] D.M. Hepburn, I.J. Kemp, A.J. Shields, IEEE Electr. Insul. Mag. 16 (2000) 19.
[28] B.J. Mulder, J. Phys. E: Sci. Instrum. 9 (1976) 724.
[29] Agar Scientific Limited.
[30] M.A. Chaudhry, A.K. Jonscher, R.M. Hill, J. Phys. D: Appl. Phys. 18 (1985) 1207.
[31] Paramount Corporation, New York, USA.
[32] B.S. Ong, Y. Wu, P. Liu, S. Gardner, N. Zhao, G. Botton, J. Am. Chem. Soc. 126 (2004) 3378.
[33] J.F. Chang, B. Sun, D.W. Breiby, M.M. Nielsen, T.I. Sölling, M. Giles, I. McCulloch, H. Sirringhaus, Chem. Mater. 16 (2004) 4772.
[34] B.S. Ong, Y. Wu, P. Liu, S. Gardner, Adv. Mater. 17 (2005) 1141.
[35] M.S.A. Abdou, F.P. Orfino, Y. Son, S. Holdcroft, J. Am. Chem. Soc. 119 (1997) 4518.
[36] Y. Qiu, Y. Hu, G. Dong, L. Wang, J. Xie, Y. Ma, Appl. Phys. Lett. 83 (2003) 1644.
[37] S. Hoshino, M. Yoshida, S. Uemura, T. Kodzasa, N. Takada, T. Kamata, K. Yase, J. Appl. Phys. 95 (2004) 5088.
[38] L.A. Majewski, J.W. Kingsley, C. Balocco, A.M. Song, Appl. Phys. Lett. 88 (2006) 222108.
[39] M. Wang, K.M. Liechti, Q. Wang, J.M. White, Langmuir 21 (2005) 1848.
[40] C.R. Kessel, S. Granick, Langmuir 7 (1991) 532.
[41] T. Manifar, S. Rohani, M. Saban, Ind. Eng. Chem. Res. 44 (2005) 970.
[42] J. Chan, X.Q. Wang, A.M. Song, J. Appl. Phys. 99 (2006) 023710.
[43] C. Balocco, L.A. Majewski, A.M. Song, Org. Electron. 7 (2006) 500.
[44] G. Lloyd, B. Eccleston, Mat. Res. Soc. Symp. Proc. 660 (2000) JJ5.12, edited by S.C. Moss.
[45] P.A. Anderson, Phys. Rev. 115 (1959) 553.
[46] Y. Wu, Y. Li, S. Gardner, B.S. Ong, Mater. Res. Soc. Symp. Proc. 871E (2005) I2.3.1.
[47] A. Zen, J. Pflaum, S. Hirschmann, W. Zhuang, F. Jaiser, U. Asawapirom, J.P. Rabe, U. Scherf, D. Neher, Adv. Funct. Mater. 14 (2004) 757.
[48] S. Cho, J. Yuen, J.Y. Kim, K. Lee, A. Heeger, Proc. SPIE 6336 (2006) 63360X-1.
[49] M.S.A. Abdou, X. Lu, Z.W. Xie, F. Orfino, M.J. Deen, S. Holdcroft, Chem. Mater. 7 (1995) 631.
[50] B.A. Mattis, P.C. Chang, V. Subramanian, Mater. Res. Soc. Symp. Proc. 771 (2003) L10.35.1.
[51] L. Bürgi, T.J. Richards, R.H. Friend, H. Sirringhaus, J. Appl. Phys. 94 (2003) 6129.

Available online at www.sciencedirect.com
ScienceDirect
Organic Electronics 9 (2008) 481–486
Organic Electronics
www.elsevier.com/locate/orgel

Air stable C_{60} based n-type organic field effect transistor using a perfluoropolymer insulator

Junhyuk Jang, Ji Whan Kim, Nohhwal Park, Jang-Joo Kim *

Department of Materials Science and Engineering and Center for OLED, Seoul National University, Seoul 151-744, Republic of Korea

Received 3 January 2008; received in revised form 2 February 2008; accepted 12 February 2008
Available online 29 February 2008

Abstract

Air stable n-type organic field effect transistors (OFETs) based on C_{60} are realized using a perfluoropolymer as the gate dielectric layer. The devices showed the field-effect mobility of 0.049 cm^2/V s in ambient air. Replacing the gate dielectric material by SiO_2 resulted in no transistor action in ambient air. Perfluorinated gate dielectric layer reduces interface traps significantly for the n-type semiconductor even in air.

PACS: 72.80.Le; 73.61.Ph; 85.30.Tv; 73.20.At

Keywords: Organic field effect transistor; n-Type; C_{60}; Air stable; Perfluorinated polymer gate insulator

1. Introduction

There has been much progress in performance of organic field effect transistors (OFETs) in recent years. A large number of semiconducting organic and polymeric materials have been reported and high field effect mobilities with high on–off ratios have been realized [1]. Most of the materials are, however, p-type and fewer n-type materials have been reported up to now [2,3]. Moreover most of the reported n-type organic semiconducting materials showed instability and sensitivity to air exposure. Moisture or hydroxy group at the interface has electron withdrawing characteristics and acts as trap sites in operation of n-type OFETs. Since accepter-like trap states induce threshold voltage shift and destroy OFETs performance, in situ measurement in high vacuum chamber or device passivation techniques are employed to characterize n-type OFETs [4,5]. Recently, hydroxyl-free gate dielectric such as divinyltetramethylsiloxane-bis (benzocyclobutene) derivative is reported to be able to yield n-channel FET conduction in most conjugated polymers. However, it is also limited to the encapsulated devices [6]. Two methods have been reported to overcome the problem. The first one is to use specially designed semiconductor materials with strong electron withdrawing groups [7–10]. It helps to increase electron affinity and prevent reaction with moisture or oxygen in ambient air. Another one is to use large grain and highly packed polycrystalline semiconductor. It reduces

* Corresponding author.
E-mail address: jjkim@snu.ac.kr (J.-J. Kim).

1566-1199/$ - see front matter © 2008 Elsevier B.V. All rights reserved.
doi:10.1016/j.orgel.2008.02.011

permeation of moisture and oxygen into the active region of film [11,12].

In this paper, we report another method to fabricate n-type OFETs stable in air without passivation, which is the use of a perfluorinated polymer as the gate dielectric layer. C_{60} was employed as an n-type semiconductor, which is reported to be unstable upon exposure to ambient air if the device is fabricated on SiO_2 dielectric layer [13,14]. We focused on the interface between semiconductor and insulator rather than semiconductor bulk itself. We selected CYTOP™ fluoropolymer as an dielectric insulator to reduce the effect of interface trap sites and fabricate ambient air-stable C_{60} OFETs. The dielectric material had been employed as the gate dielectric to eliminate gate bias stress effect in p-type rubrene single crystal field effect transistors [15].

2. Experimental

OFET devices have a top-contact and bottom-gate structure. The devices were fabricated on a heavily doped silicon wafer which works as the common gate electrode. Either thermally grown SiO_2 (3000 Å) (device 1) or spin-coated CYTOP™ (3600 Å) (device 2) was used as the dielectric layer. For the device 1, silicon dioxide layer was cleaned with H_2SO_4:H_2O_2 = 4:1 solution and rinsed with dionized water. The surface was treated with UV–O_3 for 10 min before the deposition of an organic semiconductor. For the device 2, CYTOP™ was purchased from Asahi Glass and spin-coated on a Si wafer. Native oxide of the Si wafer was removed using buffered oxide etchant before spin coating. 50 nm thick C_{60} film was deposited onto the dielectric layers with thermal evaporation under a pressure of 2.0×10^{-6} torr. Deposition rate was 0.5 Å/s. Substrate temperature was maintained at 50 °C and active region was patterned with a metal shadow mask. Au source and drain electrode were deposited by thermal evaporation under a pressure of 5.0×10^{-7} torr with the deposition rate of 2.0 Å/s. The samples were exposed to N_2 gas in a glove box to change the mask for the electrode deposition. Channel length and width were defined to 50 μm and 500 μm, respectively, with another metal shadow mask. Thickness of the electrodes was 1000 Å. Some fabricated devices were encapsulated with glass cans in a glove box. O_2 and H_2O levels in the globe box were under 1.0 ppm, respectively.

Electrical measurements were performed using an Agilent 4155 C semiconductor parameter analyzer and a Suss PM8 probe station. All electrical measurements were performed in the dark. Atomic Force Microscope (AFM) topographic images were taken in a PSIA XE-100 scanning probe microscope with non-contact mode.

3. Results and discussion

Fig. 1 shows AFM images of the C_{60} films on the insulators. The root-mean-square (RMS) roughnesses of the C_{60} films are almost the same with 5.3 Å on CYTOP™ and 5.7 Å on SiO_2, respectively. The film grown on SiO_2 dielectric layer has almost the same grain size as the film grown on CYTOP™ layer, and these grains are not large enough to prevent permeation of oxygen or moisture through the grain boundaries, one of the methods to show stable FET characteristics in ambient air [11,12].

Drain current–drain voltage (I_D–V_D) characteristics of C_{60} based FETs with the SiO_2 and CYTOP™ insulator are displayed in Fig. 2 for different gate biases (V_g). The device with the SiO_2 insulator exhibits n-type characteristics only when it was encapsulated (Fig. 2a). The device without encapsulation does not show any transistor characteristics under exposure to air (not shown), which is consistent with the previous reports [13,14]. In contrast, the device with the CYTOP™ insulator shows clear n-type I_D–V_D characteristics even in air without passivation (Fig. 2b). If the device is encapsulated, the current was increased considerably (Fig. 2c).

The transfer characteristics of the devices measured just after the fabrication of the devices ($t = 0$) in the saturation regime ($V_D = 100$ V) are shown in Fig. 3. The device with SiO_2 gate dielectric layer (Fig. 3a) shows the electron mobility of 0.08 cm^2/V s, threshold voltage of 22.5 V, and on–off ratio of 10^4, respectively. Moreover, the device showed large hysteresis of 42 V. In contrast to the device with SiO_2 insulator, the device with CYTOP™ insulator without encapsulation showed the electron mobility of 0.049 cm^2/V s and on–off ratio of 6×10^3 in ambient air (Fig. 3b), which are comparable with the encapsulated device with SiO_2 gate insulator. It is interesting to note that the device has very large threshold voltage of 64.0 V but with very small hysteresis. The encapsulated device with CYTOP™ gate insulator (Fig. 3c) resulted in the best device performance as expected. The device showed the electron mobility of 0.20 cm^2/V s, threshold voltage of 29.0 V, and on–off ratio of 10^5, respectively.

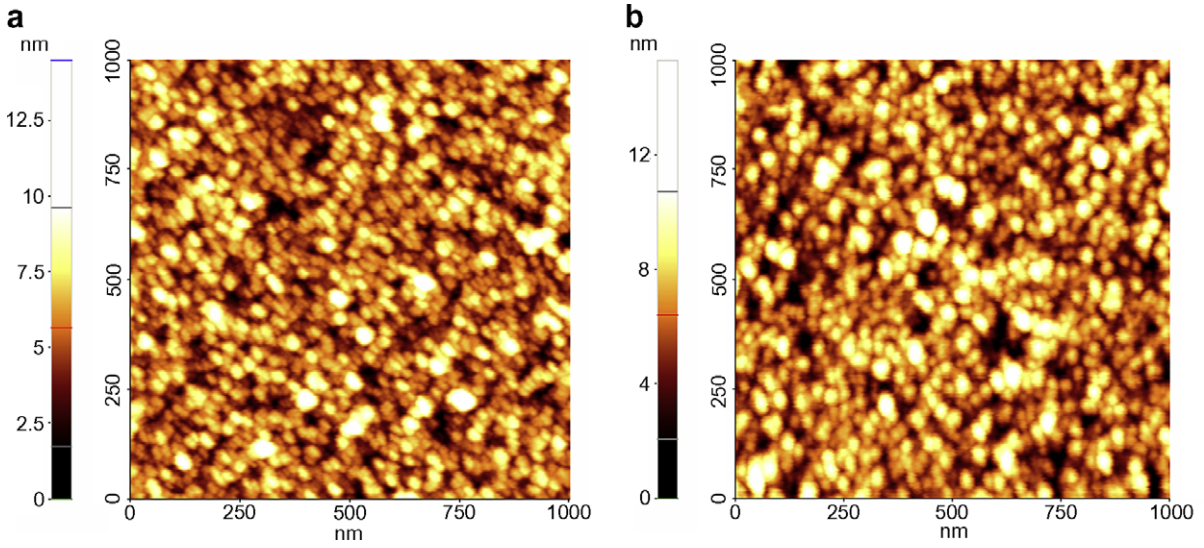

Fig. 1. Atomic force microscopy topographic images of C_{60} films grown on (a) SiO_2 and (b) CYTOP™ (scan size is 1 μm × 1 μm).

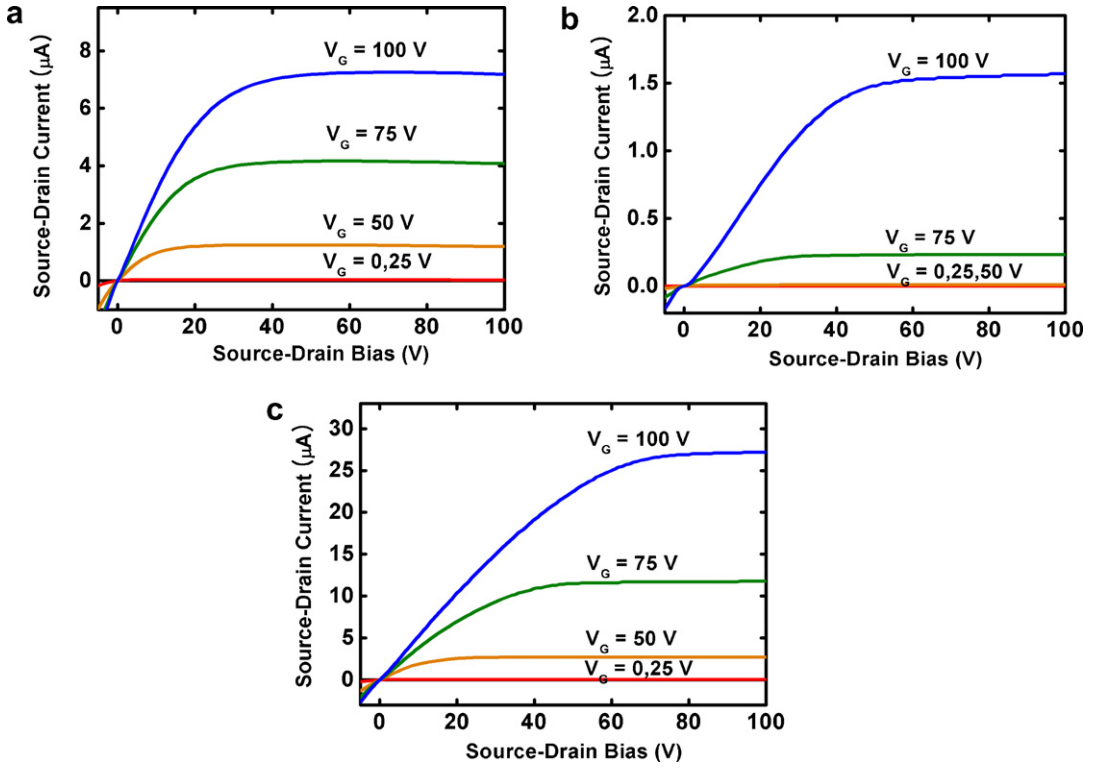

Fig. 2. Output (I_D–V_D) characteristics of C_{60} OFETs with (a) SiO_2 insulator in inert environment (passivated), (b) CYTOP™ insulator in ambient air, and (c) CYTOP™ insulator in inert environment (passivated).

To further evaluate the stability of the devices, we investigated the evolution of the transfer curves of the devices and the variation of mobility, threshold voltage and hysteresis with time are plotted in Fig. 4. Hysteresis in the figure was defined as the difference of gate bias between the forward and reverse scan at the source–drain current of 10 nA ($V_{\text{hysteresis}} = V_{\text{g}}^{\text{forward}} - V_{\text{g}}^{\text{reverse}}$ at 10 nA).

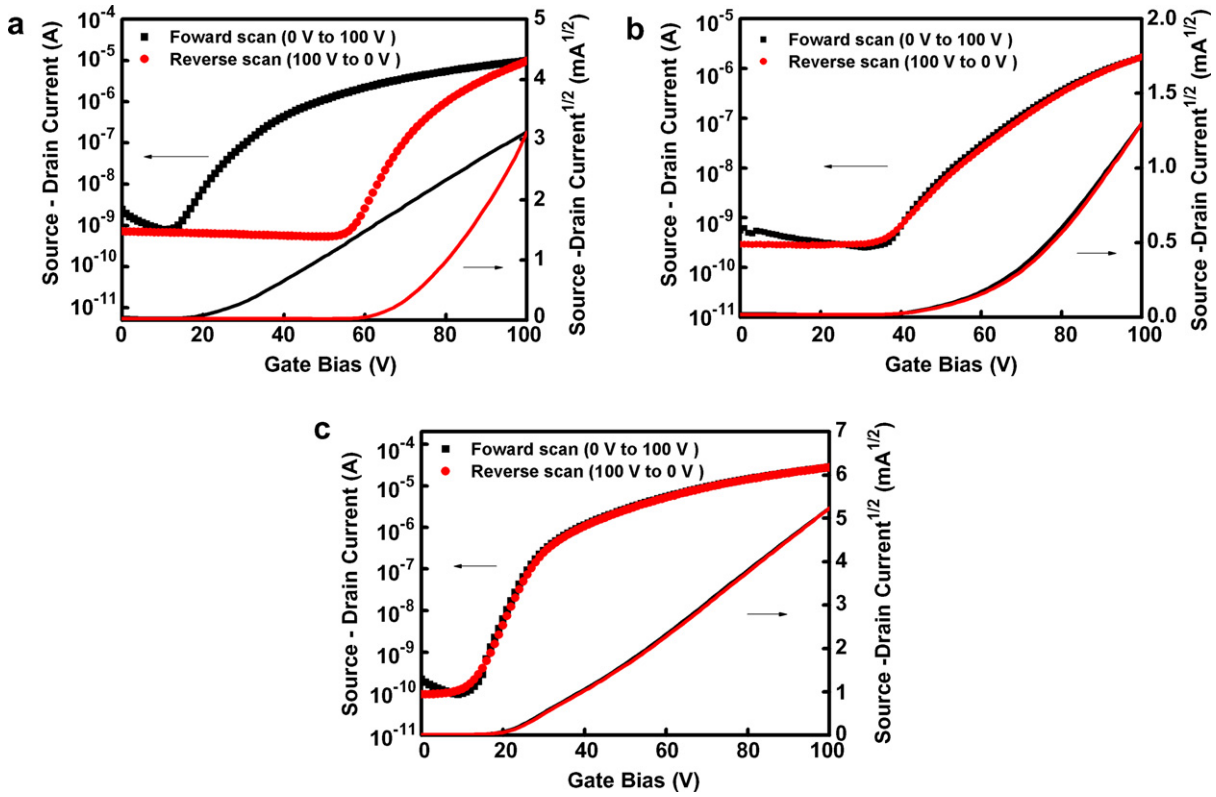

Fig. 3. Transfer (I_D–V_D) characteristics of C_{60} OFETs in saturation regime with (a) SiO_2 insulator in inert environment (passivated), (b) CYTOP™ insulator in ambient air, and (c) CYTOP™ insulator in inert environment (passivated). Both forward scan (filled rectangle) and reverse scan (filled circle) are exhibited.

The passivated device with SiO_2 insulator shows very large hysteresis of 42 V in the first scan. After the first scan, large threshold voltage shift more than 40 V was observed and hysteresis was reduced significantly to less than 5 V. Mobility was increased to 0.12 cm^2/V s at 100 s after the initial scan but slightly decreased after that point. This phenomenon can be understood by trap states at the interface between C_{60} and silicon dioxide or in the thin transporting layer near the interface. As the gate bias increases in the first scan, the trap states are filled with electrons. These trapped electrons induce the hysteresis in the first scan and large threshold voltage shift from the second scan. After the originally empty deep traps are filled, charges are trapped only in shallow states. As results, the threshold characteristics do not change much and the mobility is increased.

The device with CYTOP™ insulator in ambient air shows similar characteristics as the passivated device with SiO_2 insulator after the first scan. The device shows slowly decreasing mobility with time. The threshold voltage shift and hysteresis are maintained below 5 V until 20,000 s. Almost similar threshold voltage of the unpassivated device with CYTOP™ insulator and the passivated device with SiO_2 indicates that the trap density at the interface is almost the same between the two devices and the traps are filled by the exposure to the air in the CYTOP™ devices and by the first scan in the SiO_2 device. The source of decreasing mobility is understood by continuous generation of deep trap sites near the interface between the semiconductor and the insulators due to contact to ambient air including moisture and oxygen.

The passivated device with the CYTOP™ insulator shows most stable characteristics without any significant change up to 2000 s after initial scanning. It had very low hysteresis (<2 V) and low threshold voltage shift (<2 V) up to that time. Higher electron mobility and lower threshold voltage of the encapsulated device than un-encapsulated device indicates that the trap density in the passivated device with CYTOP™ insulator is very low and the traps at the interface or thin transporting layer near the interface are generated by the exposure of the device to ambient air.

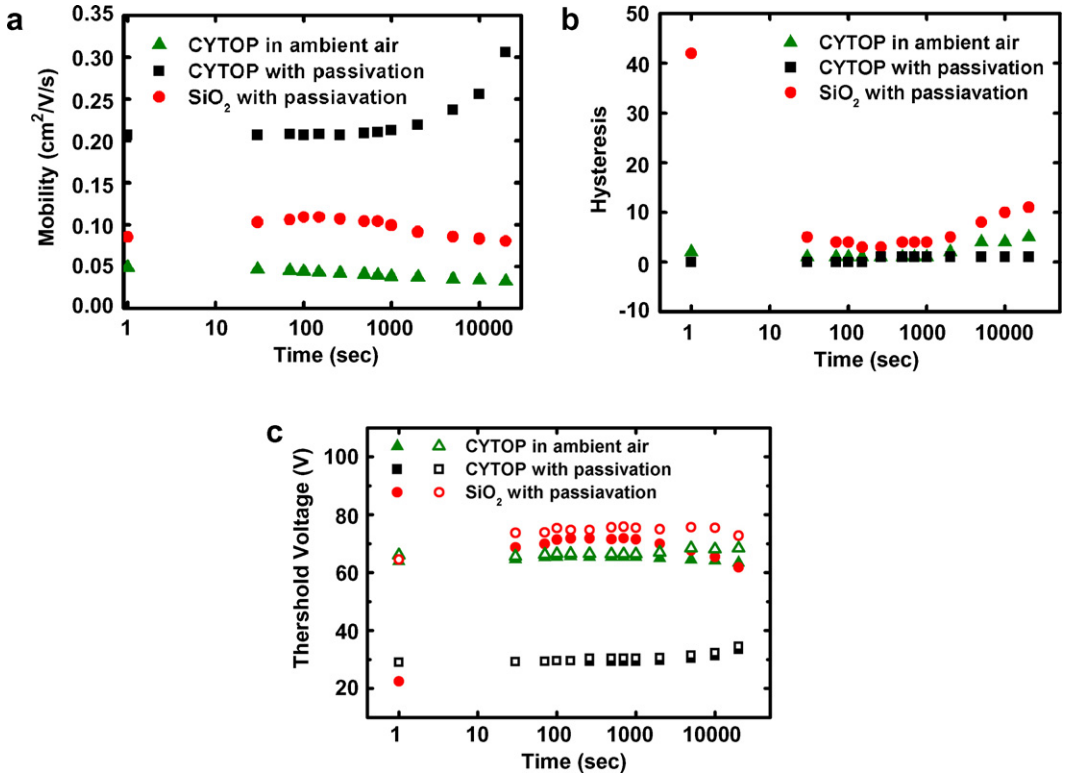

Fig. 4. Time dependence of (a) mobility, (b) hysteresis, and (c) threshold voltage for forward (filled symbols) and backward (open symbols) scan of encapsulated devices fabricated on SiO_2 (filled diamond), air exposed device on CYTOP (filled triangle) and encapsulated device on CYTOP (filled rectangle).

4. Conclusion

In summary, we demonstrated an air stable n-type C_{60} OFET by using a perfluorinated polymer, CYTOP™, as the gate dielectric layer. Replacing the gate dielectric material by SiO_2 resulted in no transistor action in ambient air. The device showed similar device characteristics as the encapsulated device fabricated on SiO_2 gate dielectric layer. This indicates that the interface trap density for electrons for n-type organic materials is significantly reduced by using the perfluorinated polymer as the gate dielectric layer even in ambient air. We believe that this finding is important for the realization of organic based complementary metal–insulator–semiconductor (CMOS) circuits.

Acknowledgements

This research was supported by a Grant (F0004071-2007-23) from the Information Display R&D Center, one of the 21st Century Frontier R&D Program funded by the Ministry of Commerce, Industry and Energy of the Korean Government.

References

[1] A.R. Murphy, M.J. Fréchet, Chem. Rev. 107 (2007) 1066 (review of FET materials).
[2] C.R. Newman, C.D. Friebie, D.A. da Silva Filho, J. Bredas, P.C. Ewbank, K.R. Mann, Chem. Mater. 46 (2004) 4436 (n-type review).
[3] S. Ando, J. Nishida, H. Tada, Y. Inoue, S. Tokito, Y. Yamashita, J. Am. Chem. Soc. 127 (2005) 5336 (n-type record).
[4] R.J. Chesterfiled, J.C. McKeen, C.R. Newman, C.D. Frisbie, J. Appl. Phys. 95 (2004) 6396.
[5] S. Kobayashi, T. Takenobu, S. Mori, A. Fujiwara, Y. Iwasa, Appl. Phys. Lett. 82 (2003) 4581.
[6] L.-L. Chua, J. Zaumseil, J.-F. Chang, E. C.-W. Ou, P. K.-H. Ho, H. Sirringhaus, R.H. Friend, Nature 434 (2005) 94.
[7] Z. Bao, A.J. Lovinger, J. Brown, J. Am. Chem. Soc. 120 (1998) 207.
[8] Y. Hosoi, D. Tsunami, H. Ishii, Y. Furukawa, Chem. Phys. Lett. 436 (2007) 139.
[9] H.Z. Chen, M.M. Ling, X. Mo, M.M. Shi, M. Wang, Z. Bao, Chem. Mater. 19 (2007) 816.

[10] Q. Tang, H. Li, Y. Liu, W. Hu, J. Am. Chem. Soc. 128 (2006) 14635.
[11] M.M. Ling, P. Erk, M. Gomez, M. Koenemann, J. Locklin, Z. Bao, Adv. Mater. 19 (2007) 1123.
[12] H.E. Katz, J. Johnson, A.J. Lovinger, W. Li, J. Am. Chem. Soc. 122 (2000) 7787.
[13] R.C. Haddon, A.S. Perel, R.C. Morris, T.T.M. Palstra, A.F. Hebard, R.M. Fleming, Appl. Phys. Lett. 67 (1995) 121.
[14] A. Tapponnier, I. Biaggio, P. Günter, Appl. Phys. Lett. 86 (2005) 12114.
[15] W.L. Kalb, T. Mathis, S. Haas, A.F. Stassen, B. Batlogg, Appl. Phys. Lett. 90 (2007) 092104.

Available online at www.sciencedirect.com
ScienceDirect
Organic Electronics 9 (2008) 487–494
Organic Electronics
www.elsevier.com/locate/orgel

1.54 μm Near-infrared photoluminescent and electroluminescent properties of a new Erbium (III) organic complex

Zhefeng Li [a,b], Jiangbo Yu [a], Liang Zhou [a,b], Hongjie Zhang [a,*], Ruiping Deng [a], Zhiyong Guo [a,b]

[a] *Key Laboratory of Rare Earth Chemistry and Physics, Changchun Institute of Applied Chemistry, Chinese Academy of Sciences, Changchun 130022, PR China*
[b] *Graduate School of the Chinese Academy of Sciences, Beijing 100064, PR China*

Received 17 January 2008; received in revised form 11 February 2008; accepted 11 February 2008
Available online 29 February 2008

Abstract

The crystal structure of $Er(PM)_3(TP)_2$ [PM = 1-phenyl-3-methyl-4-isobutyryl-5-pyrazolone, TP = triphenyl phosphine oxide] was reported and its photoluminescence properties were studied by UV–vis absorption, excited, and emission spectra. The Judd–ofelt theory was introduced to calculate the radiative transition rate and the radiative decay time of 3.65 ms for the $^4I_{13/2} \rightarrow {}^4I_{15/2}$ transition of Er^{3+} ion in this complex. The antenna-effect and phonon-assisted energy-transfer were introduced to discuss the intramolecular energy transfer from ligands to Er^{3+} ion. Based on this Er(III) complex as the emitter, the multilayer phosphorescent organic light emitting diode was fabricated with the structure of ITO/NPB 20 nm/$Er(PM)_3(TP)_2$ 50 nm/BCP 20 nm/AlQ 40 nm/LiF 1 nm/Al 120 nm, which shows the typical 1.54 μm near-infrared (NIR) emission from Er^{3+} ion with the maximum NIR irradiance of 0.21 $\mu W/cm^2$.

PACS: 78.60.Fi; 95.85.Jq; 89.75.Fb

Keywords: Electroluminescence; Near-Infrared; Erbium complex

1. Introduction

Recently, near-infrared OLEDs have attracted great attention in view of their potential applications in laser technology, optical sensors, and telecommunications [1–5]. Lanthanide based NIR OLEDs have got a great development since Curry and Gillin reported electroluminescence of the ErQ complex [4]. Several groups have demonstrated the application of lanthanide complexes and lanthanide-containing materials in NIR emitting electroluminescent diodes [1,5,6]. It is well known lanthanide ions show sharp optical-emission which is almost

* Corresponding author. Tel.: +86 431 85262127; fax: +86 431 85698041.
E-mail address: hongjie@ciac.jl.cn (H. Zhang).

1566-1199/$ - see front matter © 2008 Elsevier B.V. All rights reserved.
doi:10.1016/j.orgel.2008.02.010

independent of the environment surrounding the lanthanide ions because electrons in the 4f inner shell are shielded by the completely filled $5s^2$ and $5p^6$ outer electron shells. The characteristic emission of Er^{3+} is at 1.54 μm which coincides well with the wavelengths of the transmission-loss dispersion minima [7]. So, the development of Er(III) based near-infrared OLEDs is a challenging subject of significance from the standpoint of both basic science and technological applications.

It has long been known lanthanide emission need to be sensitized via antenna chromophore because their intra-configurational 4f–4f transitions are forbidden and absorptions are very weak. The organic ligands can be selected effectively to sensitize lanthanide ions and provide enough coordination sites to shield them from impurities in the surrounding matrix that may quench the luminescence.

The structure of pyrazolone-based ligands is similar to that of β-diketone ligands, which can enhance luminescent properties of Ln^{3+} ions well [8]. The ligand PM is easy to coordinate with Er^{3+} ion and form a stable complex with triphenyl phosphine oxide (TP) as the neutral ligand. These ligands have large conjugated structure and the isopropyl in PM ligand is the electron donor, all of which can improve the luminescent property of the complex. The single crystal of $Er(PM)_3(TP)_2$ is easy to obtain and shows good thermal stability, which is beneficial to thermal-evaporation in fabricating electroluminescent devices.

In this work, we report the structure of $Er(PM)_3(TP)_2$ and its optical properties containing UV–vis absorption, NIR luminescence, and excited spectra. By energy-transfer analysis, we found that the ligand PM can sensitize Er^{3+} ion well. With the aid of Judd–Ofelt theory [9,10], it is possible to calculate the radiative lifetime of Er^{3+} ion in this complex, and then obtain the quantum efficiency of corresponding transition. The crystal of this complex was used to fabricate the NIR electroluminescent devices, from which the 1.54 μm characteristic emission of Er^{3+} ion was detected. The devices show good performances of NIR irradiance at low voltage.

2. Experimental

2.1. Synthesis of the ligand PM

The pyrazolone-based ligand was synthesized according to the previous method [11].

2.2. Synthesis of $Er(PM)_3(TP)_2$

A mixture of PM (30 mmol), a solution of $ErCl_3$ (10 mmoL) in ethanol and TP (20 mmoL) in ethanol (200 mL) was stirred for several minutes until the solids were completely dissolved. This solution was treated with sodium hydroxide (30 ml of 1 mol/L solution), which resulted in the immediate formation of a pale precipitate, and refluxed for 5 h. The pale precipitate was then collected by vacuum filtration, washed with water, and dried under 80 °C to give the product as pale solid (11.7 g, 80%). Calcd. for $C_{78}H_{75}N_6O_8P_2Er$: C, 64.39; H, 5.16; N, 5.78. Found: C, 64.35; H, 5.29; N, 5.87%.

2.3. Fabrication of EL devices

All the organic layers were evaporated onto a precleaned ITO (with a sheet resistance of 12 Ω/sq) glass substrate with the speed of 0.05 nm/s under high vacuum ($\leqslant 3.0 \times 10^{-5}$ Pa). LiF and Al were evaporated in another vacuum chamber with different speed of 0.01 nm/s and 0.5 nm/s without being exposed to the atmosphere, respectively. The thicknesses of the deposited layers and the evaporation speed of individual materials were monitored in vacuum with quartz crystal monitors.

2.4. Apparatus

The optical absorption spectra were measured using a Carry-500 UV–vis spectrophotometer. PL and EL spectra were measured by a HORIBA Jobin Yvon FluoroLog-3 spectrofluorometer equipped with a 450 W Xe-lamp as an excitation source and a liquid-nitrogen-cooled R5509-72 PMT as detector (NIR-region). The luminescence decay curve of the emitting level of $Er(PM)_3(TP)_2$ was recorded under excitation at 355 nm with the third harmonic of a Spectra-physics Nd: YAG laser (using a 5 ns pulse width and 5 mJ of energy per pulse) as the exciting source, and the data were collected and analyzed with a LeCroy WaveRunner 6100 1 GHz Oscilloscope. The luminescence lifetime was calculated by Origin 7.0 software package. Current–irradiance–voltage properties were measured by using a computer-controlled Keithley 2400 sourcemeter and UDT Model 370 Photometer with a calibrated UDT Model 261 Germanium Detector (using an 850 nm filter to preclude the effect of visible light).

3. Result and discussion

3.1. Crystal structure of $Er(PM)_3(TP)_2$

Single crystal of complex $Er(PM)_3(TP)_2$ was obtained by recrystallization from its ethanol solution. The complex is so stable in air that it is still in the solid state over the course of several days. Thermal ellipsoid plots of $Er(PM)_3(TP)_2$ with the numbering scheme is displayed in Fig. 1a. The coordination geometry of the metal centers is best described as a distorted bicapped trigonal prism from the coordination site angles. Important experimental parameters for the structure determinations are tabulated in Table 1. The central Er^{3+} ion is coordinated by eight oxygen atoms from three PM ligands and two TP ligands. This coordination character accords with the chemical structure of the complex (Fig. 1b). Thus, the Er^{3+} ion exhibits a coordination number of eight. The average Er–O distance is 2.335 Å [2.244(2)–2.477(2) Å]. In the ligands rings, the average C–C and C–O bands are 1.403 [1.334(3)–1.533(2) Å] and 1.256 [1.244(4)–1.271(2) Å], respectively.

Table 1
Crystallographic data for $Er(PM)_3(TP)_2$

Empirical formula	$C_{78}H_{75}N_6O_8P_2Er$
Formula weight	1453.65
Temperature (K)	293(2)
Crystal system	Monoclinic
Space group	P2(1)/*n*
a (Å)	13.319(4)
b (Å)	23.141(7)
c (Å)	23.067(7)
Alpha = gamma (°)	90.000
Beta (°)	91.687(4)
Volume (Å^3)	7107(3)
Z	4
Calculated density (Mg/m^3)	1.359
Wavelength (Å)	0.71073
Absorption coefficient (mm^{-1})	1.286
Goodness-of-fit on F^2	0.949
R_1 [I > 2σ(I)]	0.0364
wR_2 [I > 2σ(I)]	0.0613
R_1 (all data)	0.0588
wR_2 (all data)	0.0661

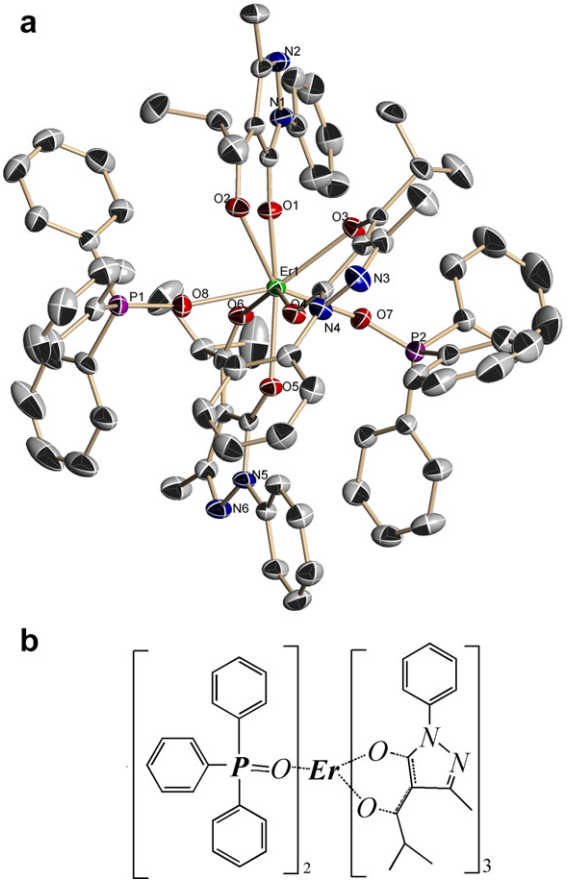

Fig. 1. (a) ORTEP plot for $Er(PM)_3(TP)_2$ with ellipsoids drawn at the 50% probability level. Hydrogen atoms were omitted for clarity. (b) Chemical structure of the complex.

3.2. Photoluminescence properties

The room-temperature absorption spectrum for $Er(PM)_3(TP)_2$ (in $CHCl_3$) is shown in Fig. 2. Below 400 nm the absorption bands of Er^{3+} ion are overlapped by the onset of the ligand absorption edge. In the 400–900 nm region, various f–f absorption bands of Er^{3+} are observed (originate from the $^4I_{15/2}$ ground state of Er^{3+}), they correspond to the energy states: $^4F_{7/2}$ (488 nm), $^2H_{11/2}$ (521 nm),

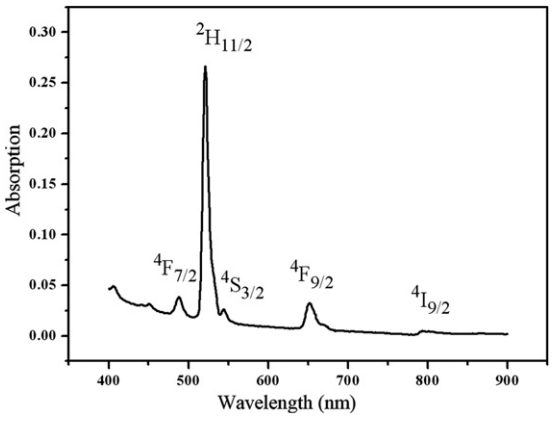

Fig. 2. Absorption spectrum of $Er(PM)_3(TP)_2$ in $CHCl_3$ solvent.

$^4S_{3/2}$ (544 nm), $^4F_{9/2}$(652 nm), $^4I_{9/2}$ (801 nm) [12]. All the observed absorption bands are numerically integrated to obtain the experimental line strength, and the values are summarized in Table 2. The excitation spectrum of $Er(PM)_3(TP)_2$ (monitored at 1538 nm) and the absorption spectra of the ligands (PM and TP) are shown in Fig. 3. As is clearly visible in Fig. 3, there are overlaps between the excitation band of the complex and the absorption bands of PM and TP, which indicates the typical sensitization of the Er^{3+} ion by the organic ligands PM, an antenna-effect, [13,14] and confirms that the Er^{3+} ion is surrounded by PM and TP in this complex [15]. In the excitation spectrum of $Er(PM)_3(TP)_2$, besides the broad band at 350 nm owing to the excitation of ligand PM, the sharp band at 377 nm and shoulder bands at 404, 448 nm can be assigning to the $^4G_{11/2}$, $^4F_{9/2}$, and $^4F_{3/2}$ excited state of Er^{3+} ion, respectively [16].

The emission spectrum of the $Er(PM)_3(TP)_2$ complex was obtained by direct excitation ($\lambda_{ex} = 350$ nm) of the ligands (shown in Fig. 3e). From the Fig. 3e, it can be found the broad emission band extending from 1450 to 1640 nm and centered at 1538 nm. The transition around 1540 nm is in the right position for telecommunications applications. The full width at half maximum (FWHM) of the emission spectrum is 70 nm, which is very wide and has potential for optical-amplification applications [17].

The lifetime of $Er(PM)_3(TP)_2$ was measured and shown in Fig. 4. Obviously, it is fit to a single exponential with a decay time of 3.3 μs at the emission wavelength 1538 nm. The nature lifetime of $^4I_{13/2} \rightarrow {}^4I_{15/2}$ transition in the $Er(PM)_3(TP)_2$ complex is calculated by Judd–Ofelt theory in Section 3.4.

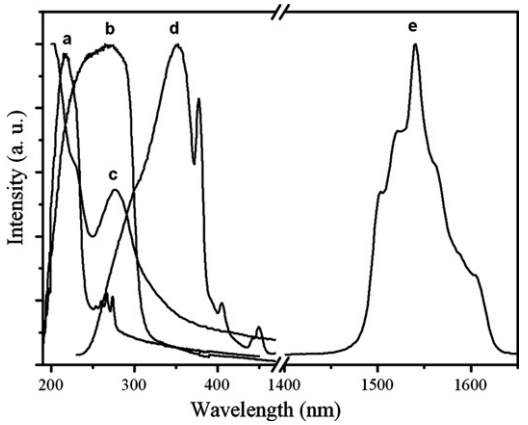

Fig. 3. The absorption spectra (thin films on quartz substrate) of ligands PM (a), TP (b), and complex $Er(PM)_3(TP)_2$(c), and the excitation (d, $\lambda_{em} = 1538$ nm) and emission (e, $\lambda_{ex} = 350$ nm) spectra of $Er(PM)_3(TP)_2$ single crystal at room-temperature.

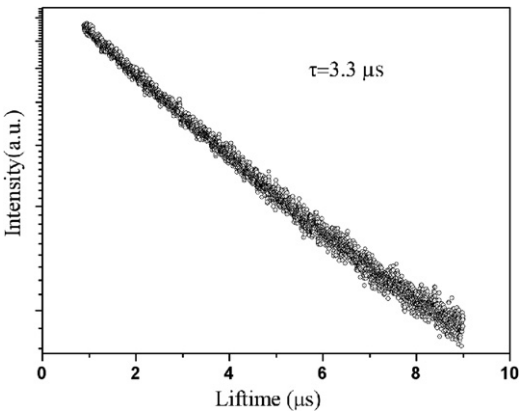

Fig. 4. The decay curve of $Er(PM)_3(TP)_2$ single crystal (emission band at 1538 nm).

3.3. Energy-transfer

In general, direct excitation on these transitions is difficult due to the low optical cross-section of lanthanide ions arising from the forbidden nature of the 4f–4f transitions. Consequently, an effort to endow the Ln^{3+} ions with high efficiency luminescence is employing strong light-harvesting ligands that can sensitize the metal ion by intramolecular energy-transfer (a mechanism-"antenna effect"). The acceptor levels of the lanthanide ions are

Table 2
Measured and calculated line strengths of Er^{3+} ion in $Er(PM)_3(TP)_2$complex (all transitions are from $^4I_{15/2}$)

S' L' J'	λ (nm)	S_{mea} ($\times 10^{-20}$ cm^2)	S_{cal} ($\times 10^{-20}$ cm^2)
$^4F_{7/2}$	488	3.7625	3.7536
$^2H_{11/2}$	521	44.8358	44.8358
$^4S_{3/2}$	544	0.6894	0.9728
$^4F_{9/2}$	652	5.7861	5.6527
$^4I_{9/2}$	801	0.7951	1.2133

rms$\Delta S = 0.3017 \times 10^{-20}$ cm^2.

important in determining the energy-transfer mechanisms from organic ligands to lanthanide ion. A choice of potential accepting levels can be made based on the energy difference between donor (sensitizer) and acceptor level (Ln^{3+}), which should not be too large for sufficient spectral overlap [18]. The selection rules for energy-transfer from sensitizer to the Ln^{3+} $^{(2S+1)}L_J$ 4f levels are $|\Delta J| = 2, 4, 6$ for the dipolar and multipolar energy-transfer (Förster type)[19] and $|\Delta J| = 0$, 1 (but forbidden for $J = J' = 0$) for the electron exchange mechanism (Dexter type) [20]. In this work, energy-transfer takes place from the triplet excited state, because the singlet state of the ligands are depopulated very fast to the triplet state and the Dexter type of transfer is in general the dominant mechanism [21,22]. The triplet state energy level (T_1) of ligand PM is 21460 cm^{-1} by examining the phosphorescence spectrum of the $Gd(PM)_3(TP)_2$ complex in 5×10^{-4} mol/L DMF solution at 77 K [23,24] whereas the $^4F_{7/2}$ energy level of Er^{3+} ion is 20420 cm^{-1} would be energetically appropriate, and is allowed by the Förster mechanism ($\Delta J = 4$ with respect to the $^4I_{15/2}$ ground state). Dexter energy-transfer is allowed only to the low-lying $^4I_{13/2}$ level ($\Delta J = 1$ from the ground state) at 6610 cm^{-1}, where the energy-transfer rate would be very slow, because of the large gap between donor and acceptor energy levels. However, according to the "phonon-assisted energy-transfer" pointed out by Güdel and coworkers [25] energy transfer can involve vibrational as well as electronic excitation of the acceptor organic ligands. So, the energy-transfer process here could be reasonable and the organic ligands could sensitize the Er^{3+} ion.

3.4. Judd–Ofelt analysis

Judd–Ofelt theory is one of the successful theories for estimating the magnitude of the forced electric-dipole transition of rare-earth ions. From the RT absorption spectrum of $Er(PM)_3(TP)_2$, we can find the optical absorption corresponds to electron transitions from the ground $^4I_{15/2}$ multiplet to the upper energy states of Er^{3+}. Five Er^{3+} ion absorption bands in the spectrum were selected to determine the phenomenological oscillator strength parameters. The band positions, along with assignments in the absorption spectrum, are shown in Table 2. The measured absorption line strengths, S_{mea}, from the ground $^4I_{15/2}$ manifold ($J = 15/2$) to the excited J' manifold can be obtained using the following Eq. (1) [26]

$$\int \mathrm{OD}(\lambda)\mathrm{d}\lambda = \frac{1}{Ln10} N_{\mathrm{Er}} L \times \frac{8\pi^3 e^2 \bar{\lambda}}{3ch(2J+1)n}\left[\frac{(n^2+2)^2}{9}\right] S_{\mathrm{mea}} \quad (1)$$

where $\mathrm{OD}(\lambda)$ is the absorption coefficient at wavelength λ; $\bar{\lambda}$ is the mean wavelength of the specific absorption band; N_{Er} is the concentration of Er^{3+} ($N_{\mathrm{Er}} = 3.01 \times 10^{17}$ cm^{-3}), L is the optical length ($L = 1$ cm); e, h, and c are the electron charge, Planck's constant, and velocity of light, respectively; and n is the refractive index of the chloroform solution ($n = 1.446$).

According to Judd–Ofelt theory, the line strength for electric-dipole (ED) transition between the initial J manifold $|(S,L)J\rangle$ and terminal J' manifold $|(S',L')J\rangle$ can be expressed by following Eq. (2) [27]

$$S = \sum_{t=2,4,6} \Omega_t |\langle (S,L)J \| U^t \| (S',L')J' \rangle|^2 \quad (2)$$

where $\langle \| U^{(t)} \| \rangle$ are the doubly reduced matrix elements corresponding to the J–J' transition. The matrix elements only depend on the angular momentum of the Er^{3+} ion states and are essentially independent of the ion's environment [16]. The oscillator strength parameters Ω_t (t = 2, 4, 6) are independent of electronic quantum numbers for the ground configuration of the Er^{3+} ion. Using Eq. (1), the experimental oscillator strength S_{mea} for the electric-dipole transition can be obtained. Then, the parameters Ω_t can be derived by least-squares fitting of Eq. (2): $\Omega_2 = 54.5998 \times 10^{-20}$ cm^2, $\Omega_4 = 2.4004 \times 10^{-20}$ cm^2, $\Omega_6 = 4.4661 \times 10^{-20}$ cm^2.

The interpretation of the physical meaning of the phenomenological oscillator strength parameters remains controversial. Ω_2 is usually related to the degree of covalence in the lanthanide-first-coordination-shell interaction [28]. The large Ω_2 value of $Er(PM)_3(TP)_2$ indicates the presence of covalent bonding between the Er^{3+} ions and the surrounding ligands [29].

Using these parameters, we recalculate the transition line strengths S_{cal} of the absorption bands using Eq. (2). The calculated line strengths are listed in Table 2. The rms (root-mean-square) deviation between the experimental and the calculated line strengths is defined by Eq. (3).

$$\mathrm{rms}\Delta S = \sqrt{\sum_{i=1}^{N} (S_{\mathrm{mea}} - S_{\mathrm{cal}})^2 / (N-3)} \quad (3)$$

where N is the number of absorption bands analyzed. A measurement of the relative error is given by the rms error $= \mathrm{rms}\Delta S/\mathrm{rms}S \times 100\%$, where $\mathrm{rms}S = (\sum S_{\mathrm{men}}^2/N)^{1/2}$. The rms error of the fitting is 1.4%, which indicates that the fitting results are in good agreement with the experimental data. The parameters Ω_t are used to determine the radiative transition rate A from the initial state J ($^4I_{13/2}$) to the terminal state J' ($^4I_{15/2}$), here $A = A_{\mathrm{ed}} + A_{\mathrm{md}}$, A_{md} is the magnetic transition rate, and the value was calculated as $3.02 \times 10^{-7}\ \mathrm{s}^{-1}$, which can be ignored because it is very small. So, $A = A_{\mathrm{ed}}$ can be calculated using Eq. (4) [30]

$$A = \frac{64\pi^4 e^2}{3h(2J+1)\bar{\lambda}^3}\frac{n(n^2+2)^2}{9} \times \sum_{t=2,4,6}\Omega_t|\langle(S,L)J\|U^t\|(S',L')J'\rangle|^2 \quad (4)$$

where n is the refractive index, and the value of $|\langle[^4I_{13/2}]\|U^t\|[^4I_{15/2}]\rangle|$ are calculated based on the intermediate-coupling wave functions obtained from the energy level fitting. The radiative lifetime for the excited $^4I_{13/2}$ state of Er^{3+} ion is determined from the radiative transition rate A using Eq. (5)

$$\tau_R = \frac{1}{A} \quad (5)$$

The radiative quantum efficiency is defined as the following $\eta_e = \tau/\tau_R$, where τ is the fluorescence lifetime. The calculated radiative lifetime and quantum efficiency are listed in Table 3. The calculated radiative decay time of 3.65 ms for the $^4I_{13/2} \rightarrow {}^4I_{15/2}$ transition of Er^{3+} ion in this complex is in excellent agreement with the reported value of 4 ms in Er organic complexes [17]. With the value for the radiative transition rate and corresponding emission spectrum, the stimulated emission cross-section σ_e is calculated using Eq. (6) [31]

$$\sigma_e = \frac{A\lambda^2}{4\pi^2 n^2 \Delta v} \quad (6)$$

where Δv is the frequency FWHM, and λ is the wavelength of the emission peak. The calculated emission cross-section of $^4I_{13/2} \rightarrow {}^4I_{15/2}$ is shown in Table 3.

3.5. Electroluminescent properties

Light emitting diodes containing $Er(PM)_3(TP)_2$ complex were prepared to characterize the EL device properties. All the current–voltage and irradiance–voltage curves for different devices are shown in Fig. 5. A device with the structure ITO/NPB 40 nm/$Er(PM)_3(TP)_2$ 60 nm/LiF 1 nm/Al 120 nm (A) was made using the NPB as the hole transport layer and the $Er(PM)_3(TP)_2$ complex as the emission layer. LiF layer is the insulating medium, which can reduce the barrier height for electron injection and then get a reduction of the driving voltage [32,33]. In Fig. 5, it is shown that device A can produce the maximum irradiance of 0.08 μW/cm^2 at the current density of 123 mA/cm^2 (21 V). To decrease the driving voltage and improve the whole performances of device, an electron trans-

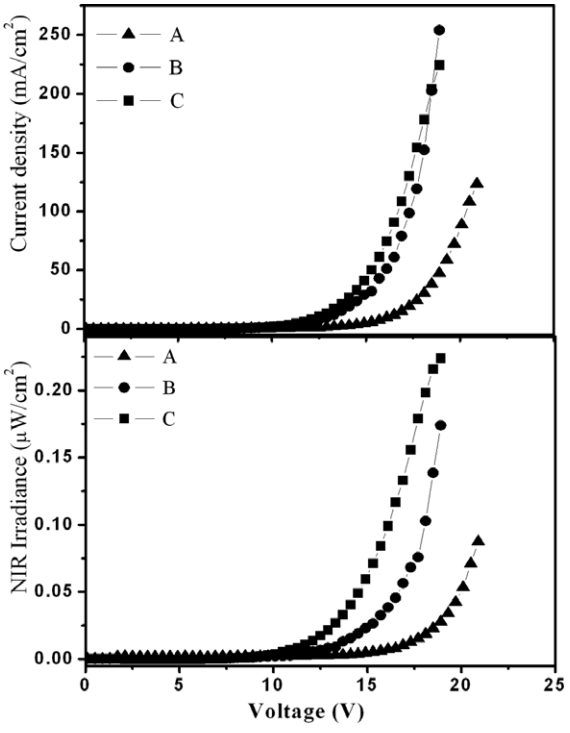

Fig. 5. Current density–voltage curves and NIR irradiance–voltage curves of device A, B, and C.

Table 3
Calculated radiative lifetime of the metastable $^4I_{13/2}$ level, the radiative transition rate, the stimulated emission cross-section, and the radiative quantum efficiency

Transition	λ (nm)	A (s^{-1})	τ_R (ms)	σ_e ($\times 10^{-21}$ cm^2)	η_e (%)
$^4I_{13/2} \rightarrow {}^4I_{15/2}$	1538	273.7	3.65	3.27	0.091

port layer AlQ was added into device B: ITO/NPB 20 nm/$Er(PM)_3(TP)_2$ 50 nm/AlQ 40 nm/LiF 1 nm/Al 120 nm. Compared with device A, device B shows higher NIR irradiance up to 0.17 μW/cm^2. At the same time, the current density of device B attained to 254 mA/cm^2 (19 V). For device C, we introduced another layer of BCP, which is usually acting as the hole-block layer in the OLEDs and helpful to confining electrons and excitons within the heterostructure emissive region and then improving characteristics of devices [34]. So device C has such structure: ITO/NPB 20 nm/$Er(PM)_3(TP)_2$ 50 nm/BCP 20 nm/AlQ 40 nm/LiF 1 nm/Al 120 nm. In fact, just as we anticipated, device C exhibited the maximum NIR irradiance of 0.21 μW/cm^2 (see Fig. 5). However, in comparison with device B, its maximum current density slightly decreases to 224 mA/cm^2 at 19 V. Therefore, we can safely say that the characteristics of device C got big improvement owing to two reasons: firstly, carriers are well confined in the emitting layer and become more balanced; secondly, reducing the total current density of device makes the device more stable and perform better. Although different thickness of the emitting layers were selected to improve the performance of the device, for example being 40 or 60 nm, these devices unfortunately show poorer performance than that of device C.

In the NIR-region, device C always shows a broad emission band peaks at 1538 nm at the different applied voltages (shown in Fig. 6), which originates from the characteristic $^4I_{13/2} - {}^4I_{15/2}$ transition of Er^{3+} ion. For the NIR EL mechanism of the Er complex based NIR devices, we believe that with the increasing of applied voltage, electrons and holes are respectively injected from the low and the high work function metal electrode into the lowest unoccupied and the highest occupied electronic levels of the organic material present at the metal–organic interface, and are respectively transported from the electron transport layer and the hole transport layer to the emission layer. Then, electrons and holes are recombined to lead to the formation of excitons, which will excite the electrons from the ground 4f states to the higher 4f excited states of Er^{3+} ion. Finally, the NIR-EL emission results from the electrons in the excited 4f state ($^4I_{13/2}$) of the Er^{3+} ion relaxing radiatively to the 4f ground state ($^4I_{15/2}$).

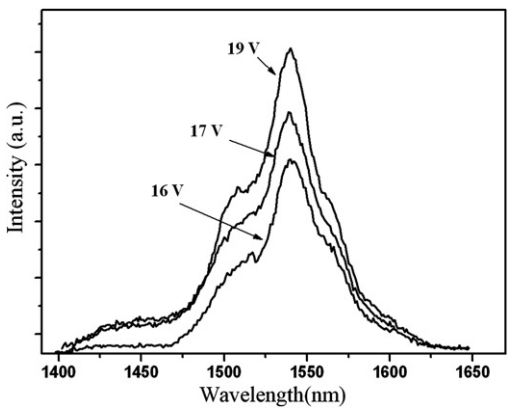

Fig. 6. EL spectrum of device C at the applied voltages of 16, 17, and 19 V.

4. Conclusions

We have conducted detail analyses of the crystal structure of the $Er(PM)_3(TP)_2$ complex. Investigating its optical properties, we found the energy-transfer from ligands to center Er^{3+} ion is possible and the characteristic emission from Er^{3+} ion is detected at 1538 nm. The FWHM of this emission is 70 nm: such a broad spectrum enables a wide gain bandwidth for optical-amplification. Judd–Ofelt theory calculation has been conducted successfully to obtain the radiative lifetime from the $^4I_{13/2}$ manifold is about 3.65 ms. The time-resolved luminescence spectrum shows monoexponential decay with a lifetime of 3.3 μs for Er^{3+} ion. The optimal device with the structure of ITO/NPB 20 nm/$Er(PM)_3(TP)_2$ 50 nm/BCP 20/AlQ 40/LiF 1 nm/Al 120 nm by using the Er complex as the emitting layer shows a strong NIR irradiance of 0.21 μW/cm^2 at 19 V. To the best of our knowledge, this is one of the best values reported of NIR OLEDs based on Erbium (III) complexes as emitters.

Acknowledgements

The authors are grateful to the financial aid from the National Natural Science Foundation of China (Grant Nos. 20490210, 206301040, 20602035 and 20771099) and the MOST of China (Grant Nos. 2006CB601103, 2006DFA42610).

References

[1] J.C. Ostrowski, K. Susumu, M.R. Robinson, M.J. Therien, G.C. Bazan, Adv. Mater. 15 (2003) 1296.

[2] L.H. Slooff, A. Polman, F. Cacialli, R.H. Friend, G.A. Hebbink, F.C.J.M. van Veggel, D.N. Reinhoud, Appl. Phys. Lett. 78 (2001) 2122.
[3] H. Suzuki, Appl. Phys. Lett. 76 (2000) 1543.
[4] R.J. Curry, W.P. Gillin, Appl. Phys. Lett. 75 (1999) 1380.
[5] T.-K. Kang, B.S. Harrison, T.J. Foley, A.S. Knefely, J.M. Boncella, J.R. Reynolds, K.S. Schanze, Adv. Mater. 15 (2003) 1093.
[6] (a) Joo Han Kim, Paul H. Holloway, Adv. Mater. 17 (2005) 91;
(b) Yuichiro Kawamura, Yuji Wada, Yasuchika Hasegawa, Mitsunori Iwamuro, Takayuki Kitamura, Shozo Yanagida, Appl. Phys. Lett. 74 (1999) 3245.
[7] A. Polman, J. Appl. Phys. 82 (1997) 1.
[8] (a) Xicum Gao, Hong Cao, Chunhui Huang, Shigeo Umitani, Guangqiang Chen, Peng Jiang, Synth. Met. 99 (1999) 127;
(b) Simone Capecchi, Olivier Renault, Dae-Gyu Moon, Mounir Halim, Mark Etchells, Peter J. Dobson, Oleg V. Salata, Victor Christou, Adv. Mater. 12 (2000) 1591.
[9] B.R. Judd, Phys. Rev. 127 (1962) 750.
[10] G.S. Ofelt, J. Chem. Phys. 37 (1962) 511.
[11] Zhe Feng Li, Liang Zhou, Jiang Bo Yu, Hong Jie Zhang, J. Phys. Chem. C 111 (2007) 2295.
[12] G.A. Kunmar, Richard E. Riman, Chem. Mater. 17 (2005) 5130.
[13] V. Bekiari, P. Lianos, Adv. Mater. 10 (1998) 1455.
[14] N. Sabbatini, M. Guardigli, J.M. Lehn, Coord. Chem. Rev. 123 (1993) 201.
[15] H.R. Li, H.J. Zhang, L.S. Fu, et al., Chem. Mater. 14 (2002) 3651.
[16] W.T. Carnall, P.R. Fields, K. Rajnal, J. Chem. Phys. 49 (1968) 4424.
[17] L.H. Slooff, A. Polman, J. Appl. Phys. 83 (1998) 497.
[18] M. Latva, H. Takalo, V.M. Mukkala, C. Matachescu, J.C. Rodriguez Ubis, J. Kankare, J. Lumin. 75 (1997) 149.
[19] T. Förster, Disc. Farad. Soc. 27 (1959) 7.
[20] D.L. Dexter, J. Chem. Phys. 21 (1953) 836.
[21] F.R. Goncalves e Silva, O.L. Malta, C. Reinhard, H.U. Güdel, C. Piguet, J.E. Moser, J.C.G. Bünzli, J. Phys. Chem. A 106 (2002) 1670.
[22] G.F. de Sá, O.L. Malta, C. de Mello Donegá, A.M. Simas, R.L. Longo, P.A. Santa-Cruz, E.F. da Silva, Coord. Chem. Rev. 196 (2000) 165.
[23] G. Crosby, R. Whan, J. Chem. Phys. 34 (1961) 743.
[24] W. Sager, N. Filipescu, J. Phys. Chem. 69 (1965) 1092.
[25] C. Reinhard, H.U. Güdel, Inorg. Chem. 41 (2002) 1048.
[26] G.H. Jia, C.Y. Tu, J.F. Li, Z.Y. You, Z.J. Zhu, B.C. Wu, Inorg. Chem. 45 (2006) 9326–9331.
[27] G.F. Wang, W.Z. Chen, Z.B. Li, Z.S. Hu, Phys. Rev. B 60 (1999) 15469.
[28] B.R.J. Judd, Chem. Phys. 70 (1979) 4830.
[29] C. Koeppen, S. Yamada, G. Jiang, A.F. Garito, J. Opt. Soc. Am. B 14 (1997) 155.
[30] X.Y. Chen, M.P. Jensen, G.K. Liu, J. Phys. Chem. B 109 (2005) 13991–13999.
[31] Li Ning Sun, Hong Jie Zhang, Lian She Fu, et al., Adv. Funct. Mater. 15 (2005) 1041.
[32] T. Mori, H. Fujikawa, S. Tokito, Y. Taga, Appl. Phys. Lett. 73 (1998) 2763–2765.
[33] M.G. Mason, C.W. Tang, L.S. Hung, P. Raychaudhuri, J. Madathil, D.J. Giesen, J. Appl. Phys. 89 (2001) 2756–2765.
[34] Jonathan G.C. Veinot, Tobin Marks, J. Acc. Chem. Res. 38 (2005) 632–643.

Available online at www.sciencedirect.com
ScienceDirect
Organic Electronics 9 (2008) 495–500
Organic Electronics
www.elsevier.com/locate/orgel

Resistive switching in Rose Bengal and other Xanthene molecules is a molecular phenomenon

Arup K. Rath, Amlan J. Pal *

Department of Solid State Physics, Indian Association for the Cultivation of Science, Kolkata, West Bengal 700 032, India

Received 10 December 2007; received in revised form 13 February 2008; accepted 13 February 2008
Available online 29 February 2008

Abstract

There has been a debate on the mechanism of resistive switching in Rose Bengal and other Xanthene class molecules. While some authors proposed that the switching was due to an oxide layer at the Rose Bengal/Aluminum interface, some inferred the switching as an extrinsic effect like filament formation. We show results from Rose Bengal and other Xanthene class molecules on doped Si. Conductance switching in such monolayers induced by Pt/Ir tip of a scanning tunneling microscope (STM) in a non-contact mode shows that resistive switching in these molecules, initially reported by us in 2003 (in thin films), is indeed a molecular phenomenon.

PACS: 73.61.Ph; 82.37.Gk; 85.35.−p; 85.65.+h

Keywords: Conductance switching; Memory phenomenon; Molecular memory

1. Introduction

From the beginning of the current decade, electrical bistability in organic molecules [1–3] has attracted much attention due to their applications as memory elements. In a bistable device, current–voltage characteristics depend on the preceding voltage pulse. In other words, current at a voltage can be used to "read" the state of a device for memory applications [4–12]. In 2003, we introduced Rose Bengal and other molecules with identical backbone in the Xanthene class that exhibited reproducible electrical bistability at room temperature [4–6]. The bistability in these materials is important due to (1) large ratio between the conductivities of the two states and (2) associated memory phenomenon for read-only and random-access memory (ROM and RAM, respectively) applications. We proposed that the high-conducting state in Rose Bengal arose due to a change in its conjugation via electroreduction or a twist between its two planes [4–6]. Formation of metal filaments through redox reaction is a general possibility in metal/organic/metal structures [13–16]. In the former cases, resistive switching in Rose Bengal can be termed as a molecular phenomenon. If metal filaments result the high-state, the switching cannot be termed as a molecular one and hence can never

* Corresponding author. Tel.: +91 33 24734971; fax: +91 33 24732805.
E-mail address: sspajp@iacs.res.in (A.J. Pal).

1566-1199/$ - see front matter © 2008 Elsevier B.V. All rights reserved.
doi:10.1016/j.orgel.2008.02.013

be extended to achieve a high-density memory elements (*a bit per molecule*). It is hence important to know the mechanism of resistive switching involved in Rose Bengal and other organic materials.

In Rose Bengal films on ZnO with Al as the top electrode, the observed electrical bistability has been explained to be due to a thin oxide layer at the interface inferring that the switching effect is completely extrinsic and not dependent on the molecular layer [16]. Since the switching mechanism is still under discussion, we aimed to take a different approach – an approach to exclude some of the proposed mechanisms. In doing so, we chose a device configuration without a possibility of oxide formation. In addition, to exclude formation of metal filaments through redox reaction, we used metals that cannot be oxidized under the voltage range of measurement. We hence deposited a monolayer of the materials on doped Si wafers and measured current–voltage (I–V) characteristics with Pt/Ir tip of a STM in a non-contact mode. Furthermore, we chose different organic materials (with a similar backbone and different substitutes) to know if the observed resistive switching truly depends on the material that is being probed.

2. Experimental

We selected disodium salts of Fluorescein, 2′,4′,5′,7′-tetraiodo Fluorescein (Erythrosin B), 2′,4′,5′,7′-tetrabromo Fluorescein (Eosin Y), 4,5,6,7-tetrachloro-2′,4′,5′,7′-tetraiodo Fluorescein (Rose Bengal), and 4,5,6,7-tetrachloro-2′,4′,5′,7′-tetrabromo Fluorescein (Phloxine B). The materials have identical backbone but varied functional substitutes. Due to the $-O^-$ and $-COO^-$ groups, we could electrostatically adsorb the materials via layer-by-layer (LbL) electrostatic assembly with poly(allyl amine hydrochloride) (PAH) as a polycation. Monolayer of the materials was grown on silicon wafers. The polished Si(1 1 1) wafers were phosphorus doped (N-type) with a resistivity of 5–10 mΩ cm. To obtain a monolayer via electrostatic assembly, a deprotonated Si substrate was first dipped in the polycationic bath (pH 6.5) for 15 min followed by thorough rinsing in deionized water baths. The Si substrate was then dipped in a bath containing the desired material (5 mM) for 15 min followed by the same rinsing protocol in a separate set of water baths. This resulted in a monolayer of the material due to electrostatic binding through its $-O^-$ and $-COO^-$ moieties. The dipping sequence was repeated to obtain multilayer films (on quartz) to record electronic absorption spectra. Monolayer of Rose Bengal and other molecules were characterized with a Pt/Ir tip of a STM (Nanosurf easyScan2) controller in a non-contact (tunneling) mode under ambient condition. Pt/Ir tip of the STM was lowered till a current of 0.5 nA was achieved at 0.5 V. The tip position was then fixed to record topographic image of the monolayer and to measure a set of I–V characteristics. Bias, applied with respect to the base electrode, was swept to both directions.

3. Results and discussion

We have characterized monolayers of different organic molecules. The monolayers were deposited via LbL film deposition technique with PAH as the polycation. To confirm formation of a monolayer, we recorded electronic absorption spectra of the films on quartz substrates. Since the value of absorbance for a monolayer should be low, we monitored the deposition process during multilayer formation. Electronic absorption spectra of PAH/Rose Bengal LbL films after deposition of different number of bilayers are shown in Fig. 1. All the spectra show a peak at 572 nm – the intensity of the band increasing with number of bilayers deposited. The band is very close to that of Rose Bengal solution (570 nm). The inset of Fig. 1 shows the absorbance of the film at peak wavelength as a function of number of Rose Bengal monolayers. A linear plot through the origin with a slope of unity confirms that the molecules were adsorbed uniformly during

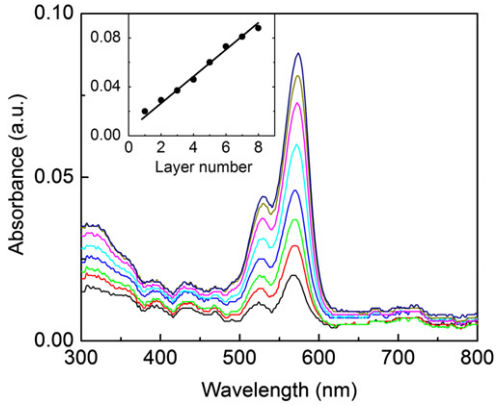

Fig. 1. Electronic absorption spectra of LbL films of PAH/Rose Bengal for different number of LbL bilayers. Inset shows absorbance at 572 nm as a function of number of bilayers.

deposition of first and every monolayer via LbL assembly. The LbL technique furthermore assures that only a monolayer of Rose Bengal was deposited in every layer. Topographic STM image of a bare wafer and a monolayer of Rose Bengal are presented in parts (a) and (b) of Fig. 2, respectively. A clear difference between the images is certainly due to deposition of Rose Bengal during electrostatic adsorption via the binding through $-O^-$ and $-COO^-$ groups of Rose Bengal with the $-NH_3^+$ moieties of PAH.

Fig. 3 shows *I–V* characteristics of Rose Bengal monolayer in two sweep directions. Multiple scans at the same point on the film for each of the sweep directions are shown in the figure to depict the level of stability. The plot shows that the current exhibits a jump at a suitable positive bias. Current at a voltage during the sweep from a positive bias is always higher than that during the sweep towards a positive voltage. The molecules lose its higher level of conductivity at around −0.5 to −1.0 V during the voltage-sweep to a negative bias. No switching occurs in the negative bias regime. The magnitude of current through the monolayer is in general high due to the parameters used during the approach of the STM tip. Also, the saturation in current at 100 nA is due to the limitation of the STM instrument used in recording *I–V* characteristics.

Memory phenomenon of the molecules has also been established. After application of suitable voltage pulse to induce either of the states, we have

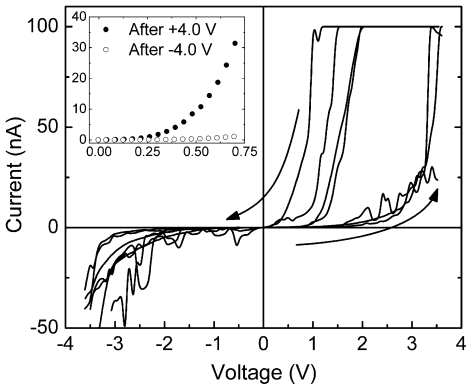

Fig. 3. Current–voltage characteristics of a monolayer of Rose Bengal for two sweep directions of applied voltage. Multiple scans at the same point is shown in the figure. Arrows represent the direction of voltage-sweep. Inset shows *I–V* plots in a small voltage window (from 0 to 0.7 V) after application of +4.0 and −4.0 V pulses (width = 2 ms), which have induced a high- and a low-conducting state, respectively.

measured *I–V* characteristics in a small (positive) voltage window. Inset of Fig. 3 shows that a +4.0 V pulse could induce a high-conducting state. Similarly, a −4.0 V pulse reinstated the initial low-state. The *I–V* plots between 0 and 0.7 V show clear difference between the states. In other words, the *I–V* plots have depended on nature of the preceding voltage pulse evidencing memory phenomenon of the molecules.

The bistability in a monolayer is reproducible over multiple voltage scans and also at different

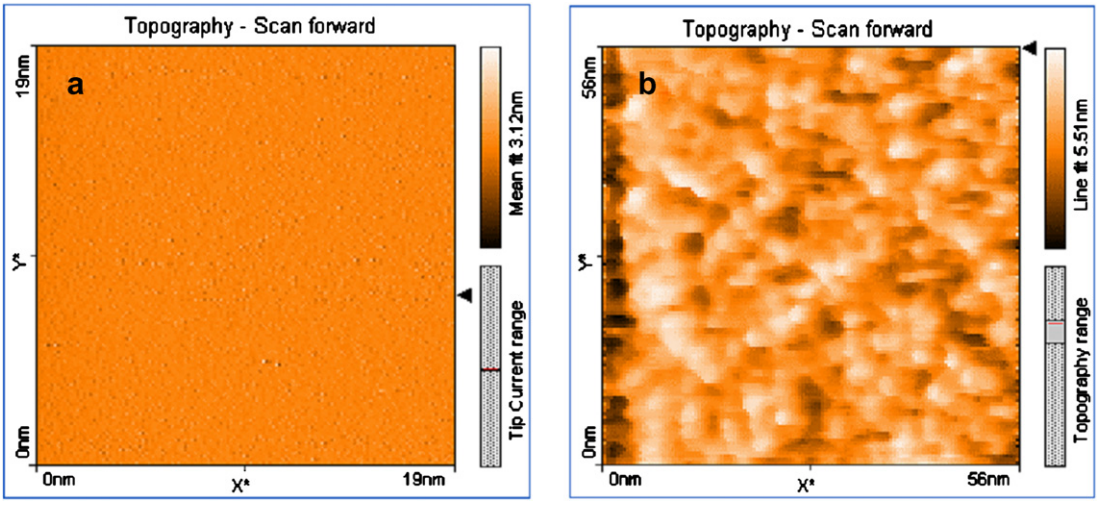

Fig. 2. Topographic STM image of (a) a bare Si substrate and (b) a monolayer of Rose Bengal on Si. The STM measurements were recorded after an approach in a constant current mode (0.5 nA at 0.5 V). The displayed scan area is 19 nm × 19 nm and 56 nm × 56 nm, respectively.

points on the monolayer film. Fig. 4, displaying results from different points on the film, shows that current at a voltage depends on the direction of voltage-sweep. The two states are clearly distinguishable when results from five points are compared. The observed resistive switching and associated memory phenomena in the present configuration (Rose Bengal between doped Si and Pt/Ir tip) are itself of interest. Since none of the involved metals can be oxidized in the voltage range of our measurement, the switching shown in Fig. 4 could not be due to metal filament formation though redox reaction. Again the measurements were carried in a non-contact mode; hence the question of filament formation via diffusion during metal deposition does not arise. The results further rule out any role of oxide layers in the resistive switching of Rose Bengal. Moreover, since we characterized only a monolayer of Rose Bengal on doped Si(1 1 1) wafers deposited via electrostatic assembly, progressive switching along the depth of the film does not occur.

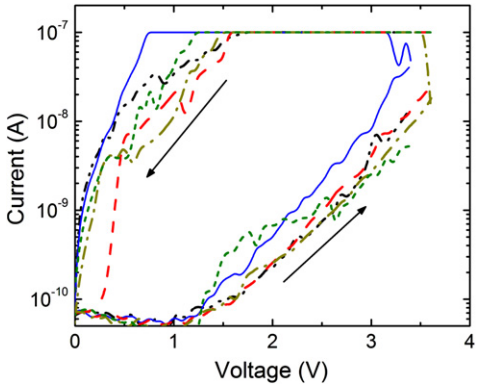

Fig. 4. Forward bias section of current–voltage characteristics of a monolayer of Rose Bengal for two different voltage-sweep directions. Results from five different points on the film are shown as different symbols. Arrows represent the direction of voltage-sweep.

As control experiments, we measured *I–V* characteristics of PAH monolayer. The *I–V* due to 1–1.5 nm native SiO_2 on Si was also measured without depositing any film. In both the cases, the *I–V* characteristics did not show any trace of resistive switching. Results presented in Figs. 3 and 4 hence show that the observed switching in Rose Bengal mono-

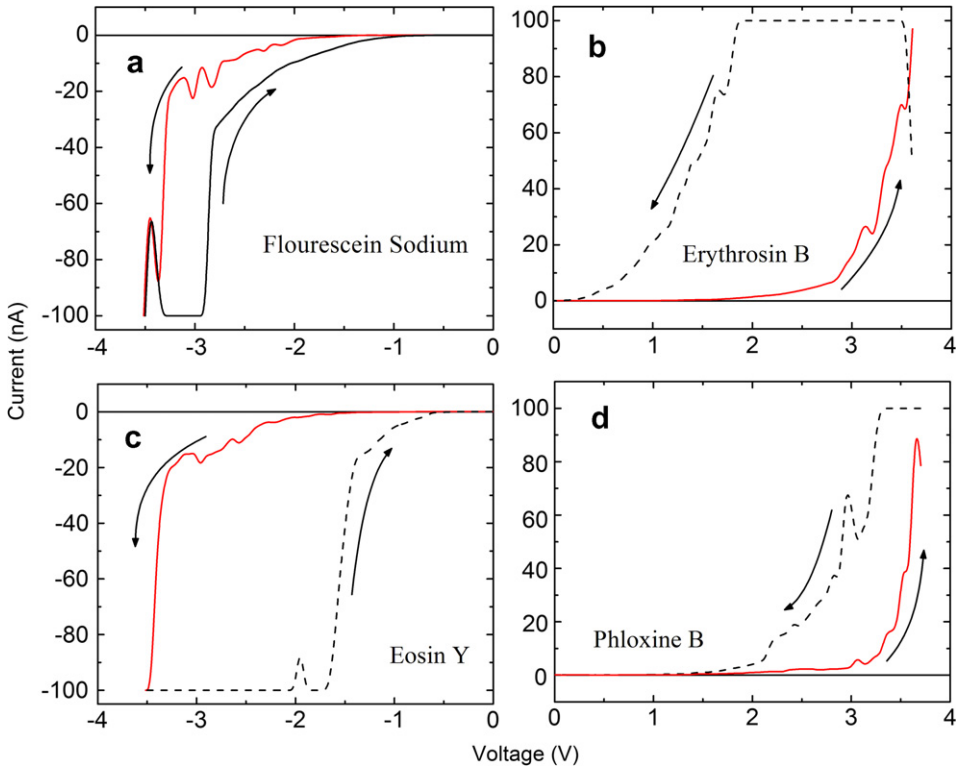

Fig. 5. Current–voltage characteristics of four different molecules in the two voltage-sweep directions. Arrows represent the direction of voltage-sweep.

layer is neither an extrinsic effect nor due to any oxide layer.

To further verify if the observed switching is a molecular effect, we characterized four other molecules, which have different substitutes than Rose Bengal. In Fig. 5, we present *I–V* characteristics of a monolayer of the four other molecules. All the four molecules along with Rose Bengal, which are in the Xanthene class, exhibit resistive switching. The bias direction of switching and the degree of it (on/off ratio) depend on the molecule (Table 1). Such dependences show that the switching in these molecules is indeed molecular in nature. If the molecular layer did not become involved during conductance switching, its parameters would have remained independent of the substitutes of the molecules.

The observed switching in these five molecules is hence molecular in nature. Since all the molecules in their ground state are biplaner in nature, upon application of bias, the molecules may get reduced and change their conformation (twist of the upper ring) to yield a high-conducting state. The on/off ratio, the ratio between the currents in the two

Table 1
Parameters of conductance switching in different molecules along with their molecular structures

Name of the molecule (substitutes)	Structure	On/Off ratio	Bias direction at which the molecule switches
Fluorescein sodium (X = H, Y = H)	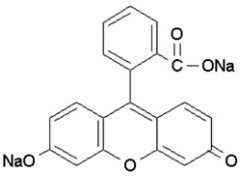	5.7 at −2 V	Switches at negative
Erythrosin B (X = H, Y = I)	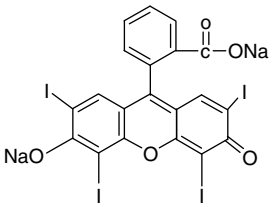	74 at +2 V	Switches at positive
Eosin Y (X = H, Y = Br)	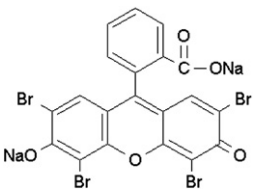	51 at –2 V	Switches at negative
Rose Bengal (X = Cl, Y = I)	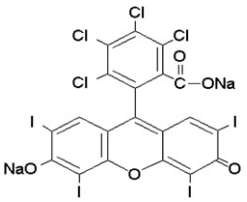	247 at +2 V	Switches at positive
Phloxine B (X = Cl, Y = Br)	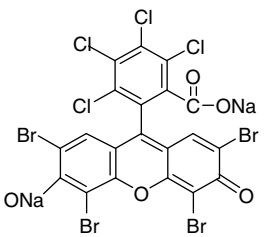	14 at +2 V	Switches at positive

stable-conformers, hence becomes dependent on the substitutes of the molecules. Moreover, since the halogen substitutes control the molecular orbitals in a predominant way, a resonance condition with the electrodes differs from a molecule to the other. Hence the direction of bias at which a molecule switches to a high-state becomes dependent on the substitutes of the molecules.

4. Conclusions

In conclusion, we have observed resistive switching in the I–V characteristics of a monolayer of Xanthene class molecules (deposited on doped Si) with Pt/Ir tip of STM as the other electrode. The use of a monolayer and the choice of electrode combination exclude the role of any oxide layer and metal diffusion in observing resistive switching. The switching strongly depends on the substitutes showing that the molecular orbitals do perturb the change in conductance. The results hence demonstrate molecular nature of electrical bistability and memory phenomena in these molecules.

Acknowledgments

AKR acknowledges CSIR Junior Research Fellowship No. 09/080(0505)/2006-EMR-I (Roll No. 503974). The Department of Science and Technology, Government of India financially supported the work through Ramanna Fellowship SR/S2/RFCMP-02/2005.

References

[1] C.P. Collier, G. Mattersteig, E.W. Wong, Y. Luo, K. Beverly, J. Sampaio, F.M. Raymo, J.F. Stoddart, J.R. Heath, Science 289 (2000) 1172.
[2] Z.J. Donhauser, B.A. Mantooth, K.F. Kelly, L.A. Bumm, J.D. Monnell, J.J. Stapleton, D.W. Price, A.M. Rawlett, D.L. Allara, J.M. Tour, P.S. Weiss, Science 292 (2001) 2303.
[3] A.O. Solak, S. Ranganathan, T. Itoh, R.L. McCreery, Electrochem. Solid State Lett. 5 (2002) E43.
[4] A. Bandyopadhyay, A.J. Pal, Appl. Phys. Lett. 82 (2003) 1215.
[5] A. Bandhopadhyay, A.J. Pal, J. Phys. Chem. B 107 (2003) 2531.
[6] A. Bandyopadhyay, A.J. Pal, Chem. Phys. Lett. 371 (2003) 86.
[7] J.S. Chen, D.G. Ma, Appl. Phys. Lett. 87 (2005) 023505.
[8] H.S. Majumdar, J.K. Baral, R. Osterbacka, O. Ikkala, H. Stubb, Org. Electron. 6 (2005) 188.
[9] M. Terai, K. Fujita, T. Tsutsui, Jpn. J. Appl. Phys. Part 1 – Regul. Pap. Brief Commun. Rev. Pap. 45 (2006) 3754.
[10] M. Caironi, D. Natali, M. Sampietro, C. Bertarelli, A. Bianco, A. Dundulachi, E. Canesi, G. Zerbi, Appl. Phys. Lett. 89 (2006) 243519.
[11] J.A. Freire, G.A. Dal Moro, R. Toniolo, I.A. Hummelgen, C.A. Ferreira, Org. Electron. 7 (2006) 397.
[12] F.L.E. Jakobsson, X. Crispin, M. Colle, M. Buchel, D.M. de Leeuw, M. Berggren, Org. Electron. 8 (2007) 559.
[13] M.N. Kozicki, M. Park, M. Mitkova, IEEE Trans. Nanotechnol. 4 (2005) 331.
[14] M. Lauters, B. McCarthy, D. Sarid, G.E. Jabbour, Appl. Phys. Lett. 87 (2005) 231105.
[15] S. Ssenyange, H.J. Yan, R.L. McCreery, Langmuir 22 (2006) 10689.
[16] S. Karthauser, B. Lussem, M. Weides, M. Alba, A. Besmehn, R. Oligschlaeger, R. Waser, J. Appl. Phys. 100 (2006) 094504.

Available online at www.sciencedirect.com
ScienceDirect
Organic Electronics 9 (2008) 501–506
Organic Electronics
www.elsevier.com/locate/orgel

Both p- and n-type dopable polymer toward electrochromic applications

Yasemin Arslan Udum [a,b], Asuman Durmus [b], Gorkem E. Gunbas [b,1], Levent Toppare [b,*]

[a] *Mersin University, Department of Chemistry, 33343, Mersin, Turkey*
[b] *Middle East Technical University, Department of Chemistry, 06531, Ankara, Turkey*

Received 19 January 2008; received in revised form 14 February 2008; accepted 17 February 2008
Available online 4 March 2008

Abstract

Synthesis and electrochemical polymerization of 8,11-bis(4-hexylthiophen-2-yl)acenaphtho[1,2-*b*]quinoxaline (HTAQ) were performed. The polymer was characterized by cyclic voltammetry, UV–Vis-NIR spectroscopy and colorimetry. Cyclic voltammetry studies revealed that the polymer was susceptible to both p- and n-doping. The electroactive polymer has fast switching time and high optical contrast. Spectroelectrochemistry also showed that the polymer is capable of being switched from bluish-green and a highly transmissive green upon p-type doping. Highly fused nitrogen containing acceptor group was utilized in the polymer backbone which was resulted in a polymer that has a significant potential for n-type doping. The existence of a true n-type doping process was proven by the results of both cyclic voltammetry and spectroelectrochemistry studies.

PACS: 82.45.Vp; 82.35.Cd; 78.20.Jq

Keywords: n-Doping; Electrochemical polymerization; Electrochromism

1. Introduction

Conducting electroactive polymers still remain a subject of intense investigation of many research groups for their technological applications [1–3]. Electrochromic polymers belong to an important class of conducting polymers which are able to change color in response to electronic signals. They are an interesting class of conjugated polymers due to their high optical contrasts [4], fast switching times [5,6], processability [7] and fine-tuning of the band gap by structure modification [8]. Such polymers can be used in devices, like multi-colored displays and image generation [9–13], antiglare rear view mirrors, vision systems or smart windows [14–16]. Most of the organic electronic materials used in these devices are highly conjugated polymers that support the injection and allow the mobility of the charge carriers (holes in the case of p-doped materials and electrons in the case of n-doped materials). To date the great majority of the electronic

* Corresponding author. Tel.: +90 3122103251; fax: +90 3122103200.
E-mail address: toppare@metu.edu.tr (L. Toppare).
[1] Present address: Department of Chemistry, University of California, Davis.

1566-1199/$ - see front matter © 2008 Elsevier B.V. All rights reserved.
doi:10.1016/j.orgel.2008.02.009

organic materials that have been investigated are p-type materials. In contrast, the selection of n-type organic materials is limited to a small number of polymers [17,18]. A polymer capable of attaining a stable n-doped state is highly desirable and this makes them useful in a variety of more complex device design such as smart windows and mirrors.

In recent years, the design and synthesis of low band gap polymers have been an area of intense interest due to their unique electrical and optical properties [19,20]. The band gap of polymer between the highest occupied electron band (valence band) and the lowest unoccupied band (the conduction band) determines the intrinsic optical properties. Recent research efforts by several groups indicate that one of the quantities that is most significant for the control of optical properties is the band gap [19,20].

Recent theoretical and experimental studies have suggested that heterocyclic copolymers with alternating aromatic–quinoid units or donor–acceptor units should be promising candidates for narrow band gap polymers [21,22]. The presence of alternating electron-acceptor and electron-donor substituents in the same polyconjugated macromolecule should lower the energy gap [23]. The high energy level for the HOMO of the donor and the low energy level for the LUMO of the acceptor results in a lower band gap due to an intra-chain charge transfer from donor to acceptor [24].

In this study, we synthesized (8,11-bis(4-hexylthiophen-2-yl)acenaphtho[1,2-*b*]quinoxaline) to obtain a polymer with a narrow band gap. Spectroelectrochemistry as well as switching properties of the polymer synthesized by electropolymerization were investigated.

2. Experimental

2.1. Materials

All chemicals were purchased from Aldrich except for tetrahydrofuran (THF) which was purchased from Across. 4,7-Dibromobenzo[1,2,5]thiadiazole [25], 3,6-dibromo-1,2-phenylenediamine [26], 5,8-dibromo-acenapthylquinoxaline [27] and tributyl(4-hexylthiophen-2-yl)stannane [28] were synthesized according to reported methods.

2.2. Equipments

A Voltalab potentiostat was used for all electrochemical studies. Electropolymerization was performed in a three-electrode cell consisting of an indium tin oxide doped glass slide (ITO) as the working electrode, platinum wire as the counter electrode, and Ag wire as the reference electrode. Tetrabutylammonium tetrafluoroborate (Bu_4NBF_4) in acetonitrile/benzonitrile (1/2 v/v) was used as the electrolytic medium. ^1H and ^{13}C NMR spectra were recorded in $CDCl_3$ on Bruker Spectrospin Avance DPX-400 Spectrometer. Chemical shifts were given in ppm downfield from tetramethylsilane. Varian Cary 5000 UV–Vis spectrophotometer was used to perform the spectroelectrochemical studies of the polymer. Colorimetry measurements were done via Minolta CS-100 Spectrophotometer.

2.3. Synthesis of 8,11-bis(4-hexylthiophen-2-yl) acenaphtho[1,2-b]quinoxaline

5,8-Bis(4-hexylthiophen-2-yl)acenapthylquinoxaline: 5,8-dibromo-acenapthylquinoxaline (0.485 mmol) and tributyl(4-hexylthiophen-2-yl)stannane (2.425 mmol) were dissolved in dry THF (100 ml), the solution was purged with argon for 30 min and $PdCl_2(PPh_3)_2$ (0.086 mmol) was added at room temperature under argon atmosphere. The mixture was stirred at 100 °C under argon atmosphere for 15 h, cooled and concentrated on the rotary evaporator. The residue was subjected to column chromatography to afford an orange solid (Scheme 1) (186 mg, 65%). ^1H NMR (400 MHz, $CDCl_3$): δ: 0.85 (t, 6H, $J = 7.4$ Hz), 1.30–1.65 (m, 12H), 1.68 (q, 4H), 2.66 (t, 4H, $J = 8$ Hz), 7.09 (s, 2H), 7.70 (s, 2H), 7.77 (t, 2H, $J = 8$ Hz), 8.01 (s, 2H), 8.02 (d, 2H, $J = 7.5$ Hz), 8.36 (s, 2H), MS: *m/e* 727 ($M^{\cdot+}$) ^{13}C NMR (400 MHz, $CDCl_3$): δ: 13.12, 21.65, 28.11, 29.62, 29.64, 30.79, 121.41, 122.65, 125.68, 127.26, 127.61, 128.40, 129.03, 131.14, 135.82, 136.86, 137.92, 141.78, 151.48.

3. Results and discussion

3.1. Cyclic voltammetry

The cyclic voltammograms during the potentiodynamic electrodeposition of monomer on ITO electrode are shown in Fig. 1. Cyclic voltammetry (CV) was obtained in acetonitrile/benzonitrile (1/2 v/v) solution containing 0.1 M tetrabutylammonium tetrafluoroborate (Bu_4NBF_4) at a scan rate of 100 mV/s. Electropolymerization was performed using multiple scan voltammetry from −0.3 V to +1.3 V at 100 mV/s. The monomer started to get

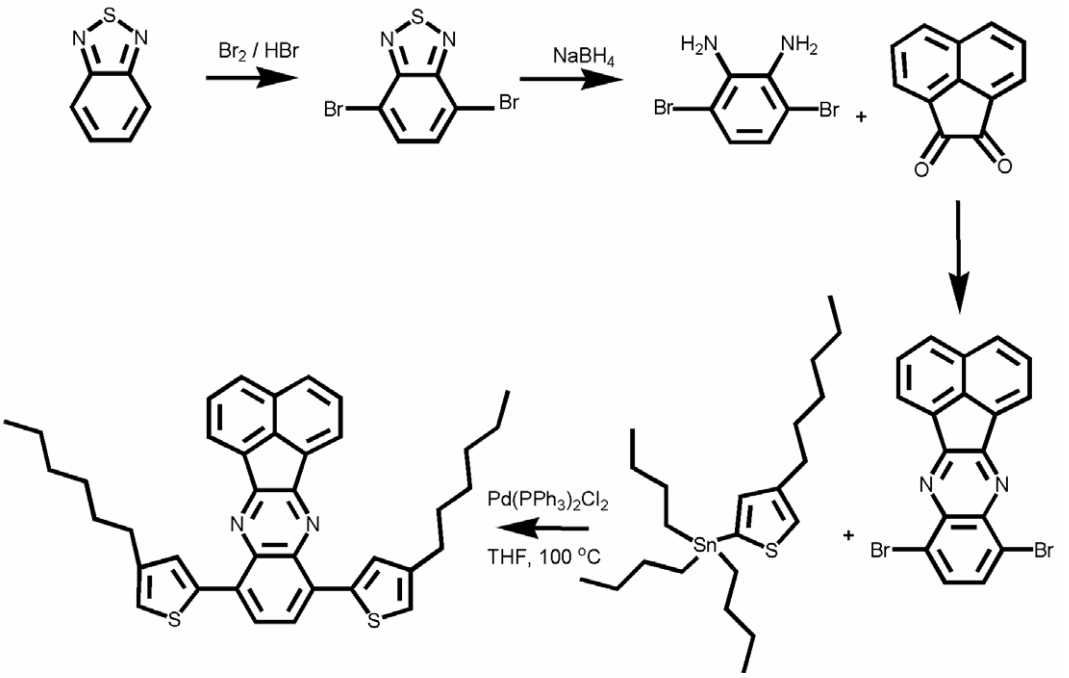

Scheme 1. Synthetic route of monomer.

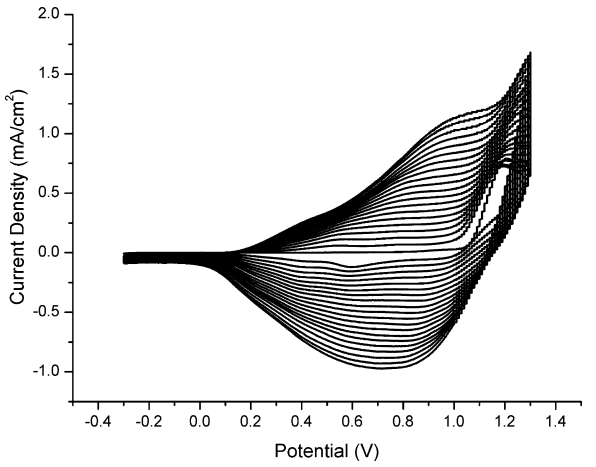

Fig. 1. Cyclic voltammogram of acetonitrile/benzonitrile (1/2 v/v) solution containing 10 mM monomer and 0.1 M Bu_4NBF_4. Scan rate: 100 mV/s.

oxidized at +1.1 V during the first anodic sweep. This oxidation corresponds to the formation of radical cations. These radical cations couple, giving oligomers, and eventually a polymeric film was deposited on the electrode surface. From the second cycle on, a broad oxidation peak was observed at +0.98 V and a reverse cathodic peak was seen at +0.72 V versus Ag wire pseudo-reference electrodes (0.35 V versus SCE). On the other hand a similar quinoxaline derivative [6] namely, poly-2,3-bis(4-tert-butylphenyl)-5,8-bis(4-hexylthiophen-2-ylquinoxaline has a monomer oxidation of 1.3 V and a polymer oxidation of 1.1 V. Functionalization of quinoxaline moiety works in lowering the oxidation potentials of both the monomer and the polymer. Moreover, this polymer revealed both p- and n-doping properties. A well-defined reversible redox couple with an E_{pa} of −1.16 V and E_{pc} of −1.34 V was observed (Fig. 2).

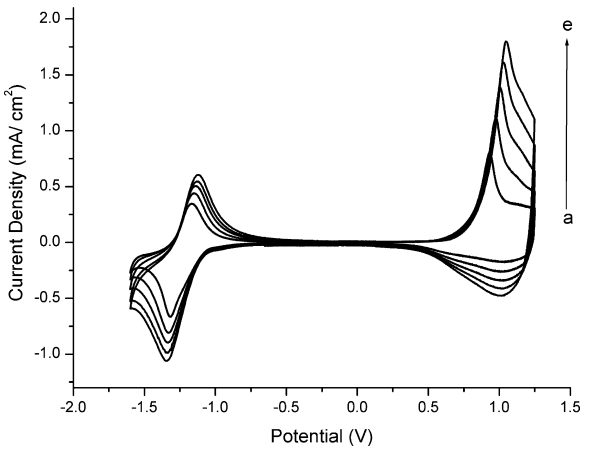

Fig. 2. Scan rate dependence of the polymer in 0.1 M Bu_4NBF_4/ACN solution: (a) 100, (b) 150, (c) 200, (d) 250, and (e) 300 mV/s.

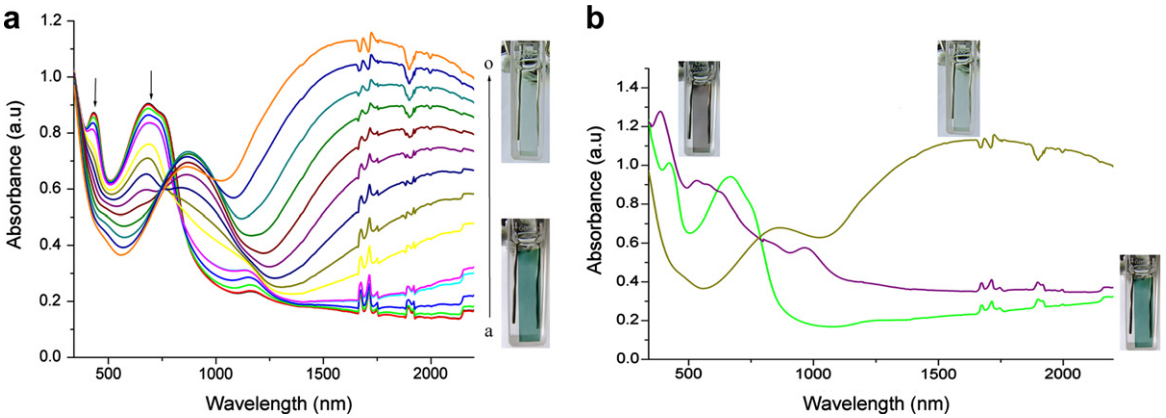

Fig. 3. (a) p-Doping: spectroelectrochemistry of polymer film on an ITO coated glass slide in monomer free 0.1 M Bu_4NBF_4/DCM electrolyte-solvent couple at applied potentials (V); (a) −0.3, (b) −0.2, (c) −0.1, (d) 0.0, (e) 0.1, (f) 0.2 (g) 0.3, (h) 0.4, (i) 0.5, (j) 0.6, (k) 0.7 (l) 0.8, (m) 0.9 and (n) 1.0. (b) n-Doping: spectroelectrochemistry at −1.5 V, −0.3 V and +1.0 V.

The cyclic voltammograms for p- and n-doping of polymer film in the monomer free solution were obtained at different scan rates. The dependence of the anodic and cathodic peak currents on the scan rates (between 100 and 300 mV/s) are shown in Fig. 2. The polymer is electrochemically active in both anodic and cathodic regions. The current was proportional to the scan rate indicating that the films were well adhered and charge transfer process was not dominated by diffusion [29].

3.2. Spectroelectrochemistry

For in situ spectroelectrochemical studies, a polymer was deposited on ITO class and spectra were recorded in a monomer free electrolyte solution (Bu_4NBF_4/dichloromethane) at various applied potentials between −0.3 V and +1.0 V. Oxidation of an electrochromic material produces radical cations (polarons) and further oxidation produces dications (bipolarons), allowing new electronic transitions thereby changing the absorption spectra. The absorbances assigned to π–π^* transitions for the neutral form of polymer are at 430 and 675 nm. These decrease as the doping proceeds while new absorbance bands evolve at 880 nm and 1700 nm due to the formation of charge carriers. Meanwhile the color of the polymer film changed from bluish-green[2] to transmissive green. The typical absorption spectra of the polymer are shown in Fig. 3a. Spectroelectrochemical studies of the polymer film demonstrate that the film's color changed during the p-doping (oxidation) and n-doping (reduction) processes. Electrochemical behavior in the cathodic region cannot be a direct evidence for n-type doping process. In addition to redox couples, an evidence for charge carrier formation upon reduction should be studied via spectroelectrochemistry or in situ conductivity measurements. True n-type doping process requires drastic changes in the NIR region upon reduction. Fig. 3b shows that PHTAQ is a true n-dopable polymer [17]. The band onsets of the polymer were calculated as 2.0 eV and 1.2 eV for the two π–π^* transitions

3.3. Kinetic studies

For optical switching studies, polymer films were synthesized electrochemically on ITO coated glass slides. Polymer was stepped between its neutral (−0.3 V) and oxidized (+1.0 V) states. While switching, the percent transmittance (T%) at λ_{max} was monitored as a function of time. A square-wave potential step method coupled with optical spectroscopy was used to investigate the switching time and the contrast. The contrast is given as the difference between T% in the neutral reduced and oxidized states and reported as ΔT%. The optical contrasts for PHTAQ in the visible region are 27% at 430 nm and 26% at 675 nm. Moreover, PHTAQ has an outstanding optical contrast of 81% at 1700 nm. These values are much better than the corresponding values for poly-2,3-bis(4-tert-butylphenyl)-5,8-bis(4-hexylthiophen-2-ylquinoxaline(10%

[2] For interpretation of color in Fig. 3, the reader is referred to the web version of this article.

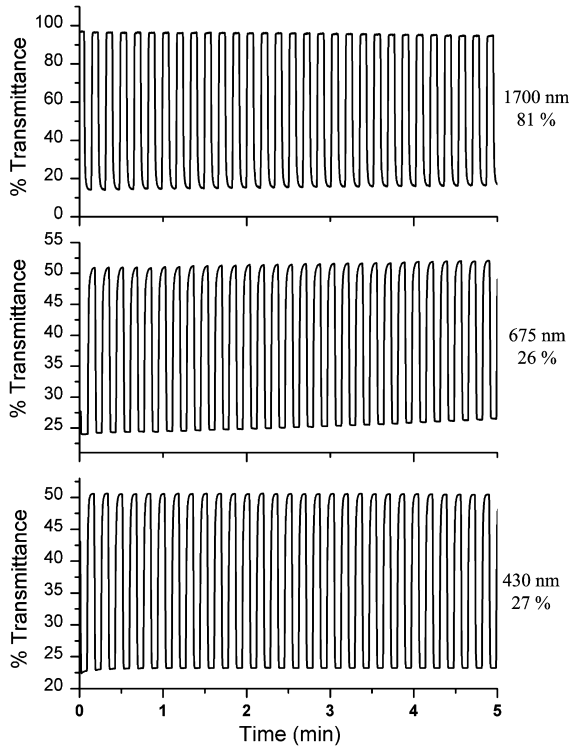

Fig. 4. Electrochromic switching, optical absorbance monitored at: (a) 430 nm (b) 675 nm and (c) 1700 nm between –0.3 V and +1.0 V in Bu_4NBF_4/ACN solution.

at 345 nm; 25% at 538 nm; 46% at NIR region). Fig. 4 shows the electrochromic switching properties of PHTAQ.

The switching time was determined by monitoring the absorption intensity changes at 430 nm, 675 nm and 1700 nm while switching the applied voltage between −0.3 V and +1.0 V and achieve 95% of their optical contrasts in the visible region in 1.2 s at 430 nm. The polymer revealed a switching time of 1.8 s at 675 nm. The polymer has also an outstanding optical contrast of 81% in NIR region with a very fast switching time of 0.6 s.

3.4. Colorimetry

A polymer's color is one of the most important properties for an application in display devices and needs to be defined precisely. For that reason, we studied the in situ colorimetric analysis of polymer by colorimetry. Colorimetry analysis, which enables numeric determination of color, is considered as a valuable method for electrochromic applications. The commonly utilized scale was set by La Commission Internationale de l'Eclairage (CIE). In CIE system, luminance or brightness, hue and saturation, symbolized with L, a, b, respectively, are determined to qualify color. At the neutral state the color of the polymer was bluish-green ($L = 34.8$, $a = -15.4$, $b = 1.5$); on the other hand, PHTAQ becomes highly transmissive green ($L = 61.7$, $a = -16.7$, $b = 7.6$) at the oxidized state and red-purple color ($L = 73.8$, $a = -3.2$, $b = 8.5$) in the reduced state.

4. Conclusion

A new low band gap conjugated polymer was synthesized and its characterization was accomplished by various techniques, including spectroelectrochemistry, kinetic and colorimetry studies. PHTAQ showed two λ_{max} values at 430 and 675 nm with band onsets at 2.0 eV and 1.2 eV, respectively. Furthermore, n-doped PHTAQ revealed a completely different optoelectrochemical spectrum at negative potentials which is a significant proof for true n-type doping process. This is an expected result for such an acceptor unit in the polymer backbone. The polymer's color varies between bluish-green, a highly transmissive green and red-purple color in neutral, p-doped and n-doped states respectively. Hence, the polymer is capable of being to both p- and n-doped and is a promising material for dual type ECD applications.

Acknowledgements

Authors gratefully thank TUBA grant. One of us (Y.A.U.) acknowledges DOSAP program of METU .

References

[1] N.S. Sariciftci, D. Braun, C. Zhang, V. Srdanov, A.J. Heeger, F. Stucky, F. Wudl, Appl. Phys. Lett. 62 (1993).
[2] T.A. Skotheim, R.L. Elsenbaumer, J.R. Reynolds, Handbook of Conducting Polymers, Marcel Dekker, New York, 1998.
[3] A. Kros, S.W.F.M. van Hövell, N.A.J.M. Sommerdijk, R.J.M. Nolte, Adv. Mater. 13 (2001) 1555.
[4] S.A. Sapp, G.A. Sotzing, J.R. Reynolds, Chem. Mater. 10 (1998) 2101.
[5] A. Kumar, D.M. Welsh, M.C. Morvant, F. Piroux, K.A. Abboud, J.R. Reynolds, Chem. Mater. 10 (1998) 896.
[6] F. Ozyurt, E.G. Gunbas, A. Durmus, L. Toppare, Org. Electron., doi:10.1016/j.orgel.2007.11.006.
[7] G. Sonmez, H.B. Sonmez, C.K.F. Shen, R.W. Jost, Y. Rubin, F. Wudl, Macromolecules 38 (2005) 669.

[8] I. Schwendeman, R. Hickman, G. Sonmez, P. Schottland, K. Zong, D. Welsh, J.R. Reynolds, Chem. Mater. 14 (2002) 3118.
[9] A.A. Argun, P.H. Aubert, B.C. Thompson, I. Schwendeman, C.L. Gaupp, J. Hwang, N.J. Pinto, D.B. Tanner, A.G. Macdiarmid, J.R. Reynolds, Chem. Mater. 16 (2004) 4401.
[10] R.J. Mortimer, A.L. Dyer, J.R. Reynolds, Displays 27 (2006) 2.
[11] R.D. Rauh, F. Wang, J.R. Reynolds, D.L. Meeker, Electrochim. Acta 46 (2001) 2023.
[12] G. Sonmez, C.K.F. Shen, Y. Rubin, F. Wudl, Angew. Chem., Int. Ed. 43 (2004) 1498.
[13] E. Sahin, E. Sahmetlioglu, I.M. Akhmedov, C. Tanyeli, L. Toppare, Org. Electron. 7 (5) (2006) 351.
[14] C.G. Granqvist, Solid State Ionics 479 (1992) 53.
[15] H.W. Heuer, R. Wehrmann, S. Kirchmeyer, Adv. Funct. Mater. 12 (2002) 89.
[16] D.R. Rosseinsky, R.J. Mortimer, Adv. Mater. 13 (2001) 783.
[17] B.C. Thompson, Y. Kim, T.D. McCarley, J.R. Reynolds, J. Am. Soc. Chem. 128 (2006) 12714.
[18] C.J. DuBois, K.A. Abboud, J.R. Reynolds, J. Phys. Chem. B 108 (2004) 8550.
[19] G. Sönmez, Chem. Commun. 42 (2005) 5251.
[20] A. Durmus, G.E. Gunbas, P. Camurlu, L. Toppare, Chem. Commun. (2007) 3246.
[21] C. Kitamura, S. Tanaka, Y. Yamashita, Chem. Mater. 8 (1996) 570.
[22] J.L. Brédas, A.J. Heeger, F. Wudl, J. Chem. Phys. 85 (1986) 4673.
[23] M. Karikomi, C. Kitamura, S. Tanaka, Y. Yamashita, J. Am. Chem. Soc. 117 (1995) 6791.
[24] M. Jayakannan, P.A. van Hal, R.A.J. Janssen, J. Polym. Sci. A: Polym. Chem. 40 (2002) 251.
[25] A.B. Da Silveria Neto, A. Lopes Sant'Ana, G. Ebeling, S.R. Goncalves, E.V.U. Costa, H.F. Quina, J. Dupont, Tetrahedron 61 (2005) 0975.
[26] Y. Tsubata, T. Suzuki, T. Miyashi, Y. Yamashita, J. Org. Chem. 57 (1992) 6749.
[27] I. Nurulla, I. Yamaguchi, T. Yamamoto, Polym. Bull. 44 (2000) 231.
[28] Q. Hou, Q. Zhou, Y. Zhang, W. Yang, R. Yang, Y. Cao, Macromolecules 37 (2004) 6299.
[29] G. Sonmez, H. Meng, Q. Zhang, F. Wudl, Adv. Funct. Mater. 13 (2003) 726.

Available online at www.sciencedirect.com
ScienceDirect
Organic Electronics 9 (2008) 507–514
Organic Electronics
www.elsevier.com/locate/orgel

Printing-induced improvements of organic thin-film transistors

A.J. Tunnell [a], D.R. Hines [b,c,*], Elba Gomar-Nadal [a], E.D. Williams [a,c]

[a] University of Maryland, Department of Physics, College Park, MD 20742, United States
[b] Laboratory for Physical Sciences, University of Maryland, College Park, MD 20740, United States
[c] University of Maryland, NanoCenter, College Park, MD 20742, United States

Received 8 June 2007; received in revised form 18 February 2008; accepted 21 February 2008
Available online 29 February 2008

Abstract

To understand the observation of improved pentacene (Pn) thin-film transistor mobility in flexible printed devices, a method for performing electrical measurements of organic thin-film transistors (OTFT) during the process of transfer printing has been developed. Different sample configurations were designed to test two aspects of the printing process: (1) the formation of the source/drain contacts a Pn thin-film, and (2) the formation of the transfer printed Pn/dielectric interface. *In situ* measurements show that pressure-induced contacts of gold (Au) electrodes result in a factor of seven mobility improvement compared with evaporation of top Au electrodes on an otherwise identical device configuration. Annealing the laminated device up to 90 °C caused no further improvement, and heating above 90 °C degraded performance. The mobility of a transfer printed device with the rough, as-grown top surface of the Pn in contact with the dielectric was found to increase dramatically with subsequent annealing for a sample temperature up to 120 °C. This is attributed to annealing-induced structural changes in the Pn film at elevated temperatures, consistent with X-ray bulk measurements showing enhanced crystal morphology in transfer printed Pn thin-films.

PACS: 81.05.Lg; 71.20.Rv; 72.80.Le

Keywords: Transfer printing; Organic electronics; Flexible electronics

Transfer printing, which allows fabrication via purely additive processing steps, is a promising method for the fabrication of flexible electronics [1–5]. Since transfer printing relies primarily on differential adhesion, it is inherently compatible with a wide range of materials [6]. Purely additive transfer printing methods have demonstrated the sequential assembly of dissimilar materials onto a plastic substrate for the fabrication of pentacene (Pn) [5], poly 3-hexylthiophene (P3HT) [7], carbon nanotube (CNT) mats [2,8] and graphene [9] thin-film transistors (TFT). Robust materials transfer onto plastic substrates has been achieved by printing near or above the glass transition temperature of the device substrate. The transfer process itself may create conditions that modify certain materials properties, thus affecting the characteristics of fabricated

* Corresponding author. Address: Laboratory for Physical Sciences, University of Maryland, College Park, MD 20740, United States. Tel.: +1 301 935 6809; fax: +1 301 935 6723.
E-mail address: hines@lps.umd.edu (D.R. Hines).

1566-1199/$ - see front matter © 2008 Elsevier B.V. All rights reserved.
doi:10.1016/j.orgel.2008.02.012

devices [10]. For the organic semiconductor Pn, we have previously shown that transfer printing can produce devices with mobilities approximately a factor of two better than devices constructed from (unprinted) vapor-deposited Pn with thermally deposited top contacts [5]. Understanding the mechanism for such changes in properties may allow further improvement in design and fabrication approaches. Here we address the question by directly measuring device characteristics during the transfer printing process. The key results show that both lamination of the source/drain (S/D) electrodes, and annealing the printed Pn/dielectric interface under pressure dramatically improve the transport properties.

In an active OTFT, an accumulation layer is generated at the semiconductor/dielectric interface by the application of a gate voltage, thus allowing a S/D current to flow in the channel. Since the active region of the OTFT device is localized to within a few nanometers of the interface between the organic semiconductor and the dielectric material [11–14], much effort has gone into improving the structure of the organic layer at this interface [15–20]. In developmental research, OTFTs have been fabricated by thermally depositing a Pn thin-film onto a doped silicon wafer with a thermal oxide surface (SiO_2/Si). With the addition of evaporated top-contact S/D electrodes, the resulting device (here referred to as the standard device) uses the oxide layer as the dielectric and the wafer itself as the gate electrode [21–26]. In this geometry, shown schematically in Fig. 1a, the as-grown bottom surface of the Pn film is in contact with the dielectric layer and the terraced top surface (see AFM image, Fig. 1c) plays little or no role in device performance. When using transfer printing techniques, the organic semiconductor layer is thermally deposited onto a sacrificial SiO_2/Si wafer (referred to as a transfer substrate), and then is transfer printed onto a plastic substrate containing an electrode subassembly with the initially terraced top surface of the Pn film in contact with the dielectric layer, as illustrated in Fig 1b. This device (here referred to as the flexible device) is configured as a bottom-contact OTFT device.

Fabrication of the flexible device involves two distinct materials processing changes compared with fabrication of the standard device. First, the forma-

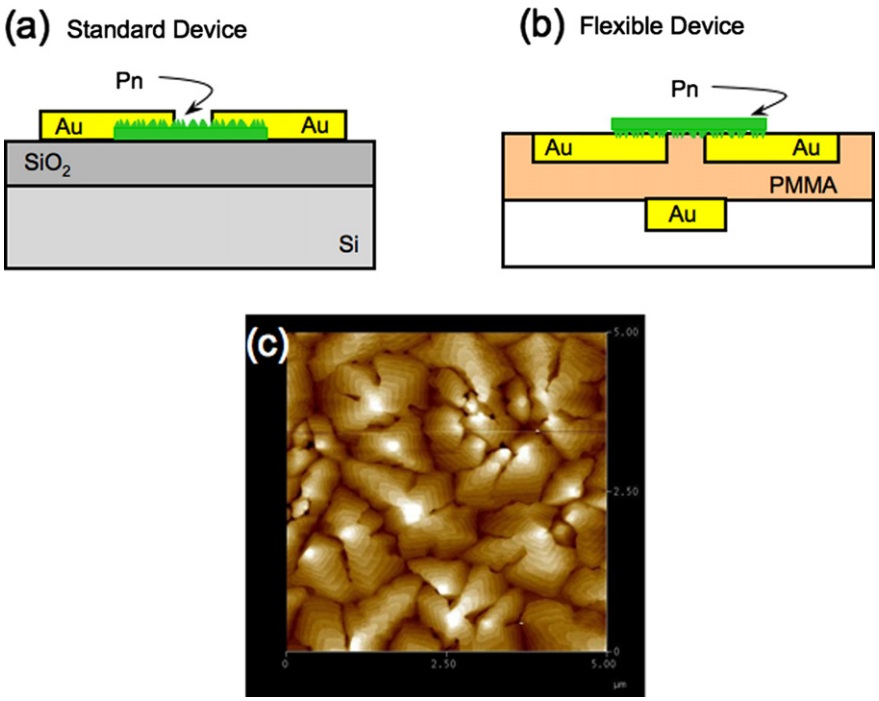

Fig. 1. (a) Cross-section illustration of the OTFT standard device geometry with thermally evaporated electrodes using the as-grown pentacene bottom surface as the active device interface. (b) Cross-section illustration of the OTFT flexible device geometry using the as-grown pentacene top surface as the active device interface. (c) An AFM image of the top surface of a 50 nm thick pentacene film thermally deposited onto a SiO_2 surface.

tion of the S/D contacts to the Pn occurs via lamination for the flexible device, as compared with direct thermal deposition for the standard device. The thermal deposition is known to result in interdiffusion of Au with the Pn, with unknown effects on the local properties. Secondly, the active interface between the Pn and the dielectric is formed by pressurized contact of a rough Pn surface for the flexible device, but direct deposition of Pn onto the SiO_2 for the standard device. To separate the effects of these two different processes on the behavior of the flexible device, we have designed two test configurations for *in situ* measurements of the evolution of the device behavior during the transfer printing process itself.

The first configuration, shown in Fig. 2a, is based on a doped Si global gate, a SiO_2 dielectric layer with the Pn grown by deposition. The printing process to be tested is the addition of top-contact S/D electrodes by lamination. Because this device is identical to the standard device, other than the processing of the electrodes, it can be used in comparison with the standard device to evaluate the effect of electrode lamination. This configuration will be referred to as the lamination test device.

The second configuration, used to test the effect of transfer printing on the interface between the Pn and the dielectric, is shown in Fig. 2b. The electrode subassembly (consisting of gate and S/D electrodes separated by a dielectric layer) is placed in contact with the thermally grown Pn thin-film. The terraced top surface of the Pn film in contact with the printed dielectric layer thus becomes the active interface for this device. To prevent cross-talk between the real gate and a ground plane on the other side of the Pn layer during *in situ* transport measurements, it was necessary to replace the SiO_2/Si substrate with a quartz substrate. This device will be referred to as the interface test device. Unfortunately, the quality of the as-grown Pn film is not as good on the quartz substrate as on the SiO_2/Si substrate. This means that the mobility values measured for the interface test device will be lower than previously reported for flexible devices [5]. In spite of this limitation, the *in situ* measurements can still be used as an important probe with which to study changes in the transport properties during the transfer printing process.

For the lamination test device, a 50 nm thick Pn film was thermally deposited onto a thermally oxidized Si transfer substrate. The doped Si wafer was used as the gate electrode and the 500 nm thick SiO_2 layer as the dielectric. A polyethylene terephthalate (PET) substrate onto which Au S/D electrodes were transfer printed formed the laminated top-contact electrodes. For the interface test device, a 50 nm thick Pn film was thermally deposited onto a quartz substrate. A separate PET substrate containing previously transfer printed Au gate and S/D electrodes separated by a 600 nm thick poly(methyl methacrylate) (PMMA) dielectric layer was placed in contact with the Pn film. The channel width was $W = 100$ μm and the channel length was $L = 6$ μm for both the lamination test and interface test devices.

Given these two device geometries, it is possible to isolate the individual effects of transfer printing

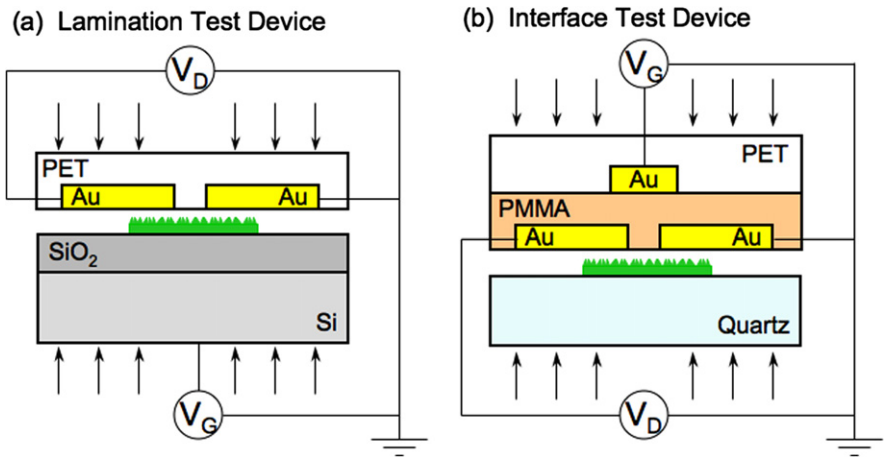

Fig. 2. (a) Cross-section illustration of the OTFT lamination test device geometry using the as-grown pentacene bottom surface as the active device interface. (b) Cross-section illustration of the OTFT interface test device geometry using the as-grown pentacene top surface as the active device interface. Arrows indicate direction of applied pressure during printing.

due to S/D lamination and Pn/dielectric interface formation. To implement these comparisons, we have developed the capability to perform *in situ* transport measurements during the transfer printing process. The transfer printing process has been implemented with a Nanonex 2500 imprint instrument, where the transfer substrate/printable layer/device substrate sample is placed between two silicone rubber sheets inside the imprint chamber. The chamber was evacuated to a pressure of 300 mtorr for 3 min and the rubber sheets pressed together by a solenoid-actuated ring in order to vacuum seal the sample. The desired transfer printing pressure was then established by filling the chamber with N_2 gas and the desired temperature established using PID controlled lamps. A detailed description of the transfer printing process has been presented elsewhere [2].

To perform *in situ* transport measurements in the imprint machine, a modification of an existing feedthrough was made to include electrical connections to the drain and gate electrodes. The source electrode was connected to a common ground contact between the imprint chamber and a source measurement unit (Keithly 2400 SourceMeter). These connections to the device were made by passing wires through a small hole in the bottom silicone sheet, which was subsequently sealed with silicone caulk. The wires were connected to the device electrodes with silver paint. To ensure a reproducible temperature profile in the imprint chamber, a blank piece of Si wafer was placed below the silicone rubber sheets as a heat sink in contact with the thermocouple. The temperatures reported in this paper are the thermocouple readings at the heat sink.

For *in situ* measurements, the printing sequence was to first increase pressure up to 600 psi, second to increase temperature in steps up to a maximum value, third to decrease temperature back down to room temperature in similar steps and finally to release the pressure. At each step of temperature or pressure, output and transfer characteristics were measured. For the lamination test and interface test devices, sets of *in situ* transport measurements are shown in Fig. 3a–c and Fig. 3d–f, respectively. These were acquired at 600 psi and 30 °C (before heating), 600 psi and 170 °C (during heating) and 600 psi and 30 °C (after heating). As can be easily seen by a comparison of Fig. 3d and f, the room temperature transistor response of the interface test device drastically increased after heating. The transport characteristics then remained essentially constant as the pressure was released. In contrast, the lamination test device (Fig. 3a and c) showed a strong OTFT response before heating and a notable decreased response after heating.

For both the lamination test device and the interface test device, pressure was applied at room temperature before heating, kept constant at 600 psi during heating and released once the thermocouple temperature returned to room temperature. During the application of pressure, transport measurements were essentially unchanged for both samples between 50 psi and 600 psi. During the removal of pressure, transport measurements were also essentially unchanged for both samples between 600 psi and 10 psi.

From data in Fig. 3, mobility as a function of printing condition is plotted in Fig. 4, where the mobility was calculated using the equation for the linear regime: $I_{ds} = \frac{WC}{L}\mu(V_g - V_T - V_{ds})V_{ds}$ where L is the channel length, W is the channel width, C is the capacitance per unit area of the insulating layer, V_T is the threshold voltage, V_g is the applied gate voltage, V_{ds} is the applied S/D voltage, I_{ds} is the measured S/D current and μ is the field-effect mobility [27]. Fig. 4a corresponds to the lamination test device and Fig. 4b corresponds to the interface test device. Several important features are evident. First, consistent with previous reports [28–31], laminated electrodes, as compared to thermally deposited electrodes (as for the standard device) result in a substantial improvement in mobility for the laminated test device before heating (compare dark column to light gray column at 30 °C in Fig. 4a). Similar improvements in mobility associated with S/D laminated electrodes have been attributed to lower contact resistance [29]. Second, for the lamination test device, the increase in mobility from 30 °C to 90 °C can be attributed to a reversible thermal activation process described by the Arrhenius equation for mobility

$$\mu = \mu_o \exp(-E_a + /k_B T) \quad (1)$$

where μ_o is the free carrier mobility, E_a is the activation energy and k_B is Boltzmann's constant. The data below 90 °C, on heating, correspond to an activation energy of 19 meV which is consistent with recently reported activation energies for Pn [24,32]. For temperatures above 90 °C, the mobility of the lamination test device decreases with increasing printing temperature and remains dramatically below what would be expected from Eq. (1) (filled circles in Fig. 4a) after cooling. The irreversible

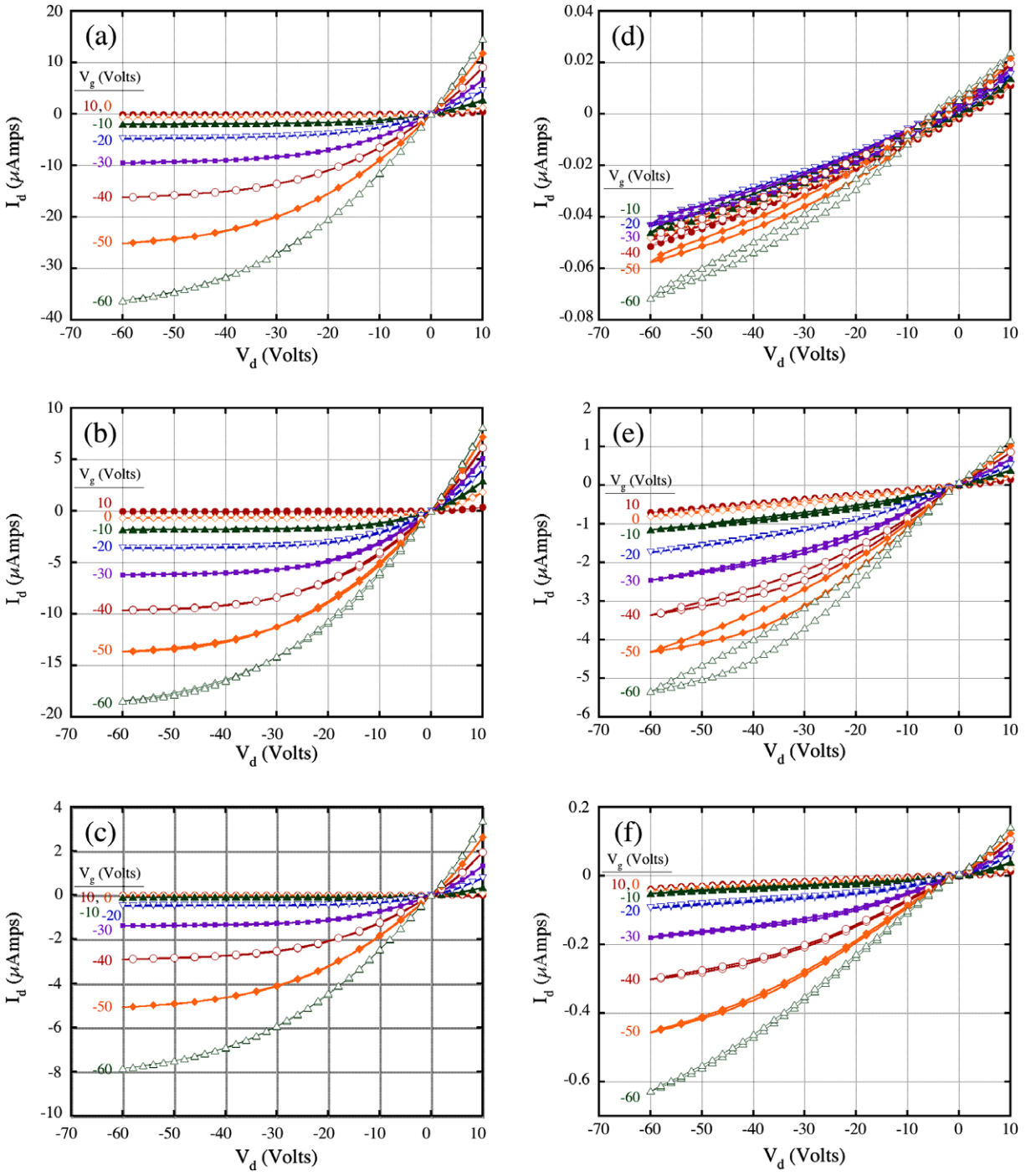

Fig. 3. *In situ* I_{ds} vs. V_{ds} transport measurements of the lamination test device for thermocouple temperatures of (a) 30 °C before heating, (b) 170 °C during heating and (c) 30 °C after heating, and of the interface test device for thermocouple temperatures of (d) 30 °C before heating, (e) 170 °C during heating and (f) 30 °C after heating. All data correspond to a pressure of 600 psi.

decrease in mobility for the lamination test device when it is heated above 90 °C is unlikely to involve changes at the S/D electrodes, since there is no corresponding effect for the interface test device (see below), which has a similar S/D electrode configuration.

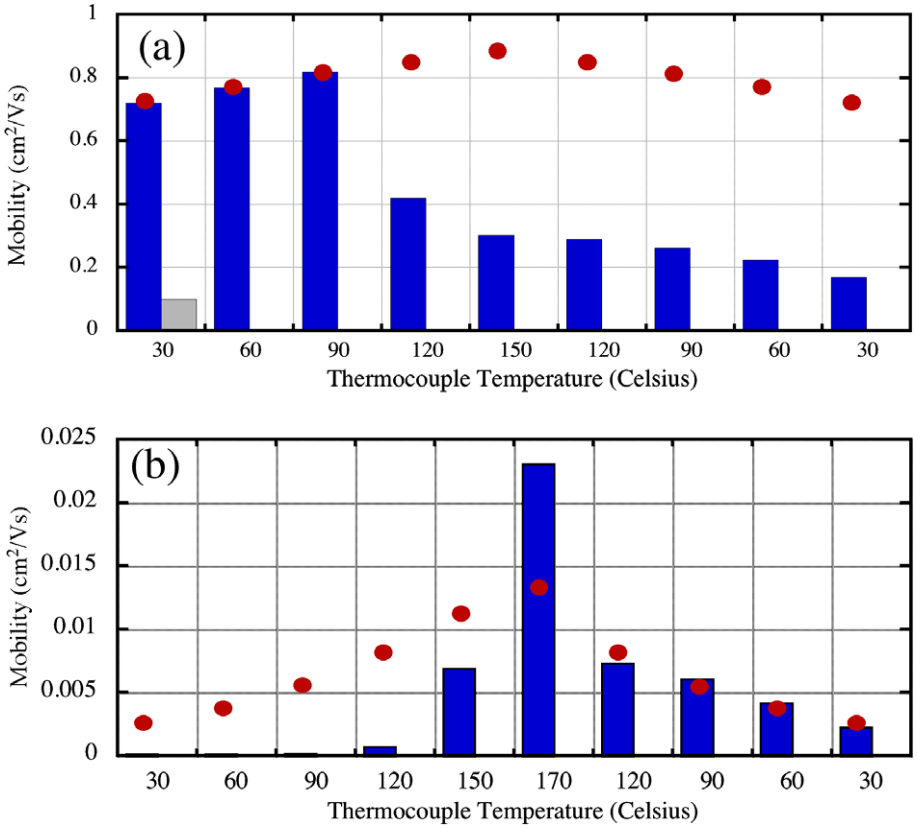

Fig. 4. Mobility of the (a) lamination test device and (b) interface test device during heating and cooling phases of the transfer printing process with pressure held at 600 psi. The filled dots correspond to the calculated mobility due only to thermal excitation. The second (light gray) bar in (a) for 30 °C corresponds to the mobility of a standard device with thermally deposited top S/D electrodes.

In contrast, the mobility of the interface test device is extremely low upon the initial contact of the electrode subassembly to the Pn film, but dramatically increases with printing temperature above 120 °C, with a net improvement in mobility remaining after the sample is cooled. The chance in mobility during cooling (120 °C to 30 °C) for the interface test device is attributed to the reversible thermal activation process described by Eq. (1) (filled dots in Fig. 4b). The larger than expected mobility at 170 °C is a transient effect (e.g. the effect does not persist upon subsequent cooling) that is a subject for further investigation.

Comparison of the lamination test device results with the interface test device results shows that improvements in mobility due to lamination occur prior to heating. Thus, changes in the S/D electrode interaction with the Pn can be ruled out as a basis for the improvements with temperature for the interface test device. Instead, the irreversible improvement in mobility for the interface test device must reflect changes taking place at the semiconductor/dielectric interface at the imprint temperatures and pressures. This may not be surprising when considering the nature of the Pn/dielectric interface. The top surface of the Pn film prior to printing exhibits a terrace structure [33] as shown in Fig. 1c. Incorporating this terraced surface into an OTFT device would result in a network of islands of Pn in contact with the dielectric layer. At such an interface, electrical transport from island to island would require out-of-plane transport. This would reduce the performance of the OTFT device and is consistent with the low mobility of the interface test device prior to an increase in printing temperature.

X-ray diffraction measurements indicate that the basal spacing correlation length of a 50 nm thick Pn film increases as much as 35% as a result of the pressure–temperature treatment of transfer printing [5,34]. This is a bulk measurement and therefore does not give a direct measure of the morphology

at the dielectric interface; however, it does show that the arrangement of Pn molecules in the film is irreversibly modified during transfer printing. We can assume therefore that the molecular ordering at the as-grown top surface, and possibly the as-grown bottom surface as well, is improved during printing. The original top surface of the Pn film has poor transport characteristics when first printed at room temperature. In this case, given sufficient molecular mobility to change the bulk crystalline order, it seems unlikely that the as-grown top surface of the Pn film would retain its original terraced structure under the transfer printing conditions of 600 psi and 120 °C (sample temperature). Smoothing of the Pn film to conform to the dielectric layer would allow the electronic transport to become more two-dimensional and is a reasonable explanation for the observed improvement of the electronic mobility of the transfer printed flexible device. Additional relaxation of the PMMA into more conformal contact with the Pn may also contribute.

In contrast to the printed Pn/dielectric interface, the initial growth parameters for the deposition of the Pn film on the SiO_2 dielectric surface were optimized for mobility at the Pn/SiO_2 interface. Thus, it is conceivable that annealing-induced rearrangement of the Pn molecules at the as-grown bottom surface could result in a less optimum structure with respect to mobility. However, other possibilities such as impurity segregation to the interface, or effects of sublimation of Pn cannot be ruled out on the basis of the present experiments.

In situ transport measurements of a Pn OTFT during the transfer printing process have been performed to determine the mechanism by which transfer printing produces flexible devices with a higher mobility than that of a standard device with thermally deposited, top S/D electrodes [2,5]. The ability to perform these *in situ* measurements provides opportunities to separate the effects of different materials processes during printing. Taken together, X-ray measurements and *in situ* measurements show that thermally-induced improvements for the flexible device can be attributed to rearrangement of the Pn molecules at the Pn/dielectric surface. It is reasonable to conclude that the thermally-induced improvement in mobility of the interface test device includes effects of evolution toward a more two-dimensional surface during the transfer printing process. However, the relaxation cannot yield as well-ordered an interface as growth, since the initial mobility (0.8 cm^2/Vs) of the lamination test device, is greater than the previously reported 0.24 cm^2/Vs measured for transfer printed flexible devices [2,5]. Nevertheless, both effects of lamination and structural relaxation must contribute to the previously observed mobility improvement in transfer printed Pn TFTs, with the lamination improvements occurring upon the initial pressurization, and the structural relaxation upon the subsequent heating. The improvements shown as a result of both effects should not be limited to transfer printed organic semiconductor films. Lamination of electrodes and thermal annealing under pressure may have benefits for other printed organic films such as those deposited using inkjet techniques.

Acknowledgments

This work has been supported by the Laboratory for Physical Sciences, and in part by NIST under contract # 70NANB6H6138.

References

[1] A.G. Blanchet, J. Rogers, J. Imaging Sci. Technol. 47 (2003) 296–303.
[2] D.R. Hines, S. Mezhenny, M. Breban, E.D. Williams, V.W. Ballarotto, G. Esen, A. Southard, M.S. Fuhrer, Appl. Phys. Lett. 86 (2005) 163101.
[3] H.E. Katz, Chem. Mater. 16 (2004) 4748–4756.
[4] D.Y. Zhou, L. Hu, G. Grüner, Appl. Phys. Lett. 88 (2006).
[5] D.R. Hines, V.W. Ballarotto, E.D. Williams, Y. Shao, S.A. Solin, J. Appl. Phys. 101 (2007) 024503.
[6] A.J. Crosby, J. Mater. Sci. 38 (2003) 4439–4449.
[7] D.R. Hines, A. Southard, M.S. Fuhrer, J. Appl. Phys. (2008), submitted for publication.
[8] V.K. Sangwan, D.R. Hines, V.W. Ballarotto, G. Esen, M.S. Fuhrer, E.D. Williams, Mater. Res. Soc. Symp. Proc. 963 (2007) 0963-Q10-57.
[9] J.H. Chen, M. Ishigami, C. Jang, D.R. Hines, M.S. Fuhrer, E.D. Williams, Adv. Mater. 19 (2007) 3623–3627.
[10] C.C. Cedeno, J. Seekampa, A.P. Kam, T. Hoffmanna, S. Zankovycha, C.M.S. Torres, C. Menozzi, M. Cavallini, M. Murgia, G. Ruani, F. Biscarini, M. Behl, R. Zentel, J. Ahopelto, Microelectron. Eng. 61–62 (2002) 25–31.
[11] A. Dodabalapur, H.E. Katz, L. Torsi, R.C. Haddon, Science 269 (1995) 1560–1562.
[12] E.L. Granstrom, C.D. Frisbie, J. Phys. Chem. B 103 (1999) 8842–8849.
[13] R. Schroeder, L.A. Majewski, M. Grell, Appl. Phys. Lett. 83 (2003) 3201–3203.
[14] R. Ruiz, D. Choudhary, B. Nickel, T. Toccoli, K.C. Chang, A.C. Mayer, P. Clancy, J.M. Blakely, R.L. Headrick, S. Iannotta, G.G. Malliaras, Chem. Mater. 16 (2004) 4497–4508.
[15] A.D. Carlo, F. Piacenza, A. Bolognesi, B. Stadlober, H. Maresch, Appl. Phys. Lett. 86 (2005) 263501.

[16] F. Eder, H. Klauk, M. Halik, U. Zschieschang, G. Schmid, C. Dehm, Appl. Phys. Lett. 84 (2004) 2673–2675.
[17] S.E. Fritz, T.W. Kelley, C.D. Frisbie, J. Phys. Chem. B 109 (2005) 10574–10577.
[18] G. Horowitz, D. Fichou, X.Z. Peng, F. Garnier, Synth. Met. 41 (1991) 1127–1130.
[19] D. Knipp, R.A. Street, A. Volkel, J. Ho, J. Appl. Phys. 93 (2003) 347–355.
[20] G. Wang, Y. Luo, P.H. Beton, Appl. Phys. Lett. 83 (2003) 3108–3110.
[21] C.D. Dimitrakopoulos, A.R. Brown, A. Pomp, J. Appl. Phys. 80 (1996) 2501–2508.
[22] D.J. Gundlach, L.L. Jia, T.N. Jackson, IEEE Electron Device Lett. 22 (2001) 571–573.
[23] R. Ruiz, A. Papadimitratos, A.C. Mayer, G.G. Malliaras, Adv. Mater. 17 (2005) 1795–1798.
[24] P.-Y. Lo, Z.-W. Pei, J.-J. Hwang, Jpn. J. Appl. Phys., Part I 45 (2006) 3704–3707.
[25] P.V. Necliudov, M.S. Shur, D.J. Gundlach, T.N. Jackson, J. Appl. Phys. 88 (2000) 6594–6597.
[26] C.D. Dimitrakopoulos, D.J. Mascaro, IBM J. Res. & Dev. 45 (2001) 11–27.
[27] S.M. Sze, Physics of Semiconductor Devices, Wiley, New York, 1981.
[28] J. Zaumseil, T. Someya, Z. Bao, Y.-L. Loo, R. Cirelli, J.A. Rogers, Appl. Phys. Lett. 82 (2003) 793–795.
[29] J. Zaumseil, K.W. Baldwin, J.A. Rogers, J. Appl. Phys. 93 (2003) 6117–6124.
[30] T.-W. Lee, J. Zaumseil, Z. Bao, J.W.P. Hsu, J.A. Rodgers, Proceedings of the National Academy of Sciences 101 (2004) 429–433.
[31] Y.L. Loo, D.V. Lang, J.A. Rogers, J.W. Hsu, Nano Lett. 3 (2003) 913.
[32] I. Yagi, K. Tsukagoshi, Y. Aoyagi, Appl. Phys. Lett. 84 (2004) 813–815.
[33] A.C. Mayer, Ricardo Ruiz, H. Zhou, R.L. Headrick, A. Kazimirov, G.G. Malliaras, Phys. Rev. B 73 (2006) 205307.
[34] Y. Shao, S.A. Solin, D.R. Hines, E.D. Williams, J. Appl. Phys. 100 (2006) 044512.

Available online at www.sciencedirect.com
ScienceDirect
Organic Electronics 9 (2008) 515–521
Organic Electronics
www.elsevier.com/locate/orgel

The modification of silver anode by an organic solvent (tetrahydrofuran) for top-emissive polymer light-emitting diodes

Lai-Wan Chong [a], Ten-Chin Wen [a,*], Yuh-Lang Lee [a,*], Tzung-Fang Guo [b]

[a] Department of Chemical Engineering, National Cheng Kung University, Tainan 701, Taiwan, ROC
[b] Institute of Electro-Optical Science and Engineering, National Cheng Kung University, Tainan 701, Taiwan, ROC

Received 31 October 2007; received in revised form 1 February 2008; accepted 24 February 2008
Available online 4 March 2008

Abstract

An organic solvent, tetrahydrofuran (THF), was employed to modify the Ag anode of a top-emissive polymer light-emitting diode (T-PLED) for improving the hole injection capability and the performance of a T-PLED device. The X-ray photoelectron spectroscope analysis shows that the THF molecules were chemically adsorbed on the Ag surface, forming oxygen-rich species by substrate-catalyzed decomposition. The THF-modification were found to enhance the hole injection on the Ag anode, decrease the threshold voltage, and increase the light intensity and luminous efficiency of a T-PLED device, attributing mainly to the increase of work function of the Ag anode.

PACS: 73.40Rw; 73.40Gk; 73.40Cg; 73.61Ph

Keywords: Top-emissive polymer light-emitting diodes; Ag modification

1. Introduction

Polymer light-emissive diodes (PLEDs) have been attracted great attentions since 1991 because of its potential applications in an easier process and a larger flat panel display in comparison with organic light-emissive diodes (OLEDs) [1]. There are two major structures according to emissive direction, bottom emissive and top-emissive PLEDs (T-PLEDs). Although bottom emissive PLEDs are most investigated, T-PLEDs attract attentions due to the advantage of using pixel circuits of thin-film transistors on opaque substrates, higher aperture ratio, more saturated color and larger light intensity [2,3]. For the common structure of T-PLEDs, an active polymer is inserted between a semi-transparent cathode and a high reflective anode. Due to the high reflectivity and low electrical resistivity, silver (Ag) is the most commonly used anode for T-PLEDs. Unfortunately, the low work function renders Ag a large hole injection barrier, causing

* Corresponding authors. Tel.: +886 6 2385487; fax: +886 6 2344496.
E-mail addresses: tcwen@mail.ncku.edu.tw (T.-C. Wen), yllee@mail.ncku.edu.tw (Y.-L. Lee).

1566-1199/$ - see front matter © 2008 Elsevier B.V. All rights reserved.
doi:10.1016/j.orgel.2008.02.014

the unbalance of carriers (hole and electron) to reduce the luminous efficiency (LE) of T-PLED [4]. Thus, the modification of interface between Ag and organic layer has attracted researchers' interesting.

In order to overcome the problem of low work function, thin-films of CF_x or Ag_2O layer deposited on the Ag anode were studied [5–8]. For preparing a CF_x and Ag_2O thin-film, various techniques including thermal evaporating, sputtering, plasma and UV-ozone were commonly used. However, all these methods do increase cost and complication in their future application. In addition, the reflectance of Ag anode decreases because of the existence of such thin-films, decaying the efficiency of a top-emissive OLEDs [8]. In order to avoid the above defects, easier methods and thinner films should be considered, such as self-assembled monolayer (SAM) on Ag surface [9–12]. In a previous work, a SAM of fluorothiophenol was employed to induce a surface dipole on an Ag anode, which increases the work function of Ag anode and improve the performance of a T-PLEDs [13].

In this study, a simpler method of anode modification is reported for enhancing the hole injection of a T-PLED. An organic solvent, tetrahydrofuran (THF) is used as a surface modifier, which chemically adsorbs on the Ag surface and improves the performance of a T-PLED. The present method offers the advantage of simple treatment which is suitable to be applied in the fabrication process of T-PLEDs.

2. Experimental

Two T-PLEDs (ITO/Ag/HY-PPV/Ca/Ag and ITO/THF-modified Ag/HY-PPV/Ca/Ag) were prepared in this study. Silver anode was deposited on an indium tin oxide (ITO) coated glass substrate for 150 nm thickness by thermal evaporation. The deposition was performed under a base pressure of 10^{-6} torr. After deposition of silver film on ITO-coated glass, the Ag anode was immediately surface modified by immersing in THF, C_4H_8O (> 99%, Mallinckrodt) for 30 min. After the reaction, the THF-modified Ag anodes were dried with a nitrogen steam and were delivered to the nitrogen-filled glove-box. "High-yellow" phenyl-substituted poly(-para-phenylenevinylene) copolymer (HY-PPV) (dissolved in toluene) was used as the light-emissive layer and was spin-coated onto the Ag anodes. Finally, a semi-transparent top cathode, Ca(12 nm)/Ag(17 nm), was vapor deposited under 10^{-6} torr. The active pixel area of the device was 6 mm^2.

Contact angle of water was measured by dynamic contact angles (DCA) instruments (Thermo Cahn DCA 300). X-ray photoelectron spectroscopy (XPS) (Perkin Elmer PHI 1600) equipped with a Mg Kα source (1253.6 eV) was used to analyze the surface composition of the modified Ag substrates. The work functions of the anode electrodes were measured by a Riken Keiki AC-2 photoelectron spectroscopy in air. The current density–voltage (J–V) and luminance–voltage (L–V) measurements were carried out by a current/voltage source measurement unit (Keithley 2400) and a calibrated silicon photodiode driven by a Keithley source. All the measurements were performed in a nitrogen-filled glove box.

3. Results and discussion

Fig. 1 presents advancing and receding contact angles of water on base Ag and THF-modified

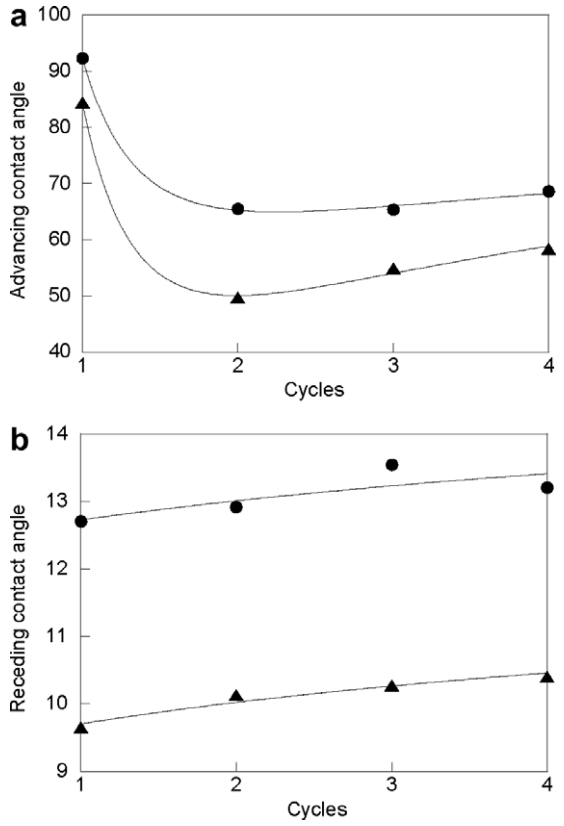

Fig. 1. Advancing (a) and receding (b) contact angles versus analysis cycles for base Ag (●) and THF-modified Ag (▲).

Ag. Four analysis cycles were performed on each specimen. The advancing contact angle on base Ag surface at the first immersion cycle is 92.4°, being attributable to the unavoidable contamination by hydrocarbon and carbonaceous impurities [14]. The advancing contact angle decreases to 65.6° at the second analysis cycle, ascribed to the partial desorption of impurities and/or to the adsorption of water molecule on the substrate surface. The advancing contact angle does not change obviously after the second cycle. For the receding contact angle, a much smaller value (13.6°), independent of the analysis cycles, was obtained for the base Ag surface. The large difference between advancing and receding contact angles, the contact angle hysteresis, indicates the heterogeneity of the Ag surface. Apparently, the adsorption of contaminant(s) causes a surface with both hydrophobic and hydrophilic regions, leading to the difference in advancing and receding contact angles. For the THF-modified Ag surface, the dependence of the contact angles with the analysis cycles of contact angle measurement is similar to that for a base Ag surface, however, smaller contact angles were obtained. It is inferred that the THF can dissolve the surface contaminant(s) of the Ag film and adsorbs instead on the Ag surface. The existence of the THF molecules on the modified Ag surface was confirmed by the XPS analysis which will be discussed in the later section. Due to the polar characteristic of the THF molecules, smaller contact angles, both advancing and receding, were anticipated on a THF-covered surface. Furthermore, the lower contact angle hysteresis measured for the THF-modified Ag surface implies that the modified surface is more uniform in surface composition compared with a contaminated one, being attributable to the formation a densely packed THF layer [15,16].

The surface compositions and binding energy of both base Ag and THF-modified Ag were analyzed by high-resolution XPS photoemission spectra. XPS C_{1s} spectra of both base Ag and THF-modified Ag are shown in Fig. 2a and b, respectively. The XPS peaks were deconvoluted with a suitable Gaussian–Lorentzian function at 284.5, 285.5 and 287.5 eV, corresponding to the feature peaks of C–C/C–H, C–O, C=O, respectively [17–19]. The area ratios of these feature peaks were calculated and listed in Table 1. For the THF-modified Ag surface, the area ratio of C–C/C–H (peak I) is lower, but the area ratios corresponding to the C–O (peak II) and C=O (peak III) species are higher in comparison with the base Ag surface. This result indicates that the contaminants adsorbing on the bare Ag surface have smaller polarity than the THF-modified Ag, which is consistent with the larger contact angle of water measured on the base Ag surface.

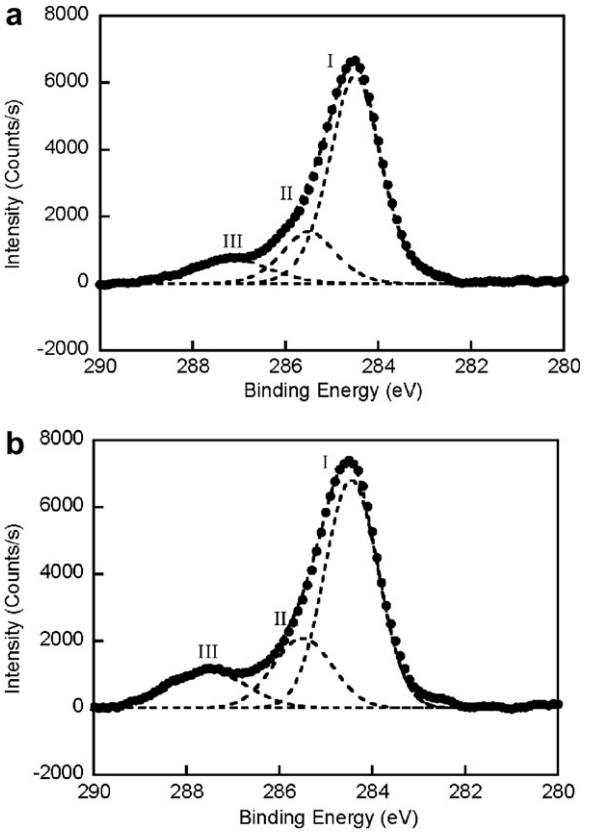

Fig. 2. High resolution XPS of C_{1s} spectra for base Ag (a), and THF-modified Ag (b).

Table 1
The peak area ratios of C_{1s} and O_{1s} spectra for base Ag and THF-modified Ag

	Peak area ratio					
XPS region	C_{1s}			O_{1s}		
Peak	I	II	III	A	B	C
Base Ag	0.71	0.18	0.11	0.27	0.73	0.00
THF-modified Ag	0.64	0.22	0.14	0.18	0.77	0.05

Fig. 3 shows the XPS O_{1s} spectra for the base Ag and THF-modified Ag surfaces. These O_{1s} spectra can be deconvoluted into two and three feature peaks, respectively, for base Ag and THF-modified Ag at 532.5, 530.7, and 529.3 eV. The feature peaks at 532.5 eV (peak A) and 530.7 eV (peak B) correspond,

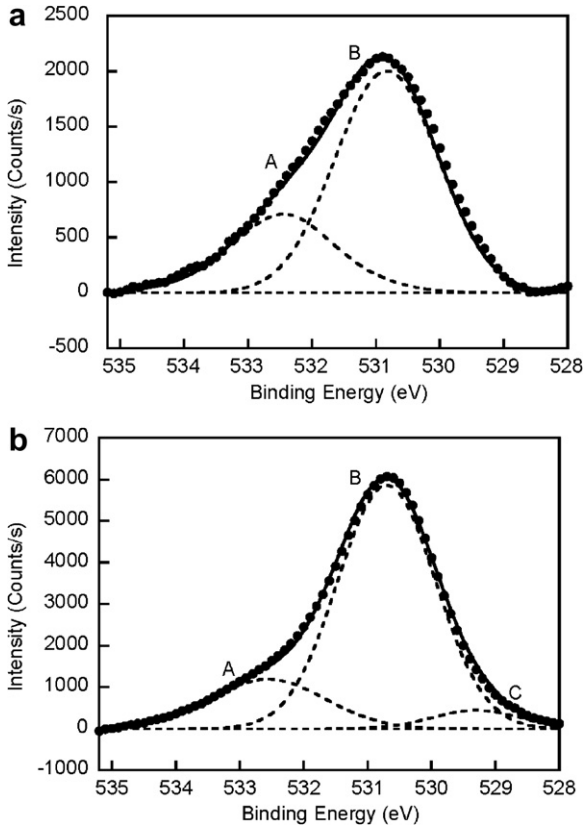

Fig. 3. High resolution XPS of O_{1s} spectra for base Ag (a), and THF-modified Ag (b).

respectively, to the adsorbed hydroxyl groups and carbonated species [17–19]. The higher ratio of the O_{1s} peak corresponding to the carbonated species (peak B) on the THF-modified Ag (Table 1) is consistent to the higher C_{1s} ratio corresponding to the C=O species. In Fig. 3b, the feature peak at 529.3 eV (peak C) was only observed on THF-modified Ag. In the literature, this feature peak was attributed to the presence of C–O–metal bonding [17–19] and the appearance this peak may imply a chemical reaction between adsorbed THF and the Ag substrate. Another evidence to the specific THF–Ag interaction can be inspected from the C/O ratio list in Table 2. The C:O ratio measured for the THF-modified Ag is 2.5, which is different from the C:O stoichiometry in THF (4.0). Since the base Ag substrate has a higher C:O ratio of 5.6, the smaller C:O ratio of the THF-modified Ag cannot be attributed to the possible contaminants, as the case on the base Ag. Therefore, a surface reaction of the adsorbed THF molecules is inferred which makes the layer became oxygen-rich by releasing a carbon-rich gas.

Table 2
Atomic concentrations and atomic ratios determined by XPS analysis for base Ag and THF-modified Ag

	Atomic concentration (%)			Atomic ratio
XPS region	Ag_{3d}	O_{1s}	C_{1s}	C/O
Base Ag	53.52	7.01	39.47	5.63
THF-modified Ag	43.99	15.99	40.02	2.50

The reaction of adsorbed THF molecules with a metal substrate (Al or Ag) had been studied as a function of substrate temperature by Wang et al. [20–22]. The C:O atomic ratio obtained at 135 K is 4.2, and decreases with increase of temperature. For temperatures from 240 to 470 K, the measured C:O ratio is about 2.8, in good agreement with the present result. The mechanism proposed for the surface reaction of THF includes the formation of ring-opening radicals through the substrate-catalyzed decomposition, followed by propagating ring-opening interactions of THF molecules. Propylene alkoxides were considered as the end compounds presented on the substrate. Although the real mechanism and products of the surface reaction are still not clear for the present system, the surface reaction of THF on the Ag surface was confirmed. That is, the THF molecules are chemically adsorbed on the Ag surface.

Table 2 also shows that the THF-modified Ag surface has a lower Ag composition in comparison with the base Ag substrate. This result implies that the adlayer on the THF-modified surface has a more condensed and/or better-covered structure. On the other hand, the contaminants on the base Ag surface were heterogeneously adsorbed, leading to the exposure of bare Ag surface and therefore, a higher measured composition of silver.

Because the property of Ag surface is changed due to the chemisorption of THF, the effect of chemisorption of THF on hole injection is interesting to knows. Thus, hole-dominated PLEDs, ITO/Ag/HY-PPV/Al and ITO/THF-modified Ag/HY-PPV/Al, were fabricated first and the corresponding J–V curves were shown in Fig. 4. The threshold voltage of the THF-modified device is lower than that of the base Ag device, attributable to the increase in work function due to the modification of THF. The work functions of both Ag anodes measured by AC-2 photoelectron spectroscopy are 4.54 eV for base Ag and 4.79 eV for the THF-mod-

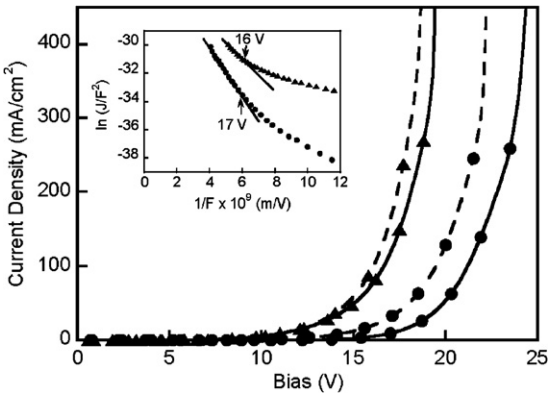

Fig. 4. J–V characteristics for the ITO/Ag/HY-PPV/Al (●) and ITO/THF-modified Ag/HY-PPV/Al devices (▲) with (---) and without (—) heat treatment at 120 °C for 1 hour. The inset is the Fowler–Nordheim plots for the devices.

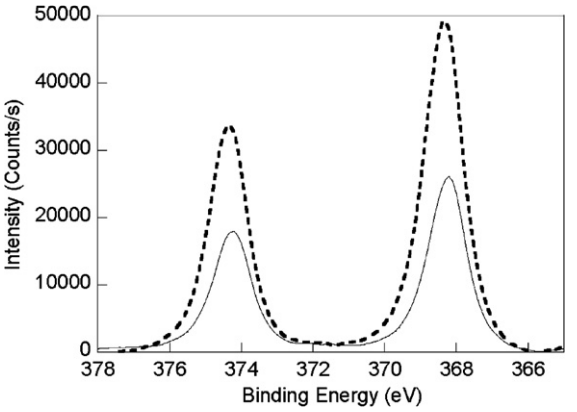

Fig. 5. High resolution XPS of Ag_{3d} spectra for base Ag with (---) and without (—) heat treatment at 120 °C for 1 h.

ified one. The higher work function of the THF-modified Ag surface is probably related to the presence of oxygen-rich species on Ag surface. Due to the high electro-negativity of oxygen atom, the oxygen-rich species are supposed to induce a surface dipole, leading to an increase of the work function.

The barrier height for the hole injection was examined using the Fowler–Nordheim (FN) tunneling theory,

$$J \propto F^2 \exp\left(\frac{-\kappa}{F}\right), \quad \text{where } \kappa = \frac{8\pi\sqrt{2m^*\varphi^{3/2}}}{3qh}, \qquad (1)$$

where J is the current density of device, F is the electric field under bias, κ is a parameter related to the shape of the injection barrier height (φ), m^* is the effective mass of holes in HY-PPV, q is the charge of hole, and h is the Planck's constant. The inset in Fig. 4 shows the plots of $\ln(J/F^2)$ versus $1/F$ for these two hole-dominated devices. The straight-line FN curves shown for these two devices indicate that the holes are injected through the tunneling process. According to Eq. (1), the slope of the line is proportional to $\varphi^{3/2}$. For the THF-modified device, the slope of FN curve is smaller than that of base Ag, indicating that THF-modified device has a lower hole injection barrier height than the base device. The hole injection barrier height measured from Eq. (1) is 0.43 eV for the THF-modified device, which is in agreement with the result measured from AC-2 photoelectron spectroscopy (0.41 eV).

The effect of heat treatment of the THF-chemisorbed layer on hole injection was also analyzed through hole-dominated PLED devices performance (Fig. 4). Before fabricating the hole-dominated devices, the THF-modified and unmodified Ag anodes were heated at a temperature of 120 °C for 1 h in a glove-box filled with nitrogen. In Fig. 4, a lower threshold voltage and a higher current density for the base Ag device with heat treatment are observed, which might be due to the decrease in resistance of hole injection by eliminating a part of hydrocarbon contaminants adsorbed on base Ag surface. This inference is sustained by XPS results (Fig. 5). After the heat treatment, the atomic concentrations of Ag significantly increase and that of carbon and oxygen decrease. The Ag_{3d} feature peaks of the base Ag with and without heat treatment do not obviously change in the peak width and the binding energy of the peak center. Moreover, the work function of the base Ag with (4.56 eV) and without (4.54 eV) heat treatment is almost the same. Therefore, it is suggested that the enhancement of the electrical properties of the base Ag devices is attributed to the decrease in resistance of hole injection by eliminating some contaminants adsorbed on base Ag surface. On the other hand, it is interested that the J–V characteristics of the THF-modified devices with and without heat treatments are similar. These results show that the enhancement of hole injection by THF-chemisorbed layer still exist at a temperature as high as 120 °C. Thus, it also implies the THF-chemisorbed layer can adsorb on Ag sturdily.

In order to clarify whether THF solvent has some in situ surface treating effects if THF is used as the solvent of HY-PPV. Four hole-dominated devices, ITO/Ag/HY-PPV (dissolved in toluene)/Al, ITO/THF-modified Ag/HY-PPV (dissolved in toluene)/Al, ITO/Ag/HY-PPV (dissolved in THF)/Al, and

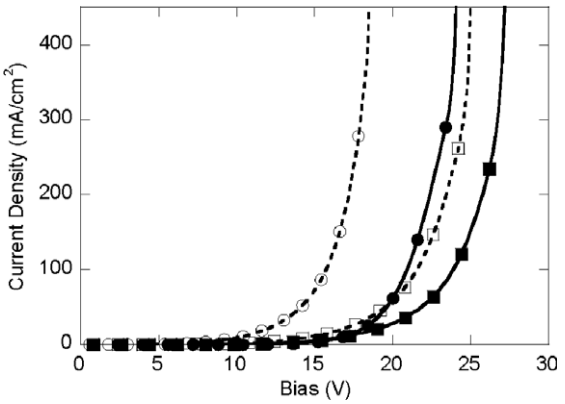

Fig. 6. *J–V* characteristics for the ITO/Ag/HY-PPV(dissolved in toluene)/Al (●), ITO/THF-modified Ag/HY-PPV (dissolved in toluene)/Al (○), ITO/Ag/HY-PPV (dissolved in THF)/Al (■), and ITO/THF-modified Ag/HY-PPV (dissolved in THF)/Al (□) devices.

ITO/THF-modified Ag/HY-PPV (dissolved in THF)/Al, were fabricated and the corresponding *J–V* curves are shown in Fig. 6. The threshold voltage of both THF-modified devices is lower than that of both base Ag devices. The devices prepared with HY-PPV dissolved in THF have the higher operating voltage and the lower current density than those in toluene. It depicts that there is not in situ effect of surface modification of Ag anode with THF as the solvent of HY-PPV. The poor performance of the device with HY-PPV dissolved in THF is attributed to the morphological effect from solvation on the polymer/metal contacts. It is clear that THF is not a good solvent for spin-coating of HY-PPV on Ag substrate. The similar results and discussion for solvation induced morphological effect on the polymer/metal contacts have been reported by Liu et al. [23,24].

After confirming the THF-modification on the hole injection, the effect of the THF-modified Ag anode on the performance of a top-emissive device was studied using a semi-transparent (Ca/Ag) cathode. Fig. 7 shows the *J–V* and *L–V* characteristics of the top-emissive devices with the structure of ITO/Ag(150 nm)/HY-PPV/Ca(12 nm)/Ag(17 nm) and ITO/THF-modified Ag/HY-PPV/Ca(12 nm)/Ag(17 nm), respectively. The *J–V* curves shown in Fig. 7a demonstrate that the effect of THF-modified layer on the threshold voltage is similar to the hole-dominated devices shown in Fig. 4. However, the effect of the THF-modification on *L–V* performance is more significant, as shown in Fig. 7b. For the THF-modified device, the maximum brightness is

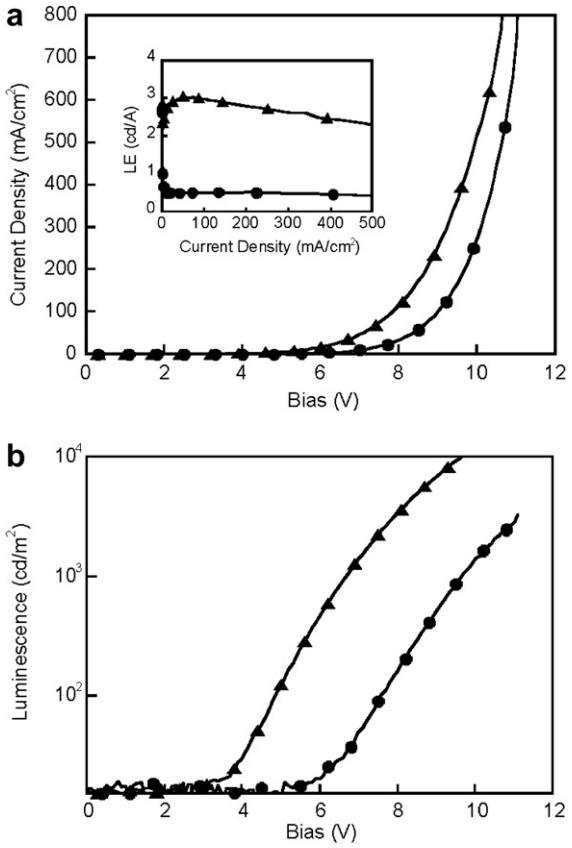

Fig. 7. *J–V* (a) and *L–V* (b) characteristics for the ITO/Ag/HY-PPV/Ca(12 nm)/Ag(17 nm) (●) and ITO/THF-modified Ag / HY-PPV/Ca(12 nm)/Ag(17 nm) devices (▲). The inset is the luminous efficiency (LE) characteristics of the top-emissive PLED devices.

15118 cd/m^2 biased at 10.7 V, which is much higher than the luminance of the unmodified Ag anode (2349 cd/m^2) operated at the same bias. The luminous efficiencies (LE) of the devices are shown in the inset of Fig. 7a. At a light intensity of 1000 cd/m^2, the LE of the THF-modified device is as high as 2.93 cd/A, which is 5-fold higher than that of the base Ag device (0.51 cd/A). The higher performance of THF-modified device is a result of a better balance of the injected holes to the injected electrons, attributed to the enhancement of hole injection on the Ag anode.

4. Conclusions

THF has been proved to be an efficient surface modifier of an Ag anode for improving the performance of a top-emissive PLED. By simply dipping an Ag anode in THF, THF molecules can chemically

adsorb on the Ag surface, forming oxygen-rich species by substrate-catalyzed decomposition. The chemically adsorbed layer increases the work function of an Ag surface, which thereby, enhances the hole injection on an Ag anode. The THF-modification was found to decrease the threshold voltage, increase the light intensity and luminous efficiency of a T-PLED device.

Acknowledgments

The authors would like to thank National Science Council (NSC) of Taiwan (NSC 96-2221-E-006-058 and NSC 96-2221-E-006-409-MY3). Dr. Ruei-Tang Chen from Eternal Chemical Co., Ltd., is appreciated for providing the HY-PPV polymer. Ms. Yu-Ting Tsai from Chi Mel EL Corporation is thankfully for detecting the work functions of the anode electrodes.

References

[1] J.H. Burroughes, D.D.C. Bradley, A.R. Brown, R.N. Marks, K. Mackay, R.H. Friend, P.L. Bruns, A.B. Holmes, Nature 347 (1990) 539.
[2] H. Riel, S. Karg, T. Beierlein, B. Ruhstaller, W. Rieβ, Appl. Phys. Lett. 82 (2003) 466.
[3] C.-C. Wu, C.-W. Chen, C.-L. Lin, C.-J. Yang, IEEE/OSA J. Display Technol. 1 (2005) 248.
[4] H.B. Michaelson, IBM J. Res. Dev. 22 (1978) 72.
[5] H. Peng, X. Zhu, J. Sun, Z. Xie, S. Xie, M. Wong, H.-S. Kwok, Appl. Phys. Lett. 87 (2005) 173505.
[6] H. Peng, J. Sun, X. Zhu, X. Yu, M. Wong, H.-S. Kwok, Appl. Phys. Lett. 88 (2006) 073517.
[7] H.-W. Choi, S.-Y. Kim, K.-B. Kim, Y.-H. Tak, J.-L. Lee, Appl. Phys. Lett. 86 (2005) 012104.
[8] C.-W. Chen, P.-Y. Hsieh, H.-H. Chiang, C.-L. Lin, H.-M. Wu, C.-C. Wu, Appl. Phys. Lett. 83 (2003) 5127.
[9] S. Khodabakhsh, D. Poplavskyy, S. Heutz, J. Nelson, D.D.C. Bradley, H. Murata, T.S. Jones, Adv. Funct. Mater. 14 (2004) 1205.
[10] B. de Boer, A. Hadipour, M.M. Mandoc, T. van Woudenbergh, P.W.M. Blom, Adv. Mater. 17 (2005) 621.
[11] M.-C. Hung, K.-Y. Wu, Y.-T. Tao, H.-W. Huang, Appl. Phys. Lett. 89 (2006) 203106.
[12] K.-Y. Wu, Y.-T. Tao, H.-W. Huang, Appl. Phys. Lett. 90 (2007) 241104.
[13] L.-W. Chong, Y.-L. Lee, T.-C. Wen, T.-F. Guo, Appl. Phys. Lett. 89 (2006) 233513.
[14] C.E. Taylor, S.D. Garvey, J.E. Pemberton, Anal. Chem. 68 (1996) 2401.
[15] C.-M. Ruan, T. Bayer, S. Meth, C.N. Sukenik, Thin Solid Films 419 (2002) 95.
[16] I.L. Liakos, R.C. Newman, E. McAlpine, M.R. Alexander, Langmuir 23 (2007) 995.
[17] D.Y. Zemlyanov, E. Savinova, A. Scheybal, K. Doblhofer, R. Schlögl, Surf. Sci. 418 (1998) 441.
[18] J.T. Wolan, G.B. Hoflund, Appl. Surf. Sci. 125 (1998) 251.
[19] G.B. Hoflund, Z.F. Hazos, G.N. Salaita, Phys. Rev. B 62 (2000) 11126.
[20] K. Wang, G.S. Chottiner, D.A. Scherson, J. Phys. Chem. 97 (1993) 11075.
[21] K. Wang, P.N. Ross Jr., Surf. Sci. 365 (1996) 753.
[22] G. Zhuang, K. Wang, P.N. Ross Jr., Surf. Sci. 387 (1997) 199.
[23] J. Liu, T.-F. Guo, Y. Shi, Y. Yang, J. Appl. Phys. 89 (2001) 3668.
[24] J. Liu, Y. Shi, L. Ma, Y. Yang, J. Appl. Phys. 88 (2000) 605.

Available online at www.sciencedirect.com
ScienceDirect
Organic Electronics 9 (2008) 522–532
Organic Electronics
www.elsevier.com/locate/orgel

Blue organic light-emitting diode with improved color purity using 5-naphthyl-spiro[fluorene-7,9′-benzofluorene]

Soon-Ok Jeon [a], Young-Min Jeon [a], Joon-Woo Kim [b], Chil-Won Lee [b], Myoung-Seon Gong [a,*]

[a] *Department of Chemistry and Institute of Basic Science, Dankook University, Chungnam 330-714, Republic of Korea*
[b] *OLED Team, Daejoo Electronic Materials, Siheung, Kyung-gi 429-848, Republic of Korea*

Received 21 January 2008; received in revised form 26 February 2008; accepted 28 February 2008
Available online 6 March 2008

Abstract

Novel spiro-type blue host material, 5-naphthyl-spiro[fluorene-7,9′-benzofluorene] (BH-1SN) and dopant material, 5-diphenyl amine-spiro[fluorene-7,9′-benzofluorene] (BH-1DPA) were successfully synthesized, and a blue OLED was made from them. The structure of the blue device is ITO/DNTPD/α-NPD/BH-1SN:5% dopant/Alq_3 or ET4/Al–LiF. Here, α-NPD is used as the hole transport layer, DNTPD as the hole injection layer, BH-1DPA or BD-1 as the blue dopant materials, Alq_3 or ET4 as the transporting layer and Al as the cathode. The blue devices doped with 5% BH-1DPA and BD-1 show blue EL emissions at 444 and 448 nm at 7 V, respectively, and a high efficiency of 3.4 cd/A at 5 V for the device was obtained from BH-1SN:5% BD-1/ET4. The CIE coordinates of the blue emission are 0.15, 0.08 at an applied voltage of 7 V for the device obtained from BH-1SN/5% BH-1DPA/Alq_3.

PACS: 42.79.Kr; 85.60.Jb; 85.45.Fd; 07.07.Hj

Keywords: Blue host material; OLED; Color purity; Spiro [fluorene-7,9′-benzofluorene]

1. Introduction

Organic light-emitting diodes are currently the subject of an intense research effort due to their promise as devices for full-color display applications [1–3]. In particular, efficient blue emission has been pursued in several different molecular systems, including metal complexes [4,5], oxadiazoles [6,7], lanthanide complexes [8], and distyrylarylenes [9–13]. In general, blue-emitting OLEDs have lower efficiencies than green or red devices, due to the larger band gap energy of the emission material, which inhibits the injection of carriers. It is often the case that poor electron injection at the cathode is the limiting factor in the efficiency.

Among the various issues involved in the fabrication of full-color OLEDs, one of the major concerns is achieving the equal performance of the three primary colors of red, green and blue. Due to their large band gap energy, blue light-emitting materials have a low affinity for the electrons from the cathode in OLED devices. Therefore, the performance of blue

* Corresponding author. Tel.: +82 41 5501476; fax: +82 41 5503431.
E-mail address: msgong@dankook.ac.kr (M.-S. Gong).

1566-1199/$ - see front matter © 2008 Elsevier B.V. All rights reserved.
doi:10.1016/j.orgel.2008.02.016

emitters is usually not satisfactory, being inferior to that of the green or red emitters. Specifically, the color purity and stability of blue OLEDs are in need of improvement. Consequently, potential new blue-emitting materials continue to receive considerable attention, because they could be utilized as a blue light source in their own right and as a host for down-hill energy transfer to green or red emitting materials [14,15]. Much of the recent research into blue-emitting materials has centered on spiro-based derivatives, because of their high solution and solid state photoluminescence quantum yields [16,17].

In this study, we report a blue organic light-emitting device made from a new spiro-type host material, BH-1SN, BH-1DPA and BD-1 as the dopant materials and Alq_3 and ET4 as the electron transporting materials in an attempt to improve the color purity.

2. Experimental

2.1. Materials and measurements

Tetrakis(triphenylphosphine)palladium(0), naphthalene-1-boronic acid, 9-fluorenone, *n*-butyllithium, diphenylamine, 1-bromo-2-iodobenzene, bromine and potassium *t*-butoxide (Aldrich Chem. Co.) were used without further purification. Palladium acetate and tri-*t*-butylphosphine (TCI Chem. Co.) were used without further purification. Naphthalene-1-boronic acid and naphthalene-2-boronic acid (Frontier Scientific Co.) were used without further purification. Tetrahydrofuran and toluene were distilled over sodium and calcium hydride. Diphenyl-[4-(2-[1,1;4,1]terphenyl-4-yl-vinyl)-phenyl]-amine (BD-1) and 2,5-bis-(2′,2″-bipyridin-6-yl)-1,1-diphenyl-3,4-diphenylsilacyclopentadiene (ET4) were used as dopant and electron transfer material, respectively, as illustrated in Scheme 1.

The FT-IR spectra were obtained with a Biorad Excaliber FTS-3000MX spectrophotometer and the ^{1}H NMR and ^{13}C NMR spectra were recorded on a Bruker Avance 500 (500 MHz) spectrometer. The photoluminescence (PL) spectra were recorded on a fluorescence spectrophotometer (Jasco FP-6500) and the UV–vis spectra were obtained by means of a UV–vis spectrophotometer (Shimadzu, UV-1601PC). The elemental analyses were performed using a CE Instrument, EA1110. The DSC measurements were performed on a Mettler DSC 822^{e} under nitrogen at a heating rate of 10 °C/min. The low and high resolution mass spectra were recorded using a JEOL, JMS-AX505WA spectrometer in FAB mode. The energy levels were measured with a low energy photo electron spectrometer (Riken-Keiki AC-2). The current–voltage characteristics of the encapsulated devices were measured on a programmable electrometer having current and voltage source (Source Measure Unit, Model Keithly 237. The luminance and EL spectra were measured with a PR650 system (Photo Research Co. Ltd.).

2.2. Synthesis of 1-(2-bromophenyl)naphthalene (*1*)

Naphthalene-1-boronic acid (10 g, 24.3 mmol), 1-iodo-2-bromobenzene (6.64 g, 29.1 mmol), tetra-

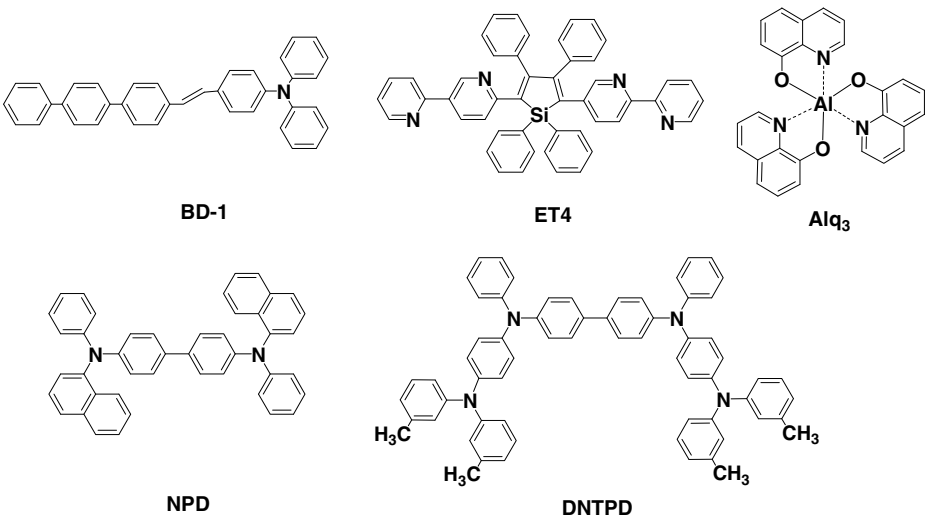

Scheme 1.

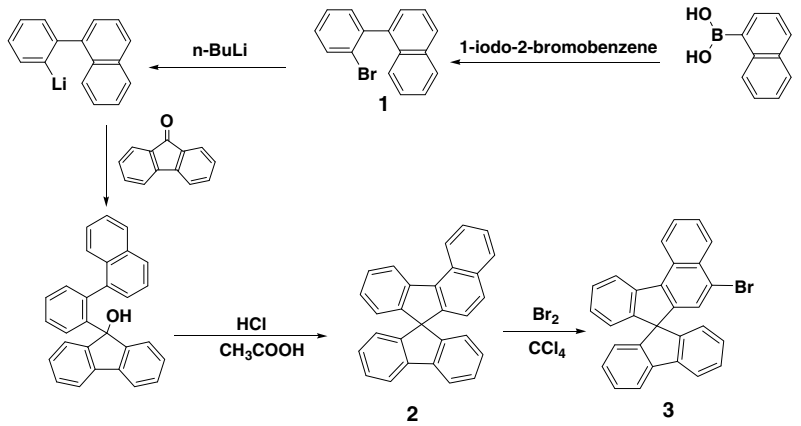

Scheme 2.

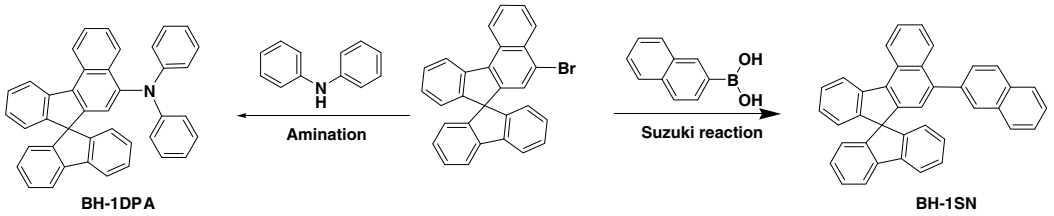

Scheme 3.

kis(triphenylphosphine)palladium(0) and THF (100 mL) were stirred in a two-necked flask for 30 min. To the above solution was added potassium carbonate (3.26 g, 29.1 mmol) dropwise over a period of 20 min. The resulting solution was refluxed overnight at 80 °C. The reaction mixture was extracted with dichloromethane and water. After the organic layer was evaporated with a rotary evaporator, the resulting powdery product was purified by column chromatography using *n*-hexane to give a white crystalline solid.

Yield 89%. Mp: 170 °C. ^{1}H NMR (500 MHz, $CDCl_3$) δ 7.91–7.89 (d, 2 H, Ar–CH–naphthalene), 7.73–7.72 (d, 2H, Ar–CH–naphthalene), 7.53–7.39 (m, 3H, Ar–CH–naphthalene), 7.36–7.34 (m, 3H, Ar–CH–benzene) 7.23 (d, 1H, Ar–CH–Br). FT-IR (KBr, cm^{-1}) 3056 (aromatic C–H), 658 (aromatic C–Br). MS (FAB) m/z 282.0 [$(M+1)^+$].

2.3. Synthesis of spiro[fluorene-7, 9′-benzofluorene] (*2*)

Into a 250 mL two-necked flask was placed a solution of 1-(2-bromophenyl)naphthalene (9.42 g, 33.2 mmol) in THF (50 mL). The reaction flask was cooled to −78 °C and *n*-BuLi (2.5 M in hexane, 14.4 mL) was added dropwise slowly. The whole solution was stirred at this temperature for 1 h, followed by the addition of a solution of 9-fluorenone (5.0 g, 27.7 mmol) in THF (30 mL) under an argon atmosphere. The resulting mixture was gradually warmed to ambient temperature and quenched by adding saturated, aqueous $NaHCO_3$ (90 mL). The mixture was extracted with dichloromethane. The combined organic layers were dried over magnesium sulfate, filtered, and evaporated under reduced pressure. A yellow powdery product was obtained. The crude residue was placed in another two-necked flask (100 mL) and dissolved in acetic acid (30 mL). A catalytic amount of aqueous HCl (5 mol%, 12 N) was then added and the whole solution was refluxed for 12 h. After cooling to ambient temperature, purification by silica gel chromatography using dichloromethane/*n*-hexane gave a white powder.

Yield 92%. Mp: 212 °C. ^{1}H NMR (500 MHz, $CDCl_3$): δ 8.87–8.86 (d, 1H, Ar–CH–benzene), 8.42–8.40 (d, 1H, Ar–CH–naphthalene), 8.35–8.33 (d, 1H, Ar–CH–benzene), 7.88–7.87 (d, 1H, Ar–CH–benzene), 7.77–7.74 (t, 2H, Ar–CH–fluorene), 7.67–7.64 (t, 2H, Ar–CH–fluorene), 7.47–7.44 (t, 2H, Ar–CH–fluorene), 7.41–7.37 (t, 2H, Ar–CH–

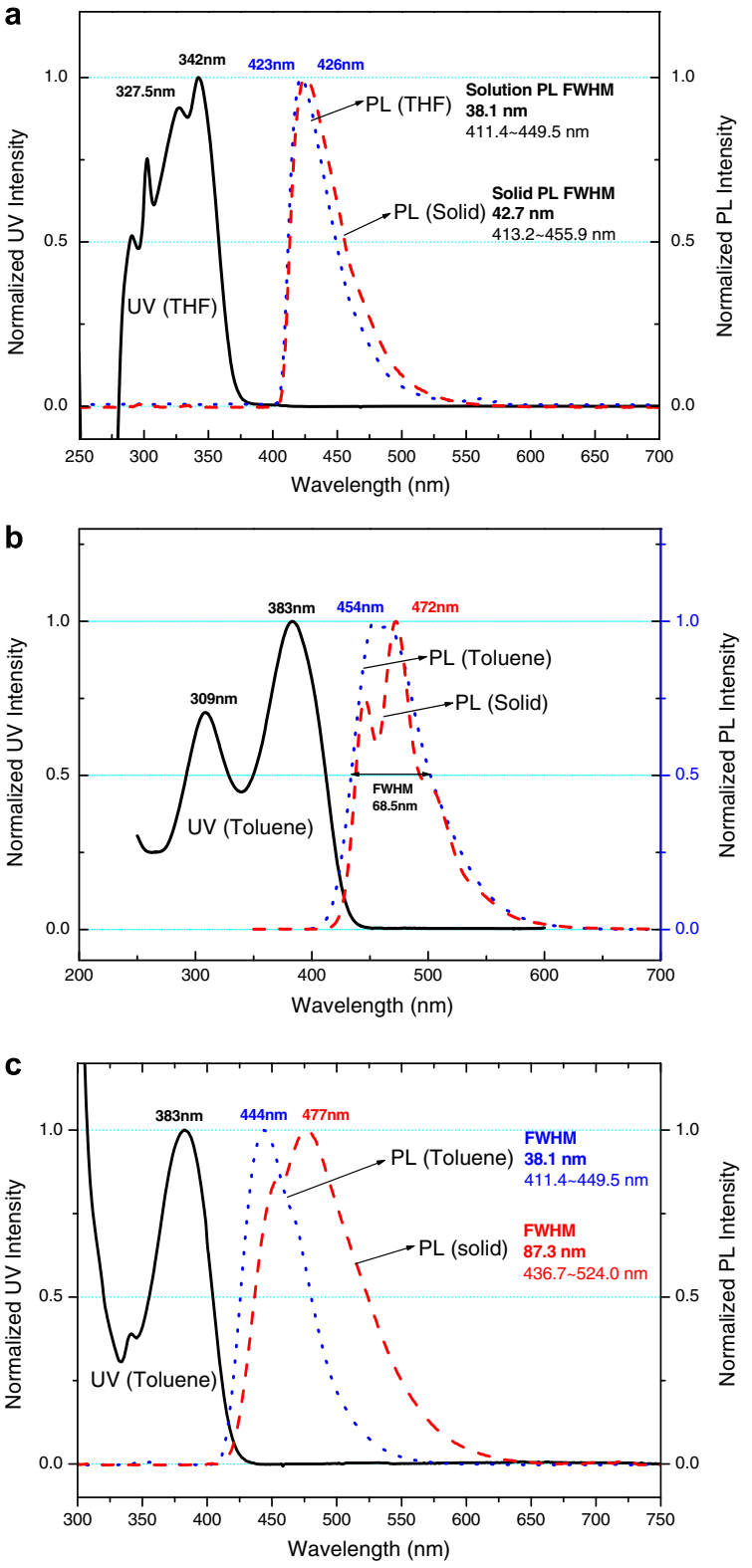

Fig. 1. The UV–vis and PL spectra of: (a) BH-1SN, (b) BD-1 and (c) BH-1DPA.

fluorene), 7.17–7.09 (m, 3H, Ar–CH–benzene), 6.70–6.70 (d, 1H, Ar–CH–benzene). FT-IR (KBr, cm^{-1}) 3059, 3018 (aromatic C–H). MS (FAB) *m/z* 366.45 [$(M + 1)^+$].

2.4. Synthesis of 5-bromo-spiro[fluorene-7,9′-benzofluorene] (3)

The spiro[fluorine-7,9′-benzofluorene] (2) was dissolved in carbon tetrachloride in a two-necked flask and then bromine was added dropwise slowly over a period of 20 min. The mixture was stirred at room temperature for 3 days. The precipitated solid was filtered and dried in vacuo to give the crude product, which was purified by recrystallization from ethyl acetate/*n*-hexane to give a white powder.

Yield 88%. Mp: 269 °C. ^{1}H NMR (500 MHz, $CDCl_3$): δ 8.87–8.86 (d, 1H, Ar–CH–benzene), 8.42–8.40 (d, 1H, Ar–CH–naphthalene), 8.35–8.33 (d, 1H, Ar–CH–benzene), 7.88–7.87 (d, 1H, Ar–CH–benzene), 7.77–7.74 (t, 2H, Ar–CH–fluorene), 7.67–7.64 (t, 2H, Ar–CH–fluorene), 7.47–7.44 (t, 2H, Ar–CH–fluorene), 7.41–7.37 (t, 2H, Ar–CH–fluorene), 7.17–7.09 (m, 3H, Ar–CH–benzene), 6.80–6.78 (d, 1H, Ar–CH–Br), 6.70–6.70 (d, 1H, Ar–CH–benzene). FT-IR (KBr, cm^{-1}) 3059, 3042, 3015 (aromatic C–H), 747 (aromatic C–Br). MS (FAB) *m/z* 444.05 [$(M + 1)^+$].

2.5. Synthesis of 5-diphenyl amine-spiro[fluorene-7,9′-benzofluorene] (BH-1DPA)

5-Bromo-spiro[fluorene-7,9′-benzofluorene] (**3**) (6 g, 13 mmol), diphenylamine (2.73 g, 16 mmol) and palladium acetate (0.087 g, 0.39 mmol) were dissolved in anhydrous toluene under a nitrogen atmosphere. To the reaction mixture was added a solution of tri-*t*-butylphosphine (1 M, 0.29 g, 1.3 mmol) and potassium *t*-butoxide (2.91 g, 26 mmol) dropwise slowly. The reaction mixture was stirred for 12 h at 100 °C. The mixture was diluted with dichloromethane and washed with distilled water (50 mL) three times. The organic layer was dried over anhydrous $MgSO_4$ and evaporated in vacuo to give the crude product, which was purified by column chromatography using *n*-hexane. The final yellow–green powdery product was obtained in 75% yield.

Yield 75%. Mp: 246 °C. ^{1}H NMR (500 MHz, $CDCl_3$) δ 8.89–8.88 (d, 1H, Ar–CH–benzene), 8.42–8.41 (d, 1H, Ar–CH–benzene), 8.04–8.03 (d, 1H, Ar–CH–Ar), 7.79–7.78 (d, 1H, Ar–CH–fluorene), 7.68–7.65 (t, 2H, Ar–CH–fluorene), 7.44–7.41 (p, 3H, Ar–CH–fluorene), 7.34–7.31 (t, 2H, Ar–CH–fluorene), 7.13–7.04 (m, 11H, Ar–CH–N–Ar), 6.89–6.87 (d, 1H, Ar–CH–N–naphthalene), 6.82–6.79 (t, 2H, Ar–CH–N), 6.76–6.73 (t, 2H, Ar–CH–N), ^{13}C NMR ($CDCl_3$): δ 150.2, 148.1, 147.8, 142.2, 131.9, 131.3, 129.1, 128.0, 127.2, 127.1 126.2, 125.8, 124.5, 124.1, 124.0, 122.9, 121.6, 121.5, 120.3, 77.4, 77.2, 76.9, 66.5 ppm. FT-IR (KBr, cm^{-1}) 3061, 3037 (aromatic C–H), 1294, 1274 (aromatic C–N). MS (FAB) *m/z* 533.0 [$(M + 1)^+$]. Anal. Calcd. for $C_{41}H_{27}N$ (533.66) C, 92.28; H, 5.10; N, 2.62. Found: C, 91.67; H, 5.08; N, 2.57. UV–vis (THF): λ_{max} (absorption) = 383 nm, λ_{max} (emission) = 444, 477 nm.

2.6. Synthesis of 5-naphthyl-spiro[fluorene-7,9′-benzofluorene] (BH-1SN)

5-Bromo-spiro[fluorene-7,9′-benzofluorene] (**3**) (5.0 g, 11.2 mmol), naphthalene-2-boronic acid (4.016 g, 13.4 mmol), tetrakis(triphenylphosphine)palladium(0) (0.64 g, 0.56 mmol) and THF (100 mL) were stirred in a two-necked flask under a nitrogen atmosphere for 1 h. To the reaction mixture was added a solution of potassium carbonate

Table 1
The various physical properties of BH-1SN, BH-1DPA and BD-1

Purity	HPLC (%)		BH-1SN	BH-1DPA	BD-1
			99.8	99.5	99
Thermal analysis	DSC	T_g[a] (°C)	133.2	110.4	–
		T_m[b] (°C)	256.5	–	–
Optical analysis	UV	Max (nm)	342	383	383
		Bg[c] (eV)	3.35	2.96	2.87
	PL	Max (nm)	423	444	454
		FWHM[d] (nm)	38.1	38.1	68.5
	Solid PL	Max (nm)	426	477	472
		FWHMd (nm)	42.7	87.3	54
Electrical analysis	AC-2	HOMO[e] (eV)	5.95	5.66	5.46
		LUMO[f] (eV)	2.6	2.70	2.57

[a] Glass transition temperature.
[b] Melting temperature.
[c] Band gap.
[d] Full width at half maximum.
[e] Highest occupied molecular orbital.
[f] Lowest unoccupied molecular orbital.

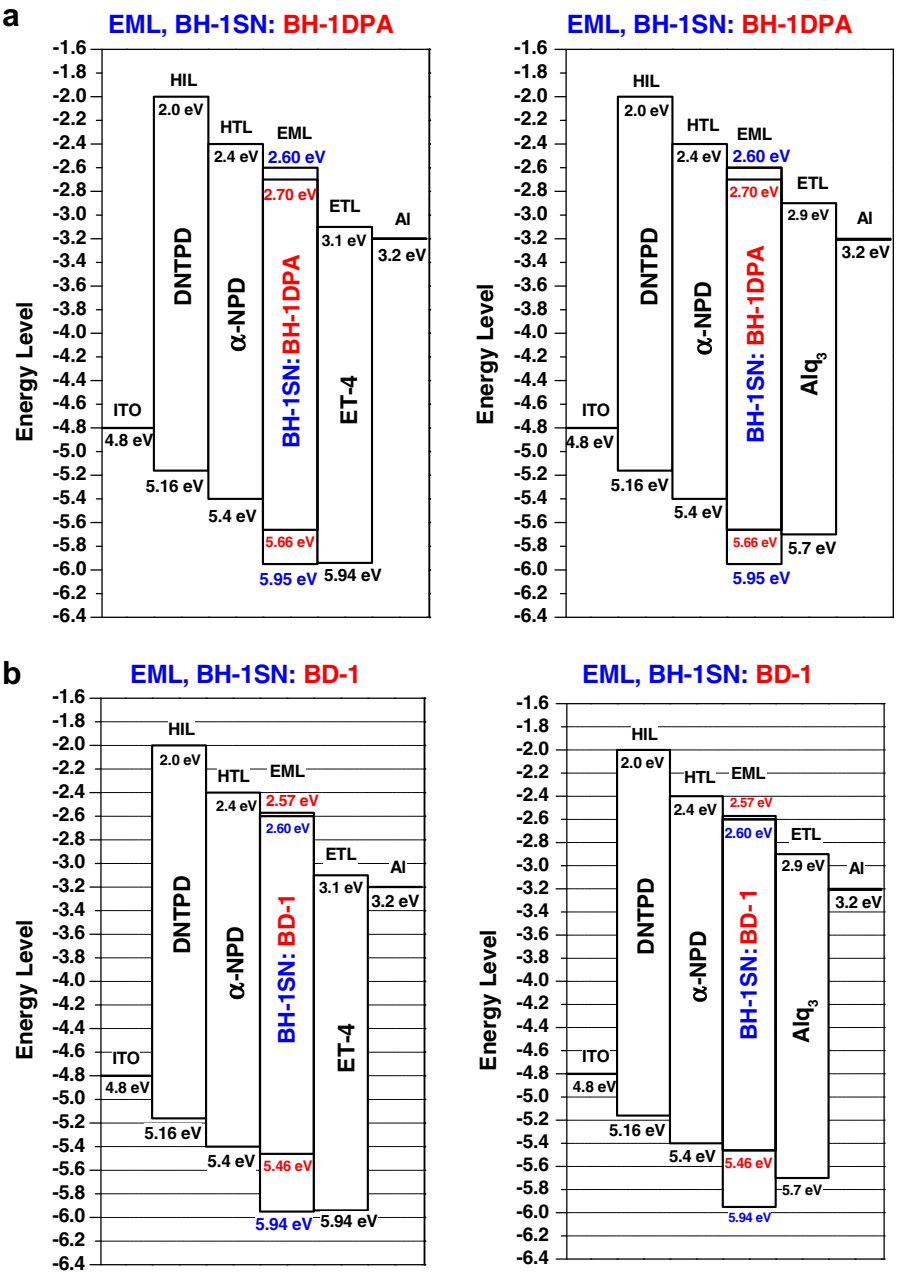

Fig. 2. The energy level of BH-1SN doped with: (a) BH-1DPA and (b) BD-1.

(2 M, 100 mL) dropwise over a period of 30 min. The reaction mixture was refluxed for 12 h at 90 °C under a nitrogen atmosphere. After cooling to ambient temperature, the reaction mixture was extracted with dichloromethane and water. The organic layer was evaporated with a rotary evaporator. The residue was subjected to column chromatography (silica gel) using *n*-hexane to afford a white powdery product.

Yield 76%. Mp: 256.5 ° C. ^{1}H NMR (500 MHz, $CDCl_3$): δ 8.96–8.94 (d, 1H, Ar–CH–benzene), 8.48–8.47 (d, 1H, Ar–CH–benzene), 8.00–7.98 (d, 1H, Ar–CH–benzene), 7.82–7.71 (m, 5H, Ar–CH–fluorene), 7.47–7.40 (m, 7H, Ar–CH–fluorene), 7.34–7.31 (t, 2H, Ar–CH–naphthalene), 7.14–7.06 (m, 5H, Ar–CH–naphthalene), 6.85–6.76 (m, 2H, Ar–CH–benzene), ^{13}C NMR ($CDCl_3$): δ 150.0, 148.1, 142.3, 138.4, 133.4, 128.9, 128.7, 128.0,

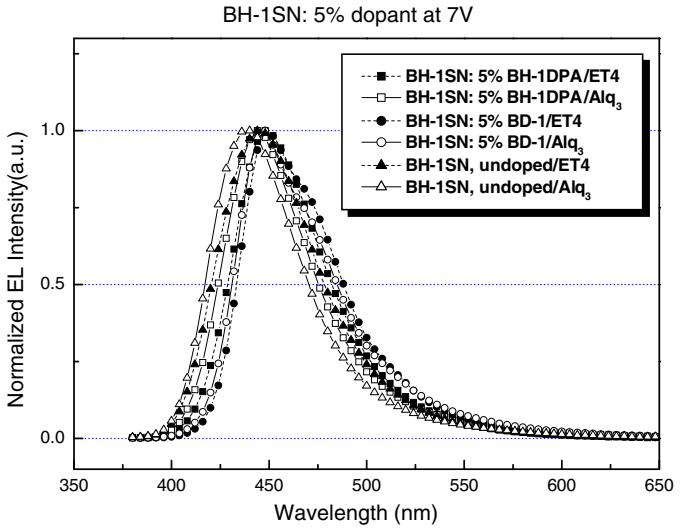

Fig. 3. The EL spectra of blue OLED obtained from BH-1SN doped with 5% dopant at 7 V.

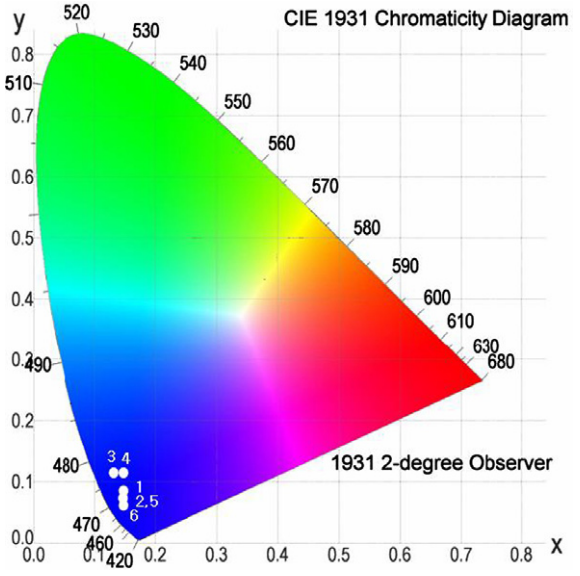

Fig. 4. The CIE 1931 coordinate diagrams of devices (1) BH-1SN:BH-1DPA/ET4 (0.15, 0.09), (2) BH-1SN:BH-1DPA/Alq_3 (0.15, 0.08), (3) BH-1SN:BD-1/ET4 (014, 0.11), (4) BH-1SN:BD-1/Alq_3 (0.15, 0.11), (5) BH-1SN/ET4 (0.15, 0.08) and (6) BH-1SN/Alq_3 (0.15, 0.07).

127.8, 127.6, 126.9, 126.4, 125.8, 124.3, 124.2, 123.5, 120.3, 77.4, 77.2, 76.9, 66.5 ppm. FT-IR (KBr, cm^{-1}) 3052, 3016 (aromatic C–H). MS (FAB) *m/z* 492.0 [$(M + 1)^+$]. Anal. Calcd. for $C_{39}H_{24}$ (492.61) C, 95.09; H, 4.91. Found: C, 94.19; H, 4.92. UV–vis (THF): λ_{max} (absorption) = 485.3, 518.5 nm, λ_{max} (emission) = 527.3 nm.

2.7. OLED fabrication

Prior to device fabrication, ITO with a resistance of 12 Ω/□ on glass was patterned as an active area with a size of 4 mm^2 (2 mm × 2 mm). The substrates were cleaned by sonication in deionized water, boiled in IPA for 20 min, and dried with nitrogen. Finally, the substrates were dry cleaned using plasma treatment in an O_2 and Ar environment. Organic layers were deposited sequentially by thermal evaporation from resistively heated alumina crucibles onto the substrate at a rate of 1.0 Å/s. The thicknesses of the DNTPD (*N*,*N*′-[*p*-di(*m*-tolyl)aminophenyl]-*N*,*N*′-diphenyl benzidine, HIL), α-NPD (*N*,*N*′-bis(1-naphthyl)-*N*,*N*′-diphenyl-1,1′-biphenyl-4,4′-diamine, HTL), host:5% dopant (EML), and Alq_3 or ET4 (ETL) layer were about 400, 200, 300 and 200 Å, respectively. Before the deposition of the metal cathode, Li–F was deposited onto the organic layers with a thickness of 10 Å. A high purity aluminum cathode was deposited at a rate of 1–5 Å/s with a thickness of 2000 Å as the top layer.

3. Results and discussion

3.1. Synthesis and characterization

New dopant material 5-diphenyl amine-spiro-[fluorene-7,9′-benzofluorene] (BH-1DPA) was synthesized by the amination reaction of 5-bromo-spiro[fluorene-7,9′-benzofluorene] (**3**) with diphenylamine. 5-Naphthyl-spiro[fluorene-7,9′-benzofluorene]

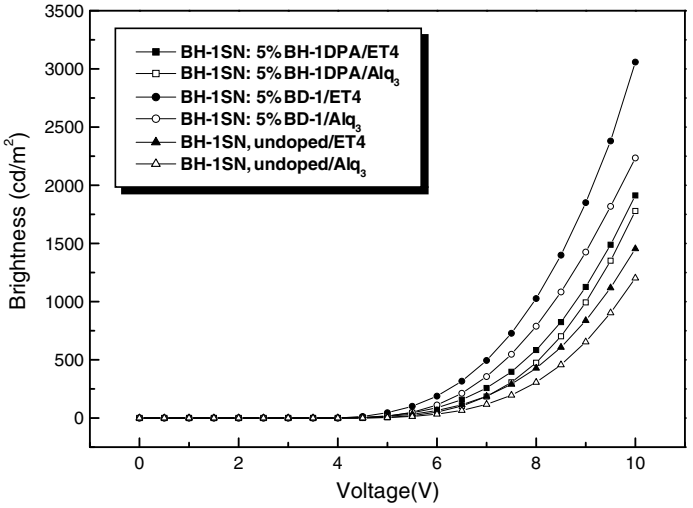

Fig. 5. The brightness–voltage characteristics of the device obtained from BH-1SN.

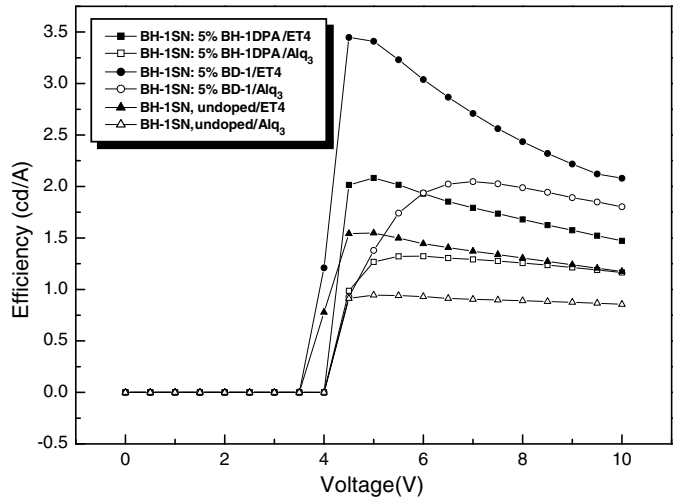

Fig. 6. The efficiency–voltage characteristics of the EL device obtained from BH-1SN.

(BH-1SN) was prepared by the Suzuki reaction of **3** with naphthalene-2-boronic acid in the presence of a palladium catalyst with good yield. The synthetic routes to BH-1DPA and BH-1SN are described in Schemes 2 and 3. The dopant and host materials, BH-1DPA and BH-1SN were identified and characterized by FT-IR, ^{1}H NMR, ^{13}C NMR, GC–MS and elemental analysis. As the acid-catalyzed cyclization reaction proceeded, the strong hydroxyl peak of 9-hydroxyl-9-(1-(2-phenyl)naphthalene)fluorene in the FT-IR spectrum disappeared. All the proton peaks were observed in the range of 6.7–8.4 ppm in the ^{1}H NMR spectra of BH-1DPA and BH-1SN. The chiral carbon peak was observed at 66 ppm in the ^{13}C NMR spectrum of BH-1DPA and BH-1SN. The results of the elemental analysis and mass spectroscopy also supported the formation of BH-1DPA and BH-1SN and matched well with the calculated data.

3.2. Optical properties

The UV–vis and photoluminescence spectra of the spiro-based compounds are shown in Fig. 1. The emission spectra of BH-1DPA obtained in the solid state are provided in the supplementary section. In the UV–vis spectra, the maximum absorption

Table 2
Electroluminescent properties of devices derived from BH-1SN Host materials at 7 and 10 V

Properties	Devices					
	1	2	3	4	5	6
EL at 7 V						
mA/cm^2	14.35	14.29	18.23	17.38	13.61	12.98
Cd/A	1.79	1.29	2.70	2.04	1.37	0.90
lm/W	0.80	0.57	1.21	0.91	0.61	0.40
Cd/m^2	257.4	184.7	494.0	356.0	186.7	117.5
CIE-x	0.15	0.15	0.14	0.15	0.15	0.15
CIE-y	0.09	0.08	0.11	0.11	0.08	0.07
EL at 10 V						
mA/cm^2	130.00	152.75	147.07	123.91	123.82	140.46
Cd/A	1.47	1.16	2.07	1.80	1.17	0.85
lm/W	0.46	0.36	0.65	0.56	0.37	0.26
Cd/m^2	1913	1779	3059	2235	1455	1202

1, BH-1SN:5% NH1-DPA/ET4; 2, BH-1SN:5% NH1-DPA/Alq3; 3, BH-1SN:5% BD-1/ET4; 4, BH-1SN:5% BD-1/Alq3; 5, BH-1SN:undoped/ET4; 6, BH-1SN:undoped/Alq3.

wavelengths of BH-1SN, BH-1DPA and BD-1 appeared at $\lambda_{max} = 342$, 383 and 383 nm in tetrahydrofuran, respectively, as shown in Table 1. Their solid state PL spectra showed strong bands in the blue[1] region at 426, 477 and 472 nm, respectively. All of the emission spectra obtained in the solid state were red-shifted compared to those obtained from the solutions. The maximum absorption spectrum of the new dopant material BH-1DPA was similar to that of BD-1. Also, the PL spectrum of BH-1DPA was shifted toward a longer wavelength than that of BD-1, which implies its good color purity. Table 1 lists the various properties of BH-1SN, BH-1DPA and BD-1.

3.3. Thermal properties

The thermal properties of BH-1SN and BH-1DPA were examined by differential scanning calorimetry (DSC) under a nitrogen atmosphere. The DSC thermogram of BH-1SN shows a melting point at 258.5 °C. The DSC measurements of BH-1DPA showed that upon the first heating, it revealed a glass transition temperature (T_g) at 112 °C and melted at 265 °C. On the second heating, no melting points were observed, even though enough time was given to cool in air. These results imply that BH-1DPA forms an amorphous yellow solid directly after the first heating. Once it becomes an amorphous solid, it does not revert to the crystalline state at all. As a result, the amorphous glassy state of the transparent film of BH-1DPA is a good candidate as an EL material.

3.4. Energy levels of materials

The highest occupied molecular orbital/lowest unoccupied molecular orbital (HOMO/LUMO) energy gap for BH-1SN was estimated to be ca. 3.35 eV from the absorption edge of the optical absorption spectrum of the BH-1SN film on a quartz substrate. The HOMO energy level of BH-1SN was determined to be 5.95 eV by AC-2. The LUMO level of BH-1SN was calculated to be 2.6 eV by subtracting the HOMO/LUMO band gap from the HOMO level as shown in Table 1. The energy levels of BH-1SN and the other organic and electrode materials used to fabricate the OLEDs in the present study are shown in Fig. 2. When the host was doped with BD-1 dopant, the efficiency was more improved than that of BH-1DPA. This result indicates that the smaller barrier between the LUMO of BH-1SN host and BD-1 dopant results in a more charge trapping when transporting the electron.

3.5. EL properties

To investigate the EL properties of BH-1SN, an EL device was fabricated using the vacuum deposition method. Fig. 3 shows the EL spectra of the six devices fabricated with various emitters in this work. The configuration of the EL device was ITO/DNTPD/α-NPD/BH-1SN:5% dopant/Alq_3 or ET4/Al–LiF. The peak for the blue light EL emission of the devices was observed at around 440–448 nm at 7 V. The peak for the device consisting of BH-1SN doped with BH-1DPA and Alq_3 as the ETL appeared at 444 nm. This result indicates that the device has good color purity and current density. The CIE color chromaticity coordinates of devices 2, 5 and 6 were (0.15, 0.08), (0.15, 0.08) and (0.15, 0.07) which are in the pure deep blue region. These OLEDs gave better color coordinate values for blue emission than the other devices as shown in Fig. 4.

3.6. OLED device properties

Fig. 5 shows the luminance–voltage characteristics of the OLEDs devices. In the case of the device doped with 5% BD-1, it was observed that the turn on volt-

[1] For interpretation of color in Figs. 1 and 4, the reader is referred to the web version of this article.

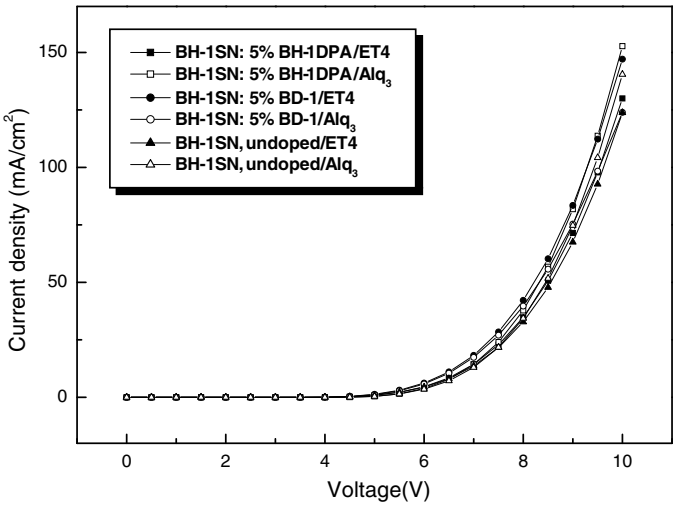

Fig. 7. The current density–voltage characteristic of devices obtained from BH-1SN host and various dopant and electron transporting materials.

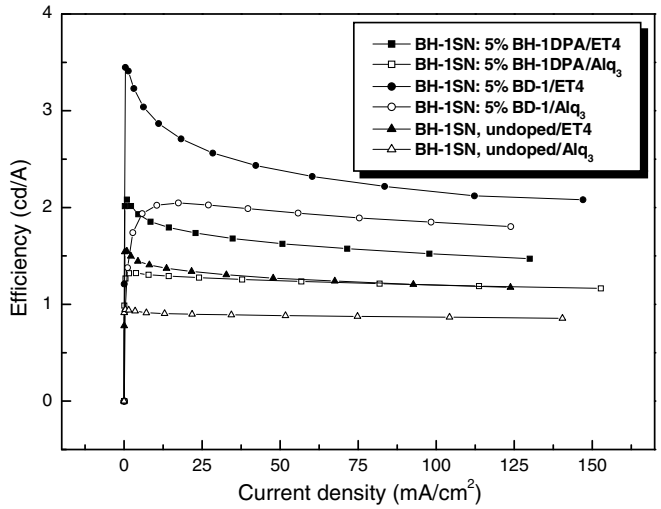

Fig. 8. The efficiency–current density characteristics of the devices using BH-1SN host and various dopant and transporting materials.

age was lowered to 4 V. The light emission occurs at about 4.5 V and the brightness is 3059 cd/m^2 at 10 V. The luminance and efficiency of the devices made using BH-1SN as the host, 5% BD-1 as the dopant and ET4 as the ETL were more than three times those of the device without the dopant, indicating that the dopant is effective in enhancing the EL properties of the spiro-type emitting layer. The threshold voltage for luminescence is about 4 V in the device with an emitting layer made of BH-1SN doped with 5% BD-1 having a thickness of 300 Å.

Fig. 6 illustrates the efficiency–voltage characteristics of the devices. The current efficiency of the BH-1SN:5% BD-1/ET4 device shows a remarkable enhancement to a maximum value of 3.4 cd/A and only a small decline when the current density increases to 152.75 mA/cm^2 as shown in Table 2. This characteristic is highly beneficial for the applications that require a high excitation density such as in the passive dot matrix devices.

The device BH-1SN:5% DPA/Alq3 also showed a maximum brightness of 3059 cd/m^2 at a current density of 152.75 mA/cm^2, as shown in Figs. 7 and 8. As the current density increased gradually, the luminescent efficiency of device BH-1SN:5% BD-1/ET4 increased abruptly to 3.4 cd/A. This phenomenon is

caused by the formation of the excitons required to emit light. The maximum power efficiency of the device obtained from BH-1SN doped with BD-1/ET4 is 1.21 lm/W, which is two times larger than that of the device without the dopant (0.61 lm/W). The efficiency rises rapidly to a maximum of about 3.4 cd/A at a low current density of about 1.21 mA/cm^2.

4. Conclusion

New blue host and dopant materials based on a spiro compound derivative were used to construct blue OLEDs. The EL emissions of the devices (doped with 5% BH-1DPA or BD-1) are observed at 444 and 448 nm, respectively. The CIE coordinates of the device made of BH-1SN:5%BH-1DPA were 0.15, 0.08, which are better color coordinate values for blue emission than the device using BD-1. As the current density increased gradually, the luminescent efficiency increased abruptly to 3.7 cd/A. The maximum power efficiency of the device obtained from BH-1SN is 1.27 lm/W, which is comparable to that of the device without the dopant (0.61 lm/W).

Acknowledgement

This work was supported by Grant No. RT104-01-02 from the Regional Technology Innovation Program of the Ministry of Knowledge Economy.

References

[1] C.W. Tang, S.A. Van Slyke, C.H. Chen, J. Appl. Phys. 65 (1989) 3610.
[2] C. Adachi, T. Tsutsui, S. Saito, Appl. Phys. Lett. 55 (1989) 1489.
[3] L.J. Rothberg, A.J. Lovinger, J. Mater. Res. 11 (1996) 3174.
[4] Y. Hamada, T. Sano, M. Fujita, T. Fujii, Y. Nishio, K. Shibata, Jpn. J. Appl. Phys. Part 2 32 (1993) 511.
[5] Y. Hamada, T. Sano, H. Fujii, Y. Nishio, H. Takahaski, K. Shibata, Jpn. J. Appl. Phys. Part 2 35 (1996) 1339.
[6] Y. Hamada, C. Adachi, T. Tsutsui, S. Saito, Jpn. J. Appl. Phys. Part 1 31 (1992) 1812.
[7] M. Strukelj, R. Jordan, A. Dodabalapur, J. Am. Chem. Soc. 118 (1996) 1213.
[8] J. Kido, W. Ikeda, M. Kimura, K. Nagai, Jpn. J. Appl. Phys. Part 2 35 (1996) 394.
[9] H. Tokailin, M. Matsuura, H. Higashi, C. Hosokawa, T. Kusumoto, Proc. SPIE 1910 (1931) 38.
[10] C. Adachi, T. Tsutsui, S. Saito, Appl. Phys. Lett. 56 (1990) 799.
[11] S.-O. Jeon, Y.-M. Jeon, J.-W.Kim, C.-W. Lee, M.-S. Gong, Synth. Met. 157 (2007) 558.
[12] N.-C. Seong, Y.-M. Jeon, T.-H. Kim, J.-W. Kim, C.-W. Lee, E.-J. Lee, J.-G. Jang, J.-Y. Lee, M.-S. Gong, Synth. Met. 157 (2007) 421.
[13] K.-S. Kim, Y.-M. Jeon, J.-W. Kim, C.-W. Lee, M.-S. Gong, Dyes Pigments 77 (2008) 238.
[14] S.M. Kelly, Flat Panel Displays: Advanced Organic Materials, Royal Society of Chemistry, Cambridge, UK, 2000.
[15] A.H. Tullo, Chem. Eng. News 78 (2000) 20.
[16] C.T. Chen, C.H. Chien, J. Am. Chem. Soc. 128 (2006) 10992.
[17] K.T. Wang, C.L. Wang, Org. Lett. 3 (2001) 2285.

Available online at www.sciencedirect.com
ScienceDirect
Organic Electronics 9 (2008) 533–538
Organic Electronics
www.elsevier.com/locate/orgel

Utilizing white OLED for full color reproduction in flat panel display

Yan Xiong, Wei Xu, Chun Li, Bo Liang, Li Zhao, Junbiao Peng, Yong Cao, Jian Wang *

Institute of Polymer Optoelectronic Materials and Devices, South China University of Technology, Key Lab of Specially Functional Materials, Ministry of Education, Guangzhou 510640, PR China

Received 16 September 2007; received in revised form 18 February 2008; accepted 25 February 2008
Available online 8 March 2008

Abstract

Full color reproduced by white OLED (organic light emitting diodes) coupled with transmission color filters for the application in flat panel display was analyzed theoretically and experimentally. A white emitter made up of three primary emission peaks was found to be superior to a white emitter made up of complementary colors, i.e. two emission peaks. However, though the full color reproduction by white emitter possesses the merit of manufacturing simplicity, it is much worse than the color reproduction by three individual primary color sub-pixels, in terms of power efficiency and the power consumption. Adjusted to the same external quantum efficiency, the full color pixel made of three primary color sub-pixels is 10 times more efficient than that made of white emitter coupled with color filters.

PACS: 72.80.Le; 78.60.Fi; 85.60.Jb; 85.60.Pg

Keywords: White organic light emitting diodes; Full color reproduction; Virtual color primary; Flat panel displays; Transmission color filters

Organic light emitting diodes (OLED) based flat panel display (FPD) technology has evolved from attractive to practical only after a little more than 10 years' research and development [1–3]. In contrast, it took approximately 30 years for liquid crystal cells to be commercialized for active matrix LCD FPD products. Since organic materials could be chemically engineered, they provide a broad emission spectrum covering the entire visible region from 400 nm to 700 nm. The solution processability of polymer OLED materials allows for the development of a full color FPD by means of a printing technique, such as inkjet printing [4,5], screen printing [6,7], or photolithographic patterning [8]. To reproduce a full color pixel, the most common practice is to use three individual primary color emission materials. Recently, white OLEDs have attracted enormous attentions for their potential applications in solid state lighting [9–16]. As the power efficiency of white polymer OLEDs increased, utilizing white OLEDs coupled with transmission filters without the need to pattern the color sub-pixels to produce full color

* Corresponding author. Tel.: +86 20 8711 4525; fax: +86 20 8711 0606.
E-mail address: jianwang@scut.edu.cn (J. Wang).

1566-1199/$ - see front matter © 2008 Elsevier B.V. All rights reserved.
doi:10.1016/j.orgel.2008.02.017

in FPD becomes feasible and attractive [17,18]. In this work, we theoretically and experimentally examined white polymer OLED full color reproduction method against the full color reproduction approach by three individual primary color emitters.

According to the principles of color matching, to achieve white emission, mixtures of three primary colors or two complementary colors, are typically required. The most common set of 'primary colors' and 'complementary colors' are red, green and blue (R, G, B), and blue and yellow, respectively [19]. To realize a full color pixel in full color display by white emission OLED coupled with transmission color filters, the white OLED functions as the backlight as same as the backlight unit in a LCD display. By applying the color filters to the white emitter, the white emission spectrum was modified by the color filters' transmission spectra. Therefore, we can treat those color filtered light emission as virtual color primaries, R, G and B to do the theoretical analysis. In addition to the modification of the emission spectrum by the color filters, the actual luminance L from the white emission is also reduced by the filters. To trace back the actual luminance, we need the following equations [17]:

$$L = K_M P_{\text{peak}} \int \frac{P(\lambda)}{P_{\text{peak}}} V(\lambda)\,\mathrm{d}\lambda$$

$$L_T = K_M P_{\text{peak}} \int \frac{P(\lambda)}{P_{\text{peak}}} T(\lambda) V(\lambda)\,\mathrm{d}\lambda$$

$$\Downarrow$$

$$L = \frac{\int \frac{P(\lambda)}{P_{\text{peak}}} V(\lambda)\,\mathrm{d}\lambda}{\int \frac{P(\lambda)}{P_{\text{peak}}} T(\lambda) V(\lambda)\,\mathrm{d}\lambda} L_T \quad L_T = \frac{\int \frac{P(\lambda)}{P_{\text{peak}}} T(\lambda) V(\lambda)\,\mathrm{d}\lambda}{\int \frac{P(\lambda)}{P_{\text{peak}}} V(\lambda)\,\mathrm{d}\lambda} \tag{1}$$

where L is the actual luminance from the white emitter while L_T is the luminance of the virtual primary (apparent luminance), K_M is a conversion factor taking the value of 683 if the radiance has the units of flux per unit solid angle and the luminance has the units of cd/m^2, $V(\lambda)$ is the photopic spectral luminous efficiency function, $T(\lambda)$ is the transmission spectral of the color filters, and $P(\lambda)/P_{\text{peak}}$ is the normalized emission spectrum. The calculations based on Eq. (1) agreed perfectly with the experimental measurements.

The transmission profiles of the color[1] filters (purchased from Haian HengXing Optical Components Factory) used in our experiments are shown in Fig. 1. Two types of polymer white light emitters produced by 'primary colors' and 'complementary colors', were fabricated with the device configurations of ITO/PEDOT:PSS/PVK/ADS329BE:Ir(Buppy)$_3$:Ir(DMFPQ)$_2$acac/Ba/Al (designated as Device A) and ITO/PEDOT:PSS/PFB2:MEH-PPV/PFB2/Ba/Al (Device B), respectively. The detailed descriptions of device making could be found in Refs. [10,20]. Though it is not important to make different devices in our current study, we replaced the blue light emitting polymer PFO-poss and red phosphorescent dye (Piq)2Ir(acaF) in Ref. [10] with ADS329BE and Ir(DMFPQ)$_2$acac in Device A [21], and replaced PFO in Ref. [20] with PFB2. The new devices have a maximum luminous efficiency of 3.62 cd/A and 1.94 cd/A for Devices A and B, corresponding to maximum external quantum efficiency (EQE) of 1.92% and 0.72%, respectively. The electroluminescence (EL) spectra of the said devices are illustrated in Fig. 2 (dot line). By applying the color filters, the white emission spectra were modified by the filters as illustrated also in Fig. 2 to produce the virtual color primaries R, G and B (solid line). The chromaticity coordinates of the virtual color primaries are listed in the inset of Fig. 2. To compare with full color pixel made of three primary color sub-pixels, the devices emitting R, G and B lights were fabricated with the structure of ITO/PEDOT:PSS/EML/Ba/Al in which the

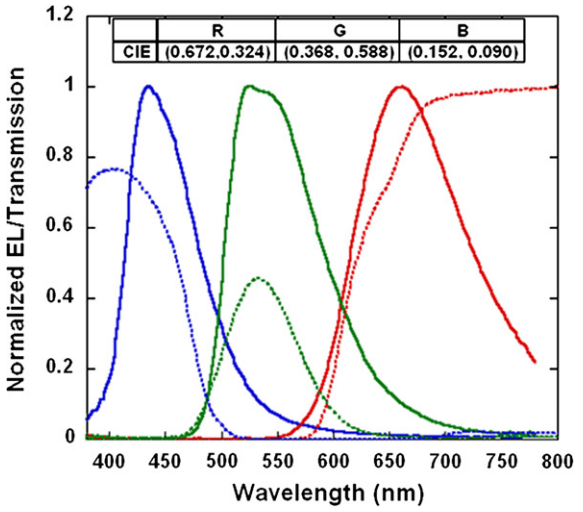

Fig. 1. Transmission profiles of the color filters (dot lines), and EL spectra of the primary red (R), green (G), and blue (B) emitters (solid lines). The inset shows the chromaticity coordinates of the three primary color sub-pixels.

[1] For interpretation of color in Figs. 1–3, the reader is referred to the web version of this article.

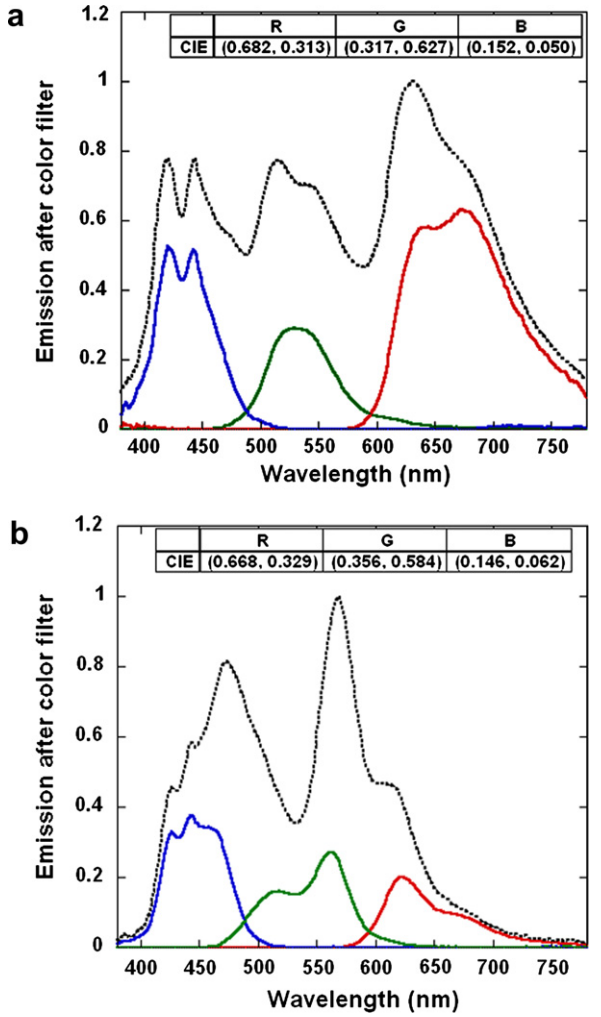

Fig. 2. EL spectra of (a) Device A and (b) Device B (dot lines) and virtual primaries produced by the color filters (solid lines). The insets show the chromaticity coordinates of the virtual color primaries.

polymer emitting layer (EML) were MEH-PPV: PFO-DBT, P-PPV, and EH-G2AN, respectively. The EL spectra are shown in Fig. 1, and the chromaticity coordinates of the three primary color sub-pixels are listed in the inset as well. For all the materials used in the experiments, PEDOT:PSS (Baytron P4083), PVK (poly(*N*-vinylcarbazole)) and ADS329BE were purchased from Bayer AG, Aldrich Co. and American Dye Sources Inc., respectively. Ir(Bu-ppy)$_3$, Ir(DMFPQ)$_2$acac, MEH-PPV, PFO-DBT, P-PPV and EH-G2AN were synthesized in our lab, and PFB2 was synthesized by Liu et al [21–23]. The current density (*J*)–operation voltage (*V*)–luminance (*L*) characteristics of the R, G, B primary color devices and the white light emitting Devices A and B are respectively shown in Fig. 3, while the EQE–*J* characteristics are shown in the insets.

To find out the performance of the fabricated devices in a real panel, we assume a full color pixel consisting of three sub-pixels in the planar configuration in which the three sub-pixels are laid side by side. The size of the full color pixel is set to 100 μm × 100 μm and each sub-pixel has the same size, i.e. 33.3 μm × 100 μm. It is deserved to note that its a common practice in OLED industry to make the area of each primary sub-pixel unequal in order to compensate the least efficient colors, e.g. blue or red. Recently, the Active Matrix Display built on TFT (thin film transistor) panel becomes the most popular driving scheme for large displays. The TFT components occupy some space of each

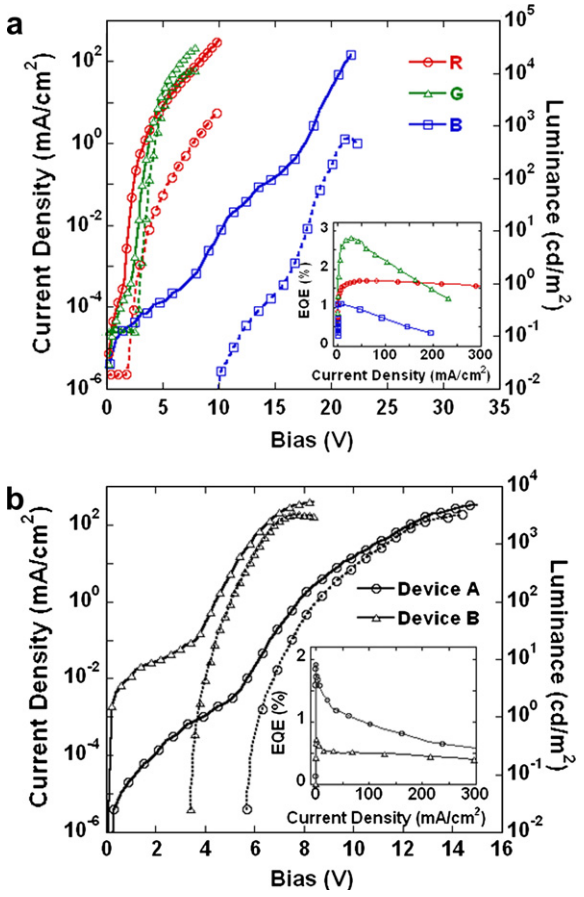

Fig. 3. Current density (*J*) (solid lines)–operation voltage (*V*)–luminance (*L*) (dot lines) characteristics of (a) the primary red (R), green (G), and blue (B) devices; (b) Devices A and B. Insets: external quantum efficiency (EQE)–*J* characteristics.

primary sub-pixel. The fill factor, which is also called aperture ratio, is defined as the ratio of the actual light emitting area to the total area of the sub-pixel. To simplify the calculation, the aperture ratio is set to 100%. The areal luminance for white is the target luminance we want to achieve for a display panel. Generally, it has a value of 200 cd/m^2 with chromaticity coordinates of D65 white at (0.313, 0.329) [24,25]. The following calculations were carried out to produce 200 cd/m^2 D65 white light, and the results are shown in Table 1. The luminous efficiency, pixel power and power efficiency of each full color pixel were calculated based on the performance of the corresponding device shown in Fig. 3.

The data in Table 1 showed that the full color pixel's luminous efficiency of 'primary colors' white emitter (0.213 cd/A) is 50% more than that of 'complementary colors' white emitter (0.139 cd/A), whereas its power efficiency (0.054 lm/W) is less than that of the latter (0.065 lm/W), and it takes more pixel power (116 μW) for 'primary colors' white emitter to produce 200 cd/m^2 D65 white light than 'complementary colors' white emitter (96.8 μW). By carefully examining the data, we found out that at the operation luminance, the operation voltage of 'primary colors' white emitter is significant higher than that of 'complementary colors' white emitter by a factor of 2, which lead to higher power consumption. The high operation voltage is due to the phosphorescent materials, Ir(Bu-ppy)$_3$, and Ir(DMFPQ)$_2$acac used in producing 'primary colors' white emitter. If the 'complementary colors' white emitter took the same J–V curve as that of the 'primary colors' white emitter, the power efficiency would be 0.048 lm/W, and it would take 138 μW of full pixel power to produce 200 cd/m^2 D65 white. In Fig. 2, its clearly seen that the emission power of the 'complementary colors' white emitter is severely cut down by the green and the red color filters. It's due to the fact that the yellow emission peak unfortunately lies between the transmission peaks of the green and the red color filters. The experimental data that the actual luminance of the full color pixel from 'complementary colors' white emitter is 12% more than that from 'primary colors' white emitter (Table 1), also proved 'primary colors' white emitter is better than 'complimentary colors' white emitter in terms of power efficiency and power consumption in flat panel display applications. From the above discussion, we learned that to further improve the power efficiency of the full color pixel, the emission peaks from the white emitter are better to be aligned with the transmission peaks of the color filters, in order to allow the maximum power transmission.

As demonstrated in Table 1, the full color reproduction approach by three individual primary color sub-pixels is far more efficient than that by white emitters coupled with transmission color filters, for the color filters severely reduced the efficiency of the white emitter. The full color pixel power efficiency from primary color sub-pixels is 0.747 lm/W,

Table 1
The characteristics of each full color pixel reproduced by different color reproduction approaches at 200 cd/m^2 D65 white

Color reproduction method	Performance	R	G	B	Full color pixel
Primary color sub-pixels	Areal luminance (cd/m^2)	26	150	24	200
	Actual luminance (cd/m^2)	78	450	72	600
	EQE (%)	1.6	2.2	1.1	–
	Luminous efficiency (cd/A)	0.628	8.77	0.864	2.31
	Pixel power (μW)	2.21	0.736	5.46	8.41
	Power efficiency (lm/W)	0.365	6.37	0.142	0.747
'Primary colors' white emitter	Areal luminance (cd/m^2)	34	153	13	200
	Actual luminance (cd/m^2)	817	1801	2346	4964
	EQE (%)	1.2	0.98	0.85	–
	Luminous efficiency (cd/A)	0.282	0.471	0.026	0.213
	Pixel power (μW)	13.2	39.7	62.7	116
	Power efficiency (lm/W)	0.080	0.121	0.006	0.054
'Complementary colors' white emitter	Areal luminance (cd/m^2)	29	156	15	200
	Actual luminance (cd/m^2)	1383	1846	2345	5574
	EQE (%)	0.50	0.49	0.47	–
	Luminous efficiency (cd/A)	0.084	0.332	0.025	0.139
	Pixel power (μW)	22	31.3	43.5	96.8
	Power efficiency (lm/W)	0.040	0.156	0.011	0.065

nearly 14 times the power efficiency from 'primary colors' white emitter of 0.054 lm/W. To achieve 200 cd/m^2 D65 white light, only 8.41 μW is required for the full color pixel of primary color sub-pixels, while it needs 116 μW for the 'primary colors' white emitter. Measurements of EQE showed that the EQE of R, G, and B primary emitters at the operation luminance are 1.6%, 2.2%, and 1.1%, respectively, while the EQE of the white emitter at the operation luminance are 1.2%, 0.98%, and 0.85%, respectively (Table 1). Adjusted to the same EQE of 1% at the operation luminance, the full color pixel's power efficiency of the primary color sub-pixels is estimated to be 10 times that of the white emitters.

Although the color reproduction method by white emission polymer coupled with color filters can greatly simplify the manufacturing process by one-step wet coating, the approach is much less power efficient than the approach of three primary color emitters in real application. The color reproduction by white OLED coupled with transmission color filters not only puts too much stress on the materials, but also requires the driver chip supplying high power to the display panel. To overcome such problems, the obvious approach is to make high efficient white OLED. The current best small molecule white OLED reached 34% EQE and 64 lm/W [15], while the current best polymer white OLED achieved 19 lm/W in power efficiency [16]. Another approach is to increase the transmission of the color filters. In Fig. 1, the maximum transmission of the green filter is only 40%. Since the green color contributed most in reproducing white, the severe reduction of the white by the green filter lead to high power consumption. We expect that doubling green filters' transmission will increase the full color pixel's power efficiency.

The common color filters are fabricated by suspending or coating organic dyes on a transparent base. The organic dyes absorbed some wavelengths and transmitted others. The tradeoff for high transmission is the full width at half maximum. A broad transmission profile will reduce the color's purity, leading to small color gamut. One way to go around the problem is to use white OLED with sharp emission peaks. It becomes a practical solution in high end LCD TV, in which LED backlights are utilized to provide large color gamut. For OLED/PLED applications, some phosphorescent emitters are demonstrated to have a smaller emission line width than that of their fluorescent counterparts, such as Eu and Tb complexes [26,27]. Making white OLED/PLED with such phosphorescent emitters is attractive to obtain saturated primary colors in flat panel display applications. Another way is to apply special color filters with high transmission and narrow line width, such as DBR (Distributed Bragg Reflector) filter. Considering the fierce price competition in consumer electronics market, this solution seems not economically feasible.

In summary, two full color reproduction approaches in the flat panel display applications were analyzed theoretically and experimentally. The full color pixel made of white emitters coupled with transmission color filters is less energy efficient due to the severe power reduction by the filters, although it possesses the advantage of manufacturing simplicity. A white emitter made up of three primary emission peaks was found to be superior to a white emitter made up of complementary colors. Adjusted to the same quantum efficiency, the full color pixel's power efficiency of three primary color sub-pixels is estimated to be 10 times more efficient than that of the white emitter.

Acknowledgements

This research was supported by the National Natural Science Foundation of China (#90201031, #50573024, and U0634003), Key Project of Science and Technology, Ministry of Education, (#104208), and the State 973 Project (#2002CB613405).

References

[1] C.W. Tang, S.A. VanSlyke, Appl. Phys. Lett. 51 (1987) 913.
[2] J.H. Burroughes, D.D.C. Bradley, A.R. Brown, R.N. Marks, K. Mackay, R.H. Friend, P.L. Burns, A.B. Holmes, Nature 347 (1990) 539.
[3] <www.pioneerelectronics.com>, <www.sony.com>, <www.kodak.com>.
[4] T.R. Hebner, C.C. Wu, D. Marcy, M.H. Lu, J.C. Sturm, Appl. Phys. Lett. 72 (1998) 519.
[5] S.-C. Chang, J. Liu, J. Bharathan, Y. Yang, J. Onohara, J. Kido, Adv. Mater. 11 (1999) 734.
[6] F. Pschenitzka, J.C. Sturm, Appl. Phys. Lett. 74 (1999) 1913.
[7] D.A. Pardo, G.E. Jabbour, N. Peyghambarian, Adv. Mater. 12 (2000) 1249.
[8] C.D. Müller, A. Falcou, N. Reckefuss, M. Rojahn, V. Wiederhirn, P. Rudati, H. Frohne, O. Nuyken, H. Becker, K. Meerholz, Nature 421 (2003) 829.
[9] F. Robert, Science 310 (2005) 1762.
[10] Y. Xu, J. Peng, J. Jiang, W. Xu, W. Yang, Y. Cao, Appl. Phys. Lett. 87 (2005) 193502.
[11] B.W. D'Andrade, S.R. Forrest, Adv. Mater. 16 (2004) 1585.

[12] X. Gong, S. Wang, D. Moses, G.C. Bazan, A.J. Heeger, Adv. Mater. 17 (2005) 2053.
[13] J. Jiang, Y. Xu, W. Yang, R. Guan, Z. Liu, H. Zhen, Y. Cao, Adv. Mater. 18 (2006) 1769.
[14] J. Huang, G. Li, E. Wu, Q. Xu, Y. Yang, Adv. Mater. 18 (2006) 114.
[15] N. Tomoyuki, H. Kunimasa, F. Keiichi, O. Hirofumi, SID Digest 38 (Bk. 2) (2007) 1018.
[16] H. Wu, J. Zou, F. Liu, L. Wang, A. Mikhailovsky, G.C. Bazan, W. Yang, Y. Cao, Adv. Mater. 20 (2008) 696.
[17] J. Wang, G. Yu, Proc. SPIE 5632 (2005) 32.
[18] K. Mitsuhiro, H. Koji, A. Reo, K. Isamu, M. Ryoko, Y. Hirokazu, Y. Tetsuro, O. Atsushi, S. Yukio, T. Shoji, Y. Jiro, S. Tatsuya, T. Shinichiro, U. Tetsuo, SID'04 Digest 35 (2004) 1017.
[19] D. Gupta, M. Katiyar, Deepak, Opt. Mater. 28 (2006) 295.
[20] G.K. Ho, H.F. Meng, S.C. Lin, S.F. Horng, C.S. Hsu, L.C. Chen, S.M. Chang, Appl. Phys. Lett. 85 (2004) 4576.
[21] L. Wang, B. Liang, F. Huang, J. Peng, Y. Cao, Appl. Phys. Lett. 89 (2006) 151115.
[22] L. Zhao, C. Li, Y. Zhang, X.H. Zhu, J. Peng, Y. Cao, Macromol. Rapid Commun. 27 (2006) 914.
[23] J. Liu, C. Min, Q. Zhou, Y. Cheng, L. Wang, D. Ma, X. Jing, F. Wang, Appl. Phys. Lett. 88 (2006) 083505.
[24] C. Poynton, Digital Video and HDTV, Morgan Kaufmann, San Francisco, 2003.
[25] R.W.G. Hunt (Ed.), Measuring Colour, second ed., Ellis Horwood, New York, 1992.
[26] M.D. McGehee, T. Bergstedt, C. Zhang, A.P. Saab, M.B. O'Regan, G.C. Bazan, V.I. Srdanov, A.J. Heeger, Adv. Mater. 11 (1999) 1349.
[27] J. Kido, Y. Okamoto, Chem. Rev. 102 (2002) 2357.

Available online at www.sciencedirect.com
ScienceDirect
Organic Electronics 9 (2008) 539–544
Organic Electronics
www.elsevier.com/locate/orgel

Large current gain and low operational voltage permeable metal-base organic transistors based on Au/Al double layer metal base

Mingdong Yi [a], Jinying Huang [a], Dongge Ma [a,*], Ivo A. Hümmelgen [b,*]

[a] State Key Laboratory of Polymer Physics and Chemistry, Changchun Institute of Applied Chemistry, Graduate School of the Chinese Academy of Sciences, Chinese Academy of Sciences, Changchun 130022, People's Republic of China
[b] Group of Organic Optoelectronic Devices, Departamento de Física, Universidade Federal do Paraná, Caixa Postal 19044, 81531-990 Curitiba PR, Brazil

Received 1 December 2007; received in revised form 25 February 2008; accepted 28 February 2008
Available online 8 March 2008

Abstract

In order to realize the common-emitter characteristics of the tris(8-hydroxyquinoline) aluminium (Alq_3)-based organic transistors, we used Au/Al double metal layer as the base, thus the vertical metal-base transistors with structure of Al/n-Si/Au/Al/Alq_3/LiF/Al were constructed. It was found that the contact properties between the base and the organic semiconductors play an important role in the device performance. The utilization of Au/Al double layer metal base allows the devices to operate at high gain in the common-emitter and common-base mode at low operational voltage.

PACS: 81.07.Pr; 73.40.Vz; 85.30.De

Keywords: Permeable; Metal base; Organic transistors; Au/Al double layer metal base

1. Introduction

Metal-base transistors (MBTs), consisting of a thin metal layer (the base) sandwiched between two semiconductors (the emitter and the collector), have been receiving much attention for the fast switching and sensor applications since 1962 [1–3]. However, largely technological difficulties in the fabrication of semiconductor–metal–semiconductor structure and the low base transport factor in MBTs based on inorganic semiconductors limit their applicability [4]. Recently, MBTs based on organic semiconductors were realized, and showed high base transport factor and significantly simpler production processes than the inorganic-based MBTs [5–10]. Importantly, this kind of vertical-type MBTs show potential application as driver in pixel OLED displays due to its higher output current density at low operational voltage. The planar-type organic thin film transistors (OTFTs) suffer from low current density, high operational voltage and low operational speed, which are

* Corresponding authors. Tel.: +86 431 85262357; fax: +86 431 85262873.
E-mail addresses: mdg1014@ciac.jl.cn (D. Ma), iah@fisica.ufpr.br (I.A. Hümmelgen).

1566-1199/$ - see front matter © 2008 Published by Elsevier B.V.
doi:10.1016/j.orgel.2008.02.018

usually due to the low carrier mobility of organic materials and long channel length. The short channel length in vertical-type transistors, which is close to the organic film thickness, leads to the superior performance in the output current and operational voltage [11–13]. However, the majority of organic-based MBTs reported so far presented yet unsatisfied characteristics when operating in the common-emitter mode, like difficulty of obtaining high common-emitter current gain and the existence of high leakage currents, characteristics that are required in applications involving amplification [14–16].

Conventional MBTs consist of a thin metal layer (the base) sandwiched between two semiconductors (the emitter and the collector). Like a general bipolar transistor, the MBT is a three-terminal device with a forward-based emitter-base junction and a reverse-based base-collector junction. However, these junctions are Schottky junction in MBTs. Generally an asymmetrical Schottky junction between emitter-base junction and base-collector junction and low electron scattering in the metal base are desirable to improve current gain. Furthermore, in the emitter-base junction, it is also expected that the hole injection current from the base to the emitter and the recombination current in the depletion region between the base and emitter are low, thus high current gain can be obtained. Obviously, the choice of the base metal and its contact characteristics with the semiconductor are very important in the determination of current gain in the cases of common-base and common-emitter operational modes.

Recently, we reported permeable-metal-base organic transistors based on tris(8-hydroxyquinoline) aluminium (Alq_3) as emitter with better common-base characteristics and by introducing an interface layer between the emitter metal and Alq_3, which can be used to greatly enhance electron injection in the emitter region, the common-emitter characteristics were realized [17,18]. In this paper, we investigated the effect of the metal base on the electrical characteristics of Alq_3-based MBTs in detail. We compared the effects of Al, Au and Au/Al as the base on the current gain characteristics and found that the Au/Al double layer metal base leads the MBTs to simultaneously well operate in the common-base and common-emitter modes with high current gain at low voltage.

2. Experimental procedures

Fig. 1 shows the studied MBTs structure. The transistors were prepared by vacuum evaporation

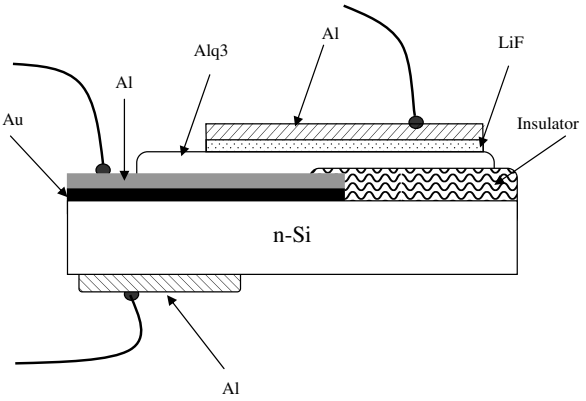

Fig. 1. Schematic structure of the Al(120 nm)/n-Si/Au(10 nm):Al(10 nm)/Alq_3(70 nm)/LiF(1 nm)/Al(120 nm) device.

under a pressure of less than 3×10^{-4} Pa. The base metal was first deposited on precleaned n-type Si(1 0 0) substrate (resistivity of 1–10 Ω cm), and then tris(8-hydroxyquinoline) aluminium (Alq_3), LiF and Al were evaporated on the metal base. Among, the Alq_3 is used as the emitter, LiF/Al as the emitter contact and n-type silicon as the collector. The base includes Au and Al single metal layers and Au/Al double metal layer. For this case of Au/Al double metal layer, the Au was first evaporated at a rate of 0.1 nm/s on n-type silicon and then the Al was evaporated at a rate of 1 nm/s in the sequence. The substrate temperature is room temperature. Before the devices were fabricated, the n-type Si substrate was first etched in a 5% HF solution to remove the surface oxide and an Al was evaporated onto the unpolished side of the Si substrate to act as Ohmic contact. The active area, which is determined by the superposition region of the strip of the base metal electrode, emitter contact electrode and Si, is $\sim 9\ mm^2$. In order to avoid short circuit between the base and the emitter, an insulator poly(methylmethacrylate) was introduced.

The thickness of the layers was measured using a surface profiler. The electric characteristics were determined using two Keithley 2400 units at room temperature. The measurement circuit is analogous to those given elsewhere [17,18]. Both the electric characteristics in common-base and common-emitter modes were obtained in this study.

3. Discussion and results

Fig. 2 shows the common-base electric characteristics of an Al/n-Si/Au/Al/Alq_3/LiF/Al device. A saturation of collection current I_c is observed at

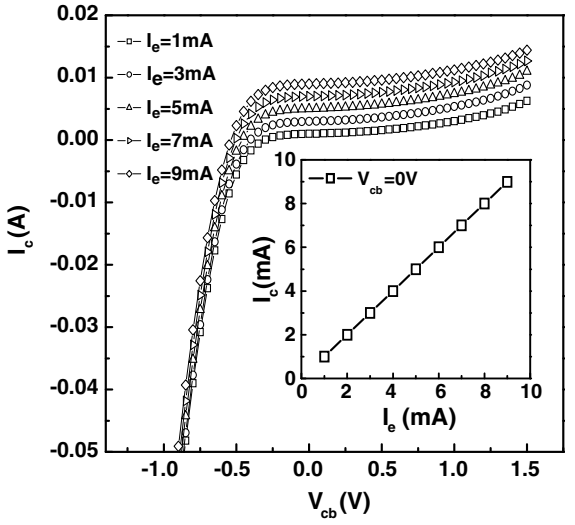

Fig. 2. Common-base mode characteristics of the Al(120 nm)/n-Si/Au(10 nm):Al(10 nm)/Alq_3(70 nm)/LiF(1 nm)/Al(120 nm) device.

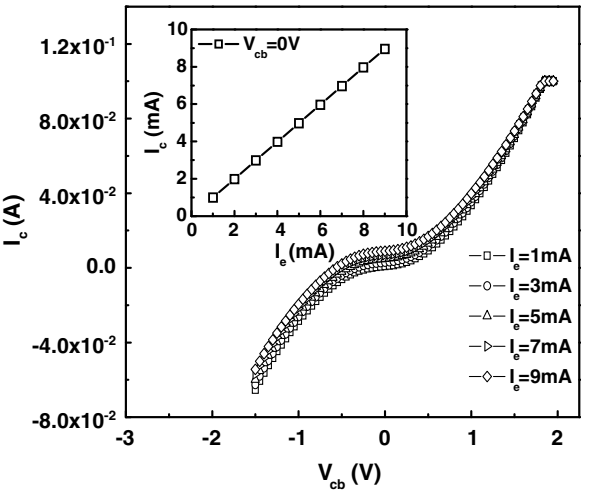

Fig. 3. Common-base mode characteristics of the Al(120 nm)/n-Si/ Al(20 nm)/Alq_3(70 nm)/LiF(1 nm)/Al(120 nm) device.

$I_c = I_e$ (I_e is the emitter current) for positive V_{cb} (V_{cb} is the potential difference between collector and base), which is due to the reverse-biased base-collector junction, resulting that almost all electrons injected by the emitter into the base arrive at the collector. There is rapid increase in negative I_c for negative V_{cb}, which is attributed to the forward-biased Au/n-Si Schottky junction, leading to the higher output current. The plot of I_c as a function of I_e at constant V_{cb} allows to calculate the common-base current gain. In order to eliminate the contribution of the leakage current, which is assumed to be constant, the common-base current gain, defined as $\alpha_0 = dI_c/dI_e$ [19], is calculated at $V_{cb} = 0$. The inset of Fig. 2 shows the calculated result. The slope α_0 equals to 0.999, which is near to the ideal common-base current gain 1. This high common-base current gain α_0 also implies that there exists a high base-transport factor α_T in the Al/n-Si/Au/Al/Alq_3/LiF/Al devices.

However, as we can see, when using Al instead of Au/Al as the base, resulting in Al/n-Si/Al/Alq_3/LiF/Al devices, although the common-base current gain α_0 of 0.995 at $V_{cb} = 0$ is obtained, there is a large leakage current, as shown in Fig. 3 where the common-base electrical characteristics and the dependence of I_c on I_e at $V_{cb} = 0$ are given. We attribute the large leakage current to the low Schottky barrier between Al and n-Si in these devices. [8] Furthermore, a high common-base current gain of near 1 and better common-base electrical characteristics with negligible leakage current are again achieved when using Au as base metal, thus in Al/n-Si/Au/Alq_3/LiF/Al devices. Fig. 4 shows the I_c as a function of V_{cb} at different I_e and the dependence of I_c on I_e at $V_{cb} = 0$ for the case of Al/n-Si/Au/Alq_3/LiF/Al devices. This indicates that Au can form better Schottky contact with n-Si, which favors the suppression of the leakage current, as expected.

It is experimentally found that the devices with Au/Al double metal layer base also exhibit better common-emitter mode characteristics. Comparatively, the expected common-emitter mode characteristics are not observed in Al/n-Si/Al/Alq_3/LiF/Al

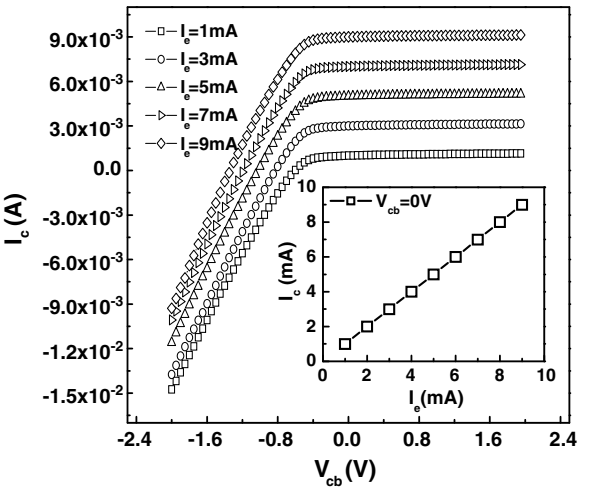

Fig. 4. Common-base mode characteristics of the Al(120 nm)/n-Si/Au(20 nm)/Alq_3(70 nm)/LiF(1 nm)/Al(120 nm) device.

and Al/n-Si/Au/Alq_3/LiF/Al devices, respectively, with Al and Au single metal layer base. Fig. 5a shows the common-emitter electrical characteristics of an Al/n-Si/Au/Al/Alq_3/LiF/Al device. Due to the large collector current I_c at $I_b = 0$, these data in Fig. 5a are replotted in Fig. 5b in the form I_c–I_L as a function of V_{ce}, where the I_L ($I_L = I_c$ at $I_b = 0$) is defined as the leakage current between the emitter and the collector. Accordingly, the dependence of the common-emitter current gain β, defined as $(I_c–I_L)/I_b$, on the V_{ce} (potential difference between collector and emitter) can be obtained, as shown in Fig. 5c. It can be clearly seen that the device shows higher common-emitter current gain at low base currents. The current gain tends to saturation at high V_{ce} bias, and decreases with the increase of the base current I_b. The maximum common-emitter current gain may reach over 4000, which is respectable even when compared to those observed in inorganic permeable metal-base transistors [20].

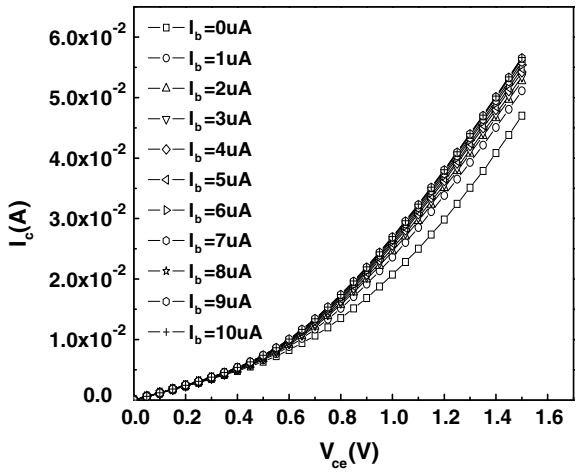

Fig. 5a. Measured common-emitter characteristics of the Al(120 nm)/n-Si/Au(10 nm):Al(10 nm)/Alq_3(70 nm)/LiF(1 nm)/Al(120 nm) device.

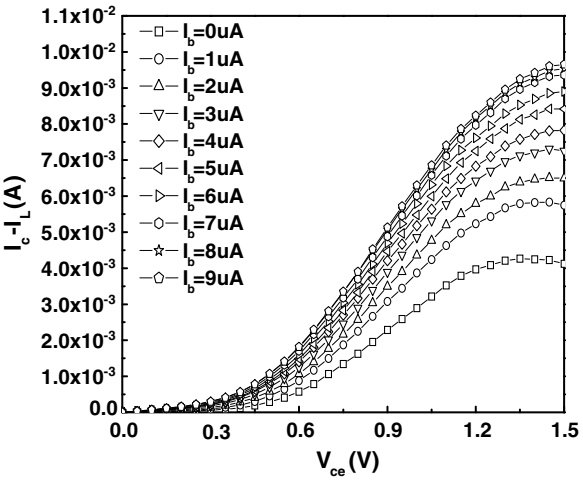

Fig. 5b. Measured common-emitter characteristics of the Al(120 nm)/n-Si/Au(10 nm):Al(10 nm)/Alq_3(70 nm)/LiF(1 nm)/Al(120 nm) device, but deducing the collector current for $I_c(I_b = 0)$.

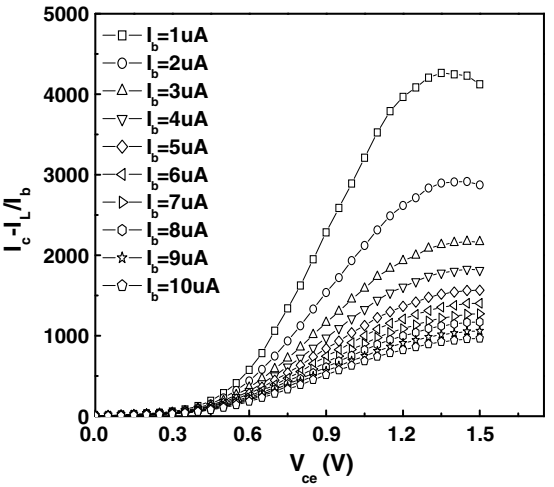

Fig. 5c. Common-emitter current gain of the Al(120 nm)/n-Si/Au(10 nm):Al(10 nm)/Alq_3(70 nm)/LiF(1nm)/Al(120 nm) device.

Fig. 6 shows the energy level diagram of the materials used in this study and the case of the contact of Au/n-Si and Alq_3/Al. It can be clearly seen that for the case of Au/Al double metal layer base, on the one hand, the Au forms a good Schottky contact with the n-Si. On the other hand, Al also forms better contact with Alq_3 at the same time, satisfying the condition that the barrier height between Alq_3 and Al is larger than that of Au and n-Si, which is desirable for an asymmetrical MBT device to improve current gain. More importantly, the utilization of Al metal in the Au/Al double metal layer base will greatly reduce the injection of the holes from Al to Alq_3 emitter with respect to the case of Au base due to the higher energy barrier in the former case. Thus, minority carrier injection and the recombination current of holes and electrons in the emitter region, which does not benefit the transistor action, are significantly decreased. Furthermore, the introduction of Al should also benefit the injection of more electrons from emitter to collector. These should be used to well explain the reason why the Au/Al double-layer metal base

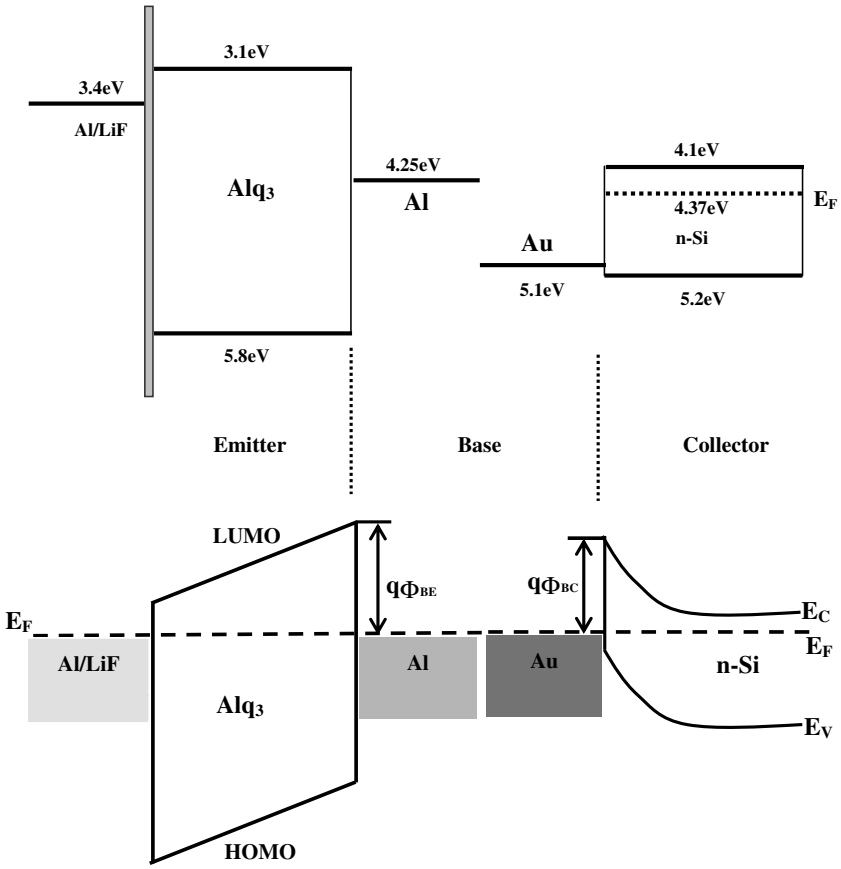

Fig. 6. Simplified energy scheme of the materials used in device production.

improves the common-base and common-emitter mode characteristics of the devices.

Like in previously reported devices based on Alq_3 [17,18], the Al/n-Si/Au/Al/Alq_3/LiF/Al devices also show permeable base characteristics, since at constant I_e, $\frac{\partial V_{be}}{\partial V_{cb}} \approx 1$ is observed. This indicates that the Au/Al double-layer metal base is also not able to shield the emitter from the electric filed changes between the base and the collector [17,18].

It is important to stress that our transistors output higher current at low operational voltage, producing lower power dissipation in the emitter layer. The high leakage current, however, constitutes a drawback and efforts are necessary to solve this problem, because it is responsible for a significant part of the dissipated power. This characteristic is especially necessary in practical application because the organic semiconductors are more sensible to the high temperatures than their inorganic counterparts and heat dissipation constitutes a general problem if higher integration is aimed.

4. Conclusions

We presented vertical architecture hybrid permeable-base transistors based on tris(8-hydroxyquinoline) aluminium (Alq_3) as the emitter with Au/Al double metal layer base that show fine characteristics of common-base and common-emitter, can be operated at low driving voltages, and allow high current density. Our results indicate that the contact of the metal base at emitter and collector interfaces plays important roles in transistor performance.

Acknowledgements

The authors would like to thank the Hundreds Talents program of Chinese Academy of Sciences, National Natural Foundation of China (50573075), National Science Fund for Distinguished Young Scholars of China (50325312), Foundation of Jilin Research Council (20050517), Science Fund for Creative Research Groups of NSFC (20621401), the

Ministry of Science and Technology of China (973 Program No. 2002CB613400), and the Brazilian institutions CNPq, Renami/CNPq and Instituto do Milênio/CNPq for Research Grants.

References

[1] M. Atalla, D. Khang, IEEE Trans. Electron. Device 9 (1962) 507.
[2] D.V. Geppert, Proc. IRE 50 (1962) 1527.
[3] D.J. Monsma, J.C. Lodder, T.J.A. Popma, B. Dieny, Phys. Rev. Lett. 74 (1995) 5260.
[4] S.M. Sze, H.K. Gummel, Solid State Electron. 9 (1966) 751.
[5] Kazuhiro Kudo, Dong Xing Wang, Masaaki Iizuka, Shigekazu Kuniyoshi, Kuniaki Tanaka, Thin Solid Films 331 (1998) 51.
[6] S. Zorba, Y. Gao, Appl. Phys. Lett. 86 (2005) 193508.
[7] Yu-Chiang Chao, Syuan-Ling Yang, Hsin-Fei Meng, Sheng-Fu Horng, Appl. Phys. Lett. 87 (2005) 253508.
[8] M.S. Meruvia, I.A. Hümmelgen, Adv. Funct. Mater. 16 (2006) 459.
[9] Tzu-Min Ou, Shiau-Shin Cheng, Chun-Yuan Huang, Meng-Chyi Wu, Appl. Phys. Lett. 89 (2006) 183508.
[10] Kiyoshi Fujimoto, Takaaki Hiroi, Kazuhiro Kudo, Masakazu Nakamura, Adv. Mater. 19 (2007) 525.
[11] M.S. Meruvia, I.A. Hümmelgen, M.L. Sartorelli, A.A. Pasa, W. Schwarzacher, Appl. Phys. Lett. 84 (2004) 3978.
[12] Liping Ma, Yang Yang, Appl. Phys. Lett. 85 (2004) 5084.
[13] Ken-ichi Nakayama, Shin-ya Fujimoto, Masaaki Yokoyama, Appl. Phys. Lett. 88 (2006) 153512.
[14] M.S. Meruvia, I.A. Hümmelgen, A.A. Pasa, W. Schwarzacher, Appl. Phys. Lett. 86 (2005) 263504.
[15] Chengang Feng, Mingdong Yi, Shunyang Yu, Dongge Ma, Tong Zhang, Michelle S. Meruvia, Ivo A. Hümmelgen, Appl. Phys. Lett. 88 (2006) 203501.
[16] M.S. Meruvia, A.R.V. Benvenho, I.A. Hümmelgen, J.A. Gómez, C. F.O. Graeff, R.W.C. Li, L.J.M.C. Aguiar, J. Gruber, Phys. Status Solidi A 202 (2005) R158.
[17] Mingdong Yi, Shunyang Yu, Dongge Ma, Chengang Feng, Tong Zhang, M.S. Meruvia, Ivo A. Hümmelgen, Org. Electron. 8 (2007) 311.
[18] Mingdong Yi, Shunyang Yu, Dongge Ma, Chengang Feng, Tong Zhang, M.S. Meruvia, Ivo A. Hümmelgen, J. Appl. Phys. 99 (2006) 106102.
[19] R. Dalven, Introduction to Applied Solid State Physics, Plenum, New York, 1980.
[20] S.L. Su, R. Fischer, W.G. Lyons, O. Tejayadi, D. Arnold, J. Klem, H. Morkoc, J. Appl. Phys. 54 (1983) 6725.

Available online at www.sciencedirect.com
ScienceDirect
Organic Electronics 9 (2008) 545–549
Organic Electronics
www.elsevier.com/locate/orgel

Letter

High air stability of threshold voltage on gate bias stress in pentacene TFTs with a hydroxyl-free and amorphous fluoropolymer as gate insulators

Tokiyoshi Umeda [a,*], Daisuke Kumaki [b], Shizuo Tokito [a]

[a] NHK Science and Technical Research Laboratories, 1-10-11 Kinuta, Setagaya-ku, Tokyo 157-8510, Japan
[b] Department of Electronic Chemistry, Tokyo Institute of Technology, 4259 Nagatsuta-cho, Midori-ku, Yokohama 226-8502, Japan

Received 4 February 2008; received in revised form 21 February 2008; accepted 24 February 2008
Available online 4 March 2008

Abstract

We investigated the air stabilities of threshold voltages (V_{th}) on gate bias stress in pentacene thin-film transistors (TFTs) with a hydroxyl-free and amorphous fluoropolymer as gate insulators. The 40-nm-thick thin films of spin-coated fluoropolymer had excellent electrical insulating properties, and the pentacene TFTs exhibited negligible current hysteresis, low leakage current, a field-effect mobility of 0.45 cm^2/Vs and an on/off current ratio of 3×10^7 when it was operated at −20 V in ambient air. After a gate bias stress of 10^4 s, a small V_{th} shift below 1.1 V was obtained despite non-passivation of the pentacene layer. We have discussed that the excellent air stability of V_{th} was attributed to the insulator surface without hydroxyl groups.

PACS: 85.30.Tv

Keywords: Organic thin-film transistor; Amorphous fluoropolymer; Cytop; Air stable threshold voltage; Bias stress; Hysteresis; Insulating properties

Organic thin-film transistors (OTFTs) have been widely studied because of their potential for low-cost and low-temperature processes and their applications to flexible large-area displays, circuits, and sensors. In particular, low-temperature processes for OTFTs of less than 150 °C enable them to be directly formed on flexible plastic substrates and they can actively drive display devices such as organic light-emitting diodes (OLEDs) [1,2], liquid crystals, and electronic inks. Ink-jet printings and roll-to-roll processes have been explored to achieve low-cost and large-area flexible displays with OTFT backplanes. These fabrication processes and the handlings of the backplanes should be carried out in ambient air to enable simple inexpensive production. Besides, the gas-barrier properties of the plastic films used as the substrates of these flexible backplanes are still insufficient to prevent oxidation and water adsorption. Therefore, OTFTs require both storage and driving stability in ambient air.

* Corresponding author.
E-mail address: umeda.t@strlstaff.strl.nhk.or.jp (T. Umeda).

1566-1199/$ - see front matter © 2008 Elsevier B.V. All rights reserved.
doi:10.1016/j.orgel.2008.02.015

However, the instabilities that are widely observed in OTFTs can be divided into three kinds; the first is the decrease in field-effect mobilities, the second is current hysteresis, and the third is threshold voltage (V_{th}) shift caused by gate bias stress. The decreases in mobilities has mainly been caused by oxidation of organic semiconductors and many attempts have been made to overcome this, such as increasing the ionization potentials of organic semiconductors to strengthen their resistance to oxidation [3,4] and protecting them with passivation layers [5]. The hysteresis are considered to be due to the short-term trapping and release of charge carriers caused by impurities and adsorbed molecules such as water at the insulator–semiconductor interfaces [6]. The V_{th} shifts induced by gate bias stress can be explained as being due to the long-term trapping and release of charge carriers caused by structural defects and impurities at the interfaces.

It has recently been reported that hydroxyl groups and/or adsorbed water related to the hysteresis and the V_{th} shifts. Hydroxyl groups and/or adsorbed water at the interfaces between SiO_2 and p-type organic single crystal increase trap densities and shift V_{th} on gate bias stressing [7,8]. Hydroxyl groups at the insulator surfaces are the trapping sites for electrons in n-type OTFTs [9,10]. OTFTs using polymer insulators containing hydroxyl groups such as poly(vinylphenol) (PVP) and poly(vinylalcohol) (PVA) have large hysteresis in ambient air [11,12]. Therefore, these results indicated that the hysteresis and the V_{th} shifts are mainly caused by the hydroxyl groups and/or adsorbed water at the interfaces between insulators and organic semiconductors.

In this letter, we report on the excellent air stability of V_{th} on the gate bias stress in pentacene TFTs with a hydroxyl-free and amorphous fluoropolymer, poly(perfluorobutenylvinylether) commercially known as Cytop (Asahi Glass Co.), as the gate insulator. This fluoropolymer can easily form uniform thin-films from solution by spin-coating. OTFTs using polymer semiconductors [13] and organic single-crystal field-effect transistors [14] with the fluoropolymer as their gate insulators have previously been reported. However, their characteristics had to be measured in a vacuum or inert atmosphere, therefore the air stability of the V_{th} on gate bias stress had not been clarified. We demonstrated that excellent air stability of V_{th} on gate bias stress in pentacene TFT with the fluoropolymer as the gate insulator is superior to that of hydrogenated amorphous silicon (a-Si:H) TFTs under similar stress conditions. In addition, previous works with the fluoropolymer as gate insulators had large operating voltage because the fluoropolymers were thick, i.e., 450–800 nm. It is very important for practical application to lowering the operating voltage. We demonstrated that spin-coated thin films of fluoropolymers with thicknesses from 15 nm to 200 nm had excellent electrical insulating properties such as low leakage current densities below 10^{-8} A/cm^2 and high electrical breakdown strengths over 5 MV/cm, resulting in low leakage current and high on/off current ratio with low operating voltage in the pentacene TFTs with the fluoropolymer as the gate insulator.

The electrical insulating properties of the amorphous fluoropolymer were measured by metal–insulator–metal structures. Thin films of fluoropolymer were spin coated from solution onto patterned aluminum (Al) electrodes deposited by thermal evaporation on glass substrates, and dried at 120 °C. The thicknesses were controlled by changing the concentrations of the solution and measured by ellipsometry and an optical profiler. Top Al electrodes were deposited by thermal evaporation orthogonal onto the films through a shadow mask and the active areas were 3×3 mm^2. The relative permittivity was 2.1 and this was not changed in a range of frequencies from 20 Hz to 100 kHz.

The bottom-gate and top-contact OTFTs were fabricated as follows. Thin fluoropolymer layers (40 nm) were formed by spin-coating onto patterned Al gate electrodes (30 nm) on glass substrates, and dried at 120 °C. The thin films of pentacene (30 nm) were evaporated onto the fluoropolymer, and 30-nm-thick gold (Au) source–drain electrodes were deposited by thermal evaporation. The channel widths (W) were 1000 μm and the lengths (L) were 50 μm, resulting in a W/L of 20. All measurements of the characteristics and gate bias stressing of the OTFTs were carried out in ambient air with a relative humidity of 60% at room temperature in the dark using a Keithley 4200-SCS semiconductor parameter analyzer.

Fig. 1 shows the current density–electric field (J–E) characteristics of the amorphous fluoropolymer, Cytop, thin films. The electrical insulating properties were not dependent on film thicknesses from 15 nm to 200 nm. The leakage current densities were lower than 10^{-8} A/cm^2 and the breakdown electric fields were larger than 5 MV/cm. The leakage current densities at 5 MV/cm are two orders of magnitudes lower than those of a plasma-grown AlO_x

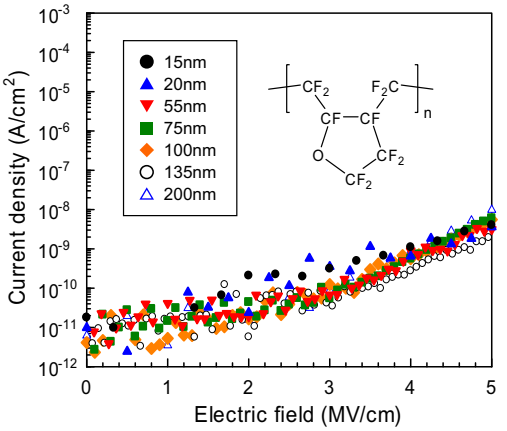

Fig. 1. Current density–electric field (J–E) characteristics of thin films of amorphous fluoropolymer, Cytop. Thin films were formed by spin coating. Inset shows chemical structure of Cytop.

insulator with a phosphonic acid-based self-assembled monolayer [15]. Furthermore, these low leakage current densities and high breakdown electric fields are substantially superior to other polymer dielectrics. For example, the breakdown electric fields of polyimide, crosslinked PVP, and crosslinked cyanoethylated PVA are around 2.5 MV/cm, and the leakage current densities at 2.5 MV/cm are three orders of magnitude higher than those of amorphous fluoropolymer [16,17].

Since the thin films of amorphous fluoropolymer have the low leakage currents and high breakdown electric fields, we can apply them to the gate insulators of OTFTs. Figs. 2a and b, show the transfer and output characteristics of a pentacene TFT with a 40-nm-thick Cytop as the gate insulator in ambient air. The transfer characteristics exhibit a steep current increase in the subthreshold region and low leakage current, and the output characteristics show good saturation behavior. Both of these exhibited negligible hysteresis despite the operation in ambient air, which will be discussed later. The field-effect mobility was calculated in the saturation regime from the linear fit of the square root of the drain current ($I_D^{0.5}$) versus gate voltage (V_G) by using equation $I_D = (C_i W/2L)\mu(V_G - V_{th})^2$, where C_i is the capacitance of the insulator, and μ is the field-effect mobility. The mobility was calculated to be 0.45 cm^2/Vs with a C_i of 46.5 nF/cm^2. The OTFT had a V_{th} of -6.3 V, an on/off current ratio of 3×10^7, and a subthreshold swing of 0.56 V/decade when V_G was swept within -20 V at a drain voltage (V_D) of -20 V. The high on-current was archived over 10 μA. It is important to apply OTFTs to the

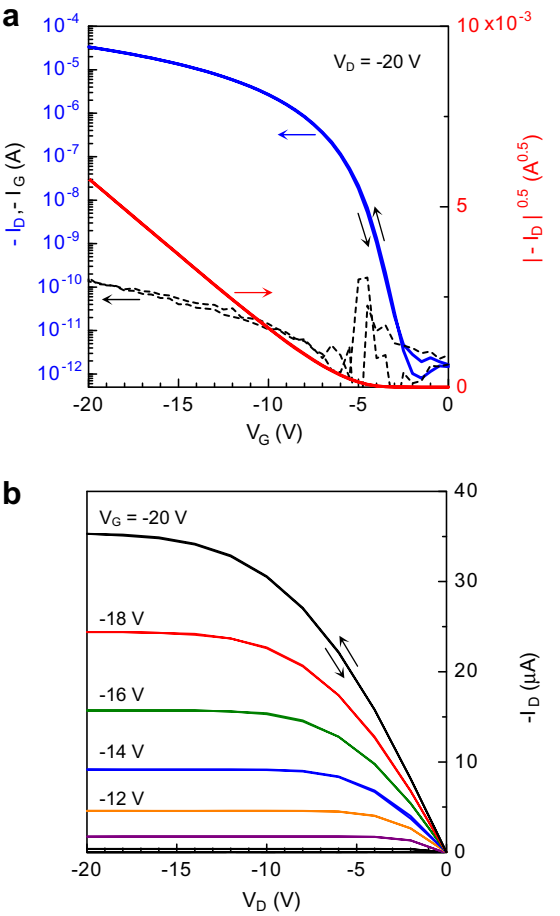

Fig. 2. (a) Transfer and (b) output characteristics of pentacene TFT with Cytop (40 nm) as gate insulator measured in ambient air. In terms of transfer characteristics, I_D is indicated by solid line and I_G is indicated by broken line. TFT has channel width of 1000 μm and channel length of 50 μm ($W/L = 20$).

driving transistors of OLED displays because a high on-current is required to drive OLEDs sufficiently well [1,2]. The operating voltage, $V_G = -20$ V, is equivalent to an electric field of 5 MV/cm because the insulator is 40-nm thick. Despite the high electric field, the gate current (I_G), which was due to leakage between the source and the gate electrodes through the gate insulator, was around 100 pA and this was five orders of magnitudes lower than the on-current. This property is due to the excellent electrical insulating properties of the amorphous fluoropolymer.

We evaluated the air stabilities of transfer characteristics on gate bias stress. Fig. 3 shows the transfer characteristics ($V_D = -20$ V) before and after bias stress at a V_G of -20 V for 100, 1000, and 10000 s in ambient air. During the stress period,

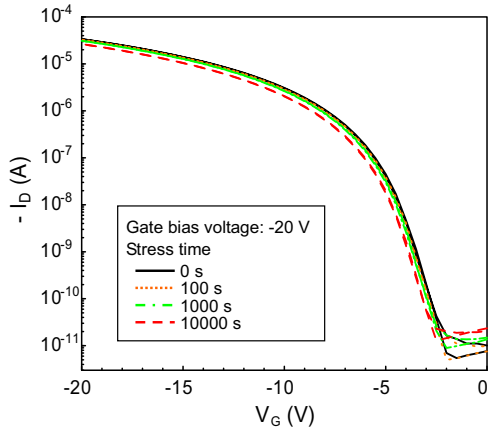

Fig. 3. Transfer characteristics ($V_D = -20$ V) before and after gate bias stress of $V_G = -20$ V ($V_D = 0$ V) for 100, 1000, and 10000 s. Bias stressing and measurements were carried out in ambient air.

V_D was held at 0 V to ensure a homogeneous electric stress field was applied throughout the channel. The transfer characteristics shifted slightly in the negative direction with the negative gate bias stress. The variations in V_{th} (ΔV_{th}) as a function of stress time are plotted in Fig. 4. The gate bias voltages were −20, −10, and −7.5 V, which were equivalent to respective electric fields of 5, 2.5, and 1.9 MV/cm. Although the electric field at the gate bias voltage of −20 V was high and the OTFT was stressed without any passivation over the pentacene layer in ambient air, the ΔV_{th} was only 1.1 V at 10000 s. These shifts are smaller than the shifts in the OTFTs with untreated SiO_2, organosilane treated SiO_2 and other

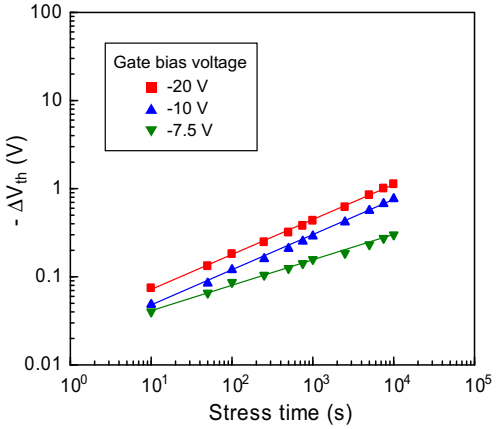

Fig. 4. Variations in threshold voltage as function of stress time plotted for gate bias voltages of −20, −10 and −7.5 V, which correspond to the electrical fields of 5, 2.5 and 1.9 MV/cm, respectively.

polymers as the gate insulators [18–20]. Even more importantly, these shifts were smaller than the shifts of V_{th} in a-Si:H TFTs under similar stress conditions [21,22].

The instabilities in OTFTs such as the hysteresis and V_{th} shifts induced by gate bias stress are generally considered to be due to short-term and long-term trapping and release of charge carriers caused by structural defects, impurities, and adsorbed molecules such as water at the insulator–semiconductor interfaces. Thermally grown SiO_2 on Si wafers are frequently used as insulators because of their superior electrical insulating properties. However, it has been reported that hydroxyl groups (Si–OH) on the SiO_2 surfaces act as trapping sites for electrons in n-type OTFTs operated even in inert atmospheres [9,10]. Besides, it have been discussed that $Si–O^-$ was created from Si–OH by water at the SiO_2 surfaces both in p-type and n-type OTFTs, which considerably shifts the V_{th} in the same positive direction [23]. Even though organosilane-treated SiO_2 is used as insulators, there are certain hysteresis and V_{th} shifts especially during operation in ambient air [4,6,8], which are considered to be caused by adsorbed water and residual hydroxyl groups on the SiO_2 surfaces, which are not substituted by organosilane agents. As is well known, OTFTs using polymer insulators such as PVP and PVA have large hysteresis [11,12]. Here, the hydroxyl groups of polymer insulators and water in ambient air are the causes of the hysteresis [12]. Although the hydroxyl groups are substituted by crosslink agents, it is difficult to completely substitute all hydroxyl groups in polymers. Unsubstituted hydroxyl groups and residual crosslink agents probably act as trapping sites. In both cases, adsorbed water and the hydroxyl groups of insulators are considered to be the causes of instabilities in these OTFTs.

The amorphous fluoropolymer used in our devices, on the other hand, does not have hydroxyl groups in its chemical structure; the films are hydrophobic due to the nature of the fluorinated material, and crosslinks are not required. Therefore, the negligible hysteresis and the small V_{th} shifts obtained in our OTFTs in ambient air are attributed to these advantages.

In conclusion, we demonstrated that pentacene TFTs with spin-coated thin films of a hydroxyl-free and amorphous fluoropolymer as the gate insulators had excellent electrical insulating properties with negligible current hysteresis and small V_{th} shifts on gate bias stressing in ambient air. The high air

stabilities of V_{th} on gate bias stress were mainly due to hydroxyl-free, hydrophobic, and non-reactive gate insulators, and these were superior to the stabilities of V_{th} in a-Si:H TFTs. These excellent air stabilities should make useful contributions to both fundamental studies for understanding insulator–semiconductor interfaces and practical applications of OTFTs to integrated circuits and flat-panel displays.

Acknowledgements

The authors would like to thank H. Kikuchi and T. Hoshi for their valuable discussions on Cytop.

References

[1] I. Yagi, N. Hirai, M. Noda, A. Imaoka, Y. Miyamoto, N. Yoneya, K. Nomoto, J. Kasahara, A. Yumoto, Tetsuo Urabe, SID Symp. Digest 38 (2007) 1753.
[2] M. Mizukami, N. Hirohata, T. Iseki, K. Ohtawara, T. Tada, S. Yagyu, T. Abe, T. Suzuki, Y. Fujisaki, Y. Inoue, S. Tokito, T. Kurita, IEEE Electron Device Lett. 27 (2006) 249.
[3] B.S. Ong, Y. Wu, P. Liu, S. Gardner, J. Am. Chem. Soc. 126 (2004) 3378.
[4] T. Umeda, S. Tokito, D. Kumaki, J. Appl. Phys. 101 (2007) 054517.
[5] S.-H. Han, J.-H. Kim, J. Jang, S.-M. Cho, M.-H. Oh, S.-H. Lee, D.-J. Choo, Appl. Phys. Lett. 88 (2006) 073519.
[6] G. Gu, M.G. Kane, S.-C. Mau, J. Appl. Phys. 101 (2007) 014504.
[7] C. Goldmann, C. Krellner, K.P. Pernstich, S. Haas, D.J. Gundlach, B. Batlogg, J. Appl. Phys. 99 (2006) 034507.
[8] C. Goldmann, D.J. Gundlach, B. Batlogg, Appl. Phys. Lett. 88 (2006) 063501.
[9] L.-L. Chua, J. Zaumseil, J.-F. Chang, E.C.-W. Ou, P.K.-H. Ho, H. Sirringhaus, R.H. Friend, Nature 434 (2005) 194.
[10] X.-H. Zhang, B. Domercq, B. Kippelen, Appl. Phys. Lett. 91 (2007) 092114.
[11] H. Klauk, M. Halik, U. Zschieschang, G. Schmid, W. Radlik, W. Weber, J. Appl. Phys. 92 (2002) 5259.
[12] S.-C. Lim, S.-H. Kim, J.-B. Koo, J.-H. Lee, C.-H. Ku, Y.-S. Yang, T. Zyung, Appl. Phys. Lett. 90 (2007) 173512.
[13] J. Veres, S. Ogier, G. Lloyd, D. de Leeuw, Chem. Mater. 16 (2004) 4543.
[14] W.L. Kalb, T. Mathis, S. Haas, A.F. Stassen, B. Batlogg, Appl. Phys. Lett. 90 (2007) 092104.
[15] H. Klauk, U. Zschieschang, J. Pflaum, M. Halik, Nature 445 (2007) 745.
[16] S.-Y. Yang, S.-H. Kim, K. Shin, H. Jeon, C.-E. Park, Appl. Phys. Lett. 88 (2006) 173507.
[17] S.-H. Kim, S.-Y. Yang, K. Shin, H. Jeon, J.-W. Lee, K.-P. Hong, C.-E. Park, Appl. Phys. Lett. 89 (2006) 183516.
[18] D. Knipp, R.A. Street, A. Volkel, J. Ho, J. Appl. Phys. 93 (2003) 347.
[19] G.H. Gelinck, H. Edzer, A. Huitema, E.V. Veenendaal, E. van Cantatore, L. Schrijnemakers, J.B.P.H. van der Putten, T.C.T. Geuns, M. Beenhakkers, J.B. Giesbers, B.-H. Hiusman, E.J. Meijer, E.M. Benito, F.J. Touwslager, A.W. Marsman, B.J.E. van Rens, D.M. De Leeuw, Nat. Mater. 3 (2004) 106.
[20] A. Salleo, F. Endicott, R.A. Street, Appl. Phys. Lett. 86 (2005) 263505.
[21] F.R. Libsch, J. Kanicki, Appl. Phys. Lett. 62 (1993) 1286.
[22] C.-H. Lee, D. Striakhilev, A. Nathan, IEEE Trans. Electron Devices 54 (2007) 45.
[23] D. Kumaki, T. Umeda, S. Tokito, Appl. Phys. Lett. 92 (2008) 093309.

Organic Electronics 9 (2008) 551–556

Contents lists available at ScienceDirect

Organic Electronics

journal homepage: www.elsevier.com/locate/orgel

Effect of molybdenum electrode annealing on the interface properties between metal and pentacene

Dong-Jin Yun, Shi-Woo Rhee *

Laboratory for Advanced Molecular Processing, Department of Chemical Engineering, Pohang University of Science and Technology, Pohang 790-784, Republic of Korea

ARTICLE INFO

Article history:
Received 27 November 2007
Received in revised form 13 February 2008
Accepted 28 February 2008
Available online 18 March 2008

PACS:
73.61.At
73.40.Cg
85.30.Tv
72.80.Le
61.72.Cc

Keywords:
Molybdenum
Contact resistance
OTFT
Pentacene
Annealing

ABSTRACT

Contact resistance between molybdenum (Mo) electrode and pentacene was studied with transmission line method (TLM). The Mo electrodes were annealed at 200 °C, 400 °C, 600 °C and 800 °C for 1 h and pentacene layer of 300 Å thickness was vacuum deposited on patterned Mo to form Mo–pentacene contact. Current–voltage measurement for Mo–pentacene contact showed linear relationship and it was confirmed that ohmic contact was formed. XRD and AFM measurements showed that Mo could be crystallized at annealing temperatures above 600 °C. 800 °C annealed Mo showed larger grains and work function was increased from 4.60 eV to 4.80 eV due to the decrease in defect density. The contact resistance was reduced down to 11.2 MΩ cm from 37.8 MΩ cm of as-deposited Mo. Also the pentacene film deposited on annealed Mo was denser with better crystallinity. Bottom contact organic field-effect transistor made with 800 °C annealed Mo showed better performance than as deposited Mo.

1. Introduction

Recently, the performance of organic thin film transistors (OTFT) has improved dramatically. The mobility of OTFT with pentacene was improved up to 1.5 cm^2/Vs and on/off ratio was also improved up to 10^5 [1,2]. Most of the researches have been focused on improving the electrical properties of components such as semiconductor, gate dielectric and source/drain electrode, but many factors are still poorly understood and controlled. One of them is contact resistance between electrode and semiconductor. Interface properties between electrode and semiconductor are critical factors for good TFT performance but with decreasing device dimensions, contact resistance has been increased [3], which degrades the device performance. Work function modification of the metal surface to lower the barrier and removal of impurities such as native oxide have been studied to lower the contact resistance [3,4]. As a source/drain (S/D) electrode, gold, silver, calcium, palladium [2,5,6] and transparent conducting oxide like indium–tin-oxide (ITO) [7] were studied and currently, gold has been mainly used as a contact metal because gold has a work function of 5.1 eV, which is close to the highest occupied molecular orbital(HOMO) level of pentacene (5.0 eV). In this case, hole injection barrier is low so that carriers can move easily in each direction between electrode and pentacene. In spite of this advantage, gold is not suitable for commercial application due to the high cost and as a noble metal, it is very difficult to etch for patterning. Molybdenum (Mo) has a low resistivity of $5 \times 10^{-6}\ \Omega$ cm and high work function of 4.6–4.9 eV and it has been

* Corresponding author. Tel.: +82 54 279 2265; fax: +82 54 279 8619.
E-mail address: srhee@postech.ac.kr (S.-W. Rhee).

1566-1199/$ - see front matter © 2008 Elsevier B.V. All rights reserved.
doi:10.1016/j.orgel.2008.02.019

studied as a source–drain electrodes of Si FET (field-effect transistor) with good performance [8]. Various groups have suggested that interface properties between metal and semiconductor could be improved through annealing process with reduced barrier height and contact resistance [9,10].

In this work, Mo has been used as a source/drain electrode metal and effect of annealing on the improvement of the interface properties between Mo and pentacene was studied. We measured the contact resistance and the *I–V* characteristics of the pentacene TFT. Crystallization of Mo was studied with X-ray diffraction (XRD) and atomic force microscopy (AFM). The work function of Mo was measured with ultraviolet photoelectron spectroscopy (UPS) and pentacene layer deposited on Mo was also investigated with XRD and AFM measurement.

2. Experimental

Pentacene was purchased from Aldrich Chemical Co. and n-type heavily doped silicon wafer with thermally grown SiO_2 (300 nm) was purchased from Silicon Materials. For the measurement of contact resistance with transmission line method (TLM), Mo (thickness: 200 nm) was deposited on glass substrate of 2 cm × 2 cm with rf sputtering and the layer was patterned with photolithography and wet etching with aqua regia. As shown in Fig. 1a, Mo was accurately patterned with length (d) of 0.1 cm and width (W) of 0.7 cm. The gap between Mo electrodes was from 50 to 90 μm with 5 μm increment between adjacent lines so that it can be used as a structure for transmission line method (TLM) as shown in Fig. 1b [7]. Mo coated glass substrate was cleaned with acetone, ethanol and IPA (*iso*-propanol) to remove organic impurities. Before the deposition of pentacene, annealing was done with Ar gas in a furnace at 200 °C, 400 °C, 600 °C and 800 °C for 1 h. Total electrode width (W, 0.5 cm) was covered with 300 Å thick pentacene film leaving 0.2 cm of Mo for probe contact. Patterned structure for TLM was checked with scanning electron microscopy (SEM). Pentacene film was deposited at 70 °C with a deposition rate of 0.3 Å/s in an organic molecular beam deposition (OMBD) system at 2×10^{-6} torr on top of this pattern.

To make a bottom contact organic thin film transistor, heavily doped Si wafer was used for gate electrode and thermally grown SiO_2 was used as a gate dielectric. SiO_2 grown n^+-Si wafer was cleaned in piranha solution (H_2SO_4: H_2O_2 = 7:4 vol%) for 1 h at 200 °C, rinsed in de-ionized water and dried using N_2 gas. Then, for S/D electrode, 100 nm thick Mo was deposited with sputtering through shadow mask to make a metal pattern with channel length of 150 μm and width of 1500 μm as shown in Fig. 1d and

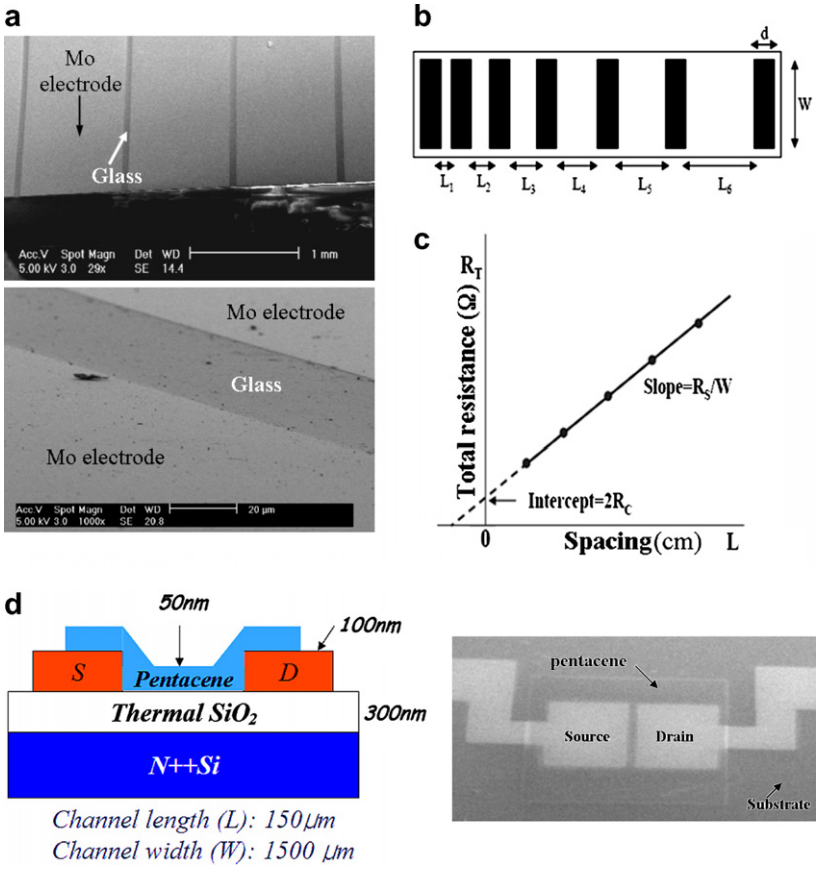

Fig. 1. (a) SEM images of Mo on SiO_2 substrate patterned using photolithography and wet etching, (b) structure of Mo lines on SiO_2 substrate, (c) plot of total resistance versus spacing between Mo electrodes, and (d) structure of bottom contact pentacene TFT with Mo source/drain electrode.

annealing process was followed. Pentacene of 50 nm was deposited at the same condition as in TLM structure formation. In order to investigate the annealing effect of Mo electrodes on device performance, pentacene TFTs with 800 °C annealed Mo was compared with as-deposited sample.

I–V measurement was done with E5270A (Agilent technology). Film morphology of Mo and pentacene were inspected with Dimension™ 3100 atomic force microscope (AFM). The work function of Mo was measured using ultraviolet photoelectron spectroscopy (UPS, Escalab 220IXL) with He(I) emission of 21.2 eV. Crystallites of Mo and pentacene were characterized with X-ray diffraction measurement (XRD, modified Philips-1880 diffractometer) using Cu Kα radiation.

3. Results and discussion

Metals could be crystallized at specific annealing temperature [9–11]. Fig. 2a shows that for as-deposited films and films annealed at 400 °C and below, (110) and (211) peaks from Mo cubic phase with the unit cell size of 3.14 Å appear from the XRD measurement [12]. At annealing temperatures of above 400 °C, (100)′, (110)′, and (200)′ peaks from Mo cubic phase with the unit cell of 3.41 Å are observed additionally. It is believed that a second phase was formed with a larger unit cell size due to the Mo crystallization. Fig. 2b shows the surface morphology of as-deposited Mo, Mo annealed at 400 °C and Mo annealed at 800 °C. Surface morphology of as-deposited Mo and 400 °C annealed Mo shows a small grain size. Surface morphology of Mo annealed at 800 °C shows a large grain size indicating crystallization of Mo. It was confirmed that Mo was crystallized at annealing temperatures above 600 °C. Fig. 3 shows the UPS spectra of Mo annealed at different temperatures and the work function of Mo could be calculated using following equation [13]:

$$\phi = h\nu(= 21.2\ eV) - E_{\text{cutoff}} + E_{\text{Fermi}} \quad (1)$$

where O, E_{cutoff} and E_{Fermi} are the work function, secondary electron cutoff and Fermi level, respectively. The work function of as-deposited Mo was measured to be 4.6 eV, and work function of Mo was increased by ~0.2 eV with annealing above 600 °C. This is probably due to the formation of the second phase as confirmed in the XRD measurement. The crystallization increased the work function of Mo closer to HOMO level of pentacene (~5.0 eV) and hole

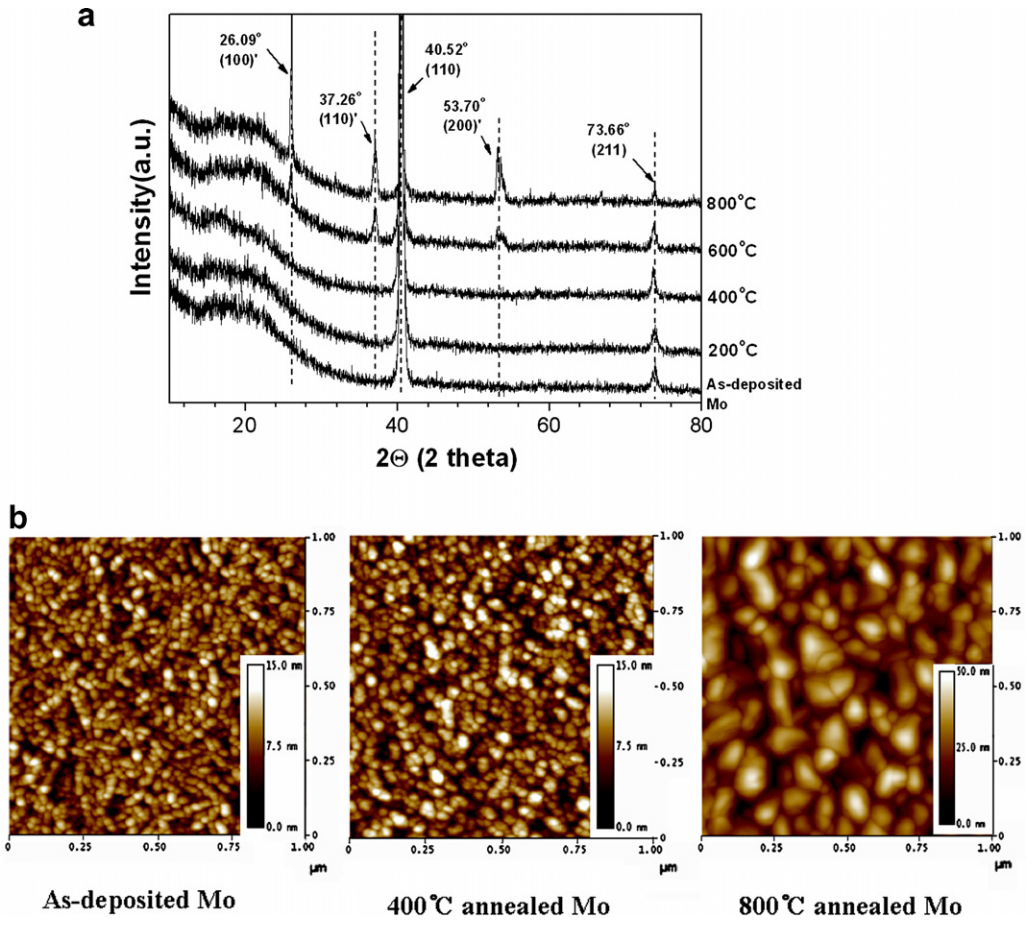

Fig. 2. (a) XRD (Cu Kα) spectra and (b) AFM images of Mo annealed at different temperatures.

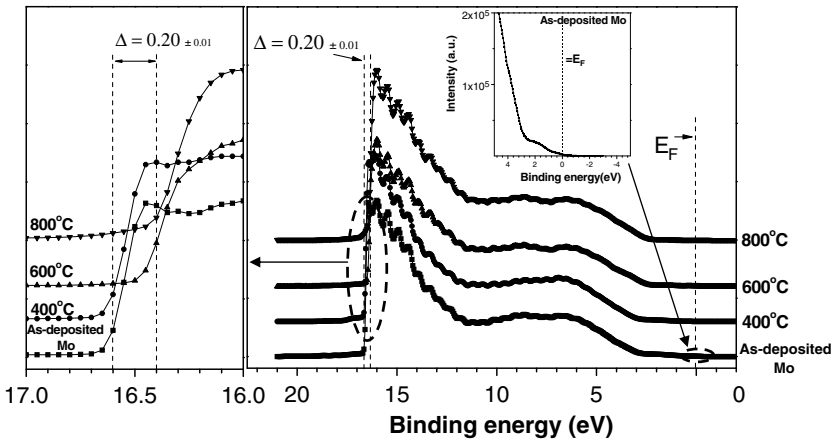

Fig. 3. Ultraviolet photoelectron spectra of Mo annealed at different temperatures.

injection barrier between Mo and pentacene was reduced. The increase in the work function is probably due to the decrease in the defect density with annealing because more energy is needed for electron emission.

Total resistance (R_T) as a function of the distance L between electrodes as shown in Fig. 1c is [14,15]

$$R_T = R_S \cdot L/W + 2R_C, \quad (2)$$

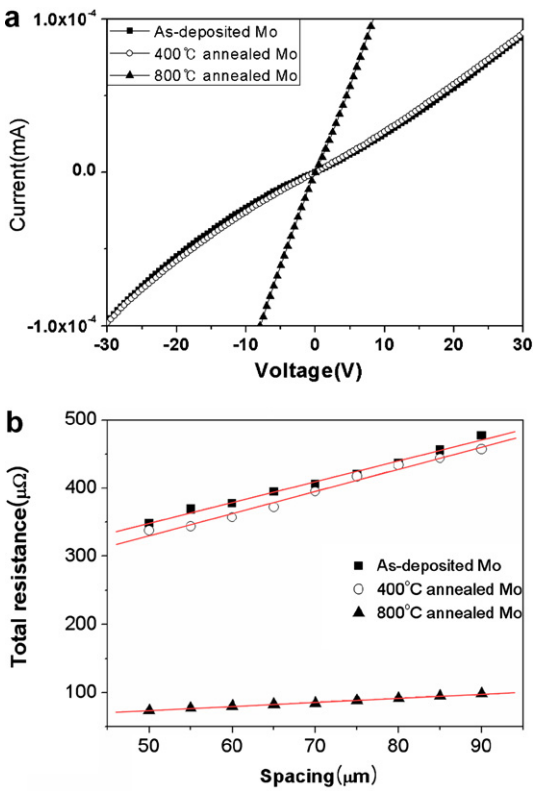

Fig. 4. (a) Current–voltage characteristics measured between the TLM electrodes with a spacing of 50 μm, and (b) plot of the measured total resistance (R_T) versus the spacing (L) between adjacent electrodes.

where R_T is the total resistance between two contacts, R_C is the contact resistance, R_S is the sheet resistance of pentacene, L is the contact spacing and W is the width of the electrode (0.5 cm). Fig. 4a shows the current–voltage characteristics measured between the two adjacent TLM electrodes with a spacing of 50 μm and Fig. 4b shows the total resistance (R_T) versus the spacing (L) between TLM electrodes. As shown in Fig. 4a, the relationship between current and voltage is almost linear, which means Mo makes ohmic contact to pentacene even though there is a hole injection barrier in the interface between Mo and pentacene. Contact resistance of as-deposited Mo has a high value of 37.8 MΩ cm. With annealing at 800 °C, contact resistance between Mo and pentacene was reduced to 11.2 MΩ cm close to the contact resistance between gold and pentacene of 5.65 MΩ cm [14].

Fig. 5a shows the XRD pattern for 50 nm-thick pentacene layer deposited on Mo. The well-known peaks [16–18] indicating single crystal and thin film phases of pentacene did not appear clearly. Peaks of (110), (111) and (022) noticeably arose on the Mo surface annealed at 800 °C and these peaks indicate the existence of flat-lying pentacene with improved adhesion on the surface of Mo [17–19]. Fig. 5b shows AFM images of 50 nm-thick pentacene layer on Mo. Compared to the pentacene layer deposited on as-deposited Mo, pentacene layer deposited on Mo surface annealed at 800 °C has denser structure with smaller grain boundaries. Grain boundaries are known to form hole traps inducing high resistance and low mobility of pentacene [20]. The improved morphology of pentacene layer deposited on Mo surface annealed at 800 °C had an effect on reducing contact resistance of the interface between Mo and pentacene.

In order to investigate the effect of improved contact resistance on device performance, pentacene TFTs with as-deposited and 800 °C annealed Mo S/D electrodes were compared. Table 1 shows the main characteristics of pentacene TFTs with as-deposited and 800 °C annealed Mo S/D electrodes which were obtained from the I–V curves in Fig. 6. A pentacene TFT with gold electrode was also made with the same procedure and characterized to

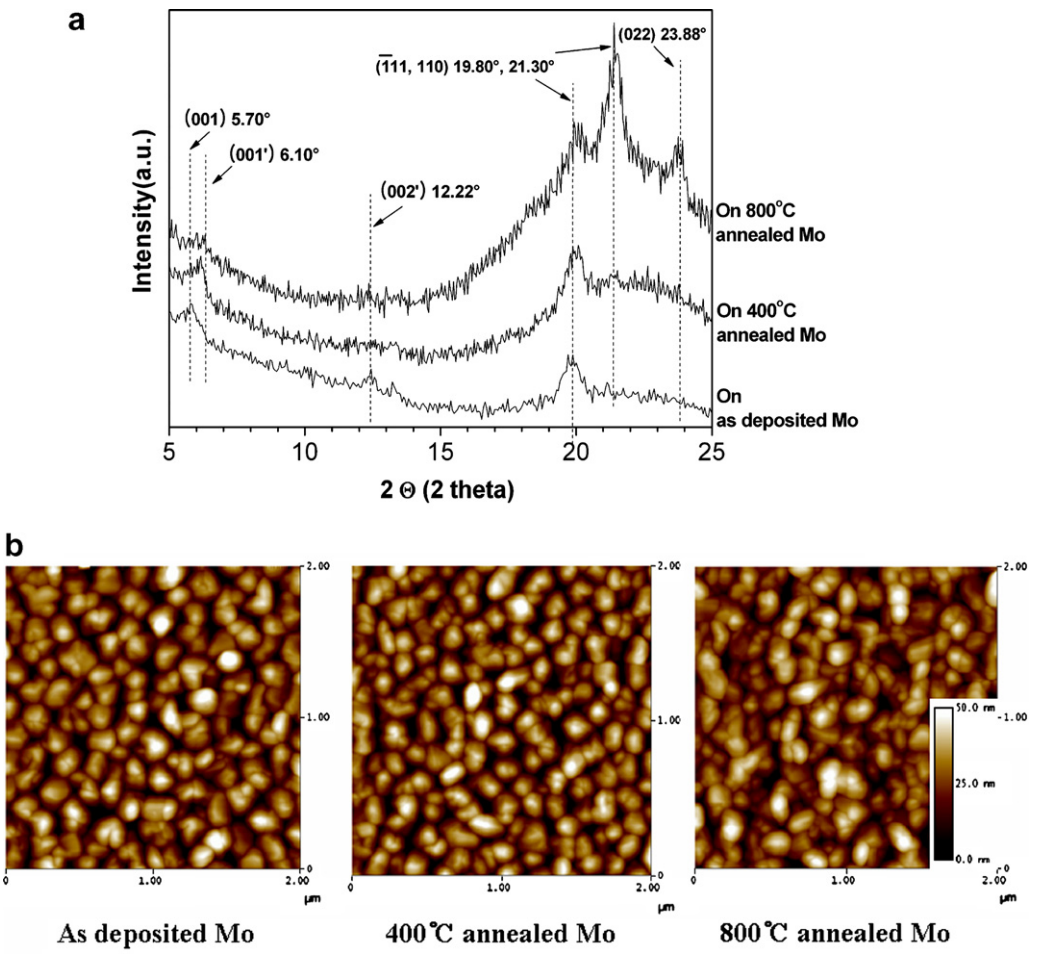

Fig. 5. (a) XRD spectra and (b) AFM images of pentacene on Mo annealed at different temperatures.

Table 1
Characteristics of pentacene TFT with as-deposited Mo, 800 °C annealed Mo and Au/Ti (50/3 nm) as a source/drain electrode

S/D electrode	Field-effect mobility (cm^2/Vs)	On/off current ratio	Threshold voltage (V)	Sub threshold swing (V/dec)
As-deposited	1.38×10^{-3}	$\sim 10^3$	−6.11	7.06
800 °C annealed	1.28×10^{-2}	$\sim 10^4$	−0.39	6.46
Au/Ti (50/3 nm)	5.22×10^{-2}	$\sim 10^5$	−2.05	1.61

compare. The field-effect mobility in the saturated regime (V_D = −40 V) was calculated from

$$I_{DS} = \frac{WC_i}{2L}(V_G - V_T)^2 \mu \quad (3)$$

where I_{DS} is the drain current at specific gate voltage (V_G), W is the channel width, L is the channel length, V_T is the threshold voltage, μ is the carrier field-effect mobility and C_i is the capacitance per unit area of the gate insulator.

Even though the hole injection barrier for Mo is greater than gold and bottom contact S/D structure usually gives inferior performance than top contact structure, good device properties were observed in pentacene TFT with 800 °C annealed Mo S/D electrode. The performance is comparable with TFT with gold electrode. The on/off ratio and the field-effect mobility of pentacene TFT were 10^4 and 1.2810^{-2} cm^2/Vs, which were about 10 times higher than with as-deposited Mo S/D (on/off ratio: 10^3, mobility: 1.3810^{-3} cm^2/Vs). Also the drain current (I_D) at saturated regime (V_D: −40 V) was increased compared with pentacene TFT with as-deposited Mo source/drain electrode, as shown in output characteristics of Fig. 6b. Annealing process of Mo reduces not only the contact resistance between Mo and pentacene but also enhances the device performance.

4. Conclusion

We have studied the annealing effect of molybdenum (Mo) metal electrode on the contact resistance between Mo and pentacene. Mo was crystallized with annealing temperature of above 600 °C and work function of Mo

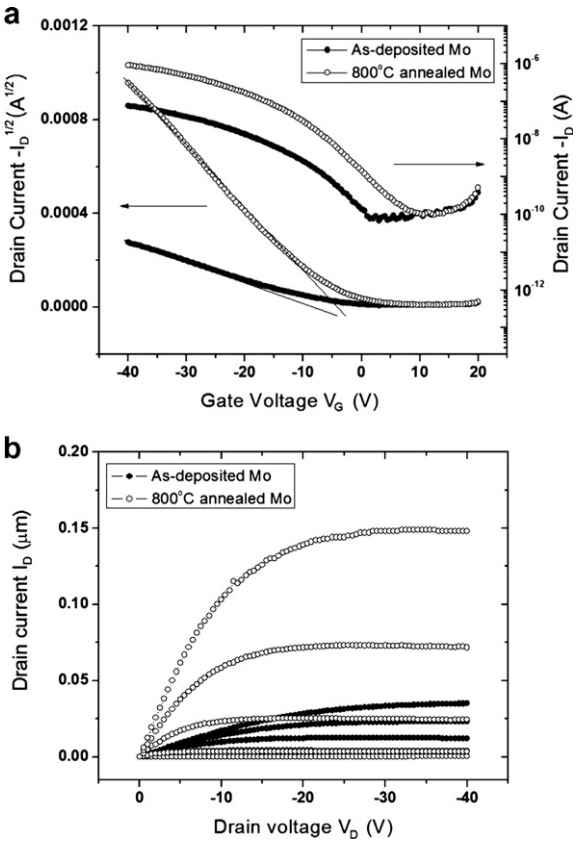

Fig. 6. (a) Comparative transfer characteristics of pentacene TFT with annealed Mo and as-deposited Mo source/drain electrode: $\log_{10}|I_D|$ versus V_G and $|I_D|^{1/2}$ versus V_G at −40 V, and (b) output characteristics of pentacene TFT with annealed Mo and as-deposited Mo source/drain electrode: drain current (I_D) versus drain voltage (V_D).

was increased with annealing closer to the highest occupied molecular orbital (HOMO) level of pentacene. Also the morphology of pentacene layer on Mo was improved with the crystallization of Mo. The contact resistance between Mo and pentacene was decreased and the TFT performance was improved substantially with annealing at 800 °C.

Acknowledgments

This research was supported by the Korea Science and Engineering Foundation (KOSEF) through the National Research Laboratory Project and Polymer Gel Cluster group of the Korea government.

References

[1] B.C. Shekar, J. Lee, S.W. Rhee, Korean J. Chem. Eng. 21 (2004) 267.
[2] G. Horowitz, J. Mater. Res. 19 (2004) 1946.
[3] H.H. Busta, J.E. Pogemiller, R.W. Standley, K.D. Mackenzie, IEEE Trans. Electr. Dev. 36 (1989) 2883.
[4] H.F. Bare, G.W. Neudeck, IEEE Electr. Dev. Lett. 7 (1986) 431.
[5] P.V. Pesavento, R.J. Chesterfield, C.R. Newman, C.D. Frisbie, J. Appl. Phys. 96 (2004) 7312.
[6] P.V. Necliudov, M.S. Shur, D.J. Gundlach, T.N. Jackson, Solid-State Electr. 47 (2003) 259.
[7] D.J. Yun, D.K. Lee, H.K. Jeon, S.W. Rhee, Org. Electr. 8 (2007) 690.
[8] R. Lin, Q. Lu, T.J. King, C. Hu, IEEE Electr. Dev. Lett. 23 (2002) 49.
[9] V.R. Reddy, P.K. Rao, C.K. Ramesh, Mater. Sci. Eng. B-Solid State Mater. Adv. Technol. 137 (2007) 200.
[10] F. Roccafortea, F. Iucolanoa, A. Albertia, F. Giannazzoa, V. Puglisib, C. Bongiornoa, S. Di Francoa, V. Raineria, Superlattices Microstruct. 40 (2006) 373.
[11] K. Jang, K. Lee, J. Kim, S. Hwang, J. Lee, S.K. Dhungel, S. Jung, J. Yi, Mater. Sci. Semicond. Process. 9 (2006) 1137.
[12] W.P. Davey, Phys. Rev. 25 (1925) 753.
[13] D. Cahen, A. Kahn, Adv. Mater. 15 (2003) 271.
[14] W.K. Kim, J.L. Lee, Appl. Phys. Lett. 88 (2006) 262102.
[15] M. Obata, T. Sakuda, K. Abe, R. Hayashibe, K. Kamimura, Surf. Coat. Technol. 180 (2004) 136.
[16] M. Shtein, J. Mapel, J. Benziger, S.R. Forrest, Appl. Phys. Lett. 81 (2002) 268.
[17] W.S. Hu, Y.T. Tao, Y.J. Hsu, D.H. Wei, Y.S. Wu, Langmuir 21 (2005) 2260.
[18] W.S. Hu, S.Z. Weng, Y.T. Tao, H.J. Liu, H.Y. Lee, L.J. Fan, Y.W. Yang, Langmuir 23 (2007) 12901.
[19] M. Oehzalt, R. Resel, C. Suess, R. Friedlein, W.R. Salaneck, J. Chem. Phys. 124 (2006) 054711.
[20] S.Y. Yang, K.W. Shin, C.E. Park, Adv. Funct. Mater. 15 (2005) 1806.

Organic Electronics 9 (2008) 557–568

Contents lists available at ScienceDirect

Organic Electronics

journal homepage: www.elsevier.com/locate/orgel

Green phosphorescent iridium dendrimers containing dendronized benzoimidazole-based ligands for OLEDs

Wei-Sheng Huang [a], Jiann T. Lin [b,*], Hong-Cheu Lin [a,*]

[a] Department of Materials Science and Engineering, National Chiao Tung University, Hsinchu, Taiwan, ROC
[b] Institute of Chemistry, Academia Sinica, Taipei, Taiwan, ROC

ARTICLE INFO

Article history:
Received 2 January 2008
Received in revised form 19 February 2008
Accepted 1 March 2008
Available online 18 March 2008

PACS:
85.60.Jb
73.61.Ph
72.80.Le

Keywords:
Iridium complexes
Dendrimers
Phosphorescence
Light-emitting diodes

ABSTRACT

A series of novel non-conjugated functionalized benzoimidazole-based dendrimers containing peripheral benzyl ether type dendrons have been synthesized and characterized. These compounds undergo cyclometalation with iridium trichloride to form iridium(III) complexes. The emission wavelengths of these dendrimers are in the range from 510 to 530 nm, and the photoluminescence quantum yields (PLQYs) in the range from 0.45 to 0.80. Dendrimers (**G*n***)$_2$**Ir**(**acac**) and (**G*n***)$_3$**Ir** exhibit a reversible one-electron oxidation wave at ~0.55 V and ~0.37 V (vs. Ag/$AgNO_3$), respectively. With a device configuration of indium tin oxide/poly(3,4-ethylenedioxythiophene):poly(styrene sulfonic acid)/4,4′-bis(*N*-carbarzolyl)biphenyl:(**G2**)$_3$**Ir** 20 wt% dopant/1,3,5-tris(2-*N*-phenyl-benzoimidazolyl)benzene/LiF/Al has a maximum external quantum efficiency (EQE) of 17.6% and a maximum current efficiency of 61.5 cd/A.

1. Introduction

Organic light-emitting diodes (OLEDs) have attracted considerable interests after Tang [1] and Burroughes's [2] report on organic (small molecule) and polymer LEDs (PLEDs). The quantum mechanical constraint sets an upper limit of the internal quantum efficiency at 25% on the fluorescence-based devices. The seminal work by Thompson demonstrated that electroluminescent devices based on heavy transition-metal complexes had great potentials to achieve an internal quantum efficiency of 100% [3]. In these complexes, both singlet and triplet excitons can contribute to emission due to efficient spin-orbit coupling which removes the spin selection regulation during radiative relaxation of the excited state. Several high performance OLEDs based on phosphorescent transition-metal complexes, including Ir [4], Pt [5], Os [6], and other metals [7], have been reported in recent years.

Small organic molecules are usually vacuum deposited for device fabrication, and the facilitation of carrier injection as well as the balance of carrier mobility can be achieved in multi-layer devices. In comparison, spin-coating technique has to be used for PLEDs due to low volatility of polymers [8]. Normally, multi-layer devices are not possible for PLEDs due to difficulty in finding appropriate solvents for casting different layers. However, spin-coating technique renders PLEDs with flexible substrates or large area displays viable. Dendrimers of appropriate molecular weights are considered to be substitutes for polymers, since they may possess similar electronic property and/or morphology as their polymer counterparts. Compared to polymers, it is relatively easy to control the molecular weights of the dendrimers precisely. Consequently,

* Corresponding authors. Tel.: +886 2 27898522; fax: +886 2 27831237 (J.T. Lin); tel.: +886 3 5712121x55305; fax: +886 3 5724727 (H.-C. Lin).
E-mail addresses: jtlin@chem.sinica.edu.tw (J.T. Lin), linhc@cc.nctu.edu.tw (H.-C. Lin).

1566-1199/$ - see front matter © 2008 Elsevier B.V. All rights reserved.
doi:10.1016/j.orgel.2008.03.001

researches on dendrimer light-emitting diodes (DLEDs) have steadily progressed in recent years.

A lot of solution processed DLEDs based on fluorescent dendrimers have been reported [9]. However, these devices only exhibit low efficiencies in most cases. In order to improve the efficiency of DLEDs, phosphorescent metal complexes encapsulated with dendrons are potential candidates. In this regard, Burn and co-workers developed a series of dendritic iridium complexes which emitted in red, green, and blue regions. The electroluminescent (EL) devices using these complexes as dopants in various hosts were reported to have good efficiencies, for example, a maximum external quantum efficiency (EQE) of 5.7% at 80 cd/m^2 for a red light-emitting device [10a], a maximum current efficiency of 55 cd/A at 400 cd/m^2 for a green light-emitting device [10b], a maximum EQE of 8.1% at 3450 cd/m^2 for a green light-emitting device [10c], and a maximum EQE of 10.4% at 100 cd/m^2 for a blue light-emitting device [10d]. Some solution processed host-free DLEDs were also reported by Burn to have high maximum EQE values around 13.6% [11]. Wang reported green-emitting phosphorescent iridium dendrimers with benzoimidazole-based ligands containing carbazolyl dendrons. The dendrimers were fabricated as high-quality films, and thus a highly efficient host-free device with a maximum EQE of 13% and a maximum luminous efficiency of 34.7 cd/A was achieved. By doping the dendrimers into a host of *N*-(4-([9,3′; 6′,9″]tercarbazo-9′-yl)phenyl)carbarzole (TCCz), the maximum EQE can be further increased to 16.6% [12].

Previously, a series of highly phosphorescent cyclometalated iridium complexes containing benzoimidazole-based ligands have been developed [13]. These complexes emit light ranging from green to red, and EL devices using these materials exhibit excellent efficiencies. In this report, we extended our study to dendrimers so as to fabricate solution-processable DLEDs. Non-conjugated Fréchet-type dendrons are used to prevent the iridium-emitting cores from changing their chroma. Green-emitting bis- and tris-cyclometalated complexes based on 1,2-diphenyl-1*H*-benzoimidazole ligands are investigated, and up to the third-generation of dendrimers have been synthesized. DLED devices based on these dendrimers are also explored.

2. Experimental

2.1. Characterization

^{1}H NMR spectra were recorded on a Bruker AMX400 spectrometer. FAB-mass spectra were collected on a JMS-700 double focusing mass spectrometer (JEOL, Tokyo, Japan) with a resolution of 3000 for low resolution and 8000 for high resolution (5% valley definition). For FAB-mass spectra, the source accelerating voltage was operated at 10 kV with a Xe gun, using 3-nitrobenzyl alcohol as the matrix. MALDI-mass spectra were collected on a Voyager DE-PRO (Applied Biosystem, Houston, USA) equipped with a nitrogen laser (337 nm) and operated in the delayed extraction reflector mode. Elemental analyses were performed on a Perkin-Elmer 2400 CHN analyzer. Cyclic voltammetry experiments were performed with a CHI-621B electrochemical analyzer. All measurements were carried out at room temperature with a conventional three-electrode configuration consisting of a platinum working electrode, an auxiliary electrode, and a nonaqueous $Ag/AgNO_3$ reference electrode. The $E_{1/2}$ values were determined as $1/2(E_p^a + E_p^c)$, where E_p^a and E_p^c are the anodic and cathodic peak potentials, respectively. The solvent used was CH_2Cl_2 and the supporting electrolyte was 0.1 M tetrabutylammonium hexafluorophosphate. Electronic absorption spectra were obtained on a Cary 50 Probe UV–visible spectrometer. Emission spectra were recorded in deoxygenated solutions at 298 K by a JASCO FP-6500 fluorescence spectrometer. The emission spectra were collected on samples with o.d. ~0.1 at the excitation wavelength. UV–visible spectra were checked before and after irradiation to monitor any possible sample degradation. Emission maxima were reproducible within 2 nm. The solution luminescence quantum yields (Φ_{PL}) were calculated relative to **Ir(ppy)**$_3$ (Φ_{PL} = 0.40 in toluene) [14]. The solid film quantum yields were measured with an integrating sphere under an excitation wavelength of 350 nm on a quartz glass. All luminescence quantum yields were taken as the average of three separate determinations and were reproducible within 10%. Luminescence lifetimes were determined on an Edinburgh FL920 time-correlated pulsed single-photon-counting instrument. Samples were degassed via freeze–thaw–pump cycle at least three times prior to measurements. Samples were excited at 337 nm from a nitrogen pulsed flashlamp with 1 ns FWHM pulse duration transmitted through a Czerny–Turner design monochromator. The solution emission was detected at 90° via a second Czerny–Turner design monochromator onto a thermoelectrically cooled red-sensitive photomultipler tube. The resulting photon counts were stored on a microprocessor-based multichannel analyzer. The instrument response function was profiled using a scatter solution and subsequently deconvoluted from the emission data to yield an undisturbed decay. Nonlinear least squares fitting of the decay curves were performed with the Levenburg–Marquardt algorithm and implemented by the Edinburgh Instruments F900 software. The reported values represent the average of at least three readings. Atomic force microscopic analyses were carried out by using a Digital Instruments Multimode III atomic force microscope. Images were captured by tapping mode with a silicon tip at a frequency of 300 kHz. For transmission electron microscopy (TEM) studies, the measurements were performed at room temperature (298 K) using a 200 kV electron microscope (JEOL JEM-2100).

2.2. Device fabrication

A layer of poly-(3,4-ethylenedioxythiophene) (PEDOT) doped with poly(styrenesulfonic acid) (PSS) with 70 nm thick was spin-coated on pre-cleaned ITO-coated glass substrates as a hole injection layer and then baked at 100 °C in air for 1 h. Then, a layer of iridium dendrimers doped into poly-(9-vinylcarbazole) (PVK, with thicknesses of ~25, ~40, and ~50 nm for **G1**–**G3**-based complexes, respectively), or 4,4′-bis(*N*-carbarzolyl)biphenyl (CBP, with thicknesses of ~30, ~45, and ~70 nm for **G1**–**G3**-based complexes, respectively) as emitters was spin-coated at a

spin rate of 3000 rpm (revolution per minute) using dichloroethane as the solvent (concentration: 10 mg mL^{-1} for the host and *x* wt% iridium dendrimer as the guest). Then the electron transporting properties of DLEDs, a layer (with a thickness of 40 nm) of 1,3,5-tris(*N*-phenylbenzimidazol-2-yl)benzene (TPBI) was vacuum deposited. Finally, a layer of LiF/Al (1 nm/ 120 nm) cathode was thermally evaporated as a cathode in a vacuum chamber (under a pressure of less than 2.5×10^{-5} torr).

3. Materials

Chemicals and solvents were reagent grades and purchased from Aldrich, Acros, TCI, and Lancaster Chemical Co. Solvents were dried by standard procedures. All reactions and manipulations were carried out under N_2 with the use of standard inert atmosphere and Schlenk techniques. All column chromatography was performed by using silica gel (230–400 mesh, Macherey-Nagel GmbH & Co.) as the stationary phase in a column which is 25–35 cm in length and 2.5 cm in diameter.

3.1. 2-(Phenol-4yl)-1-phenyl-1H-benzoimidazole

N-Phenyl-*o*-phenylenediamine (9.21 g, 50 mmol) and 4-hydroxybenzaldehyde (6.10 g, 50 mmol) were dissolved in 40 mL of 2-methoxyethanol. The mixture was heated to reflux for 48 h under N_2 atmosphere. After cooling, the reaction was quenched with water and the mixture was washed with CH_2Cl_2. The solid was then collected by filtration and pumped dry to give the desired product (5.1 g, 35%). ^{1}H NMR ($CDCl_3$, 400 MHz, ppm): δ 7.71 (d, J = 8.0 Hz, 1H), 7.57–7.51 (m, 3H), 7.36 (d, J = 8.0 Hz, 2H), 7.32 (d, J = 8.4 Hz, 2H), 7.26 (t, J = 7.2 Hz, 1H), 7.20 (t, J = 7.2 Hz, 1H), 7.11 (d, J = 8.0 Hz, 1H), 6.68 (d, J = 8.4 Hz, 2H). FABMS: m/z 287.2 ($(M+H)^+$). Anal. Calcd. for $C_{19}H_{14}N_2O$: C, 79.70; H, 4.93; N, 9.78. Found: C, 79.29; H, 5.04; N, 9.58.

3.2. General procedures for the syntheses of dendritic ligands ***Gn*** (***n*** = ***1***–***3***)

2-(Phenol-4-yl)-1-phenyl-1*H*-benzoimidazole (0.73 g, 2.5 mmol), K_2CO_3(0.35 g, 2.5 mmol), and 1.0 equiv. of various generations of **D*n*** (***n*** = **1**–**3**) were dissolved in 20 mL of dimethylformamide. The mixture was heated at 100 °C for 24 h. After cooling, the reaction was quenched by water and the mixture was extracted with CH_2Cl_2. The combined extract was then washed with brine, dried over $MgSO_4$, and evaporated to dryness. The crude product was purified by column chromatography (silica gel) using a mixture of CH_2Cl_2 and *n*-hexane (1:1 by volume) as the eluent.

G1: White solid. Yield = 87%. ^{1}H NMR ($CDCl_3$, 400 MHz, ppm): δ 7.96 (d, J = 8.0 Hz, 1H), 7.57 (d, J = 8.8 Hz, 2H), 7.54–7.52 (m, 3H), 7.39–7.26 (m, 8H), 7.20 (d, J = 8.0 Hz, 2H), 6.90 (d, J = 8.8 Hz, 2H), 5.04 (s, 2H). FABMS: m/z 377.2 ($(M+H)^+$). Anal. Calcd. for $C_{26}H_{20}N_2O$: C, 82.95; H, 5.35; N, 7.44. Found: C, 82.69; H, 5.40; N, 7.72.

G2: White solid. Yield = 87%. ^{1}H NMR ($CDCl_3$, 400 MHz, ppm): δ 7.86 (d, J = 8.0 Hz, 1H), 7.50–7.45 (m, 5H), 7.39–7.27 (m, 13H), 7.20 (d, J = 8.0 Hz, 2H), 6.85 (d, J = 8.8 Hz, 2H), 6.62 (d, J = 2.0 Hz, 2H), 6.55 (t, J = 2.0 Hz, 1H), 5.06 (s, 4H), 4.96 (s, 2H). FABMS: m/z 589.2 ($(M+H)^+$). Anal. Calcd. for $C_{40}H_{32}N_2O_3$: C, 81.61; H, 5.48; N, 4.76. Found: C, 81.46; H, 5.38; N, 4.74.

G3: White solid. Yield = 70%. ^{1}H NMR ($CDCl_3$, 400 MHz, ppm): δ 7.94 (d, J = 8.0 Hz, 1H), 7.54 (d, J = 8.8 Hz, 2H), 7.51–7.43 (m, 3H), 7.43–7.29 (m, 23H), 7.19 (d, J = 8.0 Hz, 2H), 6.87 (d, J = 8.8 Hz, 2H), 6.64 (d, J = 2.0 Hz, 4H), 6.60 (d, J = 2.0 Hz, 2H), 6.58 (t, J = 2.0 Hz, 2H), 6.52 (t, J = 2.0 Hz, 1H), 5.09 (s, 2H), 5.04 (s, 8H), 4.91 (s, 4H). FABMS: m/z 1013.6 ($(M+H)^+$). Anal. Calcd. for $C_{68}H_{56}N_2O_7$: C, 80.61; H 5.57; N, 2.76. Found: C, 80.42; H, 5.44; N, 2.87.

3.3. General procedures for the syntheses of iridium dendrimers (***Gn***)$_2$***Ir***(***acac***) (***n*** = ***1***–***3***)

To a flask containing $IrCl_3 \cdot nH_2O$ (176 mg, 0.5 mmol) and 1.0 equiv. of various generations of ligands, ***Gn***, a 3:1 mixture of 2-ethoxyethanol and water (25 mL) was added. The mixture was then refluxed for 48 h and cooled to room temperature. After cooling, the reaction was quenched by water and the mixture was washed with CH_2Cl_2. The solid formed was collected by filtration and pumped dry to give the crude product of the μ-chloro-bridged Ir(III) dimer. This crude product was mixed with Na_2CO_3 (0.30 g, 3.0 mmol), 2,4-pentanedione (0.30 g, 3.0 mmol), and 2-methoxyethanol (20 mL) in a flask. The mixture was heated to reflux for 24 h. After cooling, the reaction was quenched by water and the mixture was extracted with CH_2Cl_2. The combined extract was then washed with brine, dried over $MgSO_4$, and evaporated to dryness. The crude product was isolated by column chromatography on a silica gel column using a mixture of CH_2Cl_2 and *n*-hexane (1:1 by volume) as the eluent.

(**G1**)$_2$**Ir**(**acac**): Yellow solid. Yield = 80%. ^{1}H NMR ($CDCl_3$, 400 MHz, ppm): δ 7.67–7.59 (m, 12H), 7.49–7.45 (m, 2H), 7.25–7.20 (m, 10H), 7.18–7.08 (m, 4H), 6.79 (d, J = 8.0 Hz, 2H), 6.13–6.04 (m, 4H), 5.22 (s, 1H), 4.59 (d, J = 12.0 Hz, 2H), 4.56 (d, J = 12.0 Hz, 2H), 1.84 (s, 6H). FABMS: m/z 1042.3 (M^+). Anal. Calcd. for $C_{57}H_{45}N_4O_4Ir$: C, 65.69; H, 4.35; N, 5.38. Found: C, 65.43; H, 4.56; N, 5.51.

(**G2**)$_2$**Ir**(**acac**): Yellow solid. Yield = 55%. ^{1}H NMR ($CDCl_3$, 400 MHz, ppm): δ 7.67–7.56 (m, 12H), 7.51–7.49 (m, 2H), 7.40–7.29 (m, 20H), 7.22–7.15 (m, 3H), 7.02 (d, J = 8.0 Hz, 2H), 6.49–6.47 (m, 2H), 6.43–6.42 (m, 2H), 6.38 (d, J = 1.6 Hz, 3H), 6.20–6.07 (m, 4H), 5.22 (s, 1H), 4.88 (s, 8H), 4.51 (s, 4H), 1.84 (s, 6H). FABMS: m/z 1466.8 (M^+). Anal. Calcd. for $C_{85}H_{69}N_4O_8Ir$: C, 69.61; H, 4.74; N, 3.82. Found: C, 69.13; H, 4.92; N, 3.53.

(**G3**)$_2$**Ir**(**acac**): Yellow solid. Yield = 20%. ^{1}H NMR ($CDCl_3$, 400 MHz, ppm): δ 7.64–7.50 (m, 2H), 7.56–7.52 (m, 4H), 7.50–7.43 (m, 4H), 7.34–7.28 (m, 40H), 7.07–7.01 (m, 4H), 6.58 (d, J = 8.0 Hz, 8H), 6.52 (s, 8H), 6.47–6.37 (m, 6H), 6.24–6.20 (m, 2H), 6.08–6.02 (m, 4H), 5.21 (s, 1H), 4.99–4.93 (s, 16H), 4.81–4.77 (m, 12H), 1.84 (s, 6H). FABMS: m/z 2314.8 (M^+) Anal. Calcd. for $C_{141}H_{117}N_4O_{16}Ir$: C, 73.13; H, 5.09; N, 2.42. Found: C 72.84, H 5.00, N 2.30.

3.4. General procedures for the syntheses of iridium dendrimers (***Gn***)$_3$***Ir*** (***n*** = ***1***–***3***)

One equiv. of μ-chloro-bridged Ir(III) dimer was mixed with K_2CO_3(2.5 equiv.), ***Gn*** (2.0 equiv.), and glycerol

(5.0 mL) in a flask. The mixture was heated at 190 °C for 24 h. After cooling, the reaction was quenched by water and the mixture was extracted with CH_2Cl_2. The combined extract was then washed with brine, dried over $MgSO_4$, filtered, and evaporated to dryness. The crude product was isolated by column chromatography on a silica gel column using a mixture of CH_2Cl_2 and *n*-hexane (1:1 by volume) as the eluent.

(**G1**)$_3$**Ir**: Yellow solid. Yield = 80%. ^{1}H NMR ($CDCl_3$, 400 MHz, ppm): δ 7.64–7.55 (m, 9H), 7.47 (d, J = 8.0 Hz, 3H), 7.39 (d, J = 8.0 Hz, 3H), 7.21–7.15 (m, 15H), 7.02–6.96 (m, 6H), 6.76 (td, J = 8.4, 1.6 Hz, 3H), 6.51 (d, J = 8.4 Hz, 6H), 6.28 (d, J = 8.0 Hz, 3H), 6.14 (dd, J = 8.4, 1.6 Hz, 3H), 4.67 (d, J = 12.0 Hz, 3H), 4.62 (d, J = 12.0 Hz, 3H). FABMS: m/z 1319.3 ((M+H)$^+$). Anal. Calcd. for $C_{78}H_{57}N_6O_3Ir$: C, 71.05; H, 4.36; N, 6.37. Found: C, 70.70; H, 4.20; N, 6.43.

(**G2**)$_3$**Ir**: Yellow solid. Yield = 45%. ^{1}H NMR ($CDCl_3$, 400 MHz, ppm): δ 7.54–7.50 (m, 9H), 7.48 (d, J = 8.0 Hz, 3H), 7.40–7.35 (m, 3H), 7.29–7.23 (m, 30H), 7.08–6.96 (m, 6H), 6.76 (t, J = 8.4 Hz, 3H), 6.57 (d, J = 2.4 Hz, 3H), 6.51–6.42 (m, 9H), 6.42–6.37 (m, 6H), 6.11 (dd, J = 8.4, 1.6 Hz, 3H), 4.87 (m, 12H), 4.61 (d, J = 12.0 Hz, 3H), 4.57 (d, J = 12.0 Hz, 3H). FABMS: m/z 1954.9 (M$^+$). Anal. Calcd. for $C_{120}H_{93}N_6O_9Ir$: C, 73.71; H, 4.79; N, 4.30. Found: C, 73.68; H, 4.86; N, 4.26.

(**G3**)$_3$**Ir**: Yellow solid. Yield = 18%. ^{1}H NMR ($CDCl_3$, 400 MHz, ppm): δ 7.49–7.41 (m, 15H), 7.34–7.26 (m, 60H), 7.01–6.97(m, 6H), 6.89–6.80 (m, 6H), 6.66–6.57 (m, 12H), 6.57–6.52 (m, 6H), 6.52–6.48 (m, 6H), 6.48–6.45 (m, 6H), 6.45–6.41 (m, 6H), 5.06 (s, 12H), 4.96–4.93 (m, 12H), 4.79–4.77 (m, 12H), 4.66–4.63 (m, 6H). MADLI-TOF: m/z 3223.1(M$^+$). Anal. Calcd. for $C_{204}H_{165}N_6O_{21}Ir$: C, 75.89; H, 5.15; N, 2.60. Found: C 75.67, H 5.33, N 2.50.

4. Results and discussion

4.1. Synthesis of materials

The chemical structures of the synthesized iridium dendrimers (**G***n*)$_2$**Ir**(**acac**) and (**G***n*)$_3$**Ir** (***n*** = **0**, **1**, **2**, and **3**) are shown in Chart 1. The synthetic procedures of all dendritic ligands **G***n* (***n*** = **0**–**3**) are illustrated in Scheme 1 The zero-generation compounds **G0** [13], (**G0**)$_2$**Ir**(**acac**) [13], and (**G0**)$_3$**Ir** [12] were reported in the literatures. The reaction of *N*-phenyl-*o*-phenylenediamine with 4-hydroxybenzaldehyde provided 2-(phenol-4-yl)-1-phenyl-1*H*-benzoimidazole (Scheme 1a), which further reacted with benzyl bromide dendrons (**D***n*–**CBr**) (***n*** = **1**–**3**) in DMF at 100 °C to form dendritic ligands **G***n* (Scheme 1b), where the benzyl bromide dendrons (**D***n*–**CBr**) were prepared according to the procedure described by Fréchet and Hawker [15,16]. The synthetic procedures of iridium dendrimers (**G***n*)$_2$**Ir**(**acac**) and (**G***n*)$_3$**Ir** (***n*** = **1**–**3**) are illustrated in Scheme 2. The preparation of cyclometalated iridium dendrimers (**G***n*)$_2$**Ir**(**acac**) and (**G***n*)$_3$**Ir** involved a two-step synthesis. Firstly, $IrCl_3 \cdot nH_2O$ and dendritic ligands (**G0**–**G3**) were reacted to form a chloro-bridged dimer. The dimer

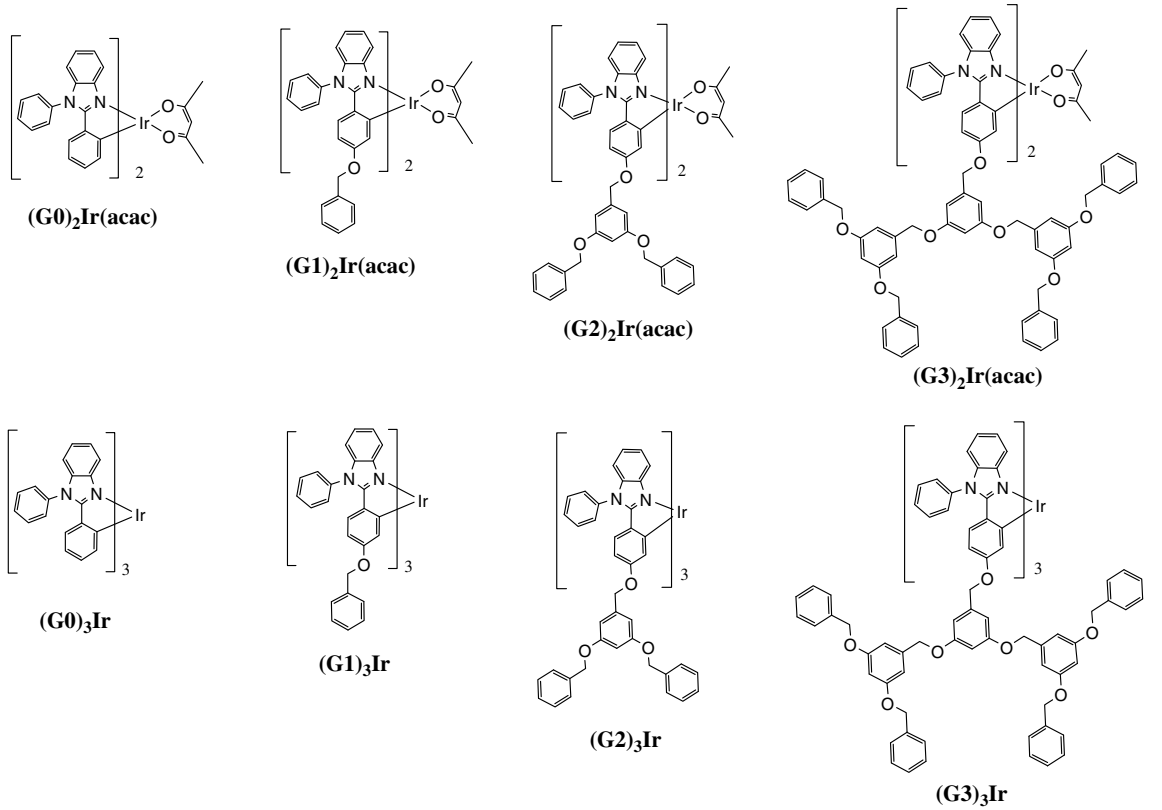

Chart 1. Chemical structures of iridium dendrimers (**G***n*)$_2$**Ir**(**acac**) and (**G***n*)$_3$**Ir** (***n*** = **0**–**3**).

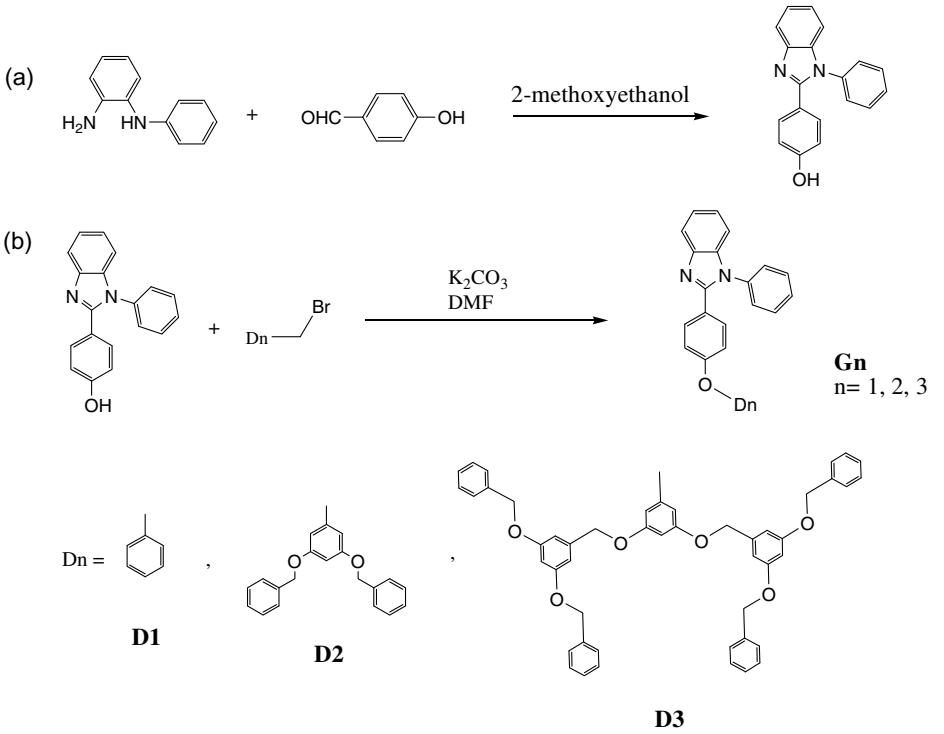

Scheme 1. Synthetic procedures of dendritic ligands **G*n*** (***n*** = **0–3**).

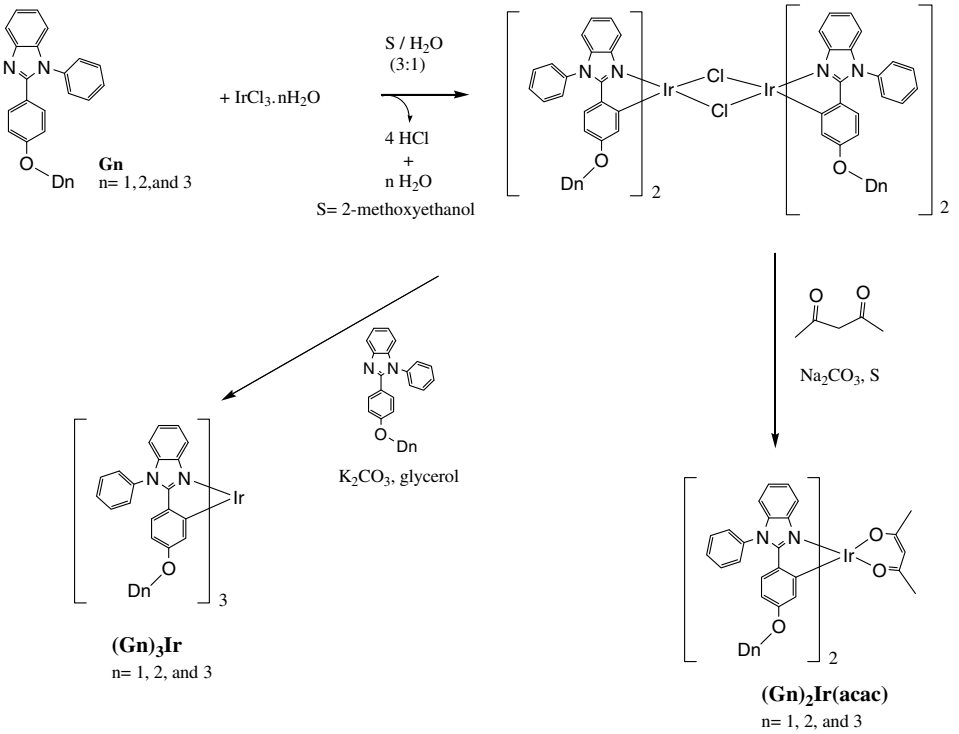

Scheme 2. Synthetic procedures of iridium dendrimers (**G*n***)$_2$**Ir**(**acac**) and (**G*n***)$_3$**Ir** (***n*** = **1–3**).

was then treated with 2,4-pentanedione in the presence of base to form (**G*n***)$_2$**Ir**(**acac**), or with additional **G*n*** in glycerol at 190 °C to give (**G*n***)$_3$**Ir**, where only facial (*fac*) isomers were obtained as evidenced from the NMR spectra.

4.2. Optical properties

The photophysical data of dendritic ligands **G*n*** and iridium dendrimers ((**G*n***)$_2$**Ir**(**acac**) and (**G*n***)$_3$**Ir**) are displayed in Table 1. Representative absorption spectra of dendritic ligands and iridium complexes are shown in Fig. 1. The ligands exhibit an absorption band at ~300 nm ($\varepsilon \sim 10^4$–10^5 M^{-1} cm^{-1}), which is characteristic of the π–π^* transition of benzoimidazolyl moieties [13]. The π–π^* transition of benzenoids from the dendrons appears as a prominent shoulder at ~285 nm for **G3**. All dendritic iridium complexes have similar absorption spectra. Besides the π–π^* transition bands of the ligands, they also exhibit weak absorption bands in the range of ~350–500 nm attributed to metal-to-ligand charge transfer transitions, i.e., ^{1}MLCT and ^{3}MLCT.

Ligands **G*n*** in CH_2Cl_2 emit light in the violet-purple region. In contrast, all dendritic iridium complexes emit green light in both toluene solutions and solid films with λ_{em} in the range of 510–530 nm. Fig. 2 shows the representative solution and neat-film photoluminescent (PL) spectra of the dendritic iridium compounds. The solution PL spectra of the iridium dendrimers resemble one another, so do the solid PL spectra. All iridium dendrimers in toluene solutions exhibit high PL quantum yields (Φ_{PL} = 0.45–0.80), indicating the efficient mixing of singlet and triplet

Table 1
Physical data of dendritic ligands **G*n*** (***n*** = **0**–**3**) and iridium dendrimers (**G*n***)$_2$**Ir**(**acac**) and (**G*n***)$_3$**Ir** (***n*** = **0**-**3**)

Compound	λ_{abs}[a] (log ε) (nm)	λ_{em} (nm)	Φ_{PL}[c] (%)	λ_{em}[d] (nm)	Φ_{PL} (film) (%)[e]	τ[f] (μs)	τ_r[g] (μs)
G0	294 (4.3)	360[a]					
G1	296 (4.4)	354[a]					
G2	296 (4.4)	354[a]					
G3	285 (4.4), 297 (4.4)	354[a]					
(**G0**)$_2$**Ir**(**acac**)[h]	300 (4.6), 314 (4.6), 348 (4.1), 387 (4.0), 415 (3.6), 459 (3.6)	523[b]	71	530	16	1.82	2.56
(**G1**)$_2$**Ir**(**acac**)	302 (4.6), 314 (4.6), 350 (4.1), 385 (4.0), 420 (3.6), 450 (3.6)	510[b]	70	530	16	1.0	1.43
(**G2**)$_2$**Ir**(**acac**)	305 (4.6), 316 (4.6), 372 (4.1), 404 (3.8), 429 (3.6)	510[b]	80	524	32	1.10	1.25
(**G3**)$_2$**Ir**(**acac**)	261 (4.8), 279 (4.8), 300 (4.6), 315 (4.6), 372 (4.1), 406 (3.8), 434 (3.6)	510[b]	68	513	41	1.13	1.66
(**G0**)$_3$**Ir**[i]	298 (4.6), 313 (4.6), 375 (4.1), 410 (3.8), 453 (3.5)	517[b]	45	534	15	1.07	2.37
(**G1**)$_3$**Ir**	299 (4.6), 312 (4.6), 376 (4.1), 385 (4.0), 411 (3.8), 454 (3.5)	523[b]	64	527	28	1.26	1.97
(**G2**)$_3$**Ir**	303 (4.6), 317 (4.6), 357 (4.1), 374 (4.1), 405 (3.8), 432 (3.5)	523[b]	65	524	40	1.11	1.71
(**G3**)$_3$**Ir**	278 (4.8), 299 (4.6), 313 (4.6), 351 (4.3), 408 (3.8), 428 (3.4)	523[b]	75	516	45	1.37	1.83

[a] Measured in CH_2Cl_2 10^{-5} M at 298 K. ε is the absorption coefficient.
[b] Recorded in toluene solutions at 298 K. Excitiaton wavelength was 410 nm for all iridium compounds.
[c] Quantum yield was measured with respect to **Ir**(**ppy**)$_3$ (Φ_p = 0.4 in toluene).
[d] Neat-film data measured at 298 K. Excitiaton wavelength was 350 nm.
[e] PL quantum efficiencies in film measured in an integrating sphere.
[f] Measured in toluene solutions at 298 K.
[g] $\tau_r = \tau/\Phi_p$.
[h] Ref. [13].
[i] Ref. [12].

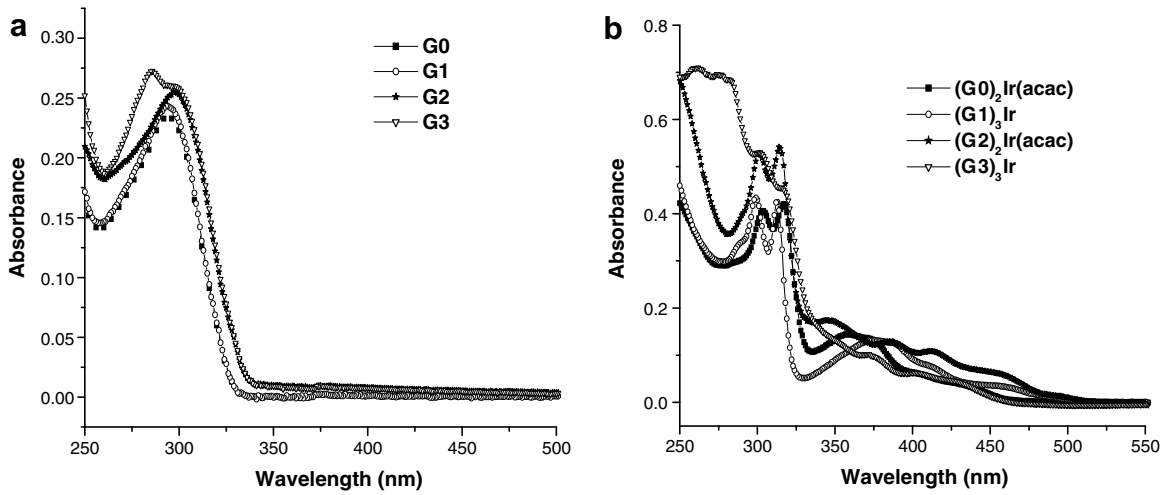

Fig. 1. Absorption spectra in CH_2Cl_2 solutions of (a) ligands **G*n***; (b) iridium dendrimers (**G*n***)$_2$**Ir**(**acac**) and (**G*n***)$_3$**Ir**.

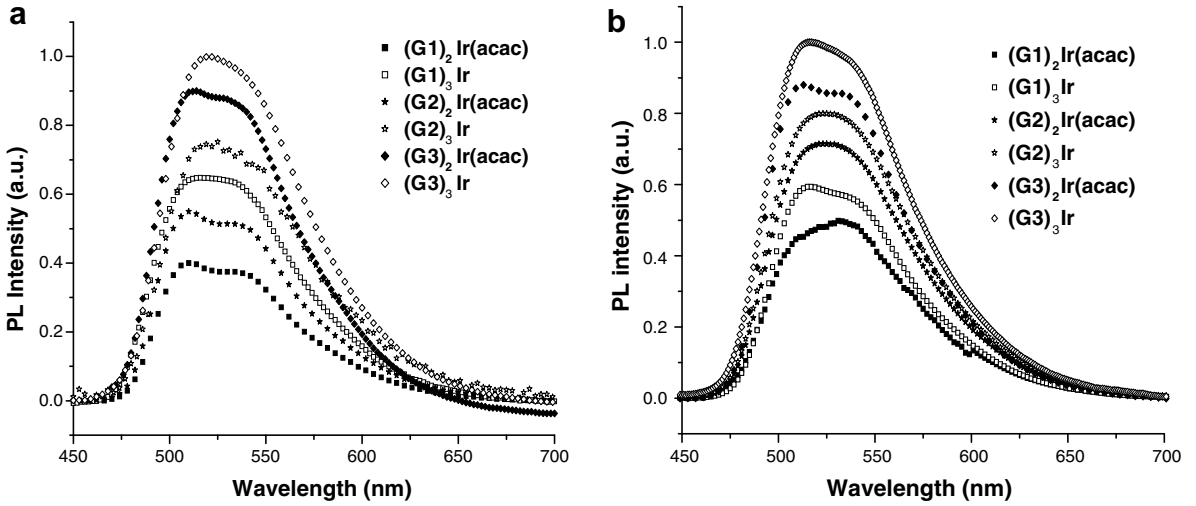

Fig. 2. PL spectra of iridium dendrimers in (a) toluene at 298 K; (b) solid films.

excited states via spin-orbit coupling. The PL quantum yields (Φ_{PL} = 0.16–0.45) in the solid films drop due to intermolecular interaction. In both the solution and solid films, the PL quantum yields increase as the dendrtric generation increases, indicating that there is less intermolecular interaction in higher generation dendrimers. The phosphorescence lifetime (τ = 1.25–1.97 μs) of these dendrimers in the solution fall in the same range as their non-dendronized congeners, i.e., (**G0**)$_2$**Ir**(**acac**) (τ = 1.82 μs) and (**G0**)$_3$**Ir** (τ = 1.07 μs).

4.3. Electrochemical studies

The electrochemical properties of these iridium dendrimers were studied by cyclic voltammetry (CV), and the electrochemical data are summarized in Table 1. A quasi-reversible one-electron oxidation wave attributed to the oxidation of iridium(III) was detected at ~550 mV for (**G*n***)$_2$**Ir**(**acac**)and ~370 mV for (**G*n***)$_3$**Ir** vs. Ag/AgNO$_3$, respectively. The dendrons in iridium complexes, (**G*n***)$_2$**Ir**(**acac**) and (**G*n***)$_3$**Ir**, appear to have negligible influence on the oxidation potentials of the iridium centers, possibly due to the non-conjugated nature of the spacers between the dendrons and the iridium centers. The energies of the highest occupied molecular orbitals (HOMOs) in (**G*n***)$_2$**Ir**(**acac**) and (**G*n***)$_3$**Ir** were calculated relative to ferrocene (Fc) which has a value of 4.8 eV with respect to the vacuum level [17]. The HOMO energies in combination with the optical band gaps derived from the absorption band edges were used to calculate the energies of the lowest unoccupied molecular orbitals (LUMOs) of the iridium dendrimers. Both HOMO and LUMO data are also collected in Table 2. No reduction waves up to −2.0 V were detected in these iridium dendrimers.

Table 2
Oxidation potentials and HOMO/LUMO energies of iridium dendrimers (**G*n***)$_2$**Ir**(**acac**) and (**G*n***$_3$)**Ir** (***n*** = **0–3**)

Compound	E_{ox} (ΔE_p) (mV)	HOMO (eV)	LUMO (eV)	Band gap (eV)
(**G0**)$_2$**Ir**(**acac**)	550 (81)	5.12	2.44	2.68
(**G1**)$_2$**Ir**(**acac**)	555 (70)	5.11	2.44	2.67
(**G2**)$_2$**Ir**(**acac**)	560 (72)	5.11	2.44	2.67
(**G3**)$_2$**Ir**(**acac**)	562 (53)	5.10	2.44	2.66
(**G0**)$_3$**Ir**	370 (76)	4.95	2.44	2.51
(**G1**)$_3$**Ir**	377 (80)	4.95	2.44	2.51
(**G2**)$_3$**Ir**	362 (76)	4.95	2.44	2.51
(**G3**)$_3$**Ir**	365 (102)	4.93	2.44	2.49

Oxidation potential reported is adjusted according to the potential of ferrocene ($E_{1/2}$ = 230 mV vs. Ag/AgNO$_3$) which was used as an internal reference. Conditions of cyclic voltammetric measurements: glassy carbon working electrode; Ag/AgNO$_3$ reference electrode. Scan rate: 100 mV/s. Electrolyte: tetrabutylammonium hexafluorophosphate. HOMO levels calculated from CV potentials using ferrocene as a standard [HOMO = 4.8 + ($E_{ox} - E_{Fc}$)]. LUMO levels were derived via eq. *Eg* = HOMO − LUMO, where *Eg* was obtained from the absorption spectra.

5. Morphology of spin-casting films

The spirit of this research is to fabricate DLEDs using spin-coating technique. Therefore, TEM and AFM were used to examine the morphology of the spin-casting films for these complexes alone or their blends with a host (PVK or CBP). Fig. 3a and b shows TEM images of the CBP and PVK solid films with a 20 wt% iridium dendrimer ((**G2**)$_3$**Ir**) dopant. Phase segregation was evident in the PVK film and the domains of the aggregate were on the scales of ~20–50 nm. Because of the larger electron-scattering cross section of the iridium atom than the carbon atom, the dark spots are likely the aggregates of the Ir complexes. In comparison, the CBP blend film appears to be more homogeneous without abrupt phase segregation. AFM studies on the films were also carried out for more direct surface topography. Fig. 3c and d shows the AFM images of the spin-coated films (~45 nm thick), obtained from a blend of CBP with various amounts of iridium dendrimer (**G2**)$_3$**Ir**, on plasma treated indium tin oxide (ITO) substrates. Both pure iridium dendrimer (**G2**)$_3$**Ir** and its CBP blends were found to be able to form thin films of good quality. In contrast, a spin-coated film from a blend of CBP

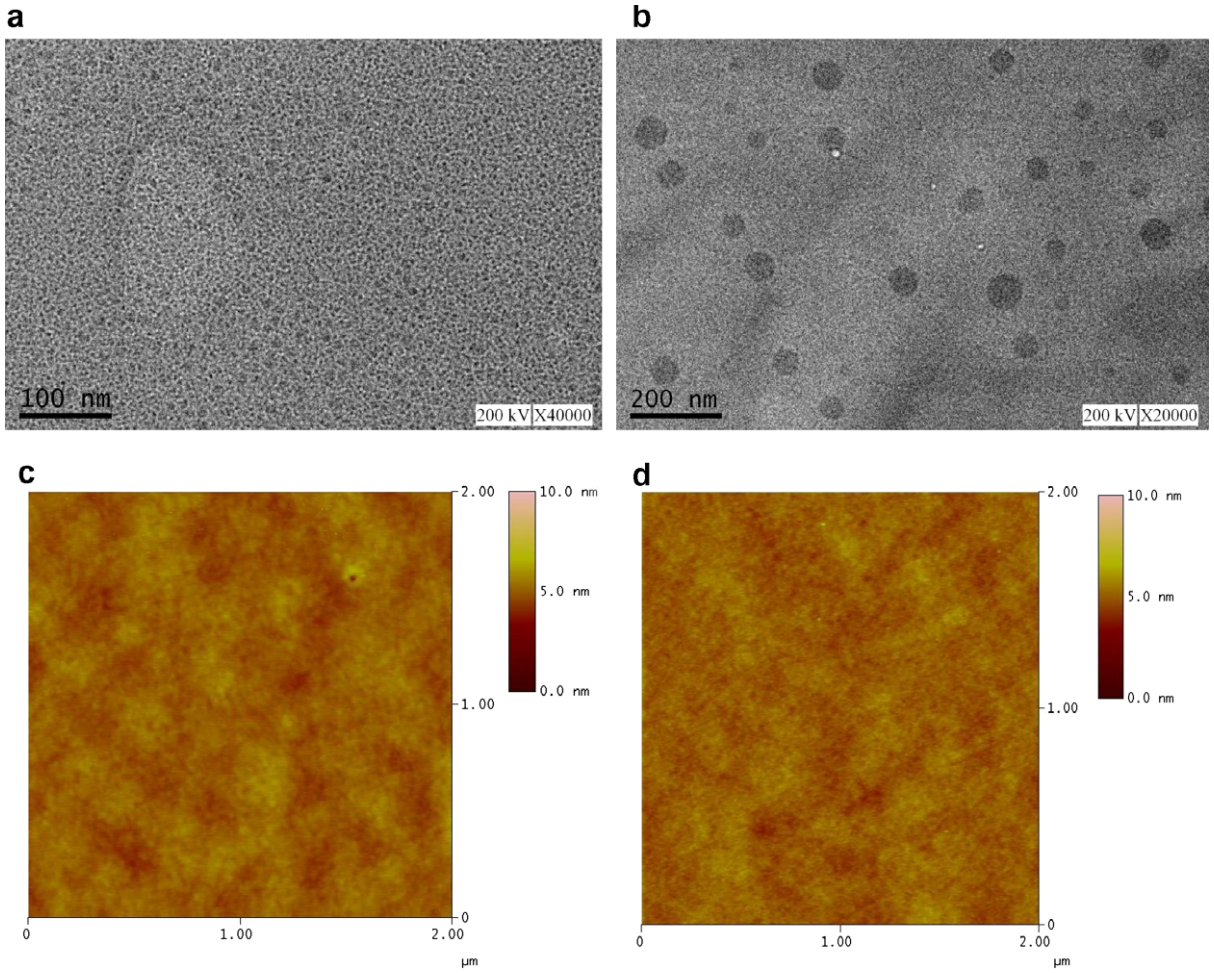

Fig. 3. TEM images of solid films of (a) 20 wt% (**G2**)$_3$**Ir** in CBP, (b) 20 wt% (**G2**)$_3$**Ir** in PVK and AFM images of solid films of (c) 20 wt% (**G2**)$_3$**Ir** in CBP, (d) pure (**G2**)$_3$**Ir**.

with 6 wt% of facial tris(2-phenylpyridine) iridium, (*fac*-**Ir**(**ppy**)$_3$), was reported to have a poor film quality [10b]. Both pure (**G2**)$_3$**Ir** film and the blend films of (**G2**)$_3$**Ir** (5–40 wt%):CBP have a similar root mean square (RMS) surface roughness of ~0.24 nm.

6. Electroluminescent (EL) properties

Because of the large triplet energy gaps, PVK (E_T = 2.5 eV) [18,19] and CBP (E_T = 2.56 eV) [20] are considered to be appropriate host for triplet green-emitters in this study. Sufficiently large triplet energy gap is essential for efficient exciton confinement inside the phosphorescent guest via energy transfer as well as suppression of back energy transfer from the triplet emitters to the host. The configurations of DLEDs using PVK and CBP as the host for the iridium dendrimers are shown in Fig. 4: (I) ITO/PEDOT:PSS (70 nm)/PVK:(**Gn**)$_3$**Ir** or (**Gn**)$_2$**Ir**(**acac**) (25–50 nm)/1,3,5-tris(*N*-phenylbenzimidazol-2-yl)benzene (TPBI) (40 nm)/LiF (1 nm)/Al (120 nm) and (II) ITO/PEDOT:PSS (70 nm)/CBP:(**Gn**)$_3$**Ir** or (**Gn**)$_2$**Ir**(**acac**) (30-70 nm)/TPBI (40 nm)/LiF (1 nm)/Al (120 nm). The structures of relevant compounds are also shown in Fig. 4, and the energy level alignments for the devices are shown in Fig. 5. Both types of the devices were fabricated by the spin-coating technique except that TPBI, the electron transporting and hole-blocking layer, was vacuum deposited. The performance parameters of DLEDs for both configurations are listed in Table 3. The representative EL spectra of devices I are shown in Fig. 6. For complete energy transfer from PVK to the iridium dendrimer, a higher mol% of the latter is needed as the dendrimer size grows larger. The better encapsulation of the emitting iridium center in the larger dendrimer apparently decreases the efficiency of the Förster energy transfer. Direction exciton formation [3c] on the dendrimer of larger generation is also expected to be less facile because of the non-conducting nature of peripheries. The best device efficiency of the devices I was found to be $\eta_{ext,max}$ = 8.6%, 9.7%, and 4.45%, and $\eta_{c,max}$ = 29.4, 32.5, and 15.3 cd/A for the DLED with 3.4, 4.6, and 6.9 mol% of (**G1**)$_3$**Ir**, (**G2**)$_3$**Ir** and (**G3**)$_3$**Ir**, respectively. The performances of devices I appeared to be inferior to those of device II, possibly due to serious phase segregation confirmed from TEM studies (vide supra).

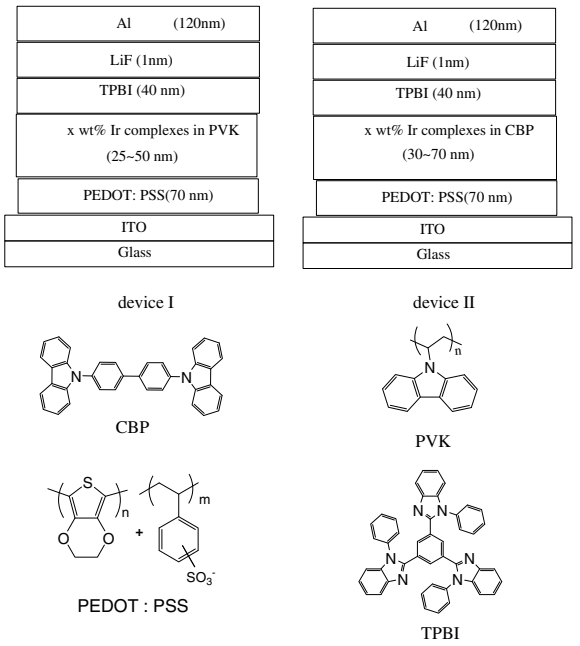

Fig. 4. The configurations of EL devices (i.e., devices I and II) and the molecular structures of the device compounds.

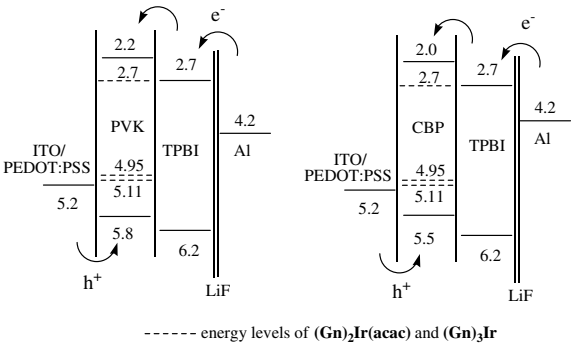

Fig. 5. Relative energy levels of the compounds utilized in the devices I and II.

Though CBP has a triplet energy gap similar to that of PVK, use of CBP is likely advantageous compared to PVK based on the following reasons: (1) the HOMO energy levels between CBP and PEDOT:PSS is smaller than those between PVK and PEDOT:PSS by ~0.3 eV and more facile hole injection from PEDOT:PSS into the host is expected. This may be beneficial to energy transfer from the host to the dendrimer; (2) CBP is ambipolar carrier-transporting [21] and better balance of charge carriers is expected in

Table 3
EL data of DLED devices with the configurations of devices I–II

Emitting layer	Brightness[a] (at V) (cd/m^2)	η_{ext}[a] (%)	η_c[a] (cd/A)	η_p[a] (lm/W)	V_{ON} (V)	λ_{em} (fwhm) (nm)	CIE at 12 V (x,y)
Device I							
PVK:(**G1**)$_3$**Ir** dopant 20 wt%	3239 (10.9);	4.8	16.2	4.6	3.5	522 (80)	0.32, 0.59
(3.38 mol%)	6061 (14.0);	1.8	6.0	1.3			
	6066 (14.5)	8.6	29.4	12.3			
PVK:(**G2**)$_3$**Ir** dopant 50 wt%	3485 (8.0);	5.2	17.5	6.8	3.5	522 (82)	0.32, 0.60
(4.56 mol%)	6046 (12.2);	1.8	6.0	1.5			
	6059 (12.5)	9.7	32.5	20.4			
PVK:(**G3**)$_3$**Ir** dopant 50 wt%	873 (12.7);	1.3	4.41	1.08	4.0	516 (74)	0.28, 0.61
(6.92 mol%)	683 (18.1);	0.20	0.68	0.12			
	996 (14.0)	4.5	15.3	6.90			
Device II							
CBP:(**G1**)$_3$**Ir** dopant 20 wt%	4540 (8.8);	6.5	22.8	8.1	3.5	522 (78)	0.31, 0.61
(7.36 mol%)	13661 (12.4);	3.9	13.7	3.5			
	22000 (16.5)	12.6	44.2	30.8			
CBP:(**G1**)$_3$**Ir** dopant 100 wt%	3355 (8.2);	5.0	17.0	6.6	3.0	528 (88)	0.33, 0.59
(36.8 mol%)	8468 (10.3);	2.6	8.6	2.6			
	11516 (7.6)	7.6	25.6	23.0			
CBP:(**G2**)$_3$**Ir** dopant 20 wt%	6213 (10.1);	8.9	31.2	9.7	3.0	518 (74)	0.29, 0.62
(4.92 mol%)	16923 (13.4);	4.9	17.0	4.0			
	20618 (15.5)	17.6	61.5	32.2			
CBP: (**G2**)$_3$**Ir** dopant 40 wt%	6213 (10.1);	10.4	30.5	9.6	3.5	518 (76)	0.29, 0.61
(9.84 mol%)	12912 (15.8);	4.4	13.0	2.7			
	13234 (17.5)	16.7	48.8	25.6			
CBP: (**G2**)$_3$**Ir** dopant 100 wt%	4617 (10.3);	6.8	23.4	7.1	3.0	524 (80)	0.31, 0.60
(24.6 mol%)	11556 (12.3);	3.4	11.7	3.0			
	12064 (13.0)	13.4	46.5	32.5			
CBP: (**G3**)$_3$**Ir** dopant 50 wt%	3279 (15.0);	5.2	16.4	3.4	7.5	510 (64)	0.24, 0.61
(7.5 mol%)	5551 (19.0);	1.8	5.6	0.9			
	5680 (18.0)	8.7	27.6	8.7			
CBP: (**G3**)$_3$**Ir** dopant 100 wt%	1876 (15.7);	2.7	9.5	1.9	9.5	528 (80)	0.30, 0.60
(15.0 mol%)	3833 (19.8);	1.1	3.8	0.7			
	3851 (20.0)	4.9	15.9	4.0			

[a] The first and second values were obtained at a current density of 20 mA and 100 mA, respectively. The third value is the maximum performance parameter of the device. fwhm, full width at half-maximum; η_{ext}, external quantum efficiency; η_c, current efficiency; η_p, power efficiency; V_{ON}, turn-on voltage, at a brightness of 1 cd/m^2.

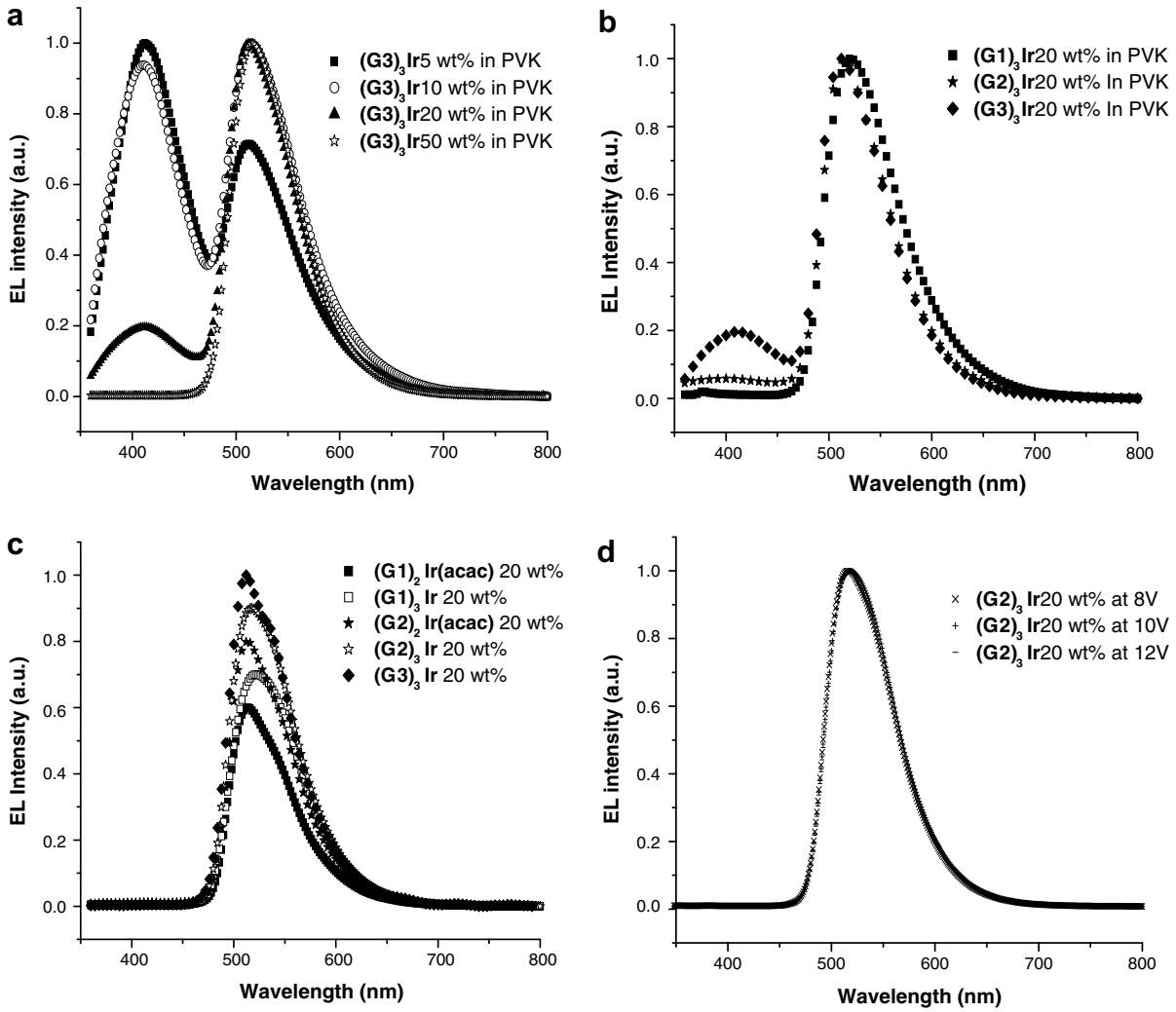

Fig. 6. (a) EL spectra of device II at a driving voltage of 12 V for various wt% of iridium dendrimer (**G3**)$_3$**Ir** in PVK; (b) EL spectra of device II at a driving voltage of 12 V for 20 wt% of various generations of iridium dendrimers (**G***n*)$_3$**Ir**in PVK; (c) EL spectra of device II at a driving voltage of 12 V for 20 wt% of various iridium dendrimers (**G***n*)$_3$**Ir** and (**G***n*)$_2$**Ir**(**acac**) in CBP; (d) EL spectra of device II at various driving voltages (8–12 V) for 20 wt% of iridium dendrimer (**G2**)$_3$**Ir** in CBP.

CBP compared to PVK which is a hole-only transporter; and (3) film from the blend of CBP and the dendrimers does not have noticeable phase segregation (vide supra). Indeed, CBP was reported to be a suitable host material for green-emitting **Ir**(**ppy**)$_3$, and the energy transfer from CBP to **Ir**(**ppy**)$_3$ was found to be efficient and the excitons were effectively confined inside **Ir**(**ppy**)$_3$ [22].

The representative EL spectra of devices II are shown in Fig. 6. Possibly due to inefficient encapsulation of emitting iridium core (the quantum yield in solid films: (**G***n*)$_2$**Ir**(**acac**) < (**G***n*)$_3$**Ir**), (**G***n*)$_2$**Ir**(**acac**)-based devices II exhibited efficiencies ($\eta_{ext,max}$ = 7.8–8.1% and $\eta_{c,max}$ = 26.8–27.7 cd/A) much inferior to those of (**G***n*)$_3$**Ir**-based devices. Therefore, only the performance of (**G***n*)$_3$**Ir**-based devices II will be discussed further. Selected current–voltage (*I*–*V*) characteristics and the external quantum efficiency and current efficiency vs. current density are shown in Figs. 7 and 8. Devices with optimal performances have dendrimers in a doping concentration of ~5.0–9.8 mol%, similar to the devices reported by Burn and co-workers [10b] using **IrppyD**:CBP blends (**IrppyD** is a dendrimer with a *fac*-tris(2-phenylpyridine) iridium core, a phenylene-based dendritic spacer, and 2-ethylhexyloxy surface groups). Selected efficiency data for the devices with the best performance are shown as follows: (1) (**G1**)$_3$**Ir**-doped device: $\eta_{ext,max}$ = 12.6%, $\eta_{c,max}$ = 44.2 cd/A, $\eta_{p,max}$ = 30.8 lm/W, and turn-on voltage (V_{ON}) = 4.0 V at 20 wt% (7.36 mol%) doping concentration; (2) (**G2**)$_3$**Ir**-doped device: $\eta_{ext,max}$ = 17.6%, $\eta_{c,max}$ = 61.7 cd/A, $\eta_{p,max}$ = 32.2 lm/w, and V_{ON} = 3.5 V at 20% (4.92 mol%) doping concentration; and (3) (**G3**)$_3$**Ir**-doped device: $\eta_{ext,max}$ = 8.7%, $\eta_{c,max}$ = 27.6 cd/A, $\eta_{p,max}$ = 8.7 lm/w, and V_{ON} = 7.5 V at 50 wt% (7.50 mol%) doping concentration. The EL performances for the device II are in order of (**G3**)$_3$**Ir** < (**G1**)$_3$**Ir** < (**G2**)$_3$**Ir**. The better EL performances of (**G2**)$_3$**Ir**-based devices than (**G1**)$_3$**Ir**-based devices may be attributed to the better encapsulation of the emitting

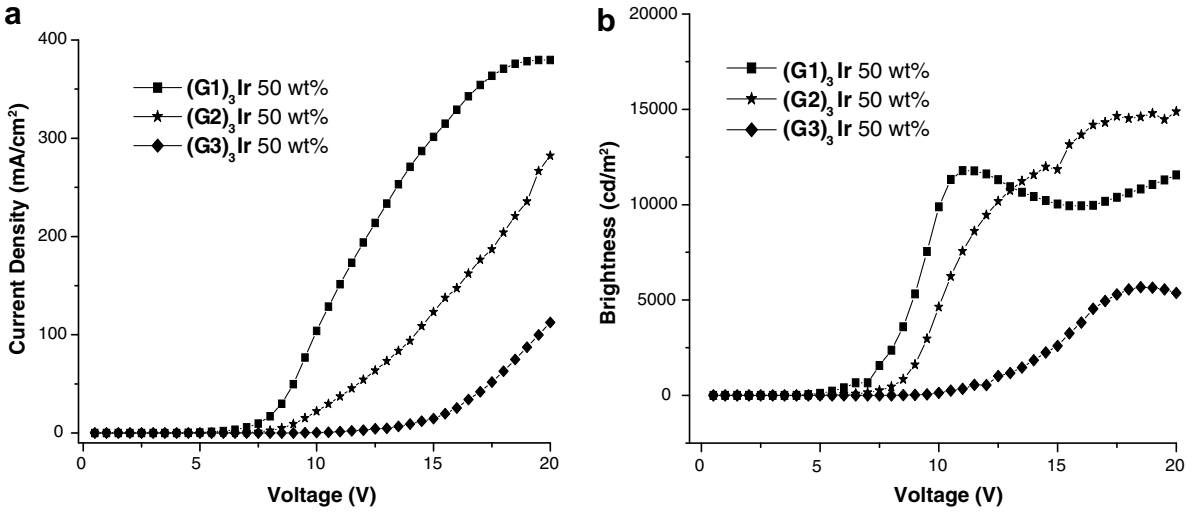

Fig. 7. EL characteristics of device II with 50 wt% of iridium dendrimers (**G*n***)$_3$**Ir** in CBP: (a) *I*–*V* plots; (b) *L*–*V* plots.

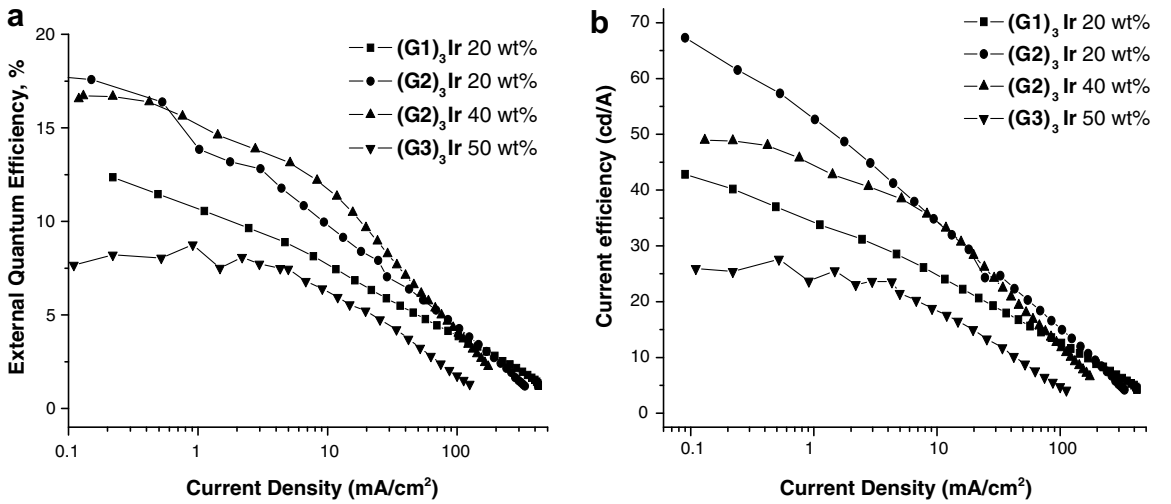

Fig. 8. EL properties of device II with selected dopant (iridium dendrimers) concentrations in CBP: (a) EQE vs. current density. (b) current efficiency vs. current density.

iridium center by the dendrons in the former. The merit of encapsulation by dendrons also reflects on suppressing the concentration quenching of the emission among (**G1**)$_3$**Ir**-based devices. As shown in Table 3, serious device deterioration occurred when the doping concentrations were increased to ca. 100 wt% for (**G1**)$_3$**Ir**-based devices II, e.g. $\eta_{ext,max}$ = 7.6% at 100 wt% of dopant concentration. In contrast, the efficiency of (**G2**)$_3$**Ir**-based devices II still retained high ($\eta_{ext,max}$ = 13.4%) even when the doping concentration was increased to around 100 wt%. Apparently, the core of iridium dendrimer (**G2**)$_3$**Ir** was better protected by the surrounding dendrons, and the intermolecular interaction and aggregation were more effectively suppressed. Though the iridium core in dendritic complex (**G3**)$_3$**Ir** was considered to have the best encapsulation by the dendrons, the EL performance of (**G3**)$_3$**Ir**-based devices was inferior to those of (**G1**)$_3$**Ir**- and (**G2**)$_3$**Ir**-based devices. In view of the larger turn-on voltage and lower current density found in (**G3**)$_3$**Ir**-based devices in Fig. 7, we speculate that the peripheral benzyl ether dendrons behave as insulating arms of the dendritic iridium emitter. Therefore, it is possible that the larger insulating peripheries of dendrons in (**G3**)$_3$**Ir** retard the transporting of electrons in the emitting layer and blockade the confinement of excitons in the emitting cores. Compared to the device I, the EL spectra of the device II fabricated from (**G*n***)$_2$**Ir**(**acac**) or (**G*n***)$_3$**Ir** were nearly superimposable with their film PL (Fig. 6c), indicating very efficient energy transfer from CBP to the iridium guest. Devices II containing iridium dendrimer (**G2**)$_3$**Ir** retained a very stable Commission Internationale de L'Eclairage (CIE) coordinate at an applied voltage ranging from 8 to 12 V (Fig. 6d). Therefore, CBP is more appropriate than PVK as

the host material for the green-emitting iridium dendrimers to be developed for highly efficient DLEDs in this study.

7. Conclusions

In summary, first-, second-, and third-generation of phosphorescent benzoimidazole-based iridium dendrimers containing peripheral benzyl ether dendrons were synthesized and characterized in this study. These iridium dendrimers emit green light and exhibit high solution quantum yields ranging from 0.45 to 0.80. The iridium dendrimers-based DLEDs fabricated by spin-coating technique exhibited promising EL performances. For highly efficient DLEDs based on green-emitting iridium dendrimers, CBP is more appropriate than PVK as the host material. The best efficiencies found in the DLEDs containing 20–50 wt% (4.5–9.8 mol%) of iridium dendrimers ($\mathbf{G}\boldsymbol{n})_3\mathbf{Ir}$ ($\boldsymbol{n}$ = **1**–**3**) doped in CBP host. Among these, the device with 20 wt% dopant has the best EL performance with a maximum EQE of 17.6% and a maximum current efficiency of 61.5 cd/A.

Acknowledgements

We thank the Academia Sinica, National Chiao Tung University and the National Science Council for supporting this work.

References

[1] C.W. Tang, S.A. Van Slyke, Appl. Phys. Lett. 51 (1987) 913.
[2] J.H. Burroughes, D.D.C. Bradley, A.R. Brown, R.N. Mackay, K. Marks, R.H. Friend, P.L. Burns, A.B. Holmes, Nature 347 (1990) 539.
[3] (a) M.A. Baldo, D.F. O'Brien, Y. You, A. Shoustikov, S. Sibley, M.E. Thompson, S.R. Forrest, Nature 395 (1998) 151;
(b) M.A. Baldo, D.F. O'Brien, M.E. Thompson, S.R. Forrest, Phys. Rev. B 60 (1999) 14422;
(c) C. Adachi, M.A. Baldo, M.E. Thompson, S.R. Forrest, J. Appl. Phys. 90 (2001) 5048.
[4] (a) H.Z. Xie, M.W. Liu, O.Y. Wang, X.H. Zhang, C.S. Lee, L.S. Hung, S.T. Lee, P.F. Teng, H.L. Kwong, H. Zheng, C. Che, Adv. Mater. 13 (2001) 1245;
(b) V.V. Grushin, N. Herron, D.D. LeCloux, W.J. Marshall, V.A. Petrov, Y. Wang, Chem. Commun. (2001) 1494;
(c) J. Ostrowski, M.R. Robinson, A.J. Heeger, G.C. Bazan, Chem. Commun. (2002) 784;
(d) J.-P. Duan, P.-P. Sun, C.-H. Cheng, Adv. Mater. 15 (2003) 24;
(e) Y.-J. Su, H.-L. Huang, C.-L. Li, C.-H. Chien, Y.-T. Tao, P.-T. Chou, S. Datta, R.-S. Liu, Adv. Mater. 15 (2003) 884;
(f) A.B. Tamayo, B.D. Alleyne, P.I. Djurovich, S. Lamansky, I. Tsyba, N.N. Ho, R. Bau, M.E. Thompson, J. Am. Chem. Soc. 125 (2003) 7377.
[5] (a) W. Lu, B.-X. Mi, M.C.W. Chan, Z. Hui, N. Zhu, S.-T. Lee, C.-M. Che, Chem. Commum. (2002) 206;
(b) B.W. D'Andrade, J. Brooks, V. Adamovich, M.E. Thompson, S.R. Forrest, Adv. Mater. 14 (2002) 1032.
[6] Y. Ma, H. Zhang, J. Shen, C.-M. Che, Synthetic Metals 94 (1998) 245.
[7] Y. Ma, C.-M. Che, H.-Y. Chao, X. Zhou, W.-H. Chan, J. Shen, Adv. Mater. 11 (1999) 852.
[8] (a) J.R. Carlise, X.-Y. Wang, M. Weck, Macromolecules 38 (2005) 9000;
(b) Y. You, S.H. Kim, H.K. Jung, S.Y. Park, Macromolecules 39 (2006) 349;
(c) C.L. Schulz, X. Chen, S.-A. Chen, S. Holdcroft, Macromolecules 39 (2006) 9157;
(d) H. Zhen, C. Luo, W. Yang, W. Song, B. Du, J. Jiang, C. Jiang, Y. Zhang, Y. Cao, Macromolecules 39 (2006) 1693;
(e) N.R. Evans, L.S. Devi, C.S.K. Mak, S.E. Watkins, S.I. Pascu, A. Köhler, R.H. Friend, C.K. Willans, A.B. Holms, J. Am. Chem. Soc. 128 (2006) 6647.
[9] (a) P.W. Wang, Y.J. Liu, C. Devadoss, P. Bharathi, J.S. Moore, Adv. Mater. 8 (1996) 237;
(b) M. Halim, J.N.G. Pillow, I.D.N. Samuel, P.L. Burn, Adv. Mater. 11 (1999) 371;
(c) A.W. Freeman, S.C. Koene, P.R.L. Malenfant, M.E. Thomson, J.M.J. Fréchet, J. Am. Chem. Soc. 122 (2000) 12385;
(d) A. Adronov, J.M.J. Fréchet, Chem. Commum. (2000) 1701;
(e) J.M. Lupton, I.D.W. Samuel, R. Beavington, M.J. Frampton, P.L. Burn, H. Bässler, Phys. Rev. B 63 (2001) 5206;
(f) C.-H. Chen, J.T. Lin, M.-C. Yeh, Org. Lett. 11 (2006) 2233.
[10] (a) T.D. Anthopoulos, M.J. Frampton, E.B. Namdas, P.L. Burn, I.D.W. Samuel, Adv. Mater. 16 (2004) 557;
(b) S.-C. Lo, N.A.H. Male, J.P.J. Markham, S.W. Magennis, P.L. Burn, I.D.W. Samuel, Adv. Mater. 14 (2002) 975;
(c) J.P.J. Markham, S.-C. Lo, S.W. Magennis, P.L. Burn, I.D.W. Samuel, Appl. Phy. Lett. 80 (2002) 2645;
(d) S.-C. Lo, G.J. Richard, J.P.J. Markham, E.B. Namdas, S. Sharma, P.L. Burn, I.D.W. Samuel, Adv. Funct. Mater. 15 (2005) 1451.
[11] S.-C. Lo, T.D. Anthopoulos, E.B. Namdas, P.L. Burn, I.D.W. Samuel, Adv. Mater. 17 (2005) 1945.
[12] J. Ding, J. Gao, Y. Cheng, Z. Xie, L. Wang, D. Ma, X. Jing, F. Wang, Adv. Funct. Mater. 16 (2006) 575.
[13] W.-S. Huang, J.T. Lin, C.-H. Chien, Y.-T. Tao, S.-S. Sun, T.-S. Wen, Chem. Mater. 16 (2004) 2480.
[14] A. Tsuboyama, H. Iwawaki, M. Furugori, T. Mukaide, J. Kamatani, S. Iawa, T. Moriyama, S. Miura, T. Takiguchi, S. Okada, M. Hoshino, K. Ueno, J. Am. Chem. Soc. 125 (2003) 12971.
[15] M. Kawa, J.M.J. Fréchet, Chem. Mater. 10 (1998) 286.
[16] C.J. Hawker, J.M.J. Fréchet, J. Am. Chem. Soc. 120 (1998) 286.
[17] J. Pommerehne, H. Vestweber, W. Guss, R.F. Mahrt, H. Bässler, M. Porsch, J. Daub, Adv. Mater. 7 (1995) 551.
[18] G. Rippen, G. Kaufmann, W. Klöpffer, Chem. Phys. 52 (1980) 152.
[19] (a) C.L. Lee, K.B. Lee, J.J. Kim, Appl. Phys. Lett. 77 (2000) 2280;
(b) S. Lamansky, R.C. Kwong, M. Nugent, P.I. Djurovich, M.E. Thompson, Org. Electron. 2 (2001) 53;
(c) Y. Kawamura, S. Yanagida, S.R. Forrest, J. Appl. Phys. 92 (2002) 87.
[20] (a) V.I. Adamovich, S.R. Cordero, P.I. Djurovich, A. Tamayo, M.E. Thompson, B.W. D'Andrade, S.R. Forrest, Org. Electron. 4 (2003) 77;
(b) K. Brunner, A.V. Dijken, H. Börner, J.J.A.M. Bastiaansen, N.M.M. Kiggen, B.M.W. Langeveld, J. Am. Chem. Soc. 126 (2004) 6035.
[21] H. Kanai, S. Ichinosawa, Y. Sato, Synthetic Metals 91 (1997) 195.
[22] M.A. Baldo, C. Adachi, S.R. Forrest, Phys. Rev. B 62 (2000) 10967.

Organic Electronics 9 (2008) 569–574

Contents lists available at ScienceDirect

Organic Electronics

journal homepage: www.elsevier.com/locate/orgel

Intrinsic and extrinsic influences on the temperature dependence of mobility in conjugated polymers

L. Mattias Andersson [a,*], Wojciech Osikowicz [b], Fredrik L.E. Jakobsson [c], Magnus Berggren [c], Lars Lindgren [d], Mats R. Andersson [d], Olle Inganäs [a]

[a] Biomolecular and Organic Electronics, Department of Physics, Chemistry and Biology, Linköping University, SE-581 83 Linköping, Sweden
[b] Surface Physics and Chemistry, Department of Physics, Chemistry and Biology, Linköping University, SE-581 83 Linköping, Sweden
[c] Organic Electronics, Department of Science and Technology, Linköping University, SE-601 74 Norrköping, Sweden
[d] Polymer Chemistry, Department of Materials and Surface Chemistry, Chalmers University of Technology, SE-412 96 Gothenburg, Sweden

ARTICLE INFO

Article history:
Received 25 January 2008
Received in revised form 27 February 2008
Accepted 7 March 2008
Available online 16 March 2008

PACS:
73.61.Ph
85.30.De

Keywords:
Polymer
Fullerene
Field effect transistor
Electrical transport
Mobility
Temperature dependence

ABSTRACT

The temperature dependence of charge carrier mobility in conjugated polymers and their blends with fullerenes is investigated with different electrical methods, through field effect transistor (FET), space charge limited current (SCLC) and charge extraction (CELIV) measurements. Simple models, such as the Gaussian disorder model (GDM), are shown to accurately predict the temperature behavior, and a good correlation between the different measurement methods is obtained. Inconsistent charge carrier concentrations in the modeling are explained through intrinsic non-equilibrium effects, and are responsible for the limited applicability of existing numerical models. A severe extrinsic influence from water in FETs with a hydrophilic insulator interface is also demonstrated. The presence of water leads to a significant overestimate of the disorder in the materials from measurements close to room temperature and erratic behavior in the 150–350 K range. To circumvent this problem it is shown to be necessary to measure under ultra high vacuum (UHV) conditions.

1. Introduction

Most conjugated polymers and molecules exhibit a mobility that is strongly decreasing with decreasing temperature. This is fully consistent with activated transport between localized states, as appropriate to the disordered polymers, and it is possible to extract information about the density of states (DOS) of the material from mobility versus temperature measurements, with some general assumptions. There are, however, frequently deviations in experimental data from low-level theoretical predictions, which leads to some confusion about data evaluation. Here, mobility versus temperature measurements from several measurement techniques and under different measurement conditions are correlated, in order to clarify their interrelationships and to aid in the future evaluation of measurement data. Field effect transistor (FET), space charge limited current (SCLC) and charge extraction (CELIV) measurements have been done under different conditions and it is shown that, when done under the appropriate conditions and evaluated properly there is a good correlation between the different methods. Furthermore it is shown that the sample geometries must be such that the measurements are done close to equilibrium and that, in the case of FETs with a hydrophilic insulator, measurements are done under ultra high vacuum (UHV) conditions in order to obtain correct data. The polymers used have been designed as solar cell materials and they are used both as pure polymers and in a mixture with

* Corresponding author. Tel.: +46 13 281253.
E-mail address: matan@ifm.liu.se (L. Mattias Andersson).

1566-1199/$ - see front matter © 2008 Elsevier B.V. All rights reserved.
doi:10.1016/j.orgel.2008.03.002

[6-6]-phenyl-C61-butyric acid methylester (PCBM), like in solar cells.

All of the polymers investigated are related, but have very varying optical and electrical properties, and they all share a relatively poor solubility. Stacked sample geometries, such as diodes thus tend to have very thin active layers, which, because the materials are intended for solar cells, is not a problem for normal devices but, as it will be shown, could conceivably cause problems during material characterization where thin samples limits the available measurement techniques and can lead to misinterpreted data. Most notably, time of flight (TOF) measurements are not possible since the samples are optically thin, which means that other techniques more prone to misinterpretation need to be relied upon more heavily. Properly evaluated data will also be shown to reveal many similarities between different but related materials.

2. Experimental

The polymers included here are selected based on their relevance to polymer photovoltaic devices [1,2] and their experimental properties, and they can each be considered as representative for a fairly large group of materials with similar characteristics. Their chemical structures are given in Fig. 1. To increase the size of the extraction currents in the CELIV measurements, blends containing 20% polymer and 80% PCBM were used.

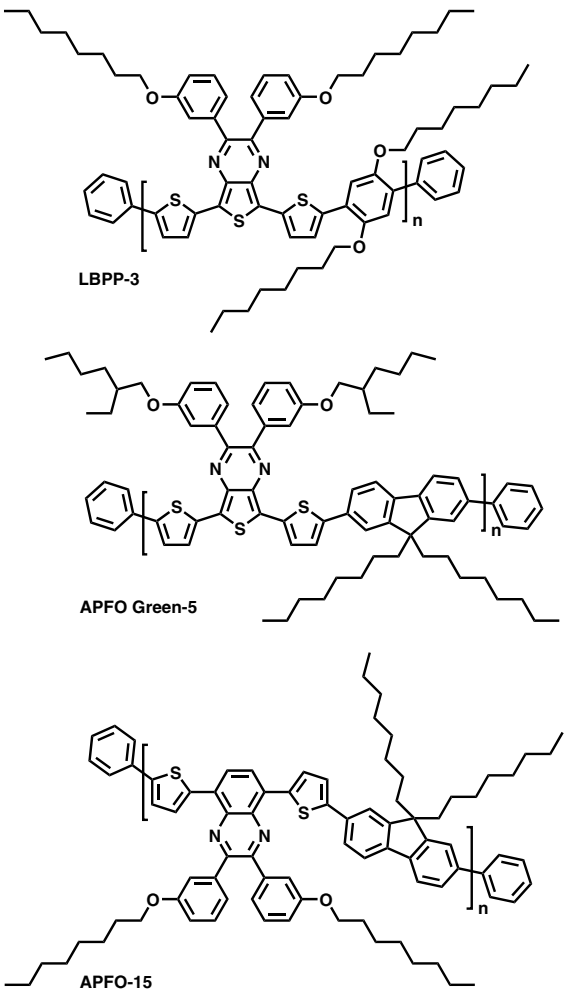

Fig. 1. Chemical structures of the included polymers.

FETs were made from thermally oxidized highly doped p-type silicon wafers with an oxide thickness of 100 nm. Gold electrodes, with a chromium buffer layer, were thermally evaporated and patterned by lithography. Channel lengths (L) were in the range between 10 and 50 μm and widths (W) around 5 mm. The active layer was spin coated on top.

Evaluation of the FET data was made in the saturated regime from derivative plots of the square root of source-drain current (I_S) versus gate voltage (V_G), through Eq. (1) [3]. C_i denotes gate capacitance. Where hysteresis or other effects prevents a constant slope, the maximum slope for outgoing (off to on) sweeps has been used. Measurements were done under high vacuum (HV, $\approx 4 \times 10^{-6}$ torr) or UHV ($\approx 2 \times 10^{-9}$ torr) conditions in different continuous flow liquid nitrogen cryostats with a Keithley 4200 semiconductor parameter analyzer. Reference measurements in air were also performed for all samples, but only vacuum measurement data is included in this paper

$$\mu = \left(\frac{\partial\sqrt{I_S}}{\partial V_G}\right)^2 \frac{2L}{WC_i} \tag{1}$$

CELIV samples were made from indium–tin–oxide (ITO) coated glass substrates with the active layer spin coated on top, and an evaporated top electrode of aluminum (60 nm). In some cases poly(3,4-ethylenedioxythiophene) poly(styrenesulfonate) (PEDOT-PSS) (EL grade, Bayer AG) was spin coated on top of the ITO and lithium fluoride evaporated as buffer layer (0.6 nm) for the aluminum. For the hole only SCLC samples, the top aluminum electrode was replaced by a palladium electrode and PEDOT was always included. All measurements on diode configuration samples were made at HV in the cryostat used for the HV FET measurements and with the Keithley 4200 semiconductor parameter analyzer, an HP 33120A arbitrary waveform generator, and a Tektronix TDS360 oscilloscope. CELIV mobility was calculated through Eq. (2) [4], where t_{max} is the time of the extraction maximum, d the sample thickness, and A the voltage rise rate. The extraction current was small compared to the capacitive current for the samples used here, and there is thus only a very small error associated with the use of Eq. (2)

$$t_{max} = d\sqrt{\frac{2}{3\mu A}} \tag{2}$$

3. Results and discussion

Electrical experiments on devices based on amorphous polymer and molecule films show that the carrier mobility is strongly dependent on temperature and carrier concentration. Photo-generated carriers with excess energy also have a higher mobility than equilibrium carriers, and the dissipation of energy can be followed as a mobility decreasing with time in for instance photo-CELIV [5]. The

reason is that charge transport occurs between localized states, and that the rate of charge transfer between those states is strongly dependent on the number of accessible states. Although difficult to measure, the DOS of these materials is usually, and with merit, approximated with an exponential [6] or Gaussian [7] function. Both of these approximations are behaving similarly near the region of occupied states and have a with energy exponentially increasing site density. The GDM describes this very well and is fairly well established, so the discussion from here on will be based on a Gaussian DOS and a Miller–Abrahams type carrier hopping [7].

At equilibrium and for low carrier concentrations, the center of the occupied density of states (ODOS) is $\sigma\hat{\sigma}$ below that of the DOS [7], where σ is the width of the DOS and $\hat{\sigma}$ is σ/kT. A first order approximation of the temperature dependence of the mobility is given by Eq. (3), which reflects the distance between DOS and ODOS and an activation energy for hopping. The prefactor 2/3 comes from Monte Carlo simulations [7]

$$\mu(T) = \mu_{0,T} \exp\left(-\left(\frac{2}{3}\hat{\sigma}\right)^2\right) \tag{3}$$

For moderate to high carrier concentrations the distance between the center of the DOS and ODOS will be smaller than $\sigma\hat{\sigma}$ and the mobility will thus be higher than expected. It is possible to describe the carrier concentration dependence of the mobility according to Eq. (4) [8,9]. Eq. (4) is based on a parameterization of the carrier concentration dependence and has limited validity, but as long as $\hat{\sigma}$ is relatively small and the carrier concentration much less than 1 it is valid [8]. There are also parameterizations of the field dependence of the mobility that are functions of $\hat{\sigma}$, and thus temperature, such as Eq. (7) [9], where e is the elementary charge, and a the lattice constant (≈1.6 nm). It is included here, but the contribution is very small

$$\mu(c) = \mu_{0,c} \exp[u(2c)^v] \tag{4}$$

$$u = \frac{1}{2}\hat{\sigma}^2 + \ln 2 \tag{5}$$

$$v = 2\frac{\ln(\hat{\sigma}^2 + \ln 4) - \ln(\ln 4)}{\hat{\sigma}^2} \tag{6}$$

$$\mu(E) = \mu_{0,E} \exp\left(0.44(\hat{\sigma}^{3/2} - 2.2)\left(\sqrt{1 + 0.8\left(\frac{Eea}{\sigma}\right)^2} - 1\right)\right) \tag{7}$$

When the temperature is changed, $\hat{\sigma}$ changes and if the carrier concentration is sufficiently high there will be deviations from the mobility temperature dependence predicted by Eq. (3). By combining Eqs. (3), (4), and (7) it is possible to fit a wide range of experimental data. The resulting function is, unfortunately, of a very general form, and could conceivably fit almost anything with the present degrees of freedom. It should also be pointed out that many alternative explanations to the functional form of experimental mobility temperature dependence data can be found in the literature; a transition to transport within a trap level [10], a dispersive to non dispersive transition [11], a transition from small to large polaron hopping [12], a transition from activated hopping to tunneling [14], and various other versions of a transition to a different hopping regime. However, most of these theories involve a transition between different regimes and although there could be a significant transition region there should, nonetheless, be distinguishable regions. In rare cases, such as in Ref. [12], this is indeed the case, but more often the data implies a single region with an exponential dependence of mobility on temperature. The fitting parameters for Eqs. (3), (4), and (7) are also frequently very reasonable for a wide range of measurement techniques, such as TOF, CELIV, SCLC and FET but there are a few discrepancies. It should be noted that there are indications that the DOS might not be modeled very well with a single Gaussian over a wide range of energies [15], and while this might be the reason for the small σ-values in most of these polymers, it would, again, introduce discernible regions in the mobility temperature dependence where the functional form of the DOS is changed, and could thus be identified if present in the studied region.

Diode i/v data can be evaluated numerically for a data set as outlined in Ref. [9], which is based on Eqs. (3), (4), and (7). The temperature range that can be thus fitted is very narrow and even though the model is predicted to break down for lower temperatures, the useful range is surprisingly small compared to data obtained through other measurement- and data evaluation techniques. A different approach to evaluate the temperature dependence of the material in terms of σ and carrier concentration from SCLC measurements is to simply use the device current values at some suitable bias and follow the temperature dependence. The mobility is proportional to the current through the Mott–Gurney law [16] (Eq. (8), with J the current density, ϵ the dielectric constant, V the applied bias, and d the sample thickness) and the field and carrier concentration dependence, both of which are also functions of temperature, can be included in a current versus $1/T^2$ curve fitting to yield σ and some sort of "effective" carrier concentration. In this way it is possible to fit a much wider temperature range (Fig. 2) and the obtained σ-value corresponds well to that obtained by the numerical model in a

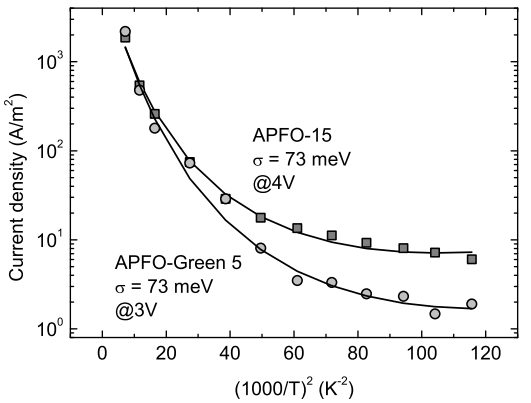

Fig. 2. Diode current at 4 V (APFO-Green 5) and 3 V (APFO-15) bias fitted with Eqs. (3), (4), and (7) with σ = 73 meV and $c = 1.1 \times 10^{-2}$ carriers per site for APFO-Green 5, and σ = 73 meV and $c = 5.0 \times 10^{-3}$ carriers per site for APFO-15. Different bias is used for figure clarity and does not greatly influence the extracted parameters.

narrow temperature range around room temperature (Fig. 3) and the value obtained from FET (Fig. 4). The obtained effective carrier concentration from this fit is, however, very much larger than the space charge limit, which is the presumed condition for extracting the mobility from Eq. (8). A very possible reason for this is that the carriers never reach energetic equilibrium, which, since the temperature dependence in the mobility reflects $\sigma\hat{\sigma}$, means that the mobility would appear higher than its predicted equilibrium value. Carriers injected at some energy independent of temperature, or with only a weak temperature dependence, suppresses the part of the temperature dependence that is due to $\sigma\hat{\sigma}$ increasing with decreasing temperature. The result is more of a $1/T$ nature as the significant contribution to the temperature dependence is then simply the change in activation energy. For the class of materials studied here, the energetic relaxation time is on the order of a few μs; photo-CELIV measurements with varying delay time between excitation and extraction on APFO-15 and APFO-15:PCBM blends, indicate a relatively fast relaxation time of 3×10^{-6} s at room temperature, and with the mobilities and layer thicknesses used here it is thus comparable to the transit time. In terms of the model, the non-equilibrium effects are mainly reflected as a perceived high effective carrier concentration as the transport occurs at an elevated energy compared to equilibrium

$$J = \frac{9}{8}\epsilon\mu\frac{V^2}{d^3} \tag{8}$$

This hypothesis is further corroborated through a couple of CELIV measurements. APFO-15 has very few free carriers, and requires illumination to generate extraction currents, and LBPP-3 has plenty of equilibrium carriers available and is possible to measure without any light. As with the SCLC carriers, the photo excited carriers are generated at an elevated energy that is independent of temperature, and similarly to the SCLC case, a curve fitting of the mobility versus $1/T^2$ yields a higher carrier concentration (4.5×10^{-3} carriers per site) than what is present according to the integral of the extraction current (8×10^{-6} carriers per site). For the measurement in the dark, there is a much better agreement (within an order of magnitude) between extracted charge and fit concentration (Fig. 5). The obtained CELIV carrier concentrations for LBPP-3 and APFO-15 under illumination for these measurements are high (Table 1), but both of the samples are based on blends, and both types of carriers are present. Blends have much larger extraction currents than the pure materials, which, for most members of this class of polymers show no extraction currents at all without photo-excitation. The increased extraction currents for the blends indicate that the two materials in the blend might act as dopants for each other, something that can also be seen as an increased hole mobility in the polymer phase of such a system [17]. Suffice to say, the carrier concentrations are high but plausible for these materials and similarly extracted carrier concentrations on single phase materials, where extraction currents are present, does indeed give much lower values; around 10^{-6} carriers per site.

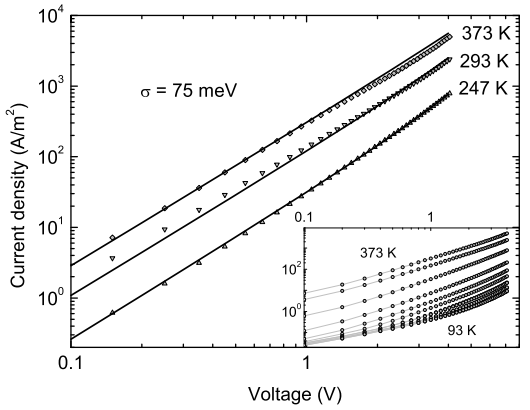

Fig. 3. APFO-15 diode i/v-characteristics fitted numerically through the model outlined in Ref. [9]. The insert shows the whole set of data covering the same temperatures as in Fig. 2. Below 247 K the model predicts a much larger spacing between the curves at all biases.

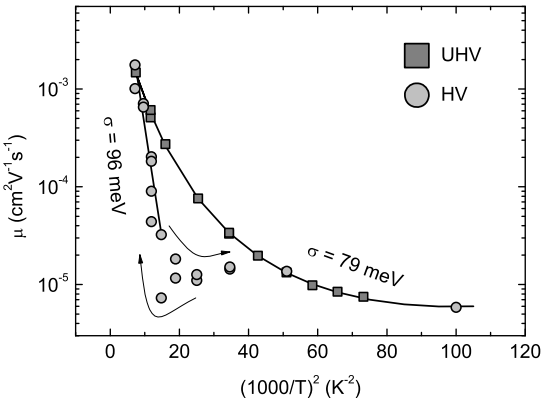

Fig. 4. APFO-Green 5 FET temperature dependence in HV and UHV. There is temperature hysteresis in the 150–350 K temperature range for the HV data but not for the UHV data. Fitting parameters for the UHV data are $\sigma = 79$ meV and $c = 1.1 \times 10^{-2}$ carriers per site.

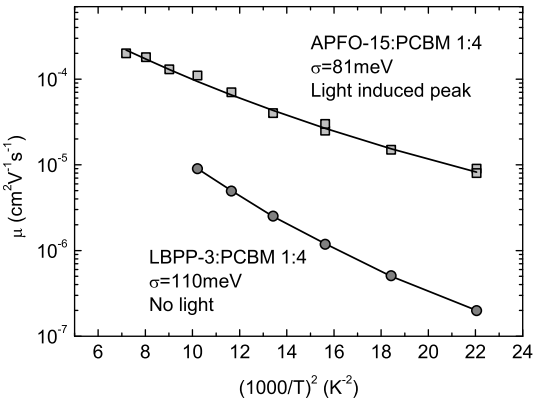

Fig. 5. CELIV temperature dependence for APFO-15 under constant illumination, and LBPP-3 in the dark. The fitting parameters are $\sigma = 81$ meV and $c = 4.5 \times 10^{-3}$ carriers per site for APFO-15, and $\sigma = 110$ meV and $c = 1.1 \times 10^{-3}$ carriers per site for LBPP-3.

Table 1
Room temperature mobility, DOS widths, and carrier concentrations for the various measurements

Measurement type	μ_{RT} ($cm^2\,V^{-1}\,s^{-1}$)	σ (meV)	c ($site^{-1}$)	Material
FET UHV	9×10^{-4}	79	1.1×10^{-2}	APFO-Green 5
FET HV (High T)	3×10^{-4}	96	n/a	APFO-Green 5
SCLC	1×10^{-4} (M–G)	73	1.1×10^{-2} (*)	APFO-Green 5
SCLC	1×10^{-4} (M–G)	73	5.0×10^{-2} (*)	APFO-15
Diode (numerical)	4×10^{-5}	75	n/a	APFO-15
CELIV light	7×10^{-5}	81	4.5×10^{-3} (*)	APFO-15:PCBM
CELIV dark	5×10^{-6}	110	1.1×10^{-3}	LBPP-3:PCBM

SCLC mobilities are evaluated through the Mott–Gurney law (Eq. (8)). Carrier concentrations marked with an (*) are not real carrier concentrations, but rather a perceived effect due to non-equilibrium.

FET data conceivably suffers from the same non-equilibrium effects as the SCLC and illuminated CELIV measurements, but there is an even more important extrinsic aspect to take into consideration, if measurements are made on hydrophilic substrates and in the presence of water. Water diffuses through the semiconductor to the insulator interface and has a profound influence on the device performance [18]. One effect is that it increases the disorder and thus the σ-value of the semiconductor [19]. Another effect is that it tends to be possible to super-cool the water to some extent [20], which gives very erratic mobility temperature dependence in the 150–350 K temperature range (Fig. 4). It turns out that even HV is not enough to prevent a significant impact from water; to get proper correlation to other measurement methods it is necessary to go to UHV. Fig. 6 shows transfer characteristics taken at room temperature and at 373 K in HV and UHV. In a way, hysteresis is a measure of disorder in the material [19], and at 373 K, where there will be very little water present in either case, the transfer characteristics are similar in that respect. At room temperature there is a much larger difference; a small hysteresis in UHV and a significant ditto in HV, indicating that the disorder is smaller in UHV. Mobility temperature dependence measurements also confirm this, and the UHV data correlate well with other types of measurements, while the HV data does not. A very important observation is that in the UHV device, neglecting any irreversible morphological contributions, hysteresis increases with temperature. This is clearly inconsistent with any simple trapping mechanism, but can be explained through non-equilibrium effects [19]. UHV and HV data coincide at high temperatures, where the water is evaporated, and at low temperatures, where it is frozen in. The HV data in Fig. 4 is obtained from a cyclic temperature scan, and when going from low to high temperatures it is possible to see an inflection point in the mobility temperature dependence such as in [12], but it is associated with the phase transition of water and not a transition to a different transport regime. Although the same issue with non-equilibrium injection as in SCLC might be present, it is probably not as pronounced in FET where the channel can be made long. The obtained carrier concentrations are a bit high, but considering that the mobility difference between FET and low carrier concentration measurements, such as CELIV, generally is about one order of magnitude [13] while Eq. (4) [8] only predicts a factor of about 2.6 for the relevant parameters it is probably not greatly overestimated.

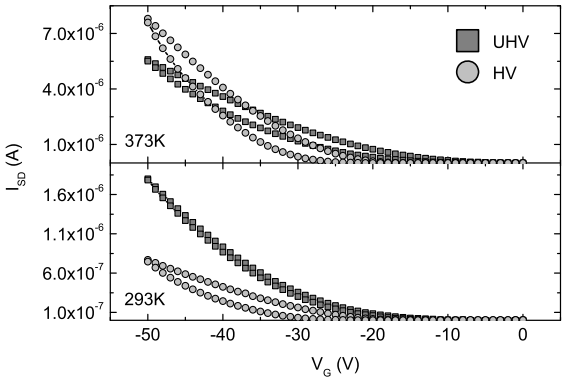

Fig. 6. FET transfer characteristics at 373 K and room temperature in HV and UHV.

Room temperature mobility as it would be measured in a direct measurement, σ-values, and temperature versus $1/T^2$ extracted carrier concentrations for all the measurements are summarized in Table 1. The considerably higher mobility in the APFO-15:PCBM blend CELIV measurement than in the pure APFO-15 SCLC measurement is consistent with previous FET measurements on different stoichiometries [1].

In conclusion, it has been shown that mobility temperature dependence measurements on conjugated polymers is well described by models such as the GDM, based on hopping transport in an exponentially increasing DOS in a rather wide temperature range without any additional considerations. It has also been indicated that different measurement techniques on the same material with films produced in a similar fashion yield similar σ-values, and that measurements on non-equilibrium carriers can lead to overestimated carrier concentrations and mobilities. For stacked sample geometries thick polymer layers should yield values closer to bulk properties. In devices such as FETs based on SiO_2 substrates, where transport occurs near an hydrophilic interface, it is necessary to go to UHV in order to obtain the proper material properties in the 150–350 K temperature range, where water will have a strong influence on the measurement and lead to overestimated σ-values and underestimated mobility values. The breakdown of parameterized models such as the one used here is dependent on $\hat{\sigma}$ and thus have a smaller useful

temperature range for materials with a large σ-value. In general, this also shows the importance of correlating different measurement techniques in order to properly characterize observed phenomena.

Acknowledgements

The authors would like to thank Abay Gadisa, Bekele Homa and Fengling Zhang for sample preparation, and the Swedish Research Council and the Strategic Research Foundation SSF for funding through COE, the Center of Organic Electronics.

References

[1] A. Gadisa, L.M. Andersson, F. Zhang, S. Admassie, W. Mammo, M.R. Andersson, O. Inganas, A new donor–acceptor–donor polyfluorene copolymer with balanced electron and hole mobility, Advanced Functional Materials 17 (18) (2007) 3836–3842.
[2] F. Zhang, W. Mammo, L.M. Andersson, S. Admassie, M.R. Andersson, O. Inganas, Low band-gap alternating fluorene copolymer/methanofullerene heterojunctions in efficient near infrared polymer solar cells, Advanced Materials 18 (2006) 2169.
[3] Ben G. Streetman, Sanjay Banerjee, Solid State Electronic Devices, Prentice Hall, Upper Saddle River, 2000, ISBN 0130261017.
[4] G. Juska, K. Arlauskas, M. Viliunas, K. Genevicius, R. Osterbacka, H. Stubb, Charge transport in π-conjugated polymers from extraction current transients, Physical Review B 62 (24) (2000) R16235.
[5] G. Dennler, A.J. Mozer, G. Juska, A. Pivrikas, R. Osterbacka, A. Fuchsbauer, N.S. Sariciftci, Charge carrier mobility and lifetime versus composition of conjugated polymer/fullerene bulk-heterojunction solar cells, Organic Electronics 7 (4) (2006) 229–234.
[6] E.J. Meijer, C. Tanase, P.W.M. Blom, E. van Veenendaal, B.H. Huisman, D.M. de Leeuw, T.M. Klapwijk, Switch-on voltage in disordered organic field-effect transistors, Applied Physics Letters 80 (20) (2002) 3838–3840.
[7] H. Bassler, Charge transport in disordered organic photoconductors – a Monte-Carlo simulation study, Physica Status Solidi B-Basic Research 175 (1) (1993) 15–56.
[8] R. Coehoorn, W.F. Pasveer, P.A. Bobbert, M.A.J. Michels, Charge-carrier concentration dependence of the hopping mobility in organic materials with gaussian disorder, Physical Review B 72 (15) (2005) 155206.
[9] W.F. Pasveer, J. Cottaar, C. Tanase, R. Coehoorn, P.A. Bobbert, P.W.M. Blom, D.M. de Leeuw, M.A.J. Michels, Unified description of charge-carrier mobilities in disordered semiconducting polymers, Physical Review Letters 94 (20) (2005) 06601.
[10] V.I. Arkhipov, J. Reynaert, Y.D. Jin, P. Heremans, E.V. Emelianova, G.J. Adriaenssens, H. Bassler, The effect of deep traps on carrier hopping in disordered organic materials, Synthetic Metals 138 (1–2) (2003) 209–212.
[11] A.J. Mozer, N.S. Sariciftci, A. Pivrikas, R. Osterbacka, G. Juska, L. Brassat, H. Bassler, Charge carrier mobility in regioregular poly(3-hexylthiophene) probed by transient conductivity techniques: A comparative study, Physical Review B 71 (3) (2005) 035214.
[12] L. Torsi, A. Dodabalapur, L.J. Rothberg, A.W.P. Fung, H.E. Katz, Intrinsic transport properties and performance limits of organic field-effect transistors, Science 272 (5267) (1996) 1462–1464.
[13] L.M. Andersson, F. Zhang, O. Inganas, Bipolar transport observed through extraction currents on organic photovoltaic blend materials, Applied Physics Letters 89 (14) (2006) 142111.
[14] G.W. Kang, K.M. Park, J.H. Song, C.H. Lee, D.H. Hwang, The electrical characteristics of pentacene-based organic field-effect transistors with polymer gate insulators, Current Applied Physics 5 (4) (2005) 297–301.
[15] O. Tal, Y. Rosenwaks, Y. Roichman, Y. Preezant, N. Tessler, C.K. Chan, A. Kahn, Threshold voltage as a measure of molecular level shift in organic thin-film transistors, Applied Physics Letters 88 (4) (2006) 043509.
[16] Murray A. Lampert, Peter Mark, Current Injection in Solids, Academic Press, New York, 1970, ISBN 0124353509.
[17] L.M. Andersson, O. Inganas, Acceptor influence on hole mobility in fullerene blends with alternating copolymers of fluorene, Applied Physics Letters 88 (8) (2006) 082103.
[18] J. Veres, S. Ogier, G. Lloyd, D. de Leeuw, Gate insulators in organic field-effect transistors, Chemistry of Materials 16 (23) (2004) 4543–4555.
[19] L.M. Andersson, O. Inganas, Non-equilibrium effects on electronic transport in organic field effect transistors, Organic Electronics 8 (4) (2007) 423–430.
[20] H.L. Gomes, P. Stallinga, M. Colle, D.M. de Leeuw, F. Biscarini, Electrical instabilities in organic semiconductors caused by trapped supercooled water, Applied Physics Letters 88 (8) (2006) 082101.

Organic Electronics 9 (2008) 575–581

Contents lists available at ScienceDirect

Organic Electronics

journal homepage: www.elsevier.com/locate/orgel

Decamethylcobaltocene as an efficient n-dopant in organic electronic materials and devices

Calvin K. Chan [a,*], Wei Zhao [a], Stephen Barlow [b], Seth Marder [b], Antoine Kahn [a]

[a] Department of Electrical Engineering, Princeton University, E-Quad, Olden Street, Princeton, NJ 08544, USA
[b] Department of Chemistry and Biochemistry, The Center for Organic Photonics and Electronics, Georgia Institute of Technology, Atlanta, GA 30332, USA

ARTICLE INFO

Article history:
Received 4 January 2008
Received in revised form 28 February 2008
Accepted 5 March 2008
Available online 21 March 2008

PACS:
72.80.Le
68.55.Ln
79.60.Fr
73.61.Ph
Keywords:
Organic semiconductor
n-Type doping
Metallocene
Photoemission spectroscopy
Phthalocyanine

ABSTRACT

n-Doping of copper phthalocyanine (CuPc), which has an electron affinity (EA) of 3.52 eV, by decamethylcobaltocene (DMC) is demonstrated. DMC has a remarkably low solid-state ionization energy (IE) of 3.3 eV, as measured by ultra-violet photoemission spectroscopy (UPS). Further UPS measurements show a large 1.4 eV upward shift of the Fermi-level within the single particle gap of CuPc between the p- and n-doped films. n-Doping is also confirmed by current–voltage (I–V) measurements, which show a 10^6-fold increase in current density due to improved electron injection and enhanced conductivity of the bulk film. An organic p–i–n CuPc homojunction is also fabricated using F_4-TCNQ and DMC as p- and n-dopants, respectively. Current–voltage characteristics demonstrate excellent rectification with a turn on voltage of approximately 1.3 eV, which is consistent with the built-in voltage measured by UPS and capacitance–voltage (C–V) measurements.

1. Introduction

Electronic doping of organic electronic materials with electron-donating or accepting compounds is an important, and increasingly used, technique for improving charge injection and transport in organic electronic devices, and for creating semiconductor device junctions. Doping also shows promise for enhancing the environmental and lifetime stability of organic devices. p-Doping, particularly with the electronegative molecule tetrafluoro-tetracyano-quinodimethane (F_4-TCNQ), has been amply demonstrated with a number of hole-transport materials [1–9]. On the other hand, n-type doping is often hindered by the energetic requirements for electron transfer from dopant to host. The paucity of compounds with adequately low ionization energy (IE) required for charge transfer to the unoccupied states of most host molecules of interest is exacerbated by the facile oxidation of these donor molecules by air.

Until recently, practical n-doping of organic semiconductors employed alkali metals (i.e., Li or Cs), which exhibit exceptionally low IEs [10–17]. However, the small size of the alkali counter-ion presents two problems: the ion diffuses readily in the organic matrix, causing difficulties in device engineering and stability; and the metal ion often remains close to the doped organic molecule, forming a Coulomb trap for the donated electron. Bulkier molecular donors could assist in circumventing both of these limitations.

Several groups have reported on molecular n-type doping using donor/host pairs with a specific match between the donor IE and the host electron affinity (EA) [18–21]. However, most of these stable molecular n-dopants have

* Corresponding author. Tel.: +1 609 258 2152; fax: +1 609 258 6279.
E-mail address: ckfchan@princeton.edu (C.K. Chan).

1566-1199/$ - see front matter © 2008 Elsevier B.V. All rights reserved.
doi:10.1016/j.orgel.2008.03.003

relatively high IEs, which limit the range of possible host materials to those with high EAs. One approach for achieving lower IE molecules uses the thermal decomposition of precursor molecular salts to sublimate molecular dopants, but this method introduces additional uncontrolled impurities into the organic film [21–24]. n-Doping with bis (terpyridine) ruthenium has also been demonstrated [19], but such compounds are not readily available and are difficult to synthesize.

We recently showed that cobaltocene ($CoCp_2$), with an IE of 4 eV as measured by ultraviolet photoemission spectroscopy (UPS), efficiently and controllably n-dopes a tris(thieno)-hexaazatriphenylene (THAP) derivative, which has an EA of 4.5 eV as measured by inverse photoemission spectroscopy (IPES). n-Doping was measured through a shift of the Fermi-level (E_F) towards the unoccupied states of the host, and through a 10^3-fold increase in the current density in $CoCp_2$-doped THAP devices [25]. Chemical composition and depth profiling experiments showed that the doping concentration is controllably varied and that dopant diffusion is negligible [26].

Gas-phase decamethylmetallocenes have previously been shown to possess considerably lower IEs as compared to their unsubstituted metallocene derivatives [27,28]. Given that the ionization energy of solid-phase cobaltocene (IE_s) is reduced by 1.5 eV with respect to the gas-phase value (IE_g), assuming a comparable polarization effect ($P = IE_g - IE_s$) for decamethylcobaltocene (DMC or $CoCp_2^*$; Fig. 1 top) would place its IE_s at only 3.2 eV. This hypothesis is verified by the measurement of the energetic levels of DMC by UPS and IPES. n-Doping of copper phthalocyanine (CuPc; Fig. 1 bottom) by DMC is demonstrated by measured shifts of the valence states towards high binding energy with respect to E_F, and by the construction of n-doped CuPc diodes and homojuction devices. CuPc has an EA of 3.52 eV, which is substantially lower than the IE of most molecular donors investigated to date. DMC is therefore introduced here as a very promising candidate for efficient n-type doping of a number of organic molecular semiconductors.

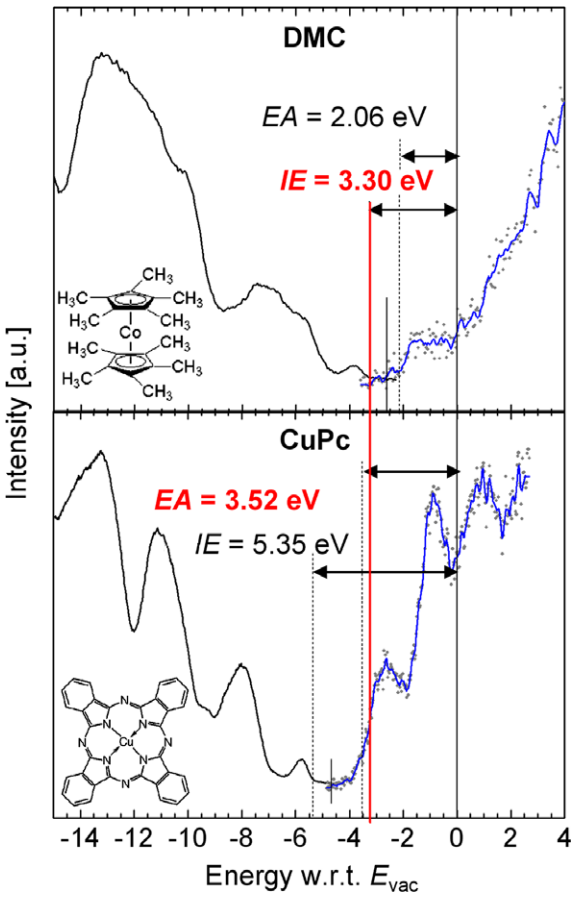

Fig. 1. UPS and IPES spectra of DMC (top) and CuPc (bottom) showing the favorable energy level alignment of the dopant donor level with the host acceptor level. The DMC and CuPc molecular structures are shown in insets.

2. Experimental

Experiments were conducted in an interconnected three-chamber ultra-high vacuum (UHV) system equipped for organic film growth, UPS and IPES analysis, and in situ current–voltage (I–V) and capacitance–voltage (C–V) measurements. DMC was loaded, as received from Sigma–Aldrich, under inert N_2 atmosphere into a sealed UHV gas-handling apparatus that allows the release of a precisely regulated amount of dopant into the vacuum chamber [25,26]. When the DMC source is heated to 100 °C, it provides a background pressure (p_d) of 10^{-6} Torr in the vacuum chamber when the gas release aperture is fully opened.

The DMC source was mounted on the sample preparation chamber equipped with a thermal evaporation cell containing CuPc (Sigma–Aldrich), which was previously purified by three cycles of gradient sublimation. This chamber, in which all doped films were grown, is connected to the growth chamber and the analysis chamber, allowing for preparation of doped films, growth of undoped and metal films, and sample characterization without breaking vacuum. Experiments were conducted at base pressures of 2×10^{-10}, 5×10^{-11}, and 1×10^{-9} Torr in the preparation, analysis, and growth chambers, respectively.

For analysis of the electronic structure of DMC, pristine films of the dopant were condensed onto indium-tin-oxide (ITO) substrates cooled to 80 K by a closed-cycle helium refrigerator. The ITO surfaces were prepared by mechanical, detergent, and solvent cleaning, followed by 1 h of UV-ozone exposure, and immediately transferred into vacuum. Doped CuPc films were obtained by evaporating the host onto a polycrystalline Au/Ti/Si(100) substrate in a controlled background pressure of DMC varying between $p_d = 10^{-8}$ to 10^{-6} Torr to obtain different doping concentrations. The deposition rate for CuPc was monitored with a quartz crystal microbalance, assuming a bulk density of 1.5 g cm^{-3}, and the background pressure of gas-phase DMC was monitored with a standard pressure ionization gauge located near the dopant source. Undoped CuPc was grown in the separate growth chamber.

Occupied electronic states of the organic films were measured with UPS using the He I ($h\nu = 21.22$ eV) and He

II ($h\nu$ = 40.8 eV) photon lines of a helium discharge lamp, while unoccupied electronic states were measured using IPES in the isochromat mode [29]. All spectra presented here are referenced to, and aligned at, the Fermi-level (E_F) of the experimental system determined by UPS and IPES measurements on a clean Au sample. The position of the vacuum level (E_{vac}) of each surface was determined using the low-energy secondary electron cut-off [30]. Experimental resolutions for UPS and IPES are 0.15 and 0.5 eV, respectively.

I–V measurements were conducted in vacuum on 100–200 nm undoped, interfacially doped, or uniformly doped CuPc films grown on solvent-cleaned Au. These Au surfaces, used as-loaded, are covered with physisorbed contaminants, particularly water and hydrocarbons, and will be hereafter referred to as Au*. Top contacts consisting of 25 nm thick circular Au pads of varying diameter were then evaporated through a shadow mask. Measurements were done in situ at room temperature using a HP4155A semiconductor parameter analyzer.

CuPc homojunction devices, structured with a 150 nm organic layer between an ITO bottom contact and a 25 nm thick Au top contact, were constructed using F_4-TCNQ as the acceptor and DMC as the donor. The devices included: (i) an intrinsic CuPc layer, and (p–i–n) a 10 nm p-region, 120 nm i-region, and a 20 nm n-region. Each device was characterized using *I–V* measurements, while p–i–n devices were additionally characterized using *C–V* measurements with a HP4274A multi-frequency LRC meter. The built-in potential in the (p–i–n) device was also determined directly via UPS measurement on the n-, i- and p-layers at various stages of the fabrication.

3. Results and discussion

3.1. Energetic levels of DMC

The occupied and unoccupied states of a ~15 monolayer films of DMC (assuming a sticking coefficient equal to unity at low temperature) measured by UPS and IPES are plotted in Fig. 1, along with the corresponding states of a 6.5 nm CuPc film on Au*. Conventionally, adiabatic IE and EA of the condensed phase materials are determined as the energy difference between the vacuum level (E_{vac}) and the onset of the highest and lowest energy features in UPS and IPES, respectively [30–32]. DMC exhibits an EA of 2.06 eV and a remarkably low IE of only 3.3 eV. This solid-state IE is in precise agreement with the hypothesized value derived from subtracting the 1.5 eV polarization energy observed for $CoCp_2$ from the 4.7 eV gas-phase IE for DMC [25,27]. CuPc shows an IE of 5.35 eV, an EA of 3.52, and therefore a transport gap E_{gap} of 1.83 eV, which is in good agreement with previously published solid-state spectroscopy data on phthalocyanines [4,5,14,15,33]. The most relevant energy level for n-type doping, i.e., the dopant IE is highlighted by a bold line spanning the two plots, and leads to the prediction of an energetically favorable electron transfer from DMC to CuPc in a simplified charge transfer model.

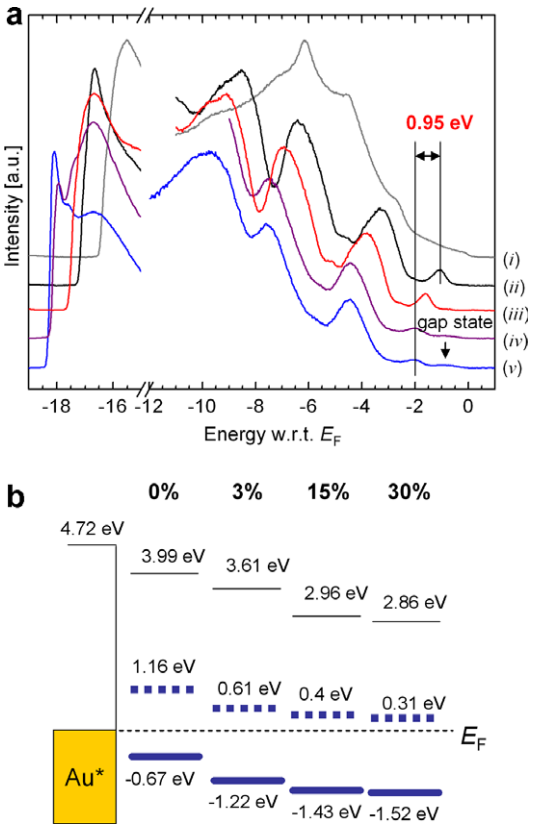

Fig. 2. (a) UPS spectra of the vacuum level onset (left) and filled valence states (right) of: (i) solvent-cleaned, as-loaded Au, "Au*"; (ii) undoped CuPc; (iii) 3% DMC-doped CuPc; (iv) 15% DMC-doped CuPc; and (v) 30% DMC-doped CuPc. (b) Corresponding energy-level diagrams showing frontier filled (thick lines) and empty (thick dashes) states, E_F and E_{vac}.

3.2. Decamethylcobaltocene as a donor in CuPc

Doping of CuPc by DMC was investigated with UPS on CuPc layers undoped or doped with varying DMC concentrations deposited on Au*. The occupied state spectrum of Au* is plotted in Fig. 2a(i). The metal work function is 4.72 eV, which is typical of a contaminated Au surface. Such a surface has been shown to produce lower hole injection barriers (ϕ_{Bh}) to organic molecular films when compared to a pristine, atomically clean Au surface [34]. In agreement with these findings, undoped CuPc deposited on the Au* substrate is found in Fig. 2a(ii) to form a 0.67 eV hole injection barrier, with the Fermi level in the lower part of the gap.

A series of 6.5 nm thick CuPc films were also deposited onto Au* substrates at 2 Å s^{-1} under DMC partial pressures of 1×10^{-7}, 5×10^{-7}, and 1×10^{-6} Torr. The interface between the doped CuPc and Au* was mediated by a 2.5 nm layer of pristine CuPc to prevent direct interaction of DMC-molecules with the substrate that could result in modification of the Au* work function. The Co2p/C1s core level peak intensity ratio measured in X-ray photoemission spectroscopy (XPS) reveals that the CuPc sample with $p_d = 10^{-6}$ Torr is doped at a concentration of ~30%. Assuming a linear extrapolation of the concentration as a function

of DMC partial pressure during growth, the varying p_d result in doping concentrations of 3%, 15%, and 30%, respectively. Previous Rutherford backscattering (RBS) experiments on THAP doped with $CoCp_2$ suggest the validity of these estimated doping concentrations [26], but the exact doping concentrations for DMC-doped CuPc remains to be confirmed.

The UPS spectra of the doped films are plotted in Fig. 2a(iii)–(v) and summarized in the energy-level diagram shown in Fig. 2b. They show the progressive shift of the CuPc molecular levels towards higher binding energy with increasing doping. This corresponds to a shift of E_F towards the unfilled CuPc states, and is indicative of significant and controlled n-doping. In the highest doping scenario, E_F shifts 0.95 eV to the upper part of the gap, with a final position only 0.31 eV below the edge of the CuPc empty states. The 1.1 eV shift of the local vacuum level, E_{vac}, is slightly larger than the molecular level shift, and is likely the result of some DMC molecules adsorbed on the CuPc surface. For the highest doping concentrations, $p_d = 5 \times 10^{-7}$ and $p_d = 1 \times 10^{-6}$ Torr, a 0.1 eV broadening of all molecular peaks is observed, which indicates a high level of dopant incorporation. Additionally, an observable density of filled states within the single-particle gap, labeled "gap state" in Fig. 2a, may be the result of the formation of charge-transfer complexes at high doping concentrations [35]. Nevertheless, the spectra of the highly doped samples retain all the features of the CuPc film.

3.3. DMC-doped CuPc devices

Undoped CuPc devices were grown on Au* and capped with freshly evaporated Au top contacts. The *I–V* measurements, normalized to current density and electric field, for the 100 nm undoped CuPc device are plotted in Fig. 3a, and show a distinctly asymmetric current in forward bias (open circles) and reverse bias (closed circles). Forward (or reverse) bias corresponds to positive bias on, and thus hole injection from, the bottom (or top) electrode. The hole

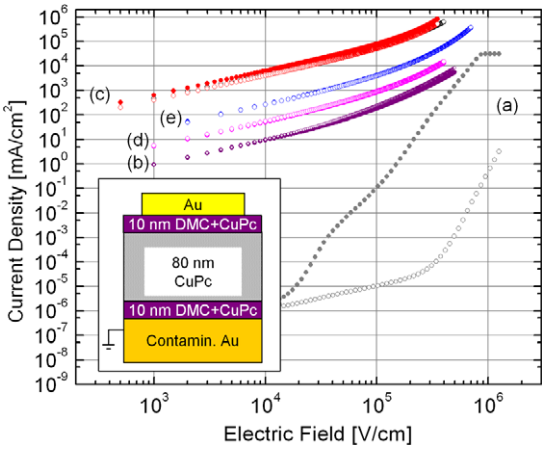

Fig. 3. Current–voltage measurements of contaminated-Au/100 nm organic/clean-Au diodes, where the organic layer consists of: (a) undoped CuPc; (b) 3% interface doped CuPc (see inset); (c) 3% homogenously doped CuPc; (d) the uniformly doped CuPc exposed to air for 15 min.; and (e) the air-exposed sample reintroduced into vacuum and pumped on for 1 h.

Table 1
Electron and hole barriers (ϕ_{Be}, ϕ_{Bh}) corresponding to undoped and doped CuPc films deposited on Au and Au*

Electrode material	ϕ_{Be} (eV)	ϕ_{Bh} (eV)
Undoped CuPc on Au* (WF = 4.72 eV)	1.16	0.67
Undoped CuPc on Au (WF = 5.20 eV)	0.92	0.91
Doped CuPc on Au* and Au	0.31	1.52

ϕ_{Bh} is the energy difference measured by UPS at the interface between the electrode Fermi level and edge of the filled states. ϕ_{Be} is obtained by subtracting ϕ_{Bh} from the single particle edge-to-edge gap of CuPc (1.83 eV in Fig. 1).

injection barriers for undoped and doped CuPc on Au and Au* listed in Table 1 are determined from the UPS data in Section 3.2. Electron injection barriers are extrapolated from the EAs assuming that CuPc has an $E_{gap} = 1.83$ eV as found from UPS and IPES in Section 3.1. As the CuPc molecular level positions at the contact interfaces indicate, the substantially lower hole injection barrier at the Au* interface ($\phi_{Bh} = 0.67$ eV) as compared to the evaporated Au interface ($\phi_{Bh} = 0.91$ eV) results in significantly improved carrier injection from the bottom interface, and therefore the observed 10^4 times increase in current density for the device under bottom hole injection. It must be emphasized that the dominant carriers in Au*/undoped CuPc/Au devices are likely to be holes, since ϕ_{Bh} is nearly 0.25 eV less than the electron injection barrier (ϕ_{Be}).

Interface-doped CuPc devices consisting of a Au* bottom contact, 10 nm of 3% DMC-doped CuPc, 80 nm of undoped CuPc, an additional 10 nm of n-doped CuPc, and a freshly evaporated Au top contact (Fig. 3, inset) was fabricated. The *I–V* measurements, shown in Fig. 3b, indicate a dramatic increase in the current density ranging from a factor of 10^3 at moderate electric fields to 10^7 at low electric fields. However, in contrast to undoped devices, this current is likely dominated by efficient electron injection and transport in CuPc, since as observed in Section 3.2, the electron injection barrier ($\phi_{Be} = 0.31$ eV) is now considerably smaller than the hole injection barrier ($\phi_{Bh} = 1.52$ eV). This is an important finding because it dispels the common misconception that CuPc is exclusively a hole transport materials. Indeed, the current density for interface-doped devices is comparable with the hole-only devices observed by Gao et al. for zinc phthalocyanine (ZnPc) [4,5], an isoelectronic analog to CuPc, suggesting that when proper electron injection contacts are formed on CuPc, the electron transport characteristics of the material are comparable to its hole transport properties. The symmetric forward and reverse bias currents indicate that the interface energetics are identical on both sides, as would be expected given that equal doping was applied to both contacts, and is dominated by the dopant-determined alignment of E_F with the empty states of CuPc. More importantly, n-doping of CuPc near the Au contacts demonstrates that use of reactive low work function anodes for electron injection can be circumvented by locally n-doping the host material at the electron injecting contact and using stable high work function metals.

Finally, devices consisting of 100 and 200 nm CuPc films doped with $p_d = 5 \times 10^{-7}$ Torr of DMC are investigated using *I–V* measurements (Fig. 3c). The superposition of

the *I–V* curves normalized to electric field for two different thickness devices indicates that the current is limited by bulk transport through the film. The homogenously doped films demonstrate an additional 10^3 times increase in current density that results from increased carrier density in the bulk of the film. The fact that curve (c) parallels curve (b) provides further indication that even in the interface-doped device, the metal–organic interface is no longer the limiting factor in charge transport.

When the fully doped CuPc devices are exposed to air for 30 min, ex situ *I–V* experiments show a 100 times decrease in current density (Fig. 3d). This effect is attributed to oxygen diffusion into the CuPc film, which traps the DMC-induced excess electrons in the bulk film [36,37]. The reduction in bulk conductivity is partially reversible when the sample is reintroduced into vacuum and measured after 1 h of pumping in situ (Fig. 3e). However, despite the negative impact of air exposure on the overall current density of the doped film, good agreement between the *I–V* curves shown in Fig. 3c, i.e. the interface-doped device, and Fig. 3d suggests that the improvement in current injection due to doping at the interfaces is not compromised. Given that improvement in carrier injection has been explained by carrier tunneling through the dopant-induced space-charge layer at the metal/organic interface [7,24], it should not be surprising that oxidizing species would negligibly affect the already electron depleted layer near the contacts.

3.4. CuPc p–i–n homojunction

The application of DMC doping of CuPc to p–i–n homojunction diodes was investigated by fabricating 150 nm thick devices with an ITO bottom contact and an Au top contact. A fully intrinsic CuPc device was fabricated as a control sample for comparison with a p–i–n device consisting of a 10 nm CuPc p-region doped at 1% with F_4-TCNQ, a 120 nm i-region, and a 20 nm n-region doped with DMC gradually from 3% at the intrinsic interface to 30% at the metal interface (Fig. 4 inset). The gradual doping was accomplished by increasing the dopant partial pressure over the course of the deposition of the n-CuPc layer. The large intrinsic region is used as a buffer layer to prevent carrier tunneling that results from the otherwise small space-charge region resulting from a direct organic p–n junction. Current density measurements of intrinsic and p–i–n devices shown in Fig. 4a and b, respectively, are plotted with respect to conventional forward and reverse diode conditions, and are in good qualitative and quantitative agreement with previous results obtained by Harada et al. on CuPc homojunctions made using a Ru compound as the n-dopant [19]. The results shown here exhibits a clear 10^3-fold increase in current density as a result of p- and n-doping, but does not demonstrate an improvement in the rectification ratio of the p–i–n device, as would have been expected. This is likely the result of an unidentified source of leakage current at reverse bias, which can also be seen at low positive biases in the horizontal reflection of the reverse bias current onto the positive bias abscissa (dotted lines). If the leakage component of the current density can be minimized, the improvements observed for the p–i–n device would directly translate into a similar increase in the rectification ratio.

For the p–i–n structure, UPS measurements were taken after deposition of the p- and n-layers to establish independently the magnitude of the built-in potential. The total shift between the two spectra is the built-in potential ϕ_{bi}, and is equal to 1.45 eV as shown in Fig. 5. Given that ϕ_{bi} in the p–i–n junction is simply given by:

$$\phi_{bi} = E_{gap} - (EA - E_{Fn}) - (E_{Fp} - IE) \quad (1)$$

where E_{Fn} and E_{Fp} are the positions of the Fermi-level in the n- and p-doped regions, respectively, the 0.38 eV difference between E_{gap} and ϕ_{bi} deviates from the sum of $EA - E_{Fn} = 0.31$ eV (Section 3.2) and $E_{Fp} - IE = 0.2$ eV [4]. Although the 130 meV discrepancy is within our experimental error, it could also be the result of UPS-induced charging in the 120 nm-thick i-layer of the device, which would result in an exaggerated energy level shift of the n-doped layer towards lower kinetic energy.

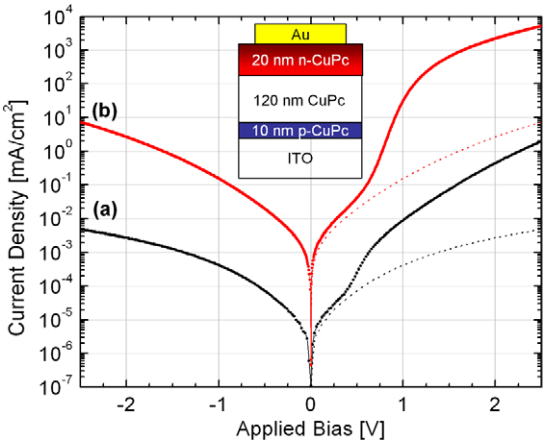

Fig. 4. Current–voltage measurements of: (a) ITO/150 nm CuPc/Au and (b) ITO/10 nm 1% F4-TCNQ:CuPc/120 nm CuPc/20 nm 3–30% graded DMC:CuPc/Au p–i–n devices. The inset shows the device structure for the p–i–n homojunction.

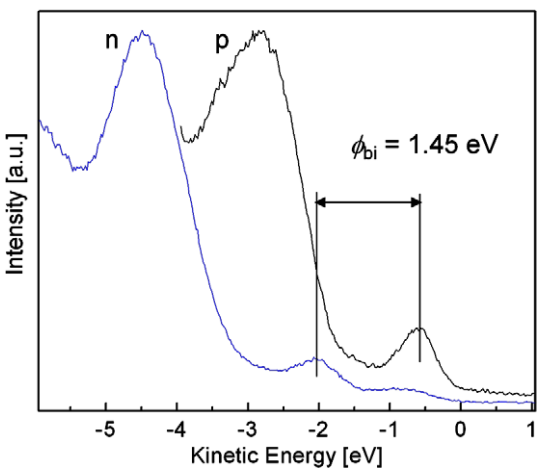

Fig. 5. UPS spectrum of the p-CuPc and n-CuPc films in the p–i–n device showing a large built-in potential.

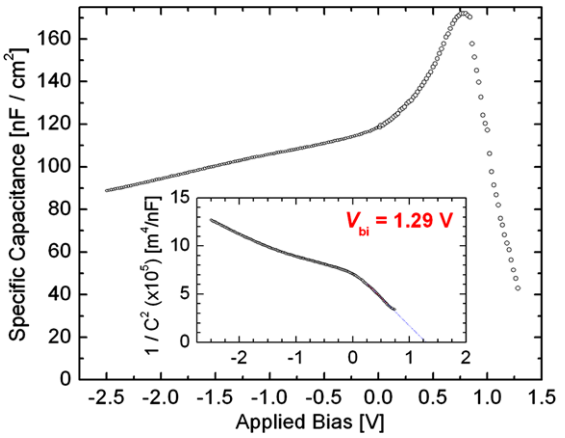

Fig. 6. Capacitance–voltage measurements of the CuPc p–i–n homojunction diode. The $1/C^2$ plot is shown in the inset.

To further investigate the value of the built-in potential of the CuPc homojunction, quasi-static *C*–*V* measurements were conducted on the p–i–n structure using a 2 kHz sinusoidal signal with an amplitude modulation of ±0.05 V. The *C*–*V* results plotted in Fig. 6 show a gradual decline of the specific capacitance of the device with increasing negative bias, and likely corresponds to an enlargement of the depleted space-charge regions at the reverse-biased p–i, i–n, and metal/organic interfaces [38]. At low positive bias, the observed exponential increase of the capacitance is correlated with the rise in diffusion capacitance, which results from the exponentially increasing current flow under forward bias found in Fig. 4b [38,39]. The drop in the capacitance at higher forward bias (>0.75 V), which is inductive in nature, has been attributed to a variety of mechanisms, including short-base diode effects [40,41], charge trapping and transport through localized trap states [42,43], injection through interfacial states [44], or carrier recombination within the film [45]. At the present time, however, it is uncertain whether any of these models apply to doped organic systems, or whether new models must be developed to explain the negative differential capacitance phenomena observed here.

Nevertheless, using the convention that the extrapolated *x*-intercept of a $1/C^2$ vs. voltage plot corresponds roughly to the built-in potential of a p–i–n diode [38], the inset of Fig. 5 suggests a 1.29 eV offset between the levels in the p- and n-regions of the CuPc homojunction. This is in excellent agreement with ϕ_{bi} = 1.32 eV expected from Eq. (1).

4. Summary

The solid-state ionization energy of decamethylcobaltocene (DMC) was found to be ~3.3 eV, which makes this compound a powerful donor for many molecular semiconductors used in organic electronics. Efficient n-type doping of CuPc by DMC was demonstrated by evaporation of the phthalocyanine films in a controlled partial pressure of the dopant. The fabrication of n-doped CuPc films was confirmed by the shift of the Fermi-level towards the unoccupied states, with a final position of only 0.3 eV below the frontier empty states of CuPc. *I*–*V* measurements were conducted on homogenously and interface-doped DMC/CuPc films sandwiched between Au contacts. These devices exhibited an increase of several orders of magnitude in current density due to enhanced injection and conductivity. Exposing the uniformly doped film to air decreases only the bulk conductivity due to the introduction of electron-trapping oxygen molecules, but this effect is found to be partially reversible. These findings have important consequences for device applications, by eliminating the need for low work function cathodes for electron injection. Finally, CuPc p–i–n homojunctions with F_4-TCNQ as the p-dopant and DMC as the n-dopant were constructed and examined with UPS, *I*–*V*, and *C*–*V* measurements. Although the exact mechanisms and theory behind the results are currently not well understood, the experiment unambiguously demonstrates the potential of molecular doping of organic films for stable, high current OLEDs and for OPVs with large open circuit voltages.

Acknowledgements

Support of this work by the National Science Foundation (DMR-0705920) and the Princeton MRSEC of the National Science Foundation (DMR-0213706) is gratefully acknowledged. Work at the Georgia Institute of Technology was supported in part by the STC Program of the National Science Foundation under Agreement Number DMR-0120967), and by the Office of Naval Research (N00014-04-1-0120).

References

[1] J. Blochwitz, M. Pfeiffer, T. Fritz, K. Leo, Appl. Phys. Lett. 73 (1998) 729.
[2] M. Pfeiffer, A. Beyer, T. Fritz, K. Leo, Appl. Phys. Lett. 73 (1998) 3202.
[3] J. Blochwitz, T. Fritz, M. Pfeiffer, K. Leo, D.M. Alloway, P.A. Lee, N.R. Armstrong, Org. Electron. 2 (2001) 97.
[4] W. Gao, A. Kahn, Appl. Phys. Lett. 79 (2001) 4040.
[5] W. Gao, A. Kahn, Org. Electron. 3 (2002) 53.
[6] W. Gao, A. Kahn, J. Appl. Phys. 94 (2003) 359.
[7] W. Gao, A. Kahn, J. Phys.: Condens. Matter 15 (2003) S2757.
[8] A. Kahn, N. Koch, W. Gao, J. Polym. Sci. Part B: Polym. Phys. 41 (2003) 2529.
[9] C. Chan, W. Gao, A. Kahn, J. Vac. Sci. Technol. A 22 (2004) 1488.
[10] J. Kido, T. Matsumoto, Appl. Phys. Lett. 73 (1998) 2866.
[11] Q.T. Le, L. Yan, Y. Gao, M.G. Mason, D.J. Giesenand, C.W. Tang, J. Appl. Phys. 87 (2000) 375.
[12] M.G. Mason, C.W. Tang, L.-S. Hung, P. Raychaudhuri, J. Madathil, D.J. Giesen, L. Yan, Q.T. Le, Y. Gao, S.-T. Lee, L.S. Liao, L.F. Cheung, W.R. Salaneck, D.A.d. Santos, J.L. Bredas, J. Appl. Phys. 89 (2001) 2756.
[13] G. Parthasarathy, C. Shen, A. Kahn, S.R. Forrest, Journal of Applied Physics 89 (2001) 4986.
[14] L. Yan, N.J. Watkins, S. Zorba, Y. Gao, C.W. Tang, Appl. Phys. Lett. 79 (2001) 4148.
[15] Y. Gao, L. Yan, Chem. Phys. Lett. 380 (2003) 451.
[16] K. Ihm, T.-H. Kang, C.-C. Hwang, Y.-J. Park, K.-B. Lee, B. Kim, C.-H. Jeon, C.-Y. Park, K. Kim, Y.-H. Tak, Appl. Phys. Lett. 83 (2003) 2949.
[17] J. Liu, A.R. Duggal, J.J. Shiang, C.M. Heller, Appl. Phys. Lett. 85 (2004) 837.
[18] A. Nollau, M. Pfeiffer, T. Fritz, K. Leo, J. Appl. Phys. 87 (2000) 4340.
[19] K. Harada, A.G. Werner, M. Pfeiffer, C.J. Bloom, C.M. Elliott, K. Leo, Phys. Rev. Lett. 94 (2005) 036601.
[20] S. Tanaka, K. Kanai, E. Kawabe, T. Iwahashi, T. Nishi, Y. Ouchi, K. Seki, Jap. J. Appl. Phys. 44 (2005) 3760.
[21] F. Li, A. Werner, M. Pfeiffer, K. Leo, X. Liu, J. Phys. Chem. B 108 (2004) 17076.
[22] A.G. Werner, F. Li, K. Harada, M. Pfeiffer, T. Fritz, K. Leo, Appl. Phys. Lett. 82 (2003) 4495.

[23] A. Werner, F. Li, K. Harada, M. Pfeiffer, T. Fritz, K. Leo, S. Machill, Adv. Funct. Mater. 14 (2004) 255.
[24] C.K. Chan, E.-G. Kim, J.-L. Bredas, A. Kahn, Adv. Funct. Mater. 16 (2005) 831.
[25] C.K. Chan, F. Amy, Q. Zhang, S. Barlow, S. Marder, A. Kahn, Chem. Phys. Lett. 431 (2006) 67.
[26] C.K. Chan, A. Kahn, Q. Zhang, S. Barlow, S. Marder, J. Appl. Phys. 102 (2007) 014906.
[27] C. Cauletti, J.C. Green, M.R. Kelly, P. Powell, J.v. Tilborg, J. Robbins, J. Smart, J. Electr. Spectr. Relat. Phenom. 19 (1980) 327.
[28] J.L. Robbins, N. Edelstein, B. Spencer, J.C. Smart, J. Am. Chem. Soc. 104 (1982) 1882.
[29] C.I. Wu, Y. Hirose, H. Sirringhaus, A. Kahn, Chem. Phys. Lett. 272 (1997) 43.
[30] D. Cahen, A. Kahn, Adv. Mater. 15 (2003) 271.
[31] I.G. Hill, A. Rajagopal, A. Kahn, Y. Hu, Appl. Phys. Lett. 73 (1998) 662.
[32] H. Ishii, K. Seki, IEEE Trans. Electron Dev. 44 (1997) 1295.
[33] T. Schwieger, Knupfer, W. Gao, A. Kahn, Appl. Phys. Lett. 83 (2003) 500.
[34] A. Wan, J. Hwang, F. Amy, A. Kahn, Org. Electron. 6 (2005) 47.
[35] E.F. Aziz, A. Vollmer, S. Eisebitt, W. Eberhardt, P. Pingel, D. Neher, N. Koch, Adv. Mater. 19 (2007) 3257.
[36] A.K. Hassan, R.D. Gould, J. Phys.: Condens. Matter 1 (1989) 6679.
[37] O.D. Jurchescu, J. Baas, T.T.M. Palstra, Applied Physics Letters 87 (2005) 052102.
[38] S.M. Sze, Physics of Semiconductor Devices, 2nd ed., Wiley-Interscience, New York, 1981.
[39] M.L. Lucia, J.L. Hernandez-Rojas, C. Leon, I. Martil, Eur. J. Phys. 14 (1993) 86.
[40] J.J.H. van den Biesen, Solid-State Electron. 33 (1990) 1471.
[41] M.-N. Tsai, T.C. Chang, P.-T. Liu, C.-W. Ko, C.-J. Chen, K.-M. Lo, Thin Solid Films 498 (2006) 244.
[42] M.S. Xu, J.N. Xu, W.Y. Cheung, Proc. of the IEEE Electron Dev. Meeting (2001) 122.
[43] K.-Y. Chiang, H.-Y. Tseng, C.-Y. Lin, C.-P. Kung, W.-H. Hou, Mater. Res. Soc. Symp. Proc. 965 (2007) S06.
[44] J. Bisquert, G. Garcia-Belmonte, A. Pitarch, H.J. Bolink, Chem. Phys. Lett. 422 (2006) 184.
[45] V. Shrotriya, Y. Yang, J. Appl. Phys. 97 (2005) 054504.

Organic Electronics 9 (2008) 582–590

Contents lists available at ScienceDirect

Organic Electronics

journal homepage: www.elsevier.com/locate/orgel

Efficient oligothiophene:fullerene bulk heterojunction organic photovoltaic cells

Jun Sakai [a,*], Tetsuya Taima [b], Kazuhiro Saito [b]

[a] Advanced Technologies Development Laboratory, Matsushita Electric Works Ltd., 1048 Kadoma Osaka, Japan
[b] Research Center for Photovoltaics, National Institute of Advanced Industrial Science and Technology (AIST), Umezono 1-1-1, Tsukuba, Ibaraki, Japan

ARTICLE INFO

Article history:
Received 10 February 2007
Received in revised form 8 March 2008
Accepted 9 March 2008
Available online 28 March 2008

Keywords:
Oligothiophene
Fullerene
Bulk heterojunction
Organic photovoltaic cells
Co-evaporation

ABSTRACT

Novel small-molecule bulk heterojunction photovoltaic (PV) cells consisting of oligothiophen (alpha-sexithiophen: 6T) and fullerene (C_{60}) have been developed. Oligothiophen is well known as a good hole-transport material, and by changing the number of thiophen rings and making chemical modifications or substitutions, its characteristics relevant to PV applications (such as carrier mobility, energy level, packing, and ordered structure) can be controlled. Thus far it has been difficult to fabricate films of oligothiophene–fullerene blends with suitable morphology by using the common co-evaporation method, because oligothiophene crystallizes easily during film deposition. The present study found that the morphology of 6T:C_{60} blends strongly depending on the composition of 6T:C_{60}. Suitable morphology was obtained only for films deposited with the co-evaporation of excess C_{60}. It is likely that excess C_{60} prevents the crystallization of 6T. By successfully controlling the film morphology, we were able to demonstrate good PV performance in oligothiophene:fullerene bulk heterojunction PV cells for the first time. Moreover, it was found that PV performance could be further improved by inserting a C_{60} layer between the blend layer and exciton blocking layer.

1. Introduction

Small-molecule organic photovoltaic (PV) cells have been significantly improved through research conducted on bulk heterojunctions, p–i–n structures, tandem structures, and exciton blocking layers [1–3]. Metal phthalocyanine (Pc)-fullerene bulk heterojunction PV cells are particularly known to exhibit high efficiency [4–9]. For the practical use of such cells, however, all parameters related to the photoelectric conversion process such as photon absorption, charge carrier mobility, and donor–acceptor blend morphology must be improved.

In this study we focused particularly on the charge carrier mobility of the organic semiconductor as one parameter that should be improved. Generally low mobility affects the carrier transport properties. As the mobility is improved, the drift length or diffusion length generally increases. Therefore, thicker layers can be used for increased photon absorption. One drawback of organic photovoltaic cells is their poor carrier transport properties. Organic transistor research has estimated the mobility of various kinds of organic semiconductors. In the Pc:C_{60} bulk heterojunction system, the field-effect electron mobility of C_{60} is about 0.3 cm^2/Vs [10]. On the other hand, the field-effect hole mobility of CuPc is about 0.02 cm^2/Vs [11]. Therefore, it follows that hole mobility should be improved to better balance the hole and electron transport properties.

We chose oligothiophene as a high hole mobility material. The basic advantages of this material are its good hole transport and the possibility of controlling mobility, energy level, packing, and ordered structure by changing the number of thiophen rings, and making chemically modifications and substitutions.

* Corresponding author. Tel.: +81 6 6906 7549; fax: +81 6 6908 9273.
E-mail address: jun-sakai@mail.mew.co.jp (J. Sakai).

1566-1199/$ - see front matter © 2008 Elsevier B.V. All rights reserved.
doi:10.1016/j.orgel.2008.03.008

Some studies on organic PV cells using oligothiophene have already been reported [12–16]. All OPV cells developed in these studies were bilayer heterojunction cells incorporating oligothiophene and n type organic material. However, good performance in an oligothiophene bulk heterojunction system has not been reported yet.

The purpose of this study was to investigate the potential for more efficient device structures employing oligothiophene as a donor material and fullerene as an acceptor material. In particular, we intended to develop a bulk heterojunction device structure of oligothiophene:fullerene similar to the phthalocyanine (Pc):fullerene system.

It is known that a good morphology of Pc:fullerene blend films can be formed through the co-evaporation of equal fractions blend of both components. For making a bulk heterojunction device employing new materials, however, new device structures and fabrication processes should be investigated.

We chose alpha-sexithiophene (6T) as the oligothiophene material because it is well known to exhibit high field-effect hole mobility, and a representative material in the oligothiophene family. Conversely, a problematic issue arises when high mobility materials are applied to PV cells. Linear molecule thin films such as oligothiophene typically are formed with a preferential orientation on the substrate, so that the long axis is perpendicular to the substrate plane. A film comprised of preferentially oriented molecules may exhibit anisotropic mobility, that is, lower mobility (intrinsic) perpendicular to the substrate than that in the substrate plane. For this reason, it is important to investigate the molecular orientation in oligothiophene:fullerene photovoltaic devices.

2. Experimental

The sample fabrication procedure is described as follows: Glass substrates with indium tin oxide (ITO) films were purchased from Kinoene-kogaku Inc. The ITO film had a film thickness of 150 nm, and sheet resistance of about 10 Ω.

Poly [3,4-ethylenedioxythiophene]-poly [styrenesulfonate] (PEDOT:PSS,Baytron Al4083) was deposited on the ITO film by spin coating (3000 rpm 120 s) and baking (135 °C 15 min). The resultant thickness was about 30 nm.

We then deposited an active layer consisting of 6T (Aldrich) and C_{60} (MTR) through sequential vacuum evaporation. The co-evaporation method was used to deposit the blend layers.

In the next step, a layer of bathocuproine (DOJINDO) 6-nm thick was deposited as an exciton blocking layer, followed by 100-nm thick Ag:Mg film deposited as a cathode metal through vacuum evaporation to complete the OPV cells.

For measuring the photovoltaic characteristics, we employed an Air Mass 1.5 Global (AM1.5G) solar simulator (Oriel) as the light source, calibrated to 100 mW/cm^2 by using a crystalline Si reference cell with an amorphous Si optical filter (Bunkoukeiki). A Keithley semiconductor parameter analyzer was used to measure the *I–V*

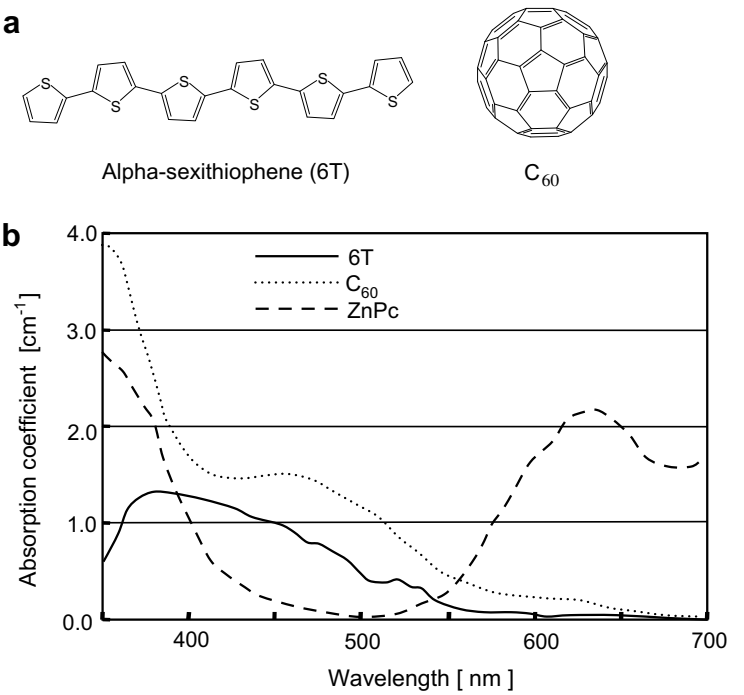

Fig. 1. (a) Chemical structure of alpha-sexithiophene and C_{60}, and (b) absorption coefficient spectra of 6T, C_{60}, and ZnPc as calculated from UV–Vis optical density and film thickness.

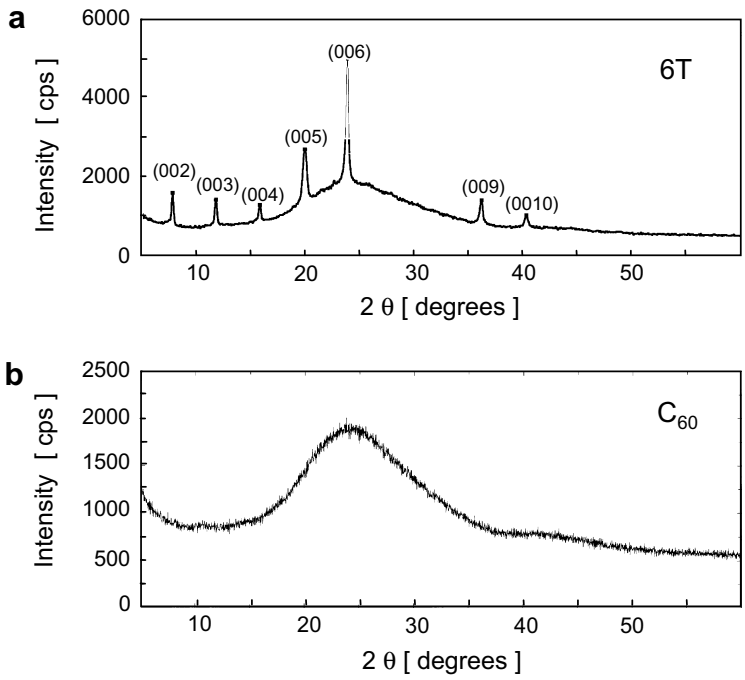

Fig. 2. (a) X-ray diffraction pattern of sexithiophene film on a glass substrate, and (b) C_{60} film on a glass substrate. The broad peak at around 25 degrees corresponds to the glass substrate.

characteristics. The effective sample area was 4 mm^2, and the prepared PV cells were measured in a vacuum chamber after deposition at room temperature without exposure to air.

The samples were further characterized by the following methods. Photo absorption spectra were measured using a UV–Vis spectrophotometer (Shimazu), and film thickness was measured by a DEKTAK surface profilemeter. Surface roughness profiles were measured by Atomic Force Microscope (AFM, Seiko instrument). Nihon Denshi provided cross-sectional Transmission Electron Microscopy (TEM) images and Energy Dispersive X-ray spectrometer (EDX) images. The samples for TEM were prepared by focused ion beam (FIB) cutting method. A highest occupied molecular orbital (HOMO) level of organic semiconductors was measured by Ultraviolet Photoelectron Spectroscopy (UPS, Bunkoukeiki) and energy gap was determined by the photo absorption edge of UV–Vis spectra.

3. Results and discussion

3.1. Characteristics of 6T and C_{60} films

First we estimated the photo absorption spectra of 6T and C_{60} in order to estimate the short-circuit current. Fig. 1a shows the chemical structure of sexithiophene and C_{60}. Fig. 1b shows the photo absorption coefficients of those materials including ZnPc. These data were calculated from the optical density and film thickness.

The peak absorption coefficient value of 6T is as high as that of ZnPc (10^5/cm order), but the peak wavelength of 6T is less than 400 nm, as compared to about 630 nm for that of ZnPc. Moreover, the main absorption wavelength of C_{60} is less than 500 nm. Since the absorption spectra do not

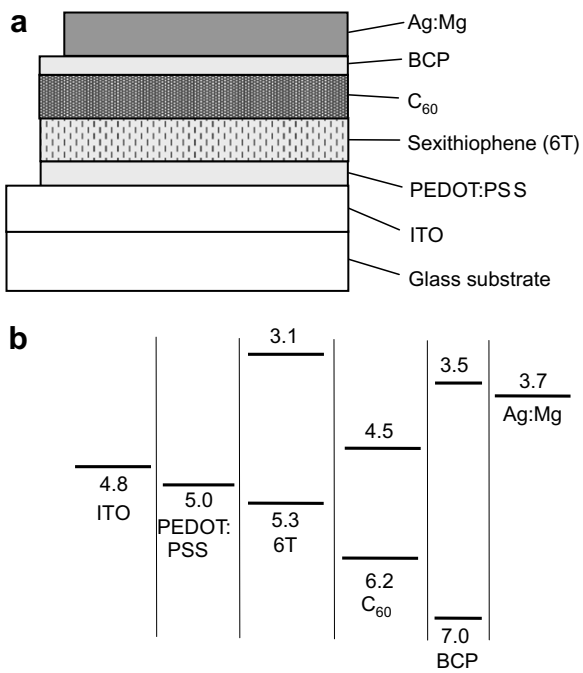

Fig. 3. (a) Schematic device structure of 6T/C_{60} bilayer heterojunction PV cell, and (b) diagram showing energy levels of the 6T/C_{60} bilayer heterojunction cell under flat band conditions.

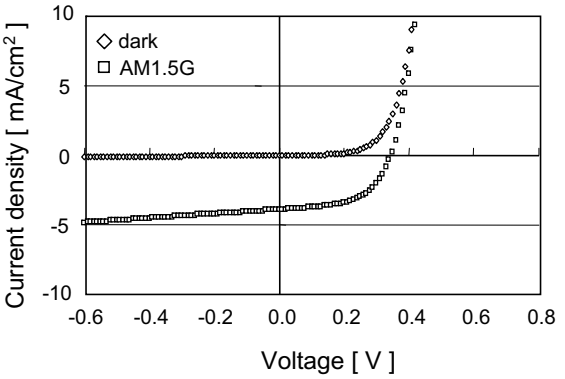

Fig. 4. Current–voltage characteristics under dark and AM1.5G, 100 mW/cm^2 for 6T/C_{60} bilayer PV cell. The *I–V* characteristics were measured in a vacuum chamber after deposition at room temperature without exposure to air. The effective sample area is 4 mm^2. Both 6T and C_{60} have a film thickness of 25 nm.

match well with the solar spectrum, high short-circuit currents such as those in the Pc-fullerene system cannot be expected in the 6T:C_{60} system.

Next we evaluated the orientation of 6T and C_{60} films deposited on a glass substrate at room temperature by

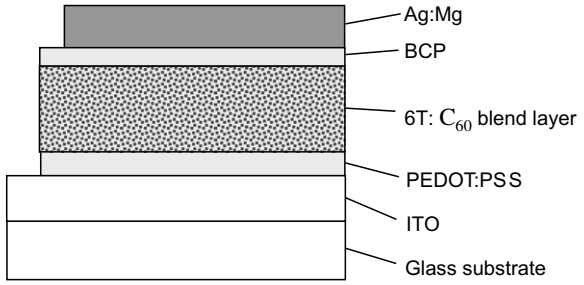

Fig. 6. Schematic device structure of 6T: C_{60} bulk heterojunction PV cells.

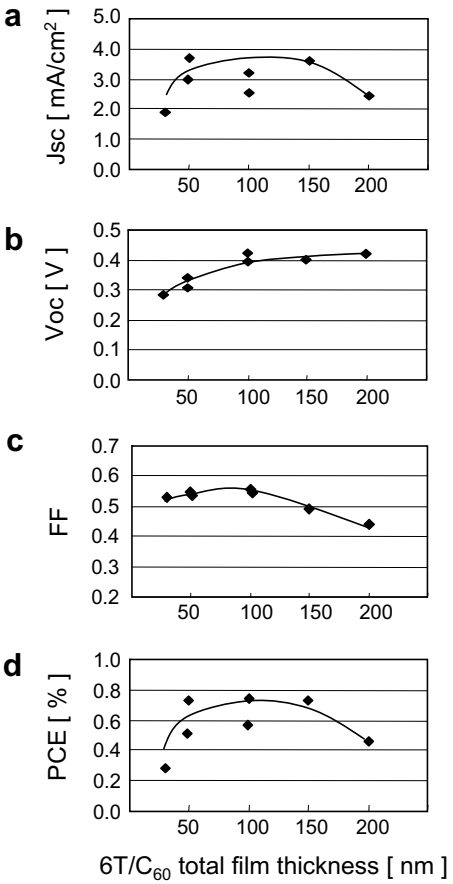

Fig. 5. Photovoltaic characteristics under AM1.5G 100 mW/cm^2 for 6T/C_{60} bilayer PV cells : (a) Jsc vs. total film thickness of the 6T and C_{60} active layer. (b) Voc vs. total film thickness of the 6T and C_{60} active layer. (c) FF vs. total film thickness of the 6T and C_{60} active layer. (d) Power conversion efficiency vs. total film thickness of the 6T and C_{60} active layer (The film thickness of 6T and C_{60} is equal in the all samples.).

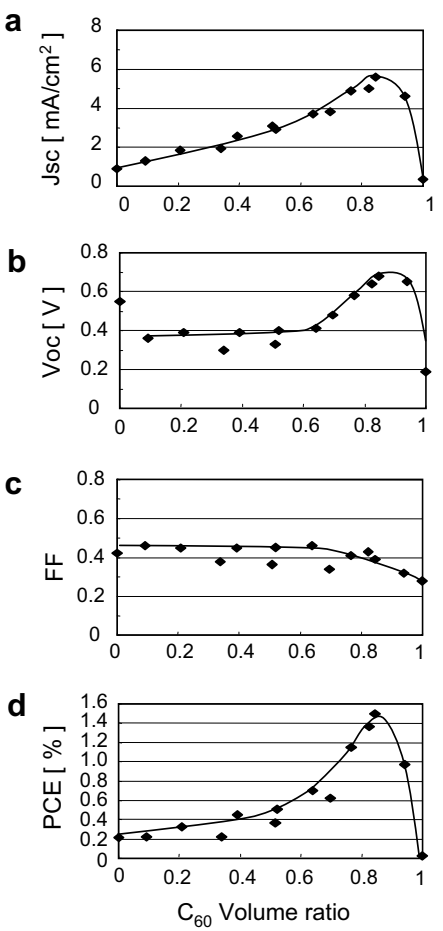

Fig. 7. Photovoltaic characteristics under AM1.5G 100 mW/cm^2 for 6T:C_{60} bulk heterojunction PV cells: (a) Jsc vs. C_{60} volume ratio. (b) Voc vs. C_{60} volume ratio. (c) FF vs. C_{60} volume ratio. (d) Power conversion efficiency vs. C_{60} volume ratio. (The volume ratio is defined as the ratio of film thickness as determined by a vacuum deposition rate monitor.)

X-ray diffraction (XRD). Fig. 2a and b shows the XRD patterns of 6T and C_{60} films, respectively. There are some sharp peaks in the 6T film pattern, indicating that the 6T molecules are crystallized with a preferred vertical orientation. Many studies on 6T film orientation have already been reported [17,18]. It is believed that hole mobility (intrinsic) in the horizontal direction is high, but lower in the vertical direction. This might prove unsuitable for photovoltaic devices. Conversely, no C_{60} peak was observed (as the broad peak at around 25 degrees corresponds to the glass substrate). This shows that the C_{60} film is almost amorphous.

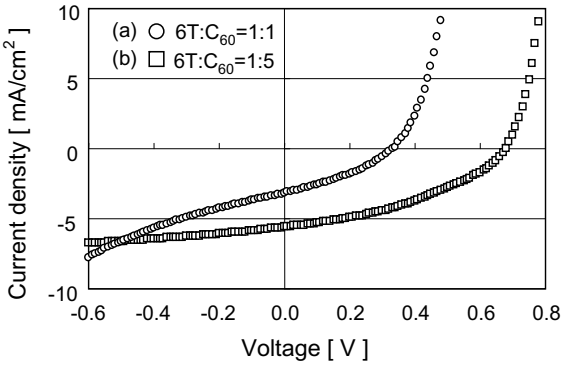

Fig. 8. Current–voltage characteristics under AM1.5G 100 mW/cm^2 for 6T:C_{60} bulk heterojunction cells. The volume ratios are (a) 6T:C_{60} = 1:1 and (b) 6T:C_{60} = 1:5.

3.2. 6T/C_{60} bilayer heterojunction PV cells

6T/C_{60} bilayer heterojunction PV cells were prepared so as to examine the heterojunction properties of 6T/C_{60} and the effects of employing high mobility material. Fig. 3 shows the device structure and an energy diagram of 6T/C_{60} PV cells. The HOMO levels of 6T and C_{60} were measured by UPS and the energy gaps were measured by the UV–Vis spectra. The work functions of the other materials are quoted from some previous literatures [19,20]. This diagram shows that 6T and C_{60} work well as a heterojunction device.

Fig. 4 shows the *I–V* characteristics of a 6T/C_{60} bilayer PV cell. This shows excellent PV characteristics: power conversion efficiency (PCE) of 0.75%, short circuit current density (Jsc) of 3.9 mA/cm^2, open circuit voltage (Voc) of 0.35 V and fill factor (FF) of 0.55 at AM1.5G 100 mW/cm^2. Thus, the combination of 6T and C_{60} was found to be a suitable heterojunction. Still, Voc was not so high considering the energy gap (0.8 eV) between HOMO of 6T and lowest unoccupied molecular orbital (LUMO) of C_{60}.

Next we investigated the dependence on film thickness in the 6T/C_{60} bilayer PV cells. The optimum thickness of the 6T/C_{60} active layer was expected to be thicker than the Pc/C_{60} active layer due to higher mobility (intrinsic) in 6T. Fig. 5 shows the relationship between the photovoltaic characteristics and total thickness of 6T/C_{60}. In this experiment, 6T and C_{60} had equal thickness.

This figure shows maximum Jsc appears when the thickness is from 50 to 150 nm; therefore, it follows that hole and electron diffusion lengths are close to optimum thickness. Voc gradually increases with thickness, while

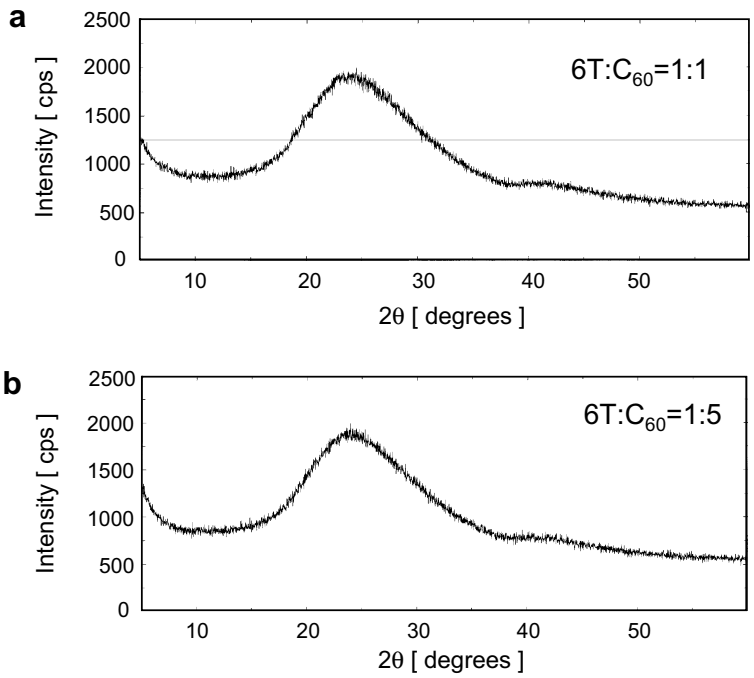

Fig. 9. X-ray diffraction patterns of 6T:C_{60} co-evaporated films on a glass substrate: (a) The volume ratio is 6T:C_{60} = 1:1 and (b) the volume ratio is 6T:C_{60} = 1:5.

FF gradually decreases with thickness due to the increase in series resistance. As a result, the optimum thickness in 6T/C_{60} was found to extend from 50 to 150 nm, while that of ZnPc/C_{60} was about 50 nm. This finding is probably due to increase of intrinsic hole mobility.

It was also found that even though the 6T film is preferentially oriented in the vertical direction, intrinsic hole mobility in the vertical direction is still higher than that of phthalocyanine.

3.3. 6T:C_{60} bulk heterojunction PV cells

3.3.1. I–V characteristics

We investigated the device structures and device fabrication procedures of 6T:C_{60} bulk heterojunction PV cells. Fig. 6 shows the basic device structure.

First we deposited a 6T:C_{60} blend layers with a fixed volume ratio of 1:1. In this study, the volume ratio is defined as the ratio of film thickness as determined by a vacuum deposition rate monitor. In the metal Pc and C_{60} system, PV characteristics were dramatically improved due to co-evaporation with a volume ratio of unity. But in the 6T:C_{60} system, contrary to our expectations, the PV characteristics with a unity volume ratio were not good (resulting in a blend film thickness of 50 nm, PCE of 0.52%, Jsc of 2.8 mA/cm^2, Voc of 0.4 V, and FF of 0.46 at AM1.5G 100 mW/cm^2). These values are inferior to those of the 6T/C_{60} bilayer heterojunction cells. In particular, Jsc of the blend type is lower than that of the bilayer type. Apparently charge separation does not occur sufficiently in the blend films due to bad blend morphology.

When we investigated the surface roughness of blend cells deposited at the unity ratio, large grains were observed in contrast to the smooth surface of the bilayer. This bad blend morphology might adversely affect the charge separation and the carrier transport.

We subsequently investigated the influence of certain different deposition conditions and found that the volume ratio of 6T:C_{60} clearly and strongly affects the blend morphology. Fig. 7 shows the relationship between the photovoltaic characteristics and 6T/C_{60} volume ratio. Jsc and Voc dramatically increase when the C_{60} volume ratio is more

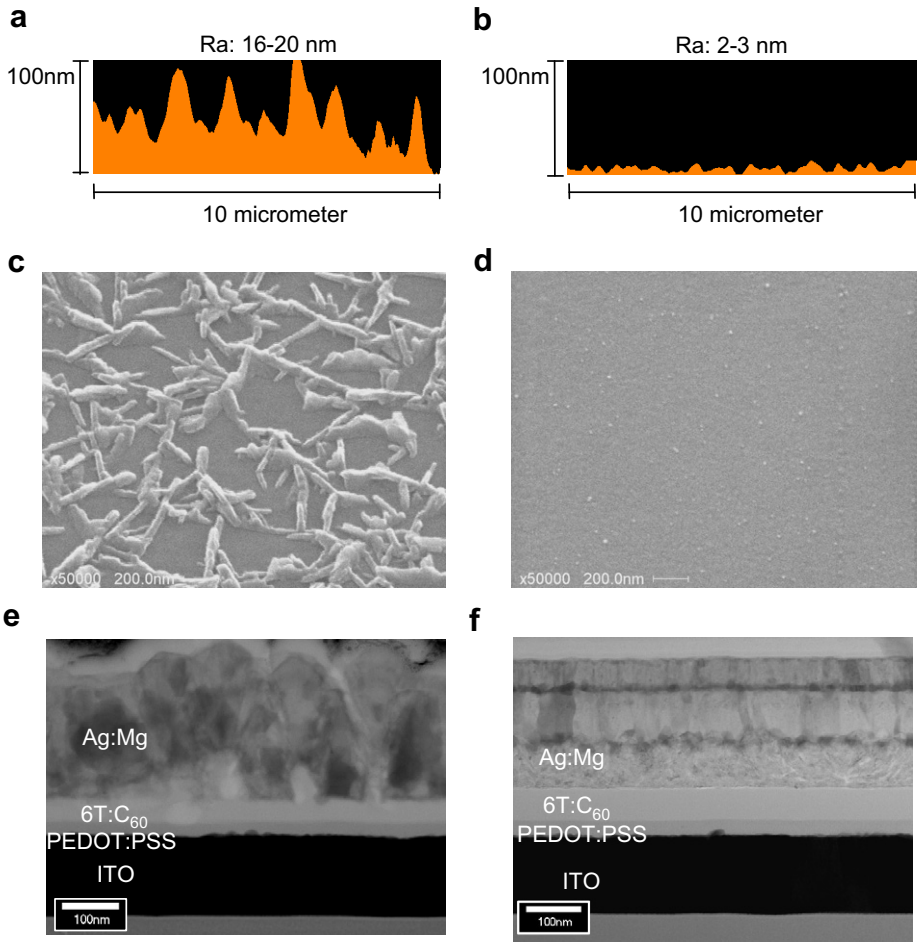

Fig. 10. AFM surface profiles of blend layers with volume ratios of (a) 6T:C_{60} = 1:1 and (b) 6T:C_{60} = 1:5. Ra is average surface roughness. SEM images (of blend layer surface) with volume ratios of (c) 6T:C_{60} = 1:1 and (d) 6T:C_{60} = 1:5. Cross-sectional TEM images with volume ratios of (e) 6T:C_{60} = 1:1 and (f) 6T:C_{60} = 1:5.

than 0.7, but FF gradually decreases as the C_{60} volume ratio increases. When the volume ratio is 0, the device structure is a 6T/metal Schottky barrier device; when the volume ratio is 1, the device structure is a C_{60}/PEDOT:PSS Schottky barrier device. Both Schottky devices work well. As can be seen in Fig. 7, the optimum C_{60} volume ratio is from 0.8 to 0.9. In particular, Jsc and Voc increase by nearly double as compared with the low volume ratio. Fig. 8 shows the *I–V* characteristics for 6T:C_{60} = 1:5 (with PCE of 1.5%, Jsc of 5.6 mA/cm^2, Voc of 0.68 V and FF of 0.39 at AM1.5G 100 mW/cm^2). The PCE of the 6T:C_{60} = 1:5 device is three times higher than that of the 6T:C_{60} = 1:1 device.

3.3.2. Blend morphology

In order to investigate the influence of volume ratio on the photovoltaic characteristics, we examined the film structure and the blend morphology by using XRD, AFM, Scanning Electron Microscope (SEM), and cross-sectional TEM images. Fig. 9 shows the XRD patterns for volume ratios of 1:1 and 1:5. Both patterns indicate that the preferred orientation of 6T is not observed in co-evaporated films, and that orientation does not depend on the volume ratio. 6T probably grows amorphously due to its interaction with C_{60}.

Fig. 10 shows the blend morphology by using AFM surface profiles, SEM surface images, and TEM cross-sectional images. These figures show significantly different morphologies between the volume ratios of 1:1 and 1:5. In the case of 1:1, small rod-shaped grains (about 200 nm in length and 40 nm in diameter) with some branches were randomly deposited [21]. Conversely, in the case of 1:5, there are no grains and a very homogeneous film is obtained.

Fig. 11 shows the distribution of carbon and sulfur by using cross-sectional TEM-EDX images. Fig. 11a shows that sulfur appears mainly in grains in the lower part of the image; therefore, these grains are composed of 6T and not C_{60}. Conversely, the 1:5 blend film is perfectly smooth with sulfur dispersed homogeneously. Fig. 11a also shows that a smooth film grows at first, followed by the growth of micro crystals from pores on the smooth film.

The growth mechanism of 6T and C_{60} blend film is as follows: As can be seen in the 6T single-film structure, 6T tends to crystallize oriented in the vertical direction. Therefore, in the case of a low C_{60} volume ratio, the micro crystals of 6T grow preferentially and do not blend well with C_{60}, due to the stronger tendency of 6T to crystallize. Apparently C_{60} molecules cover the outer surface of the 6T micro crystals. However, when the C_{60} ratio is greater than 0.7, C_{60} inhibits 6T crystallization and a nano-scale blend film is grown.

As for the relationship between the blend morphology and the photovoltaic characteristics, it is clear in the case of blend ratio 1:1 that charge separation does not occur efficiently because there are many grains and a sufficient carrier transport interpenetrating network does not exist, which explains why charge carrier transport efficiency is poor. Consequently, Jsc is low.

On the other hand, in the case of blend ratio 1:5, excess C_{60} in the blend leads to the formation of homogeneous film and the desired interpenetrating network, which results in higher Jsc.

As for increasing Voc, the maximum estimated Voc of this device is the difference between HOMO of 6T and LUMO of C_{60}, that is, 0.8 V. Therefore, it may be presumed that Voc approaches the maximum value as the blend mor-

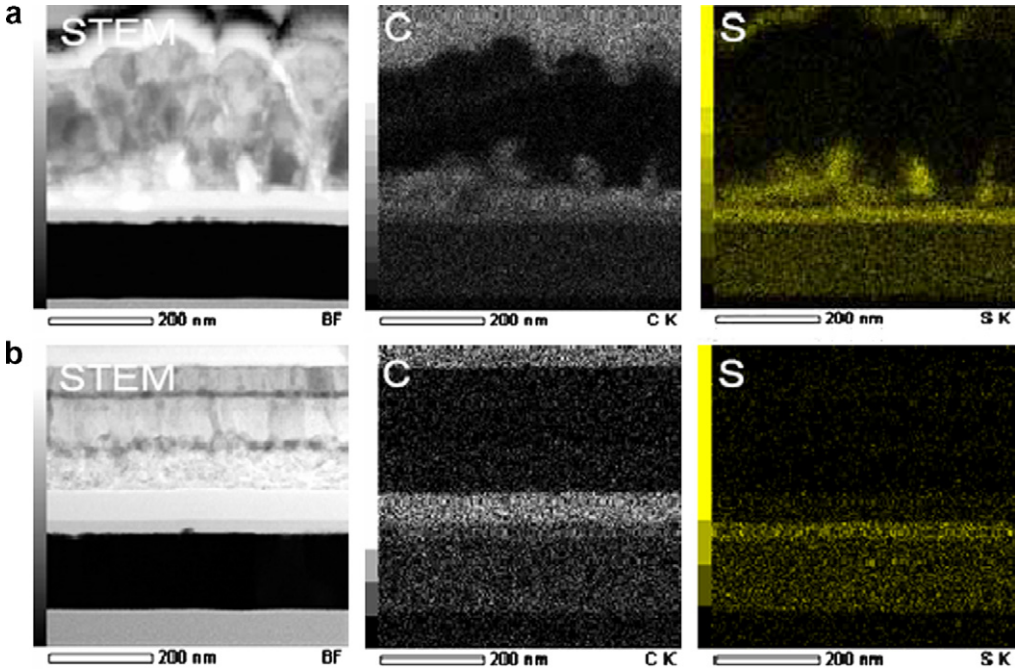

Fig. 11. Cross-sectional TEM-EDX images of STEM, carbon distribution, and sulfur distribution with volume ratios of (a) 6T:C_{60} = 1:1 and (b) 6T:C_{60} = 1:5.

phology approaches the ideal structure, along with improved interface conditions.

One more factor is the Schottky barrier between C_{60} and PEDOT:PSS. Excess C_{60} increases the interface area between C_{60} and PEDOT:PSS, which may result in an increase in the built-in potential.

3.4. MIN type (metal-intrinsic-n type) 6T:C_{60} bulk heterojunction PV cells

In metal Pc:C_{60} bulk heterojunction PV cells, a PIN (p type-intrinsic-n type) structure effectively improves the PV characteristics [22]. It has been reported that the advantage of a blend layer is high charge carrier separation efficiency with an increasing pn junction area, and the disadvantage is a poor carrier transport property due to a complex carrier path. Conversely, a planar pn junction has a smaller junction area but superior carrier transport compared to a blend film. A PIN structure has both advantages and an increase in the built-in potential parallel to the film thickness direction can be expected as well.

We tried to apply a PIN structure to 6T and excess C_{60} (1:5) bulk heterojunction PV cells as was done in the Pc:C_{60} system. This device structure is comprised of ITO/PEDOT:PSS/6T (20 nm)/6T-excess:C_{60} blend (50 nm)/C_{60} (20 nm)/BCP and metal. However, this device did not work well. All photovoltaic properties were inferior to those of devices without the PIN structure (with PCE of 0.24%, Jsc

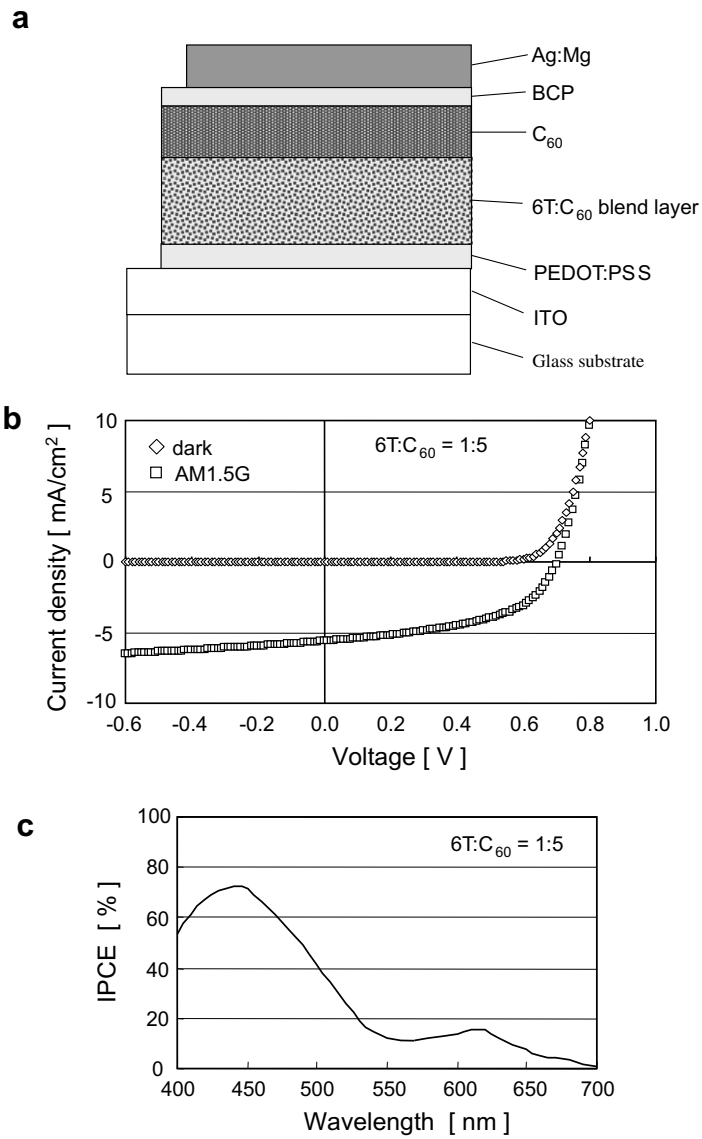

Fig. 12. (a) Schematic device structure of 6T:C_{60} MIN type bulk heterojunction PV cell. (b) Current–voltage characteristics under dark and AM1.5G100 mW/cm^2 for 6T:C_{60} MIN type bulk heterojunction PV cell. The volume ratio of the blend layer is 6T:C_{60} = 1:5. (c) IPCE spectrum of 6T:C_{60} MIN type bulk heterojunction PV cell.

of 1.7 mA/cm^2, Voc of 0.35 V and FF of 0.41 at AM1.5G 100 mW/cm^2). In order to understand this problem, we prepared a "PIM" type (p type-intrinsic-metal) device comprised of ITO/PEDOT:PSS/6T (20 nm)/6T-excess:C_{60} blend (50 nm)/BCP and metal and "MIN" type devices (consisting of ITO/PEDOT:PSS/6T-excess:C_{60} blend (50 nm)/C_{60} (20 nm)/BCP and metal) as shown in Fig. 12a. The PIM device photovoltaic characteristics were even worse than those of the PIN device (with PCE of 0.096%, Jsc of 1.8 mA/cm^2, Voc of 0.16 V, and FF of 0.34 at AM1.5G 100 mW/cm^2).

On the other hand, the MIN devices exhibited better properties than all other type devices. Fig. 12b shows the photovoltaic characteristics: PCE of 2.0%, Jsc of 5.6 mA/cm^2, Voc of 0.7 V and FF of 0.51 at AM1.5G 100 mW/cm^2. In the case of PIM type devices, large reverse current through the PI structure degrades the photovoltaic properties. Further analysis is needed to clarify this matter.

Voc and FF were better in the MIN devices. This improvement may be attributed to the fact that the C_{60} layer functions as an electron transport layer with a hole blocking effect, and serves to reduce interface resistance. Fig. 12c shows the external quantum efficiency (IPCE) of a MIN device. Photo-carrier generation probably occurs mainly in C_{60}. This is because the peak wavelength is around 450 nm, which is almost the same as the C_{60} absorption spectrum. (Fig. 1)

4. Conclusion

We have developed the new small-molecule bulk heterojunction OPV cells with a oligothiophene that is a good hole transport linear small molecule and a fullerene that has a good electron transport property for the first time. Among small-molecule OPV cells, only the Pc:C_{60} system yielded high efficiency and it was difficult to prepare bulk heterojunction OPV cells employing linear molecules, given their tendency to crystallize. Still, we succeeded in making bulk heterojunctions with linear molecules by developing an original process: the excess C_{60} blend method. Furthermore, we found that a MIN structure effectively improves 6T:C_{60} bulk heterojunction cells.

The new OPV cells developed in this study is the promising device in that there is a possibility of improving PV properties moreover with the present evaporation method and employing a higher fullerene.

The photo absorption of a fullerene mainly contributes to the photo current in the excess fullerene blending cells. So we can expect that the photo current increase more than twice by employing high photo absorption fullerene such as C_{70} and C_{84}. And also an oligothiophene is an attractive material in not only the hole mobility but also the controllability of the HOMO and LUMO levels with the design of the substituents. [16] So it's possible to increase Voc moreover by matching the energy levels of the oligothiophene to those of the fullerene.

As for the operation principle, we clarified the relation between the PV characteristics and the blend structure consists of a linear small molecule and a fullerene. Although it is said that the bulk heterojunction OPV cells employing the linear molecule such as an oligothiophen does not operate sufficiently, the cause and mechanism of low characteristics has not been clarified so far. We investigated the relation of PV characteristics and blend morphology, and it was found that the crystallization and making a few hundreds nanometer domains of a small molecule block the exciton dissociation and the charge carrier transport. And the fullerene excess blending prevents from crystallization and forms homogeneous blend morphology. Thereby the PV characteristics were dramatically improved.

We also showed that the blend morphology and such device structures as PIN, PIM, and MIN strongly influence the photovoltaic properties.

The bulk heterojunction OPV cells consist of a linear small molecule and a fullerene become the candidate of the promising OPV cells. However, from now on further analysis by measuring the photo-electron properties such as the intrinsic mobility of blend film will be needed.

Acknowledgements

This work was supported by New Energy and Industrial Technology Development Organization (NEDO) under the research and development of next-generation PV generation system technologies Project.

And we thank Dr. Yuji Yoshida for advice on the XRD analysis of 6T film.

References

[1] P. Peumans, A. Yakimov, S.R. Forrest, J. Appl. Phys. 93 (7) (2003) 3693.
[2] B. Maennig, K. Leo, N.S. Sariciftci, J. Parisi, et al., Appl. Phys. A (2004) 2494.
[3] S. Gunes, H. Neugebauer, N.S. Sariciftci, Chem. Rev. 107 (2007) 1324.
[4] S. Uchida, J. Xue, B.P. Rand, S.R. Forrest, Appl. Phys. Lett. 85 (2004) 4218.
[5] J. Xue, S. Uchida, B.P. Rand, S.R. Forrest, Appl. Phys. Lett. 85 (2004) 5757.
[6] S.R. Forrest, MRS Bull. 30 (2005) 28.
[7] B.P. Rand, J. Xue, S. Uchida, S.R. Forrest, J. Appl. Phys. 98 (2005) 124902.
[8] J. Xue, B.P. Rand, S. Uchida, S.R. Forrest, J. Appl. Phys. 98 (2005) 124903.
[9] T. Taima, K. Saito, et al, IEICE Trans. Elect. 87-C-12 (2004) 2043.
[10] R.C. Haddon, A.S. Perel, R.C. Morris, R.M. Fleming, et al., Appl. Phys. Lett. 67 (1995) 121.
[11] Z. Bao, A.J. Lovinger, A. Dodabalapur, Adv. Mater. 9 (1997) 42.
[12] N. Noma, T. Tsuziki, Y. Shirota, Adv. Mater. 7 (1996) 47.
[13] C. Videlot, A.E. Kassmi, D. Fichou, Sol. Energy Mater. Sol. Cells 63 (2000) 69.
[14] K. Schulze, C.L. Unrich, R. Schuppel, K. Leo, M.P. Pfeiffer, in: SPIE Euro 2006 Event, April, 6192.
[15] P. Liu, Q. Li, M. Huang, W. Pan, W. Deng, Appl. Phys. Lett. 89 (2006) 213501.
[16] C. Uhrich, R. Schueppel, A. Petrich, M. Pfeiffer, K. Leo, E. Brier, P. Kilickiran, P. Baeuerle, Adv. Funct. Mater. 15 (2007) 2991.
[17] S. Nagamatsu, K. Kaneko, R. Azumi, M. Matsumoto, Y. Yoshida, K. Yase, J. Phys. Chem. B 109 (19) (2005) 9374.
[18] R. Azumi, K. Kakiuchi, M. Matsumoto, Bull. Chem. Soc. Jpn. 76 (8) (2003) 1561.
[19] J.Y. Kim, S.H. Kim, H.H. Lee, K. Lee, W.M.X. Gong, A.J. Heeger, Adv. Mater. 18 (2002) 572.
[20] S. Yoo, B. Domercq, B. Kippelen, Appl. Phys. Lett. 85 (22) (2004) 5427.
[21] Y. Sun, Y. Ma, Y. Liu, Y. Lin, Z. Wang, D. Zhu, et al, Adv. Funct. Mater. (2006) 426.
[22] T. Taima, K. Saito, et al, Appl. Phys. Lett. 85 (26) (2004) 6412.

Organic Electronics 9 (2008) 591–601

Contents lists available at ScienceDirect

Organic Electronics

journal homepage: www.elsevier.com/locate/orgel

Effect of end-substitutions of distyryl-oligothiophenes by hexyl chains on environmental stability in organic thin film transistors

C. Videlot-Ackermann [a,*], H. Brisset [a], J. Ackermann [a], J. Zhang [a], P. Raynal [a], F. Fages [a], G.H. Mehl [b], T. Tnanisawa [c], N. Yoshimoto [c]

[a] Ingénierie Moléculaire et Matériaux Fonctionnels, Centre Interdisciplinaire de Nanoscience de Marseille (CINaM), CNRS-UPR-3118, Aix Marseille Université, Campus Luminy, Case 913, 13288 Marseille Cedex 09, France
[b] Department of Chemistry, University of Hull, Hull HU6 7RX, United Kingdom
[c] Graduate School of Engineering, Iwate University, 4-3-5 Ueda, Morioka 020-8551, Japan

ARTICLE INFO

Article history:
Received 23 January 2008
Received in revised form 11 March 2008
Accepted 12 March 2008
Available online 28 March 2008

PACS:
72.80.Le
33.15.−e
85.30.Tv
06.30.Ft

Keywords:
Organic thin film transistor
Organic semiconductor
Stability
Oligothiophene derivative

ABSTRACT

In this study, solution and solid-state properties as well as the organic thin film transistor (OTFT) behaviour of two α,ω-hexyl-distyryl-oligothiophenes (**DH-DS*n*T**, $n = 2, 4$) are presented. The optical and electrochemical properties of the oligomers in solution were investigated by UV–vis absorption and photoluminescence spectroscopies, and cyclic voltammetry. Liquid crystal properties were studied by differential scanning calorimetry (DSC) and optical polarising microscopy (OPM). High-vacuum evaporated thin films were studied by optical absorption, X-ray diffraction and atomic force microscopy (AFM), and implemented as p-type semiconducting layers into organic thin film transistors (OTFTs). The results are investigated to study the influence of alkyl chains on the α,ω-end positions of the distyryl-oligothiophene skeleton (**DS*n*T**). Furthermore, detailed shelf-live tests of hole mobility (μ), threshold voltage (V_t), on current (I_{ON}) and off current (I_{OFF}) under atmospheric conditions (air, temperature) of OTFTs based on **DS4T** and **DH-DS4T** show that the presence of alkyl chains in α,ω-end positions of distyryl-oligothiophenes is detrimental to the environmental stability of OTFTs over time.

1. Introduction

Over the last years, there has been a tremendously increasing interest in organic semiconductors [1]. Such materials find applications as active components in organic thin film transistors (OTFTs), solar cells and organic light-emitting diodes (OLEDs) [2]. OTFTs represent a conventional tool for studying charge transport physics in conjugated compounds, but they also reached the point of now being viable in integrated circuit applications [3]. Indeed organic transistors are expected to play a major role in printed electronics for the fabrication of devices on flexible substrates. Nevertheless in order to ensure manufacturing costs as low as possible, such processes need to be carried out under ambient conditions, which requires the materials and devices to be stable toward exposure to oxygen and moisture. The implementation of complex technologies allowing the fabrication of devices under air-free conditions would certainly lead to dramatically increased costs, thereby limiting the use of organic materials in high through-put production processes. Consequently, in view of the exploitation of organic-based devices in commercial applications, it is of paramount importance that the active materials have sufficient air stability to achieve and maintain useful functional performance characteristics without

* Corresponding author. Tel.: +33 4 91 82 95 88; fax: +33 4 91 82 95 80.
E-mail address: videlot@luminy.univ-mrs.fr (C. Videlot-Ackermann).

1566-1199/$ - see front matter © 2008 Elsevier B.V. All rights reserved.
doi:10.1016/j.orgel.2008.03.007

protective encapsulation. To be fully operative, electronic devices rely on efficient charge transport in a semiconducting material. The most fundamental figure of merit of charge transport is carrier mobility, therefore technological application of conjugated compounds depend on a thorough understanding of what controls carrier mobility in these material and its stability over time.

Recently, we reported a new series of structurally simple and readily available oligothiophene derivatives end-capped with styryl units, **DS*n*T** (n = 2–4), that were used as the semiconducting layer in OTFTs [4]. The devices not only showed very high field-effect mobility (up to 0.1 $cm^2/V\,s$) and on/off ratios (up to 10^5), but were also found to be exceptionally long-lived (more than 1 year of storage) and stable toward continuous operation, under atmospheric conditions. As these conjugated core was shown to lead to long-term stability, we thus decided the synthesize and investigate their di-*n*-hexyl-terminated analogues.

We describe herein the synthesis of two α,ω-hexyl-distyryl-oligothiophenes **DH-DS*n*T** (n = 2, 4) (Fig. 1). The solid-state structural and electronic properties of thin films obtained by high-vacuum evaporation are presented. The main purpose of this study is to delineate the influence of the alkyl chains at the α,ω-end positions of the distyryl-oligothiophene skeleton on OTFT performance and stability, as compared to the parent oligomers **DS2T** and **DS4T**.

2. Experimental part

2.1. Synthesis

Cyclohexane, methylenechloride, toluene, heptane, diethylether, dimethylformamide (DMF), tetrahydrofurane (THF), ethylacetate were purchased from CarloErba and used as received. Silica gel (240–400 mesh) was obtained from Merck. Trimethylphosphite, tri-*p*-tolylphosphine, palladium(II) acetate were purchased from Sigma–Aldrich. Dimethyl-4-*n*-hexylbenzylphosphonate **1** was synthesized as described in literature [5]. 2,2′-Bithienyl-5,5′-dicarboxaldehyde **2** and 2,2′-bithienyl-5-bromo-5′-carboxaldehyde **3** were prepared as reported by Curtis and Phillips [6]. Melting points are uncorrected and were obtained from a Electrothermal 9100 apparatus. ^1H NMR and ^{13}C NMR spectra were recorded on Bruker AC 250 at respectively 250 MHz and 62.5 MHz.

2.1.1. 4-n-Hexylbenzylalcohol

A solution of *p*-*n*-hexylbenzoic acid (1.00 g, 4.85 mmol) in dry diethyl ether (50 mL) was added to a suspension of $AlLiH_4$ (0.18 g, 4.85 mmol) in dry diethylic ether (50 mL). The mixture was refluxed for 6 h and then ethylacetate (7 mL) and water (2 mL) were added. The solid was filtered off and the organic solution was evaporated to give the title compound as an oil which was purified by distillation (0.75 g, 81%). bp = 180–185 °C/0.5 mm Hg. ^1H NMR (250 MHz, $CDCl_3$) δ: 0.81 (t, 3 H, J = 6.50 Hz, CH_3), 1.15–1.30 (m, 6H), 1.40–1.60 (m, 2H), 2.53 (t, 2H, J = 8 Hz, CH_2–C_6H_4), 4.69 (s, 2H, CH_2OH), 7.11 (d, 2H, J = 8 Hz, H_{benz}), 7.21 (d, 2H, J = 8 Hz, H_{benz}).

2.1.2. 4-n-Hexylbenzylbromide

A mixture of *p*-*n*-hexylbenzylalcohol (0.75 g, 3.90 mmol) in PBr_3 (3.17 g, 11.70 mmol) was heated to 80 °C for 10 h. After cooling, water and ice were added carefully and the mixture was extracted with diethylic ether. The organic layer was dried on $MgSO_4$ and solvent was removed under vacuum. The crude product was chromatographed on a silica gel column eluting with a 50:50 (v/v) ethyl acetate:cyclohexane mixture to give the title compound (0.85 g, 85%) as an oil. ^1H NMR (250 MHz, $CDCl_3$) δ: 0.81 (t, 3 H, J = 6.50 Hz, CH_3), 1.15–1.30 (m, 6H), 1.40–1.60 (m, 2H), 2.53 (t, 2H, J = 8 Hz, CH_2–C_6H_4), 4.55 (s, 2H, CH_2Br), 7.08 (d, 2H, J = 8 Hz, H_{benz}), 7.22 (d, 2H, J = 8 Hz, H_{benz}).

2.1.3. Dimethyl 4-n-hexylbenzylphosphonate 1

A mixture of *p*-*n*-hexylbenzylbromide (0.56 g, 2.20 mmol) and trimethylphosphite (3 mL) was refluxed for 6 h. The mixture was concentrated under vacuum to eliminate the excess of phosphite. The crude product was chromatographed on silica gel eluting with ethyl acetate to give the title compound (0.62 g, 85%) as an oil. ^1H NMR (250 MHz, $CDCl_3$) δ: 0.81 (t, 3H, J = 6.50 Hz, CH_3), 1.15–1.30 (m, 6H), 1.40–1.60 (m, 2H), 2.58 (t, 2H, J = 7.50 Hz, CH_2–C_6H_4), 3.14 (d, 2H, J = 21.25 Hz, CH_2P), 3.65 (s, 3H, OCH_3), 3.70 (s, 3H, OCH_3), 7.08 (d, 2H, J = 8 Hz, H_{benz}), 7.22 (d, 2H, J = 8 Hz, H_{benz}).

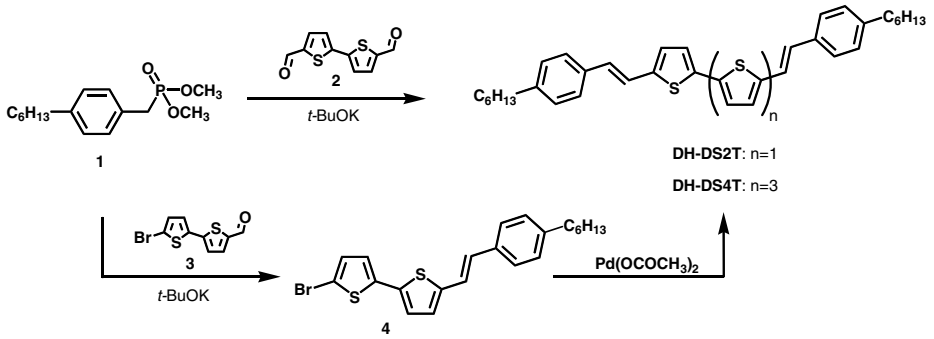

Fig. 1. Synthetic scheme for the **DH-DS*n*T** oligomers.

2.1.4. Typical procedure for Wittig-Horner olefination

2,2′-Bithienyl-5′,5′-dicarboxaldehyde **2** (0.9 mmol) and phophonate **1** (2.07 mmol) were dissolved in 60 mL of anhydrous tetrahydrofurane under argon. To this solution maintained at 0 °C was added *t*-BuOK (4.14 mmol) portionwise and the reaction mixture was stirred for 10 h at room temperature. The solvent was evaporated in *vacuo* and the residue was dissolved in methylene chloride and water was added. The mixture was extracted with methylene chloride. The combined organic extracts were washed with water, dried over $MgSO_4$, and evaporated to dryness. The product was purified on a silica gel column eluting with a mixture methylene chloride–cyclohexane mixture (1:4, v/v). The desired fractions were collected and evaporated to dryness to afford the *E* isomer.

2.1.5. E,E-5,5′-bis(2-(4-hexylphenyl)-ethenyl)-2,2′-bithiophene (DH-DS2T)

Yield: 29%. Mp 203–205 °C. ^{1}H NMR (250 MHz, $CDCl_3$) δ: 0.81 (t, 6H, J = 6.5 Hz, 2* CH_3), 1.0–1.4 (m, 12 H, 2 * $(CH_2)_3$), 1.54 (qui, 4H, 2* CH_2), 2.53 (t, 4H, J = 7.5 Hz, 2* CH_2–C_6H_4), 6.80 (d, 2H, J = 16.00 Hz, H_{eth}), 6.86 (d, 2H, J = 3.25 Hz, H_{thio}), 7.00 (d, 2H, J = 3.75 Hz, H_{thio}), 7.07 (d, 2H, J = 17.75 Hz, H_{eth}), 7.09 (d, 4H, J = 6.75 Hz, H_{ben}), 7.31 (d, 4H, J = 7.5 Hz, H_{ben}). HMRS: calc. 538.2728, found 538.2726. Elemental Analysis calcd for $C_{36}H_{42}S_2$: C, 80.24; H, 7.86; S, 11.90. Found: C, 79.13 (80.11); H, 7.73 (7.82); S, 11.92 (12.04).

2.1.6. 5-Bromo-E,5′-(2-(4-hexylphenyl)-ethenyl)-2,2′-bithiophene (4)

Yield: 57%. Mp 119–121 °C. ^{1}H NMR (250 MHz, $CDCl_3$) δ: 0.81 (t, 3H, J = 6.75 Hz, CH_3), 1.0–1.4 (m, 6 H, $(CH_2)_3$), 1.54 (qui, 2H, CH_2), 2.53 (t, 2H, J = 7.00 Hz, $C\underline{H}_2$–C_6H_4), 6.80 (d, 1H, J = 16.75 Hz, H_{eth}), 6.84 (d, 1H, J = 4.00 Hz, H_{thio}), 6.85 (d, 1H, J = 3.75 Hz, H_{thio}), 6.90 (d, 1H, J = 4.00 Hz, H_{thio}), 6.92 (d, 1H, J = 3.75 Hz, H_{thio}), 7.06 (d, 1H, J = 15.75 Hz, H_{eth}), 7.09 (d, 2H, J = 8.25 Hz, H_{ben}), 7.31 (d, 2H, J = 8.25 Hz, H_{ben}). ^{13}C NMR (67.5 MHz, $CDCl_3$) δ: 12.94 (CH_3), 21.44, 27.81, 30.19, 30.54, 34.57, 119.28, 122.83, 123.61, 125.09, 125.54, 127.58, 127.63, 129.38, 129.49, 132.94, 133.41, 137.84, 141.39, 141.73. UV (CH_2Cl_2) λ_{max} (nm), log ε: 387, 4.55. Fluorescence (CH_2Cl_2) λ_{exi} (nm), λ_{emi}: 377, 456. Mass spectrometry (FAB+) m/z: calc. 432, found 432. Elemental Analysis calcd for $C_{22}H_{23}BrS_2$: C, 61.24; H, 5.37; S, 14.86; Br, 18.52. Found: C, 62.86; H, 5.61; S, 13.80.

2.1.7. E,E-5,5‴-bis(2-(4-hexylphenyl)-ethenyl)-2,2′:5′,2″:5″,2‴-quaterthiophene (DH-DS4T)

A solution of palladium acetate (0.09 mmol) and tri-*p*-tolylphosphine (0.10 mmol) in anhydrous DMF (10 mL) was added to a mixture of compound **4** (1.67 mmol), hydroquinone (1.40 mmol), and cesium carbonate (2.10 mmol). The mixture was deaerated by the freeze-pump-thaw technique [7] and then heated at 70 °C for 4 h. Stirring was maintained for 20 h at room temperature. The solid was filtered off, washed several times with diethyl ether, and continuously extracted using a soxhlet apparatus with heptane and then with toluene. The solid residue was dried and crystallized in chloroform. Yield: 29%. Mp 296–297 °C. ^{1}H NMR (250 MHz, $CDCl_3$) δ: 0.81 (t, 6 H, J = 6.50 Hz, CH_3), 1.0–1.4 (m, 12 H, $(CH_2)_3$), 1.54 (qui, 4H, CH_2), 2.53 (t, 4H, J = 8.00 Hz, CH_2–C_6H_4), 6.80 (d, 2H, J = 16.00 Hz, H_{eth}), 6.87–7.02 (m, 8H, H_{thio}), 7.09 (d, 4H, J = 7.50 Hz, H_{ben}), 7.10 (d, 2H, J = 15.00 Hz, H_{eth}), 7.31 (d, 4H, J = 8.00 Hz, H_{ben}). Elemental analysis calcd for $C_{44}H_{46}S_4$: C, 75.16; H, 6.59; S, 18.24. Found: C, 75.46 (74.85); H, 6.67 (6.62); S, 18.68 (18.53).

2.2. Solution measurements

UV–vis absorption and fluorescence emission spectra were obtained on a Varian Cary 1E spectrophotometer and a Varian Cary Eclipse spectrofluorimeter, respectively. Corrected emission spectra were obtained on diluted solution (CH_2Cl_2, conc. $<10^{-5}$ M) upon excitation at the absorption maximum wavelength.

Cyclic voltammetric (CV) data were acquired using a BAS 100 Potentiostat (Bioanalytical Systems) and a PC computer containing BAS 100 W software (v2.3). A three-electrode system based on a platinum (Pt) working electrode (diameter 0.1 mm), a Pt counter electrode and a Ag/AgCl (with 3 M NaCl filling solution) reference electrode was used. Tetrabutylammonium hexafluorophosphate (TBHP) (Fluka) was used as received and served as supporting electrolyte (0.1 M). All experiments were carried out in anhydrous 1,2-dichlorobenzene (electronic grade purity) at 20 °C. $E_{1/2}$ redox values are determined from the cyclic voltammogram at a concentration of 1×10^{-3} M with a scan rate of 0.25 V s^{-1}. Ferrocene was used as internal standard.

2.3. Liquid crystal measurement

Thermal properties were investigated using a Mettler Toledo differential calorimeter (DSC 822^e) in nitrogen against an indium standard. Transition temperatures were determined as the onset of the maximum in the endotherm or exotherm. The mesophases were studied on an Olympus BH-2 optical polarising microscope, equipped with a Mettler FP82 HT hot stage and a Mettler FP90 central processor. Pictures of the mesophases were taken using a JVC digital video camera connected to a PC. Software *Studio Capture*, supplied by Studio86Designs was used for image capturing.

2.4. OTFTs fabrication

The "top contact" configuration, as described elsewhere [4], was used for the OTFT devices based on **DH-DS*n*T** oligomers. Highly *n*-doped silicon wafers (gate), covered with thermally grown silicon oxide SiO_2 (3000 Å, insulator layer), were purchased from Vegatec (France) and used as device substrates. Trimethylsilyl functionalization of the Si/SiO_2 surface was carried out by dipping the silicon wafers to hexamethyldisilazane (HMDS) solution overnight at room temperature. The capacitance per unit area of either untreated or HMDS-modified silicon dioxide dielectric layers was $1.2–1.3 \times 10^{-8}$ F/cm^2. Organic compounds were vacuum deposited onto the substrates, using a Edwards Auto 306 apparatus, at a rate of 4–7 nm/min under

a pressure of 1–2 × 10^{-6} mbar to a nominal thickness of 50 nm as determined with a in situ quartz crystal monitor. Substrate temperature (T_{sub}) during deposition was controlled by heating the block on which the substrates are mounted. Experimental substrate temperatures (T_{sub}) were fixed to 30, 80 or 110 °C. The Au source and drain electrodes (channel length L = 50 μm, channel width W = 1 mm) were evaporated on top of the organic thin film through a shadow mask. Current–voltage characteristics were obtained at room temperature under ambient conditions with a Hewlett-Packard 4140B pico-amperemeter-DC voltage source. The source-drain current (I_D) in the saturation regime is governed by the equation:

$$(I_d)_{sat} = (W/2L)C_i\mu(V_G - V_t)^2 \quad (1)$$

where C_i is the capacitance per unit area of the gate insulator layer, V_G is the gate voltage, V_t is the threshold voltage, and μ is the field-effect mobility. The on/off ratio values given in Table 2 were determined from the current I_D at V_G = −100 V to the current I_D at V_G = +100 V under a constant drain-source voltage V_D = −30 V. All the data in Table 2 were obtained by randomly measuring 5–7 individual OTFTs for each substrate temperature.

2.5. Thin film measurements

Atomic force microscopy (AFM) measurements were done on thin films in air with a Nanoscope III Multimode (Instrument, Inc.), operating in the tapping mode. Thin films used for AFM and OTFTs measurements are realized during the same organic vacuum evaporation.

Furthermore, thin films of **DH-DS2T** and **DH-DS4T** were analyzed by X-ray film diffractometry (XRD). Thin films were fabricated by vacuum deposition in a pressure of 5 × 10^{-5} Pa using K-cell type crucible. Si wafer (covered by a SiO_2 layer) was used as substrates which were kept at room temperature (30 °C) or 80 °C. The deposition rate was 6 nm/min, the final film thickness varied from 1 to 100 nm. The as-deposited thin films were characterized using X-ray diffraction in air using X-ray diffractometers (Rigaku Co., ATX-G and synchrotron radiation at the BL46XU ATX-GSOR in SPring-8), which were specially designed for characterization of thin films. Both in-plane and out-of-plane diffractions could be measured, because the goniometers have not only conventional $\theta/2\theta$ axes but also in-plane $\phi/2\theta\chi$ axes. The used wavelengths of X-ray in the experiments were 0.1542 nm for lab-source and 0.1000 nm in SPring-8.

3. Results and discussion

3.1. Optical and electrochemical properties

Optical absorption and fluorescence emission spectra of **DH-DS*n*T** oligomers were measured in CH_2Cl_2 solution and data are collected in Table 1. Data of **DS*n*T** (n = 2, 4) oligomers are also reported in Table 1 for comparison. Fig. 2 presents the electronic absorption and fluorescence emission spectra of **DH-DS2T**. For both substituted oligomers **DH-DS2T** and **DH-DS4T,** a weak bathochromic shift of up to 5 nm in absorption/emission maxima in solution is observed compared to the corresponding unsubstituted distyryl-oligothiophenes **DS2T** and **DS4T**, suggesting that the energy difference between the ground and excited states of distyryl-oligothiophene core is poorly sensitive to the hexyl chain substitution. As a consequence, the optical energy gap values (E_g) obtained by extrapolation of the low-energy edge of the UV–vis absorption spectra changes slightly by the introduction of electron-donating hexyl chains on conjugated cores (E_g **DS2T**/**DH-DS2T** = 2.60/2.56 eV; **DS4T**/**DH-DS4T** = 2.37/2.21 eV).

The cyclic voltammetry (CV) data for both oligomers in *o*-dichlorobenzene are listed in Table 1. The CV of **DH-DS2T** presents reversible one-electron oxidation and reduction waves corresponding respectively to the formation of the radical cation and radical anion at redox potential $E_{1/2}$ (ox1) and $E_{1/2}$ (red1), respectively. The comparison of values ($E_{1/2}$ (ox1) **DS2T**/**DH-DS2T** = 0.48/0.41 V; $E_{1/2}$ (red1) **DS2T**/**DH-DS2T** = −2.26/−2.31 V vs. ferrocene) shows that introduction of hexyl chains at the *para*-position of the terminal phenyl rings produces a negative shift of $E_{1/2}$ (ox1) and $E_{1/2}$ (red1) (70 and 50 mV, respectively) attributed to the *+I* inductive effect of the alkyl substituents. As expected in the case of the longest oligomer **DH-DS4T**, the CV contains two successive reversible one-electron oxidation waves corresponding respectively to the formation of the radical cation and the dication. The comparison of oxidation values for **DS4T** and **DH-DS4T** ($E_{1/2}$ (ox1) **DS4T**/**DH-DS4T** = 0.30/0.30 V; $E_{1/2}$ (ox2) **DS4T**/**DH-DS4T** = 0.53/0.48 V) shows that introduction of hexyl chains only affects the second oxidation step. Therefore the magnitude of $E_{1/2}(ox2) - E_{1/2}(ox1)$ that reflects the Coulombic repulsion between positive charges in the dicationic state is smaller in **DH-DS4T** (0.18 V) than in **DS4T** (0.23 V). This means the dication state is reached more easily for **DH-DS4T**. Fig. 3 gives a schematic diagram for the HOMO/LUMO energies of **DS*n*T** and **DH-DS*n*T** series estimated from the relation

Table 1
Optical and electrochemical data for **DS*n*T** and **DH-DS*n*T** oligomers in solution at room temperature

Oligomer	$\lambda_{max,abs}$ (nm)	E_g (eV)	$\lambda_{max,em}$ (nm)	$E_{1/2}$ (ox1) (V)	$E_{1/2}$ (ox2) (V)	$E_{1/2}$ (red1) (V)	HOMO (eV)	LUMO (eV)
DS2T	425	2.60	477	0.48	×	−2.26	−5.32	−2.72
DH-DS2T	430	2.56	482	0.41	×	−2.31	−5.25	−2.69
DS4T	455	2.37	524	0.30	0.53	−2.28	−5.14	−2.77
DH-DS4T	455	2.21	527	0.30	0.48	×	−5.14	−2.93

$\lambda_{max,abs}$: electronic absorption maximum, E_g optical band gap, $\lambda_{max,em}$: fluorescence emission maximum, $E_{1/2}$: electrochemical reduction/oxidation potential.
HOMO energy estimated from the following relationship: HOMO (eV) = −4.84 eV − e$E_{1/2}$ (ox1).
LUMO energy estimated from the following relationship: LUMO (eV) = HOMO + E_g [8].

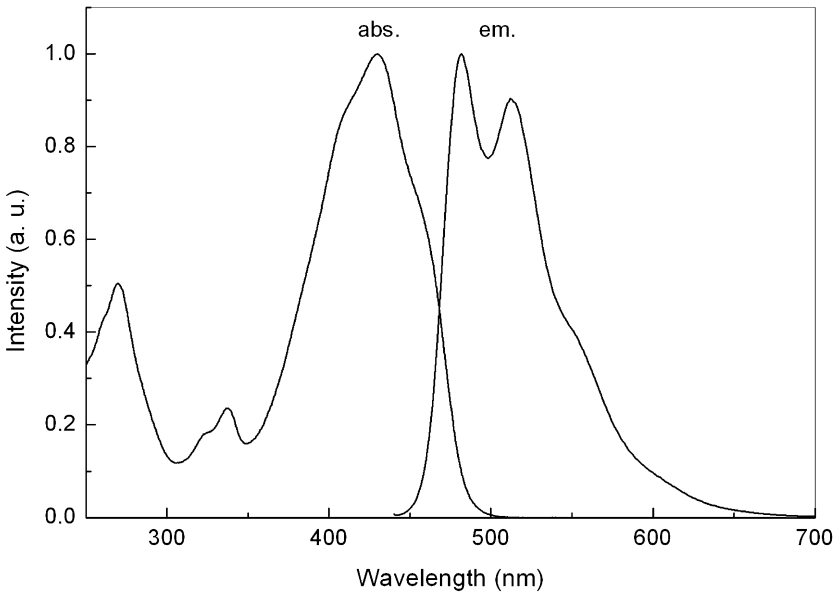

Fig. 2. Electronic absorption (abs.) and fluorescence emission (em.) spectra in solution of **DH-DS2T**.

LUMO = HOMO + *Eg*, where *E*(HOMO) is classically estimated from $E_{1/2}$ (ox) (Table 1) [8]. The analysis of UV–vis and electrochemical data for **DS2T**/**DH-DS2T** and **DS4T**/**DH-DS4T** reveals that hexyl chains increase slightly HOMO and LUMO levels only for **DH-DS2T** to compare to **DS2T**. For **DH-DS4T** compared to **DS4T**, HOMO level is controlled by the oligothiophene core (same oxidation potential for both compounds) and LUMO level by the functionnalization of the styryl group (disappearance of reduction wave for **DH-DS4T**).

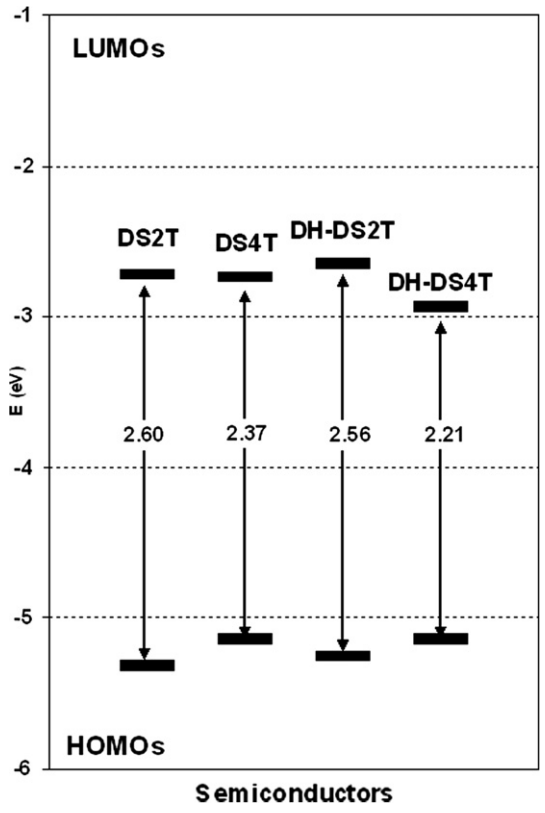

Fig. 3. HOMO and LUMO energy diagram for **DS*n*T** and **DH-DS*n*T** (*n* = 2, 4).

3.2. LC characterizations

The condensed state behaviour of the materials **DH-DS2T** and **DH-DS4T** was investigated by differential scanning calorimetry (DSC) and optical polarising microscopy (OPM) up to 300 °C. **DH-DS4T** undergoes crystal transitions at 166 °C and 197 °C and remains in a crystalline state up to 300 °C (Fig. 4a). **DS4T** shows no transitions up to 300 °C. Compared to **DS2T** which melts at 218 °C into an isotropic liquid and recrystallizes at 214 °C, **DH-DS2T** has the richest polymorphism with reversible crystalline transitions at 140 °C and 210 °C (Fig. 4a). At this temperature the material melts into a SmA phase whose texture displays focal conical defects, as typically observed for a SmA phases. This smectic phase is found stable up to 232.8 °C where a phase transition to a nematic phase, characterized by a *Schlieren* and marbled texture, can be noticed (Fig. 4b and c). At 239.8 °C **DH-DS2T** melts into an isotropic liquid. The transitions are observable on reversing the temperature, however it is noted that the thermal stability of the material in the mesomorphic state is considerably lower than in the crystalline phase. Prolonged annealing in the LC state leads to degradation, detectable as a shift of the transitions to lower temperatures and a colour change of the material. The difference in the self-assembly behaviour can be rationalized easily. Though mesomorphic behaviour for extended linear aromatic systems, such as sexiphenyls is known for many years [9], it

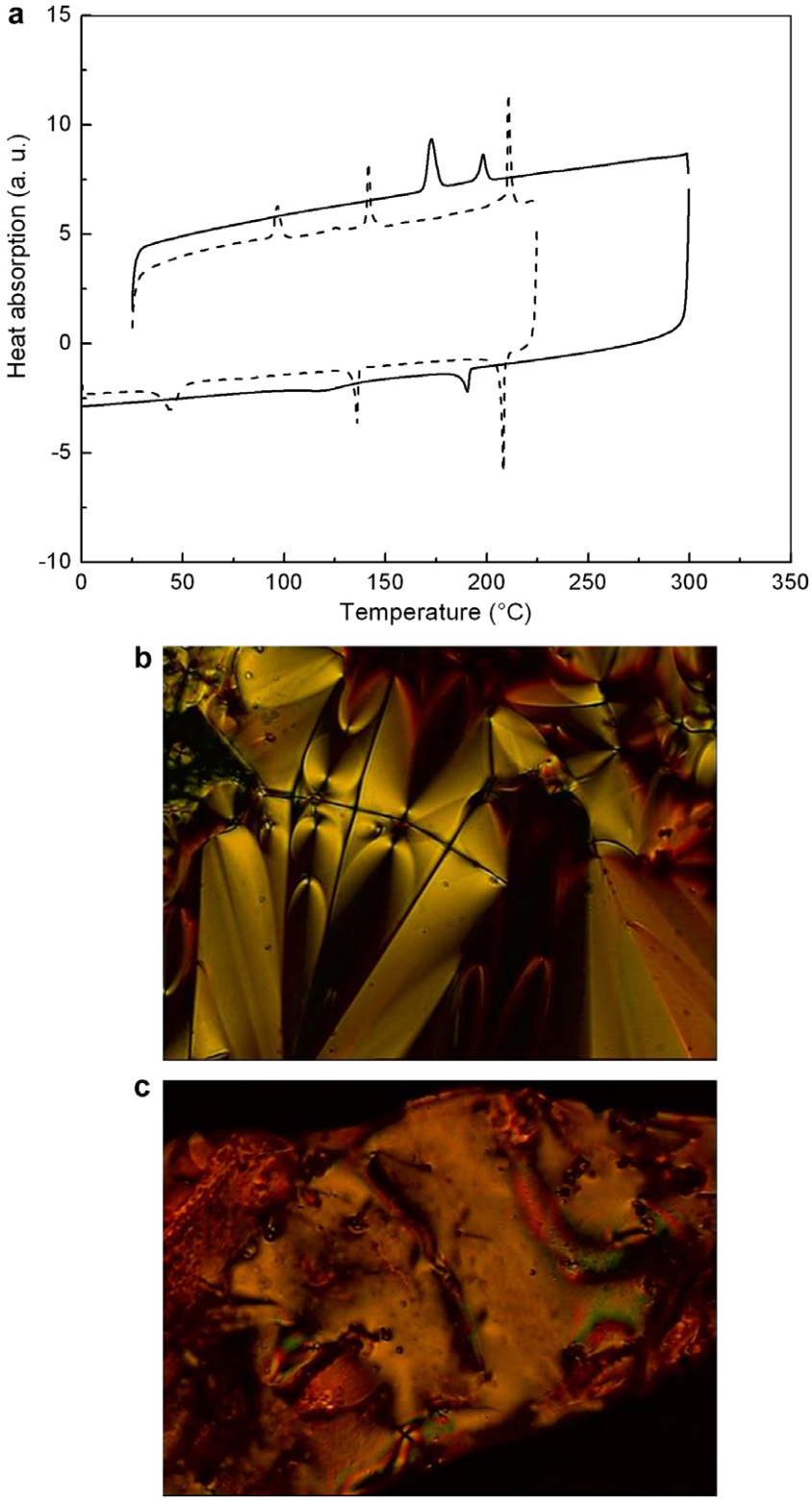

Fig. 4. (a) DSC scan of **DH-DS2T** (dashed line) and **DH-DS4T** (line). Images of focal conical defects of **DH-DS2T** at 216 °C (b) and nematic schlieren texture of **DH-DS2T** at 234 °C (c).

occurs at very high temperatures where degradation of the organic material takes place at well. Functionalization with alkyl chains at the terminal positions of the molecule enhances solubility and lowers the melting points. The

appropriate balance between the length of the aromatic groups and the alkyl chain can lead to mesomorphic behaviour, though organic materials containing more than four aromatic rings with directly connected π-electrons tend to have high transition temperatures. Materials which are structurally related to the systems of this study containing five rings both phenyl and thiophene are known to exhibit unidentified mesomorphic behaviour above 250 °C [10] and for systems incorporating perfluorinated chains a SmA phase ranging between 198 °C and 207 °C has been reported recently [11].

3.3. Thin film microstructure and morphology

The structure and morphology of vapor-deposited **DH-DS2T** and **DH-DS4T** films grown on SiO_2/Si substrate were studied by AFM and XRD. AFM pictures show a polycrystalline morphology where grain size increased with the substrate deposition temperature for both compounds. At T_{sub} = 80 °C, the monolayer terraces are clearly observed for **DH-DS4T** thin films (Fig. 5a), an average value of 4 nm being determined for the steps height. Along with these grains, a large number of needle like grains grown out of the substrates is observed (Fig. 5b) with a higher density as compared to unsubstituted **DS4T** thin films [4]. $\theta/2\theta$ X-ray diffraction spectra of **DH-DS2T** and **DH-DS4T-**based thin films vacuum deposited at 30 °C and 80 °C, respectively, with a nominal thickness of 100 nm reveal that both films are characterized by sharp and strong reflections (Fig. 6a). The peaks are tentatively indexed as (0 0 1) and higher orders which means that the *ab*-planes of the grains are oriented parallel to the substrate surface. Thin films consist of highly oriented poly-crystals having an interplanar *d*-spacings of 3.45 and 4.01 nm for **DH-DS2T** and **DH-DS4T**, respectively. These values commensurate to the molecular length. Fig. 5b shows in-plane GIXD patterns of 1 nm thick-**DS4T** and -**DH-DS4T** films. By comparison with reported crystal structure of oligothiophenes, the peaks observed in Fig. 6b can be indexed as shown in the figure with the corresponding interplanar *d*-spacing [12]. While similar *d*-spacing values are obtained for both **DS4T** and **DH-DS4T** compounds, the observed decrease of *q* values of the 200 peak shows the tendency of a lower in-plane packing density for **DH-DS4T** films as compared to **DS4T**.

The AFM images and XRD data reveal a preferential molecular orientation with the long axes along the substrate normal, where in-plane charge transport would benefit from close π–π stacking. Consequently, the molecular orientation in **DH-DS*n*T**-based thin films is favorable for charge transport across the SiO_2-semiconductor interface in OTFT configuration.

3.4. OTFTs: characterization and stability

Top contact thin film transistors of **DH-DS*n*T** (n = 2, 4) oligomers were fabricated as described in the Experimental part. All measurements were performed in air at room temperature. Table 2 collects the electrical data in terms of mobility (μ), threshold voltage (V_t) and current on/off ratio (I_{ON}/I_{OFF}) obtained with Eq. (1). Transistor responses

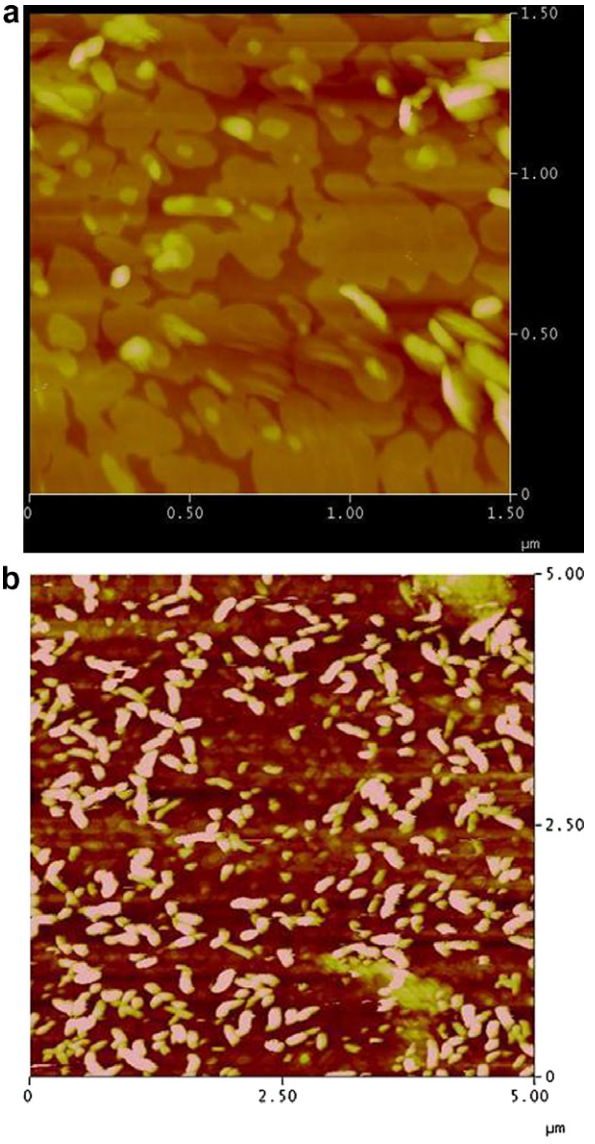

Fig. 5. PAFM picture of **DH-DS4T** thin film deposited on Si/SiO_2 substrate at T_{sub} = 80 °C. (a) Scale 1.5 µm × 1.5 µm and (b) scale 5 µm × 5 µm.

were obtained only for negative bias, which is indicative that both compounds are p-type semiconductors (Fig. 7). The devices work in the accumulation mode with the presence of a well-defined linear regime at $V_D < V_G$ followed by a saturation regime at $V_D > V_G$. The field-effect mobilities calculated in the saturation regime by Eq. (1) for **DH-DS*n*T**-based OTFTs are found to increase when the substrate deposition temperature increased from 30 °C to 80 °C (Table 2). This effect is due to the formation of better ordered thin films at elevated T_{sub} as already observed for such unsubstituted or di-*n*-hexyl-terminated rod-like molecules [13]. Typically on SiO_2/Si substrates heated to 80 °C similar mobilities are obtained. However for the longer α,ω-hexyl-distyryl-oligothiophene **DH-DS4T**, and in contrast to the case of **DS4T**, the field-effect mobilities decrease at high substrate temperature (T_{sub} = 110 °C). By

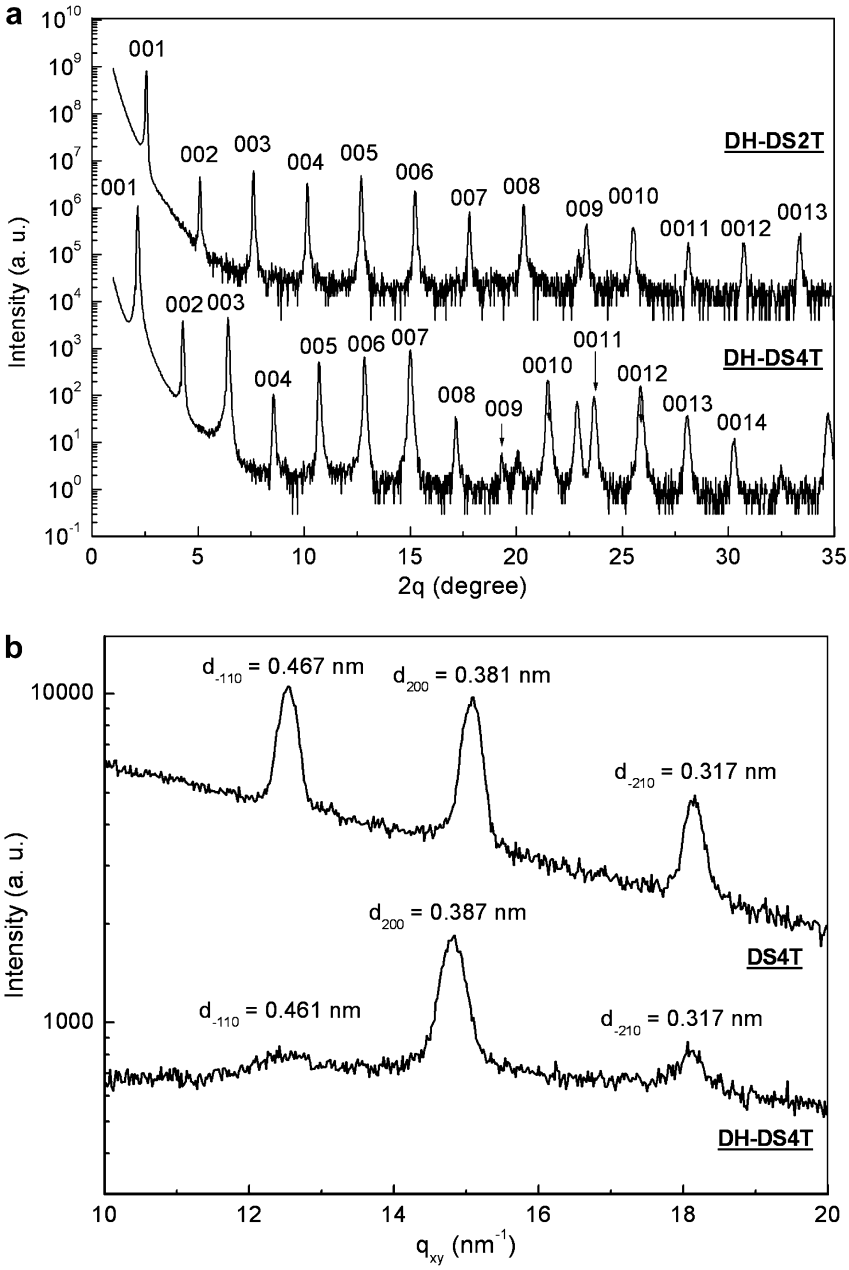

Fig. 6. (a) $\theta/2\theta$ mode of X-ray diffraction patterns of deposited **DH-DS2T** (T_{sub} = 30 °C) and **DH-DS4T** (T_{sub} = 80 °C) films on Si/SiO_2 substrates. (b) In-plane GIXD patterns of deposited **DS4T** and **DH-DS4T** films on Si/SiO_2 substrates.

Table 2
Charge carrier mobility (μ), ON/OFF ratio and threshold voltage (V_t), for OTFTs based on **DH-DS*n*T** oligomers at different substrate temperature (T_{sub}) on untreated and HMDS-treated silicon oxide (SiO_2/Si) substrates.

Oligomer	T_{sub} (°C)	Substrates	μ ($\times 10^{-2}$ cm^2/V s)	ON/OFF	V_t (V)
DH-DS2T	30	SiO_2/Si	1–1.6	0.7–1.3 $\times 10^4$	8–18
	80	SiO_2/Si	1–2.2	0.2–1.6 $\times 10^4$	11–20
		HMDS-treated SiO_2/Si	0.3–1	0.27–3 $\times 10^4$	3.1–15.7
DH-DS4T	30	SiO_2/Si	3–6	0.73–4.2 $\times 10^4$	9–13
	80	SiO_2/Si	5–7.5	0.48–5.8 $\times 10^4$	10–15.5
		HMDS-treated SiO_2/Si	2.4–5	2.7–5.1 $\times 10^3$	3.8–8.3
	110	SiO_2/Si	1–1.3	0.6–3.5 $\times 10^3$	9–15
		HMDS-treated SiO_2/Si	0.8–1.1	0.4–2.3 $\times 10^3$	10–13

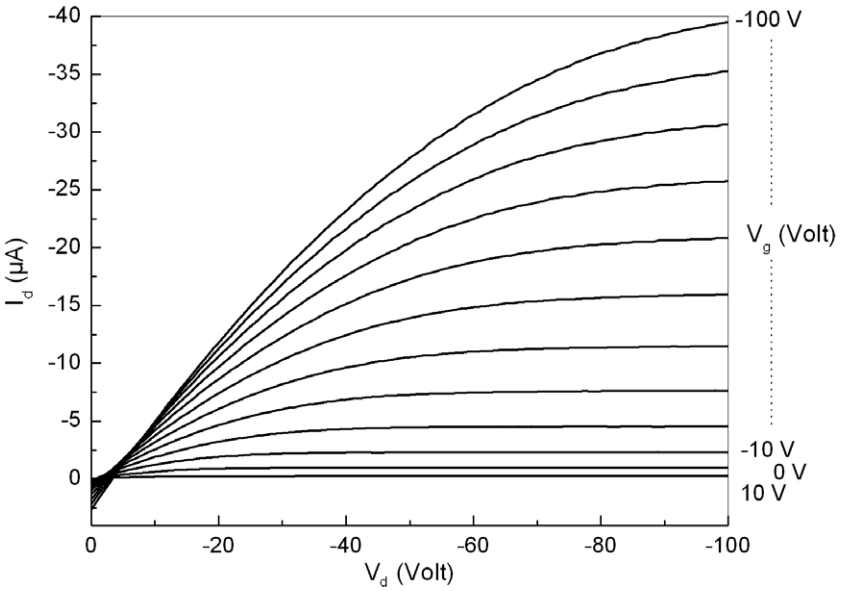

Fig. 7. Output characteristic of an OTFT device fabricated at T_{sub} = 80 °C with **DH-DS4T** on HMDS-treated Si/SiO_2 substrate.

heating the substrate up to 110 °C during the vacuum evaporation of the organic compound, desorption becomes non-negligible for compounds with a lower melting point such as **DH-DS4T** relative to **DS4T**, which impedes the formation of high-quality homogenous thin films. HMDS treatment was observed to improve the mobility and ON/OFF ratio and also to decrease the threshold voltage V_t relative to unmodified samples in the **DS*n*T** family [4]. A different behaviour was observed in the case of the **DH-DS*n*T** family. While the threshold voltage V_t decreases and ON/OFF ratio increases relative to unmodified samples, the average mobility decreases. This observation points out that in the operation of OTFTs charge carrier transport is strongly dependent on the properties of the interface between the semiconductor and the insulator. The physical contact between alkyl and HMDS chains alters the device performances in term of source-drain current (I_d) and mobility (μ).

Furthermore, OTFT devices based on **DS4T** and **DH-DS4T** were stored over 100 days in the dark under ambient conditions and device performances were measured periodically. Fig. 8 illustrates the variation of hole mobility (μ), threshold voltage (V_t), on current (I_{ON}) and off current (I_{OFF}) vs. storage days for OTFTs based on **DS4T** and **DH-DS4T** onto heated SiO_2/Si substrates (T_{sub} = 80 °C). As already reported [4] thin film field-effect transistors incorporating **DS4T** show high electrical performance, such as mobilities as high as 0.1 cm^2/V s, along with exceptional stability under ambient conditions. As shown in Fig. 8, **DS4T** gives rise to devices that show no decrease of hole mobility (μ), threshold voltage (V_t), on current (I_{ON}) and off current (I_{OFF}) after 100 days of storage. By incorporating alkyl chains, identical initial values are measured but such stability features are no longer observed, moderate stability within the 10–20 first days being recorded. While V_t and I_{OFF} remain constants over 100 days, the mobility (μ) and the on current (I_{ON}) show a plateau during the 10–20 first days followed by a decrease of about 95–98% of theirs initial values after 100 days for **DH-DS4T** based OTFTs. Although moderate, such stability was not observed for others oligomers such as octithiophene **8T** [4] and α,ω-hexyl-quaterthiophene **DH4T** [14]. The concomitant decrease of μ and I_{ON} after 20 days is representative of a decrease of device performances due to a lower density of charge carriers transported in the canal.

Several factors can explain the stability of OTFTs. The first parameter considered is the HOMO level which should lie at low-energy to limit the doping by oxygen, one of the causes of environmental degradation. However in the present case, **DS4T** and **DH-DS4T** have the same HOMO levels lying to −5.14 eV. By consequence an equal HOMO level between **DS4T** and **DH-DS4T**, estimated from solution data, is not sufficient to promote equivalent performing compounds as active layer in OTFTs. In the operation of OTFTs, charge carrier transport is especially dependent on structure and morphology of the organic semiconductor in bulk and at the interfaces (semiconductor/metal and semiconductor/insulator). Grain boundaries and defects lead to reduced electronic transport properties. The degradation of organic OTFTs in air is usually attributed to an increase in the density of localized trap density in the HOMO-LUMO gap [15]. The threshold characteristics, especially the carrier mobility, are related to the density of donor-like states with energy near the HOMO level (shallow states). The distribution and the density of donor-like states might be caused by a slight disorder in organic film. Disorder can be introduced by a different growth process which is directly correlated to the chemical structure of the oligomers. Furthermore, the formation and transport of the reactive radical cation oligomers, which are formed during the device operation as charge carriers, usually occur at the semiconductor/insulator interface, deep inside the typically 30–50 nm thick films. Such ion radical species can be readily trapped by nucleophiles as water. As a

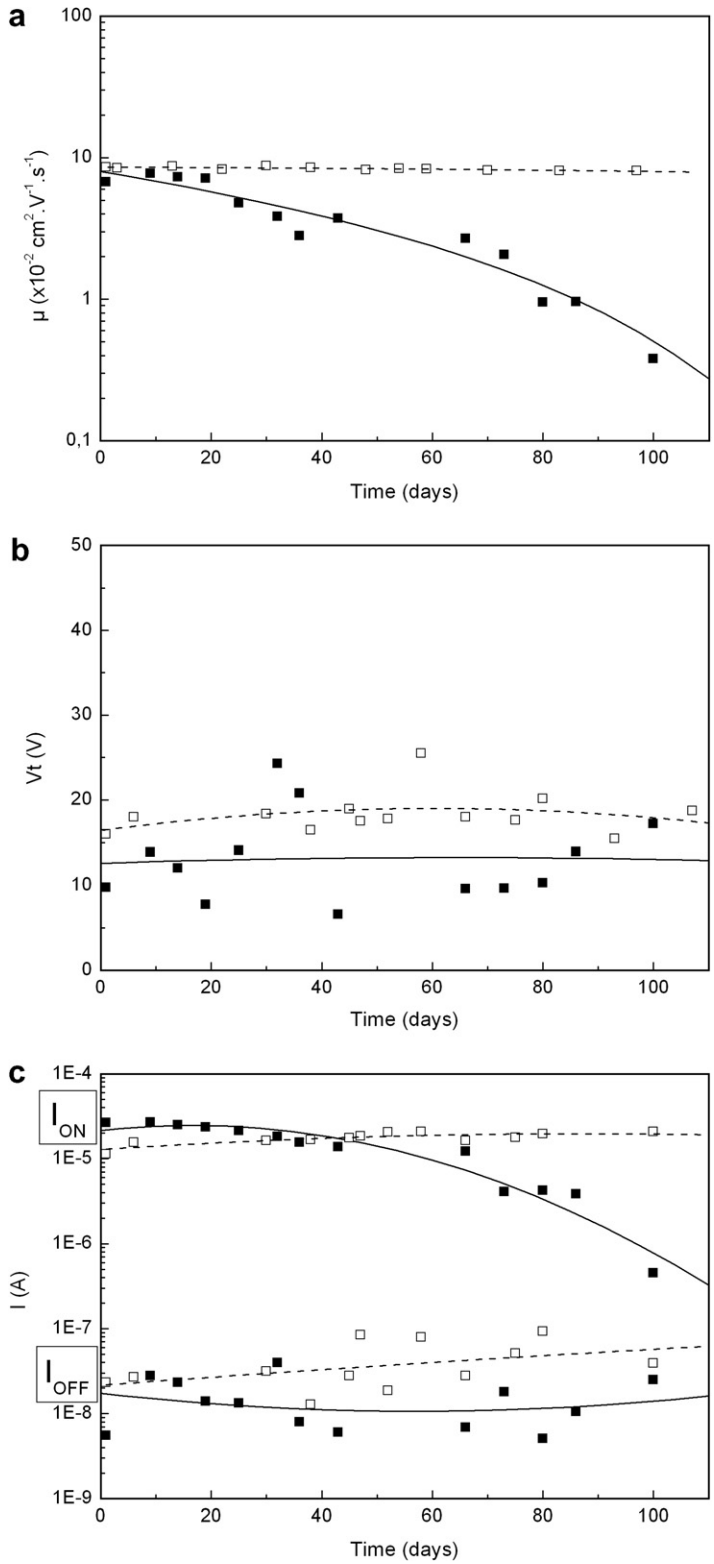

Fig. 8. Plots of hole mobility (μ), threshold voltage (V_t), on current (I_{ON}) and off current (I_{OFF}) vs. storage days for OTFTs on heated untreated Si/SiO_2 substrates (T_{sub} = 80 °C) with active layers based on **DS4T** (open square) and **DH-DS4T** (closed square).

consequence, it is expected that the morphology of the films close to the dielectric interface significantly affects the stability of the transistor during operation in air. The addition of the alkyl chains in α,ω-end positions of distyryl-oligothiophenes strongly alters the stability of OTFTs which is due to a crystalline organization leaving the place to morphological defects. Indeed AFM pictures revealed the presence of numerous needle like grains grown out of the substrates. Furthermore, the presence of alkyl chains and a lower in-plane packing density are additional morphological points likely to lead to a more efficient contaminants diffusion at semiconductor/electrode contacts and semiconductor/insulator interface, resulting in a more rapid degradation. The continuity of **DS4T** films is expected to limit the diffusion of oxygen, water and other contaminants towards the dielectric interface, thus contributing to the stability of the devices in ambient air. The flat shape and large size of **DS4T** islands reduce the density of grain boundaries which act as charge carrier traps, detrimental for charge transport as observed for pentylstyryl-tetracene derivatives to compare to tetracene [16]. These factors explain the higher stability of **DS4T** vs. **DH-DS4T** devices.

4. Conclusion

We have described the synthesis and properties of two new oligothiophene derivatives, α,ω-hexyl-distyryl-oligothiophenes (**DH-DS*n*T**, $n = 2, 4$), that behave as p-type semiconductors. The comparative analysis of the solution and solid-state properties obtained under identical conditions reveals interesting trends with regard to the **DS*n*T** parent series. The main difference is observed on OTFTs properties over time. Unlike the parent compounds **DS*n*T** which were shown to lead to stable OTFTs over very long periods of time under ambient conditions, the hexyl end-substituted compounds give rise to devices with moderate stability at least within the 10–20 first days. Therefore, the remarkable long-term stability observed with **DS*n*T** was not only due to the nature of the distyryl-oligothiophene scaffold itself, but may arise also from other factors, such as solid-state structural properties or different physicochemical properties in bulk and at the interfaces (semiconductor/metal and semiconductor/insulator). Despite the decrease in device stability, the presence of the terminal alkyl chains allows the introduction of new properties such as liquid crystal behaviour and solubility in organic solvents.

Acknowledgements

The synchrotron radiation experiments were performed at the BL13XU and the BL46XU in the SPring-8 with the approval of Japan Synchrotron Radiation Research Institute (JASRI) (Proposal No. 2007A1419/ 2007B1827).

References

[1] A.R. Murphy, J.M.J. Fréchet, Chem. Rev. 107 (2007) 1066.
[2] (a) For a recent account on organic electronics, see the special issue of Chemistry of Materials, Chem. Mater. 16(23) 2004.;
(b) C.D. Dimitrakopoulos, P.R.L. Malefant, Adv. Mater. 14 (2002) 99.
[3] (a) H. Sirringhaus, N. Tessler, R.H. Friend, Sciences 280 (1998) 1741;
(b) H. Sirringhaus, N. Tessler, R.H. Friend, Synth. Met. 102 (1999) 857;
(c) C.D. Sheraw, L. Zhou, J.R. Huang, D.J. Gundlach, T.N. Jackson, M.G. Kane, I.G. Hill, M.S. Hammond, J. Campi, B.K. Greening, J. Francl, J. West, Appl. Phys. Lett. 80 (2002) 1088;
(d) W. Fix, A. Ullmann, J. Ficker, W. Clemens, Appl. Phys. Lett. 81 (2002) 1735.
[4] C. Videlot-Ackermann, J. Ackermann, H. Brisset, K. Kawamura, N. Yoshimoto, P. Raynal, A. El Kassmi, F. Fages, J. Am. Chem. Soc. 127 (2005) 16346.
[5] C. Belluci, F. Gualtieri, A. Chiaini, Eu. J. Med. Chem. 22 (1987) 473.
[6] R.F. Curtis, G.T. Phillips, Tetrahedron 4419 (1967) 23.
[7] A. Afzali, T.L. Breen, C.R. Kagan, Chem. Mater. 14 (2002) 1742.
[8] (a) A. Miura, Z. Chen, H. Uji-i, S. De Feyter, M. Zdanowska, P. Jonkheijm, A.P.H.J. Schenning, E.W. Meijer, F. Würthner, F.C. De Schryver, Chem. Soc. 125 (2003) 14968;
(b) J. Locklin, M.M. Ling, A. Sung, M.E. Roberts, Z. Bao, Adv. Mater. 18 (2006) 2989;
(c) M.-H. Yoon, S.A. DiBenedetto, M.T. Russell, A. Faccetti, T.J. Marks, Chem. Mater. 19 (2007) 4864.
[9] (a) I.C. Lewis, C.A. Kovac, Mol. Cryst. Liq. Cryst. 51 (1979) 175;
(b) D. Vorlaender, Zeit. Phys. Chem. 126 (1927) 144.
[10] (a) S.A. Ponomarenko, S. Kirchmeyer, M. Halik, H. Klauk, U. Zschieschang, G. Schmid, A. Karbach, D. Drechsler, N.M. Alpotova, Synth. Metals 149 (2005) 231;
(b) A. Ponomarenko, S. Kirchmeyer, A. Elschner, N.M. Alpotova, M. Halik, H. Klauk, U. Zschieschang, G. Schmid, Chem. Mater. 18 (2006) 579.
[11] S. Didier, S. Sergyev, Y.H. Geerts, Tetrahedron 63 (2007) 941.
[12] (a) D. Fichou, B. Bachet, F. Demanze, I. Billy, G. Horowitz, F. Garnier, Adv. Mater. 8 (1996) 500;
(b) M. Ito, W.Y. Li, N. Yoshimoto, H. Muraoka, S. Ogawa, H. Fujishiro, Y. Asabe, J. Ackermann, C. Videlot-Ackermann, H. Brisset, F. Fages, in press.
[13] D. Fichou (Ed.), Handbook of Oligo- and Polythiophenes, Wiley-VCH, Weinheim, 1999.
[14] C. Videlot-Ackermann, J. Zhang, J. Ackermann, H. Brisset, Y. Didane, P. Raynal, A. El Kassmi, F. Fages, Curr. Appl. Phys. (2008), doi:10.1016/j.cap.2007.10.087.
[15] (a) D. Knipp, P. Kumar, A.R. Volkel, R.A. Street, Synth. Met. 155 (2005) 485;
(b) H. Klauk, U. Zschieschang, R.T. Weitz, H. Meng, F. Sun, G. Nunes, D.E. Keys, C.R. Fincher, Z. Xiang, Adv. Mater. 19 (2007) 3882.
[16] F. Cicoira, C. Santato, A. Dadvand, C. Harnagea, A. Pignolet, P. Bellutti, Z. Xiang, F. Rosei, H. Meng, D.F. Perepichka, J. Mater. Chem. 18 (2008) 158.

Organic Electronics 9 (2008) 602–608

Contents lists available at ScienceDirect

Organic Electronics

journal homepage: www.elsevier.com/locate/orgel

Electronic structure of highly crystalline polyaniline by study of tunneling conduction in n^+-Si/self-assembled monolayer/polyaniline heterostructures

D.S. Sutar [a,*], S. Lenfant [b], D. Vuillaume [b], J.V. Yakhmi [a]

[a] Technical Physics and Prototype Engineering Division, Bhabha Atomic Research Centre, Trombay, Mumbai 400 085, India
[b] Institut d'Electronique, Micro-electronique et Nanotechnologie – CNRS, Molecular Nanostructures and Devices group, BP 60069, Avenue Poincare, F-59652, Villeneuve d'Ascq cedex, France

ARTICLE INFO

Article history:
Received 3 December 2007
Received in revised form 11 April 2008
Accepted 12 April 2008
Available online 29 April 2008

PACS:
81.16.Dn
72.80.Le
87.64.Dz
73.40.Qv
73.43.Jn
71.20.−b

Keywords:
PANI
Self-assembly
MIS
C-AFM
Tunneling
Electronic structure

ABSTRACT

Highly crystalline polyaniline (PANI) films were deposited on degenerated silicon (n^+-Si) substrates covered with its native oxide (SiO_2), surface modified with amino-silane self-assembled monolayers (SAM). Scanning electron microscopy studies reveal formation of single crystal domains scattered all over the surface of film. Height and current images obtained using current-sensing AFM (C-AFM) exhibit pyramidal topography of crystallites, and inhomogeneous conductivity. As the native oxide and SAM acts as a very thin insulating layer (<2 nm) between the metal-like substrate (degenerated Si) and the PANI film, it forms n^+-Si/SiO_2/SAM/PANI metal-insulator-semiconductor (MIS) heterostructure. C-AFM probe was used for *I–V* measurements on the MIS structures and study the tunneling conduction across it. The conductance spectra derived from *I–V* characteristics corroborates well with the polaron-lattice band structure of doped PANI with presence of polaron bands between the HOMO-LUMO energy gap. These polaron bands are well-resolved from our C-AFM measurements and they are located about 0.25 eV below the LUMO and above the HOMO.

1. Introduction

Conjugated polymers are being investigated as a promising candidate for low-cost organic/molecular electronic applications [1–3]. Recently these conjugated polymers have emerged as a new class due to their self-assembly and novel electronic features [4–6]. Device structures fabricated from these polymers and other small organic molecules exhibit characteristics at par with their inorganic counter parts. In these devices the role played by the self-assembled monolayers (SAM) is of significance. In particular SAMs of alkyl-silanes are being used, as a gate dielectric or as an interfacial layer to influence the structure and morphology of active layer in these devices [4–8].

Of the various candidate conjugated polymers, polyaniline (PANI) has been one of the widely studied conducting polymers. Beauty of this polymer is its proton-doping based on its acid–base chemistry. Protonation does not change the carrier concentration and a local distortion of chemical bonds gives rise to conductivity of polymer. These distortions are commonly referred to as either a

* Corresponding author. Present address: Department of Physics, Indian Institute of Technology Bombay, Mumbai 400 076, India. Tel.: +91 22 25764545.
E-mail address: dssutar23@gmail.com (D.S. Sutar).

1566-1199/$ - see front matter © 2008 Elsevier B.V. All rights reserved.
doi:10.1016/j.orgel.2008.04.007

polaron or bipolaron and in order to explain conductive state of PANI, existence of polaron-lattice has been widely accepted [9–14]. However, there is no experimental report that adequately delineates the electronic or polaronic band structure of doped PANI or emeraldine salt form of PANI. One of the simple approaches to investigate electronic band structure of semiconductors is to study tunneling conductance by forming metal-insulator-semiconductor (MIS) device. However there are hardly any reports of band structure investigation of electronic polymers based on MIS structure.

Recently, we have prepared PANI in highly crystalline form using self-assembly route [15]. Silicon substrates were surface modified using SAM of amino-silane which provides grafting sites for growth of highly oriented crystalline PANI films. In this article, we report electrical measurements on the crystalline PANI films using conductive atomic force microscope (C-AFM). Topographic and current imaging was performed to study the surface topography and electrical homogeneity of the films surface. As the films were grown on insulating alkyl silane monolayer, it acts as a tunneling barrier for electrical conduction between metal-like substrate (degenerated Si) and PANI, and thus forms an ideal MIS structure. We study tunneling conduction in these MIS structures and investigate the electronic band structure of doped crystalline PANI.

2. Experimental

In the present study, SAMs of amino-silane (*N*-[3-Trimethoxysilylpropyl]-ethylene diamine) were grown on (100) oriented n^+-Si substrate covered with its native oxide. PANI was deposited in emeraldine salt form by chemical oxidation of aniline in an aqueous acidic medium. Our synthesis route utilizes the surface-graft polymerization that occurs at the interface between the growing polymer and the aqueous environment. The amino (NH_2) moieties of SAM act as artificial seeds for the growth of PANI and influence the structure and morphology of the PANI films. The details of SAM deposition, synthesis-processing of oriented highly crystalline PANI films and their structural-morphological characterization has been reported in our earlier article [15].

The morphology of the samples was characterized by scanning electron microscopy (SEM, Vega TeScan Digital microscope imaging system) with an accelerating voltage of 10 kV. The current-sensing atomic force microscope measurements were conducted in ambient air using a contact mode C-AFM (Veeco, model Dimension 3100 Nanoscope) equipped with a cantilever (CONT Pt-20 from Nanoworld: It is PtIr5 coated silicon cantilever with thickness 2 μm, length 450 μm, width 50 μm, force constant 0.2 N/m, and tip radius <25 nm). The load force was maintained at 50 nN. The bias was applied on the substrate and the cantilever tip which scans the polymer surface in contact mode was grounded through current amplifier. The topography and current images were recorded with 1 V bias and at a scanning rate of 1 Hz. *I–V* characteristics were measured by the C-AFM amplifier module from Veeco (controlled by the software Nanoscope 5.30). *I–V* characteristics in the voltage range −2 V to 2 V were recorded on crystals of different sizes and at different points on the same crystal. The voltage scan rate was 0.4 V/s.

3. Results and discussion

3.1. Surface morphology and topography

Fig. 1a shows the SEM micrograph of the grown PANI film. It shows well-faceted pyramid shaped crystallites distributed on a textured polycrystalline base layer [15]. Maximum size of the crystallite was about 3-4 microns. One can see that the orientation of all the pyramids is the same, implying that they are in registry with the underlying SAM and hence with the silicon substrate.

Fig. 1b is the schematic representation of C-AFM measurement, showing the MIS structure where the degenerate Si substrate acts as metal and PANI as organic semiconductor separated by thin insulating layer (alkyl SAM and native oxide on Si). It has been well established that the current transport through alkyl silane monolayers separating the electrodes, is a tunneling conduction [16,17]. Due to better order, the inter chain interaction of PANI chains makes the pi-electrons delocalized three-dimensionally, thus leading to band transport as compared to hopping transport in disordered PANI. The topographic image obtained using C-AFM is presented in Fig. 1c, which shows pyramid shaped PANI crystallite seen in SEM micrograph (Fig. 1a). It shows 3D view of pyramidal crystallite when viewed from an angle as illustrated in the background. Concurrently obtained current image with 1 V bias on the substrate is shown in Fig. 1d. The current image shows the crystallite is electrically not homogeneous. This may be also due to variation in the contact resistance between the tip and the PANI during the scan. The current non homogeneity is also clue to the inhomogeneous doping of the crystallized PANI. Similar current heterogeneities have been reported for electrochemically synthesized PANI and other polymers [18,19]. Also bulk of the film showed no current flow. Therefore, the PANI films are not homogeneously doped though they are structurally more ordered. Several measurements showed the bulk of the film (background of crystallites) to be insulating as compared to crystallites.

3.2. Electrical transport in MIS structures

The electrical transport measurements through MIS structure were performed by measuring the *I–V* characteristics at various points on the PANI surface. The *I–V* characteristics were recorded by contacting the Pt/Ir tip on PANI surface. The electrical contact between tip and PANI is expected to be ohmic as both Pt/Ir and doped PANI have similar work-functions (5.1 eV and 5.4 eV, respectively) [20,21]. Fig. 2a displays the typical *I–V* characteristics measured at different points on the films surface. The inset on upper side shows the points where the tip was contacted to perform the *I–V* measurement. The curve A which was measured at point A on the crystallite exhibit almost

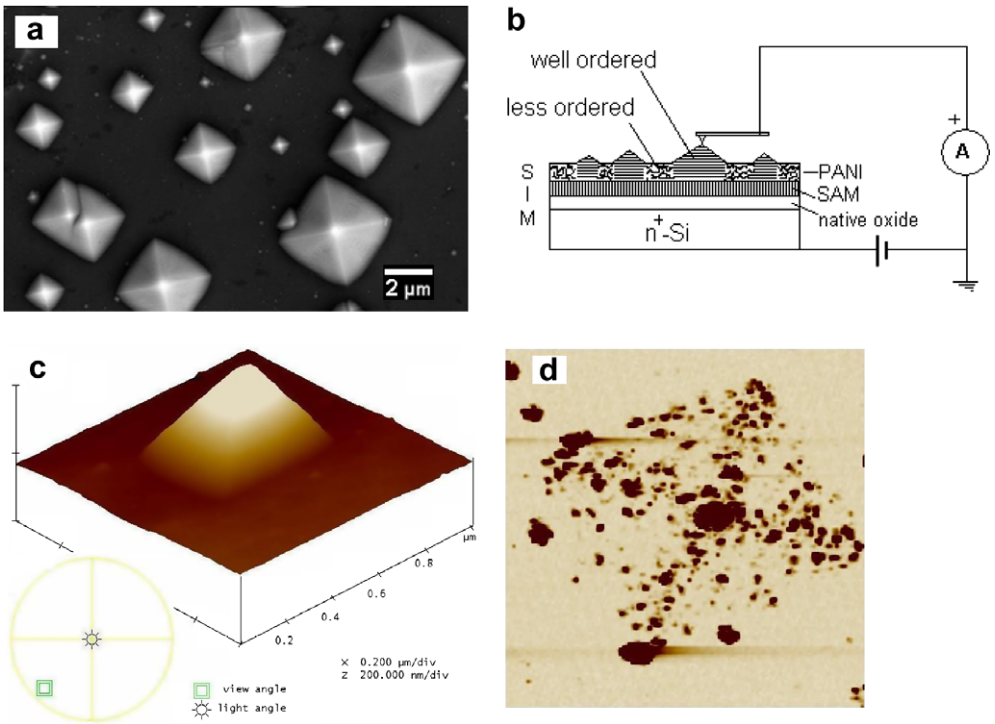

Fig. 1. SEM micrograph showing surface morphology of the PANI film formed on amino-SAM treated silicon surface. (b) Schematic of the measurement circuit. (c) C-AFM 3D topography image obtained using 1 V bias, showing pyramid shaped crystallite. (d) The current image recorded with 1 V bias on the substrate concurrently with the topography image shown in (c); the current range is 50 pA.

symmetric characteristic with an extended plateau suggestive of tunneling conduction through insulating alkyl SAM and a small shoulder in the voltage range 0.3–0.8 V on the positive bias indicative of peak in the tunneling conductance. The conductance spectra obtained from this curve is shown as inset plot of this figure. Data B (measured at the point B, shown in micrograph) shows no current flow in the measured voltage range, indicative insulating nature of this area of the film. Several measurements showed crystallites to be conducting whereas bulk of the film showed no current flow.

Fig. 2b shows plot of current observed at 1 V for different crystallites as a function of their area in contact with the organic SAM i.e., the area of the base of pyramid shaped crystallite. The current increases with size of the crystallites. This suggests that the crystallites act as submicron size pads on the organic monolayer. Thus each crystallite forms a MIS structure and electrical transport across each could be studied using the C-AFM probe to contact the crystallite. The inset of this figure is same data presented as a current density at 1 V. The scatter of almost one order in magnitude is intrinsic due to uncertainties in the size of the crystallites and the inhomogeneous doping. However, from this inset plot, it may be noted that the scatter in current density decreases with increase in crystallites size.

According to Simmons model, the tunneling current density through a barrier in the direct tunneling regime ($V < \phi_B/e$) is given by [22,23]

$$J = \left(\frac{e}{4\pi^2\hbar d^2}\right)\left\{\left(\phi_B - \frac{eV}{2}\right)\exp\left[-\frac{2(2m^*)^{1/2}}{\hbar}\left(\phi_B - \frac{eV}{2}\right)^{1/2} d\right] - \left(\phi_B + \frac{eV}{2}\right)\exp\left[-\frac{2(2m^*)^{1/2}}{\hbar}\left(\phi_B + \frac{eV}{2}\right)^{1/2} d\right]\right\} \quad (1)$$

where m^* is the effective electron mass, d is barrier width, ϕ_B is barrier height, V is applied bias.

As discussed earlier the crystallites act as conducting pads on the organic SAM, therefore, the current density was calculated using the crystallite size. As the I–V data exhibit shoulder on the positive bias, only negative bias data was used for analysis of conduction mechanism. The barrier width d was considered to be 2.23 nm (calculated length of silane molecule is 1.23 nm and native oxide thickness was assumed to be 1 nm). A typical fit to the Simmons model of tunneling conduction through an energy barrier (Eq. (1)), is shown as a solid line in Fig. 2c. We used this procedure to fit all the I–V curves measured on several crystallites and the average parameters obtained from these fits are, barrier height $\phi_B = (2.4 \pm 0.4)$ eV and effective mass $m^* = (0.5 \pm 0.08)\, m_e$ with m_e the electron mass. We observed a reduced dispersion for several I–V measurements on the same crystallite: ±0.14 eV for the barrier height and ±0.05 for the effective mass. The barrier height and effective mass are comparable to other alkyl chain molecular SAMs of similar length on silicon substrates [17,24].

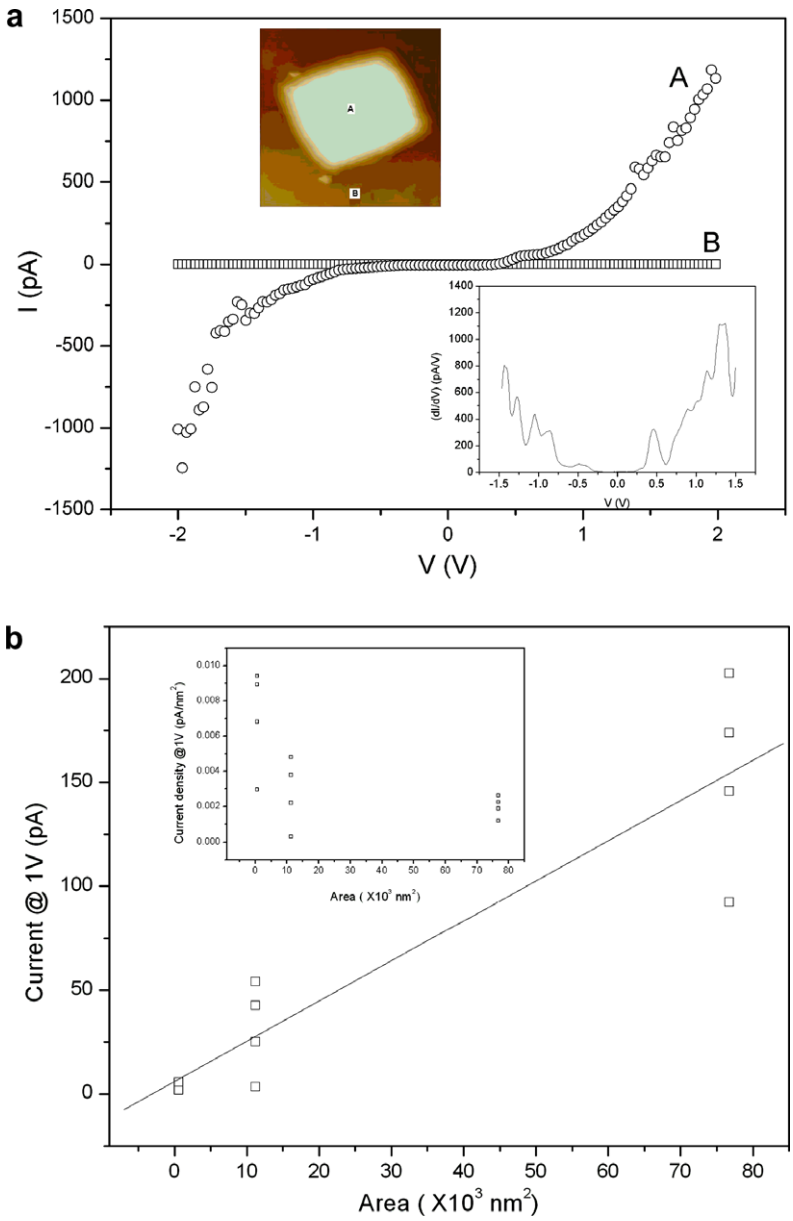

Fig. 2. (a) Typical *I–V* characteristics recorded at different points on the PANI surface. The upper inset is C-AFM micrograph showing points where the tip was contacted for *I–V* measurement. Lower inset plot is the conductance (d*I*/d*V*) spectra derived from curve A. (b) Current at 1 V as a function of size of the crystallite. The inset of this plot is current density at 1 V plotted as a function of size of the crystallite. (c) Current density Vs voltage plot for negative bias; solid line is fit to Simmons model for tunneling conduction. (d) Normalized conductance {(d*I*/d*V*)/(*I*/*V*)} spectra derived from *I–V* data (curve A in (a)).

Scanning tunneling microscopy and tunneling phenomenon in MIS structures has been used as a spectroscopic tool for the investigation of electronic band structure of the semiconductor surface [25,26]. For the MIS structure the presence of thin insulating film make the distance between the metal Fermi level and the conduction band/valence band edge of semiconductor, at the interface dependent on the applied voltage because the voltage drop across the insulating film is dependent on the applied voltage. Thus, by varying the applied bias on the metal electrode (here a role played by the highly degenerated Si substrate) one can obtain detailed information about the electronic band structure of the semiconductor.

Fig. 2d shows the normalized differential conductance (d*I*/d*V*)/(*I*/*V*) spectra numerically derived from *I–V* characteristic (Curve A in Fig. 2a) [27]. It is well known that the normalized differential conductance is a measure of the density of states (DOS). Normalization of conductance accounts for voltage dependence of the tunnel barrier at high bias, therefore, it is suppose to give better representation of DOS than direct derivative [25]. Also, at $V = 0$, the (d*I*/d*V*)/(*I*/*V*) provides a measure of DOS at Fermi level

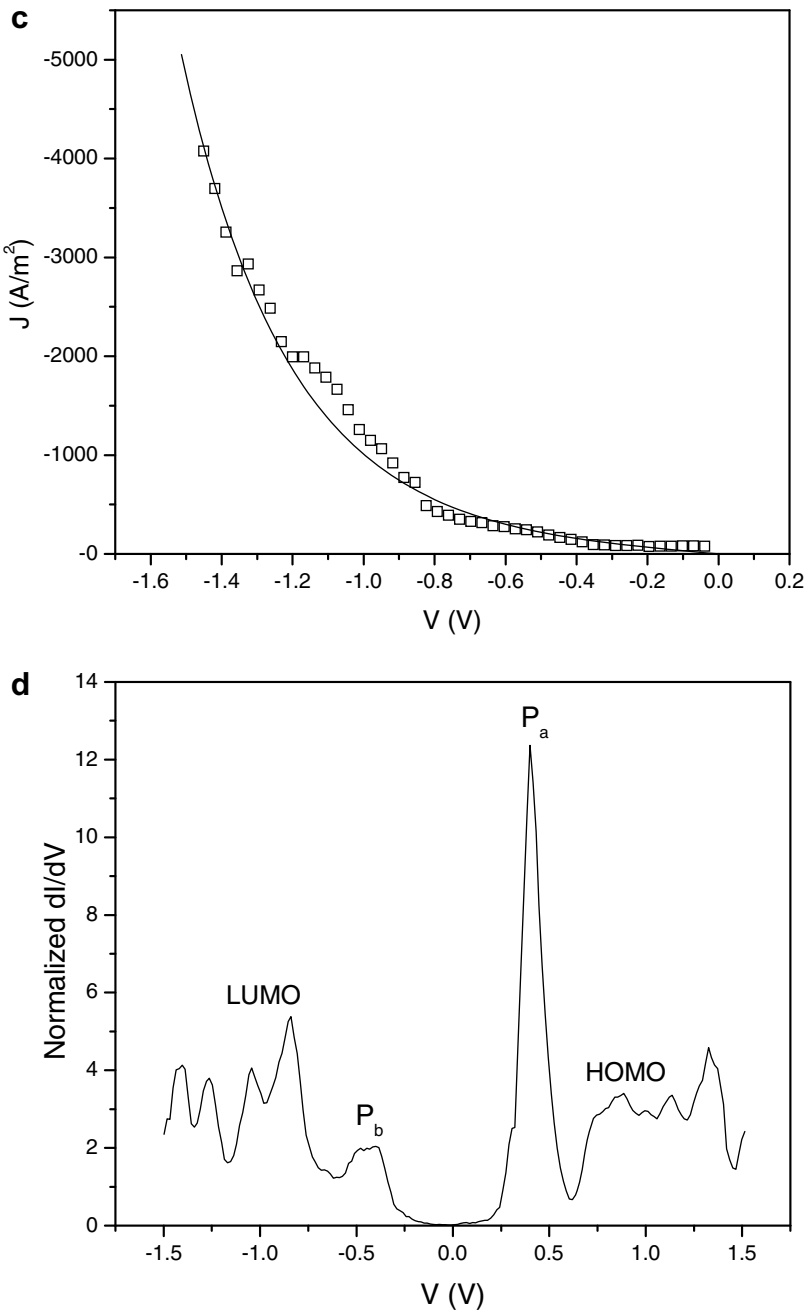

Fig. 2 (*continued*)

(E_f). Many theoretical calculations and experiments based on optical absorption suggest polaron-lattice band structure for PANI's [9–14]. Also, in doped polymers, evidence exists for formation of polarons and narrowing of the energy gap by movement of conduction and valence band states into the gap in response to distortions in the lattice caused by the presence of polarons [4,28]. The normalized differential conductance spectra clearly show the peaks which could be attributed to polaron bands in the conductance gap of HOMO-LUMO. The peak P_a corresponds to lower polaron band and peak P_b corresponds to the upper polaron band. The zero DOS gap is ~0.4 eV and the separation between the HOMO and LUMO is ~1.3 eV. The absence of DOS at the Fermi level (E_f) is indicative of semiconducting nature of crystalline PANI. All the DOS spectra obtained from the other *I–V* characteristics measured on the same PANI island and on other PANI islands show qualitatively similar structure with a conductance gap of ~1.3 eV and presence of mid gap bands attributable to polaronic structure. It may be noted that all the spectra showed

prominent lower polaron band (P_a) and lesser density upper polaron band (P_b) consistent with theoretical calculations on PANI which predict only lower polaron band to be well defined in the gap instead of two bands found in other conjugated polymers [14]. Also, the structure of the conductance spectra is qualitatively similar to earlier reported DOS spectra based on theoretical calculations by Galvao and co-workers [10,11]. In the earlier reported studies based on STM measurements of HCl doped PANI, DOS spectra showed a gap-like structure of ~1 eV width near E_f [29]. However in this case no peaks attributable to polaron bands were observed and as the doped PANI is amorphous, though substantially higher DOS appears in the gap these states are band tail states which are localized in nature. Therefore, clearly observed polaron bands, conductance gap and smaller HOMO-LUMO separation are the features arising from high structural order, increased interchain interaction and true band transport in crystalline PANI. In our study the high quality of crystals and the tunneling conduction in MIS structure both enabled to detect the polaronic features of PANI.

The schematic representation of the energy levels and band diagrams of the MIS structure is shown in Fig. 3. Fig. 3a exhibit equilibrium position of the bands. σ, π and σ^*, π^* are the HOMO and LUMO of the alkyl chain and PANI, respectively. The presence of native oxide decouple the molecular orbital levels of monolayer from the silicon energy levels, therefore, the tunneling barrier height must be a synergetic property of both native SiO_x and the alkyl monolayer [30]. Two additional bands corresponding to polaron bands are shown in PANI structure. As discussed earlier the lower polaron band is shown prominent compared to upper polaron band. The HOMO-LUMO (σ–σ^*) gap for alkyl SAM is estimated from the literature to be of 8.5 eV [31]. As the work function of PANI is ~5.4 eV [21], the HOMO is positioned at 5.4 eV and the LUMO position is estimated to be 4.05 eV using the observed band gap of PANI (1.35 eV) from our *I–V* measurements (Fig. 2d). This means that the interface dipole barrier induced by the SAM and the native oxide is about 0.6 eV. The calculated dipole moment for the amino-silane molecule is about $\mu = 1$D (PM3 calculation using MOPAC) pointing from the amino side towards the silane (see Fig. 3). The corresponding interface barrier is given by $\Phi = N\,\mu\,cos\Theta/\varepsilon$, *where* N is the density of molecule in the SAM, μ the molecule dipole, Θ the angle between the main axe of the molecule and the surface normal and ε the dielectric constant. Taking $N = 5 \times 10^{14}\,cm^{-2}$ (an upper limit for a dense, well-packed SAM), $\Theta = 0$ (ideal case) and $\varepsilon = 2.5$ (usual for organic SAM), we get $\Phi \approx 0.76$ eV in good agreement with our experimental estimation (taking in mind that we do not know the exact contribution of the native oxide). The polarity and strength of bias determines the energy level positions in subsequent band diagrams (Fig. 3b and c). On the application of positive bias on Si, the Si energy levels move down. At very low voltages there are no states in alignment with the Si CB (E_f) and hence the current is negligible. As the voltage increases Si CB (E_f) crosses the lower polaron band the holes from polaron band tunnel in to the Si CB, this reflects as prominent conductance peak. On further increase in voltage the Si CB (E_f) crosses the gap between lower polaron band and the HOMO level. During this the current saturates for a while and then continue to increase exponentially with voltage as holes from π band tunnel into the Si CB. However, with application of negative bias the Si CB (E_f) starts moving up and cross the narrow empty upper polaron band showing as a small conductance peak. Further increase in negative bias leads to exponential increase in current as the Si CB (E_f) aligns with the empty states above LUMO level (π^* band).

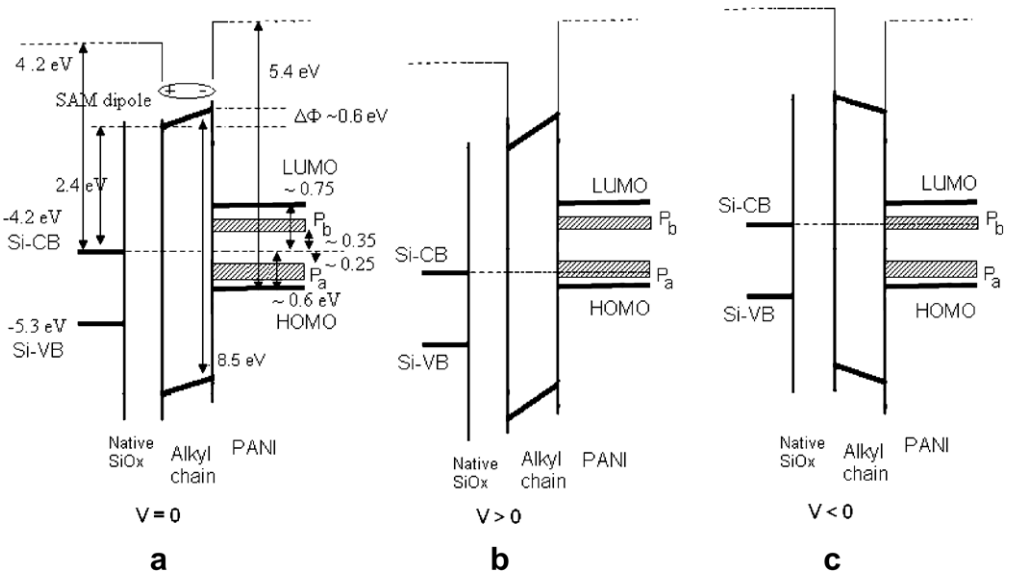

Fig. 3. Schematic representation of electron energy levels and band diagrams for a n^+-Si/alkyl-SAM/single-crystal-PANI (MIS) system: (a) At equilibrium (b) On application of positive bias at n^+-Si (metal-like) substrate (c) On application of negative bias at n^+-Si (metal-like) substrate.

4. Conclusion

The highly crystalline PANI films grown by surface-graft polymerization at the substrate polymer interface were investigated using C-AFM. The PANI films grown on amino-silane modified degenerated Si formed an ideal MIS structure. The single crystallites scattered all over the surface of film act as conductive pads on the insulating alkyl SAM. *I–V* characteristics of these MIS structures were measured and analyzed considering the tunneling conduction through the insulating alkyl SAM. Normalized conductance spectra derived from *I–V* characteristics clearly represents the band structure of PANI with presence of polaron bands in the HOMO-LUMO gap.

Acknowledgments

We would like to thank D.K. Aswal and S.K. Gupta for helpful discussions and support, and Shovit Bhattacharya for SEM. This study was supported by Indo-French Centre for Promotion of Advanced Research (IFCPAR), New Delhi, through their Project No. 3000-IT-1.

References

[1] S.R. Forrest, Nature 428 (2004) 911.
[2] C.D. Dimitrakopoulos, P.R.L. Malenfant, Adv. Mater. 14 (2002) 99.
[3] H. Sirringhaus, Adv. Mater. 17 (2005) 2411.
[4] H. Sirringhaus, P.J. Brown, R.H. Friend, M.M. Nielsen, K. Bechgaard, B.M.W. Langeveld-Voss, A.J.H. Spiering, R.A.J. Janssen, E.W. Meijer, P. Herwig, D.M. deLeeuw, Nature 401 (1999) 685.
[5] Y. Wu, P. Liu, B.S. Ong, T. Srikumar, N. Zhao, G. Botton, S. Zhu, App. Phys. Lett. 86 (2005).
[6] D.H. Kim, J.T. Han, Y.D. Park, Y. Jang, J.H. Cho, M. Hwang, K. Cho, Adv. Mater. 18 (2006) 719.
[7] R.J. Kline, M.D. McGehee, M.F. Toney, Nature Mater. 5 (2006) 222.
[8] D. Vuillaume, J. Nanosci. Nanotechnol. 2 (2002) 267.
[9] S. Stafstrom, J.L. Bredas, A.J. Epstein, H.S. Woo, D.B. Tanner, W.S. Huang, A.G. MacDiarmid, Phys. Rev. Lett. 59 (1987) 1464.
[10] D.S. Galvao, D.A. dos Santos, B. Laks, C.P. de Melo, M.J. Caldas, Phys. Rev. Lett. 63 (1989) 786.
[11] P.A. Schulz, D.S. Galvao, M.J. Caldas, Phys. Rev. B 44 (1991) 6073.
[12] R.P. McCall, J.M. Ginder, J.M. Leng, H.J. Ye, S.K. Manohar, J.G. Masters, G.E. Asturias, A.G. MacDiarmid, A.J. Epstein, Phys. Rev. 41 (1990) 5202.
[13] J.M. Ginder, A.F. Richter, A.G. MacDiarmid, A.J. Epstein, Solid State Commun. 63 (1987) 97.
[14] J. Libert, J.L. Bredas, A.J. Epstein, Phys. Rev. B 51 (1995) 5711.
[15] D.S. Sutar, N. Padma, D.K. Aswal, S.K. Deshpande, S.K. Gupta, J.V. Yakhmi, J. Colloid Interface Sci. 313 (2007) 353.
[16] D. Vuillaume, S. Lenfant, Microelectr. Eng 70 (2003) 539.
[17] A. Salomon, T. Boecking, O. Seitz, T. Markus, F. Amy, C. Chan, W. Zhao, D. Cahen, A. Kahn, Adv. Mater. 19 (2007) 445.
[18] J. Kim, S. Cho, S. Choi, S. Baek, D. Lee, O. Kim, S.-M. Park, M. Ree, Langmuir 23 (2007) 9024.
[19] S.Y. Hong, S.-M. Park, J. Phys. Chem. B. 109 (2005) 93105.
[20] B. Rezek, C.E. Nebel, Diamond Related Mater. 14 (2005) 466.
[21] P. Barta, Th. Kugler, W.R. Salaneck, A.P. Monkman, J. Libert, R. Lazzaroni, J.L. Bredas, Synth. Metals 93 (1998) 83.
[22] W. Wang, T. Lee, M.A. Reed, Phys. Rev. B 68 (2003) 035416.
[23] J.G. Simmons, J. Appl. Phys. 34 (1963) 1793.
[24] D.K. Aswal, S. Lenfant, D. Guerin, J.V. Yakhmi, D. Vuillaume, Anal. Chem. Acta 568 (2006) 84–108.
[25] R.J. Hamers, in: D.A. Bonnell (Ed.), Scanning Tunneling Microscopy and Spectroscopy: Theory, Techniques, and Applications, VCH, Weinheim, 1993, p. 51.
[26] K.C. Kao, W. Hwang, Electrical Transport in Solids, Pergamon Press, Oxford, 1981. (chapter 2).
[27] Conductance was computed numerically in Origin program and then the conductance spectrum was smoothened by five point adjacent averaging.
[28] M. Akai-Kasaya, K. Shimizu, Y. Watanabe, A. Saito, M. Aono, Y. Kuwahara, Phys. Rev. Lett. 91 (2003) 255501.
[29] D. Chaudhuri, S. Datar, R. Vishwanatha, D.D. Sarma, Appl. Phys. Lett. 87 (2005).
[30] D. Vuillaume, C. R. Physique 9 (2008) 78.
[31] L. Segev, A. Salomon, A. Natan, D. Cahen, L. Kronik, Phys. Rev. B 74 (2006) 165323.

Organic Electronics 9 (2008) 609–616

Contents lists available at ScienceDirect

Organic Electronics

journal homepage: www.elsevier.com/locate/orgel

Efficient non-doped pure blue organic light-emitting diodes based on an asymmetric phenylenevinylene with *cis* double bond

Yang Liu [a], Xutang Tao [a,*], Fuzhi Wang [b], Xiangnan Dang [b], Dechun Zou [b], Yan Ren [a], Minhua Jiang [a]

[a] State Key Laboratory of Crystal Materials, Shandong University, Jinan 250100, PR China
[b] Department of Polymer Science and Engineering, College of Chemistry, Peking University, Beijing 100871, PR China

ARTICLE INFO

Article history:
Received 19 December 2007
Received in revised form 17 March 2008
Accepted 28 March 2008
Available online 12 April 2008

PACS:
42.70.Jk
61.66.Hq
78.66.Qn
78.55.Kz

Keywords:
Organic light-emitting diodes
cis-phenylenevinylene
Structure
Pure blue
Non-doped

ABSTRACT

We reported an asymmetric phenylenevinylene with a *cis* double bond 2-(4-(*p*-tolyl)styryl)-1,4-dip-tolylbenzene (*cis*-TSDTB) and its use as efficient deep-blue emitter for organic light-emitting diodes (OLEDs) applications. The crystal structure of *cis*-TSDTB showed torsion configuration and asymmetric geometry, which make it packing in a reduced intermolecular interaction arrangement. And its single crystals showed excellent fluorescence owing to this unique molecular configuration. Typical OLEDs using *cis*-TSDTB as non-doped emitters exhibited saturated blue light with the CIE 1931 coordinates of (0.15, 0.10), which is quite close to the National Television Standards Committee (NTSC) blue standard. High luminescence efficiency (3.4 cd A^{-1}) and high brightness (9855 cd m^{-2}) have been realized in the device. All of these outstanding results indicated that *cis*-phenylenevinylene will be a promising candidate as blue light-emitting materials.

1. Introduction

Up to now, to explore of efficient and color-saturated blue-light emitters has remained the most challenging subject among the three primary emissive colors (red, green and blue) for full-color displays [1]. Owning to the intrinsic characteristic of having a wide bandgap of blue emitters, the dopping methods using suitable blue-emitting dopants is an effective approach to improve device performances; however, the undoped blue emitters are more preferable for the concise fabrication process [2]. Besides efficiency, the color saturation is most important for display applications. In order to display all colors of the visible spectrum, the three primary colors have to be as saturated as possible (that is the color coordinates have to be positioned close to the borders of the color triangle) [3]. It is ideal for the CIE coordinates of blue light-emitting materials to match with the CIE (Commission Internationale de l'Eclairage) coordinates (0.14, 0.08) specified in the NTSC (National Television Standards Committee) standard. Until recently, the reported deep-blue emitters are still rare and many of their efficiencies need to be improved further.[4] Among numerous reported blue-emitting materials, the phenylenevinylene (PV) derivates are in the most attractive ones [5]. The chemical structure of PV derivates can mostly effect their optical properties, especially in the solid state [6], e.g., the classic PPV oligomer, distyrylbenzene and its derivatives [7], exhibit a nice blue fluorescence in dilute solution with a photoluminescence (PL) efficiency up to 90%, but in the solid state the

* Corresponding author. Fax: +86 531 88574135.
E-mail address: txt@icm.sdu.edu.cn (X. Tao).

1566-1199/$ - see front matter © 2008 Elsevier B.V. All rights reserved.
doi:10.1016/j.orgel.2008.03.011

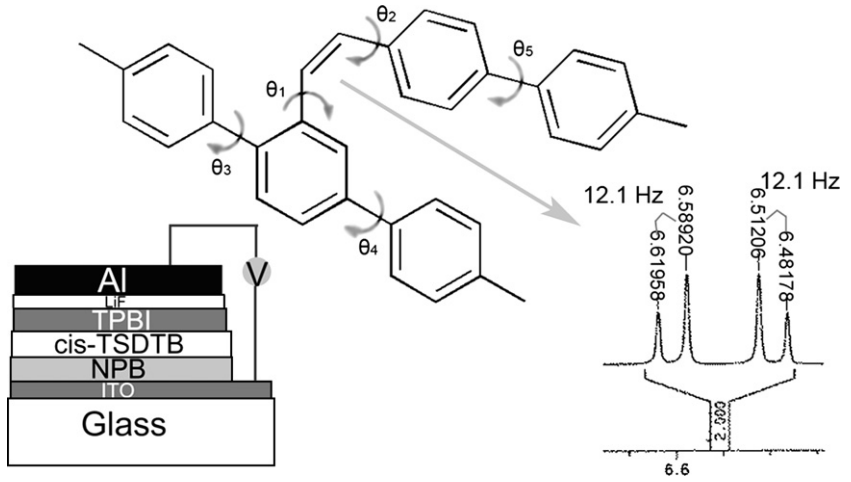

Scheme 1. Molecular structure of *cis*-TSDTB. Right-bottom shows the chemical shift of the *cis*-vinylene. Left-bottom shows one typical device configuration.

fluorescence is strongly quenched. This effect originates from the pronounced π–π interaction encountered in the crystalline lattice of these planar conjugated molecules. This architecture leads to the formation of sandwich-type dimers (H-aggregates) in the ground state and excimers in the excited state, which usually exhibit red-shifted fluorescence and low PL efficiency [8]. Various PV derivatives with different structures have been synthesized for high efficient emission in the solid state [6]. The *cis*-vinylene units in such kind of compounds are generally regarded as *cis*-defects, which usually contribute to weak luminescence [9]. Investigations have been made on the *cis*-conformation [10], whereas, the understanding on the *cis*-vinylene conformation is still incomplete, since the crystal structure with *cis*-vinylene is hard to obtain owing to their lower thermal stability [11]. In this paper, we report an asymmetric phenylenevinylene with a *cis* double bond, which have a excellent solid state fluorescence, and its utility in blue-emitting OLEDs. (As shown in Scheme 1) It is expected that, in virtue of the special conjugation configuration of the *cis*-PV, the induced unique electronic and optical properties will endow them with prospect as light-emitting materials, i.e., the comparatively shorter effective conjugation of *cis*-configuration is prone to produce more saturated blue light and molecules with the asymmetric configuration may have more tendency to adopt unconsolidated packing, which can alleviate intermolecular actions, and subsequently enhance the fluorescence yield and color purity of the solid state. These points were confirmed by following X-ray crystallographic analysis, fluorescence measurement and OLED devices results.

2. Experimental

2.1. Chemicals and instruments

All reagents and starting materials in the synthetic procedures are commercial available and used as received. The TG and DSC were measured on a SDT Q600 V8.0 Differential Scanning Calorimeter under nitrogen atmosphere. ^{1}H NMR and ^{13}C NMR spectra were recorded at 25 °C using Bruker Avance 400 spectrometer. Microanalyses (C,H,N) were performed using a German Vario EL III elemental analyzer. Electrospray mass spectrum (ES-MS) was recorded on a Finnigan LCQ mass spectrograph, and the concentration of the samples was about 1.0 mmol/mL, the diluted solution was electrosprayed at a flow rate of 5×10^{-6} L/min with a needle voltage of 4.5 kV. Electrochemical measurements were used to determine HOMOs of the material with an EG&G model 283 electrochemical system. A platinum-disk working electrode, a platinum-wire auxiliary electrode, and an Ag/AgCl reference electrode were used in a three electrode configuration with 0.1 mol/L Bu4NClO4. The LUMO energy level was calculated by subtraction of the optical band gap from the HOMO energy level. Single-crystal structural analysis was performed on a Bruker APEX2 CCD area-detector diffractometer. By SHELXL-97 program, the structures were resolved with direct method and refined by full-matrix least-squares method on F^2. Absorption measurements were carried out on a TU-1800 spectrophotometer. Photoluminescence (PL) measurements were recorded using a Hitachi F-4500 fluorescence spectrophotometer with a 150 W Xe lamp. PL efficiencies were determined using a solution of quinine sulfate as a standard (ca. 1×10^{-6} M in 0.1 M H_2SO_4, having a quantum yield of 55%). Solvents were purified and dried according to standard procedures.

2.2. Synthesis

The synthetic route to *cis*-TSDTB is shown in Scheme 2.

1-(2,5-dibromostyryl)-4-bromobenzene (*cis*-3Br). This compound was synthesized by a solventless Wittig method. 1.32 g (5 mmol) of 2,5-dibromobenzaldehyde (2BD), 3.33 g (6.5 mmol) of 4-bromobenzyl(triphenyl)phosphonium bromide and 2.8 g (25 mmol) fresh t-BuOK were placed in a dry mortar. The mixture was milled vigorously

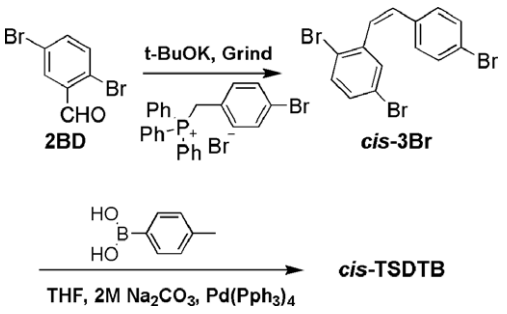

Scheme 2. The synthetic route of *cis*-TSDTB.

for about 15 min. In this process, the mortar was placed on an ice-bag to prevent violent reactions induced by high temperature. Then the mixture was dispersed in 20 mL dichloromethane and was then purified by flash chromatography on silica gel using petroleum/ethyl acetate (20:1) as elutent. 1.88 g of colorless solids was obtained. (Yield 90.2%) ^{1}H NMR (400 MHz, $CDCl_3$, ppm) δ: 6.546 (d, 1H, J = 12.0), 6.631 (d, 1H, J = 12.0), 6.989 (d, 1H, J = 8.3), 7.226 ~ 7.496 (m, 6H). ^{13}C NMR ($CDCl^3$, 100.57 M Hz, ppm) δ: 120.459, 121.268, 121.943, 127.939, 128.258, 128.998, 128.983, 130.733, 131.297, 131.393, 131.485, 132.699, 133.708. Anal. Calcd. For $C_{14}H_9Br_3$: C, 40.33; H, 2.18. Found: C, 40.79; H, 2.18. The ^{1}H NMR spectrum of *cis*-3Br shows chemical shifts at about 6.5 ppm, with a large coupling constant of 12 Hz. This indicates that the vinylene in 1-(2,5-dibromostyryl)-4-bromobenzene is with a *cis*-conformation.

2-(4-(*p*-tolyl)styryl)-1,4-dip-tolylbenzene (*cis*-TSDTB). This compound was synthesized by a Suzuki coupling method. Under argon atmosphere, to a stirred mixture of 0.833 g (2 mmol) of 1-(2,5-dibromostyryl)-4-bromobenzene and 1.63 g (12 mmol) of 4-methylphenylboronic acid in 15 ml THF and 6 ml 2 M Na_2CO_3, 0.05 g of $Pd(PPh_3)_4$ was added. The mixture was heated to 85 °C for 20 h. After cooling, the mixture was poured into water and then extracted with CH_2Cl_2 for three times, washed with water and dried with Na_2SO_4, filtrated and evaporated the solvent. The residue was purified by column chromatography (silica gel, petrol ether/ethyl acetate = 20:1) to give white solids of 0.77 g. (Yield 85%). mp 211 °C. Single crystals of *cis*-TSDTB were growed in petrol ether solutions. ^{1}H NMR (400 MHz, $CDCl_3$, ppm) δ: 2.325 (s, 3H), 2.399 (s, 3H), 2.414 (s, 3H), 6.497 (d, 1H, J = 12.1), 6.604 (d, 1H, J = 12.1), 7.118 (d, 2H, J = 8.0), 7.218 ~ 7.268 (m, 6H), 7.400 ~ 7.528 (m, 10H), 7.568 (d, 1H, J = 1.7). ^{13}C NMR ($CDCl_3$, 100.57 MHz, ppm) δ: 76.206, 76.523, 76.726, 76.841, 125.488, 126.262, 126.301, 128.206, 128.317, 128.890, 128.905, 129.013, 129.315, 129.837, 130.251, 135.450, 135.524, 136.403, 136.431, 136.568, 137.236, 137.298, 137.512, 138.960, 139.313, 139.361. MS (EI) (Calcd for C35H30, 450.61) Found, 450.7. Crystal data for *cis*-TSDTB (C35H30): Mr = 450.59, Monoclinic, space group $P_2(1)/c$, a = 11.971(5) Å, α = 90°, b = 18.163(5) Å, β = 101.051(5) Å, c = 12.311(5) Å, γ = 90°, V = 2627.1(17) Å3, Z = 4, ρcalcd = 1.139 Mg/m3, T = 293(2) K, Crystal size 0.44 × 0.38 × 0.11 mm, R_1 = 0.0746 (wR_2 = 0.2208) [I > 2 sigma(I)].

2.3. Device fabrication and characterization

OLED devices were fabricated by thermal vacuum-deposition under 1.333×10^{-4} Pa. Patterned indium tin oxide (ITO) were cleaned with detergent, de-ionized water, acetone and then de-ionized water in an ultrasonic bath (30 min each cycle), and finally treated in an ultraviolet-ozone chamber. Deposition rates were monitored with a quartz oscillation crystal and controlled at about 0.1 nm/s for organic layers and about 0.5 nm/s for metal layers. The active area of the device was about 4 mm^2. The thickness of films was measured by a Dektak surface profilometer. The EL spectra and current–voltage–luminance (J–L–V) characteristics were measured with a Spectrascan PR 650 photometer and a computer-controlled DC power supply. All the measurements of the devices were carried out under ambient conditions.

3. Results and discussion

3.1. Synthesis and characterization

Scheme 2 shows the synthesis of the asymmetric *cis*-phenylenevinylene 2-(4-(*p*-tolyl)styryl)-1,4-dip-tolylbenzene with a *cis* double bond (*cis*-TSDTB). All of the starting materials are easily available with low cost. Two kinds of classic organic reactions were adopted, Wittig and Suzuki. The product of *cis*-TSDTB was obtained as colorless crystallites in an overall yield of 77%. The molecular structure was identified by ^{1}H NMR, ^{13}C NMR, elemental analysis and electrospray mass spectrum (ES-MS). In the ^{1}H NMR spectrum, the two vinylene protons show the chemical shifts at about 6.5 ppm, (as shown in Scheme 1) with a large coupling constant of 12 Hz. This is the characteristic chemical shift and coupling constant of vinylene protons in the *cis*-configuration [11,12]. Thus, it indicates that the double bond in this compound is *cis*-conformation. It is further unequivocally confirmed by single-crystal X-ray diffraction study.

3.2. Crystal structure analysis

Fig. 1 shows the structure of *cis*-TSDTB and its packing arrangement in single crystal. Besides the *cis*-conformation, another noteworthy feature of this molecule is its torsion configuration. Due to the asymmetric geometry, each torsion angle of the molecule is different. The torsion angles between the double bond and the two adjacent phenyl rings are 36.0° (θ_1) and 49.6° (θ_2), respectively (see Scheme 1). The torsion angles between the phenyl–phenyl bond linked phenyl rings are also large, 56.8° (θ_3), 34.3° (θ_4) and 37.4° (θ_5), respectively. The torsion configuration and the asymmetric geometry are in favor of the molecules keeping non-interactions in the packing motif. As shown in Fig. 1 (down), there are four different orientations of the molecules in each of unit cells, (The figure shows two unit cells) and all the adjacent molecules are in a non-parallel arrangement. Thus, no π–π interaction or other strong intermolecular contacts are observed. This conduces to preventing the aggregation-induced fluorescence-quenching in the solid

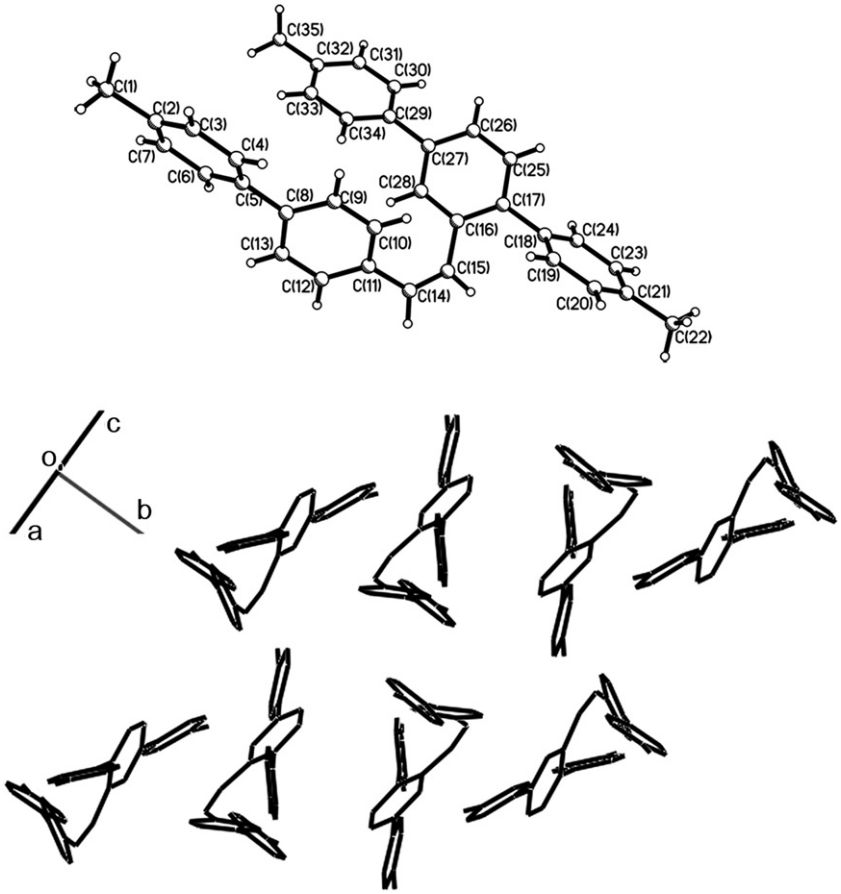

Fig. 1. The X-ray structure and packing arrangement of *cis*-TSDTB. No π–π interactions are observed.

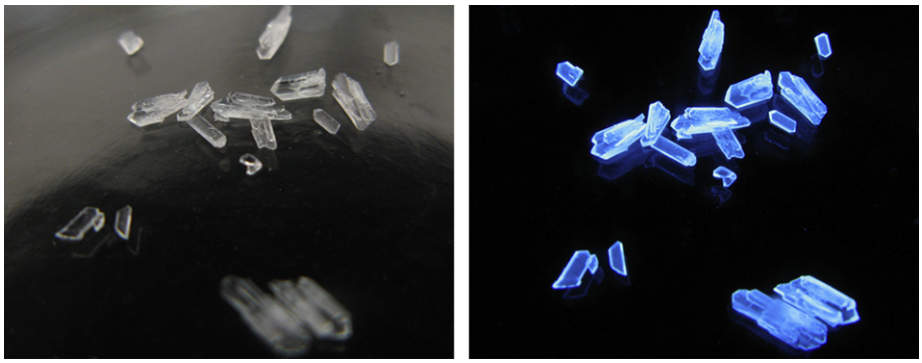

Fig. 2. The pictures of *cis*-TSDTB crystals under natural light (left) and an ultraviolet lamp (right).

state. Fig. 2 shows the picture of *cis*-TSDTB crystals under the illumination of an UV lamp, strong blue light can be seen.

3.3. Photoluminescence and thermal properties

cis-TSDTB showed nice fluorescence in dilute solutions. Violet emissions with peaks at ~380 nm and ~399 nm can be observed in several organic solvents. The photoluminescence (PL) quantum yields can be up to 41% to 60% (details see Table 1). As shown in Fig. 3 and Table 1, the absorption and PL of *cis*-TSDTB exhibit very weak solvent polarity dependences since there are no electron donor or acceptor groups in this compound. Fig. 4 shows the absorption and PL spectra of *cis*-TSDTB in THF solution and thin film. Notably, both the absorption and PL in solutions showed no changes during the course of measurement, even after the solutions being illuminated under UV light for 30 min. (The ^{1}H NMR spectrum presents no changes after being illuminated under UV light for 30 min, which indicates that there are no chemical pro-

Table 1
Optical properties of *cis*-TSDTB in different solvents (5 μM)

Solvent	λ_{max}^{abs} (nm)	λ_{max}^{PL} (nm)	Φ_f
Cyclohexane	285 (325)	397 (377)	0.51
Chloroform	287 (326)	401 (383)	0.41
THF	287 (326)	400 (381)	0.49
Ethyl acetate	285 (324)	398 (378)	0.44
Ethanol	284 (324)	398 (379)	0.60
Acetonitrile	285 (323)	398 (380)	0.35
DMF	289 (327)	402 (387)	0.54

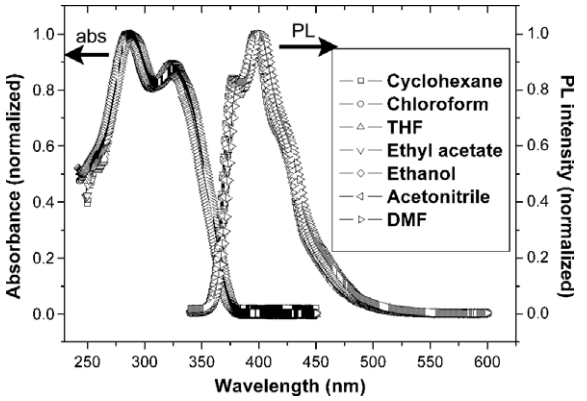

Fig. 3. Normalized absorption and PL spectra of *cis*-TSDTB in different solvents (5 μM).

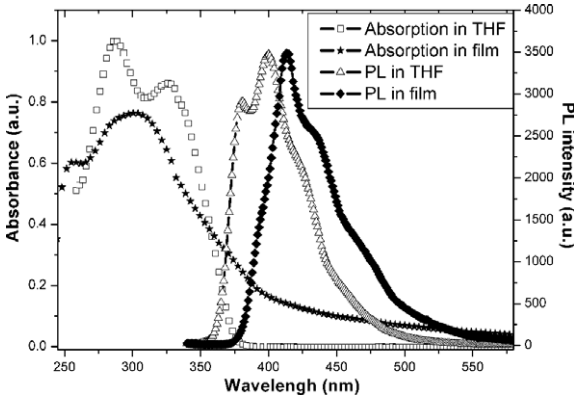

Fig. 4. The absorption and PL spectra of *cis*-TSDTB in THF solution and in thin film.

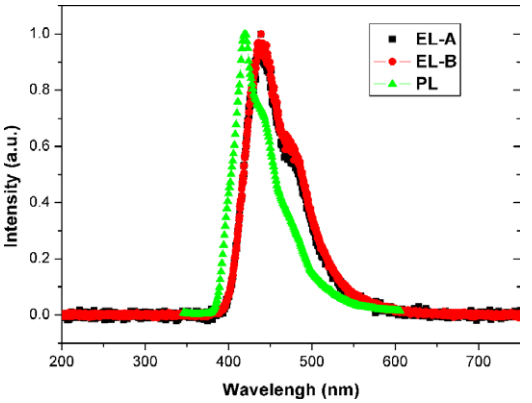

Fig. 6. PL spectrum of the film and the EL spectra of devices. Based on *cis*-TSDTB.

Table 2
EL properties of *cis*-TSDTB based devices

Device[a]	V_{onset} (V)	L_{max} (cd m^{-2})	η_{Lmax} (*cd A*$^{-1}$)	η_{Lmax} (*lm W*$^{-1}$)	CIE (*x*,*y*)	λ_{max}^{EL} (nm)
A	5	8061	2.5	1.9	(0.15, 0.11)	443
	10[b]	745[b]	1.5[b]	0.5[b]		
B	5	9855	3.4	1.9	(0.15, 0.10)	442
	10.75[b]	1468[b]	3.0[b]	0.9[b]		

[a] Configuration A: ITO/NPB(40 nm)/*cis*-TSDTB (30 nm)/BCP (10 nm)/AlQ (30 nm)/LiF (1 nm)/Al (80 nm); configuration B: ITO/NPB(40 nm)/*cis*-TSDTB (30 nm)/TPBI (40 nm)/LiF (1 nm)/Al (80 nm).
[b] At the current density of 50 mA/cm^{-2}.

cesses, such as photoisomerization or photo-cyclization taken place). This Indicates *cis*-TSDTB is stable in solutions. There are two absorption bands in *cis*-TSDTB solution (with peaks at 286 nm and 326 nm), while in film, only one absorption band with peak at ~303 nm appeared. And likewise, the profile of PL in film shows a sharp peak, without the shoulder peak at shorter wavelength. There is a small bathochromic shift, ~14 nm in the PL spectrum of solid film to that of solution. These solid state optical properties facilitate for obtaining more pure blue light. From Fig. 2, we can see the single crystals of *cis*-TSDTB are colorless and transparent, when being excited, strong and saturated blue light was obtained. Such kind of bright, saturated and pure blue crystals are desired for light-emitting and laser applications. The thermal properties of *cis*-TSDTB were

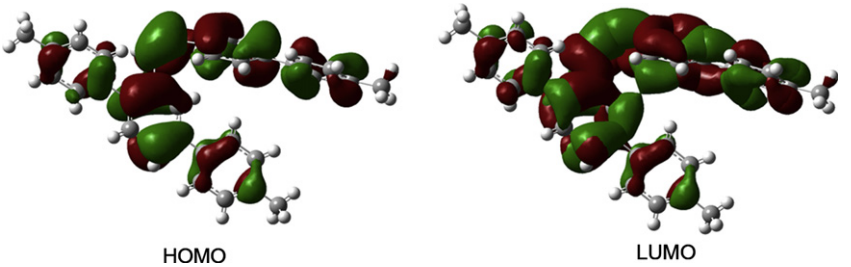

Fig. 5. HOMO and LUMO orbitals of *cis*-TSDTB.

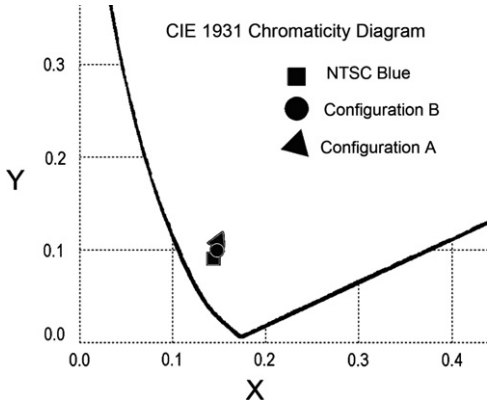

Fig. 7. CIE coordinates of the two configurations along with the NTSC blue.

investigated using differential scanning calorimetry (DSC) and thermogravimetric analysis (TGA). It showed a melting point of 211 °C and a decomposition temperature of ~300 °C. There are no other endothermic or exothermic peaks in DSC curves except the melting and decomposition points, this indicates no other thermal changes during the heating process.

3.4. Quantum chemical studies

To see insightly the effect of the *cis*-vinylene bond on the conjugation of the molecule, HOMO and LUMO orbitals of *cis*-TSDTB were inspected based on a B3LYP/6-31G Gaussian calculation. As shown in Fig. 5, both the HOMO and LUMO distribute mostly along the *cis*-bond, in despite of the terribly bent and tortile conformation of *cis*-TSDTB. Moreover, each of the phenyl rings of the molecule, including the three terminals linked by phenyl–phenyl single bond, has a non-neglectable contribution to the HOMO and LUMO. Such orbital distribution is expected partially related to the asymmetric configuration of *cis*-TSDTB, which has only one double bond on one side of the terphenyl, the limited electrons delocalization ways may produce relatively enlarged HOMO/LUMO, which is believed to be favorable for efficient fluorescence.

3.5. Electroluminescence properties

Employing *cis*-TSDTB as blue-emitting material, typical OLEDs were fabricated by thermal vacuum-deposition. The device configuration was: ITO/NPB (40 nm)/*cis*-TSDTB (30 nm)/BCP (10 nm)/AlQ (30 nm)/LiF (1 nm)/Al (80 nm) (named configuration A) (NPB = 4,4′-bis (1-naphthyl-*N*-phenylamino)-biphenyl, acted as hole transport layer; AlQ = tris(8-hydroxyquinoline)aluminum, acted as electron transport layer; BCP = 2,9-dimethyl-4,7-diphenyl-1,10-phenanthroline, acted as hole-blocking layer). To optimize the device efficiency, TPBI (2,2′,2″-(1,3,5-benzenetriyl)tris [1-phenyl-benzimidazole]), a better electron-transport layer (40 nm) was chosen to replace the BCP/AlQ layers to construct another kind of device: ITO/NPB (40 nm)/*cis*-TSDTB (30 nm)/TPBI (40 nm)/LiF (1 nm)/Al (80 nm) (named as configuration B, as illustrated in Scheme 1).

The devices emitted pure blue light with λ_{max} at ~442 nm. During the measuring process, the naked devices were found to be with good stability. Fig. 6 shows their EL spectra. A redshift of ~20 nm from the PL spectrum in film to the EL spectra was found. A high luminescence efficiency of 2.5 cd A^{-1} (1.9 lm W^{-1}) and a high brightness of 8061 cd m^{-2} were observed for the device with configuration A (details see Table 2). The performance of device using TPBI as electron transport/hole blocking layer was found to be promoted in terms of both efficiency and brightness, which was thanks to a more balanced electron/hole transport. (See the energy-level diagrams of OLEDs components in Fig. 10.) The luminescence efficiency of device with configuration B reached 3.4 cd A^{-1} and a higher brightness of 9855 cd m^{-2} was obtained (see Figs. 8 and 9). At a practical current density of 50 mA/cm^{-2} (with the operating biases of 10 V for configuration A and 10.75 V for configuration B), the devices showed only small decrease efficiency relative to the maximums, with brightness of 745 cd m^{-2} and 1468 cd m^{-2}, luminous efficiencies of 1.5 cd A^{-1} and 3.0 cd A^{-1}, for configuration A and configuration B, respectively. To the best of our knowledge, these results are among

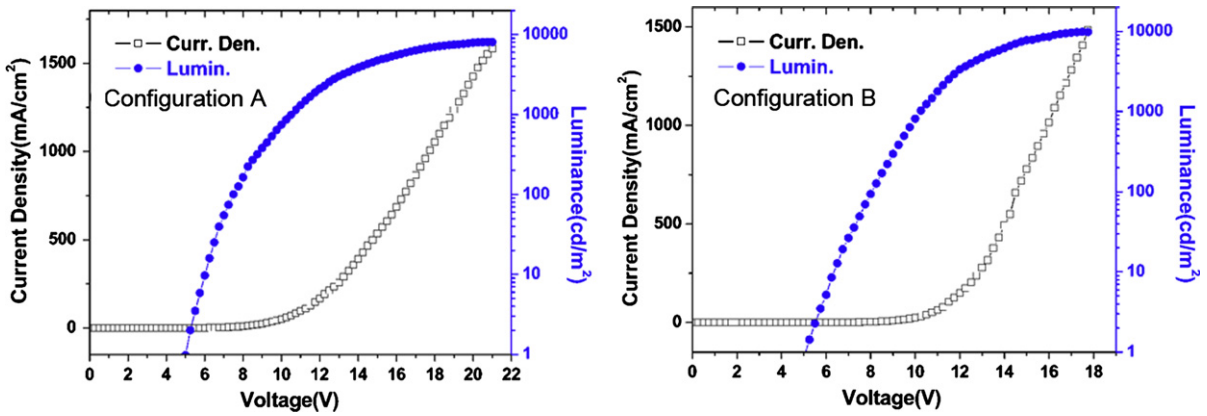

Fig. 8. Current density (*I*)–voltage (*V*) and luminance (*L*)–voltage (*V*) characteristics of devices based on *cis*-TSDTB.

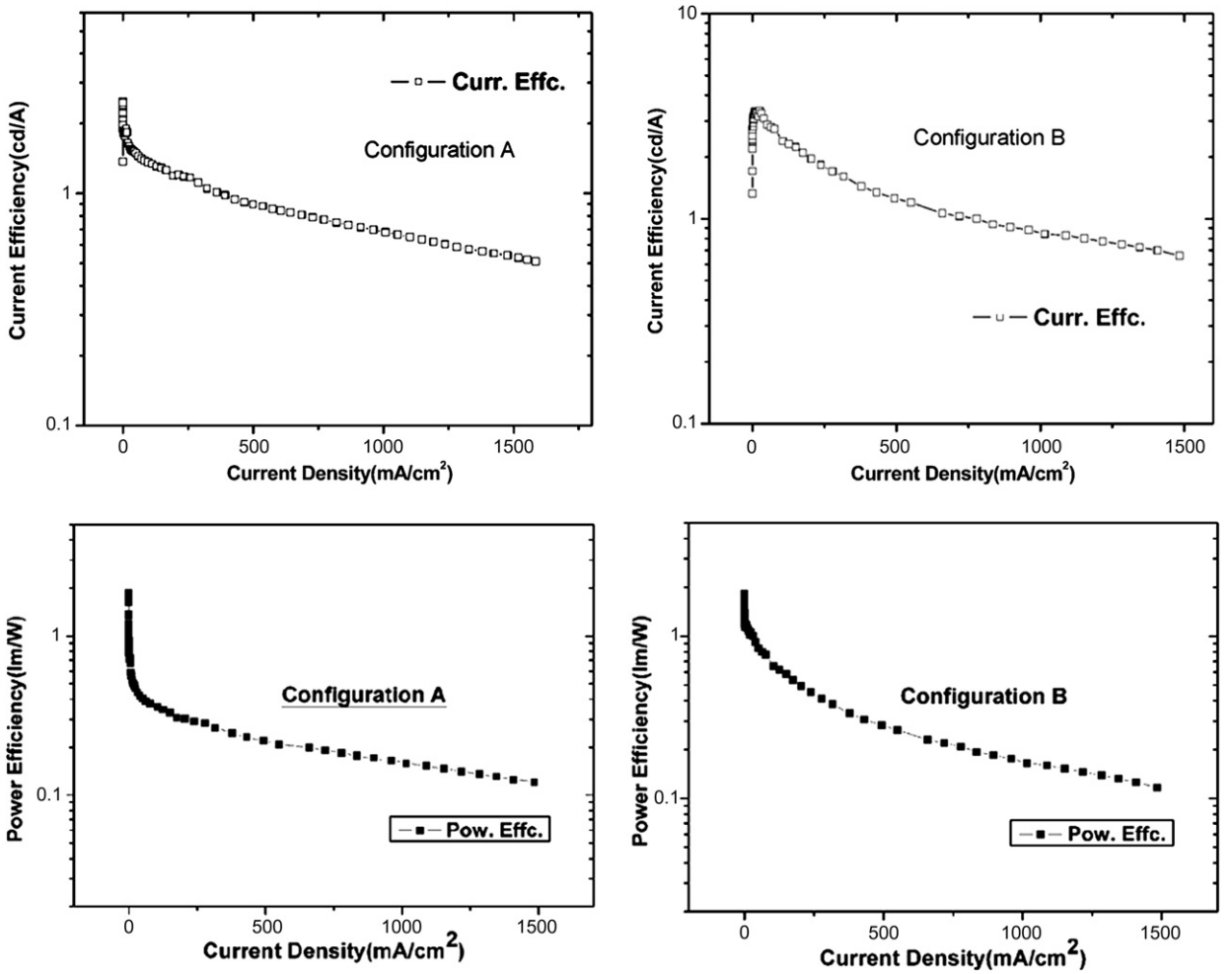

Fig. 9. Current efficiency vs. current density and Power efficiency vs. current density characteristics of devices based on *cis*-TSDTB.

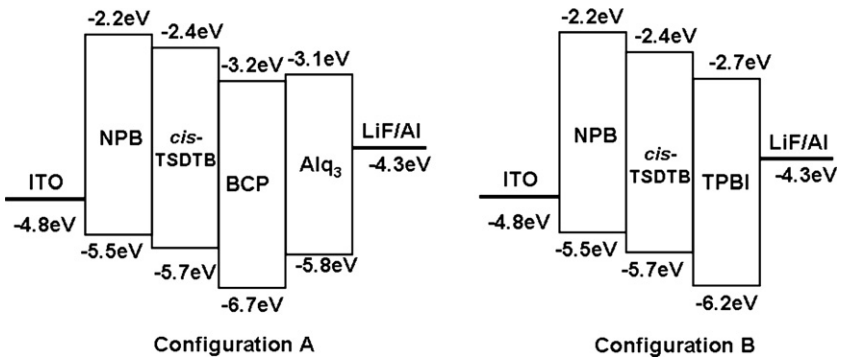

Fig. 10. Energy-level diagram of OLEDs components.

the best records in both terms of brightness and efficiency for oligomeric PPV-based devices [5,11,13]. And it is also comparable to most of the better-known blue-emitters, such as 4,4'-bis(2,2'-diphenylvinyl0-1,1'-biphenyl (DPVBi) of about 1 lm W^{-1} [14]. This indicates the prospect of *cis*-PV as light-emitting materials. Another fascinating characteristic of the *cis*-TSDTB based devices is their pure and saturated blue emissions. Commonly, the PV based blue

OLEDs gave so–so sky blue or greenish blue purity with larger CIE coordinates [5,11,13,15]. Here, owing to the novel *cis*-configuration and the eliminating of π–π interaction packing of *cis*-TSDTB, the CIE coordinates of devices with the two configurations are (0.15,0.11) and (0.15,0.10), respectively, (at the voltage of 10 V), and showed neglectable changes with applied bias. As shown in Fig. 7, both of them located quite close to the NTSC blue standard. This is craving for high performance color displays. The color purity of the *cis*-TSDTB based devices is the best for the phenylenevinylene-based devices in the literature, and can be comparable with the doped ones and the fluorene-based emitters which is well-known for their pure blue emissions [2a,4c,16]. The good performances of the *cis*-PV based OLEDs on color purity, efficiency and brightness demonstrate that the *cis*-configurated PV derivates may be not always as defects of luminescence they were thought to be [9]. More fascinating results are expected by future work on structure design.

4. Conclusion

In conclusion, an asymmetric phenylenevinylene *cis*-TSDTB was synthesized and its structure was determined. The single crystals of *cis*-TSDTB show excellent fluorescence. OLEDs using *cis*-TSDTB as undoped emitters exhibit saturated blue light with the CIE coordinates (0.15,0.10), which is quite close to the NTSC blue standard. This blue color purity is one of the best in phenylenevinylene-based materials. High luminescence efficiency (3.4 cd A^{-1}) and high brightness (9855 cd m^{-2}) indicated the *cis*-phenylenevinylene will be a promising candidate for blue light-emitting materials. Additionally, the outstanding fluorescence in crystals may render it a promising candidate for organic laser materials.

Acknowledgments

We are grateful for financial support from the National Natural Science Foundation of China (Grant No. 50325311, 50603011) and 973 program of PR China (2004CB619002), and also the NSF and 973 programs of the People's Republic of China (90401028, 50673003).

References

[1] (a) S.W. Wen, M.T. Lee, C.H. Chen, IEEE/OSA J. Display Technol. 1 (2005) 90;
(b) S.R. Forrest, Org. Electron. 4 (2003) 45.
[2] (a) S. Tao, Z. Peng, X. Zhang, P. Wang, C.-S. Lee, S.-T. Lee, Adv. Funct. Mater 15 (2005) 1716;
(b) K. Danel, T.-H. Huang, J.T. Lin, Y.-T. Tao, C.-H. Chuen, Chem. Mater. 14 (2002) 3860.
[3] T. Jü stel, H. Nikol, C. Ronda, Angew. Chem. Int. Ed. 37 (1998) 3084.
[4] (a) M.-H. Ho, Y.-S. Wu, S.-W. Wen, M.-T. Lee, T.-M. Chen, C.H. Chen, K.-C. Kwok, S.-K. So, K.-T. Yeung, Y.-K. Cheng, Z.-Q. Gao, Appl. Phys. Lett. 89 (2006) 252903;
(b) Y.H. Kim, D.C. Shin, S.H. Kim, C.H. Ko, H.S. Yu, Y.S. Chae, S.K. Kwon, Adv. Mater. 13 (2001) 1690;
(c) Y.F. Zhang, G. Cheng, Y. Zhao, J.Y. Hou, S.Y. Liu, S. Tang, Y.G. Ma, Appl. Phys. Lett. 87 (2005) 241112;
(d) C. Tang, F. Liu, Y.-J. Xia, J. Lin, L.-H. Xie, G.-Y. Zhong, Q.-L. Fan, W. Huang, Org. Electron. 7 (2006) 155;
(e) R.C. Chiechi, R.J. Tseng, F. Marchioni, Y. Yang, F. Wudl, Adv. Mater. 18 (2006) 325;
(f) B.Z. Tang, X.W. Zhan, G. Yu, P.P.S. Lee, Y.Q. Liu, D.B. Zhu, J. Mater. Chem. 11 (2001) 2974;
(g) L.H. Chan, R.H. Lee, C.F. Hsieh, H.C. Yeh, C.T. Chen, J. Am. Chem. Soc. 124 (2002) 6469;
(h) C.C. Wu, Y.T. Lin, K.T. Wong, R.T. Chen, Y.Y. Chen, Adv. Mater. 16 (2004) 61;
(i) Y. Li, M.K. Fung, Z. Xie, S.T. Lee, L.S. Hung, J. Shi, Adv. Mater. 14 (2002) 1317;
(j) W.L. Jia, T. McCormick, Q.D. Liu, H. Fukutani, M. Motala, R.Y. Wang, Y. Tao, S. Wang, J. Mater. Chem. 14 (2004) 3344;
(k) T. Oyamada, C.-H. Chang, T-C. Chao, F.-C. Fang, C.-C. Wu, K-T. Wong, H. Sasabe, C. Adachi, J. Phys. Chem. C 111 (2007) 108.
[5] (a) C. Hosokawa, H. Higashi, H. Nakamura, T. Kusumoto, Appl. Phys. Lett. 67 (1995) 3853;
(b) F. He, H. Xu, B. Yang, Y. Duan, L.L. Tian, K.K. Huang, Y.G. Ma, S.Y. Liu, S.H. Feng, J.C. Shen, Adv. Mater. 17 (2005) 2710.
[6] (a) S. Wang, W.J. Oldham, R.A. Hudack, G.C. Bazan, J. Am. Chem. Soc. 122 (2000) 5695;
(b) T. Gu, G. Accorsi, N. Armaroli, D. Guillon, J.F. Nierengarten, Tetrahedron Lett. 42 (2001) 2309.
[7] (a) P.M. Ruiz, B. Behnisch, K.H. Schweikart, M. Hanack, L. Ler, D. Oelkrug, Chem. Eur. J. 6 (2000) 1294;
(b) H.K. Ryu, W.Y. Kim, K.S. Nahm, Y.B. Hahn, Y.S. Lee, C. Lee, Synth. Met. 128 (2002) 21.
[8] F. Wurthner, C. Thalacker, S. Dieke, C. Tschierske, Chem. Eur. J. 7 (2001) 2245.
[9] (a) K.F. Won, M.S. Skaf, C.Y. Yang, P.J. Rossky, B. Bagchi, D. Hu, J. Yu, P.F. Barbara, J. Phys. Chem. B 105 (2001) 6103;
(b) Y.S. Chen, H.F. Meng, Phys. Rev. B 66 (2002) 035202.
[10] (a) M.A. Summers, P.R. Kemper, J.E. Bushnell, M.R. Robinson, G.C. Bazan, M.T. Bowers, S.K. Buratto, J. Am. Chem. Soc. 125 (2003) 5199;
(b) L. Liao, L.M. Ding, F.E. Karasz, Y. Pang, J. Polym. Sci., Part A: Polym. Chem. 42 (2004) 303.
[11] Z.Q. Xie, B. Yang, G. Cheng, L.L. Liu, F. He, F.Z. Sheng, Y.G. Ma, S.Y. Liu, Chem. Mater. 17 (2005) 1287.
[12] (a) Y. Ito, Y. Uozu, T. Dote, M. Ueda, T. Matsuura, J. Am. Chem. Soc. 110 (1988) 189;
(b) S. Jacobs, W. Eevers, G. Verreyt, H.J. Geise, Synth. Met. 61 (1993) 189.
[13] (a) M.R. Robinson, S. Wang, G.C. Bazan, Y. Cao, Adv. Mater. 12 (2000) 1701;
(b) F. He, G. Cheng, H.Q. Zhang, Y. Zheng, Z.Q. Xie, B. Yang, Y.G. Ma, S.Y. Liu, J.C. Shen, Chem. Commun. (2003) 2206.
[14] K.O. Cheon, J. Shinar, Appl. Phys. Lett. 81 (2002) 1738.
[15] Y. Duan, Y. Zhao, P. Chen, J. Li, S.-Y. Liu, F. He, Y.-G. Ma, Appl. Phys. Lett. 88 (2006) 263503.
[16] M.H. Ho, Y.S. Wu, S.W. Wen, M.T. Lee, T.M. Chen, C.H. Chen, K.C. Kwok, S.K. So, K.T. Yeung, Y.K. Cheng, Z.Q. Gao, Appl. Phys. Lett. 89 (2006) 252903.

Organic Electronics 9 (2008) 617–624

Contents lists available at ScienceDirect

Organic Electronics

journal homepage: www.elsevier.com/locate/orgel

Device operation of organic tandem solar cells

A. Hadipour, B. de Boer, P.W.M. Blom *

Molecular Electronics, Zernike Institute for Advanced Materials, University of Groningen, Nijenborgh 4, NL-9747 AG Groningen, The Netherlands

ARTICLE INFO

Article history:
Received 24 October 2007
Received in revised form 14 March 2008
Accepted 21 March 2008
Available online 4 April 2008

Keywords:
Organic solar cells
Tandem solar cells
Device physics

ABSTRACT

A generalized methodology is developed to obtain the current–voltage characteristic of polymer tandem solar cells by knowing the electrical performance of both sub cells. We demonstrate that the electrical characteristics of polymer tandem solar cells are correctly predicted for both the series and parallel connection of the sub cells. The agreement with experiments allows us to investigate the effect of a reduced open-circuit voltage, short-circuit current or fill factor in one of the sub cells on the performance of the tandem cell. A low fill factor in one of the sub cells leads to a stronger reduction of the efficiency in a series configuration as compared to the parallel tandem device.

1. Introduction

In order to make relatively cheap solar cells for large-area applications, organic materials are promising candidates. However, the narrow absorption properties combined with low charge carrier mobilities limit the performance of the organic solar cells [1,2]. One way to improve the absorption of organic solar cells is by using tandem (or multi-junction) structures [3–10]. Because of the different band gap of the active layer each sub cell then absorbs light in a different part of the solar spectrum. In order to further optimize the performance of organic tandem solar cells, it is important to understand their operation. The ability to predict the performance of tandem cells, either in series or parallel configuration, from the performance of the individual sub cells will strongly reduce the experimental work needed to reach the optimum device structure. In order to understand the electrical properties of a tandem organic solar cell, we consider here a tandem cell that is based on two sub cells with totally different electrical properties. In this general case, the bottom cell generates a higher current, but lower voltage as compared to the top cell. The presented methodology demonstrates how the electrical characteristics of tandem cells that are either connected in series or parallel, can be predicted from the characteristics of the sub cells.

In order to compare the calculated results with experiment, a 4-electrode tandem cell is used in which the bottom and top cells are separated by an optical spacer [9] (inset Fig. 5). The use of such a device structure has two advantages; first, because of the presence of 4 electrodes the *J–V* characteristics of the individual bottom and top cell as well as the tandem cell can be measured in one single device. Second, since the sub cells are electrically separated, both the series and parallel configuration can be measured within the same device. In this way the test conditions are exactly the same for all cells. In Fig. 1 the current–voltage characteristics are shown for a tandem cell based on a 250 nm blend of regioregular poly(3-hexylthiophene) (rr-P3HT) and the fullerene derivative [6,6]-phenyl-C_{61}-butyric acid methyl ester (PCBM) for the bottom cell and a 80 nm blend of poly(2-methoxy-5-(3′,7′-dimethyloctyloxy)-*p*-phenylene vinylene) (MDMO-PPV) and PCBM for the top cell. An optical spacer with a thickness of 190 nm was used to separate the sub cells. The question now is how the *J–V* characteristic of a tandem cell based on those two sub cells will look like, when they are electrically connected in series or in parallel. As a first step we consider the series configuration and subsequently the parallel tandem cell is addressed. Then the obtained

* Corresponding author. Tel.: +31 50 3634376; fax: +31 50 3638751.
E-mail address: p.w.m.blom@rug.nl (P.W.M. Blom).

1566-1199/$ - see front matter © 2008 Elsevier B.V. All rights reserved.
doi:10.1016/j.orgel.2008.03.009

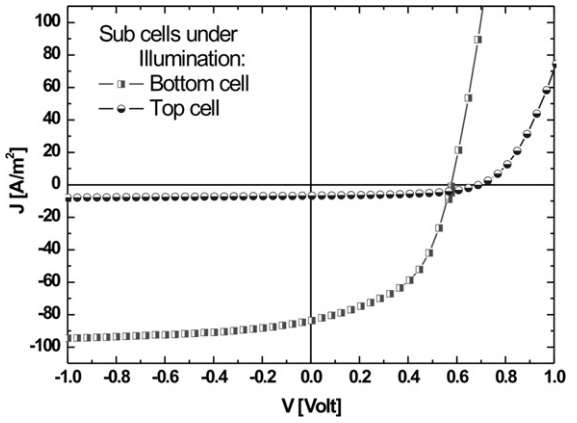

Fig. 1. The current–voltage characteristic of two sub cells under illumination. The top cell delivers higher open-circuit voltages, while its photocurrent is much lower than the bottom cell.

tandem cell *J–V* characteristics are compared to experimental data.

2. Current density–voltage characteristics for series and parallel configurations

2.1. Series configuration

When the two sub cells are connected in series, the total generated photocurrent will be constant throughout the device (conservation of charge) in steady-state. Furthermore, the voltages generated by the sub cells will add up. As a result for each point of the *J–V* characteristic of the tandem device the following relations are valid,

$$J_{\text{Tandem}} = J_{\text{Bottom}} = J_{\text{Top}} \tag{1}$$

$$V_{\text{Tandem}} = V_{\text{Bottom}} + V_{\text{Top}} \tag{2}$$

Graphically, Eq. (1) means that we can draw an arbitrary horizontal line through Fig. 1, indicating a chosen constant current density that flows through the cells. This horizontal line crosses the *J–V* curves under illumination of the individual bottom and the top cell at a specific voltage for each sub cell. Those cross-points are the values of the voltages with which the sub cells are effectively biased in order to generate the chosen constant current density. Eq. (2) then shows that we have to add those two voltage values in order to determine the bias voltage of the tandem cell in series at that constant current density. To do so, we replot Fig. 1 between zero and –10 A/m^2 in order to enlarge the vertical axis and choose three arbitrary current densities as shown in Fig. 2. The horizontal line 1 is the open-circuit condition for both sub cells in which the current densities in both of them are zero (cross-points A and B). Line 2 shows the short-circuit condition of the top cell (cross-point C), whereas the bottom sub cell is biased by a positive voltage (cross-point D). Line 3 is the condition in which the bottom cell is biased by a positive voltage (cross-point F), whereas the top is biased by a negative voltage (cross-point E).

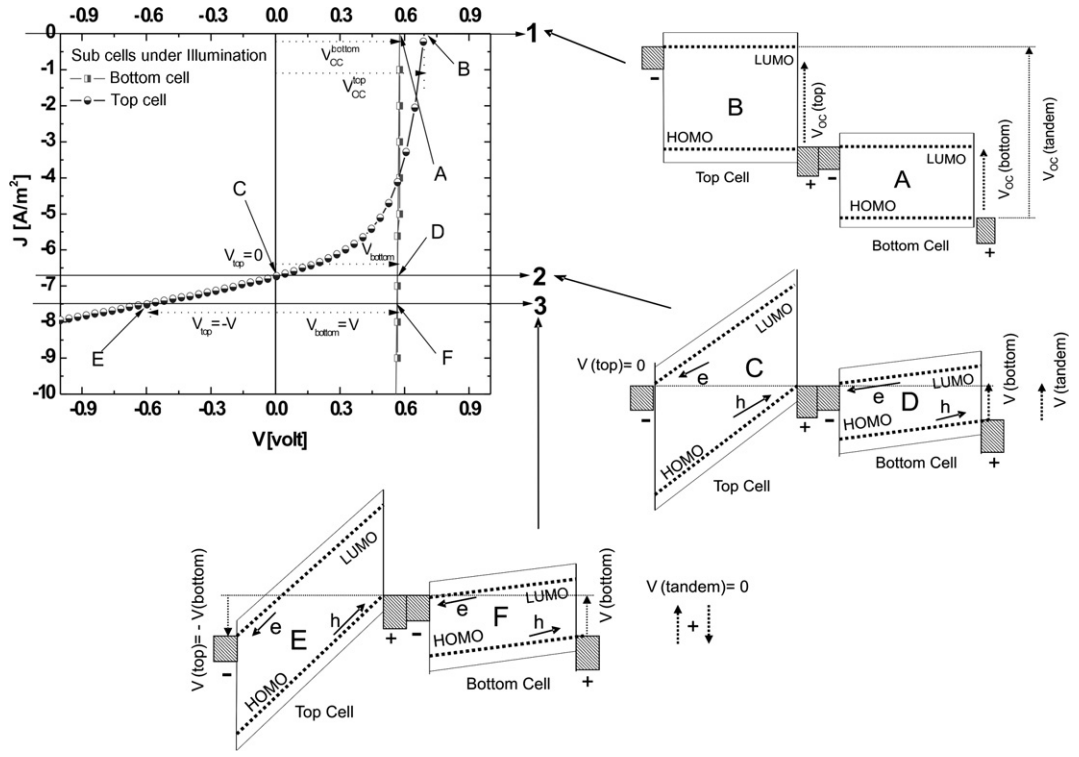

Fig. 2. A close-up of the vertical axis of Fig. 1 between 0 and −10 A/m^2. The horizontal lines 1–3 cross the curves of the bottom (A, D and F) and top cells (B, C and E), indicating a constant current density. For each line the energy-band diagrams are given.

Following Eqs. (1) and (2) we can say that,
At line 1:

$$J_{\text{Tandem}} = J_{\text{Bottom}} = J_{\text{Top}} = J_1 = 0 \ [\text{A/m}^2] \tag{3}$$

$$V_{\text{OC}}^{\text{Tandem}} = V_{\text{OC}}^{\text{Bottom}} + v_{\text{OC}}^{\text{Top}} = V_{\text{A}} + V_{\text{B}} = (0.57) + (0.7) = 1.27 \ [\text{V}] \tag{4}$$

At line 2:

$$J_{\text{Tandem}} = J_{\text{Bottom}} = J_{\text{SC}}^{\text{Top}} = J_2 = -6.68 \ [\text{A/m}^2] \tag{5}$$

$$V_{\text{Tandem}} = V_{\text{Bottom}} + V_{\text{Top}} = V_{\text{C}} + V_{\text{D}} = (0) + (0.56) = 0.56 \ [\text{V}] \tag{6}$$

At line 3:

$$J_{\text{SC}}^{\text{Tandem}} = J_{\text{Bottom}} = J_{\text{Top}} = J_3 = 7.46 \ [\text{A/m}^2] \tag{7}$$

and because for this current density of line 3 the distance from E and F to the y-axis are equal,

$$V_{\text{Tandem}} = V_{\text{Bottom}} + V_{\text{Top}} = V_{\text{E}} + V_{\text{F}} = (-0.55) + (0.55) = 0 \ [\text{V}] \tag{8}$$

In this way the open-circuit voltage (Eq. (4)), short-circuit current (Eq. (7)) and an additional arbitrary point (at short-circuit condition of the top cell) of the series tandem cell are predicted. In Fig. 2 also the energy-band diagrams are schematically depicted for these three cases. We now discuss the biasing conditions of this series tandem cell in more detail. In a series configuration the cathode of the bottom cell is electrically connected to the anode of the top cell. In the tandem cell studied here the bottom cell generates much more photocurrent than the top cell (Fig. 1) under, for example, short-circuit condition. This implies that there are not enough holes arriving from the top cell to recombine with the large amount of electrons arriving from the bottom cell. As a result, in steady-state, the excess of electrons will negatively charge the connected electrodes of the sub cells. This charging reduces the effective voltage across the bottom cell, and thus also the extracted current from the bottom cell. On the other hand, the additional electrons in the middle electrode provide a stronger voltage-drop across the top cell (the top cell is more reversed biased) and, therefore, a higher current flows through the top cell. Steady-state is reached when the lowered current in the bottom cell is equal to the enhanced current of the top cell. At the open-circuit voltage (line 1) both the sub cells are biased in such a way that the effective electric field across them is close to zero (the bias neutralizes the built-in electric field). Current matching is then achieved since both cells do not generate any current: they only act as two voltage sources of which the generated voltages add up. Line 2 shows the situation where the effective bias across the top cell is zero (C), meaning that the field across the top cell is now equal to its built-in electric field. Due to the negative charging of the middle electrode, the effective voltage across the bottom cell is strongly reduced (D) in order to balance the current with the top cell. For line 3, the electric field across the top cell is even further enhanced by the increasing amount of charge on the middle electrode, such that the top cell is now reverse (negative) biased. In this case, the electric field across the top cell is larger than its built-in electric field (E). Finally, line 3 is chosen in such a way that the negative bias across the top cell (E) is equal to the positive bias of the bottom cell (F). As a result the total voltage across the tandem equals zero, such that line 3 represents the short-circuit current of the tandem cell. By choosing sufficient horizontal lines (current levels) and extracting the voltages as mentioned above, the whole illuminated J–V curve of the series tandem cell can be constructed.

2.2. Parallel configuration

When the two sub cells are electrically connected in parallel, in steady-state, for each point of the J–V characteristics of the tandem device the following relations are valid,

$$V_{\text{Tandem}} = V_{\text{Bottom}} = V_{\text{Top}} \tag{9}$$

$$J_{\text{Tandem}} = J_{\text{Bottom}} + J_{\text{Top}} \tag{10}$$

Graphically, Eq. (9) means that we can now draw an arbitrary vertical line through Fig. 1, which indicates the chosen operating voltage for the sub cells. This vertical line crosses the J–V characteristics under illumination of the bottom and the top cell at a specific current for each cell. Those cross-points are the values of the current density generated by the sub cells at the chosen operating voltage. These two values of the current densities of the bottom and top cell then have to be added (Eq. (10)) to calculate the current of the parallel tandem cell for the chosen operating voltage. We now enlarge the horizontal axis of Fig. 1 and again draw three vertical lines, as shown in Fig. 3. The vertical line 1 is the open-circuit condition for the top cell and positive current density for the bottom cell (cross-points K and L). Line 2 shows the condition in which the sub cells have opposite current densities. At line 2, the bottom cell generates positive current due to dark injection (cross-point M), whereas the top cell generates a negative photocurrent (cross-point N). Line 3 is the short-circuit condition for all cells in which both the bottom cell (cross-point O) and the top cell (cross-point P) generate negative photocurrents.

From Eqs. (9) and (10) we obtain that:
At line 1:

$$V_{\text{Tandem}} = V_{\text{Bottom}} = V_{\text{OC}}^{\text{Top}} = V_1 = 0.69 \ [\text{V}] \tag{11}$$

$$J_{\text{Tandem}} = J_{\text{Bottom}} + J_{\text{Top}} = J_{\text{K}} + J_{\text{L}} = (87.5) + (0) = 87.5 \ [\text{A/m}^2] \tag{12}$$

At line 2:

$$V_{\text{OC}}^{\text{Tandem}} = V_{\text{Bottom}} = V_{\text{Top}} = V_2 = 0.58 \ [\text{V}] \tag{13}$$

since M and N have equal distance to the x-axis,

$$J_{\text{Tandem}} = J_{\text{Bottom}} + J_{\text{Top}} = J_{\text{M}} + J_{\text{N}} = (4.0) + (-4.0) = 0 \ [\text{A/m}^2] \tag{14}$$

At line 3:

$$V_{\text{Tandem}} = V_{\text{Bottom}} = V_{\text{Top}} = V_3 = 0 \ [\text{V}] \tag{15}$$

$$J_{\text{SC}}^{\text{Tandem}} = J_{\text{SC}}^{\text{Bottom}} + J_{\text{SC}}^{\text{Top}} = J_{\text{O}} + J_{\text{P}} = (-83.65) + (-7.1) = -90.75 \ [\text{A/m}^2] \tag{16}$$

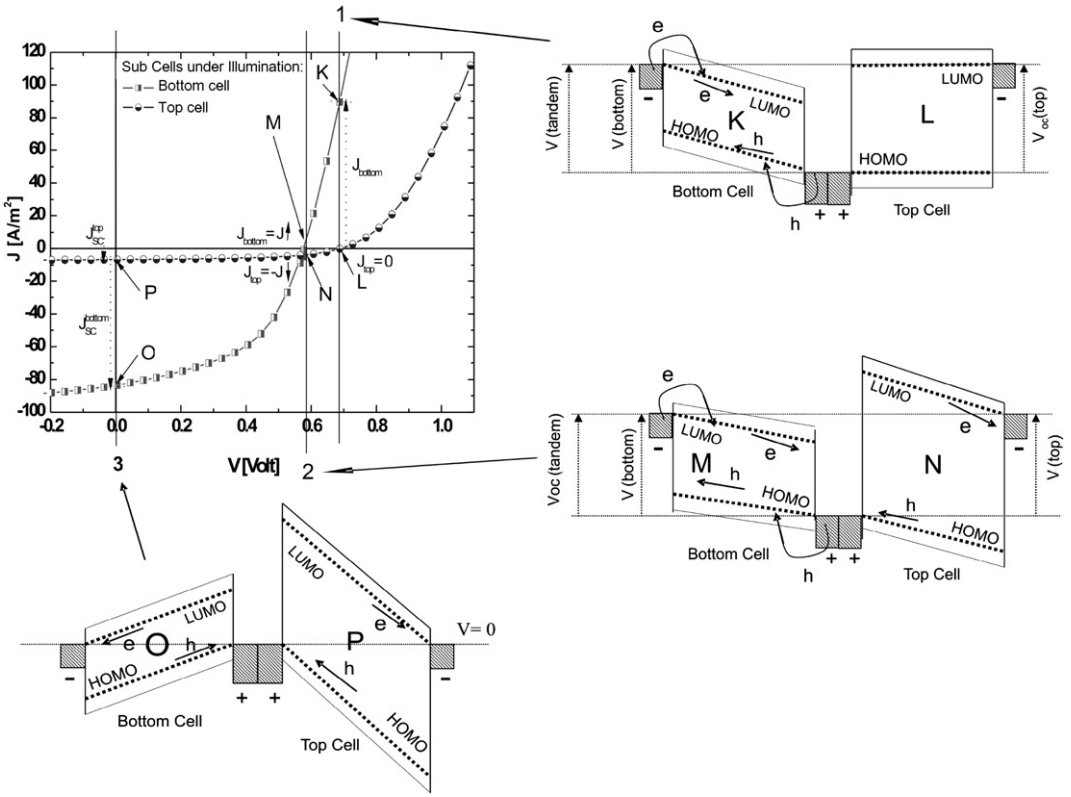

Fig. 3. Close-up of the horizontal axis of Fig. 1 between −0.2 and 1 V. By extracting the cross-points of the vertical lines with the *J–V* curve of the bottom cell (K, M and O), and the top cell (L, N and P) from the graph, the current density of the parallel tandem device can be constructed for a range of chosen voltages. The energy-band diagrams in the different operation points are also given.

With this method, the short-circuit current, open-circuit voltage and an additional point of the *J–V* characteristic are determined for a parallel tandem cell based on the sub cells mentioned before. By drawing sufficient vertical lines through the *J–V* curves of the sub cells and extracting the operation points the complete *J–V* characteristic of the parallel tandem device can be constructed. Also shown in Fig. 3 are the corresponding energy-band diagrams for the three lines. In the parallel configuration the two outer electrodes are connected and show up on an equal level in these diagrams. For line 1 the top cell is biased such that the electric field across the cell is close to zero (L). However, because of the lower built-in field in the bottom cell, the electric field in the bottom cell changes sign (K) under this bias. As a result the dark injection in the bottom cell is switched on and electrons now flow to the PEDOT:PSS in stead of to the LiF/Al electrode, leading to a positive current. For the voltage corresponding to line 2 the bottom cell is still dominated by (positive) dark current, but its current is now of equal magnitude as the (negative) photocurrent generated by the top cell. Therefore, this voltage represents the open-circuit voltage of the tandem cell and is located in between the V_{OC} is of the individual cells. Finally, line 3 shows the situation when no bias is applied across the parallel tandem. In that case both sub cells are effectively biased by their built-in electrical fields. Using the procedures described in this section, the current–voltage curve of any parallel – and series connected tandem solar cell can be derived from the electrical performance of the individual sub cells. It should be noted that this method can also be used for the prediction of the *J–V* curves of multi-junction organic solar cells with three or more active layers [1]. The constructed *J–V* curve of the series and parallel tandem cell is shown in Fig. 4, together with the characteristics of the individual sub cells.

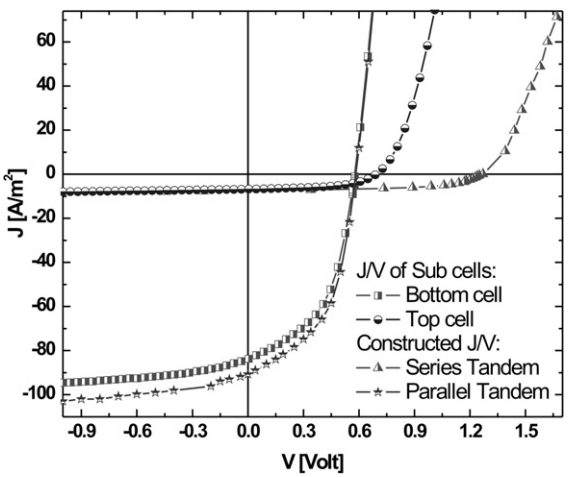

Fig. 4. Current–voltage characteristic of the two sub cells, and the constructed series and parallel tandem solar cell.

3. Comparison with experiment

To compare the calculated *J–V* characteristics of the tandem cells with experimental data we can use the measurements on the tandem device as described in Ref. [9] (inset Fig. 5). As stated above the tandem cell we consider is based on a 250 nm P3HT:PCBM blend for the bottom cell and a 80 nm MDMO-PPV:PCBM blend for the top cell, separated by an optical spacer with a thickness of 190 nm. For this thickness the optical spacer maximizes the transmitted light for the wavelengths that correspond to the absorption spectrum of the MDMO-PPV [9]. The experimental *J–V* characteristics of the individual bottom and top cell of this structure were already shown in Fig. 1. The complete structure of this tandem test device is given in the inset of Fig. 5. The two sub cells can be connected electrically in series or in parallel using external wiring. In Fig. 5, the results of the measured *J–V* curves are compared to the constructed *J–V* curves as shown in Fig. 4. The experimental *J–V* characteristics are in excellent agreement with the predicted values. To make a more quantitative comparison, we determined for the calculated and experimental *J–V* curves of Fig. 5 (series and parallel connection) the exact values for V_{OC} and J_{SC}, the voltage V_{max} and the current density J_{max} at the maximum power point, and the corresponding fill factor (FF) and efficiency η. The results are summarized in Table 1.

Clearly, all relevant solar cell parameters for the series and parallel connected tandem cells can be accurately predicted from the electrical characteristics of the individual sub cells (Table 1). Verification of the predicted characteristics with experimental data now allows us to systematically investigate the effect of a series and parallel connection of subcells with different open-circuit voltages, short-circuit currents and fill factors.

4. The efficiency of tandem solar cells with non-identical subcells

Another important question is how the performance of a tandem cell is affected, when one of the sub cells has a poor performance. Such a low performance might be the result of a low V_{OC}, J_{SC} or poor FF. To investigate the role of either a low V_{OC}, J_{SC} or FF in one of the subcells we construct a series of *J–V* characteristics in which one of these parameters is systematically varied. The other two parameters are kept constant for clarity. As an example in Fig. 6 *J–V* characteristics are shown in which the V_{OC} is systematically varied. These artificial *J–V* curves are constructed in such a way that all cells have the same FF and J_{SC}, but a large variation in V_{OC} (from 0.59 V to 0.29 V). With these 6 cells as input we can now construct on paper a series

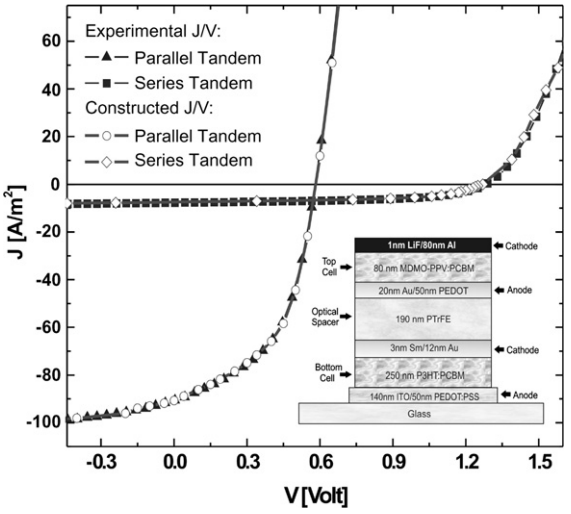

Fig. 5. The comparison between experiment and generated current–voltage characteristics. The constructed curves are in very good agreement with the experimental obtained data in both series and parallel configurations. Inset: structure of the tandem test device. The electrodes of the device can be electrically connected in parallel or in series by adjusting the external wires.

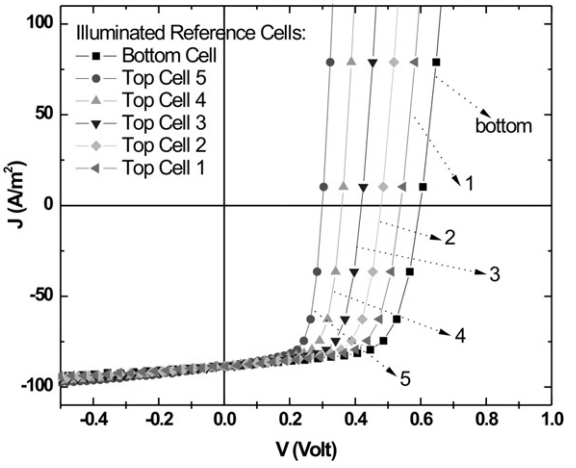

Fig. 6. Current–voltage characteristic of 6 artificial solar cells with different V_{OC}, but equal J_{SC} and fill factor. The cell with the highest V_{OC} (= -0.59 V) will be used as the bottom cell of a tandem structure. The other five cells have a V_{OC} of 0.54, 0.48, 0.41, 0.35 and 0.29 V, respectively, and will be used as top cell.

Table 1
Comparison between calculated and experimental parameters of the series and parallel tandem solar cell extracted from Fig. 5

Cell	J_{max} [A/m^2]	V_{max} [V]	J_{SC} [A/m^2]	V_{OC} [V]	FF [%]	η [%]
Calculated series	−5.64	0.91	−7.34	1.27	55	0.50
Experimental series	−6.00	0.89	−7.60	1.28	54	0.48
Calculated parallel	−66.3	0.39	−91.2	0.58	48	2.53
Experimental parallel	−64.8	0.40	−89.9	0.58	49	2.56

of tandem cells: we choose the characteristic of cell 1 (V_{OC} = 0.59 V) as bottom cell and then add all curves 2–6, subsequently as top cell. For each combination of 2 curves we then apply the method as explained above, and construct the resulting electrical tandem characteristics, when the cells are connected either in series or parallel. In this way, we can investigate the effect of a variation of the V_{OC} in one of the sub cells on the V_{OC} and performance of the tandem cells. In Fig. 7A the resulting V_{OC} of the tandem cell is plotted as a function of the V_{OC} of the top cell (ranging from 0.29 to 0.54 V). For the series connection it is evident that the V_{OC} of the tandem cell is equal to the sum of the open-circuit voltages of the different subcells. For the parallel connection the V_{OC} of the tandem cell (circles) is close, but not exactly equal to the V_{OC} of the top cell, which is the lowest of the two subcells (triangles). As shown in Fig. 3 the V_{OC} of the tandem cell is reached when the dark current of the cell with the lowest V_{OC} is cancelled by the photocurrent of the cell with the highest V_{OC}. Since, the increase of the dark current is very steep in that voltage region the V_{OC} of the tandem is slightly higher, but close to the open-circuit voltage of the cell with the lowest V_{OC}. As shown in Fig. 7B the efficiency of the series connection is considerably higher than the parallel connection. Since the J_{SC} is by definition matched and the voltages add up the efficiency of the series tandem cell is equal to the sum of the efficiencies of the subcells. Since, for the parallel connection the V_{OC} of the tandem is close to the lowest V_{OC} (Fig. 7A) the efficiency is limited by this cell. It should be noted that in these calculations we have assumed that stacking of both subcells does not change their absorption, as is the case for two subcells absorbing in a different region of the solar spectrum.

As a next step we consider the effect of a difference in the short-circuit current J_{SC} of the different subcells. In Fig. 8 a set of J–V characteristics is constructed in such a way that all cells have the same FF and V_{OC}, but a large variation in J_{SC} (from –88 A/m^2 to –26 A/m^2). Again, with these 6 cells as input we construct a series of tandem cells: we choose the characteristic of cell 1 (J_{SC} = –88 A/m^2) as bottom cell and then add all curves 2–6 (J_{SC} = –61 A/m^2 to –26 A/m^2) subsequently as top cell. In Fig. 9A the J_{SC} of the tandem cells are shown for the series and parallel connection as a function of the J_{SC} of the top cell. As expected, for the parallel connection of subcells with an equal V_{OC} the J_{SC} is equal to the sum of the J_{SC} of both subcells. For the series connection the J_{SC} of the tandem cell is slightly higher then the short-circuit current of the subcell with the lowest J_{SC} (top cell, triangles). As shown in Fig. 2 the J_{SC} of the tandem is at the point where the photocurrent in reverse bias (3rd quadrant) of the top cell is equal to the photocurrent in the top cell under forward bias (4th quadrant). Regarding the efficiency, shown in Fig. 9B, it is clear that for subcells with

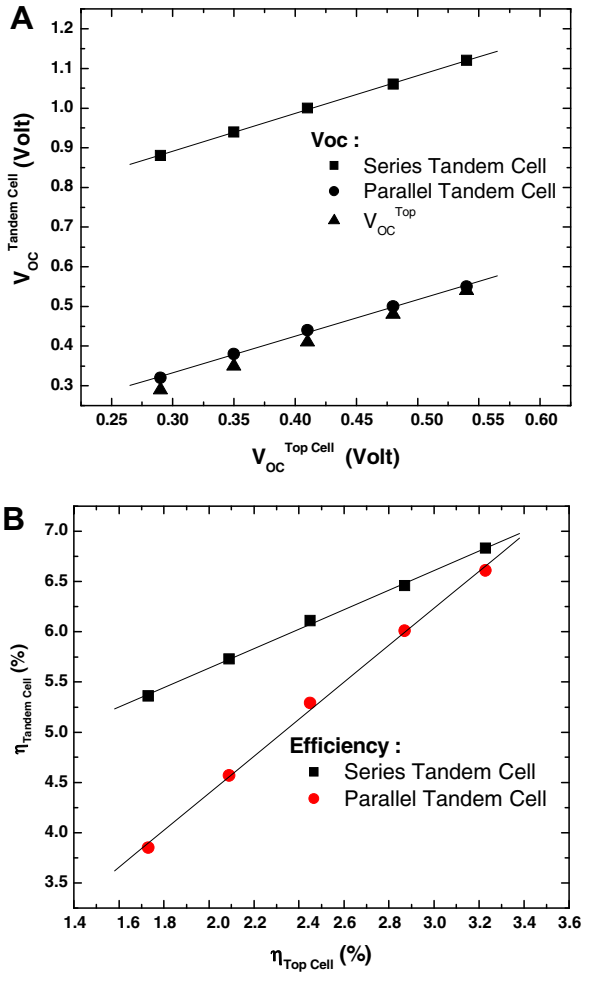

Fig. 7. (A) Open-circuit voltage of the tandem cell as a function of the V_{OC} of the top cells 1–5 from Fig. 6, both in series and parallel connection. Also shown is V_{OC} of the subcell with the lowest V_{OC} (top cell, triangles). (B) Efficiency of the series and parallel connection of the tandem cell as a function of the efficiency of the top cell. The efficiency of the parallel configuration is limited by the lower V_{OC} of the top cell.

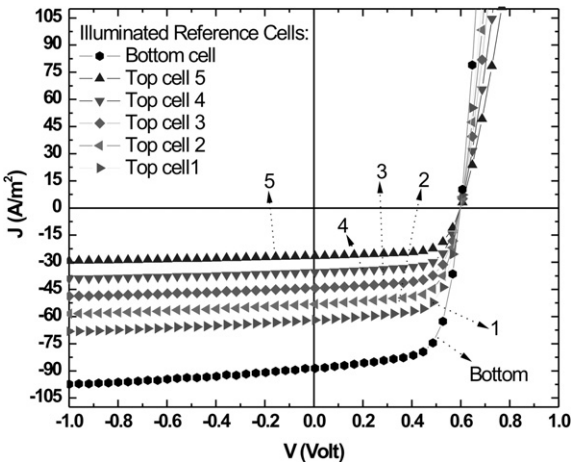

Fig. 8. Current–voltage characteristic of 6 artificial solar cells with different J_{SC}, but equal V_{OC} and fill factor. The cell with the highest J_{SC} (= 88 A/m^2) will be used as the bottom cell of a tandem structure. The other five cells have a J_{SC} of 62, 53, 44, 36 and 26 A/m^2, respectively, and will be used as top cell.

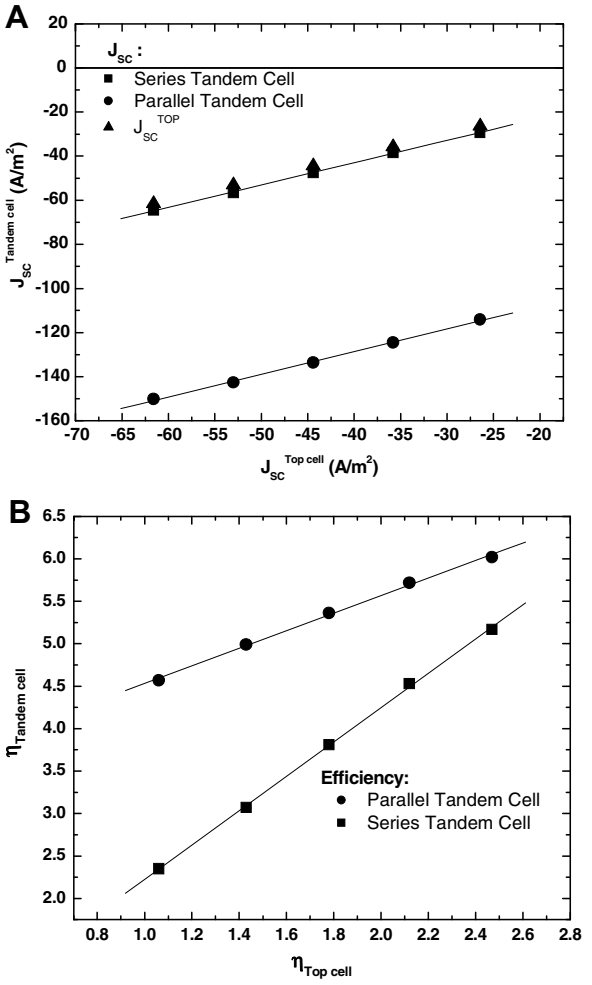

Fig. 9. (A) Short-circuit current of the tandem cell as a function of the J_{SC} of the top cells 1–5 from Fig. 8, both in series and parallel connection. Also shown is J_{SC} of the subcell with the lowest J_{SC} (top cell, triangles). (B) Efficiency of the series and parallel connection of the tandem cell as a function of the efficiency of the top cell. The efficiency of the series configuration is limited by the lower J_{SC} of the top cell.

equal V_{OC}, but varying J_{SC} the parallel connection is favorable, and the efficiency of the tandem cell is typically the sum of the efficiencies of the subcells. The efficiency of the series connection is limited (but not equal to) by the subcell with the lowest J_{SC}.

Another important question is how the fill factor of a tandem cell is affected, when one of the sub cells has a very poor FF. Will the FF of the tandem for example be closer to the highest or the lowest FF, when connected in series or parallel? To investigate this we consider a range of J–V characteristics as shown in Fig. 10. These artificial J–V curves are constructed in such a way that all cells have the same V_{OC} and J_{SC}, but a large variation in FF (from 25 to 66%). Each (artificial) solar cell has a different maximum power point (MMP), which results in a different maximum current (J_{max}) and maximum voltage (V_{max}) for each cell (Fig. 10).

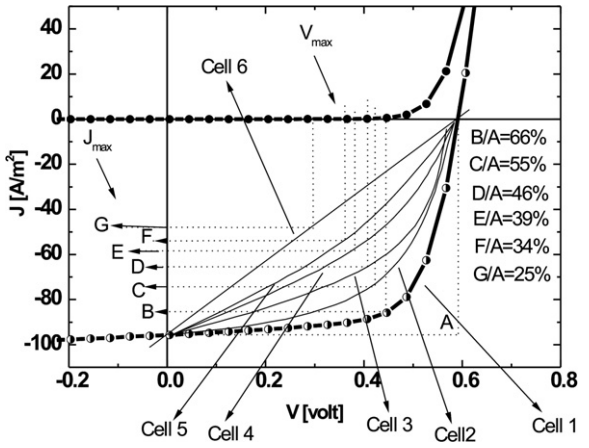

Fig. 10. Current–voltage characteristic of 6 artificial solar cells with different fill factors. The areas B/A = 0.66, C/A = 0.54, D/A = 0.44, E/A = 0.39, F/A = 0.31 and G/A = 0.25 demonstrates the fill factor of the cell 1 until the cell 6, respectively.

For the series connection the resulting J–V characteristics of the various tandem cells have the same short-circuit current ($J_{SC} = -95.3$ A/m^2) and open-circuit voltage ($V_{OC} = 1.18$ V), but different fill factors (FF) and efficiencies (η). For the parallel configuration the results of tandem cells based on the bottom cell (cell 1) with itself and the other 5 sub cells as top cells have the same short-circuit current ($J_{SC} = -190.6$ A/m^2) and open-circuit voltage ($V_{OC} = 0.59$ V) and also different fill factor (FF) and efficiencies (η). Fig. 11A demonstrates the different behavior of the series and parallel configuration tandem device when the fill factor of one sub cell is varied, in which the fill factor of the tandem devices is plotted as a function of the fill factor of the top cell. The mathematical average, which is the sum of the fill factors of the sub cells divided by two, is also plotted. When the two sub cells have an equal fill factors both the series and parallel configuration have that same fill factor. When the top cell has a significantly lower fill factor, the parallel configuration follows the mathematical average and shows a higher fill factor as compared to the series one. The lower fill factor of the top cell strongly decreases the fill factor of the series tandem device. Furthermore, the fill factors of the series tandem devices are higher than the fill factors of the top cells. Only when the bottom cell (cell 1) is combined in a tandem cell with itself, the fill factor of the tandem device equals to the fill factor of the bottom cell (cell 1, 66%). Combining the highest (66%) and lowest (25%) FF as sub cells in a series tandem device leads to a FF of 38%, which is below the average value (45.5%). The fill factor of the top cell limits the performance of the parallel tandem device as well by lowering its fill factor, equal to the series configuration. However, the fill factor of the parallel tandem cell is higher than the series configuration in all cases. The effect of the fill factors on the power conversion efficiency of the tandem cells is similar. The parallel tandem cell has higher efficiency than the series cell. The performances of all tandem cells considered are compared in Fig. 11B.

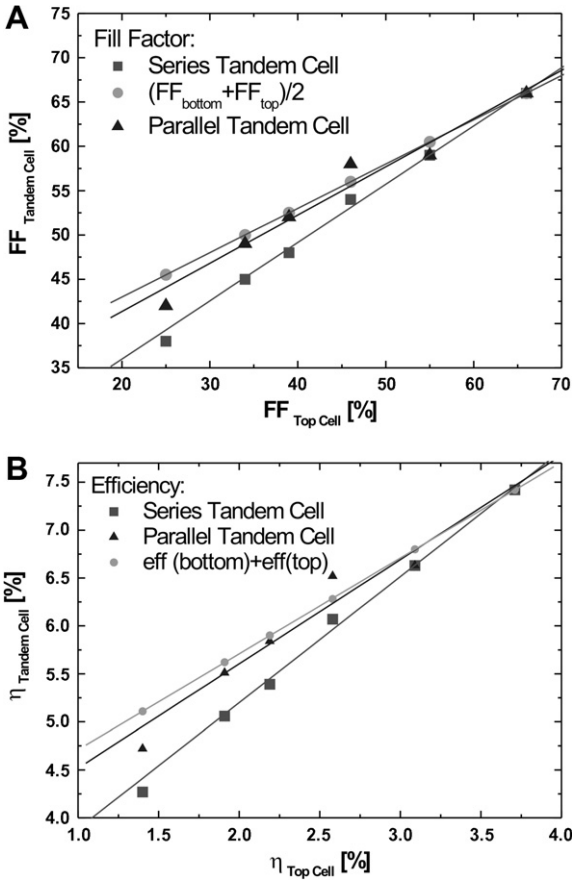

Fig. 11. (A) Fill factors of the tandem devices, series and parallel, as a function of the fill factor of the top cell and a bottom cell with a fill factor of 66%. The parallel configuration shows a higher fill factor as compared to the series configuration. (B) Efficiency of the series and parallel tandem cells considered as well as the sum of the efficiency of the sub cells as a function of the efficiency of the top cell. When both sub cells have similar electrical performance, both series and parallel configuration leads to nearly identical efficiencies. If one of the sub cells (top cell here) exhibits a lower fill factor, the parallel configuration is the better choice to fabricate.

5. Conclusions

A methodology is presented to derive the current–voltage characteristic of any arbitrary tandem device from the electrical performance of the individual sub cells. The calculated characteristics are in very good agreement with experimental data on both series and parallel connected tandem devices. In general, when both sub cells have almost the same electrical properties, series and parallel configurations lead to tandem devices with the same performance. If there are large differences in the open-circuit voltages, the series connection is a better geometry to choose since its overall efficiency is higher than the series configuration. On the other hand, for subcells with variations mainly in the short-circuit current the parallel connection is more advantageous. The mathematical average of the fill factors of the sub cells is a good approximation for the fill factor in the parallel configuration. The series configuration has significantly lower fill factor and therefore lower efficiency.

Acknowledgements

The authors gratefully acknowledge Jan Harkema and Frans van der Horst for their technical assistance, and Floris B. Kooistra and Prof. Jan C. Hummelen for providing PCBM.

References

[1] K.M. Coakley, M.D. McGehee, Chem. Mater. 16 (2004) 4533.
[2] P.W.M. Blom, V.D. Mihailetchi, L.J.A. Koster, D.E. Markov, Adv. Mat. 19 (2007) 1551.
[3] A. Hadipour, B. de Boer, P.W.M. Blom, Adv. Funct. Mater. 18 (2008) 169.
[4] M. Hiramoto, M. Suezaki, M. Yokoyama, Chem. Lett. (1990) 327.
[5] P. Peumans, A. Yakimov, S.R. Forrest, J. Appl. Phys. 93 (2003) 3693.
[6] G. Dennler, H.-J. Prall, R. Koeppe, M. Egginger, R. Autengruber, N.S. Sariciftci, Appl. Phys. Lett. 89 (2006) 073502.
[7] A. Hadipour, B. de Boer, J. Wildeman, F.B. Kooistra, J.C. Hummelen, M.G.R. Turbiez, M.M. Wienk, R.A.J. Janssen, P.W.M. Blom, Adv. Funct. Mater. 16 (2006) 1897.
[8] J.Y. Kim, K. Lee, N.E. Coates, D. Moses, T. Nguyen, M. Dante, A.J. Heeger, Science 317 (2007) 222.
[9] A. Hadipour, B. de Boer, P.W.M. Blom, J. Appl. Phys. 102 (2007) 074506.
[10] J. Gilot, M.M. Wienk, R.A.J. Janssen, Appl. Phys. Lett. 90 (2007) 143512.

Organic Electronics 9 (2008) 625–634

Contents lists available at ScienceDirect

Organic Electronics

journal homepage: www.elsevier.com/locate/orgel

Electronic structure and reactivity analysis for a set of Zn-chelates with substituted 8-hydroxyquinoline ligands and their application in OLED

Ricardo Vivas-Reyes *, Francisco Núñez-Zarur, Emiliano Martínez

Grupo de Química Cuántica y Teórica, Facultad de Ciencias Exactas y Naturales, Universidad de Cartagena, Campus de Zaragocilla, Cartagena, Colombia

ARTICLE INFO

Article history:
Received 5 February 2008
Received in revised form 31 March 2008
Accepted 1 April 2008
Available online 16 April 2008

Keywords:
OLED
Zn organometallic
Chemical descriptors
DFT

ABSTRACT

A set of four Zn organometallic complexes with aromatic substituents in the 5-position of quinoline skeleton connected through an amido linkage to the ligands were studied and compared, by using electronic descriptors such as the energy gap between the highest occupied molecular orbital (HOMO) and the energy of the lowest unoccupied molecular orbital (LUMO), molecular orbitals' surfaces, atomic charges, global hardness, local softness, Fukui function, and global and local electrophilicity indexes. All the geometries were optimized in the scheme of density functional theory (DFT) with the hybrid functional B3LYP and the 6-31G(d) basis set. The results show that the geometries of the molecules were all distorted tetrahedral, which are unaffected by substitution when they are compared with the prototypical OLED material Znq2. The frontier molecular orbitals HOMO and LUMO are delocalized over both ligands and are confined within a specific region. The reactivity analysis shows that the specific atoms prone to receive electrons are those associated with the lowest unoccupied molecular orbital (LUMO).

1. Introduction

Electronically functional organic materials have several interesting properties for their use in organic light emitting diodes (OLED) [1–9]. The structural arrangement of the simplest of these devices consists of three molecular films whose nature is essentially organic: a hole transport layer (HTL) [10], an emissive layer (EL), and an electron transport layer (ETL) [11] sandwiched between two electrodes – an anode usually made up of indium–tin oxide (ITO) and a cathode of a metal with low work function or an appropriate alloy [12a]. In an OLED, electrons and holes are injected from each electrode into ETL and HTL, respectively. These charge carriers move towards each other until they form h^+–e^- pairs in EL, called excitons, which radiate characteristic light in the visible spectrum when they become relaxed. Actually, OLED lifetimes can reach 10.000 h but for the most commercial applications 50.000 h are needed. The physical and chemical properties such as chemical reactivity, diffusion, polarization and morphology are among the most important characteristics that limit an OLED lifetimes and applications [13].

The materials frequently used in OLED devices are polymers and, recently, organometallic complexes. The tris-(8-hydroxyquinoline) aluminium(III) (Alq3) complex is a milestone for the development of OLED, which has been used as an EL and ETL in these devices since 1987 [3,14] and it comprises of an aluminium cation in formal oxidation state of +3 surrounded by three bidentate 8-hydroxyquinoline ligands in an octahedral configuration [15]. Some of the reasons for using Alq3 so frequently are because of its green emission, with photoluminescence efficiencies topping around 30%, good electron mobility and thermal

* Corresponding author. Tel./fax: +57 5 6698180.
E-mail address: rvivasr@unicartagena.edu.co (R. Vivas-Reyes).

1566-1199/$ - see front matter © 2008 Elsevier B.V. All rights reserved.
doi:10.1016/j.orgel.2008.04.004

stability up to 350 °C [14]. The existence of two geometrical isomers, meridianal and facial, is the object of debate about the film composition [16]. An analysis of the electronic structure of the Alq3 was performed by Curioni et al. on the basis of *ab initio* calculations suggesting that the coexistence of the two isomers in thin films may be a cause of its amorphous character [17]. Experimental studies has not shown evidence of the facial isomer [18,19], although recently a new crystalline phase for this isomer has been reported that is present in a few amounts [20]. Nevertheless this disagreement about the film composition, the most of both theoretical and experimental treatments refer almost exclusively to *mer*-Alq3 [21].

Another typical complex is bis-(8-hydroxyquinoline) zinc(II) (Znq2), which has also been used for OLED applications. When it is computed in the anhydrous form, the results showed a tetrahedral or planar geometry, depending on the level of theory used [22]. However, in the solid-phase, this complex is found as a tetramer, $(Znq2)_4$, with two different types of zinc cation, a pentacoordinated and a hexacoordinated [23]. One of the limitations of this compound is its insolubility in common solvents, limiting its use in solvated media for photoluminescence studies. In view of this, a new series of Znq2-derivatives whose ligands have been substituted with several aromatic groups connected through an amido linkage, which exert different electronic and/or steric effects [24,25] has been reported. This substitution, besides being a good way to modify their solubility, is a general form to alter the wavelength emission. Thus, it is necessary to know the electronic properties of these compounds in order to establish relationships between them and their optical behaviour. Moreover, it is of tremendous significance to know how these compounds capture electrons from cathode, i.e. what is the local region where electrons are injected. Recently, we have performed an analysis of the electronic structure and DFT-based reactivity for a set of analogous compounds, in order to study the electron-injection mechanism carried out in an OLED device [26].

All theses issues prompted us to wonder whether these questions could be answered or at least clarified by the use of the quantum theory calculations. First, one can hope that theoretical calculations could provide indications and trends, as to what factors affect the structural properties of these Zn organometallic complexes and get some light onto the role that has different substituents on the properties of such complexes. This investigation makes use of electronic descriptors such as the energy of the highest occupied molecular orbital (HOMO), the energy of the lowest unoccupied molecular orbital (LUMO), the gap energy HOMO-LUMO, molecular orbitals surfaces, atomic charges via natural population analysis (NPA) and DFT-based reactivity descriptors such as global hardness (η), global softness (S), local softness (s), Fukui function (f), and local and global electrophilicity indexes (ω) in order to explore the more reactive sites that could play a crucial role in the nucleophile–complex interactions for these compounds. The knowledge of such interactions is extremely significant to establish the electron-injection mechanism and to predict the OLED efficiency in the presence of impurities. [27].

2. Theoretical background and computational details

The set of four Zn–organometallic complexes with substituents in 5-position of quinoline skeleton were taken from the literature [12]. As we already commented, the set was chosen because they represent a new class of novel compounds for OLED applications. Furthermore, they were synthesized in order to find good candidates which form stable homogeneous and amorphous films for the device fabrication. Fig. 1 shows the general structure of these complexes and the keys to identify them.

All the geometries were optimized in the ground state (S_0) by using the Gaussian 03 suite of programs [28] and the B3LYP/6-31G(d) [29] model chemistry, with all the electronic and reactivity descriptors calculated at the same level of theory. Molecular orbital contributions (MOC) from different molecular parts were computed at B3LYP/6-31G(d) level by using the GaussSum program [30].

The properties of the compounds that are frequently used in OLED applications have been the object of several density functional studies, including metal–ligand bond analyses [31–33], geometrical and electronic analyses of the ground and excited states structures [16,34,35] and chemical reactivity [26], showing that functionals that include gradient corrections and hybrid functional, such as B3LYP, together with the 6-31G(d) basis set lead to good agreement with the experimental observations. DFT methods were also selected from a price/quality point of view which provide an accurate description.

A variety of reactivity descriptors such as molecular charge distribution, molecular orbitals surfaces and HOMO and LUMO energies were used in this work. The HOMO and LUMO orbitals of a molecule are called the frontier orbitals. These orbitals have a prominent role in chemical reactivity. The energy gap between the HOMO and LUMO orbitals have been found to be adequate to study the stability and chemical reactivity of a great variety of molecular systems and is an important stability index. A large gap implies high stability and a small gap implies low stability. The high stability in turn indicates low chemical reactivity and a small gap indicates high chemical reactivity.

Besides the traditional reactivity descriptors, there are a set of chemical reactivity descriptors which can be derived from density functional theory, such as the global hardness (η), global softness (S), local softness (s), Fukui function (f) and global and local electrophilicity indexes (ω). A detailed presentation and discussion of these descriptors can be found elsewhere [36–45] and only the relevant expressions used for the evaluation of different quantities are given here.

The global hardness and global softness were calculated as

$$\eta \approx \frac{\mathrm{IE} - \mathrm{EA}}{2}, \tag{1}$$

and

$$S = \frac{1}{2\eta}, \tag{2}$$

where IE and EA are the vertical ionization energy and electron affinity, respectively, for the system. The global

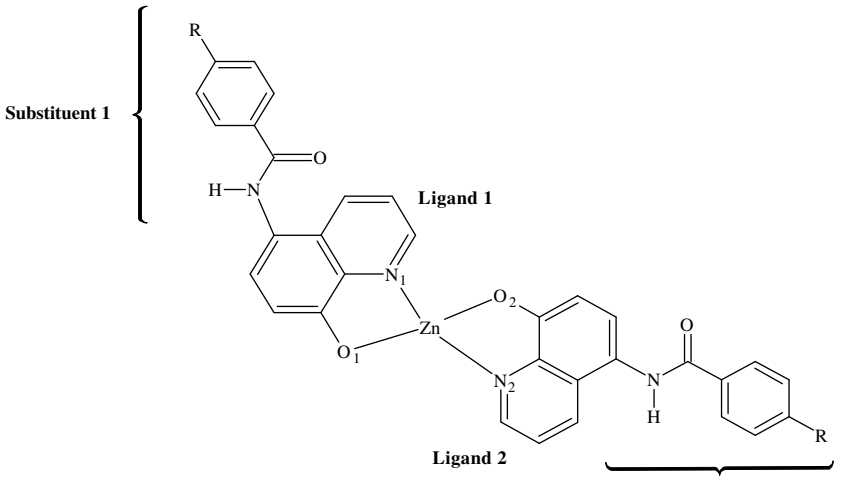

R	Compound Key
-H	HQ-I
$-NO_2$	HQ-II
$-O-(CH_2)_5-CH_3$	HQ-III
$-C(CH_3)_3$	HQ-IV

Fig. 1. General structure of the studied complexes.

hardness can be seen as the resistance of a chemical species to charge transfer or to the loss or gain of electrons and the global softness is interpreted as the inverse of global hardness. Within the framework of DFT, a general rule predicting the stability of the electronic structure of the molecules [36,37] has been established. The general rule is that chemical reactivity and stability of a molecular system evolves towards a state of greater hardness, and hence, its stability increases. Conversely, when a system evolves towards the state of lower hardness its stability decreases. The global softness (S), the inverse concept of hardness, is useful for a straightforward prediction of chemical reactivity. The soft molecules undergo changes in electron density more easily than the hard molecules and are more reactive than the hard molecules. A molecule having higher S value is more reactive than a molecule having smaller S value. In general, it can be said that the increase in softness increases the chemical reactivity and the increase in hardness decreases the chemical reactivity [36,37].

These descriptors show global properties for a system as a whole; however, in order to study selectivity and reactivity, we have carried out some calculations using local reactivity descriptors. The Fukui function can be defined as

$$f(r) = \left(\frac{\partial\rho(r)}{\partial N}\right)_{v(r)} = \left(\frac{\delta\mu}{\delta v(r)}\right)_N \tag{3}$$

The Fukui function is interpreted as the change of chemical potential (μ) given an external perturbation, or the variation of the electron density (ρ) function when the electrons number change. The Fukui function reflects the reactivity of different sites within a molecule. One assumes that the preferred direction of attack of a reagent is the one for which the variation of μ is a maximum, i.e. the preferred direction is the one with largest $f(r)$ at the reaction site. Thus, the reactivity is measured by the Fukui index of Eq. (3) [36,37]. Here, we will work exclusively with the equation for a nucleophilic attack, because the nature of interactions between the studied OLED materials and reducing agents, such as metal-based cathodes are of this type. In this context, the Fukui function of interest is

$$f^+(r) = \left(\frac{\partial\rho(r)}{\partial N}\right)^+_{v(r)} \tag{4}$$

Upon condensation to atoms [46] one obtains for a given atom k:

$$f_k^+ = q_k(N+1) - q_k(N) \tag{5}$$

with q_k as the electron population of the atom in the molecule, containing the number of electrons mentioned in parentheses. In analogy to the condensed Fukui function, the corresponding condensed local softness parameters can be easily calculated from the condensed Fukui function and the global softness, for a nucleophilic attack, s_x^+

$$s_x^+ = Sf_x^+, \tag{6}$$

where S is the global softness and f_x the Fukui function as defined above. The local softness is known as a better indicator for intermolecular reactivity sequences than the Fukui function. Since local softness is a quantity that is a product of one local and one global reactivity descriptors, it is supposed to explain the intermolecular interactions as well. Local quantities like local softness and Fukui functions are important in gaining insights into the reactivity and selectivity of a specific site in a molecule [36,37].

Another important chemical reactivity descriptor is the electrophilicity index (ω), which measures the second-order energy of an electrophile when it gets saturated with electrons, that is, the electrophilic power of the system. This is one of the so called global reactivity descriptors and is calculated as follows

$$\omega = \frac{\chi^2}{2\eta}, \tag{7}$$

where χ is the electronegativity and η is the global hardness for the given system. Eq. (7) indicates that a good electrophile will be characterized by a high electronegativity ($\chi = -\mu$), and a low value of chemical hardness. Additionally, a local electrophilicity index can be computed from an expression analogous to (6) and it has been introduced to analyze the electrophile–nucleophile reactions better

$$\omega_k = \omega f_k^+, \tag{8}$$

where f_k^+ is the nucleophilic Fukui function and ω is the global electrophilicity index. Note that the most electrophilic site in the electron acceptor coincides with the softest site in the molecule, and that the more electrophilic site is the one corresponding to the highest value of the electrophilic Fukui function, i.e. the active site of the electrophile.

Therefore, it is evident that the DFT-based descriptors of reactivity can be used for a quantitative prediction of intrinsic stability, chemical reactivity as well as the relative stabilities of the molecules. In general the local descriptors allow distinguishing one part of a molecule from other parts, we should be able to use them to differentiate the reactive behaviour of different atoms in a molecule.

3. Results and discussion

3.1. Geometries of the ground state (S_0)

For the studied complexes, all the geometries showed to be tetrahedrally distorted in the inner shell after optimization, and the zinc cation presents a general oxidation state of +2. As an example, Fig. 2 displays the optimized structure of the complex HQ-I (see key to identify in Fig. 1). In order to compare the main changes in the geometrical and electronic parameters between the compounds studied here and the prototypical OLED material Znq2, we have performed parallel calculations on the latter at B3LYP/6-31G(d) level. The results of geometrical optimization are depicted in Table 1. By inspection of these results, it should be stated that these parameters remain unchanged upon substitution. Therefore, the chemical behaviour of OLED materials have not originated from geometrical changes in the inner shell but other originated from the electronic effects of the substituents on the electronic structure, in particular, on HOMO and LUMO orbitals.

3.2. Electronic structure

For the studied complexes, the frontier orbital levels consist of sets of closely spaced "twosome", which are delocalized over the two ligands. The highest occupied molecular orbital (HOMO) and the lowest unoccupied molecular orbital (LUMO) largely preserve the electronic structure of the complex Znq2, being the complex HQ-II an exception. For intuition, the contour plots of the frontier molecular orbitals for Znq2 are depicted in Fig. 3, including the highest occupied molecular orbital (HOMO), the second highest molecular orbital ($HOMO_{-1}$), the lowest unoccupied molecular orbital (LUMO) and the second lowest molecular orbital ($LUMO_{+1}$). The complexes HQ-I, HQ-III and HQ-IV show an electron distribution similar to Znq2, while HQ-II shows a different pattern in the LUMO and $LUMO_{+1}$ orbitals.

Fig. 3 reveals the delocalized nature of the HOMOs and LUMOs orbitals. So, a large participation of phenolato ring on HOMOs and high contributions of pyridyl ring on LUMOs for HQ-I, HQ-III and HQ-IV are observed. This distribution is a consequence of the lack of conjugation through the amide linker. As it has been already stated, there is an exception with the complex HQ-II, where the LUMOs are delocalized on both substituents, with asymmetric contributions of each one. For comparison with other molecules in the set, Fig. 4 shows the molecular orbital surfaces for HQ-II. This distribution can be a consequence of electron-attractor character of the nitro group, which displaces the electron cloud of benzene ring towards itself. The nitro-substituted compound is different since the local LUMO of nitrophenyl is sufficiently low such that the molecular LUMO is localized on the nitrophenyl groups. Presumably, this has consequences for the energy (red-

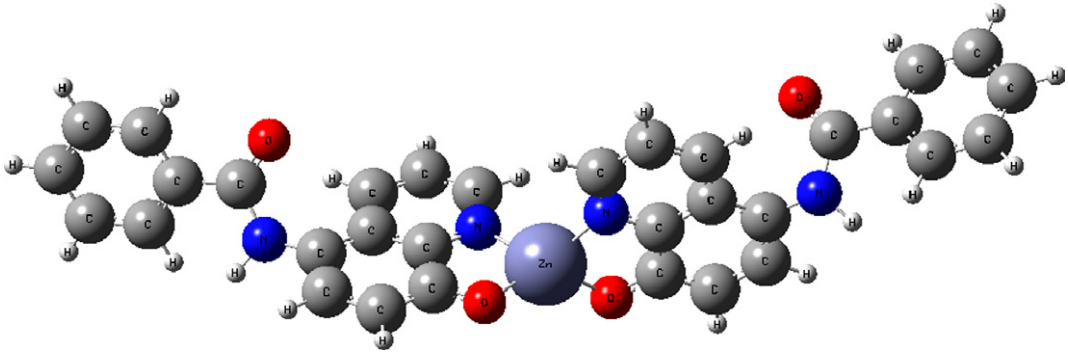

Fig. 2. B3LYP/6-31G(d) optimized geometry of the complex HQ-I. The others compounds show essentially the same geometry.

Table 1
B3LYP/6-31G(d) optimized bond lengths (Å) and angles (°) for the inner shell of the studied Zn-chelates together with those of the complex Znq2

Molecule	$Zn–O_1$	$Zn–O_2$	$Zn–N_1$	$Zn–N_2$	$O_1–Zn–O_2$	$N_1–Zn–N_2$
HQ-I	1.919	1.919	2.053	2.053	129.87	121.10
HQ-II	1.919	1.919	2.053	2.053	129.99	121.36
HQ-III	1.919	1.919	2.053	2.053	130.12	122.51
HQ-IV	1.919	1.919	2.053	2.053	129.08	120.69
Znq2	1.917	1.917	2.059	2.059	131.55	121.86

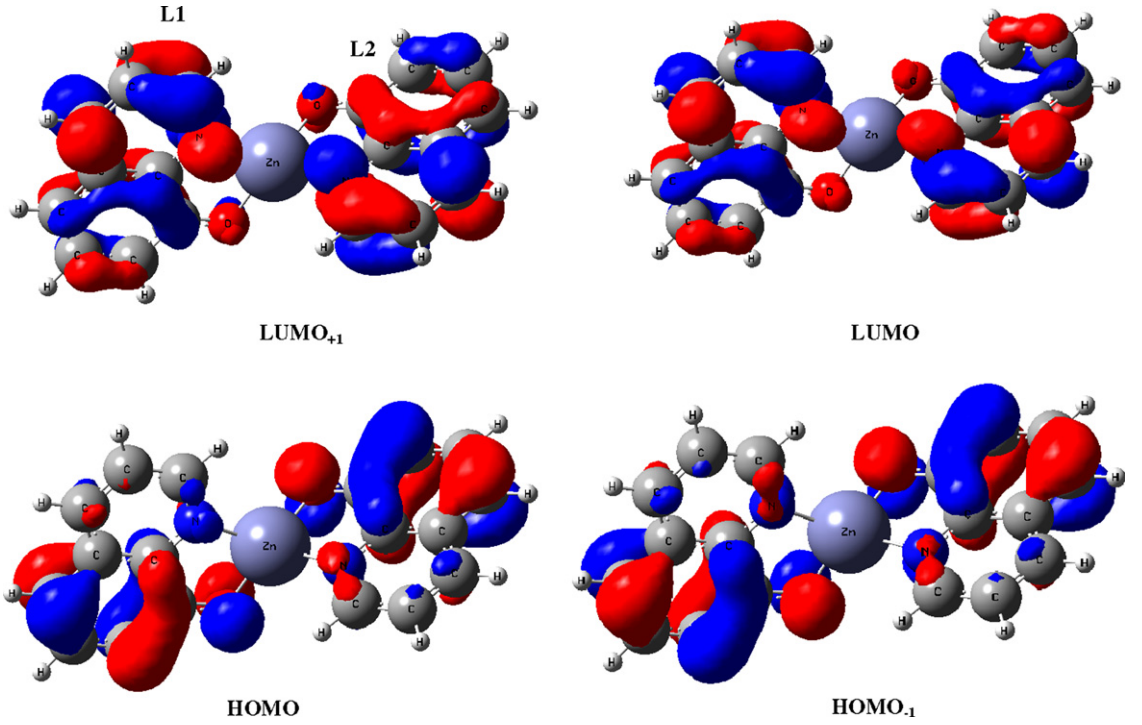

Fig. 3. Molecular orbital surfaces of the HOMOs and LUMOs for the Znq2 complex, calculated at B3LYP/6-31G(d) (isosurface value 0.03 e/au^3). L1 and L2 denote two different quinolate ligands.

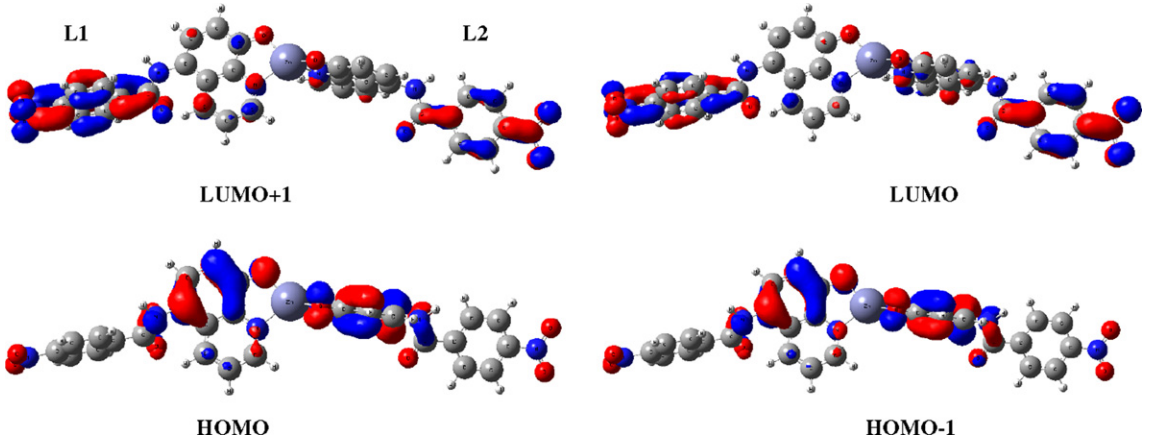

Fig. 4. Molecular orbital surfaces of the HOMOs and LUMOs for the HQ-II complex, calculated at B3LYP/6-31G(d) (isosurface value 0.03 e/au^3). L1 and L2 denote two different quinolate ligands.

shifted) and strength (weakened) of the emission from this compound.

In order to corroborate the delocalized nature and relative position of these molecular orbitals, contributions

from different molecular regions were calculated at B3LYP/6-31G(d) level. For that, all the structures were divided into seven molecular parts: 1. Zinc cation (Zn); 2. Phenolato ring of ligand 1 including O_1(Phen1); 3. Pyridyl ring of ligand 1 including N_1 (Pyr1); 4. Phenolato ring of ligand 2 including O_2 (Phen2); 5. Pyridyl ring of ligand 2 including N_1 (Pyr2); 6. Substituent group on ligand 1 (Subs1) and 7. Substituent group on ligand 2 (Subs2), which are shown in Fig. 5. The $HOMO_{-1}$ and HOMO are confined on the phenolato side at 40% on both ligands (HQ-I and HQ-IV); for HQ-II and HQ-III the distribution is a little asymmetrical, with 39 and 41% (HOMO) and 41 and 39% ($HOMO_{-1}$) on ligands 1 and 2, respectively. Very few contributions from pyridyl side, substituents and Zn cation, which are 4, 5, and 1% (all cases), in that order are also observed. These contributions from different molecular regions to HOMO set are composed mainly of p-π-type orbital from carbon and oxygen atoms in the phenolato ring; however, in the lower occupied states, the role of substituents is primary, reaching to 99% (HQ-III). The lowest unoccupied molecular orbitals LUMO and $LUMO_{+1}$ are mainly concentrated on pyridyl side of the ligands. The complexes HQ-I and HQ-IV present a contribution of 33% from pyridyl side of both ligands, while HQ-III displays an asymmetrical distribution, being 43 and 23% from the pyridyl side of the ligands 1 and 2, respectively (LUMO), and conversely, 23 and 43% from the pyridyl side of the ligands 1 and 2 ($LUMO_{+1}$). The phenolato side also shows some contribution to these orbitals, being about 14% on both ligands for HQ-I and HQ-IV, 18 and 10% (LUMO) and 10 and 18% ($LUMO_{+1}$) on ligands 1 and 2, respectively, for HQ-III. The compound HQ-II shows the more atypical electron distribution of the LUMO set. While the HOMO set is mainly dispersed on the phenolato side of the ligands, the electron cloud of the LUMO set is confined on the substituents in 30 and 50% (LUMO) and 50 and 30% ($LUMO_{+1}$) for ligands 1 and 2, respectively. The others molecular parts show only few contributions, not surpassing 7%. The electron distribution from the pyridyl side of the ligands is composed mainly of p-π^* type orbital from carbon and nitrogen atoms in the pyridyl side. Thus, for these complexes, the strongest absorptions can be assigned to transitions $\pi \rightarrow \pi^*$ localized in the ligands, in analogy to the prototypical complexes Alq3 and Znq2.

Table 2 shows the numerical values of HOMO and LUMO energy, the energy of the Gap (HOMO-LUMO), the global hardness (η) and the global electrophilicity index (ω). The general trend shown is that the substitution in the 5-position of the quinolinate skeleton increases (destabilizes) the HOMO and LUMO eigenvalues at the same time, owing to the electron-donor character of the amido bridge of the substituents (compared with Znq2). An exception to this is the complex HQ-II, in which the HOMO and LUMO eigenvalues decrease (and stabilizes), giving the larger global reactivity of the set (η = 2.43 eV). However, within any sensible estimate of error, the hardness descriptors is the same for HQ-I, HQ-III and HQ-IV, indicating that aliphatic substitutions at benzene ring exert the same effect. By inspection of the electrophilicity index in Table 2, it can be noted that all the complexes showed an electrophilicity index greater than Znq2 (except HQ-III), being the greatest for HQ-II. This can indicate that the substitution on the phenolato ring in the ligands is a favourable process in order to get improved efficiencies.

It must be noted that a simple NPA charge analysis of the ground state wave functions for the Zn cation of the molecules, including Znq2, gives a charge of 1.605 (±0.001), which is lower than their formal value of +2 from a simple ionic point of view. This feature indicates that there is a considerable covalency in the Zn–ligand interactions, and it is not affected profoundly by the substituents at 5-position on the quinoline ligands.

3.3. Interactions between cathode and the studied complexes as electron-capture materials

In this section, we will show a detailed study of the more reactive sites for the studied set of compounds.

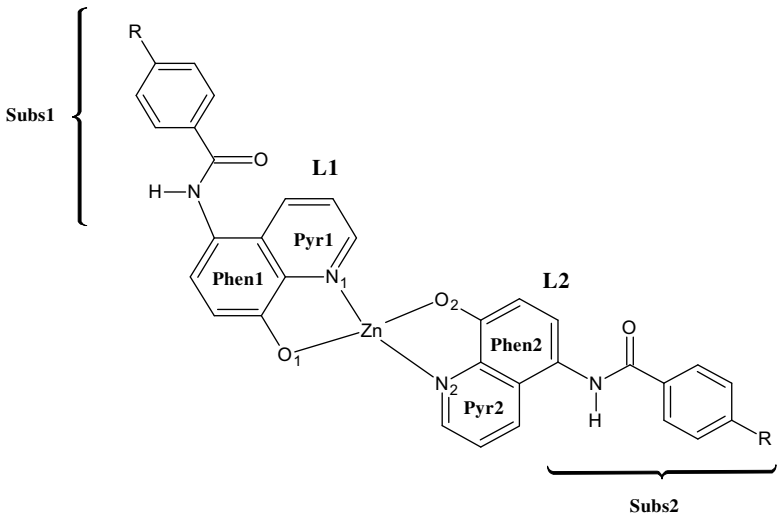

Fig. 5. Division for molecular orbital contributions (MOC) for the studied complexes.

Table 2
Energy of the HOMO, energy of the LUMO, Gap (HOMO–LUMO), global hardness, global electrophilicity index (eV) and global softness (eV^{-1}) for the studied set, calculated at B3LYP/6-31G(d) level

Molecule	E_{HOMO}	E_{LUMO}	Gap	Hardness (η)	Global electrophilicity index (ω)
HQ-I	−5.059	−1.697	3.36	2.85	2.05
HQ-II	−5.416	−2.819	2.60	2.43	3.60
HQ-III	−4.927	−1.579	3.35	2.87	1.84
HQ-IV	−5.010	−1.650	3.36	2.86	2.02
Znq2	−5.189	−1.719	3.46	3.10	1.93

Since these molecules are expected to act as electron-transport and emitting layer, this step is necessary in order to study the general mechanism of electron injection. Complexes with single metal atoms are expected to form in metal-doped complex layers and at a cathode–organic interface in the early stages of metal deposition or during degradation processes [47–50]. Since the OLED efficiency is dependent on the electron-transfer rate from the cathode to electron-transport layer, it is necessary to know the precise sites in the whole structure that could play a crucial role in the electron-capture process. So, we have to improve our knowledge about the mechanism in which a given material emits light. In this work, we have performed computational calculations of nucleophilic Fukui function (f_k^+), local softness (s_k^+) and local electrophilicity index (ω_k^+) on each one of the atoms of the investigated complexes. Fig. 6 shows the key to identify each one of the atoms of the set. The results from these calculations are summarized in Tables 3–6, where L1 and L2 denote the two different quinolate ligands as revealed in the Figs. 3 and 4. For didactic purposes, only the main atoms for each molecule are shown. From different reactivity descriptors, intermolecular and intramolecular analyses may be done. For complexes HQ-I and HQ-IV, the more

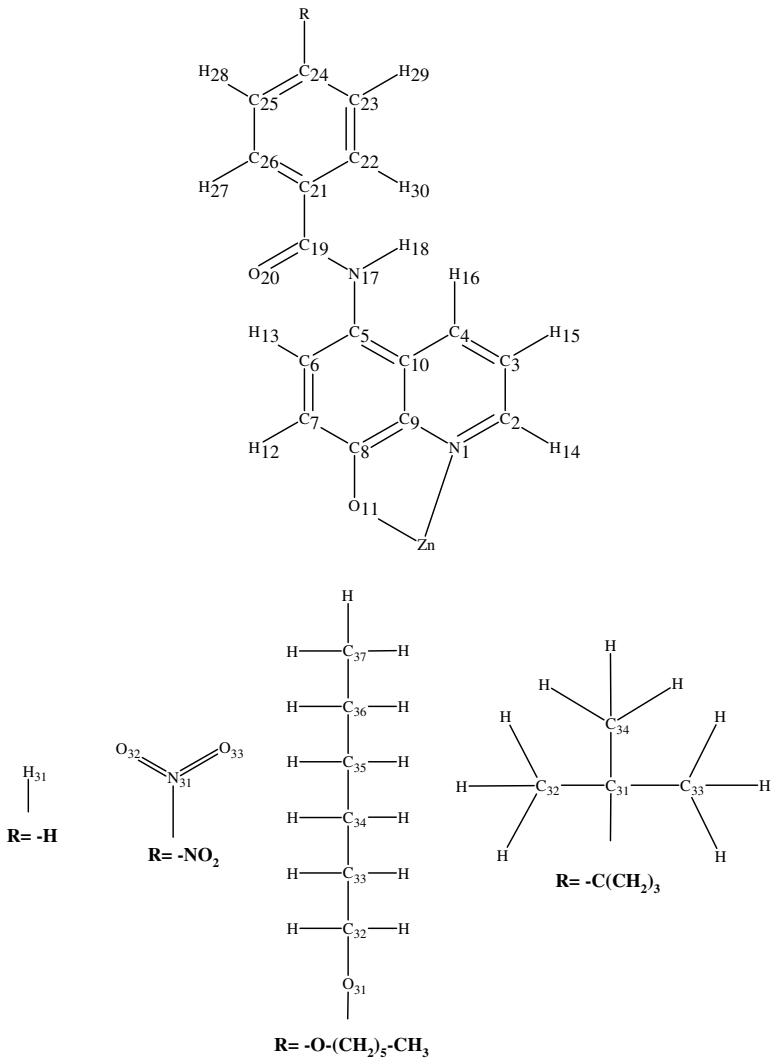

Fig. 6. Atom numeration for the investigated compounds.

Table 3
Nucleophilic Fukui function (f^+, au), local softness (s^+, eV^{-1}) and local electrophilicity index (ω^+, eV) for HQ-I

Atom	f^+ (10^{-2})		s^+ (10^{-3})		ω^+ (10^{-2})	
	L1	L2	L1	L2	L1	L2
N_1	3.4	3.4	6.0	6.0	6.98	6.98
C_2	3.5	3.6	6.1	6.1	7.18	7.21
C_4	7.1	7.2	12.5	12.8	14.57	14.61
C_5	2.3	2.3	4.0	4.0	4.72	4.72
C_6	2.7	2.7	4.7	4.7	5.54	5.54
C_{19}	2.3	2.3	4.0	4.0	4.72	4.72
C_{24}	3.2	3.1	5.6	5.4	6.57	6.55
Zn	1.2		2.1		2.46	

Table 4
Nucleophilic Fukui function (f^+, au), local softness (s^+, eV^{-1}) and local electrophilicity index (ω^+, eV) for HQ-II

Atom	f^+ (10^{-2})		s^+ (10^{-3})		ω^+ (10^{-1})	
	L1	L2	L1	L2	L1	L2
C_{21}	3.1	4.2	6.4	8.6	1.114	1.509
C_{22}	0.9	1.0	1.9	2.1	0.323	0.359
C_{23}	2.3	2.8	4.7	5.8	0.827	1.006
C_{24}	1.9	2.6	3.9	5.3	0.683	0.934
C_{25}	2.5	3.1	5.1	6.4	0.899	1.114
C_{26}	0.8	1.1	1.6	2.3	0.288	0.395
N_{31}	4.2	5.4	8.6	11.1	1.509	1.941
O_{32}	7.6	8.8	15.6	18.1	2.731	3.163
O_{33}	7.8	8.9	16.0	18.3	2.803	3.199
Zn	0.6		1.2		0.216	

Table 5
Nucleophilic Fukui function (f^+, au), local softness (s^+, eV^{-1}) and local electrophilicity index (ω^+, eV) for HQ-III

Atom	f^+ (10^{-2})		s^+ (10^{-3})		ω^+ (10^{-2})	
	L1	L2	L1	L2	L1	L2
N_1	4.4	3.2	7.7	5.6	8.10	5.89
C_2	4.3	3.1	7.5	5.4	7.92	5.71
C_3	1.1	0.6	1.9	1.0	2.03	1.11
C_4	8.8	7.0	15.3	12.2	16.21	12.89
C_5	2.7	2.4	4.7	4.2	4.97	4.42
C_6	3.1	2.5	5.4	4.4	5.71	4.61
C_7	1.9	1.9	3.3	3.3	3.50	3.50
C_8	1.8	0.9	3.1	1.6	3.32	1.66
C_{24}	3.3	2.3	5.7	4.0	6.08	4.24
Zn	1.3		2.3		2.39	

Table 6
Nucleophilic Fukui function (f^+, au), local softness (s^+, eV^{-1}) and local electrophilicity index (ω^+, eV) for HQ-IV

Atom	f^+ (10^{-2})		s^+ (10^{-3})		ω^+ (10^{-2})	
	L1	L2	L1	L2	L1	L2
N_1	3.4	3.4	5.9	5.9	6.85	6.85
C_2	3.5	3.5	6.1	6.1	7.05	7.05
C_3	0.9	0.9	1.6	1.6	1.81	1.81
C_4	7.1	7.1	12.4	12.4	14.31	14.31
C_5	2.3	2.3	4.0	4.0	4.63	4.63
C_6	2.7	2.7	4.7	4.7	5.44	5.44
C_7	1.7	1.7	3.0	3.0	3.43	3.43
C_8	1.4	1.4	2.5	2.5	2.82	2.82
C_{24}	3.5	3.5	6.1	6.1	7.05	7.05
Zn	1.2		2.1		2.42	

reactive atoms are shown to be the atoms C_4 in the quinoline ligand. This is evidenced by the Fukui function values, which are around 7.1 au. For these two compounds, numerical values of f^+ reveal that aliphatic substituents such as hydrogen and tertbutyl group exert almost the same effect on the reactivity of them. Following the sequence, the next atoms prone to capture electrons from metallic cathode are atoms N_1 and C_2, which show the same f^+ values. These values are the same for equivalent atoms of both ligands, which is a consequence of the electron distribution presented in the MOC analyses. The complex HQ-III presents the C_4 atom in L1 as the more reactive one. Atoms N_1 and C_2 are next in the reactivity trend. However, L2 shows f^+ values lower than L1. Also, this is a consequence of the asymmetrical electron distribution of this complex. An analogue result was found for the complex HQ-II, which presents the more reactive center in the atoms O_{32} and O_{33} of the nitro group in L2. Again, this is expected in view that asymmetrical distribution is observed from MOC analyses. In a global sense, the more reactive sites in the studied molecules are related to atoms contributing to the LUMO orbital, which is in line with previous experimental works [51–54]. Thus, it is expected that in the radical anion the excess electron be localized on the atoms with large LUMO coefficients.

On the other hand, the s^+ descriptor presents almost the same information as the nucleophilic Fukui function, in view that the complexes HQ-I, HQ-III and HQ-IV show almost the same global hardness (and hence, the same global softness). The local electrophilicity index, w^+, further confirms the results obtained by the s^+ and f^+ descriptors.

The chemical reactivity descriptors f^+, s^+ and ω^+ are valuable tools to describe the electron injection mechanism in an OLED, being a validity proof for the results obtained here. Moreover, the knowledge of the interactions between the OLED materials studied here and the reducing agents will be useful for predicting the OLED stability in the presence of impurities such as oxygen and water.

4. Conclusions

DFT calculations at the B3LYP/6-31G(d) level were used to study the electronic and reactivity properties of a set of OLED compounds through electronic and chemical reactivity descriptors. Several conclusions can be drawn from the results described for the theoretical investigations.

The geometries around the metal center are distorted tetrahedrally and the influence of the substituents was found negligible, when they are compared with the prototypical Znq2. The HOMO and LUMO orbitals are delocalized on both ligands, the HOMO orbital being mainly located on phenolato moieties, while the LUMO is concentrated on pyridyl moieties. For HQ-II, the LUMO is located on the *p*-nitrobenzamide group on both ligands. These qualitative results are confirmed by molecular orbital contribution (MOCs) calculations, which show the electron distribution of the frontier molecular orbitals implicated in the main transition processes.

The local reactivity analyses showed that the atoms inclined to receive electrons from the metallic cathode are atoms associated to the LUMO orbital. All these results suggest that the interaction in these Zn complexes with the ligands are principal orbital controlled.

Density functional theory is a highly valuable instrument in the interpretation of the properties of this set of four Zn organometallic complexes and as a consequence from the results described in this paper, it can be recommended to include models for the design of novel OLED complexes using high computational level (B3LYP/6-31G*) to study their properties theoretically.

Acknowledgements

The authors thank the Colombian Institute for the Science and Technology Development "Francisco Jose de Caldas" – COLCIENCIAS (Bogotá, Colombia) and the University of Cartagena (Cartagena, Colombia), as well as the Program Young Investigators and Innovators 2007 sponsored by both institutions.

References

[1] J.H. Burroughes, C.A. Jones, R.H. Friend, Nature 335 (1988) 137.
[2] S.R. Forrest, IEEE Circuits Device Mag. 5 (1989) 33.
[3] C.W. Tang, S.A. Van Slyke, Appl. Phys. Lett. 51 (1987) 913.
[4] C.W. Tang, S.A. Van Slyke, J. Appl. Phys. 65 (1989) 3610.
[5] C. Adachi, S. Tokito, T. Tsutsui, S. Saito, Jpn. J. Appl. Phys. 27 (1988). L269 and L713.
[6] J.H. Burroughes, D.D.C. Bradley, A.R. Brown, R.N. Marks, K. Mackay, R.H. Friend, P.L. Burn, A.B. Holmes, Nature 347 (1990) 539.
[7] T. Tani, Photographic Sensitivity, Oxford University Press, Oxford, UK, 1995.
[8] A. Goetzberger, J. Luther, G. Willeke, Solar Energy Mater. Solar Cells 74 (2002) 1.
[9] M.A. Díaz-García, S.F. De Ávila, M.G. Kuzyk, Appl. Phys. Lett. 80 (2002) 4486.
[10] (a) S.A. VanSlyke, C.H. Chen, C.W. Tang, Appl. Phys. Lett. 69 (1996) 2160;
(b) H. Inada, Y. Yonemoto, T. Wakimoto, K. Imai, Y. Shirota, Mol. Cryst. Liq. Cryst. 280 (1996) 331;
(c) Y. Kuwabara, H. Ogawa, H. Inada, N. Noma, Y. Shirota, Adv. Mater. 6 (1994) 677;
(d) T. Wakimoto, H. Nakada, Y. Yonemoto, S. Kawami, K. Imai, Appl. Phys. Lett. 65 (1994) 807;
(e) C. ADachi, S. Tokito, T. Tsutsui, S. Saito, Jpn. J. Appl. Phys. 28 (1988) L269.
[11] (a) J. Kido, M. Kimura, K. Nagai, Science 267 (1995) 1332;
(b) J. Kido, C. Ontaki, K. Hongawa, K. Oknyama, K. Nagai, Jpn. J. Appl. Phys. 32 (1993) L917;
(c) J. Kido, C. Ontaki, K. Hongawa, K. Oknyama, K. Nagai, Appl. Phys. Lett. 63 (1993) 2627;
(d) A.R. Brown, D.D.C. Bradley, J.H. Burroughes, R.H. Friend, N.C. Greenham, P.L. Burns, A.B. Holmes, A. Kraft, Appl. Phys. Lett. 61 (1992) 279;
(e) Y. Hamada, C. Adachi, T. Tsutsui, S. Saito, Jpn. J. Appl. Phys. 31 (1992) 1812;
(f) C. Adachi, T. Tsutsui, S. Saito, Appl. Phys. Lett. 56 (1990) 799;
(g) C. Adachi, T. Tsutsui, S. Saito, Appl. Phys. Lett. 55 (1989) 1489.
[12] (a) M. Ghedini, I. Aiello, A. Grisolia, A. Crispini, M. La Deda, Substituted 8- hydroxyquinolines metal complexes for application in organic light emitting devices. N. Russo, D.R. Salahub, M. Witko (Eds.), Metal–Ligand Interactions. Molecular, Nano-, Micro-, and Macro Systems in Complex Environment, NATO Science Series II, Math., Phys. and Chem., vol. 16, 2003;
(b) M. Ghedini, M. La Deda, I. Aiello, A. Grisolia, Inorg. Chimica Acta 357 (2004) 33–40.
[13] W. Zhao, W. Wei, J. Lozano, J.M. White, Chem. Mater. 16 (2004) 750–756.
[14] C.H. Chen, J. Shi, Coord. Chem. Rev. 171 (1998) 161.
[15] M.D. Halls, H.B. Schlegel, Chem. Mater. 13 (2001) 2632.
[16] M. Amati, F. Lelj, J. Phys. Chem. A 107 (2003) 2560–2569.
[17] A. Curioni, M. Boero, W. Andreoni, Chem. Phys. Lett. 294 (1998) 263.
[18] G.P. Kushto, Y. Iizumi, J. Kido, Z.H. Kafafi, J. Phys. Chem. 104 (2000) 3670.
[19] M. Brinkmann, G. Gadret, M. Muccini, C. Taliani, N. Masciocchi, A. Sironi, J. Am. Chem. Soc. 122 (2000) 5147.
[20] M. Braun, J. Gmeiner, M. Tzolov, M. Coelle, F.D. Meyer, W. Milius, H. Hellebrecht, O. Wendland, J.U. von Schutz, W. Brutting, J. Chem. Phys. 114 (2001) 9625–9632.
[21] L.S. Sapochak, F.E. Benincasa, R.S. Schofield, J.L. Baker, K.K.C. Riccio, D. Fogarty, H. Kohlmann, K.F. Ferris, P.E. Burrows, J. Am. Chem. Soc. 124 (2002) 6119–6125.
[22] D.V. Nicolau, S. Yoshikawa, J. Mol. Graphics Modell. 16 (1998) 83.
[23] Y. Kai, M. Moraita, N. Yasuka, N. Kasai, Bull. Chem. Soc. Jpn. 58 (1985) 1631.
[24] M. Ghedini, M. La Deda, I. Aiello, A. Grisolia, J. Chem. Soc., Dalton Trans. (2002) 3406.
[25] M. Ghedini, M. La Deda, I. Aiello, A. Grisolia, Synth. Metals 138 (2003) 189–192.
[26] (a) F. Núñez-Zarur, R. Vivas-Reyes, J. Mol. Struct.: THEOCHEM. 850 (2008) 127–134;
(b) R. Vivas-Reyes, F. Núñez-Zarur, A. Padilla, J. Chinese Chem. Soc., in press.
[27] M.H. Cohen, A. Wasserman, J. Phys. Chem. A 111 (2007) 2229–2242.
[28] M.J. Frisch, G.W. Trucks, H.B. Schlegel, G.E. Scuseria, M.A. Robb, J.R. Cheeseman, J.A. Montgomery Jr., T. Vreven, K.N. Kudin, J.C. Burant, J.M. Millam, S.S. Iyengar, J. Tomasi, V. Barone, B. Mennucci, M. Cossi, G. Scalmani, N. Rega, G.A. Petersson, H. Nakatsuji, M. Hada, M. Ehara, K. Toyota, R. Fukuda, J. Hasegawa, M. Ishida, T. Nakajima, Y. Honda, O. Kitao, H. Nakai, M. Klene, X. Li, J.E. Knox, H.P. Hratchian, J.B. Cross, C. Adamo, J. Jaramillo, R. Gomperts, R.E. Stratmann, O. Yazyev, A.J. Austin, R. Cammi, C. Pomelli, J.W. Ochterski, P.Y. Ayala, K. Morokuma, G.A. Voth, P. Salvador, J.J. Dannenberg, V.G. Zakrzewski, S. Dapprich, A.D. Daniels, M.C. Strain, O. Farkas, D.K. Malick, A.D. Rabuck, K. Raghavachari, J.B. Foresman, J.V. Ortiz, Q. Cui, A.G. Baboul, S. Clifford, J. Cioslowski, B.B. Stefanov, G. Liu, A. Liashenko, P. Piskorz, I. Komaromi, R.L. Martin, D.J. Fox, T. Keith, M.A. Al-Laham, C.Y. Peng, A. Nanayakkara, M. Challacombe, P.M.W. Gill, B. Johnson, W. Chen, M.W. Wong, C. Gonzalez, J.A. Pople, Gaussian 03, Revision B.01, Gaussian Inc., Pittsburgh, PA, 2003.
[29] (a) A.D. Becke, J. Chem. Phys. 98 (1993) 5648;
(b) C. Lee, W. Yang, R.G. Parr, Phys. Rev. B 37 (1998) 785;
(c) W.J. Hehre, R. Ditchfield, J.A. Pople, J. Chem. Phys. 56 (1972) 2257;
(d) M.M. Francl, W.J. Petro, W.J. Hehre, J.S. Binkley, M.S. Gordon, D.J. DeFrees, J.A. Pople, J. Chem. Phys. 77 (1982) 3654.
[30] N.M. O'Boyle, J.G. Vos, Gauss Sum 0.8, Dublin City University, 2004.
[31] J. Zhang, R. Wan, Synth. Metals 152 (2005) 241–244.
[32] J. Zhang, G. Franking, Chem. Phys. Lett. 394 (2004) 120–125.
[33] J. Zhang, G. Franking, J. Phys. Chem. A 108 (2004) 10296–10301.
[34] H.-Z. Gao, Z-M. Su, J. Mol. Struct.: THEOCHEM. 722 (2005) 161–168.
[35] G. Gahungu, J. Zhang, J. Phys. Chem. B 109 (2005) 17762–17767.
[36] R.G. Parr, W. Yang, Density Functional Theory of Atoms and Molecules, Oxford University Press, New York, 1989.
[37] (a) P. Geerlings, F. De Proft, W. Langenaekar, Adv. Quant. Chem. 33 (1999) 303;
(b) P. Geerlings, F. De Proft, W. Langenaeker, Chem. Rev. 103 (2003) 1793.
[38] K. Hohenberg, W. Kohn, Phys. Rev. B 136 (1964) 864.
[39] R.G. Pearson, J. Am. Chem. Soc. 85 (1963) 3533.
[40] R.G. Parr, R.G. Pearson, J. Am. Chem. Soc. 105 (1983) 7512.
[41] R.G. Parr, R.A. Donnelly, M. Levy, W.E. Palke, J. Chem. Phys. 68 (1978) 3801.
[42] R.G. Pearson, J. Am. Chem. Soc. 107 (1985) 6801.
[43] R.G. Parr, W. Yang, J. Am. Chem. Soc. 106 (1984) 4049.
[44] R.G. Parr, L.V. Szentpaly, S. Liu, J. Am. Chem. Soc. 121 (1999) 1922.
[45] (a) P. Pérez, A. Toro-Labbe, A. Aizman, R. Contreras, J. Org. Chem. 67 (2002) 4747;
(b) E. Chamorro, P.K. Chattaraj, P. Fuentealba, J. Phys. Chem. A 107 (2003) 7068.
[46] W. Yang, W. Mortier, J. Am. Chem. Soc. 108 (1986) 5708.
[47] A.Curioni, Curioni, W.Andreoni, Andreoni, IBM J. Res. Dev. 45 (1) (2001).
[48] A. Rajagopal, A. Kahn, J. Appl. Phys. 84 (1998) 355.
[49] J. Kido, T. Matsumoto, Appl. Phys. Lett. 73 (1998) 2866.
[50] M.B. Huang et al, Appl. Phys. Lett. 72 (1998) 2914.
[51] A. Greiner, Polym. Adv. Technol. 9 (1998) 371–389.

[52] M. Stoßel, J. Staudigel, F. Steuber, J. Blassing, J. Simmerer, A. Winnacker, H. Neuner, D. Metzdorf, H.-H. Johannes, W. Kowalsky, Synth. Metals 111–112 (2000) 19–24.
[53] T.A. Hopkins, K. Meerholz, S. Shaheen, M.L. Anderson, A. Schmidt, B. Kippelen, A.B. Padias, H.K.J. Hall, N. Peyghambarian, N.R. Armstrong, Chem. Mater. 8 (1996) 344–351.
[54] L.S. Sapochak, A. Padmaperuma, N. Washton, F. Endrino, G.T. Schmett, J. Marshall, D. Fogarty, P.E.Y. Burrows, S.R. Forrest, J. Am. Chem. Soc. 123 (2001) 6300–6307.

Organic Electronics 9 (2008) 635–640

Contents lists available at ScienceDirect

Organic Electronics

journal homepage: www.elsevier.com/locate/orgel

Theoretical comparative studies of charge mobilities for molecular materials: Pet versus bnpery

Caili Wang [a,b], Fuhe Wang [a], Xiaodi Yang [b], Qikai Li [b], Zhigang Shuai [b,*]

[a] Department of Physics, Capital Normal University, 100037 Beijing, China
[b] Key Laboratory of Organic Solids, Institute of Chemistry, Chinese Academy of Sciences, 100080 Beijing, China

ARTICLE INFO

Article history:
Received 14 February 2008
Received in revised form 2 April 2008
Accepted 5 April 2008
Available online 16 April 2008

PACS:
72.20.Fr
85.30.Tv
63.20.dk
82.20.Db

Keywords:
Charge mobility
Organic field-effect transistor
Marcus electron transfer theory
First-principles calculations

ABSTRACT

Charge mobility is the most important issue for organic semiconductors. We calculate the electron and hole mobilities for prototypical polycyclic hydrocarbon molecules, perylothiophene (pet) and benzo(*g*,*h*,*i*)-perylene (bnpery) using Marcus electron transfer theory coupled with a diabatic model and a homogeneous diffusion assumption to obtain the charge mobility. The first-principles DFT calculations show that the hole mobility is about an order of magnitude higher than the electron mobility in pet. However, we find that for bnpery, the electron and hole transports are balanced, namely, very close in mobility, indicating the possible application in light-emitting field-effect transistor. The crystal packing effects on the frontier orbital coupling are found to be essential to understand such differences in transport behaviors.

1. Introduction

The charge transport mechanism in organic materials has been studied for many years [1–3]. In the application of field-effect transistors (FET) [4–6], light-emitting diodes (LED) [7–9], and photovoltaic cells (PVC) [10], organic materials possess great potentials. The charge mobility is the most important parameter in the performance of electronic devices such as organic field-effect transistor [11]. Traditionally, the organic molecules or polymers are believed to have very low carriers mobility, $\sim 10^{-5}$ cm^2/Vs. However, recently tremendous progresses have been made in increasing the mobility for organic semiconductor. In the single crystal of rubrene field-effect transistors, mobility has been found to be greater than 15 cm^2/Vs [12], and for the purified pentacene single crystal, the FET mobility has been measured to be 35 cm^2/Vs [13]. These values already compete well with the inorganic semiconductors: the typical room temperature mobilities for silicon single crystals, polycrystallines, and amorphous silicon are around a few hundreds, a few tens, and a few tenth of cm^2/Vs, respectively.

In this work, we make a comparative study on the transport properties of a class of polycycle aromatic hydrocarbons, perylothiophene (pet) [14] and benzo(*g*,*h*,*i*)-perylene (bnpery) [15] through first-principles calculation, in order to gain insights in the theoretical design of organic transport materials. The structure of pet is similar to that of bnpery. Pet has been grown in micrometer single crystal wires and has been successfully applied to fabricate transistor [16] with a room temperature mobility of 0.8 cm^2/Vs. The molecular structures are shown in Fig. 1. The crystal structures can be found in Refs. [14,15]. We will

* Corresponding author. Tel.: +86 10 62521934; fax: +86 10 62525573.
E-mail address: zgshuai@iccas.ac.cn (Z. Shuai).

1566-1199/$ - see front matter © 2008 Elsevier B.V. All rights reserved.
doi:10.1016/j.orgel.2008.04.003

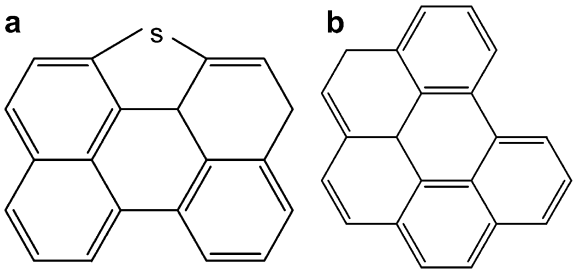

Fig. 1. Molecular structures of pet (a) and bnpery (b).

show that even though these molecules are quite similar in structure, they exhibit very different intrinsic transport properties.

2. Theoretical and computational methods

There exist two extreme models to describe the mechanism of charge transport: the coherent band model and the thermally activated hopping model. At very low temperature, the transport mechanisms in well ordered organic materials are believed to be described by a band-like model [17,18]. In this limit, the positive (hole) and negative (electron) charge carriers are fully delocalized, and the mobility can be evaluated through the effective mass approach. Even in the Holstein–Peierls model when evaluated at the first-principles level, the electron–phonon scattering induced bandwidth narrowing is not enough to give a fully localized charge picture [19]. It is found that both electron and hole transports fall in the coherent band-like regime. At room temperature, due to the thermal disorder and scattering, the transport is more appropriately described with hopping model [20–24]. In this case, the charge carriers are localized on a single molecule, jumping from one molecule to the adjacent molecule, with the hopping rate described by Marcus theory,

$$k = \frac{V^2}{\hbar}\left(\frac{\pi}{\lambda k_B T}\right)^{1/2} \exp\left(-\frac{\lambda}{4k_B T}\right) \quad (1)$$

Here, k_B is the Boltzmann constant, T is the temperature, V is the transfer integral between donor and acceptor, and λ is the reorganization energy. It indicates that the rate of charge hopping depends on two microscopic parameters: the electronic coupling term V and the reorganization energy λ The reorganization energy λ is usually expressed as the sums of internal and external contributions. The internal reorganization energy is induced by relaxation in the molecular geometry, and the external reorganization energy is caused by polarization of the surrounding medium, namely, all the other molecules in the bulk materials. The external contribution to the reorganization energy is quite complicated to evaluate, which depends on the molecular permanent dipole moments as well as the polarizability. We will simply assume some values for the external contribution to discuss the influences on the mobility. The internal reorganization energy λ_i is further divided into two parts: $\lambda_i^{(1)}$ and $\lambda_i^{(2)}$, where $\lambda_i^{(1)}$ corresponds to the geometry relaxation energy of one molecule from neutral state to charged state, and $\lambda_i^{(2)}$ corresponds to the geometry relaxation energy from charged state to neutral state, see Fig. 2 [25,26].

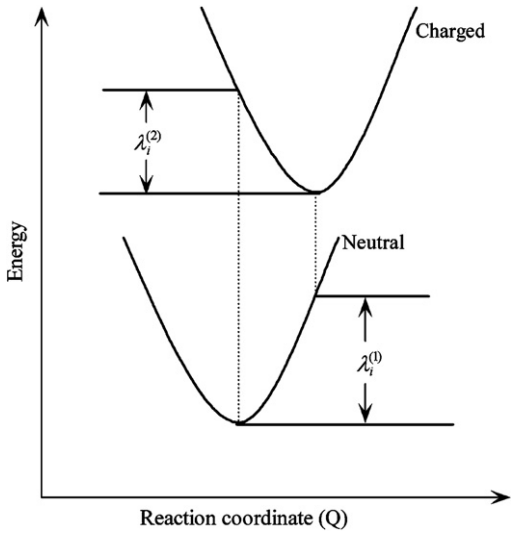

Fig. 2. Sketch of the potential energy surfaces for the neutral state and the charged state. The relaxation energies $\lambda_i^{(1)}$ and $\lambda_i^{(2)}$ are indicated.

In the evaluation of λ, the two terms were computed directly from the adiabatic potential energy surfaces [27,28],

$$\lambda = [E^{(1)}(A^+) - E^{(0)}(A^+)] + [E^{(1)}(A) - E^{(0)}(A)] \quad (2)$$

Here, $E^{(0)}(A)$, $E^{(0)}(A^+)$ are the ground-state energies of the neutral and charged states, $E^{(1)}(A)$ is the energy of the neutral molecule at the optimized charged geometry and $E^{(1)}(A^+)$ is the energy of the charged state at the geometry of the optimized neutral molecule.

Based the Einstein relation, the carrier mobility is obtained from the following Eq. (3):

$$\mu = \frac{e}{k_B T} D \quad (3)$$

where D is the diffusion constant. If we assume the charge motion is a homogeneous random walk, the diffusion constant can be evaluated as [29]:

$$D = \lim_{t\to\infty} \frac{1}{2n} \frac{\langle x(t)^2 \rangle}{t} \approx \frac{1}{2n} \sum_i d_i^2 k_i P_i = \frac{1}{2n} \frac{\sum_i d_i^2 k_i^2}{\sum_i k_i} \quad (4)$$

d is the intermolecular center-to-center distance and $n = 3$ is the spatial dimension. The hopping time between two adjacent molecules is the inverse of the rate constant $1/k$. The probability for a specific hopping route is $P_i = k_i/\Sigma_i k_i$. Namely, it is a 3-d averaged diffusion process. It is clear that the mobility is linearly proportional to the electron transfer rate. Within this mechanism, it is assumed that the localized electron can only hop between adjacent molecules, in sharp contrast to the band-like picture, where the electron is delocalized in several molecules.

The molecular structures of pet and bnpery are optimized both in the neutral and the charged states. These calculations are done at the first-principles DFT level using hybrid B3LYP functional with 6-31G* basis set [30]. All the calculations are performed in Gaussian 03 package [31].

The electronic coupling term, or the intermolecular transfer integral quantifies the electronic coupling between two interacting molecules, which is obtained through a direct approach. Namely, for the hole (electron) transport, the coupling between frontier orbitals of the two neighboring molecules is calculated from Eq. (5) [32,33].

$$V_{ij} = \langle \phi_1^0 | \hat{F}^0 | \phi_2^0 \rangle \tag{5}$$

V_{ij} is the transfer integral, ϕ_1^0 is the unperturbed frontier orbital of molecule 1, ϕ_2^0 is molecule 2 in the dimer. $\hat{F}^0$ is the Kohn–Sham–Fock operator of the dimer obtained with the unperturbed density matrix. Using the standard self-consistent-field procedure, the molecular orbitals and density matrix of the two individual molecules are calculated separately. These are used to evaluate the Kohn–Sham–Fock matrix of the dimer. This approach has been widely employed for organic molecular systems [34–36]. The calculations are carried out at the DFT level using pw91pw91 functional with 6-31G* basis set. It is shown by Huang and Kertesz, this functional gave the best description for intermolecular coupling term [37]. We have shown that this direct method for the coupling is equivalent to the site-energy corrected frontier orbital splitting method [35] and this direct method offers remarkable simplicity in computation.

3. Results and discussion

The calculated results of the relaxation energies $\lambda_i^{(1)}$ and $\lambda_i^{(2)}$ and reorganization energies λ in pet and bnpery are shown in Table 1. $\lambda_i^{(1)}$ and $\lambda_i^{(2)}$ are found to be nearly equal. It is also found that the total reorganization energy of hole for pet is slightly larger than that of bnpery. The reorganization energies for electron are nearly identical for both molecules.

Table 1
The relaxation energies $\lambda_i^{(1)}$ and $\lambda_i^{(2)}$, and the reorganization energies in pet and bnpery (in eV)

Molecular	Hole transfer			Electron transfer		
	$\lambda_i^{(1)}$	$\lambda_i^{(2)}$	λ_i	$\lambda_i^{(1)}$	$\lambda_i^{(2)}$	λ_i
Pet	0.066	0.069	0.135	0.084	0.088	0.172
Bnpery	0.063	0.062	0.125	0.082	0.082	0.164

The crystal structures for the molecules are shown in Fig. 3. The pet forms herringbone packing structure. In bnpery, two molecules form one bone in the skeleton, in place of one molecule in the herringbone structure. Starting from the crystal structure, we arbitrarily choose one molecule as the initial position for the charge to diffuse. The intermolecular transfer integrals with all the

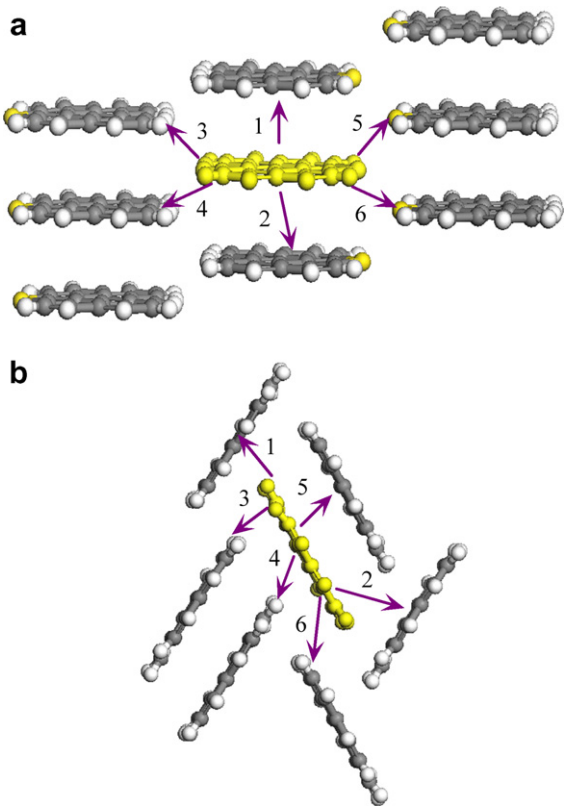

Fig. 4. Crystal structure and hopping routes in pet (a) and bnpery (b).

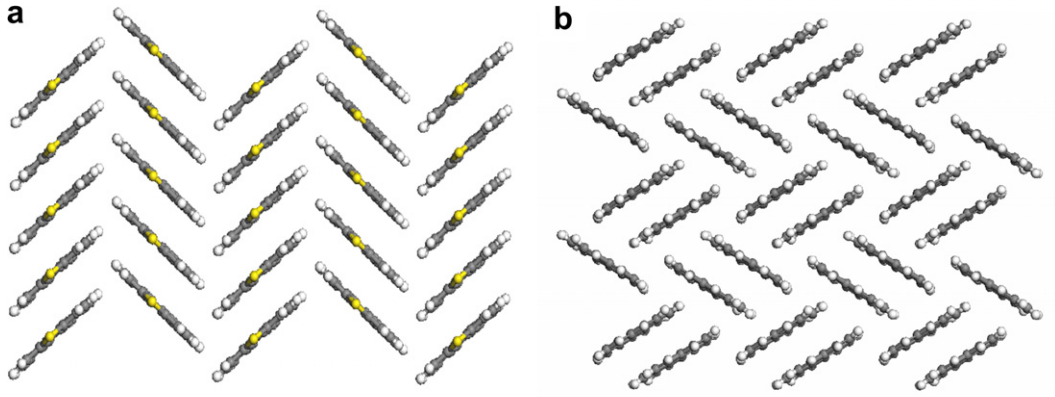

Fig. 3. (a) Herringbone structure of pet (view down the *C* axis), (b) structure of bnpery (view down the *A axis*).

Table 2
The center–center distance and the corresponding hole and electron coupling between the dimer in all the nearest neighbor pathway for pet

Pathway	Distance (Å)	Hole coupling (eV)	Electron coupling (eV)
1	4.52	0.181	6.4×10^{-2}
2	4.52	0.181	6.4×10^{-2}
3	10.21	2.8×10^{-4}	2.1×10^{-3}
4	9.18	2.0×10^{-3}	1.1×10^{-2}
5	8.76	7.8×10^{-4}	5.5×10^{-3}
6	9.89	3.4×10^{-5}	5.0×10^{-4}
Drift mobility (T = 300 K, in cm^2/Vs)		5.34	0.40

The calculated room temperature mobilities for electron and hole are given in the last line.

Table 3
The center–center distance and the corresponding hole and electron couplings between the dimer in all the nearest neighbor pathways for bnpery

Pathway	Distance (Å)	Hole coupling (eV)	Electron coupling (eV)
1	7.10	1.8×10^{-2}	3.4×10^{-3}
2	6.30	2.2×10^{-4}	7.5×10^{-3}
3	6.30	2.2×10^{-4}	7.5×10^{-3}
4	7.10	1.8×10^{-2}	3.4×10^{-3}
5	4.18	3.5×10^{-2}	8.1×10^{-4}
6	8.63	5.9×10^{-3}	2.6×10^{-2}
Drift mobility (T = 300 K, in cm^2/Vs)		0.17	0.21

The calculated room temperature mobilities for hole and electron are given in the last line.

adjacent molecules in a dimer model are evaluated. The most important six pathways (dimers) are shown in Fig. 4.

The transfer integrals for hole (for HOMO) and electron (for LUMO) are calculated, which are listed in Tables 2 and 3. The electronic coupling is determined by the relative distance and orientations of the interacting molecules. Except the case of electron coupling for bnpery, the parallel packing mode usually yields larger coupling term than the edge-corner packing, because the cofacial stacking structure is expected to provide more efficient orbital overlap.

Due to the electronic coupling for hole is much larger than for electron in pet, the calculated hole mobility is about one order of magnitude larger than that for electron. However, in bnpery, the largest transfer integral for hole is only 0.035 eV at pathway 5, and the largest transfer integral for electron is 0.026 eV at pathway 6. The hole mobility obtained is very close to and slightly less than that of electron mobility, the values being 0.17 cm^2/Vs and 0.21 cm^2/Vs, respectively. The theoretical calculation predicts that bnpery can be made as balanced transport materials. Even though the mobility is not as high as others, it can find application in light-emitting field-effect transistor.

It is intriguing to understand why bnpery behaves differently from pet. We then compare the frontier orbitals and packing modes in these two molecules, as illustrated in Fig. 5.

In pet, for the HOMO level, the wavefunction coefficients show a sign alternation for consecutive benzene along the aclinic direction, and the center-to-center offset of the two molecules of the cofacial dimer is nearly identical for benzene, and the displacement is also in the aclinic direction for pathway 1, the most efficient charge transfer route. The overall overlap is enhanced by the in-phase bonding (antibonding) of one molecular on top of the bonding (antibonding) of the other molecule for HOMO. However, for the LUMO level, the overall overlap is reduced by the cancellation of bonding (antibonding) orbital with the antibonding (bonding) interactions. Thus, the hole

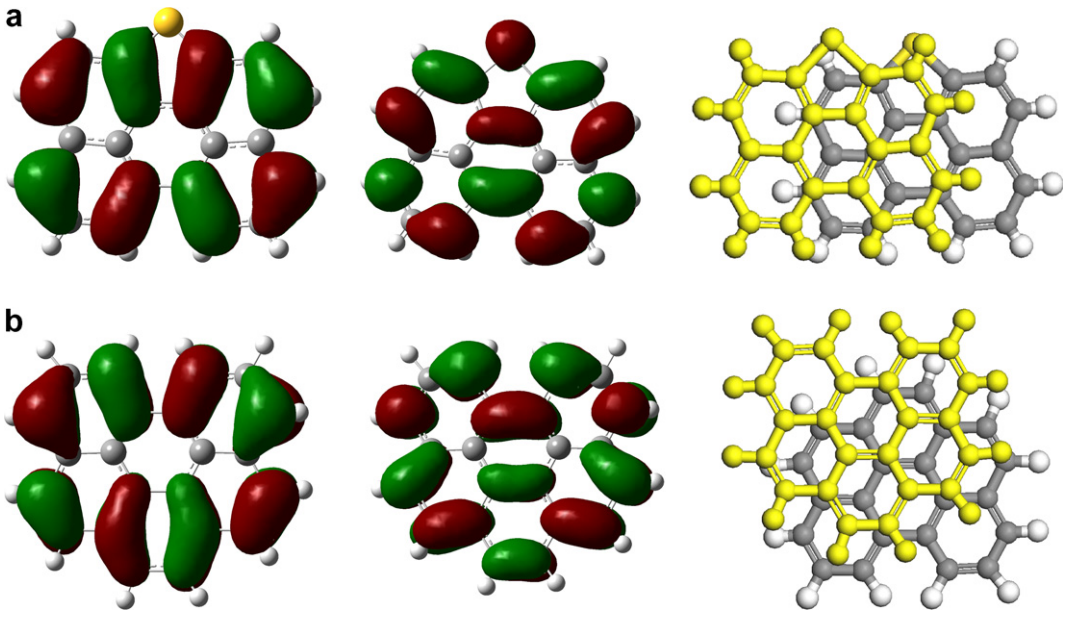

Fig. 5. HOMO, LUMO and the most important packing for (a) pet; and (b) bnpery.

transfer is more favored than the electron in pet, see Table 2. While in bnpery, the displacement between the two molecules occurs along the incline direction in pathway 5, the most efficient charge transfer route. Thus, the overall overlaps are reduced by out-phase cancellation of bonding with antibonding interaction for both HOMO and LUMO. Namely, both electron and hole possess similarly reduced charge transfer coupling terms, see Table 3. Thus, from the intermolecular interaction point of view, the hole transport character for pet and the balanced transport character for bnpery can be explained. At the same time, it also explains the reduced mobility in bnpery, namely, the cancellation of charger transfer couplings originated in packing out-phase displacement.

So far, we have completely neglected the external reorganization energy λ^e. This quantity is difficult to evaluate. Here, we simply calculate the hole mobilities for pet and bnpery as a function of λ^e, see Fig. 6. It is found that when λ^e goes from 0 to 0.2 eV, the mobility decreases about one order of magnitude. It should be borne in mind that such evaluation is too simplistic because once the polarization effect of surrounding molecules is considered, the electron coupling term should be also changed. This is out of the capability of present theoretical treatment. In addition, Marcus theory is basically a first-order perturbation in coupling term V. In fact, some of the dimer show quite strong coupling, for instance, $V = 0.181$ eV, even larger than the internal reorganization energy. We are pursuing now to develop a more rigorous approach dealing with strong coupling case.

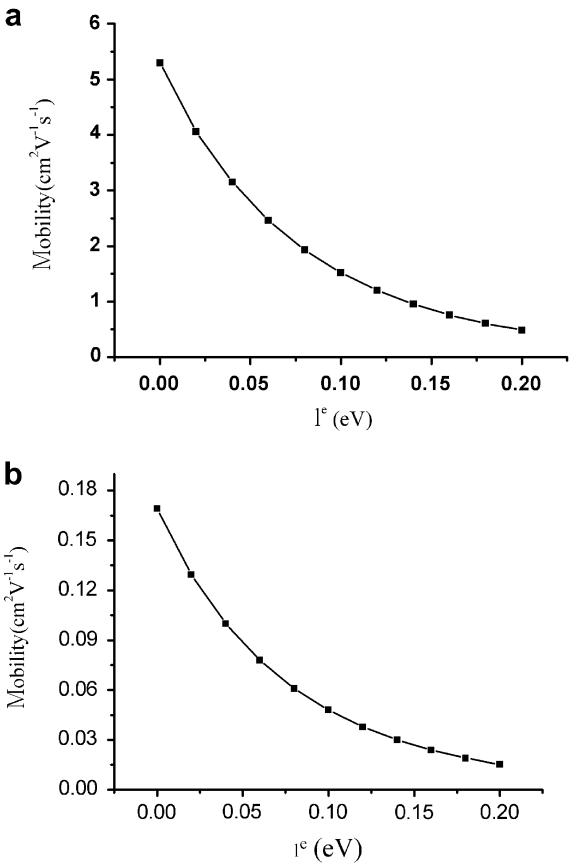

Fig. 6. Theoretical estimation of the room temperature (300 K) hole mobility as a function of external reorganization energy in the range of 0–0.2 eV.

We note that it is found that the carrier type, either electron or hole transport, in organic electronic device is determined by injection. Namely, if electron can be easily injected, then the transport will be *n*-type, and intrinsically, the materials are ambipolar in nature [38]. This view we believe is too simplistic. As we explain in the above paragraph, the intermolecular couplings for HOMO and for LUMO can be different according to the molecular structure. In solid state physics, a realistic crystal usually manifests different bandwidths for valence band and conduction band. Of course, such difference in coupling terms is not as significant as can be considered as the origin of unipolar transport, where injection plays essential role [38].

4. Conclusion

To conclude, by employing the first-principles DFT techniques and the Marcus electron transfer theory, we have comparatively investigated the transport properties for two polycyclic hydrocarbon compounds, pet and bnpery. The coupling terms are evaluated by a direct diabatic model, and the reorganization energies are calculated through adiabatic potential energy surfaces. The crystal packings are found to play essential role to determine the type of carriers in organic materials. In pet, the packing mode tends to enhance the HOMO coupling and to reduce the LUMO coupling, indicating a hole-dominant transport material. While, for bnpery, the packing mode tends to reduce both HOMO and LUMO coupling, which makes bnpery to be a promising material with great application potential in light-emitting field-effect transistor. These conclusions are drawn only based on material structures, without considering the carrier injection complexity.

Acknowledgements

The authors are indebted to Professors Daoben Zhu and Zhaohui Wang for insightful discussions on the relevant experiments. This work is supported by the Ministry of Science and Technology of China (Grant Nos. 2006CB932100 and 2006CB0N0100), NSFC, as well as the EU project MODECOM. The numerical calculation is performed at the Supercomputing Center of the Chinese Academy of Sciences.

References

[1] M. Pope, C.E. Swenberg, Electronic Processes in organic Crystals and Polymers, second ed., Oxford University Press, New York, 1999.
[2] E.A. Silinsh, V. Čápek, Organic Molecular Crystals: Interaction, Localization, and Transport Phenomena, AIP, New York, 1994.
[3] M.E. Gershenson, V. Podzorov, A.F. Morpurgo, Rev. Mod. Phys. 78 (2006) 973.
[4] C.D. Dimitrakopoulos, P.R.L. Malenfant, Adv. Mater. 14 (2002) 99.

[5] G.H. Gelinck, T.C.T. Geuns, D.M. de Leeuw, Appl. Phys. Lett. 77 (2000) 1487.
[6] Z. Bao, Adv. Mater. 12 (2000) 227.
[7] C.W. Tang, S.A. VanSlyke, App. Phys. Lett 51 (1987) 913.
[8] R.H. Friend, R.W. Gymer, A.B. Holmes, J.H. Burroughes, R.N. Marks, C. Taliani, D.D.C. Bradley, D.A. dos Santos, J.L. Brédas, M. Logdlund, W.R. Salaneck, Nature (London) 397 (1997) 121.
[9] G. Gustafson G, Y. Cao, G.M. Treacy, et al, Nature (London) 357 (1992) 477.
[10] S. Gunes, H. Neugebauer, N.S. Sariciftci, Chem. Rev. 107 (2007) 1324.
[11] F. Garnier, R. Hajlaoui, A. Yassar, P. Srivastava, Science 265 (1994) 1684.
[12] V. Podzorov, V.M. Pudalov, M.E. Gershenson, Appl. Phys. Lett. 82 (2003) 1739.
[13] O.D. Jurchescu, J. Baas, T.T.M. Palstra, Appl. Phys. Lett. 84 (2004) 3061.
[14] I.C. Santos, M. Almeida, J. Morgado, M.T. Duarte, L. Alcácer, L. Acta. Crystallogr. C 53 (1997) 1640.
[15] M. Munakata, L.P. Wu, G.L. Ning, T. Kuroda-Sowa, M. Maekawa, Y. Suenage, N. Maeno, J. Am. Chem. Soc. 121 (1999) 4968.
[16] Y.M. Sun, L. Tan, S.D. Jiang, H.L. Qian, Z.H. Wang, D.W. Yan, C.A. Di, Y. Wang, W.P. Wu, G. Yu, S.K. Yan, C.R. Wang, W.P. Hu, Y.Q. Liu, D.B. Zhu, J. Am. Chem. Soc. 129 (2007) 1882.
[17] Z. Iqbal, A.P. Webb, S. Veprek, S. Appl. Phys. Lett. 36 (1980) 163.
[18] Y.C. Cheng, R.J. Silbey, D.A. da Silva Filho, J.P. Calbert, J. Cornil, J.L. Brédas, J. Chem. Phys. 118 (2003) 3764.
[19] (a) T. Holstein, Ann. Phys. N.Y. 8 (1959) 343;
(b) K. Hannewald, P.A. Bobbert, Phys. Rev. B 69 (2004) 075212;
(c) L.J. Wang, Q. Peng, Q.K. Li, Z.G. Shuai, J. Chem. Phys. 127 (2007) 044506.
[20] R.A. Marcus, Rev. Mod. Phys. 65 (1993) 599.
[21] P.F. Barbara, T.J. Meyer, M.A. Ratner, J. Phys. Chem. 100 (1996) 13148.
[22] V. Balzani, A. Juris, M. Venturi, S. Campagna, S. Serroni, Chem. Rev. 96 (1996) 759.
[23] M. Malagoli, J.L. Brédas, Chem. Phys. Lett. 327 (2000) 13.
[24] K. Sakanoue, M. Motoda, M. Sugimoto, S. Sakaki, J. Phys. Chem. A 103 (1999) 5551.
[25] N.E. Gruhn, D.A. da Silva Filho, T.G. Bill, M. Malagoli, V. Coropceanu, A. Kahn, J.L. Brédas, J. Am. Chem. Soc. 124 (2002) 7918.
[26] J.R. Reimers, J. Chem. Phys. 115 (2001) 9103.
[27] J.L. Brédas, D. Beljonne, V. Coropceanu, J. Cornil, Chem. Rev. 104 (2004) 4971.
[28] V. Coropceanu, T. Nakano, N.E. Gruhn, O. Kwon, T. Yade, K. Katsukawa, J.L. Brédas, J. Phys. Chem. B 110 (2006) 9482.
[29] W.Q. Deng, W.A. Goddard III, J. Phys. Chem. B 108 (2004) 8614.
[30] A.D. Becke, J. Chem. Phys. 98 (1993) 5648;
C. Lee, W.T. Yang, R.G. Parr, Phys. Rev. B 37 (1988) 785.
[31] M.J. Frisch, et al. Gaussian 03, Revision A. 1, Gaussian Inc., Pittsburgh, 2003.
[32] T. Fujita, H. Nakai, H. Nakatsuji, J. Chem. Phys. 204 (1996) 2410.
[33] A. Troisi, G. Orlandi, J. Phys. Chem. A 110 (2006) 4065.
[34] S.W. Yin, Y.P. Yi, Q.X. Li, G. Yu, Y.Q. Liu, Z.G. Shuai, J. Phys. Chem. A 110 (2006) 7138.
[35] X.D. Yang, Q.K. Li, Z.G. Shuai, Nanotechnology 18 (2007) 424029.
[36] O. Kwon, V. Coropceanu, N.E. Gruhn, J.C. Durivage, J.G. Laquindanum, H.E. Katz, J. Cornil, J.L. Brédas, J. Chem. Phys. 120 (2004) 8186.
[37] J.S. Huang, M. Kertesz, Chem. Phys. Lett. 390 (2004) 110.
[38] J. Zaumseil, H. Sirringhaus, Chem. Rev. 107 (2007) 1296.

Organic Electronics 9 (2008) 641–648

Contents lists available at ScienceDirect

Organic Electronics

journal homepage: www.elsevier.com/locate/orgel

Matrix influence on the OLED emitter Ir(btp)$_2$(acac) in polymeric host materials – Studies by persistent spectral hole burning

Reinhard Bauer [a], Walter J. Finkenzeller [a], Udo Bogner [a], Mark E. Thompson [b], Hartmut Yersin [a,*]

[a] Universität Regensburg, Institut für Physikalische Chemie, 93040 Regensburg, Germany
[b] University of Southern California, Department of Chemistry, Los Angeles, California 90089, USA

ARTICLE INFO

Article history:
Received 28 January 2008
Received in revised form 2 April 2008
Accepted 5 April 2008
Available online 14 April 2008

Keywords:
Triplet emitter
OLED
Persistent spectral hole burning
Zero-field splitting
Polyvinylbutyral
Poly-*N*-vinylcarbazol
Poly(9,9-dioctylfluoren-2,7-diyl)
Ir(btp)$_2$(acac)
Phosphorescence line narrowing
Metal-to-ligand charge transfer
PVK
PVB
PFO
MLCT
ZFS
Spin–orbit coupling
SOC

ABSTRACT

Fundamental photophysical properties of the phosphorescent organometallic complex Ir(btp)$_2$(acac) doped in the polymeric matrices PVK, PFO, and PVB, respectively, are investigated. PVK and PFO are frequently used as host materials in organic light emitting diodes (OLEDs). By application of the laser spectroscopic techniques of phosphorescence line narrowing and persistent spectral hole burning – improved by a synchronous scan technique – we studied the zero-field splitting (ZFS) of the $\mathbf{T_1}$ state into the substates **I**, **II**, and **III.** Thus, we were able to probe the effects of the local environment of the emitter molecules in the different amorphous matrices. The magnitude of ZFS is determined by the extent of spin–orbit coupling (SOC) of the $\mathbf{T_1}$ state to metal-to-ligand charge transfer (MLCT) states. Only by mixings of MLCT singlets, a short-lived and intense emission of the triplet state to the singlet ground state becomes possible. Thus, sufficiently large ZFS is crucial for favorable luminescence properties of emitter complexes for OLED applications. The analysis of the spectral hole structure resulting from burning provides information about the ZFS values and their statistical (inhomogeneous) distribution in the amorphous matrices. For Ir(btp)$_2$(acac), we found a significant value of $\approx$18 cm^{-1} for the splitting between the substates **II** and **III** for all three matrices. Interestingly, for PVK the width of the ZFS distribution is found to be $\approx$14 cm^{-1} – almost twice as large as for PFO and PVB. Consequently, for a considerable fraction of Ir(btp)$_2$(acac) molecules in PVK, the ZFS is relatively small and thus, the effective SOC is weak. Therefore, it is indicated that a part of the emitter molecules shows a limited OLED performance.

1. Introduction

Phosphorescent organo-transition metal complexes are often applied as emitters in organic light emitting diodes (OLEDs) due to their high electroluminescence efficiencies [1]. Ir(btp)$_2$(acac) ((bis(2,2′-benzothienyl)-pyridinato-N,C$^{3'}$)Iridium(acetylacetonate)), (inset in Fig. 1a) is a well studied OLED emitter [2–10]. It features a saturated red emission peaked at 612 nm [2–4] and a high photoluminescence quantum efficiency. For example, in a film of CBP (4,4′-bis(carbazol-9-yl)biphenyl)) a quantum efficiency of $\approx$50% and an emission decay time of about 6 μs were measured [4,11]. Attractive photophysical properties like these are connected with a significant metal-to-ligand charge transfer (MLCT) character of the emitting $\mathbf{T_1}$ state [12–17]. In particular, the MLCT character promotes quantum mechanical admixtures of higher lying singlet states to the emitting $\mathbf{T_1}$ state via spin–orbit coupling (SOC) [17]. Such admixtures are required to open radiative decay paths from the excited triplet state $\mathbf{T_1}$ to the singlet ground state $\mathbf{S_0}(\mathbf{0})$. This means that the photophysical properties important for OLED applications, such as short emission

* Corresponding author.
E-mail address: hartmut.yersin@chemie.uni-regensburg.de (H. Yersin).

1566-1199/$ - see front matter © 2008 Elsevier B.V. All rights reserved.
doi:10.1016/j.orgel.2008.04.001

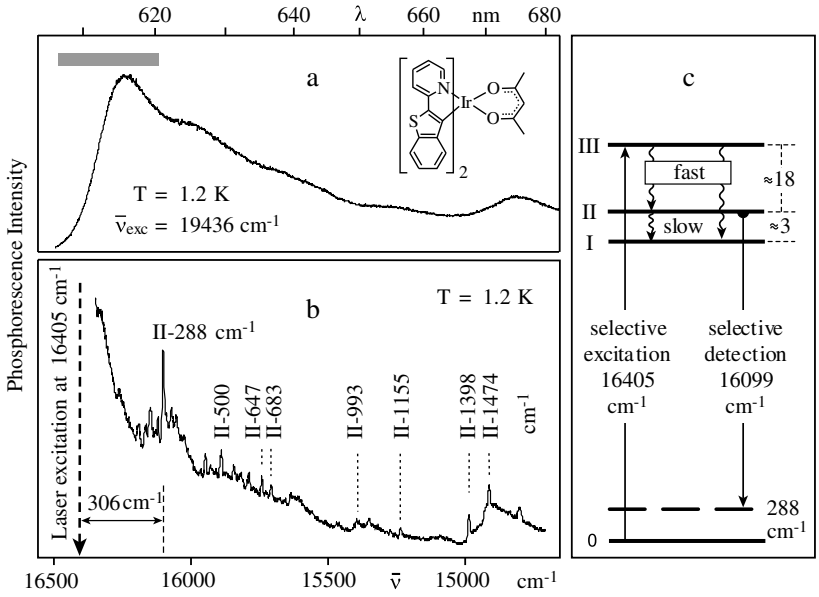

Fig. 1. Emission spectra of Ir(btp)$_2$(acac) in PFO upon excitation at (a) 19,436 cm^{-1} and at (b) 16,405 cm^{-1}. Phosphorescence line narrowing can be obtained by excitation in the region between about 16,100 cm^{-1}and 16,500 cm^{-1} (shaded bar in (a)). The intensity of the vibrational zero-phonon line (ZPL) at a spectral distance of 306 cm^{-1} from the exciting laser energy was used for probing of the spectral holes (see Fig. 2). Both spectra were measured in superfluid Helium at 1.2 K. The inset in (a) shows the chemical structure of Ir(btp)$_2$(acac). (c) Reproduces the energy level diagram for the triplet substates and depicts selected radiative and radiationless deactivation paths. The dashed line represents the vibrational level of the 288 cm^{-1} ground state mode.

decay times and high photoluminescence quantum yields, are governed by the extent of MLCT character in the emitting triplet term [12–17]. As the MLCT character is correlated to the magnitude of zero-field splitting (ZFS) of the $\mathbf{T_1}$ state into substates **I**, **II** and **III** (compare e.g. Refs. [12–17]) and as the individual features of these substates are responsible for the emission properties, it is of high interest to investigate the characteristics of the substates in more detail. Very recently, it has been shown that the photophysical properties of the triplet state of Ir(btp)$_2$ (acac) distinctly depend on the environment of the emitter complex. Emission decay times, ZFSs, spin-lattice relaxation times [18], etc., are different for different sites of the Ir complex in the matrix [12–14]. For example, the energy separations between the three $\mathbf{T_1}$ substates of Ir(btp)$_2$ (acac) have been determined on the basis of highly resolved spectra in polycrystalline hosts, such as octane or dichloromethane [12,13]. Hereby, it was found that the magnitude of ΔE(ZFS) can differ by almost a factor of two for different sites in the same host material [12]. Therefore, the influence of the host, especially of OLED relevant hosts, on the ZFS (and thus on essential photophysical properties) is of high interest.

However, with amorphous hosts – as typically used for emission layers in OLEDs – only very broad emission bands are observed. In this situation, indirect approaches of analyzing the temperature dependence of emission decay data were used to provide information about the individual properties of the triplet substates (for example, see Refs. [14,17]). On the other hand, luminescence line narrowing [19] and persistent spectral hole burning [20] represent methods which allow for high-resolution spectroscopy of dye molecules doped into amorphous hosts.[1] Most of the work published to date concerns singlet-singlet transitions (e.g. see Refs. [20–22]), but also singlet–triplet transitions [23–25] and transitions between levels of higher multiplicity [26–28] have been investigated. However, these methods have not yet been applied to OLED relevant emitter/matrix systems.

In the present study, we report on persistent spectral hole burning as a method for the investigation of the ZFS and its inhomogeneous distribution applied to the emitting triplet state of Ir(btp)$_2$(acac) doped into a common polymer (PVB = polyvinylbutyral) and two polymers which are frequently applied in OLEDs (PVK = poly-*N*-vinylcarbazol, PFO = (poly(9,9-dioctylfluoren-2,7-diyl). One goal is to obtain information on how the ZFS data obtained in Shpol'skii and Shpol'skii-like matrices relate to the properties of emitter complexes in an amorphous matrix. Further, we are interested in the inhomogeneous distribution of the ZFS values and thus of the MLCT character of the emitting triplet states. An analysis provides information about photophysical differences of the various subsets of molecules in the same amorphous matrix. The discussion indicates that a fraction of the molecules in polymer OLED matrices can exhibit less favorable emission properties for OLED applications.

2. Experimental

The samples of PVB (polyvinylbutyral, Hoechst), PVK (poly-*N*-vinylcarbazol, Acros) and PFO (poly(9,9-dioctylflu-

[1] The corresponding methods are explained in Sections 3.1 and 3.3, respectively.

oren-2,7-diyl), Aldrich) doped with $Ir(btp)_2(acac)$ at concentrations of about 10^{-3} mol/l were prepared as films of about 100 μm thickness from solution, using ethanol (PVB) or dichloromethane (PVK, PFO) as solvents. The complex was synthesized according to the procedure described in Ref. [2]. Spectral holes were burnt and probed with a (Spectra-Physics Model 380) dye ring laser with a spectral band width of about 0.1 cm^{-1}. The laser wavelength was scanned by turning the birefringent filter by means of a DC motor and recorded by a wavemeter (Burleigh WA20-VIS). For non-selective excitation, the 514.5 nm line of the Ar ion pump laser was used. The samples were immersed in an optical Helium bath cryostat which could be cooled down to $T = 1.2$ K by pumping off the He vapor. The emitted phosphorescence light was dispersed by a Spex 1401 double monochromator and detected by photon counting with a cooled RCA C7164R photomultiplier.

3. Results and discussion

3.1. Phosphorescence line narrowing for $Ir(btp)_2(acac)$ in the amorphous PFO host

The emission spectrum of $Ir(btp)_2(acac)$ doped into PFO strongly depends on the excitation energy. When a narrow-line excitation is chosen at a high energy, for example at 19,436 cm^{-1} (514.5 nm), which lies in the region of the homogeneously broadened $\mathbf{S_0} \rightarrow {}^1\mathbf{MLCT}/{}^3\mathbf{MLCT}$ transitions [12], the usual and well-known broad-band emission spectrum is obtained, even at $T = 1.2$ K (Fig. 1a). However, upon narrow-line excitation within the inhomogeneously broadened $\mathbf{S_0} \rightarrow \mathbf{T_1}$ transition range between about 16,100 and 16,500 cm^{-1} (shaded bar in Fig. 1a), for example at 16,405 cm^{-1}, a well-resolved emission spectrum can be recorded, even in this amorphous polymer host (Fig. 1b). In this case, the laser excites dominantly just that specific site of $Ir(btp)_2(acac)$ in PFO, which has an electronic 0–0 transition precisely at the chosen excitation energy. More exactly, due to the zero-field splitting of the $\mathbf{T_1}$ term into the substates **I**, **II**, and **III** and due to the much higher transition probability of the transition $\mathbf{0} \rightarrow \mathbf{III}$ compared to $\mathbf{0} \rightarrow \mathbf{II}$,**I**, specifically those molecules will be excited with preference, which have their $\mathbf{0} \rightarrow \mathbf{III}$ transition at the laser energy. (The $\mathbf{0} \rightarrow \mathbf{III}$ transition probability is by one and two orders of magnitude larger than that of the transition $\mathbf{0} \rightarrow \mathbf{II}$ and $\mathbf{0} \rightarrow \mathbf{I}$, respectively [12,13]). The structure displayed in Fig. 1b represents part of a resolved vibrational satellite structure [14] which stems from a triplet substate. Although substate **III** is excited selectively, emission from this state is not observed at low temperature. This is due to fast relaxation, i.e. fast spin-lattice relaxation (SLR), from this state to the two lower lying substates [13,14,18] (Fig. 1c). On the other hand, SLR between the substates **II** and **I** is very slow [13]. Thus, these two triplet substates both emit, even at $T = 1.2$ K. Analysis of the vibrational satellite structure of $Ir(btp)_2(acac)$ doped into a crystalline CH_2Cl_2 matrix, as carried out in Ref. [14], allows us to identify most of the satellites in the line-narrowed spectrum shown in Fig. 1b. The dominant line represents a vibrational satellite stemming from substate **II** and is induced by a 288 cm^{-1} Franck-Condon active mode (Fig. 1c) [14]. This line is found 306 cm^{-1} below the excitation energy. This value fits well, if it is assumed that substate **III** lies 18 cm^{-1} above substate **II** (288 cm^{-1} + 18 cm^{-1} = 306 cm^{-1}). The value of 18 cm^{-1} lies within the range of ΔE(ZFS) energies as determined in Ref. [12]. An independent confirmation of this splitting energy is given below. The 288 cm^{-1} vibrational satellite line – a so-called vibrational zero-phonon line (ZPL) – is accompanied by a phonon sideband at the low-energy side. This band results from couplings of low-energy vibrational modes of the complex in its matrix cage to the electronic structure/transition. These modes, often called local phonon modes (resulting from hindered rotational motions of the emitter molecules in their matrix cages), have energies in the range of 15–30 cm^{-1}. They frequently occur together with purely electronic 0–0 transitions and also – as shown in Fig. 1b – together with vibrational ZPLs [14,15].

As characteristic of phosphorescence line narrowing, the spectral shift between the exciting laser energy and the specific vibrational satellite line is almost independent of the excitation energy, when it lies within the inhomogeneously broadened absorption band. The absorption in the region of the electronic 0–0 transition depends on the excitation energy due to a varying spectral density of resonantly absorbing molecules.

For the investigations presented in this study, the vibrational satellite with a shift of 306 cm^{-1} relative to the exciting laser is selected for the detection of the spectral holes by a specific synchronous scanning method. This method will be described in the next section.

The specific vibrational satellite $\mathbf{II} \rightarrow \mathbf{0}$ + 288 cm^{-1} (representing a vibrational zero-phonon line) can be observed in the phosphorescence line-narrowed spectra of the $Ir(btp)_2(acac)$ complex for all three matrices. The width of this line is ≈ 7 cm^{-1} in PFO and PVB, while it is ≈18 cm^{-1} in PVK. The 288 cm^{-1} vibrational ZPL in the PFO matrix has the highest intensity relative to the background compared to the other matrices.

3.2. Detection of spectral holes by a synchronous excitation–detection scan technique

The intensity of a vibrational satellite (vibrational ZPL) depends linearly on the number of resonantly absorbing emitter molecules. Thus, the spectral dependence gives information about the inhomogeneous distribution. Using this relation, persistent spectral holes – after having been burnt (Section 3.3) – are probed in a luminescence excitation technique as schematically depicted in Fig. 2. Hereby, a narrow-line light source of relatively weak intensity excites a subset of molecules within the range of the inhomogeneously broadened band of the purely electronic transition. The detection energy is set to the maximum of a specific (resolved) vibrational satellite. Now scanning the excitation energy, while keeping the energy difference between detection and excitation constant, reproduces the inhomogeneous distribution function. If a persistent spectral hole has been burnt into this distribution (Section 3.3), the reduced density of resonantly absorbing molecules at the burning energy is directly displayed in the excitation spectrum (dashed structure in Fig. 2).

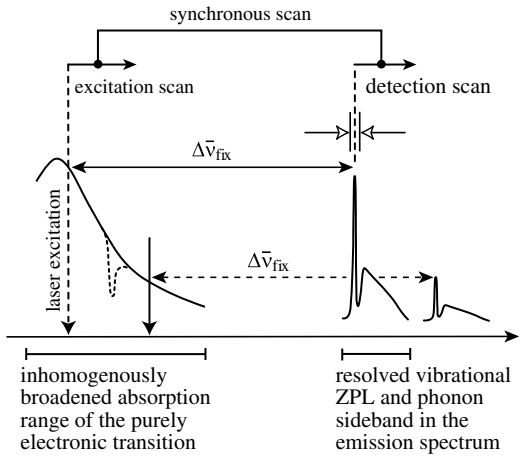

Fig. 2. Schematic diagram to illustrate the synchronous scan technique for the measurement of luminescence excitation spectra. The tunable narrow-line laser light (vertical arrow) excites preferentially a strongly absorbing subset of emitter molecules within its inhomogeneously broadened, purely electronic absorption range. At low temperature, a spectrum results, which usually consists of several vibrational zero-phonon satellite lines (ZPL, vibrational satellites) and the corresponding phonon sidebands, as explained in Section 3.1. In this diagram, only one ZPL with its phonon sideband is displayed. The inhomogeneous distribution of the purely electronic transitions is obtained by tuning the detection wavelength synchronously with a fixed energy separation $\bar{\nu}_{fix}$ relative to the excitation energy. For detection, a vibrational ZPL is chosen, which occurs with high intensity. The amplitude of the signal in emission is almost proportional to the number of resonantly excited molecules. The dashed spectral structure shows the modified band after burning of a persistent spectral hole (see Section 3.3).

For the experiments described in this investigation, the vibrational ZPL with a shift of 306 cm^{-1} was used (see Section 3.1, Fig. 1b) primarily because of the high intensity of this satellite relative to the background intensity. According to the discussion presented in Section 3.1, the resonant absorption of $\mathbf{T_1}$ substate **III** is by far the strongest among the three triplet substates of $Ir(btp)_2(acac)$ [12–14]. Therefore, we infer that this synchronous scanning technique maps dominantly the inhomogeneous distribution function (absorption) of the $\mathbf{0} \rightarrow \mathbf{III}$ transition, as long as no vibrational levels of lower lying emitters (e.g. $\mathbf{0} \rightarrow \mathbf{III} + \bar{\nu}_0$) are involved in the excitation process. In order to avoid complications due to the excitation of such vibrational levels, we performed the hole burning experiments at the long-wavelength side of the inhomogeneous distribution. This is the first time that this synchronous scan technique has been reported.

3.3. Persistent spectral hole burning of triplet substates in different amorphous hosts

Narrow-line and intense excitation within an inhomogeneously broadened electronic transition of a light absorbing species leads to reduced absorption of the sample at the excitation (laser) energy in the course of the laser excitation, and thus to the burning of a persistent spectral hole in the absorption or luminescence excitation spectrum[20]. The persistent spectral hole is a consequence of a photophysical or a photochemical burning mechanism. In addition to the spectral holes (reduced absorptions), areas of weakly increased absorption (anti-holes) are also formed. If the anti-holes lie close to the burning energy, in the spectral range of the inhomogeneously broadened electronic transition, a photophysical hole burning mechanism is indicated. This mechanism can be explained by phonon-induced barrier crossings within asymmetric double well potentials[2] which are characteristic for disordered systems [29]. Such a barrier crossing corresponds, for example, to a rearrangement of the light absorbing species in its matrix cage or of any other atom, ion or molecule in the immediate neighborhood (compare e.g. Ref. [30]). During the hole burning process, the transfer from one potential minimum to another one results in a different absorption energy of the light absorbing species. At low temperature, this new situation can be stable and a persistent spectral hole results. Persistent photophysical hole burning can occur in amorphous materials or in systems with at least local disorder [21,29–31]. Photochemical hole burning, on the other hand, is usually related to anti-holes which occur in more distant energy regions relative to the burning (laser) energy, since in this case the molecular structure is changed.

Persistent spectral holes can provide spectral structures in the absorption range of the purely electronic transition, which are several orders of magnitude narrower than the inhomogeneously broadened band. As a consequence, high-resolution spectroscopy is possible, if the absorption can be scanned over the range of the burnt hole. Since the existence of zero-phonon lines is required, most hole burning experiments are carried out at liquid He temperatures.

With $Ir(btp)_2(acac)$ doped into the amorphous PVB host, we observed persistent spectral hole burning at $T = 1.2$ K (Fig. 3). At a short burning time, e.g. of $t_b = 130$ s, a spectral hole can be seen only at the energy of the burning laser (hole A in Fig. 3a). With increasing burning time, the spectrum changes. Successively, an additional narrow hole component develops at the high-energy side and a broad hole appears at the low-energy side of the laser energy. The left part of Fig. 3 shows the spectral hole structure in PVB after three different burning times t_b with a burning intensity of about 10 W/cm^2 at 16,500 cm^{-1}. The width (FWHM) of the resonant hole A increases from 1.7 cm^{-1} after 130 s to 2.4 cm^{-1} after 2480 s. Since we observed that the width of the resonant hole depends only on the duration of the hole burning and not on the power density of the burning laser, local heating is not expected to be responsible for the increase of the width. This increase rather is attributed to dynamical processes in the double well potentials in the course of the burning, which lead to slight spectral line shifts and as a consequence to a line broadening. The side hole shifted by about 18 cm^{-1} from the resonant hole to the high-energy side has a width of 6.4 cm^{-1}. The relatively broad asymmetric hole which

[2] A more precise description requires the knowledge of the potential hypersurface. However, for the treatment of a hole burning process by a phonon induced crossing of a barrier between two minima of the potential hypersurface, it is usually sufficient to replace this hypersurface by asymmetric double well potentials. Thereby, only the knowledge of the asymmetry and the barrier height are necessary [29].

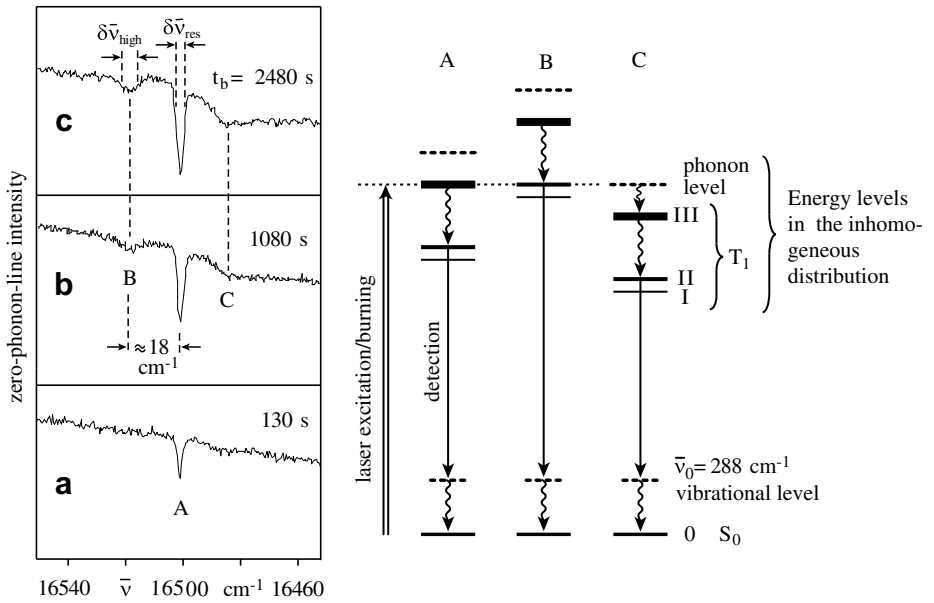

Fig. 3. Persistent spectral holes burnt at 16,500 cm^{-1} in the guest/host system $Ir(btp)_2(acac)$/PVB after different burning times t_b at $T = 1.2$ K. The spectral holes were probed by recording the intensity of the strong vibrational satellite (vibrational ZPL) shifted by 306 cm^{-1} relative to the exciting laser energy. The emission stems from substate **II** and is detected at the 288 cm^{-1} vibrational satellite. The diagram on the right hand side displays energy level schemes of three different subsets A, B, and C of molecules which lie within the inhomogeneous distribution. At a fixed laser energy, the laser burns at different levels with different absorption strengths of the doped molecules. Thus, three hole components A, B, and C result. The differences of the absorption cross sections are indicated by the thicknesses of the levels representing the triplet substates **I**, **II**, and **III**, respectively, and the dashed lines above substate **III** represent a phonon level of this substate. From the different hole components A and B and their evolution with burning time, the relative absorption cross sections of the transitions to the $\mathbf{T_1}$ substates **II** and **III**, the amount of energy splitting and, in particular, the distribution of these splittings can be determined. $\delta\bar{\nu}_{res}$ and $\delta\bar{\nu}_{high}$ represent the half widths (FWHM) of the resonant hole and of the high-energy side hole, respectively.

appears at the low-energy side is shifted by about 17 cm^{-1}. While the central component is almost saturated after 1080 s, the side components still deepen with further burning time. Quantitative analysis by fitting with Gaussian line shapes indicates that the central hole component has about the same area after 130 s burning time as the high-energy component after 1080 s (for a quantitative explanation see below).

After sufficient burning time, the measured hole spectrum shows a triple structure, with the central hole resonant with the burning laser energy, and two side holes – one low-energy and one high-energy component. Taking into account that probing displays the inhomogeneous distribution of the $\mathbf{T_1}$ substate **III** (see Section 3.1), it can be concluded that with increasing burning time different subsets of emitter molecules are involved. Burning is most efficient for molecules with highest absorption cross section, i.e. for those molecules with the energy of their substate **III** at the laser energy. Thus, the central component can be attributed to burning of molecules absorbing the laser by their $\mathbf{0} \rightarrow \mathbf{III}$ transition (compare subset "A" in Fig. 3).

$Ir(btp)_2(acac)$ complexes with their $\mathbf{T_1}$ substate **II** in resonance with the burning laser have their substate **III** blue shifted by the corresponding ZFS value of $\Delta E_{III,II}$. Therefore, the high-energy hole component can be attributed to the burning of $Ir(btp)_2(acac)$ complexes which absorb at the laser energy with their $\mathbf{0} \rightarrow \mathbf{II}$ transition (compare subset "B" in Fig. 3). The measured energy difference of both hole components represents the energy difference $\Delta E_{III,II}$. A value of about 18 cm^{-1} is found. A similar value of ZFS is reported in Refs. [12–14]. In these studies, highly resolved spectra of $Ir(btp)_2(acac)$ doped into polycrystalline dichlormethane and octane, respectively, were investigated.

The hole component shifted by 17 cm^{-1} to the red originates from molecules, which are burnt by absorption of energy levels above the $\mathbf{T_1}$ substate **III**. The most probable explanation is an absorption (burning) into a localized phonon of the excited substate **III** (compare subset C in Fig. 3), since spectral shape and energy of this low-energy side hole resemble those of typical phonon side bands [15].

From the longer build-up time of the high-energy hole component relative to the central component the ratio of absorption cross sections for the transitions to the involved triplet substates **II** and **III** can be estimated. The hole area of the central component in PVB after 130 s burning time is in good approximation the same as the area of the blue shifted component after 1080 s. Assuming the same hole burning quantum yields for both subsets of molecules, the difference of burning times can be attributed to the different absorption cross sections. Accordingly, the absorption cross section of the transition from the singlet ground state $\mathbf{S_0}$ to substate **III** can be estimated to be by a factor of ≈8 higher than that of the transition to substate **II**. This value lies in the range found for the ratios of emission decay times from the studies of different sites of $Ir(btp)_2(acac)$ in CH_2Cl_2 [13].

The absorption cross section of the **0** → **I** transition of $Ir(btp)_2(acac)$ is several times lower than those of the transitions to the substates **II** and **III**. Therefore, the observation of the corresponding side holes would require substantially longer burning times, which was not feasible with the available experimental equipment. Consequently, substate **I** is not displayed in the hole burning spectra.

For completeness, it is remarked that anti-hole areas were observed within the inhomogeneous distribution of the electronic transitions of the emitter molecules in the matrix. For example, an anti-hole is manifested in the small intensity increase in the spectral range between hole A and hole B (in Fig. 3 curve for t_b = 2480 s). This intensity increase (representing an increase of the absorption) is enhanced with further burning, i.e. the anti-hole becomes more distinct. The occurrence of anti-holes in this spectral range indicates a photophysical hole burning mechanism.

Spectral hole burning was also observed with $Ir(btp)_2$-(acac) embedded in PFO and PVK, respectively. Fig. 4 compares hole spectra for the three matrices, whereby the spectrum depicted in Fig. 4a is the same as the one shown in Fig. 3 after 2480 s burning time. The hole in PFO was burnt with an intensity of about 100 W/cm^2 for 10 min resulting in a width of 2.6 cm^{-1} of the resonant component (Fig. 4b). Here, the high-energy component is also shifted by about 18 cm^{-1} and has a width of about 8 cm^{-1}. The separation of the hole components is practically identical to the one found for $Ir(btp)_2(acac)$ doped into PVB. The low-energy component, however, has its minimum shifted by about 15 cm^{-1} and is the least pronounced one in all matrices investigated. The latter observation is in accordance with a comparatively weak electron–phonon coupling in PFO.

In the PVK matrix, $Ir(btp)_2(acac)$ showed significantly lower burning efficiency than in PFO (Fig. 4c). After 4200 s of burning with a strongly focused laser beam of about 1000 W/cm^2, the resulting central hole exhibits a width of about 4.5 cm^{-1}. This implies that a factor of about 170 more photons were used per unit area to burn the hole in PVK compared to PFO (Fig. 4). This behavior can be attributed to differences of the double well potentials in the different hosts. A more detailed explanation requires further studies.

Concerning the side holes, the spectra of the holes for the PVK matrix differ from those of the other two matrices examined here. For the high-energy hole, the blue shift of the minimum is estimated to be ≈18 cm^{-1} relative to the central component, but its width of ≈15 cm^{-1}, as determined by a fit of a Gaussian line shape, is roughly twice as large as in PFO or PVB. Local heating during burning cannot be responsible for this larger width as it is also observed with a less intense burning laser. The low-energy contribution has its minimum at ≈14 cm^{-1} red shifted relative to the central component, which is similar to the corresponding shift in PFO.

Interestingly, the half widths of the high-energy hole components – determined in good approximation as FWHM widths of Gaussian hole shapes – reveal that the ZFS values between the $\mathbf{T_1}$ substates **II** and **III** are distributed over significant ranges. For an estimation of the corresponding distributions, a convolution of Gaussian distributions and line shapes is assumed. Then, the half width (FWHM) of the distribution of the ZFS between substates **II** and **III** $\delta(\Delta E_{III,II})$ can be obtained from the half widths (FWHM) of the high-energy hole $\delta\bar{\nu}_{high}$ and of the corresponding resonant hole $\delta\bar{\nu}_{res}$ according to [32]

$$(\delta(\Delta E_{III,II}))^2 = (\delta\bar{\nu}_{high})^2 - (\delta\bar{\nu}_{res})^2. \quad (1)$$

Thus, we find values for $\delta(\Delta E_{II,III})$ of approximately 6 cm^{-1} and 7 cm^{-1} for PVB and PFO, respectively, and of ≈14 cm^{-1} for PVK. This demonstrates that the inhomogeneous distribution of the ZFS values $\Delta E_{III,II}$ is significantly broader for PVK than for the other two hosts. Obviously, $Ir(btp)_2(acac)$ exhibits a more pronounced interaction with PVK than with the other two matrices. Possibly, this is due to π-interactions of the (btp) ligand of the Ir complex with the carbazole ring system of PVK. A corresponding interaction is not present in PVB and would also be absent in PFO, if $Ir(btp)_2(acac)$ is hosted near the alkyl chains.

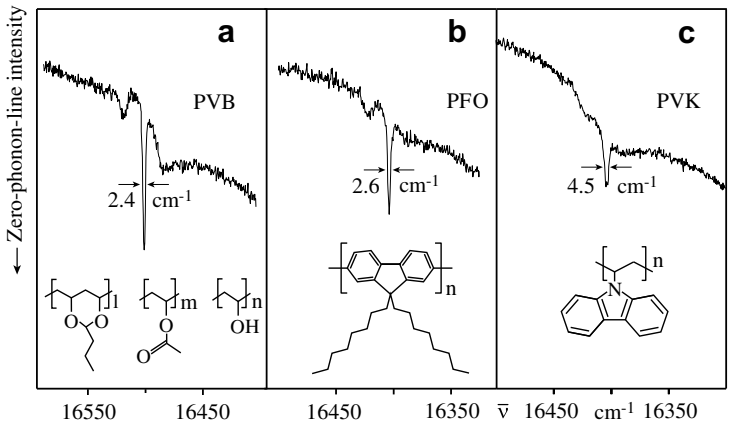

Fig. 4. Persistent spectral holes of $Ir(btp)_2(acac)$ in three amorphous polymeric matrices (a) PVB, (b) PFO, and (c) PVK at T = 1.2 K. The holes, burnt at 16,400 cm^{-1} (PVK and PFO) and 16,500 cm^{-1} (PVB), were probed by recording the intensity of an emission peak which lies 306 cm^{-1} below the energy of the probing laser. The insets show the chemical structures of the polymers. PVK and PFO are homopolymers, while PVB is built-up by three constitutional units, which are statistically distributed along the polymer chain with $l > n > m$.

The low-energy hole component is shallowest among the three investigated matrices in PFO. This is in accordance with a comparatively weak electron–phonon coupling in this matrix, which is supported by the observation that the line-narrowed spectra of $Ir(btp)_2$(acac) in PFO show well resolvable vibrational satellite lines (Section 3.1). This result is important for future investigations of other organo-transition metal complexes, if highly resolved spectra are desired.

4. Assignments and conclusion

The present study shows that persistent spectral hole burning and phosphorescence line narrowing provide powerful tools to gain insight into the splitting structure of the emitting triplet state $\mathbf{T_1}$ of $Ir(btp)_2$(acac) into substates, even when the compound is doped into amorphous matrices, which are frequently applied in OLEDs. The obtained results are in line with the findings of previous investigations in Shpol'skii and Shpol'skii-like hosts [12]. In these studies, ZFS values were determined for different discrete sites of $Ir(btp)_2$(acac) in CH_2Cl_2. $\Delta E_{III,II}$ values were found to lie between 12 and 24 cm^{-1}. In the present investigation, mean values of 18 cm^{-1} have been found for the splitting between the substates **II** and **III**. With the method of spectral hole burning, it was not possible to assess the weakly absorbing substate **I.** However, the separation between substate **I** and the next higher lying substate **II** is assumed to be also about 3 cm^{-1}, as found for Shpol'skii-like matrices [12]. In this case the (mean) total ZFS can be estimated to about 21 cm^{-1} for all three matrices. Indeed, these values lie well within the range found in the polycrystalline Shpol'skii matrices. Prior to our work, this detailed information has not been obtained for triplet emitters embedded in *amorphous* hosts.

The amount of ΔE(ZFS) is correlated with the extent of MLCT character in the emitting triplet term mixed in mainly via spin–orbit coupling [17]. Thus, a variation of ΔE(ZFS) in dependence of the compounds' environment (host cage) indicates a change of the interaction of host molecules with the electronic states of the dopant. Such a behavior is not unusual, since the host cage can alter the geometry of the dopant, cause changes of the ligand field strength, induce π–π interactions between host and guest, etc. As consequence, shifts of $^{1,3}\pi\pi^*$ and/or ^{1,3}**MLCT** states can occur. Due to such changes, state mixings will be altered and can lead to differently effective SOC. Thus, for example, smaller singlet admixtures to the emitting triplet state and also a smaller ΔE(ZFS) can result. Among the different matrices studied, PVK induces the strongest inhomogeneous spread of the splitting between the substates **II** and **III** ($\Delta E_{III,II}$). As a consequence, a substantial fraction of the $Ir(btp)_2$(acac) complexes doped into PVK have only small splittings around 10 cm^{-1}. Such values might already be too small to enable luminescence properties as required for OLED applications. This is indicated, since for emitter compounds with small ZFS values, spin–orbit coupling is relatively weak and thus, the important mixing of singlet character into the triplet substates is not effective. Therefore, such complexes exhibit comparatively small radiative decay rates and often also small quantum yields [12–14].

It should be remarked that efficient OLED triplet emitters hitherto studied exhibit significant or even large zero-field splittings of the $\mathbf{T_1}$ parent term. In this context, a value of $\approx$10 cm^{-1} may already be considered as critical.

We suppose that the results obtained for the compound in amorphous matrices at low temperature hold also at ambient temperature, if the matrices are considered to be rigid enough. This seems to be valid for host materials with a glass transition temperature T_g being significantly larger than 300 K.

In future investigations, we will use persistent spectral hole burning as a sensitive probing technique for the effects of external electric fields [31] on optical transitions in OLED emitter materials. We expect that the analysis of electric field induced shifts of the electronic levels will provide more detailed information on the interaction of the emitter complex with its closest environment, particularly, with regard to the fact that emitters in OLEDs are exposed to high electric fields.

Acknowledgements

We thank the *Bundesministerium für Bildung und Forschung (BMBF)* for providing the funding of this investigation. The *BaCaTeC* is acknowledged for financial support of the exchange with the University of Southern California.

References

[1] H. Yersin (Ed.), Highly Efficient OLEDs with Phosphorescent Materials, Wiley-VCH, Weinheim, 2008.
[2] S. Lamanski, P. Djurovich, D. Murphy, F. Abdel-Razzaq, H.-E. Lee, C. Adachi, P.E. Burrows, S.R. Forrest, M.E. Thompson, J. Am. Chem. Soc. 123 (2001) 4304.
[3] F.-C. Chen, Y. Yang, M.E. Thompson, J. Kido, Appl. Phys. Lett. 80 (2003) 2308.
[4] C. Adachi, M.A. Baldo, S.R. Forrest, S. Lamanski, M.E. Thompson, R.C. Kwong, Appl. Phys. Lett. 78 (2001) 1622.
[5] S. Lamanski, P. Djurovich, F. Abdel-Razzaq, S. Garon, D. Murphy, M.E. Thompson, J. Appl. Phys. 92 (2002) 1570.
[6] S. Tokito, M. Suzuki, F. Sato, M. Kamachi, S. Shirane, Org. Electr. 4 (2003) 105.
[7] X. Chen, J.-L. Liao, Y. Liang, M.O. Ahmed, H.-E. Tseng, S.-A. Chen, J. Am. Chem. Soc. 125 (2003) 636.
[8] S. Tokito, T. Iijima, T. Tsuzuki, F. Sato, Appl. Phys. Lett. 83 (2003) 2459.
[9] F.-C. Chen, Y. Yang, Q. Pei, Appl. Phys. Lett. 81 (2002) 4278.
[10] T. Echigo, S. Naka, H. Okada, H. Onnagawa, Jpn. J. Appl. Phys. 44 (2005) 626.
[11] Y. Kawamura, K. Goushi, J. Brooks, J.J. Brown, H. Sasabe, C. Adachi, Appl. Phys. Lett. 86 (2005) 071104.
[12] W.J. Finkenzeller, T. Hofbeck, M.E. Thompson, H. Yersin, Inorg. Chem. 46 (2007) 5076.
[13] W.J. Finkenzeller, M.E. Thompson, H. Yersin, Chem. Phys. Lett. 444 (2007) 273.
[14] H. Yersin, W.J. Finkenzeller, in: H. Yersin (Ed.), Highly Efficient OLEDs with Phosphorescent Materials, Wiley-VCH, Weinheim, 2008, p. 1.
[15] H. Yersin, D. Donges, Top. Curr. Chem. 214 (2001) 82.
[16] H. Yersin, Top. Curr. Chem. 241 (2004) 1.
[17] A.F. Rausch, H.H.H. Homeier, P.I. Djurovich, M.E. Thompson, H. Yersin, in: Z. Kafafi, F. So (Eds.), Proceedings of SPIE Optics and Photonics – Organic Light Emitting Materials and Devices XI, San Diego 2007, vol. 6655, p. 66550F.
[18] H. Yersin, J. Strasser, Coord. Chem. Rev. 208 (2000) 331.
[19] R.I. Personov, in: V.R. Agranovich, R.M. Hochstrasser (Eds.), Spectroscopy and Excitation Dynamics of Condensed Molecular Systems, North Holland, Amsterdam, 1983, p. 555.

[20] W.E. Moerner (Ed.), Persistent Spectral Hole-burning: Science and Applications, Springer, Berlin, 1988.
[21] U. Bogner, R. Schwarz, Phys. Rev. B 24 (1981) 2846.
[22] T. Attenberger, U. Bogner, M. Maier, Chem. Phys. Lett. 180 (1991) 207.
[23] S. Lin, J. Fünfschilling, I. Zschokke-Gränacher, J. Lumin. 40 (1988) 513.
[24] H. Riesen, E. Krausz, Chem. Phys. Lett. 182 (1991) 266.
[25] H. Riesen, E. Krausz, L. Wallace, J. Phys. Chem. 96 (1992) 3621.
[26] B. Kozankiewicz, J. Bernard, E. Migirdicyan, M. Orrit, M.S. Platz, Chem. Phys. Lett. 245 (1995) 549.
[27] B. Kozankiewicz, A.D. Gudmundsdottir, M. Orrit, M.S. Platz, Ph. Tamarat, J. Lumin. 86 (2000) 261.
[28] H. Riesen, Coord. Chem. Rev. 250 (2006) 1737.
[29] U. Bogner, Phys. Rev. Lett. 37 (1976) 909.
[30] K.M. Murdoch, T. Attenberger, U. Bogner, G.D. Jones, J. Phys. Chem. Solids 58 (1997) 1513.
[31] U. Bogner, in: G. Mahler, V. May, M. Schreiber (Eds.), Molecular Electronics: Properties Dynamics and Applications, Marcel Dekker, New York, 1996, p. 233.
[32] H. Cramér, Mathematische Zeitschrift 41 (1936) 405.

Organic Electronics 9 (2008) 649–655

Contents lists available at ScienceDirect

Organic Electronics

journal homepage: www.elsevier.com/locate/orgel

Asymmetrically 9,10-disubstituted anthracenes as soluble and stable blue electroluminescent molecular glasses

Li Zhao [a], Jian-hua Zou [a], Ju Huang [a], Chun Li [a], Yong Zhang [a], Chang Sun [b], Xu-hui Zhu [a,*], Junbiao Peng [a], Yong Cao [a], Jean Roncali [c]

[a] Institute of Polymer Optoelectronic Materials and Devices, Key Laboratory of Special Functional Materials, MOE, South China University of Technology (SCUT), Guangzhou 510640, China
[b] Key Laboratory of Molecular Engineering of Polymers, MOE, Fudan University, Shanghai 200433, China
[c] University of Angers, CNRS, CIMA, Linear Conjugated Systems Group, 2 Bd Lavoisier, Angers F-49045, France

ARTICLE INFO

Article history:
Received 19 February 2008
Received in revised form 7 April 2008
Accepted 12 April 2008
Available online 22 April 2008

PACS:
72.80.Le
78.60.Fi
85.60.Jb

Keywords:
Amorphous materials
Blue emission
Light-emitting diodes
Solution processibility
Device fabrication

ABSTRACT

Asymmetrically 9,10-disubstituted anthracene derivatives **1a**/**1b** have been synthesized and characterized. The new compounds exhibit a high solubility and can be easily purified by chromatographic methods. Thin solid films based on these compounds combine intrinsic amorphous morphology with pure blue emission and high solid-state photoluminescent efficiencies. These materials have been used as solution-processed active emitters in electroluminescent devices leading to interesting device performances. The effect of partial fluorination of a sub-unit of one of the compounds on the properties of the material is discussed.

1. Introduction

Solution-processible molecular emitters have become an important research topic in organic light-emitting diodes (OLEDs) [1–4]. Although appealing device efficiencies have been achieved with solution-processed fluorescent and phosphorescent molecules both in the bulk and blend, the design and synthesis of efficient and stable solution-processible pure blue electroluminescent materials still remains a challenge. To be applicable in low-cost and large-area color display, for instance, based on current inkjet-printing technology, some other special requirements have to be imposed on the emitter design such as desirable solubility in high boiling point solvents [5].

Vacuum-deposited light-emitting diodes using anthracene-based blue luminophores as bulk and host emitters have been under intensive studies [6–8], revealing promising device efficiencies and stabilities [7,8]. Thus, blue electroluminescence derived from solution-processed anthracene derivatives seem to be extremely valuable. Recently, we reported a first anthracene-cored second generation blue emitting dendrimer based on 2-ethylhexyloxy-tethered 3,5-diphenylphenyl dendrons for solution processing. While significant solubility was obtained, the lack of intrinsic morphology stability prevented its use as a favorable solution-processible host blue emitter [4c].

In this contribution novel asymmetrically 9,10-dendronized anthracene derivatives **1a**/**1b** (Chart 1) have been

* Corresponding author. Tel.: +86 20 87114346 15; fax: +86 20 87110606.
E-mail address: xuhuizhu@scut.edu.cn (X.-h. Zhu).

1566-1199/$ - see front matter © 2008 Elsevier B.V. All rights reserved.
doi:10.1016/j.orgel.2008.04.006

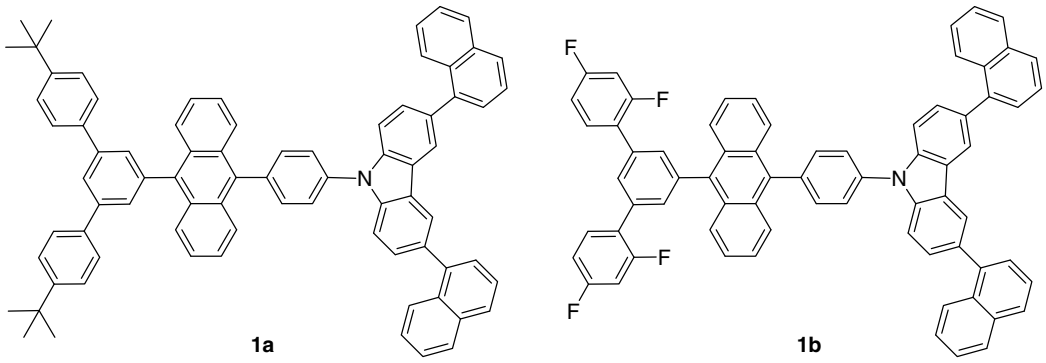

Chart 1.

designed and synthesized to afford efficient and morphologically stable solution-processed pure blue electroluminescent emitters.

A solubilizing dendron was introduced at the 9-position of anthracene of compound **1a** in order to provide the desired processability while a 4-(3,6-di(naphthalen-1-yl)carbazol-9-yl)phenyl group was attached at the opposite side of the molecule to promote glass formation, as well as to facilitate hole-injection and transport. The branched structures were expected to prevent photoluminescence quenching often associated with strong intermolecular interactions in the solid state. In addition to this, the asymmetric molecular structure can be expected to facilitate purification by chromatography when compared to the symmetrical compounds especially those carrying substituents devoid of polar groups [3,4,6]. For compound **1b**, partial fluorination of the structure was expected to possibly facilitate electron injection.

2. Results and discussion

2.1. Synthesis

The syntheses of compounds **1a**/**1b** were outlined in Scheme 1. Compound **2a** was prepared as already reported [9] and compound **2b** was synthesized in 45% yield by Suzuki coupling of 1-bromo-3,5-diiodobenzene [10] and 2,4-difluorophenylboronic acid. Precursor compounds **3a**/**3b** were prepared in 85% and 70% yield, respectively, by Suzuki coupling of compounds **2a**/**2b** with 2-(anthracen-9-yl)-4,4,5,5-tetramethyl-1,3,2-dioxaborolane (**9**). Bromo compounds **4a** and **4b** were obtained in nearly quantitative yield by treating compounds **3a** and **3b** with NBS in methylene chloride [11]. The Suzuki reagents **5a** and **5b** were prepared by two different methods. Compound **5a** was obtained in 64% yield by reacting isopropylpinacol borate (PINBOP) on the lithio-derivative obtained by treatment of **4a** with *n*-butyllithium at −78 °C. Compound **5b** was synthesized in 55% yield by reacting bis(pinacolato)diboron (PIN_2B_2) in DMSO in the presence of Pd(dppf)Cl_2. 3,6-Bis(1-naphthalenyl)carbazole **7** was prepared in 87% yield by reaction of 1-naphthalenylboronic acid with 3,6-dibromocarbazole (**8**). A Ullmann reaction [12], of **7** with an excess of 1,4-dibromobenzene gave monobromide **6** (69%). Compounds **1a**/**1b** were finally obtained in 67% and 75% yield, respectively, by reacting **5a**/**5b** with 7 under conventional Suzuki coupling conditions. The target compounds were easily purified by column chromatography due to the differences in polarity between the final products and residual starting materials or any of deboronation products (see Section 4). Another advantage of the present synthetic route is that 9-mono-dendronized anthracenes **3a**/**3b** can be easily recovered and recycled. The identity and high purity of **1a**/**1b** were then confirmed by ^{1}H NMR, microanalysis and MALDI-TOF mass spectrometry.

2.2. Solubility

The new anthracene derivatives show good solubility. For instance, 25 mg of **1a**/**1b** can be readily dissolved in 1 mL of toluene at room temperature. Good solubility in appropriate high boiling point solvent is of vital importance for device fabrication using inkjet printing [5]. In contrast to the poor solubility observed with a previous anthracenic-cored *t*-butyl-tethered second-generation dendrimer [4c], 3,5-bis(4-*t*-butylphenyl)phenyl proved to be a sufficiently solubilizing group in the case of **1a**. On the other hand, 3,5-bis(2,4-difluorophenyl)phenyl found effective in bringing about solubility to **1b** since the prearrangement of two fluorine atoms at the 2,4-positions in the phenyl ring efficiently suppresses intimate intermolecular packing.

2.3. Optical property

The UV–vis and photoluminescence (PL) spectra of **1a**/**1b** in dilute CH_2Cl_2 solutions (10^{-5} mol dm^{-3}) and in solid films are shown in Fig. 1, and the relevant data are listed in Table 1. The strong and moderate absorptions of **1a**/**1b** at ca. 258 and 303 nm in solution can be attributed to the 3,5-diphenylphenyl- [4c] and 1-naphthyl-substituted carbazolyl moiety, respectively. The multiple absorption peaks above ca. 330 nm with characteristic vibronic pattern are associated with the π–π^* transitions of the anthracenyl core [13]. Compounds **1a**/**1b** exhibit bright blue fluorescence in solution and in the solid state. The absolute solid PL quantum efficiencies were measured in an integrating sphere as 0.68 for **1a** and 0.58 for **1b** under 325-nm He–Cd laser excitation. In addition, the full width at half maxima (FWHM) for both solution and solid emission spectra are as narrow as 50–55 nm, implying

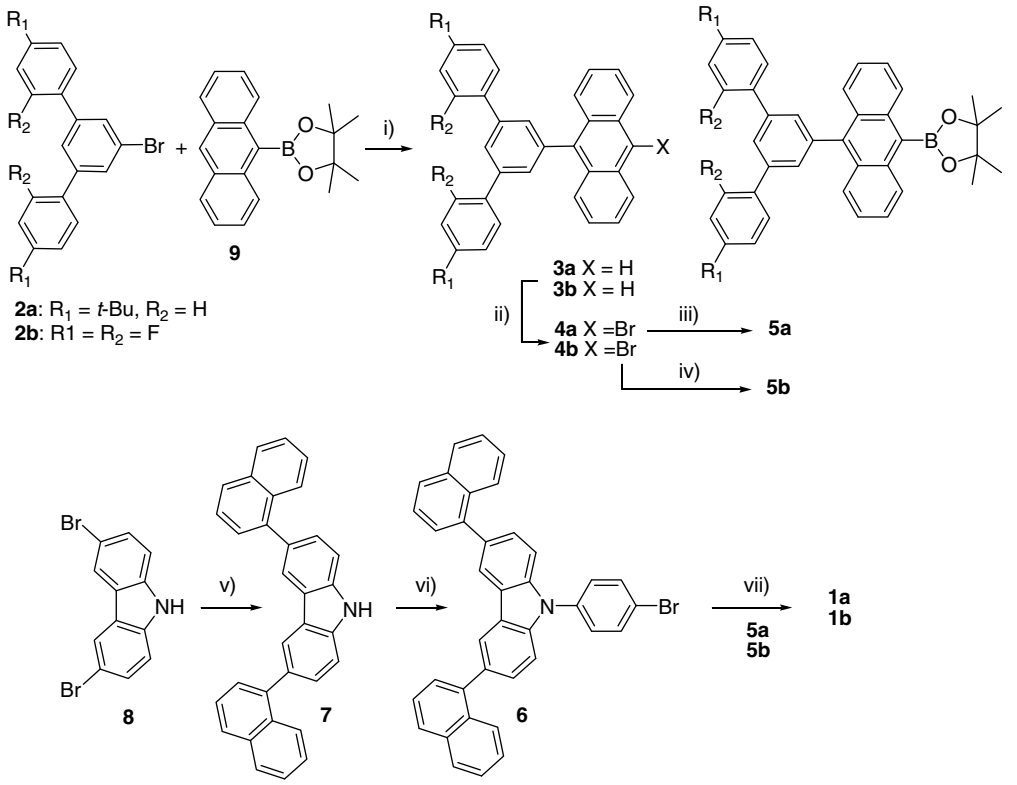

Scheme 1. Synthetic routes to **1a**/**1b**. (i) $Pd(PPh_3)_4$, Na_2CO_3, toluene, ethanol; (ii) NBS, $LiClO_4$, CH_2Cl_2; (iii) *n*-BuLi, THF, 78 °C, then PINBOP; (iv) PIN_2B_2, $Pd(dppf)_2Cl_2$, KAOc, DMSO; (v) 1-naphthalenylboronic acid, $Pd(PPh_3)_4$, Na_2CO_3, toluene, ethanol; (vi) 1,4-dibromobenzene, K_2CO_3, CuI, 18-crown-6, DMPU; (vii) $Pd(PPh_3)_4$, Na_2CO_3, toluene, ethanol.

1a/**1b** could be highly valuable fluorophores for pure blue light-emitting diodes.

2.4. Thermal and morphological stability

The thermal properties were investigated by thermal gravimetric analysis (TGA) and differential scanning calorimetry (DSC). Compounds **1a**/**1b** showed high thermal stabilities with 5%-weight-loss at 520 and 513 °C, respectively. DSC measurements were carried out on carefully dried samples and heating is avoided [4]. Glass transitions were observed in the first heating run with an outstanding T_g of 214 °C for **1a** and 187 °C for **1b** (Fig. 2). In both cases no crystallization exotherms or melting endotherms was noticed upon heating until 350 °C. It has been noted that an inherent amorphous morphology is even absent in a spirobifluorene-linked bisanthracene 2,2′-bis(10-phenylanthracene-9-yl)-9,9′-spirobifluorene [14]. Thus, for soluble molecular materials such as **1a**/**1b**, the observed high T_gs are remarkable. Apparently, the rigid bulky 4-(3,6-di(naphthalen-1-yl)carbazol-9-yl)-phenyl, together with the non-planar 3,5-diphenylphenyl-based dendron, contribute to the ease of glass formation and prominent morphological stability of **1a**/**1b**. The intrinsic amorphous characteristics were further confirmed by powder X-ray diffraction analysis (XRD). No evidence of crystallinity was observed in the angle range from 1° to 40°.

2.5. Electroluminescent properties

Compounds **1a**/**1b** were used as hole-transporting and emitting materials in simple electroluminescent devices. The emissive layer of **1a** or **1b** (55 nm) was spun-cast from toluene solution onto ITO glass slides modified by a 50 nm thick layer of poly(3,4-ethylenedioxy-thiophene):poly(styrenesulfonate) (PEDOT:PSS). A vacuum-deposited 30 nm thick layer of TPBI (1,3,5-tris(*N*-phenylbenzimidazol-2-yl)benzene, HOMO = −6.20 eV, LUMO = −2.70 eV) [15] acted as an electron transporting and hole blocking layer and the device was completed by a top electrode involving CsF (2 nm) and/Al (120 nm).

The analysis of the device performances gave the following results: V_{onset} = 4.5 V, LE_{max} = 1.88 cd A^{-1} (η_{ext} = 2.34%), λ_{max} = 448 nm with CIE coordinates (0.158, 0.104) for **1a**; and V_{onset} = 4.2 V, LE_{max} = 1.81 cd A^{-1} (η_{ext} = 2.26%), λ_{max} = 454 nm with CIE coordinates (0.162, 0.122) for **1b** (Fig. 3). The pure blue emission spectra with narrow FWHM of 64–66 nm were hardly affected in an applied voltage ranging from of 5 to 14 V (Fig. 4). At a current density of ca. 20 mA cm^{-2}, LE = 1.63 cd A^{-1}, V = 7.2 V and L = 308 cd m^{-2} for **1a** while LE = 1.60 cd A^{-1}, V = 6.6 V and L = 336 cd m^{-2} for **1b**. The lower onset and working voltages of **1b** might be related to the improved electron injection induced by the strong electron-withdrawing fluorine substituents (though not in direct conjunction with the main emissive π-backbone) and resultant molecular

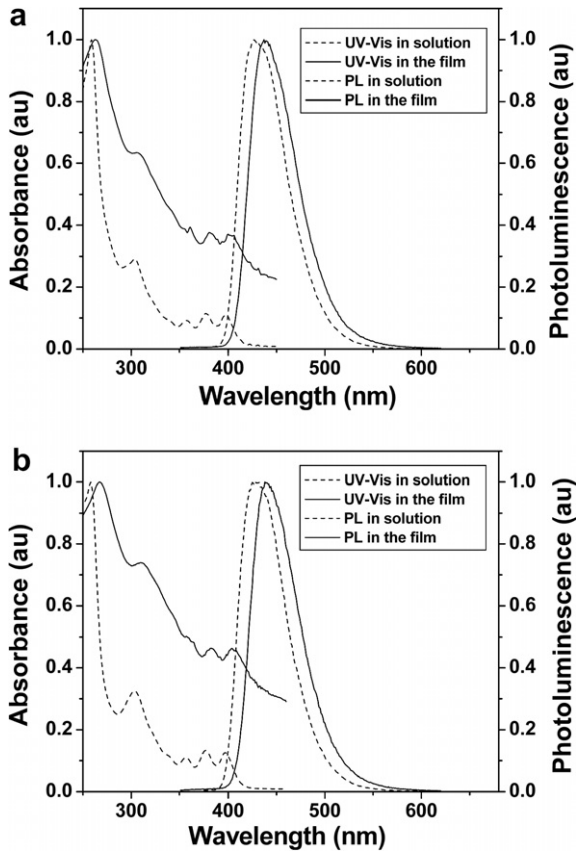

Fig. 1. The absorption and PL spectra in dilute CH_2Cl_2 solutions (10^{-5} - mol dm^{-3}) and in the films on quartz for **1a** and **1b**.

Table 1
Summary of PL and electrochemical data

	PL (λ_{max}^{em}, nm)		HOMO[a] (eV)	LUMO[b] (eV)
	Solution	Solid		
1a	427	437	−5.54	−2.54
1b	428	438	−5.56	−2.57

[a] Estimated from onset oxidation voltages with reference to ferrocene (4.8 eV vs. vacuum).
[b] Calculated from HOMO and optical band gap.

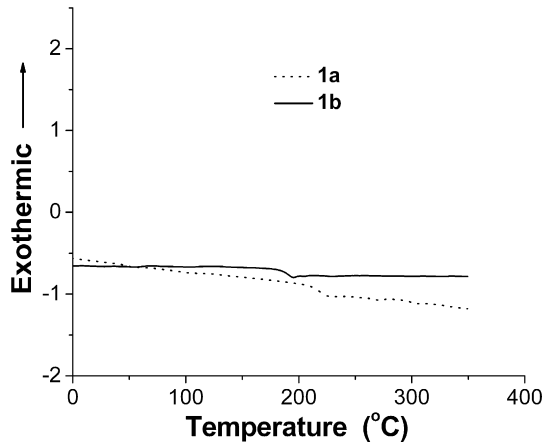

Fig. 2. The DSC curves in the first heating run of **1a**/**1b**.

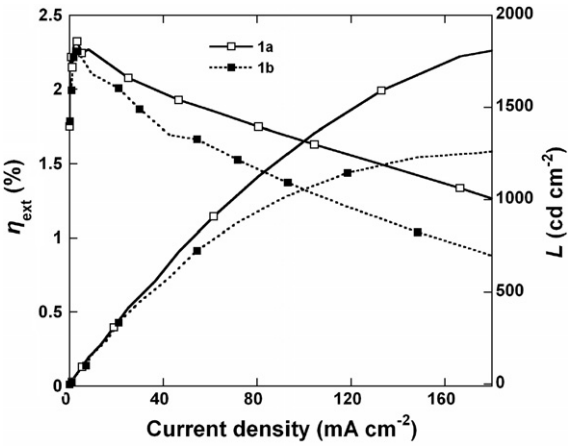

Fig. 3. The *L*–*V*–*J* characteristics of devices [ITO/PEDOT:PSS/**1a**(**1b**)/TPBI/CsF/Al].

packing leading to possible enhanced charge transport. Thus, **1a**/**1b** represent a class of solution processible non-fluorene-based blue emitters devoid of the complexity of

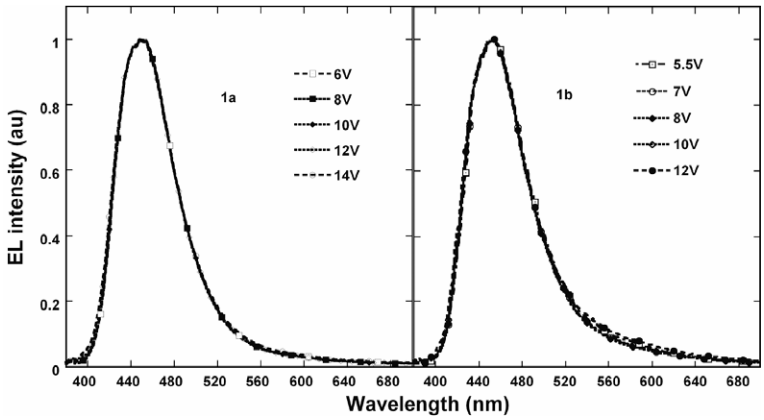

Fig. 4. The EL spectra of **1a**/**1b** under different applied voltages.

spectral instability usually present in blue-emitting 9,9-alkylated fluorenes [16].

The current properties of blue electroluminescence using solution-processed **1a**/**1b**, for instance, @ ca. 20 mA cm^{-2} compare well with some typically non-doped anthracene-based small molecules reported in multi-layered vacuum-deposited light-emitting diodes [6–8]. Hopefully, the blue EL characteristics can be further improved by blending into a soluble and amorphous conjugated wider-band gap polymer or molecular emitter. The insensitivity to emission quenching and high solid morphological stability can allow **1a**/**1b** to be used in a wide range of concentrations while ensuring homogeneous film formation [4a].

3. Conclusions

Asymmetrically 9,10-disubstituted anthracene derivatives combining synthetic accessibility, processibility and robust intrinsic morphological stability have been synthesized. The characterization of simple solution-processed electroluminescent devices based on these new materials shows that they combine efficient and stable blue emission with high spectral purity. Despite a minor effect on the HOMO and LUMO energy levels, the introduction of fluorine atoms into the structure seems to substantially lower the working voltage. The new compounds reported here represent an interesting class of solution-processible anthracene-based molecular blue emitters with high application potentials and thus should deserve intensive further research.

4. Experimental

4.1. Materials and methods

All manipulations involving air-sensitive reagents were performed under an inert atmosphere of dry nitrogen. Tetrahydrofuran (THF) was dried over Na/benzophenone and distilled prior to use. All the intermediates were isolated, analyzed by TLC (thin layer chromatography) on silica gel and ^{1}H NMR to ensure as clean an incoming reaction as possible. All starting materials, unless otherwise specified, were used as received.

^{1}H NMR spectra were recorded on a Bruker AV 300 spectrometer with deuterated solvents as the internal reference. Time-of-flight mass spectrometry (TOF-MS) was performed using a KOMPACT MALDI mass spectrometer (Shimadzu/Kratos) in the positive ion mode with matrix of dithranol. The experimentally determined and calculated masses agree within the range of accuracy of the instrument and the mass peaks with the lowest isotopic mass are reported. Elemental analyses were performed on a vario EL CHNS analyzer. UV–Vis absorption spectra were obtained on an HP 8453 spectrophotometer. Photoluminescence spectra were measured using a Jobin–Yvon spectrofluorometer JY Fluorolog-3 spectrofluorometer. For the purposes of TGA and DSC measurements, the sample was carefully dried to remove any residual aliphatic organic solvent used in the working-up procedure and to avoid heating. The absence of solvents was confirmed by ^{1}H NMR prior to analytical characterizations. Thermal gravimetric analysis (TGA) was conducted on a TG 209 F1 (NETZSCH) thermal analysis system under a heating rate of 20 °C/min from 30 to 750 °C. Differential scanning calorimetry (DSC) was run on a DSC 204 F1 (NETZSCH) thermal analysis system. The sample was heated from –60 °C to 350 °C at a rate of 20 °C/min. Powder X-ray diffraction (XRD) was performed on a Panlytical Xpert PRO X-ray diffractometer at 40 kV/40 mA. The radiation line was Cu Kα and λ = 1.5418 Å. Cyclic voltammetry was carried out on a CHI660A electrochemical workstation with platinum electrodes at a scan rate of 50 mV/s against a Ag/AgCl reference electrode with a nitrogen-saturated solution of 0.1 M n-Bu_4NPF_6 in CH_2Cl_2 using ferrocene as internal standard.

4.1.1. 3,5-Bis(2,4-difluorophenyl)phenyl bromide (**2b**)

A mixture of 1-bromo-3,5-diiodobenzene (1.8 g, 4.4 mmol), 2,4-difluorophenylboronic acid (1.39 g, 8.8 mmol), toluene (30 mL), ethanol (15 mL) and Na_2CO_3 aqueous solution (2 M, 15 mL) was degassed by N_2 bubble for 30 min. Then $Pd(PPh_3)_4$ (50 mg, 0.044 mmol) was added into the mixture rapidly. The reaction was heated at 90 °C for 12 h under N_2 atmosphere. After being cooled to room temperature, the mixture was poured into water and extracted with dichloromethane. The organic layer was separated, dried over anhydrous $MgSO_4$, filtered and concentrated. The residue was purified with silica gel column chromatography using petroleum ether as eluent to afford a white solid (0.75 g, 2 mmol) in 45% yield. ^{1}H NMR (300 MHz, $CDCl_3$, ppm) δ 6.9–7.01 (m, 4H), 7.38–7.46 (m, 2H), 7.54–7.56 (m, 1H), 7.65 (s, 2H). Anal. Calcd for $C_{18}H_9BrF_4$: C, 56.72; H, 2.38. Found: C, 57.03; H, 2.60.

4.1.2. 9-(3,5-Bis(4-t-butylphenyl)phenyl)anthracene (**3a**)

This compound was synthesized by a method similar to that for **2b**, using 2-anthracen-9-yl-4,4,5,5-tetramethyl-1,3,2-dioxaborolane and **2a** instead. The crude product was purified with column chromatography using petroleum ether as eluent to afford a white solid in 85% yield. ^{1}H NMR (300 MHz, $CDCl_3$, ppm) δ 1.36 (s, 18H), 7.35–7.38 (m, 2H), 7.44–7.49 (m, 6H), 7.65–7.68 (m, 6H), 7.83 (d, 2H, J = 9.0 Hz), 8.01 (s, 1H), 8.06 (d, 2H, J = 8.6 Hz), 8.52 (s, 1H). Anal. Calcd for $C_{40}H_{38}$: C, 92.62; H, 7.38. Found: C, 92.21; H, 7.71.

4.1.3. 9-(3,5-Bis(2,4-difluorophenyl)phenyl)anthracene (**3b**)

This compound was synthesized by a method similar to that for **2b**, using 2-anthracen-9-yl-4,4,5,5-tetramethyl-1,3,2-dioxaborolane and **2b** instead. The crude product was purified with column chromatography using petroleum ether as eluent to afford a white solid in 70% yield. ^{1}H NMR (300 MHz, $CDCl_3$, ppm) δ 6.89–6.98 (m, 4H), 7.36–7.57 (m, 6H), 7.60 (d, 2H, J = 1.1 Hz), 7.80–7.83 (m, 3H), 8.05 (d, 2H, J = 8.3 Hz), 8.51 (s, 1H). Anal. Calcd for $C_{32}H_{18}F_4$: C, 80.33; H, 3.79. Found: C, 80.46; H, 4.02.

4.1.4. 9-(3,5-Bis(4-t-butylphenyl)phenyl)-10-bromoanthracene (**4a**)

N-Bromosuccinimide (NBS) (0.8 g, 4.5 mmol) was added in one portion at room temperature to a mixture of **3a**

(2.11 g, 4.1 mmol) in dichloromethane (30 mL), $LiClO_4 \cdot 3H_2O$ (25 mg, 0.15 mmol) and silica gel (100 mg) in the absence of light. The completion of bromination was confirmed by TLC. The bromide **4a** was obtained as a yellow solid in nearly quantitative yield after purification with flash column chromatography using petroleum ether as eluent. ^{1}H NMR (300 MHz, $CDCl_3$, ppm) δ 1.36 (s, 18H), 7.38 (ddd, 2H, J_1 = 8.8 Hz, J_2 = 4.4 Hz, J_3 = 1.2 Hz), 7.46–7.50 (m, 4H), 7.57–7.62 (m, 4H), 7.65 (dd, 4H, J_1 = 8.5 Hz, J_2 = 1.9 Hz), 7.81 (d, 2H, J = 8.8 Hz), 8.02 (t, 1H, J = 1.8 Hz), 8.63 (d, 2H, J = 8.8 Hz). Anal. Calcd for $C_{40}H_{37}Br$: C, 80.39; H, 6.24. Found: C, 80.39; H, 6.53.

4.1.5. 9-(3,5-Bis(2,4-difluorophenyl)phenyl)-10-bromoanthracene (**4b**)

This compound was synthesized by a method similar to that for **4a**, using **3b** instead. The crude product was purified with column chromatography using petroleum ether as eluent to afford a yellow solid in nearly quantitative yield. ^{1}H NMR (300 MHz, $CDCl_3$, ppm) δ 6.89–6.99 (m, 4H), 7.40–7.63 (m, 8H), 7.80 (d, 2H, J = 8.8 Hz), 7.84 (t, 1H, J = 1.6 Hz), 8.63 (d, 2H, J = 8.8 Hz). Anal. Calcd for $C_{32}H_{17}BrF_4$: C, 68.96; H, 3.07. Found: C, 68.44; H, 3.31.

4.1.6. 9-(3,5-Bis(4-t-butylphenyl)phenyl)-10-(4,4,5,5-tetramethyl-1,3,2-dioxaborolane-2-yl)anthracene (**5a**)

A solution of **4a** (2.23 g, 3.73 mmol) in anhydrous THF (40 mL) was degassed with N_2 for 30 min, and then cooled to −78 °C. *n*-Butyllithium (2.5 M solution in hexane, 2.2 mL, 5.5 mmol) was added dropwise via syringe under N_2 atmosphere. The solution continued to be stirred for 30 min, and then 2-isopropoxy-4,4,5,5-tetramethyl-1,3,2-dioxaborolane (PINBOP) (1.1 mL, 5.5 mmol) was added via syringe. The reaction mixture was warmed to room temperature under stirring. After 24 h, upon concentration, water was added. The residual was extracted with dichloromethane. The organic layer was separated, dried over anhydrous $MgSO_4$, and evaporated under reduced pressure. The crude product was subject to column chromatography using silica gel and graded petroleum ether/CH_2Cl_2 eluents from 8:1 to 4:1 (v/v) to afford a yellowish solid (1.54 g, 2.39 mmol) in 64% yield. ^{1}H NMR (300 MHz, $CDCl_3$, ppm) δ 1.36 (s, 18H), 1.61 (s, 12H), 7.32 (ddd, 2H, J_1 = 8.8 Hz, J_2 = 4.4 Hz, J_3 = 1.2 Hz), 7.45–7.50 (m, 6H), 7.59 (d, 2H, J = 1.8 Hz), 7.66 (dd, 4H, J_1 = 8.6 Hz, J_2 = 1.9 Hz), 7.79 (d, 2H, J = 8.6 Hz), 7.99 (t, 1H, J = 1.7 Hz), 8.46 (d, 2H, J = 8.6 Hz). Anal. Calcd for $C_{46}H_{49}BO_2$: C, 85.70; H, 7.66. Found: C, 85.31; H, 8.10.

4.1.7. 9-(3,5-Bis(2,4-difluorophenyl)phenyl)-10-(4,4,5,5-tetramethyl-1,3,2-dioxaborolane-2-yl)anthracene (**5b**)

A two-necked round flask was charged with **4b** (1 g, 1.72 mmol), bis(pinacolato)diboron (PIN_2B_2) (0.654 g, 2.58 mmol), potassium acetate (0.506 g, 5.16 mmol), Pd(dppf)-Cl_2 (42.1 mg, 0.052 mmol). The flask was filled with N_2 and evacuated twice. Then anhydrous DMSO (10 mL) was added into the mixture. The reaction was heated at 80 °C for 12 h under N_2 atmosphere. After being cooled to the room temperature, the mixture was poured into water and extracted with dichloromethane thrice. The organic layer was combined, washed with water repeatedly, dried over anhydrous $MgSO_4$, filtered and concentrated. The crude product was subject to column chromatography with silica gel and graded petroleum ether/CH_2Cl_2 eluents from 8:1 to 4:1 (v/v) to afford a yellowish solid (0.6 g, 0.95 mmol) in 55% yield. ^{1}H NMR (300 MHz, $CDCl_3$, ppm) δ 1.61 (s, 12H), 6.91–6.99 (m, 4H), 7.35–7.40 (m, 2H), 7.47–7.56 (m, 6H), 7.79 (d, 2H, J = 8.8 Hz), 7.83 (t, 1H, J = 1.6 Hz), 8.46 (d, 2H, J = 8.7 Hz). Anal. Calcd for $C_{38}H_{29}BF_4O_2$: C, 75.51; H, 4.84. Found: C, 75.28; H, 4.93.

4.1.8. 3,6-Di(naphthalen-1-yl)carbazole (**6**)

A mixture of 3,6-dibromocarbazole (3.83 g, 11.8 mmol), 1-naphthalenylboronic acid (4.87 g, 28.3 mmol), toluene (30 mL), ethanol (15 mL) and Na_2CO_3 aqueous solution (2 M, 15 mL) was degassed by N_2 bubble for 30 min. Then $Pd(PPh_3)_4$ (80 mg, 0.07 mmol) was added into the mixture rapidly. The reaction was heated at 90 °C for 12 h under N_2 atmosphere. After being cooled to the room temperature, the mixture was poured into water and extracted with dichloromethane. The organic layer was separated, dried over anhydrous $MgSO_4$, filtered and concentrated. The residue was firstly purified with column chromatography using silica gel and graded petroleum ether/CH_2Cl_2 eluents from 8:1 to 4:1 (v/v). Upon evaporation, the solid was refluxed in petroleum ether overnight. After being cooled, the white solid was filtered, and washed with cold petroleum ether twice to afford **6** in 87% yield (4.3 g, 10.3 mmol). ^{1}H NMR (300 MHz, $CDCl_3$, ppm) δ 7.39–7.57 (m, 8H), 7.58–7.80 (m, 4H), 7.84–7.88 (m, 2H), 7.92 (d, 2H, J = 8.0 Hz), 8.01 (dd, 2H, J_1 = 8.3 Hz, J_2 = 0.69 Hz), 8.20 (s, 2H), 8.25 (s, 1H). Anal. Calcd for $C_{32}H_{21}N$: C, 91.62; H, 5.05; N, 3.34. Found: C, 91.08; H, 5.25; N, 3.62.

4.1.9. 9-(4-Bromophenyl)-3,6-di(naphthalen-1-yl)carbazole (**7**)

A mixture of CuI (114 mg, 0.6 mmol), 18-Crown-6 (79 mg, 0.3 mmol), K_2CO_3 (2.48 g, 18 mmol), 1,3-dimethyl-3,4,5,6-tetrahydro-2(1*H*)-pyrimidinone (DMPU) (1 mL), dibromo-benzene (4.25 g, 18 mmol) and 3,6-di(naphthalen-1-yl)carbazole (**6**) (2.53 g, 6 mmol) was heated at 140 °C for 18 h under nitrogen. After being cooled to room temperature, the mixture was extracted with dichloromethane, and the insoluble solid was removed with a short silica column using dichloromethane as eluent. Upon evaporation, the residual was further purified with column chromatography using silica gel and graded petroleum ether/CH_2Cl_2 eluents from 12:1 to 6:1 (v/v) to afford a pale white solid (2.39 g, 4.2 mmol) in 69% yield. TLC R_f (6:1 petroleum ether/dichloromethane v/v): 0.45. ^{1}H NMR (300 MHz, $CDCl_3$, ppm) δ 7.39–7.55 (m, 10H), 7.57–7.63 (m, 4H), 7.78–7.82 (m, 2H), 7.85–7.88 (m, 2H), 7.90–7.93 (m, 2H), 7.98–8.00 (m, 2H), 8.25 (d, 2H, J = 0.9 Hz). Anal. Calcd for $C_{38}H_{24}BrN$: C, 79.44; H, 4.21; N, 2.44. Found: C, 79.37; H, 4.69, N, 2.62.

4.1.10. 9-(3,5-Bis(4-t-butylphenyl)phenyl)-10-(4-(3,6-di(naphthalen-1-yl)carbazol-9-yl)phenyl)anthracene (**1a**)

A mixture of **5a** (0.3 g, 0.49 mmol), 7 (0.26 g, 0.45 mmol), toluene (10 mL), ethanol (5 mL) and Na_2CO_3 aqueous solution (2 M, 5 mL) was degassed by N_2 bubble for 30 min. Then $Pd(PPh_3)_4$ (30 mg, 0.026 mmol) was added

into the mixture rapidly. The reaction was heated at 90 °C for 20 h under N_2 atmosphere. After being cooled to the room temperature, the mixture was poured into water and extracted with dichloromethane. The organic layer was separated, dried over anhydrous $MgSO_4$, filtered and concentrated. The crude product was subject to column chromatography using silica gel and graded petroleum ether/CH_2Cl_2 eluents from 6:1 to 4:1 (v/v) to afford a light yellow solid (0.304 g, 0.3 mmol) in 67% yield. TLC R_f (6:1 petroleum ether/dichloromethane v/v): 0.32. ^{1}H NMR (300 MHz, $CDCl_3$, ppm) δ 1.38 (s, 18H), 7.38–7.53 (m, 12H), 7.55–7.61 (m, 4H), 7.67–7.75 (m, 8H), 7.81–8.02 (m, 14H), 8.05–8.10 (m, 3H), 8.34 (d, 2H, J = 1.1 Hz). Anal. Calcd for $C_{78}H_{61}N$: C, 92.54; H, 6.07, N, 1.38. Found: C, 92.03; H, 6.38; N, 1.56. MALDI-TOF: *m/z* 1011.8 (100%) M^+ (calcd. 1011.48).

4.1.11. 9-(3,5-Bis(2,4-difluorophenyl)phenyl)-10-(4-(3,6-di(naphthalen-1-yl)carbazol-9-yl)phenyl)anthracene (**1b**)

This compound was synthesized by a method similar to that for **1a**, using **5b** and **7** instead. The crude product was subject to column chromatography with silica gel and graded petroleum ether/CH_2Cl_2 eluents from 6:1 to 4:1 (v/v) to afford light a light yellow solid in 75% yield. TLC R_f (6:1 petroleum ether/dichloromethane v/v): 0.26. ^{1}H NMR (300 MHz, $CDCl_3$, ppm) δ 6.94–7.03 (m, 4H), 7.43–7.63 (m, 14H), 7.69–7.71 (m, 4H), 7.82 (d, 2H, J = 8.3 Hz), 7.84 (s, 1H), 7.87–7.96 (m, 10H), 8.00 (dd, 2H, J_1 = 8.3 Hz, J_2 = 1.8 Hz), 8.08 (d, 2H, J = 8.4 Hz), 8.34 (d, 2H, J = 1.5 Hz). Anal. Calcd for $C_{70}H_{41}NF_4$: C, 86.49; H, 4.25; N, 1.44. Found: C, 86.40; H, 4.40; N, 1.68. MALDI-TOF: *m/z* 972 (100%) $[M + H]^+$ (calcd. 972.33).

4.2. LED fabrication and characterizations

LED fabrication and characterizations: The fabrication process of the diodes followed a standard procedure below. The ITO-coated glass substrate underwent a wet-cleaning course in an ultrasonic bath sequentially in acetone, detergent, deionized water and isopropanol. After a 50 nm thick buffer layer of PEDOT:PSS (Baytron P4083, purchased from Bayer AG) was spin-cast on the pre-cleaned ITO substrate and dried by baking in a vacuum at 80 °C for 12 h. Then, a 55 nm thick layer of the emissive layer was spin-cast on the top of the PEDOT:PSS layer from toluene solution. Profilometry (Tencor Alfa-Step 500) was used to determine the thickness of the films. TPBI (30 nm thick) was deposited by vacuum deposition. Typically, a thin layer of CsF (2 nm thick) with a 120 nm thick Al capping layer was deposited through a shadow mask (defined active area of 0.17 cm^2) in a chamber with a basic pressure of $<3 \times 10^{-4}$ Pa. The layer thickness was monitored upon deposition by using a crystal thickness monitor (Sycon). Except the fabrication of PEDOT:PSS layer, all the processes were carried out in a N_2 atmosphere dry-box (Vacuum Atmosphere Co.). Current–voltage (I–V) characteristics were measured with a computerized Keithley 236 Source Measure Unit. The luminance of the device was measured with a photodiode calibrated by a PR-705 SpectraScan Spectrophotometer (Photo Research), with simultaneous acquisition of the EL spectra and CIE coordinates. During the calibration, the EL device was driven by a Keithley model 2400 programmable voltage–current source.

Acknowledgments

X.H.Z. is deeply grateful for the financial support of NNSF, MOE and MOST of China (Grant Nos. 50603006, 2006NCET & 2002CB613403), and thanks SCUT for a career award and SRF of MOE for a program supporting the returned overseas Chinese scholars.

References

[1] (a) J. Luo, Y. Zhou, Z.Q. Niu, Q.F. Zhou, Y. Ma, J. Pei, J. Am. Chem. Soc. 129 (2007) 11314;
(b) M.Y. Lo, C.G. Zhen, M. Lauters, G.E. Jabbour, A. Sellinger, J. Am. Chem. Soc. 129 (2007) 5808;
(c) A.C.A. Chen, S.W. Culligan, Y.H. Geng, S.H. Chen, K.P.K. Klubek, M. Vaeth, C.W. Tang, Adv. Mater. 16 (2004) 783;
(d) W.J. Oldham, R.J. Lachicotte, G.C. Bazan, J. Am. Chem. Soc. 120 (1998) 2987.
[2] P.L. Burn, S.C. Lo, I.D.W. Samuel, Adv. Mater. 19 (2007) 1675.
[3] W.Y. Lai, R. Zhu, Q.L. Fan, L.T. Hou, Y. Cao, W. Huang, Macromolecules 39 (2006) 3707.
[4] (a) J. Huang, C. Li, Y.-J. Xia, X.-H. Zhu, J.B. Peng, Y. Cao, J. Org. Chem. 72 (2007) 8580;
(b) Y.H. Sun, X.-H. Zhu, Z. Chen, Y. Zhang, Y. Cao, J. Org. Chem. 71 (2006) 6281;
(c) L. Zhao, C. Li, Y. Zhang, X.-H. Zhu, J.B. Peng, Y. Cao, Macromol. Rapid Commun. 27 (2006) 914.
[5] E. Tekin, E. Holder, D. Kozodaev, U.S. Schubert, Adv. Funct. Mater. 17 (2007) 277.
[6] (a) Y.-H. Kim, H.-C. Jeong, S.-H. Kim, K. Yang, S.-K. Kwon, Adv. Funct. Mater. 15 (2005) 1799;
(b) Y.H. Kim, D.C. Shin, S.-H. Kim, C.-H. Ko, H.-S. Yu, Y.-S. Chae, S.K. Kwon, Adv. Mater. 13 (2001) 1690.
[7] J.M. Shi, C.W. Tang, Appl. Phys. Lett. 80 (2002) 3201.
[8] (a) M.-H. Ho, Y.-S. Wu, S.-W. Wen, M.-T. Lee, T.-M. Chen, C.H. Chen, K.-C. Kwok, S.-K. So, K.-T. Yeung, Y.-K. Cheng, Z.-Q. Gao, Appl. Phys. Lett. 89 (2006) 252903;
(b) M.-T. Lee, C.-H. Liao, C.-H. Tsai, C.H. Chen, Adv. Mater. 17 (2005) 2493.
[9] (a) G.E. Greco, R.R. Schrock, Inorg. Chem. 40 (2001) 3850;
(b) C.-J. Du, H. Hart, K.-K. Ng, J. Org. Chem. 51 (1986) 3162.
[10] Y. Zhang, H.H. Shi, Y. Cao, Chin. J. Chem. 24 (2006) 1631.
[11] M. Bagheri, N. Azizi, M.R. Saidi, Can. J. Chem. 83 (2005) 146.
[12] (a) Q. Zhang, J.S. Chen, Y.X. Cheng, L.X. Wang, D.G. Ma, X.B. Jing, F.S. Wang, J. Mater. Chem. 14 (2004) 895;
(b) S. Gauthier, J.M.J. Fréchet, Synthesis (1987) 383.
[13] J.R. Lakowicz, in: Principles of Fluorescence Spectroscopy, 2nd ed., Kluwer Academic, Plennum Publishers, New York, 1999.
[14] W.-J. Shen, R. Dodda, C.-C. Wu, F.-I. Wu, T.-H. Liu, H.-H. Chen, C.H. Chen, C.-F. Shu, Chem. Mater. 16 (2004) 930.
[15] (a) Y.T. Tao, E. Balasubramaniam, A. Danel, P. Tomasik, Appl. Phys. Lett. 77 (2000) 933;
(b) Z. Gao, C.S. Lee, I. Bello, S.T. Lee, R.-M. Chen, T.-Y. Luh, J. Shi, C.W. Tang, Appl. Phys. Lett. 74 (1999) 865.
[16] U. Scherf, E.J.W. List, Adv. Mater. 14 (2002) 477.

Organic Electronics 9 (2008) 656–660

Contents lists available at ScienceDirect

Organic Electronics

journal homepage: www.elsevier.com/locate/orgel

Pentacene/fullerene (C_{60}) heterojunction solar cells: Device performance and degradation mechanisms

P. Sullivan, T.S. Jones *

Department of Chemistry, University of Warwick, Coventry CV4 7AL, United Kingdom

ARTICLE INFO

Article history:
Received 1 February 2008
Received in revised form 22 April 2008
Accepted 23 April 2008
Available online 4 May 2008

PACS:
72.40.+w
73.50.Pz
84.60.Jt

Keywords:
Pentacene
C^{60}
Solar cell
J–V characteristics
Active area
Degradation

ABSTRACT

We demonstrate power conversion efficiencies of 1.5% from molecular photovoltaic devices based on bilayer pentacene/fullerene heterojunctions under 1 sun AM1.5G simulated irradiation. Importantly, we demonstrate the independence of the device performance on active area in the range 0.05–0.65 cm^2, a critical consideration for future scaling up to manufacture. A degradation study under constant solar illumination shows two parallel mechanisms for degradation; a photooxidation resulting in a drop of the generated photocurrent, and a UV annealing effect reducing the fill factor, both of which can be eliminated by careful choice of analysis conditions.

1. Introduction

Organic semiconductors remain the focus of intense research for photovoltaic (PV) applications due to their potential for low cost, facile manufacture. Heterojunction molecular devices have traditionally been based on phthalocyanine donor layers (in particular CuPc) in conjunction with fullerene (C_{60}) acceptor layers, however the low exciton diffusion lengths have led to the requirement of blends to achieve respectable device efficiencies [1,2]. More recently, pentacene has also emerged as a promising candidate to replace phthalocyanines due to its significantly higher exciton diffusion length and charge mobility [3,4]. Whilst devices based on pentacene blends have exhibited efficiencies up to 2%, the relative improvement in performance over bilayer devices is less significant than that seen for comparable devices using phthalocyanines as the donor material [5]. The use of the more easily produced bilayers in complex device structures such as tandem cells should therefore provide less of a penalty to overall performance when using pentacene as the donor material. The need to protect devices based on pentacene/C_{60} from degradation is well known [6], however the precise mechanisms of degradation are rarely studied and a more detailed understanding is required to design suitable encapsulation methods [7].

In this paper we demonstrate efficient pentacene/C_{60} bilayer solar cells optimised for active layer thickness. The power conversion efficiency (η_p) of the best devices reaches 1.5% under true simulated 100 mW cm^{-2} AM1.5G irradiation, comparable to that reported by other groups [3,4,8]. The device performance was found to be independent of

* Corresponding author. Tel.: +44 24 7652 8265; fax: +44 24 7652 4112.
E-mail address: t.s.jones@warwick.ac.uk (T.S. Jones).

1566-1199/$ - see front matter © 2008 Elsevier B.V. All rights reserved.
doi:10.1016/j.orgel.2008.04.008

device active area for the range 0.05–0.65 cm^2 which provides optimism for future scaling up of similar devices. A study of the degradation of the devices was performed under various measurement conditions, and showed the presence of two distinct mechanisms; a photooxidation resulting in rapid loss of photocurrent, and a UV annealing effect leading to poor electrode contact and the appearance of a kink in the *J–V* curves. Analysis under vacuum conditions with UV-filtered light led to stable performance over 70 min under constant illumination.

2. Experimental details

All devices were grown by vacuum deposition in a Kurt J. Lesker Spectros system with base pressure of around 8×10^{-8} mbar. Indium tin-oxide (ITO) coated glass substrates were supplied by Psiotec with a sheet resistance of 15 Ω/□, and were solvent cleaned before use. Pentacene (Aldrich, 94%) and bathocuproine (BCP, Aldrich, 98%) were twice purified by thermal gradient sublimation before use, whilst C_{60} (MER Corp, 99.5%) was used as received. Devices for the comparison of varying pentacene thickness were prepared from fresh source material for each growth as this gave optimised performance. Devices for active area and degradation analysis were grown from used source material which gave lower, but reproducible performance. Layer thicknesses of the organic thin films were measured during growth on a quartz crystal microbalance (QCM). The QCM reading was previously calibrated to real layer thicknesses from atomic force microscope (AFM) step-edge measurements in tapping mode on a Digital Instruments Nanoscope IIIa microscope. Al electrodes were deposited in situ to a thickness of 100 nm through a shadow mask to form an active area of 8 mm × 2 mm (0.16 cm^2) except where otherwise stated. *J–V* curves were measured by a computer-controlled Keithley 2400 sourcemeter, with 1 sun (100 mW cm^{-2}) AM1.5G illumination provided by a Sciencetech solar simulator with intensity monitored by a calibrated photodiode. External quantum efficiency (EQE) measurements were also recorded via the Keithley sourcemeter, with monochromatic light provided by a Bentham tungsten lamp/monochromator combination.

3. Results and discussion

Fig. 1 shows *J–V* curves under 1 sun AM1.5G illumination and the trend in device parameters for a series of planar heterojunction devices based on an ITO/pentacene/40 nm C_{60}/10 nm BCP/Al structure grown with varying thicknesses, d_D, of pentacene. The pentacene was grown at a rate of 0.1 nm/s with no substrate heating. A 40 nm C_{60} layer was used as it matches the reported exciton diffusion length, but was also found to be the optimum thickness [9].

Peak performance is observed for a device with d_D = 43 nm, with J_{SC} = 6.7 mA cm^{-2}, V_{OC} = 0.41 V and fill factor (FF) = 0.54 leading to η_p = 1.5%. The J_{SC} value shows a significant improvement over devices we have reported previously containing CuPc as their donor layer, and this can be attributed to the improved exciton transport and

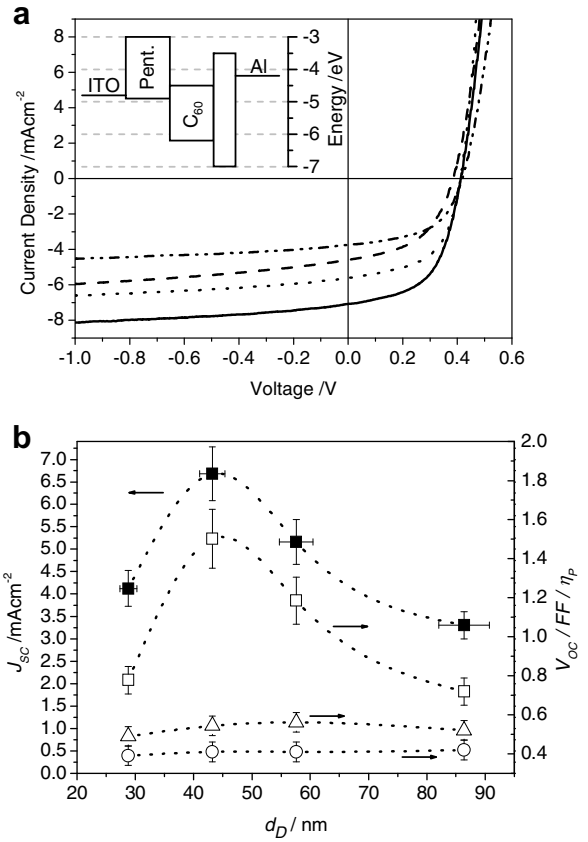

Fig. 1. (a) *J–V* characteristics of planar heterojunction devices of structure ITO/ d_D pentacene/40 nm C_{60}/10 nm BCP/Al with d_D = 29 nm (dashed line), 43 nm (solid line), 58 nm (dotted line) and 86 nm (dash-dotted line) and (inset) a schematic energy level diagram for the device. (b) A plot of J_{SC} (filled squares), V_{OC} (open circles), *FF* (open triangles) and η_p (open squares) as a function of d_D.

dissociation, higher charge mobility and improved extraction due to better matching of the donor HOMO energy level to the ITO electrode [1]. At lower pentacene thickness a loss in J_{SC} reduces performance (e.g. d_D = 29 nm; J_{SC} = 4.1 mA cm^{-2}, η_p = 0.8%) consistent with a thinner active layer reducing exciton formation, whilst a similar effect is observed at higher than optimum thickness (e.g. d_D = 58 nm; J_{SC} = 5.2 mA cm^{-2}, η_p = 1.2%) due to increased numbers of undissociated excitons. The *FF* is consistently between 0.50 and 0.55 across the full range of thicknesses. V_{OC} is seen to remain fairly constant regardless of device thickness, and this is to be expected in similar devices with no obvious source of internal field drop. It is interesting to note that V_{OC} is almost 0.1 V lower than in comparable CuPc/C_{60} heterojunctions, an effect due to the decreased interface gap (donor HOMO – acceptor LUMO difference) from 0.5 to 0.4 eV, which is considered responsible for V_{OC} in organic PV devices [10].

The optimum pentacene thickness of ~43 nm is approximately consistent with that found by Yoo et al. in a similar device structure [8], although Mayer et al. report devices with a lower optimum thickness of d_D = 20 nm [11]. The

power conversion efficiency is comparable to that estimated from EQE measurements by Yoo et al. for AM1.5G solar irradiation, which is the highest currently reported for pentacene/C_{60} heterojunction cells using unmodified ITO and metal electrodes, and is perhaps surprising after our devices were exposed to air before *J–V* characterisation. A recent report has suggested an advance in efficiency up to 2.24% in similar devices by modification of the anode by a self-assembled monolayer [12], a similar effect to that seen previously in CuPc:C_{60} heterojunction devices [13].

The EQE as a function of wavelength for a planar heterojunction device with d_D = 43 nm is shown in Fig. 2. It closely follows the electronic absorption with the features of both pentacene and C_{60} clearly visible. The high J_{SC} leads to an EQE maximum of ~55% at 670 nm, corresponding to the peak in pentacene absorption.

A wide range of device active areas have been reported in the literature with contradictory evidence on the effect this has on device performance [14,15]. Understanding the effect of active area is critical for future scaling up of organic PV technology. A series of ITO/43 nm Pentacene/40 nm C_{60}/10 nm BCP/Al devices were therefore grown simultaneously with different shadow mask areas during metal contact evaporation. Fig. 3 shows the effect of device area (up to 0.65 cm^2) on cell parameters J_{SC}, V_{OC}, η_p and FF under 100 mW cm^{-2} irradiation. The parameters remained within a 5% deviation across the series, and the scaled series resistance, R_SA, was also found to be consistent within the same error margins. The slight deviations can be accounted for by normal fluctuations within a batch of samples, and it can be concluded that device performance does not show significant dependence on active area for pentacene/C_{60} heterojunction devices as low as 0.05 cm^2. This is a promising result for the scaling-up of organic PV devices, at least as far as several square centimetres, and also implies a preference for larger area devices in research to minimise inaccuracies due to shadow masking resolution.

The stability of devices under constant illumination is a further critical consideration for eventual manufacture of organic PVs, and one which is rarely studied. Fig. 4 shows the change in *J–V* performance over a period of 70 mins

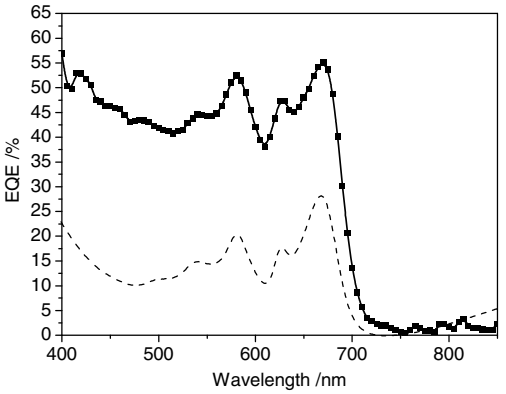

Fig. 2. EQE as a function of wavelength for a planar heterojunction device with d_D = 43 nm (solid line) and with the shape of the electronic absorption spectrum for comparison (dashed line).

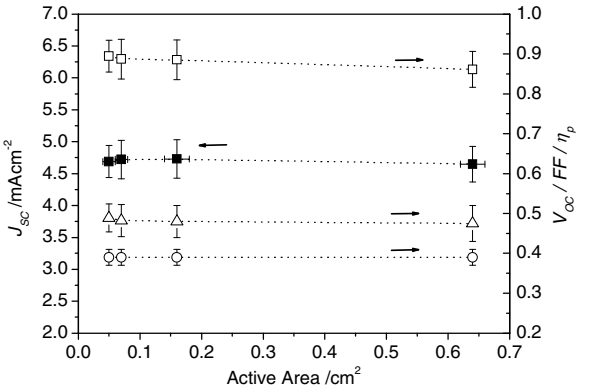

Fig. 3. The variation of device parameters for a ITO/43 nm pentacene/40 nm C_{60}/10 nm BCP/Al device with varying active area size.

for a pentacene/C_{60} planar heterojunction device (a) in air, (b) under a vacuum of ~10^{-4} mbar, and (c) under vacuum with a λ = 455 nm high-pass filter in the incident beam. The devices were all exposed to air after Al deposition before being transferred to the *J–V* setup where they were exposed to a constant illumination of 100 mW cm^{-2} throughout the 70 min period. Table 1 shows the parameters J_{SC}, V_{OC}, *FF* and η_p at the end of the 70 min period as a percentage of their starting values for each of the three analysis conditions.

The devices show much more rapid degradation than equivalent CuPc/C_{60} heterojunctions reported previously [7]. In air a rapid decrease in J_{SC} is observed, dropping to almost half its original value within 20 mins – a comparable drop in J_{SC} was not seen over the full 120 min measurement in the previous CuPc/C_{60} devices. The gradual formation of a kink in the *J–V* curve at positive bias after just a few minutes leads to a decreasing trend in FF, which itself results in a decrease in V_{OC}. The overall η_p drops very rapidly reaching less than 10% its original value within the initial 40 min.

Under vacuum the photocurrent remains constant, as seen by the overlap of all curves at negative bias. In the initial few minutes the performance is seen to increase slightly, an effect similar to that seen for a CuPc/C_{60} device under vacuum [7]. However, the increase is short lived and within 10 min a kink at positive bias begins to form, equivalent to that seen in air. The drop in FF results in a decrease in V_{OC} as well as a slight decrease in J_{SC} despite a constant photocurrent. The overall η_p decreases gradually, although less rapidly than the device in air due to the slower kink formation and stability of the photocurrent.

The differences between the evolution of *J–V* curve shapes under air and vacuum suggest two simultaneous mechanisms of degradation; (a) an oxygen induced degradation causing a decrease in photocurrent which is not observed for the device under vacuum, and (b) a purely photo-induced degradation causing the kink at positive bias that occurs regardless of the presence of oxygen.

Mechanism (a) cannot be explained purely by the photooxidation of C_{60} as the effect on photocurrent is far greater than that seen in CuPc/C_{60} devices [7]. Instead the

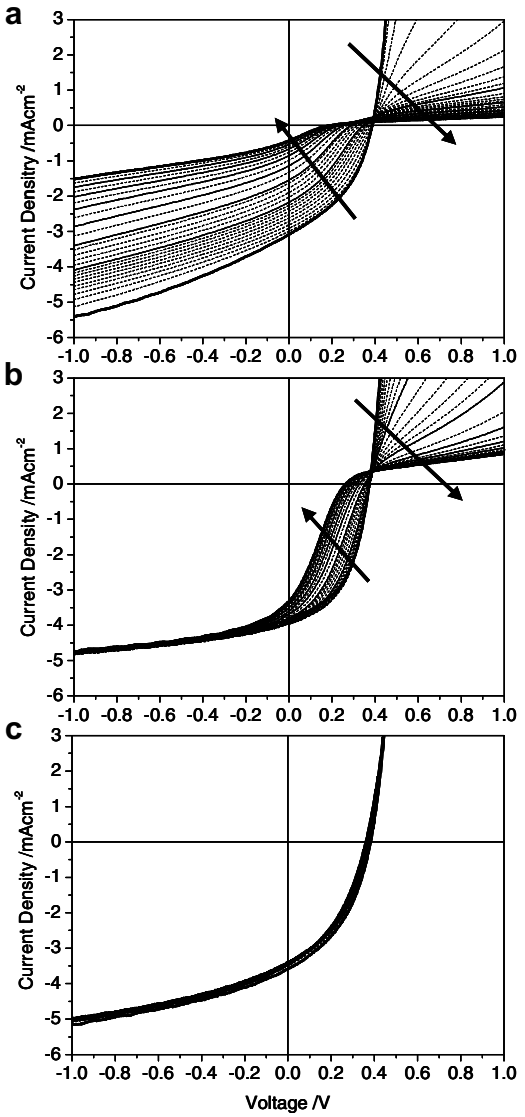

Fig. 4. *J–V* curves for a planar heterojunction device (ITO/43 nm Pentacene/40 nm C_{60}/10 nm BCP/Al) (a) in air, (b) under vacuum, and (c) under vacuum with a $\lambda = 455$ nm high-pass filter in the incident beam. Devices were exposed to constant 1 sun illumination and time progression from 0−70 mins is shown by the arrows. Thick lines indicate 0 mins and 70 - mins, with other solid lines indicating 10 min intervals.

Table 1
The device parameters of a planar heterojunction device (ITO/43 nm Pentacene/40 nm C_{60}/10 nm BCP/Al) after 70 min of constant 1 sun illumination analysed in air, under vacuum and under vacuum with a $\lambda = 455$ nm high-pass filter in the incident beam

	In air	Vacuum	Vacuum + UV blocked
J_{SC}	14.2	86.7	97.3
V_{OC}	48.7	70.3	95.9
FF	54.1	54.1	96.5
η_P	3.8	33.0	90.1

All values are expressed as a percentage of their original values before analysis.

degradation of pentacene must be having a significant effect. Pentacene has been noted to degrade in the presence of light and air to form a transannular peroxide and a dimeric peroxide amongst other compounds [16–18]. This photooxidation of pentacene will lead to a decrease in absorption and disruption of the crystal network resulting in decreased charge transport, hence explaining the drop in photocurrent in the presence of oxygen.

The kinks formed by mechanism (b) are similar to those seen in Cadmium Telluride (CdTe) solar cells [19]. In this case the kinks are a result of a barrier between the CdTe layer and the back Au contact; saturation of the junction voltage at the barrier under positive bias results in a corresponding saturation of current. During photoelectron emission microscopy (PEEM) studies Heringdorf observed that the UV radiation used to generate the photoelectrons was sufficiently energetic to desorb thin pentacene layers on a timescale of minutes, probably due to absorption of the radiation by the substrate leading to an increase in temperature [20]. For a pentacene layer grown on glass, significant substrate absorption occurs at 400 nm and below [5]. Under constant simulated solar illumination, a significant proportion of the UV radiation will be absorbed by the glass/ITO substrate causing a similar localized annealing effect. The resulting reorganisation is likely to take the form of a change in polymorph to a more thermodynamically stable form, with an associated decrease in the d(001) spacing [21]. To accommodate the decreased layer spacing, the molecules close to the electrode will be drawn away from the ITO surface (Fig. 5), and this reduction in the quality of contact between the pentacene molecules and the ITO will result in a contact barrier similar to that seen in CdTe. The difference in the rate of appearance of the kink under air and vacuum may be explained simply by the experimental setup. To hold a device under vacuum it was necessary for the incident light to pass through a sealed Perspex window on the sample holder before reaching the device. This window was found to behave as a $\lambda = 370$ nm high-pass filter and will therefore remove a portion of the UV irradiation reaching the device, reducing the rate of reorganisation at the pentacene/ITO interface and resulting in a slower onset of the *J–V* kink. Further reduction of the incident UV irradiation by the inclusion of a $\lambda = 455$ nm high-pass filter in the incident beam almost entirely removes the kink formation and leads to much more stable device performance over the full

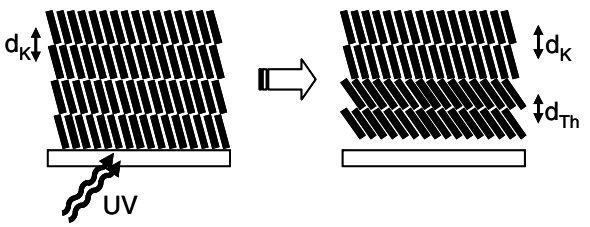

Fig. 5. The proposed reorganisation of pentacene near to the ITO substrate under UV irradiation. The layers closest to the substrate change from a kinetically favoured to a thermodynamically favoured polymorph with a corresponding decrease in the interlayer spacing ($d_{Th} < d_K$). As the top layers are held in position by the rest of the structure, the lower layers are drawn from the ITO surface to accommodate the decreased layer spacing resulting in an ITO/pentacene interface barrier.

70 mins, with J_{SC}, V_{OC} and FF remaining within 5% of their starting values, and η_p within 10%.

It is interesting to note the initial performance and J–V shape during the degradation study. The difference in performance compared to a similar device described in the active area study can be attributed to the ~30 min the devices were exposed to air during setup of the experiment before analysis, allowing oxygen to permeate through the structure. However, the initial shape of the J–V curves is good with the difference largely being due to a decrease in photocurrent. This is consistent with the devices degrading only by mechanism (a) during the storage time before analysis when the devices were not subject to UV irradiation.

4. Conclusions

To summarise, we have demonstrated pentacene/C_{60} photovoltaic devices optimised for active layer thickness showing power conversion efficiencies of 1.5%. Further, we have addressed two key issues surrounding the potential use of such devices in future PV applications; device active area and operational stability. We have shown a lack of dependence of device performance to active area over the range 0.05–0.65 cm^2 which is promising for future scaling-up. We have also identified two key degradation mechanisms which result in rapid deterioration of device performance, photooxidation and UV annealing, and demonstrated more stable device performance under conditions inhibiting both. Whilst it is clear similar general conclusions may not apply to devices based on solution cast polymer films due to the vastly different morphological effects, the results may prove useful in comparison to devices based on soluble derivatives of small molecular materials whose structural properties should more closely match those as grown by vacuum evaporation.

Acknowledgements

The authors would like to thank BP Solar and the EPSRC Excitonic Supergen consortium for funding.

References

[1] P. Sullivan, S. Heutz, S.M. Schultes, T.S. Jones, Appl. Phys. Lett. 84 (2004) 1210.
[2] J.G. Xue, B.P. Rand, S. Uchida, S.R. Forrest, Adv. Mater. 17 (2005) 66.
[3] S. Yoo, B. Domercq, B. Kippelen, Appl. Phys. Lett. 85 (2004) 5427.
[4] A.K. Pandey, J.M. Nunzi, Appl. Phys. Lett. 89 (2006) 213506.
[5] A.K. Pandey, S. Dabos-Seignon, J.M. Nunzi, Appl. Phys. Lett. 89 (2006) 113506.
[6] W.J. Potscavage, S. Yoo, B. Domercq, B. Kippelen, Appl. Phys. Lett. 90 (2007) 253511.
[7] S. Heutz, P. Sullivan, B.M. Sanderson, S.M. Schultes, T.S. Jones, Sol. Energy Mater. Sol. Cells 83 (2004) 229.
[8] S. Yoo, W.J. Potscavage, B. Domercq, S.H. Han, T.D. Li, S.C. Jones, R. Szoszklewicz, D. Levi, E. Riedo, S.R. Marder, B. Kippelen, Solid-State Electron. 51 (2007) 1367.
[9] P. Peumans, A. Yakimov, S.R. Forrest, J. Appl. Phys. 93 (2003) 3693.
[10] C.J. Brabec, A. Cravino, D. Meissner, N.S. Sariciftci, T. Fromherz, M.T. Rispens, L. Sanchez, J.C. Hummelen, Adv. Funct. Mater. 11 (2001) 374.
[11] A.C. Mayer, M.T. Lloyd, D.J. Herman, T.G. Kasen, G.G. Malliaras, Appl. Phys. Lett. 85 (2004) 6272.
[12] C.T. Tseng, Y.H. Cheng, M.C.M. Lee, C.C. Han, C.H. Cheng, Y.T. Tao, Appl. Phys. Lett. 91 (2007) 233510.
[13] S. Khodabakhsh, B.M. Sanderson, J. Nelson, T.S. Jones, Adv. Funct. Mater. 16 (2006) 95.
[14] W. Geens, T. Aernouts, J. Poortmans, G. Hadziioannou, Thin Solid Films 403 (2002) 438.
[15] J.G. Xue, S. Uchida, B.P. Rand, S.R. Forrest, Appl. Phys. Lett. 84 (2004) 3013.
[16] A. Maliakal, K. Raghavachari, H. Katz, E. Chandross, T. Siegrist, Chem. Mater. 16 (2004) 4980.
[17] M. Yamada, I. Ikemoto, H. Kuroda, Bull. Chem. Soc. Jpn 61 (1988) 1057.
[18] I.C. Lewis, L.S. Singer, J. Phys. Chem. 85 (1981) 354.
[19] A. Niemegeers, M. Burgelman, J. Appl. Phys. 81 (1997) 2881.
[20] F.J.M.Z. Heringdorf, M.C. Reuter, R.M. Tromp, Nature 412 (2001) 517.
[21] C.C. Mattheus, G.A. de Wijs, R.A. de Groot, T.T.M. Palstra, J. Am. Chem. Soc. 125 (2003) 6323.

Organic Electronics 9 (2008) 661–666

Contents lists available at ScienceDirect

Organic Electronics

journal homepage: www.elsevier.com/locate/orgel

Efficient bulk heterojunction solar cells from regio-regular-poly(3,3‴-didodecyl quaterthiophene)/$PC_{70}BM$ blends

Pardhasaradhi Vemulamada [a], Gong Hao [a], Thomas Kietzke [b,1], Alan Sellinger [b,*]

[a] Department of Materials Science and Engineering, National University of Singapore, 10 Kent Ridge Crescent, Singapore 119260, Republic of Singapore
[b] Institute of Materials Research and Engineering, (IMRE) and the Agency for Science, Technology and Research (A STAR), 3 Research Link, Singapore 117602, Republic of Singapore

ARTICLE INFO

Article history:
Received 1 January 2008
Received in revised form 10 April 2008
Accepted 10 April 2008
Available online 22 April 2008

PACS:
$PC_{70}BM$

Keywords:
Organic photovoltaics
PQT-12
C70BM

ABSTRACT

Blends of regio-regular poly(3,3‴-didodecyl quaterthiophene) (PQT-12) with (6,6)-phenyl-C_{70}-butyric acid methyl ester ($PC_{70}BM$) were investigated as active layers for application in organic photovoltaics (OPV). By optimizing the PQT-12:$PC_{70}BM$ composition ratio and annealing conditions, power conversion efficiencies (η) of 1.4% could be obtained. Effects of different preparation parameters on the incident photon conversion efficiency (IPCE), short-circuit (J_{sc}), fill factor (FF), open-circuit voltage (V_{oc}) and η are discussed.

1. Introduction

Organic photovoltaics (OPV) have become an exciting area of technology for academia, government research laboratories and industry due to their potential for low cost, light weight and large area solar cell devices [1]. From a materials perspective both small molecules and polymers are currently being investigated. Small-molecules have the advantage that they can be highly purified and vacuum deposited in multi-layer stacks, both important for device lifetime and efficiency. Polymers are generally of lower purity than small molecules but can more easily address larger device sizes at potentially lower costs by using solution-based deposition techniques such as dip, spin and spray coating, ink jet and screen printing. With regard to solution processing, one system that has gained significant attention in recent years is based on spin coated films of regio-regular poly(3-hexylthiophene) (P3HT) with fullerene derivatives [(6,6)-phenyl-C_{61}-butyric acid methyl ester ($PC_{60}BM$)]. Initial device power conversion efficiencies (η) were quite low (~0.2%) [2], but with many research groups working on this over the past 10 years, recent η values of ~5% have been achieved [3–5]. Despite these encouraging results, this system suffers from several problems, including $PC_{60}BM$s poor absorption in the visible spectrum, and most significantly rather low open-circuit voltages (~0.5–0.6 V).

P3HT has become a promising material in the field of organic solar cells over the previously extensively studied poly (*p*-phenylene vinylene) (PPV):$PC_{60}BM$ system [6,7] because of its beneficial properties such higher hole mobility (0.10 cm^2/vs) [8], enhanced photostability [9] and an improved optical absorption in the visible region. Recently another thiophene based polymer: poly(3,3‴-didodecyl quaterthiophene) (PQT-12) was reported to have nearly twice the transistor mobilities (0.18 cm^2/vs) as compared to P3HT [10]. In addition the highest occupied molecular orbital (HOMO) is lower compared to that of P3HT ($HOMO_{PQT-12}$ = −5.24 eV, $HOMO_{P3HT}$ = −5.00 eV) leading to even better ambient stability [11]. For example, it was found that

* Corresponding author. Tel.: +65 6874 4153; fax: +65 6872 7528.
E-mail address: alan-sellinger@imre.a-star.edu.sg (A. Sellinger).
[1] Merck KgaA, Frankfurter Strasse 250, 64293 Darmstadt, Germany.

1566-1199/$ - see front matter © 2008 Elsevier B.V. All rights reserved.
doi:10.1016/j.orgel.2008.04.005

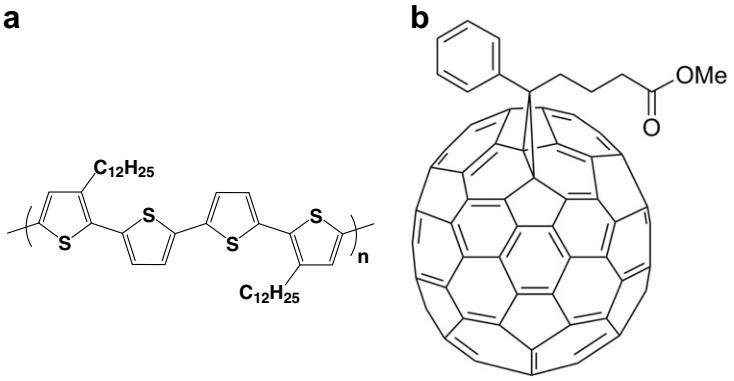

Fig. 1. The chemical structures of (a) PQT-12 and (b) $PC_{70}BM$.

organic field effect transistors (OFETs) fabricated from PQT-12 have a much greater stability in air than corresponding devices fabricated from P3HT [12]. Since the V_{oc} of organic solar cells is limited by the difference of the HOMO level of the electron donor and the LUMO level of the electron acceptor, solar cells using PQT-12 as electron donor should reach higher open-circuit voltages than those based on P3HT [11]. Hence, due to its lower HOMO and higher mobility, together with a similar broad absorption spectrum as P3HT, PQT-12 offers the potential to be used in organic solar cells with higher efficiencies and higher stability than those based on P3HT.

Currently, $PC_{60}BM$ is the most commonly investigated acceptor for solution processed organic solar cells, with only few others being reported [7,13–16]. One drawback of $PC_{60}BM$ is its low absorption in the visible range. To address this shortfall, it has been shown that PPV-based solar cells with improved light absorption, leading to enhanced J_{sc} values, can be achieved by using the fullerene derivative $PC_{70}BM$ instead of $PC_{60}BM$ [7]. This is explained by $PC_{70}BM$s stronger absorption in the visible range as compared to $PC_{60}BM$.

In the present work we report the effect of composition and annealing temperatures on the performance of solution processed solar cells made from blend films of regio-regular-PQT-12 and $PC_{70}BM$ (Fig. 1). Since both materials are used together for the first time to our knowledge, a detailed study on the optimum composition ratio was performed. It is well known that the optimum composition ratio for polymer solar cells is extremely important. For example in regio-regular-P3HT: $PC_{60}BM$ bulk heterojunction devices, considerably lower fullerene contents (1:0.8) yield optimum solar cell efficiencies [17] compared to MDMO-PPV: $PC_{60}BM$ where ratios of 1:4 are optimal. Furthermore, it has been determined that annealing significantly increases device efficiency – a parameter that was also a focus in our study [5].

2. Experimental

For device fabrication, a ≈70 nm thick layer of poly(ethylene dioxythiophene) doped with polystyrene sulfonic acid (PEDOT:PSS) was spin-coated onto commercial glass substrates covered with indium-tin-oxide (polished 140 nm ITO on SiO_2 covered soda lime glass, Merck). The PEDOT:PSS (HC Starck) films were dried on a hot plate under a nitrogen atmosphere for 10 min at 120 °C. The active layer was prepared from 2.4 wt.% solutions (24 mg/ml) in chlorobenzene. The weight ratios of PQT-12 (American Dye Source) as electron donor and $PC_{70}BM$ (American Dye Source) as electron acceptor were varied between 2:1, 1:1, 1:1.5, 1:2, 1:2.5, 1:3 and 1:4. Separate solutions of PQT-12 and $PC_{70}BM$ were stirred at 50 °C for a few hours before the solutions were mixed to form the blend solutions. The PQT-12 solutions were not completely solubilized in chlorobenzene until heated to 70 °C prior to combining the solutions. The blend solutions were stirred overnight at 50 °C and remained clear. The blend solutions were filtered through 0.22 μm-pore size PVDF syringe driven filters (Millipore) and were used to spin-coat the active layers at 2000 revolutions per minute (RPM) for 60 s. The thin films were annealed on a hot plate for 10 min and the devices completed by evaporating a 20 nm Ca layer followed by 100 nm of Ag at pressures below 8×10^{-6} mbar. The effective solar cell area as defined by the geometrical overlap between the bottom ITO electrode and the top cathode was 0.1425 cm^2. The incident photon to collected electron efficiency (IPCE) as a function of wavelength was measured with a home built system consisting of an Oriel 300 Watt Xe-lamp in combination with an Oriel Cornerstone 130 monochromator and a SRS 810 Lock-In amplifier (Stanford Research Systems). The number of photons incident on the device were calculated for each wavelength by using a calibrated Si-photodiode as a reference. The white light measurements were performed using a solar cell simulator (Steuernagel 535, Germany) and a Keithley 2400 Source/Measure unit. Details of our characterization set up used to measure white light efficiency (AM 1.5 spectrum, 100 mW/cm^2) have been previously reported [18]. All device preparation and characterization were performed under a nitrogen atmosphere.

3. Results and discussion

The highest quantum efficiency (IPCE = 28% at 475 nm) was obtained for a ratio of 1:2 (PQT-12:$PC_{70}BM$) as shown

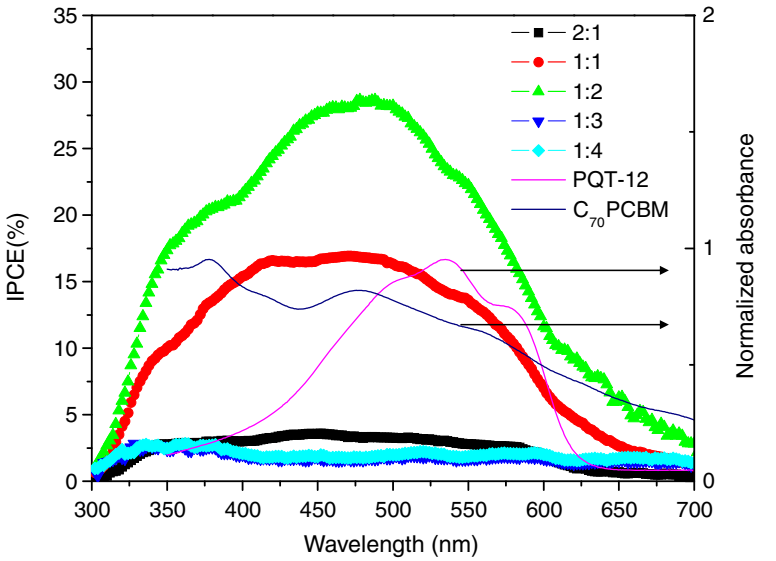

Fig. 2. Incident photon to converted electron efficiency (IPCE) spectra of OPVs: effect of donor: acceptor ratio (wt.%) (PQT-12:C_{70}PCBM) on as-deposited cells, and normalized absorbance of the pristine PQT-12, C_{70}PCBM also shown as thin lines for reference.

in Fig. 2. The spectral response extends from about 320 nm ($PC_{70}BM$ absorption) to 650 nm, indicating that both PQT-12 as well as $PC_{70}BM$ contribute to the photocurrent.

It has previously been shown that PQT-12 exhibits liquid crystalline properties with phase transitions between 120 °C and 140 °C [19]. From our differential scanning calorimeter (DSC) studies on PQT-12, two transitions were found at ~110 °C and ~140 °C. Based on these results, five different annealing temperatures were selected – room temperature (RT), 110 °C, 140 °C, 160 °C, and 180 °C – to study the influence on the device performance. Fig. 3 shows the (a) power conversion efficiency (η), (b) fill factor (FF), (c) short-circuit current density (J_{sc}), and (d) open-circuit voltage (V_{oc}) as a function of $PC_{70}BM$ weight

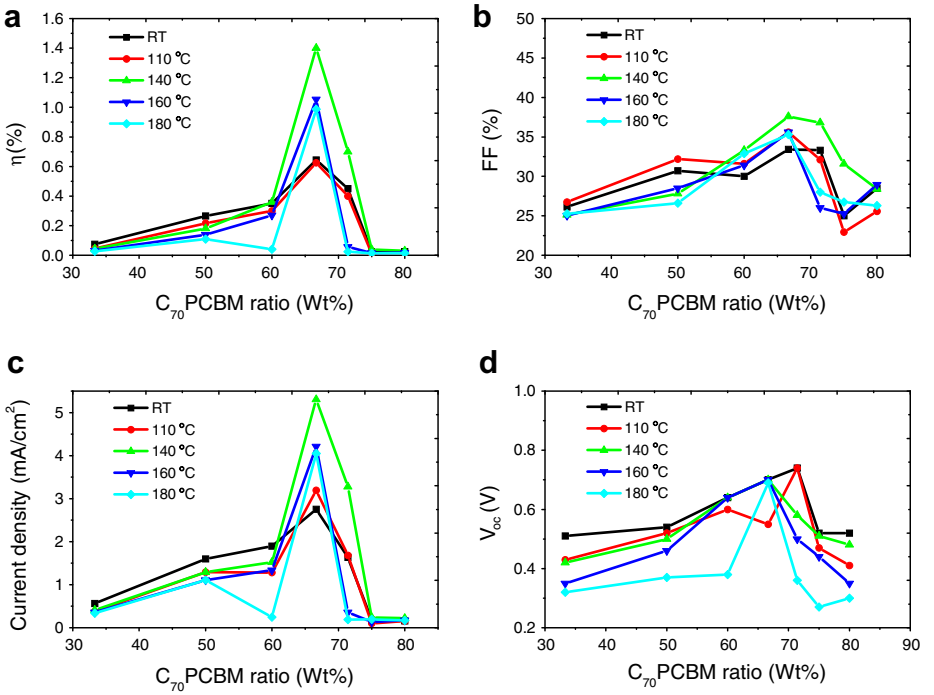

Fig. 3. (a) Power conversion efficiency (η), (b) fill factor (FF), (c) short-circuit current density (J_{sc}), and (d) open-circuit voltage V_{oc} as a function of $PC_{70}BM$ weight fraction in PQT-12:$PC_{70}BM$ OPVs when annealed at different temperatures (RT, 110 °C, 140 °C, 160 °C, and 180 °C). Annealing was done for 10 min under an N_2 atmosphere.

percentage (wt.%) in PQT-12:$PC_{70}BM$ solar cells after annealing at different temperatures. For all investigated annealing temperatures, the 1:2 PQT-12:$PC_{70}BM$ ratio yielded the best performance. The device parameters under illumination with white light (AM 1.5, 100 mW/cm^2) are summarized in Table 1. The best performance was obtained for the device annealed at 140 °C, which reached V_{oc} = 0.70 V, FF = 0.38, J_{sc} = 5.3 mA/cm^2 and η = 1.4%.

As expected a slightly higher V_{oc} compared to P3HT:$PC_{60}BM$ solar cells was achieved due to the lower HOMO level of PQT-12 compared to P3HT. The obtained efficiency is similar to previous work in which $PC_{60}BM$ and a PQT-12 based polymer (PQT-DD) were used as an acceptor and donor, respectively [20]. However in that reported work, the highest power conversion efficiency was obtained on as-deposited films (η = 1.84%), with annealing above 50 °C significantly reducing the device performance due to macro-phase separation.

Table 1
Comparison of device parameters of ITO/PEDOT:PSS/PQT-12: $PC_{70}BM$/Ca/Ag organic solar cells with different annealing temperatures processed from chlorobenzene

Annealing temperature (°C)	V_{oc} (V)	FF (%)	J_{sc} (mA/cm^2)	η (%)
RT	0.70	33.4	2.71	0.64
110	0.55	35.6	3.20	0.63
140	0.70	37.6	5.30	1.40
160	0.70	35.6	4.20	1.05
180	0.69	35.3	4.04	0.99

Annealing time was 10 min under N_2 atmosphere.

Although the open-circuit voltages reported here are higher than for P3HT:$PC_{60}BM$ based solar cells, the power conversion efficiencies have not yet reached the levels of the P3HT system yet, indicating that the nanostructures are not optimal. It is known from extensive studies on P3HT: $PC_{60}BM$ solar cells that the nanostructures formed upon evaporation of the solvents has a dramatic influence on the device efficiency [21]. An optimum nanostructure fulfills two criteria: first, the phase separation should be sufficiently small (<10 nm) to ensure that all photogenerated excitons can be dissociated at the interfaces. Second, a percolating path is needed to transport the dissociated charges to their respective electrode.

It has been frequently reported that annealing leads to improved device performance for organic solar cells as well as for organic transistors. In the case of organic transistors, it has been shown that annealing leads to better ordering of the materials resulting in higher carrier mobilities. However, the key factor leading to enhanced efficiencies in annealed OPVs is more difficult to identify. This is because unlike transistors, a blend of two materials are annealed in organic solar cells. Due to the low entropy of mixing, the two components begin to phase separate upon solvent evaporation. Once the solvent is evaporated, a meta-stable phase separated morphology is formed. Annealing at temperatures exceeding the glass transition temperature of at least one of the active materials enables the chains/molecules to take an energetically more favorable ordering (typically the formation of larger domains) leading to a change in nanostructure. Thus it was investigated if the higher efficiency after annealing is primarily caused

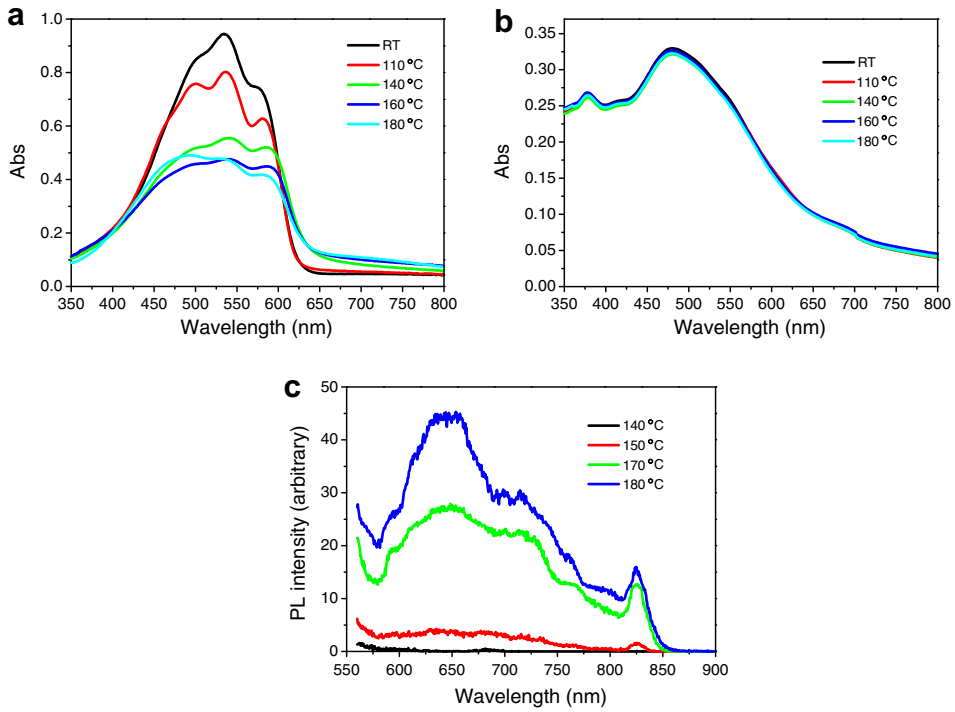

Fig. 4. Variation of absorption (Abs.) and photoluminescence (PL) with annealing temperature. (a) Abs. of pure PQT-12; (b) Abs. of 1:2 (PQT-12:$PC_{70}BM$) blend films and; (c) PL of 1:2 (PQT-12:$PC_{70}BM$) blend films (no PL observed for temperatures below 140 °C.

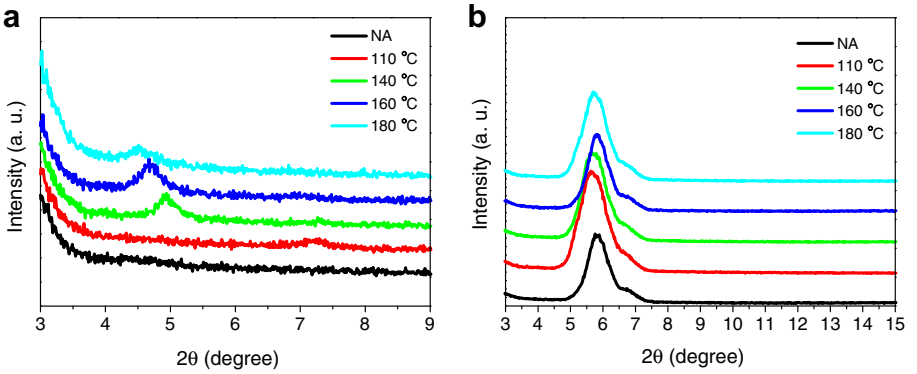

Fig. 5. XRD patterns of: (a) pure PQT-12 and (b) 1:2 (PQT-12:$PC_{70}BM$) blend films after annealing at selected temperatures for 10 min.

by enhanced ordering of the PQT-12 chains leading to higher mobilities or by changes in the nanostructure influencing the percolation of the charge carriers.

In Fig. 4 the influence of annealing temperature on the absorption (Abs.) and photoluminescence (PL) spectra is shown for 1:2 (PQT-12:$PC_{70}BM$) blend films. In the Abs. spectra for pure PQT-12 thin films (Fig. 4a), clear differences in the shape of the peaks can be observed as a function of temperature. For example, the intensity of the peak at ≈535 nm is reduced to a larger extent than that of the ≈580 nm peak. This suggests a higher degree of ordering as a function of temperature [11]. In the blend film (Fig. 4b), no difference in the Abs. spectra can be observed as a function of annealing, suggesting no influence on higher ordering of either material is taking place. Thus annealing is more likely to affect the nanostructure/morphology of the blend, rather than inducing enhanced order in PQT-12 that would result in a red shifted absorbance. In the PL spectra (Fig. 4c), the PL is completely quenched for the as-prepared film and for all annealing temperatures below 140 °C. Above 140 °C the PL signal of PQT-12 re-emerges, indicating that larger domains are formed

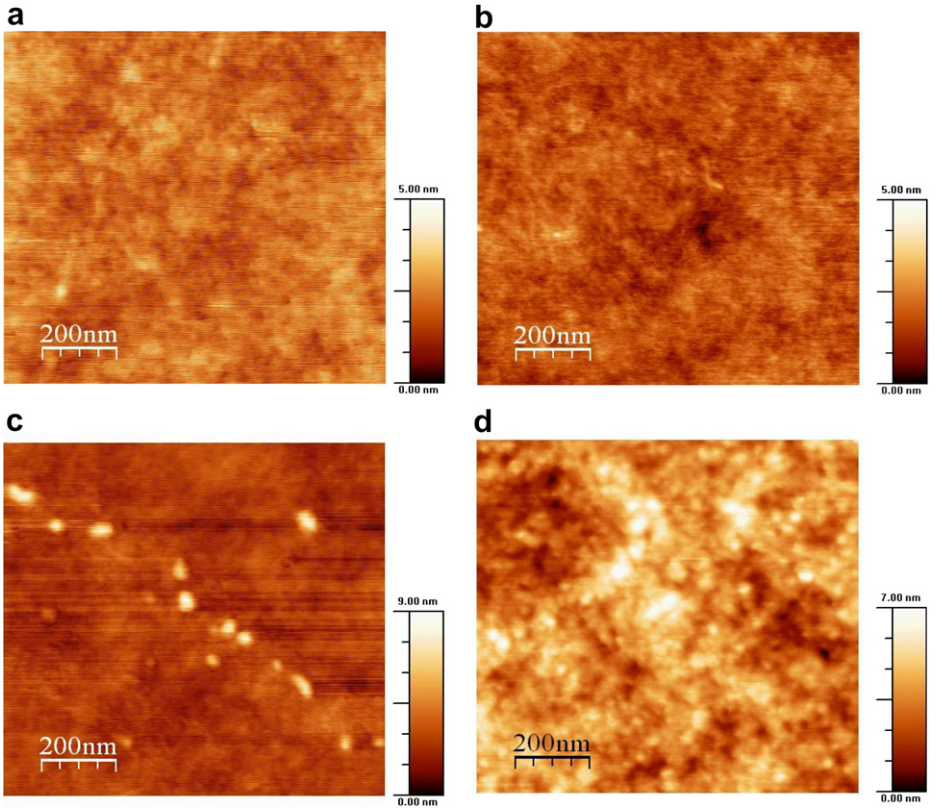

Fig. 6. Topographic atomic force microscopy (AFM) images of 1:2 (PQT-12:$PC_{70}BM$) blend films prepared from different annealing temperatures (a) RT, (b) 110 °C, (c) 140 °C and (d) 180 °C.

preventing excitons from reaching the PQT-12/$PC_{70}BM$ interfaces, which in turn reduces the J_{sc}. This temperature range corresponds to the crystalline-isotropic transition point of PQT-12 as determined by DSC.

To further study the crystallization, XRD studies of pure PQT-12, pure $PC_{70}BM$ and the blend film were performed. The PQT-12 film is amorphous as deposited with ordering appearing after annealing above 140 °C – peak appears at $2\theta = 4.9°$ (Fig. 5a). The as-deposited 1:2 blend film shows the presence of crystallinity with a peak observed at $2\theta = 5.7°$ (Fig. 5b), corresponding to the crystallization peak of the $PC_{70}BM$. No changes of the XRD signal of the blend layer on the annealing steps could be observed. It can be concluded that the presence of the $PC_{70}BM$ suppresses the ordering of the PQT-12 even after annealing above the transition temperature of 140 °C, as no peaks in the $2\theta = 4.6–4.9°$ range can be observed. This finding only partially corresponds to what is found for P3HT:$PC_{60}BM$ blends. For this combination it has been reported that $PC_{60}BM$ addition will induce disorder in the well arranged P3HT polymer chains [22]. However, annealing of the P3HT-$PC_{60}BM$ blend films will result in diffusion of $PC_{60}BM$ molecules out of the P3HT:$PC_{60}BM$ matrix [23,24] leading to better order and a red shift in the P3HT absorption spectrum.

Therefore, it can be concluded that a change of the blend nanostructure/morphology, rather than enhanced ordering of the PQT-12, is primarily responsible for the observed efficiency dependence on the annealing steps. This also explains why there is only a minor influence of annealing on the fill factor (Table 1 and Fig. 3b), which is often influenced by the mobilities of the charge carriers.

Atomic force microscopy (AFM) measurements were performed to study the layer morphology upon annealing the 1:2 blend films as shown Fig. 6. Excellent miscibility between PQT-12 and $PC_{70}BM$ was observed in the case of as-deposited blend films. No nanostructure could be identified for the film annealed below 140 °C, indicating a mixture of both phases on a scale much below the exciton diffusion length, which is thought to be <10 nm. This is in agreement with the observation of complete PL quenching at lower annealing temperatures. Beginning at 140 °C observable features are formed, and after annealing at 180 °C the whole layer is dominated by clearly identified nanostructures with domains measuring between 10 nm and 40 nm. The larger phase separation leads to a lower PL quenching, as discussed before.

It can be concluded that upon annealing at 140 °C the domain sizes are just big enough to facilitate percolating charge transport, but still small enough that significant amounts of photogenerated excitons can reach the interface. However the exact nanostructure formed cannot be determined with AFM. Furthermore, AFM can only image the surface topology which may be different from the bulk structure.

4. Conclusion

We have shown that commercially available PQT-12 and $PC_{70}BM$ semi-conducting materials can be carefully combined to produce efficient organic solar cells. The effect of blend composition and device annealing was studied with the highest power conversion efficiencies achieved for a 1:2 composition by weight. Addition of more $PC_{70}BM$ (1:3 and 1:4 compositions) significantly reduced the efficiency, while device annealing of the 1:2 blend more than doubles the power conversion efficiency from as-deposited devices 0.64% to 1.40% at 140 °C. Based on the results provided here, it is concluded that the efficiency of the PQT-12:$PC_{70}BM$ blend solar cells is limited primarily by morphology resulting in absent percolating pathways to the respective electrodes. Further processing optimization and thin film cross section studies are proposed to investigate the layer nanostructure in more detail.

Acknowledgements

This research has been supported by the Agency for Science, Technology and Research (A*STAR) and the Institute of Materials Research and Engineering (IMRE) through the VIP Program in Organic Electronics coordinated by Prof. Ananth Dodabalapur. We thank Mr. Lawrence Dunn and Mr. Zien Ooi for many helpful discussions and technical assistance.

References

[1] W.L. Ma, C.Y. Yang, X. Gong, K.H. Lee, A.J. Heeger, Adv. Funct. Mater. 15 (2005) 1617.
[2] D. Chirvase, Z. Chiguvare, M. Knipper, J. Parisi, V. Dyakonov, J.C. Hummelen, Synth. Met. 138 (2003) 299.
[3] Y. Kim, S.A. Choulis, J. Nelson, D.D.C. Bradley, S. Cook, J.R. Durrant, Appl. Phys. Lett. 80 (2005) 3885.
[4] G. Li, V. Shrotriya, Y. Yao, Y. Yang, J. Appl. Phys. 98 (2005) 043704.
[5] D. Chirvase, J. Parisi, J.C. Hummelen, V. Dyakonov, Nanotechnology 15 (2004) 1317.
[6] S.E. Shaheen, C.J. Brabec, F. Padinger, T. Fromherz, J.C. Hummelen, N.S. Sariciftci, Appl. Phys. Lett. 78 (2001) 841.
[7] M.M. Wienk, J.M. Kroon, W.J.H. Verhees, J. Knol, J.C. Hummelen, P.A. van Hal, R.A.J. Janssen, Angew. Chem. Int. Ed. 42 (2003) 3371.
[8] H. Sirringhaus, N. Tessler, R.H. Friend, Science 280 (1998) 1741.
[9] L.M. Popescu, P. van't Hof, A.B. Sieval, H.T. Jonkman, J.C. Hummelen, Appl. Phys. Lett. 89 (2006) 213507.
[10] Y.O. Wu, P. Liu, B.S. Ong, T. Srikumar, N. Zhao, G. Botton, S.P. Zhu, Appl. Phys. Lett. 86 (2005) 142102.
[11] B.S. Ong, Y. Wu, P. Liu, S. Gardner, Adv. Mater. 17 (2005) 1141.
[12] B.S. Ong, Y. Wu, P. Liu, S. Gardner, J. Am. Chem. Soc. 126 (2004) 3378.
[13] R.Y.C. Shin, T. Kietzke, S. Sudhakar, A. Dodabalapur, Z.K. Chen, A. Sellinger, Chem. Mater. 19 (2007) 1892.
[14] I. Riedel, E. von Hauff, J. Parisi, N. Martin, F. Giacalone, V. Dyakonov, Adv. Funct. Mater. 15 (2005) 1979.
[15] D. Mühlbacher, M. Scharber, M. Morana, Z. Zhu, D. Waller, R. Gaudiana, C. Brabec, Adv. Mater. 18 (2006) 2884.
[16] Y. Yao, C. Shi, G. Li, V. Shrotriya, Q. Pei, Y. Yang, Appl. Phys. Lett. 89 (2006) 153507.
[17] M. Reyes-Reyes, K. Kim, D.L. Carrolla, Appl. Phys. Lett. 87 (2005) 83506.
[18] T. Kietzke, R.Y.C. Shin, D.A.M. Egbe, Z.K. Chen, A. Sellinger, Macromolecules 40 (2007) 4424.
[19] B.S. Ong, Y. Wu, P. Liu, Proc. IEEE 93 (2005) 1412.
[20] B.C. Thompson, B.J. Kim, D.F. Kavulak, K. Sivula, C. Mauldin, J.M.J. Frechet, Macromolecules 40 (2007) 7425.
[21] X. Yang, J. Loos, S.C. Veenstra, W.J.H. Verhees, M.M. Wienk, J.M. Kroon, M.A.J. Michels, R.A.J. Janssen, Nano Lett. 5 (2005) 579.
[22] T. Erb, U. Zhokhavets, G. Gobsch, R. Raleva, B. Stuhn, P. Schilinsky, C. Waldauf, C.J. Brabec, Adv. Funct. Mater. 15 (2005) 1193.
[23] X. Yang, J.K.J. van Duren, R.A.J. Janssen, M.A.J. Michels, J. Loos, Macromolecules 37 (2004) 2151.
[24] U. Zhokhavets, T. Erb, G. Gobsch, M. Al-Ibrahim, O. Ambacher, Chem. Phys. Lett. 418 (2006) 347.

Organic Electronics 9 (2008) 667–672

Contents lists available at ScienceDirect

Organic Electronics

journal homepage: www.elsevier.com/locate/orgel

Enhanced OLED performance upon photolithographic patterning by using an atomic-layer-deposited buffer layer

Chih-Yu Chang, Feng-Yu Tsai *, Syue-Jhao Jhuo, Miin-Jang Chen

Department of Materials Science and Engineering, National Taiwan University, 1, Section 4, Roosevelt Road, Taipei, Taiwan, ROC

ARTICLE INFO

Article history:
Received 9 March 2008
Received in revised form 28 April 2008
Accepted 29 April 2008
Available online 7 May 2008

PACS:
72.80.Le
78.60.Fi
85.60.Jb
81.15.Gh
85.40.Hp

Keywords:
Atomic layer deposition
Electroluminescence
Photolithography
Conjugated polymer

ABSTRACT

This study addresses the problem of patterning-induced degradations to organic light-emitting diodes (OLEDs) by using a thin (10 Å) atomic-layer-deposited (ALD) Al_2O_3 film as both an electron-injection layer and a protecting layer for the electroluminescent material, poly[1-methoxy-4-(2′-ethyl-hexyloxy)-2,5-phenylene vinylene] (MEH-PPV). With the ALD Al_2O_3 film, the OLEDs not only withstood an aggressive photolithographic patterning process without any degradation but unprecedentedly showed increased luminous efficiency (by 100%) and lowered turn-on voltage (by 19%) afterward. Although the ALD precursor, trimethylaluminum (TMA), was found to damage the MEH-PPV layer through electrophilic addition to the vinylene groups of MEH-PPV during the deposition of the Al_2O_3 film, its damaging effect was eliminated by pre-treating the MEH-PPV surface with isopropyl alcohol (IPA), whose hydroxyl groups scavenged TMA throughout the ALD process. The performance of the photo-patterned OLEDs was further improved by using a high-conductivity hole-injection layer, which increased accumulation of holes at the EL–buffer interface to enhance electron injection. The method reported herein improves the applicability of photolithography to OLED fabrication, promising to resolve the issue of patterning that has in part impeded OLED's commercialization.

1. Introduction

Although organic light-emitting diodes (OLEDs) are finding increasing use in flat panel displays [1–4], their applications in displays are still limited due in part to the lack of an economical yet adequate method for patterning the electroluminescent (EL) materials into fine pixels. Patterning methods currently used for manufacturing or demonstrating OLED displays include evaporation through shadow masks and ink-jet printing [5–7], both of which are relatively slow [8,9], incompatible with many EL materials [10], and limited in pattern resolution [9,11]. Photolithography, the standard patterning method used in the displays industry, would also be ideal for OLEDs, but it has been shown incompatible with OLEDs due to the susceptibility of the EL materials to the typical solvents or reactive gases used in a photolithographic process [12,13]. On the other hand, an OLED device can use a thin insulator layer at the interface between the cathode and the EL layers, such as MgO [14], SiO_2 [15] and Al_2O_3 [16,17] to enhance the injection of electrons. The insulator layer, commonly referred to as the buffer layer, operates by reducing the effective barrier for electron injection and by blocking holes from the cathode [18–20], thereby lowering the operating voltage and improving the EL efficiency.

The objective of this study is to develop a photolithographic patterning (photo-patterning) technique for OLEDs that does not compromise the OLED performance. The approach adopted in this study is to use a buffer layer to both protect the EL layer of an OLED device during photo-patterning and to enhance the performance of the patterned device (see Fig. 1 for a schematic drawing of the proposed patterning process). Given that an effective buffer layer

* Corresponding author. Tel.: +886 2 33665302; fax: +886 2 2363 4562.
E-mail address: ftsai@ntu.edu.tw (F.-Y. Tsai).

1566-1199/$ - see front matter © 2008 Elsevier B.V. All rights reserved.
doi:10.1016/j.orgel.2008.04.009

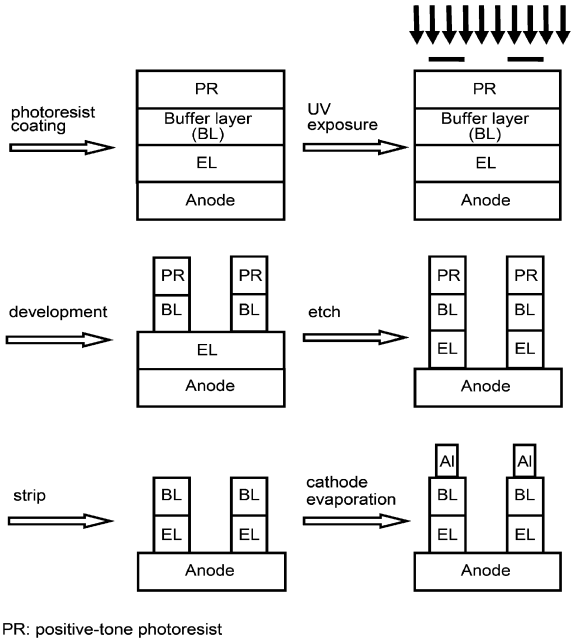

Fig. 1. Schematic drawings of the buffer-protected patterning process demonstrated in this study.

must be thin, typically in the range of 5–20 Å [21,22], it must have complete and uniform coverage over the EL layer to provide adequate protection throughout the patterning process. We used atomic layer deposition (ALD) to form Al_2O_3 films as the buffer layers, taking advantage of ALD's low defect density, high conformality, and low deposition temperatures to maximize the surface coverage of such thin films and to avoid thermally degrading the EL layer [23–25]. The content of this study is as follow: First, the minimum thickness of the ALD Al_2O_3 film required to protect the EL layer was determined by ultrasonicating Al_2O_3-coated EL films in a solvent and then inspecting their appearances. Second, the effects of the added Al_2O_3 layer on the characteristics of the OLED devices were evaluated, and the ALD process was modified, to ensure that the Al_2O_3 layer served as an effective buffer. Third, the OLED characteristics were evaluated again with devices patterned using a typical photolithography process. Finally, methods for further improving the characteristics of the photo-patterned OLEDs were explored.

2. Experimental

2.1. Device fabrication and characterization

The OLED device used in this study was segmented monochromatic display with poly[1-methoxy-4-(2′-ethylhexyloxy)-2,5-phenylene vinylene] (MEH-PPV) as the EL material. The cross-sectional structure for the control devices was indium tin oxide (ITO)/poly(3,4-ethylenedioxythiophene):poly(styrenesulfonate) (PEDOT:PSS)/MEH-PPV/Al. For the experimental devices, an Al_2O_3 buffer layer was inserted between the MEH-PPV layer and the Al cathode. The substrates were ITO-coated glass with a sheet resistance of 15 Ω/sq (purchased from Rite Displays). The substrates were cleaned by ultrasonication by turns in trichloroethylene, acetone, methanol and isopropyl alcohol, followed by rinsing with deionized water and blow-drying with nitrogen. Each of the sonication steps was carrier out at 50 °C for 15 min. Subsequently, PEDOT:PSS (Baytron P VP AI 4083, purchased from Bayer AG and used after filtering through a 0.2 μm filter) was spin-coated at 1500 rpm onto the substrates. The samples were then transferred into a glove box and baked at 160 °C for 60 min. MEH-PPV (Mn = 70,000–1,00,000 g mol^{-1}, purchased from Sigma-Aldrich and used as received) in anhydrous toluene (7 mg ml^{-1} and filtered through a 0.2 μm filter) was then spin-coated at 1100 rpm onto the PEDOT:PSS layer and baked at 70 °C for 30 min. A 250-nm-thick aluminum film was formed onto the MEH-PPV layer as the cathode by thermal evaporation through a shadow mask at 10^{-6} Torr. The devices were then encapsulated with a glass lid using photo-curable epoxy resin as sealant. The current–voltage–luminance characteristics of the devices were measured with a Keithley 2400 source meter and a Minolta CS-100 chromameter.

2.2. Spectral characterization and contact angle measurement

Ultraviolet–visible (UV–Vis) absorption spectra of MEH-PPV films were collected with a Jasco V-570 spectrometer. The MEH-PPV films (30 nm in thickness) were spin-coated at 3000 rpm on glass substrates from a 2 mg mL^{-1} solution in anhydrous toluene. Infrared spectra were collected with a Thermo Nicolet Nexus 470 Fourier transform infrared (FTIR) spectrometer, with the MEH-PPV films on KBr tablets. Water contact angles were measured using a Ramé–Hart contact angle goniometer (Model 100), where the sessile drop of 2–3 μl in volume was dispensed with a microsyringe and the contact angle was measured within 30 s after its formation.

2.3. Atomic layer deposition

Atomic layer deposition of Al_2O_3 was applied to the MEH-PPV layer using a Cambridge NanoTech Savannah 100 ALD system, with trimethylaluminum (TMA) and H_2O as the precursors. A typical deposition run consisted of a number of identical cycles, each consisting of the following steps: a 0.02 s pulse of TMA, a 5 s purge with N_2, a 0.1 s pulse of H_2O, and another 5 s purge in N_2. We also used cycles with H_2O pulsed before TMA to study the effect of the precursor sequence. The deposition temperature was 75 °C, the chamber pressure 0.1 Torr, and the N_2 flow 20 sccm. For the ALD process with the IPA pretreatment, anhydrous IPA was spun onto the MEH-PPV films at 400 rpm for 10 s, followed by the ALD process with TMA pulsed first. A cycle produced 1.2 Å of Al_2O_3, as determined using a Dektek Model 3030 profilometer. The evaporated Al_2O_3 films tested along with the ALD films were thermally evaporated from an Al source in high vacuum and then oxidized naturally in the ambient air for 10 min.

2.4. Photo-patterning process

Shipley S1813 positive-tone photoresist was spin-coated at 3000 rpm onto the MEH-PPV layer and baked for 120 s at 90 °C, followed by a 10 s exposure to a 365 nm UV light (Hsin Han Electronic R-700) through a photomask. The UV-exposed samples were developed in Shipley MF-319 developer for 30 s, rinsed in anhydrous methanol for 1 min, and then dried at 80 °C for 120 s. The Al_2O_3 buffer on the UV-exposed area was dissolved in the developer as well, and its underlying MEH-PPV was subsequently wet-etched with anhydrous toluene (120 s). After the etch step, the photoresist was stripped by sonication in anhydrous acetone for 120 s, and then dried at 100 °C for 30 min.

3. Results and discussion

To preliminarily verify the surface coverage of the ALD buffer layer over the MEH-PPV layer, several MEH-PPV film samples were overcoated with an ALD Al_2O_3 layer of various thicknesses, immersed in toluene for 10 min, and then visually inspected. The ALD layers with thicknesses $\geqslant 10$ Å kept the MEH-PPV samples intact; in contrast, an MEH-PPV sample overcoated with a 12 Å evaporated Al_2O_3 film, which was tested as a reference along with the ALD-coated samples, completely disintegrated upon the immersion in toluene. This result suggests that the excellent surface coverage of ALD would allow Al_2O_3 films with $\geqslant 10$ Å thickness to protect an underlying MEH-PPV film through the solution-based photo-patterning process.

Despite the ALD Al_2O_3 films' confirmed surface coverage, they failed to show the expected benefits of a buffer layer: the devices with a 10-Å ALD Al_2O_3 layer overcoated on the MEH-PPV layer had significantly higher turn-on voltage, lower luminance, and lower luminous efficiency than the control (see Fig. 2 and Table 1). It should be noted that control's low luminance and low luminous efficiency are intrinsic to the device structure (ITO/PEDOT:PSS/MEH-PPV/Al), and they are comparable to the optimal device characteristics reported by other researchers for the same device structure [26–28]. The adverse effects of the ALD Al_2O_3 layer are attributed to its disrupting the conjugation of MEH-PPV, which is evidenced by the blue shift and the weakened absorption occurring in the UV–Vis spectrum of MEH-PPV upon the application of the ALD Al_2O_3 layer (see Fig. 3). The affected MEH-PPV became insulating due to the disrupted conjugation, and therefore the device characteristics deteriorated drastically. By analyzing the UV–Vis spectra (Fig. 3) of MEH-PPV samples processed with different ALD conditions, we determined that exposure to TMA was the sole cause of the disruption of conjugation. As can be seen in Fig. 3, the MEH-PPV sample exposed only to TMA showed identical degradation in its UV–Vis spectrum to that of the Al_2O_3-coated sample (which was exposed to both TMA and H_2O), while the MEH-PPV sample exposed only to H_2O did not show detectable change in its UV–Vis spectrum. The significant change in the UV–Vis spectrum caused by the ALD Al_2O_3 layer indicates that the TMA exposure affected not only the top surface but also the bulk of the MEH-PPV layer.

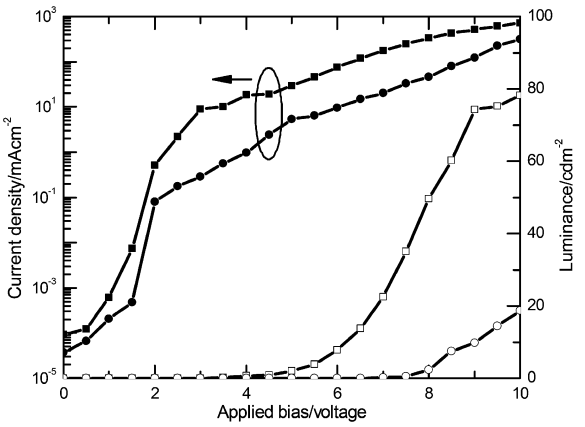

Fig. 2. Current density and luminance vs. applied bias for OLED devices: without the ALD buffer (squares), and with the ALD buffer (circles).

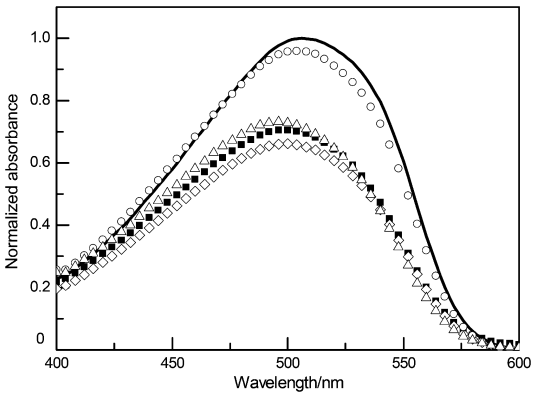

Fig. 3. UV–Vis absorption spectra of MEH-PPV films: pristine (solid lines), with a 10 Å ALD Al_2O_3 film deposited with TMA first (filled squares), with a 10 Å ALD Al_2O_3 film deposited with H_2O first (unfilled triangles), exposed only to H_2O (unfilled circles), and exposed only to TMA (unfilled diamonds).

Table 1
Characteristics of the OLED devices

Device	Turn-on voltage (V)	Maximum luminance (cd/m^2)	Luminous efficiency (cd/A)
No buffer, not patterned	4.8	78	1.4×10^{-2}
With ALD buffer, not patterned	7.7	19	9.3×10^{-3}
With IPA-pretreated ALD buffer, not patterned	3.0	242	3.0×10^{-2}
With IPA-pretreated ALD buffer, patterned	3.9	217	2.8×10^{-2}
With IPA-pretreated ALD buffer and high-conductivity PEDOT:PSS, patterned	2.8	322	4.2×10^{-2}

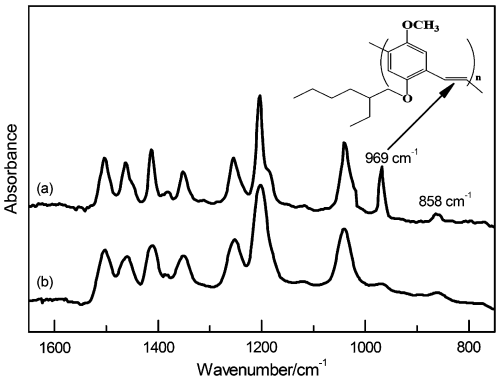

Fig. 4. IR spectra of MEH-PPV films: (a) pristine (b) TMA-exposed (150 consecutive 0.02-s pulses). The peak at 969 cm^{-1} corresponds to the vinylene double bonds of MEH-PPV, as illustrated in the margin.

This was to be expected from the elevated temperature used in the ALD process, which accelerated the permeation of TMA vapors into the MEH-PPV layer.

We further determined that the mechanism of the conjugation disruption is through electrophilic addition of TMA to the vinylene C=C groups of MEH-PPV, which can be seen by comparing the FTIR spectra shown in Fig. 4 of an MEH-PPV film before and after TMA exposure: The TMA-exposed spectrum showed significantly weakened vinylene absorption band (969 cm^{-1}). This mechanism is consistent with the fact that TMA, being a strong Lewis acid, has high reactivity for electrophilic addition to unsaturated bonds. The TMA exposure also created a new FTIR spectral feature at ~860 cm^{-1} corresponding to the Al–O bond, which was formed by oxidation of the added TMA by O_2 or H_2O upon the sample's exposure to air [29]. It should be noted that the significant change in the FTIR spectra upon the TMA exposure indicates again the deep penetration of the TMA vapors into the MEH-PPV layer.

The TMA attack on the MEH-PPV layer was reduced, but not eliminated, by introducing H_2O before TMA in the ALD cycles, as can be seen from the smaller blue shift and less weakening of the UV–Vis spectrum produced by the H_2O-first process than that of the regular TMA-first process (see Fig. 3). The H_2O-first process impeded the TMA attack by initially providing to the MEH-PPV surface a layer of adsorbed H_2O molecules, which shielded the MEH-PPV layer from TMA in the subsequent process. However, the shielding effect of the H_2O-first process was modest due to the hydrophobicity of the MEH-PPV surface, which limited the amount of the initially adsorbed H_2O molecules.

The problem of incomplete shielding of the H_2O-first process was resolved by pre-treating the MEH-PPV surface with isopropyl alcohol (IPA) immediately before the ALD process. The hydrophobic alkyl groups of IPA ensured its full adsorption onto the also hydrophobic MEH-PPV surface, while its hydroxyl groups served as reactive sites for capturing TMA during the ALD process, as illustrated in Fig. 5. The mechanism proposed in Fig. 5 agrees with the results of contact angle measurements on the MEH-PPV surface (see Fig. 6): the water contact angle reduced from 87° to 50° upon the IPA pretreatment, indicating that IPA effectively converted the hydrophobic MEH-PPV surface into a hydrophilic one. The IPA pretreatment completely prevented the TMA-induced damages, allowing ALD-processed MEH-PPV films to show identical UV–Vis spectra to that of the pristine film (Note: spectra of the IPA-pretreated, ALD-processed MEH-PPV samples was indistinguishable from that of the pristine sample and are not shown.). Furthermore, OLED devices with a 10-Å IPA-pretreated ALD Al_2O_3 buffer layer indeed showed the expected benefits of the buffer layer, i.e., decreased turn-on voltage and increased efficiency compared with the devices without the Al_2O_3 buffer (see Fig. 7 and Table 1).

The 10-Å IPA-pretreated ALD Al_2O_3 buffer layer was also effective in protecting MEH-PPV films through the photopatterning process, as evidenced by the identical UV–Vis

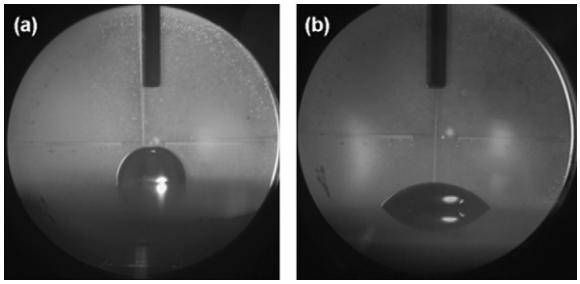

Fig. 6. Images from water contact angle measurements on MEH-PPV surface: (a) pristine (contact angle = 87°), and (b) IPA-pretreated (contact angle = 50°).

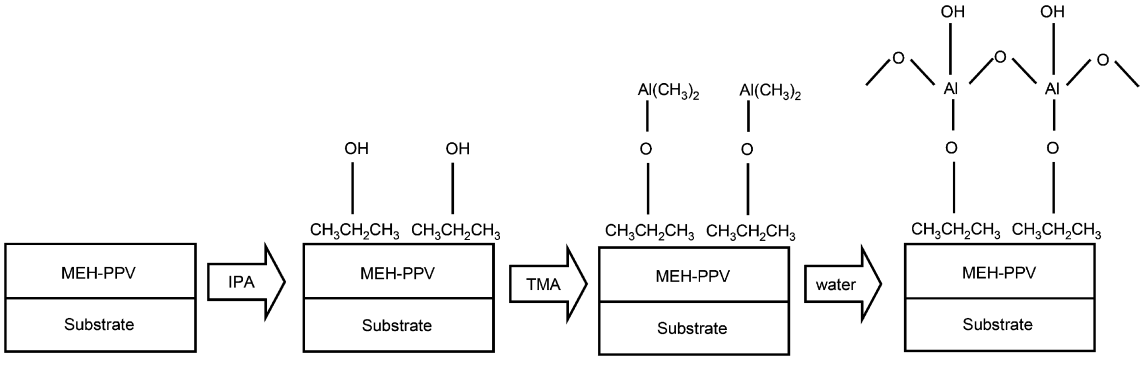

Fig. 5. Schematic drawings of the IPA-pretreated ALD process.

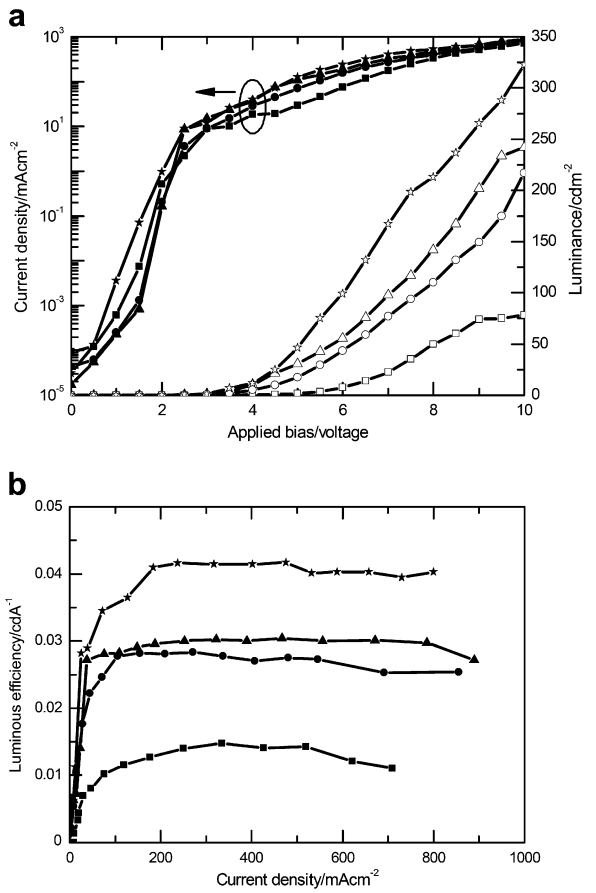

Fig. 7. (a) Current density and luminance vs. applied bias, (b) luminous efficiency vs. current density for the OLED devices: without the ALD buffer and not patterned (squares); with the ALD buffer and patterned (circles); with the ALD buffer but not patterned (triangles), and with the ALD buffer and high-conductivity PEDOT:PSS and patterned (stars). Note that the ALD buffer was deposited with the IPA pretreatment.

spectra of the photo-patterned MEH-PPV films to that of the pristine film (Note: the patterned spectra were indistinguishable from the pristine and are not shown.). More important, the OLED devices fabricated with the photo-patterned, ALD-coated MEH-PPV films showed higher luminous efficiency and lower turn-on voltage than the control devices which were not photo-patterned and without the buffer (Fig. 7 and Table 1). The above results confirm that the ALD-buffer-assisted photo-patterning process is capable of both patterning and improving OLED devices. It should be noted that the photo-patterning process did compromise part of the improvement yielded by the ALD buffer, but the net effect was still positive (Fig. 7 and Table 1).

The EL efficiency could be further improved (by 50%) and turn-on voltage further lowered (by 28%) by increasing the conductivity of the hole injection layer (HIL), PEDOT:PSS, as shown in Fig. 7 and Table 1. The conductivity of the HIL was increased by ~2 orders of magnitude by adding 5 wt.% of glycerol into the PEDOT:PSS solution [30]. The mechanism of this further improvement is explained as follow. In hole-dominated OLEDs such as the MEH-PPV-based devices studied here, a large portion of holes reach the cathode without participating in radiative recombination with electrons, thus resulting in loss of luminous efficiency. When an insulating buffer is used, holes are prevented from quenching at the cathode, and they in turn accumulate at the EL–buffer interface. The accumulated holes create interfacial dipoles that enhance electron injection from the cathode by lowering the injection barrier, while their proximity to the cathode enables them to readily capture and recombine with the injected electrons; consequently, the turn-on voltage is lowered and the EL efficiency is improved [31–33]. Increasing the conductivity of the HIL increases the accumulation of holes at the EL–buffer interface, thereby strengthening the benefits of the insulating buffer layer. We expect that more improvement can be realized with HIL with even higher conductivity, which is the subject of our on-going effort.

4. Conclusion

We demonstrated a practical solution to the heretofore unavoidable problem of patterning-induced degradations for OLEDs. OLEDs with MEH-PPV as the EL material were photo-patterned without degradation by using an ultra-thin (10 Å) ALD Al_2O_3 film overcoated on the EL layer to protect against damages induced by the solution-based photo-patterning process. Besides providing protections, the Al_2O_3 film served as an effective buffer layer to improve luminous efficiency (by 100%) and to lower turn-on voltage (by 19%) of the photo-patterned OLEDs. Although the ALD precursor, TMA, disrupted the conjugation of MEH-PPV by electrophilic addition to its vinylene moiety during the deposition of the Al_2O_3 film, this reaction was prevented by pretreating the MEH-PPV layer with IPA immediately before the ALD process, where the pre-adsorbed IPA molecules reacted with TMA to shield the underlying MEH-PPV surface. The device characteristics of the photo-patterned OLEDs were further improved by increasing the conductivity of the HIL, which increased hole accumulation at the EL–buffer interface to enhance electron injection.

Acknowledgement

This work was supported by National Science Council of Taiwan, Republic of China, under Grant No. NSC 96-2221-E-002-143-MY3.

Appendix A. Supplementary material

Supplementary data associated with this article can be found, in the online version, at doi:10.1016/j.orgel.2008.04.009.

References

[1] W. Tang, S.A. VanSlyke, Appl. Phys. Lett. 51 (1987) 913.
[2] R.H. Friend, R.W. Gymer, A.B. Holmes, J.H. Burroughes, R.N. Marks, C. Taliani, D.D.C. Bradley, D.A. Dos Santos, J.L. Brédas, M. Lögdlund, W.R. Salaneck, Nature 397 (1999) 121.

[3] D. Vak, J. Jo, J. Ghim, C. Chun, B. Lim, A.J. Heeger, D.Y. Kim, Macromolecules 39 (2006) 6433.
[4] M.T. Bernius, M. Inbasekaran, J. O'Brien, W. Wu, Adv. Mater. 12 (2000) 1737.
[5] P.F. Tian, V. Bulovic, P.E. Burrows, G. Gu, S.R. Forrest, T.X. Zhou, J. Vac. Sci. Technol. A 17 (1997) 3197.
[6] T.R. Hebner, C.C. Wu, D. Marcy, M.H. Lu, J.C. Sturn, Appl. Phys. Lett. 72 (1998) 519.
[7] D.B. Roitman, US Patent, 5,972,419, 1999.
[8] J.A. DeFranco, B.S. Schmidt, M. Lipson, G.G. Malliaras, Org. Electron. 7 (2006) 22.
[9] J. Huang, R. Xia, Y. Kim, X. Wang, J. Dane, O. Hofmann, A. Mosley, A.J. de Mello, J.C. de Mello, D.D.C. Bradley, J. Mater. Chem. 17 (2007) 1043.
[10] S.-C. Chang, J. Bharathan, Y. Yang, R. Helgeson, F. Wudl, M.B. Ramey, J.R. Reynolds, Appl. Phys. Lett. 73 (1998) 2561.
[11] Y. Yang, S.-C. Chang, J. Bharathan, J. Liu, J. Mater. Sci.: Mater. Electron. 11 (2000) 89.
[12] P.F. Tian, P.E. Burrows, S.R. Forrest, Appl. Phys. Lett. 71 (1997) 3197.
[13] D.G. Lidzey, M.A. Pate, M.S. Weaver, T.A. Fisher, D.D.C. Bradley, Synth. Met. 82 (1996) 141.
[14] H.W. Choi, S.Y. Kim, W.K. Kim, J.L. Lee, Appl. Phys. Lett. 87 (2005) 082102.
[15] Z.B. Deng, X.M. Ding, S.T. Lee, W.A. Gambling, Appl. Phys. Lett. 74 (1999) 2227.
[16] F. Li, H. Tang, J. Anderegg, J. Shinar, Appl. Phys. Lett. 70 (1997) 1233.
[17] H. Tang, F. Li, J. Shinar, Appl. Phys. Lett 71 (1997) 2560.
[18] J.H. Park, O.O. Park, J.W. Yu, J.K. Kim, Y.C. Kim, Appl. Phys. Lett. 84 (2004) 1783.
[19] T.M. Brown, R.H. Friend, I.S. Millard, D.J. Lacey, T. Butler, J.H. Burroughes, F. Cacialli, J. Appl. Phys. 93 (2003) 6159.
[20] T.-F. Guo, F.-S. Yang, Z.-J. Tsai, T.-C. Wen, S.-N. Hsieh, Y.-S. Fu, C.-T. Chung, Appl. Phys. Lett. 88 (2006) 113501.
[21] U. Wolf, H. Bässler, Appl. Phys. Lett. 74 (1999) 3848.
[22] S.T. Zhang, X.M. Ding, J.M. Zhao, H.Z. Shi, J. He, Z.H. Xiong, H.J. Ding, E.G. Obbard, Y.Q. Zhan, W. Huang, X.Y. Hou, Appl. Phys. Lett. 84 (2004) 425.
[23] M. Ritala, M. Leskelä, in: H.S. Nalwa (Ed.), Handbook of Thin Film Materials, vol. 1, Academic Press, San Diego, 2002. (Chapter 2).
[24] R.L. Puurunen, J. Appl. Phys. 97 (2005) 121301.
[25] M.D. Groner, F.H. Fabreguette, J.W. Elam, S.M. George, Chem. Mater. 16 (2004) 639.
[26] C.J. Tonzola, M.M. Alam, W. Kaminsky, S.A. Jenekhe, J. Am. Chem. Soc. 125 (2003) 13548.
[27] R. Yang, H. Wu, Y. Cao, G.C. Bazan, J. Am. Chem. Soc. 128 (2006) 14422.
[28] S.-H. Jin, S.-Y. Kang, M.-Y. Kim, Y.U. Chan, J.Y. Kim, K. Lee, Y.-S. Gal, Macromolecules 36 (2003) 3841.
[29] M.M. Frank, Y.J. Chabal, M.L. Green, A. Delabie, B. Brijs, G.D. Wilk, M.-Y. Ho, E.B.O. da Rosa, I.J.R. Baumvol, F.C. Stedile, Appl. Phys. Lett. 83 (2003) 740.
[30] J. Huang, P.F. Miller, J.S. Wilson, A.J. de Mello, J.C. de Mello, D.D.C. Bradley, Adv. Funct. Mater. 15 (2005) 290.
[31] Y.E. Kim, H. Park, J.J. Kim, Appl. Phys. Lett. 69 (1996) 599.
[32] S.T. Zhang, Y.C. Zhou, J.M. Zhao, Y.Q. Zhan, Z.J. Wang, Y. Wu, X.M. Ding, X.Y. Hou, Appl. Phys. Lett. 89 (2006) 043502.
[33] Y.-H. Niu, H. Ma, Q. Xu, A.K.-Y. Jen, Appl. Phys. Lett. 86 (2005) 083504.

Organic Electronics 9 (2008) 673–677

Contents lists available at ScienceDirect

Organic Electronics

journal homepage: www.elsevier.com/locate/orgel

Effect of water in ambient air on hysteresis in pentacene field-effect transistors containing gate dielectrics coated with polymers with different functional groups

Se Hyun Kim [a], Hoichang Yang [b], Sang Yoon Yang [a], Kipyo Hong [a], Danbi Choi [a], Chanwoo Yang [a], Dae Sung Chung [a], Chan Eon Park [a,*]

[a] Polymer Research Institute, Department of Chemical Engineering, Pohang University of Science and Technology, Pohang 790-784, Republic of Korea
[b] Rensselaer Nanotechnology Center, Rensselaer Polytechnic Institute, Troy, NY 12180, USA

ARTICLE INFO

Article history:
Received 4 March 2008
Received in revised form 2 May 2008
Accepted 2 May 2008
Available online 13 May 2008

PACS:
72.20.Jv
72.80.Le
73.20.At

Keywords:
OFETs
Pentacene
Polymer dielectrics
Hysteresis

ABSTRACT

We investigated the effect of water in ambient air on the hysteresis phenomena of pentacene field-effect transistors with polymer/SiO_2 gate dielectrics. The polarity of the polymer surface was controlled by using three different polymers: poly(styrene), poly(4-hydroxy styrene), and poly(4-vinyl pyridine). Water diffusion into the interface between the pentacene and the gate dielectric was driven by the polarity of the polymer surface, resulting in considerable hysteresis and degradation of device performances. The observed hysteresis behaviors can be explained in terms of donor- and acceptor-like trap formation by water molecules that have diffused between the pentacene and the gate dielectric. The different effects of these traps on hysteresis depending on the functional groups at the polymer surface were also investigated.

1. Introduction

Recently, organic field-effect transistors (OFETs) have received considerable interest because of their potential applications in low cost, large area and flexible electronics. The charge carrier mobility of OFET devices with a pentacene active layer has been shown to be comparable to those of amorphous silicon transistors ($\sim 3\ cm^2\ V^{-1}\ s^{-1}$) [1]. However, the utility of organic circuits has been hindered by the hysteresis phenomenon that is frequently observed during device operation. Therefore, minimizing the hysteresis effect in these circuits is a research priority in this area. When polymer layers were used as gate dielectrics, the hysteresis observed during device operation was caused by slow polarization that occurred due to application of an electric field to a film comprised polymer molecules with polar groups on either the main or side chain, and/or to a film containing ionic impurities [2,3]. Also, the functional groups at the polymer surface, which can influence semiconductor/dielectric interface properties such as semiconductor morphology [1,4] and charge traps [5], results in specific hysteresis in accordance with the applied gate bias and operational environment. In particular, oxygen and water molecules in the air induce charge traps either in the semiconductor or at the semiconductor/dielectric interface, leading to a degradation of the device performance [6–11].

In the present study, we investigated the hysteresis phenomena of pentacene FETs by measuring the electrical characteristics of pentacene FETs with polymer/SiO_2 bilayer gate dielectrics having different surface properties

* Corresponding author. Tel.: +82 54 279 2269; fax: +82 54 279 8298.
E-mail address: cep@postech.ac.kr (C.E. Park).

1566-1199/$ - see front matter © 2008 Elsevier B.V. All rights reserved.
doi:10.1016/j.orgel.2008.05.004

(polarity and functionality) in various operational environments, including a vacuum (~10^{-3} Torr), oxygen (99.9%), dry air (relative humidity (RH) ~0%) and ambient air (RH ~40%). The surface properties of the gate dielectric were controlled by applying three different ultra-thin polymer layers (~15 nm) on the SiO_2 dielectric. These systematic studies revealed that both the presence of water in the atmosphere and the polarity arising from the functional groups at the polymer surface determine the severity of hysteresis during device operation. Moreover, the observation of greater hysteresis in ambient air than in a vacuum can be accounted for in terms of the formation of long-lived donor- and acceptor-like traps by water molecules that have diffused into the interface between the semiconductor and gate dielectric, a process that is driven by the functional groups at the polymer surface.

2. Experimental

Poly(4-vinyl pyridine) (PVP), polystyrene (PS) and poly(4-hydroxyl styrene) (PHS) thin layers (see Fig. 1a–c for their chemical structures) were spin-cast onto thermally grown 300-nm-thick SiO_2 substrates, followed by annealing for 1 h at 90, 100, and 120 °C, respectively. The three types of polymer/SiO_2 bilayer gate dielectrics exhibited very smooth surfaces with root-mean-square roughnesses (Rq) of 3.6–4.5 Å, respectively, obtained by means of atomic force microscopy (AFM, Digital Instruments Multimode SPM, tapping mode, see Fig. 1d–f). The thickness of the polymer films measured by using an ellipsometer (J.A. Woollam. Co. Inc.) was of about 10–15 nm. A 50-nm-thick pentacene active layer (Aldrich), patterned through a shadow mask, was deposited onto the gate dielectrics at a rate of 0.1–0.2 Å/s by organic molecular beam deposition. Finally, the source/drain electrodes were defined on the pentacene film by thermally evaporating gold through a shadow mask. The channel length (L) and width (W) were 100 and 1000 μm, respectively. The electrical characteristics of the pentacene FETs were sequentially measured in vacuum (~10^{-3} Torr), oxygen (99.9%), dry air (RH ~0%) and ambient air (RH ~40%) using Keithley 2400 and 236 Source Meter instruments. Prior to the electrical measurement, the devices were outgassed under vacuum (~10^{-3} Torr) in the measurement chamber for at least 30 min, and then exposed to the operational environment for 30 min. The overall capacitance (C_i) for all three of the bilayer gate

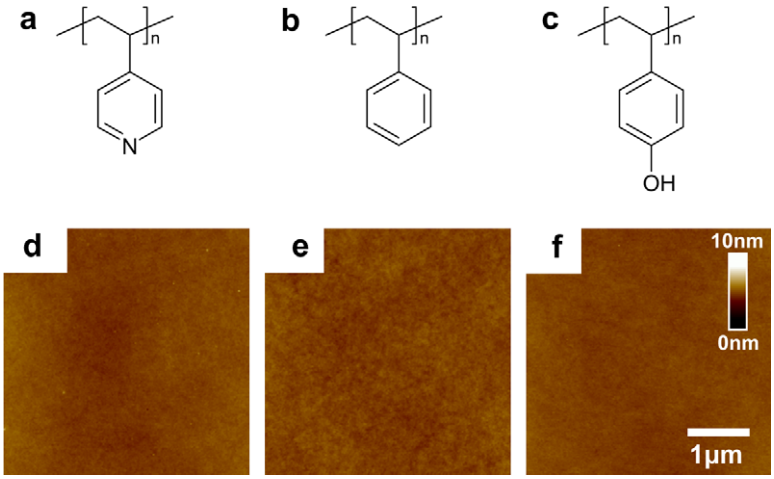

Fig. 1. Chemical structures of the polymer gate dielectrics employed in this experiment are (a) PVP, (b) PS and (c) PHS. Their surface morphologies are present in the AFM images of (c) and (d), respectively.

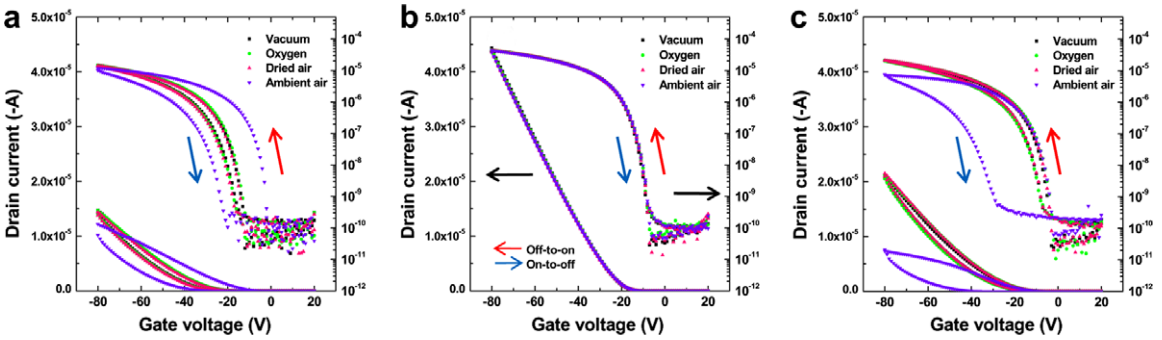

Fig. 2. Transfer characteristics of pentacene FETs in the linear regime (drain voltage, $V_D = -8$ V) using the polymer/SiO_2 bilayer gate dielectrics with various operational environments, specifically vacuum (~10^{-3} Torr), oxygen (99.9%), dry (RH ~0%) and ambient air (RH ~40%): (a) PVP, (b) PS and (c) PHS devices.

dielectrics, measured using an Agilent 4284 precision LCR meter, was 10 nF/cm^2.

3. Results and discussion

Fig. 2 shows the influence of operational environment on hysteresis in the linear regime (drain voltage $V_D = -8$ V) transfer characteristics of the devices with PVP, PS and PHS/SiO_2 bilayer gate dielectrics, and Fig. 3 shows a comparison of the device performance when the three devices were operated in the different environments. The PVP and PHS devices showed considerable hysteresis in ambient air but little hysteresis in the other environments (Fig. 2a and c). Also, operation in ambient air led to a degradation of the drain current (I_D), which resulted in a reduction in charge carrier mobility (μ) and changes in device performance indicators such as the turn-on voltage ($V_{turn\text{-}on}$), threshold voltage (V_{th}) and subthreshold swing (SS). On the other hand, compared to operation in a vacuum, devices operated in oxygen showed slightly increased I_D and SS, and shifts in $V_{turn\text{-}on}$ and V_{th} toward more positive voltages. These effects of oxygen on device performance are attributed to the acceptor-like traps created by oxygen in both pentacene films and pentacene/polymer interfaces, which attract electrons from the pentacene layer, thereby increasing the hole density in the channel region [6–8]. However, on going from a vacuum to an oxygen atmosphere, the hysteresis was not enlarged (see Fig. 2a and c), indicating that the hysteresis observed in these devices was not due to oxygen but rather to water molecules in

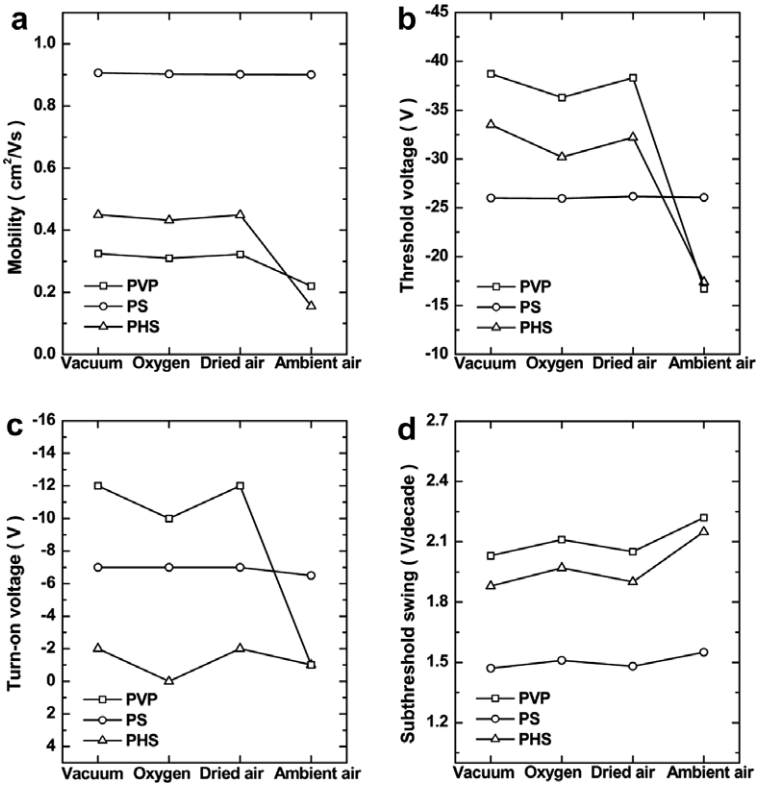

Fig. 3. Variation of the device performance characteristics for each operational environment in the PVP, PS and PHS devices. The mobility (μ) and threshold voltage (V_{th}) were calculated in the linear regime. All electrical parameters were extracted from the off-to-on sweep curves.

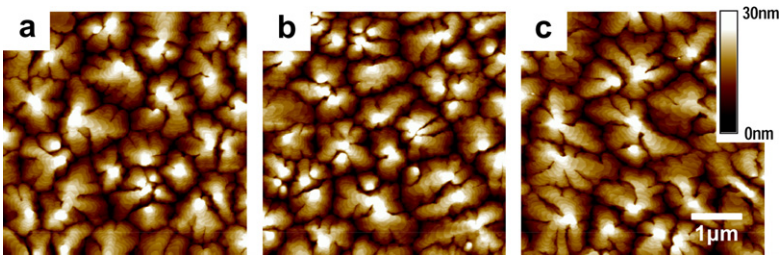

Fig. 4. AFM images in (a), (b) and (c) show the morphologies of pentacene layers (50 nm thick) on PVP, PS and PHS films, respectively.

ambient air. The influence of water in ambient air on OFETs has been previously reported [7–11]. It was found that water molecules in humid air diffuse into the grain boundary of the polycrystalline semiconductor layer and/or the interface between the semiconductor and gate dielectric, where they create both donor- and acceptor-like traps, leading to significant degradation of device performance [7]. In the present work, however, the PS device did not exhibit hysteresis in any of the operational environments (Fig. 2b), and other electrical parameters also showed almost no dependence on environment (Fig. 3). These findings indicate that the hysteresis and device performance characteristics may be crucially affected by the absorbed water in the semiconductor and the interface between the semiconductor and the gate dielectric. In addition, the diffusion of water molecules is intimately related to the density of grain boundaries in the pentacene film because small molecules migrate into the channel region through such defects [12]. As shown in Fig. 4a–c, the density of grain boundaries on the pentacene surface is similar for all of the polymer/SiO_2 bilayer gate dielectrics; thus the grain boundary effect can be excluded in our study.

To demonstrate how the functional groups at the polymer surface interact with diffusing water molecules, we investigated the surface energies of the polymers by measuring the contact angles of two test liquids, namely water and diiodomethane. Surface energy is a direct indication of intermolecular force, and consists of the sum of dispersion and polar components which are calculated by the following equation [13]:

$$1+\cos\theta=\frac{2\left(\gamma_s^d\right)^{1/2}\left(\gamma_{lv}^d\right)^{1/2}}{\gamma_{lv}}+\frac{2\left(\gamma_s^p\right)^{1/2}\left(\gamma_{lv}^p\right)^{1/2}}{\gamma_{lv}},$$

where γ_s and γ_{lv} are the surface energies of the sample and test liquid, respectively, and the superscripts d and p refer to dispersion and polar components, respectively. Also, the values of γ_{lv}, γ_{lv}^p and γ_{lv}^d for the test liquids and the procedure to solve the equation are provided in Ref. [13]. In particular, the polar component (γ_s^p) of the surface energy is attributed to polar forces arising from permanent and induced dipoles, as well as hydrogen-bonding, whereas the dispersion component (γ_s^d) is due to instantaneous dipole moments [13]. Therefore, the interaction between a polymer surface and diffusing water molecules will exhibit a greater dependence on γ_s^p rather than γ_s^d. Table 1 shows the measured contact angles of the test liquids, as well as the surface energy and polarity χ_p (i.e. the ratio of the polar component to the total surface energy) for the polymer/SiO_2 bilayer gate dielectrics. The γ_s^p and χ_p of the PS polymer are remarkably smaller than those of the PVP and PHS polymers, indicating that the surface of the PS film is more non-polar than those of the PVP and PHS films. In other words, the functional group of PS, the phenyl moiety, interacts only weakly with water molecules compared with the pyridine group in PVP and the phenol in PHS. On the other hand, the pyridine and phenol functional groups of PVP and PHS interact strongly with water molecules through hydrogen-bonding. These results indicate that the surface polarity arising from the functional group in the polymer plays an important role in determining the device performance in ambient air.

The similar surface polarities of the polymers in the PVP and PHS devices mean that the diffused water molecules give rise to hysteresis loops in the same (anticlockwise) direction (Fig. 2a and c). However, significantly different features were observed in the hysteresis depending on the functional groups at the polymer surface: In the off-to-on gate sweep of the PVP device in ambient air, a large shift of the transfer curve toward positive V_G direction is observed, whereas the on-to-off gate sweep curve is slightly moved toward the opposite direction, as compared with non-humid conditions (Fig. 2a). When the hysteresis of the PHS device in ambient air is compared with that under non-humid conditions, by contrast, the transfer curve is hardly altered during the off-to-on gate sweep, but is shifted toward negative V_G when the gate voltage is swept from on to off (Fig. 2c). These deviations of the transfer curves in ambient air from those under non-humid conditions can be attributed to the water molecules that have diffused into the interface between the semiconductor and gate dielectric, which can act as both acceptor- and donor-like traps at the interface. According to the report by Gu et al., acceptor-like traps can result in hysteresis during the off-to-on gate sweep because negative charges accumulate at the interface by filling the acceptor-like traps with electrons for positive V_G, inducing more holes than those required by the V_G and C_i to balance the stored negative charges [14]. On the contrary, the donor-like traps are occupied by holes induced by the negative V_G applied during the off-to-on gate sweep. The long life-times of the donor-like traps result in keeping the traps filled during the on-to-off gate sweep, thereby reducing I_D during the on-to-off gate sweep. In other words, the donor-like traps contribute to hysteresis during the on-to-off gate sweep [14].

Therefore, in the case of the PHS device in ambient air, the acceptor-like trap effect due to water molecules is smeared during the off-to-on gate sweep because water molecules have the same effect as the hydroxyl groups of PHS which can function as acceptor-like traps [15], making the donor-like trap effects dominate in comparison to the

Table 1
Surface energy and polarity of polymer/SiO_2 bilayer gate dielectrics

Gate dielectric	Contact angle (°)		γ_s^p (mJ m^{-2})	γ_s^d (mJ m^{-2})	$\gamma_s(\gamma_s^p+\gamma_s^d)$ (mJ m^{-2})	$\chi_p(\gamma_s^p/\gamma_s)$
	Water	Diiodomethane				
PS	90	31	0.55	43.28	44.19	0.012
PHS	56	37	17.58	32.10	49.18	0.357
PVP	49	13	18.49	39.05	57.59	0.321

non-humid conditions (Fig. 2c). On the other hand, the PVP device in ambient air shows hysteresis caused by the diffused water molecules, which act as both acceptor- and donor-like traps: the transfer curve of the PVP device in ambient air is shifted toward positive V_G in the off-to-on sweep and toward negative V_G in the on-to-off sweep, as compared with non-humid conditions. In this case, the acceptor-like trap effect on hysteresis (shift toward the positive V_G direction) is larger than the donor-like trap effect (shift toward the negative V_G direction) (Fig 2a). The decrease of I_D in the PVP device was smaller than that in the PHS device in ambient air because the acceptor-like traps created by the water molecules were more dominant than the donor-like traps in the PVP device (see Fig. 2a and c).

4. Conclusion

In conclusion, we have demonstrated the influence of water in ambient air and the functional groups at the polymer surface on the hysteresis of pentacene FETs. The polarity of the polymer surface can determine the interaction with diffused water molecules, resulting in considerable hysteresis and a degradation of device performance. Moreover, the charge traps arising from water molecules have different effects on the hysteresis depending on the functional groups at the polymer surface.

Acknowledgment

This work was supported by Grant No. RTI04-01-04 from the Regional Technology Innovation Program of the Ministry of Commerce, Industry and Energy (MOCIE).

References

[1] H.C. Yang, T.J. Shin, M.M. Ling, K. Cho, C.Y. Ryu, Z.N. Bao, J. Am. Chem. Soc. 127 (2005) 11542.
[2] J. Veres, S. Ogier, S.W. Leeming, D.C. Cupertino, S.M. Khaffaf, G. Lloyd, Proc. SPIE 147 (2003) 5217.
[3] T.B. Singh, N. Marjanović, P. Stadler, M. Auinger, G.J. Matt, S. Gűnes, N.S. Sariciftci, R. Schwődiauer, S. Bauer, J. Appl. Phys. 97 (2005) 083714.
[4] S.Y. Yang, K. Shin, C.E. Park, Adv. Funct. Mater. 15 (2005) 1806.
[5] K. Shin, S.Y. Yang, C. Yang, H. Jeon, C.E. Park, Org. Electron. 8 (2007) 336.
[6] A.R. Volkel, R.A. Street, D. Knipp, Phys. Rev. B 66 (2002) 195336.
[7] D. Knipp, A. Benor, V. Wagner, T. Muck, J. Appl. Phys. 101 (2007) 044504.
[8] O.D. Jurchescu, J. Baas, T.T.M. Palstra, Appl. Phys. Lett. 87 (2005) 052102.
[9] T. Jung, A. Dodabalapur, Appl. Phys. Lett. 87 (2005) 182109.
[10] D. Li, E. Borkent, R. Nortrup, H. Moon, H. Katz, Z. Bao, Appl. Phys. Lett. 86 (2005) 042105.
[11] C. Goldmann, D.J. Gundlach, B. Batlogg, Appl. Phys. Lett. 88 (2006) 063501.
[12] B. Crone, A. Dodabalapur, A. Gelperin, L. Torsi, H.E. Katz, A.J. Lovinger, Z. Bao, Appl. Phys. Lett. 78 (2001) 2229.
[13] A.J. Kinloch, Adhesion and Adhesives: Science and Technology, Chapman and Hall, 1987. (pp. 18–32, Chap. 2).
[14] G. Gu, M.G. Kane, J.E. Doty, A.H. Firester, Appl. Phys. Lett. 87 (2005) 243512.
[15] L.L. Chua, J. Zaumseil, J.F. Chabng, E.C.-W. Ou, P.K.-H. Ho, H. Sirringhaus, R.H. Friend, Nature 434 (2005) 194.

Organic Electronics 9 (2008) 678–686

Contents lists available at ScienceDirect

Organic Electronics

journal homepage: www.elsevier.com/locate/orgel

Effect of interfacial layer thickness on the formation of interface dipole in metal/tris(8-hydroxyquinoline) aluminum interface

Soo Young Kim, Jong-Lam Lee *

Department of Materials Science and Engineering, Pohang University of Science and Technology (POSTECH), Pohang, Kyungbuk 790-784, Republic of Korea

ARTICLE INFO

Article history:
Received 27 November 2007
Received in revised form 13 February 2008
Accepted 30 April 2008
Available online 22 May 2008

PACS:
73.61. Ph
68.37. Xy
79.60. Fr

Keywords:
Interface dipole
Alq_3
Synchrotron radiation photoemission spectroscopy
Work function
Organic light emitting diodes

ABSTRACT

We determined the interface dipole energies between interfacial layers with different thicknesses coated on indium tin oxides (ITOs) and tris(8-hydroxyquinoline) aluminum using ultraviolet and synchrotron radiation photoemission spectroscopy. After O_2 plasma treatment on 20-nm thick metal coated ITO, the work function and interface dipole energy increased. In 2-nm thick metal coated ITO, no change in the interface dipole energy was found though the work function increased. According to the valence band spectra, 2-nm thick metals are fully oxidized, but 20-nm thick metals are partially oxidized after O_2 plasma treatment. Therefore, it is considered that the contribution of the surface dipole by the deposition of Alq_3 on 2-nm thick metal is lower, resulting in a lower interface dipole. Thus, the thickness of interfacial layer has a great impact on the formation of interface dipole.

1. Introduction

Because the thin film architecture of organic based electronic devices such as organic light emitting diodes (OLEDs) [1,2], organic thin film transistor [3], and organic photovoltaic devices [4] encompasses multiple inorganic–organic and organic–organic junctions, the properties of which have a strong impact on device performance. For this reason, much of the effort in organic electronic devices has been focused on understanding and modifying the electronic properties of the interfaces. It is generally reported that a vacuum level alignment rule can not apply to the interface between metal and organic layer due to the existence of interface dipole [5–7]. Various models and mechanisms have been advocated to elucidate the formation of the interface dipole at the interface of metal with organic materials [8–10]. The concepts of interface dipole and band bending were, respectively, considered in some papers [11–15]. Other kinds of papers considered only the concept of interface dipole without considering the band bending [16–18]. The exact mechanism is not established until now.

The clean metals with few hundreds nanometer thickness were coated on glass to find the general relationship between metal work function and interface dipole energy [19]. In order to investigate realistic contacts, the metal surfaces covered with contaminants, such as carbon and oxygen, have been also used in the experiments [20,21]. The sign of interface dipole is generally negative and its magnitude linearly increases with the metal work function, corresponding to the lowering of the vacuum level by depositing the organic layer [19]. The electrical properties of OLEDs were enhanced by employing a few-nanometer-thick interfacial layers on indium tin oxide (ITO) anodes and by treating them with O_2 plasma prior to

* Corresponding author. Tel.: +82 54 279 2152; fax: +82 54 279 5242.
E-mail address: jllee@postech.ac.kr (J.-L. Lee).

1566-1199/$ - see front matter © 2008 Elsevier B.V. All rights reserved.
doi:10.1016/j.orgel.2008.04.010

the deposition of hole transport layer [22–26]. Such enhancement could contribute to the reduction of the hole injection barrier due to the increase in work function by the plasma treatment completely. According to our previous result, the thickness of hole injection layer affect the formation of interface dipole between hole injection layer and hole transport material [26]. In a cathode region, various kind of interlayer were used to reduce the electron injection barrier [27,28]. However, the role of interlayer in reducing an electron injection barrier and the effect of interlayer thickness were not understood well.

In the present work, we investigated the formation of interface dipole between metal oxide and tris(8-hydroxyquinoline) aluminum (Alq_3), and derived the general relationship between the metal work function and the interface dipole energy in OLEDs. The metal oxide layer was prepared by exposing a metal layer to O_2 plasma. Synchrotron radiation photoemission spectroscopy (SRPES) and ultraviolet photoelectron spectroscopy (UPS) were employed to observe the change of the energy level with *in situ* deposition of Alq_3 on metal layers. From this, the general relationship of interface dipole energy between O_2 plasma treated metal surfaces and organic materials is discussed.

2. Experimental

The glass coating with ITO (150-nm thick, ~20 Ω/sq.) was used as the starting substrate. The samples were cleaned in sequence with the acetone, isopropyl alcohol, and de-ionized water, and then dried with high purity nitrogen gas. In order to compare this experiment with previous one, we used similar metals with high work function such as Ir, Ru, Rh, and Ag which were used before [26]. These metals were deposited by e-beam evaporator on ITO coated glass substrate with thicknesses of 20 and 2 nm. Then, the samples were treated with O_2 plasma for 1 min with a power of 150 W in order to form a metal oxide. In order to measure SRPES spectra, the samples were sealed under vacuum condition and delivered to 4B1 beam line in Pohang Accelerator Laboratory. After breaking the vacuum condition in the air, the samples were loaded into a vacuum chamber and the organic material, Alq_3, was *in situ* deposited on the samples using a thermal evaporator. The evaporation of organic material was performed in a separately connected preparation chamber to which organic sources are attached. The organic material coverage was determined by measuring with a thickness monitor and comparing the area of the metal core level spectra. The secondary electron emission spectra, core level spectra, and valence band spectra were obtained in the main chamber using a He I excitation (21.2 eV) and an incident photon energy of 650 eV. The onset of photoemission was measured with a negative bias (−20 V) on the sample to avoid the work function of the detector. The incident photon energy was calibrated with the core level spectrum of Au 4f. Atomic Force Microscopy (AFM) was used to detect the change of film morphology after deposition of interlayer.

3. Results and discussion

Fig. 1 shows O 1s SRPES spectra of Ag samples before and after O_2 plasma treatment. In order to separate the chemical bonding states including those in the spectra, the spectral line shape was simulated using a suitable combination of Gaussian and Lorentzian functions. O 1s spectra in 20-nm thick Ag was shown in Fig. 1a. The O 1s peak separated into two components. The peak centered at 530.7 eV in 20-nm thick Ag before O_2 plasma treatment was due to chemisorbed oxygen contaminants. The other peak centered at 531.7 eV indicated O–Ag bond formed by air exposure before SRPES measurement [29]. After O_2 plasma treatment on 20-nm thick Ag, the peak intensity of O–Ag bond increased about four times and the peak indicating the chemisorbed oxygen disappeared. Furthermore, the new peak located at 532.6 eV appeared, indicating the oxidation of Ag surface by plasma treatment. The peak shifted about 0.3 eV toward the lower binding energy after O_2 plasma treatment, suggesting the increase in work function. In the case of relative amount of carbon contamination on 20-nm thick Ag, it decreased from 64% to 46% after O_2 plasma treatment (not shown here). Fig. 1b shows the O 1s spectra in 2-nm thick Ag. Before O_2 plasma treatment, O–Ag bond and chemisorbed oxygen bond were shown. The intensity ratio of O–Ag bond to chemisorbed oxygen bond is about 2.6, which is higher than that in 20-nm thick Ag (about 2.2). It is considered that ITO layer beneath 2-nm thick Ag affected the formation of O–Ag bond, which was detected by SRPES measurement due to thin thickness. After O_2 plasma treatment, the intensity of O–Ag bond increased and new peak appeared, indicating the oxidation of Ag. These results suggested that O_2 plasma treatment transformed the Ag layer into the AgO_x layer. Furthermore, it is shown that the relative amount of carbon contamination on 2-nm thick Ag decreased from 68% to 49% after O_2 plasma treatment (not shown here).

The changes of SRPES spectra with *in situ* deposition of Alq_3 on O_2 plasma treated 20-nm thick Ag layer are shown in Fig. 2. Before the deposition of Alq_3, only Ag 3d peaks were detected. After the deposition of 2-nm thick Alq_3, the intensity of Ag 3d peaks decreased and new peaks of N 1s and Al 2p appeared. When the thickness of Alq_3 reached 4 nm, Ag 3d peaks were not observed and the intensities of N 1s and Al 2p increased. This result indicated that the SRPES data at 4-nm thick Alq_3 did not mean interface properties between Ag and Alq_3, but Alq_3 properties. Therefore, the 4 nm was chosen as final thickness for calculating the interface dipole energy.

In order to observe the change of chemical composition during the deposition of Alq_3, the spectral line shape was simulated using the method mentioned above. Fig. 3a shows the change of Ag 3d peak during the deposition of Alq_3 on 20-nm thick Ag. The peak centered at 368.4 eV before the deposition of Alq_3 indicated Ag–Ag bond and the peak centered at 367.7 eV indicated Ag–O bond [29]. The intensity of Ag–Ag bond is higher than that of Ag–O bond. After the deposition of 2-nm thick Alq_3, the peak intensity of Ag 3d decreased about 70%. After the deposition of 4-nm thick Alq_3, Ag 3d peak disappeared, meaning that Ag layer

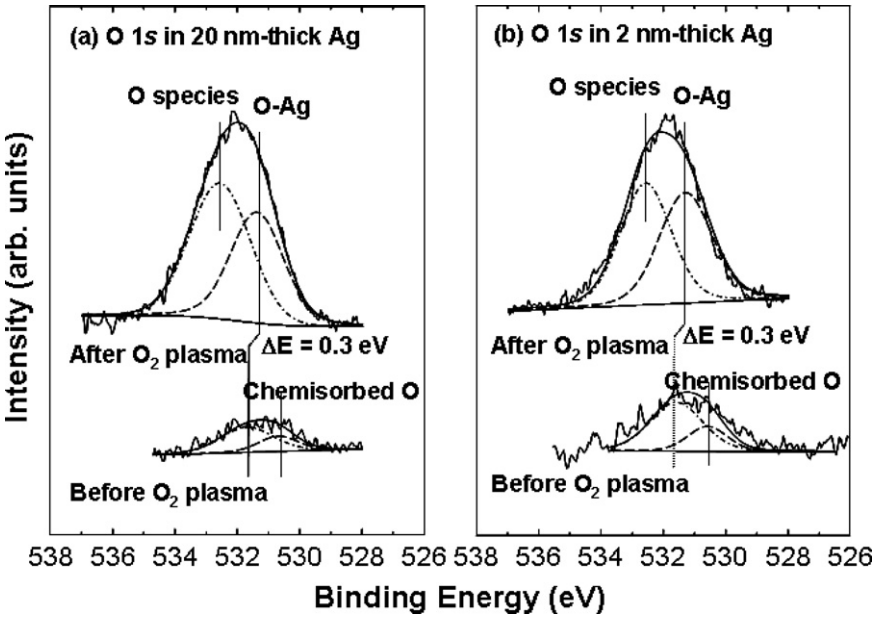

Fig. 1. The change of O 1s SRPES spectra in Ag samples before and after O_2 plasma treatment. After O_2 plasma treatment, the peak intensity indicating O–Ag bond increased and new peak appeared, indicating the oxidation of Ag surface. The peak shifted about 0.3 eV toward lower binding energy after O_2 plasma treatment, suggesting the increase in work function.

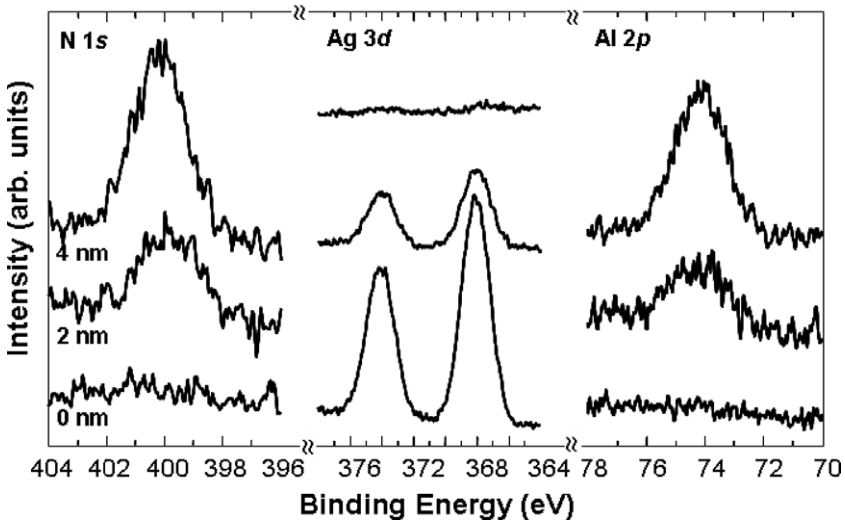

Fig. 2. Changes of SRPES spectra with the deposition of Alq_3 on O_2 plasma treated 20-nm thick Ag layer. The thickness of Alq_3 when Ag 3d peaks were not observed and the intensities of N 1s and Al 2p increased is 4 nm. This result indicated that the 4 nm thickness is good enough to calculate the interface dipole energy between Ag and Alq_3.

was wholly covered with Alq_3. The change of Ag 3d peak during the deposition of Alq_3 on 20-nm thick AgO_x is shown in Fig. 3b. The ratio of Ag–O bond to Ag–Ag bond before the deposition of Alq_3 is 0.83, which is higher than that in 20-nm thick Ag (0.23). This result indicates that Ag was oxidized after O_2 plasma treatment. As the 2-nm thick Alq_3 layer was deposited, the peak intensity of Ag 3d decreased about 67%. After the deposition of 4-nm thick Alq_3, Ag 3d peak disappeared.

Fig. 4a shows the changes of work function with *in situ* deposition of Alq_3 on 20-nm thick Ag layers. The onset of secondary electron binding energy was determined by extrapolating solid lines from the background and straight onset in the UPS spectra [30]. The work function was calculated by subtracting the onset of secondary electron binding energy from He I excitation energy. The graph was drawn with the calculated work function as horizontal axes. At as-deposited state, the work function of 20-nm

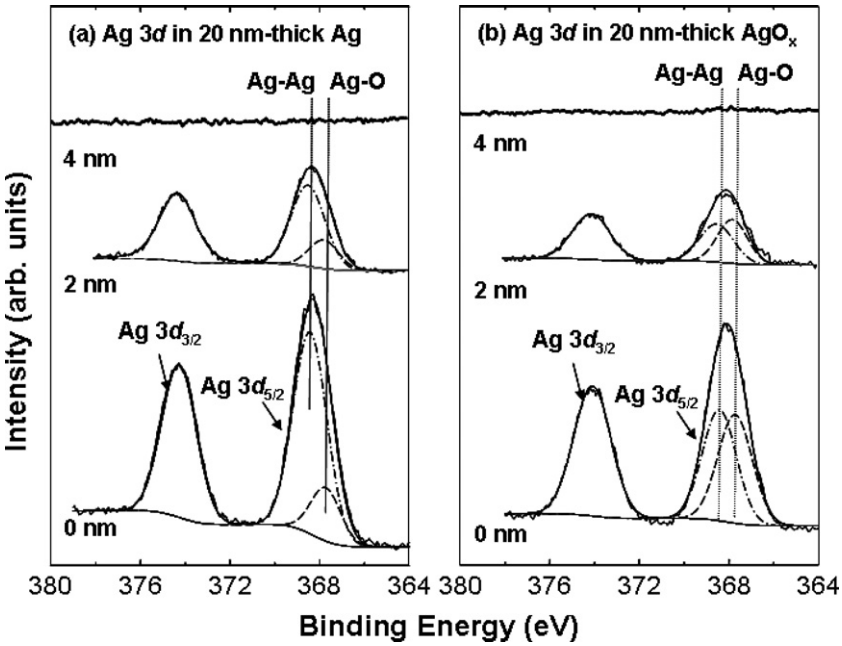

Fig. 3. The change of Ag 3d peak during the deposition of Alq_3 on (a) 20-nm thick Ag and (b) 20-nm thick AgO_x. AgO_x was fabricated by O_2 plasma treatment on Ag for 1 min with a power of 150 W.

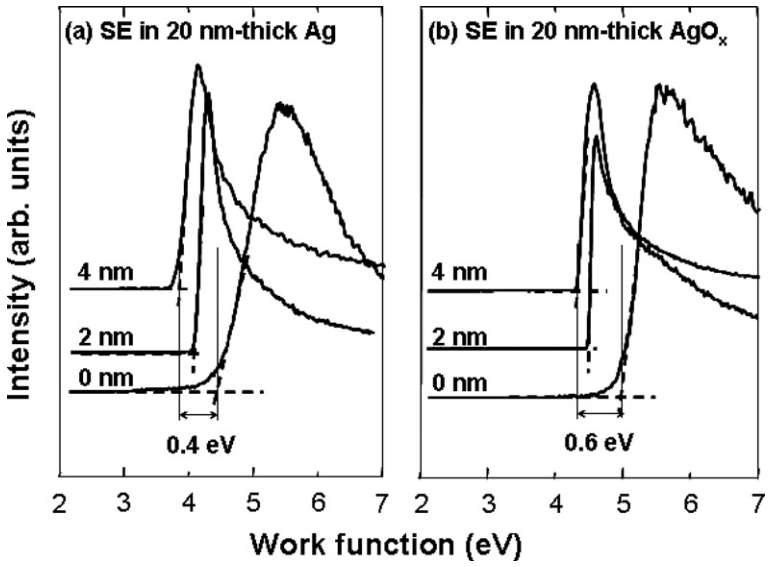

Fig. 4. The change of the onset of secondary electron spectra after deposition of Alq_3 on (a) 20-nm thick Ag and (b) 20-nm thick AgO_x. The work function was calculated by subtracting the onset of secondary electron binding energy in UPS spectra from He I excitation energy (21.2 eV).

thick Ag is 4.4 eV. With the deposition of Alq_3, the onset of secondary electron shifted about 0.4 eV, meaning the decrease in work function. Here, following the convention in surface science, the change of work function is considered as positive when the vacuum level is raised by deposition. And, the interface dipole energies are calculated by the change of work function during the deposition of organic layer without considering band bending. This means that the interface dipole energy corresponds to −0.4 eV. The changes of work function with the deposition of Alq_3 on 20-nm thick AgO_x layers are shown in Fig. 4b. At as-deposited state, the work function is 5.0 eV. This result is consistent with previous reports which stated that O_2 plasma treatment increases the work function. With deposition of Alq_3, the onset of secondary electron shifted about 0.6 eV, indicating that the interface dipole energy between 20-nm thick AgO_x and Alq_3 is −0.6 eV. It should be noted that O_2 plasma treatment on the 20-nm thick Ag

increased both the work function and the interface dipole energy.

Fig. 5a shows the changes of valence band spectra with *in situ* deposition of Alq_3 on 20-nm thick Ag. The valence band maximum (VBM) was also determined by extrapolating solid lines from the background and straight onset in the UPS spectra [30]. Before the deposition of Alq_3, the VBM was located at 0 eV, showing the metallic valence band. As Alq_3 was deposited on Ag, the VBM shifted about 2.2 eV toward the high binding energy, indicating that the energy difference between the highest occupied molecular orbital (HOMO) and the Fermi level (E_F) of Alq_3 is 2.2 eV. Because the band gap of Alq_3 (BG_{Alq3}) depend on the measuring methods, it is impossible to estimate the electron injection barrier between Ag and Alq_3 exactly [31,32]. Therefore, the injection barrier for electrons from 20-nm thick Ag to Alq_3 could be expressed to be BG_{Alq3} −2.2 eV. Fig. 5b shows the changes of VBM with *in situ* deposition of Alq_3 on 20-nm thick AgO_x. The metallic valence band is still maintained even though the sample was treated with O_2 plasma. After *in situ* deposition of 4-nm thick Alq_3, the VBM was about 1.8 eV from the E_F, meaning that the energy difference between HOMO and E_F is 1.8 eV. Therefore, the electron injection barrier at the interface of 20-nm thick Ag with Alq_3 was thought to be BG_{Alq3} −1.8 eV.

The changes of SRPES spectra with the deposition of Alq_3 on 2-nm thick AgO_x layer are shown in Fig. 6. Before the deposition of Alq_3, In 3d peaks were detected due to thin Ag layer. After the deposition of 2-nm thick Alq_3, the intensity of In 3d peaks decreased and new peaks of N 1s and Al 2p appeared. When the thickness of Alq_3 reached 4 nm, In 3d peaks were not observed and the intensities of N 1s and Al 2p increased. This result is due to that 4-nm thick Alq_3 is good enough to calculate the interface dipole energy between Alq_3 and 2-nm thick Ag.

Fig. 7a shows the change of Ag 3d peak during the deposition of Alq_3 on 2-nm thick Ag. Before the deposition of Alq_3, the peaks for Ag–Ag bond and Ag–O bond were observed. The ratio of Ag–Ag bond is higher than that of Ag–O bond. The relative ratio of Ag–O bond to Ag–Ag bond is 0.54, which is higher than that in 20-nm thick Ag (0.23). It is considered that ITO located beneath 2-nm thick Ag layer affected the oxidation of Ag, increasing the intensity of Ag–O bond. After the deposition of 2-nm thick Alq_3, the peak intensity of Ag 3d decreased about 60%. After the deposition of 4-nm thick Alq_3, Ag 3d peak disappeared, meaning that Ag layer was wholly covered with Alq_3. The change of Ag 3d peak during the deposition of Alq_3 on 2-nm thick AgO_x is shown in Fig. 7b. The ratio of Ag–O bond to Ag–Ag bond before the deposition of Alq_3 is 1.3, which is higher than that in 2-nm thick Ag (0.54). This result indicates that Ag was oxidized after O_2 plasma treatment. As the deposition of Alq_3, the peak intensity decreased about 73%. After the deposition of 4-nm thick Alq_3, Ag 3d peak disappeared.

Fig. 8a shows the changes of work function with *in situ* deposition of Alq_3 on 2-nm thick Ag layers. At as-deposited state, the work function is calculated to be 4.4 eV. With the deposition of Alq_3, the onset of secondary electron shifted about 0.3 eV, meaning the decrease in work function. Without considering band bending, this means that the interface dipole energy corresponds to −0.3 eV. The changes of work function with deposition of Alq_3 on 2-nm thick AgO_x layers are shown in Fig. 9b. At as-deposited state, the work function is calculated to be 5.0 eV. With the deposition of Alq_3, the onset of secondary electron shifted about 0.3 eV, indicating that the interface dipole energy between 20-nm thick AgO_x and Alq_3 is −0.3 eV. It should be noted that O_2 plasma treatment on 2-nm thick Ag increased the work function, but no change in interface dipole was found.

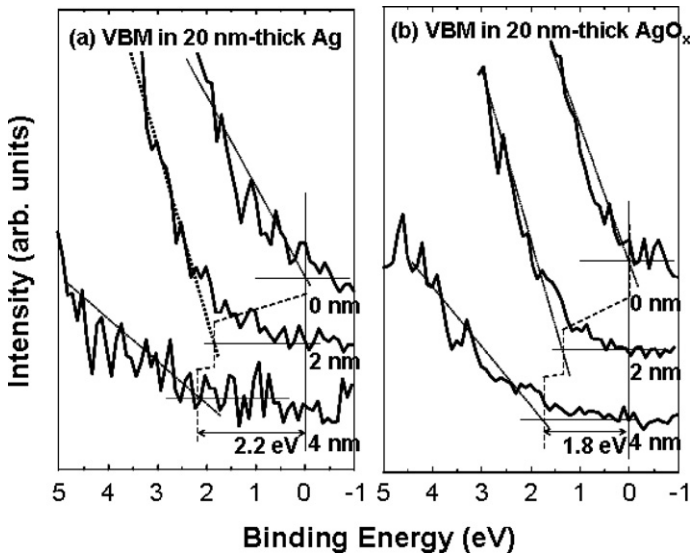

Fig. 5. The change of valence band spectra after the deposition of Alq_3 on (a) 20-nm thick Ag and (b) 20-nm thick AgO_x. The VBM was determined by extrapolating solid lines from the background and straight onset in the UPS spectra.

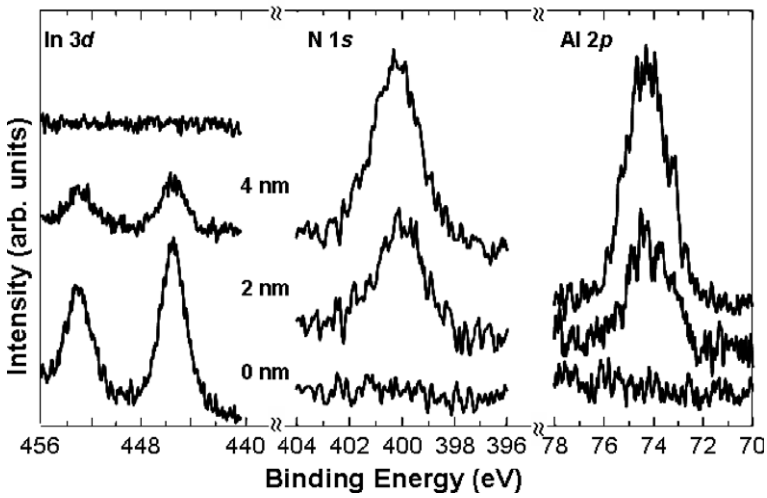

Fig. 6. Changes of SRPES spectra with the deposition of Alq_3 on O_2 plasma treated 2-nm thick Ag layer. The thickness of Alq_3 when Ag 3d peaks were not observed and the intensities of N 1s and Al 2p increased is 4 nm. This result indicated that the 4 nm thickness is good enough to calculate the interface dipole energy between Ag and Alq_3.

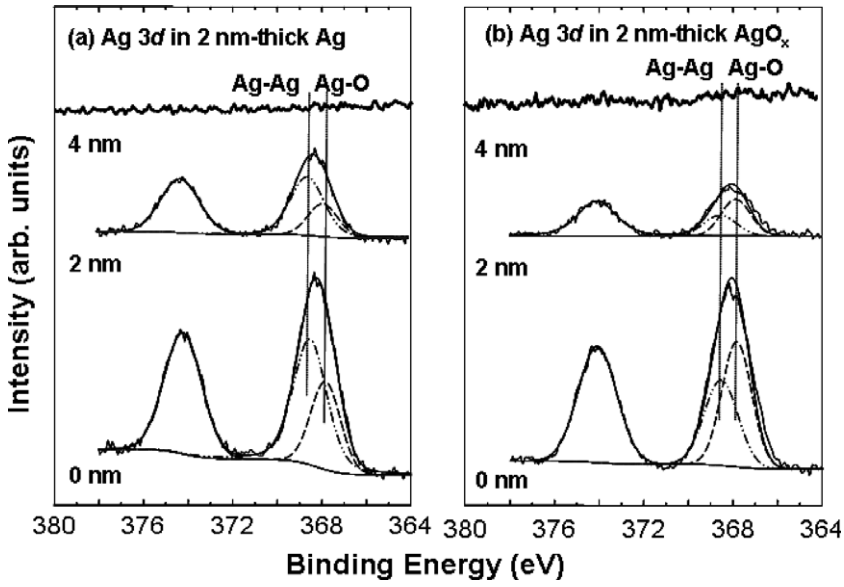

Fig. 7. The change of Ag 3d peak during the deposition of Alq_3 on (a) 2-nm thick Ag and (b) 2-nm thick AgO_x. AgO_x was fabricated by O_2 plasma treatment on Ag for 1 min with a power of 150 W.

Fig. 9a shows the changes of valence band spectra with *in situ* deposition of Alq_3 on 2-nm thick Ag. Although the Ag layer was not treated by O_2 plasma, the VBM before the deposition of Alq_3 located at 0.3 eV, indicating the formation of band gap. It is considered that ITO located beneath 2-nm thick Ag layer affected the oxidation of Ag layer. After the deposition of Alq_3, the VBM shifted about 2.2 eV toward high binding energy, meaning that the energy difference between the HOMO and E_F of Alq_3 is 2.2 eV. Therefore, the electron injection barrier was calculated to be BG_{Alq3} −2.2 eV. The changes of valence band spectra of 2-nm thick AgO_x with the deposition of Alq_3 are shown in Fig. 9b. Before the deposition of Alq_3, the VBM was located at 1.3 eV due to the band gap of AgO_x. After the deposition of 4 nm of Alq_3, the VBM shifted about 1.6 eV toward high binding energy, meaning that the energy difference between the HOMO and E_F of Alq_3 is 1.6 eV. This means that the electron injection barrier from 2-nm thick AgO_x to Alq_3 is BG_{Alq3} −1.6 eV.

In order to find the generalized relationship of interface dipole energy at the interface of O_2 plasma treated metal with Alq_3 layer, same experiments were carried out with other metals. Fig. 10a shows the interface dipole after the deposition of Alq_3 on 20-nm thick metal coated ITO as a

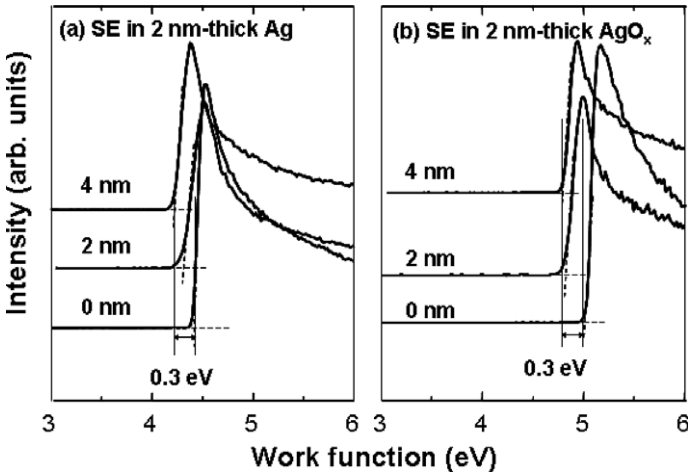

Fig. 8. The change of the onset of secondary electron spectra after deposition of Alq_3 on (a) 2-nm thick Ag and (b) 2-nm thick AgO_x. The work function was calculated by subtracting the onset of secondary electron binding energy in UPS spectra from He I excitation energy (21.2 eV).

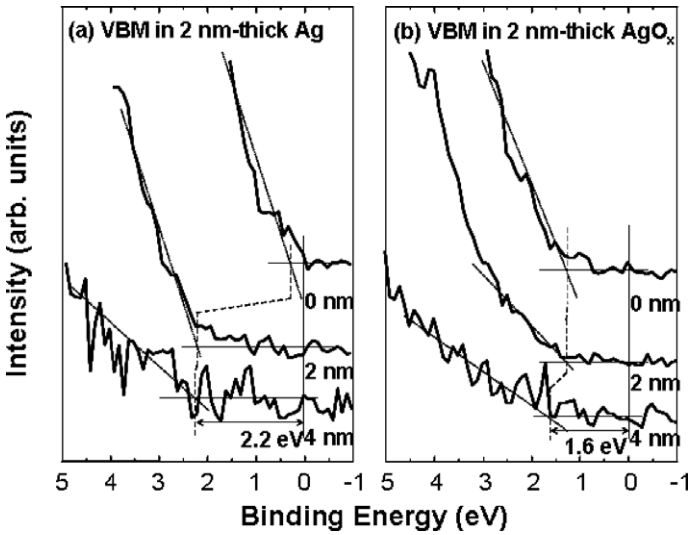

Fig. 9. The change of valence band spectra after the deposition of Alq_3 on (a) 2-nm thick Ag and (b) 2-nm thick AgO_x. The VBM was determined by extrapolating solid lines from the background and straight onset in the UPS spectra.

function of metal work function. It seems that the work function obtained from this experiment is lower than that in literature. This result indicated that 20-nm thick metals have many kinds of crystal structures. After O_2 plasma treatment, the metal work function increased due to the formation of metal oxide on the surface of metal and the interface dipole energy increased. This result is consistent with the previous report that the higher metal work function, the higher interface dipole [33]. The interface dipole energy after the deposition of Alq_3 on 2-nm thick metal coated ITO is shown in Fig. 10b. After O_2 plasma treatment, the metal work function also increased. However, the interface dipole energy maintained the same value independent of O_2 plasma treatment. It should be noted that the change of interface dipole energy between Alq_3 and 2-nm thick metal coated ITOs was not observed although the work function of 2-nm thick metal coated ITOs increased after O_2 plasma treatment. The AFM images of ITO and 2-nm thick Ir coated ITO are shown in the inset of Fig. 10b. The area is $2 \times 2\ \mu m^2$. It seems that whole surface of ITO is covered with Ir layer, suggesting that 2 nm is thick enough to cover whole surface.

Based on these experimental observations, the effect of O_2 plasma treatment on the formation of interface dipole can be explained as follows. The work function of 20-nm thick Ag and the interface dipole energy at the Ag/Alq_3 interface were calculated to be 4.4 eV and −0.4 eV (Fig. 4a). After O_2 plasma treatment, the work function increased about 0.6 eV and interface dipole also increased to be −0.6 eV (Fig. 4b). In case of 2-nm thick Ag, the work function increased by 0.6 eV after O_2 plasma treatment, but the interface dipole energy increased as small as 0.05 eV

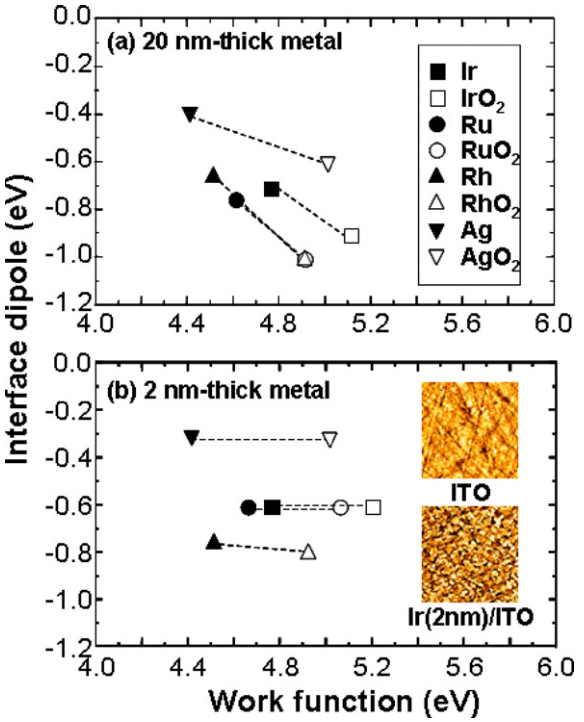

Fig. 10. The interface dipole energy after the deposition of Alq_3 on (a) 20-nm thick metal and (b) 2-nm thick metal as a function of metal work function. The kinds of metals used in this experiment are Ir, Ru, Rh, Ag, and their oxide states. The oxide states were prepared by exposing the metal layers to O_2 plasma for 1 min under 100 mTorr with a power of 150 W. The interface dipole energies are calculated by the change of secondary cutoff during the deposition of Alq_3 without considering band bending. The AFM images of ITO and 2-nm thick Ir coated ITO are shown in the inset of (b).

(Fig. 8). Similar results are shown in other metals. In 20-nm thick metal coated ITOs, metal work function increased by α and interface dipole (Δ) formed by the deposition of Alq_3 also increased from $-\Delta$ to $-(\Delta+\beta)$ with O_2 plasma treatment, as shown in Fig. 11. It is considered that the higher work function of metal substrate is, the more sensitive electron density tail exists, inducing the higher interface dipole [34]. However, the value of Δ in 2-nm thick metal coated ITOs is independent of increase in work function (α) by O_2 plasma treatment, as shown in Fig. 12.

According to the electron tail reduction model, the metal work function in a metal–organic system could be altered with a surface dipole, which originates from the tail of free electrons and depends on the number of free electrons [34]. The contribution of this surface dipole could be modified by the presence of an adsorbate. The contribution of the surface electron tail should be reduced because the metal oxide has fewer free electrons ($\sim 10^{20}/cm^2$) than the metal ($\sim 10^{22}/cm^2$) [35]. According to the valence band spectra shown in Figs. 5b and 9b, 2-nm thick Ag is fully oxidized, but 20-nm thick Ag is partially oxidized after O_2 plasma treatment. It means that the number of free electrons in 2-nm thick Ag is lower than that of 20-nm thick Ag. Therefore, the contribution of the surface dipole by the deposition of Alq_3 on 2-nm thick metal is lower, resulting in a lower interface dipole. As a result, interface dipoles in O_2 plasma treated 2-nm thick metal coated ITOs coincide with the interface dipoles in bare samples. The similar or reduced interface dipole energies were also reported between UV/O_3 treated Au and organic materials due to the formation of Au oxide layer [36]. Consequently, oxide layer plays a role in increasing the work function of electrode with identical interface dipole, leading to the increase in electron injection barrier from ϕ_B^e to $\phi_B^e + \alpha$, as shown in Fig. 12.

4. Conclusion

In conclusion, we investigated the effect of O_2 plasma treatment on the formation of interface dipole. The interface dipole energy was determined by *in situ* measurements of work function and E_F using SRPES. When the surface of 20-nm thick Ag was treated with O_2 plasma, the work function increased about 0.6 eV and the interface

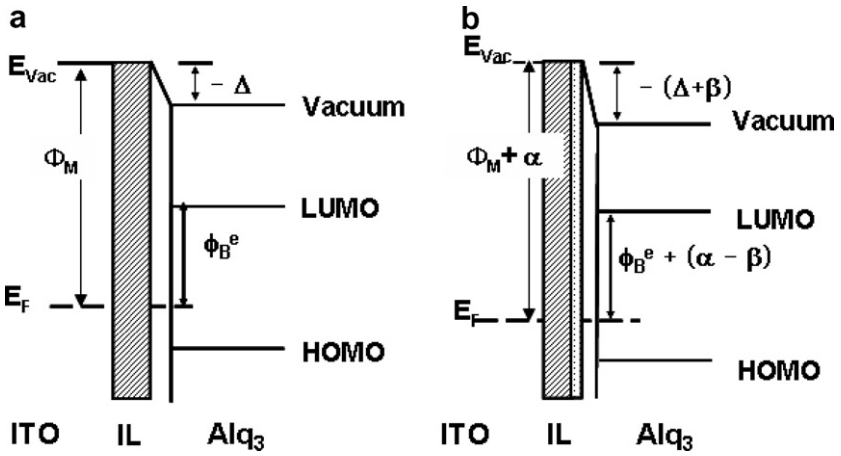

Fig. 11. The schematic band diagram in the case of (a) 20-nm thick metal interlayer and (b) O_2 plasma treated 20-nm thick metal interlayer. The work function increased about α after O_2 plasma treatment. In 20-nm thick metal interlayer, the interface dipole also increased about β, changing the electron injection barrier about α–β. The sign of α and β was considered as a positive number.

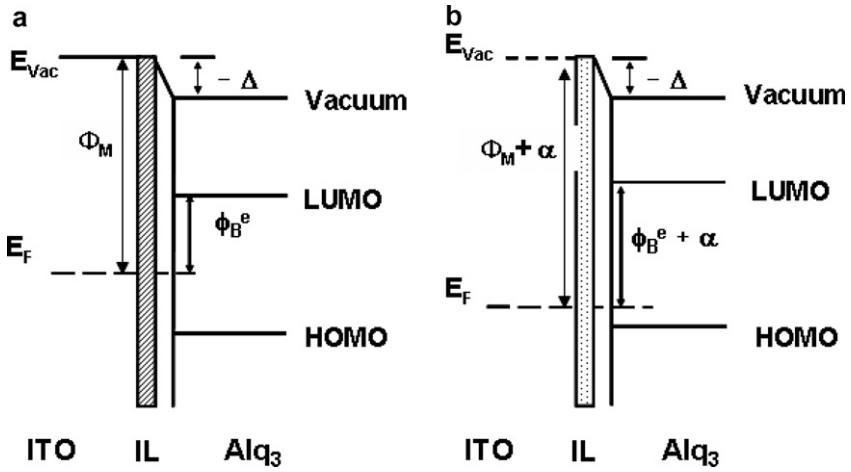

Fig. 12. The schematic band diagram in the case of (a) 2-nm thick metal interlayer and (b) O_2 plasma treated 2-nm thick metal interlayer. The work function increased about α after O_2 plasma treatment. In 2-nm thick metal interlayer, the interface dipole did not changed, increasing the electron injection barrier about α. The sign of α and β was considered as a positive number.

dipole energy also increased about 0.2 eV, indicating the increase in electron injection barrier about 0.4 eV. When 2-nm thick Ag was treated with O_2 plasma, the work function increased about 0.6 eV, but the interface dipole energy (-0.3 eV) at the Ag/Alq_3 interface almost did not change. Therefore, the work function increase (0.6 eV) in the 2-nm thick Ag by O_2 plasma treatment caused the increase of the electron injection barrier by about 0.6 eV. Similar results were found in Ir, Ru and Rh cases. The interface dipole between organic material and 20-nm thick metal coated ITOs increased after O_2 plasma treatment. However, the dipole energies of both the O_2 plasma treated 2-nm thick metal coated ITOs and bare 2-nm thick metal coated ITOs were the same with each other. These results indicated that the thickness of interfacial layer has a great impact on the formation of interface dipole.

Acknowledgments

This research was supported by a Grant (F0004180-2007-23) from the Information Display R&D Center, one of the 21st Century Frontier R&D Program funded by the Ministry of Commerce, Industry and Energy of the Korean Government and in part by the Korean Research Foundation Grant funded by the Korean Government (MOEHRD) (KRF-2005-005-J13102).

References

[1] R.H. Friend, R.W. Gymer, A.B. Holmes, J.H. Burroughes, R.N. Marks, C. Taliani, D.D.C. Bradley, D.A. Dos Santos, J.L. Bredas, M.L. Logdlund, W.R. Salaneck, Nature 397 (1999) 121.
[2] H. Burroughes, D.D.C. Bradley, A.R. Brown, R.N. Marks, K. Mackay, R.H. Friend, P.L. Burn, A.B. Holmes, Nature 347 (1990) 539.
[3] D.B. Mitzi, L.L. Kosbar, C.E. Murray, M. Copel, A. Afzali, Nature 428 (2004) 299.
[4] J.Y. Kim, S.H. Kim, H.-H. Lee, K. Lee, W. Ma, X. Gong, A.J. Heeger, Adv. Mater. 18 (2006) 572.
[5] I.G. Hill, A. Rajagopal, A. Kahn, Y. Hu, Appl. Phys. Lett. 73 (1998) 662.
[6] H. Ishii, K. Sugiyama, E. Ito, K. Seki, Adv. Mater. 11 (1999) 605.
[7] S.Y. Kim, J.-L. Lee, Appl. Phys. Lett. 89 (2006) 223515.
[8] M. Knupfer, G. Paasch, J. Vac. Sci. Technol. A 23 (2005) 1072.
[9] M. Knupfer, H. Peisert, Phys. Status Solidi A 201 (2004) 1055.
[10] X. Crispin, V. Geskin, A. Crispin, J. Cornil, R. Lazzaroni, W.R. Salaneck, J.-L. Brédas, J. Am. Chem. Soc. 124 (2002) 8131.
[11] S.Y. Kim, J.M. Baik, J.-L. Lee, Electrochem. Solid State 8 (2005) H79.
[12] M.-S. Chun, T. Teraji, T. Ito, Appl. Surf. Sci. 216 (2003) 106.
[13] H. Peisert, M. Knupfer, J. Fink, Appl. Phys. Lett. 81 (2002) 2400.
[14] L. Yan, M.G. Mason, C.W. Tang, Y. Gao, Appl. Surf. Sci. 175–176 (2001) 412.
[15] H. Ishi, N. Hayashi, E. Ito, Y. Washizu, K. Sugi, Y. Kimura, M. Niwano, Y. Ouchi, K. Seki, Phys. State Solid A 201 (2004) 1075.
[16] S. Braun, W. Osikowicz, Y. Wang, W.R. Salaneck, Org. Electron. 8 (2007) 14.
[17] O. Mcdonald, A.A. Cafolla, D. Carty, G. Sheerin, G. Hughes, Surf. Sci. 600 (2006) 3217.
[18] X. Liu, M. Knupfer, L. Dunsch, A. Tabet, H. Hartmann, Org. Electron. 7 (2006) 107.
[19] L. Yan, N.J. Watkins, S. Zorba, Y. Gao, C.W. Tang, Appl. Phys. Lett. 81 (2002) 2752.
[20] A. Wan, J. Hwang, F. Amy, A. Kahn, Org. Electron. 6 (2005) 47.
[21] M. Grobosch, M. Knupfer, Adv. Mater. 19 (2007) 754.
[22] S.Y. Kim, J.-L. Lee, Appl. Phys. Lett. 88 (2006) 112106.
[23] J. Cao, X.Y. Jiang, Z.L. Zhang, Appl. Phys. Lett. 89 (2006) 252108.
[24] S.A. Choulis, V.-E. Choong, A. Patwardhan, M.K. Mathai, F. So, Adv. Funct. Mater. 16 (2006) 1075.
[25] I.-H. Hong, M.-W. Lee, Y.-M. Koo, H. Jeong, T.-S. Kim, O.-K. Song, Appl. Phys. Lett. 87 (2005) 063502.
[26] S.Y. Kim, K. Hong, J.-L. Lee, Appl. Phys. Lett. 90 (2007) 183508.
[27] Y. Yi, S.J. Kang, K. Cho, J.M. Koo, K. Han, K. Park, M. Noh, C.-N. Whang, K. Jeong, Appl. Phys. Lett. 86 (2005) 113503.
[28] Y.Q. Zhan, Z.H. Xiong, H.Z. Shi, S.T. Zhang, Z. Xu, G.Y. Zhong, J. He, J.M. Zhao, Z.J. Wang, E. Obbard, H.J. Ding, X.J. Wang, X.M. Ding, W. Huang, X.Y. Hou, Appl. Phys. Lett. 83 (2003) 1656.
[29] G.B. Hoflund, Z.F. Hazos, Phys. Rev. B 62 (2000) 11126.
[30] S.Y. Kim, J.-L. Lee, Appl. Phys. Lett. 87 (2006) 232105.
[31] A. Rajagopal, A. Kahn, J. Appl. Phys. 84 (1998) 355.
[32] I.G. Hill, A. Kahn, Z.G. Soos, R.A. Pascal Jr., Chem. Phys. Lett. 327 (2000) 181.
[33] N.J. Watkins, L. Yan, Y. Gao, Appl. Phys. Lett. 80 (2002) 4384.
[34] N.D. Lang, W. Kohn, Phys. Rev. B 3 (1971) 1215.
[35] Z. Qiao, R. Latz, D. Mergel, Thin Solid Films 466 (2004) 250.
[36] S. Rentenberger, A. Vollmer, E. Zojer, R. Schennach, N. Koch, J. Appl. Phys. 100 (2006) 053701.

Organic Electronics 9 (2008) 687–691

Contents lists available at ScienceDirect

Organic Electronics

journal homepage: www.elsevier.com/locate/orgel

Effects of polarons and bipolarons on spin polarized transport in an organic device

Yubin Zhang [a], Junfeng Ren [c], Guichao Hu [a], Shijie Xie [a,b,*]

[a] School of Physics, Shandong University, Jinan 250100, China
[b] State Key Laboratory of Crystal Materials, Shandong University, Jinan 250100, China
[c] College of Physics and Electronics, Shandong Normal University, Jinan 250014, China

ARTICLE INFO

Article history:
Received 23 February 2008
Accepted 2 May 2008
Available online 13 May 2008

PACS:
85.75.−d
72.25.Dc
71.38.Ht
71.38.Mx

Keywords:
Organic spintronics
Spin transport
Polarons
Bipolarons

ABSTRACT

A polaron–polaron interaction model is suggested to study the spin injection and transport in an organic semiconductor (OSC) device. The evolutions of spin polarons and spinless bipolarons are calculated from the drift-diffusion equations, in which both the polaron–bipolaron transition and the spin-flipping of a spin polaron are included. Then the spin polarized current is obtained. It is found that the polarons are responsible for the spin polarized transport in an OSC. Different from the case in a normal inorganic semiconductor, spinless bipolarons will affect the spin polarization of the OSC device. Finally, effects of the spin-flip time and the mobility of the carriers on the spin polarization in an organic device are discussed.

1. Introduction

Organic semiconductors (OSCs) are a class of electronic materials that have attracted considerable attention in the last decades. They have revolutionized important technological applications including large-area electrics, owing to their processing and performance advantages compared with conventional semiconductors for low-cost or large-area device applications [1–4]. Recently, OSCs find their another application as spin transport materials. Their soft lattice structure and capability of reconstructing the structure also provide an opportunity to form a good interface with ferromagnetic metal (FM) or half-metal contacts, reducing the probability of spin scattering at the interface. In addition, the spin–orbit coupling and hyperfine interaction are very weak in the OSCs, so that the electron spin diffusion length of an OSC is expected much longer than that of a usual inorganic material [5]. A new field called organic spintronics is emerging out and attracting the attention of both physical and chemical scientists [6–16]. In 2002, Dediu's group has observed spin injection into thin films of the conjugated organic material sexithienyl (T_6) on nanostructured planar hybrid junction $La_{0.7}Sr_{0.3}MnO_3$/T_6/$La_{0.7}Sr_{0.3}MnO_3$ at room temperature [6]. The spin diffusion length in T_6 is about 200 nm at room temperature. Xiong et al. have also observed spin injection and transport in a $La_{0.7}Sr_{0.3}MnO_3$/Alq_3/Co organic spin valve. The measured magnetoresistance can be as high as 40% at low temperature [7]. Majumdar et al. have observed as much as 80% magnetoresistance (MR) at 5 K and 1.5% MR at room temperature in the structure of $La_{0.67}Sr_{0.33}MnO_3$/poly 3-hexylthiophene/Co organic spin valve [8]. They also found

* Corresponding author. Address: School of Physics, Shandong University, Jinan 250100, China. Tel.: +86 531 8837035x8321.
E-mail address: xsj@sdu.edu.cn (S. Xie).

1566-1199/$ - see front matter © 2008 Elsevier B.V. All rights reserved.
doi:10.1016/j.orgel.2008.05.005

that there is a thin spin-selective tunneling interface between LSMO and the polymer, which improves the spin injection. On the theoretical side, Yu et al. studied the influence of weak magnetic field for spin transport process in magnet/polymer/magnet structures [9]. Xie et al. suggested a model for $Re_{1-x}Sr_xMnO_3$/polymer structure and studied the spin density distribution of the system from the Su–Schrieffer–Heeger-like Hamiltonian [10]. They indicated that the carriers in OSCs contain spin polarons and spinless bipolarons. We used the spin-dependent diffusion model [9,11–13] of the electrochemical potential to study the spin polarized injection and transport in the structure of FM/OSC hetero junction and FM/OSC/FM trilayers [14,15]. By supposing that polarons and bipolarons coexist in OSCs with a given proportion r defined as $r = n_p/(n_p + n_{bp})$, we found that spin polarons are the effective carriers of the spin polarized current. A large spin polarization can be realized even that the spin polarons are minority of carriers in the OSCs.

However, in present investigations polarons and bipolarons were supposed to exist independently. In fact, due to temperature, pressure, impurity or external fields and so on, polarons and bipolarons in OSCs can transit each other. Two polarons with opposite spins can annihilate into one spinless bipolaron, while one spinless bipolaron can be decomposed into two polarons [17]. The stability and transition of polarons and bipolarons have been widely studied both from theoretical and experimental aspects [18,19]. In this paper, we do not research the transition origin of polarons and bipolarons. Instead we focus on the spin polarized transport in an OSC by considering the transition of spin polarons and spinless bipolarons. We will suggest a new mechanism about the polaron and bipolaron transition in a spin non-equivalent OSC and then build the evolution equations for polarons and bipolarons separately. Section 2 will provide a description of the model and the derivation of the relevant formulae, Numerical results are presented and discussed in Section 3, and conclusions are drawn in Section 4.

2. Model and method

We consider an OSC with a FM as contact. The spin polarized current injects from the semi-infinite FM contact ($x < 0$) into the semi-infinite organic layer ($x > 0$) as shown in Fig. 1, which will result in a non-equilibrium distribution of spins. We suppose that the spin-up electrons are the majority carriers and the spin-down electrons the minority ones. When they are injected into the organic layer, both the spin-up and spin-down electrons will evolve into either spin polarons or spinless bipolarons. Our theoretical investigation is based on the drift-diffusion model [20,23]. We assume that: (1) spin-up and spin-down polarons may transfer each other by reversing the spin; (2) a spin-up polaron may combine with a spin-down one to form a spinless bipolaron and vice versa. Therefore, the evolution equations may be written as,

$$\frac{\partial n_{\uparrow(\downarrow)}}{\partial t} = \frac{1}{e}\mathrm{div}\vec{j}_{\uparrow(\downarrow)} \pm \left(\frac{n_\downarrow}{\tau_{\downarrow\uparrow}} - \frac{n_\uparrow}{\tau_{\uparrow\downarrow}}\right) + s_{\uparrow(\downarrow)}(\vec{r},t), \tag{1a}$$

$$\frac{\partial N}{\partial t} = \frac{1}{2e}\mathrm{div}\vec{j}_N + s_N(\vec{r},t), \tag{1b}$$

where e is the electron charge, $n_{\uparrow(\downarrow)}$ the density of spin-up (spin-down) polarons, and N the density of bipolarons. The spin-flip time $\tau_{\uparrow\downarrow}$ indicates the average time of a spin-up polaron flipping its spin and $\tau_{\downarrow\uparrow}$ that of a spin-down polaron. $s_{\uparrow(\downarrow)}(\vec{r},t)$ is the source of spin polarons and $s_N(\vec{r},t)$ that of spinless bipolarons, which result from the transition between polarons and bipolarons within the OSC. $\vec{j}_{\uparrow(\downarrow)}$ is the current density of spin-up (-down) polarons and $\vec{j}_N$ that of bipolarons, which can be described by

$$\vec{j}_{\uparrow(\downarrow)} = \sigma_{\uparrow(\downarrow)}\vec{E} + eD_n\nabla n_{\uparrow(\downarrow)}, \tag{2a}$$

$$\vec{j}_N = \sigma_N\vec{E} + 2eD_N\nabla N, \tag{2b}$$

where $\sigma_{\uparrow(\downarrow)} = en_{\uparrow(\downarrow)}\mu_n$ and $\sigma_N = 2eN\mu_N$ are the conductivities of polarons and bipolarons respectively. $\vec{E}$ is the applied external electric field. D_n, μ_n, D_N and μ_N are the diffusion coefficients and mobilities of polarons and bipolarons which obey Einstein relations $D_n/\mu_n = k_0T/e$ and $D_N/\mu_N = k_0T/2e$ respectively, where k_0 is Boltzmann constant and T the temperature. We neglect the spin dependence of the diffusion coefficients and mobilities of polarons in present investigation.

As stated above, polarons and bipolarons are not independent but transit each other during their transport, which provide the sources of the carriers in the organic layer. Considering the spin non-degeneracy in present system, we propose the rate equation for polarons and bipolarons as,

$$s_{\uparrow(\downarrow)} = -kn_\uparrow n_\downarrow + bN, \tag{3a}$$

$$s_N = kn_\uparrow n_\downarrow - bN. \tag{3b}$$

The first term on the right of Eq. (3a) describes the probability that a spin-up (-down) polaron encounters a spin-down (-up) polaron to annihilate into a spinless bipolaron. The second term describes the reversed process that a bipolaron decomposes into a spin-up and a spin-down polaron. Parameter k and b express the transition strength, which are dependent on the temperature. For a spin-degenerate system, we have $n_\uparrow = n_\downarrow$ and Eq. (3) gives the result of Refs. [21,22].

Substituting Eqs. (2) and (3) into Eq. (1), we finally obtain the evolution equations for spin polarons and spinless bipolarons along the x-direction,

$$\frac{\partial n_{\uparrow(\downarrow)}}{\partial t} = D_n\frac{\partial^2 n_{\uparrow(\downarrow)}}{\partial x^2} + \mu_n E\frac{\partial n_{\uparrow(\downarrow)}}{\partial x} + n_{\uparrow(\downarrow)}\mu_n\frac{\partial E}{\partial x} \pm \left(\frac{n_\downarrow}{\tau_{\downarrow\uparrow}} - \frac{n_\uparrow}{\tau_{\uparrow\downarrow}}\right) - kn_\uparrow n_\downarrow + bN, \tag{4a}$$

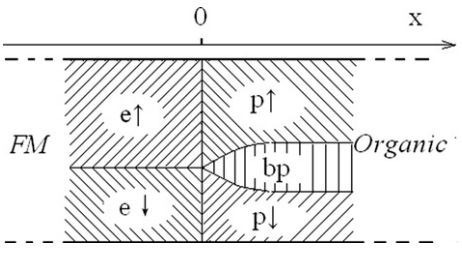

Fig. 1. A schematic diagram of the "FM/OSC" hetero structure.

$$\frac{\partial N}{\partial t} = D_N \frac{\partial^2 N}{\partial x^2} + \mu_N E \frac{\partial N}{\partial x} + N\mu_N \frac{\partial E}{\partial x} + k n_\uparrow n_\downarrow - bN. \quad (4b)$$

3. Results and discussion

First let us consider the polaron and bipolaron transition in an isolated OSC system. The sources mean the creation rates of the carriers and Eq. (3) can be solved analytically with initial condition $n_\uparrow(t=0) = n_1$, $n_\downarrow(t=0) = n_2$ and $N(t=0) = n_3$

$$n_\uparrow = \frac{\left(B + \sqrt{\frac{A}{k}}\right)e^{-Ct+C_0} + \sqrt{\frac{A}{k}} - B}{1 - e^{-Ct+C_0}}, \quad (5a)$$

$$n_\downarrow = \frac{\left(B + \sqrt{\frac{A}{k}}\right)e^{-Ct+C_0} + \sqrt{\frac{A}{k}} - B}{1 - e^{-Ct+C_0}} - n_1 + n_2, \quad (5b)$$

$$N = \frac{1}{2}(n_1 + n_2) + n_3 - \frac{1}{2}(n_\uparrow + n_\downarrow), \quad (5c)$$

where $A = \frac{k}{4}\left(n_2 - n_1 + \frac{b}{k}\right)^2 + b(n_1 + n_3)$, $B = \frac{1}{2}\left(n_2 - n_1 + \frac{b}{k}\right)$, $C = 2\sqrt{Ak}$ and $C_0 = \ln\frac{n_1+B-\sqrt{\frac{A}{k}}}{n_1+B+\sqrt{\frac{A}{k}}}$. There is a conservation condition during the transition, i.e., $n_1 - n_\uparrow = n_2 - n_\downarrow = N - n_3$.

It can be found from Eq. (5) that, after a long time evolution, the system will approach a equilibrium distribution of polarons and bipolarons. From experimental measurements [24,25], it has been known that polarons and bipolarons may coexist in most of conducting polymers. In theory [19], it was indicated that a bipolaron is energetically favorable to two isolated polarons in most polymers, which suggests a positive value of parameter k and a small positive value of b. Here we take $k = 5.6 \times 10^{-10}$ cm^3/s and $b = 1.7 \times 10^7$ s^{-1}. The evolution of carriers density with time is shown in Fig. 2. We supposed that the majority carriers are spin-up polarons with a density of $n_1 = 3.0 \times 10^{16}$ cm^{-3}, the minority ones are spin-down polarons with $n_2 = 2.0 \times 10^{16}$ cm^{-3} and there are no bipolarons with $n_3 = 0$ at the beginning. It is found that, with time evolution, the densities of both spin-up polarons and spin-down polarons decrease and, at the same time, the density of bipolaron increases, which means that the transition between polarons and bipolarons takes place. The transition approaches a dynamic equilibrium or saturation of the carriers density after a duration of $T_{p-bp} = 50$ ns in present parameters. The duration time T_{p-bp} is sensitive to the value of k. It is obtained that T_{p-bp} will be as long as seconds to reach a transition equilibrium if parameter k is smaller than 10^{-18} cm^3/s as taken in Refs. [21,22]. Parameter b mainly affects the saturation densities of polarons and bipolarons. A small value of b means that most of the spin minorities (spin-down polarons) will couple with spin majorities (spin-up polarons) to composite spinless bipolarons and at the same time the decomposition of bipolarons is small.

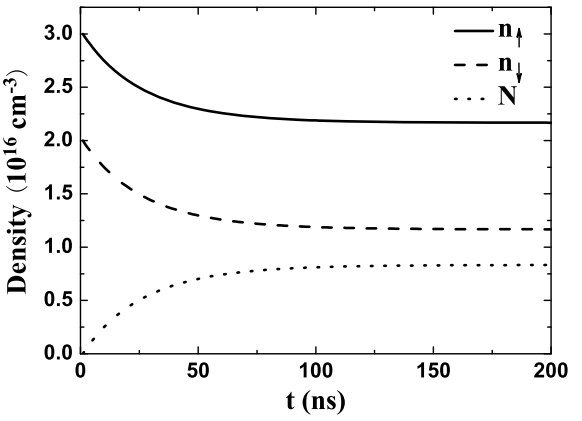

Fig. 2. The evolution of carriers density with time. The parameter is $k = 5.6 \times 10^{-10}$ cm^3/s, $b = 1.7 \times 10^7$ s^{-1}.

Now let us consider the injection and transport of spin carriers from a ferromagnetic contact to an organic semiconductor in an FM/OSC system based on Eq. (4), which could not be solved analytically. We take a numerical calculation by applying a constant driving electric field $E = 5.0 \times 10^4$ v/cm within the organic region and so $\partial E/\partial x = 0$. In addition, it is assumed that the injected electrons are completely spin polarized and are transited into spin-up polarons as soon as they are injected into the organic layer at the interface. So that we set the initial and boundary conditions as $n_\uparrow(x=0,\ t=0) = 5.0 \times 10^{16}$ cm^{-3}, $n_\downarrow(x=0,\ t=0) = 0$ and $N(x=0,\ t=0) = 0$. This assumption may be rational for a half-metal (CMR, Colossal Magnetic Resistance, such as $La_{1-x}Sr_xMnO_3$) contact if we neglect the spin-flip at the interface. All the other parameter values are listed in the captions of the corresponding figures.

To analyze the spin characteristic of the injected charges in the OSC, we define the spin polarization $P = (n_\uparrow - n_\downarrow)/(n_\uparrow + n_\downarrow)$, which is similar to that in a normal inorganic semiconductor, but with a different meaning due to the existence of bipolarons in the OSCs. As the bipolarons have not any contribution to the spin polarization, they are not included in the denominator of the definition. For example, if all the spin minorities (spin-down polarons) compose with the spin majorities (spin-up polarons) into bipolarons, there will no free spin-down carriers left in the channel. So we should have the spin polarization $P = 100\%$ which is consistent to the definition.

The evolutions of spin-up, spin-down polarons and spinless bipolarons in the OSC layer are shown in Fig. 3a. Due to the spin-flip effect and the polaron–polaron interactions, although there is only the injection of spin-up polarons, spin-down polarons and spinless bipolarons will be created during the transport. The densities of these carriers will reach a dynamic balance at a distance of about 250 nm from the interface, which reflects the spin relaxation in an organic semiconductor. It should be mentioned that the spin relaxation in an OSC is different from that in a normal inorganic semiconductor. In an OSC, the spin relaxation contains two factors: one is the spin-flipping of spin polarons, and the other is the transition between spin polarons and spinless bipolarons. Due to the spin-flip effect, the minorities (spin-down polarons) will be created in the transport along with the annihilating of majorities (spin-up polarons), which will affect the spin polarization of the injected current. In addition, due to the polaron–polaron interaction, some spin opposite polarons will annihilate into spinless bipolarons (or its inversed process), which will further affect the spin polarization. The spin polarization is shown in Fig. 3b. Apparently, it decays into the OSC.

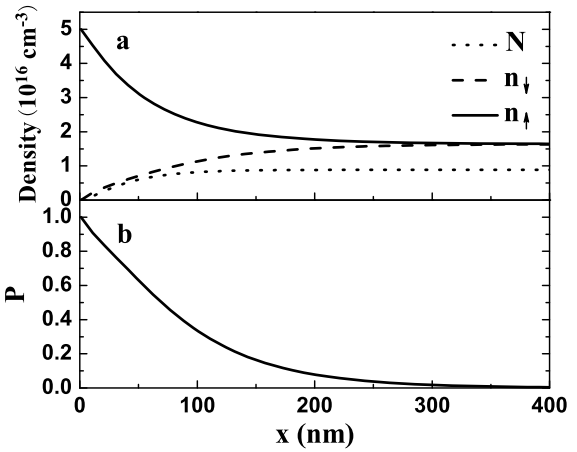

Fig. 3. The distribution of carrier densities (a) and spin polarization P (b) in the OSC layer. The solid, dashed, dot lines in fig. (a) indicate the spin-up polaron, spin-down polaron and bipolaron, respectively. The parameters are $\mu_n = \mu_N = 5.0 \times 10^{-4}$ cm^2/V s, $k = 5.6 \times 10^{-10}$ cm^3/s, $b = 1.7 \times 10^7$ s^{-1}, $\tau_{\uparrow\downarrow} = \tau_{\downarrow\uparrow} = 5.0 \times 10^{-7}$ s.

It is interesting to note that, from the present definition about the spin polarization, the appearance of bipolarons will increase the spin polarization. Effect of bipolaron density on the spin polarization P in OSC layer is shown in Fig. 4. If there are not any bipolarons during the transport, the spin polarization decays exponentially, which is consistent with that in a normal inorganic semiconductor injection if we substitute electrons in an inorganic semiconductor with spin polarons in an OSC. As the creation of bipolarons will change the distribution of spin polarons and therefore affect the spin polarization, it is found that the spin polarization will deviate from the exponential. There is an inflexion at x_0 in spin polarization curve $P(x)$, which means that at this point, the transition between polarons and bipolarons reach a dynamical equilibrium. The density of bipolarons keeps unchanged after x_0, as showed in the inset of Fig. 4. It also means that after x_0, bipolarons has no

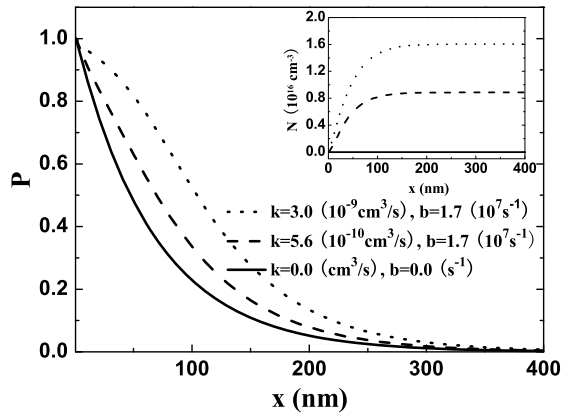

Fig. 4. The distribution of spin polarization P with the different bipolaron density. The different bipolarons density which is shown in the inset is obtained by adjusting the value of the parameter k and b, the solid line for $k = 0.0$ cm^3/s and $b = 0.0$ s^{-1}, the dash line for $k = 5.6 \times 10^{-10}$ cm^3/s and $b = 1.7 \times 10^7$ s^{-1}, and the dot line for $k = 3.0 \times 10^{-9}$ cm^3/s and $b = 1.7 \times 10^7$ s^{-1}, respectively. The other parameters are same as those in Fig. 3.

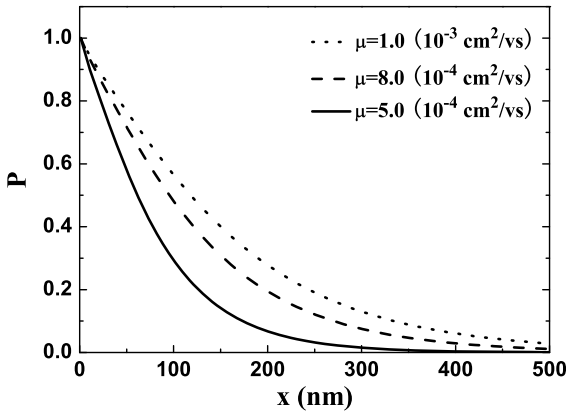

Fig. 5. The distribution of spin polarization P in the OSC layer for the different mobility. The solid, dash and dot lines indicate the different mobilities, i.e., $\mu = 5.0 \times 10^{-4}$ cm^2/V s, $\mu = 8.0 \times 10^{-4}$ cm^2/V s and $\mu = 1.0 \times 10^{-3}$ cm^2/V s, respectively. The other parameters are same as those in Fig. 3.

apparent effect on the spin polarization. Therefore, the enrollment of bipolarons in OSCs makes the spin transport more complex than that in normal semiconductors. In a normal inorganic semiconductor, there are only spin carriers, electrons or holes. At any point of the channel, one may recognise the spin-up and spin-down carriers with a spin detector. Then the spin polarization can be calculated. But in an OSC, one only could recognise the spin-up and spin-down polarons, and the spinless bipolarons could not be measured with a spin detector.

It has been indicated that a polaron moves faster than a bipolaron. We take different mobilities of polarons from bipolarons as $\mu_n = 2\mu_N = \mu$ and investigate the effect of mobility on spin polarization. The results are shown in Fig. 5. It is found that a large mobility result in a long spin diffusion in an OSC, which is consistent to that in a normal inorganic semiconductor. It should be mentioned that, due to bipolarons, the inflexion of spin polarization curve will be apart from the interface, which means that the distance

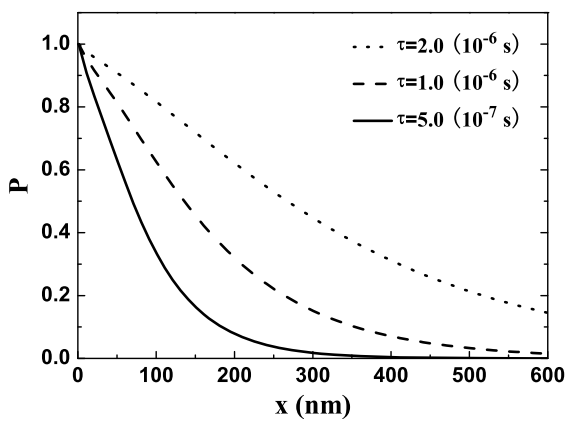

Fig. 6. The distribution of spin polarization P in the OSC layer for the different spin-flip time of the polarons when $\tau_{\uparrow\downarrow} = \tau_{\downarrow\uparrow} = \tau$. The solid, dash and dot lines indicate the different spin-flip times, i.e., $\tau = 5.0 \times 10^{-7}$ s, $\tau = 1.0 \times 10^{-6}$ s and $\tau = 2.0 \times 10^{-6}$ s respectively. The other parameters are same as those in Fig. 3.

of the effect of bipolarons on the spin polarization will increase with its mobility during the transport. The influence of the spin-flip time on the spin polarization is shown in Fig. 6. It is found that, consistent with the case of an inorganic semiconductor, a long spin-flip time will be helpful to the spin polarization in OSC. And the distance of the effect of bipolarons on the spin polarization will increase with its spin-flip time during the transport.

4. Summary

In summary, we investigated spin injection and transport from ferromagnetic contact to an OSC based on the drift-diffusion equations, where all the possible spin factors are included. Especially, a polaron–polaron interaction model is suggested to understand the polaron–bipolaron transition. This model considers the spin dependence in an organic spin device. Different from the case in an inorganic semiconductors, the relaxation of spin in the OSCs contains two factors: one is the spin-flip effect, and the other is the transition between polarons and bipolarons. By supposing that the injected electrons from the ferromagnetic contact are transited into fully spin polarized polarons when they enter an OSC, we obtain the evolutions of polarons and bipolarons during their transport in the OSC. It is found that the appearance of bipolarons decreases the density of the spin carriers (polarons) and so affects the spin polarization of the system. Polarons and bipolarons will reach a dynamical equilibrium in density during their transport. And then the spin polarization is dominated mainly by the spin-flipping of polarons. We also found that a large mobility or a long spin-flip time of spin polarons will result in a large spin diffusion length in the OSC.

Acknowledgments

The authors would like to acknowledge the financial support from the National Natural Science Key Foundation of the People's Republic of China (Grant Nos. 90403110 and 10474056) and the Research Fund for the Doctoral Program of Higher Education (No. 20070422058).

References

[1] See, e.g., I.H. Campbell, D.L. Smith, Solid State Phys. 55 (2001) 1.
[2] R.H. Friend, R.W. Gymer, A.B. Holmes, et al, Nature 397 (1999) 121.
[3] S. Forrest, P. Burrows, M. Thompson, IEEE Spectr. 37 (2000) 29.
[4] D. Voss, Nature 407 (2000) 442.
[5] S.A. Wolf, D.D. Awschalom, R.A. Buhrman, J.M. Daughton, S. von Molnár, M.L. Roukes, A.Y. Chtchelkanova, D.M. Treger, Science 294 (2001) 1488.
[6] V. Dediu, M. Murgia, F.C. Matacotta, C. Taliani, S. Barbanera, Solid State Commun. 122 (2002) 181.
[7] Z.H. Xiong, Di. Wu, Z. Valy Vardeny, Jing Shi, Nature 427 (2004) 821.
[8] Sayani Majumdar, R. Laiho, P. Laukkanen, I.J. Väyrynen, Himadi S. Majumdar, R. Őosterbacka, Appl. Phys. Lett. 89 (2006) 122114.
[9] Z.G. Yu, M.A. Berding, S. Krishnamurthy, Phys. Rev. B 71 (2005) 060408R.
[10] S.J. Xie, K.H. Ahn, D.L. Smith, A.R. Bishop, A. Saxena, Phys. Rev. B 67 (2003) 125202.
[11] D.L. Smith, R.N. Silver, Phys. Rev. B 64 (2001) 045323.
[12] P.P. Ruden, D.L. Smith, J. Appl. Phys. 95 (2004) 898.
[13] Z.G. Yu, M.A. Berding, S. Krishnamurthy, J. Appl. Phys. 97 (2005) 024510.
[14] J.F. Ren, J.Y. Fu, D.S. Liu, L.M. Mei, S.J. Xie, J. Appl. Phys. 98 (2005) 074503.
[15] J.F. Ren, J.Y. Fu, D.S. Liu, L.M. Mei, S.J. Xie, J. Phys. Condens. Matter 17 (2005) 2341.
[16] A. Saxena, T. Castan, A. Planes, M. Porta, Y. Kishi, T.A. Lograsso, D. Viehland, M. Wuttig, M. De Graef, Phys. Rev. Lett. 90 (2004) 197203.
[17] M.J. Nowak, D. Spiegel, S. Hotta, A.J. Heeger, P.A. Pincus, Macromolecules 22 (1989) 2917.
[18] Matheus Paes.Paes Lima, Geraldo.Geraldo Magela e Silva, Phys. Rev. B 74 (2006) 224304.
[19] Shi-jie Xie, Liang-mo Mei, D.L. Lin, Phys. Rev. B 50 (1994) 13364.
[20] Yuriy V. Pershin, Vlandimir Privman, Phys. Rev. Lett. 90 (2003) 256602.
[21] R.A. Street, A. Salleo, M.L. Chabinyc, Phys. Rev. B 68 (2003) 085316.
[22] A. Salleo, R.A. Street, Phys. Rev. B 70 (2004) 235324.
[23] Z.G. Yu, M.E. Flatté, Phys. Rev. B 66 (2002) 235302.
[24] T.C. Chung, J.H. Kaufman, A.J. Heeger, F. Wudl, Phys. Rev. B 30 (1984) 702.
[25] K.E. Ziemelis, A.T. Hussain, D.D.C. Bradley, R.H. Friend, J. Ruhe, G. Wegner, Phys. Rev. Lett. 66 (1991) 2231.

Organic Electronics 9 (2008) 692–698

Contents lists available at ScienceDirect

Organic Electronics

journal homepage: www.elsevier.com/locate/orgel

High-efficiency and multi-function blue fluorescent material for organic electroluminescent devices

Yu Wang [a], Yulin Hua [b,c,*], Xiaoming Wu [b,c], Lijuan Zhang [b,c], Qingchuan Hou [b,c], Feng Guan [b,c], Nan Zhang [b,c], Shougen Yin [b,c], Xiaoman Cheng [b,c]

[a] Institute of Physical Materials, Tianjin University of Technology, Tianjin 300384, PR China
[b] Key Laboratory of Display Materials and Photoelectric Devices, Ministry of Education, Tianjin 300191, PR China
[c] Tianjin Key Laboratory of Photoelectric Materials and Devices, Tianjin 300384, PR China

ARTICLE INFO

Article history:
Received 25 January 2008
Received in revised form 25 February 2008
Accepted 6 May 2008
Available online 13 May 2008

PACS:
85.60.Jb
78.60.Fi

Keywords:
Organic light-emitting devices
Efficiency
Blue fluorescent material
Multi-functional

ABSTRACT

We demonstrate one high-efficiency blue fluorescent material, *N*-(4-((E)-2-(6-((E)-4-(diphenylamino)styryl)naphthalen-2-yl)vinyl)phenyl)-*N*-phenylbenzenamine, with an emissive peak of 472 nm and the hole-transporting property speculated from different devices. It can function either as the single emissive layer or as the dye doped in *N*,*N*′-dicarbazolyl-4-4′-biphenyl (CBP). The former shows a maximum current efficiency and luminance of 7.06 cd/A (0.04 mA/cm^2) and 16930 cd/m^2, in contrast to 11.5 cd/A (4.35 mA/cm^2) and 25690 cd/m^2 for the latter. The better performance of the latter can be attributed to the bipolar carrier transport property of CBP and the hole-blocking and electron-transporting characteristic of 4,7-diphenyl-1,10-phenanthroline (BPhen), which resulting in a good balance of holes and electrons. Moreover, the Commission Internationale De L'Eclairage coordinates of the latter change slightly from (0.162, 0.3) to (0.148, 0.268) upon increasing the voltage from 3 V to 14 V.

1. Introduction

Organic light-emitting devices (OLEDs) are currently attracting considerable attention for use in flat panel displays and as solid state lighting sources. In order to achieve highly efficient OLEDs [1–4], it is essential to synthesis the red, green and blue emissive materials with the good performances. So far, the high-performance red and green emissive materials have successfully been explored, whereby the blue emissive materials remain a problem to match other colors. In order to explore the high-efficiency blue emissive materials, a heavy metal atom has been introduced to compose the phosphorescent compound and then utilizing the spin-orbit coupling transfers all excited states on the phosphor to the radiative triplet manifold, thus improving the efficiency of the devices with this emitter. For example, iridium(III)bis[4, 6difluorophenyl](pyridinatoN, C$^{2'}$)picolinate (FIrpic) [5] shows the maximum external quantum and current efficiency of 16% and 30.6 cd/A, respectively. However, the widespread use of the phosphorescent materials is limited in OLEDs by the relatively large energy barrier between the host and the blue phosphorescent dye [6], which is a need for the efficient exothermic energy transfer from host to guest [7]. As a consequence, research works are also focused on the exploitation of blue fluorescent compounds.

Recently, Idemitsu Kosan Co. Ltd. [8] has been invented a serial of blue bis-styryl derivatives, which exhibite good performances and widely used not only in industry but also academics. Lee et al. have reported an unsymmetrical

* Corresponding author. Address: Tianjin Key Laboratory of Photoelectric Materials and Devices, Tianjin 300384, PR China.
E-mail address: yulinhua@tjut.edu.cn (Y. Hua).

1566-1199/$ - see front matter © 2008 Elsevier B.V. All rights reserved.
doi:10.1016/j.orgel.2008.05.001

mono(styryl)amine fluorescent dopant, diphenyl-[4-(2-[1,1′;4′,1″]terphenyl-4-yl-vinyl)-phenyl]-amine (BD-1). By doping BD-1 in 2-methyl-9,10-di(2-naphthyl)anthracene (MADN), they produced one of the best deep blue devices with a current efficiency of 5.4 cd/A and a Commission Internationale De L'Eclairage (CIE) coordinate of (0.14, 0.13) [9].However, this high efficiency is obtained by the doping approach, which exposes some problems. For instance, while the guest and host molecules are initially homogeneously mixed, guest molecule may self-aggregate leading to phase separation during operation and/or upon heating. Phase separation increases the host–guest distance beyond available distance R (1–10 nm) or capture radius of a guest molecule for efficient host–guest energy transfer, thus rendering energy transfer ineffective [10]. This process can further degrade device stability, especially under high temperature operation. Based on these shortcomings, many efforts have been concentrated on explore the blue emitters which can function as the single active layer without a need for a host. 2,5,2′,5′,2″,5″-hexastyryl-[1,1′;4′,1″]terphenyl (HSTP), which is reported by Duan groups [11], is just one blue materials like this. By

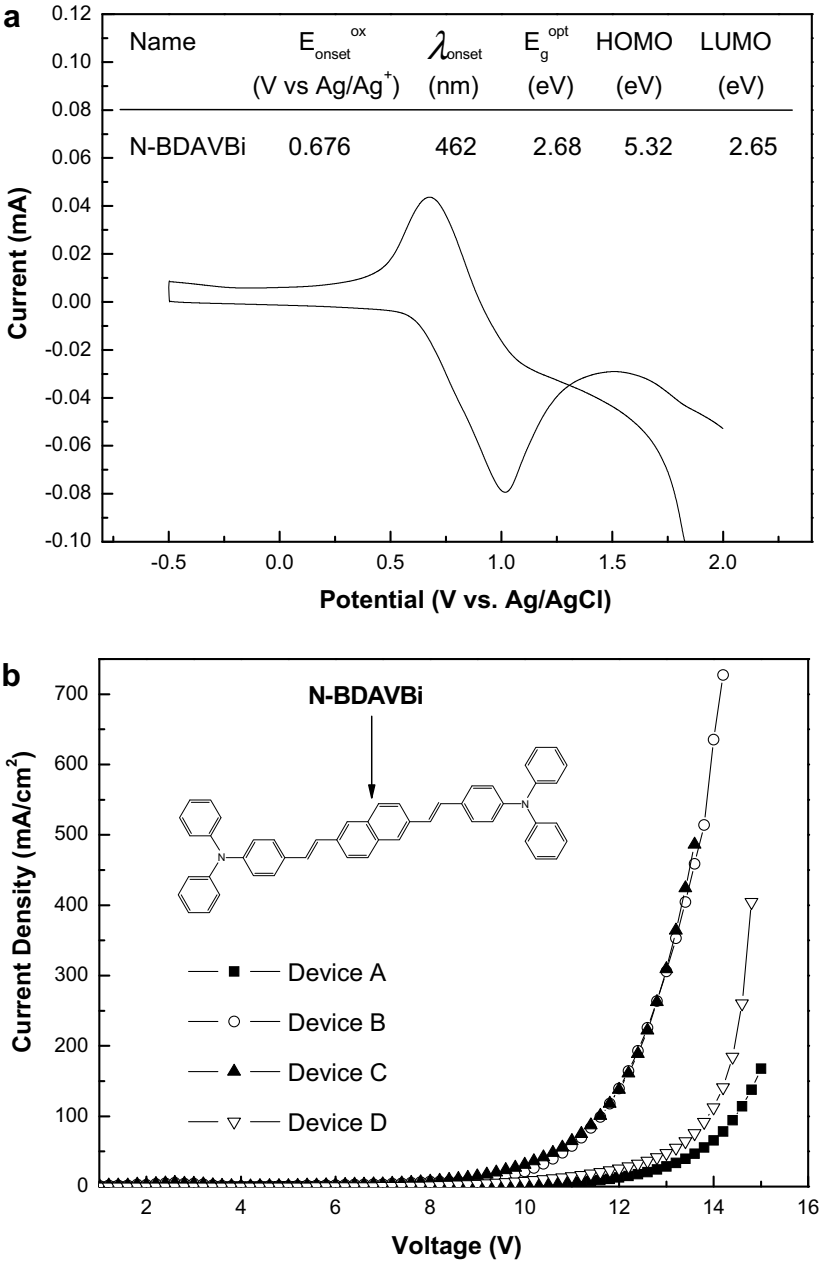

Fig. 1. (a) Cyclic voltammograms of the *N*-BDAVBi films on a platinum electrode in 0.1 M TBAP acetonitrile solution, inset: Electrochemical onset potentials and electronic energy levels of the *N*-BDAVBi films. (b) *I–V* characteristics of Device A–D; inset: chemical structures of *N*-BDAVBi.

optimizations of devices with HSTP as the emissive layer, it shows a CIE coordinate of (0.16, 0.13), maximum brightness of 15830 cd/m^2, and current efficiency of 4.88 cd/A. If we can find a blue emitter, which can be used either as the single emissive layer or the dye in the host, we can expect to design the OLEDs with different structures to meet the various needs.

In this article, we report a sky blue fluorescent material, *N*-(4-((E)-2-(6-((E)-4-(diphenylamino)styryl)naphthalen-2-yl)vinyl)phenyl)-*N*-phenylbenzenamine (*N*-BDAVBi), with both high efficiency and multi-function. This blue material is purchased from Rubipy Scientific Inc. The devices with *N*-BDAVBi as single layer or as the dye doped in the host present the maximum current efficiency of 7.06 cd/A at 0.04 mA/cm^2 and 10.5 cd/A at 1.03 mA/cm^2, respectively, corresponding to the emissive peak of 472 nm. In this work, *N*,*N*′-bis(naphthalene-2-yl)-*N*,*N*′-bis(phenyl)-benzidine (β-NPB) is used as the hole-transporting layer, while bis(2-methyl-8-quinolinolato)(para-phenylphenolato) aluminium(III) (BAlq) and 4,7-diphenyl-1,10-phenanthroline

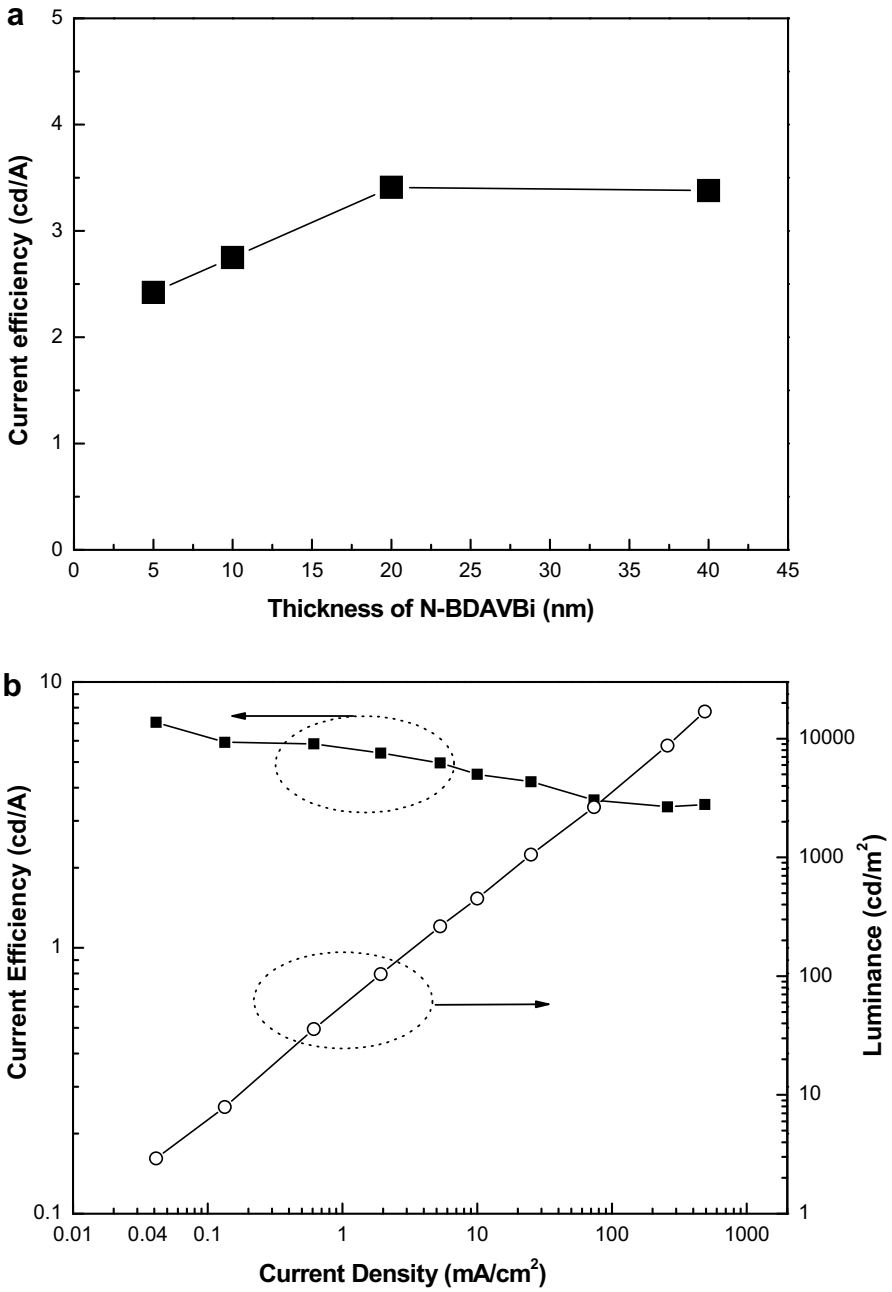

Fig. 2. (a) Current efficiency as a function of thickness of the *N*-BDAVBi layer at 100 mA/cm^2 (Device D); (b) current efficiency vs current density characteristics of Device D with the 20-nm-thick *N*-BDAVBi layer.

(BPhen) is used as the hole-blocking and electron-transport layer. *N*,*N*′-dicarbazolyl-4-4′-biphenyl (CBP) and (8-hydroxyquinoline) aluminum (Alq_3) is used as the host and electron-transporting layer, respectively.

2. Experimental

All the organic layers were deposited onto a pre-cleaned ITO glass substrate (sheet resistance 35 Ω/□) by thermal evaporation in a BOC Edwards Auto 500 Thermal Evaporation Coating System at a pressure of approximately 3×10^{-4} Pa. This was followed by an evaporated LiF buffer layer and an Al cathode (without breaking the vacuum). The deposition rates and thicknesses of the various layers were monitored using a quartz crystal oscillator. The evaporation rates were 0.2–0.3 nm/s for the organic layers and the LiF layer, and 1 nm/s for Al cathode. Electroluminescent spectra and CIE coordinates of the devices were measured by a PR650 spectra scan spectrometer. The luminance versus current and current density versus voltage characteristics were recorded simultaneously with the measurement of the EL spectra using a Keithley model 2400 programmable voltage-current source. Absorption and photoluminescence (PL) spectra of the organic materials are measured with JASCO V-570 and FluoroMax-P spectrometer. The energy levels of the materials are determined by Ecochemie μAutolab III electrochemical station through cyclic voltammogram measurements and the absorption spectra of the solid films. The electrochemical cyclic voltammetry (CV) was conducted on Ecochemie μAutolab III electrochemical station employing a Pt disk as the working electrode, Ag/Ag^+ electrode (0.01 M $AgNO_3$) as the reference electrode, and a Pt wire as the counter electrode. The reference electrode was calibrated with ferrocene ($E_{Fc/Fc^+} = 0.07$ V vs Ag/Ag^+). Tetrabutylammonium perchlorate (TBAP) was the supporting electrolyte, and the scan rate was 50 mV s^{-1}. All the measurements were carried out at room temperature in air without any device encapsulation.

3. Results and discussion

The electrochemical behavior of *N*-BDAVBi is investigated by cyclic voltammetry (CV), which is used to measure the redox potentials and evaluate the HOMO and LUMO energy level and the band gap energy of this material. The CV experiments were carried out under the protection of argon with the solid film of *N*-BDAVBi cast on the platinum disk working electrode using their acetonitrile solution (10 mg mL^{-1}) at room temperature. The onset potential is determined by taking the middle value between the peaks of the oxidation and reduction wave.

In our experiment, the HOMO level for *N*-BDAVBi is estimated using the oxidation potential whereas the LUMO energy is extrapolated from this value by using the optical band gap ($E_g^{opt} = 1240/\lambda_{onset}$) (Fig. 1(a)) [12]. Thus, the HOMO and LUMO of this material were estimated according to the following equation [13]: $HOMO = -(E_{onset}^{ox} - E_{Fc} + 4.8)$ (eV); $LUMO = HOMO - E_g^{opt}$ (eV). In which, $E_{Fc/Fc^+} = 0.32$ VvsAg/Ag^+. The results are summarized in Fig. 1 (a).

In order to ascertain the carrier transport property of *N*-BDAVBi, we fabricate three devices sorted by inserting *N*-BDAVBi to different positions. Three device structures are listed as follows: (A) ITO/*N*-BDAVBi (80 nm)/LiF/Al, (B) ITO/*N*-BDAVBi (40 nm)/Alq_3 (40 nm)/LiF/Al, and (C) ITO/β-NPB (40 nm)/*N*-BDAVBi (40 nm)/LiF/Al. As shown in Fig. 1 (b), surprisingly, Device B and C present almost the same *I*–*V* characteristics, which indicates the good carrier transport properties of *N*-BDAVBi because the hole mobility of

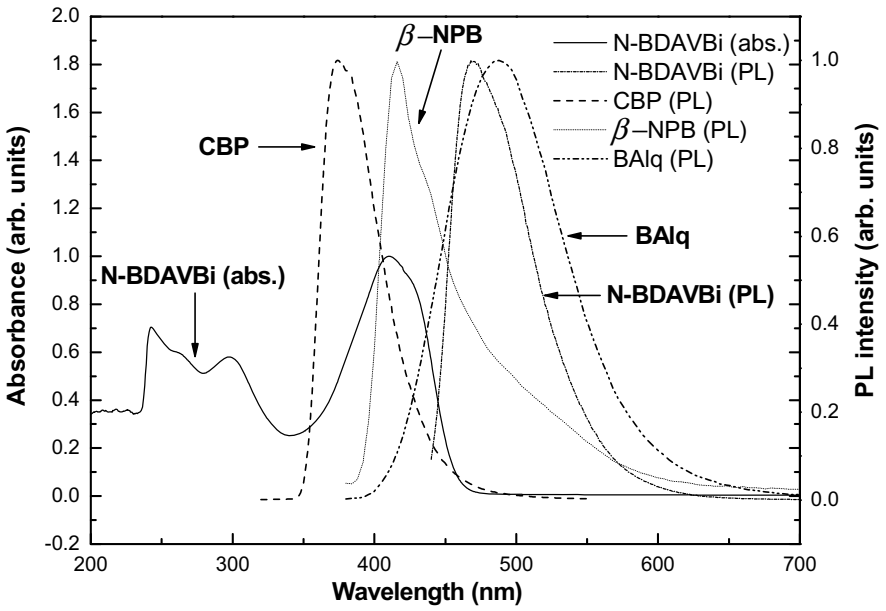

Fig. 3. Absorbance spectra of *N*-BDAVBi and Photoluminescent (PL) spectra of different materials.

NPB ($(3–6) \times 10^{-4}$ cm^2/V s) [14] is almost two order of magnitude of the electron mobility of Alq_3 ($(3–4) \times 10^{-6}$ cm^2/V s) [15]. However, no emission is observed for Device A, but a maximum current efficiency of 1.76 cd/A for Device B is found, in contrast to only 0.01 cd/A for Device C. This means *N*-BDAVBi favors the hole transport. The bad performances of Device A and C can be attributed to the residual holes injecting to the cathode, causing the cathode quenching [16].

Considering the preferable hole transport property of *N*-BDAVBi, we explore Device D (ITO/*β*-NPB (40 nm)/*N*-BDAVBi (x nm)/BAlq (30 nm)/LiF/Al) to investigate the performance of the neat *N*-BDAVBi layer by introducing BAlq as the hole-blocking and electron-transporting layer. From the inset of Fig. 2 (a), one could find that the current efficiency is improved on increasing the thickness of the *N*-BDAVBi from 5 nm to 20 nm, and then keeps constant with the 40-nm-thick *N*-BDAVBi layer. These results suggest

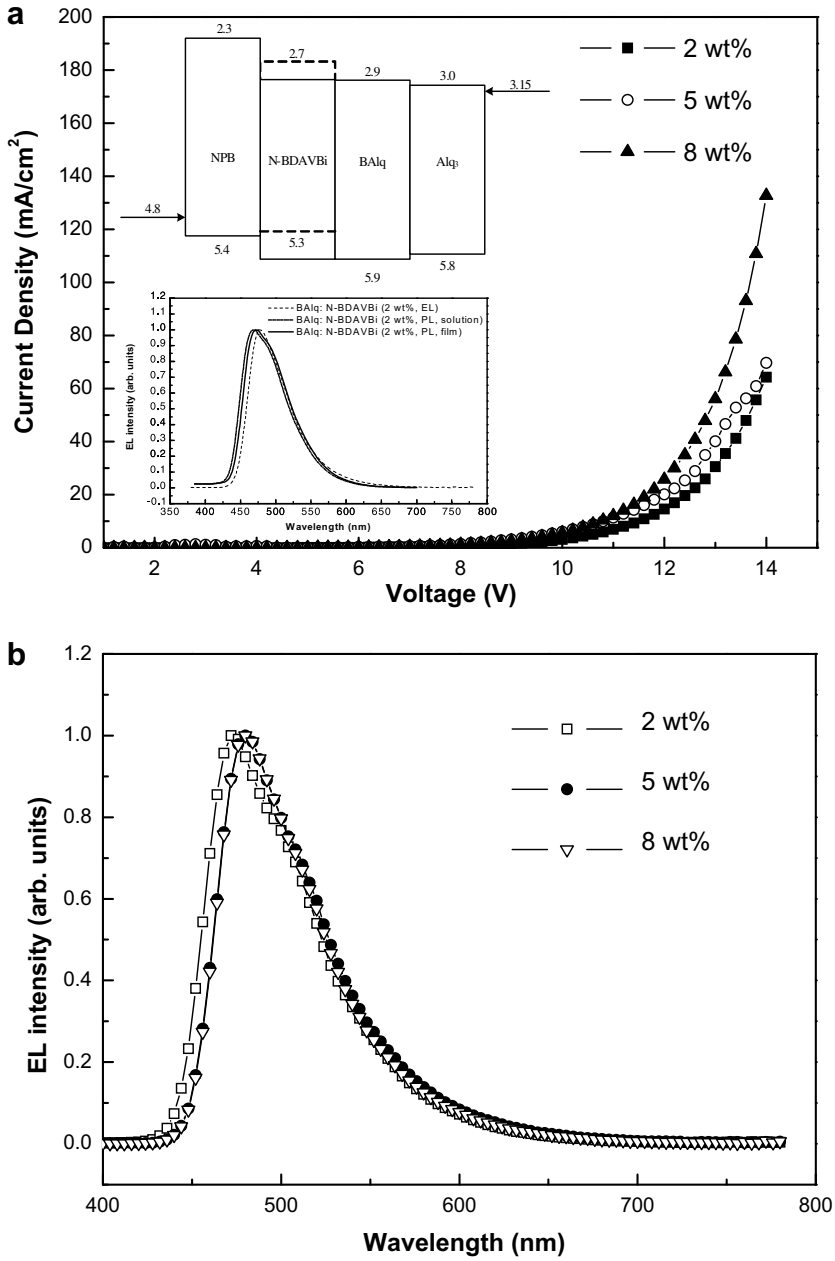

Fig. 4. (a) *J–V* characteristics of Device E with different *N*-BDAVBi: BAlq concentrations (inset: proposed energy level scheme for the device under zero applied bias; the EL spectra of Device E with the dye concentration of 2 wt% at the current density of 400 mA/cm^2, and the PL spectra of 2 wt% *N*-BDAVBi: BAlq in chloroform solution and film); (b) the EL spectra of Device E with different dye concentration at the current density of 20 mA/cm^2.

Table 1
Electroluminescent characteristic of Device D-G

Type	*x* (nm)	*y*	Maximum current efficiency (cd/A)	Current efficiency at 10 mA/cm^2 (cd/A)	Maximum luminance (cd/m^2)	CIE at 3000 cd/m^2
Device D[a]	5		3.40	3.22	5 894	(0.186,0.386)
Device D	10		3.78	3.41	10 990	(0.174,0.350)
Device D	20		7.06	4.49	16 930	(0.189,0.392)
Device D	40		5.10	3.65	10 320	(0.184,0.433)
Device E[b]		2 wt%	4.97	4.64	16 750	(0.174,0.313)
Device E		5 wt%	4.45	4.13	21 700	(0.183,0.371)
Device E		8 wt%	4.32	4.01	19 310	(0.179,0.371)
Device F[c]			10.5	8.12	20 100	(0.156,0.324)
Device G[d]			11.5	10.4	25 690	(0.148,0.291)

[a] Device D: ITO/β-NPB (40 nm)/*N*-BDAVBi (*x* nm)/BAlq (30 nm)/LiF/Al.
[b] Device E: ITO/β-NPB (40 nm)/*N*-BDAVBi: BAlq (*y* wt%, 30 nm)/BAlq (10 nm)/Alq_3 (20 nm)/LiF/Al.
[c] Device F: ITO/β-NPB (40 nm)/*N*-BDAVBi: CBP (2 wt%, 30 nm)/BAlq (10 nm)/Alq_3 (20 nm)/LiF/Al.
[d] Device G: ITO/β-NPB (40 nm)/*N*-BDAVBi: CBP (2 wt%, 20 nm)/BPhen (30 nm)/LiF/Al.

that the optimal thickness of *N*-BDAVBi layer is 20 nm. In sequence, we fixed the *N*-BDAVBi thickness of 20 nm and obtain the maximum current efficiency and luminance of 7.06 cd/A at 0.04 mA/cm^2 and 16 930 cd/m^2 at 489 mA/cm^2 (Fig. 2 (b)), respectively. This conforms that *N*-BDAVBi can effectively transport charge. However, the CIE coordinates change obviously from (0.205, 0.400) to (0.187, 0.379) as the voltages increase from 6 V to 14 V.

Generally, the efficiency can be enhanced by doping the fluorescent dye into the emissive layer, which has been broadly reported by other groups [17–19]. For this doping approach, two primary mechanisms, host–guest energy transfer and direct charge trapping followed by exciton formation at the guest, are relative to exciton formation and emission in OLEDs [20]. As shown in Fig. 3, the absorption spectra of *N*-BDAVBi overlaps well with the PL spectra of BAlq, which make the energy transfer from BAlq to *N*-BDAVBi possible. The only peak of 468 nm in the PL spectra of 2 wt% *N*-BDAVBi: BAlq in chloroform solution (Fig. 4 (a)), indeed, confirms this perfect energy transfer. In another hand, we fabricate Device E with the structure of ITO/β-NPB (40 nm)/*N*-BDAVBi: BAlq (y wt%, 30 nm)/BAlq (10 nm)/Alq_3 (20 nm)/LiF/Al. Since BAlq is usually used to block the holes and transport the electrons, the holes may mostly accumulate at the β-NPB/BAlq interface due to 0.6 eV barrier between the highest occupied molecular orbital (HOMO) of *N*-BDAVBi and BAlq. Fortunately, no β-NPB but the pure *N*-BDAVBi emission is observed in the spectra of Device E with the dye concentration of 2 wt% at the current density of 400 mA/cm^2 (Fig. 4 (a)). Such interesting phenomena can be explained in two aspects by supposing the existence of β-NPB emission or not. If we admit the existence of β-NPB emission, the efficient energy transfer must occur from β-NPB exciton to *N*-BDAVBi at the β-NPB/BAlq interface. In Fig. 3, we find the overlap between β-NPB and *N*-BDAVBi, which demonstrating this probability of energy transfer. In contrast, providing the absence of β-NPB emission, the holes must be effectively transported to the emissive layer. From the proposed energy level scheme in Fig. 4 (a), the holes tend to inject from β-NPB to *N*-BDAVBi because of the -0.1 eV barrier compared with the 0.5 eV barrier at the β-NPB/BAlq interface, thus resulting in the direct recombination of carriers in the blue dye. This is also supported in the *J*–*V* characterstics of Device E: the higher the dye concentration, the better the *J*–*V* characterstics (Fig. 4 (a)). In summary, both mechanisms work together and contribute to the pure blue emission.

Fig. 4 (b) depicts the EL spectra of Device E with different dye concentration at the current density of 20 mA/cm^2. As the *N*-BDAVBi concentration increases from 2 wt% to 8 wt%, the corresponding voltage reduces from 12.6 V to 12 V then to 11.4 V, as well the blue peak presents a red shift from 472 nm to 480 nm. In addition, the maximum current efficiency drops from 4.97 cd/A to 4.45 cd/A and then to 4.32 cd/A. The relative low efficiency of Device E (compared with Device D) may be ascribed to the 0.2 eV barrier between the LUMO of *N*-BDAVBi and BAlq (which reduce the number of the electrons transport to *N*-BDAVBi), as well the preferable electron transport property of BAlq, thus leading to the lack of enough holes recombining with the electrons in the emissive layer. In order to verify this, we adopt the bipolar host of CBP to configure Device F: ITO/β-NPB (40 nm)/*N*-BDAVBi: CBP (y wt%, 30 nm)/BAlq (30 nm)/LiF/Al. Fortunately, a good overlap between the PL spectra of CBP and the absorption spectra of *N*-BDAVBi is observed as well (Fig. 3). This suggests the possible energy transfer from CBP to *N*-BDAVBi should be expected to enhance the efficiency naturally. As shown in Table 1, this device presents a maximum current efficiency of 10.5 cd/A at 1.03 mA/cm^2, thereby revealing the lack of holes in Device E. In addition, the improved efficiency may be attributed to the bipolar carrier transport property of CBP and the preferable electron-transporting characteristic of BAlq, which resulting in an improved balance of holes and electrons. In this device, 30-nm-thick BAlq layer alleviates the holes transporting to the cathode effectively, which has been reported in our another paper [21].

From the data in Table 1, Device F shows the purer blue color than the nondoped Device D. Similar improvement of color purity and stability, due to the doping approach, has been reported by Shoustikov et al. [22] as well. The detailed reasons for these improvement are still unkown for us. A probable explanation is contributed to the improved charge balance. In order to clarify this, we introduce 4,7-diphenyl-1,10-phenanthroline (Bphen) (which has a electron

mobility of 5×10^{-4} cm^2/V s and LUMO of 6.2 eV [23]) to improve the electron injections and block the holes, thereby constructing Device G with the structure of ITO/β-NPB (40 nm)/*N*-BDAVBi: CBP (2 wt%, 20 nm)/BPhen (30 nm)/LiF/Al. This device shows the slightly changed CIE coordinates from (0.162, 0.3) to (0.148, 0.268) upon increasing the voltage from 3 V to 14 V. Furthermore, Device G exhibits the maximum current and power efficiency of 11.5 cd/A and 7.3 lm/W at 4.35 mA/cm^2, respectively, thereby indicating the improved charge balance. The improved charge balance is also proved by the improved *J*–*V*–*L* characteristics in Device F and G as compared to Device D (not shown here).

4. Conclusion

In summary, we demonstrate a high-efficiency blue fluorescent material, *N*-BDAVBi. This compound shows a blue peak of 472 nm in EL spectra and prefers the hole transport. Moreover, it can be used as the neat emissive layer with the maximum current efficiency and luminance of 7.06 cd/A and 16 930 cd/m^2. By doping *N*-BDAVBi in CBP, we obtain a maximum current efficiency of 11.5 cd/A at 4.35 mA/cm^2 and the relative stable colors.

Acknowledgements

The authors thank PH. D Jie Mao and Xin Lv (College of Chemistry, Nankai University), for help with the Absorption and PL spectra measurements. This work is supported by the National Natural Science Foundation of China (NSFC) (Grant No.60576038), the Natural Science Key Foundation of Tianjin (Grant No. 06TXTJJC14603), and the International Joint Project between NSFC and Royal Society.

References

[1] G. Cheng, Y. Zhang, Y.Y. Lin, C. Ruan, S. Liu, T. Fei, Y. Ma, Y. Cheng, Appl. Phys. Lett. 89 (2006) 043504.
[2] T.H. Liu, Y.S. Wu, M.T. Lee, H.H. Chen, C.H. Liao, C.H. Chen, Appl. Phys. Lett. 85 (2004) 4304.
[3] D.F. O'Brien, M.A. Baldo, M.E. Thompson, S.R. Forrest, Appl. Phys. Lett. 74 (1999) 0442.
[4] H. Aziz, Z.D. Popovic, N. Hu, A. Hor, G. Xu, Science 283 (1999) 1900.
[5] M. Tsai, H. Lin, H. Su, T. Ke, C. Wu, F. Fang, Y. Liao, K. Wong, C. Wu, Adv. Mater. (Weinheim, Ger.) 18 (2006) 1216.
[6] Y. Sun, N.C. Giebink, H. Kanno, B. Ma, M.E. Thompson, S.R. Forrest, Nature (London) 440 (2006) 908.
[7] R.J. Holmes, S.R. Forrest, Y.J. Tung, R.C. Kwong, J.J. Brown, S. Garon, M.E. Thompson, Appl. Phys. Lett. 82 (2003) 2422.
[8] C. Hosokawa, S. Sakamoto, T. Kusumoto, United States Patent 5389444 (1995).
[9] M.T. Lee, C.H. Liao, C.H. Tsai, C.H. Chen, Adv. Mater. (Weinheim, Ger.) 17 (2005) 2493.
[10] M.A. Baldo, D.F. O'Brien, Y. You, A. Shoustikov, S. Sibley, M.E. Thompson, S.R. Forrest, Nature (London) 395 (1998) 151.
[11] Y. Duan, Y. Zhao, P. Chen, J. Li, S. Liu, Appl. Phys. Lett. 88 (2006) 263503.
[12] J.K. Mwaura, M.R. Pinto, D. Witker, N. Ananthakrishnan, K.S. Schanze, J.R. Reynolds, Langmuir 21 (2005) 10119.
[13] Q.J. Sun, H.Q. Wang, C.H. Yang, Y.F. Li, J. Mater. Chem. 13 (2003) 800.
[14] S.C. Tse, K.C. Kwok, S.K. So, Appl. Phys. Lett. 89 (2006) 262102.
[15] S.C. Tse, K.C. Kwok, S.K. So, J. Appl. Phys. 94 (2003) 2033.
[16] F. Nüesch, D. Berner, E. Tutiš, Michel Schaer, C. Ma, X. Wang, B. Zhang, L. Zuppiroli, Adv. Funct. Mater. 15 (2005) 323.
[17] C.W. Tang, S.A. VanSlyke, C.H. Chen, J. Appl. Phys. 65 (1989) 3610.
[18] J. Littman, P. Martic, J. Appl. Phys. 72 (1992) 3610.
[19] C. Hosokawa, H. Higashi, H. Nakamura, T. Kusumoto, Appl. Phys. Lett. 67 (1995) 3853.
[20] R.J. Holmes, B.W. D'Andrade, S.R. Forrest, X. Ren, J. Li, M.E. Thompson, Appl. Phys. Lett. 83 (2003) 3818.
[21] Y. Wang, Y. Hua, X. Wu, L. Zhang, Q. Hou, Q. Liu, Org. Electr. 9 (2008) 273.
[22] A.A. Shoustikov, Y. You, M.E. Thompson, IEEE.J. Sel. Top. Quant. 4 (1998) 3.
[23] J.H. Seo, J.H. Seo, J.H. Park, Y.K. Kim, J.H. Kim, G.W. Hyung, K.H. Lee, S.S. Yoon, Appl. Phys. Lett. 90 (2007) 203507.

Organic Electronics 9 (2008) 699–710

Contents lists available at ScienceDirect

Organic Electronics

journal homepage: www.elsevier.com/locate/orgel

On the desired properties of a conjugated polymer-electrolyte blend in a light-emitting electrochemical cell

Piotr Matyba [a], Mats R. Andersson [b], Ludvig Edman [a,*]

[a] Department of Physics, Umeå University, SE-90187 Umeå, Sweden
[b] Department of Polymer Technology, Chalmers University of Technology, SE-412 96 Göteborg, Sweden

ARTICLE INFO

Article history:
Received 5 March 2008
Received in revised form 1 May 2008
Accepted 6 May 2008
Available online 23 May 2008

PACS:
85.60.Bt
85.60.Jb
72.80.Le

Keywords:
Light-emitting electrochemical cell
Conjugated polymer
Electrochemical doping
Electrochemical side reaction
Turn-on time

ABSTRACT

We present results from a systematic study on the influence of the conjugated polymer (CP) on the performance of planar light-emitting electrochemical cells (LECs) with a device structure of Au/{CP + poly(ethylene oxide) (PEO) + KCF_3SO_3}/Au. We have employed six different CPs, and we demonstrate that in order to attain a fast turn-on time and a strong light emission intensity, it is critical that the p-type doping (oxidation) potential of the CP is situated within the electrochemical stability window of the {PEO + KCF_3SO_3} electrolyte. We also find that a high ionic conductivity of the active material correlates with a small phase separation between the CP and the {PEO + KCF_3SO_3} electrolyte, and that a doping concentration of ~0.1 dopants/CP repeat unit is a generic feature of the progressing doping fronts in all investigated devices. Finally we report the first observation of a light emission zone positioned in close proximity to the positive anode in a CP-based LEC.

1. Introduction

Light-emitting electrochemical cells (LECs) have attracted increasing interest recently, mainly because they offer efficient light emission at low voltage from potentially easy-to-fabricate devices, but also because their complex and fascinating turn-on process has stirred a lot of debate regarding even its fundamental nature. Two main types of LECs exist: small-molecule based LECs, [1–14] and conjugated-polymer based LECs [15–34]. The former are commonly based on an ionic transition metal complex as the single-component active material, while the latter typically contain a three-component active material mixture, comprising a conjugated polymer (CP), an ion-solvating and ion-transporting material, and an alkaline salt.

We have recently set out on a quest to investigate and establish the desired properties of the various components in CP-based LECs for the attainment of optimized operation. We have established and reported that the physical and electrochemical properties of the electrolyte (*i.e.*, the dissolved salt together with the ion-solvating and ion-transporting material) and the electrode material play a crucial role. For instance, we find that the size of the alkaline-salt cation directly correlates to the device turn-on time and the light emission intensity [35,36], and that the electrochemical stability window of the electrode material is relevant in the context of elimination of undesired electrochemical side reactions [37]. In this paper, we extend these studies to include the core component of such devices, viz., the CP.

Our view of the *optimum* turn-on process of a CP-based LEC is as follows: when a voltage equal to or larger than the band-gap potential of the CP is applied between the two

* Corresponding author. Tel.: +46-90-7865732.
E-mail address: ludvig.edman@physics.umu.se (L. Edman).

1566-1199/$ - see front matter © 2008 Elsevier B.V. All rights reserved.
doi:10.1016/j.orgel.2008.05.010

electrodes ($V \geqslant E_g/e$), the dissolved ions redistribute in the resulting electric field to form electrical double layers (EDLs) at the electrode/active material interfaces [38]. The voltage drop over these (sub-nm-) thin EDLs is of such a magnitude that it compensates for the difference in energy between the work function of the electrode and the appropriate energy level of the CP, thus allowing for efficient oxidation of the CP (hole injection) at the anodic interface and efficient reduction of the CP (electron injection) at the cathodic interface. The injected electronic charge carriers are thereafter electrostatically compensated by the migratory motion of dissolved ions. The process of injection of holes/electrons onto the CP together with the subsequent electrostatic compensation of ions is termed electrochemical p-type/n-type doping.

At a certain doping concentration, the CP exhibits a relatively distinct transition from being an electronic insulator to become an electronic conductor, with the consequence that the metal electrodes now are in contact with a layer of highly conducting doped CP. Accordingly the electrochemical action (i.e., the injection of electronic charge carriers from an electronically conducting phase to an electronically insulating and ionically conducting phase) now takes place at the interface between the doped CP and the undoped CP (i.e., at the doping front) instead of at the metal interface. The p-type and n-type doping fronts continue to move towards each other in the inter-electrode gap, until they make contact to form a p–n junction. At this point the device has turned on, and subsequently injected electrons and holes can recombine under the emission of light at the p–n junction.

However, it is important to emphasize that the above outlined scenario represents the turn-on process of an ideal LEC, and that a number of non-desired effects can take place in a real device. For instance, it is possible that the balanced electrochemical reactions at the anodic and cathodic interfaces during device turn-on *not* correspond to p-type doping and n-type doping, respectively, of the CP, but instead involve an irreversible side reaction involving the electrode or the electrolyte material. Moreover, it has been demonstrated in a number of publications that the CP and the electrolyte phase separate [39–44], and it is not completely clear how this phase separation influences the turn-on process of an LEC.

In this paper, we have employed planar LECs with extremely large mm-sized inter-electrode gaps to enable for a direct optical probing of the device turn-on process; see Fig. 1 for a schematic of the planar device structure. We have consistently employed Au as the electrode material and KCF_3SO_3 dissolved in poly(ethylene oxide) (PEO) as the electrolyte, so that a direct correlation between device data and the chemical structure of the CP can be obtained. We have also characterized the active materials (i.e., the CP blended with the electrolyte) as regards to phase separation, electronic structure and electrochemical reversibility, and correlated these results with the acquired device data. We find that the ionic conductivity of the active material, as expected, benefits from a small phase separation between the CP and the electrolyte. More surprising, however, is that we find that an electrochemical side reaction involving the {PEO + KCF_3SO_3} electrolyte in several cases hinders, and in some cases even eliminates, the p-type doping process of the CP and the subsequent device turn on and light emission in LEC devices. We rationalize these findings by demonstrating that the p-type doping potential of the CP in these specific cases exceeds the oxidation stability potential of the electrolyte, which in turn provides an important guideline for the selection of appropriate CP/electrolyte combinations.

2. Experiment

2.1. Materials

MEH-PPV (M_w = 150,000 g/mol; Aldrich) is commercially available and was used as received. The procedures for the synthesis of BEH-PPV, BUEH-co-MEH-PPV, BUEH-PPV, BOP-PPV and BEHP-co-MEH-PPV are available in the literature [45–48]. The chemical structures of the CPs are presented in Fig. 2. Poly(ethylene oxide) (PEO, M_w = 5 ×

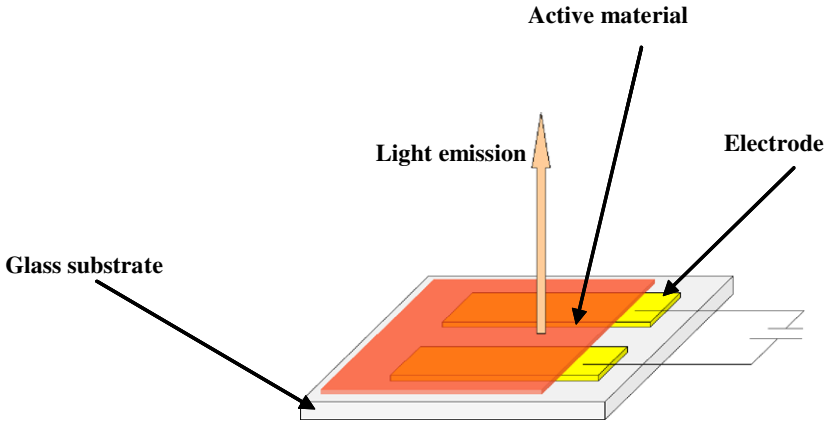

Fig. 1. Schematic of the employed planar LEC device structure deposited on a transparent glass substrate, with the electrodes positioned in a bottom-electrode configuration.

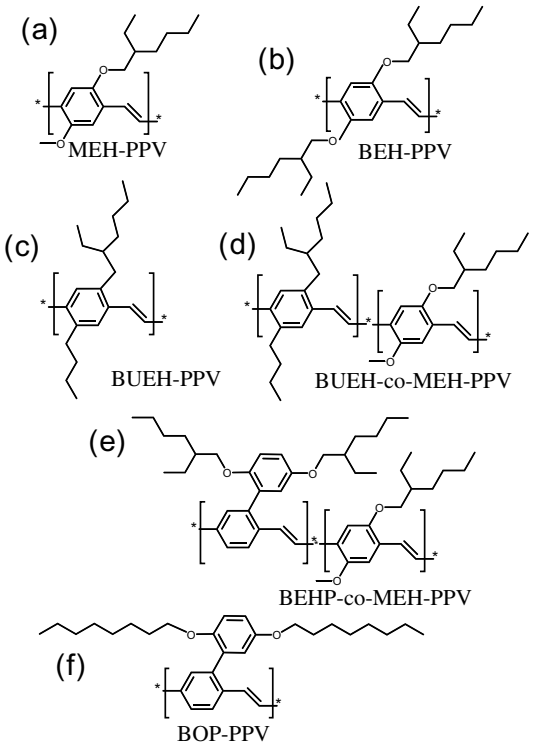

Fig. 2. Chemical structures of the conjugated polymers.

10^6 g/mol; Aldrich) was used as received, and the KCF_3SO_3 salt (99.995%; Aldrich) was dried for 12 h in a vacuum oven at $T = 473$ K before use.

2.2. Device preparation and measurements

Master solutions were prepared by dissolving each CP in chloroform (>99%, anhydrous; Aldrich) in a 10 mg/ml concentration, and PEO and KCF_3SO_3 separately in cyclohexanone (99%; Merck) in a 10 mg/ml concentration. Blend solutions were prepared by mixing the master solutions in a mass ratio of CP:PEO:KCF_3SO_3 = 1:1.35:0.25. The blend solutions were thereafter stirred on a magnetic hot plate for 5 h at $T = 323$ K.

The 1.5×1.5 cm^2 glass substrates were cleaned by subsequent ultrasonic treatments in detergent (Extran MA 01, Merck), acetone and iso-propanol. Au electrodes with a thickness of 100 nm were deposited onto the cleaned glass substrates, using thermal evaporation from a W-boat at a pressure (p) of $p \approx 1 \times 10^{-4}$ Pa. The inter-electrode distance of 1 mm was established with an Al shadow mask.

The active material films were deposited onto the electrode-coated substrates by spin-coating the blend solution (at 800 rpm for 60 s, followed by 1000 rpm for 10 s). The resulting devices were thereafter dried on a hot plate at $T = 323$ K for >5 h. All device preparation took place inside two interconnected glove boxes filled with Ar gas (O_2, H_2O< 2 ppm) and an integrated thermal evaporator. A schematic of the planar device structures positioned on a glass substrate is presented in Fig. 1. The thickness of each type of active material film was established by making a scratch in the film using a razor blade and measuring the resulting height step with an atomic force microscope operating in tapping mode. The surface morphology of the films was characterized with an optical microscope.

The device under study was transferred to an optical-access vacuum cryostat for opto-electronic characterization. Before the measurement, the device was dried in-situ in the cryostat at $T = 360$ K and $p < 10^{-3}$ Pa for >1 h. The voltage was sourced and the resulting current measured with a computer-controlled source-measure unit (Keithley 2400). Images of a device during operation were recorded under UV illumination in a dark room through the optical window of the cryostat, using a digital camera (Cannon EOS 20D) equipped with a macro lens (150 mm, f/2.8).

2.3. Cyclic voltammetry

Glass substrates were cleaned by subsequent ultrasonic treatment in detergent, acetone and isopropanol. Au electrodes (thickness: 60 nm; area: 1.0×0.5 cm^2) were deposited onto the cleaned glass substrates by thermal evaporation at $p \approx 1 \times 10^{-4}$ Pa. CP films were deposited onto the electrode-coated substrates by spin-coating a 2 mg/ml CP-in-chloroform solution at 800 rpm for 60 s. The CP-coated Au electrodes were thereafter dried on a hot plate at $T = 333$ K for 12 h.

For the cyclic voltammetry (CV) measurements, Au or CP-coated Au was used as the working electrode (WE), Pt was used as the counter electrode, and a silver wire was used as the pseudo-reference electrode. The electrolyte was either 0.1 M tetrabutylammonium hexafluorophosphate ($TBAPF_6$, $\geqslant$99%; Fluka) in CH_3CN ($\geqslant$99.8%; Aldrich) or {0.1 M KCF_3SO_3 + 2 M PEO ($M_w = 400$, Polysciences)} in CH_3CN; the molarity of PEO corresponds to the number of moles of ethylene oxide repeat units per liter of CH_3CN.

A freshly prepared electrolyte solution, a pristine WE, and carefully cleaned counter and pseudo-reference electrodes were invariably used for the CV measurements. The CV sweeps were driven and measured by an Autolab PGSTAT302 potentiostat. Directly after each (cathodic or anodic) CV scan, a calibration scan was run with a small amount of bis-(η-cyclopentadienyl)iron(II) (ferrocene, $\geqslant$98%; Fluka) added to the electrolyte ($\sim 10^{-4}$ M ferrocene concentration in CH_3CN). All potentials in the CV measurements are reported vs. the ferrocene/ferrocenium ion (Fc/Fc^+) reference redox system. The onset potentials for oxidation and reduction were calculated as the intersection of the baseline with the tangent of the current at the half-maximum of the peak. All sample preparation and CV measurements were performed under inert atmosphere in an Ar-filled glove box.

3. Results

In order to allow for a comprehensive characterization and analysis of the LEC performance as a function of conjugated polymer, we have extracted a number of data from device measurements and then correlated these findings with results obtained with CV and optical microscopy.

3.1. Device data

Fig. 3 presents the current density as a function of time for planar Au/{CP + PEO + KCF_3SO_3}/Au devices during operation at V = 5 V and T = 360 K, and Fig. 4 shows photographs of the same devices recorded at times indicated by matching Roman numerals in Fig. 3. The photographs were recorded under UV illumination in a dark room, since the UV-excited photoluminescence of the CPs is quenched by doping, and the electrochemically doped regions accordingly can be distinguished as dark regions under UV illumination [36,49–51].

The devices based on MEH-PPV (Figs. 3a and 4a) exhibit the shortest turn-on time ($t_{turn\text{-}on}$; defined as the time at which the p- and n-doped regions have met and formed a continuous p–n junction; see Table 1), the highest maximum current density, relatively balanced bipolar doping (as evidenced by the formation of both significant p-type and n-type regions in Fig. 4a), and the strongest light emission from a relatively centered p–n junction in the inter-electrode gap. It is notable that visible p-type doping is "immediately" apparent after the application of voltage at t < 1 s, while the onset of n-type doping is significantly delayed; and that the initial n-type doping, in contrast to the initial p-type doping, exhibits clearly defined finger-like features. These observations suggest that an electrochemical reaction other than n-type doping of MEH-PPV (i.e., a "side reaction") takes place at the negative cathode during the initial operation (thus the delay in n-type doping onset), and that the products of this cathodic side reaction partially block the interface of the negative cathode (thus the finger-like appearance of the initial n-type doping features). This

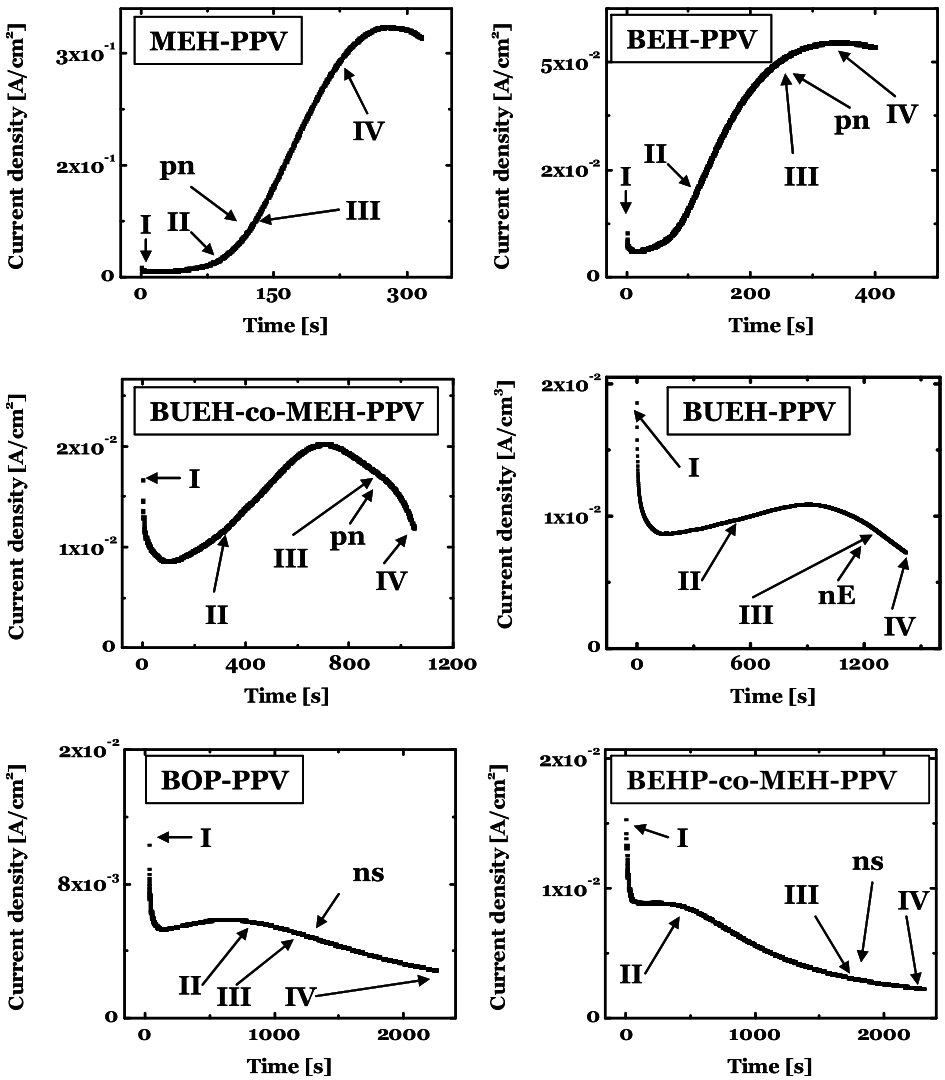

Fig. 3. Current density as a function of time for planar Au/{CP + PEO + KCF_3 SO_3}/Au devices, where the CP is identified in the inset of each graph. The devices were operated at V = 5 V and T = 360 K. The roman numerals in the graphs identify the times at which the photographs in Fig. 4 were recorded, while "pn" represents the time for for the initial p–n junction formation, "nE" represents the time for the apparent contact between the n-type doping front and the positive electrode, and "nS" represents the time at which the n-type doping front motion stops.

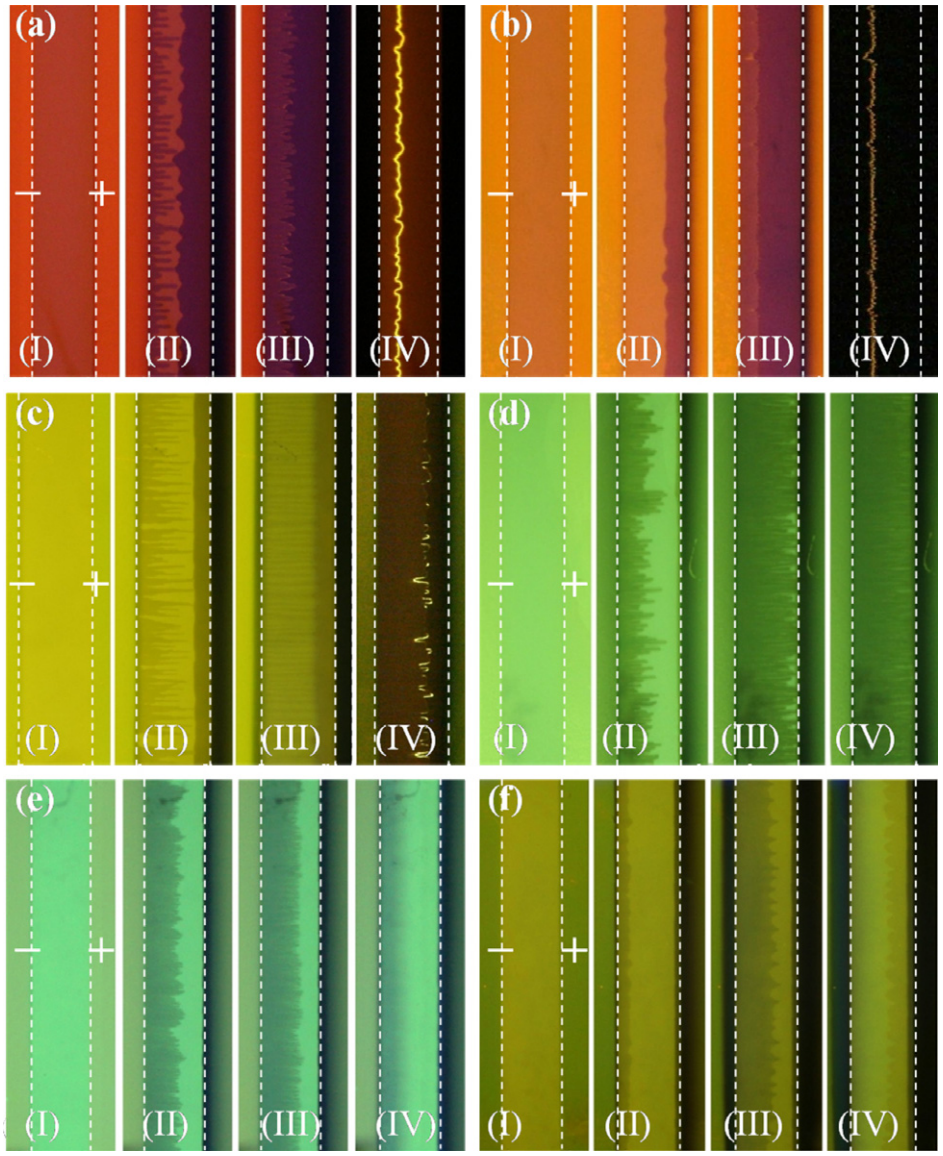

Fig. 4. Photographs of planar Au/{CP + PEO + KCF_3SO_3}/Au devices recorded during operation at $V = 5$ V and $T = 360$ K. The CPs are organized in the same order as in the other figures, i.e.: (a) MEH-PPV, (b) BEH-PPV, (c) BUEH-co-MEH-PPV, (d) BUEH-PPV, (e) BOP-PPV, and (f) BEHP-co-MEH-PPV. An electrochemically doped CP is apparent as a dark region originating from an electrode interface (marked with a dashed line).

Table 1
Device and cyclic voltammetry data as a function of conjugated polymer

Conjugated polymer	$t_{turn\text{-}on}$ (s)	σ (S/cm)	c_p (dopants/cm^3)	x_p (dopants/r.u.)	c_n (dopants/cm^3)	x_n (dopants/r.u.)	ϕ_p (V vs. Fc/Fc$^+$)	ϕ_n (V vs. Fc/Fc$^+$)
MEH-PPV	120	3.0×10^{-4}	3.1×10^{20}	0.14	4.2×10^{20}	0.18	0.1	−2.3
BEH-PPV	310	2.0×10^{-4}	4.8×10^{20}	0.26	8.6×10^{20}	0.46	0.5	−2.3
BUEH-co-MEH-PPV	440	2.8×10^{-4}	19×10^{20}	0.81	8.0×10^{20}	0.34	0.5	−2.3
BUEH-PPV	–[a]	2.9×10^{-4}	–[a]	–[a]	14×10^{20}	0.62	0.7	−2.4
BOP-PPV	–[a]	2.0×10^{-4}	–[a]	–[a]	14×10^{20}	1.0	0.7	−2.2
BEHP-co-MEH-PPV	–[a]	4.1×10^{-4}	–[a]	–[a]	20×10^{20}	1.1	0.7	−2.2

[a] No p-type doping was observed in these devices, and it was accordingly not possible to calculate the turn-on time for the p–n junction formation and the p-type doping concentration.

topic has been described in detail in a separate publication [52], but here we want to call specific attention to the absence of a similar electrochemical side reaction at the positive anode for the MEH-PPV-based devices.

The devices based on BEH-PPV (Figs. 3b and 4b) exhibit a qualitatively similar behavior as the devices based on MEH-PPV, but the turn-on time is slower by a factor of 2.6 (see Table 1), and both the maximum current density and the light intensity are significantly lower. The onset of n-type doping is significantly delayed, as was the case for the MEH-PPV devices, but it is notable that also the onset of p-type doping is slightly delayed (the first traces of p-type doping are apparent at $t \approx 5$ s).

Both MEH-PPV and BEH-PPV devices exhibit well-behaved current density–time curves (see Fig. 3a and b), with an initial decay in current corresponding to the formation of electric double layers at the two electrode/active material interfaces. This initial decay is followed by a time period of gradually increasing current up to the time of the p–n junction formation. It is during this time period that the doped regions increase in size and traverse the interelectrode gap (see Fig. 4a and b), and the increasing current is a reflection of the facts that a majority of the overpotential (defined as the applied potential subtracted by the band-gap potential) is dropping over the undoped region, and that the ionic *conductance* of this undoped region increases when its size decreases [53]. The continued increase in current and brightness after the initial p–n junction formation, and the subsequent final and irreversible decrease in current and brightness, are reflections of further electrochemical doping after the initial p–n junction formation and device failure via degradation of the material in the p–n junction region [54], respectively.

If we now turn to the BUEH-co-MEH-PPV based devices (Figs. 3c and 4c) a different behavior is observed. The turn-on time is slower, the maximum current density and the light intensity are lower, the p-type doping is very limited and its onset delayed until $t \approx 130$ s, and, most notably, the current density–time behavior is drastically different. After the initial double layer formation, the current shifts from increasing with time to decreasing with time *before* the initial p–n junction formation. Moreover, the weak and scattered light emission is observed from a *p–n junction in close proximity to the positive anode*. The last observation is noteworthy, since previously investigated planar LECs to our knowledge invariably have exhibited a p–n junction either positioned in close proximity to the negative cathode or positioned in the center of the inter-electrode gap [29,49,53,55–60].

For the final three devices based on BUEH-PPV (Figs. 3d and 4d), BOP-PPV (Figs. 3e and 4e), and BEHP-co-MEH-PPV (Figs. 3f and 4f) the common trends are that the maximum current density is very low, and that both p-type doping and light emission are absent. For the BUEH-PPV based devices, n-type doping is observed to traverse the entire inter-electrode gap, but the current reaches a maximum before the n-type front makes contact with the positive anode. For the BOP-PPV and BEHP-co-MEH-PPV based devices the n-type doping only traverses approximately two thirds of the inter-electrode gap, after which the n-type doping progression stops and eventually disappears. The current in the latter two devices is essentially constant during the early stages of the n-type doping progression, where after it begins to decrease.

From the data presented in Figs. 3 and 4, it is possible to calculate values for the ionic conductivity of the active material (σ) and the concentration of dopants in the doped regions. The immediate current density (j_0) after voltage (V) is applied over a pristine device is related to the ionic conductivity of the active material by the following equation (where d is the inter-electrode distance):

$$\sigma = \frac{j_0 \cdot d}{V}. \tag{1}$$

The average concentration of p-type and n-type dopants (c_i, $i = p, n$) in the doped regions up to the time of the *initial* p–n junction formation (t_{pn}) can be calculated by integrating the current from the initial appearance of doping (t_i) to t_{pn} (note that $t_{pn} < t_{turn\text{-}on}$, since the latter corresponds to the formation of a *continuous* p–n junction) and dividing the resulting charge with the volume of the CP in the corresponding doped region (V_i^{CP}) and the elementary charge (e):

$$c_i = \frac{1}{V_i^{CP} \cdot e} \cdot \int_{t_i}^{t_{pn}} I \mathrm{d}t. \tag{2}$$

Moreover, if we postulate that the density of all constituent materials is 1 g/cm^3 and employ the procedure outlined in Ref. [35], we find that the number of p-type dopants per CP repeat unit (r.u.) range from $x_p = 0.14$ to 0.81 dopants/r.u. in the investigated CPs, while the density of n-type dopants range from $x_n = 0.18$ to 1.1 dopants/r.u. The value for the p-type doping concentration in MEH-PPV, $x_p = 0.14$ dopants/r.u., is in good agreement with previous reports, while the n-type doping concentration in MEH-PPV, $x_n = 0.18$ dopants/r.u., is lower than in the first two of three previous reports [35,37,52]. The discrepancy in the latter case is caused by the lack of correction for the delayed n-type doping onset in the two earlier studies.

It is notable that the doping concentration values are based on the assumptions that no side reaction takes place between t_i and t_{pn} and that all doping is confined to the volume defined by the inter-electrode gap. Furthermore, it is not possible to calculate a p-type doping value or a turn-on time for p–n junction formation for BUEH-PPV, BOP-PPV and BEHP-co-MEH-PPV based devices since no p-type doping could be detected. The calculated data for σ, c_p, x_p, c_n and x_n, as well as the measured values for $t_{turn\text{-}on}$, are presented as a function of CP in Table 1.

3.2. Morphology data

Fig. 5 presents optical micrographs of the {CP + PEO + KCF_3SO_3} active material blends used in the LECs. We find, in agreement with previous reports [39,40,43,44], that these PEO based ternary materials phase separate into a CP phase (with a darker appearance) and a {PEO + KCF_3SO_3} phase (with a lighter appearance). It is clear that the surface morphology is strongly dependent on the CP. MEH-PPV based blends exhibit a comparatively minor phase separation on a ~1-μm scale, while the BUEH-PPV and BEHP-co-MEH-PPV based blends exhibit a slightly larger phase separation. The largest phase separation on the ~5-μm scale appears in the blend materials based on BEH-PPV,

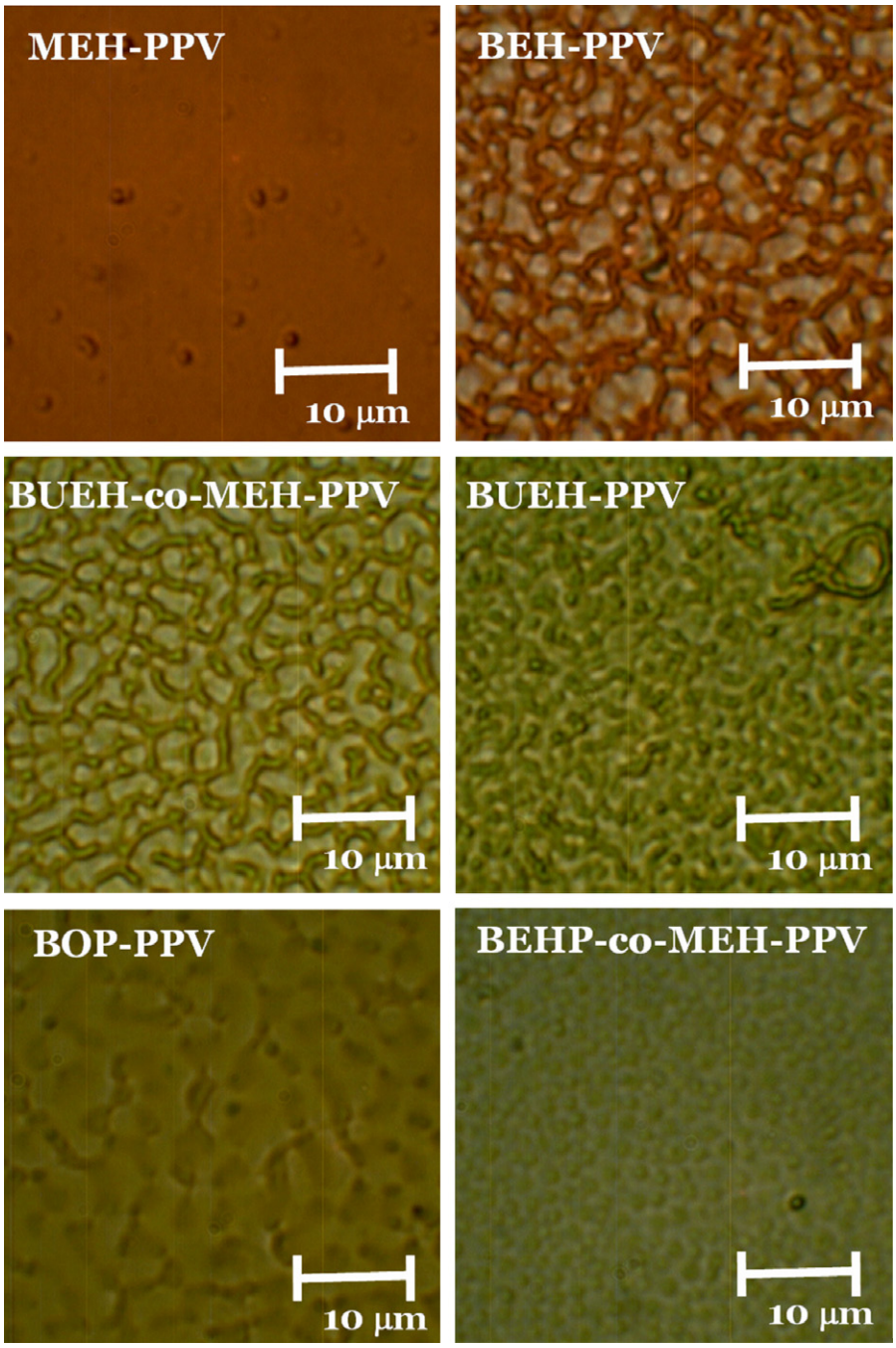

Fig. 5. Optical micrographs of the {CP + PEO + KCF_3SO_3} films, where the CP is identified in the inset of each graph.

BUEH-co-MEH-PPV, and BOP-PPV. The amount of phase separation in the {MEH-PPV + PEO + KCF_3SO_3} active material is in good agreement with a previous report employing AFM [39].

3.3. CV data

Fig. 6 presents CV data for the six different CPs, using a working electrode (WE) of Au coated with a thin film of CP and an electrolyte comprising $TBAPF_6$ in CH_3CN. Fig. 7 presents two "background" measurements performed with a WE of solely Au (and no CP film) and an electrolyte comprising either $TBAPF_6$ in CH_3CN (top graph) or {PEO + KCF_3SO_3} in CH_3CN (bottom graph). The first system in Fig. 7, employing a Au WE and a $TBAPF_6$ electrolyte, demonstrates no signs of neither reduction nor oxidation events, and it can thus be considered electrochemically inert in the probed voltage range. Accordingly, we conclude that

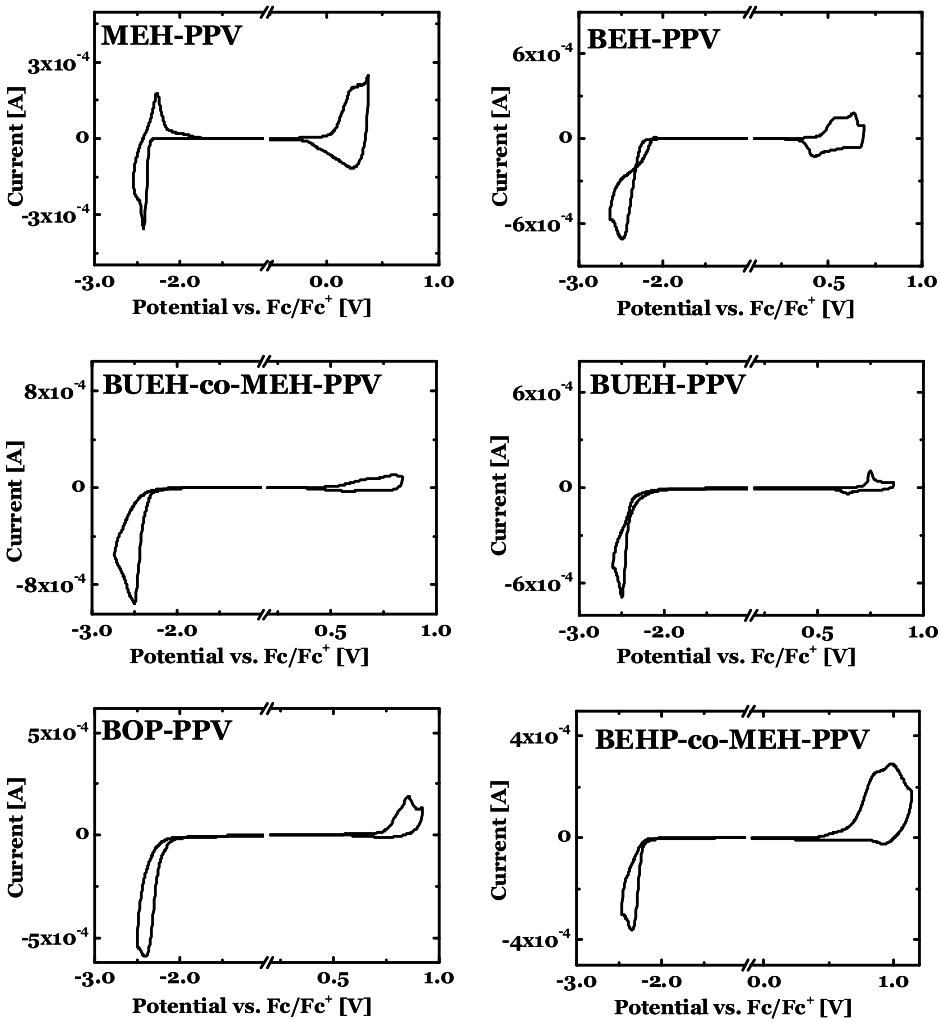

Fig. 6. CV data recorded using Au coated with a thin film of CP as the working electrode (the CP is indicated in the inset of each graph). The electrolyte was 0.1 M $TBAPF_6$ in CH_3CN, the counter electrode a Pt wire, the pseudo-reference electrode a Ag wire, and the scan rate 25 mV/s.

the oxidation and reduction peaks in Fig. 6 (detected with Au coated with a thin film of CP as the WE and a $TBAPF_6$ electrolyte) correlates to p-type doping (oxidation) and n-type doping (reduction) of the CP, respectively. The second background measurement in Fig. 7, employing a Au WE and a {PEO + KCF_3SO_3} electrolyte, exhibits a strong and irreversible reduction peak with an onset at -1.7 V vs. the Fc/Fc^+ couple and a clearly distinguishable and irreversible oxidation peak with an onset at +0.5 V vs. the Fc/Fc^+ couple. We assign both these peaks to irreversible electrochemical "side reactions" involving the {PEO + KCF_3SO_3} electrolyte, and the specific consequences of the cathodic side reaction involving the electrolyte for the operation of MEH-PPV based LECs have been discussed in a previous publication [52].

With this information at hand we return to Fig. 6. We find that all investigated CPs exhibit clearly distinguishable p-type and n-type doping peaks, albeit of significantly different magnitude, but that the apparent reversibility of the electrochemical reactions (as manifested by the existence and size of the de-doping peaks) depends strongly on the CP. However, we also observe that those electrochemical doping reactions that appear to be irreversible (based on the absence of a de-doping peak) invariably are accompanied by dissolution of the doped CP into the CH_3CN solvent, and we therefore refrain from drawing any conclusions as regards to the reversibility of the doping reactions.

To summarize, the most important and relevant information extracted from the CV measurements, in the context of the previously presented LEC device data, are that all investigated CPs are capable of both p-type and n-type doping, and that the {PEO + KCF_3SO_3} electrolyte exhibits an irreversible oxidation reaction in the probed voltage range. Fig. 8 presents the onset potentials for the p-type doping (solid circles) and n-type doping (open squares) reactions for the CPs as well as the voltage range in which the irreversible oxidation of the {PEO + KCF_3SO_3} electrolyte can be a factor (dashed region). The values for the p-type doping potential (ϕ_p) and the n-type doping potential (ϕ_n) for all investigated CP are also included into Table 1.

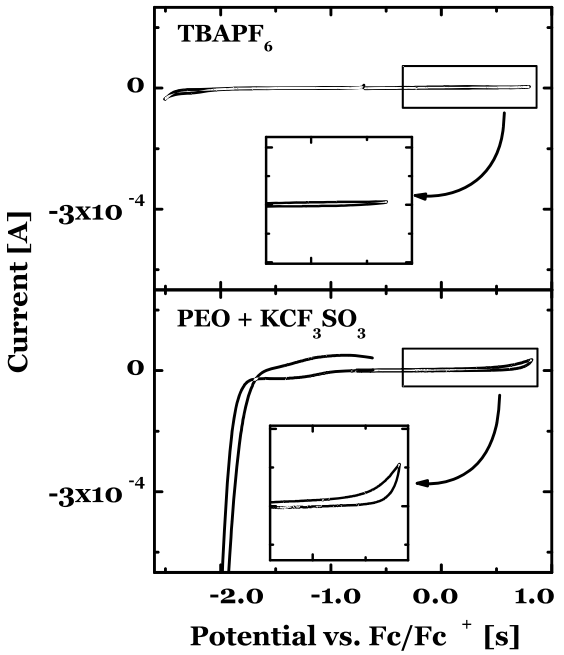

Fig. 7. CV data recorded using an electrolyte solution of 0.1 M $TBAPF_6$ in CH_3CN (top graph) and {2 M PEO + 0.1 M KCF_3SO_3} in CH_3CN (bottom graph). The working electrode was a Au film, the counter electrode a Pt wire, the pseudo-reference electrode a Ag wire, and the scan rate was 25 mV/s.

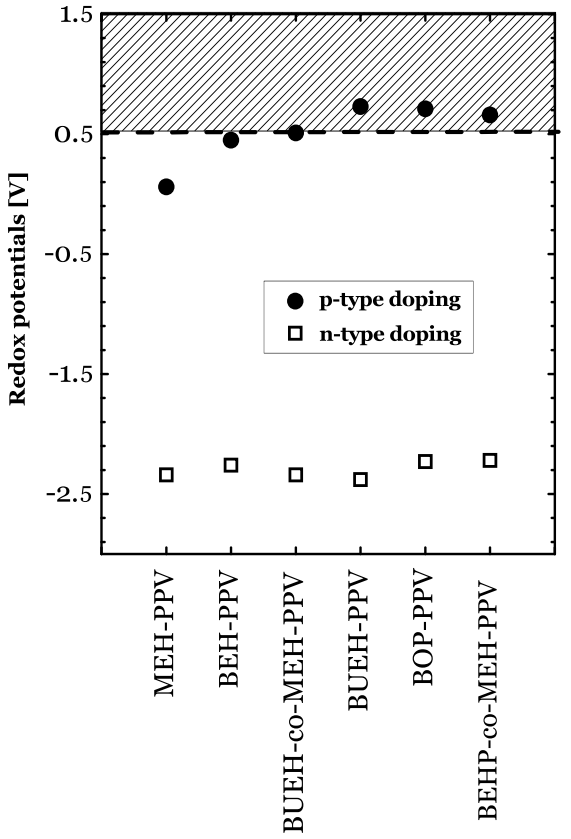

Fig. 8. Electrochemical p-type doping (oxidation) and n-type doping (reduction) potentials for the different CPs. The dashed region represents the voltage range at which the {PEO + KCF_3SO_3} electrolyte can be irreversibly oxidized. The data were extracted from the CV results presented in Figs. 6 and 7, and are reported vs. the Fc/Fc^+ couple.

4. Discussion

In the LEC literature it is often stated that it is advantageous with a small phase separation between the CP and the electrolyte in the active material, since this can be expected to correspond to a high ionic conductivity and a fast device turn-on time. In agreement with this statement, we find that the three devices with the smallest phase separation (i.e., those based on MEH-PPV, BUEH-PPV and BEHP-co-MEH-PPV; see Fig. 5) exhibit the highest ionic conductivity (see Table 1), and that the three devices with the largest phase separation (i.e., those based on BEH-PPV, BUEH-co-MEH-PPV, and BOP-PPV) exhibit a lower ionic conductivity.

However, it is notable that we find no correlation between the ionic conductivity and the device turn-on time, and that we could not even detect a p–n junction formation and light emission from the three devices based on BUEH-PPV, BOP-PPV and BEHP-co-MEH-PPV (see Fig. 4). A direct optical observation of devices during operation reveals that the origin to this undesired behavior is the absence of p-type doping. A complementary CV study demonstrates that all investigated CPs are capable of both electrochemical p- and n-type doping (Fig. 6), but that the CP in the three devices that did not turn on exhibit the highest p-type doping potential, and, importantly, that this potential exceeds the potential at which the electrolyte is irreversibly oxidized (see Fig. 8).

For the three functional LECs based on MEH-PPV, BEH-PPV and BUEH-co-MEH-PPV, which exhibit p–n junction formation and light emission, the trend is that a lower p-type doping potential of the CP corresponds to a better device performance. MEH-PPV has the lowest p-type doping potential, and devices based on this CP exhibit the fastest turn-on time, the highest current density, and the strongest light-emission; while BUEH-co-MEH-PPV has the highest p-type doping potential of the three, and accordingly such devices exhibit the slowest turn-on time, the lowest current density, and the weakest light emission. Moreover, even though we did observe p-type doping in devices based on all three of these CPs, we note that it is only for MEH-PPV that we could detect p-type doping "immediately" after the application of voltage. For BEH-PPV and BUEH-co-MEH-PPV, the onset of p-type doping is delayed, and we attribute this delay, and the overall poorer device performance, to that the electrochemical side reaction involving the electrolyte is in effect also in these devices, but that p-type doping becomes the dominant electrochemical reaction during the later stages of device operation.

We further propose that the result of the anodic electrochemical side reaction in 5 of the 6 investigated devices is the formation of a hole (and possibly ion) blocking degradation layer, and that the insulating property of the degradation layer is manifested in the shape of the current

density–time curves (see Fig. 3). We illustrate the latter point with the two extreme examples. For BEH-PPV, the degradation layer is only partially blocking since the current is observed to increase with time (after the initial double-layer formation), which demonstrates that the net effect of the electrochemical reactions is an increase in the total conductivity of the active material. For BEHP-co-MEH-PPV, on the other hand, the degradation layer becomes completely blocking with time since the current is observed to monotonically decrease to zero with time, which is the expected result if one of the electrochemical reactions at the electrodes result in the formation of a totally blocking degradation layer.

We now turn our attention to the doping concentrations in the doped regions at the time of the p–n junction formation (see Table 1). It is interesting to note that a very high doping concentration value ranging between 0.14 and 1.1 dopants/r.u. ($\sim 10^{20}$ dopants/cm^3) is a consistent feature in all investigated devices. We speculate that this high doping level, which apparently is a prerequisite for front motion in these devices, is related to a distinct increase in the electron/hole mobility at a certain doping concentration threshold. In this context, we find it interesting that Harima et al. and others report that the hole mobility in a number of different CPs exhibit a distinct increase of several orders of magnitude at a doping concentration value of ~0.1 dopants/r.u. [61–65] We are currently looking further into this fascinating subject, and we hope to be able to present our results in a future publication.

Finally, it is relevant to comment on the applicability of the herein presented results acquired on surface cells with extremely large (mm-sized) interelectrode gaps for the operation of more common-place sandwich cells with significantly smaller (sub-μm sized) interelectrode gaps. First, we propose that the main result of this study – the importance of employing device constituents that are electrochemically inert in the voltage range spanned by the oxidation and reduction potential of the CP – is applicable also for the operation of thin sandwich cells. We base this statement on the fact that the electrochemical reactions in LECs take place at interfaces between an electrode/doped CP and an undoped CP, and that the structure of these interfaces to a good approximation should be independent on the size of the interelectrode gap. Moreover, the herein studied wide-gap devices were invariably operated at a low applied voltage of 5 V, which is of a similar magnitude as the voltage used to drive sandwich cells. This implies that both the structural environment and the E-field at the interface at which the electrochemical reactions take place are rather similar in sandwich and surface cells. Second, the observed connection between a high ionic conductivity and a small phase separation between the CP and the electrolyte component in the active material is independent on the size of the interelectrode gap, and as such applicable for the operation of thin sandwich cells. Third, the fact that a high doping concentration (~0.1 dopants/CP repeat unit) is necessary in order for a doping front to progress in a wide-gap surface cell LEC should in principle also be applicable for the operation of thin sandwich cells. However, the fact that the exact thickness (and structure) of the p–n junction in surface cells is unknown is a complicating factor, since it could very well be that the thickness is of a similar, or even larger, size than the entire inter-electrode gap in thin sandwich cells. In such a scenario, it is unclear whether the observed high doping concentrations in the doped regions of surface cells exist in thin sandwich cells. This latter point also reinforces that further experimental, analytical and modelling studies on the detailed structure of the p–n junction region are needed in order to further improve the understanding and performance of LECs.

5. Conclusions

Our results clearly highlight the fact that LECs are electrochemical devices, and as such are highly sensitive to non-desired electrochemical reactions involving other device constituents than the CP, notably the electrolyte and the electrodes. The six investigated CPs all fulfill the baseline criteria for LEC operation in that they are capable of both p- and n-type electrochemical doping. However, when we optically probe planar wide-gap Au/{CP + PEO + KCF_3SO_3}/Au devices fabricated from these six CPs during operation at $V = 5$ V, we find that only three devices exhibit p–n junction formation and light emission, while the other three only exhibit n-type doping and no signs of p-type doping. Using CV, we establish that the CPs in the functional devices consistently have a lower p-type doping potential than the CPs in the non-functional devices, and that the critical oxidation stability potential of the {PEO + KCF_3SO_3} electrolyte is located in the same voltage range. Consequently, we propose that the operation of the non-functional LEC comprises n-type doping of the CP at the cathode and irreversible oxidation of the electrolyte at the anode. We also find that a small degree of phase separation between the CP and the {PEO + KCF_3SO_3} electrolyte components in the active material corresponds to a high ionic conductivity, and that the doping concentrations in the doped regions of all investigated LECs exhibit values of the order of ~0.1 dopants/CP repeat unit.

Acknowledgement

This research at Umeå University is supported by Vetenskapsrådet, Magn. Bergvalls stiftelse, and Stiftelsen J. Gust. Richert

References

[1] H.J. Bolink et al, Origin of the large spectral shift in electroluminescence in a blue light emitting cationic iridium(III) complex, Journal of Materials Chemistry 17 (48) (2007) 5032–5041.
[2] J.D. Slinker et al, Direct measurement of the electric-field distribution in a light-emitting electrochemical cell, Nature Materials 6 (11) (2007) 894–899.
[3] M.K. Nazeeruddin, M. Gratzel, Transition metal complexes for photovoltaic and light emitting applications, Photofunctional Transition Metals Complexes (2007) 113–175.
[4] J.D. Slinker et al, Electroluminescent devices from ionic transition metal complexes, Journal of Materials Chemistry 17 (29) (2007) 2976–2988.
[5] H.C. Su et al, Highly efficient orange and green solid-state light-emitting electrochemical cells based on cationic Ir-III complexes with enhanced steric hindrance, Advanced Functional Materials 17 (6) (2007) 1019–1027.

[6] H.J. Bolink et al, Stable single-layer light-emitting electrochemical cell using 4,7-diphenyl-1,10-phenanthroline-bis(2-phenylpyridine) iridium(III) hexafluorophosphate, Journal of the American Chemical Society 128 (46) (2006) 14786–14787.
[7] M.K. Nazeeruddin et al, Efficient green–blue-light-emitting cationic iridium complex for light-emitting electrochemical cells, Inorganic Chemistry 45 (23) (2006) 9245–9250.
[8] Q.S. Zhang et al, Highly efficient electroluminescence from green-light-emitting electrochemical cells based on Cu–I complexes, Advanced Functional Materials 16 (9) (2006) 1203–1208.
[9] N. Armaroli et al, Highly luminescent Cu–I complexes for light-emitting electrochemical cells, Advanced Materials 18 (10) (2006) 1313–1316.
[10] W. Zhao et al, Effect of residual solvent on $Ru(bpy)^3(ClO_4)^2$-based light-emitting electrochemical cells, Chemistry of Materials 17 (25) (2005) 6403–6406.
[11] A.B. Tamayo et al, Cationic bis-cyclometalated iridium(III) diimine complexes and their use in efficient blue, green, and red electroluminescent devices, Inorganic Chemistry 44 (24) (2005) 8723–8732.
[12] G. Kalyuzhny et al, Stability of thin-film solid-state electroluminescent devices based on tris(2,2'-bipyridine)ruthenium(II) complexes, Journal of the American Chemical Society 125 (20) (2003) 6272–6283.
[13] M. Buda, G. Kalyuzhny, A.J. Bard, Thin-film solid-state electroluminescent devices based on tris(2,2'-bipyridine)ruthenium(II) complexes, Journal of the American Chemical Society 124 (21) (2002) 6090–6098.
[14] M.T. Xianshun Zeng, F. Perepichka Igor, Andrei S. Batsanov, R. Bryce Martin, Chien-Jung Chiang, Rothe Carsten, P. Monkman Andrew, Cationic bis-cyclometallated iridium(III) phenanthroline complexes with pendant fluorenyl substituents: synthesis, redox, photophysical properties and light-emitting cells, Chemistry – A European Journal 14 (3) (2008) 933–943.
[15] J.S. Wilson et al, Supramolecular complexes of conjugated polyelectrolytes with poly(ethylene oxide): multifunctional luminescent semiconductors exhibiting electronic and ionic transport, Advanced Materials 17 (22) (2005) 2659.
[16] F.P. Wenzl et al, Thin film morphology and ion interaction behaviour of functional polymers for iontronic applications, Electrochimica Acta 52 (21) (2007) 6229–6236.
[17] Y. Shao, G.C. Bazan, A.J. Heeger, Long-lifetime polymer light-emitting electrochemical cells, Advanced Materials 19 (3) (2007) 365.
[18] L. Edman, Bringing light to solid-state electrolytes: the polymer light-emitting electrochemical cell, Electrochimica Acta 50 (19) (2005) 3878–3885.
[19] L.S.C. Pingree et al, Scanning kelvin probe imaging of the potential profiles in fixed and dynamic planar LECs, Journal of the American Chemical Society 129 (51) (2007) 15903–15910.
[20] S. Sax et al, Intrinsic electrochemical doping in blue light emitting polymer devices utilizing a water soluble anionic conjugated polymer, Organic Electronics 8 (6) (2007) 791–795.
[21] D.T. Simon, D.B. Stanislowski, S.A. Carter, Fixed p–i–n junction polymer light-emitting electrochemical cells based on charged self-assembled monolayers, Applied Physics Letters 90 (10) (2007).
[22] Y.F. Hu, J. Gao, Cationic effects in polymer light-emitting electrochemical cells, Applied Physics Letters 89 (25) (2006).
[23] J.M. Leger, D.B. Rodovsky, G.R. Bartholomew, Self-assembled, chemically fixed homojunctions in semiconducting polymers, Advanced Materials 18 (23) (2006) 3130.
[24] C. Tracy, J. Gao, Polymer bulk homojunction light-emitting electrochemical cells, Journal of Applied Physics 100 (10) (2006).
[25] F. Habrard, T. Ouisse, O. Stephan, Conjugated polymer/molten salt blend optimization, Journal of Physical Chemistry B 110 (31) (2006) 15049–15051.
[26] F. Kong et al, Fast response single-ion transport light-emitting electrochemical cell based on PPV derivative, Journal of Applied Polymer Science 101 (6) (2006) 4253–4255.
[27] J.H. Shin, S. Xiao, L. Edman, Polymer light-emitting electrochemical cells: The formation and effects of doping-induced micro shorts, Advanced Functional Materials 16 (7) (2006) 949–956.
[28] Z. Gu et al, Dual electroluminescence from a single-component light-emitting electrochemical cell, based on water-soluble conjugated polymer, Journal of Applied Polymer Science 100 (4) (2006) 2930–2936.
[29] J.M. Leger, S.A. Carter, B. Ruhstaller, Recombination profiles in poly 2-methoxy-5-(2-ethylhexyloxy)-1,4-phenylenevinylene light-emitting electrochemical cells, Journal of Applied Physics 98 (12) (2005).
[30] G. Mauthner et al, Inkjet printed surface cell light-emitting devices from a water-based polymer dispersion, Organic Electronics 9 (2) (2008) 164–170.
[31] Q.B. Pei et al, Polymer light-emitting electrochemical-cells, Science 269 (5227) (1995) 1086–1088.
[32] Y. Yang, Q.B. Pei, Efficient blue–green and white light-emitting electrochemical cells based on poly 9,9-bis(3,6-dioxaheptyl)-fluorene-2,7-diyl, Journal of Applied Physics 81 (7) (1997) 3294–3298.
[33] J.C. deMello et al, Ionic space–charge effects in polymer light-emitting diodes, Physical Review B 57 (20) (1998) 12951–12963.
[34] L. Edman et al, Single-component light-emitting electrochemical cell fabricated from cationic polyfluorene: effect of film morphology on device performance, Journal of Applied Physics 98 (4) (2005) 044502.
[35] J.H. Shin et al, Polymer light-emitting electrochemical cells: doping concentration, emission-zone position, and turn-on time, Advanced Functional Materials 17 (11) (2007) 1807–1813.
[36] J.H. Shin et al, Light emission at 5 V from a polymer device with a millimeter-sized interelectrode gap, Applied Physics Letters 89 (1) (2006) 013509.
[37] J.H. Shin et al, The influence of electrodes on the performance of light-emitting electrochemical cells, Electrochimica Acta 52 (23) (2007) 6456–6462.
[38] When $V < E_g/e$, only EDL formation (or EDL formation followed by limited unipolar doping) will take place, since bipolar doping is not energetically possible.
[39] A. Iwasiewicz-Wabnig et al, Variable-force tapping atomic force microscopy as a tool in the characterization of organic devices, Ultramicroscopy 107 (10–11) (2007) 1078–1085.
[40] L. Sardone et al, Scanning force microscopy and optical spectroscopy of phase-segregated thin films of poly(9,9′-dioctylfluorene-alt-benzothiadiazole) and poly(ethylene oxide), Journal of Materials Chemistry 17 (14) (2007) 1387–1391.
[41] L. Sardone et al, Phase segregation in thin films of conjugated polyrotaxane-poly(ethylene oxide) blends: a scanning force microscopy study, Advanced Functional Materials 17 (6) (2007) 927–932.
[42] F.P. Wenzl et al, The influence of the phase morphology on the optoelectronic properties of light-emitting electrochemical cells, Advanced Functional Materials 14 (5) (2004) 441–450.
[43] M.A. Summers, S.K. Buratto, L. Edman, Morphology and environment-dependent fluorescence in blends containing a phenylenevinylene-conjugated polymer, Thin Solid Films 515 (23) (2007) 8412–8418.
[44] J. Morgado et al, Light-emitting devices based on a poly(*p*-phenylene vinylene) derivative with ion-coordinating side groups, Journal of Applied Physics 86 (11) (1999) 6392–6395.
[45] M.R. Andersson, G. Yu, A.J. Heeger, Photoluminescence and electroluminescence of films from soluble PPV-polymers, Synthetic Metals 85 (1–3) (1997) 1275–1276.
[46] F. Hide et al, Semiconducting polymers: a new class of solid-state laser materials, Science 273 (5283) (1996) 1833–1836.
[47] D.M. Johansson et al, Synthesis of soluble phenyl-substituted poly(*p*-phenylenevinylenes) with a low content of structural defects, Macromolecules 35 (13) (2002) 4997–5003.
[48] D.M. Johansson et al, Synthesis and characterization of highly soluble phenyl-substituted poly(*p*-phenylenevinylenes), Macromolecules 33 (7) (2000) 2525–2529.
[49] J. Gao, J. Dane, Visualization of electrochemical doping and light-emitting junction formation in conjugated polymer films, Applied Physics Letters 84 (15) (2004) 2778–2780.
[50] Y.G. Zhang, J. Gao, Lifetime study of polymer light-emitting electrochemical cells, Journal of Applied Physics 100 (8) (2006).
[51] Y.G. Zhang, Y.F. Hu, J. Gao, Improving the efficiency of polymer light-emitting electrochemical cells by controlled doping relaxation, Applied Physics Letters 88 (16) (2006).
[52] J.F. Fang, N.D. Robinson, L. Edman, Identifying and alleviating electrochemical side-reactions in light-emitting electrochemical cells, Journal of the American Chemical Society 130 (2008) 4562–4568.
[53] N.D. Robinson et al, Doping front propagation in light-emitting electrochemical cells, Physical Review B 74 (15) (2006) 155210.
[54] T. Wågberg et al, On the limited operational lifetime of light-emitting electrochemical cells, Advanced Materials 20 (2008) 1744–1749.
[55] J.H. Shin, L. Edman, Light-emitting electrochemical cells with millimeter-sized interelectrode gap: low-voltage operation at room

temperature, Journal of the American Chemical Society 128 (49) (2006) 15568–15569.
[56] J. Gao, J. Dane, Imaging the doping and electroluminescence in extremely large planar polymer light-emitting electrochemical cells, Journal of Applied Physics 98 (6) (2005).
[57] D.J. Dick et al, Imaging the structure of the p–n junction in polymer light-emitting electrochemical cells, Advanced Materials 8 (12) (1996) 985–987.
[58] L. Edman et al, Polymer light-emitting electrochemical cells: doping, luminescence, and mobility, Physical Review B 70 (11) (2004) 115212.
[59] Q.B. Pei et al, Polymer light-emitting electrochemical cells: In situ formation of a light-emitting p–n junction, Journal of the American Chemical Society 118 (16) (1996) 3922–3929.
[60] Y. Kaminorz et al, Characteristics of polythiophene surface light emitting diodes, Synthetic Metals 113 (1–2) (2000) 103–114.
[61] Y. Kunugi et al, Charge transport in a regioregular poly(3-octylthiophene) film, Journal of Materials Chemistry 10 (12) (2000) 2673–2677.
[62] X.Q. Jiang et al, Influences of self-assembled structure on mobilities of charge carriers in pi-conjugated polymers, Journal of Physical Chemistry B 109 (1) (2005) 221–229.
[63] Y. Harima et al, Influence of film structure on mobilities of charge carriers in conducting polymers, Electrochimica Acta 52 (28) (2007) 8088–8095.
[64] H. Shimotani, G. Diguet, Y. Iwasa, Direct comparison of field-effect and electrochemical doping in regioregular poly(3-hexylthiophene), Applied Physics Letters 86 (2) (2005).
[65] V. Syritski, A. Opik, O. Forsen, Ion transport investigations of polypyrroles doped with different anions by EQCM and CER techniques, Electrochimica Acta 48 (10) (2003) 1409–1417.

Organic Electronics 9 (2008) 711–720

Contents lists available at ScienceDirect

Organic Electronics

journal homepage: www.elsevier.com/locate/orgel

Hybridization of a low-temperature processable polyimide gate insulator for high performance pentacene thin-film transistors

Taek Ahn *, Jin Woo Kim, Yoojeong Choi, Mi Hye Yi*

Information and Electronics Polymer Research Center, Korea Research Institute of Chemical Technology, 100 Jang-dong, Yuseong, Daejon 305-600, Republic of Korea

ARTICLE INFO

Article history:
Received 3 December 2007
Received in revised form 5 February 2008
Accepted 6 May 2008
Available online 13 May 2008

PACS:
72.80.Le
72.80.Sk

Keywords:
Organic gate insulator
Polyimide
Pentacene thin-film transistor
Hybridization

ABSTRACT

We have synthesized a novel fully soluble and low-temperature processable polyimide gate insulator (KSPI) through the one-step condensation polymerization of the monomers 5-(2,5-dioxytetrahydrofuryl)-3-methyl-3-cyclohexene-1,2-dicarboxylic anhydride and 4,4-diaminodiphenylmethane. Fully imidized KSPI was found to be completely soluble in organic solvents such as *N*-methyl-2-pyrrolidone (NMP), dimethylacetamide (DMAc), γ-butyrolactone, dimethylsulfoxide (DMSO), and 2-butoxyethanol. Thin films of KSPI can be fabricated at only 150 °C and a pentacene OTFT with KSPI as a gate dielectric was found to exhibit a field effect mobility of 0.22 cm^2/V s. To obtain a high performance organic thin-film transistor (OTFT), the KSPI surface was modified in our new technique by hybridization with a non-polar side chain containing a polyimide insulator (PI). The carrier mobility of a pentacene OTFT with a hybridized polyimide gate insulator (BPI-3) was found to be 0.92 cm^2/V s. Our new low-temperature processable polyimides show promise as gate dielectrics for OTFTs.

1. Introduction

Flexible organic electronic devices containing organic thin-film transistors (OTFTs) have received much attention of late due to the potential of this technology in smart cards, radio frequency identification (RFID) tags, nonvolatile memories, sensors, and driver circuits in flexible displays [1–10]. The significant advantage of using organic materials in electronic devices is the possibility of fabricating mechanically flexible devices on flexible substrates. However, in order for this so-called flexible technology to move forward, flexible gate dielectric materials must be developed and the performance of devices containing such materials must be optimized. However, most studies of OTFTs have employed silicon dioxide/heavily doped silicon as the insulator/gate pair. To realize flexible organic electronics, not only the organic semiconductor [11–15] but also all other components of the TFT need to be replaced with organic materials. There is therefore increasing interests in using polymeric materials as gate dielectrics in OTFTs [16–23]. The requirements of an OTFT polymeric gate dielectric are as follows: (1) a relatively high dielectric constant, (2) good heat and chemical resistance, (3) they should form pinhole-free thin films with a high breakdown voltage and long-term stability, and (4) their interfacial properties should be comparable to those of organic semiconductors. Most research into polymeric gate dielectrics has attempted to improve the performance of OTFTs by reducing the leakage current and threshold voltage or by increasing the current modulation ratio and mobility through modifications of the surface properties and variation of the dielectric constant of the gate insulator. Several polymeric gate dielectrics, such as poly(vinyl phenol) (PVP) [16,17], poly(methyl methacrylate) (PMMA) [18], poly-(vinyl alcohol) (PVA) [19,20], benzocyclobutene (BCB) [21], and polyamic acid (PAA) based polyimide (PI)

* Corresponding authors. Tel.: +82 42 860 7331; fax: +82 42 861 4151.
E-mail addresses: taekahn@krict.re.kr (T. Ahn), mhyi@krict.re.kr (M.H. Yi).

1566-1199/$ - see front matter © 2008 Elsevier B.V. All rights reserved.
doi:10.1016/j.orgel.2008.05.003

[22–26], have been investigated. Of these materials, PIs are currently considered promising gate dielectrics because of their good chemical resistance and mechanical properties. However, a major obstacle to the use of PI materials is their high processing temperature. We recently reported a new hybridization method for the modification of the surfaces of PI gate dielectrics. With this approach, a PI gate dielectric was fabricated that can be thermally treated at a minimum of 230 °C to fabricate a thin film for use in an OTFT [22]. To apply a polymeric gate insulator on a plastic substrate, the processing temperature for producing a thin film of that gate insulator should be below 200 °C. Thus, the processing temperature (of 230 °C) required to convert a polyamic-acid-based PI film into a fully imidized PI film is too high for flexible organic electronics applications.

In this paper, we report the synthesis and characterization of a new fully soluble polyimide (KSPI) for use as a gate insulator in OTFTs. KSPI was successfully synthesized with a simple one-step condensation polymerization [27] of the monomers 5-(2,5-dioxytetrahydrofuryl)-3-methyl-3-cyclohexene-1,2-dicarboxylic anhydride and 4,4-diaminodiphenylmethane. The fully imidized KSPI is soluble in *N*-methyl-2-pyrrolidone (NMP), dimethylacetamide (DMAc), γ-butyrolactone, dimethylsulfoxide (DMSO), and 2-butoxyethanol, and KSPI thin films can be fabricated with an annealing temperature of 150 °C. We fabricated pentacene OTFTs with KSPI and showed that the performance of these OTFTs can be improved by modifying the surface of the gate insulator with our hybridization technique. The new soluble polyimide (KSPI) was hybridized with a non-polar side chain containing polyimide (PI) [22] in the feed ratio KSPI/PI = 98/2 (BPI-3). The OTFT characteristics and electrical properties of this fully soluble polyimide gate insulator are discussed.

2. Experimental

2.1. Materials and measurements

4,4-Diaminodiphenylmethane was purchased from Mitsubishi Kasei Chemical Co. (Japan) and 5-(2,5-dioxytetrahydrofuryl)-3-methyl-3-cyclohexene-1,2-dicarboxylic anhydride was purchased from TCI Chemical Co. (Japan). Both compounds were dried at 100 °C for 24 h in a vacuum oven prior to use. *m*-Cresol was received from Junsei Chemical Co. (Japan) and freshly distilled under reduced pressure before use. All other chemicals required for the synthesis and purification of the monomers and polymer were also commercially available and used without any further purification. The active layer selected in this study was pentacene (98% purity), which was purchased from Aldrich Chemical Co. and used without any further purification. The solution viscosity of the polymer was measured with a Cone & Plate viscometer (Thermo HAA-KEDC 50) at 25 °C in air. The inherent viscosity of the polymer was measured with Ubbelohde viscometer at a concentration of 0.5 dL/g in NMP at 30 °C. To investigate the molecular weight of the synthesized polymer, high temperature gel permeation chromatography (GPC) analysis was conducted on a Waters Model 150C ALC/GPC equipped with Styragel columns in DMF solution at 80 °C. The ^{1}H NMR spectrum was recorded with a Bruker AMX 300 MHz spectrometer. Dimethylsulfoxide (DMSO) was used as the solvent for recording the NMR spectrum. The elemental analysis of the newly synthesized polyimide gate insulator polymer was performed on a FISONS EA-1108. The FT-IR spectrum was obtained with a Bio-Rad Digilab Division FTS-165 spectrometer after dispersing the sample in KBr. The thermal properties of the synthesized polymer were investigated with differential scanning calorimetry (DSC) and thermogravimetric analysis (TGA) performed under nitrogen at a heating rate of 10 °C/min with a Du Pont Model 910 analyzer and a Perkin–Elmer TGA 7 analyzer, respectively. The thicknesses of the polymer films were determined with an alpha-step (KLA-Tencor α-step DC 50) surface profiler. All atomic force microscopy (AFM) images of the polymer surfaces were obtained with a Digital Instrument Nanoscope IV operating in tapping mode in air using a low-force imaging technique (a small tip-sample contact area), which is useful in the high-resolution imaging of polymers. The surface tension was calculated from the contact angles of water and diiodomethane on the polymer films, which were determined with a PEONIX 300 contact angle analyzer. The output (I_{ds} vs. V_{ds}) and transfer (I_{ds} vs. V_{gs}) characteristics of the OTFT devices were measured with an Agilent E5272 semiconductor parameter analyzer. The capacitance was measured with a HP 4294A LCR meter. All these electrical measurements were carried out in air without any encapsulation.

2.2. Synthesis of the soluble polyimide (KSPI)

In a 500 mL three-neck flask containing 100 mL *m*-cresol, 5-(2,5-dioxytetrahydrofuryl)-3-methyl-3-cyclohexene-1,2-dicarboxylic anhydride (14.2 g, 54.0 mmol) and 4,4-diaminodiphenylmethane (10.7 g, 54.0 mmol) were dissolved by using a mechanical stirrer. Once the two monomers were completely dissolved, the reaction mixture was slowly heated to 70 °C over 2 h with an oil bath and maintained at that temperature for 2 h. The reaction temperature was increased to 200 °C over a 2 h period and finally fixed at 200 °C at which temperature the reaction mixture was refluxed. When the solution viscosity reached to 5000 cps (which required about 30 min after the temperature had reached 200 °C), the reaction was stopped by removing the oil bath and cooling the solution to room temperature. The polyimide (KSPI) was precipitated by adding reaction mixture dropwise to the ice-cooled excess methanol. The mixture was washed several times with methanol and filtered, and the KSPI was dried under vacuum. The KSPI was dissolved in *m*-cresol, and the KSPI was precipitated again by dropping it into an excess methanol. The mixture was filtered and the residue was collected. The procedure was repeated twice more to yield a yellowish solid. The polymer yield was 91% (21.0 g). FT-IR (KBr) ν_{max} (cm^{-1}): 3467, 3038, 2922, 1709 (C=O stretching of carbonyl), 1510 (C=C stretching of phenyl), 1380 (C–N stretching of imide), 1172, 813, 765, 665. ^{1}H NMR (DMSO, ppm): δ 7.33–7.09 (br m, 8H, Aromatic H), 5.48 (br s, 1H, CH of cyclohexene), 4.01 (br s, 2H, CH_2), 3.76–3.55 (br m, 1H, alpha CH of cyclohexene), 2.90–2.87 (br m, 4H, CH and CH_2 of succinimide, and beta CH of cyclohexene), 2.17–1.90 (br m, 6H, gamma CH_2 and

delta CH of cyclohexene, and CH_3). Anal. Calcd. for $C_{26}H_{22}O_4N_2$: C, 73.23; H, 5.20; O, 15.01; N, 6.57. Found. C, 72.58; H, 5.22; O, 15.44; N, 6.46.

2.3. Metal–insulator–metal (MIM) device fabrication

To determine the capacitance and gate leakage of the soluble and hybridized polyimide gate insulators, metal–insulator–metal (MIM) capacitor structures were prepared on patterned ITO coated glass substrates. Fully soluble KSPI and hybridized insulators (KSPI/PI in various ratios) were spin coated on top of the bottom ITO electrode and then the films were annealed at 90 °C for 10 min and at 150 °C for 30 min. The MIM devices were then completed by evaporating the top gold electrodes. The final thicknesses of all films were controlled to 300 nm. The active area of each MIM device was 50.24 mm^2.

2.4. Organic TFT device fabrication

A top-contact OTFT device geometry was used in all the electrical characterizations. Indium tin oxide (ITO) coated glass was used as the substrate and the ITO was patterned (2 mm wide stripes) to produce the gate electrode with a conventional photolithographic method: coating with a photoresist, ultraviolet light exposure, then developing and etching. The patterned ITO substrate was cleaned using a typical cleaning process for electronic applications: sonication in detergent, deionized water, acetone, and isopropanol in that order for 20 min at room temperature. KSPI was dissolved in a γ-butyrolactone/2-butoxyethanol co-solvent at a concentration of 8 wt%. In addition, a hybridized polyimide solution (KSPI/PI = 98/2) was prepared in the same co-solvent at the same concentration. The KSPI and hybridized BPI-3 solutions were spin-coated on top of the gate electrodes as gate insulators and the films were then annealed at 90 °C for 10 min and at 150 °C for 30 min. The final thickness of the polyimide gate insulator was adjusted to about 300 nm. A 60 nm thick layer of pentacene was deposited on top of the gate insulator through a shadow mask by using thermal evaporation at a pressure of 1×10^{-6} torr. The evaporation rate of pentacene was 1 Å/s and the substrate temperature was 90 °C. The OTFTs were then completed by using thermal evaporation to add 50 nm thick source and drain gold electrodes on top of the pentacene layer through a shadow mask, creating transistors with a channel length (L) and a width (W) of 50 and 1000 μm respectively.

2.5. Organic TFT devices on plastic substrates

Pentacene OTFTs on a polyethersulfone (PES) plastic substrate were also fabricated using KSPI and BPI-3. Gold (50 nm) was deposited on each polyethersulfone substrate through a shadow mask, thus creating a patterned gold electrode as the gate electrode. The polyimide insulator coating, pentacene evaporation, and source and drain electrode formation processes were carried out as for the fabrication of the OTFT devices on glass substrates.

3. Results and discussion

3.1. Syntheses and characterizations of the polymers

The synthetic routes and chemical structures of KSPI and PI are presented in Scheme 1. KSPI was synthesized with a one-step condensation polymerization [27] in *m*-cresol. The synthesis of PI has been reported previously by our group and was carried out as described [22]. PI can be classified in two categories namely, polyamic-acid-based PI which requires a high processing temperature (above 230 °C) and fully soluble PI-the final imidized state. To produce soluble PI, either long alkyl side chains should be introduced or the main chain of the polymer should be modified to adopt a kinked structure. KSPI is a fully soluble polymer. Actually, the 5-(2,5-dioxytetrahydrofuryl)-3-methyl-3-cyclohexene-1,2-dicarboxylic anhydride unit in KSPI is a key monomer which makes it soluble in organic solvents. In that monomer, dicarboxylic anhydride is linked to 3-methyl-3-cyclohexene forming a kinked structure. The linkage can make PSPI become soluble in the fully imidized state. The unit 5-(2,5-dioxytetrahydrofuryl)-3-methyl-3-cyclohexene-1,2-dicarboxylic anhydride is a key monomer in the synthesis of KSPI, making it soluble in organic solvents. In that monomer, dicarboxylic anhydride is linked to 3-methyl-3-cyclohexene forming a kinked structure. The linkage can make KSPI soluble in the fully imidized state.

KSPI was found to be soluble in organic solvents such as *N*-methyl-2-pyrrolidone (NMP), dimethylacetamide

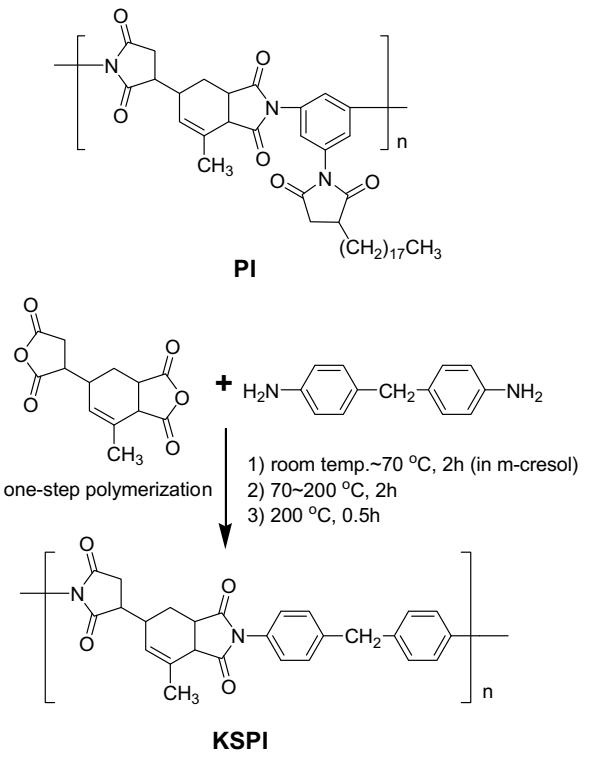

Scheme 1. Chemical structures and synthetic routes for PI and KSPI.

(DMAc), γ-butyrolactone, dimethylsulfoxide (DMSO), and 2-butoxyethanol. The number-average molecular weight (M_n) and the weight-average molecular weight (M_w) of KSPI were determined with high temperature gel permeation chromatography using polystyrene standards and DMF as an eluent, and found to be 40,000 g/mol and 85,000 g/mol, respectively, with a polydispersity index of 2.13. The inherent viscosity of KSPI was found to be 0.56 dL/g. The structure of KSPI was determined with FT-IR and ^{1}H NMR spectroscopy. The ^{1}H NMR spectrum (not shown here) of KSPI was found to contain signal broadening, but the chemical shifts are consistent with the structure of KSPI. The assignments for the ^{1}H NMR spectrum of KSPI are documented in Section 2. The amide proton peaks of poly(amic acid) were not detected at 10.0–10.5 ppm for KSPI, which means that the synthesis of KSPI with the one-step polymerization resulted in a fully imidized and completely polymerized main chain structure [27]. Fig. 1 shows the FT-IR spectrum of KSPI. The very sharp peak at 1380 cm^{-1} in the FT-IR spectrum is due to the imide C–N stretching of KSPI [28]. This peak confirms that imidized and completely polymerized KSPI was obtained with the one-step condensation route. Carbonyl (C═O) and phenyl (C═C) stretching peaks are also present at 1709 and 1510 cm^{-1}, respectively. The thermal properties of KSPI were investigated with TGA and DSC analysis. Fig. 2 shows the TGA thermogram (the inset shows the DSC curve) of KSPI. KSPI has excellent thermal stability up to almost 400 °C. The 5% weight loss temperature for KSPI was found to be 424 °C. In addition to its high thermal stability, KSPI also exhibits good mechanical properties. The glass transition temperature was found to be 264 °C. Compared to other polymeric materials that are used as gate insulators such as poly(vinyl phenol) (PVP) [16,17], poly(methyl methacrylate) (PMMA) [18], and poly(vinyl alcohol) (PVA) [14,15], KSPI has a higher T_g even though it is fully soluble in organic solvents. The lifetime and reliable operation of OTFT devices are probably closely related to T_g and the thermal stability of the gate insulator polymer. We believe that KSPI is a better candidate than these other soluble polymeric materials for gate insulators because of its superior thermal and mechanical properties.

3.2. Thin-film characterizations

Firstly, we investigated the surface morphology and the coating properties of the new soluble polyimide gate insulator, KSPI, and of the hybridized polyimide insulators. We have previously described surface modifications with the hybridization method of two different types of polymers [22]. Thin films of the following hybridized insulators with various KSPI/PI ratios (blending ratio, wt%) were fabricated, in order to investigate the hydrophobicity and morphology of their surfaces: KSPI/PI (98/2) (BPI-3), KSPI /PI (95/5) (BPI-2), and KSPI /PI (90/10) (BPI-1). Fig. 3 shows the surface morphologies of KSPI and the hybridized polymer thin films. The KSPI film has good surface roughness with a root-mean-square value of about 0.28 nm. As in our previous results [22], there are unusual wormlike patterns in the AFM images of the surfaces of the hybridized films. These patterns indicate that there is phase inversion in the hybridized films, as discussed in our previous report. However, the surface roughness of the films of BPI-2 and BPI-1 is unsatisfactory, above 1.7 nm (as shown in Fig. 3), and significant leakage current (not shown here) from their metal–insulator–metal devices was observed. These results are somewhat different to our previous results [22] for hybrids of polyamic acid (PAA) and PI. We suggest that the different annealing temperatures of the hybridized films and the different chemical structures of the main polymers (KSPI and PAA) in these hybrids result in these differences. Thus there is only a narrow KSPI/PI blending ratio range that results in hybridized films that can be utilized as thin-film gate insulators in OTFTs. A KSPI/PI

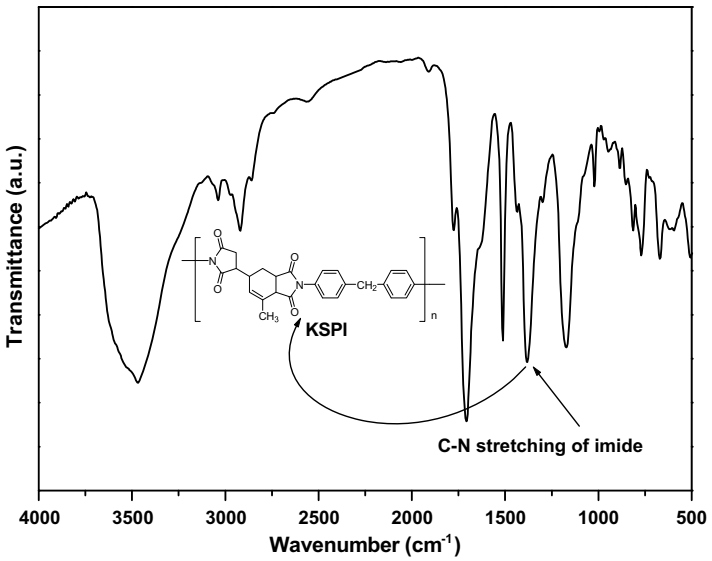

Fig. 1. FT-IR spectrum of KSPI.

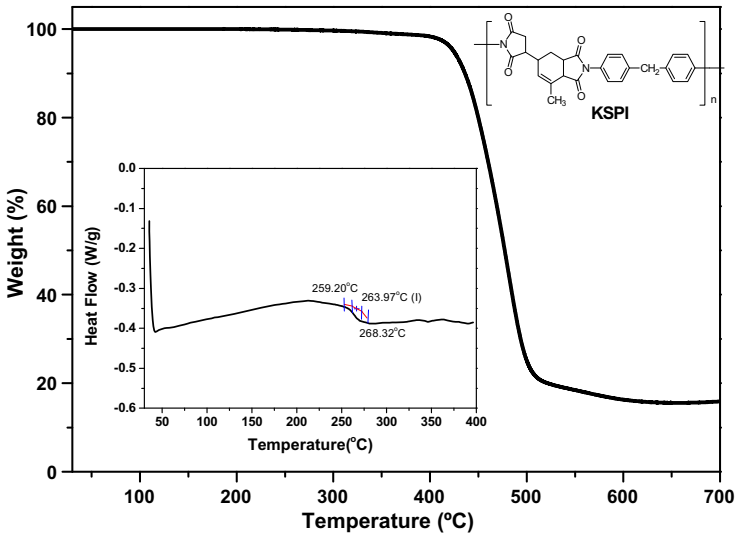

Fig. 2. TGA and DSC (inset) thermograms of KSPI.

blending ratio of 98/2 was found to provide the optimal gate insulator film. Thus the BPI-3 hybridized insulator (KSPI/PI = 98/2) was investigated in more detail and used as a gate insulator in OTFT device for comparison with KSPI.

To investigate the potential of KSPI and BPI-3 as gate insulators, we firstly checked whether their leakage currents are sufficiently low and their breakdown voltages sufficiently high by testing the corresponding metal–insulator–metal devices. Their leakage current densities and breakdown voltages were found to be less than 7.0×10^{-11} A/cm^2 at 50 V and above 2 MV/cm, respectively, which are satisfactory properties for gate insulators used in OTFTs. The capacitances of KSPI and BPI-3 were found to be 88.4 pF/mm^2 and 90.2 pF/mm^2, respectively. The root-mean-square roughness of the surfaces of the films were found to be almost identical, 0.28 nm and 0.39 nm, respectively, as shown in Fig. 3. However, the water contact angles and surface tensions of KSPI and BPI-3 are somewhat different, as expected. The surface tensions of KSPI and BPI-3 were calculated from the contact angles of water and diiodomethane and found to be 56.26 and 44.00 dyne/cm, respectively. The contact angle of water on BPI-3 is larger than that of KSPI. This means that by blending KSPI with a PI with a long alkyl side chain to create BPI-3 a more hydrophobic surface is produced. This surface modification approach is completely different from previously reported methods such as primer treatments using hexamethyldisilazane (HMDS) [29,30] or octadecyltrichlorosilane (OTS) [31–33] or the insertion of a buffer layer [34,35]. Our approach only requires a single spin-coating of the hybridized solution to complete the surface modification.

In our previous study, we used polyamic acid (PAA) as the main component of the hybridized polymer, with an annealing temperature of almost 250 °C required to convert the film to its fully imidized state [22]. In the BPI-3 system, the two polymers are completely soluble in the final imidized state so BPI-3 films can be produced by annealing at only 150 °C. This means that KSPI and BPI-3 insulators can be utilized in OTFTs with plastic substrates. The surface and electrical properties of the two films are summarized in Table 1.

Surface properties are known to influence the mechanism of the initial growth of pentacene and thus the performance of OTFTs [22,24,33,36]. AFM and X-ray diffraction (XRD) experiments were performed in order to investigate the effects of the surface properties of the gate insulators on the morphology of pentacene. AFM images of 60 nm thick pentacene on the gate insulators are shown in Fig. 4. The AFM images of 60 nm thick pentacene layers on KSPI reveal a dendritic structure with a grain size of around 0.5–1.5 μm (see Fig. 4a). The corresponding XRD pattern in Fig. 5a contains a series of sharp ($00k'$) peaks indicating that the pentacene film is highly ordered. The first peak at 5.68° (the thin-film phase) corresponds to a lattice parameter of 15.56 Å. However, no peak arising from a bulk phase was observed, indicating that the pentacene film on KSPI consists exclusively of the thin-film phase. On the other hand, the AFM image of 60 nm thick pentacene on BPI-3 does not indicate the presence of dendritic structures and its grain size is significantly lower, less than 0.5 μm (see Fig. 4b). The corresponding XRD pattern of pentacene in Fig. 5b also indicates the presence of both thin-film and bulk phases, at 5.71° and 6.07°, respectively. The measured Bragg refraction angles of 5.71° and 6.07° correspond to tilts of the *c* axis of the pentacene molecules with respect to the surface normal of 15.0° and 25.6°, respectively, indicating that the bulk phases are more tilted than the thin-film phase. The peak due to the bulk phase (6.07°) of pentacene on BPI-3 indicates that a significant fraction of the pentacene molecules are more tilted, which possibly increases the adhesion of the pentacene layer on the BPI-3 film. This increased adhesion has positive effects on the mechanism of the initial growth of pentacene and leads to the formation of a more stable

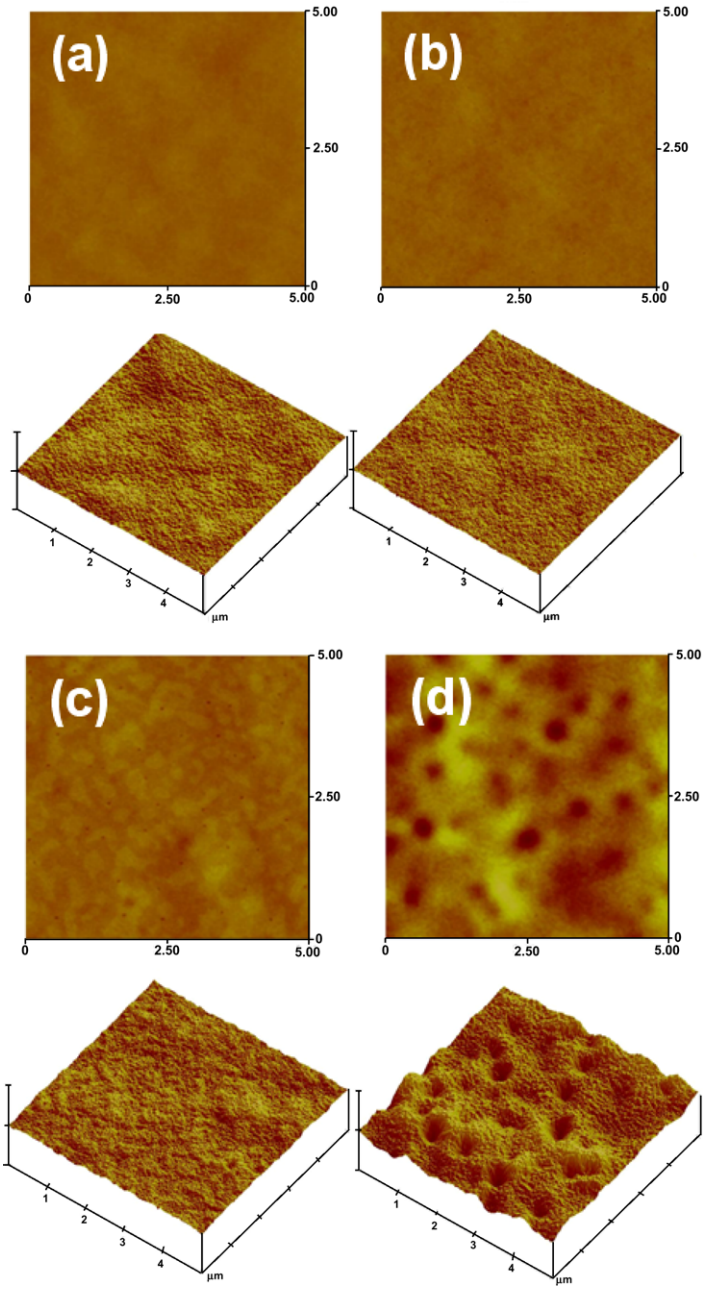

Fig. 3. AFM images (5 μm × 5 μm) of the gate insulators: (a) 100/0 (KSPI/PI in wt%, KSPI), (b) 98/2 (BPI-3), (c) 95/5 (BPI-2), and (d) 90/10 (BPI-1).

Table 1
Summary of the characteristics of KSPI and BPI-3

Gate insulator	Properties			
	Surface roughness (nm)	Surface tension (dyne/cm)[a]	Capacitance (pF/mm^2)[b]	Dielectric constant
KSPI	0.28	56.20	88.4	3.63
BPI-3	0.39	44.00	90.2	3.99

[a] Calculated from the contact angle of water and diiodomethane on the gate insulator film.
[b] Measured at 10 kHz.

interface on the BPI-3 insulator and to improved OTFT performance. Similar phenomena have been reported for the polyamic-acid-based hybrid insulator [22] and for an octadecyltrichlorosilane (OTS) treated gate insulator [32,33].

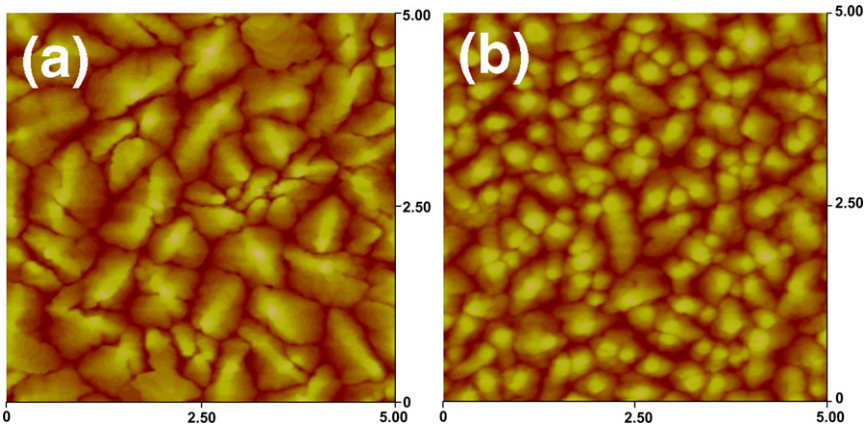

Fig. 4. AFM images (5 μm × 5 μm) of pentacene (60 nm) deposited on (a) KSPI and (b) BPI-3 insulators.

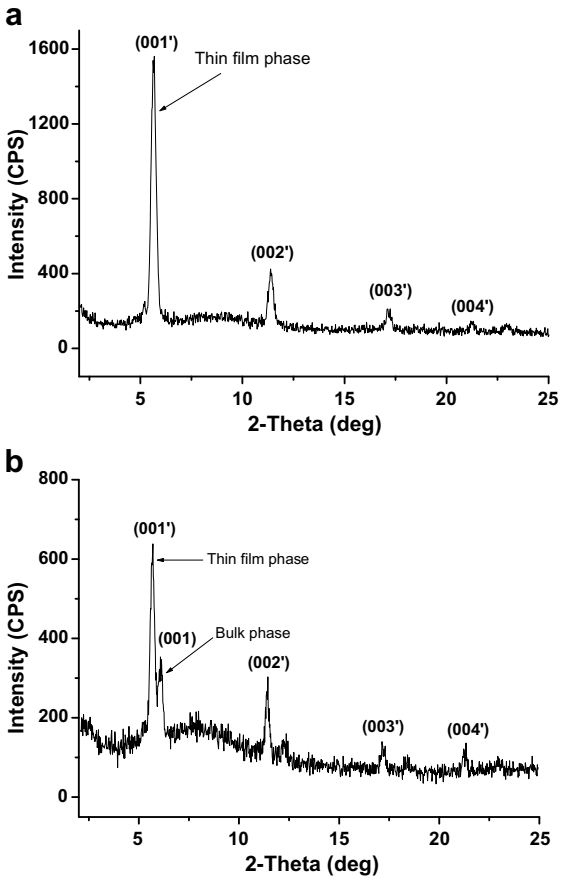

Fig. 5. X-ray diffraction patterns of pentacene deposited on 300 nm thick KSPI (a) and BPI-3 (b). The thickness of the pentacene layer was 60 nm. The deposition rate and substrate temperature were 1 Å/s and 90 °C, respectively.

3.3. TFT characteristics

Top-contact pentacene OTFTs with KSPI and BPI-3 as gate insulators were fabricated and their electrical characteristics were analyzed. The output characteristics (drain current vs. drain voltage, I_{ds} vs. V_{ds}) of the pentacene OTFTs (length L = 50 μm and width W = 1000 μm) with KSPI and BPI-3 are shown in Fig. 6 for various gate voltages. The OTFTs exhibit typical p-type characteristics with clear transitions from linear to saturation behavior. At a given negative gate voltage (V_{gs}), I_{ds} initially increases linearly with small negative V_{ds} and then saturates due to a pinch off of the accumulation layer. As the negative gate voltage (V_{gs}) increases, the device fabricated with a BPI-3 insulator exhibits a much higher drain current (I_{ds}) than the device with KSPI as an insulator. Fig. 7 shows the transfer characteristics (drain current vs. gate voltage, I_{ds} vs. V_{gs}) of the OTFTs with KSPI and BPI-3 where V_g was swept from +20 to −50 V and V_{ds} was set at −40 V. As shown in Fig. 7, the leakage current of the OTFTs with BPI-3 is lower by about one order of magnitude, 8.62×10^{-11} A, compared to 2.24×10^{-10} A for the OTFT with KSPI, and the subthreshold slope (SS) was also reduced from 3.78 to 2.27 V/dec. AFM studies (see Fig. 3) suggest that the BPI-3 system forms a film exhibiting a phase-inversion state. In other words, the BPI-3 system seems to be composed of a double-layer insulator structure which arises from the difference between the surface energies of the two polymers (KSPI and PI) in the hybrid state. The higher surface energy may facilitate the attachment of KSPI onto the ITO-patterned glass surface, and a PI thin layer is then formed on top of the KSPI layer. Therefore, the KSPI insulator can be covered with a PI polymer containing a nonpolar side chain. A similar concept and comparable phenomena were reported for surface-induced self encapsulation based on different solubilities of the hybrid polymers [37]. Consequently, the BPI-3 insulator can be obtained in the form of a more robust film relative to KSPI, which could be one of the reasons for the improved off current of the OTFT device.

The lower SS of the pentacene OTFT with BPI-3 indicates that there is a more stable interface and good contact between pentacene and BPI-3, which results from the modification of the surface of the gate insulator with the hybridization method. Since the interface charge state between an organic gate insulator and an organic semiconductor is one of the factors influencing SS [38,39], we

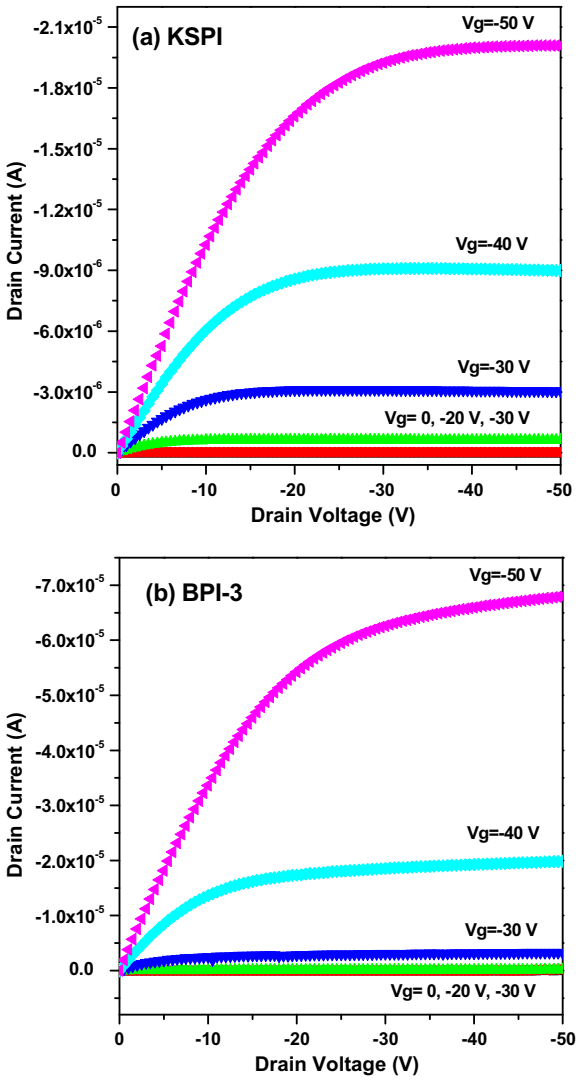

Fig. 6. Output characteristics (drain current vs. drain voltage, I_{ds} vs. V_{ds}) of OTFTs with KSPI (a) and BPI-3 (b).

believe that the lowered SS can be explained by the formation of a more stable interface between pentacene and the BPI-3 than between pentacene and KSPI. The field effect carrier mobility (μ) was extracted from a plot of $I_{ds}^{1/2}$ vs. V_{gs} in the saturation regime by using the following equation:

$$I_{ds} = \frac{WC_i}{2L}\mu(V_{gs} - V_T)^2$$

where C_i and V_T are the capacitance per unit area of the gate insulator and the threshold voltage, respectively. The carrier mobilities of the pentacene OTFTs with KSPI and BPI-3 were found to be 0.22 and 0.92 $cm^2/V\,s$, respectively. It is interesting to note that when the hybridized insulator (BPI-3) is used instead of KSPI as the gate insulator, the mobility increases by a factor of more than four even though the pentacene crystal size on BPI-3 is smaller (as shown in Fig. 4) and there is less dendritic structure than on KSPI. The overall device performance is improved dramatically by using the hybridized BPI-3 instead of KSPI as the insulator. The electrical characteristics of the pentacene OTFTs with KSPI and BPI-3 are summarized in Table 2. The performance of an OTFT can be affected by the grain size, orientation, and crystallinity of the organic semiconductor. It is clear that these properties are usually determined by the surface properties of the gate insulator, the evaporation rate of the semiconductor, the substrate temperature, the annealing process, etc [7,40,41]. If other properties are held constant a decrease in the grain size (increasing the grain boundary density) is usually thought to reduce the OTFT carrier mobility. This is contrary to our results and to some reports from other groups [7,33,40–42] that the grain size of pentacene is smaller on primer-treated gate insulators than on nontreated gate insulators, even though the overall performance of OTFTs with primer-treated gate insulators is better. In XRD studies, the peak due to the bulk phase of pentacene (at 6.07°) on our hybridized insulator indicates that a significant fraction of the pentacene molecules are lying flat on the insulator surface. Flat-lying pentacene was also observed when this material was deposited onto Cu [43,44], which implies an improved adhesion of pentacene to the insulator surface and contact between individual pentacene grains. We therefore conclude that the surface morphology and energy of the gate insulator are a further important influence on OTFT carrier mobility, because of their dramatic effect on the formation of the interface between the gate insulator and the semiconductor, which arises due to changes in the initial growth mechanism of pentacene.

In order to investigate the potential of the use of KSPI and BPI-3 in flexible OTFTs, we also fabricated and characterized OTFTs with KSPI and BPI-3 on polyethersulfone (PES) plastic substrates. The maximum processing temperature of KSPI and BPI-3 is only about 150 °C, so we were able to successfully fabricate flexible OTFTs using KSPI and BPI-3 as gate insulators on PES substrates. Patterned gold gate electrodes were used. Fig. 8 shows the transfer characteristics (drain current vs. gate voltage, I_{ds} vs. V_{gs}) of the flexible OTFTs with KSPI and BPI-3 on PES substrates, where V_g was swept from +20 to −50 V and V_{ds} was set at −40 V. The overall device performances (summarized in Table 2) of the flexible OTFTs such as the field effect mobility, the on/off ratio and the off current are somewhat worse than those of OTFT devices fabricated on glass substrates. However, the OTFT device with BPI-3 exhibits a better field effect mobility and a significantly lower subthreshold slope (SS) than the device with KSPI (in Table 2). The lower SS of the flexible OTFT with BPI-3 clearly indicates that a better interface between pentacene and BPI-3 is created by modifying the surface of the gate insulator with hybridization method. However, the off-current level of the BPI-3-based devices was slightly increased with respect to that of the KSPI-based ones. The reason for this is unclear. We believe that the increased off current observed for the devices formed on PES can be explained by the relatively bad surface roughness of the gate insulators formed on this plastic substrate. The handling of the plastic substrate in the preparation of a flexible OTFT is also a key influence

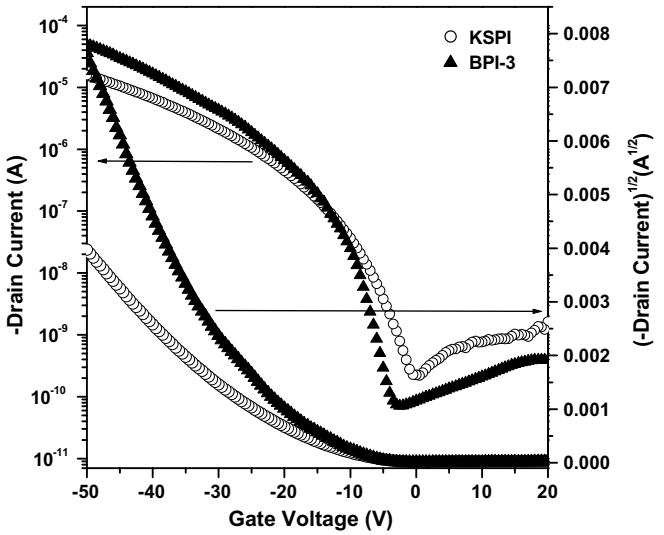

Fig. 7. Transfer characteristics (drain current vs. gate voltage, I_{ds} vs. V_{gs}, and square root of drain current vs. gate voltage, $I_{ds}^{1/2}$ vs. V_{gs}) of OTFTs with KSPI and BPI-3.

Table 2
Summary of the electrical characteristics of the pentacene OTFTs with KSPI and BPI-3 on glass and plastic substrate

Gate insulator	Performance parameter					
	Substrate	Mobility (μ)[b] (cm^2/V s)	I_{ON}/I_{OFF}[c]	Subthreshold slope (SS)	I_{OFF} (A)	Threshold voltage (V_{th})[d] (V)
KSPI (50/1000)[a]	Glass	0.22	6.9×10^4	3.78	2.24×10^{-10}	−17.6
BPI-3 (50/1000)[a]	Glass	0.92	5.7×10^5	2.27	8.62×10^{-11}	−20.8
KSPI (50/1000)[a]	Plastic	0.15	1.0×10^4	6.86	6.30×10^{-10}	−24.5
BPI-3 (50/1000)[a]	Plastic	0.25	1.4×10^4	5.54	8.40×10^{-10}	−25.7

[a] The ratio of length (L, μm) to width (W, μm).
[b] Calculated from the plot of I_{ds} vs. V_{gs} in the saturation regime by using the following relationship between the drain current and gate voltage: $I_{ds} = (WC_i/2L)\mu(V_{gs}-V_T)^2$. C_i is the capacitance of KSPI and BPI-3.
[c] The on/off ratio.
[d] V_T of the device in the saturation regime was determined from the plot of the square root of the drain current (I_{ds}) vs. the gate voltage (V_{gs}) by extrapolating the measured data to $I_{ds} = 0$.

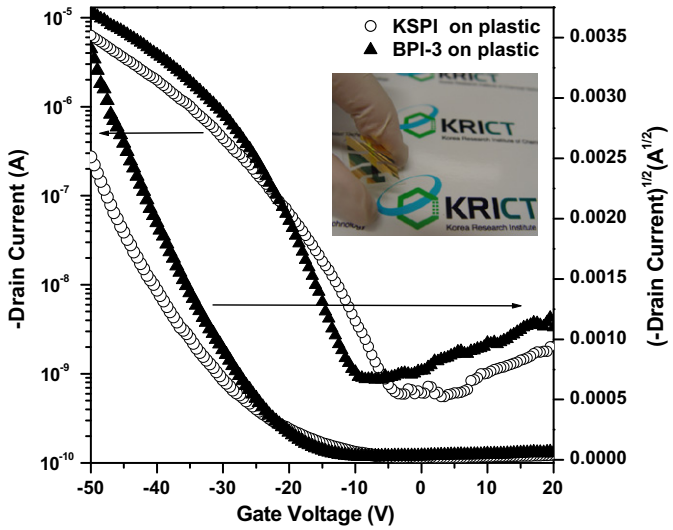

Fig. 8. Transfer characteristics (for drain current vs. gate voltage, I_{ds} vs. V_{gs}, and square root of drain current vs. gate voltage, $I_{ds}^{1/2}$ vs. V_{gs}) of OTFTs with KSPI and BPI-3 on plastic substrates. Inset: A flexible pentacene OTFT fabricated on a PES substrate.

on its performance, so we are currently optimizing the processing conditions used in the fabrication of flexible OTFTs with our newly developed gate insulators.

4. Conclusions

We have prepared a novel soluble polyimide gate insulator (KSPI) with a one-step condensation polymerization and fabricated high performance OTFTs with a hybridized gate insulator (BPI-3) on glass and plastic substrates. KSPI is completely soluble in organic solvents in the fully imidized state and forms thin films at an annealing temperature of 150 °C. An MIM device containing KSPI was found to exhibit low leakage current density and a high breakdown voltage. A pentacene OTFT with a KSPI gate insulator was found to exhibit good TFT performance with a mobility of 0.22 $cm^2/V\,s$. By carrying out the hybridization of KSPI with a PI with a long alkyl chain, we were able to modify its surface properties, which dramatically improve the formation of its interface with pentacene. The hydrophobic surface resulting from the incorporation of the PI with a long alkyl side chain results in an increase in the number of flat-lying pentacene molecules and increases the adhesion between the pentacene layer and the gate insulator, which has a positive effect on the initial growth of pentacene and results in an improvement in device performance. The increased mobility and reduced SS of OTFTs with the hybridized insulator (BPI-3) on both glass and plastic substrates indicate that a stable interface is formed between the gate insulator and the semiconductor. Unlike conventional surface modification techniques, such as primer treatments, our hybridization approach provides a very simple and facile method for modifying the surface properties. Our new low-temperature processable and fully soluble polyimide (KSPI) and hybridized polyimide polymer (BPI-3) are promising materials for gate insulators in flexible OTFTs.

Acknowledgments

Our research into gate insulators at KRICT was financially supported by the Korean Ministry of Science and Technology through the 21C Frontier program and the Top-Brand Project program.

References

[1] H. Sirringhaus, Adv. Mater. 17 (2005) 2411.
[2] C.D. Dimitrakopoulos, P.R.L. Malenfant, Adv. Mater. 14 (2002) 99.
[3] H.E. Katz, Chem. Mater. 16 (2004) 4748.
[4] G. Horowitz, J. Mater. Res. 19 (2004) 1946.
[5] P. Mach, S.J. Rodriguez, R. Nortrup, P. Wiltzius, J.A. Rogers, Appl. Phys. Lett. 78 (2001) 3592.
[6] H.E. Katz, Z. Bao, J. Phys. Chem. B 104 (2000) 671.
[7] M. Shtein, J. Mapei, J.B. Benziger, S.R. Forrest, Appl. Phys. Lett. 81 (2002) 268.
[8] C.D. Sheraw, L. Zhou, J.R. Haung, D.J. Gundlach, T.N. Jackson, M.G. Kane, I.G. Hill, M.S. Hammond, J. Campi, B.K. Greening, J. Francl, J. West, Appl. Phys. Lett. 80 (2002) 1088.
[9] T.W. Kelley, P.F. Baude, C. Gerlach, D.E. Ender, D. Muyres, M.A. Haase, D.E. Vogel, S.D. Theiss, Chem. Mater. 16 (2004) 4413.
[10] A. Facchetti, M.H. Yoon, T.J. Marks, Adv. Mater. 17 (2005) 1705.
[11] E. Lim, B.J. Jung, J. Lee, H.K. Shim, J.I. Lee, Y.S. Yang, Y.M. Do, Macromolecules 38 (2005) 4531.
[12] J.H. Park, D.S. Chung, J.W. Park, T. Ahn, H. Kong, Y.K. Jung, J. Lee, M.Y. Yi, C.E. Park, S.K. Kwon, H.K. Shim, Org. Lett. 9 (2007) 2573.
[13] Y. Li, Y. Wu, B.S. Ong, Macromolecules 39 (2006) 6521.
[14] Y. Zhu, R.D. Champion, S.A. Jenekhe, Macromolecules 39 (2006) 8712.
[15] T. Yamamoto, K. Takimiya, J. Am. Chem. Soc. 179 (2007) 2224.
[16] S. Scheinert, G. Paasch, M. Schrodner, H.K. Roth, S. Sensfub, J. Appl. Phys. 92 (2002) 330.
[17] H. Klauk, M. Halik, U. Zschieschang, F. Eder, G. Schmid, C. Dehm, Appl. Phys. Lett. 82 (2003) 4175.
[18] G. Horowitz, F. Deloffre, F. Garnier, R. Hajlaoui, M. Hmyene, A. Yassar, Synth. Met. 54 (1993) 435.
[19] R. Schroeder, L.A. Majewski, M. Grell, Appl. Phys. Lett. 84 (2004) 1004.
[20] C.A. Lee, D.W. Park, S.H. Jin, I.H. Park, J.D. Lee, B.G. Park, Appl. Phys. Lett. 88 (2006) 252102.
[21] C.D. Sheraw, D.J. Gundlach, T.N. Jackson, Mater. Res. Soc. Symp. Proc. 558 (2000) 403.
[22] S.M. Pyo, J.K. Choi, Y.N. Oh, H.S. Son, M.H. Yi, Appl. Phys. Lett. 88 (2006) 173501.
[23] S.M. Pyo, M.Y. Lee, J.H. Jeon, K.Y. Choi, M.H. Yi, J.S. Kim, Adv. Funct. Mater. 15 (2005) 619.
[24] S.M. Pyo, Y.J. Lee, J.H. Jeon, M.H. Yi, S.K. Kwon, J. Appl. Phys. 99 (2006) 073711.
[25] J.H. Shim, L.Y. Jung, S.W. Pyo, Y.K. Kim, Thin Solid Films 441 (2003) 284.
[26] W.Y. Chou, H.L. Cheng, Adv. Funct. Mater. 14 (2004) 811.
[27] M.H. Yi, W. Huang, M.Y. Jin, K.Y. Choi, Macromolecules 30 (1997) 5606.
[28] K.I. Fukukawa, Y. Shibasaki, M. Ueda, Chem. Lett. 33 (2004) 1156.
[29] H. Sirringhaus, N. Tessler, R.H. Friend, Synth. Met. 102 (1999) 857.
[30] T.C. Gorjanc, I. Levesque, M. Dlorio, Appl. Phys. Lett. 84 (2004) 930.
[31] A. Salleo, M.L. Chabinyc, M.S. Yang, R.A. Street, Appl. Phys. Lett. 81 (2002) 4383.
[32] L.A. Majewski, R. Scheroeder, M. Grell, P.A. Glarvey, M.L. Turner, J. Appl. Phys. 96 (2004) 5781.
[33] D. Knipp, R.A. Street, A. Volkel, J. Ho, J. Appl. Phys. 93 (2003) 347.
[34] S.H. Jin, J.S. Yu, J.W. Kim, C.A. Lee, B.G. Park, J.D. Lee, SID Int. Symp. Digest Tech. Papers 34 (2003) 1088.
[35] S. Uemura, M. Yoshida, S. Hoshino, T. Kodzasa, T. Kamata, Thin Solid Films 438–439 (2003) 378.
[36] K. Shankar, T.N. Jackson, J. Mater. Res. 19 (2004) 2003.
[37] A.C. Arias, F. Endicott, R.A. Street, Adv. Mater. 18 (2006) 2900.
[38] M. Halik, H. Klauk, U. Zschieschang, T. Kriem, G. Schmid, W. Radlik, Appl. Phys. Lett. 81 (2002) 289.
[39] R.J. Chesterfield, C.R. Newman, T.M. Pappenfus, P.C. Ewbank, M.H. Haukaas, K.R. Mann, L.L. Miller, C.D. Frisbie, Adv. Mater. 15 (2003) 1278.
[40] J. Lee, J.H. Kim, S. Lim, J. Appl. Phys. 95 (2004) 3733.
[41] S.J. Kang, M. Noh, D.S. Park, H.J. Kim, C.N. Whang, C.H. Chang, J. Appl. Phys. 95 (2004) 2293.
[42] K.S. Pyo, C.K. Song, Thin Solid Films 485 (2005) 230.
[43] T.J. Schuerlein, A. Schmidt, P.A. Lee, K.W. Nebesny, N.R. Armstrong, Jpn. J. Appl. Phys. Part 1 34 (1995) 3837.
[44] S. Lukas, G. Witte, C. Woll, Phys. Rev. Lett. 88 (2002) 028301.

Organic Electronics 9 (2008) 721–726

Contents lists available at ScienceDirect

Organic Electronics

journal homepage: www.elsevier.com/locate/orgel

High-performance thin-film transistor with 6,13-bis(triisopropylsilylethynyl) pentacene by inkjet printing

Sun Hee Lee[a], Min Hee Choi[a], Seung Hoon Han[a], Dong Joon Choo[a], Jin Jang[a,*], Soon Ki Kwon[b]

[a] Department of Information Display, Advanced Display Research Center, Kyung Hee University, Seoul 130-701, Republic of Korea
[b] Engineering Research Institute, School of Nano and Advanced Materials, Gyeong Sang University, Jinju 660-701, Republic of Korea

ARTICLE INFO

Article history:
Received 3 January 2008
Received in revised form 18 March 2008
Accepted 6 May 2008
Available online 13 May 2008

PACS:
05.65.+b
42.70.Jk
61.25.Hq

Keywords:
OTFT
Ink-jet printing
TIPS pentacene
Substrate temperature
Organic electronics
Flexible display

ABSTRACT

We have studied the performance improvement of organic thin-film transistor (OTFT) with a solution based TIPS pentacene (6,13-bis(triisopropylsilylethynyl)pentacene) by inkjet printing. The TIPS pentacene with 1.0 wt.% solution in 1,2-dichlorobenzene was used for printing of an active layer of OTFT. The OTFT printed at room temperature shows a shoulder-like behavior but it disappears for the OTFT printed at the substrate temperature of 60 °C. The OTFT on plastic exhibited an on/off current ratio of $\sim 10^7$, a threshold voltage of −2.0 V, a gate voltage swing of 0.6 V/decade and a field-effect mobility of 0.24 cm^2/Vs in the saturation region.

Printable thin-film transistors (PTFTs) are of increasing interest for low cost, large-area electronic applications such as active-matrix display, electronic paper and flexible microelectronics [1–3]. Inkjet printing attracts much attention in device fabrication due to its many advantages including non-contact patterning, low temperature process, low cost, low material waste so that flexible and unbreakable and light-weight plastic display is possible using PTFT. Devices like organic light-emitting diodes (OLEDs), thin-film transistors, and microlenses have been fabricated by inkjet printing [4–6].

Among the solution based organic semiconductor materials, alkyl substituted oligothiophenes and pentacene derivates with bulky side chains exhibit a good TFT performance [7,8]. Pentacene is one of the most widely studied organic semiconductor for organic thin-film transistors (OTFTs) even through pentacene cannot be prepared by solution process such as spin coating and inkjet printing due to its limited solubility. However, substitution with appropriate solubilizing ethynyl functions at the 6,13-carbon position of pentacene can lead to enhancement in solubility because it promotes extended π-electron delocalization from the pentacene nucleus [9].

Recently, a solution processed 6,13-bis(triisopropylsilylethynyl) pentacene (TIPS pentacene) semiconductor was reported to give a field-effect mobility of 1.21 cm^2/Vs of the OTFT by drop-casting process [9]. This value is similar in magnitude to that obtained from a vapor-deposited film of the same material, likely due to the strong templating effect of the silyl group [8]. On the other hand, the OTFT with inkjet printed TIPS pentacene exhibited the

* Corresponding author. Tel.: +82 2 961 0270; fax: +82 2 961 9154.
E-mail address: jjang@khu.ac.kr (J. Jang).

1566-1199/$ - see front matter © 2008 Elsevier B.V. All rights reserved.
doi:10.1016/j.orgel.2008.05.002

field-effect mobility of 0.06 cm^2/Vs [10]. Therefore, the inkjet process should be optimized to achieve a high-performance TIPS pentacene TFT.

In this study, we report the optimization of organic thin-film transistor made of TIPS pentacene using inkjet printing. Especially, overlap jetting and substrate temperature affect the performance significantly. The OTFT printed on plastic exhibited an on/off current ratio of $\sim 10^7$, a field-effect mobility of 0.24 cm^2/Vs, a gate voltage swing of 0.6 V/decade and threshold voltage of −2.0 V, indicating that the printable TFT can be applied to make flexible active-matrix displays.

Fig. 1 shows the schematic cross-section of a bottom contact TIPS pentacene OTFT used in the present work. As a gate electrode, AlNd (100 nm) was deposited on polyethersulfone (PES) substrate and patterned by photolithography. Gate insulator, photo-definable poly(4-vinylphenol) (P-PVP), spin coated from the P-PVP precursor, was patterned by photolithography process without dry etch process. Then, the sample was cured in a vacuum oven to harden the pattern [11]. It was found that the thickness and dielectric constant of P-PVP were 600 nm and 3.6, respectively. Au (50 nm) layer was deposited on the gate insulator and patterned for source/drain electrodes. To define a small pixel and keep the organic semiconductor inside of the TFT channel, a bank pattern was formed using poly(vinylalcohol) (PVA) which was patterned by photolithography process. Then, we treated gate dielectric surface with O_2 plasma to make it clean and hydrophilic surface. Finally, TIPS pentacene was coated by inkjet printing. The W/L, a ratio of channel width to channel length, of the OTFTs was fixed to 236 μm/6 μm for all the OTFTs studied in this work. After the characterization of the initial performance of TIPS pentacene TFT, the OTFT was passivated with 1-μm thick parylene-C. It was deposited on the OTFT and patterned by photolithography.

We synthesized the TIPS pentacene by 1-step reaction with starting material of 6,13-pentaquinone [12]. TIPS pentacene has bulky triisopropylsilethynyl groups at the 6,13-positions of pentacene molecule, the substituent is separated from the pentacene molecule by a rigid alkyne spacer used to hold the bulky groups away from the aromatic core to allow the closest possible approach between the aromatic rings. Therefore, it increases π-orbital overlap and reduces the inter-planar spacing compared to unsubstituted pentacene [12,13].

In order to make ink for printing, TIPS pentacene should have a high solubility and aromaticity in an organic solvent. Boiling point, viscosity, and aromaticity are important properties of solvent for solution process. Aromaticity is related with the property of organic semiconductor. For aromatic solvents such as dichlorobenzene and xylene, the solvent molecules solvate the π-electron conjugated segments of the organic molecules, so that organic semiconductors with better π-stacking and thus high electrical conduction are obtained. However, for non-aromatic solvents such as tetrahydrofuran and chloroform, the solvent molecules solvate non-conjugated segments of polymer and therefore the films with lower electrical conduction are obtained. The TIPS pentacene can be affected by solvent because it is composed of several benzene rings.

The solvent affects the morphology and crystallinity of TIPS pentacene film [14–16]. In the present work, TIPS pentacene (MW 639 g/mol) was dissolved in 1,2-dichlorobenzene having a high boiling point (179 °C) and aromaticity with a good solubility.

Inkjet printing was performed with a piezoelectric head of a Litrex Corp. 80 L (model No.). The printer can support a substrate of up to 200 × 200 mm^2 and has an optical module which can inspect the substrate condition and analyze the volume, velocity, angle deviation of in-flight drops. Piezoelectric head used in this work was a SE-128 by Spectra, Inc. Its nozzle diameter and pitch are 35 μm and 508 μm, respectively. Volume and velocity of a droplet, proper voltage waveform and frequency were optimized through a number of jetting test in advance. The optimized parameters were the droplet of 30 pl, driving voltage of 80 V, pulse width of 150 s, frequency of 500 Hz and printing speed of 20 mm/s to make stable droplets with good repeatability and absence of satellite drops before printing onto the substrate. We also tried to minimize the landing error (variation of displacement) of droplets by tuning the directionality of droplets and accurate alignment of substrate.

We printed TIPS pentacene solution at different substrate temperatures from 26 to 60 °C. After printing an active layer, the OTFT substrate was cooled down to 26 °C with the cooling rate of ∼0.5 °C /min. Printing process and measurement of the TFT performances were carried out at room temperature under ambient air condition.

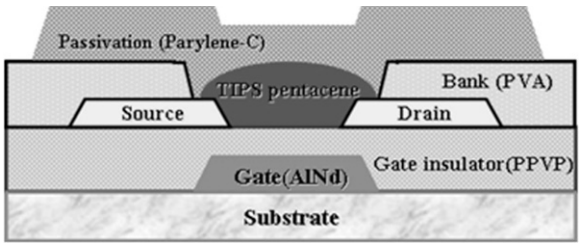

Fig. 1. A cross-sectional view of an OTFT studied in the present work.

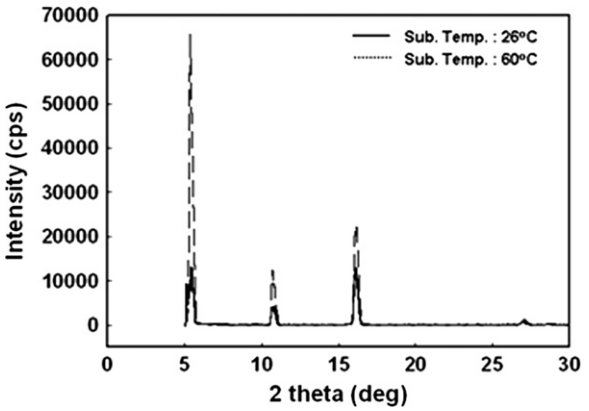

Fig. 2. XRD intensity for the printed TIPS pentacene films at different substrate temperatures: (a) 26 °C; (b) 60 °C.

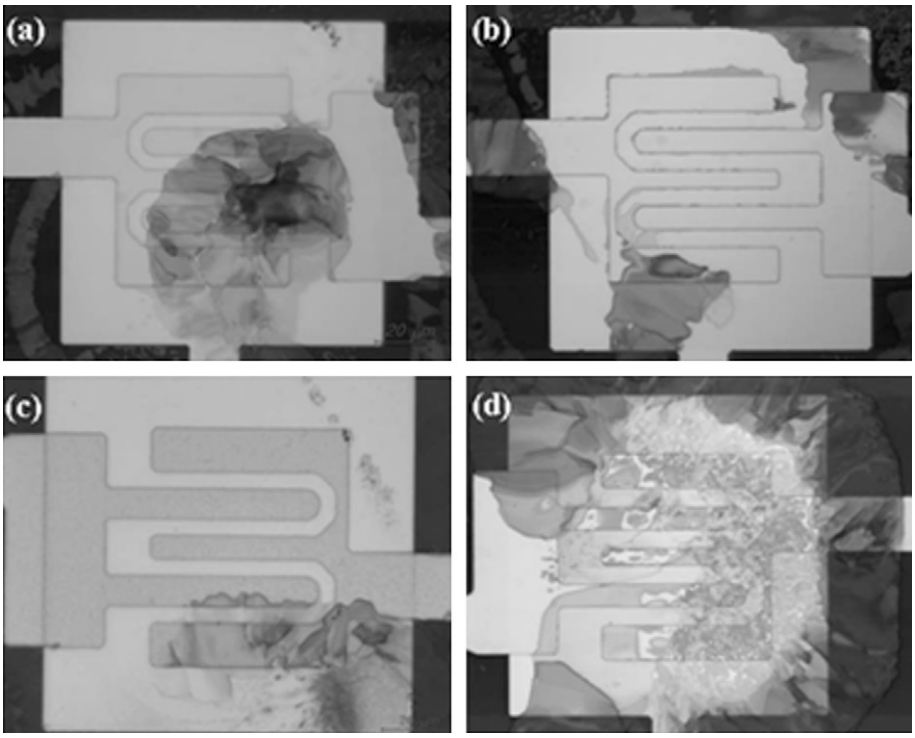

Fig. 3. Optical images of four different OTFT channels printed at 26 °C.

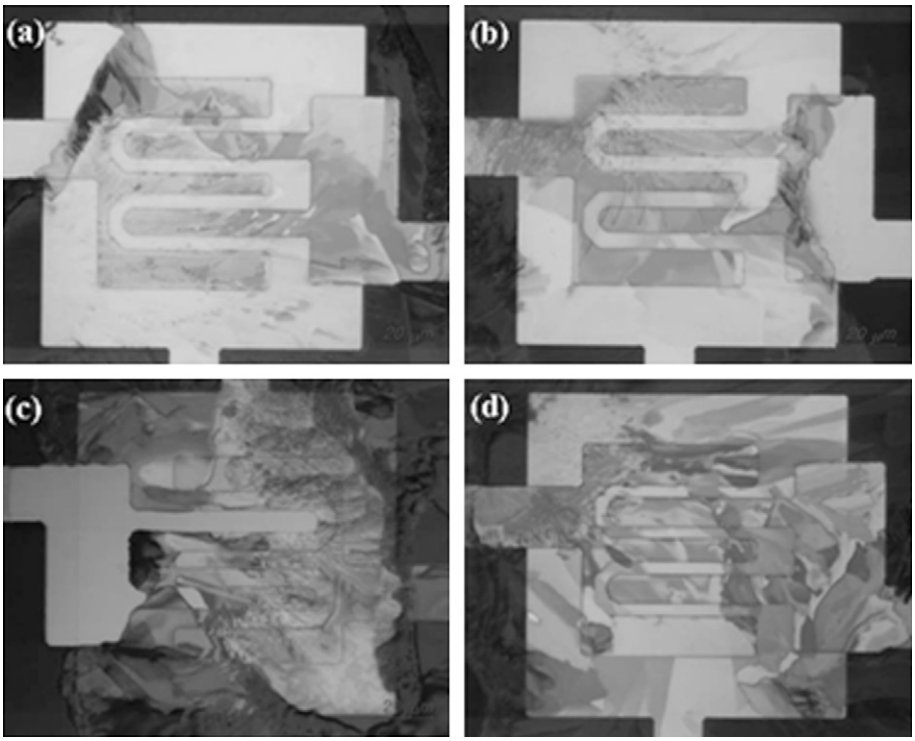

Fig. 4. Optical images of four different OTFT channels printed at 60 °C.

In our previous work, we investigated the dependence on substrate temperature during printing process using DH4T. The crystallites could not be found on the channel region by optical microscopy when jetted at 60 °C because the surface was smooth and thus the film could cover the whole channel region uniformly [17].

In this study, we used an overlap jetting method. When we jetted several drops with a separate printing method, the jetted position of each drop was not exactly the same due to the alignment deviation and thus the interface appears between the drops.

Therefore, we changed the method of printing from the separate printing of single drops to the overlapping jetting of several drops at a TFT channel. The TIPS pentacene solution printed is being dried on the TFT channel, resulting in the formation of thin-film. The advantages of the overlap jetting appear in the literature [17].

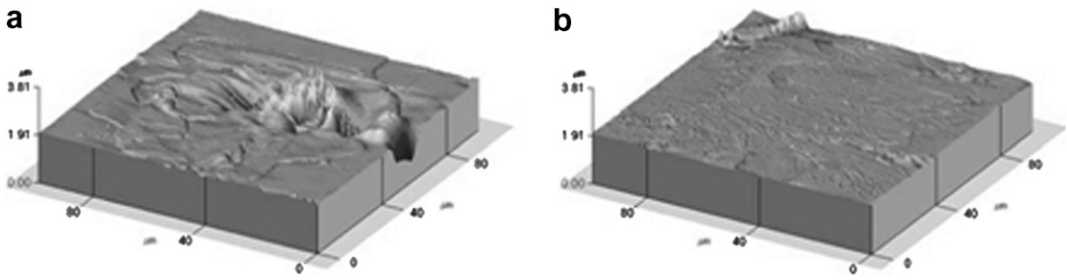

Fig. 5. AFM images of the printed TFTs at different substrate temperatures of (a) 26 °C and (b) 60 °C.

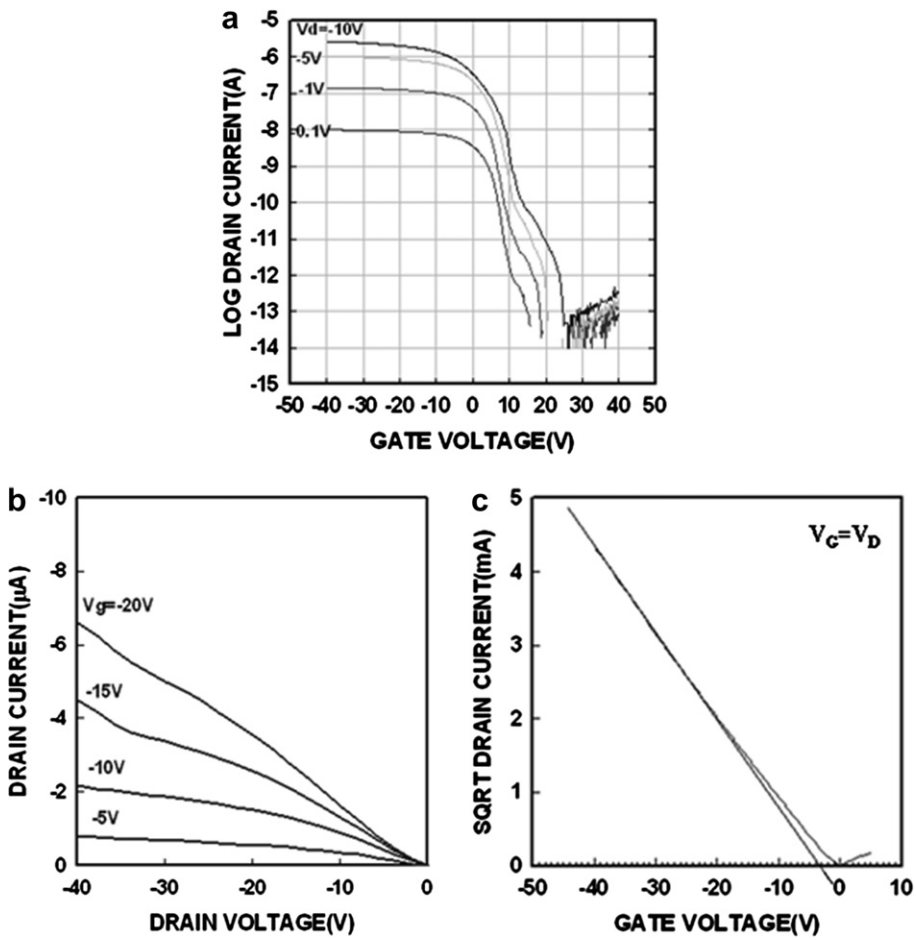

Fig. 6. The performance of the TIPS pentacene OTFT printed at 26 °C by overlap jetting method: (a) transfer; (b) output; (c) mobility characteristics.

Fig. 2 shows the intensity of X-ray diffraction (XRD) for the TIPS pentacene films printed by inkjet at the substrate temperatures of 26 and 60 °C. Single crystal TIPS-pentacene has a triclinic structure with unit cell parameters of $a = 7.5650$ Å, $b = 7.7500$ Å, $c = 16.835$ Å, $\alpha = 89.15°$, $\beta = 78.42°$, $\gamma = 83.63°$. From Bragg's law ($2d\sin\theta = n\lambda$, $\lambda = 1.54$ Å), the peak at $2\theta = 5.4°$ corresponds to a layer separation of 16.3 Å which is identical to that of the *c*-axis unit cell. The XRD results show the good molecular ordering for the inkjet printed film. A sharp and strong peak at 5.4° indicates a well organized molecular structure with vertical intermolecular spacing of 16.3 Å, which is similar to that (16.83 Å) appeared in the literatures [18,19]. Note that all the peak intensities are higher for the TIPS pentacene film printed at 60 °C.

On the other hand, the TIPS pentacene film printed at 26 °C has higher (003) peak intensity as compared to that of (001). In contrast, the OTFT printed at 60 °C has higher (001) peak intensity than that of (003). Therefore, it is concluded that the crystallite of TIPS pentacene is affected by substrate temperature during printing process such that the film printed at 60 °C has better ordering than that made at 26 °C.

We checked the coverage of the organic semiconductor on the TFT channel. Fig. 3 shows the optical images of four different TFT channels jetted with the same jetting conditions on the TFT channels prepared simultaneously, indicating that the film coverage is not uniform. The films printed at 26 °C are randomly positioned on the channel. On the other hand, the films are more uniformly formed at the channel at 60 °C as shown in Fig. 4. Note that the drying time was ~5 min and ~1 min when the substrate temperature was 26 and 60 °C, respectively. This appears to be related with the uniform formation of film over the channel region at 60 °C because fast evaporation leads to film formation near the drop point.

To confirm thickness uniformity and morphology, we measured AFM images of the TFTs printed. Fig. 5 shows the AFM images of the TFTs printed at 26 and 60 °C, respectively. We took Fig. 3a and Fig. 4a to see the AFM images. The TIPS pentacene printed at 26 °C shows non-uniform coverage over the TFT channel, but more uniform coverage

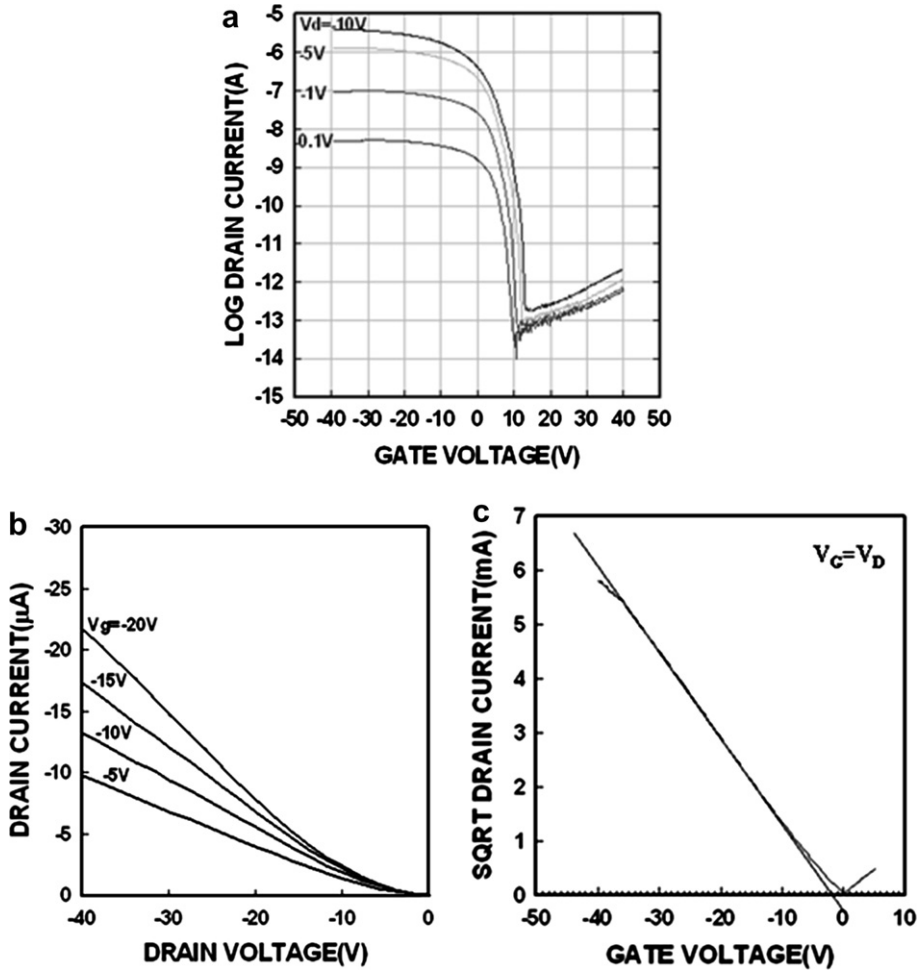

Fig. 7. The performance of the TIPS pentacene OTFT printed at 60 °C by overlap jetting method: (a) transfer; (b) output; (c) mobility characteristics.

Table 1
The characteristics of the TIPS pentacene TFTs measured after fabrication (initial value), after 120 h in air, and after parylene-C deposition in vacuum

	Initials	After 120 h	After passiyation
V_{th} (V)	−2.0	−0.6	0.05
μ_{fe} (cm^2/Vs)	0.24	0.16	0.11
I_{on}/I_{off}	$\sim10^7$	$\sim10^7$	$\sim10^7$
S (V/dec)	0.6	1.0	0.6

over the channel can be seen at 60 °C. The coverage depends on the evaporation rate of solvent and it increases with increasing temperature.

Figs. 6 and 7 show the performances of the OTFTs printed at 26 and 60 °C, respectively, with transfer (a), output (b) and mobility (c) characteristics. The OTFT printed at 26 °C exhibited the field-effect mobility (μ_{fe}) of 0.11 cm^2/Vs in the saturation region, an on/off current ratio (I_{on}/I_{off}) of 10^7, a threshold voltage (V_T) of −1.8 V and the gate voltage swing(S) of 0.8 V/dec. On the other hand, the OTFT printed at 60 °C exhibited the μ_{fe} of 0.24 cm^2/Vs, the I_{on}/I_{off} of 10^7, the V_T of −2.0 V and S of 0.6 V/dec. The performance can be improved remarkably by elevating the substrate temperature. The field-effect mobility of the printed OTFT is comparable to that of vacuum deposited OTFT [20].

Another difference in their electrical performance is the shoulder-like behavior shown in the Fig. 6a. It disappears when the jetting was done at 60 °C. This might be caused by the contamination of back surface of the OTFT because of shorter drying time at higher temperature.

Table 1 summarizes the changes in the electrical performance after being stored for 120 h in air and after parylene-C deposition. The field-effect mobility decreased, and threshold voltage shifted to positive direction due to the adsorption of O_2 and H_2O from ambient air that diffused into the organic semiconductor, and then degraded the electrical performance of OTFT significantly [21–23]. After parylene-C passivation process, the gate voltage swing recovers to the original value of 0.6 V/dec. Some water and/or water related impurities appear to be diffused out from the active layer because it was deposited in vacuum. After parylene-C passivation, the OTFT exhibited the μ_{fe} of 0.11 cm^2/Vs, an I_{on}/I_{off} of 10^7, a V_T of 0.05 V and the gate voltage swing of 0.6 V/dec. The stability of the performance of the TIPS pentacene can be seen in air until 120 h. In addition, the effect of parylene-C deposition in vacuum can be checked in the present work because its deposition was carried out in vacuum. The exposure of the OTFT in vacuum for the parylene-C deposition shifts the V_{th}, which appears to be due to the desorption of water and oxygen vapors. The result indicates that the passivation with parylene-C can be used for the application of TIPS pentacene TFT for organic electronics.

In conclusion, we studied the optimization of printing conditions for TIPS pentacene TFT. By overlap printing at 60 °C, the shoulder-like behavior in the transfer characteristics disappears. We achieved the OTFT exhibiting the μ_{fe} of 0.24 cm^2/Vs, V_T of −0.25 V, S of 0.45 V/dec. and I_{on}/I_{off} of $\sim10^7$ by introducing overlap printing of TIPS pentacene solution at 60 °C. After the passivation with parylene-C, the OTFT exhibited the μ_{fe} of 0.11 cm^2/Vs with I_{on}/I_{off} of 10^7. Therefore, the TIPS pentacene OTFT using inkjet printing can be applied to make low cost flexible electronics.

Acknowledgement

This research was supported by a Grant (F0004082-2007-23) from Information Display R&D Center, one of the 21st Century Frontier R&D Program funded by the Ministry of Commerce, Industry and Energy of Korean Government.

References

[1] K. Nomoto, N. Hirai, N. Yoneya, N. Kawashima, M. Noda, M. Wada, J. Kasahara, IEEE Trans. Electron Dev. 52 (2005) 1519.
[2] C.D. Dimitrakopoulos, D.J. Mascaro, IBM J. Res. Dev. 45 (2001) 11.
[3] D.M. deLeeuw, G.H. Gelinck, T.C.T. Geuns, van Veenendaal, E. Cantore, E. Huisman, Tech. Dig. Int. Electron Dev. Meet. 2002 (2002) 293.
[4] Y. Yang, S.-C. Chang, J. Bharathan, J. Liu, J. Mater. Sci. Mater. Electron. 11 (2000) 89.
[5] T. Kawase, H. Sirringhaus, R.H. Friend, T. Shimoda, Tech. Dig. Int. Electron Dev. Meet. 2000 (2000) 623.
[6] S. Biehl, R. Danzebrink, P. Oliveira, M.A. Aeferter, J. Sol –Gel Sci. Technol. 13 (1998) 177.
[7] M. Halik, H. Klauk, U. Zschieschang, G. Schmid, S. Ponomerenko, S. Kirchmeyer, W. Weber, Adv. Mater. 15 (2003) 917.
[8] M.M. Payne, S.R. Parkin, J.E. Anthony, C.C. Kuo, T.N. Jackson, J. Am. Chem. Soc. 127 (2005) 4986.
[9] S.K. Park, T.N. Jackson, J.E. Anthony, D.A. Mourey, Appl. Phys. Lett. 91 (2007) 063514.
[10] Y.H. Kim, Y.U. Lee, J.I. Han, S.M. Han, W.C. Lee, M.K. Han, Soc. Inform. Display 2007 (2007) 214.
[11] S.H. Lee, D.J. Choo, S.H. Han, J.H. Kim, Y.R. Son, J. Jang, Appl. Phys. Lett. 90 (2007) 033502.
[12] J.E. Anthony, J.S. Brooks, D.L. Eaton, S.R. Parkin, J. Am. Chem. Soc. 123 (2001) 9482.
[13] J.E. Anthony, D.L. Eaton, S.R. Parkin, Org. Lett. 4 (2002) 15.
[14] Y.H. Kim, Y.U. Lee, .J.I. Han, S.M. Han, M.K. Han, J. Electrochem. Soc. 154 (12) (2007) H995.
[15] J. Liu, Y. Shi, Y. Yang, Adv. Funct. Mater. 11 (2001) 420.
[16] Y. Shi, J. Liu, Y. Yang, J. Appl. Phys. 87 (2000) 4254.
[17] D.H. Song, M.H. Choi, J.Y. Kim, J. Jang, Appl. Phys. Lett. 90 (2007) 053504.
[18] J.E. Anthony, S. Brooks, D.L. Eaton, S.R. Parkin, J. Am. Chem. Soc. 123 (2001) 9482.
[19] W.H. Lee, D.H. Kim, Y.S. Jang, J.H. Cho, K.W. Cho, Appl. Phys. Lett. 90 (2007) 132106.
[20] T. Sekitani, T. Someya, T. Sakurai, J. Appl. Phys. 100 (2006) 024513.
[21] Y. Qiu, Y. Hu, G. Dong, L. Wang, J. Xie, Y. Ma, Appl. Phys. Lett. 83 (2003) 1644.
[22] R. Ye, M. Baba, K. Suzuki, Y. Ohishi, K. Mori, Thin Solid Film 464–465 (2004) 437.
[23] S.H. Han, J.H. Kim, S.M. Cho, M.H. Oh, S.H. Lee, D.J. Choo, J. Jang, Appl. Phys. Lett. 88 (2006) 073519.

Organic Electronics 9 (2008) 727–734

Contents lists available at ScienceDirect

Organic Electronics

journal homepage: www.elsevier.com/locate/orgel

Conductivity, work function, and environmental stability of PEDOT:PSS thin films treated with sorbitol

A.M. Nardes [a], M. Kemerink [a,*], M.M. de Kok [b], E. Vinken [c], K. Maturova [a], R.A.J. Janssen [a]

[a] Molecular Materials and Nanosystems, Department of Applied Physics, Eindhoven University of Technology, P.O. Box 513, 5600 MB Eindhoven, The Netherlands
[b] Philips Research Laboratories, High Tech Campus 4, 5656 AE Eindhoven, The Netherlands
[c] Laboratory of Polymer Technology, Department of Chemical Engineering, Eindhoven University of Technology, P.O. Box 513, 5600 MB Eindhoven, The Netherlands

ARTICLE INFO

Article history:
Received 20 November 2007
Accepted 7 May 2008
Available online 17 May 2008

PACS:
73.61.Ph
73.50.Dn
72.20.Ee

Keywords:
PEDOT:PSS
Conductivity
Sorbitol
Work function
Water uptake
Scanning Kelvin probe microscopy

ABSTRACT

The electrical properties of poly(3,4-ethylenedioxythiophene):poly(4-styrenesulfonate) (PEDOT:PSS) thin films deposited from aqueous dispersion using different concentrations of sorbitol have been studied in detail. Although it is well known that sorbitol enhances the conductivity of PEDOT:PSS thin films by three orders of magnitude, the origin and consequences of sorbitol treatment are only partly understood and subject of further study. By thermal annealing of spin coated PEDOT:PSS/sorbitol films and simultaneously monitoring the conductivity, we demonstrate that the strong increase in conductivity coincides with evaporation of sorbitol from the film. Hence, sorbitol is a processing additive rather than a (secondary) dopant. Scanning Kelvin probe microscopy reveals that sorbitol treatment causes a reduction of the work function from 5.1 eV to 4.8–4.9 eV. Sorbitol also influences the environmental stability of the films. While the conductivity of the pristine PEDOT:PSS films increases by about one order of magnitude at ~50% RH due to an ionic contribution to the overall conductivity, films prepared using sorbitol exhibit an increased environmental stability with an almost constant conductivity up to 45% RH and a slight decrease at 50% RH. The higher stability results from a reduced tendency to take up water from the air, which is attributed to a denser packing of the PEDOT:PSS after sorbitol treatment.

1. Introduction

The electronic properties of conducting polymers are of interest for physical concepts and technological applications. Accordingly, the development of highly conducting polymers with good stability and processability has been the focus of many recent studies [1]. Currently, a variety of conducting polymers is available for various applications, such as polyaniline, polypyrrole, and polythiophenes [2]. In this direction, poly(3,4-ethylenedioxythiophene) (PEDOT) has been found to exhibit a relatively high conductivity and appears to be the most stable conducting polymer currently available [3,4]. PEDOT itself is an insoluble material but when it is synthesized in the presence of poly(4-styrenesulfonate) (PSS) an aqueous dispersion can be obtained that can be cast into thin films. In the films the polycationic PEDOT chains are incorporated into a polyanionic PSS matrix to compensate the charges (Fig. 1). Thin films deposited from an aqueous PEDOT:PSS dispersion have been utilized in a wide range of applications [3–5], for example in antistatic coatings [6], as electrode in light-emitting diodes (LEDs) [7], photovoltaics (PV) [8], memories [9], sensors [10], and as active material for electrochromic devices [11], field-effect transistors [12] and circuits in general [13].

Thin PEDOT:PSS films are extremely hygroscopic [14] and post-deposition treatments in air by thermal annealing are generally unstable due to the fast water uptake. For example, reported conductivities measured in air are roughly one order of magnitude lower compared to those measured under an inert environment [14,15].

* Corresponding author.
E-mail address: m.kemerink@tue.nl (M. Kemerink).

1566-1199/$ - see front matter © 2008 Elsevier B.V. All rights reserved.
doi:10.1016/j.orgel.2008.05.006

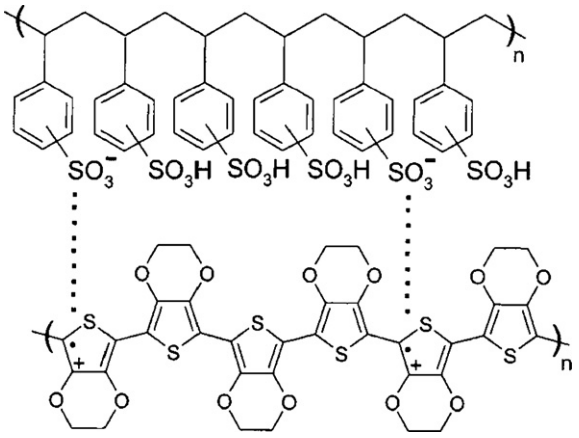

Fig. 1. Chemical structure of PEDOT (bottom) and PSS (top).

Addition of sorbitol, a polyhydroxy alcohol, to the aqueous PEDOT:PSS dispersion is known to enhance the conductivity of the thin films by several orders of magnitude, depending on its concentration [14]. The dramatic effect of sorbitol as processing additive arises from a further reorganization and stabilization of the PEDOT and PSS chains during subsequent thermal annealing of the films by a plasticizing effect [16]. While this method to enhance the conductivity has been previously studied, the reasons for the remarkable behavior are still under debate [16–22].

Apart from a change in conductivity, sorbitol treatment may also affect other properties of PEDOT:PSS relevant to device operation, e.g. the electrode work function χ. For PEDOT:PSS thin films, a range of work functions has been reported from 4.7 to 5.4 eV [23–26] and it has been found that this level can be tuned to minimize the hole-injection barrier at the anode [27] in organic LEDs [28,29] and PV cells [30]. The spread in work function values is assumed to be related to differences in the top layer, which may contain an excess of PSS [14,31–33]. Since the PSS-rich top layer may be modified by the addition of high-boiling solvents [14,31,33] or (non-) intentionally by other processing conditions [34], an effect of sorbitol treatment on the work function may be expected.

Here we investigate the conductivity and environmental stability of PEDOT:PSS thin films treated with different sorbitol concentrations. We combine *in situ* conductivity and water-uptake measurements during thermal treatment and exposure to humidity to further investigate the various properties of pristine and sorbitol-treated PEDOT:PSS thin films [14,35]. Using scanning Kelvin probe microscopy (SKPM) we find that sorbitol treatment also causes a reduction in work function from 5.1 to 4.8 eV. Furthermore, the increased conductivity by sorbitol-treatment is accompanied by an enhanced environmental stability towards uptake from water. This effect is attributed to a denser packing of the sorbitol-treated films, reducing the water uptake, in combination with a morphology that is less susceptible to swelling. The results presented here have immediate implications for device making.

2. Experimental

Soda lime glass substrates (3×3 cm^2) were grooved into pieces of 1×1 cm^2 on the back side with a diamond pen. They were cleaned with soap and then sonicated in baths of acetone and isopropanol for 20 min each and rinsed with deionized water after each process. Residual organic contaminations were removed using a 30 min UV-ozone treatment (UV-Ozone Photoreactor, PR-100, Ultraviolet Products). Four electrodes (1×6 mm^2 with 1 mm spacing) were deposited on the cleaned glass substrates using a shadow mask by evaporation of 5 nm of chromium, followed by 95 nm of gold.

A commercially available aqueous PEDOT:PSS dispersion (Baytron P VP Al 4083 from H.C. Starck) has been used. Different amounts of D-sorbitol (97%, Sigma–Aldrich) were added to the aqueous dispersion; 2.5, 5.0, or 10 wt-% (of the total solution). The solutions were stirred for at least 24 h at room temperature, filtered using a 5 μm filter, and deposited in air by spin coating, which resulted in 90–100 nm thick films as measured by a profilometer (Alpha-step 200, Tencor Instruments). For comparison, we used PEDOT:PSS without sorbitol, referred to as 'pristine', and in this case the film thickness was about 60 nm. Next, the 3×3 cm^2 substrates were cut into pieces of 1×1 cm^2 for electrical measurements.

For thermal annealing experiments, samples were transferred to a glove box (O_2 and $H_2O < 1$ ppm) and placed on a temperature-controlled metal plate. The conductivity was monitored in 10 s intervals by an Agilent 4156C semiconductor analyzer under constant bias during the entire annealing process, *i.e.* heating up to 200 °C, constant at 200 °C for 2 min, and cooling down.

The humidity experiments were carried out in a glove box that was modified to control the relative humidity up to 50% by flushing N_2 through demineralized water (degassed with He) into the box. Prior to increasing the humidity, samples were thermally annealed at 200 °C for 2 min and then rapidly cooled on a piece of metal. Only when the conductivity had stabilized after 1–2 h, the humidity levels were increased, first up to 30% for each sample (0, 2.5, 5 and 10 wt-%) and then up to 50% of relative humidity, using fresh samples.

Temperature dependent conductivity measurements were performed for a pristine sample mounted in a vacuum loading (10^{-5} mbar) cryostat (Oxford Instruments). Temperature was controlled in the 77–300 K range by an Oxford ITC 601 controller that maintained a temperature stability of ±0.1 K. Electrical measurements were performed by a Keithley 2410 source meter. The annealed sample was mounted in a cryostat (Oxford Instruments) in a glove box (O_2 and $H_2O < 1$ ppm) such that the sample was never exposed to air after bake-out.

From a comparison of 2- and 4-terminal measurements the contact resistance was found to be negligible for all our samples.

Work functions were measured by scanning Kelvin probe microscopy (SKPM) using a Veeco MultiMode AFM placed inside a glove box. Olympus OMCL-AC240TM-B2 Pt coated tips (spring constant $k \approx 2$ N/m) were used.

SKPM combines classical Kelvin probe with AFM and allows one to measure the local surface potential V_{sp}, which, for a metallic tip and sample with work functions χ_{tip} and χ_{sample} respectively, is given by $qV_{sp} = \chi_{tip} - \chi_{sample}$ with q the elementary charge. By referencing the work function of the tip to that of highly oriented pyrolytic graphite (HOPG) ($\chi_{HOPG} = 4.475 \pm 0.005$ eV [36]), the work function of the sample could be determined.

Direct insertion probe mass spectrometry analyses were carried out using a Shimadzu chromatograph (GCMS – QP5000) PEDOT:PSS were deposited into a quartz microtube, about 1–2 μl, and dried in ambient. The quartz microtube containing the sample was connected to the heating probe and subsequently inserted into the high vacuum (10^{-6} mbar) chamber for the MS analysis.

Water uptake was studied by thermal gravimetric analysis (TGA) and quartz crystal microbalance (QMB) experiments. TGA was measured with a Q500 Thermogravimetric Analyzer (TA Instruments) at a heating rate of 10 °C/min under a moisturized atmosphere created by fluxing 60 ml/min of N_2 through deionized water into the oven. For TGA experiments, free-standing 20 μm thick films of pristine and 10 wt-% of sorbitol-added PEDOT:PSS were prepared by casting the solutions on cleaned glass substrates. Here, the UV-ozone treatment step was left out in order keep the surface as hydrophobic as possible. Both samples were dried in air at 120 °C for about 20 min and 60 min for pristine and 10 wt-%, respectively, until dark blue lustrous films were obtained. By doing so, the removal of the film from the glass substrates was relatively easy. For the QMB, the pristine sample was deposited directly onto the piezoelectrical micro-crystal and dried. This experiment was conducted in an N_2 environment and the change in mass was recorded while varying the humidity level between 0% and 49% RH.

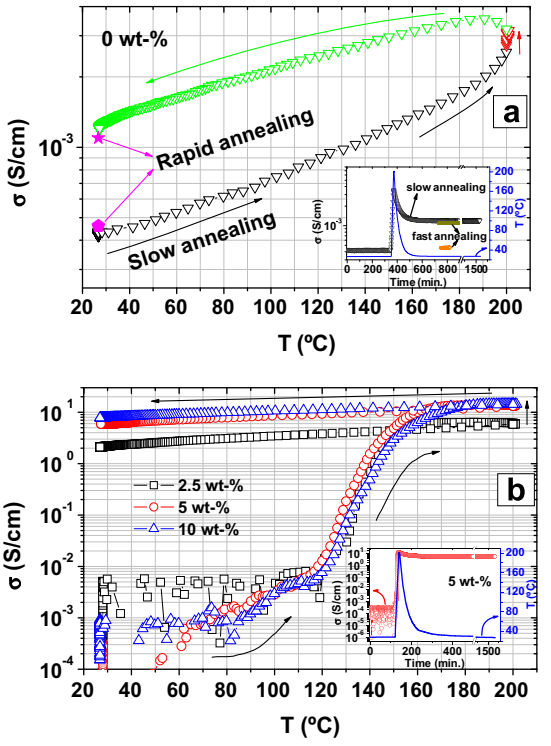

Fig. 2. Variation of the conductivity under N2 environment with temperature during slow annealing, *i.e.* heating up to 200 °C, constant at 200 °C for 2 min, and subsequent cooling of PEDOT:PSS thin films with (a) 0 wt-% (pristine film) and (b) 2.5, 5, and 10 wt-% of sorbitol concentrations. The insets show the conductivity as a function of time during the annealing process. Conductivities for pristine as-cast films and after rapid annealing (2 min at 200 °C and forced cooling) are shown by solid markers in panel (a). All the other arrows indicate the thermal cycling direction during slow annealing.

3. Results

3.1. Effect of thermal annealing

The conductivity of PEDOT:PSS films was monitored in real-time in dry N_2 environment, while gradually increasing the temperature at a rate of ~10 °C/min to 200 °C, followed by 2 min at 200 °C, and subsequent natural cooling to room temperature in about 3 h (Fig. 2).

For pristine PEDOT:PSS the conductivity increases upon annealing by about one order of magnitude from $\sim 4 \times 10^{-4}$ to 3×10^{-3} S/cm (Fig. 2a). Subsequent cooling to room temperature, results in a decrease to about 10^{-3} S/cm. Rapid thermal annealing, *i.e.* 2 min at 200 °C, followed by rapid cooling on a piece of metal affords virtually the same conductivity at the end. Hence, the annealing rate has no significant influence on the final conductivity.

For the sorbitol-treated films the behavior is significantly different (Fig. 2b). Temperatures below 120 °C do not induce significant changes in the conductivity, although the values oscillate between $\sim 10^{-4}$ and 10^{-7} S/cm. These fluctuations also occur in the majority of the sorbitol-treated samples before annealing (inset of Fig. 2b, $t < 100$ min) and are not due to instrumental noise. At about ~100 °C the fluctuations disappear and at ~120 °C the conductivity starts to increase dramatically to saturate at ~160 °C at a value close to 10 S/cm, *i.e.* 3–4 orders of magnitude higher that for the as-cast films. During the remaining part of the thermal cycle (up to 200 °C, 2 min, at 200 °C, and natural cooling) the conductivity remains at these high levels. In accordance with previous results [14], the conductivity after annealing is only weakly dependent on the amount of sorbitol in the range 2.5–10 wt-%.

We note that the fluctuations in conductivity below 120 °C for sorbitol-treated films are not observed for pristine films (inset of Fig. 2a). The detrimental effect of sorbitol on the conductivity before annealing is different from previous observations where the simple addition of a mixture of high boiling solvents had a much bigger effect in the conductivity enhancement than the following annealing step [31]. We attribute the fluctuations at room temperature to spontaneous rearrangements in the PEDOT:PSS films facilitated by the plasticizing effect of sorbitol, which may induce changes in the percolation pathways [37].

The dramatic changes in the conductivity for sorbitol-treated PEDOT:PSS thin films during by thermal annealing procedure are caused by the presence of sorbitol and rem-

nant water enabling morphological changes in the PEDOT:PSS films. Experiments in which PEDOT:PSS samples were heated while monitoring the molecules that evaporate from the film using mass spectrometry revealed that the evaporation of sorbitol (and residual water) sets in around 80 °C and reaches a maximum at ~120 °C, as evidenced from a strong increase of the $m/z = 103$ peak at 80 °C, characteristic of a sorbitol fragment (Fig. 3). The disappearance of the $m/z = 103$ peak in the mass spectrum above 160 °C indicates that virtually all sorbitol is removed from the films at this temperature. After the first run, the samples were allowed to cool down in vacuum and a second round of measurements was conducted using the same temperature profile. These measurements (not shown) revealed minor traces of the remaining sorbitol, very close to noise level.

These experiments demonstrate that sorbitol acts as a processing additive rather than as (secondary) dopant. Since the maximum rate of sorbitol loss coincides with the onset of the conductivity increase, we propose that the increased free volume in the film due to the removal of sorbitol and water, in combination with the large thermal energy during annealing and the plasticizing action of the remaining solvent mixture enables the PEDOT and PSS clusters to rearrange towards a more relaxed and compact morphology. The latter is supported by AFM and STM studies on these films, in which the lamellar arrangement of PEDOT and PSS appears to be enhanced by sorbitol treatment [16,38]. The fact that at 160 °C sorbitol and water have almost completely evaporated from the film corroborates the above interpretation of the data in Fig. 2b.

3.2. Work function

To determine the effect of sorbitol treatment on the work function of PEDOT:PSS we measured the surface potential V_{sp} of the films by scanning Kelvin probe microscopy (SKPM). The surface potential relates to the work function as $qV_{sp} = \chi_{tip} - \chi_{sample}$, where χ_{tip} and χ_{sample} are the work functions of the tip and sample, respectively. The measured work functions of PEDOT:PSS thin films range from 4.8 to 4.9 eV after sorbitol treatment as compared to 5.1 eV for the pristine PEDOT:PSS sample as shown in Fig. 4a.

The shift in work function is consistent with a removal of the PSS-rich surface layer that is present in pristine PEDOT:PPS films as explained in the band diagrams of Fig. 4b–c. The (positive) sign of the work function change upon addition of sorbitol leads to the conclusion that the PSS-rich top layer results in an inward directed surface potential dipole as indicated in Fig. 4b [39]. Compared to the situation without this dipole layer (Fig. 4c), the work function is effectively increased, the magnitude of the shift Δ depending on the surface layer thickness. Hence, upon reduction of the surface layer thickness by sorbitol treatment, the work function will decrease, *i.e.* the surface po-

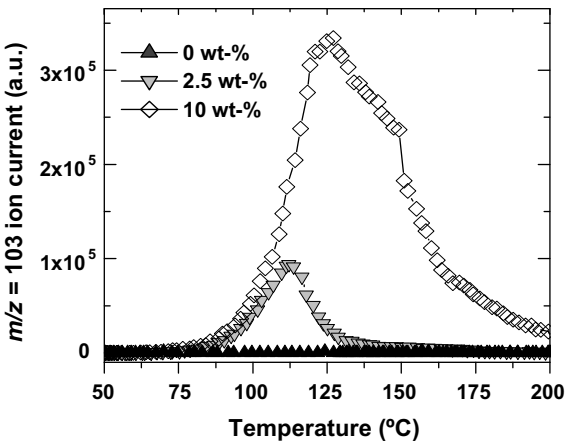

Fig. 3. Ion current of the $m/z = 103$ fragment, characteristic of sorbitol, as function of temperature for PEDOT:PSS samples treated with sorbitol (0, 2.5, and 10 wt-%) The temperature was increased at a rate of 10 °C/min.

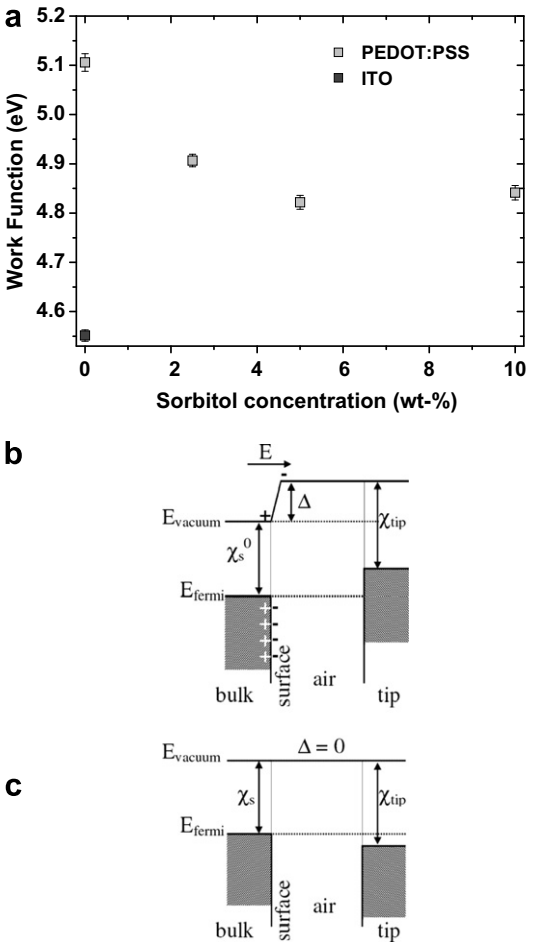

Fig. 4. (a) Work function of PEDOT:PSS thin films spin cast from solutions with different sorbitol concentrations. The work function of ITO is shown as comparison. (b, c) Schematic representation of the band diagrams during SKPM on PEDOT:PSS thin films. (b) pristine PEDOT:PSS with a PSS-rich surface layer and (c) sorbitol-treated PEDOT:PSS without PSS surface layer. χ_s^0, χ_s and χ_{tip}, are, respectively, the work functions of 'bulk' PEDOT:PSS, sorbitol-treated PEDOT:PSS thin film, and the tip. Δ is the surface dipole due to the PSS-rich surface layer, which effectively enhances the film work function to $\chi_s^0 + \Delta$.

tential will increase, as observed in the SKPM measurements. From the total absence of lateral variation in the surface potential (not shown), we conclude that the removal of the PSS top layer is homogeneous.

3.3. Effect of humidity

The change in physical, optical, and electrical properties of polymers with respect to the change of the relative humidity (RH) of the environment has been studied in many different aspects [40–43]. In general, water vapor is absorbed by the polymer when the RH increases. Evidently, if any electrical property of a material responds strongly to environmental changes, the material may be used in sensor applications [44]. On the other hand, it has been shown that uptake of water by PEDOT:PSS leads to a degradation of the device performance in solar cells that use PEDOT:PSS as an electrode material [45].

The change in conductivity as a function of RH for PEDOT:PSS thin films prepared from sorbitol-treated films is shown in Fig. 5a–c. Before introducing water vapor, all samples were thermally annealed for 2 min at 200 °C. Each panel in Fig. 5 shows two curves representing sweeps from zero to medium (up to 30%) and high (up to 50%) levels of RH. The graphs demonstrate that exposure of the samples to humidity induces a reduction in conductivity. By comparing the pristine sample (Fig. 4d) with the samples processed from sorbitol/water mixtures (Fig. 5a–c) it is clear that their sensitivity to humidity is remarkably different.

The conductivity of the pristine sample (10^{-3} S/cm) first decreases by a factor of 2.5 when increasing the RH to 30% (Fig. 5d). This is almost the same amount by which the conductivity was increased initially by thermal annealing (Fig. 2a). When the RH is then kept constant at ~30% for 1.5–2 h the conductivity decreases slightly and is not recovered when returning to RH = 0%. When increasing the RH further to 50%, a steady increase in conductivity is observed above 30% to reach a value of 10^{-2} S/cm that exceeds the initial value by about one order of magnitude, suggesting ionic conduction [46]. At RH = 50% the conductivity decreases with time and when reducing the RH to 0%, a further decrease is observed to $\sim 2 \times 10^{-5}$ S/cm.

The three sorbitol treated samples (Fig. 5a–c) show a very different behavior and their relative change in conductivity is much smaller than for pristine sample, indicating enhanced environmental stability. This is attributed to a reduced uptake of water, as will be explained in the next section. Up to 30% RH, conductivities decrease slightly (~5%) by water uptake. Exceeding ~30% RH, conductivities start to increase and reach a maximum value around 45% RH, suggesting again an ionic contribution to the overall conductivity. However, at this point, the increase in conductivity is not very high and the value barely exceeds the initial level. At maximum and constant RH level, ~50%, conductivities are lowered and some scatter is observed. Being at RH = 50% for 1.5 – 2 h causes the conductivities to reach their minimal values. During drying under N_2 atmosphere to RH = 0%, a slight recovery of the conductivities is observed, but the values always end up below the initial ones. The exact reason for this effect is unclear at present, but it seems likely that the water absorbed by the samples causes morphological changes that are irreversible with drying at room temperature.

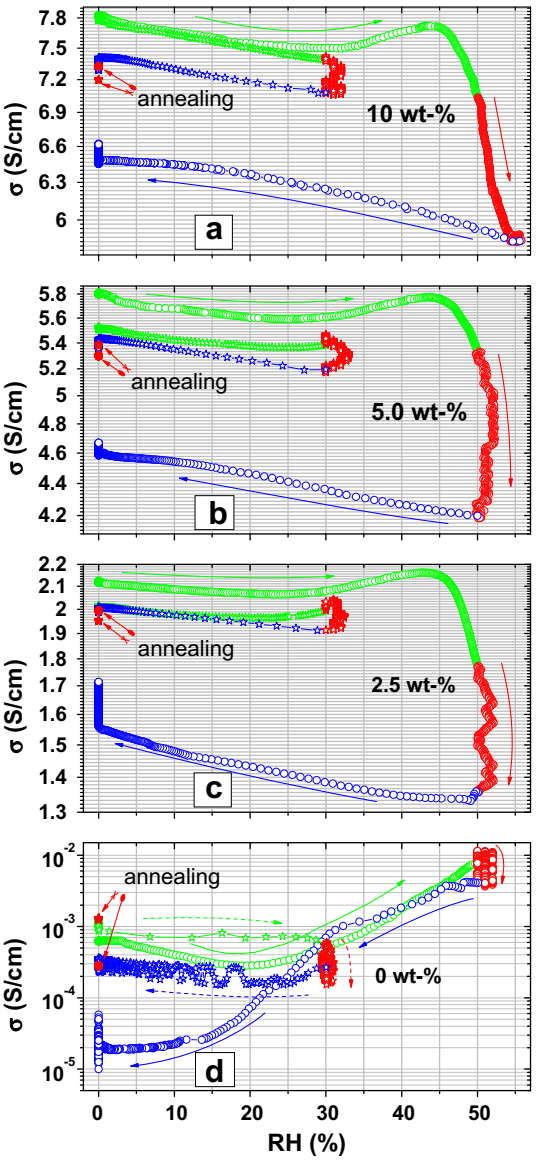

Fig. 5. Conductivity versus RH for samples with different sorbitol concentrations under medium (up to 30%, open stars) and high (up to 50%, open circles) moisture levels: (a) 10 wt-%, (b) 5 wt-%, (c) 2.5 wt-% and (d) 0 wt-%. Samples were kept at maximum moisture levels, *i.e.* 30% and 50%, during 1.5–2 h and annealed afterwards (solid markers). The arrows indicate the moisture cycling, RH(%) up (green markers), constant (red markers) and down (blue markers) and where the conductivity level ends up after a second annealing procedure at 200 °C for 2 min (solid red dots and stars for annealing after the RH sweeps up to 30% and 50%, respectively). (For interpretation of the references to colour in this figure legend, the reader is referred to the web version of this article.)

Thermal annealing of the films when the RH returned to 0% causes different effects. For the sorbitol-treated samples, thermal annealing causes a further, albeit slight, reduction of the conductivity (red dots in Fig. 5a–c) when the maximum RH was 30%, but a substantial increase

(red stars in Fig. 5a–c) for a maximum RH of 50%. The absolute values after annealing, however, are virtually identical.

3.4. Water uptake

In order to understand the (lack of) environmental stability of conductivity as described in the previous section TGA of pristine and 10 wt-% samples was carried out under a wet atmosphere to measure the release and subsequent uptake of water. In the experiments the changes in weight of the samples were monitored during two repetitive thermal cycles involving annealing at 200 °C for 6 min and subsequent cooling, followed by a longer period at room temperature.

The TGA curves in Fig. 6 show that both samples lose almost 25% of mass when increasing the temperature. During subsequent cooling a gain in mass occurs due to the re-uptake of water, which is essentially reversible, as witnessed by the second annealing step. Unlike the pristine sample, the 10 wt-% sample does not completely recover its initial mass, W_0, after the first annealing, which is due to the evaporation of sorbitol.

During the water uptake, the slope (rate of mass gain) is ~6 times higher for the pristine sample than for the 10 wt-% sample. Also the water uptake, $([W_w - W_d]/W_d) \times 100\%$, where W_w and W_d are the weights of the wet and dry samples, is much larger for the pristine sample than for the 10 wt-% sample. The values found are 35% and 13%, respectively. These observations are in line with the proposed denser morphological packing of the sorbitol-treated samples, reducing the water uptake capacity and thereby improving environmental stability.

The time scale of the experiments discussed above mainly results from the thickness of the used films. For a much thinner film of ~100 nm, as used in most devices, water uptake takes place in seconds rather than minutes as revealed by quartz crystal microbalance experiments shown by the inset of Fig. 6. More importantly, this experiment also shows that the water uptake of thin films can be totally reversed without annealing, *i.e.* by purging dry N_2. In particular, this implies that any changes in the conductivity after exposure to humidity and subsequent drying with N_2 or by pumping cannot be due to the presence of water itself.

3.5. Temperature dependence

In order to further investigate structural effects of the post-deposition treatments and exposure to moisturized environment on electrical transport properties, we have measured the temperature dependence in the 77–300 K range of the D.C. conductivity for a pristine sample before and after thermal annealing, and after subsequent exposure to 30% RH (Fig. 7).

For all conditions, the temperature dependence of the conductivity can be described by Mott's 3D variable range hopping (VRH) [47] expression $\sigma = \sigma_0 \exp[-(T_0/T)^{\alpha}]$. Here, σ_0 is the conductivity at infinite temperature, T_0 is the characteristic temperature and $\alpha = 1/(1+D) = 1/4$ in $D = 3$ dimensions as previously found [14,37]. The fact that Mott's 3D VRH applies to these each of these subsequent processing conditions confirms that the transport in dry films is electronic in nature. The slopes in Fig. 6 reflect the T_0 parameter, which is given by $T_0 = \beta/(N(E_F)\xi'^3 k_B)$ in Mott's 3D VRH model, where β is a numeral factor, k_B the Boltzmann constant, $N(E_F)$ the density of states around the Fermi level and ξ' the effective localization length [37,48]. As a result, changes in the slopes in Fig. 7 can be assigned to microscopic changes in the material upon annealing. These changes are reversible since the T_0 value prior to any treatment ($T_0 = (6.90 \pm 0.35) \times 10^6$ K) and after annealing and subsequent exposure to 30% RH ($T_0 = (7.21 \pm 0.28) \times 10^6$ K) are statistically equal. The value after annealing ($T_0 = (9.34 \pm 0.27) \times 10^6$ K), however, is higher. It must be noted that since the films were measured in a vacuum of 10^{-5} mbar, variations in T_0 cannot arise from substantial differences in the amount of water present in the film as established in the previous section.

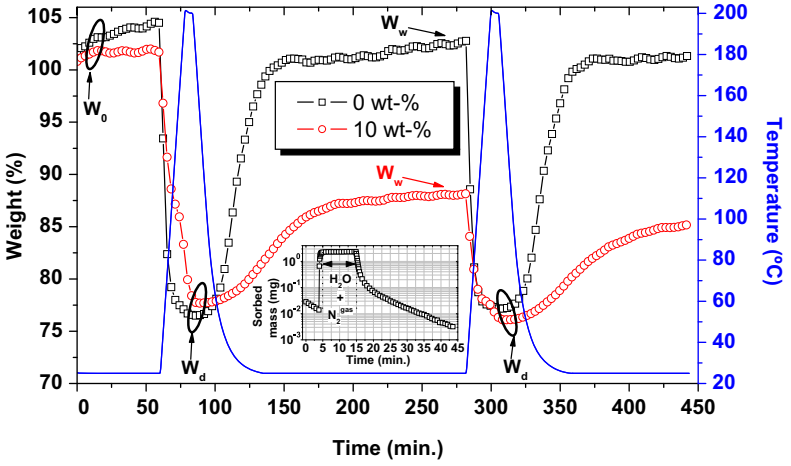

Fig. 6. TGA of pristine PEDOT:PSS (squares) and PEDOT:PSS mixed with 10 wt-% of sorbitol (circles) under a moisturized atmosphere. W_0, W_w and W_d are the weights of the fresh, wet and dry samples, respectively. The inset shows the absorbed mass of a pristine film measured with QMB when a moisturized atmosphere of 49% RH is introduced (at $t = 6$ min) and removed (at $t = 16$ min).

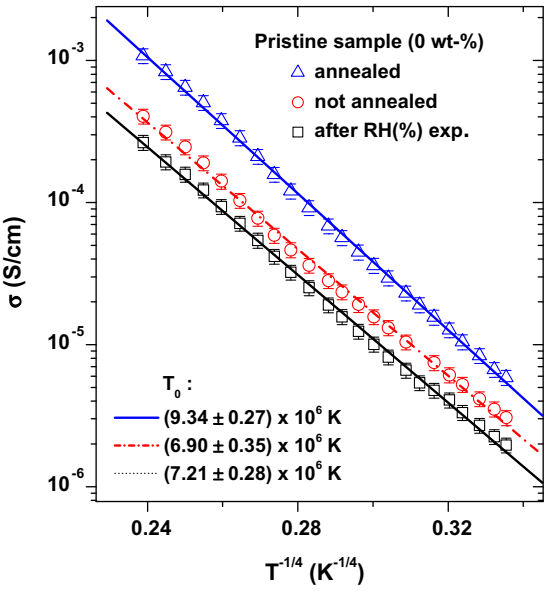

Fig. 7. Temperature dependence of the conductivity for PEDOT:PSS thin films before any treatment (○), after annealing (△), and after exposure to humidity (□). Lines are fits to Mott's VRH expression, see text.

Recalling that conduction in these materials takes place by hopping between PEDOT-rich grains of ~20 nm size [15], it is hard to imagine reversible changes in the total number of sites per unit volume N_0. Therefore we tentatively attribute the observed differences in T_0 to subtle changes in the effective localization length, most likely induced by slight de- and remixing of the PEDOT and PSS phases upon the various treatments.

4. Discussion

To clarify the complex effects of the humidity dependency presented in this paper, we recall that spin coated PEDOT:PSS films possess a phase segregated morphology, consisting of conductive PEDOT-rich grains surrounded by a shell formed by excess PSS [15,38]. PSS is a highly hydrophilic polymer electrolyte, having anionic immobile sulfonic acid groups and a proton (or Na^+ impurities, ~300 ppm) as mobile counter ion (Fig. 1). Hence, in PSS, ionic transport may occur through protons (or Na^+ [14]) that jump from one sulfonic acid group to another. When the PEDOT:PSS film is hydrated, those cations are expected to become mobile above a certain threshold. In Fig. 5, this seems to occur around 30% RH and a conductance channel parallel to the conventional electron (or hole) hopping conduction is opened. This proposition implies that below this threshold, humidity dependent changes in the conductivity must be due to changes in the conventional electron hopping channel. This seems indeed to be the case, since the reduction in conductivity when going from 0% to 30% RH in Fig. 5d is equal in magnitude to the gain in conductivity upon annealing in Fig. 7. In the discussion of Fig. 7 it was shown that the conduction both prior and after annealing follows Mott's VRH law, *i.e.* it is electronic in nature.

The relative magnitude of the ionic conduction channel, which for sorbitol-treated samples also seems to open around 30% RH is largest for pristine samples. However, the absolute magnitude of the ionic conduction channel is larger by an order of magnitude for the sorbitol-treated samples. Hence, the ionic conductivity does not scale with the presence of the segregated PSS top layer [24], being most pronounced for the 0 wt-% sample, as discussed in Section 3.2 [19,24,32,33]. The larger ionic conductivity of sorbitol-treated films corroborates our previous observation that the width of the PSS lamellas separating the granular PEDOT layers seems to be enhanced by sorbitol treatment [38]. Because of the acidic and hydrophilic nature of PSS, one expects that the ionic current is mainly carried in the PSS, with the lamellas acting as the main transport channels.

5. Conclusion

We have studied and further clarified the role of sorbitol as a typical high-boiling processing additive on the conductivity of PEDOT:PSS thin films under thermal annealing and exposure to humidity. The well-established conductivity enhancement of thin PEDO:PSS films caused by adding sorbitol to the aqueous dispersion occurs during thermal annealing and coincides with the evaporation of sorbitol from the films. The increased conductivity after annealing is accompanied by a lowering of the work function and by a remarkable increase in environmental stability after thermal annealing, as evidenced from a reduced water uptake, which we attribute to a denser packing of the PEDOT:PSS material. Up to 30% RH, the conductivity of PEDOT:PSS is dominated by conventional variable range hopping of electrons, which is negatively affected by the uptake of water. Exceeding 30% RH, a parallel ionic channel starts to contribute to the total conductivity.

Acknowledgments

We thank Dr. Albert van Breemen of TNO Science and Industry for generously providing materials, samples and for fruitful discussions and Dr. X. Lou and J. L. J. van Dongen for their assistance with mass spectrometry experiments. A. M. Nardes acknowledges the Alβan Program (the European Union Programme of High Level Scholarships for Latin America, ID#E03D19439BR) for the financial support.

References

[1] V. Saxena, B.D. Malhotra, Curr. Appl. Phys. 3 (2003) 293.
[2] T.A. Skotheim, J. Reynolds (Eds.), Handbook of Conducting Polymers, third ed., CRC, Boca Raton, FL, 2007.
[3] L. Groenendaal, F. Jonas, D. Freitag, H. Pielartzik, J.R. Reynolds, Adv. Mater. 12 (2000) 481.
[4] S. Kirchmeyer, K. Reuter, J. Mater. Chem. 15 (2005) 2077.
[5] L. Groenendaal, G. Zotti, P.H. Aubert, S.M. Waybright, J.R. Reynolds, Adv. Mater. 15 (2003) 855.
[6] F. Jonas, W. Krafft, B. Muys, Macromol. Symp. 100 (1995) 169.
[7] M.M. de Kok, M. Buechel, S.I.E. Vulto, P. van de Weijer, E.A. Meulenkamp, S.H.P.M. de Winter, A.J.G. Mank, H.J.M. Vorstenbosch, C.H.L. Weijtens, V. van Elsbergen, Phys. Status Solidi A 201 (2004) 1342.
[8] C.J. Ko, Y.K. Lin, F.C. Chen, C.W. Chu, Appl. Phys. Lett. 90 (2007) 063509.

[9] F. Verbakel, S.C.J. Meskers, R.A.J. Janssen, Chem. Mater. 18 (2006) 2707.
[10] S.C.J. Meskers, J.K.J. van Duren, R.A.J. Janssen, F. Louwet, L. Groenendaal, Adv. Mater. 15 (2003) 613.
[11] A. Kumar, D.M. Welsh, M.C. Morvant, F. Piroux, K.A. Abboud, J.R. Reynolds, Chem. Mater. 10 (1998) 896.
[12] B. Yoo, A. Dodabalapur, D.C. Lee, T. Hanrath, B.A. Korgel, Appl. Phys. Lett. 90 (2007) 072106.
[13] B. Chen, T. Cui, Y. Liu, K. Varahramyan, Solid-State Electron. 47 (2003) 841.
[14] J. Huang, P.F. Miller, J.S. Wilson, A.J. de Mello, J.C. de Mello, D.D.C. Bradley, Adv. Funct. Mater. 15 (2005) 290.
[15] A.M. Nardes, M. Kemerink, R.A.J. Janssen, J.A.M. Bastiaansen, N.M.M. Kiggen, B.M.W. Langeveld, A.J.J.M. van Breemen, M.M. de Kok, Adv. Mater. 19 (2007) 1196.
[16] S. Timpanaro, M. Kemerink, F.J. Touwslager, M.M. de Kok, S. Schrader, Chem. Phys. Lett. 394 (2004) 339.
[17] J.Y. Kim, J.H. Jung, D.E. Lee, J. Joo, Synthetic Met. 126 (2002) 311.
[18] F.J. Touwslager, N.P. Willard, D.M. de Leeuw, Synthetic Met. 135–136 (2003) 53.
[19] L.A.A. Pettersson, S. Ghosh, O. Inganäs, Organ. Electron. 3 (2002) 143.
[20] S.K.M. Jönsson, W.R. Salaneck, M. Fahlman, J. Electron Spectrosc., Relat. Phenom. 137–140 (2004) 805.
[21] J. Ouyang, C.-W. Chu, F.-C. Chen, Q. Xu, Y. Yang, Adv. Funct. Mater. 15 (2005) 203.
[22] X. Crispin, F.L.E. Jakobsson, A. Crispin, P.C.M. Grim, P. Anderson, A. Volodin, C. van Haesendonck, M. van der Auweraer, W.R. Salaneck, M. Berggren, Chem. Mater. 18 (2006) 4354.
[23] J.C. Scott, G. Malliaras, W.D. Chen, J. Breach, J. Salem, P. Brock, S. Sachs, C. Chidsey, Appl. Phys. Lett. 74 (1999) 1510.
[24] G. Greczynski, T. Kugler, M. Keil, W. Osikwicz, M. Fahlman, W.R. Salaneck, J. Electron. Spectrosc., Relat. Phenom. 121 (2001) 1.
[25] A.J. Makinen, I.G. Hill, R. Shashindhar, N. Nikolov, Z.H. Kafafi, Appl. Phys. Lett. 79 (2001) 557.
[26] N. Koch, A. Kahn, J. Ghijsen, J-J.J.-J. Pireaux, J. Schwartz, R.L. Johnson, A. Elschner, Appl. Phys. Lett. 82 (2003) 70.
[27] F. Zhang, A.P. Peisert, M. Knupfer, L. Dunsch, J. Phys. Chem. B 108 (2004) 17301.
[28] P.K.H. Ho, J-S.J.-S. Kim, J.H. Burroughes, H. Becker, F.Y.L. Sam, T.M. Brown, F. Cacialli, R.H. Friend, Nature 404 (2000) 481.
[29] H. Frohne, D.C. Muller, K. Meerholz, Chem. Phys. Chem. 3 (2002) 707.
[30] H. Frohne, S.E. Shaheen, C.J. Brabec, D.C. Muller, N.S. Sariciftci, K. Meerholz, Chem. Phys. Chem. 3 (2002) 795.
[31] S.K.M. Jönsson, J. Bigerson, X. Crispin, G. Greczynski, W. Osikowicz, A.W. Denier van der Gon, W.R. Salaneck, M. Fahlman, Synthetic Met. 139 (2003) 1.
[32] J. Hwang, F. Amy, A. Kahn, Org. Electron. 7 (2006) 387.
[33] H.J. Snaith, H. Kenrich, M. Chiesa, R.H. Friend, Polymer 46 (2005) 2573.
[34] N. Koch, A. Vollmer, A. Elschner, Appl. Phys. Lett. 90 (2007) 043512.
[35] J. Huang, P.F. Miller, J.C. de Mello, A.J. de Mello, D.D.C. Bradley, Synthetic Met. 139 (2003) 569.
[36] W.N. Hansen, G.J. Hansem, Surf. Sci. 481 (2001) 172.
[37] A.M. Nardes, M. Kemerink, R.A.J. Janssen, Phys. Rev. B. 76 (2007) 085208.
[38] A.M. Nardes, M. Kemerink, R.A.J. Janssen, Adv. Funct. Mater. 18 (2008) 865.
[39] Although PEDOT:PSS is quasi metallic, it is actually a semiconductor, which means that locally net charge densities can be formed. Only partial screening of the surface dipole by mobile cations (mostly Na^+) is expected, since, at a typical Na concentration of 300 ppm, the screening length is large compared to the surface layer thickness of a few nm.
[40] H.S. Kang, H.-S. Kang, J.K. Lee, J.W. Lee, J. Joo, J.M. Ko, M.S. Kim, J.Y. Lee, Synthetic Met. 155 (2005) 176.
[41] Y. Kudoh, K. Akami, Y. Matsuda, Synthetic Met. 98 (1998) 65.
[42] Y. Kudoh, K. Akami, H. Kusayanagi, Y. Matsuda, Synthetic Met. 123 (2001) 541.
[43] W.A. Daoud, J.H. Xin, Y.S. Szeto, Sensor Actuat. B 86 (2005) 330.
[44] D. Nilsson, T. Kugler, O. Svensson, M. Berggren, Sensor Actuat. B 86 (2002) 193.
[45] K. Kawano, R. Pacios, D. Poplavskyy, J. Nelson, D.D.C. Bradley, J.R. Durrant, Sol. Energy Mater. Sol. Cells 90 (2006) 3520.
[46] C. Carlberg, X. Chen, O. Inganäs, Solid State Ionics 85 (1996) 73.
[47] N. Mott, E.A. Davis, Electronic Processes in Non-Crystalline Materials, Clarendon Press, Oxford, 1979.
[48] J. Zhang, B.I. Shklovskii, Phys. Rev. B 70 (2004) 115317.

Organic Electronics 9 (2008) 735–739

Contents lists available at ScienceDirect

Organic Electronics

journal homepage: www.elsevier.com/locate/orgel

Determining carrier mobility with a metal–insulator–semiconductor structure

P. Stallinga [a,*], A.R.V. Benvenho [a], E.C.P. Smits [b], S.G.J. Mathijssen [b], M. Cölle [b], H.L. Gomes [a], D.M. de Leeuw [b]

[a] Universidade do Algarve, Center of Electronics, Opto-electronics and Telecommunications, Campus de Gambelas, 8005-139 Faro, Portugal
[b] Philips Research Laboratories, Professor Holstlaan 4, 5656 AA Eindhoven, The Netherlands

ARTICLE INFO

Article history:
Received 23 April 2008
Received in revised form 9 May 2008
Accepted 10 May 2008
Available online 21 May 2008

PACS:
85.30.De
85.30.Kk

Keywords:
Charge-carrier mobility
Admittance spectroscopy
MIS diode

ABSTRACT

The electron and hole mobility of nickel-bis(dithiolene) (NiDT) are determined in a metal–insulator–semiconductor (MIS) structure using admittance spectroscopy. The relaxation times found in the admittance spectra are attributed to the diffusion time of carriers to reach the insulator interface and via Einstein's relation this yields the mobility values. In this way, an electron mobility of 1.9×10^{-4} cm^2/Vs and a hole mobility of 3.9×10^{-6} cm^2/Vs were found. It is argued that the low mobility is caused by an amphoteric mid-gap trap level. The activation energy for electrons and holes from these traps is found to be 0.46 eV and 0.40 eV, respectively.

1. Introduction

The charge-carrier mobility (henceforth simply called 'mobility', or μ) is an important parameter of semiconductor materials and is the major determining factor for the speed of electronic devices. The mobility is defined as the relation of the drift velocity of the carriers to the electric field, $v = \mu E$ [1]. In semiconductors there are two types of carriers, electrons and holes, and they can have different mobilities, in crystalline materials mostly due to different effective mass (for example, in silicon the electron and hole mobility are about 1500 and 500 cm^2/Vs, respectively). In spite of its simple definition, because of the difficulty of measuring velocity, accurate determination of the mobility of the carriers is not easy and indirect ways are used, each with its own advantages and disadvantages. The most popular are current–voltage, time-of-flight, Hall measurements and field-effect-transistor.

Hall measurements are inadequate for low-mobility materials because of the tiny quantities that then have to be measured. In standard I–V curves, the mobility cannot be measured because, in the ohmic regime, the current depends on the product of charge density *and* mobility. Independent determination of mobility is impossible. This problem can be circumvented by measuring in the so-called space-charge limited current regime, which depends only on mobility [2–4]. However, when the mobility depends on electric field (for instance in the presence of traps, as in Poole–Frenkel conduction) the extraction is more complicated, because across the device the field is not constant and therefore also not a constant mobility is measured [4]. Blom et al., have used the I–V technique in systems with electron traps exponentially distributed in energy. Mobility values could then only be given for the hole-conduction SCLC regime [5].

* Corresponding author.
E-mail address: pjotr@ualg.pt (P. Stallinga).

1566-1199/$ - see front matter © 2008 Elsevier B.V. All rights reserved.
doi:10.1016/j.orgel.2008.05.007

In time-of-flight measurements, a high electron–hole density is created close to one surface of the sample by a light pulse. One type of carrier is then driven by an electrical field to the other surface. The current transient is monitored, and the characteristic time is a measure for the mobility. In highly disordered materials, the transients get distorted and extraction of the mobility more complicated [6].

A more popular technique, especially for low-mobility materials, is with a (thin-film) field-effect-transistor (TFT). The mobility is directly proportional to the derivative of a so-called transfer curve of drain–source current vs. gate–source bias. However, when traps are present, the transfer curves become highly non-linear and mobility starts being a function of bias and/or temperature, depending on the distributions of traps and conductive states [7]. In view of this, it is not clear how to define a way that will result in a unique mobility value.

Here we present a way to determine the mobility in an alternative way by means of a metal–insulator–semiconductor (MIS) diode structure. The method resembles time-of-flight, but the measurements are not done in the time domain, but in the frequency domain. Instead of measuring current transients, impedance/admittance spectra are acquired. The advantage of using MIS structures above regular diodes is that they do not have DC conductance which otherwise might mask the relevant admittance data. As a comparison, Martens et al., have endeavored to determine the electron and hole mobility by a similar technique, but instead in an LED structure [8,9], later again studied by Tsang et al. [10] (and even more recently by Schmeits [11] and an elaborate example by Nguyen et al. [12]). These devices need dual injection of carriers, *i.e.*, both electrons and holes simultaneously. The analysis becomes thus complicated and leaves room for doubt, see for example their different correction factors (0.29 and 0.56, respectively) to convert the relaxation time of admittance spectroscopy to time-of-flight and thus mobility. In contrast, the MIS structure can easily be put in a one-carrier-type state (either holes *or* electrons) and this facilitates the analysis, as will be shown here.

2. Experimental

Fig. 1 shows a schematic picture of an MIS device used in this work. It consists of a "metal" for which we used, for technological reasons, a highly doped n^+-silicon single crystal. For the insulating layer, silicon oxide of thickness $d_{ox} = 200$ nm, thermally grown on the silicon substrate, with a relative permittivity (dielectric constant) of $\varepsilon_{ox} = 3.9$ [1], was used. The semiconductor used is a member of the family of organic materials nickel-bis(dithiolene) (NiDT), see Fig. 1 ($R = NMe_2$), which show ambipolar charge transport and, because of the planar nature of the molecules, can have a relatively high mobility (measured by the field-effect in a TFT) [13–15], though also low mobilities have been reported, especially when exposed to air [16]. The layer was deposited by spin-coating, with thickness d_s=50 nm. According to literature, this material has electron and hole mobility of $\mu_n = 2.0 \times 10^{-5}$ and

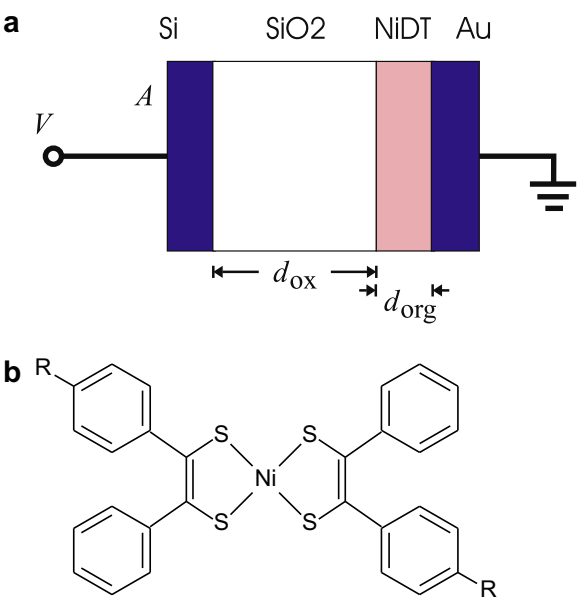

Fig. 1. Left: Schematic cross section of the MIS device consisting of (left to right): a silicon ("metal") electrode, a silicon-oxide insulating layer ($d_{ox} = 200$ nm), NiDT organic semiconductor ($d_s = 50$ nm), and gold electrode (A). The external bias V is applied to the silicon substrate relative to the gold electrode. Right: Nickel-bis(dithiolene) family. For the current work, the member used has $R = NMe_2$.

$\mu_p = 2.5 \times 10^{-4}$ (cm^2/Vs), respectively, as derived from the field-effect in FETs [15]. On top of the organic layer, a gold electrode (typical area $A = 1.3 \times 10^{-5}$ m^2) was deposited by shadow mask. The oxide capacitance is thus typically $C_{ox} = \varepsilon_{ox}\varepsilon_0 A/d_{ox} = 2.2$ nF, where ε_0 is the permittivity of vacuum, and the semiconductor layer capacitance equals $C_s = \varepsilon_{org}\varepsilon_0 A/d_s = 17.4$ nF, where a value for the relative dielectric constant of $\varepsilon_s = 5$ was used for NiDT; a typical value for organic materials. The combined geometric capacitance is thus $C_{geo} = (C_s^{-1} + C_{ox}^{-1})^{-1} = 2.0$ nF. The difference between the maximum and minimum attainable capacitance is thus of the order of 200 pF.

The nickel-bis(dithiolene) was obtained from Sensient GmbH (Germany) and has an energy gap of $E_g = 0.9$ eV, an ionization potential of $I_p = E_{vac} - E_{HOMO} = 5.2$ eV, and an electron affinity of $\chi = E_{vac} - E_{LUMO} = 4.3$ eV, where Koopmans' theorem was used linking the energies and levels [17], and E means energy and the subscripts "vac", "HOMO" and "LUMO" denote vacuum, highest-occupied-molecular-orbit (equivalent to valence band) and lowest-unoccupied-molecular-orbit (equivalent to conduction band), respectively. Considering the high resistivity of the material and the low mobility, we expect deep traps to be present that pin the Fermi level (E_F) somewhere halfway the forbidden gap. Gold has a work function of 5.1 eV [1]. The energy gap of silicon is 1.12 eV at room temperature and its Fermi level is estimated to lie 100 meV below the conduction band, which, in turn is situated 4.05 eV below the vacuum level, $\chi = E_{vac} - E_C$. With these values we are able to reconstruct the band diagram which is schematically shown in Fig. 2. The resistivity of the oxide is much higher than that of the organic layer so that nearly all the

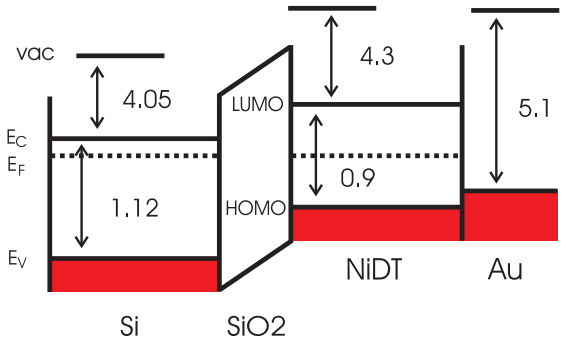

Fig. 2. Schematic band diagram of the device shown in Fig. 1. Values in eV.

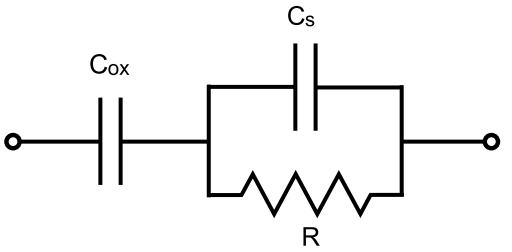

Fig. 3. Equivalent circuit used to simulate the electrical frequency behavior. For low frequencies the capacitance is equal to the oxide capacitance C_{ox}, while for high frequencies the capacitance is equal to the serial sum of C_{ox} and C_s. R does not represent the DC resistance of the organic layer but is merely a parameter that describes the frequency behavior, according to Eq. (3).

built-in voltage and applied external biases are absorbed by the oxide. It is assumed that gold is forming an ohmic contact with the organic material. For this reason we have omitted a Schottky barrier at this end of the device in the figure, although on basis of the numbers given above there should be a tiny one (of approx. 0.1 eV and built-in voltage of 0.35 V).

Electrical measurements were performed on a Keithley 487 Picoammmeter (I–V curves) and a Fluke PM 6306 RCL Bridge (impedance spectroscopy). Measurements were performed in low-vacuum (10^{-3} mbar) in a metal cryostat. All measurements were performed at room temperature ($T = 300$ K), unless otherwise specified. Positive bias signifies that the silicon electrode has a higher potential with respect to the gold counter-electrode.

3. Theory

When the organic layer is conductive by accumulation of holes or electrons, the capacitance is equal to the oxide capacitance C_{ox}. However, for the capacitance to have this value, the charges must have enough time to arrive at this interface. For high AC probing frequencies, the charges cannot follow the field oscillations. The time it takes for the charges to reach the interface is given by diffusion, for instance (for holes)

$$\tau = \frac{d_s^2}{D_p} = \frac{q}{kT}\frac{d_s^2}{\mu_p} \tag{1}$$

with D_p the hole diffusion coefficient, q the elementary charge, μ_p the hole mobility and k Boltzmann constant. Here Einstein's relation [18] was used that couples the diffusion coefficient and the mobility, $D_p = \mu_p kT/q$. A similar equation exists for electrons. Eq. (1) defines a cut-off frequency

$$f_c = \frac{1}{2\pi\tau} = \frac{\mu_p kT}{2\pi q d_s^2} \tag{2}$$

For AC-probing frequencies well below this cut-off frequency, the measured capacitance is equal to the oxide capacitance C_{ox}, while far above it, the charges do not enter the organic layer and the capacitance settles at the geometric capacitance value C_{geo}. This can also be electrically modeled by an equivalent circuit consisting of a capacitance and a resistance in series with a second capacitance, as shown in Fig. 3. The resistance R of the circuit does not represent the DC resistance of the organic layer, but merely models the frequency behavior, with

$$\tau = R(C_{ox} + C_s) \tag{3}$$

At the frequency of Eq. (2), where the capacitance drops, the loss (defined as $L = G/\omega$, with G the conductance and $\omega = 2\pi f$ the angular frequency) has a maximum. In summary, the spectrum of loss has a maximum at a frequency where simultaneously the capacitance drops. This frequency is a direct measure for the diffusion coefficient – and thus the mobility – if the device dimensions are known, see Eq. (2).

4. Results and discussion

For strong-bias, the organic layer is filled with electrons or holes and the resistivity of the organic layer is much lower than that of the insulator. The applied bias is mainly absorbed by the insulating layer and the voltage drop and electric field in the organic material are negligible. Fig. 4 shows a characteristic C–V plot which demonstrates how, under strong-bias, the capacitance at low frequencies is equal to the oxide capacitance C_{ox}. For positive bias the organic layer is full of electrons and this we call 'accumulation of electrons', whereas for strong negative bias holes are pulled into the organic layer and there exists 'accumulation of holes'. For small biases, the device is depleted, the organic layer neither has holes nor electrons and the capacitance reaches a minimum equal to C_{geo}. It is interesting to compare the device to a standard (doped) MIS device. A standard MIS goes from accumulation to inversion. The transition is abrupt when going to inversion, but stretched when going into accumulation and an asymmetric peak results [1]. Our undoped device, ideally, should go abruptly from accumulation of holes to accumulation of electrons and the dip in the C–V plot should be very narrow. The C–V plot of Fig. 4 is indeed symmetric, but the switch from accumulation of holes to accumulation of electrons is not instantaneous. This might be due to a presence of amphoteric deep levels. They can be charged either positively or negatively, thereby contributing to space charge and allowing for band bendings and stretching of the transition. More important, most of the applied

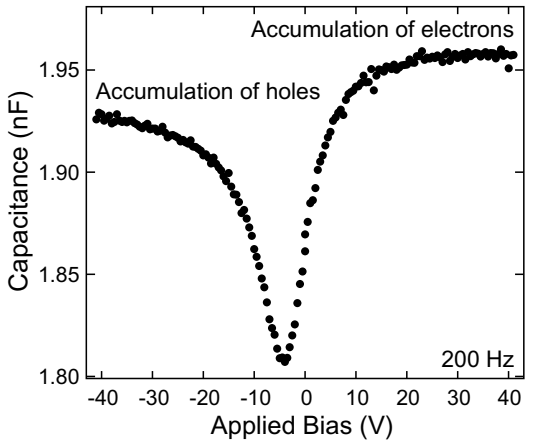

Fig. 4. *C–V* plot (measured at a frequency of 200 Hz) showing the capacitance is equal to the oxide capacitance C_{ox} for accumulation of holes or electrons. In between there is a bias where the capacitance reaches a minimum equal to the geometric capacitance C_{geo}.

bias is absorbed by the oxide layer and large voltages must be applied in order to cause any changes in the semiconductor layer. This further broadens the dip.

The minimum capacitance of Fig. 4 corresponds to the geometric capacitor formed by the silicon and gold electrodes 'filled' with the oxide and organic layers, as described in the experimental section. It happens for a bias of around −5 V, showing that at 0 V the organic layer is not completely devoid of free electrons.

As described in the theoretical section, the capacitance can be equal to the oxide capacitance C_{ox} *only* if the probing frequency is low enough. Otherwise the measured capacitance is the geometric capacitance C_{geo}. Fig. 5 shows an example of a spectrum of a device. The figure also shows a simulation of the spectrum based on the equivalent circuit given in Fig. 3. Apart from the high-frequency dispersion which we attribute to cables and other instrumental artifacts, the fit is quite well and we can see how the capacitance drops from C_{ox} to C_{geo} at a frequency where the loss has a maximum. From this frequency we can determine the (hole) mobility. The spectrum of Fig. 5 has a maximum at 640 Hz ($\tau = 250\ \mu s$). Eq. (1) with $d_s = 50$ nm then gives a hole diffusion coefficient $D_p = 1.0 \times 10^{-11}$ m^2/s, which translates via Einstein's relation into a hole mobility of $\mu_p = 3.9 \times 10^{-6}$ cm^2/Vs.

Fig. 6 shows the position of the maximum of the loss as a function of bias. At strong negative bias the frequency is constant and this gives the hole mobility as discussed above. In the same way, for strong positive bias the electron mobility can be determined. The frequency of the maximum in loss is here 31.8 kHz ($\tau = 5\ \mu s$) and this yields an electron mobility of $D_n = 5 \times 10^{-10}$ m^2/s) $\mu_n = 1.9 \times 10^{-4}$ cm^2/Vs.

The mobility is rather low and this hints at a huge abundance of deep localized states, also known as traps. When a large density of traps exists, charges spend most of their time on these localized states. To contribute to current they have to be promoted to the appropriate band. The effective mobility is then a weighed average of the trap mobility μ_T and band mobility μ_0. In other words, assuming the trap mobility is zero, the effective mobility is determined by the fraction of the time (α) a charge spends in the bands, $\mu = \alpha\mu_0$. This fraction depends on the temperature and this allows for the determination of the trap depth. Assuming the trap to be discrete and the mobility of charges residing there to be zero and a Boltzmann distribution over the levels, the activation energy of mobility is equal to the trap depth [7]. Since the frequency of the maximum in loss scales linearly with mobility (Eq. (2)), this is equal to the activation energy of this frequency.

Fig. 7 shows an Arrhenius plot of frequency of the maximum of loss as a function of temperature. From the slope we determine that the mobility of holes has an activation energy of $E_{Ap} = 400$ meV and the mobility of electrons an

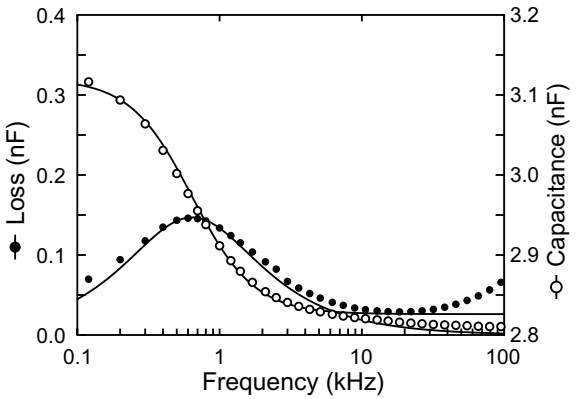

Fig. 5. Example of a spectrum of loss (•) and capacitance (○) at a bias of $V = -28$ V. For low frequencies the charges have enough time during an AC cycle to reach the interface and the measured capacitance is equal to C_{ox}, while for high frequencies the capacitance is the geometric capacitance C_{geo}, *i.e.*, charges do not move into the organic layer. The turning frequency is given by Eq. (2). At this frequency the loss has a maximum. The solid lines are simulations with $C_{ox} = 3.1$ nF, $C_s = 30$ nF and $R = 7.5$ kΩ.

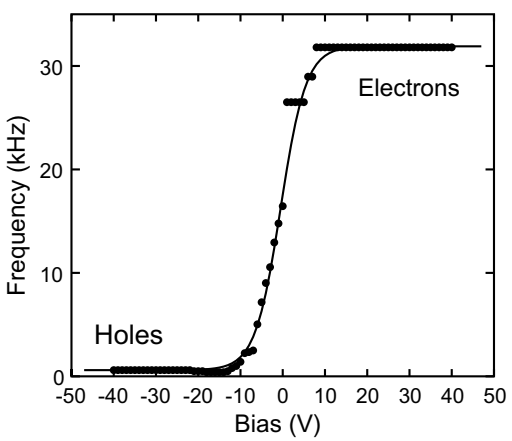

Fig. 6. Frequency of maximum of loss as a function of bias as shown in Fig. 5. The solid line is a guide to the eye. At strong positive or negative bias, the frequency is stable and this allows for the determination of the mobility via Eq. (2).

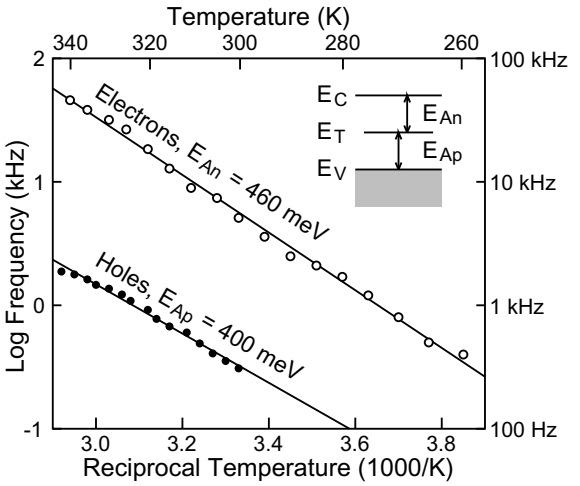

Fig. 7. Arrhenius plot of the frequency of loss as a function of temperature revealing the activation energies of mobility as indicated. The inset shows the energetic position of the responsible traps.

activation energy of $E_{An} = 460$ meV. Considering the fact that the band gap of NiDT is approximately 0.9 eV, this places the responsible traps close to mid-gap, see the energy diagram in the figure. This is in-line with the observation of an amphoteric trap mentioned earlier.

To summarize the experimental results, we have shown here how admittance spectroscopy is used to determine both the electron and hole mobilities in the same NiDT device. Compared to literature, the found mobilities are much lower. Moreover, we find the electron mobility higher than the hole mobility while it has been reported reverse [15]. The reason for this is unknown. However, it is very common that mobilities measured with different techniques result in widely different values.

What is actually measured by this technique is not the mobility, but the diffusion coefficient. They are linked by Einstein's Relation, which has its limitations. As an example, it is valid only when multiple occupancy of the electronic levels is allowed, with uncorrelated particles, like in band conduction. When the particle movements are correlated, the Einstein Relation is no longer valid and diffusion is more rapid than predicted by Einstein's Relation [19]. Another reason can be that Einstein's Relation is violated in non-equilibrium systems [20].

The combination of parameters (film thickness and mobility) puts the interesting frequencies in the range of the experimental set-up used. For materials with mobilities in the order found here the presented method is a valuable additional tool in the determination of the carrier mobility. For higher quality materials, such as crystalline silicon, the cut-off frequency falls above the measurement window, while for low-mobility materials or thick devices, the response becomes too slow and the frequency range inconvenient.

An alternative interpretation of the data which we have considered is assigning the spectral peaks to interface states. When the Fermi level is resonant with these states at the interface, the capacitance is increased and a peak in loss is observed at a frequency determined by the energetic distance of these states to the relevant band to which they communicate and with an amplitude proportional to the density of these states. Changing the bias moves the Fermi level at the interface and other interface states are probed. In this way the energetic profile of these states can be mapped [21]. However, the devices reported here do not behave in accordance to these theories and we find the analysis described here more probable.

References

[1] S.M. Sze, Physics of Semiconductor Devices, second ed., Wiley & Sons, New York, 1981.
[2] D. Ma, I.A. Hümmelgen, X. Jing, Z. Hong, L. Wang, X. Zhao, F. Wang, F.E. Karasz, J. Appl. Phys. 87 (2000) 312.
[3] A.R.V. Benvenho, R. Lessmann, I.A. Hümmelgen, R.M.Q. Mello, R.W.C. Li, F.F.C. Bazito, J. Gruber, Mater. Chem. Phys. 95 (2006) 176.
[4] D. Natali, M. Sampietro, J. Appl. Phys. 92 (2002) 5310.
[5] P.W.M. Blom, M.J.M. de Jong, J.J.M. Vleggaar, Appl. Phys. Lett. 68 (1996) 3308.
[6] H. Scher, E.W. Montroll, Phys. Rev. B 12 (1975) 2455.
[7] P. Stallinga, H.L. Gomes, Org. Electron. 7 (2006) 592.
[8] H.C.F. Martens, J.N. Huiberts, P.W.M. Blom, Appl. Phys. Lett. 77 (2000) 1852.
[9] H.C.F. Martens, H.B. Brom, P.W.M. Blom, H.F.M. Schoo, Phys. Status Solidi 218 (2000) 283.
[10] S.W. Tsang, S.K. So, J.B. Xu, J. Appl. Phys. 99 (2006) 013706.
[11] M. Schmeits, J. Appl. Phys. 101 (2007) 084508.
[12] N.D. Nguyen, M. Schmeits, H.P. Loebl, Phys. Rev. B 75 (2007) 075307.
[13] J.-Y. Cho, B. Domercq, S.C. Jones, J. Yu, X. Zhang, Z. An, M. Bishop, S. Barlow, S.R. Marder, B. Kippelen, J. Mater. Chem. 17 (2007) 2642.
[14] T. Anthopoulos, S. Setayesh, E. Smits, M. Cölle, E. Contatore, B. de Boer, P.W.M. Blom, D.M. de Leeuw, Adv. Mater. 18 (2006) 1900.
[15] E. Smits, T.D. Anthopoulos, S. Setayesh, E. van Veenendaal, R. Coehoorn, P.W.M. Blom, B. de Boer, D.M. de Leeuw, Phys. Rev. B 73 (2006) 205316.
[16] T. Taguchi, H. Wada, T. Kambayashi, B. Noda, M. Goto, T. Mori, K. Ishikawa, H. Takezoe, Chem. Phys. Lett. 421 (2006) 395.
[17] P.W. Atkins, Quanta, A Handbook of Concepts, second ed., Oxford University Press, Oxford, 1991.
[18] A. Einstein, Ann. Phys. 17 (1905) 549.
[19] S.E. Guidoni, C.M. Aldao, Eur. J. Phys. 23 (2002) 395.
[20] T. Speck, U. Seifert, Europhys. Lett. 74 (2006) 391.
[21] P. Stallinga, H.L. Gomes, M. Murgia, K. Müllen, Org. Electron. 3 (2002) 43.

Organic Electronics 9 (2008) 740–746

Contents lists available at ScienceDirect

Organic Electronics

journal homepage: www.elsevier.com/locate/orgel

Bulk heterojunction organic solar cells based on soluble poly(thienylene vinylene) derivatives

Claudio Girotto [a,b,*], David Cheyns [a,b], Tom Aernouts [a], Fateme Banishoeib [c], Laurence Lutsen [d], Thomas J. Cleij [c], Dirk Vanderzande [c,d], Jan Genoe [a], Jef Poortmans [a,b], Paul Heremans [a,b]

[a] IMEC vzw, Polymer and Molecular Electronics, Kapeldreef 75, B-3001 Leuven, Belgium
[b] ESAT, Katholieke Universiteit Leuven, Kasteelpark Arenberg 10, B-3001 Leuven, Belgium
[c] University of Hasselt, Institute of Material Research (IMO), Agoralaan, Building D, B-3590 Diepenbeek, Belgium
[d] IMEC, IMOMEC Division, Wetenschapspark 1, B-3590 Diepenbeek, Belgium

ARTICLE INFO

Article history:
Received 13 February 2008
Accepted 10 May 2008
Available online 29 May 2008

PACS:
84.60.Jt
73.61.Ph
78.20.Ci

Keywords:
Bulk heterojunction organic solar cells
Low bandgap polymer
PTV
Soluble derivatives
Poly-(2,5-thienylene vinylene)

ABSTRACT

We report on the comparison of photophysical and photovoltaic properties of three different soluble alkyl derivatives of the low bandgap poly(2,5-thienylene vinylene) (PTV), synthesized using the dithiocarbamate precursor route. The solubility of the precursor material in dichlorobenzene is enhanced by the addition of hexyl, dihexyl and dodecyl sidegroups to the polymer chain. The materials were characterized in solid state by means of absorption, ellipsometry and atomic force microscopy of films made from both the pristine alkyl-PTVs and alkyl-PTVs:([6,6]-phenyl C_{61}-butyric acid methyl ester) (PCBM) mixtures in a 1:1 ratio. The materials showed an optical bandgap below 1.7 eV, derived from the absorption spectrum of the polymers. Field-effect transistors made of these materials showed hole mobilities in the range of 10^{-7} to 10^{-6} cm^2/Vs. Bulk heterojunction solar cells made with the polymer:PCBM blend reached efficiencies above 0.6%.

1. Introduction

In recent years, organic photovoltaic (OPV) devices are gaining interest as power conversion efficiencies (η) approach 5% [1–6]. The increased efficiency achieved in the last years, together with the potential reduction of production costs that this class of devices offer, make them particularly interesting for mass-production of low-cost self-powered electronics.

Bulk heterojunction solar cells are one of the most promising concepts to produce OPV devices. These devices are composed by a mixture of two organic materials that are deposited from solution and act as the active layer of the solar cell. Recently, the focus of most of the research has been on the poly(3-hexylthiophene) (P3HT) and ([6,6]-phenyl C_{61}-butyric acid methyl ester) (PCBM) mixture, as this combination can yield devices with $\eta > 4\%$ [5–7]. The absorption of P3HT, however, does not allow to optimally harvest the red part of the incident solar spectrum. Therefore, designing new materials shifted to the red and near infrared regions could be beneficial [8]. In fact, to generate more current the optical bandgap of the absorbing material should be less than 1.8 eV [9,10].

New materials with a bandgap lower than that of P3HT have already shown that this approach can increase the efficiency of the solar cells to 5.5% and is expected to reach values up to 7% [11,12]. Other polymers with low bandgaps are under investigation, in order to broaden this class of

* Corresponding author. Address: IMEC vzw, Polymer and Molecular Electronics, Kapeldreef 75, B-3001 Leuven, Belgium.
E-mail address: Claudio.Girotto@imec.be (C. Girotto).

1566-1199/$ - see front matter © 2008 Elsevier B.V. All rights reserved.
doi:10.1016/j.orgel.2008.05.014

materials. Poly(2,5-thienylene vinylene) (PTV) is one of these materials, and has already been employed in thin film transistors owing to its high charge carrier mobility [13,14].

Various synthetic routes have been proposed in the last two decades for the PTV family, but the high reactivity of intermediates or even the monomer itself precluded the development of a reproducible, versatile and high yield polymerization process [15]. Several attempts were also conducted to synthesize alkyl-substituted PTVs [16–18], but only a few reports were focused on the photovoltaic response of these materials and these showed limited performance [19].

Nevertheless, this electron rich conjugated polymer still attracts interest due to its low oxidation potential, which should stabilize the charge-separated state and therefore be advantageous in polymer solar cells [17]. For this reason, we recently introduced the use of the dithiocarbamate (DTC) precursor route as a successful synthesis route for the PTV derivatives, demonstrating good yield, low polydispersity, low chemical defect content and satisfactory molecular weight [15,20,21].

In previous reports, this material shows an onset of absorption at around 750 nm (1.65 eV) and solar cells made with this material show short-circuit currents (J_{SC}) up to 4 mA/cm^2 and an overall efficiency of 0.6%, markedly higher than the values found in literature [22,23]. A more recent work shows that higher molecular weight seems to have an effect on the performance of bulk heterojunction solar cells, that could be enhanced to 0.76% [21]. In these studies, PTV depositions were typically made via a soluble precursor polymer, since PTV is not soluble and therefore not processable. After deposition, the precursor polymer was then converted with a heat treatment into the conjugated polymer by elimination of the leaving group, generally rendering it insoluble in the solid state [24].

These promising results obtained with solar cells based on the precursor material suggested to extend the DTC precursor route to side chain functionalized PTVs using lithium bis(trimethylsilyl)amide (LHMDS) in order to obtain soluble PTV derivatives [15,20]. The synthesis produced three derivatives consisting of either hexyl, dihexyl or dodecyl alkyl side chains (Fig. 1).

The influence of the side chain functionalization has been shown to be crucial for the characteristics of a polymer, as has been demonstrated by several studies for the poly(3-*n*-alkylthiophene) (P3AT) class, showing that the length of the alkyl group influences the electronic, electrochemical, and optical properties of the materials [25–27]. The focus of this paper is, then, on the comparison of the optical, electrical and solar cell devices characteristics of the three soluble PTV derivatives with different side chain we obtained from the DTC precursor route.

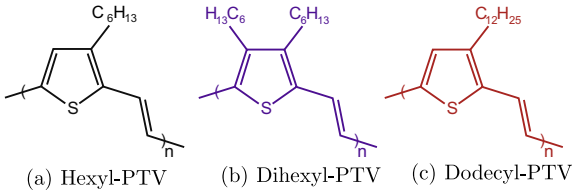

Fig. 1. Chemical structure of the PTV derivatives studied in this work. Three different sidegroups have been added to the PTV conjugated polymer to enhance its solubility. (a) Hexyl-PTV. (b) Dihexyl-PTV. (c) Dodecyl-PTV.

2. Experimental

2.1. Synthesis of PTV derivatives

The soluble alkyl-PTV derivatives used in this work were synthesized according to procedures described in literature [15]. The polymerization results of the three materials are reported in Table 1.

2.2. Device preparation

Solar cell structures were prepared according to the following procedure. Indium–tin-oxide (ITO) coated glass substrates, purchased from Merck Display Technologies with 20 Ω/□, were first patterned and then cleaned thoroughly with a sequence of detergent, de-ionized water, acetone and boiling isopropanol, each step for 10 min in an ultra sonic bath. The cleaned substrates were purified further by oxygen plasma treatment with an oxygen pressure of 0.26 Torr and a power of 100 W for 10 min. The substrates were then spin coated with a 0.45 μm filtered poly(3,4-ethylenedioxythiophene):poly(styrenesulfonate) (PEDOT:PSS) solution, purchased from HC Starck, at 3000 rpm for 30 s to produce a 30 nm thick layer. The substrates were subsequently heated on a hotplate in air at 120 °C for 10 min to remove excess water.

The further steps of the production process and the current/voltage characterization occurred in a glove box under a controlled nitrogen environment. The active layer containing a mixture of one of the PTVs derivatives and PCBM, purchased from Solenne bv, was spin coated from a dichlorobenzene solution, which was prepared under N_2 environment and stirred on a hotplate at 50 °C for at least 24 h.

LiF (0.6 nm) and Al (100 nm) top electrodes were deposited by thermal evaporation in ultra high vacuum (10^{-8} Torr) through a shadow mask to define eight separate cells on each substrate. The active areas were measured using an optical microscope, resulting in a range between 3.1 and 3.4 mm^2.

Field-effect transistor structures were made by spin coating the organic layer on n++ Si/Al substrates. The substrate itself was used as gate, with 100 nm of thermally

Table 1
Polymerization results for the three PTV derivatives used in this work: weight average molecular weight (M_w), number average molecular weight (M_n) and polydispersity (PD)

Polymer	M_w	M_n	PD
Hexyl-PTV	54,000	9600	5.6
Dihexyl-PTV	71,400	7700	9.3
Dodecyl-PTV	79,500	13,400	5.9

grown oxide as gate dielectric and patterned Au source and drain electrodes in a bottom contact configuration. The channel width was 5000 μm, the channel length was 10 μm. Mobilities were extracted from the saturation regime.

2.3. Measurements and characterization

The photovoltaic characteristics were measured under nitrogen atmosphere using an Agilent 4156C parameter analyzer under 100 mW/cm^2 AM1.5 simulated illumination using a LOT-Oriel Group Europe solar simulator with a 1000 W Xenon arc lamp, filtered by a Newport OD 0.8 neutral density filter.

UV–visible absorption spectra were obtained using a Shimadzu UV-1601PC UV–visible spectrophotometer. Thin polymer films were spin coated onto previously cleaned quartz slides from the same solutions used for the solar cells structures. A Headway Research Inc. spin coater was used to spin coat the films at 1000 rpm for 60 s.

Atomic force microscopy (AFM) images were recorded on a Picoscan PicoSPM LE scanning probe microscope in tapping mode.

Ellipsometry measurements were performed with a GES5 Variable Angle Spectroscopic Ellipsometer (VASE) from SOPRA.

3. Result and discussions

3.1. Solvent and spin coating parameters

The solubility of the PTV derivatives was found to be similar for tetrahydronaphthalene and 1,2-dichlorobenzene, and both solvents showed analogous results. For this reason, 1,2-dichlorobenzene was chosen for the comparison between the three different polymers. Hexyl-PTV showed the most critical solubility, indicating that a side chain longer than hexyl was necessary to keep the polymer in solution. Solubility was enhanced only at very high solution temperatures ($T > 150$ °C), but was nevertheless limited to 10 mg/ml. At this concentration, particles were still visible and the solution needed to be filtered with a 0.45 μm PTFE filter.

Doubling the hexyl side chain improved the solubility of the polymer: dihexyl-PTV was easily solvable up to 20 mg/ml and more, showing a clear solution without aggregates. Longer side chains increased the amount of polymer that could be dissolved as well: dodecyl-PTV reached almost the same solubility level as the dihexyl-PTV, although showing a few unsolved clusters. Nevertheless, in order to keep consistency in the experiments, all these solutions underwent the same filtration process.

Due to the low polymer concentration, the viscosity of the solutions was low, limiting the choice of parameters for spin coating. In order to get a film thicknesses of approximately 100 nm, samples had to be spin coated at a low speed of 1000 rpm, resulting in 60 nm thickness for the hexyl-PTV and 130 nm for both the dihexyl- and dodecyl-PTV.

3.2. UV–vis absorption and ellipsometry

The solid state optical absorption spectra of the three pristine polymers and their mixture with PCBM at 1:1 weight ratio are shown on Fig. 2.

The three polymers were dark blue and exhibited similar absorption profiles, as expected, but revealed a shift in the absorption peak λ_{max} from 607 (hexyl-PTV) to 622 and 630 nm (dodecyl- and dihexyl-PTV, respectively). The effect of the substituent appeared to be not simply steric, as longer side chains led to red-shifting of the absorption, as already observed for P3AT films [25]. The optical bandgaps confirmed the red shift for dihexyl-PTV, resulting in onsets at 739 nm (1.68 eV, hexyl- and dodecyl-PTV) and 749 nm (1.66 eV, dihexyl-PTV).

The three polymers presented prominent shoulders at energies higher than the absorption peak. Similar characteristics are found in P3HT and are typically ascribed to π–π interactions [28,29], thus we suggest that the PTV derivatives could be affected by significant self-organization as well. Secondary additional shoulders are present at energies lower than the absorption peak. The smooth shoulders in the spectrum of hexyl-PTV, at 577 and 684 nm, were more pronounced in dodecyl-PTV, and even red-shifted to 583 and 693 nm in dihexyl-PTV. This suggested that a longer single side chain may promote solvation of the polymer, leading to expanded chain structures with longer π-conjugation lengths and improved side-chain ordering, as observed for P3ATs [25,29]. The presence of two side chains, as in the case of dihexyl-PTV, may enhance even more this property.

The addition of PCBM in hexyl-PTV did not vary the absorption of the polymer and just superimposed the absorption spectra of the two materials. When mixed to dihexyl- and dodecyl-PTV, PCBM smoothed the peaks and the shoulders of the polymer absorption spectrum, combined it with a strong absorption to the UV range, and added a constant background absorption, especially perceptible above 700 nm. This absorption can be ascribable to light scattering induced by a nanoscale phase separation of the polymer:PCBM mixture, not visible in the

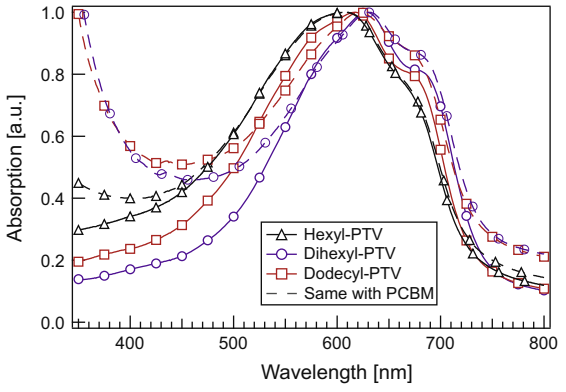

Fig. 2. Solid state absorption spectra of the three PTV derivatives and their mixtures with PCBM. Solid lines show the spectra of pristine hexyl-PTV (△), dihexyl-PTV (○) and dodecyl-PTV (□) films, while dashed lines represent their mixtures in 1:1 ratio with PCBM.

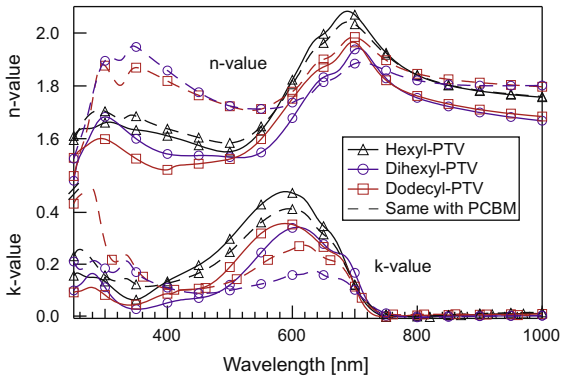

Fig. 3. Ellipsometry measurements (top: *n*-value; bottom: *k*-value) of the three PTV derivatives and their mixtures with PCBM. Solid lines show the values of pristine hexyl-PTV (△), dihexyl-PTV (○) and dodecyl-PTV (□) films, while dashed lines represent their mixtures in 1:1 ratio with PCBM.

hexyl-PTV:PCBM film, due to its homogeneity. Since morphology of the active layer is crucial for high efficiency solar cells, these differences could already suggest that the device performance would be seriously affected by the miscibility of the PTV derivatives with PCBM.

The ellipsometry measurements shown in Fig. 3 confirmed the results obtained from UV–vis spectra, showing a red shift in the *k*-value with the same trend above mentioned. Noticeably, favored by the intrinsic characteristics of ellipsometry, the scattering component measured with UV–vis spectroscopy in the case of dihexyl- and dodecyl-PTV mixed with PCBM was not present in these measurements, confirming that this signal is derived from the nanoscale intermixing of the blend rather then being a property of the materials themselves. Additional information could be drawn concerning the absorption coefficient, equal for pristine dihexyl-PTV and dodecyl-PTV and markedly higher for hexyl-PTV. The cause of this difference could be ascribed again to the introduction of the inert alkyl substituent with increased segmental volume, resulting in a dilution of the polymer backbone concentration in the film [30]. Considering the mixtures in PCBM, this effect gave noticeable reduction of the extinction coefficient *k* in the case of dihexyl- and dodecyl-PTV.

3.3. AFM imaging

Morphology analysis of films obtained from spin coating of pristine polymers and polymers:PCBM mixtures by AFM is reported in Figs. 4 and 5, respectively. Small differences in the morphology of the films were noticed for the three different polymers. The film composed of hexyl-PTV (root mean square roughness (RMS) = 0.36 nm) was smoother than the films of dodecyl-PTV (RMS = 0.76 nm) and that of dihexyl-PTV (RMS = 1.44 nm); the smooth hexyl-PTV film is indicative of an amorphous film, providing further evidence to confirm the effect of side groups to the stacking of polymer chains.

When mixed with PCBM (Fig. 5), the hexyl-PTV film shows little evidence of phase separation, which did not change substantially the surface roughness (RMS = 0.69 nm). Dodecyl-PTV:PCBM surface morphology remained almost unvaried as compared to the pristine film (RMS = 0.85 nm), and showed a slightly heterogeneous phase distribution. Dihexyl-PTV exhibited the most

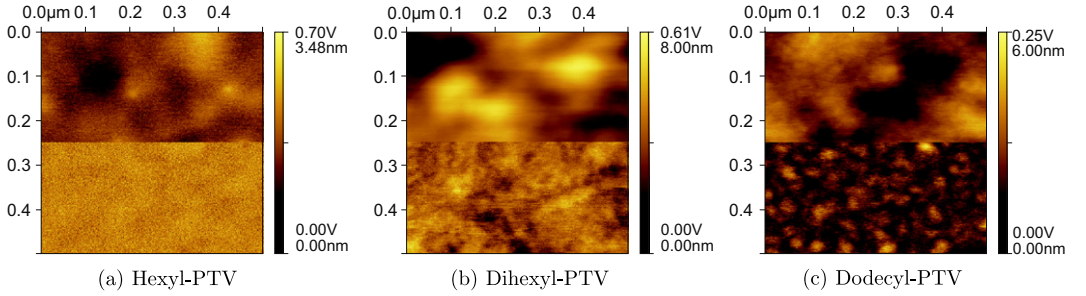

Fig. 4. Topography (top) and phase (bottom) atomic force microscopy scans of pristine layers of the three PTV derivatives.

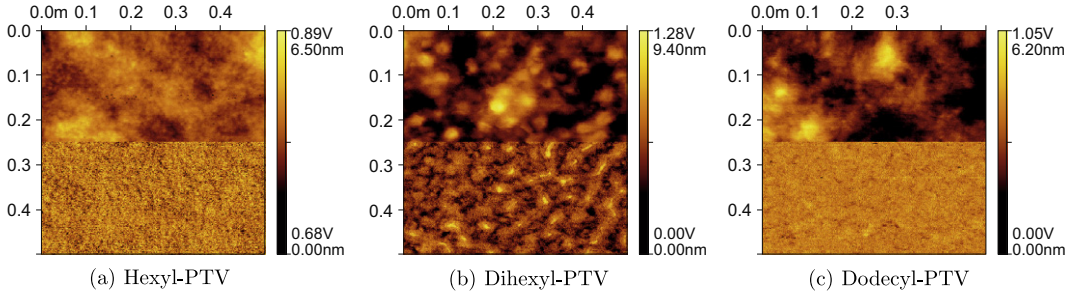

Fig. 5. Topography (top) and phase (bottom) atomic force microscopy scans of layers of the three PTV derivatives mixed in 1:1 ratio with PCBM.

pronounced phase separation, while still keeping a homogeneous interface (RMS = 1.19 nm). These observations should correlate with an improvement in J_{SC} and efficiency for bulk heterojunction devices with dihexyl-PTV, thanks to the positive effect of segregation on charge separation and transport, as has been reported by Ma et al. for the P3HT:PCBM blend system [5].

3.4. Current–voltage and mobility measurements

Good transport properties of the individual composites of the active layer are important for efficient photovoltaic performance of a specific blend [11]. Hole mobility obtained from field-effect transistors is a useful measurement that facilitates the screening and development of materials that can potentially be interesting for solar cell applications [31]. Moreover, this technique has effectively been used for the characterization of P3AT with different side chain lengths to characterize the dependence of the transport properties on the alkyl group, confirming P3HT as a good candidate for OPVs due to its optimal properties [26,27].

We also use this technique to verify the transport properties of both intrinsic PTV films and their mixtures with PCBM. Measurements show values in the range 10^{-5} to 10^{-7} cm^2/Vs, lower than that obtained previously with the precursor material [13,14]. Mobilities improve for dihexyl-PTV and dodecyl-PTV when the polymers are mixed with PCBM, increasing by values between 3 and 10, while the mobility of hexyl-PTV is decreased by the introduction of PCBM in the solution [32,33]. The complete data extracted from measurements are reported in Table 2.

Solar cells were made with the different PTV derivatives mixed with PCBM in 1:1 ratio by spin coating from dichlorobenzene solution. Every run included one sample produced with each PTV derivative and one P3HT:PCBM reference sample. From the analysis of the results, it was concluded that the best power conversion efficiency could be obtained from blends of dihexyl-PTV. Fig. 6 shows the best set of solar cells, produced with the three different PTV derivatives, measured in dark and under illumination, while Table 3 summarizes the results. Compared to the devices made by Nguyen et al., the increased open-circuit voltage (V_{OC}) obtained with the soluble derivatives discloses a characteristic of the conjugated polymer that was not revealed by the precursor route [22,23].

Hexyl-PTV shows limitations in both current generation and extraction, being characterized by a large series resistance. The reduced thickness of the active layer (60 nm)

Table 2
Results from field-effect transistor measurements: field-effect mobility (μ) and threshold voltage (V_T)

Cell	μ [cm^2/Vs]	V_T [V]
Hexyl-PTV	8×10^{-7}	−5.5
Dihexyl-PTV	7×10^{-6}	−4.6
Dodecyl-PTV	2.8×10^{-6}	−5
Hexyl-PTV:PCBM	1.8×10^{-7}	−6
Dihexyl-PTV:PCBM	2.3×10^{-5}	−1.8
Dodecyl-PTV:PCBM	2.3×10^{-5}	−0.7

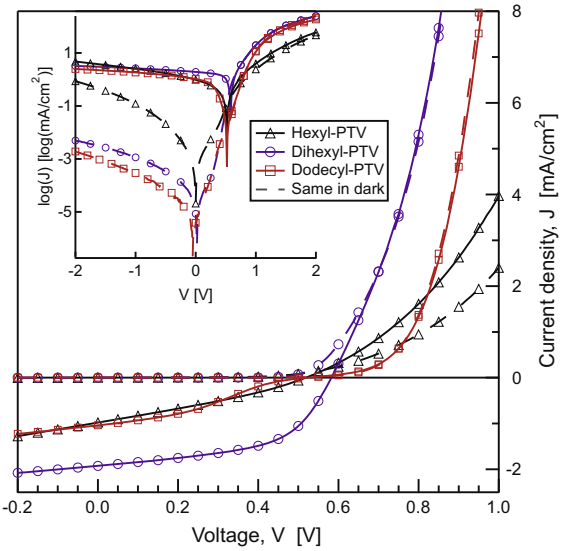

Fig. 6. The photovoltaic response of the best solar cells made with the three soluble PTV derivatives in mixture with PCBM. Solid lines show the curve under 100 mW/cm^2 AM1.5 simulated illumination of hexyl-PTV (△), dihexyl-PTV (○) and dodecyl-PTV (□) devices, while dashed lines represent their curves in dark. The inner graph shows a semi-log plot of the same curves.

Table 3
Results from photovoltaic measurements under illumination

Cell	V_{OC} [mV]	J_{SC} [mA/cm^2]	FF [%]	η [%]
Hexyl-PTV	520	0.98	30	0.15
Dihexyl-PTV	580	1.93	54	0.61
Dodecyl-PTV	520	1.03	31	0.17
Precursor-PTV*	350	3.9	40	0.5

* is derived from the work of Nguyen et al. for a 1:1 ratio with PCBM [22,23].

could explain the low short-circuit current (J_{SC}), but is in contradiction with the problems in charge collection. The low mobility of the material, nevertheless, could be the limiting factor for these devices.

Dodecyl-PTV performance is characterized by an s-shaped curve that limits the fill factor (FF): this is usually ascribed to a thin current-limiting layer due to impurity doping of the absorber or corrosion of the top contact [34]. Since all our samples were produced with the same procedure and were kept in the same controlled environment during the whole process, we exclude problems with the cathode and assume that the dodecyl-PTV could contain some impurities from the synthesis process or could have been contaminated by external agents before the preparation of the solutions, since the other two materials never showed this characteristic in the *iv*-curves.

Dihexyl-PTV devices are characterized by the highest FF, above 50%, and V_{OC}, ranging between 580 and 590 mV. J_{SC} is still limited but improvements could be achieved with thicker depositions (actual thickness: 130 nm), optimized ratio in the mixture with PCBM and enhanced morphology of the active layer at the nanoscale

level, by thermal annealing or by varying the choice of the solvent.

4. Conclusions

Three different soluble PTV derivatives have been tested and their photovoltaic response has been investigated. The insoluble PTV, typically processed from its soluble precursor, has been successfully rendered soluble by the addition of three different side chains, namely a hexyl, a dihexyl and a dodecyl group.

Materials have been characterized by absorption, ellipsometry and atomic force microscopy, and field-effect transistors and solar cells have been produced. Hexyl-PTV shows a critical solubility, and its overall performances are limited to hole mobility in the order of 8×10^{-7} cm^2/Vs and photovoltaic power conversion of around 0.15%. Dodecyl-PTV is easily soluble up to 20 mg/ml and shows an increased hole mobility, while still demonstrating limited photovoltaic response due to possible contamination. Dihexyl-PTV is the most promising of the three materials, with a power conversion efficiency exceeding 0.6%.

Further investigations could extend this first comparison between these materials to the optimization of the ratio in the mixture with PCBM in order to enhance the performance of the devices. In addition, thermal annealing treatments and the use of different solvents could improve the morphology of the active layer, a crucial factor for highly efficient solar cells.

Acknowledgments

We thank the IWT SBO-project 030220 "NANOSOLAR", funded by the Institute for the Promotion of Innovation by Science and Technology in Flanders (IWT), and the "Fonds voor Wetenschappelijk Onderzoek" (FWO-Vlaanderen), for financial support. This work, as part of the European Science Foundation EUROCORES Programme SONS (SOHYDs) was also supported by funds from the "Fonds voor Wetenschappelijk Onderzoek" (FWO-Vlaanderen) and the EC Sixth Framework Programme, under Contract N. ERAS-CT-2003-980409.

References

[1] J. Xue, B.P. Rand, S. Uchida, S.R. Forrest, A hybrid planar-mixed molecular heterojunction photovoltaic cell, Adv. Mater. 17 (1) (2005) 66–71.
[2] J. Drechsel, B. Maennig, F. Kozlowski, M. Pfeiffer, K. Leo, H. Hoppe, Efficient organic solar cells based on a double p-i-n architecture using doped wide-gap transport layers, Appl. Phys. Lett. 86 (2005) 244102.
[3] H.H.P. Gommans, D. Cheyns, T. Aernouts, C. Girotto, J. Poortmans, P. Heremans, Electro-optical study of subphthalocyanine in a bilayer organic solar cell, Adv. Funct. Mater. 17 (15) (2007) 2653–2658.
[4] B.P. Rand, J. Genoe, P. Heremans, J. Poortmans, Solar cells utilizing small molecular weight organic semiconductors, Prog. Photovoltaics 15 (2007) 659–676.
[5] W. Ma, C. Yang, X. Gong, K. Lee, A.J. Heeger, Thermally stable, efficient polymer solar cells with nanoscale control of the interpenetrating network morphology, Adv. Funct. Mater. 15 (2005) 1617–1622.
[6] J.Y. Kim, K. Lee, N.E. Coates, D. Moses, T.-Q. Nguyen, M. Dante, A.J. Heeger, Efficient tandem polymer solar cells fabricated by all-solution processing, Science 317 (5835) (2007) 222–225.
[7] G. Li, V. Shrotriya, J. Huang, Y. Yao, T. Moriarty, K. Emery, Y. Yang, High-efficiency solution processable polymer photovoltaic cells by self-organization of polymer blends, Nat. Mater. 4 (2005) 864–868.
[8] C. Winder, N.S. Sariciftci, Low bandgap polymers for photon harvesting in bulk heterojunction solar cells, J. Mater. Chem. 14 (7) (2004) 1077–1086.
[9] M.C. Scharber, D. Mühlbacher, M. Koppe, P. Denk, C. Waldauf, A.J. Heeger, C.J. Brabec, Design rules for donors in bulk-heterojunction solar cells – towards 10% energy-conversion efficiency, Adv. Mater. 18 (2006) 789–794.
[10] E. Bundgaard, F.C. Krebs, Low band gap polymers for organic photovoltaics, Sol. Energy Mater. Sol. Cells 91 (11) (2007) 954–985.
[11] D. Mühlbacher, M. Scharber, M. Morana, Z. Zhu, D. Waller, R. Gaudiana, C.J. Brabec, High photovoltaic performance of a low-bandgap polymer, Adv. Mater. 18 (21) (2006) 2884–2889.
[12] J. Peet, J.Y. Kim, N.E. Coates, W.L. Ma, D. Moses, A.J. Heeger, G.C. Bazan, Efficiency enhancement in low-bandgap polymer solar cells by processing with alkane dithiols, Nat. Mater. 6 (7) (2007) 497–500.
[13] H.E.A. Huitema, G.H. Gelinck, J.B.P.H. van der Putten, K.E. Kuijk, K.M. Hart, E. Cantatore, P.T. Herwig, van Breemen, D.M. de Leeuw, Plastic transistors in active-matrix displays, Nature 414 (2001) 599.
[14] H.E.A. Huitema, G.H. Gelinck, J.B.P.H. van der Putten, K.E. Kuijk, K.M. Hart, E. Cantatore, D.M. de Leeuw, Active-matrix displays driven by solution processed polymeric transistors, Adv. Mater. 14 (17) (2002) 1201–1204.
[15] F. Banishoeib, P. Adriaensens, S. Berson, S. Guillerez, O. Douheret, J.V. Manca, S. Fourier, T.J. Cleij, L. Lutsen, D. Vanderzande, The synthesis of regio-regular poly(3-alkyl-2,5-thienylene vinylene) derivatives using lithium bis(trimethylsilyl)amide (LHMDS) in the dithiocarbamate precursor route, Sol. Energy Mater. Sol. Cells 91 (11) (2007) 1026–1034.
[16] R.S. Loewe, R.D. McCullough, Effects of structural regularity on the properties of poly(3-alkylthienylenevinylenes), Chem. Mater. 12 (10) (2000) 3214–3221.
[17] K. Van De Wetering, C. Brochon, C. Ngov, G. Hadziioannou, Design and synthesis of a low band gap conjugated macroinitiator: toward rod-coil donor–acceptor block copolymers, Macromolecules 39 (13) (2006) 4289–4297.
[18] J.J. Apperloo, C. Martineau, P.A. van Hal, J. Roncali, R.A.J. Janssen, Intra- and intermolecular photoinduced energy and electron transfer between oligothienylenevinylenes and *n*-methylfulleropyrrolidine, J. Phys. Chem. A 106 (1) (2002) 21–31.
[19] A.P. Smith, R.R. Smith, B.E. Taylor, M.F. Durstock, An investigation of poly(thienylene vinylene) in organic photovoltaic devices, Chem. Mat. 16 (23) (2004) 4687–4692.
[20] F. Banishoeib, S. Fourier, T.J. Cleij, L. Lutsen, D. Vanderzande, The synthesis of poly(thienylene vinylene) derivatives via the dithiocarbamate route: low band gap p-type conjugated polymers for photovoltaics, Eur. Phys. J. Appl. Phys 37 (2007) 237–240.
[21] F. Banishoeib, A. Henckens, S. Fourier, G. Vanhooyland, M. Breselge, J.V. Manca, T.J. Cleij, L. Lutsen, D. Vanderzande, L.H. Nguyen, H. Neugebauer, N.S. Sariciftci, Synthesis of poly(2,5-thienylene vinylene) and its derivatives: low band gap materials for photovoltaics, Thin Solid Films 516 (12) (2008) 3978–3988.
[22] L.H. Nguyen, S. Günes, H. Neugebauer, N.S. Sariciftci, F. Banishoeib, A. Henckens, T.J. Cleij, L. Lutsen, D. Vanderzande, Low-bandgap poly(thienylene vinylene) for organic solar cells: photophysics and photovoltaic performance, in: P. Heremans, M. Muccini, E.A. Meulenkamp (Eds.), Organic Optoelectronics and Photonics II. Proceedings of the SPIE, vol. 6192, 2006.
[23] L.H. Nguyen, S. Günes, H. Neugebauer, N.S. Sariciftci, F. Banishoeib, A. Henckens, T.J. Cleij, L. Lutsen, D. Vanderzande, Precursor route poly(thienylene vinylene) for organic solar cells: photophysics and photovoltaic performance, Sol. Energy Mater. Sol. Cells 90 (17) (2006) 2815–2828.
[24] A. Henckens, M. Knipper, I. Polec, J.V. Manca, L. Lutsen, D. Vanderzande, Poly(thienylene vinylene) derivatives as low band gap polymers for photovoltaic applications, Thin Solid Films 451–452 (2004) 572–579.
[25] R.D. McCullough, S.P. Williams, S. Tristram-Nagle, M. Jayaraman, P.C. Ewbank, L. Miller, The first synthesis and new properties of regioregular, head-to-tail coupled polythiophenes, Synth. Met. 69 (1–3) (1995) 279–282.
[26] Y.D. Park, D.H. Kim, Y. Jang, J.H. Cho, M. Hwang, H.S. Lee, J.A. Lim, K. Cho, Effect of side chain length on molecular ordering and field-effect mobility in poly(3-alkylthiophene) transistors, Org. Electron. 7 (6) (2006) 514–520.

[27] A. Babel, S.A. Jenekhe, Alkyl chain length dependence of the field-effect carrier mobility in regioregular poly(3-alkylthiophene)s, Synth. Met. 148 (2) (2005) 169–173.
[28] P.J. Brown, D.S. Thomas, A. Köhler, J.S. Wilson, J.-S. Kim, C.M. Ramsdale, H. Sirringhaus, R.H. Friend, Effect of interchain interactions on the absorption and emission of poly(3-hexylthiophene), Phys. Rev. B 67 (6) (2003) 064203.
[29] C.-K. Shin, H. Lee, Effect of alkyl side-chain length and solvent on the luminescent characteristics of poly(3-*n*-alkylthiophene), Synth. Met. 140 (2-3) (2004) 177–181.
[30] L. Liao, Y. Pang, Poly[(1,4-phenylenevinylene)-alt-(1,3-phenylenevinylene)]s with different length of side chain: their synthesis and optical properties, Synth. Met. 144 (3) (2004) 271–277.
[31] M. Morana, P. Koers, C. Waldauf, M. Koppe, D. Mühlbacher, P. Denk, M. Scharber, D. Waller, C. Brabec, Organic field-effect devices as tool to characterize the bipolar transport in polymer-fullerene blends: the case of P3HT-PCBM, Adv. Funct. Mater. 17 (16) (2007) 3274–3283.
[32] V.D. Mihailetchi, L.J.A. Koster, P.W.M. Blom, C. Melzer, B. de Boer, J.K.J. van Duren, R.A.J. Janssen, Compositional dependence of the performance of poly(*p*-phenylene vinylene):methanofullerene bulk-heterojunction solar cells, Adv. Funct. Mater. 15 (5) (2005) 795–801.
[33] S.M. Tuladhar, D. Poplavskyy, S.A. Choulis, J.R. Durrant, D.D.C. Bradley, J. Nelson, Ambipolar charge transport in films of methanofullerene and poly(phenylenevinylene)/methanofullerene blends, Adv. Funct. Mater. 15 (7) (2005) 1171–1182.
[34] M. Glatthaar, M. Riede, N. Keegan, K. Sylvester-Hvid, B. Zimmermann, M. Niggemann, A. Hinsch, A. Gombert, Efficiency limiting factors of organic bulk heterojunction solarcells identified by electrical impedance spectroscopy, Sol. Energy Mater. Sol. Cells 91 (5) (2007) 390–393.

Organic Electronics 9 (2008) 747–752

Contents lists available at ScienceDirect

Organic Electronics

journal homepage: www.elsevier.com/locate/orgel

Organic photovoltaic cells with high open circuit voltages based on pentacene derivatives

Leonidas C. Palilis [a,1], Paul A. Lane [a,*], Gary P. Kushto [a], Balaji Purushothaman [b], John E. Anthony [b], Zakya H. Kafafi [a,2]

[a] US Naval Research Laboratory, 4555 Overlook Avenue SW, Washington, DC 20375-5611, United States
[b] Department of Chemistry, University of Kentucky, Lexington, KY 40506-0055, United States

ARTICLE INFO

Article history:
Received 4 March 2008
Received in revised form 8 May 2008
Accepted 10 May 2008
Available online 16 June 2008

PACS:
73.50.Gr
78.40.Me
84.60.Jt

Keywords:
Pentacene
Organic photovoltaics
Fullerene
Morphology

ABSTRACT

Heterojunction organic photovoltaic devices were fabricated using C_{60} as the electron acceptor and several pentacene derivatives with triisopropylsilylethynyl functional groups as the electron donor. The open circuit voltage (V_{oc}) of functionalized pentacene-based cells is significantly higher (0.57–0.90 V) than for cells based on unsubstituted pentacene (0.24 V), due to the higher oxidation potentials of these pentacene derivatives. The performance of pentacene derivative cells is limited by lower current densities than the reference pentacene/C_{60} cell. The absorption spectra of films and solutions of pentacene derivatives closely resemble one another, leading us to conclude that these films are amorphous in nature. Weak intermolecular coupling in the derivative films results in lower charge mobility and shorter exciton diffusion lengths relative to pentacene.

Published by Elsevier B.V.

1. Introduction

Organic photovoltaics based on molecular semiconductors have attracted significant scientific and commercial interest due to their potential use for low cost flexible solar cells. The primary device architecture used in molecular solar cells is a multi-layer structure where charge photogeneration occurs at interfaces between electron donor and acceptor molecules [1,2]. Materials employed in solar cells should ideally have strong absorption overlapping the solar spectrum, efficient exciton diffusion to the interface and high charge carrier mobility. Fused acenes comprise a class of materials that have recently been used in organic photovoltaics. Tetracene [3,4] and pentacene [5–9] have been used in cells with efficiencies of ~2% under simulated solar illumination. Pentacene is a particularly promising material due to its strong absorption in the visible part of the solar spectrum [10] and high field-effect mobility, as high as 3 $cm^2/V\,s$ in thin film transistors [11]. The performance of pentacene-based solar cells has been limited by their relatively low open circuit voltage (V_{oc}), a direct consequence of the small offset between the highest occupied molecular orbital (HOMO) of pentacene (4.9 eV) [12] and the lowest unoccupied molecular orbital (LUMO) of C_{60}.

Recently, Anthony and co-workers modified the chemical structure of pentacene in order to change its optical and electronic properties [13–15]. They sought to increase the

* Corresponding author.
E-mail addresses: lpalil@imel.demokritos.gr (L.C. Palilis), paul.lane@nrl.navy.mil (P.A. Lane).
[1] Present address: Institute of Microelectronics, National Center for Scientific Research "Demokritos", P.O. Box 60228, 15310 Aghia Paraskevi, Attiki, Greece.
[2] Present address: National Science Foundation, 4201 Wilson Boulevard, Suite 1065 North, Arlington, VA 22230, United States.

1566-1199/$ - see front matter Published by Elsevier B.V.
doi:10.1016/j.orgel.2008.05.015

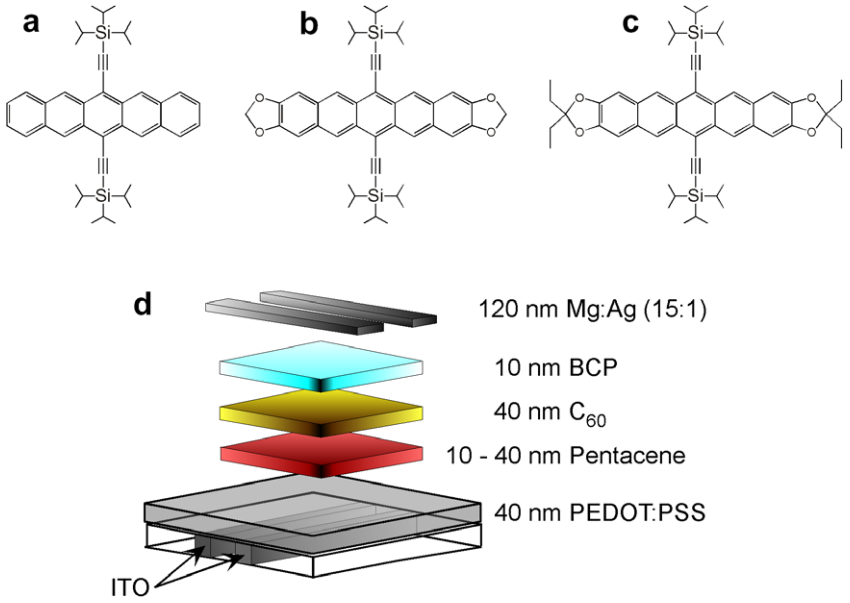

Fig. 1. Chemical structures of (a) TIPS, (b) TP-5, (c) EtTP-5, and (d) schematic diagram of the photovoltaic cells.

intermolecular π-orbital overlap in the crystalline form in order to improve carrier mobility, lower the energy of the HOMOs in order to increase the open circuit voltage of solar cells, and modify the absorption spectrum in order to harvest more solar light. To this end, triisopropylsilylethynyl functional groups were added at the 6,13-positions of pentacene and 1,3-dioxolane moieties were fused to the terminal benzenoid rings of the pentacene molecule. The chemical structures of (a) 6,13-bis(triisopropylsilylethynyl)-pentacene (TIPS), (b) 6,14-bis(tri-isopropylsilylethynyl)-1,3,9,11-tetraoxacyclopenta[*b*,*m*]pentacene (TP-5) and (c) 2,2,10,10-tetraethyl-6,14-bis(tri-isopropylsilylethynyl)-1,3,9,11-tetraoxacyclopenta[*b*,*m*]pentacene (EtTP-5) are shown in Fig. 1. These pentacene derivatives have been used as fluorescent dopant molecules in organic light-emitting diodes [16–18]. More recently, Lloyd et al. investigated multi-layer, solution-processed solar cells using TIPS as an electron donor [19]. In this study, we report on the fabrication and characterization of organic solar cells using this series of pentacene derivatives as electron donors. Our approach differs from that of Lloyd et al. in that all layers in our cells are formed by vacuum sublimation. We obtain significantly higher V_{oc} from the derivative-based cells than for reference pentacene-based cells and correlate this increase with their higher oxidation potentials. Despite the lower short circuit photocurrent (J_{sc}) of the derivative-based cells, a power conversion efficiency of 0.74% was obtained from a dioxalane-based pentacene with high V_{oc}, comparable to that of a reference cell (0.82%).

2. Experimental

The synthesis of TIPS and TP-5 was previously reported [13]. EtTP-5 was prepared by the addition of triisopropylsilyl acetylide to the corresponding quinone [20], followed by deoxygenation with aqueous stannous chloride/10% H_2SO_4. C_{60} was purchased from SES (Houston, TX) while both pentacene and 2,9-dimethyl-4,7-diphenyl-1,10-phenanthroline were purchased from Aldrich (Milwaukee, WI). All materials were purified twice via vacuum train sublimation prior to use. The oxidation potential measurements were performed by cyclic voltammetry in dichloromethane solution vs ferrocene as the internal standard.

Fig. 1d shows the multi-layer device architecture we employed for organic photovoltaics. Indium tin oxide (ITO) coated by poly(3,4-ethylenedioxythiophene):poly(styrenesulfonate) (PEDOT:PSS) was used as the anode. The ~40 nm thick PEDOT:PSS layer was spin-cast from a pre-filtered aqueous solution onto ozone-cleaned ITO-coated glass substrates (ITO thickness = 100 nm, sheet resistance = 15 Ω/square) and then annealed in air at 130 °C for 10 min. Pentacene or one of its derivatives acted as the electron donor and hole transport material and C_{60} as the electron acceptor and electron transport material. A 10 nm thick layer of 2,9-dimethyl-4,7-diphenyl-1,10-phenanthroline, also known as bathocuproine (BCP), was deposited on top of the C_{60} layer to prevent exciton quenching at the C_{60}/cathode interface. The organic layers were sequentially deposited onto the ITO/PEDOT:PSS substrates by vacuum thermal evaporation under a background pressure of $<10^{-6}$ Torr at a rate of ~0.5–1 Å s^{-1}. The thickness of the pentacene layer was varied between approximately 10 and 40 nm while that of C_{60} was fixed at 40 nm. Finally, a ~130 nm thick metal Mg:Ag cathode (10:1 by weight) was co-deposited through a shadow mask from separate evaporation sources. The active device area was 4 mm^2. Optical absorption spectra were measured with an HP 8423 UV–vis spectrophotometer.

The photovoltaic devices were spectroscopically and electrically characterized in an inert atmosphere, N_2 glove

box (O_2 and H_2O < 1 ppm) at room temperature, immediately following their fabrication. The current–voltage characteristics, both in the dark and under simulated AM 1.5 solar illumination at 100 mW/cm^2 (1 sun), were measured by a Keithley multimeter. The series resistance was calculated by a linear regression to the dark JV curve above 1 V. A good fit to the Schockley equation, modified for series and shunt resistance, could not be obtained for these devices. The solar light intensity was measured with a calibrated silicon photodiode and varied using neutral density filters. The spectral response of the cells was characterized by incident photon-to-current efficiency (IPCE) measurements.

3. Results and discussion

Fig. 2 shows the extinction spectra of (a) thin films and (b) dilute toluene solutions of the pentacene derivatives; the thin film extinction spectrum of pentacene is shown for comparison. TIPS has a peak at $\lambda \approx 650$ nm with an extinction coefficient close to 20,000 cm^{-1} and vibronic side bands at 554 and 602 nm. The extinction spectra of both TP-5 and EtTP-5 are similar to that of TIPS in the red and contain an intense, sharp peak in the blue; $\alpha = 74{,}000$ cm^{-1} at $\lambda = 470$ nm for TP-5 and $\alpha = 62{,}000$ cm^{-1} at $\lambda = 458$ nm for EtTP-5. There is a similar, but much weaker absorption feature in the blue for TIPS ($\alpha = 9700$ cm^{-1} at $\lambda = 442$ nm). The oscillator strength of this transition is dramatically affected by the dioxolane moiety. By comparison, the pentacene absorption spectrum is red-shifted from that of the derivatives and is much stronger. The significant red-shift of the pentacene film absorption compared to its solution spectrum has been proposed to be a direct result of strong intermolecular interactions [5]. This coupling results in increased absorption in the red portion of the solar spectrum, which enhances photocurrent generation. In contrast, the thin film and solution spectra of the pentacene derivatives are remarkably similar, suggesting that solid state interactions are relatively weak in these films. The solid state spectra are slightly broader than the solution spectra and only the absorption spectrum of TP-5 has a limited red-shift (~20 nm) from solution to thin film. Ostroverkhova et al. [21] studied the morphology and photoconductivity of TIPS films prepared under different conditions and showed that it is possible to obtain larger crystalline domains, particularly by crystallization from solution. Such films exhibit significantly red-shifted absorption, with an absorption edge at ~750 nm. Films prepared by sublimation under vacuum onto a heated substrate also showed evidence of crystallization. The limited red-shift and absence of new features strongly suggest that the films sublimed onto an unheated substrate are essentially amorphous, though the presence of some crystallinity cannot be completely ruled out.

Fig. 3 shows the dark current density–voltage (J–V) characteristics for the various photovoltaic cells with a 40 nm thick layer of pentacene or one of its derivatives. The pentacene derivative-based cells have significantly higher series resistance (R_s) than the pentacene-based cell. Cells based on pentacene exhibited a low R_s of 4.0 Ω cm^2 compared to 21.7 Ω cm^2 for TIPS, 29.8 Ω cm^2 for TP-5 and 26.2 Ω cm^2 for EtTP-5. The lower current density of devices made with pentacene derivatives vis-à-vis pentacene re-

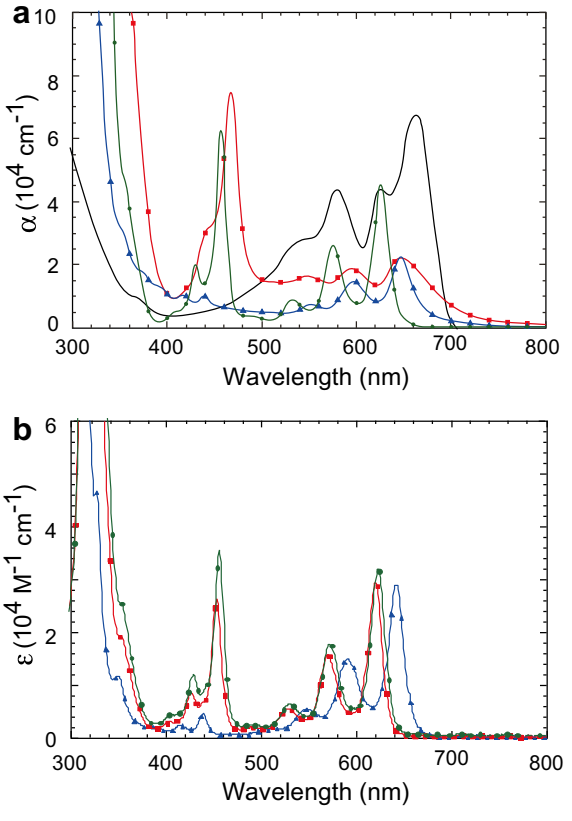

Fig. 2. (a) Thin-film extinction spectra of the pentacene derivatives TIPS (green, circles), TP-5 (red, squares), and EtTP-5 (blue, triangles). The extinction spectra of pentacene is shown for comparison (black line). (b) Solution extinction spectra of TIPS (green, circles), TP-5 (red, squares), and EtTP-5 (blue, triangles). (For interpretation of the references to colour in this figure legend, the reader is referred to the web version of this article.)

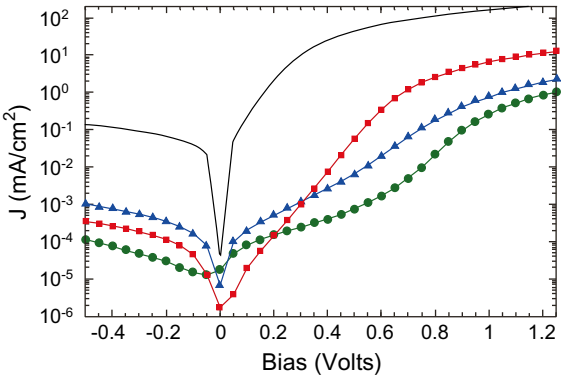

Fig. 3. Dark current density–voltage characteristics for the pentacene/C_{60} (black line) and derivative/C_{60} photovoltaic cells [TIPS (green, circles), TP-5 (red, squares), and EtTP-5 (blue, triangles)]. (For interpretation of the references to colour in this figure legend, the reader is referred to the web version of this article.)

flects the relative hole mobility in these films. The room temperature hole mobility of pentacene exceeds 1 cm^2/V s, [11], whereas Park et al. [22] measured a field-effect hole mobility of 0.02 cm^2/V s for TIPS sublimed onto a substrate at room temperature. Higher field-effect mobility from TIPS has been observed when grown from solution onto a functionalized substrate [23], although this structure differs significantly from that of a photovoltaic cell. More recently, transient THz absorption studies by Ostroverkhova et al. have also shown that the charge carrier mobility of a crystalline film of TIPS can be as high as one-third that of pentacene [21]. The much lower current densities obtained here are in agreement with the conclusion drawn from the absorption spectra – pentacene derivative films prepared by sublimation onto an unheated substrate have weak intermolecular coupling.

Fig. 4 shows the *J–V* characteristics of the various pentacene-based devices under AM1.5 illumination; Table 1 summarizes their performance. The power conversion efficiency η and the fill factor (*ff*) of the cells were calculated using

$$\eta = J_{sc} V_{oc} ff / P_0 \quad (1)$$

where J_{sc} is the short circuit current density, V_{oc} is the open circuit voltage, *ff* is the fill factor and P_0 is the incident light intensity. The fill factor is defined as the ratio between the maximum output power (P_{max}) and the product of J_{sc} and V_{oc}. The pentacene device shows good performance with V_{oc} = 0.24 V, J_{sc} = 7.6 mA/cm^2, *ff* = 0.46, and η = 0.82%. The small V_{oc}, almost half that of the more commonly reported copper phthalocyanine (CuPc)/C_{60} cell (~0.45 V) [2], reflects the lower ionization potential of pentacene (4.9 eV) [12] compared to CuPc (5.1 eV) [24]. The efficiency of the pentacene/C_{60} cell is comparable to that of similar device architectures, though the open circuit voltage is slightly lower than that reported by Mayer et al. (0.30 V) [5] and Yoo et al. (0.36 V) [6]. These variations arise from slightly different structures and fabrication conditions, particularly

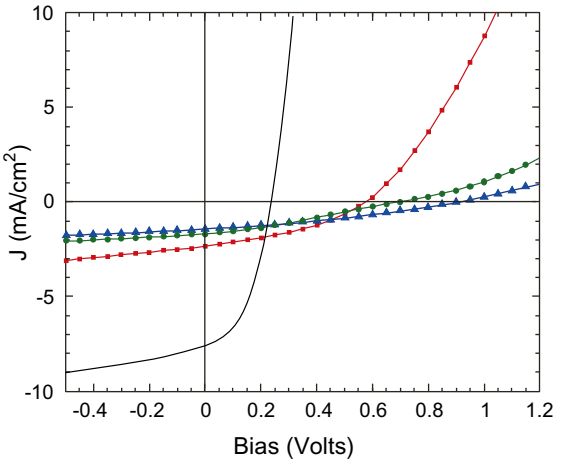

Fig. 4. Illuminated *J–V* characteristics (AM1.5, 100 mW/cm^2) for the pentacene/C_{60} (black line) and derivative/C_{60} photovoltaic cells [TIPS (green, circles), TP-5 (red, squares), and EtTP-5 (blue, triangles)]. (For interpretation of the references to colour in this figure legend, the reader is referred to the web version of this article.)

Table 1
Photovoltaic parameters of our solar cells obtained in the dark (Fig. 3) and under AM1.5 (100 mW/cm^2) solar illumination (Fig. 4)

Electron donor	E_{ox} (V)	V_{oc} (V)	J_{sc} (mA/cm^2)	*ff*	η (%)
Pentacene	0.100	0.24	7.59	0.46	0.82
TP-5	0.217	0.57	2.32	0.37	0.50
EtTP-5	0.180	0.69	1.68	0.29	0.34
TIPS	0.390	0.90	1.42	0.33	0.42

The layer thicknesses are 40 nm for the electron donor, 40 nm for C_{60}, and 10 nm for BCP. The oxidation potential data for the pentacene derivatives are listed for comparison.

the use of a different cathode, Mg:Ag in our case and either aluminum [6] or cesium fluoride capped by aluminum [5] in other studies. In comparison, the cells based on the pentacene derivatives showed a lower performance in terms of the overall cell efficiency being equal to 0.34% for EtTP-5, 0.42% for TIPS, and 0.50% for TP-5. Lloyd et al. achieved an efficiency of 0.52% from a cell using solution-processed TIPS [19], comparable to what we report here. The lower efficiency of cells based on pentacene derivatives is mainly due to the lower J_{sc}, and is also affected by the lower fill factor, owing to the larger R_s of the derivative-based cells. All the cells based on the pentacene derivatives showed a significant increase of V_{oc}, compared to that of pure pentacene (0.24 V), ranging from 0.57 V for TP-5, 0.69 for EtTP-5, and 0.90 V for TIPS. The open circuit voltage for the TIPS/C_{60} cell is among the highest reported to date for small molecule-based organic photovoltaics [2,25]. Examples of electron donors yielding values of V_{oc} approaching 1 V in cells with C_{60} include 4,4-bis[*N*-1-naphthyl-*N*-phenyl-amino]biphenyl (α-NPD) [26] and subphthalocyanines [27]. We note that the photocurrent density and dark current density are similar above V_{oc} for all devices, suggesting that there is no significant photoenhanced conductivity. J_{sc} is proportional to the illumination intensity, indicating that exciton-exciton annhilation was not a significant loss mechanism in these cells.

Fig. 5 shows a qualitative correlation between V_{oc} and the oxidation potential of pentacene and the derivatives. TIPS has the highest oxidation potential of 0.39 V while pentacene the lowest of 0.10 V, measured relative to a ferrocene standard. Gas phase photoemission measurements

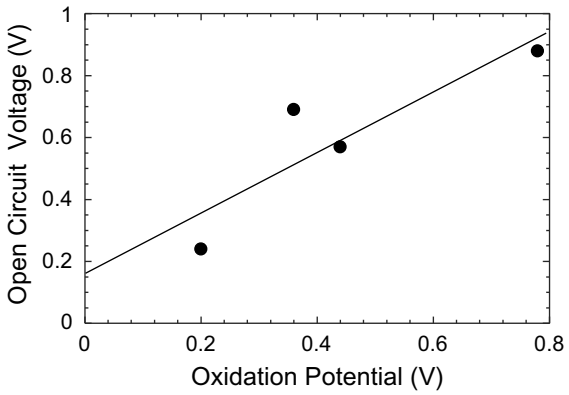

Fig. 5. Variation of V_{oc} with the oxidation potential of the electron donor molecules.

show a similar trend with the vertical ionization energy being higher for TIPS (6.38 eV) than for TP-5 (6.20 eV) or EtTP-5 (6.01 eV) [28]. It is worth noting that there is not a 1:1 correspondence between V_{oc} and the oxidation potentials of the various pentacene derivatives. This can be partly attributed to the effect of polarization energy in the solid state, which can be as high as a few tenths of eV. The injection conditions at the interface between PEDOT:PSS and electron donor should also be considered. V_{oc} depends on the amount of injected holes according to Eq. (2), which is a rearrangement of the Shockley equation [2]

$$V_{oc} = \frac{nk_BT}{q} \ln\left(1 + \frac{I_{ph} - V_{oc}/R_{sh}}{I_0}\right) \quad (2)$$

where k_B is the Boltzmann constant, q the electron charge, T the temperature in Kelvin, I_{ph} the photocurrent and I_0 is the reverse saturation current. Increased hole injection from the anode would result in a larger dark current opposing the photocurrent. The shunt resistance of the pentacene derivative cells, determined by a linear fit to the reverse bias dark current, exceeded $10^5\ \Omega\ cm^2$ and thus the leakage current will be of order $\mu A/cm^2$, two orders of magnitude lower than the photocurrent. Hence, the shunt resistance only plays a minor role in determining the open circuit voltage of these cells.

Fig. 6a compares the IPCE spectra of the various cells. Pentacene cells show the highest efficiency of 72% at 660 nm suggesting that exciton diffusion and charge transfer are efficient processes. The strong contribution of unsubstituted pentacene is consistent with the long exciton diffusion length ($\geqslant$50 nm) that has been reported [6]. On the other hand, all pentacene derivatives have much lower efficiencies, 16% or less within the longer-wavelength absorption bands, where excitons are generated in the pentacene layers. The IPCE spectra of the pentacene derivative cells follow the absorption spectrum of C_{60} with some additional contributions in the red. It is quite surprising that there is no evidence of the strong absorption in the blue for TP-5 and EtTP-5 in the IPCE spectra of devices based on these derivatives. These spectra demonstrate that the primary charge generation pathway is absorption by C_{60} followed by charge transfer at the organic heterojunction. Fig. 6b compares the IPCE spectrum of the TP-5 device with the calculated absorption of a bi-layer film consisting of 40 nm of C_{60} and 40 nm of TP-5. The two spectra diverge where TP-5 absorbs strongly between 400 and 500 nm. The sharp absorption peak of TP-5 permits a rough estimation of the diffusion length by taking the absorbance as a function of the depth profile of the bi-layer structure (neglecting thin film interference effects). A very short exciton diffusion length should result in a dip in the IPCE spectrum at λ = 470 nm, as the TP-5 layer will filter light from the heterojunction. Likewise, an exciton diffusion length comparable to the film thickness, should result in a peak at this wavelength. A good fit to the IPCE spectrum between 400 and 500 nm could be obtained for an exciton diffusion length of 18–20 nm (Fig. 6b). We propose that the weaker intermolecular coupling in the derivative films inhibits exciton diffusion, in which case thicker layers increase the series resistance, but do not yield additional photocurrent.

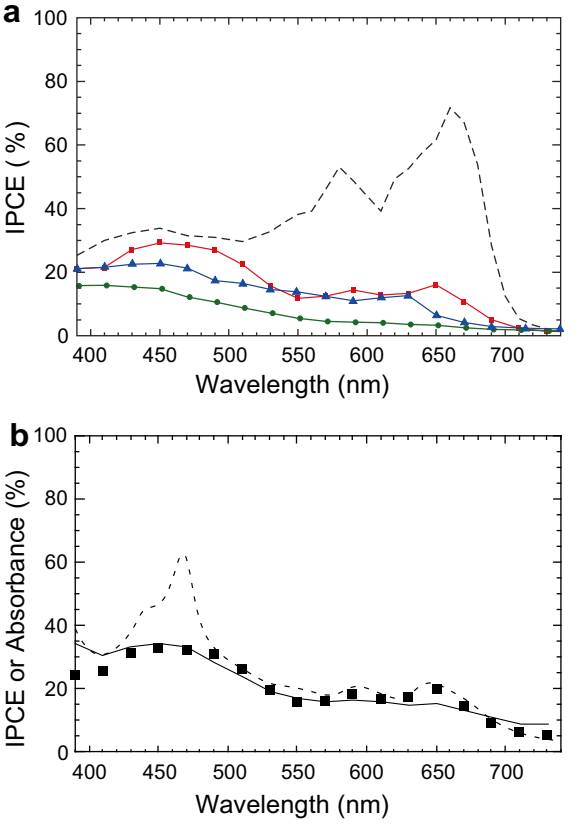

Fig. 6. (a) IPCE spectra of solar cells based on pentacene (black line) and its derivatives [TIPS (green, circles), TP-5 (red, squares), and EtTP-5 (blue, triangles)]. (b) Comparison of the IPCE spectrum of a TP-5 based cell (symbols) to the calculated absorbance of a TP-5/C_{60} bilayer film (dashed line) and a simulated IPCE spectrum taking into account the exciton diffusion length of TP-5 (solid line). (For interpretation of the references to colour in this figure legend, the reader is referred to the web version of this article.)

This hypothesis was confirmed by examining the effect of the thickness of the pentacene derivative layer on cell performance. The thicknesses of the C_{60} and BCP layers were fixed at 40 nm and 10 nm, respectively. Table 2 compares V_{oc}, J_{sc}, and η for TP-5 and EtTP-5 based pentacene/C_{60} cells with different TP-5 and EtTP-5 layer thicknesses. V_{oc} is unaffected by the thickness of the EtTP-5 layer, indicating that the offset between the HOMO of EtTP-5 and LUMO of C_{60} plays a determining role in this system. The

Table 2
Dependence of the photovoltaic cell parameters of TP-5 and EtTP-5 based solar cells on the thickness of the pentacene derivative layer

Electron donor (thickness)	V_{oc} (V)	J_{sc} (mA/cm^2)	*ff*	η (%)
TP-5 (12 nm)	0.45	1.81	0.41	0.33
TP-5 (23 nm)	0.56	2.46	0.41	0.56
TP-5 (38 nm)	0.57	2.32	0.37	0.50
EtTP-5 (12 nm)	0.72	2.40	0.43	0.74
EtTP-5 (23 nm)	0.72	1.97	0.40	0.57
EtTP-5 (38 nm)	0.69	1.68	0.29	0.34

All devices have 40 nm thick C_{60} and 10 nm thick BCP layers.

fill factor and current density, however, decrease monotonically with cell thickness. Increased absorption by EtTP-5 is more than offset by poor carrier extraction owing to the particularly low hole mobility of this material. Thus, the primary role played by EtTP-5 is to sensitize charge photogeneration at the organic heterojunction. The maximum efficiency ($\eta = 0.74\%$) therefore occurs for the thinnest (13 nm) EtTP-5 layer. For TP-5, the maximum efficiency is ($\eta = 0.56\%$) for a thickness of 24 nm, in good agreement with the estimated diffusion length. For the thinnest cell, efficiency is limited by light absorption of TP-5 and as its thickness increases, the series resistance limits the cell efficiency. These maximum efficiencies are slightly below that of the reference pentacene cell (0.82%).

4. Conclusions

In summary, we have demonstrated organic solar cells based on a series of pentacene derivatives functionalized by triisopropylsilylethynyl and dioxolane substitution. High open circuit voltages and reasonable power conversion efficiencies were obtained for solar cells based on these materials. V_{oc} of these cells correlates nicely with the oxidation potential of the donor pentacene derivative. The power conversion efficiency of these cells reached 0.74% and was limited by the series resistance and photocurrent generation efficiency. We attribute these effects to the amorphous nature of pentacene derivative films prepared by sublimation onto unheated substrates. As improved charge transport within the pentacene derivative layer has been demonstrated [21,23], significant improvements in efficiency may be expected with optimization of both the deposition conditions and the device architecture.

Acknowledgements

The authors would like to thank Dr. Mason Wolak for measuring the absorption spectra of TIPS and Olga Lobanova and Dennis Lichtenberger for providing preliminary gas phase photoemission data. This work was supported by the Office of Naval Research.

References

[1] C.W. Tang, Appl. Phys. Lett. 48 (1986) 183–185.
[2] P. Peumans, A. Yakimov, S.R. Forrest, J. Appl. Phys. 93 (2003) 3693–3723.
[3] C.-W. Chu, Y. Shao, V. Shrotriya, Y. Yang, Appl. Phys. Lett. 86 (2005) 243506.
[4] Y. Shao, S. Sista, C.W. Chu, D. Sievers, Y. Yang, Appl. Phys. Lett. 90 (2007) 103501.
[5] A.C. Mayer, M.T. Lloyd, D.J. Herman, T.G. Kasen, G.G. Malliaras, Appl. Phys. Lett. 85 (2004) 6272–6274.
[6] S. Yoo, B. Domercq, B. Kippelen, Appl. Phys. Lett. 85 (2004) 5427–5429.
[7] A.K. Pandey, J.-M. Nunzi, Appl. Phys. Lett. 89 (2006) 213506.
[8] Y. Kinoshita, T. Hasobe, H. Murata, Appl. Phys. Lett. 91 (2007) 083518.
[9] J. Yang, T.Q. Nguyen, Org. Electron. 8 (2007) 566–5674.
[10] A. Maliakal, K. Raghavachari, H. Katz, E. Chandross, T. Siegrist, Chem. Mater. 16 (2004) 4980–4986.
[11] H. Klauk, M. Halik, U. Zschieschang, G. Schmid, W. Radlik, J. Appl. Phys. 92 (2002) 5259–5263.
[12] N.J. Watkins, L. Yan, Y.L. Gao, Appl. Phys. Lett. 80 (2002) 4384–4386.
[13] J.E. Anthony, J.S. Brooks, D.L. Eaton, S.R. Parkin, J. Am. Chem. Soc. 123 (2001) 9482–9483.
[14] C.D. Sheraw, T.N. Jackson, D.L. Eaton, J.E. Anthony, Adv. Mater. 15 (2003) 2009–2011.
[15] M.M. Payne, J.H. Delcamp, S.R. Parkin, J.E. Anthony, Org. Lett. 6 (2004) 1609–1612.
[16] M.A. Wolak, B.B. Jang, L.C. Palilis, Z.H. Kafafi, J. Phys. Chem. B 108 (2004) 5492–5499.
[17] L.C. Palilis, J.S. Melinger, M.A. Wolak, Z.H. Kafafi, J. Phys. Chem. B 109 (2005) 5456–5463.
[18] M.A. Wolak, J. Delcamp, C.A. Landis, P.A. Lane, J. Anthony, Z.H. Kafafi, Adv. Funct. Mater. 16 (2006) 1943–1949.
[19] M.T. Lloyd, A.C. Mayer, A.S. Tayi, A.M. Bowen, T.G. Kasen, D.J. Herman, D.A. Mourey, J.E. Anthony, G.G. Malliaras, Org. Electron. 7 (2006) 243–248.
[20] J.E. Anthony, J. Gierschner, C.A. Landis, S.R. Parkin, J.B. Sherman, R.C. Bakus, Chem. Commun. 45 (2007) 4746–4748.
[21] O. Ostroverkhova, S. Shcherbyna, D.G. Cooke, R.F. Egerton, F.A. Hegmann, R. Tykwinski, S.R. Parkin, J.E. Anthony, J. Appl. Phys. 98 (2005) 033701.
[22] J.G. Park, R. Vasic, J.S. Brooks, J.E. Anthony, J. Appl. Phys. 100 (2006) 044511.
[23] S.K. Park, T.N. Jackson, J.E. Anthony, D.A. Mourey, Appl. Phys. Lett. 91 (2007) 063514.
[24] I.G. Hill, A. Kahn, J. Appl. Phys. 86 (1999) 2116–2122.
[25] B.P. Rand, J. genoe, P. Heremans, J. Poortmans, Progr. Photovolt. 15 (2007) 659.
[26] G.P. Kushto, W.H. Kim, Z.H. Kafafi, Appl. Phys. Lett. 86 (2005) 093502.
[27] K.L. Mutoloo, E.I. Mayo, B.P. Rand, S.R. Forrest, M.E. Thompson, J. Am. Chem. Soc. 128 (2006) 8108–8109.
[28] O. Lobanova, private communication.

Organic Electronics 9 (2008) 753–756

Contents lists available at ScienceDirect

Organic Electronics

journal homepage: www.elsevier.com/locate/orgel

Fabrication of high-mobility organic single-crystal field-effect transistors with amorphous fluoropolymer gate insulators

Mayumi Uno [a,b], Y. Tominari [b], J. Takeya [b,*]

[a] Technology Research Institute of Osaka Prefecture, Izumi, Osaka 594-1157, Japan
[b] Graduate School of Science, Osaka University, Toyonaka, Osaka 560-0043, Japan

ARTICLE INFO

Article history:
Received 17 February 2008
Received in revised form 7 May 2008
Accepted 12 May 2008
Available online 20 May 2008

PACS:
73.61.Ph
72.80.Le
73.40.-c

Keywords:
Organic transistor
Organic single-crystal
Rubrene
High-mobility

ABSTRACT

High-mobility rubrene single-crystal field-effect transistors are built on highly water- and oil-repellent fluoropolymer gate insulators. Roughness is introduced at the surface once to provide good adhesion to metal films and photoresist polymers for stable electrodes. Before constructing interfaces to crystals, smoothness of the fluoropolymer surface is recovered by annealing at a moderate temperature to maximize carrier mobility. Mobility values estimated in the saturation region reproducibly exceeded 15 $cm^2/V\,s$ for all the 10 devices, reaching 30 $cm^2/V\,s$ for the best two devices. The results demonstrate that the water-repellency and smoothness of the dielectric polymers are favorable for the excellent transistor performance.

Organic semiconductors are attracting considerable attention in the industry owing to their applicability to low-cost and flexible electronic devices such as field-effect transistors. In order to accelerate development of the organic field-effect transistors (OFETs) toward commercial use for matrix controlling devices of ultra-thin displays, for example, tremendous efforts are being made to improve their reproducibility and stability in ambient atmosphere as well as their current-amplifying performances themselves. Although material development is by all means essential along this line, equally important is searching for gate insulating materials, as the interfaces between the semiconductor and gate dielectric insulators play the central part in their operation. Very recently, it was reported that devices with fluoropolymer dielectric insulators showed significant improvement in bias-stressing and subthreshold properties, as compared with the common OFETs with SiO_2 gate dielectrics [1–3]. The use of the water- and oil-repellent fluoropolymer can be favorable in the device stability, as moisture and other contaminants are reported to provide trap levels at the interface between semiconductors and gate dielectrics [4]. The drawback of the fluoropolymer insulators, however, is difficulty in some device fabrication processes, such as photolithography and deposition of metal electrodes, because of their high water- and oil-repellency itself.

In this paper, we report a method to essentially improve the device fabrication processes, so that the photolithography technique works on the fluoropolymer gate insulators and highly air-stable OFETs are available with a-few-micrometer scale channels. The method incorporates the processes of (1) dry etching the fluoropolymer surface to stabilize the source and drain contacts by improving adhesion of the metals and (2) annealing at a temperature above the glass transition temperature

* Corresponding author.
E-mail address: takeya@chem.sci.osaka-u.ac.jp (J. Takeya).

1566-1199/$ - see front matter © 2008 Elsevier B.V. All rights reserved.
doi:10.1016/j.orgel.2008.05.008

after preparation of the metal electrodes to minimize the roughness of the gate dielectric surface, so that scattering of the carriers induced near the interface becomes less probable.

To make the best use of the dielectric surfaces with minimized trap density, we examine the device performances using rubrene single-crystal transistors, for which we reported very high carrier mobility incorporating carefully deposited silane-based self-assembled monolayers at the interfaces [5]. As a result of these processes, the single-crystal OFETs (SC-OFETs) exhibit excellent performance as transistor devices with a maximum mobility μ of 30 $cm^2/V\,s$ in the saturation regime. We note that the result marks the best performance factor of real current amplification among any OFETs ever reported, though we measured even higher values to represent potential material property disregarding the contact resistances at source and drain electrodes, using the method of the four-terminal measurements [5]. Hystorically, SC-OFETs have been used to demonstrate the maximum intrinsic properties of the organic semiconductors as they exclude complications due to grain boundaries, providing an insight into the fundamental mechanism of carrier transport [6–9]. In addition to such approaches, recently emerging are attempts to push forward the SC-OFETs for applications to realize an ultimate performance preserving the high intrinsic properties of transporting carriers in semiconductor materials. For example, integration techniques are being developed to grow organic single-crystals simultaneously at many positions on patterned electrodes in a substrate [10], which contrast conventional methods of preparing SC-OFET samples manually one by one [11–13]. Therefore, it becomes to make more sense these days to discuss SC-OFETs as candidates for practical use in the future.

We purchased a solution of fluoropolymer resin Cytop™ (CTL-813NMX) from Asahi Glass Company, and spin-coated it on 500-nm thick SiO_2/n-Si substrates. The films were dried at 90 °C for 10 min and annealed in an oven at 200 °C for 1 h to evaporate the solvent completely. Then, the surface of the fluoropolymer film was dry-etched with CHF_3 and oxygen-gas plasma for 2 min, using a SAMCO RIE-10N reactive ion chamber to facilitate the subsequent processes of photolithography and deposition of metal electrodes by improving the adhesion. The use of the mixed gas is effective in ashing away organic impurities and removing the residual inorganic impurities during the reactive ion-etching process. Fig. 1a and b shows scanning electron microscopy (SEM) images of the fluoropolymer surfaces before and after the dry etching process, respectively. More surface features (i.e. roughness) are observed after the etching process, which enhance the adhesion.

Source and drain electrodes of Au/Cr were fabricated to a total thickness of 20 nm on the fluoropolymer films by vacuum deposition and through the lift-off technique. Because of the strong adhesion to rough surfaces, the electrodes adhere to the polymer well, and thus can withstand the lift-off process even in an ultrasonic bath. After forming the electrodes, the substrates were annealed above the glass transition temperature of the polymer (at 120–200 °C) for 20 min to recover their original repellency. The flatness of the resultant film can be seen in the SEM image shown in Fig. 1c. We measured the water contact angle on the film at each stage of the process to determine the water repellency. The contact angle of the as-coated polymer was 111°. It decreased to 96° after the etching process and recovered to 107° upon annealing. The final thickness of the gate insulators was typically ~1 μm, as measured with a profilometer for all the devices. The relative dielectric constant ϵ of the Cytop™ was ~2.15, as determined through independent ac impedance measurements. The relatively low ϵ value may be advantageous for accumulating high-mobility carriers, because of less significant polaronic coupling to dynamic polarization at the fluoropolymer surface [14].

Thin platelets of rubrene single-crystals are grown to a thickness of about 2 μm by physical vapor deposition [15]. Sublimation is repeated at least twice to purify the crystals. The thin crystals are electrostatically laminated on the substrates to obtain bottom-contact rubrene SC-OFETs [12]. The channel width W and length L are both fixed to 100 μm for all the devices. We note that the channel is restricted to the square region between the electrodes by removing the area from the channel using laser-etching equipment [16]. We measured the transfer and output characteristics of the devices using an Agilent E5270 semiconductor parameter analyzer under ambient conditions.

The main panel of Fig. 2a shows the output characteristics of a typical rubrene SC-OFET sample with a fluoropolymer film measured in the crystallographic b axis direction at various gate voltages V_G. The drain current I_D exhibits a saturating trend with increasing drain voltage $|V_D|$ above $|V_G|$. In order to evaluate the mobility μ in the saturation

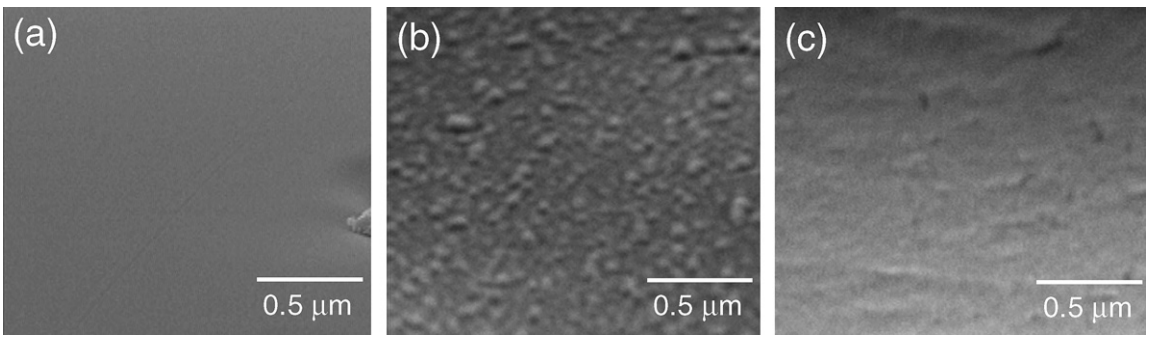

Fig. 1. Scanning electron microscope images of the Cytop™ films: (a) as formed, (b) after dry-etching, and (c) after annealing.

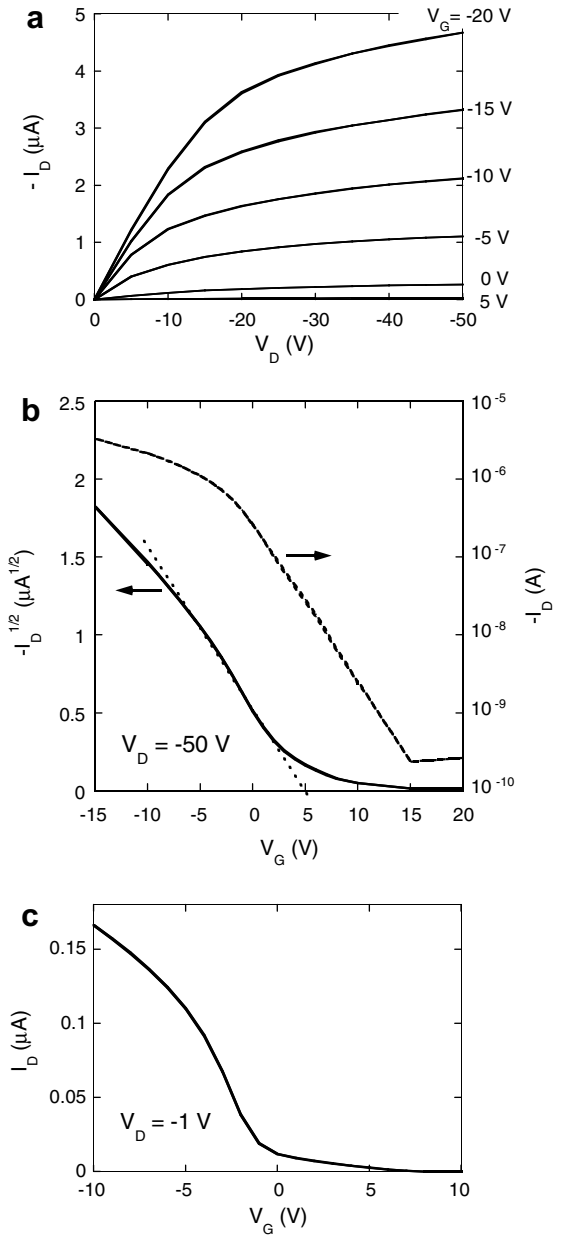

Fig. 2. (a) Output characteristics of a typical rubrene single-crystal transistor with a fluoropolymer gate dielectric insulator. (b) Transfer characteristics of the same sample in the saturation regime. The solid line represents the square root of the drain current scaled by the left axis, and the dashed line is a logarithmic plot of the drain current scaled by the right axis. The mobility value is estimated from the slope of the dotted line. (c) Transfer characteristics of the same sample in the linear regime. The mobility value is estimated from the slope of the dotted line.

regime, I_D is measured as function of V_G. Sweeping V_G back and forth gives almost no hysteresis. This indicates that the bias-stress effect in the fluoropolymer devices is negligible, which agrees with the results reported in [2]. Using the standard equation

$$\mu = \frac{L}{W}\frac{2}{C_i}\left(\frac{\partial\sqrt{I_D}}{\partial V_G}\right)^2 \quad (1)$$

the mobility μ of the present device is estimated to be $\sim$17 cm^2/V s, taking the rate of $\partial\sqrt{I_D}/\partial V_G$ at weak gate electric fields. C_i is the capacitance of the gate dielectric per unit area. Almost the same value is evaluated for the linear region, which is shown in Fig. 2c. As we have argued previously [5,9], in high-mobility SC-OFETs, the rate of $\partial I_D/\partial V_G$ tends to decrease as the applied V_G increases, since the carriers are more confined to the interface to the gate insulators and suffer from scattering by random potentials at the surface of the amorphous insulators. Thus, the estimated μ also reflects the extent of carrier distribution inside the crystals, in addition to the amount and energy levels of shallow traps at the interfaces. The μ values for eight devices prepared by the same procedure are in the range of $\sim$15–20 cm^2/V s, indicating the good reproducibility of the fluoropolymer devices. On the basis of the logarithmic plot in Fig. 2b, the normalized subthreshold swing SC_i is typically 6 V/nF decade and the on–off ratio is $\sim 10^4$, demonstrating the high switching performance of the present devices. The main panel of Fig. 3 shows the same plot as Fig. 2b for one of the two samples, in which the device platform was prepared in a slightly different way. The fluoropolymer substrates were annealed after photolithography but before deposition of the Au/Cr electrodes, which sacrifices the adhesion of the metal to the fluoropolymer surfaces. Though the resistance to the lift-off process decreases, this method prevents thermal deformation of the Au/Cr electrodes on the polymer surfaces. Using Eq. (1), μ is estimated to be as high as $\sim$30 cm^2/V s in the saturation region. The μ of the other sample is estimated to be $\sim$28 cm^2/V s. The fact that these values are much higher than those of the previous eight samples suggests that some microscopic inhomogeneity of the dielectric surface related to the metal deformation is responsible for the mobility of the carriers in the rubrene

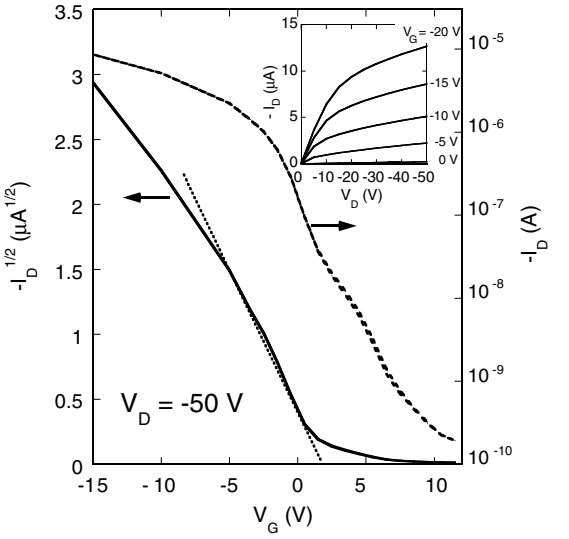

Fig. 3. Main panel: Transfer characteristics of the best rubrene single-crystal transistor with fluoropolymer gate dielectric insulator. The solid line represents the square root of the drain current scaled by the left axis, and the dashed line is the logarithmic plot of the drain current scaled by the right axis. The mobility value is estimated from the slope of the dotted line.

crystal transistors. We also prepared several devices as references on the rough polymer surfaces skipping the annealing process. The μ values are all less than or equal to 10 $cm^2/V\,s$ for these devices, which indicates that the micromorphology of the fluoropolymer surface is responsible for the performance of the SC-OFETs. The output characteristics plotted in the inset of Fig. 3 also show current saturation, though the saturating trend is not as obvious as that inFig. 2b.

In our devices with SiO_2 gate dielectrics, μ in the saturation region was much lower than that in the linear region, though the maximum mobility of the linear region (measured by the two-terminal method) reached ~18 $cm^2/V\,s$ for one of the SiO_2 SC-OFETs [5]. One can find non-ideal properties of the current saturation in the literature for other high-mobility rubrene SC-OFETs with μ values as high as 19 $cm^2/V\,s$ [17]. Given that the pinch-off region near the drain electrode responsible for current saturation is defined by the presence of high-concentration impurities in SiO_2–silicon metal-oxide-semiconductor field-effect transistors [18], the mechanism to form the pinch-off in organic semiconductors is non-trivial because of the absence of explicit impurities. Thus, the experimental results on the organic single-crystal transistors raise the question of how compatible high-mobility carrier transport with minimized impurity scattering and the ideal current saturation with a well-defined pinch-off region in the channel are. The present fluoropolymer OFET is a successful example of a high-mobility device with fairly good saturation. It is to be further investigated for compatibility, for the saturation properties are crucial in such applications as a current source in the back panels of organic displays. We also note that the mobility value exceeds 15 $cm^2/V\,s$ for all 10 fluoropolymer devices. As compared to our previous SiO_2 devices, which were highly influenced by moisture and other contaminants, the fluoropolymer SC-OFETs show much better reproducibility. Thus, the incorporation of a fluoropolymer gate dielectric layer in SC-OFETs facilitates experiments such as the evaluation of electronic properties of newly synthesized compounds for organic transistors [19].

In conclusion, we have established a method to incorporate water- and oil-repellent fluoropolymer gate dielectrics in high-performance organic single-crystal transistors: the formation of stable metal electrodes and the use of photolithography have become possible by intentionally introducing surface roughness. By recovering the surface smoothness through post-annealing, a high-mobility of up to 30 $cm^2/V\,s$ was achieved in the saturation region, which directly leads to excellent current amplification performance in real devices. In addition to high reproducibility, the technique of interfacing organic single-crystals and fluoropolymer layers enables reliable platforms for experiments, for example, the assessment of newly synthesized organic materials and investigation of the ultimate carrier mobility at the surfaces of organic semiconductors.

Acknowledgements

The authors acknowledge Asahi Glass Company for technical information on Cytop™. This work was financially supported by the Industrial Technology Research Grant Program in 2006 of NEDO, Japan, and a Grant-in-Aid for Scientific Research (Nos. 17069003, 18028029, and 19360009) from MEXT, Japan.

References

[1] J. Veres, S.D. Ogier, S.W. Leeming, D.C. Cupertino, Adv. Mater. (Weinheim, Germany) 13 (2003) 199.
[2] W.L. Kalb, T. Mathis, S. Haas, A.F. Stassen, B. Batlogg, Appl. Phys. Lett. 90 (2007) 092104.
[3] T. Umeda, D. Kumaki, S. Tokito, Org. Electr. 9 (2008) 545.
[4] C. Goldmann, C. Krellner, K.P. Pernstich, S. Haas, D.J. Gundlach, B. Batlogg, J. Appl. Phys. 99 (2006) 034507.
[5] J. Takeya, M. Yamagishi, Y. Tominari, R. Hirahara, Y. Nakazawa, T. Nishikawa, T. Kawase, T. Shimoda, Appl. Phys. Lett. 90 (2007) 102120.
[6] V. Podzorov, E. Menard, A. Borissov, V. Kiryukhin, J.A. Rogers, M.E. Gershenson, Phys. Rev. Lett. 93 (2004) 086602.
[7] J. Takeya, K. Tsukagoshi, Y. Aoyagi, T. Takenobu, Y. Iwasa, Jpn. J. Appl. Phys. 44 (2005) L1393.
[8] V. Podzorov, E. Menard, J.A. Rogers, M.E. Gershenson, Phys. Rev. Lett. 95 (2005) 226601.
[9] J. Takeya, J. Kato, K. Hara, M. Yamagishi, R. Hirahara, K. Yamada, Y. Nakazawa, S. Ikehata, K. Tsukagoshi, Y. Aoyagi, T. Takenobu, Y. Iwasa, Phys. Rev. Lett. 98 (2007) 196804.
[10] A.L. Briseno, S.C.B. Mannsfeld, M.M. Ling, S. Liu, R.J. Tseng, C. Reese, M.E. Roberts, Y. Yang, F. Wudl, Z. Bao, Nature 444 (2006) 913.
[11] V. Podzorov, V.M. Pudalov, M.E. Gershenson, Appl. Phys. Lett. 82 (2003) 1739.
[12] J. Takeya, C. Goldmann, S. Haas, K.P. Pernstich, B. Ketterer, B. Batlogg, J. Appl. Phys. 94 (2003) 5800.
[13] R.W.I. de Boer, T.M. Klapwijk, A.F. Morpurgo, Appl. Phys. Lett. 83 (2003) 4345.
[14] I.N. Hulea, S. Fratini, H. Xie, C.L. Mulder, N.N. Iossad, G. Rastelli, S. Ciuchi, A.F. Morpurgo, Nat. Mater. 5 (2006) 982.
[15] Ch. Kloc, P.G. Simpkins, T. Siegrist, R.A. Laudise, J. Cryst. Growth 182 (1997) 416.
[16] I. Yagi, K. Tsukagoshi, Y. Aoyagi, Appl. Phys. Lett. 84 (2004) 813.
[17] C. Reese, W.-J. Chung, M.-M. Ling, M. Roberts, Z. Bao, Appl. Phys. Lett. 89 (2006) 202108.
[18] S.M. Sze (Ed.), Semiconductor Devices: Physics and Technology, John Wiley & Sons, New York, 1985.
[19] K. Yamada, T. Okamoto, K. Kudoh, A. Wakamiya, S. Yamaguchi, J. Takeya, Appl. Phys. Lett. 90 (2007) 072102.

leading to the formation of stable anions and dianions [19]. This property of PDIs makes them attractive materials in chemiluminescence, near-infrared emitters and electrochromic devices [14,16,20]. The majority of studies on optical and electrochemical properties of PDIs are carried out in solution [16,19,21] and the number of solid state electrochemistry studies are limited [15,22–25]. Additionally, macroscopic oxide films are under intensive investigation due to their use in optoelectronic applications such as dye-sensitized solar cells, electrochromic and electroluminescent displays [26–33]. The electrochemistry of self-assembly films of polyether derivatives of PDIs was previously reported by Gregg [25], but we could find no report on the electrochemistry of polyether substituted PDI doped nanocrystalline metal oxide films.

On the other hand, the research field of electrochromic materials includes organic, inorganic, and polymeric materials as well as several hybrid materials [34,35]. The most common applications of EC materials include a variety of displays, smart windows, optical shutters, and mirror devices. Electrochromic materials include organic small molecules, such as the bipyridiliums (viologens), which are a class of materials that are transparent in the stable dicationic state. Electrochromism is observed for the thin films of polyviologens and N-substituted viologens such as heptyl viologen [34]. Recently, improved electrochromic properties have been observed with composite systems, where organic molecules are adsorbed on mesoporous nanoparticles of doped metal oxides [35,36–38]. To the best of our knowledge, electrochromic effect of perylenediimides adsorbed on mesoporous surfaces was not reported. Previously, we reported spectroelectrochemical properties of perylenemonoimidemonoanhydride derivatives but not for perylenediimides [38,39].

In this paper, series of PDI derivatives are synthesized, electrochemical and spectral behavior of PDIs on nanocrystalline metal oxide particles are investigated. The stability of mono and dianionic species on mesoporous metal oxide surface is presented. PDI 1–4 include polyether side chain ending with amino groups and PDI 5 includes phenyl substituted polyether side chain attached from phenyl units to perylene core. Free amino substituents are chosen for their reactive features that allow functionalization and/or they provide a site for attaching on different substrates. Phenyl substituted polyether derivative is chosen for its low fluorescent feature and compare with PDI 1–5. In order to determine the solid state behavior of synthesized dyes, the optical and electrochemical properties are studied on semiconductor (nc-TiO_2), insulator (nc-Al_2O_3), amorphous Si surfaces and self-assembly films and that compared with their solutions in $CHCl_3$ The chemical structures and their names of synthesized PDIs are given in Scheme 1.

2. Experimental section

2.1. Chemicals and instruments

Perylene-3,4:9,10-tetracarboxylic dianhydride (PDA), tetraethylene glycol di(*p*-toluene sulphonate) (TEGdTs), pentaethylene glycol di(*p*-toluene sulphonate) (PEGdTs), sodium (Na), ethanolamine, 1-amino-2-propanol, triethylene glycol monomethyl ether, aluminum oxide (neutral) and silicagel 60 for column chromatography, tetrabutylammonium hexafluorophosphate ([TBA][PF_6]), titanium (IV) isopropoxide [Ti(O^iPr)$_4$], poly(ethyleneoxide) (MW 100.000), glacial acetic acid, tetraethyl orthosilicate (TEOS) were obtained from Fluka. Potassium carbonate (K_2CO_3), dimethyl formamide (DMF), *p*-nitrophenol (*p*-NO_2PhOH), hydrazine monohydrate ($NH_2NH_2.H_2O$), imidazole, thionyl chloride ($SOCl_2$), benzene, and pyridine were obtained from Merck. Organic solvents chloroform ($CHCl_3$), dichloromethane (CH_2Cl_2), acetonitrile (MeCN), ethanol (EtOH), methanol (MeOH), 2-propanol (^{i}PrOH), tetrahydrofuran (THF), ethyl acetate (EtOAc), toluene ($C_6H_5CH_3$) were of spectroscopic grade and used as received. Ferrocene (Fc) was from Aldrich and used as standard for the determination of LUMO energy levels of synthesized PDI derivatives.

PDI derivatives were analyzed by using Nicolet Magna 550 FTIR spectrophotometer, Bruker DPX-400 and 400 MHz HP Digital FT–NMR spectrometer, Analytic Jena S 600 UV spectrophotometer, PTIQM1 fluorescence spectrophotometer and Picoquant Time-Harp 100 instrument equipped with PDL 800-B laser/LED pulse lamb. CH Instruments 660B model potentiostate was used for electrochemical measurements under nitrogene atmosphere at various scan rates. Tencor Alpha Step 500 profilometer was used in thickness measurements of the films.

2.2. Synthetic methods

PDIs were synthesized according to the published literature procedures [41a–d].

2.3. Preparation of PDI doped nanocrystalline titania film (NT)

The nanocrystalline TiO_2 films were prepared according to the procedure described in literature [42a]. The autoclaving process was carried out at 235 °C, instead of 200 °C and colloidal solution condensed to 10% by weight of TiO_2. Anatase TiO_2 colloids were obtained from a sol-gel hydrolysis by autoclaving and condensation of Ti(O^iPr)$_4$ in acetic acid solution. 160 ml of H_2O and 51 ml glacial acetic acid were mixed in a flask and stirred at 0 °C. 6 ml of ^{i}PrOH and 24 ml Ti(O^iPr)$_4$ were mixed in a dropping funnel. The Ti(O^iPr)$_4$ / ^{i}PrOH solution was dripped into acetic acid-H_2O mixture, which was previously prepared and kept at 0 °C, at a rate of 1–2 drops/s. The mixture was refluxed for 4 h and then recovered colloidal solution was placed into an autoclave chamber equipped with a Teflon beaker and heated at 235 °C for 12 h. After this treatment the colloidal solution was sonicated and evaporated to a final concentration of 10% of TiO_2 by weight. In order to act as a binding agent poly(ethyleneoxide), 20% by weight with respect to the amount of TiO_2, was added to this final colloidal solution. The paste was coated onto microscope glass slides by doctor blade technique. TiO_2 films were dried at room temperature and then sintered at 450 °C for 30 min. Final thickness of porous TiO_2 films were ~5 μm. Doping of the PDIs onto TiO_2 films were performed by soaking

glass slides into 0.5 mM MeCN solution of PDIs and keeping in the solution for 3 h. PDI adsorbed TiO_2 films finally washed with fresh MeCN.

2.4. Preparation of PDI doped silica films (PS)

TEOS (22.4 ml, 0.1 mol) and dry EtOH (11.2 ml) were mixed in a flask and stirred for 10 min under N_2 atmosphere (Solution A). A mixture of 7.2 ml H_2O (0.4 mol) and 1 ml HCl (37%) were added to absolute EtOH (11.2 ml) in a flask and stirred for 10 min (Solution B). Solution A was added dropwise to Solution B that was under vigorous stirring. Synthesized PDIs were dissolved in this sol–gel solution to obtain 0.5 mM final dye concentration. After obtaining an individual complete dissolution of each PDI, 1 ml Triton-X 100 surfactant was added to sol–gel solution in order to prevent the films from cracking. After stirring for 5 min, resulting silica sol-gel solution was coated onto microscope glass slides by dip coating. The films were dried at 100 °C for 30 min. Final thickness of silica films were measured and found to be ~4.5 μm.

2.5. Preparation of PDI doped nanocrystalline alumina film (NA)

Nanocrystalline Al_2O_3 (alumina) films were prepared by Yoldas et. al. route [42b]. Aluminium tri-*iso* propylate (51 g 0.25 mole) hydrolyzed in 450 ml (25.5 mole) hot water at 75–80 °C under vigorous stirring. 1.46 ml (0.0175 mole) HCl (36.5%) added into solution and peptized for 3 days at 90 °C. At the end a clear solution (sol) was obtained. The sol was concentrated to 17.5% Al_2O_3 (w/w) at 50 mbar and 50 °C with rotary evaporator. 8% PEG 20000 was added to obtain a better film and stirred overnight to get homogeneous paste. The paste was coated on the conductive FTO coated glass electrodes by doctor blade technique. Scotch 3M Polymer tape was used as a spacer. Prepared films were heated at 500 °C for 30 min. Thickness of the films was found as 8 μm.

2.6. Preparation of self-assembly PDI films (SA)

THF solutions of the PDIs with a concentration of 15–20 mg PDI/ml THF were used for spin-coating (1600 rpm). Glass microscope slides were used as support material.

3. Results and discussion

Synthesized PDIs were waxy and very soluble in common organic solvents ranging from alcohols to toluene. Their solubility in polar and protic solvents was better than aprotic and non-polar ones. This might be because of the polar side chains of the dyes and their capability of making hydrogen bonds with protic solvents.

3.1. Absorbance and luminescence properties of PDIs

The absorption and fluorescence spectra of the PDIs were recorded in four different organic solvents ($C_6H_5CH_3$, $CHCl_3$, MeOH, and MeCN) and four different thin

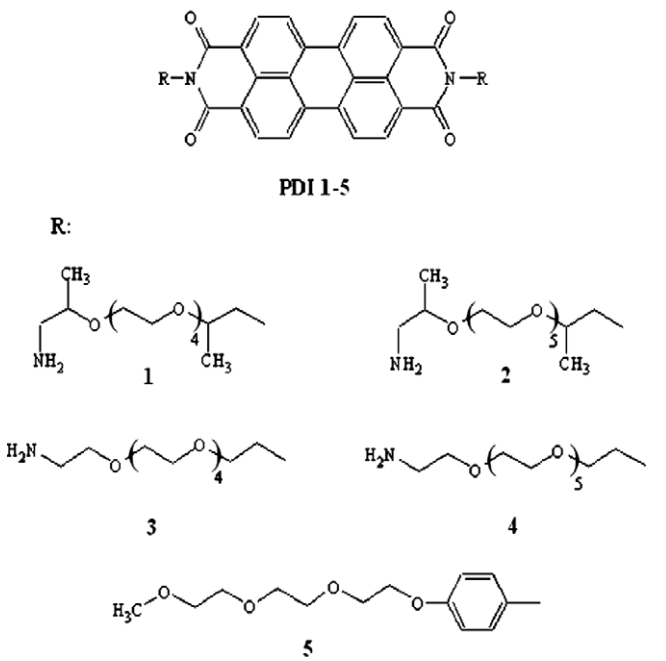

Scheme 1. N,N′-Bis{2-[2-(2-{2-[2-(2-amino-1-methylethoxy) ethoxy]ethoxy}ethoxy) ethoxy] propyl}-perylene-3,4:9,10- tetracarboxydiimide, (PDI 1); N,N′-bis(2-{2-[2-(2-{2-[2-(2-amino-1-methylethoxy)ethoxy]ethoxy}ethoxy)ethoxy]ethoxy}propyl)-3,4:9,10-perylene tetracarboxydiimide, (PDI 2); N,N′-bis{2-[2-(2-{2-[2-(2-aminoethoxy)ethoxy]ethoxy}ethoxy)ethoxy]ethyl}-3,4:9,10-perylene tetracarboxydiimide, (PDI 3); N,N′-bis(2-{2-[2-(2-{2-[2-(2-aminoethoxy)ethoxy]ethoxy}ethoxy)ethoxy] ethoxy}ethyl)-3,4:9,10-perylene tetracarboxydiimide, (PDI 4); N,N′-bis(4-{2-[2-(2-methoxyethoxy) ethoxy]ethoxy}phenyl)-3,4:9,10-perylene tetracarboxydiimide, (PDI 5).

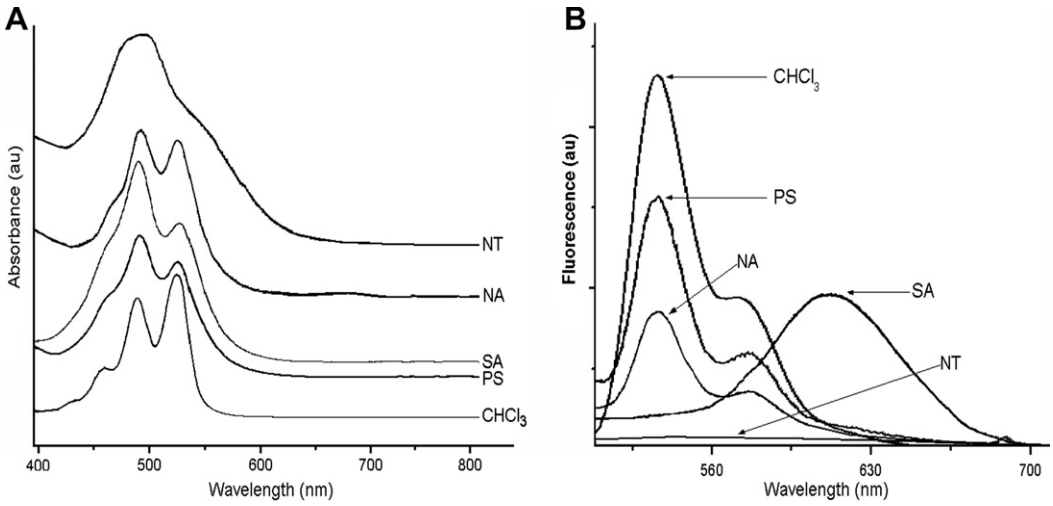

Fig. 1. (A) Absorption spectra of PDI 3 in $CHCl_3$, PS, SA, NA and NT films and (B) fluorescence emission spectra of PDI 3 in $CHCl_3$, and the films (PS: silica film, SA: self-organized film, NT: nanocrystalline titania film, and NA: nanocrystalline alumina film).

films (NT, PS, self-assemblied (SA), and NA) at room temperature. Fig. 1A shows the absorption spectra of PDI 3 in $CHCl_3$ solution and films. The UV–vis absorption spectra of the PDIs in solution have three bands at 459, 488 and 522 nm, which are characteristic for all symmetric PDI derivatives [1–5]. The maximum absorption and fluorescence emission wavelengths of the PDIs have slightly blue-shifted (about 5–6 nm) with increasing solvent polarity. Strong broadening of absorption peaks due to exciton–phonon coupling was observed in the case of film and the absorption maximum shifts blue by 0.21 eV (from 522 to 488 nm) due to the π-orbital overlaps between dye molecules [44]. The broadening of the absorption spectrum was mostly dominant in NT films when compared to NA, PS and SA films. The absorption maxima are changed from 522 to 488 nm whenever the dye environment is changed from $CHCl_3$ solvent to film matrix. Although the nature of this shift is not very well known, it is related to the intermolecular interactions and aggregation tendency of these dyes in thin films [45–48]. The ratio of absorbances of 522 to 488 nm band decreases, which often indicates aggregation of these dye molecules [48].

The fluorescence emission spectra (Fig. 1B) of PDIs were obtained in $CHCl_3$ solutions ($\lambda_{exc} = 488$ nm) and in thin films. The emission spectra of the PDI derivatives were all the same except the SA and NT films. In SA and NT films, the three emission bands that are characteristic for PDIs were seen. The emission spectra of SA films were broadened and strongly red-shifted, whereas the emission in NT films was almost disappeared (Fig. 1B).

The fluorescence quantum yields (Φ_f) of PDIs in $CHCl_3$ were calculated according to the published procedure and N-DODEPER was used as the reference [43]. The Φ_f of the PDIs in $CHCl_3$ was determined as 0.95–1.0 for PDI 1–4, however for PDI5 this value was calculated as 0.024. Determinations of fluorescence quantum yields of the dyes in solution are relatively easy in comparison to thin films. In thin films many corrections, such as self-quenching of the emission and the total internal reflection of the emission due to high refractive indices must be done for acceptable determination of quantum efficiencies. On the other hand, Tirapattur et al. calculated the fluorescence quantum yield by using time-resolved fluorescence measurements obtained in both phases (solution and thin films) assuming that the fluorescence decay constants (k_f) are similar in both phases [49,50]. But this approach may not be valid since the fluorescence decays are multi exponentials.

Fig. 2 shows fluorescence decay curves (bir tane decay var) of PDI 3 in $CHCl_3$ solution. The fluorescence lifetimes (τ_f) were measured to be 5, 17, 2.8 and 1.7 ns in solution ($CHCl_3$), and in the SA, PS and NA films, respectively (Table 1). The fitting procedure applied to the fluorescence decay profiles yield acceptable statistic ($X^2 < 1.2$) with a single-exponential function in $CHCl_3$ solutions and multi exponentials in thin films.

The red-shift observed for PDIs in SA films was about 90 nm. Liu et al. observed that PDIs including polyether side chains form highly ordered thin films [51]. The strong tendency of PDIs to form π–π stacking arrangement may yield strong interactions between PDIs in the films resulting in a red-shift in spectra and a longer fluorescence lifetime [52]. Similar red-shifted emission band was observed for PDI polymers by De Witte et al. [53]. The fluorescence lifetime of SA films are measured to be between 15.7–18.2 ns, which are significantly longer than those in $CHCl_3$. The longer fluorescence lifetime in SA films is in agreement with literature and explained by the formation of excimer type species in films [48,53] The experimental data clearly points that the presence of new species which could be an excimer type of aggregates or complexes of PDIs in SA films. The fluorescence spectra of PDIs in PS and NA thin films are similar to those in solutions but lower in fluorescence intensity. Furthermore, the fluorescence lifetimes of PDIs in PS and NA thin films are shorter than those of in solution and measured to be 2.8 and 1.7 ns for PS and NA films, respectively. Shorter lifetimes are consisted with

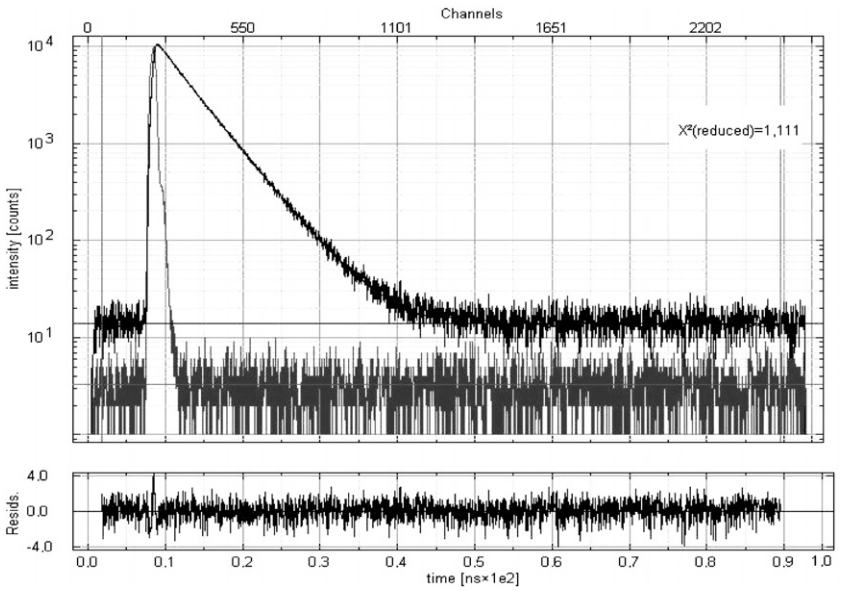

Fig. 2. The fluorescence decay curve of PDI 3 (in $CHCl_3$, concentration $<10^{-5}$).

Table 1
Spectroscopic data for the PDIs in solution and thin films

PDI	τ_f (ns)				Φ_f
	$CHCl_3$	SA	PS	NA	$CHCl_3$
1	4.74	18.2	2.85	1.78	0.99
2	4.99	16.3	2.78	1.76	0.95
3	4.72	15.7	2.81	1.82	1.00
4	4.67	17.3	2.92	1.77	0.99
5	0.06	–	–	–	0.024

τ_f values are fluorescence lifetimes and Φ_f values are quantum yields.

lower intensity of fluorescence, pointing that rate of nonradiative transitions, regardless of their nature, are faster than the radiative transitions. The low Φ_f of PDI 5 arises from the electron-rich aromatic substituent, which leads to a strong fluorescence quenching, as reported and described in literature [32,33,54–58]. It must be noted that, the fluorescence lifetime of PDI 5 in PS and NA films were not reported because of poor statistics even with multiexponential decay curves.

Extremely weak fluorescence intensity of the synthesized PDIs may be attributed to the strong electrostatic interactions between TiO_2 and dye molecules [59]. It also indicates the possibility of efficient photo-energy/electron transfer processes from the excited PDI molecules to the nanostructured TiO_2 surface. Bossman et al. reported that $Ru(bpy)_3^{2+}$ complexes located near TiO_2 do not emit light [60]. HOMO and LUMO energy levels of $Ru(bpy)_3^{2+}$ (−5.9 and −3.9 eV) [40] are very similar to those of PDIs, (−5.9 and −3.8 eV) [54]. The quenching mechanism of our dyes can be explained by the injection of excited electrons to electron traps below the band edge of TiO_2. Thus the injected electrons recombine by non-radiative processes resulting in a very weak emission and very fast fluorescence decay that is faster than our instrument response. Solid state electrochemical studies support our approach and these results will be discussed in following sections.

3.2. Electrochemistry of PDIs in solution

Determination of HOMO and LUMO energy levels is crucial for the selection of anodic and cathodic materials in organic electronics [61]. Electrochemical potentials provide these information. The electrochemical measurements of PDIs were performed by the use of 0.1 M $[TBA][PF_6]$ as electrolyte in $MeCN/CHCl_3$: 5/1 solvent mixture. Glassy carbon electrode (GCE) was used as working, platinum wire as counter and Ag/AgCl as reference electrodes. Calculation of LUMO and HOMO energy levels were based on the value of 4.8 eV for ferrocene with respect to vacuum level and following equations were used [62]

$$E_{LUMO} = -e(E_{1/2(red.,dye)} - E_{1/2(Fc)} + 4.8),$$
$$E_{HOMO} = -e(E_{1/2(ox.,dye)} - E_{1/2(Fc)} + 4.8).$$

The onset potentials ($E_{red.1}$ and $E_{red.2}$) were determined from the intersection of two tangents drawn at the rising reduction current and background current in the cyclic voltammograms. The first reduction peak was used to calculate the LUMO energy level as it belongs to the reduction of neutral molecule whereas the second peak belongs to the reduction of monoanion of parent molecule. HOMO energy values of PDIs were estimated from oxidation potentials. The electrochemical band gap values are calculated by subtracting the onset potential of the first reduction and the first oxidation.

Two reversible reductions of PDIs are observed on the voltammograms. The redox potentials and HOMO–LUMO energy levels of the dyes are given in Table 2. The cyclic voltammogram of PDI 1 in $CHCl_3$ solution (as inset) is shown in Fig. 3. Two reversible reduction peaks around −0.57 and −0.77 V and one irreversible oxidation peak

Table 2
Peak potentials of PDIs in $CHCl_3$ and films

PDI	$E_{ox.}$ (V)	$E_{red.1}$ (V)				$E_{red.2}$ (V)				LUMO (eV)[c]	HOMO (eV)[c]	Band gap (eV)
	$CHCl_3$	$CHCl_3$	SA	NT	NA	$CHCl_3$	SA	NT	NA	$CHCl_3$	$CHCl_3$	$CHCl_3$
1	+1.68	−0.57	−0.81	−0.85	−0.84	−0.77	−1.07	−1.15	−1.06	−3.95	−6.07	2.25[a] 2.12[b]
2	+1.72	−0.56	−0.82	−0.83	−0.86	−0.75	−1.05	−1.16	−1.09	−3.96	−6.14	2.24[a] 2.18[b]
3	+1.73	−0.54	−0.80	−0.85	−0.85	−0.72	−1.05	−1.13	−1.05	−3.93	−6.12	2.25[a] 2.19[b]
4	+1.79	−0.53	−0.79	−0.85	−0.82	−0.74	−1.07	−1.15	−1.10	−3.95	−6.07	2.25[a] 2.12[b]
5	+1.60	−0.58	−0.76	−0.88	−0.86	0.72	−1.09	−1.19	−1.08	−3.88	−6.06	2.25[a] 2.18[b]

[a] Optical band gaps.
[b] Electrochemical band gaps.
[c] (Fc/Fc^+ is 0 and 42 V vs Ag/AgCl).

around 1.68 V are observed for PDI 1. The peak separations between two reduction potentials are 14–20 mV. ΔE_p values are 79 mV for first reduction and 82 mV for second reduction. Integration of peak shapes shows that each reduction refers to one electron process. No significant change at the peak currents is observed after several cycles (15 times). LUMO energy values of PDIs in solution are calculated to be between −3.88 and −3.96 eV. The electrochemical and optical band gap values are in good correlation and observed to be between 2.1 and 2.3 eV (Table 2). Although the LUMO energy levels, calculated from the redox potentials for liquid phase seem to be favorable for photovoltaic applications, the solid state electrochemistry data is required to support it. That is why the position of conduction band edge of TiO_2 is dependent on the amount the ions adsorbed at inner Helmholtz double layer of TiO_2/electrolyte interface [63]. The amount of ions, adsorbed at Helmholtz layer, maybe, is affected by the adsorbed dye on TiO_2 surface. The electrochemistry of the thin films will be discussed in Section 3.3.

3.3. Electrochemistry of thin films

Solid state electrochemistry is a useful tool to understand whether there is an interaction between electroactive groups of organic molecule and metal oxide surfaces or not. NA, SA and NT films were prepared on FTO glasses and used as working electrode. Fig. 3 shows cyclic voltammetry of SA, NT an NA films. Since PDI 1–4 are soluble in common solvents, the SA films of them are not stable in electrolyte and just only one cyclic scan can be performed with high scan rates (⩾200 mV/s). However, the very low solubility of PDI 5 in CH_3CN allowed us to make the spectroelectrochemical experiments in SA films. Therefore, the results in SA films were given and discussed only for PDI 5.

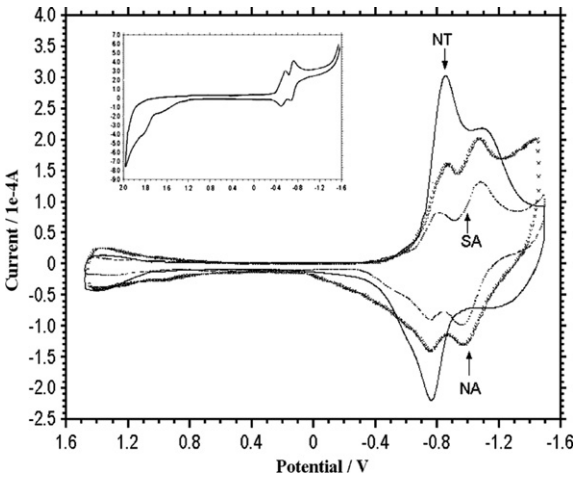

Fig. 3. Cyclic voltammogram of NT (PDI 1), NA (PDI 1) and SA (PDI 5) films. The inset is cyclic voltammogram of PDI 1 in solution (supporting electrolyte is 0.1 M [TBA][PF_6] in MeCN/$CHCl_3$:5/1).

The redox potentials of films shows approximately 25 mV negative shift when compared with solution phase. This shift may be explained by the limited percolation of electrolyte cations. TBA^+ cations are quite large and its percolation inside the film is more difficult than that of smaller cations, such as Li^+, Na^+ etc. Gregg et al. reported that, because of its large size and the nonreactive alkyl groups on its periphery, TBA^+ neither adsorbs on the TiO_2 surface nor reacts chemically with it [64]. On the other hand, polyether side chain oxygen atoms with unpaired electrons may be attractive centers for electrolyte cations. Electrostatic interactions between electrolyte cations and unpaired electrons on oxygen atoms may decrease the mobility of cations. In order to understand this approach better, amino precursor (PEGDA1), which contains pentaethyoxy chain and non-electroactive in studied potential region, is doped onto TiO_2 film and electrochemical behavior of the films are monitored. Fig. 4 shows the cyclic voltammograms of bare TiO_2, bare alumina and PEGDA1 doped TiO_2 films. The alumina films show a weak background current but it is negligible in comparison with that of TiO_2 film. The TiO_2 films show a capacitive current starting from −0.60 V. Because of the electron traps below bulk conduction band edge of TiO_2, the electrons flow from F:SnO_2 electrode to TiO_2 particles. These accumulated electrons are immobile unless they are thermally excited to the conduction band [65]. The capacitive current of TiO_2 film slightly increases when doped with PEGDA1. As mentioned above, polyether side chains including oxygen atoms may act as attractive centers for electrolyte cations. Although TBA^+ cations do not like TiO_2 surface, the etheric oxygens may facilitate their movement though the film surfaces that results in more capacitance.

CV measurements were also carried out by using $LiClO_4$ as electrolyte and the results (not shown here) supported our approach. Influence of electrolyte cations on redox behavior is another topic for future studies. Here, we fo-

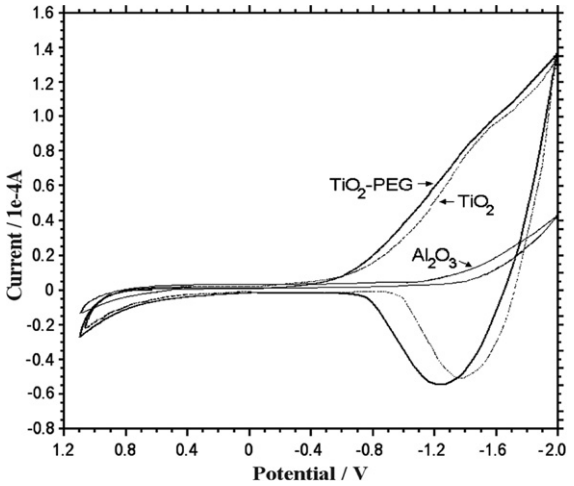

Fig. 4. Cyclic voltammogram of bare TiO_2, alumina and amino precursor (PEGDA1) doped TiO_2 film.

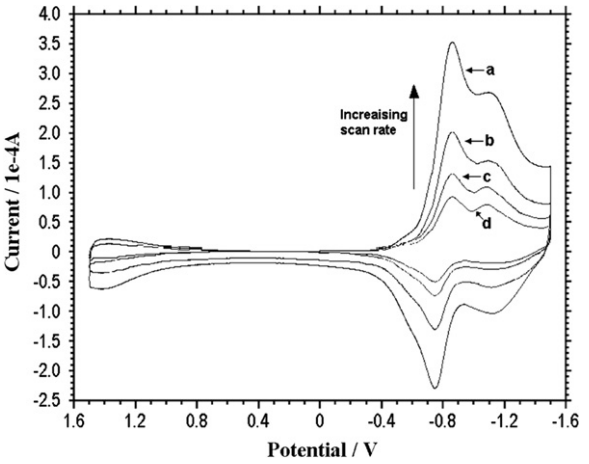

Fig. 5. Cyclic scans of PDI 5 at 200 (a), 100 (b), 50 (c) and 25 (d) mV/s scan rate.

cused on the influence of the film matrix on redox behaviors. Therefore, the potentials in 0.1 M $TBAPF_6$ were considered.

As expected, SA and NA films show two reversible reductions. The reduction peaks are separated by ~30 mV. The peak separations are ~15 mV larger than that of solution phase. This can be attributed to a dimer anion ($dimer^-$) formation between monoanion and neat perylene molecules after the first reduction step. Thus, the formation of dianion becomes more difficult (requires more negative voltage) in SA and NA films. The NT films show different behavior during voltammetric time scale. The second reduction onset voltage shifts slightly to more negative potentials than those of SA and NA films. Moreover, the first reduction is reversible but the reversibility of the second reduction changes depending on the scan rate. Integration of the peaks shows that approximately 30% of monoanion does not convert to dianion. The onset potential of capacitive current on NT films is nearly at the same potential with that of PDIs and the electron accumulation on TiO_2 particles continues during the voltammetric scan. The first reduction onset of PDI may not be influenced by the accumulated electrons due to the small amount of accumulation. However the amount of accumulated electrons increases by the increasing negative voltage and this may supply some negative charge for positively charged non-reduced carbonyl groups. Thus the second reduction potentials of PDI might be expected to shift more negative potentials than those of SA and NA films. Reversibility of the reduction waves depends on the scan rate in NT films. The reduction waves are almost fully reversible at high scan rates (>100 mV/s). However, the oxidation waves disappear when the scan rate is decreased (Fig. 5). At very low scan rates, desorption of adsorbed PDI is also observed. The cyclic scans at various (5, 10, and 25 mV/s) scanning rates shows that the desorption starts below −1.0 V that approximately corresponds to the second reduction peak of PDI. We applied −1.0 V for 3 min to a 2 cm^2 TiO_2 film in order to desorb enough amount of dye to the solution phase that will allow cyclic scan. The cyclic voltammogram of the desorbed dye gave only one reversible reduction peak at around −0.5 V. It indicates that a degradation process exists after the second reduction. Gosztola et al. observed some degradation of PDI dianion during bulk electrolysis in OTTLE cell and they attributed that some residual oxygen in OTTLE cell can lead a photodegradation process [20]. Since SA and NA films did not show such degradation in our working condition, it is clear that TiO_2 plays an active role. We think that the PDIs, presented in this study, are not convenient for Greatzel type organic dye-sensitized photovoltaic applications since the onsets of capacitive current of TiO_2 and the first reduction of PDI are nearly at the same potential. That is why the onset of capacitive current is related with the Fermi level of TiO_2 and it is clear that the LUMO energy level of PDIs lies under the conduction band of TiO_2. It is a known the fact that the LUMO level of dye must be located slightly above the conduction band edge of n-type semiconductor for electron injection [26].

3.4. Spectroelectrochemistry of thin films

The changes in absorption spectra of the films depending on applied voltage were also characterized. Spectroelectrochemical measurements were carried out with NT and NA films. The working electrode was $F:SnO_2$ – metal oxide – PDI with ~1 cm^2 area. The counter and quassi-reference electrodes were prepared by stripping 5 mm of $F:SnO_2$ coating in the middle of the $F:SnO_2$ coated glass, and coating the separated parts by platinum and silver paste, respectively. The working electrode and counter/quassi-reference electrode were sealed with surlyn agent at 110 °C. Nitrogen saturated supporting electrolyte was filled from previously prepared holes to system under vacuum. The prepared systems were placed into the holder of UV–vis spectrophotometer and connected to potentiostat.

Both NA and NT films display striking electrochromism during the reduction process. A color change from red to blue and from blue to violet is observed while the potential decreases from 0 to −1.8 V. Blue color appears at the first

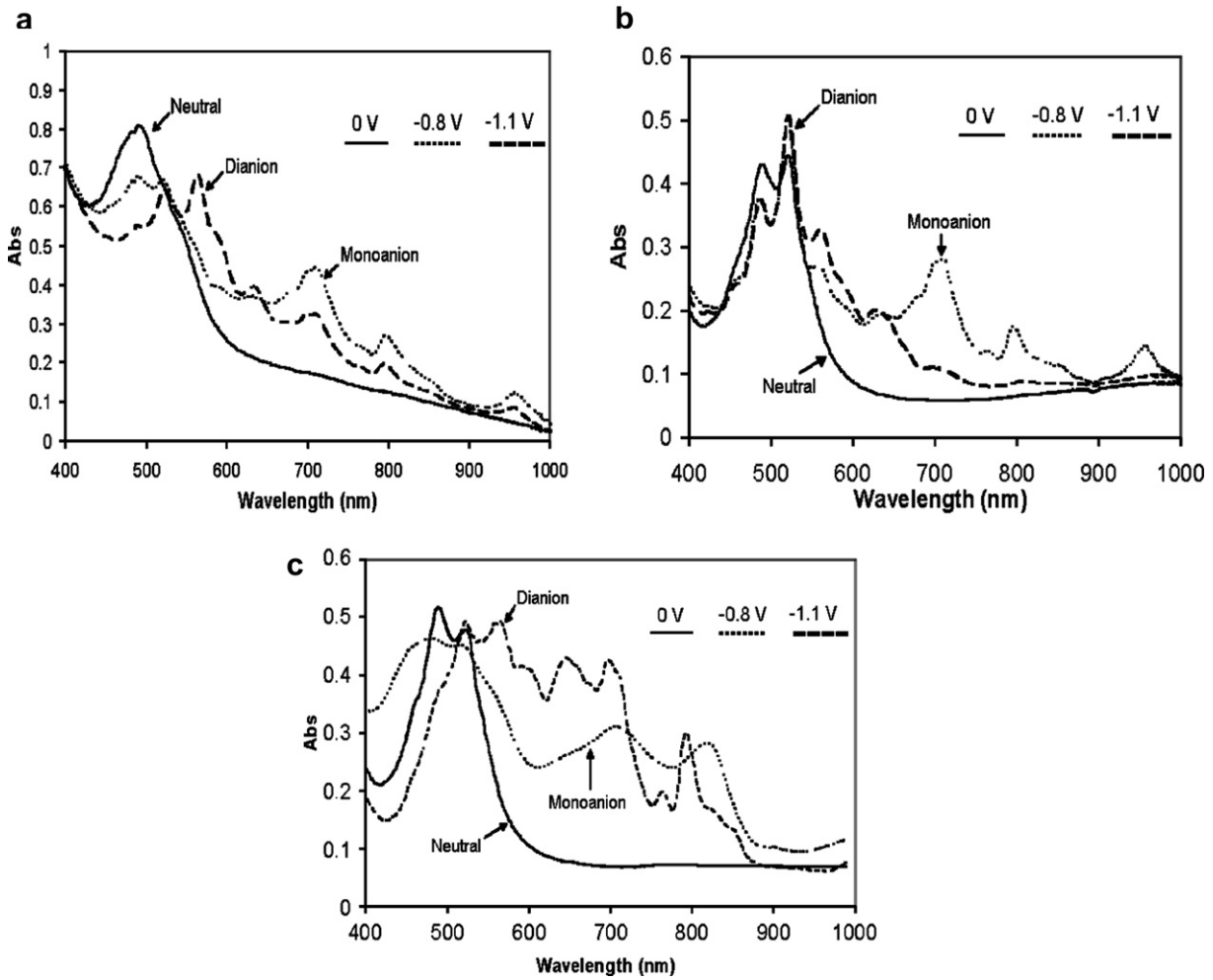

Fig. 6. Absorption spectra of NT–PDI 1 (a), NA–PDI 1 (b) and SA–PDI 5 (c) films with respect to applied voltage.

reduction potential which correspond to monoanion. The color change from blue to violet (dianion) appears down to −1 V. Several cycles were carried out at high scan rates (>100 mV/s) and complete color change is observed in both NA and NT films. However, due to possible degradation of the dye at NT films, color loss occurs at scan rates lower than 100 mV/s. At more positive potentials (∼0 V) compared to the offset of monoanion re-oxidation potential, color change from violet to red is observed in NT films. No additional peak corresponding to color change observed. That means, the electrons do not move to F:SnO_2 electrode, probably remain in TiO_2 traps, thus no current (or peak on cyclic scale) appears. The form of cathodic and anodic current in bare TiO_2 electrode supports our approach (Fig. 4). While the cathodic scan shows a linear increase, the anodic scan shows peak-like discharge of accumulated electrons. The offset of anodic scan is observed to be more negative than the onset of the cathodic scan. It indicates that the discharge of accumulated electrons occurs faster than accumulation. Thus, most of the traps become empty before the complete oxidation of monoanions of PDI. On the other hand, the color change is reversible in NA films. The complete color change from blue (monoanion) to red (neutral) terminates close to 0 V. In agreement with color change, the oxidation peak tail appears up to 0 V in NA films (Fig. 3). These observations also indicate that TiO_2 particles mostly capture a couple of electrons given by monoanion under the negative voltage. Fig. 6 shows the absorption spectra of NA and NT films with respect to the applied voltage conditions. New absorption peaks at 631, 674, 710, 773, 796 and 956 nm grow up to −1.0 V. These are characteristic monoanion peaks as reported by other authors, with the exception that the peak at 631 nm does not decline by the applied voltage below −1.0 V [20,25,66]. As mentioned above, ∼30% of monoanion remains in NT films. Therefore the absorption peaks related to monoanion is observed below −1.0 V which is onset potential for dianion formation. By the formation of dianions, the peaks at 523, 563 and 590 nm are observed. The maximum absorption band of dianion in NA films appears at 523 nm, while this value is 563 nm in NT films. The peak at 523 nm is characteristic maximum absorption band for dianion of PDI in solution [20]. As discussed above, the degradation of PDI starts by the forma-

tion of dianion. The decrease of the characteristic absorption maxima is due to the degradation of PDIs. The NA films show similar absorption bands of dianion formation in solution. The peaks corresponding to neutral species still appear during the monoanion formation in NA and NT films. It is most probably due to the formation of dimeric species between monoanion and neutral species.

The absorption spectra of SA films (for PDI 5) show structureless and broad peaks especially for dianion. The absorption spectra of monoanion show more or less definable broad peaks. By the formation of monoanion, the absorption peaks of neutral PDI become broad and new broad peaks appear at 700 and 820 nm. The peaks become more complicated by the formation of dianion. Self-assembly films of PDIs which are chemically reduced show similar results [45].

4. Conclusion

In this study, electrochemical and spectroscopic properties of polyether derivatives of PDIs adsorbed on metal oxide surface are presented. Electrochromism of PDIs is clear and stable on NA films. The observation of red and blue color in the systems presented in this study, especially in NA films, maybe an advantage for the design of RGB molecular electrochromic devices. On the other hand, the onset potential of the first reduction LUMO of PDIs and the onset potential of capacitive current (Fermi level) of TiO_2 are almost equal. It indicates the LUMO level of PDIs is under the conduction band of TiO_2. Therefore, these dyes may not be convenient for photovoltaic applications.

Acknowledgements

We acknowledge partial funding by the European Commission (FP6 MOLYCELL project-SES-CT-2003-502783), Scientific and Technical Research Council of Turkey (TUBITAK, NATO A-2 support funds) and Alexander von Humbolt Foundation of Germany. We appreciate the project support funds of the State Planning Organization of Turkey (DPT).

References

[1] H. Langhals, S. Sprenger, M.T. Bradherm, Liebigs Ann. (1995) 481.
[2] H. Langhals, W. Jona, Eur. J. Org. Chem. (1998) 847.
[3] K.D. Belfield, K.J. Schafer Jr., M.D. Alexander, Chem. Mater. 12 (2000) 1184.
[4] A.M. Van de Craats, J.M. Warman, P. Schlichting, U. Rohr, Y. Greets, K. Müllen, Synth. Met. 102 (1999) 1550.
[5] P. Pösch, M. Thelakkat, H.W. Schmidt, Synth. Met. 102 (1999) 1110.
[6] W. Huang, D. Yan, Q. Lu, Y. Huang, Eur. Polym. J. 39 (2003) 1099.
[7] Y. Shibano, T. Umeyama, Y. Matano, H. Imahori, Org. Lett. 9 (2007) 1971.
[8] T. Edvinsson, C. Li, N. Pschirer, J. Schöneboom, F. Eickemeyer, E. Sens, G. Boschloo, A. Herrmann, K. Müllen, A. Hagfeldt, J. Phys. Chem. C Lett. 111 (2007) 15137.
[9] H. Icil, S. Icli, J. Polym. Sci. A: Polym. Chem. 35 (1997) 2137.
[10] M.J. Ahrens, L.E. Sinks, B. Rybtchinski, V. Liu, B.A. Jones, J.M. Giaimo, A.V. Gusev, A.J. Goshe, D.M. Tiede, M.R. Wasielewski, J. Am. Chem. Soc. 126 (2004) 8284.
[11] S. Mackinnon, M.Z.Y. Wang, J. Polym. Sci. A: Polym. Chem. 38 (2000) 3467.
[12] H. Dincalp, S. Icli, J. Photochem. Photobiol. A: Chem. 141 (2001) 147.
[13] C. Karapire, C. Timur, S. Icli, Dyes Pigments 50 (2003) 135.
[14] M.E. Williams, R.W. Murray, Chem. Mater. 10 (1998) 3603.
[15] G. Tamizhmani, J.P. Dodelet, Chem. Mater 3 (1991) 1046.
[16] W. Lu, J.P. Gao, Z.Y. Wang, Y. Qi, G.G. Sacripante, J.D. Duff, P.R. Sundararajan, Macromolecules 32 (1999) 8880.
[17] C.W. Struijk, A.B. Sieval, J.E.J. Dakhorst, M. Van Dijk, P. Kimkes, R.B.M. Koehorst, H. Donker, T.J. Schaafsma, S.J. Picken, A.M. Van de Craats, J.M. Warman, H. Zuilhof, E.J.R. Sudhölter, J. Am. Chem. Soc. 122 (2000) 11057.
[18] R.A. Cormier, B.A. Gregg, J. Phys. Chem. B 101 (1997) 11004.
[19] S.K. Lee, Y. Zu, A. Herrmann, Y. Geerts, K. Müllen, A.J. Bard, J. Am. Chem. Soc 121 (1999) 3513.
[20] D. Gosztola, M.P. Niemcyzk, W. Svec, A.S. Lukas, M.R. Wasielewski, J. Phys. Chem. A 104 (2000) 6545.
[21] W.E. Ford, H. Hiratsuka, P.V. Kamat, J. Phys. Chem 93 (1989) 6692.
[22] K.J. Cho, H.K. Shim, Y.I. Kim, Synth. Met. 117 (2001) 153.
[23] J. Danziger, J.P. Dodelet, N.R. Armstrong, Chem. Mater. 3 (1991) 812.
[24] D.K. Slattery, C.A. Linkous, N.E. Gruhn, J.C. Baum, Dyes Pigments 49 (2001).
[25] B.A. Gregg, R.A. Cormier, J. Phys. Chem. B 102 (1998) 9952.
[26] B. O'Reagan, M. Gratzel, Nature 353 (1991) 737.
[27] M. Graetzel, Nature 414 (2001) 338.
[28] Q. Wang, S. Zakeeruddin, .M. Cremer, J. Baeuerle, P. Humphry-Baker, R.M. Graetzel, J. Am.Chem. Soc 127 (2005) 5706.
[29] P. Bonhote, E. Gogniat, F. Campus, L. Walder, M. Graetzel, Displays 20 (1999) 137.
[30] Y.S. Huang, L. Kavan, I. Exnar, M. Graetzel, J. Electrochem. Soc. 142 (1995) L142.
[31] W. Gopel, K.D. Schierbaum, Sens. Actuators B 26 (1995) 1.
[32] M.T. Möller, S. Asaftei, D. Corr, M. Ryan, L. Walder, Adv. Mater. 216 (2004) 1558.
[33] R. Cinnsealach, G. Boschloo, S.N. Rao, D. Fitzmaurice, Sol. Energ. Mater. Sol. Cells 55 (1998) 215.
[34] C.A. Bignozzi, M. Biancardo, P.F.H. Schwab, Semiconductor photochemistry and photophysics, in: V. Ramamurthy, K.S. Schanze (Eds.), Molecular and Supramolecular Photochemistry, vol. 10, Marcel-Dekker, New York, 2003.
[35] A.A. Argun, P.H. Aubert, B.C. Thomson, I. Schwendeman, C.L. Gaupp, J. Hwang, N.J. Pinto, D.B. Taner, A.G. MacDiarmit, J.R. Reynolds, Chem. Mater. 16 (2004) 4401.
[36] M. Biancardo, P.F.H. Schwap, R. Argazzi, C.A. Biagnozzi, Inorg. Chem 42 (2003) 3966.
[37] D. Corr, U. Bach, D. Fay, M. Kinsella, C. McAtamney, F. O'Reilly, S.N. Rao, N. Stobie, Solid State Ionics 165 (2003) 315.
[38] U. Bach, D. Corr, D. Lupo, F. Pichot, M. Ryan, Adv. Mater. 14 (2002) 845.
[39] M. Kus, S. Demic, C. Zafer, G. Saygili, H. Bilgili, S. Icli, Eur. J. Phys.: Appl. Phys. 37 (2007) 277.
[40] K. Ocakoglu, C. Zafer, B. Cetinkaya, S. Icli, Dyes and Pigments 75 (2007) 385.
[41] (a) D.J. Chadwick, I.A. Cliffe, I.O. Sutherland, J. Chem. Perkin Trans. I 565 (1984) 1707;
(b) C.J. Pedersen, J. Am. Chem. Soc. 89 (1967) 7017;
(c) J.P. Dutasta, J.P. Declerg, C.E. Calderon, B. Tirant, J. Am. Chem. Soc. 111 (1989) 7136;
(d) B.H. Langhals, W. Jona, F. Einsield, S. Wahnlich, Adv. Mater. 10 (1998) 1022.
[42] (a) M.G. Kang, N.G. Park, Y.J. Park, K.S. Ryu, S.H. Chang, Solar Energ. Mater. Solar Cells 75 (2003) 475;
(b) B.E. Yoldas, J. Am. Ceram. Soc. Bull. 54 (1975) 286.
[43] C. Karapire, C. Zafer, S. Icli, Synth. Met. 2145 (2004) 51.
[44] Y. Luo, J. Lin, J. Coll. Int. Sci. 297 (2006) 625.
[45] R.O. Marcon, S. Bronchsztain, Langmuir 23 (2007) 11972.
[46] B. Janey, S.K. Asha, J. Phys. Chem. B 110 (2006) 20937.
[47] E.M. Calzado, J.M. Villalvilla, P.G. Boj, J.A. Quintana, R. Gomez, J.L. Segura, M.A. Diaz-Garcia, J. Phys. Chem. C. 111 (2007) 13595.
[48] R. Gomez, D. Veldman, R. Blanco, C. Seoane, J.L. Segura, R.A.J. Janssen, Macromolecules 40 (2007) 2760.
[49] S. Tirapattur, M. Belletete, N. Drolet, M. Leclerc, G. Durocher, Chem. Phys. Lett. 370 (2003) 799.
[50] S. Tirapattur, M. Belletete, N. Drolet, M. Leclerc, G. Durocher, Macromolecules 35 (2002) 8889.
[51] (a) S.G. Liu, G. Siu, R.A. Cormier, R.M. Leblane, B.A. Gregg, J. Phys. Chem. B 106 (2002) 1307;
(b) R.A. Cormier, B.A. Gregg, Chem. Mater. 10 (1998) 1309.
[52] C. Burgdorff, H.G. Löhmannsröben, R. Reisfeld, Chem. Phys. Lett. 197 (1992) 358.
[53] P.A.J. De Witte, J. Hernando, E.E. Neuteboom, E.M.H.P. van Dijk, S.C.J. Meskers, R.A.J. Janssen, N.F. van Hulst, R.J.M. Nolte, M.F. Garcia-Parajo, A.E. Rowan, J. Phys. Chem. B. 110 (2006) 7803.
[54] D. Uzun, M.E. Ozser, K. Yuney, H. İcil, M. Demuth, J. Photochem. Photobiol. A: Chem. 156 (2003) 45.

[55] Y. Liu, S. Xiao, H. Li, Y. Li, H. Liu, F. Lu, J. Zhuang, D. Zhu, J. Phys. Chem. B 108 (2004) 6256.
[56] H. Quante, Y. Geerts, K. Müllen, Chem. Mater. 9 (1997) 495.
[57] M.O. Vysotsky, V. Bohmer, F. Wurthner, C.C. You, K. Rissanen, Org. Lett. 4 (2002) 2901.
[58] K.D. Belfield, M.V. Bondar, O.V. Przhonska, K.J. Schafer, J. Photochem. Photobiol. A: Chem. 151 (2002) 7.
[59] G. Ramakrishna, H.N. Ghosh, J. Phys. Chem. B 105 (2001) 7000.
[60] S.H. Bossman, C. Turro, C. Schnabel, M.R. Pokhrel Jr., L.M. Payavan, B. Baumeister, M. Wörner, J. Phys. Chem. B 105 (2001) 5374.
[61] A.R. Watkins, J. Phys. Chem. 78 (1974) 2555.
[62] D.O. Cowan, R.L.E. Drisko, J. Am. Chem. Soc. 192 (1970) 6281.
[63] B.A. Gregg, S.G. Chen, R.A. Cormier, Chem. Mater. 16 (2004) 4586.
[64] B.A. Gregg, Si-G. Chen, S. Ferrere, J. Phys. Chem. B 107 (2003) 3019.
[65] H.G. Agrell, G. Boschloo, A. Hagfelt, J. Phys. Chem. B 108 (2004) 12388.
[66] R.O. Marcon, S. Brochsztain, Langmuir 23 (2007) 11972.

We observe the formation of a very large interface dipole of −1.2 eV for the interface between α-6T and clean Pd, which is confined to a thin interfacial region and a barrier for hole injection of about 0.7 eV. Our core level photoemission spectroscopy results indeed indicate a chemical reaction between the thermally deposited α-6T and the palladium surface due to the decomposition of a small amount of α-sexithiophene molecules upon adsorption on the palladium surface after the first deposition step.

To complete our knowledge about the interface between the organic semiconductor α-sexithiophene and polycrystalline palladium as metal electrode, we have also performed X-ray photoemission spectroscopy as well as ultraviolet photoemission spectroscopy at the interface between α-6T and contaminated palladium substrates. Contaminations will often occur in the fabrication of devices, which is in many cases not carried out under good vacuum conditions, and the knowledge of the impact of contaminations on the energy level alignment is important to understand the corresponding device performance. For this interface we determine a reduced interface dipole of −0.4 eV and hole injection barrier of 0.5 eV. Our combined X-ray photoemission spectroscopy and ultraviolet photoemission spectroscopy studies show no evidence of a chemical interaction for this kind of interface.

2. Experimental details

For our combined X-ray photoemission (XPS) and ultraviolet photoemission spectroscopy (UPS) studies we have used a commercial PHI 5600 spectrometer, which is equipped with two light sources. Photons with energy of 1486.6 eV from a monochromatized Al K_α source for XPS and photons from a helium discharge lamp with energy of 21.21 eV for UPS measurements are provided. All ultra-violet photoemission spectroscopy measurements were done by applying a sample bias of −5 V to obtain the correct, sample determined, secondary electron cutoff. The recorded spectra were corrected for the contributions of He satellite radiation. The total energy resolution of the spectrometer was determined by analyzing the width of the Pd Fermi edge to be about 350 meV (XPS) and 100 meV (UPS), respectively. The binding energy (BE) scale was aligned by measuring the Fermi edge (0 eV) and the $Pd3_{5/2}$ emission feature (335.1 eV) of a polycrystalline palladium substrate. Applying several cycles of Ar^+ sputtering (3 keV, 10^{-8} mbar), the polycrystalline palladium foils were cleaned. Additionally, we have checked the surface composition of the sputter cleaned substrates by using X-ray photoemission spectroscopy and did not monitor any sign of contaminations. To probe the contaminated palladium electrodes we have treated polycrystalline palladium foils in an ultrasonic bath with acetone for 15 min and rinsing with ethanol for 1 min before putting it into the ultra-high vacuum chamber. The so prepared palladium foils we have also characterized by XPS taking a full range spectra. As a result, we found an overall composition of the contamination layer of carbon (75%), oxygen (20%), and nitrogen (5%) on the ex-situ treated palladium foils. The thickness of the contamination layer is about 1–2 nm.

In a preparation chamber (base pressure 5.5×10^{-10} mbar), which is directly attached to the spectrometer system, thin α-sexithiophene (purchased from Sigma Aldrich) films with different thicknesses have been prepared by in situ thermal evaporation with a typical evaporation rate between 1 Å/min. und 2.5 Å/min. on the clean as well as on the contaminated palladium substrates. Subsequently, the films were transferred to the analyzer chamber (base pressure 1×10^{-10} mbar) without breaking the vacuum and characterized taking a full range XPS spectrum. The number of impurities in the films was very small and below the detection limit of the XPS due to the ultra-high vacuum conditions during the preparation process of the organic films. To estimate the thickness of every individual α-sexithiophene overlayer we have monitored the attenuation of the intensity of the $Pd3_{5/2}$ substrate peak due to the organic film. Considering the procedure of Seah and Dench [14] we have calculated the mean free path of the electrons in the α-6T films to be about 2.5 nm for the kinetic energy of 1152 eV for the $Pd3_{5/2}$ signal from the substrate and a density of 1.5 g/cm^3 for α-sexithiophene [15,16]. We point out that this procedure to determine the thickness of the organic layers is only correct for a layer-by-layer growth. If the organic films does not grow uniformly this methods underestimates the film thickness.

3. Results and discussion

3.1. XPS: Clean Pd surface

On the left hand side of Fig. 1, we present the evolution of the carbon C1s emission feature with a gradual increase in the thickness of the α-sexithiophene overlayer. We observe for many film thicknesses a clear fine structure in the C1s core level spectra. Going from very low coverage, where the fine structure is lost, this structure becomes more and more pronounced with an increase in the film thickness. The C1s core level consists of two components assigned to the two different carbon sites in the α-6T molecule. The contribution (C_C) at the lower binding energy side is attributed to carbon atoms that are bound to other carbon atoms only. The component placed at higher binding energies (C_S) corresponds to carbon atoms attached to sulphur atoms in the thiophene ring. The binding energy of the C1s core level excitation as measured using the C_C as well as the C_S-component is constant at about 284.5–285.4 eV and 285.2–285.1 eV, respectively. These energy positions as well as the observation of the fine structure in the C1s emission feature are in good agreement with previously reported values for thiophene based organic materials [17–22]. We observe a higher spectral weight for the C_S-component in comparison to the C_C-component on going from a thickness of 0.9 nm up to the thickest α-sexithiophene films. This observation can be directly followed by analyzing the peak shape as a function of film thickness. An analysis of the spectral weight ratio between the C_C and C_S component in the C1s core level for the thinnest α-sexithiophene film indicate that on average 2.2 S atoms per molecule are bonded to the Pd surface. We could also observe a change in the peak shape between thin and

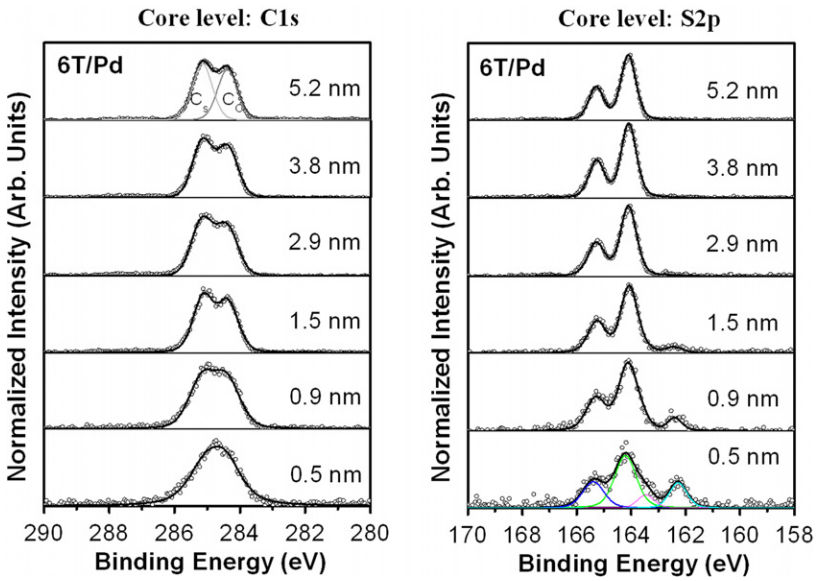

Fig. 1. Left panel: Evolution of the C1s emission feature with increasing α-6T layer thickness on Pd. Right panel: Evolution of the S2p peak of α-6T with progressive deposition of α-sexithiophene onto the polycrystalline palladium.

thick α-6T films. These points are an indication for a chemical reaction between the α-sexithiophene molecules and the palladium substrate in the first molecular layer.

Furthermore, we have determined the behaviour of the S2p spectra dependent on the α-6T film thickness going from low coverage to thick films shown in the right panel of Fig. 1. The spectra reveal that there are two types of sulphur-containing species present at this interface especially for the thin α-6T films. We were able to distinguish these two species by fitting the spectra width with two pairs of spin-orbit components $S2p_{3/2}$ and $S2p_{1/2}$. For the fit we assume a Gaussian: Lorentzian (70:30) line shape, an area ratio of 2:1, as well as an energy splitting fixed at 1.18 eV which reflects the multiplicity of these energy levels [23]. The results of these fits are depicted in the bottom spectrum (for 0.5 nm α-sexithiophene film thickness) on the right hand side in Fig. 1. The first spin-orbit doublet at the higher binding energy side is located for all overlayer thicknesses at almost constant binding energy at about 164.2–164.1 eV for $S2p_{3/2}$ as well as at about 165.4–165.3 eV for the $S2p_{1/2}$ spin-orbit component. These energy positions are in good agreement with previous studies using photoemission spectroscopy, which were performed on thiophene containing organic molecules [18–20,24–27]. The observed binding energy of the $S2p_{3/2}$ component at ~164 eV [25] is in very good agreement with previously reported results for flat lying thiophene based organic molecules on metallic substrates [18,28–30]. From this point we conclude that the α-sexithiophene molecules adsorb on the Pd surface with the molecular axis parallel to the surface plane. The energy width of this spin-orbit doublet is independent of the film thickness with a FWHM (full width at half maximum) of about 0.7–0.8 eV. The second species, which can be observed up to a film thickness of about 1.5 nm, has $S2p_{3/2}$ and $S2p_{1/2}$ components at 162.3–162.5 and 163.5–163.7 eV, respectively, 1.9 eV lower than the main line in the S2p core level of α-6T. The full width at half maximum for the additionally observed doublet is also constant at 0.7–0.8 eV independent of the thickness of the organic overlayer. Only for the thinnest film of α-6T (0.5 nm) the FWHM amounts to 0.9 eV. The energy of the $S2p_{3/2}$ (~162 eV) component represents the typical binding energy of S atoms atomically bonded to the palladium substrate [31–33]. In contrast to the adsorption of S_2 and SO_2 on different palladium surfaces (see Ref. [31,32]) we did not observe a large change in the energy position of the Pd3d core level emission feature and we did not observe a broadening of the Pd3d features upon the adsorption of the α-6T molecules on polycrystalline palladium. We show the Pd3d core level emission feature in Fig. 2, which exhibits a very slight change in the energy position only by about 0.1 eV after the first deposition step.

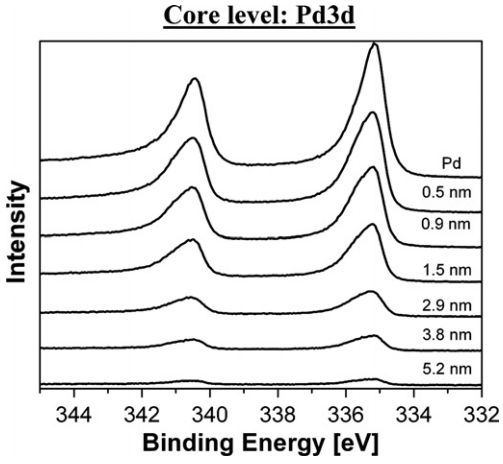

Fig. 2. Core level photoemission spectra for the Pd3d feature dependent on the increasing α-sexithiophene overlayer thickness.

Afterwards the binding energy remains constant at 335.2 eV for the $Pd3_{5/2}$ component. In addition, the FWHM is constant at about 0.6 eV. From this, we conclude that only a small amount of sulphur atoms is atomically bonded to the palladium surface due to the decomposition of the α-sexithiophene molecules on defect sites of the polycrystalline palladium surface. Our conclusion is in consensus with the results of Terada et al. [29], who have investigated the adsorption for submonolayer thiophene on Pd(1 1 1) and Pd(1 1 0) surfaces by S K-edge soft X-ray adsorption fine structure spectra. They report a small amount of atomically bonded sulphur atoms on Pd(1 1 1) and Pd(1 0 0) surfaces due to a decomposition upon the adsorption of thiophene molecules, possible on the step edges. The appearance of an additional S2p feature in the core level data for thiophene based organic materials were also observed for other metal surfaces [34]. Liu et al. [34] have published results for the adsorption of sulphur-containing molecules like thiophene on the Au(1 1 1) surface investigated using a combination of thermal desorption spectroscopy and synchrotron-based high-resolution soft X-ray photoelectron spectroscopy. They show that also for the adsorption of thiophene on a Au(1 1 1) surface a $S2p_{3/2}$ weak feature additionally appears at a binding energy near 161 eV, which they attribute to atomically bonded sulphur on defect sites of the Au(1 1 1) surface. They also mentioned that this effect would be larger for polycrystalline gold surfaces.

The constant binding energy of the two S2p species as well as of the Pd3d core level emission feature in this work is consistent with a description, in which only a small fraction of the sulphur atoms is strongly bonded to the palladium atoms due to the decomposition of the α-6T molecules upon the adsorption after the first deposition step. The additional sulphur species, which is clearly revealed in the XPS data can not be associated to a known bulk binary phase, such as the common PdS phase. This reasoning can be justified with the very small quantity of sulphur atoms in the according coverage of α-6T up to 1.5 nm.

3.2. UPS: Clean Pd surface

To complete our knowledge about the interface between the organic semiconductor α-sexithiophene and clean polycrystalline palladium we now turn to our valence band photoemission studies at this interface. In the left panel of Fig. 3 we show the valence spectra for α-6T on polycrystalline Pd as a function of increasing organic film thickness. For the clean polycrystalline palladium surface we find a work function $\Phi = 5.1$ eV within an absolute error of 0.1 eV. This is in good agreement with previously published results for polycrystalline palladium surfaces [13]. After the initial deposition of α-6T we can observe an abrupt and rigid shift of the work function by about 1 eV. We deduce that the α-6T/Pd interface is characterized by a very large interface dipole confined to a thin interfacial region. Furthermore, we can observe only a slight shift in the work function with a further increase in the α-sexithiophene film thickness. After the film thickness has reached a value of 2 nm it remains essentially constant. Such an abrupt shift in the work function upon the initial deposition of the organic material is additionally a clear indication for the formation of a first, most likely closed monolayer of α-6T on palladium. In the past such abrupt shifts in the work function were reported for thiophene based organic materials on gold [18,19,27,35,36] and on silver [20] as well as for other organic overlayers grown layer-by-layer on metal substrates [37]. From the panel (a) in Fig. 3 it is clearly visible that the main valence band features of α-sexithiophene are fully developed at a film thickness larger than 2 nm whereas at lower coverage the contributions from the Pd substrate must be taken into account. The valence band spectra of the sputter cleaned polycrystalline palladium surface show a prominent Fermi edge, which defines the binding energy axis. The lowest lying peak structures of α-6T arise at 1.3, 2.0, and 3.6 eV. Our results are in good agreement to former publications on the valence band structure of α-6T [18,38–40]. By using the spectral onset of the lowest lying valence band feature a direct measure of the hole injection barrier across this interface is possible. The low binding energy emission edge of the valence band onset was determined by linear extrapolation. Across the α-6T/palladium interface we find a hole injection barrier Φ_{Bh} of 0.7 eV. Moreover, we estimate the electron injection barrier to be about 1.9 eV taking into account the exiton binding energy E_b in α-6T of about 0.4 eV [41,42] and the onset of the electron-hole excitation E_{eh} of about 2.2 eV [43,44] to determine the band gap of α-6T to be $E_g = E_{eh} + E_b = 2.6$ eV. Our valence band photoemission spectra show no evidence for chemical interactions like the formation of new features related to interface induced electronic levels. To have a look closer to the possible existence of interface states for the thin α-sexithiophene film thicknesses due to a chemical interaction at the interface, we have additionally removed the valence band signal coming from the palladium substrate by subtracting of the signal of the clean Pd surface. We did not find any evidence of interface induced electronic levels resulting in new features. This is in contrast to our results for core level photoemission spectroscopy on the C1s and S2p emission features, where we find a chemical reaction between sulphur atoms of α-sexithiophene and the polycrystalline palladium substrate for very low coverage. We attribute this to two points, which are: (i) the fact, that only a small fraction of the sulphur atoms is strongly bonded to the palladium atoms, as concluded from our core level photoemission experiments and (ii) the small fraction of sulphur atoms, which are directly bonded to the palladium surface for low coverage only results in a drop in the density of states of the Pd 4d population near the Fermi edge but not in the formation of new electronic levels in the energy gap of the organic semiconductor α-6T, i.e. those with low binding energy. This is in agreement with published results for S_2 on palladium surfaces, e.g. S_2 on Pd(1 1 1) [32] and S_2 and SO_2 on Pd/Rh(1 1 1) surfaces [31].

The energy level alignment for the metal/organic interface between clean palladium and the thiophene based organic semiconductor α-sexithiophene is summarized on the left hand side in Fig. 4 (panel a) for a film thickness of 2 nm. This thickness is large enough to avoid the impact of image charge screening on the interface electronic levels

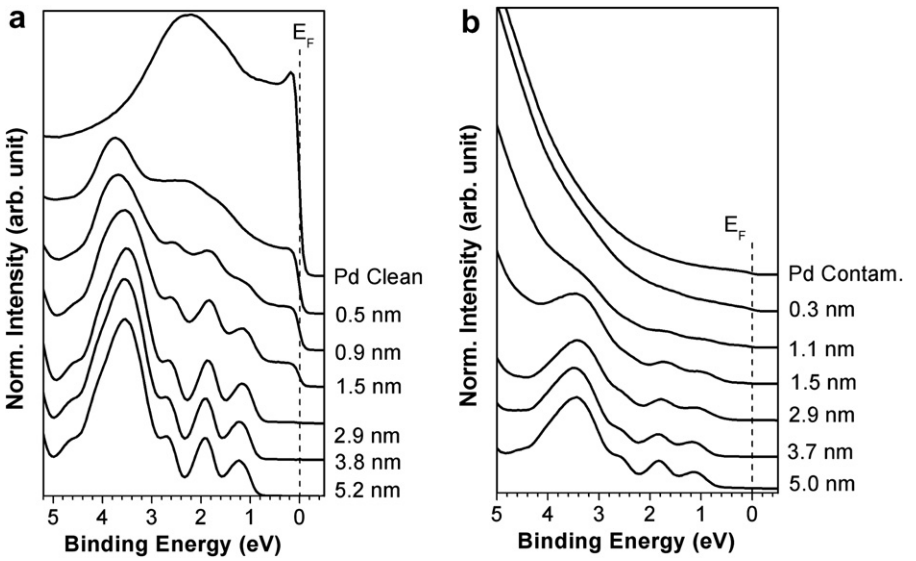

Fig. 3. UPS spectra of α-6T on polycrystalline palladium as a function of the overlayer thickness. The dotted line indicates the position of the Fermi level at a binding energy 0 eV. Left panel (a): Valence band photoemission spectra (UPS) of α-6T on clean palladium. Right panel (b): Valence band photoemission spectra (UPS) of α-6T on ex-situ prepared contaminated palladium.

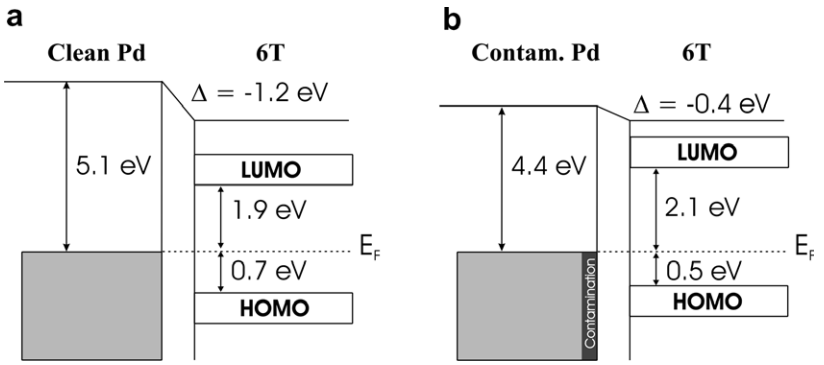

Fig. 4. Schematic energy level diagrams of the clean 6T/Pd interface (left side) and the contaminated 6T/Pd interface (right side) as obtained from photoemission spectroscopy investigations.

[45]. The interface is characterized by the presence of a large interface dipole of about −1.2 eV and a hole injection barrier of 0.7 eV. We point out that such high interface dipoles have been reported previously for other interfaces between thiophene based organic materials and metal electrodes [18,19,27,36,46–48]. Commonly, for many other organic/metal interfaces such quite large interface dipoles are also found [4–6]. In the literature several possible contributions to the interface dipole are discussed [4–6,10,11,49]. These contributions can be: (i) reduction of the metal work function upon the adsorption of the organic material [50–53], (ii) appearing of chemical interaction between the α-sexithiophene molecules and the palladium surface, and (iii) an induced density of interface states, which defines the charge neutrality level (CNL) of the organic semiconductor, while there is a tendency to align the Fermi level and the charge neutrality level [9,49,54–56].

More insight can be gained by a comparison of our data to those obtained for an interface with gold. The results of the photoemission studies of the 6T/Au interface discussed here have been published previously [18,36]. This comparison to the interface with gold as metal contact [18,36] shows the same interface dipole of −1.2 eV. In contrast to this similarity, a larger hole injection barrier of 1.2 eV is found for 6T/Au, in comparison to 0.7 eV for the 6T/Pd interface. In spite of the fact that the two interfaces 6T/Au and 6T/Pd have a very similar work function of the metal contact they show different electronic interface properties, which can be explained to be a consequence of the strength of the chemical reactions at the interfaces. At the interface between α-sexithiophene and gold relatively small chemical interactions take place. Such interfaces can be described within the model of the induced density of interface states (IDIS) [9,54–57]. In the context of this model for weakly-interacting interfaces, the interface

dipole as well as the hole injection barrier is related to the tendency at metal/organic interfaces to align the charge neutrality level and the metal work function [9,54–56]. This is driven by a finite density of states, which is induced in the gap of the organic semiconductor by weak interactions, and which also determines the position of the charge neutrality level. There is a tendency for the CNL and the metal work function to align and this tendency is screened by the induced density of states. In previous publications it has been demonstrated that this scenario can successfully explain the interface electronic characteristic of a number of organic/metal interfaces [9,54–57]. In contrast, at the interface between α-sexithiophene and palladium the chemical interactions, which can be observed in the way of interfaces states most likely pin the interface Fermi level and thus they also predominantly determine the interface energy level alignment.

3.3. XPS and UPS: Contaminated Pd surface

In a separate experiment, we have studied the interface between the organic semiconductor α-6T and contaminated palladium substrates using photoemission spectroscopy in order to gain insight into the impact of contaminations on the interface reaction and the energy level alignment. Our X-ray photoemission studies reveal a surface composition of ex-situ cleaned palladium substrates with 75% carbon, 20% oxygen, and 5% nitrogen. In Fig. 5, we show the emission in the $Pd3d_{5/2}$ and $Pd_{3/2}$ region on the left hand side as well as the $Pd3p_{3/2}$ and O1s core level in the right panel. The obvious broadening as well as the changed peak shape of the Pd3d emission feature of the contaminated palladium surface in comparison to the clean palladium substrates indicates the presence of two more peaks in Pd3d emission region. The surface of the ex-situ prepared palladium foils is characterized by a mixture of three Pd3d5/2 peaks located 335.2 eV (A), 335.9 eV (B) and 336.9 eV (C). The first contribution (A) at the lower binding energy side of the $Pd3d_{5/2}$ peak at 335.2 eV we assign to metallic Pd in agreement with previously reported results [23,58–60]. The first contamination induced Pd3d emission at higher binding energy side with the spin-orbit doublet $Pd3_{5/2}$ and $Pd3_{3/2}$ at 336.9 eV and 342.1 eV (C), respectively is shifted by 1.7 eV from the position of metallic Pd (335.2 eV). This contribution to the Pd3d emission feature of a contaminated palladium surface is assigned to oxidized palladium. The chemical shift of this oxygen induced contribution attributed to PdO agrees well with earlier studies on oxidized Pd [58,59,61–64]. The observed chemical shift of 1.7 eV in this study is not consistent with a chemical shift previously reported for either PdO_2 (2.1–2.9 eV) or higher palladium oxides (3.5–3.6 eV) [23,58,61,62]. The second oxygen induced $Pd3_{5/2}$ feature (B), which appears at 335.9 eV, is shifted towards higher binding energy by 0.7 eV. We assign this emission feature, in agreement to the work of Kim et al. [58] to PdO_{ads}.

On the right hand side in Fig. 5 we show the X-ray spectra of $Pd3p_{3/2}$ and O1s. The O1s emission (A) is not well resolved from the broad $Pd3p_{3/2}$ peak and occurs as a shoulder at 530.9 eV. This value agrees well with the binding energy for metal oxides and absorbed oxygen [59,62]. Two contributions to the $Pd3p_{3/2}$ signal are determined in our study at 532.2 eV (B) and 533.6 eV (C) attributed to pure metallic Pd and to the oxygen induced PdO [59]. The observed chemical shift of ~1.4 eV is rather similar to the one of the Pd3d emission feature. From these results, we conclude that the ex-situ cleaned contaminated palladium surface has been covered with carbon, nitrogen, and oxygen resulting in a contaminated and oxidized Pd layer at the surface.

In Fig. 6 we present the evolution of the S2p emission feature with a gradual increase in the thickness of the α-sexithiophene overlayer on top of contaminated palladium substrate. The S2p spin-orbit doublet appears at 163.3 eV for the $S2p_{3/2}$ component and is shifted towards higher binding energy by ~0.3 eV with an increase in the α-sexithiophene film thickness. The observed binding energy of the $S2p_{3/2}$ and the $S2p_{1/2}$ component at 163.9–164.2 eV and 165.1–165.4 eV agrees well with previous reported results for thiophene based organic materials studied by photoemission spectroscopy [18–20,24–27] as well as with the results for the interface between α-6T and clean palladium. For thicker α-6T (thickness > 2.5 nm) films the binding energy of the $S2p_{3/2}$ and the $S2p_{1/2}$ components remains constant between 164.1–164.2 eV and 165.3–165.4 eV, respectively. In addition, the energy width of this spin-orbit doublet is independent of the film thickness with a FWHM (full width at half maximum) of about

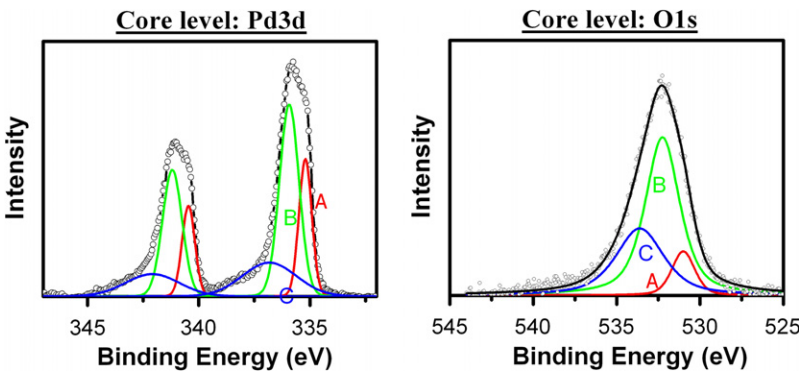

Fig. 5. X-ray photoemission spectra of a contaminated palladium surface. Left panel: XPS spectra of the $Pd3d_{5/2}$ and $Pd3d_{3/2}$ core level. Right panel: XPS spectra of the $Pd3p_{3/2}$ and O1s emission region. The components A–C for both panels are discussed in the text.

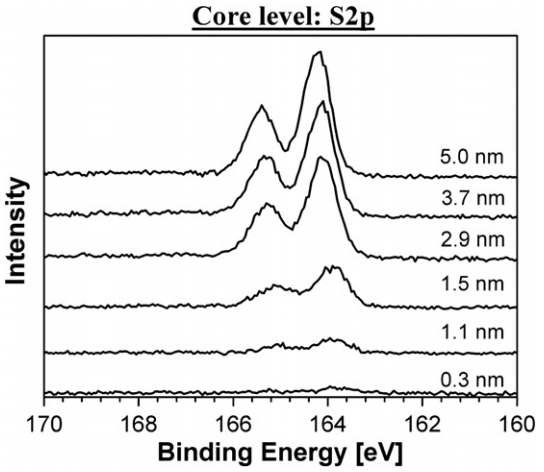

Fig. 6. Core level photoemission spectra for the S2p emission feature dependent on the increasing overlayer thickness for the interface α-6T/contaminated Pd.

0.7–0.8 eV. From our core level spectroscopy data, we conclude a chemical reaction free interface between α-sexithiophene and contaminated palladium substrates. The shift in the binding energy of the S2p feature might be introduced by the presence of the palladium surface oxide layer. The absence of interactions as compared to the clean Pd surface can be rationalized by the presence of the contamination layer that decouples Pd and α-6T and thus prevents chemical reactions.

The valence band spectra of the interface of contaminated palladium and the organic semiconductor α-sexithiophene are presented on the right hand side (panel (b)) in Fig. 3. In comparison to the clean palladium surface the valence band spectrum of the ex-situ cleaned palladium foils is not characterized by a prominent Fermi edge. Due to the contamination layer at the contaminated Pd surface the density of states of the Pd4d population near the Fermi edge is suppressed as revealed in the top spectrum in Fig. 3 (panel) (b). Moreover, we observe a decreased work function of 4.4 eV for the contaminated palladium surface corresponding to a work function reduction by 0.7 eV compared to clean palladium due to the contamination layer. With a rising film thickness of α-6T, new features due to photoemission from the molecular orbitals of the α-sexithiophene appear. At 2.5 nm coverage of α-6T the characteristic valence band structure of α-sexithiophene is fully developed. The lowest lying peak structures of α-6T arise at energy positions of 1.1 eV, 1.8 eV, and 3.4 eV. The valence band spectra for the interface with contaminated palladium substrates agree to the literature [18,20,38–40,65] and to the observed valence band spectrum α-6T on clean palladium. Also in the case of the contaminated palladium substrate we use the spectral onset of the lowest lying valence band feature to measure the hole injection barrier by linear extrapolation. We determine the barrier for hole injection across the 6T/contaminated palladium interface to be 0.5 eV and the electron injection barrier to be 2.1 eV. We find no evidence of chemical reactions like the formation of new features related to induced electronic levels in our valence band photoemission spectra. This fact is in agreement with core level spectroscopy results above where we find also no evidence of chemical reactions.

The energy level alignment of the corresponding interface is presented in the right diagram in Fig. 4 (panel (b)). We observe a reduction of the interface dipole and of the hole injection barrier as compared to the interface between α-6T and clean Pd. This observation is in agreement with what have been reported by Wan et al. [66] for gold recently and for further interfaces of α-6T with different contaminated metal substrates [67]. We assign the reduction of the interface dipole by 0.8 eV from −1.2 eV for the interface α-6T/clean Pd to −0.4 eV for α-6T/contaminated Pd predominantly to the reduction of the metal surface dipole [10] as a consequence of the contamination layer. This parallels a reduction of the metal surface work function upon the deposition of rare gases [68]. The origin of the remaining interface dipole and charge injection barrier for the contaminated palladium substrates might still be related to the tendency for the organic charge neutrality level (CNL) and the metal work function to align at metal/organic interfaces [54–56]. On the other hand, at the interface between α-6T and contaminated palladium, the contamination layer results in a separation of the two materials such that there is only little overlap of the metal and the organic wave functions. From this point of view, the induced density of states might be essentially eliminated by introducing the contamination layer. Consequently, the remaining interface dipole could also be due to a pinning of the Fermi level by electronic states of the organic semiconductor that extend into the gap above the highest occupied molecular orbital or by the existence of band bending as a consequence of valence band tails in the gap, probably because of disorder or defects, as has been discussed recently [69–71].

4. Summary

We have presented a combined valence band and core level photoemission study of the interface between the organic semiconductor α-sexithiophene and polycrystalline palladium. In this study, we have analyzed the interface to clean, and ex-situ prepared and consequently contaminated palladium surfaces. For the interface with clean Pd our X-ray photoemission experiments reveal a decomposition of a small quantity of α-6T molecules upon the adsorption on the polycrystalline palladium surface after the first deposition. Furthermore, our data allow the determination of the energy level diagram at the α-6T/Pd interface. We have found a very large interface dipole of about −1.2 eV as well as a hole injection barrier of 0.7 eV, while the barrier for electron injection was obtained to be about 1.9 eV. In the case of the contaminated palladium, we find oxidation of the Pd surface due to the ex-situ treatment of the palladium foils. Our core level spectroscopy data as well as valence band spectroscopy results show no evidence of chemical reactions at this interface. The results of the ultraviolet photoemission spectroscopy demonstrate that under ex-situ cleaning conditions the work function of the palladium substrate is much smaller than that of the atomically clean material. The energy level alignment at

the interface to contaminated Pd shows a smaller interface dipole of −0.4 eV as well as a reduced injection barrier of 0.5 eV. We attribute this due to the separation of the two materials at the interface and a consequent little overlap of the corresponding wave functions. We mainly ascribe the interface dipole to the consequences of electronic states of the organic semiconductor that extend into the gap above the highest occupied molecular orbital, due to disorder or defects.

Acknowledgements

We gratefully thank R. Hübel, S. Leger, and R. Schönfelder for technical support. We acknowledge financial support by the Deutsche Forschungsgemeinschaft under No. KN393/5.

References

[1] S. Scheinert, G. Paasch, Phys. Status Solidi A 6 (2004) 1263.
[2] G. Horowitz, J. Mater. Res. 19 (2004) 1946.
[3] W. Clemens, I. Fix, J. Ficker, A. Knobloch, A. Ullmann, J. Mater. Res. 19 (2004) 1963.
[4] W.R. Salaneck, K. Seki, A. Kahn, J.J. Pireaux, Conjugated Polymer and Molecular Interfaces: Science and Technology for Photonic and Optoelectronic Applications, Marcel Dekker, New York, 2002.
[5] H. Ishii, K. Sugiyama, E. Ito, K. Seki, Adv. Mater. 11 (1999) 605.
[6] W.R. Salaneck, M. Fahlman, J. Mater. Res. 19 (2004) 1917.
[7] D. Cahen, A. Kahn, E. Umbach, Mater. Today 8 (2005) 32.
[8] A. Kahn, N. Koch, W. Gao, J. Polym. Sci. B 41 (2003) 2529.
[9] H. Vazquez, Y.J. Dappe, J. Ortega, F. Flores, J. Chem. Phys. 126 (2007) 144703.
[10] M. Knupfer, G. Paasch, J. Vac. Sci. Technol. A 23 (2005) 1072.
[11] M. Knupfer, H. Peisert, Phys. Status Solidi A 201 (2004) 1055.
[12] D. Cahen, A. Kahn, Adv. Mater. 15 (2003) 271.
[13] H.B. Michaelson, J. Appl. Phys. 48 (1977) 4729.
[14] M.P. Seah, W.A. Dench, Surf. Interface Anal. 1 (1979) 2.
[15] B. Servet, S. Ries, M. Trotel, P. Alnot, G. Horowitz, F. Garnier, Adv. Mater. 5 (1993) 461.
[16] D. Oeter, C. Ziegler, W. Göpel, Synth. Metals 61 (1993) 147.
[17] G.J. Herrera, G.J. Whitten, Synth. Metals 128 (2002) 317.
[18] T. Schwieger, X. Liu, H. Peisert, B. Adolphi, N. Kiriy, M. Knupfer, J. Appl. Phys. 97 (2005) 123712.
[19] X. Liu, M. Knupfer, B.H. Huisman, Surf. Sci. 595 (2005) 165.
[20] M. Grobosch, M. Knupfer, Org. Electron. 8 (2007) 625.
[21] G. Koller, F.P. Netzer, M.G. Ramsey, Surf. Sci. 421 (1999) 353.
[22] M.G. Ramsey, G. Koller, I. Kardinal, F.P. Netzer, Surf. Sci. 352–354 (1996) 128.
[23] J.F. Moulder, W.F. Stickle, P.E. Sobol, K.D. Bomben, Handbook of X-ray Photoelectron Spectroscopy, Perkin–Elmer Cooperation (1992).
[24] K.M. Baumgärtner, M. Volmer-Uebing, J. Taborski, P. Bäuerle, E. Umbach, Berichte der Bunsengesellschaft 95 (1991) 1488.
[25] A. Nambu, H. Kondoh, I. Nakai, K. Amemiya, T. Ohta, Surf. Sci. 530 (2003) 101.
[26] A.J. Cascio, J.E. Lyon, M.M. Beerbom, R. Schlaf, Y. Zhu, S.A. Jenekhe, Appl. Phys. Lett. 88 (2006) 062104.
[27] J.E. Lyon, A.J. Cascio, M.M. Beerbom, R. Schlaf, Y. Zhu, S.A. Jenekhe, Appl. Phys. Lett. 88 (2006) 222109.
[28] M. Kiguchi, S. Entani, K. Saiki, Appl. Phys. Lett. 84 (2004) 344.
[29] S. Terada, T. Ykokoyama, M. Sakano, A. Imansishi, Y. Kitajima, M. Kiguchi, Y. Okamoto, T. Ohta, Surf. Sci. 414 (1998) 107.
[30] H. Orita, N. Itoh, Surf. Sci. 550 (2004) 177.
[31] J.A. Rodriguez, T. Jirsak, S. Chaturvedi, J. Chem. Phys. 110 (1999) 3138.
[32] J.A. Rodriguez, S. Chaturvedi, T. Jirsak, Chem. Phys. Lett. 296 (1998) 421.
[33] J.C. Love, D.B. Wolfe, R. Haasch, M.L. Chabinyc, K.E. Paul, G.M. Whitesides, R.G. Nuzzo, J. Am. Chem. Soc. 125 (2003) 2597.
[34] G. Liu, J.A. Rodriguez, J. Dvorak, J. Hrbek, T. Jirsak, Surf. Sci. 505 (2002) 295.
[35] X. Liu, M. Knupfer, L. Dunsch, A. Tabet, H. Hartmann, Org. Electron. 7 (2006) 107.
[36] M. Knupfer, X. Liu, Surf. Sci. 600 (2006) 3978.
[37] T.S. Ellis, K.T. Park, S.L. Hulbert, M.D. Ulrich, J.E. Rowe, J. Appl. Phys. 95 (2004) 982.
[38] H. Fujimoto, U. Nagashima, H. Inokuchi, K. Seki, Y. Cao, H. Nakahara, J. Nakayama, M. Hoshino, K. Fukuda, J. Chem. Phys. 92 (1990) 4077.
[39] C.E. Heiner, J. Dreyer, I.V. Hertel, N. Koch, H.H. Ritze, W. Widdra, B. Winter, Appl. Phys. Lett. 87 (2005) 093501.
[40] Y. Ge, J.E. Whitten, Chem. Phys. Lett. 448 (2007) 65.
[41] L.M. Blinov, S.P. Palto, G. Ruani, C. Taliani, A.A. Tevosov, S.G. Yudin, R. Zamboni, Chem. Phys. Lett. 232 (1995) 401.
[42] I.G. Hill, A. Kahn, Z.G. Soos, R.A. Pascal Jr., Chem. Phys. Lett. 327 (2000) 181.
[43] M. Knupfer, T. Pichler, M.S. Golden, J. Fink, M. Murgia, R.H. Michel, R. Zamboni, C. Taliani, Phys. Rev. Lett. 83 (1999) 1443.
[44] P. Lang, F. Kouki, J.P. Roger, J.C. Martinez, G. Horowitz, F. Garnier, Synth. Metals 101 (1999) 536.
[45] H. Peisert, M. Knupfer, T. Schwieger, J.M. Auerhammer, M.S. Golden, J. Fink, J. Appl. Phys. 91 (2002) 4872.
[46] A.J. Makinen, I.G. Hill, T. Noda, Y. Shirota, Z.H. Kafafi, Appl. Phys. Lett. 78 (2001) 670.
[47] A.J. Makinen, I.G. Hill, M. Kinoshita, T. Noda, Y. Shirota, Z.H. Kafafi, J. Appl. Phys. 91 (2002) 5456.
[48] F. Baier, F. von Ludowig, A. Soukopp, C. Vaterlein, J. Laubender, P. Bauerle, M. Sokolowski, E. Umbach, Opt. Mater. 12 (1999) 285.
[49] H. Vázquez, W. Gao, F. Flores, A. Kahn, Phys. Rev. B 71 (2005) 041306.
[50] X. Crispin, V. Geskin, A. Crispin, J. Cornil, R. Lazzaroni, W.R. Salaneck, J.L. Bredas, J. Am. Chem. Soc. 124 (2002) 8131.
[51] X. Crispin, Sol. Energy Mater. Sol. Cells 83 (2004) 147.
[52] K. Wandelt, Appl. Surf. Sci. 111 (1997) 1.
[53] N. Koch, A. Kahn, J. Ghijsen, J.J. Pireaux, J. Schwartz, R.L. Johnson, A. Elschner, Appl. Phys. Lett. 82 (2003) 70.
[54] H. Vázquez, F. Flores, R. Oszwaldowski, J. Ortega, R. Pérez, A. Kahn, Appl. Surf. Sci. 234 (2004) 107.
[55] H. Vázquez, R. Oszwaldowski, P. Pou, J. Ortega, R. Pérez, F. Flores, A. Kahn, Europhys. Lett. 65 (2004) 802.
[56] H. Vázquez, F. Flores, A. Kahn, Org. Electron. 8 (2007) 241.
[57] O.V. Molodtsova, M. Grobosch, M. Knupfer, V.Y. Aristov, Appl. Phys. Lett. 91 (2007) 244103.
[58] K.S. Kim, A.F. Gossmann, N. Winograd, Anal. Chem. 46 (1974) 197.
[59] M. Peuckert, J. Phys. Chem. 89 (1985) 2481.
[60] V.A. Bondzie, P. Kleban, D.J. Dwyer, Surf. Sci. 347 (1996) 319.
[61] J.M. Tura, P. Regull, L. Victori, M.D. Decastellar, Surf. Interface Anal. 11 (1988) 447.
[62] B.A. Banse, B.E. Koel, Surf. Sci. 232 (1990) 275.
[63] P. Legare, F. Finck, R. Roche, G. Maire, Surf. Sci. 217 (1989) 167.
[64] W.E. Moddeman, W.C. Bowling, D.C. Carter, D.R. Grove, Surf. Interface Anal. 11 (1988) 317.
[65] N. Koch, G. Heimel, J. Wu, E. Zojer, R.L. Johnson, J.-L. Bredas, K. Müllen, J.P. Rabe, Chem. Phys. Lett. 413 (2005) 390.
[66] A. Wan, J. Hwang, F. Amy, A. Kahn, Org. Electron. 6 (2005) 47.
[67] M. Grobosch, M. Knupfer, Adv. Mater. 19 (2007) 754.
[68] A. Zangwill, Physics at Surfaces, Cambridge University Press, Cambridge, 1988.
[69] O. Tal, Y. Rosenwaks, Y. Preezant, N. Tessler, C.K. Chan, A. Kahn, Phys. Rev. Lett. 95 (2005) 256405.
[70] G. Paasch, H. Peisert, M. Knupfer, J. Fink, S. Scheinert, J. Appl. Phys. 93 (2003) 6084.
[71] H. Fukagawa, S. Kera, T. Kataoka, S. Hosoumi, Y. Watanabe, K. Kudo, N. Ueno, Adv. Mater. 19 (2007) 665.

structures from ordered polymer chains [10,15,16]. P3HT fibers, obtained from highly concentrated solution, are reported to increase the photovoltaic performance of polymer/fullerene solar cells [17]. In general it is possible to control the formation of a phase separated morphology with crystalline P3HT and PCBM domains inside the active layer of bulk-heterojunction solar cells can be achieved by following ways:

(1) By choosing the appropriate solvent with required boiling point for either slow or high evaporation rate [11,18,19].
(2) By reducing the drying speed of spin-coated films [20–22].
(3) By melting of bilayers [23].
(4) By thermal annealing of produced films with or without applied external voltage [12,13,24].
(5) By using chemical additives [2,25,26].

The observed correlation between domain formation and photovoltaic device performance indicates that a certain degree of phase separation of the two organic components (polymer and PCBM) is beneficial and increases the power conversion efficiency of organic solar cells. However, the alternative and simpler method of controlling the morphology of the blends is possible by adding a third material to the blend of polymer and PCBM. It has been already shown before, that the photoconductivity response is strongly increased in polymer/fullerene composites by adding a small amount of the alkyl thiol to the solution prior to the film deposition [1]. Also strongly improved photovoltaic performance and efficiency enhancement through improved morphology and interpenetrating network was observed in organic solar cells fabricated from the low band gap polymer poly[2,6-(4,4-bis-(2-ethylhexyl)-4H-cyclopenta[2,1-b;3,4-b′]-dithiophene)-alt-4,7-(2,1,3-benzothiadiazole)] (PCPDTBT) and PCBM blends [2].

In order to further to optimize the performance of organic solar cells fabricated from polymer/fullerene mixtures with alkyl thiols it is necessary to understand the influence of the additive to the molecular rearrangement as well as to the optical and electrical properties of the blends. We have chosen to use P3HT and PCBM for solar cells fabrication because these are well known and widely studied materials for efficient organic photovoltaic devices.

In this paper, we use comparative optical and electrical techniques to probe the properties of organic solar cells fabricated from regioregular P3HT and PCBM bulk-heterojunction by adding alkyl thiols. We have studied four different solar cells: (1) as produced films of P3HT and PCBM (untreated, no alkyl thiol), (2) thermally annealed films (treated, no alkyl thiol), (3) as produced films with alkyl thiol (untreated, with alkyl thiol) and (4) thermally annealed films with alkyl thiol (treated, with alkyl thiol).

Incident photon to current conversion efficiency (IPCE) is measured for all films together with the photovoltaic response. The morphology was studied using AFM, whereas current–voltage (I–V) characteristics were measured together with the charge extraction using linear increase of voltage (CELIV) and photo-CELIV technique to determine the electrical properties of these four different types of bulk-heterojunction solar cells. The results clearly show that alkyl thiol addition can substitute the post production treatment for increasing the efficiency.

2. Results and discussion

In Fig. 1 the optical absorption coefficient as a function of wavelength is shown for all four different solar cells. The increase in optical absorption upon post production treatment by annealing and simultaneous applying a constant current during treatment as has been already shown before [27–29]. The red-shift of the absorption is clearly seen for treated cells as well as for cells with alkyl thiol additive. The difference in absorption in treated and untreated solar cells, with alkyl thiol additive, is negligible indicating the final optimum structure can be achieved by the additive alone. Characteristic vibronic peaks, which are barely visible in untreated films, are clearly pronounced in treated cells and cells with alkyl thiol (at around 517 nm, 556 nm and 603 nm). The increased optical absorption allows harvesting more energy for treated cells and cells with alkyl thiol, therefore, apart from improved transport and recombination properties, these cells are expected to have better photovoltaic performance.

Current–voltage (I–V) characteristics for all cells under illumination with a solar simulator are shown in Fig. 2. To allow a comparison, the fabrication procedures were kept the same for all four types of cells. Untreated solar cells have the worst performance with the lowest short circuit current (5.2 mA/cm^2) and low fill factor. However, these cells demonstrate a relatively higher open circuit voltage (0.64 V), but, due to a low short circuit current and a low fill factor, their power conversion efficiency is only around 0.9%. Open circuit voltage has been observed to increase using the post production treatment in earlier reports [24]. This was not observed in our studies. Our as-produced untreated solar cells show slightly higher efficiency (0.9%) as compared to the earlier reported cells

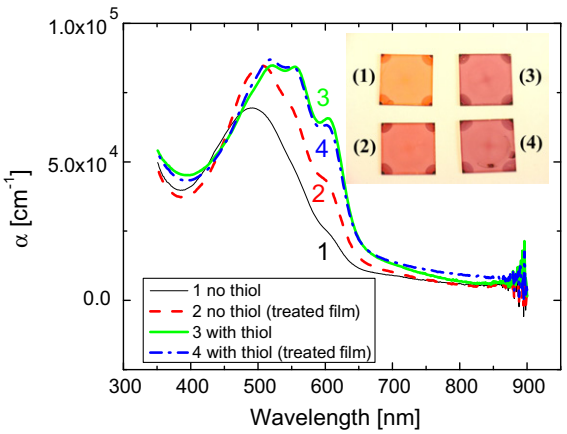

Fig. 1. Optical absorption coefficient of 4 different RR-P3HT/PCBM bulk-heterojunction solar cells: as produced (thin line), annealed (thick dashed line), thiol added (thick line), thiol added and annealed film (thick dash dot line).

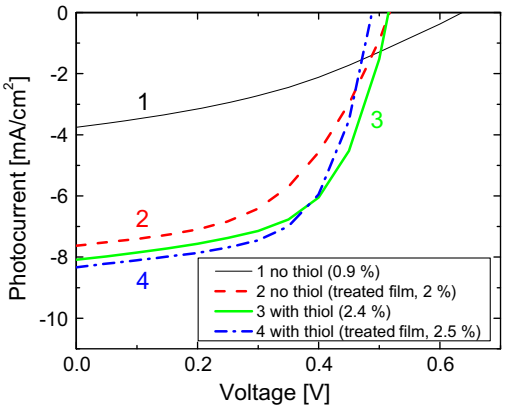

Fig. 2. Current–voltage (*I–V*) curves in the fourth quadrant of 4 different RR-P3HT/PCBM bulk-heterojunction solar cells under illumination with solar simulator (1000 W/m^2, 1.5 AM): as produced (thin line), annealed (thick dashed line), thiol added (thick line), thiol added and annealed film (thick dash dot line).

making this difference plausible. The difference in photocurrents between treated cell and cells with alkyl thiol is rather small, except that treated cells have lower fill factors and therefore slightly lower efficiency (2%) as compared to cells with alkyl thiol additive (2.4–2.5%).

Significant improvement of power conversion efficiency in treated cell and cells with alkyl thiol might arise from two effects:

(1) the increased absorption,
(2) the improved charge carrier transport and/or reduced losses, when charge carrier lifetime must be longer than the slower carrier transit time.

We have measured the incident photon to collected electron efficiency (IPCE) in all four types of cells and the results are shown in Fig. 3. Earlier studies have already shown the IPCE depends on post production treatment

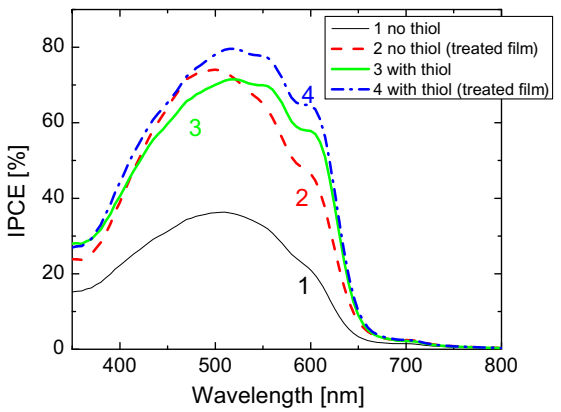

Fig. 3. Incident photon to current efficiency of 4 different RR-P3HT/PCBM bulk-heterojunction solar cells: as produced (thin line), annealed (thick dashed line), thiol added (thick line), thiol added and annealed film (thick dash dot line).

and can be up to 70–80% [24,27–30]. In all samples studied here, the IPCE is increasing at short wavelengths following the increase in optical absorption in polymer/PCBM blend, reaches a maximum and suddenly decreases following the edge of the absorption curve. The same characteristic absorption peaks seen in the optical absorption spectra (Fig. 1) are also clearly seen in the IPCE spectra. The IPCE values for the untreated cell are much smaller compared the rest of the cells, reaching a maximum of around 35%, whereas cells with treatment or alkyl thiol additives reach up to slightly below 80% IPCE. IPCE results do not allow distinguishing between improved carrier mobility and increased charge carrier lifetime, since both parameters would increase the IPCE. From the IPCE studies it can be concluded that the improvement is not only due to the increased optical absorption, but probably also due to improved transport and/or reduced recombination losses (e.g. due to longer charge carrier lifetime).

Charge transport in bulk-heterojunction solar cells usually strongly depends on the nanomorphology of the polymer/PCBM films, where the interpenetrating network formed between polymer and PCBM is created from polymer and PCBM rich phases [9,12,14,27–30]. Tapping mode AFM images (2.5 μm × 2.5 μm) of all studied cells are shown in Fig. 4. In cells without alkyl thiol the coarse morphology is stronger in treated films, with the surface roughness staying similar (on the same 5 nm scale). Both treated and untreated cells with alkyl thiol show much coarser surface as compared to the cells without alkyl thiol. Apparently, as it has already been shown before [2], polymer and PCBM rich phases is advantageous for charge transport and photovoltaic performance for films with alkyl thiol additive. As has been already shown before, the fact that addition of alkyl thiols strongly influences the structure of the interpenetrating network most likely is the reason for the improved IPCE and power conversion efficiency. The electron and hole transport to the electrodes might be improved, since pronounced polymer and PCBM phases will create well defined pathways for the transport of the respective charges.

Dark current–voltage (*I–V*) curves recorded for all 4 different solar cells are shown in Fig. 5a. The dark current, shown in the region of negative applied voltage, representing the reverse bias (positive voltage on Al, negative on ITO), is similar for all cells. The current in forward bias is much larger compared to the reverse bias current. The rectification ratio for the treated cells and for cells with alkyl thiol is more than two orders of magnitude, whereas for untreated cells the rectification ratio is one order of magnitude less compared to other cells.

Due to the different nanomorphology of the interpenetrating network, the dark conductivity is expected to increase in the cells with higher conversion efficiency, because of improved conductivity of the films (assuming the injection is not limited by the contact). This effect has been already observed in the case of postproduction treatment [24,30]. The dark injection current (at large forward bias) is much lower in untreated cells without alkyl thiol, suggesting that either the carrier mobility or equilibrium carrier concentration is smaller compared to treated cells and cells with alkyl thiol:

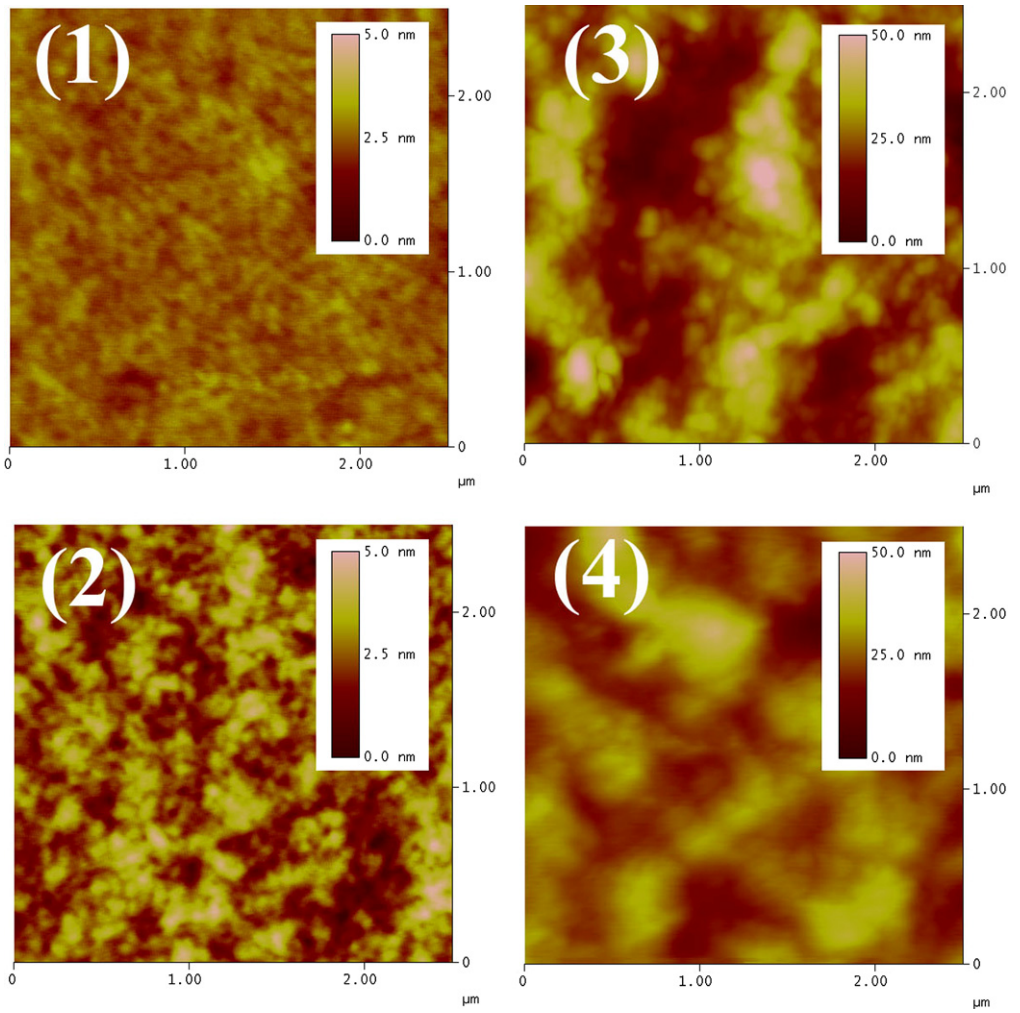

Fig. 4. Tapping mode AFM images of 4 different RR-P3HT/PCBM bulk-heterojunction solar cells: as produced (1), annealed (2), thiol added (3), thiol added and annealed film (4). The RMS surface roughness for all solar cells is 0.2 nm (cell 1), 0.6 nm (cell 2), 7.1 nm (cell 3), and 4.3 nm (cell 4).

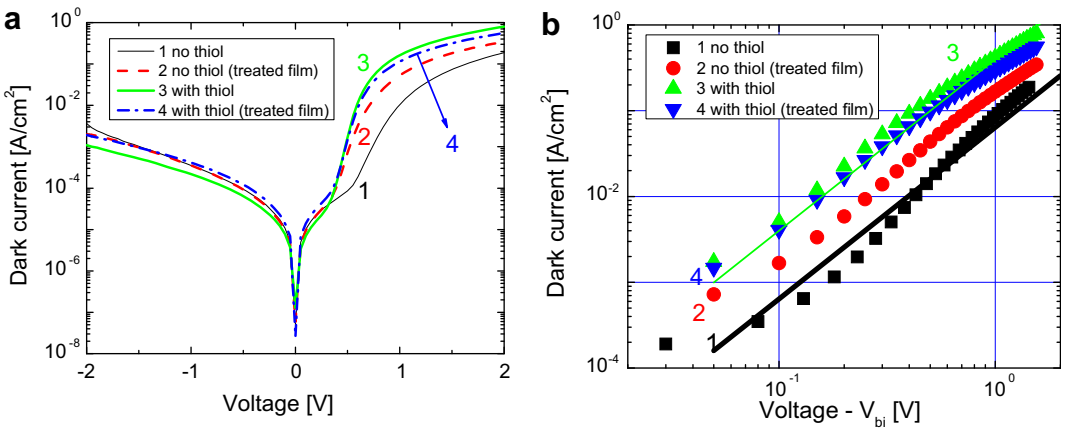

Fig. 5. Dark current–voltage (*I*–*V*) curves (a) and same dependencies plotted in log–log scale with built-in voltage subtracted (b) of 4 different RR-P3HT/PCBM bulk-heterojunction solar cells: as produced (thin line), annealed (thick dashed line), thiol added (thick line), thiol added and annealed film (thick dash dot line). Straight lines (thick for sample 1 and thin for sample 3) are calculated ideal Mott's space charge limited currents using carrier mobility at long time obtained from photo-CELIV (Fig. 7).

$$(j = \mathrm{en}\mu_n E + \mathrm{ep}\mu_p E), \quad (1)$$

where j is the current density, e is electron charge, n and p are the electron and hole concentration, respectively, μ_n and μ_p are the electron and hole mobilities, respectively, and E is the electric field). In principle, another possibility for a smaller dark current in forward bias in untreated cells without alkyl thiol could be due to a contact limited injection. The post production thermal treatment and/or the alkyl thiol addition could have altered the contact properties between the interpenetrating network and the electrode. However, treated cells without alkyl thiol (which also have high dark injection current) were annealed without the aluminum electrode, which was thermally evaporated afterwards. Therefore, at least Aluminum electrode interface cannot be responsible for the lower dark current in forward bias in the untreated cells.

In Fig. 5b the same dark current–voltage curves with subtracted built-in voltage (taken from the open circuit voltage of the I–V curves under illumination) are plotted in log–log scale in order to characterize the current–voltage dependence. For voltages above 1 V the current seems to approach a square dependence but deviates at larger voltages in treated cell and cells with alkyl thiol. As it will be shown later from Fig. 6a, at given geometry and intrinsic conductivity, a space charge limited current already dominates at 1 V in all our cells, due to low intrinsic carrier concentration (SCLC condition is reached when the charge on the electrodes (CU) is larger than the charge present inside the film, $Q > CU$).

The straight line in Fig. 5 shows the calculated SCLC current for sample 1 and sample 3, where the carrier mobility is taken at longest delay times from the photo-CELIV technique (shown below in Fig. 7) because of the dispersive nature of charge transport in organic materials. The following equation was used to calculate SCLC [31]:

$$j = \frac{9}{8}\varepsilon\varepsilon_0\mu\frac{U^2}{d^3}, \quad (2)$$

where ε and ε_0 are the relative and vacuum's dielectric permittivity respectively, U is applied external voltage and d is the film thickness. The dark current measured in untreated solar cells (Fig. 5b) is lower as compared to treated cell and cells with alkyl thiol, so is the carrier mobility (at longer times) as shown in Fig. 7. The calculated SCLC values and current measured from I–V curves are in rather good agreement within the experimental error, showing that the photo-CELIV experiment rather well estimates the steady-state carrier mobility. It is important to note that usually in steady-state space-charge-limited conduction models [31] a carrier transport with carrier mobility independent on the electric field is assumed, which is rarely the case in disordered materials like in solution processed films.

In order to find out whether the increased dark current in treated cell and in cells with alkyl thiol is due to higher carrier intrinsic concentration (due to doping, impurities or similar effects) or due to improved charge carrier mobility, we have studied the cells using dark charge carrier extrac-

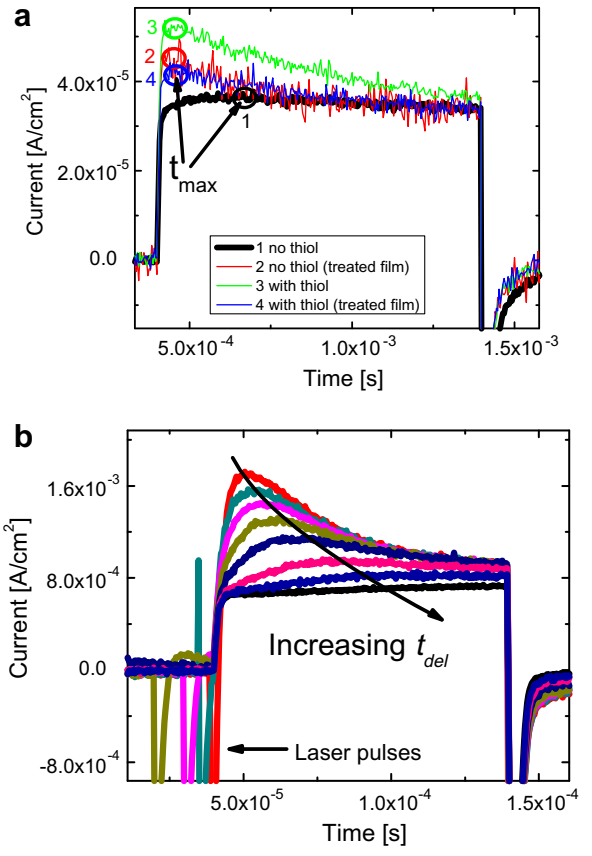

Fig. 6. (a) CELIV dark current transient response to an applied triangle-shaped voltage pulse in reverse bias of 4 different RR-P3HT/PCBM bulk-heterojunction solar cells: as produced (thin line), annealed (thick dashed line), thiol added (thick line), thiol added and annealed film (thick dash dot line). Circles mark the position of current extraction maximum (t_{max}) for all four different type of films. (b) Photo-CELIV current transients recorded for various delay times t_{del} between the laser and triangle-shaped voltage pulses. The extraction maximum time shift is guided with an arrow.

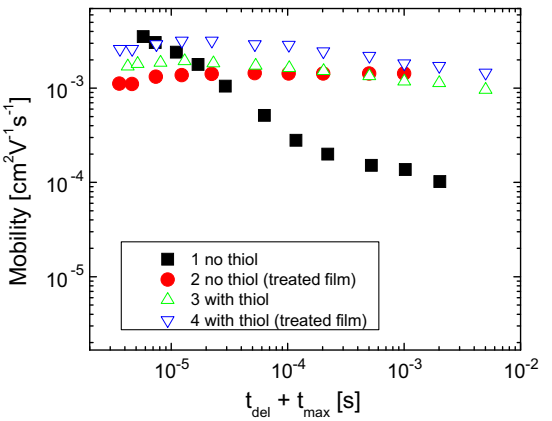

Fig. 7. Charge carrier mobility of 4 different RR-P3HT/PCBM bulk-heterojunction solar cells: as produced (filled squares), annealed (filled circles), thiol added (open up-pointing triangles), annealed film with thiol (open down-pointing triangles).

tion by linearly increasing voltage (dark CELIV) technique [32]. This technique allows to measure the charge carrier concentration and the mobility simultaneously [33]. The dark CELIV current transients are shown in Fig. 6a. In CELIV experiments a triangle-shaped voltage pulse is applied in reverse bias. The film acts as a capacitor, and the current is measured with an Oscilloscope's load resistance forming all together a differentiating RC circuit. The current response would show a constant current pulse if the capacitor would be ideal without mobile charges between the capacitor plates. However, if there is an intrinsic carrier concentration inside the film, the dark current response would be seen as a conductivity current on top of the constant capacitive displacement current step. The charge mobility can then be estimated from the current extraction maximum and charge concentration is estimated and by integrating the current over time [32,33]. The current transient response shown in Fig. 6a is different for the untreated cells without alkyl thiol and the other cells. At the initial time the current is rapidly increasing in the treated cell and cells with alkyl thiol, whereas later the current decreases forming an extraction maximum (t_{max}). The extraction current in the untreated cell is much smaller and the extraction maximum is at longer times showing less equilibrium charge with slower mobility in the untreated solar cells.

From Fig. 6a the equilibrium (intrinsic) charge concentration is estimated $5.6 \times 10^{14}\,cm^{-3}$ in the untreated sample (1), $1.3 \times 10^{15}\,cm^{-3}$ in the treated sample (2), $3.8 \times 10^{15}\,cm^{-3}$ in the untreated sample with thiol (3), and $1.7 \times 10^{15}\,cm^{-3}$ in the treated sample with thiol (4). The charge present in the film are calculated to be below $4 \times 10^{-10}\,C$, whereas the charge due to the geometrical capacitance at 1 V is around $3 \times 10^{-9}\,C$ (for contact area around $5\,mm^2$). Therefore, the charge on the electrodes for all samples (samples were made with similar geometries) at 1 V is much larger than the equilibrium intrinsic charge stored in the film, which justifies using the model of a space charge limited current (as discussed above). This observation is in agreement with high purity organic semiconductors where the steady state SCLC is easily reached at rather low applied external electric field [34,35].

For measuring the mobilities of photogenerated charge carriers, we have used the photo-CELIV technique [36]. This technique is able to probe dispersive transport which is typical in all disordered materials. As an additional advantage, the charge carrier mobility can be measured in <100 nm thin films, where typical time-of-flight (TOF) technique is not applicable [37]. The main advantage of this method is that it allows measuring the carrier mobility and density simultaneously. The charge carriers are photogenerated with a short laser light pulse prior to their extraction with a triangle-shaped voltage pulse. The delay between the laser and triangle voltage pulses (t_{del}) is changed and the current transients are recorded in the oscilloscope for different delay times. Experimentally measured photo-CELIV transients were recorded for all four types of solar cells and where the transients for untreated solar cells without thiol are shown in Fig. 6b. The charge carrier mobility is then estimated using the following equation:

$$\mu = \frac{2d^2}{3At_{max}^2}, \tag{3}$$

where A is the slope of triangle-shaped voltage pulse.

Fig. 7 shows the charge carrier mobilities for all four types of films experimentally measured from the photo-CELIV current transients. Mobility is plotted as a function of time, which is the sum of both the delay time between the laser pulse and triangle voltage pulse and the extraction maximum. The carrier mobility in the untreated film without alkyl thiol has a very strong time-dependence, whereas the carrier mobilities in the other films show a rather time-independent behavior. Interestingly, the carrier mobility at very short time is very similar in all films. In untreated films, this similar value might arise from the unfinished carrier relaxation in the broad density of states (DOS). The relaxation of the photogenerated charge carriers and the carrier mobility saturates when DOS has a Gaussian distribution, as described by Bässler's theory of charge transport in disordered organic materials [38,39]. At longer times, when the carrier mobility approaches the dynamic equilibrium, the difference between the untreated film and the rest of the films becomes larger.

In CELIV experiments the measured current is determined as a sum of both faster and slower carrier mobilities as shown in Eq. (1), therefore, the plotted mobility in Fig. 7 is presumably from the faster carriers [40]. The dark injection current will be mostly dominated by carriers with faster mobility, so we can use the photo-CELIV mobility to calculate the SCLC current which is shown as a line in Fig. 5b).

3. Conclusions

Addition of alkyl thiols to P3HT/PCBM solar cells results in improved photovoltaic performance and efficiency compared to pristine untreated and even to thermally annealed cells. Therefore, substitution of postproduction treatment of bulk-heterojunction solar cells can simplify the solar cell fabrication process. Solar cells fabricated with alkyl thiol show red-shifted absorption compared to untreated and even to thermally annealed cells. In addition, the optical absorption coefficient increases in the cells with alkyl thiol. Both effects allow for a better overlap with the solar spectrum and for a larger portion of energy absorbed. IPCE spectra and current–voltage characteristics show a large difference between untreated solar cells without alkyl thiol and the cells with the additive. In this study the power conversion efficiency in unoptimized solar cells with alkyl thiol was found to be 2.5% whereas for the untreated P3HT/PCBM cells around 0.9% (under AM1.5 standard illumination conditions) were obtained. We found that thermal treatment and alkyl thiol addition strongly increases dark current, which is mainly due to improved charge carrier mobility, as seen from time resolved carrier mobility measurements with photo-CELIV. Untreated solar cells show much a strong decay of carrier mobility with time. Treated cells and cells with alkyl thiol mobility is nearly time-independent suggesting reduced losses. The relaxed carrier equilibrium mobility is in rather good agreement with

the steady state space charge limited current in the current–voltage characteristics. The improved carrier equilibrium mobility is explained by the differences in the morphology of the cells. Treated cells and cells with alkyl thiol, show improved interpenetrating network and well defined pathways for the electron and hole conduction to the electrodes.

4. Experimental

Bulk-heterojunction solar cells were prepared according to the following procedure: indium tin oxide (ITO) coated glass substrates with surface resistance of $\sim$15 square^{-1} (purchased from Merck) were cut to square pieces 1.5 cm $\times$ 1.5 cm and approximately half of ITO was chemically etched away. Substrates were then first mechanically cleaned using Kodak lens cleaning tissue and afterwards washed in the ultrasonic bath using organic solvents and dried in a nitrogen flow. A thin layer of high quality poly(3,4-ethylenedioxythiophene)-poly(styrenesulfonate) (PEDOT:PSS) in aqueous solution (purchased from Bayer AG) was spin-coated on the substrates using 2000 RPM spin-coater speed. The thickness of PEDOT is below 50 nm. Substrates with PEDOT were annealed on the hotplate for several minutes at 120 °C. The photoactive layer of polymer and PCBM was spin-coated on top with typical thicknesses of 100–200 nm. Four different photoactive layers were used in the experiment: first 10:8 mg/ml ratio of P3HT and PCBM in toluene was prepared, well dissolved in the ultrasonic bath. The solution was separated into two glass bottles and 5% by volume of *n*-octylthiol was added to one of the solutions. Both solutions were filtered through 0.45 μm filter and deposited on to the prepared substrates: 2 samples were made from pristine solution and 2 samples from solution with *n*-octylthiol. One sample from each pair was later thermally annealed on the hotplate at 120 °C for several minutes. During all measurements the samples were kept at room temperature. For visualization of the postproduction treatment and alkyl thiol addition effects the experiments were performed for all four fabricated bulk-heterojunction solar cells. To finalize the preparation of solar cell, the top electrode consisting of 0.5 nm LiF and subsequently Al was evaporated in the vacuum below 10^{-5} mbar. The size of the active area of the solar cells was between 3 mm^2 and 12 mm^2.

For film preparation spincoater obtained from Specialty Coating Systems Inc. model P6700 was used. Optical absorption spectra and absorption coefficient were measured using Cary 3G UV–Visibile Spectrophotometer and film thickness (as well as film morphology) was determined Veeco Nanoscope DI 3100 AFM. Current–voltage curves were measured with a Keithley SMU 236 in the dark and under an illumination intensity of 1000 Wm^{-2} with a Steuernagel Lichttechnik GmbH solar simulator providing the AM1.5 sun spectrum. In the IPCE measurements were using standard setup. During the CELIV measurement the triangle-shaped voltage pulses were generated using Agilent 33250A arbitrary pulse generator controlled by Stanford Research Systems DG535 pulse generator. In the photo-CELIV measurements Coherent Infinity 40–100 Nd:YAG 5ns 532 nm laser was used together with supporting optics. Custom written Labview control program controlled the timing between the laser and triangle voltage pulses.

Acknowledgements

The financial support of Austrian Foundation for Advancement of Science (FWF Project No. S9711-N08) Valuable discussions with Alan Heeger, Dan Moses and G. Bazan is gratefully acknowledged.

References

[1] J. Peet, C. Soci, R.C. Coffin, T.Q. Nguyen, A. Mikhailovsky, D. Moses, G.C. Bazan, Appl. Phys. Lett. 89 (2006) 252105.
[2] J. Peet, J.Y. Kim, N.E. Coates, W.L. Ma, D. Moses, A.J. Heeger, G.C. Bazan, Nat. Mater. 6 (2007) 497.
[3] G.A. Chamberlain, Sol. Cells 8 (1983) 47.
[4] D. Wöhrle, D. Meissner, Adv. Mater. 3 (1991) 129.
[5] C.J. Brabec, N.S. Sariciftci, J.C. Hummelen, Adv. Funct. Mater. 11 (2001) 15.
[6] J.J.M. Halls, R.H. Friend, in: M.D. Archer, R. Hill (Eds.), Imperial College Press, London, UK, 2001.
[7] J. Nelson, Curr. Opinion. Solid State Mater. Sci. 6 (2002) 87.
[8] J.-M. NunziC.R. Physique 32002 523.
[9] W. Ma, C. Yang, X. Gong, K. Lee, A.J. Heeger, Adv. Funct. Mater. 15 (2005) 1617.
[10] Y. Kim, S. Cook, S.M. Tuladhar, S.A. Choulis, J. Nelson, J.R. Durrant, D.D.C. Bradley, M. Giles, I. Mcculloch, C.-S. Ha, M. Ree, Nat. Mater. 5 (2006) 197.
[11] S.E. Shaheen, C.J. Brabec, N.S. Sariciftci, Appl. Phys. Lett. 78 (2001) 841.
[12] H. Hoppe, N.S. Sariciftci, J. Mater. Chem. 16 (2006) 45.
[13] H. Hoppe, N.S. Sariciftci, J. Mater. Res. 19 (7) (2004).
[14] X. Yang, J. Loos, S.C. Veenstra, W.J.H. Verhees, M.M. Wienk, J.M. Kroon, M.A.J. Michels, R.A.J. Janssen, Nano. Lett. 5 (4) (2005) 579.
[15] H. Sirringhaus, P.J. Brown, R.H. Friend, M.M. Nielsen, K. Bechgaard, B.M.W. Langeveld-Voss, A.J.H. Spiering, R.A.J. Janssen, E.W. Meijer, P. Herwig, D.M. de Leeuw, Nature 401 (1999) 685.
[16] R. Österbacka, C.P. An, X.M. Jiang, Z.V. Vardeny, Science 287 (5454) (2000) 839.
[17] S. Berson, R. De Bettignies, S. Bailly, S. Guillerez, Adv. Func. Mater. 17 (2007) 1377.
[18] G. Yu, J. Gao, J.C. Hummelen, F. Wudl, A.J. Heeger, Science 270 (1995) 1789.
[19] Y. Kim, S.A. Choulis, J. Nelson, D.D.C. Bradley, S. Cook, R. Durrant, Appl. Phys. Lett. 86 (2005) 063502.
[20] G. Li, V. Shrotriya, J. Huang, Y. Yao, T. Moriarty, K. Emery, Y. Yang, Nat. Mater. 4 (2005) 864.
[21] P. Vanlaeke, G. Vanhoyland, T. Aernouts, D. Cheyns, C. Deibel, J. Manca, P. Heremans, J. Poortmans, Thin Solid Films 511 (2006) 358.
[22] V.D. Mihailetchi, H. Xie, B. de Boer, L.M. Popescu, J.C. Hummelen, P.W.M. Blom, L.J.A. Koster, Appl. Phys. Lett. 89 (2006) 012107.
[23] K. Kim, J. Liu, D.L. Carroll, Appl. Phys. Lett. 88 (2006) 181911.
[24] F. Padinger, R.S. Rittberger, N.S. Sariciftci, Adv. Funct. Mater. 13 (2003) 1.
[25] A.J. Moulé, K. Meerholz, Adv. Mater. 20 (2008) 240.
[26] S. Cook, A. Furube, R. Katoh, Jap. J. Appl. Phys. 40 (2008) 1238.
[27] D. Chirvase, J. Parisi, J.C. Hummelen, V. Dyakonov, Nanotechnology 15 (2004) 1317.
[28] G. Li, V. Shrotriya, Y. Yao, Y. Yang, J. Appl. Phys. 98 (2005) 043704.
[29] I. Riedel, V. Dyakonov, Phys. Status Solidi (A), Appl. Res. 201 (6) (2004) 1332.
[30] M.R. Reyes, K. Kim, D.L. Carroll, Appl. Phys. Lett. 87 (2005) 083506.
[31] A. Rose, Phys. Rev. 97 (1955) 1538.
[32] G. Juška, K. Arlauskas, M. Viliūnas, J. Kočka, Phys. Rev. Lett. 84 (2000) 4946.
[33] A. Pivrikas, R. Osterbacka, G. Juska, K. Arlauskas, H. Stubb, Synthetic Met. 155 (2005) 15.
[34] S.C. Jain, W. Geens, A. Mehra, V. Kumar, T. Aernouts, J. Poortmans, R. Mertens, M. Willander, J. Appl. Phys. 89 (2001) 3804.
[35] V.I. Arkhipov, H. von Seggern, E.V. Emelianova, Appl. Phys. Lett. 83 (2003) 5074.

[36] R. Österbacka, A. Pivrikas, G. Juška, K. Genevičiusb, K. Arlauskas, H. Stubb, Curr. Appl. Phys. 4 (2004) 534.
[37] G. Juška, K. Genevičius, K. Arlauskas, R. Österbacka, H. Stubb, Phys. Rev. B 65 (2002) 233208.
[38] H. Bässler, Phys. Status Solidi (B), Basic Res. 175 (1993) 15.
[39] S.V. Novikov, D.H. Dunlap, V.M. Kenkre, P.E. Parris, A.V. Vannikov, Phys. Rev. Lett. 81 (1998) 4472.
[40] G. Juška, K. Genevičius, G. Sliaužys, A. Pivrikas, M. Scharber, R. Österbacka, J. Appl. Phys. 101 (2007) 114505.

Recently, Vázquez et al. proposed the induced density of interface states (IDIS) model which is developed for the weakly-interacting O/M interface, especially organic/Au (O/Au) interface, to describe the energy level alignment [3–5]. Several simplified assumptions are made, i.e. (i) the energy levels of the highest occupied molecular orbital (HOMO) and the lowest unoccupied molecular orbital (LUMO) are broadened to form continuous levels, which is called the IDIS, in the original HOMO–LUMO gap by the interaction with the 6s-state of Au. (ii) The relative energy of the charge neutrality level (CNL), which is defined as the topmost occupied level in the IDIS by two electrons originally occupying the HOMO, is independent of the surface. They reported that there is little difference between Au(1 1 1) and polycrystalline Au. (iii) The VL shift is given so that some electrons are transferred between the metal and the IDIS to achieve the equilibrium by the change of the electron occupation and the potential built up by the electron transfer.

Hence, the VL shift (Δ) is given in the IDIS model as

$$\Delta = -(1 - S)(\Phi_M - E_{CNL}), \tag{1}$$

where Φ_M is the work function of the metal, E_{CNL} is the energy of the CNL and S is the slope parameter defined as

$$S = \frac{d\Phi_B}{d\Phi_M} = \frac{1}{1 + 4\pi e^2 D(E_F)\delta/A}, \tag{2}$$

where Φ_B is the barrier for electron injection, i.e. the energy separation between the metal Fermi level (E_F) and the LUMO, e is the elementary charge, $D(E_F)$ is the local density of state at the E_F, δ is the distance between the charges induced in the metal and the organic molecule and A is the area associated with a PTCDA molecule. We note that in their articles [5–7], the sign of Δ is defined positive as the work function decreases, and the values of E_{CNL} and Φ_M are measured with respect to the VL, and are negative. Since the definition of the sign of Δ in their articles is opposite to the original definition of Δ [1], we changed the sign of the right-hand side of Eq. (1) from that in Refs. [5–7] to avoid confusion. The original definition of negative Δ for VL lowering and Eq. (1) will be used throughout the following part of this article. The slope parameter changes in the range of $0 < S < 1$.

More recently, these authors have incorporated the contribution of the push-back effect into their framework [6,7]. Thus, the updated model explains the interface dipole formation by the following processes: (i) the VL shift due to the push-back effect, (ii) the level broadening to form the IDIS and (iii) the charge transfer.

In spite of its rather simple assumptions, this model shows fairly good agreement with the experimental data for the O/Au interfaces, and we admit that it is a great contribution to the discussion on the origin of the interface dipole layer for these interfaces. However, it has been still unclear whether the IDIS model can be generally applied to various metal substrates. Within the framework of the IDIS model, E_{CNL} on other metals are expected to be almost the same as on Au, because (i) only the valence s-orbital is taken into account in the IDIS model, and the d-orbital is not taken into account, (ii) the interactions between these s-orbitals and the frontier orbitals (HOMO and LUMO) of the organic molecules are very similar since the character of the s-orbital is common, which is well known for small molecule adsorption, e.g. carbon monoxide (CO) and H_2 [8–10], on noble and transition metals and (iii) E_{CNL} does not depend on δ [4]. It was also reported that $D(E_F)$ becomes larger as δ becomes smaller [4]. However, the magnitude of S does not vary so much because of the compensating variations of $D(E_F)$ and δ. Therefore, from Eq. (1), a linear relation between Δ and Φ_M can be expected. Actually, the observed Δ simply depends on Φ_M as previously reported for perylene-3,4,9,10-tetracarboxylic dianhydride (PTCDA, see Fig. 1) for the combination of Au with simple metals such as Sn, In and Mg [11]. Thus, the IDIS model may be applicable for the simple metals in which the d-bands locate very deep below the E_F (Sn, In, etc.), or which have no d-electron (Mg, Al, etc.), since the effect of the d-band can be neglected.

On the other hand, some recent experimental works have shown very different results about the interfacial electronic structure depending on the metal surface (e.g. Ag(1 1 1) [12–15,17], Ag(1 1 0) [12], Cu(1 1 1) [15,17] and Au(1 1 1) [15–17]). They reported that the molecular orbitals (MOs) of PTCDA are significantly modified by the interaction with the metal surface [12–15,17]. It was also reported that the metal d-band plays an important role in the formation of the interface states at the O/M interface, and thus in the energy level alignment [12]. Therefore, it is clear that the IDIS model cannot be simply applied to these interfaces, and that further studies are necessary to develop an improved model which takes into account the metal d-band.

As an example for such interaction with the metal d-band, we consider the H_2 adsorption on noble and transition metals [8–10]. The hydrogen 1s-state is broadened into resonances and shifted down in energy by the interaction with the broad continuum of metal sp-bands, and the broadened adsorbate state interacts with the metal d-band states resulting in the formation of the bonding and anti-bonding states. For these systems, it is well known that three parameters, (i) the centroid of the metal d-band states (ε_d), (ii) the filling of the metal d-band (f_d) and (iii) the coupling matrix element (V_{ad}) between the adsorbate states and the metal d-band states, govern the interaction energy between the adsorbate state with the filling f_a at the energy ε_a and the metal d-band state with the filling f_d at the energy ε_d as

$$E_{d\text{-hyb}} = -C(f_a, f_d)\frac{V_{ad}^2}{|\varepsilon_a - \varepsilon_d|} + \alpha V_{ad}^2, \tag{3}$$

where $C(f_a, f_d)$ only depends on the number of electrons in the adsorbate state and the metal d-band state. The first

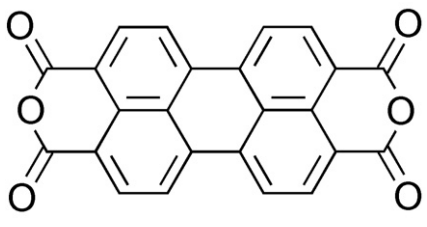

Fig. 1. Molecular structure of PTCDA.

term gives the hybridization energy leading to the attraction if the anti-bonding state is not completely filled, while the second term gives the repulsion due to the orthogonalization between the adsorbate states and the metal d-band states. We can see that ε_d is a key parameter to investigate such interaction with the metal d-band. For a given adsorbate f_a is fixed, and for noble metals f_d is also fixed; the interaction energy $E_{d\text{-hyb}}$ between the adsorbate states and the metal d-band states is governed by the delicate balance of $|\varepsilon_a - \varepsilon_d|$ and V_{ad}^2.

The physical picture for the hydrogen/metal interface described above is applied not only to hydrogen but also to any atom or molecule [8]. Then we consider the case of organic molecule adsorption on noble metals in the simple model shown in Fig. 2. We should consider the whole interactions between the adsorbate states and the metal states to precisely investigate the interfacial electronic structure. Since the magnitude of the interaction, however, depends on the inverse of the energy separation between the corresponding states, HOMO and LUMO are the most important for the interaction with the metal d-band. Therefore, HOMO and LUMO should be taken into account as the adsorbate states, while for the case of H_2 adsorption only the hydrogen 1s-state is taken into account in Ref. [8]. As in the case of the 1s-state of hydrogen, the original molecular states (Fig. 2a) are broadened into resonances and shifted down in energy by the interaction with the broad continuum of the metal sp-bands (Fig. 2b). Then, these broadened states interact with the metal d-band states resulting in the formation of the bonding and anti-bonding states (Fig. 2c). We note that the energy shift, the split width of the energy levels and the interface E_F position depend on the system. As shown in Fig. 2, we can expect that both the HOMO-derived bonding and the anti-bonding states are completely filled for the noble metal interfaces. On the other hand, the occupation of the LUMO-derived anti-bonding state depends on the metal, that is, the interface Fermi level varies with metal. Therefore, the hybridization between the LUMO of organic molecule and the metal d-band states is dominant for determining the interfacial interaction. From these expectations and from Eq. (3), two important parameters that determine the interfacial interaction at the organic/noble metal interface are derived: (i) the energy separation between the LUMO of organic molecule (ε_{LUMO}) and the centroid of the metal d-band states ($\varepsilon_{d\text{-LUMO}} = |\varepsilon_{LUMO} - \varepsilon_d|$), which results in the attractive effect due to the hybridization and (ii) the coupling matrix element (V_{ad}) between the adsorbate states and the metal d-band states, which results in the repulsive effect due to the orthogonalization.

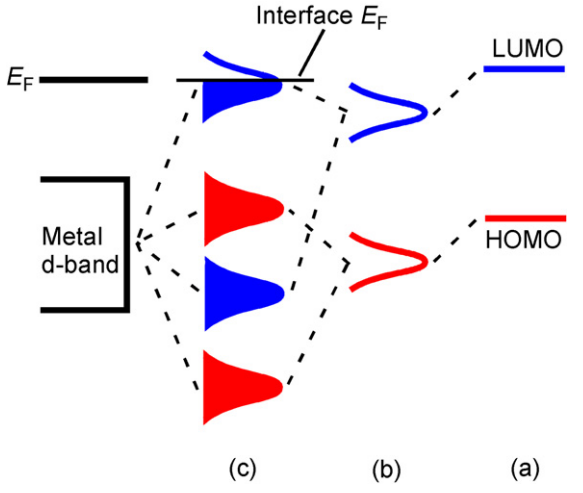

Fig. 2. Schematic illustrations of the interactions between the metal d-band and the HOMO and LUMO of the organic molecule: (a) original molecular states; (b) formation of the broadened molecular states by the interaction with the broad continuum of the metal sp-bands; (c) formation of the bonding and anti-bonding states by the interaction with the metal d-band states. The interface E_F position depends on the system. The interfacial interaction is governed by the occupation of the anti-bonding state originated from the hybridization between the LUMO and the metal d-band states.

However, there has not been such research in which the role of the metal d-band in the formation of the interfacial electronic structures for organic/noble metal interfaces is considered in terms of two factors of the attractive and repulsive interactions described above. Its examination will shed light on the mechanism of the energy level alignment at the interfaces of these metals. In this paper, we report the detailed analysis of the electronic structure (such as the VL shift and the formation of the interface states) at the interfaces between PTCDA and noble metals (Au, Ag and Cu) from the view point of the role of the metal d-band.

2. Experimental

The sample of PTCDA purchased from Aldrich was purified by using two times of vacuum sublimation. Polycrystalline metal substrates were prepared by vacuum deposition of respective metal on a Si(1 1 1) substrate in the preparation chamber (base pressure $<8.0 \times 10^{-7}$ Pa). PTCDA was vacuum deposited on the polycrystalline metal substrates. The film thickness and the deposition rate (~0.1 nm/min) were monitored by a quartz crystal oscillator by assuming that the density of the film is similar to that of the single crystal (1.70 g/cm^3). UPS measurements were performed in the measurement chamber (base pressure $<6 \times 10^{-8}$ Pa) using a He discharge lamp ($h\nu = 21.22$ eV) and synchrotron radiation (SR) ($h\nu = 20$–40 eV) as the excitation sources. The SR experiments were carried out at the beam line BL8B2 of the UVSOR facility at the Institute for Molecular Science. The monochromatic SR is obtained by the plane-grating monochrometer [18]. Energy analyses of photoelectrons were performed using high-resolution electron energy analyzers; AR65 (Omicron, $\Delta E \approx 100$ meV) in the laboratory and ARUPS10 (VG, $\Delta E \approx 150$ meV) in the UVSOR. The sample was biased (−4.0 V) to accelerate the slow secondary electrons when the low energy electron cutoff was measured.

3. Results and discussion

Fig. 3 shows the film thickness dependence of the VL energy (E_{vac}^F) of the PTCDA film relative to the E_F of the metal substrates. The values of E_{vac}^F for the film thickness of 0 nm correspond to the Φ_M. The VL shift (Δ) in the 1 ML

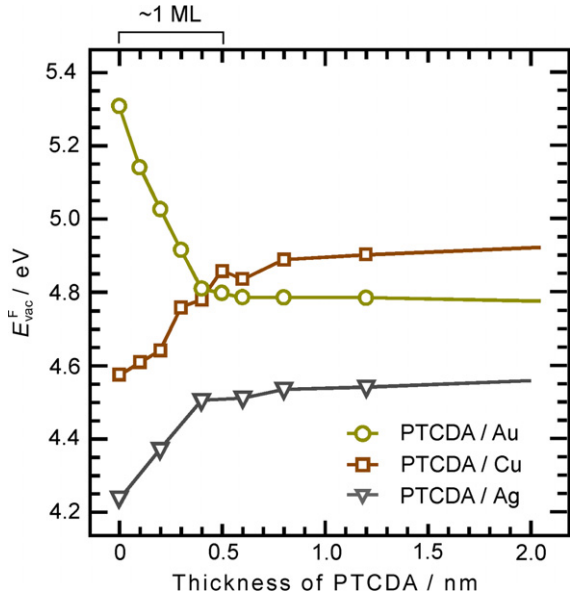

Fig. 3. Energy change of the vacuum level at the PTCDA/metal interfaces depending on the film thickness of PTCDA. The energy of the vacuum level is relative to the Fermi level of the clean metal substrates.

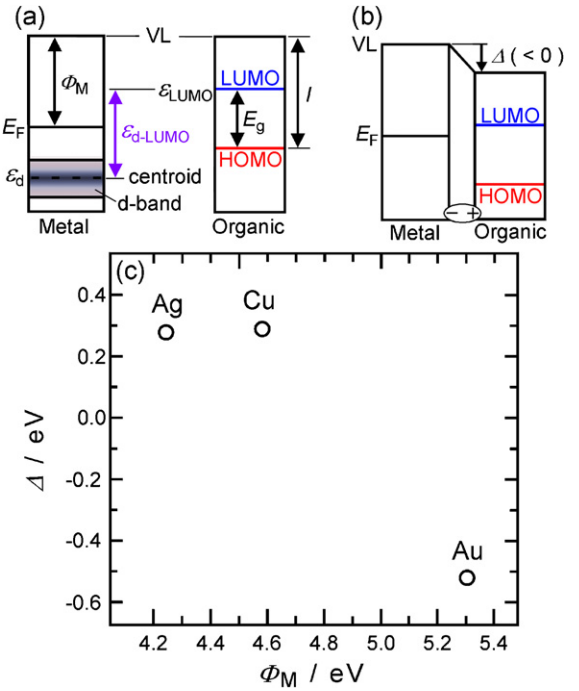

Fig. 4. (a) Vacuum level aligned energy diagram before contacting with the metal for estimating $\varepsilon_{d\text{-}LUMO}$. (b) Energy diagram after contacting with the metal. The vacuum level shifts by Δ due to the formation of the interface dipole layer. (c) Plots of Δ as a function of Φ_M. The values are listed in Table 1.

region at the PTCDA/Au, Ag and Cu interfaces is −0.52, 0.27 and 0.29 eV, respectively (summarized in Table 1). The negative interface dipole layer, which lowers the E^F_{vac}, is formed at the PTCDA/Au interface, while the positive ones are formed at the PTCDA/Ag and PTCDA/Cu interfaces. Duhm et al. previously reported that the Δ for PTCDA on the (1 1 1) surfaces of Au, Ag and Cu is −0.45, −0.10 and −0.15 eV, respectively [15]. Their results are inconsistent with our results. This discrepancy may come from the differences in the substrates, that is, between the single crystal substrate and the polycrystalline one. As already noted about Eq. (1), Δ is defined negative for work function decrease, following the original definition of Δ [1] (see Fig. 4a and b). We note that 0.5 nm film thickness corresponds to the 1 ML region.

The observed values of Δ are plotted as a function of Φ_M in Fig. 4c. If the IDIS model is applicable for these interfaces, we can expect a linear relation between Φ_M and Δ as described in Eq. (1). However, the results do not show the linear relation indicating that the IDIS model cannot explain the dipole layer formation at these interfaces.

Table 1
Experimentally obtained and estimated energy parameters

	Φ_M	Δ	ε_d	$\varepsilon_{d\text{-}LUMO}$
Au	5.31	−0.52	3.56	4.98
Ag	4.24	0.27	4.30	4.58
Cu	4.58	0.29	2.67	3.40

Φ_M and Δ are the observed values of the metal work function and the vacuum level shift; ε_d is the reported value of the centroid energy of the metal d-band with respect to the Fermi level [10] and $\varepsilon_{d\text{-}LUMO}$ is the estimated energy separation between the LUMO of PTCDA and the ε_d. All values are written in eV.

The UPS spectra in the vicinity of the E_F of the metal for the PTCDA/Au, Ag and Cu interfaces are shown in Fig. 5. The abscissa is the electron binding energy relative to the E_F. The spectra were taken in the normal emission condition. We observed the formation of the interface states at the 1 ML PTCDA/Ag and Cu interfaces (indicated by the vertical bars), while there was no indication of such a formation in the case of Au. These results agree well with the reported electronic structures for the PTCDA/Au(1 1 1), Ag(1 1 1) and Cu(1 1 1) interfaces [12,15]. The interface states for the Ag(1 1 1) and Cu(1 1 1) interfaces are more clearly observed than those for the polycrystalline Ag and Cu interfaces, and we found that the interface states formed at the Ag(1 1 1) and Cu(1 1 1) interfaces cannot be explained by the IDIS model, that is, the observed interface states are not the broadened states but the split states. From these results, we can expect that the picture described in Fig. 2 is realized for the PTCDA/Ag and Cu interfaces. Therefore, we have to consider the effect of the metal d-band which is not taken into account in the IDIS model.

In order to consider the attractive interfacial interaction, we estimate the value of $\varepsilon_{d\text{-}LUMO}$. As shown in Fig. 4a, ε_{LUMO} is deduced as

$$\varepsilon_{LUMO} = I - E_g - \Phi_M, \quad (4)$$

where I is the ionization potential of PTCDA deduced from the HOMO peak of the thick PTCDA film, E_g is the reported peak-to-peak HOMO–LUMO gap (E_g = 3.2 eV [3]) and the values of ε_d are taken from Ref. [10]. They are summarized

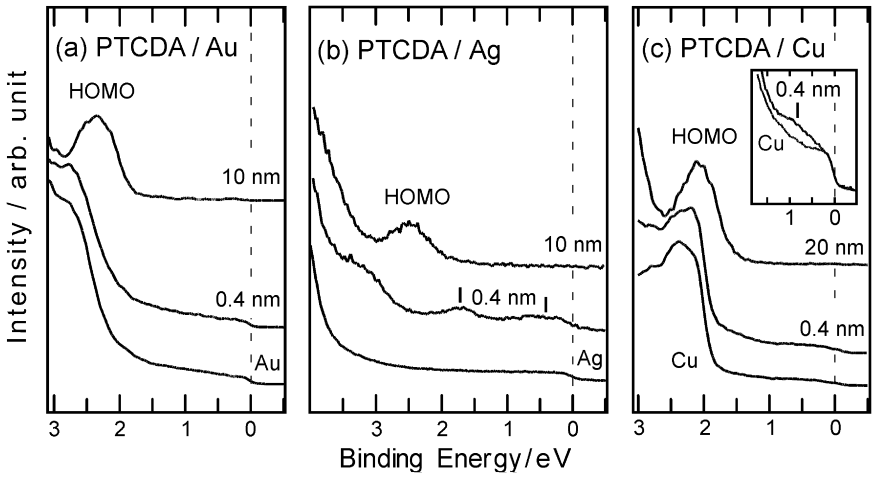

Fig. 5. Normal emission UPS spectra for (a) PTCDA/Au, (b) PTCDA/Ag and (c) PTCDA/Cu interfaces, respectively. The bottom, middle and top spectra show the clean metal substrates, the 1 ML PTCDA film and the thick PTCDA film, respectively. The abscissa is the electron binding energy with respect to the Fermi level.

in Table 1. The magnitude of the attractive interaction, which depends on $1/\varepsilon_{\text{d-LUMO}}$ (Eq. (3)), for the PTCDA/Cu interface is expected to be the largest, while that for the PTCDA/Au interface is expected to be the smallest. The observed values of Δ are plotted as a function of $1/\varepsilon_{\text{d-LUMO}}$ shown in Fig. 6. Although the values of Δ for the Ag and Cu interfaces are found to be almost identical, Δ for the Au interface is quite different from those on Ag and Cu.

One may ask why the PTCDA/Au interface is so different from the PTCDA/Ag interface despite the values of $\varepsilon_{\text{d-LUMO}}$ for the PTCDA/Au and Ag interfaces not being different so much as seen in Fig. 6 and Table 1. As a factor examining this, we consider the coupling matrix element (V_{ad}) between the adsorbate states and the metal d-band states which increases with the principal quantum number (n). Since the orthogonalization energy ($\varepsilon_{\text{orth}}$) between the adsorbate states and the metal d-band states increases monotonically with V_{ad}^2 [8], the $\varepsilon_{\text{orth}}$ for the 5d-metal (Au) is considerably larger than the 3d and 4d metals (Cu and Ag). Thus, the repulsive interaction for the PTCDA/Au interface is expected to be large, while that for the PTCDA/Ag and Cu interfaces is expected to be small.

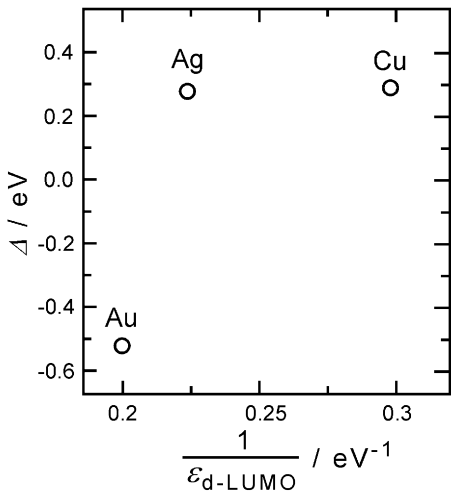

Fig. 6. Plots of Δ as a function of $1/\varepsilon_{\text{d-LUMO}}$. The values are listed in Table 1.

Since the magnitude of the interaction should have a relation with the adsorption states of the molecules, we consider the adsorption states of the PTCDA molecule on the metal substrates. The average carbon bonding distance (d_C) of the PTCDA molecule on Au(111), Ag(111) and Cu(111) deduced from the results of the X-ray standing wave (XSW) experiments was reported to be 0.327, 0.286 and 0.266 nm, respectively [19,20]. By defining $\sum r$ to be the sum of the van der Waals radii (r_{vdW}) of the metal atom and the carbon atom forming PTCDA [21], we can judge the adsorption states by comparing $\sum r$ and d_C. The values of d_C, r_{vdW} and $\sum r$ are listed in Table 2. We can see that PTCDA molecules are physisorbed on Au because $\sum r \approx d_C$, while they are chemisorbed on Ag and Cu because $\sum r > d_C$, if we use the value of d_C for the (111) surface also for the polycrystalline surface. These results are consistent with our estimation by the magnitude of $1/\varepsilon_{\text{d-LUMO}}$ and V_{ad}^2 described above, and also consistent with the temperature programmed desorption results [22,23]. The 1 ML film of the PTCDA molecule on Au(111) desorbs at the sample temperature above 673 K [22], while no intact molecular desorption of the 1 ML film occurs for PTCDA on Ag(111)

Table 2
Molecular adsorption parameters

	r_{vdW} (nm)		$\sum r$ (nm)	d_C (nm)
	Metal	Carbon		
Au(111)	0.166		0.336	0.327
Ag(111)	0.172	0.170	0.342	0.286
Cu(111)	0.140		0.310	0.266

r_{vdW} is the van der Waals radii [21]; $\sum r$ is the sum of the r_{vdW} of the metal atom and the carbon atom and d_C is the average carbon bonding distance of the PTCDA molecule on the metal surface determined by the XSW experiments [19,20].

[23]. For PTCDA on Cu(1 1 1), similar results with PTCDA/Ag(1 1 1) are expected, because the strong chemical interaction is also observed [12].

According to the discussion made above, since $\varepsilon_{\text{d-LUMO}}$ and V_{ad}^2 for the PTCDA/Au interface are large, the interaction between PTCDA and Au is very weak (physisorption). According to the study of the physisorbed Xe atom on the metal surface [2,24], the possible origins of the interface dipole for the physisorbed system are the rearrangement of the surface charge due to the push-back effect and the mirror effect. Therefore, we suppose that the origins of the interface dipole for the PTCDA/Au interface are the repulsive orthogonalization interaction (the push-back effect and the mirror effect), that is, $\Delta \approx \Delta_{\text{orth}}$. On the other hand, since $\varepsilon_{\text{d-LUMO}}$ and V_{ad}^2 for the PTCDA/Ag and Cu interfaces are small, the attractive hybridization interactions (chemical interaction) between PTCDA and Ag, Cu are rather strong. These chemical interactions cause the formation of the interface states and resulting charge re-distribution, which results in the dominant origin of the positive Δ formations, that is, $\Delta \approx \Delta_{\text{chem}}$. Therefore, it is natural that the nonlinear relation between Δ and Φ_{M} is observed in Fig. 4c since the origins of the interface dipole are completely different between the PTCDA/Au interface and the PTCDA/Ag and Cu interfaces. Note that free PTCDA molecule is nonpolar, but the distortion into the nonplanar configurations on Ag(1 1 1) and Cu(1 1 1) due to the chemical interaction [19,20] may cause some permanent dipole. In our study, however, since we used the polycrystalline metal substrates on which there is no definite adsorption structure, we cannot discuss the permanent dipole formation induced by the molecular deformation separately. Therefore, we include the molecular deformation effect in Δ_{chem}.

The observed correlations among $\varepsilon_{\text{d-LUMO}}$, V_{ad}, d_{C} and $\varepsilon_{\text{orth}}$ are schematically described in Fig. 7. We found that two factors, (i) the energy separation between the LUMO of PTCDA and the metal d-band states ($\varepsilon_{\text{d-LUMO}}$), which results in the attractive effect due to the hybridization, and (ii) the coupling matrix element (V_{ad}) between the adsorbate states and the metal d-band states, which results in the repulsive effect due to the orthogonalization, are important for determining the interfacial electronic structure. Consequently, the interactions at the PTCDA/noble metal interfaces are governed by not only one factor such as Φ_{M} but also a variety of factors which are related to the d-band states such as $\varepsilon_{\text{d-LUMO}}$ and V_{ad}.

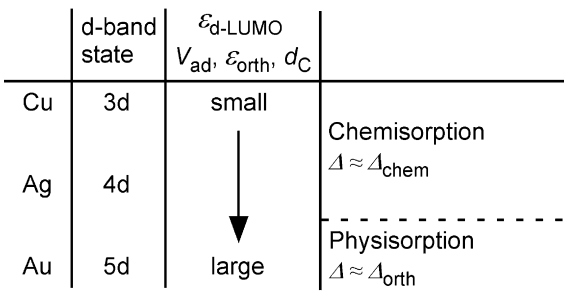

Fig. 7. Schematic view of the correlation among $\varepsilon_{\text{d-LUMO}}$, V_{ad}, d_{C} and $\varepsilon_{\text{orth}}$. These parameters increase with n. The dominant origins of Δ are determined by the delicate valence of these factors.

Finally, we mention the charge injection barrier. The ionization potential and the electron affinity of the 1 ML PTCDA film on Ag and Cu are different from those of the neutral PTCDA since the electronic structures of the 1 ML PTCDA film on Ag and Cu are modified by the interaction with the metal. Therefore, the charge injection barrier between the metal and the 1 ML PTCDA film is governed by the interface states formed at the PTCDA/metal interface. On the other hand, the charge injection barrier between the metal and the thick PTCDA film is governed by the energy position of the HOMO and the LUMO. As shown in Fig. 3, the Fermi level for the PTCDA/Ag interface is the closest to the LUMO. Therefore, the electron injection barrier for the PTCDA/Ag interface is expected to be the smallest among the Au, Ag and Cu interfaces.

4. Conclusion

We examined the role of the metal d-band in the energy level alignment at the PTCDA/noble metal (Au, Ag and Cu) interfaces, and found that two factors, (1) the energy separation between the LUMO of PTCDA and the centroid of the metal d-band states ($\varepsilon_{\text{d-LUMO}}$) and (2) the coupling matrix element (V_{ad}) between the adsorbate states and the metal d-band states, are important for determining the interfacial electronic structure. The attractive hybridization energy between the LUMO of PTCDA and the metal d-band states is proportional to $1/\varepsilon_{\text{d-LUMO}}$, and the repulsive orthogonalization energy increases with V_{ad}^2. Thus, the hybridization (orthogonalization) interaction for the PTCDA/Ag and Cu interfaces is strong (weak) because of its small value of $\varepsilon_{\text{d-LUMO}}$ and V_{ad}^2, which results in the chemisorption and the formation of the interface states for these interfaces. On the other hand, the hybridization (orthogonalization) interaction for the PTCDA/Au interface is very weak (very strong) because of its large value of $\varepsilon_{\text{d-LUMO}}$ and V_{ad}^2, which results in the physisorption for this interface. Therefore, we conclude that the push-back effect and the mirror effect originated from the orthogonalization are dominant for the interface dipole formation for the physisorbed PTCDA/Au interface. On the other hand, the formation of the interface states and resulting charge re-distribution is dominant for the interface dipole formation for the chemisorbed PTCDA/Ag and Cu interfaces. From these results, we found that the metal d-band state-related parameters, $\varepsilon_{\text{d-LUMO}}$ and V_{ad}, should be taken into account when we consider the origins of the vacuum level shift at the O/M (here, M denotes noble and transition metals) interfaces, and that the IDIS model in which the metal d-band is not taken into account cannot explain the interfacial phenomena at these interfaces.

Acknowledgements

The authors thank Prof. Morikawa of Osaka University for the fruitful discussion. This work was partly supported by the Grant-In-Aid for Scientific Research (S) (No. 19105005) from Japan Society for the Promotion of Science

(JSPS) and Global COE in Chemistry at Nagoya University (No. B-021) from the Ministry of Education, Culture, Sports, Science and Technology of Japan. E.K. thanks JSPS for the Research Fellowship for Young Scientists.

References

[1] S. Narioka, H. Ishii, D. Yoshimura, M. Sei, Y. Ouchi, K. Seki, S. Hasegawa, T. Miyazaki, Y. Harima, K. Yamashita, Appl. Phys. Lett. 67 (1995) 1899.
[2] H. Ishii, K. Sugiyama, E. Ito, K. Seki, Adv. Mater. 11 (1999) 605.
[3] H. Vázquez, F. Flores, R. Oszwaldowski, J. Ortega, R. Pérez, A. Kahn, Appl. Surf. Sci. 234 (2004) 107.
[4] H. Vázquez, R. Oszwaldowski, P. Pou, J. Ortega, R. Pérez, F. Flores, A. Kahn, Europhys. Lett. 65 (2004) 802.
[5] H. Vázquez, F. Flores, A. Kahn, Org. Electron. 8 (2007) 241.
[6] H. Vázquez, Y.J. Dappe, J. Ortega, F. Flores, J. Chem. Phys. 126 (2007) 144703.
[7] H. Vázquez, Y.J. Dappe, J. Ortega, F. Flores, Appl. Surf. Sci. 254 (2007) 378.
[8] B. Hammer, J.K. Nørskov, Nature 376 (1995) 238.
[9] B. Hammer, Y. Morikawa, J.K. Nørskov, Phys. Rev. Lett. 76 (1996) 2141.
[10] A. Ruban, B. Hammer, P. Stoltze, H.L. Skriver, J.K. Nørskov, J. Mol. Catal. A: Chem. 115 (1997) 421.
[11] I.G. Hill, A. Rajagopal, A. Kahn, Appl. Phys. Lett. 73 (1998) 662.
[12] Y. Zou, L. Kilian, A. Schöll, Th. Schmidt, R. Fink, E. Umbach, Surf. Sci. 600 (2006) 1240.
[13] R. Temirov, S. Soubatch, A. Luican, F.S. Tautz, Nature 444 (2006) 350.
[14] A. Kraft, R. Temirov, S.K.M. Henze, S. Soubatch, M. Rohlfing, F.S. Tautz, Phys. Rev. B 74 (2006) 041402(R).
[15] S. Duhm, A. Gerlach, I. Salzmann, B. Bröker, R.L. Johnson, F. Schreiber, N. Koch, Org. Electron. 9 (2008) 111.
[16] J. Kroger, H. Jensen, R. Berndt, R. Rurali, N. Lorente, Chem. Phys. Lett. 438 (2007) 249.
[17] F.S. Tautz, Progr. Surf. Sci. 82 (2007) 479.
[18] K. Seki, H. Nakagawa, K. Fukui, E. Ishiguro, R. Kato, T. Mori, K. Sakai, M. Watanabe, Nucl. Instrum. Methods Phys. Res. A 246 (1986) 264.
[19] S.K.M. Henze, O. Bauer, T.-L. Lee, M. Sokolowski, F.S. Tautz, Surf. Sci. 601 (2007) 1566.
[20] A. Gerlach, S. Sellner, F. Schreiber, N. Koch, J. Zegenhagen, Phys. Rev. B 75 (2007) 045401.
[21] A. Bondi, J. Phys. Chem. 68 (1964) 441.
[22] P. Fenter, F. Schreiber, L. Zhou, P. Eisenberger, S.R. Forrest, Phys. Rev. B 56 (1997) 3046.
[23] L. Kilian, E. Umbach, M. Sokolowski, Surf. Sci. 573 (2004) 359.
[24] K. Wandelt, J.E. Hulse, J. Chem. Phys. 80 (1984) 1340.

on the other hand PL intensity variation under an applied field gives an estimate of the built in field near the interface. In addition, thermally activated processes can also cause changes in PL intensity. A bias dependent PL can be used to study the different competing mechanisms of exciton generation, diffusion and dissociation [14,15]. Thus a bias dependent PL spectrum is of critical importance as it gives information regarding the electro-luminescence (EL), photoconduction and photovoltaic effects. EL efficiency is a determining factor for the performance of PLEDs and is directly related to PL efficiency [16], as both originate from the same intermediate state, i.e. excitons [17].

LiF:Al electrodes are widely used for the enhancement of the efficiency of PLEDs and PSCs. However, the underlying mechanisms are still under investigation. Several mechanisms have been suggested thus far [18-22], including (i) the lowering of work function of Aluminum; (ii) dissociation of LiF and subsequent chemical reaction (doping) of the organic semiconductor; (iii) formation of a dipole layer leading to a vacuum level offset between the organic layer and the Al; and (iv) protection of the organic layer from the hot Al atoms during thermal deposition. Despite of these proposed mechanisms the exact role of LiF is not yet completely understood. Although a good deal of efforts have been devoted to clearly explain the role of LiF in the efficiency enhancement of PLEDs, but the underlying mechanisms for the PSCs efficiency improvement by LiF inclusion has not yet been discussed in much detail.

In this article, we report the effect of coating Al on to P3HT. The blue shift in the peak energy and a relative increase in the shoulder peak at higher energy in PL emission have been explained on the basis of increase in the degree of intrachain disorder, resulting in a relatively higher population of intrachain excitons. We further report the different types of PL quenching pattern obtained for the two types of schottky cells fabricated with and without a thin layer of LiF. The difference has been explained on the basis of the nature of interface of P3HT with Al alone and that of Al in the presence of a thin layer of LiF.

2. Experiment

Six different types of samples namely A, B, C, D, E and F, have been fabricated as shown in Fig. 1 (a, b, c, d, e and f) for the purpose of PL measurements. Prior to sample fabrication, glass substrates (for samples A, B, C and D) and ITO coated glass substrates (for samples E and F) were cleaned using NH_3 and H_2O_2 followed by sonication in chloroform and iso propanol solution. Samples A and B were spin coated at {1500 (30 s), 3000 (10 s)} rpm with a thin film of regioregular (rr) P3HT (Merck Lisicon SP001, having an average Molecular weight of 44000, and 96% regioregularity) from its chloroform solution on to the cleaned glass substrate followed by annealing at 100 °C (under vacuum for 2 h). Samples A were divided into two lots. First lot was coated with 2.5 nm Al (under vacuum, $P = 2.0 \times 10^{-6}$ Torr). The second lot was coated with 1 nm LiF prior to coating 2.5 nm Al under identical conditions. Similarly Sample B was divided into two lots, first lot was coated with 30 nm Al while the second lot was coated with 1 nm LiF followed by 30 nm Al. Sample C was divided into three lots, while first lot was spin coated with regioregular (rr) P3HT (as obtained from Merck) at {1500 (30 s), 3000 (10 s)} rpm, the second lot was spin coated with non-regio controlled (nrc) P3HT (synthesized, using $FeCl_3$ method [31,38], having a regioregularity of 88%) at {1500 (30 s), 3000 (10 s)} rpm [31] and the third lot was spin coated at {1500 (30 s), 3000 (10 s)} rpm with regiorandom (rrnd) P3HT (used as obtained from Aldrich, having 1:1 HT:HH

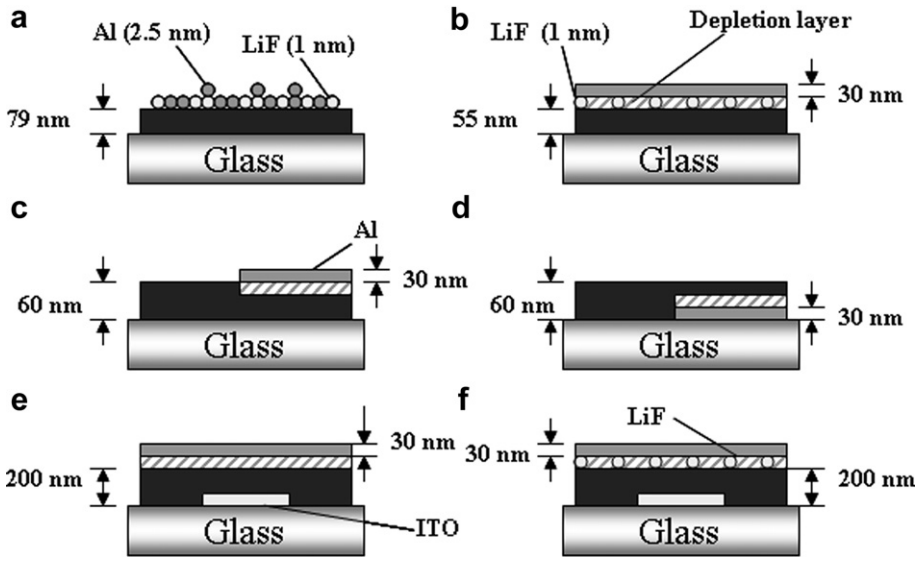

Fig. 1. Shows the Schematic diagram of (a) (Sample A) Island deposition of LiF (1 nm) followed by Al (2.5 nm) on a P3HT coated glass substrate (b) (Sample B) Island deposition of LiF (1 nm) followed by Al (30 nm) on a P3HT coated glass substrate (c) (Sample C) Half coated with Al (30 nm) on the top (the hashed portion shows the depletion layer formed at the Al/P3HT interface) (d) (Sample D) Half coated with Bottom Al (30 nm) electrode (e) (Sample E) a diode cell having ITO/P3HT/Al configuration (f) (Sample F) a diode cell having ITO/P3HT/LiF:Al configuration.

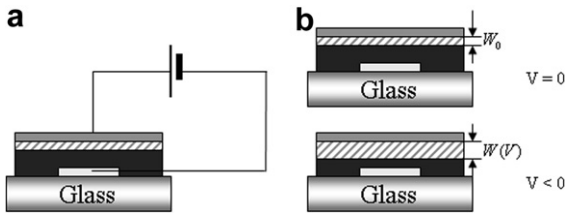

Fig. 2. (a) Shows the typical biasing arrangement under the reverse bias conditions (b) Shows the effect of increasing reverse bias on the depletion layer width leading to PL quenching.

coupling). While the first lot of sample C was half coated 30 nm thick Al on to the top of the film, However, sample D was half coated with 30 nm thick Al prior to spin coating at {1500 (30 s), 3000 (10 s)}rpm the rr P3HT film, as is also clear from Fig. 1c and d. On one hand all the lots of Sample C were used to study the effect of intrachain disorder on the absorption and emission spectra. The first lot of Sample C coated with rr P3HT was also used to compare with Sample D for the effect of coating Al on top and bottom of the film as will be discussed in detail in the next section. Fig. 1e and f show the schematic diagram of the sample fabricated for the bias dependent PL spectra of the schottky cell. It should be noted that the Cells E and F were fabricated in ITO/P3HT/Al and ITO/P3HT/LiF:Al type device configurations, as is also shown in Fig. 1e and f, respectively. Both LiF and Al were deposited by thermal evaporation. For the fabrication of ITO based sandwich cells, ITO coated glass substrates were patterned by etching in dilute HCl solution with Zinc powder to fabricate the ITO bottom electrodes, which were subsequently spin coated at {1500 (30 s), 3000 (10 s)}rpm with chloroform solution of rr P3HT. The Thickness of these films was later determined to be 200 nm. All the film Thicknesses were measured using Dektak Surface Profiler. Thicknesses of sample A and B were determined to be 79 and 55 nm, respectively, while both samples C and D were of identical thickness of 60 nm.

PL measurement was done under ambient conditions using photonic multi channel analyzer (Hamamatsu PMA-11), kept at a distance of 70 cm from the sample. A He–Cd Laser (300 mW, CW, 442 nm, Kimmon IK4121R) was used as a light-pumping source. The intensity of photons incident on the sample was later calculated to be 0.15 W/cm^2 incident at an inclination of about 30 degrees to the normal. In situ electrical bias was applied on the cells using Keithley 6517 A electrometer. ITO was biased as a cathode under the reverse bias direction, as is shown in Fig. 2a. Care was also taken to avoid over exposure of the sample to the laser beam. It should also be noted that all the samples except sample D were illuminated from the glass side. However, Sample D was illuminated from the film side. The details of which will be discussed in the next section.

3. Results and discussion

Fig. 3 shows the effect of an island deposition of LiF (1 nm) and LiF (1 nm) followed by Al (2.5 nm) on rr P3HT

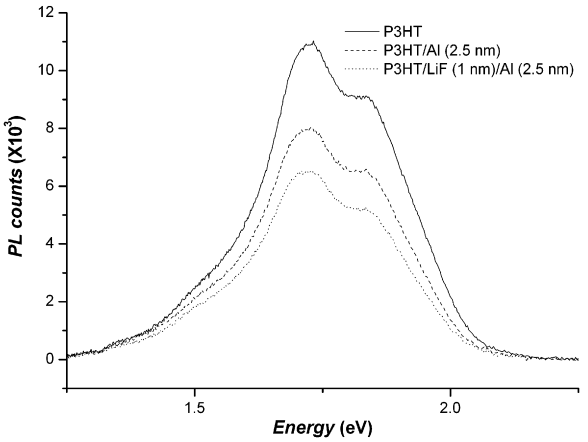

Fig. 3. PL Quenching effect due to island deposition of Al and LiF:Al on pristine P3HT film.

film. It was observed that coating LiF and Al both separately onto a P3HT film results in the quenching of the PL signal [24]. The PL emission intensity I_{PL} is given by

$$I_{PL} = \eta_{PL}\eta_C I_{abs} \quad (1)$$

where η_{PL}, η_C and I_{abs} denote the PL efficiency [25,26,39], efficiency of the detector and the intensity of the light absorbed, respectively. It should be noted that η_{PL} itself is given by the relation under the similar assumptions as in [26,39].

$$\eta_{PL} = \left(\frac{K_R}{K_R + K_{NR}}\right) \quad (2)$$

where K_R and K_{NR} denote the radiative and non radiative decay rate constants of excitons. The observed effects in Fig. 3 can be explained on the basis of the fact that deposition of a small amount of external species leads to an increase in the non radiative decay paths near the interface, which then leads to decrease in the PL efficiency resulting in the observed PL quenching. Our previous report [24] also indicates that the PL quenching was observed by coating the Al and LiF over layers on a P3HT film separately. Although the extent of PL quenching was different in the two cases. It was observed that coating LiF leads to increase in the K_{NR} while coating Al leads to PL quenching due to dissociation of excitons near the Al/P3HT interface due to high built in field of the depletion layer. Similarly Fig. 3 shows that increasing the population of the impurities i.e. coating LiF (1 nm) and then further coating Al (2.5 nm) resulted in increasing level of PL quenching. However, when the thickness of Al was increased from 2.5 nm to 30 nm the PL intensity increased as can be seen in Fig. 4. This effect has been observed due to double excitation of the film by the incident laser beam due to a strong reflection occurring from the top coated Al layer [26]. It is important to note that unlike Fig. 3, In Fig. 4 the PL counts for P3HT/LiF:Al samples were higher than that of P3HT/Al samples. Fig. 4 also shows an increase in the high energy shoulder peak occurring due to the Al coating on to the top of pristine P3HT film. Another significant point is the blue shift shown by the peak PL emission (E = 1.702 eV) spectra due to Al coating.

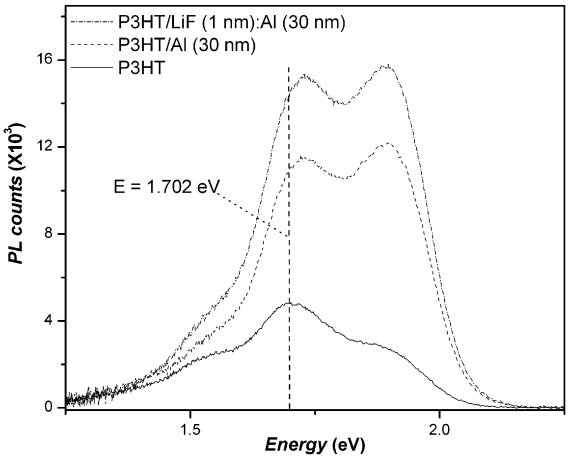

Fig. 4. The effect of coating 30 nm thick Al on pristine and LiF (1 nm) coated P3HT films on the PL of P3HT.

In order to ascertain the exact origin of this behavior another experiment was performed in which both top and bottom Al coated samples, namely samples C and D were fabricated. While sample C was illuminated by laser light from the glass facing side contrary to the sample D which was illuminated from the film facing side. This was done primarily because the bottom Al layer (sample D) would screen the intensity of the laser light and would also largely block the PL emissions from the underlying P3HT bulk layer, if illuminated from the glass side. It is a general observation that intensity of PL signal is also correlated with the degree of roughness near the interface. As can be clearly seen from Fig. 5, the PL counts for pristine P3HT film was higher in the case of sample C compared to that of sample D. It should be noted that both sample C and D showed an increase in the PL intensity, a clear cut evidence of dual excitation of the bulk in the two cases. However, unlike sample C, Sample D did not show any increase in the high energy shoulder peak, clearly indicating that such an effect is taking place due to the thermal deposition of Al over the pristine P3HT films. The results were similar to the one observed by Thakur et al. [37], although in their case they studied the effect of coating gold (Au) on Pristine P3HT film. In another similar report Brown et al. [30] also observed that the high energy peak in the PL emission occurs due to the intrachain excitons [33,34] and that the intrachain excitons are highly affected by the intrachain disorder contrary to the interchain excitons. Thus it can be concluded that coating Al on to the top of a film results in an increase in the intrachain disorder due to the thermal energy transfer from the hot Al atoms coated on P3HT film during the thermal evaporation process. It is known that the spin coated P3HT films are composed of microcrystalline domains embedded in an amorphous matrix. Inside these domains the polymers π -stack in one direction and form lamella of interlocking chains in the other direction. Usually the alkyl side chains try to orient themselves in a least strained position (energetically). Although this type of rearrangement is less pronounced in spin coated P3HT films as compared to dip coated or casted P3HT films [34-36]. However, as a result of this energy transfer between Al and immediate P3HT, polymer chains tend to have a more strained structure of the hexyl group attached to the polymer backbone, resulting in an increase in the intrachain disorder. Also, since some of these chains may be part of a micro crystalline domain, thus an intrachain disorder may result in a decrease of degree of π-stacking of these microcrystalline domains and hence of the films at the macro level, resulting in the blue shift of the PL emission peak occurring at 1.702 eV, as shown in Fig. 4. However, the absence of any such blue shift in Fig. 3 in which island deposition of Al and LiF:Al was done is probably due to the fact that the thickness of Al and LiF in these cases were too less to result in any observable changes.

In order to have detailed insight about the intrachain disorder effects on PL, we further fabricated three types of films, first was coated with rr P3HT, the second one was coated with non-regio controlled (nrc) P3HT and the third with rrnd P3HT (as obtained from Aldrich). The normalized absorption and emission spectra of these films have been shown in Fig. 6. It is clearly evident from

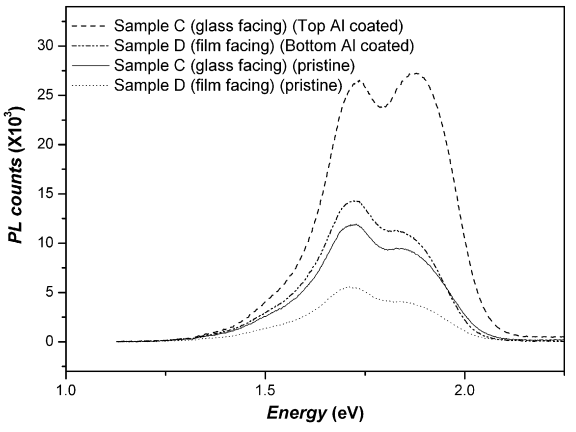

Fig. 5. Effect of top and bottom coating of Al (30 nm) on the PL spectra of P3HT films taken from glass side (glass facing) or from film side (film facing).

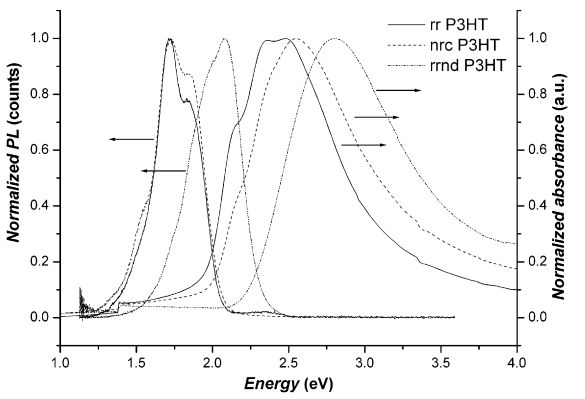

Fig. 6. Normalized absorption and emission spectra of rr P3HT, nrc P3HT and rrnd P3HT films.

this figure that the π–π^* transition band of the films was blue shifted [31] in the increasing order of their regio randomness, suggesting that higher degree of regioregularity leads to decrease in the band gap. This effect is attributed to the lesser degree of π conjugation on the parent chain in rrnd P3HT. Even the Band edge appears to be blue shifted in the increasing order of regio randomness of these P3HT films. Another striking feature is that the absorption of rr P3HT has three distinct peaks occurring at (E = 2.13, 2.33 and 2.50 eV), respectively. Pandey et al. [31] have demonstrated that the lowest energy peak in the absorption spectra (at 2.13 eV) corresponds to 0–0 transition and is related to the conformational order in the chains, while the peak at 2.33 eV corresponds to 0–1 transition and is related to the interchain ordering or the π-stacking of the various chains. While the main peak near 2.50 eV corresponds to the 0–2 transition. Compared to the rr P3HT these peaks were less pronounced in nrc P3HT and nearly vanished in rrnd P3HT film. It should also be noted that a clear blue shift in the absorption spectra was obtained for rrnd P3HT. However, only a little blue shift was obtained in nrc P3HT. This is probably due to high degree of regio regularity in these samples despite of being synthesized by $FeCl_3$ method.

Further if we look at the PL emission spectra of these films, we find that there is almost no shift in the emission spectra of rr P3HT and nrc P3HT, on the contrary a large blue shift was obtained in the emission spectra of rrnd P3HT as compared to that of rr P3HT. Further it must be noted that the 0–0, 0–1 and 0–2 transitions for the emission spectra of rr P3HT and nrc P3HT occur at E = 1.89, 1.7 and 1.5 eV, respectively. However, the corresponding 0–0, 0–1 and 0–2 transitions for rrnd P3HT occur at E = 2.07, 1.98 and 1.74 eV, respectively. As can also be seen from Fig. 6 that the intensity of shoulder peaks at 1.5 eV and 1.89 eV increase in the case of nrc P3HT compared to the rr P3HT. Brown et al. [30] have emphasized that the high energy peak at E = 1.89 eV is highly affected by the intrachain disorder, i.e. the degree of regioregularity of the polymer. Thus, the relative increase of the high energy peak as can be seen from the normalized PL spectra of the two films from Fig. 6 is owing to the lower degree of regio regularity on a single polymer chain in nrc P3HT. However, Brown et al. also pointed out that the peak in the emission spectra corresponding to interchain excitons (at E = 1.702 eV) doesn't get affected by the local order that is the regioregularity, as clearly corroborated by the Fig. 6. In the case of rrnd P3HT the highest energy peak at E = 2.07 eV corresponding to 0–0 transition has relatively higher intensity as compared to the 0–1 transition at E = 1.98 eV. This is because the intrachain disorder is highest in rrnd P3HT and hence the 0–0 transition in rrnd P3HT has a higher intensity as compared to 0–1 transition. Kaneto et al. [32] presented the PL spectra of an electrochemically synthesized polymer, which showed very low contributions from the interchain emissive state. At the same time it must be noted that the emission at E = 1.5 eV is also relatively increased in the case of nrc P3HT. This peak relates to the conformational order and as we know that the conformational order decreases in the nrc P3HT film resulting in relatively higher values of observed PL intensity (at E = 1.5 eV). In another interesting work Tanaka et al. [34] have demonstrated a clear cut change in the characteristic PL emission spectra by the fine control of the blending ratios of rr and rrnd P3HT.

In order to clearly understand the difference in the nature of interface we fabricated two types of cells E and F, for the purpose of study of the bias dependent photoluminescence quenching in the two cells. Fig. 2b shows the effect of increasing reverse bias voltage results in increasing the depletion layer thickness from w_0 (at 0 V) to w (V) at any reverse bias voltage V and hence resulting in PL quenching due to lessening of the thickness of active P3HT layer. It should be noted that although the depletion width at zero bias for cell E $(w_0)_E$, has been found to be slightly less than the depletion width at zero bias for cell F $(w_0)_F$. However, the higher value of PL counts in cell E is primarily due to the significant difference in the value of the parameter χ as has been defined in Ref. [26]. Although at present the exact origin of this behavior is not completely understood.PL quenching Q_{PL} [26-28,39] as defined by Eq. (3)

$$Q_{PL} = (I_{PL}(0) - I_{PL}(V))/I_{PL}(0) \quad (3)$$

where I_{PL} (0) and I_{PL} (V) denote the PL intensity at zero bias and at a bias V, respectively. Fig. 7 shows the quenching pattern for cell E and F and exhibits that a relatively higher level of quenching was observed in cell E as compared to that in cell F with the increasing reverse bias voltage. Similar results have been observed by Markov et al. [23] also. Although there are reports of PL quenching due to injected charge carriers [39–41] but such an effect is negligible in the present case as our discussion here concerns only with the reverse bias regime. Therefore, from Eq. (3) it is clear that the quenching directly relates to the amount of light absorbed by the bulk of semiconductor. Using the similar analysis as was given in Ref. [26], the depletion width dependence of bias voltage was plotted for cells E and F using the bias dependence of quenching of these cells. The change in the depletion width $\delta w(V)$ has been found to be related to Q_{PL} as is given by Eq. (4),

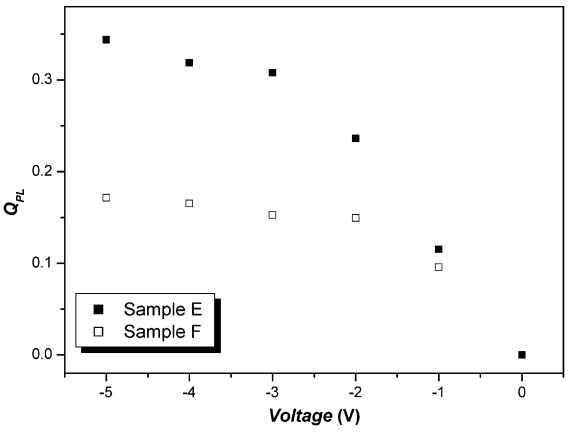

Fig. 7. Plot of PL quenching Q_{PL} versus the reverse bias voltages V for cell E and F.

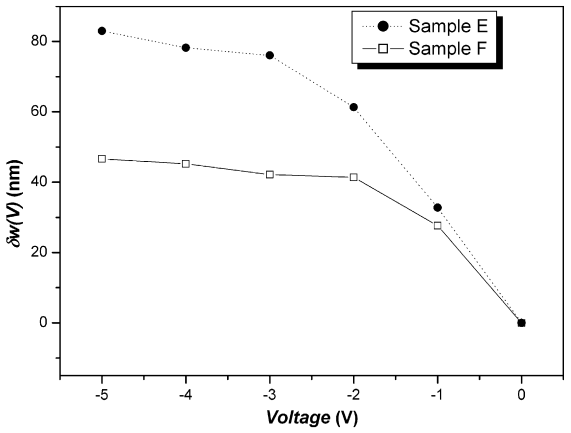

Fig. 8. Change in depletion width δw as a function of voltage for cell E and F.

$$\delta w(V) = \frac{1}{\alpha} \ln \left| \frac{\sqrt{(A+2B)^2 + 4BQ_{PL}} - A}{2B} \right| \quad (4)$$

where the constants A and B were determined as described in Ref. [26,39]. The plot of $\delta w(V)$ against the applied bias V for the two cells has been shown in the Fig. 8. The change in the depletion width as a function of voltage was found to be more prominent in the cell E as compared to cell F. Thus it can be concluded that the presence of LiF near the interface limits the extent of modulation of the depletion layer with the applied reverse bias voltage. Fig. 8 shows a clear cut deviation of the depletion width from Eq. (5) [26,29], that itself has been derived assuming a uniform charge carrier density. However, in a polymeric semiconductor like P3HT the charge carrier density is non uniform, thus resulting in the observed deviation. Takshi et al. also demonstrated similar observations in Ref. [29].

$$W = \sqrt{2\varepsilon_s(V_{bi} - V)/qN_A} \quad (5)$$

where w denotes the depletion layer width. ε_s, q, V_{bi}, N_A denote the dielectric permittivity, charge of an electron, built in potential and Acceptor charge density, respectively. Fig. 9 on the other hand shows higher level of photocurrents in cell F as compared to that for the cell E. The photocurrents are found to increase with the increasing application of reverse bias voltage for the two cells. Here, it must be noted that the improvement in the PLEDs is mainly due to the improved injection of the electrons from the cathode into the LUMO of n-type semiconductor. However in our study only p-type material i.e. P3HT was used, and the IV characteristics reflect the hole transport. The holes are injected from ITO into the HOMO of P3HT and from there into the Fermi level of Al. Thus, a decrease in the forward bias current was observed for cell F as is shown in inset of Fig. 9, although the built in voltage V_{bi} was found to increase upon the LiF coating.

Brabec et al. [21] studied the effect of LiF in Bulk hetero junction solar cells. It was observed that including a thin layer of LiF improved the solar cell efficiency of the PSCs considerably. In their final conclusion they attributed this effect to either the orientation of LiF or chemical reactions leading to charge transfer across the interface, thus resulting in the formation of dipole moment across the junction. However, the absence of memory currents in LiF coated photo induced memory devices [24] clearly rules out any such possibility. Thus, we conclude that it is the orientation of LiF near the interface that results in the dipole moment across the junction. At the same time it is this dipole moment of LiF that leads to high localized field as is shown by the offset level Δ in the band diagram in Fig. 10. The lesser values of depletion width of the cell F probably resulted due to the less steep band bending of P3HT in cell F as is shown in the Fig. 10. However, the high localized field near the interface in cell F resulted in higher values of photocurrents, as photocurrents are generated by the field assisted dissociation of excitons. A highly localized Field near the interface ensures effective dissociation of excitons. Thus we conclude that it is the dipole moment of the LiF molecule itself that leads to a highly localized field, resulting in the improvement of the Solar cell efficiency.

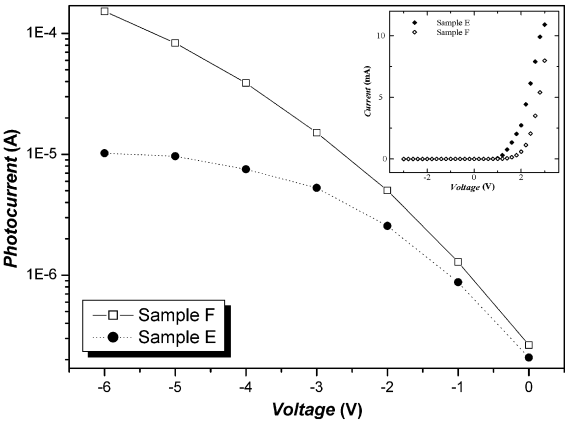

Fig. 9. Photocurrents as a function of reverse bias voltages for cell E and F. Inset shows the forward bias currents for cell E and F.

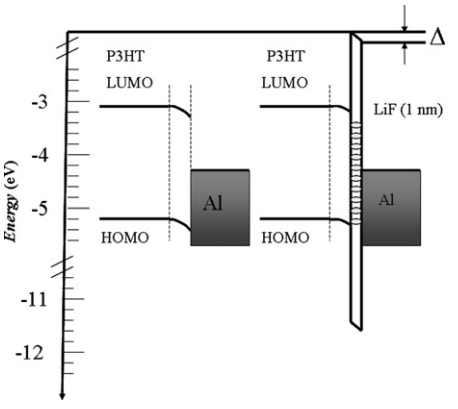

Fig. 10. Band diagram for the cell E and F at zero bias condition.

4. Conclusion

Finally we would like to conclude two main points. First is that the Al coating on to the top of polymer pristine film has identical effects as that observed by decreasing regio regularity of the polymer chain. Both of these effects actually originate from the intrachain excitons which are highly dependent on the local order on a chain. The second point is that the depletion layer is less modulated in cell F compared to cell E. Although an overall high Electric field is developed near the interface in cell F. Inclusion of LiF improves the solar cell efficiency of PSCs due to the fact that LiF is a strong ionic molecule having high dielectric constant, which results in a strong localized electric field due to the dipole formation by these molecules, further resulting in the observed lower values of depletion layer and higher values of the photocurrents in LiF:Al modified cathode type Schottky devices.

Acknowledgements

This work was supported by Grant in Aid for Science and Research in priority area "Super hierarchical structures" from Ministry of education, culture, sports, science and technology, Japan. One of the authors (V.S.) would further like to thank Heiwa Nakajima Foundation for providing the scholarship.

References

[1] H. Spanggaard, F.C. Kerbs, Sol. Energy. Mat. Sol. Cells 83 (2004) 125.
[2] Y. Kim, S.A. Choulis, J. Nelson, D.D.C. Bradley, S. Cook, J.R. Durrant, J. Mater. Sci. 40 (2005) 1371.
[3] T.F. Guo, Y. Yang, Appl. Phys. Lett. 80 (2002) 148.
[4] P. Pneumans, A. Yakimov, S.R. Forrest, J. Appl. Phys. 93 (2003) 3693.
[5] V. Singh, M. Yano, W. Takashima, K. Kaneto, Jpn. J. Appl. Phys. 45 No. 1B (2006) 534.
[6] D.A. Bernards, T. Biegala, Z.A. Samuels, J.D. Slinker, G.G. Malliaras, S.F. Torres, H.D. Abruna, J.A. Rogers, Appl. Phys. Lett. 84 (2004) 3675.
[7] T.W. Lee, S. Jeon, J. Maria, J. Zaumseil, J.W.P. Hsu, J.A. Rogers, Adv. Func. Mat. 15 (2005) 1435.
[8] J.C. Scott, J. Vac. Sci. Tech. A21 (2003) 521.
[9] W.R. Siliveira, J.A. Marohn, Phys. Rev. Lett. 93 (2003) 116104.
[10] S. Grecu, M.R. Buck, A. Opitz, W. Brutting, Org. Elec. 7 (2006) 276.
[11] T.P.I. Saragi, T.F. Lieker, J. Salbeck, Synth. Met. 148 (2005) 267.
[12] B. Deveaud, A. Regreny, J.Y. Emery, A. Chomette, J. Appl. Phys. 59 (1986) 1633.
[13] B.S. Elmann, E.S. Koteles, C. Jagannath, Y.J. Chen, S. Charbonneau, M.L.W. Thewalt, Proc. SPIE 794 (1987) 44.
[14] R. Kersting, U. Lemmer, M. Deussen, H.J. Bekker, R.F. Mahrt, H. Kurz, V.I. Arkhipov, H. Bassler, E.O. Gobel, Phys. Rev. Lett. 73 (1994) 1440.
[15] G. Yu, J. Gao, J.C. Hummelen, F. Wudl, A.J. Heeger, Science 270 (1995) 1789.
[16] M. Segal, M.A. Baldo, R.J. Holmes, S.R. Forrest, Z.G. Soos, Phys. Rev. B68 (2003) 075211.
[17] N.S. Sariciftci, L. Smilowitz, A.J. Heeger, F. Wudl, Science 258 (1992) 1474.
[18] Y.D. Jin, X.B. Ding, J. Reynaert, V.I. Arkhipov, G. Borghs, P.L. Heremans, M. Van der Auweraer, Org. Elec. 5 (2004) 271.
[19] T. Yokoyama, H. Ishii, Y. Ouchi, Surf. Rev. Lett. 9 (1) (2002) 425.
[20] M.A. Baldo, S.R. Forrest, Phys. Rev. B64 (2001) 085201.
[21] C.J. Brabec, S.E. Shaheen, C. Winder, N.S. Sariciftci, P. Denk, Appl. Phys. Lett. 80 (7) (2002) 1288.
[22] S. Sohn, K. Park, D. Lee, D. Jung, H.M. Kim, U. Manna, J. Yi, J. Boo, H. Chae, H. Kim, Jpn. J. Appl. Phys. 45 (4B) (2006) 3733.
[23] D.E. Markov, P.W.M. Blom, Phys. Rev. B72 (2005) 161401(R).
[24] V. Singh, A.K. Thakur, S.S. Pandey, W. Takashima, K. Kaneto, Jpn. J. Appl. Phys. 47 (2B) (2008) 1251.
[25] H. Becker, S.E. Burns, R.H. Friend, Phys. Rev. B56 (1997) 1893.
[26] V. Singh, A.K. Thakur, S.S. Pandey, W. Takashima, K. Kaneto, Appl. Phys. Exp. 1 (2008) 021801.
[27] S. Tasch, G. Kranzelbinder, G. Leising, U. Scherf, Phys. Rev. B55 (8) (1997) 5079.
[28] M.C.J.M. Vissenberg, M.J.M. de Jong, Phys. Rev. B57 (1998) 2667.
[29] A. Takshi, A. Dimopoulos, J.D. Madden, Appl. Phys. Lett. 91 (2007) 083513.
[30] P.J. Brown, D.S. Thoma, A. Kohler, J.S. Wilson, J.S. Kim, J.S.C.M. Ramsdale, H. Sirringhaus, R.H. Friend, Phys. Rev. B67 (2003) 064203.
[31] S.S. Pandey, W. Takashima, S. Nagamatsu, T. Endo, M. Rikukawa, K. Kaneto, Jpn. J. Appl. Phys. 39 (2000) L94.
[32] K. Kaneto, Y. Kohno, K. Yoshino, Solid State Commun 51 (1984) 267.
[33] R. Hidayat, A. Fuji, M. Ozaki, K. Yoshino, Jpn. J. Appl. Phys. part 1 40 (12) (2001) 7103.
[34] H. Tanaka, Y. Yoshida, T. Nakao, N. Tsujimoto, A. Fujii, M. Ozaki, Jpn. J. Appl. Phys. 40 (2006) L1077.
[35] W. Takashima, S.S. Pandey, T. Endo, M. Rikukawa, N. Tanigaki, Y. Yoshida, K. Yase, K. Kaneto, Thin Solid Films 393 (2001) 334.
[36] G. Wang, T. Hirasa, D. Moses, A.J. Heeger, Synth. Met. 146 (2004) 127.
[37] A.K. Thakur, A.K. Mukherjee, D.M.G. Preethichandra, W. Takashima, K. Kaneto, J. Appl. Phys. 101 (2007) 104508.
[38] M.R. Anderson, D. Selse, M. Berggeren, H. Jarvinen, T. Hjertberg, O. Inganas, O. Wennerstrom, J.E. Osterholm, Macromolecules 27 (1994) 6503.
[39] V. Singh, A.K. Thakur, S.S. Pandey, W. Takashima, K. Kaneto, Synth. Met. 158 (7) (2008) 283.
[40] Y. Luo, H. Aziz, G. Xu, Z.D. Popovic, Chem. Mater. 19 (2007) 2288.
[41] H.S. Majumdar, C. Botta, A. Bolognesi, A.J. Pal, Synth. Met. 148 (2) (2005) 175.

spirofluorene-linked anthracene [25], heteroatom- and aromatic amine-substituted spiro compound [26], pyrene-substituted spiro compound [27] and difluorene-indenofluorene compound [28].

In this paper, we report the synthesis of new host and dopant materials 2-(10-biphenylanthracene)-spiro[fluorene-7,9′-benzofluorene] (BH-3B) and 2-[4′-(phenyl-4-vinylbenzeneamine)phenyl-spiro[fluorene-7,9′-benzofluorene] (BH-3BD) by Suzuki reaction. Various properties such as UV–Vis absorption, photoluminescence, electroluminescence including EL efficiency and color purity were evaluated.

2. Experiment

2.1. Material and measurements

9-(4-Biphenylanthracene)-10-boronic acid was synthesized according to the method previously reported [7–9]. Tetrakis(triphenylphosphine)palladium(0) and potassium carbonate (Aldrich Chem. Co.) were used without further purification. Tetrahydrofuran was distilled over sodium and calcium hydride. 1-(2-Bromophenyl)naphthalene (**1**) was prepared by the method previously reported [29,30]. Diphenyl-[4-(2-[1,1;4,1]terphenyl-4-yl-vinyl)-phenyl]-amine (BD-1) was used as one of the dopants.

^{1}H NMR and ^{13}C NMR spectra were recorded on a Bruker, Avance 500 (500 MHz) spectrometer. Photoluminescence (PL) spectra were recorded on a fluorescence spectrophotometer (Jasco FP-6500) and UV–Vis spectra were obtained by a UV–Vis spectrophotometer (Shimadzu, UV-1601PC). Energy levels were measured with a low-energy photo-electron spectrometer (Riken-Keiki AC-2). The FT-IR spectra were obtained with a Biorad Excaliber FTS-3000MX spectrophotometer and elemental analyses were performed using a CE Instrument, EA1110. The DSC measurements were performed on a Mettler DSC 822^e under nitrogen at a heating rate of 10 °C/min. Low and high resolution mass spectra were recorded using a JEOL, JMS-AX505WA spectrometer in FAB mode.

2.2. Synthesis of 2-bromo-spiro[fluorene-7,9′-benzofluorene] (*2*)

To a two-necked flask (250 mL), was placed a solution of 1-(2-bromophenyl)naphthalene (10 g, 35.3 mmol) dissolved in THF (50 mL). The reaction flask was cooled to −78 °C and *n*-BuLi (2.5 M in hexane, 16.8 mL) was added dropwise slowly. The whole solution was stirred at this temperature for 1 h, followed by addition of a solution of 2-bromo fluorenone (10.8 g, 41.7 mmol) dissolved in THF (30 mL) under argon atmosphere. The resulting mixture was gradually warmed to ambient temperature and quenched by saturated, aqueous $NaHCO_3$ (80 mL). The reaction mixture was extracted with dichloromethane. The combined organic layers were dried with magnesium sulfate, and filtered. After the solvent was evaporated under reduced pressure, the yellow powdery product was obtained.

The above solid product was placed in a two-necked flask (100 mL) and dissolved in acetic acid (30 mL). Catalytic amount of aqueous HCl (5 mol%, 12 N) was then added and the whole solution was refluxed for 12 h. After having been cooled to ambient temperature, the purification by silica gel chromatography using dichloromethane/*n*-hexane (1/1) gave a white powdery product. Yield 73%. Mp 152 °C. ^{1}H NMR (500 MHz, $CDCl_3$) δ 8.85-8.83 (d, 1H, Ar-*H* in fluorene), 8.44–8.43 (d, 1H, Ar-*H* in fluorene), 7.92–7.90 (d, 1H, Ar-*H* in benzofluorene), 7.85–7.83 (d, 1H, Ar-*H* in fluorene), 7.73–7.70 (t, 2H, Ar-*H* in benzofluorene), 7.64–7.62 (d, 1H, Ar-*H* in benzofluorene), 7.57–7.54 (t, 1H, Ar-*H* in fluorene), 7.50–7.46 (t, 2H, Ar-*H* in benzofluorene), 7.39–7.36 (t, 1H, Ar-*H* in fluorene), 7.17–7.15 (t, 1H, Ar-*H* in benzofluorene), 7.12–7.09 (t, 1H Ar-*H* in fluorene), 6.82–6.78 (m, 2H, Ar-*H* in benzofluorene), 6.70–6.69 (d, 1H, Ar-*H* in fluorene). FT-IR (KBr, cm^{-1}) 3055 (aromatic C-*H*), 1580 (aromatic C=C), 657 (aromatic C–Br).

2.3. Synthesis of 2-(10-biphenylanthracene)-spiro[fluorene-7,9′-benzofluorene] (BH-3B)

Compound **2** (5.0 g, 11.18 mmol) and 9-(4-biphenylanthracene)-10-boronic acid (5.01 g, 13.41 mmol) and tetrakis(triphenylphosphine)palladium(0) (0.68 g, 0.59 mmol) were dissolved in THF (100 mL) in a two-necked flask under nitrogen atmosphere for 30 min. A solution of potassium carbonate (1.63 g, 11.18 mmol) dissolved in distilled water (50 mL) was added dropwise over a period of 20 min. The resulting solution was refluxed overnight at 80 °C. The reaction mixture was extracted with dichloromethane and water. The organic layer was evaporated with a rotary evaporator. The resulting powdery product was purified by column chromatography from *n*-hexane to give a white crystalline solid. Yield 60%. Mp 350 °C. ^{1}H NMR (500 MHz, $CDCl_3$) δ 8.75–8.33 (2d, 2H, Ar-C*H*-benzofluorene), 8.12–7.99 (2d, 2H, Ar-C*H*-benzofluorene), 7.88–7.73 (2d, 2H, Ar-C*H*-benzofluorene), 7.71-7.45 (m, 8H, Ar-C*H*-anthracene), 7.66–7.64 (m, 4H, Ar-*H* in fluorene), 7.63–7.49 (2d, 2H, Ar-C*H*-benzofluorene), 7.41–7.39 (d, 1H, Ar-*H* in fluorene), 7.39–7.38 (t, 1H, Ar-*H* in fluorene), 7.21–7.18 (m, 4H, –*Ph*–Ph), 7.18–7.15 (m, 5H, –Ph–*Ph*), 7.02–6.84 (2d, 2H, Ar-C*H*-benzofluorene), 6.79–6.78 (d, 1H, Ar-*H* in fluorene). ^{13}C NMR ($CDCl_3$) δ 148.6, 147.5, 141.0, 138.8, 131.8, 129.4, 129.1, 129.0, 127.5, 127.3, 127.2, 127.0, 126.9, 125.2, 125.1, 124.4, 120.4, 77.4, 77.2, 76.9, 66.5 ppm. FT-IR (KBr, cm^{-1}) 3059, 3040, 3012 (aromatic C–H), 1578 (aromatic C=C). MS (FAB) m/z 694.0 [$(M + 1)^+$]. Anal. Calcd. for $C_{55}H_{34}$ (694.86): C, 95.07; H, 4.93. Found: C, 94.53; H, 4.87. UV–Vis (THF) λ_{max} (Absorption) = 369, 388 nm, λ_{max} (Emission) = 432, 447 nm.

2.4. Synthesis of 2-[4′-(phenyl-4-vinylbenzeneamine)phenyl]-spiro[fluorene-7,9′-benzofluorene](BH-3BD)

Compound **3** (5.0 g, 12.13 mmol), *N*-[4-[2-(4-bromophenyl)vinyl]phenyl]-*N*,*N*-diphenylamine (4.3 g, 10.11 mmol) and tetrakis(triphenylphosphine)palladium(0) (0.58 g, 0.51 mmol) were dissolved in THF (100 mL) under nitrogen atmosphere for 30 min. To an above solution, was added a solution of potassium carbonate (1.40 g, 10.11 mmol) dissolved in distilled water

(50 mL) dropwise over a period of 20 min. After the resulting solution was refluxed overnight at 80 °C, the reaction mixture was extracted with dichloromethane and water. After the organic layer was evaporated with a rotary evaporator, the resulting powdery product was purified by column chromatography from *n*-hexane to give a yellow crystalline solid. Yield 58%. Mp 308.3 °C. ^{1}H NMR (500 MHz, $CDCl_3$) δ 8.88–8.86 (d, 1H, Ar-*H* in benzofluorene), 8.46–8.44 (d, 1H, Ar-*H* in benzofluorene), 7.94–7.88 (m, 2H, Ar-*H* in benzofluorene), 7.72–7.34 (2d, 2H, –Ph–C*H*=C*H*–), 7.63–7.62 (m, 2H, Ar-*H* in fluorene), 7.55–7.38 (t, 1H, Ar*H* in fluorene), 7.38–7.34 (d, 1H, Ar-C*H*-vinyl), 7.32-6.77 (m, 4H, Ar-*H* in fluorene), 7.25–7.07 (2d, 4H, –*Ph*–CH=CH–), 7.22-7.15 (m, 6H, Ar-*H* in benzofluorene), 7.18-6.97 (m, 10H, –N(*Ph*)$_2$), 7.24–6.85 (2d, 4H, –*Ph*–N(Ph)$_2$). ^{13}C NMR ($CDCl_3$) δ 149.7, 148.5, 147.7, 140.6, 136.7, 129.5, 129.4, 128.2, 128.1, 128.0, 127.5, 127.3, 126.9, 126.7, 124.6, 124.2, 123.7, 123.2, 122.5, 120.6, 120.3, 77.4, 77.2, 66.5 ppm. FT-IR (KBr, cm^{-1}) 3059, 3040, 3012 (aromatic C-H), 1580 (C=C), 1491 (C-N). Anal. Calcd. for $C_{55}H_{37}N$ (711.89): C, 92.79; H, 5.24; N, 1.97. Found: C, 91.12; H, 5.17; N, 1.88. UV–Vis (THF): λ_{max} (Absorption) = 375 nm, λ_{max} (Emission) = 469, 476 nm.

2.5. Synthesis of 4-[2-naphthyl-4′(phenyl-4-vinylbenzeneamine)]phenyl (BD-1N)

A solution of naphthalene-1-boronic acid (3.39 g, 19.7 mmol), 4-bromo-4′-(1,2-diphenylvinyl)biphenyl (7.0 g, 16.4 mmol) and tetrakis(triphenylphosphine)palladium (0) (0.95 g, 0.82 mmol) were dissolved in THF (150 mL) in a two-necked flask under nitrogen atmosphere for 30 min. To an above reaction mixture, was added a solution of potassium carbonate (2.27 g, 16.4 mmol) dissolved in distilled water (50 mL) dropwise over a period of 20 min. The resulting solution was refluxed overnight at 80 °C. The reaction mixture was extracted with dichloromethane and water. The organic layer was evaporated with a rotary evaporator. The resulting powdery product was purified by column chromatography from hexane to give a yellow crystalline solid. Yield 73%. Mp 204.8 °C. ^{1}H NMR (500 MHz, $CDCl_3$) δ 7.96–7.94 (d, 1H, Ar-*H* in naphthalene), 7.90–7.89 (d, 1H, Ar-*H* in naphthalene), 7.85–7.84 (d, 1H, Ar-*H* in naphthalene), 7.61-7.59 (d, 2H, –C*H*=C*H*–), 7.53–7.47 (m, 4H, –*Ph*–CH=CH–), 7.44–7.40 (m, 4H, Ar-*H* in naphthalene), 7.16–6.83 (m, 10H, –N(*Ph*)$_2$), 7.12–6.92 (m, 4H, –*Ph*–N(Ph)$_2$). ^{13}C NMR ($CDCl_3$) δ 147.7, 147.6, 139.9, 136.8, 130.6, 129.5, 128.5, 127.8, 127.6, 127.0, 126.8, 126.4, 126.2, 126.0, 125.6, 124.7, 123.7, 123.2, 77.4, 77.2, 76.9 ppm. FT-IR (KBr, cm^{-1}) 3059, 3040, 3012 (aromatic C–H), 1580 (aromatic C=C), 1491 (C–N). MS (FAB) m/z 473.0 [$(M + 1)^+$]. Anal. Calcd. for $C_{36}H_{27}N$ (473.61): C, 91.30; H, 5.75; N, 1.97. Found: C, 91.25; H, 5.72; N, 2.11. UV–Vis (THF): λ_{max} (Absorption) = 369.5 nm, λ_{max} (Emission) = 442, 452 nm.

2.6. OLED fabrication and measurement

Prior to device fabrication, ITO with a resistance of 12 Ω/□ on glass was patterned as an active area of 4 mm^2(2 mm × 2 mm). The substrates were cleaned by sonication in deionized water, boiled in IPA for 20 min, and dried with nitrogen. Finally, the substrates were dry cleaned using plasma treatment in an O_2 and Ar environment. Organic layers were deposited sequentially by thermal evaporation from resistively heated alumina crucibles onto the substrate an a rate of 1.0 Å/s. The thicknesses of *N,N′*-bis-[4-(di-*m*-tolylamino)phenyl]-*N,N′*-diphenylbiphenyl-4,4′-diamine (DNTPD, HIL), bis[*N*-(1-naphthyl)-*N*-phenyl]benzidine (NPD, HTL), host:5% dopant (EML) and aluminum tris(8-hydroxyquinoline)(Alq_3, ETL) layer were about 400, 200, 300 and 200 Å, respectively. Before the deposition of metal cathode, LiF was deposited onto the organic layers with the thickness of 10 Å. A high-purity aluminum cathode was deposited at a rate of 1 ∼ 5 Å/s with the thickness of 2000 Å as the top layer. After the evaporation chamber was vented with nitrogen gas, the device was immediately transferred to a glove-box upon fabrication. A thin bead of epoxy adhesive was applied from a syringe around the edge of a clean cover glass. To complete the package, a clean cover glass was placed on the top of the device. The epoxy resin was cured under intense UV radiation for 3 min. The current–voltage characteristics of the encapsulated devices were measured on a programmable electrometer having current and voltage sources (model Keithley 237). The luminance and EL spectra were measured with a PR650 system (Photo Research Co. Ltd.).

3. Results and discussion

3.1. Synthesis and characterization

2-(10-Biphenylanthracene)-spiro[fluorene-7,9′-benzofluorene] (BH-3B) was prepared through Suzuki reaction of 2-bromo-spiro[fluorene-7,9′-benzofluorene] (**2**) with

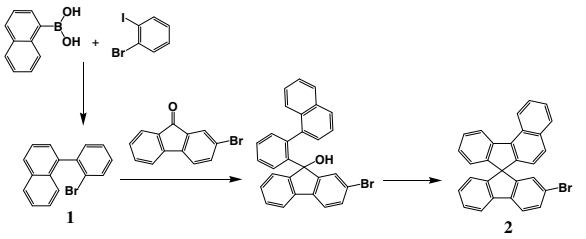

Scheme 1.

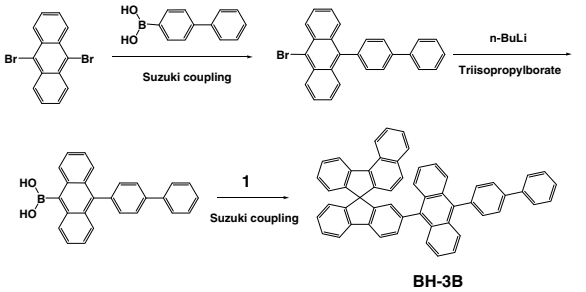

Scheme 2.

9-(4-biphenylanthracene)-10-boronic acid using palladium catalyst as shown Schemes 1 and 2. The general synthetic routes of the two dopant materials, 2-[4′-(phenyl-4-vinylbenzeneamine)phenyl-spiro[fluorene-7,9′-benzofluorene] (BH-3BD) and 4-[2-naphthyl-4′(phenyl-4-vinylbenzeneamine)]phenyl (BD-1N) are shown in Scheme 3. The conversion of **2** into spiro[fluorene-7,9′-benzofluorene]-2-boronic acid (**3**) was achieved by a two step synthesis: lithiation of **2** with an excess of *n*-BuLi, followed by treating it with triisopropyl borate. BH-3BD and BD-1N prepared by reacting 4-bromo-4′-(1,2-diphenylvinyl)biphenyl with **3** and naphthalene-2-boronic acid via the Suzuki reaction, respectively. BH-3B, BH-3BD and BD-1N were characterized by ^{1}H NMR,^{13}C NMR, FT-IR, GC-MS and elemental analysis.

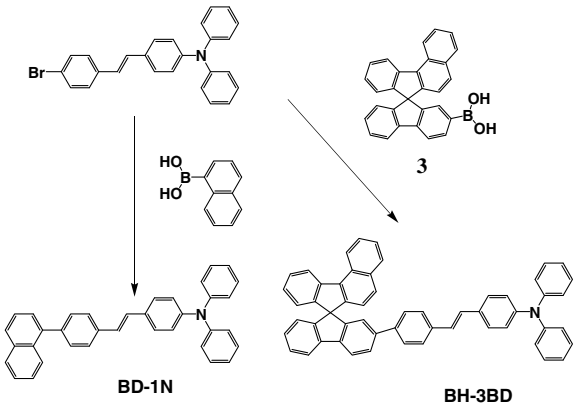

Scheme 3.

Table 1
Thermal properties data of new spiro host and dopant materials

	Temperature (°C)	BH-3B[d]	BD-1[e]	BD-1N[f]	BH-3BD[g]
Thermal properties	T_g[a]	282.4	—	68.93	—
	T_c[b]	—	—	97.7	—
	T_m[c]	350	306.9	204.8	308.3

[a] Glass transition temperature.
[b] Crystallization temperature.
[c] Melting temperature.
[d] 2-(10-biphenylanthracene)-spiro[fluorene-7,9′-benzofluorene].
[e] Diphenyl-[4-(2-[1,1;4,1]terphenyl-4-yl-vinyl)-phenyl]amine.
[f] 4-[2-naphthyl-4′(phenyl-4-vinylbenzeneamine)]phenyl.
[g] 2-[4′-(phenyl-4-vinylbenzeneamine)phenyl-spiro[fluorene-7,9′-benzofluorene].

3.2. Thermal properties

The thermal properties of the BH-3B, BH-3BD and BD-1N were investigated by differential scanning calorimetry (DSC). DSC was performed in the temperature range of 25–500 °C. The DSC results are summarized in Table 1. The DSC thermograms of BH-3B and BH-3BD exhibited endothermic melting peaks (T_m) during the first heating scan at 350 and 308.3 °C, respectively. BH-3BD shows higher glass transition temperature (282.4 °C), which is comparable to BD-1N at 68.9 °C. This result indicates that rigid and bulky spiro[fluorene-7,9′-benzofluorene] group having tetrahedral spirobifluorene skeleton in BH-3B might mitigate the intermolecular cohesion among the molecules in the solid state. As a consequence, BH-3B is able to form homogeneous and stable amorphous film by thermal evaporation which is a basic requirement for material to be used as host material in OLEDs.

3.3. Optical properties

UV–Vis absorption and photoluminescence spectral data of BH-3B, BH-3BD and BD-1N were shown in Fig. 1 and Table 2. BH-3B showed an UV–Vis absorption maximum at 369 nm and on-set at 388 nm (corresponding band gap is 3.02 eV). The emission spectrum shows a broad peak centered at 432 nm. The emission spectra of the BH-3B thin film, prepared by spin-coating from a toluene solution onto a quartz plate, was similar to those in dilute solution but exhibit a red-shifts of 35 nm (λ_{max} = 447 nm). Fig. 1(b) and (c) depicts the absorption and PL spectra of dopants BH-3BD and BD-1N, which have resemblance to BD-1, in dilute solution and solid thin film. They show absorption maxima at around 375 nm and 369 nm, respectively. The emission spectrum of the solid thin film shows red-shifted

Table 2
Optical and EL properties new host and dopant materials

Properties	Materials	Units	BH-3B	BD-1	BD-1N	BH-3BD
Optical properties	Abs (THF)[a]	λ_{max} (nm)	388	383	369.5	375
	Em (THF)[b]		432	454	452	469
	Em (SF)[c]		447	472	442	476.5
	Φ_f[d]	%	69	71	75	78
EL properties	Blue host: BH-3B at 7 V	EQE(%)	1.7	3.6	2.9	3.9
		mA/cm^2	19.46	24.82	23.19	24.46
		cd/A	2.11	3.06	2.13	3.43
		lm/W	0.94	1.37	0.95	1.54
		cd/m^2	411.2	760.7	496	840
		CIE-*x*	0.15	0.15	0.16	0.15
		CIE-*y*	0.10	0.14	0.12	0.14

[a] Absoption in THF.
[b] Emission in THF.
[c] Emission in solid film.
[d] Fluorescence quantum efficiency, relative to 9,10-diphenylanthracene in cyclohexane (Φ_f = 90%).

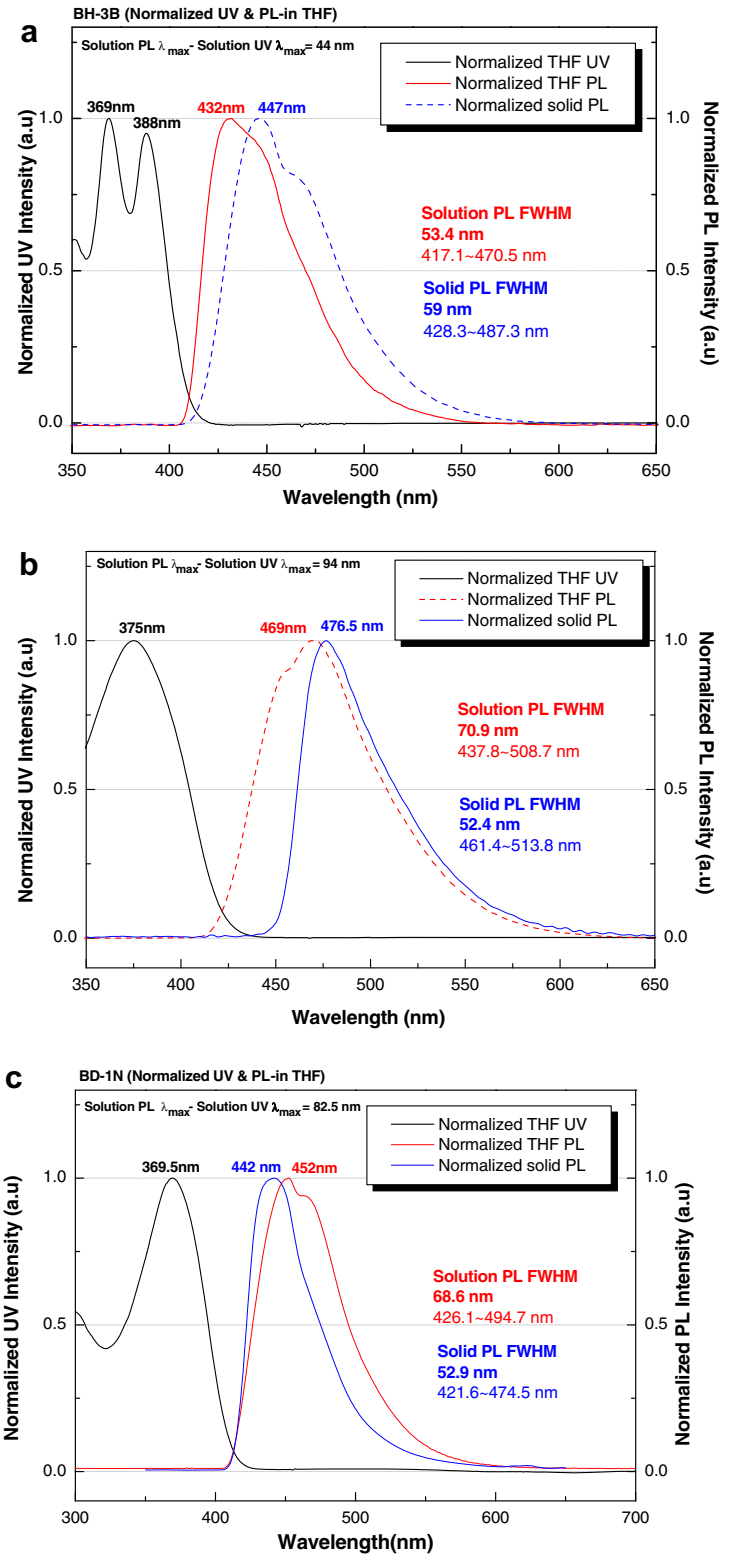

Fig. 1. Normalized absorption and photoluminescence spectra of (a) BH-3B, (b) BH-3BD, and (c) BD-1N in solution and thin solid film.

by 7.5 nm for BH-3BD and blue-shifted by 10 nm for BD-1N in comparison to its PL spectrum in dilute solution. The solution fluorescence quantum efficiency (Φ_f) of host and dopant materials, all of which fall in the range of were

determined relative to 9,10-diphenylanthracene in cyclohexane ($\Phi_f = 0.90$) [31].

3.4. The estimation of the HOMO and LUMO energy levels

A low-energy photoelectron spectrometer was used to obtain information about HOMO energy values of host and dopant materials. The HOMO energy level of BH-3B is approximately 5.80 eV. The band gaps were determined to be 3.02 eV from the absorption edge of the optical absorption spectrum of BH-3B thin solid film on quartz substrate. The LUMO energy level of BH-3B was estimated to be 2.78 eV. The energy levels of BH-3B, BH-3BD, BD-1N and BD-1 materials used to fabricate OLEDs in the present study are shown in Fig. 2. BH-3BD have slightly higher LUMO levels than BD-1 and BD-1N leading to an additional injection barrier for electrons: the LUMO of BH-3BD lies at 2.59 eV, while the LUMOs of BD-1 and BD-1N are located around 2.57 and 2.53 eV, respectively. This causes the increased driving voltage for OLEDs with BD-1N.

3.5. EL properties

In this study, an EL device was fabricated using DNTPD as a hole injection layer, α-NPD as the hole transport layer, Alq_3 as the electron transport layer, BH-3B host:5% dopant as an emitting layer, ITO as the anode, LiF as the buffer layer, and Al as the cathode to form a structure of ITO/DNTPD/NPB/BH-3B:5% dopant/Alq_3/Al-LiF.

In Fig. 3, the EL spectra of the devices derived from blue host BH-3B doped with BD-1, BD-1N and BH-3BD dopants were compared. The device provides a main EL peak at around 444 ~ 456 nm at 7 V. The EL spectrum of device without dopant was very similar with those of devices doped with three other dopants. The emitting color of device with BH-3B:5% dopant as emitting layer showed the deep blue emission $(x, y) = (0.15, 0.14)$, $(0.16, 0.12)$ and $(0.15, 0.14)$ at 24.82, 23.19 and 24.82 mA/cm^2, respectively, in CIE (Commission Internationale de l'Eclairage) chromaticity coordinates as shown in Fig. 4. It was observed that undoped device displayed a better color purity but poor efficiency. The CIE coordinates are (0.15, 0.10) at 19.46 mA/cm^2.

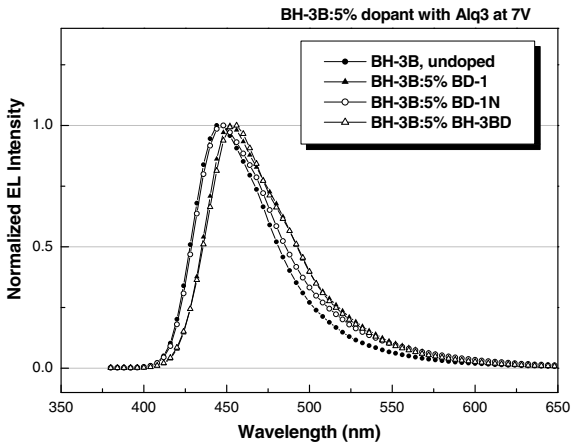

Fig. 3. EL spectra of the devices obtained from BH-3B host doped with various dopants.

The EL emission spectra from emitting layers of BH-3B as the host and 0%, 3%, 5% or 7% BD-1N as the dopant at 7 V are measured. The CIE coordinates of the four devices made of 7%, 5%, 3%, 0% BD-1N were (0.15, 0.10), (0.15, 0.12), (0.16, 0.12) and (0.17, 0.14), respectively. The best brightness was 731 and 3200 cd/m^2 at 7 and 10 V, respectively, for the BH-3B:7% BD-1N. This value is more than 1.8 times the luminance of the device without the dopant at 7 V, indicating that increase of the dopant concentration

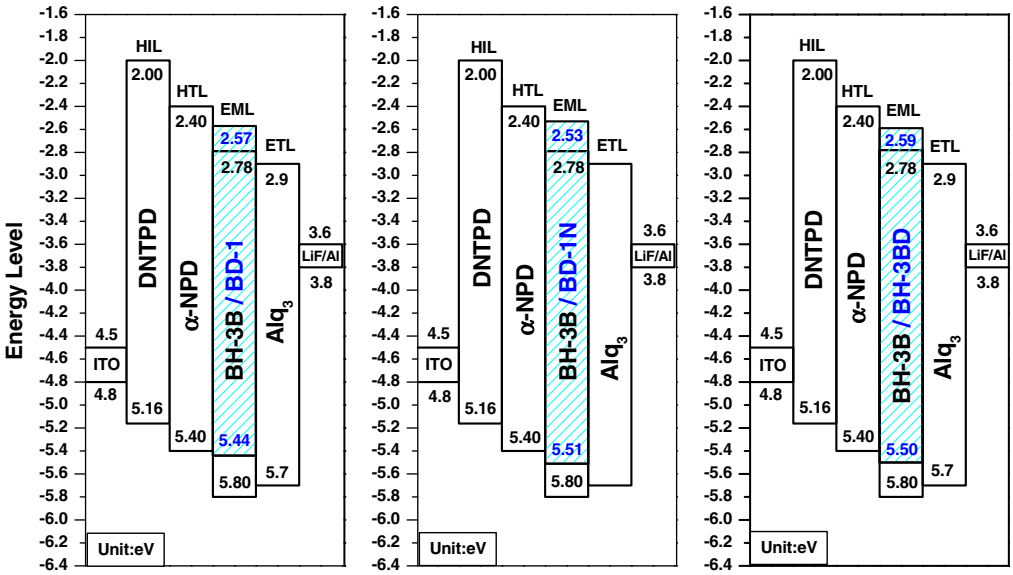

Fig. 2. Energy diagram of BH-3B doped with (a) BD-1, (b) BD-1N, and (c) BH-3BD.

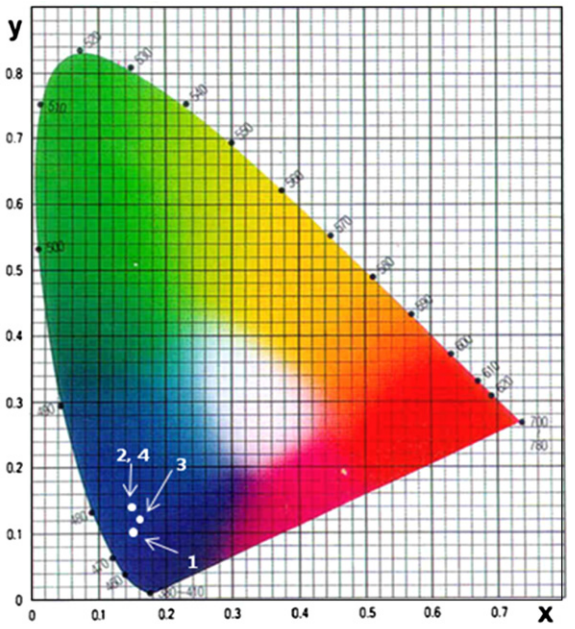

Fig. 4. CIE 1931 coordinates diagram of devices: (1) BH-3B, undoped (0.15, 0.10), (2) BH-3B:5%BD-1 (0.15, 0.14) (3) BH-3B:5%BD-1N (016, 0.12), (4) BH-3B:5%BH-3BD (0.15, 0.14).

enhances the EL properties of the BH-3B emitting layer doped with BD-1N. The current density vs. EL efficiency characteristics of the doped devices showed a similar pattern to that of undoped device. As the content of BD-1N was increased from 0% to 7%, the EL efficiency was increased from 2.11 cd/A to 2.92 cd/A at 20 mA/cm^2.

3.6. Luminance-voltage characteristics

The threshold voltage for luminescence is about 4 V in the device with an emitting layer made of BH-3B:5% BH-3BD having a thickness of 300 Å. Fig. 5 shows the luminance-voltage characteristics of the BH-3B doped with 5% BD-1, BD-1N and BH-3BD. The maximum luminance values of 2140, 4072, 2436 and 5407 cd/m^2 at 10 V were observed, respectively. ITO/DNTPD/NPB/BH-3B:5%BH-3BD/Alq$_3$/Al-LiF device showed EL spectrum at 455.6 nm and luminance was increased to 5407 cd/m^2 from 2140 cd/m^2 (the device without dopant). This result suggests that BH-3BD can be a promising dopant material for blue EL device.

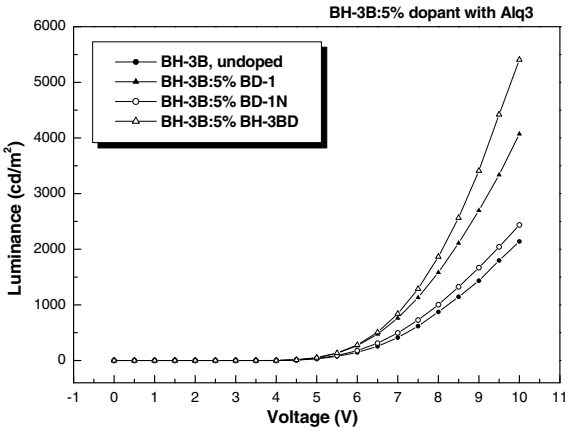

Fig. 5. Brightness–voltage curves of the device using BH-3B host.

3.7. Current density vs. EL efficiency characteristics

Application of a voltage between the electrodes should induce the injection of charges into the organic layer (holes from the anode and electrons from the cathode); their recombination will create excitons; a fraction of them will decay radiatively. The dependence of the current density on the voltage for the devices obtained from BH-3B doped with BD-1, BD-1N and BH-3BD is shown in Fig. 6.

The operating voltage of the device obtained from BH-3B:5%BH-3BD at a luminance of 840 cd/m^2 was 7 V with a current density of 24.46 mA/cm^2, which was comparable

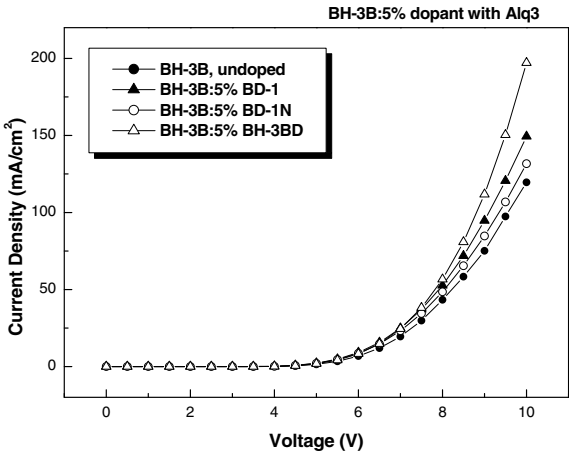

Fig. 6. Current density–voltage curves of the device using BH-3B host.

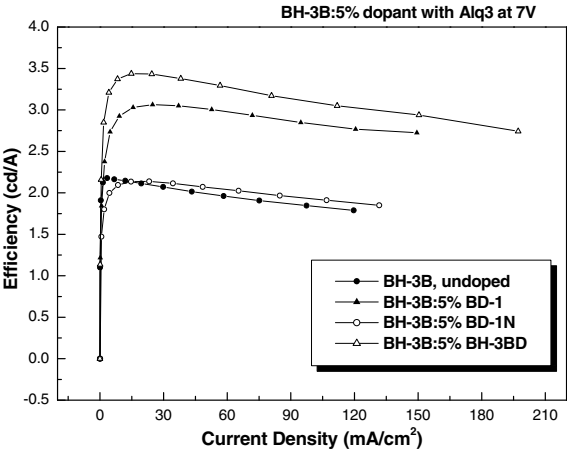

Fig. 7. Efficiency–current density characteristics of the device using BH-3B.

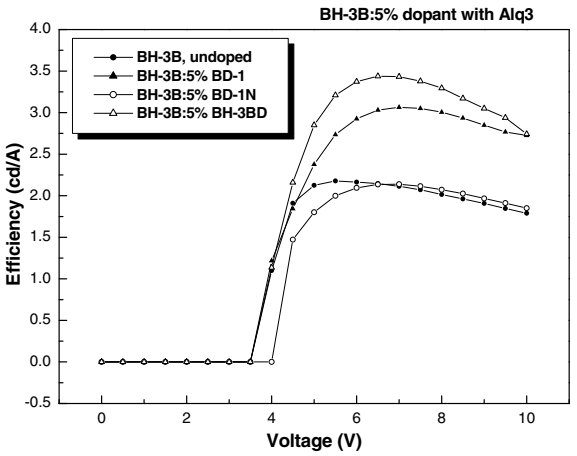

Fig. 8. Efficiency–voltage characteristics of the device using BH-3B host material.

to that of the undoped device 411.2 cd/m^2 at a current density of 19.46 mA/cm^2 as listed Table 2. Fig. 7 shows the dependence of efficiency on the current density of four devices. It can be seen that BH-3B doped with BH-3BD shows the highest efficiency and a little decrease of efficiency as the current density increased from 0 to 200 mA/cm^2, e.g., a weak current induced fluorescent quenching. It reached a current efficiency of 3.43 cd/A (1.54 lm/W).

ITO/DNTPD/NPB/BH-3B:5%BD-1/Alq_3/Al-LiF device showed deep blue EL spectrum at 452 nm and efficiency of 3.06 cd/A, but the device obtained from 5% BH-3BD exhibited relatively higher efficiency 3.43 cd/A as shown in Fig. 8. Based on the result, it was found that spiro-type host and dopant materials are efficient to improve EL efficiency in the structure of BH-3B:5% BH-3BD/Alq_3 device.

4. Conclusion

New blue light-emitting spiro-type host and dopant materials were prepared to construct a blue, organic light-emitting diode. The devices made using BH-3B as the host and BD-1, BD-1N and BH-3BD as the dopant showed blue light emission with a maximum PL emission at around 432, 454, 452 and 469 nm. An OLED made using BH-3BD as a dopant with the structure of ITO/DNTPD/α-NPD/BH-3B:5% BH-3BD/Alq_3/Al-LiF was fabricated and characterized. The device has a maximum luminance of 5407 cd/m^2 at a current density of 197.18 mA/cm^2(2.74 cd/A) at 10 V. The CIE coordinates are $x = 0.15$, $y = 0.14$. Lifetime measurement tests are now in progress. These results will be present elsewhere in the future.

Acknowledgement

This work was supported by Grant No. RTI04-01-02 from the Regional Technology Innovation Program of the Ministry of Knowledge Economy(MKE).

References

[1] Q. Pei, Y. Yang, J. Am. Chem. Soc. 118 (1996) 7416.
[2] Y. Ohmori, M. Uchida, K. Muro, K. Yoshino, Jpn. J. Appl. Phys. 30 (1991) 1941.
[3] J.I. Lee, V.Y. Lee, R.D. Miller, ETRI J. 24 (2002) 409.
[4] S.M. Kelly, Flat Panel Displays: Advanced Organic Materials, Royal Society of Chemistry, Cambridge, UK, 2000. p. 1.
[5] A.H. Tullo, Chem. Eng. News 78 (2000) 20.
[6] Tobat P.I. Saragi, Till Spehr, Achim Siebert, Thomas Fuhrmann-Lieker, Josef Salbeck, Chem. Rev. 107 (2007) 1011.
[7] H. Xiao, H. Shen, Y. Lin, J. Su, Dyes Pigments 73 (2007) 224–229.
[8] C.-T. Chen, Y. Wei, J.-S. Lin, M.V.R.K. Moturu, W.-S. Chao, Y.-T. Tao, C.-H. Chien, J. Am. Chem. Soc. 128 (2006) 10992.
[9] J. Pei, J. Ni, X.-H. Zhou, X.-Y. Cao, Y.-H. Lai, J. Org. Chem. 67 (2002) 4924.
[10] J.-H. Fournier, T. Maris, J.D. Wuest, J. Org. Chem. 69 (2004) 1762.
[11] K.-T. Wong, Z.-J. Wang, Y.-Y. Chien, C.-L. Wang, Org. Lett. 3 (2001) 2285.
[12] D. Horhant, J.-J. Liang, M. Virboul, C. Poriel, G. Alcaraz, J. Rault-Berthelot, Org. Lett. 8 (2006) 257.
[13] H. Lee, J. Oh, H.Y. Chu, J.-I. Lee, S.H. Kim, Y.S. Yang, G.H. Kim, L.-M. Do, T. Zyung, J. Lee, Y. Park, Tetrahedron 59 (2003) 2773.
[14] C.T. Chen, C.H. Chien, J. Am. Chem. Soc. 128 (2006) 10992.
[15] K.T. Wang, C.L. Wang, Org. Lett. 3 (2001) 2285.
[16] F. Milota, C. Warmuth, A. Tortschanoff, J. Sperling, T. Fuhrmann, J. Salbeck, H.F. Kauffmann, Synth. Met. 121 (2001) 1497.
[17] V. Prelog, D. Bedekovic, Helv. Chim. Acta 62 (1979) 2285.
[18] N. Harada, H. Ono, T. Nishiwaki, H. Uda, J. Chem. Soc. Chem. Commun. (1991) 1753.
[19] V. Alcazar, F. Diederich, Angew. Chem. 104 (1992) 1503.
[20] T. Spehr, A. Siebert, T. Fuhrmann-Lieker, S. Salbeck, T. Rabe, T. Riedl, H.H. Johannes, W. Kowalsky, J. Wang, T. Weimann, P. Hinze, Appl. Phys. Lett. 87 (2005) 161103.
[21] K.T. Wong, Y.L. Liao, Y.T. Lin, H.C. Su, C.C. Wu, Org. Lett. 7 (2005) 5131.
[22] T.C. Chao, Y.T. Lin, C.Y. Yang, T.S. Hung, H.C. Chou, C.C. Wu, K.T. Wong, Adv. Mater. (Weinheim, Ger.) 17 (2005) 992.
[23] W.J. Shen, R. Dodda, C.C. Wu, F.I. Wu, T.H. Liu, H.H. Chen, C.H. Chen, C.F. Shu, Chem. Mater. 16 (2004) 930.
[24] D. Gebeyehu, K. Walzer, G. He, M. Pfeiffer, K. Leo, J. Brandt, A. Gerhard, P. Stoessel, H. Vestweber, Synth. Met. 148 (2005) 205.
[25] Y.H. Kim, D.C. Shin, S.H. Kim, C.H. Ko, H.S. Yu, Y.S. Chae, S.K. Kwon, Adv. Mater. 13 (2001) 1690.
[26] R. Pudzich, J. Salbeck, Synth. Met. 138 (2003) 21.
[27] S. Tao, Z. Peng, X. Zhang, P. Wang, C.S. Lee, S.T. Lee, Adv. Funct. Mater. 15 (2005) 1716.
[28] D. Horhant, J.J. Liang, M. Virboul, C. Poriel, G. Alcaraz, J. Rault-Berthelot, Org. Lett. 8 (2006) 257.
[29] S.-O. Jeon, Y.-M. Jeon, J.-W. Kim, C.-W. Lee, M.-S. Gong, Org. Electron. 9 (2008) 522.
[30] S.-O. Jeon, Y.-M. Jeon, J.-W. Kim, C.-W. Lee, M.-S. Gong, Synth. Met., submitted for publication.
[31] S. Hamai, F. Hirayama, J. Phys. Chem. 87 (1983) 83.

injection barrier. Also halide materials with strong electron affinity such as antimony pentachloride ($SbCl_5$) [16], ferric chloride ($FeCl_3$) [17] or Iodine (I_2) [18] showed enhancement in hole injection.

In this paper, we report a new p-type dopant of copper iodide (CuI) to enhance the hole injection from a Ag metal anode. High efficiency TEOLEDs were realized using the doped HIL. Relatively low melting temperature (606 °C) of CuI than other metal oxides (800 °C for MoO_3 and 1470 °C for WO_3) facilitates coevaporation with organic materials.

2. Experimental

Thermally grown SiO_2 (3000 Å) on Si wafer was used as the substrate and cleaned with acetone and isopropyl alcohol. The TEOLEDs were fabricated by thermal evaporation under 10^{-7} torr without breaking vacuum. A patterned silver (50 nm) electrode was prepared as the bottom contact anode by thermal evaporation through a shadow mask. The organic multilayer structure was formed by sequentially depositing organic layers on the anode, which consists of 10 nm thick CuI doped NPB as the hole injection layer (HIL), 20 nm thick undoped NPB as the hole transport layer (HTL), 25 nm thick *N*,*N*′-dicarbazolyl-4,4′-biphenyl (CBP) doped with 6 wt% tris-(2-phenylpyridyl)iridium(III) ($Ir(ppy)_3$) as the emitting layer (EML), 7 nm thick 2,9-dimethyl-4,7-diphenyl-1,10-phenanthroline (BCP) as the hole blocking layer (HBL), and 44 nm thick tris-(8-hydroxyquinoline)aluminum (Alq_3) as the electron transport layer (ETL), respectively. Ytterbium (1 nm) and silver (20 nm) were used as the cathode to achieve efficient electron injection and semi optical transmittance. Finally 45-nm-thick Alq_3 was deposited as the capping layer to enhance the out-coupling efficiency of the device. The fabricated devices were encapsulated prior to the measurement.

The current density–voltage–luminance (*J*–*V*–*L*) characteristics of the devices were measured by a Keithley 2400 semiconductor parameter analyzer and a Photo Research PR-650 spectrophotometer. The absorption spectra were measured by UV–Vis–NIR spectrophotometer Cary 5000. Angular distribution of intensity and spectra were measured by an optical fiber and a S2000 miniature fiber optic spectrometer (Ocean Optics).

3. Results and discussion

Fig. 1 shows the UV–Vis–NIR absorption spectra of the CuI, undoped NPB and 20 wt% CuI doped NPB films. The absorption spectrum of the undoped NPB film shows only absorption peak by π–π^* transition near 400 nm wavelength. In contrast, the absorption spectrum of the CuI doped NPB film shows additional absorption peaks at around 506 nm and 1430 nm, which indicates the formation of charge transfer (CT) complexes [11,13,15]. Enhanced hole injection from the Ag anode to HTL through CuI doped NPB HIL was confirmed using hole only devices with the device structure of Ag/NPB:X% CuI (80 nm)/NPB (20 nm)/Ag (50 nm). Fig. 2 shows *J*–*V* characteristics of the hole only devices consisting of 0, 20 and 25 wt% CuI

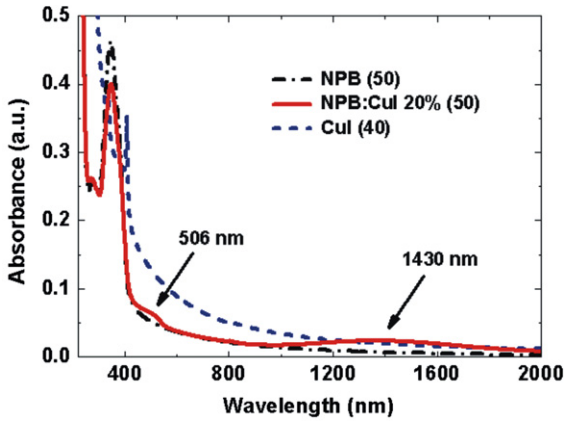

Fig. 1. UV–Vis–NIR absorption spectra of CuI (dashed line), undoped NPB (dot-dashed line) and CuI 20 wt% doped NPB films (solid line), respectively.

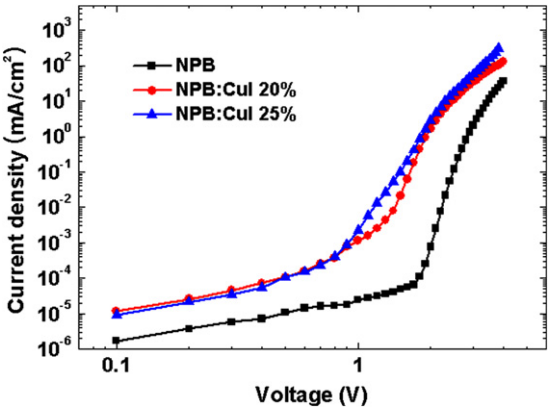

Fig. 2. Current density–voltage characteristics of the hole only devices [Ag (50 nm)/NPB:CuI X% (80 nm)/NPB (20 nm)/Ag (50 nm)] with the doping concentration of 0 wt% (rectangle), 20 wt% (circle) and 25 wt% (triangle), respectively.

doped HILs, respectively. The devices with a CuI doped HIL exhibit significantly enhanced the hole injection compared to the device without the CuI doped layer. The turn-on voltage for hole injection was reduced by about 1 V and current density is dramatically enhanced at low voltage region.

To understand the formation of CT complexes of CuI with hole transporting materials, we doped CuI in the three different hole transport materials of NPB, 4,4′,4″-tris-(*N*-(2-naphthyl)-*N*-phenyl-amino)triphenylamine (2-TNATA) and 1,1-bis-(4-methylphenyl)-aminophenyl-cyclohexane (TAPC). Fig. 3 shows the difference absorption spectra between CuI doped (20 wt%) HIL and undoped HIL. Apparently 2-TNATA and NPB films doped with CuI form charge transfer complexes effectively. However, TAPC shows little change in absorption by the doping. This behavior can be easily understood based on the energy levels of the materials. NPB and 2-TNATA have high HOMO level of 5.4 eV and 5.0 eV, respectively. On the other hand TAPC has much lower HOMO level of 5.8 eV [19]. These re-

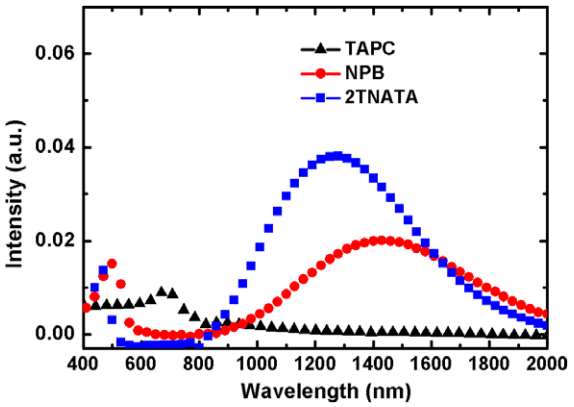

Fig. 3. The difference of absorbance between 20 wt% CuI doped HIL (50 nm) and undoped HIL (50 nm) for NPB (rectangle), 2TNATA (circle) and TAPC (triangle) as the hole transporting materials, respectively.

sults indicate that the Fermi level of p-type CuI is located between the HOMO levels of NPB and TAPC, which is consistent with the recent report of the Fermi level of CuI [20].

Fig. 4a shows current density–voltage–luminance characteristics of the TEOLEDs consisting of Ag/NPB:X% CuI (10 nm)/NPB (20 nm)/CBP:6 wt% $Ir(ppy)_3$ (25 nm)/BCP (7 nm)/Alq_3 (44 nm)/Yb (1 nm)/Ag (20 nm). The undoped 20 nm thick NPB layer was inserted between HIL and EML to prevent the quenching of exciton at the interface between the doped NPB and EML. The device without CuI doped HIL requires high voltage to inject current through the device and no light was detected up to 10 V, indicating that the hole injection is very small if the doped injection layer is absent. However much improved luminance in the devices with CuI doped HIL indicates that hole injection becomes efficient by the doping. Turn-on (at 1 cd/m^2) and operating voltage (at 1000 cd/m^2) were 2.9 V and 5.6 V, respectively. The current efficiency as a function of luminance is shown in Fig. 4b. All the devices with CuI doped NPB layer showed high current efficiencies. The maximum current efficiency of 69 cd/A was achieved from the device with the 20 wt% CuI doped HIL at 0.14 mA/cm^2. The efficiency corresponds to the external quantum efficiency of 17.5% as the angular dependence of emission intensity from the device is Lambertian. The current efficiency was enhanced by about 10% if the glass cap is removed. Roll-off of the efficiency was not significant in the device with the efficiency of 64.6 cd/A at 1000 cd/m^2, and 57.5 cd/A even at 5000 cd/m^2. The highest luminance efficiency was obtained by setting the normal direction resonant wavelength at about 20 nm longer than the peak wavelength of the intrinsic emission as described by Wu et al. [2]. The devices with different doping concentrations in NPB resulted in lower current efficiency, which can be interpreted based on optical effect related to the shift of recombination zone and less charge balance in the devices coming from the variation of hole injection current. The EL emission spectra and *J–V* characteristics do not change much with doping concentration. However, increasing doping concentration can lead to the shift of the recombination zone toward the hole blocking layer because the hole transport becomes faster with increasing doping concentration as shown in Fig. 2. Our optical calculation showed that the external quantum efficiency increases significantly as the recombination zone shifts toward the HBL without changing the emission spectrum. Therefore, the external quantum efficiency is improved with increasing doping concentration. If the hole transport is too fast, however, the recombination zone can penetrate into the HBL to reduce the efficiency again, which is the case for 25% doping. These are the reasons why the 20% doping gives the highest efficiency.

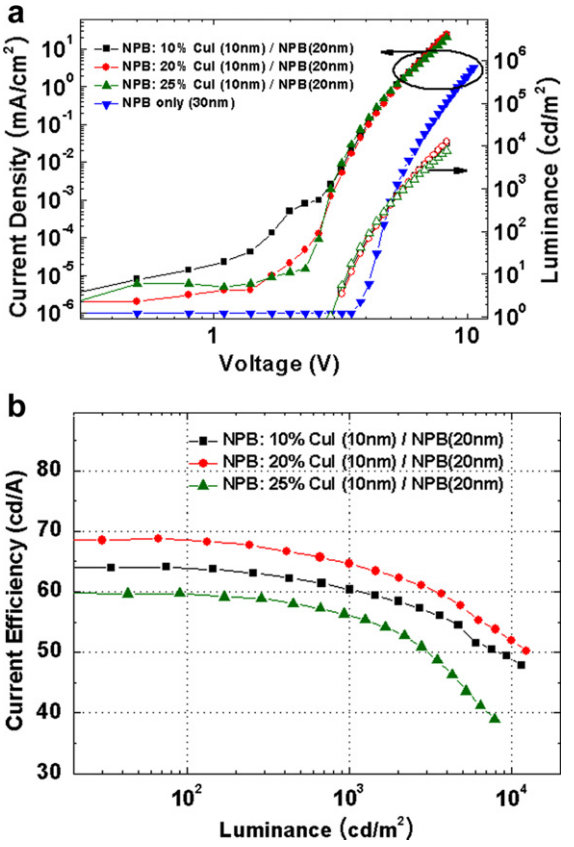

Fig. 4. (a) Current density–voltage–luminance characteristics and (b) current efficiency–luminance of the TEOLEDs adopting CuI doped NPB HILs with the doping concentration of 0 wt% (inverse triangle), 10 wt% (rectangle), 20 wt% (circle) and 25 wt% (triangle).

Angular dependence of emission spectrum and intensity of TEOLEDs is important because they are sensitive to the dimension of the devices and related to the viewing angle problem. Fig. 5 shows the electroluminescence spectra measured at the current density of 20 mA/cm^2 at different viewing angles of 0°, 20°, 40° and 60° off from the normal direction for the device with CuI 20 wt% doped HIL. The peak wavelength shifts from 537 nm at 0° to 516 nm at 60°. This spectrum shift with viewing angle might be originated from the microcavity effect of TEOLEDs [21]. It is interesting to note that the angular distribution of the EL intensity of the CuI doped TEOLEDs is similar with the Lambertian distribution as shown in the inset of Fig. 5, while usual TEOLEDs have a distribution with enhanced intensity in the forward direction. The spectrum shift and angular distribution of the emission could be im-

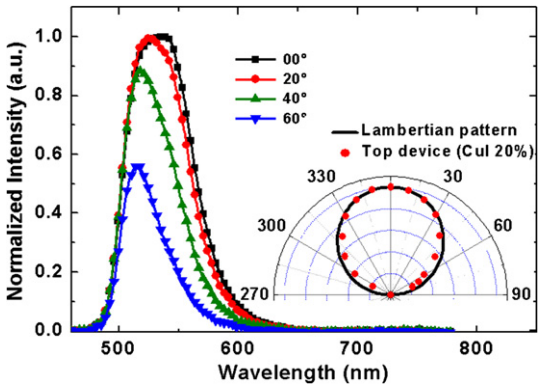

Fig. 5. Spectra of TEOLEDs at different viewing angles. Inset: angular distribution of EL intensity for the TEOLEDs.

proved by an optimization of the reflectance of the cathode and the thickness of each organic layer.

4. Conclusion

In summary, we have developed a new p-type dopant of CuI and demonstrated high efficiency top-emitting OLEDs using CuI doped NPB as the HIL. Hole injection from the Ag metal anode to NPB was dramatically enhanced by the formation of charge transfer complex between NPB and CuI. The device with 20 wt% CuI doped HIL showed high current efficiency of 69 cd/A, EQE of 17.5% at 0.14 mA/cm^2 and operating voltage of 5.6 V at 1000 cd/m^2. The angular distribution of EL intensity is close to the Lambertian.

Acknowledgement

This research was supported by a Grant (F0004071-2007-23) from the Information Display R&D Center, one of the 21st Century Frontier R&D Program and the center for OLED funded by the Ministry of Knowledge Economy (MOKE).

References

[1] V. Bulović, G. Gu, P.E. Burrows, S.R. Forrest, M.E. Thompson, Nature 380 (29) (1996).
[2] C.-J. Yang, S.-H. Liu, H.-H. Hsieh, C.-C. Liu, T.-Y. Cho, C.-C. Wu, Appl. Phys. Lett. 91 (253508) (2007).
[3] Q. Huang, K. Walzer, M. Pfeiffer, K. Leo, M. Hofmann, T. Stubinger, J. Appl. Phys. 100 (064507) (2006).
[4] M. Zhang, H. You, W. Wang, J. Shi, S. Guo, M. Liu, D. Ma, Semicond. Sci. Technol. 21 (1094) (2006).
[5] X. Zhu, J. Sun, X. Yu, M. Wong, H.-S. Kwok, Jpn. J. Appl. Phys. 46 (1033) (2007).
[6] H. Kanno, Y. Sun, S.R. Forrest, Appl. Phys. Lett. 86 (263502) (2005).
[7] S.Y. Kim, J.-L. Lee, K.-B. Kim, Y.-H. Tak, Appl. Phys. Lett. 86 (133504) (2005).
[8] C.-W. Chen, P.-Y. Hsieh, H.-H. Chiang, C.-L. Lin, H.-M. Wu, C.-C. Wu, Appl. Phys. Lett. 83 (5127) (2003).
[9] H. Peng, J. Sun, X. Zhu, X. Yu, M. Wong, H.-S. Kwok, Appl. Phys. Lett. 88 (073517) (2006).
[10] L.-W. Chong, Y.-L. Lee, T.-C. Wen, T.-F. Guo, Appl. Phys. Lett. 89 (233513) (2006).
[11] J. Guo, N. Koch, S.L. Bernasek, J. Schwartz, Chem. Phys. Lett. 426 (370) (2006).
[12] X.L. Zhu, J.X. Sun, H.J. Peng, Z.G. Meng, M. Wong, H.S. Kwok, Appl. Phys. Lett. 87 (153508) (2005).
[13] C.-C. Chang, M.-T. Hsieh, J.-F. Chen, S.-W. Hwang, C.H. Chen, Appl. Phys. Lett. 89 (253504) (2006).
[14] J. Cao, X.Y. Jiang, Z.L. Zhang, Appl. Phys. Lett. 89 (252108) (2006).
[15] D.-S. Leem, H.-D. Park, J.-W. Kang, J.-H. Lee, J.-W. Kim, J.-J. Kim, Appl. Phys. Lett. 91 (011113) (2007).
[16] C. Ganzorig, M. Fujihira, Appl. Phys. Lett. 77 (4211) (2000).
[17] J. Endo, T. Matsumoto, J. Kido, Jpn. J. Appl. Phys. Part 2 41 (L358) (2002).
[18] F. Huang, A.G. MacDiamid, B.R. Hsieh, Appl. Phys. Lett. 71 (2415) (1997).
[19] M. Aonuma, T. Oyamada, H. Sasabe, T. Miki, C. Adachi, Appl. Phys. Lett. 90 (183503) (2007).
[20] A.R. Kumarasinghe, W.R. Flavell, A.G. Thomas, A.K. Mallick, D. Tsoutsou, C. Chatwin, S. Rayner, P. Kirkham, S. Warren, S. Patel, P. Christian, P. O'Brien, M. Grätzel, R. Hengerer, J. Chem. Phys. 127 (114703) (2007).
[21] N. Tessler, S. Burns, H. Becker, R.H. Friend, Appl. Phys. Lett. 70 (556) (1997).

affinities [4], and hybrid blends of polymers with inorganic materials [5].

Devices formed from blending materials give good efficiencies, but controlling the morphology in a reproducible way during processing and long-term device operation presents challenges [6]. Indeed the best bulk heterojunction devices are comprised of poly(3-*n*-hexylthiophene): fullerene blends in which complicated solvent and annealing processes are used to achieve the optimized performance. One strategy that has been studied to improve the stability of the active film is to covalently tether the donor and acceptor [7–9], although there is no strong evidence that this leads to improved device performance. The materials studied here differ from these tethered donor and acceptors, which are mostly connected by non-conjugated linkers and hence considered as individual chromophores, in that the donor and the acceptor are in conjugation. Although there have been polymers that have electron donating and electron withdrawing units within the polymer main chain these latter polymers have been synthesized to have a low optical transition energy [10–15]. In contrast, the polymers for this work have been designed to enhance intramolecular exciton dissociation. The preparation of poly(1,4-phenylenevinylene)s (PPVs) that have electron donating and withdrawing groups in a *para* arrangement on the phenyl ring of the polymer backbone and their use in simple photovoltaic devices have been previously reported [16]. With these new polymers it was found that the presence of the electron donating and withdrawing groups in conjugation led to a quenching of the luminescence and here we use LEPR to unambiguously identify the products of photoinduced charge separation. The electron accepting unit was a nitro group attached to the 7-position of the fluorenyl side group. In addition, control polymers without the nitro group were also studied. In the materials containing a nitro group, light induced EPR showed that photoexcitation resulted in positive polarons on the polymer backbone and the generation of localized radical anions centered on the nitro group. In contrast, only a weak positive polaron center was observed for the polymers without the nitro groups. This indicates that having electron donating and withdrawing groups in conjugation can give an intramolecularly charge separated state.

Electron magnetic resonance methods can identify paramagnetic electronic states, and may provide detailed information on the local structure. For the $S = 1/2$ centers relevant to this work, spectra can be analyzed using the spin-Hamiltonian [17],

$$\hat{\mathbf{H}} = \mu_B \mathbf{B} \cdot \mathbf{g} \cdot \hat{\mathbf{S}} + \sum_i (\hat{\mathbf{S}} \cdot \mathbf{A} \cdot \hat{\mathbf{I}}_i + g_{n,i} \mu_N \mathbf{B} \cdot \hat{\mathbf{I}}_i) \quad (1)$$

which includes the electronic Zeeman term, hyperfine interactions, and nuclear Zeeman interactions, respectively, and where μ_B is the Bohr magneton and μ_N the nuclear magneton, and the sum includes relevant magnetic neighbor nuclei. The sample is exposed to highly monochromatic microwave photons, typically in the 9–10 GHz range, and an external magnetic field is swept. Performing the experiment at higher microwave frequencies increases the field values required to observe resonance and results in an improved ability to resolve different *g*-values. Splittings in the spectrum arising from the hyperfine interaction between the electron spin and magnetic nuclei are normally independent of the microwave frequency used.

Previous EPR and electron nuclear double resonance studies on PPV have established the existence of a center associated with delocalized π orbitals on the polymer chain [18,19]. Similar light induced spectra assigned to polarons have been observed for modified PPV materials, for example MEH-PPV [20], CN-PPV [20], and MDMO-PPV [3]. Measurements at 9.5 and 25 GHz on partially oriented PPV [19], and at 95 GHz on MDMO-PPV [3], have reported the polaron center to be axial with $g_{\parallel} = 2.0034$ and $g_{\perp} = 2.0024$, giving $g_{iso} = 2.0027$ ($g_{iso} = 1/3(g_x + g_y + g_z)$). The *g*-values provide characteristic information about the particular paramagnetic center. The deviation from the free-electron value of $g_e = 2.0023$ depends on the detail of the electronic state containing the unpaired spin density, including the admixture of excited states, and the degree of spin-orbit coupling. The nature and number of magnetic nuclei (for example $I = 1/2$ proton or $I = 1$ nitrogen) in the local environment of the unpaired electronic spin, along with the degree of coupling between the electronic spin and the magnetic nuclei, can result in hyperfine splitting of the EPR line. If this is unresolved it contributes to line broadening. The EPR linewidths for the polaron have been shown to be consistent with those expected from unresolved proton hyperfine splitting given the degree of localization on vinyl and phenyl sites [20]. A radical anion EPR center has been unambiguously identified only for the conjugated polymer: fullerene blends. In this case localization within the distorted fullerene gives characteristic rhombic symmetry *g*-values with an isotropic value slightly less than the free electron value [3].

2. Experimental

In this study four PPV derivatives were investigated (Fig. 1). All the derivatives contained fluorenyl and alkoxy groups in a *para* arrangement across the phenyl ring of the polymer backbone, and two of the polymers had the fluorenyl units modified by the attachment of a nitro group in the 7-position. The materials were poly{2-[(9,9-di-*n*-propyl-9H-7-nitrofluoren-2-yl)]-5-(2-ethylhexyloxy)-1,4-phenylenevinylene} (NDPFEH-PPV) and NDPF2EH-PPV, where an additional fluorenyl unit is added to make a longer side chain. The control materials without the nitro group were poly{2-[(9,9-di-*n*-propyl-9H-fluoren-2yl)-5-(2-ethylhexyloxy)-1,4-phenylenevinylene]} (DPFEH-PPV) and DPF2EH-PPV for the polymer with the extra fluorenyl moiety in the sidechain.

Optical absorption measurements were performed on thin film samples using a Cary Varian UV–vis absorption spectrometer. Photoluminescence quantum yield (PLQY) measurements followed the method of Greenham and coworkers. [4], and used a 407 nm GaN laser as the illumination source.

Continuous wave (CW) 9.5 GHz EPR experiments used a Bruker EMX with a super-high-Q resonator (ER4122SHQ) with ER072 electromagnet. Field swept, echo-detected, pulsed EPR measurements were performed with a Bruker

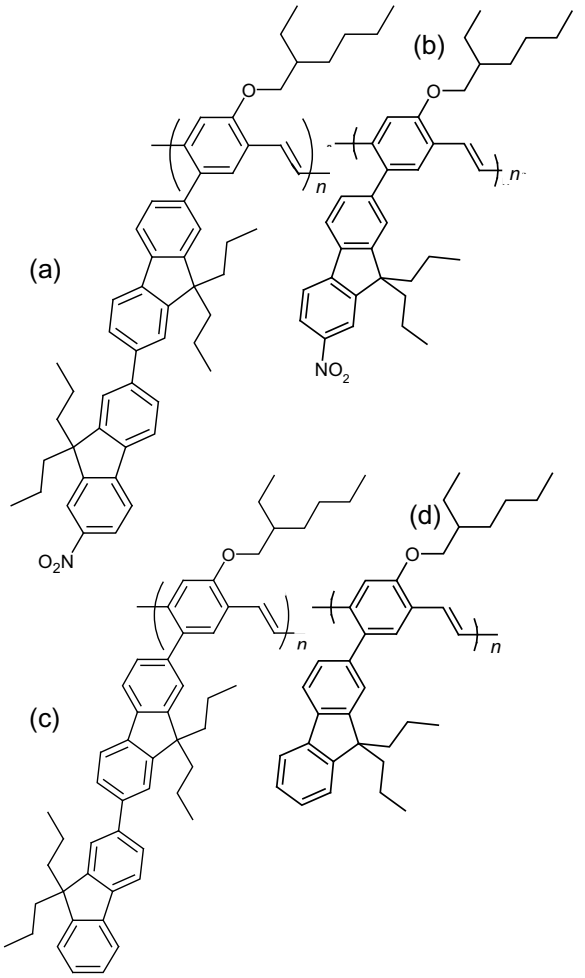

Fig. 1. Chemical structures for the materials studied, (a) NDPF2EH-PPV, (b) NDPFEH-PPV, (c) DPF2EH-PPV, and (d) DPFEH-PPV.

ELEXSYS E580 spectrometer at 9.8 and 33.7 GHz using dielectric ring resonators (ER4118X-MD5-EN and EN5107, respectively). Field swept measurements were made at 20 K. All light induced spectra used a 407 nm, 4 mW, GaN laser. Reference measurements were made on the two spectrometers using 1.6 mm diameter Coal and DPPH standard samples. The Hall field of the ER072 magnet was calibrated using an NMR magnetometer placed at the resonator position using two crossed laser beams. Both thin cast films and solution samples were studied, but were found to give identical dark and light-induced EPR spectra, the results presented here are from ~5 mg/mL frozen solutions. The solvent used was cholorobenzene. Simulation of the spectra using Eq. (1) were made with the package EasySpin [17].

3. Results and discussion

The UV–visible absorption spectra for the four PPV derivatives are shown in Fig. 2. The spectra show broad absorption over the wavelength range 200–525 nm. In

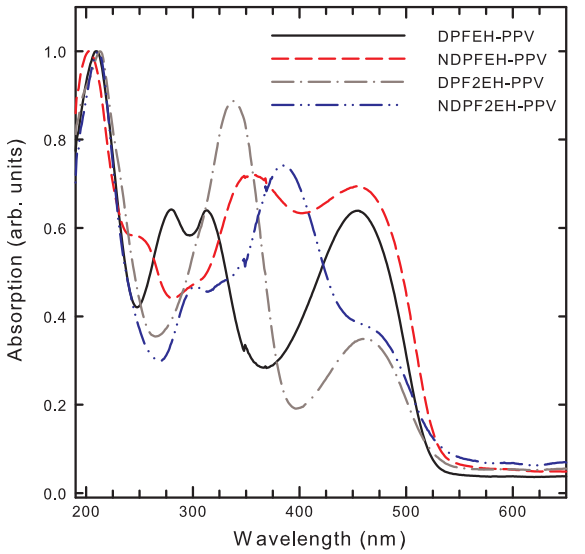

Fig. 2. Absorption spectra for DPFEH-PPV (solid), NDPFEH-PPV (dash), DPF2EH-PPV (dash-dot), and NDPF2EH-PPV (dash-dot-dot).

general for PPV based polymers there are two main absorption bands. The short wavelength region at around 210 nm corresponds to localized π–π^* transitions, and the longer wavelength absorptions are due to delocalized π–π^* transitions. In DPFEH-PPV, the absorption maximum at 209 nm is due to the localized π–π^* transitions, those at 280 nm and 313 nm correspond to the chromophore containing the phenyl ring of the polymer backbone and the fluorenyl unit, and the broad absorption around 455 nm is due to the delocalized π–π^* transitions of the polymer backbone. The optical absorption spectra of NDPFEH-PPV also shows components due to the localized π–π^* transitions (202 nm), the chromophore comprising the phenyl ring and fluorenyl unit (359 nm), and the delocalized π–π^* transitions (454 nm). The chromophore peak is red shifted compared to DPFEH-PPV due to the presence of the nitro group. DPF2EH-PPV also shows absorption features due to localized (213 nm) and delocalized (460 nm) π–π^* transitions, and has a peak at 337 nm assigned to the chromophore comprising the phenyl unit and fluorenyl moieties. This peak is red shifted compared to that of DPFEH-PPV due to the extra fluorene unit. NDPF2EH-PPV follows the same trend, with the chromophore peak red shifted relative to DPF2EH-PPV due to the presence of the nitro group.

The photoluminescence quantum yield (PLQY) results from thin films given in Table 1 shows the luminescence for nitro group containing polymers was suppressed by

Table 1
Solution photoluminescence quantum yield (PLQY) results for the four polymers, NDPFEH-PPV, NDPF2EH-PPV, DPFEH-PPV, and DPF2EH-PPV, studied

	NDPFEH	NDPF2EH	DPFEH	DPF2EH
PLQY (%)	3 ± 1	6 ± 1	19 ± 2	30 ± 2

approximately a factor of five compared to those without the electron accepting unit. The reduction in PLQY in solution could be either due to rapid loss of energy via non-radiative pathways such as energy dissipation by vibrational modes or photoinduced charge separation for NDPFEH-PPV and NDPF2EH-PPV. The PLQY values for the materials containing the longer side chain were a factor of two greater than the shorter side chain polymers, suggesting a decreased charge separation for the materials with longer side chains. It is interesting to note that the PLQY for both nitro substituted polymers is only ~20% of their unsubstituted counterparts.

Fig. 3 shows the light and dark 9.8 and 33.7 GHz echo-detected field swept pulsed EPR spectra for the nitro group containing NDPFEH-PPV in frozen solution. The light induced spectra for DPFEH-PPV (no nitro groups) at approximately the same concentration are shown in Fig. 4, with that for DPF2EH-PPV (an extra fluorenyl moiety but no nitro groups) included as an insert. Fig. 5 shows the light induced spectra for NDPF2EH-PPV (which contains the extra fluorenyl moiety and nitro group in the sidechains). A narrow Gaussian line attributed to positive polarons was observed in the light induced spectra for all samples, with the signal intensity much greater for the polymers with the nitro groups with respect to their non-nitrated equivalents. The spectra from the nitro group containing polymers, NDPFEH-PPV and NDPF2EH-PPV, also showed an additional broad component, see Figs. 3 and 5.

The LEPR spectra from DPFEH-PPV and DPF2EH-PPV (no nitro groups) at 9.8 and 33.7 GHz were simulated assuming a single $S = 1/2$ center using a Gaussian lineshape. Simultaneous fitting spectra recorded at the two microwave frequencies allowed both the frequency dependent g-value anisotropy, $g_{\|} - g_{\perp}$, and the frequency independent contributions to be determined. The g-value anisotropy for DPFEH-PPV and DPF2EH-PPV was found to be ~0.0005, see Fig. 4 and Table 2, and is slightly less than values obtained for PPV materials in previous studies [3,19]. The isotropic g-value for the polaron center observed for NDPFEH-PPV was determined to be 2.0031 ± 0.0002, simi-

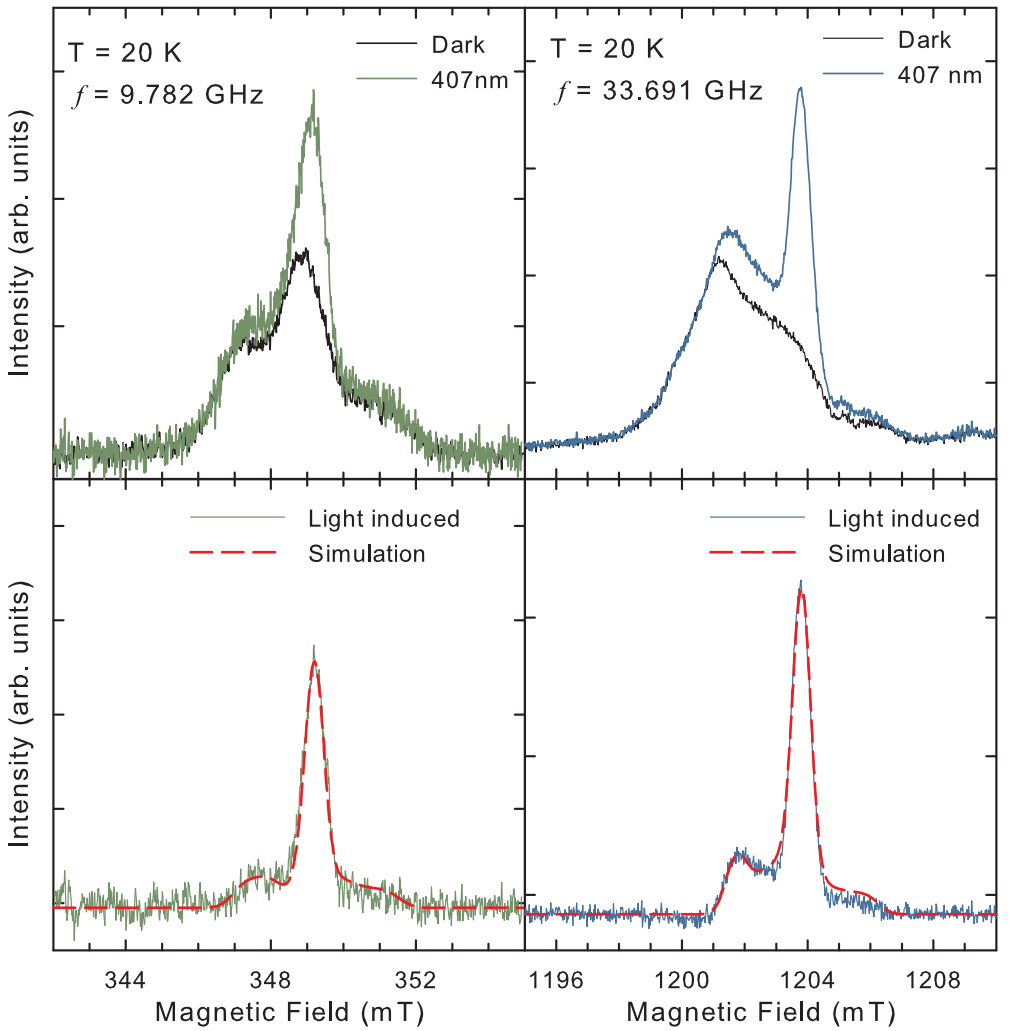

Fig. 3. Field swept pulsed EPR spectra for NDPFEH-PPV at 9.7 and 33.7 GHz. Top panels dark and 407 nm illuminated spectra (grey line), bottom panel difference spectra and simulation (dashed line).

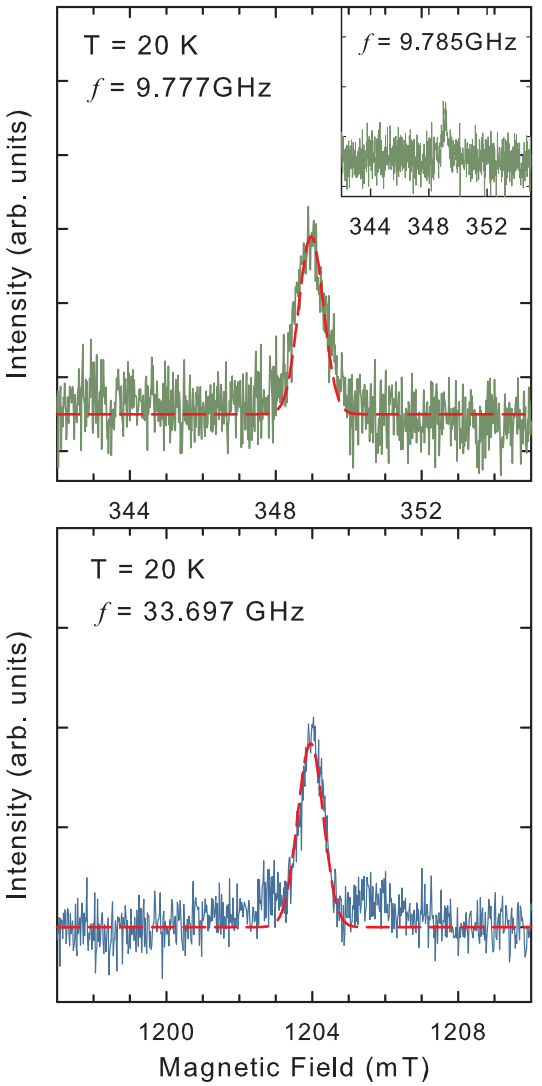

Fig. 4. Light induced EPR spectra for DPFEH-PPV at 9.7 and 33.7 GHz, simulation (dashed line). Insert shows the spectrum for DPF2EH-PPV.

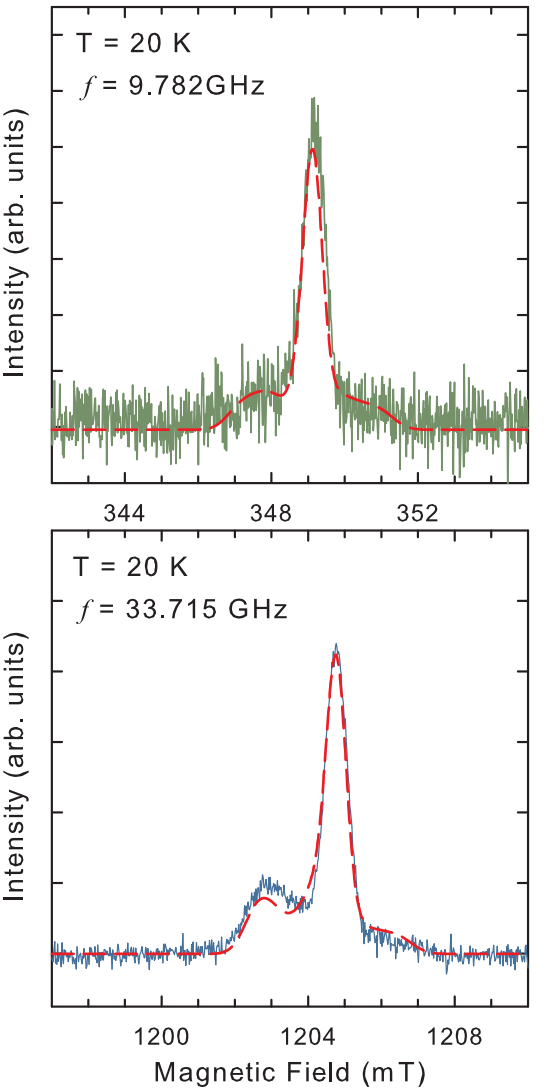

Fig. 5. Light induced EPR spectra for NDPF2EH-PPV at 9.7 and 33.7 GHz, simulation (dashed line).

lar values were observed for the four derivatives studied here (see Table 2). The experimental linewidth, 0.80 ± 0.05 mT at 9.7 GHz, is dominated by unresolved proton hyperfine structure fitted with a frequency independent value of 0.75 mT. This is slightly larger than values reported by Kuroda et al. [20] of 0.45 ± 0.01 and 0.66 ± 0.02 mT for CN-PPV and MEH-PPV, respectively, but similar to those given by De Cuester et al. [3] for MDMO-PPV (0.8 mT for the parallel component, and 0.6 mT for the perpendicular component).

For the non-nitrated derivatives (DPFEH-PPV and DPF2EH-PPV) the polaron spectra were fitted using the same *g*-value anisotropy as for the nitro group containing materials (NDPFEH-PPV and NDPF2EH-PPV), but with a smaller frequency independent width of 0.55 mT, as shown in Table 2. This quite marked reduction in the linewidth indicates a reduction in the contribution of unresolved proton hyperfine coupling. It has been reported that the dominant contributions to this are from the backbone vinylene sites [20]. The presence of the side chain nitro group alters the distribution of the polaron spin density.

Table 2
Simulation parameters for light induced EPR spectra, *g*-values and linewidths

Center	g_x	g_y	g_z	ΔB (mT)
NDPFEH				
Polaron	2.0028	2.0028	2.0033	0.55
Radical anion	2.0051	2.0032	2.0027	0.80
NDPF2EH				
Polaron	2.0028	2.0028	2.0034	0.55
Radical anion	2.0050	2.0035	2.0035	0.80
DPFEH				
Polaron	2.0028	2.0028	2.0033	0.75

The LEPR spectra for NDPFEH-PPV and NDPF2EH-PPV could be satisfactorily simulated using two centers; the polaron, and a radical center mainly localized on nitrogen, see Figs 3 and 5 and Table 2. Initial attempts to simulate the complete spectrum by assuming the broad component was due to proton hyperfine splittings or by assuming a single delocalized center with spin density on a nitrogen atom were unsuccessful [21,22]. The fits at the two frequencies shown assumed the broad component was due to a second nitro group radical center with ^{14}N hyperfine tensor principle values of 25, 15 and 64 MHz, giving an isotropic hyperfine constant of 35 MHz. This value is consistent with previous reports of radical anion centers containing a nitro group, which are typically in the range 28–35 MHz [21,22]. The simulations shown in Figs. 3 and 5 required a 55% contribution from the nitrogen radical anion center. That is, for each positive polaron created on the polymer backbone a radical anion was formed. The fact that these measurements were carried out in solution unambiguously identifies that the quenching of the luminescence is due to intramolecular charge separation. Interestingly the same results were observed for films of the polymers indicating that intermolecular interactions in the solid state has only a minor if any effect on the charge separation processes in either the non-nitrated or nitrated polymers.

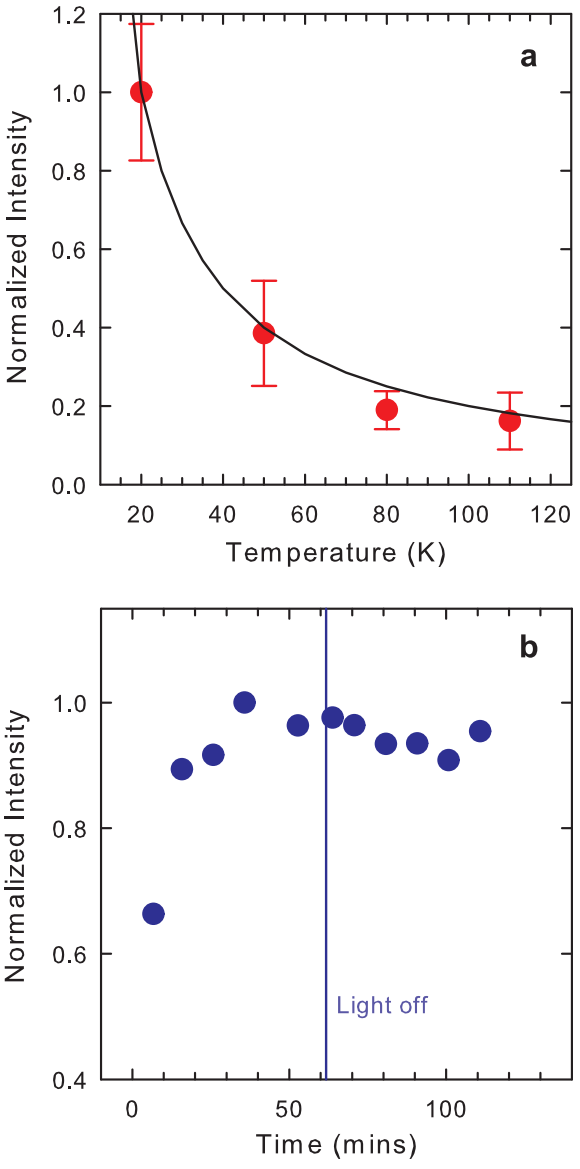

Fig. 6. Normalized double integral area of continuous wave LEPR spectra for NDPFEH-PPV, (a) against temperature, (b) against time from the start of the 407 nm illumination, the time at which the illumination was turned off is marked.

Fig. 3 also shows the presence of a dark spectrum from NDPFEH-PPV, and a comparable signal was observed for NDPF2EH-PPV (not shown). No dark spectrum was resolved for the control polymers DPFEH- and DPF2EH-PPV. The microwave frequency dependence shows that the spectral width is dominated by hyperfine interactions. The large magnitude of these interactions required to simulate the spectrum are not consistent with π–electron proton coupling expected in PPV materials [23]. These observations suggest the dark paramagnetic centers are associated with the nitro groups. A possible explanation could be the existence of different resonance contributions, including one where there is a radical cation on the nitrogen and a radical on an oxygen. It should be noted that the light induced centers are generated only in the illuminated surface layer, while the dark signal is detected from the total bulk volume of the sample and could be due to a low level impurity phase.

The decrease in the double integrated CW LEPR spectrum area with temperature shown in Fig. 6a for NDPFEH-PPV is consistent with the expected Curie behavior. The linewidth remained constant through the temperature range studied. No additional physical processes are required to account for the temperature dependence, for example enhanced recombination. Fig. 6b shows the time evolution of the LEPR signal after the start of illumination, and after it was terminated. The LEPR signal was observed to reach a maximum after approximately 40 min. At 20 K there is evidence for a small, approximately 5%, drop in intensity immediately after the illumination is turned off but the majority of the signal is persistent due to deeply trapped carriers. These observations are similar to those reported for CN-PPV and MEH-PPV [20].

4. Conclusions

In conclusion, functionalizing PPV derivatives with a nitro group results in intramolecular charge separation of the exciton. This is shown by the light-induced electron paramagnetic resonance results which detected both the positive polaron, and a radical anion mainly localized on the nitro group of the modified side chain. Approximately equal amounts of the two centers were observed to result from the photoexcitation. The control PPV derivatives, DPFEH- and DPF2EH-PPV, showed only the polaron center but with a markedly reduced intensity. The reduction in the EPR linewidth for the polaron centers in NDPFEH-PPV

and NDPF2EH-PPV compared to the control polymers provides evidence that the presence of the nitro group alters the polaron spin density distribution. The PPV derivatives NDPFEH- and NDPF2EH-PPV provide examples of an alternative method of charge separation for organic photovoltaic applications.

Acknowledgements

We thank Research Councils UK Basic Technology Programme (GR/S85726/01) and EPSRC for financial support, EAT acknowledges an ORS award.

References

[1] N.S. Sariciftci, L. Smilowitz, A.J. Heeger, F. Wudl, Science 258 (1992) 1474.
[2] S.E. Shaheen, C.J. Brabec, N.S. Sariciftci, F. Padinger, T. Fromherz, J.C. Hummelen, Appl. Phys. Lett. 78 (2001) 841.
[3] J. De Ceuster, E. Goovaerts, A. Bouwen, J.C. Hummelen, V. Dyakonov, Phys. Rev. B 64 (2001) 195206.
[4] J.J.M. Halls, C.A. Walsh, N.C. Greenham, E.A. Marseglia, R.H. Friend, S.C. Moratti, A.B. Holmes, Nature (London) 376 (1995) 498.
[5] W.U. Huynh, J.J. Dittmer, A.P. Alivisatos, Science 295 (2002) 2425.
[6] R.A.J. Janssen, J.C. Hummelen, N.S. Saricifti, MRS Bull. 30 (2005) 33.
[7] A. Cravino, N.S. Sariciftci, J. Mater. Chem. 12 (2002) 1931.
[8] J.L. Segura, N. Martin, D.M. Guldi, Chem. Soc. Rev. 34 (2005) 31.
[9] R. Gomez, D. Veldman, R. Blanco, C. Seoane, J.L. Segura, R.A.J. Janssen, Macromolecules 40 (2007) 2760.
[10] L.M. Andersson, F.L. Zhang, O. Inganas, Appl. Phys. Lett. 89 (2006).
[11] E. Perzon, X.J. Wang, S. Admassie, O. Inganas, M.R. Andersson, Polymer 47 (2006) 4261.
[12] M. Svensson, F.L. Zhang, S.C. Veenstra, W.J.H. Verhees, J.C. Hummelen, J.M. Kroon, O. Inganas, M.R. Andersson, Adv. Mater. 15 (2003) 988.
[13] S. Luzzati, M. Basso, M. Catellani, C.J. Brabec, D. Gebeyehu, N.S. Sariciftci, Thin Solid Films 403 (2002) 52.
[14] A. Dhanabalan, J.K.J. van Duren, P.A. van Hal, J.L.J. van Dongen, R.A.J. Janssen, Adv. Funct. Mater. 11 (2001) 255.
[15] S.E. Shaheen, D. Vangeneugden, R. Kiebooms, D. Vanderzande, T. Fromherz, F. Padinger, C.J. Brabec, N.S. Sariciftci, Synthetic Met. 121 (2001) 1583.
[16] B. Lochab, P.L. Burn, A. Barkhouse, K.R. Kirov, H.E. Assender, D.J. Keeble, E.A. Thomsen, A.J. Lewis, I.D.W. Samuel, Org. Electron. 8 (2007) 801.
[17] S. Stoll, A. Schweiger, J. Magn. Reson. 178 (2006) 42.
[18] S. Kuroda, T. Noguchi, T. Ohnishi, Phys. Rev. Lett. 72 (1994) 286.
[19] K. Murata, Y. Shimoi, S. Abe, S. Kuroda, T. Noguchi, T. Ohnishi, Chem. Phys. 227 (1998) 191.
[20] S. Kuroda, K. Marumoto, H. Ito, N.C. Greenham, R.H. Friend, Y. Shimoi, S. Abe, Chem. Phys. Lett. 325 (2000) 183.
[21] M.C.R. Symons, W.R. Bowman, G.W. Bradley, D.G. Morris, J. Chem. Soc. Perkin Trans. (1992) 545.
[22] M.G. Davlieva, J.M. Lu, S.V. Lindeman, J.K. Kochi, J. Am. Chem. Soc. 126 (2004) 4557.
[23] S. Kuroda, Y. Shimoi, S. Abe, T. Noguchi, T. Ohnishi, J. Phys. Soc. Jpn. 67 (1998) 3936.

extend our studies to other insulators, in particular polymethylmethacrylate (PMMA) and pentacene, and compare the devices to those based on fatty acid LB films. Although pentacene is normally used as a semiconductive layer in devices such as organic transistors [17], under certain processing conditions (flash evaporation) the resulting thin films possess small grain structures and are more electrically resistive [18].

2. Experimental details

The following materials were purchased from Sigma–Aldrich: H_2O_2, H_2SO_4 (purity 95%), $NaBH_4$ (99.99%), $HAuCl_4{\cdot}3H_2O$ (99.9%), (3-aminopropyl)-trimethoxysilane (APTMS), polymethylmethacrylate (PMMA – molecular weight 93,000), arachidic acid (purity 99%), pentacene and sodium citrate. Cadmium chloride was obtained from BDH. All glassware used in the preparation of Au nanoparticles was cleaned using freshly prepared piranha solution (70/30 H_2SO_4/H_2O_2) and rinsed thoroughly in deionised water to remove any organic residues from the surface.

The preparation of the gold nanoparticle solution involved adding 1 ml of 1% aqueous $HAuCl_4 \cdot 3H_2O$ to 100 ml of deionised water under vigorous stirring. After 1 min, 1 ml of 1% aqueous sodium citrate was added, followed by 1 ml of 0.075% $NaBH_4$ in 1% sodium citrate 1 min later. The solution was stirred for a further 5 min and then stored in the refrigerator at about 4 °C [19]. The resulting gold nanoparticles were approximately 5 nm in diameter, including the thickness of the organic capping layer.

Silicon wafers (p-type with resistivity 8–11 Ω cm, and n-type with resistivity 10–30 Ω cm, both (100) orientation and obtained from NSC Electron) were used as the substrates. Substrate cleanliness was essential to achieve reproducible electrical behaviour for the MIS structures. The silicon wafers were cleaned prior to use by ultrasonic treatment in acetone, propanol and water for 10 min each. The wafers were then placed in freshly prepared piranha solution for 30 min to remove organic impurities and rinsed thoroughly with deionised water. Wet etching using 10:1 HF was used to remove any native oxide from the silicon. Finally, the wafers were rinsed thoroughly with deionised water and dried with N_2 gas.

A thin oxide layer of 4.5 nm was thermally grown in dry oxygen at 850 °C for 10 min. An Ohmic back contact was established by the thermal evaporation of 200 nm Al followed by annealing at 350 °C for 20 min in a nitrogen ambient. To deposit Au nanoparticles, the oxidized wafers were placed in a dilute solution of APTMS (0.1 ml of APTMS in 1 ml methanol) for at least 16 h before rinsing with methanol. The wafers were subsequently immersed in the Au solution for 20 min and were again rinsed with water. Fig. 1 shows a schematic diagram of the self-assembly process. The thickness of the self-assembled APTMS layer was about 1 nm [11].

Thin organic insulating layers of 40 nm thicknesses were formed using spin-coating in the case of PMMA (8 mg ml^{-1} in chloroform, 6000 rpm spinning speed), Langmuir–Blodgett (LB) deposition for cadmium arachidate (CdAA) and flash evaporation for pentacene (evaporation rate 1.5 nm s^{-1}). The LB film deposition used a Molecular Photonics LB715 trough situated in a class 10,000 microelectronics clean room. The subphase was purified water obtained from a reverse osmosis/deionization/UV sterilization system. The film deposition was undertaken at a subphase pH of 5.8 ± 0.2 and a temperature of 20 ± 2 °C. A cadmium arachidate monolayer was obtained by spreading arachidic acid on a water subphase containing 5.0×10^{-4} M cadmium chloride (in practice, this floating layer was a mixture of the fatty acid and its salt). The deposition surface pressure was 22 mN m^{-1}.

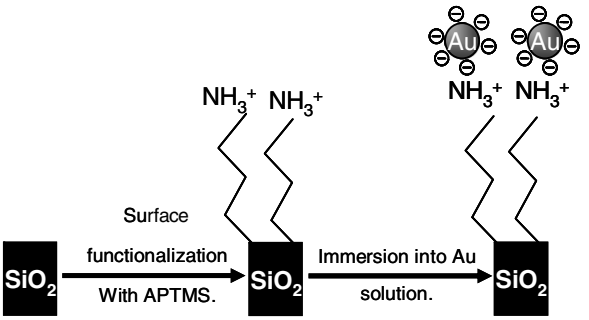

Fig. 1. Schematic representation for the chemical self-assembly deposition process of Au nanoparticles.

Following the deposition of the organic insulator, Al top contacts were thermally evaporated (1 mm diameter, thickness 100 nm). Control devices of Al/SiO_2/Si and Al/insulator/SiO_2/Si were also fabricated. Double sweep capacitance–voltage (C–V) characteristics of the MIS structures were recorded at room temperature using an LCR bridge (HP4192).

3. Results and discussion

3.1. Spin-coated PMMA dielectric

Fig. 2a shows the normalized C–V characteristics of MIS structures based on a p-type Si substrate and using 40 nm PMMA thin films as the insulator. All the measurements were performed at 400 kHz and at a voltage scan rate of 50 mV s^{-1}. In each measurement, the scan was started from the inversion region and swept towards accumulation (although starting from the accumulation region did not significantly alter the device behaviour). The C–V curve for the reference Al/SiO_2/p-Si sample reveals the usual accumulation–depletion–inversion characteristics of an MIS structure; with a flat band voltage of approximately −1.2 V. Negligible hysteresis is evident at the voltage sweep rate used. The measured value of the accumulation capacitance for the reference device was 3 nF. This was consistent (within experimental errors) with the oxide thickness and the device area. Some preliminary tests on the reproducibility of the reference Al/SiO_2/Si structures have been undertaken. Devices fabricated on the same silicon substrate showed a maximum variation in SiO_2 thickness of 2% and 5% variation in the value of flat band voltage. However, a much greater variation in the thickness of SiO_2, up to 20%, was found for

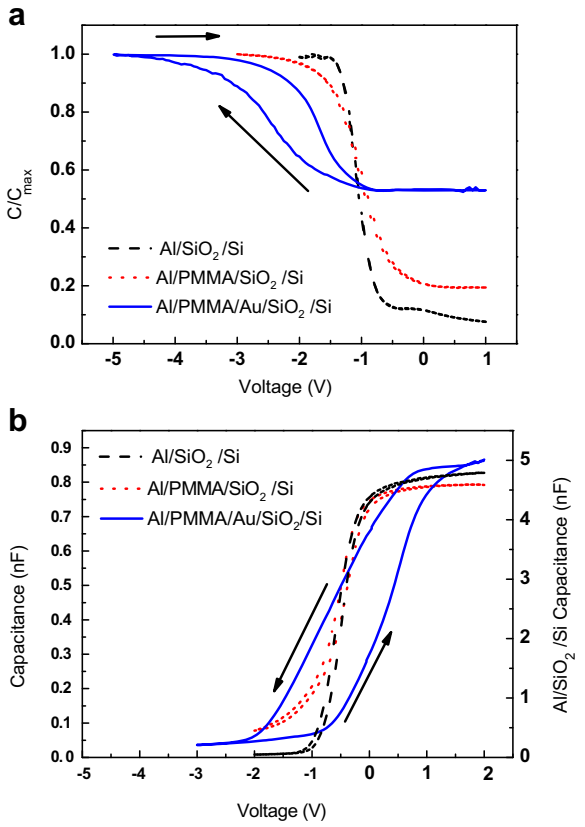

Fig. 2. *C–V* characteristics at 400 kHz for MIS capacitors with and without gold nanoparticles using PMMA as insulator and (a) p-Si and (b) n-Si as the semiconductor. (a) Normalized capacitance data and (b) absolute capacitance values.

devices fabricated on different silicon substrates. This is associated with the accuracy of the temperature of the oxidation furnace, the exact position of the silicon wafer in the furnace and the flow rate of oxygen. Accordingly, measured flat band voltages of the reference Al/SiO_2/Si structures exhibited variations from −1.2 V to −2.8 V for structures based on p-type Si and from −0.5 V to 2 V for n-type Si based structures. Therefore, reference and memory devices were always fabricated on the same silicon substrate to enable valid comparisons between device structures to be made.

The capacitance data for the Al/PMMA/SiO_2/p-Si structure also show clear accumulation–depletion–inversion regions with little hysteresis on reversing the direction of voltage scan. The measured value of the accumulation capacitance was 850 pF, as expected with the increased insulator thickness. There is very little difference in the flat band voltages for the PMMA and SiO_2 structures (a close inspection reveals, perhaps, a very small shift in the *C–V* curve to a more negative voltage for the PMMA device). This indicates that the PMMA dielectric has little incorporated charge.

The addition of Au nanoparticles (to form an Al/PMMA/Au/SiO_2/p-Si structure) results in a distinct change in the flat band voltage to about −2.5 V; this device also exhibits hysteresis in its *C–V* curve. The voltage shift in the *C–V* curve indicates the presence of positive charges within the dielectric (i.e., a more negative voltage has to be applied to the top metal electrode to achieve the flat band conditions in the semiconductor). This could be associated with either the Au nanoparticles or the self-assembled APTMS layer. Perhaps, the latter is the more likely explanation, as the nanoparticle preparation requires this layer to be positively charged. Increasing the sweep voltages to higher values (+/−8 V) resulted in a larger hysteresis window (data not shown for this device).

The clockwise nature of the hysteresis for MIS devices based on p-type semiconductors is usually associated with ion drift or polarization of the insulator. However, the lack of significant hysteresis with the reference structures strongly indicates that charge storage in the nanoparticle layer is responsible for the hysteresis effects. This is consistent with our previous results with LB film insulators [9]. We therefore suggest that, in accumulation, electrons are injected from the top electrode to the Au nanoparticles, which subsequently become negatively charged. The opposite effect occurs in inversion and electrons are extracted from the nanoparticles to the top electrode. Although charge injection might be expected to occur via the SiO_2 layer (leading to a counter-clockwise hysteresis) the carrier transport distance is greater than 5 nm when the additional thicknesses of the organic nanoparticle capping layer and the self-assembled APTMS layer are taken into consideration. This is too large for effective tunnelling and carrier transport through the PMMA dominates. Counter-clockwise hysteresis has been observed during this investigation by using thermally grown SiO_2 layer at 800 °C for 20 min (data not shown). Although the measured thickness of the oxide layer was about 7 nm, AFM images of the film surface showed many voids (in some cases greater than 1 μm) compared to the relatively smooth features of the oxide used in structure in Fig. 2a. This is almost certainly the result of the lower oxidation temperature used (800 °C instead of 850 °C). Consequently, when a positive voltage was applied to the MIS structure, electrons were injected from the inversion layer on the p-Si surface into the Au nanoparticles through this 'leaky' oxide.

Fig. 2b shows the *C–V* curves for MIS devices fabricated on n-type Si. These data are shown in the form of absolute capacitance values versus voltage. The results are consistent with those described above for the p-Si substrates. Significant hysteresis is observed only when Au nanoparticles are included in the MIS device, as shown in Fig. 2b. In this case, the hysteresis is counter-clockwise, but again suggests charging of the nanoparticles through the gate insulator: in the inversion region (negative gate bias) the nanoparticles are charged, and in accumulation they are discharged. An interesting feature in Fig. 2b is the shift in the *C–V* curve to a more positive voltage on addition of the Au nanoparticles. This is opposite to the observation for the p-type substrate and suggests some incorporated negative charge associated with the nanoparticles. These are perhaps partially charged during the MIS device fabrication.

3.2. Cadmium arachidate LB film dielectric

Capacitance versus voltage data for MIS devices with a LB film insulator are depicted in Fig. 3; Fig. 3a for

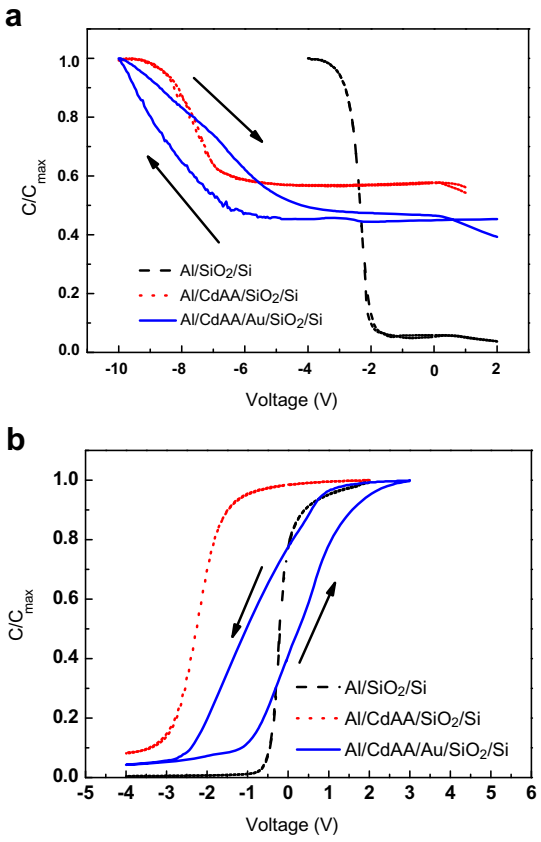

Fig. 3. Normalized *C–V* characteristics at 400 kHz for MIS capacitors with and without gold nanoparticles using CdAA as the insulator. (a) p-Si substrate. (b) n-Si substrate.

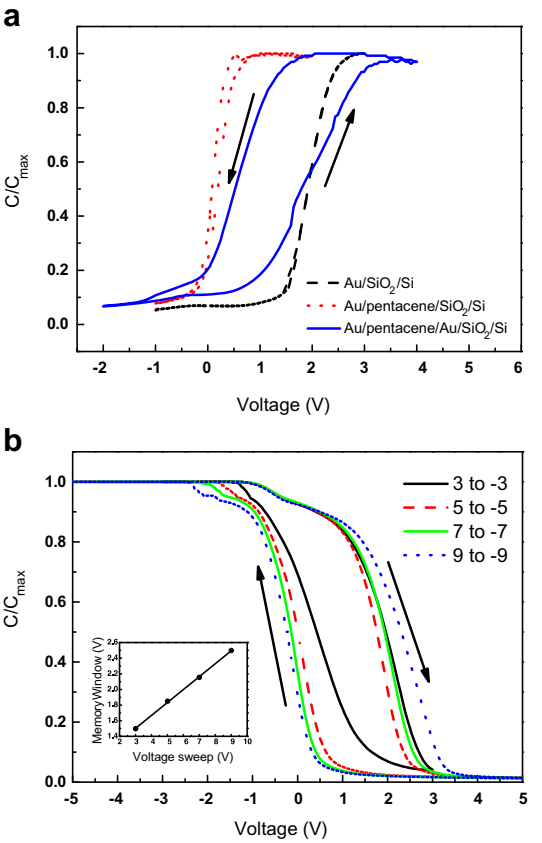

Fig. 4. (a) Normalized *C–V* characteristics at 400 kHz for MIS capacitors with and without gold nanoparticles using pentacene as the insulator and n-Si as the semiconductor. (b) *C–V* characteristics at 400 kHz under different scan voltage ranges for an MIS capacitor incorporating gold nanoparticles and using pentacene as the insulator.

p-Si substrates and Fig. 3b for n-type substrates. The main features are very similar to those in Fig. 2, i.e., hysteresis effects are only evident for the nanoparticle-containing structures, although the details (degree of hysteresis, flat band voltage shifts) are somewhat different for the two different types of device structure.

The *C–V* curves in Fig. 3a (p-Si substrate) are similar to those we reported previously [9]. A large negative shift in the flat band voltage is revealed with the cadmium arachidate insulator, suggesting that this layer is positively charged. This phenomenon is also evident for the n-type substrate, Fig. 3b, but to a lesser extent. In the case of the n-Si substrate, the *C–V* curve is shifted towards positive voltage on incorporation of the nanoparticles, an effect noted above for the Al/PMMA/Au/SiO_2/n-Si structure, Fig. 2b. The result is an MIS device with the hysteresis centred on approximately 0 V, which should prove useful for memory operation.

3.3. Evaporated pentacene dielectric

High speed (flash) evaporation of pentacene has been reported to result in comparatively insulating films [18]. The results of using this material as the insulating layer in our MIS structures are shown in Fig. 4. Again, negligible hysteresis effects were observed in our reference devices, e.g., Fig 4a for an n-Si substrate. This suggests a relatively clean (in an electronic sense) interface between the semiconductor and the dielectric. The interface between the SiO_2 layer and pentacene has been reported to cause relatively large hysteresis effects in devices in which pentacene is exploited as a semiconductor, i.e., field effect transistors [20]. However, in the case of the MIS device used in this study, the most important interface will be that between the silicon semiconductor and the silicon dioxide layer. Our results suggest that either charge carriers do not move freely between the silicon (or the top electrode) and the SiO_2/pentacene interface or that there are relatively few trapping states between the SiO_2 and the flash-evaporated pentacene. The shape of the hysteresis curves are much 'squarer' than those for the other organic insulators used in this work. This may reflect the higher charge transport mobilities for carriers in the pentacene layer, leading to rapid charge and discharge of the Au nanoparticles.

Fig. 4b shows the effect of scanning the voltage between different limits. As shown in the inset to Fig. 4b, the hysteresis window of the *C–V* curves increases linearly with increasing voltage sweep in the measured range (3–9 V).

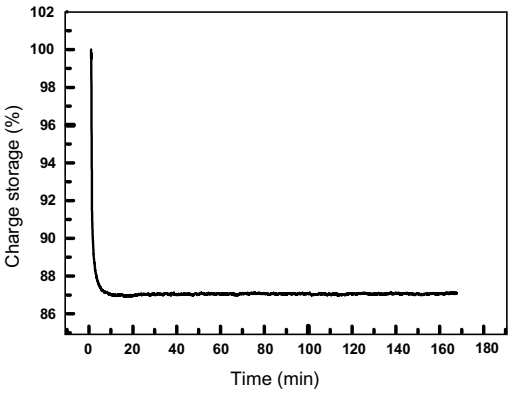

Fig. 5. Charge retention characteristics of the device used in Fig. 4b. The ordinate corresponds to the capacitance of the MIS structure.

For example, the memory window is about 1.5 V for ±3 V, and 2.5 V for ±9 V (scan rate of 50 mV s^{-1} used in all cases). At lower voltage sweeps (below ±3 V), the memory windows becomes very small; the memory device exhibits no hysteresis at sweep voltages below ±1.3 V since the *C–V* curves cannot reach the accumulation region (accounting for the fact that the curve inset in Fig. 4b does not pass through the origin). The amount of charge stored in the nanoparticles Q can be estimated from $Q = C\Delta V_{FB}$, where ΔV_{FB} is the flat band voltage shift; this gives a figure for the number of charge carriers stored of 3.6×10^{12} cm^{-2} for a sweep voltage of ±9 V.

The charge storage characteristics of the nanoparticle-containing MIS structures can be observed by monitoring the capacitance with time following charging the devices for few seconds and then applying a bias voltage. A charging voltage of −4 V (accumulation region) was applied for 3 s to the device whose *C–V* behaviour is depicted in Fig. 4b. The capacitance was then measured at a bias voltage of 3.5 V over a period of about 3 h. Fig. 5 shows the change in normalized capacitance of the device. The charge loss over the first 3 min is estimated to be 3.5% min^{-1}. The capacitance then reached a constant value (about 87% of the charging capacitance) after 6 min. The relatively small subsequent change in the capacitance after 3 h demonstrates that the MIS memory device has a good retention time, and indicates that there is very low leakage current in the memory capacitor. The origin of the fast decay in capacitance during the first few minutes has been attributed to the Coulomb repulsion between electrons confined in nanoparticles [21]. The subsequent slow change in capacitance may be due to the movement of charges from the Au nanoparticles to the bulk silicon of the MIS device through the SiO_2 layer.

4. Conclusions

Metal–insulator–semiconductor memory structures have been fabricated incorporating self-assembled gold nanoparticles as the charge storage elements. Three different organic insulators, each deposited using a different method, have been used as the dielectric in the MIS structures. Using *C–V* measurements, all the devices exhibited memory characteristics, with a memory window depending on the range of the sweep voltage. Relatively wide memory windows with square-shaped hysteresis curves were achieved for Al/pentacene/Au/SiO_2/Si structures, regardless of the silicon substrate type. This was attributed to the good charge transport properties of the pentacene (compared to the other insulators used in this work). However, wide hysteresis windows centred around 0 V were also observed for Al/PMMA/Au/SiO_2/n-Si and Al/CdAA/Au/SiO_2/n-Si MIS structures. These results augur well for the development of memory devices based on charge storage in nanoparticles, although further work is clearly needed on the storage lifetimes and on the long-term stability of the structures.

Acknowledgements

We would like to thank the Science and Engineering Research Council for funding this work (Grant Number EP/D039924/1). One of us (D.K.) would also like to thank the School of Engineering, Durham University for the provision of a studentship. We would like also to thank Dr. Xiaojun Han and Prof. Steve Evans, School of Physics and Astronomy, University of Leeds, UK, for their valuable help in the preparation of Au nanoparticles.

References

[1] B. Park, K. Cho, B. Moon, S. Kim, Microelectron. Eng. 84 (2007) 1627.
[2] S. Duguay, S. Burignat, P. Kern, J.J. Grop, A. Souifi, A. Slaoui, Semicond. Sci. Technol. 22 (2007) 837.
[3] S. Paul, A. Kanwal, M. Chhowalla, Nanotechnology 17 (2006) 145.
[4] K. Müller, K. Henkel, I. Paloumpa, D. Schmeißer, Thin Solid Films 515 (2007) 7683.
[5] S. Fujisaki, H. Ishiwara, Y. Fukisaki, Appl. Phys. Lett. 90 (2007) 162902.
[6] E. Cagin, D.Y. Chen, J.J. Siddiqui, J.D. Phillips, J. Phys. D Appl. Phys. 40 (2007) 2430.
[7] W. Guan, S. Long, M. Liu, Z. Li, Y. Hu, Q. Liu, J. Phys. D Appl. Phys. 40 (2007) 2754.
[8] Ch. Sargentis, K. Giannakopoulos, A. Travlos, D. Tsamakis, Physica 38 (2007) 85.
[9] S. Paul, C. Pearson, A. Molloy, M.A. Cousins, M. Green, S. Kolliopoulou, P. Dimitrakis, P. Normand, D. Tsoukalas, M.C. Petty, Nano Lett. 3 (2003) 533.
[10] Y. Yang, J. Ouyang, L. Ma, R.J.H. Tseng, Ch.W. Chu, Adv. Funct. Mater. 16 (2006) 1001.
[11] W.L. Leong, P.S. Lee, S.G. Mhaisalkar, T.P. Chen, A. Dodabalapur, Appl. Phys. Lett. 90 (2007) 042906.
[12] Z. Liu, C. Lee, V. Narayanan, G. Pei, E.C. Kan, IEEE Trans. Electron. Dev. 49 (2002) 1606.
[13] J.J. Lee, X. Wang, W. Bai, N. Lu, D.L. Kwong, IEEE Trans. Electron. Dev. 50 (2003) 2077.
[14] S. Kolliopoulou, P. Dimitrakis, P. Normand, H.-L. Zhang, N. Cant, S.D. Evans, S. Paul, C. Pearson, A. Molloy, M.C. Petty, J. Appl. Phys. 94 (2003) 5234.
[15] S. Kolliopoulou, P. Dimitrakis, P. Normand, H.-L. Zhang, N. Cant, S.D. Evans, S. Paul, C. Pearson, A. Molloy, M.C. Petty, D. Tsoukalas, Microelectron. Eng. 73–74 (2004) 725.
[16] S. Kolliopoulou, P. Dimitrakis, D. Goustouridis, P. Normand, C. Pearson, M.C. Petty, H. Radamson, D. Tsoukalas, Microelectron. Eng. 83 (2006) 1563.
[17] S.Y. Yang, S.H. Kim, K. Shin, H. Jeon, C.E. Park, Appl. Phys. Lett. 88 (2006) 173507.
[18] D.J. Gundlach, Y.Y. Lin, T.N. Jackson, S.F. Nelson, D.G. Schlom, IEEE Electron. Dev. Lett. 18 (1997) 87.
[19] Y. Jin, X. Kang, Y. Song, B. Zhang, G. Cheng, S.Dong, Anal. Chem. 73 (2001) 2843.
[20] J.W.H. Smith, I.G. Hill, J. Appl. Phys. 101 (2007) 044503.
[21] B. Park, K. Cho, H. Kim, S. Kim, Semicond. Sci. Technol. 21 (2006) 975.

by using a small-size rubbing device. The nanorubbing process, which consists in the deformation of a polymer thin film by scanning an Atomic Force Microscopy (AFM) tip operating in contact mode, has been first used to align polyimide layers. The structural anisotropy resulting from nanorubbing was demonstrated to be sufficiently strong to induce efficient liquid crystal orientation even at a moderate load force [9,10].

In this paper, we report on the application of the nanorubbing technique to P3HT thin films. Our aim is to study the effect of chain orientation on the field-effect transistor (FET) properties by nanorubbing P3HT thin deposits that constitute the active layer in the FET channel. It has been shown previously that charge transport in polymer FETs is highly dependent on the orientation of the crystalline domains relative to the carrier transport direction (from source to drain) [11]. We critically test the nanorubbing technique and find that, indeed, FETs display different properties, depending on the orientation of the alignment process [12].

2. Experimental section

2.1. Thin film preparation

RR–P3HT with a regioregularity of 99.8% was obtained from Aldrich. P3HT thin films were prepared by dip-coating clean silicon substrates into chloroform solutions (5 mg/ml) of RR–P3HT; the substrate is immersed one time and stays 30 s in the polymer solution; the retracting speed is 70 mm/min. Typical film thicknesses are in the 5–10 nm range, as determined by ellipsometry and AFM. The FETs are designed in the bottom-gate bottom-contact configuration. The devices were fabricated from a doped silicon substrate, which plays the role of the gate supporting a 100 nm thick SiO_2 dielectric. The SiO_2 layer capacitance C_i was measured to be 33 nF/cm^2. The source and drain electrodes were deposited by electron-beam evaporation of 70 nm Pd with a 1 nm thick Ti adhesion layer. Typical channel width (W) dimensions are 25- and 100-μm with corresponding channel length (L) sizes of 1- and 30-μm. The P3HT active layers were formed by dipping those structures in chloroform solutions, following the above described protocol.

2.2. Nanorubbing

The nanorubbing process was performed with a Nanoscope IIIa AFM microscope working in contact mode. The tips are made of antimony-doped silicon with a spring constant of 2 ± 0.5 N/m. [13] Typically 10 consecutive rubbing scans were carried out with the AFM tip in order to induce a sufficient deformation on the P3HT deposits. The loading force applied by the tip on the film during nanorubbing is approximately 200 nN, as calculated from the approach–retract curves.

2.3. AFM imaging

The AFM imaging was performed in "Tapping-mode" (TMAFM). In this mode, the cantilever holding the probe tip oscillates close to the resonance frequency (ca. 300 kHz) above the sample surface so that the tip is in intermittent contact with the surface at the lower end of the oscillation. Since no lateral force is applied by the tip on the surface during TMAFM operation, no further surface modification is expected to occur in those conditions. The phase of the oscillating tip is very sensitive to the nature of the interaction with the surface. It has been shown that the phase lag is related to the mechanical response of the material when the amplitude is only slightly damped upon contact with the surface. [14–16] Therefore, simultaneous acquisition of the phase and the height image provides a map of the local mechanical response. The AFM images were recorded with a Nanoscope IIIa microscope operated at room temperature in air using commercial cantilevers made of antimony-doped silicon with a spring constant of 30 N/m. The images were digitally sampled at the maximum number of pixels (512) in each direction, and the Nanoscope image processing software was used for image analysis. Unless otherwise stated, image treatment was limited to a "flattening" operation, whereby a first-order surface representing height variations related to a possible tilt of the sample is subtracted from the original image.

2.4. FET characterization

The drain current I_d vs. drain bias V_d (output) and I_d vs. gate bias V_g (transfer) characteristics have been collected in ambient conditions with an Agilent 4156C Precision Semiconductor Parameter Analyzer.

3. Results and discussion

In a typical experiment, we have unidirectionally rubbed, with the AFM tip in contact mode, a $(10 \times 10)\ \mu m^2$ area on a P3HT film prepared by dip-coating. Afterwards, the morphology of the rubbed regions was investigated by TMAFM. Fig. 1a shows height and phase images in an area across the modified region. The rubbed area is barely visible in the height image (left) and appears more clearly in the phase image (right). This phase contrast originates from local differences in tip-sample interactions, which indicates that the nanorubbing process induces a modification in the polymer mechanical response. Since rubbing favors polymer crystallization via chain alignment [17] and we observe a clear optical signature of P3HT chain alignment in the rubbed areas (see below), it is most likely the change in TMAFM phase signal over the rubbed areas is due a local increase in stiffness, as a result of P3HT chain ordering.

Upon closer inspection, we observe that the rubbed area presents, both in the height and phase images, a regular pattern made of grooves parallel to the rubbing direction (Fig. 1b). From the Fourier transform of the height image (see inset), the period of the pattern is found to be about 40 nm. This value is directly related to the experimental conditions of the rubbing process. The $(10 \times 10)\ \mu m^2$ area was scanned by 256 parallel lines and the lateral shift between two lines is therefore (10,000 (nm)/256 = 39 (nm)), which corresponds to the period of the pattern formed in

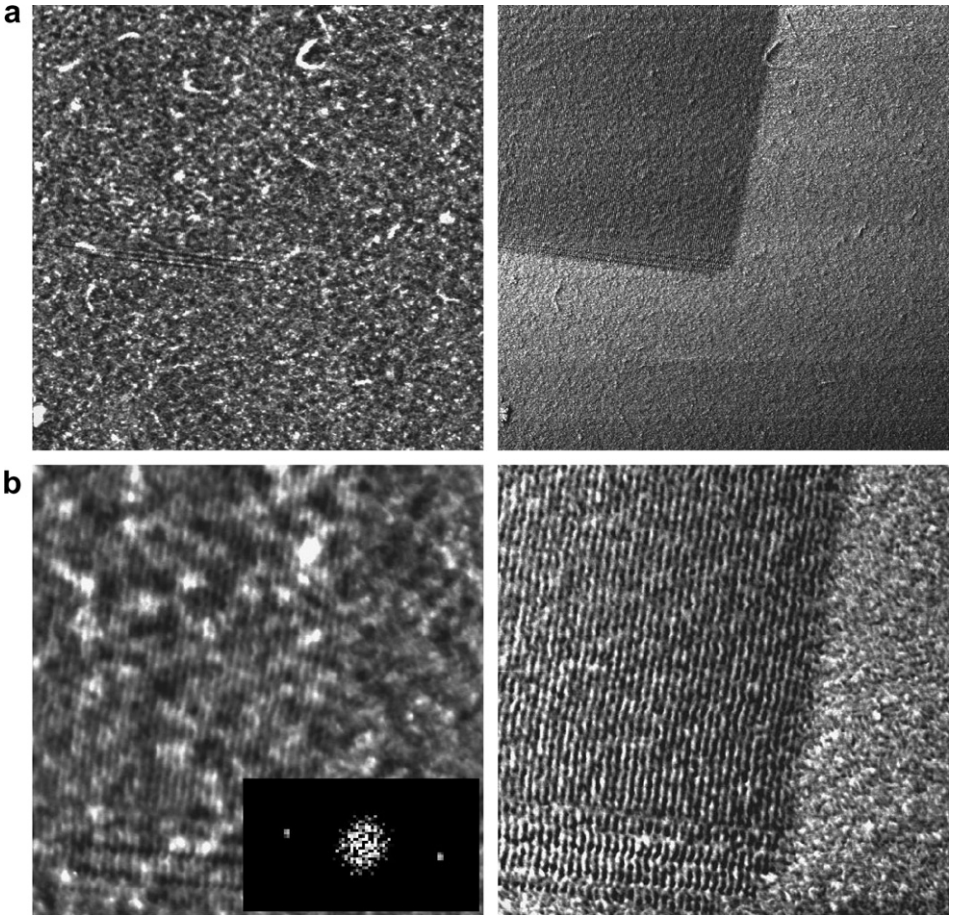

Fig. 1. (a) $(10 \times 10)\ \mu m^2$ and (b) $(2.5 \times 2.5)\ \mu m^2$ TMAFM height (left) and phase (right) images of a nanorubbed area. The vertical gray scale is 10 nm and 20° for the height and phase image, respectively. Inset: Fourier transform of the height image.

the rubbed zone. Under the conditions used here (10 rubbing scans with a load of 200 nN), the vertical amplitude of the pattern is 1.5 ± 0.5 nm.

Based on these observations, it therefore becomes possible to generate patterns with a well-defined periodicity, by selecting the size of the rubbed area and the resolution of the scanning during the rubbing operation. Two examples are shown in Fig. 2. In image Fig. 2a, a square of $(5 \times 5)\ \mu m^2$ was rubbed with a resolution of 32 lines/scan. Accordingly, the grooves period is around 150 nm (5000 (nm)/32 = 156 (nm)). A closer look reveals that the lines are not perfectly parallel, but correspond to a very tight zig–zag pattern. This is even clearer upon further reducing the resolution to 16 lines/scan (Fig. 2b). This reflects the actual tip displacement during the rubbing: the tip scans back and forth in the fast scan direction while slowly moving in the orthogonal direction (Fig. 2c), giving rise to the zig–zag pattern. Nevertheless, for more realistic rubbing conditions (256 lines/scan) used for FET characterization, the lines can be considered to be parallel.

In order to highlight a possible orientation of the polymer chains within the rubbed zone, the samples were analyzed with optical microscopy between crossed polars. As an example, two P3HT films with four $(10 \times 10)\ \mu m^2$ rubbed square areas are shown in Fig. 3; all the nanorubbed domains appear with a high birefringence. In addition, complete extinction of these squares is observed when the polars are oriented either parallel or perpendicular to the rubbing direction. These observations clearly testify the orientation of the polymer chains induced by the rubbing process.

When using a single polar, we observe that the rubbed areas appear darker when it is oriented parallel to the rubbing direction while they are brighter when the orientation is perpendicular to the rubbing direction. This difference in the light absorption indicates that the chains are oriented along the rubbing direction, since it is well known that the first optical transition in conjugated polymers is polarized along the chain axis [18]. The polymer chains orientation is most probably due to the combination of the shear stress induced by the tip displacement and the ability of the regioregular polymer to crystallize.

Since regioregular P3HT is partly crystalline [19], we propose that the anisotropy appearing upon rubbing is due to the alignment of preexisting crystalline domains and/or to the stretching and crystallization of chains in

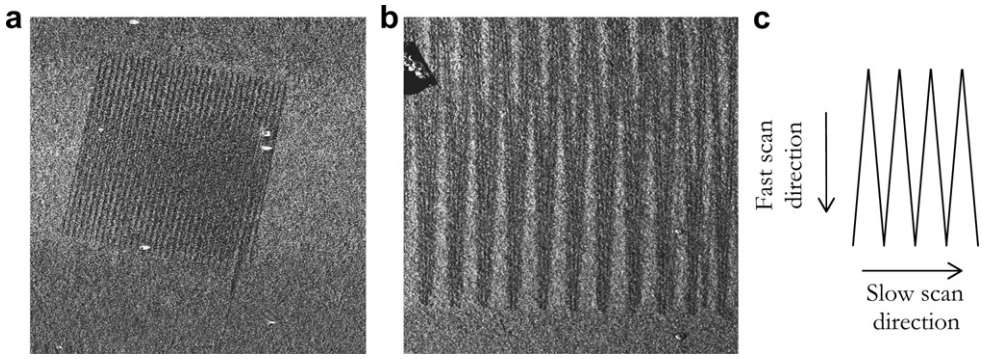

Fig. 2. (a) (10×10) μm^2 TMAFM phase image of a nanorubbed P3HT film with a resolution of 32 lines/scan. The vertical gray scale is 30°. (b) (4×4) μm^2 TMAFM phase image of a nanorubbed P3HT film with a resolution of 16 lines/scan. The vertical gray scale is 15°. (c) Scheme of the tip scan pattern. The dark regions in images (a) and (b) correspond to the zones where the tip has rubbed the film surface.

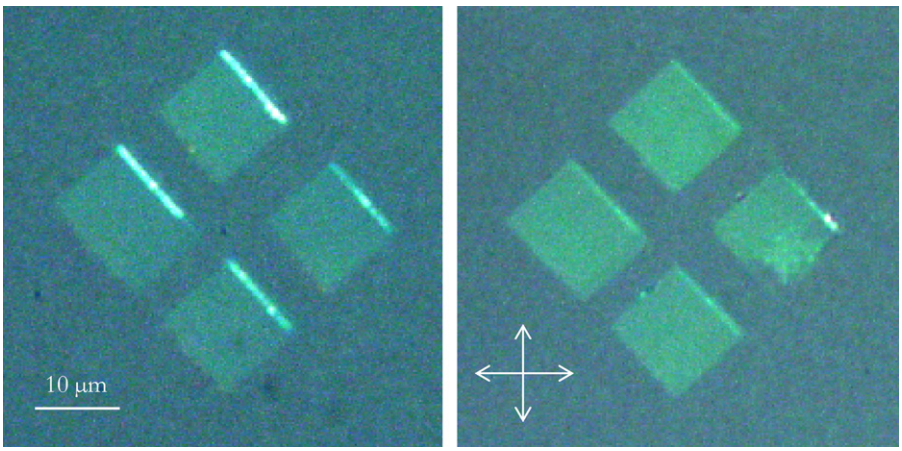

Fig. 3. Optical micrographs between crossed polars for P3HT films with four (10×10) μm^2 rubbed squares. The crossed polars are oriented as shown by the white arrows.

the amorphous regions. In a control experiment, nanorubbing has been carried out on thin films of regiorandom P3HT, which cannot crystallize due to the random arrangement of the hexyl side groups. In that case, neither changes in the surface morphology nor birefringence are observed, which is consistent with the absence of polymer chain orientation. In the regiorandom system, the polymer chains that are stretched by the tip displacement most probably relax back to the coiled state very quickly afterwards.

In order to study the effect of chain orientation on the device electrical properties, we applied the nanorubbing technique to P3HT thin films defining the channel of FETs. The rubbed area includes the P3HT channel and a part of the electrodes, because the polymer layer, deposited by dip-coating, covers the devices entirely. The TMAFM height image (top left) in Fig. 4a shows the P3HT channel as the dark horizontal region comprised between the source and drain electrodes, which appear in gray. The corresponding phase image (top right) shows no contrast between the channel and the electrodes, consistent with the fact that the whole device surface is covered with P3HT. The pattern generated by the rubbing is clearly observed in the close-ups (Fig. 4b); it is very similar to that obtained on the 'free' P3HT films.

Fig. 5 displays optical micrographs of a P3HT FET with a nanorubbed zone across the channel. Rubbing has been performed over a (25×25) μm^2 area, with the scan direction along the electrodes, as indicated by the arrow in the right micrograph. Between crossed polars, the electrodes appear in pale blue and the rubbed area is very bright (yellow over SiO_2 and blue over Pd source and drain electrodes) when the rubbing direction is at 45° with respect to the polars (left image), which indicates that also in this system the rubbed polymer is birefringent. Consistently, a complete extinction of the rubbed square is observed when the rubbing direction is either parallel or perpendicular to the polarization directions, testifying to the polymer chain orientation within the rubbed domain and so within the P3HT channel.

4. FETs properties

The typical output (a) and transfer (b) characteristics of P3HT FETs fabricated with $W = 25$ μm, $L = 1$ μm and

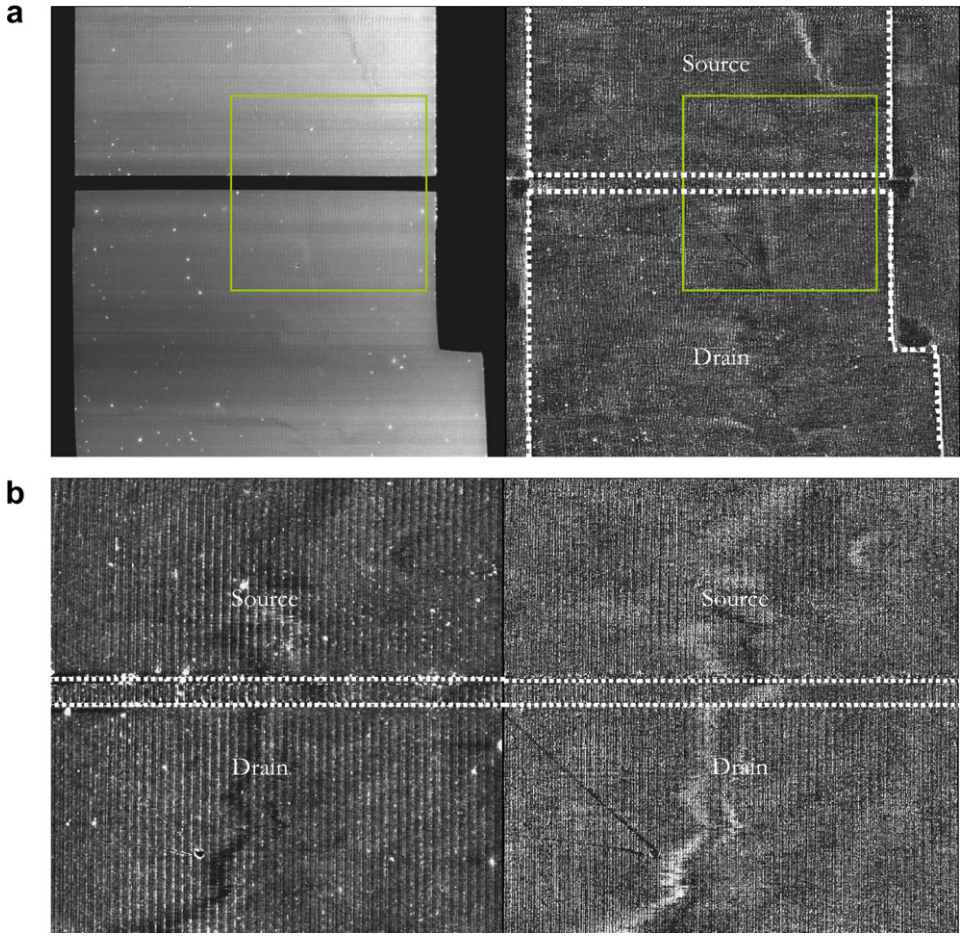

Fig. 4. (a) $(35 \times 35)\,\mu m^2$ and (b) $(15 \times 15)\,\mu m^2$ TMAFM height (left) and phase (right) images of a channel-rubbed field-effect transistor. Images (b) correspond to green squared areas in images (a). The vertical gray scale is 7 nm for height images and 25° for phase images.

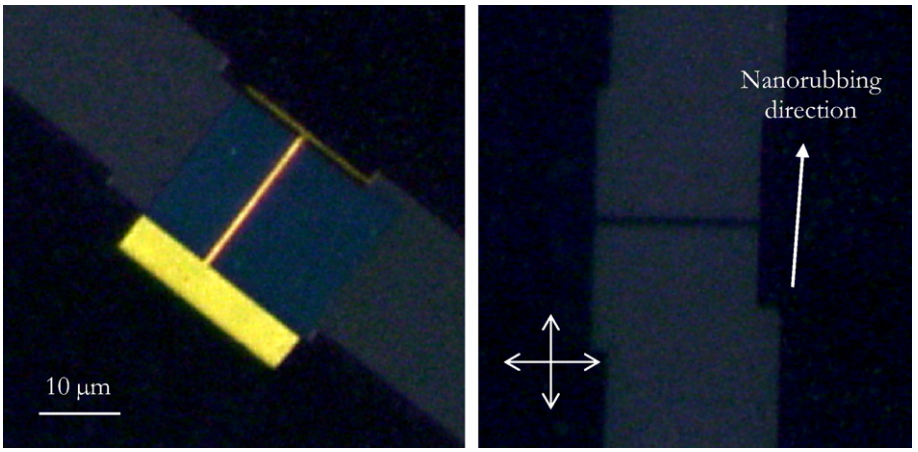

Fig. 5. Optical micrographs between crossed polars of a P3HT field-effect transistor with the channel structured by nanorubbing. The crossed polars are oriented as shown by the white arrows.

pristine SiO_2 dielectrics [20,21] are given in Fig. 6. These transistors display short channel effects [22,23], in other words inability of the drain current to saturate above the pinch-off. We have consequently determined the field-effect mobility at both low and high drain voltages, as shown hereafter. The on/off current ratio of our FETs is

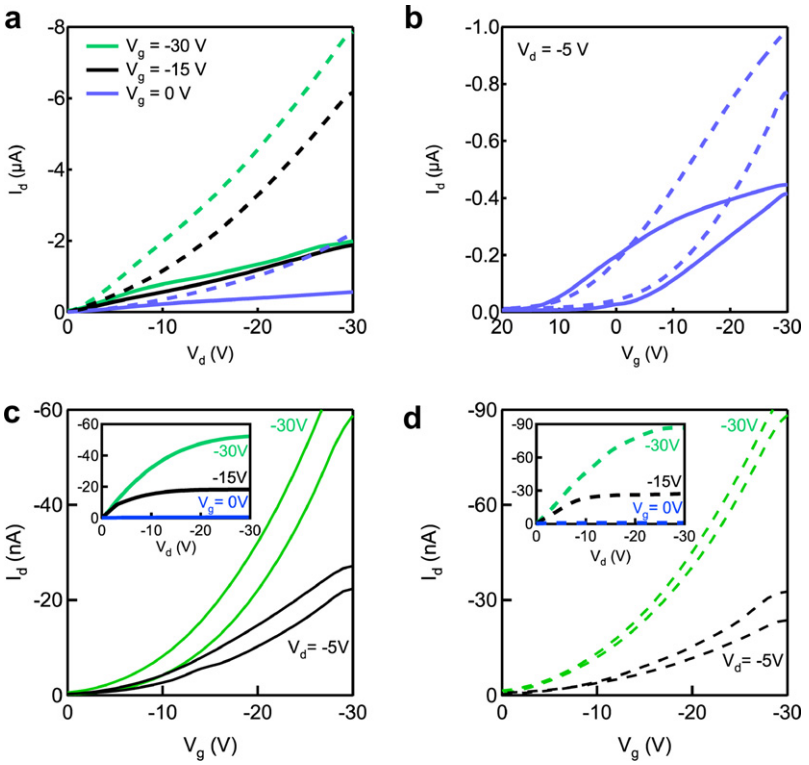

Fig. 6. Output (a) and transfer (b) characteristics of P3HT FETs with $W = 25$ μm, $L = 1$ μm and pristine SiO_2 dielectrics. (c) and (d) Transfer behavior of P3HT FETs with $W = 100$ μm, $L = 30$ μm and hexamethyldisilazane-treated SiO_2 dielectrics. Insets display their respective output response. Before rubbing (continuous curves) and after rubbing (dashed curves).

below 1000, similar to previous reports, which affirmed unintentional doping of the P3HT when processed in ambient conditions [24,25]. This unfortunately precludes the extraction of certain parameters, such as maximum transconductance and cut-off frequency, i.e., a more in-depth analysis of the electrical changes induced by the nanorubbing process. Note that the transfer characteristics (Fig. 6b) show a pronounced hysteresis, typical of thick SiO_2 dielectrics, which indicates a relatively high density of traps at the organic/dielectric interface and within the dielectric [26]. As proper treatment of the dielectric reduces the hysteresis, we have also tested devices with $W = 100$ μm, $L = 30$ μm, and hexamethyldisilazane-coated 100-nm-thick SiO_2 dielectrics. Their corresponding current–voltage characteristics are given in panels (c) and (d) of Fig. 6. Indeed, they display lower hysteresis with respect to pristine SiO_2 devices together with a well-defined saturation of the $I_d - V_d$ curves (see insets).

To quantify the impact of nanorubbing process on the FET characteristics, we have determined the linear mobility μ_{lin} using the equation $I_d = W/L{*}C_i{*}\mu_{lin}{*}(V_g - V_{th}){*}V_d$, where the threshold voltage V_{th} has been extracted from plots of $I_d/g_m^{1/2}$ vs. V_g. Here $g_m = \partial I_d/\partial V_g$ is the transconductance. Given the presence of superlinearities at low V_g in the output characteristics of the $L = 1$ μm FETs, the extracted values for the linear mobility might be questionable. We therefore provide the field-effect mobility also at high gate voltages, using the equation $I_d = W/2L{*}C_i{*}\mu_{sat}{*}(V_g - V_{th\ sat})^2$. The $V_{th\ sat}$ has been extracted from plots of $I_d^{1/2}$ vs. V_g. Table 1 compares all these parameters for the homogeneous and nanorubbed devices (along the electrode direction). We observe two times or higher mobilities for the nanorubbed FETs, comparable with published data for standard bottom-contact P3HT devices [27]. From the transfer plots we have also extracted the source-drain series resistance (R_{sd}), using the technique detailed by Rhayem and collaborators [28] and found values in

Table 1
Electrical properties of the homogeneous and nanorubbed P3HT FETs (along the electrode direction)

Device		V_{th} (V)	μ_{lin} (cm^2/V s)	R_{sd} (MΩ)	$V_{th\ sat}$ (V)	μ_{sat} (cm^2/V s)
$W = 25$ μm $L = 1$ μm	Homogeneous	12	2.6×10^{-3}	5	−4	7×10^{-3}
	Nanorubbing//	7	6.4×10^{-3}	1	2	20×10^{-3}
$W = 100$ μm $L = 30$ μm	Homogeneous	−6	2.0×10^{-3}	50	0	1×10^{-3}
	Nanorubbing//	−10	3.0×10^{-3}	35	0	2×10^{-3}

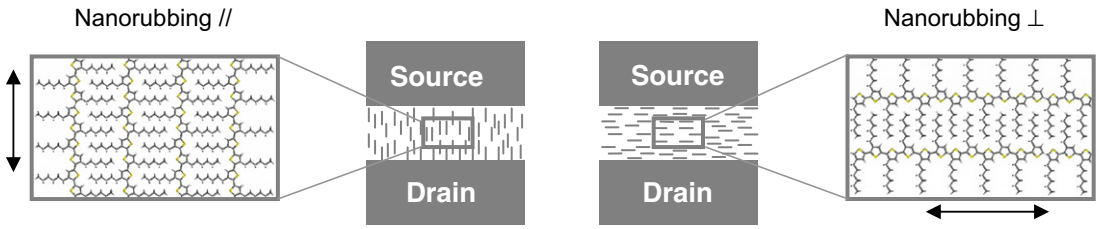

Fig. 7. Schematic representation of the P3HT chain arrangement when the nanorubbing is performed parallel (left) and perpendicular (right) to the source–drain axis. The polymer chains and the electrodes are not to scale. The double arrows indicate the rubbing direction.

the MΩ range, consistent with previous reports on P3HT films deposited by spin coating [29,30]. This indicates that the nanorubbing process provides a gentle modification of the metal/polymer charge–injection interface. Finally, we have checked that the mobility value does not depend on the direction of the dip-coating operation, i.e., either parallel or perpendicular to the electrodes. In other words, in the conditions we used, the dip-coating does not induce significant orientation of the P3HT film.

After rubbing the P3HT channel along the electrode direction (i.e., as indicated in Fig. 5), the transistors operate nicely, with improved parameters (see Table 1). In contrast, when the nanorubbing is performed perpendicular to the electrode direction, the mobility has consistently been found lower and approaching 10^{-4} cm^2/V s. This contrast in mobility is most probably related to the difference in chain orientation induced by the rubbing. It has been shown previously [8] that rubbing P3HT films leads to a global orientation of the chains at the surface, with the (100) plane perpendicular to the polymer layer. This means that the plane of individual polymer molecules is parallel to the surface. Let us note that such arrangement is not the most favorable for charge transport in the plane of the polymer film (a 'edge-on' organization has been shown to lead to the highest mobilities) [11]. When rubbing is carried out perpendicular to the source–drain axis, the chains are therefore arranged flat on the surface and perpendicular to the transport direction (Fig. 7, right). In such configuration, charge transport in the source-drain direction implies chain-to-chain hopping over a large distance (because of the presence of the alkyl groups), which is consistent with the low mobility observed. In contrast, when nanorubbing is performed parallel to the source–drain axis, the chains are oriented parallel to the transport direction (Fig. 7, left). Intramolecular transport is favoured and only a few inter-chain hopping events are necessary for charges to cross the channel. This is consistent with the twofold increase in mobility with respect to the homogeneous layer, in which the chain orientation is random. This behavior is similar to that recently observed when the chain orientation is promoted in poly(3,3‴-didodecyl-quaterthiophene) by embossing the polymer layer in the liquid-crystalline state [31]. Finally, we note that additional mechanisms could affect the mobilities of nanorubbed transistors. Precisely, the surface roughness induced to the polymer films constituting the FET channel by the rubbing process is likely to induce a nonuniformity in the electric field and, hence, a modification of their respective field-effect mobilities. This side effect cannot be ruled out and might play a role in our experiments. Yet, we believe that it should be strongly related to the magnitude of the corrugation (depth of the nanogrooves) as well as the periodicity of the surface deformation, and this has been not observed in the experiments.

5. Conclusions

We have applied the nanorubbing process, which uses an AFM tip operating in contact mode, to structure regioregular P3HT thin films. Rubbing induces a slight deformation on the surface, showing up as grooves to the fast scan direction, along with a modification of the mechanical response corresponding most probably to shear-induced orientation of crystalline domains. Polarized optical microscopy clearly indicates that the P3HT chains are oriented along the rubbing direction. Consistently, thin films of regiorandom P3HT, which cannot crystallize, show no morphological modifications and no optical anisotropy upon nanorubbing.

In order to study the effect of chain orientation on the electrical properties of P3HT devices, we applied the nanorubbing technique to structure the P3HT film deposited in the channel of FETs. When nanorubbing is carried out parallel to the source–drain axis, the electrical performances of the devices (such as the linear and saturation mobilities) are improved with respect to FETs employing isotropic P3HT films. In contrast, when nanorubbing is performed perpendicular to the source–drain direction, the mobility decreases. These effects are related to the polymer chain orientation: in the latter case, the chains are perpendicular to the transport direction and the charge transport implies chain-to-chain hopping over large distance, which leads to low mobilities. When the nanorubbing is performed parallel to the source-drain axis, the chains are parallel to the transport direction, intramolecular transport is favored, leading to higher mobilities.

Acknowledgments

This work was supported by the Belgian National Fund for Scientific Research (F.R.S. – FNRS), by the Belgian Federal Science Policy Office in the framework of the 'Pôle d'Attraction Interuniversitaire' program (PAI 6/27), and by Région Wallonne (ETIQUEL project). P. Damman, Ph. Leclère and S. Melinte are Research Associates of the F.R.S. – FNRS. G. Derue is grateful to FRIA for a doctoral fellowship.

References

[1] G.M. Wang, J. Swensen, D. Moses, A.J. Heeger, J. Appl. Phys. 93 (2003) 6137.
[2] H.G.O. Sandberg, G.L. Frey, M.N. Shkunov, M.M. Nielsen, C. Kumpf, Langmuir 18 (2002) 10176.
[3] H. Sirringhaus, P.J. Brown, R.H. Friend, M.M. Nielsen, K. Bechgaard, B.M.W. Langeveld-Voos, A.J.H. Spiering, R.A.J. Janssen, E.W. Meijer, Synth. Met. 111 (2001) 129.
[4] H. Yang, T.J. Shin, L. Yang, K. Cho, C.Y. Ryu, Z. Bao, Adv. Funct. Mater. 15 (2005) 671.
[5] J. Mardalen, E.J. Samuelsen, O.R. Gautun, P.H. Carlsen, Synth. Met. 48 (1992) 363.
[6] S.K. Sharma, R. Singhal, B.D. Malhotra, N. Sehgal, A. Kumar, Electrochim. Acta 49 (2004) 2479.
[7] S. Nagamatsu, W. Takashima, K. Kaneto, Macromolecules 36 (2003) 5252.
[8] G. Derue, S. Coppée, S. Gabriele, M. Surin, V. Geskin, F. Monteverde, Ph. Leclère, R. Lazzaroni, P. Damman, J. Am. Chem. Soc. 127 (2005) 8018.
[9] J.-H. Kim, M. Yoneya, J. Yamamoto, H. Yokoyama, Nanotechnology 13 (2002) 133.
[10] J.-H. Kim, M. Yoneya, H. Yokoyama, Nature 420 (2002) 159.
[11] H. Sirringhaus, P.J. Brown, R.H. Friend, M.M. Nielsen, K. Bechgaard, B.M.W. Langeveld-Voss, A.J.H. Spiering, R.A.J. Janssen, E.W. Meijer, P. Herwig, D.M. de Leeuw, Nature 401 (1999) 685.
[12] S. Scheinert, T. Doll, A. Scherer, G. Paasch, I. Hörselmann, Appl. Phys. Lett. 84 (2004) 4427.
[13] We have also used AFM cantilevers with higher or smaller spring constants to perform the nanorubbing process; we have observed that the cantilevers with intermediate spring constant (around 2 N/m) give the best results in terms of reproducibility and control of the applied force, with lower risk of damaging the polymer surface.
[14] G. Bar, Y. Thomman, R. Brandsch, H.J. Cantow, M.H. Whangbo, Langmuir 13 (1997) 3807.
[15] S.N. Magonov, V. Elings, W.H. Whangbo, Surf. Sci. Lett. 375 (1997) 385.
[16] N.A. Burnham, O.P. Behrend, F. Oulevey, G. Gremaud, P.-J. Gallo, D. Gourdon, E. Dupas, A.J. Kulik, H.M. Pollock, G.A.D. Briggs, Nanotechnology 8 (1997) 67.
[17] S. Coppée, V.M. Geskin, R. Lazzaroni, P. Damman, Macromolecules 37 (2004) 244.
[18] J. Gierschner, M. Ehni, H.-J. Egelhaaf, B. Miliàn Medina, D. Beljonne, H. Benmansour, G.C. Bazan, J. Chem. Phys. 123 (2005) 144914.
[19] A. Zen, M. Saphiannikova, D. Neher, J. Grenzer, S. Grigorian, U. Pietsch, U. Asawapirom, S. Janietz, U. Scherf, I. Lieberwirth, G. Wegner, Macromolecules 39 (2006) 2162.
[20] A. Facchetti, M.-H. Yoon, T.J. Marks, Adv. Mater. 17 (2005) 1705.
[21] Thinner dielectrics could have been employed in order to increase the gate-induced electric field. For reproducible electrical characteristics, we avoided on purpose very thin dielectrics that might be stressed by the nanorubbing process.
[22] M.L. Chabinyc, J.P. Lu, R.A. Street, Y. Wu, P. Liu, B.S. Ong, J. Appl. Phys. 96 (2004) 2063.
[23] J.N. Haddock, X. Zhang, S. Zheng, Q. Zhang, S.R. Marder, B. Kippelen, Org. Electron. 7 (2006) 45.
[24] Z. Bao, A. Dodabalapur, A.J. Lovinger, J. Appl. Phys. Lett. 69 (1996) 4108.
[25] H. Sirringhaus, N. Tessler, D.S. Thomas, P.J. Brown, R.H. Friend, Adv. Solid-State 39 (1999) 101.
[26] A.R. Brown, C.P. Jarrett, D.M. de Leeuw, M. Matters, Synth. Met. 88 (1997) 37.
[27] J. Veres, S. Ogier, G. Lloyd, D.M. de Leeuw, Chem. Mater. 16 (2004) 4543.
[28] J. Rhayem, M. Valenza, D. Rigaud, N. Szydlo, H. Lebrun, J. Appl. Phys. 83 (1998) 3660.
[29] B.H. Hamadani, D. Natelson, Appl. Phys. Lett. 84 (2004) 443.
[30] E.J. Meijer, G.H. Gelinck, E. van Veenendaal, B.-H. Huisman, D.M. de Leeuw, T.M. Klapwijk, Appl. Phys. Lett. 82 (2003) 4576.
[31] Z. Hu, B. Muls, L. Gence, D.A. Serban, J. Hofkens, S. Melinte, B. Nysten, S. Demoustier-Champagne, A.M. Jonas, Nano Lett. 7 (2007) 3639.

may provide an explanation for the huge variation in the reported switching times.

Pristine MIM diodes (Fig. 1) consisted of an Al bottom electrode, a sputtered layer of Al_2O_3 (10 nm), a spirofluorene polymer (80 nm), and a Ba/Al (5 nm/100 nm) top electrode that forms an Ohmic contact with the polymer. The devices with an active area of 9 mm^2 were encapsulated to exclude O_2 and H_2O. In all cases, positive bias voltage refers to the bottom electrode being poled positive with respect to the top electrode. The memories were 'formed' by applying a 15 V pulse, which was terminated immediately after the current through the device reaches a compliance level of 10 mA. The J-V characteristics after forming are presented in Fig 1. They show a symmetric, voltage controlled negative differential resistance (NDR). Reliable switching is obtained at the top and bottom of the NDR [21,22]. Using a pulse with 4–6 V amplitude, the memory switches to the low resistance ON state. A pulse with 8–10 V amplitude, corresponding to the end of the NDR regime, switches the memory to the high resistance OFF state.

Already in 1967, Simmons and Verderber studied the switching dynamics of SiOx memories. The J-V characteristics were measured using a saw tooth bias profile. At low repetition frequencies a clear NDR was observed. With increasing frequency the magnitude of the NDR gradually decreases, and vanishes at about 1 kHz. They concluded that a dead time was responsible for the disappearance of the NDR [22,23]. After programming, a waiting time of at least 1 ms is needed to switch the resistance again. The J-V characteristics of similar saw tooth measurements on our memories are presented in Fig. 2. In perfect agreement with Simmons and Verderber, the NDR disappears at a repetition rate of about 1 kHz. The data shows that when the programming voltage is cycled too fast the device remains always in the OFF state, as will be shown later.

Before investigating the dead time, we measured single switching events using a waiting time >10 s between events. In these experiments, the device with a capacitance of 2.7 nF is coupled directly to a pulse generator (50 ohm) when applying the programming pulse. This gives a time constant for charging of the dielectric (τ_{DC}) of 1.4×10^2 ns. The current density is measured before and after switching using a low reading bias of 1 V. The current density as a function of pulse length for switching from the high resistance OFF state to the low resistance ON state is shown in Fig. 3A, and from the ON to the OFF state in

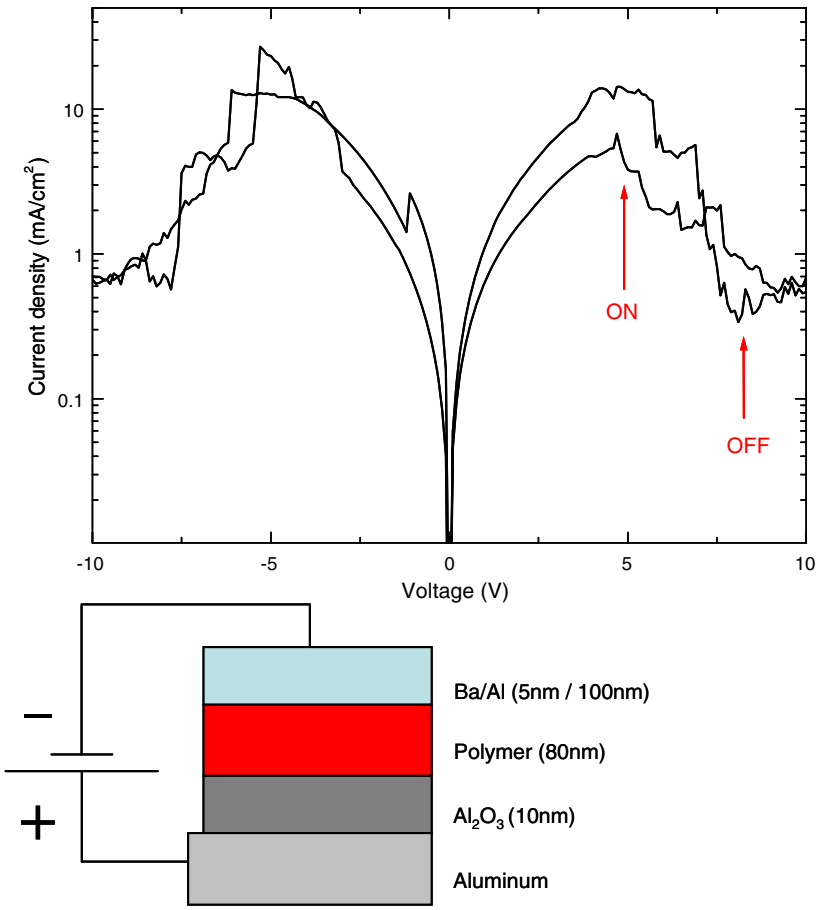

Fig. 1. (top) J-V characteristics of a device scanned from 0 V → +10 V → −10 V → 0 V. Arrows indicate the voltage levels applied to switch the device to the low resistance ON and high resistance OFF state in pulse experiments. (bottom) Lay-out of the memory diode.

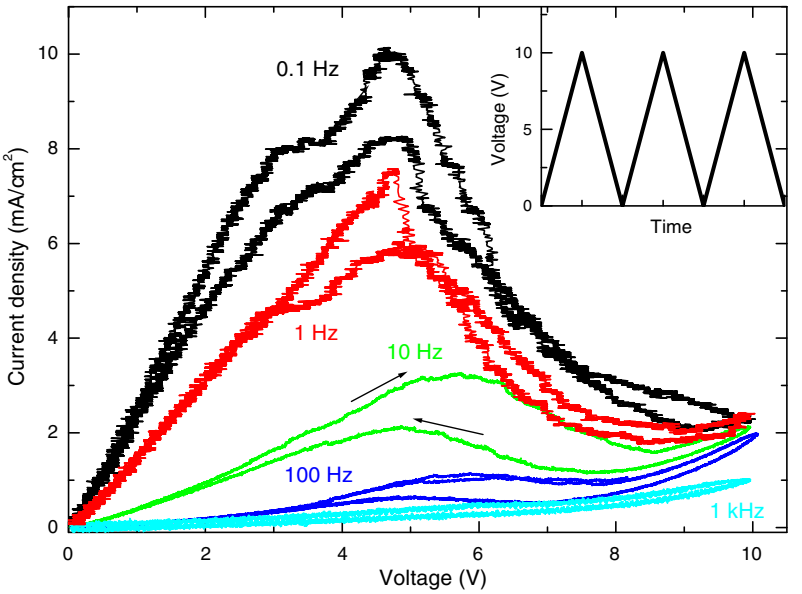

Fig. 2. J-V characteristics measured using a time modulated voltage with a saw tooth waveform (see inset) with modulation frequency from 0.1 Hz to 1 kHz, averaged over more than five cycles. A 50 Ω resistor is used to measure the current.

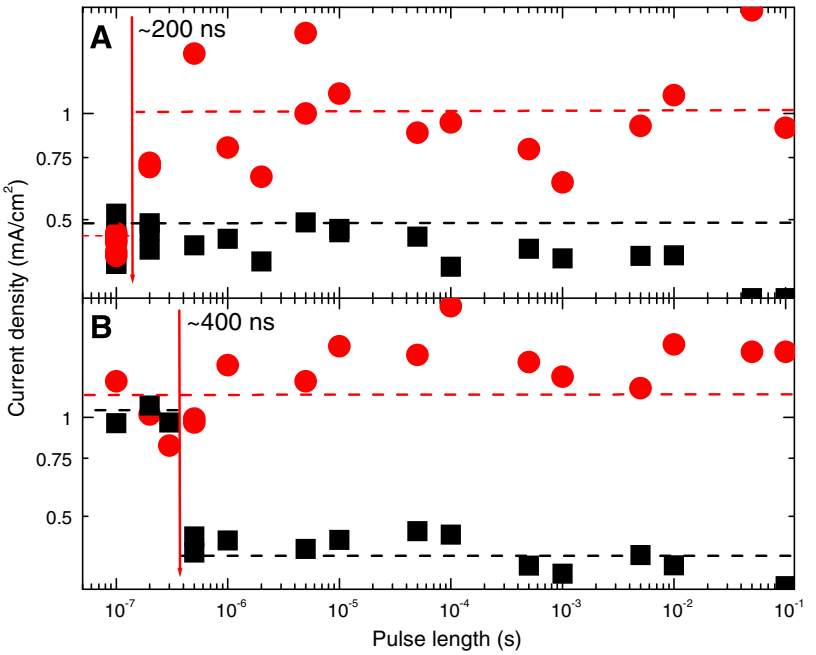

Fig. 3. The current density measured using a low reading bias of 1 V before and after switching after a ON or OFF voltage pulse with varying length.: (A) OFF (■) to ON (●)switching with a +4 V pulse; (B) ON (●) to OFF (■) switching with a+8 V pulse. The initial states were prepared >10 s before the start of the experiment with a pulse of fixed length (100 ms).

Fig. 3B. In these experiments, the initial state has been prepared by a pulse of fixed length (100 ms). Fig. 3A shows that a minimum pulse length of 200 ns is needed to induce a change in resistance. Fig. 3B shows that the switching time from the ON to the OFF state is 400 ns. These times are of the same order of magnitude as τ_{DC} and therefore, it may well be possible to achieve switching times shorter then 400 ns by, e.g. lowering τ_{DC} through reduction of the electrode area. The fastest switching times reported for organic memories are on the order of 10 ns [5].

Subsequently, the dynamics of repeated switching events were investigated using a fixed programming pulse length of 0.5 ms and varying the delay time between the programming cycles. The voltage sequence is shown in

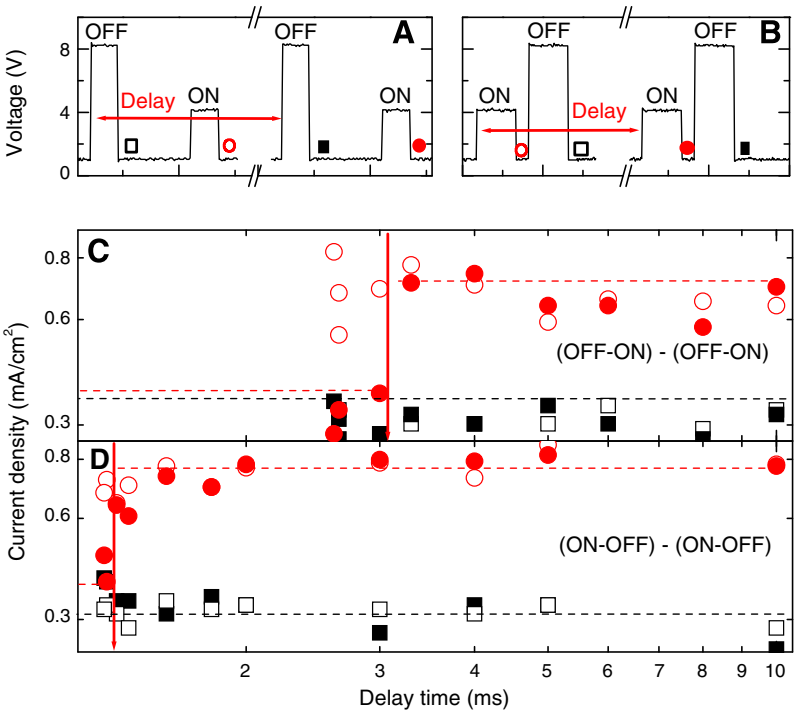

Fig. 4. (A, B) Pulse sequence for (OFF–ON)-(OFF–ON) and (ON–OFF)-(ON–OFF) switching, and (C, D) Current density under application of +1 V bias voltage monitoring the conductivity state after : □ first +8 V OFF pulse ; ○ first +4 V ON pulse ; ■ second +8 V OFF ; ● second +4 V, ON pulse.

Fig. 4. Using a high bias of 8 V, the memory is switched OFF. After 1 ms, the memory is switched back to the ON state. This pulse sequence is repeated after a variable delay time. In these experiments, the device is coupled to the pulse generator via a resistor (1 kΩ), resulting in a τ_{DC} of 3 μs. The current density is measured after each pulse with an oscilloscope using a low reading voltage of 1 V. Fig. 4 shows the current density in the first cycle (open symbols) and the second cycle (closed symbols) as a function of delay time between the cycles. Repeated OFF–ON switching is presented in Fig. 4C. For times longer than 3 ms the current densities in the first and second cycles are identical; the closed symbols overlap the open symbols. For shorter delay times the memory can be switched in the first cycle (open symbols) but not anymore in the second programming cycle (closed symbols). This demonstrates the presence of a dead time of about 3 ms for OFF–ON switching. Similarly, Fig. 4D shows a dead time of about 1.5 ms for repeated ON–OFF switching. The difference between repeated OFF–ON and repeated ON–OFF switching is not yet understood. We note that the dead times obtained from the pulse measurements agree very well with the dead time obtained using a saw tooth bias profile and are several orders of magnitude longer than τ_{DC} Therefore, the millisecond dead time can only be due to an intrinsic, slow process within the active layer(s) of the diode and puts a limitation on the access time of the memory.

In systems exhibiting voltage controlled NDR, domains with high and low resistivity form spontaneously, leading to an inhomogeneous distribution of charge density inside the material [24]. The domain boundaries relocate when changing the applied voltage [25] and the "dead time" can now be interpreted in terms of a time needed for domain boundary relocation and redistribution of charge density, in such a way that a next switching event can occur. The huge variation in reported switching times can be explained by the different measuring protocols. Measurements of single switching events yield microsecond switching times. The use of repeated switching cycles invariably leads to millisecond switching times dominated by the dead time.

We note that the occurrence of a dead time is a key ingredient to observe unipolar switching. At high bias the memory is programmed in the high resistance OFF-state. When the bias voltage is ramped down on a time scale smaller than the dead time, the memory cannot switch back to the ON-state. The OFF-state is preserved. Thus, a dead time is a prerequisite for unipolar memory operation.

Acknowledgments

We thank Michael Büchel for device preparation. This research forms a part of the research programme of the Dutch Polymer Institute (DPI), project #523. We gratefully acknowledge financial support from the EC (project Poly-Apply IST-IP-507143), and Fundação para a Ciência e Tecnologia , research unit 631, CEOT.

References

[1] J.C. Scott, L.D. Bozano, Adv. Mater. 19 (2007) 1452.
[2] A. Prakash, J. Ouyang, J.-L. Lin, Y. Yang, J. Appl. Phys. 100 (2006) 054309.

[3] R. Müller, R. Naulaerts, J. Billen, J. Genoe, P. Heremans, Appl. Phys. Lett. 90 (2007) 063503.
[4] M. Cölle, M. Büchel, D.M. de Leeuw, Org. Electron. 7 (2006) 305.
[5] L.P. Ma, J. Liu, Y. Yang, Appl. Phys. Lett. 80 (2002) 2997.
[6] L. Ma, S. Pyo, J. Ouyang, Q. Xu, Y. Yang, Appl. Phys. Lett. 82 (2003) 1419.
[7] L. Ma, Q. Xu, Y. Yang, Appl. Phys. Lett. 84 (2004) 4908.
[8] D. Ma, M. Aguiar, J.A. Freire, I.A. Hümmelgen, Adv. Mater. 12 (2000) 1063.
[9] H.K. Henisch, W.R. Smith, Appl. Phys. Lett. 24 (1974) 589.
[10] F.L.E. Jakobsson, X. Crispin, M. Cölle, M. Büchel, D.M. de Leeuw, M. Berggren, Org. Electron. 8 (2007) 559.
[11] J. Chen, D. Ma, Appl. Phys. Lett. 87 (2005) 23505.
[12] H.X. He, X.L. Li, N.J. Tao, L.A. Nagahara, I. Amlani, R. Tsui, Phys. Rev. B 68 (2003) 45302.
[13] B. Mukherjee, S.K. Batabyal, A.J. Pal, Adv. Mater. 19 (2007) 717.
[14] R. Müller, R. Naulaerts, J. Billen, J. Genoe, P. Heremans, Appl. Phys. Lett. 90 (2007) 063503.
[15] F. Verbakel, S.C.J. Meskers, M. Cölle, M. Büchel, H.L. Gomes, R.A.J. Janssen, D.M. de Leeuw, Appl. Phys. Lett. 91 (2007) 192103.
[16] A. Beck, J.G. Bednorz, C. Gerber, C. Rossel, D. Widmer, Appl. Phys. Lett. 77 (2000) 139.
[17] R. Waser, M. Aono, Nature Mater. 6 (2007) 833.
[18] S. Karthäuser, B. Lüssem, M. Weides, M. Alba, A. Besmehn, R. Oligschlaeger, R. Waser, J. Appl. Phys. 100 (2006) 094504.
[19] T. Oyamada, H. Tanaka, K. Matsushige, H. Sasabe, C. Adachi, Appl. Phys. Lett. 83 (2003) 1252.
[20] H.L. Gomes, A.R. Benvenho, D.M. de Leeuw, M. Cölle, P. Stallinga, F. Verbakel, D.M. Taylor, Org. Electron. 9 (2008) 119.
[21] L.D. Bozano, B.W. Kean, V.R. Deline, J.R. Salem, J.C. Scott, Appl. Phys. Lett. 84 (2004) 607.
[22] J.G. Simmons, R.R. Verderber, Proc. R. Soc. Lond. Ser. A 301 (1967) 77.
[23] R.D. Gould, C.A. Hogarth, Phys. Status Solidi (a) 23 (1974) 531.
[24] B.K. Ridley, Proc. Phys. Soc. 82 (1963) 954.
[25] K.J. Lou, H.T. Grahn, K.H. Ploog, Phys. Rev. B 57 (1998) R6838.

the electron injection electrode, and by judiciously selecting the right material for the gate insulator [7,8].

These approaches are interesting from a scientific viewpoint. However, when a single material system takes charge of both the luminescence and the charge transportation functions, either the luminescence performance or the electric performance is sacrificed, because, in many cases, the quantum yield of luminescence and electrical performance of material are related to trade-off. Moreover, it is also a problem that the EL efficiency of OLET is lower than that of general organic light-emitting diodes (OLEDs) when most carrier doses not contribute EL, if there is a significant difference between the mobility of the electron and the hall. To increase the EL efficiency and reduce the driving voltage by improving electrical performance of the devices, externally controllable carrier balance and enough high quantum yield of luminescence at recombination/light-emitting site are required.

Specialized OLETs were earlier reported by the authors with a horizontal PN-hetero-boundary combined with electron and hole transport materials along the carrier channels (PN-OLETs) [1]. In this device structure, the carrier recombination and thus photon generation happen at the interface between two organic semiconductor materials with different polarity or at a thin light-emitting layer inserted between them. It is by deliberate insertion of PN-boundary that the carrier balance and EL efficiency can be enhanced. Moreover, the role of light-emission and charge transport is split up with multiple materials, resulting in a decrease of the driving voltage. The EL efficiency may improve, because enough distance exists between the light-emitting area and the metal electrodes absorbing the light. In addition, by applying the hole-source with the patterned p-type semiconductor to an injection electrode of minority carriers, the diverging current by hole as miner carrier at the low gate voltage region, which can be seen with a general ambipolar transistor, is expected to be suppressed and the on/off ratio of the current and the luminance maintained high.

However, during actual investigation of PN-OLET there was a problem in the controllability of the current and the EL intensity by the gate. The light-emitting surface of the PN-OLETs consists of the liner-emitting area arranged to move side by side. Consequently, it was necessary to narrow down the width of this liner-emitting area, namely channel length, and to arrange it in a high density to obtain high EL intensity from the light-emitting surface. Yet, when the length of the channel was actually shortened, it was found that the on/off ratio of the current and the EL intensity decreased significantly. It was realized that this problem originated in a similar effect to the short channel effect caused by the influence of parasitic resistance in the device.

Hence, in this research, an attempt was made to improve the carrier balance and the on/off ratio of the current and the luminance by controlling injection of each carrier independently with the split-gate structure [9]. It was proved that the on/off ratio of the current and the luminance could be improved from 10 or less with the single-gate structure up to 1000 with the split-gate structure without substantial change in the maximum luminance and the external quantum efficiency.

2. Experiment

The conceptual structure of the PN-OLET with the split-gate is shown Fig. 1.

The fabrication process of our device is as follows. First, a 100 nm-thick aluminum–tantalum alloy gate electrode, split into two, was formed with photolithography on the insulating substrate, and then a 250 nm-thick layer of SiO_2 was formed on the gate electrode through chemical vapor deposition. Next, the 50 nm-thick electron-source––a comb-shaped mesh––and hole-source were formed on the gate insulator to the split of gate located between the two sources. The gap-length of the split-gate and the channel length of the transistor are l μm and 3 μm, respectively. The line-density of the light-emitting area was 166 line/mm.

The horizontal PN-boundary structure was fabricated by photolithographic lift-off patterning of thin-films of organic semiconductor on the electrode substrate aforementioned. This patterning was done using the alkaline water as a lift-off solvent, instead of the organic solvent, to minimize the damage to the organic semiconductor film. The details of the patterning process of organic films were given in an earlier report [1]. By this technique, fine slit pattern of pentacene, with at least 0.5 μm-width, could be formed so far, although more minute patterns were considered possible. Therefore, this lift-off patterning can possibly be applied not only to fabrication of PN-hetero-boundary OLETs, but also to the isolation processing of organic thin-film transistors (OTFTs) for preventing current leakage between adjacent devices in integrated circuits, in high-definition pixel patterning for OLEDs display, and so on.

The organic semiconductor pattern, which covered one of the comb-shaped source electrodes, consists of a 3 nm-thick copper phthalocyanine (CuPc) film stacked on 47 nm-thick pentacene film as p-type material. The CuPc layer was inserted to decrease the influence of interfacial barrier on continuous deposition of the organic EL layer, and to decrease the driving voltage. Subsequently, 15 nm-thick *N*,*N*′-bis(3-methylphenyl)-*N*,*N*′-diphenylbenzidine (TPD) as hole transport layer, 2.5 nm-thick 2 wt% 4-(dicyanomethylene)-2-methyl-6-(4-dimethylaminostyryl)-4H-pyran (DCM) doped tris(8-hydroxyquinolinato)aluminum(III) (Alq_3) as a light-emitting layer and 12.5 nm-thick Alq_3 as an electron transport layer were formed on the whole area of the substrate with the patterned CuPc/pentacene. Finally, 50 nm-thick *N*,*N*′-dihexyl-1,4,5,8-naphthaleneterracarboximide (C6-NTC), as an n-type organic

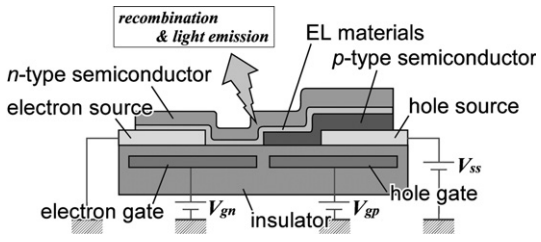

Fig. 1. The schematic structure of the PN-hetero-boundary organic light-emitting transistor with the split-gate structure.

semiconductor, was formed after the deposition of 3 nm-thick 2,9-dimethyl-4,7-diphenyl-1,10-phenanthroline (bathocuproine: BCP), which was inserted for avoiding the quenching of the excitons at the interface of Alq_3 and C6-NTC that disturbs the EL from the Alq_3 layer [10].

The energy level diagram along the expected charge pass in the device was shown in Fig. 2. By the large LUMO level gap at the interface of TPD/Alq_3 and the large HOMO level gap at the interface of Alq_3/BCP, it is expected that the electron and the hole are confined into the Alq_3 layer and contribute to the EL from the Alq_3 layer. Moreover, the step-like profile of HOMO on the hole injection side (left side) seems to contribute to smooth transportation of the hole. On the other side, the ragged profile of LUMO on the electron injection side (right side) seems to causes a high operation voltage as considered in the discussion part.

The optical and electrical properties of the devices were measured in probe station TTP4 (Lake Shore Cryotronics, Inc.) under 1×10^{-3} Pa pressure. For source–source current (I_{ss}) and the luminance (L) measurement, the combination of semiconductor parameter analyzer 4155C (Agilent Technologies, Inc.) and low-power detector 818-UV (Newport Corporation) was employed.

In this study, the device was driven by sweeping the potential of the hole-source like a drain electrode in driving for measurement of static characteristics of OTFTs, when the electron-source was fixed to the ground potential. Then, the potential of the electron-gate was changed at regular intervals. During each setting of the electron-gate potential, the source–source voltage (V_{ss}) sweeping, and similarly, the potential of the hole-gate were kept constant. We expected balanced carrier injection and high on/off ratio of the current and the luminance to be achieved by the appropriately selected hole-gate potential.

The device was designed to be suitable for n-type driving polarity. Applying the hole-source with the patterned p-type semiconductor to an injection electrode of minority carriers is important to achieve high on/off ratio of the I_{ss} and emission intensity, and to keep down the diverging current of minority carriers at the low gate voltage region, as normally observed in conventional organic ambipolar transistors. Why the n-type semiconductor for a top layer was used, rather than the p-type, was because the naphthaleneterracarboximide derivatives as n-type semiconductor, by virtue of their unique charge transmission mechanism [11], showed sufficient electric performance, even if the molecular orientation was disordered under the influence of the ragged surface of the lower layer.

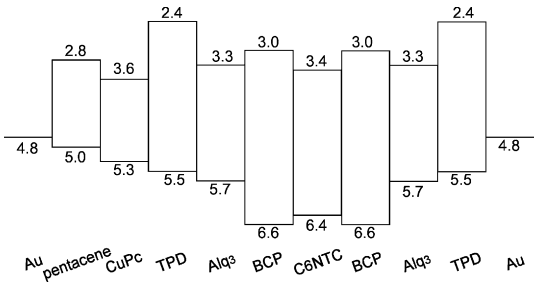

Fig. 2. The energy diagrams along the expected carrier pass in the PN-OLETs.

3. Discussion of results

The V_{ss} dependence of the I_{ss} and the L of the conventional single-gate PN-OLETs and the split-gate PN-OLETs with hole-gate voltage of +60 V were shown in Fig. 3a and b, respectively. Both PN-OLETs were fabricated on the same substrate, and all the organic active layers were deposited at the same time. By introducing the split-gate, the I_{ss} and the L at a low electron-gate voltage were successfully suppressed while those at a high electron voltage were kept almost constant. Incidentally, the L of about 100 cd/m^2 was obtained at 15 V in the V_{ss} with turn-on voltage of less than 10 V.

By the way, in the typical organic ambipolar transistor, it is anticipated that the accumulation of the hole occurs only when the potential of the hole-source becomes higher than that of the hole-gate. However, this is not coherent to our experimental result that the EL was observed by the V_{ss} of 10 V or less. This discrepancy between typical organic ambipolar transistors and our device might originate in the patterned and multilayered complex organic semiconductor layer of our device. To clarify the operation mechanism of our device, we plan to study the characteristic of the split-gate transistors with simpler semiconductor layer structure in the future.

The ratios of I_{ss} and L at the electron-gate voltage of −10 V (off) and at +30 V (on) of split-gate PN-OLET were shown in Fig. 4a and b. In both 15 V and 30 V in the V_{ss}, the on/off ratio improved exponentially with change in the hole-gate voltage into positive direction, and the on/off ratio of 1000 or more was achieved at +60 V in the hole-gate voltage for both the I_{ss} and the L. On the other hand, the on/off ratio became less than that of the single-gate PN-OLET with change in hole-gate voltage into negative direction. The criterion of suitable hole-gate voltage was based on the assumption that the off-current and the off-luminescence observed at low electron-gate voltage originated mainly and unexpectedly in the hole current. Therefore, the objective of controlling the off-current was achieved by fixing the hole-gate voltage to positive potential that depresses the accumulation of the hole.

The V_{ss} dependences of the external quantum efficiency (η_{ext}) of conventional single-gate PN-OLETs and split-gate PN-OLETs were shown in Fig. 5a–c. When the V_{ss} was varied, a single peak appeared in the η_{ext}. Such phenomenon may originate from an inversion of the amount of accumulated electrons and holes in response to variance in the potential of gate and hole-sources. This inversion caused by the device is characteristic of ambipolar OTFTs in which one of the charge currents draws the saturation curve, when the other charge current exponentially increases with change in the V_{ss}. The timings of the inversion of the amount of carrier depend on the relation between the potentials of different electrodes. Hence, in conventional single-gate PN-OLETs, the V_{ss}, at which the peak η_{ext} appears, changes depending on the gate voltage, especially at the low gate voltage region. Such a trend was observed

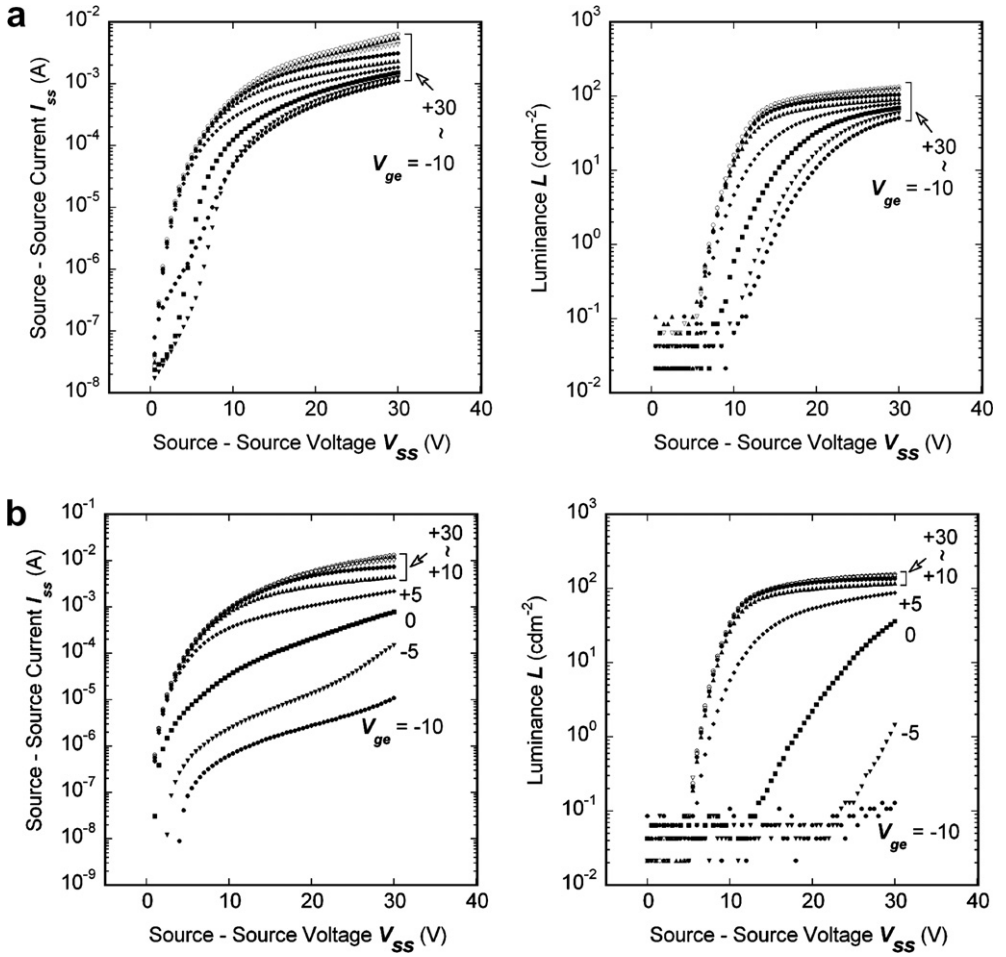

Fig. 3. The dependence on the source to source voltage for the source–source current and the luminance of (a) the conventional single-gate PN-OLETs and (b) the split-gate PN-OLETs with hole-gate voltage of +60 V.

in the split-gate type device too. Additionally, in the split-gate type device, the electron-gate dependency of peak position rises when the potential of the hole-gate changes into positive direction and falls when the potential of the hole-gate changes into negative direction. This experimental result implies that the amount of hole carrier at the low electron-gate voltage region decreases as the potential of hole-gate increases in the positive direction, and as a result the off-current is depressed.

The major problem in improving the device performance of PN-OLETs is that the η_{ext} of PN-OLETs is significantly lower than that of OLEDs of the same EL materials. When the split-gate structure was introduced to PN-OLET, considerable improvement was expected in the EL efficiency in terms of achieving independent control of the potential of the two gates. However, as shown in Fig. 4, not only was there practically no difference in the single-gate device, but also the control of the potential of the hall gate was not fully independent. The incompleteness of confinement of exciton that contributes to the luminescence of the EL layer is considered possibly responsible for the low EL efficiency, because the EL layer is thinner than OLEDs (especially Alq_3 layer). However, no substantial change in η_{ext} was observed when the thickness of the EL layer was doubled or halved. It follows, therefore, that the chief cause for low EL efficiency could be something else.

Surprisingly, the parasitic resistance that exists in the present PN-OLETs structure is now considered the possible cause for low EL efficiency. Based on the energy diagram (Fig. 2), it is believed that there has been a significant voltage drop between the electron-source and the hole-source in the EL layer, because the resistance of the organic semiconductors, such as pentacene and C6-NTC, is small as compared to that of the emitting layer such as TPD and Alq_3. The EL layer located at the interface of the electron-source/the n-type material is possibly deleterious to the device performance. It is conjectured that the EL layer at the electron-source/the n-type material interface causes a big parasitic resistance, because the EL layer has a reverse bias against the direction of the charge migration at that interface. The parasitic resistance at this point changes the ideal electric field distribution in the device significantly and disturbs the control of the carrier balance by the gate and/or degenerate the EL efficiency by generating, for instance, the unexpected charge pass. For studying these problems, it is necessary to fabricate a device with

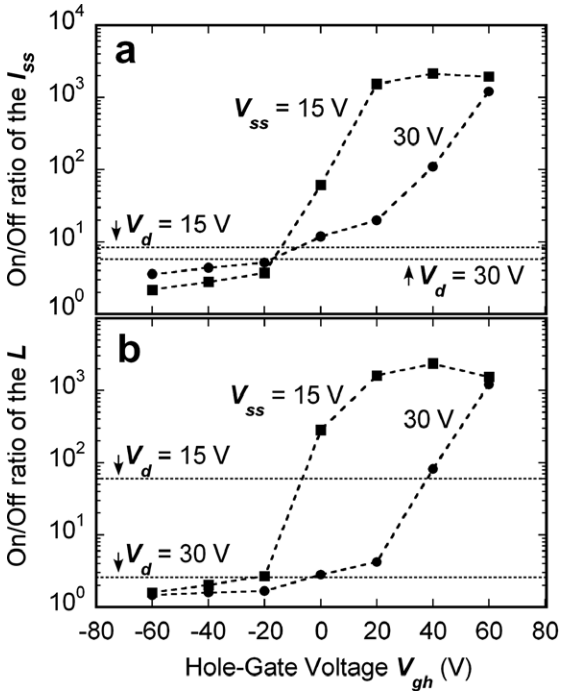

Fig. 4. The on/off ratios of I_{ss} and L at the electron-gate voltage of −10 V (off) and at +30 V (on) in the split-gate PN-OLETs.

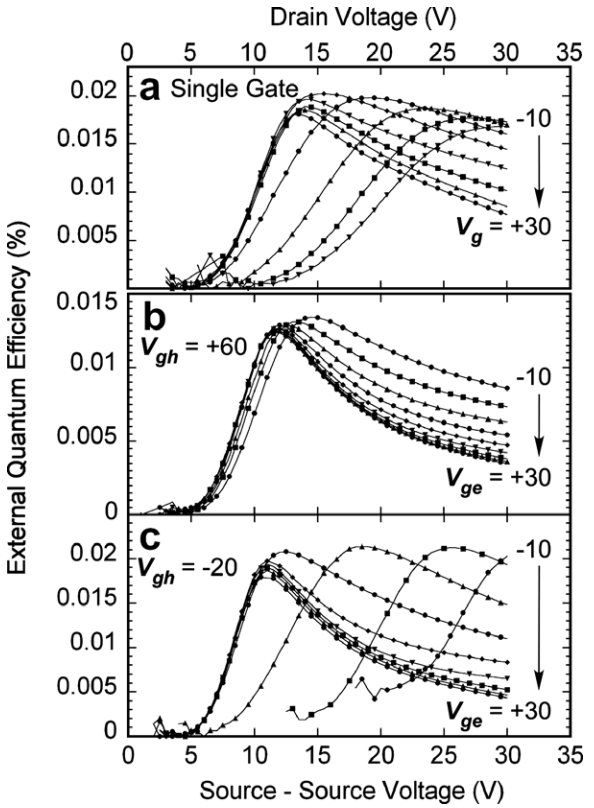

Fig. 5. The dependence on the source to source voltage for the external quantum efficiency of (a) the single-gate PN-OLETs, (b) the split-gate PN-OLETs with the hole-gate voltage of +60 V and (c) −20 V.

no EL layer on the electron-source/the n-type material interface. Accordingly, a new fabrication process is being developed where this extra layer is not formed. By eliminating parasitic resistance, the split-gate structure is expected to contribute to the improvement of not only the on/off ratio, but also the carrier balance.

4. Conclusions

In this research, the on/off ratio of the I_{ss} and the L of the original device structure were successfully improved by introducing the split-gate structure into the PN-OLETs. This split-gate structure can be expected to contribute to improve not only the on/off ratio but also the EL efficiency by improving the charge balance in the PN-OLETs with the parasitic-resistance-less structures that are being developed by the author. In addition, it is emphasized that the split-gate structure may prove useful not only for PN-OLETs but also for general MOS-type OLETs that have the single material systems for active layer.

Acknowledgments

This work was supported by the Integrative Industry-Academia Partnership (IIAP) including Kyoto University, Nippon Telegraph and Telephone Corporation, Pioneer Corporation, Hitachi, Ltd., Mitsubishi Chemical Corporation, and Rohm Co., Ltd., as well as by the Special Coordination Funds for Promoting Science and Technology from the Ministry of Education, Culture, Sports, Science and Technology of Japan.

References

[1] N. Suganuma, N. Shimoji, Y. Oku, K. Matsushige, Novel organic light-emitting transistors with PN-heteroboundary carrier recombination sites fabricated by lift-off patterning of organic semiconductor thin films, J. Mater. Res. 22 (2007) 2982;
N. Suganuma, N. Shimoji, PCT Int. Appl. WO2007/010925;
N. Suganuma, PCT Int. Appl. WO2007/026703.
[2] A. Hepp, H. Heil, W. Weise, M. Ahles, R. Schmechel, H. von Seggern, Light-emitting field-effect transistor based on a tetracene thin film, Phys. Rev. Lett. 91 (2003) 157406.
[3] M. Ahles, A. Hepp, R. Schmechel, H. von Seggern, Light emission from a polymer transistor, Appl. Phys. Lett. 84 (2004) 428.
[4] T. Sakanoue, E. Fujiwara, R. Yamada, H. Tada, Visible light emission from polymer-based field-effect transistors, Appl. Phys. Lett. 84 (2004) 3037.
[5] T. Sakanoue, E. Fujiwara, R. Yamada, H. Tada, Preparation of organic light-emitting field-effect transistors with asymmetric electrodes, Chem. Lett. 34 (2005) 494.
[6] T. Oyamada, H. Sasabe, C. Adachi, S. Okuyama, N. Shimoji, K. Matsushige, Electroluminescence of 2,4-bis(4-(2-thiophene-yl) phenyl)thiophene in organic light-emitting field-effect transistors, Appl. Phys. Lett. 86 (2005) 093505.
[7] J.S. Swensen, C. Soci, A.J. Heeger, Light emission from an ambipolar semiconducting polymer field-effect transistor, Appl. Phys. Lett. 87 (2005) 253511.
[8] J. Zaumseil, R.H. Friend, H. Sirringhaus, Spatial control of the recombination zone in an ambipolar light-emitting organic transistor, Nat. Mater. 5 (2006) 69.
[9] C. Adachi, N. Suganuma, PCT Int. Appl. WO2005/072018.
[10] A. Nollau, M. Hoffmann, T. Fritz, K. Leo, Dissociation of excitons in organic dye layers of perylene derivatives, Thin Solid Films 368 (2000) 130.
[11] H. Tachikawa, H. Kawabata, R. Miyamoto, K. Nakayama, M. Yokoyama, Experimental and theoretical studies on the organic–inorganic hybrid compound: aluminum-NTCDA co-deposited film, J. Phys. Chem. B 109 (2005) 3139.

standard planar structure has remained virtually unchanged and still is the most widely used device geometry. Planar OFETs can have either a top gate (TG) or bottom gate (BG) configuration, yet processing an OFET with both top and bottom gate present enables the study of a whole new device structure. Moreover, the dual gate OFET (DG-OFET) could further improve the performance of organic TFTs, without adding a significantly higher complexity to the processing of devices.

One of the main bottlenecks for the practical applications of OFETs in the electronic industry is the instability of the materials during operation under environmental conditions and the limited control of the electrical parameters of the device. A very important issue is the control of the threshold voltage (V_{TH}), which becomes crucial for proper operation, low power consumption and increasing the noise margin, especially in complicated organic circuitry. The first issue is often solved either by using an environmentally stable organic semiconductor [7,8] or by coating the device with a passivating material. The second issue is often more difficult and can be achieved, to a limited extend, by modifying the surface of the dielectric with self-assembled monolayers [9]. A DG-OFET solves both problems at once: the top insulator acts as a passivating layer by protecting the semiconductor from ambient, and the top gate can be used to accurately control the threshold voltage. The use of DG-OFET devices has already been exploited to significantly improve the noise margin in organic circuitry [10]. Furthermore, the DG-OFET has the potential to expand the possibilities of what has already been achieved and thoroughly studied with common organic TFT devices.

Dual-gate transistors, and even triple gate FETs, have already been researched extensively in the field of inorganic, e.g. silicon, electronics [11]. Modeling and analysis of organic dual-gate transistors however has only been recently developed [12–16], mostly on devices with evaporated pentacene as semiconductor rather than polymer semiconductors cast from solution. Recently, a linear dependence between the threshold voltage of the bottom channel (V_{TH}) and the applied top gate (V_{GT}) was proposed and observed, with the slope of the linear fit equal to the ratio between the capacitances of both dielectric layers [14]. In this work, DG-OFETs (Fig. 1) processed from solution with p-type polymeric semiconductors and polymeric top dielectrics are investigated. We demonstrate that a single linear relationship between V_{TH} and V_{GT} is incomplete for a DG-OFET with both the top and bottom channels active, since the influence of the top gate potential on the bottom channel is screened by the charge carriers in the top channel and vice versa. Furthermore the transfer characteristics of the DG-OFET will be discussed in which a transition region is clearly observed when both channels are properly working.

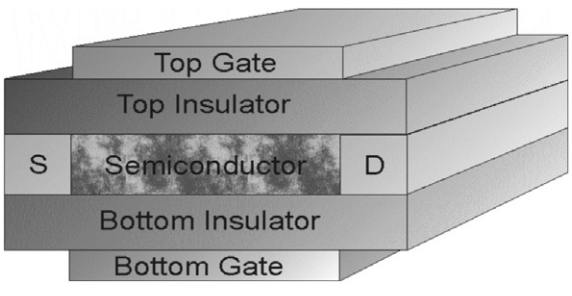

Fig. 1. Schematic structure of the dual-gate organic field-effect transistor.

2. Experimental procedure

The DG-OFETs were processed using heavily n-doped silicon wafers as bottom gate electrode, with a 200 nm thick thermally grown silicon oxide layer as bottom insulator with a capacitance of 17 nF cm^{-2}. Gold source and drain electrodes were patterned on top of the oxide layer by conventional lithography. An interpenetrating finger structure was used with channel lengths varying from 5 to 40 μm and a constant channel width of 10,000 μm. The oxide layer was treated with the primer hexamethyldisilazane (HMDS) in order to make the surface hydrophobic to improve wetting and prevent charge trapping at the interface [17]. The described FET-substrates were provided by Philips Research Laboratories Eindhoven.

The polymer semiconductors used were poly(4,4′-didecylbithiophene-*co*-2,5-thieno[2,3-*b*]thiophene) (PDTT) [18], poly(2-methoxy-5-(2′-ethylhexyloxy)-1,4-phenylene vinylene) (MEH-PPV), both synthesized at the University of Groningen, and regioregular poly(3-hexylthiophene) (rr-P3HT, electronic grade; 98.5% regioregular; Rieke Metals, Inc.). rr-P3HT was dissolved in distilled toluene, dedoped with hydrazine at 60 °C and precipitated in methanol. The fraction collected was Soxhlet extracted for at least 64 h with methanol, *n*-hexane, dichloromethane and finally with chloroform. The chloroform fraction was precipitated in methanol, dried under vacuum and stored in a glove box under N_2 atmosphere. All polymers are shown in Fig. 2.

PDTT, rr-P3HT and MEH-PPV were dissolved in 1,2-dichlorobenzene, chloroform and toluene, respectively, and spin coated on top of the prefabricated substrates. The PDTT films were annealed at 125 °C on a hotplate for 30 min. Subsequently, the dielectric film was spin coated on top of the semiconductor. The dielectrics used were polystyrene (PS) and polymethylmethacrylate (PMMA) dissolved in methylethyl ketone (MEK). The dielectrics were spin coated at different speeds in order to achieve different layer thicknesses. Finally, 60 nm Ag was evaporated through a shadow mask as top gate electrode. Transfer and output characteristics of the DG-FETs were recorded in vacuum (<10^{-5} mbar) and in the dark at room temperature, using a Keithley 4200 semiconductor parameter analyzer. The lowest current limit measurable by the Keithley 4200 is 1–10 nA.

3. Results and discussion

The fundamental principles of the operation of the DG-OFET do not differ from that of a common organic TFT. In a single gate OFET (SG-OFET) the charges are induced by the gate potential at the semiconductor/insulator interface

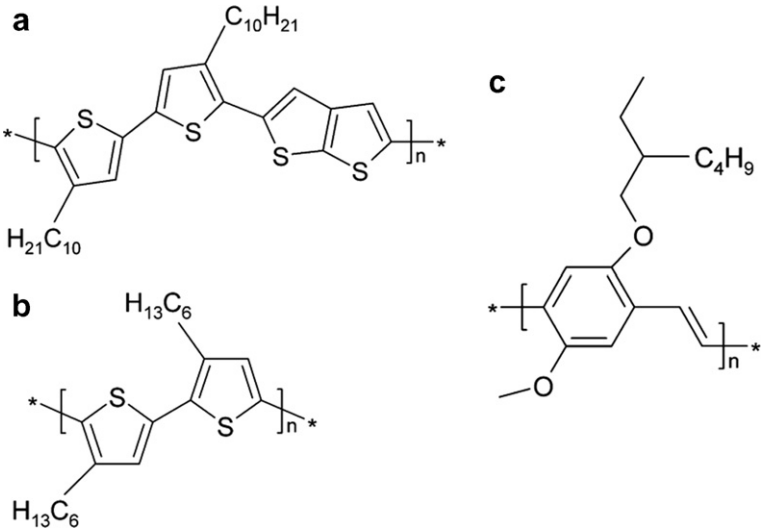

Fig. 2. Chemical structure of: (a) poly(4,4′-didecylbithiophene-*co*-2,5-thieno[2,3-*b*]thiophene) (PDTT); (b) regioregular poly(3-hexylthiophene) (rr-P3HT) and (c) poly(2-methoxy-5-(2′-ethylhexyloxy)-1,4-phenylene vinylene) (MEH-PPV).

forming a conducting channel. The induced charges are mostly confined in the first 5 nm from the interface [19], hence the conduction is dominated by this thin channel rather than by the bulk. This implies that the two channels in DG-OFETs with semiconductor layers thicker than ~15 nm will thus remain independent and will not merge. The formation of the channel, in addition to creating a conducting path between the source and drain electrodes, also screens the gate potential similar to the operation of a plate capacitor. This means that when a channel is in the accumulation regime, the gate that causes the accumulation is fully screened by the charges within the first 5 nm and the second channel will not feel the presence of this gate.

Sweeping single gate potentials in a dual-gate device, leaving the other gate floating, will therefore give separate and independent characteristics for the two channels. The results for the single-gate measurements of a typical DG-OFET with PDTT (25 nm) as the semiconductor and PS (430 nm) as top dielectric are shown in Fig. 3. The figure shows the output and transfer characteristics of the top and bottom channels of the DG-OFET measured independently. The currents of both channels are of the same order of magnitude, hence the conduction in the channels is similar. The mobilities calculated from the transfer characteristics in the linear regime are also similar since the capacitances of both dielectrics are comparable. The mobilities found (for $V_D = -5$ V and $V_G - V_{TH} = -20$ V) are 7.3×10^{-3} cm^2 V^{-1} s^{-1} for the bottom channel and 2.2×10^{-3} cm^2 V^{-1} s^{-1} for the top channel. The threshold voltage of the bottom channel is −5.3 V at $V_D = -5$ V and −6.0 V at $V_D = -45$ V. The threshold voltage of the top channel is +3.0 V at $V_D = -5$ V and +3.9 V at $V_D = -45$ V. Crucial for analyzing the true properties of a dual-gate device is that a DG-OFET is obtained in which both channels exhibit similar mobilities. We also note that in Fig. 3a and b the saturation of the output characteristics occurs earlier than expected: for $V_G = -40$ V the source-drain bias that marks the onset of saturation is around −30 V rather than −40 V. This is explained by the fact that one gate is not connected. Consequently, this floating gate will have an effective potential which lies between the source and drain bias, depending on the leakage resistances between source-gate and drain-gate, The potential of the floating gate results in an additional electrostatic coupling. Fig. 4 shows the forward and backward scans of the transfer characteristics of two DG-OFETs with different materials and layer thicknesses, when the bottom gate potential is swept while keeping the top gate potential constant at different top gate potentials. There is almost no hysteresis present in the scans of both of the devices.

From Fig. 4 we extract the bottom channel threshold voltage (V_{TH}). The threshold voltage is defined as the onset of strong inversion [20]. Although most organic transistors only operate in accumulation mode and show no current in inversion, the classical metal-oxide-semiconductor field-effect theory is used to extract the V_{TH} from the transfer characteristics of the transistor in accumulation mode, where the current depends quadratically on the gate voltage: $I_D \sim (V_G - V_{TH})^2$. The square root of the saturation current is then plotted against the gate voltage, V_G. This curve is fitted linearly and the intercept on the V_G-axis is defined as the V_{TH} of the transistor. At the threshold voltage the amount of accumulated charges in and organic semiconductor, Q_G, is equal to zero and this point defines the onset of the charge accumulation. The threshold voltage, for the device depicted in Fig. 4b is plotted as a function of the top gate voltage in Fig. 5 and clearly demonstrates the shift in threshold voltage.

The linear relationship previously reported [13–15] is also found here, yet a more detailed analysis of the data demonstrates two linear relationships to be present. The intercept of the two linear fits is close to zero top gate bias.

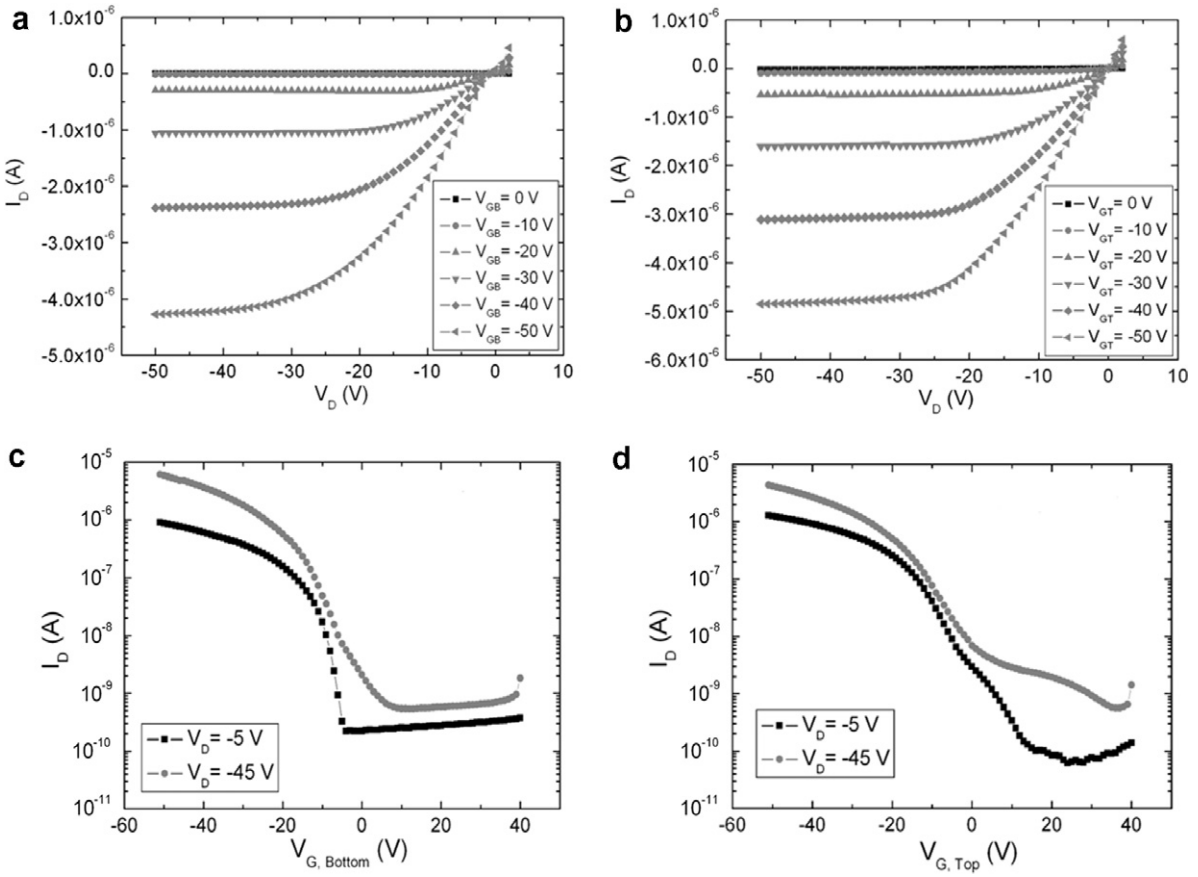

Fig. 3. Device characteristics of the bottom and top channel in a DG-OFET, measured separately. (a) and (c) are the output and transfer characteristics of the bottom channel, respectively. (b) and (d) are the output and transfer characteristics of the top channel. The device is a finger FET with $L/W = 20/10{,}000$ with PDTT as semiconductor (thickness 25 nm) and polystyrene as the top dielectric (thickness 430 nm). The mobilities obtained (for $V_G - V_{TH} = -20$ V) are 7.3×10^{-3} cm^2 V^{-1} s^{-1} for the bottom channel and 2.2×10^{-3} cm^2 V^{-1} s^{-1} for the top channel.

This double linear relationship can be readily explained from the working principle of the DG-OFET having two active channels.

The current in the channel is dependent on the amount of charges, Q_G, which are induced by the gate potential. If one of the channels is depleted (or 'OFF'), screening of the field does not occur and, consequently, the other channel will depend on *both* gates via:

$$Q_G = C_2 V_{GT} + C_1 V_{GB} \quad (1)$$

where C_2 is the capacitance of the layer between the channel and the top gate, C_1 the capacitance of the layer between the channel and the bottom gate, and V_{GT} and V_{GB} are the top and bottom bias, respectively. Note that C_1 or C_2 can consist of the capacitance of a dielectric layer in series with the capacitance of the semiconducting layer. In these devices, the bottom gate potential is swept while the top gate voltage is held constant. If the bottom gate voltage, V_{GB}, is more positive than the threshold voltage V_{TH}, no appreciable accumulation of charges in the channels is expected. The point where $V_{GB} = V_{TH}$ marks the onset for charges to accumulate at the semiconductor-insulator interface. At this point no charges have accumulated and $Q_G = 0$. Then, from rearranging Eq. (1), the threshold voltage, when sweeping V_{GB}, will depend on V_{GT} in the following way:

$$V_{GB} = V_{TH} = -\frac{C_2}{C_1} V_{GT} = -\Delta \cdot V_{GT} \quad (2)$$

where $-\Delta$ is the slope of the line obtained by plotting V_{TH} versus V_{GT}. As shown in Fig. 5, we obtain two cases by sweeping the bottom gate bias and stepping the top gate bias at fixed values. We note that p-type semiconductors are used in these devices.

Now several scenarios are possible, depending on the different regimes of screening within the DG-OFET:

(1) When the top gate potential is held *negative*, the top channel is in the accumulation regime. However, by setting the bottom gate at sufficiently positive values we can fully deplete the top channel. This is observed in Fig. 4 for bottom gate voltages larger than +20 V. Thus when the bottom gate is sufficiently positive both channels are depleted and the top channel is sensitive for both gate potentials since no charge in the bottom channel is present to screen the bottom gate. According to Eq. (1) sweeping V_{GB}

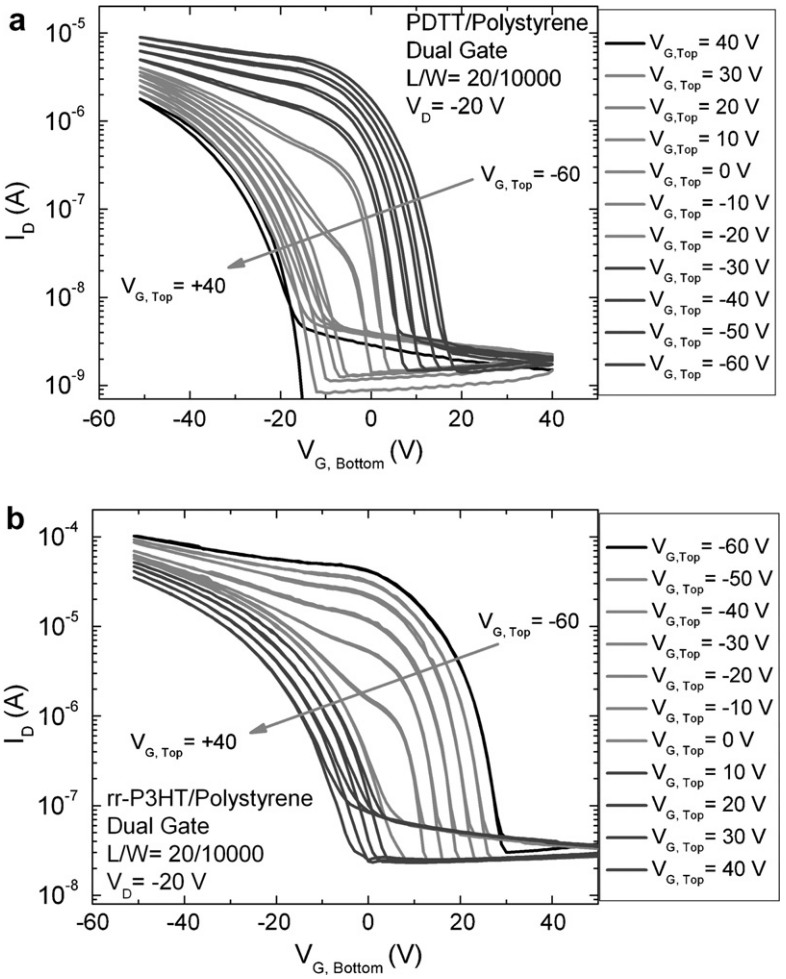

Fig. 4. Forward and backward scans of the transfer curves for two DG-OFET with different capacitance ratios and materials in dual-gate mode. The bottom gate bias was swept from +40 to −50 V while the top gate bias was held constant. The sweeps were repeated for different top gate biases, varied with steps of 10 V from +40 to −60 V. The devices shown are: (a) a finger transistor with $L/W = 20/10{,}000$ with PDTT as semiconductor (thickness 25 nm) and polystyrene (thickness 430 nm) as the top dielectric, and (b) a finger transistor with $L/W = 20/10{,}000$ with rr-P3HT as semiconductor (thickness 75 nm) and polystyrene (thickness 450 nm) as the top dielectric. The drain–source voltage was equal to −20 V for both devices.

to less positive values will lead to the point where $V_{GB} = V_{TH}$ and charges will start to accumulate in the *top channel* while the bottom channel will still be depleted. The accumulation of charges will occur in the top channel first because of a constant negative top gate potential is applied.

Since the accumulation occurs in the *top channel* from Eq. (1) it is found that the capacitance C_1, between the bottom gate electrode and the top channel, will be equal to the capacitances of the bottom insulator (C_B) and the semiconductor layers (C_S) in series: $C_1 = (1/C_B + 1/C_S)^{-1}$, while the capacitance C_2, between the top gate electrode and the top channel, will simply be the capacitance of the top insulator layer (C_T): $C_2 = C_T$. At the onset where $V_{GB} = V_{TH}$, no charge carriers have accumulated at the bottom interface ($Q_G = 0$), and from Eq. (2) follows that:

$$\Delta = \frac{C_T(C_B + C_S)}{C_B C_S} \tag{3}$$

(2) On the other hand, if the top gate bias is held *positive*, for a p-type semiconductor, no accumulation of charges occurs in the top channel close to the semiconductor/dielectric interface and, consequently, no top channel is formed. The *bottom channel* will switch on when $V_{GB} = V_{TH}$ and charges start to accumulate according to Eq. (1). Then the capacitance C_1, between the bottom gate electrode and the bottom channel is simply the capacitance of the bottom insulator layer: $C_1 = C_B$, while the capacitance C_2, between the top gate electrode and the bottom channel is equal to the capacitance of the top insulator and semiconductor layers: $C_2 = (1/C_T + 1/C_S)^{-1}$. Hence from Eq. (2):

$$\Delta* = \frac{C_T C_S}{C_B(C_T + C_S)} \tag{4}$$

Relationships (3) and (4) confirm the two slopes that were found experimentally by plotting V_{TH} against V_{GT}. The

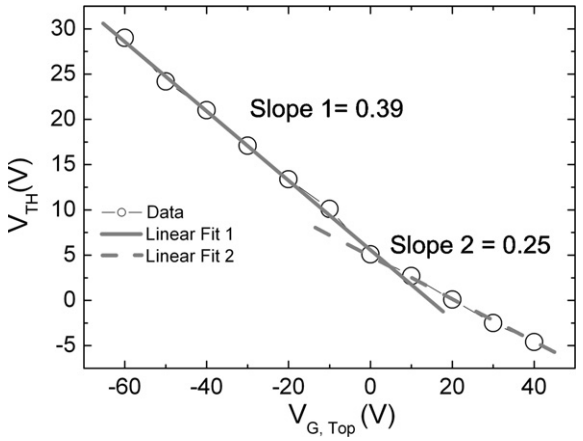

Fig. 5. Plot of the bottom channel threshold voltage versus the top gate bias for a finger transistor with $L/W = 20/10{,}000$ with rr-P3HT (75 nm) as semiconductor and polystyrene (450 nm) as the top dielectric (see Fig. 4b). The drain-source voltage was equal to −20 V. The plot can be fitted with two linear relationships with slopes $\Delta = 0.39$ for linear fit 1 and $\Delta^* = 0.25$ for linear fit 2. The intercept of the two fits indicates a transition in the slope and is positioned around top gate voltage between −10 V and 0 V, which corresponds to the threshold voltage of the single gate bottom channel.

transition point where the slope changes from Δ to Δ^* is the point where, due to the top gate potential, the top channel starts to accumulate charge carriers before the bottom channel. This onset of charge accumulation is around a top gate bias of approximately zero volts.

Table 1 summarizes the obtained Δ values for a series of dielectric materials, which are in good agreement with the capacitances calculated from the thickness of the layers. If the capacitance of the semiconductor, C_S, is very high with respect to C_T and C_B, we can approximate that: $\Delta \approx \Delta^* \approx C_T/C_B$, which is the relationship that was previously found [13–15]. We also extract from Table 1 that for a top dielectric layer thicker than 1 μm, hence a very low value of C_T, the difference between Δ and Δ^* becomes negligible and falls within the error of the measurements. The same analysis can be performed for sweeping the top gate potential at a fixed bottom gate bias.

Furthermore, Fig. 4 demonstrates that the drain current after the switch-on voltage, depends very strongly on the change of the bottom gate bias when the fixed top gate bias is set to values more negative than the threshold voltage. Compared to the curves of single gate devices (Fig. 3) and the curves where the top gate is positive, the increase (or decrease) in current occurs at much faster rate. This increased change in current can be explained by the penetration of the unscreened field of the (positive) bottom gate. The local field in the top channel, controlled by the change in the bottom gate bias, will vary to a larger extend than that for a single gate devices since the contribution of the negative top gate field is also present, leading to a faster increase or decrease in the accumulated charges in the channel, amd hence a faster increase or decrease in the current. On the other hand when the top gate is fixed to values more positive than then threshold voltage it will never induce any accumulation in the channels and the change in the field in the bottom channel, since the top channel will not reach accumulation, will be the same as in a single gate device.

In addition, from the transfer curves in Fig. 4, a flattening can be observed around the point where the bottom gate bias is zero and the top gate bias is negative. This feature is depicted more clearly by replotting the data in Fig. 6 as a decrease of the differential of the current against the bottom gate bias, $\delta I_D/\delta V_{BG}$. For the replotted curves at a negative top gate bias, the differential $\delta I_D/\delta V_{BG}$ starts to decrease around a bottom gate bias of zero Volts and continues to decrease until a bottom gate bias of −15 V. This feature of the DG-OFET transfer curves marks the *transition region*. This feature is similar to the transfer characteristics of a OFET with doped semiconductor where there are also two channels present: a proper field-effect interface channel and a bulk current resulting from dopant density present in the semiconductor [21]. Despite the similarities in transfer characteristics, the system here analyzed is not significantly doped, since no intentional dopants were added and the measurements were performed in high vacuum and dark, so the second channel arises from a second interface field-effect channel and not from bulk conduction. The transition region in the transfer curves is present only when the top channel is accumulating charge carriers, and is caused by the screening of the bottom gate potential by the charges accumulating in the bottom channel. When a negative top gate bias and a positive

Table 1
Comparison between the calculated Δ and Δ^* and the corresponding experimentally found linear fits for the relationship between V_{TH} and V_{GT}

Device Semiconductor/top dielectric	C_S (F cm^{-2})	C_T (F cm^{-2})	Δ	Fit 1	Δ^*	Fit 2
PDTT(25 nm)/PS (375 nm)	1.1×10^{-7}	5.9×10^{-9}	0.40	0.33 ± 0.03	0.33	0.23 ± 0.03
P3HT(22 nm)/PS (1250 nm)	1.1×10^{-7}	1.8×10^{-9}	0.13	0.14 ± 0.01	0.10	0.09 ± 0.02
rr-P3HT(22 nm)/PS (800 nm)	1.1×10^{-7}	2.7×10^{-9}	0.19	0.17 ± 0.02	0.16	0.15 ± 0.08
rr-P3HT(25 nm)/PS (460 nm)	1.1×10^{-7}	4.8×10^{-9}	0.33	0.24 ± 0.02	0.27	0.20 ± 0.03
rr-P3HT(25 nm)/PS (410 nm)	1.1×10^{-7}	5.4×10^{-9}	0.37	0.39 ± 0.05	0.30	0.31 ± 0.08
rr-P3HT(25 nm)/PS (395 nm)	1.1×10^{-7}	5.6×10^{-9}	0.38	0.36 ± 0.05	0.31	0.35 ± 0.06
rr-P3HT(75 nm)/PS (605 nm)	3.4×10^{-8}	3.6×10^{-9}	0.33	0.29 ± 0.05	0.19	0.20 ± 0.04
rr-P3HT(75 nm)/PS (560 nm)	3.4×10^{-8}	4.0×10^{-9}	0.35	0.34 ± 0.02	0.21	0.22 ± 0.03
rr-P3HT(75 nm)/PS (450 nm)	3.4×10^{-8}	4.9×10^{-9}	0.43	0.41 ± 0.03	0.25	0.26 ± 0.04
MEH-PPV(86 nm)/PMMA (354 nm)	3.1×10^{-8}	9.0×10^{-9}	1.07	1.08 ± 0.01	0.61	0.64 ± 0.02

The bottom capacitance (C_B) is fixed by using 200 nm thermally grown SiO_x at 1.7×10^{-8} F cm^{-2}.

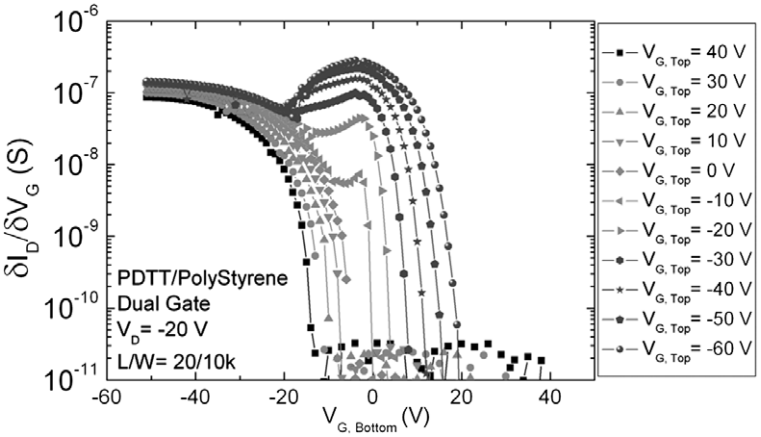

Fig. 6. Transconductance $\delta I_D/\delta V_{BG}$ of the transfer characteristics shown in Fig. 4a. For bottom gate bias between 0 and −15 V, a clear decrease in the transconductance is observed for a fixed negative top gate bias.

bottom gate bias are applied, there will be no accumulation in the bottom channel; hence no screening of the bottom gate and the top channel will depend on both gate potentials. Sweeping the bottom gate bias from high positive values towards less positive values will lead to accumulation in the top channel. As explained above, this happens when $V_{GB} = V_{TH}$, the point where the sum of the fields influencing the top channel, which depend on the gate potentials and the capacitances of the layers between the gates and the channel, will start accumulating charges. Current will then start to flow between the source and the drain electrodes. Keeping the top gate bias constant, the current will increase according to the change in bottom gate bias and will depend on the capacitance of the layers between the top channel and the bottom gate (C_S and C_B). The bottom channel will be insensitive for the top gate potential since the charges accumulated in the top channel screen the top gate potential. However, when a negative V_{GB} bias is reached for $-V_{GB} > -V_{TH}$, the bottom channel will start to accumulate charge carriers and switch on. These charges will partially screen the influence of the bottom gate potential on the top channel, causing a decrease in the transconductance of the top channel. This is marked by the transition region where the bottom channel depends on the bottom gate only and the top channel will depend on both gates. Eventually when V_{GB} is negative and sufficiently large, the charges accumulated in the bottom channel will completely screen the influence of the bottom gate potential on the top channel and the change in overall drain current will depend only on the change of the current of the bottom channel. The current in the top channel will not be modified since V_{GT} is held constant.

If the top gate bias is positive, no accumulation in the top channel is feasible; hence no transition region will appear since the device operation will depend on the bottom channel only. The bottom channel-only dependence for very negative V_{GB} is clearly visible from Figs. 4 and 6 where for both positive and negative V_{GT}, the change in the current and its differential converges for $V_{GB} < -15$ V.

We note that the considerations stated above hold only for a DG-OFET for *two* working channels of comparable conductance, i.e., the mobility in one channel is within two orders of magnitude of the other channel. If only *one* channel is active or if one of the channel is far worse performing than the other (for example a difference in mobilities of four orders of magnitude), then the presence of the transition region in the transfer characteristics of the DG-FET will disappear, and only one Δ-factor for the relationship between V_{TH} and V_{GT} will be found. Obviously, when only one channel is active and influenced by the gates, the presence of the second channel is negligible.

4. Conclusions

In conclusion, we have demonstrated that the dependence of the bottom threshold voltage on the top gate bias presents two linear relationships depending on which channel of the DG-OFET is switching on first. Furthermore a decrease in transconductance marks a transition region caused by the screening of the second channel that switches on. We demonstrate that the change in the threshold voltage depends on the top gate bias with two linear relationships for two different regimes.

If one of the gate potentials is positive and the channel is in depletion, while the other channel is in accumulation, then both gate potentials will influence the active channel.

If both channels are in accumulation, the gate potentials are screened by the accumulated charge carriers closest to that gate and both channels operate individually: no mutual influences are observed.

For a dual-gate OFET with its top channel in accumulation, we demonstrate a drop in the transconductance when the bottom gate potential becomes negative. This transition regime between both linear regimes is marked by a drop in the transconductance, where the bottom channel depends on the bottom gate only and the top channel will depend on both gates. The transition regime results from the fact that the charges accumulated in the bottom channel will start to screen the influence of the bottom gate potential on the top channel and the change in overall drain

current will depend only on the change of the current of the bottom channel.

Acknowledgments

The authors thank K. Asadi and E.C.P. Smits for fruitful discussions, J. Harkema and F. van der Horst for the technical support, J. Wildeman for providing MEH-PPV and Philips Research for providing the substrates for the DG-OFET. The Zernike Institute for Advanced Materials is acknowledged for financial support. We acknowledge financial support by the EC under FP6 contract no. NMP-032652 (BioDot).

References

[1] Z. Xu, S.H. Li, L. Ma, G. Li, Y. Yang, Appl. Phys. Lett. 91 (2007) 92911.
[2] C. Rost, S. Karg, W. Riess, M.A. Loi, M. Murgia, M. Muccini, Appl. Phys. Lett. 85 (2004) 1613.
[3] E. Cantatore, T.C.T. Geuns, G.H. Gelinck, E. van Veenendal, A.F.A. Gruijthuijsen, L. Schrijnemakers, S. Drews, D.M. de Leeuw, IEEE J. Solid State Circ. 42 (2007) 84.
[4] H. Rost, J. Ficker, J.S. Alonso, L. Leenders, I. McCulloch, Synth. Met. 145 (2004) 83.
[5] G.H. Gelinck, A.W. Marsman, F.J. Touwslager, S. Setayesh, D.M. de Leeuw, R.C.G. Naber, P.W.M. Blom, Appl. Phys. Lett. 87 (2005) 92903.
[6] N. Stutzmann, R.H. Friend, H. Sirringhaus, Science 299 (2003) 1881.
[7] T.D. Anthopoulos, G.C. Anyfantis, G.C. Papavassiliou, D.M. de Leeuw, Appl. Phys. Lett. 90 (2007) 122105.
[8] A.J.J.M. van Breemen, P.T. Herwig, C.H.T. Chlon, J. Sweelssen, H.F.M. Schoo, E.M. Benito, D.M. de Leeuw, C. Tanase, J. Wildeman, P.W.M. Blom, Adv. Funct. Mater. 15 (2005) 872.
[9] K. Suemori, S. Uemura, M. Yoshida, S. Hocino, N. Takada, T. Kodzasa, T. Kamata, Appl. Phys. Lett. 91 (2007) 192112.
[10] M. Spijkman, E.C.P. Smits, P.W.M. Blom, D.M. de Leeuw, Y. Bon Saint Côme, S. Setayesh, E. Cantatore, Appl. Phys. Lett. 92 (2008) 143304.
[11] A. Kranti, G.A. Armstrong, Semicond. Sci. Technol. 21 (2006) 409.
[12] L.L. Chua, R.H. Friend, P.K.H. Ho, Appl. Phys. Lett. 87 (2005) 253512.
[13] S. Iba, T. Sekitani, Y. Kato, T. Someya, H. Kawaguchi, M. Takamiya, T. Sakurai, S. Takagi, Appl. Phys. Lett. 87 (2005) 23509.
[14] G.H. Gelinck, E. van Veenendaal, R. Coehoorn, Appl. Phys. Lett. 87 (2005) 73508.
[15] M. Morana, G. Bret, C. Brabec, Appl. Phys. Lett. 87 (2005) 153511.
[16] J.B. Koo, K.S. Suh, I.K. You, S.H. Kim, Jpn. J. Appl. Phys. Part 1 46 (2007) 5062.
[17] H. Sirringhaus, P.J. Brown, R.H. Friend, M.M. Nielsen, K. Bechgaard, B.M.W. Langeveld-Voss, A.J.H. Spiering, R.A.J. Janssen, E.W. Meijer, P. Herwig, D.M. de Leeuw, Nature 401 (1999) 685.
[18] M. Heeney, C. Bailey, K. Genevicious, M. Shkunov, D. Sparrowe, I. McCulloch, J. Am. Chem. Soc. 127 (2005) 1078.
[19] C. Tanase, E.J. Meijer, P.W.M. Blom, D.M. de Leeuw, Org. Electron. 4 (2003) 33.
[20] S.M. Sze, Physics of Semiconductor Devices, Wiley, New York, 1981.
[21] E.J. Meijer, C. Detcheverry, P.J. Baesjou, E. van Veenendaal, D.M. de Leeuw, T.M. Klapwijk, J. Appl. Phys. 93 (2003) 4831.

Models which regard polymer semiconductors as undoped materials should be then revised to include the effect of band bending (depletion zones) and minority carrier injection and storage in the diode bulk.

The central magnitude that informs about carrier accumulation is the capacitance, which can be readily determined by impedance spectroscopy. This is because in all solar cells the generation of positive and negative carriers creates a splitting of Fermi levels that is ultimately responsible for the photovoltage [9]. In silicon solar cells, for instance, the capacitance shows two main components as a function of the bias [10,11]: a Mott–Schottky characteristic, due to the modulation of the Schottky barrier, at reverse and moderate forward bias, and a chemical capacitance [9], that increases exponentially for intense forward bias. The first characteristic indicates the presence of doping whereby the solar cell device is able to accumulate substantial minorities. Such carrier storage is manifest in the second characteristic, the chemical capacitance, which directly reflects the carrier statistics [9]. In standard dye-sensitized solar cells (DSC) based on nanostructured TiO_2, the shape of the voltage dependence of the capacitance is somewhat different, since the "hole conductor" is a liquid electrolyte with high ionic concentration, so that the Schottky barrier in the active semiconductor layer is not found. However, the chemical capacitance is very clearly observed and shows the density of states of electrons accumulated in the electron-transporting material (TiO_2) [12,13]. The identification of the voltage-dependent capacitance has become then a major tool for assessing the energetics in a DSC [14] and for interpreting the recombination lifetime [15]. The strong accumulation associated with the unconstrained rise of the Fermi level with bias appears in high performance solar cells [13], while in many other cases, the charge storage is inhibited by additional mechanisms and the solar cell capacitance may become *negative* at strong forward bias [10].

Given the general significance of the capacitance for interpretation of the fundamental transport and recombination mechanism governing the operation of new classes of solar cell devices, in this paper we present direct measurements and interpretation of the capacitance under reverse and forward voltages of a BHJ structure of the type ITO/PEDOT:PSS/P3HT:PCBM/Al. Reverse bias capacitance exhibits Mott–Schottky-like behavior signaling the formation of a Schottky junction (band bending) at the P3HT:PCBM-Al contact. Impedance modeling allows to extract both the recombination time and mobility of the minority carriers (electrons) at forward bias in the dark.

2. Experimental

We have built diodes with structure ITO/PEDOT:PSS/P3HT:PCBM/Al following the next procedure: RR-P3HT from Rieke Materials and PCBM from Nano-c were dissolved in xylene in a weight ratio of (1:0.75). The solution was heat up to 65 °C and continuously stirred for 3 h. In parallel, ITO substrates from Diamond Coatings with a sheet resistance of 40 Ω/□ were cleaned in 5 min subsequent ultrasonic baths of acetone, methanol and isopropanol. They were later introduced in oxygen plasma for 5 min. Baytron P CH8000 from HC Starck was spin-coated on top of the ITO substrate giving a film thickness of ~50 nm. The resulting film was annealed at 120 °C for 5 min in order to remove any possible water residual on the film. The P3HT:PCBM film was then spin-cast from the previously prepared solution at 800 rpm. The active layer thickness was measured to be $L \sim 200$ nm. The film was pre-annealed at 85 °C for 5 min to remove any solvent remaining on the film after deposition. Samples were then taken to a vacuum chamber to thermally evaporate the aluminium contacts through a shadow mask. The evaporation was done at $\sim 3 \times 10^{-6}$ atm at rates between 2 and 10 Å/s. The active area of the diode, given by the overlap between ITO and aluminium, is 9 mm^2. The finalized devices were immediately encapsulated with an epoxy resin

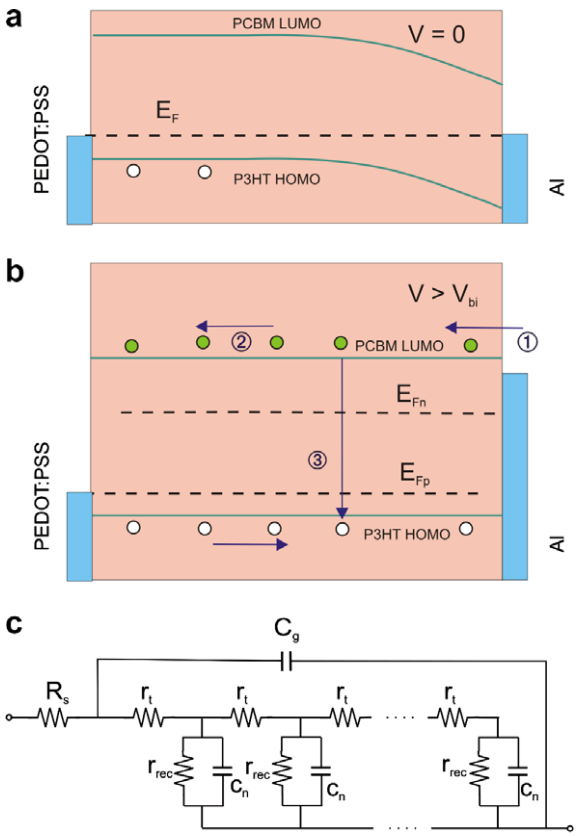

Fig. 1. (a) Band structure of the P3HT:PCBM heterojunction in equilibrium ($V = 0$). Band bending appears near the cathode and holes can occupy HOMO states of the P3HT within the neutral region. (b) Main dynamic processes occurring in the diode bulk layer for $V > V_{bi}$. Holes (majority carriers) are able to occupy the whole active layer. Electrons (minority carriers) are injected (1) into the LUMO of the PCBM, diffuse along the diode bulk (2), and eventually recombine with holes (3). (c) Equivalent circuit accounting for the diffusion–recombination mechanism used for fitting. Modulation of stored excess minority carriers gives rise to distributed chemical capacitances c_n. Bimolecular recombination of conduction band electrons and valence band holes are modeled by resistive elements r_{rec}. Transport of electrons is represented by means of r_t. An additional series resistance is needed to model contact and wire effects, R_s. Finally a capacitor $C_g \approx \varepsilon\varepsilon_0 A/L$ represents dielectric contribution of the diode.

and glass. Even though encapsulation took place right after evaporation, it has to be stressed that devices were briefly in contact with air. Nevertheless, repetitive measurements of dark *J–V* characteristics (inset of Fig. 2a) gave identical results over several weeks. The impedance measurements were carried out in the air and room temperature, using an Autolab PGSTAT-30 equipped with a frequency analyzer module in the frequency range between 1 MHz and 1 Hz. Ac oscillating amplitude was as low as 10 mV (rms) in order to maintain the linearity of the response.

3. Results and discussion

It is well-known that P3HT is a conjugated polymer that in exposure to oxygen and/or moisture results p-doped [7,8]. Under such conditions, it has been suggested that the P3HT-Aluminum contact shows a Schottky diode behavior. Band bending with a corresponding depletion zone is formed at the contact as indicated in Fig. 1a [16,17]. For a Schottky diode [18] the junction capacitance, which appears as a consequence of the modulation of the depletion layer, exhibits a bias dependence according to the Mott–Schottky relation

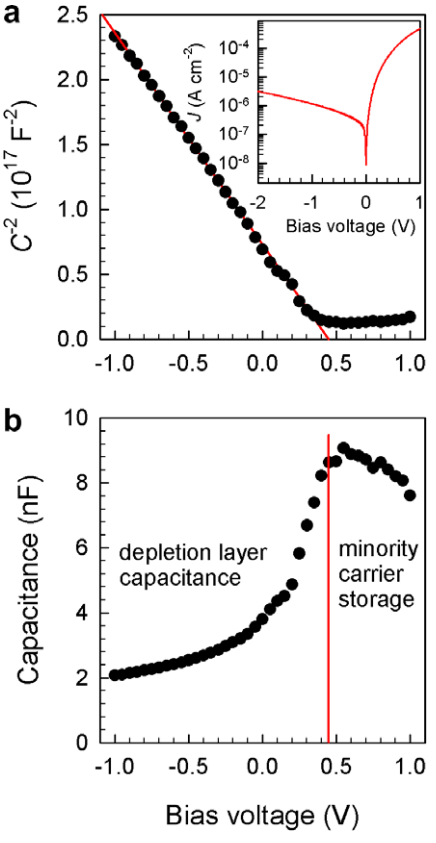

Fig. 2. (a) Mott–Schottky curve (100 Hz) which exhibits a straight line yielding $V_{bi} = 0.43$ V and $N_A = 3.5 \times 10^{16}$ cm^{-3}, assuming $\varepsilon = 3$ for P3HT:PCBM. In the inset: *J–V* characteristics measured in the dark. (b) Capacitance (100 Hz) as a function of bias. Vertical line separates voltage regions for which capacitance is determined either by the depletion layer modulation ($V < V_{bi}$) or the storage of minority carriers ($V > V_{bi}$).

$$C^{-2} = \frac{2(V_{bi} - V)}{A^2 e \varepsilon \varepsilon_0 N_A} \quad (1)$$

where V_{bi} is the built-in potential, V is the applied voltage, A corresponds to the device active surface (9 mm^2), e accounts for the elementary charge, ε is the relative dielectric constant, ε_0 the permittivity of the vacuum, and N_A the concentration of acceptor impurities. Our experimental results follow Eq. (1) (Mott–Schottky curve) which exhibits a straight line over a wide bias voltage range (Fig. 2a) yielding $V_{bi} = 0.43$ V and $N_A = 3.5 \times 10^{16}$ cm^{-3}, assuming $\varepsilon = 3$ for P3HT:PCBM. In this case the depletion region for a reverse bias voltage between 0 and 1 V results to be varying between 63 and 115 nm, compatible with an active layer thickness of 200 nm. At $V = V_{bi}$ (flat-band conditions) the depletion layer adjacent to the P3HT:PCBM/Al contact disappears and the neutral, doped region extends along the whole diode bulk (Fig. 1b).

As commented in the Introduction, when the Schottky barrier vanishes at $V > V_{bi}$ it is expected that the device capacitance is governed by a chemical capacitance due to the excess minority carriers C_μ [11,19,20], that is related to the change of the occupancy of electrons in the LUMO of the PCBM, as follows

$$C_\mu = e^2 \frac{dn}{dE_{Fn}} \quad (2)$$

Here the capacitance is given per unit volume, n corresponds to the electron concentration, and E_{Fn} accounts for the electron quasi-Fermi level (see Fig. 1b). According to Eq. (2), the capacitance should increase as a function of forward bias. For ideal statistics, the increase is exponential [10]. However, it has been shown in classic Schottky diodes [21] that under moderate to large forward bias conditions, minority carrier injection can be *limited* depending on the barrier heights at the metal–semiconductor junction. Oxidation of the aluminium cathode (due to the preparation conditions) leads to the formation of an Al_2O_3 layer between the aluminium and the P3HT:PCBM. Electron injection from aluminium to PCBM might be blocked to some extent by this tunneling barrier, and could limit charge collection under illumination This injection-limiting effect yields a peak in the capacitance–voltage characteristics, and eventually a strong negative capacitance component [21].

Fig. 2b shows the measured capacitance at low frequency (100 Hz) as a function of the bias. The capacitance increases in the forward direction, reaching a peak for voltages of approximately 0.6–0.7 V. At this point the capacitance decreases caused by the limitation upon the concentration of minority carriers in the neutral regions of the device. Alternative explanations of a large low-frequency capacitance at forward bias point to the occurence of charge blocking caused by slow injection/extraction at the contacts [22]. Although these effects cannot be completely discarded, such interpretations are however based on increasing capacitance values at forward bias in opposition to our observations in Fig. 2.

Fig. 3 displays the measured electrical impedance in the complex plane for different forward bias voltages from 0.5 to 1 V. It can be seen that the impedance spectra are com-

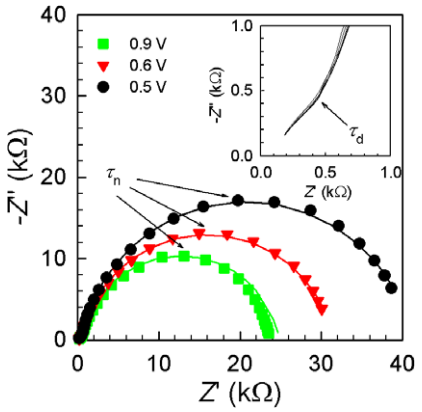

Fig. 3. Impedance spectra measured in the dark at different bias as indicated. Experimental points and fitting results (solid line) using the equivalent circuit model of Fig. 1c. Characteristic times are marked. Inset: detail of the high-frequency interval which signals the transition between diffusion and recombination responses.

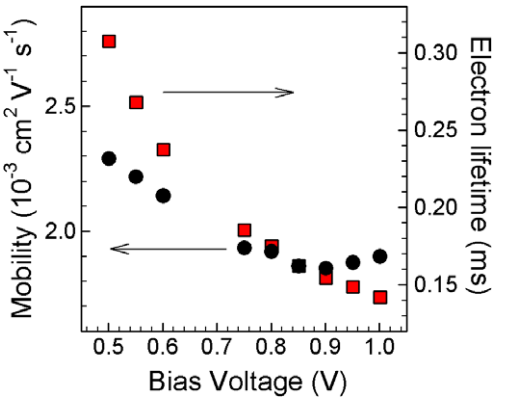

Fig. 4. Electron mobility determined from fitting parameters, using Eq. (3) and the approximation $\mu_n = eD_n/k_BT$. Electron recombination time (effective lifetime) resulting from fits.

posed of a large semicircle at low frequencies together with an almost straight line in the high-frequency part (inset of Fig. 3), which is rather independent of the applied voltage. This type of impedance pattern belongs to the responses usually encountered in systems in which carrier transport is determined by diffusion–recombination between non-absorbing contacts [23]. Injected minority carriers (electrons) from the Al contact are able to diffuse within the bulk neutral region eventually reaching the PEDOT:PSS film which acts as selective contact. Transmission line models able to represent such diffusion–recombination impedance response are well-known [23,24], and have been integrated in standard software. The impedance model (Fig. 1c) consists of an equivalent circuit which comprises distributed resistors r_t, standing for the electron transport, the distributed chemical capacitance $c_n = C_\mu$ and r_{rec} accounting for the electron recombination resistance. An additional series resistance is needed to model contact and wire effects, R_s. Finally a capacitor $C_g \approx \varepsilon\varepsilon_0 A/L$ represents dielectric contribution of the diode. The impedance model described contains two characteristic times related to the electron diffusion $\tau_d = r_t c_n$ (transit time), and the effective lifetime $\tau_n = r_{rec} c_n$, respectively [23].

By examining Fig. 3 one can observe that fitting curves match the impedance spectra in the whole measuring frequencies. The position of the characteristic times is marked in Fig. 3. $R_s \approx 100\ \Omega$, and $C_g \approx 1.0$ nF in agreement with the permittivity value assumed. The electron diffusivity (chemical diffusion coefficient) can be calculated by means of the relation [23]

$$D_n = \frac{L^2}{\tau_d} \tag{3}$$

Here $L = 200$ nm is the thickness of the diffusion layer. Assuming that the electron statistics slightly departs from dilute concentration conditions, the electron mobility might be readily calculated by using the Nernst–Einstein relationship as $\mu_n = eD_n/k_BT$ (being k_BT the thermal energy) [25,26]. Results are summarized in Fig. 4. The electron mobility extracted from fits exhibits a nearly constant value approximately equal to $2 \times 10^{-3}\ cm^2\ V^{-1}\ s^{-1}$. This value is in good agreement with that derived using PCBM electron-only devices from *J–V* measurements, for which current is considered space-charge-limited, and hence electrical field-driven rather than diffusion-determined [27]. Electron effective lifetime results within the time interval 0.3–0.1 ms, decreasing as the bias increases. Such time presumably refers to losses produced by electron–hole bimolecular recombination along the absorber layer, although surface recombination routes cannot be excluded. Alternative methods to investigate charge carrier lifetime such as photoinduced absorption [28,29] find values of similar order.

4. Conclusion

In summary, it has been shown that the P3HT:PCBM-Al contacts show a behavior consistent with a Schottky diode in the dark and under reverse bias. Furthermore, the capacitance values at forward bias are viewed as a strong indication that minority charge carriers play a significant role. With such assumption and measuring ac electrical impedance spectra we propose a model to interprete the diffusion and recombination processes which allows us to determine both the diffusion and recombination time constants. Electron mobility and effective lifetime can therefore be easily computed which permits to reach a deeper understanding of the mechanisms governing doped BHJ devices.

Acknowledgment

We thank financial support from Ministerio de Educacion y Ciencia under project HOPE CSD2007-00007 (Consolider-Ingenio 2010).

References

[1] C.J. Brabec, N.S. Sariciftci, C. Hummelen, Adv. Mater. 11 (2001) 15–26.
[2] C. Lungenschmied, G. Dennier, H. Neugebauer, N.S. Saricifti, E. Ehrenfreund, Appl. Phys. Lett. 89 (2006) 223519.

[3] L.J.A. Koster, E.C.P. Smits, V.D. Mihailetchi, P.W.M. Blom, Phys. Rev. B 72 (2005) 085205.
[4] P.W.M. Blom, V.D. Mihailetchi, L.J.A. Koster, D.E. Markov, Adv. Mater. 19 (2007) 1551–1566.
[5] W. Ma, C. Yang, X. Gong, K.-S. Lee, A.J. Heeger, Adv. Funct. Mater. 15 (2005) 1617–1622.
[6] C. Tanase, E.J. Meijer, P.W.M. Blom, D.M. de Leeuw, Phys. Rev. Lett. 91 (2003) 216601.
[7] M.S.A. Abdou, F.P. Orfino, Y. Son, S. Holdcroft, J. Am. Chem. Soc. 119 (1997) 4518.
[8] S. Hoshino, M. Yoshida, S. Uemura, T. Kodzasa, N. Takada, T. Kamata, K. Yase, J. Appl. Phys. 95 (2004) 5088.
[9] J. Bisquert, Phys. Chem. Chem. Phys. 5 (2003) 5360.
[10] I. Mora-Seró, J. Bisquert, F. Fabregat-Santiago, G. Garcia-Belmonte, G. Zoppi, K. Durose, Y. Proskuryakov, I. Oja, A. Belaidi, T. Dittrich, R. Tena-Zaera, A. Katty, C. Lévy-Clement, V. Barrioz, S.J.C. Irvine, Nano Lett. 6 (2006) 640.
[11] I. Mora-Seró, Y. Luo, G. Garcia-Belmonte, J. Bisquert, D. Muñoz, C. Voz, J. Puigdollers, R. Alcubilla, Sol. Energy Mater. Sol. Cells 92 (2008) 505–509.
[12] F. Fabregat-Santiago, J. Bisquert, G. Garcia-Belmonte, G. Boschloo, A. Hagfeldt, Sol. Energy Mater. Sol. Cells 87 (2005) 117–131.
[13] Q. Wang, S. Ito, M. Grätzel, F. Fabregat-Santiago, I. Mora-Seró, J. Bisquert, T. Bosshoa, H. Imaic, J. Phys. Chem. B 110 (2006) 19406.
[14] Q. Wang, J.-E. Moser, M. Grätzel, J. Phys. Chem. B 109 (2005) 14945.
[15] J. Bisquert, A. Zaban, M. Greenshtein, I. Mora-Seró, J. Am. Chem. Soc. 126 (2004) 13550.
[16] G. Dennler, C. Lungenschmied, N.S. Saricifti, R. Schwödiauer, S. Bauer, H. Reiss, Appl. Phys. Lett. 87 (2005) 163501.
[17] M. Glatthaar, N. Mingirulli, B. Zimmermann, T. Ziegel, R. Kern, M. Niggermann, A. Hinsch, A. Gombert, Phys. Stat. Sol. (a) 202 (2005) R125–R127.
[18] E.H. Rhoderick, R.H. Williams, Metal–Semiconductor Contacts, Clarendon Press, Oxford, 1988.
[19] S.M. Sze, Physics of Semiconductor Devices, John Wiley and Sons, New York, 1981.
[20] J. Bisquert, D. Cahen, G. Hodes, S. Rühle, A. Zaban, J. Phys. Chem. B 108 (2004) 8106–8118.
[21] M.A. Green, J. Shewchun, Solid State Electron. 16 (1973) 1141–1150.
[22] M. Glatthaar, M. Riede, N. Keegan, K. Sylvester-Hvid, B. Zimmermann, M. Niggermann, A. Hinsch, A. Gombert, Sol. Energy Mater. Sol. Cells 91 (2007) 390–393.
[23] J. Bisquert, J. Phys. Chem. B 106 (2002) 325–333.
[24] A. Pitarch, G. Garcia-Belmonte, I. Mora-Seró, J. Bisquert, Phys. Chem. Chem. Phys. 6 (2004) 2983–2988.
[25] G. Garcia-Belmonte, J. Bisquert, G. Popkirov, Appl. Phys. Lett. 83 (2003) 2178–2180.
[26] J. Bisquert, Phys. Chem. Chem. Phys. 10 (2008), doi:10.1039/b719943k.
[27] V.D. Mihailetchi, J.K.J. van Duren, P.W.M. Blom, J.C. Hummelen, R.A.J. Janssen, J.M. Kroon, M.T. Rispens, W.J.H. Verhees, M.M. Wienk, Adv. Funct. Mater. 13 (2003) 43–46.
[28] C. Arndt, U. Zhokhavets, M. Mohr, G. Gobsch, M. Al-Ibrahim, S. Sensfuss, Synthetic Metals 147 (2004) 257–260.
[29] G. Dennler, A.J. Mozer, G. Juska, A. Pivrikas, R. Österbacka, A. Fuchsbauer, N.S. Saricifti, Organic Electron. 7 (2006) 229–234.

transfer theory coupled with Einstein–Smoluchowski equation to get the orient-independent averaged mobility of organic molecular semiconductors. Olivier applied the Monte Carlo approach coupled Marcus theory to calculate the mobility of one-dimension pentacene stack model [22]. In addition, Hannewald coupled the ab initio organic crystals electron band structure with Hosltein–Peierls model to well describe the temperate-dependent anisotropic charge-carrier mobilities [7,11,23]. Regard with to the disordered pi-conjugated polymeric materials, Bässler et al. [24,25] used Monte Carlo method to simulate charger-carrier hopping transport process in the case of a Gaussian distribution site energies model (GDM). Recently, a more powerful approach by numerical solving the steady state master equation [14,15,26,27] was developed to evaluate the mobility of amorphous polymeric semiconductors. This method can get a stationary solution and readily consider the effects of charge-carrier density, electric field and traps on the mobility. To the best of our knowledge, this master equation approach solves the charge-carriers mobility of organic crystal do not be reported yet. In this paper, we restrict our research to charge-carrier mobility of organic molecular crystal in incoherent hopping region.

This article is organized as follows. In theoretical part, we briefly introduce electron transfer Marcus theory and the construction of stationary master equation. Next, the computational details are illuminated. And then the anisotropic, density-dependent and field-dependent mobilities in penitence ab-plane are issued. Finally, we conclude the paper with a summary of all results.

2. Theoretical model

In high temperature limits, the charge transfer (CT) processes belong to the incoherent hopping region. The CT rate T_{ij} from i site to j site usually be expressed by semiclassical Marcus–Hush equation [28,29]:

$$T_{ij} = V_{ij}^2 \sqrt{\frac{\pi}{\hbar k_B T \lambda_{ij}}} \exp\left(-\frac{(H_{ii} - H_{jj} - \lambda_{ij})^2}{4\lambda_{ij} k_B T}\right) \tag{1}$$

Here, V_{ij} means the electron coupling between the non-adiabatic initial state $|M_i^{e/h} M_j>$ and final state $|M_i M_j^{e/h}>$, which indicate that the electron or hole-carrier is localized at molecule i and j, respectively. For simplification, we applied one-electron approach to calculate the electron coupling V_{ij} [30,31].

$$V_{ij} = < \phi_{H/L}^{0,i} | F^0 | \phi_{H/L}^{0,j} > \tag{2}$$

$\phi_{H/L}^{0,i}$ and $\phi_{H/L}^{0,j}$ indicate the isolated (unperturbated) highest occupied molecular orbital (HOMO)s/the lowest unoccupied molecular orbital (LUMO) on ith and jth molecule. The F^0 is the Fock operator of the dimer system using the unperturbed density matrix. The detailed procedure is described in following computational detail section. This direct coupling from the dimer calculation ignores the influence of nearby other molecules coherent interaction on this coupling. In hopping region, it is reasonable to use this direct V_{ij} to calculate the charge transfer rate. λ_{ij} is the reorganization energy of the charge transfer process. It can be divided into internal reorganization energy λ_{ij}^{int} related with the ith and jth molecular geometry changes due to electron redistribution and external reorganization energy λ_{ij}^{ext} related with external environmental polarization energy relaxation. H_{ii} and H_{jj} mean the site energies of initial state and final state.

In the presence of electric field, we assume that electric field affect on the polaron site energy by linear electric potential gradient [26]. Thus, the T_{ij} approximately is calculated with following form:

$$T_{ij} = V_{ij}^2 \sqrt{\frac{\pi}{\hbar k_B T \lambda_{ij}}} \exp\left(-\frac{(H_{ii} - H_{jj} - eE \cdot R_{ji} - \lambda_{ij})^2}{4\lambda_{ij} k_B T}\right) \tag{3}$$

E is applied electric field vector and displacement vector $R_{ij} = r_j - r_i$. r_i is the center coordinate of molecule i. In supercell situation, the displacement vector R_{ji} is applied on periodic boundary condition (PBC) and then the electric field affect on this PBC applied R_{ji} to get the electric field induced difference of site energies.

After getting these electron transfer rates, we can construct the following master equation to describe the incoherent charge-carrier motions:

$$\frac{\partial p_i}{\partial t} = -\sum_j [T_{ij} p_i (1 - p_j) - T_{ji} p_j (1 - p_i)] \tag{4}$$

p_i is the probability density that i site is occupied by charge-carrier. $1-p_i$ is the Coulomb penalty factor which prevents two or more carriers occupy a site simultaneously. If we know the detailed charge-carriers injection rate from electrode to molecular crystal and escape rates from the molecules to another electrode. By solving these complicated coupled non-linear equations, we can obtain all the information about this device such as the mobility of charge-carriers, the voltage variation in the device and current density so on. But it is difficult to know the detailed knowledge of the injection and escape rates which are quite related with the couples between the electrodes and active material, fabrication technologies, and other complicated factors. These factors are out of the range of this paper. As a simplification, if we only consider that the carriers motion in internal material and ignore the complicated charge-carrier injection and escape processes, we assume that the probabilities of bulk part will soon self-arrive a pseudo-equilibrium, and then this part can be thought as time-independent quantity under a certain applied electric field. Thus, the Eq. (3) can be simplified as the following steady master equation.

$$0 = -\sum_j [T_{ij} p_i (1 - p_j) - T_{ji} p_j (1 - p_i)] \tag{5}$$

Solving this non-linear steady state master equation, we adopt following iterative procedure:

$$p_i = \frac{\sum_j T_{ji} p_j}{\sum_j T_{ij} + \sum_j (T_{ji} - T_{ij}) p_j} \tag{6}$$

We firstly give some p_i densities and can solved the some new p_i densities by Eq. (6), and then replace the old

densities with the new ones do next iteration until the densities arrive a converged value. In view of our system near homogenous and ordered onsite energies, we give same initial population to every site. Instead of Yu mentioned iterative method [32], we readily get the converged solution p_i after about 30 iterative steps related with the initial densities p_i by ordinary iteration procedure (the converge criterion set the density maximum relative error smaller than 10^{-5}). We think this probably is due to the ordered and concrete electron transfer matrix T_{ij} for pentacene molecular crystal.

Once we get the solution p_i, the average intrinsic mobility μ of charge-carrier can be obtained from following equation:

$$\mu = \frac{\sum_{ij} T_{ij} p_i (1 - p_j) R_{ji} \cdot \hat{E}}{p_{\text{tol}} |E|} \tag{7}$$

$\hat{E}$ is unit vector of applied electric field. $|E|$ is absolute value of electric field intensity. p_{tol} is the total carriers population in investigated bulk cell. Once we get the detailed CT parameters from quantum chemistry calculations according to the molecular crystal structure, then the influence of electric field and carrier density on the mobility can be unambiguously solved and discussed at molecule level by master equation approach.

3. Computation details

3.1. Single-crystal structure

In literatures, many different polymorphs are reported. As an example, we just chose the pentacene single-crystal structure whose $d(001)$ spacing is 14.1 Å [33] as our study object. The unit cell *a, b and c* vector lengths are 6.266, 7.775, 14.53 Å and cell α, β, γ angles are 76.475°, 87.682°, 84.684°, respectively. There are two slightly unequal molecules in primitive cell [000] named A and B molecule. Their fractional coordinates are (0,0,0) for A and (1/2, 1/2, 1/2) for B. The other molecules can be considered as their respective equivalent molecules by translational symmetry.

3.2. The electron coupling terms

Here, we calculated all possible non-zero the electron/hole carriers transfer integrals V_{ij} coupled with [000] cell A or B molecules, that is, the pairs one molecule is from the A or B in [000] cell and another is from its most adjacent molecule. For transfer integrals related to other cell molecules, they can be obtained from the translational symmetry. We firstly obtain the isolated molecular orbits of the M1 and M2 in [000] cell by two separately self-consistent field (SCF) calculations. Then, based on these isolated molecular orbits and molecular pair relative space position, we can solve the HOMO/LUMO electron couplings of this pair by constructing their zeroth-order Fock matrix without SCF iteration [30,31]. The isolated orbital energies of HOMO and LUMO are approximately thought as the hole and electron-carrier site energies.

3.3. The reorganization energies

As we discussed above, the reorganization energies consist of the internal reorganization energies ($\lambda_{ij}^{\text{int}}$) and the external energies ($\lambda_{ij}^{\text{ext}}$). The former can be regards as a sum of two separate processes with the two energetic terms λ_1 and λ_2 related to the internal reorganization energy for a neutral molecule and charged molecule showed in Fig. 1. For more detail, we need get the energies of neutral molecule at its balance geometry and its charged molecular balance geometry. The difference of these two energies is the λ_1. The same way to solve the λ_2. Then we can get the internal reorganization energies for hole and electron are 83.6 and 125.5 meV. The external reorganization energy is related with the lattice relaxation due to the electron transfer reaction. It is not easy to directly be obtained from the quantum chemical calculation. For organic solids and weak polar media, the medium contribution to the relaxation energy is up to 0.1 eV [34]. Based on the referent [35] calculations, the lattice relaxation of the localized charged state in pentacene-like anthracene molecular crystal are 15 meV, which are far smaller than its internal reorganization energy. Thus, in this paper we actually set the internal reorganization energy as the total reorganization energy in solid phase.

3.4. Steady state master equation

We build supercell of the ab-plane of pentacene single-crystal whose size is 10×10. This means the size of supercell is 10 units a vector lengths, 10 unit *b* vector lengths and 1 unit *c* vector length. The periodic boundary condition (PBC) is applied in order to keep the total carriers conversation in studied supercell. In addition, 20×20, 30×30, 60×60 supercells also be used as a test. We found that the calculated mobilities from larger sizes surfaces are exactly same as that of 10×10 supercell. As for ordered pentacene ab surface, size 10×10 is large enough to express the two-dimension charge-carrier mobility character.

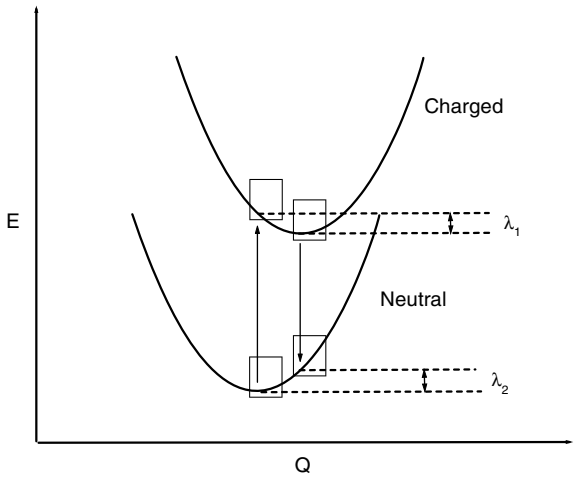

Fig. 1. The four energy values to be calculated in neutral ground and charged (hole/electron) states at neutral and charged optimized geometries to deduce the two components of the internal reorganization energy.

3.5. Quantum calculation method

All the quantum chemical calculation are used the B3LYP hybrid functional with 6-31g(d) basis set and are performed on Gaussian 03 package [36].

4. The results and discussion

4.1. Electron couplings and site energies

For our chosen pentacene single-crystal, the possible non-zero coupling terms between the molecular pairs one from the primitive cell [000] are calculated by the method mentioned above. Each coupling term are identified by five labels M1 M2 [$n_a n_b n_c$]. M1 M2 means the two molecular labels of this electron transfer pathway. The former molecule M1 is in the primitive [000] cell. The M2 belongs to [$n_a n_b n_c$] cell, that is, M2 are translated n_a unit along a vector, n_b unit along b vector and n_c unit along vector c. For example, A B [001] is the coupling between the A molecule in [000] cell and B molecule in [001] cell. Under tight binding approximation, we calculated the cell labels n_a, n_b, and n_c from –1 to 1. When absolute value of cell label larger than 2, the couplings are zero. All the nonzero couplings are listed in Table 1.

Firstly, as for the couplings in right side of Table 1 whose the cell labels n_c for molecule M2 are 1 or −1, the couplings for HOMOs or LUMOs are far smaller than nonzero those of n_c label is 0. The reason is that vector c length (14.53 Å) is near to twice of vector a (6.266 Å), or b (7.775 Å) lengths. The translation along vector c makes the distance of M1 and M2 far larger than translation along vector a or b. The orbital spatial overlaps for left side pairs are far less that those of right side. Thus, the charge-carriers prefer to transport in ab-plane with two-dimension form rather than three-dimension form. And the charge-carrier mobilities measured by most single-crystal FET experiments data are near two-dimension. It is also this reason that we focus our research on the mobility in ab-palne of pentacene crystal.

Secondly, the coupling terms for n_c label is 0 in left side of Table 1. At first glance, we note the couplings for hole or electron-carriers are not remarkably different. The largest coupling for electron-carriers is pair AB [000] −73.6 meV, while the largest couplings for hole carriers are pairs AB [−100] and BA [100] and AB [0−10] and BA [010] 81.6 meV. Here, pairs AB [−100] and BA [100] and pairs AB [0−10] and BA [010] are equivalent pairs by translation operate [16]. However, from these coupling values, we can not conclude hole or electron which one is more readily transported as charge-carriers. For more detailed character about the couplings, for electron-carriers, the ratio of the largest coupling AB [000] to the smallest nonzero coupling BB [−100] in ab-plane is 1.96, while the ratio for hole carriers is 2.58. This means that the transfer integrals for hole carriers are more dependent on the direction than those of electron-carriers. We will talk about this property in later part.

With regard to the site energies, at single electron approximation, we take the isolated HOMO and LUMO energies as site energies of hole-carrier and electron-carrier. Because the isolated HOMOs orbital energies are −4.5610 and −4.5029 eV for A and B molecules and LUMOs orbital energies are −2.2766 and −2.3135 eV for A and B molecules. Thus, we can set two different site energies both HOMO and LUMO for A molecule as zero and for B molecule HOMO as 58.1 meV and −36.9 meV, respectively. These energy differences for HOMOs and LUMOs are due to the geometry differences between A and B molecules in triclinic $P\bar{1}$ symmetry pentacene crystal.

4.2. Anisotropy of the mobility in pentacene ab-plane

Once we got the all the electron couplings between different sites, we can obtain the charge transfer rate using Marcus theory (Eq. (3)). Then we can solve the steady state master equation (Eq. (5)) to obtain the solution of probability density p_i. Finally, based on the Eq. (7), we can get the mobility of charge-carriers. Before solving the rate of electron transfer, we need know the detailed quantity of some parameters such as the applied electric filed vector, temperature, and initial carriers occupied density p_i so on.

As we talked in introduce part, the freestanding organic single-crystal EFT provide with a power experimental tool to explore the intrinsic mobility of charge-carriers. Lee et al. [10] use fan-shaped electrodes on Si/SiO_2 substrate to measure and get the very good anisotropic field effect mobility of hole carriers in pentacene single-crystal ab-plane. Unfortunately, the concrete direction of mobility

Table 1
The transfer integrals of the hole-carrier (HOMO) and electron-carrier (LUMO)

CT pathway	HOMO (meV)	LUMO (meV)	CT pathway	HOMO (meV)	LUMO (meV)
AB [−1−10]	−52.7	−73.6	AA [−1−11]	−0.2	−2.0
AA [−100]	34.5	−40.2	BB [−1−11]	−0.1	−0.9
BB [−100]	31.6	−37.6	AB [−1−11]	−0.3	6.6
AB [−100]	81.6	69.9	AA [0−11]	−2.8	0.2
AB [0−10]	81.6	69.8	BB [0−11]	−1.5	0.0
AB [000]	−52.7	−73.6	BA [001]	−0.3	6.6
BA [000]	−52.7	−73.6	AB [00−1]	−0.3	6.6
BA [010]	81.6	69.8	AA [00−1]	−2.8	0.2
AA [100]	34.5	−40.2	BB [00−1]	−1.5	0.0
BB [100]	31.6	−37.6	AA [00−1]	−0.2	−2.0
BA [100]	81.6	69.9	BB [00−1]	−0.1	−0.9
BA [110]	−52.7	−73.6	BA [00−1]	−0.3	6.6

can not be decided because the crystal axes of single-crystal pentacene were not measured directly in their experiment. In order to compare the experimental data and assign the detailed mobility direction angle, we choose our intensity of electric field as 500 V/cm because the $E = V_{SD}/L = 1$ V/20 μm = 500 V/cm [10] and temperature as 300 K. The applied electric field is in ab-plane whose direction are expressed by the angle (θ) between with vector *a*. The initial occupied density varies with the different applied gate voltages [3]. The single-crystal organic FET allows a broad range of charge density to be explored based on the applied gate voltage. Here, we firstly set charge density as 0.1 carrier per molecule to study the anisotropic mobility of pentacene ab-plane.

According to these concrete parameters, we can unambiguously obtain the mobility of hole and electron-carriers at different direction of applied electric field i.e. θ angle. When θ is equal to zero, the direction of electric field is same as that of a vector. The results are showed in Fig. 2. From the Fig. 2, we can note that both the mobilities of electron and hole are the elliptical shape with the θ angle. But their direction angles θs related with the maximum mobility and minimum mobility are quite different for electron and hole carriers. For example, for hole-carrier, the θ is 150 or its opposite orient 330° related to maximum mobility 7.78 cm^2/Vs and 60 or its opposite orient 240° related to the minimum mobility 4.69 cm^2/Vs. While for electron-carriers, the 30 or it opposite orient 210 is related to the maximum mobility 6.87 cm^2/Vs and 120 or its opposite orient 300 is related to the minimum mobility 5.13 cm^2/Vs. The ratios of maximum mobility to minimum one is 1.34 for electron-carrier smaller than that of hole-carrier 1.63. This can be rationalized by the anisotropic properties of transfer integrals for electron and hole in this pentacene crystal structure. As we discussed above, the ratios of the largest coupling to the smallest one 1.96 for electron is smaller than that of hole 2.58. Thus, the hole-carrier mobility is more dependent with the orientation that electron-carrier mobility.

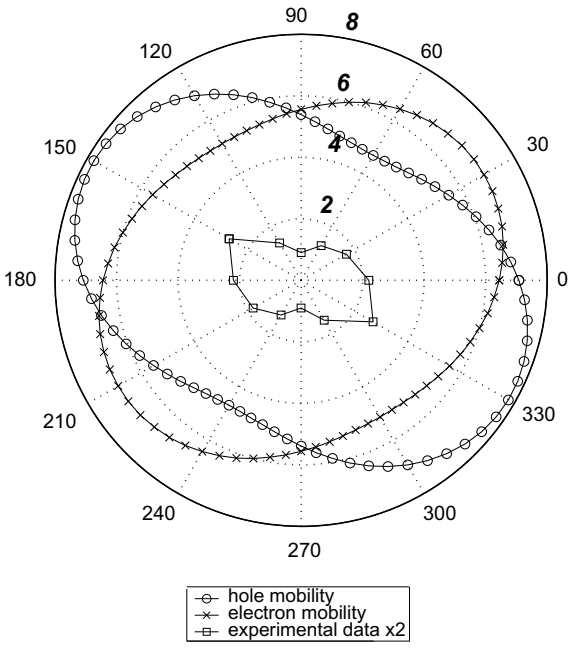

Fig. 2. Polar plot of the calculated hole mobility, electron mobility and experimental hole mobility from Ref. [10] are, respectively showed by circle, cross and square lines. The experimental values are multiplied by 2 for explicit contrast. The modeling electric filed is 500 V/cm and the density of charge-carriers is 0.1/molecule. The italic bold numbers 2, 4, 6 and 8 scale the mobility by the circle dash line and unit is cm^2/Vs. The θ is labeled by the normal number from 0 to 330°.

In view of the absolute values of electron-carrier and hole-carrier mobility, we noted that the intrinsic mobility of hole is slightly bigger than that of electron but basically they are very close to each other. This character agrees with the Cornil's recent conclusion [34].

As a contrast, the experimental hole-carrier mobility at −10 V gate voltage are also plotted in Fig. 2. Here, we assign the direction angle θ of the highest hole mobility as 150° i.e. the open square line. For clear, the experimental values are multiplied by 2. Compared the Lee's experimental polar plot [10], our hole-carrier mobility (circle line) give basically similar anisotropic character i.e. elliptical profile though the our absolute values are near six times of the experimental data. This big difference in values is probably due to the influence of carrier traps. Moreover in our calculations, we assume the pure hopping process in pentacene and neglect influences of lattice vibration on the charge transfer integrals. But carefully looking into the experimental and theoretical figures, we can find the following differences:

(a) The angle between the directions of the highest mobility and lowest mobility is 180–120 = 60° for experiment result but our result is 150–60 = 90°.
(b) The ratio of the maximum mobility to the minimum mobility in experiment is about 1.35/0.45 = 3 larger than our result 1.63.
(c) The experimental elliptical polar plot profile is not very smooth. There are two concave parts nearby its lowest mobility at 120 and 300 degree. But our anisotropic mobility is very smooth curve.

We think that these differences are probably due to the presence of texture in their pentacene single-crystal FET device measurement. It makes the direction of the lowest hole-carrier mobility exist small departure with out result and makes the experimental polar plot profile not very smooth. In our results, the calculated mobilities are intrinsic charge-carrier mobilities based on the perfect pentacene crystal structure in the absence of any structure trap or energy trap. In addition, in our theoretical model, neglect of the fluctuation of charge transfer integrals from lattice vibration and the electron coherent also probably results in the different angles discussed in a part and different smoothness of the anisotropy plot for experiment and our calculations.

As for the reason why the electron mobility in experiment are far smaller than the mobility of hole carriers, it most probable due to higher density of carrier trap and easier charge injection ability from electrode to pentacene for electron-carriers than hole carriers [34].

4.3. The density-dependent mobility

Scientists currently realized that the charge–carrier density also is very important factor to effect on the mobility. Tanase et al. [37] systemically investigated the relationship of the hole mobility of amorphous polymer and charge–carrier density in diodes and FETs. The experiment showed that the mobility can differ up to three-orders of magnitude between the diode and FET. For single-crystal molecular materials, the density-dependent mobility was few investigated by the single-crystal FET devices recently [21]. In theoretical field, the steady state master equation provide with a power tool to explore the density-dependent intrinsic mobility. We vary the average charge density from 10^{-7} carriers per molecule (very low density region) to 0.6 carriers per molecule (quite high density region) to study the charge-carrier mobilities. When the charge density exceeds 0.6 carriers per molecule, the master Eq. (4) cannot readily get the converged solution within 100 iterations. The calculated mobilities are showed in Fig. 3. From the Fig. 3, we can readily note that at low density region (smaller than 10^{-3}), both mobilities for electron and hole monotonously almost are independent with the carriers density while they are remarkably decreased with the increasing of average charge-carrier density at high density region (larger than 10^{-2}). This density-dependence for single-crystal is different from the relationship of amorphous polymer [37]. However, these exactly agree with Zhou's et al. recent Monte Carlo simulation [38] conclusions that at high densities, the Coulomb penalty factor $1-p_j$ in (Eq. (5)) will reduce the carriers mobility in materials with low intrinsic disorder and enhance the mobility in materials with high intrinsic disorder.

4.4. The electric field-dependent mobility

As we known, the electric field dependence of mobility is also different for single-crystal and disordered materials [21]. Time-of-flight mobility measurements showed that the field dependence in many conjugated polymers approximates the Poole–Frenkel form i.e. $\mu = \mu_0 \exp(\gamma\sqrt{E})$ [39]. For molecular crystal, the electric field dependence is quite different from conjugated polymer system and observed only in ultrapure crystals along the directions with the maximum charge mobilities [21,40]. Based on the Eqs. (3) and (4)–(7), we investigated the intensity of electric field-dependent mobilities of hole and electron-carriers at different electric field directions (θ angles). We found that the charge-carrier mobilities at different directional angles θ and charge densities are quite similar. As an example in Fig. 4, we only draw the plot of the mobilities of hole and electron-carrier with logarithmic electric field fixing the charge density as 0.1 charge-carrier per molecule and direction angle θ as 0° i.e. $\vec{E}//\vec{a}$. From the Fig. 4, we noted that the mobilities of charge-carrier in pentacene crystal remarkably decrease when the electric field are stronger than 5×10^5 V/cm, while at usually applied electric field region 300–3×10^5 V/cm, the mobilities of hole and electron-carrier are nearly independent with the electric field. At hopping region, the electric field dependence of the mobility in our case can not be described by the Poole–Frenkel behavior observed in most disordered amorphous materials. This is due to our large site energies gap and small reorganization energies properties. Here, we regard the A molecular site energies as 0 for hole and electron-carriers, and set the B molecular site energies as the HOMO and LUMO energies gap between A and B molecules i.e. 58.1 and −36.9 meV for hole and electron-carriers. And the internal reorganization energies for hole and electron are 83.6 and 125.5 meV. These site energies gaps are near to the respective reorganization energies. Unlike homogeneous site energies, the charge transfer driven force ($eE \cdot R_{ji}$) induced by electric field do not consistently increase or decrease charge transfer hopping rate along the electric field direction. Thus, the field dependence neither looks like the Poole–Frenkel nor Marcus inverted region behavior mentioned in Ref. [22]. However, if we set the external reorganization energies for

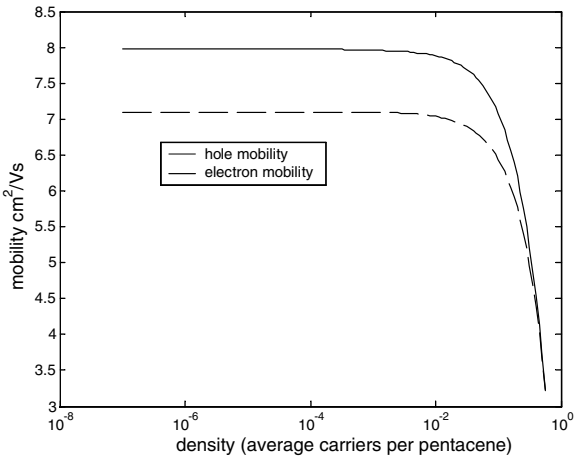

Fig. 3. The curve of average charge density with the mobility of hole carriers (solid line) and electron-carriers(dash line) where intensity of electric field is 500 V/cm and $\theta = 0°$.

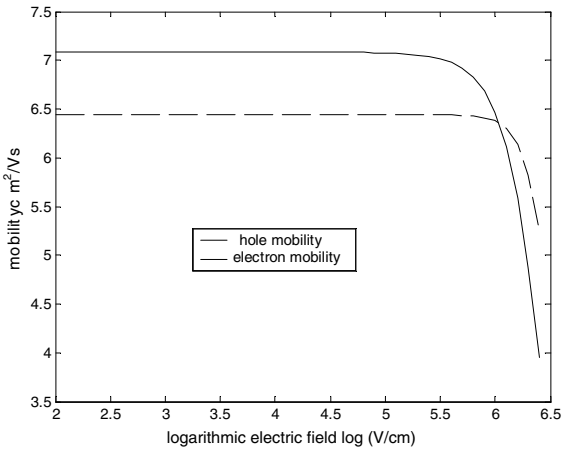

Fig. 4. The relationship of logarithmic electric field and the mobility of hole carriers (solid line) and electron-carriers (dash line) where the average charge density is 0.1 and $\theta = 0°$.

electron and hole as 100 meV which makes the reorganization energies are larger than site energies gaps between A and B site, then we noted that the mobility shows Poole–Frenkel behavior in low intensity electric field and Marcus inverted region behavior in strong intensity electric field. These are very similar with Oliver's 1D pentacene model field-dependant results [22] (we do not draw them here). Comparing with the mobility of electron, the mobility of hole more remarkably decrease with an increase of the electric field when the electric field becomes strong enough. It also can be rationalized by the charge transfer micro-parameters the reorganization energies. In our situation, the reorganization energy of electron-carrier is larger than that of hole. Thus, based on the Eq. (3), we can find that the electric field will more remarkably influence the charge transfer rate of hole than that of electron when $|eE \cdot R_{ij}|$ are comparable or larger than the reorganization energy. In Marcus inverted region [28] increasing the electric field will more remarkably decrease the electron hopping rate than hole hopping. Based on the relationship of the CT rate and the mobility i.e. Eq. (7), we can understand the strong field will decrease the charge-carrier mobilities, especially for the mobility of hole carrier.

5. Conclusion

The two-dimension charge-carrier mobilities of pentacene ab-plane are calculated by numerically solving the steady master equation method. Unlike the experimental results, the calculated the mobilities of hole-carrier and electron-carrier are the same order of magnitude in absolute values. The anisotropic mobility of hole-carrier in ab-plane well agrees with the Lee's experimental result. The various properties of transfer integrals for electron and hole carriers result in the different anisotropic field induced mobilities for electron and hole carriers. The density and electric field dependences on the mobility are also discussed in this paper. For pentacene crystal, the usual electric field and not too high carrier density will not influence on the mobility values. But at very strong electric field and huge carrier density region, increasing of them will decrease the charge-carrier mobilities. In conclusion, the master equation method provide with a powerful and efficient method to numerically solve the mobility from the molecular packing structure. And the dependences of electric field, charge density and traps (which will be talked about later) on the mobility all can be clearly issued.

Acknowledgements

The authors are thankful to Dr. Jérôme Cornil for reading this paper and giving some good advices. This work is supported by the SNU research Grants Nos. 999212 and 801741.

References

[1] C.W. Tang, S.A. Vanslyke, Appl. Phys. Lett. 51 (1987) 913.
[2] J.H. Burroughes, D.D.C. Bradley, A.R. Brown, R.N. Marks, K. Mackey, R.H. Friend, P.L. Burn, A.B. Holmes, Nature (London) 347 (1990) 539.
[3] M.E. Gershenson, V. Podzorov, A.F. Morpurgo, Rev. Mod. Phys. 78 (2006) 973.
[4] C.W. Tang, Appl. Phys. Lett. 48 (1986) 183.
[5] N. Karl, Synthetic Met. 133 (34) (2003) 649.
[6] Y.C. Cheng, R.J. Silbey, D.A.D.S. Filho, J.P. Calbert, J. Cornil, J.L. Bredas, J. Chem. Phys. 118 (2003) 3764.
[7] K. Hannewald, P.A. Bobbert, Phys. Rev. B 69 (2004) 075212.
[8] A. Troisi, G. Orlandi, J. Phys. Chem. A 110 (2006) 4065.
[9] C. Reese, Z.N. Bao, Mater. Today 10 (2007) 20.
[10] J.Y. Lee, S. Roth, Y.W. Park, Appl. Phys. Lett. 88 (2006) 252106.
[11] K. Hannewald, P.A. Bobbert, Appl. Phys. Lett. 85 (2004) 1535.
[12] R. Silbey, R.W. Munn, J. Chem. Phys. 72 (1980) 2763.
[13] V.M. Kenkre, J.D. Andersen, D.H. Dunlap, C.B. Duke, Phys. Rev. Lett. 62 (1989) 1165.
[14] J.A. Freire, G. Voss, J. Chem. Phys. 122 (2005) 124705.
[15] W.F. Pasveer, J. Cottaar, C. Tanase, R. Coehoorn, P.A. Bobbert, P.W.M. Blom, D.M. de Leeuw, M.A.J. Michels, Phys. Rev. Lett. J1 - PRL 94 (2005) 206601.
[16] A. Troisi, G. Orlandi, J. Phys. Chem. B 109 (2005) 1849.
[17] A. Troisi, Adv. Mater. 19 (2007) 2000.
[18] X.D. Yang, Q.K. Li, Z.G. Shuai, Nanotechnology 18 (2007) 424029.
[19] A. Datta, S. Mohakud, S.K. Pati, J. Chem. Phys. 126 (2007) 144710.
[20] J.L. Bredas, D. Beljonne, V. Coropceanu, J. Cornil, Chem. Rev. 104 (2004) 4971.
[21] V. Coropceanu, J. Cornil, D.A.D.S. Filho, Y. Olivier, R. Silbey, J.-L. Bredas, Chem. Rev. 107 (2007) 926.
[22] Y. Olivier, V. Lemaur, J.L. Bredas, J. Cornil, J. Phys. Chem. A 110 (2006) 6356.
[23] K. Hannewald, V.M. Stojanovic, J.M.T. Schellekens, P.A. Bobbert, G. Kresse, J. Hafner, Phys. Rev. B 69 (2004) 075211.
[24] B. Hartenstein, H. Bassler, S. Heun, P. Borsenberger, M. Vanderauweraer, F.C. Deschryver, Chem. Phys. 191 (1995) 321.
[25] U. Albrecht, H. Bassler, Phys. Status Solid B: Basic Res. 191 (1995) 455.
[26] Z.G. Yu, D.L. Smith, A. Saxena, R.L. Martin, A.R. Bishop, Phys. Rev. Lett. J1 - PRL 84 (2000) 721.
[27] J.A. Freire, Phys. Rev. B 72 (2005) 125112.
[28] R.A. Marcus, Rev. Mod. Phys. 65 (1993) 599.
[29] N.S. Hush, Electrochim. Acta 13 (1967) 1005.
[30] S.W. Yin, Y.P. Yi, Q.X. Li, G. Yu, Y.Q. Liu, Z.G. Shuai, J. Phys. Chem. A 110 (2006) 7138.
[31] A. Troisi, G. Orlandi, Chem. Phys. Lett. 344 (2001) 509.
[32] Z.G. Yu, D.L. Smith, A. Saxena, R.L. Martin, A.R. Bishop, Phys. Rev. B 63 (2001) 085202.
[33] C.C. Mattheus, A.B. Dros, J. Baas, A. Meetsma, J.L. de Boer, T.T.M. Palstra, Acta Crystallogr. Sec. C: Cryst. Struct. Commun. 57 (2001) 939.
[34] J. Cornil, J.L. Bredas, J. Zaumseil, H. Sirringhaus, Adv. Mater. 19 (2007) 1791.
[35] I.V. Brovchenko, Chem. Phys. Lett. 278 (1997) 355.
[36] G.W.T.M.J. Frisch, H.B. Schlegel, G.E. Scuseria,, J.R.C.M.A. Robb, J.A. Montgomery, Jr., T. Vreven,, J.C.B.K.N. Kudin, J.M. Millam, S.S. Iyengar, J. Tomasi,, B.M.V. Barone, M. Cossi, G. Scalmani, N. Rega,, H.N.G.A. Petersson, M. Hada, M. Ehara, K. Toyota,, J.H.R. Fukuda, M. Ishida, T. Nakajima, Y. Honda, O. Kitao,, M.K.H. Nakai, X. Li, J.E. Knox, H.P. Hratchian, J.B. Cross,, J.J.C. Adamo, R. Gomperts, R.E. Stratmann, O. Yazyev,, R.C.A.J. Austin, C. Pomelli, J.W. Ochterski, P.Y. Ayala,, G.A.V.K. Morokuma, P. Salvador, J.J. Dannenberg,, S.D.V.G. Zakrzewski, A.D. Daniels, M.C. Strain,, D.K.M.O. Farkas, A.D. Rabuck, K. Raghavachari,, J.V.O.J.B. Foresman, Q. Cui, A.G. Baboul, S. Clifford,, B.B.S.J. Cioslowski, G. Liu, A. Liashenko, P. Piskorz,, R.L.M.I. Komaromi, D.J. Fox, T. Keith, M.A. Al-Laham,, A.N.C.Y. Peng, M. Challacombe, P.M.W. Gill,, W.C.B. Johnson, M.W. Wong, C. Gonzalez, J.A. Pople, Gaussian 03, Revision B.05, Gaussian, Inc., Pittsburgh, PA, 2003.
[37] C. Tanase, E.J. Meijer, P.W.M. Blom, D.M. de Leeuw, Phys. Rev. Lett. J1 – PRL. 91 (2003) 216601.
[38] J. Zhou, Y.C. Zhou, J.M. Zhao, C.Q. Wu, X.M. Ding, X.Y. Hou, Phys. Rev. B 75 (2007) 153201.
[39] P.W.M. Blom, M.J.M. de Jong, M.G. van Munster, Phys. Rev. B 55 (1997) R656 LP.
[40] W. Warta, N. Karl, Phys. Rev. B 32 (1985) 1172 LP.

and thiolated molecules. As a result, it is not a generic method for all electrodes. Furthermore, the precise environmental control (i.e. cleanness of the electrode surface) is crucial for SAM formation and the reproducibility has always been a concern for large-scale fabrication.

Poly(3,4-ethylenedioxythiophene) (PEDOT) displays extraordinary electrical properties and is currently applied in various electronic products such as antistatic coatings for cathode ray tubes, hole transport layers for light-emitting diodes, photovoltaic devices, organic thin film transistors, and sensors [17–20]. Here, we show that the work functions of two commonly used electrodes, Au and indium-tin-oxide (ITO), are modified by surface-electropolymerization using ethylenedioxythiophenes (EDOT) or its derivatives (EDOT–OH and EDOT–COOH as shown in Fig. 1a). The EDOT monomers with various functional side-chains were tested to understand the effect of functional groups to the work function tuning. The resulting work function is tunable by varying the electropolymerization condition and polymer side-chain functional groups. Most importantly, the process is applicable for a wide range of electrodes, not only limited to Au and ITO. Interestingly, the value of work function of ITO (or Au) electrodes can be adjusted to decrease by 0.6 eV (or increase by 0.4 eV) when the deposited film is thinner than 40 nm. When the deposied film is thin, the surface dipole is dominantly resulted from the interaction between electrodes and PEDOT and irrelevant to the side chain of the EDOT monomers. In contrast, when the film deposited with thickness greater than 40 nm, the work function is contolled by the intrinsic property of the functionalized polymers regardless of the electrode materials.

2. Results and discussion

Fig. 1b shows the values of the measured work function (relative to a reference Au) for sputtered Au and ITO electrodes electropolymerized with EDOT, EDOT–OH and EDOT–COOH as a function of electropolymerization time from 0 to 160 s. In our previous studies, we concluded that the materials deposited on the surface of the electrode are proportional to the electropolymerization time [21,22]. The original work function of ITO is ~4.55 eV and the work function of the electrode is raised up to 5.05 eV when the EDOT monomer is electropolymerized for 5 s. Similar changes in work function are also observed for EDOT–OH and EDOT–COOH, proving that the method is feasible for work function engineering on electrodes. We observed that the initial change in work function for three monomers are almost identical, indicating that the surface dipoles are formed on ITO electrodes and they are not strongly related to the side chains when the polymer film is thin (thickness < 40 nm). Therefore it is likely that the formation of the surface dipole is due to the interaction between ITO and PEDOTs (polymer main chain of the polymerized films). For the Au electrodes, the measured work function was also similar for three monomers when only thin films were deposited, where the work functions were decreased from 5.2–5.3 eV to 4.9–5.1 eV. When thicker films were deposited after electropolymerization for a longer period of time, the values of work function are determined by the composition of polymer films regardless the electrode materials underneath. The work function values measured on Au elecrode when PEDOT films were deposited for 160 s were identical to those on ITO electrodes, which could be

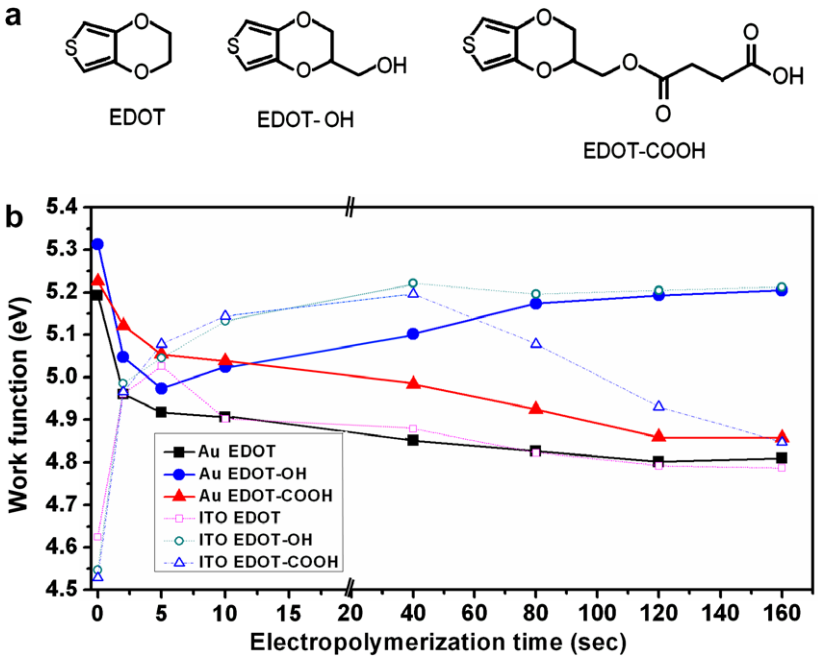

Fig. 1. (a) Chemical structures of EDOT, EDOT–OH and EDOT–COOH. (b) Measured work function for sputtered Au and ITO electrodes electropolymerized with EDOT, EDOT–OH and EDOT–COOH as a function of electropolymerization time.

due to that the penetration depth of electric dipole is short. Besides, from the point of view of band bending, the Fermi level alignment between electrodes and PEDOT introduces a local exchange of charges, where the effect is pronounced when the PEDOT is very thin. However, when a thick film of PEDOT is formed, the intrinsic surface property of polymers will dominate the workfunction value [11,23]. Therefore, thick PEDOT films from three different monomers clearly showed different work functions.

The AFM images in Fig. 2 show the effect of polymerization time on the surface morphology for EDOT–COOH and EDOT–OH coated Au electrodes. With longer electropolymerization time, it was observed that the grain size was larger and the morphology became very different for both polymers. The combination of the differences in surface morphology and the polymer intrinsic properties could be the reason why the measured work function was different with deposited polymer film and deposition time.

ITO is widely used in the organic electronic devices due to its high conductivity and transparency. Normally, ITO serves as anode for hole-injection. Therefore increasing the work function of ITO is able to enhance the injection of carriers. We have fabricated the diodes with the structure of Au (thermal evaporated 100 nm)/pentacene (50 nm)/PEDOT–COOH/ITO (schematically shown in the inset of Fig. 3a) to demonstrate the effect of work function shift on the electrical performance of the diodes. Fig. 3b plots the current density of the diodes driven by different voltages as a function of electropolymerization time on ITO electrodes. The device containing PEDOT layer from electropolymerization of EDOT–COOH for 40 s displays the highest current density. This obervation agrees with the experimental data in Fig. 1b that the work function of ITO after tuning (~5.2 eV) with electropolymerization is close to the pentacene (literature value: 5.1–5.2 eV) [24,25]. The matching of work function resulted in a lower charge-injection barrier, thereby lowering contact resistance between ITO and pentacene [24]. Fig. 3b clearly shows that the evolution of current density of the diodes is consistent with our experimental work function data when the polymerized film is very thin, where the interface dipole between ITO and PEDOT is siginificantly contributing to the charge-injection process. Although Fig. 3b also demonstates that the current desnity of the diodes modifed with thicker PEDOT (>40 s electropolymerization) is consistent with the work function data, other contributing factors which may reduce the current density such as increasing thickness of the PEDOT or the interface dipole between PEDOT and pentacene, are necessary to be taken into consideration. The effects of these factors warrant further studies. In brief, the simple hole-injection barrier, simply estimated by the work function difference between the electrode and the pentacene, is able to explain the electrical characteristics for this diode.

3. Experimental

Unfunctionalized EDOT was purchased from Sigma–Aldrich and the EDOT functionalized with carboxylic acid group (EDOT–COOH) were synthesized from the known hydroxymethyl-EDOT (EDOT–OH) [26] incorporating an ester linkage [27]. (Fig. 1a). Electropolymerization of all monomers were performed in acidic aqueous microemulsion solution containing 10 mM of the respective monomer and 0.1 M lithium perchlorate ($LiClO_4$), 0.01 M HCl, and 0.05 M sodium dodecyl sulfonate (SDS) as supporting electrolyte. The electropolymerization on electrode surface was carried out when the electrolysis potential was kept at 0.9 V (vs. Ag/AgCl) on Au electrodes and 1.0 V on ITO electrodes. The work function before and after electrolysis was measured by Kelvin probe method (SKP system) [23], conducted in air with a 3 mm diameter of stainless head coated with Au as a reference electrode. The contact potential difference (CPD) was taken as the averaged value over 30 repeated measurements at one position. The standard deviation of the experiment was 10 mV. The work function was calculated relative to a reference Au (5.0 eV). For the fabrication of diode device, the pentacene was thermally

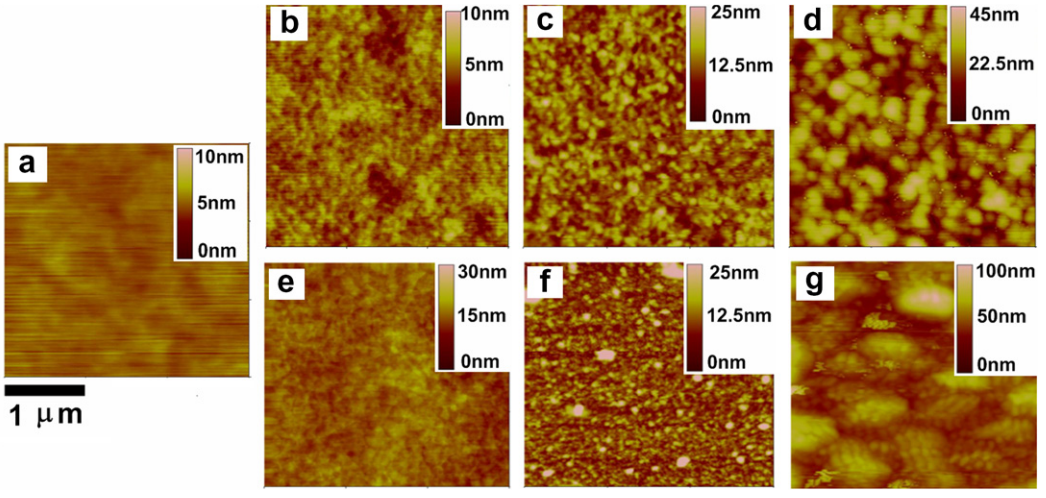

Fig. 2. AFM images for (a) plain Au, and those electrpolymerized with (b) 5 s (c) 10 s and (d) 40 s of EDOT–COOH monomer. AFM images for those electrpolymerized with (e) 5 s (f) 10 s and (g) 40 s of EDOT–OH monomer.

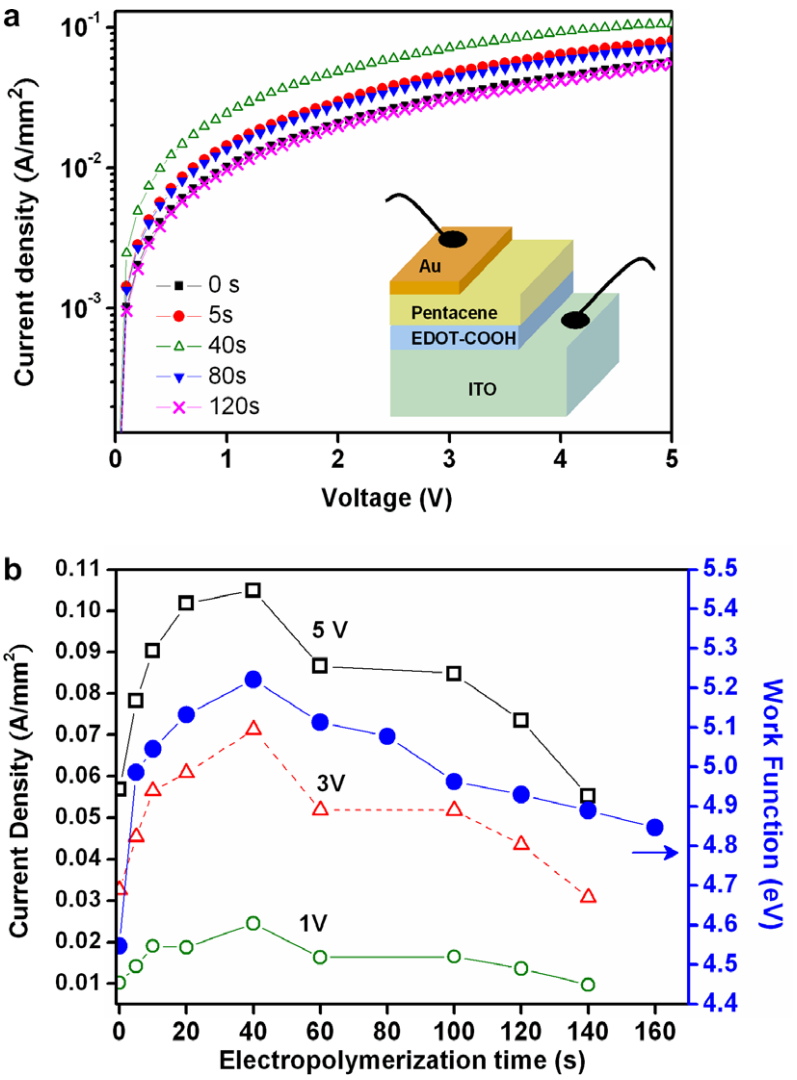

Fig. 3. (a) Current density of the diodes with the structure of Au (thermal evaporated 100 nm)/Pentacene(50 nm)/PEDOT–COOH/ITO. Inset shows the schematic illustration for the device. (b) The current density of the diodes driven by different voltages as a function of electropolymerization time on ITO electrodes.

evaporated onto the ITO electrodes with or without electropolymerized films.

4. Conclusion

In summary, we demonstrate that the work function of Au and ITO can be tuned continually by electropolymerization using EDOT, EDOT–COOH and EDOT–OH. This method is controllable and suitable for wide-range selections of electrodes. A thin layer of polymer (~40 nm) results in a most pronounced effect on work function change. Furthermore, the diode devices with EDOT–COOH modified on ITO surface demonstrate the possibility of improving contact property in organic electronics. It requires more studies to reveal details of the mechanism of short-range dipole formation and the study of the work function tuning method to other types of organic devices are currently underway.

Acknowledgment

This research was supported by Nanyang Technological University, Singapore.

References

[1] N. Jackson, Y.Y. Lin, D.J. Gundlach, H. Klauk, IEEE J. Sel. Top. Quantum Electron. 4 (1998) 100.
[2] A. Dodabalapur, Solid State Commun. 102 (1997) 259.
[3] M. Arai, K. Nakaya, O. Onitsuka, T. Inoue, M. Codama, M. Tanaka, H. Tanabe, Synth. Met. 91 (1997) 21.
[4] J.R. Sheats, Science 277 (1997) 191.
[5] K. Mullen, U. Scherf, Organic Light Emitting Devices: Synthesis Properties and Applications, Wiley-VCH, 2006.
[6] C.W. Tang, S.A. VanSlyke, Appl. Phys. Lett. 51 (1987) 913.
[7] J.H. Burroughes, D.D.C. Bradley, A.R. Brown, R.N. Marks, K. Mackay, R.H. Friend, P.L. Burns, A.B. Holmes, Nature 347 (1990) 539.
[8] D. Braun, A.J. Heeger, Appl. Phys. Lett. 68 (1991) 1982.

[9] F. Garnier, A. Yassar, R. Hajlaoui, P. Srivastava, Science 265 (1994) 1684.
[10] J. Morgado, N. Barbagallo, A. Charas, M. Matos, L. Alcacer, F. Cacialli, J. Phys. D: Appl. Phys. 36 (2003) 434.
[11] P.A. Cox, The Electronic Structure & Chemistry of Solids, Oxford University Press, 1987.
[12] I.H. Campbell, J.D. Kress, R.L. Martin, D.L. Smith, N.N. Barashkov, J.P. Ferraris, Appl. Phys. Lett. 71 (1997) 3528.
[13] R.W. Zehner, B.F. Parsons, R.P. Hsung, L.R. Sita, Langmuir 15 (1999) 1121.
[14] A.A. Dhirani, R.W. Zehner, R.P. Hsung, P. Guyot-Sionest, L.R. Sita, J. Am. Chem. Soc. 118 (1996) 3319.
[15] I.H. Campbell, S. Rubin, T.A. Zawodzinski, J.D. Kress, R.L. Martin, D.L. Smith, N.N. Barashkov, J.P. Ferraris, Phys. Rev. B54 (1996) 14321.
[16] C.W. Lee, K. Zhang, H. Tantang, A. Lohani, T. Nagahiro, K. Tamada, Y. Chen, S.G. Mhaisalkar, L.J. Li, Appl. Phys. Lett. 91 (2007) 103515.
[17] L. Groenendaal, F. Jonas, D. Freitag, H. Pielartzik, J.R. Reynolds, Adv. Mater. 12 (2000) 481.
[18] L. Groenendaal, G. Zotti, P.-H. Aubert, S.M. Waybright, J.R. Reynolds, Adv. Mater. 15 (2003) 855.
[19] J. Roncali, P. Blanchard, P. Frère, J. Mater. Chem. 15 (2005) 1589.
[20] S.-C. Luo, E. Mohamed Ali, N.C. Tansil, H.-h. Yu, S. Gao, E.A.B. Kantchev, J.Y. Ying, Langmuir (2008), doi:10.1021/la800333g..
[21] E. Mohamed Ali, E.A.B. Kantchev, H.-h. Yu, J.Y. Ying, Macromolecules 40 (2007) 6025.
[22] S. Kirchmeyer, K. Reuter, J. Mater. Chem. 15 (2005) 2077.
[23] I.D. Baikie, S. Mackenzie, P.J.Z. Estrup, J.A. Meyer, Rev. Sci. Instrum. 62 (1991) 1326.
[24] D.-J. Yun, D.-K. Lee, H.-K. Jeon, S.-W. Rhee, Org. Electron. 8 (2007) 690.
[25] L. Diao, C.D. Frisbie, D.D. Schroepfer, P.P. Ruden, J. Appl. Phys. 101 (1991) 014510.
[26] A. Lima, P. Schottland, S. Sadki, C. Chevrot, Synth. Met. 93 (1998) 33.
[27] The compound was reported separately by F. Mouffouk, S.J. Higgins, Electrochem. Commun. 8 (2006) 3.

drain electrodes. Also, we discussed the mechanism of reduction in the contact resistance by examining crystallinity of pentacene on the electrodes, and hole-injection barrier between pentacene and the electrodes.

2. Experimental

OFETs with bottom-contact configurations were fabricated on heavily doped silicon wafers covered by thermally grown 300 nm-thick silicon-dioxide layers. Poly(4-methyl styrene) (PMS) ($M_w \approx 72{,}000$, Aldrich) was then spin-coated on the silicone oxide (with a thickness of 75 nm). Subsequently, a 3 nm-thick titanium film (adhesion layer) was formed on the PMS-coated silicon-oxide substrate by means of thermal evaporation. The gold source/drain electrodes (with a thickness of 30 nm) were then deposited using a shadow mask. The channel length (L) and width (W) were 200 and 2000 μm, respectively. Afterwards, a water-based PEDOT:PSS (Baytron® P) solution (0.25 wt.%) was spin-coated on the gold-patterned substrates. Since the PEDOT:PSS solution was wetted only on the hydrophilic gold surface (but dewetted on the hydrophobic PMS surface), the polymer mixture could be specifically spin-coated on the gold electrodes with various thicknesses (between 20 and 100 nm). However, the thickness effect was found to be minimal due to the conductivity of PEDOT:PSS (i.e., 0.4 S/cm). A 30 nm-thick pentacene (Aldrich) film was then deposited as the active layer using a shadow mask (at 0.1 Å/s and a pressure of less than 10^{-6} Torr). The electrical characteristics of the OFETs were measured in air using Keithley 2400 and 236 source/measure units. Also, the crystallinities and film structures of the pentacene film on bare gold and the PEDOT:PSS-coated gold substrates were investigated by means of atomic force microscopy (AFM, Digital Instruments Multimode SPM) and grazing incidence angle X-ray diffraction (GIXD) experiments performed with the 10C1 XRS II beamline (wavelength 1.54 Å) at the Pohang accelerator laboratory (PAL). The hole-injection barrier between pentacene and gold (or PEDOT:PSS-coated gold) was evaluated by means of ultraviolet photoemission spectroscopy (UPS) performed using the 4B1 PES II beamline at PAL upon varying the thickness of the pentacene film between 0.4 and 25.6 nm.

3. Results and discussion

Fig. 1a shows a schematic cross-section of the OFETs fabricated using the PEDOT:PSS-coated gold electrodes whereas Fig. 1b and c shows their transfer and output characteristics, respectively. The carrier mobility was calculated in the linear regime from the slope of a plot of the drain current versus the gate voltage by fitting the data to the following equation: $I_D = (WC_i/L)\mu(V_G - V_{th})V_D$, where I_D is the drain current, μ is the carrier mobility, V_{th} is the threshold voltage, and V_D is the drain voltage (−4 V). The measured capacitance, C_i, was 7.7 nF/cm^2. The carrier mobility of the pentacene OFETs containing PEDOT:PSS-coated gold electrodes was 0.218 cm^2/V s whereas that of the devices based on bare gold substrates was 0.031 cm^2/V s. As shown in Fig. 1c, an ohmic-contact behavior was observed for the devices based on PEDOT:PSS-coated gold, whereas non-ohmic-contact characteristics were measured for the transistors based on bare gold (due to large contact resistance).

The contact resistance was evaluated by means of a four-probe measurement, as described previously [13,14]. The potential probes were patterned on the OFET devices by depositing 100 nm-thick gold films with a shadow mask (each probe was approximately 20 μm in width). The values of the contact resistances, normalized to the channel width, are summarized in Fig. 2. The OFETs composed

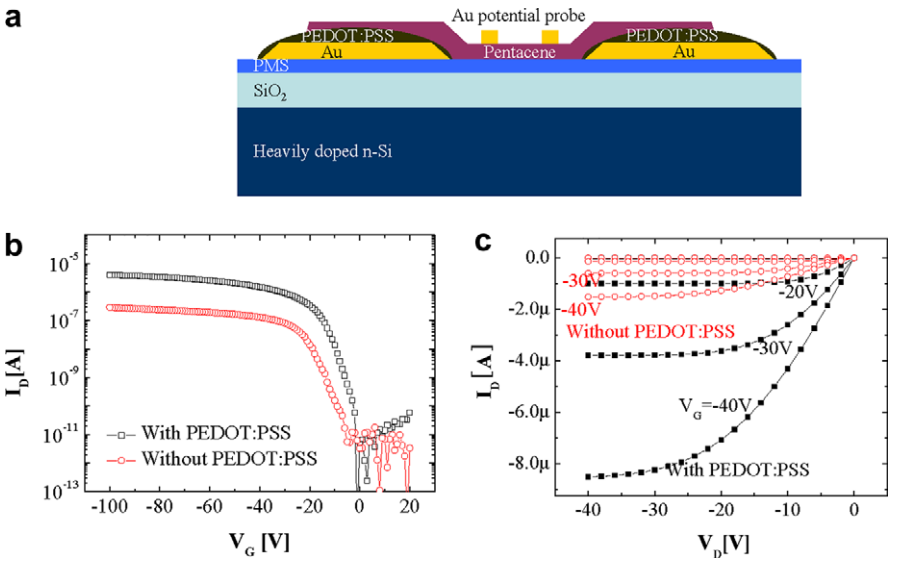

Fig. 1. (a) Schematic diagram of a bottom-contact pentacene OFET containing PEDOT:PSS-coated gold electrodes; (b) transfer characteristics in the linear region (V_D = −4 V) of OFETs with/without PEDOT:PSS-coated gold electrodes; and (c) output characteristics of OFETs with/without PEDOT:PSS-coated gold electrodes.

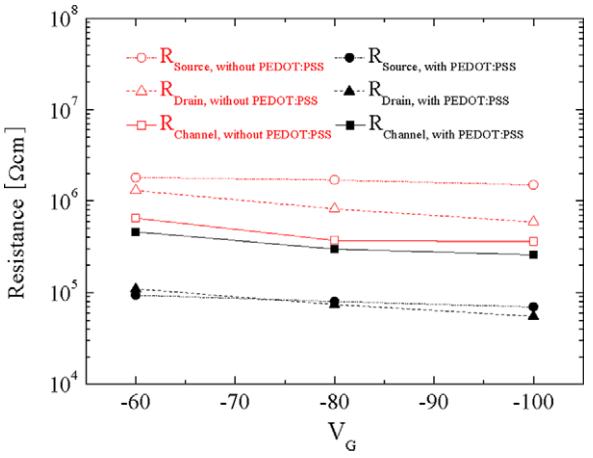

Fig. 2. Width-normalized film resistance and source/drain contact resistances as a function of the gate bias, V_G for OFET devices with/without PEDOT:PSS-coated gold electrodes.

of bare gold electrodes showed large contact resistances of about $1.5 \times 10^6\ \Omega$ cm at the source region and $5.9 \times 10^5\ \Omega$ cm at the drain region (at a gate bias of -100 V), whereas those containing PEDOT:PSS-coated gold electrodes exhibited contact resistances of about $7.0 \times 10^4\ \Omega$ cm and $5.5 \times 10^4\ \Omega$ cm, respectively (at the same gate bias). However, the channel resistance was similar for both types of devices. These results indicate that the increased mobility of the OFETs containing the PEDOT:PSS-coated gold electrodes originates from the reduced contact resistance. Since the morphology and crystallinity of the pentacene film may vary depending on whether electrodes with or without PEDOT:PSS coating are used, the effects of these two parameters on the contact resistance were also investigated.

As shown in Fig. 3a and b, the pentacene film is composed of small grains (with dimensions between 50 and 100 nm) when deposited on bare gold and of larger grains when deposited on the PEDOT:PSS-coated surface, which implies a higher crystallinity of pentacene on the modified

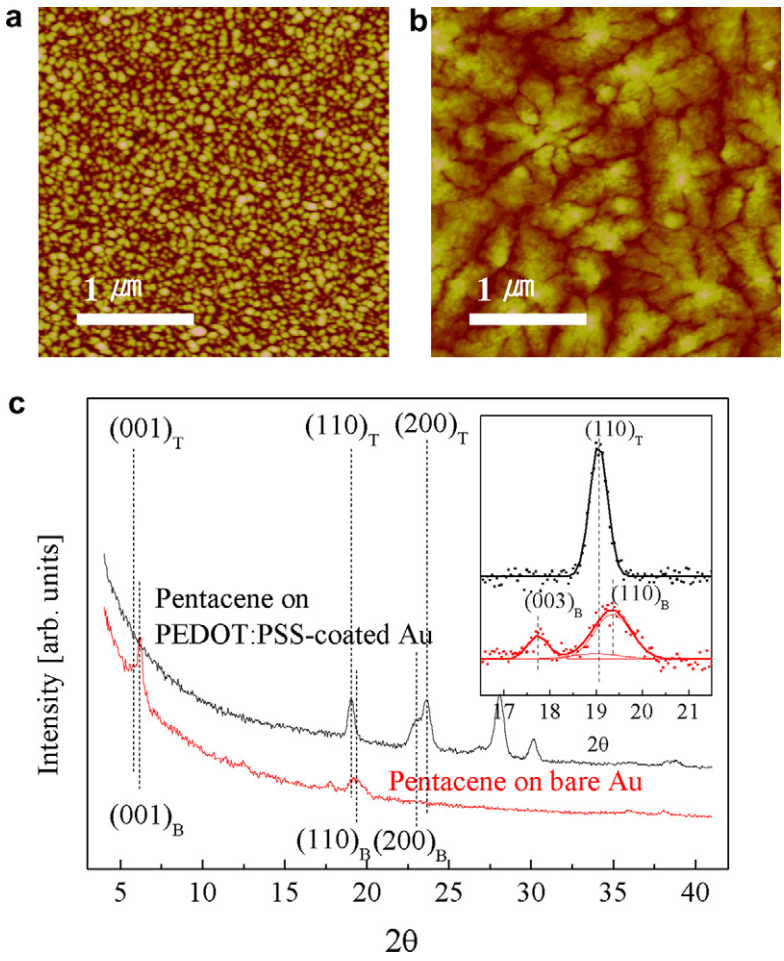

Fig. 3. (a) AFM image of pentacene on bare gold; (b) AFM image of pentacene on PEDOT:PSS-coated gold; and (c) GIXD patterns of pentacene on PEDOT:PSS-coated gold and bare gold. T represents the thin-film phase and B the bulk phase. The inset shows details of the (1 1 0) peaks (the base lines of the GIXD pattern were subtracted and the peaks were fitted by using a Gaussian distribution).

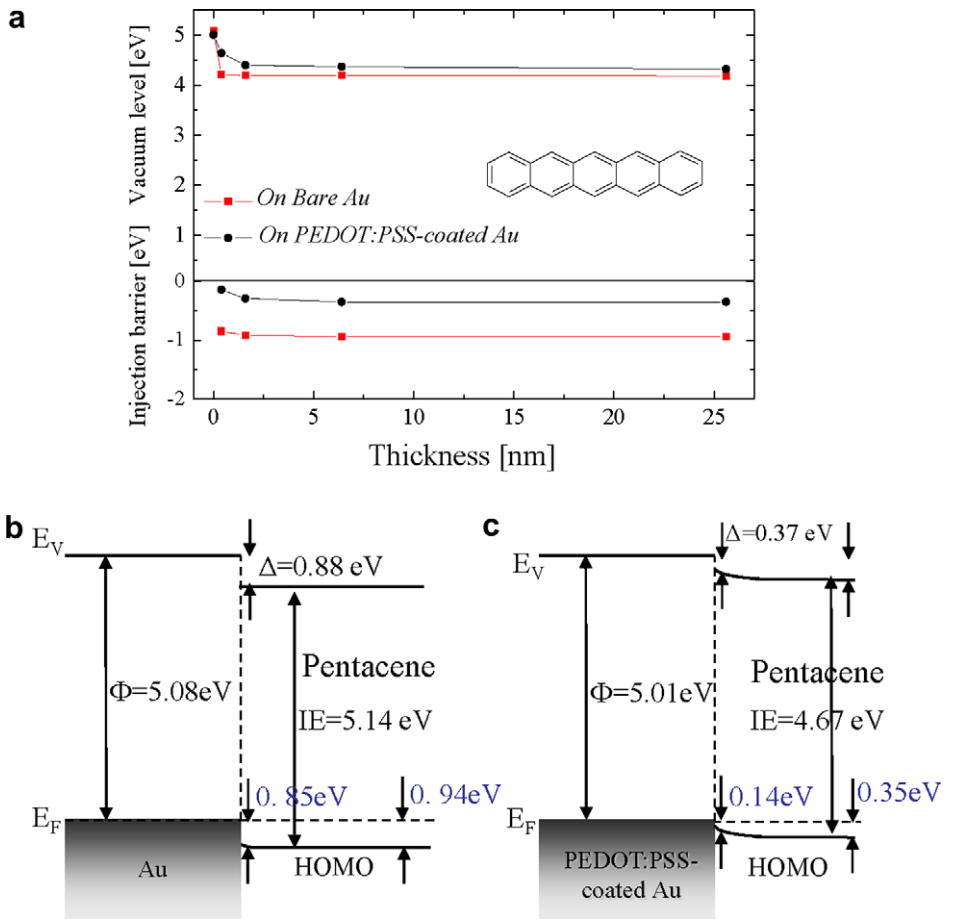

Fig. 4. (a) Vacuum level of pentacene and hole injection barrier between bare gold/PEDOT:PSS-coated gold and pentacene upon varying the pentacene thickness; (b,c) band diagrams of the interface between gold and pentacene and between PEDOT:PSS-coated gold and pentacene.

electrodes. To clarify this result, we performed GIXD experiments on both types of electrodes (see Fig. 3c). On bare gold, the pentacene molecules were found to lay parallel to the surface (as inferred from $(00k)_B$ in GIXD), consistent with previous reports [15,16]. Furthermore, these molecules exhibited a predominant bulk-phase structure (having a 14.4 Å d-spacing of $(00k)_B$) [15–18] with a small portion of a thin-film-phase structure (having a 15.6 Å d-spacing of $(00k)_T$) [19]. On PEDOT:PSS-coated gold, the pentacene molecules were arranged perpendicular to the surface, thereby exhibiting a predominant thin-film-phase structure (with only very few peaks corresponding to the bulk phase) – a result inferred from $(110)_T$, $(200)_T$, and $(200)_B$ in the GIXD patterns [15,17,18]. From the GIXD patterns, we also calculated the coherence length of pentacene (i.e., the distance over which order is maintained). In the (110) direction, this length was determined to be about 10.4 nm (bulk phase) and 7.5 nm (thin-film phase) on the bare gold substrate and 20.8 nm (thin-film phase) on the PEDOT:PSS-coated surface (the coherence length for the bulk phase on the PEDOT:PSS-coated electrode could not be determined because the peak corresponding to the (110) direction was too small). In all cases, the coherence lengths were determined from the half-widths of the (110) peaks by using Scherrer's formula (see the inset of Fig. 3c) [19]. Given that the coherence length is proportional to the size of the domains, much larger domains are present on the PEDOT:PSS-coated gold surface; these represent a higher crystallinity of pentacene. We think this higher crystallinity of pentacene on PEDOT:PSS-coated gold surface could come from weaker interaction between pentacene and PEDOT:PSS-coated gold and reduced roughness of gold surface after PEDOT:PSS coating [3,15].

The vacuum level of pentacene and the injection barrier between bare gold/PEDOT:PSS-coated gold and pentacene were investigated by means of UPS upon varying the pentacene thickness up to 25 nm (see Fig. 4a). The band diagrams of the interface between bare gold/PEDOT:PSS-coated gold and pentacene are shown in Fig. 4b and c. The work functions of bare gold and PEDOT:PSS-coated gold are 5.08 and 5.01 eV, respectively. The hole-injection barrier between pentacene and bare gold is 0.85 eV, whereas a much smaller barrier (of 0.14 eV) is observed between pentacene and PEDOT:PSS-coated gold. This value is smaller than that reported previously [19], probably because of the thickness of the pentacene film. The low hole-injection barrier comes from the very small shift in the vacuum level which results from the drastically

reduced induced density of interface states between PEDOT:PSS-coated gold and pentacene [20–24]. Also, the 0.47 eV smaller ionization energy of pentacene on PEDOT:PSS-coated gold may significantly contribute to the lower hole-injection barrier as a result of the increased crystallinity of the semiconductor on the modified gold surface [21].

Contact resistance in the drain region is originated from the lower crystallinity of pentacene on the gold electrode (with respect to that in the channel region) as a result of the absence of an energy barrier for the holes to transfer from the highest occupied molecular orbital of pentacene to the Fermi level of the electrode. Thus, the reduced contact resistance (from 5.9×10^5 to $5.5 \times 10^4\ \Omega$ cm) observed in the drain region of the OFETs based on PEDOT:PSS-coated electrodes (at a gate bias of -100 V) is due to the increased crystallinity of pentacene – a result that was confirmed by means of AFM and GIXD experiments. Contact resistance in the source region arises from both the hole-injection barrier between pentacene and the gold electrode and the low crystallinity of the organic semiconductor on the metal substrate. Therefore, the contact resistance of OFETs fabricated with bare gold electrodes is higher in the source region than in the drain region, the difference being about $9.1 \times 10^5\ \Omega$ cm (at a gate bias of -100 V). This difference comes from the large hole-injection barrier (namely, 0.85 eV) between pentacene and bare gold. Thus, the contact resistance at the source decreases from 1.5×10^6 to about $5.9 \times 10^5\ \Omega$ cm as a result of a reduction in the injection barrier and further from 5.9×10^5 to about $7.0 \times 10^4\ \Omega$ cm as a result of an increase in the crystallinity of pentacene upon coating PEDOT:PSS on the gold electrode. The decrease in the contact resistance caused by the reduction of the hole-injection barrier (i.e., $9.1 \times 10^5\ \Omega$ cm) is comparable to that due to the increase in crystallinity (i.e., $5.2 \times 10^5\ \Omega$ cm). However, since the increase in crystallinity significantly contributes to a smaller hole-injection barrier (from 0.85 to 0.14 eV) by lowering the ionization energy by 0.47 eV (see Fig. 4) [21], this parameter appears to be the major origin of the reduction of the contact resistance.

4. Conclusion

We reduced the contact resistance of pentacene OFETs by coating PEDOT:PSS on gold electrodes. Through AFM, GIXD and UPS experiments, we found out that the PEDOT:PSS-coating improved crystallinity of pentacene on PEDOT:PSs-coated gold electrode as well as the hole injection property. By the increased crystallinity and the reduced hole injection barrier (from 0.85 to 0.14 eV), the field-effect mobility of the fabricated pentacene OFET with PEDOT:PSS-coated gold electrodes was improved from 0.031 to 0.218 cm^2/V s. Though the contributions of increased crystallinity and reduced hole-injection barrier to contact resistance were comparable to each other, the increased crystallinity appears to be the major origin of the reduction of the contact resistance since the crystallinity also reduces the hole-injection barrier.

Acknowledgment

This work was supported by a Grant (F0004020-2006-22) from the Information Display R&D Center, one of the 21st Century Frontier R&D Program funded by the Ministry of Commerce, Industry and Energy of the Korean Government.

References

[1] F. Eder, H. Klauk, M. Halik, U. Zschieschang, G. Schmid, C. Dehm, Appl. Phys. Lett. 84 (2004) 2673.
[2] W. Fix, A. Ullmann, J. Ficker, W. Clemens, Appl. Phys. Lett. 81 (2002) 1735.
[3] I. Kymissis, C.D. Dimitrakopoulos, S. Purushothaman, IEEE Trans. Electron. Dev. 48 (2001) 1060.
[4] David J. Gundlach, LiLi Jia, Thomas N. Jackson, IEEE Trans. Dev. Lett. 22 (2001) 571.
[5] F. De Angelis, S. Cipolloni, L. Mariucci, G. Fortunato, Appl. Phys. Lett. 86 (2005) 203505.
[6] K. Ihm, B. Kim, T. Kang, K. Kim, M.H. Joo, T.H. Kim, S.S. Yoon, S. Chung, Appl. Phys. Lett. 89 (2006) 033504.
[7] B.H. Hamadani, D.A. Corley, J.W. Ciszek, J.M. Tour, D. Natelson, Nano Lett. 6 (2006) 1303.
[8] C. Di, G. Yu, Y. Liu, X. Xu, D. Wei, Y. Song, Y. Sun, Y. Wang, D. Zhu, J. Liu, X. Liu, D. Wu, J. Am. Chem. Soc. 128 (2006) 16418.
[9] T. Maeda, H. Kato, H. Kawakami, Appl. Phys. Lett. 89 (2006) 123508.
[10] W. Kim, K. Hong, J.L. Lee, Appl. Phys. Lett. 89 (2006) 142117.
[11] H.S. Lee, J.H. Cho, W.-K. Kim, J.-L. Lee, K. Cho, Electrochem. Solid-State Lett. 10 (2007) H239.
[12] R. Schroeder, L.A. Majewski, M. Grell, J. Maunoury, J. Gautrot, P. Hodge, MikeTurner, Appl. Phys. Lett. 87 (2005) 113501.
[13] P.V. Pesavento, R.J. Chesterfield, C.R. Newman, C.D. Frisbie, J. Appl. Phys. 96 (2004) 7312.
[14] P.V. Pesavento, K.P. Putambekar, C.D. Frisbie, H.C. McKeen, P.P. Ruden, J. Appl. Phys. 99 (2006) 094504.
[15] D. Käfer, L. Ruppel, G. Witte, Phys. Rev. B 75 (2007) 085309.
[16] W.S. Hu, Y.T. Tao, Y.J. Hsu, D.H. Wei, Y.S. Wu, Lanmuir 21 (2005) 2260.
[17] R.B. Campbell, J.M. Robertson, J. Trotter, Acta Crystallogr. 15 (1962) 289;
R.B. Campbell, J.M. Robertson, J. Trotter, Acta Crystallogr. 14 (1961) 705.
[18] T. Kakudate, N. Yoshimoto, Appl. Phys. Lett. 90 (2007) 081903.
[19] R. Ruiz, A.C. Mayer, G.G. Malliaras, Appl. Phys. Lett. 85 (2004) 4926.
[20] N. Koch, A. Kahn, J. Ghijsen, J.-J. Pireaux, J. Schwartz, R.L. Johnson, A. Elschner, Appl. Phys. Lett. 82 (2003) 70.
[21] K. Hong, J.W. Lee, S.Y. Yang, K. Shin, H. Jeon, S.H. Kim, C. Yang, C.E. Park, Org. Electron. 9 (2008) 21.
[22] H. Vazquez, R. Oszwaldowski, P. Pou, J. Ortega, R. Perez, F. Flores, A. Kahn, Europhys. Lett. 65 (2004) 802.
[23] H. Vazquez, F. Flores, R. Oszwaldowski, J. Ortega, R. Perez, A. Kahn, Appl. Surf. Sci. 234 (2004) 107.
[24] A. Wan, J. Hwang, F. Amy, A. Kahn, Org. Electron. 6 (2005) 47.

the degraded PLED showed island-like structures of tens-of-micrometer size. Based on the SPEM analysis results, we suggest that the main degradation mechanism of the PLED is out-diffusion of sulfur (S) towards the cathode, resulting in effective generation of conduction paths between the electrodes.

2. Experimental

The staking sequence of the PLED was ITO/50–60 nm thick poly(3,4-ethylene dioxythiophene) poly(4-styrene-sulfonate) (PEDOT:PSS)/10 nm thick poly(9,9-dioctylfluorene-co-bis-*N*,*N*-(4-butylphenyl)-bis-*N*,*N*-phenyl-1,4-phenyl enediamine) (PFB)/70–80 nm thick poly(9,9′-di-2-ethylhexy l-2′,3′,6′,7′-tetraoctyloxy-spriofluorene-co-*N*-octyl-oxy-phenoxazine (TS9)/BaF_2/Ca/Al. The polymers were spin coated and the cathode materials were thermally deposited under a vacuum. The PLED was operated under packaged and air-ambient conditions until the luminescence decreased by 50%. Then, the cathode layers were removed by chemical etching in order to investigate the chemical states of the surface of the TS9 emission layer (EML) using SPEM, at the Pohang Light Source [12]. The base pressure of the SPEM chamber was 2×10^{-10} Torr, and the sample was mildly sputtered in order to remove any air contamination on the EML surface. The incident photon energy was 620 eV. The X-ray was focused by a Fresnel zone plate, and the diameter of the X-ray focused on the sample surface was 0.5–1.0 μm. Pristine, or undriven, PLED was also prepared and investigated according to the same procedure. In order to remove the cathode layers of both the driven and undriven PLEDs, the PLEDs were chemically etched for 1–2 min using solvent containing H_2SO_4 and HCl with volume ratio of 2:1. It is noticeable that if cathode layers were re-deposited after the chemical etching, then the electric and luminescent property was almost the same as that of unetched PLED. Schematic of the SPEM investigation is shown in Fig. 1.

3. Results and discussion

In SPEM the photoelectrons generated by the focused X-rays were collected by an electron energy analyzer. Escape depth or probing depth of the photoelectrons is only less than 1 nm and, thus, the SPEM images and the space-resolved spectra are results based on the electrons generated from the topmost surface of the sample. As expected, for the pristine PLED, the SPEM images of the surface of the EML showed a uniform contrast, indicating no sign of degradation (at least on the surface of the TS9 layer): a typical image obtained at the C 1s binding energy is shown in Fig. 1a. By contrast, for the degraded PLED, the images obtained at the C 1s and S 2p core-levels showed island-like structures, as shown in Fig. 1b and c. The observation of S in the island-like structures was unexpected, because this implies that S atoms exist at the top surface of the TS9 layer. The contrast obtained at the S 2p core-level (c) was more enhanced than that obtained at the C 1s core-level (b) because, unlike the carbon (C) atoms, the S atoms exist only in island-like structures (see Fig. 3a)

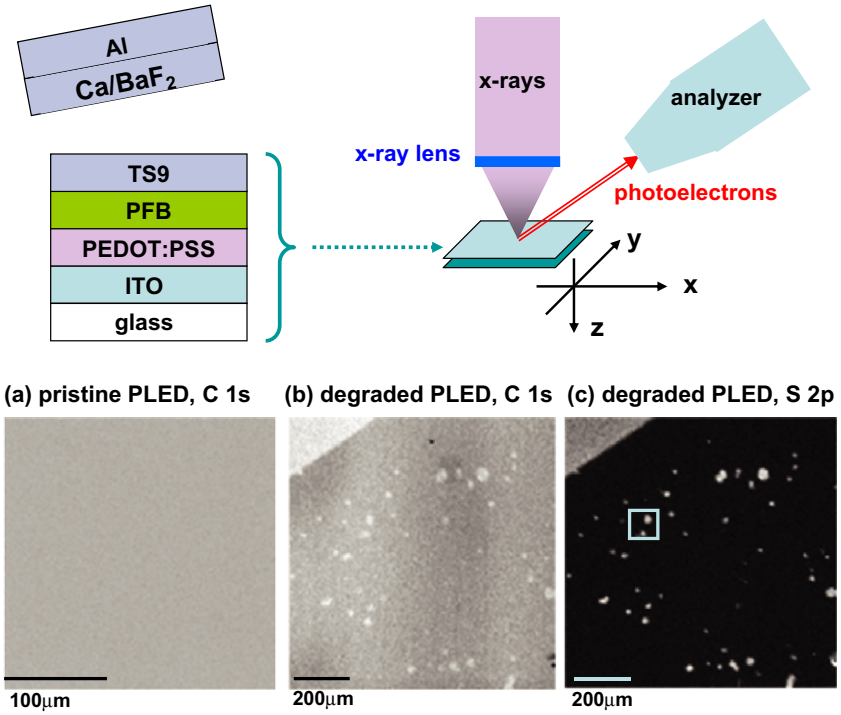

Fig. 1. Schematic of SPEM investigation of the PLED and the SPEM images obtained with 620 eV X-ray energy. (a) C 1s photoelectron image obtained for pristine PLED. (b) C 1s photoelectron image obtained for degraded PLED driven to 50% luminescence, or half life. (c) S 2p photoelectron image for the degraded PLED. The energy window of each photoelectron image is 12.8 eV. The triangular shape in the left upper edge of the (b) and (c) images is the ITO anode structure for outside electric connection.

within the probing depth (<1 nm) of SPEM and possibly also deeper.

It was found that each island-like structure has the same spectral feature. Fig. 2a–e is detailed SPEM images of the island-like structure. The images in Fig. 2a and b were obtained at the S 2p and C 1s core-levels, respectively. The intensity of any SPEM image is affected by the electron yield, as well as by the conductivity of the insulating layer or the charging effect. Contrasting images (a) and (b), the main difference between inside and outside the island-like structure is the existence of the S component and the lesser charging inside, which allow for a relatively higher electron yield. Also shown is the sample current image (c), the contrast change of which indicates any change in the absorption coefficient or electron yield. Thus, the sample current image (c) and both the S 2p and C 1s images show similar features.

The chemical states of the island-like structure were obtained by measuring the S 2p and C 1s photoelectron spectra in detail, as shown in Fig. 3a and b. The survey spectrum (data not shown in the figure) obtained inside the island-like structure was dominated by the C 1s peak with some intensity of S 2p peak and traces of O 1s and N 1s peaks. Outside the island-like structure and for the undriven PLED, they were respectively dominated by the C 1s peak with traces of O 1s and N 1s peaks. Since the SPEM probing depth for the C 1s and S 2p photoelectrons is less than 1 nm, the spectra thus represent the chemical states of the surface of the TS9 EML layer. As shown in Fig. 3a, there was no trace of S in the pristine PLED, 'A'', nor any trace outside the island-like structure, 'A'. Only in the island-like structure, 'B', and also in 'C', was S 2p observed. The S 2p spectrum could be deconvoluted with two components, each component having a spin-orbit doublet. The binding energy of the main component was 164 eV, and that of the other component, ~162.3 eV. It has been reported that the S 2p main peak (S $2p_{3/2}$) occurred at ~164 eV for the S in the PEDOT (sulfide (C–S–C)) configuration, and at 168.5 eV for the PSS (sulfonate (SO_3^- and SO_3H)) configuration [7,13]. This difference in binding energy can be explained by the amount of charge transfer from S to nearby elements having different electro-negativities (ENs). For example, compared with the case of sulfonate, where S strongly bonds with O (EN ~ 3.5 eV) [14], in sulfide, where S bonds less strongly with C (EN ~ 2.5 eV) [14], the lesser charge transfer leads the S 2p peak position to appear at a ~4.5 eV-lower binding energy. When S bonds with H to form the –C–S–H configuration, the binding energy of the S 2p can be lower than that of the –C–S–C– configuration due to the weaker bonding and lower EN of H (EN ~ 2.2 eV) [14] compared with that of C. Thus, the S 2p peak at 162.3 eV could be assigned to the C–S–H configuration. Xu reported that after operation, the PSS phase segregates from the PEDOT:PSS layer towards the anode [7]. Contrarily, Martin reported that the PSS chain segregates towards the interface of the emission layer and the PEDOT:PSS layer [6]. Our result indicates that S out-diffused further to the cathode-fronting surface of the emission layer and formed sulfide and thiol configurations in the EML layer. It is not yet clear in what configuration the S out-diffused from the PEDOT:PSS layer towards

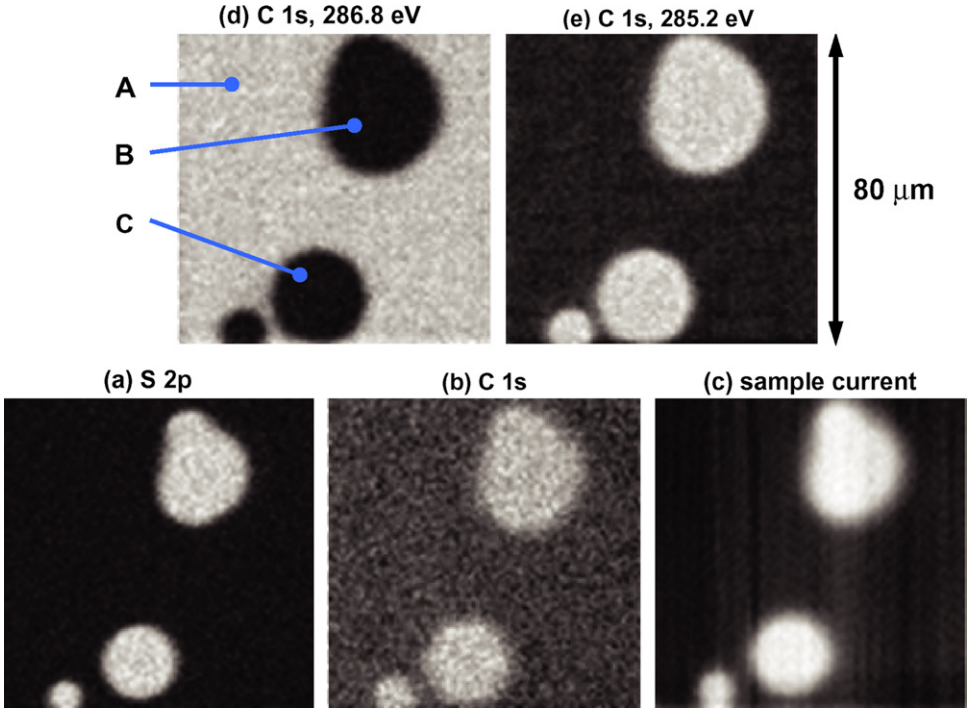

Fig. 2. SPEM images obtained from the boxed area of the image in Fig. 1c. (a) S 2p image. (b) C 1s image. (c) Sample current image obtained by measuring the total electron yield. (d) C 1s image centered at 286.8 eV. (e) C 1s image centered at 285.2 eV. The energy window for the (a) and (b) images is 12.8 eV, and for the (d) and (e) images, 0.8 eV.

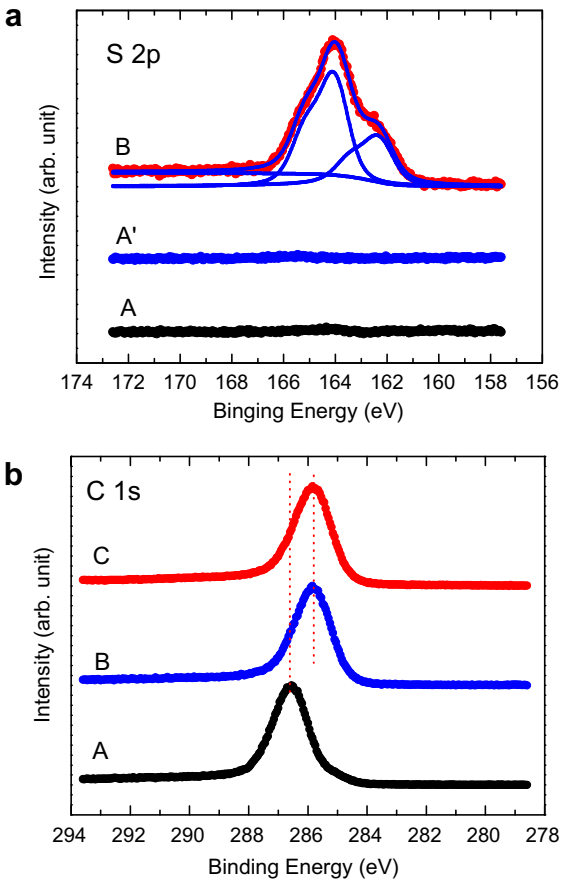

Fig. 3. (a) S 2p photoelectron spectra obtained for the pristine PLED 'A'', outside the island-like structure 'A' and inside the island-like structure 'B'. (b) C 1s photoelectron spectra obtained for outside the island-like structure 'A', inside the island-like structure 'B', and inside another island-like structure 'C'. For clarity, each spectrum was shifted in its vertical axis.

the TS9 layer. It is likely that HSO_3 and SO_3^-, which are singly bonded with the aromatic ring, dissociated more easily from the PSS than the S in the PEDOT configuration, in which S bonds with C in the C–S–C configuration. Then, we may suggest that HSO_3 and SO_3^- out-diffused towards the cathode, and that S or HS further dissociated from HSO_3 and SO_3^- during the out-diffusion process because oxygen, the EN of which is higher than S (EN ~ 2.5 eV) [14], can bond with surrounding neighbors. Near the interface between the cathode and the TS9 layer, then, the dissociated S and SH can be stabilized by forming sulfide and thiol configurations. It maybe suggested that one of the main driving forces of the dissociation and out-diffusion of the HSO_3 and SO_3^- is the 'local heat' generated by the local and strong current flow; the local heat generation caused by strong current flow was also regarded as the main degradation mechanism of the top-emission OLED [11].

The polymers are not good conductors, and photoelectrons are charge-shifted, especially when investigated with SPEM. Several electron-volts of charging shift was observed when the thickness of the poly(methyl methacrylate) (PMMA) was about 100 nm [15]. TS9 is comprised predominantly of C, and thus the C 1s spectral shapes both outside, A, and inside, B and C, the island-like structure are similar, as shown in Fig. 3b, except for the slight broadening of the spectra for B and C due to the additional C–S–C and C–S–H configurations that have slightly lower binging energies. The amount of S relative to C, measured from the S 2p and C 1s spectral intensity, was ~5%. Thus, the main peak positions of the B and C should be almost the same as that of spectrum A. However, as shown in Fig. 3b, the difference of the peak position was ~1 eV, larger than expected. This indicates that the charging effect is much smaller inside the island-like structure. This fact resulted in the contrast reversal in the C 1s images, measured at 285.2 eV and 286.8 eV as shown in Fig. 2d and e. This indicates that the conduction path length through the island-like structure became shorter compared with that outside the island-like structure. This shortness of path between the cathode and the anode further indicates the generation of effective conduction-bypass channels for the device current, lowering device efficiency and resulting in device degradation.

4. Conclusions

In conclusion, we provided direct spectromicroscopic data on the degradation mechanism of a PLED based on the spin-coated PEDOT:PSS polymer. On the surface of the emission layer, we found island-like structures containing S in the –C–S–C– and –C–S–H configurations. We posit that S out-diffused from the PEDOT:PSS layer towards the cathode, resulting in an increase of conductance effecting current bypass and eventual device degradation. Our results imply that preventing the out-diffusion of S is one of the main strategies for improving PLED stability.

References

[1] C.W. Tang, S.A. VanSlyke, C.H. Chen, J. Appl. Phys. 65 (1989) 3610.
[2] J.H. Burroughes, D.D.C. Bradley, A.R. Brown, R.N. Marks, K.D. Mackay, R.H. Friend, P.L. Burn, A.B. Holmes, Nature 347 (1990) 539.
[3] Hiroshi Okada, Japanese R&D Trend Analysis – Advanced Materials Phase XVII, Report No. 2: Electro conductive Polymers (Update VII), KRI, Inc., 2005, pp. 109.
[4] J.S. Kim, R.H. Friend, F. Cacialli, Appl. Phys. Lett. 74 (1999) 3084.
[5] C. Giebeler, S.A. Whitelegg, D.G. Lidzey, P.A. Lane, D.D.C. Bradley, Appl. Phys. Lett. 75 (1999) 2144.
[6] S.J. Martin, R.A.L. Jones, M. Geoghegan, A.M. Higgins, I. Grizzi, J.J.M. Halls, S. Kirchmeyer, R.M. Dalgliesh, Phys. Rev. B 71 (2005) 081308(R).
[7] X. Xu, R.A. Register, S.R. Forrest, Appl. Phys. Lett. 89 (2006) 142109.
[8] C. Garditz, A. Winnacker, F. Schindler, R. Paetzold, Appl. Phys. Lett. 90 (2007) 103506.
[9] F.A. Boroumand, A. Hammiche, G. Hill, D.G. Lidzey, Adv. Mater. 16 (2004) 252.
[10] H.J. Shin, M.C. Jung, J. Chung, K. Kim, J.C. Lee, S.P. Lee, Appl. Phys. Lett. 89 (2006) 063503.
[11] H.J. Shin, H.J. Song, J. Lee, H.J. Yoon, J. Chung, J.C. Lee, J. Appl. Phys. 100 (2006) 084504.
[12] M.K. Lee, H.J. Shin, Rev. Sci. Instrum. 72 (2001) 2605.
[13] S.K.M. Jonsson, J. Birgerson, X. Crispin, G. Greczynski, W. Oskiowicz, A.W. Denier van der Gon, W.R. Salaneck, M. Fahlman, Synthetic Metals 1 (2003) 10361.
[14] F.A. Cotton, G. Wilkinson, P.L. Gans, Basic Inorganic Chemistry, second ed., John Wiley & Sons Inc., 1987. p. 62.
[15] H.J. Shin, H.J. Song, M.K. Lee, G.B. Kim, C.K. Hong, J. Appl. Phys. 93 (2003) 8982.

Coupling of optical and electrical properties may be a direction in this regard. Since a little percent of molecules changes its conformation upon switching, electronic absorption of organic films responds poorly [19]. Measurement of photoluminescence spectrum to "read" a state is too impractical considering the length of time scale required to record a spectrum. Since some of the heterostructure devices yield photovoltage upon illumination [20–23] measurement of photovoltage or photocurrent may be a process of probing the states. Since open-circuit voltage (V_{OC}) or short-circuit current (I_{SC}) of a photovoltaic device may also be measured without an external bias, the "read" process would not influence or interfere the "write" procedure. In this article, we introduce non-interacting "write" and "read" processes in organic memory devices based on a heterostructure of organic materials.

2. Experimental

2.1. Materials and devices

Copper phthalocyanine (CuPc) and disodium salt of 4,5,6,7-tetrachloro-2′,4′,5′,7′-tetraiodo fluorescein (Rose Bengal) were purchased from Sigma–Aldrich and were used without further purification. Devices were fabricated on stripped indium tin oxide (ITO) coated glass substrates, which were cleaned and processed following standard protocol. First CuPc was thermally evaporated on the substrates at a pressure below 10^{-6} Torr. With CuPc being insoluble in acetone, Rose Bengal solution in acetone (2 mg/ml) was spun on CuPc films at a speed of 1500 rpm. Thickness of both the materials was kept at 50 nm each. The bilayer films were annealed in vacuum at 60 °C. As upper electrodes, aluminum (Al) was thermally evaporated at a pressure below 10^{-6} Torr by using a shadow mask (to obtain strips of Al). Apart from the heterostructure devices, single layer devices based on the components, i.e., CuPc (50 nm) and Rose Bengal (50 nm) films, were also fabricated with the same pair of electrodes. Area of each of the devices, as defined by the overlap of ITO and Al strips, was 6 mm^2.

2.2. Characterization

All the measurements were carried out in a shielded vacuum chamber, which had a quartz window. Current–voltage (I–V) characteristics were recorded with a Keithley 6517A electrometer. Bias was applied with respect to the Al electrode. Sweep speed of applied voltage was 50 mV/s. A Newport-Stratford solar simulator (model 96000) was used to shine the devices. I–V characteristics were recorded under dark and various illumination conditions. Intensity of the incident beam was varied in the 10–100 mW/cm^2 range with the help of neutral density filters. To record spectral response of photocurrent or action spectrum, a Jobin–Yvon monochromator model H20 was used. UV–vis absorption spectra of different films deposited on quartz substrates were recorded with a Shimadzu UV-2550 spectrophotometer. For memory applications, voltage pulse of suitable amplitude and width was used to "write" a state. To "read" a state, either the I_{SC} or the V_{OC} of the device was measured as a function of time.

3. Results and discussion

Since we wanted unrelated "write" and "read" processes, we aimed to use photogenerated functions as parameters to read the states. Heterostructures between two organic materials was hence the direction to follow. We first characterized the CuPc, Rose Bengal, and their heterojunction (CuPc/Rose Bengal) films. Electronic absorption spectra of the heterojunction and its components are shown in Fig. 1. While the components show spectra corresponding to their electronic absorption bands, the spectrum of the heterojunction was a sum of that of CuPc and Rose Bengal. The spectrum not only evidenced presence of the components in the heterojunction film but also identified the spectral range where photoresponse would have to be probed and matched.

I–V characteristics of a heterostructure device (ITO/CuPc/Rose Bengal/Al) under dark and illumination conditions are shown in Fig. 2. Photoresponse of the device along with those based on its components have been zoomed and presented in the inset of Fig. 2. The results show that the degree of photoresponse in the heterojunction-device is much more than those in ITO/CuPc/Al and ITO/Rose Bengal/Al devices. The band-diagram, as presented in the inset of Fig. 2, show that the heterojunction based on CuPc and Rose Bengal is favorable for the generation of photocurrent. V_{OC} and I_{SC} of the heterojunction reach up to 0.4 V and 0.045 mA/cm^2, respectively. The values of I_{SC} in the devices based on the individual components are several orders lower in magnitude. V_{OC} was marginally lower in the ITO/CuPc/Rose Bengal/Al device as compared to ITO/CuPc/Al and ITO/Rose Bengal/Al devices. When intensity of illumination was varied, I_{SC} in all the devices responded linearly with it.

To ensure that photo-absorption in the dye layers has indeed contributed to the observed photocurrent, we

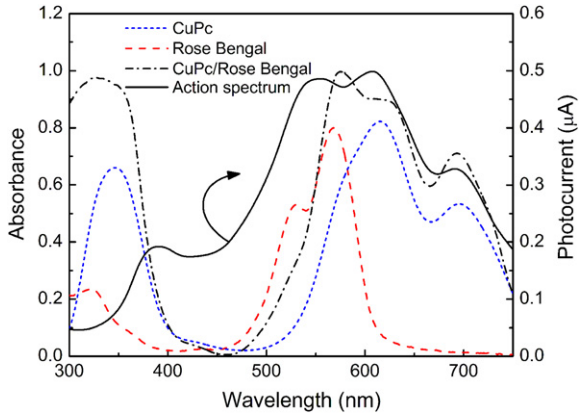

Fig. 1. Electronic absorption spectra of CuPc, Rose Bengal, and CuPc/Rose Bengal heterojunction films on quartz and photoaction spectrum of an ITO/CuPc/Rose Bengal/Al device with −1.0 V as applied voltage.

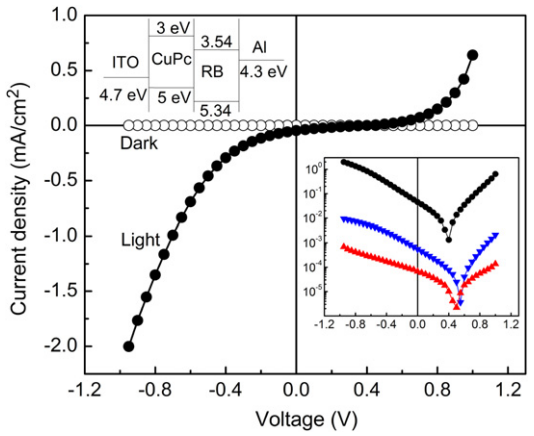

Fig. 2. *I–V* characteristics under dark and illumination (100 mW/cm^2) conditions of a device based on CuPc/Rose Bengal heterojunction film sandwiched between ITO and Al electrodes. Inset shows the characteristics of the device along with that of ITO/CuPc/Al (blue down-triangles) and ITO/Rose Bengal/Al (red up-triangles) under illumination in a log-linear scale. Energy band-diagram of an ITO/CuPc/Rose Bengal/Al device is also shown in the inset.

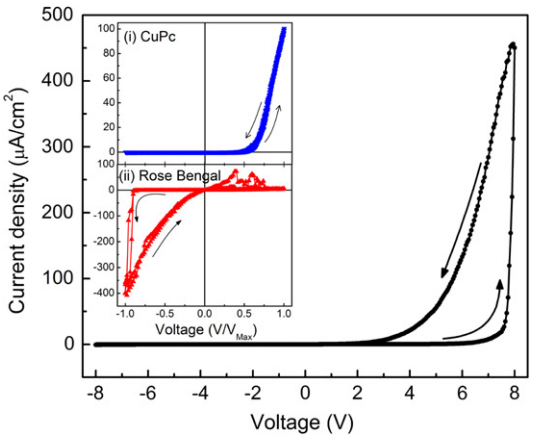

Fig. 3. *I–V* characteristics of an ITO/CuPc/Rose Bengal/Al device in dark condition under a voltage loop. Characteristics of devices based on CuPc and Rose Bengal are shown in the insets with V_{Max} being 9.0 and 2.5 V, respectively. Arrows mark the direction of voltage sweep.

recorded photocurrent as a function of incident wavelength. The spectrum, when compared with the electronic absorption spectrum of the heterojunction film (Fig. 1), shows bands corresponding to the components of the device. Excitons generated at the dye layers have hence became dissociated in electrons and holes; due to the dissimilar metal electrodes, the carriers travel to the opposite electrode to yield photocurrent in the external circuit. The relative intensity of the bands, however, did not exactly match with the electronic absorption spectrum. This could be due to additional effects raised due to exciton dissociation probabilities in CuPc and Rose Bengal layers and carrier mobilities in them in observing photocurrent in the external circuit.

Having proven that the devices based on CuPc/Rose Bengal heterojunctions can act as photovoltaic solar cells, we studied electrical bistability of the devices. *I–V* characteristics of an ITO/CuPc/Rose Bengal/Al heterostructure device under dark condition and under a voltage loop are shown in Fig. 3. The results show that the device exhibits electrical bistability in the positive bias direction. Device current during the sweep towards a positive bias was a couple of orders in magnitude lower than that during the sweep from a positive voltage. In other words, a positive voltage actually switches the conductivity of the heterojunction layer to a higher value. Again, at a suitable negative bias, the heterostructure device switches off to its low-conducting state.

We further have evaluated the components of the heterojunction that could be responsible for the electrical bistability. To do so, we characterized devices based on CuPc and Rose Bengal separately. *I–V* characteristics of the ITO/CuPc/Al and ITO/Rose Bengal/Al devices in dark and under multiple voltage loops are presented in the inset of Fig. 3. While the former device do not evidence any bistability with V_{Max} up to 9.0 V, the latter one expectedly exhibits a typical conductance switching. Here device current switched to a high-value at a threshold voltage of −2.5 V. Since the high-conducting state is retained even after withdrawal of bias and up to some positive voltage, the conductance-switching in Rose Bengal is referred to as memory-switching phenomenon.

It is intriguing to compare the bistability of ITO/Rose Bengal/Al and ITO/CuPc/Rose Bengal/Al along devices with the *I–V* characteristics of an ITO/CuPc/Al one to shed some light on the mechanism involved. Since the electrode combination in the three devices are the same, the absence of bistability in the CuPc case immediately rules out any role of Al oxide or Al penetration [18,24] in observing conductance switching. The results furthermore emphasize the importance of xanthene class molecules (Rose Bengal is a member of this class of molecules) in conductance switching and memory applications. Moreover, the direction of bias at which switching to a high-state occurs differed in ITO/Rose Bengal/Al and ITO/CuPc/Rose Bengal/Al devices. Barrier height for carrier injection from the ITO electrode has hence an immense effect in switching the conductivity of the molecules.

Mechanism of bistability in Rose Bengal has been explained in terms of conformational change with or without electroreduction [1,16]. The molecule is electron-accepting in nature due to the halide functional groups. In a device, when electron injection from an electrode is possible, some of the molecules undergo a change in their conformation. The molecules' HOMO and LUMO change resulting in a decrease in its band gap. Barrier heights with the electrodes hence decrease resulting in a higher flow of current across the device (high-conducting state). At a suitable negative bias, the molecules switch off to its low-conducting state. Switching at opposite bias directions in ITO/Rose Bengal/Al and ITO/CuPc/Rose Bengal/Al devices in fact arises due to dissimilar barrier heights from the ITO electrode. In the former case, where switching to a high-state occurs at a negative bias, electron injection from the ITO electrode to Rose Bengal is favorable than that from the Al side. In the ITO/CuPc/Rose Bengal/Al device, ITO is in contact with

CuPc, which has a higher LUMO and HOMO than the respective levels of Rose Bengal (inset of Fig. 2). This results in an increase in the electron barrier-height from the ITO electrode (while keeping Rose Bengal/Al barrier the same). Hence, electron injection from the Rose Bengal becomes favorable in the ITO/CuPc/Rose Bengal/Al device leading to the observation of conductance switching at a positive voltage.

Several research groups have exemplified memory phenomenon in devices based on Rose Bengal [1,2,8,24,25]. To evidence read-only memory (ROM) and random-access memory (RAM) applications, a bias is applied to "write" a state following "read" process by measuring current under small voltage pulses. A high- and a low-state are also often flip-flopped ("write" and "erase") with a "read" process in-between them to generate a "write-read-erase-read" sequence. Here we aimed to decouple "write" and "read" processes by employing non-interacting functionalities. To check if V_{OC} and/or I_{SC} can be employed as a parameter to "read" the state of the heterojunction device, we first measured the effect of conductance switching on photovoltaic effects. Before and after switching an ITO/CuPc/Rose Bengal/Al device, its I–V characteristics have been measured under dark and illumination conditions (Fig. 4). In the dark condition, there is the usual change (increase) in device current due to the conductance switching. Under illumination condition, both I_{SC} and V_{OC} exhibited a clear increase. The effect of conductance switching on photovoltaic parameters was repeatable and reproducible over many cycles.

The responses of I_{SC} and V_{OC} with conductance switching are itself of interest. Considering the fact that the origin of V_{OC} in a heterojunction device is a combined effect of HOMO and LUMO of the components and the electrode workfunctions, an increase in V_{OC} during the conductance-switching marks that HOMO and/or LUMO of the molecule must have changed during switching. This supports molecular nature of electrical bistability in Rose Bengal and other similar molecules in the xanthene class. The increase in I_{SC} in a high-conducting device, on the other hand, can be due to two aspects: (1) rise in V_{OC} and (2) decrease in device resistance. The magnitude of increase cannot solely be due to the increase in V_{OC}. Fortunately both the factors contributed positively leading to a clear increase in I_{SC}.

We next aimed to use photovoltaic parameters, namely V_{OC} and I_{SC} to "read" the states of the devices. Since measurement of none of them requires application of an external bias, the processes have not interacted the "write" process. In other words, we have applied a suitable voltage pulse to switch the device; we then have measured V_{OC} and I_{SC} separately for ROM and RAM applications. Fig. 5a and b, respectively show V_{OC} and I_{SC} of an ITO/CuPc/Rose Bengal/Al device before and after switching Rose Bengal as a function of time. The plots show that while probing the high- and low-states of the device, both V_{OC} and I_{SC} remained clearly different. The results hence show that the photovoltaic parameters could read the states of the device over a considerable period of time displaying ROM application. The parameters have also been measured while flip-flopping between the two states (Fig. 6). Here a high- and a low-conducting state are written with suitable voltage pulses and the states are "read" by measuring V_{OC} and I_{SC} of the device under illumination. The figure shows that V_{OC} and I_{SC} remained different for the two states evidencing that both V_{OC} and I_{SC} can be the "read" parameter during RAM application of a memory device.

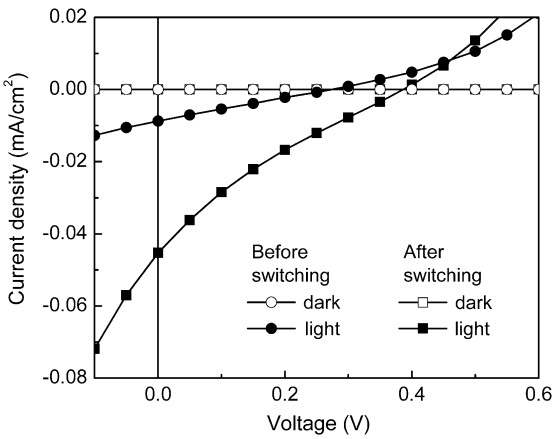

Fig. 4. I–V characteristics under dark and illumination (100 mW/cm^2) conditions of an ITO/CuPc/Rose Bengal/Al device before and after conductance switching. A 9.0 V pulse (10 s) was applied to switch the device.

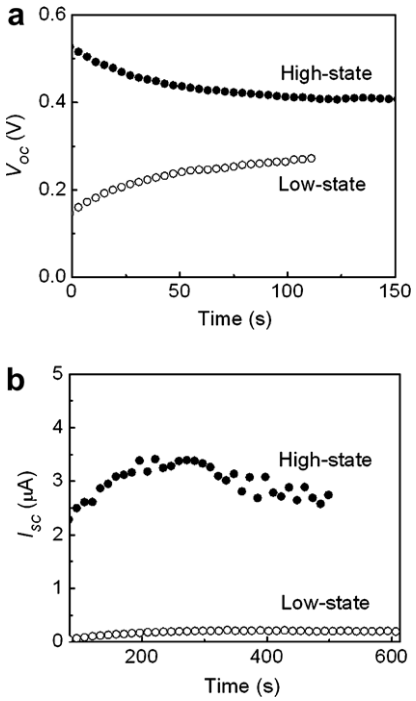

Fig. 5. ROM application using photovoltage and photocurrent. (a) Photovoltage and (b) photocurrent were directly measured after switching the device to a high-conducting state (9.0 V, 10 s) or to a low-state (−9.0 V, 10 s).

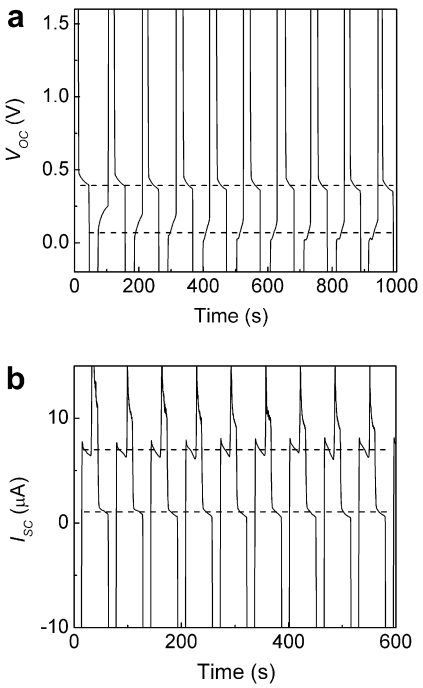

Fig. 6. RAM application using photovoltage and photocurrent. After the high- and the low-states were flip-flopped, (a) V_{OC} and (b) I_{SC} were measured in between. Broken lines represent the two states in the figures.

4. Conclusions

In conclusion, we have fabricated and characterized organic memory devices based on a heterojunction between copper phthalocyanine and Rose Bengal. Devices based on the heterojunction have exhibited electrical bistability. The combination of the materials in addition has yielded photovoltage under solar light illumination. When Rose Bengal of the heterojunction was switched to a high-conducting state by applying a suitable voltage pulse, the parameters of the photovoltaic cell, namely V_{OC} and I_{SC} showed an increase in their magnitude. This has prompted us to club the two effects so that the electrically bistable device can be switched by a voltage pulse and probed by measuring photovoltage or photocurrent. Since the latter parameters can be measured without applying any voltage, the results exemplify non-interacting "write" and "read" processes in organic memory devices.

Acknowledgements

SS acknowledges CSIR NET Fellowship No. F.NO.9/80(468)/2004-EMR-I (Roll No. 507170). The authors also acknowledge financial supports through projects 03(1044)/05/EMR-II, SR/S2/RFCMP-02/2005, and 2007/37/2/BRNS.

References

[1] A. Bandhopadhyay, A.J. Pal, J. Phys. Chem. B 107 (2003) 2531.
[2] A. Bandyopadhyay, A.J. Pal, Adv. Mater. 15 (2003) 1949.
[3] Y. Yang, L.P. Ma, J.H. Wu, MRS Bull. 29 (2004) 833.
[4] J. Lin, M. Zheng, J.S. Chen, X.A. Gao, D.G. Ma, Inorg. Chem. 46 (2007) 341.
[5] M. Caironi, D. Natali, M. Sampietro, C. Bertarelli, A. Bianco, A. Dundulachi, E. Canesi, G. Zerbi, Appl. Phys. Lett. 89 (2006) 243519.
[6] B. Mukherjee, A.J. Pal, Appl. Phys. Lett. 85 (2004) 2116.
[7] M. Lauters, B. McCarthy, D. Sarid, G.E. Jabbour, Appl. Phys. Lett. 87 (2005) 231105.
[8] F.L.E. Jakobsson, X. Crispin, M. Berggren, Appl. Phys. Lett. 87 (2005) 063503.
[9] M. Terai, K. Fujita, T. Tsutsui, Jpn. J. Appl. Phys. Part 1 – Regul. Pap. Brief Commun. Rev. Pap. 45 (2006) 3754.
[10] J.A. Freire, G.A. Dal Moro, R. Toniolo, I.A. Hummelgen, C.A. Ferreira, Org. Electron. 7 (2006) 397.
[11] B. Mukherjee, S.K. Batabyal, A.J. Pal, Adv. Mater. 19 (2007) 717.
[12] C.P. Collier, G. Mattersteig, E.W. Wong, Y. Luo, K. Beverly, J. Sampaio, F.M. Raymo, J.F. Stoddart, J.R. Heath, Science 289 (2000) 1172.
[13] Z.J. Donhauser, B.A. Mantooth, K.F. Kelly, L.A. Bumm, J.D. Monnell, J.J. Stapleton, D.W. Price, A.M. Rawlett, D.L. Allara, J.M. Tour, P.S. Weiss, Science 292 (2001) 2303.
[14] A.O. Solak, S. Ranganathan, T. Itoh, R.L. McCreery, Electrochem. Solid State Lett. 5 (2002) E43.
[15] B.C. Das, A.J. Pal, Org. Electron. 9 (2008) 39.
[16] A.K. Rath, A.J. Pal, Org. Electron. 9 (2008) 495.
[17] S. Ssenyange, H.J. Yan, R.L. McCreery, Langmuir 22 (2006) 10689.
[18] F. Verbakel, S.C.J. Meskers, R.A.J. Janssen, H.L. Gomes, M. Colle, M. Buchel, D.M. de Leeuw, Appl. Phys. Lett. 91 (2007) 192103.
[19] A. Bandyopadhyay, A. Chowdhury, A.J. Pal, Opt. Mater. 28 (2006) 1432.
[20] P. Peumans, A. Yakimov, S.R. Forrest, J. Appl. Phys. 93 (2003) 3693.
[21] K. Colladet, S. Fourier, T.J. Cleij, L. Lutsen, J. Gelan, D. Vanderzande, L.H. Nguyen, H. Neugebauer, S. Sariciftci, A. Aguirre, G. Janssen, E. Goovaerts, Macromolecules 40 (2007) 65.
[22] J.K. Mapel, M. Singh, M.A. Baldo, K. Celebi, Appl. Phys. Lett. 90 (2007) 121102.
[23] D.E. Markov, E. Amsterdam, P.W.M. Blom, A.B. Sieval, J.C. Hummelen, J. Phys. Chem. A 109 (2005) 5266.
[24] S. Karthauser, B. Lussem, M. Weides, M. Alba, A. Besmehn, R. Oligschlaeger, R. Waser, J. Appl. Phys. 100 (2006) 094504.
[25] G.S. Bang, J. Park, J. Lee, N.J. Choi, H.Y. Baek, H. Lee, Langmuir 23 (2007) 5195.

nanoparticle-embedded MIS capacitors with gate insulating layers made of parylene-C layers were fabricated. Current density versus voltage (*J*–*V*) and capacitance versus voltage (*C*–*V*) curves of a representative gold nanoparticle-embedded MIS capacitor are characterized and discussed in this paper.

2. Synthesis and fabrication

Gold nanoparticles were synthesized in toluene using the colloidal method [9]. A mixture of 30 mL of 30 mM hydrogen tetrachloroaurate aqueous solution and 80 mL of 50 mM tetraoctylammonium bromide in a toluene was vigorously stirred. A freshly prepared 25 mL of 0.5 M sodium borohydride aqueous solution was added to the mixture and vigorously stirred for 3 h. Fig. 1a shows the high resolution transmission electron microscopy (HRTEM) image of gold nanoparticles synthesized by the colloidal method. Their average diameter is about 5 nm, their shape is largely spherical, and the gold nanoparticles are separated from each other. And their regular arrangement is closely packed. No aggregation of the gold nanoparticles was observed. In the HRTEM image, the estimated density of the gold nanoparticles is 2.86×10^{12} cm^{-2} and the average distance between neighboring nanoparticles is about 2 nm.

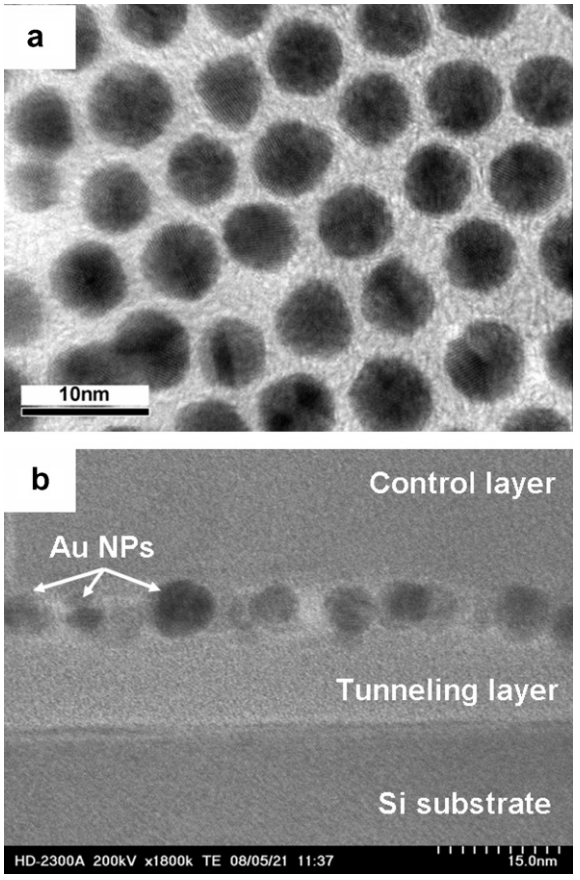

Fig. 1. (a) The top-view HRTEM image of gold nanoparticles (synthesized by the colloidal method) dispersed on a SiO_2/Si substrate and (b) a cross-sectional TEM image of gold nanoparticles presented between the tunneling and control layers.

To determine the electrical characteristics of the polymer gate dielectric material, we have prepared the MIS capacitor structures with parylene-C layers present in between the top electrodes and the silicon substrates. Gold nanoparticles were dispersed by a spin coating method on SiO_2 layers with a thickness of 6.3 nm on top of silicon (p-type, (1 0 0)) wafers and the SiO_2 layers were utilized as the tunneling ones. A 6.3 nm SiO_2 layer was grown on a Si wafer by in situ steam generation oxidation in which oxygen and hydrogen were used as process gases with a flow rate of 4.98 and 0.2 slm, respectively. The oxidation was performed at a wafer temperature of 950 °C and at a chamber pressure of 10 Torr. After the dispersion of the gold nanoparticles, all the samples under study were directly put in an oven to dry off the solvent at 70 °C. Some selected from the samples were treated with an UV–O_3 process to remove the surfactants and organic residues presented on the surface of the gold nanoparticles. Parylene-C layer was deposited as a control gate dielectric. The parylene-C layer was deposited by the chemical vapor deposition at room temperature in 0.1 mTorr. The CVD starting material was parylene-C dimer (DPX-C, Parylene Korea Co. Ltd.). First, parylene-C dimmer was vaporized at 150 °C, forming a dimmer gas. The gas molecules were subsequently cleaved to the monomer form by heating up to 650 °C. And the active monomer gas was then introduced to a deposition chamber where it was dispersed and polymerized spontaneously on the substrate at room temperature to form a parylene film. The thicknesses of the parylene-C layers were about 100 nm. The size of top gold electrodes was 1.93×10^{-3} cm^2. In order to confirm well-dispersed gold nanoparticles of the fabricated MIS capacitor, a cross-sectional HRTEM of the MIS capacitor was carried out (shown in the Fig. 1b). A schematic diagram of a representative MIS capacitor embedded with gold nanoparticles and the chemical structure of parylene-C is shown in Fig. 2. The current density versus voltage and capacitance versus voltage measurements were performed with a semiconductor parameter analyzer (Agilent 4155 C) and a precision LCR meter (HP 4285A) at room temperature.

3. Results and discussion

The UV–visible absorption spectrum of the gold nanoparticles dispersed in a toluene is shown in Fig. 3. A broad surface plasmon band is present at 520 nm in the absorption spectrum. As the size of the gold nanoparticles decreases, the peak position shifts toward the shorter wavelength region. The broadening of the absorption band is due not only to the inhomogeneous size distribution but also to the size shrinkage [10].

A significant limitation that gate insulating materials including polymer gate insulating materials face is gate leakage. Leakage current density (*J*) of the MIS capacitor is examined here. Fig. 4 shows the leakage current density versus voltage obtained from a representative MIS capacitor with a 100 nm thick parylene-C layer. Electric field

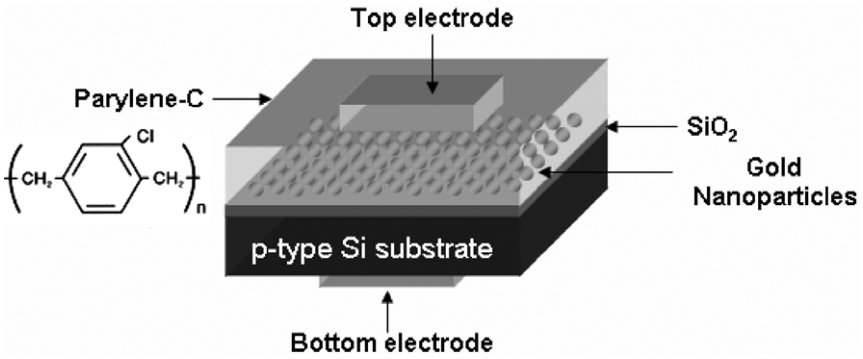

Fig. 2. A schematic diagram of the MIS capacitor embedded with gold nanoparticles and the chemical structure of parylene-C.

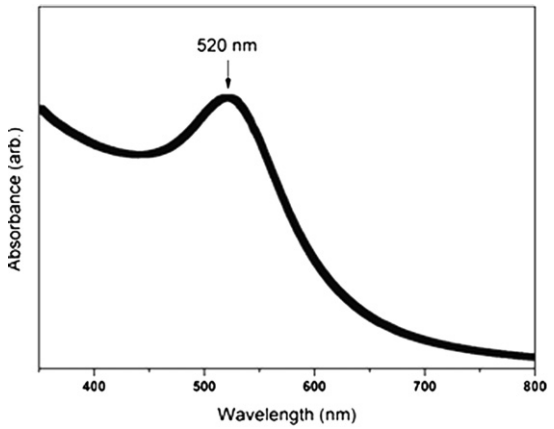

Fig. 3. A UV–visible absorption spectrum obtained from gold nanoparticles dispersed in toluene.

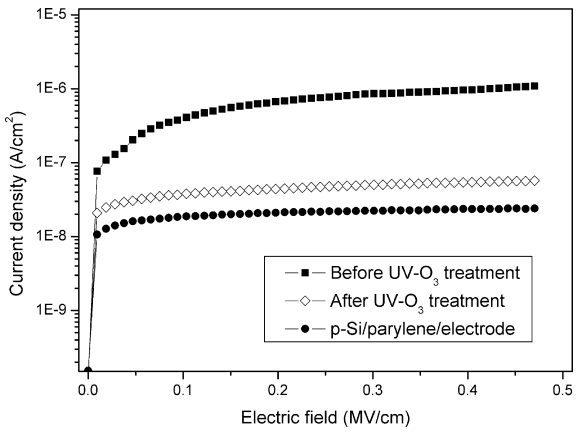

Fig. 4. Current density as a function of the electric field when the gate bias field sweeps from 0 to 0.5 MV/cm flowing through the gate insulator of the MIS capacitors.

varies from 0 to 0.5 MV/cm. A sample without the UV–O_3 treatment exhibits the larger current density as a function of electric field, compared to that with the UV–O_3 treatment. This result may be caused by the presence of the remanent residues. The organic residues are interfered with a deposition of the parylene-C layer. Fig. 4 also shows the current density through the gate insulating layer as a function of the electric field applied across the parylene-C layer when the electric field sweeps from 0 to 0.5 MV/cm. The observed leakage current density of the MIS capacitor is smaller than other reported polymer and polymer/inorganic gate insulators (PVA, PVP, P(VDF-TrFE) and PVP/YO_x, etc.) [11–13]. The current density of the cross-linked PVP is about 0.17 μA/cm^2 at an electric field of 0.5 MV/cm. However, the current density of our fabricated sample is less than 10^{-7} A/cm^2 in magnitude, at the same electric field. Our room temperature parylene-C deposition does not give thermal or chemical damages to metal nanoparticles suitable to nodes of memory devices. The deposition of conventional insulators (especially, SiO_2) requires high temperature processes, giving serious thermal damages to the surface of gold nanoparticles.

The capacitance versus voltage (*C–V*) curves taken for a reference sample without gold nanoparticles and the MIS capacitor embedded with gold nanoparticles at a frequency of 1 MHz are plotted in Fig. 5. The *C–V* curve of the reference sample shows a little flat-band voltage shift of about 0.1 V (Fig. 5a). Any threshold voltage shifts have not been shown in the *C–V* curves of MIS capacitors. However, if the charge traps exist in the interface of between a tunneling layer and a control layer or in the center of gate dielectric layers, the charge carriers can be stored in those traps and the threshold voltage is shifted by these trapped charge carriers [14]. In this case, the main concern with the charge traps is a role of the polymer insulating material as a gate material. However, the *C–V* curve of the MIS capacitor exhibits a threshold voltage window of 2.1 V when the gold nanoparticles without UV–O_3 treatment are present as the floating gate layer (Fig. 5b). After the UV–O_3 treatment, the threshold voltage shift of the MIS capacitor was reduced because of the removal of organic residues around the gold nanoparticles. The window of the *C–V* loop indicates the magnitude of the trapped charge carriers in the floating gate layer. The estimated number of trapped charges in the gold nanoparticles for a threshold voltage shift is about 0.64×10^{11} cm^{-2}. And these trapped charge carriers were injected from the p-type Si substrate. Furthermore, the dips in the weak inversion of the *C–V*

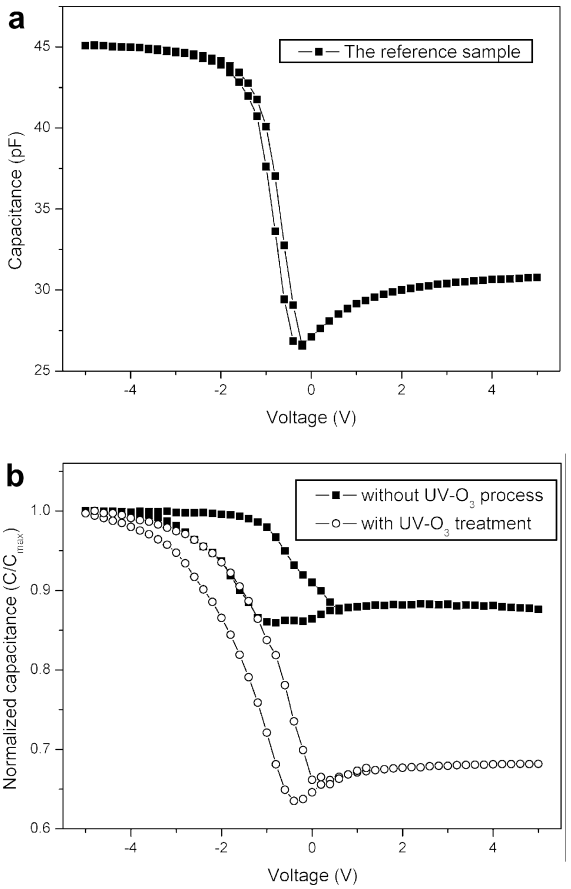

Fig. 5. High frequency *C–V* curves of the fabricated MIS capacitors without (a) and with gold nanoparticles (b).

loops can be seen in Fig. 5. These dips are related with the deep depletion of MIS capacitors [15]. The capacitance approaches the C_{min} of the MIS capacitors as the positive gate voltage increases.

In order to investigate the retention characteristics of the MIS capacitor embedded with gold nanoparticles, charge remains versus time (*C–t*) measurement was performed (Fig. 6). The charge remains is defined as charge remains = $\{C(t) - C_{FB}\}/\{C(0) - C_{FB}\} \times 100$ where $C(t)$ is the capacitance at measurement time and C_{FB} is the flat-band capacitance during forward bias sweeping. The MIS capacitor embedded with nanoparticles was charged for 1 s at a bias voltage of +7 V. Then, the *C–t* measurement was made under a bias voltage of 0 V applied to the top electrode. The general feature of the *C–t* curve consists of two decay regimes; the first is the initial fast decay and the second is the subsequent slow decay. There are two possible mechanisms explaining the initial fast decay, the lateral charge loss [16] and the Coulomb repulsion between electrons confined in nanocrystals [17]. In this case, the first possible mechanism is excluded since the lateral charge loss of the floating gate layer cannot be formed due to the separation between the gold nanoparticles (see the HRTEM image of Fig. 1). Hence, we suggest that the origin of the initial fast decay is the Coulomb repulsion between the confined electrons. Furthermore, the subsequent slow decay may be due to the transfer of electrons from the gold nanoparticles to the electrode through the control oxide layer. After applying a bias, the initial decay for the MIS capacitor embedded with gold nanoparticles over a period of 10^3 s is about 17%. However, the subsequent decay is only 3% after 3×10^5 s. These retention characteristics come from the higher work function of gold nanoparticles and those of most semiconductor nanoparticles. Gold nanoparticles with high work function enhance their data retention characteristics, which are comparable values to that of nonvolatile memory devices.

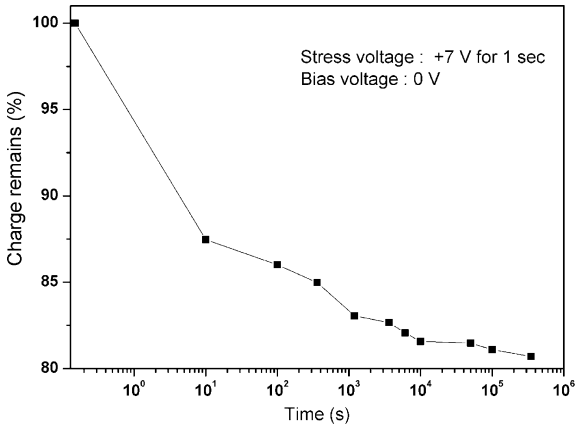

Fig. 6. Charge retention characteristics of the MIS capacitor embedded with gold nanoparticles after applying a gate voltage bias of +7 V for 1 s.

4. Conclusions

In summary, gold nanoparticles synthesized by the colloidal method were dispersed on an oxidized p-type Si wafer. The estimated charge density of the dispersed gold nanoparticles was about 0.64×10^{11} cm^{-2}. In the case of *J–V* curves obtained for the MIS capacitor, parylene-C insulating material showed good performance as gate insulator, compared with other polymer gate materials. The *C–V* curves taken for the MIS capacitor embedded with gold nanoparticles demonstrated a threshold voltage shift of about 1.1 V. In addition, the initial charge loss for the MIS capacitor embedded with gold nanoparticles exhibited a fast decay rate due to the Coulomb repulsion effect. Nevertheless, the subsequent decay of the capacitance was only 3% after 3×10^5 s. We showed the possibility to fabricate memory devices using gold nanoparticle-embedded MIS capacitors based on the low temperature process.

Acknowledgments

This work was supported by the Center for Integrated-Nano-Systems (CINS) of the Korea Research Foundation (KRF-2006-005-J03601), and the Korea Science and Engineering Foundation (KOSEF) through the National Research Lab. Program (R0A-2005-000-10045-02 (2007)) and the nano R&D program (M10703000980-07M0300-98010).

References

[1] S. Tiwari, F. Rana, H. Hanafi, A. Hartstein, E.F. Crabbe, K. Chan, Appl. Phys. Lett. 68 (1996) 1377.
[2] H. Hanafi, S. Tiwari, I. Khan, IEEE Trans. Electron Dev. 43 (1996) 1553.
[3] T. Hori, T. Ohzone, Y. Odark, J. Hirase, IEEE IEDM Tech. Dig. 92 (1992) 469.
[4] Min She, T.-J. King, IEEE Trans. Electron Dev. 50 (2003) 1934.
[5] Y.-C. King, T.-J. King, C. Hu, IEEE Trans. Electron Dev. 48 (2001) 696.
[6] Z. Liu, C. Lee, V. Narayanan, G. Pei, E.C. Kan, IEEE Trans. Electron Dev. 49 (2002) 1606.
[7] C. Lee, A. Gorur-Seetharam, E. Kan, IEDM Tech. Dig. 3 (2003) 557.
[8] C.D. Dimitrakopoulos, P.R.L. Malenfant, Adv. Mater. 14 (2002) 99.
[9] M. Brust, D. Bethell, C.J. Kiely, D.J. Shifffin, Langmuir 14 (1998) 5425.
[10] S. Link, M.A. El-sayed, J. Phys. Chem. B 103 (1999) 4212.
[11] H. Klauk, M. Halik, U. Zschieschang, G. Schmid, W. Radlik, W. Weber, J. Appl. Phys. 92 (2002) 5259.
[12] Y.X. Li, L. Yan, R.P. Shrestha, D. Yang, E.A. Irene, J. Vac. Sci. Technol. A 25 (2007) 275.
[13] D.K. Hwang, K. Lee, J.H. Kim, S. Im, C.S. Kim, H.K. Baik, J.H. Park, E. Kim, Appl. Phys. Lett. 88 (2006) 243513.
[14] T. Hori, Gate Dielectrics and MOS ULSIs-Principles, Technologies, and Applications, Springer-Verlag, Berlin, 1997.
[15] B.G. Streetman, S. Banerjee, Solid State Electronics, Prentice Hall International, Inc, 2004.
[16] J.K. Kim, H.J. Cheong, Y. Kim, J.-Y. Yi, H.J. Bark, S.H. Bang, J.H. Cho, Appl. Phys. Lett. 82 (2003) 2527.
[17] O. Winkler, F. Merget, M. Heuser, B. Hadam, M. Baus, B. Spangenberg, H. Kurz, Microelectron. Eng. 61–62 (2002) 497.

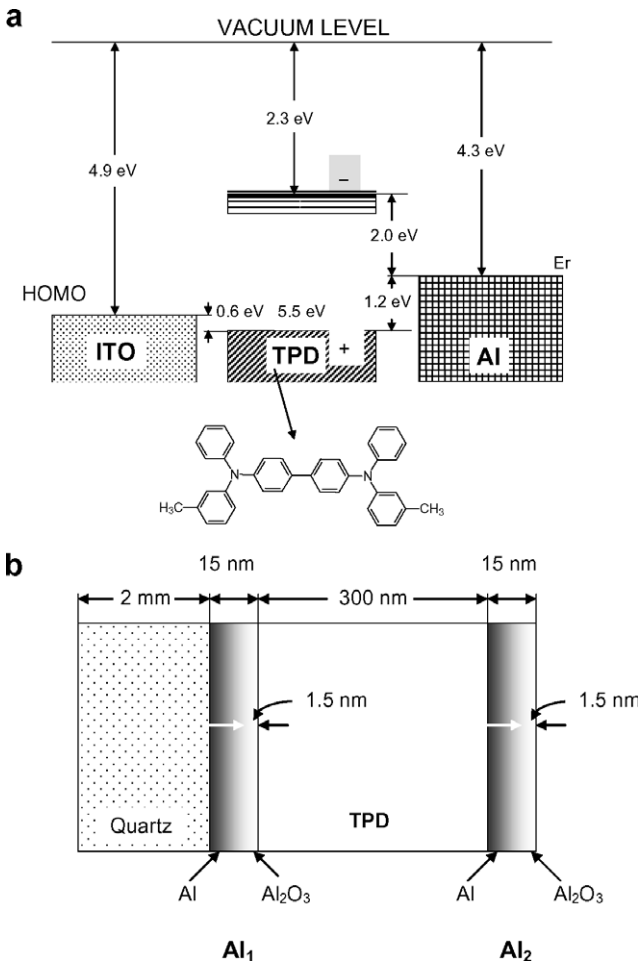

Fig. 1. The energy levels diagram for TPD and electrode materials (ITO, Al) in thin film structures used in the present study (a). The electrode sequence at substrate (Quartz) (in brief Al_1) and non-substrate (TPD) (in brief Al_2) deposited Al for structure (A) (b).

and structure (B): Quartz/ITO/TPD/Al. They consist of a semitransparent, vacuum-evaporated, 15 nm-thick Al layer on a quartz (Q) substrate for structure (A) and a transparent 20 Ω/sq ITO glass substrate for structure (B), a 300 nm TPD, and a 15 nm-thick Al top metal layer. The electrically active area of the cells was 0.09 cm^2. The surface contact conditions of Al electrodes were found to be an important factor governing the dark current (j_{dark})–electric field (F) characteristics. The substrate aluminum electrode (Al_1) was evaporated in a vacuum chamber with a base pressure 5×10^{-6} hPa. The deposition rate was typically 0.3–0.5 nm/s. Such prepared layers have been kept for about 2 h under ambient atmosphere to oxidize their upper segments to Al_2O_3. A TPD film was evaporated in the same chamber with a deposition rate of around 0.3 nm/s. A 15 nm-thick aluminum layer (Al_2) was then evaporated on top of TPD and Al_2O_3 was grown within close to the surface segments by simple 1 h exposure of the layer to the air. As a consequence the TPD layer contacted with the substrate electrode (Al_1) through the sequence of Al_2O_3/Al, but through the reverse sequence of Al/Al_2O_3, with the top electrode (Al_2). The situation is illustrated in Fig. 1b.

3. Results

Fig. 2 presents typical current density (j_{dark})–electric field (F) plots for structure (A) (a) and structure (B) (b) at different electrode biases. The built in potential correction (4.9−4.3 = 0.6 eV) for sample (B) has been neglected since due to the relatively thick samples the resulting field ($<2 \times 10^4$ V/cm) yields only an insignificant effect on the effective field in the samples. Low-field regime theoretical fits (see Section 4.1) are given by the black point curves. In addition to an obvious asymmetry for ITO^+ and ITO^- bias for structure (B), resulting from a large difference in the hole (=0.6 eV) and electron (=2.6 eV) injection barrier heights (see Fig. 1a), a distinct asymmetry in the plots is seen for structure (A) with Al_1^+ and Al_1^- biased Al_1 electrode. A difference of about three orders of magnitude in the current density and a difference in the j_{dark}–F characteristics shape suggest that while in the ITO^+-biased structure (B) the hole injection from ITO^+ determines the current flow, the hole injection at the Al^+ anode is responsible for the current flow with the ITO^--biased structure (B) (the barrier height for the hole injection from Al^+ = 1.2 eV). We believe that the asymmetry for structure (A) comes out from oppo-

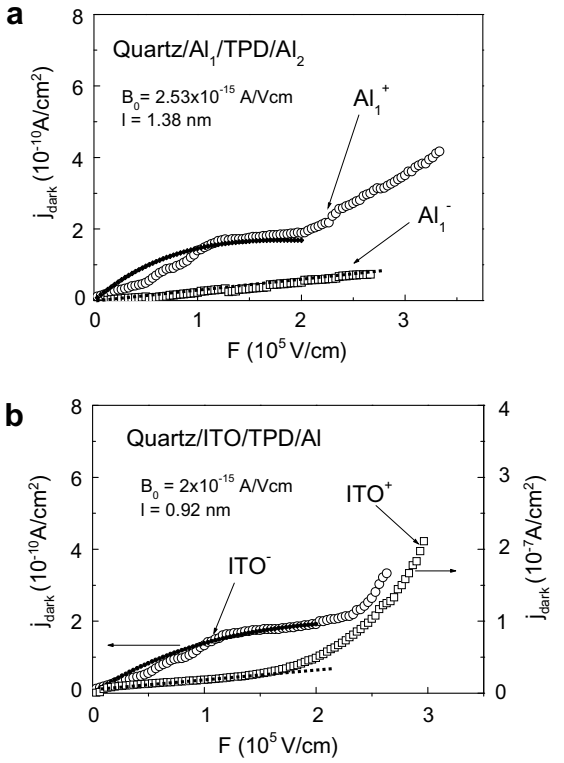

Fig. 2. Experimental current–electric field characteristics (open data points) for two 300 nm-thick TPD films sandwiched between Quartz/Al/Al (a) and Quartz/ITO/Al (b) electrodes at their (+, −) and reversed (−, +) bias. Black point curves represent theoretical fits of low- and moderate-field (LMF) approximation based on Eq. (4). The fitting parameters B_0 and l are given in the figure.

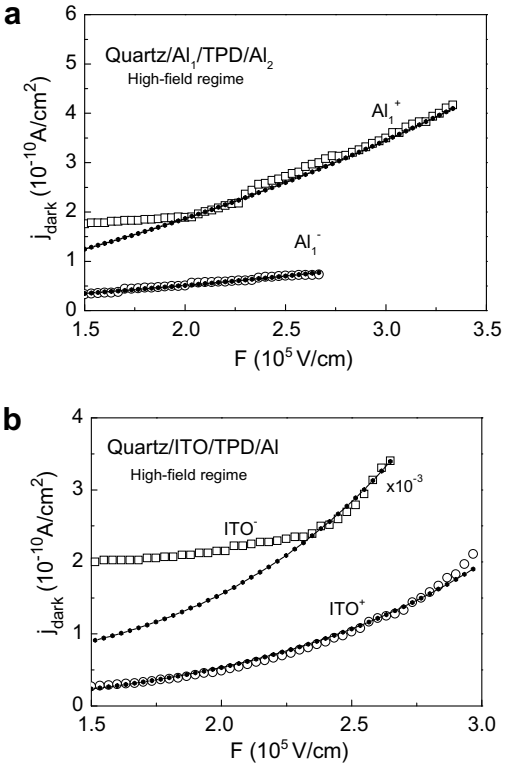

Fig. 3. High-field regime current density-electric field profiles for structures (A) (a) and (B) (b). Open point figures stand for the experimental data, black point curves are theoretical fits using Eq. (6), $j = BF^{3/4}\exp(aF^{1/2})$. The best fits yield $B = 4.9 \times 10^{-15}$ A/cm$^{5/4}$ V$^{3/4}$, $a = 3.1 \times 10^{-3}$ (cm/V)$^{1/2}$ (case Al_1^+) and $B = 1.55 \times 10^{-15}$ A/cm$^{5/4}$ V$^{3/4}$, $a = 2.8 \times 10^{-3}$ (cm/V)$^{1/2}$ (case Al_1^-) for structure (A), and $B = 6.4 \times 10^{-14}$ A/cm$^{5/4}$ V$^{3/4}$, $a = 1.0 \times 10^{-2}$ (cm/V)$^{1/2}$ (case ITO$^+$) and $B = 7 \times 10^{-17}$ A/cm$^{5/4}$ V$^{3/4}$ and $a = 1.1 \times 10^{-2}$ (cm/V)$^{1/2}$ (case ITO$^-$) for structure (B).

site sequence of Al and Al_2O_3 layers composing the substrate (Al_1) and non-substrate (Al_2) deposited electrodes as depicted in Fig. 1b (for discussion see Section 4.3). In Fig. 3, the high-field j_{dark}–F segments from Fig. 2 are shown and compared with the theoretical plots (black point curves) for both structure (A) and structure (B) at the electrode biases the same as those in Fig. 2. We note that there is no one common strictly defined electric field strength (F_H) where the high-field regime sets in though it falls somewhere between 2 and 2.5 × 10^5 V/cm. A slight shift towards higher values of F_H can be noted at decreasing currents. For Al_1^- case with structure (A) the high-field behavior has not been observed (up to 2.75 × 10^5 V/cm) because of a very low-current flow.

4. Analysis of results and discussion

4.1. Injection-limited current

In the absence of surface states the energy barriers that control carrier injection from a metal (semiconductor) of work function Φ to the valence band of an organic solid located at an energy I_i below the vacuum level (HOMO) and conduction level at an electronic affinity level A below the vacuum level (LUMO) are $\chi_h = I_i - \Phi$ for holes and $\chi_e = \Phi - A$ for electrons (see Fig. 1a). In the present system χ_e (ITO) ≈ 2.6 eV, χ_e(Al) ≈ 2.3 eV, and χ_h (ITO) ≈ 0.6 eV, χ_h (Al) ≈ 1.3 eV for ITO and Al, respectively. This indicates that the remarkable injection current can be expected only for holes with positively biased ITO. The measured (collected) current (j_{dark}), flowing in direction "x" perpendicular to the injecting interface, is determined by the source current (j_s) and the drift current (j_{df}) of thermalized carriers if the diffusion current can be neglected. To explain electric field (F) characteristics of the current flowing through an insulating sample, the functional dependence $j_s(x)$ must be accounted for as a boundary condition in the theoretical model of carrier injection [14]. The results presented in Section 3 can be explained employing a commonly used model of the 1D-Onsager theory based on the external field-dependent escape probability (dissociation efficiency) of the injected charge from its image counterpart in the electrode at a given distance x from the contact/insulator interface [15]. These charges bound by the Coulombic attraction can be considered as an interface charge pair (CP) state formed by the charge transfer between contact and insulator. The 1D-Onsager injection process assumes usually the source current to be a δ-like function defined as

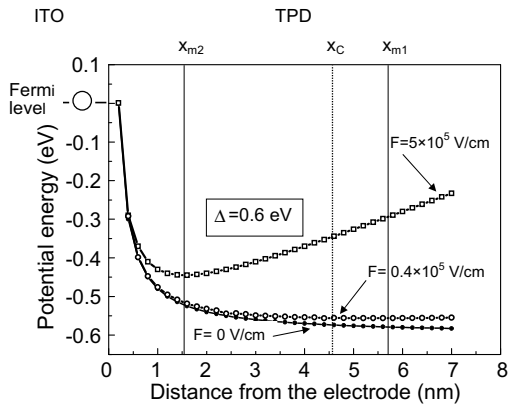

Fig. 4. Potential energy distribution and characteristic distances x_m and x_C (for definitions see text) for hole injection at the ITO–TPD interface at low- and high-electric fields selected in a way showing the case $x_m > x_C$ (with x_{m1}) and the case $x_m < x_C$ (with x_{m2}). For discussion see Section 4.2. The injection energy barrier is given in the frame.

$$j_s(x) = j_0 \quad \text{for} \quad x \le l \quad \text{and} \quad j_s(x) = 0 \quad \text{for} \quad x > l \tag{1}$$

where l is the primary separation of charges in the interface CP state (also known as the thermalization length). Once injected, the carriers can either recombine with their electrode image counterparts or contribute to the collected current if they are able to overcome the Coulombic barrier formed by a combination of the inter-pair Coulombic attraction and the applied external voltage, and located at (see Fig. 4)

$$x_m = (\beta/\gamma)^{1/2} \tag{2}$$

where

$$\gamma = \frac{eF}{kT} \quad \text{and} \quad \beta = \frac{e^2}{16\pi\varepsilon_0\varepsilon kT} \tag{3}$$

There is no general analytical solution to the current equation invoking such a charge carrier formation process. Its general form [14]

$$j_{dark} = j_0 \frac{\int_0^l \exp(-\gamma x - \beta/x)dx}{\int_0^\infty \exp(-\gamma x - \beta/x)} = j_0\eta(l,F) \tag{4}$$

tells us that the collected current amounts to a fraction $\eta(l,F)$ of the source current j_0, the function $\eta(l,F)$ defining the field-dependent escape probability (dissociation efficiency) of the injected hole from its image counterpart in the electrode, at the distance l from the interface. However, for a common situation of $x_m \gg l$, simple analytical solutions follow from expression (4) in the low-field regime $[2(\beta\gamma)^{1/2} < 1]$ [14]

$$j_{dark} = j_0(el^2/\beta kT)F\exp[-(el/kT)F - \beta/l)] \tag{5}$$

and in the high-field regime $[2(\beta\gamma)^{1/2} \gg 1]$ [14]

$$j_{dark} = j_0\{[l^2(e/kT)^{3/4}/\pi^{1/2}\beta^{5/4}]\exp(-\beta/l)\}F^{3/4} \times \exp[2(\beta e/kT)^{1/2}F^{1/2}] \tag{6}$$

with room-temperature $a = 2(\beta e/kT)^{1/2} = 8.9 \times 10^{-3}$ (cm/V)$^{1/2}$ calculated with the TPD dielectric constant $\varepsilon = 3$ [12].

Fig. 2 represents typical current density–electric field characteristics for our film structures (A) and (B) within low- and moderate-electric fields reaching in the upper limit the high-field regime. Within the whole electric field range, a non-linear relationship between current density and electric field is observed, except for low-current densities for structure (A) with negative polarization of the substrate electrode Al_1^-, where the experimental dependence $j(F)$ can well be approximated by a linear plot. Moreover, the shape and current level for the positive Al_1^+, resemble closely those with ITO^- polarized structure (B). As a guideline for the analysis of these $j_{dark}(F)$ characteristics, theoretical plots of both low- and moderate-field (LMF) approximation (5), and high-field (HF) approximation (6) are presented in Figs. 2 and 3, respectively. Fig. 2 shows that LMF approximation persists up to $F \approx 2 \times 10^5$ V/cm and then HF approximation (6) reproduces reasonably the experimental data (Fig. 3). As adjustable parameters, the theoretical Eq. (5) contains a constant $B_0 = j_0(el^2/\beta kT)$ and the primary injection distance l. The values of $l_A = 1.38 \pm 0.05$ nm and of $l_B = 0.98 \pm 0.05$ nm were found for structure (A) and (B), respectively. They, within the experimental accuracy, are very close each other and comparable with two intermolecular spacings, though a higher value of l could be expected for l_A since the isolating buffer Al_2O_3 layer reduces the hole attraction by its image counterpart in the Al anode. These values seem to reflect the general feature of charge injection in organic solids. A value of 1.2 nm has been obtained for the distance in the singlet exciton dissociation by electron transfer at an anthracene crystal/metal interface [16]. The reason for the excessive theoretical current values within the lowest field region is discussed in Section 4.2. The fitting parameter a_{exp} for the high-field regime characteristics (Fig. 3), within 20% agrees with the theoretical prediction 9×10^{-3} (cm/V)$^{1/2}$ for structure (B), but is by a factor of 1.5 smaller than that for structure (A). The origin of this discrepancy is not quite clear at present. One can speculate an increase of the effective dielectric constant caused by its high value ($\varepsilon \approx 9$) for the Al_2O_3 layers or a specific disorder (trap) effect at Al/TPD interface [14]. The metal deposition on organic layers is known to affect the energetics of the charge injection process [17]. Of particular concern are reactive alkali metals deposited on electron acceptor materials. In contrast, the Al contact on electron donor materials has been shown to form rather a physisorbed layer leading only to a little valence level shift, e.g. of ~0.1 eV for *p*-sexiphenyl [18]. Based on the literature reports of UPS but also on other studies (e.g. the injection evolution in time and frequency dependence of the contact capacitance [19]), we assumed it to show only an insignificant activity preserving to a large extent geometrical properties of TPD/Al contact. Therefore, we do not expect Al atoms penetrating TPD films to change the basic injection mechanisms, thus functional shapes of the current–voltage characteristics. Indeed, the good fits we obtain with experimental data suggest that the underlying dependencies of the current–voltage characteristics are correctly described in this paper. However, a local, near-contact disorder in TPD induced by vacuum evaporation

of Al still can affect the model fitting parameters like B_0, β, a_{exp}. This could contribute to the observed deviation of a_{exp} from its theoretical value. The exact value of the electric field starting the HF approximation of the current–voltage characteristics might also be affected by the interfacial electronic structures (see discussion in Section 4.3).

4.2. Effect of electrode recombination

An apparent discrepancy between theory and experiment seen in the lowest field region in Fig. 2 can be rationalized taking into account the back flux of the injected carriers which undergo electrode recombination. Such a process has already been considered to modify the current–voltage characteristics in the high-field region, but the results not verified experimentally [1,14,20,21]. In general, the surface recombination rate (η_r) is a distance-dependent quantity, e.g. $\eta_r(x) = \eta_r(0)\ \exp(-\alpha_2 x)$, where $\eta_r(0)$ is the recombination rate at $x = 0$ and α_2 is a characteristic parameter dependent on the type of electrical contact [1,14]. It can reflect physically probable tunneling mechanism of recombination. But then even an approximate solution for the current is not tractable analytically and requires numerical calculations [20]. A way to simplify the surface recombination description has been demonstrated by Scott and Malliaras [21]. It consists in the near-surface averaging the charge density and placing it at the distance $x_C = (1/4)\ r_C$, where $r_C = e^2/4\pi\varepsilon_0\varepsilon kT$ is the 3D bi-molecular capture radius at which the charge carrier-image binding energy is equal to kT. The factor ¼ takes into account the average velocity of the carrier motion towards the injecting contact. At room temperature ($kT \approx 0.025$ eV) and for typical dielectric constant $\varepsilon = 3$, $x_C \approx 4.6$ nm, which is ~10 times larger than an intermolecular distance and the primary injection distance, l. The 'average' charge that approaches the interface within x_C disappears efficiently (according to Ref. [21], inevitably) at the interface by a field-enhanced diffusion process that resembles Langevin bimolecular recombination which often is the case for disordered organic solids at low-electric fields [22,23]. This charge back flux reduces the current flowing through the sample. Then, the measured (j_{exp}) net (j_{net}) current can be defined as

$$j_{net} = j_{exp} = j_{inj} - j_{rec} \tag{7}$$

where

$$j_{rec} = en_C\mu F(x_C) \tag{8}$$

and

$$F(x_C) = F - \frac{e}{16\pi\varepsilon_0\varepsilon x_C^2} \tag{9}$$

where $n_C \approx n_0$ represents the charge concentration at $x = x_C$ and is considered as an 'average' charge density within the 0–x_C region [21].

In order to determine the recombination current we use Eq. (7) and the data of Fig. 2. Accordingly, its field dependence can be calculated and as such is shown in Fig. 5a. A broad maximum of j_{rec} is apparent within the (0.5–1.0) × 10^5 V/cm field range, an abrupt roll-off (down to 10^{-12} A/cm^2), observed above 10^5 V/cm, reflects a strong drop in the charge concentration

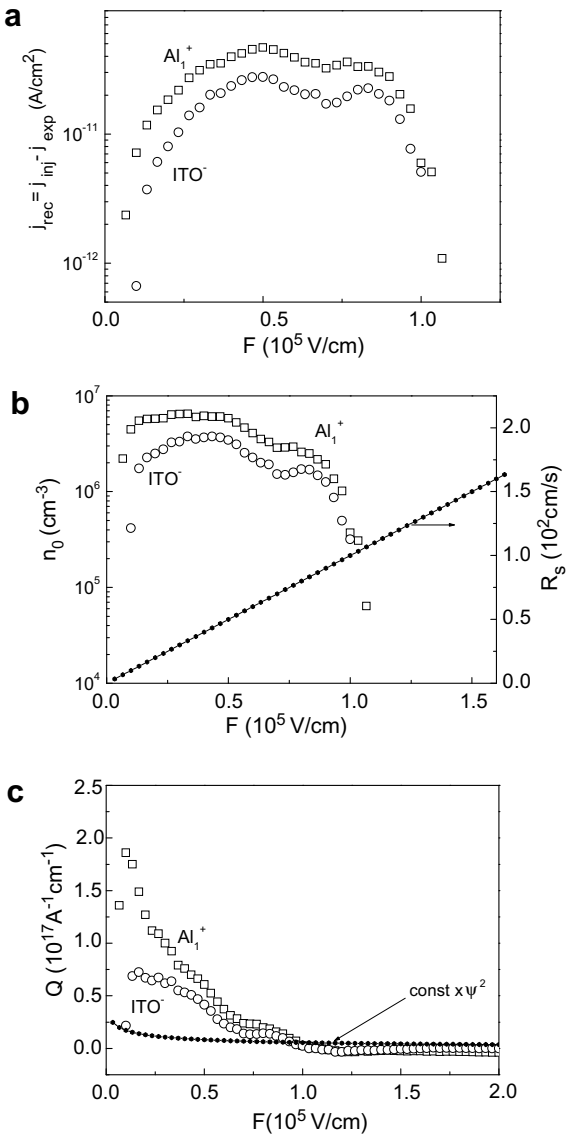

Fig. 5. Surface recombination current density (a), charge concentration at $x = x_C$ (b) and factor $Q = n_0/j_{inj}$ (c) as functions of applied electric field for the TPD films, obtained from the data of Fig. 2 using Eqs. (7) and (10), respectively. The black point line in part (b) shows the surface recombination rate derived from Eq. (11) with a field-independent hole mobility in amorphous TPD, $\mu \approx 10^{-3}$ cm^2/Vs, taken from field-independent time-of-flight mobility measurements by Stolka et al. [26]. The black point curve in part (c) represents a factor proportional to the theoretical quantity ψ^2 calculated using Eq. (13).

$$n_C = \frac{j_{rec}}{e\mu F} \tag{10}$$

as shown in Fig. 5b.

The surface recombination rate

$$R_S = \frac{j_{rec}}{n_0 e} = \frac{\gamma_{eh}}{4\pi r_C} F \tag{11}$$

is determined by the bimolecular (second order) recombination rate constant of the carrier (γ_{eh}) which, according to a Langevin-like recombination model [1], is governed by

the carrier diffusion (D), $\gamma_{eh} = 4\pi D r_C$. If, in addition, the validity of the Einstein's relation is assumed ($eD = \mu kT$), R_S becomes simply a drift velocity of the carrier $R_S = \mu F$.

The non-monotonic field evolution of the recombination current (Fig. 5a) can be explained by invoking the probability $w(F)$ of a hole located at $x \leqslant x_C$ to reach the potential maximum located at the field-dependent x_m (see Eq. (2)). The recombination current is then proportional to the recombination probability

$$P_R = 1 - w(F) = 1 - w_0 \exp\left[\frac{eF(x_C - x_m)}{kT}\right] = 1 - w_0 \exp\left[\frac{eFx_C}{kT} - \frac{e}{4kT}\sqrt{\frac{eF}{\pi\varepsilon_0\varepsilon}}\right] \quad (12)$$

where $w_0 = \exp(\Delta/kT)$ and Δ is the barrier height in the absence of both the external field and the image charge effect. As the electric field increases from low values with $x_m > x_C$ (the case exemplified in Fig. 4 by x_{m1}), $w(F)$ decreases and the recombination current is expected to increase. At still increasing field P_R reaches its broad maximum at $x_m = x_C$ (corresponding to the electric field $F \approx 0.6 \times 10^5$ V/cm) and then decreases as $x_m < x_C$ (the case exemplified in Fig. 4 by x_{m2}). This is what we observe for j_{rec} in Fig. 5a. The origin of the shallow local minimum at about 0.75×10^5 V/cm is not quite clear and one can speculate as it would be due to an instability in the measured current caused by the formation of the injecting contact [19]. In the high-field regime the recombination current is expected to strongly drop down and it indeed does so for $F > 10^5$ V/cm. The high-field region approach including the surface recombination relates the charge density at x_C to the injection current as $n_0 \sim \psi^2 j_{inj}(F)$, where the proportionality factor is given by [21]

$$\psi(f) = f^{-1} + f^{-1/2} - f^{-1}(1 + 2f^{1/2})^{1/2} \quad (13)$$

and accounts for the field-dependent surface recombination velocity through the reduced electric field $f = eFr_C/kT$. Assuming a similar relation to hold in the whole electric field range, $n_0 = Q(F)\ j_{inj}$, yields good agreement of the experimental $Q(F)$ derived from the data of Figs. 2 and 5 with the theoretical prediction of $C\psi^2$ only at high fields, showing essential discrepancy at low fields as presented in Fig. 5c. This confirms the crucial role of the surface recombination for the injection currents at low fields and only their insignificant modification at high fields (>0.75×10^5 V/cm) as demonstrated in Fig. 3.

4.3. Asymmetry for substrate and non-substrate deposited Al electrodes

The asymmetric behavior of structure A (Quartz/Al_1/TPD/Al_2), demonstrated in Fig. 2, results from the difference in electron–hole balance within the sample, holes being injected from the Al_1^+ or Al_2^+ anodes and electrons injected either from the Al_2^- or Al_1^- cathodes, respectively. The measured current (j_{exp}) in these cases can be approximated by the hole injection current, j_h, diminished by the volume recombination current, j_{VR}, $j_{exp} \approx j_h - j_{VR}$. The electron injection from Al^- has been shown to vary upon its oxidation [24]. The X-ray photoelectron spectroscopy shows that a 1.5 nm-thick Al layer exposed to air (oxygen) for more than 5 min converts completely in Al_2O_3 [24]. Accordingly, in our structure (A) the cathode Al_1 consists of a sequence Quartz/Al^- (13.5 nm)/Al_2O_3 (1.5 nm) and cathode Al_2 of a sequence Al^- (13.5 nm)/Al_2O_3(1.5 nm)/air (see Fig. 1b). Consequently, the electron injection at Al_2^- can be considered as the direct thermionic emission into TPD, and the electron injection at Al_1^- requires electron transmission through the 1.5 nm-thick film of Al_2O_3 prior entering TPD. The electron injection barrier height between the organic film and cathode is determined by the difference between the work function Φ of the latter and the lowest unoccupied molecular orbital (LUMO) A of the former. In the case of Al and TPD, $\Phi = 4.3$ eV and $A = 2.3$ eV, so the barrier height is a rather large 2 eV. Hence the thermionic emission of electrons from the cathode Al_2^- is very weak. The total cell current $j \approx j_h$ ($j_{VR} \to 0$). Thus, for the Al_1^+ bias the current behaves like that for structure (B) with ITO^- cathode, where due to the high-injection barrier (4.9−2.3 eV = 2.6 eV) practically no electron injection in TPD can be expected. In fact, both Al_1^+ and ITO^- characteristics are quasi-identical (see Fig. 2a and b). In contrast, when a high-ionization potential 8.7 eV Al_2O_3 layer is added (Al_1), considerable voltage drops across this layer, which can align the Fermi level of Al with the LUMO of TPD and enable electron tunneling through the thin Al_2O_3 layer. The opposing effects of the voltage drop and the barrier width render optimization of the thickness of the buffer layer Al_2O_3 at which the electron injection reaches a maximum. This has been found to amount ≈1.2 nm [24] close to ≈1.5 nm in the cathode Al_1 of our structure (A). As a result the electron density in the sample becomes significantly increased. In turn, the increased electron density enhances the electron–hole recombination rate (an increase of the recombination current) that leads to a significant reduction of the total cell current. Indeed, the measured current of the Al_1^--biased structure (A) is much lower and its field dependence follows the hole injection current from the Al_1^+ anode (Fig. 2a) accounted for their surface recombination (see Section 4.2). The bi-molecular electron–hole recombination in the sample bulk may be a reason of the observed shift in the critical electric field (F_H) where the high-field regime sets in (see Figs. 2 and 3). At low-electron injection levels, Al_1^+ for structure (A) and ITO^- for structure (B), the recombination current can be neglected ($j_{VR} \to 0$), we practically deal with single positive currents (j_h) limited by weak injection of holes over a relatively high (1.2 eV) barrier at Al^+ anodes. The effect of the injection barrier on the onset of the high-field regime behavior (a steep increase) of the current has been already observed in single-layer (280–300 nm thick) Alq_3 and TTN LEDs provided with two Mg electrodes [25]. A much lower F_H for the Alq_3 structure correlated with the lower electron injection barrier (≈0.9 eV) at the Mg/Alq_3 interface than that suggested for the Mg/TTN/Mg structure.

5. Summary and conclusions

We have been able to observe the hole injection from both ITO and Al electrodes within low-, moderate-, and high-electric field regimes of the current flow. A theoretical modeling is presented based on the hole and electron injection-limited current accounted for the surface and bi-molecular recombination of injected holes with their contact image charge or Al-injected electrons, respectively. In addition to an obvious asymmetry in the current behavior of Quartz/ITO/TPD/Al structure a distinct asymmetry has also been observed for Quartz/Al/TPD/Al structure.

The injection currents have been treated in the approximation of the 1D version of Onsager's approach of geminate recombination modified by the surface and bi-molecular recombination assuming the validity of Einstein's relation for diffusion and drift in the vicinity of Coulomb barrier placed at $x = x_m$ and involving a near-surface demarcation plane $x = x_C = (1/4)r_C$ being a 1D equivalent of the 3D Onsager radius $r_C = e^2/4\pi\varepsilon_0\varepsilon kT$. Theory is in good agreement with collected experimental data. From the fitting procedures in the low- and moderate-field regions ($<10^5$ V/cm) the primary injection distance on $\sim$1 nm has been inferred – a reasonable value corresponding to about two intermolecular spacings characteristic of electron transfer reactions at the metal/organic solid interface.

This work also provided evidence that the electrons injected at the Al^- /TPD interface form negative recombination centers for oppositely injected hole currents rather than contribute directly to the currents. This confirms electrons to be almost immobile carriers in TPD, which in the bi-molecular recombination reduce the hole flux reaching the cathode and thus the total cell current.

Once having recognized injection of holes from both ITO and Al electrical contacts, we have shown that proper accounting of surface and bi-molecular electron–hole recombination leads to consistent analysis of the electrical characteristics of thin film structures with nominally different electrodes and procedures of their preparation.

References

[1] J. Kalinowski, Organic Light Emitting Diodes: Principles, Characteristics, and Processes, Marcel Dekker, New York, 2005.
[2] C.W. Tang, S.A. VanSlyke, Appl. Phys. Lett. 51 (1987) 913.
[3] C.W. Tang, S.A. VanSlyke, C.H. Cheng, J. Appl. Phys. 65 (1989) 3610.
[4] P.E. Burrows, S.R. Forrest, Appl. Phys. Lett. 64 (1993) 2285.
[5] P.E. Burrows, Z. Shen, V. Bulovic, B.M. McCarty, S.R. Forrest, J.A. Cronin, M.E. Thompson, J. Appl. Phys. 79 (1996) 7991.
[6] J. Kalinowski, N. Camaioni, P. Di Marco, V. Fattori, G. Giro, Int. J. Electron. 81 (1996) 377.
[7] S.R. Forrest, P.E. Burrows, M.E. Thompson, in: S. Miyata, H.S. Nalwa (Eds.), Organic Electroluminescent Materials and Devices, Gordon & Breach, Amsterdam, 1997 (Chapter 13).
[8] C. Giebeler, H. Antoniadis, D.D.C. Bradley, Y. Shirota, J. Appl. Phys. 85 (1999) 608.
[9] G. Giro, M. Cocchi, J. Kalinowski, V. Fattori, P. Di Marco, P. Dembech, G. Seconi, Adv. Mater. Opt. Electron. 9 (1999) 189.
[10] J. Kalinowski, in: S. Miyata, H.S. Nalwa (Eds.), Organic Electroluminescent Materials and Devices, Gordon & Breach, Amsterdam, 1997. Chapter 1.
[11] Y. Shirota, K. Okumoto, Proc. SPIE 4105 (2001) 158.
[12] A.J. Campbell, D.D.C. Bradley, J. Laubender, M. Sokolowski, J. Appl. Phys. 86 (1999) 5004.
[13] J. Kalinowski, W. Stampor, J. Szmytkowski, D. Virgili, M. Cocchi, V. Fattori, C. Sabatini, Phys. Rev. B74 (2006) 085316.
[14] J. Godlewski, J. Kalinowski, Jpn. J. Appl. Phys. (Part 1) 28 (1989) 24.
[15] D.F. Blossey, Phys. Rev. B9 (1974) 183.
[16] H. Killesreiter, H. Bässler, Chem. Phys. Lett. 11 (1971) 411.
[17] H. Ishii, K. Sugiyama, E. Ito, K. Seki, Adv. Mater. 11 (1999) 605.
[18] N. Koch, L.M. You, P.V.R. Lazzaroni, R.L. Johnson, G. Leising, J.J. Pireaux, J.L. Brédas, Adv. Mater. 10 (1998) 1038.
[19] A. Ioannidis, J.S. Facci, M.A. Abkowitz, J. Appl. Phys. 84 (1998) 1439.
[20] J. Godlewski, J. Kalinowski, G. Mancini, S. Stizza, Physica Status Solidi B183 (1994) 233.
[21] J. Campbell Scott, George G. Malliaras, Chem. Phys. Lett. 299 (1999) 115.
[22] J. Kalinowski, Mol. Cryst. Liq. Cryst. 355 (2001) 231.
[23] J. Kalinowski, M. Cocchi, V. Fattori, P. Di Marco, G. Giro, Jpn. J. Appl. Phys. (Part 2) 40 (2001) L282.
[24] F. Li, H. Tang, J. Anderegg, J. Shinar, Appl. Phys. Lett. 70 (1997) 1233.
[25] S.D. Wang, K. Kanai, E. Kawabe, Y. Ouchi, K. Seki, Chem. Phys. Lett. 423 (2006) 170.
[26] M. Stolka, J.F. Janus, D.M. Pai, J. Phys. Chem. 88 (1984) 4707.

[5,6] are better suited for improving the hole-injection properties because we anticipate that a higher work function will be compatible with the smaller resistance in p-type materials. From this view, Mg-doped LaCuOSe (LaCuOSe:Mg) is an attractive candidate because it is a transparent p-type semiconductor that shows a degenerate conduction with conductivities as high as 910 S cm^{-1} [7] and large work functions of ~5 eV.

Herein we report that a low E_{HIB} of 0.3 eV is formed at LaCuOSe:Mg/*N*,*N*′-diphenyl-*N*,*N*′-bis(1,1′-biphenyl)-4,4′-diamine (NPB) interfaces. The E_{HIB} values were measured by ultraviolet photoemission spectroscopy (UPS), and the interface electrical properties were characterized using hole-only devices composed of a LaCuOSe:Mg/NPB/Al structure. These observations substantiated that employing LaCuOSe:Mg as an anode improves the electrical characteristics; i.e., a low threshold voltage of <0.2 V and a high current drivability of 250 mA cm^{-2} at 2 V were obtained.

Epitaxial films of LaCuOSe:Mg fabricated on (001) MgO single crystals were employed in this study to determine the fundamental interface properties with a well-defined structure. The epitaxial films of LaCuOSe:Mg were prepared on single-crystalline MgO(001) substrates by a reactive solid-phase epitaxy (R-SPE) process [8–10]. In this process, a thin Cu layer (5 nm in thickness) was initially deposited on an MgO(001) substrate under a high vacuum of 10^{-5} Pa at 400 °C by pulsed laser deposition (PLD). An amorphous LaCuOSe:Mg layer was then deposited on the thin Cu layer at room temperature sequentially in the same PLD chamber. A sintered ceramic disk of LaCuOSe:Mg was used as the PLD target. The obtained films were annealed at 1000 °C with a small amount of LaCuOSe powder in evacuated silica glass ampoules. The surfaces of the obtained films were polished by chemical–mechanical polishing (CMP), which produced an atomically flat, terrace-and-step surface with root-mean-square roughnesses (R_{rms}) of 0.6–1.5 nm. The film thickness was fixed between 30 and 50 nm because it was confirmed that LaCuOSe:Mg exhibits the largest hole concentration and the highest conductivity for thicknesses less than 50 nm [7]. It should be noted that the small thickness of the LaCuOSe:Mg layer causes a somewhat high series resistance for hole-only devices, as will be discussed later. However, the series resistance is small enough to obtain a large injection current, which demonstrates the improved injection properties of the LaCuOSe:Mg/NPB interface. The electrical conductivity, hole concentration, and Hall mobility of the LaCuOSe:Mg films used in this study were >500 S cm^{-1}, >1 × 10^{21} cm^{-3}, and ~3 cm^2 V^{-1} s^{-1}, respectively, at room temperature. Details of the optical and electrical properties are reported in Ref. [7].

The LaCuOSe:Mg films were then transferred to a multichamber system equipped with two preparation chambers, two organic/metal evaporation chambers, an X-ray photoemission spectroscopy (XPS)/ultraviolet photoemission spectroscopy (UPS) chamber, and an electrical/light-emission measurement chamber connected in an ultra-high vacuum at 10^{-6} Pa. Residual atmospheric contaminants and polishing residues on the surfaces of the LaCuOSe:Mg films were removed in the preparation chamber by an oxygen plasma treatment (radio frequency (RF) plasma in a pure O_2 gas at 6.0 × 10^{-1} Pa for 30 s with an RF power of 50 W). Observations of C 1s peak intensities by XPS confirmed that carbon contaminants were removed by the oxygen plasma treatment. XPS measurements also revealed that the oxygen plasma treatment oxidized the LaCuOSe:Mg surface, and the valence state of Cu^+ at the surface of LaCuOSe:Mg changed to Cu^{2+}. The LaCuOSe:Mg films maintained the same high conductivity after the treatment.

Sublimation-purified NPB (Lumtec, Taiwan) was deposited by thermal vacuum evaporation at deposition rates of 0.07–0.15 nm s^{-1}, a pressure of 2 × 10^{-6} Pa, and a substrate temperature of room temperature. The thickness of the NPB film was monitored with a pre-calibrated quartz-oscillator thickness meter. UPS measurements under an ultra-high vacuum (5 × 10^{-8} Pa) and thin layer depositions of NPB were alternately repeated by transferring the sample between the UPS chamber and the deposition chamber in vacuum to collect UPS spectra as a function of NPB thickness.

Single-crystalline (sc-) ITO films prepared by PLD [11] and commercially-available polycrystalline (pc-) ITO films (Asahi Glass Co., Ltd.) were examined for comparison. Before the deposition of NPB, the sc- and pc-ITO films were treated by the oxygen plasma (50 W, 6.0 × 10^{-1} Pa with durations of 30 s for sc-ITO and 3 min for pc-ITO), and annealed in vacuum in the other preparation chamber (250 °C, ~5 × 10^{-6} Pa, 5 min) to obtain conductive ITO films with large work functions (~5 eV). An Al/NPB interface was also examined by *in situ* UPS measurements.

Fig. 1 shows the UPS spectra of the LaCuOSe:Mg/NPB interfaces as a function of NPB thickness (*t*). The work

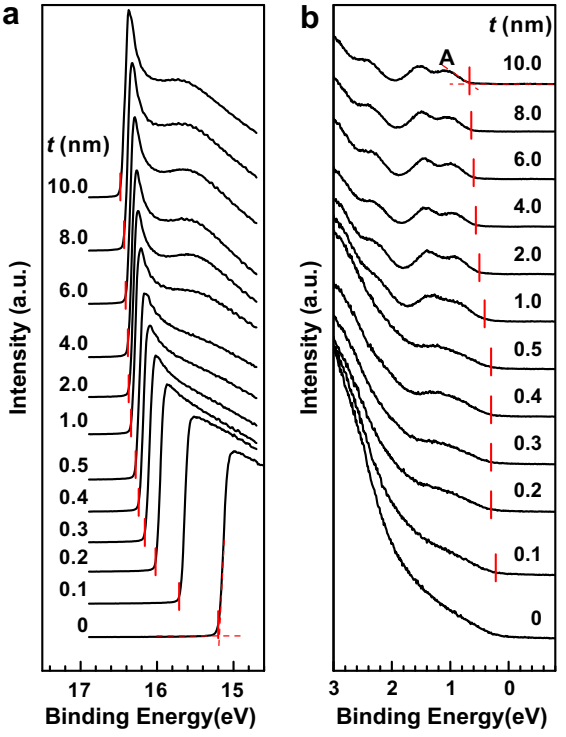

Fig. 1. Variation of UPS spectra of LaCuOSe:Mg/NPB interface with NPB thickness. (a) Cut-off and (b) valence region.

functions were evaluated from the energy difference between the excitation energy (He I, 21.2 eV) and the cut-off energy (indicated by vertical bars in Fig. 1a) [12]. On the other hand, the energy levels of the HOMO of the NPB films were evaluated as the onset energies of peak A in Fig. 1b. It was found that the oxygen plasma treatment increased the work function of the LaCuOSe:Mg film to ~6.0 eV, which is much higher than those of a bulk LaCuOSe:Mg surface (~5.0 eV) and ITO film surfaces (4.1–5.4 eV) [1–4]. Fig. 1a shows that the cut-off energy dropped sharply from 15.2 to 16.1 eV as t increased only to 0.3 nm. The HOMO energy gradually shifted to deeper energies from 0.2 to 0.6 eV as the NPB thickness increased to 4.0 nm. These results indicate that the vacuum level (E_{vac}) and the HOMO energy of the NPB move to deeper energies with respect to the Fermi level (E_F) of the bulk region in the LaCuOSe:Mg film.

Fig. 2a shows the energy level diagram built from the above UPS measurements for a LaCuOSe:Mg/NPB interface. It is noted that E_{HIB}, which is defined as the energy difference between E_F and the HOMO energy of the NPB film at the interface, is as low as 0.3 eV. The E_{HIB} values of our sc-ITO/NPB and pc-ITO/NPB interfaces were 0.6 and 0.7 eV, respectively, and significant differences were not found between them. In addition, these values are consistent with reported ones [2,3], confirming the validity of the data obtained with our apparatus and procedures. Consequently, we concluded that the oxygen plasma treated LaCuOSe:Mg/NPB interfaces realize approximately half the E_{HIB} of an ITO/NPB interface. It should also be noted that the HOMO level decreased as the NPB thickness increased in the vicinity of the interface, which will be discussed later with the derived carrier concentration shown in Fig. 2b.

Fig. 3 schematically illustrates the energy level alignments of the LaCuOSe:Mg/NPB interface before and after contact. E_F of the LaCuOSe:Mg (i.e., the work function) and the HOMO energy of an isolated NPB [14] were located at 6.0 and 5.2 eV from E_{vac}, respectively. If the Schottky–Mott rule is assumed (Fig. 3a), then these values predict a negative E_{HIB} value −0.8 eV, which suggests that an ohmic contact may be formed. Unfortunately, the experimental result showed that a discontinuous energy down shift (often referred to as 'vacuum level shift' [15,16]) of 1.1 eV occurred at the interface upon contact, which results in a positive E_{HIB} value of 0.3 eV (Fig. 3b).

To evaluate the hole-injection properties electrically, hole-only devices with an MgO/LaCuOSe:Mg (50 nm in thickness)/NPB (200 nm)/Al (100 nm) structure were fabricated. Metal contacts for the LaCuOSe:Mg anodes were formed with Au electrodes, which were vacuum evaporated on the exposed area of the LaCuOSe:Mg layer, as illustrated in the inset of Fig. 4a. The area of the Al electrode was 1.0 mm^2. If positive forward voltages are applied (i.e., a positive potential for the LaCuOSe:Mg anode), electron injection from the Al cathode to the NPB layer is blocked due to the large electron injection barrier (E_{EIB}) at the NPB/Al interface. The E_{EIB} value of 2.8 eV was estimated from the energy difference between E_F of Al and LUMO* of NPB as shown in Fig. 3b. The LUMO* was determined from the HOMO level measured by UPS and the transport gap of NPB [13].

Fig. 4 shows the current density (J)–voltage (V) curves of the hole-only devices. For LaCuOSe:Mg/NPB/Al (closed circles in (a) and (b)), J began to rise at ~0.2 V, and then increased linearly as the applied voltage increased. The obtained J values (e.g., 250 mA cm^{-2} at 2 V) were two orders of magnitude larger than those of ITO/NPB/Al hole-only devices [17]. We also confirmed similar smaller currents on our pc-ITO/NPB/Al devices (open circles in (b)), and found that the J–V curves follow the linear

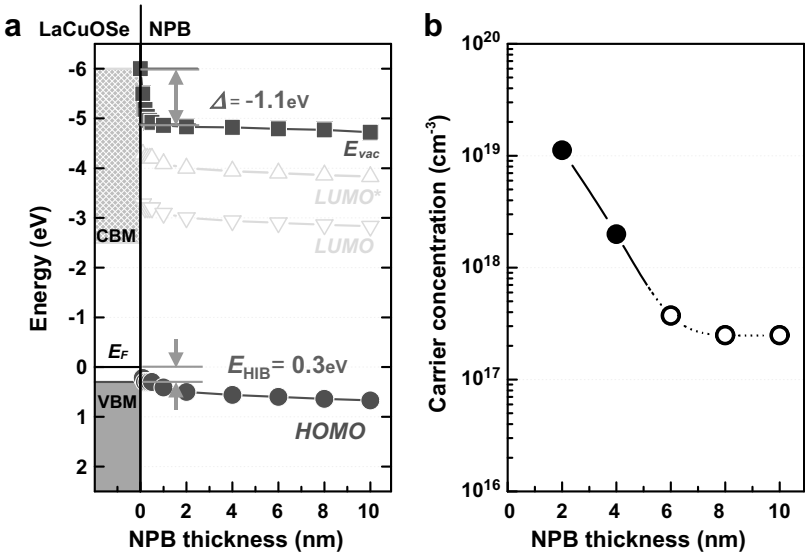

Fig. 2. (a) Energy level alignment in the vicinity of LaCuOSe:Mg/NPB interface. Locations of the lowest unoccupied molecular orbital (LUMO) and the LUMO energy after an electron occupies the LUMO state (LUMO*) estimated from the data in ref. 13 are shown for reference. CBM and VBM denote the conduction band minimum and the valence band maximum of LaCuOSe:Mg, respectively. (b) Variation of the acceptor concentration with NPB thickness estimated from second-order derivatives of the HOMO level bending curve and Poisson's equation.

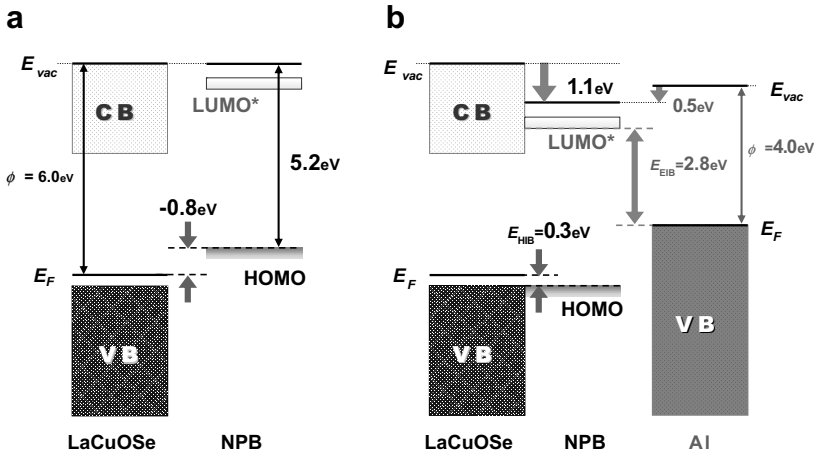

Fig. 3. Relevant energy levels of LaCuOSe:Mg and NPB (a) before and (b) after contact. Electron injection barrier (E_{EIB}) at the Al/NPB interface was also measured by UPS.

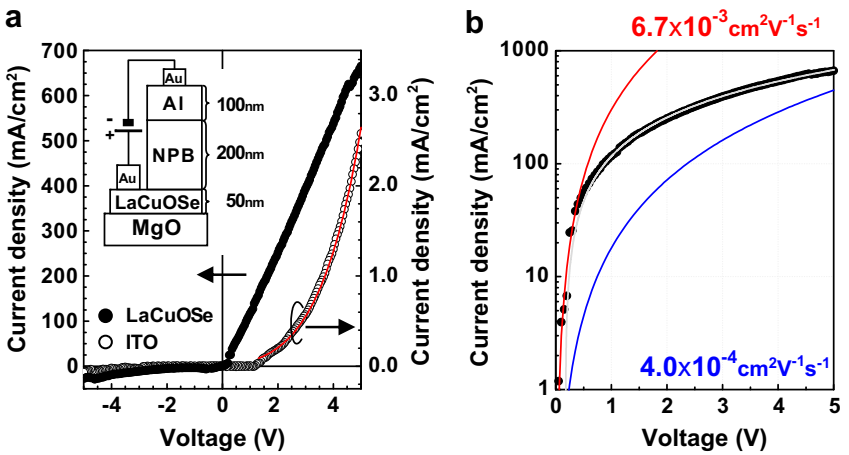

Fig. 4. *J–V* curve of LaCuOSe:Mg/NPB/Al hole-only device. (a) For comparison, that of a pc-ITO/NPB/Al device is shown along with the fitted result to the Schottky model. Inset is the structure of the hole-only device. (b) Semi-logarithmic plot of the *J–V* curve of the LaCuOSe:Mg/NPB/Al device. Blue and red curves show SCLC curves for $\mu_{NPB} = 4 \times 10^{-4}$ cm^2 V^{-1} s^{-1} and 6.7×10^{-3} cm^2 V^{-1} s^{-1}, respectively. Gray curve shows ohmic currents with a differential resistance of 714 Ω. (For interpretation of the references to color in this figure legend, the reader is referred to the web version of this article.)

$\ln J - \sqrt{E}$ relation (E denotes the average electric field applied in the NPB layer) with a slope parameter (β_s/k_BT) of 1.3×10^{-3} (the fitting result is shown by the red line in (a)). The slope parameter agrees roughly with that of the Schottky model (0.77×10^{-3}, calculated using the relative dielectric constant of NPB of 3.6 [18]). This result indicates that the hole injection is still limited by the Schottky barrier even in the current ITO/NPB interface. In contrast, such a Schottky injection was not observed for the LaCuOSe:Mg/NPB interface. We confirmed that the bottom LaCuOSe:Mg layer causes a high series resistance (~650 Ω) due to its thin thickness (~50 nm). This series resistance is almost the same as the differential resistance (714 Ω) of the LaCuOSe:Mg/NPB/Al device at >0.2 V. These results indicate that the interface does not limit the hole injection in this device, and hence, the two orders larger currents are achieved. However, considering the reported mobility (μ_{NPB}) of 4×10^{-4} cm^2 V^{-1} s^{-1} [19], the obtained current is too large for a 200-nm-thick intrinsic NPB layer. The largest current flowing in an intrinsic layer is limited by space charge formed by injected carriers, and therefore, can be estimated by the space charge limited current (SCLC) model. The blue line in Fig. 4b shows the SCLC curve for the reported μ_{NPB} value of 4×10^{-4} cm^2 V^{-1} s^{-1}, which demonstrates that the SCLC current is much lower than the observed current. A much higher mobility of 6.7×10^{-3} cm^2 V^{-1} s^{-1} must be assumed to explain the observed currents (the red line in Fig. 4b), but this mobility value is unrealistic. Another possibility is that the NPB layer is slightly doped. In this case, the conductivity of the NPB layer must be larger than the value estimated from the apparent conductivities of the LaCuOSe:Mg/NPB/Al device in the forward bias region (3×10^{-6} S cm^{-1}), which corresponds to the doped hole concentration of >10^{16} cm^{-3} using the reported μ_{NPB} value. This model would be plausible because the conductivity of (ReO_3)-doped NPB is

reported to be 7.5×10^{-6} S cm^{-1} [17]. Furthermore, the hole concentration distribution in the NPB layer can also be estimated from the second-order derivatives of the HOMO level bending curve $\phi(x)$ in Fig. 2a by following Poisson's equation $d^2\phi(x)/dx^2 = \rho(x)/\varepsilon$ where $\rho(x)$ denotes the background charge (assumed to be the acceptor density in a fully depleted layer) and ε the dielectric constant of the NPB layer. Fig. 2b gives the obtained result. In the vicinity of the interface ($t < 6$ nm), the hole concentration decreased with increasing the NPB thickness, and leveled off at $\sim 10^{17}$ cm^{-3} at $t > 6$ nm. It should be noticed that the HOMO level bending is small, only $\sim$0.1 eV, at $t > 6$ nm, and the accuracy of the absolute value is not high. In addition, similar HOMO level shifts can be occurred by a charging effect during the UPS measurements. In the present study, however, we confirmed reproducibility and reliability of the results by repetitive measurements and time dependence of the spectra, and no indication of the charging effect was observed. Therefore, we conclude that the NPB film is doped also at $t > 6$ nm, but the hole concentration can be less than 10^{17} cm^3. This discussion is still consistent with the above value of $>10^{16}$ cm^{-3} estimated from the *J–V* curve. It is speculated that the high-density holes are generated from copper ions diffused from the LaCuOSe:Mg layer. Further investigation is required to reveal the origin of the high-density current and the HOMO level bending.

In summary, we achieved a low hole-injection barrier (0.3 eV) to NPB using an oxygen plasma treated LaCuOSe:Mg film as an anode. The hole-only device demonstrated a low threshold voltage and a high-density current drivability. The present results demonstrate that LaCuOSe:Mg has great potential as an efficient transparent anode for OLEDs and other organic electronic devices.

Acknowledgement

We are indebted to Dr. Kenji Nomura (ERATO-SORST, JST) for his help in the preparation of sc-ITO films.

References

[1] Y. Park, V. Choong, Y. Gao, B.R. Hsieh, C.W. Tang, Appl. Phys. Lett. 68 (1996) 2699.
[2] X.M. Ding, L.M. Hung, L.F. Cheng, Z.B. Deng, X.Y. Hou, C.S. Lee, S.T. Lee, Appl. Phys. Lett. 76 (2000) 2704.
[3] S.M. Tadayyon, H.M. Grandin, K. Griffiths, P.R. Norton, H. Aziz, Z.D. Popovic, Org. Electron. 5 (2004) 157.
[4] K. Sugiyama, H. Ishii, Y. Ouchi, K. Seki, J. Appl. Phys. 87 (2000) 295.
[5] H. Kawazoe, M. Yasukawa, H. Hyodo, M. Kurita, H. Yanagi, H. Hosono, Nature 389 (1997) 939.
[6] A. Kudo, H. Yanagi, H. Hosono, H. Kawazoe, Appl. Phys. Lett. 73 (1998) 220.
[7] H. Hiramatsu, K. Ueda, H. Ohta, M. Hirano, M. Kikuchi, H. Yanagi, T. Kamiya, H. Hosono, Appl. Phys. Lett. 91 (2007) 012104.
[8] H. Hiramatsu, K. Ueda, H. Ohta, M. Hirano, T. Kamiya, H. Hosono, Appl. Phys. Lett. 82 (2003) 1048.
[9] H. Hiramatsu, K. Ueda, H. Ohta, M. Orita, M. Hirano, H. Hosono, Appl. Phys. Lett. 81 (2002) 598.
[10] H. Hiramatsu, H. Ohta, T. Suzuki, C. Honjo, Y. Ikuhara, K. Ueda, T. Kamiya, M. Hirano, H. Hosono, Cryst. Growth Des. 4 (2004) 301.
[11] H. Ohta, M. Orita, M. Hirano, H. Hosono, J. Appl. Phys. 91 (2002) 3547.
[12] P. Yu, M. Cardona, Fundamentals of Semiconductors, Springer, Berlin, 2003. pp. 438–439.
[13] I.G. Hill, A. Kahn, Z.G. Soos, R.A. Pascal Jr., Chem. Phys. Lett. 327 (2000) 181.
[14] S.T. Lee, Y.M. Wang, X.Y. Hou, C.W. Tang, Appl. Phys. Lett. 74 (1999) 670.
[15] A. Rajagopal, C.L. Wu, A. Kahn, J. Appl. Phys. 83 (1998) 2649.
[16] H. Ishii, K. Sugiyama, E. Ito, K. Seki, Adv. Mater. 11 (1999) 605.
[17] D.-S. Leem, H.-D. Park, J.-W. Kang, J.-H. Lee, J.-W. Kim, J.-J. Kim, Appl. Phys. Lett. 91 (2007) 011113.
[18] Y.F. Xu, Y.S. Tao, H.J. Zhang, X.Z. Chen, G.H. Cao, Z.A. Xu, H.Y. Li, S.N. Bao, P. He, Physica B 362 (2005) 35.
[19] S.C. Tse, S.W. Tsang, S.K. So, Proc. SPIE 6333 (2006) 63331P.

Gundlach et al. also observed the complete transition of the thin film phase into the bulk phase when the pentacene film was post-exposed to ethanol, degrading the performance of TFTs severely [19]. However, systematic studies on the correlation between the onset of the bulk phase and the electronic transport in pentacene TFTs were not well established in their work. In this letter, we report a phase transition in pentacene induced by postannealing process, correlating it to the film morphology and the electronic transport. Moreover, we suggest that this transition from the thin film phase to the bulk phase could be another main factor causing the mobility degradation after high temperature annealing other than the physical desorption of pentacene as previously observed in Refs. [8,9].

Pentacene TFTs based on a bottom-contact configuration have been fabricated on a highly doped n type silicon wafer (<0.005 Ωcm; ⟨100⟩ orientation) as shown in Fig. 1a. The highly doped silicon and 200 nm of thermal SiO_2 serves as the gate electrode and dielectric, respectively. A 120 nm thick layer of palladium was first e-beam evaporated, and patterned to define the source/drain contacts. Then, pentacene obtained from Aldrich (97% purity) without further purification was deposited onto the gate oxide by thermal evaporation following the treatment of the oxide surface with octadecylthrichlorosilane (OTS). The nominal channel length and width of TFTs, in which the pentacene active layer is exposed to air without any encapsulation, is 60 and 300 μm, respectively. The detail description of the fabrication procedure is provided in Ref. [2]. Besides pentacene TFTs, thin pentacene films also were grown on the OTS treated oxide to be used for atomic force microscopy (AFM) and X-ray diffraction (XRD) measurements, which were processed in the same batch along with the TFT devices.

From the transfer curve of the bottom-contact pentacene TFTs measured at room temperature (see Fig. 1b), we extract a saturation mobility 0.086 cm^2/Vs, and an on/off current ratio >10^7 at a drain-source voltage (V_D) of −60 V. For annealing tests, the TFTs were kept for 1 h at a given annealing temperature, and cooled down to RT (30 °C) to measure the transfer curves. This procedure was repeated with the same device for different annealing temperatures of 50, 70, 100, 120, and 160 °C. The dependences of resulting mobilities on annealing temperatures for three other TFT samples that were processed together on the same substrate are well shown in Fig. 2 (left), where the carrier mobilities are normalized with respect to their highest mobility value ($N_\mu = \mu/\mu_{max}$). The mobility values of all the samples tend to increase with increasing annealing temperature, and reach to peak values ($N_\mu = 1$) at 70 °C even though the highest values range from 0.092 to 0.12 cm^2/Vs. They then start to decrease beyond that, and drop close to $N_\mu = 0.6$ at 160 °C. The right plot of Fig. 2 shows the XRD patterns that are collected on the pentacene films annealed at RT (30 °C), 70, 100, 120, and 160 °C, respectively, which were carried out along with AFM analysis in order to gain more insight on the degradation mechanism of transistor mobility at high annealing temperatures.

The diffraction peaks of the RT sample indexed as (00l′) indicate that the film consists mainly of the thin film phase, and is highly oriented in the out-of-plane direction with periodicity of a lattice spacing $d(00l')$ of 15.4 Å. There is also seen a second set of diffraction peaks (00l) corresponding to a $d(001)$ of 14.4 Å of the bulk phase, but their intensities are negligible when compared to the thin film phase. The peak patterns remain similar as long as the annealing temperatures stay below 100 °C. A further increase of the annealing temperature, however, triggers the evolution of the bulk phase. This is interestingly consistent with the mobility decrease observed in the TFT de-

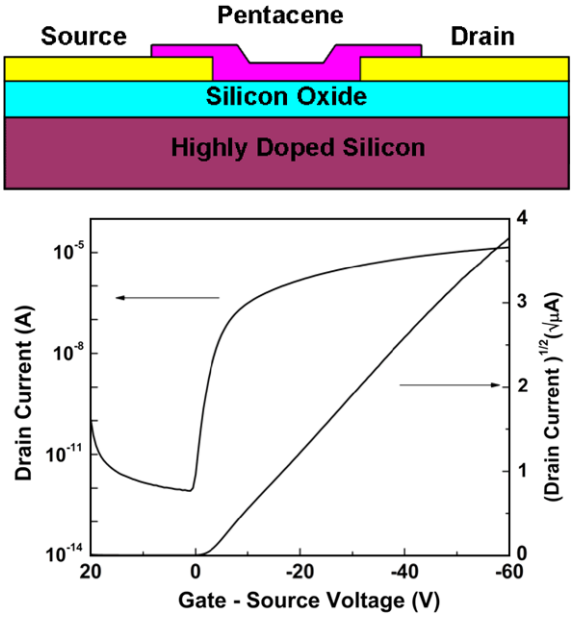

Fig. 1. (a) Schematic cross-sectional view of a bottom-contact pentacene TFT without encapsulation. (b) Transfer characteristic, measured at RT, of such a bottom-contact pentacene TFT with a channel length and width of 60 and 300 μm, respectively.

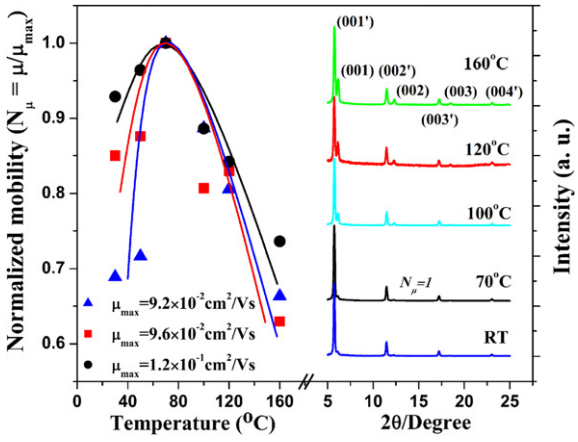

Fig. 2. (Left) Normalized carrier mobility ($N_\mu = \mu/\mu_{max}$) variation for three other TFT samples without encapsulation as a function of annealing temperature. (Right) XRD patterns of bare pentacene films without encapsulation that were postannealed at RT, 70, 100, 120, and 160 °C for 1 h.

vices and the onset of the lamellar-like structure seen in the AFM measurements that will be discussed more below. The ratio of the first order XRD peak intensities between the two phases [(001)/(001′)] changes from 0.057 to 0.31 while the annealing temperature increases from RT to 160 °C. This is different from the observation made in Refs. [6,9] where only the thin film phase peak was detected and its intensity was decreased beyond a certain critical annealing temperature without any evolution of the bulk phase.

Fig. 3 is AFM pictures illustrating the surface morphology of pentacene films that were heat-treated at the given annealing temperatures for 1 h. Before annealing (RT), the pentacene film is terrace-like multilayered with a typical dendritic structure in which the average grain size ranges from 2 to 4 μm. The film remains morphologically similar until the annealing temperature reaches to 100 °C whereas a striking difference in the morphology is revealed when the annealing temperature exceeds beyond 100 °C. It is seen that lamellar-like plates start to grow from the film surface, thus, strongly suggesting that another phase nucleates. This lamellar-like structure is very similar to that found in the as-grown pentacene film at high substrate temperatures (Ref. 18), where it was identified as the bulk phase. The comparison with the XRD results for the films suggests that this annealing induced phase can be also interpreted as the bulk phase in pentacene. The corresponding height profile reveals that the lamella observed on the film surface regrows to a thickness of 140 nm at 100 °C annealing temperature. Most of portions, however, still remain similar. The lamella, then, propagates onto all over the surface, forming a series of multilayered lamellar structures when the annealing temperature further increases to 160 °C at which the height of the protrusive lamellas reaches close to 400 nm.

In order to further confirm the correlation between the onset of the bulk phase and the mobility deterioration after high temperature annealing, another set of pentacene TFTs and films were prepared identical to those described above except that they are encapsulated with photo-sensitized polyvinyl alcohol (PVA) by spin coating. The right plot of Fig. 4 shows the XRD results for the PVA-encapsulated pentacene films. The peak patterns at RT remains unchanged except the slight decrease in peak intensity due to the PVA layer as compared to the PVA-less film, but still providing clear information on the film crystallite. It is interesting to note that, with encapsulation, the annealing induced evolution of the bulk phase is suppressed to higher temperature (120 °C), and accordingly the corresponding mobilities measured from three other PVA-encapsulated TFTs, keep increasing up to 0.064–0.079 cm^2/Vs ($N_\mu = 1$) until the annealing temperature reaches to 120 °C. The mobilities, then, precipitously drop to $N_\mu = 0.1–0.35$ with further increasing temperature up to 160 °C at which the bulk phase becomes appreciable in the XRD patterns. These observations made in both samples with and without encapsulation strongly suggest that the nucleation of the bulk phase that must be correlated to the lamellar-structure observed in the AFM pictures is another cause for the deterioration in carrier transport other than the pentacene desorption during high temperature postannealing treatment. Moreover, it is clear that encapsulation helps to retard the nucleation of the bulk phase that may induce structural defects, and/or to prevent the film from re-evaporating, leading to a better thermal stability to TFT devices.

In order to quantitatively investigate the evolution of the two polymorphs in pentacene, we calculated the minimum crystal size and the quality of each phase perpendicular to the (00l) planes in PVA-less pentacene films using the paracrytal theory [11]. Both the parameters of interest can be extracted from the following equation by taking the slop and the ordinate intercept of the lines, respectively:

$$(\delta s)^2 = (\delta s)_c^2 + (\delta s)_{II}^2 = \frac{1}{\overline{L}_{hkl}^2} + \frac{\pi^4 g_{II}^4 m^4}{\overline{d}_{hkl}^2}, \quad (1)$$

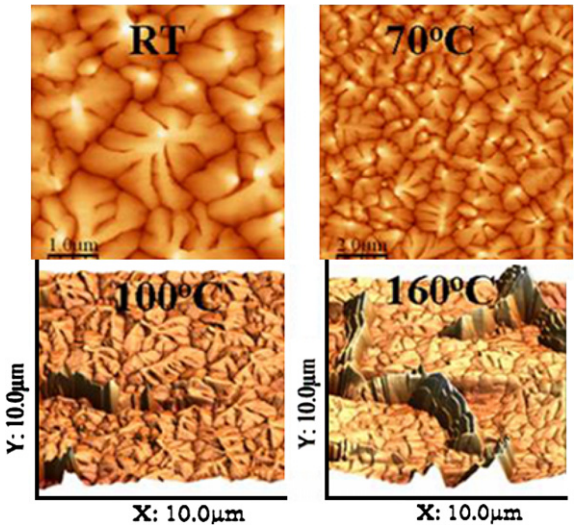

Fig. 3. AFM images of pentacene films annealed at RT (30 °C), 70 °C, 100 °C, and 160 °C.

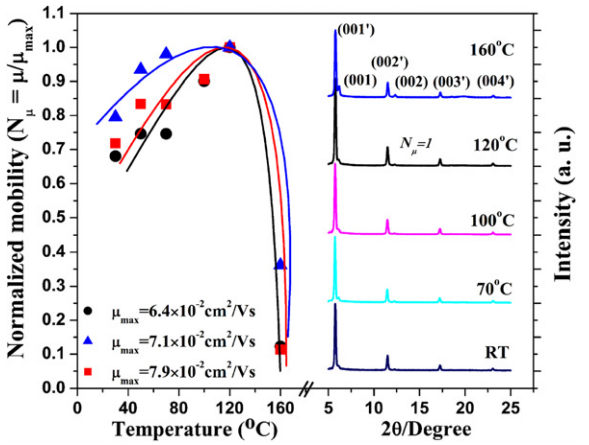

Fig. 4. The left plot shows the normalized carrier mobility ($N_\mu = \mu/\mu_{max}$) variation as a function of annealing temperature for three other TFT samples encapsulated. The XRD patterns of pentacene films with PVA encapsulation postannealed at RT, 70, 100, 120, and 160 °C, respectively, are shown in the right plot.

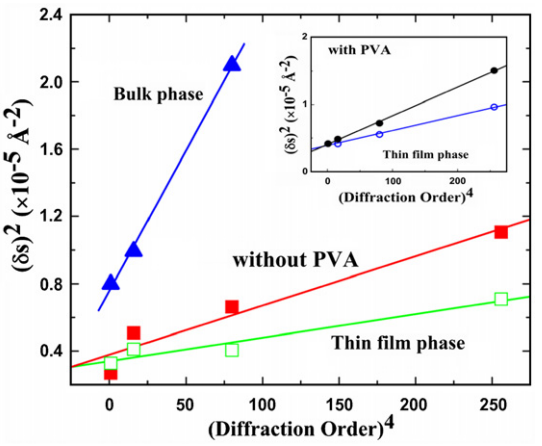

Fig. 5. Variations of $(\delta s)^2$ as a function of the fourth power of the diffraction order and their linear fits for the thin film phase and the bulk phase in pentacene films without PVA encapsulation annealed at RT (open data points) and 160 °C (filled data points). The inset is for the thin film phase in PVA-encapsulated pentacene films annealed at RT (open data points) and 160 °C (filled data points).

and

$$\delta s = 2\cos\theta\ \delta\theta/\lambda, \tag{2}$$

where δs is the overall broadening, $(\delta s)_c$ and $(\delta s)_{II}$ are the broadenings due to the average crystal size and the structural disorder, respectively, $\overline{L}_{hkl}$ is the average crystal size normal to the (hkl) planes, g_{II} is the mean distance fluctuation between successive (hkl) planes, $\overline{d}_{hkl}$ is the average (hkl) plane spacing, θ is the diffraction angle, $\delta\theta$ is the half width of the peak at half maximum, and λ is the X-ray wavelength. Fig. 5 shows the variations of $(\delta s)^2$ as a function of the fourth power of the diffraction order for both phases in the PVA-less pentacene films annealed at RT, and 160 °C, respectively. It is found that with increasing annealing temperatures, the average crystallite size of the thin film phase calculated from the plot in Fig. 5 decreases from 540 to 510 Å while the bulk phase crystallite evolves up to 360 Å. The crystallite size of the thin film phase in the PVA-encapsulated pentacene films extracted from the inset of Fig. 5 for comparison also exhibits a decrease from 510 to 500 Å as the annealing temperature increases up to 160 °C. The reduction in the crystal size perpendicular to the surface plane that occurs more in the PVA-less pentacene may be ascribed either to physical desorption or to phase transition from the thin film phase to the bulk phase. It should be noted that the XRD peak intensity of the bulk phase measured in the PVA-encapsulated pentacene is still weak even for the 160 °C annealed sample, indicating that the bulk phase crystallite created in the film must be very small. The extracted g_{II} of 1.6% and 2.4% for both the thin film and bulk phase of the 160 °C annealed film without encapsulation confirms that the structural perfection normal to the film surface is rather high regardless of the crystallite polymorph.

In summary, we have fabricated pentacene based TFTs to investigate the postannealing effects on the device performance. It is found that the nucleation of the bulk phase in pentacene that sets in at high annealing temperatures is another main factor, other than the sublimation of pentacene, causing degradation to the mobility of TFTs. The thermal stability of TFT devices can be improved by encapsulation, which appears to suppress the onset of the bulk phase in pentacene. Without encapsulation, the bulk phase crystallite is found to grow up to about 70% of the as-grown film thickness when the sample is postannealed at 160 °C.

Acknowledgment

This work was supported by NSF EPSCoR Grant (Award No. EPS-0701890 and CFDA# 47.080).

References

[1] D. Knipp, R.A. Street, A. Völkel, J. Ho, J. Appl. Phys. 93 (2003) 347.
[2] S. Jung, T. Ji, V.K. Varadan, Appl. Phys. Lett. 90 (2007) 062105.
[3] R.J. Chesterfield, J.C. McKeen, C.R. Newman, P.C. Ewbank, D.A. da Silva Filho, J.L. Bredas, L.L. Miller, K.R. Mann, C.D. Frisbie, J. Phys. Chem. B 108 (2006) 19281.
[4] G. Horowitz, M.E. Hajlaoui, R. Hajlaoui, J. Appl. Phys. 87 (2000) 4456.
[5] P.Y. Lo, Z.W. Pei, J.J. Hwang, H.Y. Tseng, Y.J. Chen, Jpn. J. Appl. Phys. 45 (2006) 3704.
[6] R. Ye, M. Baba, K. Suzuki, Y. Ohishi, K. Mori, Jpn. J. Appl. Phys. 42 (2003) 4473.
[7] T. Komoda, Y. Endo, K. Kyuno, A. Toriumi, Jpn. J. Appl. Phys. 41 (2002) 2767.
[8] S.J. Kang, M. Noh, D.S. Park, H.J. Kim, C.N. Whang, C.H. Chang, J. Appl. Phys. 95 (2004) 2293.
[9] D. Guo, S. Ikeda, K. Saiki, H. Miyazoe, K. Terashima, J. Appl. Phys. 99 (2006) 094502.
[10] T. Sekitani, S. Iba, Y. Kato, T. Someya, Appl. Phys. Lett. 85 (2004) 3902.
[11] C.C. Mattheus, A.B. Dros, J. Baas, G.T. Oostergetel, A. Meetsma, J.L. de Boer, T.T.M. Palstra, Synthetic Met. 138 (2003) 475.
[12] C.C. Mattheus, G.A. de Wijs, R.A. de Groot, T.T.M. Palstra, J. Am. Chem. Soc. 125 (2003) 6323.
[13] C.D. Dimitrakopoulos, A.R. Brown, A. Pomp, J. Appl. Phys. 80 (1996) 2501.
[14] A.C. Mayer, A. Kazimirov, G.G. Malliaras, Phys. Rev. Lett. 97 (2006) 105503.
[15] L.F. Drummy, D.C. Martin, Adv. Mater. 17 (2005) 903.
[16] M. Shtein, J. Mapel, J.B. Benziger, S.R. Forest, Appl. Phys. Lett. 81 (2002) 268.
[17] R. Ruiz, A. Papadimitratos, A.C. Mayer, G.G. Malliaras, Adv. Mater. 17 (2005) 1795.
[18] I.P.M. Bouchoms, W.A. Schoonveld, J. Vrijmoeth, T.M. Klapwijk, Synthetic Met. 104 (1999) 175.
[19] D.J. Gundlach, T.N. Jackson, D.G. Schlom, S.F. Nelson, Appl. Phys. Lett. 74 (1999) 3302.

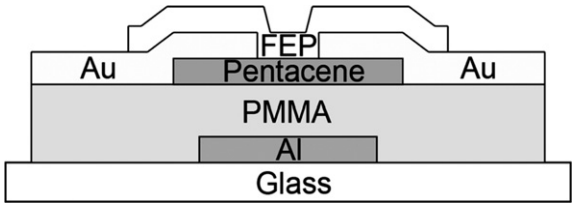

Fig. 1. Schematic illustration of the bottom-gate and top-contact pentacene OTFT with FEP capping.

mobility. We also investigated the level of threshold voltage shift as a function of the coverage of FEP film on the surface of the pentacene and the effects of further covering the device with a polymer multilayer to improve air resistivity.

We used a bottom-gate and top-contact OTFT as shown in Fig. 1. The glass substrate was washed with detergent solution rinsed with de-ionized water and placed in trichloroethylene, acetone, and isopropyl alcohol. An aluminum gate (50 nm) was deposited onto the glass substrate by thermal evaporation. Optical PMMA in toluene was then spin-coated for a gate dielectric layer (1 μm) in air. After annealing at 80 °C for 1 h, the device was transferred into an argon-purged glove box. Pentacene (70 nm) and gold electrode (70 nm) were thermally evaporated on the PMMA surface in a sequential manner. Subsequently, FEP was deposited by thermal evaporation on the pentacene layer, which was located between the source and the drain electrode (Fig. 1). The rate of deposition was 0.5–0.7 Å/s as measured by a quartz-crystal deposition monitor (Sycon Instruments, STM-100/MF). Thermal evaporation was performed in a high vacuum of 5×10^{-6} Torr. All measurements were made in an argon-purged glove box to avoid the influence of oxygen and moisture. The carrier mobility in the saturated region was determined by the following equation:

$$I_D = \frac{WC_i}{2L}\mu_e(V_G - V_T)^2 \quad (1)$$

where I_D is the drain current; W and L are the channel width and length, respectively; μ_e is the effective mobility;

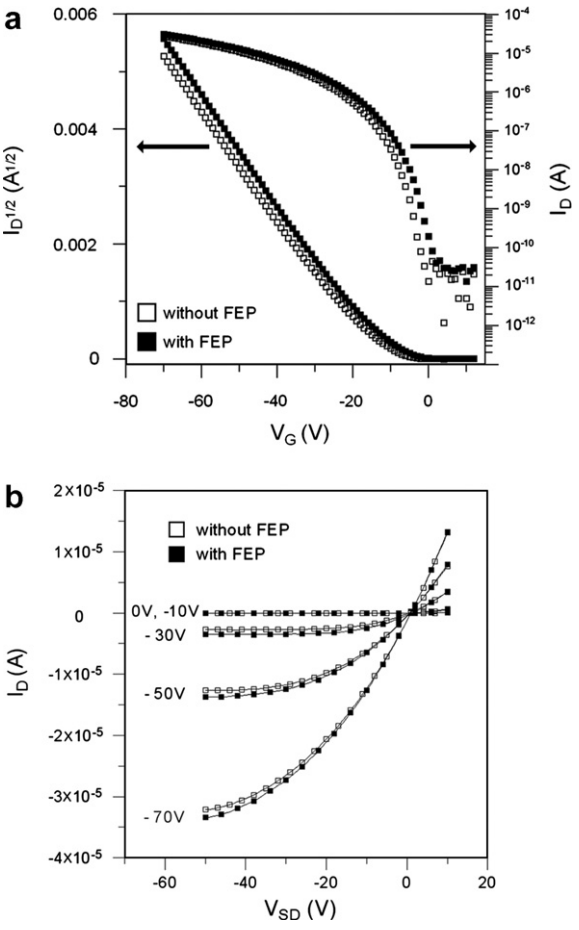

Fig. 2. Electrical characteristics of the pentacene OTFTs without and with FEP layer. (a) Drain current (I_D) (right y-axis, logarithmic scale) and the square root of I_D (left y-axis) versus gate voltage (V_G) curves. The data points were obtained while the gate voltage was scanned from +10 to −70 V. (b) Drain current (I_D) versus source–drain voltage (V_{SD}) curves.

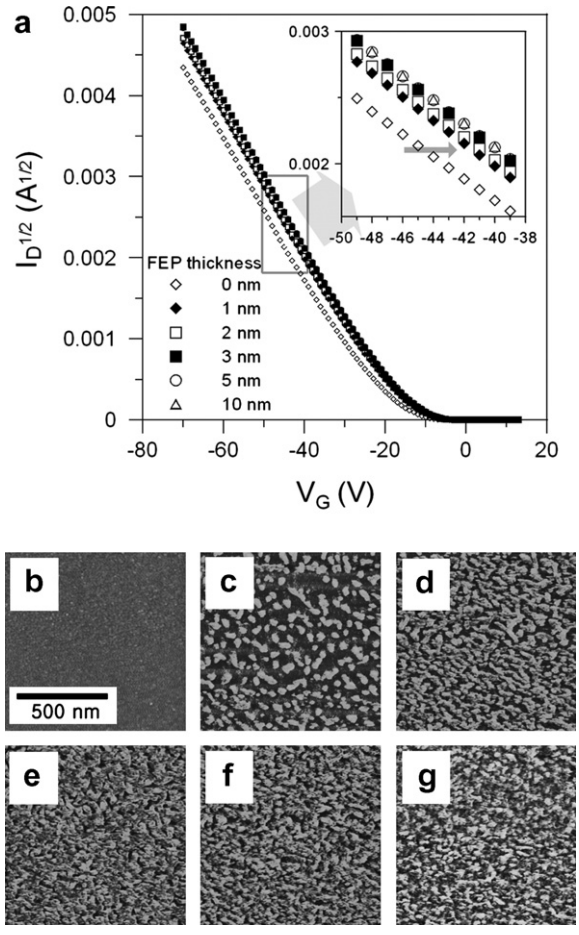

Fig. 3. (a) Characteristics of the pentacene OTFT with varying FEP thickness of 0, 1, 2, 3, 5 and 10 nm. Inset is the zoom image of the indicated area. (b–g) AFM images of the pentacene surface, where FEP is deposited with different thickness: (b) 0, (c) 1, (d) 2, (e) 3, (f) 5 and (g) 10 nm.

C_i is the capacitance per unit area; V_G is the gate voltage; and V_T is the threshold voltage. In our experiment, the carrier mobility was kept constant in the saturated region.

Fig. 2a and b shows the current–voltage characteristics of the device before and after FEP passivation. We calculated mobility using Eq. (1) at a source–drain voltage of −40 V. The mobility of the device appeared to be the same with and without FEP (0.18 $cm^2 V^{-1} s^{-1}$). Small increases in on current (from 2.7×10^{-5} to 3.0×10^{-5} A) and off current (from 2.5×10^{-11} to 3.1×10^{-11} A) were observed after passivation. The ratio of on current to off current was about 10^6. The threshold voltage shifted from −14.7 V to −12.5 V. We believe that the main cause of this shift was the high electronegativity of FEP. FEP is a polymer with the molecular formula $[-(CF_2CF_2)_n\ CF_2C(CF_3)F-]_n$, with a significant fraction of fluorine atoms included in the main chain backbone. Since fluorine atoms have the highest electronegativity of all the elements, they weakly attract electrons from the adjacent pentacene molecules. It has been reported that this localization of electrons produces more positive carriers within the pentacene layer [12] and therefore provides a greater output current capability than would occur without FEP at the same source–drain voltage. We also observed a shift in threshold voltage during low-voltage operation of other organic transistors including a plasma-treated aluminum gate and a thin poly(4-vinylphenol) (PVPh) film as a dielectric layer. The threshold voltage shifted from −0.90 V to −0.72 V during operation below 4 V.

The characteristic curves shown in Fig. 3a illustrate the way in which the shift in threshold voltage depended on the degree of coverage by the FEP film. As a reference, the threshold voltage of the pentacene transistor was measured before the deposition of FEP. A thin film of 1 nm FEP was then deposited onto the pentacene surface, and the threshold voltage was measured again. By repeating the deposition on the same sample, we obtained six characteristic curves as a function of thickness at 0, 1, 2, 3, 5 and 10 nm, respectively. All the characteristic curves with FEP passivation shifted to the right when compared with the curve without the FEP layer, showing greater (i.e., more positive) threshold voltages than the reference sample. The

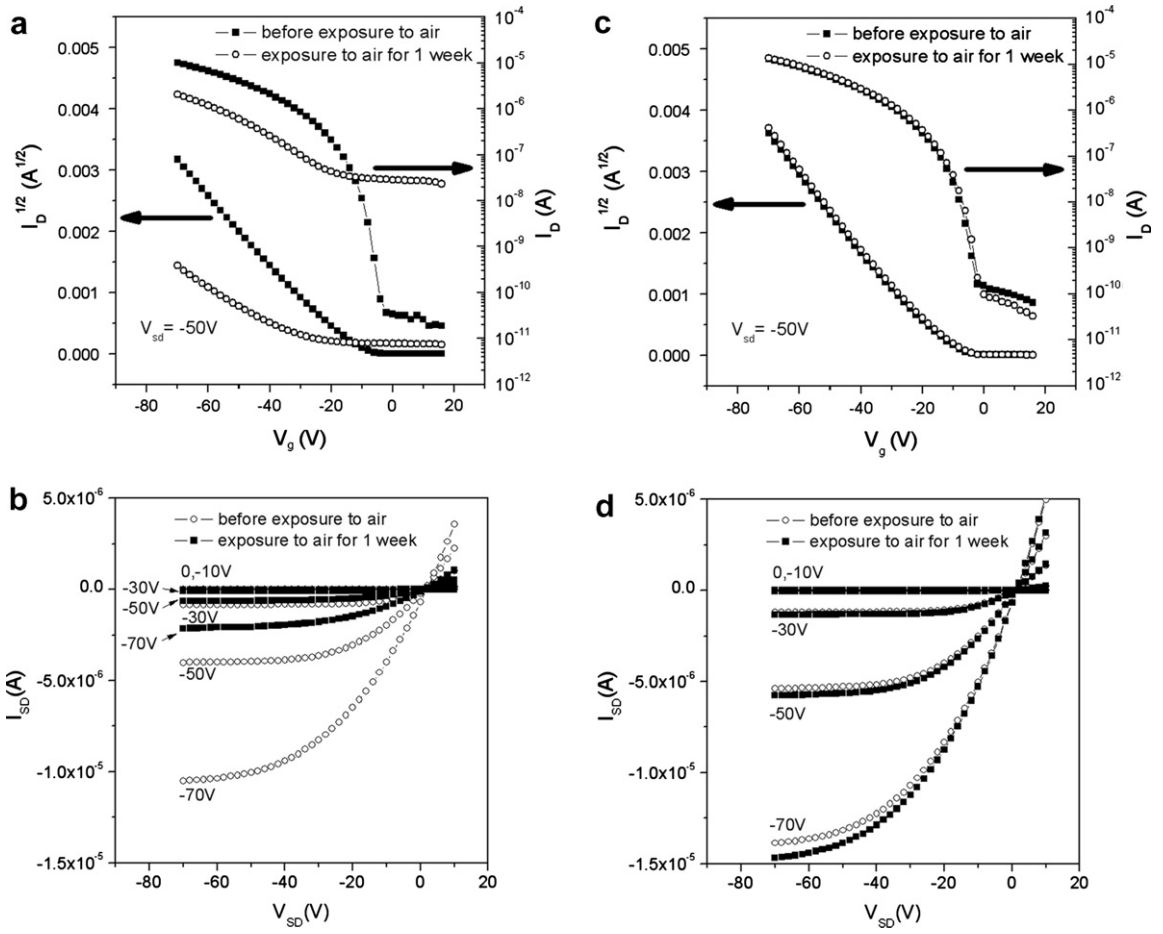

Fig. 4. Electrical characteristics of the pentacene OTFTs measured before and after exposure to air for one week. (a) Drain current (I_D) (right y-axis, logarithmic scale) and the square root of I_D (left y-axis) versus gate voltage (V_G) curves for the non-encapsulated OTFT. The data points were obtained while the gate voltage was scanned from +20 to −70 V. (b) Drain current (I_D) versus source–drain voltage (V_{SD}) curves for the non-encapsulated OTFT. The curves were obtained before and after one week of exposure to air. (c) I_D and the square root of I_D versus V_G curves for the encapsulated device (d) I_D versus V_{SD} curves for the encapsulated device.

shift in threshold voltage resulted in increased current, which has a positive effect on the operation of p-type transistors.

The level of shifting increased with increasing FEP film thickness up to 3 nm; beyond that level, the FEP film thickness effect became saturated. The enlarged images of the pentacene surface shown in Fig. 3b–g illustrate this effect. Fig. 3b is an AFM image of the flat substrate. The morphology of the surface passivated by FEP with different film thicknesses is shown in Fig. 3c–g: FEP molecules first form islands consisting of disordered lumps; with more FEP deposition, the size of islands grows, increasing domain-to-domain connectivity. The surface was completely covered by FEP when the thickness of the film reached 3 nm. No further shift of the threshold voltage was observed after full coverage of the surface was reached, showing that the shifting is more relevant to the coverage of FEP rather than to film thickness.

In another experiment, we also found that FEP passivation helps to encapsulate pentacene OTFTs without deterioration. In this experiment, the performance of the devices was not affected by PMMA coating (10 wt% in toluene) on the FEP-passivated pentacene transistor. Two FEP-passivated OTFTs were prepared: One was encapsulated with a polymer multilayer [PMMA/poly (urethane acrylate) (PUA)/poly (ethylene terephthalate) (PET)], and the other was used as a control. The encapsulation process for the FEP-passivated pentacene OTFT was as follows. The PMMA layer (1 μm) was spin-coated on the surface of the FEP-passivated pentacene OTFT at a speed of 3000 rpm for 30 s, and then annealed on a hot plate at 80 °C for 1 h. A droplet of UV-curable PUA was placed on the PMMA-coated surface, slightly pressed against a PET film, and cured under UV light (365 m, 350 $\mu W/cm^2$) for 1 min. The device was then taken out of the argon-purged box and exposed to an air environment. Fig. 4 demonstrates the current–voltage characteristics of the encapsulated and the non-encapsulated devices as measured before and after exposure to air for 1 week. The characteristic curves for the non-encapsulated device in Fig. 4a and b show on current values measured before and after exposure of 1.0×10^{-5} A and 2.1×10^{-6} A, respectively, and off current values of 3.2×10^{-11} A and 2.7×10^{-8} A, respectively. Mobility decreased from 0.12 $cm^2 V^{-1} s^{-1}$ to 0.05 $cm^2 V^{-1} s^{-1}$, and the on–off current ratios decreased from 3.2×10^5 to 7.7×10^2. In contrast, as shown in Fig 4c and d, the effect of oxygen and moisture on the encapsulated device was negligible. At a source–drain voltage of −50 V, the mobility values for the encapsulated device before and after exposure were 0.15 $cm^2 V^{-1} s^{-1}$ and 0.16 $cm^2 V^{-1} s^{-1}$, respectively. The on currents before and after exposure were 1.3×10^{-5} A and 1.4×10^{-5} A, respectively; with off currents of 1.2×10^{-10} A and 8.1×10^{-11} A, respectively. The on–off current ratios before and after exposure were also very similar. Thus, there was no noticeable change in performance of the encapsulated device after exposure to air for 1 week, whereas the non-encapsulated device showed serious degradation.

In summary, we have demonstrated that the deposition of non-charged FEP on the pentacene surface shifts the threshold voltage of the pentacene OTFT upward without diminishing the on–off current ratio and charge-carrier mobility. A slight increase of current was observed after the FEP deposition. The level of shift for the threshold voltage was closely related to the coverage of the pentacene surface by FEP. No further shifting was observed after complete coverage of the surface was reached at a thickness of 3 nm of FEP. We have also demonstrated that the encapsulation of the FEP-covered pentacene OTFT with a multilayer of PMMA/PUA/PET leads to prevention of deterioration of the device in an air environment for a period of at least 1 week.

Acknowledgments

This research was supported by the Kyungwon University Research Fund in 2007 and the Korea Science and Engineering Foundation (KOSEF) grant funded by the Korea government (MOST) (No. 2007-04373).

References

[1] H. Sirringhaus, N. Tessler, R.H. Friend, Science 280 (1998) 1741.
[2] P. Mach, S.J. Rodriguez, R. Nortrup, P. Wiltzius, J.A. Rogers, Appl. Phys. Lett. 78 (2001) 3592.
[3] B. Crone, A. Dodabalapur, A. Gelperin, L. Torsi, H.E. Katz, A.J. Lovinger, Z. Bao, Appl. Phys. Lett. 78 (2001) 2229.
[4] P. Peumans, S.R. Forrest, Appl. Phys. Lett. 79 (2001) 126.
[5] C.D. Dimitrakopoulos, P.R.L. Malenfant, Adv. Mater. 14 (2002) 99.
[6] S.Y. Park, M. Park, H.H. Lee, Appl. Phys. Lett. 85 (2004) 2283.
[7] K.K. Han, S.Y. Park, M.J. Kim, H.H. Lee, Appl. Phys. Lett. 87 (2005) 253502.
[8] D.J. Gundlach, T.N. Jackson, D.G. Schlom, S.F. Nelson, Appl. Phys. Lett. 74 (1999) 3302.
[9] Y.H. Noh, S.Y. Park, S.M. Seo, H.H. Lee, Org. Electron. 7 (2006) 271.
[10] J.H. Lee, G.H. Kim, S.H. Kim, S.C. Lim, Y.S. Yang, J. Oh, J.H. Youk, J. Jang, T. Zyung, Curr. Appl. Phys. 5 (2005) 348.
[11] M. Scharnberg, V. Zaporojtchenko, R. Adelung, F. Faupel, C. Pannemann, T. Diekmann, U. Hilleringmann, Appl. Phys. Lett. 90 (2007) 013501.
[12] S.H. Han, J.H. Kim, J. Jang, S.M. Cho, M.H. Oh, S.H. Lee, D.J. Choo, Appl. Phys. Lett. 88 (2006) 073519.

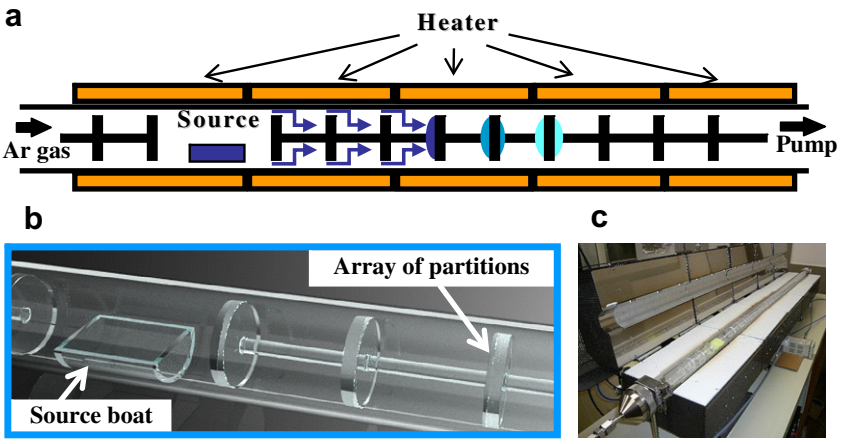

Fig. 1. (a) A schematic diagram of the new sublimation purification system where arrays of partitions is installed inside of the tube, and photographs of (b) the tube and (c) the new purification system.

from impurities is urgently needed for the realization of low-cost and high-performance organic electronic devices. In this paper, we report a new concept of sublimation purification system for the efficient separation of the target material from impurities; installing arrays of partitions in the sublimation tube.

Fig. 1 shows the new sublimation purification system schematically and photographs of the tube and the system. The five independent heating-bands control the temperature of the glass tube sectionally for the segregation of the deposition positions of target materials and impurities. Two arrays of partitions made of glass were installed inside of the 110 cm long pyrex tube; shorter one is near the inert gas inlet and the longer one is in the place of material deposition. This array of partitions promotes the separated deposition of target materials from impurities. The source boat was located at 15 cm far from gas inlet between two arrays of partitions. The Ar gas flow was controlled from 30 ml/min to 400 ml/min, and the pressure from 80 Pa to 0.1 MPa. With this new system, we have tried to purify some organic materials such as tris(8-hydroxyquinolinato) aluminum(III) (Alq_3) and 1,3-bis[2-(2,2′-bipyridine-6yl)-1,2,4-oxadiazol-5*yl*]benzene (Bpy-OXD), and compared with the result of the conventional method without the arrays of partitions.

In the conventional method, the purified materials are deposited on the inside wall of the tube rather broadly. For example, the deposition range of the purified Alq_3 was from 10 cm to 30 cm depends on the pressure and the gas flow, and some other materials seem to be impurities were deposited about 10 cm far or even continuously from the purified Alq_3 region. In the new method, the deposition range was from 5 cm to 15 cm for Alq_3 mainly depends on the gas flow; larger the gas flow broader the deposition range. We could not get any distinct relation between the deposition range and the pressure. However, there is no distinct difference in final yield after purification between the two purification methods. We are able to get about 70% materials after one cycle purification from about 1 g source materials from both of the methods. The purified materials are deposited on the inside wall of the tube and on the array of partition simultaneously in the new method; from 30% to 50% of the purified materials were deposited on the inside wall of the tube after the sublimation. Although the new purification system could not enhance the final yield, it clearly improved the purity of the purified materials as below described.

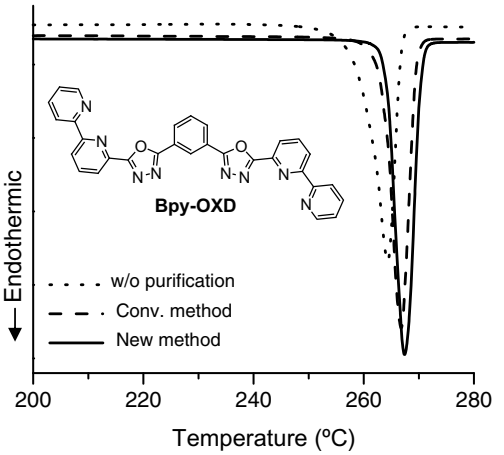

Fig. 2. Chemical structure of Bpy-OXD, and DSC curves of Bpy-OXD before (dot) and after purification by the conventional method (dash) and by the new method (solid).

Table 1
Summary of DSC and purity data of three kinds of Bpy-OXD

	T_m (°C)	Purity	
		From HPLC (%)	From DSC (mol%)
w/o Purification	264.3	99.04	98.4
Conventional method	266.8	99.37	99.7
New method	267.4	99.73	99.9

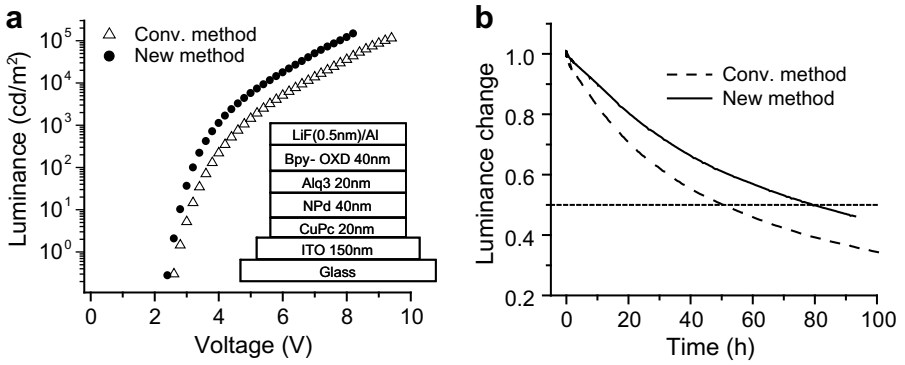

Fig. 3. (a) Luminance-voltage and (b) lifetime curves under 75 mA/cm^2 of EL cells made of two kinds of Bpy-OXD; purified by the conventional method (Δ, dash) and by the new method (●, solid). The inset in (a) shows EL cell structure used.

One of the results for Bpy-OXD was shown in Fig. 2 and Table 1. Fig. 2 shows the differential scanning calorimetry (DSC, Seiko Instruments, DSC6200) curves of three kinds of Bpy-OXD; raw material without further purification purchased from Hodogaya Chemicals, purified one by the conventional purification method without the array of partitions, and purified one by the new purification method. From the DSC data, we have calculated the purity of target materials using the simplified van't Hoff equation [12] expressed as follows:

$$T_0 - T = \frac{RT_0^2 x}{\Delta H_f} \times \frac{1}{F} \quad (1)$$

where T_0 is the melting point of the pure material, T is the temperature of the sample during melting, R is the gas constant, ΔH_f is the enthalpy of fusion of the pure material, x is the mole fraction of impurity, and F is the liquid fraction at T. The calculation process was explained elsewhere [12]. The calculated purity data were summarized in Table 1. For the comparison, we have also checked the purity by high-performance liquid chromatography (HPLC) [13], which were shown in Table 1 together. From both of data, it is clear that the new system improve the purity of Bpy-OXD. Although the difference of purity seems to be very slight, the difference of EL properties of those materials was very distinct.

Fig. 3 shows the luminance-voltage curves of EL cells made of two kinds of Bpy-OXD as the electron transport layer. From those curves, one can easily grasp that Bpy-OXD purified by the new system has much better electron transporting property than that purified by the conventional method. The turn-on voltage was lowered about 1 V to get a luminance of 1000 cd/m^2 by using Bpy-OXD purified by the new system; from 4.7 V to 3.9 V. Because impurities usually play charge traps or interrupt charge transporting, the enhancement of material purity by using the new system resulted in this large enhancement of luminance in EL cell. Note that the luminance efficiency of both devices are almost the same of about 11 cd/A.

We have also checked the lifetime of the cells, and Fig. 3 (b) shows the luminance changes under a constant current density of 75 mA/cm^2, where we chose a high current density to accelerate the test due to decreasing influences of extrinsic factors like defects of sealing. The half-life time was increased about 1.5 times (from 50 h to 79 h). Note that the test devices were encapsulated with a fresh desiccant in a highly inert glove box (dew point of below −50 °C and O_2 concentration of 5 ppm). This enhancement can be explained by the lowering of the driving voltage comes from the purity enhancement of Bpy-OXD. From these results, we can conclude that the new purification system was improved sufficiently to enhance the device performance largely by improving the purity of materials.

In summary, we developed a new sublimation purification system using arrays of partitions in the tube. Although the final yield was almost the same with that of the conventional method, the purity of material was improved as largely as the turn-on voltage of EL device was lowered about 1 V and the lifetime was increased about 1.5 times.

Acknowledgment

This work was supported by the Cooperative Link for Unique Science and Technology for Economy Revitalization (CLUSTER) and CLUSTER (the second stage) of Ministry of Education, Culture, Sports, Science and Technology, Japan.

References

[1] S.R. Forrest, Nature 428 (2004) 911.
[2] J.R. Sheats, J. Mater. Res. 19 (2004) 1974.
[3] C.W. Tang, S.A. Van Slyke, Appl. Phys. Lett. 51 (1987) 913.
[4] S.R. Forrest, Org. Elect. 4 (2003) 45.
[5] B. Geffroy, P. le Roy, C. Prat, Polym. Int. 55 (2006) 572.
[6] D.A. Pardo, N. Peyghambarian, G.E. Jabbour, Jpn. J. Appl. Phys. 40 (2001) 4922.
[7] O.D. Jurchescu, J. Baas, T.T.M. Palstra, Appl. Phys. Lett. 84 (2004) 3061.
[8] H.J. Wagner, R.O. Loutfy, C.-K. Hsiao, J. Mater. Sci. 17 (1982) 2781.
[9] W. Warta, R. Stehle, N. Karl, Appl. Phys. A 36 (1985) 163.
[10] C. –Y. Liu, A.J. Bard, Chem. Mater. 12 (2000) 2353.
[11] S.R. Forrest, Chem. Rev. 97 (1997) 1793.
[12] K. Yamamoto, M. Momota, H. Kiitamura, K. Narita, Anal. Sci. 12 (1996) 893.
[13] The experimental condition of HPLC is as follows; Column: Inertsil ODS-SP (5 μm, 4.6 × 250 mm), Carrier: CH_3CN: 0.05% TFAaq = 35: 65, Rate: 1 ml/min, Temp.: 40 °C, Det.: 254 nm.

not contribute to light emission, and it can also result in an enhanced non-radiative recombination due to interactions between the excitons and charge carriers. Moreover, charge transport is one of the main limiting factors in determining the operating voltage and the luminance efficiency. Therefore, understanding the relationship between molecular structure and charge transport properties of a material is a key point in providing guideline for device design.

The charge-transfer rate can be described by Marcus theory via the following equation [9,10]:

$$k_{et} = \frac{4\pi^2}{h}\frac{1}{\sqrt{4\pi\lambda k_B T}}t^2 \exp\left\{-\frac{(\Delta G^0 + \lambda)^2}{4\lambda k_B T}\right\} \quad (1)$$

where λ is reorganization energy, t is transfer integral, T is temperature, ΔG^0 is the free energy between the initial and the final sites, and h and k_B are the Planck and Boltzmann constants, respectively. For this study, all sites are equivalent, ΔG^0 is zero. Therefore, in terms of Eq. (1), there are two major parameters determining the charge-transfer rate: (i) the intermolecular transfer integral t, which should be maximized; and (ii) the reorganization energy λ, which needs to be small for the efficient transport.

1. Experimental

1.1. Synthesis and structure characterization

$BeSO_4 \cdot 4H_2O$ (1.2 mmol) was dissolved in 20 ml of deionized water in a flask. 2-(2-hydroxyphenyl)benzothiazolate (BTZ) (2.4 mmol) was dissolved in 40 ml of ethanol in another flask. The $BeSO_4 \cdot 4H_2O$ solution was slowly poured into the BTZ solution under stirring. $Be(BTZ)_2$ was precipitated after the mixed solution was adjusted to pH 9–10 using triethylamine at room temperature. The final yellow powder was purified by vacuum sublimation method. ^{1}H NMR ($CDCL_3$, δ, ppm): 8.23(2H, m); 8.12 (2H, m); 7.55(4H, m); 7.31 (2H, d); 7.05(2H, m); 6.88(2H, m); 6.79(2H, m). Anal. Calcd for $C_{26}H_{16}BeN_2O_2S_2$ (%): C, 67.66; H, 3.49; N, 6.07. Found: C, 67.64; H, 3.40; N, 6.13. FT IR (in KBr) (cm^{-1}) 3063, 1608, 1547, 1490, 1426, 1336, 1235, 1155, 1030, 951, 745, 671. The ^{1}HNMR spectrum was recorded on the Switzerland Bruker DRX300 spectrometers. Elemental analysis was performed on a Perkin-Elmer 240C elemental analyzer. FT-IR spectrum of the complex dispersed in KBr disks was recorded on Nicolet 7199B spectrometer. Diffraction intensities for $Be(BTZ)_2$ were collected at 183 K on a Bruker Smart CCD diffractometer (Mo Kα λ = 0.71073 Å). The crystal structure was solved by direct method with SHELXL97 program and refined with full-matrix least-squares method.

1.2. Calculation details

All the calculations were performed at the density functional theory (DFT) [11,12] with the Dmol3 program. The DND (the double numerical plus *d*-function) basis set and PW91exchange correlating function of general gradient approximate (GGA) were chosen (for selected optimized geometric parameters, see Table 2).

1.3. Device preparation

The OLED structure employed in this study was single layered. Emitting layer was fabricated by high-vacuum (10^{-4} Torr) thermal evaporation onto a glass substrate precoated with an indium-tin-oxide (ITO) layer. Prior to use, the ITO surface was ultrasonicated in a detergent solution followed by deionzed water rinse and dip into acetone. Aluminum was evaporated as cathode.

2. Results and discussion

2.1. Crystal structure

The single crystal of $Be(BTZ)_2$ was grown by vacuum sublimation in a tube furnace under a base pressure at 390 °C for 5 h. The colorless single crystal was collected at room temperature, with typical size of 0.20 × 0.20 × 0.10 mm. Crystal data, the details of data collection and refinements were summarized in Table 1. The crystal data for $Be(BTZ)_2$ are monoclinic, a = 24.522(3) Å, b = 12.0546(14) Å, c = 14.7981(17) Å, α = 90°, β = 93.476(2)°, γ = 90°; space group $C2/c$. The anhydrous $Be(BTZ)_2$ crystals have a monomer structure with one Be^{2+} ion center. The single crystal structure is described in Fig. 1. The selected bond lengths and bond angles are listed in Table 2. The Be^{2+} ion are four-coordinated to two 2-(2-hydroxyphenyl)benzothiazolate and have a distorted tetrahedral geometry. The Be–O distances are 1.571(4) Å/1.573(5) Å, which falls in the typical Be–O lengths (1.56–1.63 Å). Meanwhile, the Be–N bond lengths both are 1.743(5) Å, within the 1.65–1.80 Å range of Be–N bond. The N–Be–N and O–Be–O bond angles of 104.1(2)–115.7(3)° are all of typical values for tetrahedral geometry. The optimized structure parameters are in good agreement with the experimental data (in Table 2). Crystallographic data for the structure reported in this paper have been deposited with the Cambridge Crystallographic Data Centre as supplementary publication no. CCDC-620423. The data can be obtained free of charge from

Table 1
Crystal and structure refinement data for $Be(BTZ)_2$

	$Be(BTZ)_2$
Empirical formula	$C_{26}H_{16}BeN_2O_2S_2$
Fw	461.54
Cryst syst	Monoclinic
Space group	$C2/c$
a (Å)	24.522(3)
b (Å)	12.0546(14)
c (Å)	14.7981(17)
β (°)	93.476(2)
V Å^3	4366.3(9)
Z	8
F(000)	1904.0
D(calcd.) (mg m^{-3})	1.404
λ (Å)	0.71073
μ (mm^{-1})	0.271
Temperature (K)	273(2)
2θ range (°)	1.88–28.58
Final R indices ($I > 2\sigma(I)$)	$R1$ = 0.0576, $wR2$ = 0.1045
R indices (all data)	$R1$ = 0.1510 $wR2$ = 0.1308
Goodness-of-fit on $F_\lambda 2$	0.921

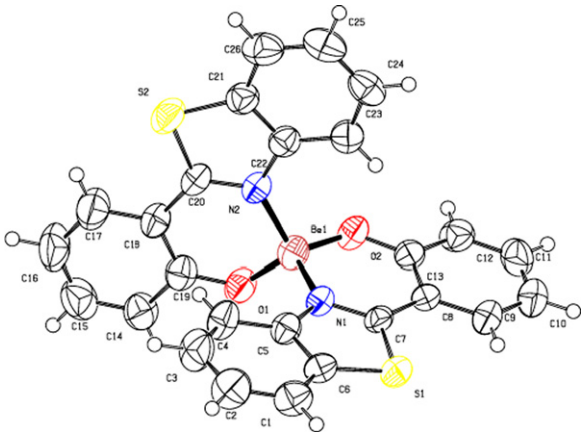

Fig. 1. Single crystal structure of $Be(BTZ)_2$.

www.ccdc.cam.ac.uk/conts/retrieving.html (or from the Cambridge Crystallographic Data Center, 12 Union Road, Cambridge CB 1EZ, UK; Fax: +44 1223 336 033; deposit@ccdc.cam.uk).

Table 2
Experimental and optimized structure parameters

Parameter	Exptl.	Cacld.
O(2)–Be(1)	1.571(4)	1.566
N(1)–Be(1)	1.743(5)	1.724
O(1)–Be(1)	1.573(5)	1.567
N(2)–Be(1)	1.743(4)	1.710
O(2)–Be(1) –O(1)	115.7(3)	115.66
O(2)–Be(1)–N(2)	111.9(2)	110.45
O(1)–Be(1)–N(2)	104.1(2)	104.79
O(2)–Be(1)–N(1)	105.2(2)	105.21
O(1)–Be(1)–N(1)	111.7(2)	112.16
N(2)–Be(1)–N(1)	108.2(2)	108.48

Bond lengths are reported in angstroms and bond angles in degrees.

2.2. Electronic structure

The features of the highest occupied molecular orbital (HOMO) and the lowest unoccupied molecular orbital

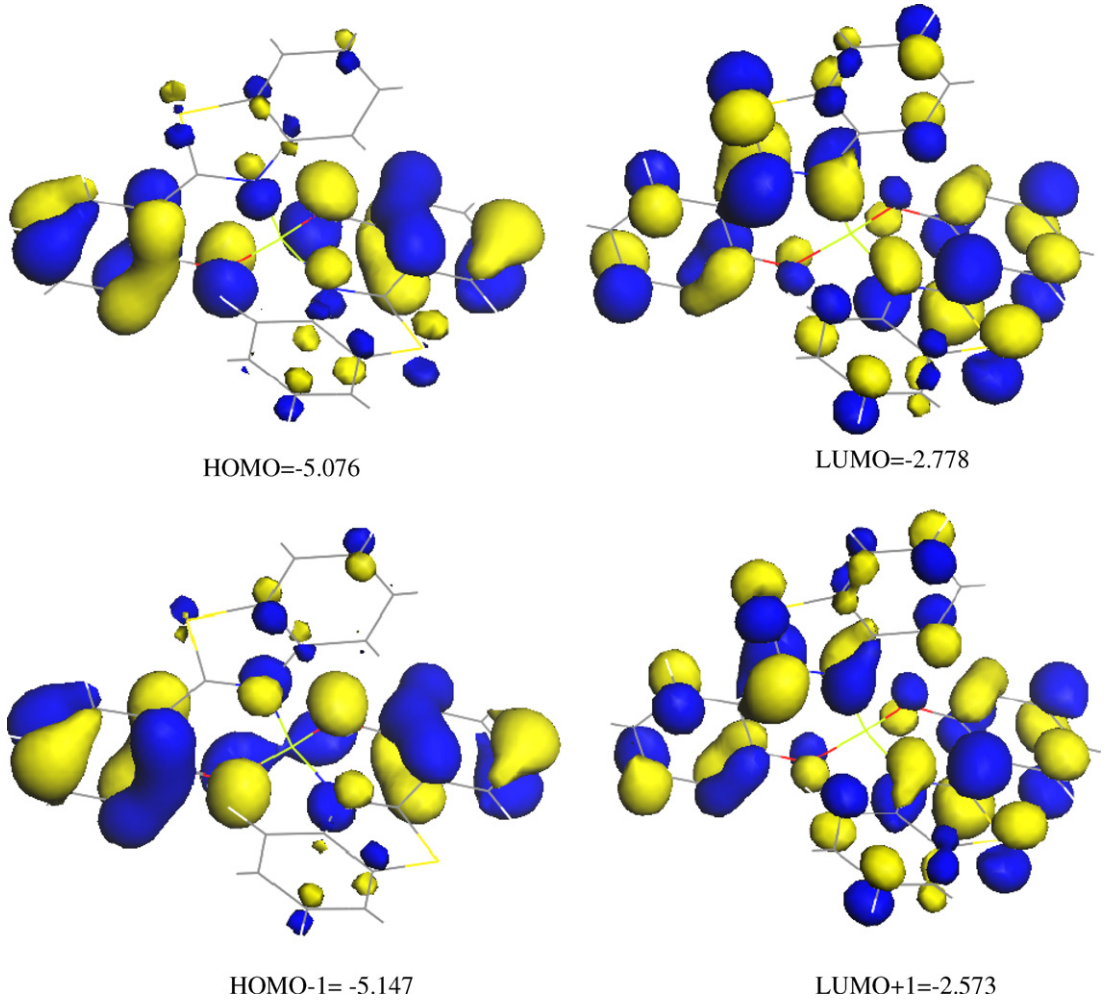

Fig. 2. Molecular Orbitals amplitude and corresponding values in HOMO, HOMO − 1, LUMO and LUMO + 1.

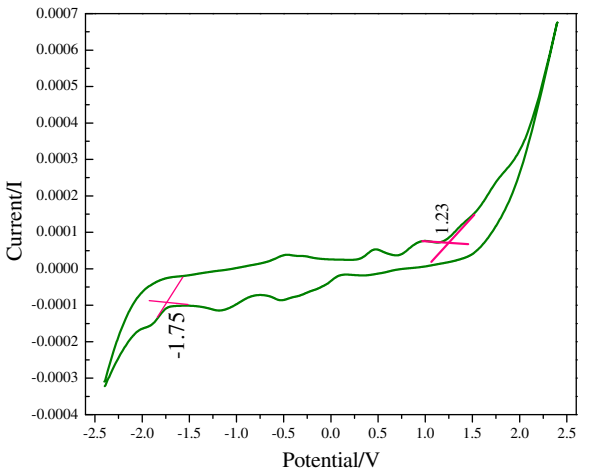

Fig. 3. Cyclic voltammograms of $Be(BTZ)_2$ in 0.1 M $TBAPF_6$, at a scan rate of 50 mv/s.

(LUMO) of $Be(BTZ)_2$ are presented in Fig. 2. The HOMO density is mostly located on the phenoxide site, in particular, at C13 and C19 of ligand. Accordingly, the LUMO density can be found at the phenoxide and thiazolyl rings. The contribution of Be^{2+} ion to orbitals is vanishing, indicating that the π–π^* transition occurs from phenoxide to thiazolyl.

The emission color of the organic materials is a function of HOMO–LUMO energy gap (E_g) of electroluminescent molecule. In addition, the charge injection barriers are due largely to energy differences between the work function of the electrodes and energy of the HOMO or LUMO (E_{HOMO} or E_{LUMO}) in organic material. The empirical values of E_{HOMO} or E_{LUMO} can be obtained by cyclic voltammetry, which is one of the simplest and most practical methods to give much information needed to reveal the electronic structures of materials. Oxidation potential (E_0^{ox}) and reduction potential (E_0^{red}) were measured directly by cyclic voltammetry (Autolab/PG STAT302). The values of E_0^{ox}, E_0^{red} are 1.23 V and −1.75 V, respectively (in Fig. 3). Therefore, E_{HOMO} is −5.97 eV, and E_{LUMO} is −2.99 eV in terms of Eq. (2) [13] below the vacuum energy level. E_g is calculated to be 2.98 eV as $E_g = E_{LUMO} - E_{HOMO}$.

$$E_{HOMO}/E_{LUMO} = -(E_0^{ox}/E_0^{red} + 4.74)\ eV \quad (2)$$

The calculated values of E_{HOMO}, E_{HOMO-1}, E_{LUMO}, E_{LUMO+1} and E_g are −5.076 eV, −5.147 eV, −2.778 eV, −2.573 eV and 2.298 eV, respectively. Theoretical values, within the tolerance of calculation, are in agreement with measured values.

Table 3
Calculated variations of structural parameters in both cation and anion relative to the neutral molecule and their total energy

Parameters	Cation	Anion
N(1)–Be(1)	−0.02	−0.01
N(2)–Be(1)	−0.02	−0.01
O(2)–Be(1)	0.01	0.009
O(1)–Be(1)	0.01	0.008
Total energy/Ha	−2071.478	−2071.766

Bond lengths are reported in angstroms.

2.3. Charge-transfer property

The structural and electronic properties of both the anion and the cation were studied by DFT in order to reveal the effect of charge injection on the molecular conformational stability. The neutral state will become cation when a hole is injected into and will become anion when an electron is trapped. The bond strength parameters of optimized neutral state was used as reference and was set to zero, the others with respect to this reference are listed in Table 3. The reorganization energy λ corresponds to the sum of geometry relaxation energy upon going from the neutral state geometry to the charge-state geometry, or vice versa. The geometry modifications upon cation are more pronounced (Be–N: 0.02 Å; Be–O: 0.01 Å) than upon anion (Be–N: 0.01 Å; Be–O: 0.0085 Å). This indicates that adding a hole has stronger effect than adding an electron. It is rationalized that the reorganization energy of anion is much smaller than that of cation by the fact of geometry modifications. In addition, the charge-transfer integral t is equal to the half of energy splitting values between E_{HOMO} and E_{HOMO-1} (for hole carrier) or between the E_{LUMO} and E_{LUMO+1} (for electron carrier). The value of t_h is 0.071 eV and t_e is 0.205 eV. Thereby, the electron-transfer rate is larger than hole-transfer rate according to Eq. (1). From the view of energy, the total energy of neutral state is −2071.7139825Ha. The total energy of anion is smaller (as seen in Table 3). Therefore, it is reasonable that the anion of $Be(BTZ)_2$ is of the most stability. This indicates that electron-transfer property of $Be(BTZ)_2$ is of advantage over hole-transfer property.

2.4. Optical property

PL and EL spectra are almost identical, as can be seen in Fig. 4 PL of powder and EL spectra of single layer structured device of $Be(BTZ)_2$ were measured. PL emission maximum is located at 456 nm and maximum value of EL emission is at 460 nm.

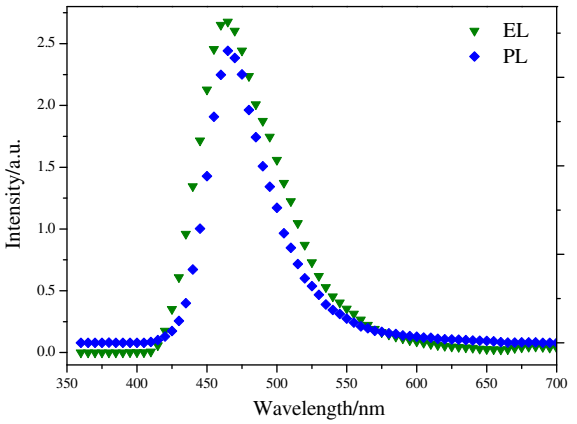

Fig. 4. The PL spectrum (♦) of powder and EL spectra (▼) of device (Device structure: ITO/Be(BTZ)2/Al).

Compared with PL wavelength of $Be(BTZ)_2$ powder, EL spectrum has a very small red shift of 4 nm and a bigger FWHM (full wave at half maximum) (PL: 48.9 nm, EL: 61.9 nm). This difference is resulted from the congregated molecular state. Intermolecular interaction is very weak for powder due to the larger intermolecular distance. The CIE coordinates for single layer structured device are $X = 0.1525$, $Y = 0.1803$.

In summary, the single crystal of $Be(BTZ)_2$ was grown by the vacuum sublimation method. The details of the single crystal structure, electronic structure, charge-transfer and luminescent properties were studied. The conclusions indicate that the crystal of $Be(BTZ)_2$ is monoclinic, space group $C2/c$, $a = 24.522(3)$ Å, $b = 12.0546(14)$ Å, $c = 14.7981(17)$ Å, $\alpha = 90°$, $\beta = 93.476(2)°$, $\gamma = 90°$. According to density functional theory calculations on $Be(BTZ)_2$, the HOMO is located largely on the phenoxide and the LUMO mainly distributes on the phenoxide and thiazolyl rings. $Be(BTZ)_2$ is a good electron-transport material. In terms of the EL spectrum, the wavelength of emission is localized in blue light region. Therefore, it would be a good candidate for luminescent material.

Acknowledgements

This work was financially supported by National Natural Scientific Foundation of China (20671068); Natural Science Foundation of Shanxi Province (20041066); Shanxi Scientific Research Foundation for Returned Scholars (200523); Scientific and Technical Key Project of Shanxi (2006031121).

References

[1] M. Gross, D.C. Muller, U. Scherf, S. Ulrich, D. Neher, C. Brauchle, K. Meerholz, Nature 405 (2000) 661.
[2] B. S Xu, Y.Y. Hao, X. H Fang, H. Wang, X.G. Liu, Appl. Phys. Lett. 90 (2007) 053903.
[3] B.S. Xu, H.X. Xu, L.Q. Chen, X.H. Fang, X.G. Liu, H. Wang, Org. Electron. 9 (2008) 267.
[4] Z.L. Shen, P.E. Burrows, V. Bulovic, S.R. Forrest, M.E. Thompson, Science 276 (1997) 2009.
[5] M. Brinkmann, G. Gadret, M. Muccini, C. Taliani, N. Masciocchi, A. Sironi, J. Am. Chem. Soc. 122 (2000) 5147.
[6] J. Hullger, Angew. Chem. 106 (1994) 151.
[7] X.M. Zhang, M.L. Tong, X.M. Chen, Angew. Chem. Int. Ed. 41 (2002) 1029.
[8] G.C. Yang, Y. Liao, Z.M. Su, H.Y. Zhang, Y. Wang, J. Phys. Chem. A 13 (2006) 1286i.
[9] R.A. Marcus, Rev. Mod. Phys. 65 (1993) 599.
[10] B. Jason, B. Yelizaveta, L. Sergey, I.D. Peter, T. Irina, B. Robert, E.T. Mark, Inorg. Chem. 41 (2002) 3055.
[11] M.H. Ho, C.M. Chang, T.Y. Chu, T.M. Chen, C.H. Chen, Org. Electron. 9 (2008) 101.
[12] G. Yu, S.W. Yin, Y.Q. Liu, Z.G. Shuai, D.B. Zhu, J. Am. Chem. Soc. 125 (2003) 14816.
[13] Y.S. Yao, J. Xiao, X.S. Wang, Z.B. Deng, B.W. Zhang, Adv. Funct. Mater. 16 (2006) 709.

are reported. In recent years, impedance spectroscopy has showed to be a powerful tool to investigate the behavior of multilayer devices, disclosing the contributions of the different layers and the related interfaces [10,11]. The structure of the investigated devices is depicted in Fig. 1a. Glass substrates covered with 120 nm thick ITO patterned strips were used for ITO based devices. LSMO films (40 nm thick) were grown by pulsed electron deposition (pulsed plasma enhanced configuration – PPD) on $SrTiO_3$ substrates, through a shadow mask with a width of approximately 1 mm. LSMO films grown by PPD have been extensively investigated [9,12], showing typical room temperature conductivity of 10^2 S/cm and Curie T_c temperatures of about 340 K. Magnetic properties of LSMO films were checked by Magneto-Optical Kerr Effect (MOKE) and found to be in accordance with the existing literature. For any evaporation run, one ITO and one LSMO sample were introduced together in the chamber after a rinse in acetone and isopropanol ultrasonic bath. Before the deposition, the samples were annealed following the procedures established by XPS investigations [12], in order to remove the surface carbon contamination and to restore the surface oxygen stoichiometry in LSMO films. Then, 80 nm thick Alq3 (SIGMA–ALDRICH) films were deposited on ITO and LSMO substrates at room temperature, by sublimation from a Knudsen cell at 10^{-8} to 10^{-9} mbar and growth rate of 0.1–0.2 Å/s. Finally, Al films (~60 nm thick) were evaporated on the top of Alq3 by using a shadow mask to obtain the final crossbar structure. The device area was 1 mm^2 and, hence, all the reported magnitudes are referred to this value.

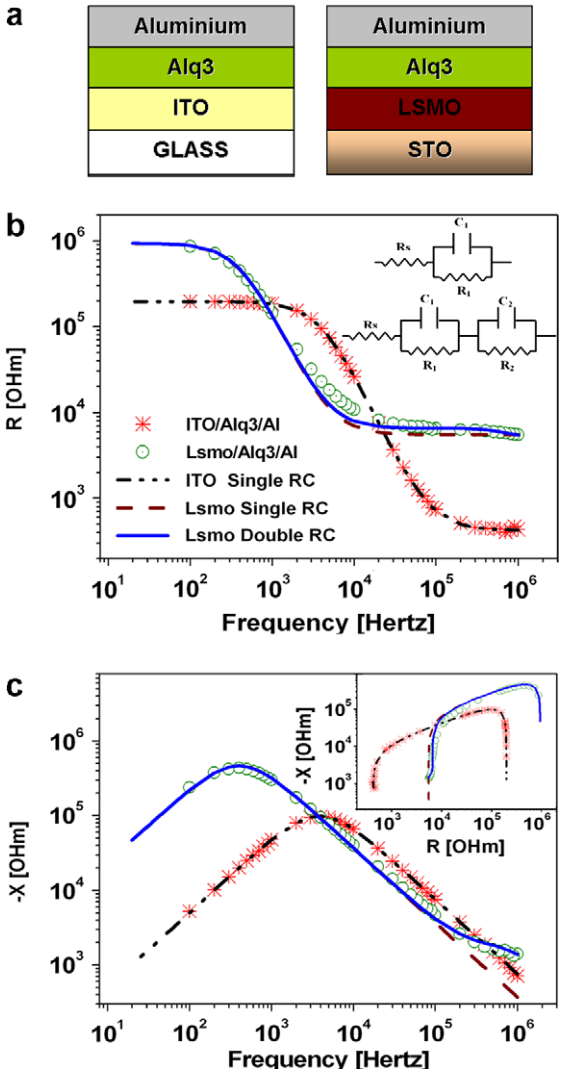

Fig. 1. (a) Structure of the investigated devices, (b) real and (c) imaginary parts of the complex impedance of ITO/Alq3/Al and LSMO/Alq3/Al devices, compared with the fitting curves obtained by the equivalent circuits in the inset in Fig. 1b. In the inset in Fig. 1c, the impedance spectra are reported in a log–log Nyqvist plot.

Impedance spectra were collected in vacuum by an Agilent LCR meter, mounting the samples in a cryogenic probe station or in a closed cycle cryo-generator equipped with RF probes [13,14]. The oscillating voltage in measuring process was fixed at 100 mV, in order to test the device response in the injection limited current regime where MR phenomena are usually investigated [8]. We have focused on Alq3, since, so far, the combination LSMO/Alq3 showed to provide the most interesting results in organic spintronics, even if an exhaustive explanation for this occurrence is still lacking. Furthermore, the widely investigated behaviour of ITO/Alq3/Al devices, which were used in many cases to analyze the Alq3 intrinsic electrical parameters, represents a reliable reference to evidence the features related to the LSMO/Alq3 interface [11,15–18].

Room temperature real and imaginary parts of the complex impedance, $Z(f) = R(f)+jX(f)$ for two typical ITO/Alq3/Al and LSMO/ALq3/Al structures are shown in Fig. 1b and c, respectively. The inset in Fig. 1c represents the same curves in a log–log Nyqvist plot. For both structures, $R(f)$ spectra stay constant in the low frequency range even if at different values. Then, $R(f)$ begin to decrease rapidly as frequency is increased. The corresponding −3 dB cut-off frequencies are 400 Hz and 3.5 KHz for LSMO and ITO based devices, respectively. These differences are also reflected in the position of local maxima in $-X(f)$ spectra. The non zero values of $R(f)$ in the upper frequency edge reveal a limiting resistance Rs, which has been estimated to be 300 Ohm for ITO structures and about 5 KOhm for LSMO ones. For comparison, it is clear that the distinguishing features of the LSMO/Alq3/Al device can only be ascribed to the peculiar properties due to the combination between LSMO and Alq3.

With the aim to better address this fundamental issue, the equivalent circuits in the inset in Fig. 1b have been considered to fit the experimental impedance measurements. The fitting curves are also reported in Fig. 1b and c. As shown, the ITO device ac response is well fitted by a single circuit, involving a parallel resistor R_1 and a capacitor C_1, with the Rs in series. This description is in agreement with previous studies, where the ITO/Alq3/Al response has been investigated also as function of temperature and applied bias voltages [15–18]. In our case, R_1 (coinciding with $R(f)$ value at low frequencies) is about 200 KOhm and the extracted equivalent conductivity (4×10^{-9} S/cm) is very close to the data reported in Ref. [15].

On the contrary (see the dashed lines in Fig. 1b and c), the same equivalent circuit is not suitable to describe the impedance measurements of LSMO/Alq3/Al structures, where, for all investigated devices, the ac response shows a peculiar behavior in the frequency region above 100 KHz. Indeed, both $R(f)$ and $-X(f)$ spectra exhibit a slope change at high frequencies, so that adding an extra R_2C_2 component (continuous line) to the above discussed equivalent circuit improves considerably the fitting. This slope change is particularly clear in the $-X(f)$ spectrum which is not sensitive to the value of the in series resistance Rs. For the investigated devices, R_2 was about 1.5 KOhm, while C_2 ranged between 180 pF and 210 pF. By comparison with the ITO device, it comes out the conclusion that the R_2C_2 component has to be attributed to the specific electrical properties of the interface region between LSMO and Alq3.

It seems clear that, despite the nominally similar work function values (4.8–4.9 eV), ITO and LSMO form considerably different interface regions with Alq3. Once again, this experimental evidence confirms that the simple energy barrier heights, coming from the energy gap between the clean electrode work function and the molecular HOMO or LUMO values, offer only a simplified scenario to describe the electrical properties of every specific interface.

The alignment of the energy levels at both ITO/Alq3 and LSMO/ALq3 interfaces has been recently investigated by X-ray (XPS) and ultraviolet (UPS) photoemission spectroscopy studies [19,9]. These accurate analysis disclosed the occurrence of a significant vacuum level shift (0.9 eV) between LSMO and Alq3, indicating the presence of a strong interface dipole. On the contrary, the same effect is much more limited for ITO/Alq3 interface, where the dipole strength is only 0.1 eV. Considering the annealing procedure followed for our LSMO films before the deposition of the organic film [12], we are able to rule out that the LSMO/Alq3 dipole is due to extrinsic effects such as a contamination layer or unwanted chemical reactions [20]. Although the occurrence of large interface dipoles between organic and conducting electrodes seems to be a general feature of many interfaces, their physical origin is still widely debated in literature and many intrinsic factors (charge transfer, orientation of permanent dipoles, band bending, i.e.) have been invoked to provide an explanation for this phenomenon [21]. To this regard, as far as Alq3 is concerned, the specific polar properties of the molecule have usually been cited to justify its widespread capability to produce interface dipoles. Recent experiments seem to prompt a basic scenario where a density of intermediate states, energetically localized between the electrode Fermi level and the Alq3 LUMO, is induced by the presence of the interface local dipoles [22]. More specifically, a direct relation between the interface states energy distribution parameters and the disorder level of the dipole layer was also found. This occurrence has been demonstrated to strongly affect the charge injection process in the related devices, with the supposed possibility to generate even different conducting states as a function the applied electric field [23].

Despite the agreement with many experimental studies, further research is needed to develop this general theoretical framework and to clarify, in particular, the role of the specific electrode surface electronic properties in affecting the dipole formation and its strength. Recent models suggest that the interface states induction can be considerably mediated by the density of states near the Fermi level of the considered electrode [24]. Although further investigations are required, we believe the R_2C_2 contribution is the electrical representation of the interface charge distribution and the consequent local field related to the interfacial dipole. This result reflects the importance of ac conductivity measurements as a new way of investigating interface physics.

Depending on the sample, R_1 parameter values range between 400 KOhm and 900 KOhm for LSMO devices, thus resulting always larger than the values evaluated for ITO devices. Independent DC measurements (not shown here) confirm this result. Similarly C_1 values (between 350 pF and 400 pF) in LSMO devices are higher than that deduced for ITO devices (220 pF).

In order to further examine the electrical properties of the interface between LSMO and Alq3, impedance spectra of the LSMO/Alq3/Al devices have been also recorded at different temperatures between 295 K and 35 K. These measurements reported in Fig. 2a and b evidence the different temperature dependences in the low and high frequency range, where the contribution of series resistance

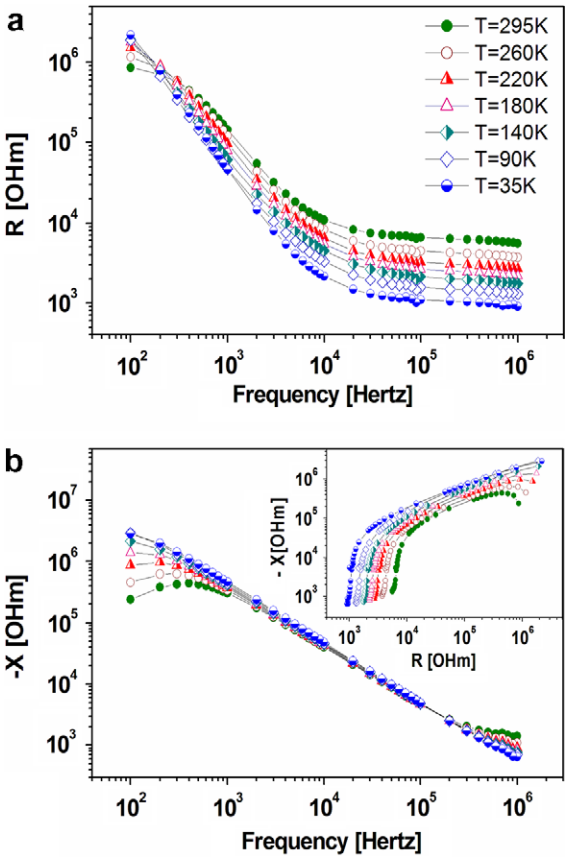

Fig. 2. (a) Real and (b) imaginary parts of impedance spectra recorded for LSMO/Alq3/Al device at different temperatures. In the inset in Fig. 2c, the same spectra are reported in a log–log Nyqvist plot.

Rs and of R_2C_2 component become dominant. To clarify the specific temperature dependence of the various components, the experimental curves have been fitted by the equivalent circuit at any investigated temperature.

Fig. 3 reports the obtained R_1 and R_2 temperature dependence, while the log–log Nyqvist plot of the experimental impedance spectra between 100 KHz and 1 MHz and the corresponding fitting curves is shown in the inset in Fig. 3. Interestingly, the data reveal the complementary behavior of R_1 and R_2. The former follows a semiconducting trend and its value increases up to 5 MOhm at cryogenic temperatures, supporting the idea that R_1 is mainly related to the organic film electrical properties. On the contrary, R_2 temperature dependence is metallic-like and its value is about 400 Ohm at 35 K. A complementary behavior is also followed by C_1 and C_2, since the former decreases of 30% from room temperature to 35 K and the latter tends to increase of about 20% in the same range.

Following the basic assumption of the proposed circuit geometry (see Fig. 1b), the R_2C_2 component is related to the electrical properties of the interface region between LSMO and Alq3. The metallic-like temperature dependence of the parameter R_2 is apparently quite surprisingly and, so far, there are not any available models able to explain it. Nevertheless, such behavior has been reported in many LSMO based devices, both fully inorganic [25,26] and organic–inorganic devices. Just as an example, it has been found that LSMO/polymer based organic light-emitting diodes showed metallic-like temperature behavior [27], while the light emission was proportional to the electrical current, thus ruling out the short circuits occurrence. While additional investigations are required in order to reveal the basis of this behavior, we can speculate on the influence of the peculiar band structure of the manganite close to the Fermi level. As the metallic character of LMSO is strongly increased when the temperature is reduced, it is expected to lead to considerably higher injection efficiency at low temperatures. At higher temperatures, the metallic characteristics become increasingly complicated as the metal-insulator transition is approached at around 340 K. Focusing on this subject, it is to remember that the temperature dependence of the spin valve effect has not been satisfactorily explained so far. Usually, MR values decrease drastically with temperature and the phenomenon is explained by invoking the corresponding LSMO superficial magnetization reduction. Fine details are elusive and, up to date, the question seems still open. To this regard, in Fig. 4, we compare our experimental MR temperature dependence (symbols) with LSMO superficial magnetization variation with temperature (dashed line), as obtained from existing literature, in particular from the seminal paper of Park et al., in which magnetization in the superficial 5 Å of a LSMO film was measured by spin-resolved photoemission spectroscopy [28]. Although the superficial magnetization data is indeed coming from a different sample, this kind of behavior is accepted in the community. As shown, the quantitative agreement between both trends is very poor.

In the attempt to overcome this limitation and motivated by recent theoretical studies suggesting the direct proportionality relation between the spin injection efficiency and the interfacial conductivity in manganite/organic systems [29], we tentatively present here a phenomenological model where the interface effect is combined with LSMO magnetization to explain the MR behavior with temperature. To this end, the implicit basic assumptions that both the spin diffusion time inside the organic and the spin injection efficiency of the Cobalt electrode decrease very weakly with temperature in the interval studied [4], are reasonably satisfied.

Then, magnetoresistance MR_{th} temperature dependence has been directly expressed by $MR_{th} = M_{sup} \times G_{int}$, where M_{sup} is LSMO superficial magnetization and G_{int} is the interfacial conductance given by $1/R_{2N}$. Here, R_{2N} is the LSMO/Alq3 interfacial resistance normalized at $T = 20$ K, as extracted from R_2 data in Fig. 3. R_1 is not taken into account in the model, since, as we have demonstrated above, it represents a contribution coming from the bulk of the organic semiconductor. The theoretical MR_{th} data (solid line) calculated by our model are also plotted in Fig. 4.

Although this very simple model cannot aim to contain all the relevant and complex physics of spin injection from

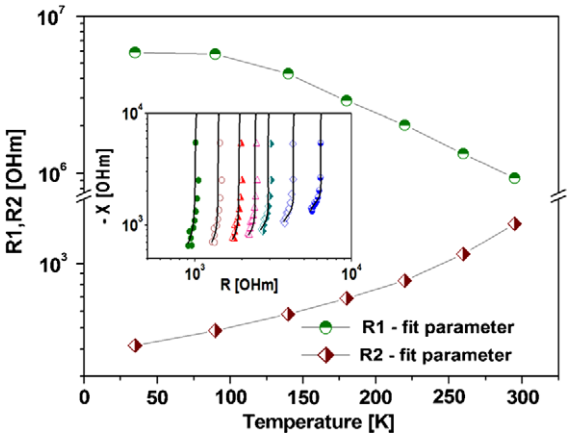

Fig. 3. Temperature dependence of R_1 and R_2 for LSMO/Alq3/Al equivalent circuit. In the inset, high frequency impedance spectra (symbols) and fitting (solid) curves are reported in a log–log Nyqvist plot.

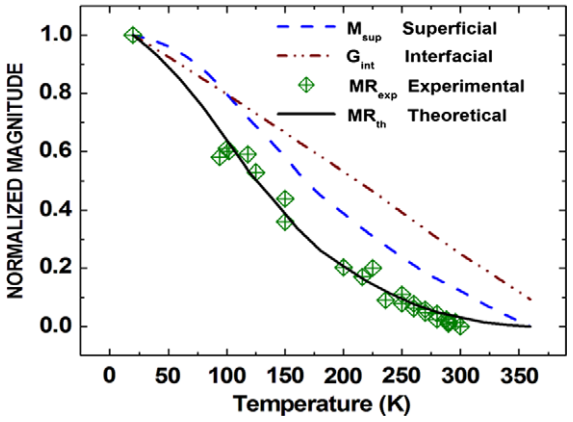

Fig. 4. Experimental (symbols) MR temperature dependence compared with the theoretical data (solid line) calculated by multiplying superficial magnetization M_{sup} (dashed line, Ref. [28]) with the normalized interfacial conductance G_{int} (dash dot line).

manganites into organic semiconductors, the good quantitative agreement between experimental and predicted MR_{th} data obtained in this case confirms the importance of the interfacial resistance in the interpretation of magnetoresistance data for organic spin valves.

In summary, the electrical properties of the LSMO/Alq3 interface region were investigated by comparing impedance measurements on ITO/Alq3/Al and LSMO/Alq3/Al devices. The presence of an interfacial resistance is associated with the interfacial dipole between LSMO and Alq3. The temperature dependence of this resistance evidences the complex character of the half-metal/organic hybrid systems and gives some indication of the critical issues for the development of organic spintronics. In this line, a simple model is presented to show how this occurrence affects the final magnetoresistance response of LSMO/Alq3 hybrid structures. Further studies, in which the intrinsic molecular dipole and hence the interfacial resistance could be modified by deposition parameters, are envisaged.

Acknowledgement

L.E.H, P.G and V.D. acknowledge financial support from EU OFSPIN project. M.B, A.C. and P.D. are partially supported by the MIUR PRIN 2007 "Microfluidi e tecniche di processo per la realizzazione di dispositivi Lab-on-chip". Important support from Ilaria Bergenti, Yiqiang Zhan, Carmela Aruta and Federico Bona is also gratefully acknowledged.

References

[1] V. Dediu, M. Murgia, F.C. Matacotta, C. Taliani, S. Barbanera, Sol. State Commun. 122 (2002) 181.
[2] Z.H. Xiong, Di Wu, Z.V. Vardeny, J. Shi, Nature 427 (2004) 821.
[3] A. Riminucci, I. Bergenti, L.E. Hueso, M. Murgia, C. Taliani, Y. Zhan, F. Casoli, M.O. de Jong, V. Dediu, arxiv:cond-mat/0701603.
[4] F.J. Wang, C.G. Yang, X.G. Li, Z.V. Vardeny, Phys. Rev. B 75 (2007) 245324.
[5] W. Xu, G.J. Szulczewski, P. LeClair, I. Navarrete, R. Schad, G. Miao, H. Guo, A. Gupta, Appl. Phys. Lett. 90 (2007) 072506.
[6] S. Majumdar, E. Laiho, P. Laukkanen, I.J. Varrynen, H.S. Majumdar, R. Obsterbacka, Appl. Phys. Lett. 89 (2006) 122114.
[7] D. Wu, Z.H. Kiong, X.G. Li, Z.V. Vardeny, J. Shi, Phys. Rev. Lett. 95 (2005) 016802.
[8] L.E. Hueso, I. Bergenti, A. Riminucci, Y. Zhan, V. Dediu, Adv. Mater. 19 (2007) 2639.
[9] Y.Q. Zhan, I. Bergenti, L.E. Hueso, V. Dediu, M.P. de Jong, Z.S. Li, Phys. Rev. B 76 (2007) 045406.
[10] J. Mc Donald, E. Barsoukov, Impedance Spectroscopy: Theory, Experiments and Applications, John Wiley & Sons, 2005.
[11] W. Brutting, S. Berleb, A.G. Muckl, Org. Elec. 2 (2001) 1.
[12] M.P. de Jong, V. Dediu, C. Taliani, W.R. Salaneck, J. Appl. Phys. 94 (2003) 7292.
[13] P. D'Angelo, M. Barra, M. Nicodemi, A. Cassinese, J. Appl. Phys. 101 (2007) 044910.
[14] M. Barra, M. Biasiucci, P. D'Angelo, A. Cassinese, A.C. Barone, A. Carella, A. Rovello, J. Appl. Phys. 102 (2007) 093712.
[15] A. Moliton, W. Rammal, B. Lucas, Eur. Phys.: J. Appl. Phys. 33 (2006) 175.
[16] A. Moliton, W. Rammal, B. Lucas, Eur. Phys. J. Appl. Phys. 32 (2005) 95.
[17] J.H. Ahn, J.U. Lee, T.W. Kim, Curr. Appl. Phys. 7 (2007) 509.
[18] V.M. Silva, S.K. Mendiratta, L. Pereira, J. Non-Cryst. Solid 352 (2006) 1652.
[19] A.S. Wan, A.J. Makinen, P.A. Lane, G.P. Kushto, Chem. Phys. Lett. 446 (2007) 317.
[20] M. Grobosh, K. Dorr, R.B. Gangineni, M. Knupfer, Appl. Phys. Lett. 92 (2007) 023302.
[21] H. Ishii, K. Sugiyama, E. Ito, K. SEki, Adv. Mater. 11 (1999) 605.
[22] M.A. Baldo, S.R. Forrest, Phys. Rev. B 64 (2001) 085201.
[23] I. Thurzo, H. Mendez, C. Iacovita, D.R.T. Zhan, Synth. Metals 156 (2005) 1108.
[24] H. Vazquez, F. Flores, A. Khan, Org. Elec. 8 (2007) 241.
[25] M.-H. Jo, N.D. Marthur, N.K. Todd, G. Blamire, Phys. Rev. B 61 (2000) R14905.
[26] Y. Ishii, H. Yamada, H. Sato, H. Akoh, Y. Ogawa, M. Kawasaki, Y. Tokura, Appl. Phys. Lett. 89 (2006) 042509.
[27] A. Hayer, A. Kohler, E. Arisi, I. Bergenti, A. Dediu, C. Taliani, M. Al-Suti, M.S. Kahn, Synth. Metals 147 (2004) 155.
[28] J.H. Park, E. Vescovo, H.J. KIm, C. Kwon, R. Ramesh, T. Venkatesan, Phys. Rev. Lett. 81 (1998) 1953.
[29] J.F. Ren, J.Y. Fu, D.S. Liu, L.M. Mei, S.J. Xie, J. Appl. Phys. 98 (2005) 074503.

thin film and Alq_3/Al interface and explain the experimental results obtained. Besides, the simple structure of the reported device indicates that it can be easily embedded into the well-developed semiconductor fabrication processes.

2. Experiments

The bistable device consists of an organic layer interposed between two electrodes. The fabrication process of the device is described as follows. First, a 150-nm-thick Alq_3 organic layer is deposited on a cleaned 1 Ωcm resistivity n-type silicon wafer by thermal deposition method in a vacuum below 3×10^{-6} Torr at room temperature. Then an 80-nm-thick aluminum top-electrode is deposited on the organic layer through a shadow mask. The size of each Al electrode is 0.64 mm^2. The deposition rates of the Alq_3 thin film are 0.05 nm/s, 0.15 nm/s, 0.2 nm/s, and 0.3 nm/s. The deposition rate is controlled by the setting temperature of the crucible and the corresponding setting temperature for each deposition rate is listed in Table 1. The current–voltage (I–V) characteristics are measured using a Hewlett Packard 4156A semiconductor parameter analyzer in an ambient environment. The capacitance–voltage (C–V) characteristics are recorded by an Agilent 4284A Precision LCR meter at a frequency of 1 MHz and amplitude of 25 mV. The surface morphology of the Alq_3 thin film on the Si wafer is obtained by using an atomic force microscope (AFM, DI-Veeco Instruments). The composition in the Alq_3/Al and the atomic concentration of the Alq_3 are analyzed using X-ray photoemission spectroscopy (XPS), while structural information is obtained via gracing incidence X-ray diffraction (GIXRD) analysis.

3. Results and discussion

Fig. 1 shows typical I–V characteristics of the fabricated Al/Alq_3/n-type Si structure. As can be seen, this device exhibits two different conductance states at an identical applied voltage. The silicon electrode is kept at 0 V, and all bias conditions are applied on the aluminum electrode. At the first bias (black curve in Fig. 1), the voltage sweeps from 0 V to 10 V. Initially, the device exhibits low conductance (OFF state). However, with an increased voltage, a transition from low conductance to high conductance (ON state) occurs at a threshold voltage of about 5 V, and then the device is maintained at a high conductance state. At the next bias (red curve in Fig. 1), the device still holds at high conductance. Therefore, this device possesses the nature of bistablity. Furthermore, by applying a negative voltage form 0 V to −10 V, the device can be switched from high conductance back to low conductance. The plot of ON/OFF current ratio as a function of reading voltage is shown in the inset of Fig. 1. It is obvious that the device has a very wide reading voltage range with large ON/OFF current ratio which may reduce reading errors and increase the reliability of the device. For this reason, the tolerance of this device is large enough for external surrounding circuitry to adopt. The corresponding reading currents after "writing" and "erasing" for the first four cycles are shown in Fig. 2.

Table 1
Alq_3 thin film properties obtained from XPS measurements for different deposition rates of Alq_3 thin film under different setting temperatures

Deposition rate (nm/s)	Setting temperature (°C)	N (atom%)	N/C
0.05	251	6.8	0.075
0.15	267	6.2	0.068
0.2	274	6	0.066
0.3	281	5.9	0.065

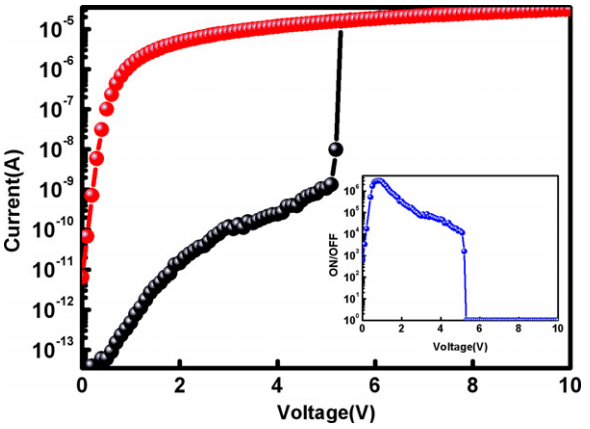

Fig. 1. Current–voltage characteristics of the fabricated device. The black and red curves represent writing and reading biases, respectively. The inset shows the voltage-dependent ON/OFF current ratio curve.

At low bias of the first bias, the current is very small because electrons are obstructed by a barrier formed between the Si substrate and Alq_3. Thus, only a few electrons can be injected into the organic active layer. Then most of them are further trapped by the defects in the bulk Alq_3 thin film and at the interface of Schottky junction. As a result, the device stays at high resistance. By applying a voltage above the threshold, the barrier can be overcome, and this enables numerous electrons to be injected into the active layer and the defects can be filled. Accordingly, electrons are transported easily into the active layer and drift unobstructedly towards the other end of the device. At the next bias, the device exhibits a resistance-like

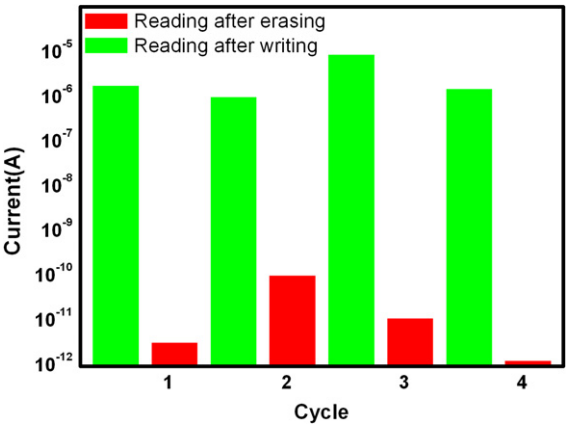

Fig. 2. The reading currents after "writing" and "erasing" of the reported device for the first four cycles.

characteristic when the reading voltage is larger than the energy barrier between Si and Alq_3, that is, ohmic relation. Thus, the ON state can be obtained for any reading voltage larger than the iso-type hetero-junction barrier between n-type silicon and Alq_3, which is about 0.65 eV from Fig. 1.

The bistable characteristic of the Al/Alq_3/n-type Si structure mainly originates from the defects at the interface of Schottky junction. Fig. 3 shows the *C–V* characteristic of the device. It can be seen from the curve that the device is kept at some capacitance value while the applied voltage is below the threshold. Then, the value changes into another lower capacitance value when the voltage exceeds its threshold. The variation of capacitance could be ascribed to the defects in the bulk Alq_3 thin film and at the interface of Schottky junction. At the initial stage of the applied voltage, few electrons are trapped by the defects in the low electrical field. Then, more and more electrons are trapped by the defects as the voltage increases. While the applied voltage is near the threshold, defects are filled sufficiently to make the device possess a metal-like property; consequently, the capacitance is converted into a lower value. In addition, the *I–V* curve of the Al/Alq_3/n-type Si structure with one small Al drop as the top electrode does not exhibit bistability but rather diode behavior. This indicates that the interface property between Al electrode and Alq_3 thin film plays an important role for bistability. A significant chemical reaction occurs

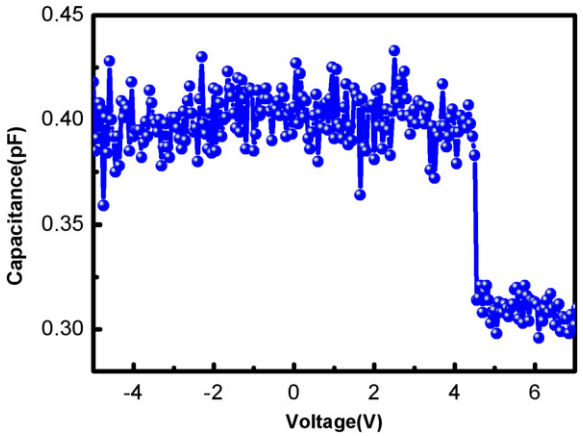

Fig. 3. Capacitance–voltage characteristic of the device at a frequency of 1 MHz. The Si electrode is kept at 0 V, and the voltage on the Al electrode is swept form −5 V to 7 V.

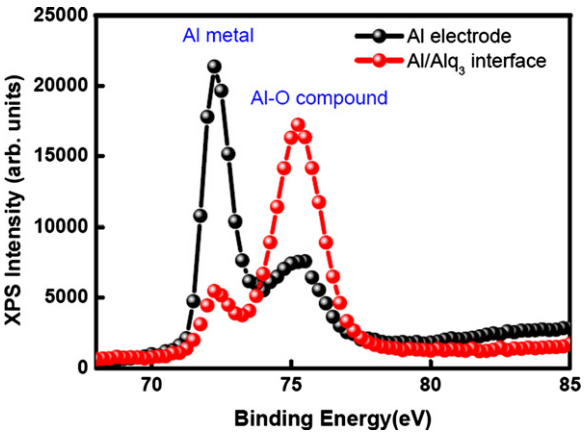

Fig. 4. XPS curves of Al electrode and Al/Alq_3 interface of our reported device.

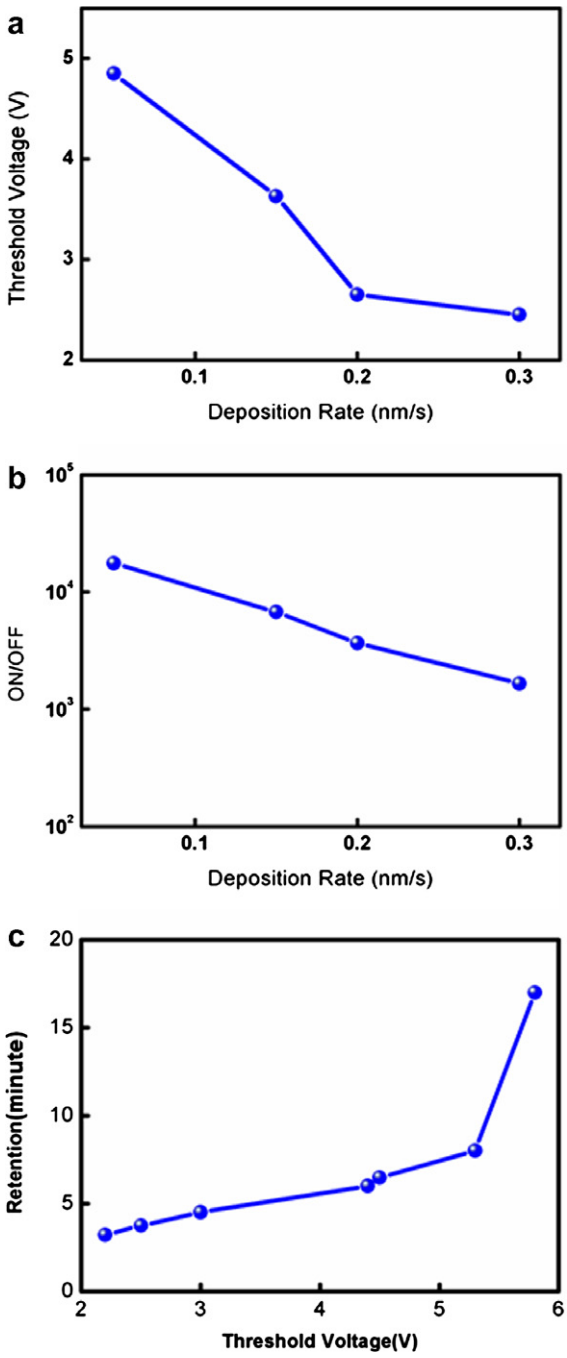

Fig. 5. Electrical properties of the device with different deposition rates of the Alq_3 thin film: (a) deposition-rate dependent threshold voltage, (b) deposition-rate dependent ON/OFF current ratio, and (c) threshold–voltage dependent retention time. Data points shown in (a) and (b) are average values measured from our fabricated devices.

at the interface when aluminum is thermally deposited on the Alq_3 thin film [15]. The resulting product, supportively consisting of Al–O interactions, serves as interface traps and makes carriers be poorly injected through the Schottky junction interface. For this reason, trapping charges at the interface between Alq_3 and Al primarily control the switching mechanism. Fig. 4 shows the XPS curves of the Al electrode and the Alq_3/Al interface of the reported device, which clearly confirms the existence of Al–O compound at the Alq_3/Al interface.

The electrical behavior of the device can be modified by varying the deposition rate of the organic active layer. Fig. 5a and b shows the deposition rate effect on the threshold voltage and ON/OFF current ratio of the device: both decrease with an increase in the deposition rate of Alq_3 thin film. In addition, as can be seen in Fig. 5c, the retention time is dependent on the threshold voltage of the device. Since the threshold voltage can be tuned by adjusting the deposition rate of the organic thin film, the retention time can be extended by reducing the deposition rate of the organic thin film.

Previous reports on the morphology of the organic thin film indicate that roughness decreases with the deposition rate [16,17]. That is to say, the effective surface area between Alq_3 and Al can be adjusted by regulating the deposition rate of Alq_3. For that reason, a higher deposition rate introduces a relatively small amount of defects at the Schottky junction interface. Fig. 6 shows the AFM images of the Alq_3 thin films deposited at 0.05 nm/s, 0.15 nm/s, 0.2 nm/s, and 0.3 nm/s, respectively. The corresponding surface roughness means are 0.38 nm, 0.35 nm, 0.31 nm, and 0.17 nm. These reveal that the deposition rate of the Alq_3 thin film is a major factor in the adjustment of effective contact surface area between Alq_3 and Al. Effective contact surface area will affect the amount of the interface defects of the device. As a result, the relative amount of the defects at the Schottky junction interface can be modified by controlling the deposition rate of the organic thin film. Furthermore, Fig. 7 shows gracing incidence X-ray diffraction curves of the Alq_3 thin film deposited at different rates. It is obvious that all Alq_3 thin films are with amorphous diffraction patterns. In other words, crystallization does not occur in all organic thin films. That is, threshold voltage, ON/OFF current ratio, and retention time are not related to crystallization quality of thin film. They are closely related to the film roughness, as shown by the AFM images in Fig. 6. Besides, it has been demonstrated that the atomic N/C ratio of the Alq_3 thin film changes with the deposition rate of the Alq_3 thin film [16,17]. At a higher deposition rate, that is, higher temperature condition, the Alq_3 molecule structure disintegrates to release *N*-containing species due to the decomposition energy of Alq_3 being smaller than its sublimation energy. It is also shown that the Alq_3 thin film deposited at a lower deposition rate

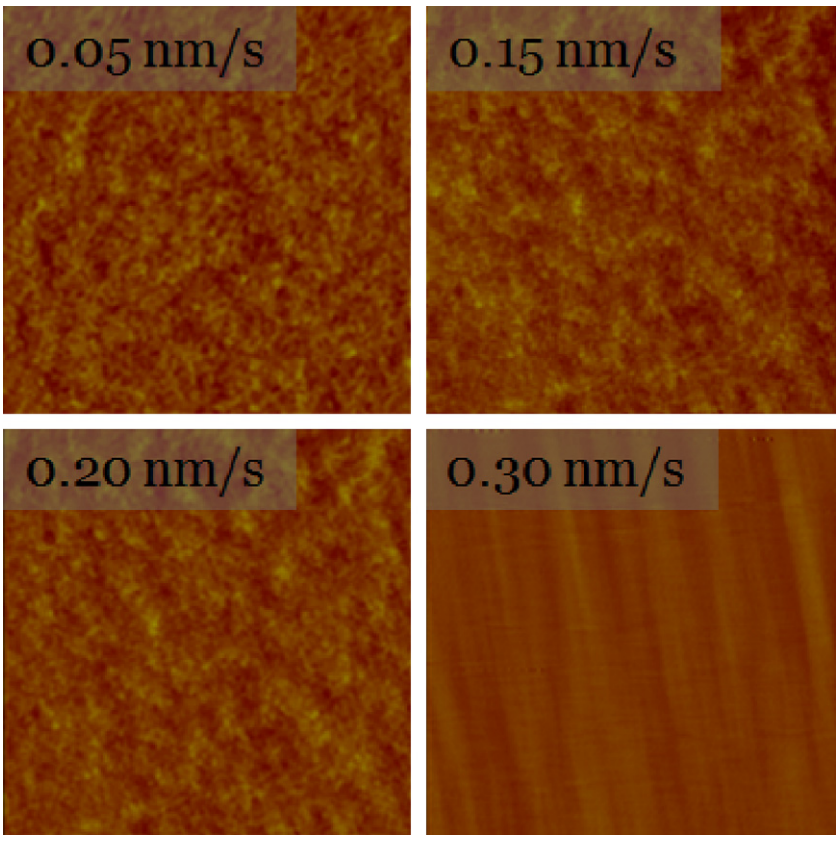

Fig. 6. AFM images of the Alq_3 thin film deposited on n-type Si wafer at four different deposition rates. Surface roughness means are 0.38 nm, 0.35 nm, 0.31 nm, and 0.17 nm for deposition rates at 0.05 nm/s, 0.15 nm/s, 0.2 nm/s, and 0.3 nm/s, respectively.

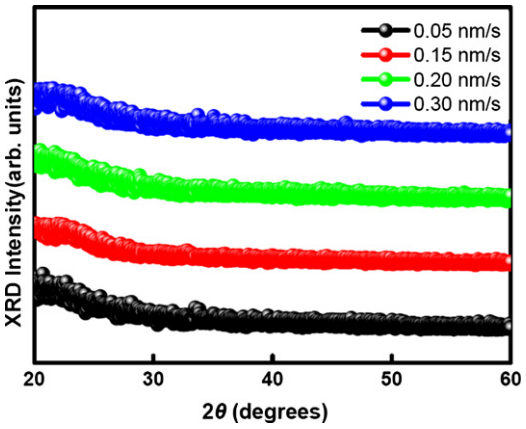

Fig. 7. Gracing incidence X-ray diffraction (GIXRD) curves of the Alq_3 thin films for different deposition rates.

contains a greater atomic concentration of nitrogen and a higher atomic *N*/*C* ratio. The corresponding concentrations of *N* and atomic *N*/*C* ratios from XPS measurements for different deposition rates of Alq_3 thin film are given in Table 1, which clearly indicates the same trend discussed above. Moreover, the electrons being injected into the Alq_3 thin film undergo a repulsive force generated by the negatively charged nitrogen atoms which is the result of the electronegativity of a nitrogen atom being larger than that of a carbon or oxygen atom for a neutral Alq_3 molecule [18]. Hence, the electrons in the Alq_3 thin film with smaller *N*/*C* ratio experience less repulsive force [17]. In other words, an increase in the deposition rate of the Alq_3 thin film can extend the hopping distance and raise hopping frequency of electrons in the Alq_3 thin film.

From above discussions, two findings can be made to explain the results obtained in Fig. 5a and b. First, it is obvious that threshold voltage decreases with increasing deposition rate because of a smaller amount of defects at the Schottky junction interface at a higher deposition rate. Second, the same relationship for the ON/OFF current ratio is because a smaller amount of nitrogen atoms are available to prevent the electrons from hopping in the Alq_3 thin film, hence increase the low conductance state current and decrease the ON/OFF current ratio at a higher deposition rate. Additionally, the distribution of defects at the interface corresponds to the trapping energy [19]. These defects can be classified roughly into two groups: low trapping energy defects (E_{low}) and high trapping energy defects (E_{high}). Higher deposition rate of Alq_3 thin film introduces smoother Alq_3 surface roughness, and may produce less E_{high}. A sample with a smaller threshold voltage, resulting from higher deposition rate and smaller surface roughness of Alq_3, exhibits shorter retention time probably due to less E_{high}. The trapped electrons are more easily released from the E_{low} defects at the Schottky junction interface. Therefore, the electrons can not be kept longer in the E_{low} defects and the device has shorter retention time, as shown in Fig. 5c. Consequently, the deposition rate of Alq_3 thin film has a significant effect on the electrical properties of the organic bistable devices, e.g., threshold voltage, ON/OFF current ratio, and retention time. The electrical characteristics of the device can be optimized and tuned according to our needs for different situations based on the trends obtained in these experiments. Of course some tradeoffs must be made.

4. Conclusions

In summary, the current–voltage characteristics of the organic bistable device, Al/Alq_3/n-type Si, are investigated. This bistability results from the interface defects at the Alq_3/Al junction. Promising results for thermal deposition with controllable film quality by varying the deposition rate of Alq_3 thin film are also provided. The properties of Alq_3 thin film and Alq_3/Al interface are obtained by XPS, AFM, and GIXRD measurements. Owing to the simple structure of the device, the organic electronic memory device can be embedded into the conventional silicon-based fabrication processes. Furthermore, this device has great potential for high-density data storage, low-cost memory applications in future nanoelectronics.

References

[1] C.W. Tang, S.A. VanSlyke, Appl. Phys. Lett. 51 (1987) 913.
[2] G. Yu, J. Gao, J.C. Hummelen, F. Wudl, A.J. Heeger, Science 270 (1995) 1789.
[3] C.D. Dimitrakopoulos, S. Purushothaman, J. Kymissis, A. Callegari, J.M. Shaw, Science 283 (1999) 822.
[4] B. Eitan, P. Pavan, I. Bloom, E. Aloni, A. Frommer, D. Finzi, IEEE Electron. Dev. Lett. 21 (2000) 543.
[5] R.S. Potember, T.O. Poehler, D.O. Cowan, Appl. Phys. Lett. 34 (1979) 405.
[6] L.P. Ma, J. Liu, Y. Yang, Appl. Phys. Lett. 80 (2002) 2997.
[7] S. Möller, C. Perlov, W. Jackson, C. Taussig, S.R. Forrest, Nature 426 (2003) 166.
[8] A. Bandyopadhyay, A.J. Pal, Adv. Mater. 15 (2003) 1949.
[9] R.J. Tseng, J. Huang, J. Ouyang, R.B. Kaner, Y. Yang, Nano. Lett. 5 (2005) 1077.
[10] C.W. Chu, J. Ouyang, J.-H. Tseng, Y. Yang, Adv. Mater. 17 (2005) 1440.
[11] Q. Ling, Y. Song, S.J. Ding, C. Zhu, D.S.H. Chan, D.-L. Kwong, E.-T. Kang, K.-G. Neoh, Adv. Mater. 17 (2005) 455.
[12] C.-H. Tu, Y.-S. Lai, D.-L. Kwong, IEEE Electron. Dev. Lett. 27 (2006) 354.
[13] S. Paul, A. Kanwal, M. Chhowalla, Nanotechnology 17 (2006) 145.
[14] L. Li, Q.-D. Ling, S.-L. Lim, Y.-P. Tan, C. Zhu, D.S.H. Chan, E.-T. Kang, K.-G. Neoh, Org. Electron. 8 (2007) 401.
[15] M.G. Mason, C.W. Tang, L.-S. Hung, P. Raychaudhuri, J. Madathil, D.J. Giesen, L. Yan, Q.T. Le, Y. Gao, S.-T. Lee, L.S. Liao, L.F. Cheng, W.R. Salaneck, D.A. dos Santos, J.L. Brėdas, J. Appl. Phys. 89 (2001) 2756.
[16] L.F. Cheng, L.S. Liao, W.Y. Lai, X.H. Sun, N.B. Wong, C.S. Lee, S.T. Lee, Chem. Phys. Lett. 319 (2000) 418.
[17] C.B. Lee, A. Uddin, X. Hu, T.G. Anderson, Mater. Sci. Eng. B 112 (2004) 14.
[18] R. Trensch, F.J. Himpsel, S. Kakar, L.J. Terminello, C. Heske, T. van Buuren, V.V. Diuh, H.W. Lee, K. Pakbaz, G. Fox, I. Jiménez, J. Appl. Phys. 86 (1999) 88.
[19] S.M. Sze, Physics of Semiconductor Devices, second ed., Wiley, New York, 1981. Chapter 7, p. 380.

was measured by the photoemission spectroscopic measurement in air. The mobility of the top-contact 2A-TFT was improved to 1.0 cm^2/Vs by careful treatment of the gate-insulator surface with octyltrichlorosilane (OTS). We also report on the reduction of contact resistance of the bottom-contact 2A-TFT by employing MoO_x as the carrier injection layer for the S–D electrodes. The bottom-contact 2A-TFT with the MoO_x/Au electrode showed a high mobility of 1.0 cm^2/Vs, which is comparable to that in the top-contact 2A-TFT.

Cross sections of the (a) top- and (b) bottom-contact 2A-TFTs are shown schematically in Fig. 1. We employed a highly doped silicon wafer with thermally grown SiO_2 (200 nm) as the common gate electrode and the gate insulator. After immersing the substrate in a piranha solution at 80 °C for 10 min, it was ultrasonicated for 5 min with deionized water, acetone, and isopropyl alcohol, in that order. In the bottom-contact 2A-TFTs, two types S–D electrodes consisting of MoO_x/Au and Cr/Au were fabricated on the substrate. The MoO_x layer was deposited by thermal evaporation from MoO_3 powder at a pressure below 5.0×10^{-5} Pa (deposition rate: 0.05 nm/s). Then, Au was formed on the MoO_x layer in the same vacuum chamber. The S–D electrodes were patterned by photolithography and a lift-off process. The Cr/Au electrodes were deposited by e-beam evaporation and patterned by the same procedure. In the cases of both substrates used for the top- and bottom-contact TFTs, the SiO_2 gate-insulator surface was treated with the OTS solution (20 mM) for 15 h. These treated substrates were ultrasonicated in anhydrous toluene, acetone, and isopropyl alcohol for 10 min and was then cleaned with the ethanol moisture. Anthracene oligomer (2A) was purified twice by train sublimation, and it was deposited as 30-nm thick layer by thermal vapor deposition at 80 C (deposition rate: 0.01 nm/s). After the deposition of the 2A layer, for fabricating the top-contact TFT, 50-nm-thick Au source–drain electrodes were deposited through a shadow mask on the active layer at a rate of 0.1 nm/s. The channel length and width (L/W) of the top- and bottom-contact TFTs were 50 μm/1 mm and 50 μm/500 μm. The electrical characteristics were measured at room temperature by an HP4140 source-meter system. Electrical characterizations were carried out under vacuum without exposure to air after the device fabrication.

Fig. 2a shows plots of drain current (I_D) and square root of I_D vs. gate voltage (V_G) at a drain voltage (V_D) of −100 V

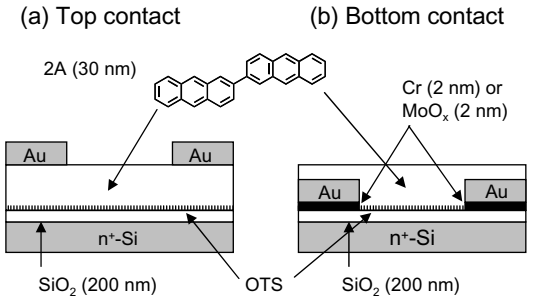

Fig. 1. Schematic cross sections of (a) top- and (b) bottom-contact 2A-TFTs.

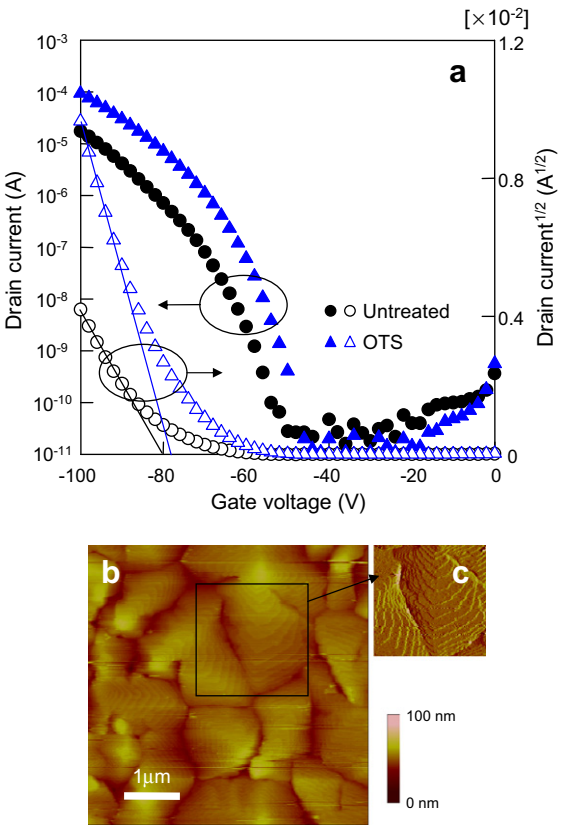

Fig. 2. (a) Drain current (left) and square root of drain current (right) vs. gate voltage at a drain voltage of −100 V for top-contact 2A-TFTs fabricated on the OTS-treated and untreated SiO_2. (b) Normal (5×5 μm) and (c) high-pass-filtered (2×2 μm) AFM image of a 2A layer deposited on the OTS-treated SiO_2.

for the top-contact 2A-TFTs with and without OTS treatment. Drain current of the 2A-TFT fabricated on the OTS-treated SiO_2 was nearly one order of magnitude higher than that of the 2A-TFT fabricated on the untreated SiO_2. The field-effect mobility in the saturation regime was improved from 0.25 to 1.0 cm^2/Vs with a current on/off ratio of 10^7. Threshold voltages for 2A-TFTs fabricated on the untreated and OTS-treated substrate were −80 and −77 V, respectively. Fig. 2b and c shows AFM images of a 2A film with a thickness of 30 nm deposited on the OTS-treated SiO_2. Large grains more than 3 μm and clear step structures corresponding to the molecular length of 2A were observed. The improvement of mobility is attributed to the highly ordered crystal growth due to the low-surface energy of the SiO_2 gate-insulator surface [13].

Although the top-contact TFT shows high mobility of 1.0 cm^2/Vs, the bottom-contact TFT is more feasible for practical application. The bottom-contact TFT is suitable for high-resolution and integration of OTFTs, because a photolithographic method can be used in its fabrication process. It is therefore important to achieve high mobility in the bottom-contact OTFT. However, we found that the increase of injection barrier caused by the deep HOMO level of 2A (5.55 eV) leads to the significant decrease of drain current in the bottom-contact TFT. Fig. 3a shows the out-

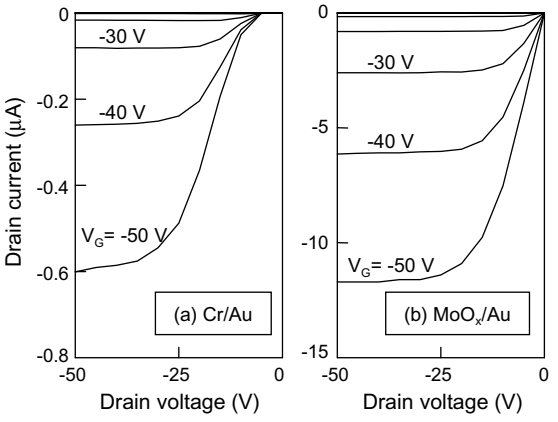

Fig. 3. Output characteristics of bottom-contact 2A-TFTs with (a) Cr/Au and (b) MoO_x/Au S–D electrodes. The gate voltage was measured from 0 to −50 V.

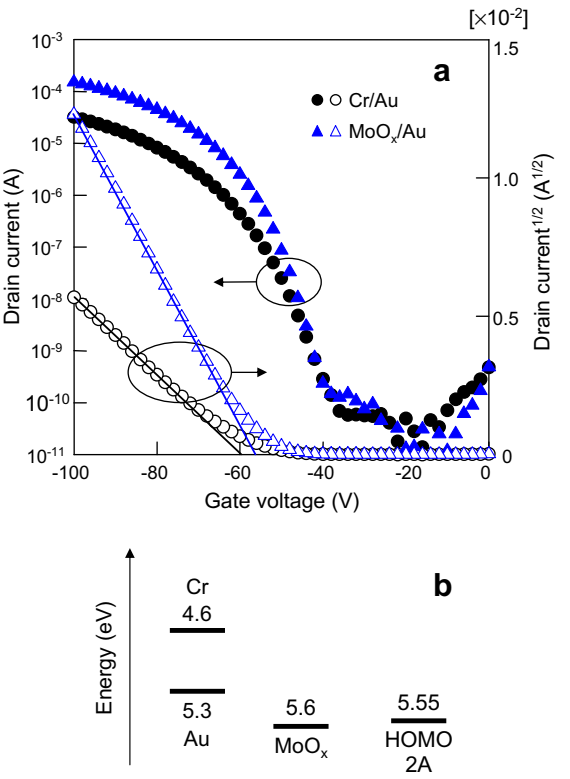

Fig. 4. (a) Drain current (left) and square root of drain current (right) vs. gate voltage at a drain voltage of −100 V for bottom-contact 2A-TFTs with MoO_x/Au (triangles) and Cr/Au (circles) S–D electrodes, and (b) energy-level diagram of 2A and electrode materials.

put characteristics for a bottom-contact 2A-TFT fabricated on the OTS-treated substrate with Cr (2 nm)/Au (50 nm) S–D electrodes. Owing to the large injection barrier, drain current showed a non-linear rise at a low-drain voltage. In addition, the turn-on voltage shifted nearly 10 V to the high-voltage side. The decrease of drain current caused by the large injection barrier in the bottom-contact TFT will become a serious problem not only in the 2A but also in other organic semiconductors with a deep HOMO level. To reduce the injection barrier between the S–D electrodes and the organic semiconductor, we reported on the bottom-contact OTFT with a MoO_x carrier injection layer for S–D electrodes [14]. The MoO_x layer not only enhances the carrier injection but also acts as an adhesive layer, as shown in Fig. 1b and Fig. 3b shows the output characteristics for a bottom-contact 2A-TFT with a MoO_x carrier injection layer. It is clear that non-linearity of drain current at low-drain voltage is significantly improved by employing the MoO_x carrier injection layer. In addition, the drain current of the bottom-contact 2A-TFT with a MoO_x/Au electrode was increased up to twenty times compared to that of the Cr/Au electrode. Fig. 4a shows the transfer characteristics for bottom-contact 2A-TFTs with Cr/Au and MoO_x/Au electrodes. The mobility improved from 0.22 (Cr/Au) to 1.0 cm^2/Vs (MoO_x/Au), which is comparable to that of the top-contact 2A-TFT. This result indicates that the high injection barrier results in the significant decrease of the mobility calculated from the I_D–V_G characteristics.

The contact resistance depends on the physical-contact condition and injection barrier height at the interface between the organic semiconductor and S–D electrodes. The high contact resistance of the bottom-contact 2A-TFT is mainly attributed to the large injection barrier between the 2A and S–D electrodes. We estimated the HOMO level of 2A and the work function of electrode materials by photoemission spectroscopy in air (AC-3: Rikenkeiki), as shown in Fig. 4b. The HOMO level of 2A was 5.55 eV. The work function of Au was found to be 5.3 eV after UV/O_3 cleaning. The MoO_x is known to be a wide gap semiconductor. The position of the valance band was estimated to be 5.6 eV, which was deeper potential than the work function of Cr (4.6 eV). It can thus reduce the injection barrier and enhance hole injection. The contact area between the 2A and MoO_x layer is extremely small (2 nm). However, the injection barrier height in this area affects significantly the contact resistance, because the effective channel region in the organic semiconductor layer localizes at a thickness of few nanometers on the gate-insulator surface [15]. These results also suggest that the increase of the contact resistance caused by the Cr layer is comparatively large.

In summary, we fabricated top- and bottom-contact TFTs based on 2,2-bianthryl (2A). The top-contact 2A-TFT showed high mobility of 1.0 cm^2/Vs with a current on/off ratio of 10^7 as a result of OTS treatment. Large grains and clear step structures corresponding to the molecular length of 2A were observed in the AFM image of a 2A film deposited on the OTS-treated SiO_2. Although a high contact resistance due to the deep HOMO level of 2A was observed in the case of the bottom-contact 2A-TFT with Cr/Au S–D electrodes, we successfully reduced the injection barrier by employing the MoO_x layer. The mobility was improved to 1.0 cm^2/Vs, which is comparable to the mobility in the top-contact 2A-TFT.

Acknowledgments

We are grateful to Dr. Yuan Gao and Taisuke Uemura (Kanto Denka Kogyo Co., LTD.) for the synthesis of the anthracene oligomers.

References

[1] L. Zhou, A. Wanga, S.C. Wu, J. Sun, S. Park, T.N. Jackson, Appl. Phys. Lett. 88 (2006) 083502.
[2] M. Mizukami, N. Hirohata, T. Iseki, K. Ohtawara, T. Tada, S. Yagyu, T. Abe, T. Suzuki, Y. Fujisaki, Y. Inoue, S. Tokito, T. Kurita, IEEE Electr. Device Lett. 27 (2006) 249.
[3] C.D. Sheraw, L. Zhou, J.R. Huang, D.J. Gundlach, T.N. Jackson, M.G. Kane, I.G. Hill, M.S. Hammond, J. Campi, B.K. Greening, J. Francl, J. West, Appl. Phys. Lett. 80 (2002) 1088.
[4] P.F. Baude, D.A. Ender, M.A. Haase, T.W. Kelley, D.V. Muyres, S.D. Theiss, Appl. Phys. Lett. 82 (2003) 3964.
[5] T. Someya, H.E. Katz, A. Gelperin, A.J. Lovinger, A. Dodabalapur, Appl. Phys. Lett. 81 (2002) 3079.
[6] Zheng-Tao Zhu, J.T. Mason, R. Dieckmann, G.G. Malliaras, Appl. Phys. Lett. 81 (2002) 4643.
[7] H. Tian, J. Shi, D. Yan, L. Wang, Y. Geng, F. Wang, Adv. Mater. 18 (2006) 2149.
[8] K. Takimiya, H. Ebata, K. Sakamoto, T. Izawa, T. Otsubo, Y. Kunugi, J. Am. Chem. Soc. 128 (2006) 12604.
[9] T. Yamamoto, K. Takimiya, J. Am. Chem. Soc. 129 (2007) 2224.
[10] H. Klauk, U. Zschieschang, R.T. Weitz, H. Meng, F. Sun, G. Nunes, D.E. Keys, C.R. Fincher, Z. Xiang, Adv. Mater. 19 (2007) 3882.
[11] K. Ito, T. Suzuki, Y. Sakamoto, D. Kubota, Y. Inoue, F. Sato, S. Tokito, Angew. Chem. Int. Ed. 42 (2003) 1159.
[12] Y. Inoue, S. Tokito, K. Ito, T. Suzuki, J. Appl. Phys. 95 (2003) 5795.
[13] T. Umeda, D. Kumaki, S. Tokito, submitted for publication.
[14] D. Kumaki, T. Umeda, S. Tokito, Appl. Phys. Lett. 92 (2008) 013301.
[15] R. Ruiz, A. Papadimitratos, A.C. Mayer, G.G. Malliaras, Adv. Mater. 17 (2005) 1795.

devices with polymeric semiconductor as well as high capacitance dielectrics which were all processed by solution method and cured at low temperature.

In this work, we have initially prepared soluble TiO_2 nano-particles as high-k gate dielectric on substrate at low temperature to enhance the capacitance of OFETs. For a high performance OFETs, generally, a low-k polymer at the insulator/semiconductor interface is desirable, as low interface polarity has been shown to increase carrier mobility [16,17]. In addition, the polymer could further smooth the TiO_2 dielectric surface and suppress the leakage current from grain boundary of TiO_2 films. Accordingly, a layer of the low-k polymer was spin-coated on top of the TiO_2 nano-particles film and a stacked structure (bilayer) of low-k/high-k dielectrics was fabricated in this study. With regioregular poly(3-hexylthiophene) (RR-P3HT) as active semiconductor, good FET characteristics were obtained at low drive voltage.

The polymer FETs were fabricated on N++ type low-resistance Si wafers as substrate and acts as a common gate electrode. An oleic acid surface-modified TiO_2 nanoparticles (TiO_2-oleic) with high solublility in chlorobenzene or toluene was solution-deposited on wafer as high-k gate dielectrics. This TiO_2-oleic was synthesized and modified from literatures [18]. The TiO_2-oleic were reported as anatase phase ($k = 31$) and were cylindrical in shape (20 nm in length and 4 nm wide, measured by transmission electron Microscopy (TEM), Fig. 1a). The high-k TiO_2-oleic layers were obtained by spin-coating of TiO_2-oleic solution (10 wt% in Cl–benzene) at 1000 rpm for 30 s, followed by a baking process at 120 °C in oven for 0.5hr. Subsequently, another layer of the cross-linking PVP ($k = 4.1$) was applied on TiO_2-oleic film to smoother the interface and as the low-k materials. The uniformity of the TiO_2-oleic film was examined by using scanning electron microscopy (SEM) imaging of fracture edge. As shown in Fig. 1b, the TiO_2 layer by solution process exhibit uniform film with homogeneous nano-particle dispersions, suggesting a good candidate for high-k insulator for OFETs devices.

The transistors with bilayer dielectric films with different thickness were fabricated (transisor 2: TiO_2-oleic (317 nm)/PVP (317 nm); transisor 4: TiO_2-oleic (317 nm)/PVP (85 nm)). The cross-linked PVP material (the top layer of bilayer dielectric) shows good dielectric performance and chemical resistance to many solvents and bases which typically found in positive photoresist developers, indicating that the cross-linked PVP in this study were suitable for use in photolithography and wet etching process. Hence, we defined the region of electrodes with channel width/length = 1000 um/10 um on top of the PVP layer by photolithography/Pt-deposition (20 nm)/lift-off process (acetone), leading to a patterned source and drain electrode with fine accuracy and the surface of underlying PVP films remain intact. Before spin-deposition of P3HT, the PVP films were further treated with octyltrichlorosilane (OTS) or hexamethyldisilazane (HMDS) as a SAM modification layer [19]. After spin-coating of the P3HT (3 mg/1 mL in toluene, 500 rpm, 60 s) as semiconductor, a bottom gate, bottom contact configuration of the unpatterned P3HT-OFETs was fabricated and shown in Fig. 2. All current–voltage (I–V) measurements for our OFETs were performed

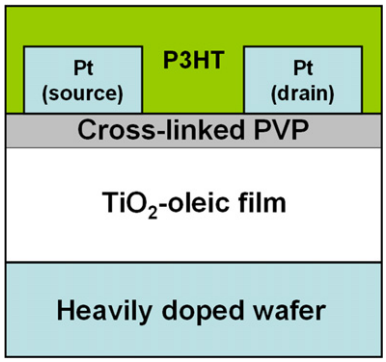

Fig. 2. Devices structure of bottom gate, bottom contact configuration OFETs in this study.

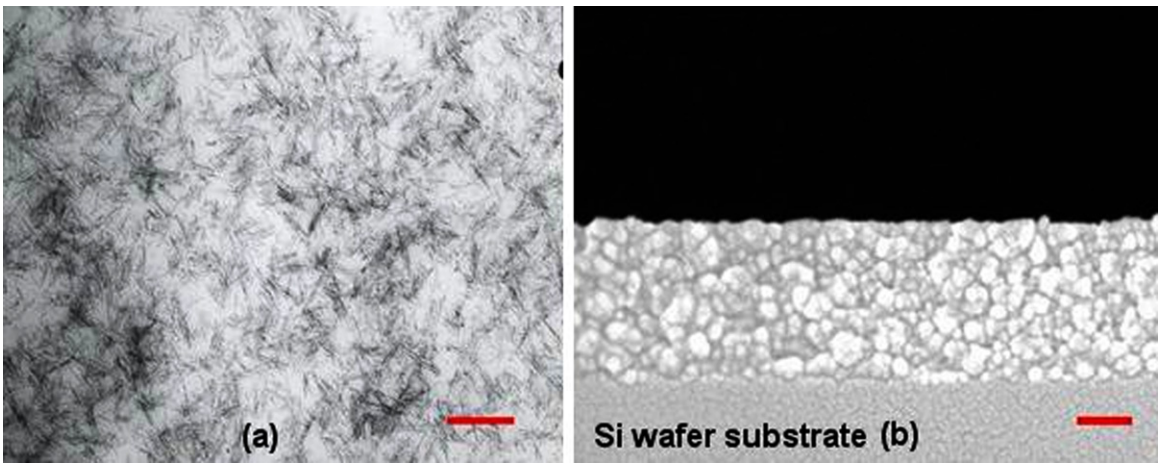

Fig. 1. (a) TEM image of TiO_2-oleic nano-particle (b) cross-sectional SEM image of TiO_2-oleic layer. All scale bars are 100 nm.

Table 1
Summary of dielectric properties (100 kHz) and field effect transistor data

Sample	Condition	Oleic-TiO_2 (nm)	PVP (nm)	C_{ox} (nF/cm^2)	u cm^2/V s	On/off ratio	Ss V/dec	V_t (V)
Transistor 1	Operated at V_{ds} −40 V	–	580 (OTS-treated)	6.3	0.0074	7.90×10^3	5.50	−4.46
Transistor 2		317	317 (OTS-treated)	10.0	0.0260	2.96×10^3	2.60	−6.33
Transistor 3		317	317 (HMDS-treated)	10.0	0.0028	1.90×10^3	4.26	1.54
Transistor 2	Operated at V_{ds} −10 V	317	317(OTS-treated)	10.0	0.0072	5.40×10^2	1.44	1.26
Transistor 4		317	85 (OTS-treated)	28.0	0.0140	1.00×10^3	1.89	1.14

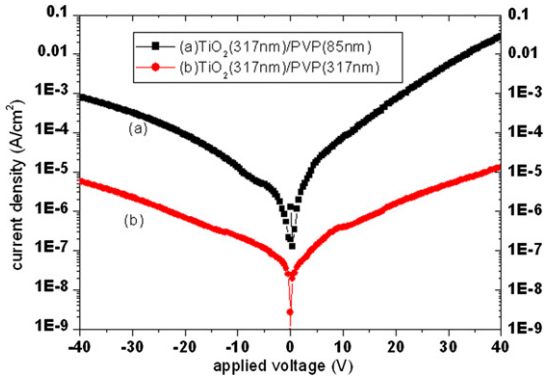

Fig. 3. Leakage currents of the bilayer film: (a) (TiO_2-oleic (317 nm)/PVP (85 nm)) and (b) (TiO_2-oleic (317 nm)/PVP (317 nm)).

with semiconductor parameter analyzer (4156 C, Agilent) at room temperature in air. To characterize leakage currents and capacitances of TiO_2-oleic/PVP films, we have made a capacitor structure (MIM) by sandwiching the bilayer materials between indium tin oxide (ITO) and Au electrode. The effective gate capacitances (C_{ox}) were measured by capacitance analyzer (590 CV, Keithley) at 100 k MHz and listed in Table 1. We found that transisor 2 and transisor 4 exhibit the capacitances of 10 nF/cm^2 and 28 nF/cm^2, respectively, which are close to the theoretical values for serially connected capacitor layers.

The current-density–voltage (J–V) characteristics of these MIM structures (ITO/TiO_2-oleic (317 nm)/PVP (317 nm)/Au and ITO/TiO_2-oleic (317 nm)/PVP (85 nm)/Au) were investigated and shown in Fig. 3. With a thicker capped layer of cross-linked PVP, the TiO_2-oleic (317 nm)/PVP (317 nm) have lower current densities (10^{-5} A/cm^2 at 40 V) than that

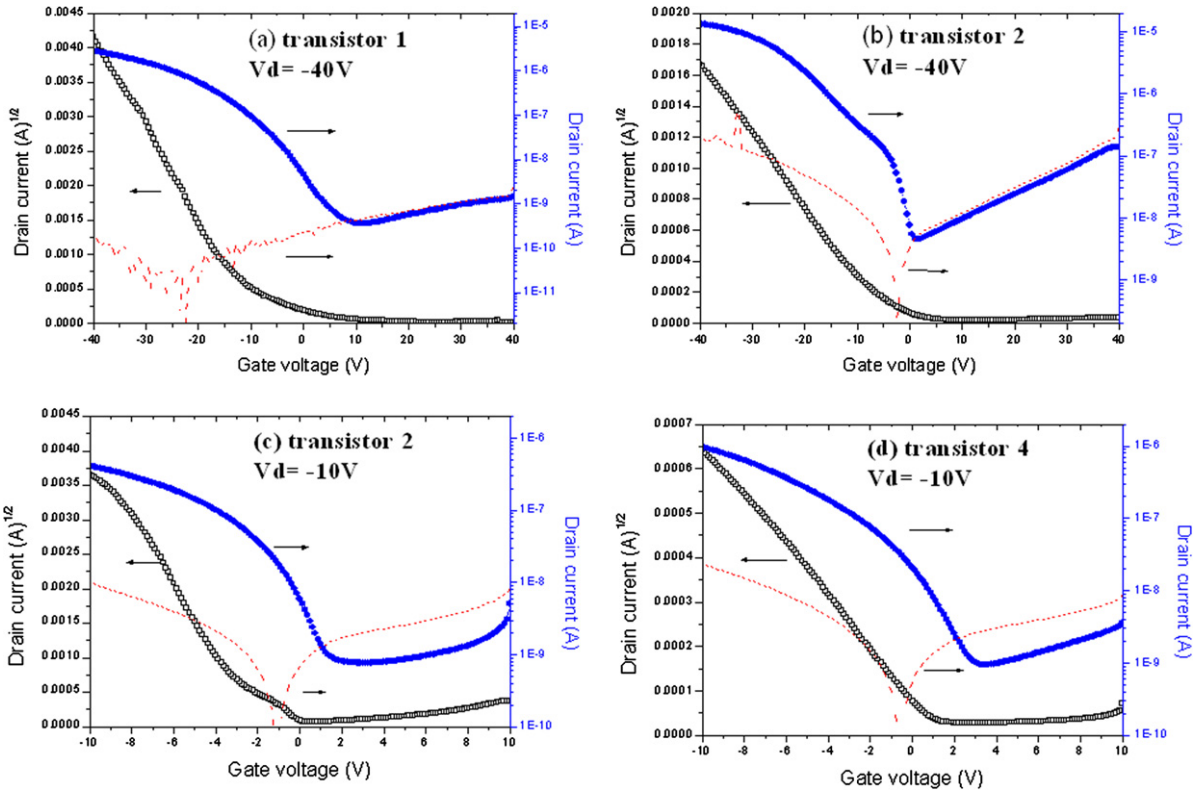

Fig. 4. Transfer characteristics (solid line) and the leakage current (dashed line) of (a) transistor 1 (insulator: PVP (580 nm)) with V_d = −40 V (b) transistor 2 (insulator: TiO_2-oleic (317 nm)/PVP (317 nm)) with V_d = −40 V (c) transistor 2 with V_d = −10 V (d) transistor 4 (insulator: TiO_2-oleic (317 nm)/PVP (85 nm)) with V_d = −10 V.

of TiO_2-oleic (317 nm)/PVP (85 nm) (10^{-3} A/cm^2 at 40 V) by two orders of magnitude. Although the current density of 10^{-3} A/cm^2 (at 40 V) is high, the TiO_2-oleic (317 nm)/PVP (85 nm) film have an acceptable current density of 10^{-5} A/cm^2 (at 10 V), a value good enough for a gate insulator for OFETs operation within 10 V. It should be noted that the bilayer dielectric structure is necessary in this study because the MIM structure of ITO/TiO_2-oleic (317 nm)/Au show high leakage current, thus not able to be an insulator solely in this study.

The surface roughness of the dielectric layers was characterized by an atomic force microscope ((AFM) Nanoscope IIIa, digital Instruments). The root-mean-square (rms) roughness of the TiO_2-oleic film on silicon wafer is 1.72 nm. When top-coating layer (PVP) was applied on TiO_2-oleic film, the rms was further reduced to 0.61 nm which was close to that of SiO_2 surface on Si substrate.

All of the electrical parameters of the OFETs in this study were listed in table 1. The devices of transistor 1, 2, and 3 were operated at V_{ds} = −40 V, V_{gs} = 40 V to −40 V. In addition, for low voltage operating, the electric properties of transistor 2 and transistor 4 were measured within 10 V. The carrier mobility u and the threshold voltage V_t were determined by using the following Eq. (1):

$$\sqrt{I_{D,SAT}} = \sqrt{\frac{W\mu C_{OX}}{2L}}(V_G - V_t) \quad (1)$$

Where $I_{D,SAT}$ is the saturated drain current, C_{ox} is the gate capacitance per unit area, W and L are the conducting channel width and length, V_G denotes the gate applied voltage. The mobility was extracted from the slope of the linear plots of the square root of the drain current versus the gate voltage (Fig. 4).

All of the transfer characteristics of P3HT-OFETs in this study are shown in Fig. 4. As to the transistor 2 with OTS-treated insulator, the mobility in the saturation region and the threshold voltage were 0.0260 cm^2/V s and −6.33 V, respectively. The on/off ratio was about 2.96×10^3. This mobility and on/off ratio were similar to unpatterned P3HT-based OFETs with SiO_2 as gate dielectric [6]. For the HMDS-treated transistor 3, the mobility and the threshold voltage were 0.0028 cm^2/V s and 1.54 V, respectively, with on/off ratio 1.9×10^3. It is obviously that devices with OTS-treated insulator show better performance than HMDS one. Transistor 1 was the device with single layer of cross-linked PVP as gate dielectric. The mobility and the threshold voltage are 0.0074 cm^2/V s and −4.46 V, respectively, with on/off ratio 7.90×10^3. The mobility of transistor 1 was about 4 times lower than that of transistor 2.

To achieve high performance, low operating voltage OFETs, transistor 2 and transistor 4 were tested within 10 V (V_{ds} = −10 V, V_{gs} = 10 V to −10 V). The transfer characteristics are shown in Fig. 4c and d and output characteristics are shown in Fig. 5. The transistor 2 with capacitance of 10 nF/cm^2 exhibited mobility of 0.0072 cm^2/V s and the threshold voltage was 1.26 V. The on/off ratio was 5.4×10^2. On the other hand, the transistor 4 (capacitance of 28 nF/cm^2) had twice the field-induced current at the same gate voltage as shown in Fig. 5b. The mobility of transistor 4 was better than for transistor 2, namely, 0.0140 cm^2/V s and the threshold voltage was 1.14 V with on/off ratio 1.0×10^3. According to the work by Wang et al., [13] they demonstrated P3HT-OFETs with sputtered TiO_2 and bilayer SiO_2/TiO_2 as gate insulators which operate at 10 V and show mobility of 0.005 cm^2/V s and 0.032 cm^2/V s, respectively. Although transistors with lower mobility were obtained in our cases, this is the first example of polymeric semiconductor based FETs that were made by a simple, solution-processable TiO_2 gate dielectric which fabricate at low temperature.

We have also investigated the hysteresis of the P3HT-OFETs with bilayer TiO_2-oleic/PVP gate insulators. The gate-to-source voltage (V_{GS}) is continuously swept in steps of 0.12 V, starting from 10 V, passing through −10 V, and finally arriving at 10 V. The maximum difference of V_G for a constant current in the forward and reverse scans was designated as the amount of hysteresis (ΔV_{hys}) [20]. The polymer gate dielectric OFETs usually result in large hysteresis in the I–V characteristics. In our cases, the transistor 4 with thin PVP (85 nm) and the transistor 2 with thicker PVP (317 nm) both show the similar hysteresis behavior and the ΔV_{hys} is 4.10 V and 4.24 V, respectively, as shown in Fig. 6. The parameters of both the two OFETs include carrier mobility, subthreshold slope, and on/off ratio are unaffected by the hysteresis. It is believed that OFETs with

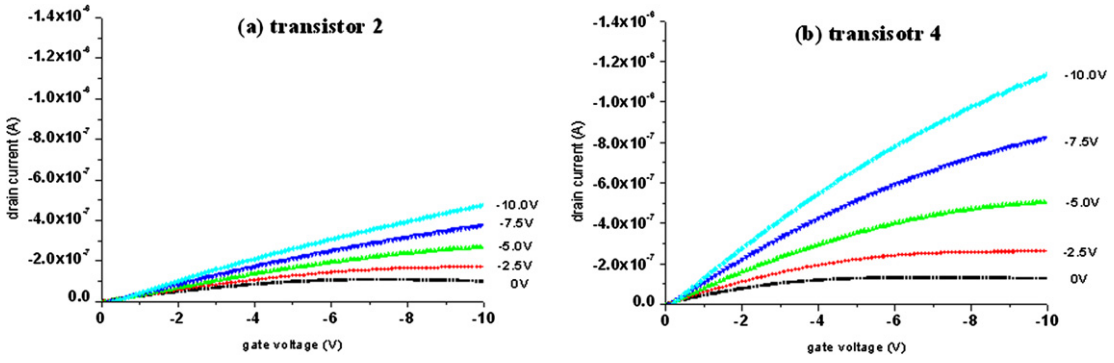

Fig. 5. ID-VG transfer curves of OFETs with bilayer dielectrics. (a) transistor 2 (TiO_2-oleic (317 nm)/PVP (317 nm)) and (b) transistor 4 (TiO_2-oleic (317 nm)/PVP (85 nm)).

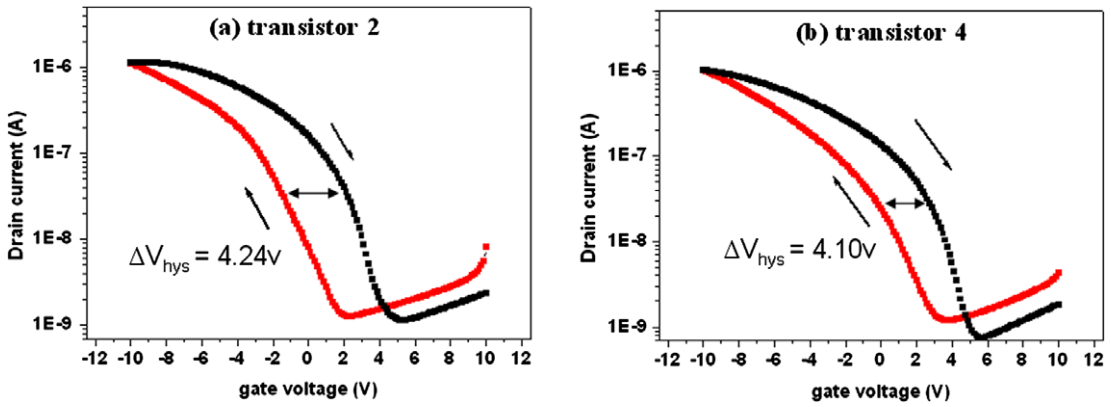

Fig. 6. The Hysteresis behavior of OFETs with bilayer dielectrics. (a) transistor 2 (TiO_2-oleic (317 nm)/PVP (317 nm)) and (b) transistor 4 (TiO_2-oleic (317 nm)/PVP (85 nm)).

hysteresis may arise from the migration of the negative ions in the PVP gate insulator and surface polarization [21,22].

In conclusion, we have successfully demonstrated a polymeric semiconductor-based transistor with low-*k* polymer/high-*k* metal-oxide (TiO_2) bilayer as gate dielectric. The metal-oxide (TiO_2) layers are readily processable from solution and cured at low temperature, instead of traditionally sputtering or high temperature sintering process, thus may suitable for a low-cost OFETs manufacture. The low-*k* polymer capped on TiO_2 layer could further smooth the TiO_2 dielectric surface and suppress the leakage current from grain boundary of TiO_2 films. The resulting unpatented P3HT-OFETs could operate with supply voltage less than 10 V and the mobility and threshold voltage were 0.0140 cm^2/V s and 1.14 V, respectively. The on/off ratio was 1.0×10^3.

References

[1] H. Sirringhaus, T. Kawase, R.H. Friend, T. Shimoda, M. Inbasekaran, W. Wu, E.P. Woo, Science 290 (2000) 2123.
[2] L.-L. Chua, J. Zaumseil, J.-F. Chang, E.C.W. Ou, P.K.H. Ho, H. Sirringhaus, R.h. Friend, Nature 434 (2005) 194.
[3] B. Crone, A. Dodabalapur, Y.-Y. Lin, R.W. Filas, Z. Bao, A. LaDuca, R. Sarpeshkar, H.E. Katz, W. Li, Nature 403 (2000) 521.
[4] J.H. Burroughes, D.D.C. Bradley, A.R. Brown, R.N. Marks, K. Mackay, R.H. Friend, P.L. Burns, A.B. Holmes, Nature 347 (1990) 539.
[5] L. Herlogsson, X. Crispin, N.D. Robinson, M. Sandberg, O.-J. Hagel, G. Gustafsson, M. Berggren, Adv. Mater. 19 (2007) 97.
[6] A. Facchetti, M.H. Yoon, T.J. Marks, Adv. Mater. 17 (2005) 1705.
[7] L.L. Chua, P.K.H. Ho, H. Sirringhaus, R.H. Friend, Appl. Phys. Lett. 84 (2004) 3400.
[8] M.H. Yoon, H. Yan, A. Facchetti, T.J. Marks, J. Am. Chem. Soc. 127 (2005) 10388.
[9] S.Y. yang, S.H. Kim, K. Shin, H. Jeon, C.F. Park, Appl. Phys. Lett. 88 (2006) 173507.
[10] M. Halik, H. Klauk, U. Zschieschang, G. Schmid, C. Dehm, M. Schutz, S. Maisch, F. Effenberger, M. Brunnbauer, F. Stellacci, Nature 431 (2004) 963.
[11] C.D. Dimitrakopoulos, S. Purushothaman, J. Kymissis, A. Callegari, J.M. Shaw, Science 283 (1999) 822.
[12] L.A. Majewski, R. Schroeder, M. Grell, Adv. Funct. Mater. 15 (2005) 1017.
[13] G. Wang, D. Moses, A.J. Heeger, H.-M. Zhang, M. Narasimhan, R.E. Demaray, J. Appl. Phys. 95 (2004) 316.
[14] J. Lee, J.H. Kim, S. Im, Appl. Phys. Lett. 29 (2003) 2689.
[15] C.S. Kim, S.J. Jo, S.W. Lee, W.J. Kim, H.K. Baik, Appl. Phys. Lett. 88 (2006) 243515.
[16] J. Veres, S.D. Ogier, G. Lloyd, D.M. de Leeuw, Chem. Mater. 16 (2004) 4543.
[17] J. Veres, S.D. Ogier, S.W. Leeming, D.C. Cupertino, S.M. Khaffaf, Adv. Funct. Mater. 13 (2003) 199.
[18] P.D. Cozzoli, A. Kornowski, H. Weller, J. Am. Chem. Soc. 125 (2003) 14539.
[19] S.C. Lim, S.H. Kim, J.H. Lee, M.K. Kim, D.J. Kim, T. Zyung, Synthetic Met. 148 (2005) 75.
[20] Y.H. Noh, S.Y. Park, S.M. Seo, H.H. Lee, Org. Electronics. 7 (2006) 271.
[21] J. Jang, S.H. Han, SID Int. Symp. Digest Tech. Papers 37 (2006) 108.
[22] S.Y. Park, M. Park, H.H. Lee, Appl. Phys. Lett. 85 (2004) 2283.

Organic Electronics 9 (2008) 930

Contents lists available at ScienceDirect

Organic Electronics

journal homepage: www.elsevier.com/locate/orgel

Corrigendum

Corrigendum to 'Magnetic field release of trapped charges in poly(fluorenylenevinylene)s' [Org. Electr. 8 (2007) 695–701]

Michelle S. Meruvia [a], José A. Freire [a], Ivo A. Hümmelgen [a,*], Jonas Gruber [b], Carlos F.O. Graeff [c]

[a] Group of Organic Optoelectronic Devices, Departamento de Física, Universidade Federal do Paraná, Caixa Postal 19044, 81531-990 Curitiba-PR, Brazil
[b] Instituto de Química, Universidade de São Paulo, Caixa Postal 26077, 05513-970 São Paulo-SP, Brazil
[c] Departamento de Física, FC, Universidade Estadual Paulista, 17033-360 Bauru-SP, Brazil

The correct structures of the polymers shown in Fig. 1 of the article are presented below. We apologize any inconvenience this mistake may have caused.

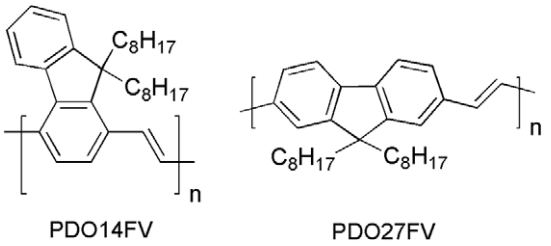

PDO14FV PDO27FV

Fig. 1. Structures of poly(9,9-dioctyl-1,4-fluorenylenevinylene), PDO14FV and poly(9,9-dioctyl-2,7-fluorenylenevinylene), PDO27FV.

DOI of original article: 10.1016/j.orgel.2007.05.007
* Corresponding author. Tel./fax: +55 41 33613645.
E-mail address: iah@fisica.ufpr.br (I.A. Hümmelgen).

1566-1199/$ - see front matter
doi:10.1016/j.orgel.2008.04.002

that most of the material ends up as waste. Reverse gravure (RG) coating, on the other hand, is a roll-to-roll technique suitable for mass fabrication. This method produces thin homogeneous multi-layers over large areas for a wide range of ink viscosities [9,10].

Recently, we presented a low-voltage hygroscopic insulator field effect transistor (HIFET) printed and coated on a pre-patterned plastic substrate in air [10]. While traditional organic FETs usually operate at high voltages and require very smooth substrates for achieving high yield in the fabrication, the HIFET operates at low-voltage [11,12] and is rather insensitive to the roughness of the substrate [13] due to the operation principle [14] and the large thickness of the insulator. This ion modulated transistor is an excellent candidate for low-cost roll-to-roll manufacturing and can e.g. be used in humidity sensing applications [15] and when high switching speed is not necessary.

In this work we present a five-step process for fabricating all-printed HIFETs on plastic substrates completely by means of mass fabrication methods in room atmosphere. The RG coating technique was used to apply the semiconductor and insulator layers, while the electrodes were IJ printed. The transistors have been fabricated completely by roll-to-roll compatible printing and coating methods that are used in the printing industry.

2. Experimental

The HIFET geometry and process steps (Step 1–5) are shown in Fig. 1a. The substrate, a 50 μm thick Mylar® A film from DuPont Teijin Films, was washed with distilled water, acetone and isopropanol before printing. The IJ printer was a drop-on-demand Dimatix™ Materials Printer (DMP-2800) and the cartridge (DMC-11610) consisted of 16 nozzles with effective diameters of 21.5 μm. In Step 1, transistor S/D electrodes were fabricated by IJ printing a silver nanoparticle dispersion from Cabot with a drop spacing of 30 μm. The finger width (see Fig. 1b) of the electrodes was 200 μm, the channel width (W) was 1.5 mm and the channel length (L) was about 40 μm. A sheet resistance of 1–2 Ω/□ was achieved after sintering the electrodes at 120 °C on a hotplate for 20 min.

A low viscosity (~1 mPa s) semiconductor solution was obtained by dissolving 1.0 wt.% regioregular poly(3-hexylthiophene) (P3HT) from Plextronics in toluene and p-xylene (1:1). The solvent mixture was used to combine a lower evaporation rate (p-xylene) with a higher solubility (toluene). The insulator solution consisted of 10 wt.% of poly(4-vinyl phenol) (PVP) from ChemFirst/DuPont mixed with isopropanol. The viscosity was measured to about 10 mPa s by a Bohlin VOR rheometer. The P3HT- and PVP-layers were subsequently RG coated (Step 2 and Step 3) with a tabletop Mini-Labo™ test coater at a web speed (v_{web}) of 1.6 m/min and a roll speed (v_{roll}) of 0.6 m/min. A 20 mm diameter metal gravure roll with continuous trihelical grooves, 4.7 lines/mm, was used.

For IJ printing the gate electrode, the print head was optically aligned to print on the transistor channel area. As gate electrode material the conductive polymer poly(3,4-ethylene dioxythiophene) and poly(styrene sulfonate) (PEDOT:PSS) was used. In Step 4, a layer of the low-conductive Baytron P (Jet PE FL from H.C. Starck) was first IJ printed. This PEDOT:PSS water dispersion had a solid content of 1.49 wt.%, a viscosity of 8.5 mPa s and a conductivity of 1.4 mS/cm [16]. The non-crosslinked PVP was protected by this layer, when the more conductive, but ethanol containing, Baytron P (Jet HC) was IJ printed in Step 5. The ink had a solid content of 0.7 wt.%, a viscosity of 12 mPas and a conductivity of 74 S/cm [16].

All electrical characterizations of the HIFET were done in air in darkness at a relative humidity of 31–33% using an Agilent 4142B parameter analyzer and the conductivity measurements were done in a two probe configuration. The HIFET was stored in ambient air and in darkness between the measurements. The thickness of P3HT- and PVP-layers was determined from the absorption spectra and the surfaces were imaged with an atomic force microscope (AFM) (Park Scientific). The work function of evaporated silver on a Mylar® A substrate was measured in air as a function of time with the Kelvin probe technique. To determine the chemical composition of the IJ printed silver electrodes and to evaluate the P3HT coating on the electrodes, X-ray photoelectron spectroscopy (XPS) (Physical Electronics) was used.

3. Results and discussion

The characteristics of an all-printed HIFET measured two and 48 days after fabrication are shown in Fig. 2. The transistor switches between on- and off-state with a ratio

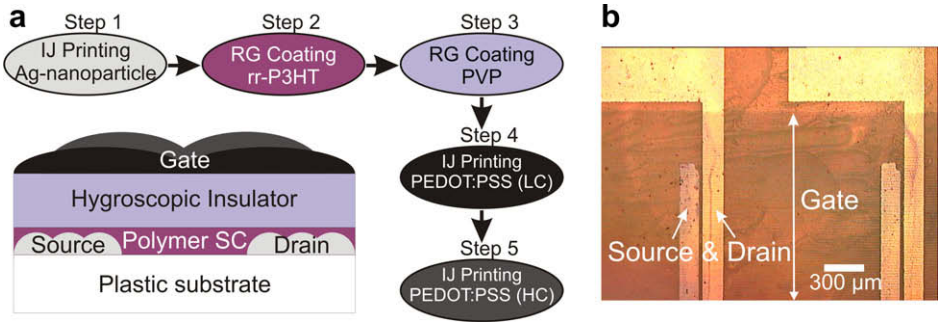

Fig. 1. (a) A five-step process flow for the fabrication of all-printed low-voltage organic transistors and a schematic image of a cross section of the transistor. Semiconductor is denoted as SC, while low- and high-conductive is denoted as LC and HC and (b) An optical microscope top-view picture of two all-printed devices.

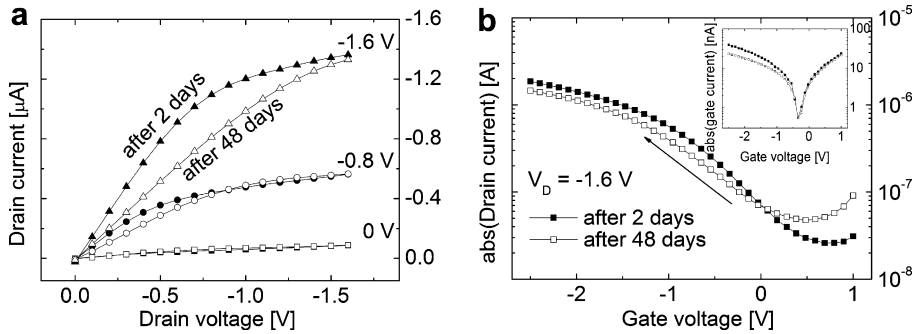

Fig. 2. (a) Output and (b) transfer curves for an all-printed HIFET measured in air two and 48 days after fabrication. The inset in (b) shows the gate current for the same measurements.

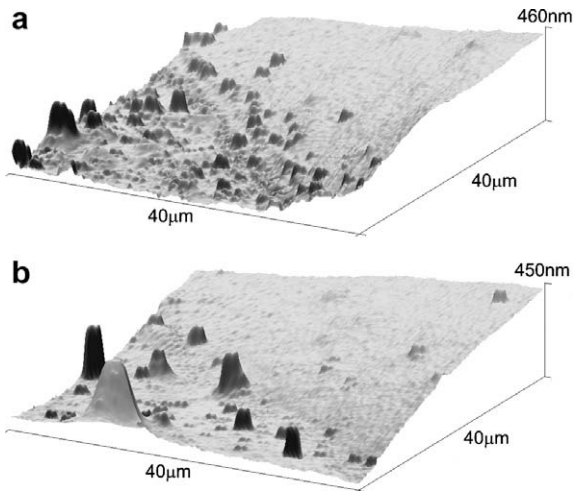

Fig. 3. AFM images of the edge of an IJ printed silver electrode on the Mylar® A substrate (a) before and (b) after it was RG coated with the semiconductor.

of 10^2. For both measurements the threshold voltage (V_T) was estimated to 0.5 V, by extrapolating the linear part of $\sqrt{I_D}$ in the transfer curve to the x-axis.

Two AFM images of IJ printed silver electrodes on the Mylar® A substrate are shown in Fig. 3, with and without the coated P3HT layer. The thickness of the electrodes increase gradually and no sign of the unwanted "ring stain effect" is seen [3]. The height of the IJ printed contacts was measured to 200–400 nm, while the size of the not fully sintered silver nanoparticles was close to 50 nm. We noted that, although the thickness of the contacts were almost one third of the insulator thickness, no clear increase in the gate leakage was observed as compared to when much thinner evaporated gold contacts [10] were used.

The RMS roughness of the Mylar® A substrate was measured with the AFM to 25-50 nm and only slightly lower values on the RG coated P3HT surface. However, it has been shown that the charge transport in the HIFET is as good on this rather rough substrate as on a smoother substrate [13].

The thickness of the RG coated layers was determined to 25–35 nm for P3HT and 1.2–1.3 μm for PVP. These values are consistent with results documented earlier for the same coating parameters [10]. By e.g. changing the coating speed or the concentration of the solution, it is possible to adjust the coating thickness.

Since the S/D electrodes were about ten times thicker than the P3HT layer, a large contact resistance due to poor step coverage at the contact edges could have been expected. This effect was noticed by Richards et al. [17] with the same geometry when the thickness of the spin coated semiconductor layer was similar to or smaller than the evaporated gold electrodes. However, in this work, such effects were not seen. Despite the rough appearance, the RG coated P3HT layer covered both the channel area and the electrodes. The latter was not only observed optically, but was also supported by XPS measurements on the P3HT coated silver electrodes, which showed very clear sulphur peaks but no detectable silver signal, indicating a complete P3HT coverage to a thickness of several nanometres all over the investigated area (100 μm × 100 μm). The good P3HT coverage can be explained by the lower surface tension of the P3HT solution as compared to the surface energy of the Mylar® A substrate and the silver electrodes as well as the smoothening properties of the RG coating method.

The IJ printed S/D electrodes in this work consist of silver and are thicker than the evaporated gold electrodes

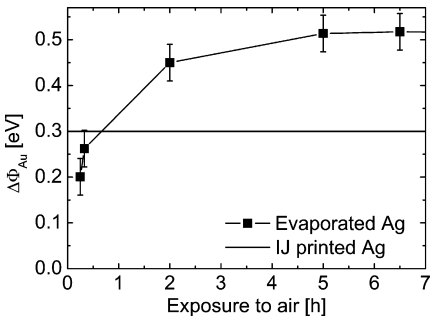

Fig. 4. The relative work function ($\Delta\Phi$) of evaporated silver on a Mylar® A substrate as measured by the Kelvin probe technique in air as a function of time. The absolute value of the work function increased upon exposure to air and saturated at a level approximately 0.5 eV above a reference sputtered gold sample. The measured work function for the annealed IJ printed silver nanoparticle dispersion is indicated at 0.3 eV.

used in Ref. [10]. To investigate the effect on the contact resistance from the material change, the work function of silver electrodes was measured and compared to that of gold. Kelvin probe measurements in air of evaporated silver showed a change in the work function during exposure to air, as can be seen in Fig. 4. The work function of silver increased rapidly the first hours and saturated at a level approximately 0.5 eV above a reference gold sample. For the annealed IJ printed silver the work function was measured to about 0.3 eV above the gold sample.

According to literature, the work function of sputtered gold is 5.1–5.2 eV, while silver should have a work function of approximately 4.3 eV. However, these values originate from measurements in ultra-high vacuum and on clean non-oxidized surfaces. The work function of gold that had been exposed to air has been measured to values around 4.7 eV [18] and the difference was explained by the hydrocarbon adsorption on the surface in air. If this is used as a reference value of the sputtered gold sample, the absolute work function value of the annealed IJ printed silver electrodes from the Kelvin probe measurements would then be roughly 5.0 eV. This value is consistent with what others have measured for oxidized silver [19,20].

The presence of adsorbed oxygen on the silver electrodes was confirmed by the XPS measurement. On the surface, the atomic concentrations were determined to about 46% carbon, 34% silver, 14% oxygen and 6% nitrogen, while no oxygen was detected in the bulk after sputtering with argon ions. Since the work function of the silver electrodes seem to be almost equal to the ionization potential of P3HT (5.1 eV), a very low energy barrier should be expected, which can explain why no Schottky barrier originating super-linear behaviour at low S/D voltage (V_D) was seen in the transistor characteristics in Fig. 2. Instead the contact is ohmic and an estimation of the upper value of the contact resistance in the transistors of less than 100 kΩ cm (after two days) is obtained by looking at the drain current (I_D) in the linear regime at a gate voltage (V_G) of −1.6 V. Since twice as large slope was measured already at a gate voltage of −0.8 V on all-printed HIFETs with a thicker gate electrode [13], the upper value of the contact resistance can be reduced with a factor of two to less than 50 kΩ cm. The true contact resistance is, however, most likely even smaller, since the channel length was rather long (~40 μm) and the channel resistance therefore can be explained by the resistance of the semiconductor.

The large charge injection area associated with the chosen top-gate bottom-contact geometry is also a reason why the contact resistance is significantly smaller than the channel resistance [17]. There is also a small contribution to the contact resistance from the charge transport through the silver oxide and the bulk of P3HT. Silver is easily oxidized, but in contrary to most metal oxides, silver oxide is slightly conductive with a value of about 50 μS/cm and the oxide layer protects the metal from further oxidation [21].

The non-crosslinked PVP layer was dissolved by the ethanol containing high-conductive Baytron P (Jet HC) formulation. Therefore, a protective Baytron P (Jet PE FL) layer (Step 4) was introduced between the PVP layer and the high-conductive Baytron P (Jet HC). The IJ printable PEDOT:PSS water dispersion Baytron P Jet PE FL is insoluble after drying, but has a low conductivity. Consequently, with the two-layer gate electrode, most of the transistors were working and showing similar transistors characteristics. A different approach was used in Ref. [10], where a one layer gate contact was IJ printed from an ink consisting of Baytron P, water and a small amount of a non-polar surfactant (Triton X-100). This resulted, however, in a large hysteresis in the transistor characteristics, but was not seen in this work when the low-conductive Baytron P (Jet PE FL) layer was used.

In Fig. 2a, a decrease in the output current is noticed 48 days from fabrication, especially in the linear part of the curves. No major changes have earlier been observed for shorter ageing time when stored below 65% relative humidity in air. The channel conductance (g_D) is derived from the analytical expression of the drain current (I_D) in the linear region:

$$g_D = \frac{dI_D}{dV_D} = \left(\frac{W}{L}\right) C_i \mu (V_G - V_T), \quad (1)$$

where C_i is the dielectric capacitance per unit area and μ is the hole mobility in the active channel. Since W, L and V_T were constant, the decrease in conductance with time is either due to a decrease in μ, C_i or V_G. In Fig. 2, the channel conductivity at $V_G = 0$ V is identical at both measurements. If assuming that the unintentional doping of P3HT is saturated, which is reasonable when both solutions and fabrication steps are done in air, then μ is constant. Therefore, we do not consider a change in the mobility as a major contributor to a reduced channel conductance, which also a constant V_T supports. The gate current, on the other hand, in the inset of Fig. 2b, has decreased between the measurements, while the conductivity of the PEDOT:PSS gate electrode was reduced by a factor of three. Hence, the observed degradation can be ascribed to a reduced conductivity of the gate electrode and can, therefore, be solved simply by IJ printing a thicker or more stable conductive ink on top of the protective layer. Yet, the reduced gate conductivity cannot explain all the results, since the saturated drain currents are equal at both measurements. Consequently, a difference in the effective capacitance, between the two measurements cannot be ruled out. Nevertheless, the HIFET has been documented to work even after one year in ambient air [15].

4. Summary

We have presented a five-step method of printing and coating low-voltage organic transistors in air, where all fabrication steps are suitable for roll-to-roll manufacturing. Although, the IJ printed S/D electrodes were of silver and rather thick, the contact resistance was small and complete semiconductor coverage on the S/D electrodes was confirmed by XPS measurements. After 48 days of storing the HIFET in ambient air it still showed low-voltage behaviour. The channel conductance was, however, slightly reduced due to a reduced conductivity of the IJ printed PEDOT:PSS gate electrode. This cost-effective fabri-

cation method generates organic transistors operating at low-voltage and with a high yield.

Acknowledgments

The authors would like to thank Dr. Himadri Majumdar for help with the AFM and for fruitful discussions. This work is financed by the National Center of Excellence via Åbo Akademi Foundation and the Academy of Finland.

References

[1] H. Sirringhaus, T. Kawase, R.H. Friend, T. Shimoda, M. Inbasekaran, W. Wu, E.P. Woo, Science 290 (2000) 2123.
[2] Y. Liu, K. Varahramyan, T. Cui, Macromol. Rapid Commun. 26 (2005) 1955.
[3] H. Ko, H. Pan, C.P. Grigoropoulos, C.K. Luscombe, J.M.J. Fréchet, D. Poulikakos, Nanotechnology 18 (2007) 345202.
[4] Y.-Y. Noh, N. Zhao, M. Caironi, H. Sirringhaus, Nature Nanotech. 2 (2007) 784.
[5] A. Knobloch, A. Manuelli, A. Bernds, W. Clemens, J. Appl. Phys. 96 (2004) 2286.
[6] T. Mäkelä, S. Jussila, H. Kosonen, T.G. Bäcklund, H.G.O. Sandberg, H. Stubb, Synth. Met. 153 (2005) 285.
[7] A.C. Huebler, F. Doetz, H. Kempa, H.E. Katz, M. Bartzsch, N. Brandt, I. Hennig, U. Fuegmann, S. Vaidyanathan, J. Granstrom, S. Liu, A. Sydorenko, T. Zillger, G. Schmidt, K. Preissler, E. Reichmanis, P. Eckerle, F. Richter, T. Fischer, U. Hahn, Org. Electron. 8 (2007) 480.
[8] A. Blumel, A. Klug, S. Eder, U. Scherf, E. Moderegger, E.J.W. List, Org. Electron. 8 (2007) 389.
[9] R.W. Hewson, N. Kapur, P.H. Gaskell, Chem. Eng. Sci. 61 (2006) 5487.
[10] N.J. Kaihovirta, D. Tobjörk, T. Mäkelä, R. Österbacka, Adv. Eng. Mater. 10 (2008) 640.
[11] H.G.O. Sandberg, T.G. Bäcklund, R. Österbacka, H. Stubb, Adv. Mater. 16 (2004) 1112.
[12] T.G. Bäcklund, R. Österbacka, H. Stubb, J. Bobacka, A. Ivaska, J. Appl. Phys. 98 (2005) 074504.
[13] N.J. Kaihovirta, D. Tobjörk, T. Mäkelä, R. Österbacka, Appl. Phys. Lett. 93 (2008) 053302.
[14] T.G. Bäcklund, H.G.O. Sandberg, R. Österbacka, H. Stubb, Appl. Phys. Lett. 85 (2004) 3887.
[15] H.G.O. Sandberg, T.G. Bäcklund, R. Österbacka, S. Jussila, T. Mäkelä, H. Stubb, Synth. Met. 155 (2005) 662.
[16] Technical data sheet received from H.C. Starck GmbH.
[17] T.J. Richards, H. Sirringhaus, J. Appl. Phys. 102 (2007) 094510.
[18] S. Rentenberger, A. Vollmer, E. Zojer, R. Schennach, N. Koch, J. Appl. Phys. 100 (2006) 053701.
[19] K. Seki, T. Tani, H. Ishii, Thin Solid Films 273 (1996) 20.
[20] L. Bürgi, T.J. Richards, R.H. Friend, H. Sirringhaus, J. Appl. Phys. 94 (2003) 6129.
[21] D.R. Lide, CRC Handbook of Chemistry and Physics, 83rd ed., CRC Press, Boca Raton FL, 2002.

Charge injection through electrode/semiconductor contacts plays a crucial role for the device performance of OTFTs. The charge injection strongly depends on the energy alignment [17–19] and the film morphology of organic semiconductors [14,15,20–23] at electrode/semiconductor contacts. As good molecular ordering of organic semiconductors results in the high charge mobility [1,13,24–27], it is desirable that the distribution of the molecular ordering is continuous and uniform in the entire active layer. When an organic semiconductor active layer contacts bottom metal electrodes, however, the interfacial interaction of organic semiconductor with electrode contacts usually breaks the molecular ordering and disrupts the continuity of the molecular ordering distribution bordering the electrodes. The interfacial interaction results in the inferior device performance of bottom-contact OTFTs compared to top-contact OTFTs [14,15] (in top-contact OTFTs, the molecular ordering is mainly modulated by dielectric/semiconductor interfaces and its distribution may be continuous and uniform in the entire active layer). To improve the device performance of bottom-contact pentacene thin-film transistors (TFTs), self-assembled monolayers (SAMs) of alkanethiol have been used to modify the surfaces of gold (Au) electrodes, improving the morphology of pentacene bordering the electrodes [15,20,21]. On the other hand, SAMs have been demonstrated to be a versatile technique for modulation of Shottky barrier height at metal/semiconductor contacts [28–33]. By chemisorbing SAMs of molecules with an intrinsic electric dipole moment and forming a highly ordered molecular layer on a metal surface, Schottky barrier height at a metal/semiconductor contact can be raised or lowered to significantly affect the charge injection. Thus, SAMs may be effective technique to improve the charge injection at electrode/semiconductor contacts for TFTs of poly(3,3‴-didodecylquaterthiophene) (PQT-12), which is a novel high per- formance polymeric semiconductor with strong environmental stability [8].

Recently, high performance PQT-12 TFTs have been demonstrated in top-contact device configuration with mobilities up to 0.18 $cm^2 V^{-1} s^{-1}$ on silane-modified silicon substrates [8,13]. In bottom-contact devices with bare Au electrodes, PQT-12 TFTs showed reduced mobilities of about 0.02–0.09 $cm^2 V^{-1} s^{-1}$ on silane-modified silicon substrates [34,35]. Employing printable metal conductors from thiol-stabilized Au and organic acid-stabilized silver nanoparticles precursors as bottom S–D electrodes, PQT-12 TFTs gave enhanced mobilities of 0.07–0.16 $cm^2 V^{-1} s^{-1}$ in bottom-contact device configuration [36–38]. It was suggested that the improved contacts between PQT-12 and printable metal conductors resulted in the improved performance of bottom-contact devices [36–38]. However, no study of the electrode/PQT-12 contacts has been reported yet.

Here we report the modification of Au S–D electrode surfaces by SAMs of an alkanethiol and a perfluorinated alkanethiol for bottom-contact PQT-12 TFTs. The SAMs modifications of Au surface can modulate Schottky barrier height at electrode/PQT-12 contacts and improve the molecular ordering of PQT-12 adjacent to the Au S–D electrodes. The SAMs modifications led to significant improvements in device performance of PQT-12 TFTs. Despite the higher hole Schottky barrier, PQT-12 TFTs with Au electrodes surface-modified with alkanethiol SAMs showed much higher mobilities, up to 0.09 $cm^2 V^{-1} s^{-1}$, than those of PQT-12 TFTs with bare Au electrodes (~0.015 $cm^2 V^{-1} s^{-1}$), due to the improved molecular ordering of PQT-12 at electrode/PQT-12 contacts. With Au electrodes surface-modified with perfluorinated alkanethiol SAMs, PQT-12 TFTs exhibited dramatically increased mobilities of up to 0.19 $cm^2 V^{-1} s^{-1}$, which was attributable to the combined effect of the lower hole Schottky barrier and the improved PQT-12 molecular ordering.

2. Experimental

1-Decanethiol (96%) (DT) and 1*H*,1*H*,2*H*,2*H*-perfluorodecanethiol (97%) (FDT) were used as received from Sigma–Aldrich without further purification. Bottom-contact OTFTs were fabricated on a heavily n-doped silicon (Si) wafer with Au (50 nm) S–D electrodes adhered on a titanium layer (1 nm) and patterned using lift-off technique. The silicon wafer and its surface SiO_2 layer (100 nm) served as gate electrode and gate dielectric, respectively. The channel width was maintained as 10,000 μm and the channel lengths were 20, 40, 60, 80, 100 μm. For PQT-12 TFTs with bare Au S–D electrodes, the electrodes were cleaned successively with ultrasonication in acetone, methanol, and de-ionized water. The SiO_2 surfaces with patterned Au electrodes were briefly plasma-cleaned and treated with 3 mM solution of octyltrichlorosilane (OTS-8) in hexane at room temperature for 15 min, rinsed with hexane and isopropanol, and dried with nitrogen gas. For OTFTs with Au–DT and Au–FDT S–D electrodes, the patterned Au electrodes were then immersed into 3 mM solution of DT and FDT in absolute ethanol at room temperature for 24 h, rinsed with hexane and ethanol, and dried with nitrogen gas. Finally, PQT-12 semiconductor layers of about 60 nm were deposited on the bare Au, Au–DT, and Au–FDT electrode patterns by spin-coating a solution of PQT-12 in dichlorobenzene (0.3 wt%). The semiconductor layer was then dried, annealed at 125 °C for 30 min, and cooled to room temperature overnight in vacuum. The OTFTs were characterized using an Agilent 4157B Semiconductor Parameter Analyzer System. The AFM experiments were conducted with a Nanoscope IIIa MultiMode scanning probe microscope (Digital Instruments) in tapping mode with a scan rate of 0.5 Hz. The device mobilities in linear and saturation regimes were extracted from the following equations neglecting contact resistance entirely: [1,7].

Linear regime :

$$(V_{ds} \ll V_{Gs} - V_T) : I_{DS} = V_{DS} C_i \mu (V_{GS} - V_T) W/L;$$

Saturation regime :

$$(V_{ds} > V_{Gs} - V_T) : I_{DS} = C_i \mu (V_{GS} - V_T)^2 W/2L$$

where I_{DS} is the drain current, C_i is the capacitance per unit area of the gate dielectric layer, and V_{GS} and V_T are gate voltage and threshold voltage.

3. Results and discussion

1-Decanethiol (DT) and 1*H*,1*H*,2*H*,2*H*-perfluorodecanethiol (FDT) SAMs were employed to modify Au electrode surfaces for PQT-12 TFTs. Fig. 1 shows output characteristics of representative PQT-12 TFTs with Au, Au–DT, Au–FDT S–D electrodes, generally following p-type enhanced mode of metal-oxide semiconductor field-effect transistors (MOSFETs). The output characteristics of the device in Fig. 1a show pronounced curvatures at low V_{DS}, indicating that the charge injection process is non-Ohmic and contact-limited [39,40] due to the inefficiency of charge injection at Au/PQT-12 contacts. The device with bare Au S–D electrodes had linear and saturation mobilities of only about 0.0012 and 0.015 $cm^2\ V^{-1}\ s^{-1}$ (Fig. 2), respectively, and a current on/off ratio of about 10^5. The linear and saturation device mobilities were estimated by ignoring contact effect. The mobility of bottom-contacts PQT-12 TFTs with bare Au electrodes here is lower than those of the bottom-contact PQT-12 TFTs previously reported [34,35]. The relative low mobility is probably due to the slight degradation of high performance PQT-12 semiconductor [8], which has been stored under ambient atmosphere for almost 2 years. The environmental stability of PQT-12 is much higher than that of regioregular poly(3-hexylthiophene) (P3HT) under the same ambient condition [8].

The device with Au–DT S–D electrodes showed a much higher linear and saturation mobilities of 0.04 ± 0.01 and 0.08 ± 0.01 $cm^2\ V^{-1}\ s^{-1}$, respectively, and a current on/off ratio of about 10^6 with nearly Ohmic injection in Fig. 1b. On the other hand, the device with Au–FDT electrodes gave a dramatically improved device linear and saturation mobilities of 0.08 ± 0.01 and 0.17 ± 0.02 $cm^2\ V^{-1}\ s^{-1}$ respectively, and a current on/off ratio of about 10^6. The linear and saturation device mobilities for Au–DT and Au–FDT electrodes were also estimated by ignoring contact effect. Generally, the band bending at high gate voltages could dominate the energy offset at the electrode/semiconductor contacts. As shown in Fig. 1, the saturation drain currents for devices with Au, Au–DT, and Au–FDT S–D electrodes under $V_G = -40$ V are significantly. This result suggests that the influence of SAMs is significant in present work. The role of SAMs under high gate voltage is not well-understood yet. As shown in Fig. 2, the characteristics of improved mobilities in linear and saturation regimes due to Au–DT and Au–FDT S–D electrodes are widespread in the V_{GS} regime. The device mobility of 0.17 ± 0.02 $cm^2\ V^{-1}\ s^{-1}$ observed here is parallel to those of the high performance PQT-12 TFTs in both top-contact and bottom-contact device configurations [8,13,34–38].

To understand electrode/PQT-12 contacts, where the contact resistance can be associated with the device performance, the contact resistances of PQT-12 TFTs with bare Au, Au–DT, and Au–FDT electrodes were compared by channel length scaling analysis (transfer line method). The device resistance dependence on the channel length was analyzed in the linear regime ($V_{DS} \ll V_{GS} - V_T$). In this regime, device "on" resistance, R_{on}, can be approximately expressed as [41–43]:

$$R_{on} = \frac{\partial V_{DS}}{\partial I_{DS}}\bigg|_{V_{DS}}^{V_{GS}} = R_{Ch} + R_C = \frac{L}{W\mu_i C_i (V_{GS} - V_T)} + R_C, \qquad (1)$$

where R_{Ch} and R_c are the channel length L dependent channel resistance and the channel length L independent contact resistance, respectively. μ_i is the intrinsic mobility of the semiconductor.

Fig. 3 shows a plot of width normalized Ron of devices with bare Au, Au–DT, and Au–FDT electrodes as a function of L at $V_{GS} = -40$ V and $V_{DS} = -3$ V. The experimental data are well expressed by Eq. (1) in first order, with Ron · W linearly depending on L. As determined from the intercept of linear fitting, the contact resistances for bare Au, Au–DT, and Au–FDT electrodes are about 580 kΩ, 19 kΩ, and 4 kΩ, respectively. The reduction of the contact resistance for Au–DT and Au–FDT electrodes is consistent with the observation by electrostatic force microscopy that charge injection from Au electrode into pentacene was improved due the SAMs modification of Au electrodes [21]. The corrected mobilities from Fig. 3 for PQT-12 TFTs with bare Au, Au–DT, and Au–FDT electrodes are about 0.05, 0.09, and 0.19 cm2 V−1 s−1, respectively. The channel length scaling analysis suggests that the surface-modifications of Au

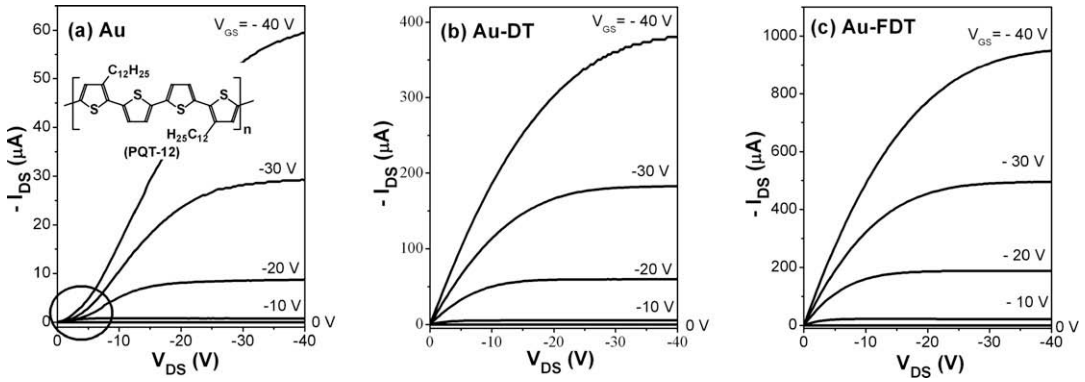

Fig. 1. Source–drain current I_{DS} *vs* source–drain voltage V_{DS} as a function of gate voltage V_{GS} for bottom-contact PQT-12 TFTs with (a) bare Au, (b) Au–DT, and (c) Au–FDT S–D electrodes. The channel length and width are, respectively, 20 μm and 10,000 μm for all PQT-12 TFTs. The insert in (a) is chemical structure of PQT-12.

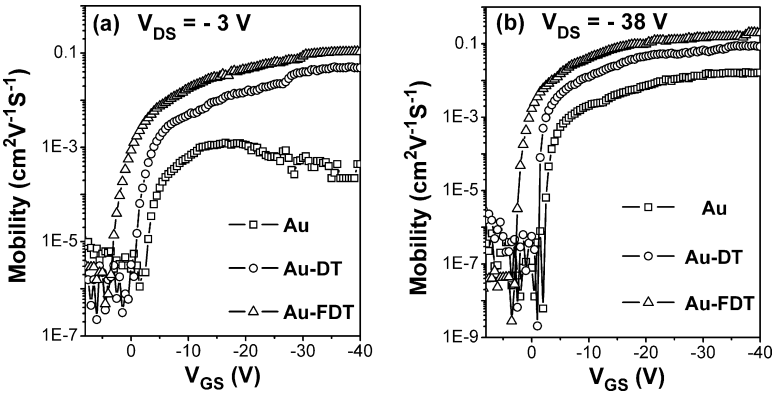

Fig. 2. (a) Linear (V_{ds} = −3 V) and saturation (V_{ds} = −38 V) device mobilities of PQT-12 TFTs with Au, Au–DT, and Au–FDT S–D electrodes. V_T of PQT-12 TFTs with bare Au, Au–DT, and FDT are about −14.7 V, −12.1 eV, and −11.6 V, respectively. The channel length and width are, respectively, 20 and 10,000 μm for all PQT-12 TFTs.

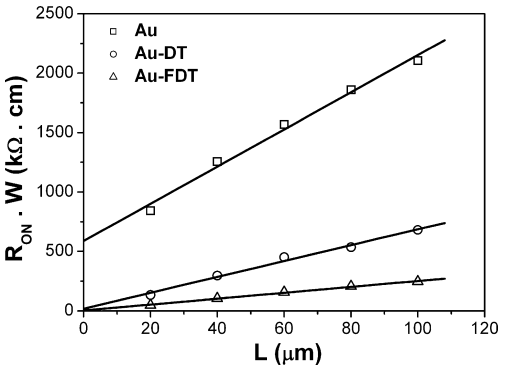

Fig. 3. Relationship between the width normalized "on" resistance and channel length at V_{GS} = −40 V and V_{DS} = −3 V for bottom-contact PQT-12 TFTs with bare Au, Au–DT, and Au–FDT S–D electrodes.

S–D electrodes by DT and FDT SAMs significantly decrease the contact resistance for bottom-contact PQT-12 TFTs, resulting in improved device performance. The different contact resistances with Au, Au–DT, and AU–FDT electrodes should be associated with the properties of electrode/PQT-12 contacts, which determine the charge injection in PQT-12 TFTs.

DT and FDT SAMs on Au surfaces (schematically illustrated in Fig. 4) have opposite intrinsic dipoles [28], which can result in opposite Schottky barrier height modulations for charge injection at electrode/PQT-12 contacts. When alkanethiol chemisorbs onto Au(111), the thiol group generally loses its proton upon adsorption and binds to the Au as a thiol anion. DT SAMs with densely-packed 2D structure on the Au(111) usually form a commensurate $\sqrt{3} \times \sqrt{3}R30^{\circ}$ hexagonal lattice with an off-normal tilt angle, α, of ~30° [44]. The sulfur atoms have a distance of 4.97 Å and the DT grafting density is about 4.7×10^{18} m^{-2} on Au(111). On the other hand, densely-packed FDT SAMs form a commensurate hexagonal lattice with a lattice constant of about 5.8 Å and an off-normal tilt angle is about 12° [45]. The FDT grating density on Au(111) is estimated to be about 3.4×10^{18} m^{-2}.

At electrode/semiconductor contacts, Schottky barrier heights for electron injection, φ_{Bn}, and hole injection, φ_{Bp}, may be expressed in the relations by Eqs. (2), (3) [17], respectively:

$$\phi_{Bn} = \phi_M + \Delta\phi_{Dipole} - \chi \quad (2)$$

$$\phi_{Bp} = E_g - (\phi_M + \Delta\phi_{Dipole} - \chi) \quad (3)$$

$$\Delta\phi_{Dipole} = N\left(\frac{\mu_{\perp}}{\varepsilon_0\kappa} + \frac{\mu_{Au-S}}{\varepsilon_0\kappa_{Au-S}}\right)(SAMs) \quad (4)$$

where φ_M is the work function of the electrode, χ and E_g are, respectively, the electron affinity and band gap of the organic semiconductor, and $\Delta\varphi_{Dipole}$ is the Schottky barrier height change due to an interface dipole at electrode/semiconductor contacts. For $\Delta\varphi_{Dipole}$ due to the thiol SAMs dipole on Au surfaces in Eq. (4), the first term represents

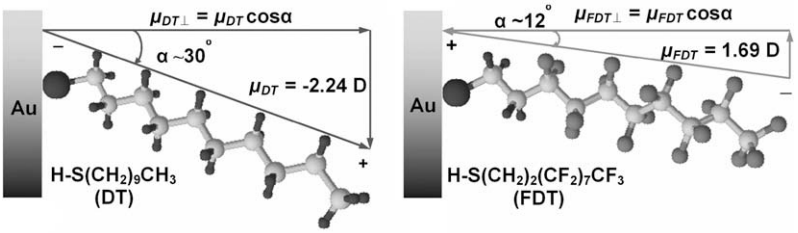

Fig. 4. Schematic illustration of dipole moments of (a) 1-decanethiol (DT) and (b) 1*H*,1*H*,2*H*,2*H*-perfluorodecanethiol (FDT) on Au(111) surfaces.

the barrier change due to the effective dipole moment of the SAMs (there may be depolarization effect on the effective dipole moment of SAMs due to the charge transfer between SAMs and the substrate.[46]), and the second term represents the barrier change taking into account the intrinsic Au-S dipole moment. [28,29] N is grafting density, $\mu_{\perp}$ is the component of the dipole moment of the SAMs normal to the Au surface, ε_0 is the permittivity of the vacuum, κ is the dielectric constant of the dipole layer of DT or FDT SAMs, μ_{Au-S} is the dipole moment due to the Au–S charge-transfer interaction, and κ_{Au-S} is dielectric constant of the Au–S layer. The Schottky barrier height change at electrode/PQT-12 contacts is defined to be positive if the direction of the effective dipole moment points to the Au surface, as shown in Fig. 4b.

The schematic energy-level diagrams of Au/PQT-12, Au–DT/PQT-12, and Au–FDT/PQT-12 interfaces were illustrated in Fig. 5a–c, respectively. Since the effective dipole moment of FDT SAMs and Au–S layers both have the same

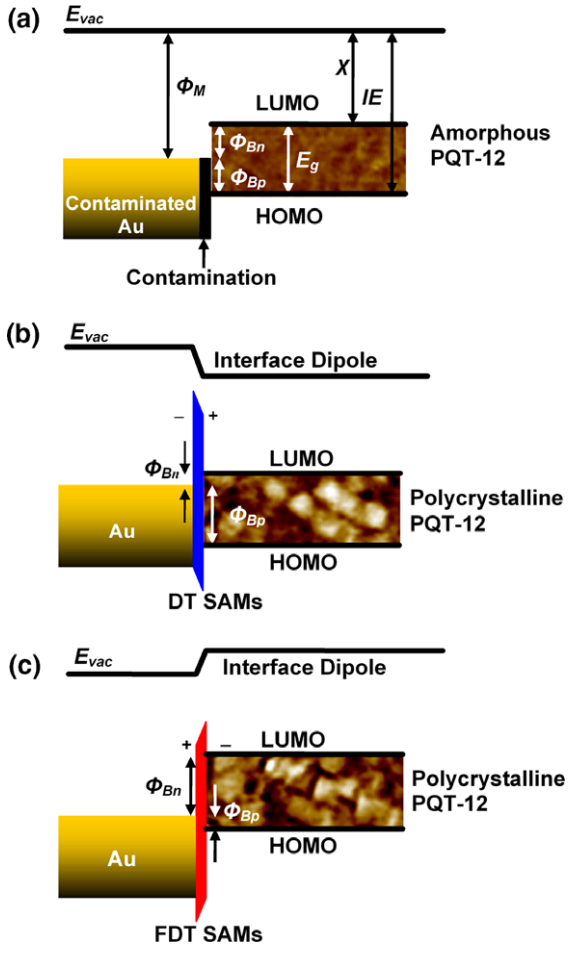

Fig. 5. Schematic energy-level diagrams of: (a) Au/PQT-12, (b) Au–DT/PQT-12, and (c) Au–FDT/PQT-12 interfaces. Local vacuum energy levels (E_{vac}) of Au and PQT-12 in (a) were set at the same level for illustrative clarity of Schottky barrier height modulation due to DT and FDT SAMs in (b) and (c). + and – denote the direction of the interface dipole. φ_M: Au work function; IE: ionization energy; χ: electron affinity.

direction and point from the SAM to the Au surface, the chemisorption of FDT SAMs onto Au surface can induce a positive $\Delta\varphi_{Dipole}$ at electrode/semiconductor contacts. The Schottky barrier height change due to interfacial FDT SAMs can be estimated to be about 1.0 eV [47]. This suggests that the interfacial FDT SAMs can decrease φ_{Bp} for hole injection (Fig. 5c). On the other hand, the chemisorption of DT SAMs onto Au surface may induce a negative $\Delta\varphi_{Dipole}$ at an electrode/semiconductor contact because the effective dipole moment of Au–S layers is smaller than that of DT SAMs [28]. The interfacial DT SAMs may induce about –1.3 eV change of Schottky barrier height [47] and produce an increase of φ_{Bp} for hole injection (Fig. 5b). The modulation tendency of Schottky barrier height by DT and FDT SAMs could be opposite,[28] although the change of the Schottky barrier height might compromised by the possible depolarization effect on effective dipole moments of DT and FDT SAMs [46].

The solution-processable devices were usually fabricated under ambient condition and the impact of contamination from ambient exposure cannot be negligible for the work function of Au electrodes. The work function of Au electrodes contaminated from ambient exposure will be reduced by 0.7–0.9 eV from that of the clean Au electrodes under ultra-high vacuum (~5.1 eV) [19,48]. When the TFTs devices operates with polycrystalline Au electrode, the Au contacts could introduce a distribution in the interfacial states due to interactions and charge transfer between electrodes and semiconductors at contacts [19]. Energy-level alignment at electrode/semiconductor interface can give rise to an injection barrier for charge injection [49]. The HOMO level of PQT-12 locates at about 5.2 eV [8,50]. The injection barrier formed at bare Au/PQT-12 contacts is illustrated in Fig. 5a.

Charge transport across metal/semiconductor contacts can be described by thermionic emission-diffusion model [51,52]:

$$J_p \propto \mu \exp(-q\phi_{Bp}/kT), \tag{5}$$

where J_p and φ_{Bp} are current density and Schottky barrier height for hole injection; k is the Boltzmann constant and T is temperature. FDT SAMs on Au surface forms a layer with positive dipole moment, giving rise to a decrease of φ_{Bp} at electrode/PQT-12 contacts, which may improve the hole injection for PQT-12 TFTs. Conversely, DT SAMs on Au surface imposes a thin layer with negative dipole moment between Au and PQT-12, resulting in an increase of φ_{Bp} for hole injection at electrode/PQT-12 contacts.

Recently, Stoliar et al. have demonstrated a SAM-assisted charge injection via a tunneling mechanism at electrode/pentacene contacts for pentacene TFTs [21]. charge carrier injection at Au–DT/ or Au–FDT/PQT-12 contacts comprises mainly two steps: (1) tunneling of charge carrier through DT or FDT SAMs and (2) charge injection into HOMO or LUMO of PQT-12 semiconductor. On the other hand, Stoliar et al. have also shown that the charge injection is very sensitive to the ordering of pentacene semiconductor at the interface [21]. To understand the improved hole injection in Fig. 1b, the morphologies of PQT-12 at electrode/PQT-12 contacts are investigated in this work.

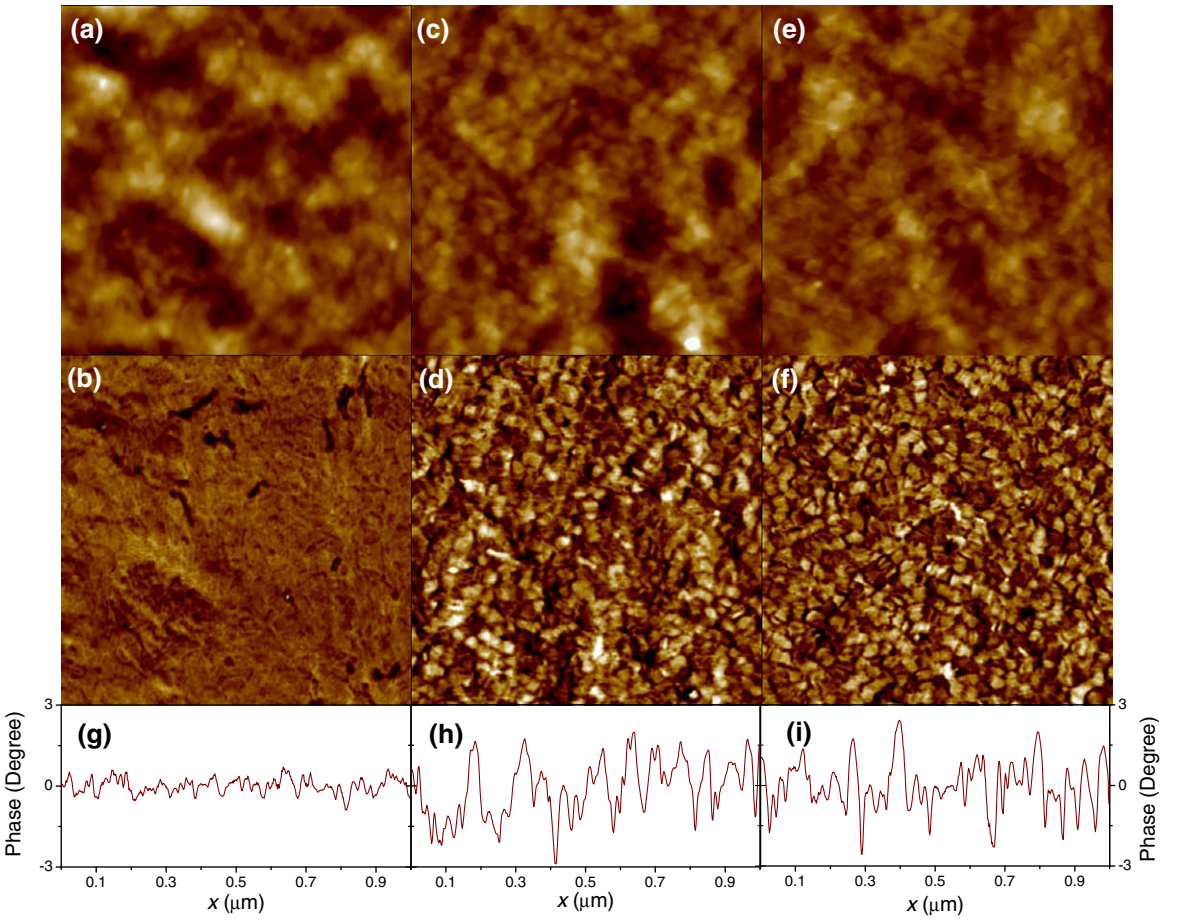

Fig. 6. (a) and (b) are, respectively, AFM topography and phase images (1 μm × 1 μm) of PQT-12 thin film on untreated Au surface after annealing; (c) and (d) are, respectively, AFM topography and phase images (1 μm × 1 μm) of PQT-12 thin film on Au–DT surface after annealing; (e) and (f) are, respectively, AFM topography and phase images (1 μm × 1 μm) of PQT-12 thin film on Au–FDT surface after annealing. The PQT-12 films are 20-30 nm in thickness on Au, Au–DT, and AU–FDT surfaces. Height-scale of images: z = 20 nm in (a), (c), and (e); 5 degree in (b), (d), and (f). (g), (h), and (i) are representative surface phase profiles of AFM phase images of (b), (d), and (f), respectively.

Fig. 6a and b show, respectively, AFM topography and phase images of PQT-12 thin film (20–30 nm) on bare Au surfaces after post-deposition annealing. The post-deposition annealing temperature of about 125 °C is well below the temperature of about 180 °C, at which thiol monolayers desorbs from Au surfaces.[53] The phase image in Fig. 6b appears to be featureless with amorphous or disordered polymer morphology, which is probably due to the interaction between the PQT-12 and the Au surface [14,15,54]. In sharp contrast, the phase images of PQT-12 thin film (20–30 nm) on Au–DT and Au–FDT surfaces after post-deposition annealing (Fig. 6d and f) show highly polycrystalline films with extensive nano-crystalline domains. As shown in Fig. 6g–i, the surface phase profiles of PQT-12 films on Au–DT and Au–FDT surfaces are significantly rougher than that on bare Au surface. The size of PQT-12 domains on Au–DT and Au–FDT surfaces are generally larger than 30 nm × 30 nm, suggesting that interface morphology of PQT-12 is close to the surface polycrystalline morphology of PQT-12. The formation of PQT-12 nano-crystalline domains is similar to the polycrystalline formation of PQT-12 and other polythiophene-based semiconductors on silane-modified oxide silicon surfaces and probably due to the self-organizations of PQT-12 polymer on Au–DT and Au–FDT surfaces (the π–π stacking of PQT-12 polymer chains: lamellar stacks) [8,13,50,55,56].

The difference in molecular ordering or structural order between crystalline and amorphous organic semiconductor can result in several orders of magnitude difference in charge mobility [1,13,24–27]. Charge transport in amorphous or disordered organic semiconductors is generally hopping transport and charge carriers are scattered at every hopping step, resulting in low charge mobility. On the other hand, π–π stacking of polymer chains may allow charge carrier delocalization between chains and give two-dimensional transport within a lamella stack. Charge transport in polycrystalline or highly ordered organic semiconductors favor bandlike transport as in conventional inorganic semiconductors over hopping, accounting for high mobility in polycrystalline or highly ordered organic semiconductors. It has been shown that the charge injected current is proportional to the charge mobility of

the organic semiconductor at the electrode/semiconductor contacts (as described in Eq. (5)) [51,52]. Thus, by inducing the formation of polycrystalline PQT-12 semiconductor at the electrode/PQT-12 interfaces, DT SAMs on Au electrodes can improve the charge injection through the electrode/PQT-12 contacts, despite the unfavorable dipole moments of DT SAMs for hole injection. The FDT SAMs on Au electrodes can further improve the hole injection for devices, assisted by the favorable dipole moment of FDT SAMs for hole injection. The results suggest that the improved molecular ordering due to the SAMs modification could compensate the negative effect stemmed from insulating properties and/or energy-mismatch of SAMs and improve charge injection for devices. These phenomena are also consistent with the recent report of mobility-dependent charge injection into organic semiconductors [57].

At electrode/PQT-12 contacts in PQT-12 TFTs, hole injection process consists mainly of hole tunneling through DT SAMs, FDT SAMs, or the contamination layer and hole injection into HOMO of PQT-12 semiconductor. Investigating the charge injection through electrode/PQT-12 contacts and morphologies of PQT-12 on different Au surfaces, it is suggested that the hole injection barrier and the amorphous PQT-12 at Au/PQT-12 contacts has contributed to the non-Ohmic charge injection in PQT-12 TFTs with Bare Au electrodes (Fig. 1a). Although there is a higher Schoottky barrier for hole injection at Au–DT/PQT-12 contacts, the devices with Au–DT S–D electrodes shows much improved device performance with nearly Ohmic charge injection in Fig. 1b. This result suggests the beneficial effect of the PQT-12 polycrystalline morphology at Au–DT/PQT-12 contacts. With lower Schottky barrier for hole injection and PQT-12 polycrystalline morphology at Au–FDT/PQT-12 contacts, the device with Au–FDT electrodes gave a further improved device performance. The clear correlation between the PQT-12 morphologies and the charge injection properties at electrode/PQT-12 contacts in present study also could be an explanation to the enhanced mobility in bottom-contact PQT-12 TFTs with printable metal conductors (S–D electrodes) from thiol-stabilized Au or organic acid-stabilized silver nanoparticles precursors [36–38]. The thiols and organic acid immobilized on the printable metal conductor surfaces probably gave rise to the improved PQT-12 morphologies at the electrode/PQT-12 contacts, resulting in improved charge injections and the enhanced mobilities compared to those of bottom-contact PQT-12 TFTs with bare Au S–D electrodes. These results suggest that the Schoottky barrier and morphologies of organic semiconductors at electrode/semiconductor contacts can play important roles for the charge injection for organic TFTs.

4. Conclusion

We have demonstrated that surface modification of Au electrodes with alkanethiol and perfluorinated alkanethiol SAMs is an effective method for dramatic improvement of device performance of bottom-contact PQT-12 TFTs. The thiol SAMs modification of Au electrodes modulates Schottky barrier height and promotes the formation of polycrystalline PQT-12 at electrode/semiconductor contacts. The combination of these effects results in significant improvement of charge injection at the electrode/semiconductor contacts for high performance bottom-contact PQT-12 TFTs. The work presented here may help to understand the charge injection in organic electronics and provide a simple path to the fabrication of high performance, low-cost, and solution-processable bottom-contact OTFTs using fine lithography technology.

Acknowledgment

This work is financially supported by Singapore A*STAR under Grant No: 052 117 0031.

References

[1] C.D. Dimitrakopoulos, P.R.L. Malenfant, Adv. Mater. 14 (2002) 99.
[2] E. Menard, M.A. Meitl, Y. Sun, J.U. Park, D.J.L. Shir, Y.S. Nam, S. Jeon, J.A. Rogers, Chem. Rev. 107 (2007) 1117.
[3] J. Zaumseil, H. Sirringhaus, Chem. Rev. 107 (2007) 1296.
[4] C.R. Newman, C.D. Frisbie, D.A. Da Silva Filho, J.L. Bredas, P.L. Ewbank, K.R. Mann, Chem. Mater. 16 (2004) 4436.
[5] H.E. Katz, Chem. Mater. 16 (2004) 4748.
[6] J.T. Mabeck, G.G. Malliaras, Anal. Bioanal. Chem 384 (2006) 343.
[7] D. Gamota, P. Brazis, K. Kalyanasundaram, J. Zhang (Eds.), Printed Organic and Molecular Electronics, Kluwer, Dordrecht, Netherlands, 2004. and references therein.
[8] B.S. Ong, Y. Wu, P. Liu, S. Gardner, J. Am. Chem. Soc. 126 (2004) 3378.
[9] I. Mcculloch, M. Heeney, C. Bailey, K. Genevicius, I. Macdonald, M. Shkunov, D. Sparrowe, S. Tierney, R. Wagner, W.M. Zhang, M.L. Chabinyc, R.J. Kline, M.D. Mcgehee, M.F. Toney, Nature Mater. 5 (2006) 328.
[10] M.H. Yoon, S.A. DiBenedetto, A. Facchetti, T.J. Marks, J. Am. Chem. Soc. 127 (2005) 1348.
[11] H. Meng, F. Sun, M.B. Goldfinger, F. Gao, D.J. Londono, W.J. Marshal, G.S. Blackman, K.D. Dobbs, D.E. Keys, J. Am. Chem. Soc. 128 (2006) 9304.
[12] H. Sirringhaus, P.J. Brown, R.H. Friend, M.M. Nielsen, K. Bechgaard, B.M.W. Langeveld-Voss, A.J.H. Spiering, R.A.J. Janssen, E.W. Meijer, P. Herwig, D.M. de Leeuw, Nature 14 (1999) 685.
[13] Y. Wu, P. Liu, B.S. Ong, T. Srikumar, N. Zhao, G. Botton, S. Zhu, Appl. Phys. Lett. 86 (2005) 142102.
[14] G.R. Dholakia, M. Meyyappan, A. Facchetti, T.J. Marks, Nano Lett. 6 (2006) 2447.
[15] I. Kymissis, C.D. Dimitrakopoulos, S. Purushothaman, IEEE Trans. Electron Devices 48 (2001) 1060.
[16] M.M. Ling, Z. Bao, Chem. Mater. 16 (2004) 4824.
[17] H. Ishii, K. Sugiyama, E. Ito, K. Seki, Adv. Mater. 11 (1999) 605.
[18] J.E. Lyon, A.J. Cascio, M.M. Beerbom, R. Schlaf, Y. Zhu, S.A. Jenekhe, Appl. Phys. Lett. 88 (2006) 222109.
[19] M. Grobosch, M. Knupfer, Adv. Mater. 19 (2007) 754.
[20] C. Bock, D.V. Pham, U. Kunze, D. Kafer, G. Witte, Ch. Woll, J. Appl. Phys. 100 (2006) 114517.
[21] P. Stoliar, R. Kshirsagar, M. Massi, P. Annibale, C. Albonetti, D.M. de Leeuw, F. Biscarini, J. Am. Chem. Soc. 129 (2007) 6477.
[22] Q. Cao, Z.T. Zhu, M.G. Lemaitre, M.G. Xia, M. Shim, J.A. Rogers, Appl. Phys. Lett. 88 (2006) 113511.
[23] L.W. Chong, Y.L. Lee, T.C. Wen, Thin Solid Films 515 (2007) 2833.
[24] R.A. Street, Nature Mater. 5 (2006) 171.
[25] R.A. Street, J.E. Northrup, A. Salleo, Phys. Rev. B 71 (2005) 165202.
[26] V. Coropceanu, J. Cornil, D.A. da Silva Filho, Y. Olivier, R. Silbey, J. Bredas, Chem. Rev. 107 (2007) 926.
[27] J.M. Warman, M.P. de Haas, G. Dicker, F.C. Grozema, J. Piris, M.G. Debije, Chem. Mater. 16 (2004) 4600.
[28] I.H. Campbell, S. Rubin, T.A. Zawodzinski, J.D. Kress, R. L Martin, D.L. Smith, N.N. Barashkov, J.P. Ferraris, Phys. Rev. B. 54 (1996) 14321.
[29] R.W. Zehner, B.F. Parsons, R.R. Hsung, L.R. Sita, Langmuir 15 (1999) 1121.
[30] L. Zuppiroli, L. Si-Ahmed, K. Kamaras, F. Nuesch, M.N. Bussac, D. Ades, A. Siove, E. Moons, M. Gratzel, Eur. Phys. J. B 11 (1999) 505.
[31] B. de Boer (a), A. Hadipour, M.M. Mandoc, T. van Woudenbergh, P.W.M. Blom, Adv. Mater. 17 (2005) 621.

[32] K. Asadi, F. Gholamrezaie, E.C.P. Smits, P.W.M. Blom, B. de Boer, J. Mater. Chem. 17 (2007) 1947.
[33] B.H. Hamadani, D.A. Corley, J.W. Ciszek, J.M. Tour, D. Natelson, Nano Lett. 6 (2006) 1303.
[34] A. Salleo, T.W. Chen, A.R. Volkel, Y. Wu, P. Liu, B.S. Ong, Phys. Rev. B 70 (2004) 115311.
[35] M.L. Chabinyc, F. Endicott, B.D. Vogt, D.M. DeLongchamp, E.K. Lin, Y. Wu, P. Liu, B.S. Ong, Appl. Phys. Lett. 88 (2006) 113514.
[36] Y. Wu, Y. Li, B.S. Ong, P. Liu, S. Gardner, B. Chiang, Adv. Mater. 17 (2005) 184.
[37] Y. Wu, Y. Li, P. Liu, S. Gardner, B.S. Ong, Chem. Mater. 18 (2006) 4627.
[38] Y. Wu, Y. Li, B.S. Ong, J. Am. Chem. Soc. 128 (2006) 4202.
[39] B.H. Hamadani, D. Natelson, Appl. Phys. Lett. 84 (2004) 443.
[40] B.H. Hamadani, D. Natelson, J. Appl. Phys. 97 (2005) 064508.
[41] S. Luan, G.W. Neudeck, J. Appl. Phys. 72 (1992) 766.
[42] M. Lefenfeld, G. Blanchet, J.A. Roger, Adv. Mater. 14 (2003) 1188.
[43] D.J. Gundlach, L. Zhou, J.A. Nichols, T.N. Jackson, P.V. Necliudov, M.S. Shur, J. Appl. Phys 100 (2006) 024509.
[44] A. Ulman, Chem. Rev. 96 (1996) 1533.
[45] G.Y. Liu, P. Fenter, C.E.D. Chidsey, D.F. Ogletree, P. Eisenberger, M. Salmeron, J. Chem. Phys. 101 (1994) 4301.
[46] D. Cahen, R. Naaman, Z. Vager, Adv. Funct. Mater. 15 (2005) 1571.
[47] Schottky barrier height change was calculated from Eq. (4) and excluding the Au–S dipole moment. Dielectric constant of DT and FDT SAMs layer is assumed to be 2.5 and 2.1, respectively. $D \approx 3.33564 \times 10^{-30}$ C m; $\varepsilon_0 = 8.854 \times 10^{-12}$ f/m.
[48] A. Wan, J. Hwang, F. Amy, A. Kahn, Organ. Electron. 6 (2005) 47.
[49] H. Vazquez, F. Flores, A. Kahn, Organ. Electron. 8 (2007) 241.
[50] B.S. Ong, Y. Wu, P. Liu, S. Gardner, Adv. Mater. 17 (2005) 1141.
[51] S.M. Sze, K.K. Ng, Physics of Semiconductor Devices, third ed., Wiley, New York, 2007.
[52] J.C. Scott, G.G. Malliaras, Chem. Phys. Lett. 299 (1999) 115.
[53] F. Bensebaa, T.H. Ellis, A. Badia, R.B. Lennox, Langmuir 14 (1998) 2361.
[54] Z.Y. Yang, H.M. Zhang, C.J. Yan, S.S. Li, H.J. Yan, W.G. Song, L.J. Wan, Proc. Natl. Acad. Sci. USA 104 (2007) 3707.
[55] N. Zhao, G.A. Botton, S. Zhu, A. Duft, B.S. Ong, Y. Wu, P. Liu, Macromolecules 37 (2004) 8307.
[56] M.L. Chabinyc, M.F. Toney, R.J. Kline, I. McCulloch, M. Heeney, J. Am. Chem. Soc. 129 (2007) 3226.
[57] Y. Shen, M.W. Klein, D.B. Jacobs, J.C. Scott, G.G. Malliaras, Phys. Rev. Lett. 86 (2001) 3867.

be achieved using (mostly two-dimensional) organic molecules that stack with their planes parallel to the surface, such as columnar materials with strong π-stacking. Among molecules recently used for that purpose, triphenylene, hexazatriphenylene, and hexaazatrinaphthylene derivatives stand out as very attractive candidates [11–13]. With proper functionalization, these electron-transport materials can form films with various morphologies, such as amorphous, crystalline, or columnar discotic liquid-crystalline, and different electronic properties [14–17]. Moreover, it has been shown that a high electron-affinity example, tris{2,5-bis(3,5-bis-trifluoromethyl-phenyhl)thieno}[3,4-*b,h,n*]-1,4,5,8,9,12-hexaazatriphenylene (THAP), can be *n*-doped with the molecular donor cobaltocene, resulting in enhanced electron-injection [14,18].

In this work, we investigate the electronic properties of tris{2,5-bis(3,5-bis-trifluoromethyl-phenyl)thieno}[3,4-*b,h,n*]-1,4,5,8,9,12-hexaazatriphenylene films adsorbed on Ag and Au, two noble metals with significantly different work functions. The chemical structure of the molecule is given in Fig. 1. Both crystalline and non-crystalline substrates are used in order to probe for any effect of orientation and order of the molecular film on its electronic structure. Recent investigations of well-ordered molecular systems show that molecular orientation can have a profound influence on the electronic properties of the film, such as its ionization energy (IE) [19,20].

Ultraviolet photoemission spectroscopy (UPS) and X-ray photoemission spectroscopy (XPS) data are recorded as a function of THAP thicknesses. With Ag substrates, an interface state induced by electron transfer from the metal to the molecule is observed. Based on the XPS data, we suggest that the transferred charge is distributed mostly over the inner ring of the molecule. No evidence of charge transfer or chemical reaction is observed for THAP on Au, and no evidence is obtained of any significant difference being induced by the crystalline vs. non-crystalline nature of the substrate. Finally, we calculate the position of the charge neutrality level of THAP to be 5.2 ± 0.3 eV below the vacuum level (E_{vac}), and correlate this position with measured values of Schottky barrier heights.

2. Experimental

All experiments were performed in ultra-high vacuum (UHV), in a dual chamber system equipped with organic evaporation sources, UPS, XPS, low-energy electron diffraction (LEED), and ion sputtering and annealing. Base pressures were 1×10^{-9} Torr in the organic deposition chamber and 2×10^{-10} Torr in the analysis chamber. Non-crystalline Au and Ag substrates (a-Au and a-Ag, respectively) were prepared by metal evaporation on a Si(100) wafer with the following structures: Au(1500 Å)/Ti(500 Å)/Si(100) and Ag(1500 Å)/Si(100). The crystalline Au and Ag substrates were flame-annealed Au(111)/mica purchased from Molecular Imaging, and a Ag(110) single crystal purchased from Mateck (misorientation $\leqslant 0.1°$), respectively. All substrates were prepared in final form by several repeated cycles of Ar ion-sputtering (beam voltage of 500 V) and annealing (710 K for Au and 600 K for Ag). These procedures produced clean and well-ordered metallic surfaces exhibiting a rectangular (1×1) unit cell in the case of the Ag(110) and the standard $(22 \times \sqrt{3})$ reconstruction of Au(111) as observed by LEED. No diffraction patterns were observed in the case of non-crystalline substrates.

THAP was synthesized and purified as previously described [14], and placed in a quartz crucible in the preparation chamber. The molecules were deposited on the clean metal surfaces by thermal evaporation (~480 K) at a rate of 0.3 Å/min for the first layers and ~3 Å/min for the last layers of the thicker films. Rates and thicknesses were estimated using a quartz crystal microbalance calibrated by X-ray photoemission spectroscopy. During deposition, the substrates were held at room temperature.

UPS measurements were performed using He I ($h\nu$ = 21.22 eV) and He II ($h\nu$ = 40.8 eV) radiation from a discharge lamp. XPS was carried out with the non-monochromatized Al Kα line ($h\nu$ = 1486.6 eV) of an X-ray tube. The emitted photoelectrons were counted using a double-pass cylindrical mirror analyzer. To measure the onset of photoemission, or cut-off of the secondary emission peak, and determine the position of E_{vac}, UPS spectra were collected while biasing the sample at −3 V. The resolution in UPS and XPS measurements, determined from the width of the Fermi step on the metallic substrates, were 0.15 and 0.8 eV, respectively.

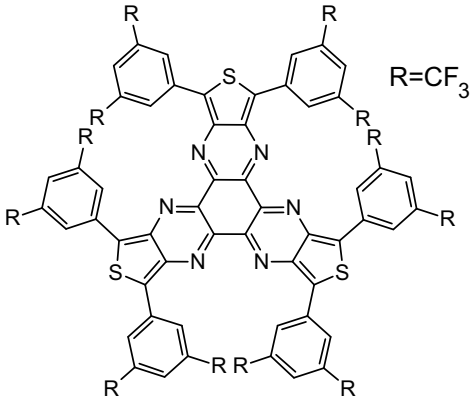

Fig. 1. Chemical structure of THAP.

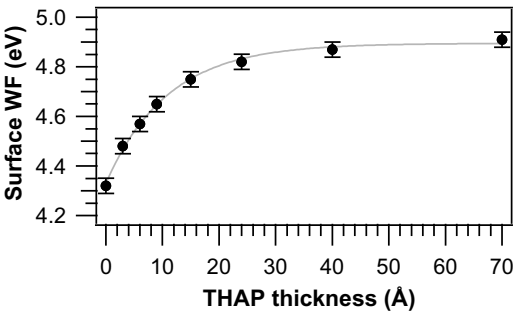

Fig. 2. WF of the THAP/Ag(110) surface as a function of THAP thickness.

3. Results

3.1. THAP on Ag

The evolution of the work function (WF) of the THAP/Ag(1 1 0) system as a function of THAP thickness is shown is Fig. 2. The WF of the clean Ag(1 1 0) surface, measured from the cut-off of the secondary emission peak, is 4.32 eV. This value is smaller than the adiabatic electron affinity (EA) of THAP molecular film (4.59 eV, as measured by inverse photoemission spectroscopy [18]). Accordingly, the deposition of THAP is accompanied by an upward realignment of the molecular levels due to an electron transfer from the metal to the organic, resulting in the formation of an interface dipole with a dipole moment pointing from the molecule toward the metal. The vacuum level, measured on Ag covered with a sub-monolayer THAP film (effective evaporated thickness 3 Å), shifts upwards by 0.16 eV, indicating an increase in the WF of THAP/Ag with respect to that of the clean metal surface. An additional 0.17 eV increase in WF is achieved when the effective THAP thickness reaches 9 Å. Upon further evaporations, the WF slowly increases, reaching a final value of 4.91 eV for a 70 Å thick film. The change in the overall slope of the plot of WF vs. THAP thickness at around 9 Å suggests that this thickness corresponds to the completion of the first monolayer (ML). This value is in good agreement with the value produced by previous scanning tunneling microscopy experiments [21].

The He II UPS spectra measured for different thicknesses of THAP on Ag(1 1 0) are shown in Fig. 3a. The clean metal surface features (bottom spectrum) located between −8 eV and −4 eV are associated with the Ag 4d levels. As the thickness of the THAP layer increases, the intensity of the Ag(1 1 0) valence band (VB) features and Fermi step decreases. New peaks characteristic of the THAP electronic structure, labeled A, B and C, appear at effective thicknesses as low as 3 Å. As the THAP thickness increases, the VB progressively shifts by up to 0.25 eV towards higher binding energy (BE). Since E_{vac} shifts upward by 0.43 eV over the same thickness range, the IE of the THAP increases by 0.68 eV. The physical origin of this modification will be discussed later. The energy band diagram of this system is given in Fig. 4a.

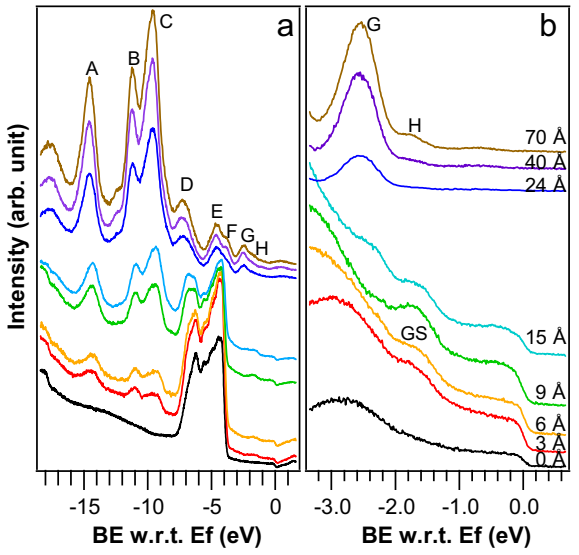

Fig. 3. (a) He II spectra of the THAP/Ag(1 1 0) interfaces as a function of THAP thickness and (b) corresponding He I spectra of the valence states close to E_F.

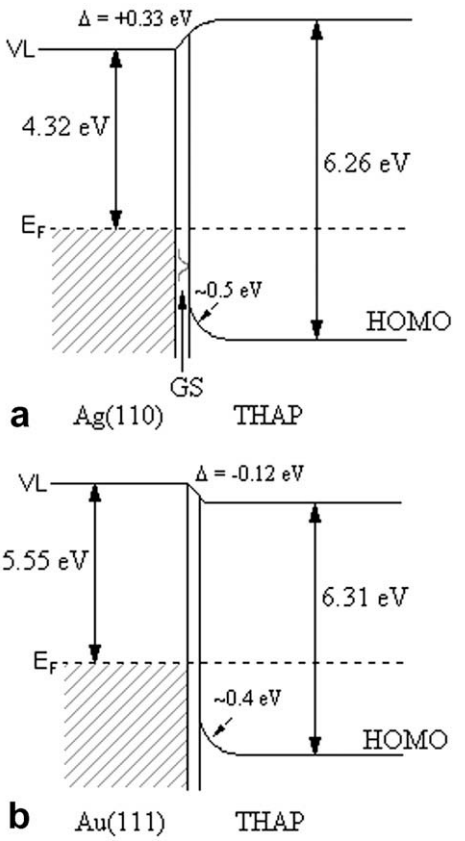

Fig. 4. (a) Schematic energy band diagrams of the THAP adsorbed on (a) Ag(1 1 0) and (b) Au(1 1 1).

The VB spectrum of the 70 Å thick THAP film presents a number of features, of which the one labeled H is attributed to ionization from the highest occupied molecular orbital (HOMO). The adiabatic IE of the THAP film, estimated from the leading edge of this feature, is 6.26 eV, consistent with values previously determined for thick films deposited on PEDOT:PSS [14,18]. In addition, the measured IE is, as expected, smaller than the computed value of 7.04 eV (vertical IP) obtained by density functional theory (DFT) B3LYP/6-31G** calculations for molecules in gas phase [14]; the difference can be largely attributed to the stabilization of the positive charge of the THAP radical cation by polarization of the surrounding molecules in the solid [22,23]. An expanded plot of the VB in the vicinity of the Fermi level (E_F) is shown in Fig. 3b. The feature labeled GS and seen at −1.73 eV on the 3–9 Å spectra is not an intrinsic VB feature of the molecular compound, but is a result of the strong molecule-substrate interaction, and will be discussed later in this paper.

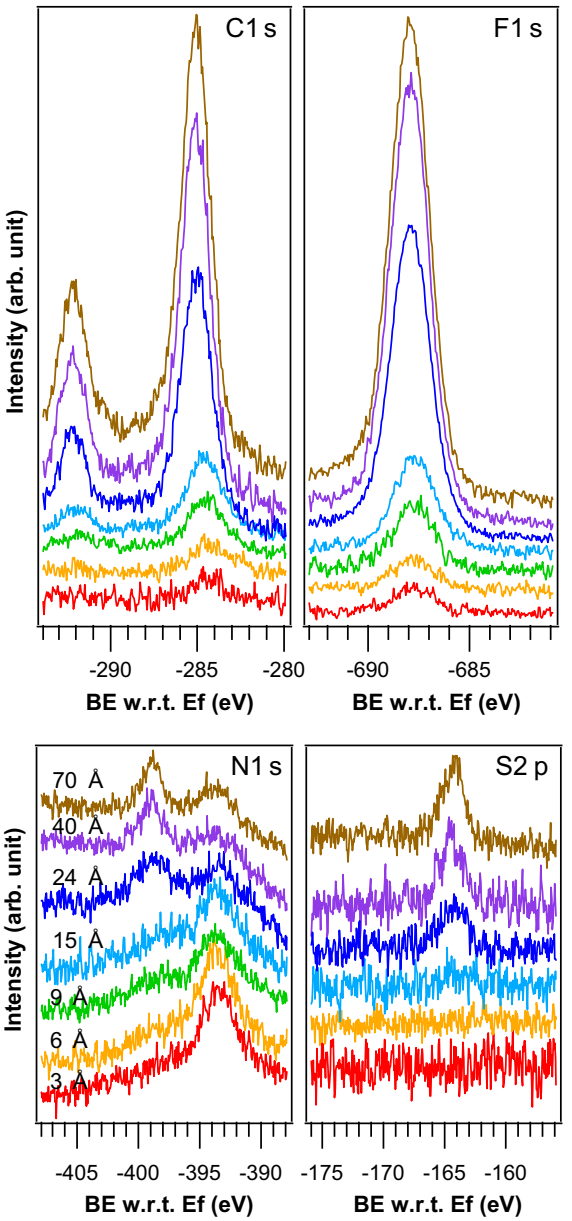

Fig. 5. Ag3d, F1s, C1s, S2p and N1s core levels for increasing THAP thickness on Ag(110).

The Ag3d, F1s, C1s, S2p and N1s core levels (CL) recorded for different THAP thicknesses are shown in Fig. 5. The S and N signals are weak, due to low photoionization cross sections with Al Kα photons, and low density in THAP (3 sulfur and 6 nitrogen atoms per molecule vs. 36 fluorine and 66 carbon atoms). Note that the −394 eV peak in the N spectrum is an artifact of the measurement and corresponds to a Mo3$p_{3/2}$ ionization from the molybdenum clip holding the sample. The N1s peak is that located at higher energy (about −400 eV).

Two C1s peaks can be seen for thicknesses of 6 Å and above. The peak centered at lower BE is attributed to carbon atoms of the core of the molecule (C_C), while the one centered at higher BE corresponds to carbon atoms of the trifluoromethyl groups (C_F). The resolution of the XPS system is insufficient to fully resolve the carbon atoms bound to nitrogen (C_N), which usually appear at ca. 1.3 eV higher BE than C_C [24,25]. Also, the 1.1 eV spin splitting of the S2p core level (CL) is not resolved, although the sulfur peak exhibits a clear asymmetric shape, with an average peak center corresponding to BE equal to −165 eV. The F1s CL appears at 688 eV BE, and shifts by about 0.2 eV toward higher BE as the thickness increases. This shift is consistent with the shift observed in the UPS spectra, as well as in the N1s and S2p CLs. However, the shifts of the C1s spectra differ from those of the fluorine, sulfur and nitrogen core levels. The center of the C_C1s feature shifts by 0.6 eV towards higher BE, reaching the final value of 285 eV for a 70 Å thick film, while the center of the C_F1s peak shifts by only 0.4 eV and appears at 292.2 eV for the same film thickness. All the shifts reported here are summarized in the Fig. 6a. Assuming that 0.2 eV of these shifts corresponds to the shift of the VB and other CLs, the net chemical shifts of the C_C1s and C_F1s CLs are therefore 0.4 eV and 0.2 eV, respectively. These shifts show that the carbon atoms of molecules close to the Ag surface are in a more electron-rich environment than those of the bulk or surface molecules. This change underlines the substantial interaction with the substrate, as is explained in the discussion section.

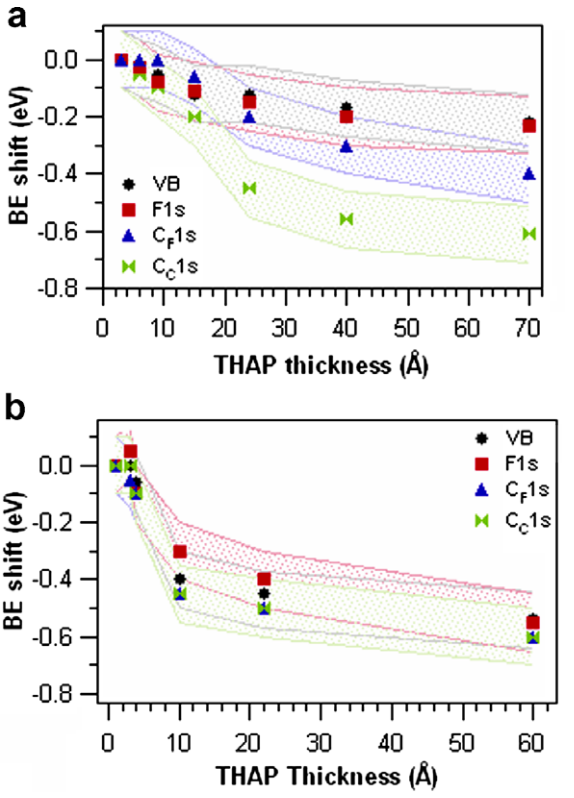

Fig. 6. Energy level shifts as a function of the THAP film thickness deposited on (a) Ag and (b) Au. In the figures, each set of data points is displayed in a sleeve representing the approximate experimental error in determining the value of each data point.

THAP molecules form ordered films on Ag(1 1 0) [21], and the investigation of the impact of the crystalline nature of the substrate on the electronic properties of the film is of interest. The above experiments are, therefore, repeated on a-Ag, on which no particular THAP order is expected. The WF of the clean a-Ag surface is measured to be 4.43 eV, and increases by 0.19 eV with the evaporation of 3 Å of THAP. As in the case of Ag(1 1 0), this corresponds to the formation an interface dipole with a dipole moment pointing from the molecule towards the metallic surface. This dipole is the result of an electron transfer from Ag to the molecular layer, which also induces the formation of electronic interface states as in the case of Ag(1 1 0) (*cf.* Fig. 7). Similarly to the previous system, we observe a rigid shift of the VB and the F1s, C1s, S2p and N1s core levels by up to 0.2 eV towards higher BE as the film thickness increases up to 60 Å.

3.2. THAP/Au

The WF of the clean polycrystalline Au(1 1 1) surface is 5.55 eV, intermediate between the THAP IE and EA. The deposition of a 3 Å layer of THAP leads to a decrease of the WF by 0.12 eV. Contrary to the case of THAP/Ag, the corresponding E_{vac} shift corresponds to the formation of an interface dipole with a dipole moment pointing from the metallic surface toward the molecule. Further THAP evaporations induce a gradual decrease of the WF down to 5.39 eV (Fig. 8). This evolution is characteristic of a physisorptive organic-metal system, and will be further discussed below. The THAP IE measured on the 60 Å film is 6.31 eV, in good agreement with the value given above.

The evolution of the part of the VB close to the Fermi level as a function of the THAP coverage is shown in Fig. 9. In contrast to the case of a Ag substrate, no interface gap state is observed in the low-thickness regime. However, as the film thickness increases, the VB shifts by 0.6 eV toward higher BE, with no apparent concomitant E_{vac} shift. This shift is consistent with those observed for the F1s and C1s (Figs. 6b and 10) as well as N1s and S2p CLs (not shown here), although no evidence of a chemical reaction can be inferred from these XPS data, in support of the claim that the molecules are physisorbed on the Au(1 1 1) surface. Upon further evaporation, E_{vac} shifts back by 0.06 eV, which together with the 0.6 eV shift of the VB towards higher BE gives rise to a 0.54 eV increase of the IE of the THAP film. This value, which is smaller than the one observed in the case of the Ag (0.68 eV), results also in part from a polarization effect, as will be explained in the dis-

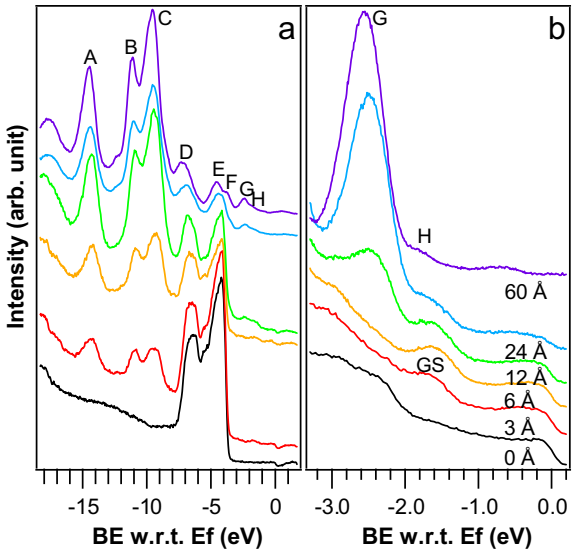

Fig. 7. (a) He II spectra of the THAP/a-Ag interfaces for various THAP thicknesses and (b) top of the valence band of the THAP/a-Ag interfaces.

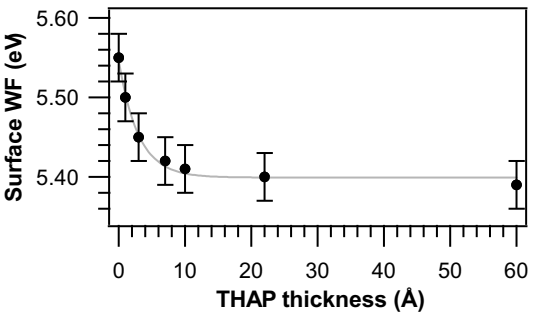

Fig. 8. WF of the THAP/Au(1 1 1) surface as a function of THAP thickness.

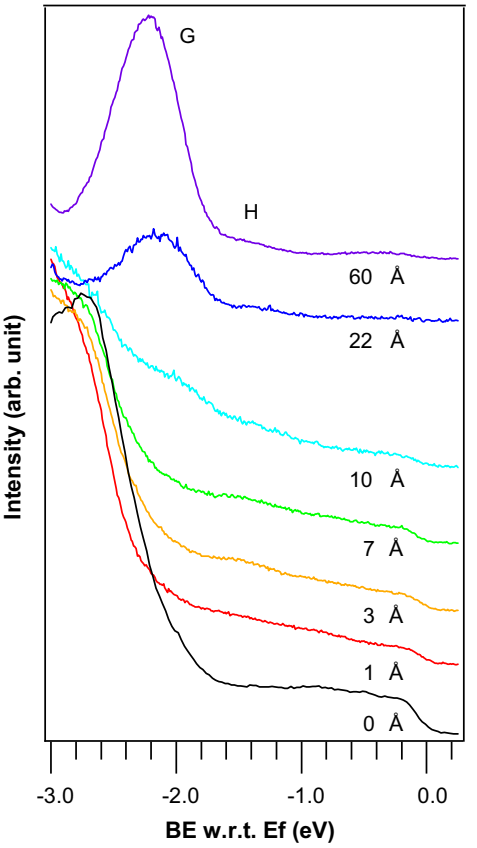

Fig. 9. He I spectra of the valence states close to E_F for THAP/Au(1 1 1).

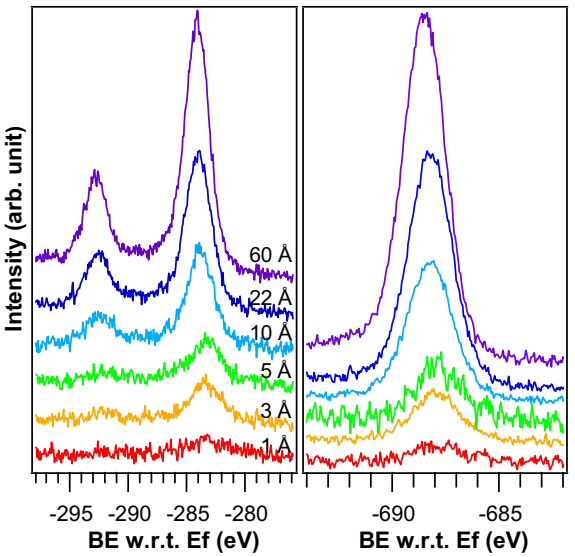

Fig. 10. F1s and C1s core levels for increasing THAP thickness on Au(1 1 1).

cussion section. The energy band diagram of this system is given in Fig. 4b.

Since an ordered layer-by-layer growth of THAP can be achieved on Au(1 1 1) [26], the experiment is repeated on a-Au to investigate the influence of molecular order on the electronic structure of the film. The WF of the sputtered and annealed a-Au is measured at 5.27 eV. The WF drops by 0.1 eV after the first evaporation, and remains nearly constant upon further THAP deposition. As the THAP layer thickness increases, both XPS and UPS features shift by 0.5 eV towards higher BE. These observations are in good agreement with those described in the case of Au(1 1 1).

4. Discussion

The evaporation of a very thin layer of THAP on both Ag(1 1 0) and α-Ag results in the formation of an electronic state labeled GS (Figs. 3, 4 and 7). This state does not correspond to an intrinsic energy level of the molecule. Since the WF of the pristine Ag surface is smaller than the EA of the THAP film, electrons are expected to be transferred from the metal into the lowest unoccupied molecular orbital (LUMO) of THAP to raise the molecular levels and achieve thermodynamic equilibrium. Presumably, the partially-occupied LUMO relaxes into the gap, forming the observed GS interface state. The rapid attenuation of this peak with increasing THAP thickness demonstrates that the transferred charge and the state are localized at the interface [27].

The XPS measurements confirm this charge transfer. The C1s core level shifts for THAP on both Ag(1 1 0) and a-Ag imply a change in oxidation state and a modification of the carbon electronic environment as the molecular film grows. The dominant 0.4 eV chemical shift of the C_C1s with increasing THAP thickness suggests that the transferred electron charge is predominately localized on the inner ring of the molecules at the interface with Ag, and that this charge diminishes on molecules positioned further away from the metal. The inferred position of the charge is consistent with the fact that the LUMO, i.e. the molecular orbital that is occupied first by the transferred electron, is mostly localized on the inner core of the molecule [28].

The VB shifts towards higher BE as the thickness of the organic film increases, on both crystalline and non-crystalline Ag and Au substrates. Charging can be ruled out, as no variation of the molecular levels as a function of time nor photon flux can be detected during the experiment, and as the shift begins to appear at thicknesses as low as 6–9 Å. The substantially different final HOMO and VB positions obtained on Ag and Au following the initial shift (Figs. 3, 7 and 9) also precludes the possibility that the VB shift be due to an unintentional doping by residual impurities in the THAP material.

The similarity between photoemission results obtained for THAP on crystalline and non-crystalline substrates suggests that the shift does not originate from molecular order. Although no structural data from the THAP layer were obtained in the present work, our recent experience with THAP grown under similar conditions on Au(1 1 1) [21] and Ag(1 1 0) [18] is that molecular order is easily obtained on these crystalline substrates, whereas no order is expected on a-Au and a-Ag.

We suggest, therefore, that polarization and/or a change in molecular orientation with film thickness are responsible for the observed shift. Polarization naturally occurs when a hole or electron either hops on a molecule in a transport process, or is left behind by the photoemission process. The polarization is a result of screening of the positively-charged molecules by the surrounding molecules in the film and depends on molecular packing and position with respect to, for example, the interface with a metallic substrate [29,30]. In the cases examined here and at low THAP thickness, the positively-charged molecules lay close to the metal and are well screened by the negative image-charges in the metal, resulting in a relatively low BE and IE. As the thickness of the organic film increases and UPS increasingly probes molecules further from the interface, the screening weakens and the energy levels of the molecular ion probed by photoemission shift towards higher BE. The shift of the hole state and VB due to the polarization, together with the E_{vac} shift, cause the IE of the THAP film to increase as a function of film thickness. This variation is more significant for Ag than for Au substrates. At the THAP/Ag interface, the first molecular layer(s) are negatively charged due to the electron transfer from the metal, and the IE of these molecules is already lower than that of neutral molecules. The total change in IE, from interface to bulk and surface of the thicker films, is, therefore, larger in the case of Ag.

A change in molecular orientation, e.g. from lying flat on the metal surface to "standing up" has recently been shown to have a significant impact on the IE of molecular films [19] as well as on the position of the molecular levels [20]. The latter in particular can be explained through a transition between two molecular films, i.e. the first one made of the (presumably flat-lying) molecules in direct contact with the metal (the first 3–6 Å in the present case), and the second constituting the remainder of the film.

Vacuum level alignment at the "heterojunction" between these two films with different IEs leads to the apparent shift of the VB. Although no structural data on molecular orientation are available here, the possibility of a molecular orientation-based effect cannot be ruled out.

The position of the Fermi level at the interface between the first molecular layer and the substrate as a function of the substrate WF is shown in Fig. 11. The linear dependence defines the interface, or screening, parameter $S = \frac{dE_F}{d\Phi_M}$ which is often used to describe the dependence of energy barriers at metal-semiconductor interfaces [1,2,31,32,6]. In this work, S is found to be equal to 0.59. This value can be used to estimate the position of the charge neutrality level (CNL) of THAP. It has been found that the energy position of the CNL in the gap of organic semiconductors does not depend sensitively on the formed interfaces, and thus can be approximated by an intrinsic value. In the induced density of interface states (IDIS) model, this value can be assimilated with the chemical potential of the organic material [1,2,33,34]. As described in previous works [1,35,36], the energetic position of the CNL with respect to E_{vac}, E_{CNL} can be determined in first approximation using the following equation:

$$E_{CNL} = \frac{(E_F - S \cdot \Phi_M)}{(1 - S)} \quad (1)$$

where E_F is the Fermi level position of the THAP/metal system, S is the screening parameter and Φ_M is the substrate work function prior to THAP evaporation. Based on (1), the value of E_{CNL} is found to be -5.2 ± 0.3 eV, in good agreement with the value proposed by Zhao et al. [36]. As expected, this value is lower than that obtained by estimating the chemical potential of a molecule as the average of the first ionization energy (IE) and electron affinity (EA) [33,37,38], which in the present case gives -5.47 eV. This concept, which was used by Pauling to determine atomic electronegativities [39] and pursued by Crispin et al. [37,38] to study metal/organic interfaces within a chemisorption approach, yields a mid-gap position of the CNL. Yet, in organic semiconductors the induced density of states in the proximity of the HOMO is larger than that of the LUMO, causing the CNL to be positioned in the upper half of the gap and resulting in a slightly smaller absolute value of E_{CNL} (CNL closer to the vacuum level).

The determination of the CNL position provides a rationale for the small WF decrease observed in the case of THAP/Au. Typically, in a physisorbed molecule-on-metal system, a decrease in the WF upon interface formation is explained in part in terms of the compression of the tail of the electronic wave function extending from the metal surface by the molecule due to Pauli exclusion principle, also known as the "pillow" effect [27,34,40]. Usually, the magnitude of this effect is of the order of 0.5–1.0 eV. For instance, the WF of a UHV cleaned Au sample is about 5.2–5.4 eV while the WF of an air-exposed Au sample, on which contaminant species compress this electronic tail, is about 4.7 eV. In the case of THAP/Au, the WF of the clean metallic substrate is reduced by only 0.1 eV, implying that the decrease cannot be solely attributed to the "pillow" effect. We suggest that it is limited by the alignment of the Au Fermi level with the CNL. The THAP E_{CNL} is relatively low with respect to E_{vac} (-5.2 eV) as compared to that of many other organic molecules studied in similar contexts, such as CuPc (-3.8 eV), CBP (-4.4 eV) and PTCBI (-4.4 eV) [41]. Therefore, the THAP molecular levels cannot move significantly down with respect to the metal Fermi level without inducing an electron transfer into the organic film, which then counteracts the "pillow" effect. A similar situation is encountered with compounds like perylene-3,4,9,10-tetracarboxylicdianhydride (PTCDA) deposited on Au, the PTCDA E_{CNL} being also being relatively low (-4.8–-5.0 eV) [1,42].

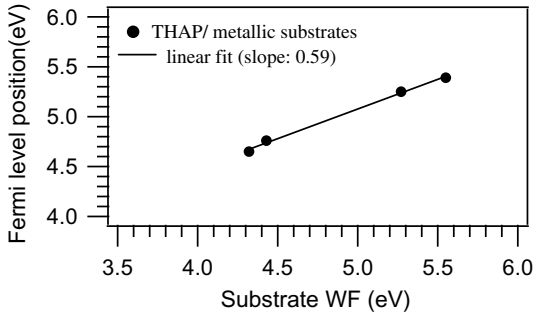

Fig. 11. Fermi level position at the first layer of THAP vs. substrate work function.

5. Conclusion

The electronic properties of THAP films deposited layer-by-layer on medium and high work function metallic substrates (i.e. Ag and Au) was investigated by means of ultraviolet and X-rays photoemission spectroscopies. With both Ag(1 1 0) and a-Ag, a charge transfer occurs from the metal to the LUMO of the THAP molecule, leading to the occupation of a new interface gap state. Core level spectroscopy analysis suggests that the transferred charge is mainly localized on the inner ring of the molecules. No evidence of charge transfer or chemical reaction is observed for THAP adsorbed on Au(1 1 1) and a-Au. Within the resolution of these angle-integrated photoemission data, no significant difference is obtained between the electronic structures of THAP films grown on crystalline and non-crystalline substrates. In all cases, the molecular levels shift with increasing thickness, a phenomenon attributed to a decrease in polarization away from the metal interface. A change in molecular orientation, from flat on the metal surface to standing-up for thicker films, is also a potential origin for this shift. The charge neutrality level of the THAP is estimated to be at -5.2 ± 0.3 eV below vacuum level. The determination of this level, which in the framework of the induced density of interface state model represents the chemical potential of the organic semiconductor, provides a rationale for both the barrier height and interface dipole formed at the Au interface.

Acknowledgements

The Princeton group gratefully acknowledges support from the National Science Foundation (DMR-0705920)

and the Princeton MRSEC of the National Science Foundation (DMR-0213706). Work at the Georgia Institute of Technology was supported by the National Science Foundation (ECCS-0309131 and the STC Program under Agreement Number DMR-0120967), Lintec Corporation, and by the Office of Naval Research (N00014-04-1-0120). We also thank Yana Vaynzof for her help during the photoemission measurements.

References

[1] H. Vázquez, R. Oszwaldowski, P. Pou, J. Ortega, R. Pérez, F. Flores, A. Kahn, Europhys. Lett. 65 (2004) 802.
[2] H. Vázquez, F. Flores, R. Oszwaldowski, J. Ortega, R. Pérez, A. Kahn, Appl. Surf. Sci. 234 (2004) 107.
[3] D. Cahen, A. Kahn, E. Umbach, Materials Today, 2005, July/August issue, 32.
[4] H. Lüth, Surface and Interfaces of Solids, Springer-Verlag Edition, 1992.
[5] C. Shen, A. Kahn, I.G. Hill, in: A. Kahn, J.-J. Pireaux, W.R. Salaneck, K. Seki (Eds.), Conjugated Polymer and Molecular Interfaces, Marcel Dekker, Inc., 2001, p. 351.
[6] S. Braun, W. Osikowicz, Y. Wang, W.R. Salaneck, Org. Electron. 8 (2007) 14.
[7] J.X. Tang, C.S. Lee, S.T. Lee, J. Appl. Phys. 101 (2007) 064504.
[8] H. Ishii, H. Oji, E. Ito, N. Hayashi, D. Yoshimura, K. Seki, J. Luminesc. 87–89 (2000) 61.
[9] K. Seki, K. Hayashi, H. Oji, E. Ito, Y. Ouchi, H. Ishii, Thin Solid Films 393 (2001) 298.
[10] I.G. Hill, J. Hwang, C. Huang, A. Kahn, J.E. McDermott, J. Schwartz, Appl. Phys. Lett. 90 (2007) 012109.
[11] A.M. Van de Craats, L.D.A. Siebbeles, I. Bleyl, D. Haarer, Y.A. Berlin, A.A. Zharikov, J.M. Warman, J. Phys. Chem. B 102 (1998) 9625.
[12] Z. Ke-Qing, W. Bi-Qin, H. Ping, L. Quan, Z. Liang-Fu, Chin. J. Chem. 23 (2005) 767.
[13] S. Kumar, Chem. Soc. Rev. 35 (2006) 83.
[14] S. Barlow, Q. Zhang, B.R. Kaafarani, C. Risko, F. Amy, C.K. Chan, B. Domercq, Z.A. Starikova, M.Y. Antipin, T.V. Timofeeva, B. Kippelen, J.-L. Brédas, A. Kahn, S.R. Marder, Chem. Eur. J. 13 (2007) 3537.
[15] B.R. Kaafarani, T. Kondo, J. Yu, Q. Zhang, D. Dattilo, C. Risko, S.C. Jones, S. Barlow, B. Domercq, F. Amy, A. Khan, J.-L. Brédas, B. Kippelen, S.R. Marder, J. Am. Chem. Soc. 127 (2005) 16358.
[16] V. Lemaur, D.A. de Silva Filho, V. Coropceanu, M. Lehmann, Y. Geerts, J. Piris, M.G. Debije, A.M. van de Craats, K. Senthilkumar, L.D. Siebbeles, J.M. Warman, J.-L. Brédas, J. Cornil, J. Am. Chem. Soc. 126 (2004) 3271.
[17] M. Lehmann, G. Kestemont, R.G. Aspe, C. Buess-Herman, M.H.J. Koch, M.G. Debije, J. Piris, M.P. de Haas, J.M. Warman, M.D. Watson, V. Lemaur, J. Cornil, Y.H. Geerts, R. Gearba, D.A. Ivanov, Chem. Eur. J. 11 (2005) 3349.
[18] C.K. Chan, F. Amy, Q. Zhang, S. Barlow, S.R. Marder, A. Kahn, Chem. Phys. Lett. 431 (2006) 67.
[19] H. Yamane, Y. Yabuuchi, H. Fukagawa, S. Kera, K.K. Okudaira, N. Ueno, J. Appl. Phys. 99 (2006) 093705.
[20] S. Duhm, G. Heimel, I. Salzmann, H. Glowatzki, R.L. Johnson, A. Vollmer, J.P. Rabe, N. Koch, Nature Mater. 7 (2008) 326.
[21] E. Salomon, Q. Zhang, S. Barlow, S.R. Marder, A. Kahn, J. Phys. Chem. C 112 (2008) 9803.
[22] N. Sato, H. Inokuchi, E.A. Silinish, Chem. Phys. 115 (1987) 269.
[23] J.D. Anderson, E.M. McDonald, P.A. Lee, M.L. Anderson, E.L. Ritchie, H.K. Hall, T. Hopkins, E.A. Nash, J. Wang, A. Padias, S. Thayumanavan, S. Barlow, S.R. Marder, G. Jabbour, S. Shaheen, B. Kippelen, N. Peyghambarian, R.M. Wightman, N.R. Armstrong, J. Am. Chem. Soc. 120 (1998) 9646.
[24] N. Papageorgiou, Y. Ferro, E. Salomon, A. Allouche, J.M. Layet, L. Giovanelli, G. Le Lay, Phys. Rev. B 68 (2003) 235105.
[25] V. Yu Aristov, O.V. Molodtsova, V.M. Zhilin, D.V. Vyalikh, M. Knupfer, Phys. Rev. B 72 (2005) 165318.
[26] S.D. Ha, Q. Zhang, S. Barlow, S.R. Marder, A. Kahn, Phys. Rev. B 77 (2008) 085433.
[27] A. Kahn, N. Koch, W. Gao, J. Polym. Sci., Polym. Phys. 41 (2003) 2529.
[28] S. Barlow, Q. Zhang, B.R. Kaafarani, C. Risko, F. Amy, C.K. Chan, B. Domercq, Z.A. Starikova, M.Y. Antipin, T.V. Timofeeva, B. Kippelen, J.-L. Brédas, A. Kahn, S.R. Marder, Chem. Eur. J. 13 (2007) 3537. (supporting information).
[29] F. Amy, C.K. Chan, A. Kahn, Org. Electron. 6 (2005) 85.
[30] E.V. Tsiper, Z.G. Soos, W. Gao, A. Kahn, Chem. Phys. Lett. 360 (2002) 47.
[31] S.M. Sze, Physics of Semiconductor Devices, second ed., Wiley, 1981.
[32] W. Mönch, Surf. Sci. 299 (1994) 928.
[33] H. Vázquez, F. Flores, A. Kahn, in: Proceedings of the International Symposium Super-Functionality Organic Devices, IPAP Conference Series, vol. 6, 2005, p. 1.
[34] H. Vázquez, F. Flores, A. Kahn, Org. Electron. 8 (2007) 241.
[35] H. Vázquez, W. Gao, F. Flores, A. Kahn, Phys. Rev. B 71 (2005) 041306.
[36] W. Zhao, E. Salomon, Q. Zhang, S. Barlow, S.R. Marder, A. Kahn, Phys. Rev. B 77 (2008) 165336.
[37] X. Crispin, Solar Energy Mater. Solar Cell 83 (2004) 147.
[38] X. Crispin, V. Geskin, A. Crispin, J. Cornil, R. Lazzaroni, W.R. Salaneck, J.-L. Brédas, J. Am. Chem. Soc. 124 (2002) 8131.
[39] L. Pauling, The Nature of the Chemical Bond, third ed., Cornell University Press, 1960.
[40] H. Vazquez, Y.J. Dappe, J. Ortega, F. Flores, J. Chem. Phys. 126 (2007) 144703.
[41] H. Vazquez, Y.J. Dappe, J. Ortega, F. Flores, Appl. Surf. Sci. 254 (2007) 378.
[42] I.G. Hill, A. Rajagopal, A. Kahn, Y. Hu, Appl. Phys. Lett. 73 (1998) 662.

high-charge carrier mobility and good stability has become a focus of research into organic electronic materials [2–4]. Fluorene-based copolymers have recently emerged as promising materials for polymer TFTs [5–7]. Fluorene-based polymers such as poly(9,9′-dioctylfluorene-*alt*-bithiophene) (F8T2) have better stability than thiophene-based polymers because of their rigid structures and lower HOMO levels, as well as good film-forming and hole-transporting properties. On the other hand, organic small molecules have also been introduced as active layers in solution-processed OTFTs, through the introduction of various alkyl side chains or by using precursor systems containing thermally removable solubilizing groups. Some of these compounds have exhibited promising behavior as solution-deposited semiconductors with hole mobilities on the order of 0.1 $cm^2 V^{-1} s^{-1}$, however, the number of organic small molecules with good solubility and TFT performance is limited so far [8–10].

The use of blends of π-conjugated polymers has proven effective in improving the electronic and optoelectronic properties of OLEDs and photovoltaic devices [11,12]. Recently, blends and other multicomponent systems are also introduced in solution-processable OTFT applications for tuning and improving the properties of TFTs. For example, solution-processed blends of an n-type polymer, poly(benzobisimidazobenzophenanthroline) (BBL) and a p-type small molecule, copper phthalocyanine resulted in ambipolar thin-film transistors that transport both holes and electrons [13]. The incorporation of polyethylene into regioregular P3HT yielded mechanically robust, high-performance TFTs, owing to a highly favourable, crystallization-induced phase segregation of the two components [14]. Moreover, solution-processed rubrene based transistor exhibited saturated mobilities of up to 0.7 $cm^2 V^{-1} s^{-1}$ and on/off ratios of over 10^6 by incorporating a glass-inducing diluent, diphenylanthracene [15]. Therefore, blending two or more electrically active materials can offer multiple advantages into active semiconductor for realizing solution-processable, high-performance OTFTs.

Here, we report the synergistic effect of the blend systems consisting of fluorene–thiophene based copolymer F8T2 and thiophene-based oligomer DH4T in OTFTs. Despite of its high-on/off ratio and low-off current, on the order of pA, F8T2 is known to be unsuitable for real applications because of the relatively low-charge carrier mobility on the order of 10^{-3} $cm^2 V^{-1} s^{-1}$, without the use of additional alignment techniques. Thus our approach is to incorporate the polymer/oligomer blend system into the fluorene-based polymer semiconductor with the aim of improving the hole mobility of this class of polymers while preserving its high-on/off ratio. The morphologies and charge carrier mobilities of a series of binary blends of polymeric and oligomeric semiconductors are investigated. Moreover, comparison of these characteristics with those of the polyfluorene homopolymer and terfluorene oligomer devices enables us to further investigate the charge carrier transport in the blend devices. These results demonstrate that the use of polymer/oligomer blend systems is an effective way to increase the performance of solution-processable OTFTs.

2. Experimental section

2.1. Materials

The fluorene–thiophene based copolymer, F8T2, and the thiophene-based oligomer, DH4T, were prepared with methods described in a previous report, through the Suzuki coupling reaction [16]. Polyfluorene homopolymer, PF8, and the fluorene-based oligomer, 3FL, were also prepared for comparison. The number-average molecular weight (Mn) of F8T2 was found to be 38,000. F8T2 was found to exhibit a crystallization peak at 159 °C and a melting endothermal peak at 268 °C.

2.2. Physical measurements

The number-average molecular weight was determined by gel permeation chromatography (GPC) on a Waters GPC-150C instrument calibrated with polystyrene standards, with THF used as the eluent. Differential scanning calorimetry (DSC) was performed under a nitrogen atmosphere at a heating rate of 10 °C min^{-1}. UV–vis spectra were obtained using an MPS2000 (SHIMADZU) UV/vis spectrometer. The morphological characterizations with XRD and AFM were performed on the same films as used in the OTFT measurements. The XRD measurements were carried out with a Rigaku Denki RU-300 using Cu Kα radiation (40 kV, 200 mA) in the θ–2θ scan mode with 0.01° steps in 2θ and 0.6 s per step. Non-contact mode (Dynamic Force Mode) AFM images were recorded using a Seiko Instruments SPA-300/SPI3800 probe system, equipped with a Si cantilever (Seiko Instruments SII-DF20, force constant 15 N m^{-1}, resonance frequency ~130 kHz, and tip curvature radius = 10 nm).

2.3. Fabrication of the TFT devices

TFTs were fabricated using the bottom contact geometry. Gold was used for the source and drain contacts and silicon oxide (SiO_2) with a thickness of 300 nm was used as the dielectric. The SiO_2 surface was cleaned with UV–ozone treatment (UV irradiation for 20 min in an oxygen atmosphere) and pretreated with hexamethyldisilazane (HMDS) to produce apolar and smooth surfaces onto which the polymer could be spin-coated. The polymer and/or oligomer solutions were dissolved in 0.5 wt.% *o*-dichlorobenzene, and filtered through a 0.45 μm pore size polytetrafluoroethylene (PTFE) membrane syringe filter before use. The polymer solutions were applied dropwise onto the substrates and spin-coated at 1500 rpm. The films were dried on a hot plate at 150 °C for 20 min in a glovebox. The electrical characteristics of the OTFT devices were measured in a glovebox using an Agilent 4155C Semiconductor Parameter Analyzer.

3. Results and discussion

3.1. Optical properties of the F8T2/DH4T blends

The chemical structures of all the semiconducting materials used in this study are shown in Fig. 1. The UV–

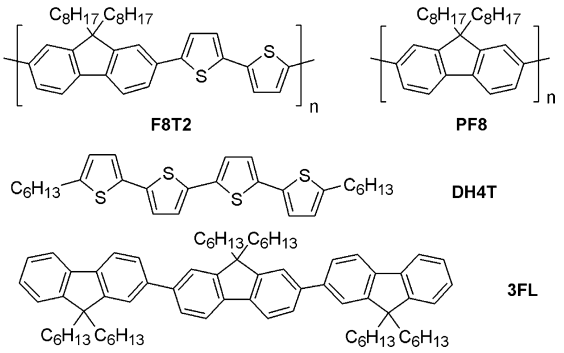

Fig. 1. Chemical structures of the semiconductors.

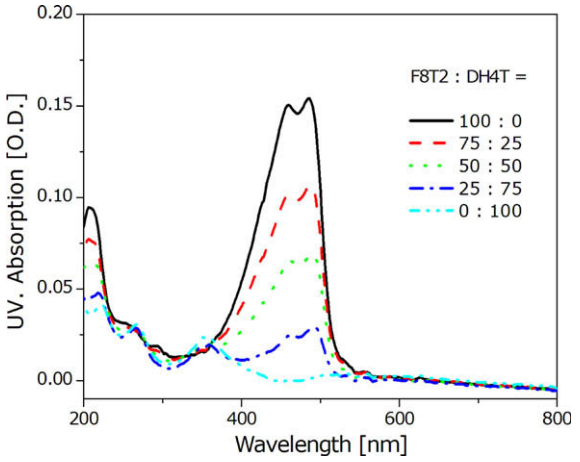

Fig. 2. UV–vis absorption spectra of the F8T2, DH4T, and F8T2/DH4T blend films.

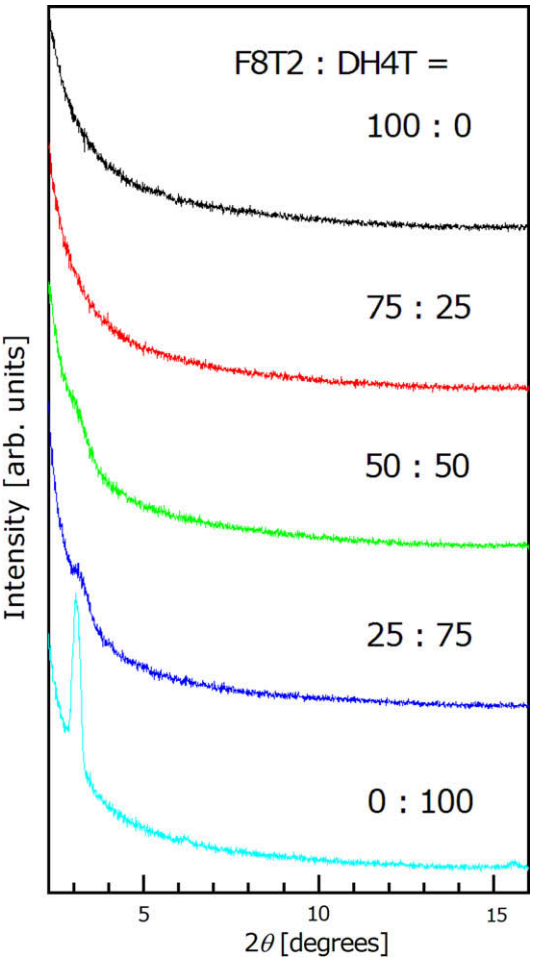

Fig. 3. XRD patterns of the F8T2, DH4T, and F8T2/DH4T blend films.

vis absorption spectra of the F8T2/DH4T blend films are shown in Fig. 2 with those of the F8T2 and DH4T films. The absorption peaks of F8T2 are at 210, 460 and 485 nm and those of the DH4T film are at 220, 268, and 355 nm. The absorption peaks of the blend films can be understood as the superpositions of those of the F8T2 and DH4T films. The intensities of the absorption peaks vary with the blend ratios. As more DH4T is incorporated, the intensities of the absorption peaks originating from F8T2 and DH4T decrease and increase, respectively.

3.2. Morphological characteristics of the F8T2/DH4T blend films

Crystallization of the polymer and oligomer was confirmed with film X-ray diffraction (XRD), which enabled the identification of the nature of the mesophase. As shown in Fig. 3, the DH4T film produces multiple ($h00$) reflections with a (100) reflection at $2\theta = 3.1°$, indicating a d spacing of 28.5 Å, which is comparable to the molecular length of DH4T calculated using MOPAC-PM3 (31.0 Å). In other words, the molecules in the spin-coated DH4T film are oriented normal to the surface, which is a similar result to that reported previously for a vacuum-deposited DH4T film with a d spacing of 27.8 Å [17]. Interestingly, blend films containing 50% or more DH4T also exhibit the peak at $2\theta = 3.1°$ as shoulder. This means that the vertical alignment of the D4HT molecules is somewhat maintained in 50% and 75% DH4T blend films. As more DH4T was incorporated, the intensity of the reflection at 3.1° was found to increase. In contrast, there is no peak for the 25% DH4T blend film in the low-angle region of the XRD pattern, which indicates that the minor DH4T phase in the 25% DH4T blend film is not aligned as in the 50% and 75% DH4T films, and so might act as an impurity disturbing the alignment of F8T2. This result is consistent with the relatively low-thin-film mobility of the 25% DH4T film, even though its domain size is comparable to that of the 50% DH4T film.

The morphologies of the F8T2/DH4T blend films were also investigated using atomic force microscopy (AFM). As shown in Fig. 4, the morphologies of the blend films are clearly different to those of the polymer and oligomer films. Whereas the F8T2 and DH4T films have a smooth and homogeneous surface morphology, two distinct phases can be seen in the blend films. During the evaporation process, the oligomer and polymer components separate due to differences in solubilities as the solution is concentrated [18]. The bright features in Fig. 4b–d

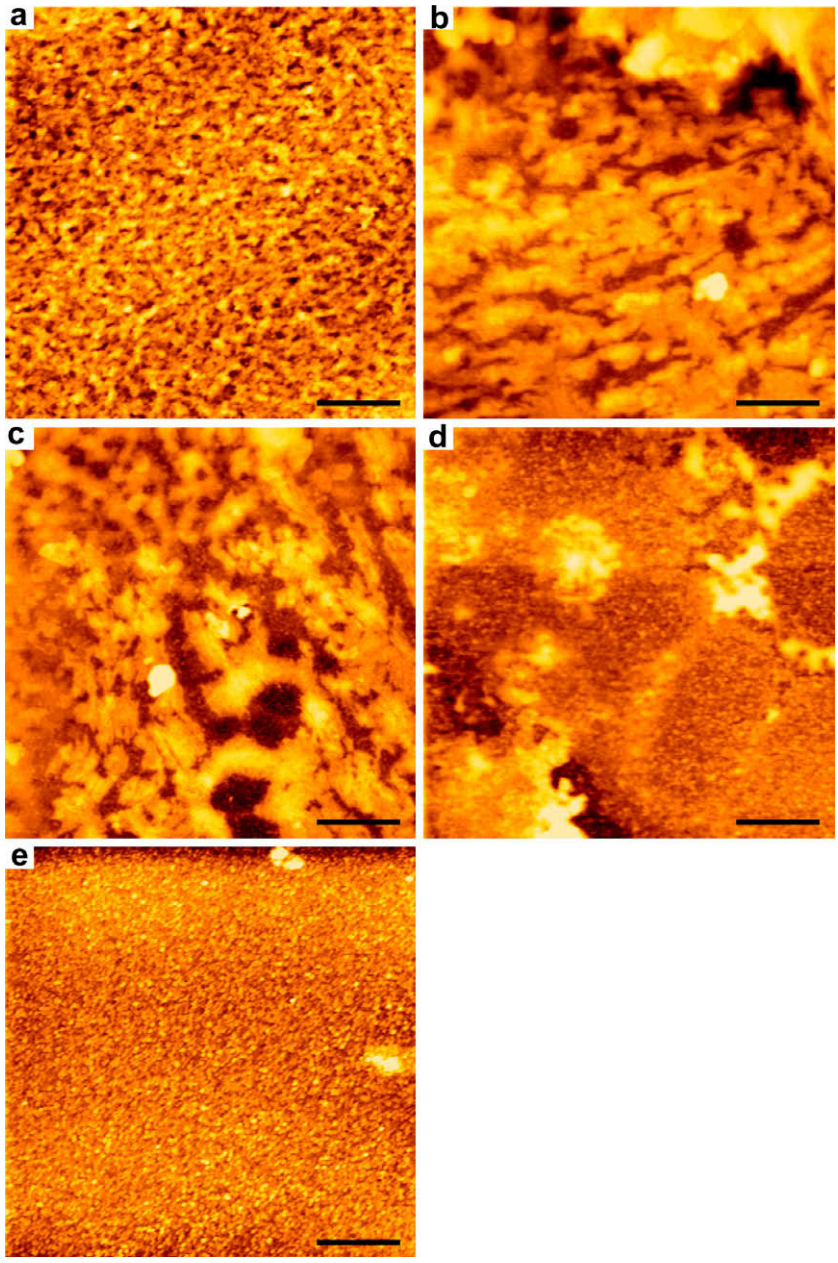

Fig. 4. AFM images of the (a) F8T2 film, (b) 25% DH4T, (c) 50% DH4T and (d) 75% DH4T blend films and (e) DH4T film (10 μm × 10 μm). The scale bar represents 2 μm.

decrease with increasing DH4T content in the blends, indicating that the brighter regions correspond to the F8T2 polymer phase. The surface morphologies of the 75% and 50% F8T2 films are similar with those previously reported for P3HT and dibenzotetrathiafulvalene (DBTTF) blends, in which the film surfaces became rough and branching domains such as dendrite and seaweed appeared by blending [19]. The morphologies of polymer/oligomer blends are comparable to those of two polymer blends. Binary blends of P3HT with poly[2-methoxy-5-(2-ethylhexyloxy)-1,4-phenylenevinylene] (MEH-PPH) and with polystyrene formed spherical domains or a bicontinuous network on the length scale of 100–600 nm depending on the blend composition [20].

3.3. Transistor properties of the F8T2/DH4T blends

The TFT devices of DH4T/F8T2 blend films were fabricated and compared with those of DH4T and F8T2 films. The output characteristics of the devices at different gate voltages are shown in Fig. 5. The devices of the blend films showed typical p-type behaviors with clear saturation currents. A contact resistance, likely due to the relatively low solubility of DH4T, was however observed at low source-

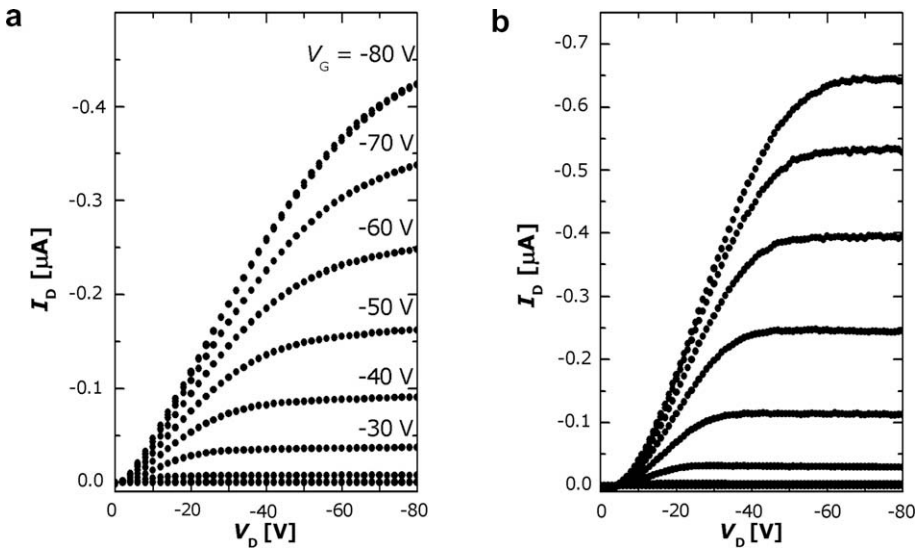

Fig. 5. Output characteristics of the (a) F8T2 film and (b) 50% DH4T blend film (channel width W = 100 μm and length L = 10 μm).

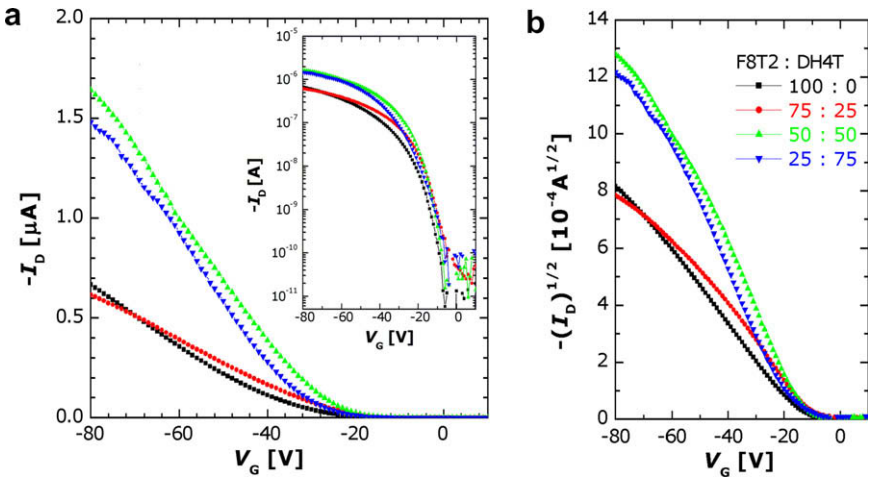

Fig. 6. Plots of the transfer curves for the F8T2 and F8T2/DH4T films at constant V_D = −80 V; (a) $-I_D$ versus V_G (inset: semilogarithmic plot) and (b) $(-I_D)^{1/2}$ versus V_G (channel width W = 100 μm and length L = 10 μm).

drain voltages. Plots of the transfer curve [i.e., $I_D = f(V_G)$] at constant V_D = −80 V are shown in Fig. 6. The field-effect mobilities were calculated in the saturation regime at V_D = −80 V using the conventional TFT equation proposed by Horowitz for saturation regimes [21].

The TFT fabricated with F8T2 under the same conditions as used for the blend devices was found to have a hole mobility in the range 0.001–0.003 $cm^2 V^{-1} s^{-1}$ with an on/off ratio of the order of 10^5, which is in close agreement with the reported hole mobilities of F8T2 devices fabricated under similar conditions [5]. On the other hand, as expected, the field-effect mobility of the TFT device fabricated with a spin-coated DH4T film could not be measured. This result can be compared with that of our previous report for a vacuum-deposited DH4T film, which found a hole-mobility of 0.02 $cm^2 V^{-1} s^{-1}$ using the same DH4T batch and bottom-contact device as used in the blend devices [17]. The absence of TFT characteristics for the spin-coated DH4T film can be explained by the poor quality of the film, which results from DH4T's low solubility. Blending the oligomer with a polymer can improve the low solubility of the oligomer as well as the relatively poor TFT performance of the polymer.

The compositional dependence of the hole mobility of the F8T2/DH4T blend films is shown in Fig. 7. The 50% and 75% DH4T blend films produce better TFT performances than the F8T2 and DH4T films. The hole mobilities of the 50% and 75% DH4T blends were found to be 0.011 $cm^2 V^{-1} s^{-1}$, which is four times higher than that of the F8T2 polymer film. Three channel widths (W) and

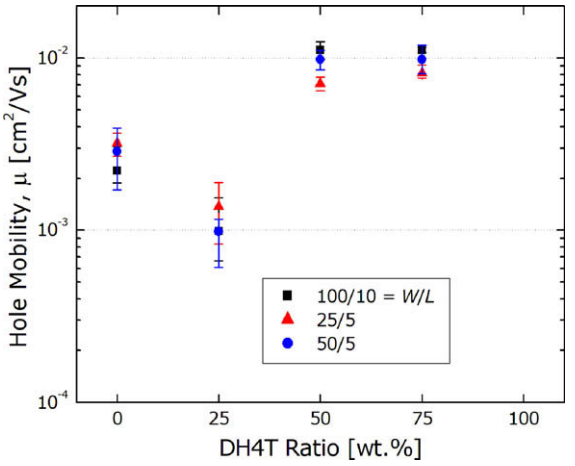

Fig. 7. Dependence of the hole mobility of F8T2/DH4T blend devices on the DH4T concentration.

lengths (L) [W(μm)/L(μm) = 100/10, 50/5 and 25/5] were used in one device: only slight variation of the hole mobilities with the W/L ratio was observed, resulting in the same dependence of the hole mobility on DH4T composition. As shown in Fig. 6, the incorporation of the oligomer into the polymer causes an increase in the on current without much increase in the off current. The 50% and 75% DH4T blend films exhibit on-currents of up to 1.5 μA, which are two and a half times higher than that of the F8T2 film. At the same time, the off-currents of the 25% and 50% DH4T blend films were still in the range 10–20 pA, which is apparently lower than that of the other thiophene-based polymers (e.g., >100 pA for stable polythiophene semiconductors incorporating thieno[2,3-*b*]thiophene [22]). As a result, the F8T2/DH4T blend devices have on/off ratios in the range 10^4–10^5, and in particular the on/off ratio of the 50% DH4T blend film device (0.9×10^5) was found to be close to that of the F8T2 film device. The optimal blend ratio for our polymer/oligomer blend system was found to be 50/50 with a hole mobility of 0.011 $cm^2\ V^{-1}\ s^{-1}$, a high-on/off ratio of about 10^5 and a low-off current of 17 pA. The TFT characteristics of the blend films are summarized in Table 1. The improvements in the TFT characteristics that result from the incorporation of 50% or 75% oligomer were also observed with other thiophene-based oligomers, T2TT and T2FL. (The chemical structures of T2TT and T2FL are shown in Ref. [17].)

3.4. Comparative study

At this point the question arises as to which mechanism predominantly controls the TFT characteristics of the polymer/oligomer blends. To assess the roles of the polymer and the oligomer in the blend films, polyfluorene homopolymer, poly(9,9′-dioctylfluorene) (PF8) and the fluorene-based oligomer, 9,9,9′,9′,9″,9″-dihexyl-[2,2′;7′,3″]terfluorene (3FL) were used in blends instead of F8T2 and DH4T, respectively.

The TFT devices fabricated with only PF8 or 3FL were found to have no TFT characteristics, because of their relatively low-HOMO levels, which result in difficult hole injection from the Au electrode. This result is consistent with those of previous reports, which found a high barrier to charge injection from the Au electrode to PF8. Although PF8 is a liquid crystalline polymer that tends to be highly ordered in thin films, PF8 devices are known to have no TFT characteristics [23].

Films of PF8/DH4T and F8T2/3FL blends were fabricated under the same conditions as used for the F8T2/DH4T blends. While all the PF8/DH4T blend films were found to exhibit no TFT characteristics, the F8T2/3FL blend films were found to exhibit TFT characteristics with hole mobilities of 0.001–0.002 $cm^2\ V^{-1}\ s^{-1}$. This result indicates that the polymer component controls the TFT characteristics

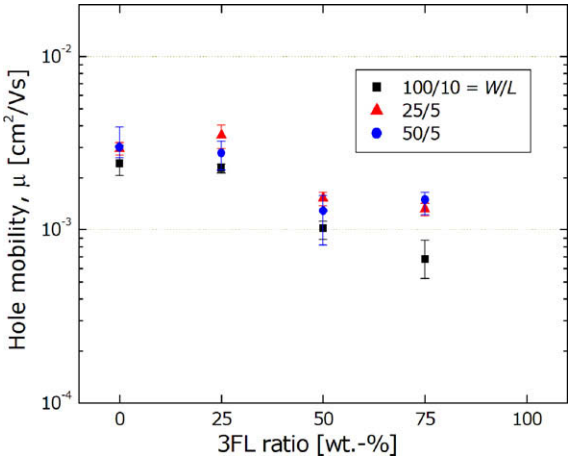

Fig. 8. Dependence of the hole mobility of F8T2/3FL blend devices on the 3FL concentration.

Table 1
TFT characteristics of the polymer/oligomer blend films (channel width W = 100 μm and length L = 10 μm)[a]

		Blend ratios (polymer:oligomer, wt.%)				
		100:0	75:25	50:50	25:75	0:100
F8T2:DH4T	μ/$cm^2\ V^{-1}\ s^{-1}$	0.0026	0.0011	0.011	0.011	–[b]
	I_{on}/I_{off}	1.3×10^5	0.3×10^5	0.9×10^5	0.3×10^5	–[b]
	I_{off}/pA	−5.2	−20.3	−17.4	−49.1	–[b]
	I_{on}/μA	−0.67	−0.62	−1.6	−1.5	–[b]
F8T2:3FL	μ/$cm^2\ V^{-1}\ s^{-1}$	0.0026	0.0023	0.0010	0.0007	–[b]
PF8:DH4T	μ/$cm^2\ V^{-1}\ s^{-1}$	–[b]	–[b]	–[b]	–[b]	–[b]
PF8:3FL	μ/$cm^2\ V^{-1}\ s^{-1}$	–[b]	–[b]	–[b]	–[b]	–[b]

[a] Determined from the transfer characteristics at V_D = −80 V. The mobilities (μ) were calculated in the saturation regime.
[b] No TFT characteristics was observed.

of the polymer/oligomer blend system, which is consistent with a previous report, in which the transport in such a blend system was analyzed using percolation theory and found to be dominated by the performance of the polymer [24].

On the other hand, it is worth noting that the TFT performances of the F8T2/DH4T and F8T2/3FL blend films were found to be different. The dependence of the hole mobility of the F8T2/3FL blend devices on the 3FL concentration is shown in Fig. 8. Whereas the hole mobility of the 50:50 F8T2/DH4T blend film was found to be four times higher than that of the F8T2 film, that of the 50:50 F8T2/3FL blend film is half that of the F8T2 film. The difference can be explained by the nature of the incorporated oligomers. The reduced TFT performance of the F8T2/3FL blend can be attributed to the relatively low-HOMO levels of the 3FL oligomer, which result in difficult hole injection, and the position of the introduced alkyl groups at the 9-position of fluorene. It has been reported that the thin-film morphologies and TFT characteristics of oligothiophene films depend on the position and bulkiness of the introduced side groups. Due to the ease of solid-state core packing, α,ω-dihexyl-substituted systems exhibit better TFT performance than β,β-dihexyl-functionalized systems [25,26]. The positions of the substituted alkyl chains in DH4T and 3FL correspond to those of α,ω-dihexyl-substituted and β,β-dihexyl-functionalized thiophene derivatives, respectively.

The comparative study of the TFT characteristics of PF8/DH4T, F8T2/3FL and F8T2/DH4T blends shows that (1) the main pathway for hole transport in polymeric and oligomeric semiconductors blend systems is the polymer and (2) the nature of the blended oligomer affects the OTFT performance of the blends.

4. Conclusions

We successfully produced synergistic effects in polymer and oligomer semiconductor blend systems without compromising their other OTFT characteristics. The good solubility of the polymer was found to complement the high performance of the small molecules. The F8T2/DH4T blends were found to exhibit good solubility and could be introduced onto the substrate by simple spin-coating. The 50:50 F8T2/DH4T blend film device was found to have a hole mobility of 0.011 $cm^2 V^{-1} s^{-1}$ and a high-on/off ratio of up to 10^5. The F8T2/DH4T blend films were found to have improved on-currents – about twice that of F8T2 – without much increase in the off-currents. The enhanced TFT performances of the blend films were explained in terms of morphological characteristics revealed by the XRD and AFM analyses. A comparative study with polyfluorene homopolymer and terfluorene showed that carrier transport in the blend systems is mainly controlled by the polymer component and that the nature of the blended oligomer affects the OTFT performance of the blends.

Acknowledgements

This research was supported by a Grant (No. AOD-02-A) from the Information Display R&D Center, one of the 21st Century Frontier R& D Program funded by the Ministry of Commerce, Industry and Energy of the Korean Government. We gratefully acknowledge Professor I.-N. Kang (Catholic University), Dr. M. Misaki (AIST) and Dr. Y.-Y. Noh (ETRI) for the fruitful discussion. E. Lim was supported by the Winter Institute Program of KJF and JISTEC for visiting research at AIST.

References

[1] H. Sirringhaus, P.J. Brown, R.H. Friend, M.M. Nielsen, K. Bechgaard, B.M.W. Langeveld-Voss, A.J.H. Spiering, R.A.J. Janssen, E.W. Meijer, P. Herwig, D.M. de Leeuw, Nature 401 (1999) 685.
[2] B.S. Ong, Y. Wu, P. Liu, S. Gardner, J. Am. Chem. Soc. 126 (2004) 3378.
[3] I. Mcculloch, M. Heeney, C. Bailey, C.K. Genevicius, I. Macdonald, M. Shkunov, D. Sparrowe, S. Tierney, R. Wagner, W. Zhang, M.L. Chabinyc, R.J. Kline, M.D. Mcgehee, M.F. Toney, Nat. Mater. 5 (2006) 328.
[4] H. Pan, Y. Li, Y. Wu, P. Liu, B.S. Ong, S. Zhu, G. Xu, J. Am. Chem. Soc. 129 (2007) 4112.
[5] H. Sirringhaus, R.J. Wilson, R.H. Friend, M. Inbasekaran, W. Wu, E.P. Woo, M. Grell, D.D.C. Bradly, Appl. Phys. Lett. 77 (2000) 406.
[6] E. Lim, B.-J. Jung, J. Lee, H.-K. Shim, J.-I. Lee, Y.S. Yang, L.-M. Do, Macromolecules 38 (2005) 4531.
[7] Y.M. Kim, E. Lim, I.-N. Kang, B.-J. Jung, J. Lee, B.W. Koo, L.-M. Do, H.-K. Shim, Macromolecules 39 (2006) 4081.
[8] K.C. Dickey, J.E. Anthony, Y.-L. Loo, Adv. Mater. 18 (2006) 1721.
[9] A. Afzali, C.D. Dimitrakopoulos, T.L. Breen, J. Am. Chem. Soc. 124 (2002) 8812.
[10] Y. Li, Y. Wu, P. Lin, Z. Prostran, S. Gardner, B.S. Ong, Chem. Mater. 19 (2007) 418.
[11] M. Berggren, O. Inganäs, G. Gustafsson, J. Rasmusson, M.R. Andersson, T. Hjertberg, O. Wennerström, Nature 372 (1994) 444.
[12] C.J. Brabec, N.S. Sariciftci, J.C. Hummelen, Adv. Funct. Mater. 11 (2001) 15.
[13] A. Babel, J.D. Wind, S.A. Jenekhe, Adv. Funct. Mater. 14 (2004) 891.
[14] S. Goffri, C. Muller, N. Stingelin-Stutzmann, D.W. Breiby, C.P. Radano, J.W. Andreasen, R. Thompson, R.A.J. Janssen, M.M. Nielsen, P. Smith, H. Sirringhaus, Nat. Mater. 5 (2006) 950.
[15] N. Stingelin-Stutzmann, E. Smits, H. Wondergem, C. Tanase, P. Blom, P. Smith, D. de Leeuw, Nat. Mater. 4 (2005) 601.
[16] E. Lim, B.-J. Jung, H.-K. Shim, Macromolecules 36 (2003) 4288.
[17] E. Lim, B.-J. Jung, H.-K. Shim, T. Taguchi, B. Noda, T. Kambayashi, T. Mori, K. Ishikawa, H. Takezoe, L.-M. Do, Org. Electron. 7 (2006) 121.
[18] R.H. Pater, M.G. Hansen, U.S. Patent 5770676, 1998.
[19] T. Kambayashi, H. Wada, M. Goto, T. Mori, B. Park, H. Takezoe, K. Ishidawa, Org. Electron. 7 (2006) 440.
[20] A. Babel, S.A. Jenekhe, Macromolecules 37 (2004) 9835.
[21] C.D. Dimitrakoupoulos, P.R.L. Melenfant, Adv. Mater. 14 (2002) 99.
[22] M. Heeney, C. Bailey, K. Genevicius, M. Shkunov, D. Sparrowe, S. Tierny, I. McCulloch, J. Am. Chem. Soc. 127 (2005) 1078.
[23] A. Babel, S.A. Jenekhe, Macromolecules 36 (2003) 7759.
[24] D.M. Russell, C.J. Newsome, S.P. Li, T. Kugler, M. Ishida, T. Shimoda, Appl. Phys. Lett. 87 (2005) 222109.
[25] H.E. Katz, Z. Bao, S.L. Gilat, Accounts Chem. Res. 34 (2001) 359.
[26] A. Facchetti, M. Mushrush, M.-H. Yoon, G.R. Hutchison, M.A. Ratner, T.J. Marks, J. Am. Chem. Soc. 126 (2004) 13859.

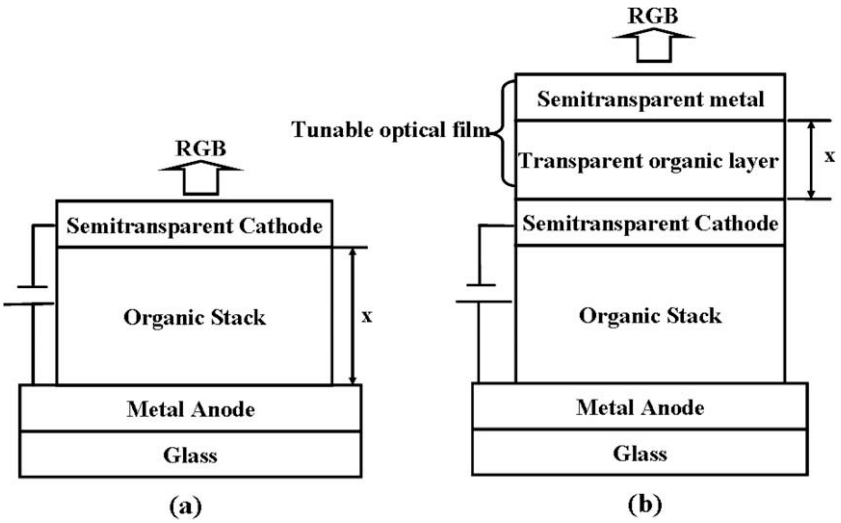

Fig. 1. (a) Conventional top-emitting OLED; (b) top-emitting OLED with TOF.

reflective mirrors in the microcavity. In order to achieve the three primary colors in this kind of device configuration, it needs to change the organic layer thickness between the two electrodes to adjust the resonant wavelength of the cavity. However, the electrical characteristics and the power consumption of an OLED are strongly dependent on the thickness of organic layers, especially for organic materials with low charge mobilities. The microcavity OLED with thick organic layers would cause the increase of driving voltages and power consumption. And the device with thin organic layers may result in large leakage current and low light-emitting efficiency. The performance of top-emitting microcavity OLEDs would be further enhanced if the optical and electrical characteristics of the OLEDs can be optimized individually. Xie et al. reported high contrast OLEDs with semitransparent cathode covered with low-reflection multiple layers [16]. The overlaid multiple layers in their devices can reduce effectively the ambient reflection while they do not influence the electrical performance of the device. Here, we developed an approach to realize RGB emission from a top-emitting OLED. The device configuration is shown in Fig. 1b, which consists of a top-emitting white OLED overlaid by a multi-layer tunable optical films (TOF). The TOF can effectively varying the emission color and does not influence the electrical performance of the underlying OLEDs. Blue, green and red emission has been obtained by covering TOF on top-emitting OLEDs based on both green and white emitters.

2. Experiment

The configuration of the color tunable top-emitting OLEDs we designed is shown in Fig. 1b which consists of an anode, an organic stack, a semitransparent cathode and a TOF. The anode of Al(10 nm)/Ag(80 nm) is thermally deposited on the pre-cleaned glass substrate. The commonly used hole-transporting *N*,*N*′-bis-(1-naphthl)-diphenyl-1-1′-*N*,*N*′-diamine (NPB) (30 nm) and electron-transporting/emissive tris(8-quinolinolato) aluminum (Alq_3) (60 nm) are used to form an organic stack. A 20-nm-thick Ag is used as the semitransparent cathode. A 1.7-nm vanadium oxide (V_2O_5) and a 10-nm Samarium (Sm) are introduced at Ag anode/NPB and Alq_3/Ag cathode interfaces as buffer layers to enhance hole and electron injection, respectively. The TOF includes a transparent organic layer and a semitransparent metal layer. Here Alq_3 and Ag are used as the transparent layer and the semitransparent metal layer, respectively. The top-emitting white OLED has an organic stack of 40 nm poly(ethylenedioxythiophene):poly(styrene sulfonic acid)(PEDOT:PSS)/40 nm 1,3-bis(9-carbazolyl)benzene(mCP):10 wt% bis[(4,6-difluorophenyl)-pyridinato-N,C^2](picolinato)Ir(III)(FIrpic):1 wt% bis(2,4-diphenyl-quinoline)iridium(III)acetylan-etonate-[$Ir(ppq)_2(acac)$]/10 nm 2,9-dimethyl-4,7- diphenyl-1,10-phenanthroline (BCP)/20 nm Alq_3. All layers were deposited by thermal evaporation at a base pressure about 5×10^{-4} Pa except the PEDOT:PSS layer and the mCP: 10 wt% FIrpic: 1 wt% $Ir(ppq)_2(acac)$ layer which were deposited via spin-coating. The current–voltage–luminance (*I*–*V*–*L*) characteristics and electroluminescent (EL) characteristics of the devices were measured using Keithley 2400 source meter and PR650 Spectroscan spectrometer. All the measurements were carried out at room temperature under ambient conditions.

3. Results and discussion

It is crucial to determine the thickness of semitransparent Ag cathode and the individual layers in TOF for achieving optimized device performance. We investigated the influence of semitransparent Ag cathode on the top-emitting OLEDs. Three top-emitting OLEDs with 10-, 20-, and 30-nm Ag semitransparent cathodes were fabricated. The device with 20-nm Ag semitransparent cathode showed a better device performance than the other two devices. This may be attributed to its good conductivity and high transmittance. The transmittance of the multiple layer structure

of Ag 20 nm/Alq_3/Ag 20 nm is calculated to determine thickness of Alq_3 in TOF for achieving its maximum transmittance in blue, green and red region. In modeling, the refractive index data for Ag were taken from the reference [17]. The refractive index of Alq_3 is fixed at 1.73 in the range of 400–700 nm [18]. The calculation of the transmittance of multilayer films was carried out by using the transfer matrix method [19]. The calculated results are shown in Fig. 2. The Ag 20 nm/Alq_3/Ag 20 nm multilayer film shows a wavelength-dependent transmittance. It is found that the maximum transmittance at blue, green and red region can be achieved when the Alq_3 thickness is 60, 90, and 120 nm, respectively. Their transmittance ranges from 55% to 60%. The wavelength-dependent transmittance of Ag/Alq_3/Ag structure may be attributed to the interference effect between the two metals. For comparison studies, the measured transmission spectra of the Ag/Alq_3/Ag structure with different Alq_3 thickness are also shown in Fig. 2. The calculated and measured transmission spectra coincide with each other very well.

The EL spectra of the color tunable top-emitting OLED with a structure of Al 10 nm/Ag 80 nm/V_2O_5 1.7 nm/NPB 30 nm/Alq_3 60 nm/Sm 10 nm/Ag 20 nm/Alq_3 × nm/Ag 20 nm are shown in Fig. 3. It can be seen that the resulted top-emitting OLEDs can exhibit blue, green and red emission when the Alq_3 layer thickness in TOF are 60, 90 and 120 nm, respectively. The blue, green and red emission peaks at 500, 552 and 632 nm with a full width at half maximum (FWHM) 73, 50 and 80 nm, respectively. And their corresponding Commission Internationale de L'Eclairage (C.I.E) coordinates are (0.24,0.54), (0.37,0.59), and (0.51,0.43), respectively.

Since the bottom anode in this kind of OLEDs is highly reflective Ag, the microcavity effect between Ag anode and Ag/Alq_3/Ag multi-layer may influence the EL emission. In order to explore the influence of the microcavity effect, the OLEDs with the same structure based on indium tin oxide (ITO) anode are also fabricated and the EL spectrum measured from the top is also shown in Fig. 3. As seen from Fig. 3, the EL spectrum of the device with ITO anode is similar to the OLED with Ag anode when the Alq_3 thickness in TOF is 60 nm. When the Alq_3 layer is 90 and 120 nm, the top-emitting OLEDs using ITO as anode show broad emission compared to those of the top-emitting OLEDs using Ag anode. This indicates that the microcavity effect between Ag anode and the TOF favors narrowing the EL spectrum and realizing three primary color RGB emission.

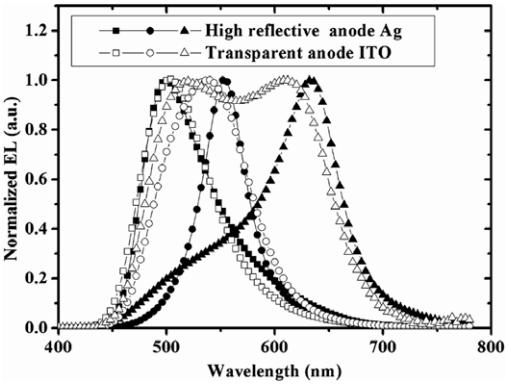

Fig. 3. Normalized EL spectra of the top-emitting OLEDs based on NPB/Alq_3 stack with highly reflective Ag anode (close symbol) and transparent ITO anode (open symbol) at 10 V. The thicknesses of Alq_3 in TOF are 60, 90, and 120 nm, respectively.

Fig. 4a shows the *J–V–L* characteristics of the color tunable top-emitting OLEDs with different Alq_3 thickness in

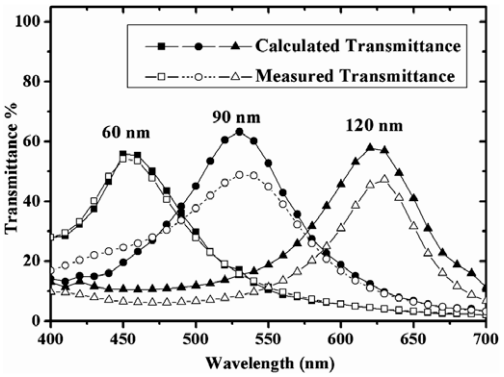

Fig. 2. Calculated (closed symbol) and measured (open symbol) transmission spectra for Ag 20 nm/Alq_3 × nm/Ag 20 nm with different thickness of Alq_3 layer.

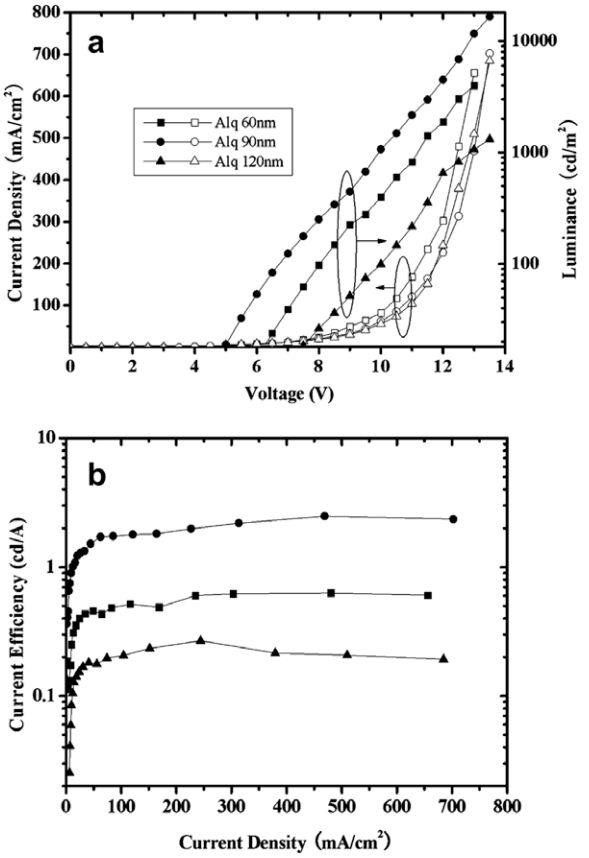

Fig. 4. (a) *J–V–L* and (b) current-luminous efficiency characteristics of the color tunable top-emitting OLEDs based on NPB/Alq_3 stack.

the TOF. It can be seen that the RGB top-emitting OLEDs show almost identical *I–V* characteristics. This is due to that the three devices have the same electrodes and organic EL stack. The overlaid exterior TOF does not influence the electrical characteristics of the underlying OLEDs. The current-luminous efficiency curves of the color tunable top-emitting OLEDs are shown in Fig. 4b. The current efficiencies of the blue, green and red OLEDs are 0.6, 2.0 and 0.2 cd/A, respectively. Since Alq_3 is green fluorescent material, its emission spectrum locates mainly in green region. Although red and blue emission can be achieved via microcavity effect by overlying the TOF film, the C.I.E coordinates are not very pure. If the TOF film is overlaid on a white OLED, RGB emission with good C.I.E coordinates may be achieved. The white top-emitting OLEDs with a structure of Glass/Al 10 nm/Ag 80 nm/V_2O_5 7 nm/PEDOT:PSS 40 nm/ mCP: 10 wt% FIrpic: 1 wt% $Ir(ppq)_2(acac)$ 40 nm/ BCP 10 nm/Alq_3 20 nm/Sm 10 nm/Ag 20 nm is fabricated and the normalized EL spectrum is shown in Fig. 5. It can be seen that the EL spectrum of the white top-emitting OLED covers from 450 nm to 650 nm with corresponding C.I.E coordinates of (0.34, 0.41). When a TOF film is deposited onto this white top-emitting OLED, the pure RGB emission are realized. Fig. 5 also exhibits the EL spectra of the top-emitting OLEDs with different thickness of the Alq_3 layer in the TOF. The blue, green and red emission is achieved with emission peaks at 470, 520 and 620 nm and an FWHM of 40, 32 and 55 nm, respectively. And their corresponding C.I.E coordinates are (0.17, 0.25), (0.22, 0.51) and (0.62, 0.35), respectively, much better than the OLEDs based on NPB/Alq_3 stack. The *J–V–L* characteristics and current-luminous efficiency curves are shown in Fig. 6. It can be seen that the blue, green and red OLEDs exhibit almost identical *V–I* characteristics. Since the light-emitting efficiency of the white top-emitting OLED is merely about 1.95 cd/A, the resulting blue, green and red OLEDs are a little low and the corresponding efficiencies are 0.3, 1.0 and 0.5 cd/A, respectively. The light-emitting efficiencies of blue, green and red emission are about 15%, 51% and 26% of the white top-emitting OLED. If high efficiency white top-emitting OLED can be fabricated, efficient three primary color RGB emission would be realized. In addition,

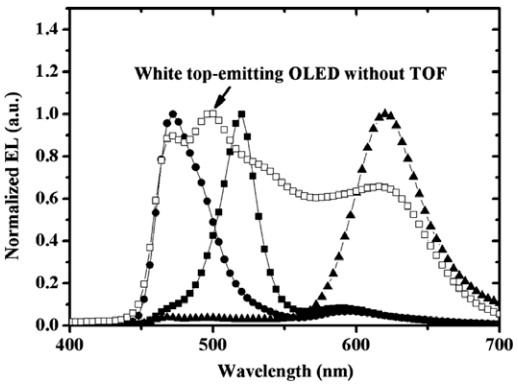

Fig. 5. Normalized EL spectra of the white top-emitting OLEDs and color tunable top-emitting OLEDs based on white emissive organic stack at 10 V.

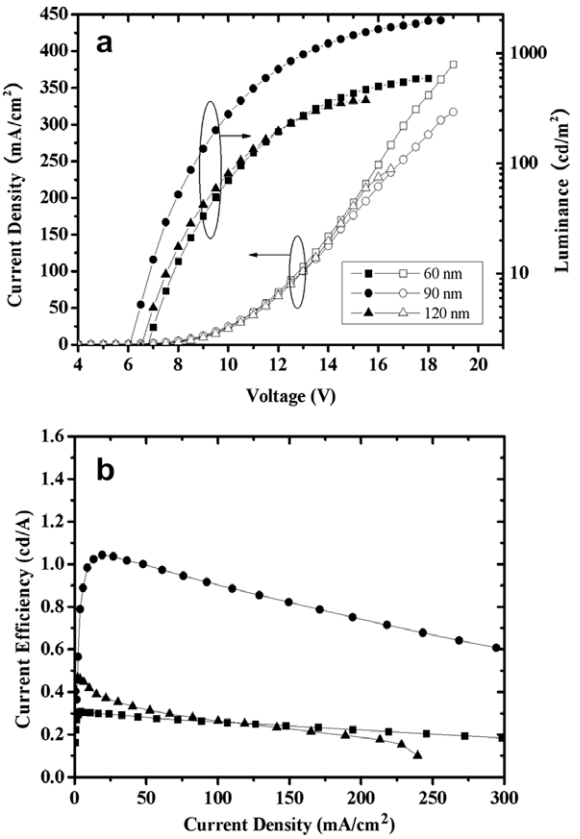

Fig. 6. (a) *J–V–L* and (b) current-luminous efficiency characteristics of color tunable top-emitting OLEDs based on white emissive organic stack.

though the microcavity effect can enhance theoretically the light-emitting efficiency for this kind of microcavity OLED, the loss of light-emitting efficiency related to metal absorption in TOFs consisting of metal films is inevitable. If TOFs is further optimized to reduce the metal thickness or metals with relatively low absorption coefficient such as Au is utilized, the light-emitting efficiency may be to some extent enhanced.

Since the microcavity OLEDs commonly show viewing angle dependent emission, the angular dependence of EL emission from the top side of this kind of RGB OLEDs is investigated. Fig. 7 shows the measured angular dependence of the peak emission for this kind of RGB top-emitting OLEDs based on the white emissive organic stack. The OLEDs are mounted on a rotating arm at a distance of 1 cm from a fiber connected to a spectrometer and the angular emission pattern is measured at 10 V. As depicted in Fig. 7, the peak wavelength is gradually blue shifted when the viewing angle increases from 0° to 60° since the resonant wavelength of the microcavity is proportional to the value of the $\cos\theta$, where θ is the angle to the normal of the device. The peak wavelengths are blue shifted about 26, 59 and 29 nm, respectively, for blue, green and red emission when the viewing angle increases from 0° to 60°. Interestingly, the viewing angle dependence of red and blue emission is smaller than the green emission. This

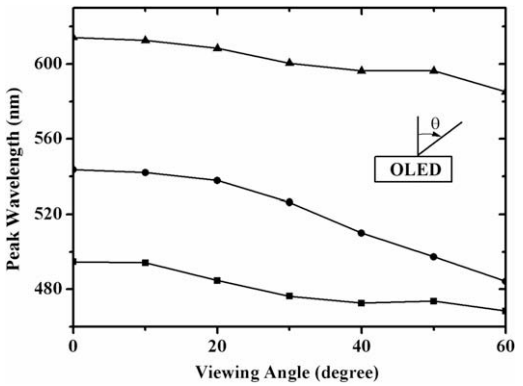

Fig. 7. The emission peak wavelength changes as a function of the viewing angle for the red (triangles), green (circles), and blue (squares) emission top-emitting OLEDs based on the white emissive organic stack.

may be attributed to that the white emissive stack contains only the blue and red phosphorescent dopants. If a green emitter is incorporated, the viewing angle dependence of green emission may be improved. Nevertheless, the viewing angle dependence for this kind of device is still a drawback for full color display. For further suppressing the angular dependence, the material with high refractive index or with large dispersive refractive index that effectively reduced the blue shift [20] can be selected to replace the Alq_3 layer between the two Ag layers.

4. Conclusions

In summary, we developed an approach to realize RGB full color emission from a top-emitting white OLED with TOFs. The advantage of this device configuration is that the optical and electrical performance can be optimized individually. Compared to the inorganic dielectric mirrors that must be fabricated via radio-frequency magnetron sputtering at high substrate temperature, this approach is more suitable for top-emitting OLEDs since the TOFs can be fabricated easily by thermal evaporation and would not destroy the underlying organic layers. If the light-emitting efficiency and the angular dependence of emission can be further improved, this may become a simple way to realize full color display by using white top-emitting OLEDs without color filters.

Acknowledgement

This work has been supported by the National Natural Science Foundation of China (Nos. 50573076, 20621401).

References

[1] L.S. Hung, C.H. Chen, MSE Reports 39 (2002) 143.
[2] C.W. Tang, D.J. Williams, J.C. Chang, U.S. Patent No. 5 294 870 (1994).
[3] Z. Shen, P.E. Burrows, V. Bulovic, S.R. Forrest, M.E. Thompson, Science 276 (1997) 2009.
[4] J. Kido, M. Kimura, K. Nagai, Science 267 (1995) 1332.
[5] F. Wang, P. Wang, X. Fan, X. Dang, C. Zhen, D. Zou, Appl. Phys. Lett. 89 (2006) 183519.
[6] C.C. Wu, C.W. Chen, Y.T. Lin, H.L. Yu, J.H. Hsu, T.Y. Luh, Appl. Phys. Lett. 79 (2001) 3023.
[7] M. Yoshida, A. Fujii, Y. Ohmori, K. Yoshino, Appl. Phys. Lett. 69 (1996) 734.
[8] S. Han, D. Grozea, C. Huang, Z.H. Lu, R. Wood, W.Y. Kim, J. Appl. Phys. 96 (2004) 709.
[9] Y.Q. Li, J.X. Tang, Z.Y. Xie, L.S. Hung, S.S. Lau, Chem. Phys. Lett. 386 (2004) 128.
[10] T. Nakayama, Y. Itoh, A. Kakuta, Appl. Phys. Lett. 63 (1993) 594.
[11] A. Dodabalapur, L.J. Rothberg, T.M. Miller, E.W. Kwock, Appl. Phys. Lett. 64 (1994) 2486.
[12] A. Dodabalapur, L.J. Rothberg, R.H. Jordan, T.M. Miller, R.E. Slusher, J.M. Phillips, J. Appl. Phys. 80 (1996) 12.
[13] V. Bulovic, V.B. Khalfin, G. Gu, P.E. Burrows, D.Z. Garbuzov, S.R. Forrest, Phys. Rev. B 58 (1998) 3730.
[14] S. Tokito, T. Tsutsui, Y. Taga, J. Appl. Phys. 86 (1999) 2407.
[15] S. Han, C.J. Huang, Z.H. Lu, J. Appl. Phys. 97 (2005) 093102.
[16] Z.Y. Xie, L.S. Hung, Appl. Phys. Lett. 84 (2004) 1207.
[17] D.W. Lynch, W.R. Hunter, Handbook of Optical Constants of Solids, vol. 3, Academic, San Diego, 1998, p. 235.
[18] P.E. Burrows, G. Gu, S.R. Forrest, E.P. Vicenzi, T.X. Zhou, J. Appl. Phys. 87 (2000) 3080.
[19] M. Born, E. Wolf, Principles of Optics, MacMillan, New York, 1964, p. 254.
[20] N. Tessler, S. Burns, H. Becker, R.H. Friend, Appl. Phys. Lett. 70 (1997) 556.

electroluminescent (EL) efficiency is enhanced and the EL spectrum is narrowed with respect to the ITO case, indicating that metal/metal oxide/metal can be the better anode in OLEDs.

2. Experiment

Al/WO_3/Au was fabricated by thermal deposition in vacuum system. To gain more knowledge about the transmission, Al/WO_3/Au structures with different thicknesses of Al, WO_3 and Au were deposited on glass substrates, and the transmittance dependence can be determined. Fig. 1 shows the transmittance spectra of Al/WO_3/Au structures in the wavelength range of 400–800 nm. The OLED structure with the composite anode is Al/WO_3/Au/V_2O_5/NPB (*N*,*N*′-diphenyl-*N*,*N*′-bis(1-naphthyl)-(1,1′- biphenyl)-4,4′-diamine)(60 nm)/Alq_3(*Tris* (8-hydroxyquinoline) aluminum(III))(50 nm)/LiF(1 nm)/Al(100 nm). For comparison, the control device with structure of ITO/V_2O_5/NPB/Alq_3/LiF/Al was also fabricated. All OLEDs were fabricated on pre-cleaned glass. All thin films were deposited by thermal evaporation at pressure less than 3×10^{-3} Pa, and deposited continuously without vacuum breaks. All the organics were evaporated at the rate of 0.2–0.3 nm/s, and the metallic electrodes were evaporated at the rate of 2–3 nm/s. The emissive area of the devices was 3.57 mm^2. The current–voltage–brightness characteristics were measured using a computer controlled sourcemeter (Keithley 2400) and photometer (IL1400A) with a calibrated silicon photodiode. The EL spectra were measured by Instaspec spectrometer. All the measurements were carried out in ambient atmosphere at room temperature.

3. Results and discussion

Fig. 1 shows the optical transmission spectra of ITO, Al/Au and Al/WO_3/Au structures in the wavelength range from 400 to 800 nm. It is interesting to note that the transmittance of the composite structure is significantly improved by inserting WO_3 between Al and Au layers with respect to the corresponding Al/Au structures. The maximum transmittance reaches over 55% for the case of Al(7 nm)/WO_3(3 nm)/Au(13 nm). It is well known fact that the utilization of Au favors the formation of ohmic contact and hole injection. Our results in Fig. 2 also show that, the current injection of the device improves by increasing the thickness of Au. For example, the current injection of Al(11 nm)/WO_3(3 nm)/Au(14 nm) is higher than that of the device with Al(11 nm)/WO_3(3 nm)/Au(6 nm) at the same applied voltage. With the capability of tuning the transmittance by modifying the thickness of layer in the composite electrode structure as shown in Fig. 1, we can optimize the hole injection and transmittance properties of Al/WO_3/Au and thus realizing high efficiency OLEDs.

The current density–voltage characteristics of Al/WO_3/Au OLEDs are shown in Fig. 2. The thickness of Al, WO_3 and Au has significant influence on the electrical characteristics of the OLEDs. For example, the current injection of Al(7 nm)/WO_3(3 nm)/Au(13 nm) OLED, is higher than that of Al(7 nm)/WO_3(5 nm)/Au(13 nm), also Al(8 nm)/WO_3(3 nm)/Au(13 nm) is higher than that of Al(7 nm)/WO_3(3 nm)/Au(13 nm), at the same applied voltage. Although the introduction of the WO_3 reduces the injection current with respect to both the corresponding Al/Au and ITO electrodes such as the case of Al(7 nm)/WO_3(3 nm)/Au(13 nm) in Fig. 2, the current efficiency is considerably enhanced primarily due to the improvement of the transmittance as discussed later. This indicates that beside the conductivity property of metal electrode, the transmittance is also very important in device performance.

Fig. 3 shows the brightness–current density characteristics of the devices with Al/WO_3/Au and ITO anodes. The brightness and efficiency are improved by using the optimized Al/WO_3/Au as the anode in the OLED structure of V_2O_5/NPB/Alq_3/LiF/Al compared to the ITO one. In our results, the Al/WO_3/Au structures with thickness of 7/3/13 (in nm) and 8/3/13 show the highest brightness at the same current density. Fig. 4a shows the current efficiency–current density characteristics of the Al/WO_3/Au and ITO OLEDs. The maximum efficiency reaches 3.25 cd/A for the structure of Al(7 nm)/WO_3(3 nm)/Au(13 nm), while the highest efficiency of the ITO OLED is only

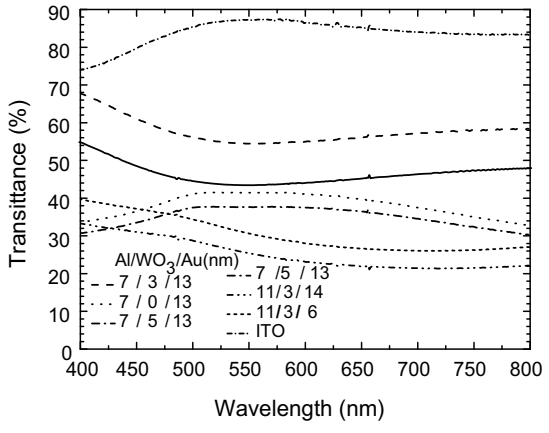

Fig. 1. Transmittance spectra of various thickness Al/WO_3/Au and Al/Au.

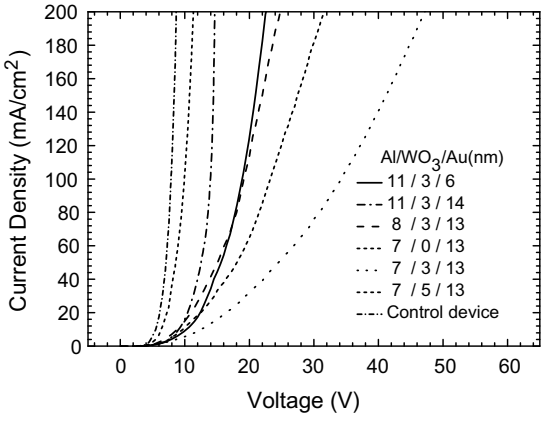

Fig. 2. Current density–voltage characteristics of Al/WO_3/Au with different Al, WO_3 and Au thickness and Al/Au device.

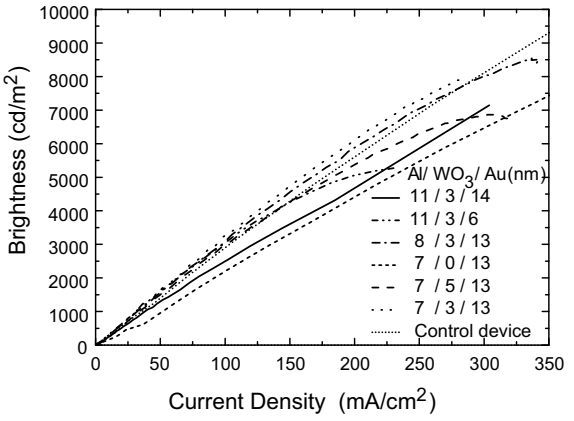

Fig. 3. Current density–brightness characteristics of Al/WO_3/Au and Al/Au device.

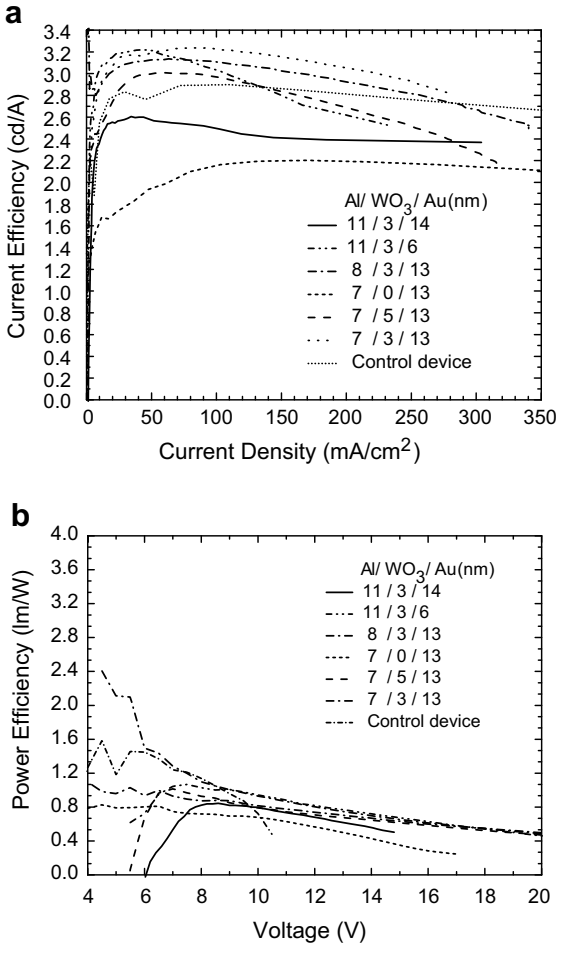

Fig. 4. (a) Current density–current efficiency characteristics of Al/WO_3/Au and Al/Au device and control device. (b) Power efficiency–voltage characteristics of Al/WO_3/Au, Al/Au device and control device.

2.8 cd/A and the Al(7 nm)/Au(13 nm) is 2.6 cd/A. The current efficiency of the devices with Al(7 nm)/WO_3(3 nm)/Au(13 nm) anode is higher than that of the devices with Al(7 nm)/Au(13 nm) anode because the insertion of WO_3 thin layer between the metal Al and Au not only offer a better electron and hole balance [17,18] as shown in Fig. 2 but also improve the transmission of the composite anode as shown in Fig. 1. However, when the thickness of WO_3 is further increased from 3 nm to 5 nm, the current efficiency will reduce and become lower than that of the Al(7 nm)/WO_3(3 nm)/Au(13 nm) case due to the reduction of the transmission (see Fig. 1). Consequently, in order to enhance the current efficiency of the Al/WO_3/Au OLEDs, both the transmission and electrical properties have to be considered simultaneously and not either one of them. In addition, our results show that the insertion of WO_3 into the composite layer does play important role in the improvement of the device performance. Besides the current efficiency, the power efficiency of the two Al/WO_3/Au devices is higher than that of the corresponding Al/Au OLED and almost the same as that of the control device at the same control voltage (see Fig. 4b).

Fig. 5 shows the EL spectra of the Al/Au and Al/WO_3/Au-based anode devices and the ITO-based anode device in normal direction. It can be seen that the utilization of Al/WO_3/Au and Al/Au anodes narrows down the EL spectrum, from 100 nm for ITO device to 70 nm for Al/Au, and 60 nm for Al/WO_3/Au. Besides, the peak wavelength is blue-shifted, from 546 nm for ITO device to about 538 nm for both Al/Au and Al/WO_3/Au. The phenomena of the spectral narrowing and blue shift is due to the microcavity effect, which are consistent with those reported [8,9]. It can be seen that the WO_3 layer also further narrows the EL spectrum with respect to the case of Al/Au without significantly blue shifting the EL spectrum further. This implies that the color purity is further improved for the case of Al/WO_3/Au. Moreover, as shown in Fig. 6, the EL spectrum of Al(7 nm)/WO_3(3 nm)/Au(13 nm) case only shifted by approximately 10 nm when the viewing angle increases from 0 to 50°. However, the spectral shift is small as compared with the OLEDs with a strong microcavity effect. Take the OLED with distributed Bragg reflector (DBR) as an example [19], the spectral shift can be 30 nm when the viewing angle increases only from 0 to 40° as shown in Fig. 6b for the OLED structure of DBR/ITO/NPB(80 nm)/Alq_3(70 nm)/

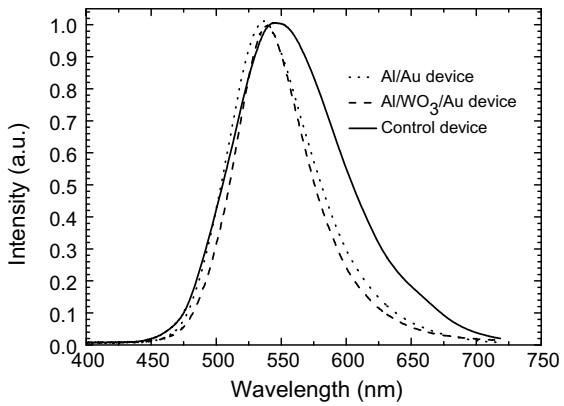

Fig. 5. EL spectra of Al(7 nm)/WO_3(3 nm)/Au(13 nm) and Al(7 nm)/Au(13 nm) OLEDs and the control device.

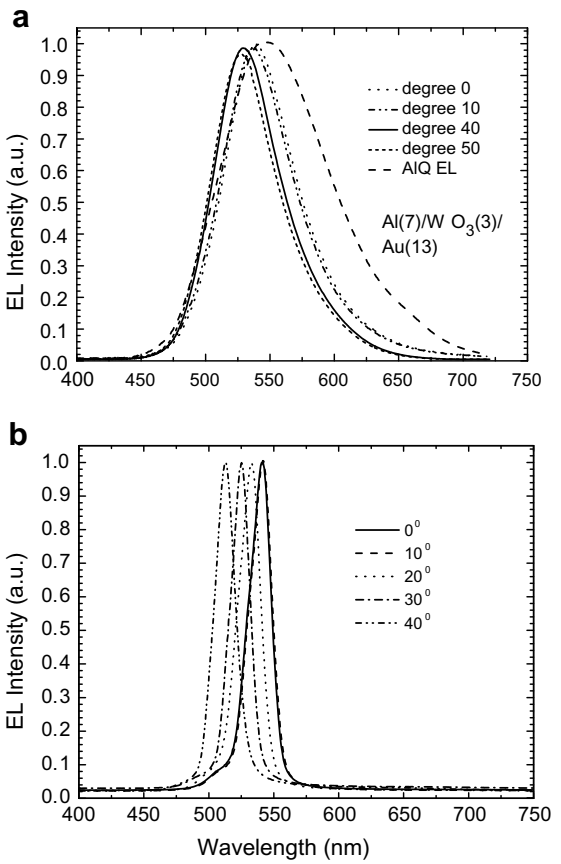

Fig. 6. (a) EL spectra of Al(7 nm)/WO_3(3 nm)/Au(13 nm) OLEDs at different viewing angles. (b) The EL spectra of microcavity OLEDs using DBR grating taken from Ref. [19].

LiF(1 nm)/Al (130 nm) where DBR consists of alternative quarter wavelength SiO_2 and TiO_2 layers.

4. Conclusion

We have developed a metal/metal oxide/metal (MIM) composite anode for high efficiency OLEDs. Our results show that the MIM structure not only shows higher transmittance, but also considerably enhances the brightness and EL efficiency. The importance is that the introduction of the metal oxide between metals greatly reduces the angular dependence caused by microcavity effect. The MIM composite layers should also be a good method as anode in top-emitting OLEDs, and due to its conductivity and transparency, and function as an effective interconnecting layer in tandem OLEDs.

Acknowledgement

We acknowledge the support of the Grant (#14300.324.01) from the Research Grant Council of the HK Special Administrative Region, China. We thank e-Ray Optoelectronics for supplying part of the organic materials at special prices.

References

[1] H. Antoniadis, J.N. Miller, D.B. Roitman, I.H. Campbell, IEEE Trans. Electron. Devices 44 (1997) 1289.
[2] A. Andersson, T. Kugler, M. Logdlund, A.B. Holmes, X. Li, W.R. Salaneck, Surf. Interface Anal. 28 (1999) 186.
[3] S.T. Lee, Z.Q. Gao, L.S. Hung, Appl. Phys. Lett. 75 (1999) 1404.
[4] K.W. Wong, H.L. Yip, Y. Luo, K.Y. Wong, W.M. Lau, K.H. Low, H.F. Chow, Z.Q. Gao, W.L. Yeung, C.C. Chang, Appl. Phys. Lett. 80 (2002) 2788.
[5] M.P. de Jong, L.J. van IJzendoorn, M.J.A. de Voigt, Appl. Phys. Lett. 77 (2000) 2255.
[6] P. Melpignano, A. Baron-Toaldo, V. Biondo, S. Priante, R. Zamboni, M. Murgia, S. Caria, L. Gregoratti, A. Barinov, M. Kiskinova, Appl. Phys. Lett. 86 (2005) 041105.
[7] G. Gu, V. Bulovic, P.E. Burrows, S.R. Forrest, Appl. Phys. Lett. 68 (1996) 2606.
[8] C.W. Chen, P.Y. Hsieh, H.H. Chiang, C.L. Lin, H.M. Wu, C.C. Wu, Appl. Phys. Lett. 83 (2003) 5127.
[9] X.L. Zhu, J.X. Sun, H.J. Peng, Z.G. Meng, M. Wong, H.S. Kwok, Appl. Phys. Lett. 87 (2005) 153508.
[10] S. Han, Y. Yuan, Z.H. Lu, J. Appl. Phys. 100 (2006) 074504.
[11] K. Fehse, G. Schwartz, K. Walzer, K. Leo, J. Appl. Phys. 101 (2007) 124509.
[12] H. Peng, X. Zhu, J. Sun, Z. Xie, S. Xie, M. Wong, H.S. Kwok, Appl. Phys. Lett. 87 (2005) 173505.
[13] R.B. Pode, C.J. Lee, D.G. Moon, J.I. Han, Appl. Phys. Lett. 84 (2004) 4614.
[14] S. Han, X. Feng, D. Johnson, R. Wood, Z.H. Lu, Appl. Phys. Lett. 82 (2003) 2715.
[15] J.X. Sun, X.L. Zhu, H.J. Peng, M. Wong, H.S. Kwok, Organic Electron. 8 (2007) 305.
[16] G.J. Kovacs, G.D. Scott, Phys. Rev. B 16 (1977) 1297.
[17] H.H. Fong, W.C.H. Choy, K.N. Hui, Y.J. Liang, Appl. Phys. Lett. 88 (2006) 113510.
[18] H.M. Zhang, W.C.H. Choy, IEEE Trans. Electron. Devices, in press.
[19] H.M. Zhang, H. You, J.W. Shi, W. Wang, S.X. Guo, M.D. Liu, D.G. Ma, Optical Quantum Electron., in press.

high cost and difficulty of its process limit their practical use in commercial products. Very recently, a polymer solar cell with graphene-based film as anode was also reported but its efficiency is still much less than 1% [9]. Accordingly, one of the important advantages of using semiconductive conjugated polymer as a transparent electrode is that conducting polymers can be easily fabricated by inkjet printing, screen printing, roll-to-roll coating or other economical solution processes [10–12].

Among the numerous conducting polymers, the polythiophene derivative, poly(3,4-ethylenedioxythiophene) (PEDOT) has high conductivity and excellent environmental stability, but it is insoluble in many solvents. Water-dispersible PEDOT:poly(styrenesulfonate) (PSS) complex has been extensively used as a hole-transport layer in organic optoelectronic devices because of its ease of process and suitable work function [13]. PEDOT:PSS exhibits significant optical transparency to visible light of 80% [14], and its conductivity can be improved by the addition of polyalcohols or high dielectric solvents [15–21]. Several polymer solar cells using PEDOT:PSS as a transparent electrode have recently been demonstrated [16,20–22]. However, its highest conductivity is still about 20 times of magnitude lower than that of ITO (~3800 S/cm) [20].

Although PEDOT:PSS has shown favorable optical transparency, its conductivity is still too low to support high device performance because of the existence of insulating PSS component. Winther-Jensen and West recently synthesized a PEDOT thin film without insulating PSS by vapor-phase polymerization [23]. This process utilizes iron(III) toluenesulfonate ($Fe(OTs)_3$) as an oxidant and pyridine as a basic inhibitor. The polymer solar cells based on such PEDOT electrodes exhibit usable device performance [24]. In addition, Ha et al. demonstrated a simple process for preparing highly conductive PEDOT thin films on a glass substrate [25]. This method utilizes iron(III) toluenesulfonate ($Fe(OTs)_3$) as an oxidant and imidazole as a base to reduce the reactivity of $Fe(OTs)_3$, reducing the rate of polymerization and the doping level. At optimal conduction, the conductivity of this PEDOT thin film is approximately 750 S/cm. This easily prepared and highly conductive PEDOT electrode can be further applied in the soft electronics industry, in which inorganic materials are unsuitable. This work demonstrates a series of P3HT:PCBM-based solar cells with PEDOT anode of various thicknesses (Fig. 1) and measures their current–voltage characteristics, including their solar power conversion efficiency, resistance and incident photon to electron conversion efficiency (IPCE), to investigate the effect of light intensity, PEDOT transparency and sheet resistance.

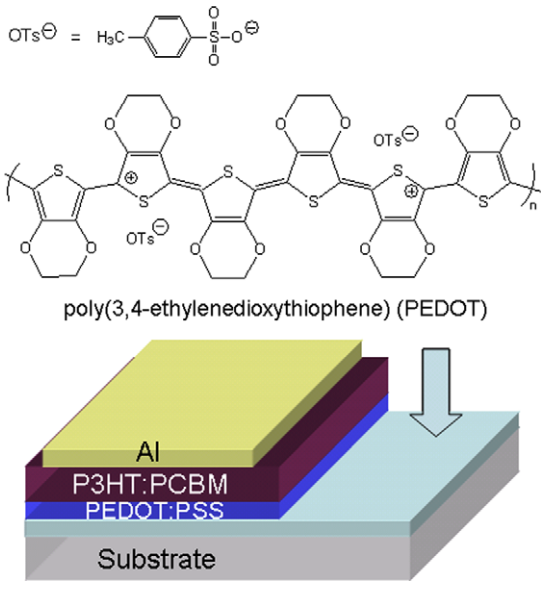

Fig. 1. Schematic representation of the P3HT:PCBM-based solar cell with PEDOT anode.

2. Experimental

The PEDOT films were polymerized in a manner similar to that employed by Ha et al. [25]. 3,4-Ethylenedioxythiophene (EDOT) (Baytron M, Bayer) was first purified by distillation, yielding a clear colorless liquid, and the glass substrate was cleaned with detergent, acetone and isopropyl alcohol in an ultrasonic bath, before being dried in an oven. $Fe(OTs)_3$ (4 g, 40 wt.% in *n*-butanol, Baytron C, Bayer) and imidazole (0.36 g, 5.25 mmol) were dissolved in *n*-butanol (7.4 mL) with stirring at 50 °C for 30 min. The distilled EDOT (0.43 g, 3.00 mmol) was then added to the solution. The mixture was rapidly spin-coated onto the pre-cleaned glass substrate at various spin rates, and then moved onto a digitally controlled hotplate for EDOT polymerization at 110 °C for 1 h. Finally, the PEDOT/glass substrates were cooled to room temperature. They were washed twice with methanol to remove the residual imidazole and oxidant and then dried on a hot plate at 110 °C for 5 min. Regioregular P3HT was prepared using the Grignard metathesis approach, providing regiocontrol in each coupling step in the polymeric reaction [26]. The regioregularity was determined by ^1H NMR to be greater than 96%. The number-average molecular weight was 43000 g/mol and the polydispersity index was 1.5, based on GPC analysis (THF eluent, polystyrene standard). PCBM was prepared in our laboratory using a method described elsewhere [27].

Polymer solar cells with an ITO (15 Ω/sq, Merck Display) or PEDOT anode were prepared as follows. PEDOT transparent films of various thicknesses were prepared as in the above experiment without further cleaning. The ITO glass was cleaned as the glass substrate described above. PEDOT:PSS (Baytron P, Bayer) was spin-coated on thus-prepared anode substrates to modify the anode surface, affording a hole-collection layer of 60 nm, after drying at 140 °C for 10 min. Then, the P3HT:PCBM blend (10 mg P3HT and 8 mg PCBM in 1 mL chlorobenzene) was spin-coated on top of the hole-collection layer at 700 rpm for 60 s, forming an active layer with a thickness of 90 nm. A 100 nm aluminum electrode was then deposited on top of the active layer using a thermal evaporator. The active area of the device, defined using a shadow mask was 0.09 cm^2. After the cathode was deposited, the devices were annealed using a digitally controlled hotplate at 150 °C for 30 min, and then slowly cooled to room temperature.

The optical transparent spectra of the PEDOT films on glass substrate were measured using a Hitachi U-3410 spectrophotometer. The surface morphology of the electrode films was observed by atomic force microscopy (AFM) using a Digital Instruments NanoScope IIIa. All images were captured in height-contrast mode, revealing the surface roughness of the films. The sheet resistances of PEDOT films were measured using a four-point probe meter, Quatek QT50, and the thickness of each sample was measured using a Dektak 6 M profilometer after a cut had been made on the film surface by a razor blade to expose the glass surface. Averages of at least four measurements made at different locations on the sample were taken to determine film thickness and calculate sheet resistance. The work functions of materials were measured using an AC2 photoelectron spectrometer (Riken Keiki Co.). The ITO sample was cleaned before any measurement was made. The PEDOT sample was prepared as in the above experiment and without further cleaning.

The current–voltage characteristics were measured using a Keithley 236 source measurement unit. The solar simulator comprised an Oriel xenon arc lamp with an AM1.5G solar filter, and the intensity was calibrated using a mono-Si reference cell with a KG5 color filter. A set of neutral density filters with a constant optical density over the spectral range of the light source was used to vary the light intensity from 50 mW/cm^2 to 6 mW/cm^2. The IPCE spectra were recorded under illumination by a xenon lamp with a monochromator (TRIAX 180, JOBIN YVON), and the light intensity was calibrated using an OPHIR 2A-SH power meter.

3. Results and discussion

In-situ oxidative polymerization was adopted to prepare PEDOT films on glass substrate using $Fe(OTs)_3$ and imidazole as oxidant and base, respectively. The function of imidazole is to reduce the reduction potential of the Fe^{3+}/Fe^{2+} couple and then the polymerization rate by reducing the pH of a reaction medium and forming a coordination complex with $Fe(OTs)_3$. Additionally, the presence of imidazole promotes formation of polymer chains with high molecular weights through a faster quench on monomer radicals than on oligomeric radicals during polymerization, thus increasing the conductivity of the PEDOT film [25]. The as-synthesized polymer film did not dissolve in water and common organic solvents, preventing the dissolution of PEDOT in the subsequent device fabrication process. The surface roughness of the PEDOT film was determined from its AFM images, shown in Fig. 2. It was found to be around 1.5 nm which was ~3.1 nm less than that of the ITO surface (The AFM image of the ITO surface is not shown.).

PEDOT films of four thicknesses were obtained by varying the spin rates – 256 nm, 169 nm, 81 nm and 28 nm. Fig. 3 plots the sheet resistances and transparency of the PEDOT films on a glass substrate. The sheet resistances were measured by the four-point probe method. The results show that the sheet resistances increased as the PEDOT film thickness decreased. The values ranged from 76 to

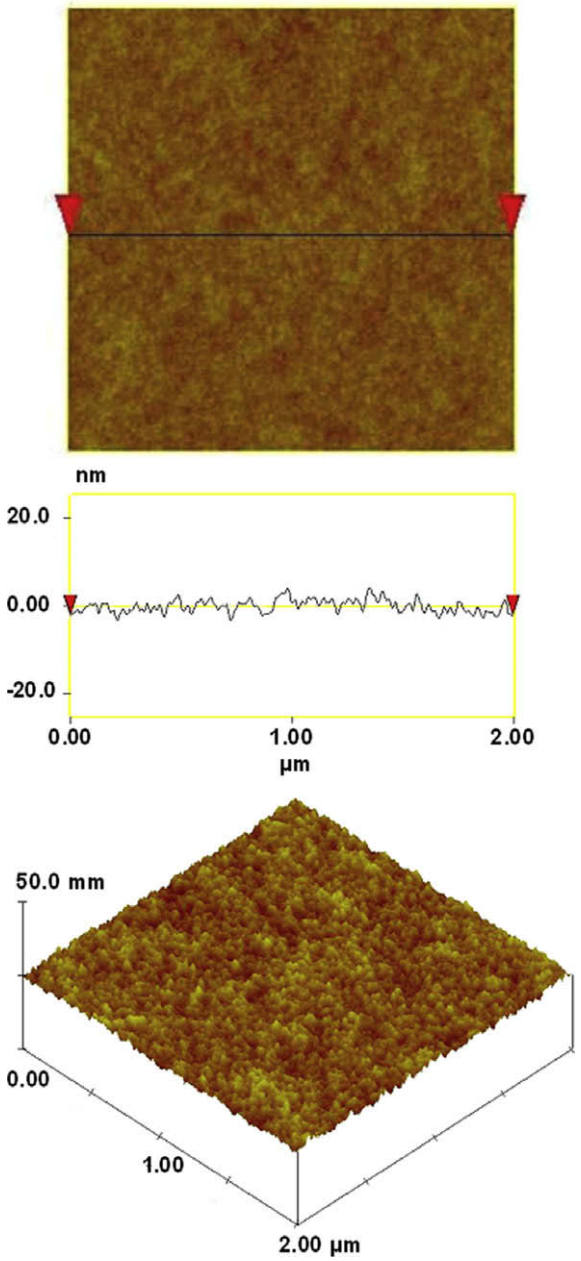

Fig. 2. AFM images of the PEDOT film.

761 Ω/sq, and corresponding to thicknesses of 256–28 nm, with an average conductivity of about 500 S/cm. In these cases, the conductivity of PEDOT was closer to, but lower than, that of ITO (15 Ω/sq, 3800 S/cm), but it still exceeded those of the other doped PEDOT:PSS conductive materials, presented in the literature [15–21]. The absorption spectrum of photoactive P3HT has a main absorption wavelength in the range of 400–650 nm with a maximum absorption wavelength at 510 nm. Therefore, Fig. 3 also plots the transmittance of PEDOT film on glass at the wavelength of 510 nm to examine the effect of PEDOT on the absorbance of P3HT in a polymer solar cell. As expected,

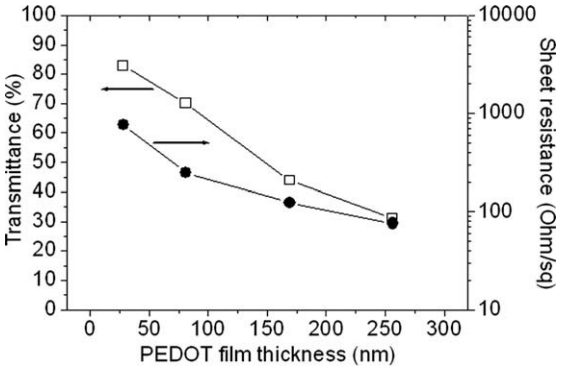

Fig. 3. The influences of the thickness of PEDOT film on its transmittance at 510 nm (□) and sheet resistance (●).

the transmittance increased as PEDOT film thickness declined, allowing more sunlight to penetrate to the active layer of the solar cells. Thinner PEDOT electrodes can act positively as transparent electrodes with good transmittance; however, the larger resistance increases the total series resistance of the diodes. Obviously, the primary task in improving device efficiency is to identify the optimal balance condition between thickness and resistance.

The work function of the electrode material is also a key parameter in determining device performance. In this work, a UV source was employed to measure the ionization potential of materials in air using an AC2 photoelectron spectrometer. Fig. 4 plots the square root of the counting rate (CR) as a function of the photon energy and the photoemission threshold energy, which is also called the work function, was determined from the crossing point of the background and the yield line. The work functions of PEDOT and ITO were found out to be 4.97 eV and 4.94 eV, respectively. Because measurements of the samples were made in air, the value of ITO measured herein was slightly higher than that reported in the literature, ~4.7 eV, as determined by ultraviolet photoelectron spectroscopy in an ultra-high vacuum [7,28]. Since the work function of the as-prepared PEDOT is very close to that of ITO, the additional adjustment on energy levels of photoactive ingredients can be minimized as using PEDOT replaces ITO as the anode of photovoltaic cells. Herein, a series of devices with a PEDOT/PEDOT:PSS/P3HT:PCBM/Al structure (as shown in Fig. 1) were fabricated to investigate the effect of the thickness of the PEDOT anode on device performance.

An ideal high-efficiency solar cell would have a series resistance (R_S) of close to zero [29]. For a real solar cell, a smaller R_S is associated with a better fill factor (FF) and short circuit current density (J_{SC}), and therefore higher power conversion efficiency (PCE) of devices [29,30]. The calculation of R_S from the dark current–voltage curves of the devices with various PEDOT thicknesses (Fig. 5) reveals that the R_S of the PEDOT anode-based devices increased as the PEDOT thickness declined. The values ranged from 40 to $10^3\ \Omega\ cm^2$ and corresponded to electrode thicknesses of 256–28 nm; they remained higher than that of the ITO anode-based device (<10 $\Omega\ cm^2$). R_S varies in a manner similar to the sheet resistance of PEDOT films (Fig. 3) because R_S is the sum of the contact resistance and the bulk resistance of the materials, ($R_S = R_{anode} + R_{PEDOT:PSS} + R_{P3HT} + R_{PCBM} + R_{Al}$) [31]. All devices were fabricated with the same photoactive components under identical process, so it is reasonable to assume that the resistances of PEDOT:PSS, P3HT:PCBM and Al stayed constant in devices. Therefore, the R_S of the device changes only with the sheet resistance of the PEDOT anode.

Fig. 6a–d display the effect of PEDOT film thickness on the open-circuit voltage (V_{OC}), FF, J_{SC} and PCE of the devices under AM 1.5G illumination at various light intensities. Fig. 6a demonstrates that the anode thickness does not affect V_{OC} when the light intensity is fixed. However, when the light intensity increases from 6, 18, 29, 38 to 50 mW/cm^2; V_{OC} monotonically increases from 0.41, 0.47, 0.50, 0.52 to 0.54 V, respectively, as for general polymer solar cells [32,33]. Fig. 6b plots the dependence of FF on the PEDOT thickness under various light intensities. For fixed anode thickness, the FF of the PEDOT anode-based devices increased slightly as the light intensity decreased, which characteristic is similar to that of typical solar cells [33]. The data also indicate that the FF fell from ~36% to ~25% as the PEDOT thickness decreased from 256 to 28 nm, because a thinner anode thickness leads to a higher sheet resistance and a higher R_S. Fig. 6c plots the dependence of J_{SC} on the PEDOT anode thickness under different light intensities. As expected, J_{SC} increased as the light intensity

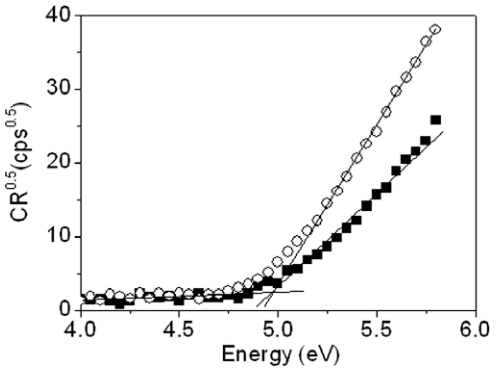

Fig. 4. Photoelectron yield spectroscopy for PEDOT (○) and ITO (■) films.

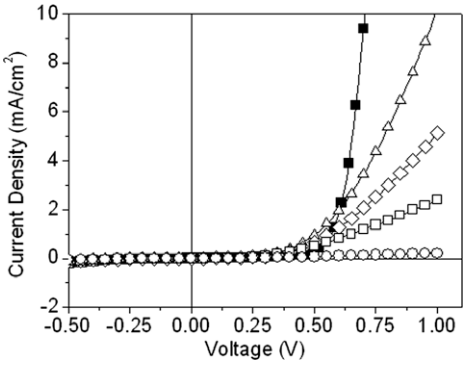

Fig. 5. Dark current characteristics of anode/PEDOT:PSS/P3HT:PCBM/Al devices with different anodes: ITO (■); PEDOT with thicknesses of 256 nm (△); 169 nm (◇); 81 nm (□); and 28 nm (○).

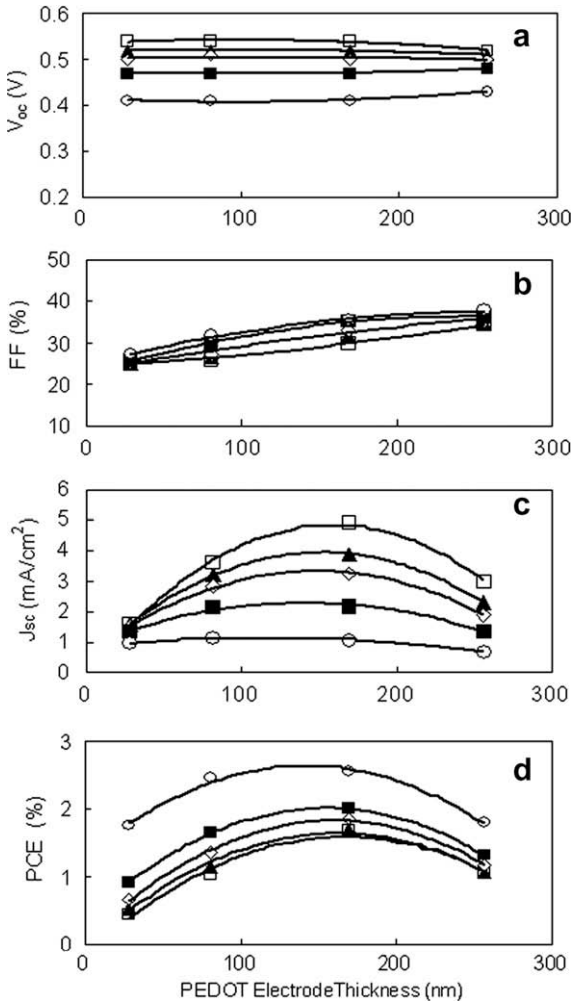

Fig. 6. Dependence of (a) open-circuit voltage (V_{OC}), (b) fill factor (FF), (c) short-circuit current density (J_{SC}) and (d) power conversion efficiency (PCE) on the thickness of PEDOT anode in the anode/PEDOT:PSS/P3HT:PCBM/Al devices under AM1.5G solar simulated irradiation at power intensities of 50 mW/cm^2 (□); 38 mW/cm^2 (▲); 29 mW/cm^2 (◇); 18 mW/cm^2 (■); and 6 mW/cm^2 (○).

raised from 6 to 50 mW/cm^2 (Fig. 6c). J_{SC} also increased with PEDOT anode thickness from 28 to 169 nm because a thicker PEDOT has a lower resistance and yields a higher J_{SC}. However, as the PEDOT anode thickness continues to increase to 256 nm, the resistance may become favorable, but a thicker film corresponds to an inferior transmittance, and therefore poor light absorption and photocurrent generation, causing the photocurrent of a 256 nm-thick PEDOT anode-based device to be lower than that of a 169 nm-thick device. Accordingly, J_{SC} is largest for a PEDOT anode-based device with a thickness of 169 nm, suggesting that the PEDOT anode has the optimal balance between the transmittance and the resistance at this thickness. In brief, as the cell is operated under a high-intensity illumination, a thicker PEDOT associated with a lower sheet resistance will conduct more photocurrent out of the cell. Conversely, as the cell is illuminated with a low-intensity

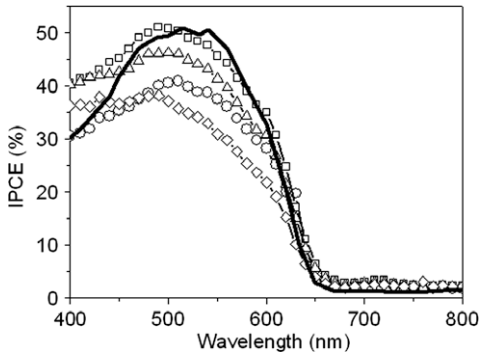

Fig. 7. (a) Incident photon-to-current conversion efficiency (IPCE) spectra of anode/PEDOT:PSS/P3HT:PCBM/Al devices with different anodes: ITO (black line), 256 nm-thick PEDOT (◇), 169 nm-thick PEDOT (△), 81 nm-thick PEDOT (□) and 28 nm-thick PEDOT (○).

light, a thinner PEDOT will allow more light to reach the photoactive layer and produce more excitons and, thus, increase photocurrent. Therefore, at a fixed light intensity, PEDOT thickness must be carefully adjusted to balance the series resistance of the cell and the exciton generation rate inside the photoactive layer to optimize cell efficiency. Fig. 6d plots the calculated PCE of devices with various PEDOT thicknesses under different light intensities. Basically, the trend is similar to those of V_{OC}, FF and J_{SC}. Since the resistance limited the photocurrent output under high light intensity, PEDOT anode-based devices herein perform best when the anode thickness is 169 nm under 6 mW/cm^2 of AM 1.5G irradiation; the highest PCE is 2.6% with an FF of 35.5%.

Fig. 7 presents the IPCE spectra of the devices with an anode/PEDOT:PSS/P3HT:PCBM/Al structure using ITO or PEDOT of various thicknesses as the anode. The efficiency under monochromatic illumination with a power density of 63–480 μW/cm^2, depending on the irradiation wavelength, was calculated. All IPCE curves closely follow the absorption spectrum of the P3HT:PCBM blend and maximum efficiency wavelength of the IPCE located at around 500 nm. The IPCE spectra of the devices were sensitive to the change in PEDOT anode thickness. When the PEDOT anode thickness was 81 nm, the IPCE reached maxima over the full range of wavelengths due to the optimal equilibrium between the sheet resistance and the light transmittance. Very interestingly, these IPCEs were comparable to those of the ITO anode-based device, directly establishing the feasibility of using this organic-based PEDOT as the anode in fabricating high-efficiency flexible devices.

4. Conclusions

This work demonstrated a polymer solar cell with a conductive PEDOT anode synthesized by *in-situ* polymerization of EDOT on a glass substrate using $Fe(OTs)_3$ and imidazole as oxidant and base, respectively. The results reveal that the thickness of PEDOT is a key factor in determining the device performance. Thinner PEDOT electrodes are more effective transparent electrodes with better transmittance,

allowing more sunlight to be incident on the active layer of the solar cells, but increasing the series resistance, thus reducing the photocurrent of the devices. Thicker PEDOT electrodes have a lower resistance, but transmittance limits the sunlight absorption of the devices. When the thickness of the PEDOT anode is optimized, a PCE of 2.6%, under AM1.5G irradiation is obtained. Furthermore, the IPCE results demonstrate that these PEDOT anode-based devices have a similar efficiency to that of an ITO anode-based device, suggesting the feasibility of replacing ITO with PEDOT as the anode of a polymer solar cell. This transparent and flexible polymer electrode can be further used to develop completely organic solar cells or other electronic devices using an easy and economic solution process on flexible plastic substrates.

Acknowledgements

The authors would like to thank National Taiwan University, Academia Sinica and National Science Council of Republic of China for financially supporting this research.

References

[1] C.J. Brabec, N.S. Sariciftci, J.C. Hummelen, Adv. Funct. Mater. 11 (2005) 15.
[2] H. Spanggaard, F.C. Krebs, Sol. Energy Mater. Sol. Cells 83 (2004) 125.
[3] E. Bundgaard, F.C. Krebs, Sol. Energy Mater. Sol. Cells 91 (2007) 954.
[4] S. Günes, H. Neugebauer, N.S. Sariciftci, Chem. Rev. 107 (2007) 1324.
[5] B.C. Thompson, J.M.J. Fréchet, Angew. Chem. Int. Ed. 46 (2007) 2.
[6] J.S. Kim, M. Granström, R.H. Friend, N. Johansson, W.R. Salaneck, R. Daik, W.J. Feast, J. Appl. Phys. 84 (1998) 6859.
[7] M.G. Mason, L.S. Hung, C.W. Tang, S.T. Lee, K.W. Wong, M. Wang, J. Appl. Phys. 86 (1999) 1688.
[8] M.W. Rowell, M.A. Topinka, M.D. McGehee, H. Prall, G. Dennler, N.S. Sariciftci, L. Hu, G. Gruner, Appl. Phys. Lett. 86 (2006) 233506.
[9] X. Wang, L. Zhi, N. Tsao, Z. Tomović, J. Li, K. Müllen, Angew. Chem. Int. Ed. 47 (2008) 2990.
[10] C.N. Hoth, S.A. Choulis, P. Schilinsky, C.J. Brabec, Adv. Mater. 19 (2007) 3973.
[11] F.C. Krebs, J. Alstrup, H. Spanggaard, K. Larsen, E. Kold, Sol. Energy Mater. Sol. Cells 83 (2004) 293.
[12] S.S. Kim, S.I. Na, J. Jo, G. Tae, D.Y. Kim, Adv. Mater. 19 (2007) 4410.
[13] J.S. Huang, P.F. Miller, J.S. Wilson, A.J. de Mello, J.C. de Mello, D.D.C. Bradley, Adv. Funct. Mater. 15 (2005) 290.
[14] B.L. Groenendaal, F. Jonas, D. Freitag, H. Pielartzik, J.R. Reynolds, Adv. Mater. 12 (2000) 481.
[15] L.A.A. Pettersson, S. Ghosh, O. Inganäs, Org. Electron. 3 (2002) 143.
[16] F. Zhang, M. Johansson, M.R. Andersson, J.C. Hummelen, O. Inganäs, Adv. Mater. 14 (2002) 662.
[17] W.H. Kim, A.J. Makinen, N. Nikolov, R. Shashidhar, H. Kim, Z.H. Kafafi, Appl. Phys. Lett. 80 (2002) 3844.
[18] J.Y. Kim, J.H. Jung, D.E. Lee, J. Joo, Synth. Met. 126 (2002) 311.
[19] S.K.M. Jönsson, J. Birgerson, X. Grispin, G. Greczynski, W. Osikowicz, A.W.D. van der Gon, W.R. Salaneck, M. Fahlman, Synth. Met. 139 (2003) 1.
[20] J. Quyang, C.W. Chu, F.C. Chen, Q. Xu, Y. Yang, Adv. Funct. Mater. 15 (2005) 203.
[21] E. Ahlswede, W. Mühleisen, M.W. bin Moh Wahi, J. Hanisch, M. Powalla, Appl. Phys. Lett. 92 (2008) 143307.
[22] B. Zimmermann, M. Glatthaar, M. Niggemann, M.K. Riede, A. Hinsch, A. Gombert, Sol. Energy Mater. Sol. Cells 91 (2007) 374.
[23] B. Winther-Jensen, K. West, Macromolecules 37 (2004) 4538.
[24] B. Winther-Jensen, F.C. Krebs, Sol. Energy Mater. Sol. Cells 90 (2006) 123.
[25] Y.H. Ha, N. Nikolov, S.K. Pollack, J. Mastrangelo, B.D. Martin, R. Shashidhar, Adv. Funct. Mater. 14 (2004) 615.
[26] R.S. Loewe, S.M. Khersonsky, R.D. McCullough, Adv. Mater. 11 (1999) 250.
[27] J.C. Hummelen, B.W. Knight, F. Lepeq, F. Wudl, J. Org. Chem. 60 (1995) 532.
[28] D.J. Milliron, I.G. Hill, C. Shen, A. Kahna, J. Schwartz, J. Appl. Phys. 87 (2000) 572.
[29] C.J. Brabec, V. Dyakonov, J. Parisi, N.S. Sariciftci, Organic Photovoltaics: Concepts and Realization, Springer, New York, 2003. Chapter 5, pp. 214.
[30] W. Ma, C.Y. Yang, X. Gong, K. Lee, A.J. Heeger, Adv. Funct. Mater. 15 (2005) 1617.
[31] J. Rostalski, D. Meissner, Sol. Energy Mater. Sol. Cells 63 (2000) 37.
[32] L.J.A. Koster, V.D. Mihailetchi, R. Ramaker, P.W.M. Blom, Appl. Phys. Lett. 86 (2005) 123509.
[33] J.Y. Kim, K. Lee, N.E. Coates, D. Moses, T.Q. Nguyen, M. Dante, A.J. Heeger, Science 317 (2007) 222.

FET current–voltage characteristics [4,9]. However, the available experimental data have not yet been described by a unified general model, and the proposed ones vary from band-like polaronic transport (due to coherent motion of charge carriers in extended states) to incoherent hopping regime, depending on the temperature and the crystal packing and structure [2,10]. In fact, polarons in organic semiconductors interact strongly with the lattice structure, and the processes of polaron trapping and scattering in an organic anisotropic crystal are more complex and less understood than those related to the more usual phonons [5]. On the other hand, the observation of anisotropic transport properties in single crystals has been usually considered the signature of band-like transport processes, not limited by extrinsic defects, structural disorder or fabrication-induced defective states [2,4,9,11].

Another factor to be considered is the interaction of organic semiconductors with photons that may induce sensible alteration of their transport properties: the energy of defect creation in organic semiconductors is smaller than for their inorganic counterparts [12] and the extent of such interactions is still not understood.

Bearing these considerations in mind, we have grown from solution organic single crystals based on 4-hydroxy-cyanobenzene (4HCB). The crystals grow in the form of rectangular-shaped platelets of tunable sizes and thicknesses, having two almost perpendicular crystallographic axes (namely *a* and *b*) constituting the main planar face. 4HCB presents three major features of interest: it's a solution-grown single crystal (easily and readily available), it forms macroscopic, easy-to-handle platelets, and it possesses an intrinsic dipolar charge distribution, due to the presence of the electron-attractor cyano group connected via a conjugated benzenic bridge to an electron-donor group, the hydroxylic one (Fig. 1). The N atom tends to attract electrons, and represents a perturbation in the electronic density distribution around the molecule. Moreover, its lone electron pair and its spatial position are different, with respect to the π-electron system of the benzenic rings, along the two crystallographic axes *a* and *b*.

The focus of this work was hence to investigate the effects on the macroscopic transport properties of (i) the anisotropic molecular packing of the crystal and (ii) the presence of a polar molecule within the crystal lattice. To these aims, charge transport along the two planar crystallographic axes was investigated both with the aid of a transverse electric field provided by a FET and by applying an external optical excitation. The results evidenced an anisotropic transport along the two axes, as well as an anisotropic influence of the optical excitation. The effects of the presence of a polar molecule in the crystal, and of its different alignment along the two axes, are discussed and correlated to the observed mobility behaviour.

2. Experimental

Organic single crystals based on 4-hydroxy-cyanobenzene (4HCB, Fig. 1) have been grown from a solution of ethylic ether/petroleum ether 80:20 V:V, as described elsewhere [13]. The so-obtained rectangular-shaped platelets tunable in size (up to a few mm^2) and thickness (up to 1 mm), are flat in the *a*–*b* plane, and ideal for device fabrication. Crystals of about 1–2 mm of side and 150–400 μm of thickness were used for this study. The crystal structure for this compound (Fig. 1), known since a long time [14], has been confirmed by X-ray diffraction (XRD).

In particular, along the direction *a*, the distance between two benzenic rings is 9.2 Å, while along the direction *b* is 10.7 Å. A marked difference between the two crystallographic axes is that along the direction *a*, a N atom

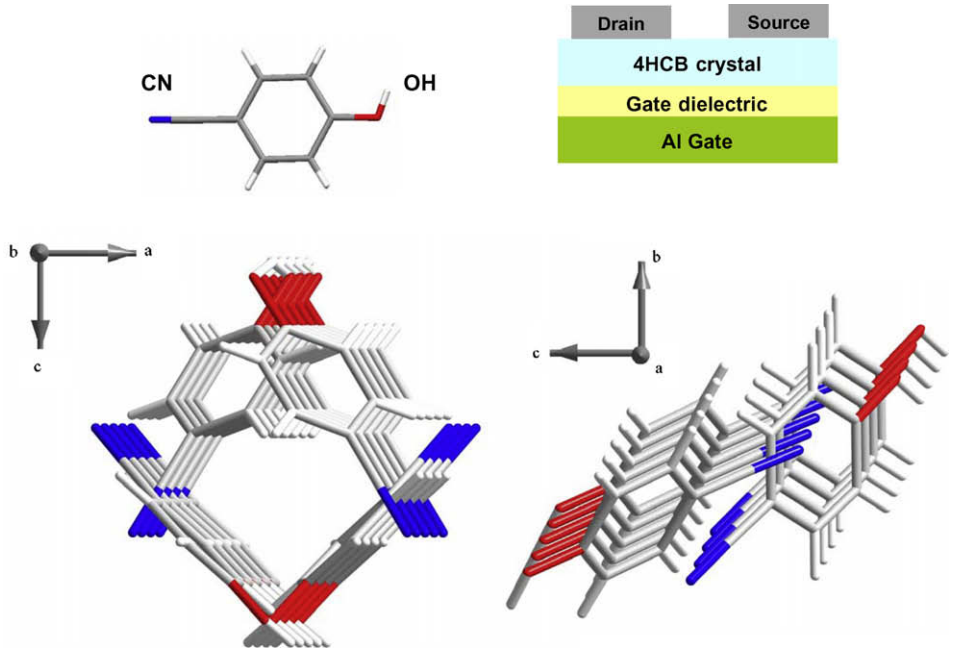

Fig. 1. 4HCB molecule and its packing in the crystals along directions *a* and *b*. The layout of the SCFET is also reported on the top left.

is sandwiched between two adjacent overlapping rings. FTIR analyses of freshly prepared single crystals did not reveal the presence of impurities. The top-contact, bottom-gate FET device was obtained by fabricating the source and drain contacts directly onto the crystal surface with silver epoxy [3,15]. The crystals were positioned on an aluminum electrode, and the thin air-filled gap left between the bottom of the crystal and the gate electrode played the role of the gate dielectric [7,16]. The presence of a thin native Al oxide layer on the metal surface cannot be excluded, and could have contributed to the formation of the gate dielectric capacitance. As already reported in the literature, [3,6,15] the effects of contact resistance are not relevant at the high drain–source voltages typically used in our two-terminal FET measurements. All the measurements were performed with a Keithley Source-meter 2400 and Electrometer 6517, at 295 K, in air and in the dark. Spectral photocurrent (PC) measurements were carried out in the planar configuration with an optical flux of 1×10^{13} photons/cm^2 at $\lambda = 450$ nm. PC spectra were recorded in air at 295 K with a bias of 150 V. The low-level injection conditions ensured that no alteration in the crystal electrical response was induced by the PC measurements, as assessed by comparing many consecutively acquired PC spectra. A good reproducibility of the electrical measurements has been assessed over many tested crystals. No sign of permanent ageing or degradation of the crystals was observed, neither from the I–V curves nor from XRD measurements performed after the electrical ones.

3. Results and discussion

The transport properties of 4HCB crystals were studied by performing I–V analyses, first in the dark and then under exposure to light, in a 2-terminal configuration between the top source and drain contacts along the two crystallographic directions *a* and *b*. The results are reported in Fig. 2 as solid symbols and confirm the presence of a charge transport anisotropy. A higher current flows along the direction *a*, as expected due to its closer molecular packing. Moreover, along direction *a* the nitrogen atom of the cyano group intersects the current flow through the π-stacking of the aromatic rings, with the molecular dipole transverse with respect to benzenic rings pile. On the contrary, along axis *b* the molecular dipole is partially aligned along the direction of the current flow (Fig. 1): the presence of an electric dipole and its different orientation with respect to the direction of the carrier flow along the two axes, locally modify the electric field experienced by the charge carriers, and are thus likely to affect the carrier transport behaviour.

When the crystal is exposed to white light, a different effect is induced along the two axes: the current remains almost constant along *b*, while along *a* it decreases of an almost constant factor (20%). Moreover, we have observed degradation and hysteresis effects in the I–V curves only if repeated measurements were carried out under or after exposure to white light. The degradation effects almost completely recover after storage in the dark for a few hours. These observations suggest that the interaction with photons induces the electrical activation of charge trapping states that: (i) are more effective along direction *a*, (ii) are able to reduce the collected current, and (iii) are characterized by a long emission time constant.

We have then investigated the effects of applying a bias to the Al gate of the structures sketched in Fig. 1. In this way, the device behaves like a FET, and the transverse electric field affects the conduction between the drain and source top contacts. The conduction is enhanced for negative gate voltages, indicating that the crystal has a p-type conductivity. No evident hysteresis effects were detected after repeated bias scans were carried out in the dark. The saturation regime could not be reached in our FETs due to the relatively large thickness of the measured crystals ($\geqslant 150$ μm), that induces a high series resistance in the top-contact bottom-gate configuration here used. The crystallographic orientation of the electrical contacts has been assessed by XRD analyses on the tested crystals. We have estimated the mobility in the dark, along the two crystallographic directions *a* and *b*, from the linear region of the I–V curves, and we observed a mobility anisotropy in the two directions, with $\mu_a \approx 5 \times 10^{-2}$ cm^2/Vs and $\mu_b \approx 5 \times 10^{-3}$ cm^2/Vs. We observe relatively large off-currents that may be attributed to extrinsic dopants, but the observation of anisotropic transport both in the 2-terminal configuration

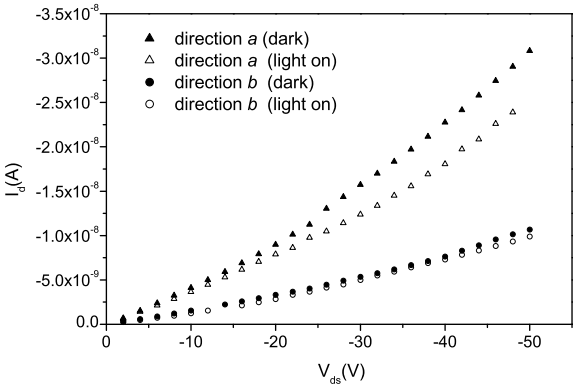

Fig. 2. Current voltage curves for the two planar directions *a* and *b*, in the dark (solid markers) and under constant white light illumination (open marks).The distance between the contacts is 350 μm.

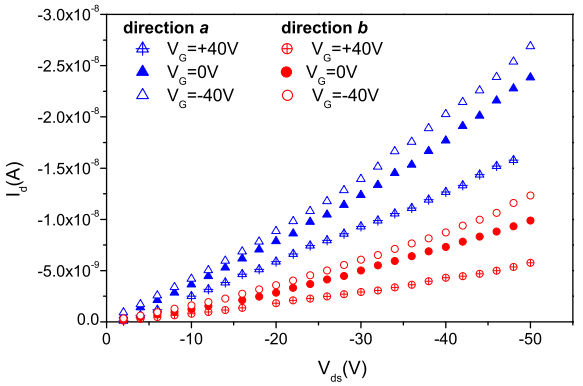

Fig. 3. FET curves measured under exposure to white light on the same crystal along the two directions *a* and *b*. The channel width is 500 μm and its length is 350 μm. The crystal thickness is 150 μm.

and in the FET-like operational mode confirms that their possible presence does not significantly affect the charge transport processes [3,11].

We then carried out the same measurements on the same crystals but under constant exposure to white light (Fig. 3). Strong hysteresis effects were observed when repeated measurements were carried out under optical excitation. Moreover, in these conditions, the anisotropy of charge transport along the two planar directions was still present, but the estimated mobility values became comparable along the two directions, with a value of $\mu \approx 3 \times 10^{-3}$ cm^2/Vs, indicating that the mobility along *a* decreases during exposure to light, while along *b* the transport is not seriously affected.

If we focus our attention on the experimental results: (i) the reduction of the current along a under optical excitation (Fig. 2), (ii) the reduction of the mobility only along *a* under optical excitation, and (iii) the appearance of hysteresis effects only after the interaction with photons, we can advance a hypothesis on the origin of this trapping site. We refer to the molecular arrangements along directions *a* and *b*, shown in Fig. 1, where the more significant difference is the presence along direction *a* of the N atom sandwiched between two adjacent benzene rings. This characteristic implies a local electrostatic distortion that may induce the formation of trapping sites able to interact with a photon. If we take into account both the effects induced by optical excitation, i.e. the current reduction along axis *a* and the I–V curves deterioration along both axes, we can hypothesize that the traps are neutral in their ground state and that they become electrically active only after the interaction with photons. In this case the interaction with photons may induce the emission of an electron from the trapping state, thus emptying the level and leaving it in a positive charged state. This behaviour is typical of a donor level and induces a twofold effect. First, there is an increase in the concentration of conduction electrons that may readily recombine with the injected holes. These electrons cannot contribute to the collected current since the band offset at the Ag/crystal contacts favours hole injection. Secondly, after exposure to light, the center is positively charged, and may affect the collected hole current via an enhanced charge carrier scattering process, thus also contributing to the observed reduction of the collected current.

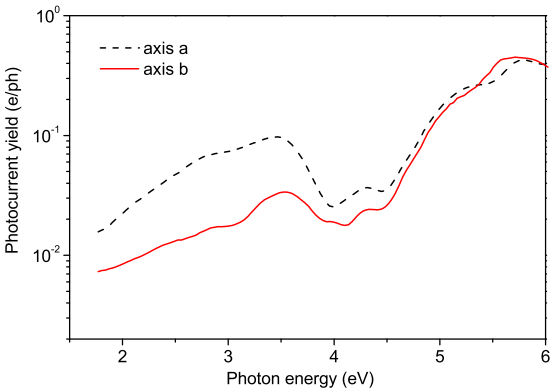

Fig. 4. Photocurrent yield (electron/photon) as a function of the incident photon beam energy for 4HCB single crystals, along axis *a* (dotted line) and axis *b* (solid line).

In order to investigate the presence of deep electrically active states, we carried out spectral PC analyses along directions *a* and *b* on the same crystal and the photoconductivity yield spectrum is reported in Fig. 4. The HOMO–LUMO transport edge is located at 4.5 eV, followed by exciton related features at lower energies [17]. A large band of deeper states is clearly visible at lower energies in the spectrum, starting at $E = 3.9$ eV, i.e. 0.45 eV from the HOMO–LUMO gap. It is noteworthy that the number of electrons excited per incident photon is larger along axis *a* than along axis *b*, and that the photoinduced current does not return to zero even for smaller photon energy values for both axes (Fig. 4). PC analyses therefore confirm the presence in the crystal of photo-activated donor-like defective states, more effective in influencing the collected current along axis *a* than along *b*. Since the main structural difference between the axes *a* and *b* is the geometrical orientation of the 4HCB intrinsic dipole with respect to the π–π stacking, we suggest that the lack of mobility anisotropy observed in our crystals under optical excitation is due to the light-induced electrical activation of deep states related to the presence and to the orientation of the molecular dipole and to the balance along the two axes *a* and *b* of two factors:

- axis *a* has a higher charge current transport very likely due to a stronger π-orbital stacking and to the presence of the electron-rich nitrogen atom sandwiched between consecutive benzenic rings (see Fig. 1);
- along axis *b* the electric molecular dipole is partially aligned along the direction of current flow, facilitating the latter, while along axis *a* the same dipole is transverse to the current flow. The latter spatial arrangement introduces a geometrical distortion of the π-clouds, very likely enhancing the carrier scattering and lowering the mobility when electrically activated by optical excitation.

Such a hypothesis implies that the charge carrier mobility in organic single crystals is not uniquely controlled by the molecular packing of the lattice, but it is also affected by the electronic properties of the single atoms constituting the basic packed molecules, as well as by their mutual orientation in the three-dimensional space.

4. Conclusions

In conclusion, we have investigated the charge carrier transport properties of organic, solution-grown single crystals based on 4-hydroxy-cyanobenzene, a molecule that possesses an intrinsic dipolar charge distribution. In order to correlate the charge carrier transport behaviour to the molecular functionality, we have fabricated air-gap FET devices that induce a transverse electric field on the planar *a*–*b* crystallographic directions. An anisotropic transport behaviour has been observed along axes *a* and *b* both in the dark and under white light, and it has been correlated to the molecular lattice packing by XRD measurements.

The exposure to visible light induced a different effect along the two directions that we have attributed to the presence and alignment of the molecular dipole. We suggests that this structure originates trapping centers that behave like deep donors and that are more efficient along axis *a*. A band of optically activated deep traps, located at 0.45 eV from the HOMO–LUMO transport edge, was identified by PC analyses that also confirm the occurrence of a persistent light-induced conductivity. The mobility along the two axes is anisotropic if measured in the dark, while it becomes comparable when the crystals are exposed to white light. We ascribed this behaviour to the intrinsic 4HCB molecular electric dipole that may originate deep electronic states electrically activated by optical excitation. Since the molecular dipole is differently oriented along the two crystallographic axes, it differently affects the current flow along the two directions. The results here presented suggest that future studies on carrier transport of SCFETs should consider the presence of molecular static dipoles, even of non intrinsic ones (i.e. of the so-called induced dipoles), as one of the parameters that can affect the device transport behaviour, in addition to anisotropic molecular packing and fabrication-induced defects.

References

[1] (a) N. Karl, in: R. Farchioni, G. Grosso (Eds.), Organic Electronic Materials, Springer, Berlin, 2001, pp. 215–239, 284–326;
(b) N. Karl, K.-H. Kraft, J. Marktanner, M. Munch, F. Schatz, R. Stehle, H.-M. Uhde, J. Vac. Sci. Technol. A 17 (1999) 2318.
[2] V. Podzorov, E. Menard, A. Borissov, V. Kiryukhin, J. Rogers, M. Gershenson, Phys. Rev. Lett. 93 (2004) 86602.
[3] R. de Boer, M. Gershenson, A. Morpurgo, V. Podzorov, Phys. Status Solidi A 201 (2004) 1302.
[4] V. Sundar, J. Zauseil, V. Podzorov, E. Menard, R. Willett, T. Someya, M. Gershenson, J. Rogers, Science 303 (2004) 1644.
[5] S. Mannsfeld, J. Locklin, C. Reese, M. Roberts, A. Lovinger, Z. Bhao, Adv. Funct. Mater. 17 (2007) 1627.
[6] V. Podzorov, V. Pudalov, M. Gershenson, Appl. Phys. Lett. 83 (2003) 4345.
[7] E. Menard, V. Podzorov, S. Gaur, M. Gershenson, J. Rogers, Adv. Mater. 16 (2004) 2097.
[8] C. Reese, Z. Bhao, Mater. Today 10 (2007) 27.
[9] (a) R. Zeis et al., Chem. Mater. 18 (2006) 244;
(b) J. Anthony, J. Brooks, D. Eaton, S. Parkin, J. Am. Chem. Soc. 123 (2001) 9482;
(c) M. Mas-Torrent, P. Hadley, S. Bromley, X. Ribas, J. Tarres, M. Mas, E. Molins, J. Veciana, C. Rovira, J. Am. Chem. Soc. 126 (2004) 8546.
[10] G. Horowitz, Adv. Mater. 10 (1998) 365.
[11] J. Lee, S. Roth, Y. Park, Appl. Phys. Lett. 88 (2006) 252106.
[12] (a) D.V. Lang, X. Chi, T. Siegrist, A. Sergent, A. Ramirez, Phys. Rev. Lett. 93 (2004) 76601;
(b) J. Northrup, M. Chabinyc, Phys. Rev. B 68 (2003) 41202.
[13] A. Fraleoni-Morgera, B. Fraboni, I. Mencarelli, L. Setti, C. Femoni, R. DiPietro, A. Cavallini, submitted for publication.
[14] T. Higashi, K. Osaki, Acta Cryst. Sec. B: Struct. Crystallogr. Cryst. Chem. 33 (1977) 607.
[15] V. Butko, X. Chi, D.V. Lang, A. Ramirez, Appl. Phys. Lett. 83 (2003) 4773.
[16] M. Kotani, K. Kakinuma, M. Yoshimura, K. Ishii, S. Yamazaki, T. Kobori, H. Okuyama, H. Kobayashi, H. Tada, Chem. Phys. 325 (2006) 160.
[17] D.V. Lang, X. Chi, T. Siegrist, A. Sergent, A. Ramirez, Phys. Rev. Lett. 93 (2004) 86802.

due to extrinsic trap states and the bias stress effect must be separated in data analysis.

In conventional silicon metal oxide semiconductor FET (MOSFET) technology, no hysteresis is observed on the I_D-V_G (drain current–gate voltage) or I_D-V_D (drain current–drain voltage) characteristics. Moreover, when a constant gate voltage and drain-source voltage are applied on the device, no variation of the drain current with the time is observed. On the other hand, hysteresis effect is observed in high K dielectrics development. To characterize and to measure the I_D-V_G hysteresis behavior, a gate pulse technique has been proposed by Leroux et al. [14].

In this paper, we take advantages of a gate pulse method introduced by Leroux et al. [14] and we demonstrate how to adapt this technique to the specific behavior of OFET. We present and analyze a study on transient current characteristics under constant gate and drain-source voltage. From this study, we try to explain the hysteresis in the current-voltage characteristics due to the measurement method, and we propose a gate pulse electrical measurement method derived of the one proposed in the high K dielectrics, to perform I_D-V_G and I_D-V_D characteristics.

2. Device fabrication and experimental details

The OTFTs used in this work are fabricated on highly doped n-type silicon substrate (<0.005 Ω cm) covered with a thermally grown silicon oxide (SiO_2) layer. The back Si serves as a gate electrode and the SiO_2 as a gate insulator. Bottom contact source-drain contacts (Ti/Au) were patterned by e-beam lithography with a ratio W/L (channel length L and channel width W) equal to 200 μm/1 μm for device A and by optical lithography with a ratio W/L 1000 μm/50 μm for device B. The silicon oxide thicknesses were equal to 10 nm for device A and 250 nm for device B. All the wafers were treated with UV/O_3 plasma treatment before pentacene deposition. A pentacene layer was vacuum evaporated at 0.1 Å/s on drain/source (D/S) titanium/gold electrodes and with a substrate maintained at the room temperature. The thickness of the active layer of pentacene was 25 nm in device A and 60 nm in device B.

Device characteristics were measured in a shielded dark box in ambient air and at room temperature with a micromanipulator probe station. Sense measurements, constant voltages and pulse gate voltages were performed with an Agilent 5270B semiconductor parameter analyser. A function of this analyser allows to carry out pulsed sweep measurements. The making of the pulsed gate measurements is given below.

3. Characterization of the hysteresis

Fig. 1 shows the transfer characteristics (I_D-V_G) for device A (W/L = 200/1 μm) with the static method using a step voltage of 100 mV/s (Fig. 1a), and using the pulse gate method (Fig. 1b), the details of the measurements are given below. With the static method we can observe a hysteresis in the current–voltage characteristic, whereas by using the pulse method, the hysteresis effect practically disappears. With the static method, we therefore can ex-

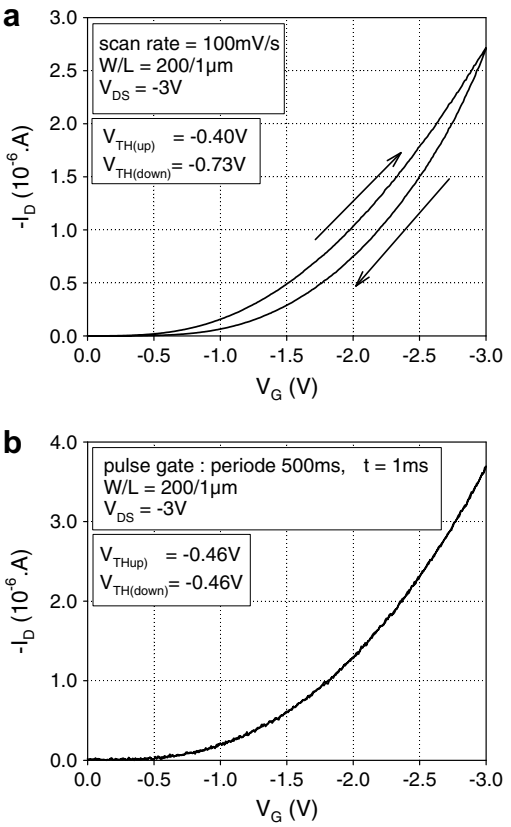

Fig. 1. Drain current versus gate voltage characteristics I_D-V_G for device A (W/L = 200/1 μm) in saturated regime (V_D = −3 V), (a) with the static method for a sweep rate of 100 mV/s, $V_{TH(up)}$ is equal to −0.40 V and $V_{TH(down)}$ is equal to −0.73 V. (b) With a gate pulse electrical method, $V_{TH(up)} = V_{TH(down)}$ = −0.46 V.

tract two values of threshold voltage (V_{TH}) and two values of carrier mobility (μ), the first for the up scan and the second for the down scan. We can see in Fig. 1b that V_{TH} and μ values are identical and independent of the measurement scan when done with the pulse voltage method.

Fig. 2 shows the transient drain current (I_D) as a function of the time when "on-state" and "off-state" cycles of 500 s are successively applied to the OFET. V_G = −3 V and V_D = −6 V corresponds to the "on-state" and V_G = 0 V and V_D = 0 V corresponds to the "off-state", where V_G and V_D are the gate voltage and the drain-source voltage, respectively. In the "on-state", the drain current decreases with the time. When a negative voltage is applied to the gate, an accumulation channel is formed and under the effect of the electric field between drain and source, a hole current circulates. In principle, this current should remain constant. In the saturated regime (V_G = −3 V and V_D = −6 V), as well as in the linear regime (not shown here), the I_D versus time curve shows a decay of the drain current as a function of the time. In logarithm scale, shown in the inset of Fig. 2, this current decay follows a power law, $I_D = At^{-\alpha}$, with α equal to around 0.11. This decrease is usually explained by the presence of traps at the interface between the semiconductor and the oxide, and/or in the bulk of the organic semiconductor [15]. In the literature, some authors [11] suggested

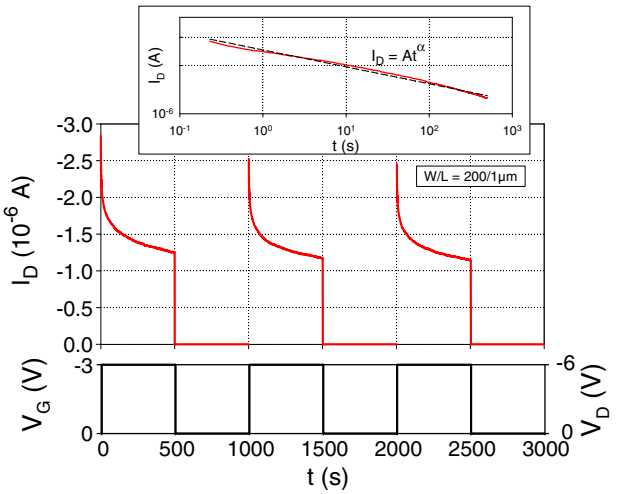

Fig. 2. Gate pulse voltage and time dependence of the drain current under on-state ($V_G = -3$ V, $V_D = -6$ V) and off-state ($V_G = 0$ V, $V_D = 0$ V) regime. In the insert, in solid line, I_D versus time in logarithm scale in the on-state regime, and in dotted lines, the data are fitted by a power low $I_D = At^{-\alpha}$.

that for the SiO_2 dielectric films, I_D decay was caused by electron traps at the organic-channel/inorganic-dielectric interface. In similar devices, other authors [16,17] suggested that the decrease of the drain current with time is due to the bias stress effect, and some of the possible causes for the bias stress are trapping inside the pentacene or at the dielectric interface.

This behavior is well reproducible for successive application of "on-state and off-state", with almost the same initial I_D value at the beginning after each "on-state". However, it is important to note that although the relaxation of the drain current is very fast when we switch from the on-state to the off-state (not seen on Fig. 2), if the duration of off-state is too short compared to that of on-state, I_D does not regain its initial value at the next off-state to on-state switching. As proposed by several authors [10,11], we can consider that the on-state corresponds to a charge-trapping period and the off-state corresponds to a detrapping of the previously trapped charges.

Moreover, we have observed, not shown here, that if we apply a gate pulse train at a frequency of 10 Hz (with a gate voltage magnitude from 0 to −3 V), with a duty cycle below 10%, no drain current decrease is observed as a function of the time while with a static gate voltage (100% gate duty cycle), the decrease in drain current is around 65% after 1000 s.

The last observations have consequences during I_D–V_G transfer characteristics measurement. In the static mea-

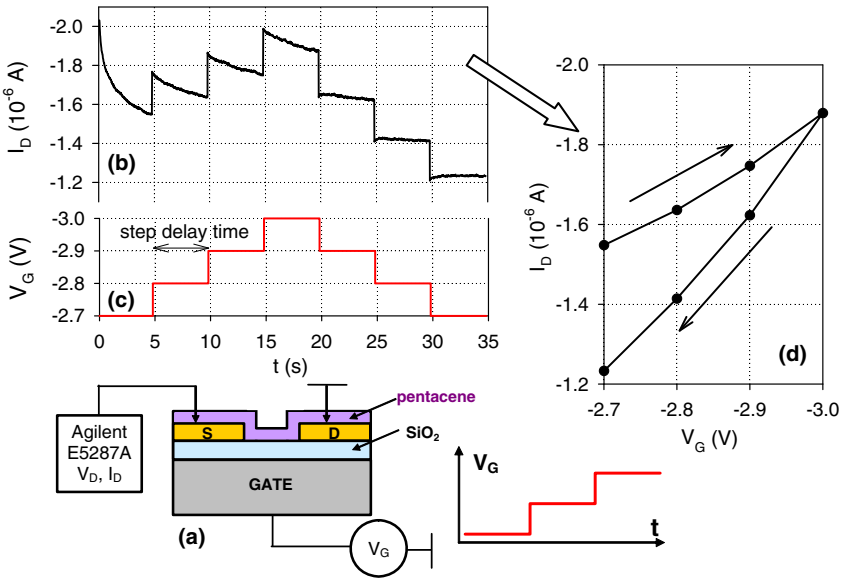

Fig. 3. (a) Experimental setup describing the static method. (b) Drain current as a function of the time for the up and down sweeps when successive steps are applied to the gate. (c) Successive steps gate voltage (characterized by the sweep rate in V/s). (d) Transfer characteristics I_D–V_G for the up and the down scans. The points correspond to the value of the current I_D at the end of the step voltage V_G.

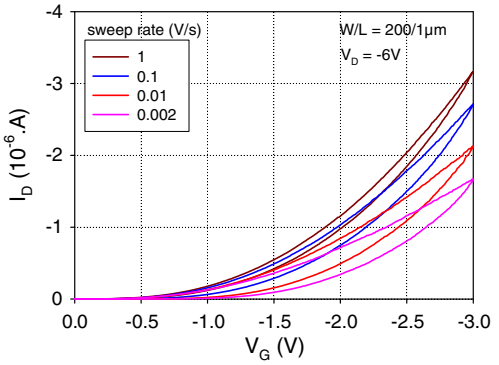

Fig. 4. Drain current versus gate voltage characteristics I_D–V_G for different sweep rate values (0.002 to 1 V/s) for device A ($W/L = 200/1$ µm) in the saturated regime ($V_D = -6$ V).

surement (Fig. 3), when the gate bias V_G switches, step by step, from a negative value to a more negative value (up scan in Fig. 1a), we observe an extra drain current [12] and during the step delay time (measurement), this drain current decays. On the other hand, the measurement at the time $t + 1$ is affected by the trapping/detrapping phenomenon occurring during the measurement at the time t. When V_G switches from a negative value to a less negative value, the drain current stays about constant during the step delay time. Consequently, for the same V_G, more current is measured during the up scan than during the down scan, causing the observed hysteresis. Fig. 4 shows the transfer characteristics obtained on the same device for different sweep rates. We can observe that the threshold voltage (V_{TH}) shift, between the up and down sweeps, depends on the sweep rate, and so on the measurement conditions. From this result, we can conclude that the lower the value of the sweep rate is, the more important the hysteresis would be.

In order, to avoid the detrimental of hysteresis and trapping/detrapping effects in the extraction of the device parameters, we propose a dynamic method based on gate voltage pulse. We saw earlier that if we applied on/off cycles on the OFET, the drain current regains its initial value if the on-off time ratio is properly chosen. Consequently, it should be possible to measure the drain current as a function of the gate voltage, without that the measurement at the time $t + 1$ is affected by the measurement at the time t.

The principle of the experiment is shown in Fig. 5. A voltage pulse with a magnitude V_G, a pulse width Δt and a period P is applied to the gate. The drain-source voltage V_D, in saturated or linear regime, is held constant and we measured the drain current during the pulse. To perform the measurements, we use a function of the Agilent 5270B. This function sets the setup parameters (magnitude of the peak, width and period) which determine the pulsed sweep measurement conditions as shown in Fig. 5a. The drain current measurement is performed during the pulse width, one measurement by pulse is realized (the integration time setting is ignored).

Charge trapping on bulk and/or interface traps occurs during the width pulse Δt. During (P–Δt), the bulk and/or interface traps effects are annealed. The annealing of whole or a part of these effects is observed during the time, i.e. when V_G is equal to 0 V. If the duty cycle is correctly adapted, the hysteresis phenomenon is not observed (see Fig. 5d), V_{Th} and μ values become independent to the measurement conditions.

4. Experimental results using the pulse gate method

We used this technique to measure the transfer characteristics of two different devices (A and B, see Section 5) in both the saturation and linear regimes. The saturation data were analyzed by plotting the square root of the drain cur-

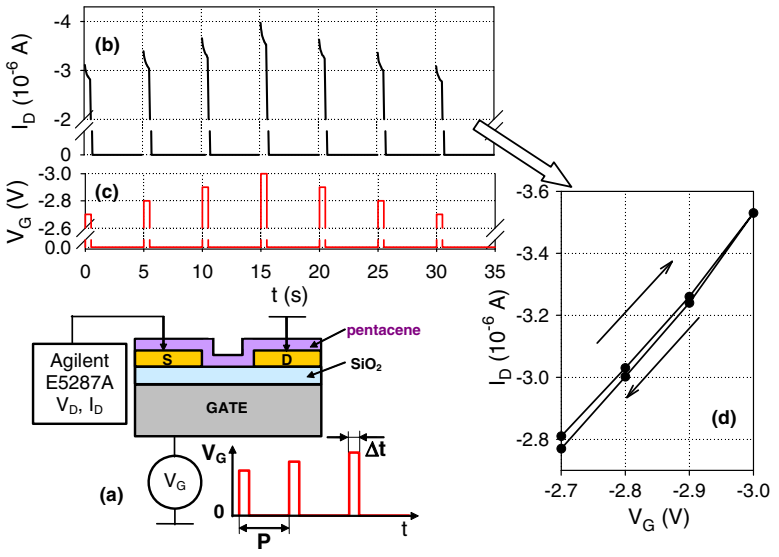

Fig. 5. (a) Experimental setup describing the dynamic method. (b) Drain current as a function of the time for the up and down sweeps when successive pulses are applied to the gate. (c) Successive gate pulses (characterized by a magnitude V_G, a pulse width Δt and a period P). (d) Transfer characteristics I_D–V_G for the up and down scans. The points correspond to the value of the current I_D at the end of each pulse V_G.

rent (I_D) as a function of the gate voltage. The slope of the fit to the linear portion of this plot, above the threshold, yields the field effect mobility, while the gate voltage intercept of the fit line determines the threshold voltage. The mobility, μ, was evaluated in the saturation region by the classical equation:

$$I_D = \frac{W}{2L}\mu C_i (V_G - V_{TH})^2,$$

where I_D is the drain current density, W and L are the channel width and length, respectively, C_i is the insulator capacitance, and V_G and V_{TH} are the gate and threshold voltage, respectively. Fig. 6a shows the I_D–V_G characteristics for device A, obtained with the dynamic method based on gate voltage pulse, for a period P equal to 1 s and three values of Δt equal to 1, 100 and 500 ms, corresponding to a duty cycle of 0.1, 10 and 50%, respectively. Fig. 6b represents the relative shift between the up and down sweeps $\Delta V_{TH}/V_{TH0}$, with $\Delta V_{TH} = V_{TH(down)} - V_{TH(up)}$ and V_{TH0} is the value of the threshold voltage with a duty equal to 0.1% (the up and down curves are superimposed), as a function of the duty cycle. In the same figure, we have also represented the relative variation of μ between the up and down sweeps $\Delta\mu/\mu_0(\Delta\mu = \mu_{down} - \mu_{up})$ and μ_0 is the carrier mobility with a duty cycle equal to 0.1%. For a duty cycle equal to 0.1% (also for 0.5 and 1%, but not shown here), we show that the I_D–V_G up and down curves are superimposed. As a result, for a duty cycle lower than 1%, V_{TH} and μ are not affected by trapping/detrapping hysteresis effects and so are independent to the measurement conditions. Moreover, it is important to note that, compared to V_{TH} variation, the carrier mobility variation is less affected by these effects.

Fig. 7a and b show the results of the same experiments for device B, the transfer characteristics for different duty cycles ranging from 1% to 75%, and $\Delta V_{TH}/V_{TH0}$ and $\Delta\mu/\mu_0$ extracted from the I_D–V_G characteristics, as a function of the duty cycle. As shown in device A, $\Delta V_{TH}/V_{TH0}$ and $\Delta\mu/\mu_0$ remain approximately constant for a duty cycle lower than 5% and a large variation of V_{TH} and a small variation of μ are observed when the duty cycle is increased above 5%. The last results show that to characterize the OFETs, the gate pulse electrical method can be applied whatever the device geometries (e.g. for large and submicrometer OFET).

The previous experiments showed the effect of charge trapping on the OFET parameter extraction. If we assume, as discussed previously and in Refs. [11,12], that the bulk and/or interface trapping occurs during the pulse width Δt and the detrapping occurs during the time (P–Δt), whole or a part of the bulk and/or interface traps effects can be annealed. By keeping Δt constant and by varying the pulse period, we can investigate the detrapping effect on the OFET parameters. We report in Fig. 8 the results of such experiments where I_D–V_G characteristics are measured at two constant pulse durations (Δt = 1 ms and

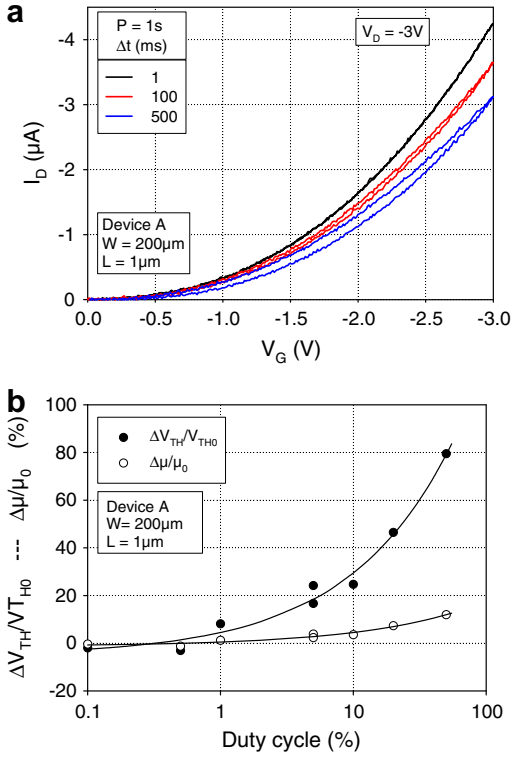

Fig. 6. (a) Drain current versus gate voltage characteristics I_D–V_G as a function of the duty cycle (0.1, 10 and 50%) for device A (W/L = 200/1 µm) in saturated regime (V_D = −3 V). (b) Relative variation of V_{TH} and relative variation of μ between the up and down sweeps as a function of the duty cycle. The lines are only a guide for eyes.

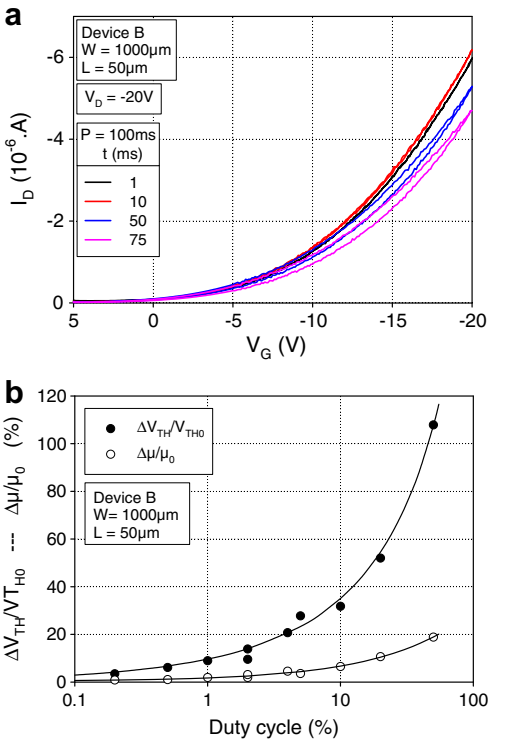

Fig. 7. (a) Drain current versus gate voltage characteristics I_D–V_G for different duty cycle values (ranging from 1 to 75%) for device B (W/L = 1000/50 µm). (b) Relative variation of V_{TH} and relative variation of μ for the up and down scans as a function of the duty cycle for device B. The lines are only a guide for eyes.

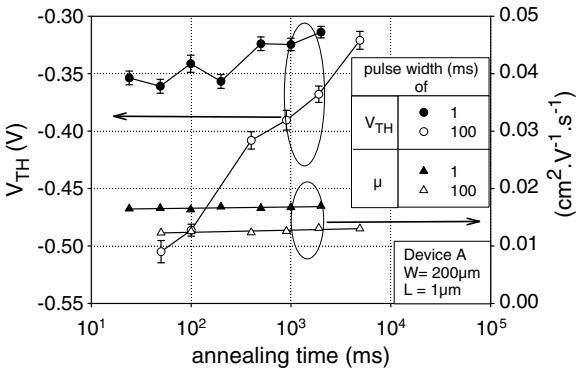

Fig. 8. Threshold voltage and carrier mobility as a function of the annealing time for two value of the trap-effect time of 1 and 100 ms.

100 ms) while varying the period of the pulses between 10 ms and 5 s. During the pulse duration, charges are trapped and during the time $P-\Delta t$, charges are detrapped. For the same quantity of trapped charges, it is possible to see the annealing time effect on V_{TH} and the carrier mobility (μ). It is clear that μ is weakly affected by the annealing time, while V_{TH}, which varies as a function of the ratio between annealing and trapping times, is much more affected and, especially when using a long pulse duration (i.e. allowing a larger charge carrier trapping). After a long period (detrapping), V_{TH} tends to its "intrinsic value". These experimental results demonstrate that the trapping/annealing mechanism must be considered to explain the V_{TH} variations in the hysteresis phenomena.

5. Conclusion

In summary, we have shown that when a gate pulse voltage, with an appropriated duty cycle, is applied on the gate of an OFET, no drift of the drain current is observed which is not the case in a constant voltage. We also demonstrated that with a gate pulse electrical method, it is possible to perform I_D-V_G characteristics on OFET and to limit the hysteresis effects due to up and down sweeps. The device parameters (threshold voltage, charge carrier mobility) can be extracted without suffering from the hysteresis effect induced by the charge trapping/detrapping phenomenon (during the up and down scans), especially before and after bias stress studies. We applied this technique on OFET with a large range of channel length, i.e. from 50 μm down to 1 μm. Finally, we saw that with this dynamic method based on gate voltage pulse, it is possible to investigate the trapping/detrapping phenomenon in OFET.

References

[1] T.N. Jackson et al, IEEE J. Sel. Top. Quant. Electron. 4 (1998) 100.
[2] Y. Watanabe, K. Kudo, Appl. Phys. Lett. 87 (2005) 223505.
[3] G. Horowitz, J. Mater. Res. 19 (2004) 1946.
[4] C.D. Dimitrakopoulos, P.R.L. Malenfant, Adv. Mater. 14 (2002) 1999.
[5] C.R. Newman, C.D. Frisbie, D.A. da Silva Filho, J.-L. Bredas, P.C. Ewbank, K.R. Mann, Chem. Mater. 16 (2004) 4436.
[6] F. De Angelis, L. Mariucci, S. Cipolloni, G. Fortunato, J. Non-Cryst. Solids 352 (2006) 1765.
[7] A.R. Völkel, R.A. Street, D. Knipp, Phys. Rev. B 66 (2002) 195336.
[8] S. Cipolloni, L. Mariucci, A. Valletta, D. Simeone, F. De Angelis, G. Fortunato, Thin Solid Films 515 (2007) 7546.
[9] T. Jung, A. Dodabalapur, R. Wenz, S. Mahapatra, Appl. Phys. Lett. 87 (2005) 182109.
[10] D.K. Hwang, K. Lee, J.H. Kim, S. Im, Appl. Phys. Lett. 89 (2006) 093507.
[11] G. Gu, M.G. Kane, J.E. Doty, A.H. Firester, Appl. Phys. Lett. 87 (2005) 243512.
[12] G. Gu, M.G. Kane, S.-C. Mau, J. Appl. Phys. 101 (2007) 014504.
[13] C. Erlen, F. Brunetti, P. Lugli, M. Fiebig, S. Schiefer, B. Nickel, in: Proceedings of the Sixth IEEE Conference on Nanotechnology, 2006, IEEE-NANO 2006.
[14] C. Leroux, J. Mitard, G. Guibaudo, X. Garros, G. Reimbold, B. Guillaumot, F. Martin, IEDM Tech. Dig. (2004) 30.1.7.
[15] S. Scheinert, K.P. Pernstich, B. Batlogg, G. Paasch, J. Appl. Phys. 102 (2007) 104503.
[16] T. Jung, A. Dodabalapur, R. Wenz, S. Mohapatra, Appl. Phys. Lett. 87 (2005) 182109.
[17] L.L. Chua, J. Zaumseil, J.-F. Chang, E.C.-W. Ou, P.K.-H. Ho, H. Sirringhaus, R.H. Friend, Nature (London) 434 (2005) 194.

that the use of MoO_3 and MoO_3 doped hole-transporting material as anode modification layers significantly reduces the operational voltage and improves the efficiency and lifetime of OLEDs [23–31].

The first introduction of MoO_X layer between ITO and hole-transporting layer was reported by Tokito et al. in 1996 [23]. They found that the operation voltage was reduced and the efficiency was enhanced. They attributed the improvement to the lower energy barrier for hole injection at the metal oxide/hole-transporting layer interface. In 2002, Reynolds et al. used MoO_3 as electron extraction barrier layer in polymer light-emitting diodes (PLEDs) [24]. The same improvement in device efficiency and brightness was obtained, which was attributed to the buildup of electrons at the MoO_3/emissive polymer layer interface, resulting in local field and a consequent enhancement of the hole injection and recombination. In 2006, Ikeda et al. reported that the use of MoO_3 doped NPB composite as a buffer layer on ITO could also reduce the operational voltage and enhance the brightness and efficiency of device [25]. Importantly, they found that the composite buffer layer greatly suppressed the pixel defects. The use of MoO_3 as the hole injection layer in top-emitting OLEDs/PLEDs and invertible PLEDs was also reported. It was found that the device efficiency was greatly improved, owing to the enhancement of the hole injection [26–29]. Matsushima et al. [30] reported the effect of a MoO_3 buffer layer on the hole injection properties by current–voltage (I–V) characteristics of hole-only devices. They found that a 0.75 nm-thick MoO_3 layer on ITO led to an Ohmic contact formation, and the enhancement of hole injection was attributed to the electron transfer from ITO and organic molecule to MoO_3, which was supported by X-ray photoelectron and ultraviolet/visible/near-infrared absorption measurements. However, all the reported work are lack of systematic investigations into the mechanism and the relationship between the characteristics of the MoO_3 interfacial layer and electroluminescence (EL) performance of OLEDs.

In previous work [31], we reported high efficiency and long lifetime of OLEDs with MoO_3 as the anode buffer layer and used the I–V characteristics of hole-only devices and polarized optical microscopy data to initially demonstrate the enhancement of the hole injection and the improvement of the morphology stability of the hole-transporting layer. In this work, we carried out systematic studies on the role of MoO_3 and MoO_3 doped *N*,*N*′-di(naphthalene-1-yl)–*N*,*N*′-diphenyl-benzidine (NPB) as the interface modification layers on ITO in OLEDs by atomic force microscopy (AFM), polarized optical microscopy, transmission spectra, ultraviolet photoemission spectroscopy (UPS) and X-ray photoemission spectroscopy (XPS). The studies on the energy level and the film morphology show that the MoO_3 and MoO_3:NPB layers can reduce the hole injection barrier, improve the interfacial stability and suppress the crystallization of the hole transport layer NPB. As a result, the efficiency and stability of OLEDs are improved.

2. Experimental

The device structure used in this study was ITO/MoO_3:NPB (10 wt.%, 40 nm) or MoO_3 (6 nm)/NPB (100 nm)/tris(8-hydroxyquinoline) aluminum (Alq_3) (60 nm)/LiF (1 nm)/Al (120 nm). For comparison, ITO/CuPc (10 nm)/NPB/Alq_3/LiF/Al and ITO/NPB/Alq_3/LiF/Al devices were also studied. The OLEDs and thin films for the thermal annealing studies were prepared by thermal evaporation in a high-vacuum system with pressure less than 5×10^{-4} Pa. For OLED devices, the commercial ITO-coated glass with a sheet resistance of 100 Ω/□ was used as the anode. The 40 nm

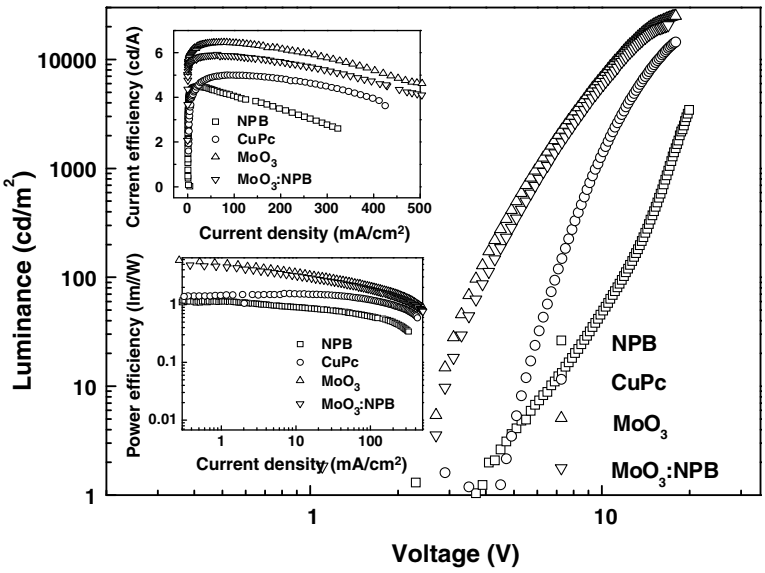

Fig. 1. Luminance-voltage of ITO/buffer layer/NPB/Alq_3/LiF/Al devices with buffer layers of CuPc (circle), MoO_3 (up triangle), MoO_3:NPB (down triangle) and without buffer layer (square) at room temperature. The current efficiency–current density and the power efficiency–current density of above devices are shown in the inset.

MoO_3:NPB or 6 nm MoO_3, 100 nm NPB, 60 nm Alq_3, 1 nm LiF and 150 nm Al were evaporated onto ITO in turn. The concentration of MoO_3 in NPB was controlled at 10 wt.%. The evaporation rates were monitored by frequency counter and calibrated by Dektak 6M Profiler (Veeco). The overlap between ITO and Al electrodes was 16 mm^2 as the emissive size of devices. For the measurements of transmittance, energy level and morphology of NPB, CuPc/NPB, MoO_3/NPB and MoO_3:NPB/NPB thin films at different temperatures, these films were deposited on ITO-coated glass substrates. The current–voltage-brightness characteristics were measured using a Keithley source measurement unit (Keithley 2400 and Keithley 2000) with a calibrated silicon photodiode. All devices were measured at room temperature without encapsulation.

Thermal treatment was done in two ways: thermal annealing in an oven and heating the substrate during the film deposition. For thermal annealing, the films were first deposited on substrate, and then heated in an oven at 90 °C or 110 °C for 2 h. In another way, the substrate was first put in a vacuum chamber, and then heated to 80 °C or 120 °C under a vacuum less than 5×10^{-4} Pa. When the substrate reached the final temperature, the film deposition composite or device fabrication began. The

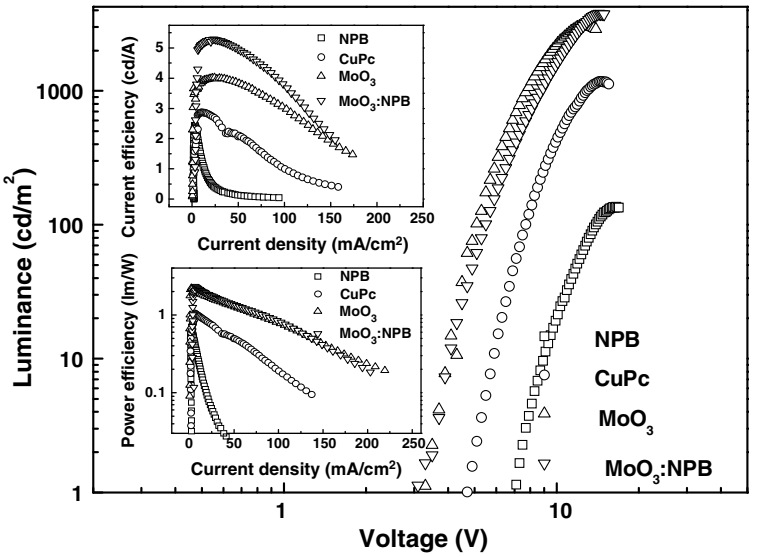

Fig. 2. Luminance-voltage of ITO/buffer layer/NPB/Alq_3/LiF/Al devices with buffer layers of CuPc (circle), MoO_3 (up triangle), MoO_3:NPB (down triangle) and without buffer layer (square) fabricated at substrate temperature of 80 °C. The current efficiency–current density and the power efficiency–current density of above devices are shown in the inset.

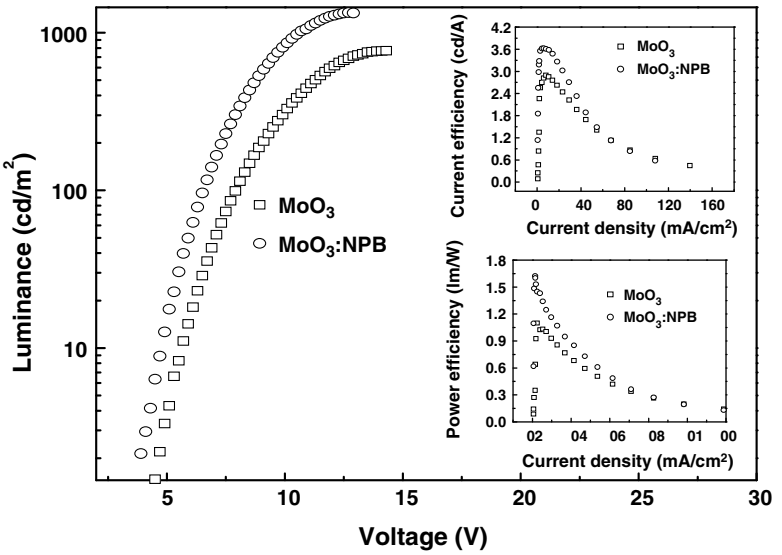

Fig. 3. Luminance-voltage of ITO/buffer layer/NPB/Alq_3/LiF/Al devices with buffer layers of MoO_3 (square) and MoO_3:NPB (circle) fabricated at substrate temperature of 120 °C. The current efficiency–current density and the power efficiency–current density of above devices are shown in the inset.

films or devices were taken out and measured after cooling to room temperature.

The transmission spectra were performed by UV–Vis–NIR Spectrophotometer (SHIMADZU UV-3600). The morphology and localized crystallization were measured by atomic force microscopy (AFM) (SIINT, SPA400) in tapping mode and polarized optical microscopy (OLYMPUS BX51), respectively. The interface electronic structure and variation in the work function were performed by XPS with Al *Ka* X-ray source (1486.6 eV) and UPS with He discharge lamp (UV light of 21.22 eV) (Thermo ELECTRON CORPORATION, ESCALAB 250). The resolution of the spectra was 0.3 eV for XPS and 0.1 eV for UPS. The UPS measurements were performed with a −4 V bias applied to the sample in order to enable the measurement of the secondary electrons cutoff.

3. Results and discussion

3.1. Electroluminescence properties of OLEDs at different temperatures

The electroluminescent (EL) properties of OLEDs with different anode modification layers at different temperatures were first investigated. Fig. 1 shows the current density–luminance–voltage characteristics of ITO/NPB/Alq_3/LiF/Al and ITO/CuPc, MoO_3 or MoO_3:NPB/NPB/Alq_3/LiF/Al devices at room temperature. The current efficiency–current density and power efficiency–current density characteristics of the same devices are shown in inset of Fig. 1. It is clearly that the turn-on voltage (defined as the voltage required for the luminance of 1 cd/m^2) is significantly reduced when inserting the MoO_3 and MoO_3:NPB buffer layers. The turn-on voltage is reduced to 2.7 V of devices with MoO_3 andMoO_3:NPB buffer layers from 4.0 V of devices without buffer layer. Meanwhile, the utilization of CuPc layer does not reduce the turn-on voltage, even increasing the turn-on voltage, it can be seen that the luminance is greatly enhanced at high voltage, which is in agreement with the literature [32]. In the case of MoO_3 as a buffer layer, we found that a low turn-on voltage can be kept in a wide range of MoO_3 thickness [31]. This also demonstrates the practical applicability of MoO_3 as a buffer layer

Table 1
The comparison of the EL performance of OLEDs with different buffer layers at different substrate temperatures[a]

		$V_{turn\text{-}on}$ (V)	L_{max} (cd/m^2)	CE_{max} (cd/A)	PE_{max} (lm/W)
At room temperature	A	3.7	8420	4.49	1.14
	B	4.5	14,480	5.01	1.57
	C	2.7	25,050	6.47	6.06
	D	2.7	20,700	5.92	4.84
At 80 °C	A	7.1	140	2.44	0.62
	B	4.7	1170	2.87	1.04
	C	3.3	3090	4.02	2.22
	D	3.1	3780	5.29	2.31
At 120 °C	A	–	–	–	–
	B	–	–	–	–
	C	4.3	770	2.92	1.04
	D	3.7	1341	3.64	1.64

[a] The EL properties of device A and B fabricated at substrate temperature of 120 °C cannot be obtained, which is shown by "–". In the table, A represents the device without buffer layer, and B, C and D represent the devices with the CuPc, MoO_3, and MoO3:NPB buffer layer, respectively.

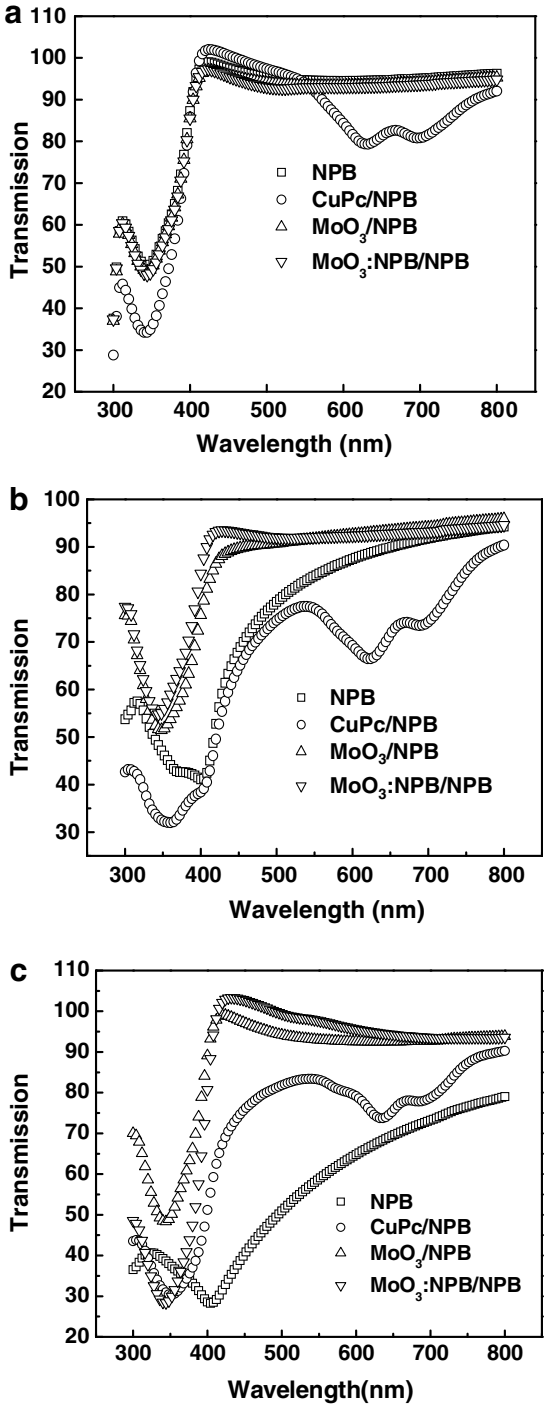

Fig. 4. Transmission spectra of NPB (50 nm), CuPc (10 nm)/NPB (50 nm), MoO_3 (6 nm)/NPB (50 nm) and MoO_3:NPB (40 nm)/NPB (50 nm) at room temperature (a), after annealing at 110 °C for 2 h (b), and fabricated at substrate temperature of 120 °C (c).

in OLEDs. Due to the high luminance at low operational voltage and low current density, it can be seen that the EL current efficiency of the devices with MoO_3 and MoO_3:NPB buffer layers is enhanced to 6.45 cd/A and 5.88 cd/A, respectively, as shown in the inset of Fig. 1, which are higher than 5.00 cd/A of device with CuPc buffer layer and 4.49 cd/A of device without a buffer layer. Furthermore, the power efficiencies are also greatly enhanced when using MoO_3 or MoO_3:NPB as the buffer layer. The power efficiency of the devices with MoO_3 and MoO_3:NPB buffer layers reaches 5.65 lm/W and 4.84 lm/W, respectively. In comparison, the power efficiencies of the devices with CuPc buffer layer and without a buffer layer are only 1.55 lm/W and 1.14 lm/W, respectively.

More importantly, it is found that the devices fabricated at high temperature may yet operate well when utilizing the MoO_3 and MoO_3:NPB buffer layers, whereas the luminance and efficiency are rapidly degraded at high treatment temperature when using CuPc as a buffer layer and no buffer layer in devices. Fig. 2 shows the luminance-voltage characteristics of ITO/NPB/Alq_3/LiF/Al and ITO/CuPc, MoO_3 or MoO_3:NPB/NPB/Alq_3/LiF/Al devices fabricated at substrate temperature of 80 °C, which is near the glass transition temperature of NPB. The current efficiency–current density and power efficiency–current density characteristics of the same devices fabricated at the same conditions are shown in inset of Fig. 2. It is clearly seen that the devices can yet operate well with efficiency of 4.00 cd/A (2.22 lm/W) in the case of MoO_3 buffer layer and 5.29 cd/A (2.31 lm/W) in the case of MoO_3:NPB buffer layer, whereas the efficiencies of the devices with CuPc buffer layer and no buffer layer are reduced to 2.86 cd/A (1.04 lm/W) and 2.31 cd/A (0.61 lm/W), respectively. Although the luminance of the devices with MoO_3 and MoO_3:NPB buffer layers decreases, the decrease in luminance of the devices with CuPc buffer layer and no buffer

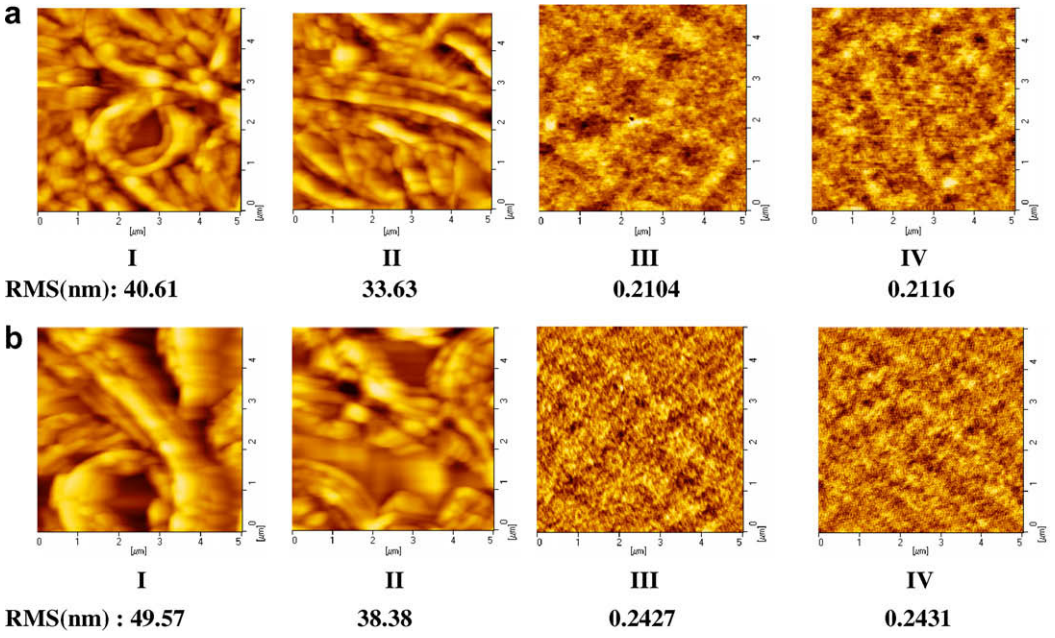

Fig. 5. Atomic force microscopy images of NPB (50 nm) (I), CuPc (10 nm)/NPB (50 nm) (II), MoO_3 (6 nm)/NPB (50 nm) (III) and MoO_3:NPB (40 nm)/NPB (50 nm) (IV) for annealing temperature at 90 °C (a) and 110 °C (b) for 2 h.

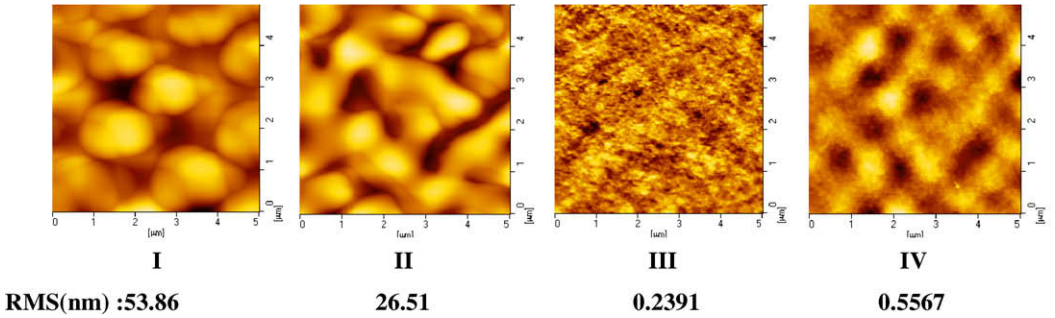

Fig. 6. Atomic force microscopy images of NPB (50 nm) (I), CuPc (10 nm)/NPB (50 nm) (II), MoO_3 (6 nm)/NPB (50 nm) (III) and MoO_3:NPB (40 nm)/NPB (50 nm) (IV) fabricated at substrate temperature of 120 °C.

layer is more pronounced. It has been proven experimentally that the device degradation at high temperature is originated from the crystallization of NPB, and the CuPc buffer layer again easily induces the crystallization of NPB at elevated temperature [33]. Clearly, the utilization of the MoO_3 or MoO_3:NPB buffer layer restrains the NPB from the crystallization, as demonstrated below.

Evidently, when the devices are fabricated at a substrate temperature of 120 °C, which is above the glass transition temperature of NPB, the emission of the devices with CuPc buffer layer and no buffer layer disappears, but the devices with MoO_3 and MoO_3:NPB buffer layers can still operate with luminance of 770 cd/m^2, efficiency of 2.95 cd/A and luminance of 1340 cd/m^2, efficiency of 3.66 cd/A, respectively, as shown in Fig. 3. These results adequately demonstrate that MoO_3 and MoO_3:NPB as anode interfacial modification materials in OLEDs play an important role in the improvement of EL efficiency and stability of OLEDs.

Table 1 summarizes the electroluminescence properties of OLEDs with different buffer layers at various temperature treatment conditions. It can be seen that the utilization of the MoO_3 and MoO_3:NPB buffer layers can reduce the turn-on voltage and enhance the luminance and efficiency, and the improvement is further obvious at high substrate temperature. The fact that the devices with MoO_3 and MoO_3:NPB as buffer layers can yet operate at higher luminance and efficiency even after treatment at high temperature also indicates strongly a better stability of these devices.

3.2. Effects of anode buffer layer on transmission spectra and morphology

To fully understand the mechanism of MoO_3 in the improvement of efficiency and stability in OLEDs, the effects of MoO_3 and MoO_3:NPB on the transmission and the morphology of NPB hole-transporting layer were studies in detail. As expected, a high transmission of interfacial modification film is necessary to the coupling efficiency of light output. Fig. 4 shows the transmission spectra of NPB, CuPc/NPB, MoO_3/NPB and MoO_3:NPB/NPB at different treatment temperatures. It can be seen that at room temperature (Fig. 4a), the insertion of MoO_3 or MoO_3:NPB buffer layer hardly changes the transmittance of the whole films in a wide range of 400–800 nm compared to the case of NPB, while the utilization of CuPc as the buffer layer significantly reduces the transmission in the range of 500–800 nm, which should be originated from the absorption of CuPc. Furthermore, as shown in Fig. 4b, the transmission of MoO_3/NPB and MoO_3:NPB/NPB films have hardly decrease after thermally annealing at 110 °C for 2 h, whereas NPB and CuPc/NPB films show larger reduction in the transmission. Similarly, the transmission of MoO_3/NPB and MoO_3:NPB/NPB films also did not show any change, but the transmission of NPB and CuPc/NPB films were greatly reduced as these films were deposited at the substrate temperature of 120 °C (Fig. 4c). A decrease in the transmission of CuPc/NPB and NPB films after thermal treatment is attributed to the NPB crystallization. A slight change in the transmission of MoO_3/NPB and MoO_3:NPB/

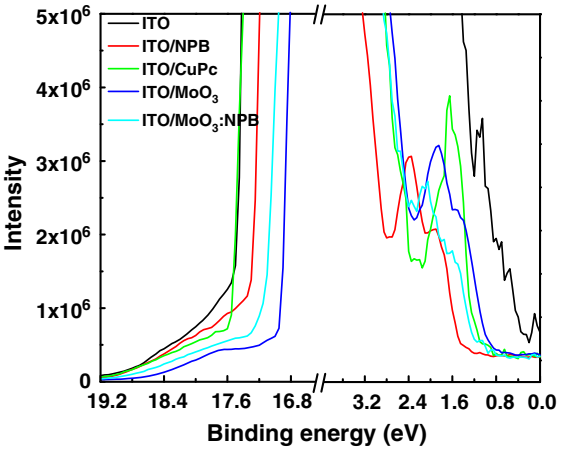

Fig. 8. UPS spectra in the cases of ITO, ITO/NPB, ITO/CuPc, ITO/MoO_3 and ITO/MoO_3:NPB.

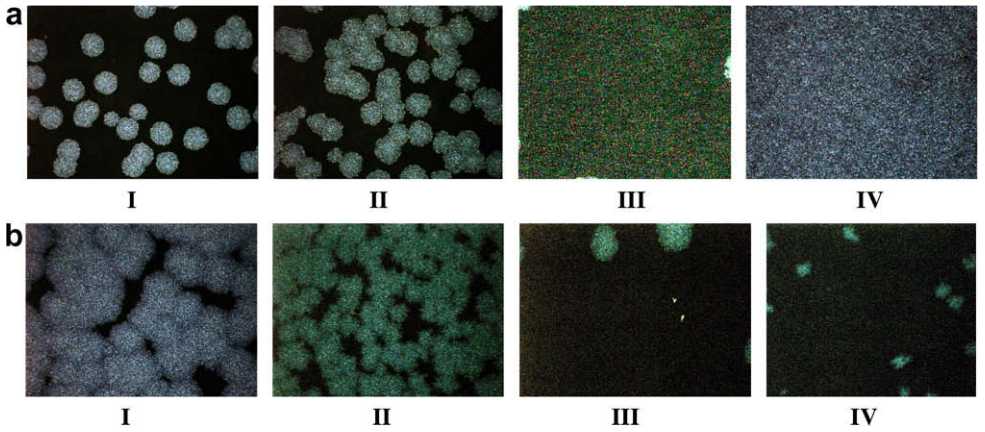

Fig. 7. Polarized optical microscopic image of NPB (50 nm) (I), CuPc (10 nm)/NPB (50 nm) (II), MoO_3 (6 nm)/NPB (50 nm) (III) and MoO_3:NPB (40 nm)/NPB (50 nm) (IV) for annealing temperature at 90 °C (a) and 110 °C (b) for 2 h.

NPB films should demonstrate that the MoO_3 and MoO_3:NPB as the buffer layer does play an important role in suppressing the NPB crystallization, which favors the improvement of efficiency in OLEDs.

The effects of the interfacial modification layers on the morphology of NPB films can be used to further prove the advantages of the MoO_3 and MoO_3:NPB as buffer layers in OLEDs. MoO_3 and MoO_3:NPB buffer layers greatly improve the morphology stability and quality of NPB film, and effectively suppress the crystallization of NPB film. Fig. 5a and b shows the AFM images of NPB, CuPc/NPB, MoO_3/NPB and MoO_3:NPB/NPB films after annealing, respectively, at 90 °C and 110 °C for 2 h. Fig. 6 shows the AFM images of NPB, CuPc/NPB, MoO_3/NPB and MoO_3:NPB/NPB films fabricated at 120 °C. It is clearly seen that the surface of NPB film with CuPc buffer layer and without buffer layer displays higher roughness (higher root mean square, RMS), and some NPB crystallization areas are obviously observed, while the NPB with MoO_3 and MoO_3:NPB buffer layers show a smooth and featureless morphology, similar to the case of the NPB film at room temperature. Although the processes of the NPB crystallization and the suppression of NPB crystallization in Figs. 5 and 6 are different due to the different treatment conditions, the introduction of the MoO_3 and MoO_3:NPB buffer layers can effectively suppress the crystallization of NPB film, fully demonstrating the improvement mechanism in device stability.

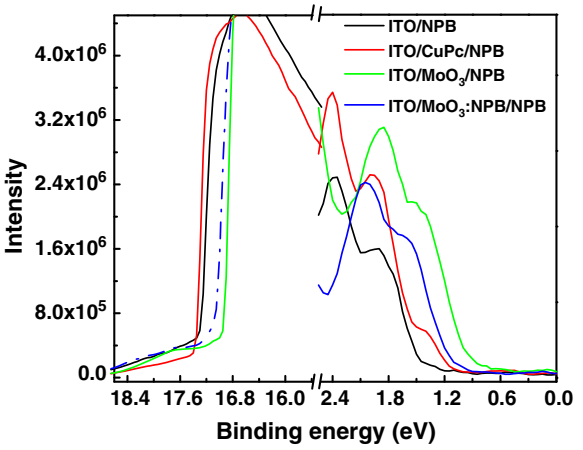

Fig. 9. UPS spectra in the cases of ITO/NPB, ITO/CuPc/NPB, ITO/MoO_3/NPB, ITO/MoO_3:NPB/NPB.

The suppression of NPB crystallization by the MoO_3 and MoO_3:NPB buffer layers can be further revealed from the polarized optical microscopic images of NPB films under different treatment conditions (Fig. 7). The films of NPB on ITO and CuPc display a large crystallization area, which become larger with the increase of the annealing temperature. However, the crystallization area is significantly reduced for the NPB film on MoO_3 and MoO_3:NPB. As we know, the vacuum-deposited CuPc thin film is a polycrystalline structure. It is easy to induce the nucleation and

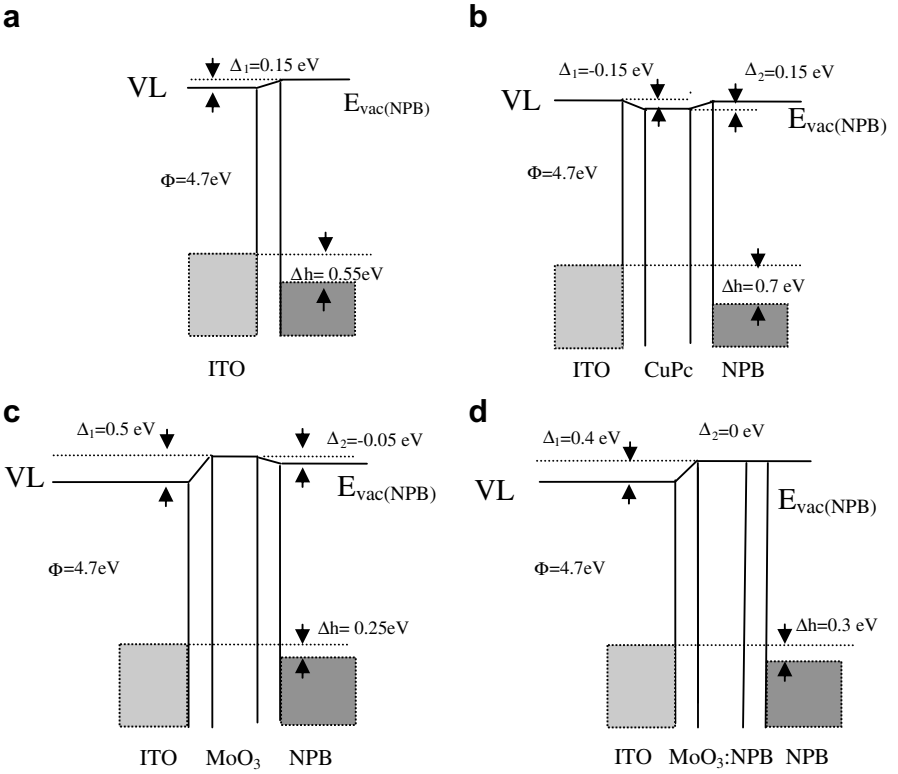

Fig. 10. Schematic energy diagrams of ITO/NPB (a), ITO/CuPc/NPB (b), ITO/MoO_3/NPB (c), ITO/MoO_3:NPB/NPB (d) constructed from the UPS.

the crystallization of semi-crystalline NPB film, especially at high temperature, which is consistent with the literature [34,35]. Differently, the film of the vacuum-deposited MoO_3 has amorphous morphology, and the amorphous film can effectively suppress the NPB crystallization within the critical thickness. This further proves the important role of MoO_3 and MoO_3:NPB as buffer layers in improving the device stability.

3.3. Injection barrier at interfaces

Besides the effect of the interfacial modification layer on the morphology, which directly determines the device stability, large numbers of experiments have also demonstrated that the introduction of the interfacial layer at electrodes can significantly influence the injection of charge carriers by the change of the interfacial barrier at electrodes [36,37]. To clearly demonstrate the effects of MoO_3 and MoO_3:NPB as buffer layers on the charge carriers injection, UPS is used to determine the interfacial energy level. Fig. 8 shows the UPS spectra of NPB, CuPc, MoO_3, MoO_3:NPB on ITO as well as ITO. From the UPS spectra, the work functions (Φ_{buffer}) of ITO are calculated to be 4.7 eV, and the modification of CuPc, MoO_3 and MoO_3:NPB on ITO leads to the energy level to shift to 4.55 eV, 5.2 eV and 5.1 eV, respectively. It can be seen from these level values that the utilization of CuPc layer results in the vacuum level shift down, whereas the modification of MoO_3 or MoO_3:NPB makes the vacuum level shift up. This level shift has been attributed to the formation of interfacial dipoles (Δ) between ITO and CuPc, MoO_3, MoO_3:NPB, which reaches −0.15 eV, 0.5 eV and 0.4 eV, respectively.

In order to evaluate the hole injection barriers in an actual device, the UPS spectra were taken for the devices with a structure of ITO/NPB, ITO/CuPc/NPB, ITO/MoO_3/NPB and ITO/MoO_3:NPB/NPB films (Fig. 9). It can be calculated that the interfacial dipole Δ of 0.15 eV is generated at ITO/NPB and CuPc/NPB interfaces, the interfacial dipole Δ of −0.05 eV is formed at MoO_3/NPB interface, whereas there is no dipole formation at MoO_3:NPB/NPB interface. The energy diagrams of ITO/NPB, ITO/CuPc/NPB, ITO/MoO_3/NPB, ITO/MoO_3:NPB/NPB extracted from the UPS are shown in Fig. 10. It can be seen that the hole injection barrier from ITO to NPB is 0.55 eV in the case of ITO/NPB (Fig. 10a). The introduction of CuPc buffer layer increases the barrier to 0.7 eV, which is consistent with the reported explanation where the utilization of CuPc buffer layer blocks the hole injection [38]. However, the hole injection barrier is reduced from 0.55 eV to 0.25 eV and 0.3 eV after inserting MoO_3 and MoO_3:NPB buffer layer, respectively. Obviously, the utilization of MoO_3 and MoO_3:NPB on ITO greatly reduces the hole injection barrier, which should be attributed to the reduction of operational voltage and the improvement of EL efficiency.

The enhancement mechanism of the work function of ITO modified by interfacial layer could be well elucidated by XPS spectra of ITO, ITO/MoO_3 (1 nm), ITO/MoO_3:NPB (1 nm), as shown in Fig. 11. It can be seen that the In 3d and Sn 3d peaks shift towards higher binding energy after depositing MoO_3 (1 nm) and MoO_3:NPB (1 nm) on ITO. This shift of binding energy indicates that there occurs electron

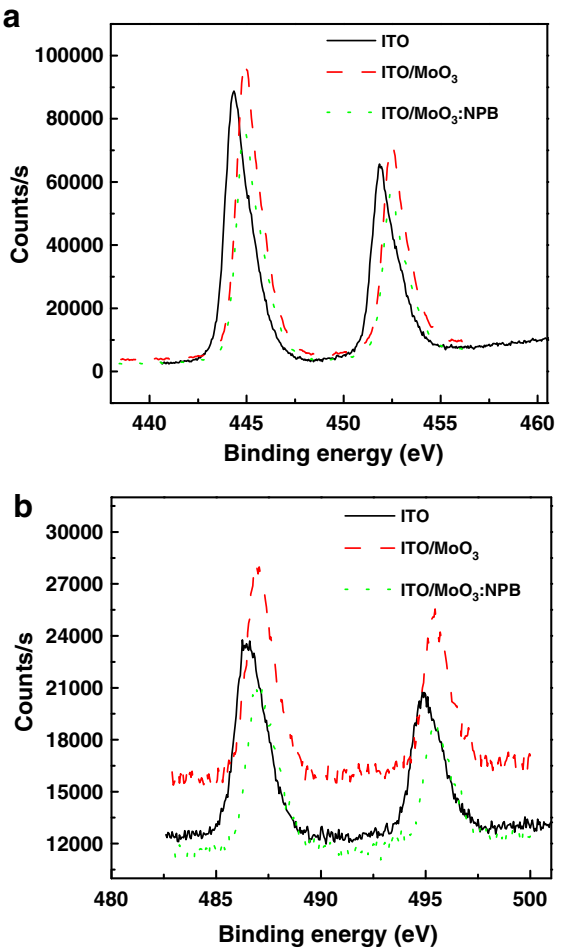

Fig. 11. XPS spectra of ITO (solid), ITO/MoO_3 (dash), ITO/MoO_3:NPB (dot) films.

transfer from ITO to MoO_3 and MoO_3:NPB at the interface. As a result, a dipole layer is formed right at the interface. With such interfacial dipole formation, there will be an abrupt shift of the potential across the dipole layer [39], leading to an up-shift of 0.5 eV and 0.4 eV in the vacuum level, as shown in Fig. 10c and d. Therefore, the hole injection barrier is greatly reduced, as a result of a shift in the vacuum level caused by electron transfer from ITO to MoO_3 or MoO_3:NPB at interface. Accordingly, the introduction of MoO_3 and MoO_3:NPB interfacial layers also effectively reduces the driving voltage of OLED device and thus improves the power efficiency, which are very beneficial for practical applications of OLEDs.

4. Conclusions

We have systematically studied the role of MoO_3 and MoO_3 doped *N*,*N*′-di(naphthalene-1-yl)–*N*,*N*′-diphenyl-benzidine (NPB) used as the interface layer on ITO in improving the efficiency and lifetime of organic light-emitting diodes (OLEDs). The investigations into the energy level and the film morphology under different thermal

treatment conditions clearly reveal that the MoO_3 and MoO_3:NPB on ITO can reduce the hole injection barrier, suppress the crystallization of hole-transporting NPB, thus resulting in higher efficiency and better stability of OLEDs. The reduction of the hole injection barrier can be attributed to the formation of the interfacial dipole due to the occurrence of electron transfer at interface. The results demonstrated that the MoO_3 and MoO_3:NPB are a practical valuable interfacial modification layer on ITO in OLEDs.

Acknowledgments

We would like to thank the support from the Hundreds Talents Program of Chinese Academy of Sciences, the National Science Fund for Distinguished Young Scholars of China (50325312), Foundation of Jilin Research Council (20050517), Science Fund for Creative Research Groups of NSFC (20621401) and Ministry of Science and Technology of China (973 Program No. 2002CB613404 and 863 Program No. 2006AA03A161).

References

[1] Y. Yang, E. Westerweele, C. Zhang, P. Smith, A.J. Heeger, J. Appl. Phys. 77 (1995) 694.
[2] L.S. Hung, C.W. Tang, M.G. Mason, Appl. Phys. Lett. 70 (1997) 152.
[3] M.G. Mason, L.S. Hung, C.W. Tang, S.T. Lee, K.W. Wong, M. Wang, J. Appl. Phys. 86 (1999) 1688.
[4] S.K. Heeks, J.H. Burroughes, C. Towns, S. Cina, N. Baynes, N. Athanassopoulou, J.C. Carter, S. Miyashita, J. Soc. Inf. Disp. 10 (2000) 139.
[5] N.K. Patel, S. Cina, J.H. Burroughes, IEEE J. Sel. Top. Quantum Elect. 8 (2002) 346.
[6] M. Ishii, T. Mori, H. Fujikawa, S. Tokito, Y. Taga, J. Lumin. 87–89 (2000) 1165.
[7] K. Sugiyama, H. Ishii, Y. Ouchi, K. Seki, J. Appl. Phys. 87 (2000) 295.
[8] M. Rottmann, K.H. Heckner, J. Phys. D: Appl. Phys. 28 (1995) 1448.
[9] J. Cui, Q. Huang, Q. Wang, T.J. Marks, Langmuir 17 (2001) 2051.
[10] S.A. Van Slyke, C.H. Chen, C.W. Tang, Appl. Phys. Lett. 69 (1996) 2160.
[11] S.Y. Kim, J.M. Baik, H.K. Yu, J.L. Lee, J. Appl. Phys. 98 (2005) 093707.
[12] C.A. Di, G. Yu, Y.Q. Liu, X.J. Xu, Y.B. Song, D.B. Zhu, Appl. Phys. Lett. 89 (2006) 033502.
[13] J. Li, M. Yahiro, K. Ishida, H. Yamada, K. Matsushige, Synthetic Met. 151 (2005) 141.
[14] C.C. Chang, M.T. Hsieh, J.F. Chen, Appl. Phys. Lett. 89 (2006) 253504.
[15] Y. Luo, H. Aziz, G. Xu, Z.D. Popovic, J. Appl. Phys. 101 (2007) 054512.
[16] S.W. Shi, D.G. Ma, Semicond. Sci. Technol. 20 (2005) 1213.
[17] J. Huang, G. Li, E. Wu, Q. Xu, Y. Yang, Adv. Mater. 18 (2006) 114.
[18] S.Y. Chen, T.Y. Chu, J.F. Chen, C.Y. Su, C.H. Chen, Appl. Phys. Lett. 89 (2006) 053518.
[19] X.D. Feng, C.J. Huang, V. Lui, R.S. Khangura, Z.H. Lu, Appl. Phys. Lett. 86 (2005) 143511.
[20] D. Grozea, A. Turak, Y. Yuan, S. Han, Z.H. Lu, W.Y. Kim, J. Appl. Phys. 101 (2007) 033522.
[21] L. Fenenko, C. Adachi, Thin Solid Films 515 (2007) 4812.
[22] R. Könenkamp, R.C. Word, M. Godinez, Nanotechnology 17 (2006) 1858.
[23] S. Tokito, K. Noda, Y. Taga, J. Phys. D: Appl. Phys. 29 (1996) 2750.
[24] K.J. Reynolds, J.A. Barker, N.C. Greenham, R.H. Friend, G.L. Frey, J. Appl. Phys. 92 (2002) 7556.
[25] H. Ikeda, J. Sakata, M. Hayakawa, T. Aoyama, T. Kawakami, K. Kamata, Y. Iwaki, S. Seo, Y. Noda, R. Nomura, S. Yamazaki, SID 06 DIGEST P-185 (2006) 923.
[26] J.H. Li, J. Huang, Y. Yang, Appl. Phys. Lett. 90 (2007) 173505.
[27] X. Zhu, J. Sun, X. Yu, M. Wong, H.S. Kwok, Jpn. J. Appl. Phys. 46 (2007) 1033.
[28] Z. Zhang, Proc. Asia Display 1 (2007) 159.
[29] H.J. Bolink, E. Coronado, D. Repetto, M. Sessolo, E.M. Barea, J. Bisquert, G.G. Belmonte, J. Prochazka, L. Kavan, Adv. Funct. Mater. 18 (2008) 145.
[30] T. Matsushima, Y. Kinoshita, H. Murata, Appl. Phys. Lett. 91 (2007) 253504.
[31] H. You, Y. Dai, Z. Zhang, D. Ma, J. Appl. Phys. 101 (2007) 026105.
[32] H. Aziz, Z.D. Popovic, N.X. Hu, A.M. Hor, G. Xu, Science 283 (1999) 1900.
[33] J. Cui, Q. Huang, J.C.G. Veinot, H. Yan, Q. Wang, G.R. Hutchison, A.G. Richter, G. Evmenenko, P. Dutta, T.J. Marks, Langmuir 18 (2002) 9958.
[34] I. Zhivkov, E. Spassova, G. Danev, S. Andreev, T. Ivanov, Vacuum 51 (1998) 189.
[35] D. Yan, J. Mol. Sci. 21 (2005) 21.
[36] N. Koch, S. Duhm, J.P. Rabe, A. Vollmer, R.L. Johnson, Phys. Rev. Lett. 95 (2005) 237601.
[37] J. Huang, Z. Xu, Y. Yang, Adv. Funct. Mater. 17 (2007) 1966.
[38] E.W. Forsythe, M.A. Abkowitz, Y. Gao, J. Phys. Chem. B 104 (2000) 3948.
[39] H. Ishii, K. Sugiyama, E. Ito, K. Seki, Adv. Mater. 11 (1999) 605.

ton formation across an expanded emission zone [12]. The red, green and blue (R, G and B) phosphor molecules are doped in separate hosts to achieve optimum efficiency and color balance. The host material in each emitting region has an energy alignment with the dopant that encourages efficient energy transfer, and also readily injects charge into the adjacent emitting region. The mechanisms leading to the extended exciton distribution are analyzed and optimized in this work.

The three-section EML phosphorescent WOLED structure differs from previous R–G–B WOLEDs that used a common host with a single exciton formation region [4], resulting in difficulties in obtaining efficient and simultaneous energy transfer from the host to all of the three dopants [8]. Also previously demonstrated 3-EML fluorescent WOLEDs have limited device efficiencies due to inefficient decay through triplet states [13], although excitons in those cases may possibly separately form in multiple regions across the EML [14,15].

This paper is organized as follows: in Section 2, the device architecture and the proposed exciton formation mechanism are described. In Section 3, we discuss the fabrication and characterization methods of the electroluminescent devices. In Section 4, we present results, and in Section 5, we analyze the results in terms of the distributed exciton formation zone in the three-section EML structure. Conclusions are presented in Section 6.

2. Theory

Fig. 1a and b shows a schematic diagram of the device and the proposed energy transfer mechanism, respectively. The hosts are arranged to form a stepped progression of HOMO and LUMO levels sandwiched between the electron and hole transport layers (ETL and HTL, respectively), leading to a series of moderate energy barriers to hole and electron transport (Fig. 1a) that distribute exciton formation across the EML. The choice of host determines the heights of the energy barriers between layers. By varying the thicknesses and doping concentrations of each section, the relative R, G and B intensity, and hence the emission color, can be precisely controlled.

Since there are no energy barriers to electron transport in the red emitting region and in the HTL (Fig. 1a), the electron density in these two layers is lower than in other regions of the device. For similar reasons, the hole density is lower in the blue emitting region and in the ETL. The majority of excitons form within the green emitting region, where holes and electrons have the highest total densities. To avoid exchange energy losses due to intersystem crossing into the blue dopant triplet state, a large energy gap host heavily doped with a blue phosphor is used in conjunction with a host material in the green emitting region whose HOMO energy is aligned to that of the blue dopant. This facilitates resonant injection of holes onto the blue dopant, resulting in a ratio of f_B blue emitting excitons to the total excitons formed [2,16]. Now, f_B is independent of the total thickness of the green emitting region, and increases with current density (J) as direct hole injection onto the blue phosphor HOMO becomes more efficient. The remaining $(1 - f_B)$ excitons form in the green emitting

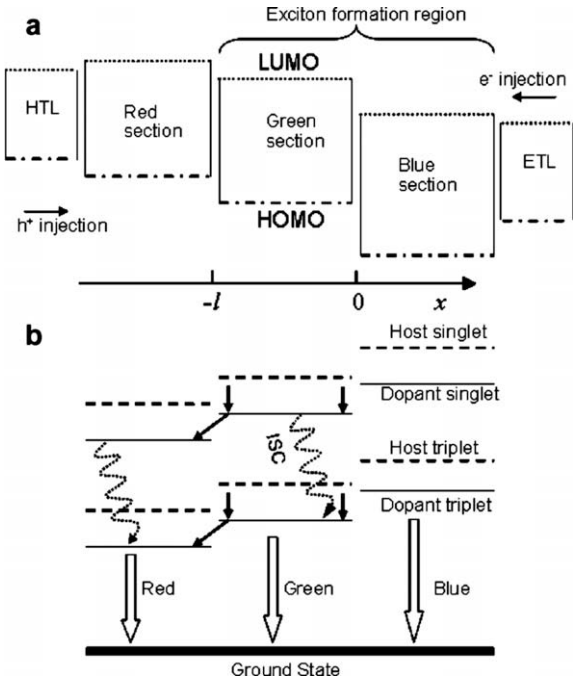

Fig. 1. (a) Schematic diagram of the highest occupied (HOMO, dash-dot) and lowest unoccupied molecular orbitals (LUMO, dotted) of hosts in the three-section emission layer (EML) structure for white organic light emitting device (WOLED). This leads to a series of small, monotonically stepped energy barriers to charge transport that allows for distributed exciton formation in multiple regions across the broad EML. (b) Proposed energy transfer in the three-section EML structure. A fraction of excitons are formed on the dopant in the blue emitting region due to direct injection of holes. The majority of excitons are formed on the host in the central green emitting region, where both holes and electrons have significant densities. Solid arrows indicate exciton transfer from host to dopant, and from higher-energy dopant to lower energy dopant in the adjacent emitting region. Dotted curved arrows illustrate intersystem crossing (ISC) from singlet to triplet state characteristic of phosphorescent dopants. Dashed lines show the host singlet and triplet states. Solid lines show the dopant singlet and triplet states. Bold line indicates the ground state energy level.

region, which can efficiently transfer from the host to the green dopant, and partly transfer from the green dopant onto the lower energy red dopant in the adjacent region (Fig. 1b, solid arrows). In Fig. 1b, the curved arrows denote intersystem crossing from the singlet to the triplet state, the dashed lines show the host singlet and triplet states, the solid lines show the dopant singlet and triplet states, and the bold line indicates the ground state energy level.

To probe the exciton distribution in the central EML region of thickness l, a thin slab of thickness $g = 4$ nm doped with the green phosphor is placed adjacent to the R/G interface, with the remaining thickness $(l - g)$ of the host left undoped. The green emission intensities of the devices with various l are then compared to determine the exciton distribution in the green host, assuming a linear relationship between the fraction of excitons in the doped slab and the amount of green emission from this region. In the blue emitting region, the doping concentration of the phosphor remains the same to ensure that f_B remains constant, independent of l. In the green emitting region,

the excitons are formed by electrons (holes) localized in traps in the vicinity of the R/G interface (G/B interface), and holes (electrons) injected from the red (blue) emitting region. We define x as the position relative to the G/B interface (at $x = 0$, see Fig. 2a). In the vicinity of the R/G interface ($x = -l$), the position-dependent exciton generation rate is then proportional to $p(x)/\tau_p(x)$, where $p(x)$ is the hole density and $\tau_p(x)$ is the mean lifetime of holes. Here, $\tau_p(x)$ increases with decreasing density of electrons ($n(x)$) in the LUMO following Shockley–Read–Hall statistics [17]. By these same arguments, other losses of holes (other than exciton formation) are also accounted for by a decrease in $\tau_p(x)$. According to the steady-state continuity equation:

$$\frac{p(x)}{\tau_p(x)} = D_p \frac{d^2 p(x)}{dx^2} - \mu_p \frac{d}{dx}[p(x)F(x)], \tag{1}$$

where D_p is the hole diffusion constant, μ_p is the hole mobility and $F(x)$ is the position-dependent electric field in the green emitting region. We also use the following relationships [18,19]:

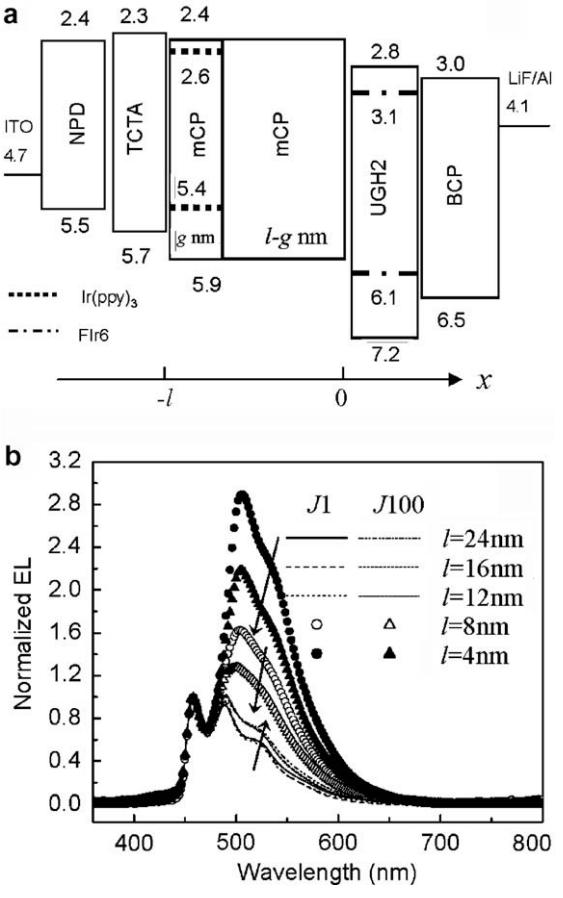

Fig. 2. (a) Proposed energy-level diagram of devices with the structures of NPD (40 nm)/TCTA (8 nm)/2 wt% $Ir(ppy)_3$:mCP (thickness $g = 4$ nm)/mCP ($l - g$, nm)/20 wt% FIr6:UGH2 (20 nm)/BCP (40 nm), where the total mCP thickness is $l = 4$, 8, 12, 16 or 24 nm. (b) Normalized electroluminescence (EL) spectra at current densities $J = 1$ and 100 mA/cm^2 for the devices in (a). Arrows indicate the trend of $Ir(ppy)_3$ intensity relative to FIr6 emission with increasing J.

$$D_p = \mu_p \frac{kT}{q}, \tag{2}$$

$$F(x) = \frac{-1}{q} \cdot \frac{dE_{HOMO}(x)}{dx}, \tag{3}$$

where k is the Boltzmann constant, T is the temperature, q is the electronic charge and E_{HOMO} is the HOMO energy. In the presence of an applied field, the hole concentration $p(x)=p_o+p_{inj}(x)$, where p_o is the hole concentration at thermal-equilibrium, and $p_{inj}(x)$ is the injected hole concentration. The corresponding hole quasi-Fermi level $E_p(x)$ is then [20]:

$$kT \ln[p(x)/P_{HOMO}] = E_p(x) - E_{HOMO}(x), \tag{4}$$

where P_{HOMO} is the density of states in the HOMO. Using Eqs. (2)–(4), Eq. (1) becomes:

$$\frac{p(x)}{\tau_p(x)} = \frac{d}{dx}\left[\frac{\mu_p}{q} kT \cdot p(x) \frac{d[\ln(p(x)/P_{HOMO})]}{dx} + \frac{\mu_p}{q} \cdot p(x) \frac{dE_{HOMO}(x)}{dx}\right] = \frac{\mu_p}{q} \frac{d}{dx}\left[p(x) \frac{dE_p(x)}{dx}\right]. \tag{5}$$

Previous studies have approximated the drift term (second term on the right hand side of Eq. (5)) by numerical integration using the regional approximation [19] in the trapped charge limit subject to the boundary conditions of zero electric field at the electrodes [20]. In this case, it has been shown that the drift term in the vicinity of the interface at $x = -l$ is approximately [19]:

$$\frac{\mu_p}{q} \frac{d}{dx}\left[p(x) \frac{dE_{HOMO}(x)}{dx}\right] = C_1 \exp\left(\frac{-(x+l)}{\mu_p \tau_p(-l)\left(\frac{dE_{HOMO}(x)}{dx}\right)\Big|_{x=-l}/q}\right), \tag{6}$$

where C_1 is a constant. The position-dependent exciton generation rate is then:

$$\frac{p(x)}{\tau_p(x)} = \frac{p(-l)}{\tau_p(-l)} \exp\left(\frac{-(x+l)}{L_1}\right) \tag{7}$$

in the vicinity of the R/G interface, where the characteristic hole decay length is $L_1 = \mu_p \tau_p(-l)\left(\frac{dE_p(x)}{dx}\right)\Big|_{x=-l}/q$.

Similarly, near the G/B interface ($x = 0$), the exciton generation rate is expressed as

$$\frac{n(x)}{\tau_n(x)} = \frac{n(0)}{\tau_n(0)} \exp\left(\frac{x}{L_2}\right), \tag{8}$$

where $n(x)$ is the electron concentration in the green emitting region, and $\tau_n(x)$ is the mean lifetime of electrons that increases with decreasing density of holes in the HOMO. The characteristic decay length in this case is $L_2 = \mu_n \tau_n(0)\left(\frac{dE_n(x)}{dx}\right)\Big|_{x=0}/q$, where μ_n is the electron mobility and $E_n(x)$ is the electron quasi-Fermi level. Combining Eqs. (7) and (8), the exciton distribution in the green emitting region is

$$\phi(x) = \phi_1 \exp[-(x+l)/L_1] + \phi_2 \exp[x/L_2]. \tag{9}$$

Here, the ratio of the constants, ϕ_1/ϕ_2, increases with J as more electrons accumulate at the R/G interface, and more holes inject directly onto the blue phosphor.

The electroluminescent (EL) spectrum can be used to extract the contributions of the emission from the green

and the blue doped regions to the external quantum efficiency (EQE). That is, the emission is proportional to the integral of $\phi(x)$ from the particular doped region normalized to the total population of excitons. Therefore, the contribution to the EQE from green emission (EQE_G) is

$$EQE_G \propto \frac{\int_{-l}^{-(l-g)} \left(\phi_1 \exp\left[\frac{-(x+l)}{L_1}\right] + \phi_2 \exp\left[\frac{x}{L_2}\right]\right) dx}{\left[\int_{-l}^{0} \left(\phi_1 \exp\left[\frac{-(x+l)}{L_1}\right] + \phi_2 \exp\left[\frac{x}{L_2}\right]\right) dx\right] \Big/ (1 - f_B)}. \quad (10)$$

The ratio of green to blue intensity is equal to the ratio of the integrals of the two regions. That is,

$$\frac{EQE_G}{EQE_B} = \frac{\int_{-l}^{-(l-g)} \left(\phi_1 \exp\left[\frac{-(x+l)}{L_1}\right] + \phi_2 \exp\left[\frac{x}{L_2}\right]\right) dx}{\left[\int_{-l}^{0} \left(\phi_1 \exp\left[\frac{-(x+l)}{L_1}\right] + \phi_2 \exp\left[\frac{x}{L_2}\right]\right) dx\right] \times \frac{f_B}{(1-f_B)}}. \quad (11)$$

Thus, by measuring the relationship of green and blue intensities as a function of the total thickness of the central EML region, l, then f_B and other parameters such as L_1, L_2, and ϕ_1/ϕ_2 can be fit to Eqs. (10) and (11), from which we infer the exciton distribution across the EML.

3. Experimental

Organic layers were deposited in high-vacuum (10^{-7} Torr) by thermal evaporation onto glass substrates precoated with a 150-nm-thick, ~20 Ω/sq indium tin oxide (ITO) layer using procedures discussed elsewhere [14]. First, a 40-nm-thick HTL of 4,4′-bis[*N*-(1-naphthyl)-*N*-phenyl-amino]-biphenyl (NPD) was deposited, followed by the multiple-section EML, and then capped by an ETL consisting of either 40-nm-thick 2,9-dimethyl-4,7-diphenyl-1,10-phenanthroline (BCP), or 20-nm-thick 4,7-diphenyl-1,10-phenanthroline (BPhen) followed by a second, 20-nm-thick BPhen layer mixed with Li in a 1:1 molar ratio. Finally, the cathode consisting of a 0.8-nm-thick LiF and a 60-nm-thick Al layer, was deposited through a shadow mask with an array of circular, 1.0 mm-diameter openings. The J *vs.* voltage (V) and luminance measurements were obtained using a semiconductor parameter analyzer and a calibrated Si photodiode following standard procedures [14].

For the three-section EML devices, the EL spectrum ($EL(\lambda)$, where λ is the wavelength) is fit to the weighted sum of the electroluminescence (EL) spectra of the monochromatic devices with the individual R, G and B dopants ($EL_R(\lambda)$, $EL_G(\lambda)$ and $EL_B(\lambda)$, respectively) via:

$$EL(\lambda) = k_R \cdot EL_R(\lambda) + k_G \cdot EL_G(\lambda) + k_B \cdot EL_B(\lambda). \quad (12)$$

With the values of k_R, k_G and k_B that minimize the mean square error between the right-hand and left-hand sides in Eq. (12), the corresponding fraction of emission from the R, G or B doped region is calculated from the ratio of the integrals of $k_R \cdot EL_R(\lambda)$, $k_G \cdot EL_G(\lambda)$ or $k_B \cdot EL_B(\lambda)$ to the integral of $EL(\lambda)$ over the wavelength range from λ = 360 to 800 nm.

4. Results

Fig. 2a shows the structure of a partially doped G/B emitting three-section EML device using 4,4′,4″-tris(*N*-carbazolyl)-triphenylamine (TCTA), *N*,*N*′-dicarbazolyl-3,5-benzene (mCP) and *p*-bis(triphenylsilyly)benzene (UGH2) as the three hosts, forming a stepped progression of HOMOs from the HTL (5.5 eV) to TCTA (5.7 eV) to mCP (5.9 eV) to UGH2 (7.2 eV) [6,10,16,21,22]. The UGH2 layer is doped with the blue emitting phosphor: 20 wt% bis(4′,6′-difluorophenylpyridinato) tetrakis(1-pyrazolyl)borate (FIr6). The complete structures employing these three hosts are: NPD (40 nm)/TCTA (8 nm)/2 wt% tris(phenylpyridine)iridium ($Ir(ppy)_3$):mCP (g)/mCP ($l - g$)/20 wt% FIr6:UGH2 (20 nm)/BCP (40 nm), where l = 4, 8, 12, 16 or 24 nm. Since the blue phosphor concentration in the UGH2 layer is large, a significant fraction of excitons form directly on the dopant molecules. The mCP region contains a thin green emitting slab of thickness g = 4 nm consisting of 2 wt% ($Ir(ppy)_3$):mCP at the TCTA/mCP interface, and an undoped mCP spacer of thickness ($l - g$) between the green and blue doped regions. When the total thickness of the mCP region, l, increases, the exciton fraction in the thin $Ir(ppy)_3$-doped slab decreases (Section 2). Fig. 2b shows the spectra at J = 1 and 100 mA/cm^2 for these devices. The peak EQE of these devices decreases from (15.5 ± 0.8)% when l = 4 nm to (6.6 ± 0.3)% when l = 24 nm (Table 1).

To examine the impact of distributed exciton formation on the device efficiencies, we fabricated a three-section R–G–B EML WOLED (WOLED1 in Fig. 3a) using the same deposition sequence of the three hosts TCTA, mCP and UGH2 as in Fig. 2, with all of the three sections uniformly doped using Ir(III) bis(2-phenylquinolyl-*N*,$C_{2'}$) acetylacetonate (PQIr), $Ir(ppy)_3$ and FIr6 as dopants for R, G and B emission, respectively. The detailed structure and layer thicknesses are provided in Table 2. As shown in Fig. 4 (circles), the peak forward-viewing EQE and power efficiency are, respectively: η_{ext} = (15.3 ± 0.8)% at $J = 1.2 \times 10^{-2}$ mA/cm^2 corresponding to a brightness of 12 cd/m^2, and η_p = (37 ± 2) lm/W at $J = 1.3 \times 10^{-3}$ mA/cm^2 and brightness of 5 cd/m^2, decreasing to (13.6 ± 0.6)% and (22 ± 1) lm/W at J = 1.6 mA/cm^2 at a brightness of 500 cd/m^2 [12]. Since efficient lamp fixtures can redirect the emitting light into the space being illuminated [2], and outcoupling can be improved by many methods such as the use of microlenses [23,24], the corresponding peak total efficiencies are $\eta_{ext,t}$ = (26 ± 1)%

Table 1
Peak external quantum efficiencies of various devices

Three-section R–G–B EML WOLEDs	WOLED1 (16.6 ± 0.8)%		WOLED2 (6.0 ± 0.3)%		
Three-section EML devices in Fig. 2	l = 4 nm (15.5 ± 0.8)%	l = 8 nm (10.2 ± 0.5)%	l = 12 nm (7.2 ± 0.3)%	l = 16 nm (7.0 ± 0.3)%	l = 24 nm (6.6 ± 0.3)%
Monochromatic devices	Red (with PQIr) (7.4 ± 0.5)%		Green (with $Ir(ppy)_3$) (9.6 ± 0.5)%		Blue (with FIr6) (10.8 ± 0.6)%

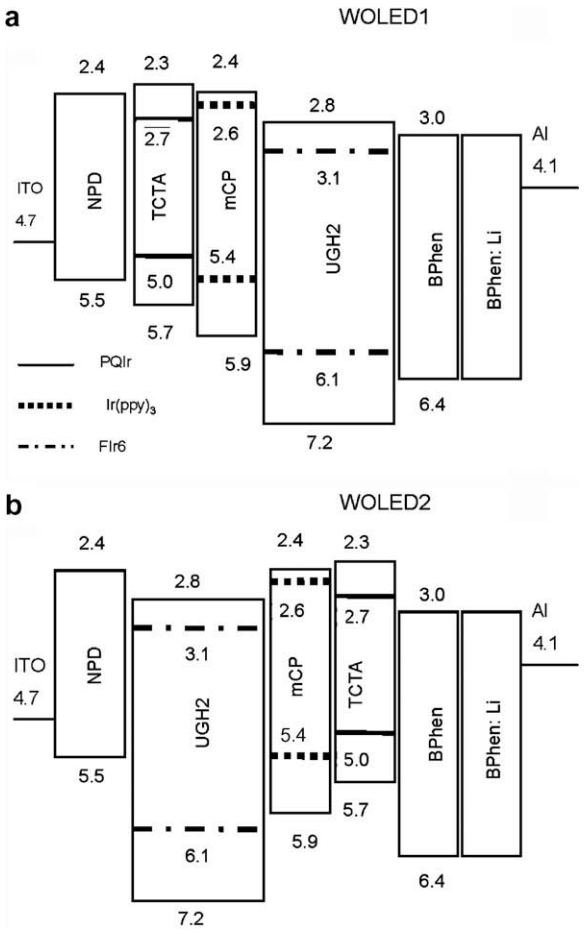

Fig. 3. Proposed energy-level diagrams of two WOLEDs with (a) the three-section EML forming a series of small energy barriers to holes across the EML (WOLED1), and (b) the three emitting regions in the opposite order (WOLED2). Numbers indicate the HOMO and LUMO energies relative to vacuum (units in eV). From Refs. [6,10,16,21,22]. Detailed structures are provided in Table 2.

Table 2
Structures of WOLED1 and WOLED2 with three-section EML

Layer function	WOLED1		WOLED2	
	Material	Thickness (nm)	Material	Thickness (nm)
Cathode	LiF/Al	60	LiF/Al	60
EIL[a]	BPhen:Li (1:1 molar ratio).	20	BPhen:Li (1:1 molar ratio)	20
ETL	BPhen	20	BPhen	20
Doped layer (B or R)	20 wt% FIr6:UGH2	20	4 wt% PQIr:TCTA	5
G doped layer	2 wt% $Ir(ppy)_3$:mCP	8	2 wt% $Ir(ppy)_3$:mCP	8
Doped layer (R or B)	4 wt% PQIr:TCTA	5	20 wt% FIr6:UGH2	20
HTL	NPD	40	NPD	40
Anode	ITO	150	ITO	150
Substrate	Glass		Glass	

Chemical names defined in text.
[a] EIL = electron injection layer, ETL = electron transport layer, HTL = hole transport layer.

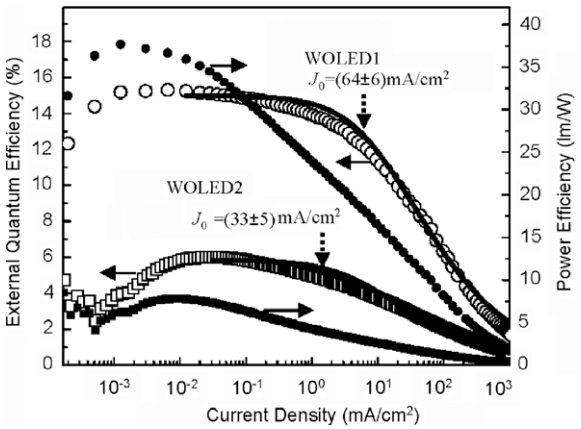

Fig. 4. External quantum efficiencies (EQE, open dots) and power efficiencies (closed dots) *vs.* current density for the two three-section EML WOLEDs in Fig. 3 (circles for WOLED1 and squares for WOLED2). The solid lines are fits using Eq. (13) in text.

and $\eta_{p,t} = (63 \pm 3)$ lm/W. The drive voltage at $J = 10$ mA/cm^2 is $V_{J10} = (5.0 \pm 0.2)$ V. When the ETL is replaced by an undoped BCP layer, η_{ext} improves to $(16.6 \pm 0.8)\%$ [12].

To determine the effect of the distributed exciton formation zone on WOLED performance, a second three-section R–G–B WOLED (WOLED2, Fig. 3b) is fabricated where the R and B emitting region positions of WOLED1 are reversed. The detailed structure of WOLED2 is also provided in Table 2. In WOLED2, the energy barriers to holes and electrons are $\geqslant 0.7$ eV at the interfaces between the EML and the HTL and ETL. Furthermore, there is no energy barrier to charges between doped regions within the EML. As a consequence, the efficiency of WOLED2 (Fig. 4, squares) is much lower than for WOLED1, peaking at $\eta_{ext} = (6.0 \pm 0.3)\%$ at $J = 3.3 \times 10^{-2}$ mA/cm^2 and $\eta_p = (10.1 \pm 0.5)$ lm/W at $J = 1.4 \times 10^{-3}$ mA/cm^2. The drive voltage for WOLED2 is higher, e.g., $V_{J10} = (6.4 \pm 0.2)$ V for WOLED2 *vs.* (5.0 ± 0.2) V for WOLED1. A comparison of the performance of these two devices is provided in Table 1.

The normalized EL spectra for both WOLEDs at several current densities are shown in Fig. 5. For WOLED1, the spectra show balanced white emission with Commission Internationale de L'Eclairage (CIE) coordinates and CRI values of, respectively (0.37, 0.41) and 81 at $J = 1$ mA/cm^2, and (0.35, 0.38) and 79 at $J = 100$ mA/cm^2. In contrast, the spectrum of WOLED2 is dominated by the red PQIr emission.

For comparison, three R, G and B emitting monochromatic devices were fabricated employing the same host-guest combinations as in the two WOLEDs. The structures of the monochromatic devices are: NPD (40 nm)/hole injection layer (HIL) (10 nm)/EML (20 nm)/BCP (40 nm), with the HIL/EML consisting of tris(phenylpyrazole)iridium ($Ir(ppz)_3$)/8 wt% PQIr:TCTA for red, TCTA/10 wt% $Ir(ppy)_3$:mCP for green and mCP/8 wt% FIr6:UGH2 for blue emission. These monochromatic devices exhibit a peak forward-viewing EQE between $(7.4 \pm 0.5)\%$ and $(10.8 \pm 0.6)\%$, as summarized in Table 1 [12]. These performances are typical of comparable electrophosphorescent OLEDs based on this set of dopants. The EL spectra for the devices are also plotted in Fig. 5. Note that WOLED1 shows a higher

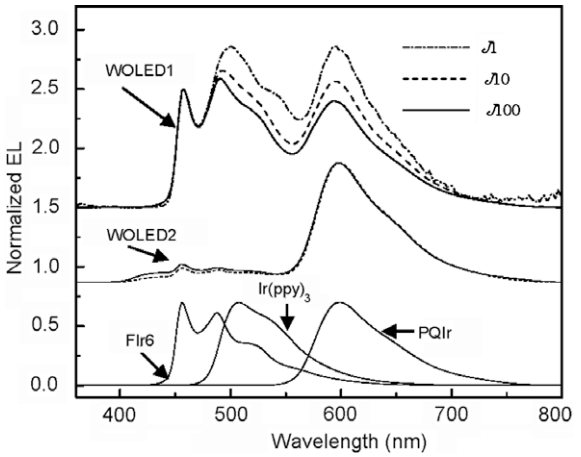

Fig. 5. Normalized EL spectra at $J = 1$, 10 and 100 mA/cm^2 for the two 3-EML WOLEDs in Fig. 3, and three monochromatic devices using the individual dopant–host combinations. Detailed structures for the monochromatic devices are provided in text.

total efficiency than any of the three individual monochromatic devices.

5. Discussion

5.1. Exciton distribution in the three-section EML

The spectra in Fig. 2b are fit using the EL spectra of the two monochromatic devices with FIr6 and Ir(ppy)$_3$ as dopants, as shown in Fig. 5, to determine the relative contributions of emission from the Ir(ppy)$_3$ and FIr6 doped regions (See Section 3). Combined with the EQE for each device measured at $J = 1$ and 100 mA/cm^2, the corresponding EQE contributed by the Ir(ppy)$_3$ emission (EQE$_G$) is plotted in Fig. 6a, which is a decreasing function of the total mCP thickness, l. The ratio of EQE$_G$ to the EQE contributed by the FIr6 emission (EQE$_B$) also decreases with increasing l (Fig. 6b).

For the devices in Fig. 2, EQE$_G$ remains unchanged when l is varied from 12 to 24 nm (Figs. 2b and 6a). This indicates that for $l \geqslant 12$ nm, Ir(ppy)$_3$ emission is primarily due to the excitons formed in the mCP region close to the TCTA/mCP (i.e., the R/G) interface. When the total mCP thickness is reduced to $l \leqslant 8$ nm, Ir(ppy)$_3$ emission is significantly enhanced, indicating an accumulation of excitons in the mCP layer close to the mCP/UGH2 (i.e., the G/B) interface, due to the accumulation of trapped holes at the large energy barrier at that location. The decrease of EQE$_G$ with increasing l is fit using Eq. (10) (Fig. 6a, lines) at various J. Since the information in Fig. 6a is insufficient to determine f_B, the ratio of EQE$_G$ to EQE$_B$ is fit to Eq. (11) (Fig. 6b, lines), assuming that the quantum yields of Ir(ppy)$_3$ and FIr6 are both unity [25,26]. The parameters obtained from the fits in Fig. 6 are $L_1 = 6.7 \pm 0.4$ nm, $L_2 = 3.8 \pm 0.2$ nm, $\phi_2/\phi_1 = 4.5 \pm 0.6$, and $f_B = (27 \pm 5)\%$ at $J = 1$ mA/cm^2, and $L_1 = 8.7 \pm 0.6$ nm, $L_2 = 4.4 \pm 0.3$ nm, $\phi_2/\phi_1 = 2.7 \pm 0.3$, and $f_B = (36 \pm 6)\%$ at $J = 100$ mA/cm^2. These results are summarized in Table 3.

To check the validity of the fits, a device with a three-section EML was fabricated with the 4-nm-thick 2 wt% Ir(ppy)$_3$:mCP slab placed at the mCP/UGH2 interface, and spaced from the TCTA/mCP interface by a 4-nm-thick layer of mCP. The detailed structure is: NPD (40 nm)/TCTA (8 nm)/mCP (4 nm)/2 wt% Ir(ppy)$_3$:mCP (4 nm)/20 wt% FIr6:UGH2 (20 nm)/BCP (40 nm). This is the same structure as the device with $l = 8$ nm in Fig. 2a, except that the positions of the Ir(ppy)$_3$-doped region and the mCP spacer are reversed. The ratio of EQE$_G$ of the test device to EQE$_G$ of the device with $l = 8$ nm in Fig. 2a is equal to the ratio between the integrals of the exciton density, $\phi(x)$, over the corresponding Ir(ppy)$_3$-doped regions in the two devices. Using

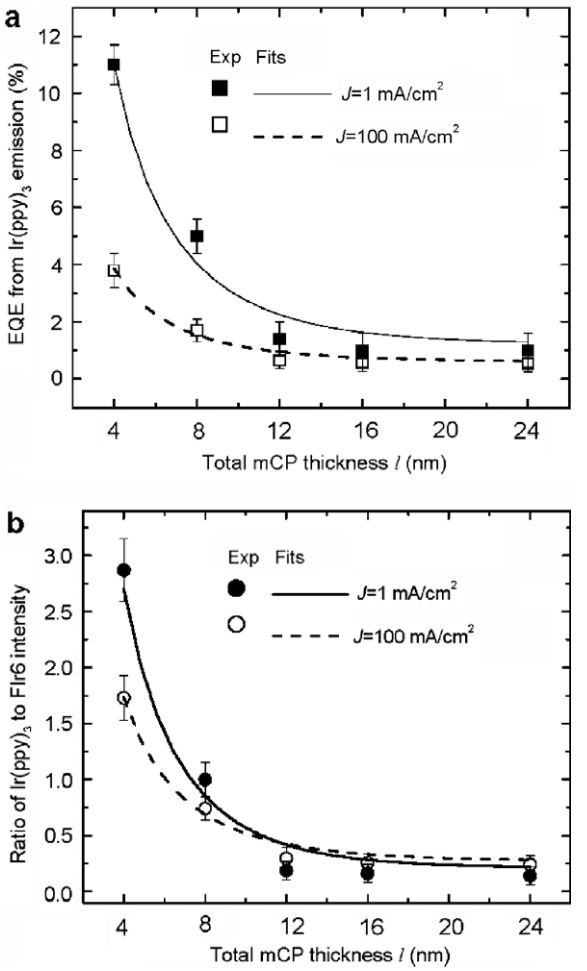

Fig. 6. (a) External quantum efficiencies (EQE) from Ir(ppy)$_3$ emission for the devices in Fig. 2a as functions of the total mCP thickness, l. Lines are fits to the points using theory in text. (b) Ratio of Ir(ppy)$_3$ to FIr6 intensity from the devices in Fig. 2a as a function of l. Lines are fits to the points using theory in text. The parameters obtained from the fits are summarized in Table 3.

Table 3
Parameters obtained from fits to the data in Fig. 6 to theory in text

Parameter	$J = 1$ mA/cm^2	$J = 100$ mA/cm^2
L_1 (nm)	6.7 ± 0.4	8.7 ± 0.6
L_2 (nm)	3.8 ± 0.2	4.4 ± 0.3
ϕ_2/ϕ_1	4.5 ± 0.6	2.7 ± 0.3
f_B (%)	27 ± 5	36 ± 6

the parameters in Table 3, the ratio is calculated to be (1.7 ± 0.1) at $J = 1$ mA/cm^2, and (1.5 ± 0.1) at $J = 100$ mA/cm^2. Based on the observed EQE_G of the latter device, we infer $EQE_G = (8.5 \pm 0.6)\%$ at $J = 1$ mA/cm^2 and $(2.5 \pm 0.2)\%$ at $J = 100$ mA/cm^2 for the test device, in agreement with the experimental observation of $(8.0 \pm 0.5)\%$ at $J = 1$ mA/cm^2 and $(2.8 \pm 0.2)\%$ at $J = 100$ mA/cm^2.

With the parameters in Table 3, we also calculate the exciton distribution in the mCP region according to Eq. (9) (Fig. 7). The integral of the exciton distribution is normalized to $(1 - f_B)$. As expected, the exciton density is high in the regions close to the two interfaces bounding the mCP region. At large J, the distribution shifts from the mCP/UGH2 interface to the TCTA/mCP interface, as inferred from the decrease in ϕ_2/ϕ_1 arising from electron pile-up at the TCTA/mCP interface. With increasing l, a larger fraction of the total exciton population is formed in the undoped spacer. This results in more excitons lost due to non-radiative decay, consistent with the observation of significantly reduced EQE of this series of devices from $(15.5 \pm 0.8)\%$ when $l = 4$ nm, to $(6.6 \pm 0.3)\%$ when $l = 24$ nm (Table 1). In addition, the increase in f_B with J indicates that direct injection of holes from the mCP HOMO to the FIr6 HOMO is more efficient at larger J, confirming that mCP acts as both a host in the green EML, and as a HIL for the blue emitting region in WOLED1.

5.2. Distributed exciton formation

Since WOLED1 (Fig. 3a) employs TCTA, mCP and UGH2 as hosts, exciton formation is distributed over the EML. That is, with f_B of the excitons formed in the FIr6-doped region $(1 - f_B)$, excitons form in the mCP region, followed by partial transfer onto the lower energy red dopant, PQIr, in the adjacent, red-emitting EML section. Thus, in principle, the three-section EML WOLED1 allows for complete radiative harvesting of excitons. This leads to a higher total efficiency for WOLED1 compared to any of the three monochromatic devices (Table 1) [12]. Since each host in the EML of WOLED1 is doped with a R, G or B emitting phosphor, energy transfer to the dopants is separately optimized, leading to balanced color and high device efficiency. Moreover, as illustrated by the three monochromatic devices, TCTA (mCP) acts as both an energy-aligned host for the red (green) dopant and an efficient HIL for the green (blue) emitting region. For the monochromatic devices, the parameters summarized in Table 3 indicates that up to 70% of the excitons form in the undoped HIL due to the energy barriers at the HIL/EML interface. Excitons formed directly in the HIL do not efficiently radiatively recombine due to inhibited transfer to the doped EML [16,27]. This leads to non-radiative decay in the HIL, and hence lower observed efficiencies compared to WOLED1.

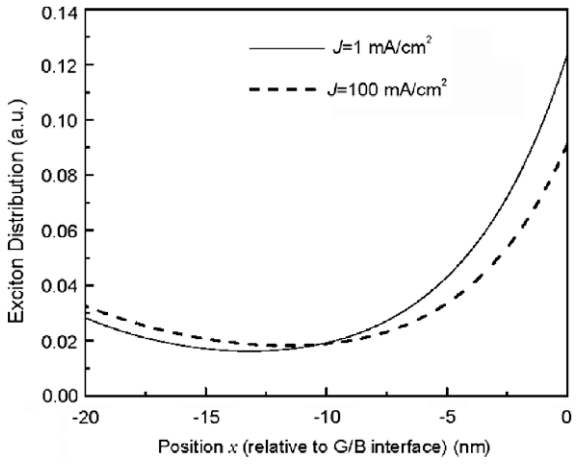

Fig. 7. Exciton distribution in the mCP region at $J = 1$ mA/cm^2 (solid line) and 100 mA/cm^2 (dashed line), based on parameters in Table 3 and theory in text. The lines corresponds to the device in Fig. 2a with a total mCP thickness of $l = 20$ nm. The integral of the area under the distribution is normalized to $(1 - f_B)$, where f_B is the fraction of the excitons generated in the blue emitting region.

The decomposition of the EL spectra of WOLED1 in Fig. 5 into the individual spectra of the R, G and B dopants (see Section 3) indicates the component ratios of R, G and B emission changes from 1:0.62:0.73 at $J = 1$ mA/cm^2 to 1:0.50:1.1 at $J = 100$ mA/cm^2. The red component emission increases with J can be attributed to (i) increased electron injection into the TCTA region may result in recombination with a small proportion of holes accumulated at the R/G interface barrier of 0.2 eV; and (ii) the distribution of excitons in the G EML section shifts from the G/B interface to the R/G interface at larger J (Fig. 7), leading to increased energy transfer to the red dopant. As in the three-section EML devices with an undoped TCTA region (Fig. 2), no TCTA emission is observed even at large J, implying that exciton formation in TCTA is negligible. This indicates that the increasing red component is mainly due to process (ii).

The structure of WOLED1 is similar to the device with $l = 8$ nm in Fig. 2a, and the test device in Section 5.1, except that the entire green EML section is doped, and the red section is also doped. Assuming energy transfer from the green to the red section is nearly 100% efficient, the EQE of WOLED1 can be calculated from the sum of EQE_G of the device with $l = 8$ nm in Fig. 2a, and EQE_G and EQE_B of the test device in Section 5.1. With the parameters in Table 3, we obtain $EQE = (16.2 \pm 0.9)\%$ at $J = 1$ mA/cm^2 and $(6.2 \pm 0.5)\%$ at $J = 100$ mA/cm^2 for WOLED1, in agreement with the experimental observation of $(14.0 \pm 0.8)\%$ at $J = 1$ mA/cm^2 and $(6.3 \pm 0.3)\%$ at $J = 100$ mA/cm^2.

Fig. 4 shows that the EQE for WOLED2 is reduced by a factor of 2.5 compared to WOLED1. In addition, the normalized EL spectra for WOLED1 and WOLED2 (Fig. 5) are significantly different, as noted in Section 3. This suggests that the energy barriers (>0.7 eV) to electron and hole transport at the edges of the EML inhibit exciton formation within the EML in WOLED2. Evidence for this is the higher drive voltage required for WOLED2 compared to WOLED1 (1.4 V higher at $J = 10$ mA/cm^2). Holes that accumulate at the NPD/UGH2 interface cannot be efficiently injected onto FIr6 molecules due to the large difference (0.6 eV) between the HOMO energies of NPD and FIr6. At the opposite edge of the EML, holes and electrons pile-up at the TCTA/ETL interface, leading to a high local density of excitons on, and emission from PQIr. The excitons, therefore, are inhibited from transfer to the G and B dopants, leading to significantly reduced efficiency.

The EQE *vs.* *J* characteristics of both three-section EML WOLEDs in Fig. 4 are fit to a model of triplet–triplet (T–T) annihilation [9]:

$$\mathrm{EQE} = \mathrm{EQE}_0 \cdot \frac{J_0}{4J}\left(\sqrt{1+\frac{8J}{J_0}}-1\right). \quad (13)$$

Here, EQE_0 is the EQE in the absence of T–T annihilation, and J_0 is the current density when $\mathrm{EQE} = \mathrm{EQE}_0/2$. From the fits (solid lines), we infer that $J_0 = (64 \pm 6)\ \mathrm{mA/cm^2}$ for WOLED1 and $J_0 = (33 \pm 5)\ \mathrm{mA/cm^2}$ for WOLED2. As the excitons accumulate in the thin TCTA layer in WOLED2, their high local density leads to enhanced T–T annihilation. In comparison, previously reported WOLEDs either have low η_p (i.e., $\eta_p = 9.9$ lm/W for a 3-EML WOLED using a common host [8]); show low EQE (i.e., 2.7% for a 3-EML fluorescent WOLED [15]); exhibit significant roll-off (i.e., $J_0 = 0.8\ \mathrm{mA/cm^2}$ for a WOLED with an abrupt energy barrier at the edge of the EML [6]); or render poor white color balance (i.e., CRI = 69 for a WOLED with a single exciton formation region [5]).

The peak efficiency of WOLED1 corresponds to an internal quantum efficiency of IQE = (87 ± 5)% [2,12,28]. As demonstrated here, the excitons can be completely harvested in the three emitting regions, showing a potential for IQE = 100% [28–30], achievable by incorporating optimized combinations of phosphorescent dopants and hosts [10,29]. This indicates that the η_p can also be increased by (15 ± 5)%. In addition, increasing the relative intensity of red and green emission can enhance the response of human eye to the emitted light by (18 ± 4)% while the CRI is maintained >75. Based on η_p achieved in WOLED1, these two factors indicate that the forward-viewing η_p can be >50 lm/W with optimized dopant–host combinations and a slightly warmer white balance.

6. Conclusions

We have demonstrated and analyzed the operation of a WOLED structure composed of three separate phosphorescent doped regions in a broad EML. The dopant and host regions are characterized by a stepped progression of HOMO levels that forms a series of small energy barriers to charge injection. This broadened EML distributes exciton formation in multiple doped regions. The selection of dopant–host combinations and their positions in the EML promote resonant injection of charges onto the dopant molecules. The distributed exciton formation zone reduces the local exciton density, thereby leading to a reduction in efficiency roll-off at large *J*. In addition, the intensities of the three colors can be separately adjusted in each of the three emitting regions in the EML without sacrificing device efficiency, such that the white color balance can be controlled as desired. The 3-EML WOLED exhibits a higher total efficiency compared to monochromatic devices using the same dopants, with the peak values of $\eta_{ext,t} = (28 \pm 1)\%$ and $\eta_{p,t} = (63 \pm 3)$ lm/W, and CRI = 81.

Acknowledgements

The authors thank the Department of Energy through a subcontract from the University of Southern California, and Universal Display Corp. for partial financial support of this work.

References

[1] B.W. D'Andrade, S.R. Forrest, Adv. Mater. 16 (2004) 1585.
[2] B.W. D'Andrade, R.J. Holmes, S.R. Forrest, Adv. Mater. 16 (2004) 624.
[3] Y. Sun, N.C. Giebink, H. Kanno, B.W. Ma, M.E. Thompson, S.R. Forrest, Nature 440 (2006) 908.
[4] J.H. Seo, J.H. Seo, J.H. Park, Y.K. Kim, J.H. Kim, G.W. Hyung, K.H. Lee, S.S. Yoon, Appl. Phys. Lett. 90 (2007) 203507.
[5] E.L. Williams, K. Haavisto, J. Li, G.E. Jabbour, Adv. Mater. 19 (2007) 197.
[6] H. Kanno, R.J. Holmes, Y. Sun, S. Kena-Cohen, S.R. Forrest, Adv. Mater. 18 (2006) 339.
[7] S. Naka, H. Okada, H. Onnagawa, Y. Yamaguchi, T. Tsutsui, Synth. Met. 111 (2000) 331.
[8] G. Cheng, Y.F. Zhang, Y. Zhao, Y.Y. Lin, C.Y. Ruan, S.Y. Liu, T. Fei, Y.G. Ma, Y.X. Cheng, Appl. Phys. Lett. 89 (2006) 043504.
[9] M.A. Baldo, C. Adachi, S.R. Forrest, Phys. Rev. B 62 (2000) 10967.
[10] G.F. He, M. Pfeiffer, K. Leo, M. Hofmann, J. Birnstock, R. Pudzich, J. Salbeck, Appl. Phys. Lett. 85 (2004) 3911.
[11] X. Zhou, D.S. Qin, M. Pfeiffer, J. Blochwitz-Nimoth, A. Werner, J. Drechsel, B. Maennig, K. Leo, M. Bold, P. Erk, H. Hartmann, Appl. Phys. Lett. 81 (2002) 4070.
[12] Y. Sun, S.R. Forrest, Appl. Phys. Lett. 91 (2007) 263503.
[13] I. Sokolik, R. Priestley, A.D. Walser, R. Dorsinville, C.W. Teng, Appl. Phys. Lett. 69 (1996) 4168.
[14] M.A. Baldo, S.R. Forrest, Phys. Rev. B 62 (2000) 10958.
[15] M.S. Kim, J.T. Lim, C.H. Jeong, J.H. Lee, G.Y. Yeom, Thin Solid Films 515 (2006) 891.
[16] R.J. Holmes, B.W. D'Andrade, S.R. Forrest, X. Ren, J. Li, M.E. Thompson, Appl. Phys. Lett. 83 (2003) 3818.
[17] W. Shockley, W.T. Read, Phys. Rev. 87 (1952) 835.
[18] R.S. Muller, T.I. Kamins, Device Electronics for Integrated Circuits, John Wiley & Sons Inc., 1986, p. 40.
[19] P.E. Burrows, Z. Shen, V. Bulovic, D.M. McCarty, S.R. Forrest, J.A. Cronin, M.E. Thompson, J. Appl. Phys. 79 (1996) 7991.
[20] M.A. Lampert, P. Mark, Current Injection in Solids, Academic, New York, 1970, p. 20.
[21] I.G. Hill, A. Kahn, J. Appl. Phys. 86 (1999) 4515.
[22] Y. Kuwabara, H. Ogawa, H. Inada, N. Noma, Y. Shirota, Adv. Mater. 6 (1994) 677.
[23] S. Moller, S.R. Forrest, J. Appl. Phys. 91 (2002) 3324.
[24] Y. Sun, S.R. Forrest, J. Appl. Phys. 100 (2006) 073106.
[25] Data provided by Dr. P.I. Djurovich, University of Southern California, 2007.
[26] Y. Kawamura, K. Goushi, J. Brooks, J.J. Brown, H. Sasabe, C. Adachi, Appl. Phys. Lett. 86 (2005) 071104.
[27] R.J. Holmes, S.R. Forrest, Y.J. Tung, R.C. Kwong, J.J. Brown, S. Garon, M.E. Thompson, Appl. Phys. Lett. 82 (2003) 2422.
[28] G. Gu, D.Z. Garbuzov, P.E. Burrows, S. Venkatesh, S.R. Forrest, M.E. Thompson, Opt. Lett. 22 (1997) 396.
[29] C. Adachi, M.A. Baldo, M.E. Thompson, S.R. Forrest, J. Appl. Phys. 90 (2001) 5048.
[30] A. Chutinan, K. Ishihara, T. Asano, M. Fujita, S. Noda, Org. Electron. 6 (2005) 3.

electrophosphorescence by blending iridium complexes with PVK and polyfluorene (PFO) as the co-host. They found that the device efficiency was very poor when using only PFO as the host and both PL and EL spectra only show the blue emission of PFO and there was almost no phosphorescence emission from the iridium complexes at all. However, the energy transfer from polyfluorene to the green phosphorescent dyes had been greatly enhanced by blending PVK into the guest/PFO film.

In this paper, we report a high-efficiency green phosphorescent PLED by doping Ir(Bu-PPy)$_3$, an Ir complex with butyl-substituted 2-phenylpyridine as a ligand, into a conjugated polymer-PFO. We fabricated the devices using PFO as the host for three device configurations: single layer (Ir complexes doped into PFO), bilayer structure (with PVK as interlayer between PEDOT and PFO layer) and blend-host (PVK + PFO as the co-host) structure. For comparison we have also made control device with PVK as the host. We found that the efficiency from the single PFO host and PFO/PVK blend-host was much lower than that of the control device with PVK as the host. However, the PFO/PVK bilayer device with PVK as an anode interlayer showed comparable efficiency as the control device with PVK as the host. The maximal luminous efficiency(LE) of 36.8 cd/A and EQE of 12.3% ph/el was achieved at the current density of 7.6 mA/cm^2 (8.7 V) from the device with a structure of ITO/PEDOT/PVK/2 wt%Ir(Bu-PPy)$_3$-PFO-30 wt%PBD/Ba/Al, which was comparable to that with PVK as the host with same dopant concentration (38.9 cd/A for ITO/PEDOT/2 wt%Ir(Bu-PPy)$_3$-PVK-25 wt%PBD/Ba/Al device). More importantly, the bilayer device has much lower operating voltage than the device with PVK as the host. We also found that the emission from Ir(Bu-PPy)$_3$ was greatly enhanced both in PL and EL processes as PVK was inserted between Ir(Bu-PPy)$_3$/PFO and PEDOT layers. Steady and transient PL spectra showed an energy transfer from PVK to the phosphorescent dyes both in the bilayer structure and in the blend-host structure. However bilayer device showed much better EL device performance than that of blend-host device. These results demonstrated that efficient green PhPLED could be realized with conjugated polymer host with a low triplet level through novel device configuration.

2. Experiment

Molecular structures under the investigation are shown in Scheme 1. The green phosphorescent Ir complex, Ir(Bu-PPy)$_3$ with butyl-substituted 2-phenylpyridine as a ligand, was synthesized in our laboratory following the method published previously [30]. PFO-POSS [31] was purchased from American Dye Sources Inc., PVK and PBD were purchased from Aldrich. All commercial available materials are used from vendors without further purification.

The device configurations in our study are following:

ITO/PEDOT(60 nm)/PVK-PBD-Ir(80 nm)/Ba(4 nm)/Al (device A)

ITO/PEDOT(60 nm)/PFO-PBD-Ir(70 nm)/Ba(4 nm)/Al (device B)

ITO/PEDOT(60 nm)/PVK(40 nm)/PFO-PBD-Ir(70 nm)/Ba(4 nm)/Al (device C)

ITO/PEDOT(60 nm)/PFO-PVK-PBD-Ir(70 nm)/Ba(4 nm)/Al (device D)

The fabrication of electrophosphorescent devices was followed a standard procedure. The ITO glass substrate was cleaned in ultrasonic bath sequentially in acetone, detergent, deionized water and isopropanol, and baked at 80 °C for 12 h. A 60 nm-thick layer of poly(ethylendioxythiophene):poly(styrene sulfonic acid) (PEDOT:PSS, Baytron P4083, Bayer AG) was spin-coated onto the precleaned ITO-glass substrates after a O_2 plasma treatment, and dried in vacuum box for over 8 h. Then, if necessary, a 40 nm thick layer of PVK (10 mg/ml) was spin-coated on the top of PEDOT and baked at 120 °C for 30 min. A mixture of the Ir(Bu-PPy)$_3$ with [PVK+PBD(25%)] or [PFO-POSS+PBD(30%)] or [PFO-POSS + PVK (1:1)+PBD(30%)]were spin-coated from the solution in chlorobenzene (for PVK+PBD) or *p*-xylene:toluene = 7:3 (for PFO + PBD), respectively. The emitting layer was spin-coated from solvent with a concentration of 20 mg/ml by adapted rotate speed. Profilometer (Tencor Alfa-Step 500) was used to measure the thickness of the films. A thin layer of Ba (4 nm thick) with about 100 nm thick Al capping layer was deposited through a shadow mask at a vacuum chamber with a base pressure of $\sim 10^{-4}$ Pa. Ba and Al layer thickness was monitored upon deposition by using a crystal thickness monitor (Sycon). Except the fabrication of

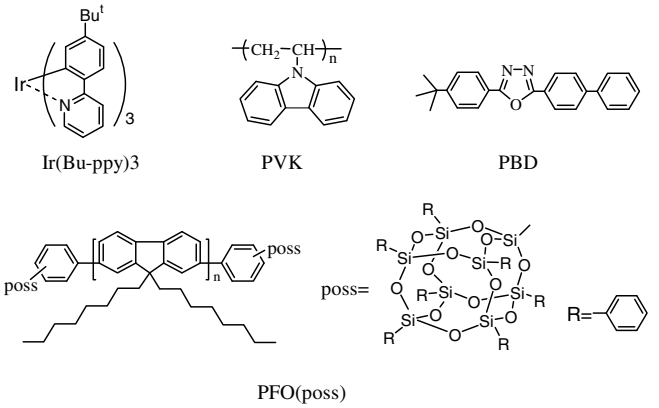

Scheme 1. The molecular structures of Ir(Bu-PPy)$_3$, PVK, PFO-POSS and PBD.

PEDOT:PSS layer, all the device fabrication was carried out in a controlled atmosphere dry-box (Vacuum Atmosphere Co.) in N_2 atmosphere. Current densities (J)–voltage (V)–luminance (L) data were collected using a Keithley 236 source measurement unit and a calibrated silicon photodiode. The luminance (cd/m^2) and luminous efficiency (cd/A) were measured by Si photodiode and calibrated by a PR-705 SpectraScan Spectrophotometer (Photo Research). PL spectra under 325 nm line excitation of HeCd laser and EL spectra were recorded by a CCD spectrophotometer (Instaspec 4, Oriel). The microscope pictures were captured by a polarizing microscope (Nikon E600w POL). Time-resolved spectra were measured by fluorescence lifetime spectrometer (FLS-920, Edinburgh Instrument Ltd.).

3. Results and discussion

3.1. EL performance of Ir(Bu-PPy)$_3$ with different device configurations

Four types of device configurations were compared, devices A, B and D are single layer devices with Ir(Bu-PPy)$_3$ doped into PVK, PFO and their blend, respectively, device C is the bilayer device with PVK inserted between PFO-Ir film and PEDOT buffer layer. Fig. 1 shows the normalized EL spectra from four devices with 2 wt%Ir(Bu-PPy)$_3$ doping concentration. Devices A, C and D showed typical phosphorescence emission of Ir(Bu-PPy)$_3$ [32] with a peak position at around 515 nm and a shoulder peak at around 540 nm, and device B showed a broadened spectrum with maximum peak at around 540 nm. Similar red shift and broadening of EL spectrum of Ir complexes in PFO host compared with that in PVK host was reported previously [23] and assigned to the extension of dopant aggregation and hence the emission from dimeric units of dopants with strong π–π interactions. Device B and D showed a trace of blue emission at around 420 nm which was responsible for the fluorescence of PFO emission, while device A, C showed complete energy transfer from PVK and PFO to Ir(Bu-PPy)$_3$ and no host emission was observed at all.

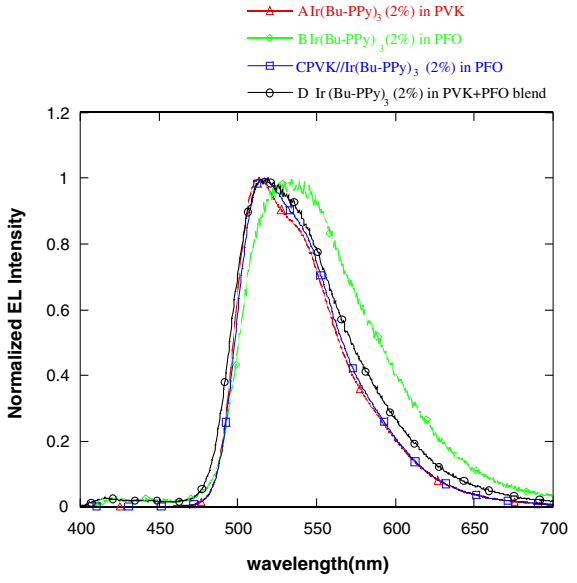

Fig. 1. The EL spectra of Ir(Bu-PPy)$_3$ doped in PVK or PFO-POSS with different device structures.

Table 1
Device performance at the maximum luminescence efficiency and at the luminescence of around 1000 cd/m^2

Host configuration (thickness)	Bias (V)	J (mA/cm^2)	L (cd/m^2)	EQE (%)	LE max (cd/A)
A: PVK-PBD(25%) (80 nm)	19.0	41.2	16028.0	13.2	38.9
B: PFO-PBD(30%) (80 nm)	7.4	1.3	44.9	1.4	3.4
C: PVK/PFO-PBD(30%) (65 nm)	8.7	7.6	2791.8	12.3	36.8
D: PVK:PFO:PBD (1:1:0.5) (80 nm)	4.6	1.8	28.8	0.62	1.56
Device performance at around 1000 cd/m^2					
A: PVK-PBD(25%) (80 nm)	16	6.4	1243	10.4	19.5
C: PVK/PFO-PBD(30%) (65 nm)	8.9	4.4	1195	14.5	27.3

The device performance observed from four devices with different configurations is summarized in Table 1. A peak luminous efficiency (LE) of 36.8 cd/A at the current density of 7.6 mA/cm^2 and the driving voltage of 8.7 V with a brightness of 2792 cd/m^2 was observed from device C with the configuration of PVK/2 wt%Ir(Bu-PPy)$_3$-PFO-30 wt%PBD, which was comparable to those from the device A with PVK host with the maximum LE of 38.9 cd/A at current density 41.2 mA/cm^2 for control device with the configuration of 2 wt%Ir(Bu-PPy)$_3$-PVK-25 wt%PBD. These values are comparable to the results reported previously by other groups from devices with Ir(PPy)$_3$ as guest and PVK as the host [11,18,19]. We also found that devices C with PVK interlayer and PFO + PBD host showed much lower operating voltage than that of the control device A with PVK + PBD host (7.9 V for PFO device vs. 15 V for PVK device at 1000 cd/m^2). In contrast, device B and device D showed very poor performance. These results indicated that the efficiency of devices with PFO as the host (device C) was significantly enhanced (compared with device with single layer structure with PFO host without PVK interlayer (device B) and with the device with PVK/PFO blend co-host configuration (device D)). In addition, the operating voltage of device C by insertion of PVK layer between PEDOT and emission layer (Ir(Bu-PPy)$_3$ in PFO blend was remarkably reduced (compared with the device using PVK as the host (device A)). The significantly lower device efficiency observed from the device with PVK + PFO co-host implies that device B with PVK + PFO co-host has different operational mechanism compared to devices C with PVK as an interlayer.

3.2. Energy transfer behavior of PVK/PFO multilayer device

3.2.1. Absorption and PL spectra

Fig. 2 shows the absorption spectrum of Ir(Bu-PPy)$_3$ and PL spectra of PFO with 30% PBD and PVK with 25% PBD. Similar good overlap between the absorption spectrum from Ir(Bu-PPy)$_3$ MLCT and PL emission spectra of PVK and PFO films were observed, which meet a requirement for the efficient Förster energy transfer from both PVK and PFO to Ir complex. However, the PL spectra of the films by both PVK and PFO with 2% (w/w) of Ir complex show

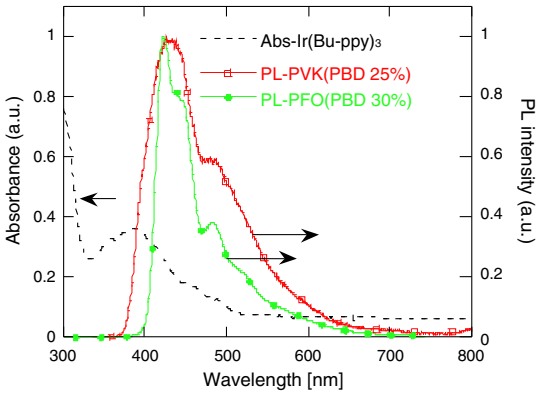

Fig. 2. The absorption of Ir(Bu-PPy)$_3$ film and the emissions of PVK-PBD(25%) and PFO-PBD(30%) films.

great difference when excited at 325 nm by HeCd laser, which is clearly depicted in Fig. 3. In the film of PVK doped with Ir complex (A film), Ir(Bu-PPy)$_3$ shows efficient phosphorescent emission with peak at around 515 nm, there is barely emission from PVK at from 400 nm to 450 nm. By contrast, the Ir(Bu-PPy)$_3$'s emission could hardly be detected in PFO-Ir complex blending film (B film), while PFO emission intensity is significantly reduced with increased concentration of the Ir complex content. This is probably due to the energy back transfer from excitons on Ir complexes to low-lying triplet states of PFO. The PFO emission quenched by doped Ir complexes was extensively investigated and reported by several groups [24,33].

Both film C, bilayer structure, and film D, PFO-PVK blend, showed a strong green emission from Ir complex with a comparable residue of blue emission from PFO. An immediate thought about origin of strong energy transfer in bilayer structure is that PFO interpenetrated into PVK

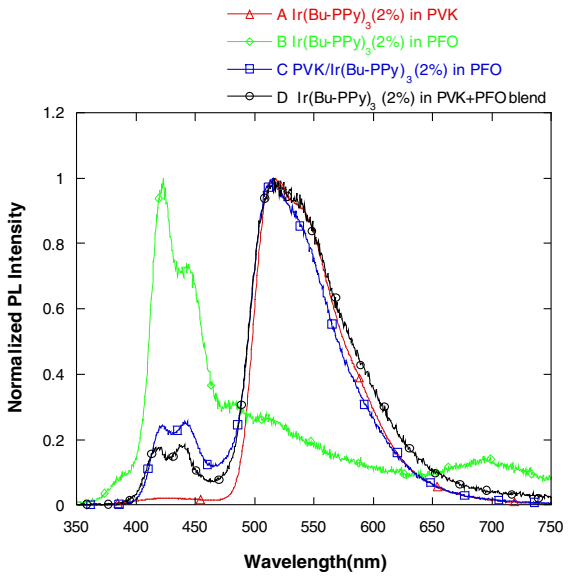

Fig. 3. PL spectra (pumped by 325 nm line of HeCd laser) of films of 2%Ir(Bu-PPy)$_3$ doped in PVK or PFO-POSS with different device structures.

layer upon spin-coating of solution of Ir/PFO on top of PVK layer and interfacial blend layer of PVK in PFO has been formed and responsible for the enhancement of the device performance as in case of regular PFO + PVK blend film. Thereby we should first to clarify whether PFO has been mixed with PVK layer underneath during spin-coating.

PVK with a molecular weight (MW) of 1,000,000 (Aldrich) used in this study is nearly insoluble in *p*-xylene mixed with toluene at 7:3 ratio, thereby the erosion of PVK layer by PFO solution is unlikely to take place. In addition, the solid film made by high MW PVK would be compact enough that not easily to be washed away by the upper non-solvent solution. This assumption was confirmed further by testing the cross section profile of the multilayer devices. When the bilayer device has been made, we cut a line on the film, and because of the different mechanic strength of PVK and PFO film and week interface interaction between unmixed PFO and PVK layers, the cross section showed a clear step between these two layers (Fig. 4). The cross section profile shape indicated that two layers were stay separated and had a clear boundary between two layers without mixing in the interface. On the other hand, EL performance from PVK + PFO blend films is significantly lower than those from PVK and PVK/PFO multilayer devices, this will further exclude possibility of interfacial blend as an origin of high efficiency of bilayer structure.

3.2.2. PL intensity versus thickness of PVK in PVK/PFO bilayer films

Fig. 5a shows the PL spectra of multilayer film with different PVK layer thickness excited at 325 nm from PVK side. As can be seen from Fig. 5a PL emissions varied dramatically with increasing thickness of PVK layer while the EL spectra did not change with the thickness of PVK layer (insert of Fig. 5a). With increasing PVK thickness, the intensity of PFO emission at 420 nm was almost not changed while the emission of Ir complex at 515 nm was increased dramatically with increasing of the PVK thickness. Compared with the PL intensity from the same film

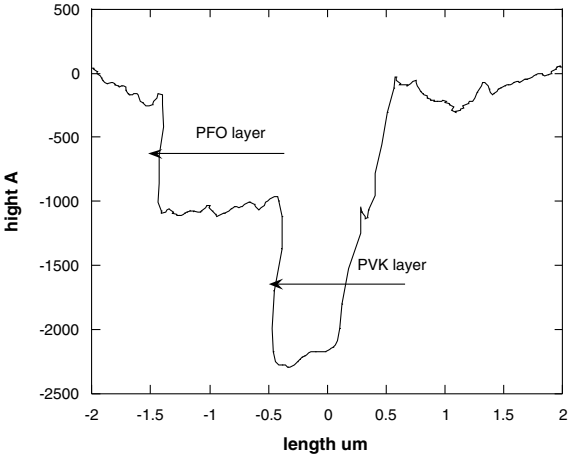

Fig. 4. Cross-section profile of PVK/PFO bilayer film.

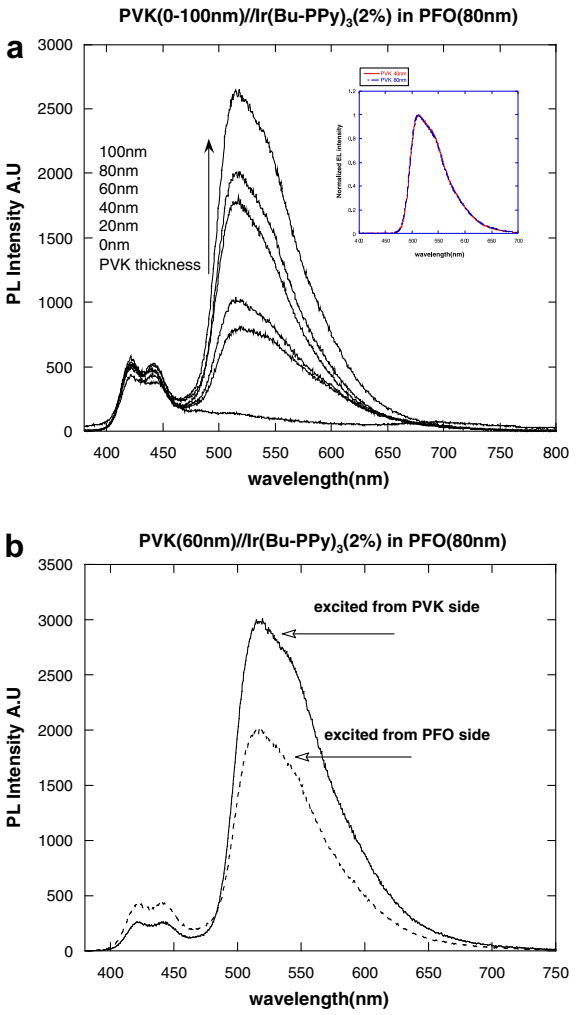

Fig. 5. (a) PL spectra of bilayer devices with PVK thickness switch from 0 nm to 100 nm. The insert shows the EL spectra of bilayer devices with 40 nm and 80 nm PVK layer and (b) PL spectra of bilayer device with 60 nm PVK layer pumped from different side of the film.

excited from PVK or PFO sides (Fig. 5b), the PL intensity at 515 nm was significantly higher when the film was excited from PVK side. These facts suggested an enhanced phosphorescent emission was originated from the excitation in the PVK layer. The excitons could be formed both in the PVK layer (excited by light absorbed in PVK layer) and the PFO-Ir layer (excited by light transmitted through PVK layer). For the excitons in the PVK layer, there were several ways to decay. Firstly, it could decay both in radiative or non-radiative way in PVK layer. Secondly, the excitons could transfer to the Ir complex through Főrster energy transfer which is effective in few nanometers. Thirdly, the singlet excitons could be transferred to triplet excitons, and diffused to the interface of the PVK and PFO-Ir, and then transferred to the Ir complex through Dexter energy transfer. The significant enhancement of green emission with increasing thickness of PVK layer clearly indicate that green emission is originated from excitons

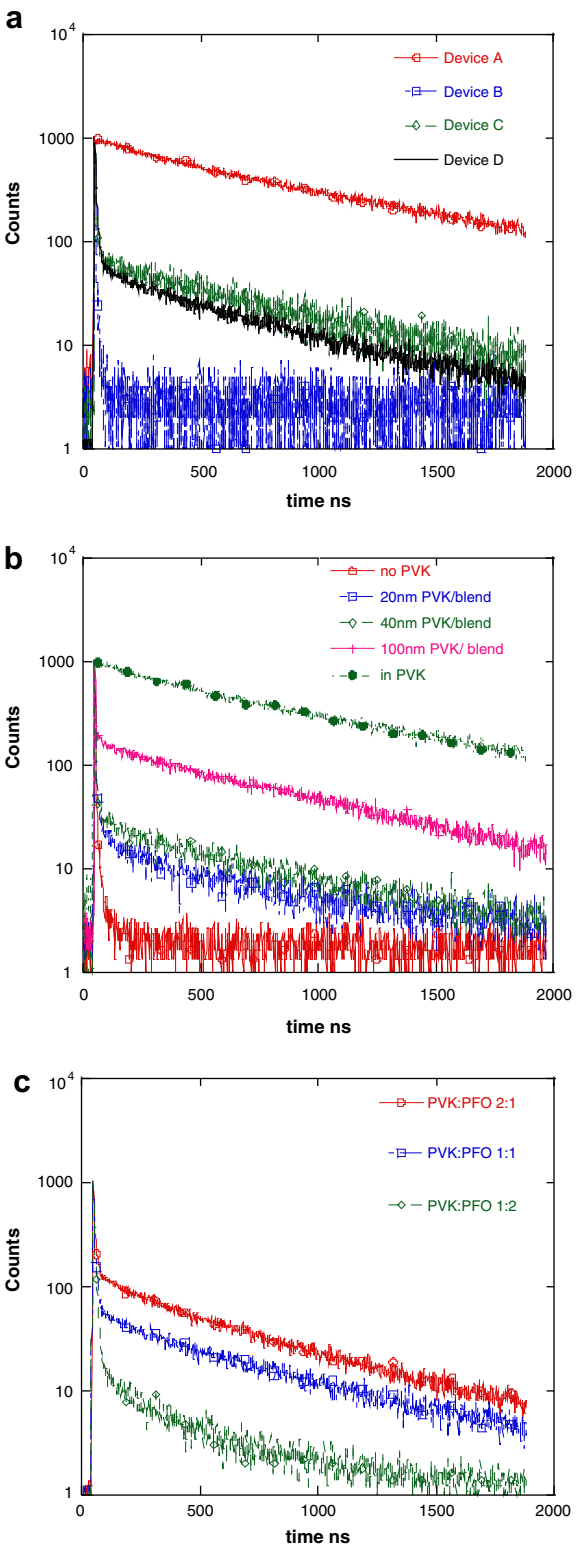

Fig. 6. Transient PL spectra of (a) Ir(Bu-PPy)$_3$ doped in PVK or PFO-POSS with different device structure, (b) bilayer device with different PVK layer thickness and (c) blend-host devices with different radiation of PVK and PFO-POSS.

Table 2
Lifetime test results of 2 wt%Ir(Bu-PPy)$_3$ doped in PVK and PFO-POSS with different configurations

Matrix or configuration	τ1	Proportion (%)	τ2	Proportion (%)
Doped PVK and PFO films				
PVK	701 ns	100		
PFO	3.55 ns	100		
Bilayer films				
PVK(20 nm)/PFO	5.24 ns	95	440 ns	5
PVK(40 nm)/PFO	2.84 ns	93	553 ns	7
PVK(100 nm)/PFO	2.34	87	699 ns	13
Blend-host films				
PVK:PFO 2:1	8.14	84	492	16
PVK:PFO 1:1	7.52	93	515	7
PVK:PFO 1:2	7.44	98	293	2

created in PVK layer and energy transferred to Ir complex by second (Főrster) or third (Dexter) routes. We also noticed that the EL spectra did not change with the thickness of PVK layer (insertion of Fig. 5a) which indicates that the PL and EL process might be dominated by different mechanism.

3.2.3. Transient PL spectra

Fig. 6a shows the time resolved PL spectra of films A, B, C, D. The excitation was at 310 nm, and the probe wavelength was at 515 nm. Film A, PVK with 2 wt%Ir(Bu-PPy)$_3$ complex showed a single exponential decay with a lifetime about 700 ns, which was comparable to that reported previously [34]. Film B, PFO blended with 2 wt%Ir(Bu-PPy)$_3$ showed a much faster decay with a lifetime of about few

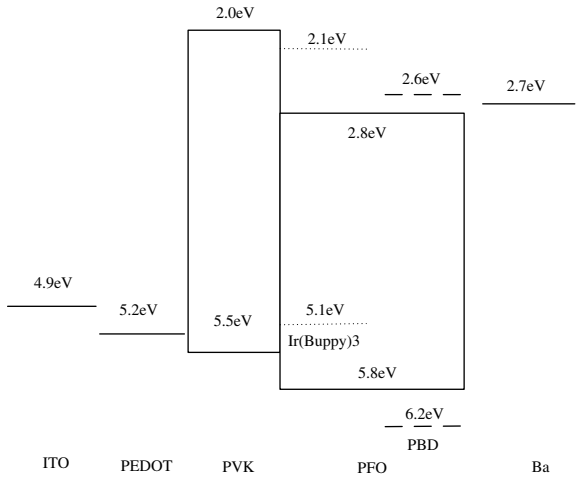

Fig. 7. Energy band diagram of Ir(Bu-PPy)$_3$, PVK, PFO-POSS and PBD.

nanoseconds. Film C, bilayer films, and film D, blend-host films with 2 wt%Ir(Bu-PPy)$_3$, both their transient PL emissions are consisted of two components: a rapid decrease (life time several ns) followed by a gentle single exponential decay (life time several hundred ns). Rapid decay was obviously from the PFO-Ir(Bu-PPy)$_3$ phase and the slow decay was from the PVK-Ir(Bu-PPy)$_3$ phase (in case of bilayer structure from PFO/PVK interface). Table 2 summarizes the life time data of PL emission from the films of different device configuration (Fig. 6a), bilayer film C with different PVK layer thickness (Fig. 6b) and blend film D with differ-

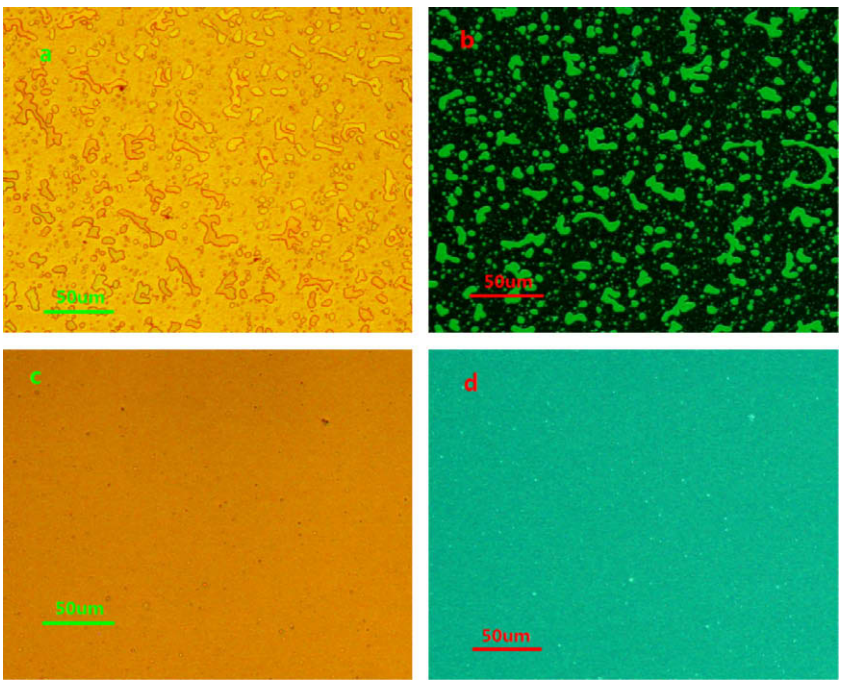

Fig. 8. Microscope photograph of film of Ir(Bu-PPy)$_3$ doped in PVK:PFO 1:1 (a) under normal lighting, (b) under ultraviolet lighting; Ir(Bu-PPy)$_3$ doped in PFO with PVK layer underneath (c) under normal lighting and (d) under ultraviolet lighting.

ent radiation of PVK and PFO-POSS (Fig. 6c) probed at 515 nm. We noted that slow component of 515 nm decay increased with increasing of PVK content in the blend. For the bilayer PVK/PFO with 2 wt%Ir(Bu-PPy)$_3$ in PFO (Film C), portion of slow decay increases with the increasing the thickness of PVK layer. This result is consistent with the report by Gong et al. [35], i.e. in a film consisted of two components with different lifetime, decay pattern changes by the relative intensity of the two different components.

3.2.4. Analysis of EL performance for the devices with different configurations

The bilayer structure device (C) and the co-host device (D) showed the similar PL spectra and time resolved spectra, this indicated that the energy transfer behavior under photoexcitation for these two different types of devices would be very similar. However we have observed a significant difference in the EL performance (Table 1). In order to address this question, we have compared the energy levels of the materials used for these devices and the morphology of the blend films. Fig. 7 is the energy band diagram of Ir(Bu-PPy)$_3$, PVK, PFO-POSS and PBD, these data were taken from the previous reports [23,36]. Since the LUMO of PFO and PVK is around −2.8 and −2.0 eV, respectively, there will be a 0.8 eV barrier for electrons between PFO/PVK interface. Thereby, PVK serves as an electron-blocking layer, and the injected electrons from PFO side would be accumulated in the PVK-PFO interface. In this case the recombination zone will be located close to the PVK layer. Since HOMO level of Ir complex is much higher than PVK level, holes injected from PVK layer could be easily trapped by Ir complexes located in the PVK-PFO interface and recombine with electrons injected from PFO side and accumulated in the interface region. As a result, the back transfer of excitons to PFO could be restrained.

Fig. 8 shows the microscope picture of the PVK and PFO blending film where severe macroscopic phase segregation of PFO and PVK components is observed, which is due to the incompatibility of PVK and PFO polymers originated from different polarity of these two polymers. Such phase segregation was reported previously also by Kim et al. for PFO/PVK blend devices [28,29]. The green phase in the micrograph responsible for Ir complex doped into PVK phase, and the dark part of the picture was the PFO phase where emission was quenched by back transfer to triplet level of PFO. Obviously, in the device with PVK and PFO blend as the co-host, the electron blocking effect of PVK was significantly reduced, and the total current was increased due to the increase in electron current, this could be clearly observed from the IV curves in Fig. 9. Therefore, the EL efficiency of device with PVK/PFO as the co-host is much lower than that of the bilayer device.

On the other hand, in contrast to monotonically increase of the 515 nm emission under photoexcitation with increasing the PVK thickness up to 100 nm in the PVK/PFO bilayer film (Fig. 5a), the device EL efficiencies increase initially with increasing the PVK thickness (0–80 nm) reaching maximum at PVK layer of 40 nm then decreases (Fig. 10). We note that EL spectra are not changing with PVK thickness in contrast of PL process showing only 515 nm emission (see inset of the Fig. 5a). This dramatic

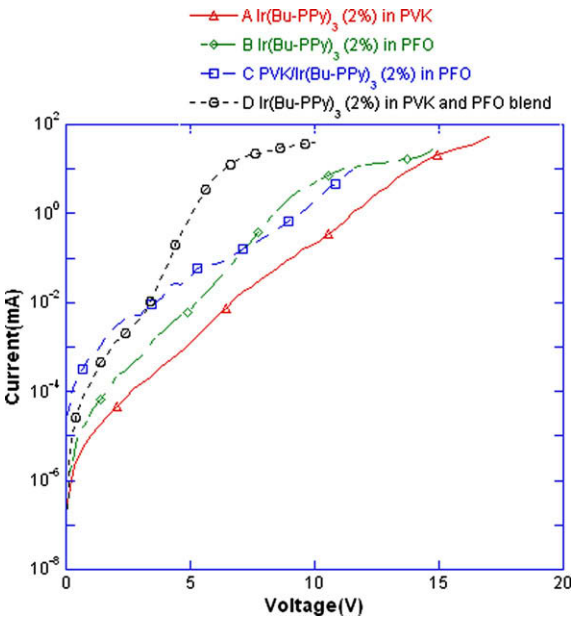

Fig. 9. IV curves of device A, B, C and D.

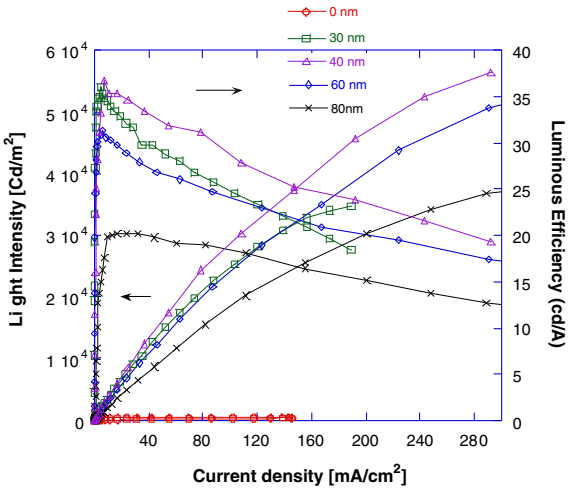

Fig. 10. Light-luminous efficiency–current density curves of bilayer devices with PVK layer varies from 0 nm to 80 nm.

difference of EL and PL process is believed to be due to carrier trapping at the dopant sites in EL process [37].

4. Conclusions

We have successfully demonstrated an efficient green phosphorescent PLED by doping Ir(Bu-PPy)$_3$ into PFO-POSS which has triplet level much lower than that of Ir(Bu-PPy)$_3$. High device efficiency as well as a greatly reduced driving voltage compared with the device with PVK as the host have been realized by inserting PVK layer between PEDOT and PFO-Ir(Bu-PPy)$_3$ layer to form a bilayer structure. It was found that PVK interlayer played important role in

energy transfer process. For the PL process, PVK could enhance the phosphorescent emission both in the bilayer structure and in the blend-host structure, but for the EL process, only the bilayer structure could provide good device performance. It was also found that PVK layer serves as an electron-blocking layer and the injected electrons from PFO side was accumulated in the PVK-PFO interface and recombination happens in the interface of PVK and PFO layer by trapping mechanism on the Ir complexes located in the interface region. We have shown that by using bilayer structure, the back transfer to low-lying PFO triplet state was substantially suppressed and high device efficiency with lower operating voltage of PhPLED can be realized. Our finding could greatly broaden the selection of host material for realizing highly efficiency green electrophosphorescent devices using conjugated polymer with relatively low triplet energy levels as the host.

Acknowledgements

The work was financially supported by Natural National Science Foundation (Project No. 50433030) and the Ministry of Science and Technology (Project No. 2002CB613405).

References

[1] M.A. Baldo, D.F. O'Brien, Y. You, A. Shoustikov, S. Sibley, M.E. Thompson, S.R. Forrest, Nature 395 (1998) 151. London.
[2] Y.G. Ma, H.Y. Zhang, J.C. Shen, C.M. Che, Synth. Met. 94 (1998) 245.
[3] M.A. Baldo, S. Lamansky, P.E. Burrows, M.E. Thompson, S.R. Forrest, Appl. Phys. Lett. 75 (1999) 4.
[4] C. Adachi, M.A. Baldo, M.E. Thompson, S.R. Forrest, J. Appl. Phys. 90 (2001) 5048.
[5] C. Adachi, R.C. Kwong, P. Djurovich, V. Adamovich, M.A. Baldo, M.E. Thompson, S.R. Forrest, Appl. Phys. Lett. 79 (2001) 2082.
[6] S. Tokito, T. Iijima, Y. Suzuri, H. Kita, T. Tsuzuki, F. Sato, Appl. Phys. Lett. 83 (2003) 569.
[7] S.J. Yeh, M.F. Wu, C.T. Chen, Y.H. Song, Y. Chi, M.H. Ho, S.F. Hsu, C.H. Chen, Adv. Mater. 17 (2005) 285.
[8] Y.R. Sun, N.C. Giebink, H. Kanno, B.W. Ma, M.E. Thompson, S.R. Forrest, Nature 440 (2006) 908.
[9] C.L. Lee, K.B. Lee, J.J. Kim, Appl. Phys. Lett. 77 (2000) 2280.
[10] M.-J. Yang, T. Tsutsui, Jpn. J. Appl. Phys. Part 2 39 (2000) L828.
[11] X. Gong, M.R. Robinson, J.C. Ostrowski, D. Moses, G.C. Bazan, A.J. Heeger, Adv. Mater. 14 (2002) 581.
[12] Y. Kawamura, S. Yanagida, S.R. Forrest, J. Appl. Phys. 92 (2002) 87.
[13] K.M. Vaeth, C.W. Tang, J. Appl. Phys. 92 (2002) 3447.
[14] X. Gong, J.C. Ostrowski, D. Moses, G.C. Bazan, A.J. Heeger, Adv. Funct. Mater. 13 (2003) 439.
[15] Y.-Y. Noh, C.-L. Lee, J.-J. Kim, K. Yase, J. Chem. Phys. 118 (2003) 2853.
[16] K.M. Vaeth, J. Dicillo, J. Polym. Sci. B 41 (2003) 2715.
[17] A. Nakamura, T. Tada, M. Mizukami, S. Yagyu, Appl. Phys. Lett. 84 (2004) 130.
[18] X.H. Yang, D. Neher, Appl. Phys. Lett. 84 (2004) 2476.
[19] X.H. Yang, D. Neher, D. Hertel, T.K. Daubler, Adv. Mater. 16 (2004) 161.
[20] H.-M. Liu, J. He, P.-F. Wang, H.-Z. Xie, X.-H. Zhang, C.-S. Lee, B.-Q. Sun, Y.-J. Xia, Appl. Phys. Lett. 87 (2005) 221103/1.
[21] J. Pina, J.S. de Melo, H.D. Burrows, A.P. Monkman, S. Navaratnam, Chem. Phys. Lett. 400 (2004) 441.
[22] F.-C. Chen, G. He, Y. Yang, Appl. Phys. Lett. 82 (2003) 1006.
[23] F.-C. Chen, S.-C. Chang, G. He, S. Pyo, Y. Yang, M. Kurotaki, J. Kido, J. Polym. Sci. B 41 (2003) 2681.
[24] M. Sudhakar, P.I. Djurovich, T.E. Hogen-Esch, M.E. Thompson, J. Am. Chem. Soc. 125 (2003) 7796.
[25] X. Gong, J.C. Ostrowski, G.C. Bazan, D. Moses, A.J. Heeger, M.S. Liu, A.K.Y. Jen, Adv. Mater. 15 (2003) 45.
[26] C. Jiang, W. Yang, J. Peng, S. Xiao, Y. Cao, Adv. Mater. 16 (2004) 537.
[27] L. Wang, B. Liang, F. Huang, J. Peng, Y. Cao, Appl. Phys. Lett. 89 (2006) 151115/1.
[28] T.-H. Kim, D.-H. Yoo, J.H. Park, O.O. Park, J.-W. Yu, J.K. Kim, Appl. Phys. Lett. 86 (2005) 171108.
[29] T.-H. Kim, H.K. Lee, O.O. Park, B.D. Chin, S.-H. Lee, J.K. Kim, Adv. Funct. Mater. 16 (2006) 611.
[30] K. Dedeian, P.I. Djurovich, F.O. Garces, G. Carlson, R.J. Watts, Inorg. Chem. 30 (1991) 1685.
[31] S. Xiao, M. Nguyen, X. Gong, Y. Cao, H. Wu, D. Moses, A.J. Heeger, Adv. Funct. Mater. 13 (2003) 25.
[32] W. Zhu, Y. Mo, M. Yuan, W. Yang, Y. Cao, Appl. Phys. Lett. 80 (2002) 2045.
[33] J. Chang, J. An, C. Im, Y.K. Kim, J. Korean Phys. Soc. 47 (2005) 1028.
[34] M.A. Baldo, S.R. Forrest, Phys. Rev. B 62 (2000) 10958.
[35] X. Gong, S.H. Lim, J.C. Ostrowski, D. Moses, C.J. Bardeen, G.C. Bazan, J. Appl. Phys. 95 (2004) 948.
[36] M. Cocchi, D. Virgili, G. Giro, V. Fattori, P. Di Marco, J. Kalinowski, Y. Shirota, Appl. Phys. Lett. 80 (2002) 2401.
[37] P.A. Lane, L.C. Palilis, D.F. O'Brien, C. Giebeler, A.J. Cadby, D.G. Lidzey, A.J. Campbell, W. Blau, D.D.C. Bradley, Phys. Rev. B 63 (2001) 235206.

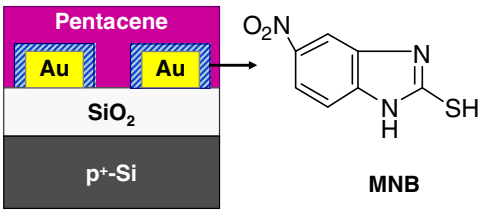

Fig. 1. The cross-sectional schematic of a pentacene BC-TFT with MNB-treated Au electrodes. The molecular structure of MNB is given in the right.

energy of the Au surface leads to poor morphology and crystalline quality of the pentacene layer, leading to the formation of a transition layer that degrades the device characteristics of pentacene BC-TFT devices [5,10]. This difficulty can be overcome through passivation of the Au layer, allowing the pentacene layer to be uniform throughout the device. Deposition of a self-assembled monolayer (SAM) onto the Au electrodes has been shown to modify the interface between the electrode and the active organic materials [3,8,13–15] and is a useful technique for improving the device characteristics. Especially, it has been reported that treating the Au electrode using 2-mercapto-5-nitro-benzimidazole (MNB) reduces contact resistance by 20–50% and significantly improve the field-effect mobility [16,17].

In this paper, we present a study of the effects of depositing a MNB–SAM onto the Au electrodes of a pentacene BC-TFTs. The structure of MNB allows the Au surface to be thiolated while leaving the active site at the opposite end of the MNB available for bonding to the pentacene (see Fig. 1). Our results show that when a pentacene thin film is deposited onto MNB-treated Au electrodes, the current–voltage (*I–V*) characteristics are significantly enhanced. We determine the structural basis for this modification of the device characteristics by examining the morphology and crystalline structure of pentacene in untreated and MNB-treated BC-TFTs using atomic force microscopy (AFM) and X-ray diffraction (XRD). In addition, the modifications of the unoccupied and occupied molecular orbitals that are associated with charge-transport in pentacene were examined using soft X-ray spectroscopy.

2. Experimental

A 100 nm-thick SiO_2 layer was synthesized on a heavily doped p^+-Si substrate using a dry oxidation process. Subsequently, the source and drain electrodes were deposited by thermally evaporating a 15 nm layer of Au at a pressure of 5×10^{-8} Torr using a shadow mask. The channel length (L) and width (W) for the electrodes were 50 μm and 1000 μm respectively. A 10 nm-thick MNB layer was evaporated onto the Au electrodes at a deposition rate of 0.01 nm/s. The MNB-deposited sample was washed in acetone in order to remove the excess MNB from the Au and SiO_2 surface. Through this process, only the MNB molecules that are bonded to the Au surface are left; the MNB is completely removed from the TFT channel and does not affect the pentacene/SiO_2 interface. The SiO_2 surface was inspected with an AFM to confirm that the MNB had been removed. The thermal evaporation of a 100 nm-thick pentacene active layer was then conducted at 165 °C at a base pressure of 5×10^{-9} Torr. The deposition rate and substrate temperature were maintained at 0.05 nm/s and room temperature, respectively. Fig. 1 shows the cross-sectional schematic of our pentacene BC-TFTs with MNB-treated Au electrodes. For comparison purposes pentacene BC-TFTs without any treatment were also prepared in the same manner.

The *I–V* characteristics of the BC-TFTs were measured using two Keithley 2400 source measurement units. The crystalline structure of the pentacene was confirmed by recording the θ–2θ XRD patterns with an incident X-ray wavelength of 1.5425 Å at beamline 10C1 of the Pohang Light Source at the Pohang Accelerator Laboratory. The C 1*s* X-ray absorption (XAS) and C $K\alpha$ X-ray emission (XES) spectra were obtained at beamline 8.0.1 of the Advanced Light Source at the Lawrence Berkeley National Laboratory. The spectra were normalized to the number of photons falling on the sample which was monitored by measuring the photocurrent produced in a highly transparent Au mesh located just upstream of the sample chamber. The charge transfer in our devices was studied by comparing MNB-treated and untreated Au layers that had been prepared for *in situ* ultraviolet photoelectron spectroscopy (UPS) measurements. Several thicknesses of pentacene (0.1, 0.2, 0.4, 0.8, 1.6, 3.2, 6.4, and 25.6 nm) were measured in regular order without breaking vacuum by depositing them in a sample preparation chamber attached to the analysis chamber. The UPS spectra were measured using He I sources with a hemispherical electron energy analyzer (PHI 5700 spectrometer) with −15 V of sample bias, and the analysis chamber and sample preparation chamber were maintained at 1×10^{-10} and 1×10^{-9} Torr, respectively.

3. Results and discussion

The *I-V* characteristics in Fig. 2 demonstrate the superior electronic characteristics of the BC-TFT device fabricated with MNB-treated Au electrodes, as compared to the untreated pentacene BC-TFT; the characteristics are summarized in Table 1. The maximum drain current (I_D) of the MNB-treated transistor, recorded with both drain (V_D) and gate (V_G) voltages at −40 V, is −16 μA – two orders of magnitude larger than that of the untreated transistor (see Fig. 2b). The influence of MNB-treatment on the carrier-transport characteristics can be determined from the $(-I_D)^{1/2}$ versus V_G plots ($V_D = -40$ V) in Fig. 2c and d. All plots are taken at $V_D = -40$ V. The $(-I_D)^{1/2}$ versus V_G relation is generally governed by [7]:

$$I_D = \frac{WC_i}{2L}\mu(V_G - V_{TH})^2, \quad (1)$$

where μ is the field-effect mobility, V_{TH} is the threshold voltage, and C_i is the capacitance of the SiO_2 gate insulator. The value of μ can be extracted from Eq. (1), and so we estimate the field-effect mobility of the MNB-treated pentacene BC-TFT to be 0.14 cm^2/Vs, an order of magnitude larger than the value determined for the untreated transistor (0.0064 cm^2/Vs). The subthreshold swings (*SS*) can also determined from the logarithmic $-I_D$ versus V_G plots by comparison with the model equation [7]:

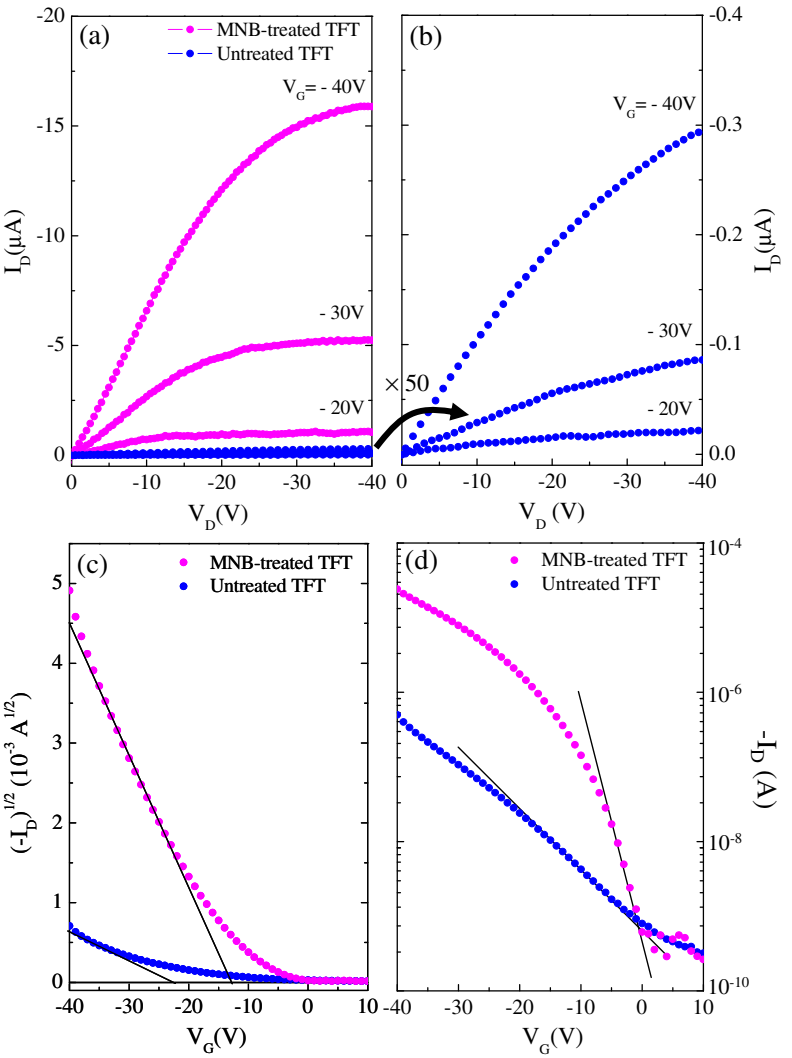

Fig. 2. (a) Plots of drain current (I_D) versus drain voltage (V_D) of untreated (pink circle) and MNB-treated pentacene BC-TFTs (blue circle) for various gate voltages (V_G) and (b) corresponding plots of untreated BC-TFTs at 50 times magnification. (c) Plots of the square root of $-I_D$ versus V_G and (d) logarithmic plots of $-I_D$ versus V_G of untreated and MNB-treated pentacene BC-TFTs.

Table 1
Summary of the device characteristics of untreated and MNB-treated pentacene BC-TFTs

Sample	μ (cm^2/Vs)	Maximum I_D (A)	On/off ratio	*SS* (V/decade)	V_{TH} (V)
Untreated BC-TFT	0.0064	-2.9×10^{-7}	2×10^3	−12.88	−21.5
MNB-treated BC-TFT	0.14	-1.6×10^{-5}	7×10^4	−3.17	−12.6

$$SS = \frac{dV_G}{d\log(-I_D)}. \quad (2)$$

Analyzing the curves in Fig. 2d, we can see that treatment of the electrodes with MNB reduces the *SS* from −12.88 V/decade in the untreated BC-TFT to −3.17 V/decade. The influence of the MNB–SAM treatment on the BC-TFT device characteristics is clear, and the following analysis will illuminate the structural and electronic effects that lead to these enhancements.

The carrier-transport characteristics of the organic active layer of these devices are related to the morphology and structure of the pentacene, specifically the crystallinity of the pentacene and the degree to which the layers on the Au electrodes match that on the SiO_2 gate dielectric [9,15–18]. Fig. 3 shows the AFM images of pentacene layers deposited on: (a) MNB-treated Au, (b) untreated Au, (c) SiO_2 on which MNB was deposited and subsequently dissolved from, and (d) clean SiO_2. The insets show the roughness profiles of each pentacene film. Importantly, there is no noticeable morphological difference between the pentacene films on the clean SiO_2 surface and the surface from which the MNB has been dissolved, confirming that the influence of the MNB treatment of the BC-TFT devices is confined to the Au electrodes. This is in accordance with

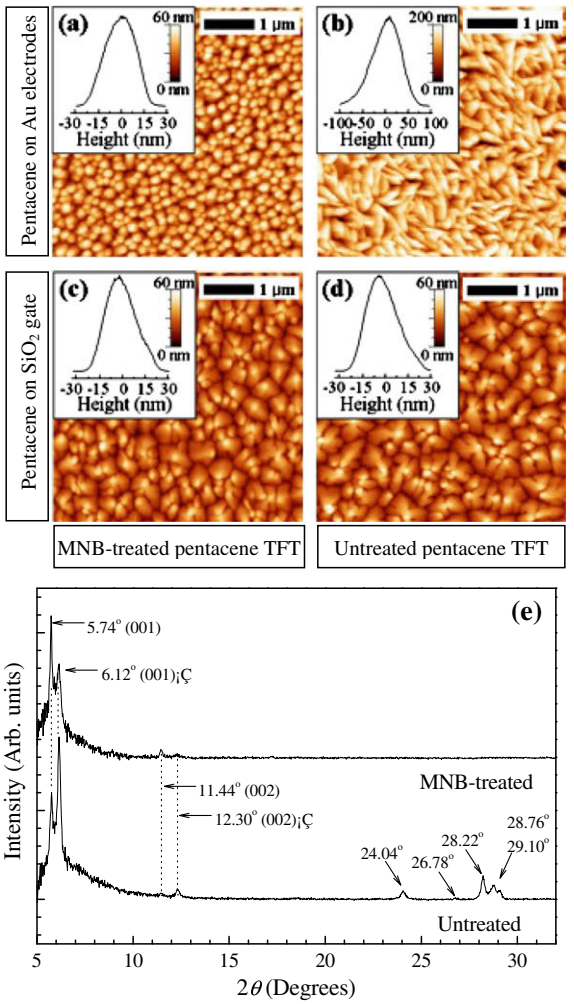

Fig. 3. AFM images of pentacene thin films on various substrates: (a) on MNB-treated Au, (b) on untreated Au, (c) on MNB dissolved SiO_2 after MNB deposition, and (d) on clean SiO_2. The insets represent the roughness profile of the pentacene surface. (e) XRD patterns of pentacene thin films on MNB-treated and untreated Au surfaces.

other reports suggesting that thiol compounds are selectively self-assembled onto the Au electrodes due to nondissociative adsorption of thiol (S-H) groups [19,20]. Depositing the MNB–SAM on the Au surface prior to the pentacene deposition causes the resultant film of round-shaped grains to have roughness similar to that of the film on the SiO_2 surfaces. The size and shape of the grains are quite similar to the films grown on OTS-treated SiO_2 substrates with highly-packed grain boundaries in a previous report [21]. The absence of the MNB–SAM has a pronounced effect on the morphology of the pentacene film deposited on the Au substrate, which has a rough surface characterized by rod-shaped grains. The effect of the MNB–SAM treatment on the morphology of the pentacene layer correlates with the variations in electronic characteristics described above, adding more evidence that the charge injection into the pentacene layer is improved as a result of structural modifications induced by the treatment of the Au electrodes.

The crystal phases of the pentacene films deposited on Au surfaces, both treated and untreated, is reflected in the XRD patterns shown in Fig. 3e. Both pentacene films are a mixture of the thin-film and the single-crystal phases described by Dimitrakopoulos et al. [9]. The structure of pentacene single crystals adopt the triclinic ($P1$ group) with the (0 0 1) plane spacing (d_{001}) of 14.5 Å, while the d_{001} of pentacene thin-films equals 15.4 Å. Although it has recently been shown that the thin-film phase is not entirely independent of the substrate identity [18], the values obtained here are very close to what has been reported for pentacene on other surfaces. The diffraction peak at 5.74° (and 11.44° for the second-order diffraction) corresponds to a d_{001} spacing equal to 15.4 Å, showing evidence for the thin-film phase, while the peak at 6.12° (12.3°) corresponds to d_{001} = 14.5 Å from the single-crystal phase. It is clear that the thin-film phase is dominant in the pentacene film grown on MNB-treated Au, as in the pentacene thin film on SiO_2 surface. In addition to the alignment of the pentacene molecules along the long axes of 14.5 Å and 15.4 Å, the pentacene films grown on the bare Au surface exhibit several more diffraction peaks at 24.04°, 26.78°, 28.22°, 28.76°, and 29.10°, corresponding to a much lower plane-spacing of about 3 Å. The peaks with high Bragg angles come from the first monolayer of pentacene molecules on bare Au surface lying almost parallel to the Au surface; these peaks do not appear in the XRD patterns measured from the pentacene on the MNB-treated Au surface or on the SiO_2 surface [10,11]. The dominant presence of the thin film phase and the absence of the flat-lying phase are characteristic of the pentacene film deposited on the treated Au surface, demonstrating the relationship between the quality of the crystalline structure and the improved device characteristics that are brought about by the MNB–SAM electrode treatment.

Taking the above morphological and structural results into account, it is quite clear that changes in electrode surface energy occur in the pentacene BC-TFTs owing to the MNB treatment, and that this change enhances the packing of pentacene grains, making them similar to what is observed on SiO_2. A more highly-packed pentacene grains at the Au electrodes' surfaces leads to the reduction of grain boundary scattering, resulting in better charge-transport characteristics and a smooth pentacene surface contribute to the enhancement of injection efficiency. Since the injection and transport of charge carriers in TFT devices are strongly related to the delocalized molecular orbital states of the organic layer, we expect to see evidence of a correlation between the device properties and the molecular orbital states of pentacene films deposited on treated and untreated Au surfaces.

The partial density of the unoccupied carbon 2p molecular orbital states of pentacene is probed by the C 1s XAS spectra shown in Fig. 4a. The π^* states are represented by the sharp resonant absorption features in the region 283–287 eV; the broad features in the region above 288 eV are σ^* resonances. The location of the lowest unoccupied molecular orbital (LUMO) is marked by a vertical line at 284.1 eV. As is expected from the previous structural and functional characterization, the C 1s XAS spectrum of the pentacene thin film on MNB-treated Au

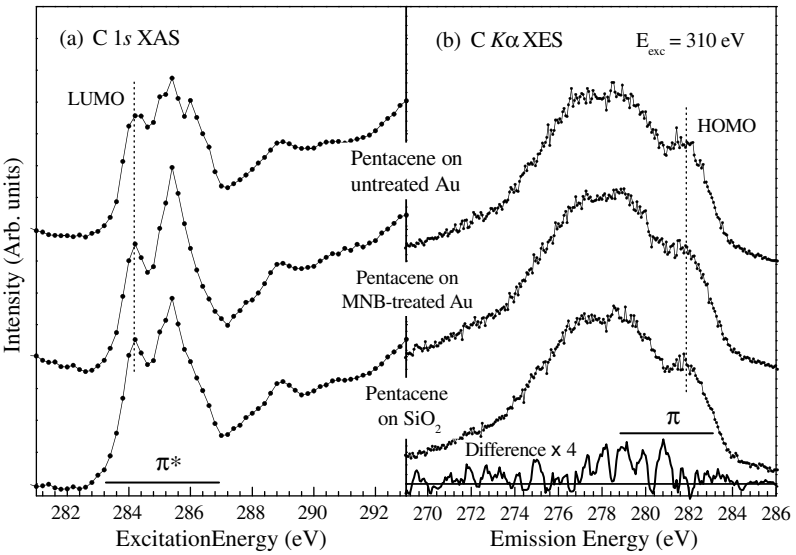

Fig. 4. (a) C 1*s* XAS spectra of pentacene thin films on MNB-treated Au, untreated Au, and SiO_2 substrates and (b) C *K*α non-resonant XES spectra of corresponding samples excited at 310 eV.

resembles that of well-ordered pentacene films on SiO_2 substrates. Since the incident angle of linearly polarized X-rays was set to 30° with respect to the sample's normal direction, the XAS measurements mostly probe the *p*-characteristics of the molecule parallel to the sample surface. Therefore, two intense features at 284.2 and 285.4 eV suggest that unoccupied π^* orbitals are aligned nearly parallel to the plane of the sample's surface. This agrees well with results for pentacene films grown on SAM-modified Au surfaces reported by Hu et al. [11]. For pentacene films grown on untreated Au, the spectrum exhibits some additional features at 285 and 286 eV. These sub-features most likely stem from a different packing arrangement of the pentacene molecules. As seen in Fig. 3, a pentacene film deposited on Au contains randomly-oriented grains possessing rod-like shapes. By examining the spectral features is therefore able to determine the various pentacene alignments present in the samples.

The C *K*α XES spectra in Fig. 4b describe the partial density of the occupied molecular orbitals. The excitation energy (E_{exc}) was set to 310 eV, well above the absorption threshold, in order to ensure that the X-ray absorption and emission processes are entirely decoupled and the resulting fluorescence spectra is free from resonant scattering effects. The emission from transitions originating from the highest occupied molecular orbital (HOMO) occurs at 281.8 eV, marked with a vertical line. One can see that there is a discernable increase in π orbital states around 279–281 eV when pentacene is deposited on MNB-treated Au. This π-state enhancement is highlighted in the bottom spectrum which is obtained by subtracting the spectrum of pentacene film on untreated Au from that on the MNB-treated Au. Before the subtraction, all spectra were normalized to the number of photons falling on the sample monitored by the photocurrent of a highly transparent gold mesh. The delocalization boundary of π molecular states is enlarged as their binding energy increases [12]. Therefore the enhancement of π orbital states at lower emission energy (higher binding energy) represents a large intermolecular overlapping of π orbitals. These spectroscopic results provide excellent evidence in explaining the superior electronic characteristics found for MNB-treated pentacene BC-TFTs in comparison to those of untreated BC-TFTs.

For further evaluation of the electronic structure at the interface of the pentacene and the treated or untreated Au surfaces, UPS measurements were performed. Although it is a surface-sensitive technique, the UPS spectra of various thicknesses of pentacene (Fig. 5) demonstrate a clear effect of the MNB–SAM treatment on the electronic structure of the organic active layer. A double-stepped high binding energy cutoff (E_{cutoff}) is observed in the UPS spectra of pentacene on MNB-treated Au. This phenomenon is a spectral signature caused by MNB molecules bonded to Au molecules and also to exposed, unbounded Au, both of which are detectable because complete surface coverage cannot be obtained. There is a clear shift in E_{cutoff} as a function of pentacene thickness on both MNB-treated and untreated Au. The direction of shifts are opposite, however; on MNB-treated Au the pentacene E_{cutoff} shifts towards lower binding energy with increasing thickness, while the opposite shift occurs for pentacene on untreated Au. The E_{cutoff} shifts at maximum pentacene coverage (25.6 nm) are −0.59 eV and 1.07 eV on MNB-treated and untreated Au, respectively. These results indicate that the vacuum level of pure pentacene is higher than that of MNB-treated Au but lower than that of untreated Au, and so a dipole is formed at each interface. The dipole has an opposite direction in the two cases, however, which has a direct effect on the device characteristics. The reversal of the interfacial dipole as a result of the MNB–SAM treatment of the Au comes about as a result of the change in Au surface energy, and provides a direct indication of the treatment's effect on the electronic characteristics of the device [22].

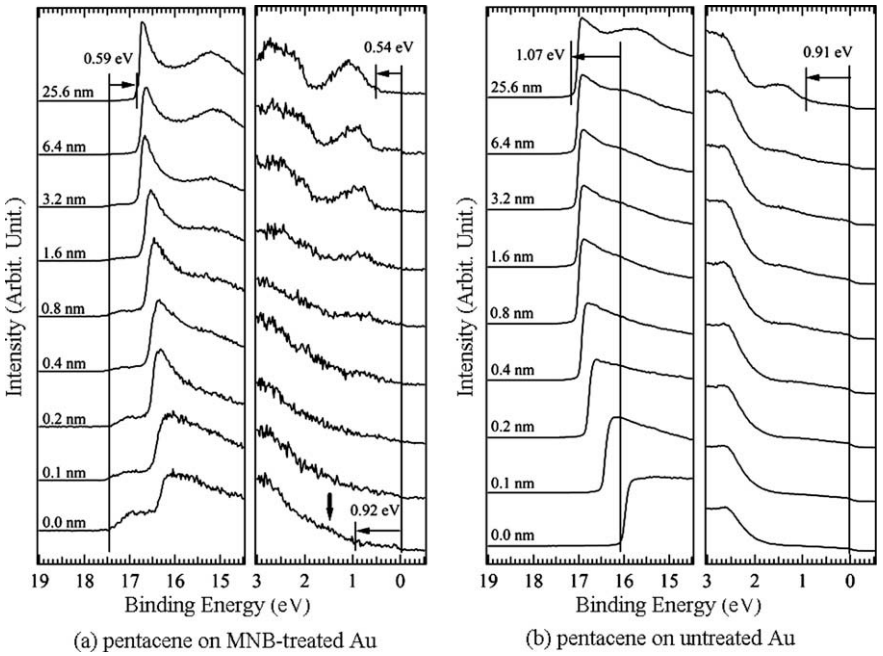

Fig. 5. UPS spectra of a series of thicknesses of pentacene (0.1, 0.2, 0.4, 0.8, 1.6, 3.2, 6.4, and 25.6 nm) (a) on MNB-treated Au and (b) on untreated Au.

The HOMO region (0–3 eV) is displayed in Fig. 5 on a binding energy scale relative Fermi energy level (E_F). Once the pentacene thickness has reached 3.2 eV there is a clear signal from the HOMO level. The gaps between E_F and the HOMO onset of pentacene can thus be determined to be 0.54 eV and 0.91 eV on MNB-treated Au and on untreated Au, respectively. The reduction in the gap as a result of the MNB–SAM deposition reflects the lowering of the height of the injection hole injection barrier, coinciding with the reduced *SS* of the BC-TFT that was fabricated with MNB-treated Au electrodes. In addition, the HOMO level of MNB can be observed in the spectra of MNB-treated Au without pentacene deposition (0.0 nm pentacene thickness); it is found at 0.92 eV relative to E_F and is indicated with an arrow at Fig. 5a. The agreement between the MNB and pentacene HOMO levels ensures that there is

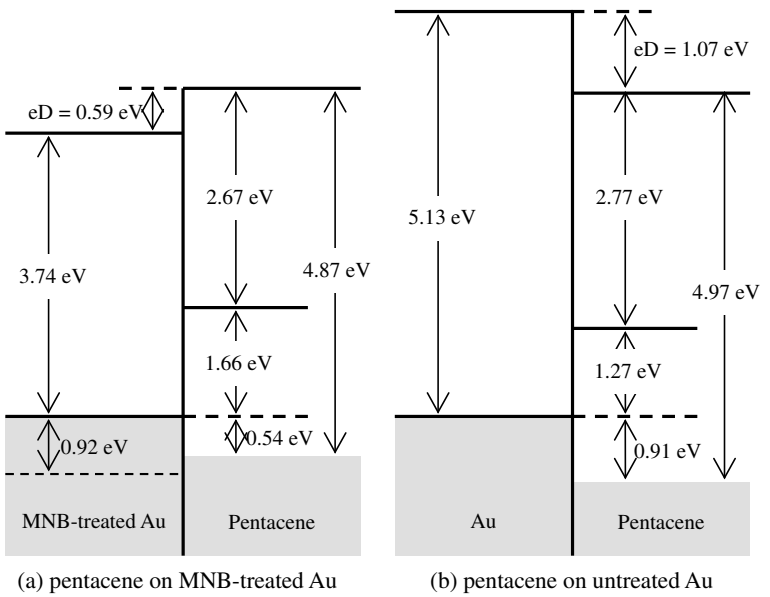

Fig. 6. Band diagrams of pentacene (a) on MNB-treated Au and (b) on untreated Au.

an efficient coupling between the two, and that no hole injection barrier exists at the pentacene/MNB interface [23].

The information provided by the UPS spectra can be summarized and interpreted in terms of the energy diagram for pentacene/MNB/Au that is shown in Fig. 6. The energy of the LUMO of pentacene was determined in relation to the HOMO level by adding the value of a previously-reported HOMO–LUMO gap (2.2 eV) [24]. The ionization potential (I_P) of pentacene is determined from the UPS spectra by using the following equation:

$$I_P = h\nu - E_{cutoff} + E_{HOMO}, \quad (3)$$

where $h\nu$ indicates the incident photon energy of 21.2 eV, and E_{HOMO} is the onset energy of the HOMO level. According to the equation, the I_P of pentacene on MNB-treated Au and on untreated Au are 4.87 eV and 4.97 eV, respectively. The slight decrease in the I_P of pentacene on MNB-treated Au is attributed to the increasing delocalization of π molecular states.

4. Conclusions

We have investigated the influence of a MNB treatment on the electronic characteristics of pentacene thin film transistors fabricated with a bottom-contact structure. The *I-V* characteristics of the BC-TFT devices are greatly improved by the treatment of the Au electrodes with an MNB–SAM prior to the deposition of the pentacene active layer. The morphological and spectroscopic investigations reveal a strong correlation between the enhanced electronic characteristics and the structural and morphological changes brought about by the MNB–SAM treatment. The treatment causes the pentacene layer on the Au electrode to closely resemble that of the layer deposited on the SiO_2 gate dielectric, eliminating any transition regions and accompanying barriers. The close-packed grains and enhanced molecular order of the pentacene film gives rise to the improvement of carrier-transport characteristics, leading to more efficient device performance. The presence of the MNB layer also reduces the injection barrier at the interface between the electrode and the pentacene, which improves the device performance as well.

Acknowledgements

This work was supported by the Brain Korea 21 (BK21) project of the Korea Research Foundation (KRF), and the Korea Science and Engineering Foundation (KOSEF) through the National Core Research Center for Nanomedical Technology. We gratefully acknowledge the Natural Sciences and Engineering Research Council of Canada and the Canada Research Chair program.

References

[1] H.E.A. Huitema, G.H. Gelinck, J.B.P.H. van der Putten, K.E. Kuijk, K.M. Hart, E. Cantatore, D.M. de Leeuw, Adv. Mater. 14 (2002) 1201.
[2] C.D. Sheraw, L. Zhou, J.R. Huang, D.J. Gundlach, T.N. Jackson, M.G. Kane, I.G. Hill, M.S. Hammond, J. Campi, B.K. Greening, J. Francl, J. West, Appl. Phys. Lett. 80 (2002) 1088.
[3] K. Nomoto, N. Hirai, N. Yoneya, N. Kawashima, M. Noda, M. Wada, J. Kasahara, IEEE Trans. Elect. Dev. 52 (2005) 1519.
[4] R. Wisnieff, Nature 394 (1998) 225.
[5] P.F. Baude, D.A. Ender, M.A. Haase, T.W. Kelley, D.V. Muyres, S.D. Theiss, Appl. Phys. Lett. 82 (2003) 3964.
[6] J.M. Shaw, P.F. Seidler, IBM J. Res & Dev. 45 (2001) 3.
[7] D.A. Neamen, Semiconductor Physics and Devices, Second ed., Irwin, Chicago, 1997.
[8] X. Liu, Z. Luo, S. Han, T. Tang, D. Zhang, C. Zhou, Appl. Phys. Lett. 86 (2005) 243501.
[9] C.D. Dimitrakopoulos, A.R. Brown, A. Pomp, J. Appl. Phys. 80 (1996) 2501.
[10] D. Käfer, L. Ruppel, G. Witte, Phys. Rev. B 75 (2007) 085309.
[11] W.S. Hu, Y.T. Tao, Y.J. Hsu, D.H. Wei, Y.S. Wu, Langmuir 21 (2005) 2260.
[12] S.J. Kang, Y. Yi, C.Y. Kim, K.-H. Yoo, A. Moewes, M.H. Cho, J.D. Denlinger, C.N. Whang, G.S. Chang, Phys. Rev. B 72 (2005) 205328.
[13] J.H. Kang, D. da Silva Filho, J.-L. Bredas, X. –Y. Zhu, Appl. Phys. Lett. 86 (2005) 152115.
[14] I. Kymissis, C.D. Dimitrakopoulos, S. Purushothaman, IEEE Trans. Elect. Dev. 48 (2001) 1060.
[15] K. Ihm, B. Kim, T.-H. Kang, K.-J. Kim, M.H. Joo, T.H. Kim, S.S. Yoon, S. Chung, Appl. Phys. Lett. 89 (2006) 033504.
[16] A. Benor, D. Knipp, Org. Electron. 9 (2008) 209.
[17] S.H. Kim, J.H. Lee, S.C. Lim, Y.S. Yang, T. Zyung, Jpn. J. Appl. Phys. 43 (2004) L60.
[18] S. Schiefer, M. Huth, A. Dobrinevski, B. Nickel, J. Am. Chem. Soc. 129 (2007) 10316.
[19] C.-K. Song, B.-W. Koo, S.-B. Lee, D.-H. Kim, Jpn. J. Appl. Phys. 41 (2002) 2730.
[20] J. Zhou, F. Hagelberg, Phys. Rev. Lett. 97 (2006) 045505.
[21] M. Shtein, J. Mapel, J.B. Benziger, S.R. Forrest, Appl. Phys. Lett. 81 (2002) 268.
[22] K.P. Pernstich, S. Haas, D. Oberhoff, C. Goldmann, D.J. Gundlach, B. Batlogg, J. Appl. Phys. 96 (2004) 6431.
[23] B.S. Kim, J.M. Beebe, Y. Jun, X.–Y. Zhu, C.D. Frisbie, J. Am. Chem. Soc. 128 (2006) 4970.
[24] N.J. Watkins, Y. Gao, J. Appl. Phys. 94 (2003) 1289.

bipolarons [11]. Several models for MR in OSCs have been proposed [7–10]. Theoretical studies on spin-dependent injection and transport in OSCs from spin diffusion theory have just begun [12–15], and a comprehensive understanding is still lacking.

Carriers in OSCs were usually supposed to have spin 1/2 from the spin diffusion theory just like that in inorganic semiconductors [12–14]. However, there are instinct differences for carriers in OSCs from that in inorganic ones. Carriers are extended electrons or holes with 1/2 spin in inorganic semiconductors. OSC has the character of low dimension. Due to strong electron-lattice interactions, injected electrons can induce the distortion of the lattice and result in some charged self-trapped states called polaron or bipolaron excitations. These excitations have been obtained theoretically from the Su-Schrieffer-Heeger-like Hamiltonian [11,16–18]. Experimental evidence for polarons and bipolarons has also been given through ESR (electron-spin-resonance) studies [19,20]. These excitations have different electron-spin relations and act as carriers in OSCs. Due to the effect of temperature, pressure and external electric field, polarons and bipolarons in OSCs are not stable but can transform each other. Two spin polarons can annihilate into one spinless bipolaron, while one spinless bipolaron can be dissociated into two spin polarons. Therefore, the coexistence of spin and spinless carriers is the main characteristic of organic semiconductors and is the main difference of an organic spin device from a normal inorganic one. In this paper, we do not study the formation mechanism of polarons and bipolarons and just suppose that they coexist in OSCs with a given polaron proportion γ defined as $\gamma = n_p/(n_p + n_{bp})$. Based on the spin diffusion theory, we have developed our previous simple ferromagnetic/organic model and built the structure of ferromagnetic/OSC/ferromagnetic (FM/OSC/FM) to study the spin-polarized injection and transport. Charge current polarization (CCP) and the MR ratio are obtained with two symmetric FM layers. The article is organized as follows: Section 2 provides a description of the model and the derivation of the relevant formulae. Numerical results are presented and discussed in Section 3. A conclusion is given in Section 4.

2. Model

The system we consider here is a simple one-dimensional spin injection sandwich device, which comprises of two semi-infinite FM layers ($x < 0$ and $x \geqslant x_0$) and one layer of the OSC with the length x_0. The two FM layers are in parallel or antiparallel magnetization alignment. Spin-polarized electrons in the left FM layer are injected into the OSC layer and they will transform into spin polarons and spinless bipolarons. Therefore in the OSC layer there would be three carrier transport channels, i.e., a spin-up polaron, spin-down polaron and spinless bipolaron channel, respectively. When they are ejected out and go into the right FM layer, these carriers (spin polarons and spinless bipolarons) would completely converted into spin-polarized electrons. The whole transport picture is shown schematically in Fig. 1.

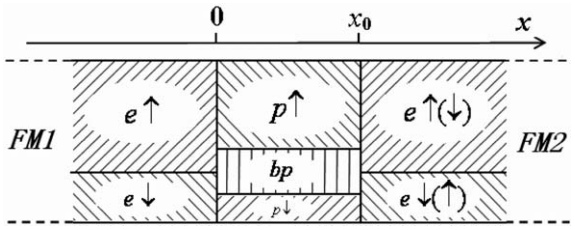

Fig. 1. A schematic diagram of the "FM/OSC/FM" device.

Our analysis is based on the spin diffusion theory for spin-polarized electrons in the FM and spin polarons in the OSC layer. Here we write the diffusion equation for the electrochemical potential μ_s ($s = \uparrow,\downarrow$) in three layers as [12–15],

$$\frac{\partial^2(\mu_\uparrow - \mu_\downarrow)}{\partial x^2} = \frac{\mu_\uparrow - \mu_\downarrow}{\lambda^2} \tag{1}$$

where λ is the spin diffusion length in FM and OSC layer. The difference of the electrochemical potential $(\mu_\uparrow - \mu_\downarrow)$ decays exponentially inside the FM layer and approaches zero at $x = \pm\infty$, i.e. $\mu_\uparrow(\pm\infty) = \mu_\downarrow(\pm\infty)$.

For spin-polarized electrons in the FM layer and spin polarons in the OSC layer, we write the solutions as follows:

$$\begin{aligned}
&\mu_{FM1\uparrow} - \mu_{FM1\downarrow} = Ae^{x/\lambda_{FM}}, \quad x < 0,\\
&\mu_{p\uparrow} - \mu_{p\downarrow} = B_1 e^{-x/\lambda_p} + B_2 e^{(x-x_0)/\lambda_p}, \quad 0 \leqslant x < x_0,\\
&\mu_{FM2\uparrow} - \mu_{FM2\downarrow} = De^{-(x-x_0)/\lambda_{FM}}, \quad x \geqslant x_0,
\end{aligned} \tag{2}$$

where λ_{FM} and λ_p are the corresponding spin diffusion lengths in the two FM layers and the OSC layer, respectively. Coefficients A, B_1, B_2, and D are determined by the continuity of the electrochemical potential at the interfaces.

The space charge distribution in the OSC layer is neglected as the device is usually operated at low voltages. We assume that there is no strong spin-flip scattering as electrons traverse the interfacial layer [12,21–23]. From Ohm's law, the current densities can be written as:

$$j_s = -\sigma_s \frac{\partial(\mu_s/e)}{\partial x}, \quad j_{bp} = -\sigma_{bp} \frac{\partial(\mu_{bp}/(2e))}{\partial x}, \tag{3}$$

where σ_s is the conductivity of spin-polarized carriers and σ_{bp} that of bipolarons. The current in the FM layer is $j = j_{FM\uparrow} + j_{FM\downarrow}$, while in the OSC layer $j = j_{p\uparrow} + j_{p\downarrow} + j_{bp}$. Here j_{bp} is the current contributed from the spinless bipolarons in OSCs.

A conductivity is proportional to the density of the carriers. If the effect of the boundary magnetic field of the contact is neglected, we have approximately, $\sigma_{p\uparrow} = \sigma_{p\downarrow} = \gamma \cdot \sigma/2$, $\sigma_{bp} = (1-\gamma)\sigma$ where $\sigma_{p\uparrow}(\sigma_{p\downarrow})$ is the conductivity for polarons with spin $\uparrow(\downarrow)$. Defining the spin polarization in the FM bulk as $\beta_0 = (\sigma_{FM\uparrow} - \sigma_{FM\downarrow})/(\sigma_{FM\uparrow} + \sigma_{FM\downarrow})$. Conductivity for spin-up and spin-down carriers in the FM layer can be written as, $\sigma_{FM\uparrow} = (1 + \beta_0)\sigma_{FM}/2$, $\sigma_{FM\downarrow} = (1 - \beta_0)\sigma_{FM}/2$ where $\sigma_{FM} = \sigma_{FM\uparrow} + \sigma_{FM\downarrow}$ is the total conductivity of the FM layer.

At the interfaces of the FM/OSC or OSC/FM, the total current is written as

$$j = -\sum_{s}(\Delta\mu_s/e)/R_s - (\mu_{bp}/(2e))/R_{bp}, \tag{4}$$

where R_s and R_{bp} are the interfacial resistance for spin and spinless carriers, respectively.

The CCP is defined as $\alpha(x) = (j_{p\uparrow} - j_{p\downarrow})/(j_{p\uparrow} + j_{p\downarrow} + j_{bp})$ in the OSC layer and $\alpha(x) = (j_\uparrow - j_\downarrow)/(j_\uparrow + j_\downarrow)$ in the FM layer. CCP at the two interfaces are symmetric because of the two symmetric FM layers used here. From Eqs. (2) and (3) and the boundary condition Eq. (4), we can obtain the expression of CCP α_0 at the interfaces,

$$\alpha_0 = \frac{4\beta_0 \cdot \frac{\lambda_{FM}}{\sigma_{FM}} + (1-\beta_0^2)\cdot(R_\downarrow - R_\uparrow)}{\frac{4}{\gamma}\cdot\frac{\lambda_p}{\sigma}\cdot\frac{1\mp e^{-x_0/\lambda_p}}{1\pm e^{-x_0/\lambda_p}}\cdot(1-\beta_0^2) + 4\frac{\lambda_{FM}}{\sigma_{FM}} + (R_\downarrow + R_\uparrow)\cdot(1-\beta_0^2)}, \tag{5}$$

where "∓"and "±" are corresponding for parallel and antiparallel magnetization alignment of the two FM layers. From the interfacial CCP, we can give the expression of the coefficients A, B_1, B_2, and D. Finally the position dependence of the CCP for the FM/OSC/FM device can be derived as

$$\begin{cases} \alpha(x) = \beta_0 + [\alpha_0 - \beta_0]\cdot e^{x/\lambda_{FM}}, & x < 0, \\ \alpha(x) = \frac{\alpha_0}{1\pm e^{-x_0/\lambda_p}}\cdot(e^{-x/\lambda_p} + e^{(x-x_0)/\lambda_p}), & \\ \quad 0 \leqslant x < x_0, & \\ \alpha(x) = \pm\beta_0 \pm [\alpha_0 - \beta_0]\cdot e^{-(x-x_0)/\lambda_{FM}}, & \\ \quad x \geqslant x_0. & \end{cases} \tag{6}$$

To get the MR ratio, we have to calculate the individual electrochemical potential across the device. It is done by substituting $\alpha(x)$ of Eq. (6) into j_s of Eq. (3) and then integrating over the three regions to obtain,

$$\begin{cases} \mu_{FM1\uparrow}(x) = -\frac{ejx}{\sigma_{FM}} - \frac{ej\lambda_{FM}}{\sigma_{FM}}\frac{\alpha_0-\beta_0}{1+\beta_0}(e^{x/\lambda_{FM}} - 1), & x < 0, \\ \mu_{p\uparrow}(x) = -\frac{ejx}{\sigma} - \frac{ej\lambda_p\alpha_0}{\gamma\sigma}\frac{[-(e^{-x/\lambda_p}-1)\pm e^{-x_0/\lambda_p}(e^{x/\lambda_p}-1)]}{1+e^{-x_0/\lambda_p}} + \Delta\mu_\uparrow(0), & \\ \quad 0 \leqslant x < x_0, & \\ \mu_{FM2\uparrow}(x) = -\frac{ej(x-x_0)}{\sigma_{FM}} \pm \frac{ej\lambda_{FM}}{\sigma_{FM}}\frac{\alpha_0-\beta_0}{1\pm\beta_0}(e^{-(x-x_0)/\lambda_{FM}} - 1) & \\ \quad + \mu_{p\uparrow}(x_0) + \Delta\mu_\uparrow(x_0), \quad x \geqslant x_0. & \end{cases} \tag{7}$$

Here $\Delta\mu_\uparrow(0)$ and $\Delta\mu_\uparrow(x_0)$ are the electrochemical potential discontinuities at the interfaces, as stated in Eq. (4). The corresponding electrochemical potentials for the spin-down carriers (electrons in FM layer and polarons in OSC layer) can be obtained in a similar way.

We now consider the MR ratio of the FM/OSC/FM device. The MR ratio is given by,

$$MR = \frac{\Delta R}{R_{anti}} = \frac{R_{anti} - R_{par}}{R_{anti}}, \tag{8}$$

where R_{anti} and R_{par} are resistances of the FM/OSC/FM device for antiparallel and parallel magnetization alignment of the two FM layers. The resistance is expressed as

$$R_{anti(par)} = \frac{\mu_{0_{anti(par)}}(-\lambda_{FM}) - \mu_{0_{anti(par)}}(x_0 + \lambda_{FM})}{e\cdot j}. \tag{9}$$

Here μ_0 is the spin-independent component of the electrochemical potential, which is related to the measured voltage drop across the device. To obtain μ_0, we consider the expression for either $\mu_\uparrow(x)$ (Eq. (7)) or $\mu_\downarrow(x)$ and extract the linear (ohmic) part [24].

3. Results and discussion

3.1. Charge current polarization

As the conductivity of an OSC is usually much smaller than that of a FM metal, we set $\sigma_{FM} = 1\ (\Omega\,cm)^{-1}$ and $\sigma = 10^{-2}\ (\Omega\,cm)^{-1}$. The spin-diffusion length is set to be $\lambda_{FM} = 100$ nm and $\lambda_P = 200$ nm in the FM and OSC layer, respectively. The thickness of the OSC layer is set to be $x_0 = 100$ nm and the spin polarization in the FM bulk $\beta_0 = 0.9$. The position dependence of the CCP for a parallel magnetization alignment of the two FM layers is calculated and the results are shown in Fig. 2. The spin-dependence of the interfacial resistance is such that $R_\uparrow$ for spin-up carriers is set at $0.1 \times R_\downarrow$ for spin-down carriers (at both FM/OSC interfaces). It is found that the CCP $\alpha_p(x)$ decreases exponentially from the FM layer into the OSC layer. The existence of an spin-dependent interfacial resistance may improve the CCP. For example, the value of interfacial CCP α_{p0} increases to 0.2 with an interfacial resistance $R_\downarrow = 10^{-3}\ \Omega\,cm^2$ from 0.04 without any interfacial resistances. The interfacial CCP would give the whole information in FM/OSC/FM device.

Next, we perform the calculations for the antiparallel magnetization alignment of the two FM layers. All corresponding parameters are keeping the same as that used in the parallel configuration case of Fig. 2. The position dependence of the CCP $\alpha_{ap}(x)$ plotted in Fig. 3 reflects the antisymmetry of the FM magnetization. For the case of the zero interfacial resistance, there is zero-CCP across the entire OSC layer. In the presence of spin-dependent interfacial resistance, the results are similar to the parallel case. There are, however, two main differences: (a) in the parallel case CCP keeps nearly unchanged in the OSC layer, while in the antiparallel case it decreases rapidly and reaches zero at $x = x_0/2$, (b) the CCP is not sensitive to interfacial resistance in the antiparallel case, where a high value of CCP is obtained at $R_\downarrow = 10^{-1}\ \Omega\,cm^2$.

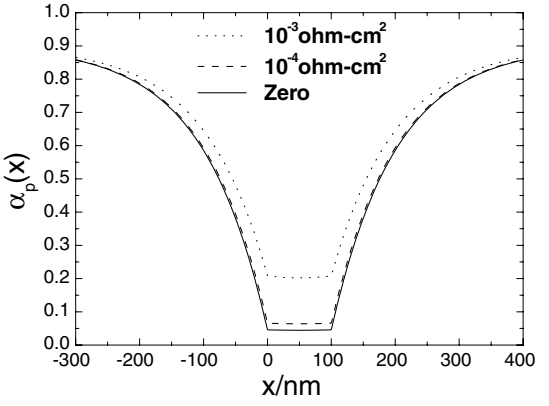

Fig. 2. Position dependence of CCP for various values of spin-down $R_\downarrow$ with parallel magnetization alignment of the two FM layers. $R_\uparrow$ is set at $0.1\ R_\downarrow$, and the polaron proportion is $\gamma = 0.5$.

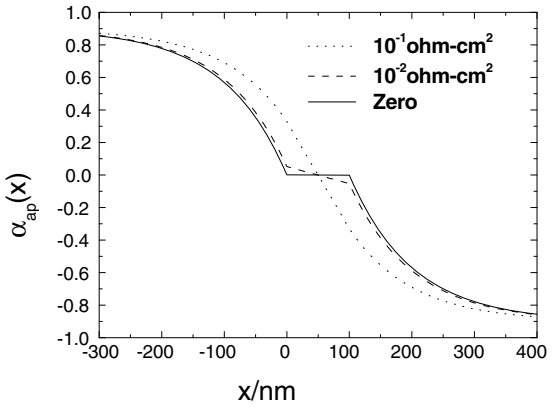

Fig. 3. Position dependence of CCP for various values of spin-down $R_\downarrow$ with antiparallel magnetization alignment of the two FM layers. $R_\uparrow$ is set at 0.1 $R_\downarrow$, and the polaron proportion is $\gamma = 0.5$.

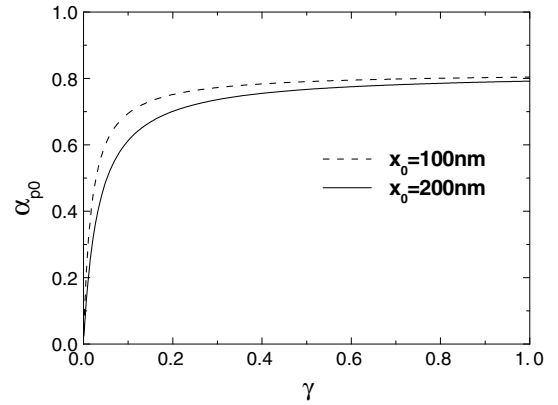

Fig. 4. Dependence of interfacial CCP α_{p0} on the polaron proportion γ with $R_\downarrow = 10 \times R_\uparrow = 10^{-1}\ \Omega\,\mathrm{cm}^2$, Other parameters are the same as those in Fig. 2.

Dependence of the interfacial CCP for parallel magnetization alignment α_{p0} on the polaron proportion γ is calculated, as shown in Fig. 4, with $R_\downarrow = 10 \times R_\uparrow = 10^{-1}\ \Omega\,\mathrm{cm}^2$. Apparently, CCP is zero at $\gamma = 0$ because carriers in the OSC are spinless bipolarons. The maximum CCP is obtained at $\gamma = 1$ which means that a maximum CCP in an organic spin device will be reached if all the carriers are spin polarons. In addition, it is also found that a significant CCP would appear as soon as there exist polarons. For example, even if polarons only comprise 20% of all carriers, the spin polarization will be over 90% of the value attainable with all spin polarons. Therefore, the spinless bipolarons has no apparent effect on the CCP in an organic spin device. The spin polarons are effective carriers of a spin-polarized current, even if they constitute only a fraction of all carriers. As stated above, the polaron proportion γ in OSCs depends upon the concrete material as well as the external circumstance such as temperature and external electric field. Polarons and bipolarons can transfer each other under certain conditions. For example, a bipolaron can be dissociated into two spin polarons through photo exciting. Maybe the present prediction could be experimentally confirmed by photo-irradiating the device. This may initiate a variety of exciting new applications in organic spintronics.

CCP is dependent upon the thickness of the OSC, as shown in Fig. 5. From the figure, it is found that there will be a high value of CCP when the thickness of the OSC is small. For example, α_{p0} is about 0.8 when the thickness of OSC $x_0 < 10$ nm for interfacial resistance $R_\downarrow = 10 \times R_\uparrow = 10^{-3}\ \Omega\,\mathrm{cm}^2$. It is obviously that the CCP α_{p0} decreases with the increasing of the OSC thickness x_0. CCP decreases rapidly when the thickness of the OSC in the range of $0 < x_0 < 200$ nm. It will go to nearly zero when x_0 is much longer than the spin diffusion length in OSCs. The interfacial CCP will be enhanced by several orders when the spin-dependent interfacial resistance is included in the model.

3.2. Magnetoresistance

Fig. 6 plots the MR ratio as a function of the polaron proportion γ with the OSC layer thickness $x_0 = 100$ nm. From the figure, one finds that MR is small when $\gamma \to 0$ be-

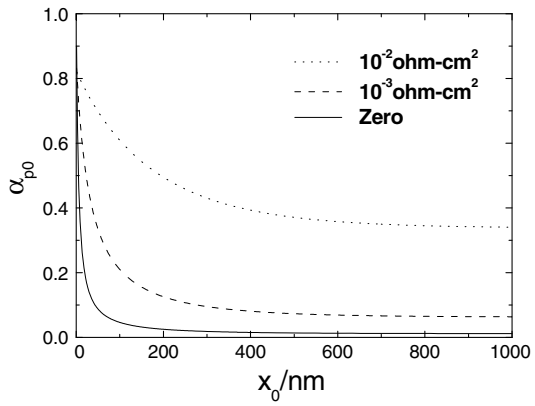

Fig. 5. Dependence of interfacial CCP α_{p0} on the organic thickness x_0 for various values of spin-down $R_\downarrow$. $R_\uparrow$ is set at 0.1 $R_\downarrow$, and the polaron proportion is $\gamma = 0.5$.

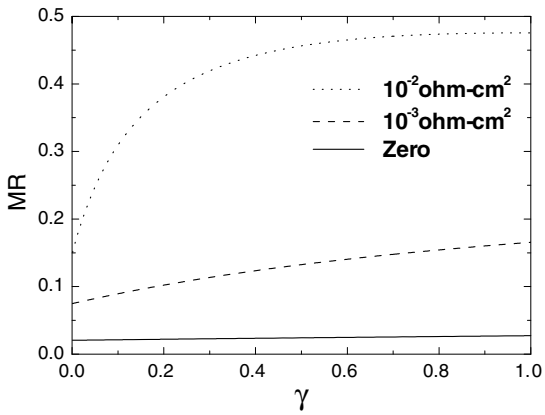

Fig. 6. MR ratio as a function of the polaron proportion γ for various values of spin-down $R_\downarrow$. $R_\uparrow$ is set at 0.1 $R_\downarrow$, and the organic thickness is $x_0 = 100$ nm.

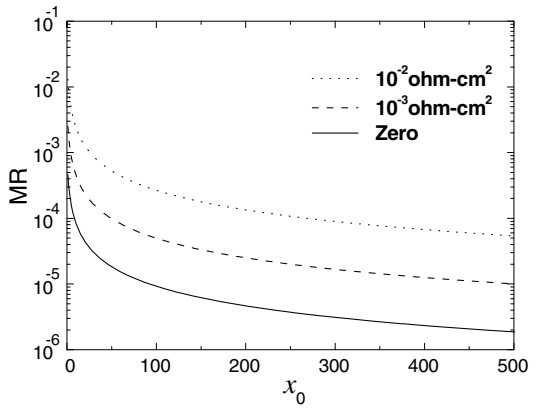

Fig. 7. MR ratio as a function of the OSC thickness x_0 for various values of spin-down $R_\downarrow$. $R_\uparrow$ is set at 0.1 $R_\downarrow$, and the polaron proportion is $\gamma = 0.5$.

cause carriers in organic layer in this case are nearly all spinless bipolarons, and the two FM layer has little spin correlation. MR increases with the increasing of the polaron proportion and the maximum MR is obtained at $\gamma = 1$ which means that a maximum MR in an organic spin device will be reached if all the carriers are spin polarons. From the figure, one also finds that a spin-dependent interfacial resistance will enhance the MR ratio remarkably. In addition, it is also found that a remarkable MR ratio would appear when there is a big spin-dependent interfacial resistance even the polaron proportion γ is small. For example, even when polaron proportion $\gamma = 0.2$, the MR ratio will be about 80% of the value attainable with all spin polarons at the condition of $R_\downarrow = 10 \times R_\uparrow = 10^{-2}\ \Omega\,\mathrm{cm}^2$. Therefore, a big spin-dependent interfacial resistance and the existence of the spin polarons are very important for achieving remarkable MR in the structure of FM/OSC/FM.

It has been obtained that the spin diffusion length in an OSC is about one hundred nanometers. If the thickness of the organic interlayer is larger than the spin diffusion length, the MR ratio will be affected. Fig. 7 gives the dependence of the MR ratio on the OSC thickness. The polaron proportion is $\gamma = 0.5$. From the figure, one finds that the MR ratio decreases with the increasing of the OSC thickness. For a thick interlayer, the MR ratio tends to zero, which means that there is no apparent spin correlation between the magnetic layers. When the spin-dependent interfacial resistance is considered, the MR ratio is enhanced. Therefore, to get an apparent MR in an organic device, it is better to adopt a spin-dependent interface, and the thickness of the organic interlayer is much smaller than the spin diffusion length.

4. Conclusions

Stimulated by the experimental observations about spin-polarized injection and transport in OSCs, we studied the CCP and the MR ratio in a structure of symmetric FM/OSC/FM device, according to Ohm's law and the spin diffusion theory. Spin polarons and spinless bipolarons are assumed to be the main carriers in OSCs. Our calculations suggest that CCP decreases exponentially from the FM layer into the OSC layer and a spin-dependent interfacial resistance is beneficial for achieving efficient CCP and high MR ratio in the device. For effect of special carriers on spin injection and transport in FM/OSC/FM device, it is predicted that polarons are effective spin carriers in OSCs for polarized charge current. The existence of spin polarons will be available for gaining remarkable MR in FM/OSC/FM devices. The MR ratio will tend to zero when the thickness of the organic interlayer is larger than the spin diffusion length.

Acknowledgments

This work was supported by the National Natural Science Foundation of China (Grant No. 10747143) and Shandong Distinguished Middle-aged and Young Scientist Encourage and Reward Foundation (Grant No. 2007BS01017).

References

[1] See e.g. I.H. Campbell, D.L. Smith, Solid State Phys. 55 (2001) 1.
[2] S.A. Wolf, D.D. Awschalom, R.A. Buhrman, J.M. Daughton, S. von Molnár, M.L. Roukes, A.Y. Chtchelkanova, D.M. Treger, Science 294 (2001) 1488.
[3] V. Dediu, M. Murgia, F.C. Matacotta, C. Taliani, S. Barbanera, Solid State Commun. 122 (2002) 181.
[4] Z.H. Xiong, Di Wu, Z. Valy Vardeny, Jing Shi, Nature 427 (2004) 821.
[5] T.S. Santos, J.S. Lee, P. Migdal, I.C. Lekshmi, B. Satpati, J.S. Moodera, Phys. Rev. Lett. 98 (2007) 016601.
[6] Y. Sheng, T.D. Nguyen, G. Veeraraghavan, O. Mermer, M. Wohlgenannt, Phys. Rev. B 75 (2007) 035202.
[7] Y. Wu, Z.H. Xu, B. Hu, X.G. Li, Phys. Rev. B 75 (2007) 035214.
[8] F.J. Wang, C.G. Yang, Z.V. Vardeny, Phys. Rev. B 75 (2007) 245324.
[9] A.R. Rocha, S. Sanvito, J. Appl. Phys. 101 (2007) 09B102.
[10] M. Nishioka, Y.B. Lee, A.M. Goldman, Y. Xia, C.D. Frisbie, Appl. Phys. Lett. 91 (2007) 092117.
[11] S.J. Xie, K.H. Ahn, D.L. Smith, A.R. Bishop, A. Saxena, Phys. Rev. B 67 (2003) 125202.
[12] P.P. Ruden, D.L. Smith, J. Appl. Phys. 95 (2004) 4898.
[13] Z.G. Yu, M.A. Berding, S. Krishnamurthy, J. Appl. Phys. 97 (2005) 024510.
[14] Z.G. Yu, M.A. Berding, S. Krishnamurthy, Phys. Rev. B 71 (2005) 060408.
[15] J.F. Ren, J.Y. Fu, D.S. Liu, L.M. Mei, S.J. Xie, J. Appl. Phys. 98 (2005) 074503.
[16] A.J. Heeger, S. Kivelson, J.R. Schrieffer, W.P. Su, Rev. Mod. Phys. 60 (1988) 781.
[17] P.S. Davids, A. Saxena, D.L. Smith, J. Appl. Phys. 78 (1995) 4244.
[18] Geraldo Magela e Silva, Phys. Rev. B 61 (2000) 10777.
[19] J.C. Scott, P. Pfluger, M.T. Krounbi, G.B. Street, Phys. Rev. B 28 (1983) 2140.
[20] F. Genoud, M. Guglielmi, M. Nechtschein, E. Genies, M. Salmon, Phys. Rev. Lett. 55 (1985) 118.
[21] P.C. van Son, H. van Kempen, P. Wyder, Phys. Rev. Lett. 58 (1987) 2271.
[22] D. Hägele, M. Oestreich, W.W. Rühle, N. Nestle, K. Eberl, Appl. Phys. Lett. 73 (11) (1998) 1580.
[23] G. Schmidt, D. Ferrand, L.W. Molenkamp, A.T. Filip, B.J. van Wees, Phys. Rev. B 62 (2000) R4790.
[24] S. Agrawal, M.B.A. Jalil, K.L. Teo, Y.F. Liew, J. Appl. Phys. 97 (2005) 103907.

active layer and the upper electrode. The role and function of C_{60} in the devices are investigated.

2. Experimental

Photovoltaic devices were fabricated in a typical sandwich structure. The ITO-coated glass substrates were cleaned by ultrasonic treatment in deionized water, acetone, detergent, and isopropyl alcohol sequentially, followed by spin coating a 40 nm thin layer of poly(3,4-ethylenedioxythiopene) (PEDOT):poly(styrenesulfonate) (PSS) (Bayer Baytron P 4083). After baking at 80 °C for 10 h, the substrates were transferred into a nitrogen-filled glove box. MEH-PPV (made in our lab) was dissolved in chlorobenzene (CB), followed by blending with PCBM (1:4 w/w). The blend was stirred for 10 h in the glove box, and spin-coated onto the surface of the PEDOT:PSS. The typical film thickness was about 80–100 nm. At last, the C_{60} layer and 100 nm Al cathode layer, was then thermally evaporated on top of the blend film under vacuum of 3×10^{-4} Pa. The active area of the device was 0.15 cm^2. The BHJ cells with the sandwich structure ITO/PEDOT:PSS/MEH-PPV:PCBM/C_{60}/Al were fabricated as shown in Fig. 1.

The spectral response of the devices was measured with a photomodulation spectroscopic setup (model Merlin, Oriel). The ECE of Solar cell was measured under an illumination of 100 mW cm^{-2} with an AM1.5 solar simulator (Oriel model 91192). The current–voltage (*J–V*) characteristics were measured with a Keithley 236 source-measure unit.

3. Results and discussion

Fig. 2 shows the illuminated (a) and the dark (b) *J–V* characteristics under AM 1.5 illumination for a calibrated solar simulator with an intensity of 100 mW cm^{-2} for photovoltaic device A and device B. The device performance depends on whether the device possesses the C_{60} layer as clearly seen from the Fig. 2. The device A without the C_{60} layer shows performance with V_{oc} = 0.8 V, I_{sc} = 4.25 mA cm^{-2}, and $FF = 46.16\% \cdot \eta$ for this device is therefore only 1.57%. Inserting C_{60} layer, the performance of device B increases. The device B with C_{60} layer exhibits some improvement with I_{sc} = 4.63 mA cm^{-2}, and FF = 51.11%, while V_{oc} remains at 0.8 V. The corresponding power conversion efficiency is 1.89%.The *J–V* curves measured in the dark reveal the device B has higher the rectification ratio than the device A, and possesses the smaller series

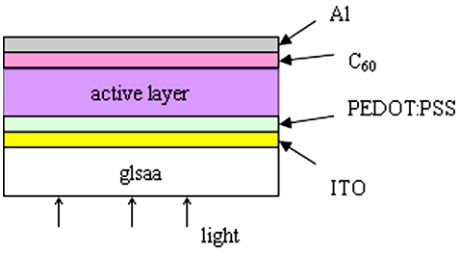

Fig. 1. Structure of the device ITO/PEDOT:PSS/MEH-PPV:PCBM/C_{60}/Al.

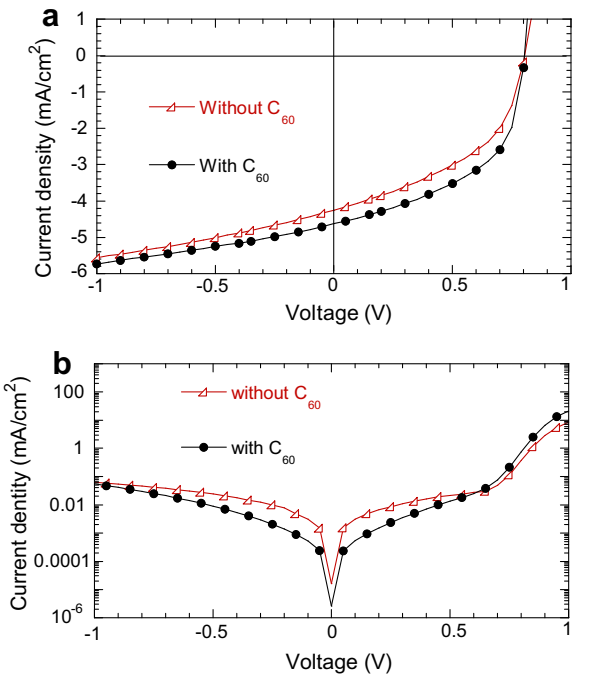

Fig. 2. *J–V* characteristics of the photovoltaic cells with and without the C_{60} layer, illuminated (a) and dark (b).

resistance, bigger shunt resistance, which shows the device B has the higher injection current at the positive voltage of 1.0 V and lower leakage current at the negative voltages. The summary of device performance in this work is provided in Table 1.

There are some reasons for the performance improvement by the insertion of C_{60} layer. Firstly, when incident light transmits through the active layer, the optical field intensity has the different distribution as a function of the position in the device. Since the position of the maximum optical field intensity is at a distance from the metal cathode, the C_{60} inserting layer moves the MEH-PPV:PCBM blend layer farther away from the metal cathode and into regions of higher optical field intensity. So the MEH-PPV:PCBM composite film can absorb more incident light, and create more photogenerated charge carriers in the layer, therefore increasing the device performance. Secondly, a layer of C_{60} is a very good electron conductor, when the C_{60} layer is inserted between the active layer and the electrode layer, from the energy level diagram shown in Fig. 3, we can see that the electrons can cross through it very easily and quickly, while the holes are blocked by the C_{60} layer. Because the C_{60} has a large highest occupied molecular orbital (HOMO) level at 6.2 eV,

Table 1
Summary of the photovoltaic cells performance with and without the C_{60} layer

Device	V_{oc} (V)	I_{sc} (mA cm^{-2})	FF (%)	η (%)	R_S Ω cm^2
Device A (without C_{60})	0.80	4.25	46.16	1.57	11.24
Device B (with C_{60})	0.80	4.63	51.11	1.89	8.36

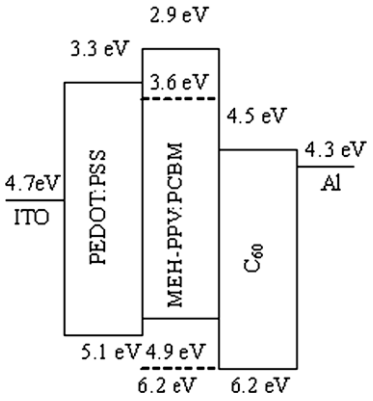

Fig. 3. Energy lever diagram of the device B with the C_{60} layer.

while that of the MEH-PPV, at 4.9 eV. Therefore, the recombining ratio between electrons and holes reduces and the charge extraction efficiency enhances significantly. The Table 1 shows the device with C_{60} layer has the lower series resistance (R_s), which increases the device *FF* and I_{sc}, Series resistances were derived from the slope of the *J–V* characteristic curve under dark conditions close to 1 V [14]. Furthermore, it has been shown that C_{60} layer prevents the underlying organic layer from being damaged during metal deposition.

Fig. 4 compares the photosensitivity(PS) spectra of the device A and device B. The PS maximum of 0.189 A/W at 537 nm was observed for device B, the PS maximum of device A decreases to 0.174 A/W. The PS of the device B with C_{60} layer shows some enhancement at the 430–650 nm photosensitive wavelength range. This increase in the PS contributes to the increase in the performance of our devices. The increase of the PS values could be benefited from the increasing photogeneration charges in the active layer and transport mechanism of charge carriers in the device with the C_{60} layer.

The C_{60} layer could not only increase the device performance but also improve the lifetime of the device. The device A and B without encapsulation were placed in nitrogen-filled glovebox. After three days, the performance of the device B reduces slightly, I_{sc} of the device B dropped from 4.62 to 4.58 mA/cm^2, *FF* declined from 51.11% to 49.31%, V_{oc} remained 0.8 V and ECE decrease from 1.89% to 1.81%. However, the device A performance impaired significantly, The device A shows descending performance with V_{oc} = 0.75 V, I_{sc} = 3.95 mA cm^{-2}, and $FF = 42.5\% \cdot \eta$ for this device is therefore only 1.26%. The ECE of the device lost almost 20% of its initial maximum power output.

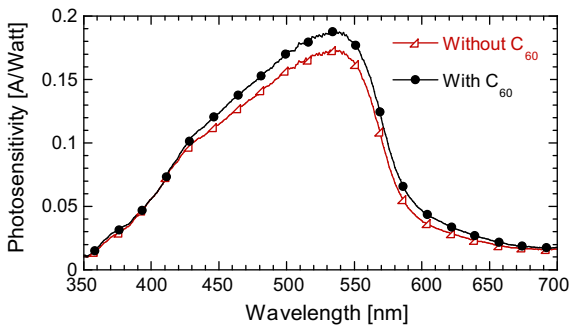

Fig. 4. Photosensitivity spectrum of the solar cell with and without the C_{60} layer.

Some possible reasons explain the lifetime delay by the insertion of C_{60} layer. Firstly, the possible complex chemical reaction between the PPV and the aluminium electrode at the interface is responsible for the degradation of the device performance [15,16], when incident light irradiates the device, the active layer of the solar cell would generate many radical cations and radical anions [17–19], These radical species are likely to react with aluminium metal thus gradually dissolving the metal electrode in the organic material leading to disruption of the conjugation in the MEH-PPV system [20]. The C_{60} inserting layer may efficiently prevent chemical reactions between the active layer and the reactive electrode metal to take place. Secondly, although the device without encapsulation were placed in nitrogen-filled glovebox for three days, there are a little oxygen in the chamber (2.9 ppm), these oxygen diffuse into the active layer of the device, the oxygen diffusing into the active layer oxidizes the vinylene double bond by cycloaddition, leading to the formation of carbonyl units and scission of the polymer backbone, with a shortening in the conjugation length of the polymer. Loss of conjugation in the polymer leads to a degradation of charge-carrier mobility, The oxidation of the active layer also creates more deep traps in the polymer, which bring about the degradation of the device performance [21]. The C_{60} layer delays oxygen diffusion into the active layer of the device.

4. Conclusion

In summary, we have investigated the function of the modifying layer of C_{60} on photovoltaic performance of solar cells based on MEH-PPV:PCBM. It is found that the device performance can be enhanced with the C_{60} layer inserted between the polymer blend and the cathode electrode. The improved solar cell performance can be attributed to the C_{60} layer works as an optical spacer and a charge blocking layer. In addition, owing to the C_{60} layer may efficiently prevent chemical reactions between the active layer and the reactive electrode metal to take place, and delays oxygen diffusion into the active layer of the device, the C_{60} insertion layer also could improve the lifetime of the devices.

Acknowledgements

This work is financially supported by the National Natural Science Foundation of China (Project No. 90201023) and the MOST National Research Project (No. 2002CB613405).

References

[1] C.J. Brabec, N.S. Sariciftci, J.C. Hummelen, Adv. Funct. Mater. 11 (2001) 15.
[2] K.M. Coakley, M.D. McGehee, Chem. Mater. 16 (2004) 4533.

[3] G. Yu, J. Gao, J.C. Hummelen, F. Wudl, A.J. Heeger, Science 270 (1995) 1789.
[4] C.J. Brabec, A. Cravino, D. Meissner, N.S. Sariciftci, T. Fromherz, M.T. Rispens, L. Sanchez, J.C. Hummelen, Adv. Funct. Mater. 11 (2001) 374.
[5] V.D. Mihailetchi, P.W.M. Blom, J.C. Hummelen, M.T. Rispens, J. Appl. Phys. 94 (2003) 6849.
[6] H. Frohne, S.E. Shaheen, C.J. Brabec, D.C. Muller, N.S. Sariciftci, K. Meerholz, ChemPhysChem 3 (2002) 795.
[7] L.S. Roman, M. Berggren, O. Inganas, Appl. Phys. Lett. 75 (1999) 3557.
[8] C.J. Brabec, S.E. Shaheen, C. Winder, N.S. Sariciftci, P. Denk, Appl. Phys. Lett. 80 (2002) 1288.
[9] S. Alem, R. Bettignies, J.M. Nunzi, Appl. Phys. Lett. 84 (2004) 2178.
[10] J.Y. Kim, S.H. Kim, H.-H. Lee, K. Lee, W. Ma, X. Gong, A.J. Heeger, Adv. Mater. 18 (2006) 572.
[11] J. Gilot, L. Barbu, M.M. Wienk, R.A.J. Janssen, Appl. Phys. Lett. 91 (2007) 113520.
[12] Y. Li, Y.B. Hou, Y. Wang, L.F. Qin, Z.H. Feng, B. Feng, F. Teng, Synth. Met. 157 (2007) 956.
[13] P. Peumans, A. Yakimov, S.R. Forrest, J. Appl. Phys. 93 (2003) 3693.
[14] F. Shirland, Adv. Energy Convers. 6 (1966) 201.
[15] H. Aziz, G. Xu, Synth. Met. 80 (1996) 7.
[16] M. Logdlund, J.L. Bredas, J. Chem. Phys. 101 (1994) 4357.
[17] P.M. Allemand, G. Srdanov, A. Koch, K. Khemani, F. Wudl, Y. Rubin, F.N. Diederich, M.M. Alvarez, S.J. Anz, R.L. Whetten, J. Am. Chem. Soc. 113 (1991) 2780.
[18] N.S. Sariciftci, L. Smilowitz, A.J. Heeger, Science 258 (1992) 1474.
[19] V. Dyakonov, G. Zoriniants, M.C. Scharber, C.J. Brabec, R.A.J. Janssen, J.C. Hummelen, N.S. Sariciftci, Phys. Rev. B 59 (1999) 8019.
[20] F.C. Krebs, J.E. Carle, N. Cruys-Bagger, M. Andersen, M.R. Lilliedal, M.A. Hammond, S. Hvidt, Sol. Energy Mater. Sol. Cells 86 (2005) 499.
[21] R. Pacios, A.J. Chatten, K. Kawnao, J.R. Durrant, D.D.C. Bradley, J. Nelson, Adv. Fnuct. Mater. 16 (2006) 2117.

eventually be more important for practical applications [8–10]. The microscopic mechanisms of carrier transport, injection, and traps pertaining to any new organic semiconductor and its interaction with the metal and insulator surfaces has an important implication on the organic transistor performance, and understanding of those could be exploited to improve the device performance through various engineering routes. For example, contact barriers, mobility variation with the electric field, traps and fixed charges are known to significantly affect the electrical characteristics of transistors [11–13]. However, due to the complexity involved in the transistor operation, it is often difficult to identify the actual physical mechanisms that have significant impact on the device characteristics, solely by a simple analysis of the experimental data based on one-dimensional analytical models. These analytical models can predict the overall device behavior, but are often unable to identify the underlying microscopic behavior. The associated inaccuracies in correctly predicting the device behavior may cause an ambiguous characterization of the material's intrinsic properties and it may lead to a premature discarding of a potentially important organic semiconductor material. In this respect, two-dimensional physics-based numerical simulation has proven to be of great help not only in understanding the detailed microscopic processes in the interior of the device, but also in enhancing the possibility of the investigations of those physical quantities that would otherwise be difficult to obtain [11–13]. Such examinations lead to the analysis of the cause of the non-ideal performance of the device behavior incorporating a new organic material and its optimization towards obtaining the best electrical characteristics. Towards these goals, in this article, we build on the previous theoretical efforts by combining detailed device simulation with experiments to help characterize TIPS-pentacene OTFTs. A physics-based 2 D numerical simulation is used to link the effect of contact barrier, field-dependent mobility, and traps to the observed output and transfer characteristics that are different from those corresponding to ideal MOSFET equations [12,13].

2. Experiment

A schematic cross section of the TFTs under study is depicted in Fig. 1. TIPS-pentacene OTFTs were fabricated in bottom-contact geometry on a 100 nm thick SiO_2 layer thermally grown on heavily doped n-Si wafers that also function as the gate (G) electrode. The source (S) and drain (D) electrodes consisting of 5 nm titanium adhesion layer and 100 nm gold layer were patterned on the silicon wafers through photolithography and lift-off process. For deposition of active layers, a 2 wt.% TIPS-pentacene solution in toluene was drop-cast in ambient air over the patterned electrodes and allowed to dry slowly in a solvent-rich environment at 50 °C to promote ordered molecular arrangement [4]. The solvent vapor environment was created by pouring toluene into the bottom of a glass petri-dish and heating it at 50 °C. The drop-cast transistors were then attached to the lid of petri-dish and kept over the pool of the solvent. The electrical measurements were performed in the dark at the ambient conditions with a parametric analyzer (HP 4156).

3. Device simulation and material parameters

For simulation, we have used the commercial device simulator Silvaco-Atlas® which predicts the electrical characteristics associated with a specified physical structure and bias conditions by solving systems of Poisson's equation and continuity equation which are a set of coupled, partial differential equations given for holes by Eqs. (1) and (2) below

$$\varepsilon\nabla^2\psi = -pq \tag{1}$$

$$\frac{\partial p}{\partial t} = \frac{1}{q}\nabla \cdot J_p + G_p - R_p \tag{2}$$

where ε is the dielectric constant, ψ is the potential, p is the local hole density, q is the fundamental electronic charge, G_p is the charge generation rate, R_p is the charge recombination rate, and J_p is the current density which is given considering its drift and diffusion components by Eq. (3)

$$J_p = qp\mu_p F + qD_p\nabla p \tag{3}$$

where μ_p is the mobility of holes, F is the local electric field, and D_p is the hole diffusion coefficient.

The material parameters of TIPS-pentacene used in the simulation were borrowed from literature: dielectric constant, bandgap, and electron affinity were given by 4.0,

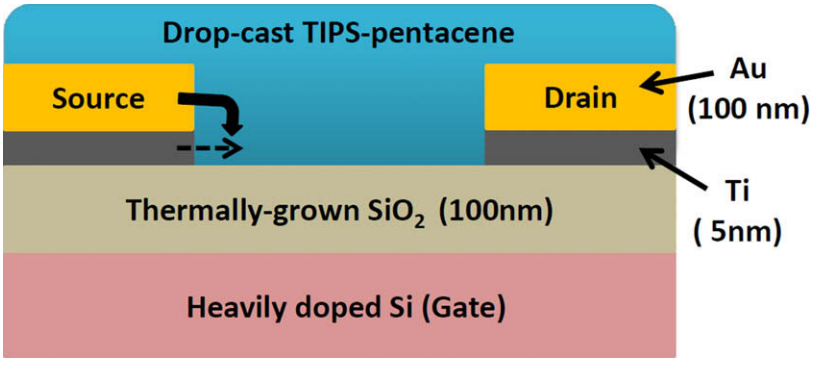

Fig. 1. Schematic illustration of the cross-section of the TIPS-pentacene OTFT. The arrows on the source contact depict possible charge injection routes from the gold (solid) and titanium (dashed) layers.

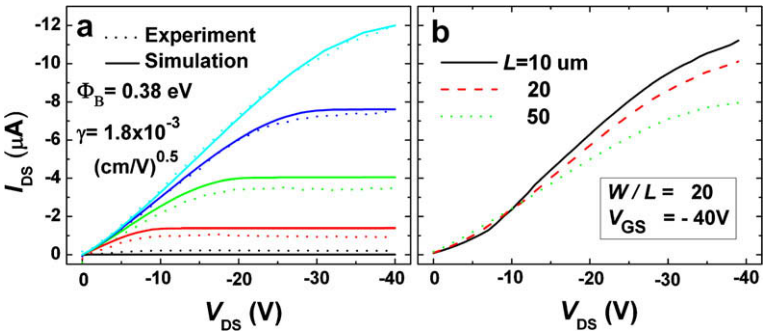

Fig. 2. (a) Output characteristics of TIPS-pentacene TFTs: experimental (dotted) vs. numerical simulation (solid) results. Simulation was done in consideration of both a contact barrier height Φ_B of 0.38 eV and the field-dependence of mobility given by Eq. (4) with $\mu_o = 0.061$ cm^2/Vs and $\gamma = 1.8 \times 10^{-3}$ (cm/V)$^{0.5}$. V_{GS} is varied from 0 to −40 V in −10 V steps (b) Experimental output characteristics for devices with a channel length L of 10, 20 and 50 μm and with W/L of 20 and V_{GS} of −40 V.

1.8 eV, and, 2.9 eV respectively, and the effective density of states in the conduction band (=N_C) and valence band (=N_V) were both assumed to be 2×10^{21} cm^{-3} [12–14]. In this study, TIPS-pentacene was considered as intrinsic, undoped semiconductors. The work-function of the gate electrode was taken as 4.5 eV, while the work-functions of source and drain contacts were adjusted to match the experimentally obtained drain currents during device simulation.

4. Results and discussion

Dotted lines in Fig. 2a show the experimental output characteristics of a TIPS-pentacene OTFT with the channel width W of 1.5 mm and length L of 50 μm in the forward sweep (off to on) at an incremental gate voltage (V_{GS}) from 0 to −40 V in a step of −10 V. According to a standard procedure for extracting mobility values and threshold voltage using the MOSFET equations, the linear-region field-effect mobility μ_{lin} and the saturation mobility μ_{sat} are estimated to be 7×10^{-3} cm^2/V s and 2×10^{-2} cm^2/V s, respectively, whereas the threshold voltage V_T is obtained as 2.4 V. They exhibit a clear pinch-off and ideal saturation behavior at high drain voltages (V_{DS}), but one can easily observe the so-called "current crowding" at low-V_{DS}, which corresponds to the non-ohmic behavior of the drain current (I_{DS}) in the linear region. From Fig. 2b showing the I_{DS}–V_{DS} curves for different values of L with the W/L ratio and V_{GS} fixed at 20 and −40 V, respectively, one can also see that I_{DS} in low-V_{DS} region for devices with shorter channels increase more superlinearly than devices with longer channels, consistent with the presence of a contact barrier, because the relative effect of contacts will be larger in devices with shorter channels [13,15].

This may be explained mainly by a limited carrier injection from metal contacts to semiconductors, especially in bottom-contact OTFTs where the effect of barrier height Φ_B, from metal to semiconductor is known to be more pronounced than that of top-contact equivalents due to smaller-contact area, etc [15,16]. Φ_B is defined as the difference between the metal work-function (Φ_S) and ionization level (E_v) of the semiconductor. Ideally, the choice of Ti/Au should be a good Ohmic contact to TIPS-pentacene because there is a proper energy level alignment between the work-function of gold ($\equiv \Phi_{AU} \approx 4.7$–5.0 eV) and a value of 4.7 eV of E_v for TIPS-pentacene, provided that Ti, having the work-function Φ_{Ti} of 4.3 eV, is sufficiently thin so that Au layer can get close to the dielectric/semiconductor interface where most of the induced charges are accumulated [17]. Presented in Fig. 3a is the simulated output characteristics with Φ_{Ti} and Φ_{AU} set at 4.3 eV and 5.0 eV, respectively, for the current device geometry of Ti(5 nm)/

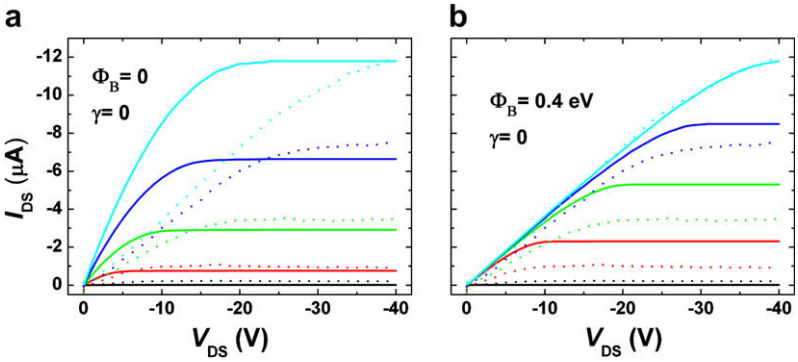

Fig. 3. Output characteristics of TIPS-pentacene TFTs: experimental (dotted) vs. numerical simulation (solid) results. (a) Simulated characteristics with $\Phi_B = 0$ and $\gamma = 0$ (no field-dependence) and (b) Simulated characteristics with $\Phi_B = 0.4$ eV and $\gamma = 0$. In (a) and (b), the mobility value is scaled to match the value of I_{DS}(V_{DS} = −40 V) for V_{GS} = −40 V. V_{GS} in (a) and (b) is varied from 0 to −40 V in −10 V steps.

Au(100 nm). The fact that it does not show any sign of injection-limited behavior in its linear region indicates that the current Ti-thickness is thin enough to ensure that major injection occurs from Au layer as depicted with a solid, bent arrow in Fig. 1 *in this ideal case* where there is no energy barrier between Au and TIPS-pentacene. The origin of the big difference between the observed characteristics and the simulated one may then be found from the presence of the contact barrier between Au and TIPS-pentacene. In fact, many groups have reported on the existence of energy barrier on the order of 0.5–1.0 eV between pentacene and Au, and such barriers have mostly been explained using a formation of interfacial dipoles [18–20] that effectively modifies the energy barrier at the metal–semiconductor interfaces. The reasons for the formation of this interfacial dipole is not properly understood, but is believed to be due to the complex chemical interaction between the organic semiconductor and metal resulting in charge transfer, screening, or hybridization effects [19,20].

On the basis of the above discussion, we can now define an effective contact barrier to reproduce the output characteristics at low-drain voltages in the output curves. However, our simulation results indicate that the contact barrier effect alone cannot explain the whole output characteristics in both linear and saturation regions over the range of V_{GS} used in this study. As shown in Fig. 3b, for example, an attempt to simulate the non-linear behavior of I_{DS} in the linear region only by increasing Φ_B typically requires adjustment of mobility towards a larger value in order to fit the current level comparable to the experimental data in the saturation region for a specific value of V_{GS}, but it in turn fails to provide the fit that is consistent over different values of V_{GS}. The subtle yet still observable curvature of the output characteristics in the low-V_{DS} region is also hard to explain solely by the contact barrier for the given device geometry. Previous studies using two-dimensional numerical simulations, however, showed that the non-linearity of the output curves in the low-V_{DS} region may result from the combined effect of both the contact barrier and field-dependent mobility [13,21,22]. In addition, the larger current observed in devices with a shorter channel in Fig. 2b suggests that there may be a field-induced enhancement in mobility.

To underline the presence of field-dependent mobility in TIPS-pentacene OTFTs, we extracted a field-effect mobility of devices with L of 10, 20, and 50 μm at several values of V_{DS} in linear region and plotted it as a function of $(V_{DS}/L)^{0.5}$, as shown in Fig. 4. The logarithmic variation of mobility with $(V_{DS}/L)^{0.5}$ for a series of channel lengths suggests that it follows the Poole–Frenkel (PF)-type field-dependence given by

$$\mu = \mu_o \exp(\gamma\sqrt{F}) \tag{4}$$

where μ_0 is the zero-field mobility, F is the electric field and γ is the characteristic parameter for the field-dependence [21,22]. Note that F is a function of position inside the TFT channel and can be influenced by local charge density but here it is taken as V_{DS}/L for simplicity. Apparent linear fit [dashed line in Fig. 4] yielded field-dependent parameters of $\mu_o = 0.035$ cm^2/Vs and $\gamma = 1.7 \times 10^{-3}$ (cm/V)$^{0.5}$. It is noted that this PF field-dependence is often observed in disordered organic semiconductors. Although it is known that drop-cast TIPS-pentacene films typically consist of platelet-like structures each of which may be regarded crystalline [See AFM and optical microscopy images and X-ray diffraction patterns in Fig. 5], it may still be plausible to model TIPS-pentacene films as a partially disordered system in that such platelets are distributed in TFT channels in a random, disordered fashion [3,4].

In this respect, we have incorporated the field-dependence of mobility given by Eq. (4), in addition to the contact barrier effect, into our numerical simulation. Line curves in Fig. 2a shows the simulated output curves which take into account both the PF mobility and contact barriers. The best fit to the experimental data was obtained with Φ_B of 0.38 eV, μ_o of 0.061 cm^2/Vs, and γ of 1.8×10^{-3} (cm/V)$^{0.5}$, respectively. It is noted that the field-dependent parameters obtained in this way are different from the values obtained from Fig. 4. Such discrepancy is rather natural because the latter is obtained using the simple MOSFET equations and does not consider the detailed spatial electric field distribution in channels. Another thing to note is that the energy barrier of 0.38 eV between Au and TIPS-pentacene now almost equals to the energy barrier between Ti and TIPS-pentacene, as long as there are no significant interfacial dipoles, etc. between Ti and TIPS-pentacene to create the additional injec-

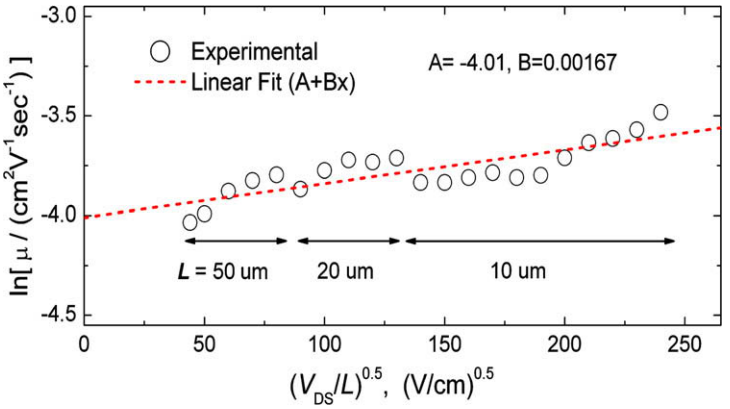

Fig. 4. Natural logarithm of field-effect mobility for devices in Fig. 3a, as a function of $(V_{DS}/L)^{0.5}$. Dashed line is a linear fit with which the field-dependent parameters in Eq. (4) are estimated to be $\mu_o = 0.035$ cm^2/Vs and $\gamma = 1.7 \times 10^{-3}$ (cm/V)$^{0.5}$.

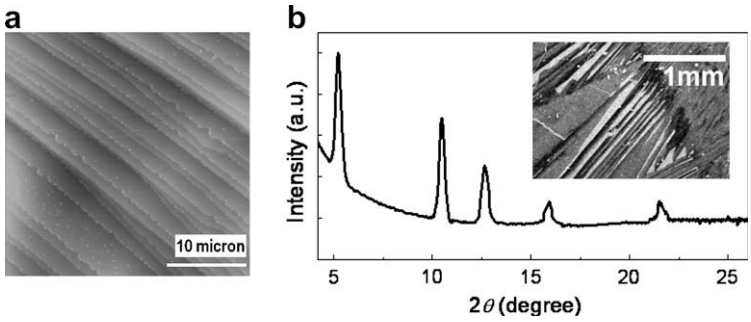

Fig. 5. (a) Atomic force microscopy (AFM) image and (b) X-ray diffraction data, and optical microscope image (inset) of TIPS-pentacene film.

tion barrier at that interface. In such case, injection from Ti, which is depicted with a dashed, straight arrow in Fig. 1, can become significant and in fact can be the dominant route, as Ti is in more close contact with the charge accumulation layer than Au layer is [17].

Although the simulated curves in Fig. 2a show a reasonable match to the experimental data, it is noted that the simulated curves at low $|V_{GS}|$ still exhibits a significant deviation, suggesting that one may need to include additional factors for the complete TFT model. Moreover, the I_{DS}–V_{GS} transfer curve shown in Fig. 6a exhibits a hysteresis loop when one scans V_{GS} from 0 to −40 V and then back from −40 to 0 V at V_{DS} = −40 V. Both observations, i.e., deviation in subthreshold region and the hysteresis behavior of the transfer characteristics, indicate the existence of traps, which may come from dielectric-semiconductor interface or from structural defects in TIPS-pentacene films [11,12]. In order to explain such trap-related phenomenon, we have adopted the spatially uniform density of trap states (DTS) or $g(E)$ in the TIPS-pentacene films that is modeled by an exponential distribution of acceptor-like traps as follows

$$g(E) = N_{TA} \exp[(E - E_C)/W_{TA}] \quad (5)$$

where E refers to the energy measured from the valence band edge, and N_{TA} and W_{TA} refer to the coefficient and the characteristic energy width of the exponential trap distribution, respectively. E_C represents the energy level of conduction band minimum. It was previously discussed that oxygen is the chemical origin of acceptor-like traps in pentacene and that acceptor-like traps provide extra hole current in the subthreshold region in pentacene OTFTs [11,12,23,24]. Additionally, we have included a positive interface trapped charge (N_{it}), which may arise due to impurities such as moisture, oxygen or mobile charges in the dielectric [12,13].

Line curve 1 in Fig. 6a, which includes non-ideal contact and field-dependent mobility but no trap effects, shows the underestimation of I_{DS} in the subthreshold region and a sharp increase of I_{DS} near threshold (small subthreshold swing), which are quite different from actual observation. On the other hand, much better match to the experimental curve was realized upon consideration of traps in addition to contact barrier and PF mobility as can be seen in line curves 2 and 3 which are the simulated transfer curves for forward and backward sweeps, respectively. Curve 2 was obtained with $N_{TA} = 1.0 \times 10^{18}\ cm^{-3}\ eV^{-1}$, $W_{TA} = 0.55$ eV and $N_{it} = 8.0 \times 10^{11}\ cm^{-2}$. At this stage, a slight decrease in μ_o to 0.052 cm^2/Vs was also required to produce a better fit. The forward-sweep output characteristics shown in Fig. 6b also exhibits the improved fit to the experimental data in all the range of V_{GS} with the above trap parameters. As observed from the simulated results, the dominance of deep acceptor-like traps in determining the subthreshold characteristics is essentially similar to the reports made for pentacene OTFTs, and consistent with experiments done on TIPS-pentacene by Ostroverkhova et al., where the temperature dependence and time scale of transient photoconductivity signal was linked to presence of deep traps [23,24,9].

Finally, the reverse bias sweep [curve 3 in Fig. 6a] was modeled with $N_{TA} = 8.0 \times 10^{17}\ cm^{-3}\ eV^{-1}$, $W_{TA} = 0.55$ eV,

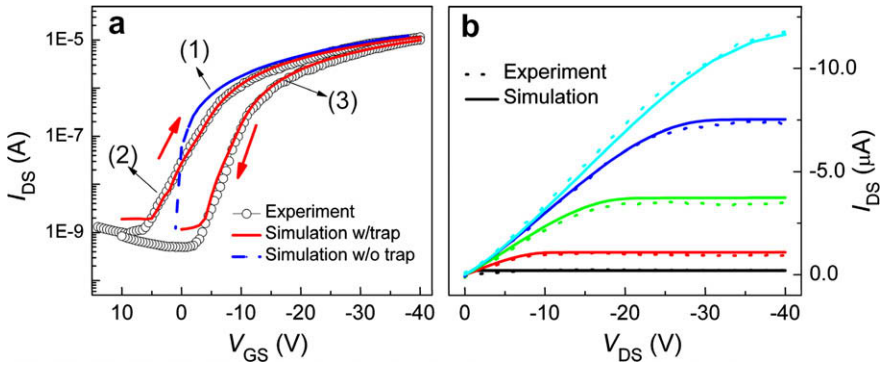

Fig. 6. (a) Numerical fit to the transfer curves (curve 1 is without traps, while curves 2 and 3 are plotted using trap distribution given by Eq. (5) and interface charges in forward (2) and reverse (3) bias sweep). (b) Output curves with DTS distribution and contact barrier height of 0.38 eV, μ_o = 0.052 cm^2/Vs and $\gamma = 1.8 \times 10^{-3}\ (cm/V)^{0.5}$.

$N_{it} = 2.0 \times 10^{12}$ cm^{-2}, and $\mu_o = 0.058$ cm^2/Vs. The increase in N_{it} in the reverse sweep is a result of a relatively slow discharging of the trap states when compared to the sweep speed (=5 V/s) used in this study and is mainly responsible for the shift in threshold voltage [12]. The decrease in N_{TA} was required to match the subthreshold slope in the reverse sweep. This might be connected to an actual sweep-induced decrease in trap density, but its physical origin is unclear at the moment, and it might be similar to metastable defect alteration in pentacene or amorphous silicon films by the gate-induced bias stress. However, it might simply be an effective change that is required to simulate the reduction of available trap states due to the slow discharging [23,25]. In addition, one may note the slight increase in the zero-field mobility in the reverse gate bias scan. Although this change resulted in the least-squared-error fit to the experimental data, its effect on the transfer characteristics is less visible than that of the change in N_{TA} and N_{it}, and thus it may be regarded insignificant although one may not completely rule out the possibility of the stress-induced change in the transport properties.

5. Conclusion

In conclusion, we have modeled the output and transfer characteristics of OTFTs made of TIPS-pentacene. TIPS-pentacene channels being the partially disordered system, the non-linear behavior of output curves at low-V_{DS} was confirmed to be a result of both contact barriers and field-dependent mobility. We then implemented the trap model to account for the whole region of the transfer characteristics as well as its hysteresis behavior. The work presented here will help to build an integral picture of injection, transport, and traps in TIPS-pentacene in a context of OTFT operation, and will serve as a starting point for further optimization of the performance of TIPS-pentacene OTFTs.

Acknowledgements

This work was supported by the Brain Korea 21 Project, School of Information Technology, KAIST, 2007, by the ERC Program of the Korea Science and Engineering Foundation (KOSEF) Grant funded by the Korea Ministry of Education, Science and Technology (MEST) (No. R11-2007-045-01001-0), and by the KOSEF Grant funded by the same (No. R01-2007-000-11023-0).

References

[1] T.W. Kelley, D.V. Muyres, P.F. Baude, T.P. Smith, T.D. Jones, Mater. Res. Soc. Symp. Proc. L65 (2003) 771.
[2] K. Itaka, M. Yamashiro, J. Yamaguchi, M. Haemori, S. Yaginuma, Y. Matsumoto, M. Kondo, H. Hoinuma, Adv. Mat. 18 (2006) 1713.
[3] C.D. Sheraw, T.N. Jackson, D.L. Eaton, J.E. Anthony, Adv. Mat. 15 (2009) 2009.
[4] S.K. Park, T.N. Jackson, J.E. Anthony, D.A. Mourey, Appl. Phys. Lett. 91 (2007) 63514.
[5] C.C. Matthews, G.A. de Wijs, R.A.D. Groots, T.T.M. Palstra, J. Am. Chem. Soc. 125 (2003) 6323.
[6] J.E. Anthony, J.S. Brooks, D.L. Eaton, S.R. Parkin, J. Am. Chem. Soc. 123 (2001) 9482.
[7] R.C. Haddon, X. Chi, M.E. Itkis, J.E. Anthony, D.L. Eaton, T. Siegrist, C.C. Mattheus, T.T.M. Palstra, J. Phys. Chem. B 106 (2002) 8288.
[8] J.S. Brooks, T. Tokumoto, E.S. Choi, D. Graf, N. Biskup, D.L. Eaton, J.E. Anthony, S.A. Odom, J. Appl. Phys. 96 (2004).
[9] O. Ostroverkhova, D.G. Cooke, S. Scherbyna, R.F. Egerton, F.A. Hegmann, R.R. Tykwinski, J.E. Anthony, Phys. Rev. B 71 (2005) 35204.
[10] J.G. Park, R. Vasic, J.S. Brooks, J.E. Anthony, J. Appl. Phys. 100 (2006).
[11] M.A. Alam, A. Dodabalapur, M.R. Pinto, IEEE Trans. Elec. Dev. 44 (1997) 1332.
[12] S. Scheinert, G. Paasch, Phys. Status Solidi. A 201 (2004) 1263.
[13] A. Bolognesi, A.D. Carlo, P. Lugli, Appl. Phys. Lett. 81 (2002) 4646.
[14] T. Okamato, Z. Bao, J. Am. Chem. Soc. 129 (2007) 0308.
[15] I.G. Hill, Appl. Phys. Lett. 91 (2007) 63514.
[16] N. Tessler, Y. Roichman, Appl. Phys. Lett. 79 (2001) 2987.
[17] N. Yoneya, M. Noda, N. Hirai, K. Nomoto, M. Wada, J. Kasahara, Appl. Phys. Lett. 85 (2004) 4663.
[18] K. Hong, J.W. Lee, S.Y. Yang, K. Shin, H. Jeon, S.H. Kim, C. Yang, C.E. Park, Org. Elect. 9 (2008) 21.
[19] A. Kahn, N. Koch, W. Gao, J. Polym. Sci. Part B: Polym. Phys. 41 (2003) 2529.
[20] H. Ishii, K. Sugiyama, E. Ito, K. Seki, Adv. Mater. 11 (1999) 605.
[21] S. Cherian, C. Donley, D. Mathine, L. LaRussa, W. Xia, N. Armstrong, J. Appl. Phys. 96 (2004).
[22] L. Wang, D. Fine, D. Basu, A. Dodabalapur, J. Appl. Phys. 101 (2003) 54515.
[23] D. Knipp, R.A. Street, A. Volkel, J. Ho, J. Appl. Phys. 93 (2003) 347.
[24] R.A. Street, D. Knipp, A. Volkel, Appl. Phys. Lett. 80 (2002) 1658.
[25] M.J. Powell, C. van Berkel, A.R. Franklin, Phys. Rev. B 45 (1992) 4160.

in organic LEDs in general, we decided to examine dissociation of optically-excited singlet excitons in TPD leading to intrinsic and/or interface photocarrier production by a steady-state photoconduction study in single layer TPD structures of ITO/Al and Al/Al combinations of electrical contacts with varying bias. A theoretical modeling is presented based on the diffusion equation for the excitons and applying the 1D-Onsager model of geminate recombination of electrons with their image countercharge in the electrode, and the bulk intrinsic charge generation analysed in terms of the Poole–Frenkel approximation of the 3D-Onsager theory of geminate charge pairs produced by dissociation of singlet excitons. The experimental results are in agreement with the model predictions.

2. Experimental details

Fig. 1a shows two organic film – electrode structures studied in this work. Structure (A): Quartz/Al_1/TPD/Al_2, and structure (B): Quartz/ITO/TPD/Al. They consist of a semitransparent, vacuum-evaporated, 15 nm-thick Al layer on a quartz (Q) substrate for structure (A) and a transparent 20 Ω/sq ITO glass substrate for structure (B), a 300 nm TPD, and a 15 nm-thick Al top metal layer. The energy level scheme of the materials used and possible charge photogeneration mechanisms are shown in Fig. 1b (for details see Section 4). The electrically active area of the cells was 0.09 cm^2. The surface contact conditions of Al electrodes were found to be an important factor governing the dark current (j_{dark}) – electric field (F) characteristics

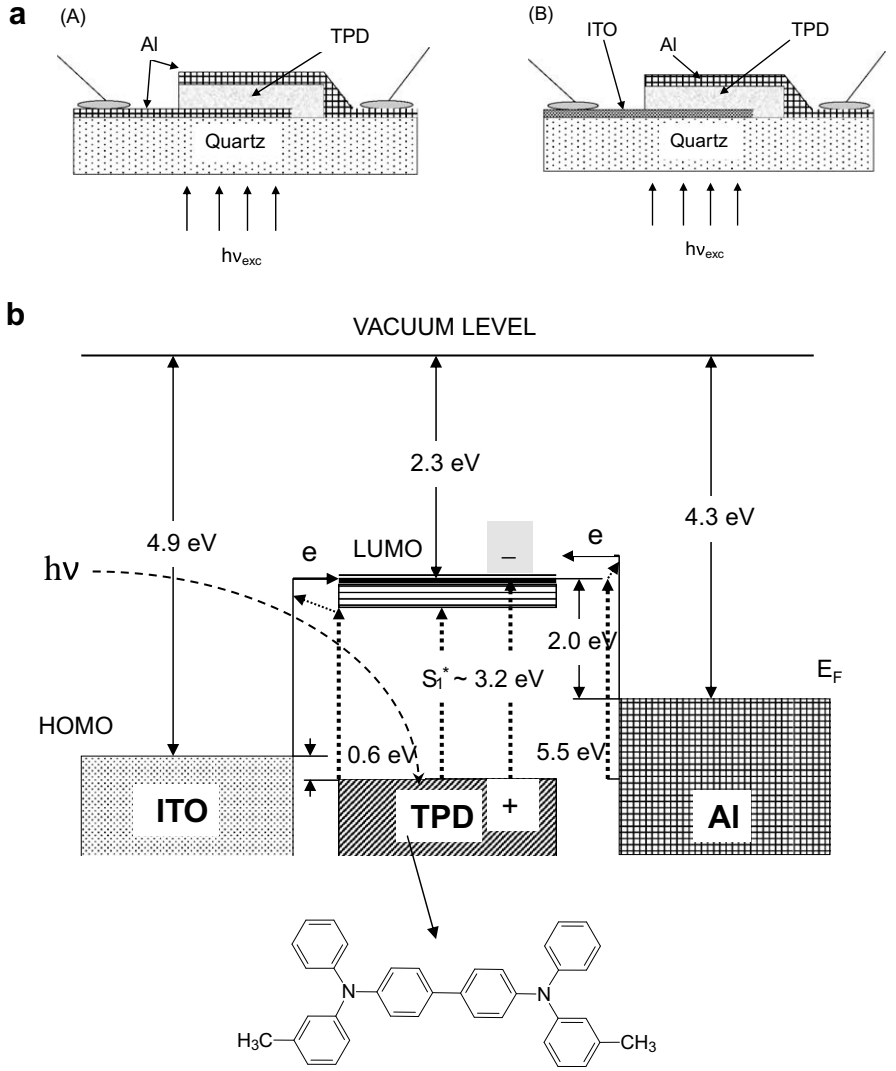

Fig. 1. (a) Schematic of the two TPD film structures studied and way of their illumination; (b) energy levels diagram. Possible charge photogeneration processes are depicted: (i) intrinsic (bulk) photogeneration – a photon of the exciting light (hν) creates an electron–hole pair, (ii) the vibrationally-relaxed excited singlet exciton (S_1) dissociates at the electrodes injecting electrons (**e**).

[13]. The substrate aluminum electrode (Al_1) was evaporated in a vacuum chamber with a base pressure 5×10^{-6} hPa. The deposition rate was typically 0.3–0.5 nm/s. Such prepared layers have been kept for 2 h under ambient atmosphere to oxidize their upper segments to Al_2O_3. A TPD film was evaporated in the same chamber with a deposition rate of around 0.3 nm/s. A 15 nm-thick aluminum layer (Al_2) was then evaporated on top of TPD and a 1.5 nm-thick Al_2O_3 layer was grown within close to the surface segments by simple 1 h exposure of the layer to the air. As a consequence the TPD layer contacted with the substrate electrode (Al_1) through the sequence of Al_2O_3 (1.5 nm)/Al, but through the reverse sequence of Al/Al_2O_3 (1.5 nm), with the top electrode (Al_2) [13].

The steady-state photoconduction measurements were conducted upon irradiation of the TPD film structures (A) and (B) through the Quartz substrate and following it layers of Al_1 or ITO which could be either positively or negatively biased electric contact. An Osram 150 W Xenon lamp was used as a light source. The photocurrent was measured within the quantal intensity range $10^{12} < I_0 < 10^{15}$ quanta/cm^{2}s and a d.c. field range between 10^3 and 3×10^5 V cm^{-1}. The values of I_0 were accounted for the transmission characteristics of the illuminated electrodes ITO and Al. The action spectra of the photocurrent were measured in the wavelength (λ) range between 300 and 500 nm, comprising the penetration depth between 57 nm (λ = 355 nm) and 4 μm (λ = 425 nm). For λ > 450 nm the photocurrent fell in the electrical noise range. All measurements were carried out in ambient atmosphere conditions. The photocurrents were "pure" photocurrent values (j_{ph}) obtained as the difference between the sample current measured under illumination and its dark current. As a rule these values were lower than the dark currents, the j_{ph}/j_{dark} ratio fell down to 10^{-2} for the $ITO^+/TPD/Al^-$ structure.

3. Results

Upon illumination of an interface between a substrate deposited electrode and TPD film a photocurrent is generated. The following notations will be used: $j_{ph}^{(+)}$ is the photocurrent density with illuminated electrode positive, and $j_{ph}^{(-)}$ is the photocurrent density with illuminated electrode negative. The indices (+) and (−) are not, in general, identical with the sign of charge carriers, each of them can refer either to a hole or electron current originating at the back

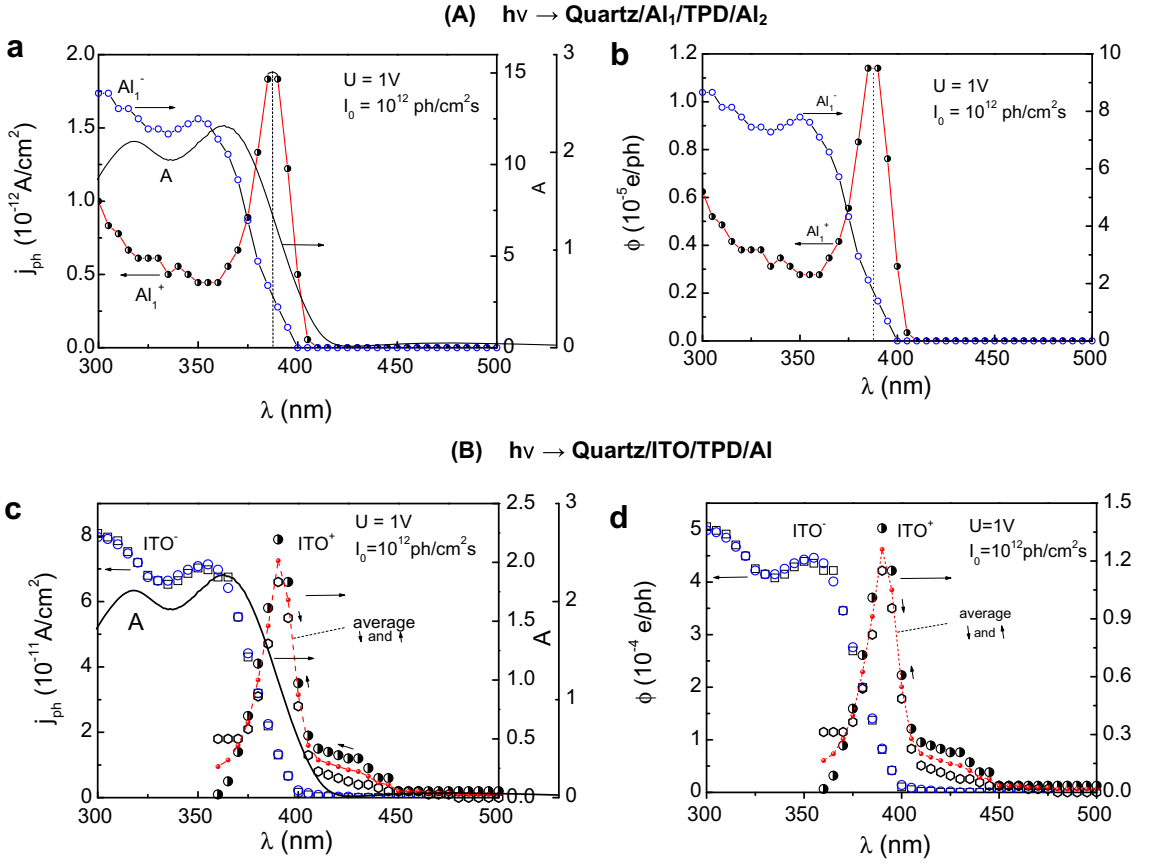

Fig. 2. Action spectra of the photocurrent (j_{ph}) and the charge photogeneration efficiency (φ) for TPD film structure (A) (a and b, respectively), and TPD film structure (B) (c and d, respectively) for negative (−) and positive (+) electrical bias of the illuminated electrodes Al_1 and ITO. While the solid lines in parts a and b are guides to the eyes, the dashed curves in parts c and d represent the average values of respective quantities when scanning the λ towards long (↓) and short (↑) – wavelength wings of the applied spectral range. The absorption spectrum (A) of a 300 nm thick TPD film is added for comparison. The applied voltage and excitation light intensity are given in the figure.

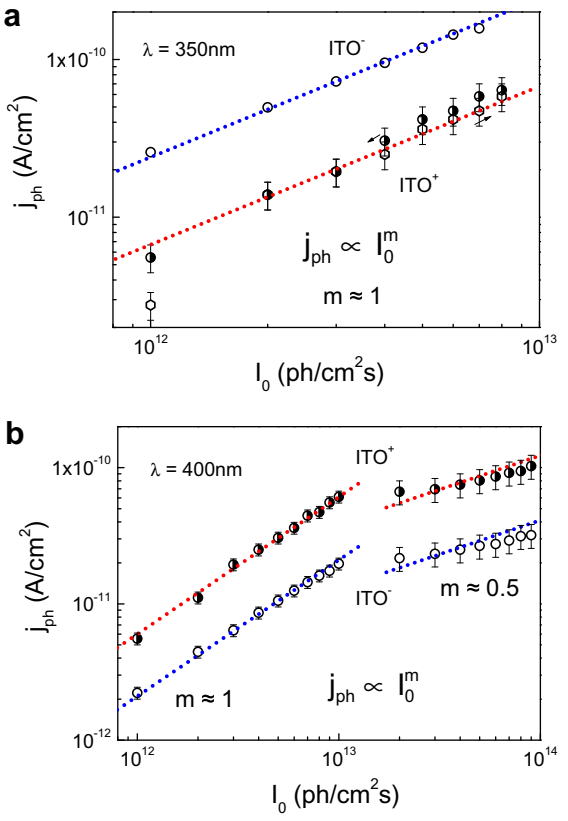

Fig. 3. The excitation light intensity dependence of the photocurrent for TPD structure (B) illuminated either through electrode ITO^+ or ITO^- at wavelengths 350 nm (a) and 400 nm (b), both at an electric field of $\approx 3.3 \times 10^4$ V/cm.

electrode. Fig. 2 shows the photocurrent action spectra for structure (A) and (B). It is strongly antibatic with the TPD absorption spectrum for $j_{ph}^{(+)}$ and shows symbatic features that is resembles the TPD absorption spectrum for $j_{ph}^{(-)}$. The light intensity (I_0) dependence of the photocurrents fits a $j_{ph} \propto I_0^m$ relationship with m varying from ≈1 for the low light intensity region (<10^{13} ph/cm^{2}s), tending to ≈0.5 for $I_0 > 10^{13}$ ph/cm^{2}s (Fig. 3). The dependence of the photocurrent on the applied electric field is complex but can be approximated by a linear $\ln j_{ph} \propto F^{1/2}$ function in the high field regime ($F > 1.5 \times 10^5$ V/cm) (Fig. 4).

4. Discussion

Photocurrents in solid organic films can arise from various processes: (i) optical release of trapped space charge in the bulk (photo-enhancement of space-charge-limited currents, SCLC), (ii) extrinsic unipolar carrier generation by exciton dissociation at the contact or the surface, and (iii) generation of carrier pairs in the bulk involving host or impurity molecules. The first possibility can be disregarded because the concentration of a volume space charge resulted from the dark current injection ($n = j_{dark}/e\mu F \approx 10^{10}$/cm^3 with $j \sim 10^{-7}$ A/cm^2 [13], the hole mobility in TPD $\mu = 10^{-3}$ cm^2/Vs [12], and e standing for the electron charge) appears to be much lower than the capacitor charge ($n = (3/2)\varepsilon_0\varepsilon F/ed \approx 10^{15}$/cm^3) which argues against SCL limitation of the dark current. Furthermore, it would lead to sublinear excitation intensity dependence with ($0.5 < m < 1$) which is not the case (see Fig. 3). The observed antibatic correlation with a strong maximum at ≈390 nm for $j_{ph}^{(+)}$ (ITO^+, Al_1^+) (Fig. 2) is compatible only with mechanism (ii). A symbatic response to the absorption spectrum of the current $j_{ph}^{(-)}$ (ITO^-, Al_1^-) between 370 and 400 nm passes into apparent antibatic behavior at the short-wavelength wing of he absorption spectrum below 330 nm (Fig. 2). This suggests the current to be governed by a combination of the carrier generation and bi-molecular recombination in the sample volume corresponding to mechanism (iii). However, at moderate and high light intensities ($\geqslant 10^{13}$ ph/cm^2 s), the photocurrents generated by lower photon energies, e.g. corresponding to the energy of S_1 exciton (≈3.1 eV → 400 nm), can be dominated by mechanism (iii) as well, their light intensity dependence $j_{ph} \propto I_0^m$ with $m \approx 0.5$ provides an experimental support for such a suggestion (see Fig. 3).

4.1. Exciton-induced electron injection

Carrier generation in accord with case (ii) can be described assuming that singlet excitons of the Frenkel type, produced by light absorbed in the TPD layer, diffuse towards the positive and/or negative electrode, where they can dissociate introducing a hole or an electron into TPD. Though singlet exciton-induced injection of holes at the anodes is energetically feasible (see Fig. 1b), a strongly antibatic correlation of the photocurrent for the ITO^+- and Al_1^+- biased structures (A) and (B), respectively (Fig. 2), indicates this process to be very inefficient. Therefore, the antibatic correlation of $j_{ph}^{(+)}$ has to be associated with electron injection at the respective cathodes (Al^-, Al_2^-). Calculation of either $j_{ph}^{(-)}$ or $j_{ph}^{(+)}$ requires solution of the diffusion differential equation for the exciton concentration, $N(x)$:

$$D\left(\frac{d^2N}{dx^2}\right) - \frac{N}{\tau} + \frac{I_0}{\ell_a}\exp\left(-\frac{x}{\ell_a}\right) = 0 \qquad (1)$$

where D is the diffusion coefficient of the excitons, τ is their intrinsic lifetime, $\ell_d = (2D\tau)^{1/2}$ the diffusion length for the one-dimensional diffusion, I_0 the incident light intensity, and $\ell_a = \alpha^{-1}$ the penetration depth of exciting light, where α is the linear absorption coefficient defined by the Bouguer–Lambert law $I = I_0\exp(-\alpha d)$. It has been shown that the solution of Eq. (1) under the conditions $\ell_d << d$ (such that $\exp(-d/\ell_d) \to 0$), where d stands for the film thickness, and $\ell_a < d$, yields [16]:

$$N(x) = \frac{I_0\tau}{\ell_d^2 - \ell_a^2}\left[\frac{\ell_d^2 + \ell_a\ell_d^2/c}{\ell_d + \ell_d^2/c}\exp\left(-\frac{x}{\ell_d}\right) - \ell_a\exp\left(-\frac{x}{\ell_a}\right)\right] \qquad (2)$$

Here, $\ell_d^2/c = \ell_q$ stands for the "quenching length" that is the length necessary for an exciton to be quenched at the interface. The diffusion motion is considered as a nearest-neighbor random walk on a simple cubic lattice with

the diffusion coefficient given by $D = (1/6)c^2/t_h$, where c is the lattice spacing and t_h is the mean time between hopping steps of length c.

The photocurrent densities are given by

$$j_{ph}^{(-)} \propto N(x=0) = G\frac{I_0\ell_d}{\ell_a+\ell_d} \tag{3}$$

and

$$j_{ph}^{(+)} \propto N(x=d) = G\frac{I_0\ell_d}{\ell_a-\ell_d}\exp\left(-\frac{d}{\ell_a}\right) \tag{4}$$

with $G = e\xi\eta/(1+\ell_d/k_{eff}c\tau)$ being a fraction of exciton flux transformed into the current flux, where the factor $(1+\ell_d/k_{eff}c\tau)$ gives the fraction of the excitons reaching the surface that is annihilated there, ξ is the probability that a charge carrier is produced as a result of surface reaction, and η is the factor accounting for the probability of the created carrier to contribute to the current. The factor $(1+\ell_d/k_{eff}c\tau) \to 1$ for the effective reaction constant $k_{eff} \to \infty$ or $(\ell_d/k_{eff}c\tau) \ll 1$, and equals zero for $k_{eff} \approx 0$.

While the $j_{ph}^{(-)}(\lambda)$ for $\lambda > 320$ nm follows roughly the absorption curve, the current $j_{ph}^{(+)}$ has a maximum at $\ell_a(\max) = (1/2)d + [(1/4)d^2 - \ell_d d]^{1/2} < d$ if $(\ell_d/\ell_a) \neq 0$, and $\ell_a(\max) \cong d$ if $(\ell_d/\ell_a) \to 0$ $(\ell_d \ll \ell_a)$. This is the case in Fig. 2, where $j_{ph}^{(+)}$ reaches its maximum at $\lambda \approx 390$ nm corresponding to $\ell_a(\max) \cong 300$ nm coinciding with the sample thickness. From the ratio of $j_{ph}^{(+)}(\max)/j_{ph}^{(+)}(\lambda)$ at a given λ chosen between $j_{ph}^{(-)}(\max)$ and $j_{ph}^{(+)}(\max)$, e.g. $j_{ph}^{(+)}(\max)/j_{ph}^{(+)}(\lambda) \approx 3.7$ at $\lambda = 375$ nm ($\ell_a = 91$ nm), $\ell_d = 32 \pm 5$ nm can

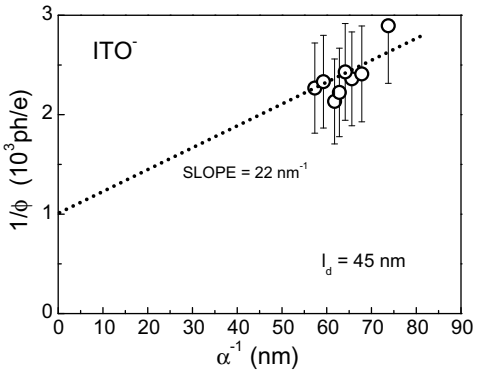

Fig. 5. The linear plot of the inverse of charge photogeneration efficiency vs the light penetration depth $\ell_a = \alpha^{-1}$ for the strictly symbatic part of the photocurrent efficiency action spectrum from Fig. 2d. $F = 3.3 \times 10^4$ V/cm and $I_0 = 10^{12}$ ph/cm^{2}s have been applied throughout the whole range of α^{-1} in the figure.

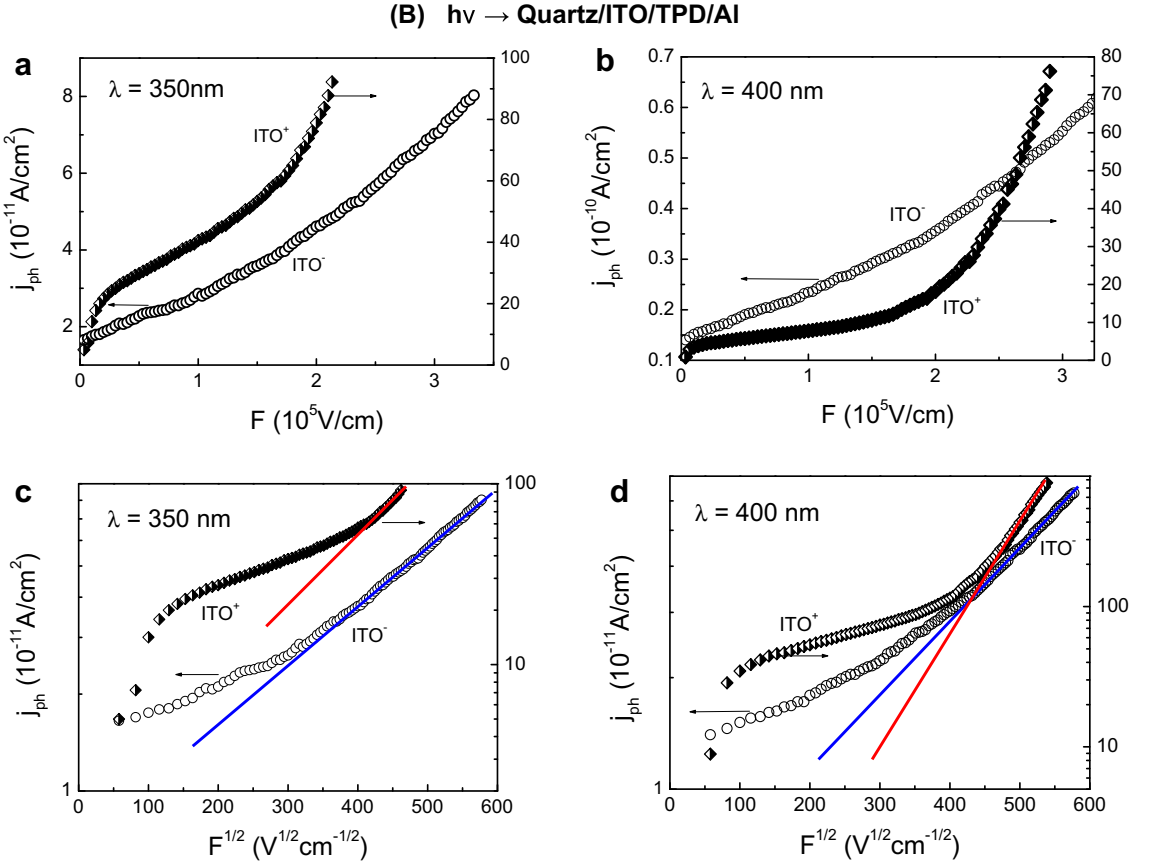

Fig. 4. The electric field dependence of the photocurrent in TPD structure (B) for the excitation intensity of 10^{12} ph/cm^{2}s at two different wavelengths and ITO electric biases given in the figure. The data are represented by two different plots: $j_{ph} \sim F$ (a and b) and $\log j_{ph} \sim F^{1/2}$ (c and d). The theoretical predictions following the 1D (ITO$^-$) and 3D (ITO$^+$) Onsager theory are indicated by solid lines.

be calculated using Eq. (4). A slightly larger value of $\ell_d = 45 \pm 8$ nm follows from the $1/\varphi$ versus $\ell_a = \alpha^{-1}$ plot which according to Eq. (3) is expected to be a straight line $1/\varphi^- = A + S\ell_a$ with the slope S (nm^{-1}) and intercept A (ph/e) (note that by definition $\varphi^- = j_{ph}^{(-)}/eI_0$). Indeed, this is the case presented in Fig. 5 for $j_{ph}^{(-)}$ (ITO^- case of structure (B)) where the intercept-to-slope ratio gives $A/S = 45 \pm 8$ nm. These are reasonable numbers comparable with the value of $\ell_d = 30 \pm 10$ nm obtained earlier for TPD films utilizing the quenching of the TPD fluorescence by a thin Alq_3 layer and its fluorescence as a detector of the quenched S_1 excitons of TPD [15]. A slightly larger present values of ℓ_d might be associated with the fact that neither $j_{ph}^{(-)}$ nor $j_{ph}^{(+)}$ are pure exciton-induced injection currents at the electrodes; they contain a weak component of bulk-generated currents. From $\ell_d = 32 \pm 5$ nm $D = \ell_d^2/2\tau = (5 \pm 1) \times 10^{-3}$ cm^2/s follows with $\tau = 1 \pm 0.1$ ns determined experimentally on pure TPD films [15]. This value of D is comparable with surface quenching experimental data on D for crystalline anthracene whenever the measured diffusion length of singlet excitons has been found to reach large values between 200 and 800 nm [17]. The shorter diffusion length of singlet exciton in TPD is due to the short lifetime as compared with anthracene singlets (9–27 ns) [17]. On the other hand, it is close to the diffusion coefficient $D_{c'} = 3.3 \times 10^{-3}$ cm^2/s of singlet excitons moving perpendicularly to the (ab) plane of single crystal of tetracene with singlet exciton lifetime $\tau_S \approx 2 \times 10^{-10}$ s at room temperature [18]. This indicates that excitons in TPD migrate by incoherent hopping, the mechanism generally thought to be appropriate for organic solids at room temperature. From the directly measured diffusion length and intrinsic lifetime, it is natural to use the diffusion constant for a nearest-neighbor random walk, which gives the hopping time $t_h = c^2/6D = 3 \times 10^{-13}$ s if the average distance between molecules of glassy TPD, $c = 0.9$ nm [12] is used in the calculation.

In the system metal-organic solid the dipole–dipole quenching mechanism (k_q) dominates usually over the charge-transfer (dissociation) mechanism (k_{dis}) in the exciton quenching [19], unless an organic solid is a strong electron acceptor like a molecular p-chloranil crystal [20], where charge transfer is a dominating quenching mechanism. Consequently, the surface photogeneration efficiency, φ, indicates the fraction of charge-transfer reactions, $\varphi \approx k_{dis}/k_q$. From the data of Fig. 2b and d the maximum values of φ for surface-injected currents follow: φ_{max} $(Al_1^-) \approx 7.5 \times 10^{-5}$ e/ph, φ_{max} $(Al_1^+) \approx 1.2 \times 10^{-5}$ e/ph for structure (A), and φ_{max} $(ITO^-) \approx 4.5 \times 10^{-4}$ e/ph, φ_{max} $(ITO^+) \approx 1.3 \times 10^{-4}$ e/ph for structure (B). To calculate the corresponding values of k_{dis} one needs to know k_q which has been shown to be a steep power decreasing function of the distance (δ) of the exciton from the metal interface, $k_q = 10^{-9}$ $cm^3 \times \delta^{-3}$ [21]. Its value is expected to differ for Al_1^-, Al_1^+, ITO^- and ITO^+ – illuminated electrodes because in addition to the natural asymmetry of ITO/Al electrode system, the 1.5 nm-thick layers of Al_2O_3 make structure with Al_1/Al_2 electrode system asymmetric too [13]. The k_q $(\delta = 1.5\ nm) \approx 3 \times 10^{11}$ s^{-1} at Al_1^- and $k_{dis}(Al_1^-) \approx 2 \times 10^7$ s^{-1}. We note that $k_q(\delta = 1.5$ nm) constitutes a fraction ≈ 0.1 of the average exciton jump frequency $\nu = t_h^{-1} = 3.3 \times 10^{12}$ s^{-1} that is only one of about 10 excitons impinging on the layer transfers its energy to Al. By this the Al_2O_3 layer appears to be a rather strong exciton reflector with the reflection coefficient ≈ 0.9.

If the quantum mechanical tunneling of the electron is the rate determining step of the exciton dissociation process, its rate constant can be expressed as $k_{dis}(\delta) = k_{dis}(0)\exp(-\delta/\delta_0)$, where $k_{dis}(0)$ is $k_{dis}(\delta)$ at $\delta = 0$ and $\delta_0 = \hbar/2(2m^*\Delta E)^{1/2}$, m^* being the effective electron mass and ΔE the energy gap between the tunneling electron and the electron acceptor level within the barrier. At low electric fields applied the metal electron has to traverse the rectangular barrier of thickness δ and height $\Delta E = E_c(Al_2O_3) - (I_{TPD} - E_S)$, where $E_c(Al_2O_3)$ is the conduction level (relative to vacuum) in Al_2O_3, I_{TPD} is the ionization potential of TPD (≈ 5.5 eV) and E_S is the energy of singlet exciton (≈ 3.2 eV). The wide gap ($E_g = 8.7$ eV) insulator Al_2O_3 contains a large concentration of electron traps extended from the conduction band edge down into the band gap, reaching a maximum concentration of more than 10^{18} cm^{-3} at 3.4 eV below this energy [22]. They act as the electron acceptor and electron conducting centers, so that $E_c \approx 3.4$ eV can be assumed. Then, $\Delta E \approx (3.4 - 2.3)$ eV = 1.1 eV and $\delta_0 = 0.35$ nm as calculated with $m^* = 0.35\ m_e$ (m_e – electron rest mass) [23]. Once having $k_{dis}(\delta = 1.5$ nm) and δ_0, the $k_{dis}(0) \approx 1.5 \times 10^9$ s^{-1} can be calculated with the barrier transparency 1.4×10^{-2}. These numbers differ from those for injection of holes in anthracene/fatty acid/Al system ($\delta_0 = 0.22$ nm, $k_{dis}(0) = 3 \times 10^{13}$ s^{-1}) [21]. The difference comes from different electrical properties of the barrier layers (m^* and ΔE). The much lower value of $k_{dis}(0)$ for the present system might be associated with an argument that an electron injection from the metal into an excited electron–hole pair located at a molecule may be considered as a three particle process which by definition is less effective than hole ejection which is a two-particle process. A lower value of φ_{max} $(Al_1^+) \approx 1.2 \times 10^{-5}$ e/ph can be explained by the electron injection from Al_2^- devoid the Al_2O_3 buffer at the TPD/Al contact. The probability of the electron injection is here proportional to the coupling matrix elements between the singlet exciton neutral bound state and an ionized state in TPD [24]. It is determined by the density of states in the continuum (metal) and by the penetration depth of one-dimensional Bloch waves in the forbidden gap of the organic layer. The latter is given by $\delta_B = \hbar/2(2m^*\Delta E)^{1/2}$ which yields a value $\delta_B \approx 0.07$ nm if $m^* = m_e$ and $\Delta E = E_F$ (Al) $- A_{TPD} = 2$ eV is assumed with $A_{TPD} = 2.3$ eV standing for the electron affinity of TPD (see Fig. 1). Clearly, the rate constants for exciton quenching and dissociation will depend on its distance δ on the interface as in the case of the above discussed tunneling effect. An effective critical quenching distance (δ_c) for an exciton can be defined at which the probability of energy transfer equals the probability of reflection, $k_q(\delta = \delta_e) = 10^{-9}$ $\delta_c^{-3} = \ell_d/c\tau$, $\delta_c \approx 3$ nm. The exciton dissociation at this distance would be rather an inefficient exciton decay channel since the exciton–ion coupling elements, being proportional to $\exp(-\delta/\delta_B)$, are very small ($\approx 10^{-19}$ for $\delta = \delta_c$). Assuming the dissociation to proceed from the first molecular layer adjacent to the Al_2^- (Al_1^+) electrode ($c \approx 0.9$ nm), we arrive at $k_q(\delta =$

0.9 nm) $\approx 1.4 \times 10^{12}\ s^{-1}$, $k_{dis}(\delta = 0.9\ nm) = \varphi(Al_1^+) \times k_q(\delta = 0.9\ nm) \approx 1.2 \times 10^{-5} \times 1.4 \times 10^{12}\ s^{-1} \approx 2 \times 10^7\ s^{-1}$, and $k_{dis}(0) \approx 7.7 \times 10^{12}\ s^{-1}$. In contrast to the anthracene/Al system, $k_{dis}(0)$ within a factor of two is comparable with the average jump frequency of the exciton between neighboring hopping sites, $t_h^{-1} = 3 \times 10^{12}\ s^{-1}$. This suggests that the yield of dissociation reaction is determined by diffusion of excitons towards the surface rather than by the strong exciton–ion coupling.

Interestingly, the charge photogeneration yield in structure (B) exceeds by an order of magnitude of that in structure (A) (Fig. 2b and d). The reasons are two fold: (i) a greater charge dissociation contribution to the total quenching process of singlet excitons at the ITO^-/TPD contact, and (ii) increasing of the concentration of singlet excitons at the Al^- cathode (ITO^+/TPD) due to the recombination of holes injected efficiently at the ITO^+ anode and electrons located nearby the Al^- cathode. The first reason is understood in view of the lower electron concentration in ITO as compared with metal electrodes and better matching of its HOMO-to-TPD LUMO gap with singlet exciton energy level. A more detailed study of exciton quenching processes at the ITO/organic solid contact is needed to get more quantitative insight in the electron traffic through this interface. The second reason gets its strong support from a relatively efficient hole injection at the ITO^+ anode and a large difference between hole and electron mobilities in TPD [12]. The high mobility holes reach in a microsecond the close neighborhood of Al^- cathode, where they recombine with quasi immobile electrons there accumulated. A quite a large number of singlet excitons created as a result of this recombination process contributes to the electron injection at Al^-, enhancing the observed effective photogeneration yield.

4.2. Intrinsic photocarrier generation

The general expression for the photocurrent density including the bulk generation mechanism (iii) is defined by [25]

$$j = \frac{2e\eta I_0[1 - \exp(-\alpha d)]}{1 + \tau_t/\tau_{rec}}, \tag{5}$$

where $\tau_t = d/2\mu F$ is the average transit time of carriers to electrodes and $\tau_{rec} = (\gamma n)^{-1}$ is the recombination time of oppositely charged carriers populated at concentration n and annihilating with the second order rate constant, γ, related indirectly to the carrier mobility, μ. The following limits for Eq. (5) can be distinguished: (a) $\tau_t/\tau_{rec} << 1$, thus

$$j \cong 2e\eta I_0[1 - \exp(-\alpha d)], \tag{6}$$

and (b) $\tau_t/\tau_{rec} >> 1$, thus

$$j \cong 2eI_0\ [1 - \exp(-\alpha d)]\frac{\tau_{rec}}{\tau_t} = \frac{4e\mu F}{d}\left(\frac{\eta I_0}{\alpha\gamma}\right)^{1/2}[1 - \exp(-\alpha d)] \tag{7}$$

obtained with the average recombination time $\tau_{rec} \cong \alpha \int_0^{1/\alpha} dx/\gamma n(x)$, and $n(x) \cong \alpha\eta I_0/\gamma)^{1/2}\exp(-\alpha x/2)$.

While Eq. (6) represents the lower light intensity limit featured by linear increase of the current with excitation intensity, I_0, Eq. (7) stands for the upper limit for high light intensities with the current following the square root of the exciting light intensity. The latter comes from the carrier kinetics assuming the bi-molecular recombination to dominate the carrier decay. The second limit with $j_{ph} \sim I_0^{1/2}$ is identified above $I_0 \cong 10^{13}$ ph/cm^{2}s (Fig. 3b). Fig. 4 shows that upon application of increasing electric field, photocurrent increases in different manner dependent on the polarization of the illuminated electrode ($j_{ph}^{(-)}, j_{ph}^{(+)}$) and the wavelength of the active light. The field dependence of the photocurrent is expected to include that for the photogeneration efficiency, η, (see Eq. (7)). It is likely that in the high field region ($F > 1.5 \times 10^5$ V/cm), the photocurrent plots reflect either the surface generated currents described by $j = A_0F^{3/4}\exp(aF^{1/2})$ and based on the 1D version of the Onsager theory of geminate recombination, where A_0 is a constant dependent on I_0 and $a_{theor} = (e/kT)(e/4\pi\varepsilon_0\varepsilon)^{1/2} = 8 \times 10^{-3}$ (cm/V)$^{1/2}$ obtained with $\varepsilon = 3$ [12,26]. A bulk photogeneration process is often interpreted in terms of the 3D-Onsager model which, in general, provides a complex expression for $\eta(F)$ (see e.g Ref. [1]). However, it can be approximated by a Poole–Frenkel type function if the separation distance of the geminate e...h pairs is short enough, i.e. less than one or two intermolecular spacings [19,27]

$$\eta_{PF}(F) = \eta_0\frac{\exp(\beta_{PF}F^{1/2})}{A_{PF} + \exp(\beta_{PF}F^{1/2})} \cong \eta_0\frac{k_{eh}(F=0)}{k_R}\exp(\beta_{PF}F^{1/2}) \tag{8}$$

where η_0 is the primary quantum yield in carrier pairs for the absorbed photon (assumed to be independent of the applied field), $A_{PF} = k_R/k_{eh}(F = 0)$ is a constant determining the branching ratio of recombination (k_R) and pair generation (k_{eh}) channels at $F = 0$, and $\beta_{PF} = (e^3/\pi\varepsilon_0\varepsilon)^{1/2}$ a characteristic PF parameter with the value of two times of the Schottky parameter, a, $\beta_{PF} = 2a$. On the PF formalism premise, the absence of the high field saturation tendency in $j_{ph}(F)$ curves in Figs. 4c,d means that $A_{PF} > \exp(\beta_{PF}F^{1/2})$. Interestingly, the slopes of the high-field segments of the $\ln j_{ph}^{(-)} - F^{1/2}$ plots with the ITO^--biased structure (B) amount an average value (for two different excitation wavelengths) $\partial \log j_{ph}^{(-)}/\partial F^{1/2} \approx (5 \pm 2) \times 10^{-3}$ cm/V, approaching within a factor of 0.6 ± 0.3 the theoretical value of a, while the average slope $\partial \log j_{ph}^{(+)}/\partial F^{1/2} \approx (10 \pm 2) \times 10^{-3}$ cm/V for $j_{ph}^{(+)}$ exceeds this value by a factor of about 2, suggesting $j_{ph}^{(+)}$ to follow the 3D and $j_{ph}^{(-)}$ the 1D Onsager formalism for the photocarrier production. We explain this result at the premise of different contributions of two photocurrent components, one originating from the near-cathode surface regions, thus dominating the ITO^--biased current flow, and the second from a bulk photogeneration process dominating the photocurrent with ITO^+ bias. A systematic deflection of a and β_{eff} from their calculated values has no simple explanation though one can speculate an increased local effective temperature caused by the excited states or a specific disorder (trap) effect [26] at the electronically active interface to be responsible for these differences.

5. Concluding remarks

The excitation light wavelength-, light intensity-, and applied electric field-dependent photoconduction of solid TPD (the archetype of the hole transporting material for organic LEDs) sandwiched between two semitransparent Al electrodes (Quartz/Al_1/Al_2) and Quartz/ITO/Al electrodes has been shown to be underlain by either injection of electrons or intrinsic bulk photogeneration process. The results have been analyzed in terms of a kinetic model for electric-field-assisted dissociation of singlet excitons, TPD^*, at the negatively biased electrodes, and their dissociation in the bulk, based on the 1D and a Poole–Frenkel approximation of the 3D version of the Onsager theory of geminate recombination, respectively. The satisfactory agreement between experiment and theory of charge-transfer exciton reactions on the surface is obtained with the singlet exciton diffusion length $\ell_d = 32 \pm 5$ nm (thus the diffusion coefficient $D = 5 \pm 1 \times 10^{-3}$ cm^2/s). The high field region ($F > 1.5 \times 10^5$ V/cm) dependence follows either the 1D-Onsager model for electron injection, or 3 D-Onsager model for the bulk generation well illustrated by the structure Quartz/ITO/Al with negative and positive electrical ITO bias, respectively. The data follow well $\log j_{ph} - F^{1/2}$ straight lines with the slopes ratio ≈ 0.5 as predicted by the high field approximations of $j_{ph}(F)$ in these two models.

References

[1] J. Kalinowski, Organic Light Emitting Diodes: Principles, Characteristics and Processes, Marcel Dekker, New York, 2005.
[2] C.W. Tang, S.A. VanSlyke, Appl. Phys. Lett. 51 (1987) 913.
[3] C.W. Tang, S.A. VanSlyke, C.H. Cheng, J. Appl. Phys. 65 (1989) 3610.
[4] P.E. Burrows, S.R. Forrest, Appl. Phys. Lett. 64 (1993) 2285.
[5] P.E. Burrows, Z. Shen, V. Bulovic, B.M. McCarty, S.R. Forrest, J.A. Cronin, M.E. Thompson, J. Appl. Phys. 79 (1996) 7991.
[6] J. Kalinowski, N. Camaioni, P. Di Marco, V. Fattori, G. Giro, Int. J. Electron. 81 (1996) 377.
[7] S.R. Forrest, P.E. Burrows, M.E. Thompson, in S. Miyata, H.S. Nalwa (Eds.), Organic Electroluminescent Materials and Devices, Gordon & Breach, Amsterdam, 1997 (Chapter 13).
[8] C. Giebeler, H. Antoniadis, D.D.C. Bradley, Y. Shirota, J. Appl. Phys. 85 (1999) 608.
[9] G. Giro, M. Cocchi, J. Kalinowski, V. Fattori, P. Di Marco, P. Dembech, G. Seconi, Adv. Mater. Opt. Electron. 9 (1999) 189.
[10] J. Kalinowski, in S. Miyata, H.S. Nalwa (Eds.), Organic Electroluminescent Materials and Devices, Gordon & Breach, Amsterdam, 1997 (Chapter 1).
[11] Y. Shirota, K. Okumoto, Proc. SPIE 4105 (2001) 158.
[12] M. Stolka, J.F. Janus, D.M. Pai, J. Phys. Chem. 88 (1984) 4707.
[13] J. Kalinowski, K. Szybowska, Org. Elecr. 9 (2008) 883.
[14] A.J. Campbell, D.D.C. Bradley, J. Laubender, M. Sokolowski, J. Appl. Phys. 86 (1999) 5004.
[15] J. Kalinowski, G. Giro, P. Di Marco, N. Camaioni, V. Fattori, Chem. Phys. Lett. 265 (1997) 607.
[16] B.J. Mulder, Philips Res. Rep. Supplement 4 (1968).
[17] R.C. Powell, Z.G. Soos, J. Lumin. 11 (1975) 1.
[18] G. Vaubel, H. Bässler, Mol. Cryst. Liq. Cryst. 12 (1970) 47.
[19] M. Pope, C.E. Swenberg, Electronic Processes in Organic Crystals, Oxford University Press, Oxford, 1982.
[20] H. Killesreiter, H. Bässler, Phys. Status Solidi (b) 51 (1972) 657.
[21] H. Killesreiter, H. Bässler, Chem. Phys. Lett. 11 (1971) 411.
[22] D.A. Mehta, S.R. Butler, F.J. Fegl, J. Appl. Phys. 43 (1972) 4631.
[23] L. Braginsky, V. Sklover, H. Hofmann, P. Bowen, Phys. Rev. B 70 (2004) 134201.
[24] J. Singh, H. Bässler, Phys. Stat. Solidi (b) 62 (1974) 147.
[25] J. Kalinowski, W. Stampor, J. Szmytkowski, M. Cocchi, D. Virgili, V. Fattori, P. Di Marco, J. Chem. Phys. 122 (2005) 154710.
[26] J. Godlewski, J. Kalinowski, Jpn. J. Appl. Phys. (Part 1) 28 (1989) 24.
[27] J. Kalinowski, W. Stampor, P. Di Marco, J. Chem. Phys. 96 (1992) 4136.

OTFT. Note that organic single and bilayers using PVA, PA and parylene have the WVTR of 10^{-1}–10^{-2} g/m^2/day according to our measurements.

Fig. 1 shows the process flow for the hybrid passivation layer on OTFT backplane on plastic. The backplane was fabricated by photolithographic process. Polyethylenenaphthalate (PEN, Dupont Teijin) was used as a substrate after annealing at 180 °C for 4 h for degassing, and then 100 nm-thick silicon–nitride (SiN_x) was deposited on both sides as gas barriers. Ductile metal, AlNd, was sputtered on the gas barrier as a gate electrode and patterned by photolithography. On gate electrodes, dielectric layer of poly(4-vinylphenol) (PVP) with cross-linking agent was spin-coated and cured in a vacuum oven at 180 °C for 4 h. Then, PVP was etched by oxygen plasma to make holes for electrical contacts. As source/drain electrodes, Cr (5 nm)/Au (50 nm) were deposited by sputtering and patterned by photolithography. The ratio of channel width to length ratio (W/L) was fixed at 100 μm/8 μm for all the samples shown in this paper.

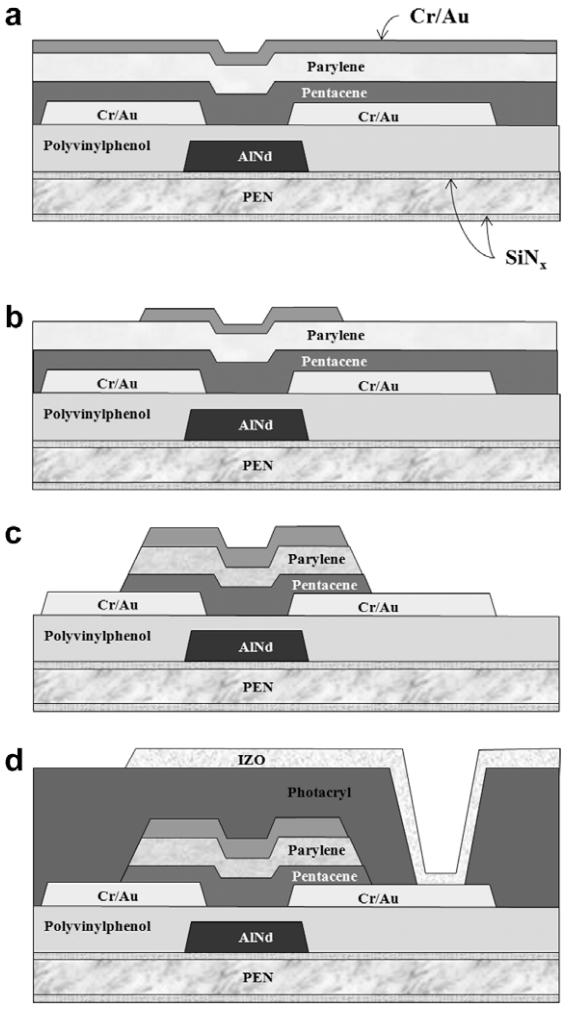

Fig. 1. Process flow for HML passivation layers for OTFT array on plastic (a) deposition of pentacene, parylene and Cr/Au, (b) patterning of top Cr/Au, (c) dry etching of parylene and pentacene, (d) deposition and patterning of PA and IZO.

Prior to pentacene deposition, the substrate was treated with octadecyltrichlorosilane to enhance the performance of pentacene OTFT [12]. After the treatment, three layers of pentacene (100 nm), parylene (1.5 μm) and Cr (5 nm)/Au (80 nm) were deposited on the substrate as shown in Fig. 1a. In our equipment a pentacene chamber is connected to a parylene chamber, therefore, both materials can be deposited without vacuum break. Here, pentacene was deposited by organic flow deposition (made by ADP Engineering) at the pressure of 1 Torr and parylene was polymerized in a vacuum chamber. Metal layer of Cr/Au was deposited by DC magnetron sputtering.

The top Cr/Au was patterned by photolithography using potassium iodine based etchant as shown Fig. 1b. Then, parylene and pentacene layers were isolated by dry etching at the pressure of 16 mTorr and the power of 50 W (Fig. 1c). After the isolation, 1 μm-thick PA (Dongjin Semichem) was spun on the substrate and patterned by UV exposure to make holes for electrical contacts. The patterned PA was cured at 150 °C for 1 h. Finally, 100 nm-thick IZO was sputtered and patterned on the substrate. After the whole fabrication process, the OTFTs were annealed at 150 °C and 180 °C, respectively, for 1 h in vacuum and measured in ambient air with storage time. During the time, the average relative humidity and temperature were 45% and 25 °C, respectively.

Fig. 1d shows the OTFT structure in a pixel with the hybrid passivation layer. Pentacene layer is sandwitched between IZO/PA/Au(/Cr)/parylene (top) and SiN_x/PEN/SiN_x/AlNd/PVP (bottom). Therefore, the organic semiconductor is passivated by organic/inorganic layers, showing a good barrier performance against water and oxygen permeations.

Moreover, the TFT structure can be in a pixel of the backplanes for LCD and EPD, where the pixel electrode of ITO or IZO is overlapped with OTFT. This is a kind of a field-shielding pixel structure, which shields the electric field of the common electrodes from the LCD and EPD. It can increase the aperture ratio [13], however, the capacitive coupling between Au and IZO changes the threshold voltage (V_T) because a top-gate of Au is floating. From the design used in this work, the capacitance between drain and top Cr/Au metal is 18% of the capacitance between drain and bottom gate. This means that a typical driving voltage of 10 V yields a maximum V_T shift of 1.8 V by capacitive coupling. This value does not affect display image seriously because the maximum V_T shift is occurred only when V_D changes from high to low or vice versa. Note that the overlap between source/drain electrodes and gate electrode is 3 μm, which is the conventional design rule in the manufacturing of amorphous silicon TFT backplane.

In contrast to EPD process of simple lamination, LCD processes such as curing of LC alignment layer and hot-pressing require high temperature (~180 °C) process. Therefore, the backplane based on OTFT should endure such a high temperature heating and maintain its initial performance.

Fig. 2 shows the change in the transfer characteristics of the passivated OTFT annealed at 150 °C and 180 °C for 1 h, respectively. Here, 180 °C is the maximum process temperature because of the PEN substrate used in the present

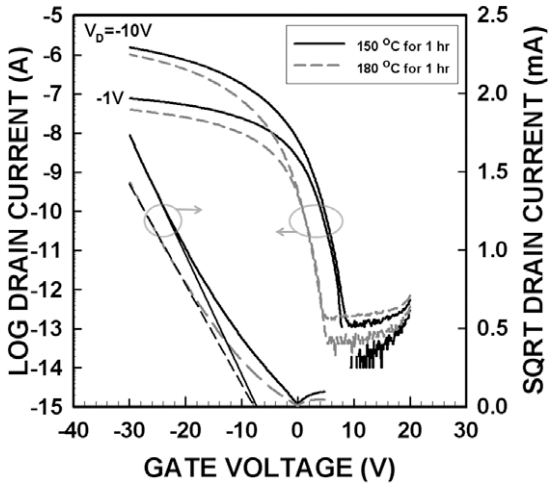

Fig. 2. Transfer and mobility characteristics of the HML-passivated OTFT annealed at 150 °C (–) and 180 °C, (---) for 1 h.

work. The electrical performances of OTFTs annealed at 150 °C exhibited a field-effect mobility (μ_{fe}) of 0.2 ~ 0.3 cm^2/V s, V_T of −8.0 to −11 V and an on/off current ratio (I_{on}/I_{off}) of 10^7. After annealing at 180 °C, μ_{fe} were slightly decreased by 0.03 cm^2/V s, however, the change in V_T was negligible. The devices on a plastic substrate have a hundred of OTFTs with channel widths of 100, 200 and 500 μm with length of 8 μm. Even though the values of mobility and threshold voltage for the TFTs are slightly different, there was no dependence on the channel width. All the performances of the TFTs reported in this paper have the same W/L ratio of 100 μm/8 μm.

Another important observation is V_{on} enhancement. The difference between V_T and V_{on} is related to a distribution of shallow traps in the gap states, therefore, $|V_T - V_{on}|$ is zero in ideal case [14]. In the case shown in Fig. 2, $|V_T - V_{on}|$ was decreased from 17 V to 13 V by 4 V after 180 °C annealing. This indicates that the gap states, which might be caused by structural defects and impurities, are partially deactivated and/or reduced after the annealing.

In spite of the degradation in μ_{fe}, the performance is suitable for driving displays and it is turned out that the maximum process temperature is limited by not the fail of OTFT but the PEN substrate.

Fig. 3a shows the transfer characteristics of the HML-passivated OTFT measured in ambient air until the storage for 781 h. The changes in I_{off}, S and V_{on} are negligible during the storage, and this indicates that HML using organic/inorganic combination has a good barrier performance against water and oxygen permeations.

Fig. 3b shows the I_{on} and I_{off} at drain voltage (V_D) of −10 V as a function of storage time, which was extracted at V_G of −30 V (I_{on}) and + 4 V (I_{off}). In our previous work, the bilayer of PVA and PA was used for OTFT passivation [7]. In that case, V_T shifted to positive direction and thus compensated for the degradation in μ_{fe}. That effect was explained by oxygen doping effect. In the present work, the changes in μ_{fe} and I_{off} were negligible after the storage of 781 h in air. This means that the doping effect is not dominant because of excellent barrier performance of HML. The

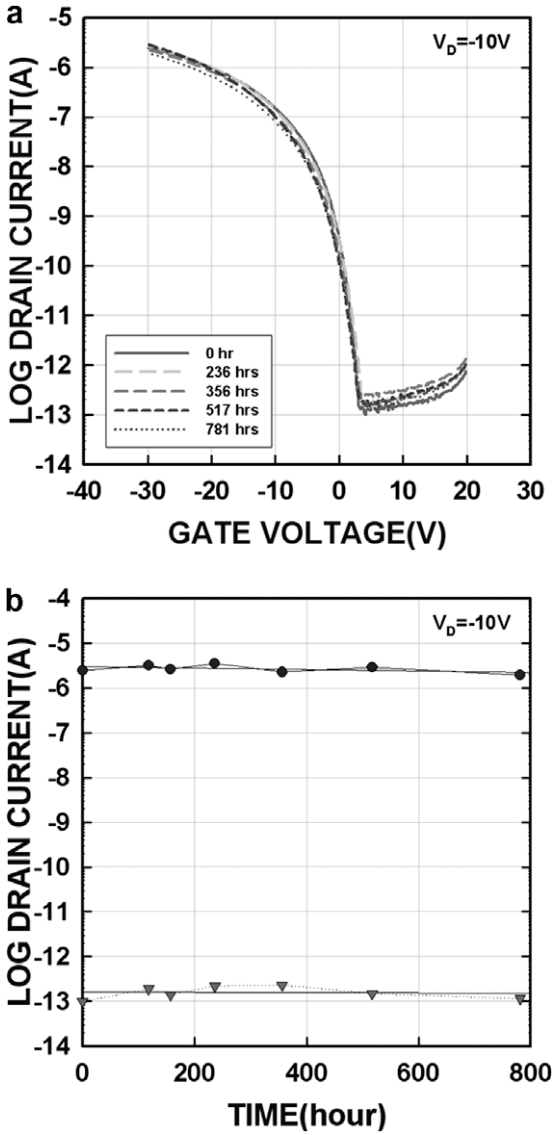

Fig. 3. Transfer characteristics (a) and I_{on}/I_{off}, (b) of the HML-passivated OTFT measured in ambient air.

small negative shift of V_T seems to be caused not by impurities from ambient air but bias-stress effect during the repeated measurement.

Fig. 4 shows the hysteresis in the transfer characteristics after storage in ambient air for 781 h. The hysteresis of OTFT can be caused by various origins such as charge trapping, mobile ion and dielectric polarization and become larger when the OTFT is exposed to ambient air [15]. As shown in Fig. 4, HML-passivated OTFT showed a small hysteresis less than 1 V in the transfer characteristics although it was exposed to ambient air for 781 h. This small hysteresis is consistent with the stability in subthreshold region as shown in Fig. 3a and the HML is effective against impurity adsorption from ambient air.

In our previous work, we developed a method to extract the storage lifetime of OTFTs from the I_{on} variation [7], and the storage lifetime of 11,000 h was obtained using PVA/PA

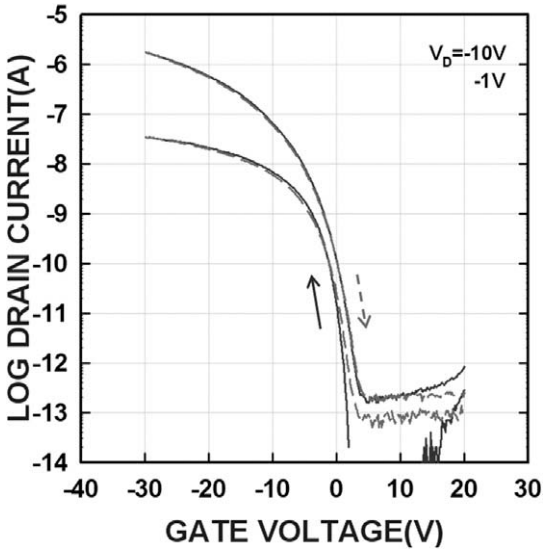

Fig. 4. Hysteresis in the transfer characteristics after storage in ambient air for 781 h.

passivation. The long lifetime is mainly due to the oxygen doping effect which shifted the V_T. This increases the currents in the subthreshold region. In the present work, the TFT performance is quite stable in on- and off-states due to better barrier performance of HML.

In conclusion, we fabricated pentacene OTFTs using HML of parylene/Au/PA/IZO, organic/inorganic multi-layer. The HML-passivated OTFT exhibited μ_{fe} of 0.20–0.30 cm^2/V s with high I_{on}/I_{off} of 10^7. After annealing at 180 °C the HML-passivated OTFT was stable during the storage time of 781 h and the changes in on-, off- and subthreshold currents were negligibly small. The hysteresis in transfer characteristics was less than 1 V, after the expose of the OTFT to ambient air for 781 h. These indicate that HML-passivation is suitable for making stable OTFT array.

This work was supported by a grant from Information Display R&D Center, one of the 21st Century Frontier R&D Program funded by the Ministry of Commerce, Industry and Energy of Korean government.

References

[1] K. Nomoto, N. Hirai, N. Yoneya, N. Kawashima, M. Noda, M. Wada, J. Kasahara, IEEE Trans. Electron. Dev. 52 (2006) 1519.
[2] Y. Fujisaki, H. Sato, T. Yamamoto, H. Fujikake, S. Tokito, T. Kurita, J. Soc. Inf. Display 15 (2007) 501.
[3] L. Zhou, A. Wanga, S.-C. Wu, J. Sun, S. Park, T.N. Jackson, Appl. Phys. Lett. 88 (2006) 083502.
[4] M. Mizukami, N. Hirohata, T. Iseki, K. Ohtawara, T. Tada, S. Yagyu, T. Abe, T. Suzuki, Y. Fujisaki, Y. Inoue, S. Tokito, T. Kurita, IEEE Electron. Device Lett. 27 (2006) 249.
[5] I. Yagi, N. Hirai, Y. Miyamoto, M. Noda, A. Imaoka, N. Yoneya, K. Nomoto, J. Kasahara, A. Yumoto, T. Urabe, J. Soc. Inf. Display 16 (2008) 15.
[6] H. Maeda, M. Matsuoka, M. Nagae, H. Honda, T. Suzuki, K. Ogawa, H. Kobayashi, SID Symposium Digest Tech. Papers 23 (2008) 314.
[7] S.H. Han, J.H. Kim, J. Jang, S.M. Cho, M.H. Oh, S.H. Lee, D.J. Choo, Appl. Phys. Lett. 88 (2006) 073519.
[8] T. Sekitani, T. Someya, Jpn. J. App. Phys. 46 (2007) 4300.
[9] W. Kim, W. Koo, S. Jo, C. Kim, H. Baik, J. Lee, S. Im, Appl. Surf. Sci. 252 (2005) 1332.
[10] H. Jung, T. Lim, Y. Choi, M. Yi, J. Won, S. Pyo, Appl. Phys. Lett. 92 (2008) 163504.
[11] P.E. Burrows, G.L. Graff, M.E. Gross, P.M. Martin, M.K. Shi, M. Hall, E. Mast, C. Bonham, W. Bennett, M.B. Sullivan, Displays 22 (2001) 65.
[12] H.Y. Choi, S.H. Kim, J. Jang, Adv. Mater. 16 (2004) 732.
[13] G.H. Gelinck, H.E.A. Huitema, M. van Mil, E. van Veenendaal, P.J.G. van Lieshout, F. Touwslager, S.F. Patry, S. Sohn, T. Whitesides, M.D. McCreary, J. Soc. Inf. Display 14 (2006) 113.
[14] C.R. Newman, C.D. Frisbie, D.A.da S. Filho, J.-L. Brédas, P.C. Ewbank, K.R. Mann, Chem. Mater. 16 (2004) 4436.
[15] J.B. Koo, C.H. Ku, S.C. Lim, S.H. Kim, J.H. Lee, Appl. Phys. Lett. 90 (2007) 133503.

provide a large on-state current, which is often limited by the low carrier mobility, and a high on/off ratio. A proper tailoring of material properties is therefore required. On the other hand, organic systems offer large flexibility in their synthesis, since new materials can be chemically synthesized it is reasonable to assume that the desired properties can be eventually reached. Another important limitation for the use of organic materials in microelectronic industry is the lack of an appropriate integration scheme. Therefore, developing a compatible route for the integration of these materials is highly desirable.

The integration of polymers into microelectronic devices is still a challenging task, because most of the standard processes used in device fabrication, most notably photolithography, are not fully compatible with this kind of materials. These incompatibilities are mostly due to the conventional photolithographic techniques, generally used for patterning inorganic materials, that often involve harsh chemical treatments with acids and wet based processing steps. These treatments may deteriorate the optical and electrical properties of typical functional organic materials. This damage occurs mostly because polymers undergo photodegradation and oxidation in the presence of strong UV radiation, oxygen and acids [9]. In addition, during device patterning some chemical reactions between the conducting polymer and the photoresist required for optical lithography are possible, especially if a thermal treatment or exposure to UV light is employed. Finally, some interactions with the solvents used (i.e. acetone, isopropanole) might affect the final result, e.g. inducing peeling, swelling, or cracking. To overcome these drawbacks, several alternative approaches have been proposed in literature. Among them, inkjet printing is a very promising low cost technique for device fabrication from solution processable materials [10,11]. However, the spatial resolution that can be achieved can barely follow the aggressive scaling required by the microelectronic industry. Nonetheless, in this direction some recent publications are reported with very promising results [12,13]. Microcontact printing is another potential patterning approach where the pattern of a self assembling monolayer (SAM) is transferred from an elastomeric stamp onto the substrate [14–16]. Finally, screen printing has attracted considerable attention since it is a fast, low cost coating technique [17]. However, the compatibility of the above mentioned techniques with standard CMOS technology is still an issue. Device patterning by UV lithography still remains the most attractive technique, since it is a well established method for large scale manufacturing and allows the fabrication of complex structures, such as vertically stacked devices. The possibility of applying this technique in a non destructive manner for the integration of organic devices is highly desirable and eventually could lead to the fabrication of inexpensive devices using existing production equipment.

In this study we demonstrate a possible route for the integration of small size polymeric Schottky diodes in a crossbar architecture by standard UV lithography. Poly(3-hexylthiophene) (P3HT) was chosen as the model organic material since it is widely studied, it has a relatively high charge carrier mobility [18], also many publications can be found in the literature concerning its properties [19]. In addition, we also tested our strategy on different materials comprising oligomers of polyphenylenevinylene (OPV) in order to investigate the compatibility of the process with several compounds. In Fig. 1 the molecular structures of the compounds, which were tested in this study, P3HT and OPV5, are presented. The proposed approach is based on the deposition of a passive dielectric matrix on top of the bottom electrode of the junction; in this layer via-holes are opened and subsequently filled with the organic material, before the top electrode fabrication step. Consequently, the active layer is deposited only at the intersection between the top and the bottom electrode of the junction. By applying this approach, it is possible to integrate micron size junctions in a reproducible way by avoiding the deterioration of the functional materials during the sequence of the lithographic steps. The electrical characteristics of the as prepared junctions reveal the successful patterning of the material and demonstrate the compatibility of the process with the tested compounds.

2. Integration approach

Several approaches can be found in literature regarding the application of UV lithography for the integration of organic molecules in electronic devices. Recently, an approach was proposed for OLED applications [20] employing the sequential deposition of many of the re-

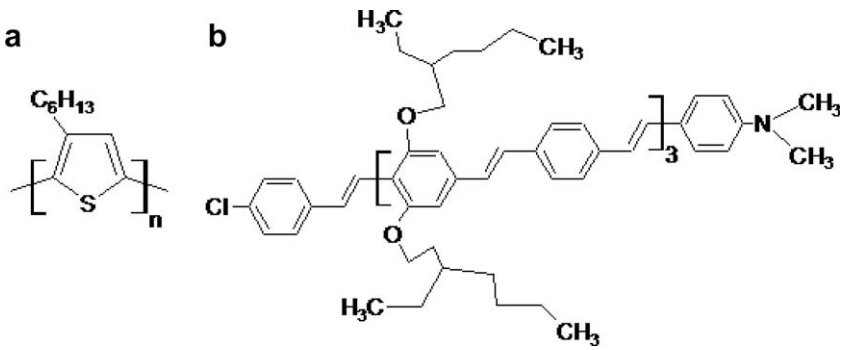

Fig. 1. Molecular structures of the organic compounds that were investigated in this work: (a) P3HT and (b) OPV5.

quired layers on top of the organic compound, which then act as a capping layer; finally, the full stack is patterned by UV lithography and dry etched. The final structure was obtained without damaging the organic material. This method is quite effective and can be applied for simple patterning but in case of a more complicated structure a more elaborate approach may be required. Another approach that has been proposed involves the deposition of an intermediate protective layer (a buffer layer) on top of the polymeric compound to protect it from the potential aggressive steps [21]. Well defined geometric features could be produced by applying this scheme. However, this method involves the use of an additional process step, the deposition of the capping layer, a parylene layer, by CVD method, which may not be compatible with some materials and moreover may damage the polymeric compound during the mechanical peeling of the buffer layer. In a recent report it is claimed that the direct exposure of P3HT (at an energy of about 150 mJ/cm^2) does not deteriorate its electrical properties [22], and therefore direct patterning of the polymeric compound is proposed. Eventhough this approach is very attractive and would simplify the patterning process, we decided to focus on the development of a method that is compatible with several different organic compounds and not only with P3HT.

Before discussing our strategy, we also address the difficulties of the crossbar structure when a polymer is involved. In crossbar architectures the active material is placed between the intersections of two perpendicular metal lines, therefore a top electrode patterning is required. In case of an inorganic compound a conventional patterning can be performed in both the active material and the top electrode. When a polymer is involved in the process, conventional patterning is possible only if the polymer is fully protected from any exposure to chemicals, i.e. the basic developer or the acidic solution that is used for the top electrode etching. In a recent approach, molecular crossbar junctions are prepared in the holes of a lithographically patterned photoresist and the junction is fabricated by inserting a conducting polymer between a self assembled monolayer and the top electrode, which is then deposited through a shadow mask [23,24]. Excellent stability is reported because of the encapsulation of the diodes by the photoresist, which is not removed and acts as a dielectric matrix.

In this study we adopted a similar approach, i.e. the use of a passive layer where via-holes are created by UV lithography and filled with the polymer. The passive layer is a deposited dielectric film with known properties and controlled thickness. To fulfill the above-mentioned requirements and to avoid degrading the polymeric compound, the most suitable approach for the polymer patterning is the lift-off method, which also allows minimizing the number of the integration steps [25]. Therefore, after via-holes etching, the photoresist is not removed and is used as a mask. The polymer is deposited on top of it and then, by performing a lift-off process, the semiconductor is finally kept only in the desired areas. The desired pattern is achieved without performing an additional lithographic step, the structure is self-aligned and possible misalignments related to an additional patterning of the polymer layer are avoided.

In Fig. 2 a detailed schematic process flow of the patterning steps sequence, which was used in order to integrate P3HT Schottky junctions, is presented. At the first step the bottom electrode is deposited through e-beam assisted or thermal evaporation and then is being patterned through the lift-off method (A). In the second step the dielectric matrix is deposited, subsequently patterned by UV lithography and wet etching (B), in order to achieve the desired pattern. At the next step the polymer is deposited on top of the already patterned photoresist (C) then is lifted-off with an appropriate solvent (D). Finally, at the last stage, the top electrode is deposited by thermal evaporation and subsequently patterned by UV lithography and

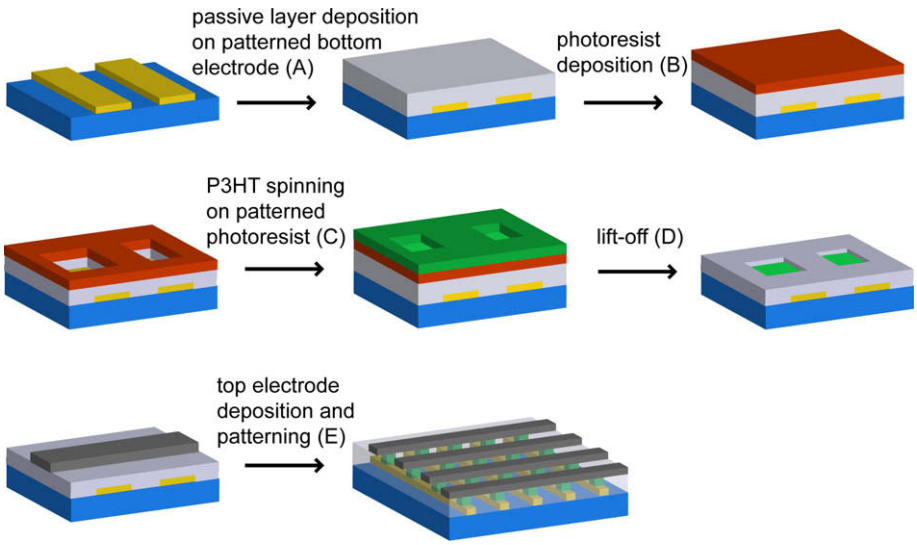

Fig. 2. Schematic diagrams of the lithographic steps sequence in order to pattern polymers films in a crossbar architecture.

wet etching (E). Experimental details for each integration step are given in the text below.

3. Device fabrication

In this study a Si-n^+ wafer coated with 100 nm thermally grown silicon dioxide was used as the substrate. A 35 nm layer of Au was deposited by e-beam assisted evaporation and patterned through UV lithography and lift-off. A thin layer of Ti (15 nm) was previously evaporated on top of the oxide in order to promote the adhesion of Au on the substrate. The dielectric layers used in this study were silicon dioxide (SiO_2) and aluminium oxide (Al_2O_3) deposited by e-beam assisted evaporation with a thickness of 50 nm. Prior to the oxide deposition, a thin layer of Ti (3 nm) was deposited on top of Au in order to promote the adhesion of the passive layer. In the subsequent process step, a positive-tone photoresist was spun onto the substrate, exposed through a dark-field chrome mask, and developed to produce an array of different size holes (20×20, 10×10, 4×4 μm^2) on the top of the silicon layer. The photoresist used in this study was the AZ5214, purchased from AZ Electronic Materials. The opening of the via-holes in the dielectric matrix, after UV lithography process, was obtained by wet etching with the Buffered Oxide Etchant solution (BOE, NH4 F:HF, 7:1). A modification of the standard lithography process was made in this step. More precisely, the post-baking time of the photoresist was reduced to 30 s, instead of the typical 120 s. This change was necessary since we observed a better lift-off of the polymer from the undesired areas. Moreover, we also modified the etching solution; instead of using the standard BOE we diluted it with water (1BOE:1H_2O, v/v) in order to avoid possible over-etching of the oxide layer because of the decreased time of post-baking of the photoresist. The thin intermediate Ti layer was also etched by BOE, in order to reach the bottom Au electrode. We did not observe any significant difference in the integration process between the two dielectrics. After completing the lithography process, P3HT was deposited by spin coating technique, from a solution with a concentration of 5 mg/ml in toluene, at a rotational speed ranging from 800 to 1000 rpm. The regioregular P3HT (97–98%) used in this study was synthesized by the McCollough route [26]. Prior to the deposition, the solution was heated at 60 °C for 10 min and then filtered through a 0.02 μm pore size PTFE membrane syringe filter. The molecular weight was 35,600 and the polydispersity of the compound 1.9. A low rotational speed during spin coating was found to be necessary as we observed that a higher rotational speed resulted in poor filling at the desired areas. Finally, it was observed that a successful polymer patterning is strongly related to the combination of the rotational speed, the acceleration of the spinning and the viscosity of the polymer solution, since these parameters could strongly affect the wettability of the solution inside the dots. Another critical parameter is the solvent that is used for the lift-off process. We replaced acetone, which is the commonly used solvent, with a mixture of acetone with isopropanol (1:3), in order to prevent the removal of P3HT layer from the desired areas. A similar modification was also proposed by another group [25], who employed a mixture of acetone and methanol, instead of pure acetone. We do not expect any deterioration of the

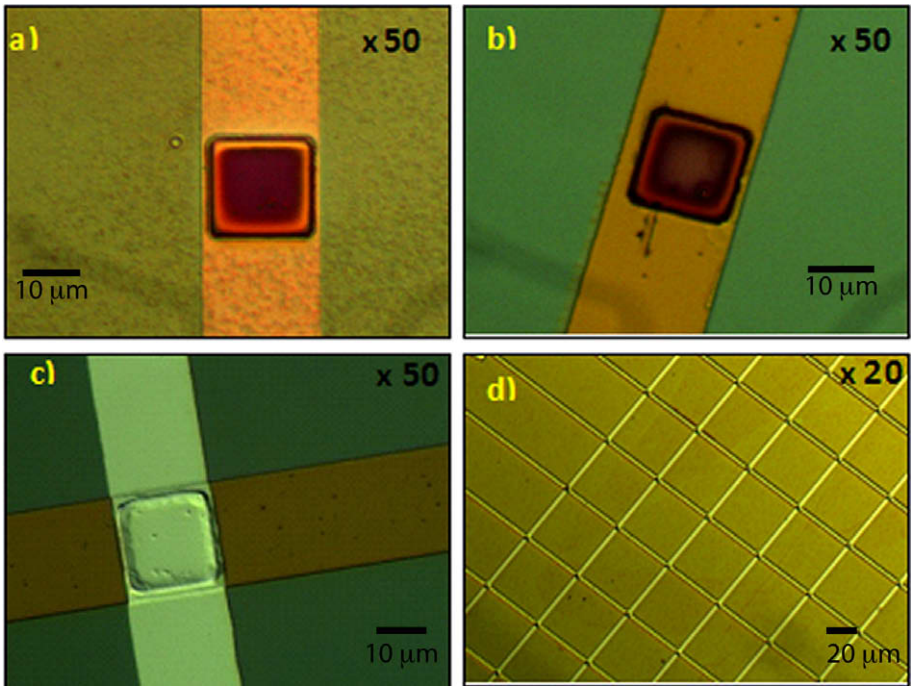

Fig. 3. (a–c) Optical microscope images of a 20×20 μm^2 junction illustrating the sequence of process integration steps: (a) after P3HT spinning; (b) after photoresist removal; (c) after top electrode patterning; (d) full crossbar structure with 4×4 μm^2 junctions.

device performance after the immersion of the devices into acetone and isopropanol mixture. In fact, in a recent paper it is demonstrated that polar solvents do not deteriorate the P3HT properties [27]. In Fig. 3 we report optical microscope images of a device with a $20 \times 20\ \mu m^2$ cross point area, showing the patterning before and after the lift-off of the photoresist (Fig. 3a and b) and the final crossbar structure of the device (Fig. 3c). In Fig. 3d a crossbar array with a cross point area of $4 \times 4\ \mu m^2$ is shown. The experiments were performed using toluene as solvent for P3HT without the need of replacing it with xylene, which leads to lower carrier mobility, as Chan et al. [25] proposed in their study. The use of a poorer solvent was not necessary since we did not observe any reaction of the photoresist we used with toluene. On the other hand, we also observed some lift-off difficulties when chloroform was used as solvent, as also reported by Chan et al. [25]. After photoresist removal, P3HT thickness was measured using a stylus profilometer. It was determined that P3HT thickness inside 50 nm deep holes was 30 nm, corresponding to a filling of 50–60%, independently from hole size. This is related to the fact that, although initially holes are completely filled with the polymer solution, after spinning and evaporation of the solvent only the solute remains inside the holes.

In order to investigate the compatibility of the process with other compounds, the sequence of steps described above was used to pattern OPV5, a *p*-phenylene–vinylene oligomer [28]. OPV5 was deposited using the same conditions of P3HT, i.e. by spin coating technique, from a solution with a concentration of 5 mg/ml in toluene, at a rotational speed ranging from 800 to 1000 rpm. A successful patterning was easily achieved for these materials with only one minor change to the full process. Warm isopropanol (40 °C) was used as a lift-off solvent instead of acetone and isopropanol mixture, since OPVs are slightly soluble in acetone. The photoresist used in this study allowed this change. The hole filling factor in this case was the same as P3HT, i.e. 50–60%.

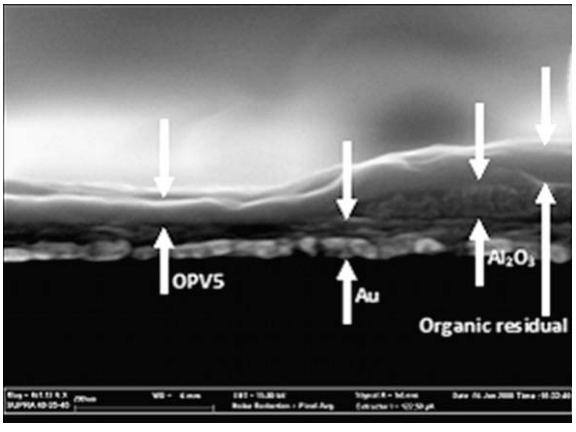

Fig. 4. Cross sectional SEM image of the border of a $20 \times 20\ \mu m^2$ patterned hole after the lift-off process. The scale bar corresponds to 200 nm.

The lift-off patterning method can sometimes result in some residuals of the photoresist and the organic compound around the patterned area, on top of the dielectric layer. This can be explained considering that the organic compounds and the photoresist have a strong adhesion, mainly because of the same nature of the compounds. In addition, the degree of the residuals is strongly dependent on the molecular structure of the chosen organic compound. In Fig. 4 a cross-sectional SEM image is presented, showing the border of a patterned hole ($20 \times 20\ \mu m^2$) after the lift-off process of OPV5. The dielectric matrix in this device is Al_2O_3. The scale bar presented in the image corresponds to 200 nm. It can be clearly observed that after the removal of the photoresist some organic residuals remain on top of the passive layer. This can also be explained considering the fact that the lift-off in our case is performed in a less effective manner than the conventional process, where boiling acetone is employed for the removal of the photoresist. As discussed above, boiling acetone was found to damage the exposed organic layer. Similar effects were observed with P3HT patterning, as also reported by other authors [25], who attributed the effect to the mechanical way of lift-off rather than dissolution. As an alternative approach this group proposed the direct patterning of the P3HT [22]. Despite the presence of residuals at the hole edges, we did not observe significant problems for the device integration. We obtained a uniform deposition of the top electrode (aluminium or titanium), through thermal evaporation or e-beam assisted evaporation, with the metal following the morphology of the organic compound without any discontinuity of the lines. This is further supported by the electrical characterization results presented in the next paragraphs. On the other hand, since the crossbar architecture is highly appealing for vertical stacking, these imperfections might lead to integration difficulties when several layers are involved. As a possible remedy, we tested a simple post deposition treatment under a solvent vapor saturated environment, an approach which is used in block copolymer research [29]. More precisely, the already patterned samples were placed in a vessel with a solvent saturated environment, toluene in case of P3HT, (at 45 °C) for ~5 h. During this treatment the interaction occurring between the vapors of the solvent and the organic compound leads to a rearrangement of the polymer inside the patterned dots. Indeed, after this treatment we observed better defined structures in case of P3HT patterned arrays. In parallel, Schottky diodes were prepared, after vapor annealing, in order to investigate in which manner this treatment affects the electrical properties of the material and whether it is worth pursuing this approach. The results are presented in the following section. We found that the selection of the suitable solvent and temperature is strongly related to the organic compound used in the device. This is a subject of further study.

After the successful patterning of the P3HT, the final step to be addressed is the deposition of the top electrode and patterning, without damaging the polymeric compound beneath. We chose aluminium as top electrode for P3HT Schottky junctions. The metal layer was deposited by thermal evaporation and patterned by UV lithography end wet etching. To prevent the diffusion of Al inside the

P3HT and to avoid some possible damaging of the functional material because of the thermal evaporation a thin layer of a polymeric dielectric (poly-vinyl-phenol, PVP) was deposited by spin coating on top of the polymeric compound [30]. This PVP layer is expected to enhance the adhesion of Al to the P3HT film, since the OH groups that contains react chemically with Al, resulting in an improvement of the metal patterning with the wet etching process. PVP was spin cast from ethyl-acetate on the P3HT film at a concentration of 0.4% wt/wt. Ethyl-acetate was chosen since P3HT is insoluble in this solvent. The resulting thickness of the PVP is expected to be around 10 nm [30], so that the total thickness of the P3HT/ PVP stack is about 40 nm. For the top electrode patterning a wet etching process is necessary since the photoresist cannot be deposited directly on top of the polymer. The design of the lithographic masks that was used in this study allows the use of the wet chemistry, since the area of the organic compound is smaller compared to the bottom and top metal lines. As a consequence, since the polymer is placed inside the holes, it is completely covered and protected from the chemical attack of the acidic solution (80% H_3PO_4:5%CH_3COOH:5% HNO_3:10% H_2O) that is used for the Al etching. To ensure full compatibility with the organic compounds, we avoided heating the samples above 100 °C during the lithography process.

The same sequence of steps was carried out in order to fabricate the OPV5 Schottky junctions. Although, in the latter we chose Ti as top contact, deposited by e-beam assisted evaporation, since it is known that Al is more reactive and easily diffuses into PPVs [31,32]. Using Ti we did not observe any shorts in our devices, therefore the PVP protecting layer was not necessary.

4. Electrical characteristics

The electrical results reported here refer to devices that were fabricated using SiO_2 dielectric layer. Fig. 5 presents the *J–V* characteristics of the as prepared Schottky diode with a structure of Au/P3HT/PVP/Al. Electrical measurements were performed at room temperature under dark conditions. The current was measured starting from zero to positive voltage and then brought back (forward current), and from zero to negative voltage and then brought back (reverse, or leakage, current). The rectification ratio was defined in this structure as the ratio between current values at 2.2 and −2.2 V. Aluminium was chosen as top electrode since it has a low work function (WF = 3.9–4.3 eV) and is expected to form Schottky contact with P3HT [33]. On the other hand, gold is a metal with a high work function (WF = 4.9–5.3 eV) and the Au/P3HT contact produces a small barrier [34] and as a result Au acts as an Ohmic contact. The *J–V* characteristics confirm the rectifying behaviour expected for this structure. A good rectification ratio was obtained, with an I_{on}/I_{off} ratio of 1×10^2–2×10^3, which demonstrates the successful patterning of P3HT into crossbar architecture, without damaging the material electrical properties. Consequently, it is confirmed that the PVP-Al stack successfully protected P3HT from the acidic etching solution and the basic developer. However, by adding the PVP dielectric layer we introduce one extra resistance in the structure that might lead to a decrease in the current density at both forward and reverse voltages. On the other hand, this resistance does not affect the I_{on}/I_{off} ratio since the contribution is the same for both voltages regions. The obtained current densities are in good agreement with previously published values for similar diode structures [35]. This also confirms the feasibility of the UV lithographic patterning without affecting the material properties. Finally, we must underline the fact that no metal selection optimization or polymer thermal annealing was performed in order to optimize the electrical performances, since the main goal of this work was the demonstration of the integration route. Therefore, it is likely that the junction characteristics can be further optimized through an annealing of the organic layer or a more accurate choice of the electrode materials.

In Fig. 5 the *J–V* characteristics of a Schottky diode that was prepared after the vapor treatment of the P3HT, as described in the previous section, are also reported. As it can

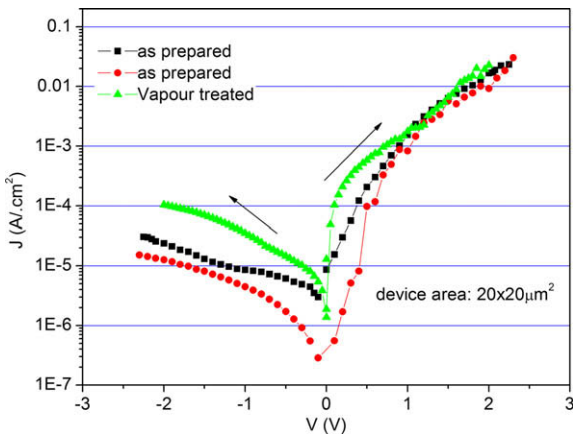

Fig. 5. Typical *J–V* characteristics of a Schottky diode with a structure of Au/P3HT-PVP/Al.

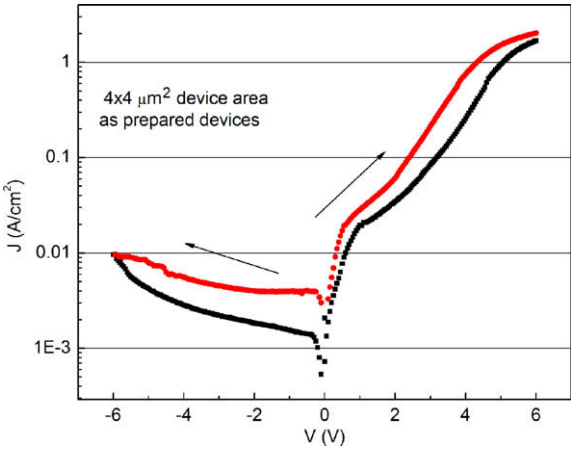

Fig. 6. Typical *J–V* characteristics of a Schottky diode with a structure of Au/OPV5/Ti.

be observed, the forward current density is of the same order of magnitude compared with the untreated diodes, suggesting that no degradation occurred. This result indicates that the vapor annealing is suitable as a post deposition treatment to improve some patterning imperfections. On the other hand, a slight degradation of the reverse current density is observed, which might be either attributed to this treatment, or to the spread of characteristics in different devices. This is a subject of further study.

The accomplishment of the integration scheme is further supported by the electrical characteristics of an OPV5 Schottky diode that are reported in Fig. 6, with a diode structure of Au/OPV5/Ti. Au was chosen as ohmic contact and Ti is expected to form a Schottky contact with the organic material. The obtained rectification ratio is above 10^2 at 4 V with a high current density of 0.3–0.8 A/cm^2. This confirms the applicability of the proposed integration route to a variety of organic semiconductors with different molecular structures.

In both P3HT and OPV5 devices we observed a spread of the characteristics, as it can be observed in Figs. 5 and 6, where we reported the curves with the largest variation. This spread could be attributed to thickness variation of the organic compounds inside the patterned holes after the spinning process. In fact, since for each organic compound the measured devices belonged to the same 2×2 cm^2 substrate, some non-uniformities of the organic layer thickness arising from the spinning process might occur. Further analyses are in progress to better understand this behaviour and improve device reproducibility.

5. Conclusions

In this study a process was developed for the integration of polymers into crossbar arrays by standard UV lithography. The approach was illustrated using P3HT and OPV5 as organic compounds, proving the compatibility of the process with different organic materials. Good rectification ratios of $I_{on}/I_{off} = 1 \times 10^2$-$2 \times 10^3$ were obtained from the fabricated Schottky junctions, demonstrating the successful patterning of the functional materials without deteriorating their electrical properties. The obtained current densities are in the range of the values that are generally reported in literature for these materials. Moreover, the high current density obtained in OPV5 Schottky junctions shows promise for the future use of these materials in as selectors in crossbar based non-volatile memories.

Acknowledgement

This work was performed in the framework of the EU FP6 project "VERSATILE", Contract No.: 026714.

References

[1] C.D. Dimitrakopoulos, D.J. Mascaro, IBM J. Res. Dev. 45 (2001) 11–27.
[2] A.R. Brown, A. Pomp, C.M. Hart, D.M. De Leeuw, Science 270 (1995) 972.
[3] M. Johnson, A. Al-Shamma, D. Bosch, M. Crowley, M. Farmwald, L. Fasoli, A. Ilkbahar, B. Kleveland, T. Lee, Tz-yi Liu, N. Quang, R. Scheuerlein, K. So, T. Thorp, IEEE J. Solid-State. Circ. 38 (11) (2003).
[4] J. Campbell Scott, L. Bozano, Adv. Mater. 19 (2007) 1452–1463.
[5] Q.-D. Ling, D.-J. Liaw, E. Yeow-Hwee Teo, C. Zhu, D. Siu-Hung Chan, E.-T. Kang, K.-G. Neoh, Polymer 48 (2007) 5182–5201.
[6] J.H. Burroughes, D.D.C. Bradley, A.R. Brown, R.N. Marks, K. Mackay, R.H. Friend, P.L. Burns, A.B. Holmes, Nature 347 (1990) 539.
[7] H. Spanggaard, F.C. Krebs, Sol. Energy. Mater. Sol. C 83 (2004) 125–146.
[8] E. Bundgaard, F.C. Krebs, Sol. Energy. Mater. Sol. C 91 (2007) 954–985.
[9] J. Ficker, H. von Seggern, H. Rost, W. Fix, W. Clemens, I. McCulloch, Appl. Phys. Lett. 85 (2004) 1377.
[10] H. Sirringhaus, T. Kawase, R.H. Friend, T. Shimoda, M. Inbasekaran, W. Wu, E.P. Woo, Science 290 (2000) 2123–2126.
[11] N. Stutzman, R.H. Friend, H. Sirringhaus, Science 299 (2003) 1881.
[12] T. Sekitani, Y. Noguchi, U. Zschieschang, H. Klauk, T. Someya, Proc. Nat. Acad. Sci. 105 (13) (2008) 4976.
[13] S.P. Li, C.J. Newsome, T. Kugler, M. Ishida, S. Inoue, Appl. Phys. Lett. 90 (2007) 172103.
[14] J.A. Rogers, Z. Bao, K. Baldwin, A. Dodabalapur, B. Crone, V.R. Raju, V. Kuck, H. Katz, K. Amundson, Proc. Nat. Acad. Sci. 98 (2001) 4835.
[15] U. Zschieschang, H. Klauk, M. Halik, G. Schmid, C. Dehm, Adv. Mater. 15 (2003) 1147.
[16] U. Zschieschang, M. halik, H. Klauk, Labgmuir 24 (2008) 1665.
[17] D.A. Pardo, G.E. Jabbour, N. Peyghambarian, Adv. Mater. 12 (2000) 1249–1252.
[18] H. Sirringhaus, P.J. Brown, R.H. Friend, M.M. Nielsen, K. Bechgaard, B.M.W. Langeveld-Voss, A.J.H. Spiering, R.A.J. Janssen, E.W. Meijer, P. Herwig, D.M. de Leeuw, Nature 401 (1999) 685.
[19] H. Sirringhaus, N. Tessler, R.H. Friend, Science 280 (1998) 1741.
[20] B. Lamprecht, E. Kraker, G. Weirum, H. Ditlbacher, G. Jakopic, G. Leising, J.R. Krenn, Phys. Status Solidi (RRL) 2 (2008) 16–18.
[21] John A. DeFranco, Bradley S. Schmidt, Michal Lipson, George G. Malliaras, Org. Elect. 7 (2006) 22–28.
[22] C. Balocco, L.A. Majewski, A.M. Song, Org. Elect. 7 (2006) 500–507.
[23] H.B. Akkerman, P.W.M. Blom, D.M. de Leeuw, B. de Boer, Nature 441 (2006) 69.
[24] H.B. Akkerman, A.J. Kronemeijer, P.A. van Hal, D.M. de Leeuw, P.W.M. Blom, B. de Boer, Small 4 (2008) 100.
[25] J.R. Chan, X.Q. Huang, A.M. Song, J. Appl. Phys. 99 (2006) 023710.
[26] R.D. McCullough, R.D. Lowe, M. Jayaraman, D.L. Anderson, J. Org. Chem. 58 (1993) 904.
[27] L.A. Majewski, A.M. Song, J. Appl. Phys. 102 (2007) 074515.
[28] J. Alstrup, K. Norrman, M. Jørgensen, F.C. Krebs, Sol. Energy. Mater. Sol. C 90 (2006) 2777–2792.
[29] J. Peng, D.H. Kim, W. Knoli, Y. Xuan, B. Li, Y. Han, J. Chem. Phys. 125 (2006) 064702.
[30] S. Ferrari, F. Perissinotti, E. Peron, L. Fumagalli, D. Natali, M. Sampietro, Org. Elect. 8 (2007) 407–414.
[31] K. Norrman, F.C. Krebs, Sol. Energy. Mater. Sol. C 90 (2006) 213.
[32] A. Crispin, A. Jonsson, M. Fahlman, W.R. Salaneck, J. Chem. Phys. 115 (2001) 252.
[33] S.P. Spekaman, G.G. Rozenberg, K.J. Clay, W.I. Milne, A. Ille, I.A. Gardner, E. Bresler, J.H.G. Steinke, Org. Elect. 2 (2001) 65.
[34] C.H. Lei, A. Das, M. Elliott, J.E. Macdonald, M.L. Turner, Synth. Met. 145 (2004) 217–220.
[35] K. Kaneto, W. Takashima, Curr. Appl. Phys. 1 (2001) 355–361.

sandwich-like structure of the type dielectric/semiconductor/insulator created in PMMA upon 50 keV silicon ion implantation at doses ranging from 3.2×10^{14} to 10^{17} ions/cm^2. For some electrical applications, e.g. for sensing, large-area flat panels are desirable, that is why we examine herein relatively large samples of Si$^+$-implanted PMMA.

2. Experimental

Two series of samples (plates) of identical size 10 mm × 10 mm were cut from two PMMA materials of optical quality: (i) 5 mm thick UV-grade PMMA containing a small amount of polyvinyltoluene, prepared to be used as a charged particles detector-scintillator, and (ii) UV-opaque PMMA (Röhm Plexiglas GS-233), 2 mm thick. Since the 50% light cut-off of these materials is at ~300 nm and ~380 nm, respectively, in the following they will be referred to as UVB-PMMA and UVA-PMMA, respectively (according to the definitions proposed by ISO International Standard ISO/CD 21348). The samples were implanted with silicon ions at an energy of 50 keV under identical conditions. The variety of implantation doses was the same for both series: $D_1 = 3.2 \times 10^{14}$, $D_2 = 1 \times 10^{15}$, $D_3 = 3.2 \times 10^{15}$, $D_4 = 1 \times 10^{16}$, $D_5 = 3.2 \times 10^{16}$ and $D_6 = 1 \times 10^{17}$ ions/cm^2. The experimental details have been described elsewhere [19]. Both pristine and Si$^+$-implanted PMMA samples were characterized by various spectroscopy techniques. Additionally to transmittance, fluorescence, photo-luminescence and specular reflectance (data reported in [19]), the samples were subjected to diffuse reflectance, attenuated total reflectance (ATR) and FTIR specular reflectance spectroscopy, UV-visible Raman, and FT-Raman.

The direct current (DC) experiments were carried out by standard two-point method using computer-controlled Keithley 617 Programable Electrometer with the capability of measuring resistance up to 10^{15} Ω. Narrow, 1 cm-long silver paste electric contacts were deposited at the two opposite edges of the implanted surface of the PMMA samples, as shown in Fig. 1a. Since the width of the contacts is 1 mm, they completely cover the two layers formed by the ion implantation: a low-conductive porous layer (1) and a buried conductive ion-implanted layer (2), both of thickness of few tens of nanometers and with no sharp boundary between them. The DC transconductance of Si$^+$-implanted PMMA was studied upon applying a gate voltage on a copper electrode (3 mm width, 1 cm length) placed on the implanted PMMA surface between the side-electrodes (the drain and the source) (Fig. 1b). In this arrangement, the width-to-length ratio for the channel situated within the layer (2) is $W/L \approx 3$.

Additionally, the electrical response of the Si$^+$-implanted PMMA was probed by sinusoidal alternating current (AC) measurements accomplished by phase-sensitive lock-in technique. The sampling signal from a Stanford Research Systems SR830 DSP lock-in build-in generator was acquired by a computer that controls the frequency sweep. These measurements consisted in determination of the frequency dependent current flowing through the samples

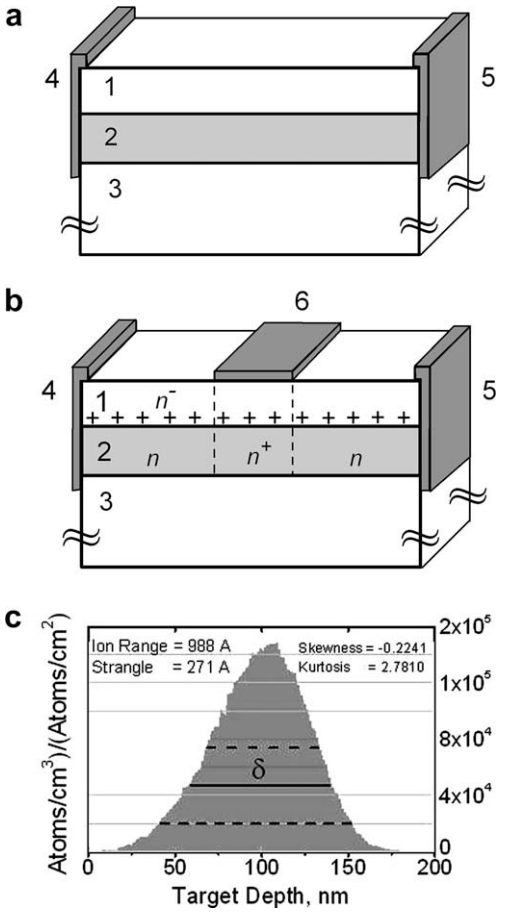

Fig. 1. (a) Schematic view of the Si$^+$-implanted PMMA samples: (1) porous low-conductive ion-modified layer, (2) conductive ion-implanted layer, (3) pristine PMMA, (4) and (5) Ohmic contacts. (b) The corresponding field-effect structure: (1) gate dielectric, (2) channel, (3) substrate, (4) source, (5) drain and (6) gate electrodes. (c) Depth profile of the layer formed in pure PMMA by an implantation with 50 keV Si ions, as calculated using the SRIM software [32].

when the electric field was longitudinally applied to the ion-implanted layer. All measurements in this work were carried out at room temperature.

3. Results and discussion

As known, the additives to the thermoplastic PMMA, such as elastomers, acrylic modifiers, absorbers, small fraction of polycarbonate and other chemical components, can significantly change the PMMA material properties. The additives could be echoed in a different effect from the ion implantation on the electronic and electrical properties of both Si$^+$-implanted PMMA materials, even when implanted under identical conditions. That is why, the distinction between both PMMA materials used in our experiments is of importance. Clear difference was found by optical transmittance and Raman spectroscopy. Also, the effect from Si$^+$ ion implantation was best evidenced by these spectroscopy techniques. Particularly, two weak but sharp Raman bands at 1581 cm^{-1} and 1600 cm^{-1} occur

for the pristine UVB-PMMA, which are missing in the Raman spectrum of pristine UVA-PMMA. We assign these spectral features to phenyl ring vibrations, which stem from polyvinyltoluene additive in UVB-PMMA. By fluorescence analysis, an evidence for a UV absorptive component is found for UVA-PMMA (the excitation profile extends from 250 nm to 340 nm with a maximum at ~280 nm). The micro-Raman spectra at an excitation wavelength of 514 nm reveal that the average size of the carbon clusters formed by Si^+ implantation in the UVA-PMMA samples is smaller than that in UVB-PMMA, for instance, 18 Å versus 26 Å as estimated for the ion dose 10^{17} Si^+/cm^2 [19].

The transparency of PMMA allows the optical band gap of the ion-modified material to be inspected by optical absorption. In order to be isolated the pure absorption, both specular and off-specular (diffuse) reflectance of the samples were measured in addition to the transmittance. The diffuse reflectivity spectra were taken by using of DRA-2500 diffuse reflectance accessory (integrating sphere) of Varian Carry 5000 spectrophotometer and normalized by a Spectralon white standard. The light scattering from the sample could also contribute to the optical loss. The light scattering takes place when the incident light beam encounters heterogeneities, i.e., changes in the optical properties of the medium, or it hits a rough surface. Even in the simple case of a flat surface separating two homogeneous media occurs a redistribution (scattered radiation) of the incident electromagnetic energy due to the abrupt change of the initial optical properties. In the medium under consideration, the most intense part of the scattering is due to non-homogenous multiple surfaces at the unimplanted/implanted interface and Mie scattering from ion-induced roughness. The latter should be enhanced at higher ion doses and becomes significant when the surface is considerably modified by the silicon ions and the characteristic size of the surface roughness is comparable to the wavelength of the incident light. In both cases, a part of the incident radiation is redistributed in all directions. While the hemi-spherical back-scattering can be considered as included in the light intensity as measured with integrating sphere, the other part of the scattered light, i.e. the forward scattering, is generally absorbed. Comparing the spectra obtained by integrating sphere with the specular reflectance [19], we established that the scattering component of the optical loss is not present to any great extend for the examined Si^+-implanted PMMA samples at doses up to $D_6 = 10^{17}$ Si^+/cm^2 (Si^+ ion energy of 50 keV). In fact, for the samples implanted to the dose D_6, no whitening of the surface was observed and a relatively low light intensity was measured by integrating sphere (up to ~4–5% from the incident light). However, as indicated the reflectivity modification of Si^+-implanted PMMA [19], the scattering becomes sizable at the dose D_6. Since this component of the optical loss was not separately measured, reliable absorption data cannot be derived for the samples implanted to the dose D_6.

The absorption spectra of Si^+-implanted PMMA samples are shown in Fig. 2a and b. When implanted at a sufficiently high Si^+ dose (above ~10^{15} cm^{-2}), both materials exhibit a significant absorption which is not proportional to the Si^+ dose. Strongly increasing in the dose range $3.2 \times 10^{14} - 3.2 \times 10^{15}$ Si^+/cm^2, the absorption nearly saturates at doses higher than $D_3 = 3.2 \times 10^{15}$ Si^+/cm^2. This effect is well known for ion implanted PMMA [20–22] and other transparent carbon-containing polymers upon ion implantation or ion irradiation [1,2,4,23]. It is indicative of the ion-induced destruction of the polymer and carbonization of the surface layer. The strong increase of the optical absorption in the visible and the near IR is due to the formation of conjugated double C=C bonds organized in a nano-

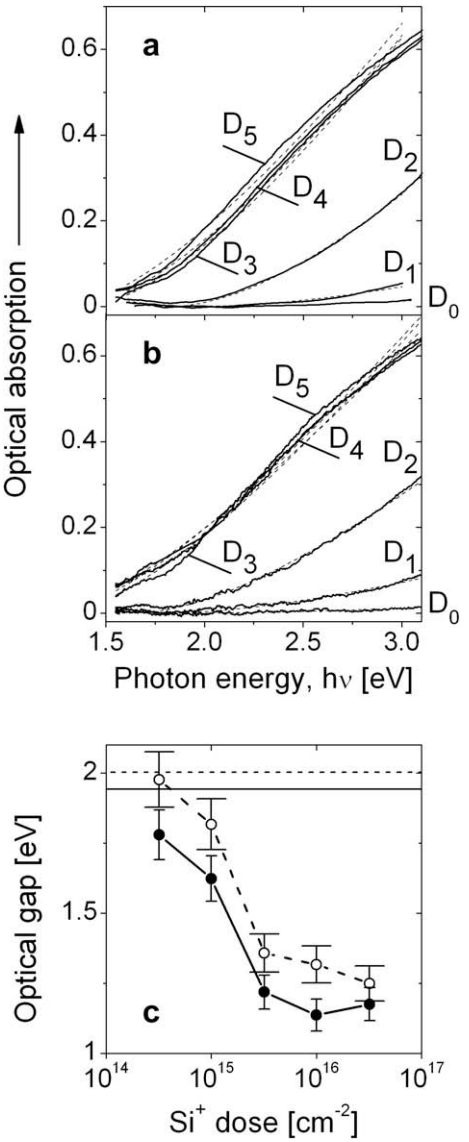

Fig. 2. Absorption spectra of the material resulting from 50 keV Si^+ ion implantation of UVA-PMMA (a) and UVB-PMMA (b). The corresponding Tauc plots are also given (dashed). The Si^+ doses [ions/cm^2] are: $D_1 = 3.2 \times 10^{14}$, $D_2 = 1 \times 10^{15}$, $D_3 = 3.2 \times 10^{15}$, $D'_4 = 1 \times 10^{16}$, $D_5 = 3.2 \times 10^{16}$, $D_6 = 1 \times 10^{17}$, D_0 stands for the pristine polymer. (c) The optical gap of the material formed in the Si^+-implanted PMMA versus the ion dose: UVA-PMMA (dashed) and UVB-PMMA (solid). The optical gap calculated for the pristine PMMA samples are also shown: UVA-PMMA (dashed line), UVB-PMMA (solid line). The error bars represent the uncertainty limits discussed in the text.

clustered hydrogenated amorphous carbon (HAC) material [23,24]. The presence of HAC phase in Si^+-implanted PMMA was confirmed by means of Raman spectroscopy [19]. The implantation-induced absorption in PMMA (Fig. 2) points out that D_3 is the dose at which the polymer degradation is nearly completed. At doses higher than D_3 aggregation of C-rich clusters with predominant sp^2 bonding takes place as supported by the reflectance, photoluminescence and micro-Raman spectra of the samples [19].

Using the absorption data corresponding to the variety of Si^+ doses, we obtained the dose dependence of optical band gap energy E_g of the material formed in PMMA by silicon ion implantation (Fig. 2c). E_g controls the imaginary part of the complex dielectric function. The of Si^+-implanted PMMA can be represented by the expression [25,26]

$$\alpha(\omega)\hbar\omega = B(\hbar\omega - E_g)^n \quad (1)$$

where a is the absorption coefficient at an optical frequency w, $\hbar w$ is the incident photon energy, B is an empirical constant, and the power factor n depends on the nature of the electronic transition, responsible for the optical absorption. Among the possible values of n [25,26], the absorption data for all samples studied herein was best-fitted by $n = 2$ (indirect allowed transition in k-space) in Eq. (1). Such an edge transition (Tauc transition) is expected for amorphous materials with a broad absorption edge and high absorption level [25] and is usually applied for description of amorphous carbon, in particular HAC layers [11,27,28]. Robertson and O'Reilly [24] have shown that the value of the optical band gap of the HAC material is correlated with the number, type and structural arrangement of the carbon atoms per molecule or per linear string, or per compact cluster. Generally, the band gap of the semiconducting HAC material decreases with the cluster size [4,24,29]. In our case, E_g can be correlated with the number (N) of carbon atoms per conjugation length. 8 N increases with the ion dose, and E_g decreases. The controllable reduction of the energy gap E_g of a polymeric material by ion implantation is of interest because of the possibility to modify its optical, electronic, and optoelectronic properties.

The accuracy of the estimated values of the optical gap is restricted by the uncertainty in the absorption, resulted from uncertainties of ±(1–1.5)% in the measured transmittance and reflectance. Significant error contributors in the measurements of these quantities could be various geometric factors. Especially, in the measurements with integrating sphere any misalignment of the sample strongly affects the results. An overall uncertainty value of ±5% for the calculated values of the optical band gap is reasonable when a perfect alignment is done and constant experimental conditions are kept. Within the uncertainty limits (represented by the error bars in Fig. 2c), the material formed in UVA-PMMA exhibits a larger band gap as compared to UVB-PMMA upon equal Si^+ dose. The standard deviation of the best-fit value E_g in fitting the absorption data does not exceed 0.3%.

The information for the electronic structure obtained by spectroscopic measurements can be related to the electrical response of Si^+-implanted PMMA. As known, the electrical conductivity of the ion-implanted polymers originates from the π-electrons in the conjugated double C=C bonds and is controlled by a hopping mechanism between the conducting carbon-rich zones, rich in π-electrons [2,4,11]. Actually, the same mechanism is responsible for the electrical conductivity of amorphous carbon and HAC near room temperature [11,30]. A variable range electron hopping conductivity through high-conducting nanoclusters separated by material with much lower conductivity in graphitized thin subsurface layer was established for PMMA subjected to low-energy ion implantation [18]. We suppose that Si^+-implanted PMMA studied herein possesses the same properties. The linear current–voltage plots for Si^+-implanted PMMA (Fig. 3a) reveal Ohmic conductance and are consistent with the hopping model [31]. The AC measurements gave the same result at a fixed frequency, for example, 500 Hz and 30 kHz. Also, the straight line passing through the origin of the current–voltage plot is a proof of the Ohmic nature of the contacts.

The ranges of 50 keV Si^+ ions in PMMA (density 1.19 g/cm^3) calculated by use of SRIM Code [32] are shown in Fig. 1c. In our case, the TRIM prediction for range distribution is close to a Gaussian distribution. It deviates slightly

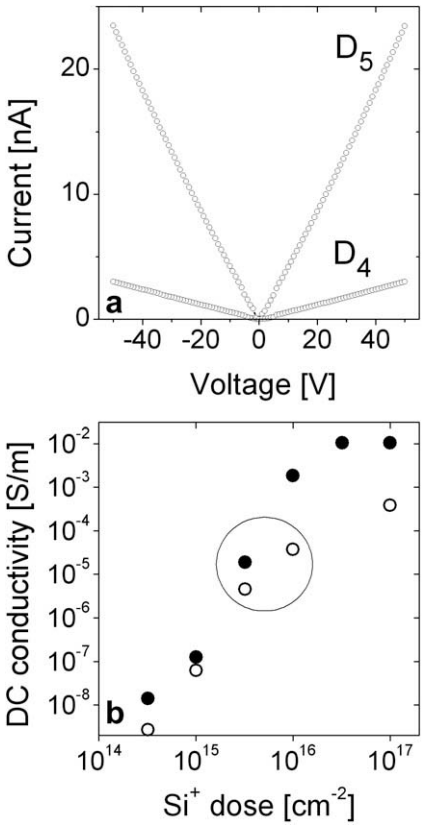

Fig. 3. (a) DC current–voltage characteristics of Si^+-implanted UVB-PMMA samples in positive and negative voltage sweep. The labels of the Si^+ doses are relevant to Fig. 2. (b) The DC conductivity of Si^+-implanted UVA-PMMA (open circles) and UVB-PMMA (solid circles) versus the ion dose. Within a circle are marked the conductivity data for the samples where an appreciable field-effect was found in this work.

from the Gaussian shape due to a slight asymmetry. In actuality, even symmetrical profile (only for light projectiles in the energy range 10–30 keV and at normal ion incidence) is not of Gaussian shape due to slightly different kurtosis [2,32]. In fact, the real ranges and profile differ from the TRIM estimate, as reported also for PMMA [33]. The TRIM calculations for the pure PMMA predict only approximate data for the polymeric materials we have used here. The additive chemical components actually present in them could change the real depth profile, a fact well known for the ion-implanted polymers [2]. Also, the thickness (δ) of the conductive ion-implanted layer (2) (Fig. 1a and c) increases with the increasing ion dose.

Alternatively we assessed the thickness of the ion-modified subsurface layer by means of FTIR specular reflectance in the mid-infrared region. The differential reflectance spectrum (DRS) $(R–R_0)/R_0$, where R_0 is the reflectance of the pristine PMMA material and R is the reflectance of the implanted material, was fit following well elaborated theoretical models [34]. A value of (140 ± 15) nm was extracted for the thickness at an implantation dose of 3.2×10^{15} Si^+/cm^2. We have to emphasize that the difference between TRIM and DRS values is due to different definitions of 'thickness'. While TRIM value reflects the effective width (at level $1/e^2$) of the ion-range distribution, DRS gives an estimate for the total thickness of the ion-modified layer. DRS rather display the whole in-depth extent of Si and recoil atoms distribution.

Being closely related to the material modification in the formed conductive layer, the in-depth distribution of the DC conductivity (σ) of this layer is non-homogenous. Thus, a real conductive channel in the host polymer PMMA is produced by the Si^+ implantation. To compare the effect of Si^+ implantation, an estimate of σ can be made for a certain fixed value of the channel width. From the ion range distribution (Fig. 1c) we adopted the value $\delta = 80$ nm being between the full width at half maximum (FWHM) ($\approx$60 nm) and the effective width ($\approx$110 nm) at level $1/e^2$ (the Gaussian full width). The other quantities necessary for the calculation of σ are the length of the electrodes and the distance between them, both equal to (10 ± 0.1) mm.

The dose dependence of so calculated σ is shown in Fig. 3b. No clear threshold dose was observed for the transition of the Si^+-implanted PMMA into conductive state. Since both the density of the delocalized π-electrons and the average size (s) of the C-rich domains (C-clusters and their aggregates) in the HAC material increase with the implantation dose [2–4], and the average distance (d) between the C-rich domains decreases, the conductivity of Si^+-implanted PMMA increases with the ion dose in accordance with the common trend known for the ion-implanted hydro-carbon polymers [3,4,8] and the predictions of the models involving the (s/d) ratio, e.g. $\sigma \sim \exp(s/d)$ [35]. From Fig. 3b one can compare the conductivity estimated for the samples of both materials being measured in analogous experiments. At equivalent Si^+ dose and energy and under identical other implantation conditions, the conductivity of the Si^+-implanted UVB-PMMA samples is higher than the conductivity of the Si^+-implanted UVA-PMMA samples whose C-domains have a smaller average size as revealed by Raman spectroscopy [19]. In context of the different initial grade of PMMA for both materials (see above), the higher conductivity of Si^+-implanted UVB-PMMA can be a result from the non-saturated C=C bonds present in this polymeric material prior to ion implantation, which promote the formation of larger sp^2 carbon domains upon implantation.

It is worthy to be noted that the conductivity enhancement (Fig. 3b) is reciprocally related to the gap closing shown in Fig. 2c since the two quantities depend (oppositely) on the C-cluster size. Both dependencies indicate a transition from insulating to semiconductor properties. From originally insulating pristine state ($\sigma_{PMMA} \sim 10^{-13}$ S/m), σ of Si^+-implanted PMMA attains at implantation dose of 10^{16}–10^{17} Si^+/cm^2 the values typical of highly conductive amorphous phase of carbon [11] and conducting polymers at room temperature and being considerably higher than the conductivity of semiconductors such as silicon ($\sim 4 \times 10^{-4}$ S/m) [36].

In view of the ion implantation performed (the mass and the energy (50 keV) of the silicon ion), a doping effect from silicon on the electrical conductivity of Si^+-implanted PMMA is not excluded at higher doses, e.g. above 10^{16} Si^+/cm^2 [37], though the Si concentration is small (<1 at.%) in comparison with those in the conventional doped polymers [38]. To best our knowledge, no data for Si doping in PMMA by silicon ion implantation have been reported in the literature. It is known, that when incorporated in HAC, the effect from silicon is negative, especially at considerably higher amount, e.g. 10 at.%. In such a case the optical gap increases due to both reduction of large sp^2 carbon clusters and the sp^3 bonding enhancement [39,40]. The efficiency of Si doping in HAC is rather low [24], however a doping effect in the classical sense could be achieved by incorporating silicon into the polymer structure (or its rests). Particularly, one can expect Si to bond to carbon at the extremes of the stopping range. No Si trace (from Si, eventual Si nanoclusters and Si bonding to the polymer or to the ion-modified polymer structure (HAC)) was detected by our spectroscopic means. Apart from the D- and G-bands of sp^2 carbon, the Raman measurements in a wide range of excitation wavelengths (1060, 647, 633, 514, 488 and 363 nm) did not reveal any spectral feature emerging upon implantation. Further, we studied our samples by means of FTIR specular reflectivity and ATR. Again, no extra absorption bands were observed in the implanted samples. Most probably, even if Si is bonded to the polymer or forms Si nanoclusters, even at higher Si^+ doses the signal from the Si-related structures is below the detection limit of the apparatus (Jobin Yvon T64000, Jobin Yvon Labram, Bruker V700). XPS survey would be useful to prove the incorporation of silicon in Si^+-implanted PMMA, but the possible role of Si doping for modification of the electrical properties of this material can be clarified by electrical measurements on the frequency domain, e.g. by admittance spectroscopy or deep level transient spectroscopy (DLTS), especially its high-sensitive and high-resolution variations such as Laplace-transform DLTS and double correlation DLTS, which allow to identify the nature of the defects and to get their depth profiles.

In addition to the DC measurements, the electrical response of the Si^+-implanted PMMA samples was probed under alternating (AC) electric field. In this case, a sinusoidal voltage with amplitude of 1 V was applied and the field frequency was swept in the range from 1 Hz to 30 KHz. The effect of the Si^+ implantation can be seen in Fig. 4 which reports the Real (the in-phase signal) and Imaginary parts of the frequency dependent current measured for the UVB-PMMA samples. A significant enhancement of AC conductivity occurs when the ion dose exceeds 10^{16} Si^+/cm^2.

The transconductance of the spatial structure formed in Si^+-implanted PMMA proven by DC measurements is also strongly conditioned by the ion dose. This is reasonable because the ion-modified subsurface region and its electrical properties are determined by the ion implantation. Particularly, as mentioned above, the in-depth variation (depth-profile) of the concentration of the (semi)conducting HAC material formed by Si^+ implantation of PMMA depends on the ion dose. Because of the diffusive spatial distribution, the ion-implanted layer has no strictly defined boundaries. Nevertheless, for the sake of simplicity one can consider the subsurface region as consisting of two layers: (1) top layer having a lower conductivity (n^-) and buried layer (2) with a higher conductivity (n) (Fig. 1b). Two circumstances are of importance in this case: (i) the possible trapping of Si at defects or due to interactions along the overlapping multiple ion tracks [2], thus producing by diffusion in the neighboring bulk material a some kind of Si-doped PMMA (still far away from materials with semiconducting quality, which only can be obtained after real doping) so modifying mostly the dielectric properties of the track-containing nanoporous layer (1) in the host polymer, and (ii) the semiconducting n-type of undoped HAC [41]. Despite we do not have well defined two side p–n junctions and the top layer (1) is not an ideal insulator, by analogy with the well known metal-oxide-semiconductor field-effect transistors (MOSFETs) the assembly composed from the channel structure of Si^+-implanted PMMA with two side electrodes (source and drain) and a top electrode (gate) can be considered as a transistor-like device. As such, we have found a field-effect transistor (FET)-like operation for one UVB-PMMA sample and for two UVA-PMMA samples, all these implanted to the doses close to the dose D_3. As examples, Figs. 5–9 show the characteristics for the former one. The output characteristics (the drain-to-source current I_{DS} versus the drain-to-source voltage V_{DS} for several values of the gate-to-source voltage V_{DS} (Fig. 5a) is similar to that of conventional MOSFETs and corresponds to an n-channel with electron accumulation mode at positive voltage V_{GS}. With increase of the positive gate voltage the electron concentration in the layer (2) under the metal gate increases. This layer can be thought as composed of two n-regions and one n^+-region defined by the gate (Fig. 1b).

The channel current I_{DS} can be controlled also by applying V_{GS} of opposite polarity. The current–voltage characteristics at negative gate voltages (Fig. 5b) are quite different

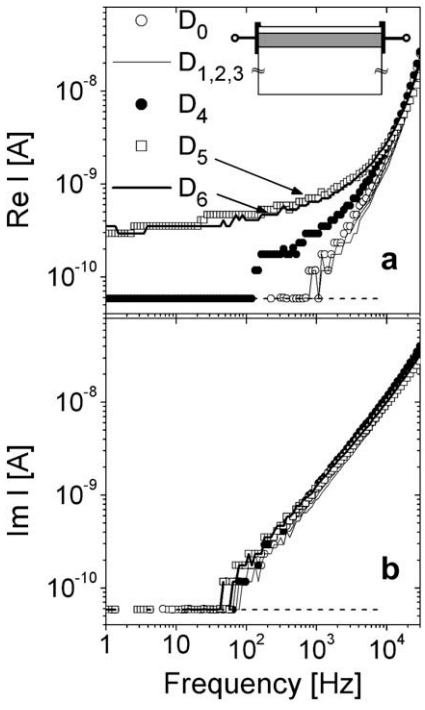

Fig. 4. The frequency dependence of the Real (a) and Imaginary (b) parts of the alternating current in Si^+-implanted UVB-PMMA. The labels refer to the doses as in Fig. 2, D_0 – the data for pristine UVB-PMMA given for comparison. The dashed lines indicate the sensitivity limits of the apparatus.

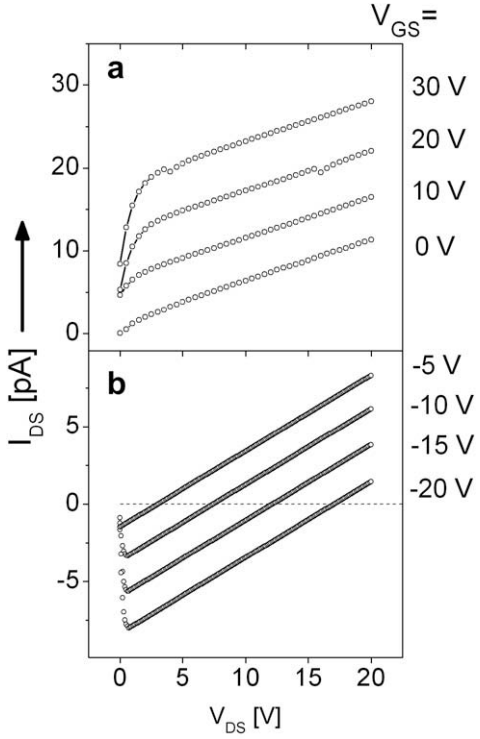

Fig. 5. (a) Output characteristics $I_{DS}(V_{DS})$ of a FET-like operation of Si^+-implanted UVB-PMMA (dose $D_3 = 3.2 \times 10^{15}$ Si^+/cm^2 for various values of the gate-to-source voltage V_{GS}. Panel (b): $I_{DS}(V_{DS})$ for negative values of V_{GS}.

from the case with positive V_{GS} Particularly, I_{DS} becomes switchable with the gate voltage. By increase of the drain voltage the sign of I_{DS}, i.e. the direction of the current flow can be changed what is of practical interest (transistor-like invertor). Thus, the current I_{DS} can be reduced to zero when V_{DS} approaches the value V^0_{DS}, i.e. a peak of the channel resistance occurs at that switching voltage which can be linearly tuned by change of V_{GS} (Fig. 6). Such a transistor-like switch has been reported for similar electronic devices based on ion-implanted polymers, e.g. polyethylene and polyamide-6 films [4,7] implanted with B^+ and Sb^+ at ion energy and doses comparable to those we have used here. In terms of our treatment, the switching function can be explained by zero equivalent voltage drop in the electron-enriched n^+ channel region under the gate (see Fig. 1b). Unlike the FET-like regime described above, the Si^+ dose is not critical for that switching function. The channel transconductance for Si^+-implanted PMMA samples, calculated by the slope ($\partial I_{DS}/\partial V_{GS}$) at a constant drain voltage exhibits a dose dependence (Fig. 7) which correlates to that of DC conductivity (recall Fig. 3b).

Further information provides the change of the output characteristics upon electrical stress (Fig. 8). The stress by a negative gate voltage results in an increase of I_{DS} depending on the stressing time, while no effect from a positive V_{GS}-stress was found during the same stressing time. This feature confirms the field-effect and the *n*-type of the channel, and can be explained by generation of fixed positive charges in the layer (1) (see Fig. 1b) upon a stress by a negative gate voltage. In this case, I_{DS} increases due to both the positive V_{GS} bias applied and the electric field resulting from the generated positive charges. Through the known mechanisms of charge trapping [42,43], the positive charges can be trapped at the non-ideal interface between both layers (1) and (2), as well as in the voids of the nanoporous structure of the layer (1) near that interface like the charge trapping in submicrometer domains of thin (e.g., 80 nm) PMMA layers [44].

The transfer characteristics $I_{DS}(V_{GS})$ (Fig. 9) exhibits no clearly defined threshold for V_{GS}. A small but stable hysteresis was observed here, which indicates a some modification of the gate field. We suppose that such a modification arises from fixed charge carriers located within the bulk of the gate dielectric (the porous low-conductive subsurface layer (1)) and/or at the diffusive interface between the gate dielectric layer (1) and the conductive *n*-channel (2) in the Si^+-implanted PMMA samples (Fig. 1b). Due to the faster V_{GS}-bias, the charge effects modifying the transfer characteristics $I_{DS}(V_{GS})$ differ from the charge effects affecting the output characteristics $I_{DS}(V_{GS})$ after the relatively long electrical stress by the gate voltage (recall Fig. 8). The smaller current I_{DS} generated when the gate voltage V_{GS} is applied in descending mode is due to the reduced resultant electric field in the layer (1) owing to the additional push-pull of the positive charges from the interface. Clearly, the observed hysteresis as well as the gate on/off amplification factor (≈250) (see Fig. 9b) are smaller as compared to those reported for high-performance organic FET-memory devices employing strongly polarizable polymers and organic electrets [45–48] and ferroelectric polymers [49,50] as gate materials.

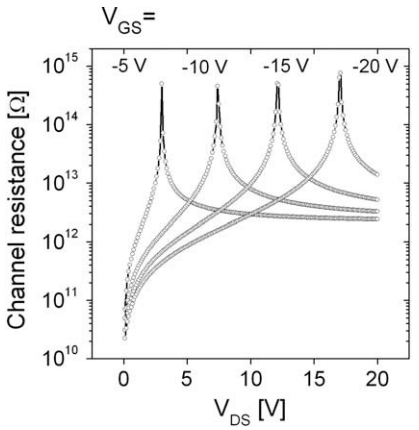

Fig. 6. The channel resistance as a function of the drain voltage V_{DS} for various values of the gate voltage V_{GS}. The implantation dose is $D_3 = 3.2 \times 1015$ Si^+/cm^2 UVB-PMMA.

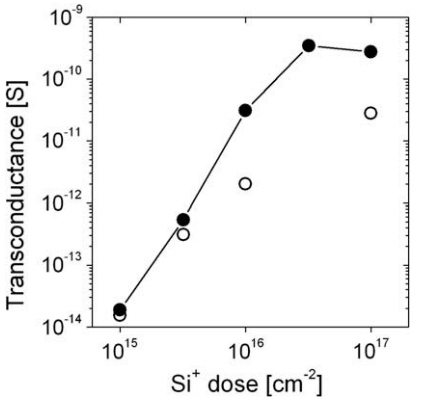

Fig. 7. Variation of the channel transconductance with the ion dose for Si^+-implanted UVA-PMMA (open circles) and UVB-PMMA (solid circles).

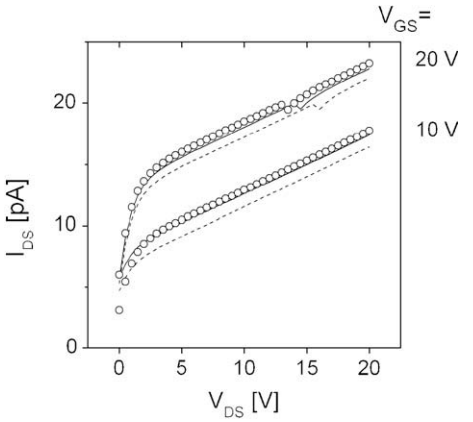

Fig. 8. As in Fig. 5, but taken before (dashed) and after a stress with a gate voltage of −40 V during stressing time 5 min (solid lines) and 15 min (circles).

Finally, compared to the organic FETs [9], the field-effect found in our Si^+-implanted PMMA samples is considerably weaker, but it could surely be enhanced by a proper choice of the implantation parameters and optimizing device architecture. The implantation conditions determine the nanostructure and electronic properties of the formed organic material, the depth profile of the layer (2) (i.e. the thickness of both layers (1) and (2), Fig. 1), the dielectric and conductive properties of the layers (1) and (2), as well as the organic interface between them. Thus, these conditions are very important for the formation of a field-effect structure and define the operation in a FET-like regime if occurs an appropriate matching of all necessary factors. That is why, an appreciable field-effect was observed in our experiments only for the samples implanted to the dose $D_3 = 3.2 \times 1015\ Si^+/cm^2$ from both PMMA materials under study, as well as the dose $D_4 = 10^{16}\ Si^+/cm^2$ from UVA-PMMA. The output characteristics of these samples are compared in Fig. 10. The relative magnitudes of I_{DS} are consistent with the corresponding values of the DC conductivity measured for these samples (recall Fig. 3b).

Really, to achieve an appreciable field-effect, a well-formed dielectric layer (1) with proper characteristics and parameters is necessary. However, the match (balance) of both conductance and transconductance of the structure is also of great importance. This is illustrated in Fig. 11 by comparison of the output characteristics measured for Si^+-implanted UVB-PMMA samples under identi-

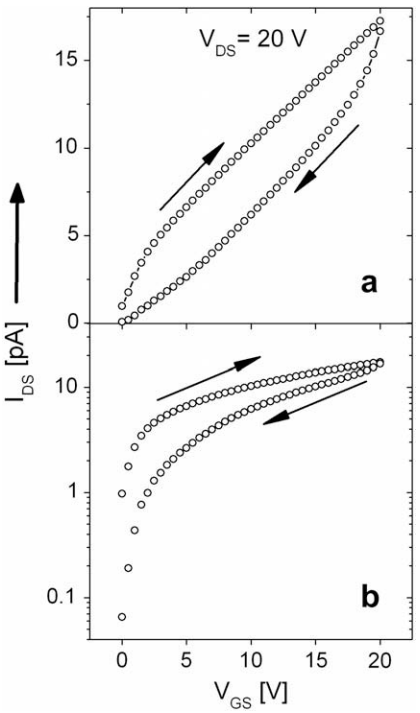

Fig. 9. (a) Transfer characteristics $I_{DS}(V_{GS})$ of the same Si^+-implanted PMMA field-effect structure as in Figs. 5, 6 and 8. The drain-to-source voltage $V_{DS} = 20$ V. Panel (b) the same, but in a logarithmic scale in order to better show the dynamic range.

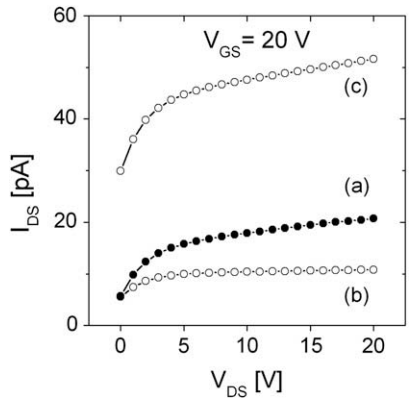

Fig. 10. Comparison of the output characteristics of a FET-like operation in Si^+-implanted PMMA: (a) dose $D_3 = 3.2 \times 10^{15}\ Si^+/cm^2$, UVB-PMMA; (b) dose $D_3 = 3.2 \times 10^{15}\ Si^+/cm^2$, UVA-PMMA; (c) dose $D_4 = 1 \times 10^{16}\ Si^+/cm^2$, UVA-PMMA.

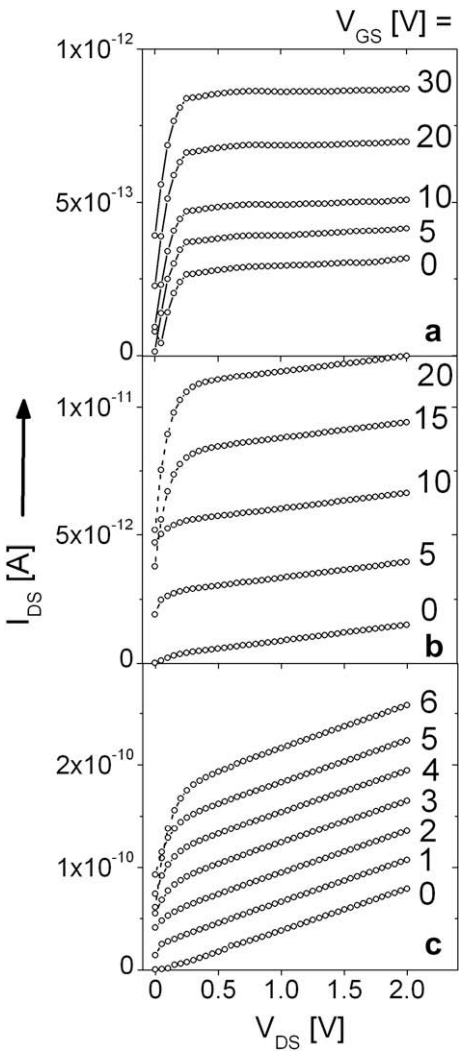

Fig. 11. Output characteristics of Si^+-implanted UVB-PMMA field-effect structures. The ion doses [Si^+/cm^2]: (a) 1×10^{15}, (b) 3.2×10^{15} and (c) 1×10^{16}.

cal experimental conditions. At a low ion dose, $D_2 = 10^{15}$ Si$^+$/cm^2 (Fig. 11a), the transconductance is low, the field-effect is weak. At the next ion dose, $D_3 = 3.2 \times 10^{15}$ Si$^+$/cm^2 (Fig. 11b), the field-effect is well pronounced and stronger, and the transconductance value is ~30 times higher. Further, the output characteristics of this sample exhibits a sizable saturation. As seen in Fig. 11c, a field-effect is also present for the sample implanted to the dose $D_4 = 10^{16}$ Si$^+$/cm^2, where the transconductance is even more (~60 times higher than that for the sample implanted to the dose D_3). However, in this case the higher transconductance is accompanied by an increased conductivity (the slope of the saturation part of the output characteristics) which does not correspond to a good-performance field-effect device. Most probably, the increased transconductance results from the increased conductivity of the dielectric layer (1). Thus, one can admit that among the Si$^+$-implanted UVB-PMMA samples, the structure formed with silicon ions at the dose D_3 best approaches the characteristics of FETs (or FET-like devices). Being no conventional organic FET, the field-effect structure in Si$^+$-implanted PMMA still provides rather low channel currents, for instance $I_{DS} \sim 10^{-11}$ A at $V_{DS} = 1$ V and $V_{GS} = 20$ V (Fig. 11b), partly due to the low W/L ratio ($W/L \sim 3$) for the channel of the configuration used. A better performance exhibits the UVA-PMMA sample implanted to the dose $D_4 = 10^{16}$ Si$^+$/cm^2, as seen in Fig. 10.

4. Conclusions

We have shown that a transconductive organic nanoscale material is formed in PMMA by low-energy silicon ion implantation at 50 keV and doses in the range of 10^{15}–10^{16} ions/cm^2. The spatial structure and the electrical properties of Si$^+$-implanted PMMA allow a field-effect to be utilized for all-organic active elements. Two layers of the ion-modified subsurface region of the polymer are responsible for the field-effect operation, one serving as a chargeable gate dielectric, and the other working as an electron transporting (n-type) active semiconductor (channel).

Our study of the electrical response of Si$^+$-implanted PMMA shows that at appropriate Si$^+$ energy and doses this material appears to be promising for applications in the integrated all-organic electronics, like fabrication of highly integrated and buried low-cost, application-specific circuits and electrical micro-switches, field-effect transistors, interconnects and other functional soft-electronic elements. Such complex-structured organic semiconductor devices can be customized by the conventional present-day microelectronics technology. Also, modifying the organic polymers by ion implantation, the application of the hydrogenated amorphous carbon material to electronic devices [51] can be combined with the properties and advantages of the plastics. Especially, the high porosity of the implanted surface, as well as the excellent bio-compatibility make Si$^+$ ion implanted PMMA attractive for electrical bio-sensor and bio-medical applications based on the detection of a field-effect induced on the subsurface region of Si$^+$-implanted PMMA when charged biomolecules are immobilized on its surface.

Acknowledgements

We acknowledge the financial support from the Swiss National Science Foundation (Project No. IB7420-110981/1 "Southern NanoEngineering Network", SONNET). This work was partially supported by PAI-RILA 2/5 French-Bulgarian bilateral project, National Science Fund of Bulgaria (Contract IRNI 21/2007) and Sofia University (Contract UFNI 075/2008).

References

[1] G. Marletta, F. Iacona, in: Y. Pauleau (Ed.), Materials and processes for surface and interface engineering, NATO-ASI Series, Series E: Applied Sciences, vol. 290, Kluwer Academic Publishers, Dordrecht, 1995, pp. 597–640.
[2] D. Fink (Ed.), Fundamentals of Ion Irradiated Polymers, Springer-Verlag, Berlin, 2004.
[3] P. Mazzoldi, G.W. Arnold (Eds.), Ion Beam Modification of Insulators, Elsevier, Amsterdam, 1987.
[4] D.V. Sviridov, V.B. Odzhaev, I.P. Kozlov, in: D.L. Wise, G.E. Wnek, D.J. Trantolo, T.M. Cooper, J.D. Gresser (Eds.), Electrical and Optical Polymer Systems – Fundamentals, Methods and Applications, Marcel Dekker, New York, 1998, pp. 387–422 (Chapter 11).
[5] D. Fink (Ed.), Transport Processes in Ion-Irradiated Polymers, Springer-Verlag, Berlin, 2004.
[6] E. Tavenner, P. Meredith, B. Wood, M. Curry, R. Giedd, Synth. Metals 145 (2004) 183–190.
[7] V.N. Popok, I.A. Karpovich, V.B. Odzhaev, D.V. Sviridov, Nucl. Instrum. Meth. B 148 (1999) 1106–1110.
[8] R.E. Giedd, M.G. Moss, J. Kaufmann, Y.Q. Wang, in: D.L. Wise, G.E. Wnek, D.J. Trantolo, T.M. Cooper, J.D. Gresser (Eds.), Electrical and Optical Polymer Systems – Fundamentals, Methods and Applications, Marcel Dekker, New York, 1998, pp. 1011–1030 (Chapter 29).
[9] C.D. Dimitrakopoulos, D.J. Mascaro, IBM J. Res. Dev. 45 (2001) 11–27.
[10] C.D. Dimitrakopoulos, P.R.L. Malenfant, Adv. Mater. 14 (2002) 99–117.
[11] S. Bhattacharyya, S.V. Subramanyam, in: D.L. Wise, G.E. Wnek, D.J. Trantolo, T.M. Cooper, J.D. Gresser (Eds.), Electrical and Optical Polymer Systems – Fundamentals, Methods and Applications, Marcel Dekker, New York, 1998, pp. 201–296 (Chapter 7).
[12] S. Uemura, M. Yoshida, S. Hoshino, T. Kodzasa, T. Kamata, Thin Solid Films 438–439 (2003) 378–381.
[13] J. Puigdollers, C. Voz, A. Orpella, R. Quidant, I. Martın, M. Vetter, R. Alcubilla, Org. Electron. 5 (2004) 67–71.
[14] K.N.N. Unni, A.K. Pandey, J.M. Nunzi, Chem. Phys. Lett. 407 (2005) 95–99.
[15] M. Na, S.W. Rhee, Org. Electron. 7 (2006) 205–212.
[16] C.A. Lee, S.H. Jin, K.D. Jung, J.D. Lee, B.G. Park, Solid-State Electron. 50 (2006) 1216–1218.
[17] X. Liu, Y. Bai, W.Q. Zhu, X.Y. Jing, Z.L. Zhang, Optoelectron. Lett. 3 (2007) 435–437.
[18] Y. Koval, M.V. Fistul, P. Müller, J. Vac. Sci. Technol. A 23 (2005) 1375–1378.
[19] G.B. Hadjichristov, V. Ivanov, E. Faulques, Appl. Surf. Sci. 254 (2008) 4820–4827.
[20] T. Venkatesan, L. Calcagno, B.S. Elman, G. Foti, in: P. Mazzoldi, G.W. Arnold (Eds.), Ion Beam Modification of Insulators, Elsevier, Amsterdam, 1987, pp. 301–379 (Chapter 8).
[21] J.P. Biersack, R. Kallweit, Nucl. Instr. Meth. B 46 (1990) 309–312.
[22] J. Davenas, P. Thevenard, G. Boiteux, M. Fallavier, X.L. Lu, Nucl. Instr. Meth. B 46 (1990) 317–323.
[23] G. Marletta, Nucl. Instr. Meth. B 46 (1990) 295–305.
[24] J. Robertson, E.P. O'Reilly, Phys. Rev. B 35 (1987) 2946–2957.
[25] J. Tauc, Amorphous and Liquid Semiconductors, Plenum Press, New York, 1974.
[26] N.F. Mott, E.A. Davis, Electronic Processess in Non-crystalline Materials, second ed., Clarendon Press, Oxford, 1979.
[27] P. Koidl, P. Oelhafen (Eds.), Amorpous Hydrogenated Carbon Films, Les Editions de Physique, Paris, 1987.
[28] C. Casiraghi, A.C. Ferrari, J. Robertson, Phys. Rev. B 72 (2005) 1–14. 085401.
[29] D. Fink, W.H. Chung, R. Klett, A. Schmoldt, J. Cardoso, R. Montiel, M.H. Vazquez, L. Wang, F. Hosoi, H. Omochi, P. Goppelt-Langer, Radiat. Eff. Def. Solids 133 (1995) 193–208.

[30] D. Dasgupta, F. Demichelis, A. Tagliaferro, Philos. Mag. B 63 (1991) 1255–1266.
[31] P. Hesto, in: G. Barbottin, A. Vapaille (Eds.), Instabilities in Silicon Devices, vol. 1, Springer, Amsterdam, 1986. p. 263 (Chapter 5).
[32] J.F. Ziegler, J.P. Biersack, U. Littmark, The Stopping and Range of Ions in Solids, Volume 1 of the Stopping and Ranges of Ions in Matter, Pergamon Press, New York, 1985, (Chapter 8). http://www.srim.org.
[33] D. Fink (Ed.), Fundamentals of Ion Irradiated Polymers, Springer-Verlag, Berlin, 2004. p. 149.
[34] D.E. McIntyre, D.E. Aspnes, Surf. Sci. 24 (1971) 417–434.
[35] B. Abeles, P. Sheng, M.D. Coutts, Y. Arie, Adv. Phys. 24 (1975) 407–461.
[36] S.M. Sze, Physics of Semiconductor Devices, Wiley, New York, 1981. Appendix H, p. 850.
[37] A. Moliton, C. Moreau, J.P. Moliton, Nucl. Instr. Meth. B 80/81 (1993) 1028–1035.
[38] J. Mort, G. Pfister, Electronic Properties of Polymers, Wiley, New York, 1982.
[39] X. Zhang, W.H. Weber, W.C. Vassell, T.J. Potter, M.A. Tamor, J. Appl. Phys. 83 (1998) 2820–2825.
[40] G.A. Abbas, P. Papakonstantinou, T.I.T. Okpalugo, J.A. McLaughlin, J. Filik, E. Harkin-Jones, Thin Solid Films 482 (2005) 201–206.
[41] D.I. Jones, D.A. Stewart, Philos. Mag. B 46 (1982) 423–434.
[42] M. Goel, Current Sci. 85 (2003) 443–453.
[43] V.N. Kestelman, L.S. Pinchuk, V.A. Goldade, Electrets in Engineering: Fundamentals and Applications, Kluwer Academic, Boston, 2000.
[44] H.O. Jacobs, G.M. Whitesides, Science 291 (2001) 1763–1766.
[45] H.E. Katz, X.M. Hong, A. Dodabalapur, R. Sarpeshkar, J. Appl. Phys. 91 (2002) 1572–1576.
[46] M. Mushrush, A. Facchetti, M. Lefenfeld, H.E. Katz, T.J. Marks, J. Am. Chem. Soc. 125 (2003) 9414–9423.
[47] Th.B. Singh, N. Marjanovic, G.J. Matt, N.S. Sariciftci, R. Schwödiauer, S. Bauer, Appl. Phys. Lett. 85 (2004) 5409–5411.
[48] K.J. Baeg, Y.Y. Noh, J. Ghim, S.J. Kang, H. Lee, D.Y. Kim, Adv. Mater. 18 (2006) 3179–3183.
[49] R. Schroeder, L.A. Majewski, M. Grell, Adv. Mater. 16 (2004) 633–636.
[50] K.N.N. Unni, R. Bettignies, S.D. Seignon, J.M. Nunzi, Appl. Phys. Lett. 85 (2004) 1823–1825.
[51] W.I. Milne, Semicond. Sci. Technol. 18 (2003) S81–S85.

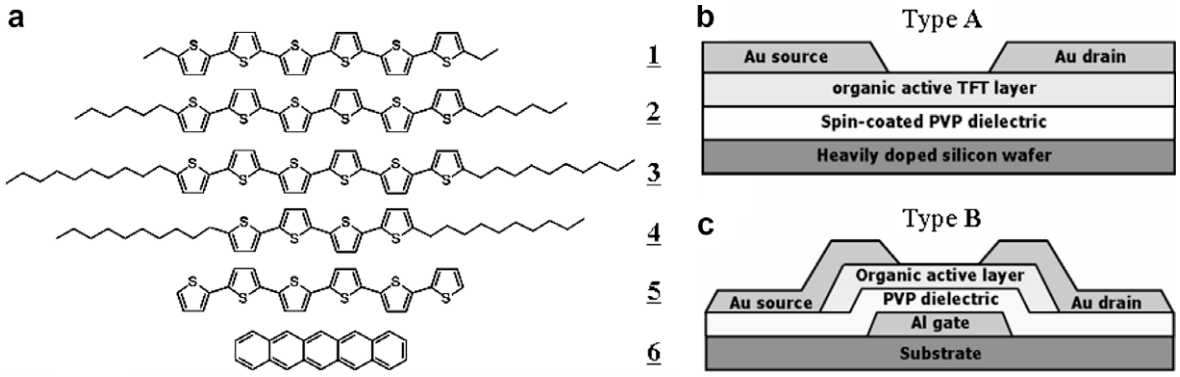

Fig. 1. (a) Chemical structure of organic semiconductor molecules; schematic cross section of a, (b) top-contact polymer gate dielectric TFT with a common gate – type A, and (c) top-contact polymer gate dielectric TFT with a patterned Al gate – type B.

5, α,α′-diethylsexithiophene **1**, α,α′-dihexylsexithiophene **2**, and α,α′-didecylsexithiophene **3**). The series was extended by α,α′-didecylquaterthiophene **4** representing a material with larger ratio between flexible insulating side chains and ridged π-conjugated chromophore and exhibits a phase transition at 98 °C [9]. All materials have been purified by sublimation prior thermal deposition on devices.

We have fabricated two different device architectures to explore the electrical characteristics in thin film transistor devices. To investigate the impact of the substrate temperature on the electrical and morphological properties, a series of transistors with a common gate – provided by a heavily doped p-type silicon wafer – and gold top contact architecture was chosen (type A in Fig. 1b). Poly (4-vinylphenol) (PVP) was used as gate dielectric layer. PVP was deposited by spin coating, and thermally cross-linked at 200 °C [10]. The final thickness of the PVP layer is 190 nm serving a smooth dielectric layer with a permittivity of 3.6. The advantage of the common gate structure is given by the large and smooth surface allowing electrical and morphological measurements on the same device without distracting effects of a patterned gate structure. The same devices of type A were used for the shelf-life measurements over a period up to 100 days. To study the device performance at elevated temperatures during operation a different architecture with a patterned gate and top-contacts was chosen (type B in Fig. 1c). These devices are not depending on back-side contact during measurement and allow the direct placement on a hot plate. The patterned gate structures were fabricated from Al (30 nm) – thermally evaporated through a stencil mask on a pre-cleaned glass wafer. The dielectric layer is served from the same PVP layer as used in fabrication of A-type devices. Organic semiconductors, aluminium (gate) and gold (source-drain layer) were deposited in a high vacuum chamber (UNIVEX300) with a pressure of $\sim 10^{-6}$ mbar, and constant deposition rates of 0.1 Å/s for the 30 nm layer of the organic compounds and approx. 0.7 Å/sec for Al and Au (30 nm). The deposition of the organic semiconductor on devices of type A was performed at constant substrate temperatures, ranging from room temperature (approx. 20 °C) to 120 °C in 20 °C steps. For devices of type B the substrate temperature was constant in all cases (approx. 20 °C).

Devices of type A have a ratio of channel width to length W/L of 150 μm/110 μm, during devices of type B exhibit a W/L of 450 μm/30 μm. Devices were characterized in air and under normal room light using an Agilent 4156 C parameter analyzer. From the electrical transfer characteristics the charge carrier mobilities were extracted from the saturated regime at a drain-source voltage of −10 V and a gate-source voltage of −8 V. The electrical characterization at elevated temperatures during operation was performed, on a hot plate, directly placed on the manual probe station. The measurements were obtained after achieving the target temperature in equilibrium at each point. *Ex situ* surface morphology was investigated by Veeco multimode atomic force microscope (AFM) with tapping mode.

3. Results and discussion

3.1. Influence of substrate heating on thin film morphology

The thin film morphology of organic semiconductors deposited on the dielectric surface is attributed to impact on the charge carrier mobility in devices. Charge transport is related to an effective ππ-overlap between conjugated molecules orientated more or less perpendicular to the surface. In thin films, a polycrystalline morphology is often observed with grains – exhibits a pronounced orientation and crystalline order of the molecules within the grains – and corresponding grain boundaries representing a mismatch in optimal ππ-stacking and break in orientation according to crystal axis parallel to the surface. Therefore, grain boundaries are attributed to represent trapping states with strong impact on carrier transport. Some publication indicate that for several organic semiconductors (pentacene, oligothiophenes or perylene carboxylic diimides) larger grain sizes lead to lower density of grain boundary and therefore to a larger carrier mobility [11–16]. Great efforts have been made to control thin film morphology by tuning the dielectric surface roughness or energy, by varying the substrate temperature [11,16] or by treating the surface with self-assembled monolayers (SAMs) [17]. The trend of "grain size–mobility-relation-

ship" is supported by results obtained on organic single crystals. Single crystals have no grain boundaries and exhibit large mobilities [18,19]. However, contradictory results have been reported as well, proving that larger grain sizes imply lower charge carrier mobilities [17,20–22]. A true statement to the "grain size–mobility-relationship" seems to be difficult because of heterogeneous set of data according to different materials, surfaces, surface treatments and deposition temperatures etc.

Here we compare the thin film morphology related to the electrical characteristics of six different semiconductor materials deposited on an amorphous polymer surface. The materials are processed identically excepting the substrate temperature during deposition. This parameter is identified to impact on the polycrystalline morphology and to affect the mobility of materials sometimes by orders of magnitude [16,23].

The AFM pictures of thin films of Et-6T-Et **1**, Hex-6T-Hex **2**, Dec-6T-Dec **3**, Dec-4T-Dec **4,** and Pentacene **6** deposited at substrate temperatures of 20 °C and 80 °C are shown in Fig. 2. Additionally, the morphology of **3** and **4** was investigated on substrates prepared at 120 °C – beyond the phase transition temperature of these materials (108 °C for **3** and 98 °C for **4**) [5,8]. Increasing substrate temperature changes the thin film morphology to larger domains in all cases. Compounds **1–3** deposited at room temperature appear with granular polycrystalline morphology. The dimensions of grains are approx. 150 nm (see Fig. 2a, c, and e). Dec-4T-Dec **4** exhibit a layered structure rather than crystalline structure with pronounced terracing of approx. 4 nm step height (Fig. 2h). This value correlates nicely to the length of a molecule **4** (l∼4.1 nm – calculated with Chem and Bio Office from CambridgeSoft®) oriented perpendicular to the surface. The layer-by-layer assembly of **4** appears randomly, rather than ordered as expected by nucleated crystalline grow. The analysis of the average domain size is difficult, but the dimensions of homogeneous areas occur larger than in 6T materials **1**–**3**. The Pentacene film (Fig. 2k) show large grains in the micrometer range in the known leaf-vein structure and exhibit pronounced terracing of around 1.4 nm step height.

Samples with materials **1**–**3** processed at 80 °C occur in the same shape of morphology for each material but with expanded grain dimensions by roughly a factor of five. Grain sizes up to 500 nm have been observed (Fig. 2b, d, and f). The domain size of homogeneous layered structure of compounds **4** (Fig. 2j) seems to be expanded as well compared to thin films deposited at low temperature. The morphology of Pentacene (at 80 °C – Fig. 2l) occurs with more bulky and larger crystalline domains but still show pronounced terracing of the same step height. Compound **4** and **5** deposited at 120 °C substrate temperature show large domains in the micrometer scale and pronounced terracing. We believe that the phase transition at 108 °C for **3** and 98 °C for **4** may provide an additional driving force to expand the order domains during deposition at temperatures above the phase transition point.

The charge carrier mobilities of thin film transistors based on all materials are summarized in Table 1. Each value is related to an average of at least three representative devices. In devices fabricated at room temperature the short alkyl-chain substituted materials **1** and **2** (μ∼0.7 cm^2/Vs) slightly outperform materials with longer alkyl side chains (**3** with μ = 0.22 cm^2/Vs and **4** with μ = 0.26 cm^2/Vs). These findings we attribute to the increased injection barrier related to the longer alkyl chains in the top contact transistor configuration [8]. A significant lower mobility of 0.02 cm^2/Vs was observed for H-substituted sexithiophene **5**. This is in good agreement with results reported by others [14,25]. Devices with Pentacene **6** exhibit a mobility of 0.54 cm^2/Vs in the set of room temperature devices. These values indicate that alkyl-substituted oligothiophenes can compete with the charge carrier mobility of pentacene, considering comparable device architectures, contact and dielectric materials and methods.

The values of charge carrier mobility, measured on devices fabricated at higher substrate temperature (40 °C, 60 °C, and 80 °C) occur without significant change or even a tendency. With exception of the value for sexithiophene **5** at 60 °C, all mobilities remain virtually constant within a factor of two (Table 1). These results are in contrast to the clear trend in occurrence of thin film morphology where an increased substrate temperatures yield larger grain sizes. Even the samples, which have been processed at 120 °C, and show a dramatic impact on their thin film morphology, do not show a significant change in the mobility.

We attribute these results to the similar tendency in film growing of our π-conjugated molecules on the PVP surfaces. The formation of the first monolayer is of particular interest, because this layer dominates the charge transport in TFTs [7]. While some materials show a pronounced nucleated 3D-crystal growing mode (Volmer–Weber) on surfaces (e.g. tetracene – making it difficult to obtain even dense film within reasonable film thickness), some other materials (e.g. pentacene, sexithiophene) prefer a layer-by-layer growing mode (Frank–van der Merve) or show a coexistence of 2D-layer growing and 3D-crystal growing (Stranski–Krastanov) [26]. The preferred mode strongly depends on the molecular structure, temperature and surface [27]. Yang et al. [28] have shown, for Pentacene, the formation of the first monolayer (2D-grow) compared to crystal grow (3D) could be controlled by the nature of the polymer surface. On PVP surfaces, a coexistence of 2D and 3D grow was observed. From the results in our study (where the semiconductor films are deposited on smooth amorphous PVP dielectrics) we conclude that the 2D-layer growing is preferred for all materials at least for the formation of the first few layers – independent from the surface temperature during deposition. In thin films based on Dec-4T-Dec **4**, the layer-by-layer growing is dominating the 3D-morphology completely. We attribute this to the weak lattice energy in **4** depending on the low concentration of π-conjugated chromophore.

A formation of a densely packed monolayer at the early beginning of deposition (film grow) should serve a homogeneous active layer at the interface causing reliable transistor characteristics. The difference in thin film morphology, observed at different temperatures, simply reflects the following crystal grow in the third dimension

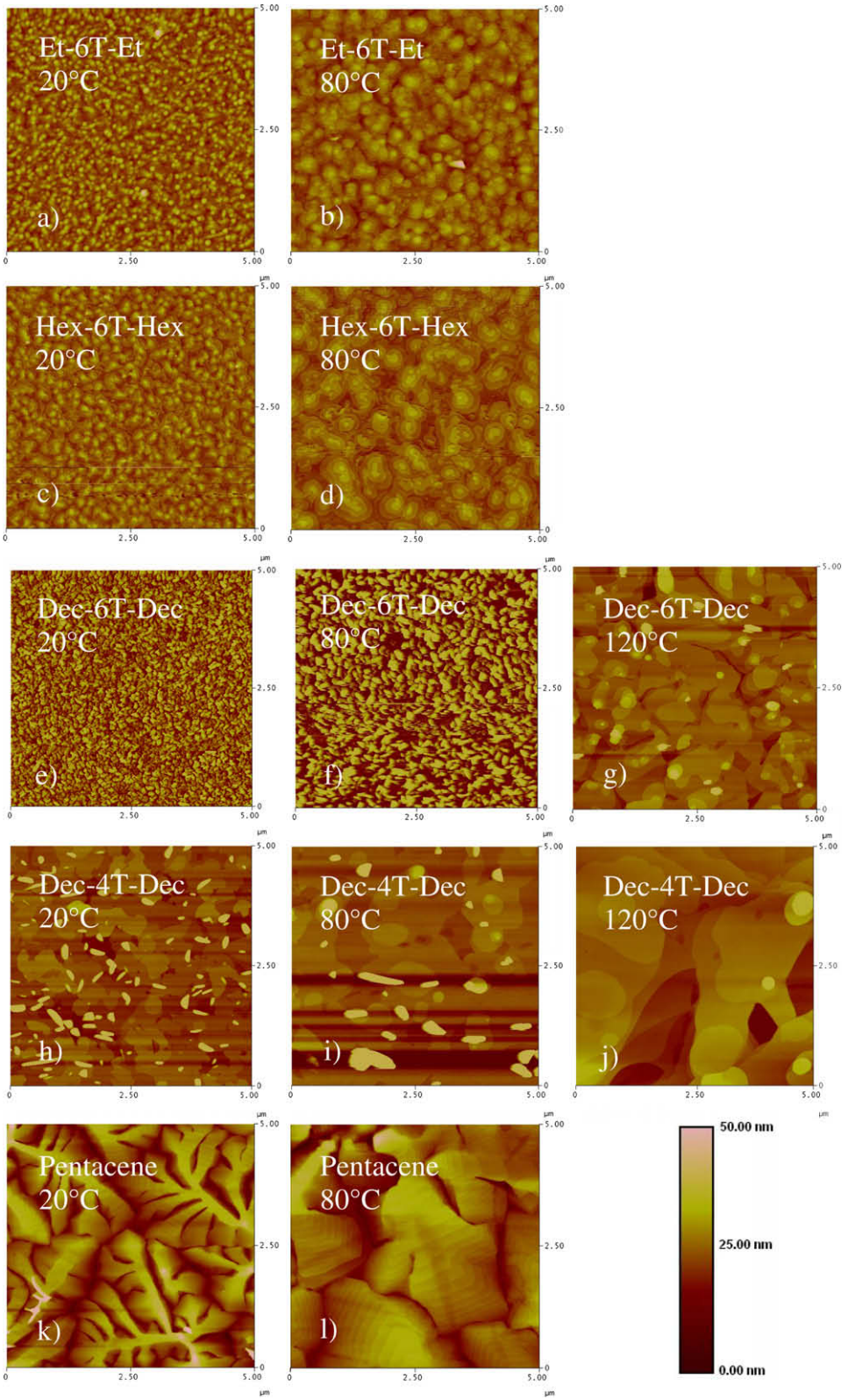

Fig. 2. Thin film AFM images of Et-6T-Et **1** (a and b), Hex-6T-Hex **2** (c and d), Dec-6T-Dec **3** (e–g), Dec-4T-Dec **4** (h–j), and Pentacene **6** (k and l) deposited at substrate temperatures of 20 °C, 80 °C, and 120 °C.

Table 1
Charge carrier mobility (cm^2/Vs) from devices with materials deposited at different substrate temperatures

Substrate temperature during deposition (°C)	Et-6T-Et **1**	Hex-6T-Hex **2**	Dec-6T-Dec **3**	Dec-4T-Dec **4**	6T **5**	Pentacene **6**
RT	0.71 ± 0.07	0.67 ± 0.08	0.22 ± 0.02	0.26 ± 0.05	0.02 ± 0.01	0.54 ± 0.06
40	0.31 ± 0.04	0.41 ± 0.17	0.19 ± 0.01	0.21 ± 0.02	–	0.66 ± 0.05
60	0.53 ± 0.06	0.31 ± 0.04	0.18 ± 0.02	0.18 ± 0.01	0.07 ± 0.01	0.59 ± 0.02
80	0.46 ± 0.06	0.60 ± 0.05	0.21 ± 0.01	0.35 ± 0.02	0.04 ± 0.01	0.46 ± 0.03
100	–	–	–	–	–	0.59 ± 0.06
120	–	–	0.38 ± 0.04	0.15 ± 0.01	–	–

on top of the previously formed monolayer and is not affecting the transistor performance.

To prove this assumption of the preferred layer growing mode of these materials we have fabricated three additional substrates. Exemplarily, Hex-6T-Hex **2** was chosen and deposited on PVP surface with sub-monolayer (~2 nm) 0.5 ML, monolayer (~4 nm) 1 ML, and supersaturated-monolayer (~6 nm) 1.5 ML in thickness. Corresponding AFM images are shown in Fig. 3a–c. We note that for very thin layers the precision of controlling the film thickness is difficult, due to the geometry of the thermal evaporator and monitoring errors. However, the AFM image (Fig. 3a–c) shows an almost half-covered surface of PVP with a thin layer of **2**. The layer thickness is around 3.5 nm – estimated from the height profiles (Fig. 3d). This value corresponds nicely to the length of **2** (~3.7 nm) and indicates the formation of a true monolayer. The monolayer domains are distributed randomly. No double or multilayer coverage is observed. Fig. 3b shows the coverage with approximately one monolayer. The former isolated domains in 0.5 ML device now occur connected, but slightly interrupted by small uncovered areas. Only some tiny areas of double layers were observed. This indicates that the material prefers to fulfil the first monolayer, before growing in 3 D. By further increasing the layer thickness up to nominal 1.5 ML, the first monolayer is densely packed (Fig. 3c) (we note that only one spot with access to the PVP substrate was found to refer the height-profile to the substrate!). A second layer starts growing on top of the first ML and sporadically the formation of a third layer is observed.

The three substrates with 0.5 ML, 1 ML, and 1.5 ML coverage of **2** were used to fabricate transistor devices. According to the incomplete coverage no transistor function was obtained for the device with 0.5 ML of **2**. TFT devices with 1 ML of **2** have a charge carrier mobility of 0.05 cm^2/Vs. The general TFT functionality is attributed to the existence of connected areas of **2**, providing a linked

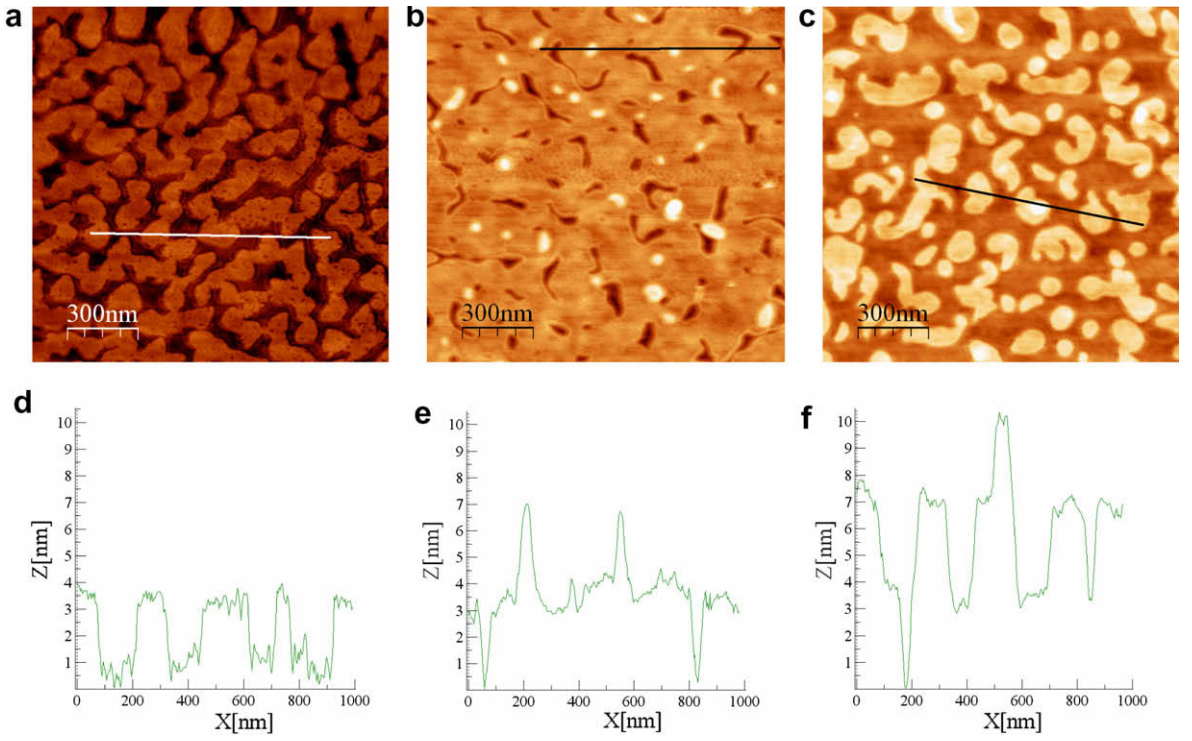

Fig. 3. AFM images of Hex-6T-Hex **2** (a) sub-monolayer (0.5 ML), (b) monolayer (1 ML), and (c) supersaturated-monolayer (1.5 ML) deposited on PVP surface, and corresponding topographic profile of chosen sections (d–f).

channel between source and drain. We address the lower mobility (compared to the thin film devices) to the existence of little uncovered areas, diluting the active channel area. Transistor devices with 1.5 ML of **2**, have an average charge carrier mobility of 0.25 cm^2/Vs. This is comparable to the values obtained from devices with polycrystalline films. From the similar mobilities, obtained with all materials at various temperatures, we conclude that 2D-layer growing is preferred for these materials for the first few layers and dominates the TFT characteristics independently from 3D-morphology [7].

In summary, we have demonstrated that oligothiophenes show large charge carrier mobilities (0.2–0.7 cm^2/Vs) independent from the substrate temperature during deposition. The substrate temperature impacts on the thin film morphology but not on the transistor characteristics. We attribute this to a preferred monolayer formation during deposition on the PVP. These findings make the oligothiophenes to attractive candidates in low cost processing with reliable performance in a wide process window.

3.2. Long-term stability

Degradation in organic TFTs is indicated by the decay of device parameters (charge carrier mobilities (μ), threshold voltage (V_{th}), subthreshold swing (S) and on/off ratio (I_{on}/I_{off})). Most degradation processes are irreversible and attributed to the damage (oxidation) of the semiconductor or changes in film morphology upon storage or operation [29–32]. Thereby the major impact is addressed to the chemical or physical interaction of water and/or oxygen with the organic semiconductor or on grain boundaries. Consequently, the modification of the chemical structure of the organic semiconductor is an important approach to improve their stability [6,33]. However, reversible changes have been reported either, related to unstressed storage or to an environmental impact (pressure, humidity, etc.) [34–38].

We have tracked our devices based on oligothiophens **1**–**5** over a period up to 100 days. During this time, the devices were stored in laboratory atmosphere without any particular protection from air, humidity, temperature variations or even light, representing a realistic test environment to obtain information on the shelf-life of devices. The shelf-life is an important property, in particular for single-use devices or devices with temporary operation (e.g. sensors or RFID-tag) were the initial device characteristics need to remain unchanged from production to the operation afterwards. The decrease in mobility (normalized) – down to 50% of the initial value – is shown in Fig. 4. To display the behaviour we have chosen results on devices prepared at room temperature during semiconductor deposition (see Table 1 for absolute values). We have observed a slow reduction in mobility values for the alkyl-substituted sexithiopenes **1**–**4** over time, which are comparable – or even slower – than observed for Pentacene devices with different inorganic or polymer dielectrics [39]. We note that – with exception of devices with 6T **5** - the time scale of degradation does not imply a complete loss in functionality. For example, Hex-6T-Hex devices tend to sustain with mobility of 0.12 cm^2/Vs after 100 days – still 20% of the initial value. Devices with 6T **5** degrade very fast (15 days) and completely. This observation is in good agreement with the larger sensitivity of 6T to oxidation at the unprotected (H-substituted) α-position of the outer thiophene rings. To investigate a potential impact of the thin film morphology (e.g. amount of grain boundaries) on device stability we have monitored the series of devices based on Et-6T-Et **1** and prepared at elevated temperatures over the same period. After 100 days, a remaining mobility of 50%, 57% and 60% was obtained for samples prepared at 40 °C, 60 °C, and 80 °C respectively, indicating that the stability is not depending on the thin film morphology (Fig. 5).

For Et-6T-Et **1**, what occurs as virtually most stable material, a more detailed set of data (including mobility and threshold voltage vs. time) is shown as insert in Fig. 4. A small variation of V_{th} between −2 V and −5 V was observed. The transfer characteristics of devices as prepared and after storage for 100 days in ambient are shown in Fig. 4b. We were not able to obtain a clear tendency in time dependent degradation from our data (mobility, V_{th}, etc.), so conclusions on the mechanism of degradation would be speculative. However, the behaviour of compound **4** is surprising. Assuming oxidation as a major mechanism, the more negative HOMO energy of −5.41 eV compared to sexithiophenes (HOMO energy app. −5.2 eV) should lead to lower sensitivity to oxidative damage and an improved stability would be expected [24]. Our observations of faster degradation might be related to the different thin film morphology of **4** compared to polycrystalline structure in the other materials. We have observed a layered structure (Fig. 2j), where larger areas of the first monolayer could be unprotected by additional layers – and therefore could be easier accessible for dopants over time.

We summarize, that transistor devices with α,α′-alkyl oligothiophenes have promising shelf-life up to 100 days. The decrease in mobility is competitive to best values reported for other small molecule semiconductors. The shelf-life is virtually unaffected from the polycrystalline thin film morphology.

3.3. Operation at elevated temperature

Besides the importance of the shelf-life of organic transistors, the behaviour of devices related to operation at different temperatures is of enormous interest, due to parameter shift under thermal and electrical stress. For organic transistors, both thermal activated and thermal deactivated carrier transport were reported, depending on various organic semiconductors, device architectures, fabrication methods and testing conditions [22,40–45]. At low temperatures, when thermal activation dominates the effect of energetic disorder in ππ-overlap, the charge carrier transport follows a thermal activated hopping transport mechanism [41]. Some literatures report on the temperature dependency of mobility as a result of permanently changed morphology of organic thin films, source/drain and organic interfaces, and semiconductor/dielectric interfaces upon thermal treatment [22,46]. Also reversible dependency in temperature operation was reported, claiming transistor applications as thermal sensors [44].

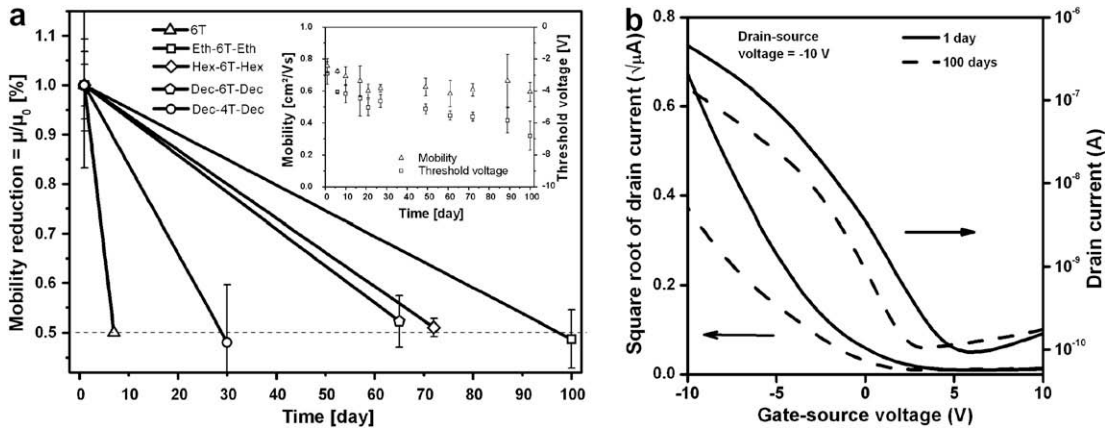

Fig. 4. (a) Decrease of mobility down to 50% of the initial values upon the time scale (*inset*: charge carrier mobility and threshold voltage of Et-6T-Et **1** TFTs measured with different storage time) and (b) transfer characteristics of TFTs with Et-6T-Et **1** directly after device fabrication and after storage for 100 days in ambient.

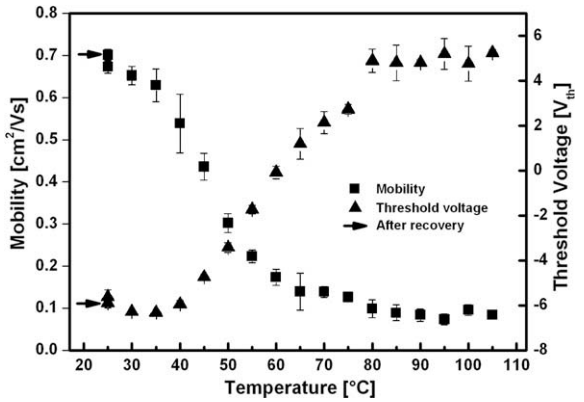

Fig. 5. Charge carrier mobility and threshold voltage of TFTs with Hex-6T-Hex **2** at different operation temperatures. Arrows mark values after cooling.

We have investigated the electrical characteristics (mobility and corresponding threshold voltage) of Hex-6T-Hex **2** in transistor devices of architecture **B**. Therefore the temperature on operating devices was increased from 25 °C to 105 °C, in 5 °C steps. For each measurement, at least three fresh transistors were characterized in order to lower the experimental error and to role out accumulating bias stress effects in devices during the experiment.

With increasing temperature during operation of the TFTs a pronounced degradation of device performance was observed. In the range of 25 °C–80 °C, the charge carrier mobility decreases from 0.68 cm^2/Vs to 0.1 cm^2/Vs and the threshold voltage shifts from −6 V to +4.5 V. By further increasing the temperature up to 105 °C the parameter shift is less pronounced and the extracted parameters remain virtually constant (μ = 0.05 cm^2/Vs and V_{th} = +5 V). After thermal treatment, the devices were stored for 20 h at room temperature in ambient. Subsequently, a complete recovery of the initial device characteristics was obtained (μ = 0.70 cm^2/Vs and V_{th} = −6 V).

The explanation of this behaviour is difficult due to the lack of access to the semiconductor/dielectric interface during the experiment. One reasonable impact could be related to a thermally enforced mismatch in the ππ-stacking between different domains in the first monolayer, comparably to grain boundaries. Possibly, a temperature induced fluctuation and vibration of the molecules inside the domains, impact on their effective ππ-overlap and lead to a temperature enhanced carrier scattering could explain the reversible behaviour. And finally, a temperature induced change of the polymer dielectric surface is reasonable, and would explain the reversible shift in threshold voltage. However this behaviour needs further investigation, due to the large importance of temperature induced parameter shift in integrated circuit applications. We summarize, that the devices are not irreversibly damaged under applied electrical stress and simultaneously elevated temperature operation up to 105 °C.

4. Conclusions

n-Alkyl substituted oligothiophenes exhibit large charge carrier mobility in the average of 0.5 cm^2/Vs in organic transistor devices. The thin film morphology of these materials depends on the substrate temperatures during deposition and the domain sizes increase with elevated temperature. The field effect mobility is virtually unaffected from the thin film morphology. We address these findings to a preferred layer grow of the materials on the amorphous polymer surface. We have obtained remarkable long term stability in ambient with a reduction in mobility of only 50% for Et-6T-Et within 100 days. The device performance depends on temperature during operation with reduction in mobility and shift in threshold voltage. The devices parameters recover to their initial values after cooling. These properties make *n*-alkyl substituted oligothiophenes to promising candidates in commercial transistor applications-fulfilling requirements as excellent electrical performance producible in a large process window, good long term stability and a suitable temperature range of device operation.

Acknowledgements

We would like to thank Dr. Stephan Kirchmeyer and Dr. Timo Meyer-Friedrichsen from H.C. Starck for providing materials **1**–**5**, and Y. Vasil for expert technical assistance.

References

[1] A. Tsumura, H. Koezuka, T. Ando, Appl. Phys. Lett. 49 (1986) 1210.
[2] G. Horowitz, D. Fichou, X. Peng, Z. Xu, F. Garnier, Solid State Commun. 72 (1989) 381.
[3] F. Garnier, G. Horowitz, X. Peng, D. Fichou, Synth. Methods 45 (1991) 163.
[4] H.E. Katz, Z. Bao, S.L. Gilat, Acc. Chem. Res. 34 (2001) 359.
[5] G. Barbarella, M. Melucci, G. Sotgiu, Adv. Mater. 17 (2005) 1581.
[6] A.R. Murphy, J.M.J. Frechet, Chem. Rev. 107 (2007) 1066.
[7] G. Horowitz, Organic Electronics: Materials, Manufacturing and Applications, Wiley VCH, 2006 (Chapter 1);
H. Klauk, Organic Electronics, Wiley VCH, 2006.
[8] M. Halik, H. Klauk, U. Zschieschang, G. Schmid, S. Ponomarenko, S. Kirchmeyer, W. Weber, Adv. Mater. 15 (2003) 917.
[9] S. Ponomarenko, S. Kirchmeyer, A. Elschner, B-H Huisman, A. Karbach, D. Drechsler, Adv. Funct. Mater. 13 (2003) 591.
[10] H. Klauk, M. Halik, U. Zschieschang, G. Schmid, W. Radlik, W. Weber, J. Appl. Phys. 92 (2002) 5259.
[11] S. Pratontep, M. Brinkmann, F. Nueesch, L. Zuppiroli, Synth. Methods 146 (2004) 387.
[12] C.D. Dimitrakopoulos, A.R. Brown, A. Pomp, J. Appl. Phys. 80 (1996) 2501.
[13] L. Torsi, A.J. Lovinger, B. Crone, T. Someya, A. Dodabalapur, H.E. Katz, A. Gelperin, J. Phys. Chem. B 106 (2002) 12563.
[14] G. Horowitz, M.E. Hajlaoui, Synth. Methods 122 (2001) 185.
[15] J. Locklin, M. Roberts, S. Mannsfeld, Z. Bao, J. Macromol. Sci. Polym. Rev. 46 (2006) 79.
[16] R.T. Weitz, K. Amsharov, U. Zschieschang, V.E. Barrena, D.K. Goswami, M. Burghard, H. Dosch, M. Jansen, K. Kern, H. Klauk, JACS 130 (2008) 4637.
[17] C. Goldmann, C. Krellner, K.P. Pernstich, S. Haas, D.J. Gundlach, B. Batlogg, J. Appl. Phys. 99 (2006) 034507/1.
[18] V. Podzorov, V.M. Pudalov, M.E. Gershenson, Appl. Phys. Lett. 82 (2003) 1739.
[19] J.E. Anthony, Angew. Chem. Int. Ed. 47 (2008) 452.
[20] S.Y. Yang, K. Shin, C.E. Park, Adv. Funct. Mater. 15 (2005) 1806.
[21] D. Knipp, R.A. Street, A. Volkel, J. Ho, J. Appl. Phys. 93 (2003) 347.
[22] D. Guo, S. Ikeda, K. Saiki, H. Miyazoe, K. Terashima, J. Appl. Phys. 99 (2006) 094502/1.
[23] J. Locklin, Z. Bao, Anal. Bioanal. Chem. 384 (2006) 336.
[24] S. Ponomarenko, S. Kirchmeyer, M. Halik, H. Klauk, U. Zschieschang, G. Schmid, A. Karbach, D. Drechsler, N.M. Alpatova, Synth. Methods 149 (2005) 231.
[25] A. Dodabalapur, L. Torsi, H.E. Katz, Science 268 (1995) 270.
[26] R. Ruiz, D. Choudhary, B. Nickel, T. Toccoli, K-C. Chang, A.C. Mayer, P. Clancy, J.M. Blakely, R.L. Headrick, S. Iannotta, G.G. Malliaras, Chem. Mater. 16 (2004) 4497.
[27] F. Dinelli, M. Murgia, P. Levy, M. Cavallini, F. Biscarini, D.M. de Leeuw, Phys. Rev. Lett. 92 (2004). 116802-1.
[28] S.Y. Yang, K. Shin, C.E. Park, Adv. Funct. Mater. 15 (2005) 1806.
[29] M. Mottaghi, G. Horowitz, Org. Electron. 7 (2006) 528.
[30] Y. Qiu, Y. Hu, G. Dong, L. Wang, J. Xie, Y. Ma, Appl. Phys. Lett. 83 (2003) 1644.
[31] X. Yan, H. Wang, D. Yan, Thin Solid Films 515 (2006) 2655.
[32] J.E. Northrup, M.L. Chabinyc, Phys. Rev. B 68 (2003) 041202/1.
[33] H. Klauk, U. Zschieschang, R.T. Weitz, H. Meng, F. Sun, G. Nunes, D.E. Keys, C.R. Fincher, Z. Xiang, Adv. Mater. 19 (2007) 3882.
[34] A. Salleo, F. Endicott, R.A. Street, Appl. Phys. Lett. 86 (2005) 263505/1.
[35] R. Ye, M. Baba, K. Suzuki, Y. Ohishi, K. Mori, Thin Solid Films 464 (2004) 437.
[36] G. Darlinski, U. Bottger, R. Waser, H. Klauk, M. Halik, U. Zschieschang, G. Schmid, C. Dehm, J. Appl. Phys. 97 (2005) 093708/1.
[37] Z-T. Zhu, J.T. Mason, R. Dieckmann, G.G. Malliaras, Appl. Phys. Lett. 81 (2002) 4643.
[38] D. Li, E-J. Borkent, R. Nortrup, H. Moon, H. Katz, Z. Bao, Appl. Phys. Lett. 86 (2005) 042105/1.
[39] H. Klauk, U. Zschieschang, J. Pflaum, M. Halik, Nature 445 (2007) 745.
[40] Y. Takamatsu, T. Sekitani, T. Someya, Appl. Phys. Lett. 90 (2007) 133516/1.
[41] G. Horowitz, M. Hajlaoui, E. Mohsen, R. Hajlaoui, J. Appl. Phys. 87 (2000) 4456.
[42] B.H. Hamadani, D. Natelson, Proc. IEEE 93 (2005) 1306.
[43] T. Minari, T. Nemoto, S. Isoda, J. Appl. Phys. 99 (2006) 034506/1.
[44] S. Jung, T. Ji, V.K. Varadan, Appl. Phys. Lett. 90 (2007) 062105/1.
[45] I.N. Hulea, S. Fratini, H. Xie, C.L. Mulder, N.N. Iossad, G. Rastelli, S. Ciuchi, A.F. Morpurgo, Nat. Mater. 5 (2006) 982.
[46] T.N. Ng, W.R. Silveira, J.A. Marohn, Phys. Rev. Lett. 98 (2007) 066101/1.

spin-coating, casting, or printing at room temperature and under ambient conditions. The mobility of the most pentacene-based OTFTs is significantly influenced and dominated by characteristics of applied gate dielectrics. PMMA is a well-known glasslike material in photonics [13]. Recently, PMMA used as a gate dielectric layer in OTFTs is also being considered, because of it shows not only good output and transfer characteristics but also potential to alternate SiO_2 as the gate dielectric in OTFTs [14–17].

In this paper, we present the study of the field-effect on pentacene-based organic TFT by using polyacrylates as dielectric layers. To control channel conductance and carrier density without using gate voltage, a series of dipole tunable polyacrylates, which are derived from PMMA matrix, are investigated as dielectric layers. By using pentacene-based OTFTs with a top-contact configuration, we will also characterize the dipole effect on the semiconductor/dielectric interface. The output and transfer characteristics related to carrier density, including field-effect mobility (μ_{sat}), on-off current ratio (I_{on}/I_{off}), turn-on voltages (V_{on}), and threshold voltages (V_{Th}), were also examined.

2. Experimental

All of the materials used in the experiment were commercially available, and solvents were used without further purification. The purity of gold and aluminum metal are 99.8%. The molecular weight of commercial poly(methylmethacrylate) (PMMA) is 15,000 g/mol. Poly(phenylacrylate)[18], poly(4-methoxyphenylacrylate) (PMPA)[19], and poly(2,2,2-trifluoroethyl methacrylate) (PTFMA)[20] were prepared according to the references. Thermal decomposition temperature (T_d), glass transition temperature (T_g), and molecular weight (M_w) of polyacrylates were determined by thermogravimetric analysis (TGA, SEIKO I TG/DTA 200), differential scanning calorimetry (DSC, SEIKO SII DSC 2000), and a Water 600 gel permeation chromatography (GPC), respectively. Surface affinity of polyacrylates thin-films was measured by using a Paul N. Gardner contact angle detector.

2.1. Device fabrication

The patterned ITO glass substrates were cleaned ultrasonically with detergent, deionized water, 2-propanol, and methanol, followed by UV-ozone pretreatment before use. For top-contact OTFTs fabrication, polyacrylates were dissolved in toluene with 12.0 wt%, spin-coated onto ITO substrates at 1000 rpm for 30 s, and dried in a vacuum oven at 80 °C for 4 h. Thereafter, pentacene was thermally deposited at 6×10^{-6} Torr (ca. 0.3–0.4 Å s^{-1}) with a film thickness of 600 Å. Top-contact Au electrodes (ca. 70 nm) were then deposited through a shadow mask. The channel length (L) and width (W) of the devices were 200 and 2000 μm, respectively. The film thickness and roughness were measured using a DI 3100 atomic force microscopy (AFM). The current–voltage (I–V) characteristics of OTFTs were measured using a Keithley 4200 semiconductor parameter analyzer and a HP 4284 CV analyzer.

3. Result and discussion

3.1. Characterization of gate dielectric surface

To investigate the effect of polyacrylates gate dielectrics on pentacence-based OTFTs, a series of polyacrylates with different ester substitutes (4-methoyxphenyl (PMPA), phenyl (PPA), and 2,2,2-trifluoroethyl (PTFMA) side chain

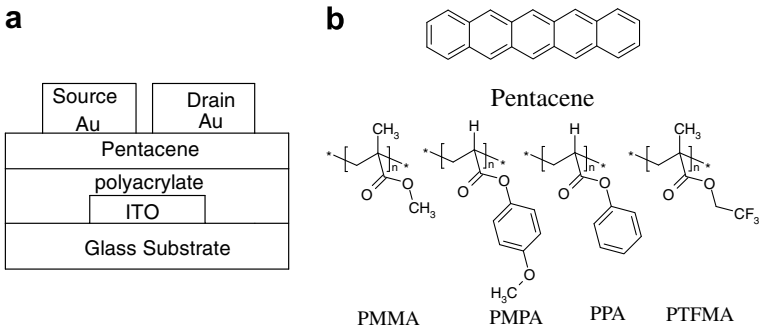

Fig. 1. (a) The schematic of top-contact OTFT and (b) chemical structures of materials used in this study.

Table 1
Gate dielectric thin-film surface characteristics

Dielectric material	T_g (°C)	Thickness (nm)	Surface roughness (R_a; nm)	Surface contact angle (°)[a]	Surface free energy (SFE; mJ m^{-2})	Dielectric constant (k)[b]
PMMA	105.2	560	0.32	74	38.19	3.2
PMPA	133.2	660	0.40	75	37.54	3.4
PPA	135.7	582	0.20	90	27.91	2.9
PTFMA	82.4	592	0.44	95	24.75	6.0

[a] Measured by using DI-water droplets.
[b] Measured at 1.0 kHz.

groups) were synthesized. Their corresponding chemical structures and the OTFT configuration are depicted in Fig. 1.

The dielectric thermal properties and thin-film surface were characterized and summarized in Table 1. In thermal analysis, both PMPA and PPA show higher T_g than that of PMMA and PTFMA, implying the rigidity of the side-chain group. All dielectrics had comparable thickness (560–660 nm) were spin-cast, and exhibited very similar topologies. The deposited dielectric thin-films were observed to be pinhole-free and smooth; whose root-mean-square roughness was within 0.20–0.44 nm.

Improved mobility could be depicted by changes in the surface energy of gate dielectrics [21]. In addition, lowering the surface energy on a gate dielectric was identified as a key factor to increasing the grain size during the growth of pentacene. To evaluate those parameters related to the thin-film surface free energy (SFE), we utilize Eq. (1), obtained from both Young's equation and the equation of state for solid/liquid interfacial tension, to estimate the surface free energy (SFE) of gate dielectrics [22].

$$\gamma_L(1+\cos\theta) = 2(\gamma_L\gamma_s)^{1/2} e^{-\beta(\gamma_L-\gamma_s)^2}, \quad (1)$$

where γ_L, γ_s, θ, and β is the surface tension of water, the surface energy of the solid, the measured contact angle, and an empirical constant with an average value of 1.06×10^{-4} $(m^2\ mJ^{-1})^2$, respectively. In estimating surface energy γ_s, the surface tension of water is substantially adopted as 72.88 mJ/m^2.

The surface contact angle of polyacrylates and their corresponding SFE, which were calculated according to Eq. (1), summarized in Table 1, are dominated by the hydrophobicity of ester groups SFE also decreases with increasing the surface contact angle. In structural modification, dielectric constant (k) is substantially increased for PMPA and PTFMA while high polar substitutes instead of methyl groups in ester linkage. The dielectric constants of PPA, PMMA, PMPA, and PTFMA were obtained as 2.9, 3.2, 3.4,

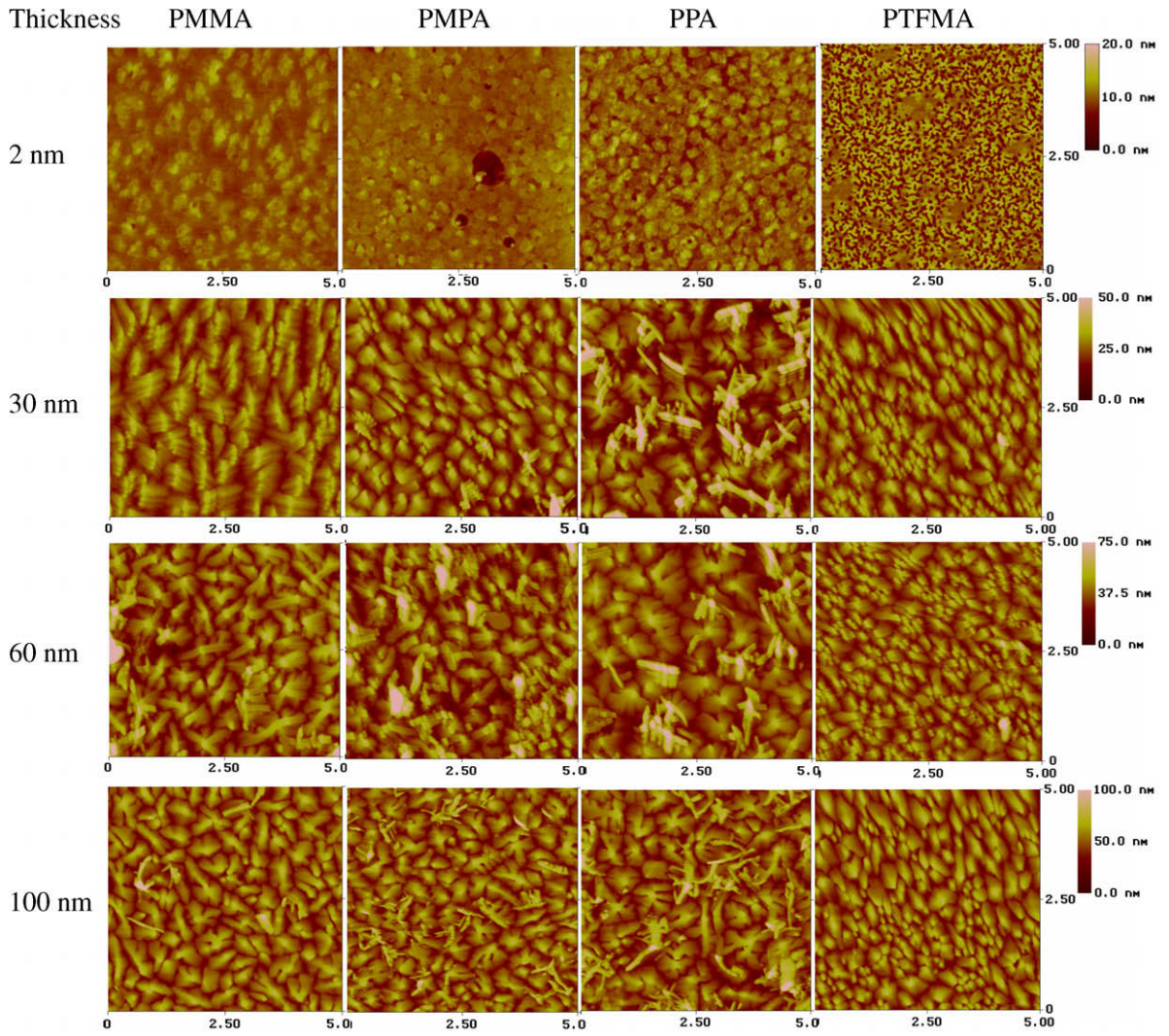

Fig. 2. AFM images of pentacene films grown on various dielectric substrates: (a) PMMA, (b) PMPA, (c) PPA and (d) PTFMA.

and 6.0, respectively. The measured k value of PTFMA is extremely high, owing to the electronegative characteristic of the 2,2,2-trifluoroethyl group.

3.2. Topography of pentacene thin-film

To study thin-film growth mechanisms during the thermal evaporation process, we utilized the AFM to measure the surface morphology of pentacenes of 2, 30, 60, and 100 nm in thickness. The profiles were measured in the channel region and are shown in Fig. 2, where grain size increases with film thickness, the grain shape is independent of pentacene film thickness. Although the surface morphology of pentacene is measured on different polyacrylate dielectrics, the typical crystallites size is remarkably similar, roughly 0.3–0.7 μm, as shown in Fig. 2. This fact is also found that the pentacene film growth mode/morphology variations are closely correlated with the surface energy of the corresponding polymer substrates. Different semiconductor film growth mechanisms are involved with different dielectric substrates, which can be associated with either formal Frank-van der Merwe (layer-by-layer) or Volmer-Weber (island) growth modes [23]. The needle-like growths, visible in the images of PMMA, PMPA, and PPA are most likely pentacene dihydride [24]. Most of the substrates show crystallites of the usual dendritic form, and their corresponding pentacene growth mechanisms show as layer-by-layer growth modes. However, the growth mechanism of PTFMA is totally different from that of mentioned above. The dendritic feature is not observed in PTFMA substrate. What displaces are dense grains with island growth mode, implying that the crystal growth of the first seeding of pentacene on the flat substrate was significantly affected when the dielectric surface energy relatively approaches to that of surface energy on pentacene crystal plane [25,26].

3.3. The output and transfer characteristics of OTFTs

The output characteristics (I_{DS} vs. V_{DS}) with various gate voltages (V_{GS}) for pentacene TFTs using polyacrylates as the gate insulator are plotted in Fig. 3. All devices show good saturation characteristics as a drain-source bias. The I_{DS}–V_{DS} output characteristics show a p-channel accumulation type field-effect transistor. Under a given gate voltage V_{GS}, the device with PTFMA gate dielectric shows similar

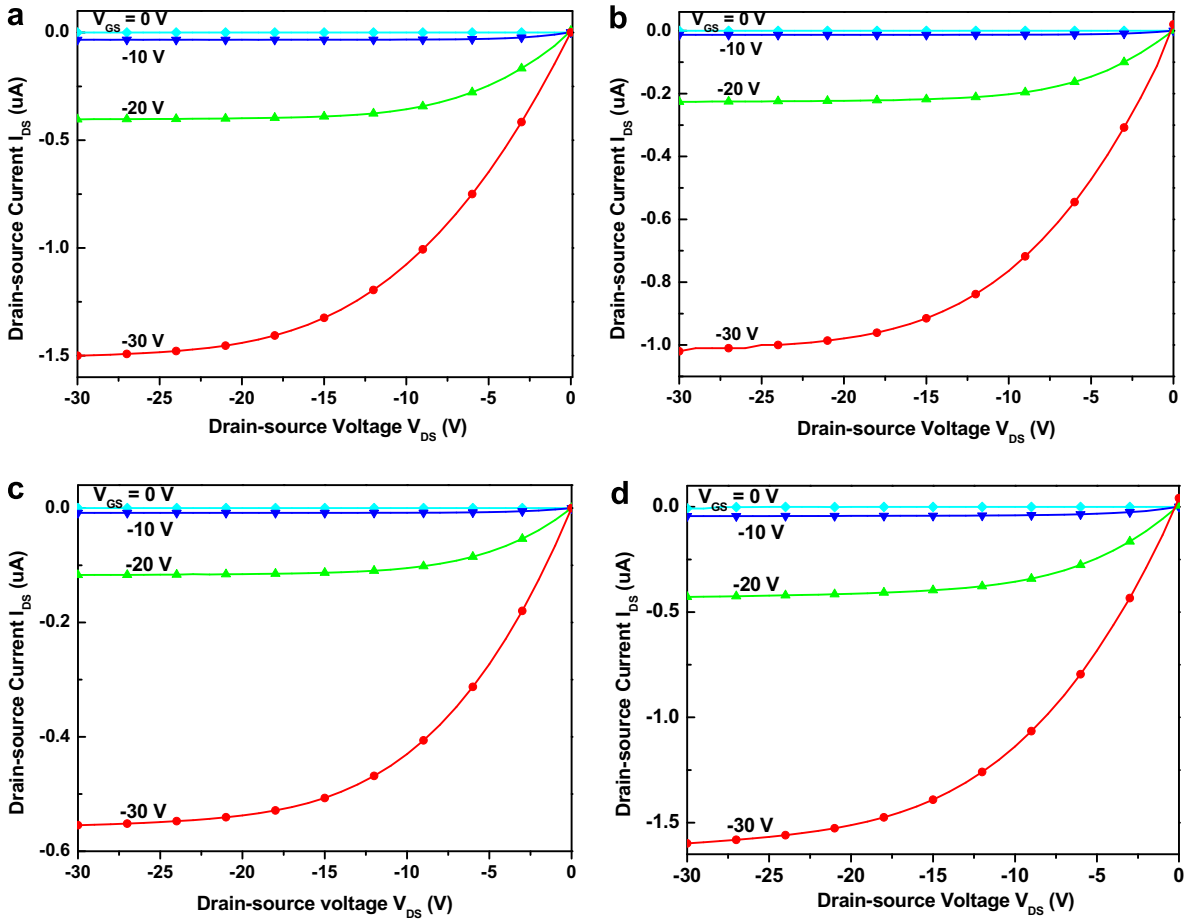

Fig. 3. Output characteristics of OTFTs with different gate dielectrics: (a) PMMA, (b) PMPA, (c) PPA and (d) PTFMA.

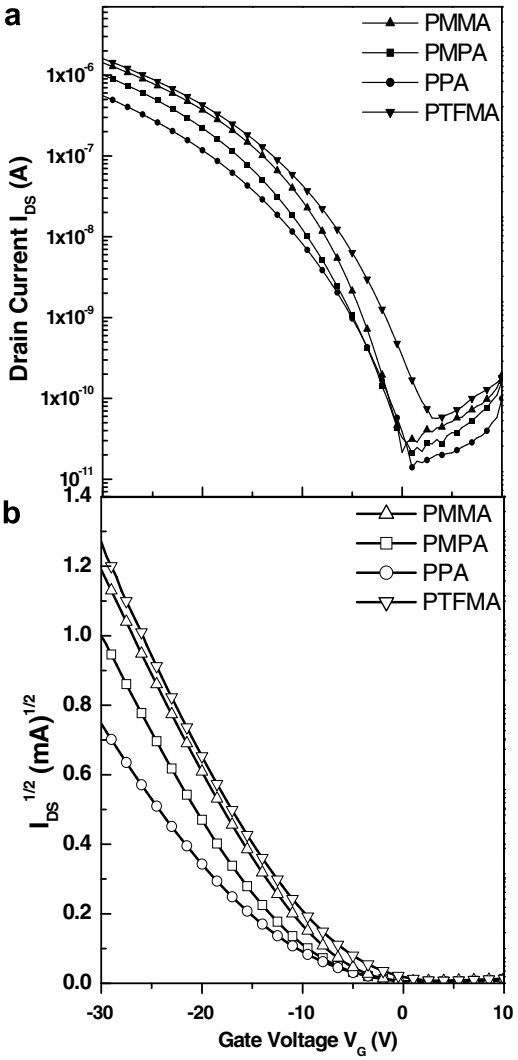

Fig. 4. Transfer characteristics of OTFTs with various gate dielectric materials. The gate voltage is swept at a constant drain-source voltage $V_{DS} = -30$ V.

features of drain-source current curves with PMMA gate dielectrics, and these devices mentioned above show higher saturation I_{DS} than that of PMPA and PPA at $V_{GS} = -30$ V.

The transfer characteristics of the devices are measured in the saturation region ($|V_{DS}| = 30\ \text{V} \geqslant |V_{GS}-V_{Th}|$), and representative transfer plots are shown in Fig. 4. The carrier mobility (μ_{sat}) and threshold voltage (V_T) are calculated from the slop and intercept of the linear part of the ($I_{DS}^{1/2}-V_G$) plot by fitting the data to Eq. (2) [27]:

$$\mu_{sat} = (2I_{DS}L)/[WC_i(V_G - V_{Th})], \quad (2)$$

where I_{DS}, L, W, C_i, V_G, and V_{Th} are the drain saturation current, channel length, channel width, gate dielectric capacitance, gate voltage, and threshold voltage, respectively. All parameters related to transfer characteristics are summarized in Table 2.

In this study, the observed charge-carrier mobility depends not only on the dielectric surface chemical characteristics but also on the dipole moment of the terminal groups on the dielectric side-chain. As shown in Table 2, gate insulators, with low surface energy and high dielectric constants, show a tendency to have high mobility due to the uniform pentacene thin-film phase and good crystallographic structure. Accordingly, PMMA and PMPA have similar dielectric constants and surface free energies. They also show similar topography with layer-by-layer crystal growing mode in AFM images (Fig. 2). Furthermore, their corresponding field-effect mobilities at the saturation region (μ_{sat}) are similar and measured at 0.153 $cm^2\ V^{-1}\ s^{-1}$ for PMMA and 0.134 $cm^2\ V^{-1}\ s^{-1}$for PMPA. In general, pentacene films grown in the layer-by-layer mode exhibit large grain sizes and relatively similar mobilities (e.g., PMMA and PMPA), but smaller grain sizes and poor mobilities in the island mode. However, pentacene film with the island mode growth in PTFMA device affords different OTFT characteristics ($\mu_{sat} = 0.195\ cm^2\ V^{-1}\ s^{-1}$) from that of the layer-by-layer mode. Thus, the field-effect mobility is relatively dropped when the thin-film phase and the single crystal phase synchronously grow and coexisted during thermal evaporation.[28]. Evidently, the topographies of PTFMA show the single crystal phase in Fig. 2. Hence, the PTFMA device has higher field-effect mobility than that of PMMA and PMPA.

The device characteristics of pentacene TFT based on different gate dielectrics are shown in Fig. 4a; the source-drain current I_{DS} in a logarithmic scale are shown against the gate voltage V_G at a constant source-drain voltage of $V_{DS} = -30$ V. All of these devices exhibit I_{on}/I_{off} values of four orders of magnitude and also show that I_{DS} values depend on the nature of polyacrylates. The I_{DS} value at $V_G = 0$ V is enhanced by one order of magnitude in devices with PTFMA compared with that of PMMA, indicating that

Table 2
Summary of the electrical performance parameter for OTFTs with different gate dielectrics

Dielectric	Mobility (μ_{sat} $cm^2\ V^{-1}\ s^{-1}$)	Capacitance (C_i; nF cm^{-2})	On–off current ratio (I_{on}/I_{off})	Turn-on voltage (V_{to}; V)	Threshold voltage (V_{Th}; V)	Dipole moment (D; Debye) [30]
PMMA	0.153	5.06	6.64×10^4	0.0	−7.03	0.94[a]
PMPA	0.134	4.56	4.72×10^4	1.0	−6.03	1.36[b]
PPA	0.093	4.41	3.97×10^4	1.0	−8.24	1.16[c]
PTFMA	0.195	5.35	2.83×10^4	3.5	−8.62	2.54[d]

Note: the side-chain group.
[a] Alkyl group ($-OCH_3$).
[b] Alkoxyaryl ($-OC_6H_5OCH_3$).
[c] Phenyl group ($-OC_6H_5$).
[d] Fluoroalkyl group ($-OCH_2CF_3$).

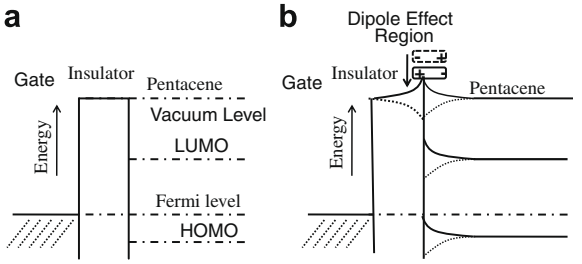

Fig. 5. Schematic energy level diagram for illustrating the interface between gate insulators and pentacene: (a) without and (b) with dipole effect between gate dielectric/pentacene interface. The "+" and "−" denote the hole and the electron, respectively.

the surface carrier is modulated by changing the terminal ester group on gate dielectrics.

The $I_{DS}^{1/2}$–V_G relations for devices are plotted in Fig. 4b. Through a linear fit for $I_{DS}^{1/2}$–V_G curves, we are able to estimate V_{Th} and μ_{sat} in the saturation region. Of particular interest is the change in V_{Th} with various polyacrylates. V_{Th} and V_{to} shift positive as dielectrics go from PPA through PMMA to PTFMA.

The observed V_{Th} and V_{to} shift correlates to the electron affinity of the polymeric insulators end group. The dipole structures synchronously form a built-in dipole-dipole field, and the induced field is equivalent to a gate voltage applied in the transistor channel. The electronegativity of the terminal functional group on polymeric dielectrics influences the charge distribution within the gate insulator and pentacene. This can lead to the formation of an electric dipole within the dielectric/pentacene interface. The field induced phenomenon was also studied by Campbell et al. [29], who proposed the charge distribution within similar molecules and found a dipole moment whose strength significantly depended on the functional group of the investigated molecules. In this presented circumstance, the electron affinity of a close-packed organized organic monolayer can differ from the properties of the isolated molecules. As a result, the charge density at the insulator-organic semiconductor interface has been organized in advance so that it would affect device performance dramatically. The change in surface potentially modifies interface properties, as illustrated in the schematic band diagram shown in Fig. 5. When pentacene is deposited onto a dielectric layer without the dipole effect, the vacuum levels are aligned and no bending of the HOMO and LUMO level occurs, as shown in Fig. 5a. When a negative gate voltage is applied, the Fermi level of the gate electrode shifts towards higher (electron) energies. A part of the applied gate voltage is dropped across the gate insulator, and since the band alignment of the HOMO and LUMO level is fixed with respect to the vacuum level, the remaining gate voltage bends HOMO and LUMO levels. As a result, mobile charge carriers can be accumulated and formed in the conducting channel. For a polymeric dielectric with a permanent dipole field inserted between the gate electrode and the pentacene, as shown in Fig. 5b, the dipole field of the polymeric insulator modifies the surface potential which has the same effect as applying a (negative) gate voltage. For a p-type OTFT, therefore, V_{Th} and V_{to} will shift to more a positive region when a polymer with high dipole moment is used as a gate dielectric layer.

4. Conclusion

We have demonstrated that the single-layered polyacrylate with electronegative side groups significantly induces a built-in field within the semiconductor/dielectrics interface in p-type organic TFTs. This built-in field also shifts both threshold voltage (V_{Th}) and turn-on voltage (V_{to}) to positive bias voltage in pentacene-based devices with increasing the dipole moment of the dielectric. Although SAMs approach was also employed as gate dielectrics and the ultrathin monolayer less than 10 nm would be effective for reducing the operational voltage, it would be a technical challenge for making a pin-hole free monolayer film in a large area. Accordingly, we find that our study provides a simple way of controlling channel charge density at very low density levels and consequently the V_{Th} value, which should be useful for fabricating OTFTs with improved functionality. Permittivity tunable polymeric dielectrics are also a promising route to alternative SAM processed, and they will also open up exciting possibilities for fabrication of large area TFT devices by inkjet printing.

Acknowledgement

This work was supported by the MOE ATU Program "Aim for the Top University" # 97W802 and NSC-96-2628-E009-021-MY3.

References

[1] F. Ebisawa, T. Kurokawa, S. Nara, J. Appl. Phys. 54 (1983) 3255.
[2] A. Tsumura, H. Koezuka, T. Ando, Appl. Phys. Lett. 49 (1986) 1210.
[3] A. Assadi, S. Svensson, M. Willander, O. Inganas, Appl. Phys. Lett. 53 (1988) 195.
[4] K. Kudo, M. Yamashina, T. Moriizumi, Jpn. J. Appl. Phys. 23 (1984) 30.
[5] G. Horowitz, D. Fichou, X.Z. Peng, Z.G. Xu, F. Garnier, Solid State Commun. 72 (1989) 381.
[6] H.E.A. Huitema, G.H. Gelinck, J.B.P.H. van der Putten, K.E. Kuijk, C.M. Hart, E. Cantatore, P.T. Herwig, A.J.J.M. van Breemen, D.M. de Leeuw, Nature 414 (2002) 99.
[7] C.D. Sheraw, L. Zhou, J.R. Huang, D.J. Gundlach, T.N. Jackson, M.G. Kane, I.G. Hill, M.S. Hammond, J. Campi, B.K. Greening, J. Francl, J. West, Appl. Phys. Lett. 80 (2002) 1088.
[8] C. Bartic, A. Campitelli, S. Borghs, Appl. Phys. Lett. 82 (2003) 475.
[9] B. Crone, A. Dodabalapur, Y.Y. Lin, R.W. Filas, Z. Bao, A. LaDuca, R. Sarpeshkar, H.E. Katz, W. Li, Nature 403 (2000) 521.
[10] H. Klauk, M. Halik, U. Zschieschang, F. Eder, G. Schmid, C. Dehm, Appl. Phys. Lett. 82 (2003) 4175.
[11] S. Kobayashi, T. Nishikawa, T. Takenobu, S. Mori, T. Shimoda, T. Mitani, H. Shimotani, N. Yoshimoto, S. Ogawa, Y. Iwasa, Nature Mater. 3 (2004) 317.
[12] K.P. Pernstich, S. Haas, D. Oberhoff, C. Goldmann, D.J. Gundlach, B. Batlogg, A.N. Rashid, G. Schitter, J. Appl. Phys. 96 (2004) 6431.
[13] D.L. Keyes, R.R. Lamonte, D. McNally, M. Bitritto, Photonics Spectra 30 (2001) 131–134.
[14] T.-S. Huang, Y.-K. Su, P.-C. Wang, Appl. Phys. Lett. 91 (2007) 92116.
[15] G.-W. Kang, K.-M. Park, J.-H. Song, C.H. Lee, D.H. Hwang, Curr. Appl. Phys. 5 (2005) 297.
[16] C.-S. Chuang, S.-T. Tsai, Y.-S. Lin, F.-C. Chen, H.-P.D. Shieh, Jpn. J. Appl. Phys. 46 (2007) L1197.
[17] K. Müller, I. Paloumpa, K. Henkel, D. Schmeißer, Mater. Sci. Eng. 26 (2006) 1028.
[18] D.-J. Liaw, R.-S. Lin, J. Macro. Sci. Part A 31 (1994) 715.
[19] B.S.R. Reddy, J. Poly. Mater. 16 (1999) 271.
[20] M. Raihane, B. Ameduri, J. Fluorine Chem. 127 (2006) 391.

[21] I. Kymissis, C.D. Dimitrakopoulos, S. Purushothaman, IEEE Trans. Electron Dev. 48 (2001) 1060–1064.
[22] M. Gindl, G. Sinn, W. Gindl, A. Reiterer, S. Tschegg, Colloids Surf. A: Physicochem. Eng. Aspects 181 (2001) 279.
[23] D.L. Smith, Thin-Film Deposition: Principles and Practice, McGraw-Hill, New York, 1995 (Chapter 5).
[24] C. Mattheus, J. Baas, A. Meetsma, J.L. de Boer, C. Kloc, T. Segrist, T.M. Palstra, Acta Crystallogr. E58 (2002) o1229.
[25] W.Y. Chou, C.W. Kuo, H.L. Cheng, Y.R. Chen, F.C. Tang, F.Y. Yang, D.Y. Shu, C.C. Liao, Appl. Phys. Lett. 89 (2006) 112126.
[26] J.E. Northrup, M.L. Tiago, S.G. Louie, Phys. Rev. B Phys. 66 (2002) 121404.
[27] S.M. Sze, Semiconductor Devices, Wiley, New York, 1985 (Chapter 5).
[28] C.D. Dimitrakopoulos, A.R. Brown, A. Pomp, J. Appl. Phys. 80 (1996) 2501.
[29] I.H. Campbell, S. Rubin, T.A. Zawodzinski, J.D. Kress, R.L. Martin, D.L. Smith, N.N. Barashkov, J.P. Ferraris, Phys. Rev. B 54 (1996) 4321.
[30] G.W. Gokel, Dean's Handbook of Organic Chemistry, second ed., McGraw-Hill, USA, 2004.

solid state [7]. It has been reported that this disadvantage can be modulated dramatically by introducing twisted geometry or noncoplanar configurations directly into the conjugated backbones of the molecules [8].

Tröger's base (TB), an old compound first synthesized by Tröger in 1887, [9] has recently received renewed interests as new applications of its derivatives and analogues continue to emerge due to their inherent chirality, C_2 or approximate C_2 symmetry and particular rigid, concave A-shaped framework [10]. This A-shaped twisted configuration is theoretically disadvantageous for the formation of π–π close stacking, which may lead to fluorescence quenching in the solid state. Our recent study on the aggregation-induced emission (AIE) phenomenon of a pyridinium salt with A-shaped TB scaffold prompted us to continuously explore TB analogues as emissive materials [11]. With this in mind, we have designed and synthesized two fluorene based TB analogues which incorporate large π-conjugated aryl substituted fluorene group with concave A-shaped TB scaffold in order to exploit their potentials as light emitting material. It is confirmed that the two fluorene based TB analogues show strong fluorescence both in dilute solutions and aggregated states (including polycrystalline powders and amorphous films). Unusually, the amorphous films of the two compounds show multiple blue–green emissions similar to the emissions of some polyfluorenes and oligofluorenes while both dilute solutions and polycrystalline powders of the two compounds show single blue–violet emissions, furthermore, the amorphous film emissions are red-shifted in comparison with their polycrystalline counterpart. Meanwhile, both TB analogues exhibit high glass transition temperature (T_g) (147 °C for TBFB-BP and 128 °C for TBFB-FB) and excellent thermal stability. The thin films of both compounds prepared by vacuum thermal evaporation are amorphous and smooth without pinhole. Our results indicate that the two compounds would be promising candidates as light-emitting materials. The potentials of the two TB analogues as light-emitting materials are demonstrated by the high luminance (22047 cd/m^2 for TBFB-BP and 13434 cd/m^2 for TBFB-FB), high efficiency (2.78 cd/A, 1.82 lm/W for TBFB-BP and 2.76 cd/A, 1.93 lm/W for TBFB-FB) and relative low turn-on voltage (4.6 V for TBFB-BP and 4.5 V for TBFB-FB) of devices using them as emitting layers.

2. Results and discussion

2.1. Synthesis and characterization

The synthesis of the two TB analogues TBFB-BP and TBFB-FB is depicted in Scheme 1. 2-Amino-7-bromofluorene was first alkylated to enhance the solubility. 2-Amino-7-bromo-9,9-bibutylfluorene was prepared by alkylation of 2-amino-7-bromofluorene using aqueous NaOH and *n*-butylbromid in stirring dimethyl sulphoxide (DMSO) [12]. Then, the intermediate TBFB-Br was prepared by condensation of 2-amino-7-bromo-9,9-bibutylfluorene and hexamethylenetetramine (HMTA) under trifluoroacetic acid (TFA) conditions and argon (Ar) atmosphere. And then, TBFB-Br underwent Suzuki coupling reaction with corresponding aryl boronic acid to achieve the two key TB analogues were verified by ^{1}H and ^{13}C NMR spectroscopy, matrix assisted laser desorption/ionization time of flight (MALDI-TOF) mass spectrometry and elemental analysis. The two compounds are readily soluble in common

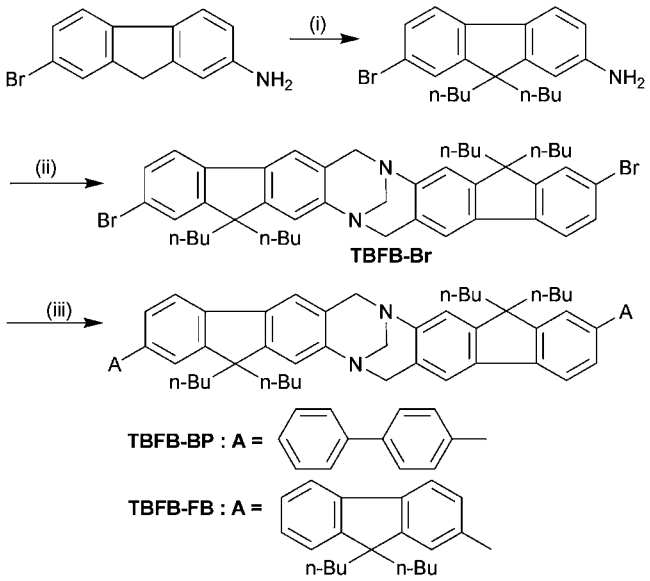

Scheme 1. Synthetic route to TBFB-BP and TBFB-FB.

organic solvents such as dichloromethane (DCM), tetrahydrofuran (THF), *N*,*N*-dimethyl formamide (DMF).

2.2. Condensed state structures, thermal properties and morphology

To understand the framework and arrangement of the molecules in the aggregated crystalline state, single crystals of TBFB-BP suitable for X-ray analysis, a representative case, were obtained by carefully layering the DCM solution of TBFB-BP with ethanol. The molecular structure of TBFB-BP and its packing arrangement in single crystal are given in Fig. 1. Details of the solution and refinement of the X-ray structure are presented in Table 1. As shown in Fig. 1a, there are two crystallographically independent molecules A and B in its structure. Each molecule involves two molecular units: a central methylene diazocine bridge and a pair of aromatic rigid rings. The central methylene diazocine bridge imposes approximate C_2 symmetry on the molecule, and provides a twisted A-shaped conformation. The dihedral angles between the two benzene rings adjoining the central diazocine are 84.1° for molecule A and 85.8 ° for molecule B. Substituted biphenyl groups show acceptable planarity as angles between the two constituent benzene rings fall in 4.7–21.1°, while the biphenyl moieties in the wings are twisted relative to the fluorene rings by angles in the range from 30.4° to 58.0°. These twist angles suggest that some electrons delocalize among the biphenyl groups and the noncoplanar configuration of the wings would bring the steric effect.

The packing structure shows that TBFB-BP forms racemic crystals as (R,R)-enantiomers and (S,S)-enantiomers in their packing structure are equal in amount (Fig. 1b and c). Due to the A-shaped twisted configuration and the steric effect of the substituted biphenyl groups of the compound, there is no classical strong face-to-face π–π interaction between the neighboring molecules revealing from its crystal packing structure.

Thermal properties of the two TB analogues were investigated by differential scanning calorimetry (DSC) (Fig. 2a) and thermogravimetric analysis (TGA) (Fig. 2b). DSC scans were performed in the temperature range from 25 to

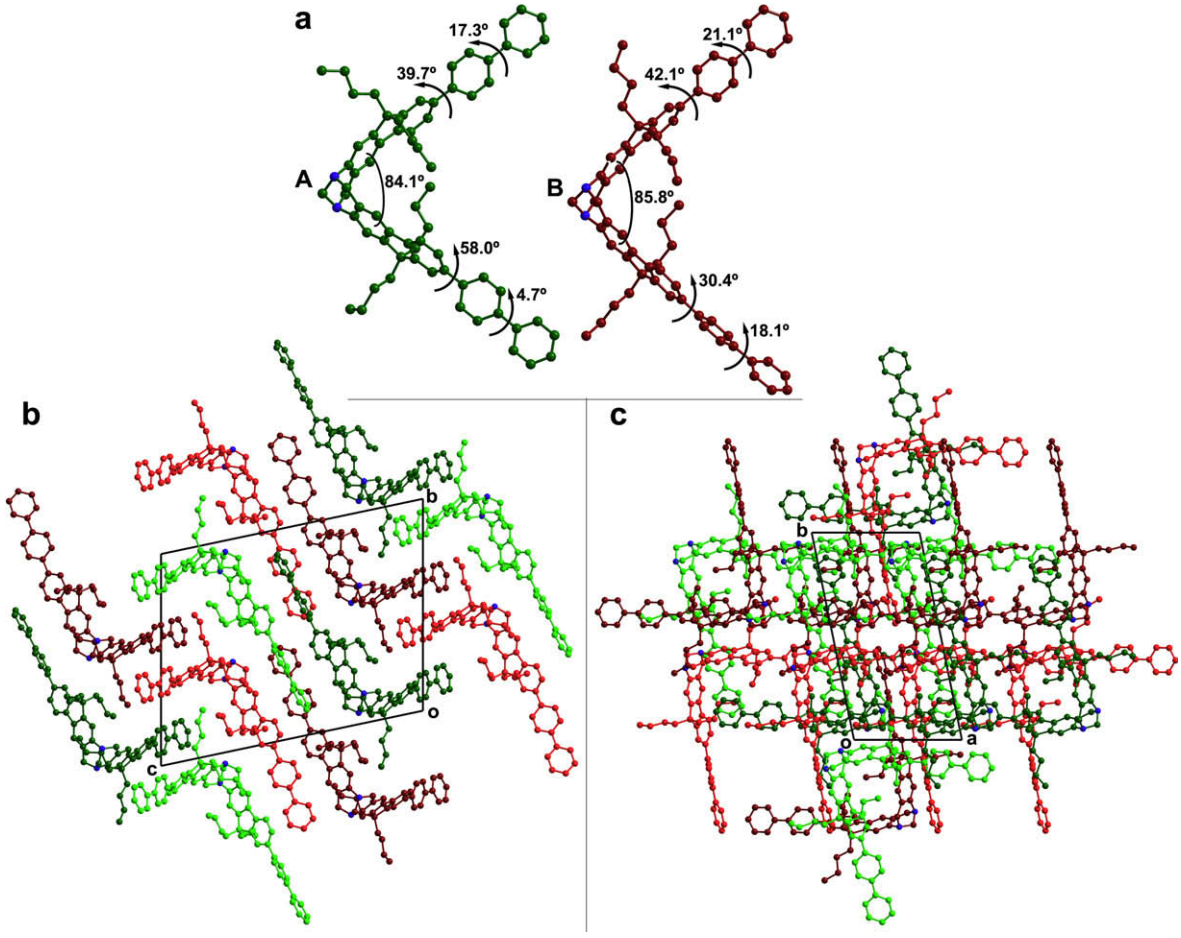

Fig. 1. (a) Molecular structure of TBFB-BP. (b) The crystal packing diagram of TBFB-BP projected onto the bc plane. (c) The crystal packing diagram of TBFB-BP projected onto the ab plane. Hydrogen atoms are omitted for clarity. The two crystallographically independent molecules A and B in different chirality are colored dark green (for (S,S)-A), light green (for (R,R)-A), dark red (for (S,S)-B) and red (for (R,R)-B), respectively. N atoms are colored blue. (For interpretation of the references to colour in this figure legend, the reader is referred to the web version of this article)

Table 1
Crystal data, diffraction data, and refinement data of TBFB-BP

Formula	C69 H70 N2
Formula weight	927.27
Crystal system	Triclinic
Space group	$P\bar{1}$
Unit cell dimensions	a = 10.4027(9) Å, b = 20.7657(18) Å, c = 25.804(2) Å; α = 100.930(5)°, β = 94.168(6)°, γ = 100.478(5)°
Volume, Z	5348.4(8) Å^3, 4
Density (calculate)	1.152 mg/m^3
Absorption coefficient	0.066 mm^{-1}
F(000)	1992
Crystal size	0.46 × 0.27 × 0.04 mm
θ range for data collection	0.81–27.55°
Limiting indices	−13 <=h <= 13, −27 <=k <=26, −32 <= l <= 33
Reflections collected/unique	82788 / 24477, [R_{int} = 0.1015]
Absorption correction	Semi-empirical from equivalents
Maximum and minimum transmission	0.9976 and 0.9705
Refinement method	Full-matrix least-squares on F^2
Data/restraint/parameters	24477/0/1288
Goodness-of-fit on F^2	0.930
Final R indices [$I > 2\sigma(I)$]	$R1$ = 0.0702, w$R2$ = 0.1632
R indices (all data)	$R1$ = 0.2162, w$R2$ = 0.2345
Largest diff. peak and hole	0.386 and −0.355 e A^{-3}

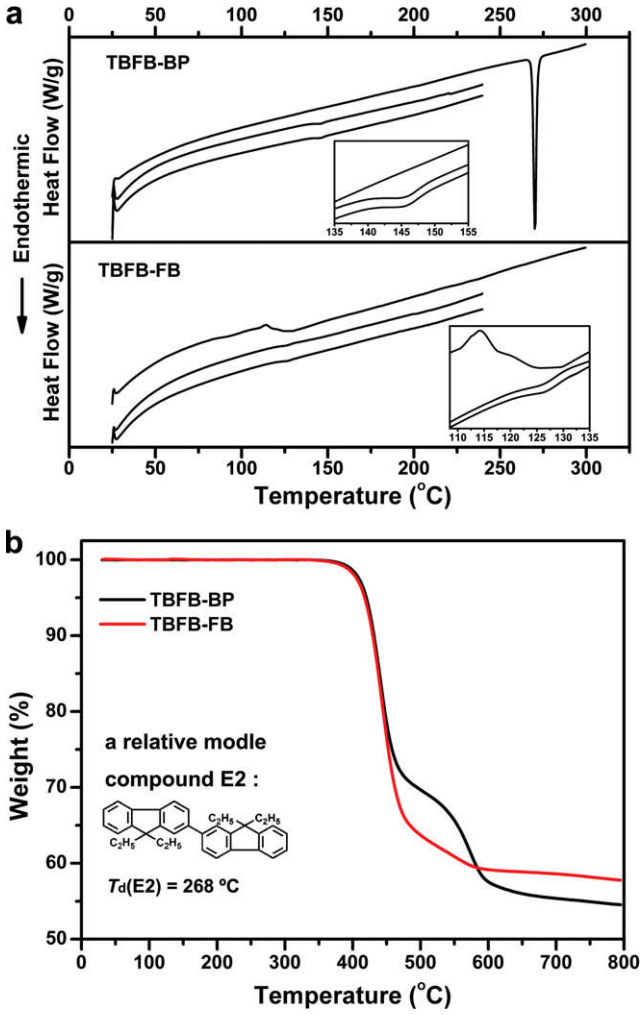

Fig. 2. (a) DSC thermograms of TBFB-BP and TBFB-FB with sequential heating and cooling cycles (first to third heating are represented from top to bottom). (b) TGA scans of TBFB-BP, TBFB-FB and informations of a relative model compound E2.

300 °C for the first heating and cooling cycle and from 25 to 240 °C for the second and third cycles. TBFB-BP melted at 271 °C on the first heating, and then it changed into a glassy state upon cooling from the melt. When the amorphous glassy sample of TBFB-BP was heated again, a glass transition occurred at 147 °C and no exothermic peak associated with crystallization can be observed up to 240 °C. TBFB-FB showed no obvious melting point but a similar glass transition during the first heating process, and when the cooled sample was heated for the second or third times, the glass transition occurred at 128 °C and no exothermic peak can be identified. On the subsequent cooling and heating cycles for the two TB analogues, just the glass transition phenomenon remained in the DSC thermogram without evidence of recrystallization. These observations indicate these two TB analogues are very stable in glass state, which can be attributed to the presence of the *Λ*-shaped TB scaffold. The two compounds also exhibit high thermochemical stability. Their decomposition temperatures (T_d) are found to exceed 350 °C and it is even impossible to completely decompose the two TB analogues by heating them to 800 °C under nitrogen atmosphere. The mass loss occurs at temperature ranging between 380 °C and 470 °C, corresponding to the loss of *n*-butyl side groups within the two molecules [13]. Indeed, the observed mass-loss values of 28% (TBFB-BP) and 36% (TBFB-FB) are in agreement with calculated weight percentages for the *n*-butyl groups of 25% for TBFB-BP and 39% for TBFB-FB. Thermogravimetric analyses indicate that the *Λ*-shaped TB scaffold has excellent thermal stability. It is reported that bi(9,9-diethylfluorene) (E2) without TB scaffold exhibits a lower tolerance to heat with a T_d of 268 °C [14]. Our results indicate that the *Λ*-shaped TB scaffold can dramatically improve morphological stability and enhance the resistance to the thermal decomposition.

To pursue the aggregation-order of the two compounds in the different aggregated states, the microstructural aspects of both powders and thin vacuum sublimated films were characterized by X-ray diffraction (XRD) (Fig. 3a). The TBFB-BP powders are highly ordered and the TBFB-FB powders are partially ordered, which suggests both powders are polycrystalline. Contrary to the powders, the thin films of both compounds (thickness below 100 nm) do not exhibit any X-ray diffraction peak, which suggests the films are amorphous. AFM tests indicate that the vacuum sublimated films are continuous and smooth. (Fig. 3b).

2.3. Photophysical and electrochemical properties

In our experiment, the two fluorene based TB analogues emit bright blue fluorescence both in dilute solutions and aggregated states (polycrystalline powders and amorphous thin films) when excited at 365 nm (as shown in the inset

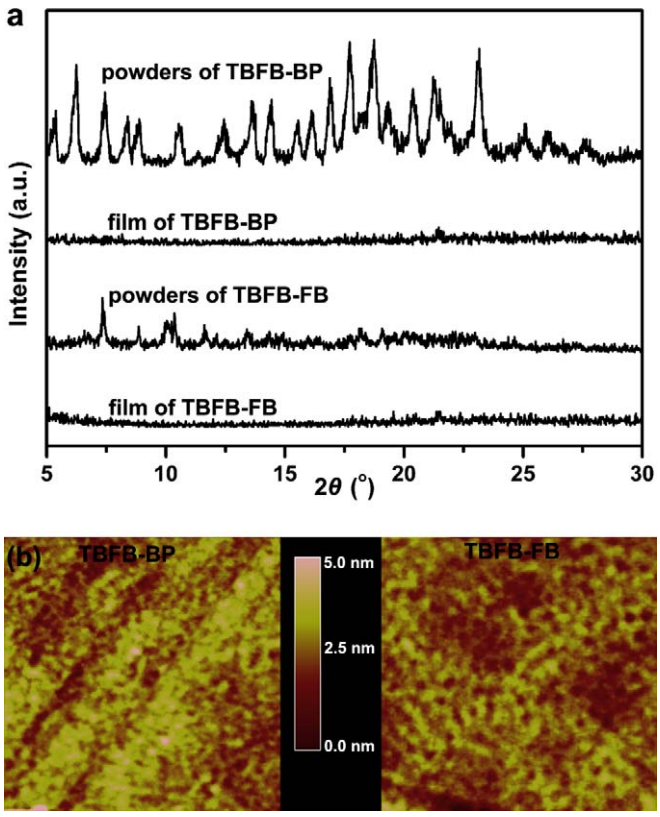

Fig. 3. (a) X-ray diffraction patterns of the two TB analogues powders in the two different aggregated states, powders and thin vacuum sublimated films. (b) AFM scans of 2 μm × 2 μm areas of vacuum sublimated films of the two TB analogues.

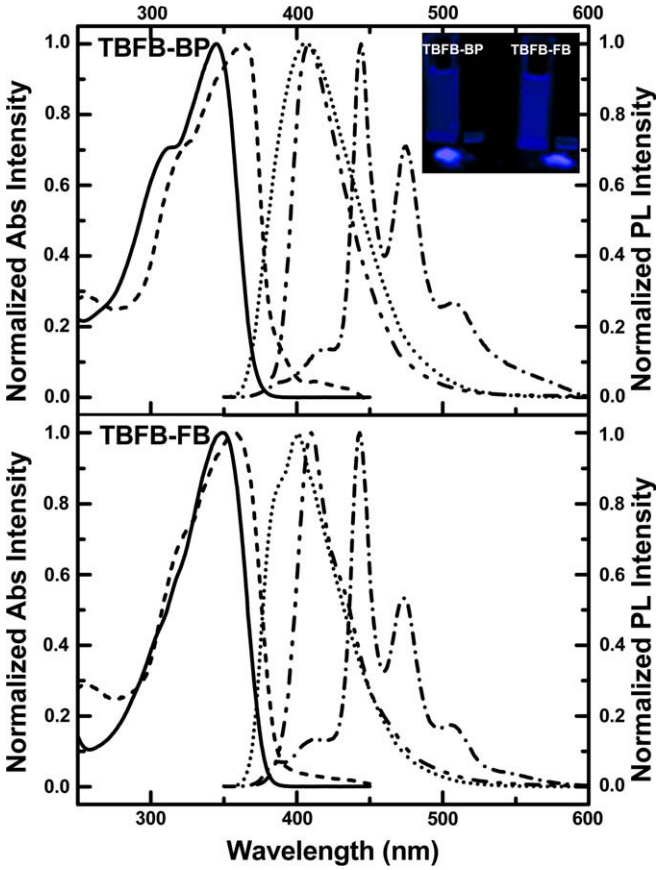

Fig. 4. Abs and PL spectra of the two TB analogues in dilute DCM solutions and aggregated states. (Solid line: Abs of solutions, dash line: Abs of films, dot line: PL of solutions, dash dot line: PL of films, dash dot dot line: PL of powders.) In the inset is shown the photograph of blue emissions from the dilute solutions and aggregated states of the two TB analogues.

photograph in Fig. 4). To have a spectrometric verification, we measured the UV–vis absorption (Abs) and photoluminescence (PL) spectra of the two compounds in dilute DCM solutions, polycrystalline powder states and amorphous thin film states as shown in Fig. 4. All the corresponding spectral data are summarized in Table 2. The absorption spectra are similar with absorption peaks located at 310–324 nm and 345–364 nm, respectively. Photoluminescence (PL) spanning blue–violet (for solutions and polycrystalline powders) and blue–green (for amorphous films) colors are obtained. The PL character is also revealed by measuring the excited state lifetimes. The PL lifetimes in dilute solutions range from 0.44 ns for TBFB-FB to 0.72 ns for TBFB-BP while they were found to vary from 1.21 to 1.23 ns for the corresponding polycrystalline powders and from 2.06 to 2.13 ns for the corresponding amorphous thin vacuum-deposited films. The band gaps (E_g) of TBFB-BP and TBFB-FB (calculated form the edges of their solution absorption spectra) are 3.34 and 3.28 eV, respectively.

Cyclic voltammetry (CV) studies of TBFB-BP and TBFB-FB in solution have been carried out in DCM by using ferrocenium/ferrocene (Fc^+/Fc) as an internal standard. Both the compounds exhibit an oxidation peak (1.17 V vs. SCE for TBFB-BP and 1.10 V vs. SCE for TBFB-FB) and a reduction peak (−0.97 V vs. SCE for TBFB-BP and −0.90 V vs. SCE for TBFB-FB) (Fig. 5). The lower oxidation of TBFB-FB indicates that it has larger conjugation extent. For TBFB-BP, the onset of oxidation starts at 0.98 V (vs. SCE) while for TBFB-FB the onset oxidation starts at 0.94 V (vs. SCE). The HOMO levels of the compounds determined by using the onset of the oxidation according to literature [15] were −5.38 and −5.34 eV, respectively. The low-lying HOMO levels confirmed the high oxidation stability of the compounds. The LUMO energy levels calculated by subtraction of the optical band gaps from the HOMO energy levels are −2.04 and −2.06 eV, respectively.

In dilute solution TBFB-BP shows an absorption maximum at 345 nm originating from the $\pi\cdots\pi^*$ transition band of the compound and a shoulder at 310 nm (Fig. 4, top). The maxima of absorption are red-shifted from 345 to 364 nm and from 310 to 324 nm when going from the solution to the amorphous thin film state. For TBFB-FB the absorption spectrum in DCM solution shows a maximum at 349 nm (Fig 4, bottom) and the film spectrum exhibiting some structured features is also red-shifted as the film absorption peak is changed to 358 nm. These facts suggest that the rigidity of the two compounds, especially TBFB-BP, is enhanced when going from the solution to the solid state.

PL spectra of the two compounds are recorded under optimized excitation wavelengths. The solution PL spectra

Table 2
Thermal, photophysical and electroluminescent properties of TBFB-BP and TBFB-FB

	TBFB-BP	TBFB-FB
T_g (°C)	147	128
λ_{Abs}[a] (nm)	345, 310	349
λ_{Abs}[b] (nm)	364, 324	358, 320
λ_{PL}[a] (nm)	406	401
λ_{PL}[b] (nm)	408	410
λ_{PL}[c] (nm)	444, 475, 508	443, 473, 506
τf[a] (ns)	0.72	0.44
τf[b] (ns)	1.23	1.21
τf[c] (ns)	2.13	2.06
Band gap[a] (eV)	3.34	3.28
Oxidation onset	0.98	0.94
Energy levels (eV) HOMO	−5.38	−5.34
LUMO	−2.04	−2.06
λ_{EL}[d] (nm)	443, 475, 511	443, 476, 514
U_{onset} (V)	4.6	4.5
L_{max}[e] (cd/m^2)	22 047	13 434
η_{Lmax} (lm/W)	1.82[f]	1.93[h]
η_{lmax} (cd/A)	2.78[g]	2.76_h
CIE[d] of OLED	(0.163, 0.136)	(0.184, 0.207)

[a] In dilute DCM solutions (1.0×10^{-5} M).
[b] In polycrystalline powders.
[c] In films by vacuum thermal vaporation method.
[d] OLEDs measured at 8 V.
[e] OLEDs measured at 17.25 V.
[f] OLEDs measured at 4.6 V.
[g] OLED measured at 5 V.
[h] OLEDs measured at 4.5 V.

reveal typical characteristics of conjugated fluorene derivatives [16]. TBFB-BP solution shows an emission peak at 406 nm, while TBFB-FB shows an emission peak at 401 nm. Comparing with biphenyl substituted compound TBFB-BP, the solution absorption spectrum of fluorene substituted TBFB-FB is red shifted but its solution fluorescence spectrum is blue shifted. This phenomenon has been reported for several other compounds, and the blue-shift of the PL spectra is thought to be associated with the asymmetrical alignment of the phenyl rings along the axis of the co-annular bond [17]. Polycrystalline powders of the two TB analogues show strong single blue–violet emissions as PL of TBFB-BP powders peaks at 408 nm while PL of TBFB-FB powders peaks at 410 nm. PL spectra of the two compounds powders show slightly red-shifted and narrower emissions comparing with their solution PL spectra. This is due to the restricted intramolecular rotations in the solid state which not only improve the conjugated length of the compounds to a certain extent but also suppress the non-radiative decay arose from the configuration transformation. It also suggests that there is no π–π stacking in the polycrystalline powders by introduction of *Λ*-shaped twisted scaffold which is in accordance with the analysis of the crystal packing structure of TBFB-BP. Unexpectedly, amorphous film PL spectra of the two TB analogues show large differences from their solution and powder states emissions. PL spectrum of amorphous TBFB-BP film consists of a slight shoulder at 413 nm corresponding to the solution and powder emissions, two relatively sharp peaks at 444 and 475 nm and a slight tail into green region (g-band). The latter triple emissions are extremely similar to that of some polyfluorenes and oligofluorenes [18]. Similar PL spectrum is observed for amorphous TBFB-FB film. It is well understood that the PL emissions of a crystal emitter will red shift relative to an amorphous one due to the formation of delocalized excitons in crystals. Uncommonly, the amorphous films of the two TB analogues show red-shifted and multiple PL emissions comparing with their polycrystalline powders. Brinkmann, Chen and coworkers have reported similar unusual cases in several compounds bearing twisted configurations, Tris(8-hydroxyquinoline)aluminum (Alq_3) [19a], Tris(8-hydroxyquinoline)gallium (Gaq_3) [19b] and 1,1-bis(2′-thienyl)-2,3,4,5-tetraphenysilole [19c]. All the authors attributed the results to a possibly denser packing of the molecules in the amorphous state that strengthened the intermolecular interactions. We think the peculiar behaviors in photophysical properties of the two TB analogues can be explained by a similar mechanism. For polycrystalline powders, the relative orientation of molecules is strictly defined, as the combined effects of the twisted *Λ*-shaped configuration and the steric effect of the biphenyl or alkylated fluorene substitutions which engender long enough distances between two adjacently chromophoric cores, excimer formation would be suppressed. Whereas in the amorphous films, as the denser packing of the molecules, intermolecular interactions such as C–H···N hydrogen bonds or π–π overlaps between the facing aromatic wings of the molecules may occur, and the large distribution of molecular environments is also likely to form excimers of different origins. The obviously red-shifted triple emissions of the amorphous films for the two TB analogues are thought to be as a result of the forming of excimers. Longer emissive lifetime τf of the amorphous films than that of polycrystalline powders and dilute solutions is also helpful to explain the forming of excimers (Table 2). Our results suggest that the PL spectral shift on aggregation order might be a characteristic of fluorene based TB analogues.

The origin of low-energy g-bands is still in dispute up to the present, and most researchers thought such g-bands and concomitant weaken emission are attributed to excimer formation or keto defects in the aggregated state [20]. Here, we are inclined to agree with the former, since such g-bands are absent in the emissions of polycrystalline powders in which excimer formation seems to be suppressed, while for the emissions of the amorphous films in which excimers are likely to form, such g-bands appear.

2.4. Electroluminescent properties

In order to investigate the electroluminescent properties of the two fluorene based TB analogues, OLEDs with device structure of ITO/NPB (30 nm)/TBFB-BP or TBFB-FB (40 nm)/TPBI (40 nm)/LiF (1 nm)/Al (80 nm) (Device 1 or 2) were preliminarily fabricated, in which 30 nm 4,4'-bis[*N*-(1-naphthyl)-*N*-phenyl-amino]-biphenyl (NPB) was the hole-transporting layer, 40 nm 1,3,5-Tris(*N*-phenylbenzimidazol-2-yl)benzene (TPBI) was the electron-transporting layer, 1 nm LiF was the electron-injection layer, and 40 nm TBFB-BP or TBFB-FB was the non-doped

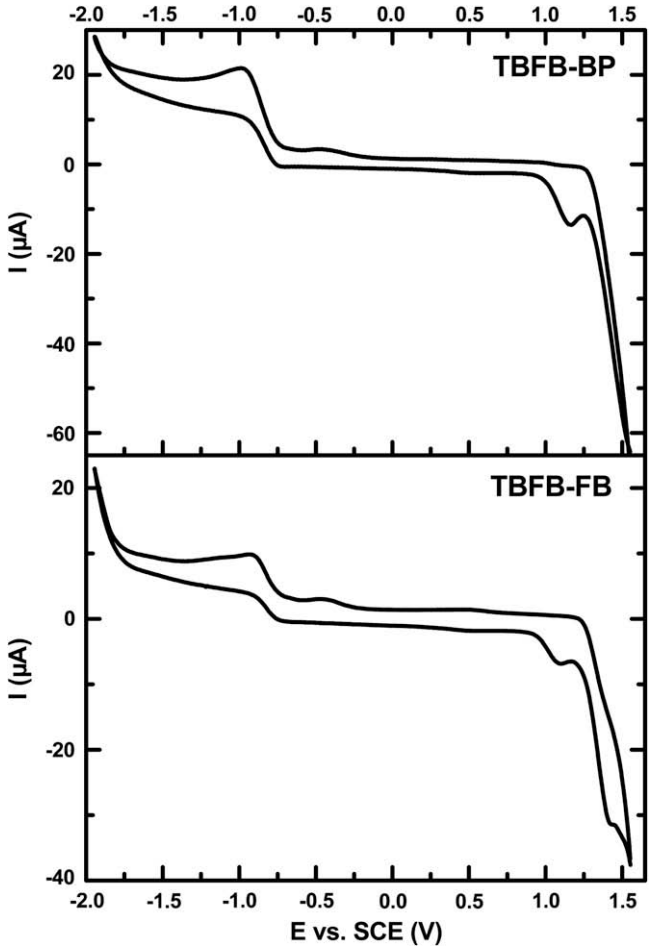

Fig. 5. Cyclic voltammogrames for TBFB-BP and TBFB-FB in DCM/[Bu_4N][ClO_4] (0.1 M) at scanning rate of 50 mV/s.

emitting layer. All the corresponding performance data are summarized in Table 2. High brightness of 22 047 cd/m^2 and 13 434 cd/m^2 were obtained for Devices 1 and 2, respectively (Fig. 6a). The two devices showed low turn-on voltages of 4.6 and 4.5 V, with high current efficiency of 2.78 (5 V) and 2.76 cd/A (4.5 V), high power efficiency of 1.82 (4.6 V) and 1.93 lm/W (4.5 V) for Devices 1 and 2, respectively (Fig. 6b). Profile of EL spectra of the two devices were similar with the corresponding films PL spectra of the two compounds (Fig. 6c), and as the voltage increasing, the low-energy g-bands of their EL spectra show a reduction. 1931 CIE coordinate are (x = 0.163, y = 0.136) and (x = 0.184, y = 0.207) at 8 V for Devices 1 and 2, respectively. An obviously stronger emission was observed for TBFB-BP as compared with TBFB-FB in the corresponding OLEDs. Meanwhile, the g-band of Device 2 is stronger than that of Device 1. This is possibly attributed to better planarity of the fluorene substituents than the biphenyl substituents which may increase the probability of forming of the excimers for the origin of the g-bands. The high brightness, high efficiency, relative low turn-on voltage, and simple architecture of the two devices make the two fluorene based TB analogues competitive emitters in non-doped OLEDs.

3. Conclusions

In summary, two new fluorene based TB analogues TBFB-BP and TBFB-FB were designed and synthesized. Both materials show high thermal stability and excellent PL and EL performances. Peculiar red-shifted and multiple emissions for amorphous films of the fluorene based TB analogues comparing with the single emissions for the corresponding polycrystalline powders are observed. Two OLEDs using TBFB-BP or TBFB-FB as emitting materials, ITO/NPB (30 nm)/TBFB-BP or TBFB-FB (40 nm)/TPBI (40 nm)/LiF (1 nm)/Al (80 nm), were obtained with high brightness (22, 047 or 13, 434 cd/m^2), high efficiency (2.78 or 2.76 cd/A, 1.82 or 1.93 lm/W) and low turn-on voltage (4.6 or 4.5 V), which indicates that the two compounds are efficient emitters in non-doped OLEDs. High efficiency and high stability in junction with easily synthesizing route render the fluorene based TB analogues a very promising class of optoelectronic materials. In addition, the method of material design, introducing A-shaped TB scaffold and large conjugated wings to the molecules, can also be applied in the design and synthesis of efficient TB analogues emitters containing other aryl groups in the wings.

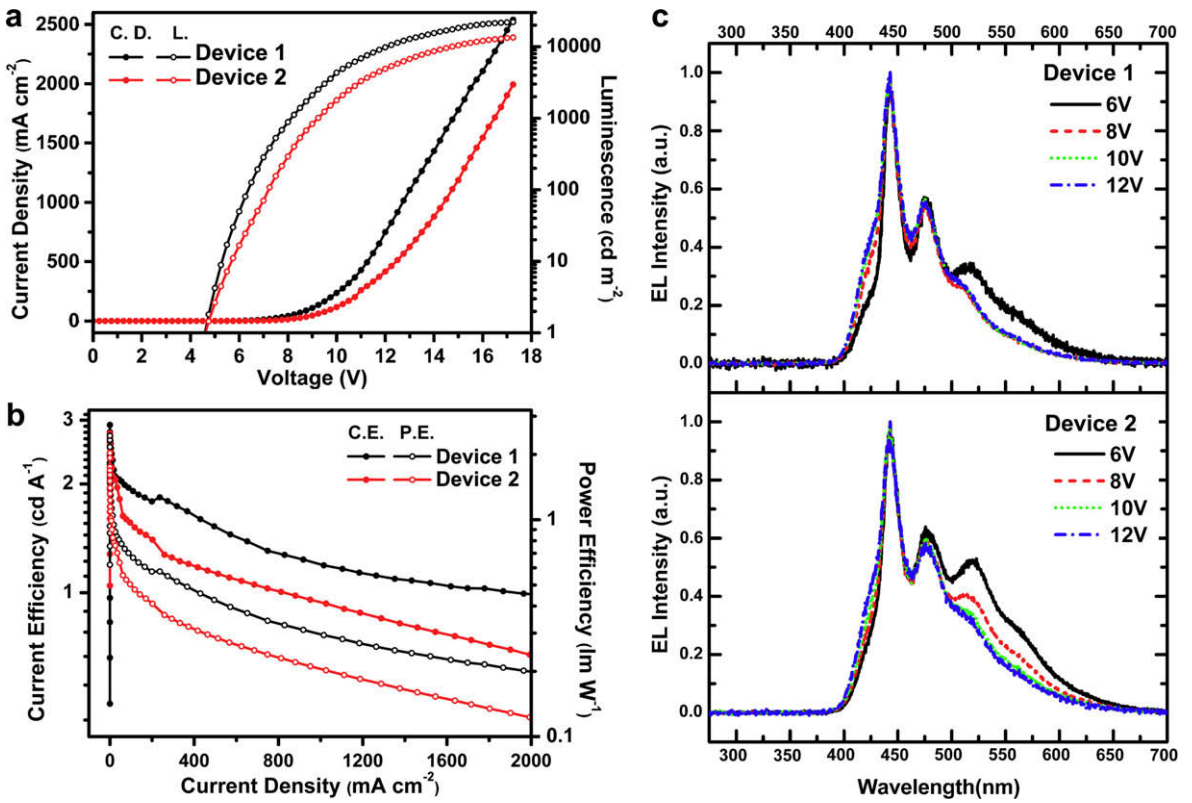

Fig. 6. (a) *I–V–L* characteristics of Devices 1 and 2; (b) current efficiency-current density-power efficiency of Devices 1 and 2 and (c) EL spectra of Devices 1 and 2.

4. Experimental

4.1. General information and materials

Commercial grade reagents except 9,9-dibutyl-fluoren-2-ylboronic acid were used as received unless otherwise stated. 9,9-Dibutyl-fluoren-2-ylboronic acid is synthesized as reported in the literature [21]. NMR spectra were recorded at 25 °C using a Bruker Advance 400 spectrometer. Coupling constants (*J*) are given in hertz (Hz). Microanalyses (C, H and N) were performed using a German Vario EL III elemental analyzer. Matrix assisted laser desorption/ionization time of flight (MALDI-TOF) mass spectra were performed using a Bruker Biflex III mass spectrometer equipped with a 337 nm nitrogen laser. The UV absorption spectra were measured on a TU-1800 SPC spectrophotometer and the fluorescence spectra were collected on a Hitachi F-4500 fluorescence spectrophotometer. The fluorescence lifetime measurements were performed on the Edinburgh FLS920 spectrofluorimeter with a hydrogen flash lamp (pulse duration 1 ns) as the excitation source on the same spectrofluorometer. Spectroscopic grade DCM was used and the dye concentration was 10^{-5} M while the solid films were prepared by thermal evaporation under vacuum (10^{-6} mbar). The cyclic voltammetry measurements were carried out with a BAS CV-50W voltammetric analyzer. An electrolyte solution of $[Bu_4N][ClO_4]$ in DCM (0.1 M) was used in the experiments. All solutions in the cell were purged with nitrogen for 10 min, and then the voltammograms were recorded at ambient temperature with a scanning rate of 50 mV/s. The working electrode was a glassy carbon-disk of 2.0 mm in diameter. A silver-wire was used as the counter electrode and an Ag/Ag^+ ($AgNO_3$) was used as a reference electrode. It was corrected by using ferrocenium/ferrocene (Fc^+/Fc) as the internal standard. Differential scanning calorimetry (DSC) scans and thermogravimetric analysis (TGA) were measured on a SDT Q600 V8.0 Differential Scanning Calorimeter, in a flowing nitrogen atmosphere and with a heating and cooling rate of 10 °C/min. AFM pictures were recorded with a Digital Instruments Nanoscope E scanning probe microscope.

The X-ray diffraction intensity data were collected at 293 K on a Bruker Smart Apex2 CCD area-detector diffractometer with graphite-monochromated Mo Kα radiation (λ = 0.71073 Å). Processing of the intensity data was carried out using the Bruker SMART routine, and the structure was solved by direct methods and refined by a full-matrix least-squares technique on F^2 using SIR-97/SHELXL-97 programs [22]. CCDC reference number 672178. Crystallographic data and refinement parameters are given in Table 1. For crystallographic data in CIF or other electronic format, see http://www.ccdc.cam.ac.uk.

4.2. Synthesis

4.2.1. 2-Amino-7-bromo-9,9-bibutylfluorene

To a stirred mixture of 2-amino-7-bromofluorene (7.42 g, 25 mmol), tetrabutylammonium bromide (0.04 g,

1.25 mmol) and DMSO (50 ml) at room temperature was added dropwise 50% aqueous NaOH (5 ml), then *n*-butylbromide (5.7 ml, 52.5 mmol) was added slowly and the reaction mixture was stirred at room temperature for 2h. An excess of diethyl ether was added, the organic layer was washed with water, diluted HCl, and saturated NaCl solution, then dried over anhydrous $MgSO_4$. The solvent was removed under vacuum and the residue was purified by column chromatography over silica gel with petroleum ether/ethyl acetate (20:1) as the eluent gave 2-amino-7-bromo-9,9-bibutylfluorene as a white solid (6.51 g, 70%). M.p. 131 °C; ^{1}H NMR (DMSO-d_6, 400 MHz): δ 0.46–0.53 (m, 4H), 0.64 (t, J = 7.34 Hz, 6H), 1.01–1.07 (q, J = 7.4 Hz, 4H), 1.79–1.83 (m, 2H), 1.88-1.93 (m, 2H), 5.27 (s, 2H), 6.51–6.56 (m, 2H), 7.35–7.49 (m, 4H). ^{13}C NMR (DMSO-d_6, 100.57 MHz): δ 13.8, 22.4, 25.7, 39.5, 54.4, 107.7, 112.9, 117.3, 119.4, 120.8, 125.3, 127.8, 129.4, 141.1, 149.2, 151.4, 151.6.

4.2.2. 4,13-Dibromo-6,6,11,11-tetrabutyl-9H,18H-8,17-methanodifluoreno(2,3-b:2′,3′-f)(1,5)diazocine (TBFB-Br)

A mixture of 2-amino-7-bromo-9,9-bibutylfluorene (3.72 g, 10 mmol) and HMTA (1.40 g, 10 mmol) in TFA (20 ml) was stirred at room temperature under Ar atmosphere for 24 h. The organic solvent was removed under vacuum and the residue was diluted with water, basified to pH 8–9 with concentrated NH_4OH and extracted with CH_2Cl_2. The organic phase was dried over anhydrous $MgSO_4$. The solvent was removed under vacuum, and the residue was purified by column chromatography over silica gel with petroleum ether/ethyl acetate (8:1) as the eluent to yield TBFB-Br as a white solid (2.5 g, 64%). M.p. 287 °C; ^{1}H NMR ($CDCl_3$, 400 MHz) δ 0.56–0.66 (m, 12H), 0.68–0.72 (m, 8H), 1.02–1.13 (m, 8H), 1.83–1.87 (m, 4H), 1.89–1.96 (m, 4H), 4.29 (d, J = 16.58 Hz, 2H), 4.42 (s, 2H), 4.85 (d, J = 16.52 Hz, 2H), 7.12 (s, 2H), 7.20 (s, 2H), 7.36–7.40 (q, 6H). ^{13}C NMR ($CDCl_3$, 100.57 MHz): δ 13.25, 13.34, 22.45, 22.57, 25.43, 25.56, 39.49, 39.56, 54.6, 58.7, 66.3, 117.2, 119.3, 120.0, 120.1, 125.8, 126.1, 129.4, 135.8, 139.1, 147.5, 149.5, 152.5. MS (MALDI-TOF) m/z, 778.2. Anal. Calcd for $C_{45}H_{52}N_2Br_2$: C, 69.23; H, 6.71; N, 3.59. Found: C, 69.21; H, 6.725; N, 3.452.

4.2.3. 4,13-Di(biphenyl-4-yl)-6,6,11,11-tetrabutyl-9H,18H-8,17-methanodifluoreno(2,3-b:2′,3′-f)(1,5)diazocine (TBFB-BP)

A mixture of TBFB-Br (1.56 g, 2 mmol) and 4-biphenylboronic acid (1.58 g, 8 mmol) in THF (20 ml) and 2 M aqueous Na_2CO_3 (10 ml) was bubbled with Ar flush for 20 min, then $Pd(PPh_3)_4$ was added quickly. The reaction mixture was stirred at 90 °C under argon atmosphere for 48 h. After cooling to room temperature, the mixture was extracted with CH_2Cl_2. The organic layer was washed with brine, and then dried over anhydrous $MgSO_4$. The solvent was removed under vacuum, and the residue was purified by column chromatography over silica gel with petroleum ether/ethyl acetate/ CH_2Cl_2 (8:1:4) as the eluent to yield TBFB-BP as a white solid (1.1 g, 59%). M.p. 271 °C; ^{1}H NMR ($CDCl_3$, 400 MHz) δ 0.66–0.79(m, 20H), 1.06–1.15 (m, 8H), 1.95 (t, J = 8. 15 Hz, 4H), 2.02 (t, J = 8.25 Hz, 4H), 4.35 (d, J = 16.60 Hz, 2H), 4.47 (s, 2H), 4.91 (d, J = 16.40 Hz, 2H), 7.29 (s, 2H), 7.36 (t, J = 7.34 Hz, 2H), 7.46 (t, J = 7.62 Hz, 4H), 7.56–7.58 (t, 4H), 7.62–7.67 (m, 8H), 7.71 (t, J = 8.57 Hz, 8H). ^{13}C NMR ($CDCl_3$, 100.57 MHz): δ 13.79, 13.86, 23.02, 23.14, 26.05, 26.18, 40.14, 40.21, 54.91, 59.23, 66.80, 117.68, 119.51, 119.83, 121.46, 125.87, 126.46, 127.04, 127.32, 127.46, 127.50, 128.83, 139.12, 139.95, 140.54, 140.77, 150.69, 151.50. MS (MALDI-TOF) m/z, 926.8. Anal. Calcd for $C_{69}H_{70}N_2$: C, 89.37; H, 7.61; N, 3.02. Found: C, 89.28; H, 7.292; N, 2.808.

4.2.4. 4,13-Di(9,9-dibutylfluorene-2-yl)-6,6,11,11-tetrabutyl-9H,18H-8,17-methanodifluoreno(2,3-b:2′,3′-f)(1,5)diazocine (TBFB-FB)

Similar procedure with TBFB-BP but 9,9-dibutyl-fluoren-2-ylboronic acid instead of 4-biphenylboronic acid is used as the reactant to yield TBFB-FB as a white solid (54%). M.p. 181 °C; ^{1}H NMR ($CDCl_3$, 400 MHz) δ 0.67–0.75(m, 40H), 1.07–1.16 (m, 16H), 1.96–2.06 (m, 16H), 4.36 (d, J = 16.59 Hz, 2H), 4.47 (s, 2H), 4.92 (d, J = 16.52 Hz, 2H), 7.20 (s, 2H), 7.29–7.37 (m, 8H), 7.59–7.66 (m, 10H), 7.72–7.77 (m, 4H). ^{13}C NMR ($CDCl_3$, 100.57 MHz): δ 13.30, 13.37, 22.54, 22.58, 22.65, 25.53, 25.60, 25.74, 39.57, 39.70, 54.42, 54.59, 58.75, 66.34, 117.15, 118.93, 119.21, 119.37, 120.80, 120.98, 122.43, 125.44, 125.52, 126.29, 126.48, 139.26, 139.56, 139.81, 139.87, 140.31, 150.24, 150.49, 150.95, 151.04. MS (MALDI-TOF) 1m/z , 1175.1. Anal. Calcd for $C_{87}H_{102}N_2$: C, 88.87; H, 8.74; N, 2.38. Found: C, 89.21; H, 8.656; N, 2.217.

4.3. OLED device fabrication

OLEDs based on the two TB analogues were fabricated and investigated. EL devices were fabricated with the configuration of ITO/NPB (30 nm)/TBFB-BP or TBFB-FB (40 nm)/TPBI (40 nm)/LiF (1 nm)/Al (80 nm), in which the TB analogues were used as emitting layer, NPB was used as hole-transporting layers (HTL) and TPBI was used as the electron-transporting layer (ETL). The ITO glass was cleaned in ultrasonic baths of detergent, deionized water and acetone in sequence, followed by oxygen plasma cleaning. The organic films and metal electrode were sequentially deposited on the substrate by thermal evaporation under a vacuum of 10^{-6} Torr. The deposition rates were 2–3 Å/s for the organic materials and 5–7 Å /s for the cathode metals. The emitting area of the device was 4 Å mm^2. The EL spectra and current–voltage–luminance (J–L–V) characteristics were measured with a Spectrascan PR 650 photometer and a computer-controlled DC power supply. All the measurements of the devices were carried out under ambient conditions.

Acknowledgments

This research was supported by the State National Natural Science Foundation of China (Grant No. 50721002, 50673003) and 973 program of China (Grant No. 2004CB619002) for financial support.

References

[1] (a) C.W. Tang, S.A. VanSlyke, Appl. Phys. Lett. 51 (1987) 913;
(b) C. Adachi, T. Tsutsui, S. Saito, Appl. Phys. Lett. 57 (1990) 913;

(c) M.T. Bemius, M. Inbasekaran, J. O'Brien, W. Wu, Adv. Mater. 12 (2000) 1737;
(d) U. Mitschke, P. Bäurele, J. Mater. Chem. 10 (2000) 1471.
[2] (a) M.D. McGehee, A.J. Heeger, Adv. Mater. 12 (2002) 1655;
(b) D. Schneider, T. Rabe, T. Reidl, T. Dobbertin, M. Kröger, E. Becker, H.-H. Johannes, W. Kowalsky, T. Weimann, J. Wang, P. Hinze, A. Gerhard, P. Stössel, H. Vestweber, Adv. Mater. 17 (2005) 31.
[3] (a) J. Cabanillas-Gonzalez, S. Yeates, D.D.C. Bradley, Synth. Met. 139 (2003) 637;
(b) R. Pacios, D.D.C. Bradley, Synth. Met. 127 (2002) 261;
(c) C.W. Tang, Appl. Phys. Lett. 48 (1986) 183;
(d) C.J. Brabec, N.S. Sariciftci, J.C. Hummelen, Adv. Funct. Mater. 11 (2001) 15.
[4] L. Zeng, E.W. Miller, A. Pralle, E.Y. Isacoff, C.J.J. Chang, Am. Chem. Soc. 128 (2006) 10.
[5] (a) K.T. Wong, Y.Y. Chien, R.T. Chen, C.F. Wang, Y.T. Lin, H.H. Chiang, P.Y. Hsieh, C.C. Wu, C.H. Chou, Y.O. Su, G.H. Lee, S.M. Peng, J. Am. Chem. Soc. 124 (2002) 11576;
(b) S.C. Chang, Y. Li, Y. Yang, J. Phys. Chem. B 104 (2000) 11650;
(c) J.M. Lupton, M.R. Craig, E.W. Meijer, Appl. Phys. Lett. 80 (2002) 4489;
(d) C.D. Mueller, A. Falcou, N. Reckefuss, M. Rojahn, V. Wiederhirn, P. Rudati, H. Frohne, O. Nuyken, H. Becker, K. Meerholz, Nature 421 (2003) 829;
(e) J.-I. Lee, H. Lee, J. Oh, H.Y. Chu, S.H. Kim, Y.S. Yang, G.H. Kim, L.-M. Do, T. Zyung, Curr. Appl. Phys. 3 (2003) 469;
(f) A.C.A. Chen, J.U. Wallace, K.P. Klubek, M.B. Madaras, C.W. Tang, S.H. Chen, Chem. Mater. 19 (2007) 4043;
(g) S. Tang, M. Liu, P. Lu, G. Cheng, M. Zeng, Z. Xie, H. Xu, H. Wang, B. Yang, Y. Ma, D. Yan, Org. Electron. 9 (2008) 241.
[6] R.H. Friend, R.W. Grmer, A.B. Holmes, J.H. Burroughes, R.N. Marls, C. Taliani, D.D.C. Bradley, D.A. Dos Santos, J.L. Brédas, M. Lögdlund, W.R. Salaneck, Nature 397 (1999) 121.
[7] K. Shirai, M. Matsuoka, K. Fukunishi, Dyes Pigments 42 (1999) 95.
[8] (a) D.H. Hwang, M.J. Park, J.H. Lee, Mater. Sci. Eng. 24 (2004) 201;
(b) J.H. Park, H.C. Ko, J.H. Kim, H.S. Lee, Syth. Met. 144 (2004) 193;
(c) Y.G. Wu, J. Li, Y.Q. Fu, Z.N. Bo, Org. Lett. 6 (2004) 3485.
[9] J. Tröger, J. Prakt. Chem. 36 (1887) 225.
[10] (a) J.C. Adrian Jr., C.S. Wilcox, J. Am. Chem. Soc. 111 (1989) 8055;
(b) M.J. Crossley, A.C. Try, R. Walton, Tetrahedron Lett. 37 (1996) 6807;
(c) A.C. Try, L. Painter, M.M. Harding, Tetrahedron Lett. 39 (1998) 9809;
(d) A. Tatibouët, M. Demeunynck, C. Andraud, A. Collet, J. Lhomme, Chem. Commun. 23 (1999) 161;
(e) Y. Kubo, T. Ohno, J. Yamanaka, S. Tkita, T. Iida, Y.J. Ishimaru, Am. Chem. Soc. 123 (2001) 12700;
(f) N.R. Deprez, K.A. McNitt, M.E. Petersen, R.G. Brown, D.E. Lewis, Tetrahedron Lett. 46 (2005) 2149;
(g) M. Valík, J. Malina, L. Palivec, J. Foltýnová, M. Tkadlecová, M. Urbanová, V. Brabec, V. Král, Tetrahedron 62 (2006) 8591.
[11] C.-X. Yuan, X.-T. Tao, Y. Ren, Y. Li, J.-X. Yang, W.-T. Yu, L. Wang, M.-H. Jiang, J. Phys. Chem. C 111 (2007) 12811.
[12] (a) M. Ranger, M. Leclerc, Chem. Commun. (1997) 1597;
(b) M. Ranger, D. Rondeau, M. Leclerc, Macromolecules 30 (1997) 7686.
[13] P.B. Balanda, M.B. Ramey, J.R. Reynolds, Macromolecules 32 (1999) 3970.
[14] T.-C. Chao, Y.-T. Lin, C.-Y. Yang, T.S. Hung, H.-C. Chou, C.-C. Wu, K.-T. Wong, Adv. Mater. 17 (2005) 992.
[15] A.K. Agrawal, S.A. Jenekhe, Chem. Mater. 8 (1998) 579.
[16] S. Janietz, D.D.C. Bradley, M. Grell, C. Giebeler, M. Inbasekaran, E.P. Woo, Appl. Phys. Lett. 73 (1998) 2453.
[17] I.B. Berlman, J. Chem. Phys. 52 (1970) 5616.
[18] (a) J. Jacob, S. Sax, T. Piok, E.J.W. List, A.C. Grimsdale, K. Müllen, J. Am. Chem. Soc. 126 (2004) 6987;
(b) A.K. Mishra, M. Graf, F. Grasse, J. Jacob, E.J.W. List, K. Müllen, Chem. Mater. 18 (2006) 2879;
(c) S.W. Culligan, Y. Geng, S.H. Chen, K. Klubek, K.M. Vaeth, C.W. Tang, Adv. Mater. 15 (2003) 1176;
(d) J.-I. Lee, H. Lee, J. Oh, H.Y. Chu, S.H. Kim, Y.S. Yang, G.H. Kim, L.-M. Do, T. Zyung, Curr. Appl. Phys. 3 (2003) 469.
[19] (a) M. Brinkmann, G. Gadret, M. Muccini, C. Taliani, N. Masciocchi, A. Sironi, J. Am. Chem. Soc. 122 (2000) 5147;
(b) M. Brinkmann, B. Fite, S. Pratontep, C. Chaumont, Chem. Mater. 16 (2004) 4627;
(c) J. Chen, B. Xu, K. Yang, Y. Cao, H.H.Y. Sung, I.D. Williams, B.Z. Tang, J. Phys. Chem. B 109 (2005) 17086.
[20] (a) M. Sims, D.D.C. Bradley, M. Ariu, M. Koeberg, A. Asimakis, M. Grell, D.G. Lidzey, Adv. Funct. Mater. 14 (2004) 765;
(b) F. Montilla, R. Mallavia, Adv. Funct. Mater. 17 (2007) 71;
(c) M. Gaal, E.J.W. List, U. Scherf, Macromolecules 36 (2003) 4236;
(d) E.J.W. List, R. Guentber, P.S. de Freitas, U. Scherf, Adv. Mater. 14 (2002) 374;
(e) H.P. Rathnayake, A. Cirpan, F.E. Karasz, M.Y. Odoi, N.I. Hammer, M.D. Barnes, P.M. Lahti, Chem. Mater. 19 (2007) 3265.
[21] A.L. Kanibolotsky, R. Berridge, P.J. Skabara, I.F. Perepichka, D.D.C. Bradley, M. Koeberg, J. Am. Chem. Soc. 126 (2004) 13695.
[22] (a) A. Altomare, M.C. Burla, M. Camalli, G.L. Cascarano, C. Giacovazzo, A. Guagliardi, A.G.G. Moliterni, G. Polidori, R. Spagna, J. Appl. Cryst. 32 (1999) 115;
(b) L.J. Farrugia, J. Appl. Cryst. 32 (1999) 837.

To improve crystallinity and ferroelectric properties of PVDF and its copolymers, methods such as mechanical stretching, thermal annealing, and electrical poling have been widely employed [4–7]. Stretching to plastic deformation at high temperatures is deemed the most efficient method to yield high crystallinity and good ferroelectricity as molecular chains can be reorganized along the stress direction to form an ordered phase. Free-standing films need to be at least 15 μm thick to possess sufficient mechanical strength and integrity. For electronic applications, dielectric films of much smaller thickness (<5 μm) are required to maintain a low switching-voltage and power consumption. Thus, the films used in such applications are mostly non free-standing and hence cannot be stretched independently. To overcome this, trifluoroethylene (TrFE) is added to PVDF polymer forming random copolymer P(VDF-TrFE). Copolymers of various compositions have been shown to crystallize into a high percentage of ferroelectric phase that only requires a facile annealing treatment at temperatures above the Curie point to yield a remnant polarization of |10| $\mu C/cm^2$ and coercive field of |50| MV/m [4,7,8]. Nevertheless one drawback is the resultant surface morphology of the working film. Due to high crystallinity of up to 80%, film topography appears with random rod-like grains creating deep valleys which are susceptible to electrical breakdown [9,13]. By combining organic ferroelectric and semiconductor materials, non-volatile memory functionality can be attained from a single field effect transistor. However, the surface roughness of the ferroelectric copolymer film is the main hindrance to device optimization [9] since the quality of the dielectric-semiconductor interface is known to be of critical importance in organic field effect transistor enabled plastic electronics applications.

This paper reports the enhanced properties of a stretched P(VDF-TrFE) film (<1 μm thickness) attached to a flexible substrate and the fabrication of organic FeFET with desirable electrical characteristics at annealing temperatures below the Curie point. Ferroelectric properties obtained by this process compare favorably with those resulting from high temperature annealing, and the surface morphology and transistor characteristics were greatly improved with the formation of flat-grain structure. These enhancements lead to a significant improvement in performance of the resultant organic FeFET devices for non-volatile memory applications.

2. Experimental

Flexible sheets (110 μm thick) of poly(ethylene terephthalate) (PET) with laminated aluminum electrode (Al-PET) (100–200 nm thick) were provided by Xerox Research Center (Canada) and cleaned by acetone, methanol and deionized water. P(VDF-TrFE) (70–30 mol%) (Solvay) solution with methyl ethyl ketone (concentration of 50 mg/cc) was filtered through 1 μm pore size and spin-coated on the Al-PET to form 900 nm thick film. An annealed sample was fabricated for reference by heating to 140 °C for 2 h in Nitrogen gas. Stretching of samples was done *in situ* using an Instron Microforce tester with heating chamber (2 kN load for stretching rate of 50 N/min). The chamber was heated to the pre-set temperature before samples were loaded and kept for 30 min to stabilize before stretching. Once the required strain was reached, the samples were maintained and heated for another 30 min followed by cooling down to ambient temperature before releasing the strain on the samples. The P(VDF-TrFE) samples were subjected to a strain ranging from 25% to 50% at temperatures of 120 °C and 70 °C. The change in Al-sheet resistance near sample failure (75% elongation), as measured by four-point probe to be 7%. Observation of the Al-surface by optical microscopy only showed the roughening of the morphology without any rupture or delamination. It was hence deemed to have a negligible contribution to the device electrical properties. Thickness of P(VDF-TrFE) film on stretched samples was verified by surface profiler to show a minor reduction of 5%. Changes in crystallinity and phases were studied by Fourier Transform Infrared (FTIR) (Perkin–Elmer) in attenuated total reflection (ATR) mode. Surface morphology was obtained by non-contact atomic force microscopy (AFM) (DI Dimensions 3100). Polarization hysteresis was measured from metal–polymer–metal (MPM) device by thermally evaporating gold (80 nm thick) through a shadow mask (1 mm diameter) and using Radiant Ferroelectric Tester with a 20 Hz triangular signal. For FeFET devices, pentacene was evaporated at pressure of 5×10^{-5} Pa and rate of 0.1–0.2 Å/s to form a 50–80 nm thick film. It was then followed by gold evaporation for source/drain electrodes formation. The devices were characterized in dark vacuum (pressure of 10^{-5} Torr) using Keithley 4200 semiconductor analyzer.

3. Results and discussion

A comparison of the FTIR spectra of stretched samples compared with spin-coated and annealed samples, Fig. 1a, displays an overall increase in the sharpness and intensity of the absorption bands after annealing; indicating amorphous–crystalline and ferroelectric–paraelectric phase transformations. The 1400 cm^{-1} band, which is most sensitive to the ordering of P(VDF-TrFE) molecular chains, exhibits the sharpest rise [10,11] along with two sharp peaks 883 and 850 cm^{-1}, which relates to the ordered phases of all-*trans* and *trans-gauche* sequences, respectively. The increment of 1286 cm^{-1} band relates to both crystallinity and *trans* sequence of more than 4 monomers, suggesting a possible polarization switching in the sample. Another band, which also displays a strong rise, 1173 cm^{-1}, has been linked to the formation of the *trans-gauche* sequence [10]. As such, changes in the 1400 and 1286 cm^{-1} band are used to compare crystallinity and ferroelectric phase transformation, respectively, for samples exhibiting long-range order.

Fig. 1a further presents the spectra of samples stretched to 50% strain at room temperature (25 °C) and 70 °C. The film crystallinity as probed by the 1400 cm^{-1} band is found to increase for the stretched samples. For samples stretched at lower temperatures, the magnitudes of the 1400 and 1173 cm^{-1} bands are smaller than the annealed samples, while the 1286 cm^{-1} band is unchanged as com-

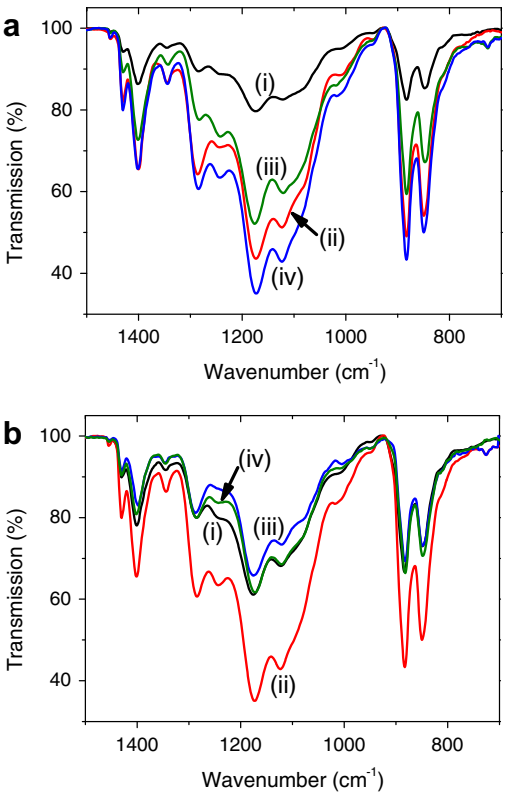

Fig. 1. (a) FTIR spectra of (i) as-spun, (ii) standard annealed at 140 °C, (iii) stretched to 50% length at 25 °C, and (iv) stretched to 50% length at 70 °C. (b) FTIR spectra of samples stretched to (i) 25%, (ii) 50%, (iii) 70% length, and (iv) stretched to breaking point (~75%) at 70 °C.

pared to the non-annealed sample. This suggests the reorganization of polymer chains only occurred in the mainly amorphous phase [11] and was limited to *trans-gauche* ordered sequence without the ferroelectric phase transformation. In the case of simultaneously stretched and annealed (50% – 70 °C) samples, the molecular chain order and hence the film crystallinity drastically increased as observed from most of the strong bands. However, certain limitations of ferroelectric phase transformation can be recognized from the smaller magnitude of the 1286 cm^{-1} band as compared to the annealed sample. This may be attributed to the lower processing temperature but could be overcome by the application of electric fields that are higher than the coercivity of the ferroelectric polymer film. From these observations, mechanical stretching is recognized in aligning the molecular chains along the stress direction by plastic extension while the simultaneous heating at low temperature allows molecular motion to facilitate polymer chain reorganization as well as the efficient phase transformation from *trans-gauche* to all-*trans* sequences.

Comparison of samples stretched to different lengths at 70 °C (Fig. 1b) indicates that the sample stretched to 70% elongation has similar characteristics as one stretched to breaking point, i.e. strong 1286 cm^{-1} but weak 1400 cm^{-1} bands. As necking was first observed in the 70%-sample, it is hence suggested that relaxation of polymer chains to short-range ordered regions was dominant during cooling. The FTIR data hence suggests that the samples stretched to 50% elongation at 70 °C should exhibit the strongest polarization properties. Assuming that the IR absorption only follows the Lambert–Beer law, the relative fraction of beta phase F_β may be estimated [10] for a standard annealed sample as 0.43. If sample is stretched to ¼ of the original length at 120 °C, the β-fraction slightly increases (0.51). Stretching is hence seen as more efficient way to facilitate molecular reordering that leads to higher fraction of β-phase for shorter duration (30 min as compared to 2 h in the standard process). This observation suggests that the working temperature can be further reduced, as confirmed by the samples exposed to a 50% strain rate at 70 °C, which yield β-fractions of 0.48.

Polarization hysteresis of the annealed sample (Fig. 2) yields a remnant polarization of |10| $\mu C/cm^2$ and coercive field of |50| MV/m in agreement with previous reports for samples on non-stretchable substrates after high temperature annealing [4,7,8]. Various combinations of strains and temperatures shown here clearly indicate their complementary effects on the crystallization of the ferroelectric phase in the P(VDF-TrFE) film. For the lower strain (25%), processing temperatures above Curie point (~100 °C) are required for formation of ferroelectric phase comparable to that obtained from standard annealing. At 120 °C, owing to greatly reduced viscosity most of polymer chains were unconstrained from disordered regions and the application of tensile strain therefore forced the reorganization of chains along the stress direction. During cooling down, phase transformation was probably identical to standard annealing but the stretched sample has slightly better ordered phase as suggested by the FTIR spectra. Once strain was increased to 50%, comparable ferroelectric behavior can still be acquired at temperature (70 °C) below the ferro-to-paraelectric transition (82–110 °C). The mechanism

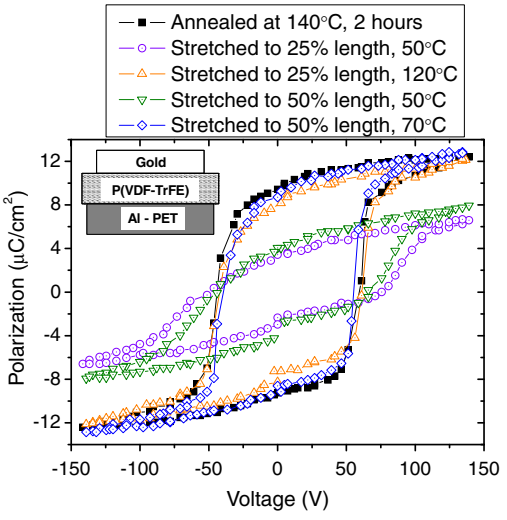

Fig. 2. Polarization hysteresis of various stretched samples as compared to standard annealed sample. Inset shows the metal–polymer–metal device structure.

of this process is different from the above. The applied strain stretches the molecular chains from the mainly amorphous phase of the as spin-coated sample at a low working temperature. As a result, the low temperature had only mild effect on chain mobility hence the reorganizing of polymer chains into ordered ferroelectric phase were solely induced by the tensile force. However, thermal activation was still necessary for the transition. As temperature was further decreased (50 °C), only partial formation of the ferroelectric phase was obtained independent of strain magnitudes and resulting in only half of the remnant polarization as compared to the annealed sample as seen in Fig. 2.

Topographical analysis using AFM imaging for standard annealed and stretched samples is shown in Fig. 3a–f. After standard annealing, Fig. 3a and e, P(VDF-TrFE) film crystallizes with rod-like grain structure on the top surface as previously reported [12,13]. The substrate flexibility does not affect the crystallization and reorganization of polymer chains during annealing. Completely different topography of the sample stretched to various strain at 70 °C is seen in Fig. 3b–d and f. The morphology is smoother with the presence of flat grains effecting a reduction of surface irregularities and a lowered surface roughness for strain level below 70%. The applied stresses are seen to effectively reduce the length while expand the width of the rod-grains. Flat-grain formation starts to take place even at the lowest strain of 25%. As the applied strain increases to 50% the grain topography becomes smoother and closer in packing. It can also be seen that the grain formation is in the vertical direction of the image which is almost perpendicular to the stretching direction. As previously discussed [12], the polymer chains have been found to fold across the long-axis of the rod grain in semi-crystalline film. As a result, the formation of flat grains seen here should be similar to rod-like grains but the growth evolves in the planar short-axis (stretching direction) to expand the width rather than developing out of the surface to form vertically steep wall as seen form comparison of Fig. 3e and f.

In general as the applied strain was raised from 25% to 50%, the density of the flat grains increased to provide better surface coverage and led to the reduction of surface roughness. Nevertheless attempt to further increase the flat-grain packing by the application of higher strains (70%) drastically exacerbated the surface morphology. As discussed, up to necking point the hardening of polymer chains took place which prevents them from further gliding. Furthermore, relaxation occurred during annealing

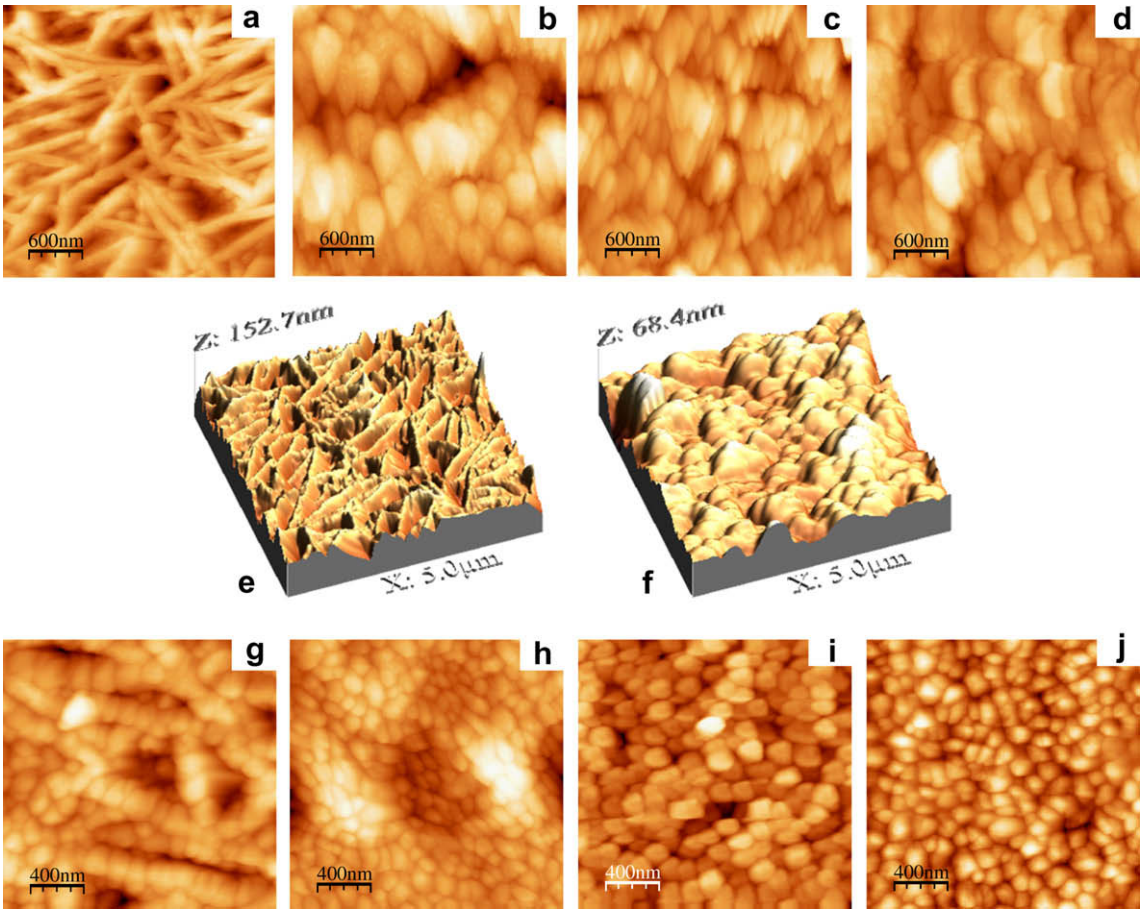

Fig. 3. AFM image comparison of samples (a) after standard annealing at 140 °C (R_{ms} = 15.6 nm), and after stretched to (b) 25% (R_{ms} = 7.74 nm), and (c) 50% (R_{ms} = 5.66 nm), (d) 70% (R_{ms} = 13.08 nm) at 70 °C. Image (e) and (f) are 3D morphology of samples shown in (a) and (c). Topography of pentacene layer on various P(VDF-TrFE) surfaces is presented for (g) annealed (140 °C – 2 h), (h) 25% – 70 °C, (i) 50% – 70 °C, (j) 70% – 70 °C.

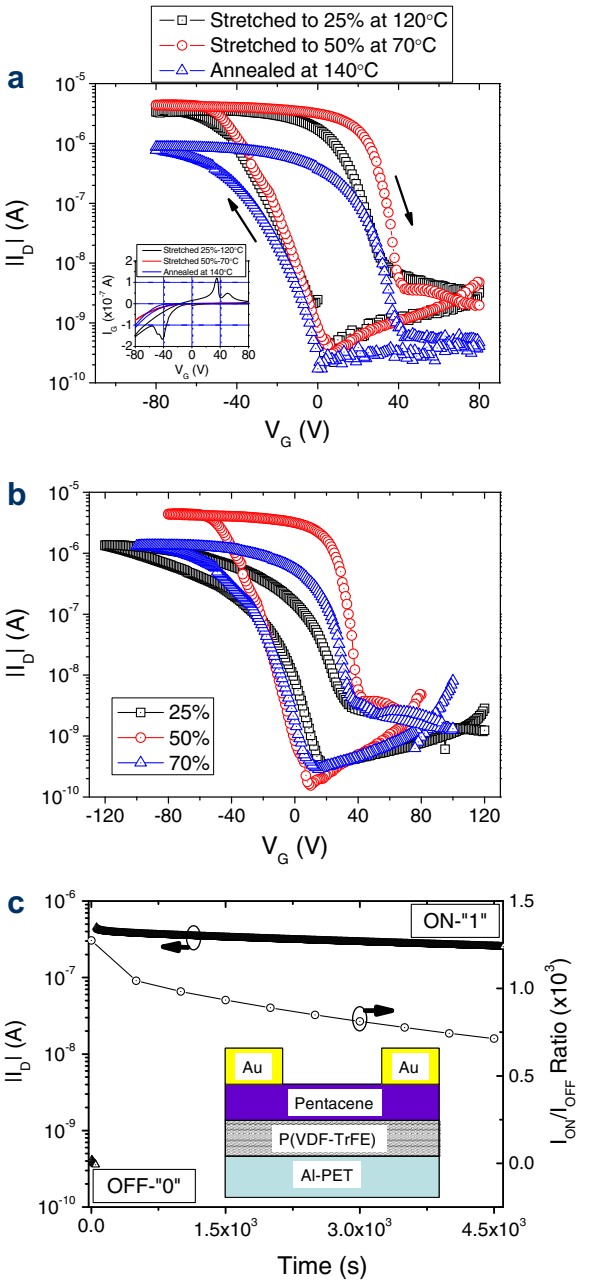

Fig. 4. Performance of ferroelectric field effect transistor devices ($W/L \sim$ 4000 μm:75 μm) measured at $V_D = -10$ V (a) I_D–V_G with inset showing I_G–V_G curves, (b) devices stretched at 70 °C to various strains, (c) current retention I_D–t (Δ) and ON/OFF ratio (O) of device on sample stretched at 50% – 70 °C with inset showing the FeFET structure.

that broke the ordered phase into regions of short-range order. This consequently leads to more irregular topography and exacerbates the surface roughness of the 70% strain sample.

Surface morphology of the pentacene layer deposited on the respective P(VDF-TrFE) samples is displayed in Fig. 3g–j. For the annealed sample, pentacene growth followed the rod-grain locations and filled up the deep valleys. At film thickness of 50 nm, the pentacene grains were unable to fully cover the irregular surface of the annealed sample resulting in the absence of transistor behavior. On the contrary, pentacene grown on the flatter surface of stretched samples is densely packed and fully cover the P(VDF-TrFE) surface. Overall almost uniformly global shape with an average size of 100–200 nm pentacene grains are observed for all the three stretched samples. The fact that the size of pentacene grains does not greatly increase even with a drastic reduction of surface roughness is probably due to the lowered surface energy of the P(VDF-TrFE) film owing to the thickening of copolymer lamellae [14,15].

Fig. 4 shows typical electrical characteristics for FeFET device which can be employed in non-volatile memory applications. The carrier mobility was calculated in the saturation regime of the I_D–V_D curves as described in previous report [9]. Value of remnant polarization by the P(VDF-TrFE) film was used for the calculation of charge mobility instead of specific capacitance. As previously reported [2], remnant polarization in the transistor device is ¼ of the value measured by the hysteresis loop. For drive voltage of |80| V, the remnant polarizations in the transistor are |0.014| C/m^2 which is equivalent to capacitance value of 1.75×10^{-4} F/m^2. Due to reduced surface roughness and better pentacene growth, ON-state drive currents are higher as seen in Fig. 4a while charge mobility is in the range of 0.072–0.12 cm^2/Vs for the stretched devices. This represents a doubling of the mobility compared to the annealed P(VDF-TrFE) reference devices comprising a 80 nm-thick pentacene film [9,16]. The enhancement may be attributed to reduced scattering of charge carriers at the pentacene grain boundaries and an improved dielectric-semiconductor interface in the stretched samples. The drain current hysteresis in Fig. 4a is consistent with polarization switching mechanism of P(VDF-TrFE) as previously described [2,9]. The gate currents from the inset of Fig. 4a show contribution from both dipole switching (peaks) and leakage during accumulation stage similar to the device with annealed P(VDF-TrFE) films [9,16]. The latter process possibly originates from charge leaking through the paths along the grain boundary defects of the flat-grain structure.

FeFET performance of the devices exposed to different stretching conditions, Fig. 4b, indicates that the current hysteresis is in concurrence with the polarization properties (Fig. 2). Due to smaller remnant polarization, current retention in 25%-strain device is less than the others leading to narrower hysteresis loop. Furthermore, as the dielectric constant is related to ferroelectricity [17], less crystalline and ferroelectric phase in 25% strain sample results in lower dielectric constant hence smaller drive current. Comparing 50% and 70% strain samples the device performance during the OFF to ON current cycles is similar; however, the 70% sample has slightly lower current retention during ON to OFF cycle. This also agrees with the above FTIR observations where the extent of crystalline phase in the 70% strain sample is smaller than that of the 50% sample due to hardening and relaxing of polymer chains in the necking regions that hinders the reorganization and leads to short-range order. Fig. 4c presents the current retention of the 50% – 70 °C device followed by 10^{-1} s voltage pulse. The current level is stable and

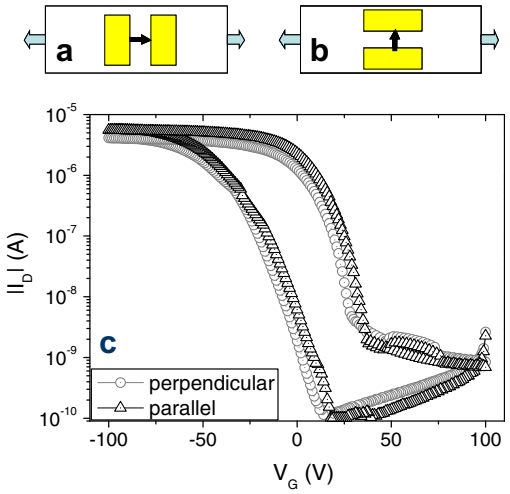

Fig. 5. Testing of drain current I_D direction (black arrows) against the stretching direction (gray arrows) (a) I_D in the same direction with the stretching, (b) I_D in the normal direction to the stretching, (c) I_D–V_G curves corresponding to each configuration measured from device of W/L ~4000 μm:75 μm at $V_D = -10$ V.

maintained up to 5000 s with the ON/OFF ratio of at least two-order difference extrapolated to more than 10^4 s. These memory behaviors are comparable to the previous report used annealed P(VDF-TrFE) film as gate dielectric layer [18].

With the whole sample being uniaxially stretched, the reorganization and alignment of P(VDF-TrFE) chains follow the stress direction. As transistor device is usually fabricated with anisometric dimensions, it is necessary to probe the dependence of device performance due to relative direction between stress and drive current flow, as demonstrated in Fig. 5a and b. The compared hysteresis of drain current in the two configurations is shown in Fig. 5c. Overall I_D–V_G current curves of parallel and perpendicular channels approximately resemble each other. A slightly smaller turn-on voltage for device in perpendicular configuration is attributed to experimental device variations. Nearly identical device performances observed here in both configurations thus indicating an absence of anisotropy which make the plastic substrate with stretched P(VDF-TrFE) films a viable solution to be integrated into organic electronic circuits with applications ranging from radio-frequency identification tags to thin film transistor based back-planes for display applications.

4. Conclusion

In summary, uniaxial stretching has been applied to P(VDF-TrFE) thin films attached to a flexible metallized PET substrate to enhance surface morphology and polarization properties of the ferroelectric polymer at lower processing temperatures. By combining stretching to plastic deformation and annealing, surface roughness can be drastically reduced. As the applied strain is sufficiently increased, annealing temperature can be decreased below the Curie transition for which crystallization and ferroelectric phase formation are greatly influenced by the strain magnitude. The reduction in roughness greatly enhances the growth of the semiconductor layer deposited on top of the stretched dielectric in the FeFET device. This process yielded charge carrier mobility values twice that of the comparable devices fabricated on dielectrics annealed at 140 °C. Furthermore, the resultant memory functionality is isotropic and yielded similar drive current hysteresis and enhanced current amplitude and ON/OFF ratio characteristics as compared to devices fabricated form the reference annealing processes.

Acknowledgements

We thank the Xerox Research Center (Canada) for supplying the Aluminum coated PET substrates. One of the authors, C.A. Nguyen, would like to acknowledge the research scholarship awarded by Nanyang Technological University. This work is supported by A*Star Grant No. 0521170037 and NTU Acrf Grant No. RG26/05.

References

[1] J.C. Scott, L.D. Bozano, Adv. Mater. 19 (2007) 1452.
[2] R.C.G. Naber, C. Tanase, P.W.M. Blom, G.H. Gelinck, A.W. Marsman, F.J. Touwslager, S. Setayesh, D.M. de Leeuw, Nat. Mater. 4 (2004) 243.
[3] R. Schroeder, L.A. Majewski, M. Voight, M. Grell, IEEE Electron Dev. Lett. 26 (2005) 69.
[4] A.J. Lovinger, Science 220 (1983) 1115.
[5] D. Naegele, D.Y. Yoon, Appl. Phys. Lett. 33 (1978) 132.
[6] T.T. Wang, J.M. Herbert, A.M. Glass (Eds.), The Application of Ferroelectric Polymers, Chapman and Hall, New York, 1988.
[7] T. Furukawa, Phase Trans. 18 (1989) 143.
[8] T. Furukawa, Adv. Coll. Int. Sci. 71–72 (1997) 183.
[9] C.A. Nguyen, P.S. Lee, S.G. Mhaisalkar, Org. Electron. 8 (2007) 415.
[10] K.J. Kim, N.M. Reynolds, S.L. Hsu, Macromolecules 22 (1989) 4395.
[11] R. Gregorio Jr., M. Cestari, J. Poly. Sci. B: Poly. Phys. 32 (1994) 859.
[12] Y.J. Park, S.J. Kang, C. Park, K.J. Kim, H.S. Lee, M.S. Lee, U. Chung, I.J. Park, Appl. Phys. Lett. 88 (2006) 242908.
[13] C.A. Nguyen, P.S. Lee, W.A. Yee, X. Lu, M. Srinivasan, S.G. Mhaisalkar, J. Electrochem. Soc. 154 (2007) G224.
[14] S.Y. Yang, K. Shin, C.E. Park, Adv. Func. Mater. 15 (2005) 186.
[15] G. Teyssedre, A. Bernes, C. Lacabanne, J. Poly. Sci. B: Poly. Phys. 33 (1995) 879.
[16] C.A. Nguyen, P.S. Lee, N. Ng, H. Su, S.G. Mhaisalkar, J. Ma, F.Y.C. Boey, Appl. Phys. Lett. 91 (2007) 042909.
[17] D. Bolten, U. Böttger, R. Waser, J. Appl. Phys. 93 (2003) 1735.
[18] R.C.G. Naber, B. de Boer, P.W.M. Blom, D.M. de Leeuw, Appl. Phys. Lett. 87 (2005) 203509.

100–200 nm typically, which is required for improving performances of electronically active devices such as OTFTs. On opposite, all other printing techniques sorely provide such thickness control.

Numerous papers [14–17] described enhancement of SCP mobility by molecular engineering and molecular self-organization [14–17]. Nevertheless, OTFT performances are also driven by interface properties between printable organic semiconductors (OSC) and source & drain (S&D) electrodes. Here, we present a full study to take advantage of this mechanism. Theoretically, the contacts should be ohmic for efficient operation. In this ideal case, the charge-injecting source electrode has no significant resistance and can supply any current required by the bulk of the OSC layer. That is to say that the OTFT performances are limited by energy barriers at the S&D/OSC interface [18–21]. As a result, the presence of contact resistances and their effect on the transistor characteristics have to be considered when developing OTFT.

Our approach is to extract the contribution of contacts in order to distinguish the contribution coming from the SCP channel resistance and that coming from S&D/SCP contact resistance, during gate-field modulation. By this way, we optimize inkjet-printed PTFT in terms of contacts independently of the intrinsic electronic properties of the SCP layer.

In addition, numerous works [22–26] give the contact resistance values for different SCP/S&D interfaces and these values often differ for the same interface. This dispersion is due to the complex superposition of the electric fields induced by the gate and the drain voltages, which is specific to each device (architecture, gate oxide thickness, etc.). Then, the relative contribution of these two fields varies from one device to another. In consequence, the extraction of contact resistances on the same device architecture is required to confront their values for different interfaces.

To our knowledge, contact effect of inkjetted S&D electrodes in PTFTs has received little attention. In this work, we compare the contact resistance obtained for two SCPs: P3HT and PQT-12; these ones in contact with different S&D electrodes: evaporated-Au, sputtered-Pt, inkjetted-silver nanoparticles and inkjetted Pedot:Pss. The influences of S&D work function, SCP ionization potential and nature of the interface (metal/polymer or polymer/polymer) on contact resistance are discussed. Moreover, it should be also observed that this work was not focused on the injecting contacts over a range of temperature, such as T. N. Jackson and D. Natelson groups did before for evaporated and/or sputtered metallic source/drain electrodes [27,28].

Finally, we talk over the limitations induced by these contact resistances as the channel length is reduced. This channel length reduction is inevitable to reach higher switching speeds, proportional to μ/L^2, for the PTFT integration in applications.

2. Experiment

Inkjet printing was performed using a custom-made piezoelectric drop-on-demand system adapted from MicroFab Technologies Inc. We used printheads with 50 and 30 μm-diameter tips and a temperature-controlled chuck. Thus, drops may be deposited onto a heated substrate, which enables a better control on the droplet spreading after contacting the surface and on the solvent evaporation rate. The driving electrical waveform applied to the piezoelectric element commands the expelled-droplet size and its velocity, and is adjusted for each electronics ink. A camera, coupled with a pulse LED, is used to optimize the formation and trajectories of droplets. A second one enables the inspection of the deposited patterns and alignment of successive printings.

Commercially available regio regular poly(3-hexylthiophene-2,5-diyl) (P3HT) and Poly(3,3‴-didodecyl-quaterthiophene) (PQT-12) were used as semiconductor without any further purification (Fig. 1). The polymer was dissolved in different organic solvents. We obtained best results with relatively high boiling point solvents, like dichlorobenzene or trichlorobenzene. Indeed, with low boiling point solvent, like chloroform or chlorobenzene, we meet frequent problems in inkjet printing process (clogging of the tip, not well-defined patterns, etc.). As well as high boiling point solvents improved the inkjet printing process reliability, their use leads to higher mobility in polythiophene deposited films [14].

First, we used metal photolithographically-patterned test-structures on doped silicon wafer (0.01–0.02 Ω cm) with a thermal oxide layer (300 nm-thick). These test-structures were used (i) to optimize inkjet printing parameters and post-treatment conditions of the SCP and (ii) to investigate inkjetted-SCP performances (Fig. 2a). Electrodes, realized by lift-off technique, were made of 100 nm-thick gold (Au) or platinum (Pt) with a 3 nm-thick titanium (Ti) adhesion layer to see the effect of electrode metal nature on PTFT performances. Surface modification of the gate oxide by octadecyltrichlorosilane (OTS) self-assembled monolayer (SAM) was done for its well-known positive impact on improved charge carrier transport and thus mobility value [29–31].

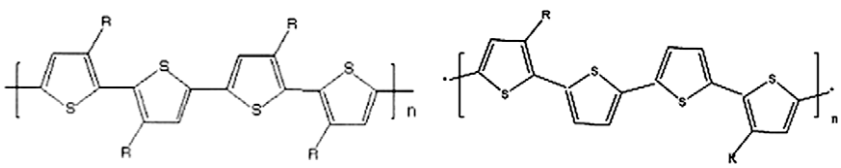

Fig. 1. Chemical structures of P3HT (R = C_6H_{13}) (a), PQT-12 (R = $C_{12}H_{25}$) (b).

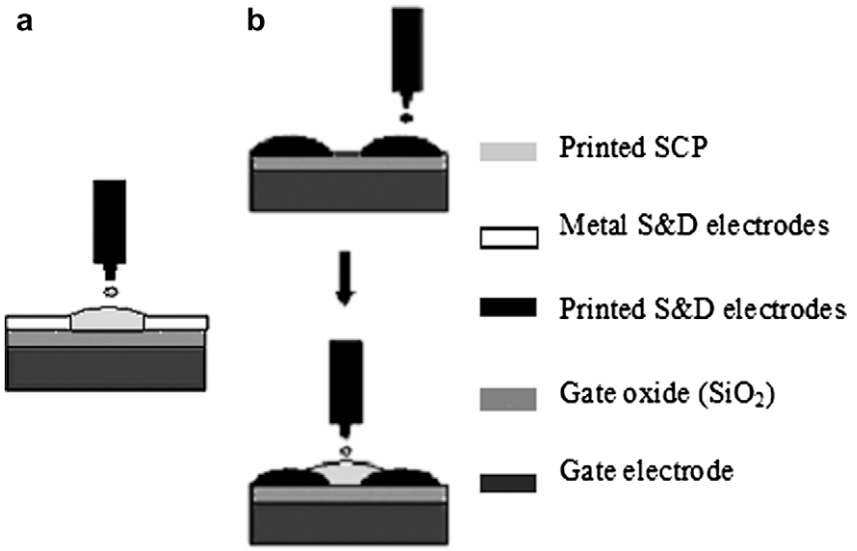

Fig. 2. Process flows used to fabricate inkjet-printed PTFTs: printing of SCP on metallized test-structures (a), printing of SCP/S&D electrodes on oxidized Si-wafer (b).

Secondly, on similar oxidized wafer, several SCP/S&D inkjetted couples were deposited to compare device performances with evaporated metal-based S&D electrodes. The process flow used to elaborate these devices is presented in Fig. 2b. We first define the S&D electrodes and then fill the channel region with the SCP, while conserving the previously-defined semiconductor deposition conditions. We investigated printable electrodes, like conducting polymers and inorganic dispersions. As conducting polymer, we used an aqueous dispersion of poly(3,4-ethylenedioxythiophene)/poly(styrenesulfonate) (Pedot:Pss) and, as inorganic material, a silver nanoparticle-based ink (Ag-NPs).

All experimental steps and OTFT electrical measurements were performed under ambient atmosphere. The cross section area of the inkjetted S&D electrodes was measured by stylus profilometry. Transistor characteristics were performed using a HP 4145A semiconductor parameter analyzer on a probe station.

3. Results and discussion

3.1. A – Electrical parameters

The mobility in the linear ($V_d \ll V_g$, Eq. (1)) and saturated ($V_d > V_g$, Eq. (2)) regimes were extracted from the following equations for the PTFTs fabricated as described in Fig. 2

$$I_{d,lin} = \frac{W}{L}\mu_{lin}C(V_g - V_t)V_d \quad (1)$$

$$I_{d,sat} = \frac{W}{2L}\mu_{sat}C(V_g - V_t)^2 \quad (2)$$

where I_d is the drain current, L the channel length, W the channel width, μ the mobility, C the oxide capacitance per unit area, V_g and V_d the gate and drain voltages and V_t the threshold voltage. Output and transfer characteristics are given for PQT-12/sputtered-Pt S&D electrodes couple in Fig. 3 and PQT-12/inkjetted Pedot:Pss S&D couple in Fig. 4. PTFT performances are summarized for each SCP/S&D couples in Table 1.

The linear resistance R_l of printed S&D electrodes was obtained from *I-V* curves. By measuring the cross section area, we estimated the printed material resistivities. The resistivity of 130 °C-annealed Ag-NPs was 17 μΩ cm, one order of magnitude higher than bulk Ag (1.6 μΩ cm), but ~3 orders of magnitude lower than Pedot:Pss (13 mΩ cm). The resistivity of Ag-NPs could be reduced by higher temperature annealing, but the main idea is to conserve plastic compatible annealing temperature for flexible electronics applications.

Contact resistances were calculated from transfer line method (TLM), which consists of measuring the channel length dependence as a function of the device resistance [22–24]. In linear regime, the total resistance R_{TOT} is the sum of the intrinsic channel resistance $R_{CH,i}$ and the contact resistance R_C (Eq. (3)):

$$R_{TOT} = \left(\frac{\partial V_d}{\partial I_d}\right)_{V_g, V_d \to 0} = R_{CH,i} + R_C = \frac{L}{W\mu_i C(V_g - V_{t,i})} + R_C \quad (3)$$

where μ_i and $V_{t,i}$ are the intrinsic mobility and threshold voltage, respectively. The contact resistance was extracted by plotting the width-normalized resistance ($R \times W$) as a function of L. Then, the slope of the linear fit gives information about the intrinsic channel resistance $R_{CH,i}$ and its extrapolation to zero channel length provides the total contact resistance R_C. TLM does not distinguish the contribution of each electrode and the extracted R_C is the sum of source and drain contributions, equally. However, scanning Kelvin probe [25] and four-probe [26] measurements

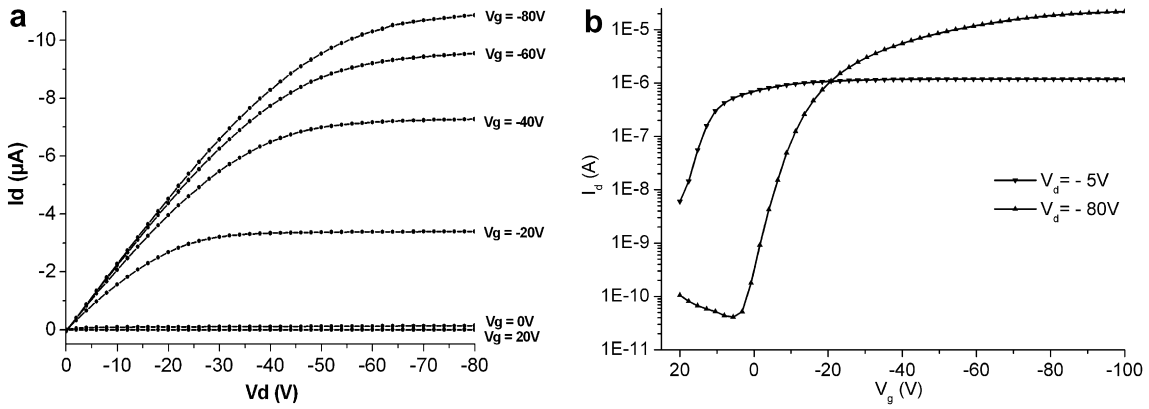

Fig. 3. Output (a) and transfer (b) curves of a PTFT made of inkjetted PQT-12 as semiconductor and sputtered-Pt S&D (L = 25 μm, W = 18 mm).

have shown that the injecting source contact resistance is high, in comparison to the drain contact resistance, especially in case of "bad" contacts.

3.2. B – Contact resistances contributions

According to the conventional Mott–Schottky model, at the source/semiconductor contact (Fig. 5), the interface energetics are controlled by the ionization potential of the semiconducting polymer IP_{SC} and the source electrode work function W_S. A Schottky barrier for hole injection, $\varphi_h = IP_{SC} - W_S$, determines the injection efficiency. We have to note that Schottky model doesn't take into account the role of trap states which exist at disordered organic semiconductor/ electrodes interface. However, in first approximation, for a qualitative discussion, we assumed that the contact barrier is equal to the one predicted by the Mott–Schottky model.

The IP_{SC} energetics level effect on contact resistance is illustrated in Fig. 6. a 0.2 eV-difference in IP_{SC} between P3HT and PQT-12 gives, in contact with the same Au source electrode, a barrier injection for hole, φ_h, 0.2 eV-

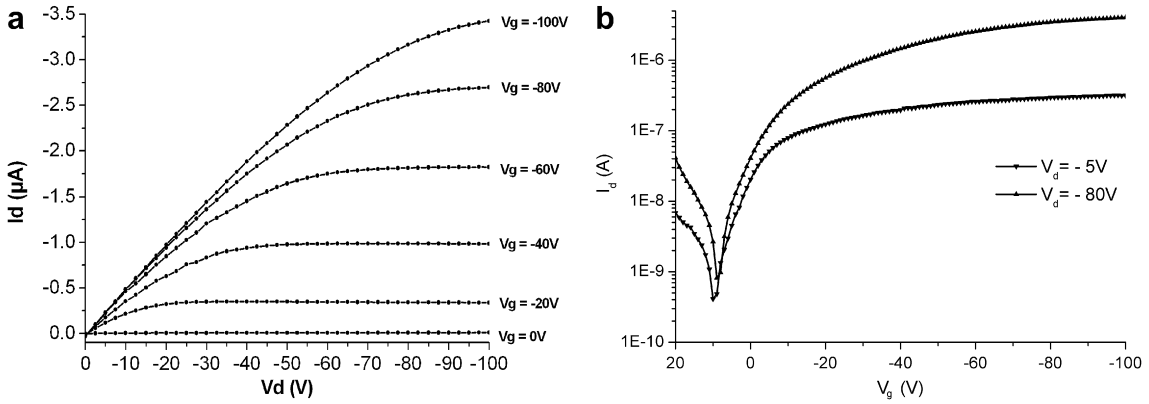

Fig. 4. Output (a) and transfer (b) curves of a PTFT with inkjetted PQT-12 as semiconductor and inkjetted Pedot:Pss S&D (L = 50 μm, W = 1.5 mm).

Table 1
Summary of PTFT performances for several SCP/S&D electrodes couples

Printed semiconductor	PQT	P3HT	PQT	PQT OTS	PQT OTS	PQT	PQT
S&D electrodes	Au	Au	Pt	Au	Pt	Printed Ag-NPs	Printed Pedot:Pss
OTS surface treatment	No	No	No	Yes	Yes	No	No
φ_h (eV)	0.2	0	−0.1	0.2	−0.1	0.7	0
μ_{sat}* (cm^2/Vs)	8×10^{-4}	1.5×10^{-3}	1.4×10^{-3}	1.4×10^{-3}	5.2×10^{-3}	4×10^{-4}	3.8×10^{-3}
I_{on}/I_{off}	1.2×10^5	9.3×10^3	2.5×10^5	6.4×10^3	3.7×10^4	1.7×10^4	7×10^3
V_t (V)	−19.5	27	−3.3	6.8	11.5	−21	−11
R_C at V_g = −80 V(M Ω cm)	6.8	0.38	0.62	2.7	0.62	15	0.36
$L_{\eta = ½}$ at V_g = −80 V (μm)	16.5	0.9	1.5	21.7	5.0	36.5	0.9

* Mobilities are derived without taking into account the channel contact resistance influence. These values are calculated from Eq. (2).

higher in the case of PQT-12. This explains the higher contact resistance observed in the PQT-12-based transistor (Table 1). SCP with relatively low ionization potential, like P3HT, leads to comparatively lower barrier of holes injection, and, in consequence, smaller contact resistances. Nevertheless, P3HT has the well-known drawback to be sensitive to ambient oxygen doping [36,37]. On the contrary, SCPs with higher ionization potential, like PQT-12, are more attractive for PTFTs because of a better stability against this doping phenomenon. However, using this high work function SCP increases the parasitic contact resistances.

At the other side of the contact, the electrode has its influence on contact resistance as shown in Fig. 7 for a PQT-12-based transistor. A 0.3 eV-difference in W_S between Au and Pt lands up in φ_h and leads up to a higher contact resistance in the case of Au ($R_{C,Au}$ = 2.7 MΩ cm, $R_{C,Pt}$ = 0.62 MΩ cm at V_g = −80 V). That also explains why the measured mobility, calculated from Eq. (2), is increased when Pt is used as contact electrode (Table 1).

For cost reductions, S&D must be also printable. Fig. 8 compares the extracted contact resistances between metal-based and inkjetted S&D in contact with PQT-12. First, low-resistive Ag-NPs-based S&D electrodes provide to the transistor a mobility divided by 3–4 compared to Pt electrodes. In making the assumption that this material has a work function close to the one of Ag bulk, φ_h is very high (0.7 eV) and the extracted contact resistance too (15 MΩ cm at V_g = −80 V, see Table 1). Secondly, the highest mobility was achieved with printed Pedot:Pss S&D, overcoming the mobility in the case of sputtered-Pt electrodes (Table 1). If we have a look at φ_h, which is more favourable to hole injection in the case of Pt (Fig. 5-a), we expect the contrary. The reason is that OTFT performances are, in this case, improved by interfacial doping of the semiconducting polymer close to the contact, which leads to a decrease of contact resistance ($R_{C,Pedot/Pss}$ = 0.36 MΩ cm at V_g = −80 V, see Table 1). Indeed, Wang et al. demonstrated that Pedot:Pss S&D electrodes offer the advantage of forming a p-doped interfacial layer with

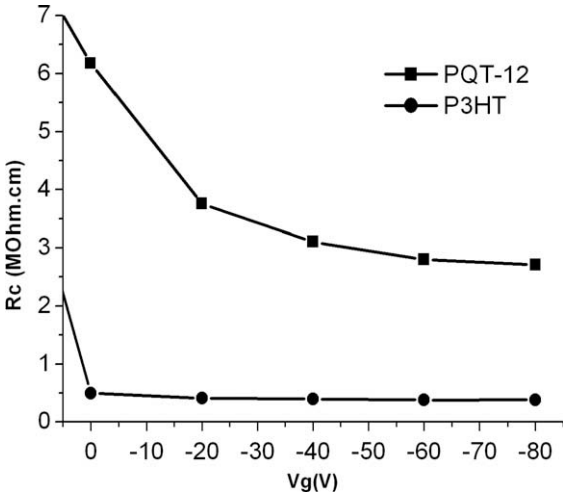

Fig. 6. Contact resistance R_C as a function of gate voltage: effect of the semiconductor (Au-based S&D electrodes).

a F8T2 organic semiconductor, and provides a very efficient charge injection at the interface [32]. Such results lead us to speculate that such doped layer is formed at the PQT-12/Pedot:Pss interface. This assumption is all the more justified, because the formation of such a layer was also observed with another SCP, like PPV [33,34]. The mechanism of barrier formation at metal/organic interfaces has been widely studied and the effective energy barrier often deviates from the Mott-Schottky model, as highlighted in this paper. In fact, an additional dipole, Δ, is created at the interface and shifts the HOMO level downward. As a result, the lowest contact resistance is obtained with inkjetted Pedot:Pss as S&D electrodes. This result explains the higher extracted mobility compared to other devices (Table 1). Consequently, through this experimental results, we see how the contact resistances engineering between SCP and S&D electrodes is crucial for the enhancement of device performance.

a

Electrodes	W_s (eV)
Pt metal	5.3
PEDOT:PSS	5.2
Au metal	5.0
Ag metal	4.5

Semiconductor	IP_{SC} (eV)
PQT12	5.2
P3HT	5

b

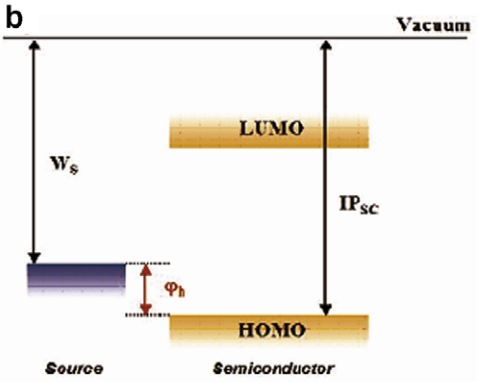

Fig. 5. (a) Work function Ws and ionization potential IP_{SC} table of involved materials at interfaces, (b) energy band diagram and injection barrier height φ_h at source/semiconductor contact.

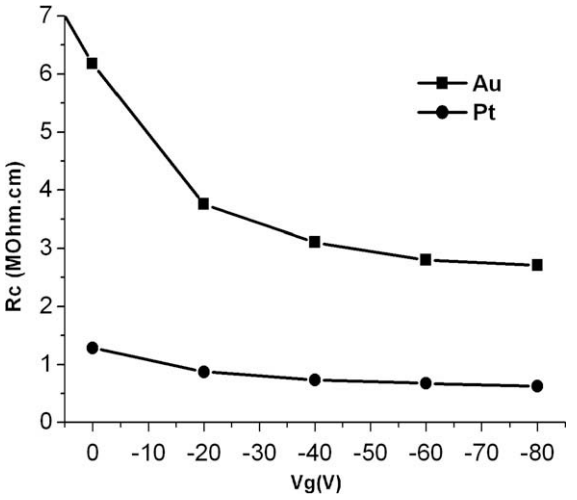

Fig. 7. Contact resistance R_C as a function of gate voltage: effect of S&D electrode metal (PQT-12-based PTFT).

The contact resistances are related to the resistivity of S&D electrodes, but the most important factor is the efficiency of charge carrier injection, governed by energy barrier height at the S&D/SCP interface. In other words, the injection process depends strongly on the magnitude of the energy barrier that is to overcome as the charge carrier across the interface. We obtain lower contact resistances when conducting polymer (Pedot:Pss) contacts the PTFT channel than evaporated metal (Au, Pt). In fact, a low-resistive material, like annealed Ag-NPs, did not confer inevitably good performances to the transistor.

Another point, as shown in Fig. 9, is that R_C can dominate R_{CH} when the channel length is reduced from 50 to 10 μm. Thereby, the benefit of reducing the channel length is limited and will be discussed hereinafter.

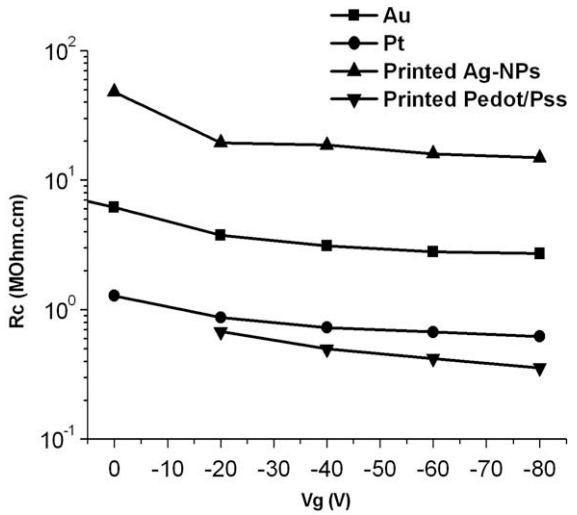

Fig. 8. Contact resistance R_C as a function of gate voltage: comparison between inkjetted and metal-based S&D electrodes (PQT-12-based OTFT).

3.3. C – Injection efficiency in PTFTs

The contact is ohmic as the injecting contact leads to any limitation of the current flow in the semiconducting bulk layer. To quantify the performance of a contact, we use the injection efficiency η as figure-of merit, which can be expressed in function of R_{CH}, the bulk resistance of the semiconductor layer, and R_C, the contact resistance (Eq. (4)) [35].

$$\eta = \frac{R_{CH}}{R_{CH} + R_C} \tag{4}$$

Several physical parameters have an impact on injection efficiency η: energy barrier height at the contact and semiconductor doping level, for example [35]. Here, we focus our attention on the device geometry dependence of injection efficiency η, especially on channel length. When L increases, R_{CH} also increases proportionally and R_C remains constant. Thus, when L is large enough, experimentally η tends towards 1 ($R_{CH} \gg R_C$) (Fig. 10). In other words, the device is less contact limited as the channel length L increases. From this observation, we define a new figure-of-merit for the PTFTs: the $L_{\eta = 1/2}$ channel length value at which the bulk resistance R_{CH} is equal to the contact resistance R_C. $L_{\eta = 1/2}$ is estimated in strong accumulation at $V_g = -80$ V. Transistor with channel length $L < L_{\eta = 1/2}$ will be seriously contact limited. That means that the ohmic nature of the contact will increase as $L_{\eta = 1/2}$ value will decrease. This figure-of-merit allows us to confront contact performances for different S&D/SCP couples (Table 1).

The first conclusion regarding $L_{\eta = 1/2}$ is the increased contact limitation as the SCP mobility increases, because the channel resistance decreases. For illustration, if we take the devices made of Pt-S&D/PQT-12 couple, $L_{\eta = 1/2}$ grows up from 1.5 to 5 μm after OTS-treatment. This limitation is amplified by the fact that the OTS-treatment reduces the contact resistance R_C, as discussed previously. The same observation can be made with Au-S&D/PQT-12 couple as $L_{\eta = 1/2}$ grows up from 16.5 μm to 21.7 μm after the

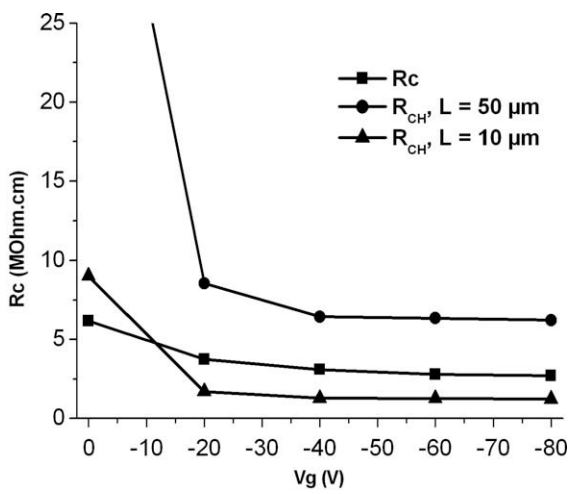

Fig. 9. Channel resistances R_{CH} and contact resistances R_C for different channel length as a function of gate voltage V_g (PQT-12-based PTFTs, Au-S&D, OTS-modified gate oxide).

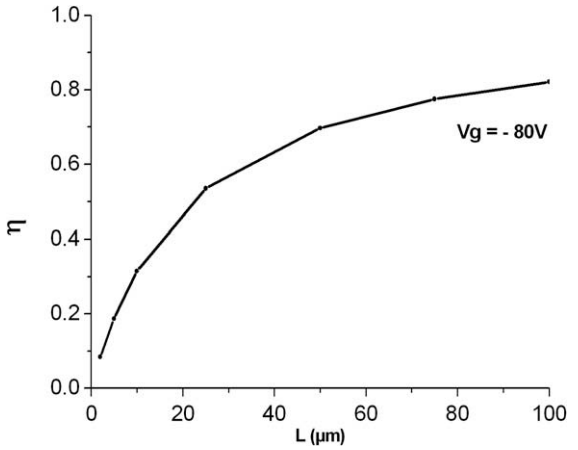

Fig. 10. Injection efficiency η as a function of the channel length L (PQT-12-based PTFTs, Au-S&D, OTS-modified gate oxide).

same treatment. Au-S&D electrodes, which perform a "good contact" in interface with P3HT ($L_{\eta = 1/2}$ = 0.9 μm), clearly limit performances of PQT-12-based PFETs, especially after gate oxide modification by OTS ($L_{\eta = 1/2}$ = 21.7 μm). Despite its relatively low resistivity, inkjetted Ag-NPs-based S&D produce the most limitating contact ($L_{\eta = 1/2}$ = 36.5 μm), due to the important mismatch between their work function and ionization potential of PQT-12. The best contact on PQT-12, i.e. the less limitating one, is achieved with inkjetted Pedot:Pss ($L_{\eta = 1/2}$ = 0.9 μm). These improved performances arise from (i) the high work function of Pedot:Pss, (ii) a small interfacial dipole Δ of the organic/organic interface [38–39] and (iii) the formation of an interfacial p-doped layer, as discussed before.

The approach of this work points out that, for optimizing PTFTs in terms of contacts, a conjunctive development of the active material (SCP) and the S&D contacts is fundamental, as the injection efficiency inheres in each SCP/S&D couple.

4. Conclusions

Here, we show that inkjet printing technique is suitable to take into account (i) cost and (ii) contact resistance reductions in PTFTs. We outlined the problem of contact resistance in these devices: a specific attention must be done to the choice of S&D material. This work demonstrates that the parasitic contact resistance associated to the inkjetted contacts in Pedot:Pss are lower than the ones with evaporated or sputtered metal in contact with SCP. Furthermore, a low-resistive inkjetted material, like annealed Ag-NPs, did not confer inevitably good performances to the transistor. In contrary, Pedot:Pss, despite higher resistivity, gave better PTFT performances owing to improved energetics level match with the semiconductor and interfacial doping. The magnitude of the contact resistance in PTFTs dominates the device performances when the channel length is reduced.

For the development of plastic electronics application, the understanding on the electrical properties of contacts and their dependence on electrode materials, organic semiconductors and processing conditions are clearly a major issue for channel length reduction perspectives.

The success in printing a couple of S&D electrodes/SCP optimized in terms of contact resistance is an important step towards low-cost and high-performance polymer devices. One of the next challenges is to confer flexibility to these PTFTs. This is in order to go towards future applications in flexible electronics.

Acknowledgments

This work was supported by fund from the 'Ministère de l'Economie des Finances et de l'Emploi' (MINEFE). The authors would also acknowledge the 'Institut d'Electronique Fondamentale' for Si-based test-structures realization.

References

[1] C.J. Drury, C.M.J. Mutsaers, C.M. Hart, M. Matters, D.M. de Leeuw, Appl. Phys. Lett. 73 (1998) 108.
[2] A. Knobloch, A. Manuelli, A. Bernds, W. Clemens, J. Appl. Phys. 96 (2004) 2286.
[3] D. Zipperer, W. Clemens, A. Ullmann, M. Böhm, W. Fix, MRS SpringMeeting, San Francisco, 2005.
[4] G.H. Gelinck, H.EdzerA. Huitema, E. van Veenendaal, E. Cantatore, L. Schrijnemakers, J.B.P.H. van der Putten, T.C.T. Geuns, M. Beenhakkers, J.B. Giesbers, B.-H. Huisman, E.J. Meijer, E.M. Benito, F.J. Touwslager, A.W. Marsman, B.J.E. van Rens, Dago M. de Leeuw, Nature Mater. 3 (2004) 106.
[5] P. van Lieshout, E. van Veenendaal, L. Schrijnemakers, G. Gelinck, F. Touwslager, E. Huitema, Solid-state circuits conference, in: Digest of Technical Papers ISSCC, vol. 1, 2005, 578.
[6] L. Zhou et al, Appl. Phys. Lett. 88 (2006) 083502.
[7] B. Crone, A. Dodabalapur, A. Gelperin, L. Torsi, H.E. Katz, A.J. Lovinger, Z. Bao, Appl. Phys. Lett. 78 (2001) 2229.
[8] H. Sirringhaus, T. Kawase, R.H. Friend, T. Shimoda, M. Inbasekaran, W. Wu, E.P. Woo, Science 290 (2000) 2123.
[9] J.Z. Wang, Z.H. Zheng, H.W. Li, W.T.S. Huck, H. Sirringhaus, Nature Mater. 3 (2004) 171.
[10] P.C. Chang, S.E. Molesa, A.R. Murphy, J.M.J. Fréchet, V. Subramanian, IEEE Trans. Electron Devices. 53 (4) (2006).
[11] S. Sanaur, A. Whalley, B. Alameddine, M. Carnes, C. Nuckolls, Org. Electron. 7 (2006) 423.
[12] D. Zielke, A.C. Hübler, U. Hahn, N. Brandt, M. Bartzsch, U. Fügmann, T. Fischer, J. Veres, S. Ogier, Appl. Phys. Lett. 87 (2005) 123508.
[13] T. Mäkela, S. Jussila, H. Kosonen, T.G. Bäcklund, H.G.O. Sandberg, H. Stubb, Synt. Met. 153 (2005) 285.
[14] J.-F. Chang, B. Sun, D.W. Breiby, M.M. Nielsen, T.I. Solling, M. Giles, I. McCulloch, H. Sirringhaus, Chem. Mater. 16 (2004) 4772.
[15] M. Funahashi, J.I. Hanna, Adv. Mater. 17 (2005) 594.
[16] P.K.-H. Ho, L. Chua, M. Dipankar, X. Gao, D. Qi, A.T.-S. Wee, J. Chang, R.H. Friend, Adv. Mater. 19 (2007) 215.
[17] H. Heil, T. Finnberg, N. von Malm, R. Schmechel, H. von Seggern, Appl. Phys. Lett. 93 (2003) 1636.
[18] S.M. Sze, Physics of Semiconductor Devices, Wiley, 1981.
[19] A. Kahn, N. Koch, W. Gao, J. Polymer Sci. Polymer Phys. 41 (2003) 2529.
[20] H. Ishii, K. Seki, IEEE Trans. Electron Devices 44 (1997) 1295.
[21] I.G. Hill, A. Rajagopal, A. Kahn, Y. Hu, Appl. Phys. Lett. 73 (1998) 662.
[22] J. Zaumseil, K.W. Baldwin, J.A. Rogers, J. Appl. Phys. 93 (2003) 6117.
[23] E.J. Meijer, G.H. Gelinck, E. van Veenendaal, B.H. Huisman, D.M. de Leeuw, T.M. Klapwijk, Appl. Phys. Lett. 82 (2003) 4576.
[24] G.B. Blanchet, C.R. Fincher, M. Lefenfeld, J.A. Rogers, Appl. Phys. Lett. 84 (2004) 296.
[25] L. Burgi, H. Sirringhaus, R.H. Friend, Appl. Phys. Lett. 80 (2004) 2913.
[26] P.V. Pesavento, R.J. Chesterfield, C.R. Newman, C.D. Frisbie, J. Appl. Phys. 96 (2004) 7312.
[27] B.H. Hamadani, D. Natelson, J. Appl. Phys. 97 (2005) 064508.
[28] D.J. Gundlach, L. Zhou, J.A. Nichols, T.N. Jackson, P.V. Necliudov, M.S. Shur, J. appl. Phys. 100 (2006) 024509.

[29] H. Sirringhaus, P.J. Brown, R.H. Friend, M.M. Nielsen, K. Bechgaard, B.M.W. Langeveld-Voss, A.J.H. Spiering, R.A.J. Janssen, E.W. Meijer, P. Herwig, D.M. de Leeuw, Nature 401 (1999) 685.
[30] R.J. Kline, M.D. McGehee, M.F. Toney, Nature Mater. 5 (2006) 222.
[31] R.J. Kline, D.M. DeLongchamp, D.A. Fischer, E.K. Lin, M. Heeney, I. McCulloch, M.F. Toney, Appl. Phys. Lett. 90 (2007) 062117.
[32] J.Z. Wang, J.F. Chang, H. Sirringhaus, Appl. Phys. Lett. 87 (2005) 083503.
[33] A.C. Fou, O. Onitsuka, M. Ferreira, M.F. Rubner, J. Appl. Phys. 79 (1996) 7501.
[34] A.C. Arias, M. Granström, D.S. Thomas, K. Petritsch, R.H. Friend, Phys. Rev. B 60 (1999) 3930.
[35] Y. Shen, A.R. Hosseini, M.H. Wong, G.G. Malliaras, Chem. Phys. Chem 5 (2004) 16.
[36] H.L. Gomes, P. Stallinga, M. Colle, F. Biscarini, D.M. de Leeuw, J. Non-Cryst. Solids 352 (2006) 1761.
[37] N. Kawashima, K. Nomoto, M. Wada, J. Kasahara, Mater. Res. Soc. Symp. Proc. 871E (2005).
[38] N. Koch, A. Kahn, J. Ghijsen, J.-J. Pireaux, J. Schwartz, Appl. Phys. Lett. 82 (2003) 70.
[39] N. Koch, A. Elschner, J. Schwartz, Appl. Phys. Lett. 82 (2003) 2281.

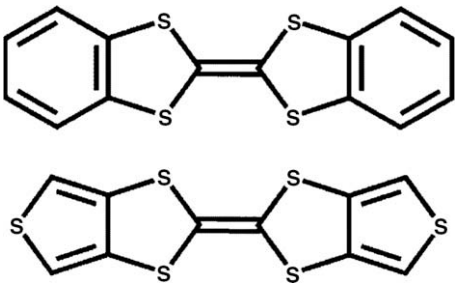

Fig. 1. Chemical structure of dibenzo- (top) and dithiophene-tetrathiafulvalene (bottom).

Fig. 1. Here we report on new results, partly in deep submicrometer devices, that are aiming to elucidate the intrinsic transport properties of DT-TTF and DB-TTF. We have fabricated OFETs based on these materials, which exhibit mobility values that are almost three times higher than previously reported for DT-TTF. Devices with channel lengths from 100 μm to below 100 nm have been analyzed in order to study the scaling properties of the devices. The performance of the OFET devices over a large temperature range (50–400 K) reveals a thermally activated transport mechanism with no or very low activation energy for temperatures smaller than 200 K and an increased activation at higher temperatures. Our results show that high performance TTF transistors can be easily fabricated from solution and used with no extra precautions to ambient conditions and to applied biases.

2. Experimental

The devices have been fabricated on thermally oxidised highly-doped silicon substrates. We use a bottom-contact setup, where the substrate serves as a common gate electrode. Metal source and drain electrodes are deposited on top of the oxide using lithography, metallisation, and lift-off. Using UV-optical lithography, we have fabricated electrode structures with channel lengths L from 100 μm down to 500 nm on 50 nm and 100 nm thick SiO_2 dielectric (cf. Fig. 2). Structures with sub 500 nm channel length are fabricated using electron beam lithography on SiO_2 with a thickness of only 20 nm. In this way, the transverse electrical field is increased, which helps to keep the devices in the long-channel regime in spite of the enhanced lateral field, cf. Ref [10]. The source and drain electrodes consist of electron gun evaporated Ti/Pt or Ti/Au, or sputtered Pt. Before deposition, the samples are cleaned in a solution of H_2O_2:H_2SO_4 (1:4) and treated with solutions of hexamethyldisilazane (HMDS) or octadecyltrichlorosilane (OTS). The resulting hydrophobic self-assembled monolayer on the oxide induces a uniform growth of micrometer size TTF crystals randomly distributed on the surface. The synthesis of DT- and DB-TTF has been reported previously [11,12]. TTF deposition is done by drop casting [8,9]. One drop (≈0.03 ml) of a 1 mg/ml solution of the TTF derivative in toluene is drop-cast on the substrate and allowed to evaporate slowly (>3 h) in a covered petri dish. This process results in the formation of a limited number of large single organic crystals that form a conducting channel between the source and drain electrodes (see Fig. 2b). Devices that are not covered by crystals show no field-effect and leakage currents in the $I \leqslant 10^{-10}$ A range. The same low leakage current is measured after mechanical removal of TTF crystals from previously functioning devices. The effective channel width W is determined by optical microscopy. Electrical characterization of the devices at room temperature is performed in air, in the dark, using a variable temperature probe station (Desert Cryogenics) and a semiconductor parameter analyzer (HP4145B). The temperature dependent measurements (50–400 K by He-flow cryostat) are carried out in vacuum (10^{-2}–10^{-4} Pa, depending on temperature) using the same equipment.

3. Results and discussion

In Fig. 3 the characteristics of a L = 30 μm channel DT-TTF transistor are presented for two measurement sequences with increasing and decreasing bias, respectively. Output and transfer characteristics both show hardly any hysteresis and follow perfect textbook behaviour. Field-effect mobilities of 3.65 $cm^2/V\,s$ were extracted from both the saturation regime ($V_{DS} = -15$ V) and the linear transfer curves ($V_{DS} = -1$ V), respectively. The fact that the values are identical shows that we can neglect limitations by charge carrier injection or displacement currents which would both result in a reduced mobility in the linear regime. Assuming ohmic contacts (cf. [13]), we can estimate the contact resistance to be approx. 30 kΩ × mm, which is rather low for OFETs. For DB-TTF-based OFETs a similarly high performance is measured except for a reduced mobility of 0.5 $cm^2/V\,s$.

For a detailed investigation of the transport properties we first apply a model of multiple trapping and release (MTR) by trap states [14]. These states induce band tails

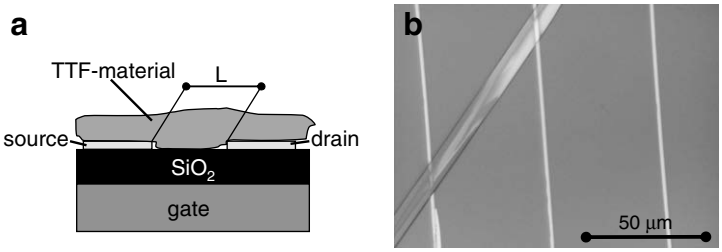

Fig. 2. (a) Schematic drawing of a transistor. The single crystal is deposited on the prefabricated electrode structure. (b) Micrograph of a TTF crystal on the source drain fingers (L = 50 μm).

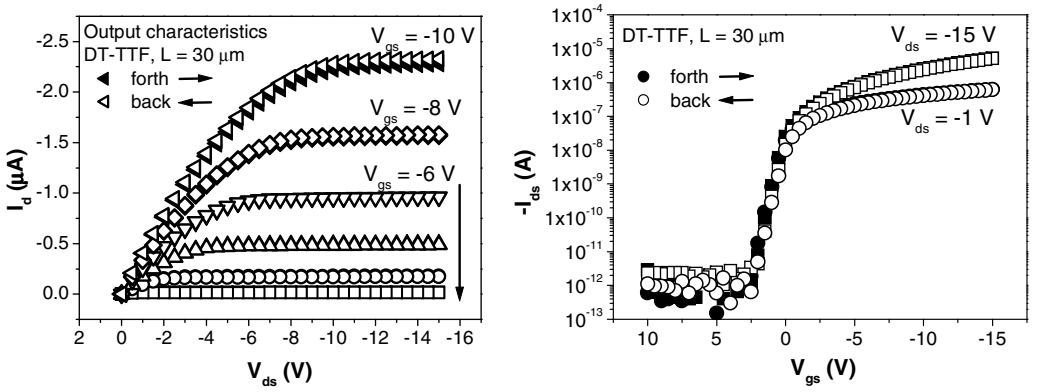

Fig. 3. Electrical output characteristics (left) and transfer characteristics (right) of a single crystal DT-TTF OFET with $L = 30$ μm at $T = 295$ K.

which often dominate the transport properties, leading to a exponential thermal activation of the mobility, characterized by the lowest energy state of the band tail [15]. This situation is generally encountered in both organic and inorganic amorphous materials [15–18,20]. Recently, it was shown that a similar exponential activation also exists in single crystalline organic semiconductors [18] where the trap states are located at or near the interface and thus can be modeled using a quasi two-dimensional density distribution whose exact properties are dependent on the gate insulator [23].

In temperature dependent mobility measurements on our devices we observe a similar exponential activation as reported for rubrene or pentacene [20]. The MTR activation energy can be extracted from the temperature dependence of the mobility shown in Fig. 4. For DB-TTF we find a constant mobility between 50 and 200 K and an exponential activation with an activation energy of 58 meV above 200 K. The mobility of DT-TTF, however, follows an activation which can be fitted using an exponential with two distinct activation energies; 15 and 108 meV.

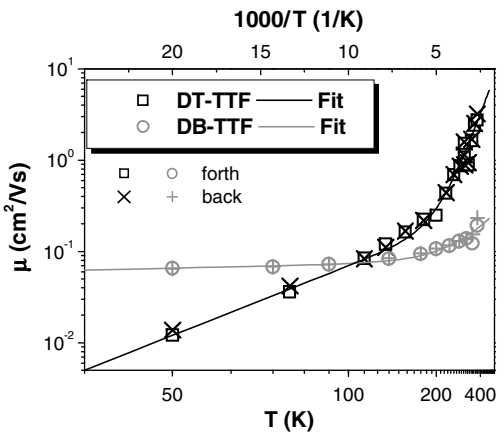

Fig. 4. Temperature dependence of the field-effect mobility as determined from transfer characteristics of DT-TTF (black) and DB-TTF (grey) OFETs for increasing (forth) and decreasing current (back) direction. The solid lines are (bi)exponential fits to the data.

We have already shown that at room temperature the mobility is not influenced by charge injection at the contacts. Given the low contact resistance one would also not expect a stronger influence at lower temperatures [21,22]. In order to make sure that this assumption is valid we can investigate the slope of the activation curves. Because charge injection does not enter the mobility analysis at room temperature, an increasing influence at lower temperature is only possible if the contact resistance has a higher activation energy than the mobility itself. However, we see only lower activation energies at lower temperatures, indicating that indeed contact effects can be neglected.

For both materials the slope of the activation curves indicate that even at low temperature the contact resistance does not influence the measurements.

This simplified analysis only suggests the presence and the approximate depth of band tails, a deeper insight, however, can be gained by using a method as in Ref. [18]. In this method the temperature dependence of the I/V characteristics is used to obtain a detailed picture of the energy distribution of the impurity levels. For this analysis, we first measure the current in saturation ($V_{DS} = -15$ V) for different values of V_{GS} and at various temperatures between 50 and 400 K.

Changing the gate voltage towards more negative values sweeps the Fermi energy through the gap towards the HOMO level. During the sweep, more and more states contribute to the transport and by analyzing the activation energy at each gate voltage we can identify the energy position of these trap states. Plotted against temperature (Fig. 5), the data reveals similar results for the two materials. For both materials we observe exponential activation with two distinct ranges of activation energies below and above 200 K, respectively.

From the thermal activation of the saturation currents we now determine the activation energy of the states in the gap which we then plot over the respective gate voltages (Fig. 6), yielding two datasets for each material corresponding to the low temperature ($T < 200$ K) and high temperature regime ($T > 200$ K). For the DB-TTF traps can be observed over the whole energy range between 10 and 180 meV. Below 10 meV the trap energies are too close

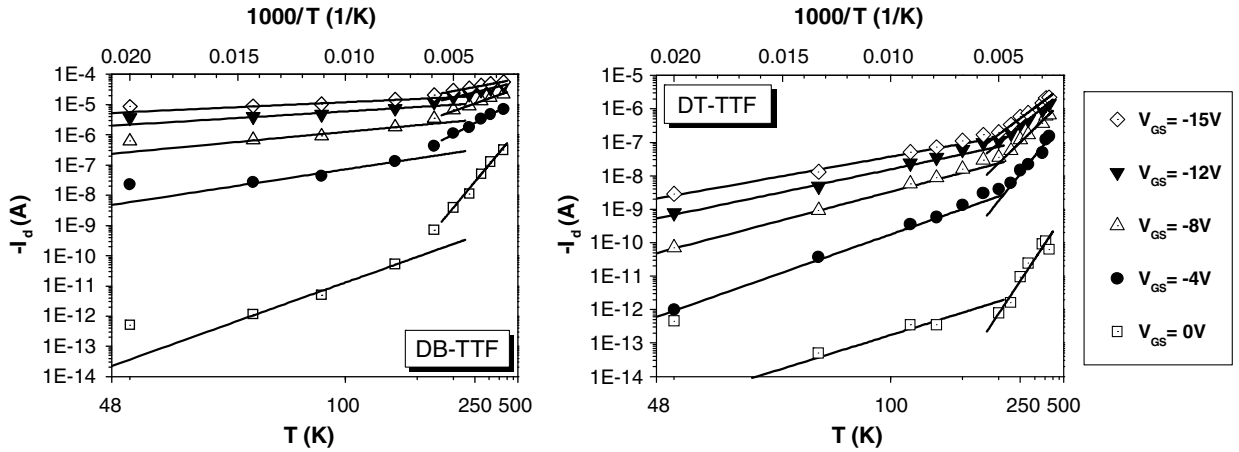

Fig. 5. Drain current I_D in saturation ($V_{DS} = -15$ V) at different V_{GS} plotted against temperature (logarithmic scale) for DB-TTF (left) and DT-TTF (right) OFETs. The straight lines correspond to exponential fits.

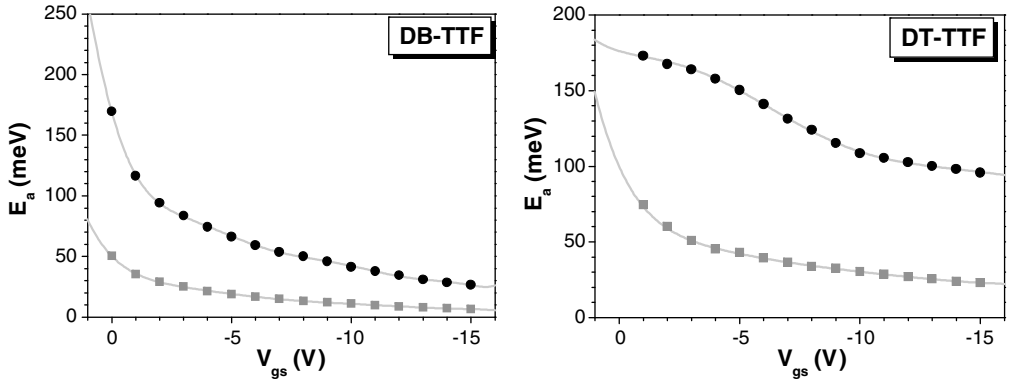

Fig. 6. Activation energy E_a (extracted from the data in Fig. 5) plotted against gate voltage for DB-TTF (left) and DT-TTF (right). For both materials we distinguish two separate regimes with different ranges of activation energies, extracted from the measurements below (grey) and above 200 K (black). E_a is the energy above the HOMO level. The solid lines are the polynomial fit.

to the HOMO to yield a useful signal. Trap energies above 180 meV are too high to be observable in the temperature regime investigated in our experiments. For the DT-TTF the situation is more complex. Here the two datasets leave an energy range between 75 and 95 meV where the density of states is too low to yield any significant influence on the I/V curves and is thus undetectable by this method.

For further evaluation we fit the data points of Fig. 6 by a continuous (polynomial) function [19] which allows us to determine its derivative at any voltage. We then use

$$N(E) = \frac{C}{e}\left(\frac{dE_a}{dV_{GS}}\right)^{-1} \quad (1)$$

in order to determine the density of states (DOS) in the gap (e is the electron charge and C the capacitance per area of our gate dielectric which we calculate to be 33 nF/cm^2 for 100 nm thick SiO_2). In order to convert this two-dimensional DOS into a volume DOS, the trap states are assumed to be concentrated within 7.5 nm of the material at the dielectric interface [18]. The results are plotted in Fig. 7. We have been careful not to evaluate parts of the fit which extend beyond or even contain the highest or lowest data points of the curve in Fig. 6. In these parts of the curve the fit typically starts to develop small ripples, usually leading to large artifacts in the extracted density of states, which is extremely sensitive to small changes in the derivative of the fit function. In the density of states of the DB-TTF (Fig. 7 left) we see a band tail extending from the HOMO which has two pronounced local maxima, one at approx. 50 meV corresponding to the activation energy determined using MTR and another maximum at approx. 85 meV. The second peak, however, indicates a much lower density of states explaining why it could not be observed using MTR.

For the DT-TTF we observe two separate regimes. The lowest observable energy region of the band tail starts at 20 meV, however, with a density of states three times higher than for the same energy in DB-TTF. We can assume that a maximum exists here, supported by the MTR evaluation (yielding 21 meV activation energy). With increasing energy the density of states decreases, becoming undetect-

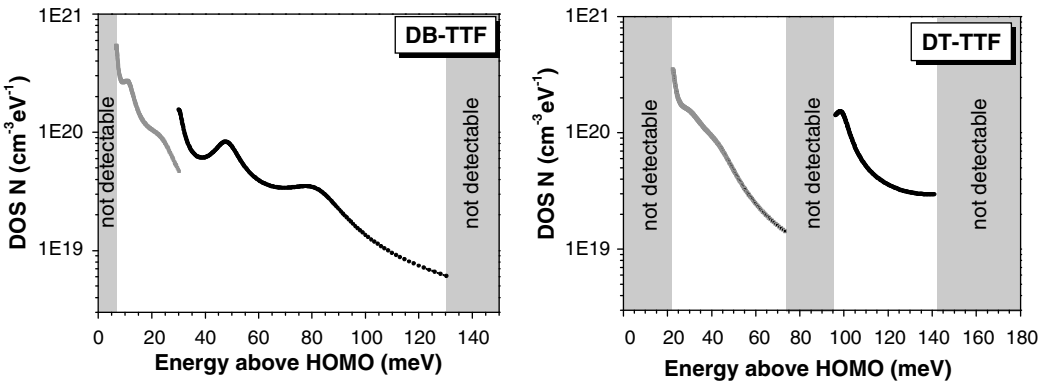

Fig. 7. Density of impurity states (DOS) plotted against their activation energy E_a above HOMO for DB-TTF (left) and DT-TTF (right). For DB-TTF a band tail emerges from the HOMO and exhibits two maxima at 50 and 85 meV. For DT-TTF there is a maximum at approx. 20 meV. The DOS decreases until it becomes undetectable at 75 meV. A second maximum can be found at 100 meV with the DOS decreasing again with increasing energy. The datapoints were calculated from the two datasets in Fig. 6 (grey: below 200 K, black: above 200 K).

able at approx. 75 meV. At 95 meV we see the density of states increasing again (now extracted from the data for $T > 200$ K) towards a maximum at 100 meV corresponding to the 104 meV activation energy determined by MTR. We see that the results obtained from MTR and the more detailed determination of the density of states are in good agreement. However, the latter yield a more detailed picture of the band structure. On the other hand the MTR model is more straight-forward and yields results which are not sensitive to polynomial fitting parameters. For example a large trap density in DT-TTF at 21 meV is clearly visible in MTR. In the density of states plot (Fig. 7), the density of states at 20 meV might just as well increase further towards lower energies without yielding a local maximum. The most reliable approach thus seems to be a combination of both methods as performed on our materials.

Besides the existence of these impurity states, we still see an untrapped carrier concentration which yields a finite current even at lower temperature. Especially in the case of the DB-TTF, mobility and carrier concentration remain more or less constant below 200 K. This finite carrier concentration also causes the weak dependence of threshold voltage on temperature. A plausible explanation would be that we observe transport either in states which are as close as a few meV to the HOMO or by pure hopping (i.e., not thermally assisted), two effects which cannot be distinguished in the investigated range of temperatures.

All transistors have proven to be relatively stable for several weeks in air. The mobility drops only by less then 50% over a timespan of several weeks. During the same period no significant changes in V_{TH} or off-current I_{off} are observed, which we found for other materials to be a main indication of an aging effect in OFET devices.

Finally, transistors with reduced channel length L were investigated in order to determine the scaling behaviour of the device properties, especially for $L < 1$ μm. Fig. 8 presents the mobility and on/off-ratio values for DT-TTF OFETs with channel lengths down to 100 nm on 20 nm thick SiO_2. The thin oxide was used in order to make sure that the gradual channel approximation [10] is still valid for these samples. We observe long-channel behaviour down to $L = 200$ nm, although the mobility starts to decrease below $L = 500$ nm, probably also due to an increasing influence of the contact resistance [21,22]. Devices with L below

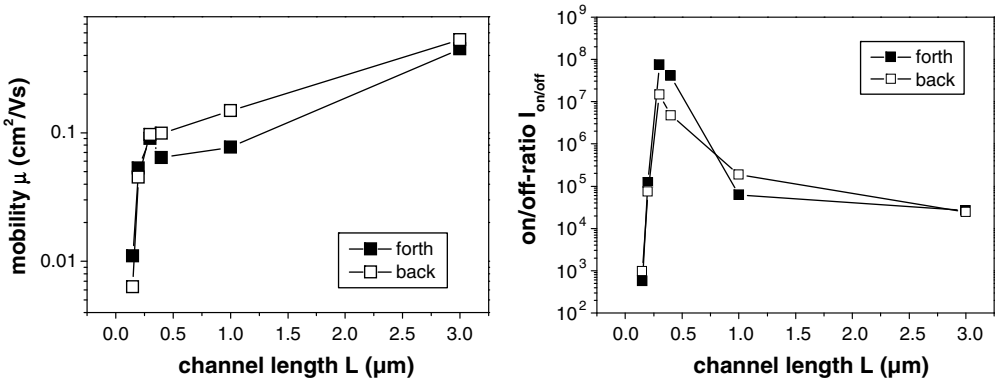

Fig. 8. Dependence of field-effect mobility (left) and on/off-current-ratio (right) of DT-TTF OFETs on 20 nm thick SiO_2 with channel lengths down to 150 nm. Full symbols correspond to values determined from transfer curves measured with increasing gate source voltage, empty ones from curves measured with decreasing voltage.

200 nm show an additional strong decrease of $I_{on/off}$. This behaviour can be attributed to short-channel effects [24,25].

4. Conclusion

We have investigated OFETs based on both DT- and DB-TTF, fabricated by drop casting from solution. These devices reveal an excellent performance and high stability. The field-effect mobility is as high as 3.6 cm^2/V s for DT-TTF, which is the highest value reported for solution-processed DT-TTF. The characteristics are textbook-like, with hardly any hysteresis in *IV*-curves and on/off-ratios of more than 10^6. Using two different approaches we were able two identify band tails and impurity bands dominating the transport at elevated temperature and a low temperature regime with non or low activation of transport. Even at $T = 50$ K the performance is outstanding, both materials exhibiting a mobility of 0.01 cm^2/V s and higher. Further analysis including the correlation between impurity levels and deposition methods or the effect of purification are ongoing.

Acknowledgements

We thank A. Morpurgo for fruitful discussions. This work was supported by the EU Integrated Project NAIMO (No. NMP4-CT-2004-500355), DGI Spain (CTQ2006-06333/BQU) and CIRIT (2005SGR-005951).

References

[1] S.R. Forrest, The path to ubiquitous and low-cost organic electronic appliances on plastic, Nature 428 (2004) 911–918.
[2] G.H. Gelinck, H.E.A. Huitema, E.V. Veenendaal, E. Cantatore, L. Schrijnemakers, J.B.P.H. van der Putten, T.C.T. Geuns, M. Beenhakkers, J.B. Giesbers, B.-H. Huisman, E.J. Meijer, E.M. Benito, F.J. Touwslager, A.W. Marsman, B.J.E. van Rens, D.M. de Leeuw, Flexible active-matrix displays and shift registers based on solution-processed organic transistors, Nature Mater. 3 (2004) 106–110.
[3] I. McCulloch, Thin films: rolling out organic electronics, Nature Mater. 4 (2005) 583–584.
[4] M. Mas-Torrent, C. Rovira, Tetrathiafulvalene derivatives for organic field effect transistors, J. Mater. Chem. 16 (2006) 433–436.
[5] O.D. Jurchescu, J. Baas, T.T.M. Palstra, Effect of impurities on the mobility of single crystal pentacene, Appl. Phys. Lett. 84 (2004) 3061–3063.
[6] V. Podzorov, S.E. Sysoev, E. Loginova, V.M. Pudalov, M.E. Gershenson, Single-crystal organic field effect transistors with the hole mobility ≈8 cm^2/V s, Appl. Phys. Lett. 83 (2003) 3504–3506.
[7] M. Pope, C.E. Swenberg, Electronic Processes in Organic Crystals and Polymers, second ed., University Press, New York, 1999.
[8] M. Mas-Torrent, M. Durkut, P. Hadley, X. Ribas, C. Rovira, High mobility of dithiophene-tetrathiafulvalene single-crystal organic field effect transistors, J. Am. Chem. Soc. 126 (2004) 984–985.
[9] M. Mas-Torrent, P. Hadley, S.T. Bromley, N. Crivillers, J. Veciana, C. Rovira, Single-crystal organic field-effect transistors based on dibenzo-tetrathiafulvalene, Appl. Phys. Lett. 86 (2005) 012110.
[10] S.M. Sze, K.K. Ng, Physics of Semiconductor Devices, third ed., John Wiley and Sons, New York, 2007.
[11] M. Mizumo, M.P. Cava, Organic metals. A study of the Hurtley–Smiles tetrathiafulvalene synthesis, J. Org. Chem. 43 (1978) 416–418.
[12] C. Rovira, J. Veciana, N. Santalo, J. Tarres, J. Cirujeda, E. Molins, J. Llorca, E. Espinosa, Synthesis of several isomeric tetrathiafulvalene π-electron donors with peripheral sulfur atoms. A study of their radical cations, J. Org. Chem. 59 (1994) 3307–3313.
[13] G. Horowitz, R. Hajlaoui, D. Fichou, A.E. Kassmi, Gate voltage dependent mobility of oligothiophene field-effect transistors, J. Appl. Phys. 85 (1999) 3202–3206.
[14] V.Y. Butko, X. Chi, D.V. Lang, A.P. Ramirez, Field-effect transistor on pentacene single crystal, Appl. Phys. Lett. 83 (2003) 4773–4775.
[15] P.G. Le Comber, W.E. Spears, Electronic transport in amorphous silicon films, Phys. Rev. Lett. 25 (1970) 509–511.
[16] J.I. Pankove, Optical Processes in Semiconductors, Dover Publications Inc., New York, 1975.
[17] G.A.N. Connell, in: M.H. Brodsky (Ed.), Amorphous Semiconductors, vol. 36, Springer, New York, 1979.
[18] D.V. Lang, X. Chi, T. Siegrist, A.M. Sergent, A.P. Ramirez, Amorphous-like density of gap states in single-crystal pentacene, Phys. Rev. Lett. 93 (2004) 086802.
[19] M.E. Gershenson, V. Podzorov, A.F. Morpurgo, Colloquium: electronic transport in single-crystal organic transistors, Rev. Mod. Phys. 78 (2006) 973–989.
[20] I.N. Hulea, S. Fratini, H. Xie, C.L. Mulder, N.N. Iossad, G. Rastelli, S. Ciuchi, A.F. Morpurgo, Tunable Fröhlich polarons in organic single-crystal transistors, Nature Mater. 5 (2006) 982.
[21] D.J. Gundlach, L. Zhou, J.A. Nichols, T.N. Jackson, P.V. Necliudov, M.S. Shur, An experimental study of contact effects in organic thin film transistors, J. Appl. Phys. 100 (2006) 024509.
[22] L. Burgi, T.J. Richards, R.H. Friend, H. Sirringhaus, Close look at charge carrier injection in polymer field-effect transistors, J. Appl. Phys. 94 (2003) 6129–6137.
[23] The polynome was chosen with the lowest possible order (6th order). Higher order polynomes can provide a slightly better fit, however, they can create oscillations at the first and last datapoints which cause massive artifacts when the derivative is taken.
[24] J.N. Haddock, X. Zhang, S. Zheng, Q. Zhang, S.R. Marder, B. Kippelen, A comprehensive study of short channel effects in organic field-effect transistors, Org. Electron. 7 (2006) 45–54.
[25] M. Leufgen, U. Bass, T. Muck, T. Borzenko, G. Schmidt, J. Geurts, V. Wagner, L.W. Molenkamp, Optimized sub-micron organic thin-film transistors: the influence of contacts and oxide thickness, Synth. Met. 146 (2004) 341–345.

specific processing additives such as, for example, 1,8-octanedithiol (ODT) or 1,8-di-iodooctane, into the host solvent, the performance of BHJ solar cells was significantly improved [17–19]. Specifically, for BHJ materials comprising the low-band gap polymer, poly[2,6-(4,4-bis-(2-ethylhexyl)-4H-cyclopenta[2,1-b;3,4-b′]dithiophene)-*alt*-4,7-(2,1,3-benzothiadiazole)] (PCPDTBT), and the soluble fullerene, [6,6]-phenyl-C_{71}butyric acid methyl ester ($PC_{71}BM$), the addition of small amounts of ODT as the processing additive increased the power-conversion efficiency of PCPDTBT: $PC_{71}BM$ solar cells by a factor of two from 2.8% to 5.5% [18].

Although BHJ BiFETs are quite different from BHJ solar cell in device structure and device operation, the use of processing additives to control the nanoscale morphology is potentially important because the charge transport of both holes and electrons in BHJ BiFETs is highly dependent on the structure of the bicontinuous networks. Motivated by the success with BHJ solar cells, in this paper we report the results of an initial study of the performance of BiFETs in which the PCPDTBT:$PC_{71}BM$ composite in the channel has been cast from solutions containing the ODT processing additive.

2. Results and discussion

The molecular structures of the low band gap polymer, PCPDTBT, the soluble fullerene, $PC_{71}BM$, and ODT are shown in Fig. 1a–c, respectively. All BHJ BiFETs were fabricated on a heavily doped n-type Si wafer with a 200 nm thick thermally grown SiO_2 layer with bottom contact geometry as shown in Fig. 1d. Based upon our previous studies of BiFETs [20,21], Aluminum (Al) was chosen to enable approximately equivalent injection of electrons (into the LUMO of $PC_{71}BM$) and holes (into the HOMO of PCPDTBT). The channel length (L) and the channel width (W) were L = 10 μm and W = 1000 μm, respectively.

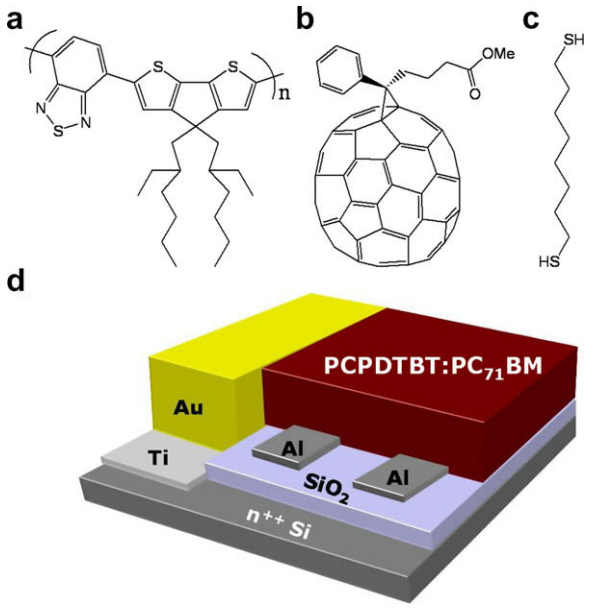

Fig. 1. Molecular structure of (a) PCPDTBT, (b) $PC_{71}BM$ and (c) 1,8-octanedithiol and (d) schematic diagram of a bottom contact bipolar field-effect transistor fabricated with PCPDTBT and; $PC_{71}BM$ mixtures.

Fig. 2 shows atomic force microscope (AFM) images in Fig. 2a and c and transmission electron microscopy (TEM) images in Fig. 2b and d of spin-cast films using blend solutions without in Fig. 2a and b and with in Fig. 2c and d the addition of 2% ODT. The PCPDTBT:$PC_{71}BM$ (1:3 ratio) BHJ films were fabricated using the fully optimized processing procedures reported in previous literature [18]. AFM and TEM images were taken from the films deposited on Si/SiO_2 substrates; details on the process of fabricating samples for TEM measurements are described elsewhere [17]. The typical thickness of the films used for AFM and TEM measurements were 60 nm. For the films obtained from the solution without the ODT additive, the AFM topography exhibits a uniform film consisting of fine, spherical grains; the film was smooth with route-mean-square (RMS) roughness value of 0.5 nm as shown in Fig. 2a. However, distinctive phase segregation morphology was observed in the film cast from solution containing the ODT additive. The grain size increased and the RMS roughness value increased to 1.0 nm, as shown in Fig. 2c.

These changes in nanoscale morphology are confirmed by TEM as shown in Fig. 2b and d. Because of the lower electron density in the polymer (relative to that in the fullerene), polymer-rich regions are the lighter regions in the TEM images [13,22]. The TEM image of the film processed with the ODT additive Fig. 2d shows phase separation clearly with the appearance of interconnected fibers which are surrounded by darker fullerene-rich regions. The TEM images of film processed without the ODT additive Fig. 2b are more finely structured without the elongated structures evident in Fig. 2d.

The fullerene derivatives are soluble in ODT while the conjugated polymers are not soluble in ODT. Thus, as discussed in detail in an earlier publication, the morphology differences observed in films cast with and without the ODT processing additive originates from the selective solubility of ODT [17,23].

To investigate the effects of the better-defined phase segregation on both electron and hole transport, BHJ BiFETs were fabricated using various ratios of PCPDTBT:$PC_{71}BM$ mixtures from 1:1 to 1:4. All transport curves are typical of BHJ BiFETs as shown in Fig. 3. The current enhancement with negative gate bias (V_{gs}) indicates hole transport (p-type mode), while the current enhancement with positive V_{gs} indicates electron transport (n-type mode). For the BiFET in which the BHJ material was cast from solutions without the use of the ODT processing additive Fig. 3a, the hole and electron currents systematically change as the PCPDTBT and $PC_{71}BM$ ratio is increased from 1:1 to 1:4. These changes in the hole and electron currents are not unexpected because, for example, a continuous network for electron transport can be formed more easily in the blend which has a higher volume percent of $PC_{71}BM$.

The corresponding changes in the hole and electron mobilities are shown in Fig. 3b [24]. The hole mobility increases and the electron mobility decreases as the volume fraction of PCPDTBT is increased. Balanced hole and electron mobilities were attained for the 1:3 ratio. In general,

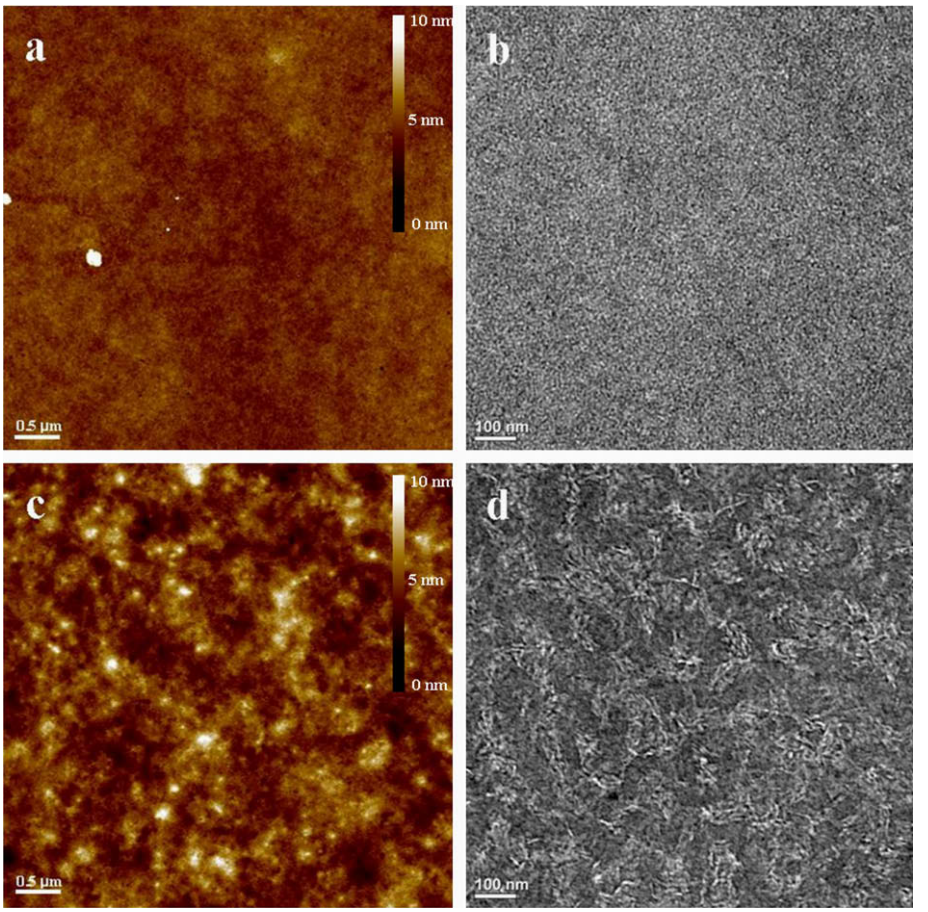

Fig. 2. Atomic force microscope (AFM) and transmission electron microscopy (TEM) images of spin-coated films cast from PCPDTBT and $PC_{71}BM$ blend solutions. (a) AFM image of the film without ODT processing, (b) TEM image of the without ODT processing, (c) AFM image of the film with ODT processing and (d) TEM image of the film with ODT processing.

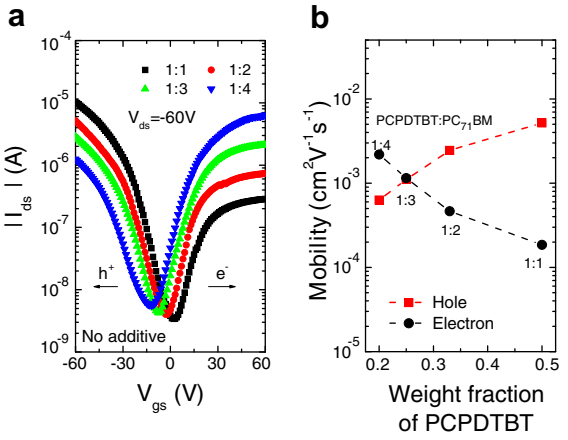

Fig. 3. (a) Transport characteristics and (b) hole and electron mobilities of the BiFETs fabricated without ODT additive with various PCPDTBT:$PC_{71}BM$ ratios.

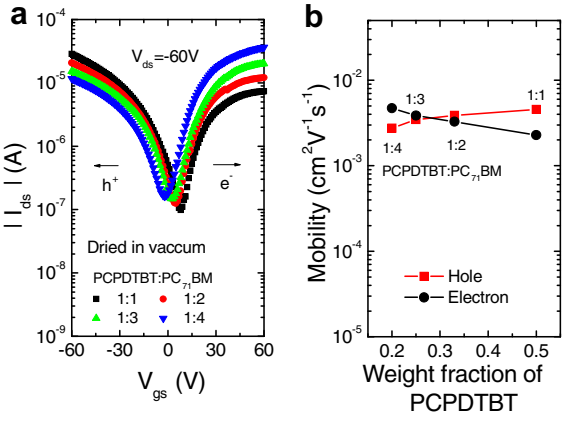

Fig. 4. (a) Transport characteristics and (b) hole and electron mobilities of the vacuum dried BiFETs fabricated with various PCPDTBT; $PC_{71}BM$ ratios processed with OTD and dried in vacuum.

balance of the hole and electron mobilities in BiFET is closely correlated with the efficiency of solar cell devices [25,26]. The most efficient solar cell fabricated with the PCPDTBT:$PC_{71}BM$ BHJ material was obtained from this volume ratio [27].

Processing with the ODT additive caused significant enhancement in the transport performance of the BiFETs. Fig. 4 shows transport characteristics (Fig. 4a) and mobility plots (Fig. 4b) obtained from BiFETs fabricated using PCPDTBT:$PC_{71}BM$ BHJ films processed with the ODT additive. Prior to measurement, all devices were kept in high vacuum (>10^{-6} torr) for 2 h to remove remaining solvent and any residual ODT additive. The ODT processing additive helps to create improved the connectivity on the phase separated bicontinuous networks. As shown in Fig. 2, there is evidence of more complete phase separation. As a result, both hole and electron mobilities are increased. Balanced hole and electron mobilities were attained at PCPDTBT:$PC_{71}BM$ ratios between 1:2 and 1:3. This is consistent with the results obtained from the solar cell measurements; the most efficient solar cell devices are obtained with ratios within the 1:2–1:3 regime [18]. In addition, use of the ODT processing additive causes the mobility values to become relatively insensitive to the ratio of PCPDTBT and $PC_{71}BM$.

In order to obtain such enhanced bipolar transport properties (higher mobilities for both holes and electrons) with ODT processing, the most important procedure during the fabrication is the vacuum drying step after deposition of active layer. Fig. 5 shows the transport characteristics (Fig. 5a) and hole/electron mobilities (Fig. 5b) of BiFET with ODT processing and without vacuum drying. The electron mobilities were significantly improved and are relatively insensitive to the PCPDTBT:$PC_{71}BM$ ratio. The hole mobilities, however, decreased by nearly an order of magnitude. Moreover, there is no possibility of obtaining balanced transport with such widely different mobilities. This result is consistent with the initial FET results that were presented as supplementary information in Ref. [18].

Residual ODT in the semiconductor layer appears to be the cause of the decrease in hole mobility. Moreover, it is known that sulphur in dithiol can attract holes (function as a hole trap) due to its proton-acceptor capability [28]. To confirm this point, we have investigated the infrared (IR) absorption spectra as shown in Fig. 6. The IR spectrum

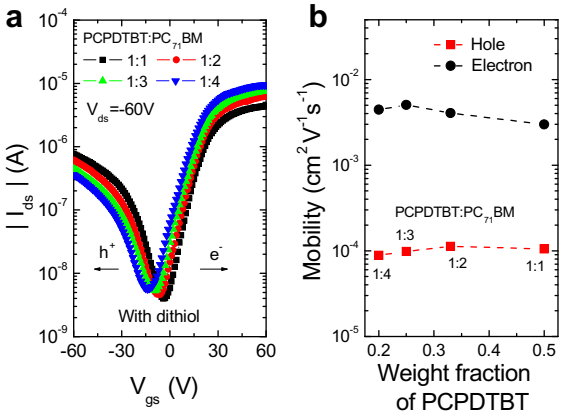

Fig. 5. (a) Transport characteristics and (b) hole and electron mobilities of the as-prepared (without vacuum drying) BiFETs fabricated with various PCPDTBT:$PC_{71}BM$ ratios and processed with OTD; see text.

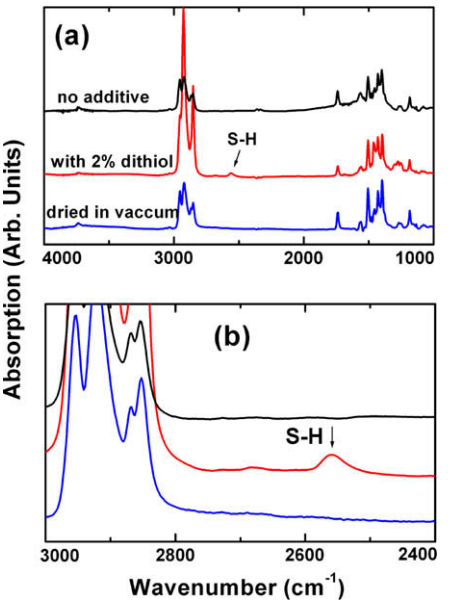

Fig. 6. (a) Infra-red (IR) absorption spectra obtained from a PCPDTBT:$PC_{71}BM$ film (1:1 ratio) with/without ODT processing and with/without vacuum drying. (b) Absorption spectra in the spectral range between 2400 cm^{-1} and 3000 cm^{-1} shown on an extended scale.

obtained from 1:1 mixture film processed with ODT shows weak absorption at 2560 cm^{-1} (see the detail absorption spectra between 2400 cm^{-1} and 3000 cm^{-1} on an extended scale as shown in Fig. 6b. The weak absorption peak appearing at 2560 cm^{-1} is associated with the stretch vibrational mode of S–H [29,30]. The existence of this peak directly indicates that ODT still remains in the mixture.

Since ODT has high boiling point (ca. 270 °C), exposure to high temperature is required in order to remove from mixture film by normal heat drying. The heat drying method, however, cannot be applied to the PCPDTBT and $PC_{71}BM$ mixture because drying at such high temperature degrades the PCPDTBT:$PC_{71}BM$ BHJ material. Thus, in order to remove ODT from the mixture, the films were dried in high vacuum (>10^{-6} torr). As demonstrated by the IR absorption spectra, vacuum drying successfully removes residual ODT from the PCPDTBT:$PC_{71}BM$ BHJ films (the S-H vibration peak completely disappears from IR absorption spectra; see Fig. 6). We conclude that residual ODT in the PCPDTBT:$PC_{71}BM$ BHJ films functions as a hole trap and thereby degrades the hole mobility. Consequently, vacuum dried BiFET shows enhanced transport properties.

3. Conclusions

In conclusion, we have demonstrated that bipolar FETs can be fabricated using various ratios PCPDTBT and $PC_{71}BM$ processed with ODT. ODT processing improves the nanoscale morphology with more complete phase separation of the components. As a result, both hole and electron mobilities are improved in bipolar FETs processed with ODT. Moreover, because of the well-defined phase

separation, the hole and electron mobilities become relatively insensitive on the ratio of p-type PCPDTBT and n-type $PC_{71}BM$. If, however, the ODT is not completely removed from the BHJ films, the hole mobility decreased by an order of magnitude, implying that residual ODT functions as a hole trap. Finally, we find that after removal of residual ODT, the PCPDTBT:$PC_{71}BM$ ratio at which the hole and electron mobility are balanced, is the same ratio required for solar cell performance (maximum efficiency) optimization.

4. Experimental

All FET structures were fabricated on a heavily doped n-type Si wafers with a 200 nm thick thermally grown SiO_2 layer; the highly doped n-type Si functioned as the gate electrode and the SiO_2 functioned as the gate dielectric insulator. Source and drain electrodes (Al) with 50 nm thickness were deposited onto the SiO_2 by e-beam evaporation; the electrodes were patterned using standard photolithographic methods. All FET devices were made with bottom contact geometry. The channel length of the devices was 10 μm and the channel width was 1 mm. Before deposition of the PCPDTBT and $PC_{71}BM$ bulk heterojunction films, the Al electrodes were etched with standard aluminum etchant to remove the aluminum oxide layer.

Active layers were deposited by spin-casting at 3000 rpm for 60 sec from a chlorobenzene solution containing various ratios PCPDTBT and $PC_{71}BM$ (from 1:1 to 1:4) with a concentration of 0.5 wt% (on the basis of PCPDTBT weight) either with 2.0 vol% ODT additives. The thickness of the active layer was around 60 nm. After active layer deposition, mild thermal treatment was carried out on a calibrated and stabilized hot plate under N_2 atmosphere at 80 °C for 15 min. All fabrication processes were carried out in the glove box filled with N_2. Electrical characterization was performed using a Keithley semiconductor parametric analyzer (Keithley 4200) under N_2 atmosphere.

Acknowledgements

This work was supported by the Heeger Center for Advanced Materials at the Gwangju Institute of Science and Technology and by the Global Research Laboratory Program of the Korean Government (M60605000005-06A0500-00510).

References

[1] E.J. Meijer, D.M. De Leeuw, S. Setayesh, E.V. Veenendaal, B.–H. Huisman, P.W.M. Blom, J.C. Hummelen, U. Scherf, T.M. Klapwijk, Nature Mater. 2 (2003) 678.
[2] Z. Bao, J. Locklin (Eds.), Organic field-effect transistors, CRC Press, Boca Raton, FL, 2007.
[3] B. Crone, A. Dodabalapur, Y.-Y. Lin, R.W. Filas, Z. Bao, A. LaDuca, R. Sarpeshkar, H.E. Katz, W. Li, Nature 403 (2000) 521.
[4] H. Sirringhaus, N. Tessler, R.H. Friend, Science 280 (1998) 1741.
[5] C.D. Dimitrakopoulos, P.R.L. Malenfant, Adv. Mater. 14 (2002) 99.
[6] A. Babel, S.A. Jenekhe, Adv. Mater. 14 (2002) 371.
[7] R.C. Haddon, A.S. Perel, R.C. Morris, T.T.M. Palstra, A.F. Hebard, R.M. Fleming, Appl. Phys. Lett. 67 (1995) 121.
[8] Y. Hayashi, H. Kanamori, I. Yamada, A. Takasu, S. Takagi, K. Kaneko, Appl. Phys. Lett. 86 (2005) 052104.
[9] K. Tada, H. Harada, K. Yoshino, Jpn. J. Appl. Phys. Part 2 36 (1997) L718.
[10] A. Babel, J.D. Wind, S.A. Jenekhe, Adv. Funct. Mater. 14 (2004) 891.
[11] W. Ma, A. Gopinathan, A.J. Heeger, Adv. Mater. 19 (2007) 3656.
[12] S. Cho, M. Surin, J. Yuen, G. Wang, R. Lazzaroni, D. Moses, K. Lee, A.J. Heeger, J. Appl. Phys. 100 (2006) 114503.
[13] W. Ma, C.Y. Yang, X. Gong, K. Lee, A.J. Heeger, Adv. Funct. Mater. 15 (2005) 1617.
[14] K. Kim, J. Liu, M.A.G. Namboothiry, D.L. Carroll, Appl. Phys. Lett. 90 (2007) 163511.
[15] F. Padinger, R.S. Rittberger, N.S. Sariciftci, Adv. Funct. Mater. 13 (2003) 85.
[16] H. Hoppe, N. Arnold, D. Meissner, N.S. Sariciftci, Thin Solid Films 451 (2004) 589.
[17] J.K. Lee, W. Ma, C.J. Brabec, J. Yuen, J.S. Moon, J.Y. Kim, K. Lee, G.C. Bazan, A.J. Heeger, J. Am. Chem. Soc. 130 (2008) 3619.
[18] J. Peet, J.Y. Kim, N.E. Coates, W.L. Ma, D. Moses, A.J. Heeger, G.C. Bazan, Nature Materials 6 (2007) 497.
[19] J. Peet, C. Soci, R.C. Coffin, T.Q. Nguyen, A. Mikhailovsky, D. Moses, G.C. Bazan, Appl. Phys. Lett. 89 (2007) 252105.
[20] S. Cho, J. Yuen, J.Y. Kim, K. Lee, A.J. Heeger, Appl. Phys. Lett. 89 (2006) 153505.
[21] S. Cho, J. Yuen, J.Y. Kim, K. Lee, A.J. Heeger, Appl. Phys. Lett. 90 (2007) 063511.
[22] X. Yang, J. Loos, S.C. Veenstra, W.J.H. Verhees, M.M. Wienk, J.M. Kroon, M.A.J. Michels, R.A.J. Janssen, Nano Lett. 5 (2005) 579.
[23] J.K. Lee, N.E. Coates, S. Cho, N.S. Cho, D. Moses, G.C. Bazan, K. Lee, A.J. Heeger, Appl. Phys. Lett. 92 (2008) 243308.
[24] These mobilities are calculated from the linear plot of $I^{1/2}$ vs. V_{gs} deduced from the measurements of the I_{ds} vs. V_{gs} using the the standard FET relation; $I_{ds}=(WC_i/2L)\,\mu(V_{gs}-V_T)^2$ where W (=1 mm) is the channel width, and L (=10 μm) is the channel length of the devices.
[25] J. Nakamura, K. Murata, K. Takahashi, Appl. Phys. Lett. 87 (2005) 132105.
[26] E. Hauff, J. Parisi, V. Dyakonov, J. Appl. Phys. 100 (2006) 043702.
[27] D. Mühlbacher, M. Scharber, M. Morana, Z. Zhu, D. Waller, R. Gaudiana, C. Brabec, Adv. Mater. 18 (2006) 2884.
[28] D.P. Long, J.L. Lazorcik, B.A. Mantooth, M.H. Moore, M.A. Ratner, A. Troisi, Y. Yao, J.W. Ciszek, J.M. Tour, R. Shashidhar, Nature Mater. 5 (2006) 901.
[29] E. Pretsch, B. Bühlmann, C. Affolter, Structural Determination of Organic Compounds, Springer, New York, 2000.
[30] R.M. Silverstein, F.X. Webster, D.J. Kiemle, Spectrometric Identification of Organic Compounds, Wiley, New York, 2005.

with a low bias and a color-saturated emission. It is worth attention that blue TEOLEDs reported recently almost use the Ag/ITO bilayer [6,8–9] as the anode, where Ag is used as the reflective anode and the resonant wavelength of the blue emission can be achieved by adjusting the ITO thickness. Chin et al. [10] reported blue TEOLEDs with the Ag/ITO anode in which the ITO thickness was fixed and the optical length in the cavity was adjusted by altering the thickness of the hole transporting layer. In our work, we find out that the reflectivity (R) of the semitransparent Sm/Ag cathode changes to a minimum value and then increases with the thickness of the 2,9-dimethyl-4,7-diphenyl-1,10-phenanthroline (BCP) layer, where the BCP layer is utilized as a light outcoupling layer. Hence, in this letter we fabricate a blue TEOLED onto the SiO_2-covered Si substrate with Sm/Ag as the cathode and the BCP layer as the light outcoupling layer. With this structure, TEOLEDs can be driven by the TFT circuits fabricated in the Si substrate. It is especially worth mentioning that the total thickness (100 nm) of organic materials sandwiched between the cathode and the anode in this TEOLED is almost same with that in a conventional BEOLED. To obtain a blue emission, the thickness of the BCP layer is designed to reach a minimum R of the cathode that means a weak multiple-beam interference occurred in the TEOLED.

2. Theory calculation

In a cavity device, both wide-angle interference and multiple-beam interference contribute to the EL spectra. For wide-angle interference there is interference between directly emitted light and reflected light that have the same wave vector, and the distance between the emission region and the reflective electrode plays an important role. Multiple-beam interference takes place when the radiation is reflected back and forth between the two electrodes.

Here, the resonant wavelength that corresponds to multiple-beam interference can be calculated with the Eq. (1) [11]

$$2\pi\left(\frac{2nd\cos\theta}{\lambda}\right) - \Phi_1(\lambda) - \Phi_2(\lambda) = 2k\pi, \tag{1}$$

where n is the refractive index of the organic layer, d is the physical thickness of the organic layer, θ is an angle in the spacer layer (Here, 0° is perpendicular to the electrode plane), λ is the resonant wavelength, $\Phi_1(\lambda)$ and $\Phi_2(\lambda)$ are the phase changes on reflection corresponding to the effective reflectivities R_1 and R_2 at the interfaces of the opaque anode/organic material and the organic material/semitransparent cathode, respectively, and k is the mode number.

In a TEOLED, when wide-angle interference is only taken into account, Eq. (1) can be simplified by ignoring $\Phi_2(\lambda)$ and only the organic layers between the emission area and the reflective anode are under consideration.

In Eq. (1), when $\theta \neq 0^0$ $\Phi_1(\lambda)$ and $\Phi_2(\lambda)$ show different values for P and S polarization, which can be calculated with the Eqs. 2 and 3, as follows [12]:

$$\Phi_{1,2}(\lambda) = \mathrm{arctg}\left(\frac{2n_0 B\cos\theta_0}{n_0^2\cos^2\theta_0 A^2 B^2}\right) \quad (\text{for } S \text{ polarization}), \tag{2}$$

$$\Phi_{1,2}(\lambda) = \mathrm{arctg}\left[\frac{2n_0\cos\theta_0\left[2N_m K_m A - B(N_m^2 K_m^2)\right]}{n_0^2(A^2+B^2) - \cos^2\theta_0(N_m^2+K_m^2)^2}\right] \quad (\text{for } P \text{ polarization}). \tag{3}$$

The above phase changes on reflection originate from the calculation of the reflectivity of the electrodes. $\Phi_1(\lambda)$ and $\Phi_2(\lambda)$ show different track under consideration of the polarization state.

For P polarization [12],

$$\eta_P = N/\cos\theta, \tag{4}$$

$$R_P = \left(|r_P|e^{j\Phi_P}\right)^2 = \left(\frac{\eta_{0P}-\eta_{1P}}{\eta_{0P}+\eta_{1P}}\right)\left(\frac{\eta_{0P}-\eta_{1P}}{\eta_{0P}+\eta_{1P}}\right)^* = \left(\frac{n_0\cos\theta_1 - N_1\cos\theta_0}{n_0\cos\theta_1 + N_1\cos\theta_0}\right)\left(\frac{n_0\cos\theta_1 - N_1\cos\theta_0}{n_0\cos\theta_1 + N_1\cos\theta_0}\right)^*. \tag{5}$$

For S polarization [12],

$$\eta_S = N/\cos\theta, \tag{6}$$

$$R_S = \left(|r_S|e^{j\Phi_S}\right)^2 = \left(\frac{\eta_{0S}-\eta_{1S}}{\eta_{0S}+\eta_{1S}}\right)\left(\frac{\eta_{0S}-\eta_{1S}}{\eta_{0S}+\eta_{1S}}\right)^* = \left(\frac{n_0\cos\theta_0 - N_1\cos\theta_1}{n_0\cos\theta_0 + N_1\cos\theta_1}\right)\left(\frac{n_0\cos\theta_0 - N_1\cos\theta_1}{n_0\cos\theta_0 + N_1\cos\theta_1}\right)^*. \tag{7}$$

Here r_P and r_S are the complex Fresnel coefficients for reflection of a wave that correspond P and S polarization, R_P and R_S are the energy reflection coefficients or the so-called reflectivities, n_0 and N_1 denote the refractive indices of the organic layer adjacent to the electrode and the electrode, where $N_1 = N_m - jK_m$ is the complex refractive index and $N_1\cos\theta_1 = A - jB$, and θ_0 and θ_1 are input and output angles in the organic and metal layers.

3. Experimental

The blue emission TEOLED is grown on Si substrates precoated with a 1600 nm thick SiO_2 layer. Prior to the device deposition, the substrates are cleaned with acetone and ethanol by using an ultrasonic bath, rinsed with deionized water, and then dried in an oven. The TEOLED architectures are Ag (100 nm)/Ag_2O (UV-ozone for 30 s)/4,4′, 4″-tris(3-methylphenylphenylamino) triphenylamine (*m*-MTDATA, 45 nm)/ 4,4′-bis[*N*-(1-naphthyl-1-)-*N*-phenyl-amino]-biphenyl (NPB, 5 nm)/4,4′-bis(2,2′-diphenylvinyl)-1,1′-biphenyl (DPVBi, 30 nm)/tris-(8-hydroxylquinoline) aluminum (Alq_3, 20 nm)/LiF (1 nm)/cathode [the Sm (11 nm)/Ag (12 nm) cathode for device A, and the BCP layer onto the SmAg cathode for device B], as shown in Fig. 1. Here, *m*-MTDATA, NPB, DPVBi and Alq_3 are utilized as a hole-injection layer, a hole-transporting layer, a blue emissive layer, and an electron-transporting layer, respectively. Sm is utilized because of both a low work function of ~2.7 eV and a relatively high transparence. All depositions are in a high vacuum above 10^{-6} Torr with a rate of 0.1–0.3 nm/s. The current–voltage–luminance characteristics are measured with a programmable

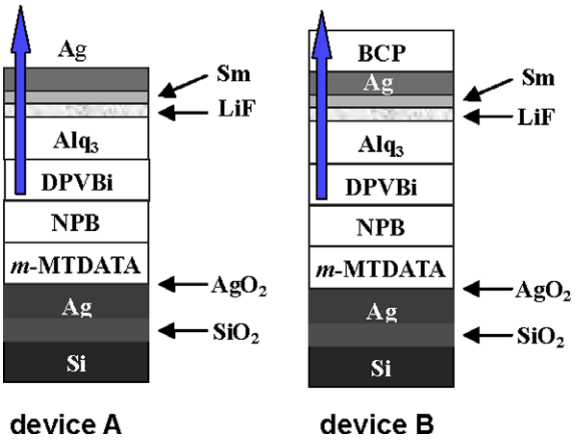

Fig. 1. Schematic illustration of devices A and B.

Keithley Model 2400 and a Photo-Research PR-650 SpectraScan Colorimeter in room-temperature air. Optical constants of the organic materials used in the work are measured with variable angle spectroscopic ellipsometry.

4. Results and discussion

The transmittivity (T) and R curves of the devices are calculated with the transfer matrix theory [13]. Here, the excitons that formed predominantly on the blue DPVBi layer are supposed to be near the DPVBi/NPB interface. The generated emission passes through DPVBi (30 nm)/Alq_3 (20 nm)/LiF (1 nm)/Sm (11 nm)/Ag (12 nm)/BCP (if with) and then escapes from the TEOLED, where the thin film of LiF is neglected. The T and R curves are shown in Fig. 2. Without the BCP layer, the maximum T value is 47% at 440 nm, while the R value is 15.6%. With the thickness of the BCP layer increases to 35–40 nm, T reaches the maximum value of 59.4% (BCP: 35 nm) and 61.4% (BCP: 40 nm) at the wavelength of 460 nm, around the emissive peak of DPVBi (~464 nm), where R is 6.7% (35 nm) and 7.4% (40 nm), respectively. Here, the microcavity effect caused by multiple-beam interference is expected as weak as possible in order to obtain a blue emission. So, the BCP thickness that we employ is controlled to be 35 nm.

Normally, multiple-beam interference mainly controls the shape of the EL spectra when the two electrodes have high reflectivities, while both multiple-beam and wide-angle interference contribute to the EL spectra when one electrode has a high reflectivity and the other one has a low reflectivity. In our paper, the low cathode reflection of devices A and B, especially for device B, may correspond to a weak multiple-beam interference and a main wide-angle interference. From Fig. 3a, the EL spectra of device A show a main peak of 468 nm with a shoulder of ~575 nm. Compared with the calculated result of the resonant wavelengths of 571 nm and 452 nm for multiple-beam and wide-angle interference, respectively, we can deduct the shoulder (~575 nm) primarily caused by multiple-beam interference, which mainly attributes to the reflection of the SmAg cathode (20.7–30.8% at the wavelength range of 500–600 nm). While the main peak at

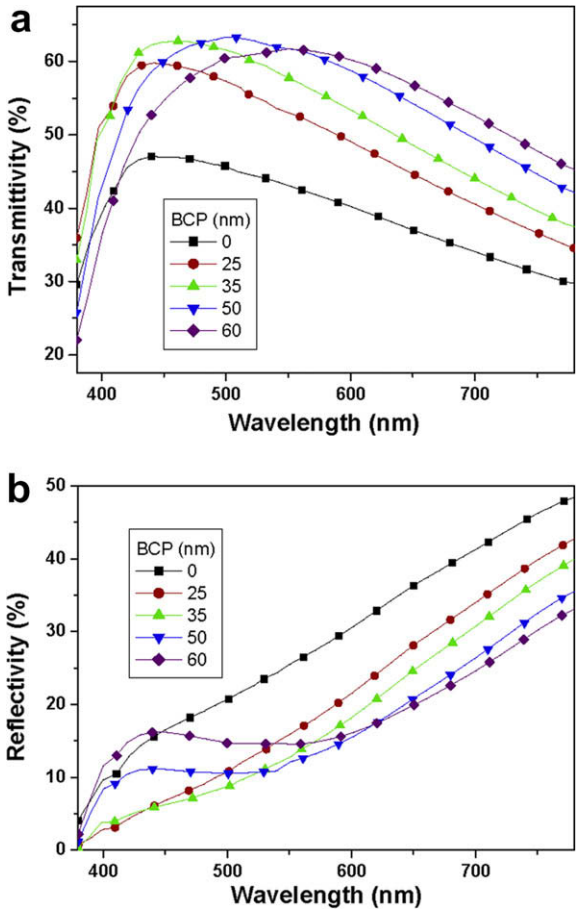

Fig. 2. Transmittivity (a) and reflectivity (b) characteristics of the DPVBi (30 nm)/Alq_3 (20 nm)/Sm (11 nm)/Ag (12 nm)/BCP/air multilayer system. Here, the thickness of the BCP layer is adjusted from 0 nm to 60 nm.

468 nm in Fig. 3a originates from the native emission of DPVBi. The resonant wavelength (452 nm) based on wide-angle interference is not obvious in this device. Device B exhibits the EL spectra with two peaks of 456 nm and 468 nm and the full width at half maximum (FWHM) of 112 nm, indicating a very weak multiple-beam interference and a relatively strong wide-angle interference (the 456 nm peak in the EL spectra may correspond to the 452 nm peak from wide-angle interference).

As can be seen in the inset of Fig. 3a, the shoulder leads to the Commission International de L'Eclairage (CIE) coordinates of (0.243, 0.315) at 6 V for device A, which locate in the white light area. When the bias increases to 17 V, the CIE coordinates shift to (0.223, 0.270) and the emission shows the greenish blue light. While in device B the blue emission show a saturated color, corresponding to CIE coordinates of (0.201, 0.263)–(0.173, 0.199) from 6 V to 17 V, which is comparative with the chromaticity coordinates of (0.165, 0.169) in the BEOLED reported by Xie [14]. This can be attributed to the suppression of multiple-beam interference together with the utilization of wide-angle interference accompanying with the BCP cover onto the SmAg semitransparent cathode.

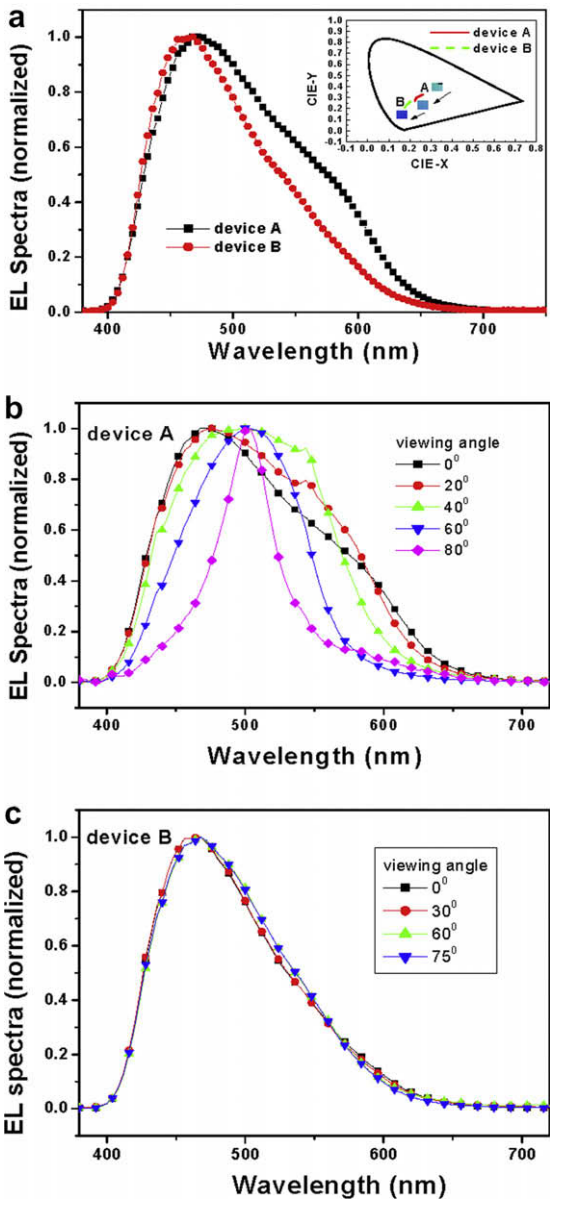

Fig. 3. (a) The EL spectra of devices A and B, and changes of the EL spectra for devices A (b) and B (c) with the viewing angle. Inset is the changes of the CIE co-ordinates for devices A and B with the bias.

We observe the EL spectra of devices A and B by changing the viewing angle from 0° to 80°, as shown in Fig. 3b and c. Here, 0° means the viewing angle is normal to the electrode surface. The main peak of device A generates a redshift of 36 nm, from 468 nm to 504 nm, obviously different from the blueshift in normal TEOLEDs [14]. The spectra are investigated with the Eqs. (1)–(3) by considering phase changes of the electrodes on reflection together with the reduction of the effective optical cavity length with a concomitantly larger viewing angle [11]. The calculated results about phase changes on reflection are shown in Fig. 4. The phase changes on reflection with *P* or *S* polarization show obvious difference when the angle is larger than 0°. Dependence of the reflectivity of the cathode and the anode for devices A and B on incident angle are shown in Fig. 5. When the angle deviates from 0°, the reflection for *P* and *S* polarization shows disparate track. As a result, a higher input angle brings a higher reflection, leading to a stronger microcavity effect. In device A, when the angle increases up to 80°, high cathode reflectivities of larger than 80% for both *P* and *S* polarization lead to significantly narrow EL spectra with the FWHM of only 44 nm. Here, the EL spectra are mainly affected by multiple-beam interference. We can also calculate the resonant peak under different angles with the Eqs. (1)–(3). From the result, the resonant wavelengths for *P* and *S* polarization at 40° are 526 nm and 483 nm in device A and their superposition contributes to the EL spectra with a main peak around 500 nm. For comparison, the BCP-covered TEOLED (device B) exhibits stable EL spectra from 0° to 75° due to weak microcavity effects, mainly decided by the relatively low reflectivity of the cathode.

Fig. 6a indicates luminance-current density–voltage (*L*–*J*–*V*) characteristics for devices A and B. The additive attachment of the BCP layer onto the SmAg cathode brings no effect on the injected current, shown as similar *I*–*V* curves. However, from Fig. 6b, the maximum *L* in device B is 28167 cd/m^2 at 18 V, which is 1.3 times higher than 21510 cd/m^2 (at 18 V) in device A. The current efficiency

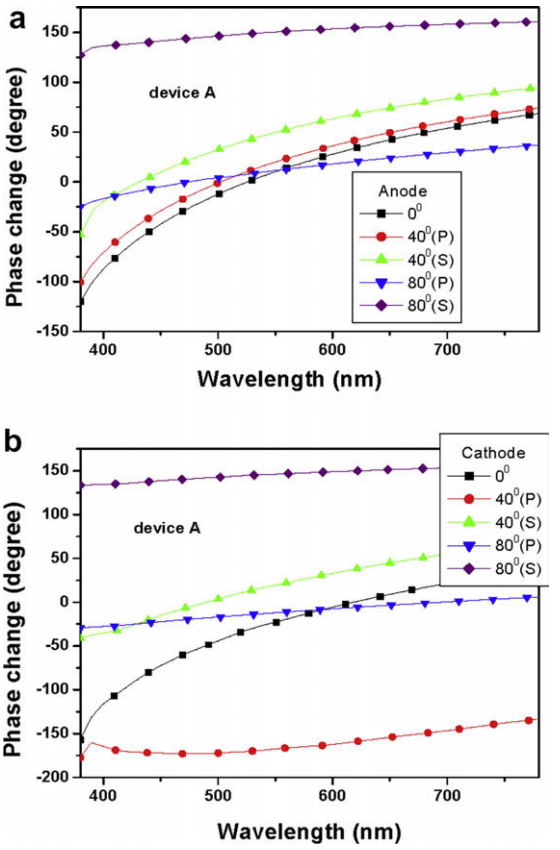

Fig. 4. Phase changes on reflection of the anode (a) and the cathode (b) for device A with changed incident angles.

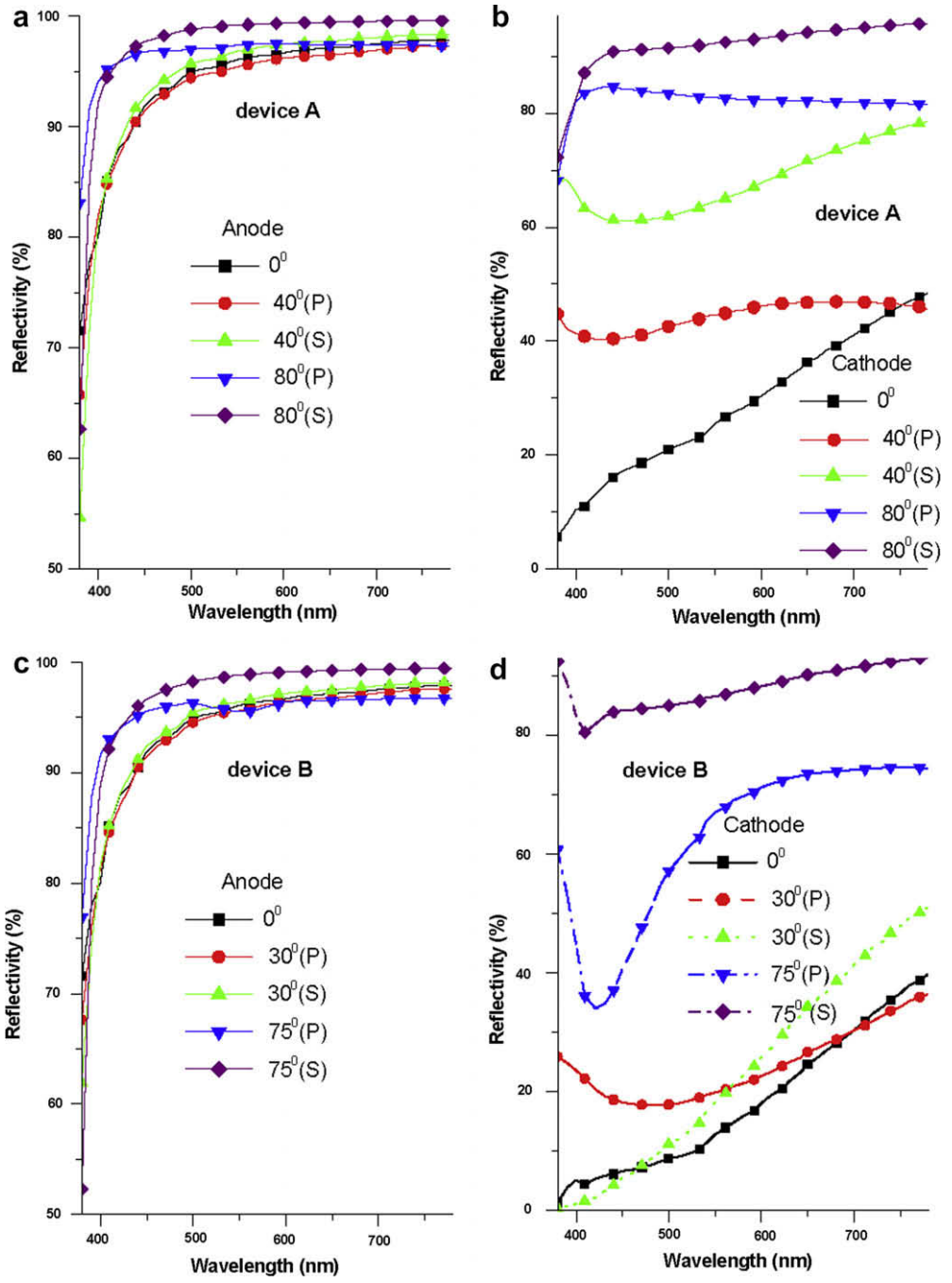

Fig. 5. Anode (a) and cathode (b) reflectivities of device A under different incident angles, and anode (c) and cathode (d) reflectivities of device B under different incident angles. The *P* and *S* polarization under variational angles show large difference.

of device B reaches 4.36 cd/A at 7 V, 1.46 times higher than that of device A.

5. Conclusion

In conclusion, we fabricate blue emission TEOLEDs based on DPVBi. Different from the conventional TEOLEDs that use ITO as a thickness adjustment layer to make the cavity length matchable with the resonant wavelength of the blue light, in this letter we construct the blue emission TEOLED with the organic compound BCP as a light outcoupling layer. With the proper thickness of the BCP layer to reduce the reflectivity of the Sm/Ag cathode, the blue emission can be obtained by suppressing multiple-beam interference to a maximum degree and utilizing wide-angle interference. The chromaticity of the blue emission in the

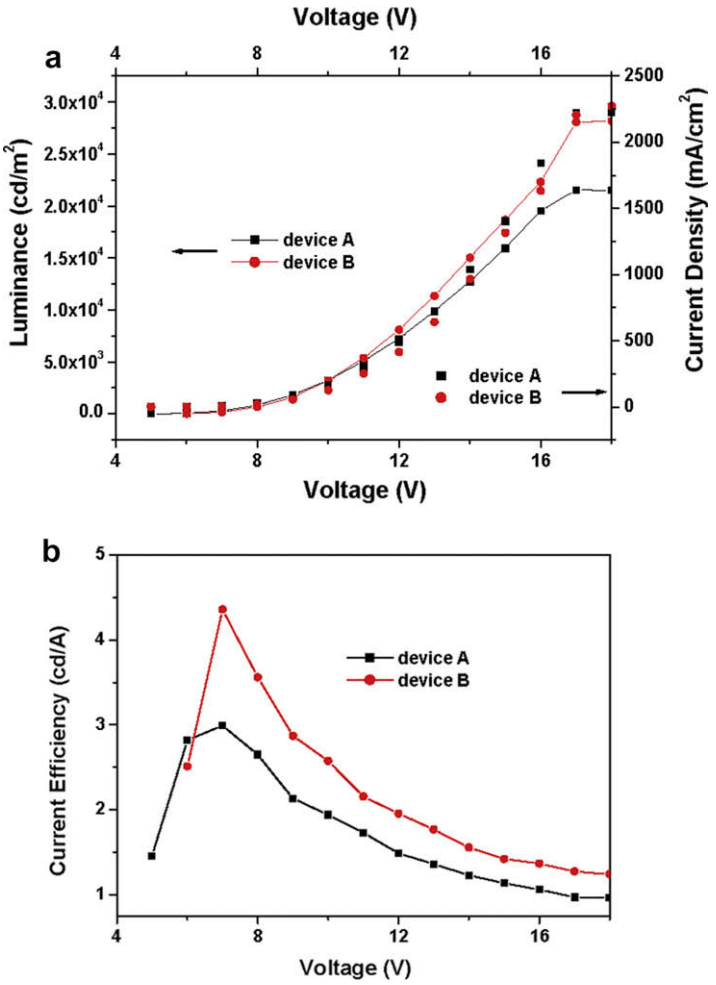

Fig. 6. *L–J–V* characteristics (a) and current efficiency curves (b) for devices A and B.

TEOLED is saturated with the CIE coordinates of (0.201, 0.263)–(0.173, 0.199) from 6 V to 17 V, comparative to that from the BEOLED. In addition, the blue emission shows stable spectra when the viewing angle alters from 0° to 75°.

Acknowledgments

This work has been supported by the Research Foundation of Nanjing University of Posts and Telecommunications under Grant no. NY207038.

References

[1] H. Riel, S. Karg, T. Beierlein, B. Ruhstaller, W. Rieß, Appl. Phys. Lett. 82 (2003) 466.
[2] C.J. Lee, R.B. Pode, J.I. Han, D.G. Moon, Appl. Phys. Lett. 89 (2006) 123501.
[3] Z. Xie, L.-S. Hung, F. Zhu, Chem. Phys. Lett. 381 (2003) 691.
[4] S. Han, X. Feng, Z.H. Lu, D. Johnson, R. Wood, Appl. Phys. Lett. 82 (2003) 2715.
[5] B.D. Lee, Y.-H. Cho, W.-J. Kim, M.H. Oh, J.H. Lee, D.S. Zang, Appl. Phys. Lett. 90 (2007) 103518.
[6] S.-F. Hsu, C.-C. Lee, A.T. Hu, C.-H. Chen, Curr. Appl. Phys. 4 (2004) 663.
[7] S. Chen, Z. Zhao, Z. Jie, W. Xie, Y. Zhao, R. Song, C. Li, S. Liu, J. Phys. D: Appl. Phys. 39 (2006) 3738.
[8] S.-F. Hsu, C.-C. Lee, S.-W. Hwang, H.-H. Chen, C.-H. Chen, A.T. Hu, Thin Solid Films 478 (2005) 271.
[9] J. Cao, X. Liu, M.A. Khan, W.Q. Zhu, X.Y. Jiang, Z.L. Zhang, S.H. Xu, Curr. Appl. Phys. 7 (2007) 300.
[10] B.D. Chin, J. Phys. D: Appl. Phys. 40 (2007) 5541.
[11] B.Y. Jung, N.Y. Kim, C. Lee, C.K. Hwangbo, C. Seoul, Appl. Opt. 41 (2002) 3312.
[12] Y.C. Lin, W.Q. Lu, Optics Theory of Thin Films, National Defence and Industry Press, Beijing, 1990. p. 63.
[13] S. Chen, W. Xie, Y. Meng, P. Chen, Y. Zhao, S. Liu, J. Appl. Phys. 103 (2008) 054506.
[14] W. Xie, Z. Wu, S. Liu, S.T. Lee, J. Phys. D: Appl. Phys. 36 (2003) 2331.

made to resolve the interface problems but these involved only cathode or anode.

In this paper, we present a method for improving the efficiency of the charge carrier injection at both electrodes of inverted TOLED. In this method, a BOLED is first fabricated on a flexible sheet. This BOLED as a whole is then transferred to a glass substrate to fabricate an inverted TOLED or ITOLED. In fact, a whole device transfer of an optimized BOLED is utilized for the fabrication of ITOLED.

We were motivated by our earlier work [13] on a bilayer transfer and the fact that a whole device can be transferred [14]. More motivating, however, was the fact that the bottom emitting OLEDs or BOLEDs are well established already in terms of materials and layer configurations because of the extensive studies carried out over the last 20 years. Therefore, the optimized results obtained through the studies can fully be taken advantage of since the ITOLED fabrication in this work involves a simple transfer of fully fabricated BOLEDs.

A schematic illustration of the ITOLED fabrication is given in Fig. 1. The mold material used for this work is poly(urethaneacrylate) (PUA) [15]. The mold properties are such that it is rigid enough to withstand the pressure applied and yet flexible enough in its film form for large area applications [16]. Onto a flat PUA mold with poly(ethyleneterephthalate) (PET) as a backing plane, a thin Teflon film (AF2400, DuPont, ~100 nm) is spin-coated to lower the surface energy. Gold is then deposited onto the Teflon coated mold by thermal evaporation under vacuum ($<10^{-6}$ Torr) followed by depositions of NPB, Alq_3, LiF, and Al cathode in succession. The device thus fabricated is a well-established, optimized green BOLED. The whole device on the flat mold is then brought into contact with a glass substrate, as shown in Fig. 1. A pressure of 0.5 MPa is applied at 50 °C for several minutes. When the flat mold is removed after cooling and relieving the pressure, the whole device on the flat mold is transferred onto the substrate. Prior to the transfer, the substrate surface is cleaned by sequential sonication in trichloroethylene, acetone, and *iso*-propyl alcohol and then it is spin coated with a 100 nm thick poly(methyl methacrylate) (PMMA) film to increase the surface energy.

This transfer of a stack of layers is always possible if the work of adhesion at the interface that forms at the substrate surface is larger than that at the mold surface [17–19] or in this case, the Teflon-coated mold surface, provided the work of adhesion at every interface of the device layers is also larger than that at the mold surface. The work of adhesion at the interface between materials i and j, W_{ij}, can be determined from contact angle measurements on the two surfaces [20,21]. The work of adhesion thus determined at the Teflon–Au interface is 21.2 mJ/m^2, whereas it is 46.0 mJ/m^2 at the PMMA–Al interface. These values clearly indicate that the device could be transferred from the Teflon-coated mold to the PMMA-coated glass substrate.

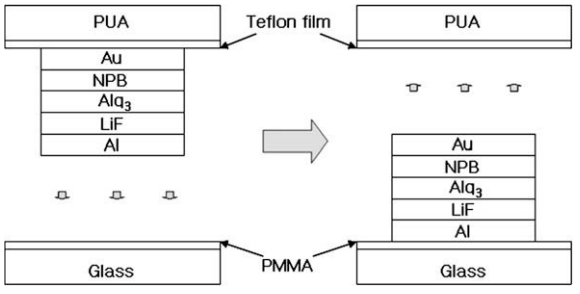

Fig. 1. Schematic illustration of fabricating ITOLED by whole device transfer method.

To clearly compare the differences in performance and at the same demonstrate the advantages that can be gained by fabricating ITOLED by the transfer method, two different ITOLEDs were fabricated. One is the ITOLED fabricated by the transfer method, following the procedure in Fig. 1, in which various layers are vapor-deposited on PUA mold in the order of Au/NPB/Alq_3/LiF/Al and then the whole device is transferred onto a glass substrate. The other is one in which the device layers are vapor-deposited on a glass substrate in the order of Al/LiF/Alq_3/NPB/Au, which is the reference device. The device structure on the glass substrate is the same for both ITOLEDs: Al (100 nm)/LiF (0.7 nm)/Alq_3 (50 nm)/NPB (50 nm)/Au (30 nm). The rates of deposition by thermal evaporation are 0.2–0.3 nm/s for organics and 1–2 nm/s for metals. Electrical measurements were carried out in an argon-filled glove box with HP 6625A and 34401A and luminance with a calibrated silicon diode. Shown in Fig. 2 are the current density–voltage, luminance–current density, and luminous efficiency–voltage characteristics of the two types of ITOLED. As shown in Fig. 2a, the turn-on voltage of the device fabricated by whole device transfer method (triangle) is much lower at 6 V than that of the reference device (circle) at 18.5 V. Fig. 2b and c shows that maximum luminance and luminous efficiency can be increased to 3700 cd/m^2 from 170 cd/m^2 and to 0.27 cd/A from 0.09 cd/A, respectively, by fabricating the ITOLED by the transfer method. There are two main reasons for the drastic improvement in the device performance. One has to do with a proper way of inserting the LiF layer. The other is related to the stability of the interface between Au and NPB.

To demonstrate the importance of deposition sequence, which is related to the two reasons for the improvement, we fabricated two TOLEDs (Al/Alq_3/NPB/Au and Al/LiF/Alq_3/NPB/Au) and two BOLEDs (Au/NPB/Alq_3/Al and Au/NPB/Alq_3/LiF/Al) and examined the current density–voltage characteristics of the devices. No device transfer was involved. As shown in Fig. 3, there is no difference between the two TOLEDs in the device characteristics, even though an LiF layer is inserted between Al and Alq_3, because of the deposition sequence (Al/LiF/Alq_3). It is well known that the release of Li by dissociation of LiF during the deposition of Al cathode and its subsequent reaction with the underlying Alq_3 layer to form Alq_3^- anions are responsible for the improvement in the device performance [22,23]. Such reaction results in an enhancement of electron injection due to the formation of a thin n-doped Alq_3 layer. In the deposition sequence of Al/LiF/Alq_3 for the TOLED, no such reaction can take place. As shown in Fig. 3 with two BOLEDs, the proper deposition sequence of Alq_3/LiF/Al (dark triangle) does result in a significant improvement in the device performance over the device without LiF (open triangle). Note in this regard that the deposition sequence

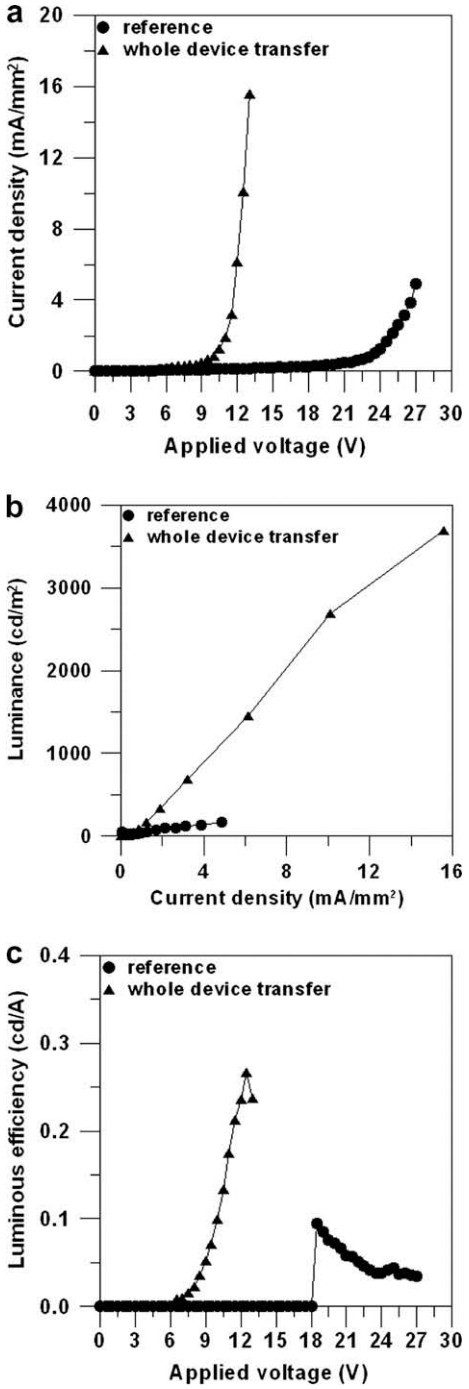

Fig. 2. Characteristics of ITOLEDs fabricated by conventional method (circle) and whole device transfer method (triangle). (a) Current density–voltage, (b) luminance–current density, and (c) luminous efficiency–voltage.

is Alq_3/LiF/Al when ITOLED is fabricated by the transfer method.

Earlier studies on the interface between Au and NPB revealed [9,10] that the metal deposited on NPB penetrates the organic layer and the metal clusters interdiffuse during the metal deposition, which results in deteriorated device

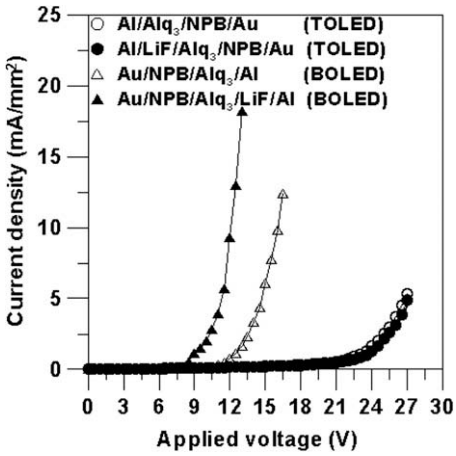

Fig. 3. Current density–voltage characteristics of the devices with four different structures of Al/Alq_3/NPB/Au (open circle, TOLED), Al/LiF/Alq_3/NPB/Au (closed circle, TOLED), Au/NPB/Alq_3/Al (open triangle, BOLED), and Au/NPB/Alq_3/LiF/Al (closed triangle, BOLED).

performance. In the fabrication by device transfer, however, NPB is deposited onto an existing gold layer, thereby avoiding the interface problem. The improvement thus realized is clear in Fig. 3 where the TOLED without LiF (open circle) is compared against the BOLED without LiF (open triangle). Similar improvement could be realized with transparent indium tin oxide (ITO), although Au was used in this work.

Another distinct advantage the device transfer method offers is that flexible substrates are not damaged, whereas they can be during metal deposition by thermal evaporation in the conventional fabrication, which makes the method more suitable for flexible applications. Shown in Fig. 4 is a green ITOLED pixel fabricated on flexible PET by whole device transfer method.

In summary, a fabrication method for top-emitting OLED (TOLED) has been presented that takes full advantage that traditional bottom-emitting OLED can offer. The perfor-

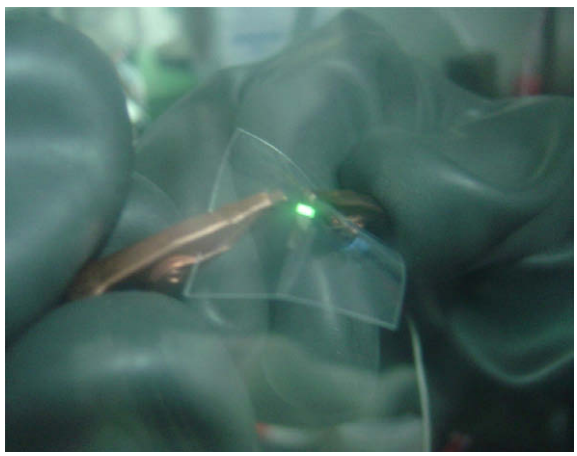

Fig. 4. Image of green light-emitting ITOLED pixel fabricated on a flexible substrate by whole device transfer method. (For interpretation of the references in color in this figure legend, the reader is referred to the web version of this article.)

mance of the inverted TOLED thus fabricated has been found to be as good as that of BOLED, which has been optimized in numerous studies over a long period of time. The whole device transfer that is involved in the fabrication allows for electrode engineering, which is otherwise not possible for fabricating ITOLED. The method also allows fabrication of ITOLED on flexible substrates without damage.

Acknowledgement

This work is supported by KOSEF [R01-2006-000-10140-0 (2006)].

References

[1] V. Bulovic, G. Gu, P.E. Burrows, S.R. Forrest, M.E. Thompson, Nature (London) 380 (1996) 29.
[2] L.S. Hung, C.W. Tang, M.G. Mason, Appl. Phys. Lett. 70 (1997) 152.
[3] G. Parthasarathy, P.E. Burrows, V. Khalfin, V.G. Kozlov, S.R. Forrest, Appl. Phys. Lett. 72 (1998) 2138.
[4] Y. Li, L.W. Tan, X.T. Hao, K.S. Ong, F. Zhn, L.S. Hung, Appl. Phys. Lett. 86 (2005) 153508.
[5] S. Chen, Z. Jie, Z. Zhao, G. Cheng, Z. Wu, Y. Zhao, B. Quan, S. Liu, X. Li, W. Xie, Appl. Phys. Lett. 89 (2006) 043505.
[6] H. Peng, J. Sun, X. Zhu, X. Yu, M. Wong, H.S. Kwok, Appl. Phys. Lett. 88 (2006) 073517.
[7] K. Hong, J.L. Lee, Electrochem. Solid-State Lett. 11 (2008) H29.
[8] C.-W. Chen, C.-L. Lin, C.-C. Wu, Appl. Phys. Lett. 85 (2004) 2469.
[9] A.C. Durr, F. Schreiber, M. Kelsch, H.D. Carstanjen, H. Dosch, O.H. Seeck, J. Appl. Phys. 93 (2003) 5201.
[10] S. Seo, C.-H. Jang, Appl. Phys. Lett. 91 (2007) 192505.
[11] T. Dobbertin, O. Werner, J. Meyer, A. Kammoun, D. Schneider, T. Riedl, E. Becker, H.-H. Johannes, W. Kowalsky, Appl. Phys. Lett. 83 (2003) 5071.
[12] H.W. Choi, S.Y. Kim, W.-K. Kim, J.-L. Lee, Appl. Phys. Lett. 87 (2005) 082102.
[13] S. Seo, J.H. Kim, H.H. Lee, Appl. Phys. Lett. 89 (2006) 253515.
[14] J. Choi, K.-H. Kim, S.-J. Choi, H.H. Lee, Nanotechnology 17 (2006) 2246.
[15] S.-J. Choi, P.J. Yoo, S.J. Baek, T.W. Kim, H.H. Lee, J. Am. Chem. Soc. 126 (2004) 7744.
[16] D. Suh, S.-J. Choi, H.H. Lee, Adv. Mater. 17 (2005) 1554.
[17] J. Rhee, H.H. Lee, Appl. Phys. Lett. 81 (2002) 4165.
[18] S.-L. Hur, D.-Y. Khang, C. Kocabas, J.A. Rogers, Appl. Phys. Lett. 85 (2004) 5730.
[19] K.-H. Kim, K.-W. Bong, H.H. Lee, Appl. Phys. Lett. 90 (2007) 093505.
[20] S. Wu, Polymer Interface and Adhesion, Marcel Dekker, New York, 1982. p. 96.
[21] Z. Wang, J. Zhang, J. Yuan, D. Yan, Y. Han, J. Am. Chem. Soc. 125 (2003) 15278.
[22] L.S. Hung, R.Q. Zhang, P. He, G. Mason, J. Phys. D 35 (2002) 103.
[23] M.G. Mason, C.W. Tang, L.S. Hung, P. Raychaudhuri, J. Madathil, D.J. Giesen, L. Yan, Q.T. Le, Y. Gao, S.-T. Lee, L.S. Liao, L.F. Cheng, W.R. Salaneck, D.A. dos Santos, J.L. Bredas, J. Appl. Phys. 89 (2001) 2756.

Two principal routes exist for the fabrication of monolithically integrated electronic circuits on arbitrarily shaped surfaces. One involves the patterning of circuits on a flat substrate, followed by deformation into its final shape [5]. This approach allows for the use of well-established patterning techniques prior to substrate deformation. Excessive strain during the deformation process may, however, cause damage to the various device layers, limiting its applicability to a narrow class of materials, and to surfaces with only limited deformation [5]. An alternative approach involves patterning directly on a preshaped substrate, such that the circuits are not subject to deformation-induced strain. This latter route is attractive because it allows for the realization of high performance devices over a nearly unlimited range of surface geometries. However, it presumes the availability of reliable patterning techniques for three-dimensional (3D) surfaces. Although various techniques for the generation of textured or patterned 3D surfaces have been reported [6–11], none have been used for the full realization of conformal electronics on nonplanar substrates. A combination of these two approaches includes partial fabrication of the circuit on a flat surface, followed by moderate deformation into its final 3D shape, at which point the fabrication is completed [12]. This typically employs wet chemical processing and conventional photolithography that are incompatible with a range of semiconductor materials and substrates.

Here, we demonstrate a material transfer technique employing elastomeric stamps and cold welding [13–15] that allows for the definition of unstrained metallic patterns directly on top of curved surfaces covered with organic semiconductor materials. This allows for the fabrication of an organic, passive matrix focal plane array (FPA) on top of a 1.0 cm radius plastic hemisphere, depicted schematically in Fig. 1a. In contrast to similar, previously reported direct 3D material transfer methods [11,16–19], our technique is compatible with the realization of high performance monolithically integrated circuits composed of organic optoelectronic devices on arbitrarily deformed substrates, requiring no wet chemistry or high processing temperatures.

The passive matrix FPA consists of two perpendicular electrode stripe arrays placed above and below continuous layers of organic semiconductor materials forming the active photodetection regions. Individual photodetectors are defined at crossings of the upper and lower stripes, where device readout is realized by probing the appropriate row and column electrodes. Fig. 1b shows an example of a completed hemispherical FPA consisting of $(500\ \mu m)^2$ copper phthalocyananine (CuPc)/C_{60} based double heterojunction photodiodes.

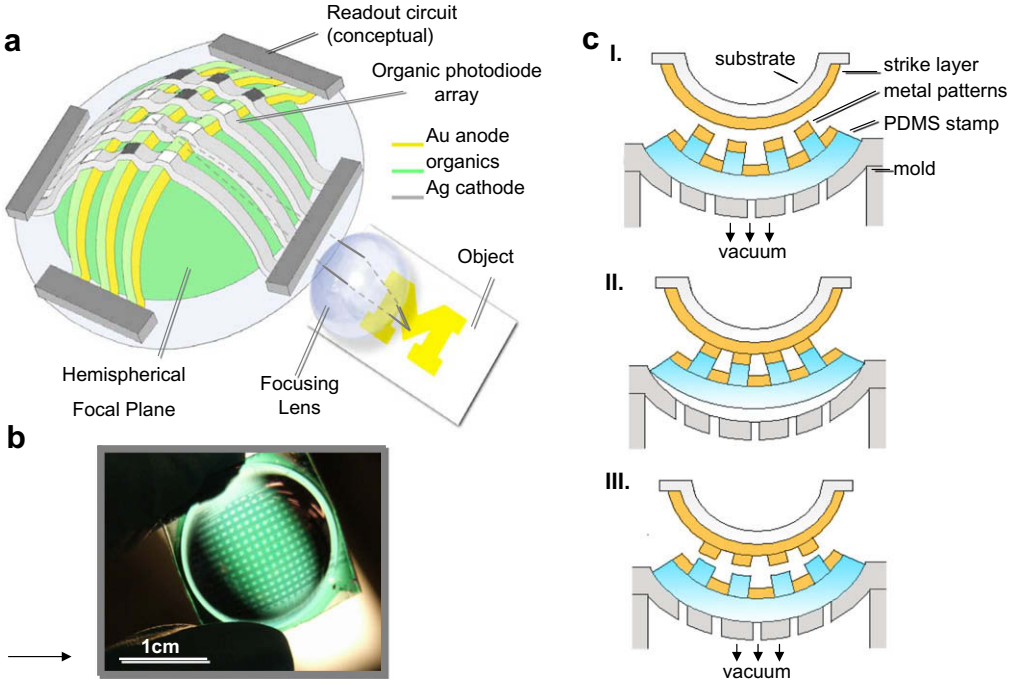

Fig. 1. (a) Schematic of the hemispherical organic photodetector focal plane array (FPA) and its incorporation into a simple imaging system. The lens produces an image of the object on the spherical focal plane, where an array of photodiodes has been defined. The readout circuits are commonly used in FPAs, but are not employed in our work. (b) Photograph of a completed hemispherical focal plane with a 11×13 array of $(500\ \mu m)^2$ photodetectors on a 1 cm radius plastic hemisphere fabricated following the process in Fig. 1c. (c) Process sequence for fabricating a hemispherical FPA. (c-I) The hemispherical plastic substrate, coated initially with a metal strike layer, is placed in proximity to a patterned PDMS stamp of the same shape, deformed by vacuum in an aluminum mold. (c-II) The vacuum holding the PDMS stamp is released, allowing the stamp to snap into contact with the substrate surface. Metallic bonds are formed between metal patterns on the stamp and strike layer on the plastic dome. (c-III) The PDMS stamp is separated from the substrate by reapplication of vacuum, leaving behind the metal patterns on the hemisphere.

The fabrication process of the FPA shown schematically in Fig. 1c proceeds as follows: A flat and transparent, glycol-modified polyethylene terephthalate (PETg) sheet is drawn by vacuum into a shaped Al mold, while being heated to 140 °C above its softening temperature. The mold is then cooled to freeze the substrate shape. Next, a 2 nm Cr adhesion layer, and a 6 nm Au strike layer are thermally deposited onto the outer surface of the hemisphere in vacuum.

A flat PDMS stamp with an array of raised ridges that corresponds to the positions of the metal columns on the FPA is fabricated using a pre-etched Si "master" consisting of an array of parallel, 40 μm or 500 μm wide by 15 μm high ridges, each separated by a distance equal to their widths [14–15]. Masters composed of a rigid material such as Si were patterned with lines of 40 μm feature size using conventional photolithography. A curing agent and PDMS prepolymer were thoroughly mixed at a 1:7 weight ratio, followed by degassing for 1 h to remove all air bubbles and to ensure complete mixing. The prepolymer is then poured onto the Si master and cured at 100 °C for 1 h to form a stamp with duplicated patterns from the master.

The stamp is coated with a 10 nm thick Au layer by vacuum thermal evaporation, and then is also deformed into a hemispherical shape by applying vacuum to its flat surface, using the same mold as before. The spherical substrate is placed onto the mold in close proximity to the deformed PDMS stamp. The vacuum is then released, causing the PDMS stamp to "snap" back onto the substrate, conformally contacting its surface, as shown in Fig. 1c. A bond is thereby formed between the metal-coated ridges on the stamp and the strike layer. The PDMS stamp is parted from the substrate through re-application of the vacuum, leaving behind the metal stripes. The strike layer is then removed by sputtering in a 30 sccm, 20 Torr and 100 W Argon plasma etching for 2 min.

Following the transfer of the bottom (anode) electrode rows, organic semiconductor layers forming the diode active region are evaporated across the full surface of the hemisphere. The double heterojunction photodetectors consisted of a 50 nm thick CuPc donor layer, a 50 nm thick C_{60} acceptor layer, a 10 nm thick bathocuproine (BCP) exciton blocking layer, and a 6 nm thick Ag strike layer grown sequentially by vacuum thermal evaporation. Finally, the top array of 20 nm thick Ag cathode columns are applied by a second, similar stamping process oriented perpendicularly to the first array of metal rows. The strike layer and the underlying organic semiconductors where then once again by exposure to an Ar plasma.

Using this process, Au or Ag stripes of thicknesses of up to 20 nm were transferred onto a 1 cm-radius hemisphere (Fig. 2a and b). Transfer of thicker metals proved to be difficult, possibly due to wrinkling of the PDMS stamp during metal deposition [21].

Fig. 2a shows an array of 10 nm thick, 500 μm wide Au stripes transferred onto a PETg hemisphere. A sheet resistance of 7 Ω/□ for 10 nm Au was estimated from measurements made between several points along the metal

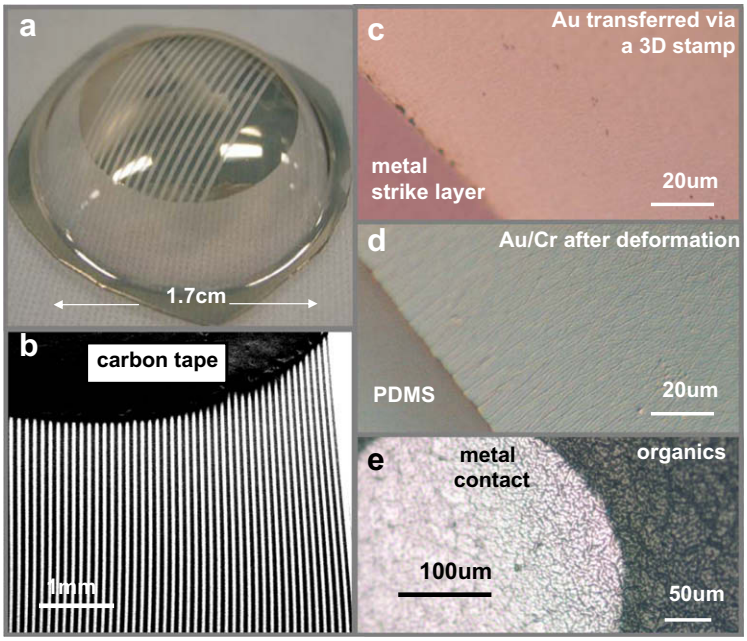

Fig. 2. (a) Optical microscope image of a 500 μm wide, cm-long and 10 nm thick Au stripe array on a PETg hemisphere produced with the process in Fig. 1c. (b) Scanning electron microscope image of an array of 40 μm wide metal stripes patterned on a hemispherically shaped substrate. The distortion of the stripe patterns at the edge of the substrate results from the PDMS stamp deformation illustrated in Fig. 1c. (c) Optical microscope image showing the edge of a metal stripe patterned via the direct material transfer illustrated in Fig. 1c, before Ar plasma etch. (d) Microscope image of Au film with a 20 Å Cr as an adhesive layer on PDMS after deforming into a 1 cm radius hemisphere. Cracking is apparent after same strain is applied as compared to Fig. 2c due to increased adhesion between metal film and PDMS. (e) Microscope image showing cracks on both metal and organic layers predeposited on a flat plastic substrate, followed by deformation to the same degree as in (c) and (d).

stripes. This corresponds to $7 \times 10^{-6}\ \Omega$ cm, consistent with that of conventional Au thin films. Since the strike layer thickness is the same as that of the transferred lines, significant fracturing of the transferred metal would lead to discontinuous electrodes created during the Ar etch, which is clearly not observed.

In Fig. 2b, we show a distortion of 40 μm wide stripe patterns along the edge of the interconnect array due to 3D deformation of the parallel stripes on the planar stamp. If desired, this distortion can be corrected by modifications to the stamp pattern. The edge features of the 40 μm metal stripes have a roughness of 1–2 μm, suggesting that pattern resolutions <10 μm are achievable.

The strain introduced on the PDMS stamp (or plastic substrate) during deformation is a function of the radius of curvature [6]. The average strain for a full hemisphere as demonstrated here, is approximately 20%, being slightly higher at the apex than at the rim. Given that free-standing metal films fracture at strains of only a few percent [22–23], the high quality metal pattern transfer suggests that significant shear slip occurs at the metal/PDMS interface during stamp deformation, due to the weak adhesion at the Au/PDMS interface. As shown in Fig. 2c, 10 nm thick Au stripe transferred by a 3D stamp shows no metal cracking. If the adhesion between metal film and PDMS is enhanced, for example, by inserting a 2 nm thick Cr adhesive layer (Fig. 2d), the metal film can not be transferred and cracks under the same amount of strain as in Fig. 2c [23]. In Fig. 2e, we show that metal contacts deposited onto plastic substrates prior to deformation also leads to significant cracking of both organic and metallic layers due to the strong metal/PETg bond that inhibits shear-induced slip.

Following the transfer of the bottom (anode) electrode rows, organic semiconductor layers forming the double heterojunction copper phthalocyanine (CuPc)/C_{60} diode [20] active region are evaporated across the full surface of the hemisphere, followed by deposition of a 10 nm thick

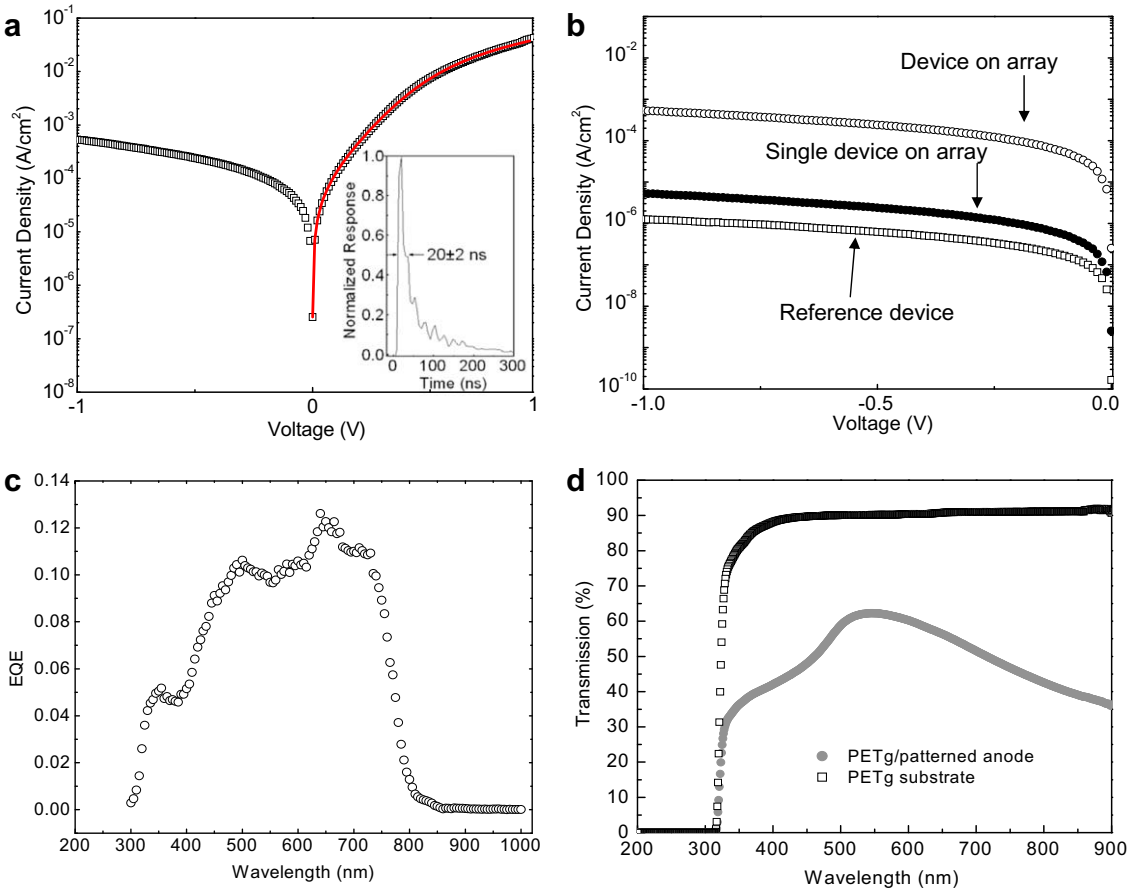

Fig. 3. (a) Current density–voltage characteristics for an individual $(40\ \mu m)^2$ organic photodetector under forward and reverse bias. The data at <0.5 V forward bias was fit (solid line) using the modified Shockley equation, $J = J_s \cdot \exp[(qV - JR_{sa})/n'kT]$, where the specific series resistance $R_{sa} = 0.33 \pm 0.01\ \Omega\ cm^2$, saturation current density $J_s = (60 \pm 2)\ \mu A\ cm^{-2}$ and $n' = 3.49 \pm 0.03$ are used. Note that $n' > 2$ results since the current is summed over the reverse currents of several diodes in the passive matrix array, and is thus affected by the sum of their resistances. *Inset*: Pulse response of a $(40\ \mu m)^2$ photodetector on the hemispherical array, showing a response time of 20 ± 2 ns. (b) Total dark current density under reverse bias (open circles), and estimated dark current of a 40 μm detector (closed circles) in a 100 × 100 focal plane array. The reverse biased dark current density of a device on a flat substrate (open squares) is shown for comparison. (c) External quantum efficiency of a transferred detector (1 mm in diameter) at 0 V bias. (d) Transmission spectrum of the PETg substrate with and without a 100 Å patterned Au anode array.

Ag strike layer. Finally, the top array of 20 nm thick Ag cathode columns are applied by a second, similar stamping process oriented perpendicularly to the first array of metal rows.

Electrical characterization of individual pixels was performed on the 100 × 100 array of $(40\ \mu m)^2$ photodetectors fabricated on a 1 cm radius hemispherical substrate. Photodetector dark currents measured along a row or column yielded a total current density of $530 \pm 20\ \mu A\ cm^{-2}$ at −1 V (Fig. 3a), which is approximately 100 times greater than for an individual diode. The dark current density for an isolated device is thus less than or equal to $5.3 \pm 0.2\ \mu A\ cm^{-2}$, which is comparable to that measured for an analogous, 1 mm-diameter control device on a flat glass/ITO substrate, as shown in of Fig. 3b.

The external quantum efficiency, shown in Fig. 3c, is >10% for wavelengths between $\lambda = 480$ nm to 740 nm, peaking at 12.6 ± 0.3% at $\lambda = 640$ nm. As shown in Fig. 3d, transmission through the 10 nm thick Au layer on PETg is 60% at $\lambda = 640$ nm, leading to a decrease of external quantum efficiency compared to previously reported CuPc/C_{60}/BCP double heterojunction photodetectors [20]. Given the reflection from the metal cathode, absorption of both metal contacts, and a calculated absorption of the organic donor/acceptor layers of 40% at $\lambda = 640$ nm [24], the internal quantum efficiency is approximately 30%. This is lower than previously reported [24] due to the thick CuPc layer used to reduce the possibility of electrical shorts between top and bottom electrodes. This, in turn, reduces the exciton diffusion efficiency, and hence the internal quantum efficiency.

The photodetector noise performance may be evaluated by determination of the detectivity $D^* = (A\Delta f)^{1/2}/\mathrm{NEP}$, where A is the detector area, Δf is the bandwidth, and NEP is the noise equivalent power [25]. In our case, shot noise limited detection at −1 V gives, $\mathrm{NEP} = (2qI_D)^{1/2}/R(\lambda)$, where q is the electronic charge, I_D is the dark current, and $R(\lambda)$ is the detector responsivity. At $\lambda = 640$ nm, we obtain $R = 0.065\ AW^{-1}$. In this case, $D^* = 5 \times 10^{10}$ cm $Hz^{1/2}\ W^{-1}$ in a 1 Hz bandwidth, which is approximately ten times less than that of a Si photodiode [26].

The current density vs. voltage characteristics of 100 pixels were measured over four different regions on the 1 cm hemisphere. None of the 100 devices was found to be electrically shorted. Indeed, devices in the center and near the edge of the matrix show less than 10% variation in average dark current, possibly due to variations in layer thickness across the hemispherical surface. This residual non-uniformity can be minimized by substrate rotation during material deposition. Among all devices, 97% have dark current densities $<20\ \mu A\ cm^{-2}$ at −1 V.

The temporal response of a photodetector in the array to an optical pulse shown in the inset of Fig. 3a, was (20 ± 2) ns. The response was characterized by illumination with a 5 Hz train of 700 ps full width at have maximum (FWHM) pulses at $\lambda = 475$ nm from a dye pumped with a N_2 laser. The average optical power was $0.29 \pm 0.02\ \mu J$ over a 5 mm diameter illuminated spot. The response is limited by the detector resistance and capacitance, where a series resistance of approximately 20 kΩ, is estimated from the forward-biased current density vs. voltage characteristic in Fig. 3a (solid line), and the capacitance measured at 10 kHz was 1.31 ± 0.01 pF. The response time is compatible with pixel readout rates of $\sim 10^7$ pixels/s, which translates into a frame readout rate in excess of the 30 frames per second video standard for a 640 × 480 pixel array. Real-time imaging applications are thus achievable with this architecture.

To demonstrate the imaging capabilities of hemispherical FPAs, we fabricated a 20 × 20 array of $(200\ \mu m)^2$ pixels spaced by 300 μm on a 1 cm radius hemisphere, a configuration that facilitated probing and readout. The detector dynamic range was extracted by measuring the photocurrent of a single device under different illumination levels at $\lambda = 633$ nm and three different bias voltages, as shown Fig. 4. Fits to the data are shown as solid lines, indicating approximately linear photocurrent variation with optical power in the range of 2 to $200\ \mu W\ cm^{-2}$. Photocurrent compression with respect to the linear fits is observed at high optical powers, while at very low optical powers, the photocurrent is noise limited, evidenced by the error bars. Note that the increasing y-axis intercept with increasing reverse bias corresponds to a larger responsivity. The dynamic range (DR) is defined as $10\log(P_1/P_0)$, where P_1 is the optical power for 1 dB photocurrent compression at high intensities, and P_0 is the lowest detectable optical power. For 0 V bias, DR = 20 dB, corresponding to a 7-bit gray-scale. At higher reverse bias, the 1 dB compression point exceeds the highest input power while P_0 remains the same. The increased linearity, therefore, leads to an increased DR due to the space charge field that sweeps out more free carriers at high intensity.

To demonstrate imaging capabilities, a rectangular, a $1.3 \times 0.8\ mm^2$ aperture placed in proximity to the hemispherical center line, was illuminated at $\lambda = 633$ nm at

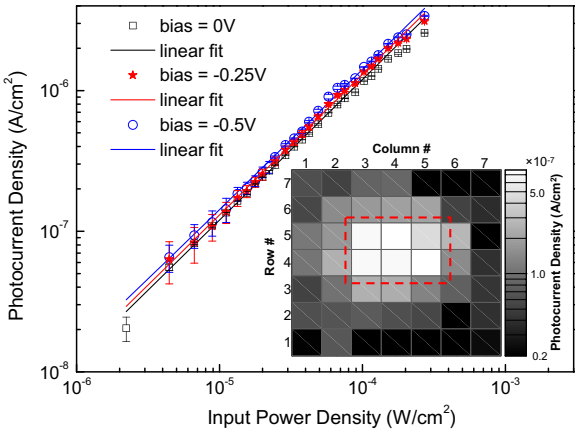

Fig. 4. Photocurrent density vs. input power density of a $(200\ \mu m)^2$ photodetector in a 20 × 20 array under various biases. Linear fits at each bias are shown as solid lines. The dynamic range, determined by the 1 dB compression point and minimum detectable power level, is approximately 20 dB, giving a 7-bit resolution. Inset: Gray scale image of a rectangular illuminated area on the hemispherical FPA, corresponding to a 2 × 3 block of photodetectors. Photocurrents of all pixels in a 7 × 7 block containing the illuminated block are depicted, showing high contrast obtained between illuminated and unilluminated pixels. Illumination was provided by a 633 nm laser beam.

120 μW cm^{-2}. The illuminated area included a 2×3 pixel block and portions of the immediately adjacent pixels. Photocurrents from pixels within a 7×7 block including the illuminated area were measured and used to generate the 7-bit gray scale image in Fig. 4, inset. The dashed rectangle illustrates the approximate extent of the illuminated area. A contrast of 99% exists between the highest and lowest pixel photocurrents located, respectively, at the center and periphery of the block. A photocurrent non-uniformity of 13% is observed among pixels in the high-illumination 2×3 pixel block, excluding the pixel at position $(5,5)$. Gray levels at partially illuminated pixels on the periphery of the rectangle exhibit a minimum contrast of 71% with respect to the maximum photocurrent. The observed non-uniformities are due to imperfections in the imaging system, light leakage, scattering from metal contact surfaces, and slight variations in the individual pixel characteristics. Given low carrier mobility of vacuum-deposited organic semiconductor materials, low pixel electrical crosstalk is expected in this passive architecture.

In summary, we have demonstrated a direct material transfer technique that is adaptable to surfaces of arbitrary 3D shape. The technique avoids introduction of excessive strain into heterogeneous material layers, thus allowing for the fabrication of high performance organic electronic devices with micrometer scale dimensions on curved surfaces with radii 1 cm or less. The technique was applied to the fabrication of a lightweight and compact hemispherical FPA. Another interesting yet challenging application is the use of curved FPAs as retinal prostheses to replace photoreceptor cell layers that have degenerated and lost sensation to different shades of light.

Acknowledgements

The authors thank the Defense Advanced Research Projects Agency, the Air Force Office of Scientific Research, the National Science Foundation and Universal Display Corporation for financial support. The authors also thank Stephane Kena-Cohen and Noel Giebink for helpful discussions.

References

[1] In an optical imaging system, the f/number is defined as the focal length of the imaging lens divided by the diameter of the entrance aperture. Larger f-numbers express lesser amounts of light per unit area reaching the image plane. The largest observable angle of the optical system defines its FOV. See, for example E. Hecht, Optics, Addison Wesley, 2002.
[2] R. Dinyari, S.-B. Rim, K. Huang, P.B. Catrysse, P. Peumans, Appl. Phys. Lett. 92 (2008).
[3] I. Sample, New Sci. 170 (2001) 23.
[4] W.J. Hamilton, P.R. Norton, E.E. Gordon, R.W. Berry, US Patent Number 6,627,865 B1, 2003.
[5] R. Bhattacharya, S. Wagner, Y.-J. Tung, J.R. Esler, M. Hack, Proc. IEEE 93 (2005) 1273.
[6] K.E. Paul, M. Prentiss, G.M. Whitesides, Adv. Func. Mater. 13 (2003) 259.
[7] P. Ruchhoeft, M. Colburn, B. Choi, H. Nounu, S. Johnson, T. Bailey, S. Damle, M. Stewart, J. Ekerdt, S.V. Sreenivasan, J.C. Wolfe, C.G. Willson, J. Vac. Sci. Technol. B 17 (1999) 2965.
[8] W.M. Choi, O.O. Park, Nanotechnology 15 (2004) 1767.
[9] W.R. Childs, R.G. Nuzzo, Adv. Mater. 16 (2004) 1323.
[10] K. Hashimoto, Y. Kaneko, T. Horiuchi, Microelectron. Eng. 83 (2006) 1312.
[11] S.M. Miller, S.M. Troian, S. Wagner, J. Vac. Sci. Technol. B 20 (2002) 2320.
[12] P.I. Hsu, R. Bhattacharya, H. Gleskova, M. Huang, Z. Xi, Z. Suo, S. Wagner, J.C. Sturm, Appl. Phys. Lett. 81 (2002) 1723.
[13] C. Kim, P.E. Burrows, S.R. Forrest, Science 288 (2000) 831.
[14] C. Kim, M. Shtein, S.R. Forrest, Appl. Phys. Lett. 80 (2002) 4051.
[15] C. Kim, S.R. Forrest, Adv. Mater. 15 (2003) 541.
[16] G.S. Ferguson, M.K. Chaudhury, G.B. Sigal, G.M. Whitesides, Science 253 (1991) 776.
[17] Y. Xia, G.M. Whitesides, Angew. Chem. Int. Ed. 37 (1998) 550.
[18] B. Michel, A. Bernard, A. Bietsch, E. Delamarche, M. Geissler, D. Juncker, H. Kind, J.P. Renault, H. Rothuizen, H. Schmid, P. Schimidt-Winkel, R. Stutz, H. Wolf, IBM J. Res. Dev. 45 (2001) 697.
[19] H.O. Jacobs, G.M. Whitesides, Science 291 (2001) 1763.
[20] P. Peumans, S.R. Forrest, Appl. Phys. Lett. 79 (2001) 126.
[21] N. Bowden, S. Brittain, A.G. Evans, J.W. Hutchinson, G.M. Whitesides, Nature 393 (1998) 146.
[22] P.H. Hsu, M. Huang, S. Wagner, Z. Suo, J.C. Sturm, Mater. Res. Soc. Symp. Proc. 621 (2000) Q8.6.1.
[23] S.P. Lacour, J. Jones, S. Wagner, T. Li, Z. Suo, Proc. IEEE 93 (2005) 1459.
[24] P. Peumans, A. Yakimov, S.R. Forrest, J. Appl. Phys. 93 (2003) 3693.
[25] NEP corresponds to the optical power required to produce a unity signal-to-noise ratio at the detector output. Photodiode noise current consists of shot and thermal noise. Shot noise is dominant at sufficiently high reverse bias.
[26] A. Rogalski, Opto-Electron. Rev. 12 (2004) 221.

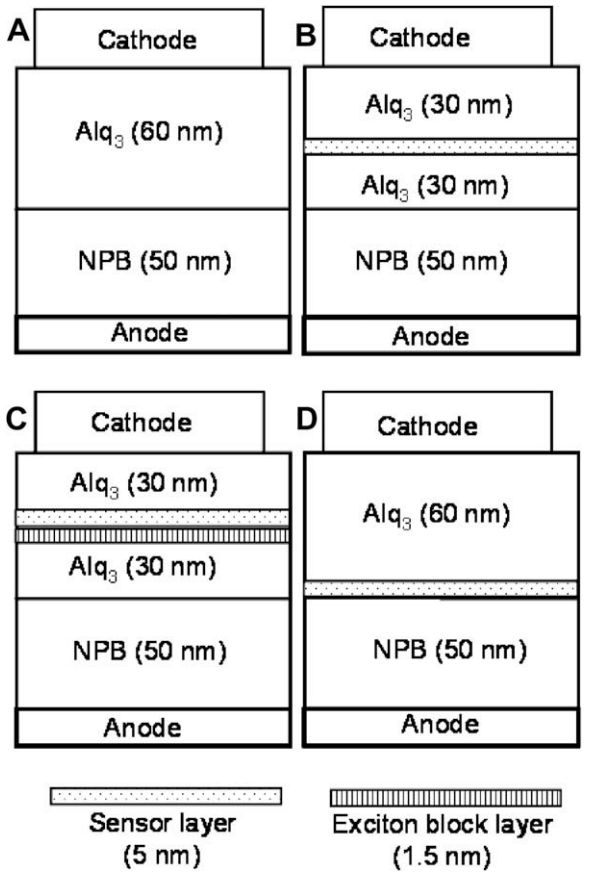

Fig. 1. Schematic diagrams depicting device structures A through D described in the text. In devices B, C, and D, red emissive fluorescent dye-doped sensor layers (5 nm) are placed in the devices to reflect exciton diffusion. In device C, a thin organic layer (1.5 nm) with wide energy gap is placed underneath the sensor layer, which functions as an exciton blocking layer but does not impede hole reaching the sensor layer, if any.

behavior. In these devices, indium–tin-oxide (ITO) is employed as anode, Mg:Ag is used for cathode, and *N,N′-di(naphthalene-1-yl)-N,N′*-diphenyl-benzidine (NPB) is utilized for forming the hole transport layer (HTL). The only difference among these devices is the emitting/electron transport layer (EML). In device structure A, a pure Alq_3 layer constitutes the entire EML. In device structure B, the EML consists of a fluorescent dye-doped sensor layer sandwiched between two pure Alq_3 layers, where the dopant is 2.0 vol.% 4-[dicyanomethylene]-2-*t*-butyl-6-(1,1,7,7-tetramethyljulolidyl-9-enyl)-4H-pyran (DCJTB). Device structure C is very similar to structure B, except that a thin exciton blocking layer (EBL) made of 2-*tert*-butyl-9,10-di-beta-naphthylanthracene (TBADN) is inserted in between the lower Alq_3 layer and the sensor layer. Device structure D is also similar to structure B, but the sensor layer in this case is located at the NPB/Alq_3 interface. Details of device fabrications and luminescence measurements are as described in our previous reports [5,7].

Fig. 2 shows the normalized EL spectra of device A operated under a DC current density of 25 mA/cm^2, at the temperatures of 21, 40 and 60 °C, respectively. As the

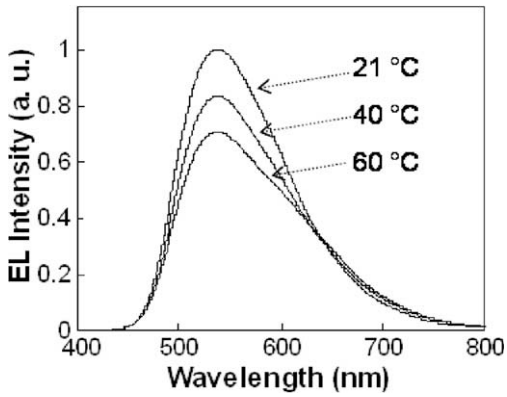

Fig. 2. Normalized EL spectra of device A operated under a DC current density of 25 mA/cm^2, at temperatures of 21, 40, and 60 °C.

temperature increases, the EL intensity of the device decreases dramatically. This observation is consistent with those of other researchers [8,9] and attributed to increased exciton diffusion at elevated temperatures. As was mentioned earlier, however, the exciton diffusion model still lacks convincing experimental verification, which is the objective of the work presented in this paper.

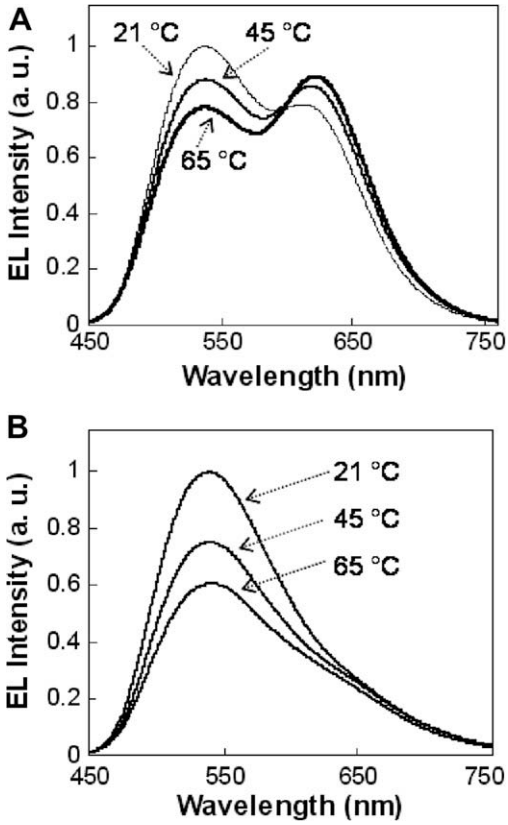

Fig. 3. (a) Normalized EL spectra of device B operated under a DC current density of 25 mA/cm^2, at temperatures of 21, 45, and 65 °C and (b) normalized EL spectra of device C under the same conditions.

Fig. 3a shows the normalized EL spectra of device B operated under a DC current density of 25 mA/cm^2, at temperatures of 21, 45 and 65 °C. There are two peaks in the spectra, where the one at 540 nm is due to the emission of the lower Alq_3 layer, and the one at 625 nm results from the red emissive sensor layer. With rising temperatures, the green portion of the spectra decreases, while the red portion of the spectra increases. In principle, there are two plausible explanations for this behavior of EL spectra with rising temperatures. The first one could be due to the drifting of charge recombination zone toward the sensor layer. In fact, this could be true when more and more holes cross the lower Alq_3 layer without recombination and reach the sensor layer at elevated temperatures. The second is based on the assumption that the majority of excitons are initially being formed at NPB/Alq_3 interface [6], but diffuse further toward the sensor layer before relaxation. As temperature increases, exciton diffusion length increases [1], which increases the number of excitons reaching the sensor layer, resulting in not only a decrease in the population of excitons relaxing inside the green emission zone but also an increase in their population in the red emitting sensor layer.

To verify which of the above explanations is true, we measured the EL spectra of device C at temperatures of 21, 45 and 65 °C. In this device, a thin (1.5 nm) exciton blocking layer (EBL), formed with a blue emitter (TBADN) is located underneath the sensor layer, thus prevents excitons from reaching the sensor layer. The purpose of using TBADN as EBL is twofold: (i) TBADN has a significantly larger energy bandgap than Alq_3, and thus effectively confines excitons inside the lower Alq_3 layer [5,10] and (ii) TBADN is a bi-polar material with a HOMO level close to that of Alq_3 [11–13], and, as such, will not substantially impede any holes from reaching the sensor layer, especially in view of its limited thickness (1.5 nm) which would also facilitate tunneling. Our measurements (data not shown here) show that the driving voltage at 25 mA/cm^2 in case of device C is 7.3 V, and is only ~0.2 V higher than in case of device B, indeed proving the validity of the second argument. In this case, we expect that the population of excitons reaching the red sensor layer of this device to be substantially reduced in comparison to the one without the EBL (device B), but the number of holes reaching the sensor layers of these two devices remain predominantly unchanged. To this end, if the change in EL spectra of device B with temperature is indeed induced by shifts in the emission zone as the result of the increased number of holes reaching the sensor layer, we should still be able to observe the same effect in device C. However, as shown in Fig. 3b, the red portion of the spectra almost completely disappears in device C, for all temperatures. This result strongly suggests that the change in EL spectra of device B with temperature (Fig. 3a) is the result of increased number of excitons reaching the sensor layer by thermally activated diffusion at the higher temperatures, rather than the shift of the charge recombination zones. In other words, it demonstrates that exciton diffusion increases with rising temperature.

Based on the above result alone, however, it is still not possible to make a definitive conclusion that the reduced EL intensity at elevated temperatures (Fig. 2) is indeed induced by the increased exciton diffusion. A possible argument to contradict this conclusion would be that the reduced EL could be derived from changes in magnitude of charge injection efficiency from the contacts at the higher temperatures, leading to a subsequent deterioration in charge balance. In order to further resolve this, we doped the Alq_3 layer adjacent to the NPB/Alq_3 interface with 2 vol.% DCJTB red emissive fluorescent dye (device D). In this device, the DCJTB doped layer is very thin in comparison to the total thickness of Alq_3, and thus we can assume that the charge injection characteristics in device D remain essentially unaltered from those in the undoped device (device A). Therefore, if the deterioration of charge balance is the main cause for the reduced EL intensity at higher temperatures of device A, we should be able to observe a similar result in device D. As shown in Fig. 4, however, device D illustrates an opposite temperature-dependence as compared to that of device A (Fig. 2), where increasing temperature leads to an increase in EL intensity, revealing that it is the increased exciton diffusion, rather than the possibly deteriorated charge balance, that is responsible for the reduced EL intensity of device A at higher temperatures.

Generally, exciton diffusion may reduce luminescence efficiency through two means: (i) exciton–exciton annihilation [14] and (ii) exciton quenching via randomly distributed nonradiative recombination sites [1,3]. In case of PL, exciton–exciton annihilation should not be a dominant factor since the exciton density is usually low, and thereby only the randomly distributed nonradiative recombination sites play an important role in quenching excitons during thermally activated diffusion. In case of EL, however, the exciton density is usually several orders of magnitudes higher, and thus both scenarios could be responsible for the reduced EL intensity at higher temperatures. We have compared the effect of temperatures on the efficiency of EL and PL for device A, and found that the temperature-dependence of EL is stronger than that of PL. This result is in agreement with the expectation that exciton–exciton annihilation process is different in EL and PL.

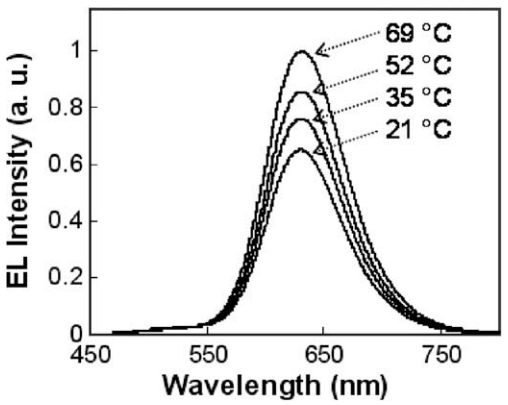

Fig. 4. Normalized EL spectra of device D operated under a DC current density of 25 mA/cm^2, at temperatures of 21, 35, 52, and 69 °C.

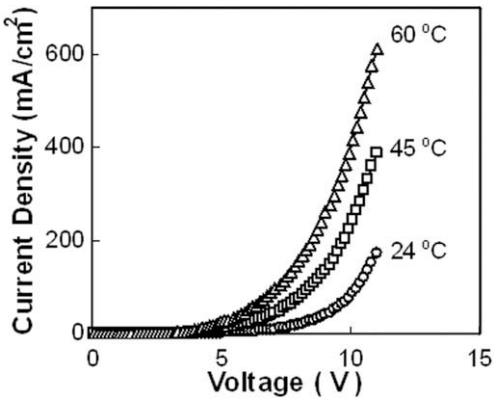

Fig. 5. Current density versus voltage (J–V) characteristics of device A, at temperatures of 24, 45, and 60 °C.

At the moment, it is still not clear what causes the increase in EL efficiency with increasing temperatures of the doped devices (Fig. 4). We plausibly attribute this observation to the combined effects of (i) limited exciton diffusion in fluorescent dye-doped systems and (ii) enhanced charge balance as a result of increased electron injection at the cathode contact at higher temperatures. As shown in device D, although only a thin layer of EML is doped with red emissive dye, it shows predominantly red emission, indicating that exciton diffusion of this device is in fact effectively limited by the doped molecules. In regards to the charge balance of a device that employs ITO as an anode and Mg:Ag as a cathode, injection of holes is usually easier, thus making electron injection the limiting factor [15]. So the possible enhancement in charge balance of this device at higher temperatures could originate from a significantly increased electron injection, evident in the shift in current density versus voltage (J–V) characteristics of the devices to higher currents as temperature increases (Fig. 5). In contrast, for the undoped device (device A) similar increase in charge balance as a result of heating may be over compensated for by significant increases in exciton diffusion, resulting in a net reduction in EL efficiency at higher temperatures (Fig. 2).

Another important issue is whether the reduced EL intensity at elevated temperatures (Fig. 2) is also due to cathode induced exciton quenching, since more excitons may diffuse toward the cathode at higher temperatures. In device C, excitons are effectively confined in the lower Alq_3 layers by the EBL, but we still observed a significant decrease in EL efficiency with increasing temperatures (Fig. 3b). This result suggests that the reduced EL intensity at elevated temperatures should not be the consequence of cathode induced exciton quenching, but rather the result of quenching phenomena in the bulk of the undoped emitting layer [5].

In summary, our experimental results strongly support a temperature-induced exciton diffusion model. In this model, the reduced EL efficiency at higher temperatures of an undoped device is attributed to the increased exciton diffusion, which leads to an intensified exciton–exciton annihilation and exciton quenching by randomly distributed nonradiative sites. For a fluorescent dye-doped device, however, the EL efficiency increases with rising temperatures. The major reason behind this discrepancy between doped and undoped devices is that excitons are effectively localized onto the doped molecules in the doped devices, which prevents excitons from being quenched during thermally activated diffusion.

Acknowledgements

One of the authors (Y.L.) acknowledges the financial support of Natural Sciences and Engineering Research Council of Canada (NSERC).

References

[1] R. Priestley, A. Walser, R. Dorsinville, Opt. Commun. 158 (1998) 93.
[2] M. Furukawa, K. Mizuno, A. Matsui, S. Rughooputh, W.C. Walker, J. Phys. Soc. Jpn. 58 (1989) 2976.
[3] U. Lemmer, R.F. Mahrt, Y. Wada, A. Greiner, H. Bässler, E.O. Göbel, Appl. Phys. Lett. 62 (1993) 2827.
[4] Y.F. Xu, H.J. Zhang, H.Y. Li, S.N. Bao, P. He, Appl. Surf. Sci. 252 (2006) 2328.
[5] Y. Luo, H. Aziz, R. Klenkler, G. Xu, Z. Popovic, Chem. Phys. Lett. 458 (2008) 319.
[6] C.W. Tang, S.A. VanSlyke, C.H. Chen, J. Appl. Phys. 65 (1989) 3610.
[7] Y. Luo, H. Aziz, G. Xu, Z. Popovic, Appl. Phys. Lett. 89 (2006) 103505.
[8] Z. Shen, P. Burrows, Vladimir Bulovic, D.M. McCarty, M.E. Thompson, S.R. Forrest, Jpn. J. Appl. Phys. Part 2 35 (1996) L401.
[9] Y. Abe, K. Onisawa, S. Aratani, M. Hanazono, J. Electrochem. Soc. 139 (1992) 641.
[10] S. Wen, M. Lee, C. Chen, J. Display Technol. 1 (2005) 90.
[11] S.C. Tse, S.K. So, M.Y. Yeung, C.F. Lo, S.W. Wen, C.H. Chen, Chem. Phys. Lett. 422 (2006) 354.
[12] Y.C. Tsai, J.H. Jou, Appl. Phys. Lett. 89 (2006) 243521.
[13] K. Okumoto, H. Kanno, Y. Hamada, H. Takahashi, K. Shibata, J. Appl. Phys. 100 (2006) 044507.
[14] M. Baldo, C. Adachi, S. Forrest, Phys. Rev. B 62 (2000) 10967.
[15] Y. Luo, H. Aziz, Z.D. Popovic, G. Xu, J. Appl. Phys. 99 (2006) 054508.

stable than Al. From the other view point of optical properties, the skin depth of Ag (~13 nm) is longer than that of Al (~7 nm) in the visible range. As a result, a thicker Ag film can be deposited to reduce the sheet resistance without compromising the light transmittance. In addition, the thicker Ag film can also provide more effective protection of the polymer films from the damage caused by ITO sputtering.

The devices were fabricated on patterned indium tin oxide (ITO)-glass substrates. After cleaning, the ITO glass was dried in an oven and then treated with UV-ozone. By spin coating, the substrates were covered with a thin layer of poly(3,4-ethylenedioxythiophene):poly(styrenesulfonate) (PEDOT:PSS), and were subsequently baked at 120 °C for 1 h. The active layer, consisting of poly(3-hexyl thiophene) (P3HT) and [6,6]-phenyl-C_{61}-butyric acid methyl ester (PCBM) dissolved in 1,2-dichlorobenzene (DCB) with a weight ratio of 1:1, was spin-coated on the top of PEDOT:PSS. The polymer blend was thermally annealed at 110 °C for 15 min. To complete the device, an ultra-thin interlayer of Cs_2CO_3 (~1 nm) and Ag were thermally evaporated under a vacuum of $\sim 6 \times 10^{-6}$ torr, sequentially, and finally capped by rf sputtered ITO. The ITO sputtering was conducted at a power of 50 W under Ar atmosphere (3×10^{-3} torr). The optimization of the thicknesses of Ag and ITO is quite crucial, since there was a trade-off between the sheet resistance and the transmittance of the electrode. After trying various thicknesses of Ag and ITO, it was found that the optimum thicknesses for Ag and ITO were 7 nm and 100 nm, respectively. In order to reduce the sheet resistance of the transparent cathode, a 60-nm thick Al counter-electrode (CE) grid was incorporated by thermal evaporation. The areas of the CE grid and the overall device defined through various shadow masks were 0.6 mm^2 (0.12 mm×5 mm) and 12 mm^2 (2 mm×6 mm), respectively. The detailed schematic illustration for the device structure is presented in Fig. 1. For some devices, the thermal post-annealing at 140 °C for 5 min was further performed in the glove box. The current density–voltage (*J–V*) characteristics of the devices were measured utilizing a Keithley 2400 source-measure unit. The photocurrent was obtained under illumination from a 150 W Thermal Oriel solar simulator (AM 1.5G). The illumination intensity was calibrated using a standard Si photodiode with a KG-5 filter (Hamamatsu, Inc.) [16]. The transmittance of the transparent cathode was measured using a Perkin Elmer Lamda 950 ultraviolet/visible/near infrared spectrometer.

Fig. 2 shows the *J–V* characteristics of the polymer solar cells under illumination in this work. The open-circuit voltage (V_{oc}), short-circuit current density (J_{sc}) and fill factor (FF) of the as-made semi-transparent OPV (Device I) with a structure of ITO/PEDOT:PSS/P3HT:PCBM/Cs_2CO_3/Ag(7 nm)/ITO(100 nm) were 0.45 V, 3.72 mA/cm^2, and 23.24%, respectively, resulting in a PCE of 0.39%. The poor performance of the semi-transparent device was probably due to the physical damage of the polymer blends caused by ITO sputtering as well as the relatively high sheet resistance of the cathode (Ag/ITO). Nevertheless, after Device I was post-annealed at 140 °C for 5 min, the device performance was dramatically improved (Device II in Fig. 2). In fact, post-annealing has been proposed to enhance the device performance of OPVs by several research groups [3,17–19]. Since no obvious variation in absorption was observed after the post-annealing treatment, we also attribute the enhanced PCE to the improvement of the organics/cathode interface as well as the increased charge mobility [3,17–19].

To understand the nature of charge transport in OPVs, the J_{sc} dependence on the incident light intensity (P_{in}) was further studied. Fig. 3a clearly shows that the J_{sc} followed a power-law dependence, $J_{sc} \propto (P_{in})^s$. After the post-annealing treatment, the exponential factor (s) deduced from the linear fit to the experimental data rose from 0.71 to 0.86. However, this value is still a little lower than that of the device with Cs_2CO_3/Ag(100 nm) cathode (s = 0.95, not shown here). This is probably due to the relatively higher sheet resistance of the cathode (Ag/ITO). In

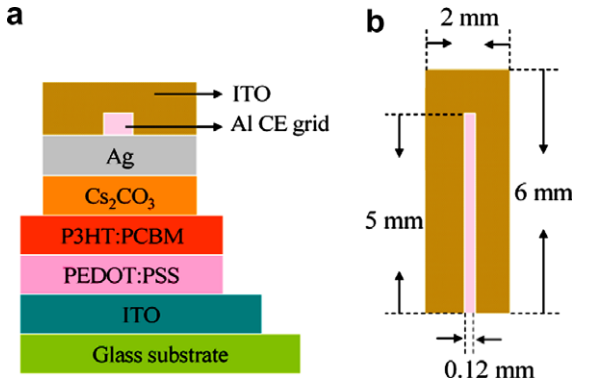

Fig. 1. (a) Device structure of the transparent polymer solar cells incorporating the Al counter-electrode (CE) grid in this study. (b) Detailed schematic illustration for the Al CE grid.

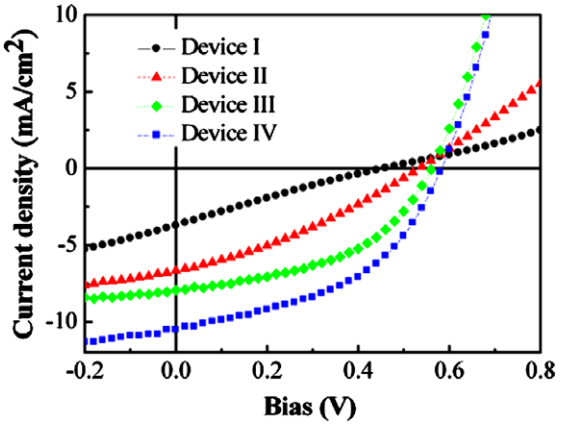

Fig. 2. *J–V* characteristics of semi-transparent polymer solar cells in this study under 100 mW/cm^2 illumination (AM 1.5G). Device I: the as-made device (●); Device II: Device I with post-annealing treatment (▲); Device III: Device II incorporating an Al CE grid (♦); Device IV: Device III with an Ag mirror underneath when illuminating (■). Note that the photoactive layers for all the devices were thermally annealed at 110 °C for 15 min and post-annealing was performed at 140 °C for 5 min for Device II, III, and IV.

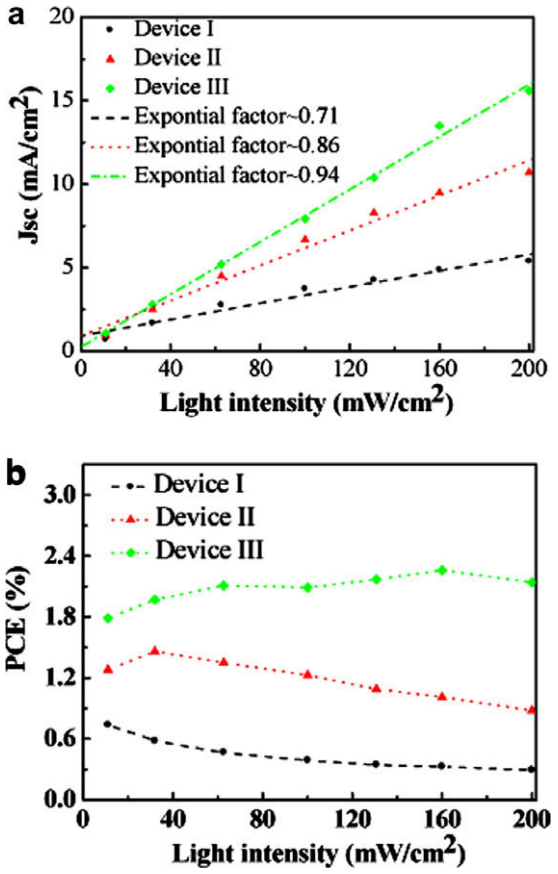

Fig. 3. (a) Short-circuit current density (J_{sc}), and (b) power conversion efficiency (PCE) as a function of incident light intensity (P_{in}).

order to overcome this problem, an Al counter-electrode (CE) grid with 5% shadow fraction was utilized to reduce the sheet resistance of the cathode. After incorporating the CE grid (Device III), the FF of the semi-transparent OPV was notably improved, yielding a PCE of 2.09% (Device III in Fig. 2). Furthermore, the exponential factor was also raised to 0.94, indicating the absence of space charges in the devices [20,21]. This assumption can be further confirmed from the dependence of the efficiency on the illumination intensity (Fig. 3b). Unlike Device I or Device II, which showed a negative correlation once the intensity was larger than 30 mW/cm^2, Device III exhibited rather stable efficiencies at higher intensities. The incident photo-to-electron conversion efficiency (IPCE) curves for the four devices are also depicted in Fig. 4. Device III, as expected, exhibited higher IPCE than Device I or II. It is worth noticing that the PCE of Device III can be further improved to 2.83% by placing an Ag mirror behind the device while illuminating (Device IV). The improved PCE is believed to be attributed to the reduced photo loss through the transparent cathode. This somehow explained why the semi-transparent OPVs are typically inferior to conventional devices with thick metals as the cathodes. All the photovoltaic characteristics are summarized in Table 1.

Fig. 5 displays the transmittance spectrum of the Cs_2CO_3/Ag(7 nm)/ITO(100 nm) transparent cathode. As

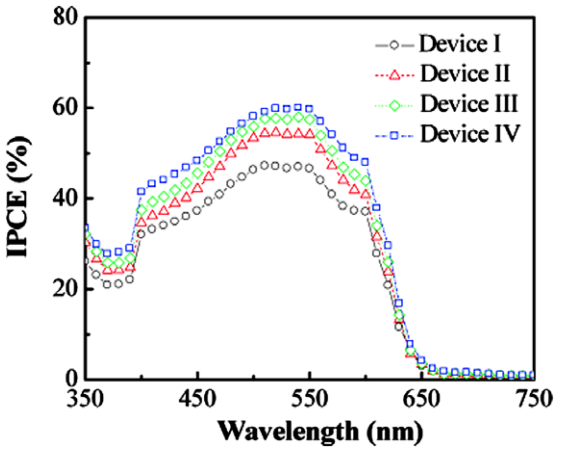

Fig. 4. The incident photo-to-electron conversion efficiency (IPCE) curves.

Table 1
The photovoltaic characteristics of the polymer solar cells in this study

	V_{oc} (V)	J_{sc} (mA/cm^2)	FF (%)	PCE (%)
Device I	0.45	3.72	23.24	0.39
Device II	0.55	6.66	33.50	1.23
Device III	0.57	7.93	46.24	2.09
Device IV	0.59	10.50	45.68	2.83

shown in Fig. 5, the transparent cathode exhibited high transmittance (~70%) in the visible regime. Further, we noted that the incorporation of a 5% CE grid did not significantly diminish the transparency. Assuming that the CE grid is completely opaque, the simulated transmittance spectrum for the transparent cathode with an Al CE grid ($T_{simu.}$) can be obtained by the following relationship: $T_{simu.} = T_{mea.} \times (1 - \tau_s)$, where τ_s is the area fraction of the CE grid ($\tau_s = 0.05$ in our case). As a consequence, with the help of the CE grid, the PCE of semi-transparent OPVs can

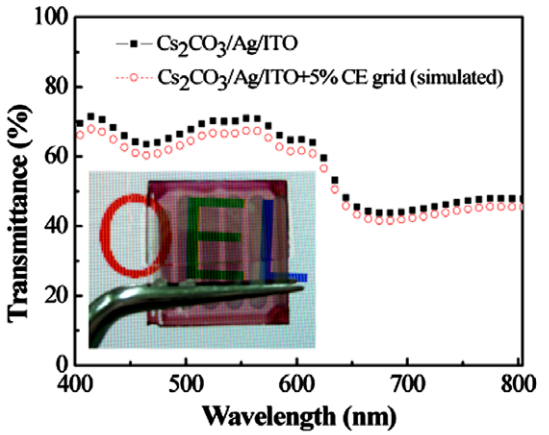

Fig. 5. The transmittance spectrum of the Cs_2CO_3/Ag(7 nm)/ITO(100 nm) transparent cathode and the simulated transmittance spectrum of transparent cathode with a 5% Al CE grid. The inset shows the picture of the semi-transparent device.

be significantly enhanced without dramatically sacrificing the overall transmittance. This is of much importance for some applications, such as stacked cells or tandem cells.

In conclusion, we demonstrated semi-transparent polymer solar cells comprising a Cs_2CO_3/Ag/ITO structure as the transparent cathode. We also found that the device performance of the semi-transparent OPVs can be significantly improved through the post-annealing treatment. Further, with the help of the Al CE grid, the semi-transparent OPV exhibited a power conversion efficiency of 2.09%.

Acknowledgements

The authors would like to thank the financial support from Ministry of Economic Affairs under Contract 96-EC-17-A-08-S1-015. F.C.C. would also like to acknowledge the support from National Science Council (NSC-97-ET-7-009-004-ET) and Ministry of Education ATU program (97W807).

References

[1] C.J. Brabec, N.S. Sariciftci, JC. Hummelen, Adv. Funct. Mater. 11 (2001) 15.
[2] G. Li, V. Shrotriya, J.S. Huang, Y. Yao, T. Moriarty, K. Emery, Y. Yang, Nat. Mater. 4 (2005) 864.
[3] W.L. Ma, C.Y. Yang, X. Gong, K. Lee, A.J. Heeger, Adv. Funct. Mater. 15 (2005) 1617.
[4] C.J. Ko, Y.K. Lin, F.C. Chen, C.W. Chu, Appl. Phys. Lett. 90 (2007) 063509.
[5] A. Yakimov, S.R. Forrest, Appl. Phys. Lett. 80 (2002) 1667.
[6] V. Shrotriya, E.H.E. Wu, G. Li, Y. Yao, Y. Yang, Appl. Phys. Lett. 88 (2006) 064104.
[7] T. Oyamada, Y. Sugawara, Y. Terao, H. Sasabe, C. Adachi, Jpn. J. Appl. Phys. 46 (2007) 1734.
[8] R.F. Bailey-Salzman, B.P. Rand, S.R. Forrest, Appl. Phys. Lett. 88 (2006) 233502.
[9] Y.Q. Li, M.K. Fung, Z.Y. Xie, S.T. Lee, L.S. Hung, J.M. Shi, Adv. Mater. 14 (2002) 1317.
[10] D. Grozea, A. Turak, X.D. Feng, Z.H. Lu, D. Johnson, R. Wood, Appl. Phys. Lett. 81 (2002) 3173.
[11] C.I. Wu, C.T. Lin, Y.H. Chen, M.H. Chen, Y.J. Lu, C.C. Wu, Appl. Phys. Lett. 88 (2006) 152104.
[12] J. Huang, T. Watanabe, K. Ueno, Y. Yang, Adv. Mater. 19 (2007) 739.
[13] G. Li, C.W. Chu, V. Shrotriya, J. Huang, Y. Yang, Appl. Phys. Lett. 88 (2006) 253503.
[14] J.S. Huang, Z. Xu, Y. Yang, Adv. Funct. Mater. 17 (2007) 1966.
[15] F.C. Chen, J.L. Wu, S.S. Yang, K.H. Hsieh, W.C. Chen, J. Appl. Phys. 103 (2008) 103721.
[16] V. Shrotriya, G. Li, Y. Yao, T. Moriarty, K. Emery, Y. Yang, Adv. Funct. Mater. 16 (2006) 2016.
[17] F. Padinger, R.S. Rittberger, N.S. Sariciftci, Adv. Funct. Mater. 13 (2003) 85.
[18] G. Li, V. Shrotriya, Y. Yao, Y. Yang, J. Appl. Phys. 98 (2005) 043704.
[19] Y. Kim, S.A. Choulis, J. Nelson, D.D.C. Bradley, S. Cook, J.R. Durrant, Appl. Phys. Lett. 86 (2005) 063502.
[20] V.D. Mihailetchi, H.X. Xie, B. de Boer, L.J.A. Koster, P.W.M. Blom, Adv. Funct. Mater. 16 (2006) 699.
[21] W.J.E. Beek, M.M. Wienk, R.A.J. Janssen, Adv. Mater. 16 (2004) 1009.

nanostructures and metal-like conductivities, conducting polymers, nanotubes, and nanofibers have attracted much attention for their potential applications in nanodevices [14].

In this study, we synthesized acid-doped [15] PANI nanotubes (a-PANINs) for use as the interfacial layer in P3HT:[6,6]-phenyl-C_{61}-butyric acid methyl ester (PCBM)-based polymer bulk heterojunction solar cells to collect holes efficiently from the active layer and transport them to the buffer layer under the internal electric fields of the fabricated ITO/buffer/a-PANINs/P3HT:PCBM/Al devices. Regioregular P3HT with 98% HT–HT coupling and PCBM (99.5% purity) were obtained from Aldrich Co. A solution of *n*-dodecylbenzenesulfonic acid (DBSA) (3 g) and ammonium persulfate (6 g) in de-ionized water (30 mL) was mixed with a solution of aniline (1 g) in HCl (ca. pH 1.5, 5 mL). The resulting dark-green mixture was gently stirred for 5 min and then a further charge of aniline (10 g) was added. After 4 h of gentle magnetic stirring, the green/black precipitate of the a-PANINs was suction-filtered and washed with copious amounts of de-ionized water and methanol. Drying under vacuum at 100 °C for 12 h yielded a dark-green powder [16–19]. A 60-nm-thick film of PEDOT-PSS (Baytron AI 4083) was spin-coated at 4000 rpm from an aqueous solution onto pre-cleaned indium tin oxide (ITO)-coated glass (sheet resistance: 15 Ω/□; Ritek) in a clean-room atmosphere (class 10000) and then dried at 180 °C for 5 min. The a-PANIN layer (30–50 nm) was then spin-coated from toluene solution (0.2 mg/mL, 5 mL) onto the ITO/PEDOT-PSS layer. Next, a P3HT:PCBM active layer was spin-coated [P3HT:PCBM, 1:1 (w/w) in *o*-xylene; 30 mg/mL] onto the a-PANIN layer and then the system was dried at 150 °C for 10 min. Subsequently, an Al cathode (200 nm) was deposited on top of the active layer through thermal evaporation at ca. 2×10^{-6} torr through a mask, defining an active area of 3 mm^2, and then dried at 150 °C for 30 min. The work functions of these materials in air were measured through photoelectron spectroscopy (PESA, AC-2). Using a Hall measurement system (ECOPI, HMS-3000), we determined that the electrical conductivities (σ_{RT}) of the as-spun a-PANIN and PEDOT-PSS films were in the ranges 3–4 and 2×10^{-4} –4×10^{-4} S/cm, respectively.

Fig. 1a displays the energy levels of the compounds used in this study. Fig. 1b and d present the device structure and chemical structures of the materials, respectively. The field-emission scanning electron microscopy (FE-SEM) image in Fig. 1c reveals that the product was composed of >12-μm-long tubes having mean and effective diameters in the ranges 300–500 and 400–600 nm, respectively. The inset to Fig. 1c indicates that the well-extended 1-D nanostructure of each a-PANIN had the form of a 1-D nanotube, the hollow tunnel of which could aid in the transport of charges further through the tubular structure, preventing interference, recombination with electrons, or defects. The length scale of phase separation in the photoactive layer is a key factor affecting the performance of polymer solar cells. To achieve high-performance cells based on P3HT:PCBM, the PCBM component must form clusters having lateral dimensions of the order of 20–50 nm within, and continuous pathways through, the whole film [20,21]. The sub-micron scale of the features in the a-PANIN surface was appropriate for the P3HT:PCBM domain, providing a well-defined contact area for the transport of

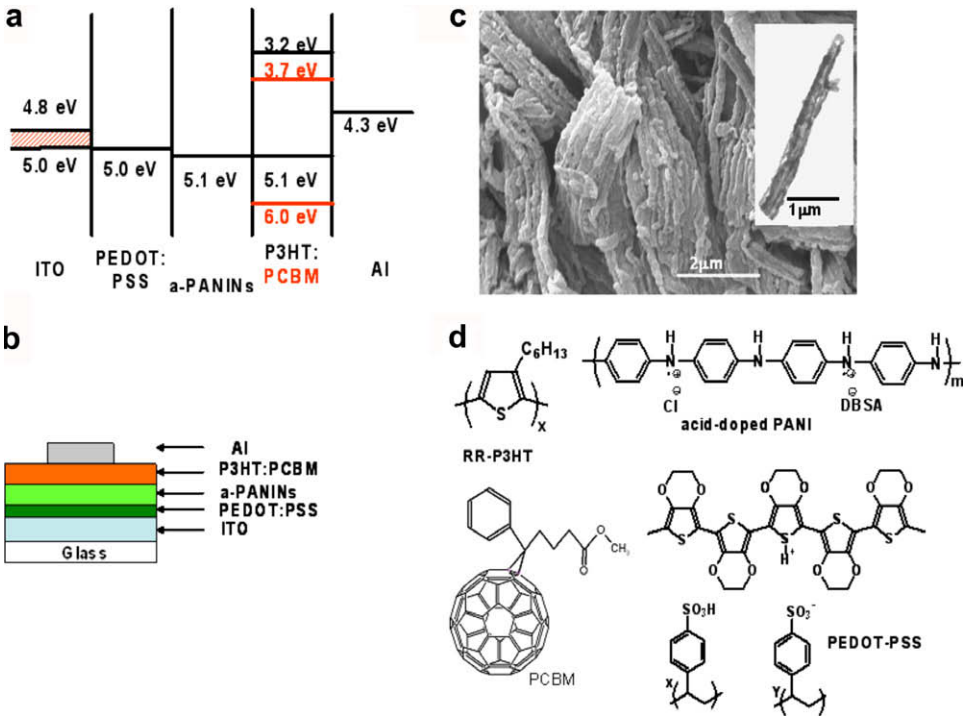

Fig. 1. (a) Energy-level diagram, (b) device structure, (c) FE-SEM image of the a-PANINs (inset: TEM image), and (d) chemical structures of the compounds used in this study.

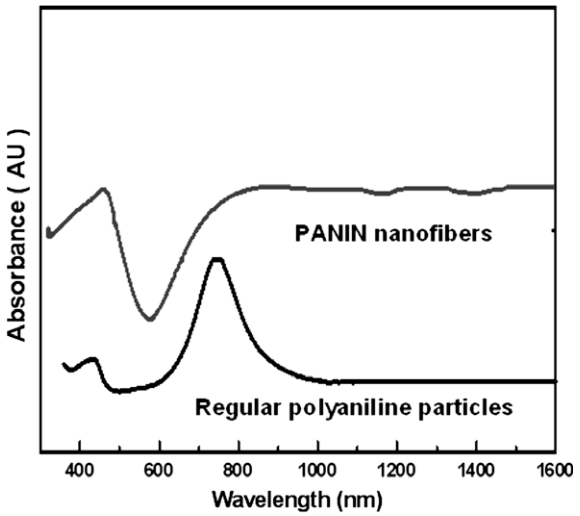

Fig. 2. UV–Vis–near-IR spectra of the regular polyaniline particles and the a-PANIN nanofibers.

free charge carriers. Fig. 2 presents the UV–Vis–near-IR spectra of the regular polyaniline particles (bulk) and the a-PANINs. The UV–Vis spectra of the a-PANINs revealed that they existed in the emeraldine oxidation state, i.e., the formation of polarons after proton doping with DBSA and Cl^- ions, with peaks centered at ca. 440 and 800–1600 nm. The emeraldine oxidation state of polyaniline, which contains 50% imino-type and 50% amino-type nitrogen atoms, can be represented by the formula in Fig. 1d. An interesting feature of the nano-polyaniline is the extended free carrier tail absorption in the near-IR region; it is usually found when polyaniline is secondarily doped by DBSA and Cl^- because of the prolonged conjugation chain length that results from rearrangement of coiled backbones into straighter conformations. The prolonged polyaniline molecules are arranged helically into nanofibers or nanotubes to prevent intra- or inter-molecular complexation and to retain the high-conjugation length (the presence of the free carrier tail), leading to the high absorbance at the near-IR region relative to that of the regular polyaniline particles. This behavior reveals that the extended conjugation length of the a-PANINs can provide longer pathway for holes to travel without exciton recombination or interference from impurities.

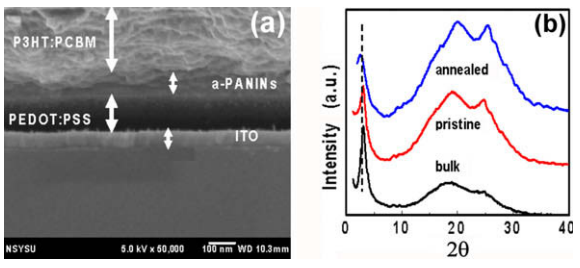

Fig. 3. (a) FE–SEM cross-sectional image of the ITO/PEDOT:PSS/a-PANINs/P3HT:PCBM layers; (b) XRD patterns of the bulk, pristine, and annealed a-PANINs films.

Fig. 3a presents a cross-sectional SEM image of the layers in the device. Because it was difficult to redissolve the a-PANIN layer into *o*-xylene after it had been dried at 150 °C, this layer survived the spin-coating of the active layer from *o*-xylene solution. Fig. 3b presents the X-ray diffraction (XRD) patterns of the bulk, pristine, and annealed a-PANIN films. We assign the sharp peak centered at a value of 2θ of 3° to the periodic distance between the dopant and the nitrogen atoms on adjacent main chains. We attribute the broad bands centered at values of 2θ of 20 and 27° to the periodicities parallel and perpendicular to the polymer chains [22], respectively. These results indicate that the a-PANIN layer was partly crystalline as a result of its special tubular morphology, which was further enhanced upon thermal treatment. We expected that this high crystallinity would result in higher charge mobility in the a-PANIN layer and, correspondingly, improved device performance.

Yang and co-workers [23] found that higher crystallinity of the interface layer results in higher solar-cell performance because of the higher charge mobility that the interface layer provides. We also prepared a p-type-only device having the structure ITO/PEDOT:PSS (80 nm)/a-PANINs (100 nm)/MoO_3(10 nm)/Al (150 nm) to investigate the hole mobility behavior in the PEDOT:PSS/a-PANINs layer. We calculated the hole mobilities from the current–voltage plots (not shown here) of this p-type-only cell structure, using the Mott–Gurney space charge limited current (SCLC) model ($J = 9\varepsilon_r\varepsilon_0\mu V^2/8L^3$; where J is the current density, ε_r is the dielectric constant, ε_0 is the vacuum permittivity, μ is the mobility, V is the applied voltage, and L is the gap of the electrodes) and the Poole–Frenkel law [$\mu = \mu_o \exp(E/E_o)^{1/2}$; where μ_o is the zero-field mobility, E is the electric field (equal to V/L), and E_o is the field coefficient] [23,24]. The zero-field hole mobility (μ_o) increased from 7.38×10^{-4} to 1.13×10^{-3} cm^2/Vs after the device had been heat-treated at 150 °C for 10 min, presumably as a result of ordering in the structure of the a-PANIN film. This finding reveals that the highly crystalline 1-D tubular morphology of the a-PANIN layer provided both a well-defined contact surface between the interfaces and efficient pathways for the transportation of free charge carriers toward their respective electrodes, thereby reducing the degree of exciton recombination within the photoactive cell.

Fig. 4 displays the *I–V* characteristics of cells incorporating and lacking the a-PANIN interfacial layer; Table 1 summarizes the performance parameters. The solvent effect resulted in a lower power conversion efficiency (PCE) relative to that described in a previous report [25] where different organic casting solvents were used. We attribute this lower photovoltaic action to the film morphology obtained from *o*-xylene, which appears to be unsuitable for the formation of an interpenetrated network [26] and disrupts the charge transport in the polymer matrix. The increase in the values of J_{sc}, V_{oc}, and PCE after thermal treatment might indicate that the molecules comprising each layer were sufficiently thermally agitated to interdiffuse, thereby increasing the heterojunction area [21,27,28]. A comparison of the cells incorporating the a-PANIN interfacial layers before (device B) and after (device D) annealing at 150 °C for 30 min reveals that thermal annealing of

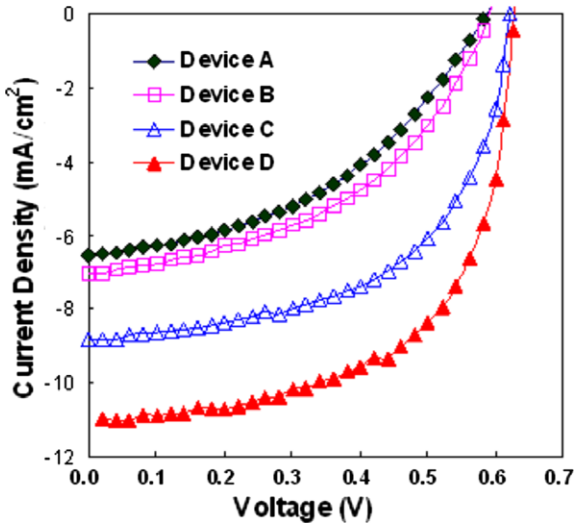

Fig. 4. Current–voltage characteristics (AM 1.5 G, 100 mW/cm^2) of the devices discussed in this report.

Table 1
Characteristics of the photovoltaic cells measured under AM 1.5 G, 100 mW/cm^2 solar illumination

Device[a]	V_{oc} (V)[b]	J_{sc} (mA/cm^2)[c]	FF (a.u.)[d]	PCE (%)[e]	R_s (Ω cm^2)[f]
A	0.58	6.33	0.44	1.67	45
B	0.60	7.09	0.45	1.91	30
C	0.64	8.83	0.55	3.39	17
D	0.64	10.96	0.60	4.26	13

[a] Devices: (A) as-cast ITO/PEDOT-PSS/P3HT:PCBM/Al; (B) as-cast ITO/PEDOT-PSS/a-PANINs/P3HT:PCBM/Al; (C) ITO/PEDOT-PSS/P3HT:PCBM/Al, annealed at 150 °C for 30 min; (D) ITO/PEDOT-PSS/a-PANINs/P3HT:PCBM/Al, annealed at 150 °C for 30 min.
[b] Open circuit voltage.
[c] Short circuit current.
[d] Fill factor.
[e] Power conversion efficiency.
[f] Series resistance.

the three-layer organic solar cell increased the crystallinity percentage of the a-PANIN layer, thereby resulting in improved photovoltaic performance. After annealing (150 °C, 30 min) the devices lacking (device C) and incorporating (device D) the a-PANIN interfacial layer, the PCE increased from 3.39% to 4.26%. These findings suggest that the 1-D nature of hole transport in the a-PANINs reduced the number of cul-de-sacs for holes [29].

We propose the following photovoltaic mechanisms for the functioning of the solar cells incorporating the a-PANIN interfacial layers: (i) The bulk heterojunction P3HT:PCBM photoactive layer accepts photons from white light and generates excitons. (ii) The partial excitons are swept to the well-contacted, highly ordered a-PANIN interfacial layer under the influence of the built-in chemical and electric potentials. The high conductivity and mobility of the annealed a-PANIN layer efficiently extracts the photo-induced holes, providing conducting pathways to the buffer layer while reducing the degree of exciton recombination and resulting in a more efficient charge separation. The enhanced hole collection can be ascribed in part to geometrical field enhancement at the a-PANIN layer, similar to the observation of a previous study using single-wall carbon nanotubes (SWNTs) as the interlayer [30]. The greater order in the structure of the a-PANINs following thermal treatment improved the degree of contact between the buffer layer and the photoactive film, decreasing the series resistance of the cell while increasing both the current and the FF [24,27,31]. (iii) The separated free charge carriers proceed toward their respective electrodes to generate electric current.

In conclusion, we have prepared polymer photovoltaic devices based on the structure ITO/PEDOT-PSS/a-PANINs/P3HT:PCBM/Al. The performance of the solar cell can be improved significantly through incorporating an a-PANIN layer into the device structure without complicating the process of device fabrication.

Acknowledgement

This study was supported by the National Science Council of Taiwan (Grant Nos. NSC-95-2113-M-151-001-MY3 and NSC-95-2113-M-110-013).

References

[1] J.J.M. Halls, K. Pichler, R.H. Friend, S.C. Moratti, A.B. Holmes, Appl. Phys. Lett. 68 (1996) 3120.
[2] T. Stubinger, W. Brutting, J. Appl. Phys. 90 (2001) 3632.
[3] N.S. Sariciftci, L. Smilowitz, A.J. Heeger, F. Wudl, Science 258 (1992) 1474.
[4] G. Yu, J. Gao, J.C. Hummelen, F. Wudl, A.J. Heeger, Science 270 (1995) 1789.
[5] H. Spanggaard, F.C. Krebs, Sol. Energ. Mater. Sol. Cells 83 (2004) 125.
[6] T.L. Benanti, D. Venkataraman, Photosynth. Res. 87 (2006) 73.
[7] S.P. Somani, P.R. Somani, M. Umeno, Appl. Phys. Lett. 89 (2006) 223505.
[8] A.J. Miller, A.R.A. Hatton, S.R.P. Silva, Appl. Phys. Lett. 89 (2006) 133117.
[9] C.G. Wu, T. Bein, Science 264 (1994) 1757.
[10] C.R. Martin, Science 266 (1994) 1961.
[11] S.P. Armes, M. Aldissi, S. Agnew, S. Gottesfeld, Langmuir 6 (1990) 1745.
[12] Z. Wei, M. Wan, Adv. Mater. 14 (2002) 1341.
[13] J. Huang, S. Virji, B.H. Weiller, R.B. Kaner, J. Am. Chem. Soc. 125 (2003) 314.
[14] S.J. Choi, S. Park, Adv. Mater. 12 (2000) 1547.
[15] Note that the backbones of the emeraldine salts of PANI nanotubes doped with both hydrochloric acid (HCl) and n-dodecylbenzenesulfonic acid (DBSA) are positively charged.
[16] J. Huang, R.B. Kaner, Angew. Chem. Int. Ed. 43 (2004) 5817.
[17] X. Zhang, W.J. Goux, S.K. Manohar, J. Am. Chem. Soc. 126 (2004) 4502.
[18] I. Sapurina, A. Riede, J. Stejskal, Synth. Met. 123 (2001) 503.
[19] J.E. Albuquerque, L.H.C. Mattoso, D.T. Balogh, R.M. Faira, J.G. Masters, A.G. MacDiarmid, Synth. Met. 113 (2000) 19.
[20] X. Yang, J. Loos, Macromolecules 40 (2007) 1353.
[21] G. Li, V. Sharotriya, J. Huang, Y. Yao, T. Moriarty, K. Emery, Y. Yang, Nature Mater. 4 (2005) 864.
[22] Y.B. Moon, Y. Cao, P. Smith, A.J. Heeger, Polym. Commun. 30 (1989) 196.
[23] Y. Shao, S. Sista, C.-W. Chu, D. Sievers, Y. Yang, Appl. Phys. Lett. 90 (2007) 103501.
[24] M.A. Lampert, P. Mark, Current Injection in Solids, Academic Press, New York, 1970.
[25] M. Reyes-Reyes, K. Kim, J. Dewald, R. López-Sandoval, A. Avadhanula, S. Curran, D.L. Carroll, Org. Lett. 7 (2005) 5749.
[26] J. Liu, Y. Shi, Y. Yang, Adv. Funct. Mater. 11 (2001) 420.
[27] W. Ma, C. Yang, X. Gong, K. Lee, A.J. Heeger, Adv. Funct. Mater. 15 (2005) 1617.
[28] F. Padinger, R.S. Rittberger, N.S. Sariciftci, Adv. Funct. Mater. 13 (2003) 85.
[29] M.M. Wienk, J.M. Kroon, W.J.H. Verhees, J. Knol, J.C. Hummelen, P.A. van Hal, R.A.J. Janssen, Angew. Chem. Int. Ed. 42 (2003) 3371.
[30] S. Chaudhary, H. Lu, A.M. Muller, C.J. Bardeen, M. Ozkan, Nano Lett. 7 (2007) 1973.
[31] M. Allbrahim, O. Ambacher, S. Sensfuss, G. Gobsch, Appl. Phys. Lett. 86 (2005) 201120.

ting diodes (OLEDs), such as surface modification using O_2 [3], Hf-doping in ITO [4], and the insertion of an organic or insulating interfacial layer [5,6].

Recently, we deposited a sub-nm-thick HfO_x layer on the surface of an ITO anode using an atomic layer deposition (ALD) process at room temperature, and found that it gave rise to a significant improvement of the OLED performance by reducing the hole injection barrier to the organic hole transport layer [7]. Based on these preliminary results obtained in OLEDs, a similar surface modification of an ITO electrode using the ALD process was applied to OTFT devices to decrease the source/drain contact resistance between ITO and pentacene channel layer. Several metal-oxides having different dielectric permittivities were deposited on the ITO surface by using an ALD process at room temperature, and the contact resistance was measured by using a simple device structure. In addition, the band alignments of pentacene/ITO structures with different metal-oxide interlayers were evaluated by using *in situ* X-ray photoelectron spectroscopy (XPS) and ultraviolet photoelectron spectroscopy (UPS) during the step-by-step deposition of pentacene.

2. Experimental

In order to measure the contact resistance between the ITO and pentacene, simple device structures without a gate dielectric layer were fabricated, as depicted in Fig. 1a. First, a 150 nm-thick ITO film was patterned on the glass substrate using a conventional photolithographic process and the channel length was varied from 50 to 250 μm with a step size of 50 μm. Before the metal-oxide treatment using an ALD process, the surface of the ITO film was sequentially cleaned in acetone and isopropyl alcohol, and dried for 1 h at 200 °C in air ambient. For the surface modification of ITO, some of the patterned samples were treated with Al_2O_3, Ta_2O_5, or TiO_2 for various numbers of cycles (3, 5, and 20) using an ALD system at room temperature. The ALD processes for Al_2O_3, Ta_2O_5, and TiO_2 were performed using TMA (trimethyl-Al), PDMAT (pentakis(dimethylamino)-Ta), and TDMAT (tetrakis(dimethylamino)-Ti) as metal precursors, respectively, and H_2O vapor was used as an oxidant. Ar was used as a purging gas and all of the precursors were maintained at room temperature except PDMAT (65 °C) during the ALD process. Each ALD cycle of metal precursor pulsing/purging/H_2O pulsing/purging was composed of 2s/3s/3s/3s for Ta_2O_5 and TiO_2 deposition, and 0.5s/8s/2s/8s for Al_2O_3 deposition, respectively. As a final step, a 70 nm-thick pentacene channel layer was deposited using a thermal evaporator and the electrical measurement was performed after carefully removing the pentacene layer present on the measurement pads using acetone.

The *I–V* characteristics of the fabricated device structures were immediately measured to avoid degradation due to air exposure using a Keithley SCS/4200 system. For the evaluation of the band alignments of the pentacene/ITO structures with different metal-oxide interlayers, pentacene was deposited using a thermal evaporator and the valence band (sample bias, −15 V), C 1s, O 1s, N 1s, and Si 2p spectra were collected *in situ* immediately after the deposition of each desired layer was completed. The XPS and UPS spectra were obtained by a PHI 5700 spectrometer using monochromatic Al Kα (1486.6 eV) and He I (21.2 eV) sources, respectively. The incident angle of photon and the take-off angle of photoelectron were maintained at 90° and 45°, respectively.

3. Results and discussion

Using a contact structure, as shown in Fig. 1a, the total resistance was first measured as a function of the channel length by scanning the applied voltage from negative to positive bias. Fig. 1b shows the measured total resistances of the ITO samples treated for 5 cycles at room temperature with the different metal-oxides as a function of the channel length. For the device structure we fabricated, the total resistance can be expressed as follows

$$R_{\text{tot}} = 2R_{\text{contact}} + R_{\text{channel}} = 2R_{\text{contact}} + \frac{\rho_{\text{channel}}}{A} L. \quad (1)$$

Here, L is the channel length and A is the cross-sectional area of the current path. Because the total resistance is linearly proportional to the channel length, the contact resistance and channel resistance per unit area can be derived from the y-axis intercept and slope, respectively. These

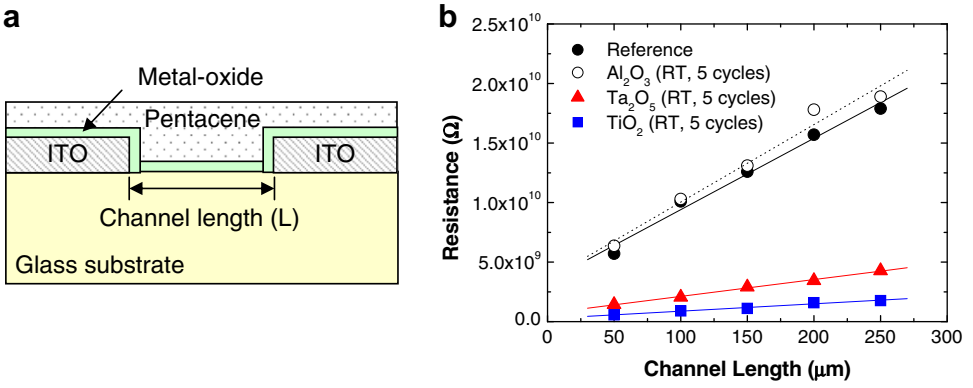

Fig. 1. (a) A schematic cross-sectional diagram of the contact structure used in this experiment and (b) the measured string resistance as a function of the channel length with different surface treatments using various metal-oxides.

Table 1
The summarized contact and channel resistances after ALD treatment at room temperature using various metal-oxides for different numbers of cycles

Sample	Treatment condition	Contact resistance (R_c, Ω)	Channel resistance (ρ_{ch}/cm^2)
ITO (reference)	–	1.70×10^9	6.00×10^{11}
Al_2O_3	RT, 5 cycles	1.76×10^9	6.51×10^{11}
TiO_2	RT, 3 cycles	5.79×10^7	2.02×10^6
	RT, 5 cycles	1.80×10^8	6.18×10^6
	RT, 20 cycles	$>10^{10}$	–
Ta_2O_5	RT, 3 cycles	4.22×10^8	1.07×10^7
	RT, 5 cycles	3.54×10^7	1.41×10^7
	RT, 20 cycles	5.61×10^9	2.16×10^7

measured values are summarized in Table 1 as a function of the number of deposition cycles for the various metal-oxides. According to Fig. 1b, compared to the reference sample without any treatment, the contact resistance was significantly reduced (by two orders of magnitude) for the ITO samples treated with Ta_2O_5 and TiO_2 for 5 cycles. However, Al_2O_3 treatment did not lead to any improvement showing a similar behavior to the reference one. According to the bulk data, the dielectric constants of Al_2O_3, Ta_2O_5 and TiO_2 are known to be around 9, 26, and 80, respectively [8]. Although the dielectric permittivity values of ultra-thin metal-oxide films may be significantly lowered due to the thin film effect, the degree of improvement of the contact resistance is strongly dependent on the magnitude and number of dipole moments in the case of metal-oxides deposited on an ITO electrode. By increasing the total number of deposition cycles, the contact resistance was significantly increased again because of the increase in the physical thickness of the insulating metal-oxide films, as was confirmed in another experiment using HfO_2 in OLEDs [7].

In our experimental conditions, the numbers of deposition cycles resulting in the lowest contact resistance were 5 and 3 for the Ta_2O_5 and TiO_2 treatment, respectively, as listed in Table 1. The difference in the optimum condition for the different metal-oxide treatments is believed to be caused by the difference in the growth rates; the growth rate of TiO_2 is over two times higher than that of Ta_2O_5 at 200–250 °C [9]. The intensity difference of In $3d_{5/2}$ peaks coming from the TiO_2/ITO and Ta_2O_5/ITO samples measured by XPS also confirmed that the thickness of TiO_2 was higher than that of Ta_2O_5. In addition to the improvement of the contact resistance, the channel resistance was also decreased by one order of magnitude as shown in Fig. 1b and Table 1. Because the resistivity of the pentacene layer is strongly dependent on the surface roughness, atomic force microscopy (AFM) measurement of the deposited pentacene thin film was performed on all of the samples with different underlying metal-oxide layers. All of the pentacene layers showed island structures with polycrystalline-like surface morphology having a grain size of 1–2 μm, and no noticeable difference of surface morphology was found among them within the range of experimental error (data not shown here). Recently, several research groups reported that the use of a gate insulator with a high dielectric constant enhances the polarization of the subsequently deposited pentacene layer and, as a consequence, increases the carrier concentration and mobility [10,11]. Therefore, the introduction of an ultra-thin high-*k* layer under the pentacene may enhance the carrier mobility of the OTFT device as an additional benefit in our experimental results and a more detailed study is currently under way to investigate this.

In order to verify the chemical structure of the metal-oxide interface layer, XPS measurement was performed before the *ex situ* deposition of the pentacene layer (Fig. 2). Only the Al 2p and Ta 4f core peaks are shown in Fig. 2 because all of the Ti core peaks were overlapped with other elemental peaks originating from the underlying ITO substrate. Although the deposition temperature was extremely low compared to the typical ALD processing conditions (over 200 °C), no metallic component was ob-

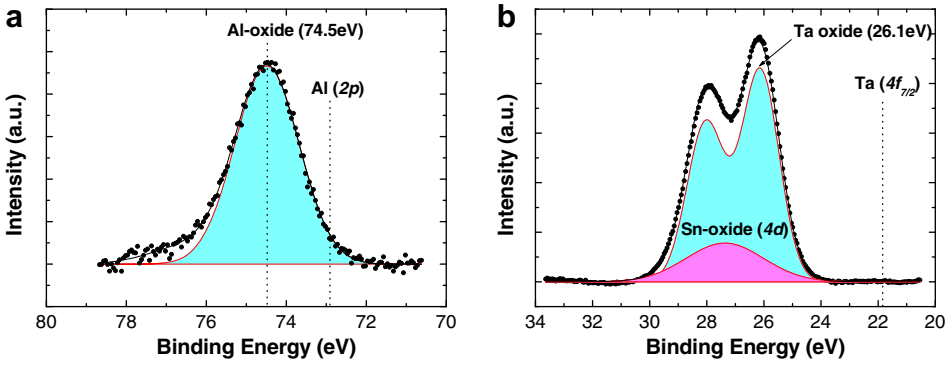

Fig. 2. The XPS spectrum of the ITO surface after ALD treatment for 5 cycles at room temperature: (a) Al 2p core peak from Al_2O_3 and (b) Ta 4f core peak from Ta_2O_5.

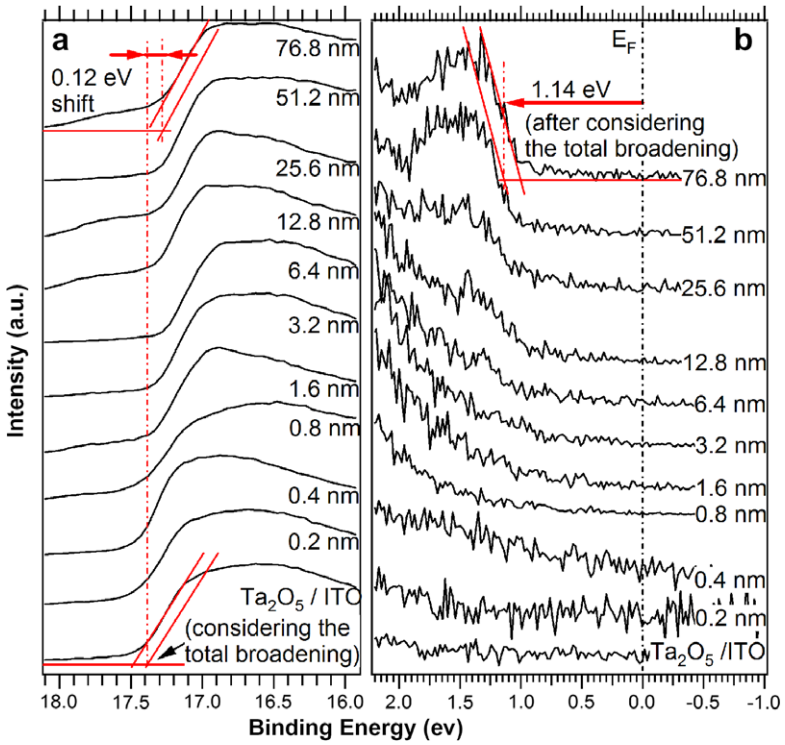

Fig. 3. The PES spectra (a) near the high energy binding cutoff region and (b) near the HOMO region collected during the step-by-step deposition of pentacene on ITO treated with Ta_2O_5 using ALD process for 5 cycles at room temperature.

served, due to the fast oxidation of the reactive metal precursors with H_2O during the deposition or the subsequent exposure to air ambient.

One possible reason for the improvement of the contact resistance between pentacene and ITO is the reduction of the barrier height for hole injection from ITO to pentacene. In order to confirm this mechanism, a series of XPS and UPS measurements were performed *in situ* during the step-by-step deposition of pentacene on clean or ALD-treated ITO samples with the various high-*k* metal-oxides. For the treatment of the ITO substrates, Al_2O_3 having a medium-range *k* value and Ta_2O_5 having a high-range *k* value were deposited on ITO for 5 cycles at room temperature. The photoemission spectroscopy (PES) spectra obtained during the growth of pentacene on Ta_2O_5-treated ITO are shown in Fig. 3. Fig. 3a shows the spectra of the secondary electron cutoff region as a function of the pentacene thickness. The cutoff position was determined by fitting the cutoff tail of the spectra after considering the spectrometer resolution of 0.1 eV for our system (The fitting procedure is depicted with red lines) [12]. As the thickness of pentacene layer increases, the secondary electron cutoff position continuously shifted toward low binding energies and the total shift reached to 0.12 eV. Fig. 3b shows the corresponding valence band region of the same sample. The spectral features of pentacene gradually dominated the spectra with the increase of the pentacene layer thickness and the final sample with 76.8 nm-thick pentacene film showed the highest occupied molecular orbital (HOMO) onset value of 1.14 eV below the Fermi level (E_F). The HOMO onset position was also determined by line-fitting after considering the broadening effect. For the precise determination of the band alignment at the interface, the amounts of band bending of the overlayer (pentacene) and substrate (ITO) were estimated as follows. The band bending of the overlayer was estimated from the shift of the C 1s level during the step-by-step deposition of pentacene since the HOMO emissions of the early stages were not clear. This method would give reliable results since the band bending should occur through whole energy levels. We obtained the band bending of 0.54 eV toward low binding energies as the film thickened, however, the ITO substrate did not show any significant shift in core levels during the deposition.

In order to evaluate the band alignment at the interface, first, both the valence band maximum (VBM) and conduction band minimum (CBM) of ITO were determined. The VBM position relative to the E_F was determined from the In $3d_{5/2}$ peak position measured at 444.8 eV (peak not shown) since the VBM position could not be obtained from the valence band spectra due to the unclean emission features from the ITO surface. Using the known energy difference of 441.8 eV between In $3d_{5/2}$ and VBM [13], the VBM position of 3.0 eV was determined, which matches well with the reported results [14]. In addition, the CBM position was calculated to be located at 0.6 eV above the E_F considering the band gap of ITO (3.6 eV [13]).

Combining the VBM and CBM of ITO with the cutoff shift and the band bending of pentacene, we analyzed the band alignment at the pentacene/Ta_2O_5/ITO interface as follows. Since the cutoff shift contains both information of interface dipole (eD) and band bending, one should sep-

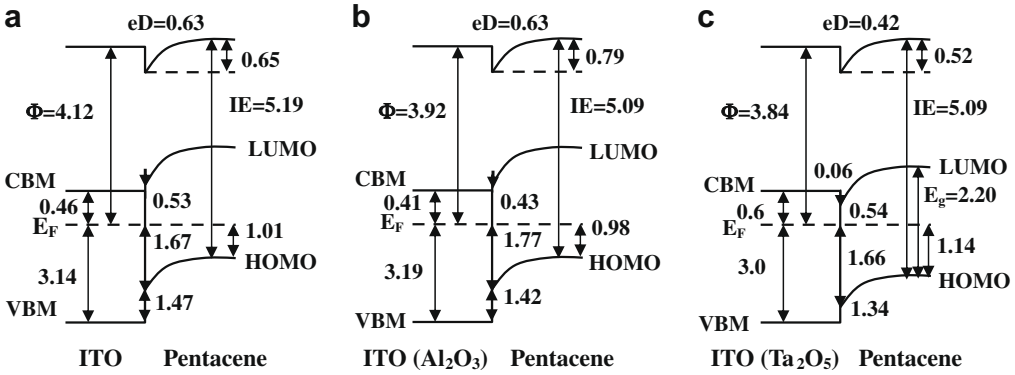

Fig. 4. The calculated energy level diagrams of the pentacene/ITO structures: (a) without any interlayer, (b) with Al_2O_3 interlayer, and (c) with Ta_2O_5 interlayer.

arate two contributions to the cutoff shift using the relation: (cutoff shift) = (interface dipole) + (band bending). The amount of the interface dipole, |eD|, was obtained to be 0.42 eV from this relation using the previously determined total cutoff shift (0.12 eV) and band bending (0.54 eV) values. This eD corresponds to the positive dipole with its negative pole pointing toward the substrate [15]. In this case, the band bending overwhelmed the interface dipole so that the cutoff positions shifted toward only one direction. The ionization energy (IE) of the final film was obtained by subtracting the cutoff position (17.25 eV) from the photon energy (21.2 eV) followed by adding the HOMO onset value (1.14 eV). The obtained IE value was 5.09 eV, which accords well with the reported value [16].

In a similar way described above, the pentacene/ITO and pentacene/Al_2O_3/ITO interfaces were also analyzed using the measured spectra, and the determined band alignments at three different interfaces (pentacene/ITO, pentacene/Al_2O_3/ITO, and pentacene/Ta_2O_5/ITO) are depicted in Fig. 4, where the pentacene energy gap of 2.2 eV was used as previously reported [17]. The hole injection barriers, which is the energy difference between the VBM of ITO and the HOMO of pentacene, were obtained by subtracting the HOMO onset and band bending values from the ITO VBM. They are 1.47, 1.42 and 1.34 eV for the interfaces of pentacene/ITO, pentacene/Al_2O_3/ITO, and pentacene/Ta_2O_5/ITO, respectively. Therefore, hole could be injected most easily at pentacene/Ta_2O_5/ITO interface having an ultra-thin dielectric interlayer with the highest dielectric constant. The thermally activated injection model indicates that the barrier reduction of 0.13 eV, comparing the pentacene/ITO with pentacene/Ta_2O_5/ITO interfaces, gives two orders of magnitude higher current ($I(Ta_2O_5)/I(ITO) = \exp(0.13\ eV/kT) \approx 1.52 \times 10^2$, at room temperature). This amount of current increment is reasonably similar to that of the contact resistance reduction (by two orders of magnitude) obtained from the device measurements (Table 1). However, in the case of Al_2O_3 treatment, the barrier reduction of 0.05 eV only increases the current by ~6.9 times due to the relatively low dielectric constant, which is believed to be within the experimental error and resulted in a similar contact resistance value to that of the reference sample (pentacene/ITO).

4. Conclusion

In summary, various ultra-thin metal-oxide films with different dielectric constants were deposited on an ITO surface using the ALD process at room temperature, and the contact resistance between the ITO and pentacene was evaluated. The contact resistance was significantly improved due to the increase of the dielectric constant of the interlayer, and the optimum number of deposition cycles depended on the growth rate of each dielectric film. The deposited interface layer had a metal-oxide binding configuration without any metallic component. Through the *in situ* XPS and UPS measurements during the step-by-step deposition of pentacene on the ITO surface, the energy level alignments of ITO and pentacene with various metal-oxide interlayers were obtained, and the magnitude of the hole injection barrier at the pentacene/Ta_2O_5 interface were found to be about 0.1 eV smaller than those at the pentacene/ITO and pentacene/Al_2O_3 interfaces, which is believed to be the direct origin of the increased hole density at the interfaces and the subsequent improvement of the contact resistance.

Acknowledgement

This work was supported by Grant No. R-11-2000-086-0000-0 (Center for Advanced Plasma Surface Technology) from the Center of Excellency Program of the KOSEF, MOST, and by the Korea Research Foundation Grant funded by the Korean Government (MOEHRD, KRF-2005-005-J11902).

References

[1] P.V. Pesavento, K.P. Puntambekar, C.D. Frisbie, J.C. McKeen, P.P. Ruden, J. Appl. Phys. 99 (2006) 094504.
[2] S. Lee, B. Koo, J.-G. Park, H. Moon, J. Hahn, J.M. Kim, MRS Bull. 31 (2006) 455.
[3] J.H. Choi, E.S. Lee, S.H. Choi, H.K. Baik, K.M. Song, Y.S. Lim, S.M. Lee, J. Vac. Sci. Technol. A 23 (2005) 1479.
[4] T.H. Chen, Y. Liou, T.J. Wu, J.Y. Chen, Appl. Phys. Lett. 85 (2004) 2092.
[5] S.A. Van Slyke, C.H. Chen, C.W. Tang, Appl. Phys. Lett. 69 (1996) 2160.

[6] C. Qiu, Z. Xie, H. Chen, M. Wong, H.S. Kwok, J. Appl. Phys. 93 (2003) 3253.
[7] S. Sohn, K. Park, D. Jung, H. Kim, H. Chae, H.M. Kim, J. Yi, M.-H. Cho, J-H. Boo, Jpn. J. Appl. Phys. 46 (2007) L461.
[8] J. Robertson, J. Vac. Sci. Technol. B 18 (2000) 1785.
[9] W.J. Maeng, H. Kim, Electrochem. Solid-State Lett. 9 (2006) G191.
[10] Y. Jang, D.H. Kim, Y.D. Park, J.H. Cho, M. Hwang, K. Cho, Appl. Phys. Lett. 87 (2005) 152105.
[11] G. Wang, D. Moses, A.J. Heeger, H.-M. Zhang, M. Narasimhan, R.E. Demaray, J. Appl. Phys. 95 (2004) 316.
[12] R. Schlaf, P.G. Schroeder, M.W. Nelson, B.A. Parkinson, C.D. Merritt, L.A. Crisafulli, H. Murata, Z.H. Kafafi, Surf. Sci. 450 (2000) 142.
[13] Y. Gassenbauer, A. Klein, Solid State Ionics 173 (2004) 141.
[14] Y. Yi, J.E. Lyon, M.M. Beerbom, R. Schlaf, J. Appl. Phys. 100 (2006) 093719.
[15] C. Shen, A. Kahn, Org. Electron. 2 (2001) 89.
[16] E.A. Silinsh, V. Cápek, Organic Molecular Crystals: Interaction, Localization and Transport Phenomena, American Institute of Physics, New York, 1994.
[17] N.J. Watkins, S. Zorba, Y.L. Gao, J. Appl. Phys. 96 (2004) 425.

films on plastics, and in many cases do not yield flexible devices due to decohesion, delamination, and/or cracking. And the conventional polymeric films generally exhibit low capacitances, and the corresponding OTFTs operate at relatively high voltages. Moreover, ultrathin self-assembled mono- or multilayers have quite a few critical issues to solve: slow formation speed, high defect density, and difficulty in producing multicomponent multilayer films.

Organic–inorganic nanohybrid thin films are drawing substantial attention due to the potential of combining the distinct properties of organic and inorganic components. The organic–inorganic hybrid superlattices are particularly attractive as the gate dielectric of low-voltage-operating OTFTs because they can provide means for combining the high-*k* and high dielectric strength (leakage resistance) properties. Systematically composed of heterogeneous materials, such hybrid superlattices exhibit unique electrical properties which differ from their constituents [18–22]. Therefore, they may provide the opportunity for developing new materials with synergic behavior, leading to improved performance or new useful properties. Recently, we developed a new vapor phase deposition method of high quality self-assembled organic layers (SAOLs), called molecular layer deposition (MLD), in order to realize precisely controlled organic–inorganic nanohybrid superlattice dielectrics for pentacene OTFTs [23–27]. MLD is a gas phase process analogous to atomic layer deposition (ALD), which is a potentially powerful method for preparing high quality multicomponent superlattices under vacuum conditions. In the MLD method, the high quality organic thin films can be quickly formed with monolayer precision under ALD conditions (temperature, pressure, etc). The MLD method can be combined with ALD to take advantages of the possibility of obtaining organic–inorganic hybrid thin films.

Herein, we report a low-temperature fabrication of mixed organic–inorganic nanohybrid superlattices on flexible plastic substrates by using MLD combined with ALD (MLD–ALD) at the same chamber on the purpose of displaying all the advantages of MLD–ALD method: accurate control of film thickness, large-scale uniformity, excellent conformality, good reproducibility, multilayer processing capability, sharp interfaces, and excellent film qualities at relatively low temperatures. And finally, we also demonstrate the performance of low voltage pentacene OTFTs delicately prepared with the dielectric superlattices on flexible plastic substrate.

2. Experimental section

2.1. Preparation of Si substrates

The Si(100) substrates used in this research were cut from n-type (100) wafers with a resistivity in the range of 1–5 Ωcm. The Si substrates were initially treated by a chemical cleaning process proposed by Ishizaka and Shiraki which involved degreasing, HNO_3 boiling, NH_4OH boiling (alkali treatment), HCl boiling (acid treatment), rinsing in deionized water, and blow-drying with nitrogen to remove contaminants and grow a thin protective oxide layer on the surface [28].

2.2. Atomic layer deposition of Al_2O_3 thin film

The oxidized Si(100) substrates were introduced into the atomic layer deposition (ALD) system Cyclic 4000 (Genitech, Taejon, Korea). The Al_2O_3 thin films were deposited onto the substrates using $[Al(CH_3)_3]$ (Aldrich; 99%) and H_2O as ALD precursors [29,30]. Ar served as both a carrier and a purging gas. The trimethyl aluminum (TMA) and water were evaporated at 20 °C. The cycle consisted of 1 s exposure to TMA, 5 s Ar purge, 1 s exposure to water, and 5 s Ar purge. The vapor pressure of the Ar in the reactor was maintained at 300 mtorr. The Al_2O_3 thin films were grown at 150 °C under a pressure of 300 mtorr.

2.3. Atomic layer deposition of TiO_2 thin film

The TiO_2 thin films were deposited onto the substrates using $[Ti(OCH(CH_3)_2)_4]$ (Aldrich; 99.999%) and H_2O as ALD precursors [30,31]. Ar served as both a carrier and a purging gas. The titanium isopropoxide (TIP) and water were evaporated at 60 and 20 °C, respectively. The cycle consisted of 2 s exposure to TIP, 5 s Ar purge, 2 s exposure to water, and 5 s Ar purge. The vapor pressure of the Ar in the reactor was maintained at 300 mtorr. The TiO_2 thin films were grown at 150 °C under a pressure of 300 mtorr.

2.4. Molecular layer deposition

Alkene-terminated self-assembled organic layers (SAOLs) were formed by exposing the Si substrates to $[CH_2{=}CH(CH_2)_6SiCl_3]$ (Aldrich; 96%) with H_2O vapor at 150 °C in the ALD chamber. The 7-octenyltrichlorosilane (7-OTS) and water were evaporated at 100 and 20 °C, respectively. Exposure times in this process were 5 s for 7-OTS with water vapor and 10 s for Ar purge. The reactor pressure during a process was about 300 mtorr. The terminal C=C groups of the SAOLs were converted to carboxylic groups with ozone treatment in the ALD chamber. The ozone was generated by an ozone-generator and dosed to the 7-OTS coated samples for 30 s at 150 °C. The C=C groups of the SAOLs reacted with ozone to convert to carboxylic acid groups. Highly active metal hydroxyl groups were formed on the COOH-terminated SAOLs by using TMA or TIP adsorption followed by exchange reaction of water molecule in order to provide highly active adsorption sites for the anchoring of the next monolayer. The molecular layer deposition of the alkylsiloxane SAOLs consisted of a repetition of three steps: adsorption of 7-OTS, modification of 7-OTS with a carboxylic group using ozone, and activation of carboxylated 7-OTS with an aluminum (or titanium) hydroxyl group.

2.5. Device fabrication

The gate electrode of transistor is formed by sputtering of 100 nm ITO on polycarbonate (PC) substrates. The 23 nm-thick dielectric layer is fabricated by MLD–ALD at 150 °C. For good crystalline pentacene channel formation, the dielectric surface was terminated with a hydrophobic SAOL. Pentacene (Aldrich Chem. Co., 99% purity) channels were patterned on the SAOLs through a shadow mask at

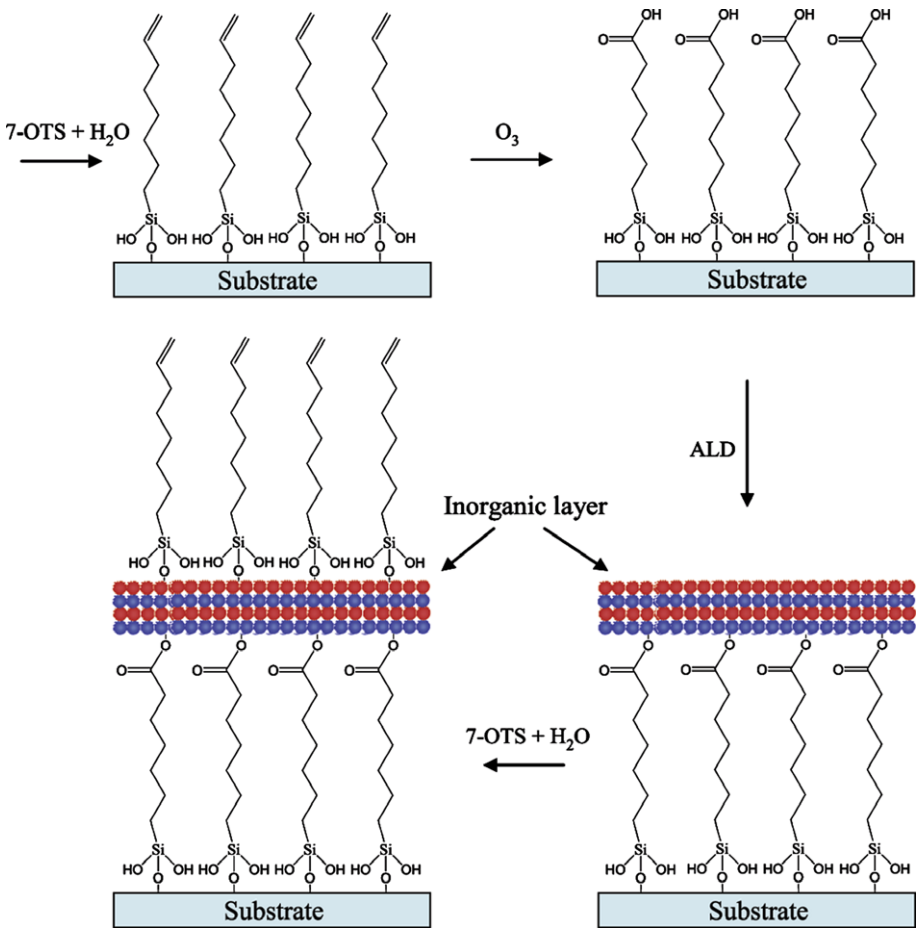

Fig. 1. Schematic outline of the procedure to fabricate organic–inorganic nanohybrid superlattices by using molecular layer deposition combined with atomic layer deposition.

a substrate temperature of RT by thermal evaporation. We fixed the deposition rate to 1 Å/s using an effusion cell (ALPHAPLUS Co., LTE-500S) in a vacuum chamber (base pressure $\sim 1 \times 10^{-6}$ Torr). The thickness of the pentacene film was 50 nm as monitored by a quartz crystal oscillator and confirmed by ellipsometry. Nominal channel length of the pentacene-TFT was 90 μm while channel width was 500 μm. Au was adopted as top-contact source/drain electrode.

2.6. Instrumentation

The samples were analyzed by a JEOL-2100F transmission electron microscopy. Specimens for cross-sectional TEM studies were prepared by mechanical grinding and polishing (~10 μm thick) followed by Ar-ion milling using a Gatan Precision Ion Polishing System (PIPSTM, Model 691). Atomic force microscopy images of the samples were obtained on a PSIA XE-100 operating in tapping mode. Contact angle analysis was performed using a model A-100 Ramé-Hart NRL goniometer to measure water contact angles in room air using the sessile drop method. All XP spectra were recorded on a VG Scientific ESCALAB MK II spectrometer using Al Kα source run at 15 kV and 10 mA. All current–voltage (*I–V*) properties of the pentacene TFTs and test structures were measured with a semiconductor parameter analyzer (HP 4155 C, Agilent Technologies), and *C–V* measurements were made with a capacitance meter (HP 4284 LCR meter, Agilent Technologies, 1 MHz) in the dark and in an air ambient (relative humidity ~45%) at 20 °C.

3. Results and discussion

Mixed-organic–inorganic nanohybrid superlattices were grown by using MLD, combined with ALD, in the same deposition chamber. The alkylsiloxane self-assembled organic layers (SAOLs) were grown under vacuum by repeated sequential adsorptions of C=C-terminated alkylsilane and titanium (or aluminum) hydroxide with ozone activation, which was called "molecular layer deposition" [23–27]. For the ideal organic layer structure with completely perpendicular, fully extended alkyl chains, the expected monolayer thickness of the SAOLs is about 12 Å. The thickness of the SAOLs versus the number of MLD cycles was measured using cross-sectional transmission

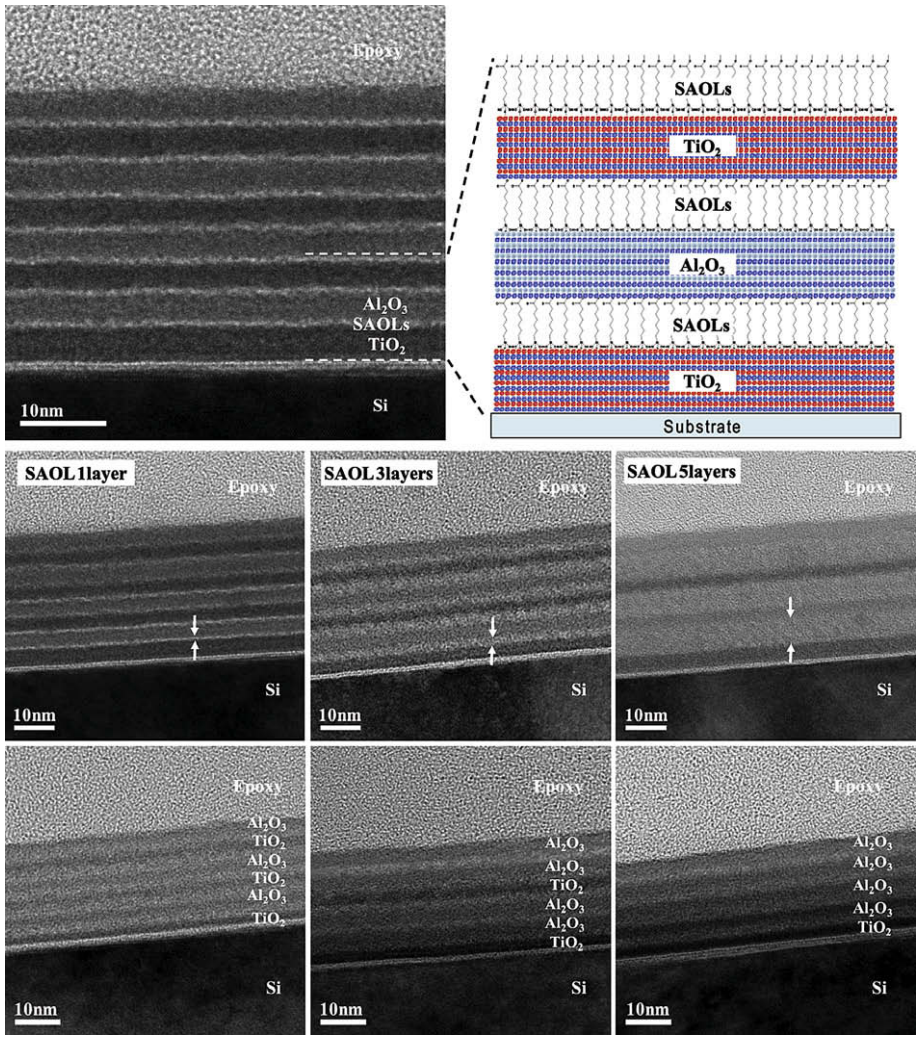

Fig. 2. TEM images of SAOLs-Al_2O_3–SAOLs-TiO_2 nanohybrid superlattices made by MLD with ALD (white is the SAOLs layer, black is the TiO_2 layer, and grey is the Al_2O_3 layer).

electron microscopy. The measured thickness of the monolayer was about 11 Å, which indicate that the chain is only tilted 20–25° from the surface normal. The quality of the monolayer was also checked by XPS and contact angle. The $^{1s}C/^{2p}Si$ peak area ratio measured by XPS is about 0.7 and the water contact angle is about 92°, which are close to those of a densely packed 7-octenylsiloxane monolayer prepared in liquid phase.

The growth of the SAOLs thickness is extremely linear relative to the number of cycles, indicating that the MLD conditions were sufficient for complete reaction [23]. The measured growth rate was about 11 Å per cycle. The AFM images of the SAOLs indicated very smooth and uniform surfaces, and the root mean square (RMS) roughness of the surfaces was as low as 3.2 Å. In comparison, the surface roughness of the initial cleaned Si substrate is about 2.1 Å. Regardless of the cycle number, the surfaces of the SAOLs are as smooth as that of the initial cleaned Si substrate, indicating that the MLD growth occurs in a two-dimensional fashion via layer-by-layer growth. These results suggest that the molecular layer deposition of the self-assembled organic layers is self-controlled and proceeds via layer-by-layer growth, and that the MLD conditions are sufficient for complete reaction at 150 °C.

Metal oxide (Al_2O_3 or TiO_2) inorganic nanolayers were grown by atomic layer deposition using self-terminating surface reactions at 150 °C, followed by deposition of the SAOLs films using MLD; we name those organic–inorganic hybrid layers as SAOLs-Al_2O_3 (or SAOLs-TiO_2). Fig. 1 shows a schematic outline of the procedure to fabricate one unit of SAOLs-Al_2O_3 (or SAOLs-TiO_2) as obtained by 1 cycle of MLD process. The inorganic nanolayer thickness per cycle is saturated when the pulse time exceeds 2 s, which indicates that the growth is self-controlled. The growth of the nanolayer thickness is extremely linear relative to the number of cycles, indicating that the ALD conditions were sufficient for complete reaction. The measured growth rates of the Al_2O_3 and TiO_2 nanolayers were 1.0 and 0.6 Å

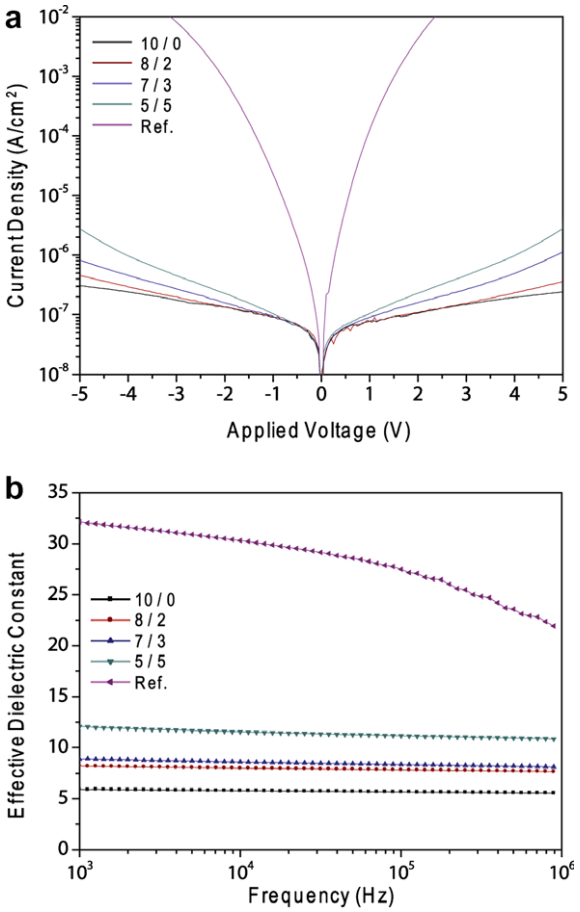

Fig. 3. Electrical properties of the SAOLs-Al_2O_3–SAOLs-TiO_2 superlattices. (a) Leakage current density as a function of applied voltage. (b) Effective dielectric constant as a function of frequency.

per cycle, respectively. Regardless of the number of the cycle, the surface morphology of the nanolayers is smooth and uniform, and the root mean square (RMS) roughness of the surface is as low as 3.0 Å. These observations indicate that the inorganic nanolayer ALD is self-controlled and extremely linear relative to the number of cycles, and the nanolayers are smooth at 150 °C.

The SAOLs-Al_2O_3–SAOLs-TiO_2 nanohybrid superlattices were grown by repeating a cyclic MLD and ALD at the same deposition chamber. Various SAOLs-Al_2O_3–SAOLs-TiO_2 nanolaminate films were deposited on Si(100) substrates at 150 °C, as shown in Fig. 2. The Si substrates were first coated with TiO_2 by ALD and the top layer of each nanolaminate film was Al_2O_3. The thicknesses of SAOLs and inorganic nanolayers in each sample were controlled by adjusting the number of MLD and ALD cycles with SAOLs, Al_2O_3, and TiO_2 growth rates of about 11, 1.0, and 0.6 Å/cycle, respectively. The TEM images provide direct observation of the superlattice structures and confirm the expectations for the individual SAOLs, Al_2O_3, and TiO_2 nanolayers in the nanolaminate films. The ability of the SAOLs-Al_2O_3–SAOLs-TiO_2 nanohybrid superlattices to survive the TEM preparation process confirms that they have excellent mechanical stability. The superlattices appear to be relatively uniform, which is confirmed by AFM. The nanohybrid superlattices were thermally stable in air up to temperatures of about 500 °C. Above 550 °C the superlattices slowly decomposed with the degradation of hydrocarbon fragments in the SAOLs.

In order to investigate the electrical properties of the SAOLs-Al_2O_3–SAOLs-TiO_2 superlattices, the nanohybrid superlattice films were sandwiched between Pt metal electrodes by using MLD–ALD. A 100 nm thick Pt film was deposited on the Si(100) substrate by radio frequency magnetron sputtering. Several nanohybrid superlattices were grown on the bottom Pt electrodes by using MLD–ALD at the same chamber. A 1.2 nm-thick Al_2O_3 (or TiO_2) film was grown on the electrodes by ALD, followed by deposition of one monolayer of the SAOLs films using MLD. In this case, one unit of the SAOLs-Al_2O_3 (or SAOLs-TiO_2) is an organic–inorganic thin film, which has a 1.1 nm-thick SAOLs as obtained by 1 cycle of MLD process and a 1.2 nm-thick Al_2O_3 (or TiO_2) nanolayer by ALD. The mixed organic–inorganic hybrid superlattices of the SAOLs-Al_2O_3 and SAOLs-TiO_2 were formed on the bottom Pt electrodes by alternating the deposition of SAOLs-Al_2O_3 and SAOLs-TiO_2. All superlattice films studied were approximately 23 nm thick and consist of 10 units of the organic–inorganic layers, where the 10 units now have four different mixing ratios of SAOLs-Al_2O_3/SAOLs-TiO_2: 10/0, 8/2, 7/3, 5/5. For comparison, an inorganic Al_2O_3–TiO_2 superlattice film without SAOLs was fabricated as a reference sample.

The patterned top Pt electrodes (100 nm) were deposited onto the superlattice films using a shadow mask, and the gate area was about 1×10^{-4} cm^2. Fig. 3a shows the leakage current density versus voltage characteristics of the Pt/SAOLs-Al_2O_3–SAOLs-TiO_2/Pt capacitors. We systematically measured the dependence of the leakage current density on the applied potential for a set of the nanohybrid superlattices with the different mixing ratios (SAOLs-Al_2O_3–SAOLs-TiO_2). The positive bias means that the top metal electrode is positive with respect to the bottom metal electrode on Si. In general, the plot shows a decrease in current density with increasing the component of SAOLs-Al_2O_3. All our samples do hardly show direct tunneling although the film with mixing ratio of 5/5 shows some inferior leakage properties. The most excellent leakage current resistance was shown from pure SAOLs-Al_2O_3 sample. However, the reference sample (Al_2O_3–TiO_2 without SAOLs) exhibited direct tunneling. Fig. 3b illustrates the frequency dependency of the dielectric constant of the superlattices at room temperature. The dielectric constant at 1 MHz for the reference sample is about 23. The dielectric constant at 1 MHz for the pure SAOLs-Al_2O_3 sample is about 6, which remained almost constant in the frequency range from 100 Hz to 1 MHz. In general, the plot shows an increase in dielectric constant with increasing the component of SAOLs-TiO_2. In particular, the film of mixing ratio of 5/5 displays the highest dielectric constant of 11. It is thus regarded that SAOLs-Al_2O_3 units tend to help reduce leakage while SAOLs-TiO_2 units help increase the dielectric constant, which is quite understandable if we consider the dielectric properties of Al_2O_3 and TiO_2.

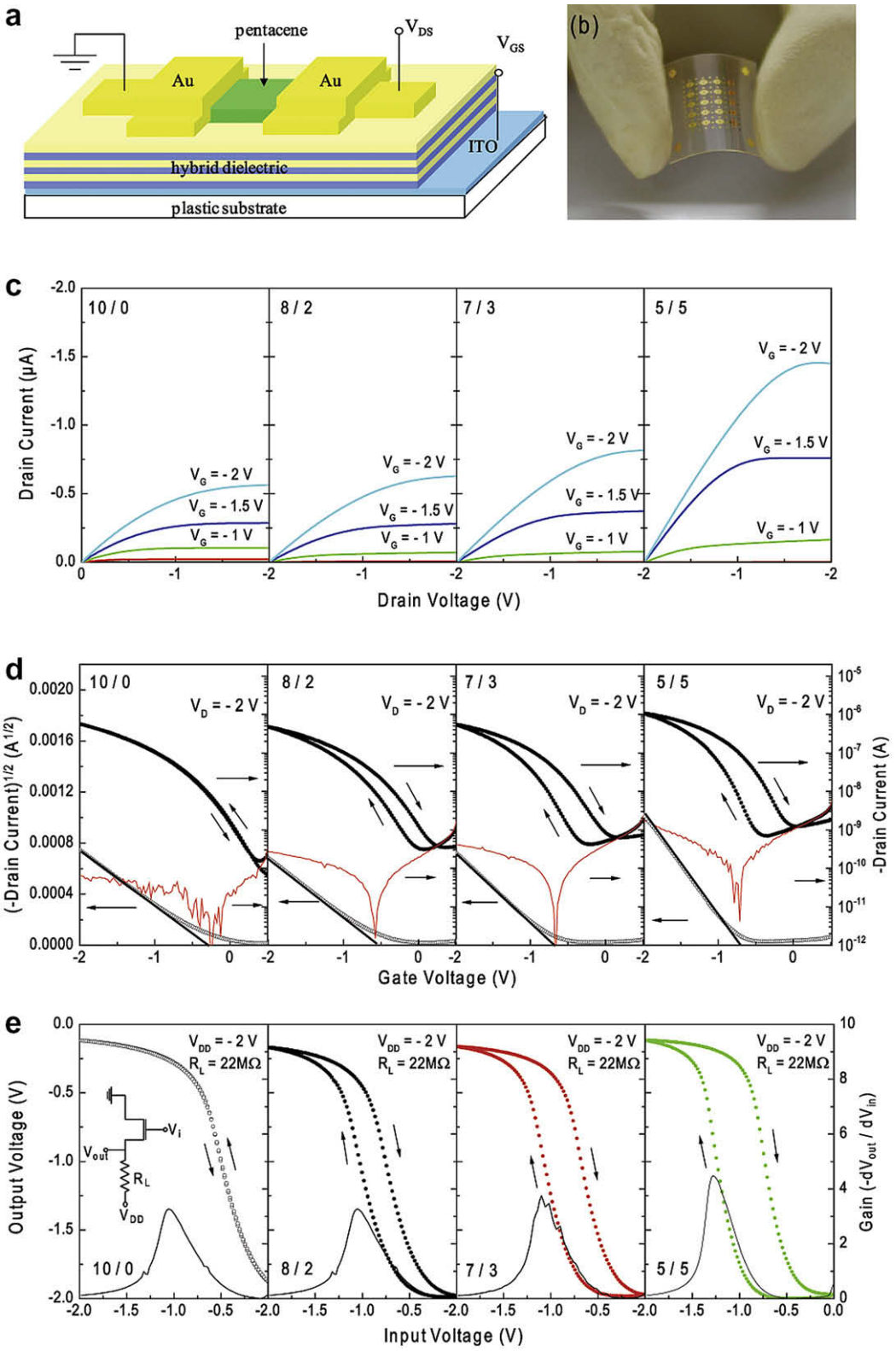

Fig. 4. (a) Schematic diagram of the OTFTs with the superlattice dielectric films on ITO-coated polycarbonate substrate. (b) Photograph of our flexible OTFT. (c) Drain current–drain voltage (I_D–V_D) output curves for our OTFTs with the nanohybrid dielectrics of four different mixing ratios: SAOLs-Al_2O_3/SAOLs-TiO_2 = 10/0, 8/2, 7/3, 5/5. (d) Drain current-gate voltage (I_D–V_G) transfer curves and the gate leakage levels of the OTFTs. (e) VTC curves and voltage gain of inverter setup with OTFTs and 22 MΩ load-resistance.

Table 1
Summary of the electrical properties of our nanohybrid dielectrics and their corresponding OTFTs

		10/0	8/2	7/3	5/5
Dielectric properties	Dielectric constant	5.5	7.6	8.1	10
	Capacitance (nF/cm^2)	221	305	325	402
	Dielectric strength (MV/cm)	−4.0	−3.0	−2.4	−1.8
OTFT properties	Saturation mobility (cm^2/V s)	0.31	0.25	0.34	0.54
	Vth (V)	−0.30	−0.60	−0.75	−0.75
	On/off ratio	3.7×10^3	1.6×10^3	1.2×10^3	1.5×10^3
	Maximum I_D (μA)	−0.50	−0.65	−0.82	−1.50
Inverter properties	VTC hysteresis (V)	0	0.3	0.4	0.5
	Gain	3.0	3.3	3.8	4.5

Based on the low electrical leakage and high dielectric constant results of Fig. 3a and b, it is very likely that the superlattice dielectric films are a good candidate for a high quality gate insulating film on flexible substrates. We thus have fabricated organic pentacene thin-film transistors (OTFTs) with the 23 nm-thick SAOLs-Al_2O_3–SAOLs-TiO_2 superlattice films of the four mixing ratios of SAOLs-Al_2O_3/SAOLs-TiO_2: 10/0, 8/2, 7/3, 5/5. Those dielectrics and organic pentacene channel were deposited on ITO-coated polycarbonate substrate, as shown in the device schematics of Fig. 4a. SAOLs offer structural flexibility, whereas inorganic layers provide the potential for dielectric properties, and thermal and mechanical stability. OTFTs with SAOLs-Al_2O_3–SAOLs-TiO_2 can endure strenuous bending, as shown in Fig. 4b, and therefore are potentially useful for flexible electronics. For good crystalline pentacene channel formation, the dielectric surface was terminated with a hydrophobic organic layer. After OTFT fabrication, we also set up load-resistance inverter using our OTFTs and 22 MΩ load. According to the output curves of Fig. 4c, transfer curves of Fig. 4d, and inverter curves (voltage transfer curves: VTC) of Fig. 4e, the OTFT with the dielectric of mixing ratio of 5/5 displays the highest properties in drain current (1.5 μA), field effect mobility (0.54 cm^2/V s), and inverter voltage gain ($-dV_{out}/dV_{in}$ = ∼4.5) operating at a low voltage of −2 V while the device also showed several other disadvantages: high gate current leakage, large gate-voltage, and VTC hysteresis. The gate-voltage induced hysteresis and leakage current decreased with increasing the mixing ratio of SAOLs-Al_2O_3, which but trades with the mobility of OTFTs; the mobility was as low as 0.25 cm^2/V s with the dielectric of mixing ratio of 8/2. In particular, the hysteresis was almost removed with the SAOLs-Al_2O_3 only dielectric (10/0 ratio) and we thus regard that the most stable OTFT is achieved with pure SAOLs-Al_2O_3 dielectric. The origin of the hysteresis attributes to the electron injection from gate electrode during negative gate bias sweep. The injected electrons make the dielectric electrically negative, staying in the dielectric and then additional holes are drawn to the channel/dielectric interface during OTFT operation. As a result, we observe clockwise hysteresis as shown in Fig. 4d. All these electrical properties of our OTFTs were expected along with the basic properties of mixed or unmixed nanohybrid dielectrics, dielectric capacitance, and dielectric strength (or leakage resistance) which were measured and shown in Fig. 3a and b. Under a same gate bias, the thin dielectric containing more SAOLs-TiO_2 component would experience higher density of charges injected from channel and gate electrode although it has higher capacitance, so that the OTFTs with such dielectrics display high mobility but large gate hysteresis as well. We summarized all the electrical properties of our dielectrics and their corresponding OTFTs in Table 1, where the dielectric strength was determined at an arbitrary leakage standard of 1×10^{-6} A/cm^2. In general, the on/off current ratio of all the OTFTs was about the same, to be $\sim 10^3$.

4. Conclusion

We have demonstrated here that the MLD–ALD method is an ideal fabrication technique for mixed organic–inorganic nanohybrid superlattices on flexible plastic substrates. The SAOLs-Al_2O_3–SAOLs-TiO_2 superlattice films prepared exhibit good thermal and mechanical stability, good flexibility, large-scale uniformity, sharp interfaces, and various unique electrical properties. The resulting pentacene OTFT delicately prepared with the 23-nm-thin dielectric superlattices on flexible plastic substrate displays the highest properties in drain current (1.5 μA), field effect mobility (0.54 cm^2/V s), and inverter voltage gain ($-dV_{out}/dV_{in}$ = ∼4.5) operating at a low voltage of −2 V.

Acknowledgements

This work was supported by the Korea Science and Engineering Foundation (KOSEF) grant funded by the Korea government (MOST) (No. 2008-02378 and No. R01-2007-000-10402-0) and by the SRC/ERC program of MOST/KOSEF (grant R11-2005-048-00000-0).

References

[1] A.E.A. Huitema et al., Nature 414 (2001) 599.
[2] M. Berggren, D. Nilsson, D.N. Robinson, Nature 6 (2007) 3.
[3] Stephen R. Forrest, Nature 428 (2004) 911.
[4] C.D. Dimitrakopoulos, P.R.L. Malenfant, Adv. Mater. 14 (2002) 99.
[5] A. Facchetti, M.-H. Yoon, T.J. Marks, Adv. Mater. 17 (2005) 1705.
[6] L.A. Majewski, M. Grell, S.D. Orier, J. Veres, Org. Electron. 4 (2003) 27.
[7] M. Shtein, J. Mapel, J.B. Benziger, S.R. Forrest, Appl. Phys. Lett. 81 (2002) 268.
[8] D. Knipp, R.A. Street, A. Völkel, J. Ho, J. Appl. Phys. 93 (2003) 347.
[9] M.-H. Yoon, H. Yan, A. Facchetti, T. Marks, J. Am. Chem. Soc. 127 (2005) 10388.
[10] Alexander Blümel et al., Org. Electron. 8 (2007) 401.
[11] L.-L. Chua, P.K.H. Ho, H. Sirringhaus, R.H. Friend, Appl. Phys. Lett. 84 (2004) 3400.

[12] F.-C. Chen, C.-W. Chu, J. He, Y. Yang, Appl. Phys. Lett. 85 (2004) 3295.
[13] Y. Liang, G. Dong, Y. Hu, L. Wang, Y. Qiu, Appl. Phys. Lett. 86 (2005) 132101.
[14] M.S. Oh, D.K. Hwang, K. Lee, S. Im, Appl. Phys. Lett. 90 (2007) 173511.
[15] M.J. Panzer, C.R. Newman, C.D. Frisbie, Appl. Phys. Lett. 86 (2005) 103503.
[16] D.K. Hwang et al., Adv. Mater. 18 (2006) 2299.
[17] D.B. Mitzi, Chem. Mater. 13 (2001) 3283.
[18] S.I. Stupp, V. LeBonheur, K. Walker, L.S. Li, K.E. Huggins, M. Keser, A. Amatutz, Science 276 (1997) 384.
[19] C.R. Kagan, D.B. Mitzi, C.D. Dimitrakopoulos, Science 286 (1999) 945.
[20] C.H. Ahn, K.M. Rabe, J.-M. Triscone, Science 303 (2004) 488.
[21] R.M. Costescu, D.G. Cahill, F.H. Fabreguette, Z.A. Sechrist, S.M. Geprge, Science 303 (2004) 989.
[22] B.H. Lee, M.K. Ryu, S. Choi, K. Lee, S. Im, M.M. Sung, J. Am. Chem. Soc. 129 (2007) 16034.
[23] K.H. Lee, J.-M. Choi, S. Im, B.H. Lee, K.K. Im, M.M. Sung, S. Lee, Appl. Phys. Lett. 91 (2007) 123502.
[24] S.H. Cha, M.S. Oh, H.K. Lee, S. Im, B.H. Lee, M.M. Sung, Appl. Phys. Lett. 92 (2008) 023506.
[25] Y. Du, S.M. George, J. Phys. Chem. C. 111 (2007) 8509.
[26] S.T. Yoshimura, W.S. Tatsuura, Appl. Phys. Lett. 59 (1991) 482.
[27] A. Ishizaka, Y.J. Shiraki, Electrochem. Soc. 133 (1986) 666.
[28] M. Ritala, K. Kukli, A. Rahtu, P.I. Räisänen, M. Leskelä, T. Sajavaara, Keinonen, Science 288 (2000) 319.
[29] Y.S. Kim, S.J. Yun, J. Cryst. Growth 274 (2005) 585.
[30] A. Rahyu, M. Ritala, Chem. Vap. Depos. 8 (2002) 21.
[31] M.H. Patk, Y.J. Jang, H.M. Sung-Suh, M.M. Sung, Langmuir 20 (2004) 2257.

ORGANIC ELECTRONICS
materials • physics • chemistry • applications

Aims and scope

An interdisciplinary journal on the physics, chemistry, and engineering of materials with applications to organic electronics and opto-electronics, **Organic Electronics** is a primary journal for physicists, material scientists and chemists who are interested in organic electronic devices such as organic light emitting diodes, thin film transistors, photovoltaic cells, etc. Papers suitable for publication in this journal cover such topics as photoconductive and electronic properties of organic materials, film growth and characterization, organic electronic and optoelectronic devices, and applications.

As an important Journal **Organic Electronics** can ensure that your most significant research receives the recognition that it deserves. As a unique publication outlet, uniting the various research disciplines involved, it provides the only forum for both applied and fundamental contributions spanning the many different disciplines addressing electronic applications of organic materials.

Abstracted/indexed in:

Current Contents: Engineering, Technology and Applied Sciences; El Compendex Plus; Engineering Index; INSPEC; Physics Briefs; Science Citation Index, expanded; Chemistry Citation Index; Current Contents: Physics, Chemistry and Engineering Science. Also covered in the abstract and citation database SCOPUS®. Full text available on ScienceDirect®.

Publication information: *Organic Electronics* (ISSN 1566-1199). For 2008, Volume 9 is scheduled for publication. Subscription prices are available upon request from the Publisher or from the Regional Sales Office nearest you or from this journal's website: (http://www.elsevier.com/locate/orgel). Further information is available on this journal and other Elsevier products through Elsevier's website: (http://www.elsevier.com). Subscriptions are accepted on a prepaid basis only and are entered on a calendar year basis. Issues are sent by standard mail (surface within Europe, air delivery outside Europe). Priority rates are available upon request. Claims for missing issues should be made within six months of the date of dispatch.

Orders, claims, and journal enquiries: please contact the Regional Sales Office nearest you:

St. Louis: Elsevier, Customer Service Department, 11830 Westline Industrial Drive, St. Louis, MO 63146, USA; phone: (877) 8397126 [toll free within the USA]; (+1) (314) 4537076 [outside the USA]; fax: (+1) (314) 5235153; e-mail: JournalCustomerService-usa@elsevier.com

Amsterdam: Elsevier, Customer Service Department, P.O. Box 211, 1000 AE Amsterdam, The Netherlands; phone: (+31) (20) 4853757; fax: (+31) (20) 4853432; e-mail: JournalsCustomerServiceEMEA@elsevier.com

Tokyo: Elsevier, Customer Service Department, 4F Higashi-Azabu, 1-Chome Bldg, 1-9-15 Higashi-Azabu, Minato-ku, Tokyo 106-0044, Japan; phone: (+81) (3) 5561 5037; fax: (+81) (3) 5561 5047; e-mail: JournalsCustomerServiceJapan@elsevier.com

Singapore: Elsevier, Customer Service Department, 3 Killiney Road, #08-01 Winsland House I, Singapore 239519; phone: (+65) 6349 0222; fax: (+65) 6733 1510; e-mail: JournalsCustomerServiceAPAC@elsevier.com

USA mailing notice: *Organic Electronics* (ISSN 1566-1199) is published bimonthly by (Elsevier B.V., Radarweg 29, 1043 NX Amsterdam, The Netherlands). Periodical postage paid at Rahway NJ and additional mailing offices.

USA POSTMASTER: Send change of address: *Organic Electronics*, Elsevier, Customer Service Department, 11830 Westline Industrial Drive, St. Louis, MO 63146, USA.

AIRFREIGHT AND MAILING in USA by Mercury International Limited, 365, Blair Road, Avenel, NJ 07001.

Printed in the Netherlands